

15 MAY 1994
PART 2B

VOLUME 75 NUMBER 10

AD-A286 751



JOURNAL OF APPLIED PHYSICS

DTIC
S ELECTE D
APR 1 3 1994
F

Proceedings of the 38th Annual Conference on Magnetism
and Magnetic Materials

This document has been approved
for public release and sale; its
distribution is unlimited.

1009 ONE THOUSAND NINE
95-01207

AMERICAN
INSTITUTE
OF PHYSICS

JOURNAL OF APPLIED PHYSICS

CODEN: JAPIAU
ISSN: 0021-8979

Editor

Steven J. Rothman
Argonne National Laboratory
Argonne, IL

Associate Editors at Argonne National Laboratory

Robert C. Birtcher
Gian P. Felcher
R. E. Holland
John N. Mundy
Simon R. Phillpot

Editorial Board

Term ending 31 December 1994

William R. Frensley (Univ. of Texas at Dallas)
Julia M. Phillips (AT&T Bell Labs, Murray Hill, NJ)
Paul M. Solomon (IBM, Yorktown Heights, NY)

Term ending 31 December 1995

Ulrich Gösele (Max Planck Inst., Halle, Germany)
William L. Johnson (Caltech, Pasadena, CA)
William F. Krupke (Lawrence Livermore Lab, CA)

Term ending 31 December 1996

Gene F. Dresselhaus (MIT, Cambridge, MA)
Allen M. Goldman (Univ. Minnesota, Minneapolis)
Klaus H. Ploog (Paul Drude Inst., Berlin, Germany)
Robert Sinclair (Stanford Univ., Stanford, CA)

Editorial Office

Diane M. Kurtz, *Editorial Supervisor*

Editorial Staff: Catherine M. Dial, *Assistant to the Editor*; Jennifer A. Smeets, *Secretary*

AIP Editorial Operations

John T. Scott, *Manager*

AIP Production

Deborah McHone, *Editorial Supervisor*
Elizabeth Belmont, *Journal Coordinator*
Julia Macklin, *Chief Production Editor*
Cindy Klingensmith, *Senior Production Editor*
Joan Eigo, *Production Editor*

The *Journal of Applied Physics* (ISSN: 0021-8979) is published semimonthly by the American Institute of Physics, 500 Sunnyside Blvd., Woodbury, NY 11797-2999. Second-class postage paid at Woodbury, NY, and additional mailing offices. POSTMASTER: Send address changes to *Journal of Applied Physics*, AIP, 500 Sunnyside Blvd., Woodbury, NY 11797-2999.

© 1994 by the American Institute of Physics.

The *Journal of Applied Physics* is the American Institute of Physics' (AIP) archival journal for significant new results in applied physics. The journal publishes articles that emphasize understanding of the physics underlying modern technology. There are two issues per month. The subject coverage includes, but is not limited to, experimental or theoretical physics applied to all aspects of materials: for example, charge and mass transport, superconductivity, magnetism; surfaces, interfaces, thin films, crystal lattice defects; electrical, optical, magnetic, and structural properties; processing; ion implantation. Materials covered include semiconductors, superconductors, metals and alloys, amorphous materials, and oxides. Other important topics are: electrical, optical, and magnetic devices; optics and lasers; nonlinear optics; electrical discharges; acoustics. The Proceedings of the Annual Conference on Magnetism and Magnetic Materials is a regular feature. *Applied Physics Reviews* is a series of occasional review articles on similar subjects.

Submit manuscripts (3 copies) to Editor, *Journal of Applied Physics*, Argonne National Laboratory, Bldg. 203, Room R-127, 9700 South Cass Avenue, P.O. Box 8296, Argonne, IL 60439-8296.

Subscription Prices* (1994)

	U.S.A. & Poss.	Can., Mex., Central & S. Amer. & Caribbean	Foreign Surface Mail	Air Freight Europe, Asia, Africa & Oceania	Optional Air Freight
Members [†]	\$190	\$270	\$270	—	\$380
Nonmembers	\$1655	\$1735	—	\$1845 [‡]	—

*The journal is available on microfiche at \$190 per year to members and \$1655 per year at the nonmember rate.

[†]AIP Member and Affiliated Societies. [‡]Includes air freight service.

Back-Number Prices: 1994 single copies: \$80. Prior to 1994 single copies: \$24 for members; \$80 for nonmembers. Prices for conference supplements available on request.

Subscription, renewals, and address changes should be addressed to *AIP Circulation and Fulfillment Division (CFD)*, 500 Sunnyside Blvd., Woodbury, NY 11797-2999. Allow at least six weeks advance notice. For address changes please send both old and new addresses and, if possible, include a mailing label from a recent issue.

Claims, Single Copy Replacement and Back Volumes: Missing issue requests will be honored only if received within six months of publication date (nine months for Australia and Asia). Single copies of a journal may be ordered and back volumes are available in print or microform. Members—contact AIP Member Services at (516) 576-2288; (800) 344-6901. Nonmember subscribers—contact AIP Subscriber Services at (516) 576-2270; (800) 344-6902.

Page Charge and Reprint Billing: Contact: AIP Publication Page Charge and Reprints—CFD, 500 Sunnyside Blvd., Woodbury, NY 11797-2999; (516) 576-2234; (800) 576-6909.

Copying Fees: Copying of articles beyond that permitted by the Fair Use provisions (Sections 107 and 108) of the U.S. Copyright Law requires payment of fees. The code at the bottom of the first page of each article gives the fee for each copy of the article. Fees should be paid through the *Copyright Clearance Center (CCC)*, 222 Rosewood Drive, Danvers, MA 01923. Persons desiring to photocopy materials for classroom use should contact CCC's Academic Permissions Service.

The item-fee code for this publication is 0021-8979/94 \$6.00.

Permission For Other Use: Permission is granted to quote from the journal with the customary acknowledgment of the source. To reprint a figure, table, or other excerpt requires in addition the consent of one of the original authors and notification to AIP. Reproduction for advertising or promotional purposes, or republication in any form, is permitted only under license from AIP, which will normally require that the permission of one of the authors also be obtained. Direct inquiries to: Office of Rights and Permissions, American Institute of Physics, 500 Sunnyside Blvd., Woodbury, NY 11797-2999.

Document Delivery: For information on obtaining copies of individual articles, contact AIP Circulation and Fulfillment Division, 500 Sunnyside Blvd., Woodbury, NY 11797-2999; phone: (516) 576-2277; (800) 344-6908; fax: (516) 394-9704; E-mail: elecprod@pinet.aip.org.

Online Availability: Abstracts of journal articles published by the AIP and its Member Societies are available in bibliographic databases on major online hosts. The abstracts are also available in the SPIN database via the AIP online service, PINET (Physics Information Network). PINET also offers Advance Abstracts, a current awareness service with abstracts of research papers up to three months prior to their publication in AIP or Member Society Journals. Call (800) 874-6383 or (516) 576-2262 for further information.

PROCEEDINGS OF THE THIRTY-EIGHTH ANNUAL CONFERENCE ON MAGNETISM AND MAGNETIC MATERIALS

PART B

**November 15-18, 1993
Minneapolis, Minnesota**

Accession For	
NTIS CRA&I	<input checked="" type="checkbox"/>
DTIC TAB	<input type="checkbox"/>
Unannounced	<input type="checkbox"/>
Justification	
By	
Distribution /	
Availability Codes	
Dist	Avail and/or Special
A-1	

**Edited by W. B. Yelon, J. L. Nix,
F. E. Pinkerton, W. M. Saslow, and R. H. Victora**

DTIC QUALITY INSPECTED 8

**Journal of Applied Physics
Volume 75, Number 10, Part II, 1994**

Library of Congress Catalog Card Number: 94-70649

International Standard Book Number: 1-56396-33~ X

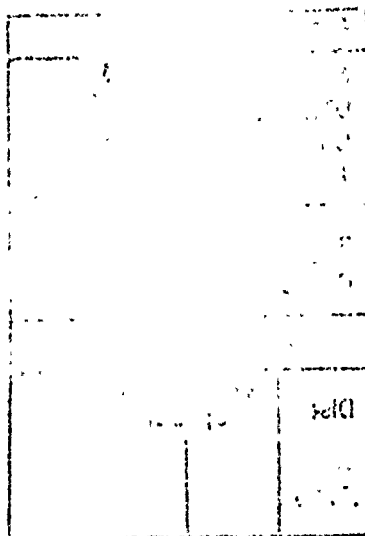
CONF-931133—Vol. 2

Copyright © 1994 by the American Institute of Physics

Published by the American Institute of Physics

500 Sunnyside Blvd., Woodbury, New York 11797-2999

Printed in the United States of America



All papers in this volume, and in previous Proceedings of the Conference on Magnetism and Magnetic Materials published in this series, have been reviewed for technical content. The selection of referees, review guidelines, and all other editorial procedures are in accordance with standards prescribed by the American Institute of Physics.

Micromagnetics and Hysteresis

- 5475 Monte Carlo simulations of remanent magnetization decay driven by interactions M. E. Matson, D. K. Lottis, E. Dan Dahlberg
- 5478 The Preisach model with stochastic input as a model for aftereffect Isaak D. Mayergoyz, Can E. Korman
- 5481 The measurement of irreversible magnetization and activation volumes R. Cammarano, P. G. McCormick, R. Street
- 5484 A phenomenological differential-relation-based vector hysteresis model A. Bergqvist, G. Engdahl
- 5487 Master equation approach to anhysteresis of noninteracting particles Ivo Klik, Ching-Ray Chang, J. Lee
- 5490 Scaling aspects of domain wall dynamics and Barkhausen effect in ferromagnetic materials G. Bertotti, G. Durin, A. Magni
- 5493 Monte Carlo simulations of the magnetocaloric effect in superferromagnetic clusters having uniaxial magnetic anisotropy L. H. Bennett, R. D. McMichael, H. C. Tang, R. E. Watson
- 5496 A phenomenological magnetomechanical hysteresis model A. Bergqvist, G. Engdahl
- 5499 Reversible transverse susceptibility of particulate recording media Jing Ju Lu, Huei Li Huang, Ching-Ray Chang, Ivo Klik
- 5502 Efficient Preisach demagnetization algorithm and its experimental testing A. A. Adly, Y. J. Zhao
- 5505 Interpreting logarithmic decay Ivo Klik, Ching-Ray Chang, J. Lee
- 5508 Magnetization processes in Co-Cr submicron samples: Hall measurements and micromagnetic simulations M. van Kooten, S. de Haan, J. C. Lodder, Th. J. A. Popma
- 5511 Frequency dependence of hysteresis curves in conducting magnetic materials (abstract) D. C. Jiles

Spin Glasses and Other Disordered Systems

- 5512 Hierarchical scaling: An analytical approach to slow relaxations in spin glasses, glasses, and other correlated systems (invited) J. Souletie
- 5517 Exchange stiffness of Ca-doped YIG I. Avgin, D. L. Huber
- 5520 Random-exchange to random-field crossover breaking in $\text{Mn}_{0.35}\text{Zn}_{0.65}\text{F}_2$ F. C. Montenegro, J. C. O. de Jesus, A. Rosales-Rivera
- 5523 Order by disorder in an anisotropic pyrochlore lattice antiferromagnet S. T. Bramwell, M. J. P. Gingras, J. N. Reimers
- 5526 A new scheme to percolation thresholds Serge Galam, Alain Mauger
- 5529 Heat capacity and magnetic properties of $\text{CoCl}_2 \cdot \text{H}_2\text{O}$ J. A. Lukin, S. A. Friedberg, S. Chardarlapaty, W. W. Brubaker, C. C. Cinquina, G. C. DeFotis
- 5532 Perturbative approximation scheme for isolated impurity bonds in the two-dimensional spin- $\frac{1}{2}$ Heisenberg antiferromagnet P. Schlottmann
- 5535 Magnetic properties of a new amorphous magnet C. P. Landee, C. M. Wynn, A. S. Albrecht, W. Zhang, G. B. Vunni, J. L. Parent, C. Navas, M. M. Turnbull
- 5538 The influence of heat treatments on order-disorder phenomena in a naturally occurring manganese-ferrite Cherie R. Bluncson, B. J. Evans
- 5541 Remanent magnetization in the diluted Ising antiferromagnet $\text{Fe}_{0.6}\text{Zn}_{0.4}\text{F}_2$ C. Djurberg, J. Mattsson, P. Nordblad
- 5544 Freezing transition in the Z_3 gauge glass Ronald Fisch

Particulate Recording Media

- 5547 Reptation and viscosity in particulate recording media in the time-limited switching regime
W. D. Doyle, L. Varga, L. He, P. J. Flanders
- 5550 Ferromagnetic resonance spectra of oriented barium ferrite tapes
Yuwu Yu, J. W. Harrell, W. D. Doyle
- 5553 Angular dependence measurement of individual barium ferrite recording particles near the single domain size
Thomas Chang, Jian Gang Zhu
- 5556 Co-Sn substituted barium ferrite particles
X. Z. Zhou, A. H. Morrish, Zheng Yang, Hua-Xian Zeng
- 5559 Magnetic properties of modified Ba-ferrite particles
H. Sadamura, N. Sugita, M. Maekawa, N. Nagai
- 5562 H_c enhancement of Co-adsorbed $\gamma\text{-Fe}_2\text{O}_3$ particles via surface treatment with sodium polyphosphate
F. E. Spada, F. T. Parker, A. E. Berkowitz, T. J. Cox
- 5565 Coercivity enhancement in $\gamma\text{-Fe}_2\text{O}_3$ by surface treatment with phosphate ions
David E. Nikles, Martin R. Parker, Elizabeth M. Crook, Terry M. Self
- 5568 Electrochemical evaluation of the effect of binder additives on iron corrosion
J. Carlos Arroyo, Hassan M. Saffarian, Garry W. Warren
- 5571 Molecular dynamics of magnetic particulate dispersions
P. A. Deymier, C. Jung, S. Raghavan
- 5574 A computer simulation of the microstructure of a particulate dispersion
G. N. Coverdale, R. W. Chantrell, A. Hart, D. Parker
- 5577 The effect of dc bias fields on the switching speed in magnetic particulate media (abstract)
W. D. Doyle, L. He
- 5577 Preparation and magnetic properties of Al-modified acicular $\alpha\text{-Fe}$ particles (abstract)
C. H. Lin, P. C. Kuo, S. C. Chen, C. S. Hsih
- 5578 Studies into the use of waterborne coating formulations for the preparation of magnetic tape (abstract)
Stacy Barrom, Ashley Bray, Song Cheng, John Elike, Hong Fan, Alan M. Lane, David E. Nikles
- 5579 Rheo-optical measurements on suspensions of magnetic recording particles (abstract)
Hyoung J. Choi, Yoon D. Park, Paul L. Frattini, Myung S. Jhon
- ## Thin and Ultrathin Films
- 5580 Growth and magnetic dynamic scaling of ultrathin ferromagnetic films: Fe/Au(001)
Y.-L. He, Y.-F. Liew, G.-C. Wang
- 5583 Mössbauer investigation of the magnetic hyperfine field distribution in Fe(100)/Ag(100) structures
P. J. Schurer, Z. Celinski, B. Heinrich
- 5586 Magnetization reversal processes in epitaxial Fe/GaAs(001) films
C. Daboo, R. J. Hicken, D. E. P. Eley, M. Gester, S. J. Gray, A. J. R. Ives, J. A. C. Bland
- 5589 Surface magnetization processes investigated by the combined surface magneto-optical Kerr effects in Fe/Cu(100) thin films
Z. J. Yang, S. D. Healy, K. R. Heim, J. S. Drucker, G. G. Hembree, M. R. Scheinfein
- 5592 The initial phases of epitaxy of fcc Fe/Cu(100): Supersurface and subsurface island formation
S. D. Healy, K. R. Heim, Z. J. Yang, G. G. Hembree, J. S. Drucker, M. R. Scheinfein
- 5595 Effect of surface layers on ferromagnetic resonance in thin Fe films: Ni, Co, Si, and $\text{YBa}_2\text{Cu}_3\text{O}_{7-\delta}$
P. Lubitz, M. Rubinstein, D. B. Chrisey, J. S. Horwitz, P. R. Broussard
- 5598 Magneto-optical Kerr effect study of ac susceptibilities in ultrathin cobalt films
A. Berger, S. Knappmann, H. P. Oepen
- 5601 Ferromagnetic resonance determination of fcc \rightarrow hcp structural change in epitaxial Co/Mn superlattices
K. Ounadjela, Y. Henry, M. Farle, P. Venneques
- 5604 Magnetization of thin Gd films on W(110) near the Curie temperature
M. Farle, W. A. Lewis

(Continued)

High Frequency and Nonlinear Phenomena

- 5607 Origin of the fine structure of subsidiary absorption in tangentially magnetized YIG films
- 5610 Instability mechanism of collective spin wave oscillations in finite-size ferrite samples
- 5613 Controlling spin-wave chaos
- 5616 Spin-wave chaotic transients
- 5619 Magnetoelastic interaction in yttrium iron garnet films with magnetic inhomogeneities through the film thickness
- 5622 Nonlinear statics and dynamics of highly anisotropic magnets
- 5625 Applications of ferrites and ferromagnets in tuning rf cavities for accelerators
- 5628 Forward volume wave microwave envelope solitons in yttrium iron garnet thin films: Peak profiles and multisoliton signatures (abstract)
- 5629 Microwave magnetic envelope solitons: Threshold powers and soliton numbers (abstract)
- 5630 Self-channeling of magnetostatic waves in ferromagnetic film (abstract)
- 5631 Spin wave solitons in an antiferromagnetic film (abstract)
- 5632 Brillouin light scattering study of spin wave instability magnon distributions in yttrium iron garnet thin films (abstract)
- 5633 Nonlinear surface spin waves (abstract)

Magnetic Properties: Tunneling

- 5634 Thermal equilibrium noise with $1/f$ spectrum and temperature-dependent magnetic viscosity in the amorphous alloy DyNi
- 5637 Time-dependent phenomena at low temperature in magnetic digital compact cassette tape
- 5639 Low-temperature magnetic relaxation of organic coated NiFe_2O_4 particles
- 5642 Quantum tunneling across a domain wall junction (abstract)
- 5642 Macroscopic quantum tunneling in antiferromagnetic horse-spleen ferritin particles (abstract)
- 5643 Magnetism of thin magnetic layers with strong anisotropy and quantum tunneling (abstract)

Magnetoelastic Behavior of Films and Crystals

- 5644 Magnetic and structural modifications in Fe and Ni films prepared by ion-assisted deposition
- 5647 Magnetostrictive hysteresis in nickel polycrystalline thick films
- 5650 Method for determining both magnetostriction and elastic modulus by ferromagnetic resonance
- 5653 Multitarget sputtering of high magnetostrictive Tb-Dy-Fe films
- 5656 Magnetostriction, elastic moduli, and coupling factors of composite Terfenol-D
- 5659 Structure and magnetic properties of mechanically alloyed SmFe_2

A. V. Pomyalov, I. Laulich

A. N. Slavin, G. Srinivasan, S. S. Cordone, V. B. Cherepanov

S. M. Rezende, F. M. de Aguiar, A. Azevedo

F. M. de Aguiar, S. M. Rezende, F. C. S. da Silva

Yu. V. Gulyaev, A. G. Temiryazev, M. P. Tikhomirova, P. E. Zil'berman

V. S. Ostrovskii

S. M. Hanna

M. A. Tsankov, M. Chen, C. E. Patton

J. M. Nash, M. Chen, M. A. Tsankov, C. E. Patton

J. Boyle, S. A. Nikitov, A. D. Boardman, A. Moghadam, K. M. Booth, J. G. Booth

A. D. Boardman, S. A. Nikitov, N. A. Waby

P. Kabos, G. Wiese, C. E. Patton

A. L. Sukstanskii, S. V. Tarasenko

B. Barbara, A. Ratnam, A. Cavalleri, M. Cerdonio, S. Vitale

X. X. Zhang, J. Tejada

R. H. Kodama, C. L. Seaman, A. E. Berkowitz, M. B. Maple

Bernard Barbara, Leon Gunther

J. Tejada, X. X. Zhang

P. Perera, M. J. O'Shea

William A. Lewis, Michael Farle, Bruce M. Clemens, Robert L. White

Isabelle Brard, Roland Georges, Gilles Le Blevnec

R. D. McMichael

E. Quandt

L. Sandlund, M. Fahlander, T. Cedell, A. E. Clark, J. B. Restorff, M. Wun-Fogle

Clive D. Milham

(Continued)

5662 High pulsed field magnetostriction in RMn_2 ($R=Gd, Tb, Nd, \text{ and } Y$)

M. R. Ibarra, C. Marquina, L. Garcia-Orza, Z. Arnold, A. del Moral

5665 An ultrasonic study of the Néel transition in dilute Cr-Al alloy single crystals

H. L. Alberts

5667 Magnetostriction of polycrystalline Co-Pd alloys

S. U. Jen, B. L. Chao

5670 Hysteretic and other relationships between technical magnetostriction and magnetization

I. J. Garshelis

5673 Micromagnetic model for the influence of biaxial stress on hysteretic magnetic properties

M. J. Sablik, L. A. Riley, G. L. Burkhardt, H. Kwun, P. Y. Cannell, K. T. Watts, R. A. Langman

5676 Modeling the effects of stress on magnetization in ferromagnetic materials (abstract)

D. C. Jiles

Hysteresis and Micromagnetics

5677 Interpretation of hysteresis curves and Henkel plots by the Preisach model (invited)

V. Basso, M. Lo Bue, G. Bertotti

5683 Experimental testing of applicability of the Preisach hysteresis model to superconductors

G. Friedman, L. Liu, J. S. Kouvel

5686 2D vector Preisach models and rotational hysteretic losses

I. D. Mayergoyz

5689 Demagnetized-state dependence of Henkel plots. I. The Preisach model

Ferenc Vajda, Edward Della Torre, R. D. McMichael

5692 Demagnetized-state dependence of Henkel plots. II. Domain wall motion

R. D. McMichael, Ferenc Vajda, Edward Della Torre

5695 Model calculations of rotational hysteresis for ferromagnetic particles with competing anisotropies

Y. Yoshida, T. L. Templeton, A. S. Arrott

5698 A hysteresis model with interactions

J. Planès

5701 Simulation of magnetization reversal in two-phase exchange coupled nanocrystalline materials

E. H. Feutrill, P. G. McCormick, R. Street

5704 Activation volume of a pair of magnetostatically coupled particles

A. Lyberatos

5707 Parameter template in local magnetic measurements

R. Kaczmarek, M. Dautain, S. Defoug

5710 3-D micromagnetic modeling of domain configurations in soft magnetic materials

Zhenzhou Guo, Edward Della Torre

5713 Magnetization in current carrying iron whiskers (abstract)

A. S. Arrott, J.-G. Lee

Magnetic Semiconductor

5714 Spin-dependent confinement in DMS-based heterostructures (invited)

A. Petrou, L. P. Fu, W. Y. Yu, S. T. Lee, B. T. Jonker, J. Warnock

5719 Optical transitions in $(ZnCo)Se$ and $(ZnFe)Se$: Role of an effective $p-d$ exchange (invited)

Chee-leung Mak, J. Bak, R. Sooryakumar, M. M. Steiner, B. T. Jonker

5725 Coexistence of Brillouin and Van Vleck spin exchange in $Zn_{1-x}Mn_xSe/Zn_{1-y}Fe_ySe$ spin superlattice structures

B. T. Jonker, H. Abad, L. P. Fu, W. Y. Yu, A. Petrou, J. Warnock

5728 Magnetic study of the diluted magnetic semiconductor $Sn_{1-x}Mn_xTe$

P. J. T. Eggenkamp, C. W. H. M. Vennix, T. Story, H. J. M. Swagten, C. H. W. Swuste, W. J. M. de Jonge

5731 Magnetic behavior of $(CuIn)_{1-x}Mn_{2x}Te_2$

P. M. Shand, P. A. Polstra, I. Miotkowski, B. C. Crooker

5734 Relaxation of magnetization in $Cd_{1-x}Mn_xTe$ diluted magnetic semiconductors under illumination

M. Smith, A. Dissanayake, H. X. Jiang, L. X. Li

5737 Theory of magnetization in IV-VI based diluted magnetic semiconductors

R. L. Hota, G. S. Tripathi, P. K. Misra

(Continued)

- 5740 Effects of oxygen vacancies on magnetic properties of Ca-substituted yttrium iron garnet (abstract)

Y. J. Song, R. E. Bornfreund, G. B. Turpin, P. E. Wigen

Magnetic Recording: Frequency, Spatial, and Tribological Effects

- 5741 Tribological studies of silicon for magnetic recording applications (invited)
- 5747 Mathematical modeling of lubrication for the head-disk interface using incompressible fluids
- 5750 Wear and stiction regimes of thin-film magnetic disks
- 5753 Recording medium properties and capacity bounds
- 5756 Direct imaging of track edge fringing fields on recorded media
- 5759 Computation of magnetic fields from recording surfaces with multiple tracks
- 5762 Micromagnetic modeling and experimental study of transition noise correlation in thin-film media
- 5765 Noise correlations in dibt recording
- 5768 Magnetic viscosity in high-density recording
- 5771 Friction and wear of ultrahigh-density magnetic tapes
- 5774 Analysis of write and read spacing loss for perpendicular recording (abstract)
- 5775 Experimental Preisach analysis of the Wohlfarth relation (abstract)

Bharat Bhushan, Vilas N. Koinkar

Paul R. Peck, Myung S. Jhon, Ralph F. Simmons, Jr., Thomas J. Janstrom

Arlen Bowen

J. A. O'Sullivan, D. G. Porter, R. S. Indeck, M. W. Muller

R. D. Gomez, I. D. Mayergoyz, E. R. Burke

E. R. Burke, R. D. Gomez, R. Madabhushi, I. D. Mayergoyz

Jian-Gang Zhu, Haiyun Wang, Thomas C. Arnoldussen

Gang Herbert Lin, H. Neal Bertram, Ralph Simmons

Pu-Ling Lu, Stanley H. Charap

Bharat Bhushan, Steven T. Patton

Yoichiro Tanaka, Tomoko Komai, Takashi Hikosaka

Ferenc Vajda, Edward Della Torre

Soft Magnetic Materials and Applications I

- 5776 Magnetic fine structure of domain walls in iron films observed with a magnetic force microscope
- 5779 Influence of rf magnetron sputtering conditions on the magnetic, crystalline, and electrical properties of thin nickel films
- 5782 Molecular magnets $V(\text{tetracyanoethylene})_x \cdot y(\text{solvent})$: Applications to magnetic shielding
- 5785 Soft magnetic properties of nanocrystalline Fe-Hf-C-N films
- 5788 Electrical characteristics of spiral coil planar inductors using amorphous alloy ribbons as magnetic layers
- 5791 Bending stresses and bistable behavior in Fe-rich amorphous wire
- 5794 Relaxation in magnetic continua
- 5797 Generalized equations for domain wall dynamics
- 5800 Magnetic induced uniaxial anisotropy in NiFe and NiFeCr films (abstract)
- 5800 Structural and magnetic properties of rf-sputtered iron nitrides using NH_3 (abstract)
- 5801 Nucleation of the nanocrystalline phase in $\text{Fe}_{73.5}\text{Cu}_1\text{Nb}_3\text{Si}_{13.5}\text{B}_9$ (abstract)

Roger Proksch, Sheryl Foss, E. Dan Dahlberg, Gary Prinz

M. S. Miller, F. E. Stageberg, Y. M. Chow, K. Rook, L. A. Heuer

B. G. Morin, C. Hahn, Joel S. Miller, A. J. Epstein

J. O. Choi, J. J. Lee, S. H. Han, H. J. Kim, I. K. Kang

K. Torigawa, H. Hirano, T. Sato, N. Tanaka

M. Vázquez, C. Gómez Polo, J. Velázquez, A. Hernando

V. L. Sobolev, I. Klik, C. R. Chang, H. L. Huang

Vladimir L. Sobolev, Huei Li Huang, Shuan Chung Chen

Terry Torng, Simon H. Liao

John Q. Xiao, C. L. Chien

J. D. Ayers, V. G. Harris, J. A. Sprague, W. T. Elam

Symposium: Magnetic Circular Dichroism

- 5802 Validity and the applicability of magnetic-circular-dichroism sum rules for transition metals (invited)

Ruqian Wu, Dingsheng Wang, J. Freeman

(Continued)

- 5807 X-ray magnetic circular dichroism studies of multilayered thin films of 3d transition metals (invited) (abstract)
- 5807 Physical information in polarized x-ray absorption spectroscopy and x-ray photoemission spectroscopy (invited) (abstract)
- 5808 Element specific magnetic hysteresis curves of Fe/Cu/Co multilayers (invited) (abstract)
- 5809 Core-level magnetic circular dichroism in 3d and 4f magnetic systems (invited) (abstract)
- 5810 Soft x-ray magneto-optical Kerr effect (invited) (abstract)
- Cooperative Phenomena: Critical Phenomena and Disordered Systems**
- 5811 Application of the spreading of damage technique to the $S=1/2$ Ising thin film
- 5814 Quantum renormalization of the XY model
- 5817 Magnetization and static structure factor behavior in a first-order helix-fan phase transition
- 5820 Magnetic properties in the Ising mixed spin-1/2-spin-1 superlattice
- 5823 Monte Carlo calculation of the correlation range for the $S=\frac{1}{2}$ isotropic Heisenberg ferromagnetic thin film
- 5826 Static critical properties of disordered ferromagnets studied by superconducting quantum interference device magnetometry and small-angle neutron-scattering techniques
- 5829 Thermodynamical properties of a Heisenberg model with Dzyaloshinski-Moriya interactions
- 5832 A unified effective-field renormalization-group framework approach for the quenched diluted Ising models
- 5835 Critical behavior of the anisotropic Heisenberg model by effective-field renormalization group
- 5838 Random decorated antiferromagnetic Ising model with mixed spins
- 5841 Phase diagrams of diluted ferromagnetic Ising films in a transverse field
- 5844 Relaxation dynamics in a reentrant (FeNi)Mn ferromagnet: A percolation analysis
- 5847 Spin glasses with cubic anisotropy
- 5850 Macroscopic random magnetic anisotropy constant in crystalline $Dy_xY_{1-x}Al_2$ ($x=0.3, 0.4$)
- 5853 Temperature dependence of the hyperfine field distributions in the $Fe_{93.5-x}Nd_xZr_{6.5}$ ($x=0, 2$) amorphous alloys
- 5856 Blocking of logarithmic temporal relaxation of magnetic remanence by piezomagnetically induced domains in $Fe_{1-x}Zn_xF_2$
- 5859 One-dimensional antiferromagnetic behavior in $AVOPO_4$ ($A=NH_4, Na$) prepared from hydrothermal conditions
- 5862 ac susceptibility on the dilute antiferromagnet $Mn_xZn_{1-x}F_2$ close to the percolation threshold (abstract)
- D. Weller, M. G. Samant, J. Stöhr, Y. Wu, B. D. Hermsmeier, G. Held, C. Chappert
- Bernard Theodoor Thole
- Y. U. Idzerda, H.-J. Lin, G. Ho, G. Meigs, A. Chaiken, G. A. Prinz, C. T. Chen
- T. Koide
- C. C. Kao, C. T. Chen, E. D. Johnson, Y. U. Idzerda, J. B. Hastings
- I. V. Rojdestvenski, U. M. S. Costa
- Alessandro Cuccoli, Valerio Tognetti, Paola Verrucchi, Ruggero Vaila
- E. Rastelli, S. Tazzari, A. Tassi
- E. F. Sarmiento, J. C. Cressoni, R. J. V. dos Santos
- I. V. Rojdestvenski, M. G. Cottam, I. A. Favorski
- S. Pouget, M. Alba, M. Nogues
- F. Lacerda, J. Ricardo de Sousa, I. P. Fittipaldi
- Douglas F. de Albuquerque, I. P. Fittipaldi
- J. Ricardo de Sousa, I. P. Fittipaldi
- Vanêssa M. Correia, Roberto J. V. dos Santos
- J. C. Cressoni, J. W. Tucker, E. F. Sarmiento
- D. Li, R. M. Roshko, G. Yang
- Z. Domański, T. K. Kopeć, F. Pázmándi, P. Erdős
- A. del Moral, M. Ciria, J. I. Arnaudas, J. S. Abell, Y. Bl
- G. K. Nicolaides, M. Pissas, D. Niarchos, R. D. Taylor, K. V. Rao
- J. Kushauer, C. Binek, W. Kleemann
- Charles J. O'Connor, Victoria Soghomonian, Robert C. Haushalter, Zhanwen Wang, Jon Zubieta
- F. L. A. Machado, F. C. Montenegro, E. Montarroyos, J. C. O. de Jesus, A. Rosales-Rivera, S. M. Rezende

(Continued)

- 5862 The frequency dependence of the ferro-to-spin-glass transition of amorphous Fe-rich Fe-Zr (abstract)
- 5863 Cooperative spin-crossover transition: Effects of the antiferro- and ferri-ordered phase (abstract)

J. Nogués, K. V. Rao

Benjamin G. Vekhter

Small Particles

- 5864 Nanocomposite formation in the Fe_3O_4 -Zn system by reaction milling
- 5867 Fe- Al_2O_3 nanocomposites prepared by high-energy ball milling
- 5870 Synthesis and properties of α'' - Fe_{16}N_2 in magnetic particles
- 5873 Magnetism and spin dynamics of nanoscale FeOOH particles
- 5876 Magnetic properties of microemulsion synthesized cobalt fine particles
- 5879 Magnetic properties of carbon-coated rare-earth carbide nanocrystallites produced by a carbon arc method
- 5882 Magnetic properties of carbon-coated, ferromagnetic nanoparticles produced by a carbon-arc method
- 5885 Structural and magnetic properties of ultrafine Fe-Pd particles
- 5888 Fine structure and magnetic properties of Mn- and Co-doped nanocrystalline γ - Fe_2O_3
- 5891 Elongated superparamagnetic particles
- 5894 Interactions between single domain particles
- 5897 Temperature dependence of switching field distribution
- 5900 Dynamics of fine particles observed in zero-field neutron scattering
- 5903 Magnetic properties of fine Ni particles coated with Pd (abstract)
- 5903 Nuclear magnetic resonance studies on the surface magnetism of vanadium ultrafine particles (abstract)

Laszlo Takacs, Martha Pardavi-Horvath

Søren Linderøth, Michael S. Pedersen

Xiaohua Bao, Robert M. Metzger, Massimo Carbucicchio

M. M. Ibrahim, G. Edwards, M. S. Seehra, B. Ganguly, G. P. Huffman

J. P. Chen, K. M. Lee, C. M. Sorensen, K. J. Klabunde, G. C. Hadjipanayis

B. Diggs, A. Zhou, C. Silva, S. Kirkpatrick, N. T. Nuhfer, M. E. McHenry, D. Petasis, S. A. Majetich, B. Brunett, J. O. Artman, S. W. Staley

E. M. Brunzman, R. Sutton, E. Bortz, S. Kirkpatrick, K. Midelfort, J. Williams, P. Smith, M. E. McHenry, S. A. Majetich, J. O. Artman, M. De Graef, S. W. Staley

L. Yiping, G. C. Hadjipanayis, C. M. Sorensen, K. J. Klabunde

Ming-Cheng Deng, Tsung-Shune Chin, F. R. Chen

Amikam Aharoni

Roger Proksch, Bruce Moskowitz

Jiang-Ching Lin, I. Klik, C. J. Chen, Ching-Ray Chang

M. Hennion, C. Bellouard, I. Mirebeau, J. L. Dormann, R. Ober

Makoto Yamaguchi, Yoshichika Otani, Hideki Miyajima

Yukihiro Hirayama, Tomoki Erata, Eiji Kita, Akira Tasaki

New Instrumentation and Measurement Techniques

- 5904 Polyphase eddy current testing
- 5907 Defect recognition in conductive materials by local magnetic-field measurement
- 5910 Component-resolved imaging of surface magnetic fields
- 5913 Measurement of Young's moduli for film and substrate by the mechanical resonance method
- 5916 A new structure of torque sensors using thin pickup head—Use of mutual coupling modulation
- 5919 A microwave transmission spectrometer

I. Marinova, S. Hayano, N. Ishida, Y. Saito, Y. Hiram, M. Yamamoto

T. Doi, S. Hayano, I. Marinova, N. Ishida, Y. Saito

R. D. Gomez, E. R. Burke, I. D. Mayergoyz

Y. H. Lee, Y. D. Shin, K. H. Lee, J. R. Rhee

I. Sasada, F. Koga

Carlo Waldfried, Scott Wadewitz, G. Dewar

(Continued)

- 5922 Measurements of intrinsic magnetic properties of materials from surface inspection (abstract)
- 5922 Three component magnetic field measurements using cubic anisotropy in (111) YIG films (abstract)
- 5923 Magnetoresistive characterization of thin-film structures by a gradient-field method (abstract)
- 5924 Dispersivity measurement of magnetic powders using the magnetic noise method (abstract)
- Symposium: Environmental Magnetism**
- 5925 Contributions of fine-particle magnetism to reading the global paleoclimate record (invited)
- 5931 Collection, measurement, and analysis of airborne magnetic particulates from pollution in the environment (invited)
- Critical Phenomena**
- 5937 Dynamics of the one-dimensional spin-1 Heisenberg antiferromagnet with exchange and single-site anisotropy
- 5940 Ferromagnetism of single crystal $\text{Fe}[\text{S}_2\text{CN}(\text{C}_2\text{D}_5)_2]_2\text{Cl}$
- 5943 Spin-1/2 Heisenberg antiferromagnet on the square and triangular lattices: A comparison of finite temperature properties
- 5946 Disorder-driven first-order phase transformations: A model for hysteresis
- 5949 Magnetic properties of the two-dimensional "triangles-in-triangles" Kagomé lattice $\text{Cu}_9\text{X}_2(\text{cpa})_6$ ($\text{X}=\text{F}, \text{Cl}, \text{Br}$)
- 5952 Magnetic properties of two copper (II)-halide layered perovskites
- 5955 Can the universal jump be observed in two-dimensional XY magnets?
- 5958 Strong thermal fluctuation effects on the dynamics of Bloch walls (abstract)
- 5959 Depth-dependent magnetic correlation length in terbium (abstract)
- Thin Film Recording Media I**
- 5960 Ba-ferrite thin-film media for high-density longitudinal recording (invited)
- 5966 Microstructural investigations of barium ferrite longitudinal thin-film media
- 5969 Low-temperature deposition of hexagonal ferrite films by sputtering
- 5972 Surface roughness and magnetic properties of *in situ* heated and postannealed thin films of perpendicular barium ferrite
- 5975 Preparation of Co-Zn ferrite films at low substrate temperature by plasma-free dc sputtering for magnetic recording media
- 5978 Magnetic and crystallographic properties of Co-Cr-(Ta,Pt)/Cr films deposited by excimer laser ablation
- 5981 Transverse susceptibility and ferromagnetic resonance of Hi-8 metal-evaporated tape
- Z. J. Chen, D. C. Jiles
- A. Ya. Perlov, A. I. Voronko, P. M. Vetoshko, V. B. Volkovoy
- P. L. Trouilloud, F. Suits, C. V. Jahnes, M. A. Russak, E. J. Spada, J. W. Chang
- V. M. Vasilyev
- Subir K. Banerjee
- Philip J. Flanders
- Shu Zhang, Yongmin Yu, V. S. Viswanath, Joachim Stolze, Gerhard Müller
- G. C. DeFotis, W. W. Brubaker, S. Chandarlapaty, K. L. Beers, G. Coffey
- N. Elstner, R. R. P. Singh, A. P. Young
- Karin Dahmen, Sivan Kartha, James A. Krumhansl, Bruce W. Roberts, James P. Sethna, Joel D. Shore
- Sanchit Maruti, Leonard W. ter Haar
- N. Sivron, T. E. Grigereit, John E. Drumheller, K. Emerson, R. D. Willett
- S. T. Bramwell, P. C. W. Holdsworth
- M. Hartl, D. Garanin, J. Koetzler
- P. M. Gehring, K. Hirota, C. F. Majkrzak, G. Shirane
- T. L. Hylton, M. A. Parker, M. Ullah, K. R. Coffey, R. Umphress, J. K. Howard
- B. Y. Wong, X. Sui, D. E. Laughlin, M. H. Kryder
- Akimitsu Morisako, Hiroaki Nakanishi, Mitsunori Matsumoto, Masahiko Naoe
- Kyusik Sin, John M. Sivertsen, Jack H. Judy
- N. Matsushita, K. Noma, S. Nakagawa, M. Naoe
- A. Ishikawa, K. Tanahashi, Y. Yahisa, Y. Hosoe, Y. Shiroishi
- C. Sürig, G. Zimmermann, K. A. Hempel

(Continued)

- 5984 Low-temperature sputter deposition of high-coercivity Co-Cr films for perpendicular recording
- 5987 Improvement of anisotropy of perpendicular magnetic recording tape by Ta addition and Kr sputtering gas (abstract)

Naoki Honda, Kazuhiro Ouchi,
Shun-ichi Iwasaki
Kiyoshi Kuga, Hideaki Yoshimoto,
Yoshiro Yoneda, Junji Numazawa,
Masahiko Naoe

Emerging Hard Magnets Based on Interstitials

- 5988 High field magnetization measurements of $\text{Sm}_2\text{Fe}_{17}$, $\text{Sm}_2\text{Fe}_{17}\text{N}_3$, $\text{Sm}_2\text{Fe}_{17}\text{D}_5$, and $\text{Pr}_2\text{Fe}_{17}$, $\text{Pr}_2\text{Fe}_{17}\text{N}_3$ (invited)
- 5994 Comparative Mössbauer effect study of several R_2Fe_{17} and $\text{R}_2\text{Fe}_{17}\text{N}_x$ compounds
- 5997 The effects of group IV B/V B/VI B additions on the magnetic properties of $\text{Sm}_{2+\delta}\text{Fe}_{17}$ carbonitrides
- 6000 Phase transformation induced by gas phase reaction in $\text{RFe}_{10}\text{SiC}_x$ alloys
- 6003 A detailed study of nitride precipitates in $\text{Nd}_2\text{Fe}_{17}$
- 6006 Aligned high anisotropy $\text{Pr}(\text{Fe},\text{Co},\text{Mo})_{12}\text{N}$ film samples
- 6009 Anisotropy and flux density enhancement in aligned ThMn_{12} -type $\text{NdFe}_{11}\text{Co}_{1-y}\text{Mo}_y\text{N}$ film samples
- 6012 Hydrogenation decomposition desorption recombination magnets based on $\text{Sm}_{2+\delta}\text{Fe}_{17}\text{M}_{0.4}$ carbonitrides ($\text{M}=\text{IVB/VB/VIB}$ group elements)
- 6015 Nitriding of melt-spun Nd-Fe-Mo alloys
- 6018 Effect of milling on the magnetic and microstructural properties of $\text{Sm}_2\text{Fe}_{17}\text{N}_x$ permanent magnets
- 6021 Magnetic properties of $\text{Y}(\text{Fe},\text{Co})_{10}\text{Mo}_2$ alloys

O. Isnard, S. Miraglia, M. Guillot,
D. Fruchart
Gary J. Long, S. Mishra, O. A.
Pringle, F. Grandjean, K. H. J.
Buschow
X. Chen, Er. Girt, Z. Altounian
E. W. Singleton, G. C. Hadjipanayis,
V. Papaefthymiou, Z. Hu, W. B.
Yelon
C. C. Colucci, S. Gama, C. A.
Hibeiro, L. P. Cardoso
R. Rani, H. Hegde, A. Navarathna,
F. J. Cadieu
A. Navarathna, H. Hegde, R. Rani,
F. J. Cadieu
X. Chen, Z. Altounian
F. E. Pinkerton, C. D. Fuerst, J. F.
Herbst
P. A. P. Wendhausen, B. Gebel, D.
Eckert, K.-H. Müller
Xie Xu, Roy Tucker, S. A. Shaheen

Field Computations

- 6024 Magnetic thin-film media response in presence of displacement eddy currents
- 6027 On finite element implementation of impedance boundary conditions
- 6030 Three-dimensional iterative solution for the multiconductor eddy current and free surface calculations
- 6033 Modeling and analysis of electric and magnetic coupled problems under nonlinear conditions
- 6036 Transformation methods in computational electromagnetism
- 6039 The effects of various magnetic materials on lamination design for stator-rotor diecasting of induction motors for electric vehicle applications
- 6042 An improved method for magnetic flux density visualization using three-dimensional edge finite element method
- 6045 Optimum design of voice coil motor with constant torque coefficients using evolution strategy
- 6048 Three-dimensional eddy current solution of a polyphase machine test model (abstract)
- 6049 Numerical methods and measurement systems for nonlinear magnetic circuits (abstract)
- 6050 Comparative analysis of two methods for time-harmonic solution of the steady state in induction motors (abstract)

A. Geri, A. Salvini, G. M. Veca
I. D. Mayergoyz, G. Bedrosian
M. Ramadan Ahmed, K. F. Ali,
Ibrahim Moustafa
A. Geri, M. La Rosa, G. M. Veca
A. Nicolet, J.-F. Remacle, B. Meys,
A. Genon, W. Legros
N. M. Elkasabgy, C. Di Pietro
Vlatko Čingoski, Hideo Yamashita
Chang Seop Koh, Osama A.
Mohammed, Jun-o Kim, Song-yop
Hahn
Uwe Pahner, Ronnie Belmans,
Vlado Ostovic
Axel Heitbrink, Hans Dieter Storzer,
Adalbert Beyer
Fobrecht DeWeerd, Kostadin
Brandisky, Uwe Pahner, Ronnie
Belmans

Spin Waves, Hyperfine Fields, and Resonance

- 6051 Selection of the ground state in CsCuCl_3 by quantum fluctuations
E. Rastelli, A. Tassi
- 6054 Scaling behavior of the homogeneous magnetization dynamics in the ferromagnetic state of EuS
R. Dombrowski, D. Görlitz, J. Kötzler, Chr. Marx
- 6057 Dynamical properties of quantum spin systems in magnetically ordered product ground states
V. S. Viswanath, Joachim Stolze, Gerhard Müller
- 6060 Magnons in ferromagnetic terbium under high pressure
S. Kawano, J. A. Fernandez-Baca, R. M. Nicklow
- 6063 Polarization analysis of magnons in CsMnI_3
Z. Tun, T. C. Hsu, J-G. Lussier
- 6066 Orientation dependence of dipole gaps in the magnetostatic wave spectrum of Bi-substituted iron garnets
Ana K. Chernakova, Andrew Cash, Jose Peruyero, Daniel D. Stancil
- 6069 Polarization analysis of the magnetic excitations in $\text{Fe}_{65}\text{Ni}_{35}$ Invar
J. W. Lynn, N. Rosov, M. Acet, H. Bach
- 6072 Temperature dependence of the magnetic excitations in ordered and disordered $\text{Fe}_{72}\text{Pt}_{28}$
N. Rosov, J. W. Lynn, J. Kästner, E. F. Wassermann, T. Chattopadhyay, H. Bach
- 6075 Theory of ferromagnetic resonance relaxation in very small solids
J. B. Sokoloff
- 6078 Crystallographic and magnetic properties of $\text{Co}_x\text{Fe}_{1-x}\text{Cr}_2\text{S}_4$
Chul Sung Kim, Min Yong Ha, Heung Moon Ko, Young Jei Oh, Heung Soo Lee, Sang Youl Lee, Jung Chul Sur, Jae Yun Park
- 6081 The effect of Co doping on spin cluster resonance in the one-dimensional Ising ferromagnet FeTAC
R. S. Rubins, T. D. Black, K. Ravindran, John E. Drumheller
- 6084 New perspective on the Green's function dipole-exchange spin wave theory for thin films (abstract)
Ming Chen, Carl E. Patton
- 6085 Ground state and spin dynamics in hexagonal antiferromagnet CsCuCl_3 (abstract)
E. P. Stefanovskii, A. L. Sukstanskii

Magnetic Bubble and VBL Memories

- 6086 Successive Bloch line write operation in a 1- μM bubble material
K. Matsuyama, T. Ohyama, H. Asada, K. Taniguchi
- 6089 Micromagnetic computation for wall and Bloch line coercivity in thin films with perpendicular anisotropy
H. Asada, K. Matsuyama, M. Gamachi, K. Taniguchi
- 6092 Phase transitions in bubble lattice under temperature lowering (abstract)
V. S. Gerasimchuk, Yu. I. Gorobets, K. De Ville
- 6093 An adaptive computational method for domain wall dynamics (abstract)
Sergey G. Osipov

Soft Magnetic Materials: Ferrites

- 6094 Wet-process preparation of amorphous Y-Fe oxide films ferromagnetic at room temperature
Q. Zhang, T. Itoh, M. Abe, M. J. Zhang
- 6097 Magnetic anomalies in single crystal Fe_3O_4 thin films
D. T. Margulies, F. T. Parker, A. E. Berkowitz
- 6100 An analysis of the high-temperature relaxation in polycrystalline magnetite
J. Castro, D. Martinez, J. Rivas, H. J. Blythe
- 6103 $\text{Dy}_3\text{Fe}_5\text{O}_{12}$ garnet thin films grown from sputtering of metallic targets
J. Ostoréro, M. Escorne, A. Pecheron-Guegan, F. Soulette, H. Le Gall
- 6106 Enhanced coercivity due to a local anisotropy increase
J. A. Jatau, M. Pardavi-Horváth, E. Della Torre
- 6109 The microwave absorbing and resonance phenomena of Y-type hexagonal ferrite microwave absorbers
H. J. Kwon, J. Y. Shin, J. H. Oh
- 6112 Effect of Er_2O_3 addition on microstructure and physical properties of Mn-Zn ferrites for high-power use
C. S. Liu, J. M. Wu, C. J. Chen, M. J. Tung

(Continued)

- 6115 Dispersion observed in electrical properties of titanium-substituted lithium ferrites
- 6118 Electrical conductivity of Mn-Zn ferrites
- 6121 Composition dependence of the elastic moduli of mixed lithium-cadmium ferrites
- 6124 Deposition and properties of NiFe_2O_4 thin films (abstract)
- 6124 Studies of stoichiometric variations of epitaxially grown $\text{Fe}_{3-x}\text{O}_4$ (abstract)
- 6125 Cation distribution of Li-Ti mixed ferrites (abstract)

Thin Film Recording Media II

- 6126 Magnetic and microstructural properties of CoCrPt/CoCrPtSi dual-layered magnetic recording media
- 6129 Bicrystal advanced thin-film media for high density recording
- 6132 AFM structure and media noise of SmCo/Cr thin films and hard disks
- 6135 Modeling of thin-film media with advanced microstructure for ultrahigh density recording
- 6138 Evaluation of the CoCrTaPt alloy for longitudinal magnetic recording
- 6141 Analysis of the electronic properties of CoCrPt thin films using parallel electron energy loss spectroscopy (PEELS)
- 6144 Noise properties and microstructure of oriented CoCrTa/Cr media
- 6147 Effects of oxide addition on magnetic and structural properties of CoNiPt alloy films
- 6150 Comparison of reproduce signal and noise of conventional and keepered CoCrTa/Cr thin film media
- 6153 Process temperature dependence of ∂M plots on Co alloy media on amorphous carbon substrates
- 6156 Friction and wear of ion-implanted diamondlike carbon and fullerene films for thin-film rigid disks
- 6159 Thin film disks for high density recording with textured underlayers (abstract)
- 6160 A study of the structural properties of sputtered CoCrPt based on x-ray diffraction, small angle x-ray scattering, XAFS, and transmission electron microscopy measurements (abstract)
- 6161 Multinuclear nonmagnetic resonance studies of perfluoro poly ether lubricants (abstract)
- 6162 The durability of new rigid disks by molded plastic substrates (abstract)

Coupling Through Nonmagnetic Layers

- 6163 Temperature-dependent non-Heisenberg exchange coupling of ferromagnetic layers (invited)

Bijoy Kumar Kuanr, G. P. Srivastava

D. Ravinder, K. Latha

D. Ravinder

R. B. van Dover, E. M. Gyorgy, J. M. Phillips, J. H. Marshall, R. J. Felder, R. M. Fleming, H. O'Bryan, Jr.

E. Lochner, K. A. Shaw, R. C. DiBari, D. Hilton, D. M. Lind, S. D. Berry

M. Bhagavantha Reddy, P. Venugopal Reddy

N. Inaba, Y. Matsuda, M. Suzuki, A. Nakamura, M. Futamoto

Tai Min, Jian-Gang Zhu

E. M. T. Velu, D. N. Lambeth, J. T. Thornton, P. E. Russell

Xiao-Guang Ye, Jian-Gang Zhu

Yuanda Cheng, Mojtaba Sedighi, Irene Lam, Richard A. Gardner, ZhiJun Yang, Michael R. Scheinfeld

Pawel Giljer, John M. Sivertsen, Jack H. Judy

R. Ranjan, W. R. Bennett, G. J. Tarnopolsky, T. Yamashita, T. Nolan, R. Sinclair

A. Murayama, S. Kondoh, M. Miyamura

Kyusik Sin, Juren Ding, Pawel Giljer, John M. Sivertsen, Jack H. Judy, Jian-Gang Zhu

Masago Kuwabara, Haydee Saffari, Mark R. Visokay, Hidetaka Hayashi, Motoharu Sato

Bharat Bhushan, B. K. Gupta

Mohammad Mirzamaani, Michael A. Russak, Christopher V. Jahnes

S. Yumoto, N. Ohshima

K. V. Viswanathan

Osamu Morita, T. Sano, Yasuyuki Imai, Naoko Hisayama, Hiroshi Takino

R. P. Erickson

(Continued)

- 6169 Photo-induced antiferromagnetic interlayer coupling in Fe superlattices with iron silicide spacers (invited)
J. E. Mattson, Eric E. Fullerton, Sudha Kumar, S. R. Lee, C. H. Sowers, M. Grimsditch, S. D. Bader, F. T. Parker
- 6174 An alternate route to giant magnetoresistance in MBE-grown Co-Cu superlattices (invited)
Roy Clarke, Darryl Barlett, Frank Tsui, Baoxing Chen, Citrad Uher
- 6178 Magnetic profile as a function of structural disorder in Fe/Cr superlattices
Michael J. Pechan, J. F. Ankner, C. F. Majkrzak, David M. Kelly, Ivan K. Schuller
- 6181 Temperature dependence of the exchange coupling in the Fe(001) whisker/11 ML Cr/20 ML Fe structure
M. From, L. X. Liao, J. F. Cochran, B. Heinrich
- 6184 Anisotropy studies of AFM coupled MBE grown Co/Cu(001) superlattices
K. Bröhl, S. Di Nunzio, F. Schreiber, Th. Zeidler, H. Zabel
- 6187 "Loose spins" in Fe/Cu/Fe(001) structures
B. Heinrich, Z. Celinski, L. X. Liao, M. From, J. F. Cochran
- 6190 Interlayer coupling and spin polarization of the nonmagnetic layers in Fe/Cu and Fe/Ag CMFs
Y. B. Xu, M. Lu, Q. Y. Jin, C. Hu, Y. Z. Miao, Y. Zhai, Q. S. Bie, H. R. Zhai, G. L. Dunifer, R. Naik, M. Ahmad
- 6193 Growth temperature dependence of biquadratic coupling in Fe/Cr(100) superlattices studied by polarized neutron reflectivity and x-ray diffraction (abstract)
M. Schäfer, J. A. Wolf, P. Grünberg, J. F. Ankner, A. Schreyer, H. Zabel, C. F. Majkrzak
- Symposium: Novel Time-Resolved Probes of Dynamical Magnetism**
- 6194 Picosecond pulsed-field probes of magnetic systems (invited)
M. R. Freeman
- 6199 Femtosecond Faraday rotation in spin-engineered heterostructures (invited)
J. J. Baumberg, D. D. Awschalom, N. Samarth
- 6205 Time-resolved scanning probe microscopy: Investigations and applications of dynamic magnetostriction (invited)
G. Nunes, Jr., M. R. Freeman
- 6211 Magnetic resonance detection and imaging using force microscope techniques (invited)
O. Züger, D. Rugar
- 6217 Measurement of thermal switching of the magnetization of single domain particles (invited)
M. Lederman, D. R. Fredkin, R. O'Barr, S. Schultz, M. Ozaki
- Hard Magnets III: Substitutional Alloys and Novel Materials**
- 6223 Magnetic phase diagram of $(\text{Tb}_{1-x}\text{Gd}_x)\text{Fe}_{11}\text{Ti}$ alloys
L. C. C. M. Nagamine, H. R. Rechenberg, P. A. Algarabel, M. R. Ibarra
- 6226 Magnetic phase diagram of $\text{Nd}(\text{Fe},\text{Mo})_{12}$ alloys
Y. Z. Wang, B. P. Hu, X. L. Rao, G. C. Liu, L. Song, L. Yin, W. Y. Lai
- 6229 Magnetic anisotropies in $\text{RFe}_{10-x}\text{Co}_x\text{Mo}_2$ compounds ($\text{R}=\text{Dy}, \text{Er}$)
Roy Tucker, Xie Xu, S. A. Shaheen
- 6232 Magnetic properties of $\text{Nd}(\text{Fe},\text{Ti})_{12}$ and $\text{Nd}(\text{Fe},\text{Ti})_{12}\text{N}_x$ films of perpendicular texture
D. Wang, D. J. Sellmyer, I. Panagiotopoulos, D. Niarchos
- 6235 ^{57}Fe Mössbauer studies of $\text{Nd}(\text{Fe}_{12-x}\text{Mo}_x)$ and $\text{Nd}(\text{Fe}_{12-x}\text{Mo}_x)\text{N}_{0.9}$ ($x=1.25$ and 1.50)
Qi-Nian Qi, Bo-Ping Hu, J. M. D. Coey
- 6238 Magnetic properties of $(\text{Er},\text{R})_2\text{Fe}_{17}\text{N}_y$ compounds ($\text{R}=\text{Y},\text{Gd}$)
J. L. Wang, W. G. Lin, N. Tang, W. Z. Li, Y. H. Gao, F. M. Yang
- 6241 Magnetic properties of $\text{Er}_2\text{Fe}_{17-x}\text{Al}_x\text{N}_y$ compounds
F. M. Yang, N. Tang, J. L. Wang, X. P. Zhong, R. W. Zhao, W. G. Lin
- 6244 Electrical and magnetic studies of (Cu/Zn) -bonded $\text{Sm}_2\text{Fe}_{17}\text{M}_x\text{N}_y$ magnets ($\text{M}=\text{B}$ or C)
Y. D. Yao, P. C. Kuo, W. C. Chang, C. J. Liu

(Continued)

- 6247 Structure and magnetic properties of interstitial compounds of the series $\text{Dy}_2\text{Fe}_{17-x}\text{Al}_x\text{Z}_y$ (Z=N or H)
- 6250 High-coercivity Sm-Fe-Ga-C compounds with $\text{Th}_2\text{Zn}_{17}$ structure by melt spinning
- 6253 A novel hard magnetic material for sintering permanent magnets
- 6256 Effect of Sm substitution on structure and magnetic properties of high-carbon $\text{Er}_2\text{Fe}_{17}\text{C}_y$ compounds
- 6259 Structure and magnetic properties of $\text{Gd}_2\text{Fe}_{17-x}\text{Ga}_x\text{C}_2$ compounds
- 6262 Effect of cobalt substitution on magnetic properties of R_2Fe_{17} silicides (R=Y, Gd, Tb, Er, and Tm)
- 6265 A contribution to the knowledge of phase equilibria and the magnetic properties of the Nd-Fe-B-X systems (X=Al, Co, V)
- 6268 Investigations of magnetic properties and microstructure of 40CeNdium-Fe-B based magnets
- 6271 Investigation of interaction mechanisms in melt-quenched NdFeB
- 6274 Crystal structure and low-temperature magnetic properties of melt-spun $\text{Sm}_2\text{Co}_7\text{B}_3$ compounds
- 6277 Saturation magnetization and anisotropy fields in the $\text{Sm}(\text{Co}_{1-x}\text{Cu}_x)_5$ phases
- 6280 SmCo (2:17-type) magnets with high contents of Fe and light rare earths
- 6283 Effect of Dy substitution on the magnetocrystalline anisotropy of GdCo_4B
- 6286 Permanent magnet film magneto-optic waveguide isolator
- 6289 Investigation of Pr-Fe-B magnets with high performance (abstract)
- 6289 *In situ* and dynamic observation of NdFeCoB magnet by high voltage transmission electron microscope (abstract)
- Magnetic Ordering and Magnetic Structure**
- 6290 Influence of electron damping and reservoir on the magnetic phase diagram of chromium alloys
- 6293 Spin fluctuation effect in the ordered Fe_2N alloy
- 6296 Isoelectronic early *n-d* impurities in Fe: Magnetic and hyperfine field properties
- 6298 Electronic structure and the Stoner *I* parameter for RPd_3 compounds (R=La, Ce, Pr, and Nd)
- 6301 Band structure calculations of heavy fermion YbSbPd and YbSbNi
- 6303 Electronic structure and Curie temperature of $\text{YFe}_{12-x}\text{Mo}_x\text{N}_y$ compounds
- 6306 The percolation limit for the disappearance of ferromagnetism in melt spun Co-B-C amorphous alloys
- 6309 High-field magnetization behavior in random anisotropy amorphous Co-Er alloys
- J. P. Liu, D. C. Zeng, N. Tang, A. J. M. Winkelmann, F. R. de Boer, K. H. J. Buschow
- Lin-Shu Kong, Bao-gen Shen, Fang-wei Wang, Lei Cao, Hui-qun Guo, Tai-shan Ning
- Bao-gen Shen, Fang-wei Wang, Lin-shu Kong, Lei Cao, Wen-shan Zhan
- Bao-gen Shen, Lei Cao, Lin-shu Kong, Tai-shan Ning, Ming Hu
- Bao-gen Shen, Fang-wei Wang, Lin-shu Kong, Lei Cao, Bo Zhang, Jian-gao Zhao
- F. Pourarian, R. T. Obermyer, S. G. Sankar
- Anders Micski, Björn Uhrenius
- S. X. Zhou, Y. G. Wang, R. Høier
- L. Folks, R. Street, R. Woodward
- C. J. Yang, W. Y. Lee, S. D. Choi
- E. Lectard, C. H. Allibert, R. Ballou
- M. Q. Huang, Y. Zheng, W. E. Wallace
- T. Ito, H. Asano, H. Ido, G. Kido
- M. Levy, R. Scarmozzino, R. M. Osgood, Jr., R. Wolfe, F. J. Cadieu, H. Hedge, C. J. Gutierrez, G. A. Prinz
- F. Z. Lian, F. Pourarian, S. Simizu, S. G. Sankar, W. E. Wallace
- Pan Shuming, Liu Jinfang, Xu Yinfan
- R. S. Fishman, S. H. Liu
- Guan-mian Chen, Ming-xi Lin, Ji-wu Ling
- N. A. de Oliveira, A. A. Gomes, A. Troper
- T. Nautiyal, A. Kashyap, S. Auluck, M. S. S. Brooks
- A. K. Solanki, Arti Kashyap, S. Auluck, M. S. S. Brooks
- A. S. Fernando, J. P. Woods, S. S. Jaswal, D. Welipitiya, B. M. Patterson, D. J. Sellmyer
- G. K. Nicolaidis, A. Inoue, V. V. Rao
- H. Lassri, L. Driouch, R. Krishnan

(Continued)

6312. Magnetic properties and crystallization of amorphous Fe-Nd-B alloys at constant Nd concentration
- 6315 Influence of applied torsion on the bistable behavior of CoSiB amorphous wire
- 6318 Details of the magnetic phase diagram of holmium from neutron diffraction in *b*-axis fields
- 6321 Critical magnetic neutron scattering above T_N in Cr+0.18 at. % Re (abstract)
- 6321 Photoinduced disaccommodation of magnetic permeability in yttrium iron garnet (abstract)
- High T_c Superconductivity: Experiment and Theory**
- 6322 Unidirectional pinning in irradiated $\text{Bi}_2\text{Sr}_2\text{CaCu}_2\text{O}_8$ (invited)
- 6328 Unusual transport and magnetic properties of Tb-doped $\text{YBa}_2\text{Cu}_3\text{O}_7$ single crystals and epitaxial thin films
- 6331 Magnetic order of Pr ions in related perovskite-type Pr123 compounds
- 6334 Collective magnetic excitations of Ho^{3+} ions in grain-aligned $\text{HoBa}_2\text{Cu}_3\text{O}_7$
- 6337 Combined electronic-nuclear magnetic ordering of the Ho^{3+} ions and magnetic stacking faults in $\text{HoBa}_2\text{Cu}_3\text{O}_x$ ($x=7.0, 6.8, 6.3$)
- 6340 Raman spectra of two-dimensional spin- $\frac{1}{2}$ Heisenberg antiferromagnets
- 6343 Vortex flux creep and magnetic hysteresis in a type-II superconductor (abstract)
- 6343 Interactions with the Dy^{3+} sublattice observed in high resistance ultrathin $\text{DyBa}_2\text{Cu}_3\text{O}_{7-x}$ films (abstract)
- 6344 Probing of the pairing state of HTSCs utilizing *a-b* plane magnetization anisotropy (abstract)
- 6345 Theory of two-dimensional antiferromagnets with a nearly critical ground state (abstract)
- Magneto-optics**
- 6346 Electronic structure and magneto-optical properties of MnBi and MnBiAl
- 6348 Low-temperature characterization of the magnetic properties of MnBiAl thin films
- 6351 The functions of Al in MnBiAlSi magneto-optical films
- 6354 Magnetic and magneto-optical properties of $\text{Mn}_5(\text{Ge}_{1-x}\text{M}_x)_3$ alloys with $\text{M}=\text{Sn}, \text{Pb}$
- 6357 Magnetic and optical characteristics of bilayered films composed of Tb-Fe-Co layer with overlayers of Co-Cr, Ni-Fe, Ta, and C
- 6360 Change of magneto-optical Kerr rotation due to interlayer thickness in magnetically coupled films with noble-metal wedge
- 6363 Chemical modification of magneto-optic garnet film properties
- 6366 Circular magnetic x-ray dichroism in rare-earth magnets
- 6369 Resonant photoemission and magnetic x-ray circular dichroism in the *M* shell of ultrathin films of Fe
- Bao-gen Shen, Lin-yuan Yang, Hui-qun Guo, Jian-gao Zhao
- J. M. Blanco, P. Aragonese, E. Irurieta, J. González, K. Kulakowski
- D. A. Tindall, C. P. Adams, M. O. Steinitz, T. M. Holden
- D. R. Noakes, E. Fawcett, B. J. Sternlieb, G. Shirane, J. Jankowska
- I. Matsubara, K. Hisatake, K. Maeda
- L. Klein, E. R. Yacoby, A. Tsameret, Y. Yeshurun, K. Kishio
- G. Cao, J. W. O'Reilly, J. E. Crow, R. J. Kennedy, D. H. Nichols
- M. Guillaume, P. Fischer, B. Roessli, A. Podlesnyak, J. Schefer, A. Furrer
- U. Staub, F. Fauth, M. Guillaume, J. Mesot, A. Furrer, P. Dosanjh, H. Zhou, P. Vorderwisch
- B. Roessli, P. Fischer, U. Staub, M. Zolliker, A. Furrer
- Stephan Haas, Elbio Dagotto, Jose Riera, Roberto Merlin, Franco Nori
- M. K. Hasan, S. J. Park, J. S. Kouvel
- K. M. Beauchamp, G. C. Spalding, W. H. Huber, A. M. Goldman
- J. Buan, N. E. Israeloff, C. C. Huang, A. M. Goldman, J. Z. Liu, R. N. Shelton
- Andrey V. Chubukov, Subir Sachdev
- S. S. Jaswal, J. X. Shen, R. D. Kirby, D. J. Sellmyer
- K. W. Wierman, J. X. Shen, R. D. Kirby, D. J. Sellmyer
- D. Huang, X. W. Zhang, C. P. Luo, H. S. Yang, Y. J. Wang
- Y. Zhang, A. P. Runge, Z. S. Shan, D. J. Sellmyer
- Kibong Song, Masahiko Naoe
- T. Katayama, Y. Suzuki, M. Hayashi, W. Geerts
- Roger F. Belt, John B. Ings, Jonathan B. Whitlock
- Xindong Wang, V. P. Antropov, B. N. Harmon, J. C. Lang, A. I. Goldman
- J. G. Tobin, G. D. Waddill

(Continued)

6372 Molecular-orbital analysis of magneto-optical Bi-O-Fe hybrid excited states

6375 A new Faraday rotation glass with a large Verdet constant

6378 Experimental investigation of the magnetic circular dichroism sum rules (abstract)

Magnetic Recording Heads: Materials, Structures, and Micromagnetics

6379 Linearity and hysteresis in the magnetoresistive response of (NiFe,NiFeCo)/Cu and Co/Cu/NiFe multilayers in patterned stripes

6382 Microstructural origin of giant magnetoresistance in a new sensor structure based on NiFe/Ag discontinuous multilayer thin films

6385 Micromagnetics of GMR spin-valve heads

6388 Micromagnetic study of narrow track orthogonal giant magnetoresistive heads

6391 Dynamic domain instability and popcorn noise in thin-film heads

6394 Dynamic response of domain walls on the air-bearing surface of thin-film heads

6397 Omega head—an experimental 120-turn inductive head

6400 Local magnetoresistance and point-source excitation of Ni-Fe thin films (abstract)

6400 Sensitivity distribution asymmetries in magnetoresistive heads with domain control films (abstract)

Anisotropy of Films and Interfaces

6401 Overlayer-induced perpendicular anisotropy in ultrathin Co films (invited)

6406 Interfacial anisotropy and magnetic transition of cobalt films on Cu(111)

6409 Local spin-density theory of interface and surface magnetocrystalline anisotropy: Pd/Co/Pd(001) and Cu/Co/Cu(001) sandwiches

6412 Perpendicular magnetic anisotropy in $\text{Co}_x\text{Pd}_{1-x}$ alloy films grown by molecular beam epitaxy

6415 *In situ* measurement of stress and surface morphology for Co/Pd multilayer films fabricated by rf sputtering

6418 Temperature-dependent interface magnetism and magnetization reversal in Co/Pt multilayers

6421 Structural and magnetic properties of Co/Cr(001) superlattices

6424 Orientational and structural dependence of magnetic anisotropy of Cu/Ni/Cu sandwiches: Misfit interface anisotropy

6427 Magnetic anisotropy in ultrathin films grown on vicinal surfaces (abstract)

6428 Theoretical predictions for magnetic anisotropy of superlattice defects (abstract)

6429 Magnetoelastic coefficients at tetragonal surfaces (abstract)

6430 Magnetic anisotropy in epitaxial Ni/Cu(001) thin films: Effects of misfit strain on perpendicular magnetic anisotropy (abstract)

Gerald F. Dionne, Gary A. Allen

Sui hua Yuan, Xiao Zhou Shu

C. T. Chen, Y. U. Idzerda, H.-J. Lin, G. Meigs, G. Ho, N. V. Smith

K. Noguchi, S. Araki, T. Chou, D. Miyauchi, Y. Honda, A. Kamijima, O. Shinoura, Y. Narumiya

M. A. Parker, T. L. Hylton, K. R. Coffey, J. K. Howard

Samuel W. Yuan, H. Neal Bertram

Yimin Guo, Jian-Gang Zhu

F. H. Liu, M. H. Kryder

X. Shi, F. H. Liu, Yuet Li, M. H. Kryder

D. D. Tang, R. E. Lee, J. L. Su, F. Chu, J. Lo, H. Santini, L. Lane, N. Robertson, M. Porro, P. Cisneroz, G. Guthmiller

R. W. Cross, A. B. Kos

N. Koyama, C. Ishikawa, Y. Suzuki, H. Aoi, K. Yoshida

Brad N. Engel, Michael H. Wiedmann, Charles M. Falco

F. Huang, G. J. Mankey, R. F. Willis

Ding-sheng Wang, Ruqian Wu, A. J. Freeman

J. R. Childress, J. L. Duvail, S. Jasmin, A. Barthélémy, A. Fert, A. Schuhl, O. Durand, P. Galtier

H. Takeshita, K. Hattori, Y. Fujiwara, K. Nakagawa, A. Itoh

Z. S. Shan, J. X. Shen, R. D. Kirby, D. J. Sellmyer, Y. J. Wang

W. Donner, T. Zeidler, F. Schreiber, N. Metoki, H. Zabel

R. Jungblut, M. T. Johnson, J. van de Stegge, A. Reinders, F. J. A. den Broeder

D. S. Chuang, C. A. Ballentine, R. C. O'Handley

R. H. Victora, J. M. MacLaren

Oh Sung Song, C. A. Ballentine, R. C. O'Handley

G. Bochi, C. A. Ballentine, H. E. Inglefield, S. S. Bogomolov, C. V. Thompson, R. C. O'Handley

(Continued)

Interlayered Exchange

- 6431 Spin-wave study of the magnetic excitations in a layered structure with bilinear and biquadratic interlayer exchange
- 6434 Temperature dependence of interlayer exchange coupling in Co/Ru/Co trilayer structures
- 6437 Oscillatory exchange coupling in Fe/Au/Fe(100)
- 6440 Oscillation of the interlayer coupling in Co/Au(111)/Co
- 6443 Theory of Brillouin light scattering from dipole-exchange spin waves in magnetic double layers with interlayer exchange coupling
- 6446 Self-stabilization of domain walls in antiferromagnetically coupled multilayered magnetic films
- 6449 Short period oscillation of the interlayer exchange coupling in sputtered Co-Re superlattices
- 6452 Hot electron spin-valve effect in coupled magnetic layers
- 6455 Magnetothermopower of $\text{Co/Cu}_{1-x}\text{Ni}_x$ multilayers
- 6458 High-field polar MOKE magnetometry as a probe of interlayer exchange coupling in MBE-grown Co/Cu/Co(111) and Fe/Cr/Fe(001) wedged trilayers
- 6461 Orientationally independent antiferromagnetic coupling in epitaxial Fe/Cr(211) and (100) superlattices
- 6464 Oscillatory interlayer coupling through (111) oriented noble metal spacers
- 6467 *Ab initio* study of the interlayer magnetic couplings in Fe/Pd(001) superlattices and of the polarization induced in the Fe and Pd layers
- 6470 Induced spin polarization on Fe/nonmagnetic metal interfaces
- 6473 The temperature dependence of the bilinear and biquadratic exchange coupling in Fe/Cu, Ag/Fe(001) structures (abstract)
- 6474 Exchange coupling through ferromagnetic bridges in magnetic multilayers (abstract)
- 6475 Exchange coupling between ferromagnetic layers: Effect of quantum well states (abstract)
- 6476 Ferromagnetic resonance studies of Py bilayers for the system (Permalloy/ Al_2O_3) (abstract)
- M. Macciò, M. G. Pini, P. Politi, A. Rettori
- Z. Zhang, L. Zhou, P. E. Wiger, K. Ounadjela
- J. Unguris, R. J. Celotta, D. T. Pierce
- J. J. de Vries, W. J. M. de Jonge, M. T. Johnson, J. aan de Stegge, A. Reinders
- A. N. Slavin, I. V. Rojdestvenski, M. G. Cottam
- Hideo Fujiwara, Tomohiro Ishikawa, W. D. Doyle
- J. L. Leal, P. P. Freitas
- R. J. Celotta, J. Unguris, D. T. Pierce
- Jing Shi, E. Kita, S. S. P. Parkin, M. B. Salamon
- A. J. R. Ives, R. J. Hicken, J. A. C. Bland, C. Daboo, M. Gester, S. J. Gray
- Eric E. Fullerton, M. J. Conover, J. E. Mattson, C. H. Sowers, S. D. Bader
- D. J. Keavney, D. F. Storm, J. W. Freeland, J. C. Walker, M. G. Pini, P. Politi, A. Rettori
- D. Stoeffler, K. Ounadjela, J. Sticht, F. Gautier
- J. L. Pérez-Díaz, M. C. Muñoz
- Z. Celinski, B. Heinrich, J. F. Cochran
- J. C. Slonczewski
- James R. Cullen, Kristi B. Hathaway
- H. Hurdequint, N. Bouterfas, A. Vaurès

Magnetic Multilayers

- 6477 Exchange coupling in [Dy|Er] metallic superlattices
- 6480 Spin-valve structures exchange biased with $a\text{-Tb}_{0.23}\text{Co}_{0.77}$ layers
- 6483 ^{151}Eu Mössbauer study on Fe/Eu multilayers
- 6486 Phase transitions in coupled double-layer systems
- 6489 Comparison of the electron-spin-resonance linewidth in multilayered CuMn spin glasses with insulating versus conducting interlayers
- W. T. Lee, H. Kaiser, J. J. Rhyne, K. Dumesnil, C. Dufour, Ph. Mangin, G. Marchal, R. W. Erwin, J. A. Borchers
- P. P. Freitas, J. L. Leal, T. S. Plaskett, L. V. Melo, J. C. Soares
- E. Baggio-Saitovitch, E. C. Passamani, K. Mibu, T. Shinjo
- Xiao Hu, Yoshiyuki Kawazoe
- D. L. Leslie-Pelecky, F. VanWijland, C. N. Hoff, J. A. Cowen, A. Gavrin, C.-L. Chien

(Continued)

- 6492 Anisotropy studies of molecular-beam-epitaxy-grown Co(111) thin films by ferromagnetic resonance
- 6495 Magnetic and magneto-optic properties of sputtered Co/Ni multilayers
- 6498 Spatial modulation of the magnetic moment in Co/Pd superlattices observed by polarized neutron reflectivity
- 6501 Electron-energy-loss spectroscopy of Fe thin films on GaAs(001)
- 6504 Effect of interface on the properties of Ti/NiFe thin films
- 6507 Magnetization reversal in compositionally modulated Tb/Fe multilayers (abstract)
- 6507 Remanence and coercivity in exchange coupled amorphous R-TM/Fe bilayers and multilayers (abstract)
- 6508 Paramagnetic/ferromagnetic transition of Co/Cu(001) films during growth (abstract)
- 6508 Photothermally modulated ferromagnetic resonance investigations of epitaxially grown thin films (abstract)
- 6509 Structural and magnetic characteristics of $\text{Co}_{81}\text{Cr}_{19}/\text{Al}$ multilayers deposited by plasma-free sputtering with Kr gas (abstract)
- Magnetotransport and Giant Magnetoresistance**
- 6510 Effects of exchange bond disorder on transport measurements
- 6513 Electrical resistivity and local magnetic order in random anisotropy amorphous ferromagnets
- 6516 *In situ* magnetic and structural analysis of epitaxial $\text{Ni}_{80}\text{Fe}_{20}$ thin films for spin-valve heterostructures
- 6519 Magnetic and magnetoresistive properties of inhomogeneous magnetic dual-layer films
- 6522 Comparison of giant magnetoresistance in multilayer systems and uranium compounds
- 6525 Preparation of Ni-Fe/Cu multilayers with low coercivity and GMR effect by ion beam sputtering
- 6528 Novel magnetoresistance behavior in single trilayer spin valves
- 6531 $1/f$ noise in giant magnetoresistive materials
- 6534 Effect of annealing on the giant magnetoresistance of sputtered Co/Cu multilayers
- 6537 Magnetoresistance and exchange effects of NiCo/Cu sandwich films with oxide overlayer
- 6540 Effect of oxygen incorporation on magnetoresistance in Co/Cu multilayers
- 6543 Giant magnetoresistance in electrodeposited Co-Ni-Cu/Cu superlattices
- F. Schreiber, A. Soliman, P. Bodeker, R. Meckenstock, K. Bröhl, J. Pelzl, I. A. Garifullin
- Y. B. Zhang, P. He, J. A. Woollam, J. X. Shen, R. D. Kirby, D. J. Sellmyer
- J. A. Borchers, J. F. Ankner, C. F. Majkrzak, B. N. Engel, M. H. Wiedmann, R. A. Van Leeuwen, C. M. Falco
- J. Yuan, E. Gu, M. Gester, J. A. C. Bland, L. M. Brown
- Shuxiang Li, Minglang Yan, Chengtao Yu, Wuyan Lai
- Roger D. Kirby, J. X. Shen, D. J. Sellmyer
- Hong Wan, A. Tsoukatos, G. C. Hadjipanayis
- F. O. Schumann, M. E. Buckley, J. A. C. Bland
- R. Meckenstock, F. Schreiber, O. von Geisau, J. Pelzl
- Takakazu Takahashi, Masahiko Naoe
- P. A. Stampe, H. Ma, H. P. Kunkel, G. Williams
- V. S. Amaral, J. B. Sousa, J. M. Moreira, B. Barbara, J. Filippi
- I. Hashim, H. A. Atwater
- John O. Oti, Stephen E. Russek, Steven C. Sanders
- H. Nakotte, K. Prokeš, E. Brück, P. F. de Châtel, F. R. de Boer, V. Sechovsky, L. Havela, H. Fujii
- Masahiko Naoe, Yasuyoshi Miyamoto, Shigeki Nakagawa
- M. Patel, T. Fujimoto, E. Gu, C. Daboo, J. A. C. Bland
- H. T. Hardner, S. S. P. Parkin, M. B. Weissman, M. B. Salamon, E. Kita
- H. Zhang, R. W. Cochrane, Y. Huai, Ming Mao, X. Bian, W. B. Muir
- T. R. McGuire, T. S. Plaskett
- K. Kagawa, H. Kano, A. Okabe, A. Suzuki, K. Hayashi
- M. Alper, K. Attenborough, V. Baryshev, R. Hart, D. S. Lashmore, W. Schwarzacher

(Continued)

- 6546 Giant magnetoresistance in melt-spun $\text{Cu}_{87}\text{Co}_{13}$
- 6548 Temperature effect on magnetoresistance in Co/Ru sandwiches
- 6551 Magnetothermopower in antiferromagnetically coupled Co-Re superlattices
- 6554 Structural and magnetotransport properties of Co/Re superlattices
- 6557 Magnetic properties of an Fe/Cu granular multilayer
- 6560 Structural and magnetoresistance studies in granular $(\text{Ni}_{81}\text{Fe}_{19}, \text{Ni}_{80}\text{Co}_{20})/\text{Ag}$ synthesized from annealed multilayers
- 6563 Giant ac magnetoresistance in the soft ferromagnet $\text{Co}_{70.4}\text{Fe}_{4.6}\text{Si}_{15}\text{B}_{10}$
- 6566 On the resistivity minimum in amorphous metallic spin-glasses (abstract)
- 6567 Dependence of the anisotropic magnetoresistance on aspect ratio in cobalt films (abstract)
- 6567 Nonoscillatory behavior in the magnetoresistance of Cu/Ni superlattice (abstract)
- Magnetic Alloys and Compounds**
- 6568 Preparation and magnetic properties of Mn_4N films by reactive facing targets sputtering
- 6571 Magnetovolume effects in strong paramagnets
- 6574 Synthesis and characterization of Fe_{16}N_2 in bulk form
- 6577 Magnetic properties of FeRhP: Influence of metallic clusters on ferromagnetism
- 6580 Magnetism in metastable bcc and fcc iron-copper alloys
- 6583 On spin-canting in maghemite particles
- 6586 Metamagnetism and spin arrangement in $\text{Nd}_6\text{Fe}_{13}\text{Sn}$
- 6589 Temperature dependence of magnetic order in single-crystalline UPdSn
- 6592 Magnetic properties of Dy-Lu alloys
- 6595 Magnetic ordering and electric polarizability of Zn-doped $\text{La}_2\text{CuO}_{4+\delta}$ single crystals
- 6598 Two-dimensional magnetic order in $\text{Pb}_2\text{Sr}_2\text{TbCu}_3\text{O}_8$
- 6601 Structure of the modulated magnetic phase of Mn_3Sn (abstract)
- 6602 Magnetic structure of NdCu_2 (abstract)
- 6603 Easy-axis transition in SmMn_2Ge_2 (abstract)
- M. A. Howson, S. O. Musa, M. J. Walker, B. J. Hickey, R. Cochrane, R. Stevens
- A. Dinia, S. Zoll, K. Ounadjela
- J. B. Sousa, R. P. Pinto, B. Almeida, M. E. Braga, P. P. Freitas, L. V. Melo, I. G. Trindade
- Y. Huai, R. W. Cochrane, X. Bian, M. Sutton
- Mark Rubinstein, J. Tejada, X. X. Zhang
- X. Bian, Z. Altounian, J. O. Stöm-Olsen, A. Zaluska, Y. Huai, R. W. Cochrane
- F. L. A. Machado, B. L. da Silva, S. M. Rezende, C. S. Martins
- J. Koetzler, G. Thummes
- Mark Tondra, B. H. Miller, E. Dan Dahlberg
- W. Abdul-Razzaq
- Shigeki Nakagawa, Masahiko Naoe
- E. G. Moroni, T. Jarlborg
- M. Q. Huang, W. E. Wallace, S. Simizu, A. T. Pedziwiatr, R. T. Obermyer, S. G. Sankar
- M. Guillot, M. Artigas, M. Bacman, D. Fruchart, D. Boursier, R. Fruchart
- P. A. Serena, N. García
- S. Linderoth, P. V. Hendriksen, F. Bødker, S. Wells, K. Davies, S. W. Charles, S. Mørup
- M. Rozenberg, R. J. Zhou, M. Velicescu, P. Schrey, G. Filoti
- R. A. Robinson, J. W. Lynn, A. C. Lawson, H. Nakotte
- B. A. Everitt, M. B. Salamon, C. P. Flynn, B. J. Park, J. A. Borchers, R. W. Erwin, F. Tsui
- G. Cao, J. W. O'Reilly, J. E. Crow, L. R. Testardi
- S. Y. Wu, W. T. Hsieh, W.-H. Li, K. C. Lee, J. W. Lynn, H. D. Yang
- J. W. Cable, N. Wakabayashi, P. Radhakrishna
- R. R. Arons, M. Löwenhaupt, E. Gratz
- R. B. van Dover, E. M. Gyorgy, R. J. Cava, J. E. Krajewski, W. F. Peck, Jr., R. J. Felder

(Continued)

6603 Neutron diffraction study of the magnetic ordering of BaCuO_{2+x} (abstract)

Xun-Li Wang, J. A.
Fernandez-Baca, Z. R. Wang, D.
Vaknin, D. C. Johnston

Granular Films

6604 Magnetic properties of metallic Co- and Fe-based granular alloys

Gang Xiao, Jian-Qing Wang

6607 Magnetic and ferromagnetic resonance studies in Co-Cu composite films

R. Krishnan, H. Lassri, M. Seddat,
M. Tessier, Sivaraman Guruswamy,
Satyam Sahay

6610 Structure and magnetism of heat-treated nanocrystalline $\text{Cu}_{80}\text{Co}_{20}$ powders prepared via chemical means

V. G. Harris, F. H. Kaatz, V.
Browning, D. J. Gillespie, R. K.
Everett, A. M. Ervin, W. T. Elam,
A. S. Edelstein

6613 Relaxation measurements and particle size determination in Co-Ag heterogeneous alloy films

S. B. Slade, F. T. Parker, A. E.
Berkowitz

6616 Studies of magnetic interactions between Gd granules in copper matrix

J. H. Hsu, Y. H. Huang

6619 Magnetic reversal in small structures

D. I. Paul, A. Cresswell

6622 Exchange interactions among ferromagnetic clusters in Cu-Co heterogeneous alloy films (abstract)

A. E. Berkowitz, F. T. Parker, D.
Rao

6622 Ferromagnetic resonance studies of granular materials (abstract)

Mark Rubinstein, Badri Das, D. B.
Chrissey, J. Horwitz, N. C. Koon

6623 Magnetic properties of cobalt clusters deposited on MgO substrates by molecular beam epitaxy (abstract)

R. Morel, A. Barthélemy, F.
Charrière, J. R. Childress, A. Fert,
B. Bellamy, A. Masson

6623 Particle interactions in granular Co films (abstract)

A. Tsoukatos, H. Wan, G. C.
Hadjipanayis

6624 Investigation of the microstructure of granular Ag-Fe and Ag-Co thin films by TEM and STEM (abstract)

Z. G. Li, H. Wan, J. Liu, T.
Tsoukatos, G. C. Hadjipanayis

Hard Magnets II: 2-14-1 and Other Hard Magnets

6625 Resonant ultrasound measurements of elastic constants in melt-spun $\text{R}_2\text{Fe}_{14}\text{B}$ compounds ($\text{R}=\text{Ce}, \text{Pr}, \text{Nd}, \text{Er}$)

C. D. Fuerst, J. F. Herbst, J. L.
Sarraf, A. Migliori

6628 Comparison of the improvement of thermal stability of NdFeB sintered magnets: Intrinsic and/or microstructural

B. M. Ma, W. L. Liu, Y. L. Liang,
D. W. Scott, C. O. Bounds

6631 Mechanical properties of hot-rolled Pr-Fe-B-Cu magnets

A. Arai, O. Kobayashi, F. Takagi, K.
Akioka, T. Shimoda

6634 Magnetocaloric dependence of magnetic viscosity measurements in NdFeB

L. Folks, R. Street, R. Woodward,
P. G. McCormick

6637 Die-upset PrCo_5 -type magnets: Enhanced coercivities

C. D. Fuerst, E. G. Brewer

6640 Nonepitaxial sputter synthesis of aligned strontium hexaferrite, $\text{SrO} \cdot 6(\text{Fe}_2\text{O}_3)$, films

H. Hegde, P. Samarasekara, F. J.
Cadieu

6643 Order-disorder and magnetic exchange interactions in substituted strontium hexaferrite $\text{SrA}_x\text{Fe}_{12-x}\text{O}_{19}$ ($\text{A}=\text{Ga}, \text{In}$)

G. K. Thompson, B. J. Evans

6646 Enhanced remanence in isotropic Fe-rich melt-spun Nd-Fe-B ribbons

L. Withanawasam, G. C.
Hadjipanayis, R. F. Krause

6649 Mechanically alloyed nanocomposite magnets

Wei Gong, G. C. Hadjipanayis,
R. F. Krause

6652 Microstructure of high-remanence Nd-Fe-B alloys with low-rare-earth content

Raja K. Mishra, V. Panchanathan

6655 Magnetic properties of sintered Alnico 5 magnet via rapid solidification technology

C. J. Yang, W. Y. Lee, S. D. Choi

6658 Effect of additives on thermal stability of Nd-Fe-B bonded magnets (abstract)

T. Nishio, H. Yagi, T. Furuya, Y.
Kasai

(Continued)

6658 Coercivity in hard magnets based on $\text{Sm}_2\text{Co}_{17}$ (abstract)

Eric Lectard, Claire Maury,
Colette H. Allibert, Lew Rabenberg

Exchange Biasing and Oxides

6659 Orientational dependence of the exchange biasing in molecular-beam-epitaxy-grown $\text{Ni}_{80}\text{Fe}_{20}/\text{Fe}_{50}\text{Mn}_{50}$ bilayers (invited)

R. Jungblut, R. Coehoorn, M. T. Johnson, J. aan de Stegge, A. Reinders

6665 Magnetic properties of epitaxial MnAl/NiAl magnetic multilayers grown on GaAs heterostructures (invited)

T. L. Cheeks, J. P. Harbison, M. Tanaka, D. M. Hwang, T. Sands, V. G. Keramidas

6670 Magneto-optical and structural properties of $\text{BiAlDyIG}/\text{Fe}$ multilayers

J. X. Shen, K. W. Wierman, Y. B. Zhang, R. D. Kirby, J. A. Woollam, D. J. Sellmyer

6673 Inverted hysteresis in magnetic systems with interface exchange

M. J. O'Shea, A.-L. Al-Sharif

6676 Magnetic and structural properties of Co/CoO bilayers

X. Lin, G. C. Hadjipanayis, S. I. Shah

6679 Resistivity anomaly in nonmagnetic metals with ferromagnetic insulator proximity layers

G. M. Roesler, Jr., Y. U. Idzerda, P. R. Broussard, M. S. Osofsky

6682 Complex magnetization processes of exchange coupled trilayers

S. Wüchner, J. Voiron, D. Givord, D. Boursier, J. J. Préjean

6685 Magnetic properties of antiferromagnetic superlattices

Shufeng Zhang, Guihua Zhang

6688 Magnetic and crystallographic properties of molecular beam epitaxially grown $\text{Fe}_3\text{O}_4/\text{NiO}$ superlattices and Fe_3O_4 films

J. J. Krebs, D. M. Lind, E. Lochner, K. A. Shaw, W. Portwine, S. D. Berry

6691 Studies of the Verwey transition in $\text{Fe}_3\text{O}_4/\text{NiO}$ superlattices by SQUID magnetometry and neutron diffraction techniques (abstract)

S. D. Berry, J. A. Borchers, R. W. Erwin, D. M. Lind, K. A. Shaw, E. Lochner

6692 Magnetic structure determination for $\text{Fe}_3\text{O}_4/\text{NiO}$ superlattices by neutron diffraction techniques (abstract)

J. A. Borchers, R. W. Erwin, J. F. Ankner, S. D. Berry, D. M. Lind, E. Lochner, K. A. Shaw

Symposium: Perpendicular Transport in Layered Structures

6693 Perpendicular magnetoresistance in magnetic multilayers: Theoretical model and discussion (invited)

Albert Fert, Thierry Valet, Jozef Barnas

6699 How to isolate effects of spin-flip scattering on giant magnetoresistance in magnetic multilayers (invited)

J. Bass, Q. Yang, S. F. Lee, P. Holody, R. Loloee, P. A. Schroeder, W. P. Pratt, Jr.

6704 Scattering theory of perpendicular transport in metallic multilayers (invited)

Gerrit E. W. Bauer, Arne Brataas, Kees M. Schep, Paul J. Kelly

6709 Perpendicular giant magnetoresistance of microstructures in Fe/Cr and Co/Cu multilayers (invited)

M. A. M. Gijs, J. B. Giesbers, M. T. Johnson, J. B. F. aan de Stegge, H. H. J. M. Janssen, S. K. J. Lenczowski, R. J. M. van de Veerdonk, J. J. M. de Jonge

6714 Spin polarization of gold films via transport (invited)

Mark Johnson

High T_c Superconductivity: Experiment and Theory

6720 Transport and magnetic properties of polycrystalline $\text{Sm}_{2-x}\text{Ce}_x\text{CuO}_{4-y}$

R. F. Jardim, C. H. Westphal, C. H. Cohenca, L. Ben-Dor, M. B. Maple

6723 Relationship between weak ferromagnetism, superconductivity, and lattice parameter in the $\text{A}_{2-x-y}\text{B}_x\text{Ce}_y\text{CuO}_4$ ($\text{A}, \text{B} \equiv \text{La}, \text{Pr}, \text{Nd}, \text{Sm}, \text{Eu}, \text{Gd}, \text{Y}$) compounds

T. Schultz, R. Smith, A. Fondado, C. Maley, T. Beacom, P. Tinklenberg, J. Gross, C. Saylor, S. Oseroff, Z. Fisk, S.-W. Cheong, T. E. Jones

6726 Alkali metals impurities influence on the magnetic and electrical properties of YBCO

I. Nedkov, A. Veneva

(Continued)

- 6729 Kinematical pairing and magnetism in layered systems
- 6731 Ground-state properties and excitations of an integrable one-dimensional model with δ -function interaction involving several bands
- 6734 Two-band model for Kondo insulators: Thermodynamic and scaling properties
- 6737 Local magnetic moments and intermediate valence state of cerium impurities in ferromagnetic rare-earth metals
- 6740 Thermoelectric power studies of a $\text{Nd}_{1.82-x}\text{Sr}_x\text{Ce}_{0.18}\text{CuO}_y$ superconducting system (abstract)
- 6740 The magnetic and superconducting properties of $\text{Pb}_2\text{Sr}_2(\text{R/Ca})\text{Cu}_3\text{O}_8$, $\text{R}=\text{Pr}$, Ce , and Cm (abstract)
- 6741 ^{57}Fe and ^{119}Sn Mössbauer studies on $\text{La}_{1.25}\text{Nd}_{0.6}\text{Sr}_{0.15}\text{CuO}_4$: Evidence for local magnetic ordering below ≈ 32 K (abstract)
- 6741 Peculiarities of inelastic neutron scattering on magnons in high- T_c materials of stoichiometrical composition Nd_2CuO_4 , La_2CuO_4 , and $\text{YBa}_2\text{Cu}_3\text{O}_6$ (abstract)
- 6742 The sign reversal of the acoustoelectric effect in anisotropic superconductors (abstract)
- 6743 Four-spin exchange in Bi_2CuO_4 (abstract)
- 6744 Antiferromagnetic spin correlation suppression and superconducting characteristics improvement in $\text{YBa}_2\text{Cu}_3\text{O}_{6+\delta}$ films under light illumination (abstract)
- 6744 ac susceptibility of $\text{Pb}_x\text{Bi}_{2-x}\text{Sr}_2\text{Ca}_2\text{Cu}_3\text{O}_{10}$ high T_c superconductors sintered for different durations (abstract)
- 6745 Spin magnetic moment of conduction quasiparticle (abstract)
- 6745 Restoration of the continuous phase transition in the vortex state due to the lattice translational symmetry: Large- N limit (abstract)
- 6746 Damping of spin waves in a square-lattice quantum antiferromagnet due to spin-phonon interaction (abstract)
- 6746 The superconducting transition temperature of layered $S_i - J_{ij} - S_j$ superconductors (abstract)
- 6747 Magnetism and superconductivity in heavy-fermion compounds (abstract)

Magneto-optic and Other Magnetic Properties

- 6748 Magnetic properties of an isolated ferromagnetic bond embedded in Heisenberg antiferromagnets
- 6751 Spin diffusion in classical Heisenberg magnets with uniform, alternating, and random exchange
- 6754 Theoretical study of magnetostriction in FeTaN thin films
- 6757 Dependence of the magnetic properties $\text{Gd}_{2-x}\text{Ce}_x\text{CuO}_4$, $0 \leq x \leq 0.15$, on their particle size
- 6760 Magnetic properties of materials in the $\text{CaO-P}_2\text{O}_5\text{-Fe}_2\text{O}_3$ system
- 6763 Magnetic properties of $\text{Y}_{3-x-y}\text{Pr}_x\text{Lu}_y\text{Fe}_5\text{O}_{12}$ garnet films
- 6766 Magnetic properties of amorphous Cr-Fe alloys prepared by thermal evaporation and mechanical milling

Valery A. Ivanov, Michail Ye. Zhuravlev, Pavel B. Z'ubin

P. Schlottmann

M. A. Continentino, G. M. Japiassu, A. Troper

C. E. Leal, A. Troper

Okram G. Singh, B. D. Padalia, Om Prakash, V. N. Moorthy, Anant V. Narlikar

J. Simon Xue, C. W. Williams, L. Soderholm

M. Breuer, B. Büchner, H. Micklitz, E. Baggio-Saitovitch, I. Souza Azevedo, R. B. Scorzelli, M. M. Abd-Elmeguid

Yu. Pashkevich, M. Larionov

A. V. Goltsev

G. Petrakovskii, V. Val'kov, K. Sablina, B. Fedoseev, A. Furrer, B. Roessli, P. Fischer

V. Eremenko, V. Fomin, I. Kachur, V. Piryatinskaya, O. Prihod'ko

S. C. Mathur, D. C. Dube, Urvija Sinha, P. K. N. Raghavan

Vladimir L. Saionov

Boris N. Shalaev, Sergey A. Kltorov

Dirk Uwe Saenger

Valery A. Cherenkov

A. V. Goltsev

S. T. Ting, S. Haas, J. E. Crow

Niraj Srivastava, Jian-Min Liu, V. S. Viswanath, Gerhard Müller

James C. Cates, Chester Alexander, Jr.

J. Mahía, C. Vázquez-Vázquez, J. Mira, M. A. López-Quintela, J. Rivas, T. E. Jones, S. B. Oseroff

Binod Kumar, Christina H. Chen

A. Azevedo, C. Cinbis, M. H. Kryder

S. K. Xia, E. Baggio-Saitovitch, C. Larica, B. V. B. Sarkissian, S. F. Cunha, J. L. Tholence

(Continued)

6769 Magnetostriction in RE-Co amorphous alloy films (abstract)

S. Uchiyama, S. Yoshino, H. Takahashi, K. Tomi-ita, T. Mori, A. Itakura, S. Iwata, S. Tsunashima
M. J. Sablik

6769 A model for the Barkhausen noise power as a function of applied field and stress (abstract)

Recording Head and System Modeling and Phenomena

6770 The effects of closure domains on flux conduction in thin film recording head

Zhenzhou Guo, Edward Della Torre

6773 Effect of recorded transition shape on spatial noise distributions and correlations

T. C. Arnoldussen, J. G. Zhu

6776 Mean interaction field in magnetic recording media

Ikuya Tagawa, Akihiko Takeo, Yoshihisa Nakamura

6779 Micromagnetic studies of medium noise mechanisms

Xiaodong Chao, H. Neal Bertram

6782 Improving ferrite MIG head read-back distortions caused by domain walls and granularity (abstract)

B. E. Argyle, R. Schäfer, P. L. Trouilloud, M. E. Re, A. P. Praino, S. Takayama, D. Dingley

Magneto-optics

6783 MO polar Kerr studies of Co rich molecular beam epitaxy grown Au/Co multilayers

S. Višňovský, M. Nývlt, V. Prosser, R. Atkinson, W. R. Hendren, I. W. Salter, M. J. Walker

6786 Magneto-optical properties and magnetization processes in superlattices

Ron Atkinson, Nikolai F. Kubrakov, Sergey N. Utochkin, Anatoley K. Zvezdin

6789 The magnetic and magneto-optical properties of Co, Cr, Mn, and Ni substituted barium ferrite films

R. Carey, P. A. Gagne Sandoval, D. M. Newman, B. V. J. Thomas

6792 Anisotropy of the magnetic and magnetooptic properties of HoIG:Al single crystals (low and high magnetic field)

J. Ostorero, M. Guillot

6795 Measurement of the Faraday effect of garnet film in alternating magnetic fields

Jia Ouyang, Ying Zhang, Huahui He

6798 An investigation on the magneto-optic and magnetic properties of Tb:YIG

Jie Hui Yang, You Xu, Guo Ying Zhang

6801 Magneto-optical properties of (BiGdY)₃Fe₅O₁₂ for optical magnetic field sensors

O. Kamada, H. Minemoto, N. Itoh

6804 Magneto-optical properties of Al and In-substituted CeYIG epitaxial films grown by sputtering (abstract)

M. Gomi, M. Abe

6804 Enhancement of the magneto-optical quality of YIG films in a structure containing a thin metal film (abstract)

A. D. Boardman, A. I. Voronko, P. M. Vetoshko, V. B. Volkovoy, A. Yu. Toporov

6805 Magnetic Davydov splitting in 2D AFM (CH₂)₂(NH₃)₂MnCl₄ (abstract)

V. Eremenko, I. Kachur, V. Piryatinskaya, V. Shapiro

Symposium: User Facilities in Magnetism

6806 Magnetic neutron scattering (invited)

J. W. Lynn

6811 Soft x-ray synchrotron radiation facilities for the study of magnetic materials (invited) (abstract)

Brian Tonner, W. O'Brien, M. A. Green, H. Höchst, R. Reininger

6812 High magnetic field research: Overview of facilities and science and technology opportunities (invited) (abstract)

J. E. Crow, H. J. Schneider-Muntau, D. M. Parkin, N. Sullivan

Magnetic Structure

6813 LiNiO₂: Quantum liquid or concentrated spin glass?

M. Rosenberg, P. Stelmaszyk, V. Klein, S. Kemmler-Sack, G. Filoti

6816 Disappearance of three-dimensional magnetic ordering in Gd₂CuO₄

T. Chattopadhyay, P. J. Brown, B. Roessli

(Continued)

- 6819 Spin-Peierls transition in CuGeO_3 : Electron paramagnetic resonance study
- 6822 Observations of magnetization reversal and magnetic clusters in copper ferrite films
- 6825 The structure and spin dynamics of lanthanide-bearing silicate glasses
- 6828 Magnetization and ferromagnetic resonance studies on amorphous films of $\text{Fe}_2\text{O}_3\text{-Bi}_2\text{O}_3\text{-Li}_2\text{O}$
- 6831 Hysteresis and magnetic aftereffect in amorphous CoZrDy films: Trends and variations versus Dy content
- 6834 First-principles calculation of orbital moment distribution in amorphous Fe
- 6837 A magnetocalorimetric study of spin fluctuations in amorphous $\text{Fe}_x\text{Zr}_{100-x}$
- 6840 Magnetic properties of colloidal silica: Potassium silicate gel/iron nanocomposites

Magneto-optic Recording

- 6843 Origin of high coercive force in rare-earth-transmission-metal thin film
- 6846 Study of the effect of defect sizes and their distribution on the coercivity of magnetic media
- 6849 Reversal mechanisms in Tb/Fe multilayers
- 6852 Write/erase cyclability of TbFeCo for mark edge recording
- 6855 Recording characteristics of Kr-sputtered Tb/FeCo multilayer magneto-optical disks
- 6858 Double compensation point media for direct overwrite
- 6861 Design and performance of magneto-optic enhanced Co/Pt-based trilayers having zero Kerr ellipticity
- 6864 Effect of substrate roughness on microstructure, uniaxial anisotropy, and coercivity of Co/Pt multilayer thin films
- 6867 Depth distribution of birefringence in magneto-optical recording disk substrates
- 6870 Growth and subsequent relaxation of the anisotropic structure of amorphous Tb-Fe (abstract)
- 6871 Macroscopic ferrimagnets as magneto-optic media (abstract)

Magnetic Imaging and Measuring Techniques

- 6872 High-resolution magneto-optic measurements with a Sagnac interferometer (invited)
- 6878 dc magnetic force microscopy imaging of thin-film recording head
- 6881 Proposed antiferromagnetically coupled dual-layer magnetic force microscope tips
- 6884 Anisotropy and magnetostriction measurement by interferometry
- 6887 New complex permeability measurement device for thin magnetic films
- 6890 Element specific magnetic microscopy with x rays (invited) (abstract)

- S. Oseroff, S-W. Cheong, A. Fondado, B. Aktas, Z. Fisk
- M. M. Ibrahim, M. S. Seehra, G. Srinivasan
- A. J. G. Ellison, C.-K. Loong, J. Wagner
- J. Chen, S. Cheney, G. Srinivasan
- G. Suran, K. Roky
- Xue-Fu Zhong, W. Y. Ching
- A. LeR. Dawson, D. H. Ryan
- R. D. Shull, H. M. Kerch, J. J. Ritter
- D. Roy Callaby, Robert D. Lorentz, Shigeki Yatsuya
- James A. Jatau, Edward Della Torre
- K. O'Grady, T. Thomson, S. J. Greaves, G. Bayreuther
- Hiroiyuki Awano, Masahiro Ojima, Katsusuke Shimazaki, Satoru Ohnuki, Norio Ohta
- Hiro Karube, Kunihiro Matsumura, Masafumi Nakada, Osamu Okada
- T. K. Hatwar, D. J. Genova, R. H. Victora
- R. Atkinson, P. J. Grundy, C. M. Hanratty, R. J. Pollard, I. W. Salter
- Chung-Hee Chang, Mark H. Kryder
- Raymond-Noel Kono, Myung S. Jhon, Thomas E. Karis
- F. Hellman, M. C. Robson, M. T. Messer
- Richard J. Gambino, Ralph R. Ruf, Nestor Bojarczuk
- A. Kapitulnik, J. S. Dodge, M. M. Fejer
- Paul Rice, John Moreland, Andrzej Wadas
- John O. Oti, Paul Rice, Stephen E. Russek
- Peter S. Harllee III, George H. Bellesis, David N. Lambeth
- S. Hayano, I. Marinova, Y. Saito
- B. Hermsmeier, J. Stöhr, Y. Wu, M. Samant, G. Harp, S. Koranda, D. Dunham, B. P. Tonner

- 6890 High spatial resolution spin-polarized scanning electron microscopy (abstract)
- 6891 An analysis of magnetization patterns measured using a magnetic force scanning tunneling microscope (abstract)
- 6892 Magnetic force microscopy of single crystal magnetite (Fe_3O_4) (abstract)
- 6893 Interpretation of magnetic force microscopic images (abstract)

Giant Magnetoresistance in Granular Materials

- 6894 Determination of para- and ferromagnetic components of magnetization and magnetoresistance of granular Co/Ag films (invited)
- 6900 Giant magnetoresistance and microstructural characteristics of epitaxial Fe-Ag and Co-Ag granular thin films
- 6903 Giant magnetoresistance and its dependence on processing conditions in magnetic granular alloys
- 6906 Theory of magnetotransport in inhomogeneous magnetic structures
- 6909 Giant magnetoresistance of dilute Cu(Co) granular films
- 6912 Dependence of giant magnetoresistance on film thickness in heterogeneous Co-Ag alloys
- 6915 Modulation-induced giant magnetoresistance in a spinodally decomposed Cu-Ni-Fe alloy
- 6918 Magnetoresistance in a granular Fe-Mg system
- 6921 Giant magnetoresistance and induced exchange anisotropy in mechanically alloyed $\text{Co}_{30}\text{Ag}_{70}$
- 6924 Correlation of x-ray diffraction and Mössbauer effect measurements with magnetic properties of heat-treated $\text{Cu}_{80}\text{Co}_{15}\text{Fe}_5$ ribbons
- 6927 Giant magnetoresistance in $\text{Ag}_{1-x}\text{Ni}_x\text{Fe}_y$ heterogeneous alloy films
- 6930 Giant and anisotropic magnetoresistance in single layer $\text{Ni}_{66}\text{Fe}_{16}\text{Co}_{18}\text{-Ag}$ films
- 6933 Giant magnetoresistance in heterogeneous $(\text{CoFe})_x\text{Ag}_{1-x}$ films (abstract)

Soft Magnetic Materials and Applications II

- 6934 The effects of film geometry on the properties of FeTaN films
- 6937 Relationship between ac and dc magnetic properties of a Co-based amorphous alloy
- 6940 Effects of nanocrystallization upon the soft magnetic properties of Co-based amorphous alloys
- 6943 Magnetic properties behaviors in $\text{Fe}_{88}\text{Zr}_7\text{B}_4\text{Cu}_1$ nanocrystalline alloy prepared by different postanneal cooling rates
- 6946 Soft-magnetic properties of amorphous tapes after dynamic current annealing
- 6949 Magnetic behavior of the amorphous wires covered by glass

H. Matsuyama, K. Koike, F. Tomiyama, H. Aoi, Y. Shiroishi, A. Ishikawa

E. R. Burke, R. D. Gomez, I. D. Mayergoyz

R. Proksch, S. Foss, C. Orme, S. Sahu, B. Moskowitz

Atsushi Kikukawa, Hiroyuki Awano, Sumio Hosaka, Yukio Honda, Ryo Imura

Mary Beth Stearns, Yuanda Cheng

N. Thangaraj, C. Echer, Kannan M. Krishnan, R. F. C. Farrow, R. F. Marks, S. S. P. Parkin

Jian-Qing Wang, Edward Price, Gang Xiao

Horacio E. Camblong, Shufeng Zhang, Peter M. Levy

R. J. Gambino, T. R. McGuire, J. M. E. Harper, Cyril Cabral, Jr.

J. R. Mitchell, A. E. Berkowitz

S. Jin, L. H. Chen, T. H. Tiefel, M. Eibschutz, R. Ramesh

Kevin Pettit, E. Kita, K. Araga, A. Tasaki, M. B. Salamon

K. Ounadjela, A. Herr, R. Poinot, J. M. D. Coey, A. Fagan, C. R. Staddon, D. Daniel, J. F. Gregg, S. M. Thompson, K. O'Grady, S. Grievies

V. G. Harris, M. Rubinstein, B. N. Das, N. C. Koon

M. L. Watson, V. G. Lewis, K. O'Grady

A. Waknis, J. A. Barnard, M. R. Parker

R. S. Beach, D. Rao, M. J. Carey, F. T. Parker, A. E. Berkowitz

Gan Qiu, J. A. Barnard

S. H. Lim, Y. S. Choi, T. H. Noh, I. K. Kang

P. Quintana, E. Amano, R. Valenzuela, J. T. S. Irvine

K. Y. Kim, J. S. Lee, T. H. Noh, I. K. Kang, T. Kang

M. A. Escobar, J. C. Perron, R. Barrué, A. R. Yavari

Horia Chiriac, Gheorghe Pop, Firuta Barariu, Manuel Vázquez

6952 Tensor components of the magnetization in a twisted Fe-rich amorphous wire

6955 A metastable ternary Nd-Fe-B compound

6958 Helical anisotropy and Matteucci effect in Co-Si-B amorphous wires with negative magnetostriction (abstract)

6959 The rf permeability of dc planar magnetron sputtered FeNi multilayer films (abstract)

Applied Superconductivity

6960 Phase transitions in the one-dimensional frustrated quantum XY model and Josephson-junction ladders

6963 Penetration of circularly polarized electromagnetic fields into superconductors with gradual resistive transitions

6966 Magnetic shielding from alternating magnetic field by NbTi/Nb/Cu superconducting multilayer composite cylinder

6969 A method of increasing magnetic energy of superconducting magnetic energy storage

6972 Synthesis of high-temperature superconducting thin films in microwave field

Applied Magnetism

6975 Estimation of fatigue exposure from magnetic coercivity

6978 Overview of applications of micromagnetic Barkhausen emissions as noninvasive material characterization technique

6981 Monitoring neutron embrittlement in nuclear pressure vessel steels using micromagnetic Barkhausen emissions

6984 Experimental study on opening compensation for magnetic shields by current superposition

6987 Effects of pole flux distribution in a homopolar linear synchronous machine

6990 Compensation of field distortion with ferromagnetic materials and permanent magnets

6993 Equivalent structures of permanent magnets and electric currents designed to generate uniform fields

6996 Thermal magnetic noise due to eddy currents in a strip wound ferromagnetic core at 4.2 K (abstract)

6996 Design of fast acting actuators for cryogenic valve applications in the ARIANE5-program (abstract)

Magnetic Domains in Soft Magnetic Materials

6997 Barkhausen transitions in single layer and bilayer thin permalloy films

7000 Equation of motion of domain walls and equivalent circuits in soft ferromagnetic materials

7003 Pinned domain-wall structure in magnetic field

7006 Susceptibility of current-carrying iron whiskers

7009 The effects of demagnetizing and stray fields on magnetoacoustic emission

Magnetic and Electronic Structure

7012 IR spectroscopy on FeNi and FePt Invar alloys

L. Kraus, S. N. Kane, M. Vázquez, G. Rivero, E. Fraga, A. Hernando, J. M. Barandiarán

B. X. Gu, B. G. Shen, H. R. Zhai

J. Yamasaki, M. Takajo, F. B. Humphrey

Craig A. Grimes, Catherine C. Ballantyne

Enzo Granato

I. D. Mayergoyz

Hiroaki Otsuka, Ikuro Itoh

T. Morisue, T. Yajima

Victor I. Kojuharoff

Z. J. Chen, D. C. Jiles, J. Kameda

L. B. Sipahi

L. B. Sipahi, M. R. Govindaraju, D. C. Jiles

I. Sasada, Y. Oonaka

M. J. Balchin, J. F. Eastham, P. C. Coles

Manlio G. Abele, Henry Rusinek, Franco Bertora, Alessandro Trequatrini

M. G. Abele

Yu. V. Maslennikov, O. Snigirev, M. Cerdonio, G. A. Prodi, S. Vitale

Peter Schiebener, Alfred Pfeiffer, Karl Smirra

G. P. Farrell, E. W. Hill

G. Aguilar-Sahagun, P. Quintana, E. Amano, J. T. S. Irvine, R. Valenzuela

Chai Tak Teh, Hui Li Huang, Vladimir L. Sobolev

J. -G. Lee, A. S. Arrott

D. H. L. Ng, C. C. H. Lo, J. P. Jakubovics

B. Buchholz, E. F. Wassermann, W. Pepperhoff, M. Acet

(Continued)

- 7015 Anti-Invar in Fe-Ni
- 7018 X-ray-absorption fine structure of selected R_2Fe_{17} nitrides
- 7021 Exchange stiffness and magnetic anisotropies in bcc $Fe_{1-x}Co_x$ alloys
- 7024 Approach to the electronic structure of antiferromagnets
- 7027 Magnetization density in URu_2Si_2 and URh_2Si_2
- 7030 Spectroscopic studies of magnetic transitions in $TbPO_4$
- 7033 Magnetic structures of itinerant electron systems (abstract)
- 7034 Electronic structure and spin-density distribution in Y_2Fe_{17} (abstract)
- 7034 Energetics of bcc-fcc lattice in Fe-Co-Ni compounds (abstract)
- Correlated f-Electron Phenomena**
- 7035 Prediction of pressure-induced changes in magnetic ordering of correlated-electron uranium systems (invited)
- 7041 Magnetic properties of the lattice Anderson model
- 7044 Effects of doping in Kondo insulators (invited)
- 7050 Structural and magnetic ordering in the cerium hydride (abstract)
- 7051 Recent developments in multi-channel Kondo physics (invited) (abstract)
- Giant Magnetoresistance in Multilayers**
- 7052 Giant magnetoresistance in $Fe_{0.95}Cr_{0.05}/Cr$ multilayer films
- 7055 The effect of Au impurities at the interfaces on the magnetoresistance of MBE-grown Co/Cu multilayers
- 7058 Low field giant magnetoresistance in discontinuous magnetic multilayers
- 7061 Epitaxial spin-valve structures for ultra-low-field detection
- 7064 Giant magnetoresistance with low saturation field in $(Ni_xCo_{100-x})/Cu$ multilayers
- 7067 Hysteresis reduction in NiFeCo/Cu multilayers exhibiting large low-field giant magnetoresistance
- 7070 Calculation of the temperature dependence of the giant MR and application to Co/Cu multilayers
- 7073 Magnetization reversal in CoFe/Ag/Fe/ZnSe thin layer sandwiches
- 7076 Effective internal fields and magnetization buildup for magnetotransport in magnetic multilayered structures
- 7079 Structure and giant magnetoresistance in sputtered and MBE grown Fe/Cr superlattices (invited) (abstract)
- M. Acet, T. Schneider, H. Zähres, E. F. Wassermann, W. Pepperhoff
- T. W. Capehart, R. K. Mishra, F. E. Pinkerton
- X. Liu, R. Sooryakumar, C. J. Gutierrez, G. A. Prinz
- J. Callaway, D. G. Kanhere, A. Kolchin
- Alessandra Continenza, Patrizia Monachesi
- G. K. Liu, C.-K. Loong, F. Trouw, M. M. Abraham, L. A. Boatner
- J. Kübler, L. Sandratskii, M. Uhl
- Ming-Zhu Huang, W. Y. Ching
- E. G. Moroni, T. Jarlborg
- Q. G. Sheng, Bernard R. Cooper
- H. Q. Lin, H. Chen, J. Callaway
- P. Schlottmann
- R. R. Arons, J. K. Cockcroft, E. Ressouche
- Kevin Ingersent, Barbara A. Jones
- L. H. Chen, S. Jin, T. H. Tiefel, R. B. Van Dover, E. M. Gyorgy, R. M. Fleming
- K. P. Wellock, B. J. Hickey, D. Greig, M. J. Walker, J. Xu, N. Wiser
- T. L. Hylton, K. R. Coffey, M. A. Parker, J. K. Howard
- A. Schuhl, O. Durand, J. R. Childress, J.-M. George, L. G. Pereira
- X. Bian, J. O. Ström-Olsen, Z. Altounian, Y. Huai, R. W. Cochrane
- S. Hossain, D. Seale, G. Qiu, J. Jarratt, J. A. Barnard, H. Fujiwara, M. R. Parker
- J. L. Duvail, A. Fert, L. G. Pereira, D. K. Lottis
- D. Bilic, E. Dan Dahlberg, A. Chaiken, C. Gutierrez, P. Lubitz, J. J. Krebs, M. Z. Harford, G. A. Prinz
- Peter M. Levy, Horacio E. Camblong, Shueng Zhang
- Ivan K. Schuller, David M. Kelly, R. Schad, M. Potter, Y. Bruynseraede

(Continued)

7079 Direct measurement of spin dependent mean free paths in metals (abstract)

7080 Giant magnetoresistance in epitaxial sputtered Fe/Cr(211) superlattices (abstract)

Magneto-optic Recording

7081 Compositional dependence of the structural and magnetic properties of PtMnSb films

7084 Secondary ion bombardment effects on the magnetic properties and microstructures of ion-beam-deposited TbFe thin films

7087 Optical and magneto-optical constants of Pr substituted TbFeCo films

7090 Thermal stability of NdGd/FeCo multilayers

7093 Physical and magnetic microstructure of rapid thermally annealed thin film bismuth-doped garnets

7096 Uniaxial anisotropy of double-layered garnet films and magneto-optical recording characteristics

7099 Anisotropy and Faraday effect in Co spinel ferrite films

7102 Magnetic and magneto-optical properties of (Tb,Dy)Nd/FeCo multilayers (abstract)

7102 Magnetization reversal dynamics in CoPt alloys and Co/Pt multilayers (abstract)

7103 Amorphous to polycrystalline transformation of (BiDy)IG films (abstract)

7104 Epitaxial Bi-content ferrite-garnet film memory (abstract)

Magnetic Alloys and Compounds

7105 Ferromagnetism of YFe_2H_x

7108 Longitudinal and transverse magnetoresistance and magnetoresistive anisotropy in ternary $(\text{Pd}_{1-x}\text{Fe}_x)_{95}\text{Mn}_5$ alloys

7111 Formation and magnetic properties of $\text{Y}_2(\text{Fe}_{0.8}\text{Ga}_{0.2})_{17}\text{C}_x$ compounds

7114 Structural and magnetic properties of $\text{Nd}_2(\text{Fe,Ti})_{19}$

7117 Possible ferrimagnetic coupling in light-rare-earth transition-metal intermetallic compounds

7120 Magnetic properties of a novel Pr-Fe-Ti phase

7122 Magnetic properties of $\text{Gd}(\text{Fe}_{1-x}\text{Co}_x)_9\text{Ti}_2$ alloys

7125 Magnetic resonance in PdFe alloys near T_c

Bruce A. Gurney, Virgil S. Speriosu, Harry Lefakis, Dennis R. Wilhoit, Omar U. Need

M. J. Conover, Eric E. Fullerton, J. E. Mattson, C. H. Sowers, S. D. Bader

R. Carey, H. Jenniches, D. M. Newman, B. W. J. Thomas

S. Yatsuya, M. B. Hintz

R. Carey, D. M. Newman, J. P. Snelling, B. W. J. Thomas

X. Y. Yu, T. Suganuma, H. Watabe, S. Iwata, S. Tsunashima, S. Uchiyama

W. R. Eppler, B. K. Cheong, D. E. Laughlin, M. H. Kryder

Katsuji Nakagawa, Seiji Kurashina, Akiyoshi Itoh

H. Y. Zhang, B. X. Gu, H. R. Zhai, M. Lu, Y. Z. Miao, S. Y. Zhang, H. B. Huang

X. Y. Yu, Y. Fujiwara, H. Watabe, S. Iwata, S. Tsunashima, S. Uchiyama

J. Valentin, Th. Kleinefeld, D. Weller

H. Y. Zhang, B. X. Gu, H. R. Zhai, Y. Z. Miao, M. Lu, T. Tang, H. B. Huang

E. I. Il'yashenko, V. P. Klin, A. D. Nickolsky, A. G. Solovjov

Kazuo Kanematsu

Z. Wang, H. P. Kunkel, Gwyn Williams

Fang-Wei Wang, Lin-Shu Kong, Lei Cao, Ming Hu, Bao-Gen Shen, Jian-Gao Zhao

J. M. Cadogan, Hong-Shuo Li, R. L. Davis, A. Margarian, S. J. Collocott, J. B. Dunlop, P. B. Gwan

Z. G. Zhao, F. R. de Boer, V. H. M. Duijn, K. H. J. Buschow, Y. C. Chuang

Hong-Shuo Li Suharyana, J. M. Cadogan, G. J. Bowden, Jian-Min Xu, S. X. Dou, H. K. Liu

Suharyana, J. M. Cadogan, Hong-Shuo Li, G. J. Bowden

A. N. Medina, V. S. Oliveira, F. G. Gandra, A. A. Gomes

(Continued)

- 7128 Effects of Co and Y substitution on magnetic properties of CeFe_2 Xianfeng Zhang, Naushad Ali
- 7131 Preparation and magnetic properties of BaM films with excellent crystallinity by Xe sputtering N. Matsushita, K. Noma, S. Nakagawa, M. Naoe
- 7134 Magnetic ordering in UCoNiSi_2 and UCoCuSi_2 studied by ac-susceptibility and neutron-diffraction measurements Moshe Kuznietz, Haim Pinto, Mordechai Melamud
- 7137 Ferromagnetic ordering in dilute PdCo alloys R. E. Parra, A. C. Gonzalez
- 7140 Magnetic susceptibility of RCo_3B_2 (R=Y, Sm, Gd, and Dy) H. Ido, M. Nanjo, M. Yamada
- 7143 ^{139}La nuclear quadrupole resonance and relaxation in Zn-doped La_2CuO_4 M. Corti, A. Lascialfari, A. Rigamonti, F. Tabak, F. Licci, L. Raffo
- 7146 ^{35}Cl nuclear-magnetic-resonance study of magnetic ordering in $\text{Sr}_2\text{CuO}_2\text{Cl}_2$ single crystal M. Corti, F. Borsa, L. L. Miller, A. Rigamonti
- 7149 Magnetic effects in Cr-Mn alloy single crystals containing 0.05 and 0.1 at. % Mn P. Smit, H. L. Alberts
- 7152 Antiferromagnetism of metastable Cr-rich Cr-Gd alloys Jen Hwa Hsu, Y. W. Fu
- 7155 Magnetic properties of two new compounds: $\text{Gd}_2\text{Ni}_3\text{Si}_5$ and $\text{Sm}_2\text{Ni}_3\text{Si}_5$ Chandan Mazumdar, R. Nagarajan, L. C. Gupta, R. Vijayaraghavan, C. Godart, B. D. Padalia
- 7158 Low-field ac magnetic susceptibility under pressure in GdMn_2 and TbMn_2 intermetallics M. R. Ibarra, Z. Arnold, C. Marquina, L. García-Orza, A. del Moral
- 7161 Time evolution of magnetization in the FeRh system near antiferromagnetic-ferromagnetic transition temperature (abstract) Shinji Yuasa, Yoshichika Otani, Hideki Miyajima
- 7161 Unusual magnetic properties and time dependent magnetization in ErCo_3Ga_2 (abstract) Naushad Ali, Xianfeng Zhang
- Blomagnetism, Magnetochemistry, and Magnetic Separation**
- 7162 Effects of magnetic fields on fibrinolysis M. Iwasaka, S. Ueno, H. Tsuda
- 7165 Early embryonic development of frogs under intense magnetic fields up to 8 T S. Ueno, M. Iwasaka, K. Shiokawa
- 7168 Influence of spreading neuronal electric sources on spatio-temporal neuromagnetic fields K. Iramina, K. Ueno, S. Ueno
- 7171 Magnetite coating prepared by ferrite plating on expanded polytetrafluoroethylene membrane for medical use Q. Zhang, T. Itoh, M. Abe
- 7174 Redistribution of dissolved oxygen concentration under magnetic fields up to 8 T S. Ueno, M. Iwasaka, T. Kitajima
- 7177 Properties of diamagnetic fluid in high gradient magnetic fields S. Ueno, M. Iwasaka
- 7180 Influence of ultraworking frequency alternating weak magnetic field on the microvasculature of mice (abstract) Ningjiang Yang, Changmin Zhang
- 7181 Enzymatic oxidation-reduction processes under magnetic fields up to 8 T (abstract) M. Iwasaka, S. Ueno
- 7181 Induction of mutations by magnetic field for the improvement of sunflower (abstract) V. Kiranmai
- 7182 The magnetic transformation of iron hydroxides under the action of micro-organism (*Azotobacter vinelandii*) (abstract) Nadezda V. Verkhovtseva, Irina V. Shpil'kina, Vyacheslav F. Babanin
- 7182 Magnetic properties of heterotrophic bacteria (abstract) Nadezda V. Verkhovtseva, Irina N. Glebova, Anatoly V. Romanuk
- 7183 Spin-glass structures in biological systems (abstract) Alexandre I. Tsapin, L. A. Blumenfeld

(Continued)

- | | | |
|------|--|--|
| 7183 | The testing of action of chemical extracts on soils by magnetic methods (abstract) | Vyacheslav F. Babanin, Irina V. Shpilkina, Alexandr V. Ivanov |
| 7184 | The magnetic diagnostics of cosmic and industrial silt in humus horizons of soils (abstract) | Vyacheslav F. Babanin, Irina V. Shpilkina, Sergei A. Shoba, Alexandr V. Ivanov |
| 7185 | Dislocation etching of flux grown strontium hexaferrite single crystals (abstract) | Urvashi Raina, Sushma Bhat, P. N. Kotru, F. Licci |
| 7186 | Dipole-dipole interactions in $\text{KEr}(\text{MoO}_4)_2$ (abstract) | A. G. Anders, S. V. Volotskii, O. E. Zubkov |
| 7186 | Database of magnetochemistry in solutions (abstract) | O. Ju. Tarasov, A. G. Vinogradov |
| 7187 | The magnetodynamic filters in monitoring the contaminants from polluted water systems (abstract) | R. Swarup, Bharat Singh |

AUTHOR INDEX

Information for Contributors

Send manuscripts to the *Journal of Applied Physics*, Argonne National Laboratory, P.O. Box 8296, Argonne, Ill. 60439-8296.

For general format and style consult recent issues of the journal and the 1990 Fourth Edition of the *AIP Style Manual*, published by the American Institute of Physics. It may be obtained for \$10.00 (payment must be enclosed) from the American Institute of Physics, c/o AIDC, 64 Depot Road, Colchester, VT 05446, 800-488-2665.

Two types of manuscripts are acceptable: **full-length** and **Communications**. The latter are short contributions not exceeding in length nine double-spaced typewritten pages or three printed pages including allowances for illustrations, references, and tables. Abstracts are required for manuscripts of both types.

The **Manuscript**, including the abstract, references, and captions, should be neatly typed in English, double-spaced, on one side of good letter-size 21.6×28-cm (8×11-in.) white paper with ample margins. It should be carefully proofread by the author. Unclear or excessive handwritten insertions are not acceptable. Number all pages in single sequence beginning with the title and abstract page. Authors should submit three clear copies of the manuscript including original India ink drawings or high contrast, glossy prints, and if necessary for the reviewer's use, a second set of equal quality.

The **Title** should be concise but informative enough to facilitate information retrieval. The **Abstract** should be self-contained (contain no footnotes). It should be adequate as an index (giving all subjects, major and minor, about which new information is given), and as a summary (giving the conclusions and all results of general interest in the article). It should be about 5% of the length of the article, but less than 500 words for full-length articles and correspondingly shorter for *Communications*. It must appear on its own sheets separate from the text.

"Part I," or simply "I," will not be included as part of the title of an article unless Part II has already been submitted for publication in this Journal. Part III, IV, ..., etc., are likewise unacceptable unless the prior parts have already been accepted or have appeared in this Journal, and are properly identified in the references.

Author's names should preferably be written in a standard form for all publications to facilitate indexing and avoid ambiguities.

Equations should be neatly typed or written in ink, punctuated and aligned to bring out their structure, and numbered on the right. Mathematical operation signs indicating continuity of the expressions should be placed at the left of the second and succeeding lines. Use \times rather than a centered dot, except for scalar products of vectors. The solidus (/) should be used instead of built-up fractions in running text, and in display wherever clarity would not be jeopardized. Use "exp" for complicated exponents.

Notation must be legible, clear, compact, and consistent with standard usage. All unusual or handwritten symbols whose identity may not be obvious must be identified in the margin the first time they appear, and at all subsequent times when confusion might arise. Superscripts are normally set directly over subscripts; authors should note where readability of the meaning requires a special order. If there is any possibility of confusion, indicate superscripts by a black pencilled V underneath the superscript and subscripts by a black pencilled \wedge over the subscript.

References and footnotes are treated alike. They must be numbered consecutively in order of first appearance in the text and should be given in a separate double-spaced list at the end of the text material. Reference should be made to the full list of authors rather than to first author followed by an abbreviation such as *et al.* References within tables should be designated by lower-case Roman letter superscripts and given at the end of the table. For the proper form, see the *AIP Style Manual* and recent issues of this journal. The number of a grant or contract is meaningless to our readers and should be omitted unless its inclusion is required by the agency that supports the research.

Separate Tables (with Roman numerals in the order of their appearance) should be used for all but the simplest tabular material; they should have captions that make the tables intelligible without references to the text. The structure should be clear, with simple column headings giving all units. Unaltered computer output and notation are generally unacceptable. Long tables should, if possible, be submitted in a form ready for direct photoreproduction. Information on the preparation of camera-ready tables appears in the back of *J. Appl. Phys.*, Vol. 73, No. 2, 15 January 1993.

Figures should not be larger than and preferably approximately the same size as the typewritten page so that they can be contained in ordinary mailing envelopes. Smaller figures are less likely to be lost if pasted on paper of this size. Figures should be planned for the 8.5-cm ($\frac{3}{8}$ -in.) column width of the journal. In some cases where the figures contain a great deal of detail, $1\frac{1}{2}$ or 2 columns may be used, at the copy editor's discretion. The lettering and plotted points on the figures should be large and clear enough so that they will be legible after reduction (their final size should be no less than 2 mm). Figures should be identified on the back, by their number, the name of the first author, and the journal. The numbering should be in the order in which they are referred to in the text. Each figure must have its own caption; list captions on a separate sheet. Graphs should have properly labeled axes with correctly abbreviated units (see *AIP Style Manual*). The form $R \times 10^3 \Omega$, for example, is ambiguous and undesirable; use either $R(10^3 \Omega)$ or $10^{-3} R (\Omega)$.

Maximum black-white contrast is necessary. We require original India-ink drawings or good clear glossy prints. Avoid small open symbols that tend to fill in upon reduction, small dots and decimal points, and lines that are not thick enough to withstand reduction. Avoid photographs of apparatus by providing schematic line diagrams instead, and replace oscillograph photographs by black-ink tracings wherever possible. For complete instructions see the *AIP Style Manual*.

Correspondence: The Editor strongly prefers to correspond directly with the author rather than through the reports division or through executives of the author's laboratory. Manuscripts returned to authors for revision should be returned to the Editor within three months. A manuscript returned later than this will generally be regarded as newly submitted and will receive a new receipt date.

Authors whose manuscripts have been accepted for publication will receive a letter informing them of the issue for which it is tentatively scheduled. All subsequent correspondence about the paper should be addressed to Editorial Supervisor, Journal of Applied Physics, American Institute of Physics, 500 Sunnyside Blvd., Woodbury, NY 11797. Please do not address correspondence about proof, reprints, return of art work, publication charges, etc., to the Editor. To do so simply delays the appropriate action and reply.

General information regarding publication charges, copyrights, and similar material may be found on the inside front cover of each issue.

Use this checklist to avoid the most common mechanical errors in submitted manuscripts.

1. The manuscript must be double-spaced *throughout*.
2. Number *all* pages in sequence.
3. Type *title* and *abstract* on a separate first page.
4. Type list of *references* (including footnotes), list of *figure captions*, and *tables* on pages separate from each other and from the main text.
5. Type *references* in the style used by AIP journals.
6. Provide marginal notes to clarify symbols and expressions for the compositor.
7. The original figures must be line drawings in India ink or high-contrast, glossy prints not larger than 21.6×28 cm.
8. Submit (a) three clear copies with clear copies of figures and (b) the original figures.

Magnetic phase diagram of $(\text{Tb}_{1-x}\text{Gd}_x)\text{Fe}_{11}\text{Ti}$ alloys

L. C. C. M. Nagamine and H. R. Rechenberg

Instituto de Física, Universidade de São Paulo, C. P. 20516, 01452-990 São Paulo, Brazil

P. A. Algarabel and M. R. Ibarra

DFMC and ICMA, Universidad de Zaragoza, Plaza de San Francisco s/n, 50009 Zaragoza, Spain

The spin reorientation transition (SRT) in $(\text{Tb}_{1-x}\text{Gd}_x)\text{Fe}_{11}\text{Ti}$ alloys has been studied by using susceptibility, angular-dependent magnetization, and Mössbauer measurements. Alloys with $x < 0.4$ are shown to undergo an axial-to-planar SRT on cooling, while alloys with $x \geq 0.4$ remain axial down to 4.2 K. $\text{TbFe}_{11}\text{Ti}$ has an easy-axis magnetization at room temperature. A theoretical magnetic phase diagram for the $(\text{Tb}_{1-x}\text{Gd}_x)\text{Fe}_{11}\text{Ti}$ system has been calculated, showing reasonable agreement with experiment.

I. INTRODUCTION

Rare earth-transition metal compounds with the ThMn_{12} structure exhibit a variety of spin reorientation (SR) phenomena arising from competition between comparable and opposite anisotropy energies of the RE and TM sublattices.¹ The former can be calculated with a single-ion model for the RE crystalline electric field (CEF) interaction and a mean-field model for the RE-TM exchange interaction. Coey and co-workers² have determined a complete set of CEF coefficients (i.e., B_2^0 , B_4^0 , B_4^4 , B_6^0 , and B_6^4) from an analysis of single-crystal magnetization data for $\text{DyFe}_{11}\text{Ti}$. The magnetic phase diagram of other (RE) Fe_{11}Ti compounds can be calculated by appropriate scaling of these coefficients for the corresponding (RE)³⁺ ions, using standard atomic parameters. Agreement with experimental data is generally good, except for $\text{TbFe}_{11}\text{Ti}$. For this compound, a first-order SR is predicted² to occur at 130 K, which is much lower than experimentally observed transition temperatures. A SR has indeed been reported to occur at 450 K by Hu *et al.*,^{1,3} at 325 K by Boltich *et al.*,⁴ at 285 K by Zhang *et al.*,⁵ at 339 K by Kou *et al.*,⁶ and at 250 K by Andreev *et al.*⁷ The significant discrepancies among these data are to be noted. On the other hand, there is general agreement that the transition is of the easy axis-easy plane-type for descending temperatures. A second, planar-to-conical transition has been reported¹ to occur at ≈ 220 K, but was not confirmed in later experiments.

In this paper we report a study of the spin reorientation in $\text{TbFe}_{11}\text{Ti}$, using three experimental techniques: Low-field ac susceptibility, angular-dependent magnetization, and Mössbauer spectroscopy. In addition, Gd-substituted alloys were also studied, in order to investigate the effect of reducing the average RE anisotropy in a controlled manner.

II. EXPERIMENT

$(\text{Tb}_{1-x}\text{Gd}_x)\text{Fe}_{11}\text{Ti}$ samples with $x=0, 0.2, 0.3, 0.4$, and 0.6 were prepared by arc melting near-stoichiometric amounts of pure metals under argon, and annealed at 850°C

for ten days. The ThMn_{12} structure was checked by x-ray diffraction. A small amount of $\alpha\text{-Fe}$ was present in some samples, but TiFe_2 was not detected.

The susceptibility of powdered samples was measured with a modified mutual inductance Hartshorn bridge operating at 15 Hz. Magnetization measurements were performed on magnetically aligned powders by means of an extraction magnetometer. Magnetic alignment was achieved by fixing the alloy powders in epoxy resin at $\approx 70^\circ\text{C}$ in a field of 5 kOe. In magnetic polar plot experiments, the oriented sample was rotated in a constant field of 5 kOe provided by an electromagnet, and both parallel (M_{\parallel}) and perpendicular (M_{\perp}) components of magnetization with respect to the applied magnetic field were measured as a function of the rotation angle.⁸ Magnetization curves with fixed sample and variable applied field (0–20 kOe) were also measured. All above-mentioned experiments could be done in the 4.2–300 K temperature range.

Mössbauer spectra were measured with a constant-acceleration spectrometer in the 78–300 K range, using a Rh^{57}Co source.

III. RESULTS AND DISCUSSION

A. $\text{TbFe}_{11}\text{Ti}$

The ternary compound is of sufficient interest to warrant a separate discussion. The first question to be addressed is whether $\text{TbFe}_{11}\text{Ti}$ is axial or planar at room temperature: As mentioned in Sec. I, opposite answers are given in Refs. 5 and 6. In the present work, it can be safely assumed that the alloy was easy axis at the powder alignment temperature of ≈ 345 K. The magnetization curves, measured at room temperature with H_{ext} both parallel and perpendicular to the alignment direction, revealed substantial anisotropy, giving us a first evidence that the magnetization remained axial at 296 K.

We next consider Mössbauer spectra. The intensities of the absorption lines in an ^{57}Fe magnetically split six-line spectrum are in the ratio $3:a:1:1:a:3$, where

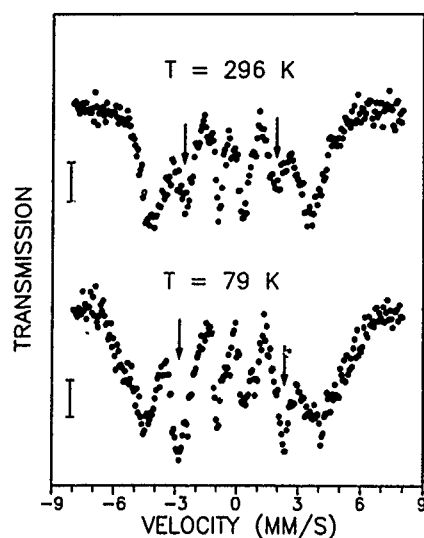


FIG. 1. Mössbauer spectra of aligned $\text{TbFe}_{11}\text{Ti}$ powder, with gamma-ray beam parallel to magnetic alignment direction. Vertical bars indicate 0.2% absorption. $\Delta m=0$ lines are indicated by arrows.

$$a = \frac{4\langle \sin^2 \theta \rangle}{1 + \langle \cos^2 \theta \rangle} \quad (1)$$

and θ is the angle between the hyperfine field and the gamma-ray propagation direction.⁹ Thus the relative intensities of the second and fifth lines ($\Delta m=0$ lines) provide information on the local magnetization direction.

The magnetically aligned $\text{TbFe}_{11}\text{Ti}$ sample was cut perpendicularly to the alignment axis in thin slices, which were assembled to form a flat absorber and mounted perpendicularly to the gamma radiation beam. For this geometry, the $\Delta m=0$ spectral lines are expected to be weak (totally absent for a perfectly aligned powder). Figure 1 shows spectra measured at 296 and 79 K. Owing to the poor counting statistics caused by the small sample area, a quantitative fit could not be made. Nevertheless, a marked increase of the $\Delta m=0$ lines intensity on cooling can be clearly seen. This result suggests a spin reorientation toward the absorber plane (i.e., away from the c axis) to occur between 296 and 79 K. The non-vanishing intensity of the $\Delta m=0$ lines at room temperature is due to imperfect alignment of the crystallites in our sample, and should not be taken as evidence for e.g., a conical spin structure.

Reorientation transitions are made most visible in angular dependent magnetization experiments. When a magnetically aligned sample is rotated with respect to the applied field direction, the magnetization parallel component M_{\parallel} is a maximum (minimum) if the easy direction is parallel (perpendicular) to the field. Some M_{\parallel} vs θ plots for $\text{TbFe}_{11}\text{Ti}$ are shown in Fig. 2, where $\theta=0^\circ$ or 180° denotes the alignment direction. The positions of the maxima did not change in the 296 K $>$ $T >$ 200 K range, while they are shifted by 90° below this range. At $T=200$ K the M_{\parallel} vs θ curve is nearly flat, indicating the anisotropy energy goes through zero close to this temperature, which characterizes a spin reorientation.

The canting angle α of the magnetization with respect to the c axis can be determined from the shape of the M_{\parallel} vs θ

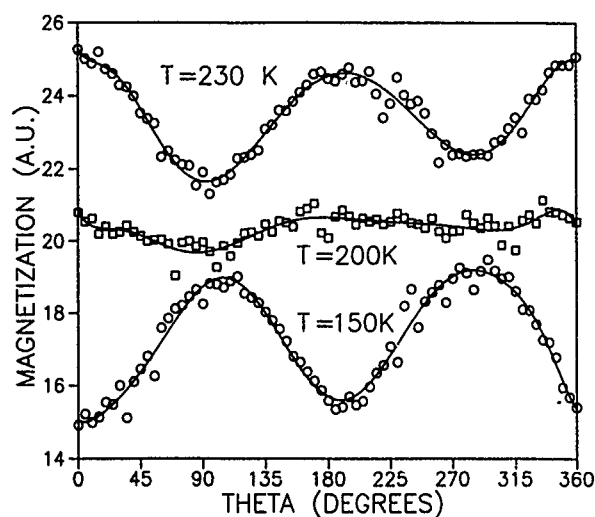


FIG. 2. Parallel magnetization component of aligned $\text{TbFe}_{11}\text{Ti}$ powder vs rotation angle with respect to the applied field ($H=5$ kOe). Continuous curves are visual guides.

pattern. Our data did not reveal an easy magnetization direction with α intermediate between 0° and 90° at any temperature. The SR in $\text{TbFe}_{11}\text{Ti}$ is thus confirmed to be an axial-to-planar or first-order transition. This result contrasts, e.g., with the $T=200$ K transition in $\text{DyFe}_{11}\text{Ti}$, which is of axial-to-conical-type, with α smoothly increasing on cooling.¹⁰

The ac susceptibility vs T curve, shown in Fig. 3, exhibits a fairly broad peak at $T=260$ K. It is reasonable to associate this anomaly with a spin reorientation. This result agrees very well with those obtained by Andreev *et al.*⁷ for a $\text{TbFe}_{11}\text{Ti}$ single crystal, from both ac susceptibility and low-field (200 Oe) angular-dependent magnetization measurements. It is noteworthy that the χ vs T curve shows no anomaly in the temperature range ($T \sim 200$ K) where a SR

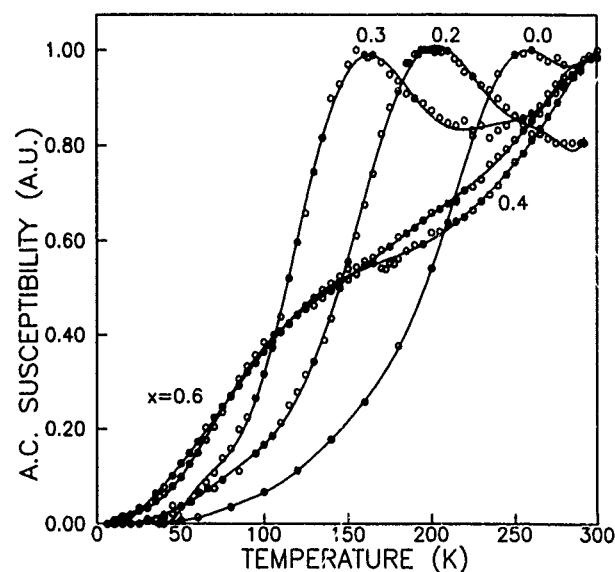


FIG. 3. Low-field susceptibility of $(\text{Tb}_{1-x}\text{Gd}_x)\text{Fe}_{11}\text{Ti}$ vs temperature (data were arbitrarily normalized for display).

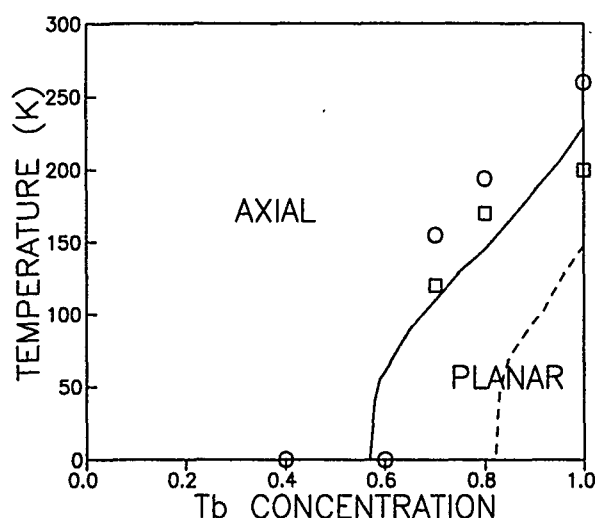


FIG. 4. Spin reorientation temperatures of $(\text{Tb}_{1-x}\text{Gd}_x)\text{Fe}_{11}\text{Ti}$ vs $(1-x)$, determined from susceptibility (○) and angular dependent magnetization (□) measurements. Curves are axial/planar boundaries, calculated with CEF coefficients from Ref. 2 (---) and with new values, cf. Table I (—).

was determined from polar plots. The striking difference between the T_{SR} values determined by the two methods can result from the static magnetic field applied during the magnetization measurements. Indeed, the sensitivity of T_{SR} to external fields has been experimentally verified for this material by Kou *et al.*,⁶ and interpreted on grounds of the anisotropy smallness near the transition temperature. Thus the axial spin orientation will acquire additional stability from an external field, depressing the SR temperature.

We should like to comment on the dispersion of T_{SR} data found in the literature for the $\text{TbFe}_{11}\text{Ti}$ alloy. The isostructural $(\text{RE})\text{Fe}_{12-x}\text{V}_x$ alloys are known to exhibit a broad x range, and it has been shown¹¹ that the V concentration has a strong influence on their magnetic properties. This effect is particularly dramatic for $\text{TbFe}_{12-x}\text{V}_x$, where the Tb sublattice anisotropy changes sign as a function of x .¹¹ Although no comparable solubility range has been reported for the Ti alloys, small stoichiometry variations cannot be ruled out, which could be responsible for the apparent irreproducibility of $\text{TbFe}_{11}\text{Ti}$ properties.

B. $(\text{Tb}_{1-x}\text{Gd}_x)\text{Fe}_{11}\text{Ti}$

Partial substitution of Gd^{3+} S-state ions for Tb^{3+} is expected to dilute the RE sublattice planar anisotropy and hence to lower the SR temperature. Our results confirm this prediction, both from susceptibility (see Fig. 3) and angular magnetization measurements. Measured SR temperatures are displayed as a function of x in Fig. 4. No transition was observed for $x \geq 0.4$.

We have calculated the theoretical magnetic phase diagram for this system with the formalism described in Ref. 12. Crystal-field and exchange-field parameters were taken from Ref. 2, with CEF coefficients scaled from Dy^{3+} to Tb^{3+}

TABLE I. Tb^{3+} crystal-field coefficients used in magnetic phase diagram calculations (K).

CEF coefficient	Scaled from Dy^{3+} data (Ref. 2)	This work
B_2^0	2.67×10^{-1}	2.85×10^{-1}
B_4^0	-2.49×10^{-3}	-1.10×10^{-3}
B_4^4	2.37×10^{-2}	3.17×10^{-2}
B_6^0	-1.97×10^{-5}	-1.97×10^{-5}
B_6^4	-4.93×10^{-6}	-4.93×10^{-6}

through the equation $B_n^m = \theta_n \langle r^n \rangle A_n^m$, where θ_n is the Stevens coefficient and A_n^m is assumed to be independent of the RE. These coefficients are given in Table I. The Fe sublattice anisotropy $K_{\text{Fe}}(T)$ was taken to be that of YFe_{11}Ti ,¹ and no external field was considered. Free energy minimization yielded the canting angle α , which was found to be either 0° or 90° , i.e., no conical structure was predicted at any temperature or concentration. It was found that a minimum Tb concentration is required to stabilize an easy-plane magnetization at $T=0$ K. The calculated SR temperatures were, however, far too low, as shown by the dashed line in Fig. 4. Agreement with experiment can be improved with small changes in the B_n^m : the solid curve in Fig. 4 has been calculated with the new coefficients given in Table I. Calculations showed little sensitivity to the 6th-order coefficients, so these were left unchanged. It is noteworthy that the largest change required was on B_4^0 and B_4^4 . This fact confirms the relative importance of the fourth-order CEF terms for the magnetic behavior of 1–12 compounds.

ACKNOWLEDGMENTS

This work was partially supported by CICYT under grant PB92-0095. L. C. C. M. N. and H. R. R. acknowledge financial support from FAPESP, CNPq, and CAPES.

¹B. P. Hu, H. S. Li, J. P. Gavigan, and J. M. D. Coey, *J. Phys.: Condens. Matter* **1**, 755 (1989).

²B. P. Hu, H. S. Li, J. M. D. Coey, and J. P. Gavigan, *Phys. Rev. B* **41**, 2221 (1990).

³B. P. Hu, H. S. Li, and J. M. D. Coey, *Hyp. Int.* **45**, 233 (1989).

⁴E. B. Boltich, B. M. Ma, L. Y. Zhang, F. Pourarian, S. K. Malik, S. G. Sankar, and W. E. Wallace, *J. Magn. Magn. Mater.* **78**, 364 (1989).

⁵L. Y. Zhang, B. M. Ma, Y. Zheng, and W. E. Wallace, *J. Appl. Phys.* **70**, 6119 (1991).

⁶X. C. Kou, T. S. Zhao, R. Grössinger, H. R. Kirchmayr, X. Li, and F. R. de Boer, *Phys. Rev. B* **47**, 3231 (1993).

⁷A. V. Andreev, N. V. Kudrevatykh, S. M. Razgonyaev, and E. N. Tarasov, *Physica B* **183**, 379 (1993).

⁸E. Joven, A. del Moral, and J. I. Arnaud, *J. Magn. Magn. Mater.* **83**, 548 (1990).

⁹N. N. Greenwood and T. C. Gibb, *Mössbauer Spectroscopy* (Chapman and Hall, London, 1971).

¹⁰L. M. García, J. Bartolomé, P. A. Algarabel, M. R. Ibarra, and M. D. Kuz'min, *J. Appl. Phys.* **73**, 5908 (1993).

¹¹L. Pareti, M. Solzi, G. Marusi, M. R. Ibarra, and P. A. Algarabel, *J. Appl. Phys.* **70**, 3753 (1991).

¹²L. C. C. M. Nagamine and H. R. Rechenberg, *J. Magn. Magn. Mater.* **104–107**, 1277 (1992).

Magnetic phase diagram of Nd(Fe,Mo)₁₂ alloys

Y. Z. Wang, B. P. Hu, X. L. Rao, and G. C. Liu

San Huan Research Laboratory, Chinese Academy of Sciences, P.O. Box 603, Beijing 100080, China

L. Song, L. Yin, and W. Y. Lai

Institute of Physics, Chinese Academy of Sciences, P.O. Box 603, Beijing 100080, China

The magnetic phase diagram of the alloy series NdFe_{12-x}Mo_x ($x=1.0\sim 2.5$) is obtained. Below the Curie temperature, the ferromagnetic phase is divided into three regions: Uniaxial, canted 1, and canted 2. At a temperature of T_{sr1} (below 200 K) a spin reorientation transition (SRT) was observed for all the samples, and at T_{sr2} (above 200 K) another SRT was found for samples with Mo concentration $1.5 < x < 1.75$. At room temperature the easy direction of magnetization (EDM) of NdFe_{12-x}Mo_x changes from the *c*-axis to a canted structure with increasing Mo concentration, with a critical composition of $x=1.56$. At low temperatures (below 100 K) all NdFe_{12-x}Mo_x compounds exhibit a canted moment structure.

I. INTRODUCTION

Among nitrided compounds having the ThMn₁₂ structure, the Nd-Fe-Mo system is the most attractive one for the study of permanent magnet materials. Recent experimental results showed that the intrinsic magnetic properties of RFe_{12-x}Mo_xN_y gets better with lower Mo concentration.^{1,2} For example the Curie temperature, the room temperature saturation magnetization $\mu_0 M_s$ and anisotropy field of the NdFe_{12-x}Mo_xN_y nitride with $x=1.0$ is 654 K, 120 JT⁻¹ kg⁻¹, and 9.5 T, respectively,¹ which makes the NdFe_{12-x}Mo_xN_y nitride be a very good candidate for permanent magnet application.³⁻⁵ However the nature of the magnetocrystalline anisotropy of the parent alloy NdFe_{12-x}Mo_x is not yet quite clear, therefore we investigated the magnetic structure of this series in detail and obtained its magnetic phase diagram.

II. EXPERIMENT

The NdFe_{12-x}Mo_x alloys with $x=1.0, 1.25, 1.5, 1.56, 1.62, 1.68, 1.75, 2.0$, and 2.5 were prepared by arc melting the elements with purity better than 99.5% under purified argon gas and annealing in vacuum at a temperature range of 1050 °–1150 °C for several hours. The quality of the compounds was checked by both powder x-ray diffraction (XRD) with Co-K α or Cu-K α radiation and by thermomagnetic analysis (TMA) methods. The spin reorientation transition was determined by TMA in the temperature range from 77 K to the Curie temperature using a vibrating sample magnetometer (VSM) in an applied field of 40 mT and also by ac susceptibility, χ_{ac} , measurements with an ac field of 0.1 mT and a frequency of 314 Hz in the temperature range of 4.2–300 K.

The nature of the magnetocrystalline anisotropy and its temperature dependence were studied by using x-ray diffraction at room temperature and using an extracting sample magnetometer in the temperature range of 4.2–300 K on magnetically aligned powders bonded using epoxy resin.

III. RESULTS AND DISCUSSION

Typical x-ray diffraction patterns for NdFe_{12-x}Mo_x are given in Fig. 1. All annealed alloys are single phase with the

ThMn₁₂ structure except $x=1$, which has a little α -Fe impurity.

The temperature dependencies of the ac susceptibility $\chi_{ac}(T)$ of different samples are shown in Fig. 2. It can be seen clearly that there are cusps on the $\chi_{ac}(T)$ curves which indicate that the spin reorientation transitions occur in all of the samples. This phenomenon is often observed in R-Fe compounds, for example, Nd₂Fe₁₄B,⁶ Tm₂Fe₁₇C_x,⁷ and DyFe₁₁Ti⁸ among others. In the alloys with Mo concentration $1.5 < x < 1.75$, two spin reorientation temperatures were observed: One is below and the other is above 200 K. The thermomagnetic analysis traces $M(T)$ at low field are shown in Fig. 3. The magnetic phase transition temperatures for different samples, Curie temperatures T_C , spin reorientation

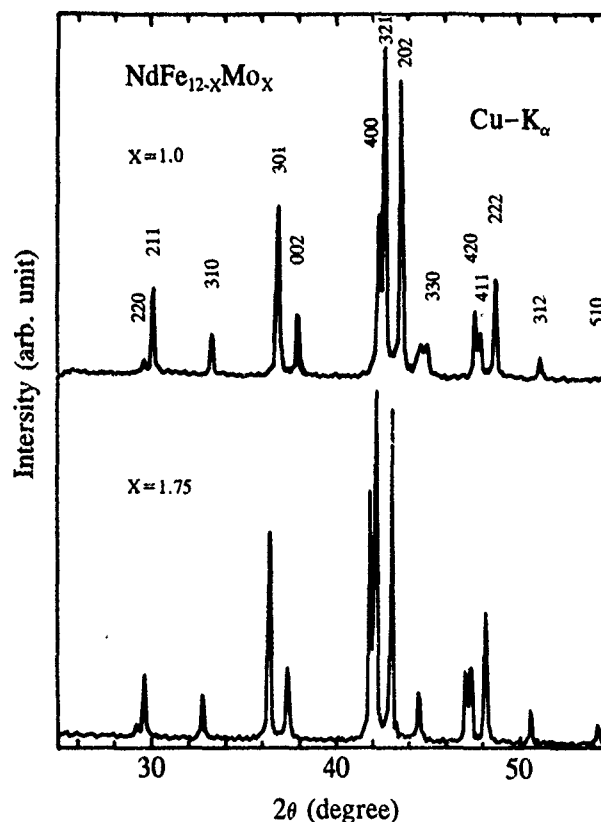


FIG. 1. X-ray diffraction pattern of powder samples for NdFe_{12-x}Mo_x with $x=1.0$ and 1.75 .

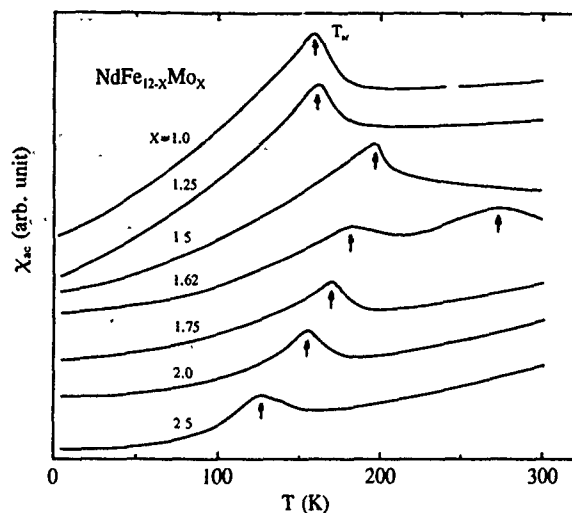


FIG. 2. Temperature dependence of the ac susceptibility $\chi_{ac}(T)$ in several $\text{NdFe}_{12-x}\text{Mo}_x$ compounds.

temperatures T_{sr1} and T_{sr2} , are listed in Table I and plotted in Fig. 4. The Curie temperature T_C increases linearly with decreasing Mo concentration, while the variations in the spin reorientation temperature T_{sr} are complex. For $x \leq 1.5$, T_{sr} increases slowly with Mo concentration. At $x = 1.5$, T_{sr} starts to split into two branches: One increases rapidly and the other decreases slowly. They divide the ferromagnetic state into three regions.

In order to distinguish the type of magnetocrystalline anisotropy in regions A and B in Fig. 4, we performed x-ray diffraction experiments on aligned powder samples at room temperature for all alloys. Figure 5 shows x-ray diffraction patterns of two typical compositions with $x = 1.5$ and 2.0, which are located in the regions A and B, respectively. The pattern of the sample with $x = 1.5$ has one dominant reflection, namely the (002) line. This result shows that the alignment direction of the sample with $x = 1.5$ is parallel to the c axis, in other words, the sample with $x = 1.5$ possesses uniaxial anisotropy. The x-ray diffraction patterns of other aligned powder samples located in region A are similar to that of $x = 1.5$, therefore the magnetocrystalline anisotropy of all alloys in region A is uniaxial. For the sample with $x = 2.0$, the x-ray diffraction pattern of the aligned powder sample is different. The pattern is similar to that of non-aligned samples (see Fig. 1). The intensity of the (400) line increases lightly and the intensities of (002), (202), and (222) obviously decreases. This pattern cannot be attributed to the uniaxial nor the easy-plane anisotropy, therefore the alloy with $x = 2.0$ has a canted moment structure. Similar x-ray patterns of all the other samples in region B show that they

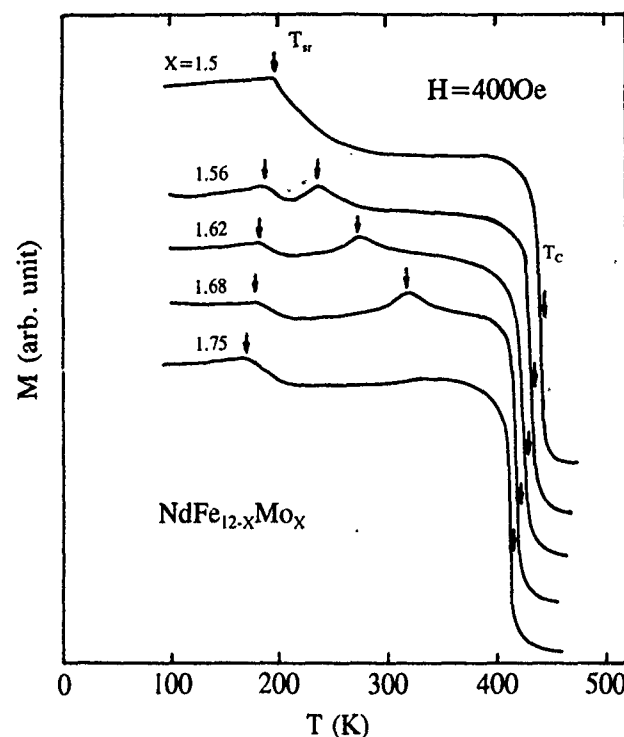


FIG. 3. Thermomagnetic analysis curves of several $\text{NdFe}_{12-x}\text{Mo}_x$ compounds in a magnetic field of 400 Oe.

have the same canted type of magnetocrystalline anisotropy. The above results were confirmed by the magnetization measurements on aligned powder samples.

Figure 6 shows magnetization curves of the aligned powder sample with Mo concentration of $x = 1.62$ in directions parallel and perpendicular to the alignment direction at 4.2, 200 and 300 K, representing the three different ferromagnetic states in the corresponding regions C, B, and A, respectively. The magnetization curves at 300 K represent a typical uniaxial anisotropy characteristic, while the magnetization curves at low temperature reflect the characteristic of the canted moment structure.⁸ At 200 K, the magnetization in the hard direction $M_{\perp}(0)$ has a considerable value of about 9% of the saturation magnetization M_s at zero field. The easy magnetization curve appears to be hardly saturated with a large susceptibility value of $\chi_{hf} = 9.87 \times 10^{-5} \text{ emu g}^{-1} \text{ Oe}^{-1}$ at high field up to 5 T due to the deviation of the easy magnetization direction from the c axis. When the temperature goes down to 4.2 K, the canted behavior appeared in magnetization curves is clearer than 200 K. Values of $M_{\perp}(0)$ and χ_{hf} increase obviously, $M_{\perp}(0)/M_s = 24\%$ and $\chi_{hf} = 34.4 \times 10^{-5} \text{ emu g}^{-1} \text{ Oe}^{-1}$, respectively. Such canted behavior can be explained by the balance between the

TABLE I. The lattice constants, a and c , Curie temperature, T_C , spin reorientation temperatures, T_{sr1} and T_{sr2} for $\text{NdFe}_{12-x}\text{Mo}_x$.

x	1.00	1.25	1.50	1.56	1.63	1.68	1.75	2.00	2.5
$T_C(\text{K})$	495	470	443	435	430	421	413	393	340
$T_{sr1}(\text{K})$	159	161	197	188	182	178	170	155	127
$T_{sr2}(\text{K})$	234	273	318

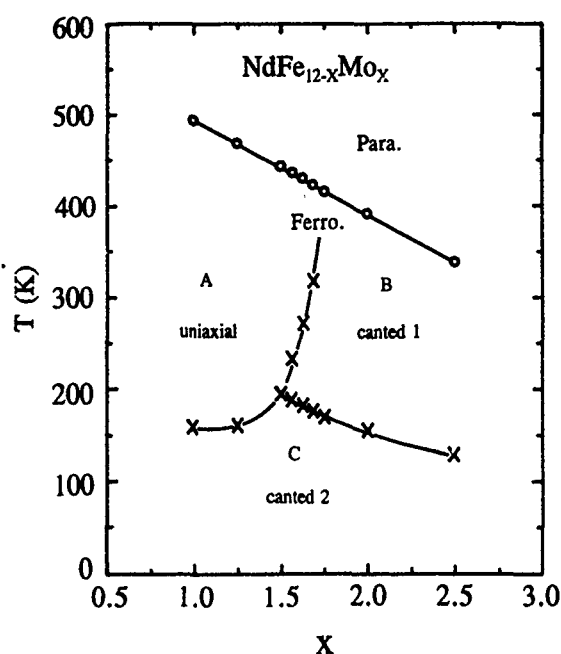


FIG. 4. Magnetic phase diagram of $\text{NdFe}_{12-x}\text{Mo}_x$ alloys.

anisotropy of the Fe sublattice and the Nd sublattice at different temperatures.⁸

The magnetic phase diagram of $\text{NdFe}_{12-x}\text{Mo}_x$ is shown in Fig. 4. The magnetic anisotropy of this alloy series is complicated. Very recently studies of the magnetocrystalline anisotropy of $\text{YFe}_{12-x}\text{Mo}_x$ ($1.0 \leq x \leq 2.5$) indicate that the easy *c*-axis anisotropy field of the Fe sublattice increases

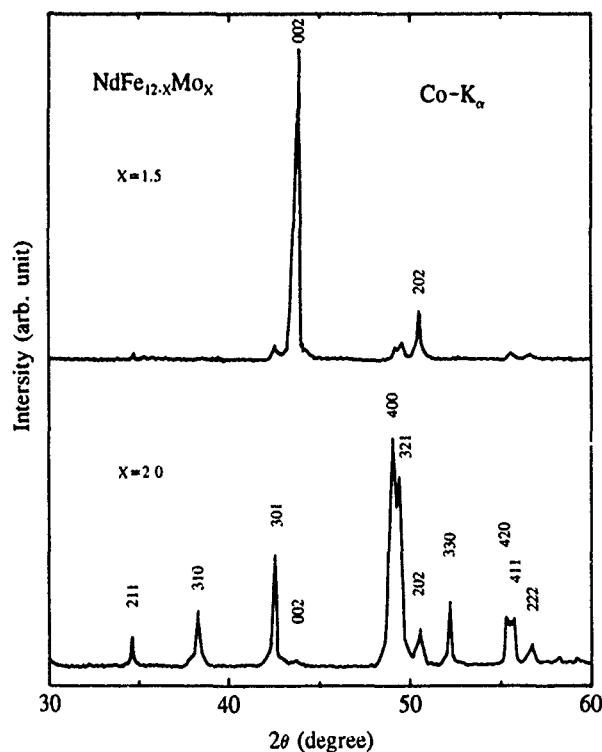


FIG. 5. X-ray diffraction patterns of magnetically aligned powder for $\text{NdFe}_{12-x}\text{Mo}_x$ with $x = 1.5$ and 2.0 . The plane of the incident and reflected x-ray is parallel to the alignment direction.

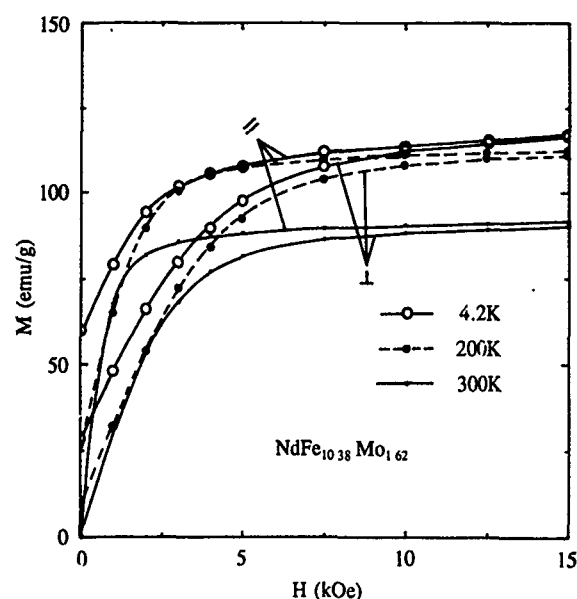


FIG. 6. Magnetization curves of $\text{NdFe}_{10.37}\text{Mo}_{1.63}$ at 4.2, 200, and 300 K.

rapidly with the decrease of Mo concentration when $x < 1.6$ and changes slowly for $x > 1.6$.¹⁰ This turning point of the anisotropy field of $\text{YFe}_{12-x}\text{Mo}_x$ is close to the triphase point of the $\text{NdFe}_{12-x}\text{Mo}_x$. Of $\text{NdFe}_{12-x}\text{Mo}_x$ with low Mo concentration, the easy *c*-axis anisotropy field of the Fe sublattice is strong enough to overcome the easy-plane anisotropy of the Nd sublattice so that $\text{NdFe}_{12-x}\text{Mo}_x$ exhibits uniaxial anisotropy. With high Mo concentration, the easy-plane anisotropy of the Nd-sublattice dominates the whole magnetic ordering temperature range. The complexity of the magnetocrystalline anisotropy of $\text{NdFe}_{12-x}\text{Mo}_x$ may also be affected by the variation of the crystal-field interaction with Mo concentration.

ACKNOWLEDGMENTS

This work is partly supported by the National Science Foundation of China and National Laboratory on Magnetism of China.

¹Y. Z. Wang, B. P. Hu, X. L. Rao, G. C. Liu, L. Yin, and W. Y. Lai, *J. Appl. Phys.* **73**, 6251 (1993).

²H. Sun, M. Akayama, K. Tatami, and H. Fujii, *Physica B* **183**, 33 (1993).

³W. Gong and G. C. Hajipanayis, *J. Appl. Phys.* **73**, 6245 (1993).

⁴B. P. Hu, P. A. P. Wendhausen, D. Eckert, W. Pitschke, A. Handstain, and K. H. Müller, *EMMA* 1993.

⁵A. Navarathna, H. Hegde, R. Rani, K. Chen, and F. J. Cadieu, *INTERMAG'93*, FC-1, Stockholm, April 1993.

⁶Y. Z. Wang, Z. X. Wang, W. Gong, and M. Y. Feng, *Chin. Phys. Lett.* **2**, 349 (1985).

⁷X. C. Kou, R. Grossinger, T. H. Jacobs, and K. H. Buschow, *J. Magn. Mater.* **88**, 1 (1990).

⁸B. P. Hu, H. S. Li, J. M. D. Coey, and J. P. Gavigan, *Phys. Rev. B* **41**, 2221 (1990).

⁹Y. Z. Wang, B. P. Hu, X. L. Rao, G. C. Liu, L. Song, L. Yin, and W. Y. Lai (unpublished).

Magnetic anisotropies in $R\text{Fe}_{10-x}\text{Co}_x\text{Mo}_2$ compounds ($R=\text{Dy, Er}$)

Roy Tucker, Xie Xu, and S. A. Shaheen

Department of Physics and Center for Materials Research and Technology (MARTECH), Florida State University, Tallahassee, Florida 32306

The effects of Co substitution on magnetic anisotropy and spin reorientation phenomena have been investigated in the $\text{DyFe}_{10-x}\text{Co}_x\text{Mo}_2$ and $\text{ErFe}_{10-x}\text{Co}_x\text{Mo}_2$ ($x=0$ to 10) series in the temperature range from 4.2 to 300 K. X-ray diffraction patterns on aligned samples indicated that the easy direction of magnetization (EDM) of the $\text{DyFe}_{10-x}\text{Co}_x\text{Mo}_2$ series is along the c axis at room temperature for all values of x . The spin reorientations were observed for all samples in the $\text{DyFe}_{10-x}\text{Co}_x\text{Mo}_2$ series except for $x=10$, and the spin reorientation temperature, T_{sr} , decreases with the increase of Co content x . The magnetic phase diagram of $\text{DyFe}_{10-x}\text{Co}_x\text{Mo}_2$ has been constructed. These results, together with the results from the $\text{YFe}_{10-x}\text{Co}_x\text{Mo}_2$ series, may lead to the conclusion that the anisotropy of Dy sublattice changes from planar to axial in the $\text{DyFe}_{10-x}\text{Co}_x\text{Mo}_2$ series with the increase of Co content. The EDM in the $\text{ErFe}_{10-x}\text{Co}_x\text{Mo}_2$ series was found to be nonaxial for $2 \leq x \leq 6$ for all temperatures below T_c . For $x < 2$ and $x > 6$ the $\text{ErFe}_{10-x}\text{Co}_x\text{Mo}_2$ compounds exhibit an axial EDM at room temperature, and spin reorientations occur at about 210 K for $x=8$ and at 140 K for $x=10$. Since Er and Dy have opposite sign of second-order Stevens factor, the above results of two systems are consistent.

I. INTRODUCTION

Recently the search for new permanent magnet materials has been focused on the ternary compounds $R\text{Fe}_{12-x}\text{M}_x$ (R =rare earth, $M=\text{Ti, V, Cr, Si, Mo}$; $x=1$ or 2),¹⁻³ which crystallize in the tetragonal ThMn_{12} structure. In this structure, the R atoms occupy the crystallographic $2a$ site and the $3d$ atoms occupy the $8i, 8j, 8f$ sites. Due to its low site symmetry, the Fe sublattice exhibits a strong uniaxial anisotropy. According to the second-order approximation of the point charge model, the short R - R distance along the c axis enables rare earths of a positive second-order Stevens factor ($\alpha > 0$) [e.g., Sm, Er, Tm, Yb] to exhibit an axial anisotropy while rare earths with $\alpha < 0$ [e.g., Nd, Tb, Dy, Ho] exhibit a nonaxial anisotropy.

Several authors have reported that the substitution of Co for Fe in the $R(\text{Fe,Co})_{11}\text{Ti}^{4,5}$ and $R(\text{Fe,Co})_{10}\text{V}_2$ (Ref. 6) systems favors a planar anisotropy, and the easy direction of magnetization (EDM) at room temperature in these alloys appears to change from axial to cone to planar with increasing Co concentration. However, our recent studies of the $\text{RCo}_{10}\text{Mo}_2$ compounds⁷ showed that the $\text{YCo}_{10}\text{Mo}_2$ and $\text{GdCo}_{10}\text{Mo}_2$ compounds exhibit an axial anisotropy from 0 K to Curie temperature. Since Y is nonmagnetic and Gd has no orbital moment, the anisotropy comes from the Co sublattice only. This means that the Co sublattice favors a uniaxial anisotropy in the $\text{RCo}_{10}\text{Mo}_2$ compounds series. We also found that at room temperature the EDM in the $\text{RCo}_{10}\text{Mo}_2$ series is along the c axis for $R=\text{Nd, Pr, and Dy}$, and it is nonaxial for $R=\text{Sm and Er}$. These results strongly indicate that in contrast to the situation in $R\text{Fe}_{12-x}\text{TM}_x$, the R sublattices with negative second-order Stevens factor ($\alpha < 0$) favor a uniaxial anisotropy, whereas those with $\alpha > 0$ favor a planar anisotropy. Ohashi *et al.* reported a similar behavior in the RCo_{11}Ti compounds series.⁸

It is interesting to observe that while the $3d$ sublattice anisotropy remains axial in both $R\text{Fe}_{10}\text{Mo}_2$ and $\text{RCo}_{10}\text{Mo}_2$ series, the R sublattice anisotropy undergoes a dramatic change. In order to understand this contrasting anisotropy behavior and to examine the effect of Co substitution on magnetic anisotropy and spin reorientations, systematic studies of the $R\text{Fe}_{10-x}\text{Co}_x\text{Mo}_2$ compounds have been made.⁹ In this paper we report the spin-reorientation behavior of the $R\text{Fe}_{10-x}\text{Co}_x\text{Mo}_2$ ($R=\text{Dy and Er, } x=0$ to 10) compounds determined by the ac susceptibility method and thermomagnetic analysis. The magnetization data on these systems are also included.

II. EXPERIMENT

$R\text{Fe}_{10-x}\text{Co}_x\text{Mo}_2$ alloys ($R=\text{Dy and Er, and } x=0, 2, 4, 6, 8, 10$) were prepared by arc melting appropriate amounts of Fe, Co, Mo, and Dy or Er under a purified argon atmosphere. As-cast samples were vacuum annealed at 1000 °C for a week. All samples are almost single phase, as determined by both x-ray powder diffraction and thermomagnetic analysis. Aligned samples for magnetic anisotropy studies were prepared by mixing fine powders in an epoxy at room temperature in the presence of a magnetic field (1 T). The room temperature EDM was deduced from the x-ray diffraction patterns of aligned samples.

A quantum design SQUID magnetometer with external field up to 5.5 T was used for the measurements of the saturation magnetization (σ_s) and anisotropy field (H_A). The value of H_A was determined by measuring the easy and hard direction of magnetization on aligned samples at room temperature. The Curie temperatures were measured using a Faraday magnetometer. Both the ac susceptibility and low field dc magnetization measurements as a function of temperature in the range from 4.2 to 300 K are used to detect possible spin reorientations.

TABLE I. Magnetic properties of the $R\text{Fe}_{10-x}\text{Co}_x\text{Mo}_2$ ($R=\text{Dy}$ and Er) compounds. The easy direction of magnetization (EDM), and values of saturation magnetization (M_s) and anisotropy field (H_A) refer to $T=300$ K.

Rare-earth element	x	T_c (K)	T_{sr} (K)	M_s ($\mu_B/\text{f.u.}$)	EDM	H_A (kOe)
Dy	0	390	130	6.16	axial	14
	2	490	100	7.42	axial	30
	4	590	75	8.01	axial	36
	6	630	58	7.46	axial	48
	8	600	40	5.53	axial	65
	10	520	...	4.34	axial	44
Er	0	330	120	5.52	axial	...
	2	450	...	8.56	planar	...
	4	510	...	8.52	planar	...
	6	550	...	8.11	planar	...
	8	610	210	7.2	axial	10
	10	480	130	5.31	axial	11

III. RESULTS AND DISCUSSIONS

The results obtained for the $\text{DyFe}_{10-x}\text{Co}_x\text{Mo}_2$ series are listed in Table I. X-ray diffraction patterns on aligned samples indicated that the EDM in the $\text{DyFe}_{10-x}\text{Co}_x\text{Mo}_2$ series is along the c axis at room temperature for all values of x . Figure 1 shows the magnetic phase diagram for the $\text{DyFe}_{10-x}\text{Co}_x\text{Mo}_2$ series. The occurrence of a maximum in the Curie temperature, which has been observed in the $\text{YFe}_{10-x}\text{Co}_x\text{Mo}_2$ and $\text{NdFe}_{10-x}\text{Co}_x\text{Mo}_2$ series^{9,10} appears to be a common feature of the $R\text{Fe}_{10-x}\text{Co}_x\text{Mo}_2$ compounds.

The spin reorientations, described as a change of the EDM from one crystallographic direction to another with varying temperature, were observed in the ac susceptibility measurements for all samples in the $\text{DyFe}_{10-x}\text{Co}_x\text{Mo}_2$ series, except for $x=10$. With the increase of Co content x , the T_{sr} decreases almost linearly at an average rate of ~ 13 K per substituted Co atom. These results, combined with the results of the $\text{YFe}_{10-x}\text{Co}_x\text{Mo}_2$ series,¹⁰ support the conclusion that the anisotropy of Dy sublattice changes gradually from pla-

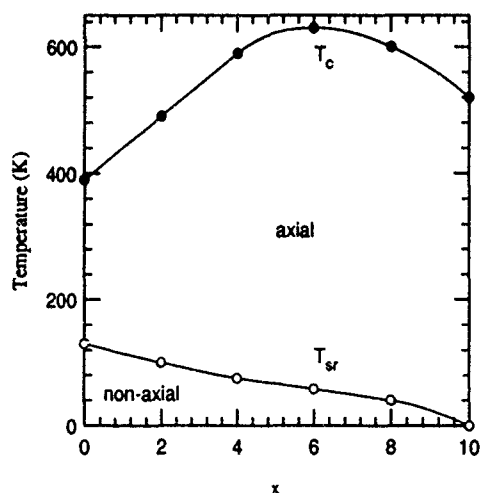


FIG. 1. Magnetic phase diagram for $\text{DyFe}_{10-x}\text{Co}_x\text{Mo}_2$.

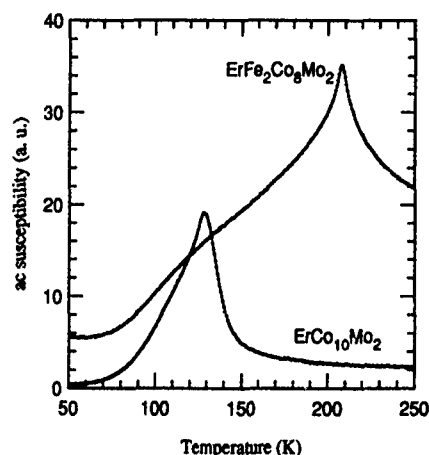


FIG. 2. Temperature dependence of the ac magnetic susceptibility of $\text{ErFe}_2\text{Co}_8\text{Mo}_2$ and $\text{ErCo}_{10}\text{Mo}_2$.

nar (in $\text{DyFe}_{10}\text{Mo}_2$) to axial (in $\text{DyCo}_{10}\text{Mo}_2$) in the $\text{DyFe}_{10-x}\text{Co}_x\text{Mo}_2$ series with the increase of Co content.

The situation in the $\text{ErFe}_{10-x}\text{Co}_x\text{Mo}_2$ series is somewhat more complex than that in the $\text{DyFe}_{10-x}\text{Co}_x\text{Mo}_2$ series. X-ray diffraction patterns on aligned samples indicated that the EDM of the $\text{ErFe}_{10-x}\text{Co}_x\text{Mo}_2$ series is nonaxial for $2 \leq x \leq 6$. For $x > 6$ the $\text{ErFe}_{10-x}\text{Co}_x\text{Mo}_2$ compounds exhibit an axial EDM at room temperature, and spin reorientations occur at about 210 K for $x=8$ and at 130 K for $x=10$, as shown in Fig. 2.

The magnetic anisotropy in $R\text{Fe}_{10-x}\text{Co}_x\text{Mo}_2$ compounds arises from two contributions: $4f$ sublattice and $3d$ sublattice anisotropies. When both R and $3d$ sublattice anisotropies favor an axial or planar arrangement of spins, then the EDM is obviously along the c axis or basal plane, respectively. However, when the R sublattice and $3d$ sublattice favor different EDM's, then the situation is complex, and the EDM of the compound is determined by the resultant of the competing sublattice anisotropies. As observed in the $\text{YFe}_{10-x}\text{Co}_x\text{Mo}_2$ series,¹⁰ the $3d$ sublattice anisotropy undergoes a change from axial at $x=0$ to planar at $4 \leq x \leq 5$ and

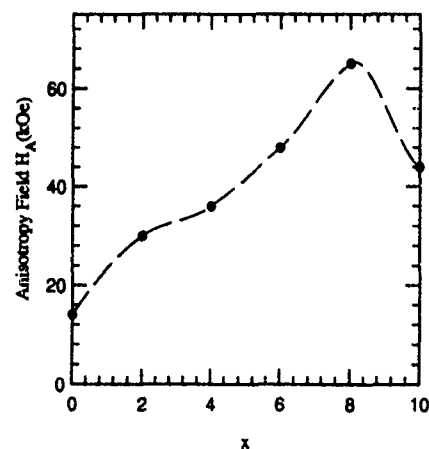


FIG. 3. The dependence of the anisotropy field H_A on Co composition x in the $\text{DyFe}_{10-x}\text{Co}_x\text{Mo}_2$ series.

back to axial at higher x values. Furthermore, the R sublattice anisotropy also undergoes a dramatic change in the $R\text{Fe}_{10-x}\text{Co}_x\text{Mo}_2$ series, and the resultant behavior is quite complex. However, it is easy to make comparisons for the terminal compounds ($x=0$ and 10) where the $3d$ anisotropy favors axial EDM for both compound series ($R=\text{Dy}$ and Er). Since Dy and Er have opposite signs of second order Stevens' factor, the magnetic anisotropy behavior of terminal compounds and the observations of spin reorientations are expected.

The field dependence of magnetization (up to 55 kOe) was measured along the easy and hard direction of magnetization on aligned samples at 300 K. The anisotropy field at 300 K for $\text{DyFe}_{10-x}\text{Co}_x\text{Mo}_2$ is listed in Table I and plotted in Fig. 3 as a function of Co content x . As seen in Fig. 3, the anisotropy field in the $\text{DyFe}_{10-x}\text{Co}_x\text{Mo}_2$ system reaches a maximum value of 6~7 T at $x=8$.

ACKNOWLEDGMENTS

We wish to thank H. Mathias for his technical assistance in x-ray measurements. The work was supported by the Florida High Tech Council and the National High Magnetic Field Laboratory.

- ¹D. B. De Mooij and K. H. J. Buschow, *Philips J. Res.* **42**, 246 (1987).
- ²K. Ohashi, Y. Tawara, R. Osugi, and M. Shimao, *J. Appl. Phys.* **64**, 5714 (1988).
- ³K. Ohashi, T. Yokoyama, R. Osugi, and Y. Tawara, *IEEE Trans. Magn. MAG-23*, 3101 (1987).
- ⁴S. F. Cheng, V. K. Sinha, Y. Xu, J. M. Elbicki, E. B. Boltich, W. E. Wallace, S. G. Sankar, and D. E. Laughlin, *J. Magn. Magn. Mater.* **75**, 330 (1988).
- ⁵V. K. Sinha, S. F. Cheng, W. E. Wallace, and S. G. Sankar, *J. Magn. Magn. Mater.* **81**, 227 (1989).
- ⁶M. Jurczyk and O. D. Chistjakov, *J. Magn. Magn. Mater.* **82**, 239 (1989).
- ⁷Xie Xu and S. A. Shaheen, *J. Magn. Magn. Mater.* **118**, L6-L10 (1993).
- ⁸K. Ohashi, H. Ido, K. Konno, and Y. Yoneda, *J. Appl. Phys.* **70**, 5986 (1991).
- ⁹Xie Xu and S. A. Shaheen, *J. Appl. Phys.* **73**, 5896 (1993).
- ¹⁰Xie Xu and S. A. Shaheen (unpublished).

Magnetic properties of $\text{Nd}(\text{Fe,Ti})_{12}$ and $\text{Nd}(\text{Fe,Ti})_{12}\text{N}_x$ films of perpendicular texture

D. Wang^{a)} and D. J. Sellmyer

Behlen Laboratory of Physics and Center for Materials Research and Analysis, University of Nebraska, Lincoln, Nebraska 68588-0113

I. Panagiotopoulos and D. Niarchos

Demokritos, National Center for Scientific Research, Institute of Materials Science, 153 10, Aghia Paraskevi Attikis, Athens, Greece

$\text{Nd}(\text{Fe,Ti})_{12}$ and $\text{Nd}(\text{Fe,Ti})_{12}\text{N}_x$ films textured with c axis perpendicular to the film plane were synthesized by sputtering. For the $\text{Nd}(\text{Fe,Ti})_{12}$ films a spin reorientation took place at about 170 K. For the $\text{Nd}(\text{Fe,Ti})_{12}\text{N}_x$ films, the anisotropy field is about 85 kOe at room temperature and 130 kOe at 5 K, corresponding to a coercivity of 2.7 and 12 kOe, respectively. Initial magnetization curves show a behavior characteristic of nucleation type of magnetization reversal mechanism. Attempts were made to fit the experimental data with Kronmüller's magnetization reversal model. The results suggest that nucleation with extended sites is responsible for the reversal.

INTRODUCTION

Higano *et al.* were probably the first to report the astonishing effect of nitriding on some rare earth-transition metal(RE-TM) compounds in 1987. They concluded that¹: "Nitriding resulted in a lattice expansion, increase in the saturation magnetization and change in Curie temperature." Coey and co-workers reported the first detailed study² of various aspects of these compounds, and their results have stimulated much of the succeeding work.³

The synthesis of SmFe_{12} films by sputtering has been reported.^{4,5} But $\text{SmFe}_{12}\text{N}_x$ or $\text{Sm}(\text{Fe,Ti})_{12}\text{N}_x$ is not a good candidate for permanent magnets because its planar magnetic anisotropy leads to a low coercivity (H_c). $\text{Nd}(\text{Fe,Ti})_{12}\text{N}_x$ is a promising candidate for permanent-magnet applications because of its high uniaxial anisotropy field (H_k), high Curie temperature and high saturation magnetization (M_s).⁶

Previously we reported the preliminary results on the $\text{Nd}(\text{Fe,Ti})_{12}$ and $\text{Nd}(\text{Fe,Ti})_{12}\text{N}_x$ films.⁷ A report on similar films has been given also recently by Navarathna *et al.*⁸ In this paper we will discuss the magnetic properties of these sputtered films. Low temperature measurements on the $\text{Nd}(\text{Fe,Ti})_{12}\text{N}_x$ films will be emphasized. The magnetization reversal mechanism will also be discussed with available models.

EXPERIMENTAL METHODS

$\text{Nd}(\text{Fe,Ti})_{12}$ films were prepared in a dc magnetron sputtering system on heated Ta substrates.⁵ The base pressure was better than 5×10^{-7} Torr. After the deposition, nitrogen gas was introduced into the chamber with a pressure up to about 200 Torr at various sample temperatures for various lengths of time; for example, a 400 °C anneal for one hour was typically used. All films reported on in this paper had a nominal thickness of about 1 μm .

RESULTS AND DISCUSSION

Figure 1 shows x-ray diffraction (XRD) patterns for films deposited at different substrate temperatures under an argon pressure of 1.5 mTorr. The XRD patterns are fitted nicely to the (002), (202), (222), and (004) lines of the tetragonal ThMn_{12} structure. The films have the c axis preferentially aligned perpendicularly to the film plane. For a substrate temperature higher than 430 °C, the small portion of α -Fe-like phase starts to increase and the (002) texture gets worse. For a substrate temperature much lower than 340 °C the films have only XRD peaks of the α -Fe-like phase. For all the measurement shown below, the films made at a substrate temperature of 390 °C were used. The XRD pattern for the nitride film was given in Ref. 7, which is similar as the

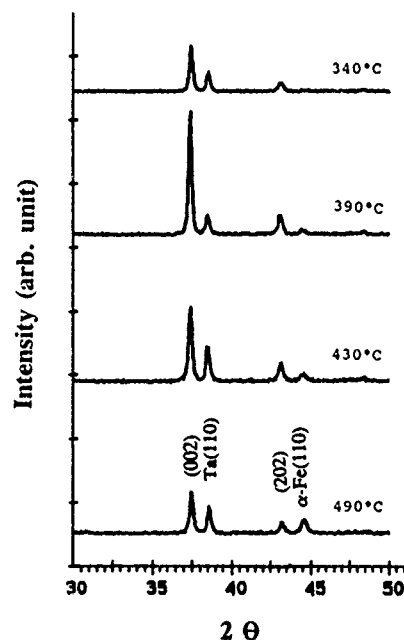


FIG. 1. XRD patterns of $\text{Nd}(\text{Fe,Ti})_{12}$ films prepared on Ta under various substrate temperatures and at a sputtering gas pressure of 1.5 mTorr.

^{a)}Present address: MINT Center, University of Alabama, Tuscaloosa, Alabama 35487-0209.

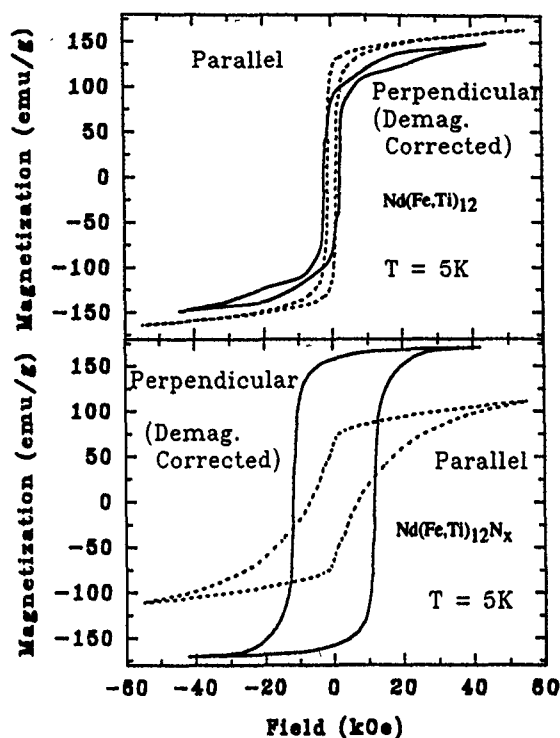


FIG. 2. Hysteresis loops of a Nd(Fe,Ti)_{12} film and a $\text{Nd(Fe,Ti)}_{12}\text{N}_x$ film of about $1 \mu\text{m}$ thick measured at 5 K with a high applied field of 55 kOe.

390 °C pattern for the film before nitriding as shown in Fig. 1 with only positions shifted to lower angles.

When films are annealed *in-situ* at a temperature of 400 °C for about one hour in a nitrogen atmosphere, a unit-cell-volume expansion of 3.6% is observed. Based on the reported data⁹ we estimated the nitrogen content to be about $x=0.9$. This accompanies a dramatic change in magnetic properties.

Figure 2 shows typical hysteresis loops for a Nd(Fe,Ti)_{12} film and a $\text{Nd(Fe,Ti)}_{12}\text{N}_x$ film of about $1 \mu\text{m}$ thick measured at a low temperature of 5 K. For the perpendicular loops the applied field has been corrected for demagnetization. It is noted that for the Nd(Fe,Ti)_{12} film the perpendicular magnetization is below the parallel magnetization, which is different from the case of room temperature measurement.⁷

Figure 3 shows the temperature dependence of the magnetization for films before and after nitriding. The procedure for this measurement was first to lower the temperature to 5 K and apply the maximum field of 55 kOe in the film plane, then decrease the field to 200 Oe, which is much lower than the coercivity, 2.7 kOe, and then measure the magnetization while increasing the temperature. A spin reorientation is observed at around 170 °C for the Nd(Fe,Ti)_{12} film. For the $\text{Nd(Fe,Ti)}_{12}\text{N}_x$ film no such phenomenon is observed. This means that the spin reorientation is suppressed by nitriding.

Figure 4 shows the initial magnetization curves of a nitride film measured at 5 K from both a thermally demagnetized and a field-demagnetized state. The hysteresis loop in the first quadrant is also shown. The magnetization for the thermally demagnetized film rises rapidly to near saturation at a field well below the coercivity. For the field-

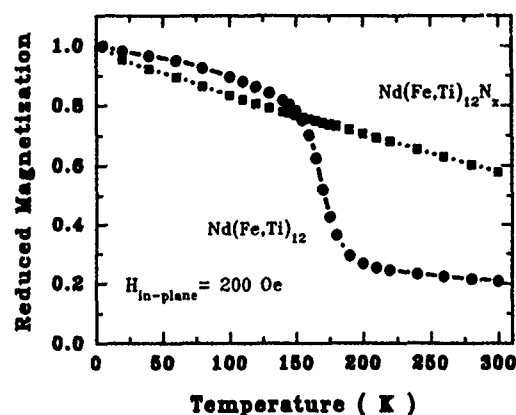


FIG. 3. Temperature dependence of magnetization for a Nd(Fe,Ti)_{12} film and a $\text{Nd(Fe,Ti)}_{12}\text{N}_x$ film under a low field of 200 Oe.

demagnetized film the initial curve is much lower. These features are similar to those observed for NdFeB sintered magnets, which are believed to be strong indications of a nucleation type of magnetization-reversal mechanism.³ Hysteresis loops were measured at different temperatures with a SQUID magnetometer. The temperature dependencies of M_s , H_k , H_c determined from the loops for a nitride film are plotted in Fig. 5. H_c decreases from 12 kOe at 5 K to 2 kOe at 350 K. At room temperature H_c is about 2.7 kOe. M_s decreases about 10% when the temperature increases from 5 K to room temperature. Kronmüller and co-workers¹⁰ have derived a simplified formula for the coercivities due both to nucleation and pinning mechanisms by assuming that there are spatial fluctuations of the first-order anisotropy constant K_1 and the exchange constant A :

$$H_c(T) = \alpha(T) \frac{2K_1(T)}{M_s(T)} - N_{\text{eff}}M_s(T), \quad (1)$$

where for pinning

$$\alpha_K^{\text{pin}}(T) = a \frac{r_0}{\delta_B} \text{ when } r_0 \ll \delta_B, \quad (2)$$

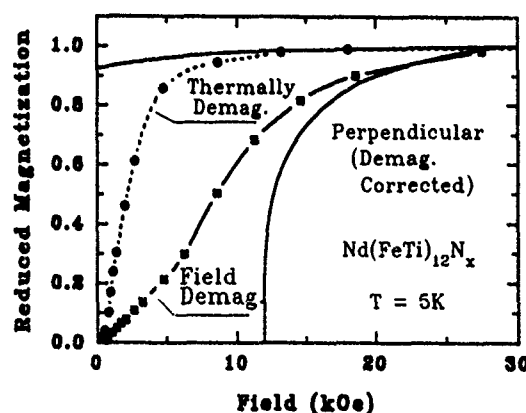


FIG. 4. Initial magnetization curve measured from a thermally demagnetized and field demagnetized state of a $\text{Nd(Fe,Ti)}_{12}\text{N}_x$ film at a low temperature of 5 K.

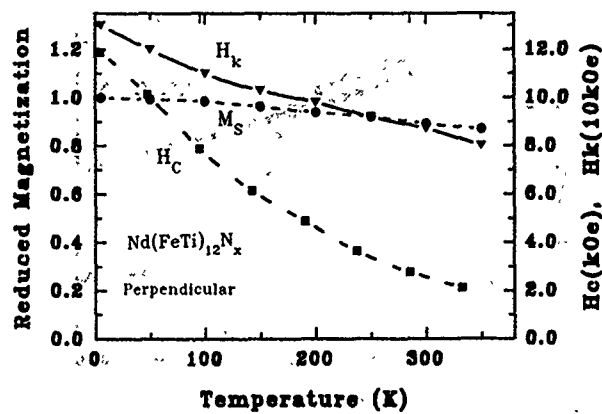


FIG. 5. Temperature dependence of the parameters M_s , H_k , H_c extrapolated from hysteresis loops for a $\text{Nd}(\text{Fe,Ti})_{12}\text{N}_x$ film.

$$\alpha_K^{\text{pin}}(T) = b \frac{\delta_B}{r_0} \text{ when } r_0 \gg \delta_B, \quad (3)$$

and where

$$\delta_B = \pi \sqrt{\frac{A}{K_1}} \quad (4)$$

is the domain-wall width for a uniaxial crystal and r_0 is the pinning-center size.

Equation (1) also applies to reversal by nucleation according to different sizes of the nucleation site (r_0):

$$\alpha_K^{\text{nuc}} = 1 - \frac{r_0^2}{\delta_B^2}, \text{ when } r_0 \ll \delta_B, \quad (5)$$

$$\alpha_K^{\text{nuc}} = \frac{\delta_B}{\pi r_0}, \text{ when } 2\pi r_0 \approx \delta_B, \quad (6)$$

$$\alpha_K^{\text{nuc}} = 1 - \frac{\Delta K}{K_1}, \text{ when } 2\pi r_0 \gg \delta_B. \quad (7)$$

We assume that the exchange constant A for the main region¹¹ is 10^{-6} erg/cm and the domain-wall thickness δ_B is given by Eq. (4). After fitting the experimental results to the cases presented in Eqs. (2) to (7), the main results of this analysis are summarized as follows: (a) Assuming reversal by pinning with small pinning centers, the fitting according to Eq. (2) gives an r_0 value of 0.03 \AA , which is unreasonably small though the H_c/M_s vs $2K/M_s^2/\delta_B$ curve shows a near linear relationship; (b) assuming reversal by pinning with large pinning centers according to Eq. (3), the experimental results are shown in Fig. 6(a). H_c/M_s does not vary linearly with $2K/M_s^2/\delta_B$, so this case can be excluded; (c) for reversal by nucleation with small nucleation sites, the experimental results are fitted according to Eq. (5). The value of r_0 obtained is 150 \AA , which is inconsistent with the small site assumption; (d) for reversal by nucleation with medium size nucleation sites, no linear relationship is expected since Eq. (6) and Eq. (3) have similar δ_B dependence; (e) for reversal by nucleation with extended nucleation sites, Fig. 6(b) gives

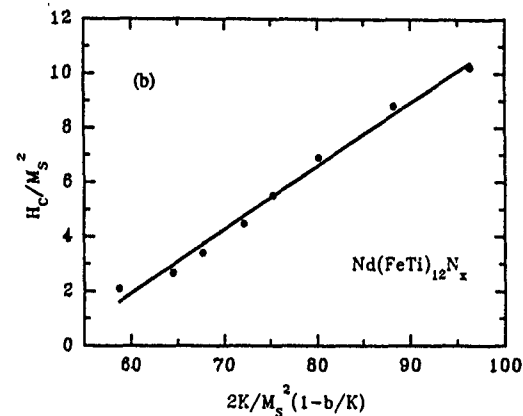
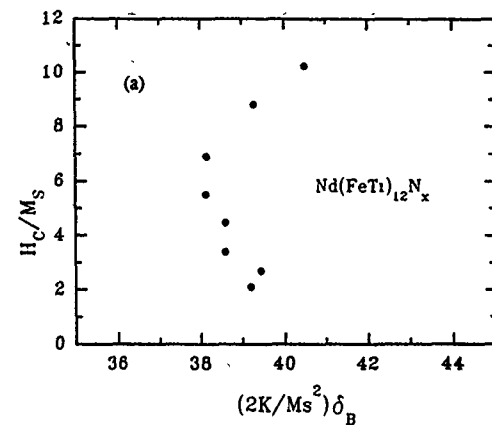


FIG. 6. (a) Experimental results for pinning with large pinning sites; (b) Experimental results and fitting results for nucleation with large sites for a $\text{Nd}(\text{Fe,Ti})_{12}\text{N}_x$ film.

the experimental results and fitting results according to Eq. (7). There is a reasonably good linear relationship between H_c/M_s and $2K/M_s^2(1-b/K)$. The prefactor in Eq. (1) is about 0.23 and N_{eff} is about 3.8.

ACKNOWLEDGMENT

Research supported by the DOE under grant DE-FG02-86ER45262.

- ¹S. Higano, K. Yamagata, K. Tokoro, M. Fukuda, and K. Kamino, IEEE Trans. Magn. **MAG-23**, 3698 (1987).
- ²J. M. D. Coey and Hong Sun, J. Magn. Magn. Mater. **87**, L251 (1990).
- ³W. E. Wallace and M. Q. Huang, IEEE Trans. Magn. **MAG-28**(5), 2312 (1992); and K. H. J. Buschow, Rep. Prog. Phys. **54**, 1123-1213 (1991).
- ⁴F. J. Cadieu, H. Hegde, R. Rani, A. Navarathna, and K. Chen, Appl. Phys. Lett. **59**, 875 (1991).
- ⁵D. Wang, S. H. Liou, P. He, D. J. Sellmyer, G. D. Hadjipanayis, and Y. Zhang, J. Magn. Magn. Mater. **124**, 62 (1993).
- ⁶Y. C. Yang, X. D. Zhang, L. S. Kong, Q. Pan, and S. L. Ge, Appl. Phys. Lett. **58**(18), 2042 (1991).
- ⁷I. Panagiotopoulos, D. Wang, D. Niarchos, and D. J. Sellmyer, Appl. Phys. Lett. **62**, 3528 (1993).
- ⁸A. Navarathna, H. Hegde, R. Rani, and F. J. Cadieu, J. Appl. Phys. **73**, 6242 (1993).
- ⁹J. M. D. Coey, Phys. Scr. **T39**, 21 (1991).
- ¹⁰H. Kronmüller, K. D. Durst, and M. Sagawa, J. Magn. Magn. Mater. **74**, 291 (1988).
- ¹¹T. Suzuki, H. Notarys, D. Dobertin, C. J. Lin, D. Weller, D. Miller, and G. Gorman, IEEE Trans. Magn. **MAG-28**, 2754 (1992), and references therein.

⁵⁷Fe Mössbauer studies of Nd(Fe_{12-x}Mo_x) and Nd(Fe_{12-x}Mo_x)N_{0.9} (x=1.25 and 1.50)

Qi-Nian Qi

Department of Pure and Applied Physics, Trinity College, Dublin 2, Ireland

Bo-Ping Hu^{a)}

Department of Pure and Applied Physics, Trinity College, Dublin 2, Ireland and Institut für Festkörper- und Werkstofforschung Dresden e.V., P.O. Box 01171, Dresden, Germany

J. M. D. Coey

Department of Pure and Applied Physics, Trinity College, Dublin 2, Ireland

Nd(Fe_{12-x}Mo_x)N_y (x=1.25 and 1.50, y=0.9) ⁵⁷Fe Mössbauer spectra of parent compounds and nitrides have been measured at 15 and 293 K. Hyperfine fields are little changed by the presence of nitrogen at 15 K, where the average value is about 25 T but at 293 K there is a change in average hyperfine field from 19 T for parent compounds to 24 T for nitrides due to the increase in Curie temperature. Spin reorientations occur in the parent compounds in the temperature range between 160–190 K but not in the nitrides, which show c-axis anisotropy throughout this range.

Recent experiments have shown that the best intrinsic magnetic properties in R(Fe_{12-x}Mo_x)N_y are found for the lowest Mo concentrations.^{1,2} The nitride with R=Nd is a candidate for permanent magnet development. Coercivities of up to 0.8 T are reported for mechanically alloyed Nd₁₀(Fe₇₅Mo₁₅)N_y (Ref. 3) and 0.64 T for milled NdFe_{10.75}Mo_{1.25}N_{0.9}.⁴ A maximum energy product of (BH)_{max}=240 kJ/m³ at room temperature has been inferred from work on thin films.⁵ In order to improve the understanding of the microscopic magnetic properties, in this work, we investigated Nd(Fe_{12-x}Mo_x) with x=1.25 and 1.50 and their nitrides by ⁵⁷Fe Mössbauer effect at the temperatures of 15 and 293 K.

The Nd(Fe_{12-x}Mo_x) alloys were prepared by arc-melting elements of purity better than 99.5% with about 10% excess of Nd to compensate the loss on melting. Buttons were then annealed in vacuum at a temperature of 1050 °C for about 5 h. The homogenized ingots were pulverized into a fine powder with an average size of about 15 μm. Nitrogenation was performed by heating the alloy powder in pure N₂ at 400–450 °C for 1–3 h. The nitrogen content was evaluated from the weight difference of the samples before and after nitrogenation.

Mössbauer absorbers consisted of about 15 mg cm⁻² of alloy powder mixed with icing sugar. Oriented absorbers were prepared by mixing alloy powder with epoxy resin and setting in an applied field of 2 T applied perpendicular to the surface of the sample. ⁵⁷Fe Mössbauer spectra were collected using a conventional constant acceleration spectrometer with a 20 mCi source of ⁵⁷Co in rhodium. The γ ray was along the alignment direction for the oriented absorbers. The velocity scale was calibrated using an α-Fe absorber at room temperature. Low temperature data were obtained using a closed-cycle two stage helium refrigerator (Air Products, model HC-2).

Figure 1 shows CuK_α x-ray diffraction patterns of Nd(Fe_{10.75}Mo_{1.25}) and Nd(Fe_{10.75}Mo_{1.25})N_{0.9}. The

magnetic characteristics of the samples are summarized in Table I.

The Nd(Fe_{12-x}Mo_x) and Nd(Fe_{12-x}Mo_x)N_{0.9} nitrides (x=1.25 and 1.50) are single phase with a ThMn₁₂-type structure⁴ as shown in Fig. 1. A detailed study of magnetization as a function of Mo concentration shows that at room temperature there is uniaxial anisotropy when x<1.55 in the parent compounds,⁶ but the corresponding nitrides have uniaxial anisotropy for all x values.¹ X-ray diffraction patterns on our oriented absorbers indicate that they all well aligned except for Nd(Fe_{10.50}Mo_{1.50}) which has a low anisotropy field at room temperature.⁶

X-ray diffraction analysis has shown that in Nd(Fe₁₀Mo₂), 8f and 8j sites are fully occupied by Fe atoms while 8i sites are shared by Fe and Mo atoms.⁷ A recent neutron diffraction study on Y(Fe₁₁Mo) showed that 20% of Mo atoms occupy 8f sites with the rest on 8i sites.⁸ The N atoms in 1:12 nitrides occupy 2b sites exclusively.^{8,9} In our work, we suppose the Mo atoms to be located on 8i sites only.

The distribution of Mo causes a distribution of Fe nearest neighbors for each Fe site, which results in quite broad outer lines in the Mössbauer spectrum due to a distribution of hyperfine fields. An acceptable fit of the spectra of isotro-

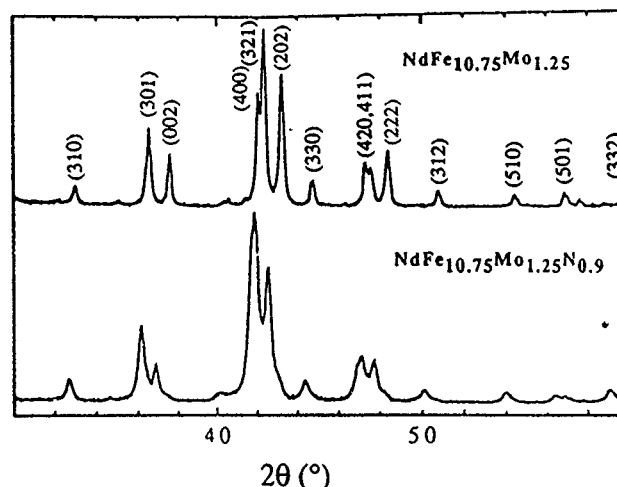


FIG. 1. CuK_α x-ray diffraction patterns of Nd(Fe_{10.75}Mo_{1.25}) and Nd(Fe_{10.75}Mo_{1.25})N_{0.9}. The peaks are indexed by using the tetragonal ThMn₁₂ symmetry (space group I4/mmm).

^{a)}Permanent address: San Huan Research Laboratory, Chinese Academy of Sciences, P. O. Box 603, Beijing 100080, China.

TABLE I. Structure and magnetic properties of $\text{Nd}(\text{Fe}_{12-x}\text{Mo}_x)$ and $\text{Nd}(\text{Fe}_{12-x}\text{Mo}_x)\text{N}_y$.^{1,6}

x	y	a (Å)	c (Å)	V (Å ³)	dV/V (%)	T_c (K)	m_s ($\mu_B/\text{f.u.}$)		T_a (K)
							10 K	295 K	
1.25	0.0	8.596	4.792	354.1	...	457	21.1	17.3	160
1.25	0.9	8.658	4.869	365.0	3.07	612	19.0	20.3	...
1.50	0.0	8.604	4.796	355.0	...	440	19.4	16.6	190
1.50	0.9	8.663	4.874	365.8	3.02	584	17.2	17.5	...

pic absorbers was achieved using just five components with a constrained intensity ratio of $12:8:4:(8-2x):(4-x)$, corresponding to $8f:8j_1:8j_2:8i_1:8i_2$. The outer line width of each sextet was varied independently from the middle and inner lines to help account for the distribution in hyperfine field at each site. The same isomer shifts and hyperfine fields are imposed for the subspectra of each site for the parent compounds and nitrides. For the spectra of oriented absorbers the same intensity constraint and Mössbauer parameters are used as for isotropic absorbers except that the angle ϕ_{Fe} between the γ -ray direction and hyperfine field was taken the same for all three iron sites due to ferromagnetic ordering.¹⁰ The hyperfine fields for the Fe sites then decrease in the order $B_{hf}(8i) > B_{hf}(8j) > B_{hf}(8f)$.^{10,11}

Figures 2 and 3 show the spectra of isotropic and oriented absorbers of $\text{Nd}(\text{Fe}_{12-x}\text{Mo}_x)$ and $\text{Nd}(\text{Fe}_{12-x}\text{Mo}_x)\text{N}_{0.9}$ ($x=1.25$ and 1.50) at 15 and 293 K together with the envelopes of the fits. The α -Fe content of the parent compounds is less than 1% and it is not included in fits, but there is about 3% α -Fe in the nitride spectra. The fitted hyperfine parameters of isotropic absorbers obtained are listed in Table II. The average hyperfine field of $\text{Nd}(\text{Fe}_{10.50}\text{Mo}_{1.50})$ is smaller by about 1 T than that of $\text{Nd}(\text{Fe}_{10.75}\text{Mo}_{1.25})$ at both 15 and

293 K, which indicates that the presence of Mo around Fe reduces the atomic magnetic moment of Fe, in accordance with the data in Table I. The increase of 24% in average hyperfine fields, from 19.3 to 24.0 T, at room temperature after nitrogenation stems from the large increase of Curie temperature, from about 450 K for parent compounds to 630 K for nitrides (Table I). At 15 K there is little change of the average hyperfine field after nitrogenation, only about 1.6 T (6%), which is much smaller than the increase of 13% found in the cases of $\text{Nd}(\text{Fe}_{11}\text{Ti})\text{N}_{0.8}$ (Ref. 11) and $\text{Nd}_2\text{Fe}_{17}\text{N}_y$.¹³

Taking the relative volume expansion values of $\delta V/V = \delta \ln V = 3.07\%$ and 3.02% for $x=1.25$ and $x=1.50$ compounds, respectively. We found that $\delta S/\delta \ln V$ on nitrogenation is 2.6 mm/s for the former and 2.0 mm/s for the latter. This is larger than that for $\text{R}_2\text{Fe}_{17}\text{N}_x$ ($\delta S/\delta \ln V = 1.7$ mm/s)¹³ and close to that for $\text{R}(\text{Fe}_{11}\text{Ti})\text{N}_x$ ($\delta S/\delta \ln V = 2.2$ mm/s)¹¹ which suggests that the interband electron transfer on nitrogenation in $\text{Nd}(\text{Fe}_{12-x}\text{Mo}_x)\text{N}_{0.9}$ ($x=1.25$ and 1.50) is stronger than in nitrides of the 2:17 series.

Comparing the spectra of oriented absorbers at two temperatures as shown in Fig. 3, the lines 2 and 5 of the spectra at 15 K are much stronger than those at 293 K for parent

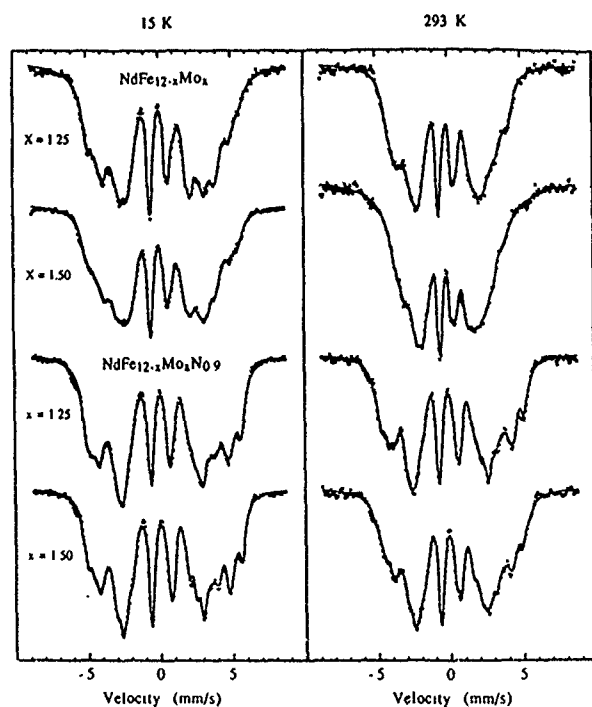


FIG. 2. The ^{57}Fe Mössbauer spectra of isotropic absorbers for $\text{Nd}(\text{Fe}_{12-x}\text{Mo}_x)$ and $\text{Nd}(\text{Fe}_{12-x}\text{Mo}_x)\text{N}_{0.9}$ ($x=1.25$ and 1.50) at 15 K (left) and 293 K (right) with the fits shown as full lines.

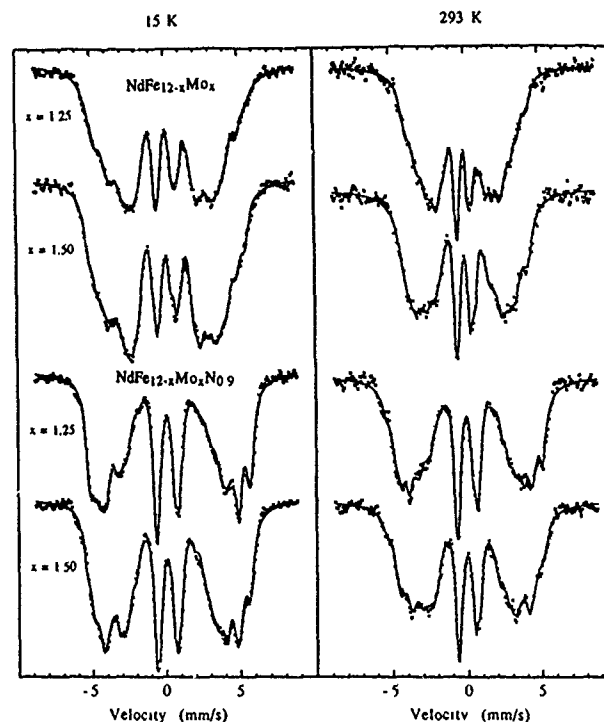


FIG. 3. The ^{57}Fe Mössbauer spectra of oriented absorbers for $\text{Nd}(\text{Fe}_{12-x}\text{Mo}_x)$ and $\text{Nd}(\text{Fe}_{12-x}\text{Mo}_x)\text{N}_{0.9}$ ($x=1.25$ and 1.50) at 15 K (left) and 293 K (right) with the fits shown as full lines.

TABLE II. Fit Mössbauer parameters for isotropic absorbers of $\text{Nd}(\text{Fe}_{12-x}\text{Mo}_x)$ and $\text{Nd}(\text{Fe}_{12-x}\text{Mo}_x)\text{N}_{0.9}$ ($x=1.25, 1.50$) measured at (a) 15 K and (b) room temperature. B_{hf} is the hyperfine field in units of tesla T, QS the quadrupole splitting, and IS the isomer shift relative to metallic iron at room temperature in units of mm/s.

Compound	Mössbauer parameters	Sites					Mean
		8 <i>f</i>	8 <i>j</i> ₁	8 <i>j</i> ₂	8 <i>i</i> ₁	8 <i>i</i> ₂	
(a) 15 K							
Nd(Fe _{10.75} Mo _{1.25})	<i>B</i> _{hf}	20.1	24.6	24.6	30.7	30.7	24.5
	IS	-0.05	-0.02	-0.02	0.02	0.02	0.03
	QS	0.17	-0.28	0.17	0.54	-0.33	
Nd(Fe _{10.50} Mo _{1.50})	<i>B</i> _{hf}	19.1	24.3	24.3	31.1	31.1	23.9
	IS	0.01	0.02	0.02	0.16	0.16	0.05
	QS	0.05	-0.20	0.22	-0.11	0.29	
Nd(Fe _{10.75} Mo _{1.25})N _{0.9}	<i>B</i> _{hf}	22.0	27.4	26.9	29.6	32.6	26.2
	IS	0.13	0.03	0.03	0.19	0.19	0.11
	QS	0.15	0.35	-0.35	0.01	0.23	
Nd(Fe _{10.50} Mo _{1.50})N _{0.9}	<i>B</i> _{hf}	21.2	28.0	25.5	29.8	29.7	25.5
	IS	0.13	0.07	0.07	0.15	0.15	0.11
	QS	0.17	0.38	-0.17	0.07	-0.32	
(b) 293 K							
Nd(Fe _{10.75} Mo _{1.25})	<i>B</i> _{hf}	17.8	18.3	18.3	24.8	24.8	19.8
	IS	0.05	-0.31	-0.31	-0.04	-0.04	-0.11
	QS	0.52	-0.69	0.03	0.19	-0.18	
Nd(Fe _{10.50} Mo _{1.50})	<i>B</i> _{hf}	14.6	18.7	18.7	22.9	22.9	18.1
	IS	-0.13	-0.14	-0.14	-0.04	-0.04	-0.11
	QS	0.15	-0.25	0.18	-0.22	0.41	
Nd(Fe _{10.75} Mo _{1.25})N _{0.9}	<i>B</i> _{hf}	19.7	25.0	27.9	31.9	30.7	25.1
	IS	-0.13	0.00	0.00	0.03	0.05	-0.04
	QS	-0.08	0.12	0.03	-0.71	0.22	
Nd(Fe _{10.50} Mo _{1.50})N _{0.9}	<i>B</i> _{hf}	18.4	23.6	24.7	29.7	27.1	23.0
	IS	-0.03	-0.02	-0.02	0.05	0.05	-0.01
	QS	0.16	-0.13	0.29	0.09	-0.01	

compounds but there is no large change for nitrides. Although the fitting angles ϕ_{Fe} at room temperature are about 35° and 39° for $\text{Nd}(\text{Fe}_{12-x}\text{Mo}_x)$ and nitrides respectively because of imperfect orientation of the powder samples, the change of more than 15° for parent compounds and less than 5° for nitrides at 15 K implies that a spin reorientation transition occurs in the parent compounds at low temperature but not in the nitrides.¹⁰ magnetization, taking account of the imperfect c -axis orientation of the absorbers. For the case where the magnetization is along c axis when the absorber is oriented at room temperature, the tilting angle θ between c axis and iron magnetization can be determined from This suggested that $\text{Nd}(\text{Fe}_{12-x}\text{Mo}_x)$ undergoes a spin reorientation away from the c axis when temperature decreases below 160 or 190 K for $x=1.25$ and 1.50, respectively. The nitrides have a magnetic structure with easy c axis between 15 and 293 K.⁶

Compared with the compounds $\text{Nd}(\text{Fe}_{12-x}\text{Ti}_x)$, the $\text{Nd}(\text{Fe}_{12-x}\text{Mo}_x)$ have a slightly larger magnetic moment, but a reduced hyperfine field. Easy c -axis anisotropy is more easily achieved in the nitrides of the Mo system since with titanium there is a 2:19 or 3:29 phase with c -plane anisotropy.¹⁵

The average hyperfine fields of nitrides $\text{NdFe}_{12-x}\text{Mo}_x\text{N}_y$ ($x=1.25$ and 1.50, $y=0.9$) are slightly larger than those of the parent compounds at 15 K and increase by 24% at room temperature. The isomer shifts increase by 0.1 mm/s mainly due to the 3% volume expansion. $\delta S/\delta \ln V$ on nitrogenation (2.3 mm/s) is larger than that in $\text{R}_2\text{Fe}_{17}\text{N}_x$ ($\delta S/\delta \ln V=1.7$ mm/s). The increase of Mo content from 1.25 to 1.50

causes a decrease of average hyperfine fields of about 1 T at 15 and 293 K for both parent compounds and nitrides. Spin reorientations occur for the parent compounds but the nitrides exhibit easy c -axis anisotropy throughout the temperature range due to the crystal field created at the neodymium by the pair of nitrogen neighbors along the c axis.

¹ Y. Z. Wang, B. P. Hu, X. L. Rao, G. C. Liu, L. Yin, and W. Y. Lai, J. Appl. Phys. **73**, 6251 (1993).

² Hong Sun, M. Akayama, K. Tatami, and H. Fujii, Physica B **183**, 33 (1993).

³ W. Gong and G. C. Hadjipanayis, J. Appl. Phys. **73**, 6245 (1993).

⁴ Bo-Ping Hu, P. A. P. Wendhausen, D. Eckert, W. Pitschke, A. Handstein, and K.-H. Müller, EMMA 1993.

⁵ A. Navarathna, H. Hegde, R. Rani, K. Chen, and F. J. Cadieu, INTERMAG'93, FC-1, Stockholm, 1993.

⁶ Y. Z. Wang, B. P. Hu, X. L. Rao, G. C. Lui, L. Song, L. Yin, and W. Y. Lai (this conference).

⁷ D. B. de Mooij and Buschow, J. Less-Common Metals **136**, 207 (1988).

⁸ Hong Sun, Y. Morri, H. Fujii, M. Akayama, and Funahashi, **48**, 13333 (1993). Phys. Rev. B.

⁹ Y. C. Yang, X. D. Zhang, L. S. Kong, Q. Pan, S. L. Ge, J. L. Yang, Y. F. Ding, B. S. Zhang, and C. T. Y. L. Jin, Solid State Commun. **78**, 313 (1991).

¹⁰ Bo-Ping Hu, Hong-Shuo Li, and J. M. D. Coey, Hyperfine Interactions **45**, 233 (1989).

¹¹ Qian Qi, D. P. F. Hurley, and J. M. D. Coey (unpublished).

¹² Qian Qi, Y. P. Li, and J. M. D. Coey, J. Phys.: CM **4**, 8029 (1992).

¹³ Bo-Ping Hu, Hong-Shuo Li, Hong Sun, and J. M. D. Coey, J. Phys.: CM **3**, 3893 (1991).

¹⁴ Qian Qi, Hong Sun, R. Skomski, and J. M. D. Coey, Phys. Rev. B **45**, 12, 278 (1992).

¹⁵ S. J. Collocott, R. K. Day, J. B. Dunlop, and R. L. Davis, Proceedings of the Seventh International Symposium on Magnetic Anisotropy and Coercivity in RE-TM Alloys (Canberra, 1992), p. 437.

Magnetic properties of $(\text{Er,R})_2\text{Fe}_{17}\text{N}_y$ compounds ($\text{R}=\text{Y,Gd}$)

J. L. Wang, W. G. Lin, N. Tang, W. Z. Li, Y. H. Gao, and F. M. Yang

Magnetism Laboratory, Institute of Physics, Chinese Academy of Sciences, P. O. Box 603, Beijing 100080, People's Republic of China

Structural and magnetic properties of the interstitial $(\text{Er}_{1-x}\text{R}_x)_2\text{Fe}_{17}\text{N}_y$ compounds with $\text{R}=\text{Y}$ and Gd , $x=0, 0.1, 0.25, 0.4, 0.5, 0.6, 0.75$, and 1.0 , $2 < y < 3$, have been investigated. All the parent compounds crystallize in the $\text{Th}_2\text{Ni}_{17}$ -type structure, except for $\text{Gd}_2\text{Fe}_{17}$ which crystallizes in the $\text{Th}_2\text{Zn}_{17}$ -structure. All nitrides preserve the same structure as the parents. Introduction of nitrogen results in an increase in lattice constants a and c , and the expansion of unit-cell volume is about 6%. The Curie temperature was found to increase distinctly after nitrogenation. Nitrogen absorption leads to an increase in saturation magnetization, the values of the saturation magnetization increase monotonically with increasing Y or Gd concentration. Nitrogenation increases the uniaxial anisotropy of the Er sublattice, and causes a spin reorientation. The Y and Gd concentration dependencies of the spin reorientation temperature T_{sr} exhibit maxima. The tentative spin phase diagrams are presented.

INTRODUCTION

Since Coey and Sun¹ reported a distinct improvement of the magnetic properties of the iron-rich R_2Fe_{17} compounds ($\text{R}=\text{rare earth or Y}$) by introducing nitrogen, the rare earth-iron nitrides of the type $\text{R}_2\text{Fe}_{17}\text{N}_y$ have attracted considerable interest, because of the excellent intrinsic magnetic properties for permanent magnet application. The structural and magnetic properties of the R_2Fe_{17} nitrides and $\text{R}_2\text{Fe}_{17}\text{N}_y$ -based pseudoternary compounds have been extensively investigated. It is well known now that introduction of nitrogen in R_2Fe_{17} compounds not only results in an increase in the Curie temperature and saturation magnetization, but also leads to a marked change of magnetocrystalline anisotropy of the compounds.²⁻⁴ Both $\text{Y}_2\text{Fe}_{17}\text{N}_y$ and $\text{Er}_2\text{Fe}_{17}\text{N}_y$ crystallize in a hexagonal $\text{Th}_2\text{Ni}_{17}$ -type structure. For $\text{Gd}_2\text{Fe}_{17}\text{N}_y$, both hexagonal $\text{Th}_2\text{Ni}_{17}$ - and rhombohedral $\text{Th}_2\text{Zn}_{17}$ -type structures may coexist.^{5,6} These compounds have similar Curie temperatures. However, the magnetocrystalline anisotropy of the three compounds are totally different. According to a crystal field theory of the anisotropy of the rare earth-transition metal intermetallic compounds,⁷ a positive second-order Stevens coefficient α_J of Er ion combining with a negative second-order crystal field coefficient A_{20} in the R_2Fe_{17} compounds⁸ results in a uniaxial anisotropy of the Er sublattice, whereas the anisotropy of the Fe sublattice is planar. The contribution to the uniaxial anisotropy which results from the Er sublattice can be enhanced by introduction of nitrogen. On the other hand, because the orbital moment of Gd is zero and Y has no magnetic moment, it can be expected that Gd or Y has no contribution to the anisotropy. Therefore, a study on the structural and magnetic properties of the $(\text{Er}_{1-x}\text{R}_x)_2\text{Fe}_{17}\text{N}_y$ series ($\text{R}=\text{Y}$ and Gd) may be helpful for a better understanding of the magnetocrystalline anisotropy in these systems.

In the present investigation we have focused our attention on the crystal structure and magnetic properties of the $(\text{Er}_{1-x}\text{R}_x)_2\text{Fe}_{17}\text{N}_y$ series with $\text{R}=\text{Y}$ and Gd , especially on magnetization and magnetocrystalline anisotropy. The results on the effect of Y and Gd substituted for Er in the $\text{Er}_2\text{Fe}_{17}\text{N}_y$

compound on the Curie temperature, saturation magnetization and magnetocrystalline anisotropy are presented.

EXPERIMENTAL METHODS

All $(\text{Er}_{1-x}\text{R}_x)_2\text{Fe}_{17}$ host compounds with $\text{R}=\text{Y, Gd}$ and $x=0, 0.1, 0.25, 0.4, 0.5, 0.6, 0.75$, and 1.0 , were prepared by arc melting starting elements with purity of 99.9%, followed by annealing in vacuum at 1423 K for 4 h. The ingots were pulverized to an average particle size of 25 μm and the powder samples obtained were heated in purified nitrogen gas under a pressure of about 1 atm at 770 K for 4 h to form the nitride compounds $(\text{Er}_{1-x}\text{R}_x)_2\text{Fe}_{17}\text{N}_y$. The value of the nitrogen content y was determined to be between 2 and 3 by weighing. X-ray diffraction was employed to determine the structure and lattice parameters of the compounds. The thermomagnetic curves were measured in a Faraday balance in the temperature region from 77 K to above the Curie temperature. The Curie temperatures T_C were derived from σ^2-T plots. Magnetization curves were measured with an extracting sample magnetometer in applied fields up to 7 T at 4.2 K. The spin reorientation temperatures T_{sr} were determined from ac-susceptibility measurements.

RESULTS AND DISCUSSION

Based on x-ray powder diffraction and thermomagnetic analysis, all the investigated $(\text{Er}_{1-x}\text{Y}_x)_2\text{Fe}_{17}\text{N}_y$ and their host compounds crystallize in the hexagonal $\text{Th}_2\text{Ni}_{17}$ -type structure, whereas $(\text{Er}_{1-x}\text{Gd}_x)_2\text{Fe}_{17}\text{N}_y$ and their host compounds crystallize in the $\text{Th}_2\text{Ni}_{17}$ -type structure for $x \leq 0.75$ and $\text{Th}_2\text{Zn}_{17}$ -type structure for $x > 0.75$ which suggests that the large size of Gd atoms makes the hexagonal $\text{Th}_2\text{Ni}_{17}$ -type structure unstable. In all compounds a small amount of $\alpha\text{-Fe}$ was detected. The typical x-ray diffraction patterns for $(\text{Er}_{0.75}\text{Gd}_{0.25})_2\text{Fe}_{17}\text{N}_y$, $\text{Gd}_2\text{Fe}_{17}\text{N}_y$ and their host compounds are shown in Fig. 1. Compared with the host, the diffraction peak positions for the nitride exhibits a clear shift toward lower angles, indicating the lattice expansion upon nitrogenation. The lattice constants a and c of the nitrides, like those of their host compounds, change very little with x . The average values of a and c of the nitrides are 8.642 Å (8.462

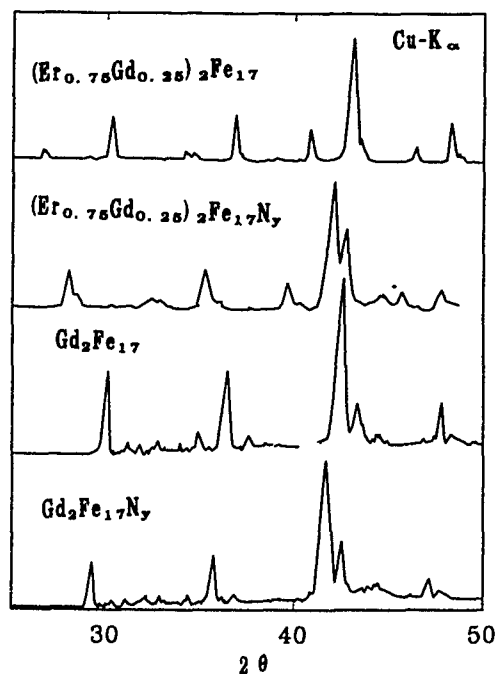


FIG. 1. X-ray diffraction patterns of $(\text{Er}_{0.75}\text{Gd}_{0.25})_2\text{Fe}_{17}$, $(\text{Er}_{0.75}\text{Y}_{0.25})_2\text{Fe}_{17}\text{N}_y$, $\text{Gd}_2\text{Fe}_{17}$, and $\text{Gd}_2\text{Fe}_{17}\text{N}_y$ compounds.

Å) and 8.458 Å (8.307 Å) for $(\text{Er}_{1-x}\text{Y}_x)_2\text{Fe}_{17}\text{N}_y$ and 8.661 Å (8.473 Å) and 8.539 Å (8.332 Å) for $(\text{Er}_{1-x}\text{Gd}_x)_2\text{Fe}_{17}\text{N}_y$ compounds, respectively. The data between parentheses pertain to the compounds before nitriding. After nitrogenation the average unit-cell volume expansion $\Delta V/V$ amounts to 6.0% for both series.

Figure 2 shows the temperature dependence of ac susceptibility χ measured at temperatures between 4.2 K and

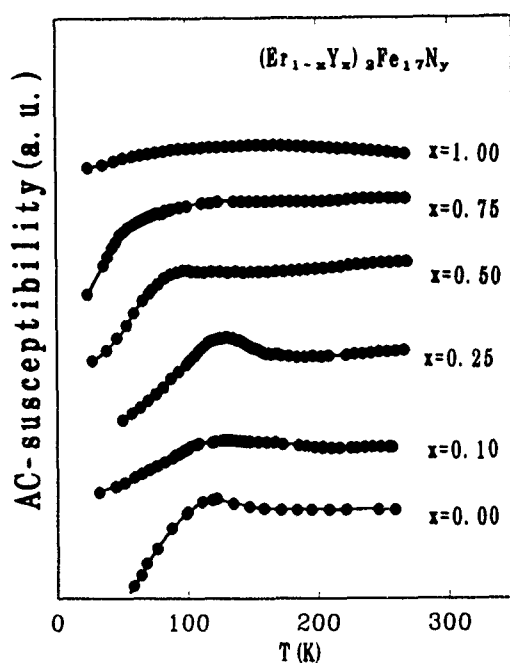


FIG. 2. Temperature dependence of the ac susceptibility (in arbitrary units) for $(\text{Er}_{1-x}\text{Y}_x)_2\text{Fe}_{17}\text{N}_y$ compounds.

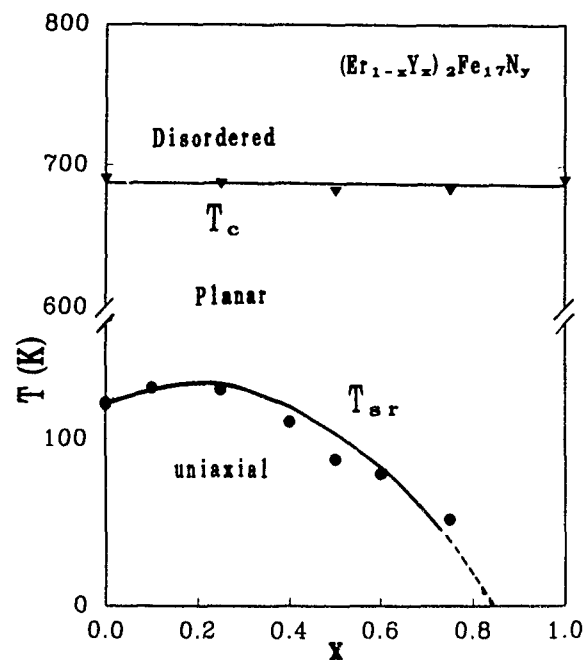


FIG. 3. Spin phase diagram of the $(\text{Er}_{1-x}\text{Y}_x)_2\text{Fe}_{17}\text{N}_y$ compounds.

room temperature, for several compositions of $(\text{Er}_{1-x}\text{Y}_x)_2\text{Fe}_{17}\text{N}_y$. Indications for spin reorientations were found in the form of maxima or jumps in the $\chi(T)$ curves. Based on the values of the spin reorientation temperature T_{sr} deduced from ac susceptibility data, the tentative spin phase diagrams are shown in Fig. 3 for $(\text{Er}_{1-x}\text{Y}_x)_2\text{Fe}_{17}\text{N}_y$ and in Fig. 4 for $(\text{Er}_{1-x}\text{Gd}_x)_2\text{Fe}_{17}\text{N}_y$ compounds. It is well known now that in the $\text{Er}_2\text{Fe}_{17}$ compound the magnetization of Er sublattice exhibits uniaxial anisotropy, whereas the magnetization of Fe sublattice has easy plane anisotropy. Because the

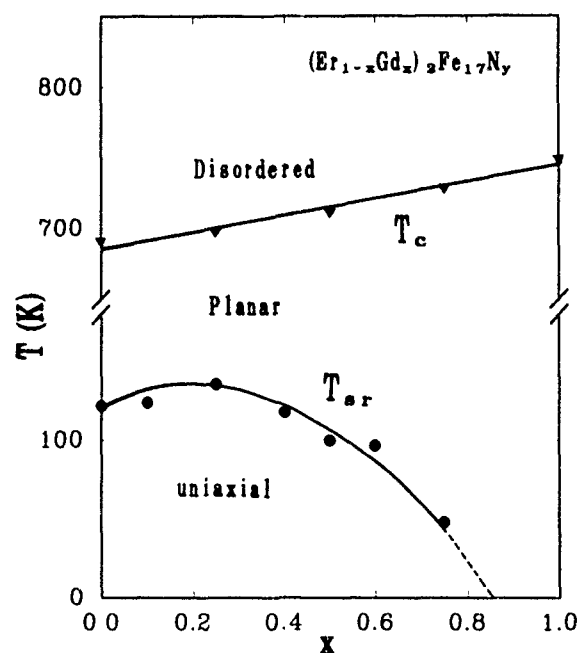


FIG. 4. Spin phase diagram of the $(\text{Er}_{1-x}\text{Gd}_x)_2\text{Fe}_{17}\text{N}_y$ compounds.

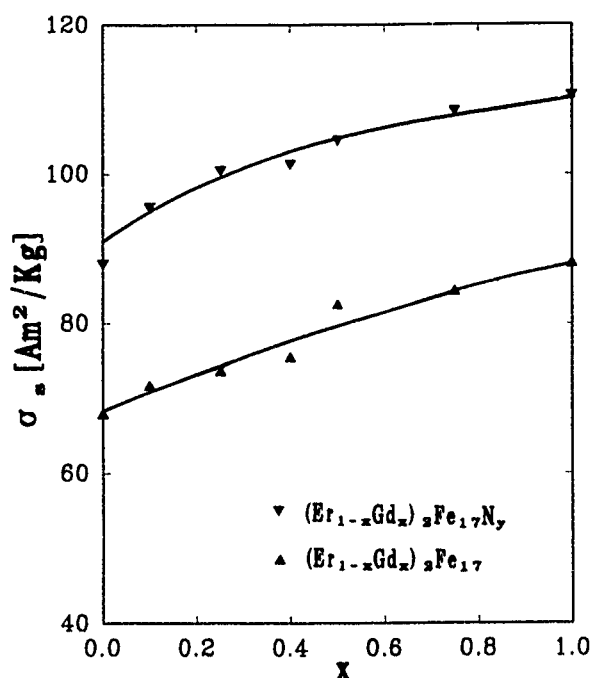


FIG. 5. Concentration dependence of the 4.2 K saturation magnetization of the $(\text{Er}_{1-x}\text{Gd}_x)_2\text{Fe}_{17}\text{N}_y$ compounds.

latter is much larger than the former, the net anisotropy of $\text{Er}_2\text{Fe}_{17}$ compound is planar in the whole magnetically ordered temperature region. Introduction of nitrogen leads to an increase in the uniaxial anisotropy of the Er sublattice and a spin reorientation from easy plane to easy axis observed at 120 K on cooling. It can be seen from Fig. 3 and Fig. 4 that the T_{sr} value increases a little with Y or Gd concentration for small x , going through a broad maximum at $x=0.25$ for both $(\text{Er}_{1-x}\text{Y}_x)_2\text{Fe}_{17}\text{N}_y$ and $(\text{Er}_{1-x}\text{Gd}_x)_2\text{Fe}_{17}\text{N}_y$ compounds, then decreases monotonically with increasing x and reaches zero at $x \approx 0.9$ for both $(\text{Er}_{1-x}\text{Y}_x)_2\text{Fe}_{17}\text{N}_y$ and $(\text{Er}_{1-x}\text{Gd}_x)_2\text{Fe}_{17}\text{N}_y$ compounds. Therefore, tentatively, we suggest, as indicated in Fig. 3 and Fig. 4, that the increase of the uniaxial anisotropy with x for a small x may be associated with the preferential substitution of Y and Gd for Er. In the hexagonal $\text{Th}_2\text{Ni}_{17}$ structure there are two crystallographically non-equivalent rare earth sites, $2b$ and $2d$. In the $\text{Tm}_2\text{Fe}_{17}$ compounds, A_{20} is negative at $2b$ sites and positive at $2d$ sites, so the Tm with a positive α_j exhibits uniaxial anisotropy at $2b$ sites and planar anisotropy at $2d$ sites.⁹ It can be reasonably assumed that such a situation is applicable for the investigated $(\text{Er,R})_2\text{Fe}_{17}\text{N}_y$ compounds. The preferential substitution of Y and Gd atoms for Er atoms on certain sites at which

Er exhibits a planar anisotropy may lead to an increase in the uniaxial anisotropy of the resultant Er sublattice. For larger x the substitution of Y or Gd for Er leads to a decrease of Er atom number at $2b$ sites which causes a decrease of uniaxial anisotropy.

The Curie temperatures of the $(\text{Er}_{1-x}\text{Y}_x)_2\text{Fe}_{17}\text{N}_y$ and $(\text{Er}_{1-x}\text{Gd}_x)_2\text{Fe}_{17}\text{N}_y$ compounds are also shown in Fig. 3 and Fig. 4, respectively. The T_c value of the $\text{Er}_2\text{Fe}_{17}\text{N}_y$ is as much as 340 K higher than that of the host. The T_c of $(\text{Er}_{1-x}\text{Gd}_x)_2\text{Fe}_{17}\text{N}_y$ compounds increases with x , whereas T_c of $(\text{Er}_{1-x}\text{Y}_x)_2\text{Fe}_{17}\text{N}_y$ compounds shows no change as x increases. A strong increase of the Curie temperature upon nitrogenation may partly be explained in terms of the lattice expansion of the nitrides which leads to an increase in the average nearest neighbor Fe-Fe distance and, therefore, to an increase of the positive Fe-Fe exchange interaction. The values for the saturation magnetization σ_s were derived by extrapolating the high field part of the magnetization curves measured at 4.2 K to $B=0$. The σ_s values have been corrected for the contribution of the α -Fe impurity phase to the magnetization, which could be deduced from the high temperature magnetization measurements. Figure 5 shows the saturation magnetization σ_s as a function of x for $(\text{Er}_{1-x}\text{Gd}_x)_2\text{Fe}_{17}\text{N}_y$ compounds. The σ_s values of the host compounds are also presented in Fig. 5 for comparison. Introduction of nitrogen leads to an increase in saturation magnetization. The σ_s values in both the $(\text{Er}_{1-x}\text{Y}_x)_2\text{Fe}_{17}\text{N}_y$ and $(\text{Er}_{1-x}\text{Gd}_x)_2\text{Fe}_{17}\text{N}_y$ compounds increase monotonically with x . However, the σ_s value increases much faster in the former than in the latter, because the moment of the heavy rare earth element exhibits an antiferromagnetic coupling with the Fe moment, the Gd moment is smaller than the Er moment, and the Y has no magnetic moment.

ACKNOWLEDGMENT

This study was supported by the National Natural Science Foundation of China.

- ¹J. M. D. Coey and Hong Sun, *J. Magn. Magn. Mater.* **87**, L251 (1990).
- ²K. H. J. Buschow, R. Coehoorn, D. B. de Mooij, K. de Waard, and T. H. Jacobs, *J. Magn. Magn. Mater.* **92**, L35 (1990).
- ³K. Schnitzler, L. Schultz, J. Wecker, and M. Katter, *Appl. Phys. Lett.* **57**, 2853 (1990).
- ⁴T. W. Capehart, R. K. Mishra, and F. E. Pinkerton, *Appl. Phys. Lett.* **58**, 1395 (1991).
- ⁵K. H. J. Buschow, *J. Less-Common Met.* **11**, 204 (1966).
- ⁶Y. Khan, *Acta Crystallogr. B* **29**, 2502 (1973).
- ⁷Bo-Ping Hu, Hong-Shuo Li, Hong Sun, J. F. Lawler, and J. M. D. Coey, *Solid State Commun.* **76**, 587 (1990).
- ⁸Y. Otani, D. P. F. Hurley, H. Sun, and J. M. D. Coey, *J. Appl. Phys.* **69**, 5584 (1991).
- ⁹P. C. M. Gubbens, A. M. van der Kraan, J. J. vanLoef, and K. H. J. Buschow, *J. Magn. Magn. Mater.* **67**, 255 (1987).

Magnetic properties of $\text{Er}_2\text{Fe}_{17-x}\text{Al}_x\text{N}_y$ compounds

F. M. Yang, N. Tang, J. L. Wang, X. P. Zhong, R. W. Zhao, and W. G. Lin

Magnetism Laboratory, Institute of Physics, Chinese Academy of Sciences, P. O. Box 603, Beijing 100080, People's Republic of China

Structural and magnetic properties of the $\text{Er}_2\text{Fe}_{17-x}\text{Al}_x\text{N}_y$ compounds ($0 \leq x \leq 3$) have been investigated. All nitrides and parent compounds crystallize in the $\text{Th}_2\text{Ni}_{17}$ structure. Al substituted for Fe leads to an increase in lattice constants a and c . Introduction of nitrogen results in a further increase of lattice constants, but the magnitude of this increase is smaller for increasing x . As Al content increases, the Curie temperature of the parent compound increases, whereas the Curie temperature of the nitride decreases. The substitution of Al for Fe results in a decrease of Fe moment in both nitrides and parent compounds. Introduction of nitrogen leads to an increase in the uniaxial anisotropy of the Er sublattice and a spin reorientation. A tentative spin phase diagram has been constructed.

INTRODUCTION

Recently the interstitial rare earth-iron nitrides $\text{R}_2\text{Fe}_{17}\text{N}_y$ have attracted much attention because of the outstanding intrinsic hard-magnetic properties as potential high-performance permanent magnets.¹ The structural and magnetic properties of these compounds have been extensively investigated.²⁻⁵ It is well known now that the magnetic moment and Curie temperature of R_2Fe_{17} compounds are strongly increased by the introduction of interstitial nitrogen. Furthermore, the absorption of nitrogen also strongly changes the magnetocrystalline anisotropy of the compounds. The introduction of nitrogen leads to the appearance of uniaxial anisotropy in the $\text{Sm}_2\text{Fe}_{17}\text{N}_y$ compounds in the whole magnetic ordering temperature region. Although Er, like Sm, possesses positive second-order Stevens coefficient α_J , the easy magnetization direction of $\text{Er}_2\text{Fe}_{17}$ compound is on the basal plane in whole temperature region up to Curie temperature. Introduction of nitrogen in the $\text{Er}_2\text{Fe}_{17}$ compound leads to an increase of uniaxial anisotropy and a spin reorientation from the easy plane to the easy axis on cooling.⁶

It has been found⁷ that the substitution of Al for Fe leads to an increase in the uniaxial anisotropy of Sm sublattice in $\text{Sm}_2\text{Fe}_{17-x}\text{Al}_x$ compounds. On the other hand, Al is also considered as an important element in improvement of magnetic performance of the permanent magnetic materials. For example, the outstanding values of magnetic hardness can be achieved at cryogenic temperature, both in powder and bulk materials of SmCo_5 , by substitution of Al for Co.⁸ As mentioned above, both substituting a third element (such as Al) for Fe and introducing the interstitial atoms (such as N, C) lead to a remarkable enhancement of the Curie temperature and the uniaxial anisotropy in the R_2Fe_{17} series with R having a positive α_J . Here, in an attempt to maximize these enhancements, we studied the $\text{Er}_2\text{Fe}_{17-x}\text{Al}_x\text{N}_y$ series to investigate the effect of the substitution of Al for Fe on the structure and magnetic properties of the interstitial $\text{R}_2\text{Fe}_{17}\text{N}_y$ nitrides. In this contribution such an effect has been determined and the results are presented.

EXPERIMENT

$\text{Er}_2\text{Fe}_{17-x}\text{Al}_x$ compounds with $x=0, 0.1, 0.2, 0.5, 0.75, 1.0, 2.0$, and 3.0 were prepared by arc melting the constituent

elements of at least 99.9% purity. The samples were homogenized by annealing in vacuum at 1370 K for 10 h. The $\text{Er}_2\text{Fe}_{17-x}\text{Al}_x\text{N}_y$ nitrides were prepared by heat treating the pulverized parent compounds in purified nitrogen gas at a pressure of one atmosphere at 773 K for different times, depending on the Al content in the parent compounds, to achieve a sufficient nitrogenation. The nitrogen content in each nitride was determined by weighting.

X-ray diffraction with $\text{Cu-K}\alpha$ radiation was used to check the crystal structure and to determine the lattice constants. Thermomagnetic analysis (TMA) was performed in the temperature range from 77 K to above the Curie temperature in a magnetic field of 0.8 T by means of a Faraday balance. The Curie temperatures were derived from σ^2 - T plots. The field dependencies of magnetization of samples consisting of powders which were free to be oriented by an applied magnetic field were measured at 4.2 K by means of an extracting sample magnetometer using a field up to 7 T produced by a superconducting magnet. The values of saturation magnetization were derived by extrapolating the high-field value to $B=0$. The spin reorientation temperatures T_{sr} were determined from ac-susceptibility measurements.

RESULTS AND DISCUSSION

X-ray powder diffraction patterns and TMA show that all investigated ternaries and their nitrides are single phase except for a small amount of α -Fe in a few samples. All $\text{Er}_2\text{Fe}_{17-x}\text{Al}_x$ compounds and corresponding nitrides crystallize in the hexagonal $\text{Th}_2\text{Ni}_{17}$ -type structure. The values of lattice constants a , c are given in Table I. Figure 1 shows the lattice constants a and c as a function of Al content for both nitrides and parent compounds. The substitution of Al for Fe results in a linear increase of lattice constants a and c in the parent compounds. This may be associated with the larger radius of the Al atom compared with that of the Fe atom. The introduction of nitrogen in $\text{Er}_2\text{Fe}_{17-x}\text{Al}_x$ leads to a further increase of lattice constants, whereas the amplitude of this increase decreases monotonically with increasing Al content, furthermore, the lattice constants a and c of the nitrides are almost independent of Al content, which suggests that the substitution of Al for Fe prevents the absorption of nitrogen. The values of nitrogen content y introduced in nitrides are

TABLE I. The lattice constants (a and c), Curie temperature (T_C), average iron magnetic moment (μ_{Fe}), spin reorientation temperature (T_{sr}) and nitrogen content (y) for $Er_2Fe_{17-x}Al_xN_y$ compounds. The data in parentheses pertain to the compounds before nitriding. Error: a and c (± 0.005 Å); T_C and T_{sr} (± 5 K); μ_{Fe} (± 0.02), $y = (\pm 5\%)$.

x	a (Å)	c (Å)	T_C (K)	T_{sr} (K)	μ_{Fe} (μ_B/Fe)	y
0.0	8.645 (8.448)	8.540 (8.291)	690 (313)	121	2.28 (1.98)	2.6
0.1	8.632 (8.475)	8.512 (8.299)	714 (355)	136	2.27 (1.97)	2.6
0.2	8.658 (8.447)	8.559 (8.313)	710 (360)	...	2.27 (1.96)	2.5
0.5	8.677 (8.472)	8.561 (8.299)	691 (363)	140	2.24 (1.95)	2.4
1.0	8.650 (8.458)	8.568 (8.326)	645 (371)	153,235	2.20 (1.94)	2.2
2.0	8.662 (8.502)	8.5673 (8.341)	609 (409)	153,287	2.10 (1.88)	1.7
3.0	8.640 (8.544)	8.550 (8.377)	559 (412)	154	1.95 (1.83)	1.2

listed in Table I. The nitrogen content y in $Er_2Fe_{17-x}Al_xN_y$ decreases monotonically with increasing Al content. According to the neutron diffraction and Mössbauer effect studies of $Nd_2Fe_{17-x}Al_x$,⁹ the Al fractional occupancy on the 18 f sites in the $Nd_2Fe_{17-x}Al_x$ increases uniformly with increasing the Al content. The occupancy of the larger Al atoms on the 18 f sites results in a decrease of 9e spacial volume and may prevent the introduction of nitrogen atoms.

The average iron magnetic moment μ_{Fe} was calculated on the basis of the saturation magnetization σ_s measured at 4.2 K. The σ_s values have been corrected for the contribution of the α -Fe impurity phase to the magnetization, which could

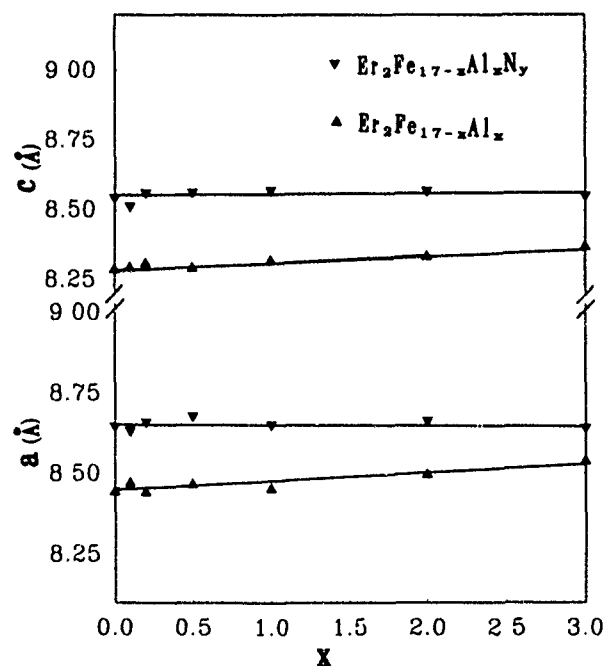


FIG. 1. Al content dependence of the lattice constants a and c of the $Er_2Fe_{17-x}Al_xN_y$ and $Er_2Fe_{17-x}Al_x$ compounds.

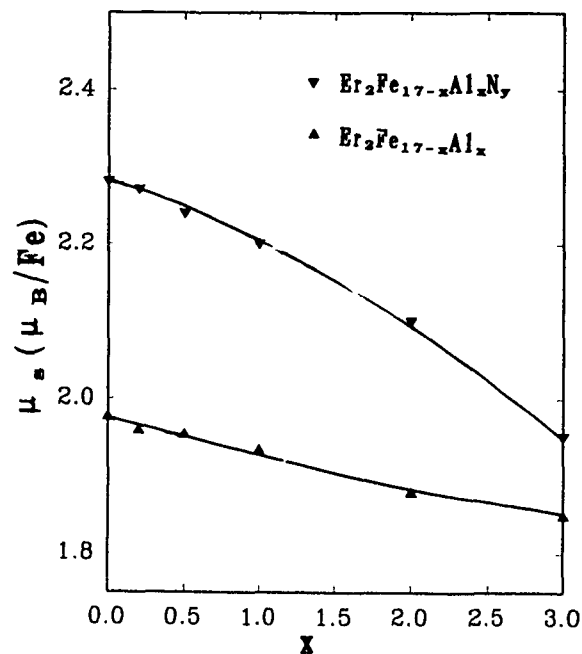


FIG. 2. The average iron magnetic moment μ_{Fe} vs the Al concentration for $Er_2Fe_{17-x}Al_xN_y$ and $Er_2Fe_{17-x}Al_x$ compounds.

be deduced from the high temperature magnetization measurements. μ_{Fe} values as a function of Al content are shown in Fig. 2. In the evaluation of the magnetic moment per iron ion it was assumed that the moment of Er ion is independent of the Al content and the value is same as that of the free Er ion. It can be seen that either in the parent compounds or in the nitrides the average Fe ion moment decreases monotonically with increasing Al content. In the case of the parent compounds, the Fe moment decreases from $1.98 \mu_B$ for $x=0$ to $1.83 \mu_B$ for $x=3$. This indicates a quenching of the Fe moment by the substitution of Al, which is similar to various analogous systems based on Al, rare earth and magnetic transition metals.¹⁰ Plusa *et al.*¹¹ explained the decrease of the average Fe moment with Al concentration in $Y_2(Fe_{1-x}Al_x)_{17}$ pseudobinary compounds by assuming that all the aluminum valence electrons populate the 3d band of the Y_2Fe_{17} compound and that one spin subband is completely full. Introduction of nitrogen leads to an increase in the average iron moment, but the amplitude of the increase upon nitridation decreases monotonically with increasing Al content, which may be associated with the decrease of the nitrogen content with increasing Al content. The values of Curie temperature T_C for both nitrides and parent compounds are also listed in Table I. T_C of the parent compounds increases with x , which may be related to the increase of lattice constants, corresponding to an increase of the positive Fe-Fe exchange coupling. Introduction of nitrogen leads to a further increase in T_C , but T_C of the nitrides decreases monotonically with increasing x . Because the lattice constants of the nitrides are nearly independent of Al content, the decrease of T_C of nitrides with Al content should be associated with the decrease of Fe moment and the decrease of the nitrogen content.

Figure 3 shows the temperature dependence of ac susceptibility χ , measured at temperatures between 4.2 K and

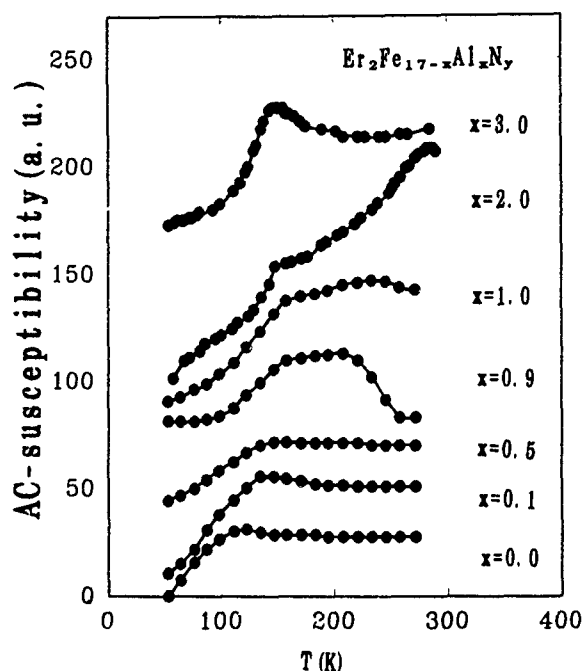


FIG. 3. Temperature dependence of the ac susceptibility (in arbitrary units) for $\text{Er}_2\text{Fe}_{17-x}\text{Al}_x\text{N}_y$ compounds.

room temperature, for several compositions. Indications for spin reorientation were found in the form of maxima or jumps in the $\chi(T)$ curves. Based on the values of the spin reorientation temperatures T_{sr} deduced from ac susceptibility data, a tentative spin phase diagram for the nitride is shown in Fig. 4. Introduction of nitrogen leads to an increase in the uniaxial anisotropy of the Er sublattice and a spin reorientation at 120 K. The spin reorientation temperature T_{sr} increases with increasing Al content. For the nitrides with $x > 0.5$, two spin reorientations can be observed at T_{sr1} and T_{sr2} , respectively, which suggests that with decreasing temperature the magnetization of the nitrides starts to depart from the c plane at T_{sr1} and coincides with the c axis at T_{sr2} . For the temperature between T_{sr1} and T_{sr2} an easy cone can be expected. Li and Cadogan¹² investigated the carbon content dependence of the crystal field coefficients for $\text{Sm}_2\text{Fe}_{17}\text{C}_{3-x}$ compounds and found that both A_{20} and A_{60} become more negative with increasing carbon content whereas A_{40} becomes more positive. It can be reasonably assumed that such a content dependence of the crystal field coefficients is applicable for $\text{Er}_2\text{Fe}_{17}\text{N}_y$ compounds. The appearance of an easy cone in the nitrides with $x > 0.5$ may be due to the fact that the decrease of nitrogen content with

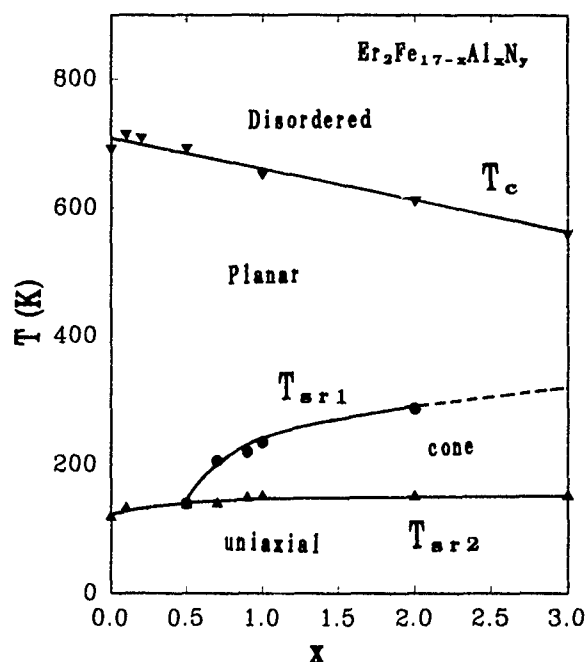


FIG. 4. The tentative spin phase diagram of the $\text{Er}_2\text{Fe}_{17-x}\text{Al}_x\text{N}_y$ compounds.

increasing Al content resulted in a shift of A_{20} toward less negative and a negative K_1 value (including the negative contribution of the Fe sublattice). In addition, a positive A_{40} gives a positive K_2 which leads, in certain x region, to the condition for easy cone, $\sin^2 \theta = -K_1/2K_2$, to be satisfied.

ACKNOWLEDGMENT

This study was supported by the National Natural Science Foundation of China.

- ¹J. M. D. Coey and Hong Sun, *J. Magn. Magn. Mater.* **87**, L251 (1990).
- ²K. H. J. Buschow, R. Coehoorn, D. B. de Mooij, K. de Waart, and T. H. Jacobs, *J. Magn. Magn. Mater.* **92**, L35 (1990).
- ³T. W. Capehart, R. K. Mishra, and F. E. Pinkerton, *Appl. Phys. Lett.* **58**, 1395 (1991).
- ⁴B.-P. Hu, H.-S. Li, H. Sun, J. F. Lawler, and J. M. D. Coey, *Solid State Commun.* **76**, 587 (1990).
- ⁵M. Katter, J. Wecker, and L. Schultz, *J. Magn. Magn. Mater.* **92**, L14 (1991).
- ⁶Bo-Ping Hu, Hong-Shuo Li, Hong Sun, J. F. Lawler, and J. M. D. Coey, *Solid State Commun.* **76**, 587 (1990).
- ⁷Z. Wang and R. A. Dunlap, *J. Phys. Condens. Matter* **5**, 2407 (1993).
- ⁸H. Oesterreicher, *Solid State Commun.* **14**, 571 (1974).
- ⁹W. B. Yelon, H. Xie, Gary J. Long, O. A. Pringle, F. Grandjean, and K. H. J. Buschow, *J. Appl. Phys.* **73**, 6029 (1993).
- ¹⁰H. Oesterreicher and D. McNeerly, *J. Less-Common Met.* **53**, 215 (1977).
- ¹¹D. Plusa, R. Pfranger, B. Wyslocki, and T. Mydlarz, *J. Less-Common Met.* **120**, 1 (1986).
- ¹²Hong-Shuo Li and J. M. Cadogan, *Solid State Commun.* **82**, 121 (1992).

Electrical and magnetic studies of (Cu/Zn)-bonded $\text{Sm}_2\text{Fe}_{17}\text{M}_x\text{N}_y$ magnets ($\text{M}=\text{B}$ or C)

Y. D. Yao

Institute of Physics, Academia Sinica, Taipei 115, Taiwan, Republic of China and Department of Physics, National Chung Cheng University, Chia-yi 621, Taiwan, Republic of China

P. C. Kuo

Institute of Materials Engineering, National Taiwan University, Taipei 107, Taiwan, Republic of China

W. C. Chang

Department of Physics, National Chung Cheng University, Chia-yi 621, Taiwan, Republic of China

C. J. Liu

Institute of Materials Engineering, National Taiwan University, Taipei 107, Taiwan, Republic of China

Samples of (Cu/Zn)-bonded and unbonded $\text{Sm}_2\text{Fe}_{17}\text{M}_x\text{N}_y$ with $\text{M}=\text{B}$ or C ($x=0, 0.25$, and 0.5 ; $y<3$) were fabricated. All the samples, besides those with B , show single Curie temperature T_C and with $\text{Sm}_2\text{Fe}_{17}$ -type crystal structure; however, multiphase structure and double T_C were observed in all the samples with B . For all the heating runs the electrical resistivity roughly above 600 K increases abruptly for all Zn-bonded samples; and decreases abruptly for all Cu-bonded samples. After these high temperature runs, the residual electrical resistivity increases for all Zn-bonded samples, and decreases for all Cu-bonded samples. The effects of Cu segregation and Zn reaction with samples are identified by the EPMA analyses.

Interstitial nitrides $\text{Sm}_2\text{Fe}_{17}\text{N}_y$ magnets discovered by Coey *et al.*¹ have been extensively studied during the past few years, e.g., Refs. 1–9. It was found that the effect of nitrogen on the structure is to expand the unit cell without changing the symmetry of the 2:17 parent compound. $\text{Sm}_2\text{Fe}_{17}\text{N}_y$ compound possesses high Curie temperature, a strong uniaxial anisotropy field, and a high saturation magnetization, which are comparable or superior to those of $\text{Nd}_2\text{Fe}_{14}\text{B}$. However, $\text{Sm}_2\text{Fe}_{17}\text{N}_y$ is metastable and decomposes to SmN and $\alpha\text{-Fe}$ at high temperatures roughly above 650 °C.¹⁰ In general, low-temperature-melting metals such as Zn, Sn, and In or organic resins such as epoxy are used to form $\text{Sm}_2\text{Fe}_{17}\text{N}_y$ bonded magnets.^{11–15}

Samples for this study were prepared from commercially available high purity Sm (99.9%), Fe (99.99%), C , B , and nitrogen gas. The $\text{Sm}_2\text{Fe}_{17}$ ingots were prepared by arc melting technique, followed by an anneal in vacuum at 1270 K for two days. For samples containing C or B , the C and B were added during the arc-melting process. These ingots were crushed and milled to powders with the average particle size of 10 μm . The temperature for nitrogenation is in the range from 700 to 800 K. In order to avoid a possible phase transition during cooling the quartz tubes were water quenched afterwards. For bonded samples, the milled samples were blended with 25 wt % of Zn or Cu powders (–325 mesh), and pressed into pellets with a pressure of 4 tons/ cm^2 in a magnetic field of 1 T. Pellets were then heat treated in N_2 for 2 h at temperatures of 620–720 K for Zn-bonded samples, and of 620–800 K for Cu-bonded samples. All the samples were characterized by powder x-ray diffraction, scanning electron microscopy (SEM) with electron probe microanalysis (EPMA) and differential scanning calorimeter (DSC), etc.

The electrical resistivity and magnetization of these samples were measured as functions of temperatures between 4 and 1200 K. For the magnetization studies, both

vibration sample magnetometer (VSM) and superconducting quantum interference device (SQUID) were used to determine the magnetization.

Powder x-ray diffraction analyses show that the $\text{Sm}_2\text{Fe}_{17}$ phase with the $\text{Th}_2\text{Zn}_{17}$ crystal structure exists in our samples; however, a small amount of $\alpha\text{-Fe}$ is always presented in most of our samples. Multiphase structure was observed in the samples with B . As an example, the powder x-ray diffraction patterns observed for $\text{Sm}_2\text{Fe}_{17}$, $\text{Sm}_2\text{Fe}_{17}\text{C}_{0.5}$, $\text{Sm}_2\text{Fe}_{17}\text{B}_{0.5}$, and $\text{Sm}_2\text{Fe}_{17}\text{N}_{2.6}$ samples are shown in Fig. 1 (a) to 1 (d), respectively. It is clearly that the 2 : 17 phase peaks in (b) and (d) are shifted to lower angles in comparison with (a) for $\text{Sm}_2\text{Fe}_{17}$; their lattice parameters a and b were roughly calculated from the powder x-ray diffraction pattern to be $a=8.58, 8.63, 8.71$ Å, and $b=12.41, 12.45, 12.61$ Å, for $\text{Sm}_2\text{Fe}_{17}$, $\text{Sm}_2\text{Fe}_{17}\text{C}_{0.5}$, and $\text{Sm}_2\text{Fe}_{17}\text{N}_y$, respectively. Curve (b) in Fig. 1 shows multiphase structure in $\text{Sm}_2\text{Fe}_{17}\text{B}_{0.5}$.

The temperature dependence of the magnetization M at 8 kG of the samples had been studied between 4 and 1100 K. The value of the magnetization at 4 K are roughly between 100 and 120 emu/g for all the unbonded samples, and between 80 and 100 emu/g for all (Zn/Cu)-bonded samples. Typically, four kinds of behaviors have been observed; as an example, Fig. 2 presents the normalized magnetization M/M_0 as functions of temperature for (a) $\text{Sm}_2\text{Fe}_{17}$, (b) $\text{Sm}_2\text{Fe}_{17}\text{C}_{0.5}$, (c) $\text{Sm}_2\text{Fe}_{17}\text{B}_{0.5}$, and (d) $\text{Sm}_2\text{Fe}_{17}\text{N}_{2.6}$. M_0 is the magnetization at 4 K and 8 kG for each sample. Clearly, the magnetization roughly above 900 K increase slowly and then drop abruptly around 1040 K with increasing temperature. This suggests that $\alpha\text{-Fe}$ is precipitated roughly above 900 K. Besides the Curie temperature T_C of $\alpha\text{-Fe}$ around 1040 K, the curves show single T_C around 390 K for $\text{Sm}_2\text{Fe}_{17}$, around 540 K for $\text{Sm}_2\text{Fe}_{17}\text{C}_{0.5}$, and around 780 K for $\text{Sm}_2\text{Fe}_{17}\text{N}_{2.6}$. However, double T_C around 400 and 600 K had

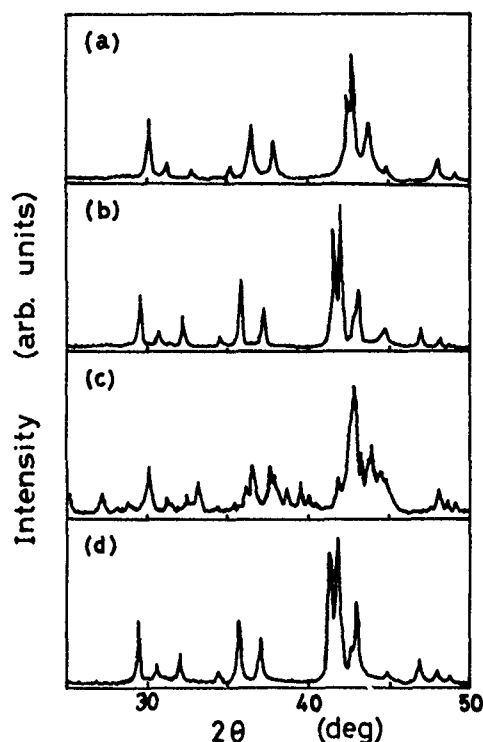


FIG. 1. The powder x-ray diffraction patterns for (a) $\text{Sm}_2\text{Fe}_{17}$, (b) $\text{Sm}_2\text{Fe}_{17}\text{C}_{0.5}$, (c) $\text{Sm}_2\text{Fe}_{17}\text{B}_{0.5}$, and (d) $\text{Sm}_2\text{Fe}_{17}\text{N}_{2.6}$ samples.

observed for all the $\text{Sm}_2\text{Fe}_{17}\text{B}_x$ samples. From the x-ray diffraction pattern, the electrical resistivity, and the magnetization studies, we conclude that besides the α -Fe phase, at least two major mixture phases with T_c around 400 and 600 K, are coexisted in the $\text{Sm}_2\text{Fe}_{17}\text{B}_x$ magnets. We guess that they may be the $\text{Sm}_2\text{Fe}_{17}$ and $\text{Sm}_2\text{Fe}_{14}\text{B}$ phases.

The electrical resistivity ρ of the bulk $\text{Sm}_2\text{Fe}_{17}\text{M}_x$ ($\text{M}=\text{C}$ or B ; $x=0, 0.25$, and 0.5) samples has been studied with increasing and decreasing temperatures between 4 and 1200 K. Each resistivity curve approaches to a constant residual resistivity near 4 K; and its value decreases after the high temperature run. This indicates that the scattering centers for the conduction electrons are decreased after high temperature runs; and also suggests that α -Fe and other ordered phases

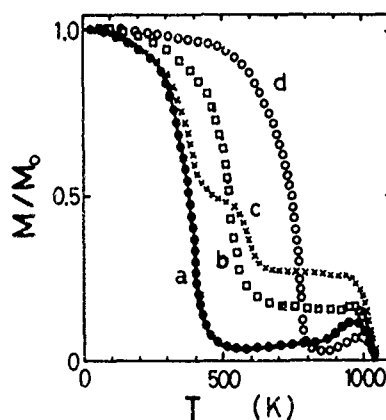


FIG. 2. The normalized magnetization as a function of temperature for (a) $\text{Sm}_2\text{Fe}_{17}$, (b) $\text{Sm}_2\text{Fe}_{17}\text{C}_{0.5}$, (c) $\text{Sm}_2\text{Fe}_{17}\text{B}_{0.5}$, and (d) $\text{Sm}_2\text{Fe}_{17}\text{N}_{2.6}$ samples.

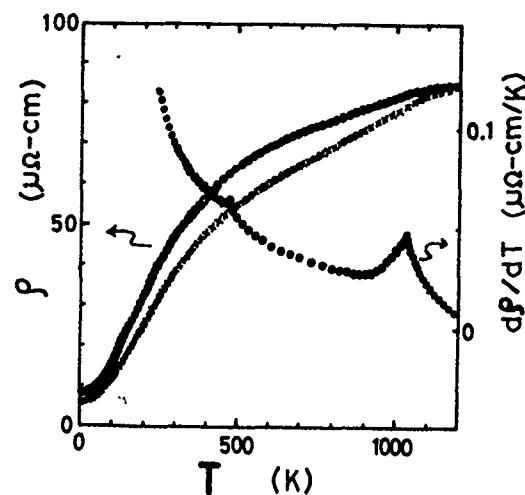


FIG. 3. The electrical resistivity and its derivative $d\rho/dT$ of the $\text{Sm}_2\text{Fe}_{17}\text{C}_{0.25}$ sample as functions of T between 4 and 1200 K. (O: heating run, \times : cooling run, and \bullet : $d\rho/dT$ for heating run.)

may be precipitated after the high temperature runs. Typically, Fig. 3 presents the electrical resistivity data of $\text{Sm}_2\text{Fe}_{17}\text{C}_{0.25}$ sample. The open circle and cross are associated with heating and cooling runs, respectively. The derivative of the electrical resistivity with respect to temperature for the heating run is plotted by dots in Fig. 3. T_c determined from the peak of $d\rho/dT$ are 480 K for $\text{Sm}_2\text{Fe}_{17}\text{C}_{0.25}$ phase and 1040 K for α -Fe phase.

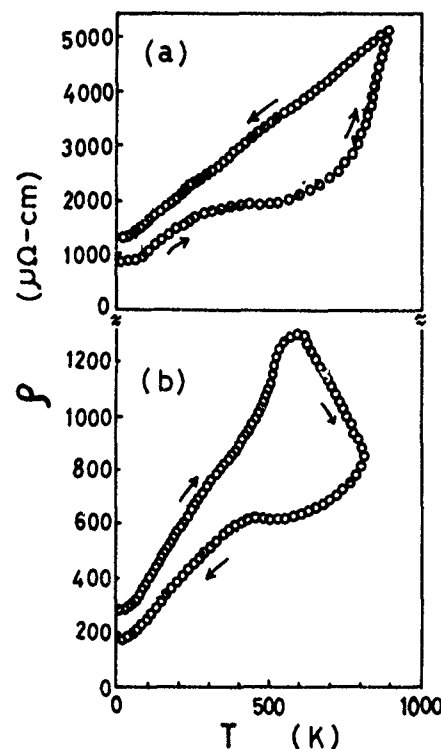


FIG. 4. The electrical resistivity as a function of T between 4 and 1000 K for (a) Zn-bonded $\text{Sm}_2\text{Fe}_{17}\text{N}_{2.0}$, and (b) Cu-bonded $\text{Sm}_2\text{Fe}_{17}\text{C}_{0.25}\text{N}_{2.6}$ (The sequence of the heating and cooling runs is indicated by arrows.)

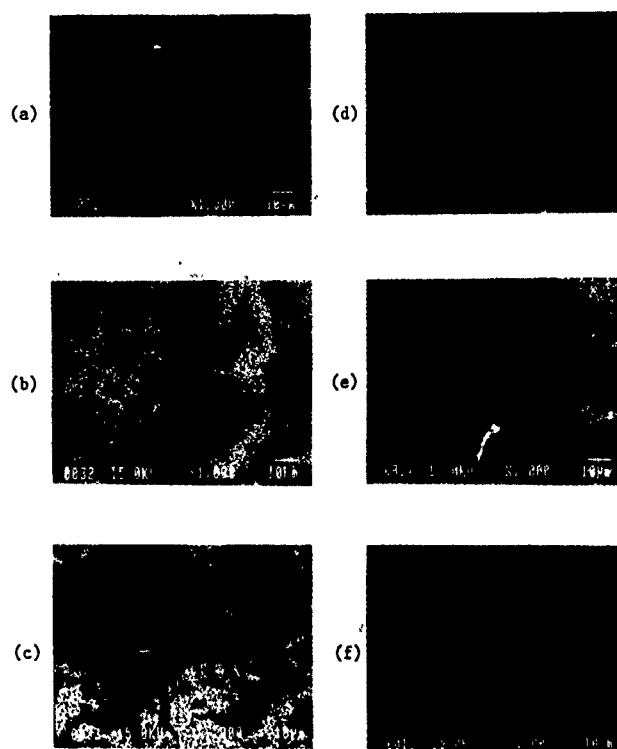


FIG. 5. (a) The SEM micrograph of the Cu-bonded $\text{Sm}_2\text{Fe}_{17}\text{C}_{0.25}\text{N}_{2.6}$ after the high temperature resistivity measurement. (b) The EPMA picture of (a) for Fe-rich distribution. (c) The EPMA picture of (a) for Cu-rich distribution. (d) The SEM micrograph of the Zn-bonded $\text{Sm}_2\text{Fe}_{17}\text{N}_{2.0}$ after the high temperature resistivity measurement. (e) The EPMA picture of (d) for Fe-rich distribution. (f) The EPMA picture of (d) for Zn-rich distribution.

The coercivity H_c of the Zn-bonded samples can be improved to 6–14 kOe after annealing them between 620 and 720 K in N_2 for 2 h. However, H_c of the Cu-bonded samples was only reached 1–3 kOe after annealing them between 620 and 800 K in N_2 for 2 h. Generally speaking, from the DSC investigations below 700 K for all the (Zn/Cu)-bonded samples, we found that an exotherm peak between 600 and 700 K for all the bonded samples, and an endothermic peak between 400 and 450 K for Cu-bonded samples only. The exotherm peak has been explained to be the onset temperature of the nitrogen absorption into $\text{Sm}_2\text{Fe}_{17}$.¹⁶ It is not clear at present about the corresponding changes correlated to the exothermic peak for all the Cu-bonded samples. However, it seems to relate the slope increase of the resistivity near 450 K with increasing temperature for all the Cu-bonded samples as shown in Fig. 4.

In general, the temperature dependence of the magnetization at 8 kG for all the (Zn/Cu)-bonded $\text{Sm}_2\text{Fe}_{17}\text{M}_x\text{N}_y$ samples behaves quite similarly to the curve d in Fig. 2 with T_c around 780 K. However, this two bonded groups show completely different behaviors for the temperature dependence of ρ with increasing and decreasing temperatures between 4 and 1000 K. The typical behaviors are that (1) for all Zn-bonded samples, the heating run ρ increases abruptly roughly above 600 K, and the value of ρ for the cooling run is always higher than that of heating run; (2) for all Cu-bonded samples, the heating run ρ decreases abruptly

roughly above 600 K, and the value of cooling run ρ is always lower than that of the heating run. In Fig. 4, as an example, curve a shows the ρ of Zn-bonded $\text{Sm}_2\text{Fe}_{17}\text{N}_{2.0}$ samples, and curve b shows the ρ of Cu-bonded $\text{Sm}_2\text{Fe}_{17}\text{C}_{0.25}\text{N}_{2.6}$ samples. The sequence of the heating and cooling runs is indicated by arrows in the figures.

From the EPMA investigations of the SEM micrographs of the (Zn/Cu)-bonded samples, we found that in the Cu-bonded samples after the high temperature measurements the Fe-rich and Cu-rich areas are completely distinguishable. As shown in Fig. 5, (a) is the SEM micrograph of the Cu-bonded $\text{Sm}_2\text{Fe}_{17}\text{C}_{0.25}\text{N}_{2.6}$ sample after the electrical resistivity measurements; (b) is the EPMA picture of Fig. 5(a) for the Fe-rich distribution (white regions); and (c) is the EPMA picture of Fig. 5(a) for the Cu-rich distribution (white regions). However, it is difficult to separate the Fe-rich and Zn-rich regions in Zn-bonded samples. As an example, Fig. 5(d) is the SEM micrograph of the Zn-bonded $\text{Sm}_2\text{Fe}_{17}\text{N}_{2.0}$ sample after the electrical resistivity measurements; (e) is the EPMA picture of Fig. 5(d) for the Fe-rich distribution (white regions); and (f) is the EPMA picture of Fig. 5(d) for the Zn-rich distribution (white regions).

Finally, for Cu-bonded samples, the main reason for the decrease of ρ after high temperature runs is due to the segregation of Cu and precipitation of Fe, so that the scattering center for conducting electrons is reduced; however, the variation of the magnetization and coercivity is small after the Cu bonding. For Zn-bonded samples, the main reason for the increase of ρ after high temperature runs is due to the chemical reactions between Zn and $\text{Sm}_2\text{Fe}_{17}\text{M}_x\text{N}_y$; and under proper annealing, the variation of magnetization is small, but the coercivity can be enhanced up to 14 kOe.

This work was supported by the National Science Council of the ROC through Grant No. NSC82-0212-M-194-016.

¹ J. M. D. Coey and H. Sun, *J. Magn. Magn. Mater.* **87**, L251 (1990).

² M. Katter, J. Wecker, L. Schultz, and R. Grossinger, *J. Magn. Magn. Mater.* **92**, L14 (1990).

³ A. Fukuno, C. Ishizaka, and T. Yoneyama, *J. Appl. Phys.* **70**, 6021 (1991).

⁴ J. Ding, P. G. McCormick, and R. Street, *Appl. Phys. Lett.* **61**, 2721 (1992).

⁵ J. P. Woods, A. S. Fernando, S. S. Jaswal, B. M. Patterson, D. Welipitiya, and D. J. Sellmyer, *J. Appl. Phys.* **73**, 6913 (1993).

⁶ K. I. Machida, Y. Nakatani, A. Onodera, and G. Y. Adachi, *Jpn. J. Appl. Phys.* **32**, L837 (1993).

⁷ R. Skomski and J. M. D. Coey, *J. Appl. Phys.* **73**, 7602 (1993).

⁸ G. J. Long, O. A. Pringle, F. Grandjean, W. B. Yelon, and K. H. J. Buschow, *J. Appl. Phys.* **74**, 504 (1993).

⁹ R. Skomski, K.-H. Müller, P. A. P. Wendhausen, and J. M. D. Coey, *J. Appl. Phys.* **73**, 6047 (1993).

¹⁰ Y. Otani, D. P. F. Hurley, H. Sun, and J. M. D. Coey, *J. Appl. Phys.* **69**, 5584 (1991).

¹¹ M. Q. Huang, L. Y. Zhang, B. M. Ma, Y. Zheng, J. M. Elbicki, W. E. Wallace, and S. G. Sankar, *J. Appl. Phys.* **70**, 6027 (1991).

¹² Y. Otani, A. Monkarika, H. Sun, J. M. D. Coey, E. Devlin, and I. R. Harris, *J. Appl. Phys.* **69**, 6735 (1991).

¹³ P. A. P. Wendhausen, A. Handstein, P. Nothnagel, D. Eckert, and K.-H. Müller, *Phys. Status Solidi A* **127**, K121 (1991).

¹⁴ W. Rodewald, B. Wall, M. Katter, M. Velicescu, and P. Schrey, *J. Appl. Phys.* **73**, 5899 (1993).

¹⁵ P. A. P. Wendhausen, D. Eckert, A. Handstein, K.-H. Müller, G. Leitner, and R. Skomski, *J. Appl. Phys.* **73**, 6044 (1993).

¹⁶ X. C. Kou, R. Grossinger, M. Katter, J. Wecker, L. Schultz, T. H. Jacobs, and K. H. J. Buschow, *J. Appl. Phys.* **70**, 2272 (1991).

Structure and magnetic properties of interstitial compounds of the series $\text{Dy}_2\text{Fe}_{17-x}\text{Al}_x\text{Z}_y$ ($\text{Z}=\text{N}$ or H)

J. P. Liu, D. C. Zeng, N. Tang, A. J. M. Winkelman, and F. R. de Boer
Van der Waals-Zeeman Laboratory, University of Amsterdam, 1018 XE Amsterdam, The Netherlands

K. H. J. Buschow
Philips Research Laboratories, 5600 JA Eindhoven, The Netherlands

The interstitial nitrides $\text{Dy}_2\text{Fe}_{17-x}\text{Al}_x\text{N}_y$ with $0 \leq x \leq 6$ and $0 \leq y \leq 2.7$ and hydrides $\text{Dy}_2\text{Fe}_{17-x}\text{Al}_x\text{H}_y$ with $0 \leq x \leq 4$ and $0 \leq y \leq 4.2$ have been synthesized by means of melting and by means of the gas-phase-interaction method. The effect of the interstitial atoms on the structure and the lattice parameters has been investigated. For the nitrogenated compounds, it is found that nitrogen can be introduced until a maximum volume expansion is reached. The magnetic properties of the interstitial compounds, including high-field magnetization at 4.2 K and Curie temperatures, have been measured. The Dy-Fe exchange interaction is found to decrease upon introduction of the interstitial atoms.

I. INTRODUCTION

Since the discovery by Coey and Sun¹ that the introduction of interstitial nitrogen greatly improves the magnetic properties of Y_2Fe_{17} and $\text{Sm}_2\text{Fe}_{17}$, much work has been done to investigate the interstitial nitrides. It has been established that nitrogenation enhances the Curie temperatures and the saturation magnetization of R_2Fe_{17} ($\text{R}=\text{rare earth}$) compounds. A similar effect has been observed earlier for the introduction of interstitial hydrogen in R_2Fe_{17} compounds (see, for instance, Ref. 2). However, the influence of the interstitial atoms on the R - T ($T=\text{transition metal}$) exchange interaction in nitrides and hydrides has not been studied in very much detail. In the present work, we have investigated the effect of interstitial nitrogen and hydrogen on the Dy-Fe coupling in $\text{Dy}_2\text{Fe}_{17-x}\text{Al}_x$ compounds.

II. EXPERIMENT

The parent compounds of the series $\text{Dy}_2\text{Fe}_{17-x}\text{Al}_x$ with $x=0.0, 1.0, 2.0, 3.0, 4.0, 5.0, 6.0$, and 7.0 were prepared by arc melting the starting materials with purities higher than or equal to 99.9%. After the melting, the ingots were annealed at 1000°C for three weeks. The homogenized ingots were checked by x-ray diffraction and found to be single phase.

The nitrogenation was carried out on fine powder particles (with diameters $\leq 40 \mu\text{m}$) in a furnace at about 500°C with flowing nitrogen gas. The time needed to reach sufficient nitrogenation varies from compound to compound. It was found that with increasing aluminum content in the parent series, the nitrogenation becomes increasingly difficult. Hydrogenation was performed by heating powdered samples for a few hours at about 250°C in flowing hydrogen gas. It was found that the hydrogenation can only be carried out for compounds with $x < 5$. The nitrogen and hydrogen contents were determined by weighing the samples. A detailed description of the synthesis of the interstitial nitrides and hydrides will be given in Ref. 3.

All nitrogenated and hydrogenated compounds have been checked by x-ray diffraction (with $\text{Cu K}\alpha$ radiation) to confirm the formation of the interstitial phases, to determine

the lattice constants, and to detect the presence of possible impurity phases.

High-field magnetization measurements up to 35 T at 4.2 K have been carried out in the Amsterdam high-field installation.⁴ The samples consisted of powder particles that were free to rotate in the sample holder. The Curie temperatures were measured by means of an automatic magnetization-temperature recorder based on the Faraday method. The magnetic field applied in the measurement was 0.14 T.

III. RESULTS AND DISCUSSION

A. Expansion of the unit cells upon the introduction of interstitial nitrogen and hydrogen

Figure 1 shows as an example the diffraction patterns of the $\text{Dy}_2\text{Fe}_{17-x}\text{Al}_x$ compound with $x=1$ and its nitride and

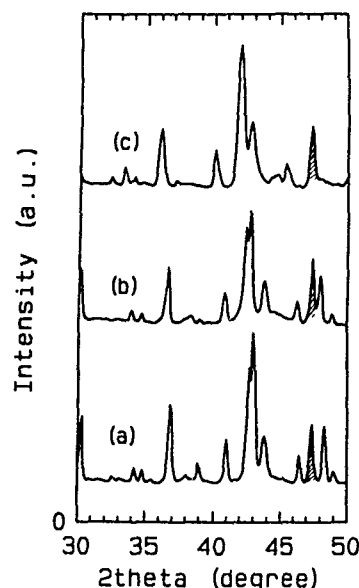


FIG. 1. X-ray diffraction patterns of the compound (a) $\text{Dy}_2\text{Fe}_{16}\text{Al}$ and its interstitial (b) hydride and (c) nitride. The dashed peaks are from the Si standard for calibration.

TABLE I. Structural data of $\text{Dy}_2\text{Fe}_{17-x}\text{Al}_x\text{Z}_y$ compounds with $x=0, 1, 2, 3, 4, 5, 6$ and 7 , and their interstitial hydrides and nitrides. The lattice parameters (a and c) are given in Å. The expansion $\Delta V/V$ is given in %.

x	Parent compounds				Z=H			Z=N			
	Type	a	c		a	c	y	a	c	y	$\Delta V/V$
0	hex.	8.476	8.312		8.552	8.408	4.0	8.648	8.473	2.7	6.1
1	hex.	8.494	8.316		8.554	8.412	3.2	8.645	8.490	2.2	5.8
2	hex.	8.538	8.344		8.575	8.438	2.6	8.652	8.472	1.7	4.3
3	rh.	8.566	12.615		8.610	12.673	2.5	8.670	12.660	1.2	2.8
4	rh.	8.609	12.564		8.615	12.674	1.8 ^a	8.665	12.682	1.3	2.3
5	rh.	8.632	12.592		8.632	12.592	0	8.668	12.949	0.7	1.7
6	rh.	8.667	12.616		8.667	12.616	0	8.659	12.716	0.3 ^a	0.8 ^a
7	rh.	8.709	12.636		8.709	12.636	0	8.709	12.636	0	0

^aThese data should be considered as less accurate.

hydride. It can be clearly seen that the unit-cell volume expands upon nitrogenation and hydrogenation, the expansion caused by the nitrogenation being the largest. Similar results have been obtained for the nitrides up to $x=6$ and for the hydrides up to $x=4$. In Table I, the structural data of the compounds are listed. In the calculation of the unit-cell volumes, the volumes of the compounds crystallizing in hexagonal structure have been multiplied by 1.5 to compare them with the unit-cell volumes of the compounds with rhombohedral structure.

It is interesting to note that the amount of interstitial atoms that can be introduced into the compounds decreases with increasing aluminum concentration. Above $x=6$ nitrogenation was not found to be possible and above $x=4$ hydrogenation was not possible, even after treatments for a very long time. All nitrogenated compounds have almost the same lattice parameters, appearing to reach a maximum expansion. The same phenomenon has previously been observed for other series.⁵ In the case of the hydrides, this "maximum expansion" phenomenon was not observed.

As is usually observed, α -Fe precipitates in the samples during the nitrogenation, which contributes to the magnetization of the compounds. A method to correct for this impurity contribution is presented elsewhere.⁶

B. Magnetic properties of the interstitial nitrides and hydrides

The Curie temperatures of the compounds $\text{Dy}_2\text{Fe}_{17-x}\text{Al}_x$ and $\text{Dy}_2\text{Fe}_{17-x}\text{Al}_x\text{N}_y$ are listed in Table II. In the range $x \leq 3$, substitution of Fe by Al causes an increase in the Curie temperature, which has been discussed in Refs. 7 and 8. The expansion of the unit cell caused by the introduction of nitrogen is accompanied by an increase of the Curie temperature. The amount of nitrogen that can be introduced, however, decreases with increasing Al concentration, which is accompanied by a reduced increase of the Curie temperature.

In R - T compounds, the magnetic properties change from ferromagnetic to ferrimagnetic when R proceeds from the light rare earths to the heavy rare earths.⁹ If the applied external field is sufficiently high, the ferrimagnetic spin structure is affected, the magnetic moments start to bend, and the magnetization increases. A simple model that describes the magnetization process of (single-crystalline) powder par-

ticles that are free to rotate in the applied field has been presented by Verhoef *et al.*¹⁰ According to this model, the intersublattice molecular-field coefficient n_{RT} can be derived directly from the magnetic susceptibility in the region where the departure from the ferrimagnetic structure occurs:

$$n_{RT} = B/M. \quad (1)$$

The exchange constant J_{RT} (the exchange parameter appearing in a nearest-neighbor Heisenberg-type Hamiltonian) can be obtained by means of the equation

$$J_{RT} = \frac{g_R \mu_B^2 N_T}{(g_R - 1) Z_{RT}} n_{RT}, \quad (2)$$

where g_R is the Landé factor of the R ion, N_T is the number of T atoms per formula unit, and the Z_{RT} is the number of nearest T -atom neighbors of an R atom.

As examples, in Fig. 2 the free-powder magnetization curves are presented for the hydride and the nitride with $x=4$. The J_{RT} values that could be derived for the investigated nitrides and hydrides are collected in Table II, together with the J_{RT} values for the parent compounds taken from Ref. 7. It can be seen clearly from the table that the introduction of hydrogen or nitrogen leads to a decrease of $|J_{\text{DyFe}}|$, which is the strongest for the nitrides. This decrease of the R - T coupling upon introduction of interstitial atoms has also been observed in other series.¹¹ The decrease may be inter-

TABLE II. Curie temperatures (T_C) and the intersublattice-coupling constants (J_{DyFe}/k), both expressed in K, for the $\text{Dy-Fe}_{17-x}\text{Al}_x$ compounds and the corresponding interstitial hydrides and nitrides. The T_C values of the parent compounds have been taken from Ref. 7.

x	Parent compounds		Z = H	Z = N	
	T_C	$-J_{\text{DyFe}}/k$	$-J_{\text{DyFe}}/k$	$-J_{\text{DyFe}}/k$	T_C
0	371	... ^a	699
1	404	671
2	436	592
3	451	10.6 ^b	9.8	8.6	525
4	436	9.04	8.5	7.5	457
5	395	8.77	...	7.3 ^b	423 ^b
6	319	9.25
7	237	10.1

^aNo values available.

^bData should be considered as less accurate.

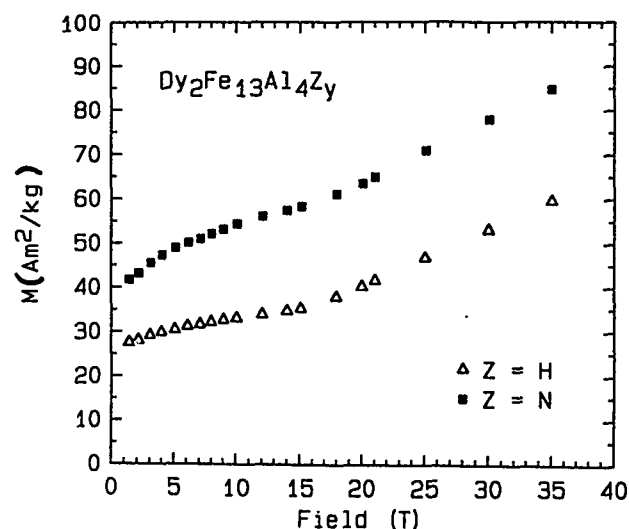


FIG. 2. Magnetic isotherms at 4.2 K of the interstitial hydride $\text{Dy}_2\text{Fe}_{13}\text{Al}_4\text{H}_{1.8}$ and nitride $\text{Dy}_2\text{Fe}_{13}\text{Al}_4\text{N}_{1.3}$.

preted to result from the increase of the unit-cell volume and the associated increase of the spatial separation of the ions. Since the $3d$ - $4f$ interaction which is mediated by the hybridization of the $3d$ - and $5d$ -electron states is distance depen-

dent, a decrease of $|J_{RT}|$ upon introduction of interstitial atoms seems natural.

ACKNOWLEDGMENTS

This work has been partially carried out within the scientific exchange program between China and the Netherlands. The authors thank Professor P. F. de Châtel for fruitful discussions.

- ¹J. M. D. Coey and H. Sun, *J. Magn. Magn. Mater.* **87**, L251 (1990).
- ²Wang Xiang-zhong, K. Donnelly, J. M. D. Coey, B. Chevalier, J. Etourneau, and T. Berlureau, *J. Mater. Sci.* **23**, 329 (1988).
- ³J. P. Liu, D. C. Zeng, A. J. M. Winkelman, F. R. de Boer, and K. H. J. Buschow (unpublished).
- ⁴R. Gersdorf, F. R. de Boer, J. C. Wolfrat, F. A. Muller, and L. W. Roeland, in *High Field Magnetism*, edited by M. Date (North-Holland, Amsterdam, 1983), p. 277.
- ⁵J. P. Liu, Ph.D. thesis, University of Amsterdam, 1994.
- ⁶J. P. Liu, F. R. de Boer, P. F. de Châtel, and K. H. J. Buschow (unpublished).
- ⁷T. H. Jacobs, K. H. J. Buschow, G. F. Zhou, and F. R. de Boer, *Physica B* **179**, 177 (1992).
- ⁸K. Itoh, N. Ohkubo, K. Kanematsu, and K-I. Kobayashi, *J. Alloys Compounds* **193**, 239 (1993).
- ⁹I. A. Campbell, *J. Phys. F: Met. Phys.* **39**, 5972 (1968).
- ¹⁰R. Verhoef, R. J. Radwanski, and J. J. M. Franse, *J. Magn. Magn. Mater.* **89**, 176 (1990).
- ¹¹J. P. Liu, F. R. de Boer, P. F. de Châtel, R. Coehoorn, and K. H. J. Buschow, *J. Magn. Magn. Mater.* (in press).

High-coercivity Sm-Fe-Ga-C compounds with $\text{Th}_2\text{Zn}_{17}$ structure by melt spinning

Lin-Shu Kong, Bao-gen Shen, Fang-wei Wang, Lei Cao, Hui-qun Guo, and Tai-shan Ning
State Key Laboratory of Magnetism, Institute of Physics, Chinese Academy of Sciences, P. O. Box 603,
Beijing 100080, China

The magnetic hardening of the $\text{Sm}_2\text{Fe}_{14}\text{Ga}_3\text{C}_x$ was investigated by melt spinning. It was found that high coercivities can be achieved by direct quenching at the optimum substrate velocity. The coercivities of 12.6–15.0 kOe were obtained in $\text{Sm}_2\text{Fe}_{14}\text{Ga}_3\text{C}_x$ ribbons with carbon contents x from 1.0 to 2.5. The as-quenched $\text{Sm}_2\text{Fe}_{14}\text{Ga}_3\text{C}_{1.5}$ ribbons had a coercivity exceeding 13 kOe within a large range of quench rates between 18 and 30 m/s. X-ray diffraction experiments indicate that the ribbons are almost entirely comprised of the $\text{Th}_2\text{Zn}_{17}$ phase. It is concluded that Ga not only stabilizes the hard magnetic phase but also is very effective in raising the coercivity in the $\text{Sm}_2\text{Fe}_{14}\text{Ga}_3\text{C}_x$ melt-spun ribbons.

I. INTRODUCTION

The rare-earth-iron intermetallic compounds based on the 2:17 structure have been attracting much attention as potential candidates for permanent magnet materials. It has been shown that $\text{Sm}_2\text{Fe}_{17}\text{N}_x$ and $\text{Sm}_2\text{Fe}_{17}\text{C}_x$ prepared by solid-gas reaction have excellent intrinsic magnetic properties.^{1,2} Unfortunately these nitrides and carbides have a poor thermal stability and degrade when heating to temperatures above about 600 °C, which may limit their widespread applications. Our early work showed that the heavy rare-earth compounds $\text{R}_2\text{Fe}_{17}\text{C}_x$ with high C content (x close to 3.0) could be obtained by melt spinning, and that they are stable at high temperatures (above 1000 °C), while the light rare-earth compounds $\text{R}_2\text{Fe}_{17}\text{C}_x$ ($x > 1.5$) are still hard to stabilize.^{3–5} The magnetic hardening of $\text{Sm}_2\text{Fe}_{17}\text{C}_x$ was studied by melt-spinning techniques a few years ago, and the coercivity of 4.6 kOe for $\text{Sm}_2\text{Fe}_{17}\text{C}_{1.5}$ alloys was reported.⁶

Recently we have found that the $\text{Th}_2\text{Zn}_{17}$ phase of Sm-Fe-C alloys with high C contents can be formed by addition of Ga.^{7,8} In this paper we report the magnetic hardening of Sm-Fe-Ga-C alloys by melt spinning. A high coercivity of up to 15 kOe was achieved by direct quenching at the optimum substrate velocity.

II. EXPERIMENT

Fe and C were first melted together in an induction furnace to form Fe-C alloys which have a lower melting temperature. Then Fe, Sm, Ga, and Fe-C alloys were melted by arc melting in an argon atmosphere of high purity. An excess of 4%–10% Sm was added to compensate for the vaporization of Sm during the melting and melt-spinning steps. For homogeneity the samples were remelted for at least four times. The ingots were melt spun in a high-purity argon atmosphere using a copper quench wheel rotating at a surface velocity v_s between 0 and 47 m/s. The ribbons were about 1 mm wide and 20–30 μm thick. The phase composition and structure were investigated with a Co K_α x-ray diffractometer. The demagnetization curves were measured by an extracting sample magnetometer with fields up to 70 kOe.

III. RESULTS AND DISCUSSION

X-ray diffraction experiments indicate that $\text{Sm}_2\text{Fe}_{14}\text{Ga}_3\text{C}_x$ ($x = 1.0, 1.5, 2.0$, and 2.5) alloys are single phase with rhombohedral $\text{Th}_2\text{Zn}_{17}$ -type structure. As an example, the powder x-ray diffraction pattern of $\text{Sm}_2\text{Fe}_{14}\text{Ga}_3\text{C}_{1.5}$ ingot is shown in Fig. 1(a). In order to obtain a high coercivity, we prepared ribbons at various quench rates. Figure 2 shows the demagnetization curves for as-quenched $\text{Sm}_2\text{Fe}_{14}\text{Ga}_3\text{C}_{1.5}$ samples by direct melt spinning at $v_s = 18$ and 30 m/s, respectively. The ribbons have an intrinsic coercivity $H_{ci} = 13.1$ kOe and remanence $B_r = 4.64$ kG for $v_s = 18$ m/s, and $H_{ci} = 15.0$ kOe and $B_r = 4.57$ kG for $v_s = 30$ m/s. The coercivities of $\text{Sm}_2\text{Fe}_{14}\text{Ga}_3\text{C}_{1.5}$ ribbons as a function of quench rates are plotted in Fig. 3. It can be seen that

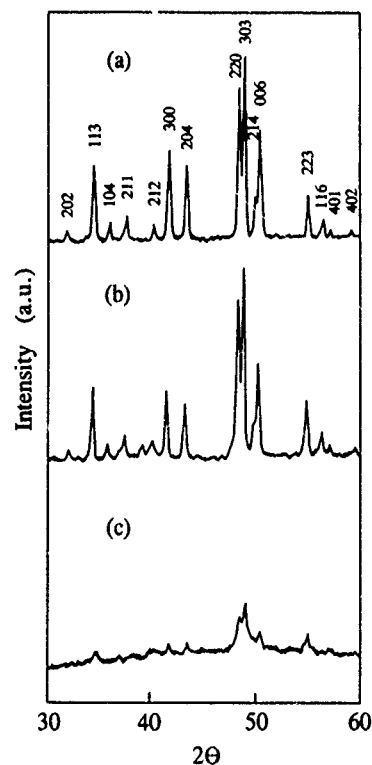


FIG. 1. X-ray diffraction patterns for $\text{Sm}_2\text{Fe}_{14}\text{Ga}_3\text{C}_{1.5}$ ingot (a), ribbons for $v_s = 30$ m/s (b), and $v_s = 40$ m/s (c).

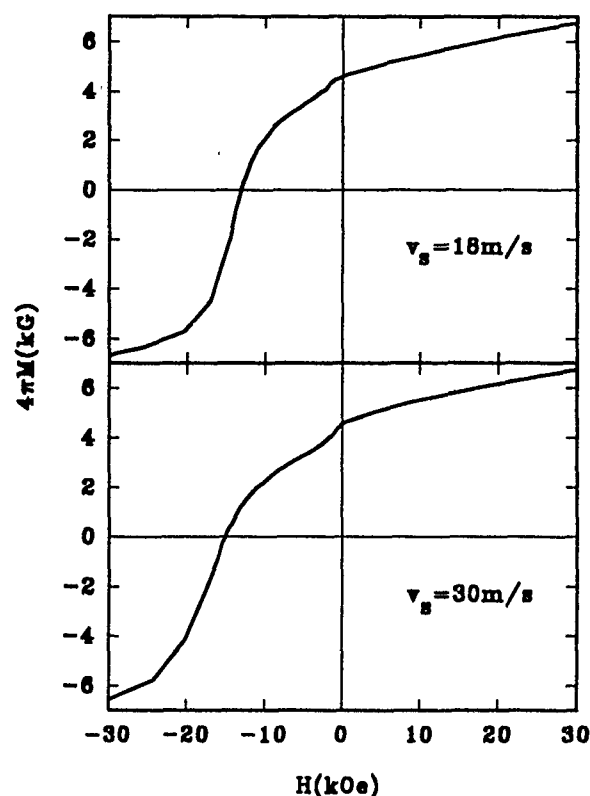


FIG. 2. Demagnetization curves for $\text{Sm}_2\text{Fe}_{14}\text{Ga}_3\text{C}_{1.5}$ ribbons.

coercivities exceed 13 kOe within a large range of quench rates between 18 and 30 m/s and are reduced when the quench rate is either slower or faster than optimum, falling to less than 100 Oe at 40 m/s. The optimum quench rate in $\text{Sm}_2\text{Fe}_{14}\text{Ga}_3\text{C}_{1.5}$ is higher than that of $\text{Nd}_2\text{Fe}_{14}\text{B}$ (near 19 m/s).⁹

The x-ray powder diffraction patterns of the as-quenched $\text{Sm}_2\text{Fe}_{14}\text{Ga}_3\text{C}$ ribbons are also included in Fig. 1. All diffraction peaks in the pattern for $v_s = 30$ m/s can be indexed to the $\text{Th}_2\text{Zn}_{17}$ -type structure, indicating that the ribbons are almost entirely comprised of hard magnetic phase.

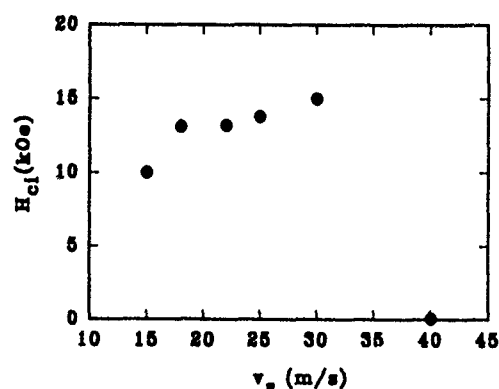


FIG. 3. Intrinsic coercivities H_{ci} as a function of quench rates v_s for $\text{Sm}_2\text{Fe}_{14}\text{Ga}_3\text{C}_{1.5}$. The data for $v_s = 40$ m/s were measured in a field of up to 8 kOe.

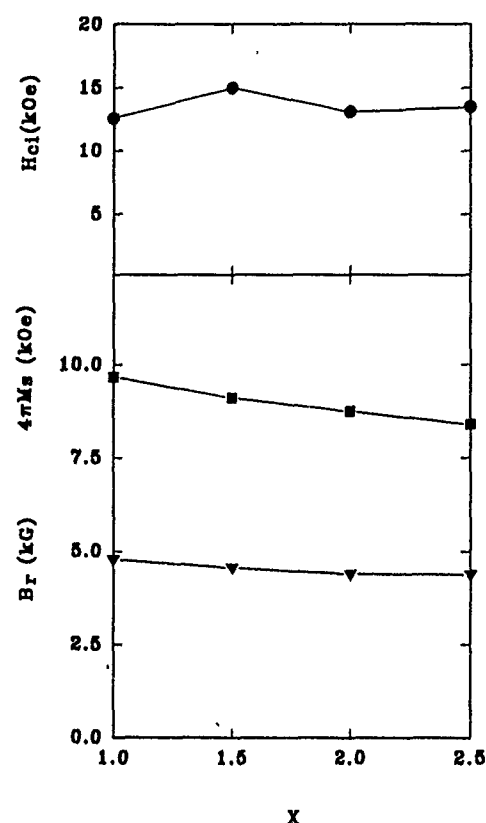


FIG. 4. Intrinsic coercivities H_{ci} , remanences B_r , and saturation magnetizations $4\pi M_s$, as a function of carbon content x for $\text{Sm}_2\text{Fe}_{14}\text{Ga}_3\text{C}_x$.

Early studies of the $\text{Sm}_2\text{Fe}_{17}\text{C}_x$ alloys showed the reasonable strength of magnetic hardening could be attained only for high-carbon compounds.⁶ However, the relatively high carbon concentration results in the formation of α -Fe and other soft magnetic phases, which prevent obtaining a higher coercivity. Because the magnetizations in the grains comprised of these soft phases are easily reversed under an external small opposite magnetic field, they induce then a cascade of demagnetization processes within adjacent grains.

The situation changes in $\text{Sm}_2\text{Fe}_{14}\text{Ga}_3\text{C}_{1.5}$. The addition of Ga helps stabilize the $\text{Th}_2\text{Zn}_{17}$ structure and reduces the soft magnetic impurity phases such as α -Fe. Thus optimum coercivities above 13 kOe, which are substantially higher than the corresponding values of Ga-free compounds $\text{Sm}_2\text{Fe}_{17}\text{C}_x$, are easily obtained in $\text{Sm}_2\text{Fe}_{14}\text{Ga}_3\text{C}_{1.5}$.

As seen in Fig. 1, the $\text{Sm}_2\text{Fe}_{14}\text{Ga}_3\text{C}_{1.5}$ ribbons for $v_s = 30$ m/s are still crystalline while an amorphous phase starts to form and only a small amount of the $\text{Th}_2\text{Zn}_{17}$ phase remains in the ribbons for $v_s = 40$ m/s. The line broadening of the diffraction peaks corresponding to the $\text{Th}_2\text{Zn}_{17}$ phase is observed in Fig. 1(c), revealing a fine-grained microstructure. The formation of the amorphous phase and the very fine grains is consistent with the substantially low coercivity (Fig. 3).

Figure 4 shows the dependences of the intrinsic coercivity H_{ci} , saturation magnetization $4\pi M_s$, and remanence B_r on the carbon content x for $\text{Sm}_2\text{Fe}_{14}\text{Ga}_3\text{C}_x$. The remanences decrease slightly with increasing carbon content x . As expected in the isotropic uniaxial materials, B_r is near half of

the saturation magnetization $4\pi M_s$. The coercivity does not change much with the carbon content x . This is not surprising. It has been shown that the substitution of Ga for Fe in $\text{Sm}_2\text{Fe}_{14}\text{Ga}_3\text{C}_x$ with lower carbon contents results in a larger increase of uniaxial anisotropy than for higher-carbon compounds.⁷ $\text{Sm}_2\text{Fe}_{14}\text{Ga}_3\text{C}_{1.0}$ exhibits an anisotropy field of 85 kOe close to that of $\text{Sm}_2\text{Fe}_{14}\text{Ga}_3\text{C}_{2.5}$ (90 kOe), which is responsible for the high coercivity.

The maximum coercivity of 15 kOe in $\text{Sm}_2\text{Fe}_{14}\text{Ga}_3\text{C}_x$ is comparable to that of $\text{Nd}_2\text{Fe}_{14}\text{B}$ (also about 15 kOe) initially reported by Croat *et al.*⁹ and higher than that of $\text{Sm}(\text{FeTiV})_{12}$ (about 9 kOe).¹⁰ The remanence of $\text{Sm}_2\text{Fe}_{14}\text{Ga}_3\text{C}_x$ is somewhat low. The reason for this is that the replacement of Fe by Ga, which is nonmagnetic, leads to a considerable reduction of saturation magnetization.

In summary, it has been found that the $\text{Sm}_2\text{Fe}_{14}\text{Ga}_3\text{C}_x$ compounds can be magnetically hardened by direct quenching. Coercivities in excess of 13 kOe for $\text{Sm}_2\text{Fe}_{14}\text{Ga}_3\text{C}_{1.5}$ are achieved within a wide range of quenching rate between 18 and 30 m/s. $\text{Sm}_2\text{Fe}_{14}\text{Ga}_3\text{C}_x$ with the C content x from 1.0 to 2.5 has a similar hard magnetic property. Further effects to improve the remanence are in progress by two ways: one is the minimization of the Ga content, and the other is the stabilization of the 2:17 phase by other elemental substitution, such as Si and Al.

ACKNOWLEDGMENTS

We are grateful to M. Hu for the assistance in the x-ray diffraction experiments. This work was supported by the National Natural Science Foundation of China and the State's Sciences and Technology Commission.

- ¹J. M. D. Coey and H. Sun, *J. Magn. Magn. Mater.* **87**, L251 (1990).
- ²J. M. D. Coey, H. Sun, Y. Otani, and D. P. F. Hurley, *J. Magn. Magn. Mater.* **98**, 76 (1991).
- ³L.-S. Kong, L. Cao, and B.-G. Shen, *J. Magn. Magn. Mater.* **115**, L137 (1992).
- ⁴B.-G. Shen, L.-S. Kong, and L. Cao, *Solid State Commun.* **83**, 753 (1992).
- ⁵L. Cao, L.-S. Kong and B.-G. Shen, *J. Phys. Condens. Matter* **4**, L515 (1992).
- ⁶J. Ding and M. Rosenberg, *J. Less-Common Metals* **166**, 313 (1990).
- ⁷B.-G. Shen, L.-S. Kong, F.-W. Wang, and L. Cao, *Appl. Phys. Lett.* **63**, 2288 (1993).
- ⁸B.-G. Shen, F.-W. Wang, L.-S. Kong, L. Cao, and H.-Q. Guo, *J. Magn. Magn. Mater.* **127**, L 267 (1993).
- ⁹J. J. Croat, J. F. Herbst, R. W. Lee, and F. E. Pinkerton, *J. Appl. Phys.* **55**, 2078 (1984).
- ¹⁰M. Okada, K. Yamagishi, and M. Homma, *Mater. Trans. JIM* **30**, 374 (1989).

A novel hard magnetic material for sintering permanent magnets

Bao-gen Shen, Fang-wei Wang, Lin-shu Kong, Lei Cao, and Wen-shan Zhan
State Key Laboratory of Magnetism, Institute of Physics, Chinese Academy of Sciences, P.O. Box 603,
Beijing 100080, China

We have discovered that the substitution of Ga or Si for Fe in $\text{Sm}_2\text{Fe}_{17}\text{C}_x$ helps the formation of high-carbon rare-earth iron compounds with 2:17-type structure. We have succeeded in preparing $\text{Sm}_2\text{Fe}_{15}\text{M}_2\text{C}_x$ ($\text{M}=\text{Ga}$, $x=0, 1.0, 2.0$, and 3.0 ; $\text{M}=\text{Si}$, $x=0, 0.5, 1.0$, and 1.5) compounds with $\text{Th}_2\text{Zn}_{17}$ -type structure by arc melting. The carbides are single phase except for $\text{Sm}_2\text{Fe}_{15}\text{Ga}_2\text{C}_{3.0}$, which contains a few percent of α -Fe. The Curie temperature T_C of $\text{Sm}_2\text{Fe}_{15}\text{Si}_2\text{C}_x$ compounds is found to increase from 550 to 590 K, as x increases from 0 to 1.5. For $\text{Sm}_2\text{Fe}_{15}\text{Ga}_2\text{C}_x$, T_C increases with x from 565 K for $x=0$ to 635 K for $x=2.0$, and then decreases with x . Room-temperature saturation magnetization of these carbides is in excess of 100 emu/g and has a small dependence on carbon content. All compounds of $\text{Sm}_2\text{Fe}_{15}\text{M}_2\text{C}_x$ studied in this work except for $\text{Sm}_2\text{Fe}_{15}\text{Si}_2$ exhibit an easy c -axis anisotropy at room temperature and show an anisotropy field of higher than 90 kOe for $x \geq 1.0$. The present work suggests the possibility of producing high-performance 2:17-type sintering permanent magnets.

INTRODUCTION

The intermetallic compounds $\text{Sm}_2\text{Fe}_{17}\text{N}_x$ and $\text{Sm}_2\text{Fe}_{17}\text{C}_x$ with higher nitrogen or carbon concentration were found to have the excellent intrinsic magnetic properties.¹ They are promising candidate for permanent magnets. However, the major drawback of the nitrides or carbides prepared by the gas-solid reaction is their high temperature instability. The aim of our work is to search for highly stable hard magnetic materials based on these nitrides or carbides. Recently, we have discovered that the carbides $\text{R}_2\text{Fe}_{17}\text{C}_x$ with carbon concentration up to $x=3.0$ can be formed by melt spinning.²⁻⁴ The melt-spun $\text{R}_2\text{Fe}_{17}\text{C}_x$ compounds were found to have a good high-temperature stability and retain $\text{Th}_2\text{Zn}_{17}$ -type or $\text{Th}_2\text{Ni}_{17}$ -type structures up to at least 1273 K. However, the carbides prepared by melt spinning are isotropic, while the high remanence and energy product can only be achieved in anisotropic materials. In order to obtain new anisotropic materials for sintering permanent magnets, we have studied the effect of the various elemental substitutions for Fe in the $\text{R}_2\text{Fe}_{17}\text{C}_x$ alloys on their formation, structure, and magnetic properties. It is found that the high-carbon $\text{R}_2\text{Fe}_{17}\text{C}_x$ compounds by the substitution of Ga, Si, Al, etc., for Fe exhibit a high thermal stability, in contrast with the carbides produced by the gas-solid reaction. We have succeeded in preparing single-phase compounds of high-carbon $\text{R}_2\text{Fe}_m\text{M}_{17-x}\text{C}_x$ ($\text{R}=\text{Y}$, Nd, Sm, Gd, Tb, Dy, Ho, Er, and Tm; $\text{M}=\text{Ga}$, Si, and Al) with $\text{Th}_2\text{Zn}_{17}$ -type or $\text{Th}_2\text{Ni}_{17}$ -type structures by arc melting.⁵⁻⁷ It was found that the arc-melted $\text{Sm}_2\text{Fe}_{14}\text{Ga}_3\text{C}_x$ compounds with $x \geq 1.5$ have a Curie temperature of higher than 600 K, and exhibit an easy c -axis anisotropy at room temperature and have an anisotropy field of higher than 90 kOe.¹ In this paper, the formation, structure, and magnetic properties of $\text{Sm}_2\text{Fe}_{15}\text{M}_2\text{C}_x$ ($\text{M}=\text{Ga}$, $x=0-3.0$; $\text{M}=\text{Si}$, $x=0-1.5$) compounds prepared by arc melting are reported.

EXPERIMENT

Iron and carbon were first arc melted into Fe-C alloys, and then Fe, Ga, Si, Sm, and Fe-C were melted by arc melting under high purified argon atmosphere into homo-

neous buttons with the compositions $\text{Sm}_2\text{Fe}_{15}\text{Ga}_2\text{C}_x$ ($x=0, 1.0, 2.0$, and 3.0) and $\text{Sm}_2\text{Fe}_{15}\text{Si}_2\text{C}_x$ ($x=0, 0.5, 1.0$, and 1.5). Elements used were at least 99.9% pure. An excess of 4.5% Sm was added to compensate the mass loss due to the evaporation of Sm during melting. The arc-melted ingots of $\text{Sm}_2\text{Fe}_{15}\text{Ga}_2\text{C}_x$ were annealed in argon atmosphere at 1450 K for 24-66 h. X-ray diffraction measurements on powder samples were performed using $\text{Co K}\alpha$ radiation to determine the crystallographic structure. The Curie temperatures were determined from the temperature dependence of the magnetization measured by a vibrating sample magnetometer or a magnetic balance in a magnetic field of 1 kOe. The saturation magnetizations were measured by an extracting sample magnetometer in a field of 70 kOe. The aligned samples for anisotropy field measurements were prepared by mixing the powder with epoxy resin and then aligning in a magnetic field of 20 kOe. The room-temperature anisotropy field was determined from magnetization curves measured along and perpendicular to the orientation direction by using the extracting sample magnetometer with a magnetic field of up to 70 kOe.

RESULTS AND DISCUSSION

X-ray diffraction measurements indicate that the $\text{Sm}_2\text{Fe}_{17}\text{C}_x$ alloys with higher carbon concentration of $x > 1.0$ have a multiphase structure with a predominant α -Fe phase. The arc-melted $\text{Sm}_2\text{Fe}_{15}\text{Ga}_2\text{C}_x$ ($0 \leq x \leq 3.0$) ingots exhibit a two-phase structure with the 2:17 type as the major phase coexisting with α -Fe. When these carbides were annealed at 1450 K for 24-66 h, they formed single-phase compounds of 2:17-type structure except for $\text{Sm}_2\text{Fe}_{15}\text{Ga}_2\text{C}_{3.0}$, which contains a few percent of α -Fe as a second phase. Figure 1 shows the x-ray diffraction patterns of the annealed $\text{Sm}_2\text{Fe}_{15}\text{Ga}_2\text{C}_x$ compounds. For $\text{Sm}_2\text{Fe}_{15}\text{Si}_2\text{C}_x$, when the carbon concentration x is lower than 1.5, the arc-melted samples are single phase with 2:17-type structure. When $x > 1.5$, a multiphase structure of the samples are shown. In previous study it has been shown that the $\text{Sm}_2\text{Fe}_{17}\text{C}_x$ compounds with high carbon concentration

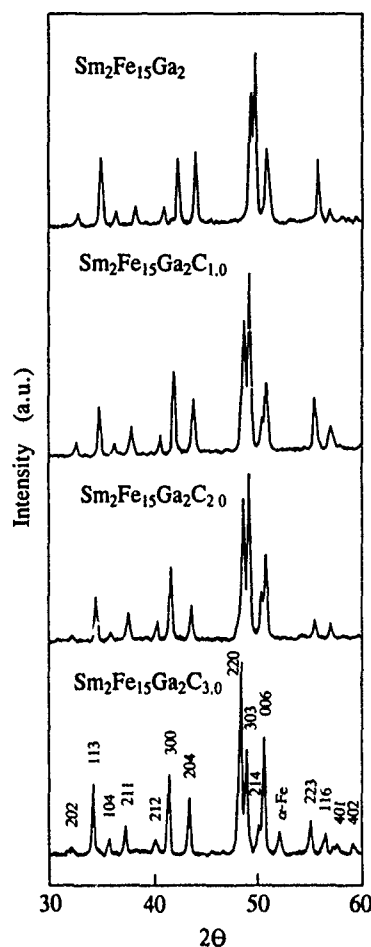


FIG. 1. X-ray diffraction patterns of $\text{Sm}_2\text{Fe}_{15}\text{Ga}_2\text{C}_x$ compounds with $x=0$, 1.0, 2.0, and 3.0.

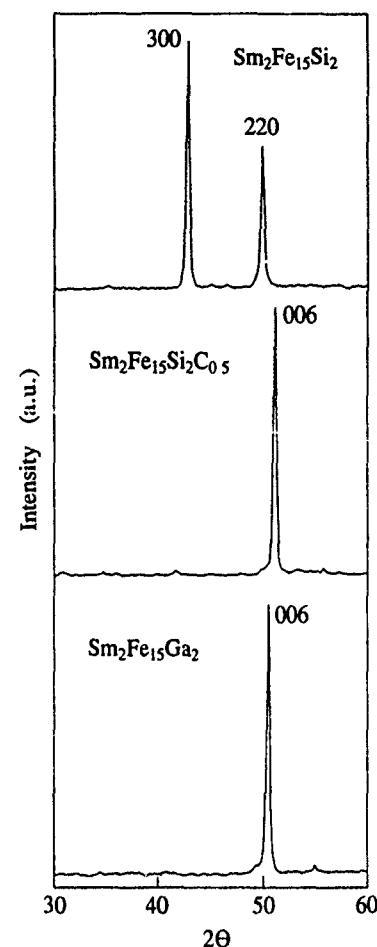


FIG. 2. X-ray diffraction patterns of magnetically aligned $\text{Sm}_2\text{Fe}_{15}\text{Si}_2$, $\text{Sm}_2\text{Fe}_{15}\text{Si}_2\text{C}_{0.5}$, and $\text{Sm}_2\text{Fe}_{15}\text{Ga}_2$ powder samples.

can be prepared by the gas-solid reaction⁸ and rapid quenching²⁻⁴ and cannot be formed by arc melting. The present studies have found that the substitution of Ga or Si for Fe has a significant effect on the stability of the crystal structure of high-carbon $\text{Sm}_2\text{Fe}_{17}\text{C}_x$ with 2:17-type structure. It is obvious that the substitution of Ga, Si, etc. for Fe in $\text{R}_2\text{Fe}_{17}\text{C}_x$ with high carbon concentration, like the substitution of Ti, V, Mo, etc., for Fe in RFe_{12} , plays an important role in the structural stability of rare-earth iron intermetallic compounds.

TABLE I. Structure and magnetic data for $\text{Sm}_2\text{Fe}_{15}\text{M}_2\text{C}_x$ ($\text{M}=\text{Ga}$ and Si).

Compound	a (Å)	c (Å)	v (Å ³)	T_C (K)	M_s (emu/g)	H_A (kOe)	Anisotropy
$\text{Sm}_2\text{Fe}_{15}\text{Ga}_2$	8.648	12.515	810.6	565			c axis
$\text{Sm}_2\text{Fe}_{15}\text{Ga}_2\text{C}_{1.0}$	8.695	12.565	822.7	619	106.0	>90	c axis
$\text{Sm}_2\text{Fe}_{15}\text{Ga}_2\text{C}_{2.0}$	8.724	12.586	829.4	635	102.3	>90	c axis
$\text{Sm}_2\text{Fe}_{15}\text{Ga}_2\text{C}_{3.0}$	8.754	12.599	836.1	622			c axis
$\text{Sm}_2\text{Fe}_{15}\text{Si}_2$	8.530	12.423	782.8	550			plane
$\text{Sm}_2\text{Fe}_{15}\text{Si}_2\text{C}_{0.5}$	8.566	12.443	790.7	561	108.1	55	c axis
$\text{Sm}_2\text{Fe}_{15}\text{Si}_2\text{C}_{1.0}$	8.607	12.447	798.5	578	104.3	≈90	c axis
$\text{Sm}_2\text{Fe}_{15}\text{Si}_2\text{C}_{1.5}$	8.648	12.478	808.2	590	101.8	>90	c axis
$\text{Sm}_2\text{Fe}_{17}$	8.559	12.410	787.3	387			plane

X-ray diffraction shows that all compounds of $\text{Sm}_2\text{Fe}_{15}\text{M}_2\text{C}_x$ have rhombohedral $\text{Th}_2\text{Zn}_{17}$ -type structure. The lattice constants a and c and unit-cell volumes v of $\text{Sm}_2\text{Fe}_{15}\text{M}_2\text{C}_x$ compounds are listed in Table I, also including the values for $\text{Sm}_2\text{Fe}_{17}$ for comparison. It can be seen from Table I that both the lattice constants and unit-cell volumes increase monotonically with increasing carbon concentrations. For $\text{Sm}_2\text{Fe}_{15}\text{Ga}_2\text{C}_{3.0}$ and $\text{Sm}_2\text{Fe}_{15}\text{Si}_2\text{C}_{1.5}$, the unit-cell volume expansion is about 3.1% and 3.2% compared with the carbon-free unit cell, respectively. For $x=0$, the substitution of Ga for Fe leads to an increase of the unit-cell volume by 3.1%, in contrast with the Si-substituted unit cell, which shows a negative increase of the unit-cell volume by 0.6%. A similar reduction of the unit-cell volume was also observed in other $\text{R}_2(\text{Fe},\text{Si})_{17}$ compounds.⁹

The Curie temperature T_C and the saturation magnetization M_s of $\text{Sm}_2\text{Fe}_{15}\text{M}_2\text{C}_x$ compounds are also listed in Table I. The room-temperature M_s of these carbides is found to be in excess of 100 emu/g and has a small dependence on carbon content. T_C of $\text{Sm}_2\text{Fe}_{15}\text{Si}_2\text{C}_x$ is found to increase from 550 to 590 K, as x increases from 0 to 1.5. For $\text{Sm}_2\text{Fe}_{15}\text{Ga}_2\text{C}_x$, T_C increases from 565 K for $x=0$ to 635 K for $x=2.0$, then decreases with x . It is commonly assumed that the Fe-Fe interaction is dominant in the Fe-rich rare-earth iron intermetallic compounds. The Curie temperature

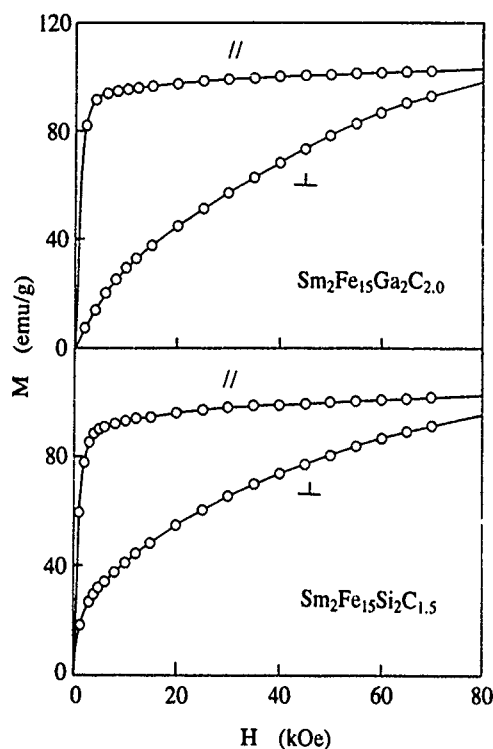


FIG. 3. The magnetization curves of the orientated $\text{Sm}_2\text{Fe}_{15}\text{Ga}_2\text{C}_{2.0}$ and $\text{Sm}_2\text{Fe}_{15}\text{Si}_2\text{C}_{1.5}$ samples measured along and perpendicular to the aligned directions.

depends strongly on the exchange interactions between Fe-Fe atoms, which is sensitive to the distance of Fe-Fe atoms. The enhancement of T_C with x in $\text{Sm}_2\text{Fe}_{15}\text{M}_2\text{C}_x$ compounds can be suggested to be mainly due to the lattice expansion induced by the introduction of carbon atoms, as with Ga- or Si-free compounds.^{2-4,8}

All compounds investigated in this work exhibit an easy c -axis anisotropy at room temperature except for $\text{Sm}_2\text{Fe}_{15}\text{Si}_2$, which shows an easy plane anisotropy. This can

be seen clearly from the x-ray diffraction patterns, shown in Fig. 2 as an example of magnetically aligned powder samples of $\text{Sm}_2\text{Fe}_{15}\text{M}_2\text{C}_x$. An important effect of the substitution Ga for Fe in the carbon-free compound on the magnetocrystalline anisotropy of $\text{Sm}_2\text{Fe}_{17}$ is found. Although the Sm sublattice in the $\text{Sm}_2\text{Fe}_{17}$ compound has an easy c -axis anisotropy, the planar anisotropy of the Fe sublattice overcomes the axial anisotropy. The role of Ga is to reduce the planar anisotropy of the Fe sublattice, resulting in a uniaxial anisotropy of the $\text{Sm}_2\text{Fe}_{15}\text{Ga}_2$ compound at room temperature. Figure 3 shows the magnetization curves of the $\text{Sm}_2\text{Fe}_{15}\text{Ga}_2\text{C}_{2.0}$ and $\text{Sm}_2\text{Fe}_{15}\text{Si}_2\text{C}_{1.5}$ samples measured along and perpendicular to the aligned directions. The room-temperature anisotropy field H_A estimated from Fig. 4 is found to be higher than 90 kOe for $x \geq 1.0$, which is about 40 kOe higher than that of $\text{Sm}_2\text{Fe}_{17}\text{C}$ (Ref. 10) and is comparable with that of $\text{Nd}_2\text{Fe}_{14}\text{B}$. Accordingly, a high-performance permanent magnet could be expected for $\text{Sm}_2(\text{Fe},\text{M})_{17}\text{C}_x$.

ACKNOWLEDGMENTS

This work was supported by the State's Sciences and Technology Commission and the National Natural Science Foundation of China.

- ¹J. M. D. Coey and Hong Sun, *J. Magn. Magn. Mater.* **87**, L251 (1990).
- ²B. G. Shen, L. S. Kong, and L. Cao, *Solid State Commun.* **83**, 753 (1992).
- ³L. S. Kong, L. Cao, and B. G. Shen, *J. Magn. Magn. Mater.* **115**, L137 (1992).
- ⁴L. Cao, L. S. Kong, and B. G. Shen, *J. Phys. Condens. Matter* **4**, L515 (1992).
- ⁵B. G. Shen, L. S. Kong, F. W. Wang, and L. Cao, *Appl. Phys. Lett.* **63**, 2288 (1993).
- ⁶B. G. Shen, F. W. Wang, L. S. Kong, L. Cao, and H. Q. Guo, *J. Magn. Magn. Mater.* **127**, L267 (1993).
- ⁷B. G. Shen, L. S. Kong, F. W. Wang, L. Cao, and W. S. Zhan, *Acta Phys. Sin.* **43** (1994) (in press).
- ⁸L. X. Liao, X. Chen, Z. Altounian, and D. H. Ryan, *Appl. Phys. Lett.* **60**, 129 (1992).
- ⁹E. E. Alp, A. M. Umarji, S. K. Malik, G. K. Skenoy, M. Q. Huang, E. B. Boltich, and W. E. Wallace, *J. Magn. Magn. Mater.* **68**, 305 (1987).
- ¹⁰X. C. Kou, R. Grossinger, T. H. Jacobs, and K. J. H. Buschow, *J. Magn. Magn. Mater.* **88**, 1 (1990).

Effect of Sm substitution on structure and magnetic properties of high-carbon $\text{Er}_2\text{Fe}_{17}\text{C}_y$ compounds

Bao-gen Shen, Lei Cao, Lin-shu Kong, Tai-shan Ning, and Ming Hu

State Key Laboratory of Magnetism, Institute of Physics, Chinese Academy of Sciences, P.O. Box 603, Beijing 100080, China

The carbides $(\text{Er}_{1-x}\text{Sm}_x)_2\text{Fe}_{17}\text{C}_y$ ($0 \leq x \leq 0.8$) with a carbon concentration up to $y=3.0$ for the Er-rich region and up to $y=1.5$ for the Sm-rich region have been successfully prepared by melt spinning. They are found to crystallize in the hexagonal $\text{Th}_2\text{Ni}_{17}$ -type or the rhombohedral $\text{Th}_2\text{Zn}_{17}$ -type structure and to be stable at high temperature. The introduction of the interstitial carbon results in a large increase in the unit-cell volumes and Curie temperatures. The room-temperature saturation magnetization is found to increase with increasing carbon or samarium concentrations. X-ray diffraction studies of magnetically aligned powder show that the samples with $x < 0.2$ or $y \leq 0.5$ exhibit easy plane anisotropy while the samples with $x \geq 0.2$ and $y \geq 1.0$ exhibit easy c -axis anisotropy at room temperature. For $(\text{Er}_{0.2}\text{Sm}_{0.8})_2\text{Fe}_{17}\text{C}_{1.5}$, the room-temperature anisotropy field is found to be 8 T, which is comparable to that of $\text{Nd}_2\text{Fe}_{14}\text{B}$.

INTRODUCTION

Introducing interstitial nitrogen or carbon atoms into R_2Fe_{17} intermetallic compounds results in a significant improvement of the magnetic properties of these compounds. The carbides $\text{R}_2\text{Fe}_{17}\text{C}_y$ ($y \approx 2.5$) prepared by the gas-solid reaction have unit-cell volumes about 6.5% larger and Curie temperatures 288–478 K higher than those of the R_2Fe_{17} compounds.¹ For $\text{Sm}_2\text{Fe}_{17}\text{C}_{2.5}$, the Curie temperature is 760 K and the room-temperature anisotropy field is 15 ± 0.5 T.¹ These carbides are promising new materials for applications in permanent magnets. However, their drawback is high-temperature instability. In our previous work, we have discovered that the carbides $\text{R}_2\text{Fe}_{17}\text{C}_x$ with high carbon concentration can be prepared by melt spinning.^{2–4} The melt-spun $\text{R}_2\text{Fe}_{17}\text{C}_x$ compounds were found to be stable at high temperature and retain still $\text{Th}_2\text{Zn}_{17}$ -type or $\text{Th}_2\text{Ni}_{17}$ -type structure up to at least 1273 K. We have successfully obtained melt-spun $\text{R}_2\text{Fe}_{17}\text{C}_y$ ($\text{R}=\text{Y}, \text{Gd}, \text{Tb}, \text{Dy}, \text{Ho}, \text{Er}, \text{and Tm}; x=0-3.0$) compounds and systematically studied their structure and magnetic properties.^{2–6} In this article, we report the formation, structure, and magnetic properties of $(\text{Er}_{1-x}\text{Sm}_x)_2\text{Fe}_{17}\text{C}_y$ compounds prepared by melt spinning.

EXPERIMENT

Iron and carbon were first arc melted into Fe–C alloys, and then Er, Sm, Fe, and Fe–C alloy were melted by arc melting in an argon atmosphere of high purity into homogeneous buttons with the compositions $(\text{Er}_{1-x}\text{Sm}_x)_2\text{Fe}_{17}\text{C}_y$ ($0 \leq x \leq 0.8, y \leq 3.0$). For homogeneity the ingots were melted several times. The purities of the elements used were at least 99.9%. An excess of 4.5% Sm was added to compensate the mass loss due to the evaporation of Sm during melting. After arc melting, the ingots were melt spun under high-purity argon atmosphere on the surface of a rotating copper wheel. The quenching rate was varied by changing the surface velocity v_s of the copper wheel between 0 and 47 m/s. The ribbons obtained are about 1 mm wide and 20–30 μm thick.

X-ray diffraction measurements were performed on the melt-spun ribbons using Co $K\alpha$ radiation to identify the phase components and determine the crystallographic structure. The Curie temperatures were determined from the temperature dependence of the magnetization measured by a vibrating sample magnetometer in a magnetic field of 1 kOe. The room-temperature saturation magnetization was measured by an extracting sample magnetometer in a field of 70 kOe. The powder samples were oriented in an applied field of 10 kOe in an epoxy resin, in order to determine the magnetocrystalline anisotropy of the $(\text{Er}_{1-x}\text{Sm}_x)_2\text{Fe}_{17}\text{C}_y$ samples. The anisotropy field was determined from magnetization curves along and perpendicular to the orientation direction by using the extracting sample magnetometer with a magnetic field of up to 70 kOe at room temperature.

RESULTS AND DISCUSSION

X-ray diffraction indicates that arc-melted $(\text{Er}_{1-x}\text{Sm}_x)_2\text{Fe}_{17}\text{C}_y$ alloys with $y \leq 1.0$ are almost single phase with hexagonal $\text{Th}_2\text{Ni}_{17}$ -type structure for $x \leq 0.3$ and rhombohedral $\text{Th}_2\text{Zn}_{17}$ -type structure for $x \geq 0.5$. For $y > 1.0$, the α -Fe phase appears coexisting with rare-earth carbides (RC) and the 2:17 phases. The amount of α -Fe increases rapidly with increasing carbon concentration y . However, we have found that by melt spinning, at an appropriate quenching rate, the $(\text{Er}_{1-x}\text{Sm}_x)_2\text{Fe}_{17}\text{C}_y$ samples with high carbon concentration crystallize in the 2:17-type structure. The formation of the 2:17 phase is found to depend strongly on the composition. The $(\text{Er}_{1-x}\text{Sm}_x)_2\text{Fe}_{17}\text{C}_y$ ($0 \leq x \leq 0.8$) compounds with carbon concentration up to $y=3.0$ for the Er-rich region and up to $y=1.5$ for the Sm-rich region can be obtained by melt spinning. For the Sm-rich end, a synthesis of high-carbon 2:17 compounds is difficult. The formation of the 2:17 phase is also sensitive to the quenching rate v_s . A low quenching rate cannot overcome the large amounts of α -Fe, whereas a high quenching rate leads to the formation of amorphous phase. For $(\text{Er}_{1-x}\text{Sm}_x)_2\text{Fe}_{17}\text{C}_y$ with

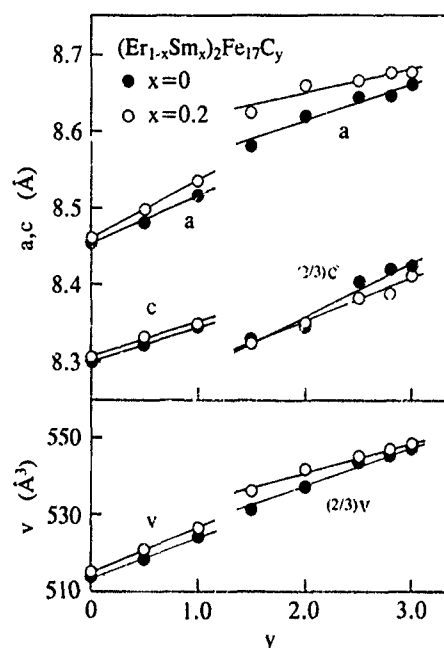


FIG. 1. The lattice parameters a and c , and the unit-cell volume v of $(\text{Er}_{1-x}\text{Sm}_x)_2\text{Fe}_{17}\text{C}_y$ with $x=0$ and 0.2 as a function of carbon concentration.

$1.5 \leq y \leq 2.8$, the optimal quenching rates to obtain the $2:17$ phase are $10\text{--}20$ m/s. It is interesting to note that the sample annealed at high temperature still maintains the $\text{Th}_2\text{Zn}_{17}$ -type structure. This demonstrates the high stability of the carbides

$(\text{Er}_{1-x}\text{Sm}_x)_2\text{Fe}_{17}\text{C}_y$ with high carbon concentration prepared by melt spinning, unlike the metastability of the carbides prepared by the gas-solid reaction.

It has been shown previously that the $\text{Er}_2\text{Fe}_{17}$ compound has a hexagonal $\text{Th}_2\text{Ni}_{17}$ -type structure, while the $\text{Sm}_2\text{Fe}_{17}$ compound has a rhombohedral $\text{Th}_2\text{Zn}_{17}$ -type structure. The substitution of Sm for Er leads to the structure change from $\text{Th}_2\text{Ni}_{17}$ type to $\text{Th}_2\text{Zn}_{17}$ type. At lower Sm concentration of $x \leq 0.2$, the structure change from hexagonal to rhombohedral with increasing carbon concentration x is also observed. The carbon concentration dependence of the lattice parameters and the unit-cell volumes for $(\text{Er}_{1-x}\text{Sm}_x)_2\text{Fe}_{17}\text{C}_y$ with $x=0$ and 0.2 , shown in Fig. 1, shows a drastic change between 1.0 and 1.5 , which results from the structure change from $\text{Th}_2\text{Ni}_{17}$ type to $\text{Th}_2\text{Zn}_{17}$ type.

The lattice parameters a and c , and the unit-cell volume v for $(\text{Er}_{1-x}\text{Sm}_x)_2\text{Fe}_{17}\text{C}_y$ are listed in Table I. It is found that the substitution of Sm for Er in the $\text{Er}_2\text{Fe}_{17}\text{C}_y$ gives rise to a small change of the unit-cell volumes, while the addition of the interstitial carbon results in a large increase of the unit-cell volume. It is apparent in Table I that the $\text{Er}_2\text{Fe}_{17}\text{C}_{3.0}$ compound has a unit-cell volume about 6.6% larger than that of $\text{Er}_2\text{Fe}_{17}$. For $(\text{Er}_{0.8}\text{Sm}_{0.2})_2\text{Fe}_{17}\text{C}_{3.0}$, the unit-cell volume expansion is about 6.5% compared with the carbon-free compound of $(\text{Er}_{0.8}\text{Sm}_{0.2})_2\text{Fe}_{17}$.

The room-temperature saturation magnetization M_s and the Curie temperature T_c for $(\text{Er}_{1-x}\text{Sm}_x)_2\text{Fe}_{17}\text{C}_y$ compounds are also summarized in Table I. The substitution of Sm for Er is found to have a relatively small effect on both M_s and T_c .

TABLE I. Structure and magnetic data for $(\text{Er}_{1-x}\text{Sm}_x)_2\text{Fe}_{17}\text{C}_y$.

Compound	Structure type	a (Å)	c (Å)	v (Å ³)	T_c (K)	M_s (emu/g)	Anisotropy
$\text{Er}_2\text{Fe}_{17}$	$\text{Th}_2\text{Ni}_{17}$	8.453	8.300	513.6	320		plane
$\text{Er}_2\text{Fe}_{17}\text{C}_{0.5}$	$\text{Th}_2\text{Ni}_{17}$	8.480	8.320	518.1	402	85.8	plane
$\text{Er}_2\text{Fe}_{17}\text{C}_{1.0}^a$	$\text{Th}_2\text{Ni}_{17}$	8.517	8.346	524.3	517		plane
$\text{Er}_2\text{Fe}_{17}\text{C}_{1.5}^a$	$\text{Th}_2\text{Zn}_{17}$	8.581	12.496	795.8	560	107.5	plane
$\text{Er}_2\text{Fe}_{17}\text{C}_{2.0}^a$	$\text{Th}_2\text{Zn}_{17}$	8.619	12.519	805.4	610	109.8	plane
$\text{Er}_2\text{Fe}_{17}\text{C}_{2.5}$	$\text{Th}_2\text{Zn}_{17}$	8.644	12.605	815.6	648	113.1	plane
$\text{Er}_2\text{Fe}_{17}\text{C}_{2.8}$	$\text{Th}_2\text{Zn}_{17}$	8.646	12.630	817.6	680	111.9	plane
$\text{Er}_2\text{Fe}_{17}\text{C}_{3.0}$	$\text{Th}_2\text{Zn}_{17}$	8.662	12.636	821.1	680		plane
$(\text{Er}_{0.8}\text{Sm}_{0.2})_2\text{Fe}_{17}$	$\text{Th}_2\text{Ni}_{17}$	8.460	8.304	514.7	337	84.7	plane
$(\text{Er}_{0.8}\text{Sm}_{0.2})_2\text{Fe}_{17}\text{C}_{0.5}$	$\text{Th}_2\text{Ni}_{17}$	8.498	8.332	521.0	404	104.8	plane
$(\text{Er}_{0.8}\text{Sm}_{0.2})_2\text{Fe}_{17}\text{C}_{1.0}$	$\text{Th}_2\text{Ni}_{17}$	8.534	8.346	526.4	512	110.6	
$(\text{Er}_{0.8}\text{Sm}_{0.2})_2\text{Fe}_{17}\text{C}_{1.5}$	$\text{Th}_2\text{Zn}_{17}$	8.625	12.485	804.3	583	114.5	c axis
$(\text{Er}_{0.8}\text{Sm}_{0.2})_2\text{Fe}_{17}\text{C}_{2.0}$	$\text{Th}_2\text{Zn}_{17}$	8.658	12.526	813.1	630	117.4	c axis
$(\text{Er}_{0.8}\text{Sm}_{0.2})_2\text{Fe}_{17}\text{C}_{2.5}$	$\text{Th}_2\text{Zn}_{17}$	8.667	12.574	818.0	668	119.4	c axis
$(\text{Er}_{0.8}\text{Sm}_{0.2})_2\text{Fe}_{17}\text{C}_{2.8}$	$\text{Th}_2\text{Zn}_{17}$	8.677	12.580	820.2	680	121.3	c axis
$(\text{Er}_{0.8}\text{Sm}_{0.2})_2\text{Fe}_{17}\text{C}_{3.0}$	$\text{Th}_2\text{Zn}_{17}$	8.677	12.618	822.7	681		c axis
$(\text{Er}_{0.7}\text{Sm}_{0.3})_2\text{Fe}_{17}\text{C}_{1.5}$	$\text{Th}_2\text{Zn}_{17}$	8.625	12.504	805.5	595	118.0	c axis
$(\text{Er}_{0.7}\text{Sm}_{0.3})_2\text{Fe}_{17}\text{C}_{2.0}$	$\text{Th}_2\text{Zn}_{17}$	8.653	12.567	814.9	640	120.6	c axis
$(\text{Er}_{0.7}\text{Sm}_{0.3})_2\text{Fe}_{17}\text{C}_{2.5}$	$\text{Th}_2\text{Zn}_{17}$	8.677	12.580	820.2	672	125.3	c axis
$(\text{Er}_{0.6}\text{Sm}_{0.4})_2\text{Fe}_{17}\text{C}_{1.5}$	$\text{Th}_2\text{Zn}_{17}$	8.635	12.510	807.8	605	118.0	c axis
$(\text{Er}_{0.6}\text{Sm}_{0.4})_2\text{Fe}_{17}\text{C}_{2.0}$	$\text{Th}_2\text{Zn}_{17}$	8.663	12.572	817.1	657	122.7	c axis
$(\text{Er}_{0.5}\text{Sm}_{0.5})_2\text{Fe}_{17}$	$\text{Th}_2\text{Zn}_{17}$	8.525	12.322	775.5	364	96.9	plane
$(\text{Er}_{0.5}\text{Sm}_{0.5})_2\text{Fe}_{17}\text{C}_{0.5}$	$\text{Th}_2\text{Zn}_{17}$	8.543	12.427	785.4	448		plane
$(\text{Er}_{0.5}\text{Sm}_{0.5})_2\text{Fe}_{17}\text{C}_{1.0}$	$\text{Th}_2\text{Zn}_{17}$	8.588	12.443	794.8	560	121.7	c axis
$(\text{Er}_{0.5}\text{Sm}_{0.5})_2\text{Fe}_{17}\text{C}_{1.5}$	$\text{Th}_2\text{Zn}_{17}$	8.648	12.504	809.9	604	126.0	c axis
$(\text{Er}_{0.5}\text{Sm}_{0.5})_2\text{Fe}_{17}\text{C}_{2.0}$	$\text{Th}_2\text{Zn}_{17}$	8.649	12.546	812.7	610		c axis
$(\text{Er}_{0.4}\text{Sm}_{0.6})_2\text{Fe}_{17}\text{C}_{1.5}$	$\text{Th}_2\text{Zn}_{17}$	8.644	12.504	809.1	602	121.1	c axis
$(\text{Er}_{0.2}\text{Sm}_{0.8})_2\text{Fe}_{17}\text{C}_{1.5}$	$\text{Th}_2\text{Zn}_{17}$	8.650	12.506	810.3	605	123.2	c axis

^aTaken from Ref. 3.

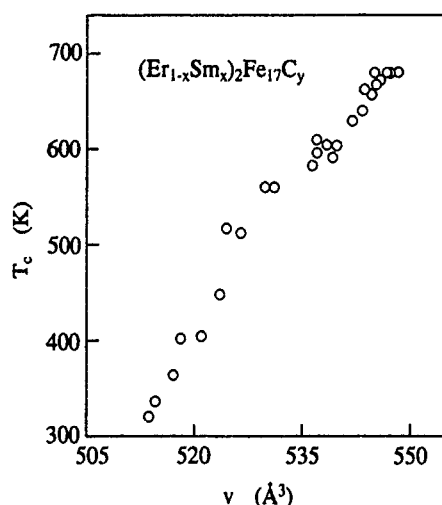


FIG. 2. The Curie temperature T_c of $(\text{Er}_{1-x}\text{Sm}_x)_2\text{Fe}_{17}\text{C}_y$ compounds as a function of unit-cell volume.

M_s and T_c increase monotonously with increasing carbon concentration y . For $x=0.2$, the saturation magnetization of the compound with $y=2.8$ has a 43% enhancement over the carbon-free compound with $y=0$. The increase of the room-temperature M_s is due to the enhancement of the Curie temperature which shifts the thermomagnetization curve to higher temperature. The strong increase of the Curie temperature with the carbon concentration y demonstrates the increase of the Fe-Fe interaction in $(\text{Er}_{1-x}\text{Sm}_x)_2\text{Fe}_{17}\text{C}_y$ by the interstitial carbon atoms. Figure 2 shows the Curie temperature of the $(\text{Er}_{1-x}\text{Sm}_x)_2\text{Fe}_{17}\text{C}_y$ compounds as a function of the unit-cell volume. An approximately linear dependence of T_c on the unit-cell volume is observed. Previous studies have shown that the relationship between T_c and volume is almost independent of the rare-earth and the interstitial atoms.⁵ From the fact that the Curie temperatures are not sensitive to the chemical composition, it seems reasonable to suggest that the enhancement of T_c in $(\text{Er}_{1-x}\text{Sm}_x)_2\text{Fe}_{17}\text{C}_y$ compounds is mainly due to the unit-cell expansion induced by the interstitial carbon atoms.

X-ray diffraction measurements on the magnetically aligned powder samples show that the $\text{Er}_2\text{Fe}_{17}\text{C}_y$ and the carbon-free compounds have an easy plane magnetocrystalline anisotropy at room temperature. An important effect of the interstitial carbon atoms on the magnetocrystalline anisotropy in the samples containing Sm is observed. The ad-

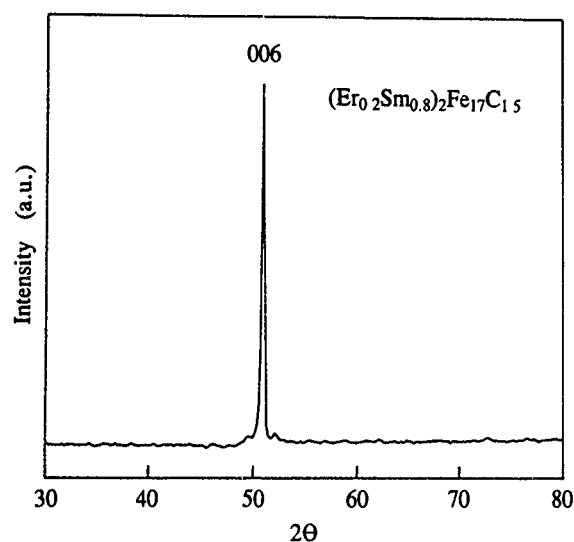


FIG. 3. X-ray diffraction patterns of magnetically aligned $(\text{Er}_{0.2}\text{Sm}_{0.8})_2\text{Fe}_{17}\text{C}_{1.5}$ powder samples.

dition of the carbon content increases the Sm sublattice anisotropy, resulting in the uniaxial anisotropy of the $(\text{Er}_{1-x}\text{Sm}_x)_2\text{Fe}_{17}\text{C}_y$. It is found that the samples with $x < 0.2$ or $y \leq 0.5$ exhibit an easy plane anisotropy, and the samples with $x \geq 0.2$ and $y \geq 1.0$ exhibit an easy c -axis anisotropy at room temperature. This can be seen clearly from the x-ray diffraction pattern of magnetically aligned powder sample of $(\text{Er}_{0.2}\text{Sm}_{0.8})_2\text{Fe}_{17}\text{C}_{1.5}$, as shown in Fig. 3 as an example. The anisotropy field rises as x or y increases. For $(\text{Er}_{0.2}\text{Sm}_{0.8})_2\text{Fe}_{17}\text{C}_{1.5}$, the room-temperature anisotropy field is found to be 8 T, which is comparable with that of $\text{Nd}_2\text{Fe}_{14}\text{B}$.

ACKNOWLEDGMENTS

This work was supported by the State's Sciences and Technology Commission and the National Natural Science Foundation of China.

¹ L. X. Liao, X. Chen, Z. Altounian, and D. H. Ryan, *Appl. Phys. Lett.* **60**, 129 (1992).

² B. G. Shen, I. S. Kong, and L. Cao, *Solid State Commun.* **83**, 753 (1992).

³ L. S. Kong, L. Cao, and B. G. Shen, *J. Magn. Magn. Mater.* **115**, L137 (1992).

⁴ L. Cao, L. S. Kong, and B. G. Shen, *J. Phys. Condens. Matter* **4**, L515 (1992).

⁵ L. S. Kong, L. Cao, and B. G. Shen, *J. Alloys Compounds* **191**, 301 (1993).

⁶ L. Cao, L. S. Kong, and B. G. Shen, *J. Phys. Condens. Matter* **5**, 2001 (1993).

Structure and magnetic properties of $\text{Gd}_2\text{Fe}_{17-x}\text{Ga}_x\text{C}_2$ compounds

Bao-gen Shen, Fang-wei Wang, Lin-shu Kong, Lei Cao, Bo Zhang, and Jian-gao Zhao
State Key Laboratory of Magnetism, Institute of Physics, Chinese Academy of Sciences,
P.O. Box 603, Beijing 100080, China

The single-phase compounds of $\text{Gd}_2\text{Fe}_{17-x}\text{Ga}_x\text{C}_2$ ($x=0, 1, 2, 3, 4, 5$, and 6) with rhombohedral $\text{Th}_2\text{Zn}_{17}$ -type structure were prepared by melt spinning for $x \leq 1$ and arc melting for $x \geq 2$. Their formation, structure, and magnetic properties were studied. The substitution of Ga for Fe in $\text{Gd}_2\text{Fe}_{17}\text{C}_2$ helps the formation of the 2:17-type structure. The addition of Ga results in the increase of the lattice constants and the unit-cell volumes. The Curie temperature has a small change when $x \leq 2$, and then decreases rapidly with increasing Ga concentration. An approximately linear decrease of the saturation magnetization with x is observed when the nonmagnetic Ga atom is substituted for Fe.

INTRODUCTION

The binary rare-earth (R) iron intermetallic compounds with $\text{Th}_2\text{Zn}_{17}$ or $\text{Th}_2\text{Ni}_{17}$ structure have not been regarded as potential permanent magnets because their Curie temperatures are very low and none of these compounds show a uniaxial anisotropy at room temperature. A large improvement of intrinsic magnetic properties has been achieved by introducing interstitial nitrogen or carbon atoms into R_2Fe_{17} compounds.^{1,2} The $\text{Sm}_2\text{Fe}_{17}\text{N}_x$ and $\text{Sm}_2\text{Fe}_{17}\text{C}_x$ compounds with higher nitrogen or carbon concentration are promising candidates for permanent magnets. However, a serious drawback of the nitrides or carbides prepared by the gas-solid reaction is their poor high-temperature stability. Recently, we have studied the effect of various elemental substitutions for Fe on the formation, structure, and magnetic properties in the $\text{R}_2\text{Fe}_{17}\text{C}_x$ alloys. We have found that the high-carbon $\text{R}_2\text{Fe}_{17}\text{C}_x$ compounds with Ga, Si, or Al, etc., substituted for Fe exhibit a high thermal stability.³⁻⁵ This is in contrast with the carbides produced by the gas-solid reaction which decompose into the equilibrium phases rare-earth carbides (RC) and α -Fe upon heating to 600–700 °C. The carbides containing Ga, Si, or Al, etc. can be formed by arc melting. We have reported some studied results of high-carbon $\text{R}_2(\text{Fe}, \text{M})_{17}\text{C}_x$ ($\text{R}=\text{Y}, \text{Nd}, \text{Sm}, \text{Gd}, \text{Tb}, \text{Dy}, \text{Ho}, \text{Er}$, and Tm ; $\text{M}=\text{Ga}$ and Si ; $x \leq 2.5$) compounds with $\text{Th}_2\text{Zn}_{17}$ -type or $\text{Th}_2\text{Ni}_{17}$ -type structures.³⁻⁵ In this article, the formation, structure, and magnetic properties of $\text{Gd}_2\text{Fe}_{17-x}\text{Ga}_x\text{C}_2$ ($0 \leq x \leq 6$) compounds prepared by arc melting or melt spinning are reported.

EXPERIMENT

The $\text{Gd}_2\text{Fe}_{17-x}\text{Ga}_x\text{C}_2$ alloys with $x=0, 1, 2, 3, 4, 5$, and 6 were prepared by arc melting in an argon atmosphere of high purity using raw materials of Gd, Fe, Ga, and Fe-C alloy of 99.9% purity. The ingots were melted several times to ensure homogeneity. The ingots with $x=0$ and 1 were then melt spun in argon atmosphere on the outside of a single copper wheel rotating with a surface speed of about 15 m/s, resulting in the formation of the single-phase compounds of the 2:17-type structure. For $2 \leq x \leq 6$, the heat treatment of the arc-melted ingots was performed in a steel tube in a highly purified argon atmosphere at 1273 K for 12 h. X-ray diffraction measurements on powder samples were performed using

Co $K\alpha$ radiation to identify the single phase and determine the crystallographic structure. The Curie temperature was determined from the temperature dependence of ac susceptibility in a field of less than 1 Oe. The saturation magnetization at 1.5 K was measured by an extracting sample magnetometer in a field of 70 kOe.

RESULTS AND DISCUSSION

Figure 1 shows x-ray diffraction patterns of arc-melted and heat-treated $\text{Gd}_2\text{Fe}_{17-x}\text{Ga}_x\text{C}_2$ samples with $0 \leq x \leq 6$. It can be seen clearly from Fig. 1 that the gallium-free sample exhibits a multiphase structure with RC, the 2:17 phase, and a predominant α -Fe phase. The substitution of Ga for Fe in these materials is found to have a significant effect on the crystal structure. The addition of Ga results in a remarkable decrease of the diffraction peaks of α -Fe. For $x=1$, the arc-melted sample is found to consist only of the rhombohedral $\text{Th}_2\text{Zn}_{17}$ and α -Fe phases. When the Ga concentration x is richer than 1, the samples prepared by arc melting are almost single phase with rhombohedral $\text{Th}_2\text{Zn}_{17}$ -type structure. No significant diffraction from impurity phases is observed. The role of Ga in the high-carbon $\text{R}_2\text{Fe}_{17-x}\text{Ga}_x\text{C}_2$ helps the formation of rare-earth iron compounds of the 2:17 type. A similar effect has been observed in other 2:17-type rare-earth iron compounds.³⁻⁵

The lattice constants a and c and the unit-cell volumes v obtained from the x-ray diffraction patterns of the melt-spun samples with $x=0$ and 1 and arc-melted and heat-treated samples with $2 \leq x \leq 6$ are shown in Fig. 2 as a function of Ga concentration. The substitution of larger Ga for Fe in the $\text{Gd}_2\text{Fe}_{17}\text{C}_2$ leads to an expansion of the unit cell. An approximately linear increase of the unit-cell volume with x is observed. The expansion of the unit-cell results from the effect of both Ga and C additions. The $\text{Gd}_2\text{Fe}_{17}\text{C}_2$ compound has a unit-cell volume about 4.9% larger than that of $\text{Gd}_2\text{Fe}_{17}$. For $\text{Gd}_2\text{Fe}_{11}\text{Ga}_6\text{C}_2$, the unit-cell volume expansion is about 3.4% compared with the gallium-free compound.

The present results of x-ray diffraction do not provide enough evidence to determine the occupancy site of the Ga atoms. However, neutron diffraction studies for $\text{Ho}_2\text{Fe}_{17-x}\text{Ga}_x\text{C}_2$ compounds have demonstrated⁶ that the Ga

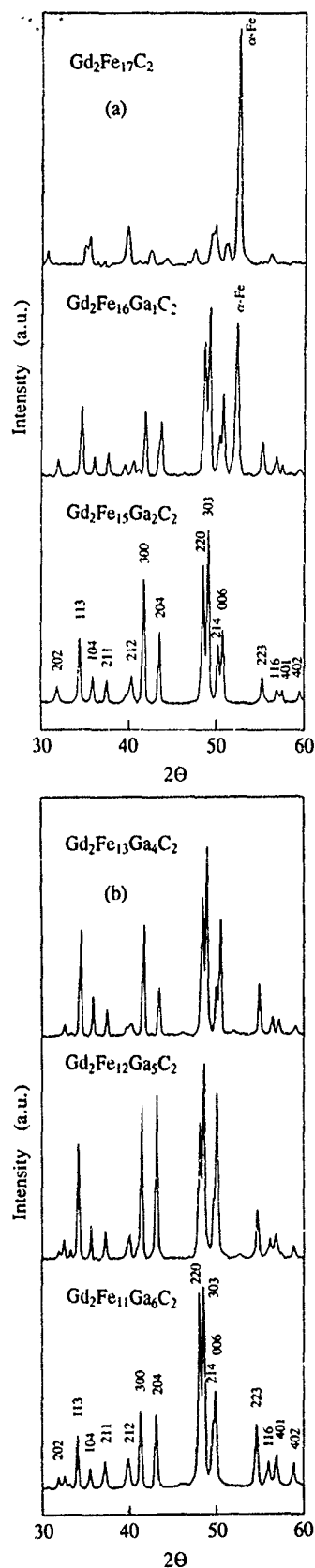


FIG. 1. X-ray diffraction patterns of arc-melted and heat-treated $\text{Gd}_2\text{Fe}_{17-x}\text{Ga}_x\text{C}_2$ samples with (a) $x=0, 1$, and 2 , (b) $x=4, 5$, and 6 .

atoms preferentially occupy $18h$ sites, when $x < 4$. For $x > 4$, the Ga atoms occupy $18h$ and $6c$ sites. In these carbides containing Ga the carbon atoms still occupy the $9e$ interstitial sites.

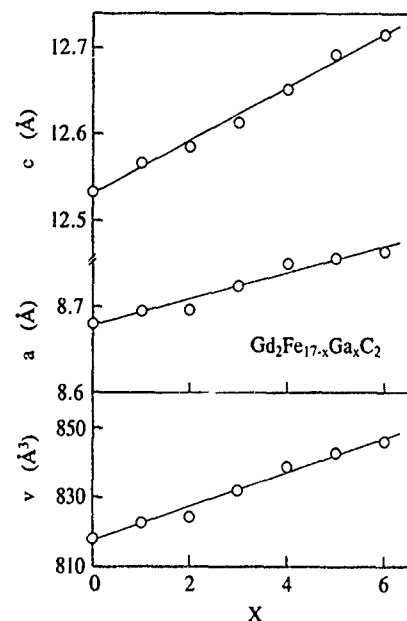


FIG. 2. The lattice constants a and c and the unit-cell volumes v of $\text{Gd}_2\text{Fe}_{17-x}\text{Ga}_x\text{C}_2$ compounds as a function of Ga concentration.

The Ga-concentration dependence of the Curie temperatures T_C of $\text{Gd}_2\text{Fe}_{17-x}\text{Ga}_x\text{C}_2$ compounds is shown in Fig. 3. The T_C is found to decrease slowly until about $x=2$ and then drop at a more rapid rate with increasing Ga concentration. It is commonly assumed that the Curie temperature of rare-earth iron compounds is determined by the Fe-Fe, R-Fe, and R-R interactions. In general, the Fe-Fe interaction is dominant, and the R-R interaction is negligible. The difference of T_C among the different rare-earth compounds indicates the influence of R-Fe interaction. It has been shown previously that the low values of the Curie temperatures of the R_2Fe_{17} compounds result from the relatively small Fe-Fe distance. The increase in Curie temperature of the nitrides or

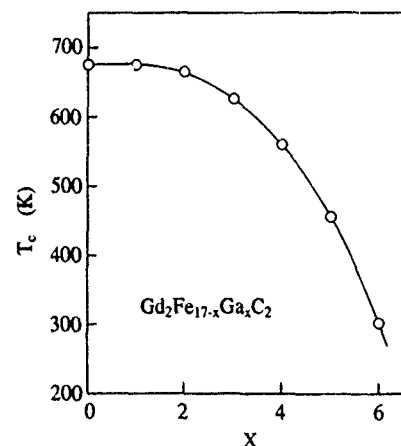


FIG. 3. The Curie temperature T_C of $\text{Gd}_2\text{Fe}_{17-x}\text{Ga}_x\text{C}_2$ compounds as a function of Ga concentration.

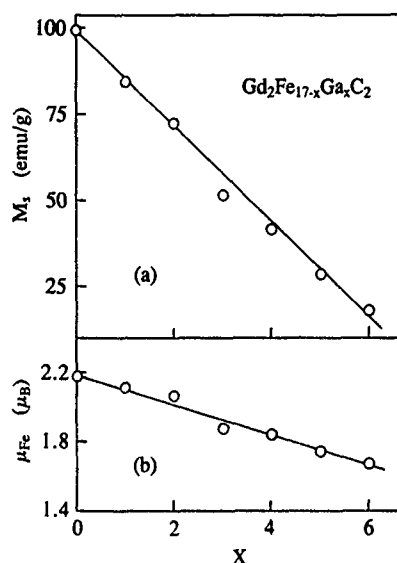


FIG. 4. (a) The saturation magnetization M_s at 1.5 K and (b) the Fe magnetic moment μ_{Fe} of $Gd_2Fe_{17-x}Ga_xC_2$ compounds as a function of Ga concentration.

carbides is mainly due to the increase of the Fe-Fe interaction which results from the increasing interatomic distance produced by the interstitial nitrogen or carbon. For $Gd_2Fe_{17-x}Ga_xC_2$ compounds with $x=0$, T_C is 200 K higher than that of Gd_2Fe_{17} .¹ However, the decrease of Curie temperature with increasing x in $Gd_2Fe_{17-x}Ga_xC_2$ is observed, although the substitution of Ga for Fe results in a monotonic increase of the unit cell. This indicates that the substitution of nonmagnetic Ga in the rare-earth iron carbides with higher carbon concentration would decrease the Fe-Fe interaction and the number of Fe-Fe atom pairs, resulting in the drop in T_C .

The saturation magnetization M_s of $Gd_2Fe_{17-x}Ga_xC_2$ compounds at 1.5 K is shown in Fig. 4(a) as a function of Ga concentration x . The M_s of the samples is found to decrease linearly with increasing x , with an approximately rate of -12 (emu/g)/at. % Ga. The antiparallel coupling between the rare-earth spin moment and the Fe moment for heavy rare-earth compounds leads to ferrimagnetism. Accordingly, the saturation moment μ_s of $Gd_2Fe_{17-x}Ga_xC_2$ compounds can be expressed by the equation

$$\mu_s = (17-x)\mu_{Fe} - 2\mu_{Gd}, \quad (1)$$

where μ_{Fe} and μ_{Gd} are the Fe and Gd magnetic moments, respectively. The μ_{Gd} can be assumed to be $7\mu_B$. Thus the Fe magnetic moment μ_{Fe} can be obtained according to Eq. (1), as shown in Fig. 4(b). It can be seen from Fig. 4(b) that μ_{Fe} of $Gd_2Fe_{17-x}Ga_xC_2$ compounds decreases linearly from $2.17\mu_B$ for $x=0$ to $1.67\mu_B$ for $x=6$ as a result of the dilution of Fe by nonmagnetic Ga atoms.

ACKNOWLEDGMENTS

This work was supported by the State's Sciences and Technology Commission and the National Natural Science Foundation of China.

- ¹H. Sun, J. M. D. Coey, Y. Otani, and D. P. F. Hurley, *J. Phys. Condens. Matter* **2**, 6465 (1990).
- ²L. X. Liao, X. Chen, Z. Altounian, and D. H. Ryan, *Appl. Phys. Lett.* **60**, 129 (1992).
- ³B. G. Shen, L. S. Kong, F. W. Fang, and L. Cao, *Appl. Phys. Lett.* **63**, 2288 (1993).
- ⁴B. G. Shen, F. W. Wang, L. S. Kong, L. Cao, and H. Q. Guo, *J. Magn. Mater.* **127**, L267 (1993).
- ⁵B. G. Shen, L. S. Kong, F. W. Wang, L. Cao, and W. S. Zhan, *Acta Phys. Sin.* **43** (1994).
- ⁶Q. W. Yan (unpublished).

Effect of cobalt substitution on magnetic properties of R_2Fe_{17} silicides ($R=Y, Gd, Tb, Er, \text{ and } Tm$)

F. Pourarian, R. T. Obermyer,^{a)} and S. G. Sankar
Carnegie Mellon Research Institute, Carnegie Mellon University, Advanced Material Corporation,
Pittsburgh, Pennsylvania 15213

Magnetic characteristics and unit-cell dimensions of the (off-stoichiometric) R_2Fe_{17} -type alloys based on $R_2Fe_{14-x}Co_xSi_2$, where $R=Gd, Tb, Er, Tm, \text{ and } Y$ and $x=4$ were determined. Partial substitution of Fe by Co slightly increases the saturation magnetization of the alloys and produces an average increase in the Curie temperature (T_c) of 55 K per Co atom. The enhancement of the Curie temperature with the addition of cobalt is attributed to the strengthening of the average $3d$ - $3d$ exchange interaction. For Er- and Tm-containing compounds, replacement of Fe by Co has a remarkable effect in shifting the observed spin reorientation temperature toward higher temperatures. These results are discussed in terms of the influence of the interaction of the $4f$ electrons of the rare-earth ions with the $3d$ electrons of the transition-metal ions, which modifies the overall anisotropy of the alloys.

I. INTRODUCTION

It is well established that binary R_2Fe_{17} compounds have basal plane anisotropy, which arises from a combination of the contribution from the $3d$ Fe and $4f$ rare-earth sublattice magnetizations.¹ Recently it was found that incorporation of Si atoms in the lattice of R_2Fe_{17} significantly enhanced the magnetic ordering temperature T_c (Refs. 2 and 3) and produced spin reorientation transition regions in the Er_2Fe_{17} alloy system.² The spin reorientation temperature T_{sr} observed in $Er_2Fe_{14}Si_2$ and in Tm-based compounds is believed to be due to a change of magnetocrystalline anisotropy from an easy axis to a basal plane with increasing temperature.³ The region of uniaxial anisotropy as determined from the spin reorientation transition is crucial for production of high-performance permanent magnet materials. The addition of Si in the lattice was also found to have a remarkable influence in reducing the unit-cell volume of $2:17$ compounds. This behavior is related to a particular Si site occupation in the lattice.⁴ In the latter reference the observation showed that the position of Si in the off-stoichiometric lattice is interestingly different from that of the stoichiometric one. This may suggest a particular influence of the Si atoms on the local anisotropy of the sublattices.

The objective of the present work is to study the effect of partial substitution of Fe by Co on the magnetic properties of off-stoichiometric R -Fe silicides. The physical and magnetic properties of the latter off-stoichiometric system was investigated before.² Results of lattice dimensions, saturation magnetization, Curie temperatures for all the studied alloys, and the spin reorientation temperatures for Er and Tm compounds are reported in detail.

II. EXPERIMENT

The starting materials were prepared by induction melting of the constituent metals in a water-cooled copper boat under a flowing argon atmosphere. As-cast ingots were heat

treated at 900 °C for 2 days and then rapidly cooled to room temperature. Powder x-ray diffraction with Cu $K\alpha$ radiation was employed to determine phase purity and lattice dimensions. The magnetic measurements were carried out at 295 and 20 K using a vibrating sample magnetometer in external fields up to 16 kOe. The saturation magnetization M_s was determined by measuring the magnetization of random and aligned powders of sizes $<38 \mu m$. The spin reorientation temperature T_{sr} was obtained from the temperature dependence of the magnetization in the temperature range 10–1100 K with a field of 0.5 kOe on both rough chunk and aligned powders. Curie temperatures T_c were also determined by plotting M^2 vs T and extrapolating the steep part of the curve to $M^2=0$.

III. RESULTS AND DISCUSSION

A. Lattice parameters

Results of x-ray diffraction on $R_2Fe_{10}Co_4Si_2$ revealed the formation of single-phase materials which have the characteristics of hexagonal crystal structure type Th_2Ni_{17} when $R=Y, Tb, Er, \text{ and } Tm$ and of rhombohedral type Th_2Zn_{17} when $R=Gd$. Table I shows results of lattice parameters compared to those of $R_2Fe_{14}Si_2$ compounds. Introduction of cobalt in the lattice (up to $x=4$) resulted in a decrease of unit-cell volume. This is expected due to the smaller size of

TABLE I. Lattice parameters and unit-cell volume of (R_2Fe_{17} -type) $R_2Fe_{10}Co_4Si_2$ compounds.

Composition	a (Å)	c (Å)	c/a	v (Å ³)
$Gd_2Fe_{14}Si_2$	8.463	12.395	1.46	768.8
$Gd_2Fe_{10}Co_4Si_2$	8.465	12.227	1.44	758.7
$Tb_2Fe_{14}Si_2$	8.473	8.257	0.97	513.4
$Tb_2Fe_{10}Co_4Si_2$	8.453	8.247	0.97	510.3
$Er_2Fe_{14}Si_2$	8.409	8.279	0.98	506.9
$Er_2Fe_{10}Co_4Si_2$	8.390	8.256	0.98	503.9
$Tm_2Fe_{14}Si_2$	8.394	8.256	0.98	503.8
$Tm_2Fe_{10}Co_4Si_2$	8.377	8.246	0.98	501.1
$Y_2Fe_{14}Si_2$	8.433	8.247	0.98	507.9
$Y_2Fe_{10}Co_4Si_2$	8.417	8.260	0.98	506.7

^{a)}Permanent address: Physics Department, Penn State University, McKeesport, PA 15132.

TABLE II. Magnetic properties of $R_2Fe_{10}Co_4Si_2$ compounds.

Composition	T_c (K)	M_s (emu/g)	
		RT	20 K
$Gd_2Fe_{10}Co_4Si_2$	753	70	58
$Tb_2Fe_{10}Co_4Si_2$	743
$Er_2Fe_{10}Co_4Si_2$	706	84	28
$Tm_2Fe_{10}Co_4Si_2$	684	101	38
$Y_2Fe_{10}Co_4Si_2$	703	123	148

the cobalt atom compared to that of iron. This reduction of lattice dimensions is also related to the preferential site occupation of cobalt in the lattice which was revealed to be the transition metal site d and h in the rhombohedral type and the f sites in the hexagonal type.⁵

B. Magnetic properties

Saturation magnetization at 20 K and room temperature and magnetic ordering temperature T_c data for $R_2Fe_{10}Co_4Si_2$ are presented in Table II. It should be noted that partial replacement of Fe by Co produces an average increase of the Curie temperature of 55 K per Co atom. The enhancement of T_c in these alloys was observed earlier when Fe is partially replaced by Si atoms.² This effect and the decrease observed in the interatomic distances of $R_2Fe_{10}Co_4Si_2$ lattice can be attributed to the modification of short Fe-Fe distances by Co atoms⁶ and concomitantly to the particular Si site occupation, which all contribute to the strengthening of the average $3d$ - $3d$ exchange interaction. Results of saturation moments for $x=4$ indicate an expected net increase relative to $R_2Fe_{14}Si_2$. The average $3d$ transition moments range between $1.9\mu_B$ and $2.0\mu_B$.

Measurements of temperature-dependent magnetization of rough chunk samples and aligned powders for Er- and Tm-based alloys are illustrated in Figs. 1–3. Er_2Fe_{17} exhibits no magnetic transition down to 4.2 K. In contrast, the Tm_2Fe_{17} alloy shows a remarkable spin reorientation transition at 72 K at which the easy direction of magnetization

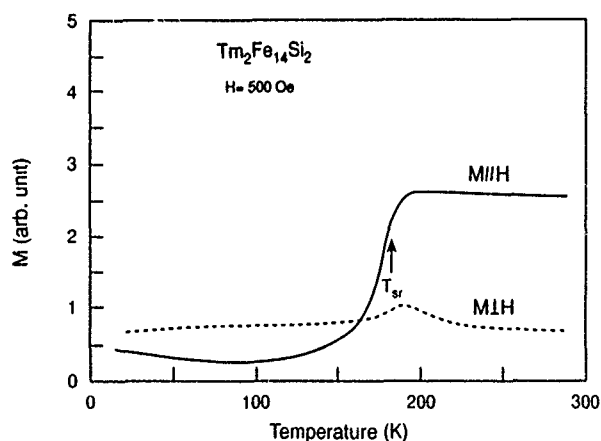


FIG. 1. Temperature dependence of the magnetization of the $Tm_2Fe_{14}Si_2$ sample with field parallel $H||M$ and perpendicular $H\perp M$ to the alignment. The arrow indicates the spin reorientation temperature T_{sr} at 180 K.

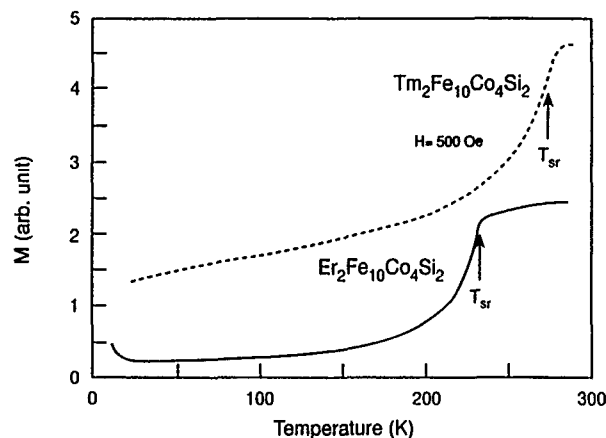


FIG. 2. Temperature dependence of the magnetization of rough chunk samples of $Er_2Fe_{10}Co_4Si_2$ and $Tm_2Fe_{10}Co_4Si_2$. The arrows indicate the spin reorientation temperatures 230 and 270 K.

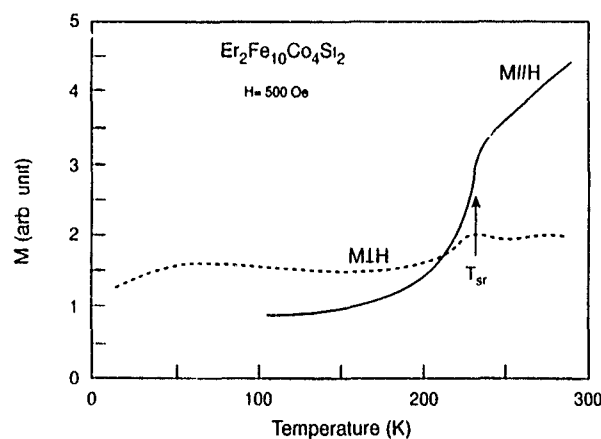


FIG. 3. Temperature dependence of the magnetization of $Er_2Fe_{10}Co_4Si_2$ with field parallel and perpendicular to the alignment. The arrow indicates the spin reorientation T_{sr} at 230 K.

TABLE III. Spin reorientation (T_{sr}) and easy direction magnetization (EDM) of $R_2Fe_{10}Co_4Si_2$ ($R=Er,Tm$) compounds.

Composition	T_{sr} (K)	EDM	
		RT	20 K
Er_2Fe_{17}	..	plane	plane
$Er_2Fe_{14}Si_2$	35(100) ^a	plane	c axis
$Er_2Fe_{10}Co_4Si_2$	230	plane	c axis
Tm_2Fe_{17}	72	plane	c axis
$Tm_2Fe_{14}Si_2$	180	plane	c axis
$Tm_2Fe_{10}Co_4Si_2$	270	plane	c axis

^a $T_{sr2}=100$ K taken from Ref. 2.

(EDM) changes from easy plane to a hard c axis.³ Addition of Si atoms ($x > 0.5$) in the lattice of the former alloy triggers a spin reorientation transition (T_{sr}) at low temperatures. In both cases the substitution of Fe by Co leads to an additional shift in T_{sr} toward higher temperatures. In fact, this behavior can be understood in these compounds, because Er and Tm, which are characterized by a positive second-order Stevens coefficient ($\alpha > 0$), together with the Co atom seek axial anisotropy. This is in contrast to the Fe moments which align in the basal plane. Therefore the axial anisotropy dominates over a wider temperature region with Co substitution. Results of T_{sr} and proposed EDM for Er- and Tm-based compounds are given in Table III. For $\text{Er}_2\text{Fe}_{10}\text{Si}_2$ the two transitions observed at $T_{sr1} = 35$ K and $T_{sr2} = 100$ K are believed to be related to the crystal structure forms rhombohedral and hexagonal type.² In $\text{Er}_2\text{Fe}_{10}\text{Co}_4\text{Si}_2$ cobalt influences the lattice and stabilizes only the hexagonal structure with a remarkable increase in the T_{sr2} value. Results indicate that both

Si and Co site occupations have a strong effect on the local anisotropy of Er (or Tm) 4f ions and induce a larger negative second-order crystal field parameter A_0^2 . The latter behavior resembles that generated in interstitial carbon in $\text{Tm}_2\text{Fe}_{17}\text{C}_x$.⁷

¹K. H. J. Buschow, Rep. Prog. Phys. **40**, 1179 (1977).

²F. Pourarian, R. Obermyer, Y. Zheng, S. G. Sankar, and W. E. Wallace, J. Appl. Phys. **73**, 6272 (1993).

³P. C. M. Gubbens and K. H. J. Buschow, Phys. Status Solidi A **34**, 729 (1976).

⁴G. J. Long, G. K. Marasinghe, S. Mishra, O. A. Pringle, F. Grandjean, K. H. J. Buschow, D. P. Middleton, W. B. Yelon, F. Pourarian, and O. Isnard, Solid State Commun. **88**, 761 (1993).

⁵J. F. Herbst, J. J. Croat, R. W. Lee, and W. B. Yelon, J. Appl. Phys. **53**, 250 (1982).

⁶H. Chen W. W. Ho, S. G. Sankar, and W. E. Wallace, J. Magn. Magn. Mater. **78**, 203 (1989).

⁷P. C. M. Gubbens, A. M. van der Kraan, T. H. Jacobs, and K. H. J. Buschow, J. Magn. Magn. Mater. **79**, 173 (1989).

A contribution to the knowledge of phase equilibria and the magnetic properties of the Nd-Fe-B-X systems (X=Al,Co,V)

Anders Micski and Björn Uhrenius

Swedish Institute for Metals Research, Drottning Kristinas väg 48, 114 28 Stockholm, Sweden

A technique based on diffusion couples for the determination of the compositions of different phases present in the Fe-Nd-B and Fe-Nd-B-Al systems was used. By this technique the composition of the liquid in equilibrium with the solid phases could be determined. Since all elements are encapsulated in an iron capsule, the study of oxidation-sensitive elements like neodymium was easily made. By using this technique, new information on the composition of the liquid phase in equilibrium with solid phases in the Fe-Nd-B system as well as the Fe-Nd-B-Al system was determined at two temperatures. This information was used to improve the representation of the liquidus surfaces of the systems. The effects of Al, V, and/or Co additions on the coercivity and energy product of sintered Fe-Nd-B magnets are also presented.

INTRODUCTION

Permanent magnets based on the Fe-Nd-B system are among the strongest available today. The excellent magnetic properties are attributed to the $\text{Nd}_2\text{Fe}_{14}\text{B}$ phase (ϕ). These magnets, however, suffer from two major drawbacks as compared to, e.g., magnets based on Sm-Co, namely, (i) poor corrosion resistance and (ii) a rapid decline in coercivity (jH_c) and magnetization above relatively low temperatures ($\approx 150^\circ\text{C}$). A major field of research is to improve these properties, which may be achieved by adding different elements to the Fe-Nd-B system, e.g., Co, V, or Al.¹⁻⁵ Co is added to improve the Curie temperature of the material and also to improve the thermal stability of the coercivity. The coercivity at room temperature, however, is reduced by Co addition. Tenaud *et al.*⁵ found that this detrimental effect could be compensated by additions of V. Al is believed to improve the wetting between the Nd-rich intergranular phase and ϕ , thus increasing the fraction of Nd-filled grain boundaries and therefore the coercivity.

When new elements are added to the Fe-Nd-B system, new phases may appear in the material. These elements may also enter the different phases already present in the material, e.g., the $\text{Nd}_2\text{Fe}_{14}\text{B}$ phase and/or the Nd-rich intergranular phase. These changes of the microstructure are of great importance for the magnetic properties of the material and may result in an improvement of the magnetic properties. To understand the influence of the different alloying elements on the microstructure, the appropriate phase diagram has to be known. The method most often used for the investigation of phase equilibria is based on differential thermal analysis (DTA), standard metallography, and electron probe microanalysis (EPMA).⁶⁻⁸ The composition of the different precipitated phases and the temperatures of the phase transformations can be determined with this technique. However, it is difficult to determine the composition of the liquid phase as well as the equilibrium composition of the solid phases present at the different temperatures. Such information is vital for the understanding of the development of the microstructure during liquid-phase sintering.

In the present study, results obtained using a complementary method involving diffusion couples are presented. Some results obtained after magnetic measurements of Nd-

Fe-B-X magnets, where X=Al, V, and/or Co, are also presented.

EXPERIMENTAL DETAILS

The diffusion-couple technique involved enclosing the elements Nd, B, and X (where X stands for any alloying element used) or alloys of the elements in an iron capsule and heat treating at the appropriate temperatures. During heat treatment the equilibrium phases between the Nd-B mixture and iron were formed. After quenching, the composition of the different phases at temperature were frozen in and were determined by EPMA. This technique made it rather easy to heat treat alloys based on oxidation-sensitive elements, like neodymium, since all elements were encapsulated in a protective capsule of iron.

Raw materials used were an iron tube (99.9% iron, wall thickness 10 mm). This was filled with neodymium (99.9%) and FeB powder (99.3%) of a Nd/B ratio which would produce the equilibrium structures of interest. The iron tube was sealed with an iron rod, which was welded to place. Heat treatments were performed at 1000 and 1100 $^\circ\text{C}$ in argon gas for ten or seven days, respectively, after which the specimens were quenched. After cutting the specimens, the microstructure was studied using metallographic techniques. The compositions of the different microstructural constituents was analyzed using a microprobe (JEOL 6400 equipped with a Tracor system 2). Four alloys with different B:Nd:Fe ratios were used as standards. These were made from rapidly quenched melt-spun ribbons produced at a cooling rate of about 10^5 K/s to ensure a homogeneous material without segregations. These standards were chemically analyzed with respect to their B, Fe, and Nd content.

The effects of Al, Co, and V additions on the magnetic properties of a Fe-Nd-B magnet with the composition $\text{Nd}_{20}\text{Fe}_{74}\text{B}_6$ was also studied. The magnets were produced from induction-melted alloys. The cast alloys were hydrogen decrepitated, milled, dried, aligned in an open coil pulse magnetizer, cold isostatically pressed at 200 MPa, and sintered in vacuum at 1080 $^\circ\text{C}$ for 1 h. The effect of a post-sinter heat treatment at 650 $^\circ\text{C}$ for 1 h in vacuum on the magnetic properties was studied. The magnetic properties

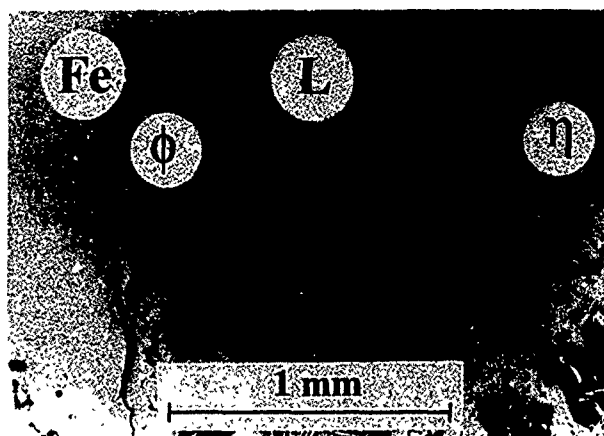


FIG. 1. Light optical micrograph of a cross section through a diffusion couple in the Fe-Nd-B system in an as-polished condition. The different phases present after heat treatment at 1000 °C for 10 days are seen. The multiphase region marked L was a homogeneous liquid phase at the heat-treatment temperature.

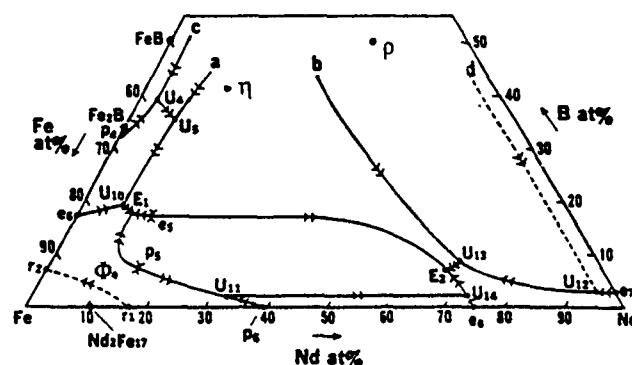
were measured in a superconducting quantum-interference device magnetometer at 273 K.

RESULTS

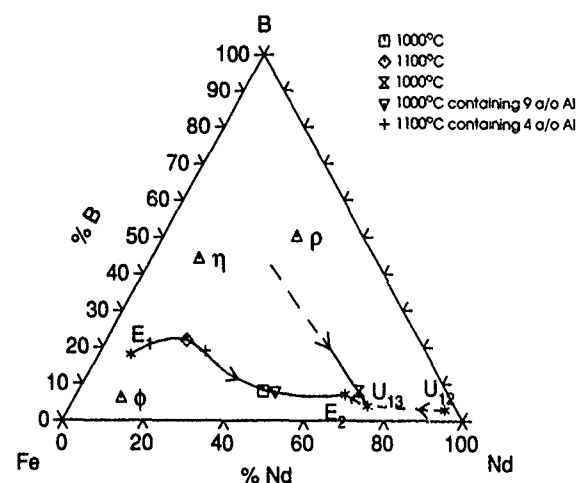
Phase relations

A picture of the part of the phase diagram along a line connecting the iron-rich corner with the Nd/B alloy could be obtained by a careful analysis of the microstructure. A typical appearance of a cross section through a diffusion couple is seen in Fig. 1. This specimen was heat treated at 1000 °C for 10 days before quenching. The iron tube is seen to the far left and has partly reacted with Nd and B at temperature. The different phases present in the microstructure are as follows: $\text{Nd}_2\text{Fe}_{14}\text{B}(\phi)$ is seen in contact (i.e., in equilibrium) with the iron to the left. Outside the ϕ phase there is a region, which at the heat treatment temperature, consisted of liquid in equilibrium with ϕ and $\text{Nd}_{11}\text{Fe}_4\text{B}_4(\eta)$, the latter phase seen to the far right. During quenching, the liquid phase decomposed to primarily precipitated needles of ϕ and an eutectic structure consisting of ϕ , η , and other intermetallic phases. The composition of the liquid phase was determined by scanning over large areas of this composite structure. An average of about 10 measurements was evaluated where each measurement was made on an area the size of about $10^4 \mu\text{m}^2$.

In Fig. 2(a), a tentative liquidus projection of the Fe-Nd-B system according to Matsuura *et al.*⁸ is shown. The positions of the three ternary phases ϕ , η , and $\text{Nd}_2\text{FeB}_3(\rho)$ are also marked. The results obtained in the present study on the Fe-Nd-B system were used to construct the diagram shown in Fig. 2(b). It was assumed that the eutectic compositions E_1 and E_2 are known from the literature.⁸ The positions of the transition composition U_{13} has tentatively been shifted to a position closer to the Fe-Nd axis, while the transition composition U_{12} is assumed to be known. The liquidus projection E_1E_2 has been drawn closer to the Fe-Nd axis as compared to Fig. 2(a) at lower temperatures, indicating a less boron-rich liquid. The composition of the



(a)



(b)

FIG. 2. (a) A tentative liquidus projection of the Nd-Fe-B system, according to Matsuura *et al.* (Ref. 8). The ternary phases ϕ , η , and ρ are also marked. (b) The liquidus projections in the Fe-Nd-B system according to the present study. Also indicated is the liquid-phase composition in the Fe-Nd-B-Al system at 1000 and 1100 °C, respectively.

liquid phases in equilibrium with the different solid phases obtained on the Fe-Nd-B is given in Table I.

The same technique was also applied to the Fe-Nd-B-Al system. Figure 2(b) shows the composition of a liquid

TABLE I. Results of the analysis of the composition of the different phases found in diffusion couples in the Fe-Nd-B and Fe-Nd-B-Al systems. L denotes the liquid phase present at the heat treatment temperature.

System	T (°C)	Phase	Composition (a/o)			
			B	Nd	Fe	Al
Fe-Nd-B	1000	L in equilibrium with ϕ and η	8	46	46	...
Fe-Nd-B	1000	L in equilibrium with η and ρ	8	70	22	...
Fe-Nd-B	1100	L in equilibrium with ϕ and η	22	20	58	...
Fe-Nd-B-Al	1000	L in equilibrium with ϕ and η	7	45	39	9
Fe-Nd-B-Al	1100	L in equilibrium with ϕ and η	18	25	53	4
Fe-Nd-B-Al	1000	ϕ in equilibrium with Fe	6	11	80	4
Fe-Nd-B-Al	1000	ϕ in equilibrium with L	6	11	77	6
Fe-Nd-B-Al	1100	ϕ (average)	6	12	79	3
Fe-Nd-B-Al	1000	ρ	49	32	14	5

TABLE II. Results obtained after magnetic measurements on alloys of different compositions.

Composition	Condition	H_c (kA/m)	$(BH)_{max}$ (kJ/m ³)
Nd ₂₀ Fe ₇₄ B ₆	as sintered	652	160
	heat treated	1039	172
Nd ₂₀ Fe ₇₄ B ₆ +3 at. % Al	as sintered	1106	206
	heat treated	1347	247
Nd ₂₀ (Fe _{0.95} Co _{0.05}) ₇₄ B ₆	as sintered	390	154
	heat treated	497	205
Nd ₂₀ (Fe _{0.95} Co _{0.05}) ₇₄ B ₆ + 2 at. % V	as sintered	414	187
	heat treated	627	212
Nd ₂₀ (Fe _{0.95} Co _{0.05}) ₇₄ B ₆ + 3 at. % Al	as sintered	434	100
	heat treated	762	123
Nd ₂₀ (Fe _{0.95} Co _{0.05}) ₇₄ B ₆ + 2 at. % V+3 at. % Al	as sintered	1225	194
	heat treated	1442	238

phase containing Al in equilibrium with ϕ and η at 1000 and 1100 °C, respectively. The composition of the liquid correspond well with the composition in the Fe–Nd–B system and is slightly shifted closer to the Nd corner. The composition of this liquid is given in Table I. In the quaternary Fe–Nd–B–Al system, the ϕ phase was found to contain aluminium, replacing iron, which is in agreement with previous work.² The composition of this phase at 1000 °C was determined both in equilibrium with pure iron and in equilibrium with the liquid. The composition can be described by the formula Nd₂Fe_{14-x}Al_xB, where $x=1.2$ in the equilibrium with the liquid, and $x=0.7$ in the equilibrium with Fe. The slightly lower Nd content obtained for this phase in the quaternary system, see Table I, as compared to the ϕ phase in the Fe–Nd–B system, might be due to the uncertainty in the EPMA analysis. Furthermore, it was not possible to determine the variation of Al content of this phase at 1100 °C due to the thin layer of the ϕ phase obtained in this case. The overall composition could, however, be described by Nd₂Fe_{14-x}Al_xB with $x=0.5$. The ρ phase was also found to dissolve aluminium on the expense of the iron content. An approximate composition for this phase at 1000 °C is Nd₂Fe_{1-x}Al_xB₃, where x is about 0.3. The Al content of the η phase was below the detection limit of the microprobe, which is believed to be less than 0.1% Al. The composition of this phase was the same in both the ternary and the quaternary systems.

Magnetic properties

The compositions of the alloys studied are listed in Table II. Tenaud *et al.*⁵ have reported that the decrease in coercivity due to a Co addition can be compensated for by additions of V. They found that the optimum V addition was critically

dependent on the B content. Based on the work by Tenaud *et al.*⁵ a V addition of 2 at. % was used in the present study. Al is known to improve the coercivity of sintered Fe–Nd–B magnets. Schneider *et al.*² have reported a coercivity maximum in sintered Fe–Nd–B magnets when the amount of Al is 3 at. %, which was used in the present study. In Table II is summarized the results from the measurements of the coercivity and energy product. The post-sintering heat treatment had a large positive effect on the measured magnetic properties. The Al additions improved the coercivity as compared to the unalloyed Fe–Nd–B magnet. The substitution of 5 at. % Co for Fe, however, decreased the coercivity substantially. The positive effect of combining Co and V additions is shown, but the coercivity is still considerably lower as compared to the unalloyed magnet. This effect is probably due to new paramagnetic phases appearing in the material after sintering. The results also show that Al and Co additions alone is not enough to obtain high coercivity. If Al, Co, and V additions are combined, however, the coercivity increases well above the value of the unalloyed and the Al alloyed magnet. The coercivity after alloying with only 2 at. % V and after alloying with Al and V was almost zero and these results were not included in Table II.

These effects on coercivity can be fully understood if the appropriate phase diagrams are known. The work at our department on this area is therefore concentrated on more phase diagram studies, and the results from these studies will be published later.

ACKNOWLEDGMENTS

The help given by Dr. Per-Olof Olsson, Swedish Military Research Establishment, during the EPMA analysis, and by Dr. Per Granberg, Solid State Physics, Uppsala University, on the magnetic measurements, is gratefully acknowledged. The financial support from the Swedish Board for Industrial and Technical Development is also gratefully acknowledged.

¹ J. M. D. Coey, H. S. Li, J. P. Gavigan, J. M. Cadogan, and B. P. Hu, in *Concerted European Action on Magnets*, edited by I. V. Mitchell, J. M. D. Coey, D. Givord, I. R. Harris, and R. Hanitsch (Elsevier, London, 1989), p. 76.

² E. Schneider, E.-T. Henig, B. Grieb, and G. Knoch, in *Concerted European Action on Magnets*, edited by I. V. Mitchell, J. M. D. Coey, D. Givord, I. R. Harris, and R. Hanitsch (Elsevier, London, 1989), p. 335.

³ M. Sagawa, *J. Mater. Eng.* **13**, 95 (1991).

⁴ K. Fritz, B. Grieb, E.-T. Henig, and G. Petzow, *Z. Metallkd.* **83**, 157 (1992).

⁵ P. Tenaud, F. Vial, and M. Sagawa, *IEEE Trans. Mag.* **26**, 1930 (1990).

⁶ G. Schneider, E.-T. Henig, G. Petzow, and H. H. Stadelmaier, *Z. Metallkd.* **77**, 755 (1986).

⁷ B. Grieb, E.-T. Henig, G. Schneider, G. Knoch, G. Petzow, and D. de Mooij, *Powder Met.* **35**, 231 (1992).

⁸ Y. Matsuura, S. Hirose, H. Yamamoto, S. Fujimura, M. Sagawa, and K. Osamura, *Jpn. J. Appl. Phys.* **24**, L635 (1985).

Investigations of magnetic properties and microstructure of 40Cedidymium-Fe-B based magnets

S. X. Zhou and Y. G. Wang

Department of Physics, The Norwegian Institute of Technology (NTH), The University of Trondheim, N-7034 Trondheim, Norway

R. Høier

Division of Applied Physics, The Foundation for Scientific and Industrial Research at the Norwegian Institute of Technology (SINTEF-Applied Physics), N-7034 Trondheim, Norway

The influence of Si, Co, and Dy_2O_3 on magnetic properties of sintered 40Cedidymium-Fe-B magnets was investigated and related to the microstructure through transmission electron microscopy (TEM) investigations. It is found that the decrease in iH_c and T_c caused by the presence of Ce in the 40Cedidymium could partly be compensated by additives. Sintered magnets with $iH_c = 9.2$ kOe and $(BH)_{\text{max}} = 28.2$ MG Oe were successfully achieved. TEM investigations show an intragranular amorphous phase within the $\text{R}_2\text{Fe}_{14}\text{B}$ (R=Nd, Pr, or Ce) grains and three new intergranular phases at grain boundaries and junctions of the $\text{R}_2\text{Fe}_{14}\text{B}$ grains. It is suggested that the deterioration in the magnetic hardening is closely related to these new phases as well as the low magnetic anisotropy field of the $\text{Ce}_2\text{Fe}_{14}\text{B}$ compound. The intragranular phase is likely to act as nucleation positions for reverse magnetic domains.

I. INTRODUCTION

Since the simultaneous discovery of Nd-Fe-B-based permanent magnets by Sumitomo Special Metals¹ in Japan and General Motors² in the United States in 1983, the R-Fe-B compounds have been of continuous interest in both technological and scientific fields because of their superior magnetic properties. Magnets with energy products as high as 45 MG Oe are commercially available, and there is a growing demand for applications related to miniaturization and more efficient devices. However, despite the outstanding magnetic properties of these magnets, their applications, especially in price-sensitive areas, have been hindered by their relatively high cost compared to the established magnets such as hard ferrite. In the past several years, many investigations³⁻⁸ have indicated that it is feasible to reduce this problem by replacing Nd with other more abundant and more inexpensive rare-earth elements, Ce, La, or unseparated rare-earth mixtures. According to Okada *et al.*,³ 40Cedidymium, which is the typical product in the extracting process of the rare-earth elements, is a good candidate for developing inexpensive R-Fe-B magnets. However, the magnetic anisotropy field, the saturation magnetization, and the Curie temperature of the $\text{Ce}_2\text{Fe}_{14}\text{B}$ compound are much lower than those of $\text{Nd}_2\text{Fe}_{14}\text{B}$. This in turn drastically reduces the coercivity, the energy product, and the thermal stability of sintered 40Cedidymium-Fe-B magnets. In our previous work,⁸ the alloy phases and the influence of Si, Co, and Dy_2O_3 on the magnetic properties of sintered 40Cedidymium-Fe-B magnets have been studied. In this paper the magnetic properties of 40Cedidymium-Fe-B sintered magnets with additions of Si, Co, and Dy_2O_3 are presented and related to the microstructure through transmission electron microscopy investigations.

II. EXPERIMENTAL PROCEDURE

40Cedidymium with the composition of 40Ce-50Nd-10Pr in wt % was synthesized using pure Nd, Ce, and Pr

metals. Two series of alloys, whose compositions are 40Cedidymium_{16.5}Fe_{77-x}Si_xB_{6.5} (alloy A) and 40Cedidymium_{16.5}Fe_{73-y}Co_ySi₄B_{6.5} (alloy B), where $x=0, 2, 4, 6$, and 8 and $y=0, 10, 20$, and 30 , were induction melted in an aluminium oxide-lined graphite crucible under argon atmosphere. The detailed procedures of sintered magnet production was described in Ref. 8. A series of Dy_2O_3 -doped alloy (alloy C) was also processed by blending the 40Cedidymium_{16.5}Fe₆₃Co₁₀Si₄B_{6.5} alloy powder with different amounts (Z wt %) of Dy_2O_3 and then the same procedure as described in Ref. 8 was followed. The magnetic properties were measured using an integrating hysteresigraph, and the Curie temperature T_c was determined by a differential scanning calorimeter (DSC) at a heating rate of $10^\circ\text{C}/\text{min}$. Electron transparent foils were prepared using argon ion milling. The specimens were then examined in a Philips CM-30 transmission electron microscope equipped with a standard energy dispersive x-ray spectroscopy (EDS).

III. MAGNETIC PROPERTIES

The composition dependence of the magnetic properties of the sintered magnets is summarized in Table I. It is clear from this table that both iH_c and T_c show a monotonic increase with increasing Si content while the remanence shows a reverse trend on Si addition. The substitution of Co for Fe gives rise to a considerable increase in T_c but a decrease in iH_c as expected. The addition of Dy_2O_3 to the Si- and Co-containing magnet substantially increases the intrinsic coercivity, from 6.0 kOe for Dy_2O_3 -free alloy to 10.5 kOe for $Z=5$ in wt % (≈ 1.8 at. % Dy in the magnet). The remanence was slightly decreased at a level of Dy_2O_3 content less than 3 wt % (≈ 1.4 at. % Dy in the magnet).

IV. MICROSTRUCTURE

The microstructure of the sintered magnet with composition of 40Cedidymium_{16.5}Fe₆₃Co₁₀Si₄B_{6.5} blended with 3

TABLE I. Magnetic properties of alloy A with increasing Si (x) content, alloy B with increasing Co (y) content, and alloy C with increasing Dy₂O₃ content (Z).

Alloy		B_r (kG)	H_c (kOe)	$(BH)_{max}$ (MG Oe)	T_c (°C)
Alloy A: x at. %	0	11.6	5.1	27.8	261
	2	11.3	5.9	28.5	268
	4	11.2	6.5	29.0	275
	6	10.8	6.9	26.4	280
	8	10.3	7.2	24.0	286
Alloy B: y at. %	0	11.2	6.5	29.0	275
	10	11.3	6.0	26.5	350
	20	11.0	5.8	25.5	418
	30	10.5	5.5	23.3	464
Alloy C: Z wt % (at. % Dy)	0(0)	11.3	6.0	26.5	350
	2 (0.7)	11.1	8.5	29.0	
	3 (1.1)	10.9	9.2	28.2	
	4 (1.4)	10.5	9.8	25.8	
	5 (1.8)	9.9	10.4	22.9	

wt % Dy₂O₃ was studied in detail. Four typical phases were found in this magnet in addition to the R₂Fe₁₄B matrix, the B-rich phase and the Nd-rich phases, which are generally observed in the sintered Nd-Fe-B magnets. These new phases can be divided into two kinds. One is present within the matrix grains and the others at the grain boundaries. The dimensions of these phases vary from several hundred nanometers to several micrometers. The phase (phase A) in Fig. 1 shows a spherical configuration (particle) and is widely distributed inside the R₂Fe₁₄B grains. The corresponding selected area electron diffraction (SAED) pattern reveals that it is an amorphous phase. This was also confirmed by high-resolution images. The composition of the A particles analyzed by EDS is given in Table II. It is clear that these particles are rich in rare-earth elements (Nd, Ce, and Pr). The reason for the occurrence of phase A is still unknown. Figure 2 shows two intergranular phases (phases B and C) fre-

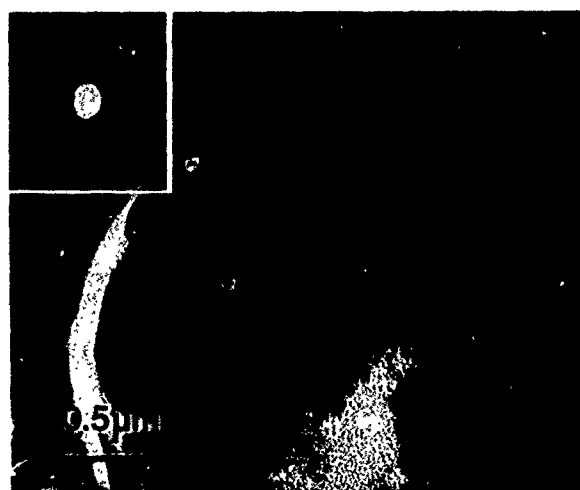


FIG. 1. TEM micrograph and SAED pattern of 40Cedidymium-Dy-Fe-Co-Si-B magnet, showing an intragranular amorphouslike phase A within the R₂Fe₁₄B grains.

TABLE II. Structure and composition of phases found in the sintered 40Cedidymium_{16.3}Fe₆₃Co₁₀Si₄B_{6.5}+3 wt % Dy₂O₃ magnet.

Phase	Structure	Composition (at %)			
		Nd	Ce	Pr	Fe
A	amorphous	40.46	37.23	2.44	19.87
B	cubic	48.25	35.40		16.35
C	trigonal	45.08	31.16	10.18	13.58
D	cubic	40.15	28.31		31.54

quently found at grain boundaries and triple point junctions between R₂Fe₁₄B matrix grains. EDS results (Table II) indicate that both phases are rich in rare-earth elements, although iron was also identified. From the SAED patterns [Figs. 2(a) and 2(b)] the crystal structure of phase B was determined to be cubic with lattice constant about 11 Å, which is close to cubic Nd₂O₃ ($a=11.04$ Å) structure, and the lattice parameters of phase C are close to trigonal Nd₂O₃ ($a=3.912$ Å, $c=6.227$ Å), a polymorph of the cubic Nd₂O₃. Because oxygen cannot be examined by EDS, it is not quite certain whether these two phases are oxides. However, R oxides are easily formed during magnet processing. At the junctions of the matrix grains we found, as shown in Fig. 3, another R-rich phase (phase D) with fcc structure and lattice param-

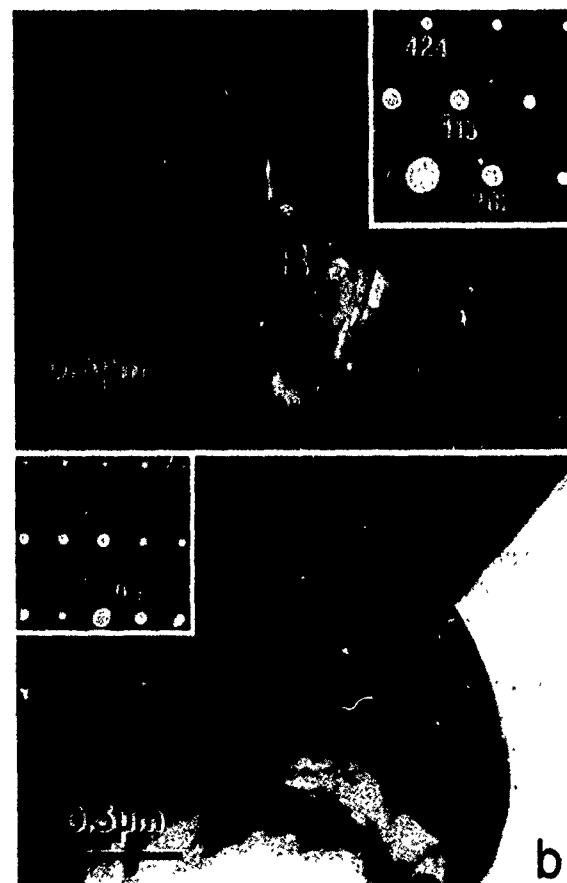


FIG. 2. Dark- and bright-field micrographs and SAED patterns of a 40Cedidymium-Dy-Fe-Co-Si-B magnet, showing two intergranular phases, B and C, with (a) cubic symmetry and (b) trigonal symmetry, respectively.



FIG. 3. Dark-field image of the intergranular phase D, found at junctions of the $R_2Fe_{14}B$ grains.

eter of about 5.4 \AA . It should be mentioned that all the four new phases observed contain a definite amount of iron.

V. DISCUSSION

It is well known that the origin of the magnetic hardening in R-Fe-B-based magnets is due to the formation of tetragonal $R_2Fe_{14}B$, with a high anisotropy field. In addition, the magnetic hardening also strongly depends on a favorable microstructure. According to Boltich *et al.*,⁹ the room-temperature anisotropy fields of $Nd_2Fe_{14}B$ and $Pr_2Fe_{14}B$ are nearly the same, 70.7 and 79.3 kOe, respectively, but the anisotropy field of $Ce_2Fe_{14}B$ is only 37.1 kOe, about half of that of $Nd_2Fe_{14}B$. From this point, the low coercivity of sintered 40Cedidymium-Fe-B magnet is likely to be attributed to the low anisotropy field of $Ce_2Fe_{14}B$. However, it should be noticed that the value of $H_c = 6 \text{ kOe}$, only about 50% of that of Nd-Fe-B sintered magnets,¹ seems anomalously low if we only consider the effect of $Ce_2Fe_{14}B$ in the sintered magnet. From this fact, it is strongly suggested that the deterioration in the magnetic hardening is not only due to the low magnetic anisotropy field of $Ce_2Fe_{14}B$, but also caused by an unfavorable microstructure. Usually sintered Nd-Fe-B-based magnets consist of three types of phases: the hard magnetic $Nd_2Fe_{14}B$ phase (matrix), the tetragonal boride phase $Nd_{1-x}Fe_4B_4$, and several intergranular Nd-rich phases. Moreover, the matrix does not contain any crystal defects and foreign phases. Based on the results of our investigation, the magnet under discussion clearly shows three new intergranular R-rich phases with different compositions and structures and an intragranular amorphous phase which is quite regularly distributed within the matrix grains. The influence of these new foreign phases on the magnetic hardening is not well understood, but it is suggested that the intragranular phase may act as nucleation positions of reverse domains due to the strong demagnetizing field around these positions, or

as pinning sites of domain walls. In this case we may infer that it is likely to act as nucleation positions of reverse domains. The enhancement of the coercivity by the substitution of Si for Fe may be attributed to the increase of the anisotropy field of $R_2Fe_{14}B$ ($R = Nd, Pr, \text{ and } Ce$) with Si content.^{10,11} The improvement on the Curie temperature T_c by Si addition may be interpreted as being due to a decrease of negative exchange interactions between $3d$ atoms. This behavior suggests that Si atoms have a strong preference for occupying the $8j_1$ and the $16k_2$ sites, which are characterized by a negative exchange interactions (antiferromagnetic) in the $R_2Fe_{14}B$ structure.

The substantial increase of the intrinsic coercivity in sintered 40Cedidymium-Fe-B magnet with increasing Dy_2O_3 content is similar to that in the Nd-Fe-B based sintered magnets reported by Ghandehari.¹² It is believed that the improvement is due to the high anisotropy field of the $Dy_2Fe_{14}B$ compound (158 kOe).

In summary, the results of the magnetic measurements indicated that the reduction of H_c and T_c caused by the Ce presented in the 40Cedidymium can be partly compensated by Si, Co, and Dy_2O_3 additions. Transmission electron microscopy (TEM) studies showed that an intragranular amorphouslike phase (phase A) is widely distributed within the matrix grains, and three new intergranular phases (phases B, C, and D) locate at grain boundaries and junctions of the matrix grains. It is inferred that these phases, especially phase A, are likely to act as nucleation positions of reverse magnetic domains.

ACKNOWLEDGMENTS

S. X. Zhou and Y. G. Wang are grateful for a grant from the Royal Norwegian Council for Scientific and Industrial Research (NTNF).

¹M. Sagawa, S. Fujimura, N. Togawa, and Y. Matsuura, *J. Appl. Phys.* **55**, 2083 (1984).

²J. J. Croat, J. F. Herbst, R. W. Lee, and F. E. Pinkerton, *J. Appl. Phys.* **55**, 2078 (1984).

³M. Okada, S. Sugimoto, C. Ishizaka, T. Tanaka, and M. Homma, *J. Appl. Phys.* **57**, 4146 (1985).

⁴B. M. Ma and C. J. Willman, *Mater. Res. Soc. Symp. Proc.* **96**, 133 (1987).

⁵W. Gong and G. C. Hadjipanyis, *J. Appl. Phys.* **63**, 3513 (1988).

⁶D. Li and V. Bogatin, *J. Appl. Phys.* **69**, 5515 (1991).

⁷M. Q. Huang, L. Y. Zhang, J. M. Elbicki, and W. E. Wallace, in *Proceedings of the 12th International Workshop on Rare Earth Magnets and their Applications*, Canberra, Australia, 1992, edited by Hi-Perm Laboratory, Research Centre for Advanced Mineral and Materials Processing, The University of Western Australia, p. 516.

⁸S. X. Zhou and R. Høier, *IEEE Trans. Magn.* (to be published).

⁹E. B. Boltich, E. Oswald, M. Q. Huang, S. Hirose, and W. E. Wallace, *J. Appl. Phys.* **57**, 4106 (1985).

¹⁰Xing Feng and Ho Wen-Wang, *J. Magn. Magn. Mater.* **74**, 271 (1988).

¹¹M. Jurczyk, *J. Magn. Magn. Mater.* **73**, 367 (1988).

¹²M. H. Ghandehari, *Appl. Phys. Lett.* **48**, 548 (1986).

Investigation of interaction mechanisms in melt-quenched NdFeB

L. Folks, R. Street, and R. Woodward

Research Centre for Advanced Mineral and Materials Processing, The University of Western Australia,
Nedlands 6009, Australia

Investigation of the magnetization processes in melt-quenched Nd₂Fe₁₄B materials has been made by analysis of measurements of the time dependence of the magnetizing curves (after thermal demagnetization) and demagnetizing curves at room temperature. The quantities S (the magnetic viscosity parameter) and χ_{irr}^i (the intrinsic irreversible susceptibility) have been determined for the commercially available materials MQI (isotropic, resin bonded), MQII (slightly anisotropic, hot pressed), and MQIII (anisotropic, hot formed) produced by Delco Remy, U.S. In addition $\delta M(H)$, which compares the fraction of irreversible processes occurring at a particular field in the magnetizing mode with those occurring at the same field in the demagnetizing mode, has been determined as a function of internal field, and the results are interpreted in terms of interactions between grains. From these results it is shown that although the magnetization and demagnetization behavior of these materials differ substantially, this may be attributed to differences in the domain structure. There is no evidence that the mechanism for hardening is different from that of the sintered materials.

INTRODUCTION

The mechanisms of magnetization in Nd₂Fe₁₄B magnets produced by melt quenching have been the subject of intensive investigation (e.g., for a review see Herbst¹). There is convincing Lorentz microscopy evidence that domain boundary walls are pinned at grain boundaries in optimally quenched ribbons and in hot-pressed and die-upset powders in the demagnetized state (Mishra²). These observations have been used to support a strong domain wall pinning model developed by Gaunt³ to explain the coercivity of melt-quenched materials (Pinkerton and Fuerst⁴). However Dürst and Kronmüller⁵ and Grönfeld and Kronmüller⁶ show by theory and experiment that in fact the coercivity of the melt-quenched materials may be explained assuming that nucleation is the dominant mechanism for magnetic hardening.

Typical melt-quenched materials exhibit two steps in the magnetization curve, suggesting that at least two distinct processes are at work, but on the demagnetization curve no steps are seen, and, from the uniformity of this behavior across compositions and microstructures, it may be assumed that only one mechanism is at work.

We have measured magnetic viscosity from the magnetization and demagnetization curves for samples of melt-quenched Nd₂Fe₁₄B, MQI (resin-bonded, isotropic), MQII (slightly anisotropic, hot pressed), and MQIII (anisotropic die upset), supplied by Delco Remy, USA. These data have been fitted to the form $M = A + S \ln(t + t_0)$ to give the magnetic viscosity parameter S as a function of internal field H_i . In conjunction with these experiments we measured the "recoil curves" by reversing the field until H_i became zero after progressively larger magnetizing fields were applied. Wohlfarth suggested that these data could be used to give an indication of the deviations from the case of noninteracting single-domain particles.⁷ Following Wohlfarth's theory, Kelly *et al.*⁸ have defined

$$\delta M = 2(P_i - P_d), \quad (1)$$

where $P_i = M_i(H)/M_i(\infty)$ and $P_d = \frac{1}{2}[1 - M_d(H)/M_i(\infty)]$,

which allows these deviations to be quantified. The isothermal remanence $M_i(H)$ and the dc demagnetization remanence $M_d(H)$ may be determined from the recoil curves, as the values of M when H_i becomes zero.

EXPERIMENT

All the magnetic measurements reported here were made using a vibrating sample magnetometer in conjunction with a 50 kOe solenoid. A cryostat was available to maintain the temperature of the sample during the measurements to ± 0.5 K. The samples were prepared in the form of spheres $\phi \sim 5$ mm with sphericity $\pm 5 \mu\text{m}$, allowing the demagnetization factor to be accurately known. Measurements were made at 298 K on the magnetization and demagnetization curves for the three materials after thermal demagnetization. In an effort to gather comprehensive information magnetic viscosity measurements were performed in conjunction with recoil curves for the initial curve and the demagnetization curve.

The values of $M_i(H_i)$ form the isothermal remanent magnetization (IRM) curve and similarly the values of $M_d(H_i)$ form the dc demagnetization (DCD) curve. If the recoil curves can be assumed to involve only reversible magnetization processes, then the values of $M_i(H_i)$ and $M_d(H_i)$ can be said to be the irreversible components of magnetization M_{irr} associated with H_i , the measurement fields.

In the case where the recoil curves for each value of H_i are parallel to each other, the value of M_{tot} at $H_i = 0$ may be adjusted to give a more accurate value of $M_{\text{irr}}(H_i)$ by taking into account the magnetic viscosity via a simple linear relation. Although this linear approximation is not ideal for other than square loop materials, the values of M_{irr} derived from this method are close (within 5%) to those derived from the method outlined by Street, McCormick, and Folks.⁹

RESULTS

For MQI the recoil curves recorded during the magnetization of the samples were largely parallel and reversible. All

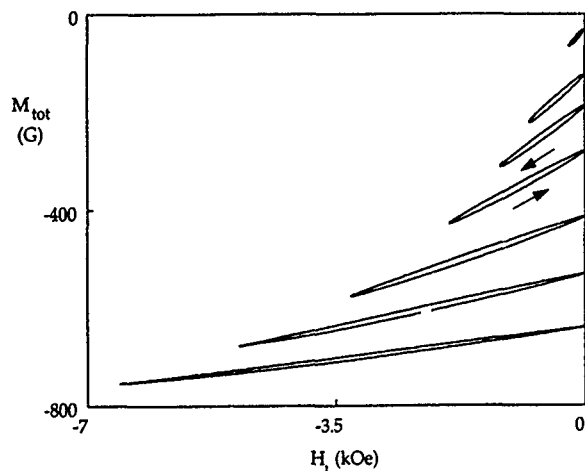


FIG. 1. A selection of recoil curves from the initial magnetization of MQIII produced by applying a magnetizing field to the sample, decreasing the field to zero, then increasing it again.

the recoil curves from both the magnetization and demagnetization measurements were slightly concave upwards at fields smaller than 2.5 kOe and linear elsewhere. For MQII and MQIII the initial recoil curves were neither parallel to each other nor truly reversible in the low-field region, as Fig. 1 shows for MQIII. At sufficiently high fields (approximately at the end of the first step) the recoil curves became parallel. For the demagnetization measurements the recoil curves were both linear and parallel to a high degree of accuracy.

The magnetic viscosity data collected for the three samples were very similar in form to that taken from conventional measurements, where no recoil curves are performed. For each of the materials the relative peak value of S is much smaller and occurs at a lower field (by ~ 1.6 kOe) on the magnetization curve than the demagnetization curve, indicating that the irreversible processes occurring are dissimilar. The shape of the S curves, shown in Fig. 2, gives no indication of the steps which appear in the initial M vs H curves.

The values of intrinsic irreversible susceptibility χ_{irr}^i , taken as the derivatives of the IRM and DCD curve with respect to H_i , are shown in Fig. 3. For the three materials the peak in χ_{irr}^i on the demagnetization curve occurs at a slightly larger field than either of the peaks on the magnetization curve, in contrast to other reports that the two peaks occur at the same field.⁶ The field at which the second peak in χ_{irr}^i occurs is the same as the field at which the single peak in S occurs during magnetization.

Figure 4 shows δM vs H_i for the materials calculated according to Eq. (1). It may be seen that the steps in the initial curves are also evident in the δM curves and that for all three materials the value of δM is positive until some point after coercivity H_c when it becomes small but negative. For each of the materials, the peaks in the δM curves coincide with the fields at which the second peak of χ_{irr}^i (and the peak of S) occur during magnetization. The sharp decreases in δM correlate closely with the peaks in χ_{irr}^i (and S) during demagnetization. These data (in agreement with the

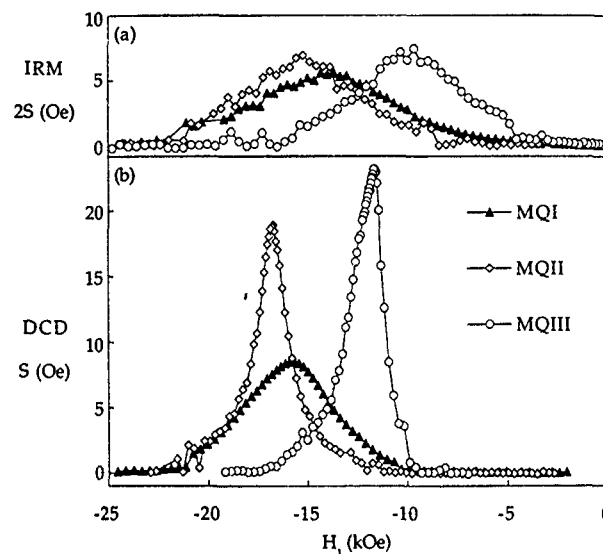


FIG. 2. Values of S vs H_i for MQI, MQII, and MQIII from (a) the initial curve (IRM) and (b) the demagnetizing curve (DCD), where S arises from fitting the time dependence data to the form $M = A + S \ln(t + t_0)$. The IRM data have been multiplied by 2 to allow direct comparison with the DCD data.

Henkel plots given by Herbst¹) show that the proportion of particles which have aligned with the field on the initial curve is greater than that on the demagnetization curve, for a given H_i , over most of the range.

SUMMARY

For MQII and MQIII the variations of S and χ_{irr}^i suggest that the first step in the initial curve is a result of largely irreversible processes but these are not sensitive to thermal activation. This is similar to the low-field behavior of sin-

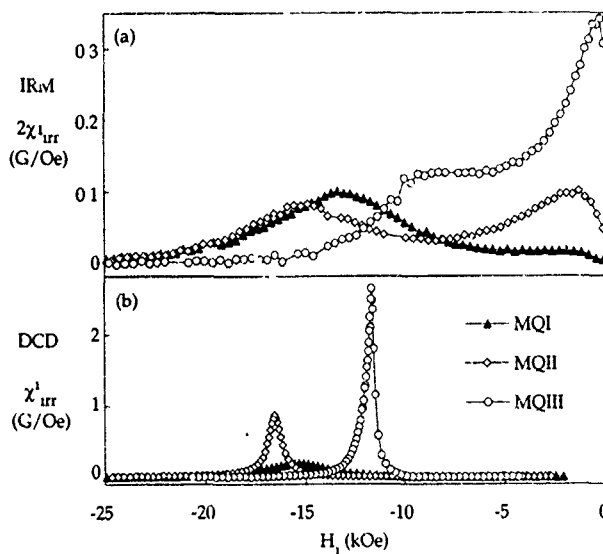


FIG. 3. χ_{irr}^i vs H_i for MQI, MQII, and MQIII from (a) the initial curve (IRM) and (b) the demagnetizing curve (DCD). The IRM data have been multiplied by 2 to allow direct comparison with the DCD data.

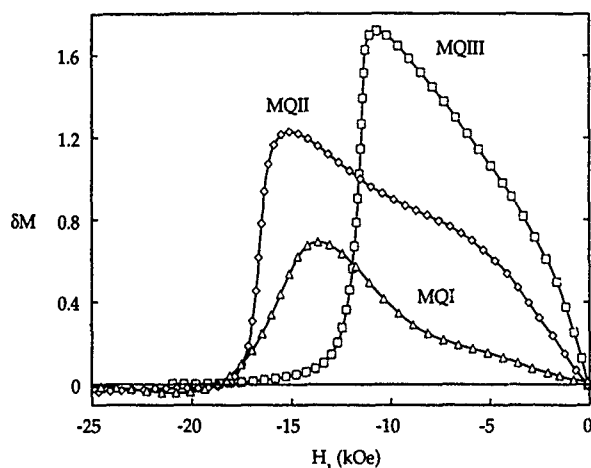


FIG. 4. δM vs H_i plot for MQI, MQII, and MQIII. The large positive values at low fields indicate the presence of larger magnetizing interactions during the initial curve than the demagnetizing curve.

tered NdFeB materials. By contrast the irreversible processes which give rise to the second step are subject to significant thermal activation, as indicated by the peak in S . This is commensurate with the opinion of Grönefeld and Kronmüller⁶ that the first step arises from the movement of domain walls within multidomain grains which result from the thermal demagnetization process. The annihilation of the domain walls will be a field-dominated process in the case where there are relatively few pinning sites within the grains, and only small time-dependent effects are expected.

If half the grains within the material are initially multidomain, and they can be assumed to be noninteracting uniaxial particles; then the value of M_{irr} after the first step will be 50% of that at saturation. Comparison of the χ'_{irr} curves with the IRM curves show that for MQII (44%) and MQIII (49%) this is approximately true, while for MQI (6%) it appears that few of the grains are multidomain after thermal demagnetization. This result may arise from the different thermal treatments of the materials, leading to either a different distribution of grain sizes or to a different density of pinning sites within the grains. However, if there were significant numbers of pinning sites within the grains, it would be expected that significant time dependence would also be evident, so the former explanation seems more likely on balance. MQIII (hot pressed and die upset) is known to have a sharp grain size distribution, and these results suggest that it is centred at some value larger than the critical size for a single domain, while the distribution for MQI appears to be centered at a size smaller than the critical size, so that only a small fraction of the grains start in a multidomain state. The average diameters of the grains in MQI, MQII, and MQIII are about 0.03 (Ref. 1), 0.08 (Ref. 10), and 0.1 (Ref. 1) μm , respectively. However, the theoretical critical domain size, below which formation of a domain wall is energetically unfavorable, is 0.3 μm (assuming no interactions with neighboring grains). These results suggest that critical domain size in bulk materials may be significantly smaller than the theoretical value for an isolated grain.

In the low-field region the recoil curves are not truly reversible, behavior which is routinely observed in strongly exchange coupled materials. This suggests that the domain wall movements within the grains (which determine the first step of the magnetization curve) are subject to exchange coupling between the hard grains and the magnetically softer grain boundary phase. The coupling energy is small compared to the magnetostatic coupling which is set in place once the domain walls have become pinned at the grain boundaries; hence it is not possible to detect this effect after saturation.

After most of the multidomain grains have been removed by the field-dominated process of domain wall annihilation, M changes slowly until some larger field, slightly smaller than H_c , when the rate of change picks up again. This point is correlated with the peak value of δM , the point at which there is the largest deviation in the behavior of the IRM and DCD curves. δM then drops rapidly to a small negative value so that the exchange coupling is in fact working to slightly demagnetize the sample at fields $> H_c$. This behavior is explained by considering that after the first step a large proportion of the grains will have adopted easy directions of magnetization close to the direction of H_a . These will be able to fully align with H_a by reversible mechanisms, leading to the small χ'_{irr} observed on the initial curve. By contrast, on the demagnetizing curve the intergranular interactions will be working to maintain a high value of M until H_c is reached.

The time dependence of M is much smaller in magnitude everywhere on the initial curves compared with the demagnetization curves. As the multidomain grains have become single-domain grains, by means of almost unimpeded domain wall motion, they will have preferentially moved to those easy directions closest to the direction of H_a so that the remaining changes in M as M_s is approached may occur mostly by reversible processes. Only 50% of the fraction of the grains which began as single-domain particles will be contributing to the time dependence which is observed.

These results give no reason to attribute magnetic hardening in melt-quenched materials to a different mechanism from that for sintered materials. Rather, the differences in the magnetization curves are attributable to differences in the domain structure alone.

ACKNOWLEDGMENTS

L.F. would like to thank Dr. K. O'Grady, S. Geoghegan, and E. Feutrill for helpful discussions.

¹J. F. Herbst, Rev. Mod. Phys. **63**, 819 (1991).

²R. K. Mishra, J. Magn. Magn. Mater. **54-57**, 450 (1986).

³P. Gaunt, Philos. Mag. B **48**, 261 (1983).

⁴E. E. Pinkerton and C. D. Fuerst, J. Appl. Phys. **69**, 5817 (1991).

⁵K.-D. Durst and H. Kronmüller, J. Magn. Magn. Mater. **68**, 63 (1987).

⁶M. Grönefeld and H. Kronmüller, J. Magn. Magn. Mater. **88**, L267 (1990).

⁷E. P. Wohlfarth, J. Appl. Phys. **29**, 595 (1958).

⁸F. E. Kelly, K. O'Grady, P. I. Mayo, and R. W. Chantrell, IEEE Trans. Mag. **25**, 3881 (1989).

⁹R. Street, P. G. McCormick, and L. Folks, J. Magn. Magn. Mater. **104-107**, 368 (1992).

¹⁰Raja K. Mishra, J. Appl. Phys. **62**, 967 (1987).

Crystal structure and low-temperature magnetic properties of melt-spun $\text{Sm}_2\text{Co}_7\text{B}_3$ compounds

C. J. Yang, W. Y. Lee, and S. D. Choi

Electromagnetic Materials Laboratory, Research Institute of Industrial Science & Technology, P.O. Box 135, 790-330 Pohang, Korea

Low-temperature magnetic properties and crystal structures of melt-spun $\text{Sm}_2\text{Co}_7\text{B}_3$ compound were characterized. The magnetic measurements in the temperature range 77–450 K indicated that a spin reorientation took place at about 150–160 K. A huge anisotropy was observed ($H_a = 135$ kOe at 300 K, 725 kOe at 77 K) for $\text{Sm}_2\text{Co}_7\text{B}_3$, although the magnetic moment is rather low. The crystal structure of the $\text{Sm}_2\text{Co}_7\text{B}_3$ compound was analyzed in detail by Rietveld analysis of powder diffraction for the first time, and revealed that B(4h) atoms are not placed in the Sm(2e) layer but in between the Sm(2e) and Co(6i₁) layers.

I. INTRODUCTION

Recently, the $\text{R}_{n+1}\text{Co}_{3n+5}\text{B}_{2n}$ ($n=1, 2, \dots, \infty$) type compounds, which are derivatives of the RCo_5 type (R=rare earth), attracted considerable interest.¹⁻³ All the previous studies suggested a huge magnetocrystalline anisotropy for $\text{R}_{n+1}\text{Co}_{3n+5}\text{B}_{2n}$ compounds. SmCo_4B ($n=1$) was reported² to show an anisotropy field of 906 kOe at 4.2 K, and $\text{Sm}_2\text{Co}_7\text{B}_3$ ($n=3$) was reported⁴ to exhibit an anisotropy field of 130 T at 4.2 K. Such huge anisotropies used to be explained in terms of the electrostatic interaction of the crystal field.^{2,5,6} The nature of the electrostatic field effect is regarded to be associated with the point symmetry of the atomic sites in the underlying crystal structure. However, no study was reported on the exact crystal structure of the $\text{R}_{n+1}\text{Co}_{3n+5}\text{B}_{2n}$ compounds. In this work we intend to refine the crystal structure of the $\text{Sm}_2\text{Co}_7\text{B}_3$ compound by using an advanced x-ray powder technique (Rietveld method) for a future study of magnetocrystalline anisotropy, and we report low-temperature magnetic behavior to examine their application as a permanent magnet.

II. EXPERIMENT

The alloy samples of $\text{Sm}_2\text{Co}_7\text{B}_3$ composition were prepared by induction melting under an Ar atmosphere using 99.95% pure raw elements. An additional 10% Sm was added to compensate for the loss caused by Sm evaporation during melting. The cast compound was homogenized at 1000 °C for 50 h to obtain single-phase $\text{Sm}_2\text{Co}_7\text{B}_3$. Furthermore, melt-spun ribbons of identical stoichiometry were made using a substrate speed of 12 m/s, which gave a single-phase 2-7-3 compound. The magnetic measurements were carried out using cylindrical powder compacts ($\phi=3$ mm, $L=10$ mm), which were magnetically aligned along the axial direction. The compact was prepared by bonding particles of an average 32 μm size under a magnetic field. A Toei vibrating sample magnetometer was used to examine the low-temperature magnetic behavior from liquid-nitrogen temperature up to 400 °C, and a Perkin-Elmer thermomagnetic analyzer was used to identify the magnetic transformation up to the Curie point. The crystal structural simulation was carried out by refining the observed x-ray diffraction pattern using the Rietveld program.^{7,8}

III. RESULTS AND DISCUSSION

A. X-ray refinement and crystal structure

The crystal structure of $\text{Sm}_2\text{Co}_7\text{B}_3$ was identified from both the cast and melt-spun samples. Figure 1 shows the powder diffraction patterns of the melt-spun $\text{Sm}_2\text{Fe}_7\text{B}_3$ compound refined by using RIETAN program. The dots refer to the observed pattern and the solid line is the calculated fit. The dotted line shown at the bottom of figure indicates the degree of deviation of the calculated fit from the observed pattern. The x-ray refinements for both cast and melt-spun compounds commonly demonstrated a good fit to the $P6/mmm$ space group with the weighted factor $R_{wp}=0.152$ and the integrated intensity factor $R_I=0.028.8$. The determined lattice parameters are $a=5.1087$ Å and $c=12.777$ Å, which are not quite the same as those reported ($a=5.088$ Å, $c=12.79$ Å) by Ido, Konno, and Ogada,⁴ who used a cast sample. The structural coordinates of the refined crystal are tabulated in Table I and the simulated model is plotted in Fig. 2. Two formula units of 24 atoms constitute one unit cell. As shown in Fig. 2, Co atoms occupy three different equivalent sites, Co(2c), Co(6i₁), and Co(6i₂). This 2-7-3 compound results from replacing the Co atoms on the plane of Sm(2e) sites in the SmCo_5 crystal structure by B(4h) atoms. However, it was found for the first time that those replaced B(4h)

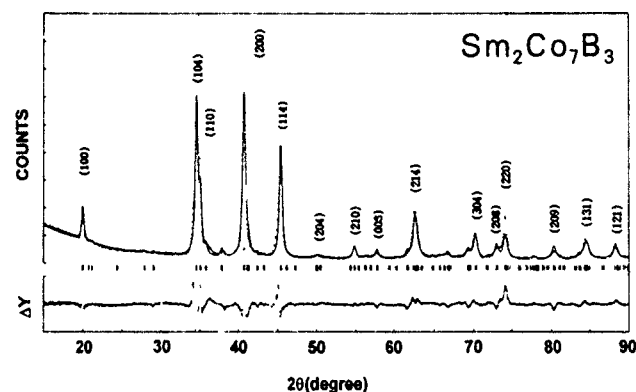


FIG. 1. Powder diffraction patterns of melt-spun $\text{Sm}_2\text{Co}_7\text{B}_3$. The dotted line refers to the observed pattern and the solid line is the calculated fit. The deviation of the calculated fit from the observed data is indicated at the bottom of the figure.

TABLE I. Refined structural coordinates of atomic sites of melt-spun $\text{Sm}_2\text{Co}_7\text{B}_3$ compounds.

Lattice parameter	Sites	Coordinates		
		x	y	z
$a=5.1087 \text{ \AA}$	Sm(1a)	0.0000	0.0000	0.0000
$c=12.770 \text{ \AA}$	Sm(1b)	0.0000	0.0000	0.5000
	Sm(2e)	0.0000	0.0000	0.2610
$P6/mmm$	Co(2c)	0.3333	0.6667	0.0000
	Co(6i ₁)	0.5000	0.0000	0.1596
$R_{wp}=0.152$	Co(6i ₂)	0.5000	0.0000	0.3857
$R_1=0.028$	B(2d)	0.3333	0.6667	0.5000
	B(4h)	0.3333	0.6667	0.1990

atoms are not placed exactly on the Sm(2e) layer but in between layers of Sm(2e) and Co(6i₂), i.e., 0.792 Å away from the Sm(2e) layer, while other B(2d) atoms substitute for the Co atoms of identical position on the Sm(1b) layer in the SmCo_5 crystal.

Unlike SmCo_5 , the interlayer distance d_2 between Sm(2e) and Co(6i₂) atoms is not the same as the distance d_1 between the Co(6i₂) and Sm(1a) layers in $\text{Sm}_2\text{Co}_7\text{B}_3$. The distances d_1 and d_2 were found to be 1.295 and 2.038 Å, respectively. Therefore the schematic crystal structure which was derived merely by replacing the layer of Co atoms by B atoms of Refs. 2 and 4 is not the correct one. The calculated interatomic distances of the refined $\text{Sm}_2\text{Co}_7\text{B}_3$ crystal are tabulated in Table II, principally regarding the hexagonal cell in Fig. 2.

B. Low-temperature magnetic properties

Figure 3 shows the low-temperature magnetic properties of melt-spun $\text{Sm}_2\text{Co}_7\text{B}_3$ measured from 77 to 350 K. The magnetic moments measured along directions both parallel

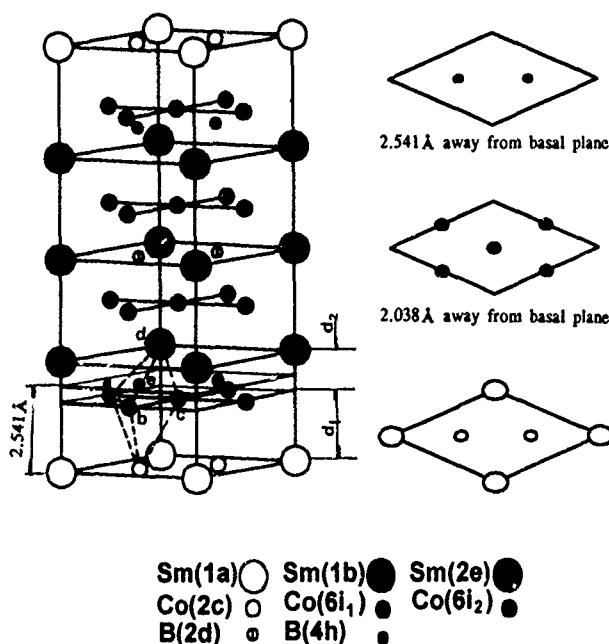


FIG. 2. The unit cell of $\text{Sm}_2\text{Co}_7\text{B}_3$ in a hexagonal cell.

TABLE II. Calculated interatomic distances of the $\text{Sm}_2\text{Co}_7\text{B}_3$ crystal (see the hexahedral cell in Fig. 2).

Atoms	Distance (Å)
Co(6i ₂)–Co(6i ₁); c axial	2.8873
Sm(2e)–Sm(1a); c axial	3.3330
Sm(2e)–Sm(1b); c axial	3.0520
Co(2c)–Co(6i ₁); a,b,c atoms	4.4021
Sm(2e)–Co(6i ₁); a,c,d atoms	2.8638
Sm(2e)–Co(6i ₁); b,d atoms	4.6099
B(4h)–Co(6i ₁); a,c,e atoms	1.5582
B(4h)–Co(6i ₁); b,e atoms	3.9342
B(4h)–Sm(2e); d,e atoms	3.0539

(||) and perpendicular (⊥) to the axial direction vary with temperature. Both the saturation and residual moments measured along the parallel direction decrease slowly with increasing temperature and drop at about 225 K, rising again at 250 K up to the previous moment observed at 225 K. Surprisingly, the magnetization curve measured along the perpendicular direction, which was monotonically flat below 225 K, rises abruptly at 225 K. The moment values observed in both directions tend to meet each other at about 350 K. We tried to explain this behavior in connection with the spin reorientation, which will be described later. The coercivity in the parallel direction at 77 K was too high (perhaps higher than 35 kOe) to be measured in the present maximum field, 16 kOe. It decreases rapidly to 8 kOe at 300 K.

To obtain the anisotropy field of $\text{Sm}_2\text{Co}_7\text{B}_3$, a field-oriented compact sample was prepared using the single-crystal powders made from a cast compound. At 300 K an anisotropy field of 135 kOe was observed, while a huge anisotropy of 725 kOe was measured at 77 K. These anisotropy fields were estimated by extrapolating the curve through polynomial fitting. However, the experimentally saturated magnetic moment by the field of 16 kOe at 300 K was only 25 emu/g although the coercivity (H_c) observed along the perpendicular direction seemed to exceed 25 kOe. One can realize that both the anisotropy field and coercivity are un-

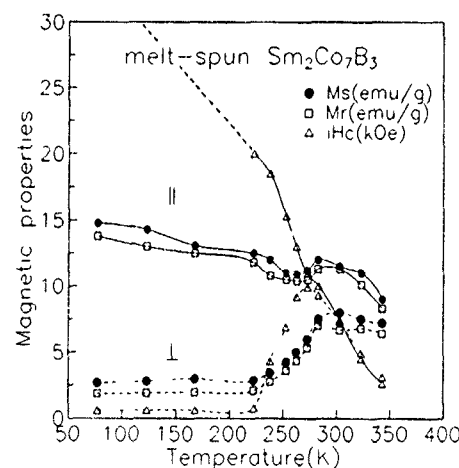


FIG. 3. Magnetic properties of melt-spun $\text{Sm}_2\text{Co}_7\text{B}_3$ as a function of temperature. || denotes the data measured along the direction parallel to the aligned axis, and ⊥ is for the perpendicular direction to the aligned axis.

TABLE III. Comparison of magnetic properties calculated from experimental data for $\text{Sm}_2\text{Co}_7\text{B}_3$.

	H_a	H_c (kOe)	M_s (emu/g)	T_c (K)	Magnetic moment	
					$\mu_B/\text{f.u.}$	μ_B/Co
Ido and co-workers ^a ($a=5.088 \text{ \AA}$, $c=12.790 \text{ \AA}$)	130 T	275		402	3.68 ^b	0.30
Present work ($a=5.1087 \text{ \AA}$, $c=12.777 \text{ \AA}$)	725 kOe	25	25	403	3.195	

^aReferences 4 and 9.

^bReference 9.

derestimated due to the weak field in this study comparing with that Ido and co-workers,^{4,9} who derived the values from the measurement at 4.2 K under a high field (30 T). Table III summarizes the calculated average magnetic moment per formula unit, $\mu_B/\text{f.u.}$ A moment of 3.195 $\mu_B/\text{f.u.}$ was obtained in the present work, which is smaller than that of Refs. 4 and 9. Ido and co-workers^{4,9} in calculating the moment assumed that the Sm ion moment is negligibly small, and an incomplete crystal model which is proved to be erroneous by our study was used. In addition, the Co atomic moment is largely decreased by neighboring B atoms.⁹ Actually this case happened between the Sm(2e) and B(4h) layers shown in Fig. 2.

In order to clarify if the magnetic anomaly observed in Fig. 3 is a symptom of spin reorientation or not, low-temperature torque curves were measured from 77 to 300 K

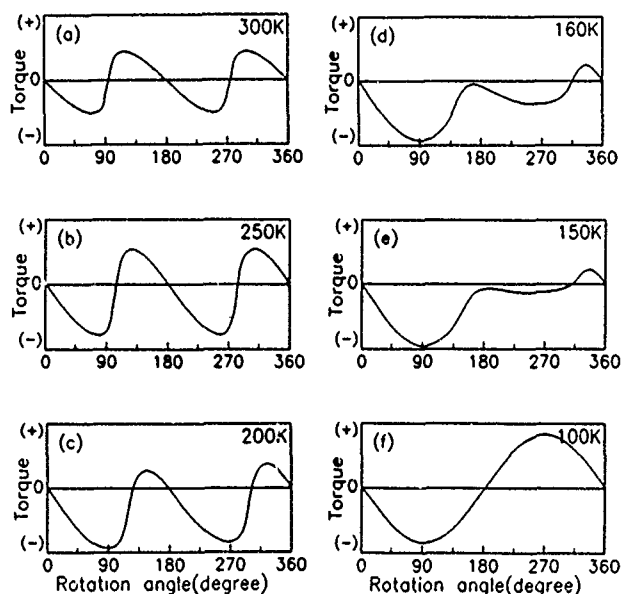


FIG. 4. Torque curves vs rotation angle of a field-oriented $\text{Sm}_2\text{Co}_7\text{B}_3$ powder compact sample measured at low temperature.

under a 16-kOe field and shown in Fig. 4. The sample used was a cylindrical powder compact, 3 mm diam \times 10 mm length. The powders of under 32 μm size were prepared from a cast ingot having a grain size larger than 30 μm and with the field oriented perpendicular to the axial direction of the sample bonded by an epoxy resin. The torque curves were measured by placing the sample with its axis parallel to rotational axis, which is perpendicular to the field direction. If the alignment is assumed to be perfect, the easy axis, [0001] of each $\text{Sm}_2\text{Co}_7\text{B}_3$ crystal, makes an angle θ with respect to the magnetization. The magnetocrystalline anisotropy in hexagonal symmetry is expressed as^{10,11}

$$E = K_1 \sin^2 \theta + K_2 \sin^4 \theta + K_3 \sin^4 \theta \cos^4 \phi + \dots,$$

where ϕ is the angle of the easy axis projected onto the crystallographic plane parallel to the field direction and perpendicular to the rotational axis. Since the sample was a multicrystalline powder compact, the last term of the right-hand side of the above expression will be disregarded. The torque $\delta E/\delta \theta$ measured at 300–200 K shown in Fig. 4 exhibits a typical variation according to the above equation. At 150–160 K the torque curve changes its periodicity, but the curve returns to its normal shape at 100 K again. Taking into account the magnetization behavior in Fig. 3 and the torque curves in Fig. 4, one can realize that some type of spin reorientation takes place at about 150–160 K. An ac susceptibility measurement also suggests the spin reorientation at 150–160 K. For such an imperfectly field-aligned condition, the magnetocrystalline anisotropy energy seems to be equilibrated with the torque exerted by the external field at instantaneous moment:¹⁰

$$\begin{aligned} \delta E/\delta \theta &= 2K_1 \sin \theta \cos \theta + 4K_2 \sin^3 \theta \cos \theta \\ &= HM(\theta) \cos \theta = HM_s(1 - p \sin^2 \theta) \cos \theta, \end{aligned}$$

where M_s is the saturation magnetization, and p is a parameter indicating the degree of anisotropy, $[(M_{\parallel c \text{ axis}}) - (M_{\perp c \text{ axis}})]/M_s$. Therefore whether the observed spin reorientation would be due to the anisotropy change from axial to plane or to cone is not clear, and its determination is beyond the scope of this paper.

¹H. Oesterreicher, F. Spada, and C. Abache, Mater. Res. Bull. **19**, 1069 (1984).

²H. H. A. Smit, R. C. Thiel, and K. H. Buschow, J. Phys. F. **18**, 295 (1988).

³H. Oesterreicher, F. T. Parker, and M. Misroch, J. Appl. Phys. **12**, 287 (1977).

⁴H. Ido, K. Konno, and H. Ogada, J. Appl. Phys. **70**, 628 (1988).

⁵T. Ito, H. Ogada, and H. Ido, J. Appl. Phys. **73**, 5914 (1993).

⁶N. M. Hong, N. P. Thuy, and T. D. Hien, J. Appl. Phys. **73**, 5917 (1933).

⁷F. Izumi, Rigaku J. **6**, 10 (1989).

⁸F. Izumi, Manual of RIETAN System (National Institute in Inorganic Materials, Tokyo, Japan, 1987).

⁹H. Ogada, H. Ido, and M. Yamauchi, J. Appl. Phys. **73**, 5911 (1993).

¹⁰J. M. Alameda, D. Givord, R. Lemaire, and Q. Lu, J. Appl. Phys. **52**, 2079 (1981).

Saturation magnetization and anisotropy fields in the $\text{Sm}(\text{Co}_{1-x}\text{Cu}_x)_5$ phases

E. Lectard and C. H. Allibert

Laboratoire de Thermodynamique et Physico-Chimie Métallurgiques, URA29 Ecole Nationale Supérieure d'Electrochimie et Electrometallurgie de Grenoble, B.P. 75, 38402 Saint Martin d'Hères, France

R. Ballou

Centre National de la Recherches Scientifique 166X Grenoble, France

The magnetic characteristics of high-anisotropy $\text{Sm}(\text{Co}_{1-x}\text{Cu}_x)_5$ phases are determined experimentally at 300 K in the range $x < 0.6$. The saturation magnetization M_s decreases and vanishes for SmCo_2Cu_3 . Identical behaviors of M_s and Curie temperature T_C versus x are observed in the range $x < 0.6$. For significant Cu substitution rate ($x > 0.35$), the decrease of the anisotropy field (H_A) when x increases is strong. For lower Cu contents, huge values of anisotropy fields make difficult the accurate determination of the substitution effect. The first anisotropy constant K_1 is calculated using the available values of H_A and M_s . A linear decrease of K_1 is observed from SmCo_5 to SmCo_2Cu_3 .

I. INTRODUCTION

The Sm-Co-based permanent magnets of the 2:17 type consist of a network of fine precipitates based on $\text{Sm}(\text{Co,Cu})_5$ distributed in a matrix based on $\text{Sm}_2(\text{Co,Fe})_{17}$. The coercivity of these magnets is related to the exchange and anisotropy characteristics of the constitutive phases. Such magnetic properties are well known for the matrix $\text{Sm}_2(\text{Co,Fe})_{17}$ (Ref. 1) but are rather scarce in $\text{Sm}(\text{Co,Cu})_5$. The phase $\text{Sm}(\text{Co}_{1-x}\text{Cu}_x)_5$ derives from the substitution for nonmagnetic Cu atoms for Co in the hexagonal compound SmCo_5 (CaCu_5 structure).² Its Curie temperature (T_C), rather well established,³⁻⁶ shows the regular decrease expected for increasing x . The few data⁵⁻⁷ reported for its saturation magnetization exhibit the same trend. As for the anisotropy, SmCo_5 is characterized by a giant axial magnetocrystalline anisotropy⁸ that results from the dominant contribution of Sm. The same feature can be predicted in the Co-rich $\text{Sm}(\text{Co,Cu})_5$ phases. The experimental results published are only for $x = 0.3$,⁷ 0.48,⁶ and 0.6.⁵ The very high value of anisotropy field H_A reported for $x = 0.3$, higher than H_A of SmCo_5 ,⁷ questions the possible evolution of H_A with x . The purpose of the present work is first to determine by experimentation at room temperature the evolution of M_s and H_A for $\text{Sm}(\text{Co}_{1-x}\text{Cu}_x)_5$ in the x range 0–0.6, then to evaluate the constants of exchange (A) and anisotropy (K_1) using the available data of T_C , M_s , and H_A .

II. EXPERIMENT

Most of the measurements of magnetization were effected at 300 K using the axial extraction technique, in external fields H_{ext} up to 7 T. Only the specimen $\text{Sm}(\text{Co}_{0.6}\text{Cu}_{0.4})_5$ was studied in H_{ext} up to 15 T. The saturation magnetization M_s was deduced from measurements on powders. The anisotropy fields H_A were obtained by comparing the magnetization curves of single crystals with the applied field oriented parallel to the basal plane and parallel to the c axis. Most of the studied specimens were obtained from alloys prepared by induction or arc melting in purified argon atmosphere. The starting materials were pieces of electrolytic

Co and Cu, 99.99%, and of Sm, 99.9%. Some Sm excess was added to balance the Sm losses by evaporation and oxidation. The cast alloys were annealed at 1100 °C for 10 h and quenched. At the annealed state, the samples were characterized by standard optical metallography, electron probe microanalysis (EPMA), and x-ray diffraction by the Debye-Scherrer method. All the specimens were checked to be single phase with homogeneous composition and presenting the CaCu_5 -type structure. When possible, single crystals were extracted from these polycrystalline materials. In other cases, powders were prepared by crushing. Several attempts were carried out to prepare single crystals using the Bridgman method in boron nitride crucibles. The EPMA characterization of the specimens often detected small amounts of precipitates with compositions $\text{Sm}_2\text{Co}_7\text{B}_3$ and $\text{Sm}_3\text{Co}_{11}\text{B}_4$. The crystal structure of these compounds presents the same symmetry and space group as SmCo_5 and appears in coherency with the $\text{Sm}(\text{Co,Cu})_5$ matrix. For this reason, only the less contaminated of the prepared specimens could be used for the measurements.

III. RESULTS

Concerning the saturation magnetization, the experimental results, consistent with the few published results, enable a plot of the variation of M_s with x at 300 K. The experimental curve compares to the evolution predicted using the Jaccarino-Walker model⁸ (Fig. 1). In this model, the magnetic moment is assumed identical to that in the binary SmCo_5 phase when one Co atom is surrounded by n Co neighbors. In the CaCu_5 structure, the Co atoms are located on the g sites (three) and c sites (two). Each Co atom is surrounded, respectively, by eight and nine Co neighbors. The random Cu for Co substitution is assumed. The best fit is obtained for five Co neighbors. It can be noted that for $x < 0.5$ the variation of the Curie temperature given by the literature data³⁻⁶ follows the same behaviour as M_s (Fig. 2). Moreover, the two curves $M_s(x)$ and $T_C(x)$ are homotetic for the low Cu contents ($x < 0.5$) that have been earlier ob-

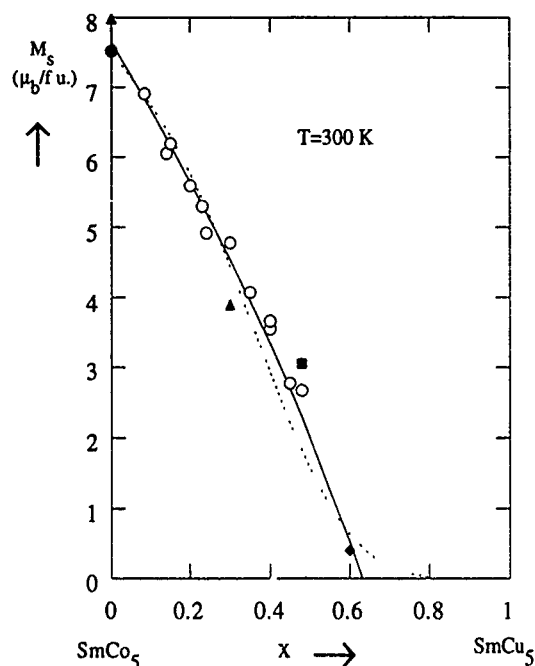


FIG. 1. x dependence at 300 K of the saturation magnetization M_s in the $\text{Sm}(\text{Co}_{1-x}\text{Cu}_x)_5$ phases: \circ , experimental data; \blacksquare Ref. 5; \blacklozenge Ref. 6; \blacktriangle Ref. 7; \bullet Ref. 10. Dashed line: simulated variation using the Jaccarino-Walker model (five neighbors).

served in the system $\text{Y}(\text{Co},\text{Ni})_5$.⁹ The phases $\text{Sm}(\text{Co}_{1-x}\text{Cu}_x)_5$ are not ferromagnetic at room temperature for $x > 0.65$.

Concerning the anisotropy, the curves plotted in the hard direction did not show any departure from the linear increase of M vs H_{ext} . Whatever the studied compositions, the

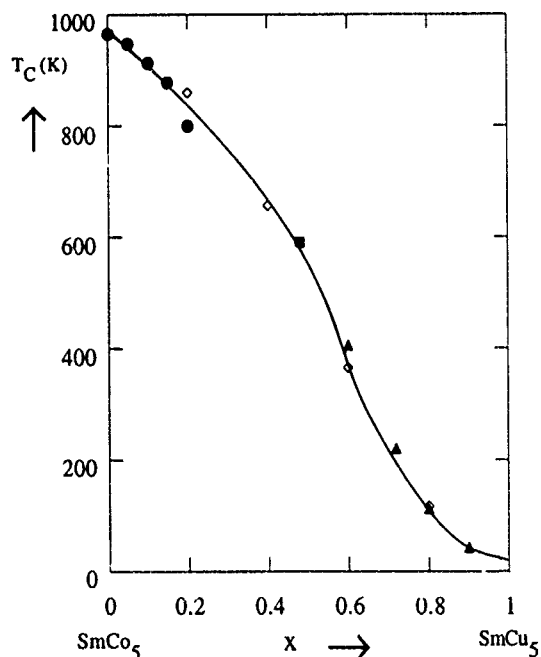


FIG. 2. Curie temperature T_C of $\text{Sm}(\text{Co}_{1-x}\text{Cu}_x)_5$ as a function of x . \bullet Ref. 3; \blacktriangle Ref. 4; \blacksquare Ref. 5; \blacklozenge Ref. 6.

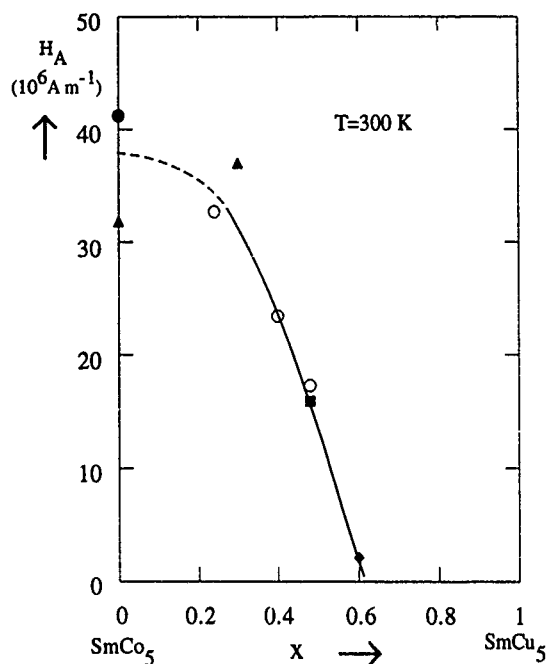


FIG. 3. Anisotropy field H_A at 300 K of $\text{Sm}(\text{Co}_{1-x}\text{Cu}_x)_5$ phases. \circ experimental data; \blacksquare Ref. 5; \blacklozenge Ref. 6; \blacktriangle Ref. 7; \bullet Ref. 10.

samples never reached the saturation. Consequently the anisotropy fields were determined by extrapolation, which involves some uncertainty. The values obtained for $x=0.4$ (23.4 MA m^{-1}) and $x=0.48$ (17.3 MA m^{-1}) are very consistent with the result given by Nagel⁵ for $x=0.48$ (15.9 MA m^{-1}). Concerning the lower Cu contents, the extrapolated value for $x=0.24$ (32.7 MA m^{-1}) is lower than that given by Uehara⁷ for $x=0.3$ (37 MA m^{-1}). Taking into account the limited precision of the determination, the discrepancy between these two values is rather slight. Much higher differences characterize the anisotropy fields published for SmCo_5 , 31.7 (Ref. 7) and 41 (Ref. 10) MA m^{-1} . The available data of anisotropy are used to plot the evolution of H_A vs x (Fig. 3). For x above 0.35 , the accuracy of the results is sufficient to evidence that the Cu for Co substitution induces a strong decrease of the anisotropy field in SmCo_5 . For the lower substitution rates, the rather scattered results do not enable one to state if Cu produces a smooth decrease or an unexpected change as suggested by the Uehara⁷ results. Using the available data of H_A and M_s , the first anisotropy constant $K_1 = \frac{1}{2} \mu_0 M_s H_A$ was calculated. The corresponding curve $K_1 = f(x)$ (Fig. 4) shows a linear decrease at 300 K from $x=0.2$ to 0.6 . A similar decrease is observed in $\text{Y}(\text{Co},\text{Ni})_5$ (Ref. 9) compounds. In the $\text{Sm}(\text{Co},\text{Cu})_5$ compound, the contribution of Sm to the anisotropy is the dominant one. It should vary with the Cu content, which should induce a change in the crystalline electric field and exchange field acting on the Sm^{3+} ion. Assuming that the colinearity of the magnetic configuration is maintained in an external field applied in the hard direction, the linear variation of K_1 suggests that the Sm contribution to the magnetocrystalline anisotropy also varies linearly with x .

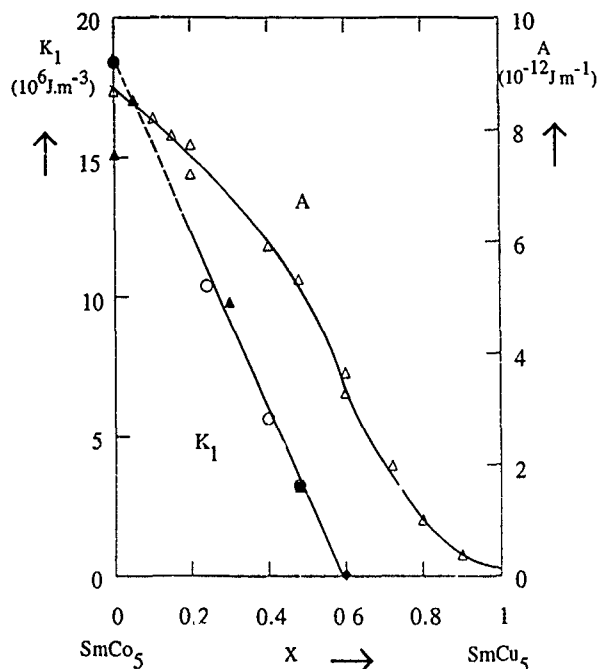


FIG. 4. Anisotropy constant K_1 at 300 K and exchange constant A variations vs x in $\text{Sm}(\text{Co}_{1-x}\text{Cu}_x)_5$. \circ experimental data; \blacksquare Ref. 5; \blacklozenge Ref. 6; \blacktriangle Ref. 7; \bullet Ref. 10.

A rough approximation of the exchange constant A was attempted from the expression $A = 10^5 \zeta^2 T_C$, where ζ is the shorter distance between two Co atoms and assumed to be 0.3 nm (Fig. 4). Using the values of A and K_1 , the Bloch wall energy γ in $\text{Sm}(\text{Co}_{1-x}\text{Cu}_x)_5$ can be evaluated using the expression $\gamma = 4\sqrt{AK_1}$. For the pinning precipitates in the permanent magnets of the 2:17 type, the composition of

which is about $\text{Sm}(\text{Co}_{0.7}\text{Cu}_{0.3})_5$, the γ value is around $32 \times 10^{-3} \text{ J m}^{-2}$.

Despite the large interest devoted to the $\text{Sm}(\text{Co}_{1-x}\text{Cu}_x)_5$ phases in the past, their intrinsic magnetic properties had not been extensively studied. This could be explained by two facts: the preparation of strictly homogeneous single-phase specimens is difficult and the huge magnetocrystalline anisotropy cannot be easily characterized. The present results, obtained on well-controlled materials, give a precise determination of the strong decrease of the saturation magnetization produced by Cu. They display a lower than expected decrease of the anisotropy field due to Cu. For this reason, only the anisotropy of the phases with a significant Cu content ($x > 0.35$) could be accurately characterized. The obtained data, complemented by the literature results, lead to the calculation of the exchange and anisotropy constants required to evaluate the domain wall energies of the 1:5 precipitates involved in the permanent magnets of 2:17 type.

¹H. F. Mildrum, M. S. Hartings, K. J. Strnat, and J. G. Tront, in *AIP Conference Proceedings*, edited by C. D. Graham and J. J. Rhyne (AIP, New York, 1972), Vol. 10, p. 618.

²I. Nishida and M. Uehara, *J. Less-Common Met.* **34**, 285 (1973).

³A. S. Yermolenko, Ye. I. Zabolotskiy, and A. V. Korolev, *Fiz. Metal. Metalloved.* **41**, 960 (1976).

⁴H. Oesterreicher, F. T. Parker, and M. Misroch, *J. Appl. Phys.* **50**, 4273 (1979).

⁵H. Nagel, *J. Appl. Phys.* **50**, 1026 (1979).

⁶S. Derkaoui, C. H. Allibert and J. Laforest, in *Proceedings of the 10th International Workshop on RE-Magnets and Their Applications*, Kyoto, Japan, May 1989, (The Society of Non-Traditional Technology, Minato-Ku, 1989), p. 277. Tokyo, 105, Japan.

⁷M. Uehara, Thesis, University of Grenoble, 1975.

⁸V. Jaccarino and L. R. Walker, *Phys. Rev. Lett.* **15**, 258 (1965).

⁹P. Gérard, Thesis, University of Grenoble, 1992.

¹⁰J. Laforest, Thesis, University of Grenoble, 1981.

SmCo (2:17-type) magnets with high contents of Fe and light rare earths

M. Q. Huang, Y. Zheng, and W. E. Wallace

Materials Science and Engineering Department, Carnegie Mellon University, Pittsburgh, Pennsylvania 15213

The magnetic properties of SmCo (2:17-type) magnets with high contents of Fe ($v = \text{Fe}/3d > 0.34$) and/or light rare earths (up to 0.4) were investigated. For magnets with compositions of $\text{Sm}(\text{Fe}_v\text{Co}_{\text{bal}}\text{Zr}_{0.02}\text{Cu}_{0.06}\{\text{Ga}\}_x)_{7.72}$, $v = 0.35$, $x = 0-0.06$, both H_c and $(BH)_{\text{max}}$ can be improved significantly by Ga doping, from 1.0 kOe and 5.4 MG Oe for $x = 0$ to 6.4 kOe and 15.4 MG Oe for $x = 0.06$. For magnets with compositions of $\text{Sm}_{0.8}\text{Pr}_{0.2}(\text{Fe}_v\text{Co}_{\text{bal}}\text{Zr}_{0.02}\text{Cu}_{0.06})_{7.67}$, $v = 0.30-0.31$, H_c can be increased strikingly by a special heat treatment, from 2.5 to over 20 kOe for $v = 0.30$ and from 0.5 to 15.5 kOe for $v = 0.31$. Examining magnets with compositions of $\text{Sm}_{0.59}\text{Pr}_{0.41}(\text{Co}_{0.68}\text{Fe}_{0.20}\text{Cu}_{0.10}\text{Zr}_{0.02})_z$ ($z = 6.68-7.75$) shows two stages of the magnetization reversal process in the range of 5.5 to 9.5 kOe and 16 to 19 kOe. Observed $(BH)_{\text{max}}$ ranged from 17 to 22.5 MG Oe.

I. INTRODUCTION

Recent progress in improving performance of 2:17-type permanent magnets has been reviewed by Ray and Liu.¹ These magnets are particularly valuable because of their high Curie temperature, low temperature coefficients of remanence B_r , and $(BH)_{\text{max}}$, compared to SmCo_5 and NdFeB magnets. Except for unconfirmed reports from Russian workers (*vide infra*), the highest achieved energy products are 32-34 MG Oe.¹⁻⁵ These are much less than that of NdFeB magnets⁶ and are very much less than the theoretical energy product of $\text{Sm}_2(\text{Co,Fe})_{17}$, 60 MG Oe. One can, of course, raise $(BH)_{\text{max}}$ by increasing B_r and H_c . The saturation magnetization of $\text{Sm}_2\text{Co}_{17}$ is easily increased by replacing Co with Fe or Sm by Pr. This improvement comes, however, at the expense of coercivity. These dopants alone effect no improvement in energy product. In the present study Al and Ga are used as additional dopants, hopefully to preserve the rise in magnetization in Fe-enriched and light-rare-earth (LRE)-doped magnets without loss of coercivity. Ga doping is particularly effective in this respect.

II. EXPERIMENT

Alloys were prepared by induction melting. The ingots were crushed and then ball milled to 3-5 μm average size. They were aligned in a 170-kOe field and then isostatically pressed at 3 tons/cm². The green compacts were then sintered under Ar at 1190-1200 °C for 1 h, followed by a solid solution treatment at 1130-1150 °C for 1-10 h and then quenched to room temperature in flowing helium. The sintered compacts were then heated to 800-850 °C for 24-50 h, followed by slow cooling to 400 °C at a rate of ~ 0.8 °C/min and then quenched to room temperature. The sintered compacts were magnetized in a 170-kOe field. The various magnetic properties were obtained by techniques that are standard in this laboratory. BH loops were traced with a Walker Hysteresograph. X-ray diffraction (XRD) information was obtained using $\text{Cr K}\alpha$ radiation.

III. RESULTS AND DISCUSSION

A. Al, Ga substitution in magnets of high Fe content

Listed in Tables I and II are the compositions of samples 1-5 and their grain size and hard magnetic properties. Comparing Ga- and Al-free samples 1 and 2, when the Fe content, designated v , increases from 0.32 to 0.35, H_A decreases from 58 to 42 kOe, and the grain size becomes much smaller. The average grain size decreases from 54 to 26 μm . Sample 1 shows excellent hard magnetic properties $H_c = 17$ kOe, $(BH)_{\text{max}} = 31.7$ MG Oe, as well as a large grain size and a fine cellular structure. However, H_c and $(BH)_{\text{max}}$ sharply diminished to 1.0 kOe and 5.4 MG Oe for sample 2. When doping with a small amount of Ga in sample 2 of high Fe content, $v = 0.35$, H_A increased from 42 to 53 kOe, and the grain size grows significantly (average grain size $d = 33$ μm). For this sample, H_c and $(BH)_{\text{max}}$ increase to 6.4 kOe and 15.4 MG Oe, respectively (sample 3). In contrast, Al doping (sample 4) does not change the microstructure. It retains a small grain size (21 μm), smaller than the Al-free sample. Even though H_A increases from 42 to 49 kOe, it exhibits poor properties: $H_c = 0.8$ kOe and $(BH)_{\text{max}} = 4.0$ MG Oe.

If Zr and Cu are omitted and only doping by Ga is involved (sample 5), no hard magnetic properties develop, even though H_A was increased as much as was produced by the substitution of Ga. This indicates that obtaining acceptable coercivity by Ga substitution in 2:17-type magnets still requires Zr and Cu. Apparently they are needed to form the critical cellular structure. Ga is a low-melting element; when it is inserted into the materials it may increase the fluidity and wettability of boundary liquid phases during the sintering process, enabling larger grains to be formed and thus enhancing H_c .

B. 2:17 magnets with substitution of Pr for Sm

1. Pr-substituted 2:17 magnets

A number of magnets represented by the formula $\text{Sm}_{1-x}\text{Pr}_x(\text{Fe}_v\text{Co}_{\text{bal}}\text{Cu}_{0.06}\text{Zr}_{0.02})_{7.67}$, $x = 0-0.4$, $v = 0.28-0.31$, were fabricated with $v = 0.28$. The magnetic properties of these magnets and their corresponding alloys are

TABLE I. Compositions of $\text{Sm}(\text{Fe}, \text{Co}, \text{Cu}, \text{Al}, \text{Ga})_{7.72}$ magnets.

Sample no.	
1	$\text{Sm}(\text{Fe}_{0.32}\text{Cu}_{0.06}\text{Zr}_{0.02}\text{Co}_{0.60})_{7.72}$
2	$\text{Sm}(\text{Fe}_{0.35}\text{Cu}_{0.06}\text{Zr}_{0.02}\text{Co}_{0.57})_{7.72}$
3	$\text{Sm}(\text{Fe}_{0.35}\text{Cu}_{0.06}\text{Zr}_{0.02}\text{Ga}_{0.06}\text{Co}_{0.51})_{7.72}$
4	$\text{Sm}(\text{Fe}_{0.35}\text{Cu}_{0.06}\text{Zr}_{0.02}\text{Al}_{0.08}\text{Co}_{0.59})_{7.72}$
5	$\text{Sm}(\text{Fe}_{0.35}\text{Ga}_{0.06}\text{Co}_{0.59})_{7.72}$

TABLE II. Magnetic properties of $\text{Sm}(\text{Fe}, \text{Co}, \text{Cu}, \text{Al}, \text{Ga})_{7.72}$ magnets.

No.	B_r (kG)	H_c (kOe)	$(BH)_{\max}$ (MG Oe)
1	12.1	17.0	31.7
2	11.8	1.0	5.4
3	10.3	6.4	15.4
4	9.7	0.8	4.0
5	11.7	<100 Oe	...

No.	M_s (emu/g) ^a	Alloys H_A (kOe) ^a	T_c (°C)	Average grain diameter (μm)
1	115.0	58.0	778	54
2	115.3	42.5	774	26
3	104.0	53.0	697	33
4	98.0	49.0	707	21
5	118.5	49.0	722	30

^aMeasured at room temperature.TABLE III. Magnetic properties of $\text{Sm}_{1-x}\text{Pr}_x(\text{Co}_{0.64}\text{Fe}_{0.28}\text{Cu}_{0.06}\text{Zr}_{0.02})_{7.67}$.

x	B_r (kG)	H_c (kOe)	$(BH)_{\max}$ (MG Oe)
0	11.5	22.0	28.0
0.1	11.6	19.5	28.4
0.2	11.9	15.5	29.8
0.3	12.2	2.4	9.3
0.4	12.4	<0.5	...

x	H_k (kOe)	Alloys M (emu/g)	H_A (kOe)
0	6.5	107	64
0.1	5.5	112	62
0.2	5.5	114	59
0.3	...	116	55
0.4	...	117	34

TABLE IV. Magnetic Properties of $\text{Sm}_{0.8}\text{Pr}_{0.2}(\text{Co}_{0.61}\text{Fe}_{0.2}\text{Cu}_{0.06}\text{Zr}_{0.02})_{7.67}$.

No.	ν	Sintering (°C)	Solid solution T (°C)	Treatment t (h)
1	0.3	1200	1130	9
2	0.3	1200	1150	3
3	0.31	1190	1130	9
4	0.31	1190	1130	9
5	0.31	1200	1150	8

No.	Isothermal T (°C)	t_{treat} (h)	H_c (kOe)	$(BH)_{\max}$ (MG Oe)
1	840	24	>20	26.0
2	840	24	2.5	...
3	840	24	15.5	24.0
4	820	24	3.5	...
5	840	24	<0.5	...

TABLE V. Magnetic properties of $\text{Sm}_{0.59}\text{Pr}_{0.41}(\text{Co}_{0.68}\text{Fe}_{0.20}\text{Cu}_{0.10}\text{Zr}_{0.02})_z$.

No.	z	B_r (kG)	H_c (kOe)
1	6.68	9.1	2.6
2	7.00	10.5	11.5
3	7.30	10.6	18.8, ~9.5
4	7.50	10.8	18.2, ~7.5
5	7.75	11.3	16.0, ~5.5

No.	$(BH)_{\max}$ (MG Oe)	Alloys M (emu/g)	H_A (kOe)
1	9.08	102.0	67.0
2	21.0	103.5	64.0
3	22.5	106.0	62.0
4	18.5	107.5	59.0
5	16.8	109.0	57.0

listed in Table III. When 20% of Sm is replaced by Pr, B_r and $(BH)_{\max}$ increase from 11.5 kG and 28.0 MG Oe to 11.9 kG and 29.8 MG Oe, respectively. This result is similar to that reported by Liu and Ray.² With increasing Pr, the moments (B_r and M) increase, as Pr has higher magnetic moment than Sm, and H_A decreases, since the Pr sublattice prefers planar anisotropy in $\text{Pr}_2(\text{Co}, \text{Fe})_{17}$ compounds. As can be seen in Table III, the H_c drops even more sharply than H_A . When the Pr content x increases to 40%, the H_c drops to 500 Oe.

It is to be noted that further increase of Fe content for these compositions will result in a deterioration of all permanent magnetic properties,² especially in H_c . In our studies for magnets corresponding to $x=0.2$ and for which the Fe content is increased to 0.30–0.31, the magnetic properties, especially H_c , can be improved significantly by optimizing the solutionizing and aging heat treatment. Results shown in Table IV show the effects of different heat treatment conditions on the magnetic properties of the $\text{Sm}_{0.8}\text{Pr}_{0.2}(\text{Co}_{0.61}\text{Fe}_{0.2}\text{Cu}_{0.06}\text{Zr}_{0.02})_{7.67}$ ($\nu=0.30, 0.31$) magnets. For $\nu=0.30$, the H_c can be dramatically increased from 2.5 kOe (sample 2) to 20 kOe (sample 1) by changing the solid solution treatment from at 1150 °C for 3 h to 1130 °C for 9 h. For the magnet of $\nu=0.31$, no hard magnetic properties were developed when sintered at 1200 °C (sample 5). H_c can be developed and increased from 3.5 kOe (sample 4) to 15.5 kOe (sample 3), if sintered at a lower temperature 1190 °C and isothermally treated at a higher temperature 840 °C. The basic principles which form the foundation of these considerations are contained in investigations and findings of numerous investigators.¹

2. Effect of variation of rare-earth content

Ivanova *et al.*,⁷ working with a pseudo-single-crystal specimen, reported some rather interesting magnetic properties: $4\pi M=1.24$ T, $H_c=896$ kA/m, and $(BH)_{\max}=288$ kJ/m³ for a magnet of composition $\text{Sm}_{0.59}\text{Pr}_{0.41}(\text{Co}_{0.68}\text{Fe}_{0.20}\text{Cu}_{0.10}\text{Zr}_{0.02})_z$ with $z=6.68$. Following up on this interesting study, a number of magnets with variation of z from 6.68 to 7.75 were fabricated. Listed in Table V are their magnetic properties. The demagnetization

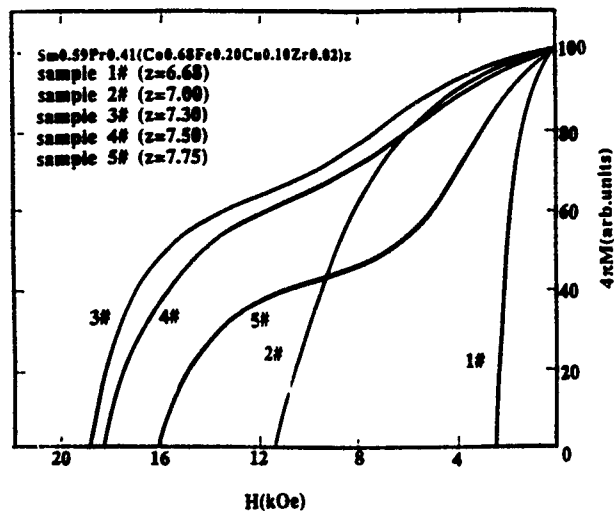


FIG. 1. $4\pi M$ vs H for samples 1,2,3,4, and 5.

curves for the samples are shown in Fig. 1. The curves for samples 1 and 2 differ from those of samples 3, 4, and 5 in that demagnetization occurs in only one stage. Microstructure for samples 1 and 3 are shown in Figs. 2 and 3.

All these magnets exhibit reasonably good hard magnetic properties. In particular, when $z > 7$, $B_r = 10.5-11.3$ kG, $H_c = 11.5-18.8$ kOe and $(BH)_{\max} = 16.8-22.5$ MG Oe. For sample 1, $z = 6.68$, the composition is much deviated from the stoichiometric composition of 2:17 compound, and a significant amount of 1:5 phase was retained in the magnet, as clearly indicated by XRD. Only a small amount of the 1:5 phase is needed to form the cellular structure needed for domain wall pinning; the rest will separate from the 2:17 phase. As seen in Fig. 2, only in some parts of

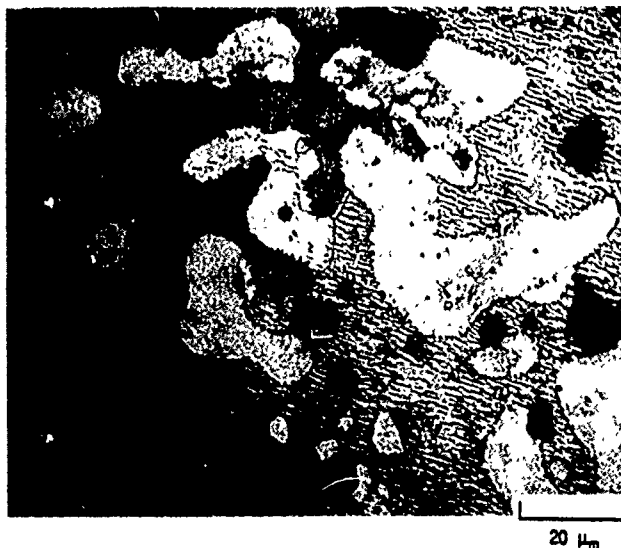


FIG. 2. Microstructure of sample 1 ($z=6.68$).

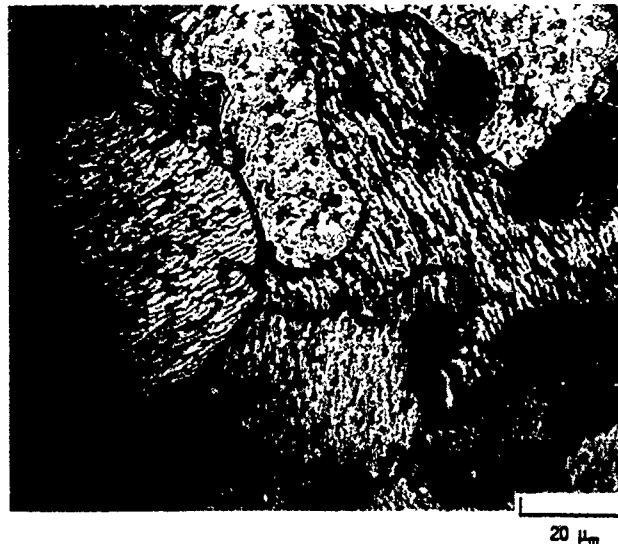


FIG. 3. Microstructure of sample 3 ($z=7.30$).

the magnet was a cellular structure formed. It exhibits a lower H_c of 2.6 kOe.

As z increases from 6.68 to 7.30, the 1:5 phase decreases (as evidenced by XRD) and the cellular structure develops more completely (see Fig. 3). As a consequence, H_c increases from 2.6 to 18.8 kOe and $(BH)_{\max}$ increases from 9.1 to 22.5 MG Oe.

For sample 3, $z = 7.30$, the demagnetization curve seems to exhibit two stages of the magnetization reversal process, a lower one at ~ 9.5 kOe and a higher one at ~ 18.8 kOe (see Figs. 1 and 2). They both can be ascribed to a mechanism of domain wall pinning, but with different pinning centers. We surmise that the lower H_c corresponds to the reversal process when the PrCo_5 -type phase acts as a pinning center, and the higher H_c for the SmCo_5 -type phase as a pinning center, since the H_A of SmCo_5 (210 kOe) is much higher than that of PrCo_5 (145 kOe).⁸ When z further increases from 7.30 to 7.75, the magnetic behavior of samples 4 and 5 are similar to that of sample 3.

ACKNOWLEDGMENT

This work was supported by a grant from the U.S. Army Research Office.

¹A. E. Ray and S. Liu, J. Mater. Engr. Perform. 1, 183 (1992).

²S. Liu and A. E. Ray, IEEE Trans. Magn. MAG-25, 3785 (1989).

³S. Liu, A. E. Ray, and H. F. Mildrum, IEEE Trans. Magn. MAG-26, 1382 (1990).

⁴S. Liu, A. E. Ray, C. H. Chen, and H. F. Mildrum, J. Appl. Phys. 69, 5853 (1991).

⁵M. Q. Huang, Y. Zheng, J. G. Sohn, J. M. Elbicki, W. E. Wallace, and S. G. Sankar, in Proceedings of the 11th International Workshop on Rare Earth Magnets and Their Applications, edited by S. G. Sankar. Vol. I, p 457, 1990.

⁶M. Sagawa, S. Hirosawa, H. Yamamoto, S. Fujimura, and Y. Matsuura, Jpn. J. Appl. Phys. 26, 785 (1987).

⁷G. V. Ivanova, A. G. Popov, L. M. Magat, V. G. Maykov, T. Z. Puzanova, Y. S. Shur, and N. V. Nikolayeva, Phys. Met. Metall. 59, 64 (1985).

⁸W. A. J. J. Velge and K. H. J. Buscho, J. Appl. Phys. 39, 3, 1717 (1968).

Effect of Dy substitution on the magnetocrystalline anisotropy of GdCo₄B

T. Ito, H. Asano, and H. Ido

Department of Applied Physics, Tohoku Gakuin University, Tagajo 985, Japan

G. Kido

Institute for Material Research, Tohoku University, Sendai 980, Japan

X-ray diffraction and magnetization measurements have been performed for powdered and field-oriented samples of Gd_{1-x}Dy_xCo₄B with $x=0, 0.05, 0.1$, and 0.2 . It has been found that Gd_{1-x}Dy_xCo₄B with $x=0.2$ has a planar magnetic anisotropy in the temperature region below room temperature; however, the samples with $x=0.05$ and $x=0.1$ have an axial magnetic anisotropy at room temperature and transform to a tilted state in the low-temperature region. By analyzing magnetization curves measured in a pulsed field up to 140 kOe at $T=4$ K and also in a static field up to 12 kOe at 78 K for the field-oriented samples with $x=0.05$ and $x=0.1$, approximate values of magnetic anisotropy constants of a Dy ion in Gd_{1-x}Dy_xCo₄B, $K_1(\text{Dy})$ and $K_2(\text{Dy})$, have been determined to be -2.1×10^{-14} erg/Dy and 1.3×10^{-14} erg/Dy, respectively. By comparing these values with those of DyCo₅, it is found that $K_2(\text{Dy})$ in the CeCo₄B-type structure is enhanced in one order by the crystallographic change from the CaCu₅- to the CeCo₄B-type structure.

I. INTRODUCTION

RCo₄B (R=rare earth) compounds have hexagonal CeCo₄B-type structure,¹ which is derived from the CaCu₅-type structure by replacing the 2c-site Co atoms by B atoms. In our previous work,² we studied the magnetic properties of GdCo₄B and found that the Gd-sublattice magnetic anisotropy is well explained by the magnetic anisotropy due to the dipole-dipole interaction. Since the magnetic anisotropy of DyCo₄B has been known to be planar at room temperature,³ it is impossible to make a field-oriented sample. The magnetic anisotropy of GdCo₄B has been clarified, so in this work, Gd_{1-x}Dy_xCo₄B compounds are prepared and the magnetization curves for field-oriented samples have been measured to study the Dy contribution to the magnetic anisotropy in these compounds.

II. SPECIMENS AND CRYSTAL STRUCTURE

Ingots of Gd_{1-x}Dy_xCo₄B were prepared by melting raw materials of 99.9% purity in an arc furnace. The melting was repeated several times to homogenize the ingots which are then annealed at 800 °C for 2 days. The crystal structure has been confirmed by x-ray diffraction to be the CeCo₄B-type structure. The field-oriented sample was prepared by solidifying the mixture of epoxy resin and the powdered specimen ($<32 \mu\text{m}$) in the magnetic field of 20 kOe at room temperature. The x-ray diffraction pattern for the field-oriented Gd_{0.95}Dy_{0.05}Co₄B is shown in Fig. 1, which shows that the sample has an axial magnetic anisotropy at room temperature.

III. EXPERIMENTAL RESULTS AND DISCUSSION

From the results of x-ray diffraction and magnetization measurements for the field-oriented samples of Gd_{1-x}Dy_xCo₄B, it has been found that Gd_{1-x}Dy_xCo₄B with $x=0.2$ has a planar magnetic anisotropy in the temperature region below room temperature; however, the samples with $x=0.05$ and $x=0.1$ have an axial anisotropy at room temperature and transform to a tilted state in the low-temperature

region. Magnetization curves for the field-oriented samples with $x=0, 0.05$, and 0.1 at 78 K are shown in Fig. 2. It is seen that the substitution of Dy for Gd in GdCo₄B has a significant effect in the magnetic anisotropy. Only 5% substitution of Dy changes the axial anisotropy of GdCo₄B to the planar or tilted one. To estimate the magnetic anisotropy constants K_1 and K_2 , the magnetization curves in Fig. 2 have been analyzed on the basis of Eq. (1) which takes the magnetic anisotropy energy including K_1 and K_2 and the Zeeman energy:

$$H = AM^3 + BM, \quad (1)$$

where H is the external magnetic field and M is the magnetization component parallel to H direction. The coefficients A and B are expressed as follows:

$$A = 4K_2/M_s^4$$

and

$$B = \begin{cases} -2(K_1 + 2K_2)/M_s^2 & \text{for } H \parallel c, \\ 2K_1/M_s^2 & \text{for } H \perp c. \end{cases} \quad (2)$$

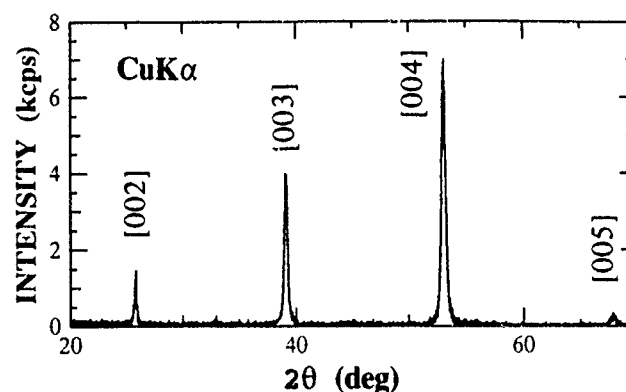


FIG. 1. X-ray diffraction pattern for the field-oriented sample of Gd_{0.95}Dy_{0.05}Co₄B

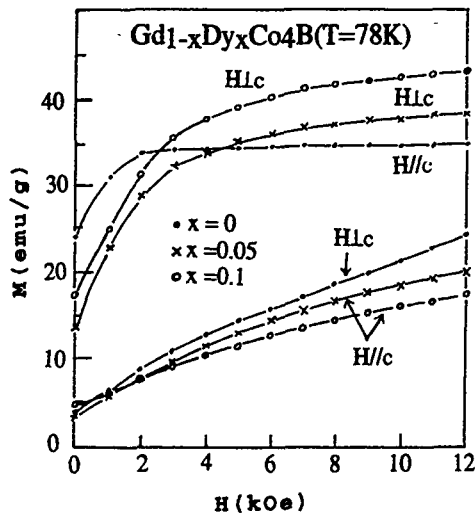


FIG. 2. Magnetization curves for the field-oriented samples of $\text{Gd}_{1-x}\text{Dy}_x\text{Co}_4\text{B}$ at $T=78$ K. The c in this figure means the field orientation direction of the sample.

To remove the magnetic domain effect, we take the data in the magnetic field larger than 3 kOe and fit Eq. (1) to them in order to estimate the values of K_1 and K_2 . The dashed curves in Fig. 3 are calculated with the values of K_1 and K_2 shown in the same figure. A similar analysis has been made for the data of the sample with $x=0.1$. Magnetization curves for the field-oriented sample in a pulsed field are shown in Fig. 4 for $x=0.1$ at 4 K. The dashed curves are calculated, where we take $K_1 = -2.3 \times 10^{-15}$ erg/f.u. and $K_2 = 1.3 \times 10^{-15}$ erg/f.u. as the best values (f.u. denotes formula unit).

Though the sample is a field-oriented one, the agreement between the observed and calculated curves is fairly good. A similar analysis has also been made for the data of the sample with $x=0.05$. The anisotropy constants K_1 and K_2 estimated by the method mentioned above are plotted against composition x in Fig. 5. The data in Fig. 5 are approximate

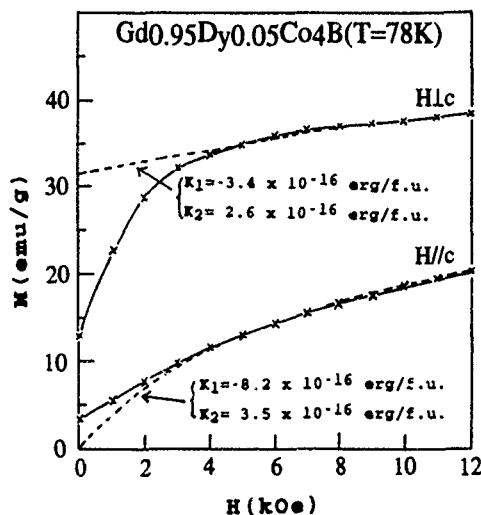


FIG. 3. Magnetization curves for the field-oriented sample of $\text{Gd}_{0.95}\text{Dy}_{0.05}\text{Co}_4\text{B}$ at $T=78$ K. The dashed curves are calculated (see the text).

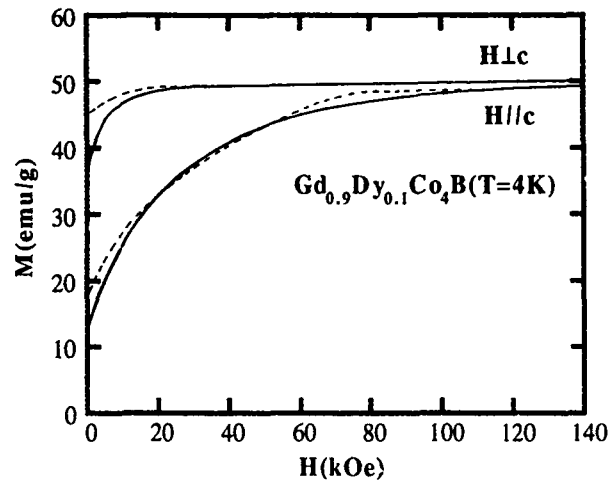


FIG. 4. Magnetization curves of the field-oriented sample of $\text{Gd}_{0.9}\text{Dy}_{0.1}\text{Co}_4\text{B}$ in a pulsed field at $T=4$ K. The dashed curves are calculated (see the text).

because the observed magnetization curves are for the field-oriented samples; however, the data at $T=4$ K and $T=78$ K seem to be consistent with each other. The anisotropy constants K_1 and K_2 in Fig. 5 can be expressed by

$$K_1 = (1-x)K_1(\text{Gd}) + xK_1(\text{Dy}) + 4K_1(\text{Co}),$$

and

$$K_2 = 4K_2(\text{Co}) + xK_2(\text{Dy}), \quad (3)$$

where $K_1(\text{Gd})$, etc., are the magnetic anisotropy constants of a Gd ion, etc. If we use $K_1(\text{Gd}) = 2.62 \times 10^{-16}$ erg/f.u., $K_1(\text{Co}) = -2.87 \times 10^{-16}$ erg/f.u., and $K_2(\text{Co}) = 1.74 \times 10^{-16}$ erg/f.u., which have been estimated from the data of GdCo_4B (Ref. 2) and YCo_4B (Ref. 4), approximate values of $K_1(\text{Dy})$ and $K_2(\text{Dy})$ can be estimated by fitting Eq. (3) to the straight lines at $T=4$ K in Fig. 5 as

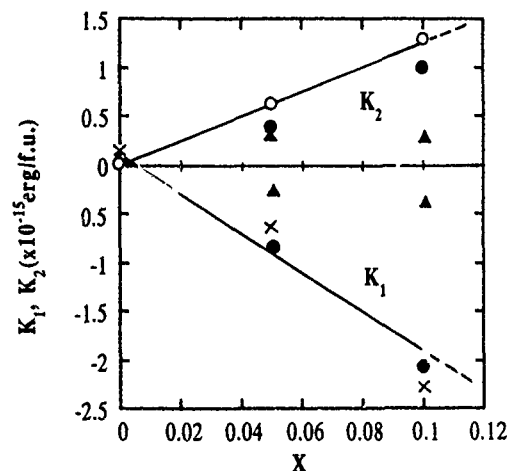


FIG. 5. Composition dependence of magnetic anisotropy constants K_1 and K_2 per formula unit in $\text{Gd}_{1-x}\text{Dy}_x\text{Co}_4\text{B}$. \circ and \times are estimated from the magnetization curves with $H\parallel c$ measured in the pulsed field up to 140 kOe at $T=4$ K, \bullet and \blacktriangle are estimated from the magnetization curves with $H\parallel c$ and $H\perp c$ measured in the low field up to 12 kOe at 77 K.

$$K_1(\text{Dy}) = -2.1 \times 10^{-14} \text{ erg/Dy}$$

and

$$K_2(\text{Dy}) = 1.3 \times 10^{-14} \text{ erg/Dy}.$$

On the other hand, $K_1(\text{Dy})$ and $K_2(\text{Dy})$ of $\text{DyCo}_{5.2}$ with CaCu_5 crystal structure have been estimated by Ermolenko and Rozhda⁵ to be -2.92×10^{-14} and 1.4×10^{-15} erg/Dy, respectively. Comparing the magnetic anisotropy constants per Dy ion in $\text{Gd}_{1-x}\text{Dy}_x\text{Co}_4\text{B}$ with those of $\text{DyCo}_{5.2}$, we can conclude that the $K_2(\text{Dy})$ is strongly enhanced by the crystallographic change from CaCu_5 -type to CeCo_4B -type struc-

tures. This fact is different from the situation of SmCo_4B and SmCo_5 , where $K_1(\text{Sm})$ is enhanced by the crystallographic change to the CeCo_4B type.⁶

¹Yu. B. Kuzuma and N. S. Bilonizhko, *Sov. Phys. Crystallogr.* **18**, 447 (1974).

²T. Ito, H. Ogata, H. Ido, and G. Kido, *J. Appl. Phys.* **73**, 5914 (1993).

³Z. Drzazga, A. Winiarska, and F. Stein, *J. Less-Common Met.* **153**, L21 (1989).

⁴H. Ogata, H. Ido, and H. Yamauchi, *J. Appl. Phys.* **73**, 9511 (1993).

⁵A. S. Ermolenko and A. F. Rozhda, *Phys. Met. Metallogr. (USSR)* **55**, 55 (1983).

⁶H. Ido, K. Sugiyama, H. Hachino, M. Date, S. F. Cheng, and K. Maki, *Physica B* **177**, 265 (1992).

Permanent magnet film magneto-optic waveguide isolator

M. Levy, R. Scarmozzino, and R. M. Osgood, Jr.

Columbia University Microelectronics Sciences Laboratory, New York, New York 10027

R. Wolfe

AT&T Bell Laboratories, Murray Hill, New Jersey 07974

F. J. Cadieu and H. Hedge

Physics Department, Queens College of City University of New York, Flushing, New York 11367

C. J. Gutierrez^{a)} and G. A. Prinz

Naval Research Laboratory, Washington, D.C. 20375

Recent advances in high-coercivity planar-magnetization film magnets and Bi-YIG (bismuth-substituted yttrium iron garnet) film technology have opened up the possibility of fabricating very small magneto-optic devices. In this article we demonstrate that these two technologies can be brought together to fabricate a high performance waveguide magneto-optic isolator for use in integrated optical circuits. The device operates at 1.55- μm wavelength and consists of a waveguide etched into a Bi-YIG film whose magnetization is saturated by a 22- μm -thick TbCu₇-type SmCo magnet with a coercivity of 4 kOe. Isolation ratios of 25 dB have been obtained in the wavelength region between 1490 and 1555 nm.

The development of optical fiber telecommunications has intensified the search for compact, low-cost magneto-optic isolators. Isolators currently in use are made of bulk crystals or thick films of modified yttrium iron garnet (YIG) and rely on bulk magnets to induce Faraday rotation in these crystals. The development of waveguide isolators, magnetized by small ferromagnetic films, would allow a considerable reduction in size and production costs.

Recent advances in Bi-YIG film technology^{1,2} have made it possible to fabricate thin-film waveguide isolators¹ with zero birefringence and isolation ratios of 30 to 35 dB. Moreover, within the last decade there have also been significant advances in the fabrication of thin and medium thickness ferromagnetic films, with high magnetization^{3,4} and high coercivity.⁴

In this article we demonstrate that these ferromagnetic films can be used as permanent magnets in a workable magneto-optic waveguide isolator. The work presented here extends results obtained by some of the authors in a previous study.⁵ We demonstrate full saturation of the magnetization in a waveguide isolator using a more powerful film magnet than in Ref. 5, and study insertion losses and the response of the film magnet isolator as a function of wavelength.

The basic structure of the device, as shown in Fig. 1, consists of a magnetic film placed on a Bi-YIG waveguide, separated by an appropriate buffering material. In order to demonstrate the feasibility of utilizing various thin-film magnet types with waveguide Bi-YIG structures we have studied the magnetic saturation induced by two different ferromagnetic films on a Bi-YIG slab waveguide. Such saturation is important because the presence of preexisting magnetic domains in the waveguide degrades the performance of the device as a result of spurious linear magnetic birefringence, induced when the magnetization in the Bi-YIG is not collin-

ear with the waveguide axis. Moreover, the magnet should saturate a length of Bi-YIG sufficient to generate 45° of Faraday rotation as the light traverses the isolator.

In this article we report on the performance of two different magnet types. The first is an iron-cobalt alloy single-crystal film, with alloy composition 30% iron and 70% cobalt, grown by molecular-beam epitaxy on a (110) GaAs substrate. Hysteresis studies of these films show a flat rectangular response to an applied magnetic field, with a zero-field remanent $4\pi M$ of about 21 kOe and a coercivity of 50 Oe. The film's thickness is approximately 1.5 μm . The second magnet is a 22- μm -thick samarium-cobalt polycrystalline film, with composition $\text{Sm}_{14}\text{Co}_{63}\text{Fe}_{20}\text{Zr}_2\text{Cu}_8$, sputtered on an aluminum oxide substrate. It has a remanent $4\pi M$ of 7 kOe and a coercivity of 4 kOe. M is in the plane of the film for both magnets.

The slab waveguide consists of a triple-layer single-crystal epitaxial Bi-YIG film¹ designed to support single TE and TM modes. The film was grown by standard liquid-phase epitaxy on a (111)-oriented gadolinium-gallium-garnet substrate. The top two epilayers have nominal composition $(\text{Bi}_{0.5}\text{Y}_{2.5})(\text{Fe}_{3.7}\text{Ga}_{1.3})\text{O}_{12}$, with a calcium content of 0.1 pfu. An index of refraction difference of 0.5% between them ensures waveguiding in the top layer. Each epilayer is approximately 3.5 μm thick. The sample was subjected to annealing processes described elsewhere¹ for near-planar

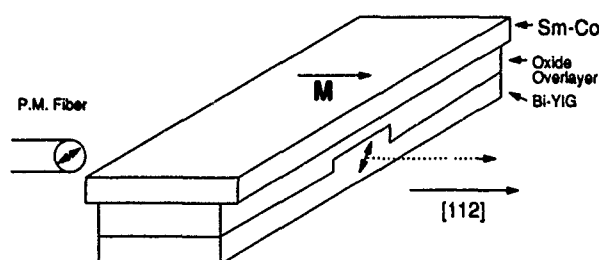


FIG. 1. Basic structure of thin-film magnet magneto-optic isolator.

^{a)}Present address: Department of Physics, Southwest Texas State University, San Marcos, TX 78666.

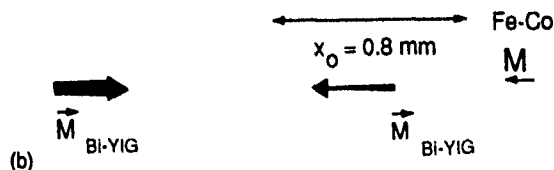
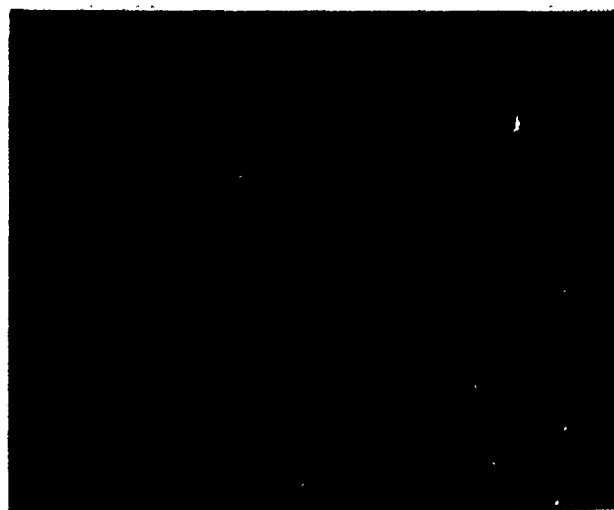
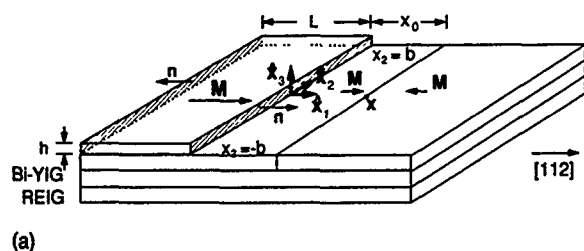


FIG. 2. (a) Shaded areas show the magnetically charged end faces of the film magnet. (b) Photomicrograph of magnetic domains in Bi-YIG epilayer (Faraday contrast) in the presence of 1.5- μm -thick Fe-Co film.

magnetization anisotropy in the upper layers, resulting in easy-magnetization axes along the [112] directions. The bottom epilayer of the three-layer structure has nominal composition $(\text{Bi}_{0.5}\text{Er}_{1.4}\text{Sm}_{0.7}\text{Pr}_{0.4})(\text{Fe}_{4.0}\text{Co}_{0.2}\text{Al}_{0.8})\text{O}_{12}$, and magnetization normal to the plane of the film. Its rare-earth composition is designed to absorb higher-order waveguide modes present in the triple-layer structure.

To study the magnetic saturation induced by the iron-cobalt alloy film in the Bi-YIG waveguide, we placed the magnetic film directly on top of the Bi-YIG sample, its magnetization parallel to the planar component of one of the easy magnetization directions of the garnet. The slab waveguide magnetization is partially saturated by the fringing field of the film magnet, which is nearly planar in the waveguide. The iron-cobalt film is found to saturate $x_0 = 0.8$ mm of the Bi-YIG sample, as shown in Fig. 2. The magnetization direction in the Fe-Co film is normal to the edge of the film, as shown in Fig. 2(a), and saturation is measured away from the magnet. The photomicrograph in Fig. 2(b) was obtained using Faraday contrast with a polarization microscope. In the figure the opposite directions of quasi-planar magnetization in the waveguiding epilayer appear as light- and dark-shaded regions parallel to the Fe-Co edge.² The maze-like pattern in the Bi-YIG corresponds to vertical magnetization domains present in the absorbing (bottom) epilayer. These domains

exhibit a higher Faraday contrast than those corresponding to the quasi-horizontal magnetization of the waveguiding epilayer because of their larger vertical components of magnetization. In the isolator, the fringing fields of these domains are neutralized by the permanent magnet and do not limit the ultimate isolation ratio of the device.

In order to obtain the micrograph shown in Fig. 2(b), a separate external magnet was first placed in proximity to the YIG sample in order to saturate the Bi-YIG magnetization in a direction opposite to that later obtained with the Fe-Co film in place. This magnet was then removed and the film magnet positioned on the YIG; the domains then relaxed to their equilibrium configuration. The resulting domain configuration in the waveguiding epilayer, observable by Faraday contrast, provides a measure of the magnetic saturation induced by the Fe-Co film in the Bi-YIG sample, and yields 0.8 mm, as indicated above.

Using the expressions in Eqs. (1) and (2) given below, for the magnetic field induced by each of the two magnetically charged pole faces in a magnetic film,^{5,6} we estimate a saturation field of 5.8 Oe for the waveguiding epilayer in the Bi-YIG sample used in these experiments. The equations, derived in Ref. 5,

$$H_1(x_1, 0, x_3) = 2\mathbf{M} \cdot \mathbf{n} \left(\arctan \frac{x_3}{x_1} - \arctan \frac{x_3 - h}{x_1} \right), \quad (1)$$

$$H_3(x_1, 0, x_3) = \mathbf{M} \cdot \mathbf{n} \ln \left[\frac{x_1^2 + x_3^2}{x_1^2 + (x_3 - h)^2} \right] \quad (2)$$

are valid for the case where the distance between the pole face and the point \mathbf{x} , where the field is evaluated, is much smaller than the lateral dimension b of the film, shown in Fig. 2(a). \mathbf{M} is the magnetization density, \mathbf{n} is the unit vector normal to the face, and the Cartesian coordinates are as shown in the figure. The pole face is at $x_1 = 0$, and the thickness of the film h is assumed to be 1.5 μm in the above calculation.

The thicker samarium-cobalt film magnet, on the other hand, has a more drastic effect on the Bi-YIG magnetization. Placed in close proximity to the edge of the garnet, its magnetization normal to the edge, the magnet's fringing field is strong enough not only to saturate the waveguiding layer, but in addition the vertical domains of the absorbing epilayer are eliminated up to a distance of 0.5 mm from the edge. Faraday contrast analysis reveals that the waveguiding epilayer remains magnetically saturated horizontally beyond a distance of 2 mm from the magnet. Calculations using Eq. (1) show that for the saturation field of 5.8 Oe calculated above, the saturation length is $x_0 = 4.2$ mm for this Sm-Co film.

A workable waveguide isolator must be long enough to generate 45° of Faraday rotation in the light input. For example, typical lengths for bismuth-substituted YIG films with near-planar magnetization range from 1 mm to several millimeters, depending on the level of bismuth doping in the Bi-YIG film. Since a single magnetically charged pole face of the samarium-cobalt magnet saturates more than 2 mm of the waveguiding epilayer, the magnet's return flux, which has additive contributions from both pole faces in the horizontal direction, will be sufficient to saturate the full length

of a channel waveguide to achieve 45° rotations.⁷ In fact, using Eq. (1) one can show that the return flux is weakest at the axial midpoint of the ridge waveguide, where the horizontal component of the field is twice that generated by each magnetic pole face.

In order to test the performance of the proposed film magnet waveguide isolator we first fabricated ridge waveguides in the Bi-YIG sample and then characterized the device performance via its isolation ratio and insertion losses. To fabricate the waveguide isolator, the linear birefringence was reduced to zero at a wavelength near $1.5\ \mu\text{m}$ by etch-tuning the thickness of the garnet film.^{1,8} Ridge waveguide patterns were then etched into the surface, parallel to one of the easy-magnetization directions, and a thin silica overlayer was sputtered over it to further tune the zero-birefringence wavelength and to provide a buffer between the magnet and the waveguide, thereby reducing absorption losses.

The Faraday rotation in the Bi-YIG waveguide was measured to be $127^\circ/\text{cm}$ at a wavelength of $1.5\ \mu\text{m}$. Thus, in order to provide 45° of rotation, the sample was cut to a length of 3.55 mm and its edges optically polished.

Performance measurements on this isolator using the $1.5\text{-}\mu\text{m}$ -thick Fe-Co magnet have been reported by some of us elsewhere.⁵ These tests showed that the magnet saturates nearly 75–90% of the length of the waveguides. Isolation ratios of 21 dB were obtained.

For the tests with the Sm-Co magnet reported here, linearly polarized light from a tunable laser source was coupled into one end of a ridge waveguide through a polarization maintaining single-mode fiber. In order to reduce the effect of the residual linear birefringence over a broad range of wavelengths, the input polarization direction was tilted by 22.5° to TE, following Dammann *et al.*⁹ The light emerging from the other end was collected by a microscope objective, passed through a metallic thin-film near-infrared polarization analyzer, and focused onto a germanium photodetector coupled to a multimeter.

Insertion losses in the isolator were measured by comparing the output of the polarization-maintaining fiber to that of the ridge waveguide. A total 6 dB of insertion loss was found, of which approximately 1.5 dB is due to reflections at the input and output facets, 1 dB is due to absorption losses in the waveguide itself, and the remainder, or 3.5 dB, is from coupling losses into and out of the waveguides. In order to reduce reflection losses, the facets of the device can be anti-reflection coated. Moreover, we expect that coupling losses can be significantly reduced with a more efficient coupling mechanism.

In order to measure the performance of the device, we cut the samarium-cobalt film together with its aluminum oxide substrate into a rectangular shape, 3.8 mm along the direction of magnetization, and 1 cm in the in-plane perpendicular direction. The structure was then placed film down on the Bi-YIG sample, its magnetization parallel to the waveguiding ridges, as shown in Fig. 1. This magnetic film was found to saturate the full length of the ridge waveguides, for 45° of rotation in the input polarization.⁷

To measure an effective isolation ratio for our device the

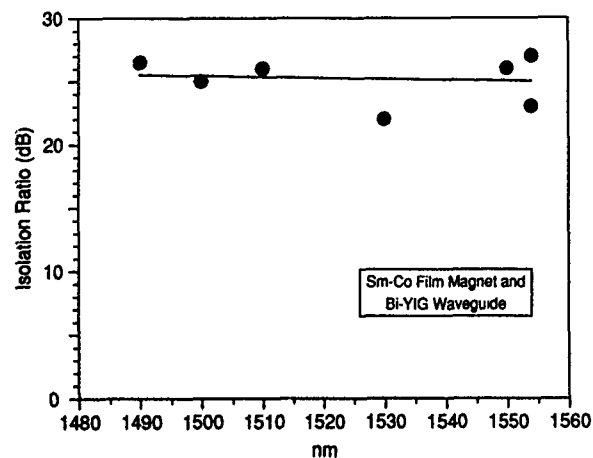


FIG. 3. Isolation ratio in Bi-YIG waveguide isolator with Sm-Co film magnet.

analyzer was set at the extinction angle. After measuring the power transmitted through the analyzer, the samarium-cobalt film was rotated 180° so that its magnetization was oriented antiparallel to the original direction of magnetization, and the transmitted power was measured again. Following Wolfe *et al.*,¹ the ratio of detected intensities for the two magnetization directions was taken as the isolation ratio for the ridge waveguide isolator. Our measurements show isolation ratios close to 25 dB in the wavelength range of our tunable laser source, from 1490 to 1555 nm. These results are plotted in Fig. 3. Forward excess losses due to birefringence are less than 0.5 dB.

M. Levy, R. Scarmozzino, and R. M. Osgood, Jr, gratefully acknowledge support by AFOSR/ARPA (Advanced Research Projects Agency) as well as the National Center for Integrated Photonics Technology (NCIPT) (DARPA) (Defense Advanced Research Project Agency) program at Columbia. F. J. Cadieu thanks AFOSR for program support, while the work at the Naval Research Laboratory was supported by ONR.

¹R. Wolfe, R. A. Lieberman, V. J. Fratello, R. E. Scotti, and N. Kopylov, *Appl. Phys. Lett.* **56**, 426 (1990).

²M. McGlashan-Powell, R. Wolfe, J. F. Dillon, Jr., and V. J. Fratello, *J. Appl. Phys.* **66**, 3342 (1989).

³C. J. Gutierrez, J. J. Krebs, and G. A. Prinz, *Appl. Phys. Lett.* **61**, 2476 (1992); C. J. Gutierrez, V. G. Harris, J. J. Krebs, W. T. Elam, and G. A. Prinz, *J. Appl. Phys.* **73**, 6763 (1993).

⁴H. Hedge, S. U. Jen, K. Chen, and F. J. Cadieu, *J. Appl. Phys.* **73**, 5926 (1993).

⁵M. Levy, I. Ilic, R. Scarmozzino, R. M. Osgood, Jr., R. Wolfe, C. J. Gutierrez, and G. A. Prinz, *IEEE Photonics Tech. Lett.* **5**, 198 (1993).

⁶Equations (1) and (2) differ from those in Ref. 5 by an overall minus sign. The equations in the present article are correct.

⁷As pointed out in Ref. 5, larger fields are needed near the ends than in the main body of the waveguide. This is achieved by taking advantage of the proximity of the magnet's pole faces to the ends of the waveguide as explained in that reference.

⁸R. Wolfe, V. J. Fratello, and M. McGlashan-Powell, *J. Appl. Phys.* **63**, 3099 (1988).

⁹H. Dammann, E. Pross, G. Rabe, and W. Tolksdorf, *Appl. Phys. Lett.* **56**, 1302 (1990).

Investigation of Pr-Fe-B magnets with high performance (abstract)

F. Z. Liañ, F. Pourarian, S. Simizu, S. G. Sankar, and W. E. Wallance

Advanced Materials Corporation, Department of Material Science and Engineering, Carnegie Mellon University, Pittsburgh, Pennsylvania 15213

Pr-Fe-B magnets with high performance based on 2:14:1 structure were investigated. The effect of fabricating processes on the oxygen content and on the magnetic properties was studied. The coercivity H_c decreases, but the B_r and $(BH)_{\max}$ of the magnets increase with the decrease of the Pr content. The decrease in the α -Fe content of the alloys annealed at 1000 °C for more than 360 h results in the enhancement of the magnetic properties of the magnets. Under the optimum conditions, the magnetic properties for $\text{Pr}_{14}\text{Fe}_{79.5}\text{B}_{6.5}$ magnets are found to be $H_c=656$ kA/m, $B_r=1.42$ T, $(BH)_{\max}=374$ kJ/m³. The microstructures of the magnets were investigated. The effect of the secondary phases in the grain boundary on the coercivity of the magnets was studied.

In situ and dynamic observation of NdFeCoB magnet by high voltage transmission electron microscope (abstract)

Pan Shuming

Research Institute of Non-Ferrous Metals, Beijing, China

Liu Jinfang

Department of Precision Alloys, Central Iron and Steel Research Institute, Beijing 100081, China

Xu Yinfan

Institute of Physics, Chinese Academy of Sciences, Beijing, China

In situ and dynamic observation of microstructural characteristics of sintered Nd-Fe-Co-B magnet has been carried out using JEM-1000X high voltage transmission electron microscope (HVTEM). Magnetic properties of the sample studied are as follows: $B_r=1.28$ T, $H_c=589$ kA/m, $(BH)_{\max}=302.4$ kJ/m³. HVTEM observation results are as follows: (1) At room temperature, the grains of the matrix phase are found to be nearly perfect crystals. In some grains, there exist some spherical inclusions that are embedded in the matrix. Structural analysis of these inclusions has been made by electron diffraction. (2) When the temperature is lower than 400 °C, we found no obvious changes. (3) When the temperature is higher than 400 °C, some small precipitates began to occur in the matrix. (4) When the temperature reaches 500 °C, the precipitates grow and become needlelike and perpendicular to each other. (5) When the temperature reaches 700 °C, the tetragonal symmetry of the matrix phase is completely damaged. (6) No remarkable changes were found for the Nd-rich grain boundary phase when the temperature increases from 25 to 600 °C. (7) Temperature dependence of coercivities of the sample has been explained by the structure changes.

Influence of electron damping and reservoir on the magnetic phase diagram of chromium alloys

R. S. Fishman

Solid State Division, Oak Ridge National Laboratory, P. O. Box 2008, Oak Ridge, Tennessee 37831-6032
and Physics Department, North Dakota State University, Fargo, North Dakota 58105-5566^{a)}

S. H. Liu

Solid State Division, Oak Ridge National Laboratory, P. O. Box 2008, Oak Ridge, Tennessee 37831-6032

The magnetic phase diagram of chromium alloys sensitively depends on both electron damping and the presence of an electron reservoir. If the damping energy Γ vanishes and the power ρ of the reservoir is infinite, then lightly doped CrMn alloys would experience a first-order transition from an incommensurate (I) to a commensurate (C) spin-density wave (SDW) state with decreasing temperature. Either damping or a finite reservoir may flip the phase boundary from one side of the triple point to the other, allowing a commensurate-to-incommensurate transition with decreasing temperature as observed experimentally. Both damping and a finite reservoir suppress the first-order jumps in the SDW order parameter and wave vector. When $\rho \leq 2$, the C-I transition is second order for all temperatures. When $\rho > 2$, the transition is second order near the tricritical point but first order at lower temperatures. Unlike electron damping, an electron reservoir does not shift the paramagnetic phase boundary and triple point.

The nesting^{1,2} of the octahedral electron and hole Fermi surfaces in chromium alloys is responsible for most of its unique properties. The Coulomb attraction³ between electrons and holes produces a spin-density wave (SDW) with wave vector close to the nesting wave vector. For pure chromium, the hole surface is slightly larger than the electron surface. Consequently, both the nesting wave vector Q and the SDW wave vector Q' are incommensurate with the lattice. The nesting of the Fermi surfaces and the Néel temperature are enhanced by doping with manganese, which adds electrons, and worsened by doping with vanadium,² which contributes holes to the conduction band.

Early experiments^{2,4} on lightly doped CrMn alloys revealed a first-order transition from commensurate (C) to incommensurate (I) phases of the SDW with decreasing temperature. By contrast, the theoretical phase diagram⁵ without damping and with a fixed chemical potential contains a first-order incommensurate-to-commensurate (I-C) transition with decreasing temperature. This phase diagram is drawn in the solid curves of Fig. 1 for the case $\rho = \infty$. Here $T_N^* \approx 77$ meV is the fictitious Néel temperature of perfectly nested chromium without impurities. The energy z_0 is proportional to the mismatch between the electron and hole surfaces in k space. As indicated, this mismatch decreases with manganese doping and increases with vanadium doping.

Two explanations have been proposed for the observed C-I transition. Because scattering from impurities breaks

electron-hole pairs,⁶ electron damping suppresses both the SDW order parameter and the Néel temperature. In previous work,⁵ we found that electron damping also favors the incommensurate over commensurate phases of the SDW. Since the ratio of the damping energy Γ to thermal energy increases with decreasing temperature, damping may flip the phase boundary from one side of the triple point to the other,

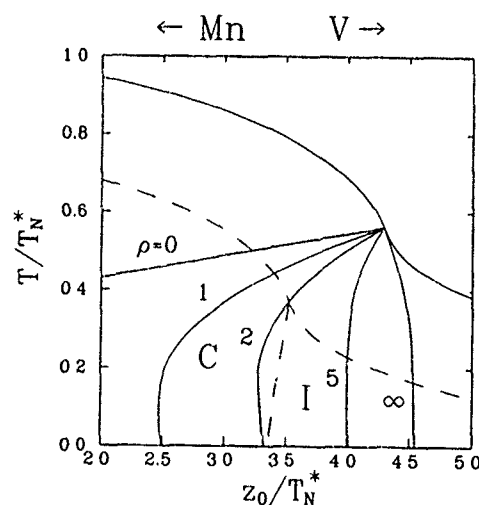


FIG. 1. T/T_N^* -vs- z_0/T_N^* phase diagram of chromium alloys. The solid curves are plotted for $\Gamma=0$ and with the indicated reservoir power. The dashed curve is plotted for $\Gamma/T_N^*=0.3$ and $\rho=\infty$. While the commensurate phase lies to the left of the boundaries, the incommensurate phase lies to the right, as shown for the dashed phase diagram with damping.

^{a)}Permanent address.

resulting in the observed first-order $C-I$ transition. The phase diagram with $\Gamma/T_N^* = 0.3$ is given by the dashed curves of Fig. 1. As well as lowering the paramagnetic phase boundary, damping also suppresses the triple point of z_0 .⁵ As Γ increases for a fixed z_0 , the size of the drop in the SDW order parameter g at the $C-I$ phase boundary decreases. When Γ exceeds some critical value $\Gamma_c(z_0)$, the Néel temperature vanishes and the alloy becomes paramagnetic. About 4% vanadium is required to drive CrV alloys paramagnetic.²

The $C-I$ transition can also be explained by imposing particle conservation. Much theoretical work on chromium alloys,^{3,6} including our previous studies,^{5,7} assumed that the chemical potential was unaffected by the formation of the SDW and the concurrent gap $\Delta \propto g$ in the electron-hole energy spectrum. This requires an infinite reservoir of electrons, which replenishes the electron-hole band and keeps the chemical potential constant. An electron reservoir is supplied^{1,8} by the electron bands midway between reciprocal-lattice points Γ and H and by the hole pockets at N . The reservoir power ρ is just the ratio of the density of states of the reservoir band to that of the electron-hole band.

When the power ρ of the electron reservoir is finite, the chemical potential will decrease and the effective mismatch \tilde{z}_0 between electron and hole surfaces will increase with decreasing temperature. As seen from Fig. 1, this increase of the energy mismatch favors the incommensurate regime. When ρ is sufficiently small, the phase boundary will flip from one side of the triple point to the other and produce a $C-I$ transition. Unlike damping, however, the reservoir does not affect the paramagnetic phase boundary or the position of the triple point.

Unfortunately, previous studies of the reservoir's effects were inconclusive. The early work of Rice⁹ approximated the octahedral hole and electron Fermi surfaces by spheres of unequal radii. While qualitatively correct, this approximation fails in the incommensurate phase, when the detailed structure of the Fermi surfaces becomes important. More recently, Angelescu, Nenciu, and Tonchev¹⁰ constructed a Ginzburg-Landau free energy which produces unphysical gaps in the T -vs- z_0 phase diagram. Machida and Fujita,¹¹ on the other hand, were primarily concerned with the effects of higher harmonics in the SDW and erroneously concluded that the phase transitions were always second order.

To clarify the effects of an electron reservoir, we have calculated the free energy of chromium alloys in the presence of a finite reservoir but without damping. The SDW wave vector must now be written

$$Q' = \frac{2\pi}{a} [1 + \delta(\Lambda - 1)] + \frac{2\pi}{a} \kappa \frac{\tilde{z}_0 - z_0}{T_N^*} (\Lambda - 1), \quad (1)$$

where $\kappa = aT_N^*/4\pi v_F \approx 0.013$, $v_F \approx 5.1 \times 10^7$ cm/s is the Fermi velocity, and $a \approx 5.45$ Å is the lattice constant of the bcc lattice. The nesting wave vector Q of the electron and hole surfaces is given by Eq. (1) with $\Lambda = 0$. The deviation of Q from the reciprocal-lattice vector $2\pi/a$ is determined by the difference $\tilde{z}_0(T) - z_0$ and by the wave-vector mismatch $\delta \approx 0.04$. For a finite reservoir, $\tilde{z}_0(T) > z_0$ and the nesting wave vector Q decreases as the temperature is lowered.

The difference between the nesting wave vector Q and the SDW wave vector Q' is determined by $0 \leq \Lambda(T) \leq 1$ and reflects the compromise⁷ between the nesting of each side of the hole octahedron with the smaller electron octahedron. When $\Lambda = 1$, the SDW wave vector is commensurate with the lattice; when $\Lambda = 0$, the nesting and SDW wave vectors are identical. For an infinite reservoir, Λ jumps to 1 as $z_0 \propto \delta v_F/a$ decreases through the phase boundary.⁵ As z_0 decreases in the commensurate regime, the nesting continues to improve and T_N continues to grow until it reaches a maximum of T_N^* when $z_0 = 0$. For a finite reservoir, the suppression of the chemical potential with decreasing temperature tends to lower Q' . By maintaining the constancy of the chemical potential and \tilde{z}_0 , the reservoir opposes the growth of the second term in Q' with decreasing temperature.

In the presence of a finite reservoir, the free energy is given by¹¹

$$F(z_0, T) = \min_{g, \Lambda} \{ \sup_{\tilde{z}_0} [F^{(0)}(\tilde{z}_0, g, \Lambda, T) - \frac{1}{32} \rho_{eh} (1 + \rho) (\tilde{z}_0 - z_0)^2] \}, \quad (2)$$

where ρ_{eh} is the density of states of the electron-hole surfaces and $F^{(0)}(\tilde{z}_0, g, \Lambda, T)$ is the free energy of chromium for an infinite reservoir with \tilde{z}_0 replacing z_0 . As defined by Eq. (2), the solution for g and Λ will minimize the free energy $F(z_0)$ subject to the constraint that it be an extremum with respect to \tilde{z}_0 . Since the reservoir power ρ does not enter $F^{(0)}(\tilde{z}_0)$, the self-consistent solutions which minimize $F(z_0)$ need only be extrema of $F^{(0)}(\tilde{z}_0)$. In fact, this set of self-consistent solutions $\{g, \Lambda\}$ may maximize the infinite-reservoir free energy $F^{(0)}(\tilde{z}_0)$. By contrast, Angelescu, Nenciu, and Tonchev¹⁰ define the free energy so that the minimization with respect to g and Λ precedes the extremization with respect to \tilde{z}_0 . As a result, the extremum condition will have *no solution* for ranges of the energy mismatch z_0 . To avoid this unphysical situation, the order of operations in Eq. (2) must be maintained.

The infinite-reservoir free energy $F^{(0)}(\tilde{z}_0)$ is taken from Ref. 5 in the absence of damping:

$$F^{(0)}(\tilde{z}_0, g, \Lambda, T) = \rho_{eh} g^2 \ln \left(\frac{T}{T_N^*} \right) - \rho_{eh} \sum_{n=0}^{\infty} \left(T \int_{-\infty}^{\infty} dz \ln \left| 1 - g^2 \frac{2i\nu_n - \tilde{z}_0 + 2z}{(i\nu_n - z) \{ (i\nu_n - \tilde{z}_0 + z)^2 - [\tilde{z}_0(\Lambda - 1)/2]^2 \}} \right| - g^2 \frac{1}{n + \frac{1}{2}} \right), \quad (3)$$

where $\nu_n = (2n+1)\pi T$ are the Matsubara frequencies. The self-consistent solutions for $\{g, \Lambda\}$ are obtained from the extremum conditions

$$\frac{\partial F^{(0)}(\bar{z}_0, g, \Lambda, T)}{\partial g} = 0, \quad (4a)$$

$$\frac{\partial F^{(0)}(\bar{z}_0, g, \Lambda, T)}{\partial \Lambda} = 0, \quad (4b)$$

just as in Ref. 5 except that now both minima and maxima sets of solutions are retained and tabulated as functions of \bar{z}_0 . The extremum condition with respect to \bar{z}_0 is given by

$$z_0 = \bar{z}_0 - \frac{16}{\rho_{eh}(1+\rho)} \frac{\partial F^{(0)}(\bar{z}_0)}{\partial \bar{z}_0}. \quad (5)$$

Notice that \bar{z}_0 is independent of ρ_{eh} and depends only on the reservoir power ρ . Since the free energy $F^{(0)}(\bar{z}_0)$ increases as \bar{z}_0 grows and the nesting worsens, we find that $\bar{z}_0 > z_0$ as anticipated earlier.

We plot the resulting phase diagram in the solid lines of Fig. 1. In the absence of a reservoir, $\rho=0$ and the incommensurate SDW is stable at $T=0$ for all z_0 . Generally, a small reservoir will suppress the jumps in the order parameter and chemical potential. When $\rho \leq 2$, the set of maxima incommensurate solutions $\{g, \Lambda\}$ smoothly joins the set of minima commensurate solutions to produce a *second-order* transition at all temperatures. In this regime, the $T=0$ phase boundary is given exactly by

$$\frac{z_0^{C-I}}{T_N^*} = 2\sqrt{2} \frac{\pi}{\gamma} \frac{\rho}{1+\rho} \approx 4.99 \frac{\rho}{1+\rho}, \quad \rho \leq 2 \quad (6)$$

where $\gamma \approx 1.78107$ is Euler's constant. Using spherical Fermi surfaces at zero temperature, Rice⁹ found that the $C-I$ phase transition becomes second order when $\rho < 0.31$, a much smaller value than obtained here with octahedral Fermi surfaces.

If $\rho > 2$, the phase transition is first order at low temperatures but becomes second order at higher temperatures, where the first-order jumps in the order parameter are smaller and more easily destroyed. For example, when $T = 0.4T_N^*$, the phase transition is second order for $\rho < 7.01$. With second-order transitions at all temperatures, the phase diagram of Machida and Fujita¹¹ exaggerates the incommensurate regime. But like Rice⁹ and the present authors, Machida and Fujita agree that the incommensurate regime is stable for all z_0 at $T=0$ when $\rho=0$.

For any value of ρ smaller than about 10, the phase boundary flips from the right to the left of the triple point, producing a $C-I$ transition. Since the reservoir power is certainly less than 10, we conclude that damping is not needed to explain the $C-I$ transition. However, damping is required to understand the decrease of the SDW wave vector and order parameter when chromium is doped with isoelectronic impurities like molybdenum or tungsten.²

The slight bulge of the $C-I$ phase boundaries to the left would seem to permit a $C-I-C$ transition with decreasing temperature. This bulge is most noticeable for intermediate values of ρ near 2 but is present for all nonzero values of ρ which allow a $C-I$ transition. We believe that even a small amount of damping will wipe out the bulge and eliminate the possibility of a $C-I-C$ transition.

This work suggests that whenever ρ is finite, the $C-I$ phase transition will become second order sufficiently close to the triple point. Experiments² on the $C-I$ transition have been performed far enough away from the triple point that the observed transition is first order. While it would be interesting to test this prediction closer to the triple point, first-order jumps in the order parameter and wave vector may be difficult to distinguish from second-order transitions in this regime.

Comparing our phase diagram with the experimentally observed $C-I$ phase transition within a narrow window of manganese concentrations, we would conclude that ρ lies between 4 and 8. By contrast, the band-structure calculations of Asano and Yamashita⁸ indicate a much smaller value of $\rho \approx 1$. However, the nested electron-hole band may itself oppose changes of the chemical potential and provide an additional, effective reservoir of electrons. Alternatively,¹² the presence of a charge-density wave which strongly favors the commensurate regime may balance the small size of the electron reservoir.

To conclude, we have investigated the effects of damping and an electron reservoir on the phase diagram of chromium alloys. While either sufficiently strong damping or a sufficiently small reservoir can explain the $C-I$ transition, we believe that a combination of the two is required to explain the detailed phase boundary. Experiments close to the tricritical point may reveal second-order $C-I$ transitions and confirm the importance of a finite electron reservoir.

We would like to acknowledge support from the U. S. Department of Energy under Contract No. DE-AC0584OR21400 with Martin Marietta Energy Systems, Inc. Useful conversations with J. F. Cooke are also gratefully acknowledged.

¹T. L. Loucks, Phys. Rev. **139**, A1181 (1965).

²W. C. Koehler, R. M. Moon, A. L. Trego, and A. R. Mackintosh, Phys. Rev. **151**, 405 (1966).

³C. Y. Young and J. B. Sokoloff, J. Phys. F. **4**, 1304 (1974).

⁴S. Komura, Y. Hamaguchi, and N. Kunitomi, J. Phys. Soc. Jpn. **23**, 171 (1967).

⁵R. S. Fishman and S. H. Liu, Phys. Rev. B **48**, 3820 (1993).

⁶J. Zittartz, Phys. Rev. **164**, 575 (1967).

⁷R. S. Fishman and S. H. Liu, Phys. Rev. B **47**, 11 870 (1993).

⁸S. Asano and J. Yamashita, J. Phys. Soc. Jpn. **23**, 714 (1967).

⁹T. M. Rice, Phys. Rev. B **2**, 3619 (1970).

¹⁰N. Angelescu, G. Nenciu, and N. S. Tonchev, Phys. Lett. **93A**, 201 (1983); J. Phys. F **14**, 2155 (1984).

¹¹K. Machida and M. Fujita, Phys. Rev. B **30**, 5284 (1984).

¹²X. W. Jiang, R. S. Fishman, and S. H. Liu (unpublished).

Spin fluctuation effect in the ordered Fe₂N alloy

Guan-mian Chen, Ming-xi Lin, and Ji-wu Ling

State Laboratory for Magnetism, Institute of Physics, Chinese Academy of Sciences, Beijing 100080, China

The temperature and field dependence of the magnetization of a Fe₂N alloy has been measured and compared with the calculation of the Moriya-Kawabata theory and Stoner-Edwards-Wohlfarth model. It is shown that Fe₂N is a very weak itinerant ferromagnet, and the Moriya-Kawabata theory and the electron gas approximation give a good description. Spin fluctuations and their interaction play a significant role in determining the thermomagnetic properties of the Fe₂N alloy.

I. INTRODUCTION

Fe₂N is an ordered interstitial alloy with orthorhombic structure¹ and the highest N content (about 11.1 wt %) in the Fe-N solid solution. Much research has been carried out on Fe₂N, but there was still controversy regarding magnetic properties^{2,3} until we identified it as a weak itinerant ferromagnet (WIF).⁴ In our previous paper, the magnetic properties of Fe₂N were analyzed based on the Stoner-Edwards-Wohlfarth (SEW) model, which gives results in agreement with the magnetization and susceptibility measured below T_c , but deviates at $T > T_c$. This is not surprising since the SEW model is essentially a mean-field theory and only single electron excitation is taken into account.

This paper reports detailed results of the temperature and field dependence of the magnetization of Fe₂N and makes a comparison with numerical calculations based on the self-consistent renormalization (SCR) theory by Moriya and Kawabata,⁵ which considers the collective excitation of the electron-hole pairs (spin fluctuations) and their interaction, and is expected to give better agreement at higher temperature.

II. FIELD DEPENDENCE OF THE MAGNETIZATION AT $T=0$

The α -FeOOH powder of average size 6 μm was reduced in pure flowing H₂ gas at 425 °C for 10 h, followed by nitriding in flowing NH₃ gas at 450 °C for 12 h. The sample was detected by x-ray diffraction as consisting of single phase and in good agreement with Jack's result¹ for Fe₂N in both line positions and intensities. Magnetization was measured from 1.5 to 30 K by the sample-drafting induction method in a superconducting solenoid with magnetic fields up to 80 kOe.

According to the SCR theory, in the electron gas approximation, the reduced magnetization ζ of the WIF can be expressed as^{5,6}

$$\frac{1}{\alpha} \left(1 + \frac{2}{27} \zeta^2 \right) = 1 + \frac{3}{2\alpha \zeta k T_F} \left(\mu_B H - \frac{\partial \Delta F}{\partial M} \right), \quad (1)$$

where the magnetization (per gram), $M = M(H, T)$, is a function of the field and temperature, the reduced moment $\zeta = \zeta(H, T) = M(H, T)/N$, with N the total electron number per gram, T_F is the Fermi temperature, $1/(\alpha-1)$ is the Stoner enhancement factor, and ΔF is the correction of the Hartree-Fock term in the free energy due to the spin fluctuation.

At $T=0$, the contribution of the spin fluctuation $\partial \Delta F / \partial M = 0$, Eq. (1) becomes

$$\zeta^2(H, 0) = \frac{27}{2} (\alpha - 1) + \frac{81}{4} \frac{\mu_B}{k T_F} H / \zeta(H, 0). \quad (2)$$

This is to be compared with the SEW model⁷:

$$\zeta^2(H, 0) = \zeta^2(0, 0) + \frac{2\chi_0}{N} \zeta^2(0, 0) H / \zeta(H, 0). \quad (3)$$

Here $\chi_0 = (\partial M / \partial H)_{H=0, T=0} = N N(E_F) \mu_B^2 / (\alpha - 1)$ is the susceptibility at zero field and temperature, and $N(E_F)$ is the density of states at the Fermi energy.

From Eqs. (2) and (3), using the experimental magnetization $\zeta(0, 0) = 0.06 \mu_B$ and $\zeta(H = 5 \text{ kOe}, 0) = 0.092 \mu_B$, we can calculate the entire field dependence of the magnetization. The result obtained is in excellent agreement with the experimental $M(H, 0)$ curve, as shown in Fig. 1, indicating Fe₂N is an unsaturated weak itinerant ferromagnet.

According to both the SCR theory [Eq. (2)] and the SEW model [Eq. (3)], the Arrott plot, i.e., the M^2 -vs- H/M curve, is a straight line for $T=0$ as shown in Fig. 2. From Eq. (2), $\alpha = \frac{2}{27} \zeta^2(0, 0) + 1 = 1.000267$ and $T_F = 1.52 \times 10^4 \text{ K}$ are determined for the SCR theory. From Eq. (3), $\chi_0 = 1.1 \times 10^{-3} \text{ emu/g Oe}$ is determined for the SEW model. In the electron gas approximation, including the Stoner enhancement, $\chi_0 = 3N \mu_B^2 / 4k T_F (\alpha - 1)$. From this expression and the experimental χ_0 value, T_F is also estimated as $1.53 \times 10^4 \text{ K}$.

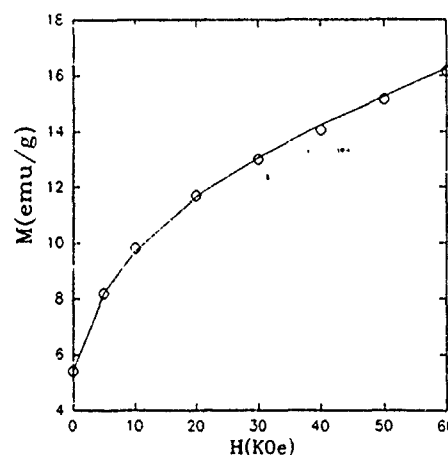


FIG. 1. Magnetization of Fe₂N as a function of field at $T=0$. Dots are the experiments and the solid line is according to the SCR theory and SEW model.

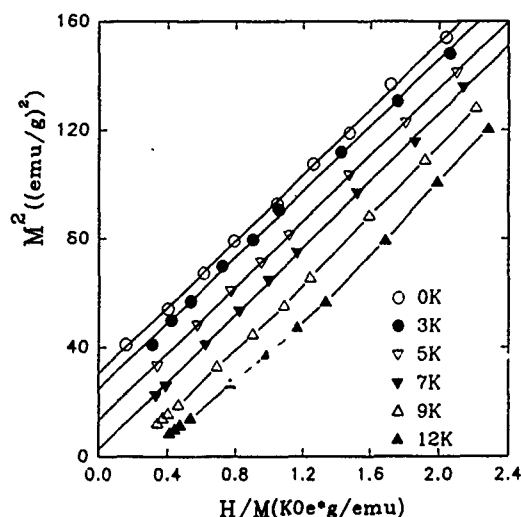


FIG. 2. Arrott plot of Fe_2N from $H=1.5$ to 20 kOe.

Thus, in the electron gas approximation, both the SCR theory and SEW model give the same description to the zero-temperature magnetization $M(H,0)$.

Table I presents those basic parameters for Fe_2N and some typical weak itinerant magnets for comparison.

III. TEMPERATURE DEPENDENCE OF THE SPONTANEOUS MAGNETIZATION AT $T < T_c$

According to the SCR theory, near T_c , the spontaneous magnetization $M(0,T)$ can be expressed as $M^2 \sim (T_c^{4/3} - T^{4/3})$, but according to the SEW model,⁸ at $T < T_c$, $M^2 \sim (T_c^2 - T^2)$.

The two relations are good criteria for verifying which model is more appropriate to describe the weak itinerant magnet. The experimental $M(0,T)$ value is obtained by extrapolating the Arrott plot (Fig. 2) to $H=0$ for $T < T_c$. However, since these parallel lines are very sharp and crowded in Fig. 2, error was introduced in the extrapolation.

$M^2(0,T)$ is plotted against $T^{4/3}$ and T^2 in Fig. 3, and they are all essentially straight lines. From Fig. 3 it is hard to tell which model is better. There are two possible reasons: First, both models are essentially able to describe the magnetic properties of Fe_2N at $T < T_c$.⁴ Second, the precision of

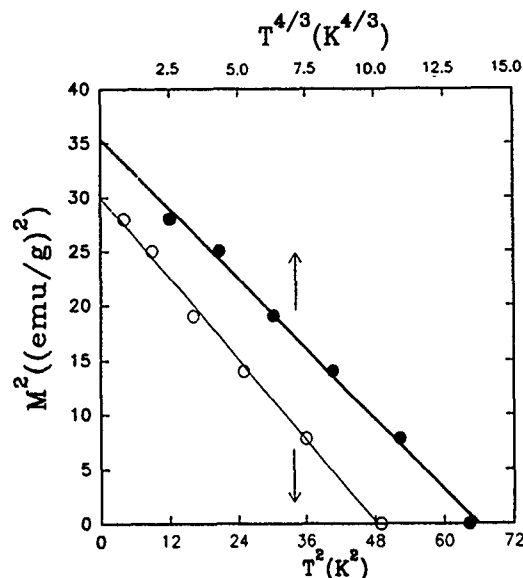


FIG. 3. Square of the magnetization of Fe_2N at $H=0$ plotted against $T^{4/3}$ and T^2 curves.

our magnetic measurement is not good enough to determine the correct expression of $M(0,T)$, especially due to the error in the extrapolation as mentioned above.

IV. MAGNETIZATION AT NONZERO FIELD AND FINITE TEMPERATURE

The Arrott plot of Fe_2N (Fig. 2) at $T < T_c$ is a series of parallel lines over a wide range of field strength. Since they are very crowded in the temperature scale, only a few points of temperature are plotted in Fig. 2 for clarity. Their slope is essentially independent of the temperature, indicating that the field dependence of the magnetization at $T < T_c$ can be described by the SEW model⁷ as given by

$$M^2(H,T) = M^2(0,0) [1 - (T/T_c)^2 + 2\chi_0 H/M(H,T)].$$

However, the Arrott plot at $T > T_c$ becomes concave and deviates from a straight line and the SEW model.

The numerical calculation of Eq. (1) was carried out according to the SCR theory [see Eqs. (6), (9), and (10) of Ref. 6] based on the electron gas approximation and $\zeta \ll 1$,

TABLE I. Basic parameters of Fe_2N and other typical itinerant ferromagnets: p_s is the zero-temperature moment [per transition-metal (TM) atom], b is the slope of the M^2 -vs- H/M curve at $T=0$, C is the Curie constant above T_c , and p_c is the effective moment deduced from the Curie constant.

	Fe_2N	ZrZn_2	Ni_3Al	Sc_3In	$\text{Ni}_{0.429}\text{Pt}$
p_s ($\mu_B/\text{TM atom}$)	0.06	0.112	0.077	0.045	0.051
T_c (K)	7	16.9	40.6	5.5	23
b ($10^{-2} \text{ emu}^3/\text{g}^3 \text{Oe}$)	6.4	0.16	0.517	0.21	0.124
C (10^{-2} emu K/g)	0.74	0.094	0.231	0.267	
p_c ($\mu_B/\text{TM atom}$)	1.2	0.65	0.39	0.26	0.88
p_c/p_s	20	5.4	5.1	5.8	17.2
α	1.000 267	1.000 93	1.000 44	1.000 15	1.000 19
χ_0 (10^{-3} emu/g Oe)	1.1	0.10	0.062	0.11	0.145
References		7, 8	9	6, 10	11

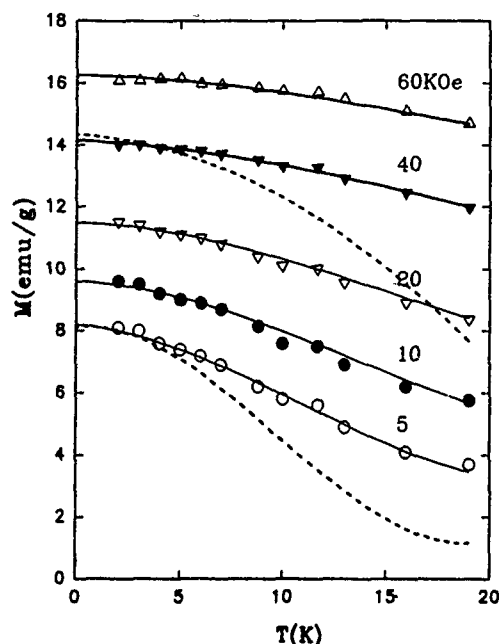


FIG. 4. Magnetization $M(H,T)$ as a function of the temperature at various fields. Solid lines are fitted to the SCR theory and the dashed lines are fitted to the SEW model.

using the α value determined above. The cutoff wave vector q_c is chosen as $\sqrt{2}$. The best fit with the experimental data is obtained when $T_F = 1.52 \times 10^4$ K.

According to both models,⁵ the Curie temperature can be determined by the following equations:

$$T_c = \left(\frac{\alpha - 1}{9.902\alpha} \right)^{3/4} T_F = 5.7 \text{ K for the SCR theory,}$$

and

$$T_c = \left(\frac{12(\alpha - 1)}{\pi^2} \right)^{1/2} T_F = 245 \text{ K for SEW model.}$$

It is easy to see that the SCR theory estimation is very close to the experimental value, 7 K, determined from Fig. 3, while the SEW model gives an estimation about 40 times larger.

The calculated $M(H,T)$ -vs- T curves (solid line) and the experimental data are shown in Fig. 4. They are in very good agreement over a wide field range. This is the second ex-

ample which shows good fit with the SCR theory among all weak itinerant magnets known up to date besides the first one (So_3In) reported earlier.⁶ For comparison, the $M(H,T)$ curve from the SEW model is also drawn in Fig. 4 (dashed lines): it deviates obviously from experiments when $T \geq T_c$.

Takeuchi and Masuda⁶ calculated the $M(H,T)$ curve of Sc_3In by the SCR theory, which coincides excellently with experiments. However, their T_F value from the $M(0,T)$ curve is ten times smaller than the value obtained from the $M(H,T)$ curve at $H=5$ and 10 kOe, i.e., 2.07×10^4 K and 2.2×10^5 K, respectively. They considered that this discrepancy probably resulted mainly from the oversimplified assumption of the electron gas model. For Fe_2N , the largest difference of T_F obtained from $M(0,T)$ and $M(H,T)$ measurement is within 20%. This indicates that the field and temperature dependence of its magnetization can be well described by the SCR theory and electron gas approximation.

In summary, it is shown that Fe_2N is a uniform, very weak itinerant ferromagnet, close to the Stoner criterion. Its T_c and zero-temperature magnetic moment p_s are among the smallest compared to other WIF (Table I). However, strongest effect of spin fluctuation is observed for Fe_2N as shown by the large effective moment p_c determined from the Curie constant above T_c . Fe_2N has the largest ratio p_c/p_s among all WIF known to date. As shown in this paper the SCR theory and electron gas approximation interpret the thermomagnetic properties of Fe_2N over a rather wide field and temperature range both below and above T_c . The SEW theory holds when $T < T_c$, but deviates at $T \geq T_c$, indicating that the spin fluctuation and its interaction play significant role.

¹ K. H. Jack, *Acta Crystallogr.* **5**, 404 (1952).

² J. B. Goodenough, A. Wold, and R. J. Arnolt, *J. Appl. Phys.* **31**, 342s (1960).

³ J. Bainbridge, D. A. Channing, W. H. Whitler, and R. E. Pendiebury, *J. Phys. Chem. Solids* **34**, 1579 (1973).

⁴ Chen Guan-mian and Li Jing-yuan, *Chinese Phys. Lett.* **2**, 365 (1985).

⁵ T. Moriya, *J. Magn. Magn. Mater.* **14**, 1 (1979); T. Moriya and Kawahata, *J. Phys. Soc. Jpn.* **34**, 639 (1973); *ibid.* **35**, 669 (1973).

⁶ J. Takeuchi and Y. Masuda, *J. Phys. Soc. Jpn.* **46**, 468 (1979).

⁷ E. P. Wohlfarth, *J. Appl. Phys.* **39**, 1061 (1968).

⁸ S. Ogawa, *J. Phys. Soc. Jpn.* **40**, 1007 (1976).

⁹ K. Suzuki and Y. Masuda, *J. Phys. Soc. Jpn.* **54**, 326 (1985); **54**, 630 (1985).

¹⁰ T. Hoiki and Y. Masuda, *J. Phys. Soc. Jpn.* **43**, 1200 (1977).

¹¹ H. L. Alberts, J. Beille, D. Bloch, and M. J. Beaus, *J. Phys. F* **4**, 1275 (1974).

Isoelectronic early n - d impurities in Fe: Magnetic and hyperfine field properties

N. A. de Oliveira, A. A. Gomes, and A. Troper

Centro Brasileiro de Pesquisas Físicas (CBPF), Rua Dr. Xavier Sigaud 150, 22290-180, Rio de Janeiro, RJ, Brazil

The hyperfine fields and the local magnetic moments in a series of alloys of isoelectronic transition impurities diluted in iron are discussed. We intend to show that, even within a very simplified model, period effects for isoelectronic impurities at the beginning of an n - d series (e.g., Sc, Y, and Lu) are dominated by the charge difference effect, inducing a very strong repulsive potential. We find that the local impurity magnetic moments are very close to each other, leading to hyperfine fields, in fair agreement with experimental data. Our calculation accounts for the general trends of the local impurity moments in ferromagnetic Fe, despite quantitative deviations that do occur, due to the very simple structure of this model. We point out, however, that our calculation is a starting point for a more refined one, dealing with rare-earth impurities (such as Eu, Gd, and Tb) placed in the Fe host, where the strong charge effects are present, together with f -spin scattering.

We focus our interest in Sc, Y, and Lu elements, which are isoelectronic d impurities at the beginning of a transition series, diluted in a Fe host to study comparatively the relative importance of period effects and the charge difference between the host and impurity. This study is a first step to discuss theoretically the whole series of rare-earth elements diluted in Fe, like GdFe and EuFe where some controversial experimental data were obtained.^{1,2} In the EuFe case, additional interest is connected to the Eu valence and its effect on the hyperfine field. Within a classical Koster-Slater formulation, the impurity problem in magnetic hosts has been discussed many years ago³ for $3d$ impurities in Fe. The change in sign of the impurity d magnetic moment with respect to the host moment could then be explained.³⁻⁵

Since intense experimental effort has been made to measure the magnetic and hyperfine field properties in such diluted alloys,² we decided to describe the observed properties within the simplest possible theoretical framework. The motivation is to check to which level our calculation gives a qualitative description of the experimental data. In particular, the case of Eu impurities diluted in Fe may be understood only by including the possibility of valence changes and thereby an orbitally induced hyperfine field.

The main difference between this work and Ref. 3 is that here we phenomenologically introduce the polarization of the s - p host conduction band, taking it as being antiparallel to the d host magnetization m_d^h . So, we put⁶

$$m_c^h = -\alpha m_d^h, \quad (1)$$

where α is a parameter obtained from a fitting of the s - p conduction-electron polarization in transition metals; this corresponds to $\alpha=0.08$.

At the impurity site, the total magnetization $\tilde{m}(0)$ is given by the sum of the impurity d moment $\tilde{m}_d(0)$ and the s - p magnetization written above. Then

$$\tilde{m}(0) = \tilde{m}_d(0) + m_c^h = \tilde{m}_d(0) - \alpha m_d^h. \quad (2)$$

Strictly speaking, the inclusion of the s - p contribution introduces a small shift in the local moment, relevant mainly

around the change in sign of the impurity moment. However, the importance of the s - p contribution concerns the hyperfine field.

The Hamiltonian of Ref. 3 is generalized here in order to include the change in Coulomb interaction due to period effects⁷:

$$H = \sum_{ij\sigma} T_{ij}^{(d)} d_{i\sigma}^\dagger d_{j\sigma} + \frac{U}{2} \sum_{i\sigma} n_{i\sigma}^d n_{i-\sigma}^d + \Delta U n_{0\sigma}^d n_{0-\sigma}^d + \sum_{ij\sigma} T_{ij}^{(c)} c_{i\sigma}^\dagger c_{j\sigma}, \quad (3)$$

where $T_{ij}^{(\alpha)}$ ($\alpha=d, c=s$ - p) are the hopping terms, and U is the host d -band Coulomb repulsion taken as 1.1 in units of the band width. $\Delta U = U_{nd}^{\text{imp}} - U_{3d}^{\text{host}}$, $n=4$ and 5 , is the change in Coulomb correlation at the impurity site (located at the origin) due to period effects. The numerical values were taken -0.8 and -1.0 , respectively, for $4d$ or $5d$ impurities.

The $c_{i\sigma}^\dagger$ and $c_{i\sigma}$ create and destroy, respectively, electrons in the wide s - p band whereas $d_{i\sigma}^\dagger$ and $d_{i\sigma}$ are creation and annihilation operators for electrons in the correlated and narrow d band. A Hartree-Fock description is assumed *ab initio* and $n_{0-\sigma} = d_{0-\sigma}^\dagger d_{0-\sigma}$ is the d occupation number at the origin of electrons with spin $-\sigma$. The solution of the Hamiltonian given by Eq. (3) is made as in Refs. 3 and 7, i.e., via the solution of the Koster-Slater problem. The next step is to obtain the Friedel sum rule for both spin-dependent

TABLE I. Calculated hyperfine fields (in kG) for isoelectronic impurities Sc, Y, and Lu in Fe. The experimental data are collected from Refs. 2, 4, and 5.

	Experimental data	Theoretical calculation		Total hyperfine field
		s - p contribution	d contribution	
ScFe	-120	-129.2	6.1	-123.1
YFe	-260	-282.2	48.4	-233.8
LuFe	-610	-796.8	130.0	-666.8

TABLE II. Calculated local moments (in Bohr magnetons) for isoelectronic impurities Sc, Y, and Lu in Fe. For comparison, the first-principles results for the same TFe systems (T=Sc, Y, and in Lu) performed in Refs. 4 and 5.

	First-principles calculation	Present calculation		
		<i>s-p</i> moment	<i>d</i> moment	Total moment
ScFe	-0.30	-0.16	-0.16	-0.32
YFe	-0.20	-0.16	-0.16	-0.32
LuFe	-0.20	-0.16	-0.17	-0.33

local potentials V_σ and the difference between these Hartree-Fock V_σ potentials and the occupation numbers.

The hyperfine fields are estimated using the Fermi-Dirac coupling constants and the core polarization terms given in Ref. 8. We emphasize the very simplified content of these descriptions, in spite that our results are quite satisfying as shown in Tables I and II.

In particular, from Table II we note that the local magnetic moments of Sc, Y, and Lu are very close, thus supporting the idea that the important effect is the charge difference between the host and impurity. Then period effects are almost wiped out in these early isoelectronic transition elements by the charge difference effect.

However, if one refines the present calculation, in this

same tight-binding scheme, to include the difference in hopping between the impurity and next-neighbor atoms, numerical values of the magnetic moment can be improved for Y and Lu. This correction accounts for the difference in the radial extent of the wave functions at the beginning and end of the *n-d* series.

Concerning experimental data, it should be noted that local magnetic moments are obtained from neutron diffraction experiments with an accuracy less than those obtained for the hyperfine fields. In view of that, our present model accounts satisfactorily for the observed hyperfine data, as shown in Table I.

Finally, calculations for magnetic and hyperfine properties for GdFe and EuFe alloys, using LuFe results as a starting point, are now in progress.⁹

¹H. Bernas, Phys. Rev. B 16, 596 (1977).

²See, for instance, G. N. Rao, Hyperfine Int. 24-26, 1119 (1985).

³I. A. Campbell and A. A. Gomes, Proc. Phys. Soc. London '1, 391 (1967).

⁴H. Akai, M. Akai, S. Blugel, B. Drittler, H. Ebert, K. Terakura, R. Zeller, and P. H. Dederichs, Prog. Theor. Phys. Suppl. 101, 11 (1990), and references therein.

⁵P. H. Dederichs, R. Zeller, H. Akai, and H. Ebert, J. Magn. Magn. Mater. 100, 261 (1991), and references therein.

⁶A. Troper, X. A. da Silva, A. P. Guimarães, and A. A. Gomes, J. Phys. F 5, 160 (1975).

⁷C. E. Leal, O. L. T. de Menezes, and A. Troper, Physica 130B, 443 (1985).

⁸I. A. Campbell, J. Phys. C 2, 1338 (1969).

⁹N. A. de Oliveira, A. A. Gomes, and A. Troper (unpublished).

Electronic structure and the Stoner I parameter for RPd_3 compounds ($R=La, Ce, Pr, \text{ and } Nd$)

T. Nautiyal, A. Kashyap, and S. Auluck
Physics Department, University of Roorkee, Roorkee 247667, India

M. S. S. Brooks
Joint Research Centre, European Institute for Transuranium Elements, Postfach 2340,
DW-7500 Karlsruhe 1, Germany

Gardner *et al.* have made measurements of the magnetic susceptibility in a large range of temperature for a complete series of RPd_3 compounds (R =rare earths). Some band structure calculations exist on $LaPd_3$ and $CePd_3$. However, the question of magnetic ordering has not been addressed in existing theoretical work. With a view to understand the magnetic behavior of these compounds we have performed self-consistent band structure calculations for $LaPd_3$, $CePd_3$, $PrPd_3$, and $NdPd_3$. Our calculations predict magnetic ordering only in $PrPd_3$ and $NdPd_3$ and hence are consistent with the experimental findings.

I. INTRODUCTION

Rare-earth (R) metals and compounds are known to possess very interesting and complicated magnetic properties.¹ The magnetic ordering in RPd_3 compounds has been studied experimentally by Gardner *et al.*² and Elsenhans *et al.*³ With a view to understand this experimental data, we have calculated the electronic structure of some RPd_3 compounds with $R=La, Ce, Pr, \text{ and } Nd$. The series of intermetallic rare-earth compounds RPd_3 has the Cu_3Au structure with Pd atoms at the face centers and R atoms at the corner of the cube. We have studied the ground-state properties of these compounds and tried to explore the magnetic ordering in these using the Stoner criterion. Our calculations also give the systematics of various band parameters (e.g., effective masses and bandwidths) as we progress through the first four members of RPd_3 series.

Earlier leading theoretical work on these compounds includes that by Koenig and Khan (KK),⁴ and Yanase and Hasegawa (YH).⁵ $CePd_3$ has a large residual resistivity ρ_0 and its resistivity $\rho(T)$ shows a maximum at 110 K with a negative $d\rho/dT$ at high temperature. Experiments show that small amounts of La, when Ce is replaced by La, halt the rapid drop in $\rho(T)$ below 110 K. YH (Ref. 5) have tried to explain the large residual resistivity of $CePd_3$ as being due to the small Fermi surface sheets arising from $4f$ electrons. They have performed the calculations using the full potential linear augmented plane wave method. KK (Ref. 4) have performed extensive linear muffin-tin orbital (LMTO) calculations for $LaPd_3$ and $CePd_3$ exploring the effects of spin-orbit (SO) coupling, and treatment of $4f$ states and $5p$ orbitals. They have calculated the optical conductivity for $LaPd_3$ and $CePd_3$. No electronic structure calculations appear to exist for $PrPd_3$ and $NdPd_3$.

II. METHOD OF CALCULATION

We have used the scalar relativistic LMTO method^{6,7} in which all relativistic terms except SO interaction have been included. KK (Ref. 4) have observed that the overall effect of including SO interaction is rather secondary as most of the data can be explained without it. We have taken the $5p$ or-

bitals of R atoms in the frozen core. Calculations are performed at the experimental value of 4.235 Å and 4.126 Å of the lattice constant for $LaPd_3$ [as quoted by KK (Ref. 4)] and $CePd_3$,⁸ respectively. For $PrPd_3$ and $NdPd_3$ the calculations were performed at a lattice constant of 4.126 Å, which is close to the experimental values of 4.1300 and 4.1181 Å, respectively.² We have used equal Wigner-Seitz (WS) radii (S) at the R and Pd sites. KK (Ref. 4) show that the f states of Pd are not very important. We have therefore used angular momentum expansion up to the f states in R atom and up to the d states in Pd atoms. This results in a 43×43 matrix, which speed up the computation. We have used 84 k points for the Brillouin zone summations for which the tetrahedron method⁹ has been used. The exchange-correlation potential used is the Barth-Hedin potential.¹⁰

III. RESULTS AND DISCUSSION

To get insight into the band structure of these compounds, we have calculated some important band parameters (Table I). μ and W are the self-consistently calculated effective mass and bandwidth, respectively, which can be calculated in terms of standard potential parameters.⁷ W_{il} is the unhybridized bandwidth that may be calculated using the canonical band theory.¹¹ A comparison of W with W_{il} enables one to analyze quantitatively the effect of hybridization on the bandwidths. For the unhybridized band of atom t and orbital quantum number l , the bandwidth W_{il} is given by¹¹

$$W_{il} = \left(\frac{12}{n_{il}} |S_{il}^{II}|^2 \right)^{1/2} \Delta_{il}$$

and

$$\Delta_{il} = 1/[\mu_{il} S_i^2 (S/S_i)^{2l+1}]$$

with $n_{il} = (2l+1)n_i$; n_i =number of t type of atoms in the unit cell; S_i =WS radius of t -type atomic sphere; μ_{il} is the corresponding effective mass, and $|S_{il}^{II}|^2$ is the second moment of the canonical tl band and in simplified form is given by¹¹

$$|S_{il}^{II}|^2 = \frac{[4(2l+1)^2](4l)!}{(2l)!(2l)!} P_{n_i n_i} (S/d_{n_i})^{2(2l+1)},$$

TABLE I. μ , effective mass (in atomic units); W_{II} , the canonical bandwidth (in mRy); W , the calculated bandwidth (in mRy); $\eta (=W/W_{II})$; and $\bar{\eta}$, the ideal ratio for f states of R atom and d states of Pd atom.

Compound	$R-f$					$Pd-d$				
	μ	W	W_{II}	η	$\bar{\eta}$	μ	W	W_{II}	η	$\bar{\eta}$
LaPd ₃	49.0	4.0	731	184.7	15.98	8.4	231	304	1.32	1.21
CePd ₃	33.7	6.1	154	25.4	15.98	7.9	258	339	1.32	1.21
PrPd ₃	34.7	5.9	109	18.4	15.98	7.9	259	340	1.32	1.21
NdPd ₃	39.1	5.2	92	17.6	15.98	7.9	258	340	1.32	1.21

where P_{nt} is the number of nearest neighbors of a t atom of the same kind and d_{nt} is the distance of this t -type atom from these nearest neighbors. The details of such a calculation for calculating W_{II} for Cu₃Au structures are given in the work of Podgorny.¹² We used $S_r/S=1$ as WS radii are the same at both the sites. η is the ratio of the calculated bandwidth and canonical bandwidth, whereas $\bar{\eta}$ is the ideal ratio when there is no difference between the two kinds of atoms. Thus a comparison of η and $\bar{\eta}$ is a good measure of degree of hybridization in a compound. As expected for these compounds, the effective mass for the f electrons is very high and canonical bandwidths very small. Our results show that there is broadening of the f bands of R atoms and d bands of Pd atoms, when $\eta > \bar{\eta}$. The broadening for the d states of Pd remains almost the same for all these compounds. However, in the case of LaPd₃, the f states of the La atom seem to be very sensitive to the presence of Pd atoms. This sensitivity is much less in CePd₃ and decreases as one goes to PrPd₃ and NdPd₃.

The l -projected charge occupancy and density of states (DOS) are presented in Table II. It shows that there is little

difference in the ionicities at the R sites and the Pd sites in the various compounds. In each compound more than one electron is lost by the R atom to the three Pd atoms in the unit cell. This is in accordance with Pauling's electronegativity difference. Interestingly, the magnitude of this charge transfer is quite large compared to that in relatively simpler systems such as transition-metal compounds, e.g., Ni₃X ($X = Al, Fe, Mn$) (Ref. 13), where the difference of the electronegativity of the two constituents is much smaller. The charge occupancies from KK (Ref. 4) (not listed in Table II) are in good agreement with ours. Inclusion of Pd f states in KK's work does not make an appreciable difference.

Since the DOS versus energy curve from our work is in good agreement with that from KK (Ref. 4) for LaPd₃ and CePd₃, we decided not to show the curves here. The angular momentum and site-resolved DOS shows a very fast rise for f states at the R site as one goes through this series. Thus the derived coefficient of electronic specific heat γ is large for PrPd₃ and NdPd₃. The γ value for LaPd₃ from this work as well as from KK (Ref. 4) is nearly eight times the experimental value.¹⁴ This is not the usual case with theory, and

TABLE II. Calculated ground state properties of RPd_3 compounds.

	LaPd ₃	CePd ₃	PrPd ₃	NdPd ₃
n_{R-s} (electrons)	0.26	0.31	0.31	0.32
n_{R-p} (electrons)	0.19	0.22	0.22	0.23
n_{R-d} (electrons)	1.04	1.26	1.23	1.19
n_{R-f} (electrons)	0.26	0.99	2.07	3.12
Ionicity of R	1.23	1.22	1.16	1.14
n_{Pd-s} (electrons)	0.75	0.76	0.75	0.75
n_{Pd-p} (electrons)	0.62	0.74	0.70	0.69
n_{Pd-d} (electrons)	9.04	8.91	8.93	8.94
Ionicity of Pd	-0.41	-0.40	-0.38	-0.36
N_{R-s} (states/Ry atom)	0.79	0.11	0.18	0.62
N_{R-p} (states/Ry atom)	0.23	0.20	0.43	0.95
N_{R-d} (states/Ry atom)	1.61	0.69	2.82	3.60
N_{R-f} (states/Ry atom)	0.18	63.24	906.73	1214.89
N_{Pd-s} (states/Ry atom)	0.63	0.13	1.63	0.97
N_{Pd-p} (states/Ry atom)	1.97	1.22	3.35	4.27
N_{Pd-d} (states/Ry atom)	0.79	0.91	13.75	15.50
$N(E_F)$ (states/Ry unit cell)	12.96	71.01	966.35	1240.80
γ (mJ mol ⁻¹ K ⁻²)	2.24	12.28	167.36	214.92
γ (mJ mol ⁻¹ K ⁻²) ^a	2.2	5.9		
γ (mJ mol ⁻¹ K ⁻²) ^b		2.5		
γ (mJ mol ⁻¹ K ⁻²) ^c	0.28	38.6		
Stoner product $IN(E_F)$	0.06	0.96	16.64	25.04
B (MBar)	1.17	1.60	1.39	1.38

^aReference 4 (theory).

^bReference 5 (theory).

^cReference 14 (experiment).

perhaps suggests the need for a higher level of sophistication for such calculations. The calculated γ values for CePd₃, however, are less than the experimental value and give a large enhancement factor of $\lambda \approx 2.1$, 5.6, and 14 for this work, KK (Ref. 4) and YH (Ref. 5), respectively. Differences in the total DOS, $N(E_F)$, values determined from the three calculations is understandable as the Fermi level (E_F) lies near a very sharp peak [Fig. 3 of KK (Ref. 4)], where the DOS changes very fast for a small shift in E_F .

The RPd₃ compounds form an interesting series in terms of their magnetic ordering behavior. Elsenhans *et al.*³ detected unusual magnetic ordering phenomena by systematic neutron scattering experiments on some members of this series in the temperature range 7 mK $\leq T \leq$ 300 K. In an effort to verify the consistency of our calculations, we have examined the Stoner criterion for these compounds. The multi-band Stoner product $IN(E_F)$, where I is the Stoner parameter and $N(E_F)$ is total DOS, appropriate for compounds is defined by¹⁵

$$IN(E_F) = N(E_F) \sum_i \sum_{ll'} \frac{N_{il}}{N(E_F)} I_{ill'} \frac{N_{il'}}{N(E_F)},$$

where the interatomic exchange integrals $I_{ill'}$ are evaluated self-consistently; and N_{il} is the site and angular momentum resolved DOS/spin. The calculated Stoner products are displayed in Table II. We obtain $IN(E_F) < 1$ for LaPd₃ and CePd₃, indicating absence of magnetic ordering in these compounds which is in agreement with experiment.² The Stoner product is > 1 for PrPd₃ and NdPd₃, implying the likelihood of magnetic ordering. Experiments² show that PrPd₃ and NdPd₃ are affected at low temperatures by the presence of crystal field. Magnetic measurements reveal that PrPd₃ shows the onset of antiferromagnetic ordering at 1.05 K. The reciprocal susceptibility-versus-temperature curve for NdPd₃ shows a negative intercept, suggesting the presence of a small antiferromagnetic exchange interaction in NdPd₃.² Measurements by Elsenhans *et al.*³ establish NdPd₃ as having an incommensurate magnetic ordering and estimate the Neel temperature of NdPd₃ as 0.73 ± 0.02 K. Simple calculations such as ours do not determine the type of magnetic ordering. Nevertheless, they are consistent with the experiments. Because of the antiferromagnetic ordering in these compounds, very large calculated values of total DOS for PrPd₃ and NdPd₃ are not alarming. It is well known¹⁶ that performing the calculations for the actual antiferromagnetic configuration would result in a dramatic drop in $N(E_F)$ because of the creation of a gap in the antiferromagnetic phase.

We also performed a calculation on these compounds for an expanded lattice to obtain a coarse estimate of the bulk modulus of these compounds as $B = -V\Delta P/\Delta V$ (P = pressure and V = volume). The estimated values, given in Table II, consistently lie between those for metals R and Pd. The LMTO method is known to give a good estimate of the

ground-state properties for compounds.¹⁷ Hence we expect these values to be reasonably accurate. Unfortunately, as far as we know, the value of B for these compounds has not yet been measured.

IV. CONCLUSIONS

We presented the systematics of some ground-state properties of the RPd₃ ($R = \text{La, Ce, Pr, and Nd}$) compounds. The calculations are for the nonmagnetic phase. We obtain a very large DOS for NdPd₃ and PrPd₃, which shows that the nonmagnetic phase is unstable to the formation of a magnetic compound. The Stoner product < 1 for LaPd₃ and CePd₃ implies absence of magnetic ordering. The results are consistent with the experiments^{2,3} that show the lack of magnetic ordering for LaPd₃ and CePd₃ and antiferromagnetic ordering for PrPd₃ and NdPd₃. η , the ratio of calculated bandwidths with the canonical bandwidths, is greater than $\bar{\eta}$ for all, indicating broadening of bands. The hybridization has maximum impact on the rare-earth f state $(\eta/\bar{\eta})_{R-f} > (\eta/\bar{\eta})_{\text{Pd-d}}$ with different magnitude in each compound. Interestingly, however, the broadening of Pd- d states in all these compounds is the same. Location of the Fermi level on a sharp peak explains the difference in the DOS values for CePd₃ from this work and earlier works.^{4,5} We have also presented an estimate for the bulk modulus of these compounds.

ACKNOWLEDGMENTS

T. N. and S. A. acknowledge the financial support from the Council of Scientific and Industrial Research, India, and also acknowledge the help extended by Dr. S. K. Dhar of Tata Institute of Fundamental Research, Bombay, India.

- ¹ E.g., see K. H. J. Buschow and E. P. Wohlfarth (eds.), *Ferromagnetic Materials*, Vol. 5 (North-Holland, Amsterdam, 1990).
- ² W. E. Gardner, J. Penfold, T. F. Smith, and I. R. Harris, *J. Phys. P* **2**, 133 (1972).
- ³ O. Elsenhans, P. Fischer, A. Furrer, K. N. Clausen, H. W. Purwins, and F. Hullinger, *Z. Phys. B* **82**, 61 (1991).
- ⁴ C. Koenig and M. A. Khan, *Phys. Rev. B* **38**, 5887 (1988).
- ⁵ A. Yanase and A. Hasegawa, *Jpn. J. Appl. Phys.* **26**, Suppl. 3, 483 (1987).
- ⁶ O. K. Andersen, *Phys. Rev. B* **12**, 3060 (1975).
- ⁷ H. L. Skriver, *The LMTO Method: Muffin-Tin Orbitals and Electronic Structure* (Springer, New York, 1984).
- ⁸ J. P. Kappler, G. Krill, M. J. Besnus, M. F. Ravet, N. Hamdaoui, and A. Meyer, *J. Appl. Phys.* **53**, 2152 (1982).
- ⁹ O. Jepsen and O. K. Andersen, *Solid State Commun.* **9**, 1763 (1971).
- ¹⁰ V. von Barth and L. Hedin, *J. Phys. C* **5**, 1629 (1972).
- ¹¹ O. K. Andersen, W. Klose, and H. Nohl, *Phys. Rev. B* **17**, 1209 (1978).
- ¹² M. Podgórny, *Acta Phys. Pol.* **A78**, 941 (1990).
- ¹³ T. Nautiyal and S. Auluck, *Phys. Rev. B* **47**, 12921 (1993), and references therein.
- ¹⁴ M. J. Besnus, J. P. Kappler, and A. Meyer, *J. Phys. R* **13**, 597 (1983).
- ¹⁵ L. Nordstrom, O. Eriksson, M. S. S. Brooks, and B. Johansson, *Phys. Rev. B* **41**, 9111 (1990).
- ¹⁶ J. Kubler, *J. Magn. Magn. Mater.* **20**, 277 (1980).
- ¹⁷ E.g., see X. Jian-hua, B. I. Min, A. J. Freeman, and T. Oguchi, *Phys. Rev. B* **41**, 5010 (1990).

Band structure calculations of heavy fermion YbSbPd and YbSbNi

A. K. Solanki, Arti Kashyap, and S. Auluck
Department of Physics, University of Roorkee, Roorkee 247 667, India

M. S. S. Brooks
Commission of the European Communities, European Institute for Transuranium Elements, Postfach 2340, W-7500 Karlsruhe, Germany

Dhar *et al.* [J. Phys. F **18**, L41 (1988); and *Proceedings of the International Conference on Strongly Correlated Electron Systems Sendai, Japan, 1992* (Plenum, New York, 1987)] have recently measured the low-temperature specific heat of YbSbPd and YbSbNi. Their measurements yield large values for the specific heat coefficient (1384 states/Ry cell for YbSbPd and 865 states/Ry cell for YbSbNi), and suggest a magnetic transition at low temperature. With a view to understand the ground state of these compounds, we have performed self-consistent scalar relativistic linear muffin-tin orbital band structure calculations. Our paramagnetic calculations for YbSbPd and YbSbNi give the density of the states at Fermi level to be 82.94 and 27.96 states/Ry cell, respectively. These give enhancement factors of 16.7 and 30.1 for YbSbPd and YbSbNi. We present results of our calculations of the band structure as well as the Stoner I parameter for these compounds.

INTRODUCTION

The properties of Yb-based ternary rare-earth compounds, characterized by $4f$ shell conduction band hybridization, have been studied extensively in recent years (see, for example, Ref. 1). One expects and does see many of the interesting Kondo related properties. These materials have been broadly classified as valence fluctuators, Kondo lattices, and heavy fermions. These compounds are characterized by an enhanced electronic coefficient of heat capacity γ , found to be an order of magnitude larger than that in ordinary metals. Keeping in view the importance of these rare-earth compounds and the fact that several interesting physical properties in YbSbPd and YbSbNi have recently been reported,^{2,3} we present scalar relativistic band structure calculations within the local density approximation (LDA), using the linear muffin-tin orbital (LMTO) method in the atomic sphere approximation^{4,5} (ASA) for these two compounds.

The salient features of these two compounds are (i) Yb ions are trivalent, (ii) their electrical resistivity shows an overall metallic behavior with large magnitude, (iii) their heat capacity shows appreciable magnetic field dependence, (iv) YbSbNi is a possible low carrier heavy-fermion compound as compared to YbSbPd, and (v) both the compounds crystallize in the MgAgAs structure.^{6,7} The cubic MgAgAs structure consists of the interpenetrating face-centered-cubic lattices with different atoms lying along the body diagonal at $(\frac{1}{4}, \frac{1}{4}, \frac{1}{4})$, $(0,0,0)$, and $(\frac{3}{4}, \frac{3}{4}, \frac{3}{4})$.

In this article, we discuss our method of calculation in Sec. II, and results and discussions are given in Sec. III. Conclusions are given in Sec. IV.

METHOD OF CALCULATION

The self-consistent LMTO-ASA method has been used. The calculations are performed semirelativistically for 89 k points in the irreducible Brillouin zone using the von Barth-Hedin exchange correlation potential.⁸ Within spheres around each atomic center the wave function is expanded in muffin-tin orbitals with the basis set of s , p , and d orbitals,

except for the Yb atom for which s , p , d , and f orbitals are chosen. Because of the open nature of the MgAgAs structure an empty sphere is included on the vacant site $(\frac{1}{2}, \frac{1}{2}, \frac{1}{2})$. We have performed calculations for the lattice constant of 6.2369 Å for both the compounds,⁹ and for simplicity the Wigner-Seitz radii for all atoms are taken to be equal (1.5356 Å). Both compounds have 29 electrons [16 of Yb, 3 of Sb, 10 of X ($X = \text{Pd or Ni}$)] in the valence states. The Yb f electrons are treated as valence electrons. Although there is controversy in literature concerning the treatment of the f electrons of Yb in the LDA, we have adopted the simplest approach (as done by other workers.^{10,11} The density of states (DOS) is calculated using the variation of the linear tetrahedral method prescribed by Jepsen and Andersen.¹²

RESULTS AND DISCUSSIONS

The band structures calculated along the symmetry direction are shown in Figs. 1 and 2, respectively, for YbSbPd and YbSbNi. Bands from 4 to 18 are plotted for YbSbPd and for YbSbNi 5 to 20 bands are plotted to keep the figures manageable. For both the compounds the bands near E_F are

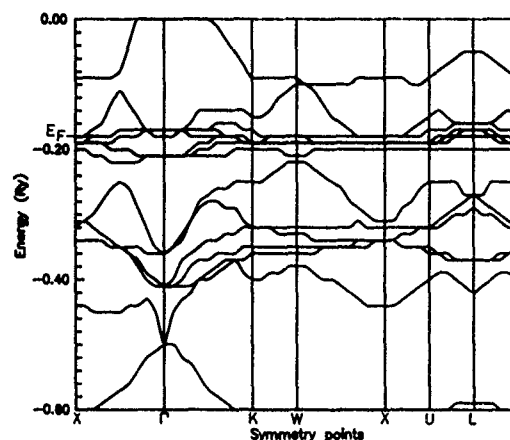


FIG. 1. Band structure of YbSbPd.

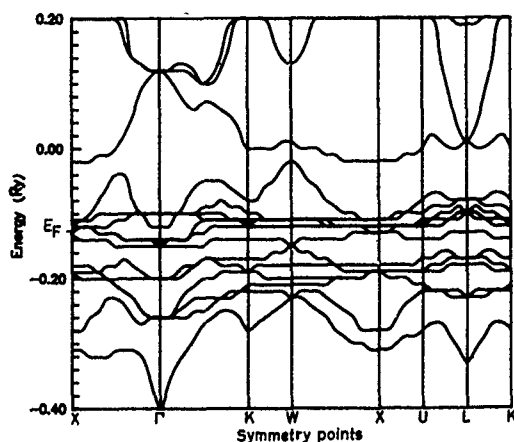


FIG. 2. Band structure of YbSbNi.

very flat, predicting a large contribution from the f bands of Yb. In the case of YbSbPd the bands near E_f ($E_f = -0.177$ Ry) are more flat as compared to YbSbNi and the bandwidths are smaller, giving a probability of higher DOS at the Fermi energy (E_f). Otherwise the band structures are similar. For both the compounds four bands (14, 15, 16, and 17) cross the Fermi level and the trend of the bands at E_f is similar; therefore one may expect similar Fermi surfaces. The calculation for the Fermi surface topology and extremal areas of the Fermi surface orbits is in progress.

The total density of states (T-DOS) for YbSbPd and YbSbNi are shown in Fig. 3. The peak in both figures at different energy sites has major contributions from different

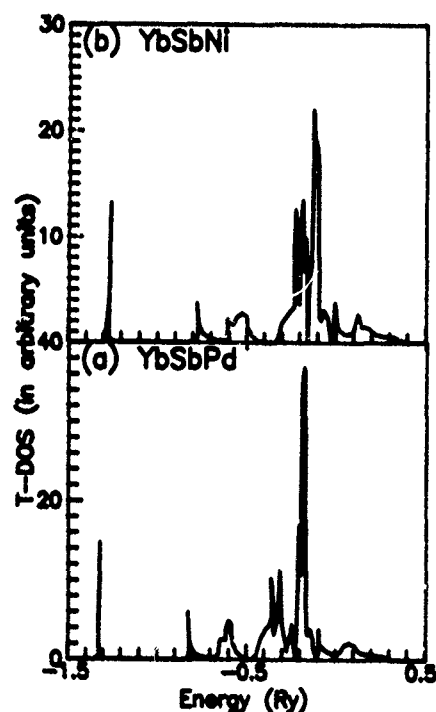


FIG. 3. Total density of states (T-DOS) (a) for YbSbPd and (b) for YbSbNi.

angular momenta corresponding to different atoms. In case of YbSbPd [i.e. Fig. 3(a)] the peak at -1.3 Ry is due to the s of Yb, at -0.6 Ry due to the s in Sb, and the next two peaks at -0.4 and -0.3 Ry have major contribution from the d states of Pd, and similarly for YbSbNi [Fig. 3(b)], the peak at -1.3 Ry is due to s of Yb, at -0.2 and -0.18 Ry are due to d 's of Ni. In both compounds the l -decomposed DOS shows a dominant Yb f character near E_f . For both compounds the E_f lies on the left of the peak in T-DOS curves. The T-DOS at E_f in case of YbSbPd is 82.94 and 27.96 states/Ry cell for YbSbPd and YbSbNi. These, when compared with the projected DOS from the heat capacity data (1384 and 865 states/Ry cell, respectively, for YbSbPd and YbSbNi), give an enhancement factor of 16.7 for YbSbPd and 30.1 for YbSbNi. These values of enhancement factors are smaller than the enhancement factor of 650 calculated by McMullan and Ray¹¹ for YbBiPt. The T-DOS at E_f for YbSbPd is found to be larger than that for YbSbNi due to the fact that for YbSbPd the bandwidth of the dominating Yb f electrons (0.267 Ry) is smaller than that for YbSbNi (0.332 Ry). The rest of the bands have more or less the same bandwidths.

Our calculations give the values of Stoner product $IN(E_f)$ to be 1.083 for YbSbPd and 0.284 for YbSbNi, respectively. Therefore, our calculations predict a possibility of a magnetic ground state for YbSbPd.

CONCLUSIONS

We have presented results of scalar relativistic LMTO-ASA calculations for two Yb-based compounds which are known to show heavy-fermion character. Band structures for both are quite similar. Our calculations give enhancement factors of 16.7 for YbSbPd and 30.1 for YbSbNi, smaller than that obtained for YbBiPt by McMullan and Ray.¹¹ Since all the atoms are heavy, there is need to do a relativistic LMTO calculation, and this may lead to change in DOS at the Fermi energy and hence in the enhancement factor. We have also calculated the Stoner I parameter. Our calculations show that for YbSbNi, $IN(E_f)$ is smaller than 1, while for YbSbPd it is larger than 1, suggesting some magnetic ground state in latter. However, relativistic calculations need to be performed before one can draw any definite conclusions.

¹S. K. Dhar, N. Nambudripad, and R. Vijayaraghavan, J. Phys. F, **18**, L41 (1988).

²S. K. Dhar, K. A. Gschneidner, Jr., and R. Vijayaraghavan, Physica B **186-188**, 463 (1993).

³O. K. Andersen, Phys. Rev. B **12**, 3060 (1975).

⁴H. L. Skriver, in *The LMTO Method* (Springer, New York, 1984).

⁵R. Marazza, D. Rossi, and R. Ferro, J. Less Common Met. **75**, 25 (1980).

⁶A. E. Dwight, in *Proceedings of the 11th Rare Earth Research Conference*, edited by J. M. Haschke, and H. A. Eick, U. S. Atomic Energy Commission Report No. CONF-741002-PS (National Technical Information Service, Springfield, VA, 1974), p. 642.

⁷U. von Barth and L. Hedin, J. Phys. C **5**, 1629 (1972).

⁸F. C. Canfield, J. D. Thompson, W. P. Beyermann, A. Lacerda, M. F. Hundley, E. Peterson, Z. Fisk, and H. R. Ott, J. Appl. Phys. **70**, 5800 (1991).

⁹O. Ericksson, J. M. Wills, and A. M. Boring, J. Alloys Compounds **185**, 145 (1992).

¹⁰G. J. McMullan and M. P. Ray, J. Phys. C **4**, 7095 (1992).

¹¹C. Jepsen and O. K. Andersen, Phys. Rev. B **29**, 5965 (1984).

Electronic structure and Curie temperature of $\text{YFe}_{12-x}\text{Mo}_x\text{N}_y$ compounds

A. S. Fernando, J. P. Woods, S. S. Jaswal, D. Welipitiya, B. M. Patterson,
and D. J. Sellmyer

*Behlen Laboratory of Physics and Center for Materials Research and Analysis, University of Nebraska,
Lincoln, Nebraska 68588-0111*

The electronic structures of $\text{YFe}_{12-x}\text{Mo}_x\text{N}_y$, where $x=1.0, 2.0$ and $y=0, 0.7$, have been studied with photoemission and spin-polarized calculations. The peak near the Fermi level in the energy distribution curves (EDC) becomes successively broader with larger Mo concentration. The features in the calculated density of state at 1.3 and 2.7 eV are not readily seen in the EDC, and this may be due to lifetime effects in these compounds. Finally, changes in Curie temperature (T_c) with the change of N or Mo concentration are compared with prediction of the theory of Mohn and Wohlfarth. Reasonable agreement is obtained in the N case but not in the Mo case, the latter most likely due to hybridization of Fe and Mo d bands.

I. INTRODUCTION

Superior permanent-magnet materials require large saturation magnetization, high Curie temperature (T_c), and large uniaxial anisotropy. The best permanent magnetic materials are rare-earth(R)-transition-metal(T) compounds. The transition metals Fe and Co have large magnetic moments and high Curie temperatures, and the R - T compounds often have large uniaxial magnetic anisotropies. The Fe-rich ternary compound $\text{Nd}_2\text{Fe}_{14}\text{R}$ has an energy product as high as 45 MgOe ,¹⁻⁴ but the relatively low T_c ($\approx 300^\circ\text{C}$) of this material limits its application. Permanent-magnet materials research is currently investigating other Fe-rich R - T compounds. The RT_{12} body-centered-tetragonal compound with the ThMn_{12} structure does not exist in the binary phase, but the structure is stabilized with the partial substitution of a nonmagnetic element (M) for Fe. The compounds $\text{RFe}_{12-x}\text{M}_x$ with $M=\text{Ti, V, Cr, Mo, W, and Si}$ have been fabricated and their magnetic properties examined.⁵ The addition of interstitial nitrogen increases the Curie temperature of the materials and the magnetic anisotropy may change.⁶ For example, T_c of $\text{NdFe}_{11}\text{Ti}$ increases by 30% upon nitriding and the magnetic anisotropy changes from in-plane to uniaxial.⁷

The magnetic properties of the compound $\text{YFe}_{12-x}\text{Mo}_x$ with $x=0.5, 1, 2, 4$ have been published.⁸ T_c decreases with increased Mo concentration, and increases with nitriding; the volume increases both with increased Mo and N concentration. The Mo atoms substitute for Fe atoms on the (i) site with the largest magnetic moment.⁹

The magnetic properties of the compounds are determined by the electronic configuration, and the increase in T_c of Y_2Fe_{17} (Ref. 10) and $\text{NdFe}_{11}\text{Ti}$ (Ref. 11) upon nitriding has been modeled using electronic structure calculations and the spin-fluctuation theory of Mohn and Wohlfarth.¹² Briefly,

$$(T_c)_{M-W} = CM_0^2/\chi_0, \quad (1)$$

where M_0 is the magnetic moment per Fe site, χ_0 is the enhanced susceptibility, and C is a constant. In earlier work the electronic structure of $\text{Sm}_2\text{Fe}_{17}\text{N}_y$ with $y=0$ and $y=2.6$ has been measured with photoelectron spectroscopy (PES), and a decrease in the density of state (DOS) at E_F is observed as nitrogen is added which agrees with the calculated DOS.¹³ In this paper the electronic structure of

$\text{YFe}_{12-x}\text{Mo}_x\text{N}_y$ with $x=1, 2$, and $y=0, 0.7$ is examined with PES, and the calculated partial DOS for Fe, Y, and Mo in YFe_{11}Mo are given. Comparison with the expected changes in T_c are presented.

II. EXPERIMENTAL PROCEDURE

Bulk samples of $\text{YFe}_{12-x}\text{Mo}_x$ with $x=1, 2$ were prepared by arc melting the elemental constituents in a water-cooled copper boat in flowing-argon gas atmosphere. All the starting elements used were at least 99.98% purity. The alloys were melted several times to insure homogeneity. The samples were wrapped separately in Ta foils and heat treated in vacuum below 3×10^{-6} Torr at 1100°C for about 50 h,⁸ and subsequently quenched in water. X-ray diffraction measurements on powder samples using $\text{Cu } K_\alpha$ radiation showed that the samples were composed of primarily the ThMn_{12} structure with a small amount of α -Fe. The magnetization of the samples was measured at 5 and 300 K with superconducting quantum interference device (SQUID) and alternating force gradient magnetometers, respectively, and the saturation magnetic moments agree with published results.⁸

The arc-melted buttons were spark cut into discs ~ 1 mm thick to expose an interior surface which was then polished to provide an optically smooth surface for PES measurements. The samples were mounted on a tungsten sample manipulator using 0.25-mm-diam tantalum wires in an ultrahigh vacuum chamber with a base pressure of 2×10^{-10} Torr. Each sample was cleaned *in situ* with several cycles of 2 keV Ar sputtering and subsequent annealing at 350°C . Auger electron spectroscopy (AES) was employed to monitor surface cleanliness and to estimate the nitrogen concentration. After cleaning the sample, nitrogen was introduced by ion implantation with a kinetic energy of 2 keV and a current density of $25 \mu\text{A}/\text{cm}^2$ for 10 min.¹⁷ The subsequent nitrogen concentration was measured with AES as $y=8.3 \pm 0.8$. The samples were then radiantly heated to 350°C for several minutes to promote nitrogen diffusion from the nitrogen-rich surface into the subsurface region. The nitrogen-rich surface layer was subsequently removed with Ar sputtering to expose the subsurface nitride and the resulting surface nitrogen concentration measured with AES was $y \approx 0.7 \pm 0.3$. Quantitatively, the nitrogen concentration per formula unit of 0.7 at the sur-

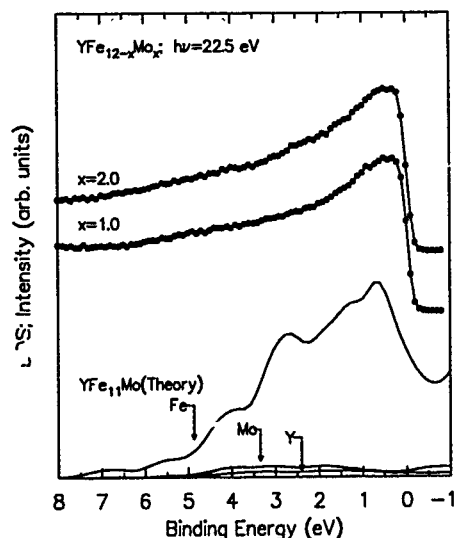


FIG. 1. Calculated partial spin-polarized DOS of Fe, Mo, and Y in YFe_{11}Mo and experimental energy distribution curves (EDC) for clean $\text{YFe}_{12-x}\text{Mo}_x$ ($x=1.0, 2.0$). The EDCs are normalized to the area under the EDC curves between 0 and 3.5 eV and shifted vertically. The zero on the binding energy axis refers to the Fermi energy (E_F).

face of 1:12 compounds here and previously published¹¹ is in agreement with published bulk values⁷ and supports the assertion that the bulk atomic structure is present up to the surface which is probed by AES and PES. The electronic structure was measured with PES experiments which were performed at the Synchrotron Radiation Center in Wisconsin. The photoelectron energy distribution curves (EDC) presented were obtained with a photon energy of 22.5 eV and a total energy resolution of 0.14 eV.

III. ELECTRONIC STRUCTURE

The EDCs from the Ar-sputter-cleaned and annealed $\text{YFe}_{12-x}\text{Mo}_x$ samples with bulk values of $x=1.0, 2.0$, and the calculated partial DOS for each element in YFe_{11}Mo are shown in Fig. 1. The EDC curves have been normalized to the same areas between 0 and 3.5 eV binding energy and the baseline for each EDC is shifted vertically. The DOS are determined with self-consistent spin-polarized calculations using linear-muffin-tin orbitals in the scalar relativistic approximation.¹⁴ A supercell consisting of four formula units was used to simulate the ternary compound with correct stoichiometry. The total DOS (not shown) is the sum of the three partial DOS curves, and the total DOS is dominated by the Fe DOS, due to the large atomic percentage (85%) of Fe in the compound. The present Fe DOS is substantially different from Fe DOS in $\text{NdFe}_{11}\text{Ti}$ compounds¹¹ and the difference is due to the strong hybridization with Mo.

The EDCs are comparable to the calculated DOS with a 1–2 eV wide peak at the Fermi energy. The features in the calculated DOS at 1.3 and 2.7 eV are not readily discernible in the EDC, and this may be due to lifetime effects in these compounds.¹⁵

The change in EDCs at E_F after nitriding YFe_{11}Mo and $\text{YFe}_{10}\text{Mo}_2$ compounds are shown in Fig. 2. The YFe_{11}Mo

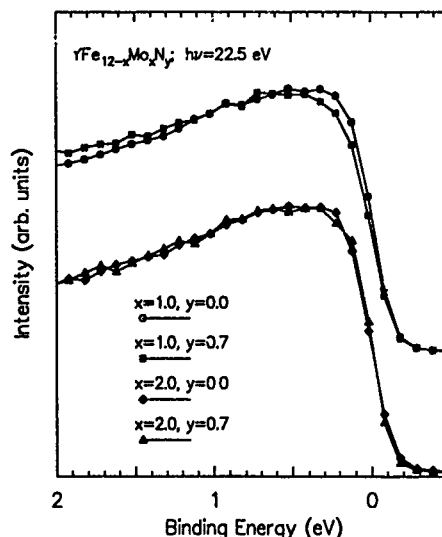


FIG. 2. Expand view of the experimental EDCs of $\text{YFe}_{11}\text{MoN}_y$ for $y=0.0, y=0.7$ (upper two curves) and of $\text{YFe}_{10}\text{Mo}_2\text{N}_y$ for $y=0.0, y=0.7$ (lower two curves). The zero on the binding energy axis corresponds to the Fermi energy.

sample (upper two curves) shows a significant decrease in EDC at E_F upon nitriding; the $\text{YFe}_{10}\text{Mo}_2$ sample (lower two curves) does not show any significant change in EDC at E_F upon nitriding. The comparison of EDCs for $x=1$ and $x=2$ without nitrogen (upper two curves) and with nitrogen (lower two curves) are shown in Fig. 3. The EDCs at E_F for YFe_{11}Mo and $\text{YFe}_{10}\text{Mo}_2$ show no significant change; the nitrided samples $\text{YFe}_{11}\text{MoN}_{0.7}$ and $\text{YFe}_{10}\text{Mo}_2\text{N}_{0.7}$ show a slight increase in EDC at E_F as the Mo:Fe ratio is increased.

In previous experiments on 1:12 and 2:17 compounds^{11,13} the change in the EDCs at E_F was compared

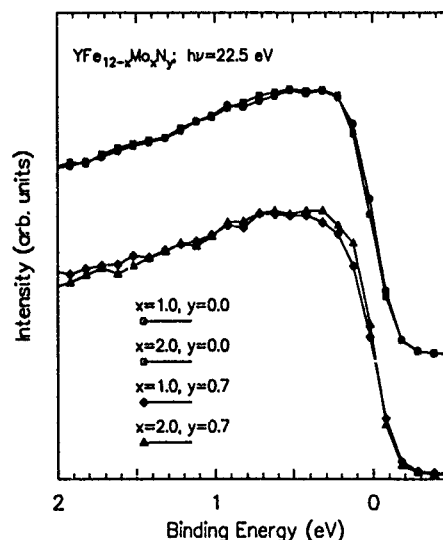


FIG. 3. Expand view of EDCs of unnitrided (upper two curves) and nitrided (lower two curves) samples of $\text{YFe}_{12-x}\text{Mo}_x$ ($x=1.0, 2.0$). The zero on the binding energy axis refers to the Fermi energy.

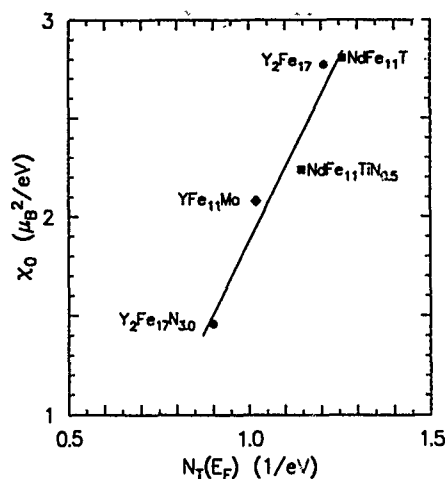


FIG. 4. Calculated χ_0 vs calculated $N_T(E_F)$ for the samples listed.

to the calculated^{10,16} total DOS, $N_T(E_F) = N_{\uparrow}(E_F) + N_{\downarrow}(E_F)$, where $N_{\uparrow}(E_F)$ and $N_{\downarrow}(E_F)$ are the up- and down-spin DOS at the Fermi level, respectively. The calculated DOS, Stoner parameter, and magnetic moments used with Mohn and Wohlfarth theory predict a change in T_c upon nitrogeation which agrees very well with measured change in T_c . In the present experiment the calculated DOS is available only for the YFe_{11}Mo compound, and a comparison of changes in $N_T(E_F)$ as the nitrogen concentration or the Fe:Mo ratio changed is not possible.

In order to compare changes in the measured electronic structure with changes in the magnetic properties (T_c and M_0), a dependence of χ_0 on $N_T(E_F)$ is required. Calculated values of χ_0 for listed samples, where $\chi_0^{-1} = [1/N_{\uparrow}(E_F) + 1/N_{\downarrow}(E_F) - 2I]/4\mu_B^2$ are plotted as a function of $N_T(E_F)$ in Fig. 4. There is a linear dependence between χ_0 and $N_T(E_F)$ in the small range of $N_T(E_F)$ for the 1:12 and 2:17 Fe-based compounds considered. With this plot, the electronic structure is related to T_c and M_0 as $M_0^2/T_c \propto \chi_0 = AN_T(E_F) + B$, where A and B are constants and $B/A = -0.48 \text{ eV}^{-1}$. Upon alloying with either N or Mo, the new value of T_c (T'_c) can be related through Eq. (1) to the measured changes in magnetization and electronic structure by

$$(T'_c/T_c)_{M-W} = (M_0'^2/M_0^2)(\chi_0/\chi_0'), \quad (2)$$

where χ_0/χ_0' is given by $[N_T(E_F) - 0.48]/[N_T(E_F) - 0.48]$. The values of $N_T(E_F)$ are obtained from the experimental EDC curves. The ratio $(T'_c/T_c)_{\text{exp}}$ measured directly, and $(T'_c/T_c)_{M-W}$ are shown in Table I.

As shown in Table I, these two values agree fairly well when nitrogen is added to the two parent compounds. However, when the nitrogen concentration is held fixed and the Fe:Mo ratio is varied, there is a large disagreement between these two values. The disagreement is due to the fact that substitution of Mo for Fe in going from YFe_{11}Mo to $\text{YFe}_{10}\text{Mo}_2$ lowers the Fe concentration and causes a strong hybridization of the Fe and Mo d bands thus changing the proportionality constant in Eq. (1).

TABLE I. Calculated values of $(T'_c/T_c)_{M-W}$ and $(T'_c/T_c)_{\text{exp}}$ for $\text{YFe}_{12-x}\text{Mo}_x\text{N}_y$ samples.

x, y	$(M'_0/M_0)^2$ ^a	(χ_0/χ'_0) ^b	$(T'_c/T_c)_{M-W}$ $\pm 8\%$	$(T'_c/T_c)_{\text{exp}}$ ^a
1,0,0	1.10	1.24	1.36	1.41
1,0,7				
2,0,0	1.59	0.98	1.56	1.48
2,0,7				
1,0,0	0.44	0.95	0.42	0.68
2,0,0				
1,0,7	0.62	0.75	0.46	0.72
2,0,7				

^aReference 8.

^bBased on experimental $N_T(E_F)$ values.

IV. CONCLUSIONS

PES experiments probing the electronic structure agree approximately with the calculated DOS. The samples with fixed Mo concentration follow the Curie-temperature theory of Mohn and Wohlfarth upon nitriding. However, the theory does not correctly predict changes in T_c on alloying with Mo. The reason for this appear to be that nitrogen goes into the lattice interstitially and mainly expands the lattice, whereas Mo substitution for Fe causes a significant change in the electronic structure of the material.

ACKNOWLEDGMENTS

We are grateful to the United States Department of Energy for support under Grant No. DE-FG02-86ER45262, Nebraska Energy Office and to the Cornell National Supercomputing Facility which is funded by the National Science Foundation. The authors thank the staff of the Synchrotron Radiation Center at the University of Wisconsin.

- M. Sagawa, S. Fujimura, N. Togawa, and Y. Matsuura, *J. Appl. Phys.* **55**, 2083 (1984).
- G. C. Hadjipanayis, R. C. Hazeton, and K. R. Lawless, *Appl. Phys. Lett.* **43**, 797 (1983).
- J. J. Croat, J. F. Herbst, R. W. Lee, and F. E. Pinkerton, *Appl. Phys. Lett.* **44**, 148 (1984).
- K. S. V. L. Narasimhan, in *Proceedings of the 8th International Workshop on Rare-Earth Magnets and their Applications*, edited by K. J. Strnat (University of Dayton, Dayton, OH, 1985), p. 459.
- D. B. de Mooij and K. H. J. Buschow, *J. Less Common Met.* **136**, 207 (1988).
- J. M. D. Coey, H. Sun, and D. P. F. Hurley, *J. Magn. Magn. Mater.* **101**, 310 (1991).
- Y.-C. Yang, X.-D. Zhang, L.-S. Kong, and Q. Pan, *Solid State Commun.* **78**, 317 (1991).
- H. Sun, M. Akayama, K. Tatami, and H. Fujii, *Physica B* **183**, 33 (1993).
- C. J. M. Denissen, R. Coehoorn, and K. H. J. Buschow, *J. Magn. Magn. Mater.* **87**, 51 (1990).
- S. S. Jaswal, W. B. Yelon, G. C. Hadjipanayis, Y. Z. Wang, and D. J. Sellmyer, *Phys. Rev. Lett.* **67**, 644 (1991).
- A. S. Fernando, J. P. Woods, S. S. Jaswal, B. M. Patterson, D. Welipitiya, A. S. Nazareth, and D. J. Sellmyer, *J. Appl. Phys.* **73**, 6919 (1993).
- P. Mohn and E. P. Wohlfarth, *J. Phys. F* **17**, 2421 (1987).
- J. P. Woods, A. S. Fernando, S. S. Jaswal, B. M. Patterson, D. Welipitiya, and D. J. Sellmyer, *J. Appl. Phys.* **73**, 6913 (1993).
- H. L. Skriver, *The LMTO Method*, Vol. 41 of the Springer Series in Solid State Sciences (Springer, New York, 1984).
- M. M. Steiner, R. C. Albers, L. J. Sham, *Phys. Rev. B* **45**, 13272 (1992).
- S. S. Jaswal, *Phys. Rev. B* **48**, 6156 (1993).

The percolation limit for the disappearance of ferromagnetism in melt spun Co-B-C amorphous alloys

G. K. Nicolaides

National Center for Scientific Research "Demokritos," Institute of Material Science Aghia Paraskevi, Athens 153 10, Greece

A. Inoue

Institute of Materials Research, Tohoku University, Sendai, Japan

K. V. Rao

Royal Institute of Technology, Department of Condensed Matter, S-10044 Stockholm, Sweden

Low-temperature magnetic properties of the $\text{Co}_{56-x}\text{B}_{32+x}\text{C}_{12}$, $x=0, 2, 4$, and 4.5 ternary amorphous alloys are investigated by using low-field ac magnetic susceptibility measurement techniques and also a superconducting quantum interference device magnetometer. The ac susceptibility data show that these alloys undergo a paramagnetic to ferromagnetic state transition at cryogenic temperatures. The Curie temperature T_c decreases linearly with decreasing Co content at a rate $31 \text{ K per } \%$ Co, suggesting a percolation limit for the disappearance of ferromagnetism at around $50 \text{ at } \%$ Co. A scaling analysis performed on magnetic isotherms obtained near T_c ; even for the sample almost close to the percolation limit, yields critical exponent values consistent with the 3D-Heisenberg model for an ideal ferromagnet. Thus in these Co-based amorphous alloys, long-range order persists to the concentrations almost at the percolation limit and the mean-field theory is found to describe well the paramagnetic to the ferromagnetic state phase transitions.

I. INTRODUCTION

The ternary amorphous Co-B-C system with stoichiometry in the extended concentration regime provides us a unique opportunity to study the magnetic properties of Co close to the percolation limit for the disappearance of ferromagnetism. It has been found^{1,2} that the amorphous alloys $\text{Co}_{88-y}\text{B}_y\text{C}_{12}$, with $y=12, 16, 24$, and 32 are simple ferromagnets, and the T_c decreases linearly with decreasing Co content. Contrary to the results of magnetic studies of similar but Fe-based transition metal-metalloid amorphous alloys like $(\text{Fe}_x\text{Ni}_{1-x})_{75}\text{P}_{16}\text{B}_6\text{Al}_3$,³ no spin-glass behavior has been observed in all the above-mentioned Co-based amorphous alloys. The absence of spin-glass behavior in Co-based alloys could be expected from the well-known phenomenological Bethe-Slater curve⁴ predicting the dependence of the exchange coupling constant J with the Co-Co separation distance.

In order to have a better picture of the ferromagnetic state of the CoBC amorphous alloys near the percolation limit for the disappearance of ferromagnetism, we attempt a scaling analysis near the paramagnetic (PM) to ferromagnetic (FM) state transition of the amorphous alloys $\text{Co}_{56-x}\text{B}_{32+x}\text{C}_{12}$ with $x=0, 2, 4$, and 4.5 . The extracted values of the critical exponents β and δ are compared with those predicted⁵ by the 3D-Heisenberg model. In addition we present the magnetic phase diagram of the above CoBC amorphous alloys.

II. EXPERIMENTAL

Ingots of nominal composition $\text{Co}_{56-x}\text{B}_{32+x}\text{C}_{12}$, with $x=0, 2, 4$, and 4.5 were prepared in a arc-melting furnace under continuous flow of argon gas, and subsequently melt spun under a very low pressure of argon atmosphere. This

was necessary, since the melting of these alloys is relatively difficult because of the high metalloid content resulting in a low electrical conductivity for these ingots. The obtained ribbons were $5\text{--}60 \text{ cm}$ in length, $10 \mu\text{m}$ thick, 0.5 mm wide, and shiny. They were found to be x-ray amorphous, while the composition was determined with energy dispersive x-ray analysis (EDAX) using a scanning electron microscope. ac susceptibility measurements were performed using a calibrated and balanced mutual inductance bridge, employing a two phase PAR lock-in signal analyzer, so we were able to measure both components of χ_{ac} , the real (χ'), and the imaginary (χ'') simultaneously. The results were corrected for demagnetizing effects. For the dc magnetic studies we employed a Quantum Design superconducting quantum interference device (SQUID) magnetometer.

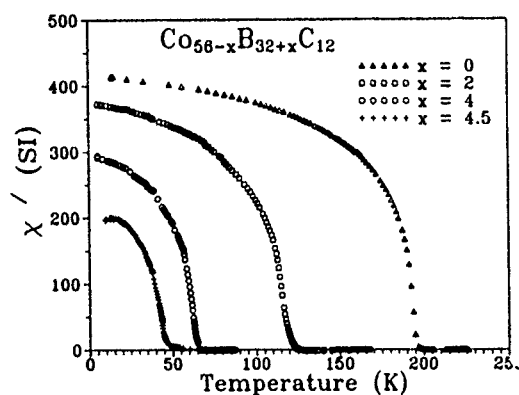


FIG. 1. Real part, $\chi'(T)$ of ac susceptibility for $\text{Co}_{56-x}\text{B}_{32+x}\text{C}_{12}$ with $x=0, 2, 4$, and 4.5 .

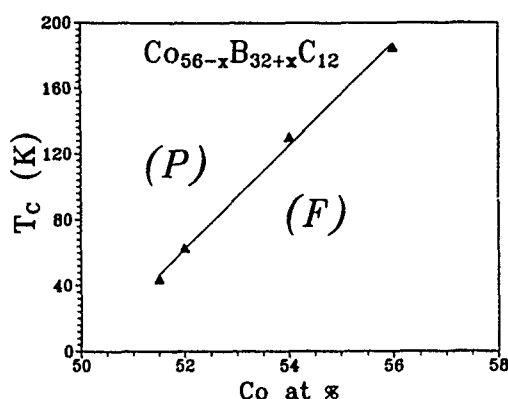


FIG. 2. Magnetic phase diagram of $\text{Co}_{56-x}\text{B}_{32+x}\text{C}_{12}$ with $x=0, 2, 4$, and 4.5 . Actually the x axis is the Co at %.

III. RESULTS AND DISCUSSION

In Fig. 1 are presented the real part χ' of the ac susceptibility data of the amorphous alloys $\text{Co}_{56-x}\text{B}_{32+x}\text{C}_{12}$ where $x=0, 2, 4$, and 4.5 . For all of the alloys studied, $\chi'(T)$ shows a single transition from a paramagnetic to a ferromagnetic state as the temperature decreases. It is obvious that, below the Curie transition temperature (T_c), that $\chi'(T)$ increases monotonically down to 4.2 K, with no indication of spin-glass behavior. Only in the $\chi'(T)$ data of the alloys with 51.5 at % Co there is some indication of decreasing of $\chi'(T)$ at around 6 K. However, we did not find any clear signature for the possible existence of a spin-glass state and $\chi''(T)$, for example, is zero. The magnetic phase diagram for the composition range studied is obtained and is shown in Fig. 2. It is found that the Curie temperature (T_c) decreases with decreasing Co content at a rate of 31 K per at % Co, suggesting a percolation limit for the disappearance of the ferromagnetism in these alloys at around 50 at % Co. In order to perform a scaling analysis near the paramagnetic to ferromagnetic state transition, we obtained a set of magnetic isotherms around $T=T_c$, for the alloys with 52 at % and 54 at % of Co content. By plotting the magnetization $M^{1/\beta}$ versus the ratio of the field over the magnetization $(H/M)^{1/\gamma}$, where the critical exponents values β and γ have been varied in the range $\beta=0.3-0.6$ and $\gamma=1.2-2$, we obtained the

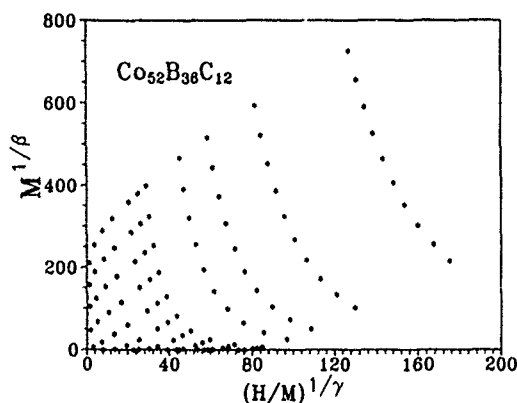


FIG. 3. Modified Arrott plots for $\text{Co}_{52}\text{B}_{36}\text{C}_{12}$.

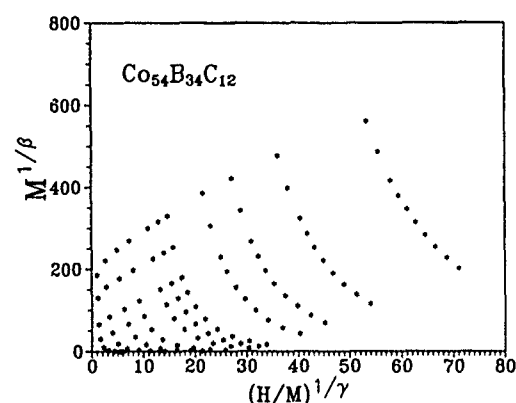


FIG. 4. Modified Arrott plots for $\text{Co}_{54}\text{B}_{34}\text{C}_{12}$.

modified Arrott plots which are presented in Figs. 3 and 4. These plots are indeed straight lines near the transition temperature as should have been expected for ideal ferromagnets. To cross examine now the values of the critical exponents β and γ , the isotherms are plotted according to the scaling relation $\log_{10}(m)$ vs $\log_{10}(h)$. Here m and h are the reduced magnetization and the reduced field, respectively, where

$$m = M(\epsilon, H)/|\epsilon|^\beta, \quad h = H(\epsilon, M)/|\epsilon|^{\beta+\gamma}, \quad \epsilon = (T - T_c)/T_c.$$

We have varied the T_c by 0.5 K, the β from 0.3 to 0.6, the γ from 1.2 to 2.5, and $|\epsilon|=0.02-0.2$. The correct values of T_c , β , and γ are the values which in the high-field regime cause the collapse of the two branches of the isotherms in a $\log_{10}(m)$ vs $\log_{10}(h)$ diagram almost onto the same line (in reality the two branches for the high-field regime converge towards the same limit). The obtained values of the exponents β , γ are found to be the same with those found using the modified Arrott plots method and are presented in the Table I, while the scaling is presented in the Figs. 5 and 6. In addition to this, assuming that the static scaling hypothesis is valid, then we can calculate the value of δ from the relation $\beta + \gamma = \beta \cdot \delta$, which also is shown in the Table I. Comparing the obtained values of the critical exponents β , γ , and δ , with those predicted for the 3D-Heisenberg model (these values are also included in Table I), we see that in the case of $x=4$ (52 at % Co), there is excellent agreement between experiment and theory, while in the case of $x=2$ (54 at % Co) there is a slight deviation. The latter might indicate that this particular alloy, below T_c , exhibits a nonideal ferromagnetic order.

TABLE I. Critical exponents for $\text{Co}_{56-x}\text{B}_{32+x}\text{C}_{12}$ amorphous alloys. Numbers in the parentheses denote the uncertainty in the least significant figure.

x	β	γ	δ	$1+\gamma/\beta$
2	0.450 ± 0.003	1.60 ± 0.02		4.55
4	0.368 ± 0.003	1.40 ± 0.02		4.80
3D-Heisenberg ^a	0.365(3)	1.405(2)	4.85(4)	...

^aRef. 5.

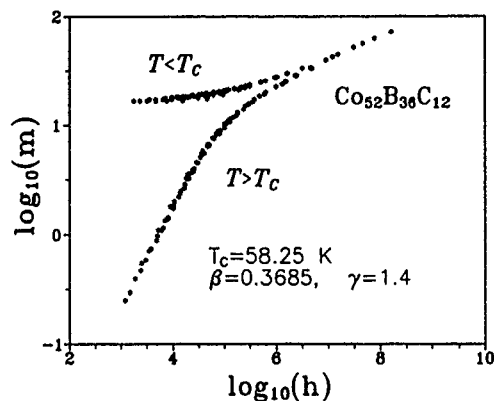


FIG. 5. $\log_{10}(m)$ vs $\log_{10}(h)$ for $\text{Co}_{52}\text{B}_{36}\text{C}_{12}$.

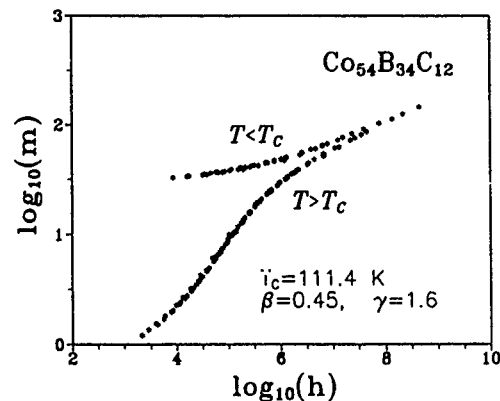


FIG. 6. $\log_{10}(m)$ vs $\log_{10}(h)$ for $\text{Co}_{54}\text{B}_{34}\text{C}_{12}$.

IV. CONCLUSION

Successfully melt-spun $\text{Co}_{56-x}\text{B}_{32+x}\text{C}_{12}$ ($x=0, 2, 4$, and 4.5) amorphous alloys have been found to exhibit a single paramagnetic to ferromagnetic state transition, at temperatures below room temperature. In addition it is found that T_c is decreasing with decreasing Co content at a rate of 31 K per Co at %. A scaling analysis performed near T_c showed that one alloy ($x=4$) has critical exponent values in excellent

agreement with values predicted by mean-field theory, while these values for the $x=2$ alloy deviate slightly from theory.

¹A. Inoue, T. Nakamura, and T. Masumoto, *J. Mater. Sci. Lett.* **5**, 1178 (1986).

²M. Pont, Ph.D. thesis, University of Auton, Barcelona, 1990.

³O. Beckman, E. Figueroa, K. Gramm, L. Lundgren, K. V. Rao, and H. S. Chen, *Phys. Scr.* **25**, 726 (1982).

⁴K. Moorjani and J. M. D. Coey, *Magnetic Glasses* (Elsevier, New York, 1984).

⁵M. Ferer, M. A. Moore, and M. Wortis, *Phys. Rev. B* **4**, 3954 (1971).

High-field magnetization behavior in random anisotropy amorphous Co-Er alloys

H. Lassri, L. Driouch, and R. Krishnan
Laboratoire de Magnétisme, C.N.R.S. 92195 Meudon, France

Amorphous $\text{Co}_{1-x}\text{Er}_x$ ribbons with $x=55$ and 65 were prepared by the melt-spinning technique. Magnetization measurements were carried out in the temperature range $4\text{--}100\text{ K}$ under high magnetic fields up to 20 T . Even at 20 T the saturation is not fully attained. Assuming that Co has no moment in the alloy with $x=65$ the Er moment is found to be $7.0\mu_B$ which indicates a speromagnetic spin structure. The Co moment in the alloy with $x=55$ is then found to be $0.1\mu_B$, which is negligibly small. By analyzing the approach to saturation using Chudnovsky's theory we have extracted some fundamental parameters.

I. INTRODUCTION

Amorphous alloys based on rare-earth metals are interesting materials to study the various fundamental parameters, such as ferromagnetic, antiferromagnetic interactions, random anisotropy, etc.^{1,2} We have reported on the amorphous Co-Er-B alloy,³ where we have shown that Er has a conical spin structure resulting from strong random anisotropy and that under sufficiently high magnetic fields the antiferromagnetic interaction between Er-Co breaks down. It has also been shown that for rare-earth metal concentrations higher than about $60\text{ at } \%$, the transition metal moment would vanish.⁴ Therefore we wanted to study the binary Co-Er system rich in Er, in order to get more information on the magnetic state of Er. The magnetization of this system was studied earlier⁴ but under an external field of only 1.4 T which, as it will be shown here, is far too small for saturation. We report here our magnetization studies on amorphous $\text{Co}_{45}\text{Er}_{55}$ and $\text{Co}_{35}\text{Er}_{65}$ alloys under applied fields up to 20 T . We have also analyzed the approach to saturation using Chudnovsky's theory and obtained some magnetic parameters of interest.

II. EXPERIMENTAL DETAILS

Amorphous $\text{Co}_{1-x}\text{Er}_x$ alloys with $x=55$ and 65 were prepared by the usual melt spinning technique under inert atmosphere. Linear velocity of the copper wheel was in the range $30\text{--}40\text{ m/s}$. The diameter of the orifice of the quartz crucible was 0.5 mm .

The amorphous state was verified by x-ray diffraction. The exact composition was determined by electron probe microanalysis. The magnetization was measured in the temperature range $4\text{--}100\text{ K}$ and under applied fields up to 20 T .

III. RESULTS AND DISCUSSION

The ribbons were about 1 mm wide and $30\text{ }\mu\text{m}$ thick and were all amorphous as shown by the characteristic broad x-ray diffraction peak.

The field dependence of the magnetization at different temperatures for the two alloys was similar and Fig. 1 shows the result for the alloy with $\text{Er}=65\text{ at } \%$. It can be seen that even at 20 T , the saturation is not yet complete. So the saturation magnetic moment M_0 was calculated at H_∞ , using H^{-2} dependence, which will be justified in the next section. The magnetization of the alloy with $x=65$ can be considered

to arise only from the Er atoms as we pointed out earlier. Under this assumption, from the alloy moment of $4.56\mu_B$ we find the Er moment $\mu_{\text{Er}}=7.0\mu_B/\text{atom}$, which is smaller than $9.0\mu_B$, theoretically expected for the ground state. This indicates that the Er spin structure is not collinear. This spin structure arises from the random anisotropy which is larger than the ferromagnetic $J_{\text{Er-Er}}$ interaction. It is interesting to note that this situation is different from what we had observed earlier for Co-Er-B alloys,³ where the Co atoms bear a strong moment and therefore a fairly strong antiferromagnetic interaction $J_{\text{Co-Er}}$ tends to maintain the Er spins in one hemisphere.³ It is to be noted that our value of μ_{Er} is much higher than that reported by Xingbo and Miyazaki,⁴ as is expected, because their measurements were carried out under fairly low fields. Now taking our experimental value of $\mu_{\text{Er}}=7.0\mu_B$ for the alloy with $x=55$, and from the alloy moment of $3.8\mu_B$, the Co moment is calculated to be $0.1\mu_B$ which is indeed negligibly small.

The Curie temperature (T_C) of the alloys was obtained from the Arrott's plots and the result for $x=65$ is shown in Fig. 2. The Curie temperature T_C was found to be 30 and 40 K for $x=65$ and 55 , respectively. These relatively low values indicate the weak ferromagnetic Er-Er interactions.

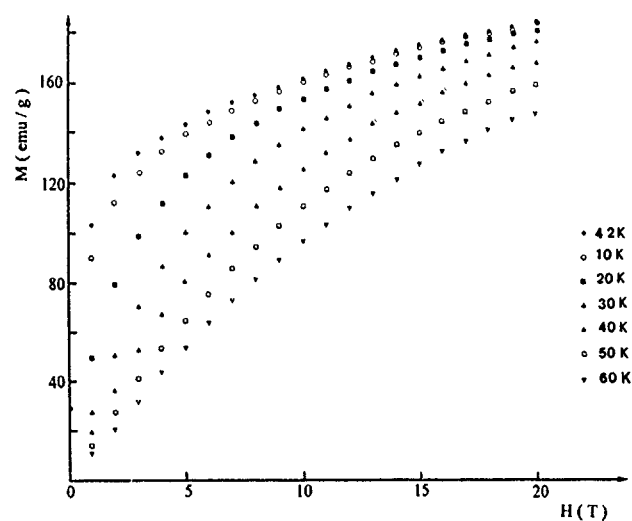


FIG. 1. The field dependence of the magnetization at various temperatures for the alloy $\text{Co}_{35}\text{Er}_{65}$.

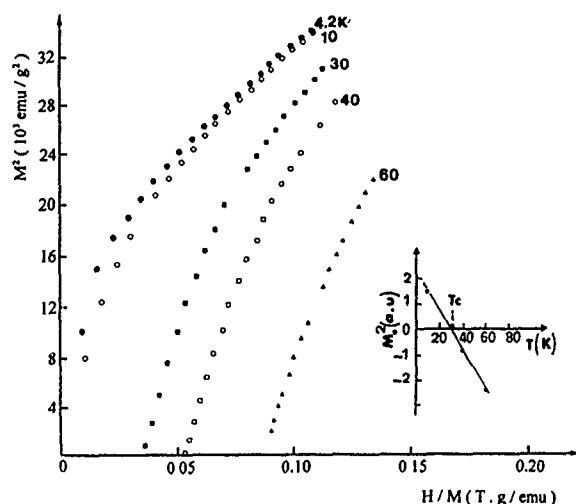


FIG. 2. The Arrott plot for the alloy $\text{Co}_{35}\text{Er}_{65}$. The inset shows M^2 vs T .

Chudnovsky^{5,6} has proposed a theory to explain the approach to saturation in terms of various fundamental parameters, which has been applied by several authors to analyze their results.^{7,8} Two cases are to be distinguished; first when the applied field is smaller than the exchange field ($H_{\text{app}} < H_{\text{exch}}$) and the second when ($H_{\text{app}} \gg H_{\text{exch}}$). In our present case considering the low Curie temperatures of the Er-Co samples, the second case is more appropriate. In this high-field regime one can write

$$(M_0 - M)/M_0 = \delta M/M_0 = 1/15 [H_r/(H + H_{\text{ex}})]^2, \quad (1)$$

where M_0 is the magnetization extrapolated value to H_∞ and H_r is the random local anisotropy field and is related to the local anisotropy energy K_r by the relation

$$2K_r/M = H_r. \quad (2)$$

In some cases H_{ex} has been neglected since it is small compared to the external field and H_r has been calculated.⁸ However, with some algebraic manipulations, as we describe below, it is also possible to consider H_{ex} and obtain not only H_r but also H_{ex} .

Equation (1) can be rewritten as

$$(\delta M/M_0)^{-0.5} = B(H + H_{\text{ex}}), \quad (3)$$

where $B = \sqrt{15} \times (H_r)^{-1}$. So by plotting $(\delta M/M_0)^{-0.5}$ as a function of H , one can obtain H_r from the slope B and the exchange field H_{ex} from the intercept. Figure 3 shows such a plot for $\text{Er}=65$. The data points align well in the high-field regime $H_{\text{app}} \gg H_{\text{ex}}$. But one observes a deviation from the linear dependence in the intermediate regime where the random anisotropy and the exchange field influence the magnetization behavior. This field region is known as the crossover field H_{co} and will be discussed later. The value of H_r was obtained by linear regression. Table I shows the various magnetic parameters calculated from the Fig. 3. It must be cautioned, however, that the value of H_{ex} should be taken with some caution and considering the relatively low value *vis a vis* H_{app} it could vary by a factor of 2 or 3. Nevertheless, this gives an order of magnitude of the parameter. For $x = 65$, we

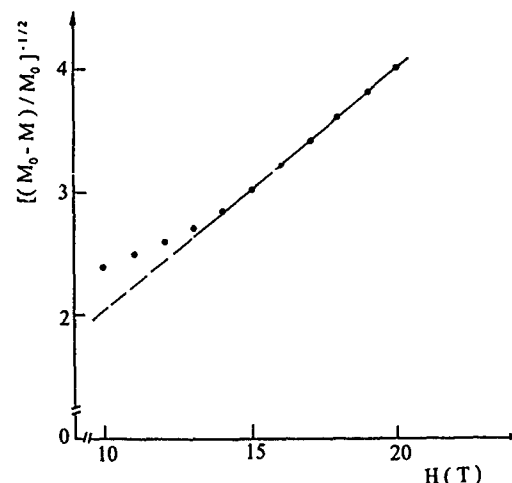


FIG. 3. The H dependence of the quantity $[(M_0 - M)/M_0]^{-1/2}$ for the sample $\text{Co}_{35}\text{Er}_{65}$ at 4 K.

find $K_r = 1.8 \times 10^8 \text{ erg cm}^{-3}$ (which has been calculated from H_r) and this agrees well with the value obtained by Hadjipanayis *et al.*⁸ for an amorphous Er-Au-B alloy, where Er are the only magnetic atoms.

From the crossover field H_{co} mentioned above, it is possible to calculate the important structural parameter l_c , which is the distance over which the local anisotropy axes are correlated. From Chudnovsky's theory⁹ we can write

$$H_{\text{co}} = 2A/M_0(R_a)^{-1/2}, \quad (4)$$

where A is the exchange constant. However, generally this crossover field is difficult to observe experimentally in crystalline and amorphous materials where T_C and hence the exchange field is high.⁹ Fortunately the present alloys offer a possibility to observe H_{co} . As we had mentioned when discussing the M dependence on H^2 , one observes a deviation from the linear behavior (Fig. 3), which precisely corresponds to the crossover field where the regime changes to the low field one. From Fig. 3 H_{co} is found to be close to 11 T. In Eq. (3) all parameters except A are known. It is possible to calculate by combining the models proposed by Hasegawa,¹⁰ Heiman *et al.*¹¹ as described below. From the mean-field model the exchange constant A can be written¹⁰ (considering only Er since Co has no moment) as

$$A = n_{\text{Er-Er}} J_{\text{Er-Er}} (g_{\text{Er}} - 1)^2 J^2 x^2 / a_{\text{Er-Er}}, \quad (5)$$

where x is the Er concentration, $n_{\text{Er-Er}}$ indicates the number of maximum permissible pairs of Er atoms per volume extending to the first nearest neighbors, $a_{\text{Er-Er}}$ the interatomic distance between Er atoms, x the Er concentration, and the

TABLE I. Some magnetic properties of $\text{Co}_{1-x}\text{Er}_x$ alloys at 4 K.

x	M_0 (emu g ⁻¹)	T_C (K)	A (10 ⁻⁸ erg cm ⁻¹)	H_{ex} (T)	H_r (T)	K_r (10 ⁸ erg cm ⁻³)
55	179	40	1.9	0.4	19	1.5
65	197	30	1.7	0.4	20	1.8

rest of the symbols have the usual meaning. Several authors¹² have assumed that $n_{\text{Er-Er}}=2$ and $a_{\text{Er-Er}}=3.5 \text{ \AA}$.

One can express the Curie temperature, after Heiman *et al.*¹¹ as

$$3kT_C = 2xZ_{\text{Er-Er}}J_{\text{Er-Er}}J_{\text{Er}}(g_{\text{Er}}-1)^2(J_{\text{Er}}+1), \quad (6)$$

where $Z_{\text{Er-Er}}$ denotes the number of Er neighbors around Er atom which is generally taken as 12 in such amorphous alloys and the other symbols have their usual meaning. $g_{\text{Er}}=1.2$, $J_{\text{Er}}=7.5$.

Combining Eqs. (5) and (6) we can eliminate the term $J_{\text{Er-Er}}$ and get

$$A = xJ_{\text{Er}}kT_C/[4(J_{\text{Er}}+1)a_{\text{Er-Er}}]. \quad (7)$$

Knowing all the parameters in the above Eq. (7) A can be calculated. For example, for $x=65$, A is found to be $1.7 \times 10^{-8} \text{ erg cm}$. Using this value of A in Eq. (4), we calculate $R_a = 1.5 \text{ \AA}$. This rather small value indicates that there is practically no correlation in the direction of the easy axis from one rare-earth site to another. This is in agreement with the fact that this alloy is a speromagnet. One finds in transition metal-rich alloys, generally, that R_a is about 5 \AA , which corresponds to a few atomic sites.¹³

ACKNOWLEDGMENT

This work was performed under the European collaboration programme CEAM 3, which is gratefully acknowledged.

¹K. Moorjani and J. M. D. Coey, *Magnetic Glasses* (North Holland, Amsterdam, 1984), Chap. VI.

²D. J. Sellmyer and S. Nafis, *J. Appl. Phys.* **57**, 3584 (1985).

³R. Krishnan and H. Lassri, *Solid State Commun.* **69**, 803 (1989).

⁴Yang Xingbo and T. Miyazaki, *J. Magn. Magn. Mater.* **73**, 39 (1988).

⁵E. M. Chudnovsky and R. A. Serota, *Phys. Rev. B* **26**, 2697 (1982).

⁶E. M. Chudnovsky, W. M. Saslow, and R. A. Serota, *Phys. Rev. B* **33**, 251 (1986).

⁷H. Lassri and R. Krishnan, *J. Magn. Magn. Mater.* **104-107**, 157 (1992).

⁸G. Hadjipanayis, D. J. Sellmyer, and B. Brandt, *Phys. Rev. B* **23**, 3349 (1981).

⁹E. M. Chudnovsky, *J. Magn. Magn. Mater.* **79**, 127 (1989).

¹⁰R. Hasegawa, *J. Appl. Phys.* **45**, 3109 (1974).

¹¹N. Heiman, K. Lee, R. Potter, and S. Kirkpatrick, *J. Appl. Phys.* **47**, 2634 (1976).

¹²Y. Mimura, N. Imamura, T. Kobayashi, A. Okada, and Y. Kushihiro, *J. Appl. Phys.* **49**, 1208 (1978).

¹³See, for example, E. M. Chudnovsky, *J. Appl. Phys.* **64**, 5770 (1988).

Magnetic properties and crystallization of amorphous Fe-Nd-B alloys at constant Nd concentration

Bao-gen Shen, Lin-yuan Yang, Hui-qun Guo, and Jian-gao Zhao

State Key Laboratory of Magnetism, Institute of Physics, Chinese Academy of Sciences, P.O. Box 603, Beijing 100080, People's Republic of China

The B-content dependence of magnetization, Curie temperature, and crystallization temperature for amorphous $(\text{Fe}_{1-x}\text{B}_x)_{100-y}\text{Nd}_y$ alloys with $y=4, 7$, and 12 were studied. Spontaneous magnetization shows a monotonic decrease with x , and the noncollinear spin structures have been proposed to explain the observed results. It is found that the Curie temperature of the samples increases at first with increasing B concentration x , and shows a maximum value at a certain B concentration, then decreases monotonically with x . The composition dependence of T_c is explained by the average molecular-field model. An exceptionally strong rise of crystallization temperature with x is found, and demonstrates that the thermal stability of amorphous Fe-Nd-B alloys has a remarkable enhancement by the substitution of B for Fe.

I. INTRODUCTION

Since the discovery of the Fe-Nd-B permanent magnet materials, the magnetic properties of rapidly quenched Fe-Nd-B alloys have been studied extensively. Recently, some researchers have developed an interest in the study of magnetic properties of rapidly quenched Fe-Nd-B alloys with lower Nd concentration. Most of these studies focus on their hard magnetic properties, while investigations on magnetic properties and crystallization of amorphous Fe-Nd-B alloys are relatively fewer. To obtain more information about magnetic behaviors of rapidly quenched Fe-Nd-B alloys, we extended the study of amorphous Fe-Nd-B alloys to a wide composition range.¹ In our previous paper, a study on magnetic properties and crystallization of amorphous $(\text{Fe}_{1-x}\text{Nd}_x)_{100-y}\text{B}_y$ with $y=6, 18.5$, and 25 as well as the effects of heat treatment on their hard magnetic properties has been reported.²⁻⁶ This paper focuses on the study of B-concentration dependence of magnetization, Curie temperature, and crystallization temperature of amorphous $(\text{Fe}_{1-x}\text{B}_x)_{100-y}\text{Nd}_y$ alloys at constant Nd concentration of $y=4, 7$, and 12 .

II. EXPERIMENTAL

Alloys with composition $(\text{Fe}_{1-x}\text{B}_x)_{100-y}\text{Nd}_y$ ($0.104 \leq x \leq 0.365$, $y=4$; $0.065 \leq x \leq 0.323$, $y=7$; $0.067 \leq x \leq 0.413$, $y=12$) were prepared by arc melting in a purified argon atmosphere. The ingots were melted several times to insure the homogeneity, and then melt spun in an argon atmosphere on the outside of a rotating copper drum of 20 cm diameter with a surface speed of about 47 m/s, resulting in ribbons about 1 mm wide and 20–30 μm thick. No crystallinity in the ribbon samples was detectable by x-ray diffraction. The Curie temperature of the samples was determined from the magnetization curve in a field of about 45 Oe or the temperature dependence of the ac susceptibility in a weak field lower than 1 Oe. The measurements on the low-temperature magnetization were performed by an extracting sample magnetometer at fields up to 65 kOe. The crystalli-

zation temperature of the samples was determined from the differential scanning calorimetry (DSC) traces with a heating rate of 20 K/min.

III. RESULTS AND DISCUSSION

Figure 1 shows the B-concentration dependence of the Curie temperature T_c of amorphous $(\text{Fe}_{1-x}\text{B}_x)_{100-y}\text{Nd}_y$ alloys at constant Nd concentration of $y=4, 7$, and 12 , together with that of amorphous $\text{Fe}_{1-x}\text{B}_x$ alloys for comparison. Pronounced effects of the composition on Curie temperature are observed. It can be seen from Fig. 1 that the T_c of the samples increases at first with increasing B concentration x , and shows a maximum value at a certain B concentration, then decreases monotonously with x . This variation of T_c is similar to those of amorphous $\text{Fe}_{1-x}\text{B}_x$ alloys,⁷ in which T_c showed a maximum at about 30 at. % B. The

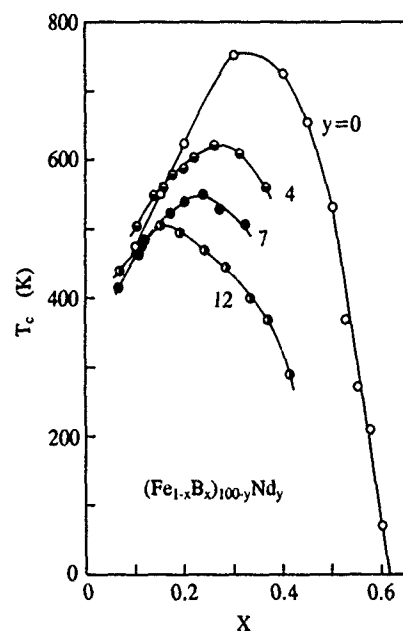


FIG. 1. B-concentration dependence of the Curie temperature T_c of amorphous $(\text{Fe}_{1-x}\text{B}_x)_{100-y}\text{Nd}_y$ alloys with $y=0$ [7] (\circ), $y=4$ (\odot), 7 (\bullet), and 12 (\bullet).

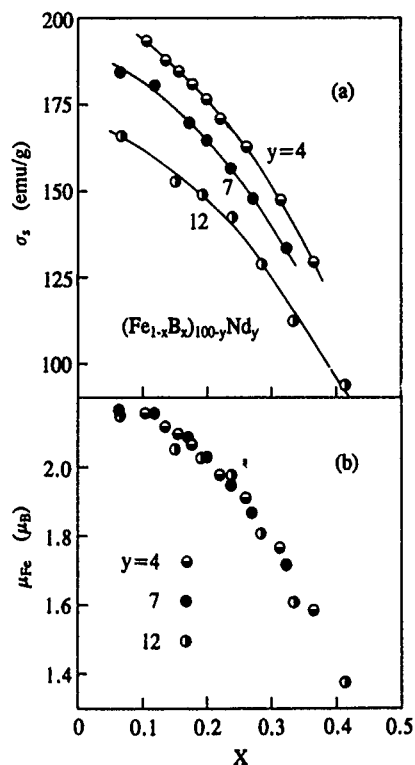


FIG. 2. B-concentration dependence of the spontaneous magnetization $\sigma_s(1.5)$ at 1.5 K (a) and the average magnetic moment μ_{Fe} per Fe atom (b) for amorphous $(Fe_{1-x}B_x)_{100-y}Nd_y$ alloys with $y=4$ (○), 7 (●), and 12 (○).

maximum value of T_c is found to shift to lower B concentration, when the neodymium is added in the Fe-B alloys. According to the average molecular-field model, the Curie temperature is directly proportional to the exchange integral between magnetic atoms and the number of nearest-neighbor magnetic atoms. The exchange integral of alloys is affected by element species and interatomic distance. For the Fe-rich amorphous Fe-Nd-B alloys, the T_c depends mainly on Fe-Fe exchange interactions. The addition of Nd is found to decrease the T_c of amorphous Fe-B alloys with the same B concentration, as shown in Fig. 1. This implies that the substitution of Nd for Fe would decrease the exchange interactions between Fe-Fe atoms. For $(Fe_{1-x}B_x)_{100-y}Nd_y$, the increase of T_c with x at lower B concentration can be attributed to the increase of the Fe-Fe interaction as a result of the increase in Fe-Fe spacing by the interstitial B atoms. At higher B concentration, the decrease of T_c with x may be due to the decrease of Fe-Fe interactions and the number of Fe-Fe atom pairs.

The magnetization data at 1.5 K were measured for amorphous $(Fe_{1-x}B_x)_{100-y}Nd_y$ alloys at constant Nd concentration. The spontaneous magnetization $\sigma_s(1.5)$ was obtained by fitting the magnetization curves according to the approach to the saturation law,

$$\sigma(H) = \sigma_s(1.5)(1 - a/H - b/H^2). \quad (1)$$

The $\sigma_s(1.5)$ as a function of B concentration is shown in Fig. 2(a). The $\sigma_s(1.5)$ is found to decrease monotonously with increasing B concentration x . It has been shown previously that in the amorphous $(Fe_{1-x}Nd_x)_{81.5}B_{18.5}$ and

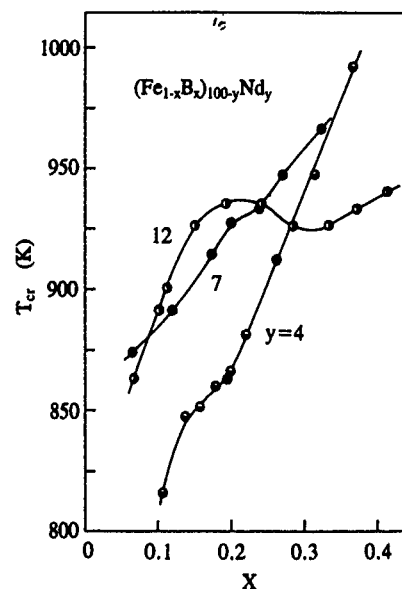


FIG. 3. B-concentration dependence of the crystallization temperature T_{cr} of amorphous $(Fe_{1-x}B_x)_{100-y}Nd_y$ alloys with $y=4$ (○), 7 (●), and 12 (○).

$(Fe_{1-x}Nd_x)_{94}B_6$ alloys by a smooth extrapolation of the $\sigma_s(1.5)$ vs x curves to $x=1.0$, the values of $\sigma_s(1.5)$ of both the $Nd_{81.5}B_{18.5}$ and $Nd_{94}B_6$ are obtained to be 40 emu/g.⁶ Therefore, the Nd atom moment is found to be $1.02\mu_B$, which is only about 30% of the moment of a free Nd^{3+} ion ($3.27\mu_B$). This implies the existence of a noncollinear spin structure in amorphous Fe-Nd-B alloys. The fact that the magnetization curves are difficult to saturate, especially at higher Nd concentration, supports the existence of the noncollinear spin structures in the amorphous Fe-Nd-B alloys. The Nd moment is distributed on a cone of half angle θ_{Nd} , which is 112° as calculated from the formula $\mu_{Nd} = (1/2)\mu_{Nd}^{3+}(1 + \cos \theta_{Nd})$. It is found that the value of θ_{Nd} in amorphous $Fe_{1-x}Nd_x$ films is 106° – 111° as x increases from 0.04 to 0.9.⁸ These results demonstrate that in amorphous Fe-Nd-B alloys the Nd moment is slightly influenced by the boron concentration. Accordingly, the θ_{Nd} is roughly constant for all x due to the very strong local random anisotropy of Nd. For amorphous $(Fe_{1-x}B_x)_{100-y}Nd_y$ alloys, if the θ_{Nd} is assumed to be 112° , that is, the Nd magnetic moment is $1.02\mu_B$, the average magnetic moment per Fe atom μ_{Fe} is found to drop monotonically with increasing B concentration, as shown in Fig. 2(b). The decrease of μ_{Fe} with x can be attributed to the decrease of the number of Fe atoms and the coordination of the nearest Fe atoms.

Figure 3 shows the B-concentration dependence of the crystallization temperature T_{cr} measured at a scanning rate of 20 K/min for amorphous $(Fe_{1-x}B_x)_{100-y}Nd_y$ alloys at constant Nd concentration of $y=4, 7$, and 12 . The T_{cr} is found to depend strongly on B concentration. The substitution of B for Fe plays an important role in the enhancement of the thermal stability of amorphous Fe-Nd-B alloys. In the samples with $y=4$ and 7 , the T_{cr} increases monotonically with increasing B concentration x . For $y=12$, the T_{cr} first increases sharply with increasing B concentration x , it goes through a broad maximum at about $x=0.29$ (17 at % B) to

lower values and then increases again with x . A similar concentration dependence of T_{cr} was observed in amorphous $Fe_{1-x}B_x$ alloys.⁹ Previous studies have shown that in many metal-metalloid amorphous alloys T_{cr} exhibits a maximum near the equilibrium eutectic composition. The maximum value of T_{cr} in the $(Fe_{1-x}B_x)_{100-y}Nd_y$ alloys with $y=12$ is exhibited near 17 at % B, which is just the eutectic composition of the ternary Fe-Nd-B system. It is found that the T_{cr} of amorphous Fe-Nd-B alloys studied in this work are 120–210 K higher than those of amorphous Fe-B alloys with the same B concentration. This demonstrates that the thermal stability of amorphous Fe-Nd-B alloys has a remarkable enhancement by the substitution of some Nd for Fe. When a small amount of Nd, having a great affinity to B and its atomic radius being larger than Fe, is added in the Fe-B alloys, the viscosity of the alloy increases and the diffusion coefficient reduces, therefore the thermal stability of the amorphous alloys is enhanced. In general, the ternary amorphous alloys would be more stable against crystallization than the binary ones, and the corresponding crystallization temperature would become higher.

ACKNOWLEDGMENTS

This work was supported by the State's Sciences and Technology Commission and the National Natural Science Foundation of China.

- ¹B. G. Shen and L. Y. Yang, *Prog. Natural Sci.* **3**, 130 (1993).
- ²B. G. Shen, J. X. Zhang, L. Y. Yang, F. Wo, T. S. Ning, S. Q. Ji, J. G. Zhao, H. Q. Guo, and W. S. Zhan, *J. Magn. Magn. Mater.* **89**, 195 (1990).
- ³B. G. Shen, J. X. Zhang, L. Y. Yang, H. Q. Guo, and J. G. Zhao, *Mater. Sci. Eng. A* **133**, 162 (1991).
- ⁴B. G. Shen, L. Y. Yang, and H. Q. Guo, *Acta Physica Sinica (Overseas Edition)* **1**, 57 (1992).
- ⁵L. Y. Yang, B. G. Shen, J. X. Zhang, J. G. Zhao, H. Q. Guo, and F. M. Yang, *J. Magn. Magn. Mater.* **104-107**, 1191 (1992).
- ⁶B. G. Shen, L. Y. Yang, J. G. Zhao, and H. Q. Guo, *Chin. Phys. Lett.* **10**, 620 (1993).
- ⁷C. L. Chien and K. M. Unruh, *Phys. Rev. B* **25**, 5790 (1982).
- ⁸D. S. Dai, R. Y. Fang, L. T. Tong, Z. X. Lui, Z. J. Zhou, and Z. H. Lin, *J. Appl. Phys.* **57**, 3589 (1985).
- ⁹R. Ray, R. Hasegawa, C.-P. Chou, and L. A. Davis, *Scr. Metal.* **11**, 973 (1977).

Influence of applied torsion on the bistable behavior of CoSiB amorphous wire

J. M. Blanco and P. Aragonés

Departamento de Física Aplicada I, EUITI, Universidad del País Vasco, 20011 San Sebastián, Spain

E. Irurieta, J. González, and K. Kulakowski^{a)}

Departamento de Física de Materiales, Facultad de Químicas, Universidad del País Vasco, 20009 San Sebastián, Spain

Experimental results are reported on the torsion dependence of bistability of CoSiB amorphous alloys. Switching field and remanence magnetization are measured with applied torsion up to 20π rad/m for as-quenched wire as well as for stress-annealed wire, with and without preannealing. Measurements are performed both for M_z - H_z and M_z - H_ϕ hysteresis loop. The results show that the bistability of Co-rich amorphous wire strongly depends on the torsion-induced helical anisotropy.

I. INTRODUCTION

Bistability of magnetic state of amorphous 3d wires makes these systems attractive for applications.¹ In particular, the influence of tension and torsion to the effect is of current interest.^{2,3} If magnetostriction is small, remagnetization processes can be very sensitive to actual distribution of local magnetic anisotropy in the wire. Such dependence was found recently⁴ in nearly zero-magnetostrictive CoFeSiB amorphous wires. In Co-based wires, magnetostriction is one order of magnitude smaller than in Fe-rich ones. Then, experimental data are needed to evaluate the usefulness of these wires as bistable elements.

Recently, we have reported on the influence of applied tension^{5,6} on the hysteresis loop of current annealed cobalt-based amorphous wire. Special attention has been paid to the switching field H^* , namely, the value of the applied magnetic field, for which the bistability takes place. The aim of the present paper is to perform a similar study on the influence of torsion stress on the bistable behavior of the same current-annealed cobalt-based alloy wire previously investigated in Refs. 5,6, in order to establish the mechanisms responsible for the bistability.

II. EXPERIMENTAL TECHNIQUE

Amorphous wires of nominal composition $\text{Co}_{72.5}\text{Si}_{12.5}\text{B}_{15}$ were obtained by means of the in-rotating-water technique by UNITIKA Ltd. Co, Japan. The diameter of wires is $120\ \mu\text{m}$ and its length is 10 cm. The shape magnetostriction λ of this wire is known to be about -3.5×10^{-6} . Hysteresis loops M_z - H_z and M_z - H_ϕ are obtained by conventional induction method with frequency 50 Hz. During measurement, a torsion ζ is applied up to one turn (20π rad/m). Circular magnetic field H_ϕ is produced by ac electric current, flowing along the sample. The values of switching field, due to this current, are calculated at the surface of a wire. More details on the measurement technique are described in Ref. 3.

Two kinds of thermal treatment have been applied: stress annealing with and without preannealing. Both kinds of annealing are by means of electric current. The current of pre-

annealing is 525 mA. Annealing conditions are: stress of 550 MPa, current I_{ann} of 400 or 450 mA. The value 400 mA corresponds to Curie temperature of the alloy (593 K).

III. EXPERIMENTAL RESULTS

Remanence magnetization m_r is found to be very similar for M_z - H_z (Fig. 1) and M_z - H_ϕ experimental data. Also, the data on m_r are almost the same for both annealing currents, 400 and 450 mA. For as-quenched sample, remanence magnetization is remarkably lower, than that for the annealed wire. Both curves saturate with torsion about $\zeta=35$ rad/m. Above this value of ζ , the data on m_r for annealed sample do not depend on annealing time. For lower values of torsion, the differences between the curves $m_r(\zeta)$ for different annealing times are significant only for preannealed samples. There, $m_r(\zeta=0)$ for M_z - H_ϕ experiment shows a maximum with annealing time at about $t_{\text{ann}}=15$ min (Fig. 2). For M_z - H_z data this dependence also exists, but its character is not clear.

The torsion dependence of the switching field H^* for the M_z - H_ϕ experiment is regular, almost linear and at first sight

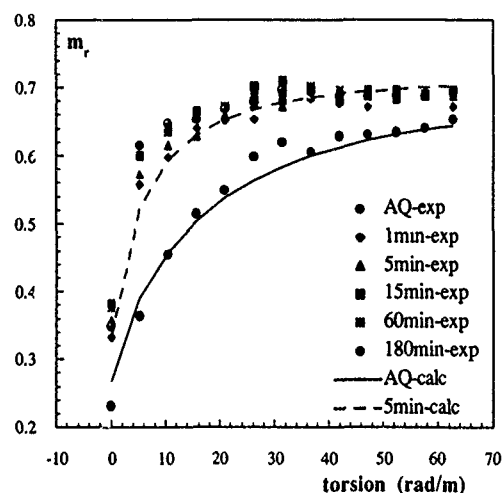


FIG. 1. Remanence magnetization against applied torsion. Annealing current is 400 mA. Experimental data from the M_z - H_z hysteresis loop are compared with calculations according to the paper (Ref. 3). The values of the parameter r_0 are $31\ \mu\text{m}$ (as-quenched) and $35\ \mu\text{m}$ ($t=5$ min).

^{a)}On leave from the Faculty of Physics and Nuclear Techniques, University of Mining and Metallurgy, Cracow, Poland.

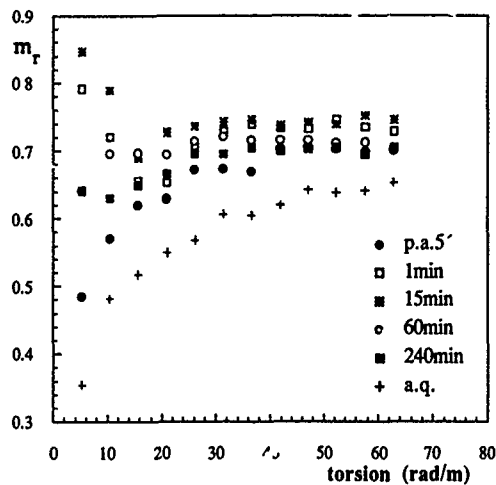


FIG. 2. Remanence magnetization for preannealed wire, measured in M_z - H_ϕ experiment, for $I_{ann}=450$ mA.

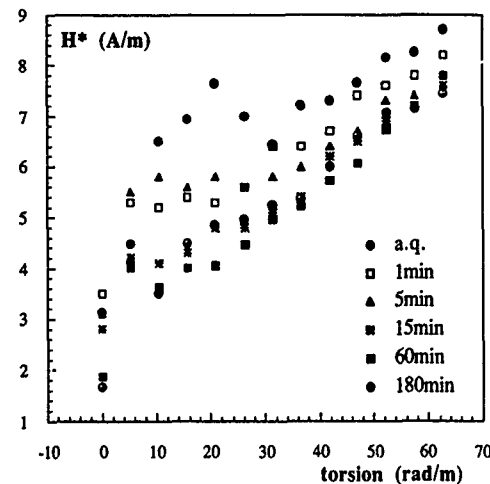


FIG. 4. Switching field from M_z - H_z measurement, against torsion, for $I_{ann}=400$ mA.

does not depend on thermal treatment (Fig. 3). The slope of the curve $H^*(\zeta)$ is slightly reduced with torsion only for short annealing times. For M_z - H_z experiment, the switching field H^* for $I_{ann}=400$ mA decreases with annealing time. For $I_{ann}=450$ mA the dependence $H^*(\zeta)$ does not change with t_{ann} . On the contrary, for as-quenched wire this curve shows a maximum at about $\zeta=21$ rad/m (Fig. 4). For $I_{ann}=400$ mA we can observe how this maximum is shifted towards smaller values of applied torsion, when annealing time increases. For $I_{ann}=450$ mA this maximum is visible only for as-quenched wire (Fig. 5). The values of H^* for the M_z - H_ϕ experiment are close to those for the M_z - H_z one.

IV. DISCUSSION

Experimentally observed difference between remanence magnetization m_r for as-quenched sample and annealed samples (Fig. 1) indicates that for as-quenched sample a kind of instability of amorphous structure is present. Its existence

is confirmed by the maximum of switching field H^* in M_z - H_z experiments. In the case of H^* , this instability can be removed in a continuous way by annealing in Curie temperature, or immediately by annealing in higher temperatures. In the case of m_r , the effect disappears immediately even for short annealing time and $I_{ann}=400$ mA. This indicates that the switching field is much more sensitive to the details of local distribution of magnetization in the region between inner core and outer shell. The same effect, but much more strong, was found recently⁴ in nearly zero-magnetostrictive amorphous wires.

Thermal treatment changes magnetic softness and initial ($\zeta=0$) value of remanence magnetization. But, as ζ increases, torsion-induced helical anisotropy is expected to stabilize the radius of inner core and the spatial distribution of internal stresses. To describe the effect of torsion on remanence magnetization, we approximate the distribution of the density of magnetic anisotropy within the wire by a function

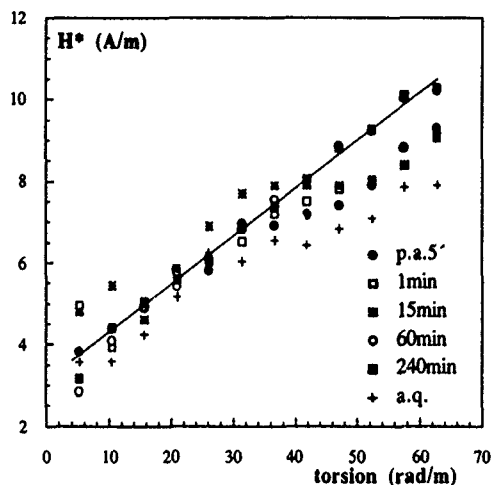


FIG. 3. Switching field from M_z - H_ϕ measurement, for $I_{ann}=450$ mA, with preannealing. The data for $t_{ann}=240$ min are fitted with straight line.

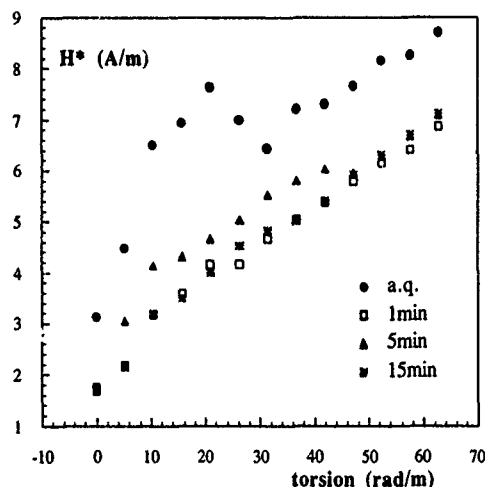


FIG. 5. Switching field from M_z - H_z measurement, without preannealing, for $I_{ann}=450$ mA.

$$k(r) = k_0[1 - (r/r_0)^n],$$

where k_0 is the density of anisotropy at the wire axis, r_0 is the initial ($\zeta=0$) value of the radius of inner core, and n is a parameter introduced to describe the shape of the function $k(r)$. This parametrization was found to be useful⁶ to describe the tension dependence of bistability in the wire with the same composition. With this function, remanence magnetization can be calculated³ as an average of the cosine of local magnetization with the wire axis. Actually, we get good accordance with experimental data, applying the same values of the parameters k_0 and n , which were found previously⁶ from tension dependence of m_r and H^* ($k_0 = -1575$ and -1785 MPa, $n = 0.4$ and 0.2 for as-quenched wire, and for $t_{\text{ann}} = 5$ min, respectively). However, the fitting values of r_0 are changed (example giving, from 24 to 31 μm for as-quenched wire). The results of the calculations are presented in Fig. 1. These values indicate that reduced remanence magnetization is remarkably larger than the ratio of the volume of inner core to the volume of a wire.

The torsion dependence of switching field is known³ to be dominated by torsion-induced helical anisotropy $k\zeta$. The order of magnitude of both densities of magnetic anisotropy, $k(r)$ and $k\zeta$, is the same in the average over the volume of a wire. However, the latter dominates near $r=r_0$, where nucleation processes occur. These processes are known to determine the value of switching field for the propagation mechanism.⁷ Still, our measurements of H^* can hardly be fitted by a square root of torsion-induced anisotropy. This difficulty is particularly clear for long annealing times (Fig. 3). Additional enhancement of the curve $H^*(\zeta)$ for higher values of torsion can be produced by the torsion-induced canting of local magnetic moments by an angle α . In such a case, appropriate expression for switching field is known⁸ to contain the multiplying factor $(\cos \alpha)^{-1/2}$. According to our evaluations, this correction is of order of 3%.

The values of switching field measured from the M_z - H_ϕ hysteresis loop should be evaluated at the radius of inner

core. This radius cannot be determined accurately. However, any reasonable estimation gives the value of H^* lower, than this one for M_z - H_z experiment. More detailed discussion on this difference for nearly zero-magnetostrictive wires is given elsewhere,⁴ and those arguments are valid only partially for the nonzero-magnetostrictive system, which is discussed in this paper. Here we would like to state only, that these differences are expected to be enhanced by helical magnetization in the region between inner core and outer shell.

Concluding, measurements of torsion dependence of bistability in Co-rich amorphous wires indicate that the domain structure of a wire is stabilized by torsion. Switching field measured from the M_z - H_z hysteresis loop is found to be sensitive to local magnetic state of the boundary between inner core and outer shell. Outer shell gives remarkable contribution to remanence magnetization.

ACKNOWLEDGMENTS

One of the authors (K. K.) is grateful to the Ministry of Education and Science of Spain for financial support from the program "Profesor en Año Sabático." This work has been supported by C.I.C.Y.T. Project MAT 93/0437 and the Excma Diputación Foral de Guipúzcoa.

¹K. Mohri, IEEE Trans. Magn. MAG-20, 942 (1984).

²A. Mitra and M. Vázquez, J. Phys. D 23, 228 (1990).

³M. Vázquez, J. González, J. M. Blanco, J. M. Barandiarán, G. Rivero, and A. Hernando, J. Magn. Magn. Mater. 96, 321 (1991).

⁴J. González, K. Kulakowski, P. Aragonese, J. M. Blanco, and E. Irurieta (unpublished).

⁵P. Aragonese, J. M. Blanco, J. González, and M. Vázquez, INTERMAG'93, Stockholm 1993, paper BD-07.

⁶K. Kulakowski, J. González, and P. Aragonese (unpublished).

⁷M. Vázquez, C. Gómez-Polo, and D. X. Chen, IEEE Trans. Magn. MAG-20, 3147 (1992).

⁸S. Chikazumi, *Physics of Magnetism* (Krieger, Huntington, New York, 1978), p. 289.

Details of the magnetic phase diagram of holmium from neutron diffraction in b -axis fields

D. A. Tindall and C. P. Adams

Department of Physics, Dalhousie University, Halifax, Nova Scotia, Canada B3H 3J5

M. O. Steinitz

Department of Physics, St. Francis Xavier University, Antigonish, Nova Scotia, Canada B2G 1C0

T. M. Holden

Neutron and Condensed Matter Science, AECL Research, Chalk River, Ontario, Canada K0J 1J0

We report measurements of the intensity and position of the satellites arising from the helimagnetic structure of Ho in 1.4 and 3 T b -axis magnetic fields. There are a number of lock-in effects at commensurate values of the spiral wave vector τ ; here we report on those in the temperature range 115–132 K. We confirm our previous observation of the lock-in at $\tau=5/18$ between 125 K and the Néel temperature (132 K). We have discovered a two-phase region in which the $5/18$ phase coexists with an incommensurate phase. In this two-phase region, the proportion of the $5/18$ phase increases with temperature from onset at 119 K to full lock-in at 125 K. The existence of this two-phase region may have significant influence on interpretation of the magnetic phase diagram.

There is, by now, a large body of results obtained using neutron scattering to study the magnetic phases of holmium,^{1–9} in addition to research with ultrasonic,^{10–12} magnetization,¹³ specific heat,¹⁴ x-ray,^{15,16} and dilatometric^{17–19} techniques. Yet there is much that is undiscovered about the magnetic structure of this rare earth metal. Our recent studies^{6–8} have focused on the lock-in behavior of the spiral wave vector τ . In a c -axis magnetic field we have discovered lock-ins at commensurate values of $\tau=1/5$ and $1/4$ reciprocal lattice units (rlu) at 43 and 96 K, respectively. Investigations^{8,9} in a b -axis field have shown lock-ins at $\tau=1/4$ rlu, and a higher temperature lock-in at $\tau=5/18$ rlu at about 125 K which persists up to the Néel transition. It is interesting to note that this value of $5/18$ also appears to be the ultimate value reached in zero field, or c -axis fields up to 3 T.⁵ In this case, however, the width of any commensurate region must be small as it has, so far, evaded detection. There are also intensity anomalies of the (10τ) peaks at the boundaries of these locked-in regions that have not yet been explained. The work reported here concentrates on the temperature region from 115 K to the Néel transition in 1.4 and 3 T b -axis magnetic fields. We have refined our earlier observation of the lock-in at $\tau=5/18$ rlu and have also observed an anomalous intensity variation as the lock-in is approached. We have found evidence that, before full lock-in is achieved, there is a temperature region in which two phases coexist; one with an incommensurate value of τ and the other commensurate (at $\tau=5/18$ rlu). We find, based on these and previous measurements, that this effect is not caused by inhomogeneity of the applied field or in the sample. A two-phase region enables us to interpret the meaning of phase boundaries previously observed¹³ in the phase diagram.

The experiments were performed at the Chalk River Laboratories of AECL Research in Chalk River, Ontario, using the N5 triple-axis neutron spectrometer. The measurements were made at zero-energy transfer (elastic scattering) with the monochromator set to an energy of 8.2 THz. The sample, a single crystal of holmium with dimensions roughly $2\times 1\times 1$ cm, was mounted in the M2 cryostat²⁰ that allows

350° access for the neutron beam and a temperature range from 4.2 K to room temperature. The sample orientation was such that we could observe $(h0l)$ reflections. The temperature was read and controlled with a platinum resistance thermometer mounted in the base of the probe (the temperatures were high enough that magnetoresistance effects in the thermometer were negligible).

The helimagnetic structure of holmium below the Néel transition is generally incommensurate with the period of the lattice, with a temperature-dependent wave vector τ . Thus, a τ of $1/4$ rlu represents four lattice units along the c axis in real space before the structure repeats. The magnetic satellites are a distance $\pm\tau$ rlu in the c^* direction away from the nuclear scattering peaks in reciprocal space. All of the peaks move in reciprocal space as the temperature changes, because of thermal expansion. We therefore measured τ as the distance between the nuclear peak at (100) and its satellite at (10τ) . The (100) peak and the satellite at (10τ) were scanned in the c^* direction. Gaussian fits were made to the peaks, and the difference between the centers of the peaks yielded our value for τ . The fits to the centers of the peaks show a standard deviation of 0.0001 rlu and we estimate our absolute values of τ to be good to ± 0.0005 rlu. τ generally varies smoothly with temperature, but in a magnetic field the temperature dependence decreases as τ locks in at certain commensurate values.

The lock-in studied here extends from the Néel temperature down to a lower, field-dependent temperature which is 125 K in a 3 T b -axis field. This is the first known transition from a paramagnetic phase directly to a commensurate phase observed in a rare earth metal. Some previous work⁴ had suggested that this lock-in occurred with $\tau=8/29=0.2757$ rlu but our measurements⁹ have previously indicated that the correct τ value for this lock-in is $5/18=0.2778$. Our latest results, shown in Fig. 1, confirm that $5/18$ is indeed the lock-in value and that $8/29$ is outside the error range. We have also observed this lock-in in a 1.4 T b -axis field. The temperature region where the lock-in occurs in 1.4 T is smaller, since the energy gained by transition to the commen-

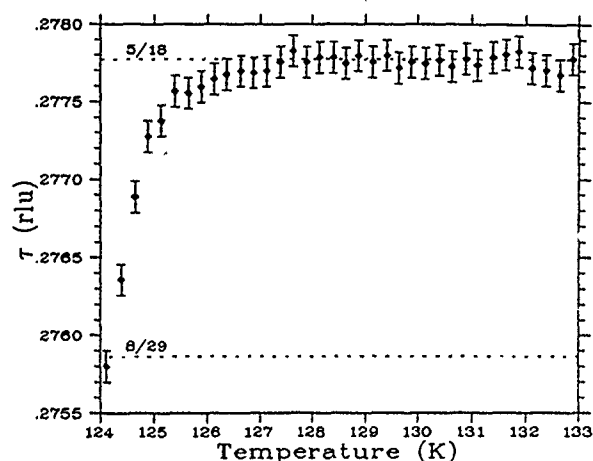


FIG. 1. τ vs temperature in a 3 T b -axis applied magnetic field. τ values of 5/18 and 8/29 are shown by dashed lines. These data clearly support a lock-in at $\tau=5/18$.

surate structure is smaller in the lesser field. The ratio of the temperature widths at 3 T and 1.4 T (7 K/1.5 K) is equal to the square of the ratio of the fields $(3\text{ T}/1.4\text{ T})^2$. The τ value at lock-in is still very close to 5/18 rlu in 1.4 T b -axis field.

Figure 2 shows that the peak widths arising from fits to the (10τ) peak with a single Gaussian have a curious feature. Outside the 119–125 K range, the full width at half maximum (FWHM) of both the (10τ) and the (100) peaks are stable at 0.0072 rlu. However, inside this temperature region the width of the (10τ) peak rises strongly while the width of the nuclear (100) peak stays constant. The intensity of the (10τ) satellite also shows an anomaly here (Fig. 3). This is similar to intensity variations we have found at the boundaries of other lock-in regions. The smooth curve, of a critical exponent form, in Fig. 4 shows the anomaly clearly: the fit is good everywhere except in the 119–125 K range. If we look at the single Gaussian fit to the scan (shown by the dashed

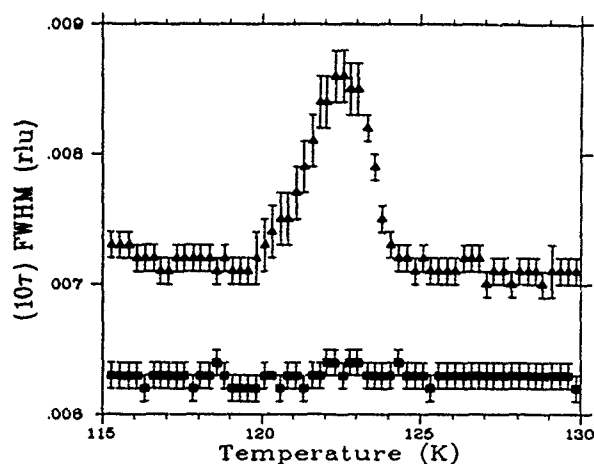


FIG. 2. The full width at half maximum vs temperature for the (10τ) satellite peak (Δ) and the (100) nuclear peak (\blacksquare), using a single Gaussian fit in a 3 T b -axis field. Notice the sharp rise in apparent width of (10τ) in the two-phase region. The data for (100) have been displaced downwards by 0.001 rlu, for clarity.

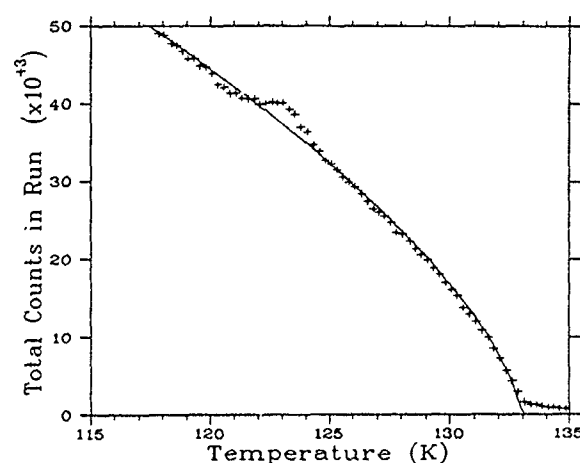


FIG. 3. A plot of total counts in each run vs temperature. The curve is a fit to $A(1 - (T/T_N))^{2\beta}$, with $\beta=0.327$ and $T_N=132.9$ K. The anomaly in the two-phase region has some similarity to that seen on entering other locked-in regions.

line in Fig. 4) we see that it is clearly lopsided. This led us to believe that a two-Gaussian fit might be more suitable: If this widening arises from the coexistence of two phases with different τ 's, then a two-Gaussian fit is a more appropriate representation of the physical situation. The width of each of the two Gaussians should then be the same as that outside the two-phase region (0.0072 rlu). We also assumed that, rather than having two coexisting incommensurate phases, one of the phases should be commensurate, because of the proximity to the commensurate lock-in at $\tau=5/18$ rlu. We therefore fixed the position of one peak at $\tau=5/18$ rlu and allowed the other, incommensurate, peak to move (from an initial value of $\tau=0.2668$ rlu to 5/18). These restrictions reduce the number of parameters in the fitting procedure to the same number that were used previously with the single-Gaussian fit. The solid line in Fig. 4 shows that the two-Gaussian fit to the data is, indeed, much better than the single-Gaussian fit. The in-

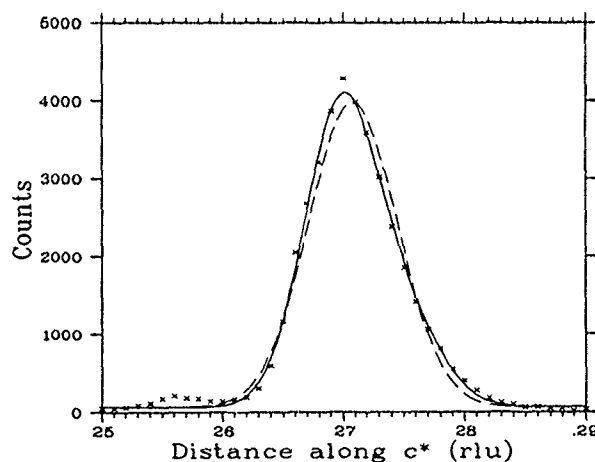


FIG. 4. The dashed line shows a single-Gaussian fit to the (10τ) peak in the two-phase region at 122.3 K. Notice the lopsidedness of the fit. The solid line shows a two-Gaussian fit to the same data. Although the number of free parameters remains the same, the result is a far better fit. At this temperature the peaks are separated by only 0.005 rlu.

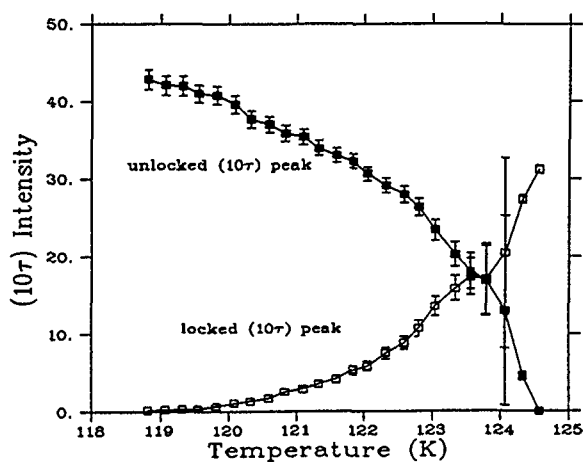


FIG. 5. Intensity of the unlocked (10τ) peak (■) and the intensity of the locked (10τ) peak (□) vs temperature over the two-phase region.

tensities of the commensurate and incommensurate phases are shown in Fig. 5. The intensity of the locked-in phase increases smoothly up to 125 K while that of the incommensurate phase decreases in a similar manner, disappearing rapidly at 125 K. In the region above 123.6 K (where the incommensurate peak is very close to the commensurate value and becoming very weak) the fits to the individual peaks become quite uncertain although, of course, the total is fitted well.

We had some doubt as to whether or not this two-phase region is genuine or is merely a result of an inhomogeneous internal magnetic field in the sample. By measuring the slope of the coexistence curve on the b -axis field phase diagram (Fig. 4 of the paper by Willis *et al.*¹³) near 125 K and 3 T, we found that the field would have to vary by at least 10% over the volume of the sample to give a two-phase region that was 5 K wide. However, the applied field profile varies by less than 2% over the sample volume so this, in itself, cannot account for the effect. Another possibility is that the irregular shape of the sample leads to internal field inhomogeneity. Supposing that it did, and noting that Willis *et al.*¹³ show [in their Fig. 2(b)] that the magnetization does not change significantly between 100 and 125 K and that the magnitude of the slope of the coexistence curve at the $\tau=1/4$ rlu lock-in is very similar to that at 125 K and 3 T, the same field inhomogeneity would give the same 5 K distribution in phases at the two different temperatures. This would completely smear out the $\tau=1/4$ lock-in, which is not the case.⁹ Thus, internal field inhomogeneity cannot account for the two-phase region. This also demonstrates that the demagnetization factors

arising from sample shape are negligible. However, there remains the possibility that this two-phase region is a sample-dependent feature, as has so often plagued experiments in the rare earths. Further experiments to investigate this region, with other samples, are desirable.

In summary, the measurements reported here allow us to identify one of the phases previously observed and reinterpret the b -axis magnetic phase diagram in this region, as a new phase is present in the 120–125 K region at 3 T. There may be a splitting of one of the coexistence curves as seen earlier for the c -axis phase diagram.^{5,6}

The authors gratefully acknowledge the financial support of the Natural Sciences and Engineering Research Council of Canada and the Canadian Institute for Neutron Scattering. Once again, we would like to thank AECL Research, Chalk River for the use of their excellent facilities and the expert advice and assistance of their employees; especially Larry MacEwan, Peter Moss, Mel Potter, and Don Tennant. We are obliged to M. J. Pechan and C. Stassis for the loan of the sample.

- ¹W. C. Koehler, J. W. Cable, M. K. Wilkinson, and E. O. Wollan, *Phys. Rev.* **151**, 414 (1966).
- ²W. C. Koehler, J. W. Cable, H. R. Child, M. K. Wilkinson, and E. O. Wollan, *Phys. Rev.* **158**, 450 (1967).
- ³M. J. Pechan and C. Stassis, *J. Appl. Phys.* **55**, 1900 (1984).
- ⁴J. A. Tarvin and J. Eckert, *Solid State Commun.* **30**, 375 (1979).
- ⁵D. R. Noakes, D. A. Tindall, M. O. Steinitz, and N. Ali, *J. Appl. Phys.* **67**, 5274 (1990).
- ⁶D. A. Tindall, M. O. Steinitz, M. Kahrizi, D. R. Noakes, and N. Ali, *J. Appl. Phys.* **69**, 5691 (1991).
- ⁷D. A. Tindall, M. O. Steinitz, and T. M. Holden, *Phys. Rev. B* **47**, 5463 (1993).
- ⁸D. A. Tindall, M. O. Steinitz, and T. M. Holden, *J. Phys. Cond. Matt.* **4**, 9927 (1992).
- ⁹D. A. Tindall, M. O. Steinitz, and T. M. Holden, *J. Appl. Phys.* **73**, 6543 (1993).
- ¹⁰M. C. Lee, R. A. Treder, and M. Levy, *J. Phys. Chem. Solids* **36**, 1281 (1975).
- ¹¹A. M. Simpson, M. H. Jericho, and M. C. Jain, *Can. J. Phys.* **54**, 1172 (1976).
- ¹²S. B. Palmer and E. W. Lee, *Proc. Roy. Soc. London Ser. A* **327**, 519 (1972).
- ¹³F. Willis, N. Ali, M. O. Steinitz, M. Kahrizi, and D. A. Tindall, *J. Appl. Phys.* **67**, 5277 (1990).
- ¹⁴K. D. Jayasuriya, S. J. Campbell, and A. M. Stewart, *J. Phys. F* **15**, 225 (1985).
- ¹⁵D. Gibbs, D. E. Moncton, K. L. D'Amico, J. Bohr, and B. H. Grier, *Phys. Rev. Lett.* **55**, 234 (1985).
- ¹⁶J. Bohr, D. Gibbs, D. E. Moncton, and K. L. D'Amico, *Physica* **140A**, 349 (1986).
- ¹⁷J. J. Rhyne, S. Legvold, and E. T. Rodine, *Phys. Rev.* **154**, 266 (1967).
- ¹⁸D. A. Tindall, M. O. Steinitz, and M. L. Plumer, *J. Phys. F* **7**, L263 (1977).
- ¹⁹M. O. Steinitz, M. Kahrizi, and D. A. Tindall, *Phys. Rev. B* **36**, 783 (1987).
- ²⁰D. C. Tennant, N. Kerley, and N. Killoran, *Rev. Sci. Instrum.* **60**, 136 (1989).

Critical magnetic neutron scattering above T_N in Cr+0.18 at. % Re (abstract)

D. R. Noakes

Physics Department, Virginia State University, Petersburg, Virginia 23806

E. Fawcett

Physics Department, University of Toronto, Toronto, Ontario M5S 1A7, Canada

B. J. Sternlieb and G. Shirane

Brookhaven National Laboratory, Upton, New York 11973

J. Jankowska

Institute of Nuclear Research SWIERK, 05-400 Otwock, Poland

Magnetic critical neutron scattering from a single crystal of Cr+0.18 at. % Re¹ was observed above its Néel transition (323 K) to an incommensurate spin density wave state. The data were analyzed in terms of the critical susceptibility model that successfully fit analogous data from single crystals of pure chromium and Cr+0.2 at. % V.² An additional complication in this case is the fact that a small portion of the sample becomes commensurate antiferromagnetic at a temperature well above 323 K, which causes a commensurate magnetic Bragg peak that partially obscures the critical scattering near 323 K. The "Sato-Maki"² form of incommensurate critical susceptibility fits the data reasonably well.³ The intensity of magnetic critical scattering in Cr+0.18 at. % Re is about a factor 2 stronger than in pure Cr, whereas in Cr+0.2 at. % V it is about the same factor weaker.

¹K. Mikke and J. Jankowska, *J. Phys. F* **10**, L159 (1980).

²D. R. Noakes, E. Fawcett, T. M. Holden, and P. C. de Camargo, *Phys. Rev. Lett.* **65**, 369 (1990).

³D. R. Noakes, E. Fawcett, B. J. Sternlieb, G. Shirane, and J. Jankowska (unpublished).

Photoinduced disaccommodation of magnetic permeability in yttrium iron garnet (abstract)

I. Matsubara, K. Hisatake, and K. Maeda

Department of Physics, Kanagawa Dental College, Yokosuka, Kanagawa 238, Japan

After illuminating a single crystal of yttrium iron garnet grown by a modified floating zone method at 77 K, the complex permeability was measured from 77 to 300 K under low alternating field. As well as the decreasing of permeability and the appearance of a peak in μ'' - T curve, disaccommodation (DA) or the change of permeability with time was found to be induced around 140 and 210 K. As the result of the superposition of disaccommodation, the peak in the μ'' - T curve is observed to be divided. These photoinduced magnetic effects cannot be attributed to a single origin, for only photoinduced DA disappears in the process of warming. The origins are discussed and a model is proposed, taking account of the mobility of oxygen vacancy depending on the charge state and the photoexcited electron.

Unidirectional pinning in irradiated $\text{Bi}_2\text{Sr}_2\text{CaCu}_2\text{O}_8$ (invited)

L. Klein, E. R. Yacoby, A. Tsameret, and Y. Yeshurun
Department of Physics, Bar-Ilan University, 52900 Ramat-Gan, Israel

K. Kishio
Department of Industrial Chemistry, University of Tokyo, Bunkyo-ku, Tokyo 113 Japan

$\text{Bi}_2\text{Sr}_2\text{CaCu}_2\text{O}_8$ crystals were irradiated with heavy ions (Pb, Xe) to produce columnar defects along the c direction or at 45° with respect to it. We describe the dependence of the critical currents, irreversibility fields, pinning force, and magnetic relaxation rates on the dose and on the type of ions. The irreversible properties of the Pb-irradiated samples are more enhanced than those of the Xe-irradiated sample at low temperatures, and vice versa at high temperatures. At low temperatures the efficiency of the columnar defects is enhanced with the ion dose but, at high temperatures, the maximum dose (2.5×10^{11} ions/cm²) is less efficient than intermediate doses. The unidirectional nature of the columnar pinning centers serves to demonstrate that the vortices maintain linelike features. For most of the irradiated samples, the pinning force density data are reduced to a single curve below 45 K. The relaxation rates at low temperatures reflect thermal reduction of the effective pinning barriers.

I. INTRODUCTION

$\text{Bi}_2\text{Sr}_2\text{CaCu}_2\text{O}_8$ (BSCCO) is characterized by weak flux pinning even relative to other high-temperature superconductors (HTS). This is reflected in its low critical currents and low irreversibility fields,¹ which hinder high-current applications. Therefore, the possibility of enhancing the pinning force is important not only for studying the flux properties, but also as an indication of the possibility of reaching critical currents that will enable high-current applications. BSCCO is also one of the most anisotropic compounds among the known cuprate HTS, due to the weak coupling between the Cu-O layers. The effect of the coupling on the vortex properties is still debated. In particular, it is still unclear in what range of field and temperature the coupling is important and the vortices are linelike, and at what range the coupling can be neglected and the vortices are two dimensional "pancakes".² References 3–15 list some of the experimental works dealing with this issue.

Columnar defects are now a common probe for studying flux properties in HTS.^{12–20} These defects, induced by heavy-ion irradiation, have several advantages. Columnar defects are very efficient pinning centers; thus their effect indicates how much the pinning force may be artificially enhanced. In addition, these defects are oriented and it is possible to distinguish between linelike vortices and pure two-dimensional pancakes by looking for the dependence of pinning properties on the angle between the applied field and the defects.^{13–15} Linelike vortices are most efficiently pinned when they are oriented along the defect, and tilting them away from the defects should decrease pinning. On the other hand, no angular dependence is expected for two-dimensional pancakes, since the density of pinning centers in each Cu-O plane is what matters, and the correlation of pin-

ning centers at different planes is not relevant. Thus, important information concerning the vortices dimensionally may be obtained by studying the angular dependence of the pinning properties.^{13–15}

In previous works^{13–15} we have demonstrated the unidirectional nature of the columnar defects in BSCCO via the hysteresis loops, $M(H)$. Typical results are shown in Fig. 1. The figure describes the evolution of the unidirectional pinning with temperature via the difference between the hysteresis loops recorded for field in the direction of the columnar defect ($+45^\circ$) and for the field perpendicular to it (-45°) for sample B3 (see Table I). We find that the magnetization is largest for fields applied along the defects and conclude that this unidirectional pinning indicates the linelike nature of

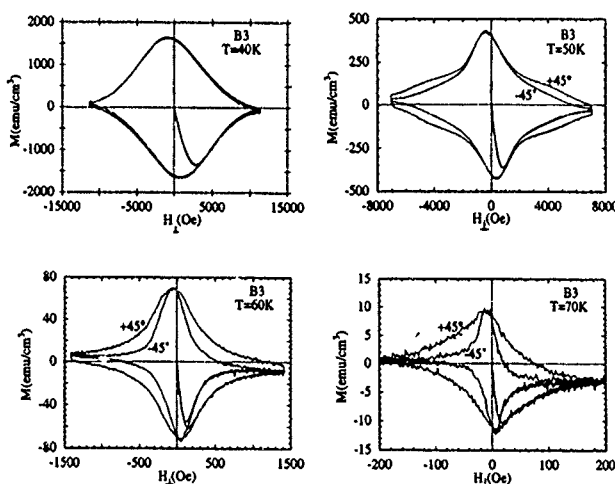


FIG. 1. Magnetization curves for sample B3 with the applied field at $\pm 45^\circ$ relative to the c direction at 40, 50, 60, and 70 K.

TABLE I. Information on the samples under investigation. Dimensions, ion type, dose, angle of irradiation, and the effective pinning at $T=20$ K.

	Dimensions (mm ³)	Ion	Dose (ions/cm ²)	ϕ (deg)	U_{eff} (e / $T=20$ K)
B0	1.25×0.75×0.05	—	—	—	0.0065
B1	1.5 × 1×0.044	Pb	10 ¹⁰	0	0.049
B2	1.6 × 0.95×0.046	Pb	10 ¹¹	0	0.045
B3	1.6×0.9×0.046	Pb	10 ¹¹	45	0.056
B4	1×0.95×0.042	Pb	2.5×10 ¹¹	0	0.055
B5	1.3×0.66×0.0835	Xe	10 ¹¹	45	—

vortices in BSCCO. In this article we pursue these previous works and describe extensive magnetic measurements on BSCCO crystals irradiated with Pb or with Xe ions. We report on (i) the dependence of the critical current and (ii) the dependence of the irreversibility line on the dose and on the type of irradiation; (iii) the scaling properties of the pinning force density; (iv) the angular dependence of J_c and the irreversibility line; and (v) a preliminary study of relaxation of the remanent magnetization.

II. EXPERIMENT

The measurements were performed on BSCCO crystals irradiated with 5.8-GeV Pb ions or 6-GeV Xe ions along the c direction or at 45° with respect to it. Irradiation was carried out at the Grand Accélérateur National d'Ions Lourds (GANIL, Caen, France). The Pb ions produce *continuous* columnar defects along their paths. The Xe ions did not produce columnar defects, but only clouds of clusters dispersed around the ion trajectory. In the case where the diameter of these clouds is smaller than the distance between two neighboring ion trajectories, the Xe ions tracks act as correlated disordered defects.²¹ All our measurements were performed on an Oxford Instruments vibrating sample magnetometer (VSM). The sample preparation is described in Ref. 22. The transition temperature $T_c=85$ K of the unirradiated samples is reduced by less than 0.5 K after irradiation. Table I lists the samples under investigation, their dimensions, and the details of ion irradiation.

III. RESULTS AND DISCUSSION

A. Critical currents

The critical currents were estimated from the width of the magnetization curves, using the Bean model²³ for rectangular samples.²⁴ The main response of the sample magnetization is in the Cu-O planes, i.e., the response due to H_{\perp} (the component of the field perpendicular to the planes). Therefore, in comparing magnetization curves with the applied field at different angles relative to the c direction, we use H_{\perp} values. Figure 2(a) shows the critical current J_c as a function of temperature, at a constant field $H_{\perp}=0.75$ T, applied along the defect, for the BSCCO crystal under investigation. Note that H_{\perp} is larger than the self-field²⁵ $H_s \approx J_c d$ (d is the shortest dimension of the sample), in order to avoid uncertainties in determination of J_c . The figure shows that (I) the critical current increases with the dose and (II) the Pb irra-

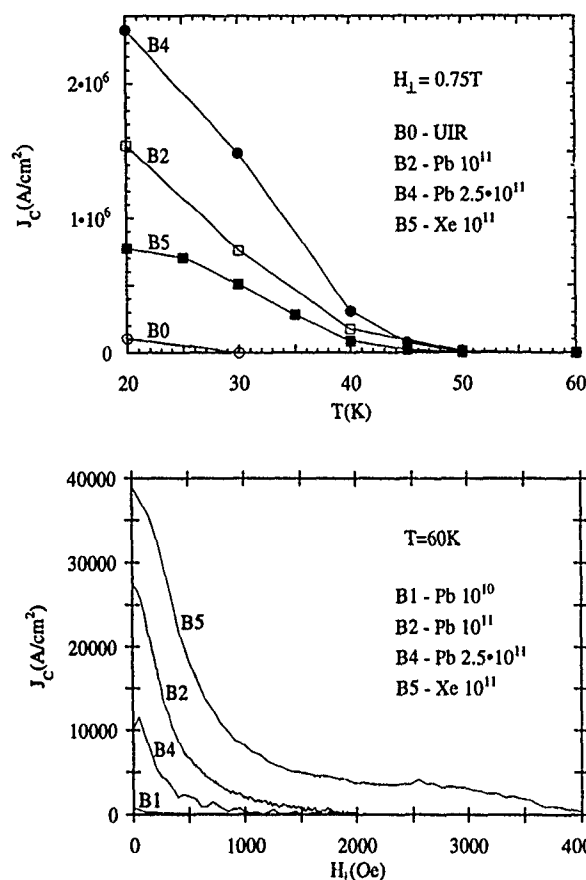


FIG. 2. (a) The critical current density as a function of temperature at $H_{\perp}=0.75$ T for various samples. (b) The critical current density at $T=60$ K as a function of magnetic field for the irradiated samples.

diation is more efficient in enhancing J_c than the Xe irradiation. As we show below, these two observations hold only below 50 K.

Figure 2(b) shows the critical current as a function of field, for the isotherm $T=60$ K, for irradiated BSCCO crystals. We note that H_s at 60 K in these samples is not larger than 300 Oe. At this temperature, J_c of sample B4 (Pb-irradiated, 2.5×10^{11} ions/cm²) is smaller than that of B2 (Pb, 10^{11}). Also, it is apparent that the critical current of sample B5 (Xe-irradiated, 10^{11}) is higher than the critical current of all other irradiated samples. Thus, at approximately 50 K there are two crossover phenomena: first, in the efficiency of the columnar defect, the maximum dose becomes relatively less efficient at high temperatures; second, in the efficiency of the defects created by the Xe irradiation: at low temperatures, columns produced by Pb ions are more efficient in flux trapping than defects produced by Xe ions, whereas at high temperatures the reverse situation is observed. Insight into these phenomena is obtained from the analysis of the irreversibility line and the pinning force density, which follows below.

B. Irreversibility line (IRL)

The irreversibility field was determined from the hysteresis loops with a criterion of $J_c < 100$ A/cm². Figure 3 shows the irreversibility field as a function of temperature for different doses and types of irradiation. Note that in this figure

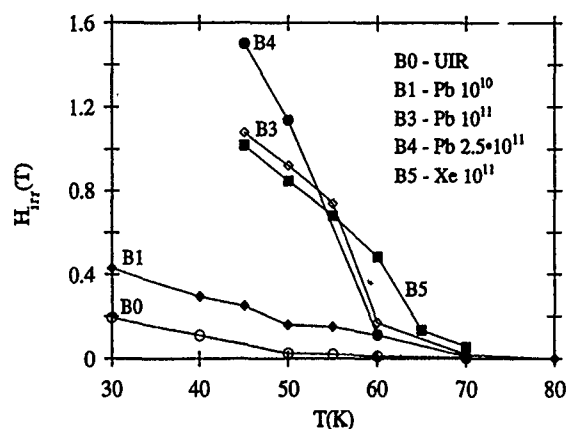


FIG. 3. The irreversible field H_{ir} as a function of temperature for various samples.

we present the IRL of sample B3; the IRL of sample B2 (the same dose but irradiated in the c direction) is almost the same. The irradiation shifts the irreversibility field upwards in a significant way. At low temperatures, the shift is more pronounced for higher doses of irradiation. However, at temperatures above 55 K this is not the case. Between 50 and 60 K there is a crossing of the irreversibility lines of the samples irradiated by Pb ions with doses of 10^{11} and 2.5×10^{11} ions/cm² (samples B3 and B4, respectively). This crossover indicates that there is an optimum irradiation dose of Pb ions at high temperatures above which the critical current becomes smaller.

The crossover can probably be related to a transition between two mechanisms of nonlogarithmic creep processes. It was theoretically shown²⁶ that a creep process in the presence of columnar defects is governed by a nucleation motion of vortex lines. Such a motion can be realized by two different mechanisms. At a low density of columnar defects, when the transverse localization length of a vortex line L_{\perp} is smaller than d_c , the averaged distance between the columnar defects, the creep process is dominated by the motion of vortex lines to the bulk after being liberated from the columnar defect. At high density of columnar defects, when L_{\perp} is comparable with d_c , the creep process is dominated by a motion of flux lines via a sequence of hops from one columnar defect to an adjacent one. The increase of columnar defects density results therefore in a suppression of the effective barrier for flux creep and in the enhancement of the relaxation rate. The crossover temperature between the two processes depends on the density of defects and occurs at lower temperatures for the larger dose. This crossover in the flux-creep process, which was identified experimentally²⁷ in BSCCO crystals with columnar defects, is probably responsible for the crossovers of J_c and of the IRLs between samples B3 and B4.

Another interesting feature apparent from Fig. 3 is the crossing of the IRLs of the Xe-irradiated sample (B5) and those of the Pb-irradiated samples (B3 and B4) at 55 K. At low temperatures the IRL of the Xe-irradiated sample (B5) follows the IRL of the sample irradiated by Pb ions with the same dose (10^{11} , B3). At 55 K, however, the IRLs of the

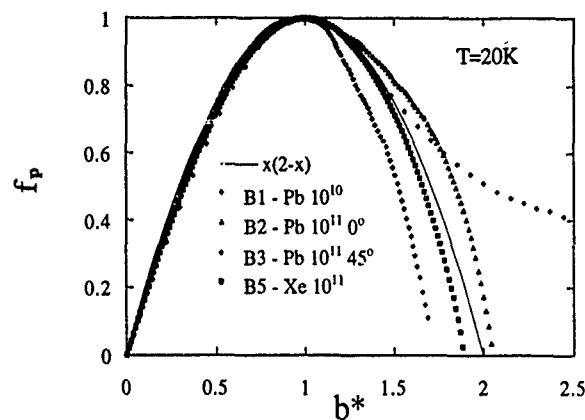
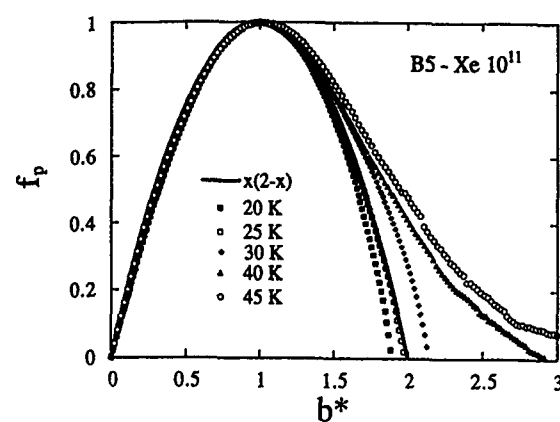


FIG. 4. (a) The rescaled pinning force density $f_p = F_p/F_{p,max}$ as a function of the reduced field $b^* = H/H_{max}$, for sample B5 at various temperatures. The solid line denotes the function $b^*(2-b^*)$. (b) The rescaled pinning force density $f_p = F_p/F_{p,max}$ as a function of the reduced field $b^* = H/H_{max}$, for various irradiated samples at $T = 20$ K. The solid line denotes the function $b^*(2-b^*)$.

Pb-irradiated samples decrease rapidly whereas the IRLs of the Xe-irradiated sample decrease quite slowly with T . This indicates that the efficiency of columnar defects produced by the Pb ions decreases strongly at high temperatures. Also, the irreversibility lines of all the samples irradiated by Pb ions tend to converge at the high-temperature regime of the irreversibility line. This convergence, first observed by Hardy *et al.*,²⁸ provides another indication of the rapid decrease, at high temperatures, of the efficiency of the defects produced by the Pb ions. The surprising observation that the IRL of the Xe sample (B5) decreases more moderately than that of the Pb samples suggests that a new pinning mechanism becomes dominant at high temperatures in the Xe-irradiated sample.

The difference between the irradiation by the Pb and Xe ions can provide an explanation for the above observations. Since the Xe ions produce only clouds of dispersed anisotropic defects, while the Pb ions produce continuous defects, we expect that at low temperatures the Pb irradiation provides more efficient defects. At high temperature, however, vortices start to wander inside and between the clouds. Above some threshold temperature, when the mean amplitude of thermal fluctuations becomes larger than the spacing of clusters within clouds, the defects created by the Xe irradiation become equivalent to columnar defects with the diameter of the clouds.²¹ The efficiency of these columnar de-

fects at high temperatures is higher than those of the columnar defects created by the Pb ions, since the diameter of the clouds seems to be larger. We suggest, therefore, that the origin of the new pinning mechanism in the Xe-irradiated sample is the columnarlike defects created at high temperatures.

C. Density of the pinning force

Figure 4(a) shows F_p as a function of H (we assume that $H \approx B$) for sample B5, irradiated by Xe ions. The data are presented in the normalized coordinates $f_p = F_p/F_{p,max}$ vs $b^* = H/H_{max}$, where $F_{p,max}$ is the maximal value of F_p , and H_{max} is the value of H at $F_{p,max}$. The figure demonstrates that below H_{max} the data for all isotherms below 45 K can be reduced to a single curve. The scaling of the pinning force density for the irradiated samples at temperatures below 45 K indicates that a single dominant pinning mechanism is involved.^{29,30}

The general shape of the curves for $T < 45$ K closely resembles the parabola $f_p(b^*) = b^*(2 - b^*)$. A similar function (though with H_{c2} as the scaling field) has been analytically derived and used for samples with $\Delta\kappa$ pinning of volume defects.³⁰ Different functional forms of $f_p(b^*)$ were recently identified in unirradiated and proton-irradiated $\text{YBa}_2\text{Cu}_3\text{O}_7$ (YBCO) crystals.^{31,32} The difference in the scaling functions is clearly consistent with the difference in the pinning size (point or cloud) taking place in these systems.

The similarity in the functional form of the curves is lost for large fields at $T > 40$ K: the pinning force density does not drop sharply to zero, as is the case for $T < 40$ K, but rather decreases slowly so that a "tail" originates at high fields [see Fig. 4(a)]. For even higher temperatures the scaling in the range $H < H_{max}$ also breaks down.

A similar scaling was also found in the other irradiated crystals (B1, B2, and B3), at low temperatures. This is demonstrated in Fig. 4(b), which shows f_p vs b^* for the samples B1, B2, and B3 together with B5, at $T = 20$ K. The scaling in the range $H < H_{max}$ is clearly evident. The general shape of the curves, except for sample B1, follows the function $f_p(b^*) = b^*(2 - b^*)$. At higher temperatures, however, the $f_p(b^*)$ curve develops a tail in the large-field regime, and as the temperature is further increased the scaling in the low-field regime does not hold any more. It is interesting to note that both the unirradiated sample and the sample with the largest dose of irradiation (B4) do not exhibit the scaling discussed above.

The absence of the scaling of the pinning force at temperatures higher than 45 K can possibly be related to the appearance of a tail in the pinning force density curve at high temperatures ($T > 45$ K). A tail in the pinning force density was recently observed in irradiated YBCO crystals,³² and was attributed, using flux creep models, to an increase in the thermal activation. We suggest an alternative explanation, namely that a different pinning mechanism starts to be important for $T > 45$ K. This possibility is consistent with the increase of the critical current of the sample irradiated by Xe ions in comparison to the rapid decrease of the J_c of the samples irradiated by Pb ions, at high temperatures [see Fig. 2(b)].

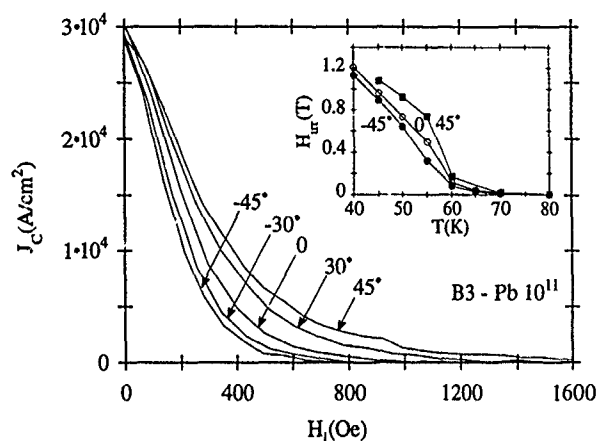


FIG. 5. The critical current density of sample B3, at $T = 60$ K, as a function of H_L for different field directions. Inset: The irreversible field H_{irr} as a function of temperature for sample B3 for different field directions.

We note that there are several difficulties in our attempt to obtain information from the functional form of $f(b^*)$. First, the scaling holds only up to H_{max} , and deviations from scaling are observed at high fields. Second, the functional form to which we compare $f(b^*)$ was derived for low-temperature superconductors, for which the scaling field is the upper critical field H_{c2} . Further study is therefore needed in order to establish the relevance of the functional form of $f(b^*)$ to the pinning mechanism in HTS.

D. Angular dependence

The angular dependence of J_c is described in Fig. 5, which shows the critical currents of sample B3 for different angles between the field and the columnar defects. The maximum critical current is obtained for the external field in the direction of the defects (45°), thus demonstrating the unidirectional nature of J_c .

Another demonstration of the unidirectional features is provided in the inset of Fig. 5, which shows the dependence of the irreversibility field on the direction of the field relative to the defect. It is clear that the irreversibility field decreases as the angle between the field and the defect increases. This is a clear indication of the presence of coupling between the layers, which yields the possibility of tilting vortices by an external field; without this coupling the component of the field parallel to the planes penetrates freely and no tilting is possible.^{14,15} At low temperatures, it might be quite difficult to observe unidirectional pinning.¹⁵ However, a closer look reveals angular dependence, also in this temperature regime.

E. Relaxation

In this section we present preliminary results on relaxation measurements for Pb-irradiated samples. In these measurements the sample is cooled in the presence of a field of 1.6 T. The field is then turned off and the relaxation is measured. The results should be treated with caution due to the possible effect of self-fields in this procedure. However, the consistency of results of different shapes implies that the effect of self-fields is not dominant. Moreover, we wish to

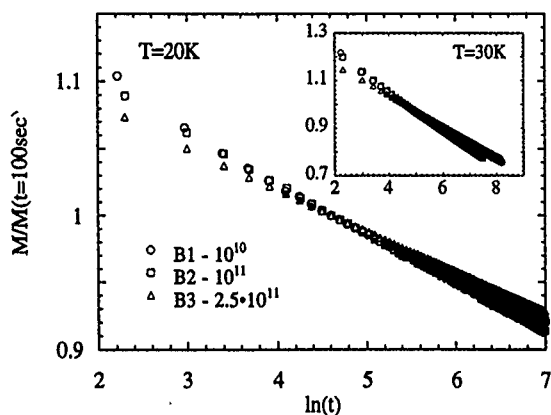


FIG. 6. The magnetic relaxation for the Pb-irradiated samples at $T=20$ K and 30 K (inset). Note: The magnetic moment was divided by its value at $t=100$ sec in order to compare data obtained from different samples.

compare our results to other reports²⁰ in which relaxation at zero field was used. At low temperatures, the relaxation of the irradiated samples in the experimental time window are logarithmic with time. We thus can extract the effective barrier by using $U=kT/(d \ln M/d \ln t)$ and neglect corrections of the interpolation formula. The effective barriers that are extracted from these relaxation rates show a strong decrease as temperature is increased. In Fig. 6 we present the logarithmic relaxation of the remanent magnetization in irradiated samples for 20 and 30 K (inset). It is apparent that at constant temperature the relaxation rates at the various samples are very similar (see an example in Table I), although there are apparent differences in the magnitude of the magnetization. A similar result of converging effective barriers for samples with different irradiation was obtained by Gerhauser *et al.* at $T=10$ K.²⁰ The convergence was interpreted as an indication that the intervortex interactions are not important and thus the effective barrier should reflect only the effective barrier for the depinning of a single vortex from the defect.

In our previous works¹³⁻¹⁵ we reported on apparent unidirectional pinning deduced from the different hysteresis loops for different field directions with respect to the columnar defects. This unidirectional pinning was more apparent above 50 K. At lower temperatures the hysteresis loops look almost identical (see Fig. 1), i.e., the relative anisotropy in $M(H)$ decreases as temperature is decreased. The reduction in the pinning barrier as temperature increases can explain the difference in the relative anisotropy between high and low temperatures. At low temperatures, when the applied field is not in the direction of the defect, the pinning potential is high enough to overcome the Gibbs free energy, and thus the hysteresis loops overlap for various field directions.^{12,15} When the temperature increases the Gibbs energy plays the major role, and unidirectional pinning is observed at all fields.

IV. SUMMARY AND CONCLUSIONS

In this article we have shown that columnar defects created by heavy-ion irradiation can improve the irreversible properties of HTS BSCCO crystals i.e., their J_c , U_{eff} , and

IRL. There is an optimum dose of irradiation (approximately 10^{11} ions/cm²) above which these properties suffer a reduction. Defects produced by Xe ions, although they consist of clouds of clusters, can be treated in the high-temperature range as columnar defects with a diameter defined by the cloud's diameter. We conclude that at the range of temperatures where scaling of the pinning force density holds, a single pinning mechanism (probably $\Delta\kappa$ pinning of volume defects) affects the magnetic behavior. The angular dependence of J_c and IRL leads us to conclude that the vortices in the BSCCO system are linelike vortices. The temperature dependence of U_{eff} can explain the temperature dependence of the relative anisotropy of pinning efficiency of columnar defects.

ACKNOWLEDGMENTS

Extensive collaboration and discussions with M. Konczykowski are acknowledged. The work in Israel is supported by the Ministry of Science and Technology.

- ¹ Y. Yeshurun, A. P. Malozemoff, T. K. Worthington, R. M. Yandroski, L. Krusin-Elbaum, F. H. Holtzberg, T. R. Dinger, and G. V. Chandrasekhar, *Cryogenics* **29**, 258 (1989).
- ² J. R. Clem, *Phys. Rev. B* **43**, 7837 (1991).
- ³ J. C. Martinez, S. H. Brongersma, A. Koshelev, B. Ivlev, P. H. Kes, R. P. Griessen, D. G. de Groot, Z. Tarnavski, and A. A. Menovsky, *Phys. Rev. Lett.* **69**, 2276 (1992).
- ⁴ T. Fukami, K. Miyoshi, T. Nishizaki, Y. Horie, F. Ichikawa, and T. Aomine, *Physica C* **202**, 167 (1992).
- ⁵ Y. Iye, S. Nakamura, and T. Tamegai, *Physica C* **159**, 433 (1989).
- ⁶ Y. Iye, I. Oguru, T. Tamegai, W. R. Datars, N. Motohira, and K. Kitazawa, *Physica C* **199**, 154 (1992).
- ⁷ P. H. Kes, J. Aarts, V. M. Vinokur, and C. J. van der Beek, *Phys. Rev. Lett.* **64**, 1063 (1990).
- ⁸ H. Raffy, S. Labdi, O. Laborde, and P. Monceau, *Phys. Rev. Lett.* **66**, 2515 (1991).
- ⁹ S. Martin, A. T. Fiory, R. M. Fleming, G. P. Espinosa, and A. S. Cooper, *Phys. Rev. Lett.* **62**, 677 (1989); *Appl. Phys. Lett.* **54**, 72 (1989).
- ¹⁰ R. Kleiner, F. Steinmeyer, G. Kunkel, and P. Mueller, *Phys. Rev. Lett.* **68**, 2394 (1992).
- ¹¹ M. J. Naughton, R. C. Yu, P. K. Davies, J. E. Fischer, R. V. Chamberlin, Z. Wang, T. W. Jing, N. P. Ong, and P. M. Chaikin, *Phys. Rev. B* **38**, 9280 (1988).
- ¹² J. R. Thompson, Y. R. Sun, H. R. Kerchner, D. K. Christen, B. C. Sales, B. C. Chakoumakos, A. D. Marwick, L. Civale, and J. O. Thompson, *Appl. Phys. Lett.* **60**, 2306 (1992).
- ¹³ L. Klein, E. R. Yacoby, Y. Yeshurun, M. Konczykowski, and K. Kishio, *Physica C* **209**, 251 (1993).
- ¹⁴ L. Klein, E. R. Yacoby, Y. Yeshurun, M. Konczykowski, and K. Kishio, *Physica A* **200**, 413 (1993).
- ¹⁵ L. Klein, E. R. Yacoby, Y. Yeshurun, M. Konczykowski, and K. Kishio, *Phys. Rev. B* **48**, 3523 (1993).
- ¹⁶ V. Hardy, D. Groult, J. Provost, M. Hervieu, B. Raveau, and S. Boffard, *Physica C* **178**, 255 (1991).
- ¹⁷ L. Civale, A. D. Marwick, T. K. Worthington, M. A. Kirk, J. R. Thompson, L. Krusin-Elbaum, Y. Sun, J. R. Clem, and F. Holtzberg, *Phys. Rev. Lett.* **67**, 648 (1991).
- ¹⁸ M. Konczykowski, F. Rullier-Albenque, E. R. Yacoby, A. Shaulov, Y. Yeshurun, and P. Lejay, *Phys. Rev. B* **44**, 7167 (1991).
- ¹⁹ D. Prost, L. Fruchter, I. A. Campbell, N. Motohira, and M. Konczykowski, *Phys. Rev. B* **47**, 3457 (1993).
- ²⁰ W. Gerhauser, G. Ries, H. W. Newmueller, W. Schmidt, O. Eibl, G. Saemann-Ischenko, and S. Klaumunzer, *Phys. Rev. Lett.* **68**, 879 (1992).
- ²¹ M. Konczykowski (private communication).
- ²² N. Motohira, K. Kuwahara, T. Hasegawa, K. Kishio, and K. Kitazawa, *J. Ceram. Soc. Jpn. Int. Ed.* **97**, 994 (1989).
- ²³ C. P. Bean, *Phys. Rev. Lett.* **8**, 250 (1962); *Rev. Mod. Phys.* **36**, 31 (1964).
- ²⁴ A. M. Campbell and J. E. Evetts, *Adv. Phys.* **21**, 199 (1972).
- ²⁵ M. Daumling and D. C. Larbalestier, *Phys. Rev. B* **40**, 9350 (1989).

- ²⁶D. R. Nelson and V. M. Vinokur, Phys. Rev. Lett. **68**, 2398 (1992).
- ²⁷M. Konczykowski, N. Chikumoto, V. M. Vinokur, and M. Feigel'man (unpublished).
- ²⁸V. Hardy, Ch. Simon, J. Provost, and D. Groult, Physica C **205**, 371 (1993).
- ²⁹A. M. Campbell and J. E. Evetts, *Critical Currents in Superconductors* (Taylor & Francis, London, 1972), Chaps. 7 and 8; H. Ullmaier, *Irreversible Properties of Type II Superconductors* (Springer, Berlin, 1975), Chaps. 3-5.
- ³⁰D. Dew-Hughes, Philos. Mag. **30**, 293 (1974).
- ³¹L. Klein, E. R. Yacoby, Y. Yeshurun, A. Erb, G. Müller-Vogt, U. Breit, and H. Wühl, Phys. Rev. B (to be published).
- ³²L. Civale, M. W. McElfresh, A. D. Marwick, F. Holtzberg, C. Feild, J. R. Thompson, and D. K. Christen, Phys. Rev. B **43**, 13732 (1991).

Unusual transport and magnetic properties of Tb-doped $\text{YBa}_2\text{Cu}_3\text{O}_7$ single crystals and epitaxial thin films

G. Cao, J. W. O'Reilly, and J. E. Crow

National High Magnetic Field Laboratory, Florida State University, Tallahassee, Florida 32306-4005

R. J. Kennedy

Department of Physics, 1800-3 Dirac Drive, Florida A&M University, Tallahassee, Florida 32310

D. H. Nichols

National High Magnetic Field Laboratory, Florida State University, Tallahassee, Florida 32306-4005

The electrical resistivity $\rho(T)$ and magnetic susceptibility $\chi(T, H)$ ($1.8 \leq T \leq 350$ K and $0 \leq H \leq 5.5$ T) have been measured on single crystals and epitaxial thin films of $\text{Y}_{1-x}\text{Tb}_x\text{Ba}_2\text{Cu}_3\text{O}_7$. The T_c is 92 K and irrespective of Tb doping up to $x=0.50$. For $T > T_c$, $\rho(T)$ has a linear dependence, i.e., $\rho(T) \approx A + BT$, with the reduced resistivity $\rho(T)/\rho(250 \text{ K})$ for $x=0.10, 0.25$, and 0.50 , being independent of Tb doping. The results of magnetic susceptibility along with the computation of effective moment of Tb in the presence of crystal electric fields (CEF) tend to suggest that the Tb is mixed valent. The insensitivity of T_c to the Tb doping and the possibility that Tb may be mixed valent are in sharp contrast to the case of Pr and Ce doping which have been shown to be very deleterious to superconductivity. The magnetic susceptibility $\chi(T)$ is extremely anisotropic, and this anisotropy cannot be explained by simple models with CEF effects.

Among the striking features of the high- T_c superconductor $\text{YBa}_2\text{Cu}_3\text{O}_7$ (YBCO) are the insensitivity of the superconducting properties to rare-earth substitutions for Y since many of the rare-earth elements possess magnetic moments, normally leading to conditions deleterious to superconductivity. The exceptions to this behavior are Ce, Pr, and Tb, where Pr forms a nonsuperconducting isostructural compound and Ce and Tb do not form the YBCO structure at all. The valence instability of Ce and Tb in many metallic compounds and oxides is a common occurrence, e.g., CeO_2 and Tb_4O_7 . The fact that $\text{CeBa}_2\text{Cu}_3\text{O}_{7-\delta}$ and $\text{TbBa}_2\text{Cu}_3\text{O}_{7-\delta}$ do not form has been attributed to Ce and Tb entering the lattice as a tetravalent or mixed-valent ion and thus driving the system unstable. However, Pr, of which Pr_6O_{11} is the stable oxide and strongly suggestive of unstable valence behavior, does form the $\text{PrBa}_2\text{Cu}_3\text{O}_{7-\delta}$ phase. $\text{PrBa}_2\text{Cu}_3\text{O}_{7-\delta}$ although being crystallographically identical to all the other rare-earth-based superconductors of the series, is an insulator, and substitution of Pr for Y in $\text{Y}_{1-x}\text{Pr}_x\text{Ba}_2\text{Cu}_3\text{O}_{7-\delta}$ suppresses T_c with superconductivity disappearing at $x \approx 0.55$.

The mechanism(s) responsible for the depression of T_c with x has been the subject of considerable interest and controversy. Numerous investigations have been carried out with the objective of developing an understanding of Pr in the $\text{RBa}_2\text{Cu}_3\text{O}_{7-\delta}$ compounds. Most of the discussion of the T_c depression centers on the Pr valence and/or possible magnetic pair breaking due to a $4f$ -electron and conduction-hole interaction which is absent in the other rare-earth-doped $\text{YBa}_2\text{Cu}_3\text{O}_{7-\delta}$ systems. Results of these investigations tend to conclude that Pr is slightly mixed valent and hybridizes with the charge carriers within the adjacent CuO_2 planes, and thus depresses T_c by a combination of dynamic hole filling and pair breaking.¹⁻⁴ Evidence from electron-energy-loss spectroscopy⁵ and x-ray absorption spectroscopy indicates that the valence of Pr is close to $3+$, which is consistent with the thermodynamic studies if strong hybridization is also included.

Based on our recent study of electrical resistivities of thin films of $\text{Y}_{1-x}\text{Pr}_x\text{Ba}_2\text{Cu}_3\text{O}_{7-\delta}$ and $\text{Nd}_{1-x}\text{Ce}_x\text{Ba}_2\text{Cu}_3\text{O}_{7-\delta}$,¹⁴ $\rho(T, x)$ behavior of the Ce-doped samples closely follows the behavior seen for the Pr-doped compounds, strongly suggesting that the depression of T_c is due to a common mechanism and that hole filling or $4f$ -electron hybridization with CuO planes rather than magnetic pair breaking may be the dominant mechanism (see Fig. 4).

As mentioned above, Tb, like Ce and Pr, is also known to show mixed-valent behavior in many oxide systems and other compounds with two possible magnetic ground states ($J=6$ for Tb^{3+} and $J=\frac{7}{2}$ for Tb^{4+}). As a natural extension of our study of hole filling and pair breaking in these systems, we have focused our attention on Tb-doped $\text{YBa}_2\text{Cu}_3\text{O}_{7-\delta}$ single crystals and thin films. Our earlier study of this system has already revealed some interesting and unexpected phenomena. In this paper, we report our recent results of transport and magnetic measurements with an emphasis on the unusual behavior observed in this Tb-doped system.

The $\rho(T)$ for $\text{Y}_{1-x}\text{Tb}_x\text{Ba}_2\text{Cu}_3\text{O}_{7-\delta}$ films is shown in Fig. 1 for $x=0.1, 0.25$, and 0.50 . The substitution of the magnetic Tb for Y surprisingly does not shift T_c (92.5 K) even for x as high as 0.50 . However, $\rho(T, x)$ for all x displays a linear- T behavior, i.e., $\rho(T) \approx A + BT$ for $T > T_c$ although the magnitude of the normal-state resistivity increases systematically with Tb concentration x . The superconducting transition for all x is very sharp with the temperature width of the transition being less than 1.2 K. The results of the resistivity experiments presented here are somewhat unexpected in that magnetic susceptibility results for $\text{Y}_{1-x}\text{Tb}_x\text{Ba}_2\text{Cu}_3\text{O}_{7-\delta}$ single crystals to be presented next strongly suggest that Tb may be mixed valent. The resistivity behavior and the apparent insensitivity of T_c to the Tb doping is thus perplexing.

It is interesting to note that the T -linear slope of $\rho(T, x)$ for $T > T_c$ increases rapidly with increasing x , and a fit of $\rho(T, x)$ to $A + BT$ shows that the Tb doping primarily alters

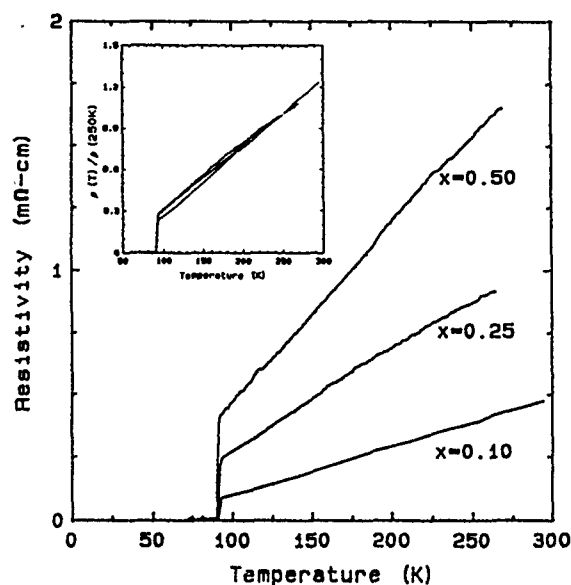


FIG. 1. The resistivity $\rho(T)$ vs temperature of thin films of $Y_{1-x}Tb_xBa_2Cu_3O_{7-\delta}$ for $x=0.10, 0.25$, and 0.50 . Inset: The reduced resistivity $\rho(T)/\rho(250\text{ K})$ vs temperature.

the slope and much more weakly impacts on the $T \rightarrow 0$ intercept. This can be seen in a plot of a reduced resistivity $\rho(T)/\rho(250\text{ K})$ versus temperature for $x=0.10, 0.25$, and 0.50 (see inset in Fig. 1) where an approximately universal curve is seen, reflecting a common reduced slope. This suggests that the scattering mechanism for carrier transport in the CuO_2 planes leading to the linear- T dependence is dependent on Tb doping, and this coupled with the independence of T_c on Tb doping is puzzling, considering many of the models proposed to explain the linear- T dependence of $\rho(T)$ are based on excitations which also mediate the pairing.

Shown in Fig. 2 is magnetic susceptibility $\chi(T)$ (defined as M/H) versus temperature for $2 \leq T \leq 100\text{ K}$ at $H_{||c}=20\text{ Oe}$ for a single crystal with $x=0.3$. As can be seen, the onset

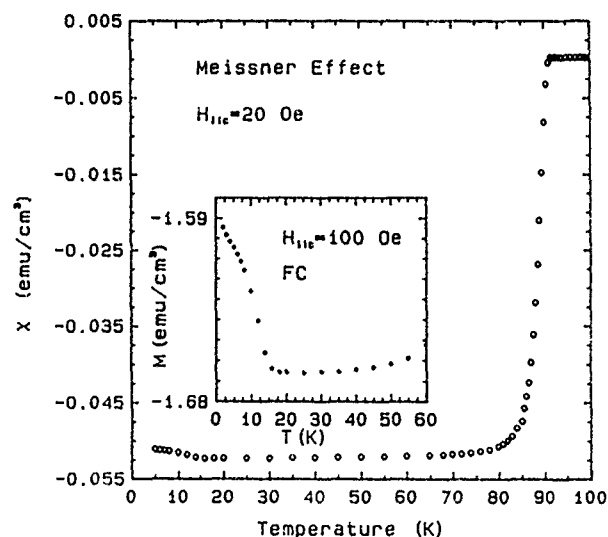


FIG. 2. The magnetic susceptibility $\chi(T)$ vs temperature for an oxygenated single crystal with $x \approx 0.30$ at $H_{||c}=20\text{ Oe}$. Inset: Magnetization M vs temperature at $H_{||c}=100\text{ Oe}$.

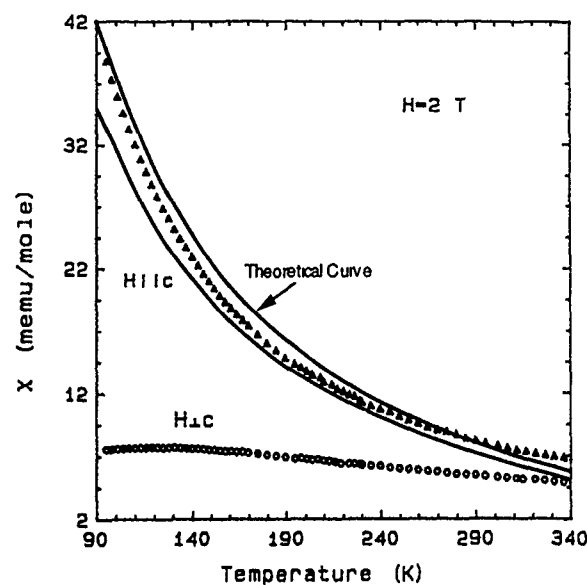


FIG. 3. The magnetic susceptibility $\chi(T)$ vs temperature for the oxygenated single crystal of $Y_{1-x}Tb_xBa_2Cu_3O_{7-\delta}$ with $x \approx 0.30$ for $H_{||c}$ (triangle) and $H_{\perp c}$ (circle) at $H=2.0\text{ T}$. The solid lines are the single-ion CEF theoretical predictions assuming a Tb^{4+} in the system for the two directions of the field.

of T_c is at 90.5 K with a width of T_c less than 2 K , implying a full or nearly full oxygen content in the sample. The value of T_c is in good agreement with the results of electrical resistivity measurements on epitaxial thin films presented above. The flux expulsion (Meissner effect) is 70% (of $1/4\pi$), which was obtained on cooling the sample through T_c in the magnetic field. In addition, it is interesting to note that there is a sharp up-turn that developed at $T \leq 15\text{ K}$ in $\chi(T)$ which becomes more evident in higher fields (see the inset in Fig. 1, where a plot of magnetization M versus temperature at $H_{||c}=100\text{ Oe}$ is shown). This behavior may suggest magnetic ordering associated with Tb. It is not uncommon for rare-earth ions to be ordered at low temperatures, for instance, $T_N \approx 1.5\text{ K}$ for $NdBa_2Cu_3O_7$ and $T_N \approx 2.5\text{ K}$ for $GdBa_2Cu_3O_7$. However, ordering at such a relatively high temperature is normally not expected for Tb as well as for the majority of rare earths. Yet, it is well known that Pr anomalously orders at $T_N \approx 17\text{ K}$ in $PrBa_2Cu_3O_7$. Other probes, such as low-temperature specific heat, can certainly help to clarify this issue.

Shown in Fig. 3 is $\chi_c(T)$ and $\chi_{ab}(T)$, where $\chi_c(T)$ is for $H_{||c}$ and $\chi_{ab}(T)$ for $H_{\perp c}$, for the single crystal with $x \approx 0.30$ and $T_c=90.5\text{ K}$. As can be seen, $\chi(T)$ for this sample is extremely anisotropic with $\chi_{ab}(T)$ nearly T independent and $\chi_c(T)$ displaying a strong Curie-Weiss-like response. $\chi_c(T)$ can be fitted to a modified Curie-Weiss law, i.e., $\chi(T) = \chi_0 + C/(T - T^*)$, with $\chi_0 = 3.7 \times 10^{-3}\text{ emu/mol}$, $\mu_{eff} = 8.10\mu_B$, and $T_c^* \approx 60\text{ K}$ for $H_{||c}$. The value of χ_0 obtained for $H_{||c}$ is unusually large in contrast to those reported for $YBa_2Cu_3O_{7-\delta}$.⁶ The μ_{eff} is close to a value expected for Tb^{4+} . This value is also consistent with that obtained for the fully oxygenated polycrystalline sample which gives $8.25\mu_B$. The measured value of μ_{eff} is closer to the Hund's-rule value of $7.90\mu_B$ for Tb^{4+} than $9.72\mu_B$ for Tb^{3+} , suggesting a nearly tetravalent Tb in this compound.

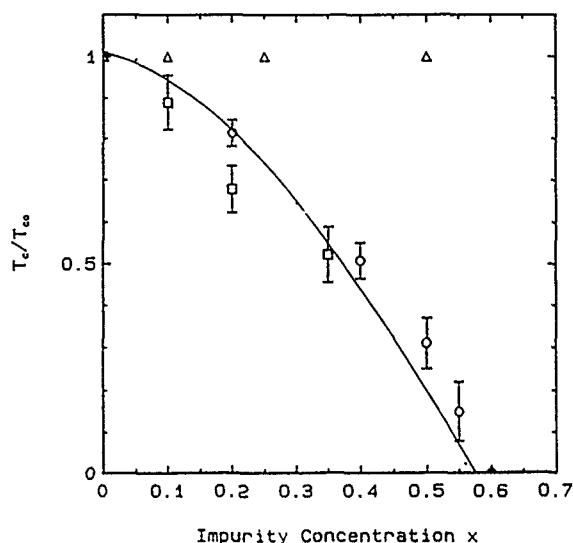


FIG. 4. The superconducting transition temperature T_c with dopant concentration x for $Y_{1-x}Tb_xBa_2Cu_3O_{7-\delta}$ (triangle), $Y_{1-x}Pr_xBa_2Cu_3O_{7-\delta}$ (circles), and $Nd_{1-x}Ce_xBa_2Cu_3O_{7-\delta}$ (squares) (see Ref. 6). The vertical bars indicate the transition width. The solid line is the smoothed variation of T_c vs x for polycrystalline $Y_{1-x}Pr_xBa_2Cu_3O_{7-\delta}$.

An analysis of $\chi(T)$ for the same temperature range used to determine the measured μ_{eff} and using crystal electric field (CEF) parameters extrapolated from measured CEF excitation for $DyBa_2Cu_3O_{7-\delta}$ and $HoBa_2Cu_3O_{7-\delta}$ gives $\mu_{eff}=9.1\mu_B$ for the effective paramagnetic moment for Tb^{3+} , including CEF effects. Thus, at this time CEF effects seem unable to account for the discrepancy between the measured paramagnetic moment and that expected for a Tb^{3+} ion.

If Tb is tetravalent, or at least mixed valent as suggested by $\chi(T)$, the effects observed in this Tb-doped system are quite unusual and in strong contrast to the case of the Pr- and Ce-doped compounds. For the Pr- and Ce-doped $YBa_2Cu_3O_{7-\delta}$ the 4f electrons are extremely deleterious to the superconductivity state (see Fig. 4). The insensitivity of T_c for $Y_{1-x}Tb_xBa_2Cu_3O_{7-\delta}$ would seem to suggest that Tb enters the $YBa_2Cu_3O_{7-\delta}$ as a stable 3+ valent ion with negligible exchange coupling between the 4f electrons and charge carriers in the CuO_2 planes. If Tb is trivalent, then the nonformation of an orthorhombic 1:2:3 Tb structure similar to that formed with Y and most of the other rare earths is puzzling. Also, the analysis of $\chi(T)$ data both for the oxygenated polycrystalline and the single-crystal samples leads to a effective paramagnetic moment suggestive of mixed-valent behavior. If we accept the premise that Tb is mixed valent in this system, then why is T_c insensitive to Tb doping? At the present stage we are not able to give a conclusive explanation as to why Tb does not depress T_c , but issues related to how the 4f electrons hybridize with other states may provide an answer to this dilemma. Intuitively, the extraordinarily small spatial extent of the 4f shell of Tb (compared to those of Pr and Ce) may be the cause, resulting in a hybridization significantly different from that in the other systems, and thus unexpected phenomena.

Indeed, this point becomes more interesting by considering CEF models of Tb^{4+} and Tb^{3+} (see Fig. 3). As can be seen, the theoretical analysis of $\chi(T)$ for the Tb^{4+} -doped system (solid lines in Fig. 3) using CEF parameters extrapolated from measured CEF excitation for $DyBa_2Cu_3O_{7-\delta}$ and $HoBa_2Cu_3O_{7-\delta}$ fails to predict a behavior similar to that observed in the Tb-doped system, and the same analysis of $\chi(T)$ assuming a trivalent Tb in the system (not shown) is also inconsistent with the experimental observation. CEF effects alone, evidently, cannot account for the anomalously large anisotropy in this system, strongly suggesting that additional effects possibly associated with the details of the 4f-electron hybridization absent in other high- T_c systems and Pr-doped YBCO are required to characterize the actual behavior in the Tb-doped system. It has been thought that in cuprate superconductors the anisotropy of $\chi(T)$ is primarily caused by the anisotropy in the Van Vleck terms, which are a reflection of the anisotropy induced due to the spatial orientation of the Cu d orbitals and driven by CEF effects.⁸ If Tb is tetravalent, the hybridization between the 4f electrons and charge carriers within the planes would impact heavily on the anisotropy of the Van Vleck contributions.

Relevantly, the other major phenomenon also shown in Fig. 3 is the non-Curie-Weiss behavior for $T > T_c$ when an external field H perpendicular to the c axis is applied. As can be seen, $\chi_{ab}(T)$ is unusually linear for $T > 150$ K, and thus significantly different from the Curie-Weiss law. For $T < 150$ K, in addition, a well-defined peak or a plateau is repeatedly seen at low fields. In contrast, for $H \parallel c$, $\chi(T)$ retains normal Curie-Weiss behavior. This behavior is apparently unusual in that in other high- T_c materials at $T > T_c$ the Curie-Weiss law is always well obeyed irrespective of the direction of the applied field H , and that the deviation from the Curie-Weiss law is generally an indication of a nonparamagnetic behavior. It cannot be ruled out that the unusual observation found in $\chi(T)$ may represent the presence of spin fluctuations or weak magnetic correlations in CuO planes due to the unusual 4f-electron hybridization with some states. Further efforts are required in order to reach a conclusive explanation as to why the magnetic properties of the Tb-doped superconductor behave so unusually.

¹ Azusa Matsuda, Kyoichi Kinoshita, Takao Ishii, Hiroyuki Shibata, Takao Watanabe, and Tomoaki Yamada, Phys. Rev. B **38**, 2910 (1988).

² J. J. Neumeier, T. Bjornholm, M. B. Maple, and I. K. Schuler, Phys. Rev. Lett. **63**, 2516 (1989).

³ D. P. Norton, D. H. Lowndes, B. C. Sales, J. D. Budai, B. C. Chakoumakos, and H. R. Kerchens, Phys. Rev. Lett. **66**, 1537 (1991).

⁴ D. E. MacLaughlin, A. P. Reyes, M. Takigawa, P. C. Hammel, R. H. Heffner, J. D. Thompson and J. E. Crow, Physica B **171**, 245 (1991); A. P. Reyes, D. E. MacLaughlin, M. Takigawa, P. C. Hammel, R. H. Heffner, J. D. Thompson, J. E. Crow, A. Kebede, T. Mihalisin, and J. Schwegler, Phys. Rev. B **42**, 2600 (1990).

⁵ L. Soderholm and G. L. Goodman, J. Solid State Chem. **81**, 121 (1989).

⁶ G. Cao, J. Bolivar, R. J. Kennedy, J. W. O'Reilly, J. E. Crow, and Pernambuco-Wise, Physica B **186-188**, 1004 (1993).

⁷ G. Cao, Ph.D. dissertation, Department of Physics, Temple University, 1992.

⁸ W. C. Lee, R. A. Klemm, and D. C. Johnston, Phys. Rev. Lett. **63**, 1012 (1989).

Magnetic order of Pr ions in related perovskite-type Pr123 compounds

M. Guillaume, P. Fischer, B. Roessli, A. Podlesnyak, J. Schefer, and A. Furrer
*Laboratorium für Neutronenstreuung, Eidgenössische Technische Hochschule Zürich und Paul Scherrer
 Institut, CH-5232 Villigen PSI, Switzerland*

The magnetic order of Pr ions in polycrystalline, tetragonal $\text{PrBa}_2\text{Cu}_3\text{O}_{6.2}$ has been studied by neutron-diffraction measurements. The basic ordering consists of an antiferromagnetic arrangement with the propagation vector $\mathbf{k}=[1/2, 1/2, 1/2]$, but the magnetic ordering is imperfect due to finite correlation length $\xi_c=(10\pm1)$ Å along the c axis. The Néel temperature is determined to be $T_N=(12\pm1)$ K, and the magnetic saturation moment of the Pr ions turns out to be $(1.9\pm0.2)\mu_B$. The distance Pr-O(2) compared in several related perovskite-type Pr compounds correlates with the Néel temperature in accordance with the superexchange interaction.

I. INTRODUCTION

Neutron-diffraction measurements¹ on the nonsuperconducting $\text{PrBa}_2\text{Cu}_3\text{O}_7$ yield an exceptionally high Néel temperature T_N of 17 K which exceeds the T_N value derived for the isostructural compound $\text{GdBa}_2\text{Cu}_3\text{O}_7$ (Ref. 2) by an order of magnitude, in disagreement with the de Gennes scaling law. The basic ordering of $\text{PrBa}_2\text{Cu}_3\text{O}_7$ (Ref. 1) consists of a simple antiferromagnetic arrangement with the propagation vector $\mathbf{k}=[1/2, 1/2, 1/2]$ and magnetic moment orientation $[0,0,1]$. The magnetic moment at saturation is $0.74\mu_B$ (Ref. 1), which is small compared to the free-ion value of $gJ=3.2\mu_B$.

For the polycrystalline compound $\text{PrBa}_2\text{Cu}_3\text{O}_6$ susceptibility measurements yield $T_N(\text{Pr})=10.8$ K (Ref. 2) for the ordering of the Pr sublattice, whereas recently for a single crystal of $\text{PrBa}_2\text{Cu}_3\text{O}_6$ Uma *et al.*³ observed $T_N\approx 12$ K. From single-crystal neutron-diffraction studies on $\text{PrBa}_2\text{Cu}_3\text{O}_{6.2}$,⁴ the copper ions exhibit long-range magnetic ordering according to $\mathbf{k}=[1/2, 1/2, 1/2]$ below $T_N(\text{Cu})\approx 370$ K. The Cu spins are oriented approximately perpendicular to the c axis, and the temperature dependence of the $1/2, 1/2, 3/2$ magnetic peak indicates normal saturation below ~ 100 K. So far there is no information concerning the magnetic moment and the easy axis of magnetization of the Pr ions.

From recently published neutron-diffraction results⁵ of $\text{RBa}_2\text{Cu}_3\text{O}_7$ (R = rare earth) we determined by extrapolation for the interionic distances Cu(2)-Cu(2), Cu(2)-O(3), Pr-O(2) an intermediate valence for Pr in the $\text{PrBa}_2\text{Cu}_3\text{O}_7$ sample of +3.4, whereas for $\text{PrBa}_2\text{Cu}_3\text{O}_6$ we obtained a valence of +3.0. We assume that this extrapolated valence is a structural effect associated with strong hybridization of Pr with the oxygen ligand atoms in the CuO_2 planes. On the other hand, neutron spectroscopy⁶ and electron-energy-loss spectroscopy (EELS)⁷ measurements show clear evidence for an effective valence of +3. How do these structural changes in the Pr compound from oxygen 7 to the oxygen 6 influence the magnetic ordering? With these motivations we report in the present paper on long-range antiferromagnetic order of Pr ions in $\text{PrBa}_2\text{Cu}_3\text{O}_6$ by neutron diffraction and present an interpretation of the results based on the present knowledge of the crystalline electric field in this system. We observed a correlation in several related perovskite-type Pr compounds between the distance Pr-O(2) and the Néel temperature. Magnetic neutron-diffraction studies on a tetragonal

$\text{PrSrBaCu}_3\text{O}_7$ sample yielded similar results as obtained for the $\text{PrBa}_2\text{Cu}_3\text{O}_7$ compound.

II. EXPERIMENTAL RESULTS

Sample preparation and experimental details have been described elsewhere.⁸ For $\text{PrBa}_2\text{Cu}_3\text{O}_{6.2}$ we performed neutron-diffraction measurements at $T=18$ K and $T=1.5$ K, i.e., well above and well below the Néel temperature. In the difference pattern of the two temperatures shown in Fig. 1 we clearly observe a magnetic peak at $2\theta=18.3^\circ$ which may be indexed in the magnetic unit cell as (1,1,1) with the

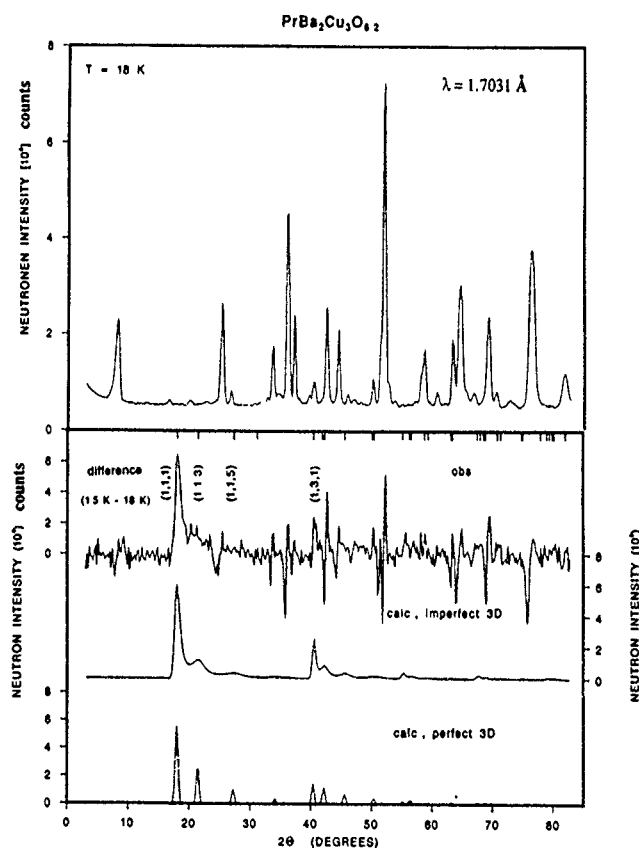


FIG. 1. Upper part: Neutron-diffraction pattern of $\text{PrBa}_2\text{Cu}_3\text{O}_{6.2}$ measured at 18 K. Lower part: Magnetic difference neutron-diffraction pattern (1.5 K-18 K) for $\text{PrBa}_2\text{Cu}_3\text{O}_{6.2}$ (indices h, k, l referring to the magnetic unit cell). The observed intensities are compared with a calculation for both imperfect and perfect 3D ordering.

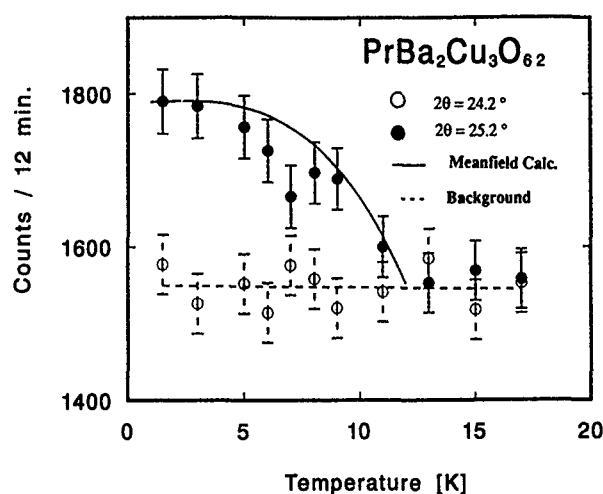


FIG. 2. Temperature dependence of the magnetic neutron intensity of the $(1/2, 1/2, 1/2)$ peak observed for $\text{PrBa}_2\text{Cu}_3\text{O}_{6.2}$ yielding, $T_N = (12 \pm 1)$ K. The line is the result of a mean-field crystal-field calculation.

propagation vector $\mathbf{k} = [1/2, 1/2, 1/2]$ as in nonsuperconducting $\text{PrBa}_2\text{Cu}_3\text{O}_7$. The neighboring negative and positive differences in the intensities which appear at the nuclear Bragg position are due to the change of the lattice parameters when changing the temperature from $T = 18$ K to $T = 1.5$ K. Since all three Miller indices are half-integer, the magnetic unit cell is doubled along all basic translations compared to the chemical unit cell, corresponding to antiferromagnetic coupling along all three crystallographic directions. Pronounced line broadening of the magnetic peaks was observed. The widths at half maximum of the magnetic lines depend on the reflection index (h, k, l) and the scattering angle 2θ . We emphasize that these linewidth anomalies only affect the magnetic peaks.

The measurement of the temperature dependence of the dominant $(1/2, 1/2, 1/2)$ peak (indices h, k, l referring to nuclear unit cell) yields a Néel temperature $T_N = (12 \pm 1)$ K, see Fig. 2.

III. DATA ANALYSIS

The unusual line shapes observed in the magnetic neutron diffraction pattern of $\text{PrBa}_2\text{Cu}_3\text{O}_{6.2}$ can be shown to result from finite magnetic correlations along the c axis, equivalent to the occurrence of magnetic intensity for a particular reflection (h, k, l) turns out to be a Lorentzian:

$$I_{hkl}(\mathbf{q}) \propto F(\mathbf{Q})^2 \frac{\Gamma}{\Pi(\Gamma^2 + |\tau_{hkl} - \mathbf{Q}|^2)} \delta(q_a) \delta(q_b),$$

$$\mathbf{q} = (q_a, q_b, q_c) = \tau_{hkl} - \mathbf{Q}. \quad (1)$$

$F(\mathbf{Q})$ = neutron magnetic form factor, \mathbf{Q} = scattering vector.

Figure 1 shows the result of the least-squares refinement of the magnetic difference intensities based on Eq. (1) and the magnetic form factor⁹ of Pr^{3+} which excellently reproduces the observed data. From our diffraction results we cannot decide whether the Pr^{3+} magnetic moments are directed parallel or perpendicular to the c axis (both fits yield ap-

proximately the same goodness of fit χ^2), and the (average) correlation length along the c axis is $\xi_c = 2/\Gamma = (10 \pm 1)$ Å.

The nuclear and magnetic intensities at 1.5 K yield the best fit for the magnetic moment of $\text{Pr}: \mu_{\text{Pr}} = (1.9 \pm 0.2) \mu_B$.

A similar calculation for perfect three-dimensional (3D) long-range magnetic order yields a saturated moment of about $0.8 \mu_B$; however, the calculated intensities clearly do not correspond to the measurement as can be seen from Fig. 1.

IV. DISCUSSION

By means of neutron-diffraction investigations we have established for $\text{PrBa}_2\text{Cu}_3\text{O}_{6.2}$ imperfect three-dimensional "long-range" magnetic ordering due to finite c correlation length of 10 Å, with a magnetic moment of saturation at $1.9 \mu_B$ of Pr^{3+} .

Compared to $\text{PrBa}_2\text{Cu}_3\text{O}_7$ the rather unusual and unexpected increase of the magnetic moment in $\text{PrBa}_2\text{Cu}_3\text{O}_{6.2}$ can be explained by the drastic change of the low-lying crystal-field levels when going from the O_7 to the O_6 compound. The corresponding crystal-field parameters have been worked out by Nekvasil *et al.*⁶ from neutron spectroscopic experiments. A mean-field calculation based on their crystal-field parameters yields saturated magnetic moments of $1.1 \mu_B$ and $2.1 \mu_B$ for the O_7 and O_6 compounds, respectively, which reasonably compare to the moment values determined by neutron diffraction. The crystal-field interaction for the tetragonal O_6 compound [with vanishing "orthorhombic" crystal-field parameters B_2^2 and B_4^2 , Ref. (6)] produces an extremely anisotropic single-ion susceptibility, yielding the c axis as the easy axis of magnetization. The calculated temperature dependence of the magnetic Bragg intensities (which are linearly related to the square of the ordered moment) is also in excellent agreement with the experimental findings, see Fig. 2.

Jostarndt *et al.*¹⁰ showed that the magnon peak position of $\text{PrBa}_2\text{Cu}_3\text{O}_6$ (splitting of Γ_5 doublet ground state due to the antiferromagnetic ordering of Pr ions) as a function of temperature decreases drastically to 0 at around $T = 12$ K. This extrapolation yields a Néel temperature of (12 ± 2) K which is in good agreement with our neutron-diffraction result with T_N of 12 K.

The exceptionally high Néel temperatures of the $\text{PrBa}_2\text{Cu}_3\text{O}_x$ compounds is still a matter of debate. It may be related to strong hybridization of the $4f$ electrons with the p orbitals of the ligand oxygen ions in the CuO_2 planes which enhances the superexchange interaction between the Pr ions. Hybridization is presumably also the reason for the unusually large line widths of the crystal-field transitions.^{10,11}

The surprising imperfect magnetic ordering in $\text{PrBa}_2\text{Cu}_3\text{O}_{6.2}$ is to some extent similar to the magnetic Dy ordering discovered recently in a single crystal of $\text{DyBa}_2\text{Cu}_3\text{O}_6$ which shows below ~ 1.5 K "short-range" magnetic order along the c axis and even at 70 mK a finite c -correlation length of about 13 Å together with 2D long-range antiferromagnetic ordering below 0.55 K.¹² The same behavior was recently observed (but not quantitatively analyzed) in $\text{PrBa}_2\text{Cu}_3\text{NbO}_8$,¹³ which shows a Néel temperature of 12.6 K similar to $\text{PrBa}_2\text{Cu}_3\text{O}_{6.2}$. The imperfect antiferro-

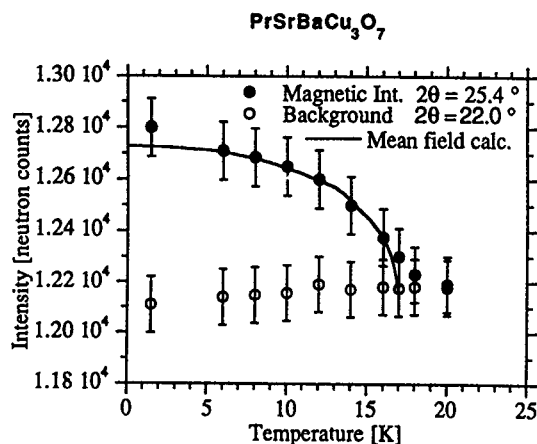


FIG. 3. Temperature dependence of the magnetic neutron intensity of the $(1/2, 1/2, 1/2)$ peak observed for $\text{PrSrBaCu}_3\text{O}_7$, yielding $T_N = (17 \pm 1)$ K.

magnetic ordering has a correlation length of about 7 Å along the c axis. Also polycrystalline $\text{HoBa}_2\text{Cu}_3\text{O}_7$ (Ref. 14) exhibits an imperfect three-dimensional magnetic ordering, existing below $T_N = 190$ mK due to a finite correlation length $\xi_c = 29$ Å along the c axis.

The observed anomalies of perovskite-type Pr compounds are not unique. Similar results were also observed for PrO_2 (Ref. 15) which shows a Néel temperature of 14 K. An even higher Néel temperature $T_N = 21$ K was reported for PrCu_2Si_2 .¹⁶ The Pr compounds (PrO_2 , PrCu_2Si_2 , $\text{PrBa}_2\text{Cu}_3\text{O}_x$) showed a large value of the linear electronic specific heat capacity coefficient^{16,17} which indicates a heavy-fermion-like behavior. Anomalous is furthermore the absence of the spin-Kondo effect in PrCu_2Si_2 in contrast to other RCu_2Si_2 (R =rare earth) compounds which clearly show the spin-Kondo effect.¹⁶

We have also started neutron-diffraction investigations on a $\text{PrSrBaCu}_3\text{O}_7$ compound which has a tetragonal symmetry. Despite the disorder produced by Sr entering the Ba sites, we still observe a T_N of 17 K, as shown in Fig. 3, i.e., as high as for the $\text{PrBa}_2\text{Cu}_3\text{O}_7$ compound. From the magnetic difference neutron-diffraction pattern intensities for $T = 20$ K subtracted from those at $T = 1.5$ K we clearly observed a magnetic peak at $(1/2, 1/2, 1/2)$ which does not show asymmetric line broadening. In $\text{PrSrBaCu}_3\text{O}_7$ the antiferromagnetic ordering is therefore of longer range than in $\text{PrBa}_2\text{Cu}_3\text{O}_{6.2}$. On the other hand, the low-energy spectrum of the crystalline electric field of $\text{PrSrBaCu}_3\text{O}_7$ looks similar to the $\text{PrBa}_2\text{Cu}_3\text{O}_7$ compound. We have calculated the temperature dependence of the magnetic moment using the crystal-field parameters worked out by Nekvasil *et al.*¹⁸ for the $\text{PrBa}_2\text{Cu}_3\text{O}_7$ compound. Our result is in good agreement with the experimental findings, see Fig. 3. Thus the substitution of Ba^{3+} by Sr^{2+} which leads to disorder does not change the magnetic ordering of the Pr ions in $\text{PrSrBaCu}_3\text{O}_7$.

TABLE I. The distance $\text{Pr-O}(2)$ Å at $T = 10$ K for several Pr compounds, related with the Néel temperature.

	$\text{Pr-O}(2)$ (Å)	T_N (K)
$\text{PrBa}_2\text{Cu}_3\text{O}_7$ (Ref. 1)	2.449(5)	17.0 ± 1
$\text{PrSrBaCu}_3\text{O}_7$	2.439(5)	17.0 ± 1
$\text{PrBa}_2\text{Cu}_3\text{O}_{6.2}$	2.480(4)	12.0 ± 1
$\text{PrBa}_2\text{Cu}_2\text{NbO}_8$ (Ref. 10)	2.487(6)	12.6 ± 1

A comparison of the Néel temperatures of several related Pr perovskite-type compounds, see Table I, indicates a systematic correlation with the variation of the distance $\text{Pr-O}(2)$. The higher the T_N values are the smaller $\text{Pr-O}(2)$ distances have been determined by neutron diffraction (at $T = 10$ K) as expected from the superexchange interaction.

ACKNOWLEDGMENTS

We would like to thank X. Z. Wang, B. Hellebrand, and D. Bauerle from J-Kepler University of Linz for providing us the ceramic sample $\text{PrSrBaCu}_3\text{O}_7$ for neutron-scattering experiments. Corresponding detailed results will be published later. Financial support by the Swiss National Science Foundation is gratefully acknowledged.

- ¹W.-H. Li, J. W. Lynn, S. Skanthakumar, T. W. Clinton, A. Kebede, C.-S. Jee, J. E. Crow, and T. Mihalisin, *Phys. Rev. B* **40**, 5300 (1989).
- ²A. Kebede, J. P. Rodriguez, I. Perez, T. Mihalisin, G. Myer, J. E. Crow, P. P. Wise, and P. Schlottman, *J. Appl. Phys.* **69**, 5376 (1991).
- ³S. Uma, T. Sarkar, M. Seshasayee, G. Rangarajan, C. R. Venkateswara Rao, and C. Subramanian, *Solid State Commun.* **87**, 289 (1993).
- ⁴N. Rosov, J. W. Lynn, G. Cao, J. W. O'Reilly, P. Pernambuco-Wise, and J. E. Crow, *Physica C* **204**, 171 (1992).
- ⁵M. Guillaume, P. Allenspach, J. Mesot, B. Roessli, U. Staub, P. Fischer, and A. Furrer, *Z. Phys. B* **90**, 13 (1993).
- ⁶V. Nekvasil, E. Holland-Moritz, H.-D. Jostarndt, U. Walter, and G. Hilscher, *J. Magn. Magn. Mater.* **117**, 11 (1992).
- ⁷J. Fink, N. Nucker, H. Romberg, and M. Alexander, *Phys. Rev. B* **42**, 4823 (1990).
- ⁸M. Guillaume, P. Fischer, B. Roessli, A. Podlesnyak, J. Schefer, and A. Furrer, *Solid State Commun.* **88**, 57 (1993).
- ⁹E. J. Lisher and J. B. Forsyth, *Acta Crystallogr. A* **27**, 545 (1971).
- ¹⁰H.-D. Jostarndt, U. Walter, J. Harnisch-macher, J. Kalenborn, A. Severing, and E. Holland-Moritz, *Phys. Rev. B* **46**, 14872 (1992).
- ¹¹L. Soderholm, C.-K. Loong, G. L. Goodman, and B. D. Dabrowski, *Phys. Rev. B* **43**, 7923 (1991).
- ¹²T. W. Clinton, Ph. D. thesis, University of Maryland, 1992.
- ¹³N. Rosov, J. W. Lynn, H. B. Radonsky, M. Bennahmias, T. J. Goodwin, P. Klavins, and R. N. Shelton, *Phys. Rev. B* **47**, 15256 (1993).
- ¹⁴B. Roessli, P. Fischer, U. Staub, M. Zolliker, and A. Furrer, *Europhys. Lett.* **23**, 511 (1993).
- ¹⁵J. B. MacChesney, H. J. Williams, R. C. Sherwood, and J. F. Potter, *J. Chem. Phys.* **41**, 3177 (1964).
- ¹⁶E. V. Sampathkumaran and I. Das, *Physica B* **186-188**, 328 (1993).
- ¹⁷For a review of superconductivity on $\text{YBa}_2\text{Cu}_3\text{O}_7$ -type compounds, see *High-Temperature Superconductivity*, edited by J. W. Lynn (Springer, New York, 1989).
- ¹⁸V. Nekvasil, E. Holland-Moritz, H.-D. Jostarndt, U. Walter, and G. Hilscher, *J. Magn. Magn. Mater.* **117**, 11 (1992).

Collective magnetic excitations of Ho^{3+} ions in grain-aligned $\text{HoBa}_2\text{Cu}_3\text{O}_7$

U. Staub,^{a)} F. Fauth, M. Guillaume, J. Mesot, and A. Furrer

*Eidgenössische Technische Hochschule Zürich, Laboratorium für Neutronenstreuung,
CH-5232 Villigen PSI, Switzerland*

P. Dosanjh and H. Zhou

Department of Physics, University of British Columbia, Vancouver British Columbia, Canada

P. Vorderwisch

Hahn Meitner Institut, D-1000 Berlin, Germany

Inelastic neutron scattering has been employed to study the magnetic excitations of Ho^{3+} in a grain-aligned sample of $\text{HoBa}_2\text{Cu}_3\text{O}_7$. The lowest lying branch exhibits dispersion for spin waves propagating in the (a,b) plane, whereas excitations along the c axis remain constant in energy. The data are analyzed in the random phase approximation in terms of the Heisenberg and an anisotropic model, resulting in an enormous spatial anisotropy of the magnetic coupling parameters, which are weakly ferromagnetic, antiferromagnetic, and almost zero for nearest-neighbor Ho^{3+} pairs along the a , b , and c axes, respectively. In addition, we have been able to separate the spin wave excitations in longitudinal and transverse parts.

It is now well known that for nearly all high- T_c compounds $\text{RBa}_2\text{Cu}_3\text{O}_{7-\delta}$ (R denotes rare earth) superconductivity and magnetic ordering of the R ion sublattice coexist at low temperatures. In order to understand the interplay of magnetism and superconductivity in these systems, information on both the electronic ground state of the R^{3+} ions and the coupling mechanism between the R^{3+} ions is highly desirable. While the ground-state wave functions in these systems are well established particularly through neutron spectroscopic investigations of the crystalline-electric-field (CEF) interaction,¹ there is a lack of unambiguous information concerning the nature and size of the magnetic pair interactions. It is usually argued that the large separation of the R^{3+} ions along the c axis gives rise to an essentially two-dimensional character of the magnetic correlations. In fact, there are numerous examples for the two-dimensional magnetic behavior of the R^{3+} ions in the $\text{RBa}_2\text{Cu}_3\text{O}_{7-\delta}$ systems,² however, for some compounds a three-dimensional long-range magnetic order was clearly observed in neutron diffraction experiments.^{2,3}

Several mechanisms could be involved in the coupling of the R^{3+} ions to form two- or three-dimensional spin structures: Dipolar, Ruderman-Kittel-Kasuya-Yosida (RKKY), and superexchange interactions. Calculations based on dipolar interactions alone result in Néel temperatures which are much lower than the observed ordering temperatures, and there are controversies as to the importance of either RKKY or superexchange interactions. Some qualitative information on the coupling of the R^{3+} ions has been obtained from magnetization and low-temperature specific-heat measurements which indicate large anisotropies of the exchange interaction in the (a,b) plane.⁴ A more detailed insight into the coupling mechanism results from studying the spin dynamics through the measurement of the collective magnetic excitations or spin waves which inherently contain information on the nature and size of the magnetic coupling between the R^{3+}

ions. Inelastic neutron scattering (INS) provides the most direct access to this property and thereby allows a very direct determination of exchange parameters.

Preliminary INS data of the low-lying magnetic excitations observed in a grain-aligned sample of $\text{HoBa}_2\text{Cu}_3\text{O}_7$ have been published in Ref. 5. Here we present new experimental data taken under improved energy resolution. We have chosen $\text{HoBa}_2\text{Cu}_3\text{O}_x$ for two specific reasons. First, a recent low-temperature neutron diffraction study⁶ of $\text{HoBa}_2\text{Cu}_3\text{O}_7$ indicates the existence of three-dimensional magnetic correlations associated with the Ho^{3+} sublattice below $T_N=0.19$ K as well as a three-dimensional or mean-field type behavior of the zero-field magnetization with a critical exponent $\beta=0.4\pm0.1$, so that we may expect the magnetic excitations to exhibit dispersion effects. Second, and most importantly, the CEF level scheme of $\text{HoBa}_2\text{Cu}_3\text{O}_7$ is characterized by a series of low-lying states¹ which can be sufficiently resolved within the small range of energy dispersion anticipated for these systems. In particular, we have studied in great detail the lowest ground-state CEF excitation $\Gamma_3\rightarrow\Gamma_4$ with energy $\Delta\approx0.5$ meV, which has by far the largest dipole transition matrix element and therefore exhibits the largest dispersion effects.

The preparation and characterization of the $\text{HoBa}_2\text{Cu}_3\text{O}_7$ sample is published elsewhere.⁵ The INS experiments were performed at the reactor BerII at the Berlin Neutron Scattering Center with use of the triple-axis spectrometer FLEX operating in the neutron energy-loss configuration. The energy of the outgoing neutrons was kept fixed at 3.5 meV. No collimation was used, giving rise to an energy resolution of 0.09 meV at $\Delta E=0$. A beryllium filter was inserted between monochromator and sample to eliminate higher order contamination. The samples were oriented with the $[001]$ axis in the scattering plane and mounted in an "orange ILL-type" helium cryostat to achieve temperatures $T\geq 1.5$ K. Constant Q scans were employed throughout the experiments, where $Q=2\pi(x/a, y/b, z/c)$ is the scattering vector. Due to the random orientation of the sample in the (a,b) plane, however, we could not distinguish between the com-

^{a)}Present address: Chemistry Department, Argonne National Laboratory, Argonne IL 60439.

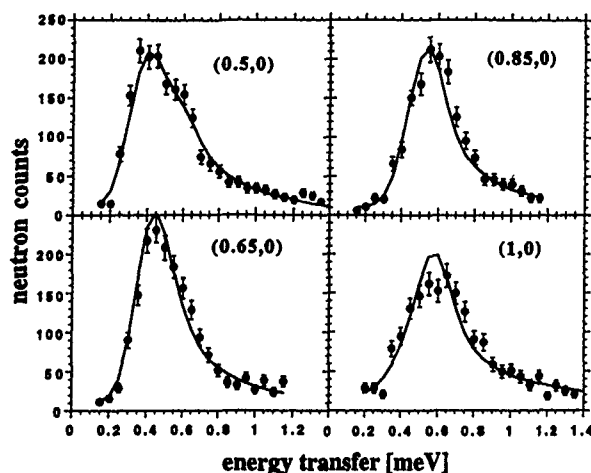


FIG. 1. Normalized and form factor corrected energy spectra of neutrons scattered from grain-aligned $\text{HoBa}_2\text{Cu}_3\text{O}_7$, taken at $T=1.5$ K and constant analyzer energy $E_A=3.5$ meV, for propagation vectors along the $[x',0]$ direction. The lines correspond to the calculated (x,y) -averaged excitation spectra as explained in the text.

ponents of the scattering vector \mathbf{Q} perpendicular to the z axis, i.e., the actual scattering vector was $\mathbf{Q}=2\pi(x'/a, z/c)$ with $x' = \sqrt{x^2+y^2}$ (assuming $a=b$).

We covered a large region of reciprocal space in the (x',z) -plane. For all \mathbf{Q} the ground-state CEF excitation $\Gamma_3 \rightarrow \Gamma_4$ shows up as a well resolved inelastic line as exemplified in Figs. 1, 2, and 3. Its peak shape is broad and often asymmetric for \mathbf{Q} perpendicular to the z axis (Fig. 1), whereas for \mathbf{Q} involving a zero x' component narrow lines are observed (Fig. 2). The energy of maximum peak intensity of this excitation varies typically between 0.4 and 0.6 meV

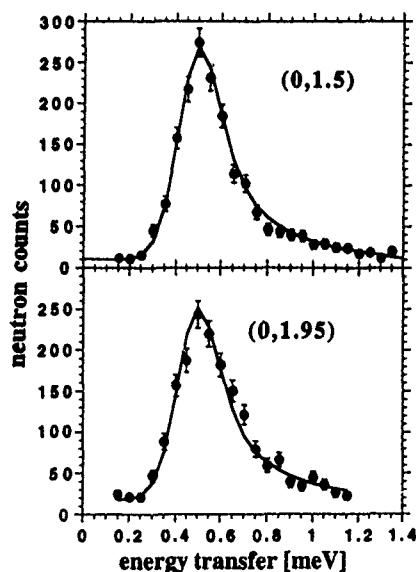


FIG. 2. Normalized and form factor corrected energy spectra of neutrons scattered from grain-aligned $\text{HoBa}_2\text{Cu}_3\text{O}_7$, taken at $T=1.5$ K and constant analyzer energy $E_A=3.5$ meV, for propagation vectors along the $[0,z]$ direction. The lines are the result of the anisotropic line shape fits to the dispersion-free CEF excitations.

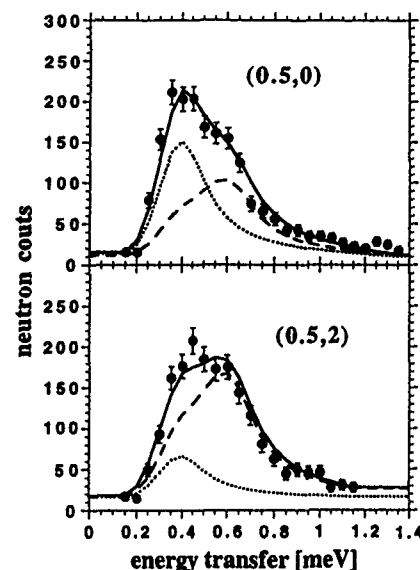


FIG. 3. Normalized and form factor corrected energy spectra of neutrons scattered from grain-aligned $\text{HoBa}_2\text{Cu}_3\text{O}_7$, taken at $T=1.5$ K and constant analyzer energy $E_A=3.5$ meV, for propagation vectors along the $[0.5,z]$ direction. The dotted lines corresponds to the transverse branch of the excitation, the broken lines corresponds to the longitudinal branch of the excitation and the full lines are the result of the total (x,y) -averaged calculation as explained in the text.

when following \mathbf{Q} along the x' axis, whereas it remains more or less constant upon variation of \mathbf{Q} along the z axis.

In the random phase approximation the magnetic excitation energies are determined by the poles of the dynamic magnetic susceptibility,⁷

$$\chi(\mathbf{Q}, \omega) = \chi_0(\omega) [1 - J(\mathbf{Q})\chi_0(\omega)]^{-1}, \quad (1)$$

where $J(\mathbf{Q})$ is the Fourier transform of the exchange coupling and $\chi_0(\omega)$ the single-ion susceptibility. For $x=7$, the calculation becomes particularly simple for an effective two-level system:

$$h\omega(\mathbf{Q}) = \left\{ \Delta \left[\Delta - 2M^2 J(\mathbf{Q}) \tanh\left(\frac{\Delta}{2k_B T}\right) \right] \right\}^{1/2}. \quad (2)$$

Here, Δ corresponds to the energy separation between the CEF ground state Γ_3 and the first-excited CEF state Γ_4 , and $M^2=27$ is the dipole transition matrix element between the two CEF states.¹ For the calculation of $J(\mathbf{Q})$ we took into account Heisenberg-type exchange parameters J_a , J_b , and J_c , coupling the central Ho^{3+} ion pairwise with the Ho^{3+} ions at the nearest-neighbor positions $\pm a$, $\pm b$, and $\pm c$ along the x , y , and z directions, respectively. Our choice of Heisenberg-type exchange is fully supported by the above mentioned behavior of the zero-field magnetization observed by neutron diffraction.⁶ From the absence of dispersion along the z axis (Fig. 2) we immediately conclude that $J_c=0 \pm 0.2$ μeV , as actually expected from the large separation of the Ho^{3+} ions along that axis. The experimental uncertainty associated with J_c results from the standard deviation of the peak positions of Fig. 2 inserted into Eq. (2). Information on J_a and J_b is more difficult to obtain because of the random orientation of the x and y axes in our sample, thus the mag-

netic excitation spectra cannot be analyzed directly according to Eq. (2), but we have to average Eq. (2) in the (x, y) plane, what is explained in detail in Ref. 5. In addition, it is obvious that we have an asymmetric lane shape, as also was seen in the earlier works.^{1,8} This asymmetry is explained due to Cu spin fluctuations at the Ho site.⁸ However, we have to include this lane shape in our data analysis. The energy spectra of Fig. 1 were least-squares fitted to the model outlined above. The only fitting parameters were an overall scaling factor for the intensity, a constant background level, a half-width parameter for the Gaussian type of the intrinsic broadening of the CEF line, an anisotropic line shape factor and the two model parameters J_a and J_b . Δ was kept fixed at the pure CEF energy ($\Delta=0.49$ meV) determined in a $\text{Y}_{0.9}\text{Ho}_{0.1}\text{Ba}_2\text{Cu}_3\text{O}_7$ sample.⁸ We obtained for $J_a=0.5\pm0.1$ μeV and for $J_b=-1.6\pm0.2$ μeV . Due to the random orientation of the x and y axes another solution is possible by interchanging the parameters J_a and J_b . However, the analysis of a recent low-temperature neutron diffraction study⁶ of the magnetic ordering in $\text{HoBa}_2\text{Cu}_3\text{O}_7$ is consistent with our choice of ferromagnetic and antiferromagnetic coupling along the a and b axes, respectively. We derive from our data the molecular-field parameter $J(\mathbf{Q}_0)=2(J_a-J_b-J_c)$ to be $J(\mathbf{Q}_0)=4.2\pm0.6$ μeV , which is in good agreement with the mean-field value $J(\mathbf{Q}_0)=5.2\pm0.5$ μeV calculated from the zero field magnetization.⁶

Our model parameters can reproduce the \mathbf{Q} dependence of the observed energy spectra reasonably well (see Fig. 1). Improvements of the data analysis are possible by going beyond the simple Heisenberg model. For example, the exchange interaction can be generalized to include anisotropies in the coupling of the spin operators S^α ($\alpha=x, y, z$). As a result the response function is split into transverse and longitudinal components which can be separated in INS experiments through the polarization factor in the neutron cross-section or by use of polarized neutrons, however, our present data would clearly be over interpreted by the application of a full anisotropic model. Nevertheless, with the good energy resolution and many spectra taken with different \mathbf{Q} in reciprocal space we can improve our Heisenberg model. As shown in Fig. 3, the spectra for constant x' values ($x'\neq 0$) and different z values should look like exactly the same for the Heisenberg model ($J_c\approx 0$), what is obviously not correct.

A step between the full anisotropic model and the Heisenberg model is to express the spin operators \mathbf{S} in \mathbf{S}^\perp and \mathbf{S}^\parallel , which results in a transverse and longitudinal component, respectively. Therefore the number of model parameters is increased from two to five ($J_a^\perp, J_a^\parallel, J_b^\perp, J_b^\parallel$, and $M^\parallel, M^\perp = M^\parallel^2 + M^\perp^2 = 27$). On the other hand, we are now able to fit all 21 measured energy spectra simultaneously (Fig. 1), as compared two the Heisenberg model, where we can only fit spectra with $\mathbf{Q}=(x', 0)$. We obtain the following results:

$$J_a^\parallel = 0.0 \pm 0.4 \text{ } \mu\text{eV}, \quad M^\parallel = 7.8 \pm 0.6,$$

$$J_a^\perp = -6.9 \pm 0.7 \text{ } \mu\text{eV}, \quad M^\perp = 19.2 \pm 0.4,$$

$$J_b^\parallel = 3.3 \pm 0.8 \text{ } \mu\text{eV},$$

$$J_b^\perp = -2.6 \pm 0.3 \text{ } \mu\text{eV}.$$

Again we find a good agreement between the exchange parameter determined from the dimer excitation,⁸ where they can extract only the transverse exchange parameters ($J_a^\perp = -J_b^\perp = 2.6 \pm 0.3$ μeV).

We have been able to prove directly the essentially two-dimensional nature of the magnetic coupling between the Ho^{3+} ions in $\text{HoBa}_2\text{Cu}_3\text{O}_7$. The coupling of the Ho spins for $x=7$ turns out to be extremely anisotropic in the (a, b) plane, i.e., there is a strong antiferromagnetic coupling along the b axis and a smaller ferromagnetic coupling along the a axis. This is in close analogy to the results obtained by fitting the specific-heat anomaly due to magnetic ordering of other $\text{RBa}_2\text{Cu}_3\text{O}_7$ compounds.⁴ However, our results are considerably more detailed with respect to the size and the nature of the exchange interaction in the (a, b) plane. In addition, we have been able to separate the spin wave excitations in longitudinal and transverse parts. We get for the transverse component a ferromagnetic and an antiferromagnetic coupling in the a and b direction, respectively, whereas we get for the longitudinal component no and a strong antiferromagnetic coupling in the a and b direction, respectively. The strong magnetic anisotropy in the (a, b) plane can be reproduced neither by dipolar nor by RKKY interactions, thus the coupling of the Ho^{3+} ions is presumably dominated by nearest-neighbor superexchange interactions mediated by the $O(2)$ and $O(3)$ ions as oxygen bridges, which—at the same time—also take part in the superconducting processes. The charge distribution at the plane oxygen sites is therefore one of the most crucial quantities towards a detailed understanding of the relevant physical properties of the $\text{RBa}_2\text{Cu}_3\text{O}_7$ compounds.

Financial support by the Swiss National Science Foundation is gratefully acknowledged.

¹A. Furrer, P. Brüesch, and P. Unternährer, Phys. Rev. B **38**, 4616 (1988).

²H. Maletta, E. Pörschke, T. Chattopadhyay, and P. J. Brown, Physica C **166**, 9 (1990).

³P. Fischer, B. Schmid, P. Brüesch, F. Stucki, and P. Unternährer, Z. Phys. B: Condensed Matter **74**, 183 (1989).

⁴K. N. Yang, J. M. Ferraira, B. W. Lee, M. B. Maple, W.-H. Li, J. W. Lynn, and R. W. Erwin, Phys. Rev. B **40**, 10963 (1989).

⁵U. Staub, F. Fauth, M. Guillaume, J. Mesot, A. Furrer, P. Dosanjh, and H. Zhou, Europhys. Lett. **21**, 845 (1993).

⁶B. Rössli, P. Fischer, U. Staub, M. Zolliker, and A. Furrer, Europhys. Lett. **23**, 511 (1993).

⁷J. Jensen and A. R. Mackintosh, *Rare Earth Magnetism, Structures and Excitations*, edited by J. Birman, S. S. Edwards, C. H. L. Smith, and M. Rees (Oxford Science, Oxford, 1991).

⁸M. Guillaume, U. Staub, F. Fauth, J. Mesot, A. Furrer, and C. J. Carlile (to be published).

Combined electronic-nuclear magnetic ordering of the Ho^{3+} ions and magnetic stacking faults in $\text{HoBa}_2\text{Cu}_3\text{O}_x$ ($x=7.0, 6.8, 6.3$)

B. Roessli, P. Fischer, U. Staub, M. Zolliker, and A. Furrer

Laboratorium für Neutronenstreuung, Eidgenössische Technische Hochschule Zürich and Paul Scherrer Institut, CH-5232 Villigen PSI, Switzerland

Magnetic ordering of $\text{HoBa}_2\text{Cu}_3\text{O}_x$ ($x=7.0, 6.8, 6.3$) was investigated by means of neutron diffraction. Long-range antiferromagnetism is found for $x=7.0$ below $T_N=190$ mK and for $x=6.8$ below $T_N=100$ mK corresponding to propagation vector $\mathbf{K}=[0, 1/2, 1/2]$ with magnetic moment directions parallel to the a axis. The observed temperature dependence of the magnetic order parameter is in excellent agreement with mean-field calculations taking into account crystal field, exchange, and hyperfine interactions. No magnetic superlattice reflections were detected for $x=6.3$. A highly unusual ordering behavior is observed in $\text{HoBa}_2\text{Cu}_3\text{O}_x$ ($x=7.0, 6.8$) where the three-dimensional magnetic ordering is imperfect, due to finite correlation length $\xi_c=29$ and 129 Å, respectively, along the c axis.

I. INTRODUCTION

Long-range antiferromagnetic rare-earth ordering has been determined in $\text{RBa}_2\text{Cu}_3\text{O}_7$ by means of neutron diffraction for $R=\text{Pr, Nd, Gd, Dy, Er, and Yb}$.¹ However, the magnetic ordering of the $\text{HoBa}_2\text{Cu}_3\text{O}_x$ system with singlet-crystal-field ground state² and presumably combined nuclear (^{165}Ho)-electronic ordering below $T_N \approx 170$ mK (Ref. 3) could not be solved unambiguously.^{4,5} First neutron-diffraction experiments⁴ on $\text{HoBa}_2\text{Cu}_3\text{O}_{6.8}$ revealed a single magnetic peak at temperatures below $T_N=140$ mK in agreement with heat-capacity measurements;³ however, the detailed nature of the antiferromagnetic correlations could not be established. On the other hand, μSR measurements on $\text{HoBa}_2\text{Cu}_3\text{O}_7$ (Ref. 5) claimed the existence of 3D antiferromagnetic order below $T_N \approx 5$ K, corresponding to $\mathbf{K}=[1/2, 1/2, 1/2]$ and alignment of the magnetic moments of Ho along the a axis. Below 100 mK the μSR data indicated $\mathbf{K}=[0, 1/2, 1/2]$, easy axis of magnetization $[0, 0, 1]$, and an ordered Ho moment of $\sim 2.6 \mu_B$. Therefore new systematic neutron-diffraction measurements were performed on $\text{HoBa}_2\text{Cu}_3\text{O}_x$ ($x=7.0, 6.8$, and 6.3). First results for $x=7.0$ have been published in Ref. 6.

II. EXPERIMENTAL

The $\text{HoBa}_2\text{Cu}_3\text{O}_x$ ($x=7.0, 6.8, 6.3$) samples were prepared by standard sintering techniques. From resistivity measurements the critical temperatures were found to be $T_c=93, 53$, and 0 K for $x=7.0, 6.8$, and 6.3 , respectively. The same samples have previously been used to determine the crystal-field interaction by means of inelastic neutron scattering.⁷ The present experiments were performed on the multicounter diffractometer DMC⁸ at the reactor Saphir of the Paul Scherrer Institut at Würenlingen (Switzerland) operating in the high-intensity mode [vertically focusing Ge(311) monochromator, collimations $-/-12'$, wavelength 1.7036 Å]. The single-phase quality of the polycrystalline samples was confirmed and the structure parameters were determined by neutron diffraction at 10 K in the high-resolution mode. In particular, the oxygen concentrations $x=7.00 \pm 0.02, 6.77 \pm 0.02$, and 6.25 ± 0.02 resulted for the three samples. For the low-temperature experiments the specimens were mounted inside

a bottom loading $^4\text{He}/^3\text{He}$ dilution refrigerator attaining 7 mK. To achieve good thermal contact ^4He was condensed into the sample voids. The raw data were corrected for absorption according to the measured transmission.

III. RESULTS

The magnetic structures were determined at $T=7$ mK. In order to visualize the peaks due to magnetic ordering of Ho^{3+} ions we calculated the difference patterns for $T=7$ mK and $T>T_N$. Figures 1 and 2 show the results obtained for $x=7.0$ and 6.8 , respectively. The magnetic peaks can be indexed with increasing scattering angle 2θ as $(0, 1/2, 1/2)$, $(0, 1/2, 3/2)$, $(0, 1/2, 5/2)$, $(1, 1/2, 1/2)$, etc., with reference to the chemical cell. Combined with intensity calculations the corresponding antiferromagnetic structure of $\text{HoBa}_2\text{Cu}_3\text{O}_x$ ($x=7.0, 6.8$) is unambiguously described by the propagation vector $\mathbf{K}=[0, 1/2, 1/2]$, i.e., the magnetic cell is doubled along the b and c directions compared to the chemical one, and the Ho^{3+} magnetic sublattice consists of antiferromagnetic (a, c) layers stacked according to antitranslation $[0, 1, 0]$ as schematically displayed as insert in Fig. 1. This antiferromagnetic structure is in agreement with the anisotropic exchange parameters determined recently by inelastic neutron scattering experiments on grain-aligned powers of $\text{HoBa}_2\text{Cu}_3\text{O}_x$.⁹ The sequence of magnetic peaks observed for $x=6.8$ is the same as for $x=7.0$.

In the refinement of the magnetic diffraction patterns we took into account nuclear (^{165}Ho) polarization effects. The magnetic part of the cross section for neutron diffraction from magnetic samples with polarized nuclei and unpolarized neutrons is given by⁶

$$\frac{\sigma}{4\pi} = A^2 M_{\perp}^2 + 2Ab_N / M_{\perp} \cdot \mathbf{P} + b_N^2 I^2 P^2, \quad (1)$$

where $A=0.2696 \times 10^{-12}$ cm is the electronic magnetic scattering length. $\mathbf{M}_{\perp} \equiv \mathbf{M} \perp (\mathbf{Q}) = \mathbf{M}(\mathbf{Q}) - [\hat{\mathbf{Q}} \cdot \mathbf{M}(\mathbf{Q})]\hat{\mathbf{Q}}$ with $\mathbf{M}(\mathbf{Q}) = g_J f(\mathbf{Q}) \mathbf{J}$ is the component of the magnetization perpendicular to the scattering vector \mathbf{Q} and \mathbf{J} the total angular momentum vector. $f(\mathbf{Q})$ is the electronic form factor and \mathbf{P} the polarization vector of the nuclei. b_N is the scattering

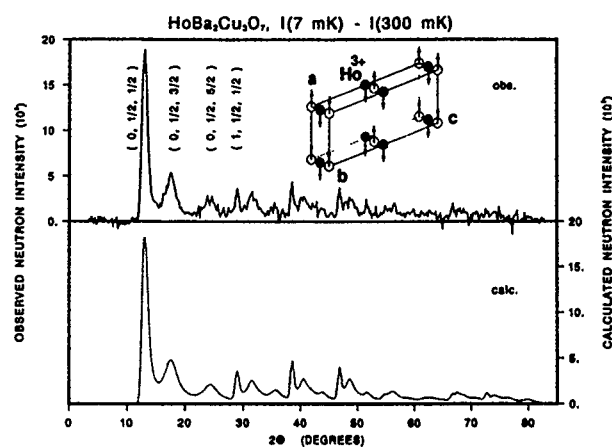


FIG. 1. Observed and calculated magnetic neutron-diffraction difference pattern $I(7 \text{ mK}) - I(300 \text{ mK})$ of $\text{HoBa}_2\text{Cu}_3\text{O}_7$. The calculated line corresponds to the model explained in the text. Inset: Magnetic sublattice of $\text{HoBa}_2\text{Cu}_3\text{O}_7$. The magnetic moments are oriented parallel to the a axis. The statistics correspond to about three days measurements.

length of a thermal neutron by a nuclear spin I .¹⁵ The least-squares refinements of the observed magnetic diffraction patterns were carried out by means of a modified version of the program MINREF¹⁰ including instrumental resolution and using Eq. (1). The electronic form factor of Ho^{3+} was used in the relativistic dipole approximation.¹¹

The unusual line shapes observed in the magnetic neutron diffraction pattern of $\text{HoBa}_2\text{Cu}_3\text{O}_7$ (and to a lesser extent in $\text{HoBa}_2\text{Cu}_3\text{O}_{6.8}$) can be shown to result from finite magnetic correlations along the c axis which is equivalent to the occurrence of magnetic stacking faults along that direction. In that case, the shape of the magnetic intensity for a particular reflection (h, k, l) can be described by a Lorentzian:¹²

$$I_{hkl}(\mathbf{q}) \propto \frac{\Gamma}{\pi(\Gamma^2 + |\tau_{hkl} - \mathbf{Q}|^2)} \delta(q_a) \delta(q_b) \quad (2)$$

with $\mathbf{q} = (q_a, q_b, q_c) = \tau_{hkl} - \mathbf{Q}$.

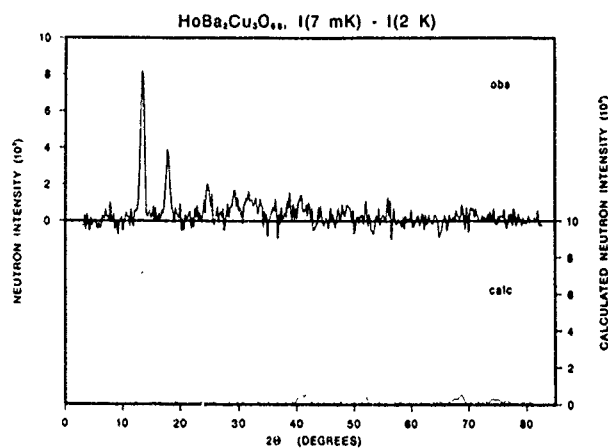


FIG. 2. Observed and calculated magnetic neutron-diffraction difference pattern $I(7 \text{ mK}) - I(2 \text{ K})$ of $\text{HoBa}_2\text{Cu}_3\text{O}_{6.8}$. The magnetic structure is the same as for $\text{HoBa}_2\text{Cu}_3\text{O}_7$. The statistics correspond to about three days measurements.

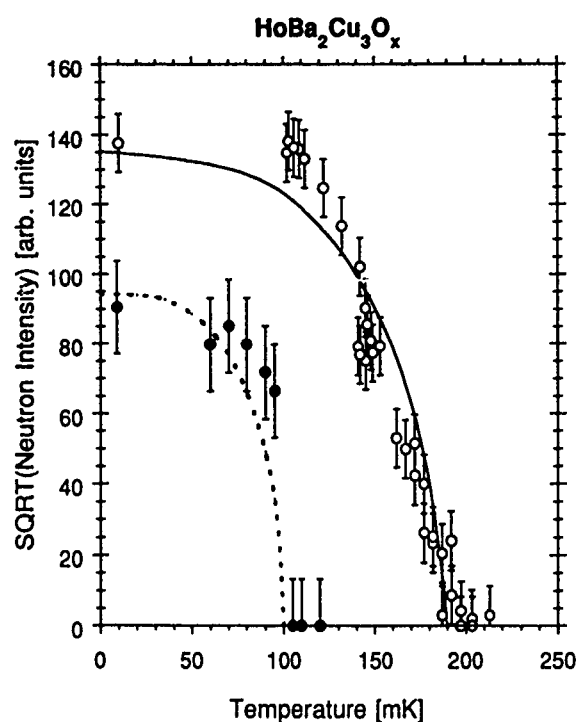


FIG. 3. The open (full) points represent the observed and the (dotted) line the calculated square root of the magnetic neutron intensity for the $(0, 1/2, 1/2)$ peak of $\text{HoBa}_2\text{Cu}_3\text{O}_x$, $x=7.0$ with $T_N=190 \text{ mK}$ ($x=6.8$ with $T_N=100 \text{ mK}$).

Figure 1 shows the results of the least-squares refinement based on Eqs. (1) and (2) (and using the Laue theorem for diffraction in polycrystalline samples), which excellently reproduces the data observed for $\text{HoBa}_2\text{Cu}_3\text{O}_{7.0}$. The Ho^{3+} magnetic moments are directed parallel to the a axis, and the (average) correlation length along the c axis is $\xi_c = 2/\Gamma = (29 \pm 4) \text{ \AA}$. By scaling the magnetic diffraction pattern with the nuclear reflections we obtain an electronic zero-field moment $\mu = 2.8(3) \mu_B$ at $T=7 \text{ mK}$. A least-squares refinement of the $\text{HoBa}_2\text{Cu}_3\text{O}_{6.8}$ data yields $\mu = 1.7(2) \mu_B$ and $\xi_c = (129 \pm 10) \text{ \AA}$ at $T=7 \text{ mK}$ (see Fig. 2).

Figure 3 shows the temperature dependence of the observed neutron intensities for the $(0, 1/2, 1/2)$ magnetic reflection. For a mean-field analysis of these data we base our calculations on a Hamiltonian which includes crystal field, exchange, and hyperfine interactions:

$$H = V_c - \lambda \langle J_x \rangle J_x + a J_x I_x. \quad (3)$$

V_c is the crystal-field operator, λ the molecular field parameter, a the hyperfine coupling constant, and x the easy axis of magnetization. The crystal field as determined by neutron spectroscopy^{2,7} yields Γ_3 and Γ_4 singlets as ground and first excited states, respectively, with energy separation Δ . As the remaining crystal-field states lie far above Δ , we can restrict our calculations to an effective two-level system. H is then diagonalized in the subspace spanned by the vectors $\{\Gamma_3, m_I\}, \{\Gamma_4, m_I\}; m_I = -I, \dots, I; I = 7/2\}$. At finite temperature the induced electronic and nuclear polarizations are given by¹³

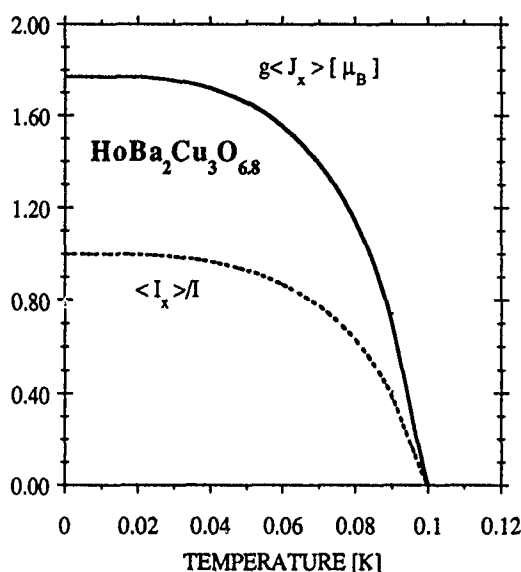


FIG. 4. The lines are the calculated electronic magnetization $\mu(T)$ and the (reduced) polarization of the nuclei $P = \langle I_x \rangle / I$, respectively, for $\text{HoBa}_2\text{Cu}_3\text{O}_{6.8}$, as explained in the text. The same calculations were carried out for $\text{HoBa}_2\text{Cu}_3\text{O}_7$ and are published in Ref. 6.

$$\langle J_x \rangle = \sum_{m_I} z^{m_I} \text{sh} \left(\frac{\Delta_{m_I}}{kT} \right) / \sum_{m_I} \text{ch} \left(\frac{\Delta_{m_I}}{kT} \right),$$

$$\langle I_x \rangle / I = \sum_{m_I} m_I \text{ch} \left(\frac{\Delta_{m_I}}{kT} \right) / \sum_{m_I} \text{ch} \left(\frac{\Delta_{m_I}}{kT} \right). \quad (4)$$

Δ_{m_I} is the energy separating two eigenstates of Eq. (3) with same nuclear spin states m_I , and z^{m_I} is the solution of the self-consistent equation for the induced electronic moment of the new quantum states at $T=0$ K:

$$z^{m_I} = |w| \frac{x \langle J_x \rangle + m_I \alpha}{\sqrt{1 + (x \langle J_x \rangle + m_I \alpha)^2}},$$

$$\alpha = -2|w| \frac{a}{\Delta}, \quad x = \frac{2|w|}{\Delta} \lambda, \quad (5)$$

with $|w| = |\langle \Gamma_4 | J_x | \Gamma_3 \rangle|$. The hyperfine coupling constant has been determined by electron paramagnetic resonance (EPR) measurements¹⁴ to be $a = 39$ mK, and the value of $|w|$ and Δ are known from neutron spectroscopic experiments on $\text{HoBa}_2\text{Cu}_3\text{O}_x$.^{2,7} The only adjustable parameter is then the molecular-field constant λ which we have chosen such as to correctly predict the Néel temperature T_N . For both $x=7.0$ and $x=6.8$ we find $\lambda=65$ mK. Figure 4 shows the results of our calculations based on Eqs. (4) and (5), with the model parameters summarized in Table I. At $T=7$ mK the calcu-

TABLE I. Parameter values concerning crystal field, magnetic ordering, and hyperfine interactions in $\text{HoBa}_2\text{Cu}_3\text{O}_x$.

	$\text{HoBa}_2\text{Cu}_3\text{O}_{6.8}$	$\text{HoBa}_2\text{Cu}_3\text{O}_7$	Refs.
Δ (K)	7.31	5.60	4,10
$ w $	4.97	5.08	4,10
λ (mK)	65	65	present work
a (mK)	39	39	18
T_N (mK)	100	190	present work
μ_{calc} (μ_B)	1.77	2.68	present work
μ_{obs} (μ_B)	1.7(2)	2.8(3)	present work

lated electronic moments turn out to be $\mu=1.77\mu_B$ and $\mu=2.68\mu_B$ for $x=6.8$ and 7.0 , respectively, in excellent agreement with the derived values from the diffraction data (see text and Table I). For $x=6.3$ the calculation (assuming $\lambda=65$ mK as for $x=6.8$ and $x=7.0$) yields $T_N=60$ mK and $\mu=0.4\mu_B$ at saturation. This value is too small to give significant contributions to the magnetic diffraction pattern, in agreement with the observed diffraction data for $\text{HoBa}_2\text{Cu}_3\text{O}_{6.3}$. Similar calculations carried out including the full crystal-field level scheme gave essentially identical results as obtained from the effective two-level model, Eqs. (4) and (5).

ACKNOWLEDGMENTS

This work was partly supported by the Swiss National Science Foundation. The authors are indebted to S. Fischer for expert technical assistance in the dilution refrigerator experiments.

- ¹ J. W. Lynn, in *High Temperature Superconductivity*, edited by J. W. Lynn (Springer, Berlin, 1990), p. 268.
- ² A. Furrer, P. Bruesch, and P. Unternährer, *Phys. Rev. B* **38**, 4616 (1988).
- ³ B. D. Dunlap, M. Slaski, D. G. Hinks, L. Soderholm, M. Beno, K. Zhang, C. Segre, G. W. Crabtree, W. K. Kwok, S. K. Malik, I. K. Schuller, J. D. Jorgensen, and Z. Sungaila, *J. Magn. Magn. Mater.* **68**, L139 (1987).
- ⁴ P. Fischer, K. Kakurai, M. Steiner, K. N. Clausen, B. Lebeck, F. Hulliger, H. R. Ott, P. Bruesch, and P. Unternährer, *Physica C* **152**, 145 (1988).
- ⁵ P. Birrer, F. N. Gygax, B. Hitti, E. Lippolt, A. Schenek, M. Weber, S. Barth, F. Hulliger, and H. P. Ott, *Phys. Rev. B* **39**, 11449 (1989).
- ⁶ B. Roessli, P. Fischer, U. Staub, M. Zolliker, and A. Furrer, *Europhys. Lett.* **23**, 511 (1993).
- ⁷ U. Staub, P. Allenspach, J. Mesot, A. Furrer, H. Blank, and H. Mutka, *Physica B* **180&181**, 417 (1992).
- ⁸ J. Schefer, P. Fischer, H. Heer, A. Isacson, M. Koch, and R. Thut, *Nucl. Instrum. Methods A* **288**, 477 (1990).
- ⁹ U. Staub, F. Fauth, M. Guillaume, J. Mesot, A. Furrer, P. Dosanjh, and H. Zhou, *Europhys. Lett.* **21**, 845 (1993).
- ¹⁰ O. Elsenhans, *J. Appl. Cryst.* **23**, 73 (1990).
- ¹¹ A. J. Freeman and J. P. Desclaux, *J. Magn. Magn. Mater.* **12**, 11 (1990).
- ¹² M. Goldman, *J. Phys. (Paris)* **41**, 885 (1980).
- ¹³ J. Hamann and P. Manneville, *J. Physique* **34**, 615 (1973).
- ¹⁴ A. Abragam and B. Bleaney, *Electron Paramagnetic Resonance of Transition Ions* (Clarendon, Oxford, 1970).

Raman spectra of two-dimensional spin- $\frac{1}{2}$ Heisenberg antiferromagnets

Stephan Haas and Elbio Dagotto

Department of Physics and Supercomputer Computations Research Institute, Florida State University,
Tallahassee, Florida 32306

Jose Riera

Physics Division and Center for Computationally Intensive Physics, Oak Ridge National Laboratory,
Oak Ridge, Tennessee 37831-6373

Roberto Merlin and Franco Nori

Department of Physics, University of Michigan, Ann Arbor, Michigan 48109-1120

The Raman spectrum of two-dimensional spin- $\frac{1}{2}$ Heisenberg antiferromagnets is calculated by exactly diagonalizing clusters of up to 26 sites. The obtained spectra are compared to experimental results for various high- T_c precursors, such as La_2CuO_4 and $\text{YBa}_2\text{Cu}_3\text{O}_{6.2}$. In spite of good agreement in the position of the main excitation in the B_{1g} channel, i.e., the two-magnon peak around 0.4 eV, an additional mechanism has to be invoked to account for the broad and asymmetric shape of the overall spectrum. Here, we consider the phonon-magnon interaction which, in a quasistatic approximation, renormalizes the Heisenberg exchange integral. This mechanism is motivated in part by recent experimental observations that the Raman linewidth broadens with increasing temperature. Our results are in good agreement with Raman scattering experiments performed by various groups; in particular, the calculations reproduce the broad line shape of the two-magnon peak, the asymmetry about its maximum, the existence of spectral weight at high energies, and the observation of nominally forbidden A_{1g} scattering.

Raman scattering is a powerful technique for the study of electronic excitations in strongly correlated systems. Recently, much attention has been given to the anomalous magnetic scattering with a very broad and asymmetric line shape observed in the Raman spectra of high- T_c precursors, such as La_2CuO_4 , and $\text{YBa}_2\text{Cu}_3\text{O}_{6.2}$ at around 3230 and 3080 cm^{-1} , respectively.¹ The selection rules associated with this peak are also anomalous. While the spin-pair excitations scatter predominantly in the allowed B_{1g} channel, there is also a significant contribution in the nominally forbidden A_{1g} configuration.¹

Previous theoretical studies²⁻⁴ of Raman scattering in the nearest-neighbor spin- $\frac{1}{2}$ Heisenberg model on a two-dimensional square lattice have shown good agreement with experiments in the position of the two-magnon peak, but they have failed to account for the enhanced width observed in the spectra. Several schemes have been proposed to resolve this problem. Initially, it was believed that strong quantum fluctuations were responsible for the broadening.³ However, recent studies of spin-pair excitations in a spin-1 insulator, NiPS_3 , show a relative width comparable to that of two-dimensional cuprates.⁵ This leads us to question the view that the observed anomaly is due to large quantum fluctuations intrinsic to spin- $\frac{1}{2}$ systems. Instead, we propose that a magnon-phonon coupling is responsible for the experimentally observed large widths. We remark that the measured widths are 3-4 times larger than the ones predicted within the spin-wave theory using the Dyson-Maleev transformation, even when processes involving up to four magnons are taken into account.⁴

The isotropic Heisenberg Hamiltonian is given by

$$H_0 = J \sum_{\langle ij \rangle} \mathbf{S}_i \cdot \mathbf{S}_j, \quad (1)$$

where the notation is standard, and only nearest-neighbor interaction is assumed. For the cuprates, the exchange integral is $J \approx 1450 \text{ K} \approx 0.12 \text{ eV}$.

In our study, we obtained the ground state $|\phi_0\rangle$ of H_0 using a Lanczos algorithm on finite two-dimensional square clusters ($N=16, 18, 20$, and 26) with periodic boundary conditions. We studied zero-temperature spectra associated with the scattering Hamiltonian¹⁻⁴

$$H_{\text{Raman}} = \sum_{\langle ij \rangle} (\mathbf{E}_{\text{inc}} \cdot \hat{\sigma}_{ij})(\mathbf{E}_{\text{sc}} \cdot \hat{\sigma}_{ij}) \mathbf{S}_i \cdot \mathbf{S}_j, \quad (2)$$

where $\mathbf{E}_{\text{inc,sc}}$ corresponds to the electric field of the incident and scattered photons, and $\hat{\sigma}_{ij}$ is the unit vector connecting sites i and j . We concentrated on the case of polarizations perpendicular to each other, $\mathbf{E}_{\text{inc}} \propto \hat{x} + \hat{y}$ and $\mathbf{E}_{\text{sc}} \propto \hat{x} - \hat{y}$, giving B_{1g} scattering.

The spectrum of the scattering operator can be written as

$$I(\omega) = \sum_n |\langle \phi_n | H_{\text{Raman}} | \phi_0 \rangle|^2 \delta(\omega - (E_n - E_0)), \quad (3)$$

where ϕ_n denotes the eigenvectors of the Heisenberg Hamiltonian with energy E_n . In practice, the dynamical spectrum $I(\omega)$ is extracted from a continued-fraction expansion of the quantity

$$I(\omega) = -\frac{1}{\pi} \text{Im} \langle \phi_0 | H_{\text{Raman}} \frac{1}{\omega + E_0 + i\epsilon - H_0} H_{\text{Raman}} | \phi_0 \rangle, \quad (4)$$

where ϵ is a small real number introduced in the calculation to shift the poles of Eq. (4) into the complex plane.

Our results for B_{1g} scattering are shown in Figs. 1 and 2. The experimentally observed two-magnon excitation lies around $3J$, which is in good agreement with the location of the main peak in the exactly diagonalized 16-site square lat-

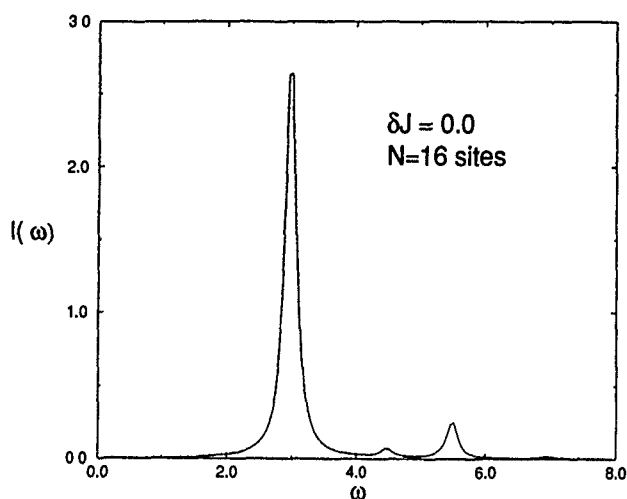


FIG. 1. B_{1g} Raman spectrum in the 4×4 lattice for the pure Heisenberg model. The peaks have been given a finite width $\epsilon = 0.1J$, and ω is given in units of J .

tice shown in Fig. 1. The position of this peak can be understood in terms of the Ising model, which corresponds to the limit of the anisotropic Heisenberg Hamiltonian where no quantum fluctuations are present. In its ground state, the Ising spins align antiferromagnetically for $J > 0$. Within this model and for a two-dimensional (2D) square lattice, it is well known that the incoming light creates a local spin-pair flip at an energy $3J$ higher than the ground-state energy. This argument remains valid even in the presence of quantum fluctuations. Our results indicate that the two-magnon excitation is at $2.957J$, $3.426J$, and $3.037J$ for the 16-, 20-, and 26-site square lattices, respectively. We believe that the somewhat large shift for the 20-site cluster is due to an artifact inherent to the symmetry of the cluster.

While there is good agreement with experiments in regard to the two-magnon peak position, the calculated widths are too small. Thus, it seems necessary to invoke an additional process to account for the observed wide and asymmetric line shape. Here, we propose that the important inter-

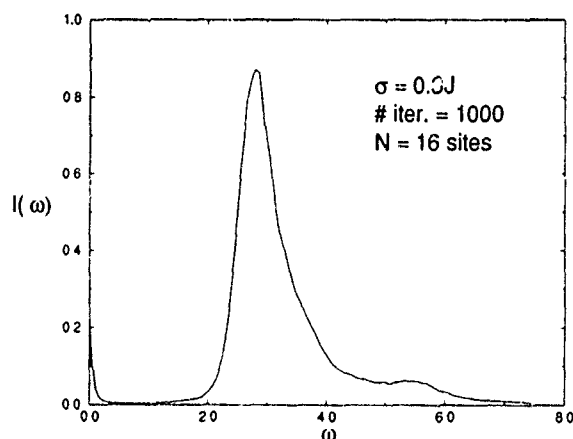


FIG. 2. B_{1g} Raman spectrum for the Heisenberg model on a 4×4 lattice in the presence of randomness in the exchange integral; this represents the effect of the spin-pair-phonon interaction; ω is given in units of J .

action is between the magnon pair and phonons. The phonons distort the lattice and renormalize the spin-spin exchange interaction in H_0 . This mechanism relates to that proposed by Halley⁶ to account for two-magnon infrared absorption in, e.g., MnF_2 . The calculations in Fig. 2 correspond to the Raman spectra of a disordered lattice, or alternatively, to the quenched phonon approximation. This approximation is valid for the cuprates because there is a clear separation of energies between the fast modes (magnons) and the slow modes (phonons). For instance, in $YBa_2Cu_3O_6$ the characteristic Debye frequency is about 340 cm^{-1} while the two-magnon excitation is $\approx 3080 \text{ cm}^{-1}$. The Born-Oppenheimer approximation focuses on the fast modes and freezes the slow ones.

In our approach, we consider quantum fluctuations and, more important, finite temperatures, which distort the lattice. In turn, these lattice distortions induce changes, δJ_{ij} , in the exchange integral J of the perfect undistorted lattice. Here, δJ_{ij} represents the instantaneous value of $\mathbf{Q} \cdot \nabla_{\mathbf{Q}} J_{ij}(\mathbf{R})$, where \mathbf{R} denotes the equilibrium position of the ion carrying the spin, and \mathbf{Q} is the deviation from the equilibrium. In the quenched disorder approximation, we obtain the effective Hamiltonian

$$H_i = \sum_{\langle ij \rangle} (J + \delta J_{ij}) \mathbf{S}_i \cdot \mathbf{S}_j, \quad (5)$$

where $|\delta J_{ij}| < J$ is a random variable reflecting the motion of the ions. Owing to this motion, the translational invariance of the original Heisenberg Hamiltonian [Eq. (1)] breaks down. This corresponds to taking a snapshot of the lattice, i.e., to a Born-Oppenheimer-type approximation which focuses on the fast (high-energy) modes and freezes the slow (low-energy) phonon modes.

In our study, the random couplings δJ_{ij} were drawn from a Gaussian distribution

$$P(\delta J_{ij}) = \frac{1}{\sqrt{2\pi}\sigma} \exp[-(\delta J_{ij})^2/2\sigma^2].$$

For a typical optical phonon frequency ($\approx 340 \text{ cm}^{-1}$ for $YBa_2Cu_3O_6$), we expect $\sigma \approx 0.3J$.⁷ $I(\omega)$ was obtained as the quenched average over $m \approx 1000$ realizations of the randomly distorted lattice. The quenched average of an operator \hat{O} is defined by

$$\langle\langle \hat{O} \rangle\rangle = \frac{1}{m} \sum_{j=1}^m \langle \phi_0(j) | \hat{O} | \phi_0(j) \rangle, \quad (6)$$

where $\phi_0(j)$ is the ground state of the j th realization of the disordered system.

In Fig. 2, we show the Raman spectrum for the 16-site square lattice in the presence of random exchange couplings drawn from a Gaussian distribution with $\sigma \approx 0.3J$, which we found to agree best with experimental spectra.¹

We find that the three main features observed in the experiments,¹ namely, the broad line shape of the two-magnon peak, the asymmetry about its maximum, and the existence of spectral weight up to $\omega \sim 8J$ are well reproduced. Beyond the two-magnon peak, there is a continuum of phonon-multimagnon excitations. The small feature

around $\omega \sim 5.5J$ is tentatively assigned to a four-magnon excitation. We are currently investigating this point. In addition, the calculated A_{1g} component (not shown), which becomes allowed due to disorder, also shows good agreement with experiments.

Finally, we would like to stress that not every kind of disorder gives rise to the observed broadening of the spectrum. For instance, disorder by point defects or twinning planes will not produce such an effect. Also, it is observed in experiments that the Raman linewidth broadens with increasing temperature.⁸ This is a strong indication of a phonon mechanism for the broadening.

In summary, we find strong evidence of phonon-induced broadening of the two-magnon Raman scattering peak by treating the low-energy phonons as a static random distortion of the lattice. Our results are in good agreement with experimental spectra.

S. H. acknowledges support by the Southeastern University Research Association (SURA) and by the Supercomputer Computations Research Institute (SCRI). J. R. has been supported in part by the U.S. Department of Energy (DOE) Office of Scientific Computing under the High Performance Computing and Communications Program (HPCC), and in part by DOE under Contract No. DE-AC05-84OR21400

managed by Martin Marietta Energy Systems, Inc., and under Contract No. DE-FG05-87ER40376 with Vanderbilt University. The work of E. D. is partially supported by the ONR Grant No. N00014-93-1-0495, and by the donors of The Petroleum Research Fund.

¹K. B. Lyons *et al.*, Phys. Rev. Lett. **60**, 732 (1988); Phys. Rev. B **39**, 2293 (1989); I. Ohana *et al.*, *ibid.* **39**, 2293 (1989); P. E. Sulewski *et al.*, *ibid.* **41**, 225 (1990); S. Sugai *et al.*, *ibid.* **42**, 1045 (1990); R. Liu *et al.* (unpublished).

²R. R. P. Singh *et al.*, Phys. Rev. B **62**, 2736 (1989); S. Bacci and E. Gagliano, *ibid.* **42**, 8773 (1990); S. Bacci and E. Gagliano, *ibid.* **43**, 6224 (1991).

³E. Dagotto and D. Poilblanc, Phys. Rev. B **42**, 7940 (1990).

⁴C. M. Cannali and S. M. Girvin, Phys. Rev. B **45**, 7127 (1992).

⁵M. J. Massey *et al.*, Phys. Rev. Lett. **69**, 2299 (1992); S. Rosenblum *et al.*, Phys. Rev. B (to be published).

⁶J. W. Halley, Phys. Rev. **154**, 458 (1967).

⁷For conventional transition metal oxides and halide magnets, the dependence of the superexchange integral J on the spin-spin separation r is approximately given by $J(r) \sim r^{-10}$. This decay law can be extracted from experiments probing the pressure dependence of J ; see, e.g., M. J. Massey *et al.*, Phys. Rev. B **41**, 8776 (1990). However, for the cuprates the exact value of the decay exponent is still not agreed upon. For instance, recent results of M. Aronson *et al.*, Phys. Rev. B **44**, 4657 (1991), predict an exponent of about -6.4 ± 0.8 . Nevertheless, any of these values for the decay exponent gives a very strong dependence of J on the spin-spin separation, and our estimate for σ is not significantly affected by them.

⁸P. Knoll *et al.*, Phys. Rev. B **42**, 4842 (1990).

Vortex flux creep and magnetic hysteresis in a type-II superconductor (abstract)

M. K. Hasan, S. J. Park, and J. S. Kouvel^{a)}

Physics Department, University of Illinois, Chicago, Illinois 60680

Upon reversal of the external magnetic field H during any hysteretic cycling of a type-II superconductor in its vortex state, the rate at which the magnetic flux density B varies with H is typically seen to start from zero and then change gradually. Measurements have now been made of the time dependence of B (the vortex flux creep) at many fixed- H points on several hysteresis loops of a grain-oriented $\text{YBa}_2\text{Cu}_3\text{O}_7$ sample at 4.2 K (with \mathbf{H} and \mathbf{B} along the c axis), and it is observed that the size of the logarithmic dB/dt drops abruptly to zero, before proceeding to change in sign, whenever H is reversed. This curious similarity between the hysteretic behavior of dB/dt at fixed H and that of the nearly instantaneously measured dB/dH can be understood qualitatively in terms of the vortex pinning. As rotational magnetization measurements have recently shown,¹ the unpinning and repinning of moving vortices is manifested macroscopically as a frictional process. Thus, the reversal of vortex motion involves the reversal of frictional forces, during which the vortex population in the superconducting sample (which is proportional to B) does not change with time or field.

^{a)}Work supported in part by NSF Grant No. DMR-90-24416.

¹H. P. Goeckner and J. S. Kouvel, J. Appl. Phys. 73, 5860 (1993), and references therein.

Interactions with the Dy^{3+} sublattice observed in high resistance ultrathin $\text{DyBa}_2\text{Cu}_3\text{O}_{7-x}$ films (abstract)

K. M. Beauchamp, G. C. Spalding, W. H. Huber, and A. M. Goldman

University of Minnesota, Minneapolis, Minnesota 55455

A low-temperature anomalous magnetoresistance has previously been reported in disordered ultrathin $\text{DyBa}_2\text{Cu}_3\text{O}_{7-x}$ films. This unusual behavior was associated with interactions between the charge carriers and a magnetic lattice. Here, new results are presented showing a peak in the temperature dependence of the resistivity near the Dy^{3+} Néel temperature. A calculation is included which shows that the peak in $R(T)$ is consistent with spin disorder scattering from the Dy^{3+} ions as they order antiferromagnetically. These observations lend support to the suggestion, based on neutron scattering studies, that the Dy^{3+} interactions are not strictly dipolar and that the electrons may contribute to the magnetic ordering of the Dy^{3+} sublattice.

Probing of the pairing state of HTSCs utilizing *a-b* plane magnetization anisotropy (abstract)

J. Buan, N. E. Israeloff, C. C. Huang, and A. M. Goldman

*Center for Science and Application of Superconductivity and School of Physics and Astronomy,
University of Minnesota, Minneapolis, Minnesota 55455*

J. Z. Liu and R. N. Shelton

Department of Physics, University of California, Davis, California 95616

We have performed measurements of the *a-b* plane longitudinal and transverse magnetization anisotropy on an untwinned, high quality single crystal of $\text{LuBa}_2\text{Cu}_3\text{O}_{7-x}$ in magnetic fields below H_{c1} as a function of temperature, from 2 K to the transition temperature and the angle between the field and a fixed direction in the *a-b* plane. When the superconducting order parameter has nodes on the Fermi surface, such as the case of the spin-singlet $d_{x^2-y^2}$ order parameter, nonlinear effects associated with low-energy quasiparticles should become important.¹ It was pointed out by Yip and Sauls that these effects will be most important at low temperatures. They should be observable in a measurement of the anisotropy of the magnetization or the magnetic torque. The magnetization is predicted to develop an anisotropic component transverse to the applied field. Anisotropic transverse magnetization with $d_{x^2-y^2}$ symmetry is not seen in the temperature regime 5 to 25 K. Our results set stringent limits on the anisotropy of the transverse magnetization in this range. Within the resolution of our experiment no evidence for *d*-wave pairing is observed.

Supported in part by the Materials Research Group Program of the NSF under Grant No. NSF/DMR-8908094.

¹S. K. Yip and J. A. Sauls, Phys. Rev. Lett. **69**, 2264 (1992).

Theory of two-dimensional antiferromagnets with a nearly critical ground state (abstract)

Andrey V. Chubukov^{a)} and Subir Sachdev

Departments of Physics and Applied Physics, P. O. Box 2157, Yale University, New Haven, Connecticut 06520

We present the general theory of clean, two-dimensional, quantum Heisenberg antiferromagnets which are close to the zero-temperature quantum transition between ground states with and without long-range Néel order. For Néel-ordered states, "nearly-critical" means that the ground state spin stiffness, ρ_s , satisfies $\rho_s \ll J$, where J is the nearest-neighbor exchange constant, while "nearly-critical" quantum-disordered ground states have an energy gap, Δ , towards excitations with spin-1, which satisfies $\Delta \ll J$. The allowed temperatures, T , are also smaller than J , but *no* restrictions are placed on the values of $k_B T / \rho_s$ or $k_B T / \Delta$. Under these circumstances, we show that the wave vector /frequency-dependent uniform and staggered spin susceptibilities, and the specific heat, are completely universal functions of just three thermodynamic parameters. On the ordered side, these three parameters are ρ_s , the $T=0$ spin-wave velocity c , and the ground state staggered moment N_0 . Explicit results for the universal scaling functions are obtained by a $1/N$ expansion on the $O(N)$ quantum nonlinear sigma model. These calculations lead to a variety of testable predictions for neutron scattering, NMR, and magnetization measurements. Our results are in good agreement with a number of numerical simulations and experiments on undoped and lightly doped $\text{La}_{2-x}\text{Sr}_x\text{CuO}_4$.

^{a)}Also with the P. L. Kapitza Institute for Physical Problems, Moscow, Russia.

Electronic structure and magneto-optical properties of MnBi and MnBiAl

S. S. Jaswal, J. X. Shen, R. D. Kirby, and D. J. Sellmyer

Behlen Laboratory of Physics and Center for Materials Research and Analysis, University of Nebraska,
Lincoln, Nebraska 68588-0111

MnBiAl films are of considerable current interest for possible magneto-optical applications because of their perpendicular anisotropy, large polar Kerr rotation, reduced grain size, and structural stability. We report here experimental and theoretical studies of the effect of Al alloying on the electronic structure and magneto-optical properties of MnBi. Our measured spectral dependencies of the polar Kerr rotation in the two systems are similar. We carried out relativistic self-consistent spin-polarized electronic structure calculations on MnBi and MnBiAl, and the calculated densities of states are in good agreement with available x-ray photoemission spectroscopy data for both materials. The spin magnetic moment of Mn increases and the overall orbital moment decreases with the addition of Al to MnBi. The latter effect implies the lowering of spin-orbit interactions upon alloying MnBi with Al, and the two effects together suggest that the spectral dependencies of the Kerr rotation should be similar, as is observed experimentally.

MnBi has been known for several decades as a material with a large Kerr rotation. Recently, efforts have been made to improve its magneto-optical properties by alloying with other metals such as Al.¹⁻⁴ The electronic structure of MnBi has been calculated by Coehoorn and deGroot,⁵ and a cluster study on the electronic and magnetic properties of MnBi and MnBiAl has been reported.⁶ We report here theoretical and experimental studies of the electronic structure and magneto-optical properties of MnBi and MnBiAl.

MnBi crystal is hexagonal with four atoms per unit cell and the space group symmetry is $P6_3/mmc$ with sites a and c occupied. MnBiAl also has the same structure, and the distance between the hexagonal planes remains essentially unchanged upon alloying MnBi with Al. Unfortunately, little information is available on the change in the a lattice constant with the addition of Al. Also, the sites occupied by the Al atoms are unknown, but the interstitial sites in the hexagonal NiAs structure are thought to be the most likely candidates. In the present calculations we assume MnBiAl to be an ordered structure with all the interstitial (d) sites occupied by Al atoms. We had to make the a lattice constant of MnBiAl 15% larger than that of MnBi to stabilize the electronic structure calculations.

The relativistic self-consistent spin-polarized electronic structure calculations are based on the linear muffin-tin orbitals method (LMTO) in the local density approximation.⁷ MnBi and MnBiAl have four and six atoms per unit cell, respectively. With s , p , and d as basis functions, the relativistic Hamiltonian gives 72×72 and 108×108 matrices for MnBi and MnBiAl, respectively.

The results for total and partial spin-polarized densities of states (DOS) for MnBi are shown in Fig. 1. The Mn $3d$ states dominate the spectrum with a peak around 3 eV below the Fermi level in the occupied states. The magneto-optical properties of MnBi are primarily determined by transitions between Mn d and Bi p states. The present results are similar

to those of Coehoorn and deGroot⁵ based on the augmented spherical wave method.

The MnBiAl DOS, plotted in Fig. 2, are qualitatively similar to those of MnBi. The differences in the two spectra arise because of the additional hybridization mainly between the s - p states of Bi and Al in MnBiAl. The calculated DOS for the two systems are in good agreement with the x-ray photoemission spectroscopy data of Wang *et al.*²

The calculated magnetic moments in MnBi and MnBiAl are listed in Table I. The Mn moment in MnBiAl is about 5% larger than that in MnBi, whereas the induced moment on Bi goes down. This is due to the reduced hybridization between Mn and Bi states, which results from the hybridization of the Bi and Al states mentioned in the preceding paragraph.

The Kerr rotation in the two systems is primarily due to the magnetism of Mn and the spin-orbit interactions of Bi.⁸

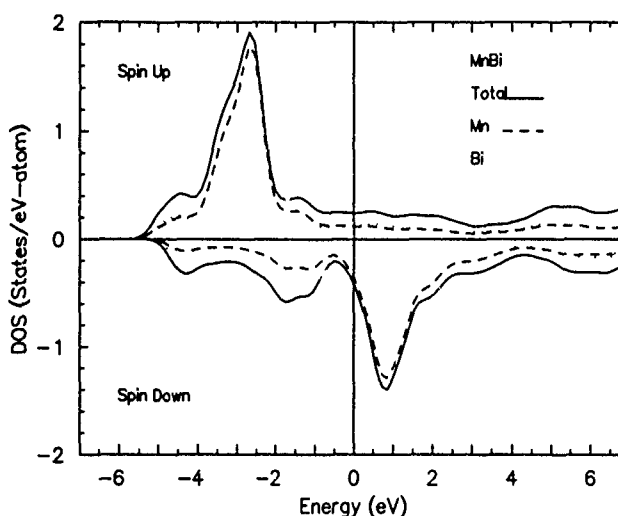


FIG. 1. Total and partial spin-polarized densities of states of MnBi.

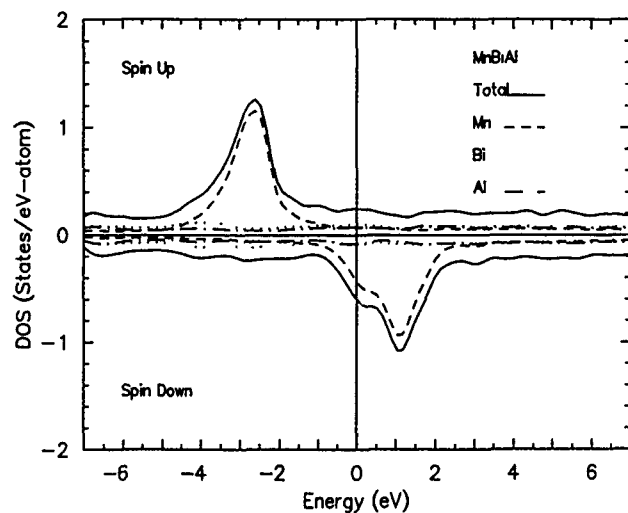


FIG. 2. Total and partial spin-polarized densities of states of MnBiAl.

We have seen above that the addition of Al to MnBi enhances the Mn magnetic moment. To study the effect of Al on spin-orbit interactions, we have calculated the orbital moments in the two systems, which are given by

$$l_z = \sum_{\sigma l m_l} n_{m_l}^{\sigma} m_l,$$

where m_l is the magnetic quantum number corresponding to the orbital quantum number l and $n_{m_l}^{\sigma}$ is the occupied number density for spin σ .⁹ The calculated values of the orbital moment (in μ_B) for MnBi and MnBiAl are 0.129 and 0.057 per unit cell, respectively. Thus the addition of Al to MnBi lowers the spin-orbit interactions due to the hybridization of Al and Bi states.

The present calculations are based on 33.3 at. % Al in MnBiAl, while the experimental results are for Al concentrations of typically 15 at. %. Thus the increase in the magnetic

TABLE I. Magnetic moments (in μ_B) for different sites in MnBi and MnBiAl.

	MnBi		MnBiAl
	Present calculations	Ref. 5	Present calculations
Mn	3.78	3.61	4.08
Bi	-0.20	-0.09	-0.01
Al			-0.02

moment of Mn and the decrease in spin-orbit interactions for the experimental concentrations of Al in MnBi are expected to be small. Since the changes in the magnetic moments and spin-orbit interactions due to aluminization of MnBi have

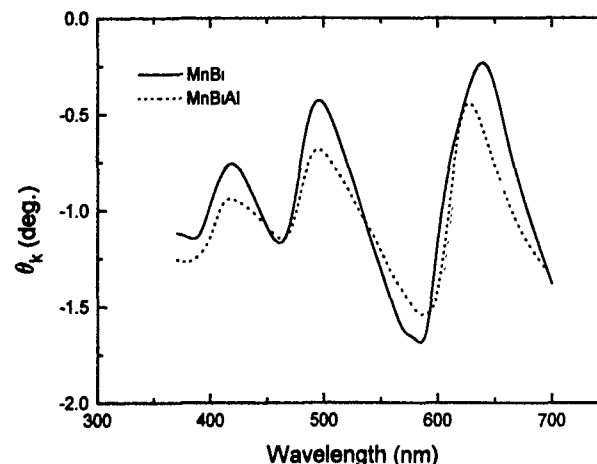


FIG. 3. Measured polar Kerr rotation as a function of the wavelength in MnBi and MnBiAl. The oscillations in the rotation are due to optical interference effects in the SiO_x overcoat. The nominal compositions were $\text{Mn}_1\text{Bi}_{0.8}$ and $\text{Mn}_1\text{Bi}_{0.8}\text{Al}_{0.4}$.

opposite effects on the Kerr rotation, we expect Kerr spectra of MnBi and MnBiAl to be quantitatively similar.

Our experimental results for the Kerr rotation as a function of wavelength are plotted in Fig. 3. The oscillations in the data are due to multiple reflections from the ~ 150 nm thick SiO_x overcoat. Taking the average values of these oscillations, we note that the Kerr rotations for MnBi and MnBiAl are similar, in agreement with our theoretical predictions. Our experimental results are also in agreement with those of Di *et al.*⁴ The experimental results of Wang *et al.*^{1,2} are somewhat similar to the above data except for a low value of 0.7° for MnBi at 633 nm.

In conclusion, the electronic structure calculations predict that the Kerr rotations in MnBi and MnBiAl should be similar, which is in agreement with the experimental data.

This work is supported by the National Science Foundation under Grant No. DMR-9222976, ARPA Grant No. MDA 972-93-1-0009 to the National Storage Industry Consortium, the NSF Experimental Program to Stimulate Competitive Research, and the National Supercomputing Facility at Cornell University. We are grateful to Hans Skriver for the copies of relativistic LMTO programs.

¹Y. J. Wang, J. Magn. Magn. Mater. **84**, 39 (1990).

²Y. J. Wang, C. Luo, L. C. Kong, X. Qi, D. Huang, and Y. Chen, J. Magn. Soc. Jpn. Suppl. **17** (S1), 294 (1993).

³J. X. Shen, R. D. Kirby, D. J. Sellmyer, and Y. J. Wang, J. Appl. Phys. **69**, 5984 (1991).

⁴G. Q. Di, S. Iwata, S. Tsunashima, and S. Uchiyama, J. Magn. Magn. Mater. **104-107**, 1023 (1992).

⁵R. Coehoorn and R. A. de Groot, J. Phys. F **15**, 2135 (1985).

⁶L. Zhiqiang, L. Helie, L. Wuyan, Z. Zhi, and Z. Qingqi, J. Magn. Magn. Mater. **98**, 47 (1992).

⁷H. L. Skriver, *The LMTO Method*, Vol. 41 of *Springer Series in Solid State Sciences* (Springer, New York, 1984).

⁸D. K. Misemer, J. Magn. Magn. Mater. **72**, 267 (1988).

⁹M. S. S. Brooks and P. J. Kelly, Phys. Rev. Lett. **51**, 1708 (1983).

Low-temperature characterization of the magnetic properties of MnBiAl thin films

K. W. Wierman, J. X. Shen, R. D. Kirby, and D. J. Sellmyer

Behlen Laboratory of Physics and Center for Materials Research and Analysis, University of Nebraska, Lincoln, Nebraska 68588-0111

The magnetic properties of thin-film samples of $\text{MnBi}_{0.8}\text{Al}_x$ with aluminum concentrations of $x=0.0, 0.4, 0.6$, and 0.8 were systematically studied over a temperature range of 20 to 300 K. The as-deposited films are amorphous and nonmagnetic, but highly textured polycrystalline films that are ferromagnetic are formed by annealing at 350 °C. Our measurements show that the coercivity of such films rapidly decreases, then approaches a constant value (4 kOe for $x=0.4$) with increasing annealing time. Magnetic measurements show that both anisotropy and coercivity decrease with decreasing temperature. Unlike bulk MnBi, our $\text{MnBi}_{0.8}\text{Al}_x$ thin films do not have a spin reorientation transition at low temperatures. This may be due to impediment of the lattice contraction by the Al atoms doped into the interstitial sites of the MnBi lattice.

INTRODUCTION

MnBiAl has been proposed as a possible magneto-optical storage candidate due to its large Kerr rotation and perpendicular magnetic anisotropy. Wang reported that (Al,Si) doping increased the Kerr rotation, improved the thermal stability, and reduced the polycrystalline grain size.¹ Roberts² carried out neutron diffraction studies on bulk MnBi and found that the c axis contracted by more than 1% as the temperature was lowered from 300 to 5 K. Recent work by Guo *et al.*³ on bulk MnBi showed that the uniaxial anisotropy constant decreases substantially with decreasing temperature, and the lattice contraction may be a major contributing factor to this decrease. It is also of interest to ascertain what role aluminum doping plays in determining the anisotropy energy and its temperature dependence.

EXPERIMENT

$\text{MnBi}_{0.8}\text{Al}_x$ thin films with nominal Al contents $x=0.0, 0.4, 0.6$, and 0.8 were made by sequential evaporation of Bi, Mn, and Al from a tungsten boat onto a room-temperature glass substrate. The base pressure of the vacuum chamber was 3×10^{-7} Torr, and the film thickness was typically 80 nm. After evaporation, the thin films were covered with a 150-nm-thick SiO_x protective layer. Samples were annealed in vacuum for 4 h at 350 °C. X-ray diffraction measurements show large intensities for the (002) and (004) MnBi peaks, indicating that the annealed films have the NiAs-type hexagonal structure with the c axis highly oriented along the film normal. The c -axis lattice parameter of $\text{MnBi}_{0.8}\text{Al}_{0.8}$ (6.06 Å) is the same as that of MnBi_{0.8} (6.07 Å) within measurement error, similar results were obtained for $x=0.4, 0.6$. In the measurements reported here, the temperature dependencies of the perpendicular anisotropy constant K_u , coercive force H_c , and remnant magnetization were determined from hysteresis loops generated by an alternating-gradient force magnetometer (AGFM). Kerr rotation versus total annealing time measurements were made using an apparatus described elsewhere.⁴

RESULTS AND DISCUSSION

Figure 1 shows the perpendicular and parallel hysteresis loops as measured with the AGFM for $\text{MnBi}_{0.8}\text{Al}_{0.4}$ at three different temperatures. These loops clearly show that perpendicular anisotropy is maintained down to low temperatures for $x=0.4$, and similar loops were obtained for the $x=0.0, 0.6$, and 0.8 samples. No evidence of the spin reorientation transition reported for bulk MnBi is found in these measurements.⁵

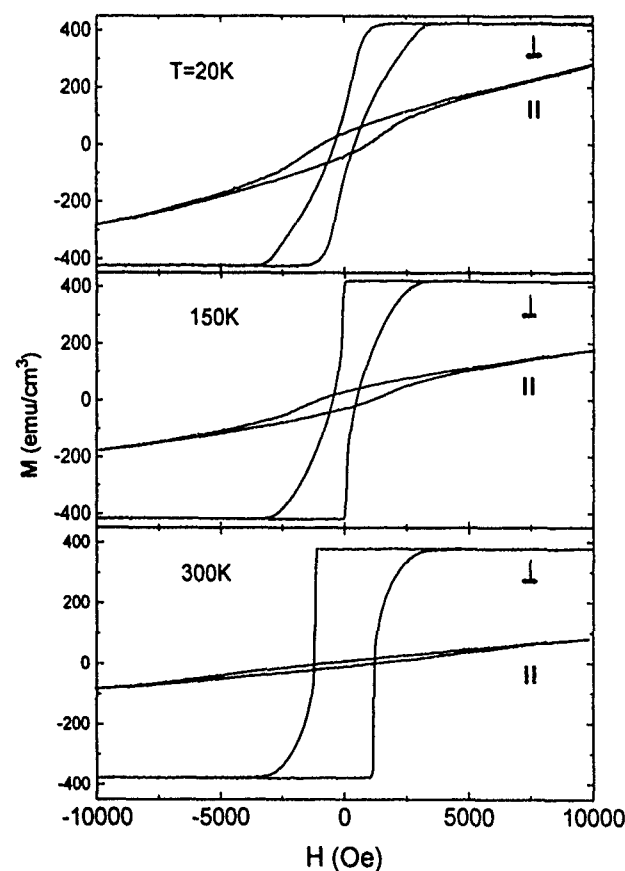


FIG. 1. Parallel and perpendicular magnetization loops for $\text{MnBi}_{0.8}\text{Al}_{0.4}$. The parallel and perpendicular loops are indicated.

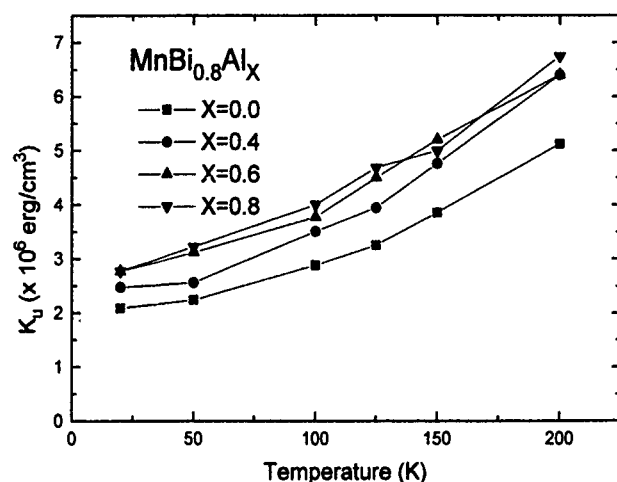


FIG. 2. Temperature dependence of the anisotropy constant K_u of $\text{MnBi}_{0.8}\text{Al}_{0.4}$ for four different sample compositions.

The area between the perpendicular and parallel hysteresis loops was used to determine the magnetic anisotropy constant K_u , and Fig. 2 shows the temperature dependence of K_u for $x=0.0, 0.4, 0.6$, and 0.8 . It can be seen that for each sample K_u increases with increasing temperature, as was found for bulk MnBi ,^{3,5} with the $x=0.8$ sample showing the largest increase. K_u could not be reliably determined for temperatures above 200 K because of the limited magnetic field available on the AGFM. Assuming the decrease in K_u with decreasing temperature is due to contraction of the c axis, then Al doping appears to hinder this contraction. This would be consistent with the Al atoms residing at the interstitial sites as opposed to in the grain boundaries.

Figure 3 plots the ratio of the remnant magnetization to the saturation magnetization (M_r/M_s) as a function temperature. The sharp drop in this ratio as T goes below 150 K is likely associated with the rapid reduction in K_u as the temperature is lowered. However, even at 50 K the anisotropy field ($2K_u/M_s$) is still a factor of two to three larger than the demagnetizing field ($H_d = 4\pi M_s$), suggesting that the rapid

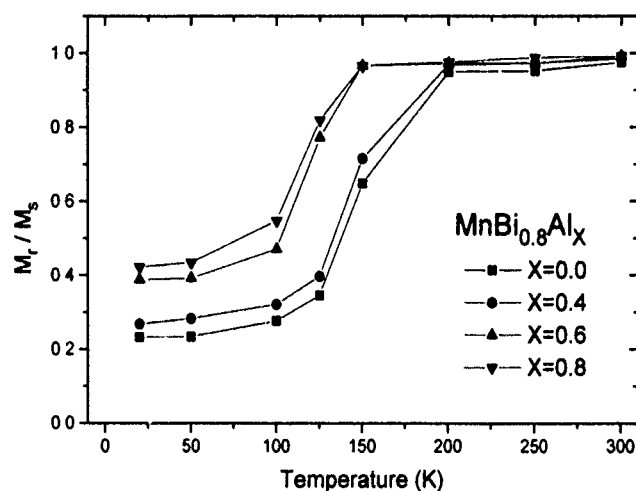


FIG. 3. Temperature dependence of the remnant magnetization M_r for four different sample compositions.

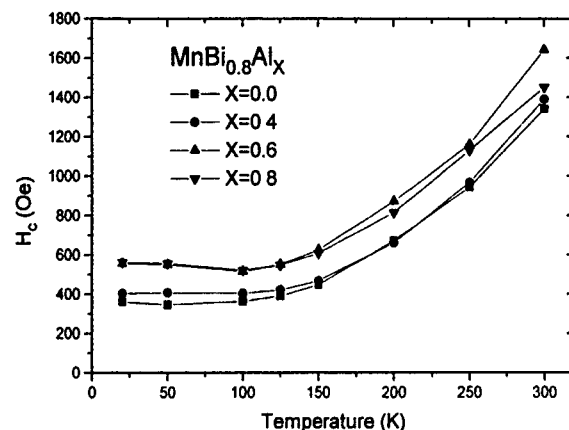


FIG. 4. Coercivity of $\text{MnBi}_{0.8}\text{Al}_{0.4}$ vs temperature for four different sample compositions.

drop in the remnant magnetization near 150 K is due to domain formation. It should also be noted that Al doping seems to only moderately improve loop squareness.

Figure 4 shows the coercivity as a function of temperature for all four samples. It should be noted that the $x=0.8$ sample has a slightly smaller coercivity than the $x=0.6$ at 300 K, even though it has a larger value of K_u . This suggests that physical properties other than the anisotropy field, such as crystalline microstructure and small variations in composition, are important in determining the magnitude of the coercivity.

Figure 5 shows the coercivities of $\text{MnBi}_{0.8}$ and $\text{MnBi}_{0.8}\text{Al}_x$ as a function of annealing time at 350 °C. The initial rapid decreases in the coercivities are consistent with crystallization of small particles, followed by growth of the particles. After annealing for about 6 h, no additional reductions in the coercivities are observed, suggesting that the crystallization process is completed and the particle sizes have reached their maximum values. The magnitude of the Kerr rotation (not shown) shows a behavior consistent with this interpretation. It rises rapidly from zero as a function of annealing time, finally saturating after 6 h of annealing. The

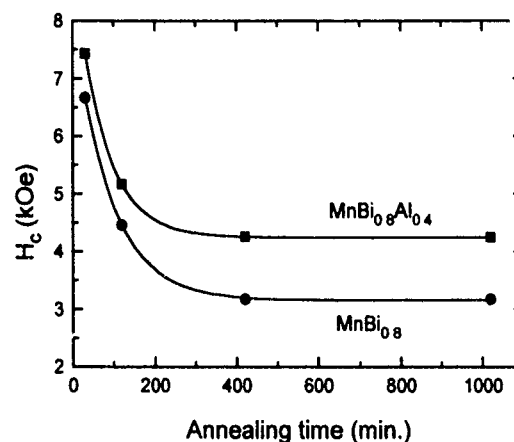


FIG. 5. Coercivity vs annealing time for $\text{MnBi}_{0.8}\text{Al}_{0.4}$ and $\text{MnBi}_{0.8}$.

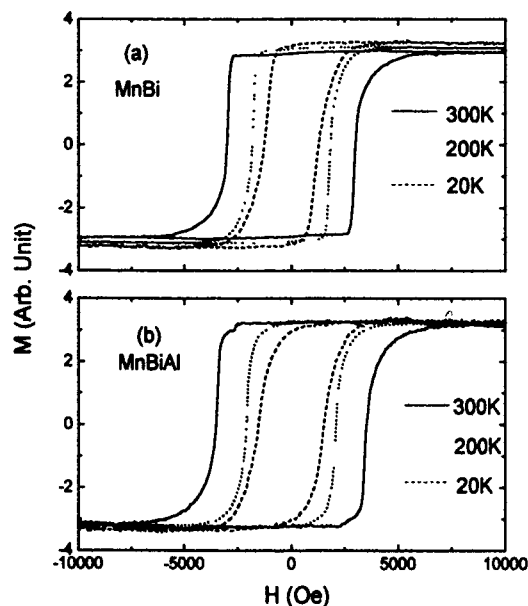


FIG. 6. Hysteresis loops obtained with an AGFM for (a) $\text{MnBi}_{0.8}$ and (b) $\text{MnBi}_{0.8}\text{Al}_{0.4}$ after 45 h of annealing at 350 °C.

Al-doped sample has a larger coercivity for all annealing times, which may be a reflection of the smaller grain sizes expected with Al doping.¹

Figure 6 shows the temperature dependencies of the hysteresis loops for $\text{MnBi}_{0.8}$ and $\text{MnBi}_{0.8}\text{Al}_{0.4}$ after 45 h of annealing. Notice that both samples have nearly 100% remnant magnetization, even at the lowest temperature of 20 K. These results show that annealing conditions can have a larger effect on the remnant magnetization than does Al doping. The

similar results here for $\text{MnBi}_{0.8}$ and $\text{MnBi}_{0.8}\text{Al}_{0.4}$ may be a consequence of diffusion of Si from the SiO_x overcoat into the bulk of the sample, as has been suggested by Wang.¹

In summary, we have studied the magnetic properties of $\text{MnBi}_{0.8}\text{Al}_x$ for four different compositions over the temperature range 20 to 300 K. The values of the uniaxial anisotropy constant K_u were found to increase with Al content at room temperature and below. Our measurements showed no evidence of the low-temperature spin-reorientation transition previously observed in bulk MnBi. Coercivity measurements versus annealing time were obtained showing the sensitivity of the magnetic properties to annealing conditions. Further x-ray diffraction and electron microscopy studies are needed to determine the positions of the Al atoms and further to determine the effects that annealing conditions have on the crystal structure and microstructure. These studies are under way.

ACKNOWLEDGMENTS

We are indebted for financial support of this work to the National Science Foundation under Grant No. DMR-9222976, and to the Advanced Research Projects Agency/National Storage Industry Consortium under Grant No. MDA972-93-1-0009.

¹Y. J. Wang, *J. Magn. Magn. Mater.* **84**, 39 (1990).

²B. W. Roberts, *Phys. Rev.* **104**, 607 (1956).

³X. Guo, X. Chen, Z. Altounian, and J. O. Ström-Olsen, *Phys. Rev. B* **46**, 14578 (1992).

⁴J. X. Shen, R. D. Kirby, and D. J. Sellmyer, *J. Magn. Magn. Mater.* **81**, 107 (1989).

⁵R. S. Tebble and D. J. Craik, *Magnetic Materials* (Wiley-Interscience, New York, 1969), p. 125.

The functions of Al in MnBiAlSi magneto-optical films

D. Huang, X. W. Zhang, C. P. Luo, H. S. Yang, and Y. J. Wang

State Key Laboratory of Magnetism, Institute of Physics, Chinese Academy of Sciences, Beijing 100080, China

This article reports the effect of Al doping into MnBiSi films on the structure and magneto-optical properties of the parent. Under suitable Al doping, the x-ray diffraction peaks of (002) and (004) move to a larger 2θ value related to that of MnBiSi. Moreover, two satellite peaks appear beside the main (002) and (004) peaks of MnBiAlSi. Such structural distortion due to Al doping results in an increased Kerr rotation angle, an effective perpendicular anisotropy constant K_u , as well as improvement of the thermal stability of MnBiSi.

I. INTRODUCTION

Since 1973 great attention has been paid to the amorphous rare-earth (RE)-transition-metal alloy film because of its large magneto-optical (MO) recording density.¹⁻³ These materials are used in practical MO disk products on the market today. However, a number of basic deficiencies remain, which include domain stability, thermal stability, and corrosion resistance. Moreover, these materials have small Kerr rotation angle and poor figure of merit around 400 nm. Apparently, RF-TM alloys must be replaced by a new medium because the short-wavelength recording is the trend for the MO disk since realization of the 420-nm recording will make it possible to increase the area density by a factor of 4.⁴

Nowadays, finding a new recording medium suitable for short-wavelength MO recording is of great interest. Several candidates such as Pt/Co multilayers and doped garnet are competing as the second generation recording medium. Pt/Co multilayers especially have a good figure of merit at about 400 nm (Ref. 5) as compared to the amorphous film.

Much of the earlier work on MO media was about MnBi (Ref. 6) since it satisfies some requirements of MO media such as large Θ_K , perpendicular anisotropy, and rectangular hysteresis loop. The major factor that obstructs the progress of MnBi as an available MO medium is that it has two crystal phases with the transition temperature close to its Curie temperature and thermomagnetic writing will result in thermal instability. In 1988, Wang reported on the (Al,Si)-doped MnBi film.^{7,8} With the doping of Al and Si, the phase transition of MnBi is successfully suppressed. Meanwhile, the Θ_K is greatly increased to 2.04° at 6328 \AA , 1.6° at $0.4 \text{ }\mu\text{m}$. Comparatively, at $0.4 \text{ }\mu\text{m}$, it is about three times as large as that of Pt/Co multilayers and six to seven times of TbFeCo. As a result, (Al,Si)-doped MnBi film becomes a promising candidate.⁹

In this article, using the data from the homogeneous saturated samples, we have systematically studied the effect of Al doping, concerning the MO properties, crystal structure, and temperature dependence of some material parameters.

II. EXPERIMENTAL PROCEDURE

As our previous reports showed,^{7,8} $\text{Mn}_{1.0}\text{Bi}_{0.7}\text{Al}_{0.3}$ (named MnBiAlSi) and $\text{Mn}_{1.0}\text{Bi}_{1.0}$ (MnBiSi) films were prepared by thermal evaporating pure metals Bi, Al, and Mn, respectively, on glass substrate from multiple Ta boats. The

area of substrate is $8 \times 8 \text{ mm}^2$. Silicon oxide film as a protective layer was then deposited on these samples. The base pressure of the vacuum system is about 5×10^{-6} Torr.

The composition of the films was controlled by a quartz crystal monitor during evaporation, Bi, Al, Mn, and SiO were approximately 50, 9, 30, and 150 nm, respectively. The as-deposited films were annealed at about 600 K for 6 h in a vacuum of 1×10^{-6} Torr for alloying.

Magnetic domain structure was examined by using a polarization microscope (PM) in polar reflective mode. The polar Θ_K spectra and hysteresis loop were obtained by using modulation method through glass substrates. The crystalline structure was detected by a x-ray diffractometer (XRD). Torque was also employed to measure the effective perpendicular anisotropy constant K_u at different temperature. The annealing experiment was designed to study the thermal stability.

III. RESULTS AND DISCUSSION

The typical magnetic domain images of MnBiAlSi film are given in Fig. 1, in which Fig. 1(a) is taken just after annealing. Figures 1(b) and 1(c) are taken after the sample was magnetized under 6 kOe along the vertical direction, corresponding to both the remanence states with positive and negative M_r . It reveals that the samples are uniformly saturated. The domain picture of MnBiSi is similar to Fig. 1.

Figures 2(a) and 2(b) are the x-ray diffraction profile of MnBiAlSi and MnBiSi films. The extremely strong (002)

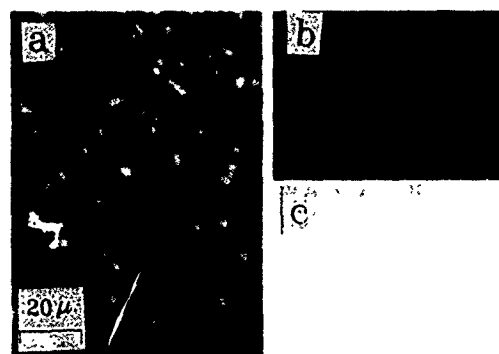


FIG. 1. Magnetic domain images of a MnBiAlSi film, in which (a) is taken just after annealing and (b) and (c) are taken after the domain images are saturated along the vertical with the opposite contrast.

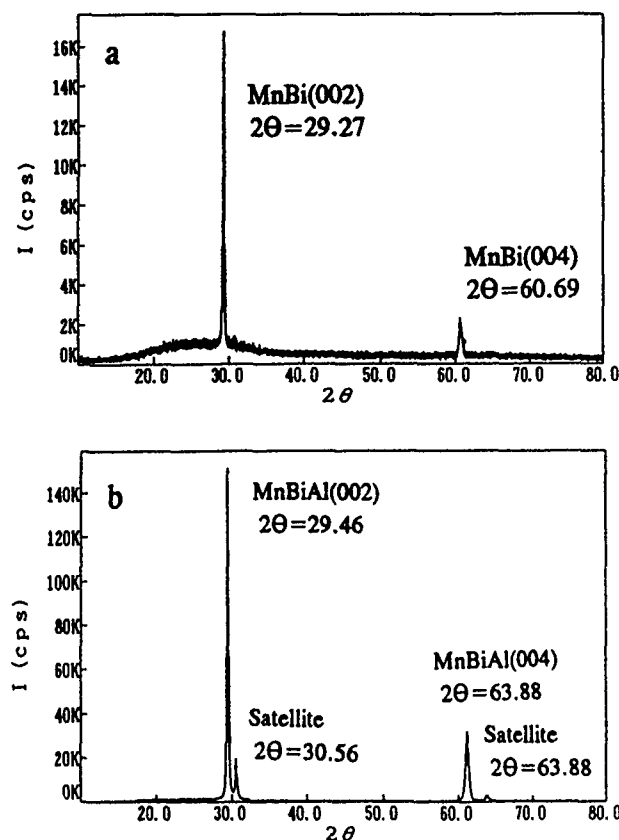


FIG. 2. X-ray diffraction profiles.

and (004) peaks are their common feature. It means that the perfect (002) texture with the c axis normal to the film plane is formed. Meanwhile, the c -axis orientation is also fine, which can be confirmed by $\delta\theta \approx 1.9^\circ$ from the θ - 2θ curve (rocking curve) of the MnBiAlSi sample.

The other structural feature for Al doping into MnBiSi is that two new small satellite peaks appear beside the (002) and (004) peaks of MnBiAlSi on the x-ray profile, and they belong to the same crystal face family. These two peaks are surely not from any peak of Mn, Bi, or MnBi crystalline. They are effect of Al doping and may be of an unknown second new phase, at present. Below we can see that this second phase is stable in structure during the repeatedly heating-quenching circles.

Moreover, it is also found that the index d of MnBiAlSi between the two nearest hexagonal base planes is slightly reduced, from 6.10 Å (MnBiSi) to 6.04 Å (MnBiAlSi). This is evidence of Al in corporation in the MnBi structure.

It is well known that the Al-doped MnBi film has much larger Θ_K than MnBi film.^{7,8} Figure 3 is the Kerr rotation spectra of MnBiAlSi and MnBiSi for our new homogeneous saturated samples. The reflectivity spectra of MnBiAlSi is also shown. Besides the different Θ_K value, we can see that the spectra of MnBiAlSi has an apparent peak structure around 6300 Å, but the peak of MnBiSi is poorly defined. In order to make it clearer, we show the curves in the insert where just the shape of both Kerr spectra are compared. Since the magneto-optical MO effect comes from the transition of the polarized electron,^{10,11} the difference between the spectra suggests that Al doping modulates the structure of the electronic state of MnBi near the Fermi level.

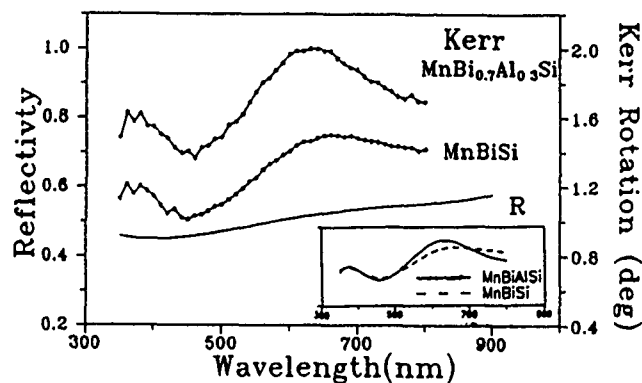


FIG. 3. Kerr rotation and reflectivity spectra. In the insert the shape of Kerr spectra for both samples are compared.

From the hysteresis loops measured by surface magneto-optical Kerr effect (SMOKE) at 6328 Å, as indicated in Fig. 4, we can see that the coercivity increases from about 1.4 kOe of MnBiSi to 2.3 kOe of MnBiAlSi. Also, the rectangular shape is highly improved with the doping of Al atoms. These will make the MnBiAlSi more suitable for MO recording.

At room temperature, K_u of MnBiAlSi is 2.5×10^6 erg/cm³ and $K_u = 1.2 \times 10^6$ erg/cm³ for MnBiSi. The temperature dependence of the normalized anisotropy constant $K_u(T)/K_u(300 \text{ K})$ is given in Fig. 5 for MnBiAlSi and MnBiSi, respectively, for the range 80 to 300 K. From it, we can see that when the temperature varies from 300 down to 80 K, K_u of MnBiSi decreases by 80% from 2.5×10^6 to 0.5×10^6 erg/cm³, similar to the previous report on MnBi alloy film.¹² Comparatively, K_u of MnBiAlSi has only a little change on the whole temperature.

As a magneto-optical recording medium, the thermal stability is very significant. Consequently, the experiment of about 750 K annealing on MnBiAlSi and MnBiSi were done, which approaches to the temperature of MnBi phase transition. The annealing procedure is that the samples were annealed in vacuum about 1×10^{-6} Torr for different durations from 10 to 3000 min at 750 K and then were cooled down to room temperature at the rate of -1.6 K/s . Figure 6 shows the Θ_K value versus the annealing time. It is clear that with the

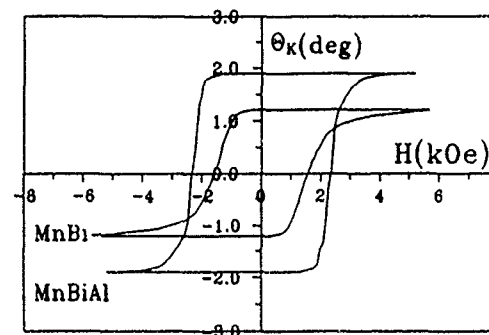


FIG. 4. Kerr hysteresis loops.

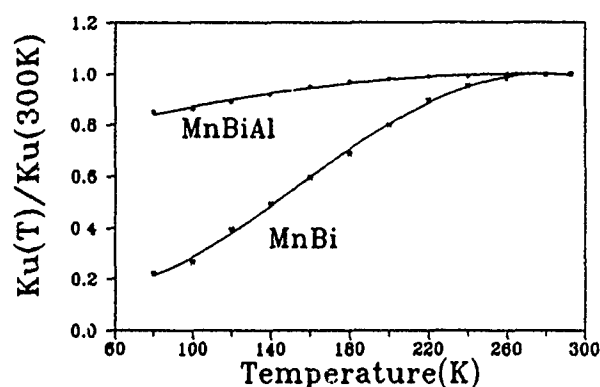


FIG. 5. Temperature dependence of anisotropy constant.

increase of annealing time, Θ_K of MnBiSi decreases continuously from 1.5° to 1.06° , while Θ_K of MnBiAlSi is almost unchanged.

As mentioned above, the Al doping into MnBiSi greatly improves the MO properties and stability, and this improvement maybe resulted from the structure change.

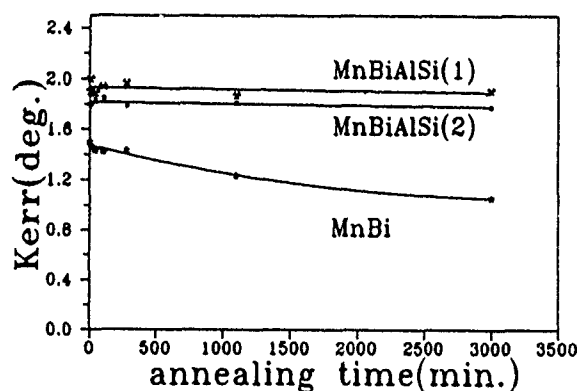


FIG. 6. Effect of thermal annealing on the value of Θ_K .

In the close-packed hexagonal structure of MnBi, there are a total of 14 Mn atoms on two neighboring hcp basal planes and three Bi atoms located at the intermediate between the hcp basal planes in a crystal unit cell. There are three interstitial sites that are identical to the site of three Bi atoms.¹³

In a solid solution if a large atom like Bi is replaced by a small atom like Al, the lattice constant decreases. The change or distortion of the crystal structure must carry out the change of the properties. We know that MO effect of MnBi mainly comes from the interband transition. Its large Θ_K value comes from Mn 3d electrons, which are strongly hybridized with Bi 6p electrons.¹⁴ We consider that the doped Al atoms will surely affect the hybrid states, and consequently will produce the better MO properties including the larger Kerr rotation. The entrance of Al atoms into the lattice of MnBi including the Bi sites and the interstitial sites also affect the bonding between the nearest Mn atoms. The suppression of the phase transition could be related to the improvement of the bonding.

ACKNOWLEDGMENT

We would like to acknowledge the financial support of the joint optical disk laboratory and the state key laboratory of magnetism, Chinese Academy of Sciences, respectively.

- ¹P. Chaudhari, J. J. Cuomo, and R. J. Gambino, Appl. Phys. Lett. **22**, 337 (1973).
- ²S. Matsushita, K. Sunago, and Y. Sakurai, Jpn. J. Appl. Phys. **14**, 1851 (1975).
- ³Y. Mimura, N. Imamura, and T. Kobayashi, Jpn. J. Appl. Phys. **15**, 933 (1976); Y. Mimura, N. Imamura, T. Kobayashi, A. Okada, and Y. Kushiro, J. Appl. Phys. **49**, 1208 (1978).
- ⁴D. Rugar, C.-J. Lin, and R. Geiss, IEEE Trans. MAG-23, 2263 (1987).
- ⁵J. A. M. Greidanus and W. Bas Zeper, Mater. Res. Bull. **15**, 31 (1990).
- ⁶D. Chen, J. F. Ready, and E. Bernal, J. Appl. Phys. **39**, 3916 (1968).
- ⁷Y. J. Wang, J. Magn. Mater. **84**, 39 (1990).
- ⁸Y. J. Wang, J. X. Shen, and Q. Tang, J. Phys. C8, 1725 (1988).
- ⁹S. Uchiyama, J. Magn. Soc. Jpn. **17**, Suppl. S1 (1993).
- ¹⁰P. S. Pershan, J. Appl. Phys. **38**, 1482 (1967).
- ¹¹J. L. Erskine and E. A. Stern, Phys. Rev. Lett. **30**, 1329 (1973).
- ¹²C. Guillaud, Thesis, University of Strasbourg, 1943.
- ¹³B. T. M. Willis and H. P. Pookiby, Proc. Phys. Soc. Sect. B **67**, 290 (1954); P. R. Heikes, Phys. Rev. **99**, 446 (1955).
- ¹⁴R. Coehoorn and R. A. de Groot, J. Phys. F **15**, 2135 (1985).

Magnetic and magneto-optical properties of $\text{Mn}_5(\text{Ge}_{1-x}\text{M}_x)_3$ alloys with $\text{M}=\text{Sn}, \text{Pb}$

Y. Zhang,^{a)} A. P. Runge, Z. S. Shan, and D. J. Sellmyer

Behlen Laboratory of Physics and Center for Materials Research and Analysis, University of Nebraska, Lincoln, Nebraska 68588

We report on the magnetic and magneto-optical properties of the intermetallic alloys $\text{Mn}_5(\text{Ge}_{1-x}\text{M}_x)_3$, where $\text{M}=\text{Sn}, \text{Pb}$. Generally, these alloys were ordered ferromagnetically at $T \geq 300$ K for $x < 0.3$. The structure of $\text{Mn}_5(\text{Ge}_{1-x}\text{Sn}_x)_3$ remains in the hexagonal Mn_5Si_3 (*hP16*) phase up to $x=0.25$ and then changes to Ni_2In (*hP6*) as x approaches 1. The magnetization and Curie temperature of these alloys is largest for small x and reach a minimum value near $x=0.5$. The room temperature Polar Kerr rotation, however, increases from -0.06° at $x=0$ to maximum value of -0.12° at $x=0.1$ before decreasing toward zero for $x > 0.3$. The $\text{Mn}_5(\text{Ge}_{1-x}\text{Pb}_x)_3$ samples show a Mn_5Si_3 structure with ferromagnetic behavior for $x \leq 0.3$, and varying structure with rapidly decreasing magnetization above $x=0.3$. The magnetic behavior observed was complex for $x \geq 0.3$. The Kerr rotation of the Pb-doped alloys in the ferromagnetic region monotonically decreases from -0.06° to zero at $x \approx 0.3$.

I. INTRODUCTION

Current research of materials for use as magneto-optic storage media focuses on ferromagnetic materials that have strong uniaxial anisotropy and Curie temperatures in the range of 30–200 °C.^{1,2} The intermetallic compound Mn_5Ge_3 is ferromagnetic with a Curie temperature in the range of 27–47 °C. Favorable optical properties such as high optical absorption and large Kerr rotation might be expected largely due to the metallic character of the alloy and the high density of ferromagnetically aligned Mn^{2+} and Mn^{3+} ions present.³ Panissod and his coworkers⁴ have studied the $\text{Mn}_5(\text{Ge}_{1-x}\text{Si}_x)_3$ ferroantiferromagnetic transition as x changes from 0 to 1. They reported that Si can be substituted for Ge in Mn_5Ge_3 over the whole range of x and that these alloys are isostructural (*D8₈*). The transition is from ferromagnetic for $x < 0.85$ to antiferromagnetic for $x > 0.85$. The aim of this work is to study the effects of heavy-element alloying on the magnetic properties and magnitude of the Kerr rotation (Θ_K). We report on the preparation and properties of the compounds $\text{Mn}_5(\text{Ge}_{1-x}\text{M}_x)_3$ with $\text{M}=\text{Sn}, \text{Pb}$.

II. EXPERIMENTS

Samples were prepared from 99.995 at. % pure Mn, 99.99 at. % pure Ge, and 99.9999 at. % pure Sn or 99.999 at. % pure Pb. Stoichiometric amounts were alloyed by arc melting in an argon atmosphere. In order to obtain homogeneous alloys, each sample was melted four to five times. Mass losses during melting totaled about 2% for $\text{Mn}_5(\text{Ge}_{1-x}\text{Sn}_x)_3$ and about 3% for $\text{Mn}_5(\text{Ge}_{1-x}\text{Pb}_x)_3$. The samples were then annealed in vacuum at 700 °C for 10 days.

The structure of the samples was analyzed by x-ray diffractometry. Their magnetization and coercivity were measured using an alternating gradient force magnetometer (AGFM) and superconducting quantum interference device

(SQUID). The Curie temperatures were measured by both a high-temperature Faraday balance magnetometer and AGFM at $H=500$ Oe. The Polar Kerr rotation was determined by a home-made apparatus⁵ at room temperature and fields up to 8 kOe.

III. RESULTS AND DISCUSSION

A. Crystallographic data

Figure 1 shows x-ray diffraction measurements on representatives of the $\text{Mn}_5(\text{Ge}_{1-x}\text{Sn}_x)_3$ samples. $\text{Mn}_5(\text{Ge}_{0.90}\text{Sn}_{0.10})_3$ [Fig. 1(a)] is found to have a Mn_5Si_3 (*hP16*) type structure, as does $\text{Mn}_5(\text{Ge}_{0.70}\text{Sn}_{0.30})_3$ [Fig. 1(b)] but with a Ni_2In (*hP6*) structure phase also beginning to appear. The $\text{Mn}_5(\text{Ge}_{0.30}\text{Sn}_{0.70})_3$ sample [Fig. 1(c)] shows the Ni_2In (*hP6*) structure. Only small amounts of Mn oxides show up in the x-ray spectra. It has also been found by others that Mn_5Ge_3 has a Mn_5Si_3 structure³ and Mn_5Sn_3 has a Ni_2In structure.⁶ When Sn is substituted for Ge in Mn_5Ge_3 [i.e., $\text{Mn}_5(\text{Ge}_{1-x}\text{Sn}_x)_3$] it can be expected that for small x the compounds will maintain the Mn_5Si_3 structure and that for large x the compounds should form the Ni_2In structure. In the middle range these structures could be mixed and show various lattice distortions. Since the Sn atomic diameter is larger than that of Ge, when Sn is substituted for Ge in Mn_5Ge_3 the lattice parameter of the crystal changes. Table I gives the variations in the lattice parameters measured in our samples.

Figure 2 shows x-ray diffraction measurements on some of the $\text{Mn}_5(\text{Ge}_{1-x}\text{Pb}_x)_3$ samples. We find that, as expected, $\text{Mn}_5(\text{Ge}_{0.95}\text{Pb}_{0.05})_3$ [Fig. 2(a)] has the Mn_5Si_3 (*hP16*) structure. This structure type becomes unstable at $x > 0.3$. $\text{Mn}_5(\text{Ge}_{0.50}\text{Pb}_{0.50})_3$ [Fig. 2(b)] shows the Ni_3Sn (*hP8*) type structure, which is predominant for this composition. $\text{Mn}_5(\text{Ge}_{0.30}\text{Pb}_{0.70})_3$ [Fig. 2(c)] mainly shows the Ni_3Sn (*hP8*) type structure but broad peak is found at a position expected from a pure tetragonal Mn phase. We also note that for x larger than 0.5 the desired compounds were difficult to form. This was especially noted for Mn_5Pb_3 , which often resulted

^{a)}Permanent address. Electrical Technology Department, Huaqiao University, Quanzhou, Fujian 362011, People's Republic of China.

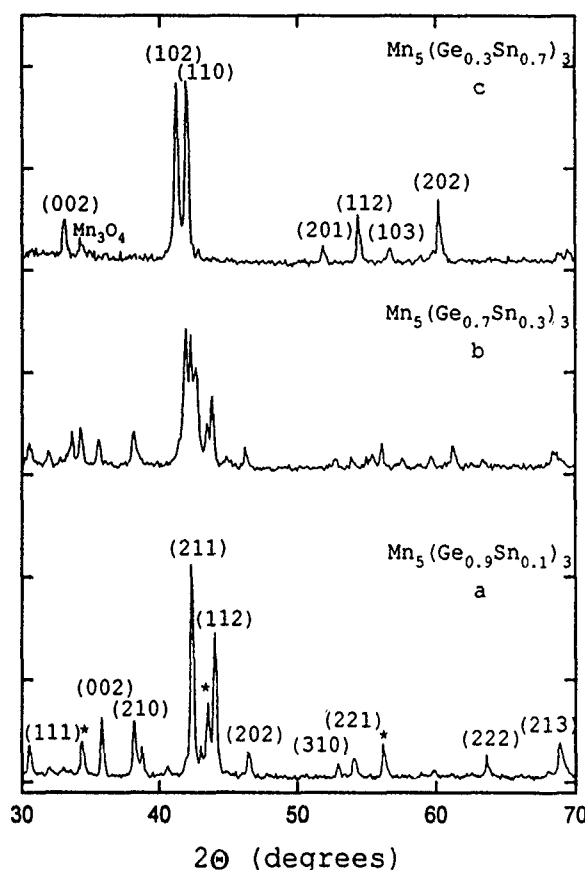


FIG. 1. X-ray diffraction patterns for several compositions of $Mn_5(Ge_{1-x}Sn_x)_3$: (a) $x=0.1$ with the Mn_5Ge_3 (*hP16* Mn_5Si_3) spectrum labeled. The asterisks denote weak peaks attributed to Mn_2Ge (*hP6* Ni_2In). (b) $x=0.3$. The spectrum shows peaks for both Mn_5Ge_3 (*hP16* Mn_5Si_3) and Mn_2Ge (*hP6* Ni_2In), with the former being dominant. (c) $x=0.7$ with peaks for $Mn_{177}Sn$ (*hP5.54* Ni_2In) labeled.

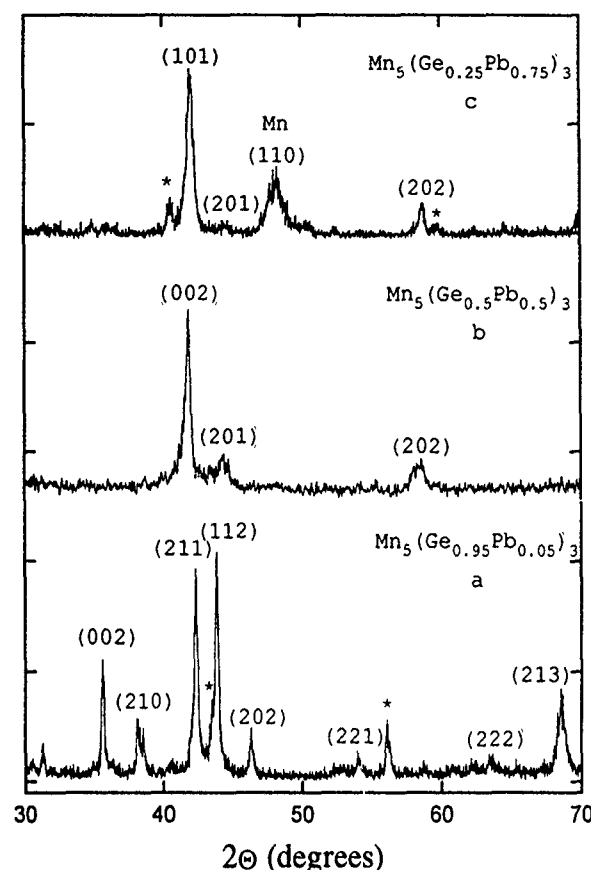


FIG. 2. X-ray diffraction patterns for several compositions of $Mn_5(Ge_{1-x}Pb_x)_3$: (a) $x=0.95$ with labels corresponding to the Mn_5Ge_3 (*hP16* Mn_5Si_3) spectrum. The asterisks denote weak peaks attributed to Mn_2Ge (*hP6* Ni_2In). (b) $x=0.5$. The labels correspond to the Mn_5Ge (*hP8* Ni_3Sn) spectrum. (c) $x=0.7$ with the labeled peaks belonging to the Mn_2Ge (*hP6* Ni_2In) structure.

in a fcc Pb structure with the main peak from the β -Mn spectrum also present. Mn has a smaller atomic diameter than Pb so it is expected that Mn_5Pb_3 in a fcc phase have a smaller lattice parameter than the pure fcc Pb lattice. These effects of alloy substitutions are confirmed by our experi-

mental results. As shown in Table I, we found that the cubic lattice parameter a changes from 4.962 Å for the pure Pb crystal to 4.955 Å for the Mn_5Pb_3 alloy.

B. Magnetic properties

Figure 3(a) shows the compositional dependence of the magnetization measured at $T=5$ K and a maximum field of 50 kOe with a SQUID magnetometer. The Curie temperatures for the compounds studied are shown in Fig. 3(b). All of the $Mn_5(Ge_{1-x}Sn_x)_3$ alloys made have a ferromagnetic transition and for $x \leq 0.3$ they are ferromagnetic at room temperature. The magnetization at $T=5$ K first generally decreases with increasing x , and then shows a slow increase above $x=0.5$. The coercivity however is maximized for $x=0.5$, reaching 1.2 kOe at $T=5$ K. The Curie temperature initially remains nearly constant, then decreases with increasing x beyond $x=0.3$, reaching a minimum at $x=0.5$, after which it increases again as x goes to 1.0.

It can be seen in Table I that as x increases, both the lattice parameter a and the average moment per Mn atom generally decrease. This is understandable since the hybridization of Mn 3d electronic states normally increases as the interatomic separation becomes smaller as given by the quantum theory.

TABLE I. Structural lattice parameters for the relevant compositions of $Mn_5(Ge_{1-x}M_x)_3$ for $M=Sn, Pb$, and the average magnetic moment per Mn atom at $T=5$ K. Data are only shown for samples from which it could be clearly calculated.

Composition	Lattice parameter		Average moment per Mn atom (μ_B)
	a	c	
Mn_5Ge_3	7.193	5.069	2.52
$Mn_5(Ge_{0.95}Sn_{0.05})_3$	7.196	4.990	2.52
$Mn_5(Ge_{0.90}Sn_{0.10})_3$	7.176	5.061	2.23
$Mn_5(Ge_{0.85}Sn_{0.15})_3$	7.116	4.978	2.23
$Mn_5(Ge_{0.80}Sn_{0.20})_3$	7.172	5.036	2.13
Mn_5Ge_3	7.193	5.069	2.52
$Mn_5(Ge_{0.95}Pb_{0.05})_3$	7.179	5.048	1.42
$Mn_5(Ge_{0.90}Pb_{0.10})_3$	7.164	5.055	2.16
$Mn_5(Ge_{0.85}Pb_{0.15})_3$	7.168	5.039	2.10
$Mn_5(Ge_{0.80}Pb_{0.20})_3$	6.755	5.212	1.23
Mn_5Pb_3	4.955	4.955	0.01
Pb	4.963	4.963	0.00

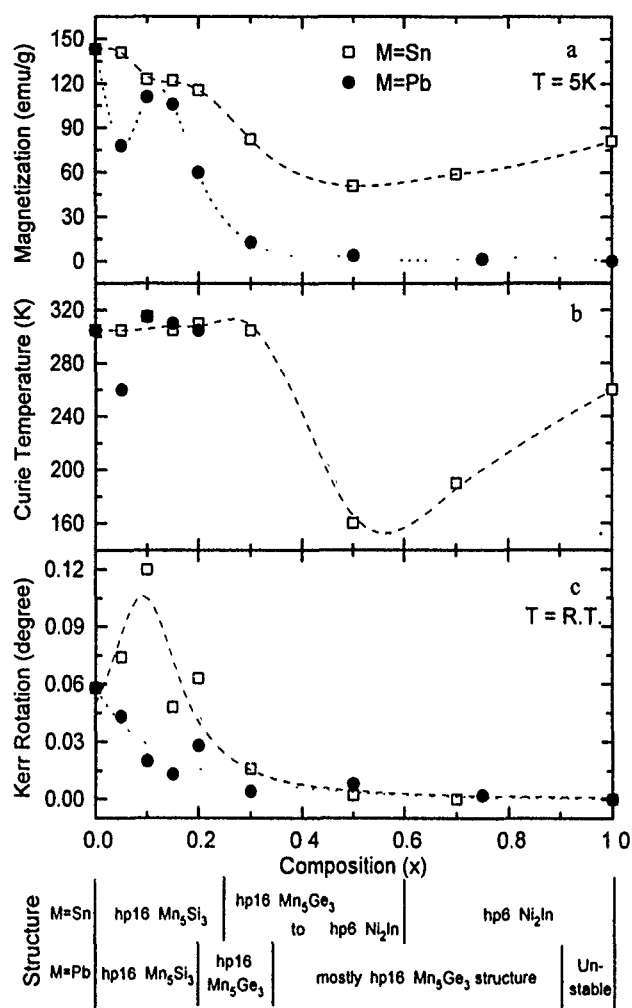


FIG. 3. Magnetic properties versus composition for $\text{Mn}_5(\text{Ge}_{1-x}\text{M}_x)_3$, $\text{M}=\text{Sn}, \text{Pb}$: (a) SQUID measurements of magnetization at $T=5$ K and $H=50$ kOe. (b) Curie temperature measurements from Faraday balance magnetometer and M vs H loops with fields up to 500 Oe. (c) Kerr rotation measurements at room temperature and fields up to 8 kOe. The curves are only meant to serve as a reference to the general trends noted. The various structure regions for each sample set are also shown for reference.

The $\text{Mn}_5(\text{Ge}_{1-x}\text{Pb}_x)_3$ alloys are ferromagnetic at room temperature only for $x \leq 0.2$. The magnetization and Curie temperature show a minimum at $x=0.05$, for reasons that are not presently clear. When $x > 0.1$ both of these properties decrease as x increases. The explanation is the same as given for the $\text{Mn}_5(\text{Ge}_{1-x}\text{Sn}_x)_3$ alloys concerning the hybridization of the Mn $3d$ states. When $x > 0.3$ the Pb substituted alloys show a complex magnetic behavior. For example, the $\text{Mn}_5(\text{Ge}_{0.25}\text{Pb}_{0.75})_3$ sample measured at $T=5$ K and up to $H=50$ kOe has a small (about 1.5 emu/g) magnetization which is unsaturated, and a coercivity of about 11 kOe, while at room temperature it still has a coercivity of about 2 kOe.

C. Magneto-optic properties

Figure 3(c) shows the relationship of the magnitude of the Polar Kerr rotation to the composition, measured at room

temperature in fields up to 8 kOe. The sign of the rotation is negative for all of the samples studied. For $\text{Mn}_5(\text{Ge}_{1-x}\text{Pb}_x)_3$, the Kerr rotation monotonically decreases from the value for the parent alloy Mn_5Ge_3 with increasing x . In agreement with the magnetization at room temperature with an applied field of 8 kOe the Kerr rotation of the Sn substituted compounds increased slightly for $x < 0.15$. The peak value of $\theta_K = 0.12^\circ$ at $x=0.1$ is enhanced above what would be expected from a direct relationship between θ_K and M . Beyond this peak the Kerr rotation drops off, going to zero rapidly outside the single phase region at $x=0.25$. The Kerr rotation values below $x=0.4$ for both cases was measured very near the Curie temperature in both series of samples which would adversely affect the magnitude of the rotation due to decreased magnetic magnetizations. However, the Polar Kerr rotation is an intrinsic quantity that depends on factors such as composition, crystal structure, and electronic structure. It is interesting that there is an enhanced maximum in θ_K for the Sn case that apparently occurs within a single phase region. Presumably this reflects subtle changes in the electronic structure. This indicates the need for at least a spin-polarized calculation on the parent Mn_5Ge_3 compound.

IV. CONCLUSION

The magnetic and magneto-optical properties strongly depend on the alloy structure. Our $\text{Mn}_5(\text{Ge}_{1-x}\text{Pb}_x)_3$ samples showed the Mn_5Si_3 structure and were ferromagnetic for $x \leq 0.3$, exhibiting complex magnetic behavior for $x > 0.3$. All of the $\text{Mn}_5(\text{Ge}_{1-x}\text{Sn}_x)_3$ alloys were also ferromagnetic, but the low-temperature magnetization showed a minimum value at $x=0.5$. Only the substitution of Sn for Ge in Mn_5Ge_3 allowed the alloy to both keep the Mn_5Si_3 structure and increase the Kerr rotation.

In general the presence of heavy elements is necessary for large spin-orbit interactions, which can aid in producing a large Kerr effect; in the case of these compounds there is a compensating effect on alloying with Sn or Pb that reduces the strength of the magnetic coupling, as evidenced by a reduction in M_s and T_c . Thus, in these compounds, any tendency for Kerr-effect enhancement is overwhelmed by the destruction of the ordered magnetic state.

ACKNOWLEDGMENTS

The authors wish to express their thanks to Y. Zheng for his assistance in the experimental work and to J. X. Shen for measuring the Kerr rotation. We are indebted to the NSF for financial support under Grant No. DMR-9222976.

- ¹G. B. Street, E. Sawatzky, and K. Lee, *J. Appl. Phys.* **44**, 410 (1973).
- ²D. Chen, J. F. Ready, and E. Bernal G., *J. Appl. Phys.* **39**, 3916 (1968).
- ³E. Sawatzky, *J. Appl. Phys.* **42**, 1706 (1971).
- ⁴P. Panissod, A. Qachaou, and G. Kappel, *J. Magn. Magn. Mater.* **31-34**, 701 (1983).
- ⁵J. X. Shen, Roger D. Kirby, and D. J. Sellmyer, *J. Magn. Magn. Mater.* **81**, 107 (1989).
- ⁶K. Yasukochi, K. Kanematsu, and T. Ohoyama, *J. Phys. Soc. Jpn.* **16**, 1123 (1961).

Magnetic and optical characteristics of bilayered films composed of Tb-Fe-Co layer with overlayers of Co-Cr, Ni-Fe, Ta, and C

Kibong Song and Masahiko Naoe

Department of Physical Electronics, Tokyo Institute of Technology, 2-12-1, O-okayama, Meguro-ku, Tokyo 152, Japan

Amorphous Tb-Fe-Co single layers and Tb-Fe-Co/M (M: Ta, C, $\text{Co}_{82}\text{Cr}_{18}$, $\text{Ni}_{81}\text{Fe}_{19}$) bilayers have been prepared by using a facing targets sputtering apparatus. The Tb-Fe-Co films deposited by Kr sputtering exhibited internal stress as low as 1×10^9 dyn/cm² even at a pressure as low as 0.2 mTorr. The Tb-Fe-Co/Ta bilayers showed a Kerr rotation angle as large as 0.85° at the thickness of Tb-Fe-Co layer of about 30 nm. The direction of magnetic moments in Tb-Fe-Co layers were arranged antiparallel by a soft magnetic $\text{Ni}_{81}\text{Fe}_{19}$ overlayer.

I. INTRODUCTION

Amorphous Tb-Fe-Co layers have been prepared in working gas such as Ne, Ar, Kr, and Xe by using a facing targets sputtering (FTS) apparatus.¹ The interfacial effects in the Tb-Fe-Co/M bilayers with various overlayer M have also been investigated. The four kinds of materials used as overlayer were paramagnetic Ta with metallic reflectivity, diamagnetic C with nonmetallic absorbability, and ferromagnetic $\text{Co}_{82}\text{Cr}_{18}$, and $\text{Ni}_{81}\text{Fe}_{19}$. The overlayers seemed to be very interesting for enhancing the Kerr effect because ^{73}Ta possesses a magnetic susceptibility χ_m as high as 154 while ^{75}Pt has a χ_m of 190 in Co/Pt multilayers for magneto-optical media. It is well known that $\text{Co}_{82}\text{Cr}_{18}$ films are semihard magnetic and exhibited large perpendicular magnetic anisotropy energy,² and that $\text{Ni}_{81}\text{Fe}_{19}$ films are very soft magnetic, exhibited very high permeability and low coercivity and revealed apparent in-plane orientation of magnetic moment.³

II. EXPERIMENTS

Specimen films of amorphous Tb-Fe-Co single layers and Tb-Fe-Co/M bilayers were deposited on glass slide substrates by using a FTS apparatus, as described in a previous article.¹ The sputtering chamber was provided with two pairs of rectangular facing targets and rotatable substrate holder, so that the bilayers could be deposited successively without breaking the vacuum. The size of the target plates was 160×100 mm².

The residual gas pressure was less than 4×10^{-7} Torr before sputtering. The Tb-Fe-Co layers with thickness t_{MO} of 100 nm were deposited at the working gas pressure of 0.1~10 mTorr, and Tb-Fe-Co/M bilayers were deposited at the Ar pressure of 0.5 mTorr. Internal stress of specimen films was measured by the bending-beam method reviewed by Blackburn and Campbell.⁴ Magnetic properties were measured by using a vibrating sample magnetometer (VSM). The Kerr rotation angle θ_K and the coercivity H_c were determined on the Kerr hysteresis loops observed from the substrate side at the wavelength of 633 nm.

III. RESULT AND DISCUSSION

Figure 1 shows the dependence of the deposition rate R_d of Tb-Fe-Co films on the atomic weight w_A and radius r_A of the working gas at the pressure of 0.5 mTorr. This depen-

dence indicated that Ar and Kr should be best for R_d among all working gases at the pressure of 0.5 mTorr.

Figure 2 shows the dependence of the absolute value of compressive internal stress $|\sigma_f|$ in Tb-Fe-Co films with thickness of 100 nm on the working gas pressure P_{wg} . The films deposited at lower P_{wg} of lighter gases such as Ne and Ar exhibited larger $|\sigma_f|$ because of the larger number and higher energy of recoiled Ne and Ar atoms.⁵ On the contrary, the films deposited at lower P_{wg} of Kr exhibited smaller $|\sigma_f|$ because of the smaller number and lower energy of recoiled Kr atoms. So, the adatoms with high kinetic energy at lower P_{wg} of Kr may cause to form a uniform and poreless film and it resulted to the reduction of $|\sigma_f|$. However, the films deposited at higher P_{wg} of Kr exhibited larger $|\sigma_f|$ because of the energy loss due to collision of sputtered atoms with heavy Kr atoms. The heaviest and largest Xe gas could scatter the sputtered atoms severely and caused larger $|\sigma_f|$ over all the range of P_{wg} in this study.

The minimum value of $|\sigma_f|$ was obtained by Kr sputtering at P_{wg} of 0.2 mTorr; however, the deposition of bilayers at P_{wg} of 0.5 mTorr seemed to be acceptable for the stability and ability of the power supply. The films deposited at this P_{wg} of Ar and Kr gases exhibited almost the same $|\sigma_f|$. Therefore, Ar was used as the working gas for depositing bilayers in this study.

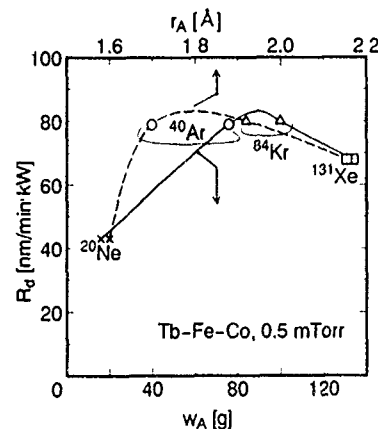


FIG. 1. Dependence of deposition rate R_d of Tb-Fe-Co layers on the atomic weight w_A and radius r_A of the working gas.

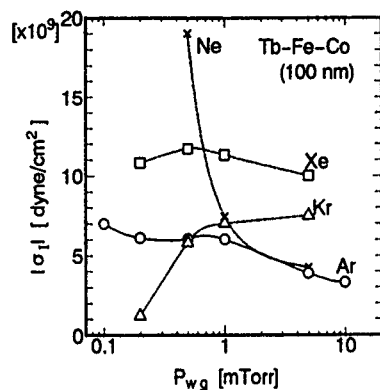


FIG. 2. Dependence of the absolute value of compressive internal stress $|\sigma_1|$ on working gas pressure P_{wg} in Tb-Fe-Co layers with a thickness of 100 nm.

Figure 3 shows the dependence of $|\sigma_1|$ in Tb-Fe-Co/M bilayers on the thickness of magneto-optical Tb-Fe-Co layers t_{MO} for a 100 nm thickness of M layers t_M . The materials of the M layer used as an overlayer were paramagnetic, metallic, and reflective Ta, diamagnetic, nonmetallic, and absorbable C, and ferromagnetic $\text{Co}_{82}\text{Cr}_{18}$ and $\text{Ni}_{81}\text{Fe}_{19}$. Bilayers with an overlayer of Ta, C, and $\text{Co}_{82}\text{Cr}_{18}$ exhibited large $|\sigma_1|$ at small t_{MO} , and it decreased with increasing t_{MO} while bilayers with a $\text{Ni}_{81}\text{Fe}_{19}$ overlayer exhibited extremely small $|\sigma_1|$.

Figure 4 shows the magnetic hysteresis loops of (a) Tb-Fe-Co (30 nm), Tb-Fe-Co (30 nm)/Ta (100 nm), Tb-Fe-Co (30 nm)/C (100 nm); (b) $\text{Co}_{82}\text{Cr}_{18}$ (100 nm); (c) Tb-Fe-Co (30 nm)/ $\text{Co}_{82}\text{Cr}_{18}$ (100 nm); (d) $\text{Ni}_{81}\text{Fe}_{19}$ (100 nm); and (e) Tb-Fe-Co (30 nm)/ $\text{Ni}_{81}\text{Fe}_{19}$ (100 nm), where (\perp) and the solid line represent the hysteresis loop observed for fields applied in the direction perpendicular to layer plane, and (\parallel) and the dashed line represent the in-plane loop. The loop shapes of the Tb-Fe-Co single layers and bilayers with paramagnetic Ta and diamagnetic C overlayers were almost the same.

The Tb-Fe-Co/ $\text{Co}_{82}\text{Cr}_{18}$ bilayer showed a shared rectangular perpendicular hysteresis loop with the coercivity H_c almost same as that of the Tb-Fe-Co single layer, where the

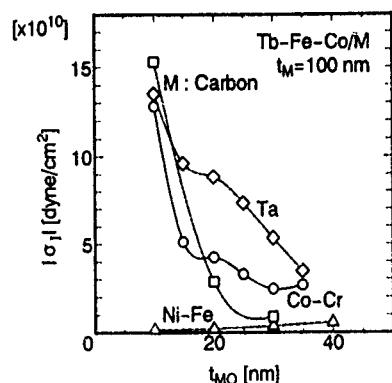


FIG. 3. Dependence of $|\sigma_1|$ on t_{MO} for Tb-Fe-Co/M bilayers, where M is Ta, C, $\text{Co}_{82}\text{Cr}_{18}$, and $\text{Ni}_{81}\text{Fe}_{19}$ layers with thickness of 100 nm.

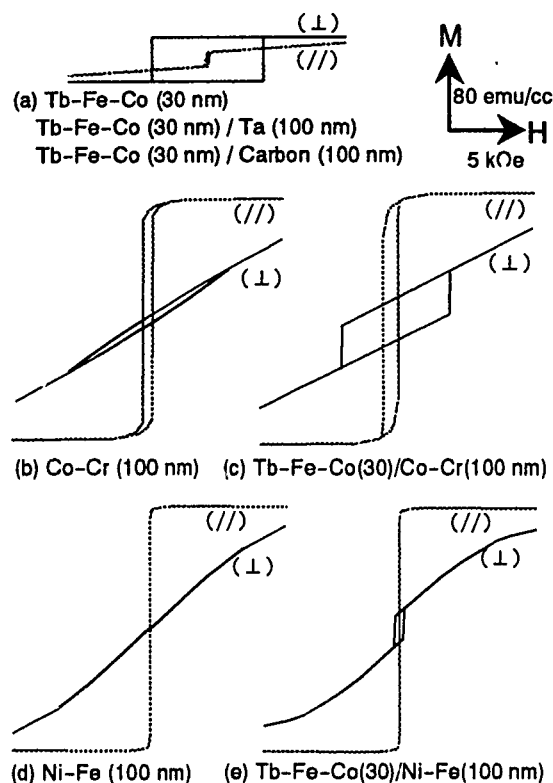


FIG. 4. Magnetic hysteresis loops of Tb-Fe-Co (30 nm)/M bilayers measured in directions normal (\perp) and parallel (\parallel) to the layer.

side of the loop was slightly sloped, and the in-plane hysteresis loop with higher H_c than those of $\text{Co}_{82}\text{Cr}_{18}$ and Tb-Fe-Co layers.

The Tb-Fe-Co/ $\text{Ni}_{81}\text{Fe}_{19}$ bilayer showed a shaped perpendicular hysteresis loop the same as that of the Tb-Fe-Co/ $\text{Co}_{82}\text{Cr}_{18}$ bilayer, but H_c was much lower than that of the Tb-Fe-Co single layer, owing to the large in-plane magnetization of the $\text{Ni}_{81}\text{Fe}_{19}$ layer. The arrangement of magnetic moment in Tb-Fe-Co layers was almost antiparallel. The in-plane hysteresis loop looked almost the same as that of the $\text{Ni}_{81}\text{Fe}_{19}$ single layer.

Figure 5 shows the dependence of Kerr rotation angle θ_K

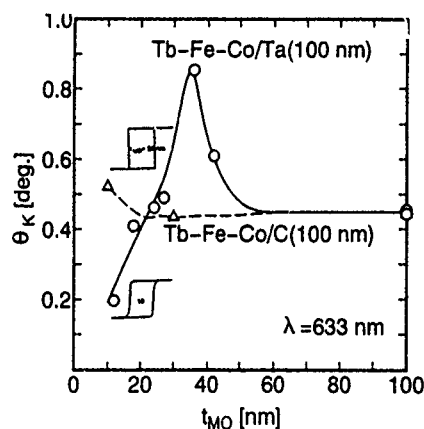


FIG. 5. Dependence of θ_K on t_{MO} and Kerr hysteresis loops for Tb-Fe-Co/M (M: 100 nm Ta and C) bilayers at a wavelength λ of 633 nm.

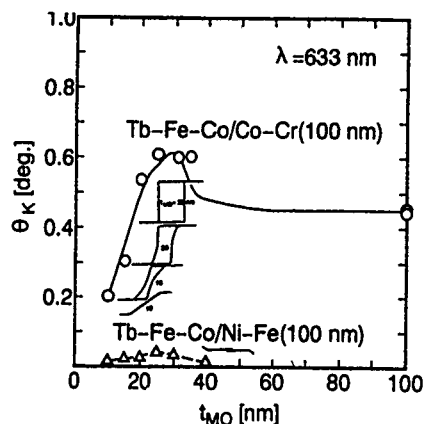


FIG. 6. Dependence of θ_K on t_{MO} and Kerr hysteresis loops for Tb-Fe-Co/M (M: 100 nm $Co_{82}Cr_{18}$, and $Ni_{81}Fe_{19}$) bilayers at λ of 633 nm.

strate side at λ of 633 nm. θ_K of these bilayers took a maximum of 0.6° and 0.04° at t_{MO} of about 30 nm. The Kerr hysteresis loops of bilayers with semihard magnetic $Co_{82}Cr_{18}$ overlayers with t_{MO} more than 25 nm revealed rectangular loop shape. The loop shape became similar to that of $Co_{82}Cr_{18}$ layers with decrease of t_{MO} .

On the contrary, the shape of Kerr hysteresis loops of bilayers with soft magnetic $Ni_{81}Fe_{19}$ overlayers was different. The shared rectangular loop was reduced about a factor

of 10, by means of the antiparallel arrangement of magnetic moments in Tb-Fe-Co layers. About 90% of the magnetic moments were arranged antiparallel by means of large in-plane magnetic moments of $Ni_{81}Fe_{19}$ layers. If the domain size of this bilayer is larger than the wavelength of the recording light, then this bilayer could be useful for very stable magneto-optical media, by means of a horseshoelike magnetic path.

IV. CONCLUSIONS

Amorphous Tb-Fe-Co single layers and Tb-Fe-Co/M (M: Tb, C, $Co_{82}Cr_{18}$, $Ni_{81}Fe_{19}$) bilayers have been prepared by using a facing targets sputtering apparatus. Results are as follows: (i) Tb-Fe-Co films deposited with Kr sputtering revealed internal stress as low as 1×10^9 dyn/cm² even at a Kr pressure as low as 0.2 mTorr; (ii) Tb-Fe-Co/Ta bilayers exhibited a Kerr rotation angle θ_K as large as 0.85° at a thickness of Tb-Fe-Co layer of about 30 nm; (iii) the direction of magnetic moments in Tb-Fe-Co layers were arranged antiparallel by a soft magnetic $Ni_{81}Fe_{19}$ overlayer.

¹K. Song, H. Ito, and M. Naoe, *Mater. Sci. Eng. A* **132**, 1264 (1991).

²S. Iwasaki, K. Ouchi, and N. Honda, *IEEE Trans. Magn.* **MAG-16**, 1111 (1980).

³T. F. Smith and I. R. Harris, *J. Phys. Chem. Solids* **28**, 1846 (1967).

⁴H. Blackburn and D. S. Campbell, *Philos. Mag.* **8**, 923 (1963).

⁵K. Song and M. Naoe, in *Ferrite: Proceedings of the 6th International Conference on Ferrites*, 1992, p. 563.

Change of magneto-optical Kerr rotation due to interlayer thickness in magnetically coupled films with noble-metal wedge

T. Katayama, Y. Suzuki,^{a)} M. Hayashi,^{b)} and W. Geerts
Electrotechnical Laboratory, Umezono, Tsukuba, Ibaraki 305, Japan

An intensity oscillation of the saturation polar Kerr rotation ϕ_K due to interlayer thickness d was observed in Fe(5 Å)/Au(d Å)/Fe(5 Å)(100) and Fe(6 Å)/Au(d Å)/Fe(6 Å)(100) sandwiched films. The periods of the oscillation are about 7–8 and 5–6 monolayers of Au thickness, respectively. The oscillation of ϕ_K can be observed only in the photon energy range 2.5–3.8 eV for Fe(6 Å)/Au(d Å)/Fe(6 Å). These phenomena are considered to be closely related to a formation of spin-polarized quantum-well states of the minority Δ_1 band in the Au layer sandwiched with two Fe barrier layers. The ϕ_K peak positions and oscillation period do not correspond exactly to those of the change in the in-plane saturation field H_s .

I. INTRODUCTION

Special attention has been focused on 3d-metal/noble-metal multilayers because they have a novel potential as materials for magneto-optical recording and giant magnetoresistance.^{1–2} In general, it has been expected that ultrathin films show a different electronic structure from that of bulk materials.³ The magneto-optical effect is very sensitive to changes of the electronic structure of the material. Bennett *et al.* reported a Kerr rotation oscillation with Cu interlayer thickness d in Fe/Cu(d Å)/Fe sandwiched films.⁴ Since their measurements were performed at only one wavelength, it provided little information about the electronic structures.

Recently, we have found a new magneto-optical transition due to the formation of quantum-well states in the ultrathin film of Fe deposited on a Au(100) surface.⁵ The new peak appears in the Fe layer thickness range between 2 and 10 Å and shifts from about 3 to 4.3 eV with increasing Fe layer thickness. We have also found an intensity oscillation of the saturation magneto-optical polar Kerr rotation ϕ_K due to the interlayer thickness d in Fe/Au(d Å)/Fe sandwiched films.⁶ This can be explained by the formation of quantum-well states (QWS) in the noble-metal layer. This is in agreement with the results as found by Ortega *et al.*^{7,8} In this article we present the results for Fe sandwiched Au samples and report on the behavior of polar Kerr rotation ϕ_K and saturation field H_s as a function of the film thickness.

II. EXPERIMENTAL PROCEDURES

All the sandwiched films with Au wedge-shaped interlayers were deposited by molecular-beam-epitaxy (MBE) method using two electron-gun sources for Fe and Au and a Knudsen cell for Ag. The MBE chamber was maintained in the range of 10^{-10} Torr during deposition. In order to make a good layer-by-layer growth of the Fe layer, Au seed layers of 4 or 10 Å were deposited for the Fe/Au/Fe(100) films. On the top of the multilayer, a 20-Å-thick Au cap layer was

deposited to prevent oxidation (see Fig. 1). The wedge-shaped Au layers were formed by means of a moving shutter method.

The thicknesses of Fe and Au films were measured and controlled by a quartz thickness monitor (IC-6000) combined with a shutter system. The growth modes and flatness of the films were monitored by observation of the high-energy electron diffraction (RHEED) patterns. ϕ_K and Kerr ellipticity η_K spectra were measured *ex situ* with a Kerr spectrometer using a piezo birefringent modulator in the photon energy range from 1.55 to 5.2 eV at RT. The incident angle of light was about 10° normal to the sample plane. The in-plane saturation field H_s was measured by the longitudinal magneto-optical Kerr effect (MOKE) method.

III. RESULTS

In Fig. 2 the ϕ_K and η_K spectra of the Fe(5 Å)/Au(23 Å)/Fe(5 Å) film are shown. A negative large ϕ_K peak is observed at about 3.8 eV. This peak is due to the plasma resonance in the Ag buffer layer. The Au interlayer thickness d dependence of ϕ_K at each energy was derived from the measured ϕ_K data.

Figure 3 shows the d dependence of ϕ_K/d_{Fe} at 3.5 eV in Fe(5 Å)/Au(d Å)/Fe(5 Å) film. ϕ_K/d_{Fe} in vertical axis shows a ϕ_K value per Fe(1 Å), normalized by the total Fe thickness (10 Å). The dashed line is a guiding base line for the eye. As shown in the figure, the large negative ϕ_K peaks are observed at around $d = 4, 20$, and 36 Å and its oscillation period is

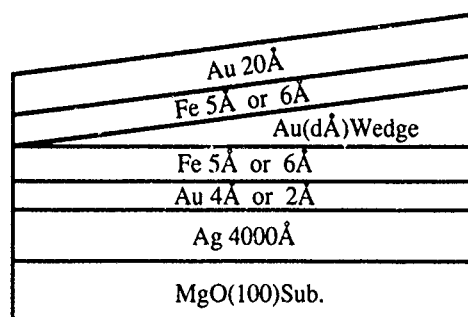


FIG. 1. Schematic drawings of cross section of the Fe/Au(d Å)/Fe sandwiched films. A cleaved MgO(100) surface is used as a substrate.

^{a)}Also with: National Institute for Advanced Interdisciplinary Research, Higashi, Tsukuba, Ibaraki 305, Japan.

^{b)}Also with: Department of Science and Technology, Nihon University, Funabashi, Chiba 274, Japan.

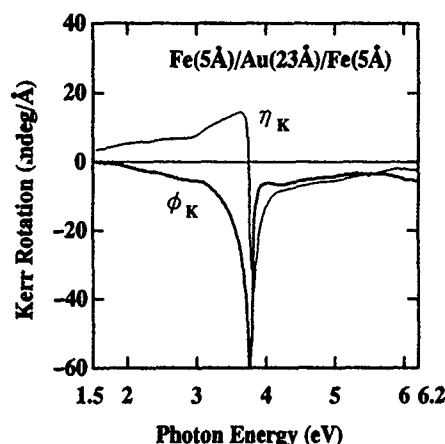


FIG. 2. The spectra of magneto-optical Kerr rotation ϕ_K and Kerr ellipticity η_K in the Fe(5 Å)/Au(23 Å)/Fe(5 Å) sandwiched film.

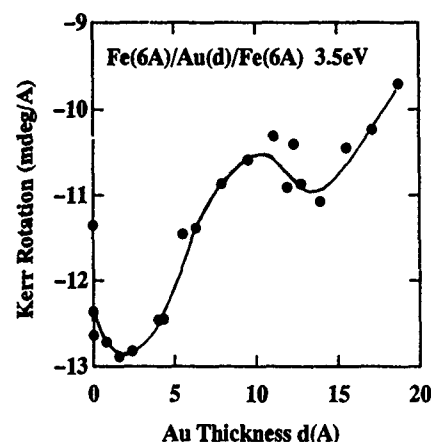


FIG. 4. The Au interlayer thickness d dependence of ϕ_K at 3.5 eV in the Fe(6 Å)/Au(d Å)/Fe(6 Å) sandwiched film.

about 7–8 monolayers (ML). In Fig. 4, the d dependence of ϕ_K at 3.5 eV in the Fe(6 Å)/Au(d Å)/Fe(6 Å) film is shown. An oscillation of ϕ_K is also observed and its period is about 5–6 ML. The ϕ_K oscillations could be only observed in the photon energy range 2.5–3.8 eV.

The oscillation period Λ in Fig. 3 is clearly larger than that of Fig. 4. As to the difference of Λ , it is found that the Λ are about 7–8 ML for Fe(3 Å)/Au(d Å)/Fe(3 Å) and 5–6 ML for Fe(9 Å)/Au(d Å)/Fe(9 Å) films, respectively. So, it is considered that the Λ changes at near Fe=5 Å from about 7–8 to 5–6 ML with increasing Fe thickness. This suggests that the period Λ is probably influenced considerably by a perfection of Fe barrier layer made with a band gap in D_1 .

Figures 5(a) and 5(b) show the d dependence of H_s in two kinds of Fe/Au(d Å)/Fe films. The behaviors of H_s in two figures are quite similar; that is, two large H_s peaks are observed around 21 and 26 Å and a small one is near 39 Å. The distance of the two peaks is about 2 ML which is thought to correspond to short oscillation of the oscillatory magnetic coupling.

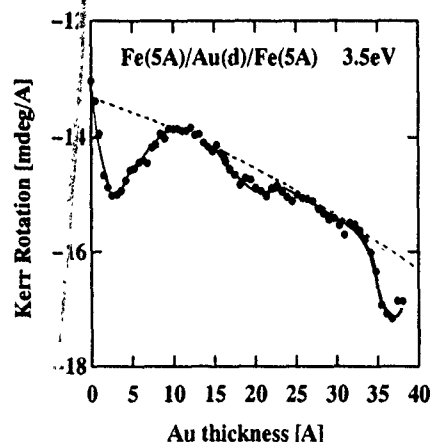


FIG. 3. The Au interlayer thickness d dependence of ϕ_K at 3.5 eV in the Fe(5 Å)/Au(d Å)/Fe(5 Å) sandwiched film. The vertical axis shows a ϕ_K per Fe 1 Å (ϕ_K/d_{Fe}), normalized by the total Fe thickness (10 Å).

IV. DISCUSSIONS

As mentioned above, an oscillation of ϕ_K as a function of d is observed in the Fe/Au(d Å)/Fe sandwiched films at various energies. Their oscillation amplitude and period Λ are very sensitive to the measuring energy. Ortega *et al.* found a quantum-well state (QWS) in ultrathin noble-metal layers such as Ag, Au, and Cu grown on Fe and Co by using an inverse photoemission spectroscopy (IPES) method.^{7,8} When the energy was fixed, for example at Fermi energy E_F , the IPES intensities oscillated with a period of about 8 ML.^{7,8}

In Fig. 6 a schematic drawing of the bulk band structures of bcc Fe and fcc Au near E_F along the film normal is shown.^{9,10} Due to presence of an energy gap between upper and lower branches of the Δ_1 minority band in Fe (shown by dotted curves), discrete QWS are formed only in the minority-spin state of the Δ_1 band of Au. The majority-spin state band in the Au is not influenced.

The QWS with different integers should cross the E_F one after another along the Δ_1 band energy dispersion with increasing Au thickness. Therefore, if the spin-polarized

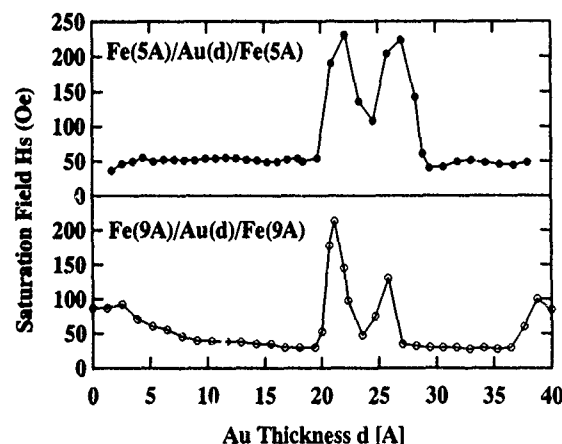


FIG. 5. The Au interlayer thickness d dependence of the in-plane saturation field H_s in (a) Fe(5 Å)/Au(d Å)/Fe(5 Å) and (b) Fe(9 Å)/Au(d Å)/Fe(9 Å) sandwiched films.

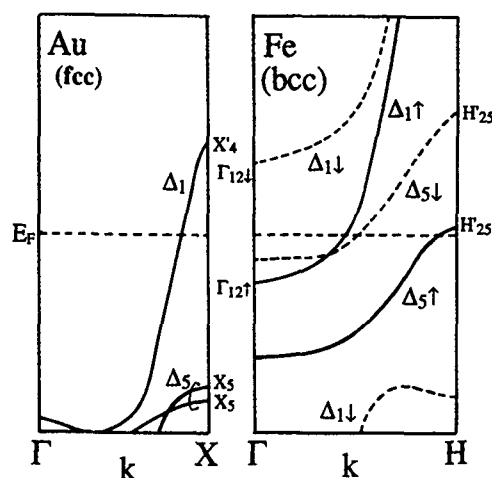


FIG. 6. A schematic drawing of the band structure of bulk bcc Fe and Au near the Fermi energy along the film normal.

QWS in noble metals behave as a final state of optical transition, a new magneto-optical (MO) transition will occur and MO intensities will oscillate periodically as QWS cross the E_F . It is considered that an optical transition from the minority-spin Δ_5 band to the Δ_1 spin-polarized QWS in the Au is a possible mechanism of the new MO transition. Assuming such a QWS model, the most reasonable energy range, in which the MO transitions occur, is above the plasma edge of the Au. However, as mentioned in a previous article,⁶ since the energy range in which the ϕ_K oscillation has been observed is rather wide (Ag case), another mechanism might be responsible for the MO effect.

Concerning the relation between IPES oscillation Λ_Q , Ortega *et al.*¹¹ have reported that Λ_Q at E_F is in good agreement with Λ_H in the Co/Cu(d Å)/Co system, but, as shown here, the H_s peak positions and its period Λ_H did not corre-

spond exactly to that of ϕ_K in Fe/Au(d Å)/Fe films. It is considered that behaviors of the ϕ_K oscillations as a function of d are more complicated than that of H_s , because ϕ_K phenomena are related to the electronic structures above E_F . Detailed studies are necessary on the relation between the oscillations of H_s and ϕ_K .

V. CONCLUSION

We reported on ϕ_K spectra and its oscillation due to d in Fe/Au(d Å)/Fe sandwiched films. As a result, the ϕ_K oscillation as a function of d was observed between about 2.5 and 3.8 eV for Fe/Au(d Å)/Fe sandwiched films. The oscillation periods are about 8 ML for less than 5 Å of Fe and 6 ML for more than 6 Å of Fe barriers. The oscillation is thought to be closely related with the formation of QWS in the Δ_1 minority-spin band in Au layers. The ϕ_K peak positions and period, however, did not correspond to that of the oscillatory magnetic coupling.

- ¹W. B. Zeper, F. J. A. M. Greidanus, P. F. Carcia, and C. R. Fincher, J. Appl. Phys. **65**, 4971 (1989).
- ²See, for instance, S. S. P. Perkin, Phys. Rev. Lett. **67**, 3598 (1991); Z. Celinski and B. Heinrich, J. Magn. Magn. Mater. **99**, L25 (1991).
- ³See, for instance, A. J. Freeman and R.-Q. Wu, J. Magn. Magn. Mater. **104-107**, 1 (1992).
- ⁴W. R. Bennett, W. Schwarzacher, and W. F. Egelhoff, Jr., Phys. Rev. Lett. **65**, 3169 (1990).
- ⁵Y. Suzuki, T. Katayama, S. Yoshida, K. Tanaka, and K. Sato, Phys. Rev. Lett. **68**, 3355 (1992).
- ⁶T. Katayama, Y. Suzuki, M. Hayashi, and A. Thiaville, J. Magn. Magn. Mater. **126**, 527 (1993).
- ⁷J. E. Ortega and F. J. Himpsel, Phys. Rev. Lett. **69**, 844 (1992).
- ⁸J. E. Ortega, F. J. Himpsel, G. J. Mankey, and R. F. Willis, Phys. Rev. B **47**, 1540 (1993).
- ⁹J. Callaway and C. S. Wang, Phys. Rev. B **16**, 2095 (1977).
- ¹⁰P. M. Laufer and D. A. Papaconstantopoulos, Phys. Rev. B **35**, 9019 (1987).
- ¹¹J. E. Ortega, F. J. Himpsel, G. J. Mankey, and R. F. Willis, Proc. MRS (to be published).

Chemical modification of magneto-optic garnet film properties

Roger F. Belt, John B. Ings, and Jonathan B. Whitlock

Airtron Division Litton Systems, 200 E. Hanover Avenue, Morris Plains, New Jersey 07950

Single-crystal magneto-optic garnet films of composition $(\text{BiTm})_3(\text{FeGa})_5\text{O}_{12}$ have applications to spatial light modulators, optical isolators, and magnetic-field sensors. These as-grown films have a coercivity under 1 Oe and can support cm-size stable domains. It has been found that chemical treatments with oxidizing or reducing gases can reversibly modify the magnetic properties. Treatments are performed at 400–700 °C for fixed times. Reducing treatments dilate the x-ray lattice constant up to 0.1%, introduce Fe^{2+} monitored by increased optical absorption at 1.00–1.06 μm and decrease Faraday rotation about 5% over the visible spectrum. Oxidation can partially or totally reverse these parameters. Magnetic measurements on the bulk film show that coercivity can be finely controlled, square hysteresis loops attained, and domain-wall mobility changed. At the same time the initial perpendicular anisotropy H_k of 8–12 kOe is decreased while the saturation magnetization ($4\pi M_s$) of 100–150 G is affected to a minor degree. For magneto-optic imaging of defects, the resolution, contrast, and device operation are assisted favorably. Magnetic measurements are presented as a function of specific chemical treatment. The data suggest that an oxygen vacancy mechanism is operative at the film surface layers.

I. INTRODUCTION

Single-crystal magneto-optic bismuth garnet films have applications to modulators, optical isolators, microwave devices, and sensors. The high perfection of these films normally leads to a low (<0.5 Oe) as-grown coercivity H_c . Various physical methods have been used to introduce controlled numbers, sizes, and distributions of defects.^{1,2} These irreversible modifications serve to increase coercivity, generate a nearly square hysteresis loop, and offer favorable effects in switching devices. In this article we examine chemical treatments in reducing atmospheres such as H_2 to attain reversible results over large areas in 3-in.-diam films.

Small changes of 1–5 Oe in dynamic H_c were measured by Metselaar and Huyberts in YIG single crystals and polycrystals.³ The likely defects were oxygen vacancies. Lotgering investigated permeability μ changes in Co- or Si-doped YIG polycrystals and developed a model of domain-wall pinning by anisotropic ions.⁴ Dixon and Kurtzig reported changes in $4\pi M_s$ with H_2 treatments of bubble films.⁵ Milani and Paroli studied specifically the H_2 diffusion in bulk YIG and films but only reported the optical properties.⁶ A later paper by Balestrino, Lagomarsima, and Tucciarone described x-ray lattice constant expansions and contractions with H_2 -annealed YIG films.⁷ A more recent effort by Kappelt *et al.* measured optical anisotropy changes in epigrown films with alternating H_2 and O_2 treatments.⁸ Since a comprehensive study of magnetization changes in our films was lacking, we concentrated on this aspect. Our investigations were motivated also by the fact that the chosen film compositions were capable of supporting large stable magnetic domains instead of the normal stripes.⁹ These films are valuable for magneto-optic imaging of fields generated around defects by eddy currents.¹⁰

II. EXPERIMENT

The film compositions used in our experiments were prepared by liquid-phase epitaxy and described thoroughly¹¹ along with various physical properties² in the as-grown con-

dition. In order to simplify any measurements, a single 3 μm layer of film on (111) GGG was used. This was obtained normally by growth on a wafer which touched the melt surface. These films were identical to those grown by total immersion and deposited on both sides of the substrate. X-ray data were obtained with a Picker diffractometer by examining (888) order reflections and measuring lattice constants with $\text{Cu K}\alpha_1$ radiation. Anisotropy fields were measured by a magneto-optic transverse susceptibility measurement on a complete wafer.¹² The magnetization, coercivity, and hysteresis curves were recorded on a Princeton Measurements Corp. Micro Mag 2900 alternating gradient magnetometer. Samples for this purpose were 15–20 mm² rectangles cut from large wafers. Data were collected with magnetic fields up to 10 kOe both perpendicular and parallel to the film plane. The former showed open loops while the latter showed only a line.

Optical absorption α of our films was measured on a Cary model 14 spectrophotometer. An evaluation of the Fe^{2+} absorption was obtained by measuring α at 1.03 μm on untreated and treated films of identical thicknesses. The relationship of Fe^{2+} and optical absorption has been discussed previously.^{13,14} An estimate of OH absorption was determined by measurements at 2.81 μm with a Nicolet model 20DXB Fourier transform infrared (FTIR) spectrometer. The Faraday rotation was measured with a polarizing microscope using a coil to generate a saturation magnetic field normal to the film plane.

Full wafer samples or portions thereof were treated in reducing atmospheres with forming gas (85% N_2 -15% H_2) and in oxidizing atmospheres by means of an oxygen ozone mixture (99 O_2 -1 O_3).¹⁵ The samples were placed in a Thermco tube furnace for specified temperatures and times. Flow rates of gas were adjusted to maintain sample temperature and insure uniform treatment over the film area. Visually the samples showed no appearance of added defects in the film when examined under a microscope.

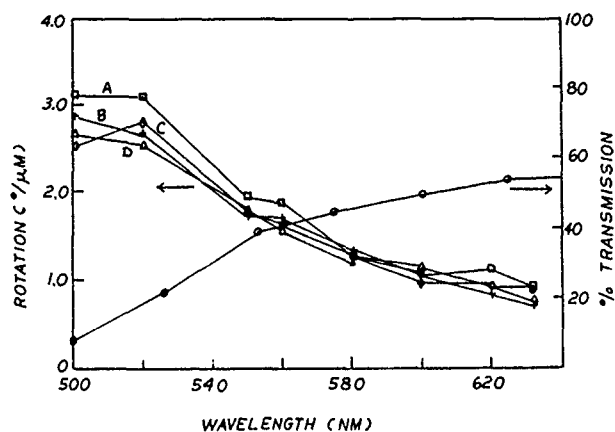


FIG. 1. Faraday rotation and transmission as a function of wavelength. A is a starting film, B, C, and D were H_2 treated for 6 min at $470^\circ C$ and then annealed in O_2 - O_3 gas mixture for 4, 9, and 14 min, respectively at $580^\circ C$.

III. RESULTS

A. X-ray lattice constants

A brief treatment of our films in forming gas (for example, 10 min at $470^\circ C$) shows some remarkable results. The entire film increases in the (111) determined x-ray lattice constant, a_f . For our films which are originally in compression, i.e., with $a_s < a_f$ where a_s is the substrate lattice constant of 12.383 \AA and $a_f = 12.390$ – 12.400 \AA , the amount of the increase is always about 0.008 \AA or nearly 0.1%. These data are consistent with the observations of Balestrino and co-workers in YIG.⁷ However, we did not observe the high-angle 2θ wings or the final contraction possibly due to our thinner films and/or shorter treatments at lower temperatures. The increased film lattice constant places the film under increasing compression and can create an easy axis of magnetization parallel to the film plane under certain conditions. In one sense, the lattice dilation with H_2 treatments is analogous to ion implantations of H^+ , He^{2+} , Ne^+ , and others; however, important distinctions are discussed later because the ion implants are not reversible.

If a H_2 -treated film is now reacted in the O_2 - O_3 gas, the x-ray lattice constant contracts until the value of the as-grown film is nearly reached. Small oscillations about this value are possible to the extent of about $\pm 0.0005 \text{ \AA}$; however, the film always remains in compression. The process of reduction oxidation is reversible because alternate treatments increase or decrease the (111) spacings, respectively. In fact, the magnetic film can be "fine tuned" by this process to yield a desirable lattice constant.

B. Optical absorption and Faraday rotation

The Faraday rotation dispersions for the as-grown and H_2 -treated films are shown in Fig. 1. The Faraday rotation exhibits a slight decrease of 5%–10% in magnitude over the visible wavelength region for H_2 -treated films. The largest decrease is in the 500–560 nm range. This happens to be near the optical transition commonly assigned to tetrahedral Fe^{3+} . It is also interesting that the sign of the Faraday rota-

tion changes as one performs the hydrogen treatment on an as-grown film. This indicates that the Bi^{3+} - Fe^{3+} interaction, which is responsible for Faraday rotation, has been changed drastically.

The optical absorption in the visible range showed no discernible changes with reducing treatments even though the films were slightly darker. However, an accurate measurement of absorption coefficients in the 1.00 – $1.06 \mu m$ range showed that increases of α by factors of 5–10 were observed in the hydrogen treated films. These data are in agreement with the observations of Milani and Paroli⁶ who attributed this absorption to the presence of Fe^{2+} . Dillon and Hansen showed the same results earlier.^{13,14} We have also examined carefully the infrared absorption at 3560 cm^{-1} and can confirm the presence of OH vibrations. However, the amount of our absorption is markedly less than Milani and Paroli report⁶ even when up to five layers (about $15 \mu m$ thickness) are examined. We do not observe at all the broad band at 2800 cm^{-1} .

C. Magnetic characterization

Our $3 \mu m$ as-grown films are reproducible in their original magnetic properties. The saturation magnetization, $4\pi M_s$, is always 100–150 G while the anisotropy field H_k is always greater than 8 kOe, and orients the magnetization perpendicular to the film plane. The characteristic stripe domains are absent and one sees only 1–2 cm^2 domains with rather few walls between crossed polarizers. The coercivity of the film is initially less than 0.5 Oe as verified by magnetometer measurements on many 5–25 mm^2 samples cut from 3-in.-diam wafers or by domain-wall movement through the entire wafer. The magnetization $4\pi M_s$, likewise undergoes small changes with chemical treatments. In oxygen at temperatures up to $1050^\circ C$, $4\pi M_s$ decreases by about 20–50 Oe, probably due to some d - a site interchange of the Ga^{3+} ions.

Magnetic parameters are summarized in Table I. Treatment of an as-grown film in either air or oxygen at $600^\circ C$ has only a slight affect on the magnetic properties even if the treatment persists for several hours. Generally, a slight increase in coercivity H_c is observed. Significantly higher anneal temperatures ($1100^\circ C$) can lead to the formation of defects which increase coercivity through a domain-wall pinning mechanism. However, the anneal treatments discussed here do not generally result in pinning defects.

Treatment in forming gas at 450 – $500^\circ C$ for short periods of time (10 min), can also increase the coercivity, as measured by noting the onset and completion of domain-wall motion as the field is varied; however, the increase is not caused by macroscopic pinning defects. As a result of the significant coercivity increase, we are not able to reliably measure H_k with our apparatus. However, upon subsequent reoxidation at $600^\circ C$, the coercivity decreases and H_k values significantly below those of the as-grown film are obtained, probably due to strain relaxation.

The most interesting changes occur in the coercivity when measured on the magnetometer. Under subsequent oxidation up to $1050^\circ C$, H_c increases gradually while upon reduction and reoxidation the coercivity decreases. By successive treatments in O_2 and H_2 , an appropriate and repro-

TABLE I. Magnetic film properties.

Sample state	Anisotropy field H_k (kOe)	Magnetization $4\pi M_s$ (G)	Coercivity H_c (Oe)
As grown	8–12	100–150	0.5–5.0
O ₂ treated 600 °C	8–12	100–150	1–5
H ₂ treated 450–500 °C	...	100	20–120
Reoxidized 600 °C	3.5–8	80–150	0.5–1.0

ducible value of H_c can be obtained. Not only does H_c change but the whole dynamics of switching process becomes more favorable, i.e., domain-wall movement is easier, faster, and more uniform over the entire film. An example of the changes incurred in the hysteresis curves with H₂ treatments is illustrated in Fig. 2. Starting with a sample having a coercivity of 300 Oe as shown in (a), samples (b), (c), and (d) were treated first in H₂ at 470 °C for six minutes and then in O₂-O₃ for 4, 9, and 14 min at 580 °C and rerun. The final coercivity at (d) is only 20 Oe. If (d) is retreated in O₂ at higher temperature or longer time, the coercivity will increase. Note also that the H₂ pretreated samples have square loops essentially, may be slightly asymmetric about $H=0$, and have limited "tails." The tails are due to residual domains and not to oblique orientation since high fields up to 10 kOe normal to the film plane eliminated them.

IV. DISCUSSION

Increases of the x-ray lattice constant in our films can be attributed to several possible reductions in the valence state (increase of ionic radius) of the original ions with H₂ treatment. For example, Bi³⁺→Bi, Fe³⁺→Fe²⁺, or Pb⁴⁺→Pb²⁺→Pb, or Pt⁴⁺→Pt, where the Pb is introduced by growth from a PbO flux and Pt from the crucible. Unfortunately, the x-ray method is not specific and one or more of these reactions can take place simultaneously. The optical evidence is more direct in that it shows the Fe²⁺ absorption and Faraday rotation are 5–10 times more and 10%–20% less, respectively. If we consider that the Pb²⁺ impurity amounts to less than 1.0 mol % of the film's composition,¹⁶ we can see that these observed optical changes are more likely to be associated with Bi³⁺ and Fe³⁺ rather than Pb²⁺ valence changes.

Recent attempts to calculate quantitatively the Faraday rotation or ellipticity have met with some success.^{17,18} These calculations were based on diamagnetic and paramagnetic transitions of the charge transfer type from 2p orbitals on

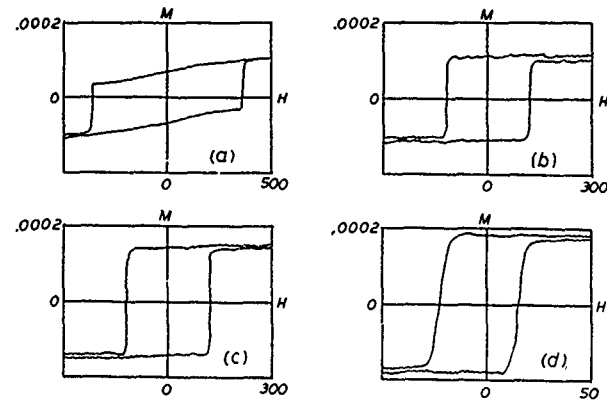


FIG. 2. Hysteresis curves of samples from Fig. 1. All curves were recorded with the field H normal to the sample plane. H is given in Oe and M in emu.

O²⁻ to 3d orbitals in Fe³⁺. Sign changes and magnitudes in BiYIG were accounted for only by adding paramagnetic terms. The sign changes generally occur at fixed ranges of Bi concentrations and fixed photon energies. Our results confirm this for $x=0.8$ bismuth levels in our films. Furthermore, our H₂ or O₂ treatments immediately affect the sign of the rotation possibly via the O₂ 2p orbitals. A larger question remains on whether we see bulk or surface effects. We are attempting to unravel this by polar Kerr-effect measurements and other data on films thinned by controlled surface removal.

- ¹J. P. Krumme, I. Bartels, B. Strocka, K. Witter, C. Schmelzer, and R. Spohr, *J. Appl. Phys.* **48**, 5191 (1977).
- ²R. F. Belt, J. B. Ings, D. C. Ferranti, and P. E. Wigen, *J. Appl. Phys.* **70**, 6398 (1991).
- ³R. Metselaar and M. A. Huyberts, *J. Phys. Chem. Solids* **34**, 2257 (1973).
- ⁴F. K. Lotgering, *J. Phys. Chem. Solids* **36**, 1183 (1975).
- ⁵M. Dixon and A. J. Kurtzig, U.S. Patent No. 3,759,745 (1973).
- ⁶E. Milani and P. Paroli, *J. Appl. Phys.* **55**, 2173 (1984).
- ⁷G. Balestrino, S. Lagomarsino, and A. Tucciarone, *J. Appl. Phys.* **59**, 424 (1986).
- ⁸R. Kappelt, H. Dotsch, A. Brockmeyer, H. P. Winkler, and B. Gather, *Proc. SPIE* **274**, 169 (1990).
- ⁹G. R. Pulliam, W. E. Ross, B. MacNeal, and R. F. Bailey, *J. Appl. Phys.* **53**, 2754 (1982).
- ¹⁰G. L. Fitzpatrick, U.S. Patent No. 4,625,167 (1986).
- ¹¹R. F. Belt and J. B. Ings, *Proc. SPIE* **753**, 142 (1987).
- ¹²R. M. Josephs, in *Proceedings of the AIP 18th Annual Conference on Magnetism and Magnetic Materials*, 1972, pp. 283–303.
- ¹³J. F. Dillon, E. M. Georgy, and J. P. Remeika, *J. Appl. Phys.* **41**, 1211 (1970).
- ¹⁴P. Hansen, W. Tolksdorf, and J. Schuldt, *J. Appl. Phys.* **43**, 4740 (1972).
- ¹⁵H. Tamada, M. Saitoh, and M. Kaneko, *J. Appl. Phys.* **67**, 949 (1990).
- ¹⁶C. Jovanovic, S. Sure, E. Clausing, C. Scharfschwerdt, M. Neumann, H. Alwes, K. Lorenz, H. Dotsch, W. Tolksdorf, and P. Willich, *J. Appl. Phys.* **71**, 436 (1992).
- ¹⁷K. Matsumoto, S. Sasaki, K. Haranga, K. Yamaguchi, T. Fujii, and Y. Asahara, *IEEE Trans. Magn.* **MAG-28**, 2985 (1992).
- ¹⁸G. Dionne and G. Allen, *J. Appl. Phys.* **30**, 6127 (1993).

Circular magnetic x-ray dichroism in rare-earth magnets

Xindong Wang, V. P. Antropov, B. N. Harmon, J. C. Lang, and A. I. Goldman

Ames Lab—USDOE and Department of Physics and Astronomy, Iowa State University, Ames, Iowa 50011

With the availability of dedicated high-intensity synchrotron radiation sources, circular magnetic x-ray dichroism (CMXD) is developing as a technique for the investigation of magnetic properties. CMXD is defined as the difference in absorption between right and left circularly polarized beams at an absorption edge and provides information about the local (element and angular momentum specific) spin and orbital magnetic moments. Both theoretical and experimental work on the CMXD spectra of rare-earth magnets is presented. The nature of the feature below the absorption edge in the rare-earth CMXD spectra for the L_2 and L_3 edges is discussed.

Circular magnetic x-ray dichroism is defined as the difference between the absorption coefficients for left- and right circularly polarized x-ray beams in a magnetized sample. With the advent of more intense synchrotron radiation sources, circular magnetic x-ray dichroism has increasingly been used as a probe of the magnetic properties of various crystalline and multilayer systems.¹⁻⁵ In the past few years, various theoretical models have been proposed for the interpretation of these spectra both qualitatively and quantitatively.⁶⁻⁸ For example, sum rules derived by Thole *et al.*⁹ and Carra *et al.*,¹⁰ which relate the integrated CMXD spectra to the ground-state expectation values of orbital and spin-dependent effective operators, have provided a theoretical basis for the interpretation of CMXD spectra and have been used to determine the spin and orbital moments of transition elements in a variety of systems.⁵ The details of the CMXD spectra at the L edges of transition elements (including $5d$ impurities in $3d$ hosts) and the M edges of the rare-earth elements can be reasonably well described by first principle calculations.^{7,8} This is not the case for the L_2 and L_3 edges of rare-earth (RE) elements. While these transitions are mainly of the $2p$ to $5d$ dipolar character, complications arise due to the existence of the $4f$ shell in these elements. In particular, features are observed below the absorption edge,¹ as well as a pronounced asymmetry between L_2 and L_3 dichroic spectra above the absorption edge for some compounds.² In this article we summarize the work which has been done on these issues and discuss some of the difficulties with the current theoretical understanding of the CMXD of rare-earth magnets.

For the L_2 and L_3 edge CMXD spectra of rare-earth elements, it is generally accepted that the prominent feature above the absorption edge arises from dipolar transitions between the $2p$ core levels and the unoccupied $5d$ states. In order to explain the feature found below the edge, electric quadrupolar transitions were introduced by Carra *et al.*⁶ This interpretation is further supported by the resonant magnetic x-ray scattering experiments.¹¹ Since the unfilled $4f$ shell in the rare-earth elements is highly localized, the quadrupolar peak appears below the edge due to strong Coulomb interactions, in the final states, between the $2p$ core hole and $4f$ electrons (excitonic state). Based on this consideration, a combined model which treats the $2p$ to $4f$ transitions using atomic multiplet theory and $2p$ to $5d$ transitions using one electron band theory was introduced.⁶ Detailed calculations

for Gd metal⁶ and later for heavy rare-earth metals¹² have been done based on this model and agree remarkably well with the experiments on the elemental metals. Encouraged by these successes, we have developed a first principles program to calculate CMXD spectra within the one electron band model, which, taken together with the atomic multiplet calculations, can be used to describe the L_2 and L_3 spectra of rare-earth elements in different compounds. The band-structure calculation was carried out within the local spin density functional approximation (LSDA) which has been shown suitable for describing the ground state properties of heavy rare-earth magnets.

Experimental spectra taken at the Gd L_2 and L_3 edges of crystalline GdFe₂ along with theoretical spectra calculated using the method described below, are shown in Fig. 1. The theoretical curves have been scaled down by a factor of 2. The CMXD measurements were taken at Cornell High-Energy Synchrotron Source (CHESS) bending magnet D line making use of the off-axis elliptical polarization of the beam. The data have been normalized to $T=0$ K saturation magnetization of the sample and full circular polarization of the x-ray beam in order to directly compare the magnitude of the experimental spectra with the theory.¹³

In our atomic-sphere-approximation tight binding linear muffin-tin orbital (ASA-TB-LMTO) band-structure code, a spin-polarized, spin-orbit-coupled, one-electron Hamiltonian is solved using the scalar relativistic spin-dependent tight-binding muffin-tin orbitals as a variational basis.¹⁴ The theoretical spectra have been convoluted with a Lorentzian of about 3.5 eV to account for the finite core hole life time and energy-dependent conduction state life time, and by a Gaussian of 1.5 eV to account for the experimental resolution. The theoretical curves, while giving the general shape, do not reproduce the experimental spectra well. We believe, however, that after taking into account of the core hole Coulomb attraction on the one electron orbitals, the agreement will be improved since the core hole effect will compress the theoretical spectrum toward the Fermi level, as observed in the experiment. The discrepancy between the absolute magnitude of the theoretical and experimental spectra (a factor of 2) can be reduced if we invoke the wave-function normalization factor to the conduction electron states. Further calculations are being undertaken to incorporate the effect of the core hole. While the full treatment of the transient impurity problem¹⁵ is still formidable for a first principles calculation,

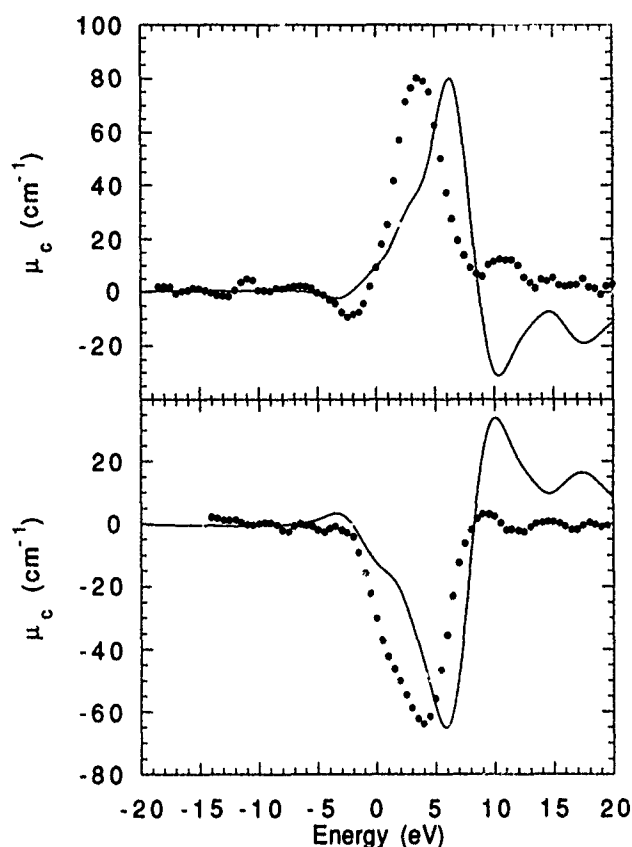


FIG. 1. Experimental (dots) and theoretical (solid line) CMXD spectra at the Gd L_3 (top), and Gd L_2 (bottom) edges. Theory curves have been scaled down by a factor of 2.

a calculation in the adiabatic approximation is essentially a static impurity problem and is well within the current computational capability. This work will be presented in a future publication.

Although the above-described model has successfully described some general features of the CMXD spectra of the L_2 and L_3 edges of heavy rare-earth elements, there are difficulties associated with it. Because of the different symmetry characteristics of the dipolar and quadrupolar transitions, the model unambiguously predicts different angular dependencies of the dipolar part (above edge) and quadrupolar part (below edge) of the CMXD spectra.^{6,16} When scaled to the magnitude of the dipolar part at different angles, theory predicts that the quadrupolar transitions should yield a pronounced angular dependence for the magnitude of the feature below the edge. To firmly establish the validity of the model, it is essential to confirm this prediction experimentally. The theory predicts that Ho and Er should demonstrate the most pronounced angular dependence.

Several experiments have been carried out and have failed to observe any angular dependence.¹⁷⁻¹⁹ This negative result has stimulated other explanations for the below edge feature, such as its assignment to the magnetic dipolar transitions involving hybridization between the $4f$ and $5d$ orbitals. Magnetic dipolar transitions, for core-level absorption spectroscopy, even when satisfying angular momenta selec-

tion rules, give basically null contributions due to a null radial matrix element as pointed out by Brouder.²⁰

We point out here several possible explanations of the observed negative results for the quadrupolar angular dependence. Recently Carra *et al.* have derived sum rules for the quadrupolar CMXD spectra,²¹ which associate the integrated quadrupolar spectrum with the expectation values of two kinds of operators in the ground state, namely the dipolar operators (not to be confused with the dipolar transitions) whose expectation values have the same angular dependence ($\cos \theta$) as the dipolar transitions and the octupolar operators whose expectation values have a different angular dependence $[(5 \cos^2 \theta - 3) \cos \theta]$. It is the contributions of the expectations values of these octupolar operators that give the quadrupolar transition a different angular dependence from the dipolar transition. The quantitative prediction on the angular dependence was made using an isolated ion calculation.⁶ When the crystal-field effects are taken into account, the ground-state expectation values of the dipolar and octupolar operators are expected to scale differently (crystal-field scaling).²¹ Further theoretical investigations are required to see if the crystal field will reduce the octupolar contribution to a greater degree than the dipolar contribution and hence reduce the difference in angular dependence between the quadrupolar and dipolar transitions. Second, as we have mentioned, the theoretical prediction was made according to an isolated ion calculation, and has completely neglected the possible hybridization of the $4f$ shell with the conduction electron states both in the ground state and the excited states. When hybridization effects are taken into account, the feature below the edge will have some dipolar mixing due to the transitions from $2p$ to the ligand states. These states hybridize with the $4f$ shell and can be a mixture of d and f character because the $2p$ core hole has broken the local crystal-field symmetry for the outer shells. The mixing of these dipolar transitions below edge will reduce the relative weight of the quadrupolar transitions and make the experimental identification of the angular dependence of the feature more difficult. Although these hybridizations have to be very small, their effects may be enhanced by the dipolar matrix element which is two orders of magnitudes larger than the quadrupolar matrix element. Finally, we want to point out here that the "shake up," due to the core hole, of the $4f$ multiplets in the $2p$ - $5d$ transitions can also modify the above edge feature as predicted by band calculations and this may be the origin for the strong asymmetry between the CMXD L_2 and L_3 edges of some heavy rare-earth compounds.

In conclusion, we believe that the combined model given in Ref. 6 gives the basic physics involved in the CMXD L_2 and L_3 edges of the heavy rare-earth compounds, although some detailed modifications are required to resolve the discrepancies between the theory and the experiment. In order to obtain a definite answer to the nature of the below edge feature of these spectra, experiments also need to be carried out at lower temperatures to reduce the thermal fluctuations, since thermal fluctuations, acting effectively as a random external field, will not only reduce the dichroic signal but also suppress the different quadrupolar angular dependence.

Note added in proof. Theoretical calculations done with the combined correction to the ASA-TB-LMTO²² have shown better agreement of the Gd L_2 and L_3 dichroic spectra between the theory and the experiment.

Ames Laboratory is operated for the United States Department of Energy by Iowa State University under Contract No. W-7405-ENG-82. Work at CHESS was supported by the National Science Foundation under Grant No. DMR-87-119764.

- ¹G. Schütz, M. Knülle, R. Wienke, W. Wilhelm, W. Wagner, P. Kienle, and R. Frahm, *Z. Phys. F* **73**, 67 (1988).
- ²P. Fisher, G. Schütz, and G. Wiesinger, *Solid State Commun.* **76**, 777 (1990).
- ³P. Rudolf, F. Sette, L. H. Tjeng, G. Miegs, and C. T. Chen, *J. Magn. Magn. Mater.* **109**, 109 (1992).
- ⁴J. Ph. Schille, Ph. Saintavi., Ch. Cartier, D. Lefebvre, C. Brouder, J. P. Kappler, and G. Krill, *Solid State Commun.* **85**, 787 (1993).
- ⁵Y. Wu, J. Stöhr, B. D. Hermsmeir, M. G. Samant, and D. Weller, *Phys. Rev. Lett.* **69**, 2307 (1992).
- ⁶P. Carra, B. N. Harmon, B. T. Thole, M. Altarelli, and G. A. Sawatzky, *Phys. Rev. Lett.* **66**, 2495 (1991).
- ⁷R. Wienke, G. Schütz, and H. Ebert, *J. Appl. Phys.* **69**, 6147 (1991).
- ⁸J. Goedkoop, Ph.D. thesis, University of Nijmegen, 1989, and references therein.

- ⁹B. T. Thole, P. Carra, F. Sette, and G. van der Laan, *Phys. Rev. Lett.* **68**, 1943 (1992).
- ¹⁰P. Carra, B. T. Thole, M. Altarelli, and X. Wang, *Phys. Rev. Lett.* **70**, 2307 (1993).
- ¹¹J. P. Hannon, G. T. Trammel, M. Blume, and Doon Gibbs, *Phys. Rev. Lett.* **61**, 1245 (1988).
- ¹²X. Wang, T. C. Lueng, B. N. Harmon, and P. Carra, *Phys. Rev. B* **47**, 9087 (1993).
- ¹³J. C. Lang, X. Wang, B. N. Harmon, A. I. Goldman, H. Wan, G. C. Hadjipanayis, and K. D. Finkelstein (unpublished).
- ¹⁴O. K. Andersen, O. Jepsen, and D. Glötzel, in *Highlights of Condensed-Matter Theory*, edited by F. Bassani, F. Fumi, and M. P. Tosi (North-Holland, New York, 1985).
- ¹⁵P. Nozières and C. T. De Dominicis, *Phys. Rev.* **178**, 1097 (1969).
- ¹⁶P. Carra and M. Altarelli, *Phys. Rev. Lett.* **64**, 1286 (1990).
- ¹⁷J. C. Lang, S. W. Kycia, X. Wang, B. N. Harmon, A. I. Goldman, D. J. Branagan, R. W. McCallum, and K. D. Finkelstein, *Phys. Rev. B* **46**, 5298 (1992).
- ¹⁸K. Shimomi, H. Maruyama, K. Kobayashi, A. Koizumi, H. Yamazaki, and T. Iwazumi, *Jpn. J. Appl. Phys.* **32-2**, 314 (1992).
- ¹⁹P. Fischer, G. Schütz, S. Scherle, M. Knülle, S. Stähler, and G. Wiesinger, *Solid State Commun.* **82**, 857 (1992).
- ²⁰C. Brouder, *J. Phys. Condens. Matter* **2**, 701 (1990).
- ²¹P. Carra, H. König, B. T. Thole, and M. Altarelli (unpublished).
- ²²J. C. Lang, Xindong Wang, V. P. Antropov, B. N. Harmon, A. I. Goldman, H. Wan, G. C. Hadjipanayis, and K. D. Finkelstein, *Phys. Rev. B* (to be published).

Resonant photoemission and magnetic x-ray circular dichroism in the *M* shell of ultrathin films of Fe

J. G. Tobin and G. D. Waddill

Lawrence Livermore National Laboratory, Chemistry and Materials Science Department, Livermore, California 94550

Using magnetic ultrathin films (2–4 monolayers) of Fe on Cu(001) and bulklike Fe, the Fe 3*p* and Fe 3*s* core states have been investigated with resonant photoemission and core-level photoemission, including magnetic x-ray circular dichroism (MXCD) experiments. The resonant photoemission experiment has been done, to probe the parentage of various spectral structures. All the observations can be explained as simply due to the presence of Auger features: It is not necessary to invoke configuration interaction combined with strong photoemission resonance.

Although the observation of spin-dependent splitting in photoelectron spectroscopy of magnetic materials has become fairly common, a complete, quantitative understanding of the underlying causes remains elusive. Consider the case of the *M* shell core levels of Fe. The Fe 3*p* state can exhibit a dichroism or variation if either circularly polarized x rays¹ or linearly polarized x rays² are used with a magnetized sample. An example of magnetic circular dichroism is shown in Fig. 1. Here the sample is 2 monolayer (ML) Fe/Cu(001) and a binding-energy shift of 0.2 eV accompanies the change from a parallel to antiparallel configuration. Alternatively, one can use true spin detection to separate contributions in the Fe 3*p* spectra.^{2–4} Each of these measurements gives a sort of “exchange splitting” but an exact analysis must await the application of full multiple scattering calculations that include spin specificity, selection rules, and band effects.⁵ The Fe 3*p* case is further complicated by the fact that the exchange splitting is of nearly the same order of magnitude as the spin-orbit splitting, inducing additional extensive mixing of *j* states.

A potentially simpler case is the Fe 3*s* “doublet,” examples of which are shown in the topmost spectra of Figs. 2 and 3. The components of this doublet or strongly asymmetric peak are associated with different spins in the local magnetic structure.⁶ In fact, it is not necessary to macroscopically magnetize the sample in order to observe the splitting of the Fe 3*s* peak; however, the samples must be magnetized in order to use spin detection to resolve the separate spin contributions.^{7,8}

The lower spectra in Figs. 2 and 3 are examples of resonant photoemission,⁹ where additional channels for electron emission have opened up as the 2*p*_{3/2} and 2*p*_{1/2} core-level thresholds were reached. The interplay of the direct and resonant channels is a means to test theories concerning the origin of the 3*s* peak splitting, as discussed in Ref. 10. Here, we present detailed resonant photoemission spectra of Fe/Cu(001) and bulklike Fe which will call into question the analysis advocated in Ref. 10.

These experiments were performed at the Stanford Synchrotron Radiation Laboratory, using the University of California/National Laboratories Participating Research Team facilities,^{11–13} on the spherical grating monochromator (SGM) beam line, 8-2. Beam line 8-2 can be used as a source of circularly polarized x rays.^{1,6,14} The data were collected in a three-tiered, two-chamber photoelectron spectrometer,¹⁵

equipped for photoemission with full energy and angular ($\pm 3^\circ$) resolution and multichannel detection.

The resonant photoemission spectra are now broken up into constant binding energy and constant kinetic-energy features. The constant kinetic-energy features are shown to be Auger peaks. The absence of strong intensity variations in the constant kinetic-energy features, as a function of photon energy, is demonstrated. This, in turn, argues against a specialized initial state (i.e., configuration-based) effect as the source of the 3*s* doublet intensity variations.

In resonant photoemission, new channels open up with the crossing of each core-level threshold. In Figs. 2 and 3, major spectral changes occur at $h\nu = 707$ eV (*L*₃ or 2*p*_{3/2} threshold) and $h\nu = 720$ eV (*L*₂ or 2*p*_{1/2} threshold). Because of finite energy broadening, the onset of these changes often occurs at photon energies just below the nominal threshold. New spectral features can be seen at the valence bands ($B^F \approx 0$; B^F is the binding energy with respect to the Fermi energy), the Fe 3*p* ($B^F = 53$ eV) and the Fe 3*s* ($B^F = 92$ eV).

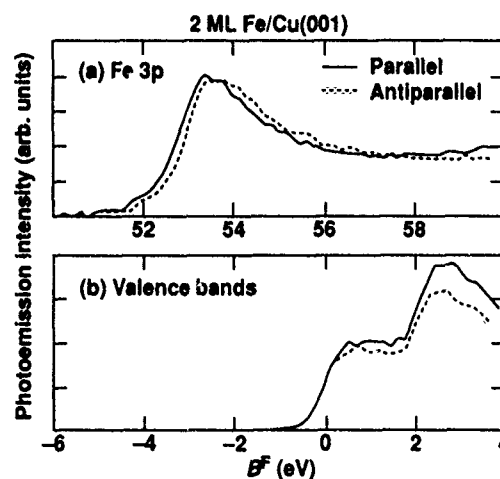


FIG. 1. Magnetic x-ray circular dichroism in photoemission of the fcc Fe 3*p* core level. The bottom panel shows the alignment of the Fermi edge, which allows for a direct comparison of the 3*p* binding energies in the top panel. The sample was 2 ML Fe/Cu(001), with perpendicular magnetization. The photon energy was 160 eV. The circularly polarized x rays were incident along the sample normal and the electron emission direction was at 55° from normal, approximately in the [210] plane. Parallel and antiparallel refer to the relative orientation of the photon helicity and sample magnetization (or minority spin) (Ref. 1). Parallel refers to both up or both down, and antiparallel is correspondingly up, down or down, up.

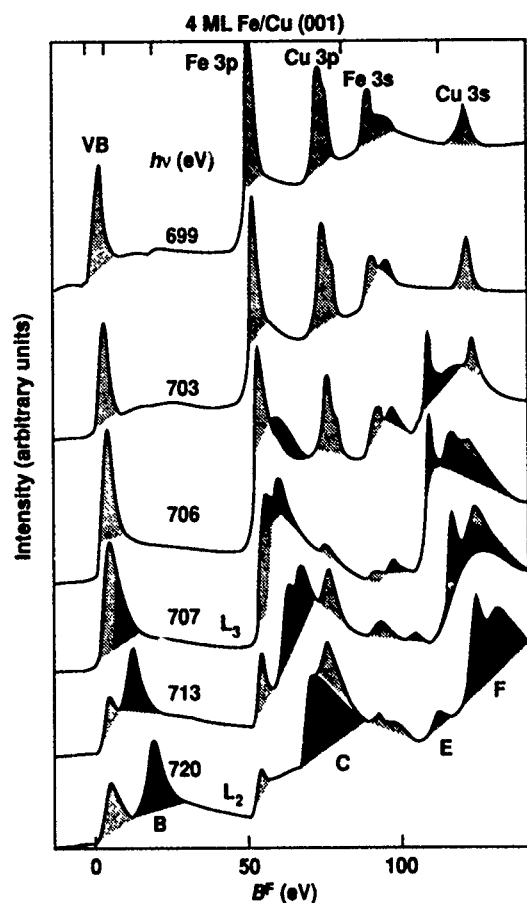


FIG. 2. Wide photoelectron emission scans of 4 ML of Fe/Cu(001) at a series of photon energies near the $2p_{3/2}$ (707 eV) and $2p_{1/2}$ (720 eV) thresholds. All scans shown were taken with linear polarization with the photons incident at 45° from the sample normal. The electrons were collected at an angle of 45° from the surface normal, with the electron momentum parallel to the photon electric polarization vector. Constant binding-energy features are shown with light shading. Constant kinetic energy reactions are shaded more darkly.

As the photon energies are increased, the new features move across the spectra, with a constant kinetic energy (KE) associated with each feature. (A summary of constant BE and constant KE features is shown in Table I.) Well above threshold, these constant KE features are identified as Auger peaks. It is only at threshold that the resonance channels and direct channel are isoenergetic. In the third column of Table I are values taken from an Auger handbook.¹⁷ All except one are printed-assigned values, with the exception being 620 eV, which corresponds to a smaller unmarked minimum. The constant difference between column 2 and column 3 arises from the measurement procedure. In this work we use peak maxima, and in Ref. 17 the minima of differential peaks is used. Thus, this shift is not unexpected and a one-to-one correspondence is found between the members of column 2 and those of column 3.

The strongest features, B, C, and F are associated with a hole in the L_3 ($2p_{3/2}$) level: $L_3M_{4,5}M_{4,5}$, $L_3M_{2,3}M_{4,5}$ and $L_3M_{2,3}M_{2,3}$ respectively.¹⁸ These are intense but broad transitions. The $L_3M_{4,5}M_{4,5}$ (KE=692 eV) and the $L_3M_{2,3}M_{4,5}$ (KE=642 and 637 eV) and the $L_3M_{2,3}M_{2,3}$ (KE=592 and 587 eV) are all intrashell interactions. The observed splitting

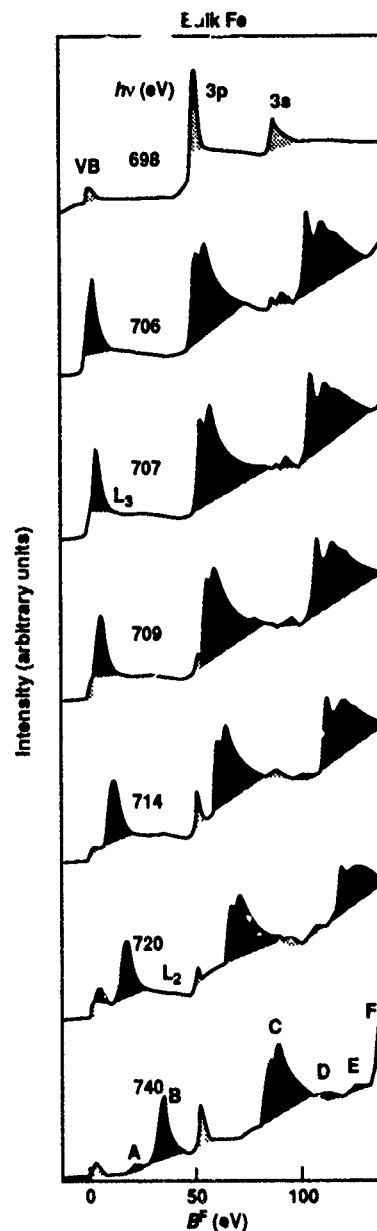


FIG. 3. Similar to Fig. 2, but here the sample is a bulklike Fe film (25 ML) on Cu(001). Note the absence of Cu spectral features. All scans were taken with linear polarization, at normal incidence, and the electrons were collected at an angle of 45° from the normal.

in C and F, which were smeared out in the lower-resolution Auger handbook spectra, is well understood.¹⁸ The other feature which first appears at the L_3 threshold is a weaker peak at KE=602 eV (E in Table I). This appears to be a $L_3M_1M_{4,5}$ transition. Also, when the L_2 threshold is reached, an additional transition will contribute intensity at this energy, as is described next.

The L_2MM transitions become accessible at $h\nu=720$ eV but in general are far less intense than their L_3MM counterparts, as discussed in Ref. 10. This is due in part to the Coster-Kronig¹⁹ decay channel, $L_2L_3M_{4,5}$, which rapidly transfers the hole into the L_3 states and thus decreases the L_2MM intensities while maintaining the L_3MM intensities. A fairly strong $L_2M_{4,5}M_{4,5}$ peak can be observed at KE = 702 eV (peak A in Table I). The other two possibilities,

TABLE I. Summary of constant B^F and KE features.

Constant	B^F , B^F (eV) ^b	Constant	KE KE (eV)	Auger features ^a KE (eV)	Frozen shell model $KE=B_1^F-B_2^F-B_3^F-\Phi$
VB ($M_{4,5}$)	~2	A	702	716	$L_2M_{4,5}M_{4,5}$ 712 eV
Fe 3p ($M_{2,3}$)	53	B ^c	692	703 ^c	$L_3M_{4,5}M_{4,5}$ 699 eV
Cu 3p	75,77	C ^c	642,637	651 ^c	$L_3M_{2,3}M_{4,5}$ 648 eV
Fe 3s (M_1)	92	D	612	(~620)	$L_2M_1M_{4,5}$ 623 eV
Cu 3s	120	E	602	610	$L_3M_1M_{4,5}$ 610 eV
		F ^c	592,587	598 ^c	$L_2M_{2,3}M_{2,3}$ 610 eV $L_3M_{2,3}M_{2,3}$ 597 eV

^aFrom Ref. 17.^cStrong feature.^bFrom Ref. 16.

$L_2M_{2,3}M_{4,5}$ and $L_2M_{2,3}M_{2,3}$ are difficult to observe, and the $L_2M_{2,3}M_{2,3}$ may overlap with the $L_3M_1M_{4,5}$ at KE = 602 eV. The final feature, D in Table I at KE = 612 eV, appears to be the $L_2M_1M_{4,5}$ peak and is fairly weak, although this is the strongest of the L_2MM features relative to its L_3MM counterpart. For the sake of argument, the results of a frozen shell model are shown in Table I. Obviously, this model is deficient and only energy differences make any sense quantitatively, e.g., $L_2M_1M_{4,5}$ vs $L_3M_1M_{4,5}$ and $L_2M_{2,3}M_{2,3}$ vs $L_3M_{2,3}M_{2,3}$. Nevertheless, it is clear that these assignments are quite reasonable. Moreover, the spectra shown here in Figs. 2 and 3 are only a part of the overall data set. A much finer grid of spectra, taken with $\Delta h\nu = 2$ eV, were also collected and were used in this analysis, although space limitation precludes their inclusion here.

Having established that the constant KE features can be assigned as Auger features, the question arises: Is there a need to invoke a specialized initial state resonance and configuration interaction to explain our observations? The answer is no. As can be seen in Figs. 2 and 3, the constant KE features generally exhibit fairly constant intensity ratios relative to each other. The constant KE features (associated with L_3MM Auger peaks B, C, E, and F are generally much more intense than the constant B^F features, with the exception of the $L_3M_1M_{4,5}$ (peak E). Peak F does seem to turn on at a slightly lower photon energy than B, C, and E, but this is not unreasonable considering the significantly different electronic structure that contributes to these features. This appears to be analogous to the delayed onset of the 3p or 3d photoemission cross sections, due to the centrifugal barrier, which is not to be expected in an s state such as the Fe 3s.²⁰ Consistent with our interpretations, recent work²¹ indicates that, resonant photoemission in Ni is also essentially due to intense Auger emission and is not actually photoemission at all.

Finally, one last observation should be made. Because x-ray absorption at the L_2 and L_3 edges is such a crucial part of the resonant photoemission process and because very strong absorption circular dichroism has been observed for both monolayers and multilayers,¹⁴ it was plausible that a magnetic circular dichroism intensity effect might be seen in resonant photoemission. Unfortunately, no such effects were observed.

An extensive resonant photoemission investigation of 4 ML Fe/Cu(001) and bulk Fe were performed. All observed resonance features can be explained by assignment as Auger

peaks; the increased intensity of the high-binding energy 3s multiplet feature at resonance appears to be related to the overlap with the $L_3M_1M_{4,5}$ (or $L_2M_1M_{4,5}$) Auger transition and does not uniquely establish this feature as arising from configuration interaction d mixing. This seriously calls into question the arguments proposed earlier in Ref. 10, where the variation in spectral intensities of the components of the 3s doublet was used to support a configuration-based model of photoelectron emission. The apparent variation of the 3s doublet components appears to be due merely to the onset of an Auger transition at the L_3 threshold.

Work was performed under the auspices of the U.S. Department of Energy by the Lawrence Livermore National Laboratory under Contract No. W-7405-ENG-48. SSRL is supported by DOE/OBES Chemical Sciences. The authors wish to thank Karen Clark for clerical support of this work.

¹D. P. Pappas *et al.*, J. Appl. Phys. **73**, 5936 (1993); the definition of parallel and antiparallel shown in Fig. 3 of this reference was wrong and has been reversed in this work.

²C. H. Roth *et al.*, Phys. Rev. Lett. **70**, 3479 (1993).

³C. Carbone and E. Kisker, Solid State Commun. **64**, 1107 (1988); F. U. Hillebrecht *et al.*, Europhys. Lett. **19**, 711 (1992); R. Jungblut *et al.*, Surf. Sci. **269/270**, 615 (1992).

⁴B. Sinkovic *et al.*, Phys. Rev. Lett. **65**, 1647 (1990).

⁵E. Tamura, P. A. Sterne, A. Gonis, G. D. Waddill, and J. G. Tobin (unpublished).

⁶G. D. Waddill *et al.*, Phys. Rev. B **46**, 552 (1992).

⁷C. Carbone *et al.*, Z. Phys. B **79**, 325 (1990).

⁸F. U. Hillebrecht *et al.*, Phys. Rev. Lett. **65**, 2450 (1990).

⁹A. Kotani and Y. Toyozawa, in *Synchrotron Radiation*, edited by C. Kunz (Springer, Berlin, 1979).

¹⁰G. Van Der Laan *et al.*, Phys. Rev. B **46**, 7221 (1992); G. Van Der Laan *et al.*, *ibid.* **46**, 9336 (1992).

¹¹K. G. Tirsell and V. P. Karpenko, Nucl. Instrum. Methods A **291**, 511 (1990).

¹²L. J. Terminello *et al.*, Nucl. Instrum. Methods A **319**, 271 (1992).

¹³T. Reich *et al.*, Rev. Sci. Instrum. **64**, 2552 (1993).

¹⁴J. G. Tobin *et al.*, Phys. Rev. Lett. **68**, 3642 (1992); A. F. Jankowski *et al.*, Symp. Proc. Mater. Res. Soc. **313**, 227 (1993); G. D. Waddill *et al.*, J. Appl. Phys. **74**, 6999 (1993).

¹⁵J. G. Tobin *et al.*, Symp. Proc. Mater. Res. Soc. **295**, 213 (1993).

¹⁶J. Kirz *et al.*, *X-Ray Data Booklet* (Center for x-ray Optics, Lawrence Berkeley Laboratory, Berkeley, CA, 1986).

¹⁷*Handbook of Auger Electron Spectroscopy* (Physical Electronics, Eden Prairie, MN).

¹⁸*Practical Surface Analysis by Auger and X-Ray Photoelectron Spectroscopy*, edited by D. Briggs and M. P. Seah (Wiley, New York, 1983).

¹⁹*Photoemission in Solids I*, edited by M. Cardona and L. Ley (Springer, Berlin, 1978); L. C. Feldman and J. W. Meyer, *Fundamentals of Surface and Thin Film Analysis* (North-Holland, New York, 1986).

²⁰J. J. Yeh and I. Lindau, At. Data Nucl. Data Tables **32**, 1 (1985).

²¹M. F. Lopez *et al.*, Europhys. Lett. **20**, 357 (1992).

Molecular-orbital analysis of magneto-optical Bi-O-Fe hybrid excited states

Gerald F. Dionne

Lincoln Laboratory, Massachusetts Institute of Technology, Lexington, Massachusetts 02173

Gary A. Allen^{a)}

Department of Physics, Massachusetts Institute of Technology, Cambridge, Massachusetts 02139

Molecular-orbital estimates of the excited-state spin-orbit coupling multiplet splitting are presented to support the theory that enhanced magneto-optical effects in $Y_{3-x}Bi_xFe_5O_{12}$ originate from covalent interactions between Bi^{3+} and Fe^{3+} ions. A self-consistent approximation is applied to a two-level bonding-antibonding hybrid formed from the excited 4P term of Fe^{3+} and the excited 3P of Bi^{3+} . For term energy values chosen from spectroscopic data, overlap integrals $s < 0.05$ are sufficient to account for bonding-state depressions that match those reported for the tetrahedral and octahedral site-enhanced transitions at 2.6 and 3.15 eV. The hybrid eigenfunctions of the upper states can contain more than 30% of the $Bi^{3+} ^3P$ orbital term. Multiplet splittings that are enhanced by the large Bi^{3+} spin-orbit coupling constant ($\lambda \approx 2$ eV) are found to be on the order of 0.5 eV with a full complement of Bi surrounding Fe in the garnet lattice, in agreement with estimates based on experiment.

I. INTRODUCTION

In a recent examination of the Kerr rotation and ellipticity enhancement in $Y_{3-x}Bi_xFe_5O_{12}$,¹ it was concluded that the principal source of the effect was large splittings of the upper states of selected optical transitions. In this interpretation, two strong lines of opposite sign with transition energies of 2.6 and 3.15 eV from Fe^{3+} in tetrahedral (d) and octahedral (a) sublattices were determined to be responsible for most of the magneto-optical enhancements across a band from 2 to 5 eV. To further this analysis, we now examine the origin of the excited-state splitting. For ferrimagnets with exchange-coupled $Fe^{3+} ^6S$ ground states, polarization rotation of a wave propagating parallel to the magnetization vector (z direction) is described mathematically as a frequency-dependent off-diagonal element of the permittivity tensor. This requires interaction between the electric vector of the optical wave and the orbital angular momentum L of the excited state. For the magnetic moments to influence nonreciprocal effects, therefore, spin-orbit coupling is a necessary component. Since the excited-state splitting is the result of spin-orbit multiplet structure, contributions from the large Bi^{3+} spin-orbit interaction reflected through covalent molecular-orbital (MO) states is the focus of this investigation.

II. TWO-LEVEL MO APPROXIMATION

For the generic two-level system sketched in Fig. 1, the covalence Hamiltonian H may be treated self-consistently following the method developed by Wolfsberg and Helmholz.² The determinant secular equation of the perturbation calculation formed from matrix elements $H_{ij} = \langle \chi_i | H | \chi_j \rangle$ is given by

$$\begin{vmatrix} H_{11} - \Lambda & H_{12} \\ H_{21} & H_{22} - \Lambda \end{vmatrix} = \begin{vmatrix} E_1 - \Lambda & B - \Lambda s \\ B - \Lambda s & E_2 - \Lambda \end{vmatrix} = 0, \quad (1)$$

where $B \approx (H_{11} + H_{22})s$ (exchange integral), and $s = \langle \chi_1 | \chi_2 \rangle$ (overlap integral). Solution of Eq. (1) yields the following eigenvalues.³

$$\Lambda_{\pm} = \frac{(E_1 + E_2)(1 - 2s^2) \pm \sqrt{(E_1 - E_2)^2(1 - s^2) + B^2}}{2(1 - s^2)}. \quad (2)$$

The MO eigenvectors $\phi_i = \sum_j c_{ij} \chi_j$ are found from the standard relation $\sum_j (H_{ij} - \Lambda_{\pm} \delta_{ij}) c_{ij} = 0$, where $\sum_j c_{ij}^2 = 1$. If $s > 0$, additional normalization factors are necessary.⁴ For the two-level case,

$$C_{ij} = c_{ij}(c_{ii}^2 + c_{ij}^2 + 2c_{ii}c_{ij}s)^{-1/2}, \quad (3)$$

and the final eigenvectors become $\phi_b = C_{11}\chi_1 + C_{12}\chi_2$ and $\phi_a = C_{21}\chi_1 - C_{22}\chi_2$ for the bonding and antibonding states, respectively. There are two important results here: (i) ϕ_b is of lower energy than χ_1 by an amount $\Lambda_- - E_1$, and (ii) the initial wave functions χ_1 and χ_2 mix in proportion to the values of C_{11} and C_{12} . For this generic example, $|\chi_2|^2$ mixes into $|\phi_b|^2$ by a fraction C_{12}^2 .

III. SUPEREXCHANGE AND SPIN-ORBIT COUPLING

As discussed previously,¹ we believe that the enhanced magneto-optical effects arise from the cooperative action of Fe^{3+} ions with degenerate excited orbital terms that are split further by covalent interactions with Bi^{3+} . Because

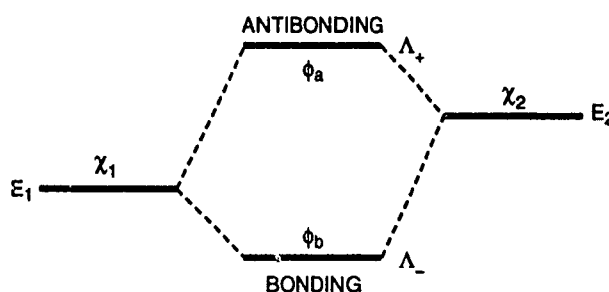


FIG. 1. Generic two-level molecular-orbital model.

^{a)}Also affiliated with Lincoln Laboratory.

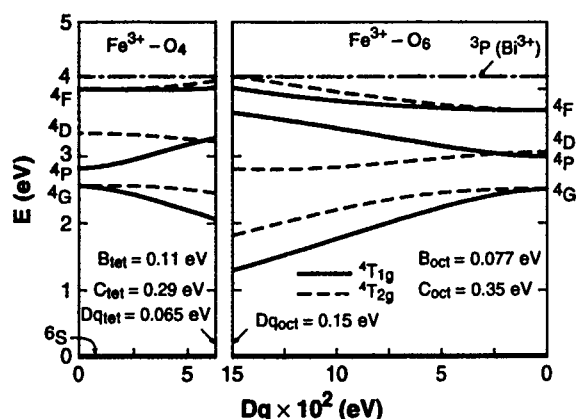


FIG. 2. Crystal-field-sensitive excited terms for (d^5) in d and a garnet sites as functions of crystal-field parameter Dq . Energies were computed from Tanabe and Sugano matrices (Ref. 7), with B and C values based on the spectral analysis of Wood and Remeika (Ref. 8).

crystal-field effects have already been accounted for (see Fig. 2), the total angular momentum J remains a "good" quantum number in each part of the hybrid state. The upper-state splitting parameter Δ for individual ions is determined principally by the eigenstates of the operator $\lambda \mathbf{L} \cdot \mathbf{S}$. The z -axis collinearity of the N magnetic moments can occur through an applied field $\mathbf{H}(=\mathbf{H}_a)$ or an exchange field $\mathbf{H}(=\mathbf{H}_{ex})$. In both cases, the degree of alignment follows a Brillouin function B , so that $N_{eff} = NB(H, T)$. There is, however, an important distinction between these two situations— \mathbf{H}_a influences J by splitting the M_J levels (Zeeman effect), but \mathbf{H}_{ex} can affect only S by splitting the M_S states.

The magnetization of the garnet is saturated in the z direction by superexchange fields,⁵ causing $B \rightarrow 1$, and $N_{eff} \rightarrow N$. Through covalent interactions, the excited states of both Fe^{3+} and Bi^{3+} should also have nondegenerate spin states. If the exchange field perturbation is applied, the lowest state M_S value enters the calculation as a multiplier when the orbital magnetic moment degeneracies of the MO states are lifted by spin-orbit coupling $\lambda \mathbf{L} \cdot \mathbf{S}$. Because S is captured by \mathbf{H}_{ex} , and is therefore aligned with the z axis, $|S| = S_z$ and $|L| = L_z$. The value of $S_z (=M_S)$ appropriate for the particular level of the $2S+1$ manifold simply multiplies each $M_L (=2L+1)$ value of the L_z manifold. Expectation values of $\lambda \mathbf{L} \cdot \mathbf{S}$ are therefore determined by

$$\phi_b | \lambda L_z S_z | \phi_b \rangle \approx \lambda M_S \langle \phi_b | L_z | \phi_b \rangle. \quad (4)$$

This situation for a 4P state is depicted in Fig. 3. For the hybrid state, the energies that determine the Δ splitting may be reduced to

$$E_\Delta(M_L) = C_{11}^2 (\lambda_1 M_{S1} M_{L1} + C_{12}^2 (\lambda_2 M_{S2}) M_{L2}), \quad (5)$$

where M_{S1} now represents the value of the lowest spin state. For the case of 4P (Fe^{3+}), $M_{L1} = 0, \pm 1$ and $M_{S1} = -3/2$; for 3P (Bi^{3+}), $M_{L2} = 0, \pm 1$ and $M_{S2} = -1$. Where $\lambda_2 \gg \lambda_1$ ($\lambda_{Bi} \gg \lambda_{Fe}$ in this case) and C_{12}^2 is significant, we may approximate $E_\Delta(M_{L2}) = C_{12}^2 (\lambda_2 M_{S2}) M_{L2}$. The magnitude of the splitting then becomes $2\Delta \approx [E_\Delta(+1) - E_\Delta(-1)]$.

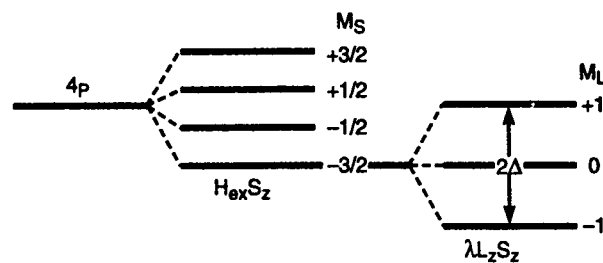


FIG. 3. Exchange field spin quenching and spin-orbit splitting of a 4P term.

IV. GROUND- AND EXCITED-STATE ENERGIES

Before we examine the excited states of the $Bi_3Fe_5O_{12}$ molecule, it is necessary to determine the stabilization energy of the ground state. This energy may be estimated from the electrostatic interactions between ions and outermost electrons in the model shown in Fig. 4. Here the binding energy of the electrons of Fe^{3+} and Bi^{3+} may be computed from the algebraic sum of the cation ionization potentials (IP) and the energy of the field from the negatively charged anion. For the outermost electron, this repulsive energy (RE) is estimated by dividing the effective lattice energy (LE) by the ionic charge. For Fe^{3+} , $IP = -54.8$ and RE from $Fe_2O_3 \approx +25.5$ eV; for Bi^{3+} and Bi_2O_3 , the corresponding values are -45.3 and $+15.8$ eV, so that a common resultant ground-state ionic energy $E_g \approx -29$ eV is estimated for both Fe^{3+} and Bi^{3+} . Stabilization energies of the excited states are found by adding -29 eV to absorption energy values from spectral data.¹

Interpreting the magneto-optical properties of $Bi_3Fe_5O_{12}$ is begun by analyzing the covalent interactions between the excited 3P term of Bi^{3+} in the dodecahedral (c) sites of the garnet lattice, and the excited states of Fe^{3+} in the d and a sites. Since isolated Bi^{3+} has an excited state ≈ 4.2 eV above the ground state,⁶ hybridization from covalence is possible with several Fe^{3+} excited states. Diagrams of the orbital terms^{7,8} as functions of the crystal-field strength parameter Dq for the d and a sites are shown in Fig. 5.

V. MOLECULAR-ORBITAL EXCITED STATES

To construct the hybrid states that represent the bands of half-width Γ between the $Bi^{3+} ^3P$ ($6s, 6p$) and $Fe^{3+} (3d^5)$ excited states that would produce electron transition matrix elements with $Fe^{3+} ^6S$ ground states, consider the following rationale: The candidates that satisfy the selection rule

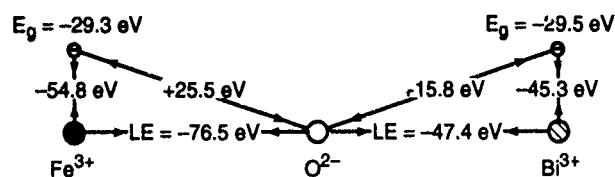


FIG. 4. Electron stabilization energies based on handbook values of ionization potentials of Bi^{3+} and Fe^{3+} and lattice energies of Bi_2O_3 and Fe_2O_3 .

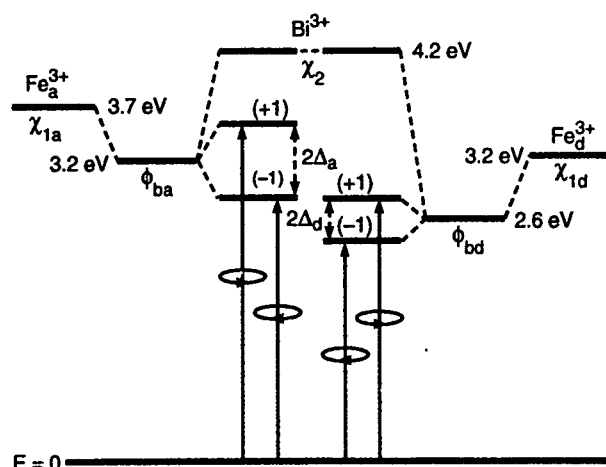


FIG. 5. Proposed molecular-orbital energy-level diagram of $\text{Bi}_3\text{Fe}_5\text{O}_{12}$. Oxygen interactions and all antibonding states have been omitted to reduce confusion. Overlap integrals can include individual Bi-O-Fe, direct Bi-Fe, and linkages between Bi and $\text{Fe}_a\text{-O-Fe}_d$ superexchange groups.

$\Delta M_L = \pm 1$, that have symmetry transformation properties similar to the $\text{Bi}^{3+} {}^3P$ state, and are crystal-field (i.e., Dq) selective are the ${}^4T_{1g}$ states. Inspection of Fig. 2 reveals three ${}^4T_{1g}$ states, associated with the 4G , 4P , and 4F terms.

For the principal transitions that appear to cause the magneto-optical anomalies at 2.6 and 3.15 eV,¹ the obvious choice is the 4P term, which has energies of 3.2 and 3.7 eV for the d and a sites, respectively, with corresponding Dq values of 0.065 and 0.15 eV. The bonding-state hybrid function is then expressed as $\phi_b = C_{11}|{}^4P\rangle + C_{12}|{}^3P\rangle$. If these quantities are used in Eqs. (1) and (2), values that agree with experiment are listed in Table I for the transition energies ($\Lambda_- - E_g$) from the ground state to the bonding states for $C_{12}^2 = 0.26$ and 0.33, and $s = 0.04$ and 0.03 for the d and a sites, respectively. The larger value of s for the d site is consistent with its shorter bond lengths. To determine the Δ values listed in Table I, we ignore the first term (the Fe^{3+} part) of Eq. (5) by assuming that $\lambda_2 \gg \lambda_1$. With $\lambda_2 = \lambda_{\text{Bi}}$ and $M_{S2} = -1$, the multiplet energies $E_{\Delta}(M_{L2}) \approx +\lambda_{\text{Bi}}C_{12}^2$, 0,

$-\lambda_{\text{Bi}}C_{12}^2$, thereby yielding $\Delta \approx \lambda_{\text{Bi}}C_{12}^2$. For $\lambda_{\text{Bi}} \approx 2$ eV,⁹ and $C_{12}^2 < 0.5$, Δ values for d and a sites are 0.52 and 0.66 eV, respectively, in general agreement with the conclusions of experiment (see footnote to Table I). Calculated values of Γ ($\approx B/4$) are also in reasonable agreement with experimental values on the order of 0.5 eV.¹

VI. DISCUSSION

From the above calculations, Fig. 5 may be constructed to illustrate the origin of the Faraday rotation peaks at 2.6 and 3.15 eV. In addition, this work presents an opportunity to suggest that the weaker transition estimated to occur at 3.9 eV initially labeled as d site,¹ may result from a partial overlap cancellation of transitions that originate from the MO states formed with the 4F terms ($E_1 \approx 4.1$ eV) of Fe^{3+} ions in both d and a sublattices. This situation would explain why the location of the second peak from the a sublattice should appear somewhere in this general energy regime. The experimental determination that the peak at 3.9 eV has the same sign as the tetrahedral peak at 2.6 eV is consistent with the ratio (3:2) of d to a sites.

Based on the notion that magneto-optical effects involving excited states are dependent on the product $N_{\text{eff}}\Delta$, we may speculate on the effects of magnetic dilution and temperature variations. If the temperature T remains below the Curie temperature T_C , N_{eff} should track with the magnetizations of the respective sublattices, subject to influence from loss of spin collinearity in the upper states of the individual transitions. Information about spin canting in both the ground and excited states may be extracted from the peak intensities as functions of Fe^{3+} content.

For other ions with a $(6s)^2$ ground-state electron configuration similar to that of Bi^{3+} , i.e., Pb^{2+} , Tl^{1+} , or neutral Hg, similar magneto-optical effects should be expected. With smaller λ values, however, the effects of the Δ splitting should be reduced somewhat from those of Bi^{3+} .

ACKNOWLEDGMENTS

This work was sponsored by the Department of the Air Force through the Lincoln Laboratory Innovative Research Program. The authors also acknowledge the support of Professor M. S. Dresselhaus and Dr. H. P. Jenssen of MIT.

TABLE I. Molecular-orbital parameters of $\text{Bi}_3\text{Fe}_5\text{O}_{12}$.

$E_1 - E_g$ (eV)	$\Lambda_- - E_g$ (eV)	s	C_{12}^2	Δ (eV)	Δ_{exp} (eV)
3.2 (d)	2.6	0.04	0.26	0.52	0.11 ^a
3.7 (a)	3.2	0.03	0.33	0.66	0.27 ^a

^aThese values were determined for $\text{Y}_{3-x}\text{Bi}_x\text{Fe}_5\text{O}_{12}$ with $x = 0.25$ (Ref. 1) For the full complement of Bi^{3+} interactions, i.e., $x = 3$, the effective s integrals, C_{12}^2 values, and Δ_{exp} magnitudes would be significantly larger.

¹G. F. Dionne and G. A. Allen, J. Appl. Phys. **73**, 6127 (1993).

²M. Wolfsberg and L. Helmholz, J. Chem. Phys. **20**, 837 (1952).

³G. F. Dionne, Technical Report TR-885, MIT Lincoln Laboratory, 19 June 1992, Appendix A, AD-A253975.

⁴C. J. Ballhausen and H. B. Gray, *Molecular Electronic Structures* (Benjamin/Cummings, Reading, MA, 1980), Chap. 2.

⁵A. M. Clogston, J. Phys. (Paris) **20**, 151 (1959).

⁶G. B. Scott, D. E. Lacklison, and J. L. Page, Phys. Rev. B **10**, 971 (1974).

⁷Y. Tanabe and S. Sugano, J. Phys. Soc. Jpn. **9**, 753 (1954).

⁸D. L. Wood and J. P. Remeika, J. Appl. Phys. **38**, 1038 (1967).

⁹S. Wittekoek and D. E. Lacklison, Phys. Rev. Lett. **28**, 740 (1972).

A new Faraday rotation glass with a large Verdet constant

Sui hua Yuan and Xiao Zhou Shu

Special Optics Laboratory, Xian Jiaotong University, Xian Chian, People's Republic of China

Heavily terbium-doped boron-silicate glasses (Tb^{3+} 10.4 at. %) with a Verdet constant (632.8 nm, room temperature) as large as -0.338 min/Oe cm, 38% larger than that of the famous FR-5 glasses, have been made. The wavelength and temperature dependencies of the Verdet constants of samples have been investigated in the ranges of 400 to 800 nm and 100 to 300 K. The results show paramagnetic Faraday rotations. The measured susceptibilities between 77 and 300 K support this point but with an effective Bohr magneton number 7% smaller than the theoretical value for free Tb^{3+} ions. Susceptibilities are further measured at temperatures from 1.5 to 100 K and magnetic fields from 0.2 to 5.0 T. The results show saturation of magnetization and give a Néel temperature of about -9 K. The effective Bohr magneton number in the state of saturated magnetization is 55% smaller than the free ion value. These results may indicate the single ion anisotropy reduction of the magnetization of the disordered Tb^{3+} ions at low temperatures. The measured indices, Abel number, and nonlinear-index coefficient are 1.745 92 (N_c), 1.746 70 ($N_{632.8}$), 1.749 84 (N_D), 1.760 31 (N_f), 49.92, and 7.638×10^{-20} m²/W, respectively. The transmittance of the sample (15.2 mm thick) is up to 85% in the range from 400 to 1500 nm. It is known that the lower transmittance is mainly due to Nd^{3+} and Pr^{3+} impurities in the raw material Tb_4O_7 by optical absorption analysis.

I. INTRODUCTION

The transparent range for visible and near infrared light Faraday rotation glasses, among which the Hoya FR-5 glass is the most famous, has attracted the attention of scientists and engineers for a long time. As a paramagnetic material, Faraday rotation glass has the disadvantage of a small Verdet constant.¹ Hoya Optics Inc. has developed FR-6 glass with better characteristics than FR-5,² but the details are not available to the author. A new Faraday rotation glass, known as the terbium glass with a Verdet constant (632.8 nm, room temperature) as large as -0.338 min/Oe cm, 38% larger than that of the FR-5 glass, has been made in this laboratory. In this glass a high concentration of terbium ions (Tb^{3+} 10.4 at. %) is doped into the boron-silicate matrices with BaF_2 and PbO_2 as flux in the melt at a temperature of about 1500 °C. Another two samples with different doping concentrations of terbium and dysprosium ions (Tb^{3+} 8.4 at. % and Dy^{3+} 7.2 at. %, respectively) were also made in the process. These three samples are known as samples I, II, and III. The light wavelength and temperature dependencies of the Verdet constants of the samples are measured to fit into a single ion theoretical model³ above 100 K. The temperature dependencies of the magnetization and the magnetic susceptibilities of samples I and II measured from 1.5 to 300 K and from 0.2 to 5.0 T show the existence of superparamagnetic clusters with antiferromagnetic structure.⁴

The indices and Abel number of sample I are, respectively, larger and smaller than those of FR-5. The nonlinear index coefficient of sample I is smaller than that of TbAlG . The optical absorptivity of sample I at 632.8 nm is larger than that of FR-5. Optical absorption spectrum analysis for sample I may indicate that the impurity neodymium and praseodymium ions in raw material Tb_4O_7 cause the larger absorptivity.

II. EXPERIMENTS

According to Crossley,³ the Verdet constant V can be written as

$$1/V = \lambda^2/C - \lambda_0^2/C, \quad (1)$$

where λ is the light wavelength, λ_0 is the resonance wavelength, and $C \propto T$ is a constant for a certain temperature. At first, the temperature was set to 303 K, the Verdet constants of samples I, II, and III were measured with a light wavelength scanned from 400 to 800 nm because of the probe limit. Second, for sample I, the temperature was set to 208 and 173 K and the wavelength was scanned again from 400 to 800 nm; the magnetic field was 0.22 T for all of the measurements. Experimental data are fit to Eq. (1) by least-squares as shown in Fig. 1. The numbers 1, 2, 3, 4, and 5 in the figure indicate samples III, II, and I at 303 K, and sample I at 208 and 173 K, respectively. The resonance wavelength λ_0 for terbium ions in samples I and II are calculated from

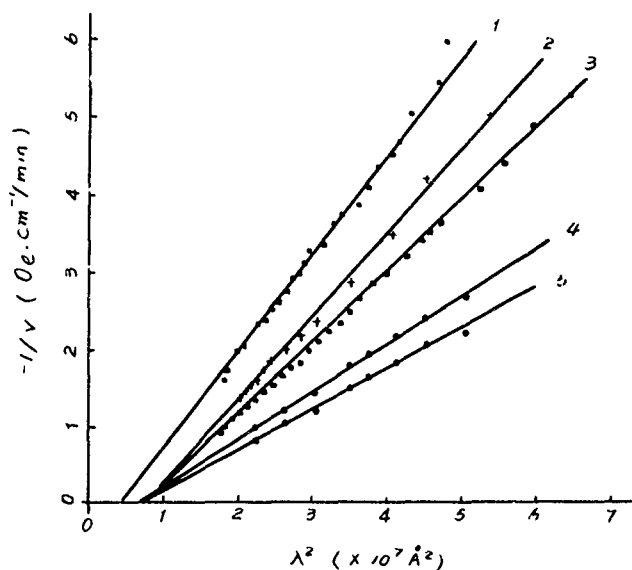


FIG. 1. The wavelength dependencies of the Verdet constants of samples I, II, and III. The numbers at the lines 1, 2, 3, 4, and 5 indicate data for samples III, II, and I at temperature 303 K and for sample I at 208 and 173 K. The applied magnetic fields are all 0.2 T.

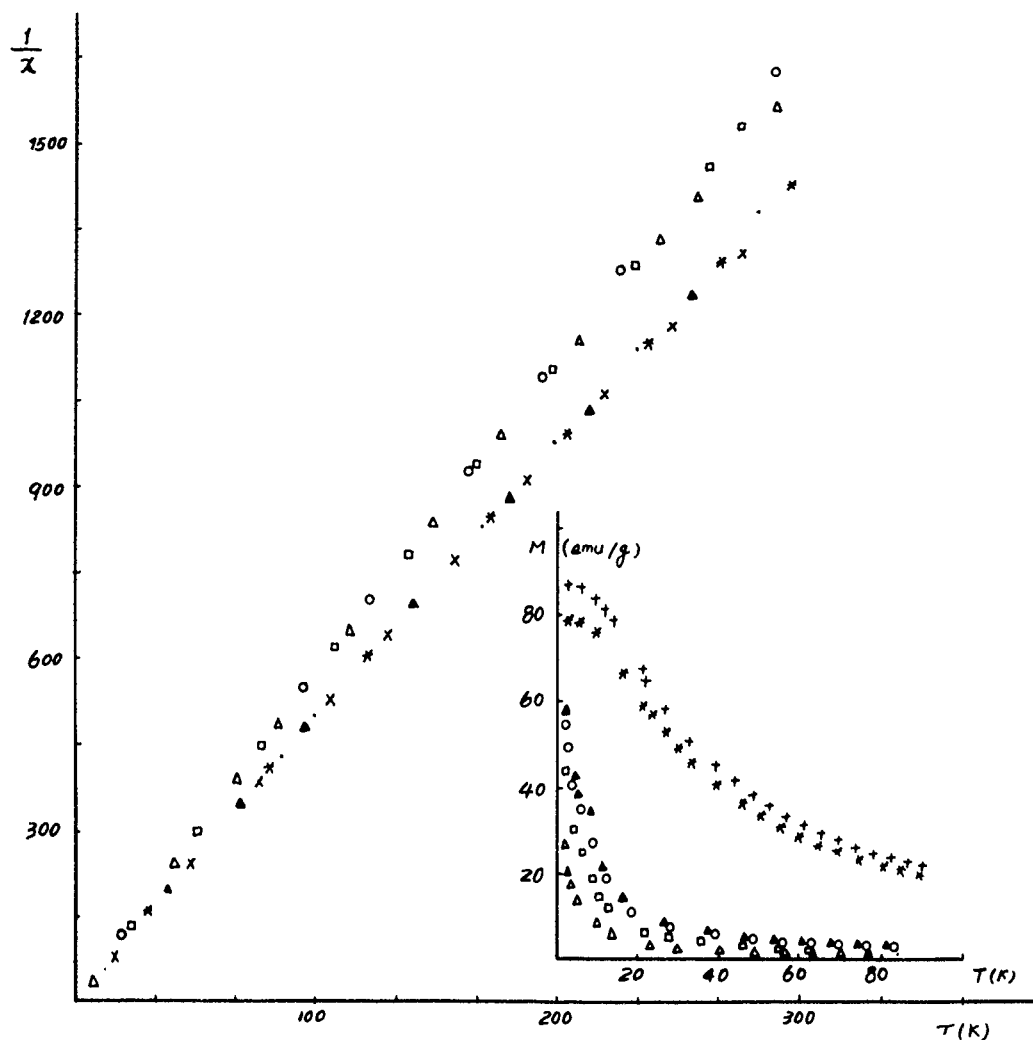


FIG. 2. The temperature dependencies of the magnetic susceptibilities of samples I and II. The upper line is for sample I and the lower sample II. The symbols Δ and \times are for the applied magnetic field 0.2 T, \square and $*$ for 0.4 T; and \circ and \blacktriangle for 0.6 T. The insert shows the temperature dependencies of the magnetization of samples I (upper) and II (lower). The symbols \dagger and $*$ are for the applied magnetic field 5.0 T; \blacktriangle and \circ for 0.6 T; and \square and Δ for 0.4 and 0.2 T, respectively

the slope and intersection of the lines 2, 3, 4, and 5 to be in the range from 258.6 to 280.0 nm with 267.6 nm as an average. This is very close to $\lambda_0=268.0$ nm for a terbium ion in TbAlG.⁵ The resonance wavelength λ_0 for the dysprosium ion in sample III is calculated from line 1 as 223.1 nm which is also close to $\lambda_0=220.5$ nm for the dysprosium ion in DyAlG.⁵ The temperature dependence of the Verdet constant of sample I was measured from 100 to 300 K to give a paramagnetic result, $1/V \propto T$. However, the hysteresis of sample I measured at 77 K is 2.5 times wider than that at 282 K. The susceptibility and magnetization of sample I were measured with a vibrating-sample magnetometer (VSM) at temperatures from 1.5 to 300 K and at applied magnetic fields from 0.2 to 5.0 T. As shown by the upper curves in Fig. 2, the magnetization at high applied magnetic fields approaches saturation at low temperature while the susceptibility curves give a negative intercept θ of about -9 K.

Using the measured density of the terbium glass and the atomic concentration of Tb^{3+} ions in the glass, the concentration of Tb^{3+} ions N is calculated to be $1.08 \times 10^{22}/\text{cm}^3$. The effective Bohr magneton number can be calculated for

sample I using the value of N and the slope of the upper line in Fig. 2. The value is $9.01 \mu_B$ which is about 7% smaller than the value for the free Tb^{3+} ion. From the insert in Fig. 2, the magnetic moment per volume of sample I below 5 K is $433.87 \text{ emu}/\text{cm}^3$. The averaged effective Bohr magneton number for each Tb^{3+} ion is thus $4.33 \mu_B$ which is 55% smaller than the free ion value.

The conventional optical parameters, of sample I, such as transmittance and index are measured with a Lambda-9 spectrophotometer. For measuring the index the sample was processed into a prism. The transmittance is up to 85% within the range between 400 and 1500 nm as shown in Fig. 3, the insert is the transit spectrum of FR-5.⁶ The indices for standard spectrum lines are 1.745 92 (N_c), 1.749 84 (N_D), and 1.760 31 (N_F), which are about 4% larger than those of FR-5 glass.⁷ The Abel number is 49.92 while the Abel number of FR-5 is 53.49.⁷ For comparison with the absorptivity, 0.0597 cm^{-1} of FR-5 at 632.8 nm,^{6,7} the index of sample I at 632.8 nm was particularly measured to be 1.746 70 and the absorptivity of the sample is calculated to be 0.0948 cm^{-1} according to the equation

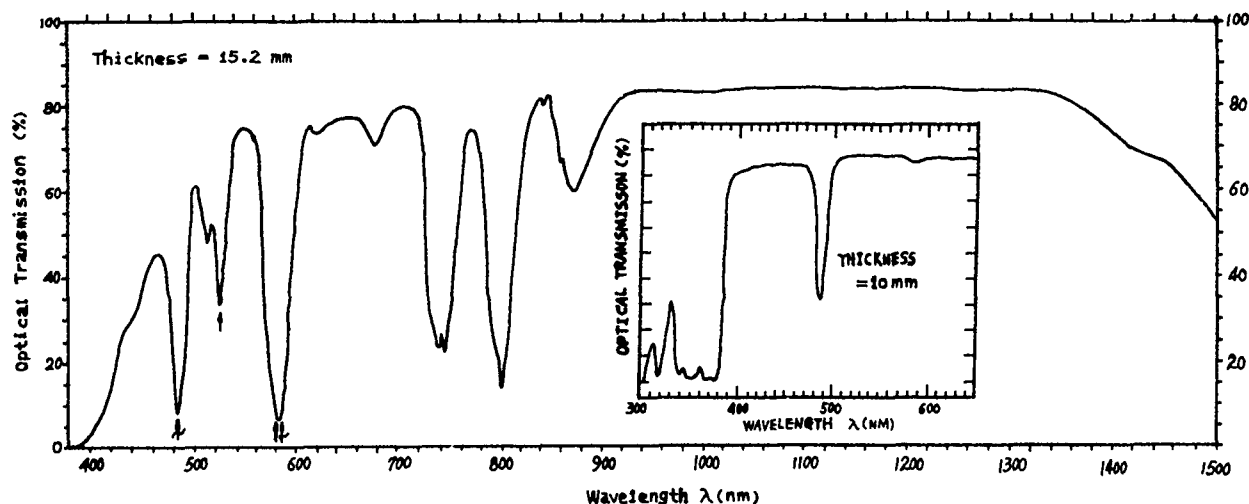


FIG. 3. The optical transmission spectrum of sample I. The insert is the optical transmission spectrum of FR-5 glass, courtesy of P. E. Sanders, SPIE 566, 317 (1985) (Fiber Optic and Laser Sensors III).

$$\eta = (1-r)^2 e^{-\alpha l}, \quad (2)$$

where η is the transmittance, $r = (N_{632.8} - 1)^2 / (N_{632.8} + 1)^2$ for normal incidence, α is the absorptivity, and $l = 15.2$ mm is the thickness of the sample. The nonlinear index coefficient of sample I is calculated according to the equation⁸

$$N_2 = K \frac{(N_D - 1)(N_D^2 + 2)^2}{\nu [1.517 + (N_D^2 + 2)(N_D + 1)N_D \nu / 6]^{1/2}} \times \frac{10^{-6}}{2.39}, \quad (3)$$

where N_2 is the nonlinear index coefficient, ν is the Abel number, N_D is the index at 589.6 nm, and K is a constant assumed as 68. The value of N_2 is $7.638 \times 10^{-20} \text{ m}^2/\text{W}$ which is a little smaller than that of TbAlG, $8.6 \times 10^{-20} \text{ m}^2/\text{W}$.⁹

III. DISCUSSION

Being different from the magnetic structure of FR-5, which is paramagnetic in the whole temperature range,⁹ the terbium glass made in our laboratory has a paramagnetic structure above 100 K and a superparamagnetic structure¹⁰ below 60 K. Like the formation of clusters composed of oxygen and gadolinium ions in germanite IR glasses,¹⁰ oxygen and terbium ions may form clusters in the terbium glass. The bigger absolute value of Néel temperature T_N , 9 K, for sample I of higher Tb^{3+} concentration 10.4 at. % than that, 6 K, for sample II of Tb^{3+} concentration 8.4 at. % may indicate a stronger magnetic interaction in sample I. The single ion anisotropy of the non-S-state Tb^{3+} ions in the disordered cluster at low temperatures may give rise to the value of the magnetic moment per Tb^{3+} ion as half of the free ion value in an applied magnetic field. Further measurements of the susceptibilities and magnetization of the samples with several different Tb^{3+} concentrations are being conducted to give the details.

The temperature dependence of the Verdet constant follows that of the susceptibility above 100 K. This fits to the single ion model.³ Further effort should be made to extend the temperature to 1.5 K in the measurement.

As seen in Fig. 3, three absorption peaks can be assigned to Nd^{3+} and Pr^{3+} ions.¹¹ The raw material Tb_4O_7 used in the process is of engineering purity only. It is considered that the higher absorptivity of the terbium glass is mainly due to the existence of the impurity ions Nd^{3+} and Pr^{3+} in the raw material Tb_4O_7 .

To support the model of the oxygen-terbium clusters microscopically, electron paramagnetic resonance (EPR) and Mössbauer studies are being conducted on the samples.

IV. CONCLUSIONS

Tb^{3+} ions may aggregate in combination with O^{2-} ions to form fine superparamagnetic clusters in Tb^{3+} heavily doped boron-silicate glasses. Simply increasing the concentration of Tb^{3+} in the glass may not result in a larger Verdet constant. Nevertheless, Tb^{3+} heavily doped glass may be useful in the study of superparamagnetism.

ACKNOWLEDGMENT

The authors are grateful to Xiaowei Chen for her nice help in drawing figures and typing the manuscript.

¹C. B. Rubinstein and S. B. Berger, J. Appl. Phys. 35, 2338 (1964).

²A. R. Tebo, Laser Focus/Electro-Optics 197, Dec. 1988.

³W. A. Crossley, R. W. Cooper, J. L. Page, and R. P. Van Staple, Phys. Rev. 181, 896 (1969).

⁴S. V. Vonsovskii, *Magnetism* (Wiley, New York, 1974), Vol. 2, pp. 975-978.

⁵C. B. Rubinstein, J. Appl. Phys. 35, 3069 (1987).

⁶P. E. Sanders, SPIE 566, 317 (1985) (Fiber Optic and Laser Sensors).

⁷Hoya Corporation Reports (1984).

⁸D. Milam, Appl. Phys. Lett. 31, 822 (1977).

⁹J. A. Davis and R. M. Bunch, Appl. Opt. 23, 633 (1984).

¹⁰S. H. Yuan and S. M. Chee, J. Appl. Phys. 70, 6272 (1988).

¹¹D. C. Stewart and D. Kato, Anal. Chem. 30, 164 (1958).

Experimental investigation of the magnetic circular dichroism sum rules (abstract)

C. T. Chen

AT&T Bell Laboratories, 600 Mountain Avenue, Murray Hill, New Jersey 07974

Y. U. Idzerda

Naval Research Laboratory, Washington, DC 20375

H.-J. Lin and G. Meigs

AT&T Bell Laboratories, 600 Mountain Avenue, Murray Hill, New Jersey 07974

G. Ho

Department of Physics, University of Pennsylvania, Philadelphia, Pennsylvania 19104

N. V. Smith

AT&T Bell Laboratories, 600 Mountain Avenue, Murray Hill, New Jersey 07974

High quality $L_{2,3}$ edges magnetic circular dichroism (MCD) data of *in situ* grown Fe, Co, and Ni ferromagnetic thin films were measured using transmission x-ray absorption technique. These data were utilized to investigate the validity of the recently proposed x-ray MCD sum-rules that offer a new means for deducing orbital- and spin-magnetic moments from MCD data.^{1,2} We find that the orbital to spin magnetic moment ratios of Fe, Co, and Ni deduced from MCD data according to the sum-rules are at $\pm 30\%$ discrepancy with those deduced from neutron scattering data. This inconsistency may be attributed to the neglecting of multi-electron excitations and band structure effects in the derivation of the sum-rules or due to uncertainties in the neutron scattering results. Caveats for MCD data taken with the fluorescence yield x-ray absorption technique will also be discussed.

¹B. T. Thole *et al.*, Phys. Rev. Lett. **68**, 1943 (1992).

²P. Carra *et al.*, Phys. Rev. Lett. **70**, 694 (1993).

Linearity and hysteresis in the magnetoresistive response of (NiFe,NiFeCo)/Cu and Co/Cu/NiFe multilayers in patterned stripes

K. Noguchi, S. Araki, T. Chou, D. Miyauchi, Y. Honda, A. Kamijima, Ø. Shinoura, and Y. Narumiya

R&D Center, TDK Corporation, 2-15-7 Higashi Owada, Ichikawa, Chiba, 272, Japan

The linearity and hysteresis in the magnetoresistive (MR) response of NiFe/Cu and NiFeCo/Cu multilayers prepared by ion beam sputtering, and Cu/Co/Cu/NiFe multilayers prepared by MBE are investigated. These characteristics in the linear regions for the second peak of antiferromagnetically coupled NiFe/Cu multilayers are almost the same as those of NiFeCo/Cu ones at 50-Hz ac applied fields. The MR amplitude at the first peak is inferior to that at the second one, whereas, the linearity and hysteresis are superior. In weakly coupled Cu/Co/Cu/NiFe multilayers, a nonhysteretic MR response is obtained at a NiFe layer thickness of 10 Å. The linearity and symmetry around the zero magnetic field of the MR curve depend on the Cu layer thickness. When the thicknesses of the NiFe and Cu layers are 10 and 45 Å, respectively, good linearity and no hysteresis are observed without biasing techniques. The output levels in the linear regions of three different multilayers are 1.5–2.5 times as large as that of the conventional Permalloy film. These multilayers are promising materials for the fabrication of MR head for ultrahigh density recording.

I. INTRODUCTION

Since the discovery of the giant magnetoresistance effect (GMR) in Fe/Cr multilayers,¹ a large number of studies have been made on the GMR effect in multilayers.^{2–5} GMR effect is attracting great interest for magnetoresistive read (MR) heads. MR heads require large resistance changes in low excitation fields. In addition, good linearity and no hysteresis of the MR curve are required to prevent distortion in the output signal wave form. Antiferromagnetically (AF) coupled NiFe/Cu and NiFeCo/Cu multilayers, which contain magnetically soft magnetic layers, exhibit MR ratio of 8%–12% with a saturation field of about 100 Oe.^{5,6} On the other hand, MR ratio of 7% has been obtained in weakly coupled Cu/Co/Cu/NiFe multilayers for fields changes of 100 Oe.⁷ However, the linearity and hysteresis in the MR curves have not been reported in these multilayers. In this paper we report the linearity, hysteresis and MR amplitude both with dc and ac applied fields at 50 Hz in three different multilayers, NiFe/Cu, NiFeCo/Cu, and Cu/Co/Cu/NiFe, and compare the results with the anisotropic magnetoresistance (AMR) of conventional Permalloy film.

II. EXPERIMENTAL DETAILS

NiFe/Cu and NiFeCo/Cu multilayers were prepared by ion beam sputtering, using Ni₈₂Fe₁₈, Ni₆₆Fe₁₆Co₁₈, and Cu targets. The films were deposited in an argon pressure of 1.5×10^{-4} Torr at R.T. with a magnetic field of 60 Oe in the film plane. The acceleration voltage of ion gun was 300 V with an ion current of 30 mA. Cu/Co/Cu/NiFe multilayers were prepared by successively depositing Cu, Co, Cu, and Ni₈₂Fe₁₈ at R.T. by evaporation in ultrahigh vacuum in a MBE system. The base pressure was below 2×10^{-10} Torr,

and the pressure during deposition was maintained at the order of 10^{-9} Torr. NiFeNb or Ta buffer layers (50 Å thick) were first grown on glass substrates in the IBS system and Cr buffer layers (50 Å thick) in the MBE. The deposition rates were controlled at 0.2–0.4 Å/s in both cases. The thicknesses of the NiFe, NiFeCo, and Co layers were varied between 10–15 Å and that of the Cu layers between 10–50 Å in all three multilayers. The periods and structures of the multilayers were investigated by measuring low angle x-ray diffraction. The magnetic properties for the films were investigated using a vibrating sample magnetometer. The MR properties with dc applied fields were measured using a standard four-terminal method on specimen with a stripe of 0.5×10 mm². The MR ratio is defined as $\Delta\rho/\rho_s$, where the ρ_s is the resistivity at the saturation magnetic field and the $\Delta\rho$ is the resistivity change. The specimens for ac MR measurements were formed into stripes with dimensions $3\text{--}7 \times 150$ μm² by photolithography. Au films were deposited on the top of the stripe as conductors by vacuum evaporation to make the track width of 4.5 μm. The magnetic field was applied in the direction of the width of the stripes in both dc and ac cases. The MR response curve with ac applied fields was measured at 50 Hz, and the sense current was 15 mA. The magnetic domain walls were observed by a magneto-optical Kerr effect apparatus.

III. RESULTS AND DISCUSSION

A. NiFe/Cu and NiFeCo/Cu multilayers

The changes of MR ratio on varying Cu layer thickness were investigated in NiFe/Cu and NiFeCo/Cu multilayers. Here, each magnetic layer thickness is fixed at 15 Å. The multilayers have 20 bilayers of NiFe or NiFeCo and Cu. The

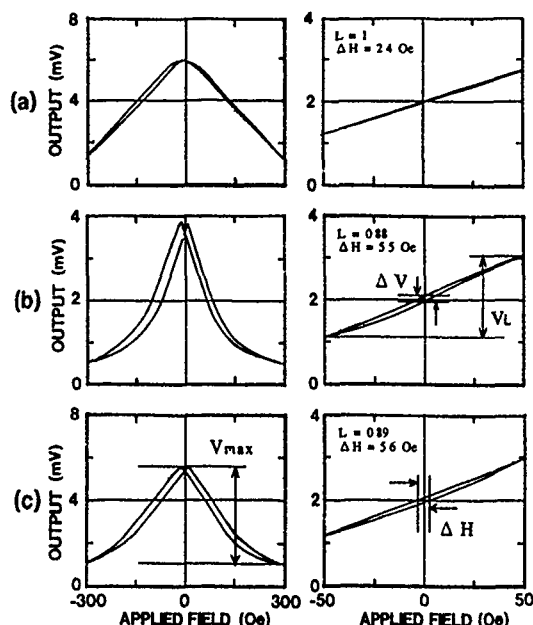


FIG. 1. MR responses with a 50-Hz applied field of ± 300 and ± 50 Oe for (a) $[\text{Cu}(9 \text{ Å})/\text{NiFe}(15 \text{ Å})]_{20}/\text{Cu}(9 \text{ Å})$, (b) $[\text{Cu}(20 \text{ Å})/\text{NiFe}(15 \text{ Å})]_{20}/\text{Cu}(20 \text{ Å})$, and (c) $[\text{Cu}(20 \text{ Å})/\text{NiFeCo}(15 \text{ Å})]_{20}/\text{Cu}(20 \text{ Å})$ with 50-Å-thick NiFeNb buffer layers.

well-defined oscillations in the changes of the MR ratio are confirmed in both multilayers.^{5,6} The peaks of the MR ratio are observed at the Cu layer thicknesses of 9 and 20 Å. At the first peak ($t_{\text{Cu}}=9 \text{ Å}$), an MR ratio of 12.3% for NiFe/Cu and 16.6% for NiFeCo/Cu multilayers are obtained. At the second peak ($t_{\text{Cu}}=20 \text{ Å}$), the MR ratios of 6.4% and 9.1% are obtained, respectively.

The MR response curves for three samples of (a) $[\text{Cu}(9 \text{ Å})/\text{NiFe}(15 \text{ Å})]_{20}/\text{Cu}(9 \text{ Å})$, (b) $[\text{Cu}(20 \text{ Å})/\text{NiFe}(15 \text{ Å})]_{20}/\text{Cu}(20 \text{ Å})$ and (c) $[\text{Cu}(20 \text{ Å})/\text{NiFeCo}(15 \text{ Å})]_{20}/\text{Cu}(20 \text{ Å})$ with 50-Å-thick NiFeNb buffer layers are shown in Fig. 1. Data are shown for the $7 \times 150 \mu\text{m}^2$ stripe with the applied fields of ± 300 and ± 50 Oe. In order to investigate the characteristics in the linear regions, a dc biasing field of about 30 Oe is applied for the low field measurement by a permanent magnet. To evaluate the linearity, hysteresis and the MR amplitude, we define the following values of the MR response: the overall MR amplitude with ± 300 Oe V_{max} , the MR amplitude with ± 50 Oe V_L , the remanent MR amplitude at zero applied field with ± 50 Oe ΔV , hysteresis of the MR response with ± 50 Oe ΔH , as indicated in Fig. 1. Therefore, we define here the linearity as $L = (V_L - \Delta V)/V_L$. The linearity becomes better when the L value is close to 1. The V_{max} value is 4.5 mV for sample (a), 3.2 mV for (b) and 4.3 mV for (c), and the V_L value is 1.59, 1.89, and 1.85 mV, respectively. The V_{max} for sample (c) is 1.5 times as large as that for (b). These values are in good agreement with the MR ratio, because the MR ratio of NiFeCo/Cu multilayers is 1.4 times as large as that of NiFe/Cu ones. However, the V_L values are almost the same. This indicates that these multilayers have the same field sensitivity in the linear regions of the MR response. In addition, the L and ΔH values are also the same in both sample (b) and (c), as shown in Fig. 1.

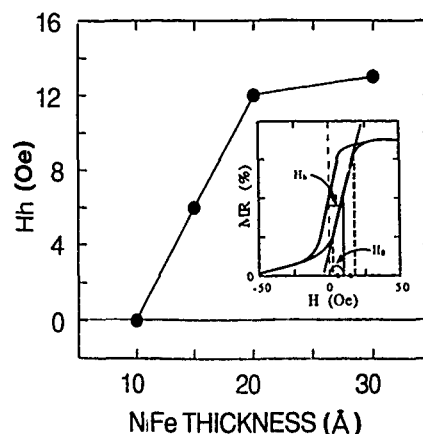


FIG. 2. The H_h values with dc applied fields on varying NiFe layer thickness for $\text{Cr}(50 \text{ Å})/[\text{Cu}(50 \text{ Å})/\text{Co}(10 \text{ Å})/\text{Cu}(50 \text{ Å})/\text{NiFe}(x \text{ Å})]_{10}$. Inset shows schematic diagram of the H_h and H_0 values in the minor loop of the MR profile.

There is no significant difference in the characteristics in the linear regions between NiFe/Cu and NiFeCo/Cu multilayers. On the other hand, a linear and nonhysteretic MR response is observed in sample (a). In particular, the ΔH value for sample (a) is smaller than that for (b). Obviously, hysteresis at the second peak is larger than that at the first peak. From domain wall observations on the specimen at the second peak, $\text{Ta}(50 \text{ Å})/[\text{Cu}(t \text{ Å})/\text{NiFeCo}(30 \text{ Å})]_2$ ($t_{\text{Cu}}=20$), domain walls nucleate and move on the specimen with changing external fields, which are applied perpendicular to the stripe axis. The observed domain walls move irregularly, not perpendicular to the stripe axis. On the contrary, the domain walls are not observed on the specimen at the first peak ($t_{\text{Cu}}=9$). This proves that domain wall displacement exists at the second peak. S. Zhang *et al.* gave a interpretation that the multilayers except for the first peak are not completely AF coupled.⁸ It is considered that ferromagnetically aligned layers locally exist at the second peak. Our results support their picture. Magnetization reversal of ferromagnetically aligned layers is caused by domain wall displacement. Consequently, the MR response with larger hysteresis are observed at the second peak.

To compare the MR responses of these multilayers with the AMR response of a Permalloy film, a trilayered MR element, consisting of an amorphous CoZrMo film as a soft adjacent layer, a Ta film as a magnetic separation layer, and a 300-Å-thick Permalloy film as a MR layer were prepared by ion beam sputtering. This film has an output level of 1.0 mV with an applied field of ± 50 Oe for the same specimen size. As a result, the output levels in the linear regions for the above multilayers obtained are 1.5–2 times as large as that of the Permalloy film.

B. Cu/Co/Cu/NiFe multilayers

MR properties of weakly coupled $[\text{Cu}(x \text{ Å})/\text{Co}(y \text{ Å})/\text{Cu}(x \text{ Å})/\text{NiFe}(z \text{ Å})]_{10}$ multilayers on varying each layer thickness were investigated. In order to evaluate the symmetry and hysteresis in the MR curve, we define the center field of the linear region and the width of the MR minor loop as

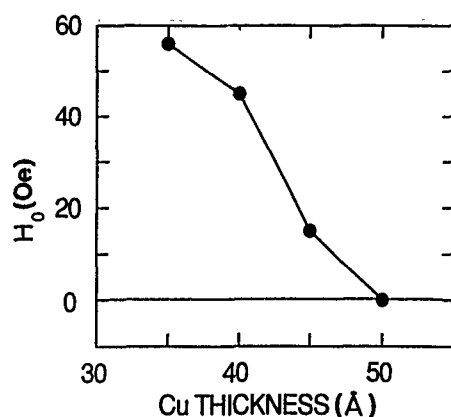


FIG. 3. The H_0 values with dc applied fields on varying Cu layer thickness for $\text{Cr}(50 \text{ Å})/[\text{Cu}(x \text{ Å})/\text{Co}(10 \text{ Å})/\text{Cu}(x \text{ Å})/\text{NiFe}(10 \text{ Å})]_{10}$.

H_0 and H_h , respectively, as indicated schematically in Fig. 2. From the technological point of view, the H_0 of zero and the H_h of zero are desirable to get a symmetric signal wave form without distortion.

Figure 2 shows the H_h values with dc applied fields on varying NiFe layer thickness, in these cases the Cu and Co thicknesses are fixed to be 50 and 10 Å, respectively. In weakly coupled Cu/Co/Cu/NiFe multilayers, the MR profile at around zero field is determined by the reversal of the magnetization of the NiFe layer. Therefore, the most effective parameter of the H_h value is the coercive force (H_c) of NiFe layer. The H_c of the NiFe layer decreases as the NiFe layer thickness decreases. For example, 10 Oe for $[\text{NiFe}(20 \text{ Å})/\text{Cu}(50 \text{ Å})]_{10}$ and 7 Oe for $[\text{NiFe}(10 \text{ Å})/\text{Cu}(50 \text{ Å})]_{20}$. The H_h values decreases with decreasing NiFe layer thickness and reaches zero at a NiFe layer thickness of 10 Å. This is in agreement with the tendency of the H_c of NiFe layers in NiFe/Cu multilayers. However, the H_c of 10-Å-thick NiFe layer is not zero. Therefore, another explanation for the H_h of zero should be considered. One reason would be a little reversal of the magnetization of the Co layers. The remanent magnetization of the Co layers was about 74% of saturated magnetization for $[\text{Co}(10 \text{ Å})/\text{Cu}(50 \text{ Å})]_{20}$. Some part of Co spins rotate at zero field, and this rotation would play a role for the H_h of zero. Figure 3 shows the H_0 values with dc applied fields on varying Cu layer thickness, in these cases the NiFe and Co thicknesses are fixed to be 10 Å. The H_0 decreases as the Cu layer increases, and becomes zero at a Cu layer thickness of 50 Å. When the Cu layer thickness is large enough, the magnetic interaction between NiFe and Co layers is negligible. However, the ferromagnetic interaction

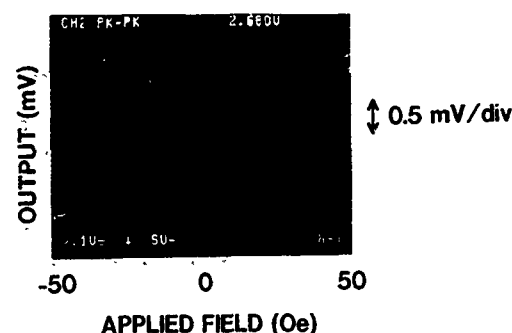


FIG. 4. MR response with a 50 Hz ac applied fields of ± 50 Oe for $\text{Cr}(50 \text{ Å})/[\text{Cu}(45 \text{ Å})/\text{Co}(10 \text{ Å})/\text{Cu}(45 \text{ Å})/\text{NiFe}(10 \text{ Å})]_{10}$.

increases with decreasing Cu layer thickness. As a result, the magnetic moment of the NiFe layer cannot rotate independently of the Co layer. Therefore, the magnetization reversal of the NiFe layer begins at larger applied field and H_0 increases with decreasing Cu layer thickness.

The MR response with ac applied fields for $(x, y, z) = (50, 10, 10)$ of $3 \times 150\text{-}\mu\text{m}^2$ stripe exhibits zero hysteresis. However, the center field of the linear region is -20 Oe, not zero. The demagnetizing field (H_d) for the ac measurement cannot be negligible because of the narrow stripe ($3 \times 150 \mu\text{m}^2$). Thus the effective external field is shifted by about H_d , so that H_0 shifts toward the negative direction. Figure 4 shows the MR response curve with ac applied fields of ± 50 Oe for $(x, y, z) = (45, 10, 10)$ of the $3 \times 150\text{-}\mu\text{m}^2$ stripe, which is the H_0 of about 20 Oe in the dc fields with $0.5 \times 10 \text{ mm}^2$ stripe. The output level with ± 50 Oe is 2.7 mV. That is roughly two and a half times as large as that of the conventional Permalloy film, which shows an output level of 1.2 mV for the same size of the specimen. A large and symmetric MR response with no hysteresis is realized in our Cu/Co/Cu/NiFe multilayers.

¹M. N. Baibich, J. M. Broto, A. Fert, F. Nguyen VanDau, F. Petroff, P. Etienne, G. Creuzet, A. Friedrich, and J. Chazealas, *Phys. Rev. Lett.* **61**, 2472 (1988).

²S. S. P. Parkin, N. More, and K. P. Roche, *Phys. Rev. Lett.* **64**, 2304 (1990).

³D. H. Mosca, F. Petroff, A. Fert, P. A. Schroeder, W. P. Pratt, Jr., and R. Laloe, *J. Magn. Magn. Mater.* **64**, 2304 (1990).

⁴S. S. P. Parkin, *Appl. Phys. Lett.* **59**, 126 (1992).

⁵M. Jimbo, T. Kanda, S. Goto, S. Tunashima, and S. Goto, *Jpn. J. Phys.* **31**, L1348 (1992).

⁶R. Nakatani, T. Dei, T. Kobayashi, and Y. Sugita, *IEEE Trans. Magn.* **MAG-28**, 2668 (1992).

⁷T. Shinjo and H. Yamamoto, *J. Phys. Soc. Jpn.* **9**, 3061 (1990).

⁸S. Zhang and P. M. Levy, *Phys. Rev. Lett.* **B 47**, 6776 (1993).

Microstructural origin of giant magnetoresistance in a new sensor structure based on NiFe/Ag discontinuous multilayer thin films

M. A. Parker, T. L. Hylton, K. R. Coffey, and J. K. Howard

IBM Fellow Program, IBM Storage Systems Division, 5600 Cottle Rd., San Jose, California 95193

The origin of giant magnetoresistance (GMR) in a new sensor structure incorporating discontinuous multilayers (DML) of NiFe thin films separated by Ag interlayers is elucidated by means of x-ray diffraction, x-ray reflectivity, and cross-section transmission electron microscopy. It is shown that the observed magnetoresistance, $\sim 4\%$ – 6% in fields on the order of 5–10 Oe at 25 °C, is associated with the breakup upon annealing of the initially dense, columnar superlattice structure into discontinuous multilayers of NiFe due to highly mobile Ag forming Ag bridges between the Ag layers. This observation supports a micromagnetic model for these structures that is based on the concept of initially large ferromagnetic domains in the as-deposited NiFe structure, exhibiting negligible GMR, breaking up into discontinuous layers, exhibiting an appreciable GMR, with antiferromagnetic ordering across the Ag interlayers.

Giant magnetoresistance (GMR) in multilayer systems is by now a well-known effect.^{1–4} The application of this effect to magnetic read-head technology, as the so-called “spin-valve,” has also been well documented.⁴ More recently, the appearance of GMR in nonmultilayer systems of granular magnetic particles in a nonmagnetic, immiscible matrix, which one might call granular GMR (GGMR or G²MR),^{5–8} has been discovered, leading many to speculate on its application to head technology, as well. In this paper, we demonstrate how to overcome the limited sensitivity of G²MR structures⁹ through a novel sensor structure¹⁰ incorporating characteristics of both multilayer GMR and G²MR in “discontinuous” multilayers (DMLs). We have previously speculated on how the low field sensitivity¹⁰ is achieved due to reduced shape anisotropy in DML as compared with G²MR, and better control of the interlayer coupling in DML, as compared with continuous multilayers (CMLs). We believe that this is a consequence of magnetostatically induced antiferromagnetic order in DMLs caused by the layer discontinuities, which distinguish these structures from their CML counterparts,¹¹ which are dominated by exchange coupling between layers. Here, we present microstructural evidence confirming the existence of these discontinuities. In addition, we demonstrate that this is a result of the high mobility of the interlayer, nonmagnetic species, Ag, migrating into the magnetic permalloy multilayers, most probably at grain boundaries in the columnar structure.

The structures consisted of the following nominal multilayer stack: Ta (100 Å)/Ag($y/2$)/[NiFe(x)/Ag(y)]₄/NiFe(x)/Ag($y/2$)/Ta(40 Å), where y was approximately 40 Å, and x , 20 Å, deposited on approximately 1000 Å of SiO₂ on Si. They were prepared by S-gun magnetron sputtering in a 4% H₂/Ar mixture at a pressure of 3 mTorr at ambient temperature. The composition of the NiFe target was nominally that of low magnetostrictive permalloy, i.e., Ni₈₁Fe₁₉. A ~ 150 Oe magnetic field was applied during deposition to give a weak uniaxial anisotropy field of ~ 3 Oe. The samples were broken into strips 8 mm \times 1.5 mm and annealed at 1 atm in 5% H₂/Ar in a rapid thermal annealer (RTA) at 305 °C, 315 °C, 325 °C, 335 °C, 345 °C, 365 °C, and 395 °C for 10 min, respectively. Magnetoresistance mea-

surements were made at room temperature with an in-line, four-point probe geometry with the magnetic field applied perpendicular to the direction of current flow, but in-plane and along the easy axis of the sample.

X-ray diffraction scans were obtained with a D-Max 1000 system equipped with a rotating anode source in the conventional θ – 2θ reflection geometry. X-ray reflectometry curves were obtained with a GIXR x-ray reflectometer in the specular scattering geometry. Cross-section TEM (XTEM) samples were prepared using conventional methods;¹² special precautions were taken during ion milling: a LN₂ cold stage was employed to preclude annealing; and a specially designed holder was used to blank the beam when incident from the film side of the sample, and to allow milling at a 5° angle of incidence to enhance uniformity. Images were taken in both bright field (BF) and dark field (DF) imaging conditions on a 4000FX with especially small apertures to allow the resolution of the superlattice reflections, giving rise to contrast from the individual NiFe and Ag layers. Care was taken to align the sample along the Si zone axis, to assure that interfaces between the multilayers were aligned approximately parallel to the beam during imaging.

Table I shows the results of annealing the multilayers in the RTA. It is significant that the as-deposited structures exhibit no GMR, although a small anisotropic magnetoresistance (AMR) was measured. Upon annealing, significant GMR develops in these structures; the highest value being $>5\%$ for the 335 °C anneal. Note, however, that the highest

TABLE I. Measured values of the magnetoresistance in NiFe/Ag multilayers as a function of annealing temperature.

Temperature	$\Delta R/R$ (%)	FWHM (Oe)	Sensitivity (%/Oe)
As-deposited	0.22	36.3	0.006
305 °C	2.33	6.2	0.370
315 °C	4.06	5.1	0.790
325 °C	4.95	12.6	0.390
335 °C	5.34	22.6	0.240
345 °C	4.90	33.3	0.150
365 °C	4.25	58.0	0.070
395 °C	2.74	130.0	0.020

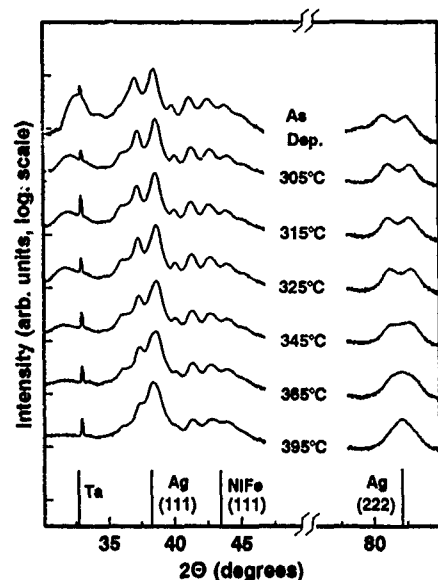


FIG. 1. High angle θ - 2θ x-ray diffractometer scans of NiFe/Ag multilayers as a function of annealing temperature.

sensitivity, i.e., $\% \Delta R/R$ per FWHM of applied field, the relevant figure of merit for a head sensor, was obtained for the 315 °C anneal with a value of 0.8%/Oe. It is also worth noting that for progressively higher temperature anneals beyond the optimum of 315 °C, the FWHM of the peak increases; also, the absolute magnitude of GMR begins to decrease.

Figure 1 shows the results of the θ - 2θ diffraction scans. The strong 111-type superlattice reflections of Ag and NiFe clearly indicate that these samples have a strong (111) fiber-axis texture. The spacing of the peaks in the as-deposited sample indicates a ~ 70 Å superlattice period. Upon annealing, it is apparent that the two dominant Ag peaks begin to shift position, while the peaks associated with NiFe remain relatively unaffected. The effect on the Ag peaks is even more pronounced when examining the Ag (222) reflections, which change from a clearly split peak in the as-deposited structure to a single broad peak near the position for the equilibrium lattice parameter of Ag for the sample annealed at 395 °C. These changes in the Ag peaks with annealing are consistent with the deterioration of the continuity of layers in the superlattice structure, and the formation of agglomerations of Ag, having the equilibrium lattice parameter within the structure. Since this occurs primarily with the Ag peaks and not the NiFe peaks, it is apparent that the deterioration is not equivalent for both the Ag and NiFe layers. This is consistent with the TEM results presented below. Thus, the Ag peaks are a complex mixture of nearly bulk-like scattering from regions of the film, where the Ag bridges across two or more NiFe layers in agglomerations, and scattering from the remnants of the initial Ag layers that are separated by the NiFe layers in the remaining superlattice structure. Since the displaced NiFe rather than bridging across the Ag tends to agglomerate on the initial NiFe layers, the spacing of the NiFe reflections tends to preserve that of the initially con-

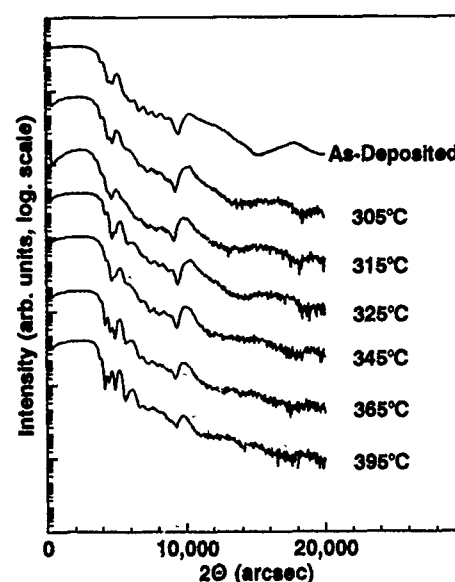


FIG. 2. Low angle x-ray reflectivity scans of NiFe/Ag multilayers as a function of annealing temperature.

tinuous multilayer structure, which is confirmed by the cross-section TEM.

The most likely way this might occur is by grain boundary migration of the Ag. Modeling of these changes based on the concept of superlattice period is problematic because this is fundamentally a new class of structure, a "discontinuous" multilayer (DML), for which no x-ray diffraction models have been published. Nevertheless, by way of analogy with continuous multilayers, one might define a "pseudoperiod" based on the position of the two dominant Ag peaks. Preliminary analysis based on this purely phenomenological parameter showed that it changed linearly with annealing time, so that an Arrhenius analysis of the change in this parameter as a function of temperature could be performed; the activation energy was found to be 1.30 ± 0.07 eV, which is close to values published for the grain boundary diffusion of Ag.¹³ However, this is not the same as identifying the mechanism with grain boundary diffusion; as in the case of Ag/Ni,¹⁴ it is likely that strain, as well as interfacial energies, provide a significant driving force for Ag migration. These observations are consistent with our earlier work⁸ on codeposited metastable NiFeAg alloys, which, upon annealing, produced large precipitate agglomerations of Ag, strong evidence for the high mobility of Ag in this system at these annealing temperatures.

Figure 2 shows the results of the GIX scans on these samples. The intensity of the higher angle Bragg peaks is reduced upon annealing, which is characteristic of "roughening" of the interfaces.¹⁵ However, as the TEM data will show below, this was not the simple interfacial "roughening" that is often seen during the annealing of superlattices, but is undoubtedly affected by the formation of Ag intrusions into the NiFe layer, as well. Due to the mutual insolubility and immiscibility of Ag with NiFe, it is problematic to use the term "intermixing" for this effect.

The XTEM micrographs of Fig. 3 show definitive micro-

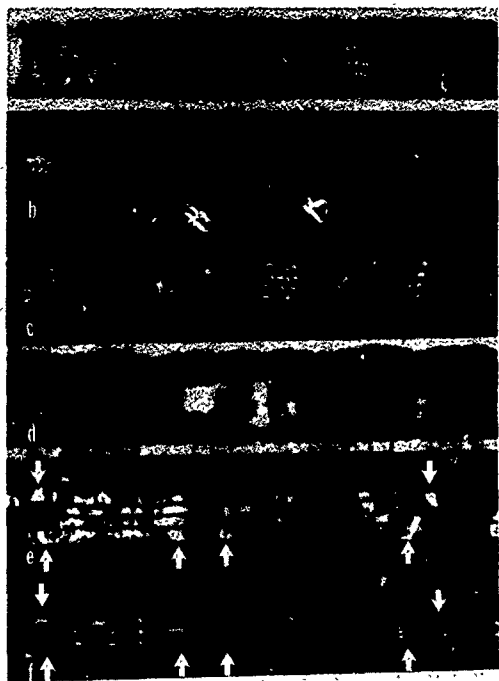


FIG. 3. Cross-section TEM micrographs of the as-deposited NiFe/Ag multilayer and the sample annealed at 395 °C for 10 mins. Legend: micrographs of the as-deposited structure (a) in BF, (b) in DF using the Ag 111* reflection, and (c) in DF using the NiFe 111* reflection; and micrographs of the post-annealed structure (d) in BF, (e) in DF using the Ag 111* reflection, and (f) in DF using the NiFe 111* reflection. "Ag-bridges" (arrowed in e) are apparent in the post-annealed structure, as are the corresponding "NiFe gaps" (arrowed in f).

structural evidence in support of the interpretation of the previous x-ray data. Figure 3(a) is a BF micrograph of the as-deposited structure; the overall thickness of the film is ~ 552 Å. Note that the interface with the substrate is rather smooth, but that the upper layer has what appears to be a relatively "rough" oxide on the Ta layer, ~ 10 Å peak to valley. The roughness of the interfaces of the intervening layers is somewhere in between these two values. Streaks are present in the image that cross the layers transversely, indicative of a columnar structure, as reported for other multilayers.¹⁶ Figure 3(b) is a DF micrograph of the as-deposited structure obtained with the Ag superlattice reflections. Columnar stacks of silver layers are clearly in evidence at the location of the previously identified streaks. The edges of these stacks are located where the film changes crystallographic orientation, and thus are most likely grain boundaries. It is clear that even though the layers are rather rough, there are no locations where a Ag layer "bridges" across the NiFe layer to make contact with an adjacent Ag layer, i.e., the layers are

well separated. The DF image of the NiFe layer [see Fig. 3(c)] likewise shows well-delimited columns, and well-separated layers. The BF image of the post-annealed sample (at 395 °C) is shown in Fig. 3(d). The DF image using the Ag superlattice reflections [see Fig. 3(e)] shows "Ag bridges" across the NiFe layers [the arrow in Fig. 3(e)]. Although "Ag bridges" were seen in structures annealed at lower temperatures, the sample annealed at 395 °C much more dramatically shows this effect. The "Ag bridges" give rise to regions where the Ag layer thickness is in excess of two times its initial value. Figure 3(f) shows that the excess intensity in the Ag DF image is complemented by a lack of intensity in the NiFe DF image at the location of "Ag bridges," indicating that "NiFe gaps" have formed, where NiFe has been displaced by Ag.

In conclusion, clear structural evidence has been presented for the attendant breakup of the NiFe layer with a concomitant appearance in GMR upon annealing. It is a reasonable inference that the formation of such discontinuous multilayers should give rise to corresponding micromagnetic changes. Magnetostatic coupling between layers in these DMLs may well give rise to the hypothesized antiferromagnetically ordered structure, accounting for the observed GMR increases.^{10,17}

- ¹ M. N. Baibich, J. M. Broto, A. Fert, F. Nguyen Van Dau, and F. Petroff, *Phys. Rev. Lett.* **61**, 2472 (1988).
- ² G. Binasch, P. Grunberg, F. Saurenbach, and W. Zinn, *Phys. Rev. B* **39**, 4828 (1989).
- ³ S. S. P. Parkin, N. More, and K. P. Roche, *Phys. Rev. Lett.* **64**, 2304 (1990).
- ⁴ B. Dieny, V. S. Speriosu, S. S. P. Parkin, B. A. Gurney, D. R. Wilhoit, and D. Mauri, *Phys. Rev. B* **43**, 1297 (1991).
- ⁵ J. Q. Xiao, J. S. Jiang, and C. L. Chien, *Phys. Rev. Lett.* **68**, 3749 (1992).
- ⁶ A. E. Berkowitz, J. R. Mitchell, M. J. Carey, A. P. Young, S. Zhang, F. E. Spada, F. T. Parker, A. Hutten, and G. Thomas, *Phys. Rev. Lett.* **68**, 3745 (1992).
- ⁷ J. A. Barnard, A. Wakis, M. Tan, E. Haftek, M. R. Parker, and M. L. Watson, *J. Magn. Magn. Mat.* **114**, L230 (1992).
- ⁸ M. A. Parker, K. R. Coffey, T. L. Hylton, and J. K. Howard, *Mat. Res. Soc. Symp. Proc.* **313**, 85 (1993).
- ⁹ T. L. Hylton, *Appl. Phys. Lett.* **62**, 2431 (1993).
- ¹⁰ T. L. Hylton, K. R. Coffey, M. A. Parker, and J. K. Howard, *Science* **261**, 1021 (1993).
- ¹¹ R. Rodmacq, G. Palumbo, and Ph. Gerard, *J. Magn. Magn. Mat.* **118**, L11 (1993).
- ¹² J. C. Bravman and R. Sinclair, *J. Electron. Micro. Technol.* **1**, 53 (1984).
- ¹³ P. G. Shewmon, *Diffusion in Solids* (McGraw-Hill, New York, 1963), p. 165.
- ¹⁴ J. A. Floro, C. V. Thompson, R. Caryl, and P. D. Bristowe (unpublished).
- ¹⁵ N. G. Basov and P. N. Lebedev, *Trudi Fiz. Inst.* **196**, 103 (1989).
- ¹⁶ S. S. P. Parkin, Z. G. Li, and D. J. Smith, *Appl. Phys. Lett.* **58**, 2710 (1991).
- ¹⁷ T. L. Hylton, K. R. Coffey, M. A. Parker, and J. K. Howard, *J. Appl. Phys.* **75**, (1994).

Micromagnetics of GMR spin-valve heads

Samuel W. Yuan

Applied Magnetics Corporation, 75 Robin Hill Road, Goleta, California 93117

H. Neal Bertram

CMRR, University of California at San Diego, La Jolla, California 92093-0401

Three-dimensional micromagnetic modeling of shielded giant magnetoresistive heads with a spin-valve sensor is presented. If the pinning field from the exchange layer is not large enough, partial unsaturation of the pinned layer occurs upon excitation from the medium, which may cause down-track output noise. Increasing the pinning strength diminishes the playback instability, however, a larger sensor height is then desirable for the ease of proper biasing, but at the expense of on-track signal level. The free layer magnetization is nominally horizontal, reducing off-track asymmetry compared to heads with smaller sensor height.

I. INTRODUCTION

The spin-valve structure exhibits giant magnetoresistance (GMR)¹ and is an ideal candidate for high density MR reproduce sensors. When placed within two soft ferromagnetic shields, such a GMR head yields significantly larger signals and sensitivities compared to conventional MR heads that utilize the anisotropic magnetoresistance effect. Recently, an unshielded spin-valve sensor was demonstrated, and its operation in a shielded environment was predicted by a two-dimensional model.² A three-dimensional micromagnetic model^{3,4} is presented here to characterize the performance and optimization criteria of such a shielded spin-valve head. Narrow gap and read track-width are assumed in this work to assess head response in ultrahigh density recording applications. Proper biasing, as well as down-track and off-track responses are simulated by the model, and design issues on final heads are addressed.

II. MODELING SCHEME

A generic spin-valve structure consists of two ferromagnetic transition metal or alloy layers separated by a nonmagnetic noble metal layer, with one of the magnetic films pinned by an adjacent exchange film. A nominal structure of NiFe (100 Å)/Cu (30 Å)/NiFe (70 Å)/AF (e.g., FeMn) is chosen in this work. A giant magnetoresistance ratio $\Delta R/R = 6\%$, and a small ferromagnetic interlayer coupling field of 10–20 Oe between the two ferromagnetic permalloy films⁵ are assumed. A schematic of the head structure is shown in Fig. 1 (the shields are not shown). Outside the track-width defining region, the current is assumed to flow horizontally only in the current leads; in the active region, the current density is distributed only in the NiFe/Cu/NiFe sandwich, mostly in the Cu spacer layer, since the resistivity of the FeMn layer is typically much higher.⁶ A detailed calculation of the current distribution for such a thin multilayer system can be carried out using semiclassical electro-transport theory.⁷ The spin-valve magnetoresistance is proportional to the cosine of the relative angle $\Delta\theta$ between the magnetizations of the two magnetic films,⁵ therefore the output response can be expressed as follows:

$$V = I \left(\frac{\Delta R}{R} \right) R_s \frac{W}{h} \frac{1 - \langle \cos(\Delta\theta) \rangle}{2}, \quad (1)$$

where R_s is the sheet resistance of the entire sandwich structure, assumed to be $20 \Omega/\square$. When the actual change of output is calculated, Eq. (1) should be subtracted by its value at the biased state. The anisotropic magnetoresistance is neglected, since the $\Delta R/R$ ratio is smaller than that of the GMR effect, typically by an order of magnitude.⁸

Only the magnetic layers are discretized for micromagnetic simulations, and a periodic boundary condition is utilized at the horizontal edges of the discretized region, to simulate a large total track width. The detailed formulation of the model has been discussed previously.⁴ The gap length is $0.18 \mu\text{m}$, and the active track width is $0.5 \mu\text{m}$. The spin-valve sensor is centered within the gap, with the center of the free layer at the midpoint. The distance between the air bearing surface (ABS) and the medium center is 250 Å , and the medium moment thickness product is 0.8 memu/cm^2 . Isolated transitions with transition width of 200 Å , and nominal recorded track width of $0.75 \mu\text{m}$ are utilized as dynamic excitation sources.

III. SHIELDED SPIN-VALVE HEAD RESPONSE

A. Proper Biasing

The biasing principle and operation scheme of the spin-valve sensor have been discussed previously.² The goal is to maintain the pinned layer in vertical saturation, while biasing the free layer magnetization in the horizontal direction as

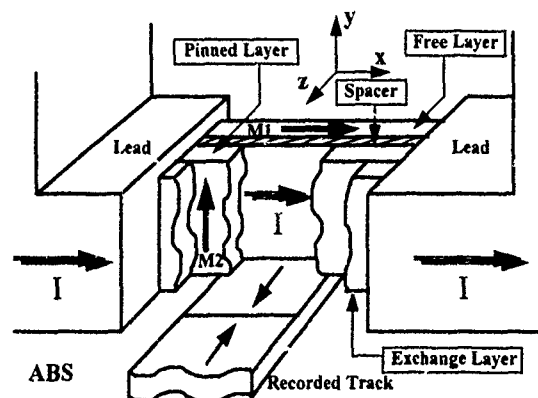


FIG. 1. Schematics of a GMR spin-valve head (shields not shown).

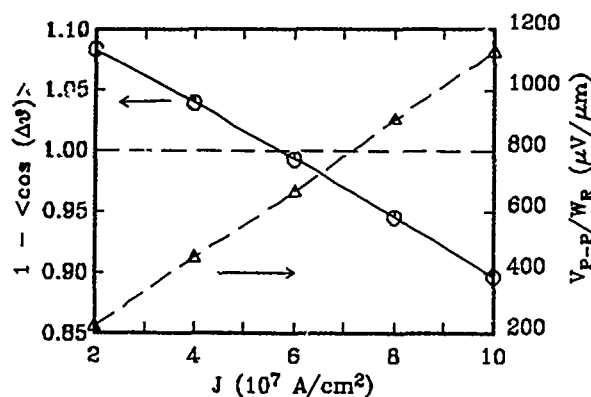


FIG. 2. Biasing level (circles) and peak-to-peak voltage (triangles) vs sense current density for $h=0.5 \mu\text{m}$, coupling field of 10 Oe, and pinning field of 100 Oe. The isolated transition width is $0.75 \mu\text{m}$.

much as possible, in order to achieve maximum response symmetry and linearity under external excitation. For a properly biased state, the magnetizations of the two magnetic layers are perpendicular to each other, therefore $\langle \cos(\Delta\theta) \rangle \approx 0$. Figure 2 shows the biasing level and on-track peak-to-peak output voltage dependencies on the sense current density when the sensor height is $0.5 \mu\text{m}$. The pinning field from the exchange layer is 100 Oe, and the interlayer coupling field is 10 Oe. The current direction is along the positive x direction, as shown in Fig. 1, in order to generate an opposing field to the demagnetizing field from the pinned layer acting on the free layer. Optimum biasing is obtained at $6 \times 10^7 \text{ A/cm}^2$ current density, at which the peak asymmetry from reading an on-track isolated transition is also minimized. With this biasing current, the output amplitude is $660 \mu\text{V}$ per micron of read track width, which exceeds the regular MR output level of $300\text{--}400 \mu\text{V}/\mu\text{m}$ for the next generation $1\text{--}2\text{-Gbit/in.}^2$ areal density read head demonstrations.^{9,10}

Figure 3 shows the magnetization configurations of the biased state with current density $J=6 \times 10^7 \text{ A/cm}^2$. For clarity, only half of the actual discretized magnetization vectors are shown. It is seen that the magnetization of the pinned layer is not fully saturated vertically, due to a large demagnetizing field and a relatively small pinning field. Correspondingly, the free layer magnetization is not horizontal, in order to be perpendicular to the pinned magnetization on the average; its biasing angle measured from the positive x axis is approximately -15° throughout the stripe height. The net horizontal magnetization components are parallel for the two films, due to the interlayer ferromagnetic coupling. This small ferromagnetic coupling field is advantageous for properly biasing the free layer, since it opposes the demagnetizing field from the pinned layer and inhibits irreversible switching of horizontal magnetizations favored by the magnetostatic coupling between the two films. However, if this field is too large, its coupling could bring the pinned layer out of saturation and induce response nonlinearity;² worse yet, if the two permalloy films are strongly coupled, their magnetizations would be nominally parallel to each other

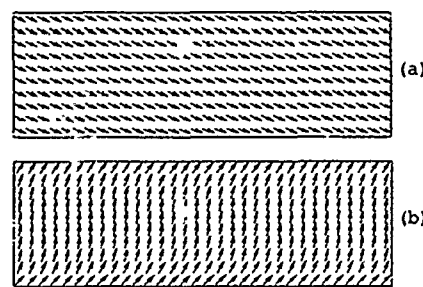


FIG. 3. Biasing magnetizations for $J=6 \times 10^7 \text{ A/cm}^2$, with head parameters identical to Fig. 2. (a) Free layer; (b) pinned layer.

under most excitations, and the spin-valve GMR effect would be lost.⁵

B. Down-track response

Figure 4 shows the down-track response to an isolated (tail-to-tail) transition with negative polarity. The solid curve represents the case with the above biasing condition. Only the change of the average normalized resistance $\cos(\Delta\theta)$ is plotted, in order to illustrate the actual swing of magnetization from its quiescent value. The maximum signal occurs before the transition center is directly underneath the free layer, and a finite reversible jump is observed on the trailing side of the gap center. As a comparison, the down-track pulse for the same transition with the following different head parameters is also included in Fig. 4: sensor height $h=1 \mu\text{m}$, sense current density $J=2 \times 10^7 \text{ A/cm}^2$, interlayer coupling field of 20 Oe, and pinning field of 1000 Oe. The maximum output now occurs when the transition center is directly underneath the free layer, and no noise spike appears. This indicates that with a weaker pinning field, the pinned layer also participates in responding to the excitation from the medium, modulating the free layer response and inducing nonlinearity or even read-back noise.

The magnetization state corresponding to the jump is shown in Fig. 5. The magnetizations of the pinned layer near the ABS come out of saturation and reverse their orienta-

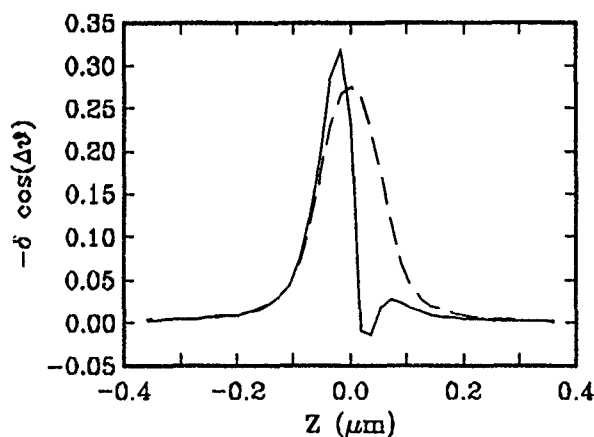


FIG. 4. Down-track responses to an isolated negative transition. Solid: head biased as in Fig. 3; dashed: $h=1 \mu\text{m}$, coupling field of 20 Oe, pinning field of 1000 Oe, and $J=2 \times 10^7 \text{ A/cm}^2$.

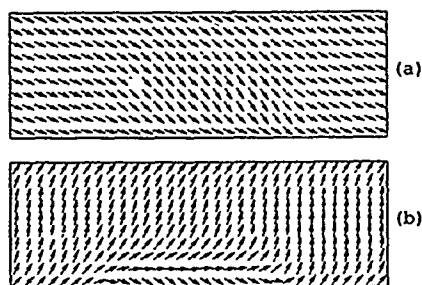


FIG. 5. Magnetization states corresponding to the noise spike in Fig. 4.

tions, forming an edge domain wall along the lower film surface. The free layer magnetization, however, does not show irregular domain activity, indicating that additional stabilization may not be necessary for this layer. The maximum transition field at the ABS is larger than 1000 Oe, for the chosen head-medium parameters, which, together with the current field, appears to overcome the demagnetizing field and the pinning field combined on the pinned layer. When a transition with positive polarity (head-on transition) is played back, the output pulse has a noise-free unipolar shape, because the transition field is now along the saturation direction of the pinned layer.

From Fig. 4, it is seen that the positive maximum change of $\cos(\Delta\theta)$ is smaller for larger sensor height (0.24 for $h=1\ \mu\text{m}$ as compared to 0.31 for $h=0.5\ \mu\text{m}$). The peak-to-peak change of the average $\cos(\Delta\theta)$ is also slightly smaller for the larger sensor height (0.60 for $h=1\ \mu\text{m}$ vs 0.61 for $h=0.5\ \mu\text{m}$), caused by the increase of biasing angle at midsensor, in agreement with Ref. 2. For the $1\text{-}\mu\text{m}$ sensor height, the biasing angle of the free layer is more than -30° at the surfaces and slightly above 0° at the midheight. The pinned layer is now almost completely saturated, with a demagnetizing field characteristic of a permanent magnet. Increasing the sense current density to $10^8\ \text{A}/\text{cm}^2$ still cannot drive the surface magnetizations of the pinned layer to the horizontal direction.

C. Off-track response

The off-track responses of the above two head configurations are compared to each other. Figure 6 shows the microtrack profiles with a record track width of $0.05\ \mu\text{m}$. The solid curves represent the case with smaller sensor height and smaller pinning field, and clearly show an offset of the magnetic center and an undershoot of peak signals on one side of the head-medium alignment, due to the nonzero biasing angle mentioned in Sec. III B. The off-track asymmetry in this case is more severe than those predicted in a conventional shielded MR-SAL head with comparable gap spacing.⁴ The head with a larger sensor height is biased better around 0° , therefore the off-track profile is more symmetric with no undershoots. The magnetic center is only slightly offset, due to the fact that the magnetizations of the free layer close to the ABS are still not horizontal. Patterned exchange biasing the free layer horizontally at the edge regions does not seem to reduce this offset substantially.

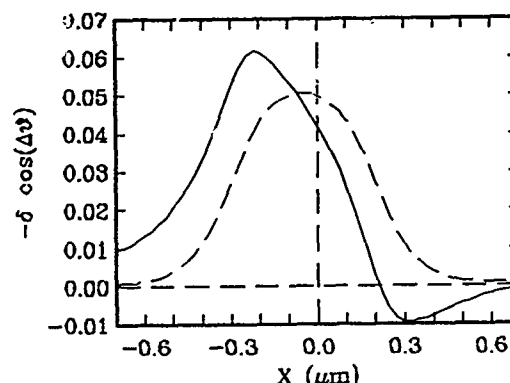


FIG. 6. Microtrack off-track profiles. Solid and dashed curves have the same correspondences as in Fig. 4.

IV. REMARKS

Given a limited biasing current density, a larger sensor height is desirable for the ease of biasing the free layer horizontally and for reducing off-track asymmetry. However, increasing the sensor height results in a loss of on-track signal due to the following two reasons: first, the required biasing current density is smaller, and the total resistance of the sandwich structure is smaller, so that the prefactor in Eq. (1) decreases; second, the peak change of the average $\cos(\Delta\theta)$ upon excitation from the medium also decreases, since the biasing angle at midsensor increases. This tradeoff must be considered when optimizing the spin-valve head design.

ACKNOWLEDGMENTS

We thank Dr. Jim Brug for helpful technical discussions. The support by Dr. Paul Frank is gratefully acknowledged. This work was funded by the National Science Foundation under Grant No. DMR-90-10908, and the National Storage and Industry Consortium under the Advanced Technology Program.

- ¹B. Dieny, V. S. Speriosu, S. Metin, S. S. P. Parkin, B. A. Gurney, P. Baumgart, and D. R. Wilhoit, *J. Appl. Phys.* **69**, 4774 (1991).
- ²D. E. Heim, R. E. Fontana, C. Tsang, V. S. Speriosu, B. A. Gurney, and M. L. Williams, *TMRC'93*, paper B5, Minneapolis.
- ³S. W. Yuan and H. N. Bertram, *Intermag'93*, paper CA-02, Stockholm.
- ⁴S. W. Yuan, H. N. Bertram, and M. K. Bhattacharyya, *TMRC'93*, paper E2, Minneapolis.
- ⁵B. Dieny, V. S. Speriosu, S. S. P. Parkin, B. A. Gurney, D. R. Wilhoit, and D. Mauri, *Phys. Rev. B* **43**, 1297 (1991).
- ⁶B. Dieny, P. Humbert, V. S. Speriosu, S. Metin, B. A. Gurney, P. Baumgart, and H. Lefakis, *Phys. Rev. B* **45**, 1297 (1992).
- ⁷R. E. Camley and J. Barnas, *Phys. Rev. Lett.* **63**, 664 (1989).
- ⁸B. Dieny, V. S. Speriosu, B. A. Gurney, S. S. P. Parkin, D. R. Wilhoit, K. P. Roche, S. Metin, D. T. Peterson, and S. Nadimi, *J. Magn. Magn. Mater.* **93**, 101 (1991).
- ⁹C. Tsang, M.-M. Chen, T. Yogi, and K. Ju, *IEEE Trans. Magn.* **MAG-26**, 1689 (1990).
- ¹⁰H. Takano, H. Fukuoka, M. Suzuki, K. Shiiki, and M. Kitada, *IEEE Trans. Magn.* **MAG-27**, 4678 (1991).

Micromagnetic study of narrow track orthogonal giant magnetoresistive heads

Yimin Guo and Jian-Gang Zhu

The Center for Micromagnetics and Information Technologies, Department of Electrical Engineering, University of Minnesota, Minneapolis, Minnesota 55455

Orthogonal narrow track magnetoresistive heads using giant magnetoresistive multilayers have been studied by micromagnetic modeling. The modeling shows that the hysteresis arises from irreversible switching of the edge-curling wall (ECW) on the side edges of the giant magnetoresistive (GMR) sensor layers. Effects of thickness and interlayer exchange coupling on the switching of the ECW are analyzed. It is also found that if the interlayer exchange coupling is ferromagnetic, the GMR orthogonal head has significant high signal amplitude.

I. INTRODUCTION

Future high track density recording requires submicron track width magnetoresistive heads. The orthogonal MR head design has been proposed for narrow track recording since its signal amplitude is independent of track width.^{1,2} However, since the current flows vertically to the air bearing surface, the recession of the magnetoresistive (MR) sensor sensing region due to the bottom conducting lead yields a reduction of the head sensitivity. Utilizing the giant magnetoresistive (GMR) film as a sensor, the small signal amplitude can be overcome by the relatively large magnetoresistance ratio of GMR films.³

In this paper, we present results of a micromagnetic modeling study on orthogonal GMR heads with narrow track width ($W=1\text{ }\mu\text{m}$). The model assumes that the sensor element is made of a giant magnetoresistive sandwich film. The study focuses on hysteresis in the GMR output response and underlying physical mechanism. Dynamic range and head sensitivity are also analyzed.

II. MODEL AND HEAD GEOMETRY

Figure 1 shows a schematics for the modeled GMR sensor. The GMR element is a trilayer film $ML(t\text{ nm})/NML(2.5\text{ nm})/ML(t\text{ nm})$, which is $4\text{ }\mu\text{m}$ in height and $1\text{ }\mu\text{m}$ in width. In the modeling, the thickness of each magnetic layer is varied in a range from 7 to 20 nm. An interlayer exchange coupling field, H_{exch} , between the two magnetic layers in the GMR film is assumed. The value of H_{exch} is varied from -30 to $+30$ Oe, i.e., from antiferromagnetic to ferromagnetic in nature. The intrinsic anisotropy easy axis is assumed to be horizontal with a magnitude of $H_k=2.5$ Oe. The vertical sensing current generates antiparallel horizontal fields (H_z) in the two magnetic layers. An additional vertical biasing field (H_y) is provided by the current flowing horizontally in a conductor over the GMR element. The sensor is placed at the center of two soft magnetic shields with assumed infinite permeability. The distance between the two shields, i.e., the gap length, is assumed to be $0.5\text{ }\mu\text{m}$.

A three-dimensional micromagnetic model⁴ is utilized to study the performance characteristics and domain structures of the GMR trilayer film. Each magnetic layer is discretized into a two-dimensional array of 200×50 elements. Within

each element, the magnetization is assumed to be always uniform. Both the magnetostatic and the exchange energies are included. The saturation magnetization of each magnetic layer in the sensor is chosen to be $M_s=800\text{ emu/cm}^3$ and the within-layer exchange energy constant $A=1.0\times 10^{-6}\text{ erg/cm}$. Coupled Landau-Lifshitz dynamic equations are integrated for the magnetization distribution in the GMR sensor.

It is assumed that external field away from the gap of shields is spatially uniform and the field along the GMR sensor is calculated exactly by using two-dimensional conformal mapping method with assuming infinite permeability for the shields. In this study, the values of the external field referred in this paper are the field intensities at the bottom of GMR element (at ABS). Keep in mind that the field at ABS is much higher than the uniform field far away due to the soft shields. Most of the calculations are performed on a Sun SPARC-2 workstation.

III. RESULTS AND DISCUSSION

A. Hysteresis mechanism and switching field

The magnetizations of the two magnetic layers are initially set antiparallel in the horizontal direction before the application of the vertical bias field. The magnitude of the

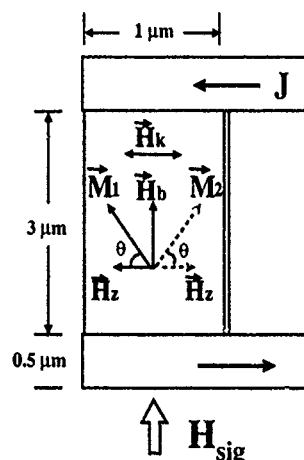


FIG. 1. The schematics of the modeled orthogonal GMR head. h is the height of the sensing region, measured between the two current leads.

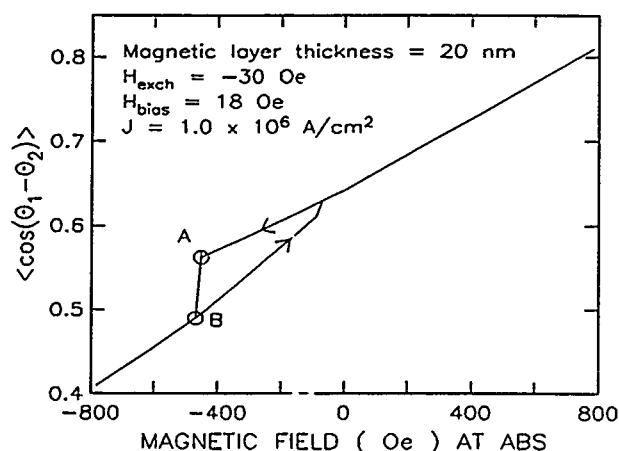


FIG. 2. Calculated GMR output for the external field varied from zero to -800 Oe and then to +800 Oe.

bias field is set such that the angle between magnetization orientations of two magnetic layers in the center region is about 90° at external field free equilibrium state. The current leads on the sensor are $0.5 \mu\text{m}$ in height. Figure 2 shows a calculated GMR output as a function of the external field. In this case, the two magnetic layers, each 20 nm thick, are separated by a nonmagnetic layer with 2.5 nm thickness. An $H_{\text{exch}} = -30$ Oe antiferromagnetic exchange field is assumed between the two magnetic layers.

The external field value is varied from zero to -800 Oe then to +800 Oe quasistatically. As shown in the figure, at -450 Oe, the GMR output, $\langle \cos \theta_{1,2} \rangle$, exhibits a large abrupt jump. As the field returns to zero, the GMR output takes a different path, starting where the jump occurred, yielding a well-pronounced hysteresis.

The simulated magnetization patterns show that the irreversible jump in the GMR output is caused by an irreversible switching of the edge-curling wall at side edges of the two-layer sensor element.⁵ Figures 3(a) and 3(b) show the corre-

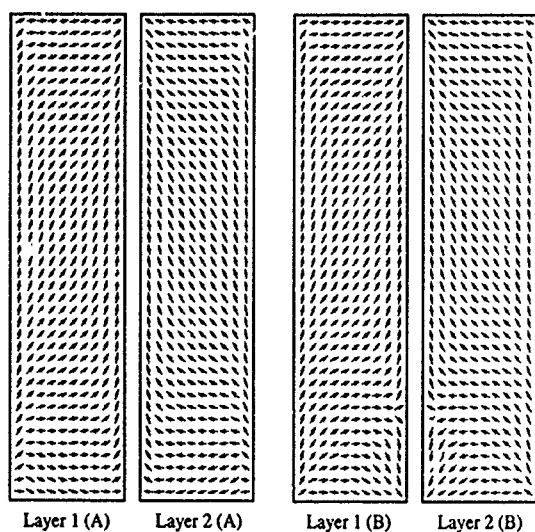


FIG. 3. (a),(b) Simulated magnetization configurations in the two magnetic layers at point A and B on the GMR output curve shown in Fig. 2.

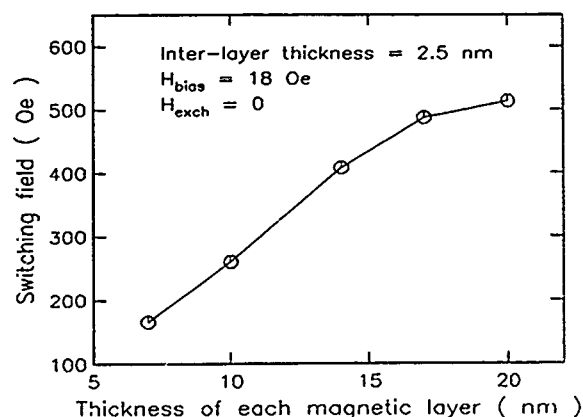


FIG. 4. Calculated switching field as a function of the thickness of each magnetic layer.

sponding magnetization patterns of the two magnetic layers before the switching (a) and after the switching (b), respectively. Prior to the application of the external field, the magnetizations in the middle region of two magnetic layers are oriented about 45° and -45° away from the vertical axis, respectively; while the magnetizations at side edges of both magnetic layers essentially point upward along the side edge due to the edge demagnetizing field, yielding formation of ECW. At point A, due to the downward external field, the magnetization near the bottom region of the sensor is almost horizontal, leaving narrow ECWs at two sides. A slight increase of the external field yields an irreversible reversal of the ECW on one of the side edges (point B). The reversal only occurs at one side edge on one layer and the opposite side edge on the other layer, because a switched ECW stabilizes the unswitched ECW in the other layer through both the interlayer magnetostatic coupling and antiferromagnetic exchange coupling. The reversal of the ECW yields a relatively large change of the magnetization orientations in the sensor, thereby resulting in a large jump in the GMR output. Further increasing the external field actually yields a steady propagation of the ECW reversal along the edge. Reducing the field magnitude, the reversed ECW reverses magnetization direction again to initial upward direction, starting from the top of the reversed segment. When the field magnitude returns to a small value, the reversed ECW irreversibly vanishes from the sensor corner, yielding a small jump in the GMR output shown in Fig. 2. The above results clearly demonstrate that the hysteresis of the GMR output is caused by irreversible switching and propagation of the edge-curling wall.

In the above case, before the external field reaches the field value where the jump occurs, referred to as switching field here after, the GMR output is completely without hysteresis. Figure 4 shows the calculated switching field as a function of the thickness of magnetic layer. It is found that the switching field increases almost linearly with the thickness. This is because that in thicker films, the width of ECW is larger due to the larger demagnetizing field, therefore a larger switching field is needed to result in ECW reversal. Figure 5 shows the calculated switching field as a function of

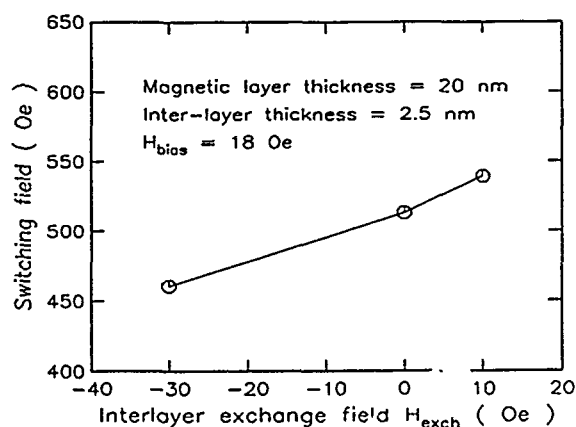


FIG. 5. Calculated switching field as a function of the interlayer exchange coupling field.

the interlayer exchange field. As the exchange coupling changes from antiferromagnetic to ferromagnetic, the switching field increases.

B. Sensitivity and flux decay length

The flux decay length, defined as λ in $\Delta M_y(y) = \Delta M_y(0)e^{-y/\lambda}$, y is the vertical distance measured from ABS, is an important factor in orthogonal head design due to the bottom current lead. In GMR head, the interlayer exchange coupling can significantly affect the flux decay length. The interlayer exchange energy density: $E_{\text{exch}} = tH_{\text{exch}}M_s \cos(2\theta) = -2tH_{\text{exch}}M_s \sin^2(\theta) + \text{constant}$, results in an effective anisotropy field $-2H_{\text{exch}}$ in the horizontal direction. Following the same approach by Wang,² the flux decay length can be approximately expressed as

$$\lambda = \sqrt{\frac{4\pi M_s g t}{H_k - 2H_{\text{exch}} + H_z / \cos^3 \theta}}, \quad (1)$$

where t is the thickness of each magnetic layer, g is the gap length between the shields, and θ is the angle of the magnetization orientation of the film with respect to the horizontal direction. Figure 6 shows the calculated sensitivity and estimated flux decay length as functions of exchange strength. As shown by the formula and curves in the figure, a ferromagnetic exchange gives rise to a larger flux decay length and consequently a higher head sensitivity.

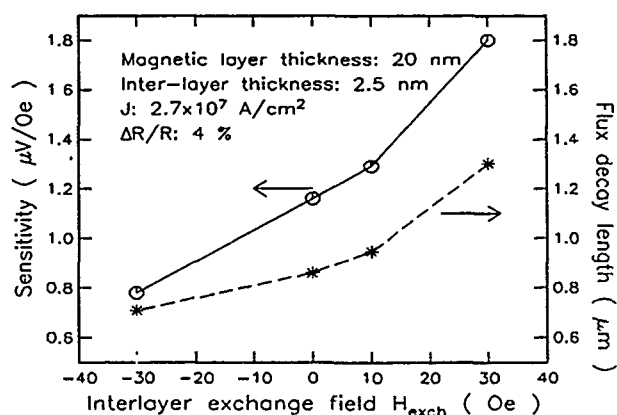


FIG. 6. Calculated sensitivity and estimated flux decay length as functions of the interlayer exchange coupling field.

IV. CONCLUSION

A micromagnetic modeling study has been performed to study a narrow track orthogonal MR head with a GMR sandwich film as the magnetoresistive sensor. It is found that irreversible switching of the edge-curling wall at the side edges of the sensor film is one mechanism for hysteresis in the orthogonal GMR output. Irreversible propagation of the edge-curling wall reversal yields a large jump in the GMR output. Reduction of antiferromagnetic interlayer exchange coupling and increase of the magnetic layer thickness can increase the critical switching field of ECWs. Ferromagnetic interlayer exchange coupling also enhances the head sensitivity.

ACKNOWLEDGMENT

This research is supported in part by the NSF Young Investigate Award (Grant ECS9358309), NIST/NSIC Heads Program and 3M Company.

¹H. Suyama, K. Tsunewaki, M. Fukuyama, N. Saito, T. Yamada, and H. Karamon, IEEE Trans. Magn. **MAG-24**, 2612 (1988).

²P. Wang, M. Krounbi, D. E. Heim, and R. Lee, Paper CA-05, Intermag'93.

³B. Dieny, V. Speriou, S. Metin, S. Parkin, B. Gurney, P. Baumgart, and D. Wilhoit, J. Appl. Phys. **69**, 4774 (1991).

⁴Y. Guo and J.-G. Zhu, Paper CA-03, Intermag'93.

⁵J. C. Slonczewski, B. Petek, and B. E. Argyle, IEEE Trans. Magn. **MAG-24**, 2045 (1988).

Dynamic domain instability and popcorn noise in thin-film heads

F. H. Liu and M. H. Kryder

Data Storage Systems Center, Carnegie Mellon University, Pittsburgh, Pennsylvania 15213

The effects of dynamic domain instability on popcorn noise probabilities were studied by correlating the measured popcorn noise probabilities with the instantaneous observations of dynamic domain states of thin-film heads during and after writing. Heads with large peak popcorn noise probabilities at intermediate values of write current amplitude were observed to exhibit asymmetric domain patterns and occasional popping wall motion in the yoke structure during writing. The occurrences of dynamic domain instability were imaged by comparing many instantaneous domain patterns at 10 μ s after a specific write current excitation. Delayed-relaxation Barkhausen wall jumps near the backgap closure were observed occasionally in several noisy heads. Quantitative correlation between the probabilities of popcorn noise and dynamic domain instability was also obtained in a very noisy head. Dynamic domain instabilities in the yoke are thus responsible for the peak popcorn noise probabilities in thin-film heads.

I. INTRODUCTION

As the areal density and data rates in magnetic recording continue to increase, it is important to limit the readback noise in thin-film heads. Popcorn noise, which consists of large noise spikes occurring shortly (on the order of microseconds) after writing, is detrimental to the reading operation immediately after write, for instance, in disk drives utilizing sector or imbedded servo schemes. This noise phenomenon has been explained to be caused predominantly by stress-induced delayed-relaxation Barkhausen wall jumps.¹ The stress changes were, in turn, explained to be caused by the rapid cooling off of thin-film heads after write. Assuming the domain patterns during writing are stable and fixed, the occurrence of popcorn noise was modeled as a Poisson process.¹ However, dynamic domain state conversions due to different write current amplitudes and frequencies as well as the dynamic domain instabilities associated with conversion boundaries between different dynamic domain states have been observed in thin-film heads.²⁻⁴ In this investigation, the effects of dynamic domain instability on the popcorn noise probabilities were studied by measuring the popcorn noise probabilities with a Barkhausen noise tester and correlating them with 0.5-ns exposure time wide-field Kerr effect microscope observations of changes in dynamic domain states of several 30-turn thin-film heads during and after writing.

II. EXPERIMENTAL APPARATUS

A Barkhausen noise tester, similar to those described in Refs. 1 and 4, was used to measure the popcorn noise probabilities in thin-film heads. A wide-field Kerr-effect microscope with a 0.5 ns exposure time was used to observe the instantaneous magnetization response on the top yoke of thin-film heads during and after the write current cycles. In this system, a pulsed laser with a pulse width of 0.5 ns is used as the light source for a wide-field polarized light microscope, equipped with a high-sensitivity TV camera and an image processor.⁵ All images in this paper were observed with magneto-optic contrast optimized to measure the component of magnetization in the trackwidth direction.

III. EXPERIMENTAL RESULTS

The effects of write current amplitude on the popcorn noise probabilities of two 30-turn heads that exemplify the heads with high and low popcorn noise probabilities are shown in Fig. 1. In head A, a very large peak popcorn noise probability at 33 mA p-p was observed to be riding on top of an exponentially increasing noise floor,⁶ whereas, in head B, a small and exponentially increasing popcorn noise probability as a function of write current amplitude was observed.

An asymmetric domain pattern with respect to the head symmetry axis and occasional popping wall motion during write current excitation were observed in head A, as depicted in Fig. 2. These images were created by subtracting two images of which one was taken with a +dc drive current of a specific amplitude and the other with a -dc drive current of the same amplitude. A pinned edge closure domain wall near the left edge of the backgap closure was clearly observed with a dc \pm 13 mA excitation, as shown in Fig. 2(a). As the excitation was increased to DC \pm 22 mA, a small displacement was observed for this wall, as shown in Fig. 2(b). When the excitation was increased to DC \pm 23 mA, this wall suddenly exhibited large displacement, as shown in Fig. 2(c). Utilizing real-time live-subtraction image processing, large

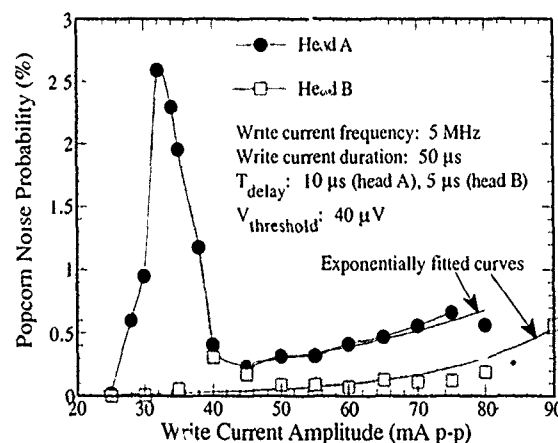


FIG. 1. The popcorn noise probabilities of heads A and B as functions of write current amplitude.



FIG. 2. The domain wall displacement images of head A with DC excitation of (a) ± 13 mA, (b) ± 22 mA, and (c) ± 23 mA, and (d) a schematic diagram of its static domain pattern.

and occasional popping motion of this wall was also observed during sine-wave current excitation of 23 mA o-p at 1 Hz. As the current amplitude was increased further, the large motion of this wall was observed to become more repeatable. A schematic diagram of the asymmetric static domain pattern in head A is depicted in Fig. 2(d). In comparison, symmetric closure domain patterns with smooth and repeatable wall motion during write current excitation were observed in head B.

By repeatedly subtracting two instantaneous domain patterns imaged $10 \mu\text{s}$ after a specific write current excitation, occasional occurrences of dynamic domain instability were actually imaged. A 256-frame-averaged image observed $10 \mu\text{s}$ after a specific write current excitation was first taken as the reference image. A large number of 32-frame-averaged images (typically 700) were also taken $10 \mu\text{s}$ after the same writing condition and then subtracted from the reference image. Occurrences of delayed-relaxation Barkhausen wall jumps after write were observed as shades of black and white contrast, as shown, for instance, in Fig. 3(a). Low stochastic occurrences of domain instability were observed as uniform gray contrast, as shown, for instance, in Fig. 3(b). The probability of domain instability after a specific write current was thus obtained by dividing the number of subtracted images that exhibited strong contrast, such as in Fig. 3(a), by the total number of images observed. The head was ac demagnetized to the same static domain state before each measurement of domain instability probability.

Probability (normalized by the peak values) of domain instability and of popcorn noise in head A as functions of write current amplitude are shown in Fig. 4. A strong correlation between the normalized probability of domain instability and popcorn noise in head A is clearly seen. In comparison, almost no domain instability was observed in head B, which has low popcorn noise probabilities for all write current excitation applied. It was also found that the probability of domain instability and popcorn noise decrease ex-

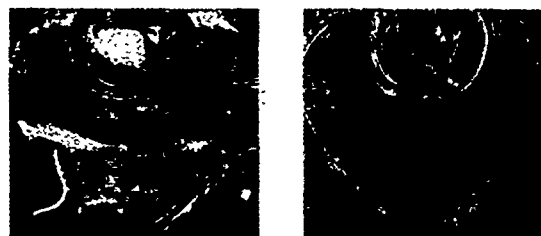


FIG. 3. Dynamic difference images of head A observed at $10 \mu\text{s}$ after the write current excitation of (a) 33 mA and (b) 43 mA, at 5 MHz.

ponentially as the delay time after write increases,¹ as shown in Fig. 5.

The specific write current amplitude that gives rise to the peak popcorn noise probability is observed to be a function of frequency, as shown in Fig. 6. The curve joined by the data points of peak popcorn noise probabilities was also observed to be the conversion boundary of two dynamic domain states, of which one contains the pinned edge closure domain wall near the left edge of the backgap closure, and the other with a large motion of the same edge closure domain wall, as indicated in the insets of Fig. 6. At the write current excitations that coincide with this conversion boundary, high probabilities of dynamic domain instability were observed.

IV. DISCUSSION

Thermal transients after write are believed to serve as a "drive" to move the walls from metastable positions just after write to their static equilibrium positions.¹ During this thermal-transient-driven relaxation process, Barkhausen wall jumps occur when walls encounter and subsequently overcome the localized pinning sites. As the write current amplitude increases, the "drive" of the thermal-transient-driven Barkhausen wall jumps increases. In the case where the initial domain states just after write are microscopically unstable, the occurrences of Barkhausen wall jumps thus increase as the write current amplitude increases. Consequently, popcorn noise probabilities increase exponentially as write current amplitude increases.¹ This mechanism

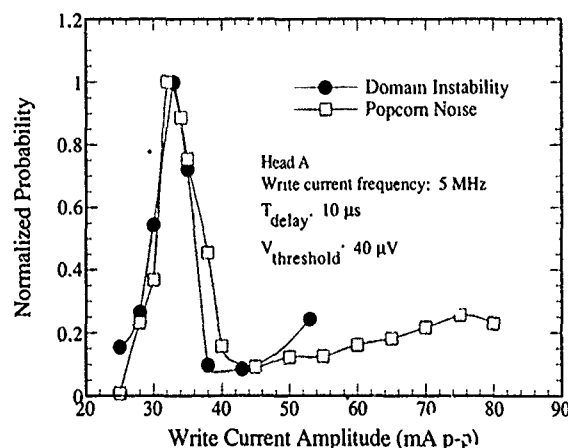


FIG. 4. Normalized probabilities of domain instability and popcorn noise in head A, as functions of write current amplitude.

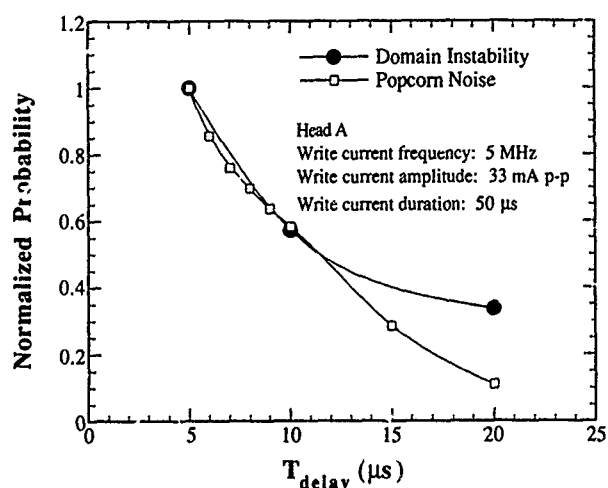


FIG. 5. Normalized probabilities of domain instability and popcorn noise in head A as functions of delay time after the write current of 33 mA p-p at 5 MHz.

of microscopic wall jumps driven by thermal transients after write is consistent with the observations of exponentially increasing popcorn noise probabilities as functions of write current amplitude in head A (between 45 to 80 mA p-p, as shown in Fig. 1) and head B, in which no large probabilities of domain instability were observed.

At the specific write current frequencies and amplitudes which coincide with the conversion boundary of two dynamic domain states, as depicted in Fig. 6, high probabilities of domain instability were observed. When domain instabilities occur during write, the initial domain states just after write are macroscopically unstable. Higher occurrences of Barkhausen wall jumps may thus occur even with moderate thermal transients after the intermediate write current amplitude. A large peak in the popcorn noise probability consequently results in addition to the exponentially increasing noise floor, as shown in Fig. 1. This mechanism of macroscopic domain instability driven by thermal transients after write is consistent with the strong correlation observed be-

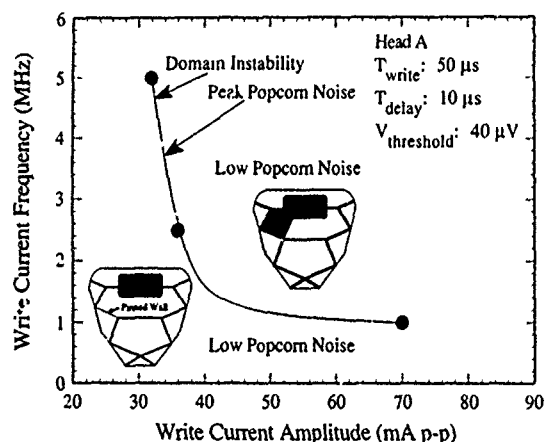


FIG. 6. The peak popcorn noise probability contour and conversion boundary of two dynamic domain states in head A, as a function of write current frequency and amplitude.

tween dynamic domain instability and popcorn noise probabilities as functions of write current amplitude and delay time after write, as shown in Figs. 4 and 5, respectively. The observed result of exponentially decreasing domain instability probability as a function of delay time in Fig. 5 indicates that domain instability is caused predominately by delayed-relaxation Barkhausen wall jumps, and not by different stable remanent domain patterns after write.

The observations of nonrepeatable domain wall displacement, as shown in Fig. 4(a), indicate that the locations of Barkhausen wall jumps, and thus the major noise sources, are fixed. In head A, the dynamic domain instability is largely related to the erratic popping wall motion near the left edge of the backgap closure, as evident by Figs. 2, 3(a), and 6. This erratic popping wall motion was observed to occur when the drive field produced by the specific write current amplitude is just enough to bring the pinned wall into motion. This specific write current amplitude was also observed to be a function of frequency. This conversion boundary between two dynamic domain states, as shown in Fig. 6, is similar with the conversion boundaries of different dynamic domain states observed by Trouilloud *et al.*² Dynamic domain instability associated with the conversion boundary of different dynamic domain patterns thus cause high probabilities of popcorn noise in thin-film heads.

V. CONCLUSIONS

Two major mechanisms of popcorn noise were observed in thin-film heads studied here. While both appear to be driven by thermal transients after write, the mechanism of microscopic wall jumps is responsible for the relatively small and exponentially increasing popcorn noise probability as a function of write current amplitude; and the mechanism of macroscopic domain instability is responsible for the large peak popcorn noise probability at intermediate write current amplitudes. The dynamic domain instability is caused mainly by the erratic popping motion of domain walls near the backgap closure of thin-film heads, and is associated with the conversion boundary of different dynamic domain states. By designing and fabricating heads with stable domain structures and dynamics, much lower probabilities of popcorn noise should result.

ACKNOWLEDGMENTS

Helpful discussions with J. Miller and A. Rice at AMC, M. Mallary at DEC and M. Schultz now at IBM are especially appreciated. This work was supported by the IBM corporation and by the National Science Foundation under grant No. ECD-8907068. The government has certain rights in this material.

¹K. Klaassen and J. van Peppen, IEEE Trans. Magn. **MAG-25**, 3212 (1989).

²P. Trouilloud, B. Argyle, B. Petek, and D. Herman, IEEE Trans. Magn. **MAG-25**, 3461 (1989).

³F. Liu, M. Schultz, and M. Kryder, J. Appl. Phys. **69**, 5414 (1991).

⁴F. Liu, P. Ryan, X. Shi, and M. Kryder, IEEE Trans. Magn. **MAG-28**, 2100 (1992).

⁵M. Kryder, P. Koeppe, and F. Liu, IEEE Trans. Magn. **MAG-26**, 2995 (1990).

⁶I. Viches, Technical Digest of DISKCON'92, p. 13.

Dynamic response of domain walls on the air-bearing surface of thin-film heads

X. Shi, F. H. Liu, Yuet Li,^{a)} and M. H. Kryder

Data Storage Systems Center, Carnegie Mellon University, Pittsburgh, Pennsylvania 15213

The domain configurations on the air-bearing surface (ABS) of inductive thin-film recording heads were studied. It was found that, instead of being a single domain structure, the ABS of a thin-film head usually has multidomains. The direction of the domain walls is neither parallel nor perpendicular to the gap plane. The magnetization was found to be in the plane of the ABS along the track width, with the magnetizations on the two sides of the domain walls either "head-to-head" or "tail-to-tail." The domain walls are slanted in order to spread the magnetic charges along the wall over a larger region, thereby reducing magnetostatic energy in this configuration. The responses of the domain walls are not all in phase, and they are generally out of phase with the rotational process along the gap edge. The magnetization configuration on the ABS and in the throat and the sloped region were investigated in one head and correlated with the domain walls on the ABS.

INTRODUCTION

Previous studies of the dynamic domain configurations and the dynamic response of domain walls in thin-film recording heads were carried out primarily on the yoke of heads and the sloped region between the yoke and the pole tip.¹⁻⁵ These earlier studies related dynamic characteristics and noise to the response of the domain walls in the yoke and in the sloped region. The work described in this paper focuses on the dynamic processes at the air-bearing surface (ABS) of thin-film heads. With a scanning magneto-optic photometer, we measured the dynamic response at the ABS of several thin-film heads and discovered the existence of complex domain configurations on the pole tips of the heads. The phase response of the domain walls relative to the response of the rotational magnetization was studied. The magnetization configurations on the ABS and in the throat and sloped region were investigated.

APPARATUS AND METHODS

The scanning magneto-optic photometer used in this work was described in detail in Ref. 6. It detects the dynamic changes in magnetization on the surface of a sample. With lock-in amplifier, both the amplitude and the phase lag of the magnetic response can be obtained. In a picture displaying the amplitude information, darker shade represents stronger magnetization response, while in a phase picture, contrast difference represents phase difference. Results measured on two different heads will be discussed. Head no. 1 is a nine-turn head with a track width of 23 μm and a pole thickness of 2 μm . Head no. 2 is a 30-turn head with a track width of 10 μm and a pole thickness of 2.5 μm .

RESULTS

The dynamic domain configuration on the ABS of head no. 1, driven by a current of 15-mA peak-peak (p-p) at 1

MHz, is shown in Fig. 1(a), (b), and (c), which correspond to three different laser configurations used in the measurements. The image in Fig. 1(a) was obtained by using the longitudinal Kerr effect. The laser beam was *s* polarized and had an incidence plane parallel to the gap plane. This laser configuration detects primarily the dynamic change in the component along the track width. The longitudinal Kerr effect was also used for obtaining the image in Fig. 1(b); however, the laser beam (also *s* polarized) had an incidence plane perpendicular to the gap plane. This laser configuration detects primarily the dynamic change in the component perpendicular to the gap plane. The polar Kerr effect was used to produce the image in Fig. 1(c). In this configuration, only the out-of-plane component of magnetization is detected.

The dynamic domain configuration on the ABS of head no. 2, driven by a current of 5 mA p-p at 1 MHz, is shown in Fig. 2. The laser configuration used is the same as that used to map Fig. 1(a). Laser configurations used to map Figs. 1(b) and (c) were also used to measure this head, and a uniform

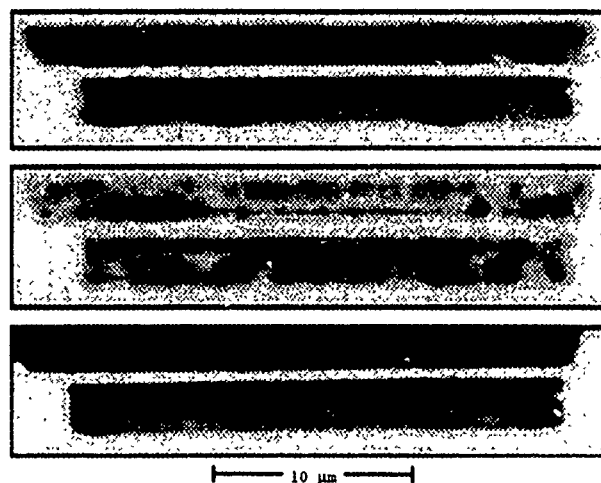


FIG. 1. (top. a) Dynamic domain pictures measured on the ABS of head no. 1.

^{a)} Now at Dept. of Electrical Engineering, University of Minnesota, Minneapolis, Minnesota 55454.

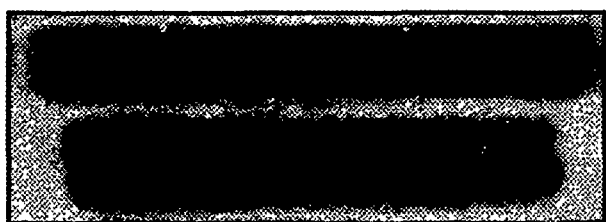


FIG. 2. Dynamic domain picture measured on the ABS of head no. 2.

response similar to the top pole tip in Fig. 2 was obtained across the track width of both pole tips.

The phase response on the ABS of head no. 2, driven by a current of 5 mA p-p at 1 MHz and a current of 10 mA p-p at 20 MHz, is shown in Figs. 3(a) and (b), respectively. Only the trailing pole is shown in Fig. 3(b). As stated previously, white and black contrasts in a phase picture indicate phase differences in the magnetic response. That the wall on the left in Fig. 3(a) has the same brightness as the gap edge suggests the response of this wall is in phase with the rotational magnetization process taking place along the gap edge. The white-black contrast between the two walls indicates that the magnetization changes caused by the two walls are out of phase. When the frequency was increased to 20 MHz, both domain walls were out of phase with the rotational magnetization process along the track edge, and the two walls were also out of phase with each other. The scanned data used to produce Fig. 3(a) indicate that the response of the domain wall on the right is 150° out of phase with the domain wall on the left and the rotational magnetization along the gap edge. At 20 MHz, the two domain walls become 180° out of phase with one another, and they both are out of phase with the rotational process.

DISCUSSION

The black stripes on the trailing pole of Fig. 1(a) are produced by the response of domain walls. The fact that no wall response was detected by using the polar Kerr effect suggests that the motion of the domain walls seen in Fig.

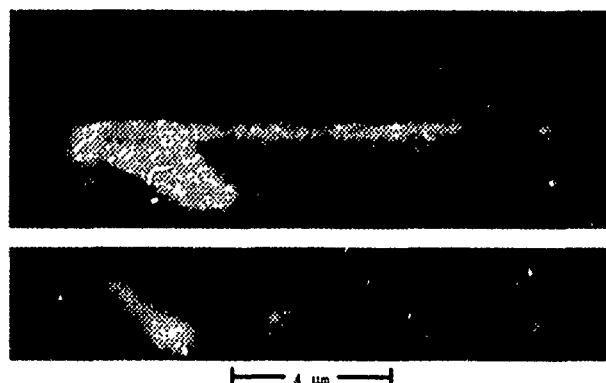


FIG. 3. Phase information in the response on the ABS of head no. 2 at (a, top) 1 MHz and (b) 20 MHz.

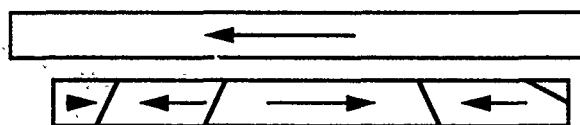


FIG. 4. Magnetization configuration on the ABS of head no. 1.

1(a) does not cause magnetization change in the direction perpendicular to the ABS, and consequently, the magnetization inside the domains is believed to be in the plane of the ABS. That the response of domain walls produced a much stronger Kerr signal in Fig. 1(a) than in Fig. 1(b) suggests that the dynamic change in magnetization caused by domain wall translation is mainly in the direction of the track width. Therefore, the magnetization configuration of this pole tip is apparently as shown in Fig. 4. The domain walls are presumably slanted because slanting spreads the magnetic charges along the walls over a longer region and thereby reduces magneto-static energy in this configuration. Based on similar reasoning, the magnetization configuration on the ABS of head no. 2 is believed to be as shown in Fig. 5.

Different phase shifts in the rotational response and the response of domain walls mean different delay times of magnetic flux conduction are associated with the two processes. As suggested by Jones,⁷ superposition of two or more pulses with different delay times produces a pulse with "wiggles." The results shown in Fig. 3(a) and (b) suggest that the read-back signal of this head could be quite noisy.

To reveal the complete domain configuration in the region near the pole tip, we mapped the domain configurations in both the ABS and the sloped region of head no. 2 with three different drive conditions: 6-mA p-p ac at 1 MHz superposed upon a dc of 20, 0, and -20 mA, and the results are shown in Figs. 6(a) and (a'), (b) and (b'), and (c) and (c'), respectively. An s-polarized laser beam with an incidence plane along the symmetry axis of the head was used to measure the sloped region. Because of the sharp angle between the throat and the sloped region, Fig. 6 does not include the surface of the throat and a short section (about $2 \mu\text{m}$) of the sloped region near the throat. However, these pictures suggest that the domain wall on the right-hand side of Fig. 6(a) is not connected to the domain wall on the right-hand side of Fig. 6(a') because they do not move in the same direction under the same dc bias. However, the domain beneath the ABS to the right of the wall in Fig. 6(a) is believed to be magnetized in the same direction as the left-hand side domain in Fig. 6(a') because they expand under the same dc drive. For the same reasons, the domain wall in Fig. 6(c) is not connected to the wall on the left-hand side of Fig. 6(c'),

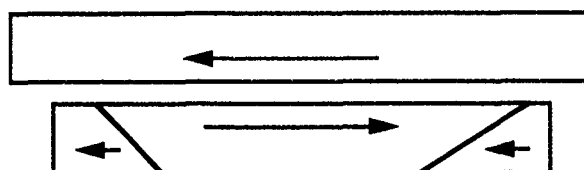


FIG. 5. Magnetization configuration on the ABS of head no. 2.

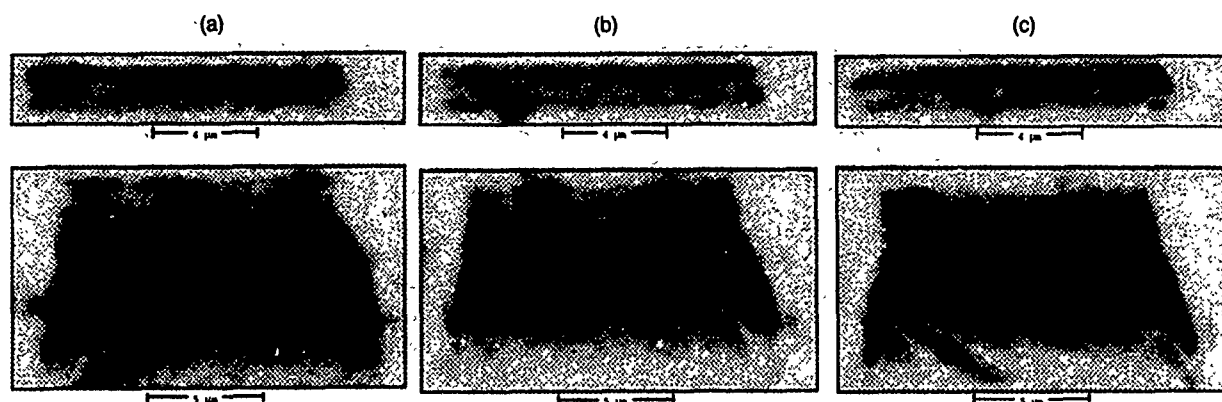


FIG. 6. Domain configuration in both the sloped region and the trailing pole tip of head no. 2. From left to right, top row: (a), (b), and (c); bottom row: (a'), (b'), and (c'). See text for detail.

and the domain to the left side of the wall in Fig. 6(c) beneath the ABS is likely magnetized in the same direction as the domain on the right-hand side of Fig. 6(c'). From the above observations, a possible complete domain configuration near the pole tip is plotted in Fig. 7. Because of the sharp angle between the throat and the sloped region, closure domain walls (a) and (a') do not extend to the corners of the pole tip. Instead, they close at the junction between the throat and the sloped region. The magnetization on the corners of the pole tip curls to reduce the large magnetostatic energy which a configuration with magnetization perpendicular to any surface would cause. The slanting of the domain walls on the ABS reduce the magnetostatic energy along the walls by spreading the magnetic charges over a longer region. Although a perfect self-closed domain configuration in the throat, like that in the sloped region, could potentially eliminate the magnetostatic energy, the need for more domain walls in such a small dimension ($1 \times 2.5 \times 10 \mu\text{m}$) may actually cause a higher energy state because of the increase in total wall energy.

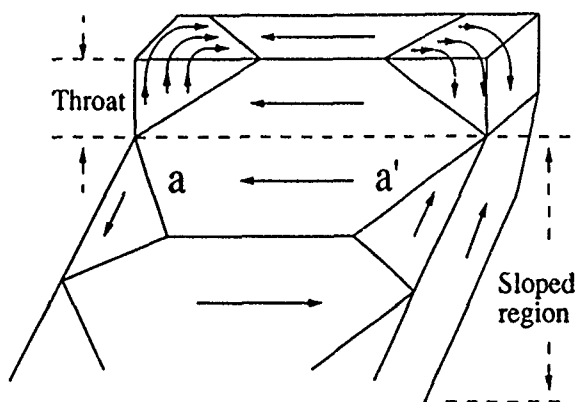


FIG. 7. Domain configuration in the region near the pole tip of head no. 2.

CONCLUSIONS

With a scanning magneto-optic photometer, the dynamic domain configurations on the ABS of several thin-film recording heads were studied. It was found that the pole tip of thin-film heads is usually a multidomain structure. The direction of the domain walls is neither parallel nor perpendicular to the gap plane. Based on the laser configuration used in the measurements and the corresponding results; the magnetization on the ABSs of most heads is believed to be in the plane of the ABS along the track width, with the magnetizations on the two sides of the domain walls either "head-to-head" or "tail-to-tail". This configuration produces strong magnetic poles along the walls. The domain walls are slanted in order to spread the magnetic charges along the walls over a larger region, thereby reducing magnetostatic energy. The responses of the domain walls are not all in phase, and they are generally out of phase with the rotational response. This phase shift phenomenon may cause "wiggles" in the read-back signal. By correspondingly measuring the domain pattern in both the sloped region and the pole tip, a possible magnetization configuration in the throat and the sloped region near the pole tip was suggested for one head. More work is required to provide a conclusive explanation for these complex domain patterns on the ABS and to understand their effect on head performance.

¹ P. L. Trouilloud, B. E. Argyle, B. Petek, and D. A. Herman, *IEEE Trans. Magn.* **25**, 3461 (1989).

² X. Shi, P. V. Koepppe, and M. H. Kryder, *IEEE Trans. Magn.* **27**, 4942 (1991).

³ F. H. Liu, P. Ryan, X. Shi, and M. H. Kryder, *IEEE Trans. Magn.* **28**, 2100 (1992).

⁴ P. Kasiraj and R. D. Holmes, *IBM Res. Rep. RJ 7805* (72187), Nov. 6, (1990).

⁵ X. Shi and M. H. Kryder, Paper HB-08, INTERMAG '93.

⁶ M. H. Kryder, P. V. Koepppe, and F. H. Liu, *IEEE Trans. Magn.* **26**, 2995 (1990).

⁷ R. E. Jones, Jr., *IEEE Trans. Magn.* **15**, 1619 (1979).

Omega head—an experimental 120-turn inductive head

D. D. Tang, R. E. Lee, J. L. Su, F. Chu, J. Lo, H. Santini, L. Lane, N. Robertson, M. Ponce, P. Cisneroz, and G. Guthmiller
IBM, 650 Harry Road, San Jose, California 95120

Experimental 120-turn thin-film inductive heads have been built. The key features of this head are the 6- μm pitch helical coils and an omega-shaped, planar yoke structure having dual easy axes. Hardbaked photoresist insulator layers are used to encapsulate the yoke and to smooth out the wafer surface topography. Micro-Kerr studies show that the easy axis remains in the transverse direction in the yokes after multiple anneals. The $P1/G/P2$ is 3.8/0.3/3.8 μm , and the yoke length is close to 1 mm. The helical coils were built with a novel process that combines yoke/stud coplating and a photoresist planarization process. The coil resistance is 68 Ω and the inductance is 5.5 μH . The yoke saturates at 5 mA. The heads were tested over disks having Mrt of 2.5 memu/cm^2 and H_c of 1500 Oe. The write threshold current is 5.3 mA (peak-to-peak) and the overwrite is 30 dB. The isolated pulse amplitude V_{pp} is 10.3 $\mu\text{V}/(T_w V)$, where track width T_w is in μm and the linear velocity V in m/s.

I. INTRODUCTION

Increasing coil turns and reducing track width of inductive heads have been the means to improve the recording density. To accommodate the increasing coil layers, the separation between $P1$ and $P2$ of today's head is typically 25 to 30 μm , beyond which it becomes increasingly more difficult to control the pole tip dimension and the composition of the plated permalloy.¹ Many different head designs were invented to tackle these problems. The most notable extension of the pancake head structure is the Diamond² design. Here, a planar head design³ was explored for higher density recording. In a planar head, the $P1$ and $P2$ yokes are separated in the plane rather than overlapping each other. Thus, the yokes can be separated farther than 30 μm and the yoke topology is kept below 12 μm . The tight winding helical coil permits much tighter inductive coupling, and therefore offers coils with lower inductance per turn square than conventional pancake heads. This paper presents exploratory work on a 120-turn planar inductive head called Omega Head (as its physi-

cal resemblance of the Greek character). The magnetic design issues, a novel head process and the recording characteristics of the head will be described.

II. MAGNETIC DESIGN ISSUES

(1) To reduce the flux leakage between $P1$ and $P2$, they should be separated far apart. Figure 1 shows the normalized flux coupling through the air (leakage) between $P1$ and $P2$ yokes based on a two-dimensional analysis. The leakage is lowered to 0.6 \times when the two yokes are offset by one yoke width, and is reduced to 0.25 \times when the yokes are on the same plane and are offset by 3 times the yoke width. Figure 2 shows the yoke configuration of the present design. The flux leakage in the back yoke is minimized. The dominant leakage of this particular design comes from the overlap portion of $P1$ and $P2$ near the throat.

(2) For small sliders, the slider height limits the coil turns to a maximum of 60 turns of 6- μm helical pitch coil³ where coils were wound on two legs of the yoke. The yoke of our Omega head is made up of two pairs of legs. The coils are wound on all four legs. The number of coil turns is no longer limited by the slider heights. To maximize the flux

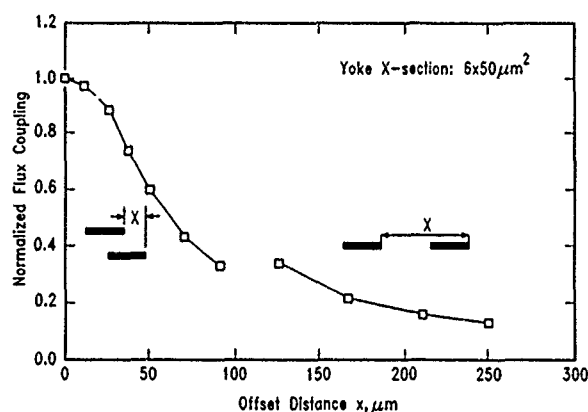


FIG. 1. Flux coupling between two yokes. Normalized to offset $x=0$. S is the vertical separation of $P1$ and $P2$. The coupling is reduced to 0.6 \times when the two yokes are offset by one yoke width, and reduced to 0.25 \times by 3 \times yoke width.



FIG. 2. SEM micrograph of an OMEGA head with 120-turn coils. Key features are helical coils, planar yoke with two easy axes, and hardbake resist encapsulated yokes.

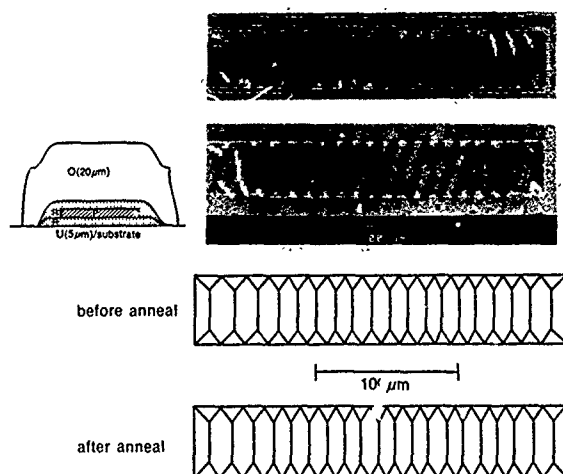


FIG. 3. μ -Kerr image of a 3- μ m permalloy film encapsulated in hardbake photoresist before and after annealing. No change in domain wall density is observed.

Omega Head Process

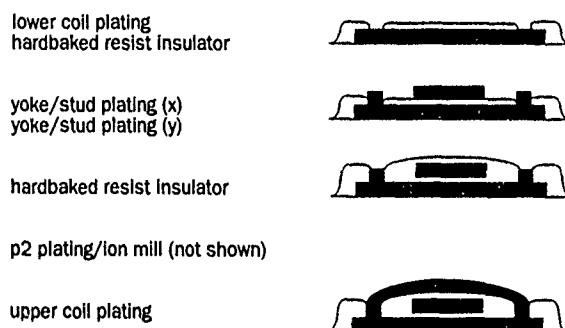


FIG. 4. Key steps of the OMEGA head process flow. Permalloy studs are plated together with the yoke in the same step. Hardbake photoresist is used for passivation.



FIG. 5. Domain images of yokes. The top and bottom yokes having easy axis in the y direction and the left and right yokes having easy axis in the x direction.

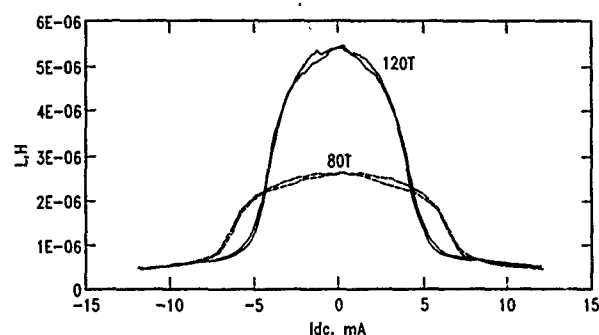


FIG. 6. Head inductance vs dc bias current in coil.

conduction efficiency, we chose a dual-axis yoke design. The easy axis of the yokes is oriented in two directions: Referring to Fig. 2, the easy axis is in the x direction for the left and right yokes, and in the y direction for the top and bottom yokes.

(3) Both hardbaked photoresist or sputtered alumina were investigated for planarizing the coil and isolating the coil from the yoke. Although the mismatch in the thermal expansion coefficient between the permalloy and the hardbaked photoresist is larger, hardbaked photoresist is much softer (Young's modulus is two orders smaller⁴) than alumina, thus, it exerts a more uniform stress to the permalloy and induces less stress anisotropy when process incurs temperature cycles. The μ -Kerr image studies (Fig. 3) confirmed that the electroplated permalloy encapsulated in the hardbaked photoresist does not show any annealing-induced changes in the domain wall density.

III. HEAD PROCESS AND CHARACTERISTICS

While the spiral coil is built over a flat surface, the helical coils must wrap around a yoke. It is more difficult to pattern many of these fine coil features over a severe topography: A new helical coil process was developed. The key concept is planarize-then-build-fine-features. In this case, we raise the lower coil contacts⁵ to the same height as the yoke with vertical coil extensions (studs), planarize the surface, and then pattern the fine features of the upper part of the coils. Figure 4 shows the major steps of the head processing.

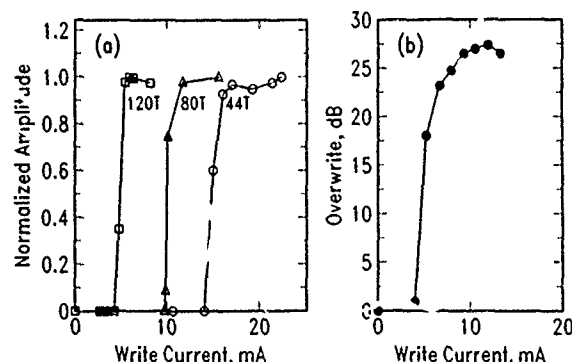


FIG. 7. (a) Threshold write current of a 120- and a 80-turn head with a 44-turn pancake head as reference, (b) overwrite characteristics of a 120-turn 3.1- μ m track width head.

TABLE I. Heads characteristics.

Head:	A	B	C	D	E	Reference (pancake)
N	120	120	120	120	80	44
Inductance (μH)	5.5	5.5	5.5	5.5	2.4	1.3
L/N^2 (nH/N ²)	0.382	0.382	0.382	0.382	0.375	0.671
T_w (μm)	8.6	6.7	3.3	4.3	8.6	8.5
V (m/s)	8	8	10	10	8	8
Overwrite (dB)	33	31	27.5	29	34	26
V_{pp} (μV)	713	542	350	399	468	280
$V_{pp}/T_w/V$ [$\mu\text{V}/\mu\text{m}/(\text{m/s})$]	10.36	10.02	10.61	9.27	6.8	4.0
PW_{50} (nm)	610	590	600	640
Estimated $a+d$ (nm)	242	230	236	240
Estimated efficiency (%)	60	59.5	60	70
Instability (%)	1.5	1.8	1.6	2.0	1.9	1.5

Co-Pt-Cr thin-film disk ($Mrt=2.5E-3$ emu/cm², $Hc=1500$ Oe).
Magnetic spacing=103.3 nm, gap length=0.3 μm .
Transition length ($W-C$ model) $a=136$ nm.

First, the lower coils are plated and later planarized with photoresist. The photoresist is patterned to expose the contacts to the lower coils and then hardbaked. Yokes and studs with easy axis in the x direction are plated in one step. Then, those in the y direction are plated by rotating the wafer 90°. A second photoresist layer is spun and exposed to open the tops of the studs for contacting the upper coils. Notice that the hardbaked photoresist fills the recess between the yoke and the studs and provides a smooth surface with a gentle slope for the subsequent construction of the upper part of the helical coils. Then two more hardbaked photoresist steps are employed to form a 3.7- μm apex spacer between the $P1$ and $P2$ in the pole tip area. Alumina gap material is then deposited and etched open at the "backgap." In this design, the "backgap" is actually located to the left of the apex spacer (see Fig. 2) $P2$ is plated. At this step, the maximum device topography is below 11 μm . The entire yoke, except the short $P2$, is encased in hardbaked photoresist passivation. The yokes have experienced three photoresist hardbake heat cycles and for those with easy axis in the y direction, the oven field is in the hard-axis direction. The micro-Kerr image of the head is shown in Fig. 5 and the domains are oriented in the transverse direction as predicted in our previ-

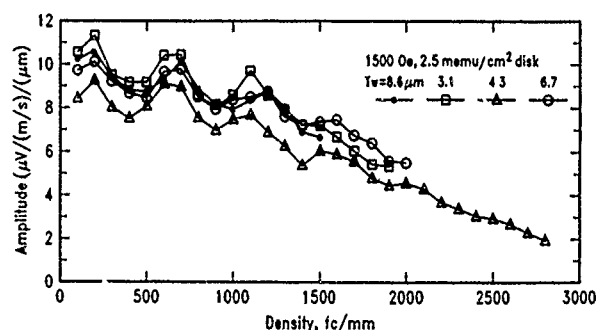


FIG. 8. Density roll-off of four 120-turn heads of different track width on thin-film disk.

ous studies. The pole tip is trimmed with an ion milling process. Upper coils are then patterned and plated to complete the coils. The head is embedded in a 30- μm -thick alumina overcoat.

The head inductance is shown in Fig. 6. The normalized head inductance is typically 0.382 nH/N², about half of today's spiral coils. The coil resistance is 68 and 38 Ω for the 120- and 80-turn heads, respectively, about half of the spiral coils. Heads were tested on Co-Pt-Cr thin-film disks with $Mrt=2.5$ memu/cm² and $Hc=1500$ Oe at a fly height of 50 nm (estimated magnetic spacing is 103 nm). Figure 7(a) shows the write threshold currents. For the 120-turn head, the threshold current (peak-to-peak) is 5.3 mA. Figure 7(b) shows the overwrite of a head with $T_w=3.1$ μm at write and overwrite flux density of 490 and 1600 fc/mm, respectively. Table I summarizes the head characteristics. The normalized readback signal is 10.3 $\mu\text{V}/(T_w V)$, where T_w is the track width in μm and V is the linear velocity in m/s. The half-height pulse width PW_{50} is 600 nm. Figure 8 shows the density roll-off plot of four heads with T_w from 8.6 to 3.1 μm . The estimated read efficiency is 60%. The head instability was measured by repeating the erase-write-read operation. The standard deviation divided by the mean value of the readback signals is in the range of 1.5% to 2%. The error rate of the heads were tested in a peak detect channel without an equalizer at a flux change of 1288 fc/mm. The on-track bit-error rate is 6.25×10^{-10} for a 80-turn 8.6- μm track width head and 7.65×10^{-9} for a 120-turn 4.3- μm track width head.

The authors would like to thank K. Ju and J. S. Best for encouragement.

¹M. Hanazono *et al.*, J. Appl. Phys. **61**, 4157 (1987).

²A trade name from Digital Equipment, Inc., see G. J. Koel, W. F. Druyvesteyn, U.S. Patent 4,165,525, Aug. 21, 1979, and also see M. Malary, European Patent 90303866.9, publication number 0 400 793 A2, May 12, 1990.

³L. T. Romankiew and G. A. Wardly, U.S. Patent 3,662,119, May 9, 1972.

⁴K. F. Young, IBM Res. Develop. **34**, 706 (1990).

⁵H. J. Hamilton, U.S. Patent 5,041,932, Aug. 20, 1991.

Local magnetoresistance and point-source excitation of Ni-Fe thin films (abstract)

R. W. Cross and A. B. Kos

Electromagnetic Technology Division, National Institute of Standards and Technology, Boulder, Colorado 80303

The magnetoresistive (MR) response was measured in Ni-Fe thin films, representative of the films used in magnetic recording read heads, with sense areas as small as $6 \times 6 \mu\text{m}$. For the bulk, central, and edge regions of the film, the MR response was measured as a function of magnitude and angle of a uniform in-plane applied magnetic field. Measurements were made using a four-contact technique which included two scanning microprobes and two orthogonal field sources.¹ The microprobes could be scanned with a resolution of $0.1 \mu\text{m}$ and positioned separately. The field sources produced a maximum field of 24 kA/m (300 Oe) that could be rotated up to $\pm 15^\circ$. From the local MR response, the local magnetic behavior was obtained and compared to micromagnetic theory.² The bulk MR response was also measured as a function of position on the film of a microfield source used for point-source excitation. The microfield source was a Fe wire electrochemically etched to a $0.1 \mu\text{m}$ tip diameter. From these results the local MR sensitivity was determined for the central and edge regions. The sensitivity profile of the film is important in optimizing the design of the device. The large variations observed in the MR response between the central and edge regions as a function of uniform field and point source excitations are indicative of the fact that magnetostatic fields dominate the response in these small structures.

¹R. W. Cross, A. B. Kos, C. A. Thompson, T. W. Petersen, and J. A. Brug, *IEEE Trans. Magn.* **28**, 3060 (1992).

²N. Smith, *J. Appl. Phys.* **63**, 2932 (1988)

Sensitivity distribution asymmetries in magnetoresistive heads with domain control films (abstract)

N. Koyama, C. Ishikawa, Y. Suzuki, H. Aoi, and K. Yoshida

Central Research Laboratory, Hitachi, Ltd., Kokubunji, Tokyo 185, Japan

Suppression of the sidetrack reading behavior is important in achieving high track-density recording with a magnetoresistive head. In the present work, we investigate the sensitivity distribution profiles of MR heads through experimentation using a microtrack technique¹ and computer simulation. Shielded, soft, adjacent-layer-biased MR heads with $3\sim 6\text{-}\mu\text{m}$ -wide tracks are used. The ends of the MR elements are coupled to antiferromagnetic or hard ferromagnetic films for domain control. In the simulation based on the Landau-Lifshitz-Gilbert equation,² the magnetization configurations in the MR elements of the domain stabilizing films are calculated to analyze the sensitivity distribution. The measured sensitivity profiles in all cases have asymmetries that are reversed when the sensing current direction or the magnetization direction of the MR element is reversed. These results agree with the simulation. The asymmetries of sensitivity profiles are explained by the magnetic poles at the domain control film edges and at the transverse edges of the element which generate a diagonal demagnetizing field distribution in the sensing region.

¹A. Wallash, M. Salo, J. K. Lee, D. Heim, and G. Garfunkel, *J. Appl. Phys.* **69**, 5402 (1991).

²Y. Nakatani, Y. Uesaka, and N. Hayashi, *Jpn. J. Appl. Phys.* **28**, 2485 (1989).

Overlayer-induced perpendicular anisotropy in ultrathin Co films (invited)

Brad N. Engel, Michael H. Wiedmann, and Charles M. Falco

Department of Physics and the Optical Sciences Center, University of Arizona, Tucson, Arizona 85721

We have used *in situ* polar Kerr effect measurements to study the magnetic anisotropy of MBE-grown $X/\text{Co}/Y$ trilayers, where X and Y are combinations of the nonmagnetic metals Ag, Au, Cu, or Pd. The competition between the perpendicular anisotropy of the initial underlayer X/Co interface and the in-plane shape anisotropy of the Co film allows us to adjust the total anisotropy of the uncovered Co to be in plane and of moderate strength. In this way, we can measure hard-axis (perpendicular) polar hysteresis curves *in situ* as a function of overlayer Y coverage, and directly deduce the anisotropy field. Polar hysteresis curves were measured *in situ* for systematically varied Co and overlayer Y layer thicknesses $2 \text{ \AA} \leq t_{\text{Co}} \leq 20 \text{ \AA}$ and $0 \text{ \AA} \leq t_Y \leq 100 \text{ \AA}$. We find, for particular combinations, the magnitude of the $X/\text{Co}/Y$ perpendicular anisotropy is strongly peaked at ~ 1 atomic layer overlayer Y coverage.

I. INTRODUCTION

One of the most interesting unresolved problems remaining in modern magnetism is the underlying mechanism of perpendicular interface anisotropy.¹ This anisotropy arises from the interface between magnetic and nonmagnetic metal films, and is observed only in particular material systems.² Possible explanations advanced for this strong anisotropy include the reduced coordination symmetry,³ altered electronic structure,⁴ and localized epitaxial strain at the interface between two different materials.⁵

In this paper we review our recent studies of interface magnetic anisotropy using *in situ* Kerr effect measurements in our molecular beam epitaxy (MBE) system. We have investigated the evolution of the magnetic and structural behavior of ultrathin Co films during the progressive formation of interfaces with different nonmagnetic overlayers.

II. BACKGROUND

There has been a great volume of research on magnetic surface and interface anisotropy since Néel's first prediction⁶ and Gradmann's first experimental observation.⁷ Investigations into the influence of nonmagnetic overlayers on the behavior ultrathin magnetic thin films have been carried out by many groups. The majority of these studies have concentrated on determinations of the magnetic moment and interface anisotropy resulting from coverage by relatively thick overlayers.

Investigations of the evolving magnetic behavior of an ultrathin film during interface formation have been performed only recently due to the stringent requirements of *in situ*, monolayer-sensitive measurements carried out in ultrahigh vacuum (UHV). Previous evidence of changes in magnetic behavior with nonmagnetic monolayer coverage include a reduction in Curie temperature of ultrathin Co(001) films when covered by Cu⁸ and an epitaxial structure-induced change in the in-plane easy axis of Fe(110) films when covered by Au.⁹

In our first work on the magnetic behavior during interface formation, we studied the perpendicular magnetism of MBE-grown Pd/Co/ Y sandwich structures where $Y = \text{Ag, Cu, and Pd}$ using *in situ* polar Kerr ellipticity measurements.¹⁰ We found the surprising result that deposition of any of the overlayers caused nonmonotonic behavior in the perpendicular coercivity H_c as a function of coverage. We found a sharp peak in H_c at a coverage of $t_Y \approx 2 \text{ \AA}$ for all materials with a monotonic increase above $t_Y \approx 4 \text{ \AA}$. The peak was most pronounced for Cu, where H_c changed by more than 200%.

The pronounced peak in coercivity we observed at ~ 1 ML suggested an abrupt change in anisotropy. We have therefore directly measured the uniaxial anisotropy of Co films *in situ* as a function of nonmagnetic overlayer coverage and confirmed the existence of a peak in the perpendicular anisotropy at ~ 1 ML coverage as well.¹¹ This unusual anisotropy behavior also recently has been independently confirmed for Au/Co/Au.¹²

III. EXPERIMENTAL TECHNIQUE

A. Film growth

We used molecular beam epitaxy (MBE) to grow single-crystalline Co films in the thickness range $2 \text{ \AA} \leq t_{\text{Co}} \leq 30 \text{ \AA}$ on single-crystalline Pd(111) and Au(111) buffer layers. The buffer layers were epitaxially grown on Co-seeded GaAs(110) substrates. The background pressure during deposition was $\leq 5 \times 10^{-10}$ Torr, and was composed predominantly of H_2 . We used effusion cells for Ag and Pd deposition at 0.1 and 0.15 $\text{\AA}/\text{s}$, respectively, and optical-feedback-controlled e -beam evaporators to deposit the Au(0.1 $\text{\AA}/\text{s}$), Co(0.25 $\text{\AA}/\text{s}$), and Cu(0.1 $\text{\AA}/\text{s}$). All deposition rates were determined from Rutherford backscattering spectrometry analysis of calibration films, and were reproducible to within $\pm 10\%$. Film quality and crystal structure were monitored during growth with reflection high energy electron diffraction (RHEED). The RHEED pattern images were captured

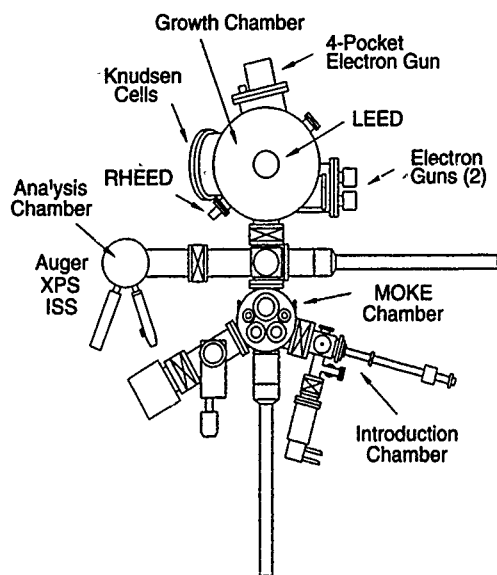


FIG. 1. Schematic representation of our modified Perkin-Elmer 433S molecular beam epitaxy system with *in situ* magneto-optic Kerr effect (MOKE).

and digitized with a computer-based video system capable of resolving changes in surface lattice spacings of 1%.

B. *In situ* Kerr effect measurement

In our MBE system, a sample can be transferred between the deposition chamber and another connected ultrahigh vacuum chamber ($P < 2 \times 10^{-10}$ Torr), where it is aligned between the poles of an external electromagnet for *in situ* Kerr effect measurements. Figure 1 is a schematic of this system. The magnetic field is applied along the sample normal with a maximum field of ± 2.2 kOe. We use a 50 kHz photoelastic modulator and lock-in-amplifier-based detection scheme with a HeNe laser to measure the polar Kerr ellipticity of the sample as a function of applied field. Measuring the ellipticity rather than the Kerr rotation eliminates the background Faraday rotation from the quartz vacuum window. Optical access is provided by a hole along the axis of one of the magnet poles. The sample can be moved repeatedly between the measurement and the deposition chambers without the need for optical realignment.

C. *In situ* anisotropy measurement

We grew our samples on Au(111) or Pd(111) buffer layers, so that the initial X/Co ($X = \text{Au, Pd}$) interface would provide a perpendicular anisotropy in competition with the in-plane shape contribution of the Co film. We could therefore adjust the initial total anisotropy of individual samples to be either perpendicular or in-plane by selecting the proper Co film thickness. This allowed us to work within the 2.2 kOe limit of our perpendicular magnetic field. Using this idea of designing samples, which balance the relatively strong shape and interface anisotropies against each other, allows us to very easily observe small changes in the total anisotropy energy due to overlayer deposition.

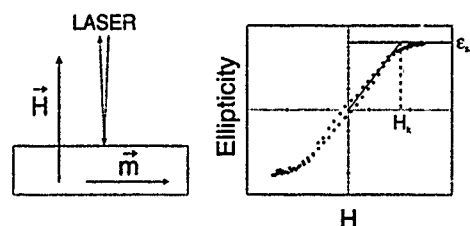


FIG. 2. Schematic of the *in situ* anisotropy energy measurement. The magnetization m lies in the plane of the sample, while the applied field H is perpendicular to the film plane.

To directly determine the total anisotropy energy, we measured hard-axis magnetization curves and deduced the anisotropy field by extrapolating the linear curves to saturation. Because our MBE system is equipped with only a 2.2 kOe perpendicular magnetic field, we are limited to making these measurements on films with in-plane easy axes of moderate anisotropy strength. However, we can create films of this type by selecting the proper Co film thickness that we grow on the Pd or Au buffer layers. Figure 2 is a schematic of this measurement technique.

The properly chosen Co thickness allows saturation of the magnetization by our 2.2 kOe field after overlayer coverage, while still maintaining an in-plane easy axis. In this way we can directly determine the anisotropy field from extrapolation of the hard-axis curves to saturation and calculate the total anisotropy energy from the relation

$$K_1 = H_k M_s / 2, \quad (1)$$

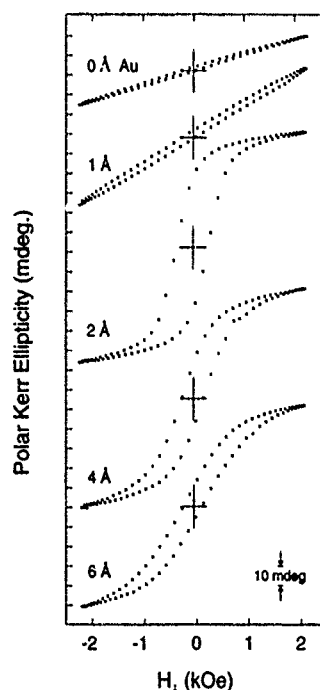


FIG. 3. Hard-axis (perpendicular) hysteresis curves from a 30 Å Co film grown on Au(111) as it is progressively covered with Au. The perpendicular anisotropy contribution from the Co/Au interface is seen to be a maximum at 2 Å Au coverage.

where $M_s = 1422 \text{ emu/cm}^3$ is the bulk saturation magnetization of Co. Refinement of this technique to include higher-order anisotropy constants was found to be unnecessary for the majority of samples studied. To assure the validity of this technique, after completing our complete set of *in situ* measurements we removed representative samples and verified the bulk magnetization behavior of the Co with a vibrating sample magnetometer. We also verified the saturation ellipticity ϵ_{sat} with an *ex situ* Kerr measurement to 10 kOe.

IV. RESULTS AND DISCUSSION

A. Anisotropy versus coverage

Figure 3 is a series of hard-axis (perpendicular) hysteresis loops of a 30 Å Co film grown on Au(111) and covered by ultrathin overlayers of Au. The top curve is that of the uncovered film; the linear behavior indicates that it has an in-plane easy axis. However, upon coverage by 1 Å of Au (slightly less than one-half of a monolayer) the slope increases. This indicates the Co/Au interface has contributed a perpendicular component to the anisotropy, although the overall easy direction still remains in plane. Continuing the coverage to 2 Å Au causes a further increase in the perpendicular component of the anisotropy, allowing the magneti-

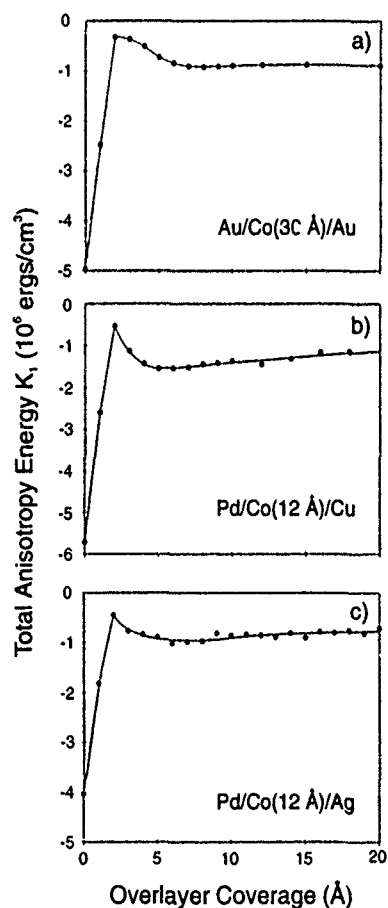


FIG. 4. Total magnetic anisotropy energy vs overlayer coverage for $X/\text{Co}/Y$ structures, where (a) $\text{Au}/\text{Co}(30 \text{ Å})/\text{Au}$; (b) $\text{Pd}/\text{Co}(12 \text{ Å})/\text{Cu}$; and (c) $\text{Pd}/\text{Co}(12 \text{ Å})/\text{Ag}$. Pronounced peak at 2 Å coverage is evident for all three overlayer materials.

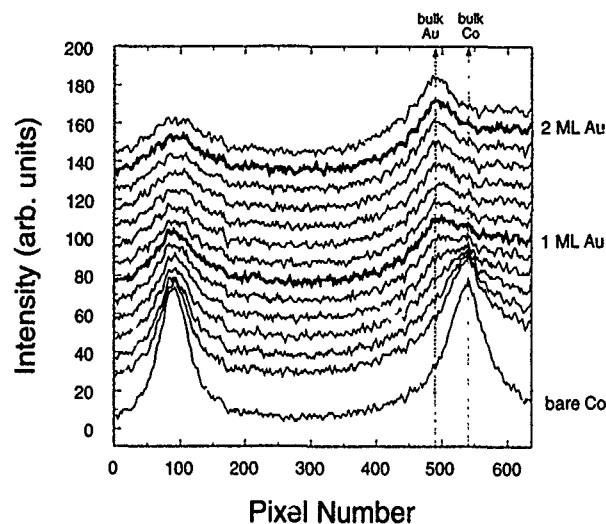


FIG. 5. Time-evolution series of line intensity profiles measured across the RHEED pattern of a Co surface as it is progressively covered by Au. Heavier traces indicate approximate coverage equivalents of 1 and 2 ML. The Au growth is found to be incoherent and strain-free from the first stages of coverages. See the text for a discussion.

zation to be saturated by our 2.2 kOe field. It is clear from the figure that further Au coverage above 2 Å then decreases the perpendicular anisotropy contribution.

Because we can saturate the moments in this sample, we are able to deduce the anisotropy field from extrapolation of the hard-axis curve to saturation and hence directly calculate the total anisotropy energy. Figure 4(a) is a plot of the anisotropy constant K_1 vs Au coverage. Here we have adopted the convention used by many researchers, where a positive K_1 indicates perpendicular anisotropy. The most striking feature is the pronounced peak at $\sim 2 \text{ Å}$ coverage, which, to within our resolution and control, is located just below 1 ML of Au. The total anisotropy energy displays the same non-monotonic behavior with Au coverage we observed in the coercivity of the perpendicular films discussed earlier.¹⁰ Above 2 Å Au coverage, the total anisotropy becomes increasingly negative, indicating a reduction of the perpendicular contribution. The overall negative anisotropy values of Fig. 4(a) indicate an in-plane easy axis was maintained throughout the coverage range for this particular Co thickness.

Figures 4(b) and 4(c) are plots of the total anisotropy energy of 12 Å Co films as a function of Cu and Ag overlayer coverage, respectively. A pronounced peak in the perpendicular anisotropy is also evident at 2 Å coverage for both of these materials.

B. Changes in crystal structure

The role of crystal structure in our observed coverage-dependent anisotropy is an important question that is difficult to address. Because magnetic anisotropy is very sensitive to the local environment, subtle changes in atomic spacings could cause significant effects. We have used RHEED to investigate coverage-dependent changes in the surface lattice spacing. However, it must be emphasized that the RHEED

geometry measures only the in-plane spacings. Information about the out-of-plane spacings can, in principle, be obtained from low energy electron diffraction (LEED) intensity versus voltage measurements. These are presently in progress and will be presented at a later date.

Figure 5 is a series of intensity profiles measured across a RHEED streak pattern showing the time evolution of a Co surface as it is progressively covered with Au. The starting surface is a freshly prepared 30 Å Co film deposited on a 500 Å Au(111) buffer layer. The RHEED images were captured every 4 s during uninterrupted Au deposition at a rate of 0.1 Å/s, giving a coverage interval between traces of ~0.4 Å. Approximate coverage equivalents of one and two atomic monolayers are indicated with heavier traces in the figure. The distance (pixel number) between the specular beam maximum on the left and the diffracted beam maximum on the right is inversely proportional to the surface lattice spacing measured transverse to the *e*-beam direction.

The first profile from the bare Co surface shows intensity maxima that are sharp and symmetric. Upon partial coverage with just 0.4 Å Au, or roughly 1/6 ML, the diffraction peak becomes asymmetric with a shoulder forming at smaller pixel number, and hence larger lattice spacing. This indicates that the Au grows incoherently and unstrained at its larger bulk lattice constant in the very early stages of deposition. This incoherent growth is similar to that seen for Co grown on bulk single-crystal Pd(111),¹³ and is not surprising in view of the large 14% lattice mismatch between Au and Co. At the coverage equivalent of 1 ML (2.4 Å), the diffraction peak is composed of contributions from both bulk Au and bulk Co spacings. After 2 ML of coverage, the peak is dominated by diffraction from the bulk Au spacing.

These measurements suggest that because the Au immediately grows incoherently and strain-free, the Co in-plane lattice spacing is unaffected by the Au overlayer. Hence, magnetoelastic anisotropy arising from an in-plane strain in the Co is unlikely to account for our observed peak in perpendicular anisotropy at 1 ML. In addition, the fact that overlayers of very different lattice mismatch with Co (2% for Cu and 14% for Au) display similar anisotropy behavior further supports this conclusion.

C. Changes in electronic structure

Another possible explanation of the observed coverage-dependent anisotropy is that the magnetic interface anisotropy is very sensitive to details of the electronic band structure.⁴ Recent photoemission measurements of Cu monolayers deposited on ferromagnetic transition metals have found electronic states that deviate significantly from bulk behavior.^{14,15} If the hybridization of electronic states at the Co/Y interface plays an important role in magnetic anisotropy, then variations of the overlayer band structure could cause significant alterations of the total anisotropy. It is interesting to note that the very recent photoemission measurements of 1 ML of Cu deposited on Co(0001) found the Cu peak at significantly lower binding energy than that of bulk (a shift of approximately 0.25 eV).¹⁴ With further Cu coverage the bulk peak rapidly emerged, so that by 2 ML only the bulk Cu peak remained. This coverage dependence of the Cu

electronic band structure is very similar to what we observe for the magnetic anisotropy of our Co/Cu structures. This suggests a possible relation between the two phenomena, although more work is needed before this can be uniquely determined.

D. Co/vacuum interface anisotropy

In Fig. 4, the initial total anisotropies of the uncovered Co films are strong and in-plane (negative K_1). As the overlayer coverage is increased from 0 to 2 Å, the magnitude of this anisotropy energy rapidly approaches zero, indicating the presence of an increasing perpendicular contribution for each of the materials Au, Cu, and Ag. In the cases of Ag and Cu, this large increase in perpendicular anisotropy after overlayer coverage is surprising, in light of the very weak interface anisotropy displayed in Co/Ag and Co/Cu multilayers.¹⁶ One possibility is the existence of a large, in-plane Co/vacuum interface anisotropy that is being replaced by a perpendicular contribution from the forming Co/Y interface. Such a large in-plane vacuum interface anisotropy has recently been observed in FCC Co(100) films.¹⁷

We can estimate the strength of the Co/UHV interface anisotropy, K_s^{UHV} , by calculating the difference between the total anisotropy energy of the uncovered and completely covered Co films of Fig. 4. The total anisotropy of the uncovered film can be written as

$$K_u = K_v + \frac{K_s^X}{t_{\text{Co}}} + \frac{K_s^{\text{UHV}}}{t_{\text{Co}}}, \quad (2)$$

where K_v is the volume anisotropy including crystalline and shape contributions, K_s^X is the interface anisotropy from the Co/substrate interface, and t_{Co} is the Co film thickness.

If we now make the reasonable assumption that there is no change in volume or substrate interface anisotropy upon complete coverage by the nonmagnetic overlayer, then K_u after coverage can be written as

$$K'_u = K_v + \frac{K_s^X}{t_{\text{Co}}} + \frac{K_s^Y}{t_{\text{Co}}}. \quad (3)$$

Here the UHV interface has been completely replaced by the Y overlayer.

Taking the difference between Eqs. (2) and (3) gives for the Co/UHV interface anisotropy

$$K_s^{\text{UHV}} = \Delta K_u t_{\text{Co}} + K_s^Y. \quad (4)$$

Using values from the multilayer literature² for K_s^Y ($Y=\text{Au}$, Ag, and Cu) yields a range of values -- $0.2 \leq K_s^{\text{UHV}} \leq -0.5$ erg/cm², depending on the substrate/overlayer combination. These variations may be due to changes in volume anisotropy not accounted for in this analysis. However, all the estimates suggest a fairly strong in-plane Co/UHV interface anisotropy for the FCC (111) face. More work is needed to refine these values.

V. SUMMARY

We have used *in situ* polar Kerr ellipticity measurements to study the perpendicular magnetic behavior of MBE-grown X/Co/Y sandwich structures, where $X=\text{Au}$ and Pd and

Y=Ag, Au, and Cu. For all three nonmagnetic overlayer materials, we find a rapid increase in the perpendicular anisotropy after only 2 Å (~1 ML) overlayer coverage. We find this perpendicular anisotropy is anomalously peaked at a coverage of ~1 ML and decreases significantly with further overlayer deposition. From these measurements, we find the Co(111)/UHV interface anisotropy to be strong and in plane. The unusual coverage-dependent anisotropy presented here will provide an additional test for theoretical explanations of the magnetic anisotropy at surfaces and interfaces in layered metallic systems.

ACKNOWLEDGMENTS

This work was supported by the U.S. Department of Energy Grant No. DE-FG02-87ER45297 and the Optical Data Storage Center at the University of Arizona. The authors gratefully acknowledge J. Leavitt for RBS measurements.

¹See the various articles in *Magnetism in the Nineties*, edited by A. J. Freeman and K. A. Gschneider, Jr. (North-Holland, New York, 1991).

- ²F. J. A. den Broeder, W. Hoving, and P. J. H. Bloemen, *J. Magn. Magn. Mat.* **93**, 562 (1991).
- ³L. Néel, *J. Phys. Radiol.* **15**, 376 (1954).
- ⁴A. J. Freeman and R. Wu, *J. Magn. Magn. Mat.* **100**, 497 (1991).
- ⁵C. Chappert and P. Bruno, *J. Appl. Phys.* **64**, 5736 (1988).
- ⁶L. Néel, *J. Phys. Radiol.* **15**, 376 (1954).
- ⁷U. Gradmann, *Appl. Phys.* **3**, 161 (1974).
- ⁸C. Schneider, P. Bressler, P. Schuster, J. Kirschner, J. J. Miguel, and R. Miranda, *Phys. Rev. Lett.* **64**, 1059 (1990).
- ⁹H. J. Elmers, T. Furubayashi, M. Albrecht, and U. Gradmann, *J. Appl. Phys.* **70**, 5764 (1991).
- ¹⁰B. N. Engel, M. H. Wiedmann, R. A. Van Leeuwen, and C. M. Falco, *J. Appl. Phys.* **73**, 6192 (1993).
- ¹¹B. N. Engel, M. H. Wiedmann, and C. M. Falco, *Phys. Rev. B* **48**, 9894 (1993).
- ¹²S. Ould-Mahfoud, R. Megy, N. Bardou, B. Bartenlian, P. Beauvillain, C. Chappert, J. Corno, B. Lecuyer, G. Sczigel, P. Veillet, and D. Weller, *Proceedings of the Materials Research Society*, Spring Meeting, San Francisco (in press).
- ¹³S. T. Purcell, H. W. van Kesteren, E. C. Cosman, and W. Hoving, *J. Magn. Magn. Mat.* **93**, 25 (1991).
- ¹⁴D. Hartmann, W. Weber, and G. Güntherodt, *Ultra Thin Films, Multilayers and Surfaces*, edited by F. J. A. den Broeder (MRS, Pittsburgh, in press).
- ¹⁵J. E. Ortega, F. J. Himpsel, G. J. Mankey, and R. F. Willis, *Phys. Rev. B* **47**, 1540 (1993).
- ¹⁶F. J. A. den Broeder, W. Hoving, P. J. H. Bloemen, *J. Magn. Magn. Mat.* **93**, 562 (1991).
- ¹⁷P. Krams, F. Lauks, R. L. Stamps, B. Hillebrands, and G. Güntherodt, *Phys. Rev. Lett.* **69**, 3674 (1992).

Interfacial anisotropy and magnetic transition of cobalt films on Cu(111)

F. Huang, G. J. Mankey, and R. F. Willis

Department of Physics, The Pennsylvania State University, University Park, Pennsylvania 16802

We measure the magnetic properties of ultrathin films of Co epitaxially grown on single crystal Cu(111) using surface magneto-optic Kerr effect. The magnetic behavior is compared with that of the same films, but covered by Cu overlayers to study the effects of film morphology on ferromagnetism. The uncapped films show mainly in-plane anisotropy, but a weak perpendicular magnetization is always present. Capping a 1.5 monolayer (ML) Co film with Cu significantly enhances perpendicular anisotropy with 1 ML of Cu overlayer eliminating the in-plane magnetization completely. The perpendicular magnetization reaches its maximum value with 3 ML of Cu overlayer, ~ 5 times higher than the uncapped films, and then decreases as more Cu is deposited. Annealing can further increase the perpendicular magnetization with the in-plane component remaining weak. In sharp contrast, this perpendicular anisotropy enhancement by Cu overlayers is not seen for Co films on Cu(100). The temperature dependence of magnetization fits to the phenomenological power law $M \sim (1 - T/T_C)^\beta$ with $\beta = 0.15 \pm 0.05$ for the uncapped 1.5 ML Co film and shows a linear behavior after the film is covered by Cu overlayers.

INTRODUCTION

Cu-coated polycrystalline thin films of Co grown on Cu(111) have been shown to have strong perpendicular anisotropy and exhibit Ising behavior over a wide temperature range.¹ This is an interesting result, since as-grown Co films generally show in-plane anisotropy,^{2,3} and Ising behavior is usually observed in highly flat single crystal films with strong uniaxial anisotropy.^{4,5} The crucial factor could be the Cu overlayer, which tends to enhance the perpendicular anisotropy. This enhancement has been previously reported in many sandwich systems, such as Au/Co/Au(111),⁶ Pd/Co/Pd(111),^{7,8} Cu/Co/Pd(111)⁸ and Ni/Co/Ni superlattices.⁹ However, the question of what happens to the magnetic phase transition behavior when the anisotropy is deliberately altered, e.g., by transition metal coating, remains open.

In this paper, we report measurements of ultrathin Co films grown on a Cu(111) single crystal. The magnetic properties are compared with those of the same films but covered by Cu overlayers. Using the magneto-optic method, we have investigated the anisotropy, magnetic transition behavior, and the effects of crystal symmetry on the magnetic properties.

EXPERIMENTAL

Thin Co films were grown at room temperature on a Cu(111) single crystal using molecular beam epitaxy (MBE). The Cu crystal was cut along the [111] direction within 0.5° using x-ray alignment. It was mechanically polished down to $0.05 \mu\text{m}$ followed by electropolishing before being introduced into the vacuum. After a few cycles of 500 eV Ar^+ bombardment and annealing to 700 K for hours, the crystal was free of contamination as determined by Auger electron spectroscopy (AES) and showed a sharp $p(1 \times 1)$ low-energy electron diffraction (LEED) pattern.

Film thickness was controlled by quartz crystal microbalance calibrated with reflection high-energy electron diffraction (RHEED) oscillations. Co on Cu(111) does not show RHEED oscillations, although it has been shown to be a good epitaxial system with metastable FCC layer-by-layer

growth up to three monolayers of Co.^{10,11} However, Co on Cu(100) does have well-resolved RHEED oscillations, and can be used to calibrate the film thickness for Co on Cu(111). Since the atomic area density of Cu(100) is 86.6% of the Cu(111) surface, the thickness on Cu(111) is 86.6% of that on Cu(100), given the same amount of deposited material.

Magnetic properties were studied *in situ* using surface magneto-optic Kerr effect (SMOKE) in the UHV chamber with a base pressure lower than 2×10^{-10} mbar. The external magnetic field can be applied both parallel and perpendicular to the film plane to detect longitudinal and polar hysteresis loops, respectively. To study the magnetic transition, the Kerr intensity (retentivity of the hysteresis loops) was measured as a function of substrate temperature, which was ramped at a constant rate of 6 K per second. Assuming the transition follows a phenomenological power law $M \sim (1 - T/T_C)^\beta$, we fit the Kerr intensity data to obtain the Curie temperature T_C and power law exponent β .

RESULTS AND DISCUSSION

The ultrathin Co films on Cu(111) have predominantly in-plane anisotropy, but a weak perpendicular magnetization with high coercivity is always present. Generally, a mild annealing reduces the coercivity and increases the perpendicular magnetization. However, a more dramatic change in anisotropy is seen from the effect of a Cu coating. As shown in Fig. 1 for a 1.5 ML of Co film, one monolayer of Cu completely wipes out the in-plane hysteresis loop and enhances the perpendicular magnetization by a factor of 3. At the same time, the coercivity of the perpendicular loop is significantly reduced. This trend continues until a Cu overlayer thickness of three monolayers, where the perpendicular magnetization is nearly five times higher than the uncovered film, Fig. 2.

The enhancement of perpendicular anisotropy by transition metal overlayers can be counted for by two competing anisotropies: a surface anisotropy that is due to reduced symmetry at the surface and favors perpendicular spin orientation; and a shape anisotropy, which tends to orient the magnetization parallel to the film plane and increases with

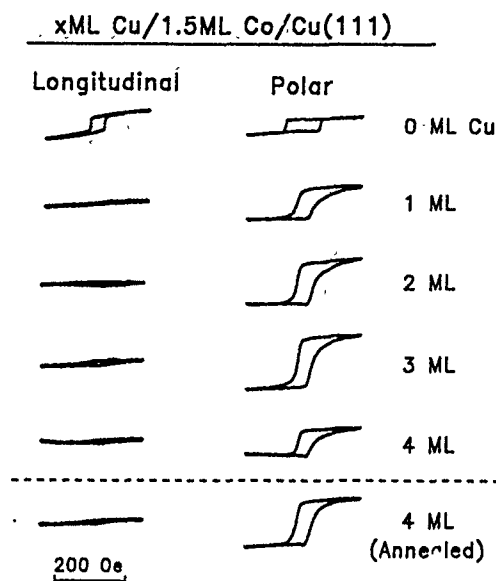


FIG. 1. Longitudinal (in-plane) and polar (perpendicular) hysteresis loops of x ML Cu/1.5 ML Co/Cu(111) measured at room temperature ($x=0,1,2,3,4$). The loops under the dashed line are for the 4 ML Cu/1.5 ML Co/Cu(111) film after annealed to 600 K.

increasing film thickness. A balance between these competing anisotropies determines the overall direction of the magnetization of the film. The Cu overlayers provide a second interface, which increases the surface anisotropy and orient the spins perpendicular to the film plane.

Also shown in Fig. 1 is the annealing effect on the thin film anisotropy. For the same Co film with 4 ML of a Cu overlayer, the perpendicular loop is much larger after annealing to 600 K. Similar results have also been observed in Fe-Pd alloy films.¹² The similarity between annealing and Cu capping suggests that annealing causes Cu segregation on top of Co to form an overlayer,¹³ and hence changes the surface anisotropy. In addition, annealing changes the microstructure of the film, such as roughness and lattice mismatch-

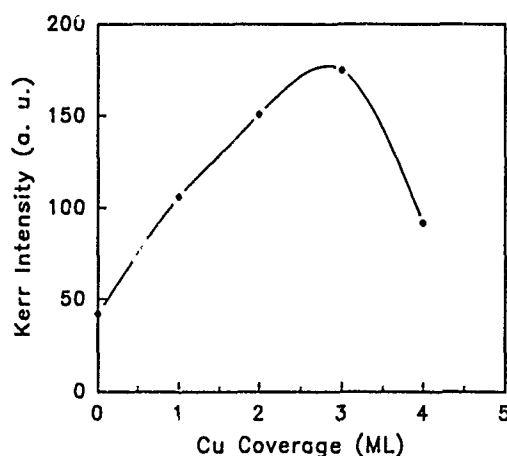


FIG. 2. Polar Kerr Intensity of x ML Cu/1.5 ML Co/Cu(111) films as a function of Cu overlayer thickness x , showing the enhancement of perpendicular magnetization by Cu capping.

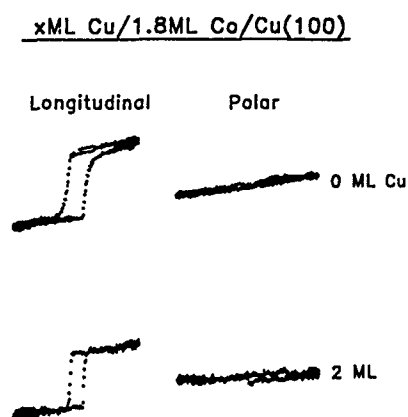


FIG. 3. Longitudinal and polar hysteresis loops of 1.8 ML Co/Cu(100) measured at 150 K before and after the coverage of 2 ML of Cu.

induced strains, which can give rise to a modified magnetocrystalline and magnetoelastic surface anisotropy.¹⁴

This is in sharp contrast to the same experiment on Cu(100) shown in Fig. 3, where the hysteresis loops of a 1.8 ML Co film are compared before and after 2 ML of Cu coverage. The magnetization of ultrathin Co films on Cu(100) lies in plane. Cu capping has little effect on both parallel and perpendicular loops. This is consistent with the Brillouin light scattering measurements,¹⁵ which showed that Cu capping can increase the perpendicular surface anisotropy (k_s from -0.46 to 0.15 erg/cm²) for the Co films on Cu(100) at thicknesses larger than $d_C \sim 2$ ML. However, below d_C , where the uncovered Co films already have positive k_s , it remains nearly the same after Cu capping.

The [111] direction is the easy axis for a bulk Co crystal. Thin films of Co grown on (111) FCC surfaces have a much stronger perpendicular anisotropy than those grown on the (100) surfaces due to magnetocrystalline anisotropy. For example, the magnetization of Co was found to experience a crossover from perpendicular to in plane at about 1–2 ML on Pd(100) and at 6 ML on Pd(111).¹⁶ Cu capping generally enhances the perpendicular anisotropy, but this change could be small compared with the strong in-plane anisotropy on the (100) surface.

Figure 4 shows the magnetic phase transition behavior of a 1.5 ML of Co on Cu(111), comparing before and after Cu capping. For the uncovered film (solid circle), the Kerr intensity was taken from the in-plane hysteresis loops. Fitting to the power law $M \sim (1 - T/T_C)^\beta$ gives $\beta = 0.15 \pm 0.05$. Although it is close to the Ising β value of 0.125, this is by no means an ideal Ising system, due to the presence of both in-plane and perpendicular anisotropy, and the pronounced finite size rounding above T_C (Fig. 4). The Cu-capped same Co film (open circle) displays a strong perpendicular anisotropy. However, the polar Kerr intensity now decreases linearly with increasing temperature. The linear decrease of magnetization with temperature is often associated with the formation of islands and clusters, which exhibit superparamagnetic behavior over a broad range of temperature and cluster sizes.^{17,18} These superparamagnetic islands and lateral inhomogeneities lead to a fast linear decrease at lower tem-

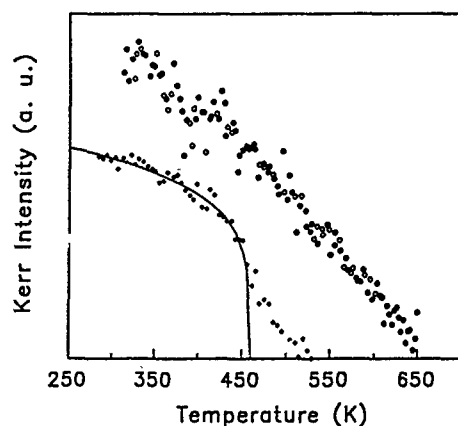


FIG. 4. Kerr intensity as a function of temperature comparing the 1.5 ML Co/Cu(111) film (●, longitudinal) and the same film but covered by 4 ML of Cu (○, polar). The solid line is the power law fit with $T_c=460$ K and $\beta=0.15$.

peratures. Similar results have also been reported in Mössbauer studies.^{19,20}

These results are very different from those reported in Ref. 1, which showed that the magnetic phase transition of a monolayer Co follows the exact Ising behavior. The Co film, quite different from our single crystal Co films, was prepared on the polycrystalline Cu(111) grains grown on sapphire (11 $\bar{2}$ 0) surface then coated with Cu before taken out to the air for the torsion oscillation magnetometry measurements. Although we cannot say for sure what has caused or destructed the Ising character, the different film surface and interface microstructure is certainly playing an important role in determining the magnetic critical behavior. More experiments are underway to study the structure-property relationships.

SUMMARY

We have observed a dramatic enhancement of the uniaxial perpendicular anisotropy by depositing Cu overlayers on Co films on Cu(111). One monolayer of Cu on top of a 1.5 ML Co(111) film can raise the perpendicular magneti-

zation by a factor of 3, reduce the coercivity by a factor of 2, and eliminate the in-plane magnetization completely. Annealing has the similar effect to Cu capping on anisotropy due to changes in film microstructure and copper segregation at the free surface. The anisotropy change induced by Cu overlayers is small for Co films on Cu(100). The uncovered film exhibits a power law behavior with $\beta=0.15\pm0.05$, in contrast to the linear temperature dependence of magnetization for the Cu-capped same film. These results emphasize the dramatic role of the interface properties in determining the magnetic behavior of magnetic superlattices and sandwich systems.

ACKNOWLEDGMENT

This work is supported by National Science Foundation Grant No. DMR 9121736.

- ¹J. Kohlhepp, H. J. Elmers, S. Cordes, and U. Gradmann, *Phys. Rev. B* **45**, 12 287 (1992).
- ²J. G. Gay and R. Richter, *Phys. Rev. Lett.* **56**, 2728 (1986).
- ³M. T. Kief and W. F. Egelhoff, Jr., *J. Appl. Phys.* **73**, 6195 (1993).
- ⁴C. Liu and S. D. Bader, *J. Appl. Phys.* **67**, 5758 (1990).
- ⁵Y. Li and K. Baberschke, *Phys. Rev. Lett.* **68**, 1208 (1992).
- ⁶C. Chappert, K. Le Dang, P. Beauvillain, H. Hurdequint, and D. Renard, *Phys. Rev. B* **34**, 3192 (1986).
- ⁷H. J. G. Draaisma, J. M. De Jonge, and F. J. A. den Broeder, *J. Magn. Magn. Mat.* **66**, 351 (1987).
- ⁸B. N. Engel, M. H. Wiedmann, R. A. Van Leeuwen, and C. M. Falco, *J. Appl. Phys.* **73**, 6192 (1993).
- ⁹M. T. Johnson, J. J. de Vries, N. W. E. McGee, J. aan de Stegge, and F. J. A. den Broeder, *Phys. Rev. Lett.* **69**, 3575 (1992).
- ¹⁰B. P. Tonner, Z. L. Han, and J. Zhang, *Phys. Rev. B* **47**, 9723 (1993).
- ¹¹Q. Chen, M. Onellion, and A. Wall, *Thin Solid Films* **196**, 103 (1991).
- ¹²F. Huang, G. J. Mankey, and R. F. Willis (unpublished).
- ¹³G. J. Mankey, M. T. Kief, and R. F. Willis, *J. Vac. Sci. Technol. A* **9**, 1595 (1991).
- ¹⁴P. Bruno and J.-P. Renard, *Appl. Phys. A* **49**, 499 (1989).
- ¹⁵P. Krams, F. Lauks, R. L. Stamps, B. Hillebrands, and G. Güntherodt, *Phys. Rev. Lett.* **69**, 3674 (1992).
- ¹⁶F. J. A. den Broeder, D. Kuiper, H. C. Donkersloot, and W. Hoving, *Appl. Phys. A* **49**, 507 (1989).
- ¹⁷D. C. Douglass, A. J. Cox, J. P. Bucher, and L. A. Bloomfield, *Phys. Rev. B* **47**, 12 874 (1993).
- ¹⁸S. N. Khanna and S. Linderroth, *Phys. Rev. Lett.* **67**, 742 (1991).
- ¹⁹G. Bayreuther, *J. Magn. Magn. Mat.* **38**, 273 (1983).
- ²⁰E. Mauri, D. Scholl, H. C. Siegmann, and E. Kay, *Phys. Rev. Lett.* **62**, 1900 (1989).

Local spin-density theory of interface and surface magnetocrystalline anisotropy: Pd/Co/Pd(001) and Cu/Co/Cu(001) sandwiches

Ding-sheng Wang,^{a)} Ruqian Wu, and A. J. Freeman

Department of Physics and Astronomy, Northwestern University, Evanston, Illinois 60208-3112

The interface magnetocrystalline anisotropy (MCA) of Cu/Co/Cu(001) and Pd/Co/Pd(001) sandwiches are investigated, employing our recently developed state tracking approach based on the full potential linearized augmented plane wave energy band method. The strong negative MCA energy for the Co monolayer is found to be decreased for Co/Cu, and even becomes positive for Co/Pd due to the interfacial hybridization, which reduces the spin orbit coupling (SOC) between the $d_{xz,yz} - d_{z^2}$ pair at \bar{M} .

Although some first principles calculations of the magnetocrystalline anisotropy (MCA) energy for interfacial systems have been carried out (e.g., for X/Co/X(111) with X=Cu, Ag, and Pd¹), a simple physical picture has not been provided due to the strong numerical random fluctuations in the results (with respect to both the occupation and number of k points).² Based on our recently proposed state tracking approach³ and the full potential linearized augmented plane wave (FLAPW) method, we found a close relationship between the MCA energy and the electronic structure for reduced symmetry systems. The strong negative MCA energy of the Co monolayer,⁴ for example, results mainly from the spin-orbit coupling (SOC) perturbation between antibonding z^2 and bonding $xz(yz)$ states near \bar{M} .^{4,5} Interfacial hybridization was found to affect the MCA in the Co layer mainly via the reduction of the SOC perturbed energy between this pair by enlarging their energy separation (in Co/Cu)⁵ or by changing their occupancies (in Co/Pd).⁶

In this paper we discuss the calculated results of the MCA energy for Cu/Co/Cu(001) and Pd/Co/Pd(001) sandwiches and reveal the underlying physics. A five layer slab model is adopted to simulate the interfaces with the Co atom lying at the ideal position in the substrate lattices (without possible atomic relaxation). From the well-converged charge density and potential obtained through the semirelativistic FLAPW calculations, the SOC induced change of the total energy is derived from a second variational procedure,³ i.e., based on a force theorem⁷ and the state tracking approach.³ Summation over 66 k points in the $\frac{1}{8}$ irreducible two-dimensional BZ (corresponding to 400 k points in the full BZ) is found to be sufficient to provide stable MCA energies.

It is well known that the MCA is determined by the SOC interaction between the occupied and the empty valence states (3d for Co). Due to the lowered symmetry at surfaces and interfaces, the MCA energy depends on the second-order perturbation of the SOC Hamiltonian ($H^{\text{SOC}} = \xi \mathbf{s} \cdot \mathbf{L}$). Therefore, any coupling through $L_{x,y}(L_z)$ will favor the in-plane (perpendicular) MCA. For the free-standing Co monolayer, the coupling (through $L_{x,y}$) between the $d_{xz,yz}$ bonding and the d_{z^2} antibonding states dominates around \bar{M} and most parts of the BZ—resulting in a strong negative MCA energy (−1.35 eV/atom).

Upon contact with a nonmagnetic substrate at the interface, the energies and the wave functions of the Co- d_{z^2} and Co- $d_{xz,yz}$ states (both point out of the plane) will be changed by the interfacial hybridization. Figure 1 presents the energy positions of the hybridized states at \bar{M} for Cu/Co/Cu(001) and Pd/Co/Pd(001) sandwiches and their components projected back to the states for the free-standing Co monolayer. For the Cu/Co/Cu system, the out-of-plane $d_{xz,yz}$ states is pulled down by the Cu d bands, while the Co- d_{z^2} state remains almost unaffected, since it separates far from the Cu- d bands in energy. By contrast, at the Co-Pd interface, both Co- $d_{xz,yz}$ and Co- d_{z^2} states are strongly affected. A substantial component (53%) the Co- $d_{xz,yz}$ wave function is now in the hybridized states, which are shifted upward by about 0.7 eV—already lying slightly above E_F .

These hybridizations are expected to affect the strength of the SOC perturbation between the Co- $d_{xz,yz}$ and the Co- d_{z^2} states, and thus the MCA energy. Figure 2 gives the band filling dependences of the MCA energies for the Cu/Co/Cu and Pd/Co/Pd sandwiches. For comparison, the MCA energy of a free-standing Co monolayer is also shown in Fig. 2, which exhibits the band filling dependence typical for 3d transition metal monolayers.³ It is characterized by the strong

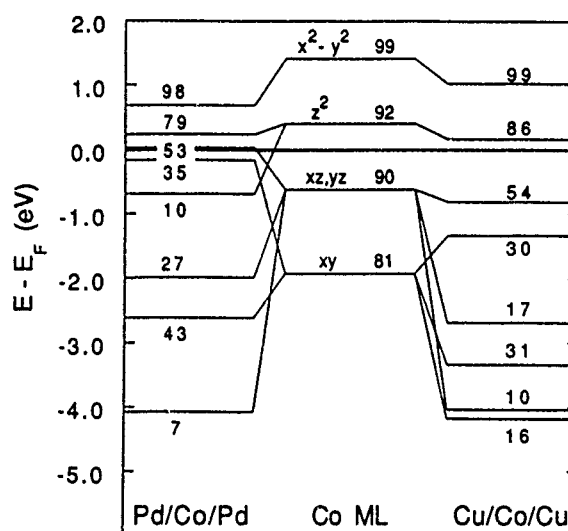


FIG. 1. Comparison of the effect of the Co-Pd and Co-Cu interface on the Co- d electron states at \bar{M} . Numbers are the percentage of the Co- d component inside the Co muffin-tin spheres.

^{a)}Present address: Institute of Physics, Academia Sinica, Beijing 100080, China.

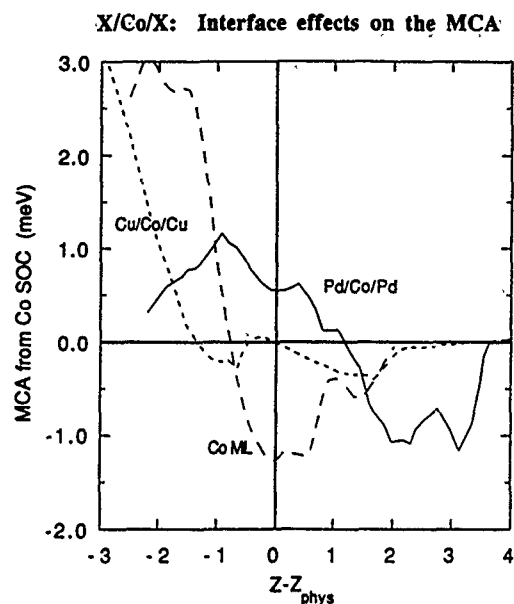


FIG. 2. Comparison of the effect of the Co-Pd and Co-Cu interface on the MCA contribution calculated when only the SOC inside the Co muffin-tin spheres is included. Results are plotted as a function of the number of valence electrons by employing a rigid band approximation. Long-dashed, short-dashed, and solid lines are for Co ML, Cu/Co/Cu, and Pd/Co/Pd sandwiches, respectively. (A Gaussian broadening with full width of 40 meV was employed.)

negative peak at about half-occupation of the spin-down d band and a change of the MCA sign at a slightly smaller occupation.

Obviously, for Pd/Co/Pd the negative peak of the MCA is still as strong as for a free-standing monolayer, but its position has been largely shifted to the larger band filling region. This behavior is caused mostly by the change of the upward shift of the out-of-plane $d_{xz,yz}$ bands (cf. Fig. 1) into the empty part, and thus the reduction in the negative MCA energy results from the SOC (through L_x) between the Co- d_{z^2} and Co- $d_{xz,yz}$ states. As a result, a positive MCA energy for Pd/Co/Pd, 0.55 meV (only SOC for a Co atom), is achieved at the physical value of band filling. This behavior is in some sense very similar to the origin of the positive MCA energy for a free standing Fe monolayer⁸ according to the relative position of the $d_{xz,yz}$ states, with respect to E_F . In the case of a free standing Fe monolayer, the $d_{xz,yz}$ is empty because there is one less electron/atom, but for the Co/Pd interface, it is due to the upward shift of the bonding Co- $d_{xz,yz}$ states.

This behavior is in clear contrast to the behavior of the Co-Cu interface, where only the magnitude of the negative MCA energy peak is greatly reduced, and the change of MCA sign is shifted to the region with lower band filling (short dashed line in Fig. 2) due to the downward shift of the out-of-plane bonding bands. This is expected, since, as shown in Fig. 1, the Co- $d_{xz,yz}$ state is drawn down by the lower-lying Cu- d bands, while the Co- d_{z^2} state remains almost unaffected.

Now it is clear that the effects of the nonmagnetic substrates on the MCA in the Co layer arise mainly from the

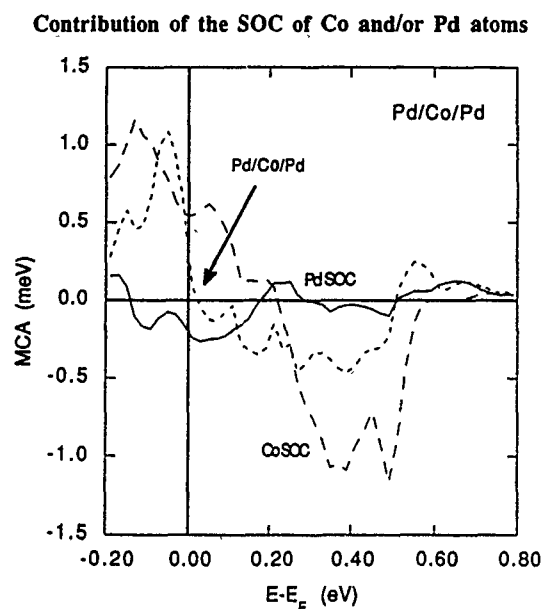


FIG. 3. MCA of the Pd/Co/Pd(001) sandwich (solid line), and the contribution of the Co SOC (long dashed line) and the contribution (per Pd atom) of the Pd SOC, plotted as a function of the highest occupation energy. (A Gaussian broadening with a full width of 40 meV was employed.)

hybridization with the Co- d_{z^2} and Co- $d_{xz,yz}$ states. Obviously, also as revealed in an effective ligand interaction model (ELIM),⁵ (i) the energy separation between the Co and substrate d bands; and (ii) the strength of the interfacial hybridization play the key roles in determining the MCA energy. The stronger the hybridization, the more the perpendicular MCA prevails. This explains the difference between two groups of substrates on the Co MCA (i.e., perpendicular MCA with Pd, Au, and Ir, and in-plane MCA with Cu and Ag).

Finally, beyond the effects of the chemical interaction discussed above, the SOC in the substrate may also affect the MCA in the magnetic layer. In the Cu/Co/Cu sandwich, the spin-polarization of the Cu bands is small, and thus the effects of the SOC in Cu muffin-tin spheres are negligible.⁵ However, in the case of Co-Pd, the strong exchange interaction produces an appreciable spin-polarization at the Pd sites ($M=0.20-0.37\mu_B$). Meanwhile, as is known, the SOC constant, ξ , of the heavier Pd atom is about three times larger than that for Co. Therefore, the contribution to the MCA of the substrate Pd atoms becomes comparable with that from the SOC in the Co layer.

The results of the MCA contribution (per Pd atom) calculated with only the SOC of the Pd atoms is given in Fig. 3. Although the magnitude of this contribution is still smaller than that from the Co SOC, it is obviously not negligible, as in the case of the Cu substrate. Since in the structure employed each unit cell contains four Pd atoms (versus one Co atom), the contribution from the Pd SOC becomes even more prominent in determining the total MCA (per unit cell). The total MCA calculated with the SOC in both Co and Pd muffin-tin spheres is also shown in Fig. 3. It is seen to be not simply the sum of the two contributions obtained by including the Co or Pd SOC separately, because the MCA comes

from the second-order SOC perturbation, and so cross terms should also exist. Note that the general trend of the variation of the total MCA with respect to the band filling follows approximately the curve of the contribution from the Co SOC only. This shows that the magnetic Co layer plays the most important role in determining the MCA behavior of this interface, although inclusion of the Pd SOC does make a difference. The resultant MCA becomes 0.23 meV (per unit cell) compared to 0.55 meV when only the Co SOC is considered.

The work at Northwestern was supported by the National Science Foundation (Grant No. DMR 91-17818 and a grant of computer time at the Pittsburgh Supercomputing

Center through its Division of Advanced Scientific Computing). One of us (DSW) acknowledges the support of the National Science Foundation of China.

- ¹G. H. O. Daalderop, P. J. Kelly, and M. F. H. Schuurmans, *Phys. Rev. B* **42**, 7270 (1990).
- ²R. Richter and J. G. Gay, *Mat. Res. Soc. Symp. Proc.* **151**, 3 (1989).
- ³D. S. Wang, R. Wu, and A. J. Freeman, *Phys. Rev. Lett.* **70**, 869 (1993).
- ⁴D. S. Wang, R. Wu, and A. J. Freeman, *J. Appl. Phys.* **73**, 6745 (1993).
- ⁵D. S. Wang, R. Wu, and A. J. Freeman, *J. Magn. Magn. Mat.* **129**, 237 (1994).
- ⁶D. S. Wang, R. Wu, and A. J. Freeman, *Phys. Rev. B* **48**, 15 886 (1994).
- ⁷M. Weinert, R. E. Watson, and J. W. Davenport, *Phys. Rev. B* **32**, 2115 (1985), and references therein.
- ⁸D. S. Wang, R. Wu, and A. J. Freeman, *Phys. Rev. B* **47**, 14 932 (1993).

Perpendicular magnetic anisotropy in $\text{Co}_x\text{Pd}_{1-x}$ alloy films grown by molecular beam epitaxy

J. R. Childress, J. L. Duvail, S. Jasmin, A. Barthélémy, and A. Fert
Laboratoire de Physique des Solides, Université Paris-Sud, 91405 Orsay Cédex, France

A. Schuhl, O. Durand, and P. Galtier
Laboratoire Central de Recherches, THOMSON-CSF, Domaine de Corbeville, 91404 Orsay, France

We have grown face-centered cubic (FCC) (111)- and (001)-oriented $\text{Co}_x\text{Pd}_{1-x}$ alloy films ($x \approx 0.20$ – 0.25) by molecular beam epitaxy on (111)Si and (001)MgO substrates, respectively, with thicknesses ≈ 200 – 1000 Å. Magnetization (SQUID) measurements show that both (111) and (100) films present a perpendicular easy axis, indicating that a strong magnetic anisotropy overcomes the demagnetizing field favoring the in-plane orientation. We have studied this magnetic anisotropy by combining SQUID and torque measurements. Our experimental results cannot be accounted for by only invoking the magnetocrystalline anisotropy of a disordered solid solution of Co in FCC Pd, and rather indicate an anisotropic distribution of Co in the Pd host.

There has been significant interest in the use of Co/Pd multilayers for magneto-optic recording, due to the observed perpendicular magnetization of ultrathin Co layers, and the large magneto-optical Kerr rotation measured in these materials.¹ More recently, it has been found that Co–Pd alloys, deposited by evaporation, electrodeposition, or sputtering with a (111) texture, also display perpendicular anisotropy and a large magneto-optical constant.^{2–5} Whereas the origin of perpendicular anisotropy in Co/Pd multilayers is usually attributed to magnetic interface anisotropy, the source of anisotropy in Co–Pd alloys has not been fully explained. In this paper, we present the fabrication and study of Co–Pd alloys fabricated, for the first time, using molecular beam epitaxy (MBE). The advantage of the MBE approach is to allow the simultaneous study of films prepared in various orientations, using different single-crystal substrates. In this manner, the dependence of the magnetic anisotropy on crystalline orientation can be explored.

Samples were grown by MBE onto single-crystal (111)Si or (100)MgO substrates, with substrate temperatures $T_s \approx 80$ °C, using separate effusion cells for Pd and Co. The growth rate of the alloy films was ≈ 6 Å/min. (111)Si substrates were cleaned chemically prior to their introduction in the vacuum, and deoxidized by heating above 800 °C in ultrahigh vacuum (UHV). Prior to the deposition of Co–Pd, a 75 Å-thick buffer layer of (111)Ag was deposited, primarily to prevent a chemical reaction of the alloy with the substrate. In the case of (100)MgO, substrates were cleaned in UHV by heating to 450 °C for 20 mins. A 15 Å Fe buffer layer was then deposited at 80 °C, to provide a flat (100) surface for the growth of the alloy.

Figure 1(a) shows the 10 keV reflection high-energy electron diffraction (RHEED) pattern obtained after growth of a 600 Å-thick nominal $\text{Co}_{0.25}\text{Pd}_{0.75}$ sample on (111)Si. This pattern, which upon rotation is found to be sixfold symmetric in the plane of the sample, is characteristic of epitaxial growth, at least over lateral distances greater than the electron coherency length (a few hundred Å). The broadening of the lines and slightly diffuse background indicates contributions from misoriented regions in the sample. The θ – 2θ x-ray diffraction pattern of this sample is shown in Fig. 2(a), where it can be seen that the main contribution to the

diffraction (besides the Si substrate) is the face-centered cubic (FCC) (111) peak of the alloy. The peak shape is slightly asymmetric, suggesting a slight distribution of Co concentrations within the area sampled by the x-ray beam, or a distribution of lattice constants due to epitaxial strain near the Ag/CoPd interface. The position of the peak maximum yields a lattice spacing of $a = 3.826$ Å, which corresponds to a Co concentration of 19 at. %, assuming a linear deviation from the bulk Pd parameter (3.890 Å) toward the bulk FCC Co parameter (3.544 Å). The electron diffraction pattern of this sample, obtained in cross section, is shown in Fig. 1(b). In addition to the bulk Si contributions, one clearly sees a strong contribution (#1) along the growth axis, which is related to the (111) FCC peak of the Co–Pd alloy. We also observe additional weak off-axis contributions (#2) from (200) and (111) peaks. Their existence and position indicate that part of the sample is well crystallized with its $\langle 110 \rangle$ FCC axis parallel to the $\langle 110 \rangle$ axis of Si. A detailed analysis of these contributions reveal that this part of the alloy is twinned along the $\langle 111 \rangle$ FCC growth axis. Finally, a close examination of the pattern reveal other contributions (#3), which are randomly located in a circle corresponding to the

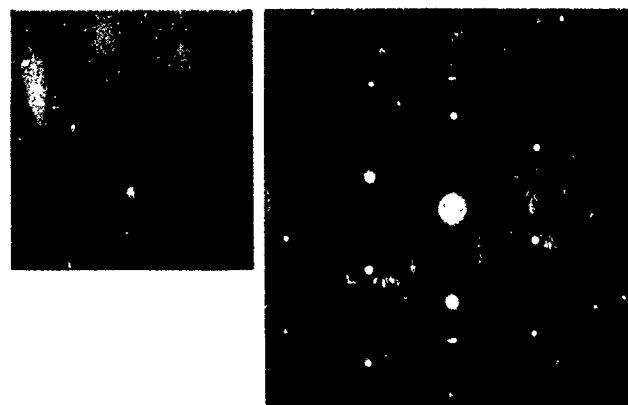


FIG. 1. (a) RHEED pattern obtained after deposition of a 600 Å film of $\text{Co}_{0.25}\text{Pd}_{0.75}$ on (111)Si with a Ag buffer layer. (b) Electron diffraction pattern of the same sample, obtained in a cross section, along the $\langle 110 \rangle$ axis of Si. The strongest peaks originate from the substrate, while the weaker ones are related to the alloy (see the text for details).

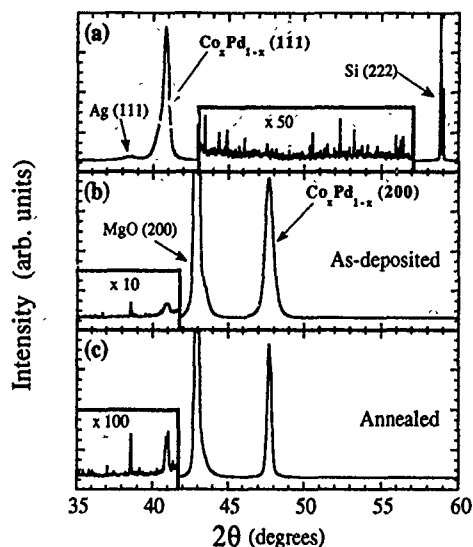


FIG. 2. (a) The θ - 2θ x-ray diffraction pattern of a (111)-oriented $\text{Co}_{0.25}\text{Pd}_{0.75}$ alloy, using $\text{Cu } K_\alpha$ radiation. The $\text{Ag}(111)$ peak comes from the Ag buffer and cap layers. (b) X-ray diffraction pattern of as-deposited (001)-oriented $\text{Co}_{0.25}\text{Pd}_{0.75}$ alloy film grown on (100)MgO. The shoulder to the right of the MgO peak is due to unfiltered substrate scattering due to the Compton effect. (c) The same (001)-oriented film after vacuum annealing at 600 °C for 2 h and rapid quenching to room temperature. The expanded views in (b) and (c) show (111) contributions, which are negligible. The other small sharp peak is due to the substrate.

(200) FCC contribution. This demonstrates that, in addition to the epitaxial structure, regions in the sample display a polycrystalline character. This may be related to the average grain size, which is only 500 Å in diameter, as observed in cross-sectional TEM imaging of the sample.

Figure 3 shows the magnetic hysteresis loops obtained at $T=15$ K for the same (111) $\text{Co}_{0.25}\text{Pd}_{0.75}$ alloy, with the field applied both in plane and out of plane of the sample. It is clear that the easy direction of magnetization is oriented out of the plane, with an anisotropy field of about 15 kOe. The coercive field is about 2 kOe, the saturation magnetization is 630 ± 30 emu/cm³, and the perpendicular remanence is about 88% of saturation.

The origin of this anisotropy, which is stronger than the demagnetization energy $2\pi M_s^2 \approx 2.5 \times 10^6$ erg/cm³, can be

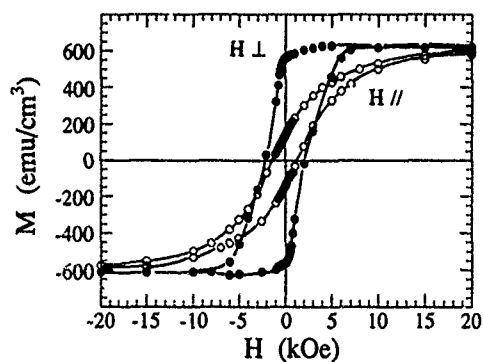


FIG. 3. Hysteresis loop at $T=15$ K of a 600 Å-thick, (111)-oriented $\text{Co}_{0.25}\text{Pd}_{0.75}$ alloy film, with the applied field H parallel (\parallel , open circles) and perpendicular (\perp , filled circles) to the plane of the film.

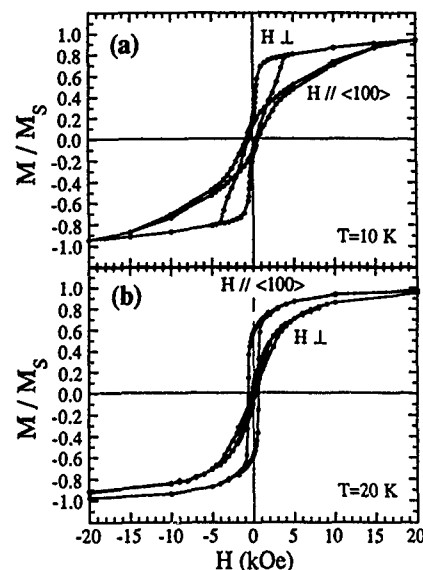


FIG. 4. (a) Hysteresis loops, with the applied field H parallel (\parallel , open circles) and perpendicular (\perp , filled circles) to the plane of the film, of (a) an as-deposited 800 Å-thick (001)-oriented $\text{Co}_{0.25}\text{Pd}_{0.75}$ alloy film, and (b) the same film after vacuum annealing at 600 °C for 2 h and rapid quenching to room temperature.

tentatively explained in several ways. At low Co concentrations, Co-Pd alloys are known to have large negative anisotropy constants K_1 and K_2 , resulting in a $\langle 111 \rangle$ easy axis.⁶ However, in a (111)-oriented single-crystal film there are, in addition to the perpendicular $\langle 111 \rangle$ axis, three other equivalent $\langle 111 \rangle$ axes at an angle of about 70° with the vertical axis, which are favored because they also reduce the shape anisotropy energy. Therefore, the expected remanence in a perfect single-crystal sample would be only about 34%. However, as shown in the electron diffraction [Fig. 2(b)], we have observed twinning of the crystal, as well as some polycrystalline contributions. In samples where the grains are small enough and oriented differently from grain to grain, exchange stiffness does not allow the magnetization to be ori-

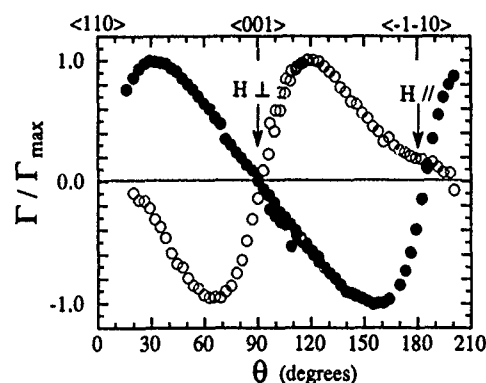


FIG. 5. Variation of the torque Γ as a function of the angle Θ between the applied field and the $\langle 110 \rangle$ axis, with rotations about $\langle -1, 1, 0 \rangle$, for as-deposited 800 Å-thick (001)-oriented $\text{Co}_{0.25}\text{Pd}_{0.75}$ alloy film (filled circles), and the same film after vacuum annealing at 600 °C for 2 h and rapid quenching to room temperature (open circles). Note that positive (negative) Γ for $0 < \Theta < 90^\circ$ corresponds to perpendicular (in-plane) anisotropy.

ented differently from grain to grain, thus favoring the $\langle 111 \rangle$ axis which is perpendicular to the film plane. With grain sizes of about 500 Å in the present sample, we cannot exclude such a possibility.

A second possible explanation for the perpendicular anisotropy is the combination of growth-induced strains, together with large magnetostriction coefficients λ_{111} reported for Co-Pd alloys.⁷ It is difficult to accurately determine the residual strains, and it is unlikely that significant strains can be sustained in these thick epitaxial films. A generous estimate may be made by considering the epitaxial strain due to the Ag/CoPd interface (8% mismatch), and assuming the classical (i.e., inversely proportional to the distance from the interfaces) relaxation to the expected bulk structure. This yields an average strain of 0.32%, which results in a significant strain-induced anisotropy energy $\approx 2.3 \times 10^6$ erg/cm³, but that is still less than one-quarter of the magnitude of the anisotropy that we have obtained from torque experiments ($\approx 9 \times 10^6$ erg/cm³).

The formation of ordered phases in Co-Pd and Co-Pt alloys has also been extensively discussed. In particular, the tetragonal $L1_0$ phase of $\text{Co}_{0.50}\text{Pd}_{0.50}$ (Ref. 8) or $\text{Co}_{0.50}\text{Pt}_{0.50}$ (Ref. 9) is uniaxial and can be at the origin of a uniaxial magnetic anisotropy, but the compositions of our samples are far from such a 50-50 alloy. The ordered phase of $\text{Co}_{0.25}\text{Pd}_{0.75}$ (close to the composition of the films studied here) is of the cubic $L1_2$ type, and cannot, by itself, produce an uniaxial anisotropy. However, this ordered phase has recently been identified in $\text{Co}_{0.25}\text{Pt}_{0.75}$ alloys with perpendicular anisotropy, suggesting that interfaces between ordered and disordered phases may provide the required symmetry breaking.¹⁰ The $L1_2$ phase has also been suggested as responsible for the perpendicular anisotropy in (111) Co/Pt multilayers, by taking into account the occurrence of atomic slip planes and the subsequent formation of oriented Co pairs.¹¹ We have thus far found no experimental evidence for the existence of the $L1_0$ or $L1_2$ phases in our samples. The final possible explanation is the existence of uniaxial short-range ordering of the Co atoms induced by the MBE growth (an explanation also suggested in the work of Weller *et al.*).² As discussed below, results obtained on (001)-oriented films are most easily explained in terms of short-range ordering of the Co-Pd alloys.

For (001)Co-Pd alloy films on (100)MgO, RHEED patterns again indicate a fully epitaxial growth mode, with the cubic axes of the alloy parallel to those of the MgO substrate and rotated by 45° with respect to the Fe seed layer. The x-ray diffraction spectrum obtained is shown in Fig. 2(b), where only the Co-Pd (200) FCC peak is observed, in addition to those due to the MgO substrate and the Fe seed layer. Furthermore, in-plane electron diffraction patterns (not shown) demonstrate the epitaxial growth of the alloy. In Fig. 4(a) we show magnetization curves for an as-deposited 800 Å-thick (001) $\text{Co}_{0.25}\text{Pd}_{0.75}$ film. The magnetization can be saturated more easily when the applied field is perpendicular to the film along the $\langle 001 \rangle$ axis. The perpendicular anisotropy is confirmed by torque measurements in which the field is rotated around the $\langle -110 \rangle$ axis, from $\langle 110 \rangle$ to $\langle -1-10 \rangle$, as shown in Fig. 5. The angular dependence of the torque is

approximately what is expected for uniaxial anisotropy, with an easy axis along the $\langle 001 \rangle$ perpendicular axis. The main point of the above results is that the perpendicular $\langle 001 \rangle$ axis is easier than the in-plane $\langle 100 \rangle$ and $\langle 010 \rangle$ axes, and this in spite of the additional demagnetizing field energy for the perpendicular orientation. Thus, our experimental results cannot be accounted for by the magnetocrystalline anisotropy of a perfectly disordered solid solution of Co in a non-distorted FCC Pd matrix.

As discussed above, if we rule out significant effects from lattice distortions, we have to consider some deviation from a disordered distribution of the Co atoms. To check that a disordered CoPd alloy does behave differently, we have vacuum annealed our (001) films at 600 °C for 2 h, and then quenched them rapidly to room temperature, which is the classic method to obtain disordered solutions.¹² The x-ray diffraction pattern [Fig. 2(c)] is essentially unchanged, except for a somewhat narrower linewidth. As can be seen from the magnetization curves after annealing [Fig. 4(b)], the magnetization is now saturated more easily by in-plane fields. Also, as shown in Fig. 5(b), there is an inversion of the torque curve, which is characteristic of the crossover from perpendicular to in-plane anisotropy (for the annealed sample, the in-plane anisotropy fields are about 7 kOe, consistent with a contribution from the demagnetization energy only). These experiments thus demonstrate that disordered alloy films do not exhibit perpendicular anisotropy, and that the results for the as-deposited samples are due to some short-range ordering of the magnetic Co atoms in the Pd matrix. Such anisotropic distributions can result from the in-plane mobility of the impinging atoms during the growth.

In conclusion, we have found a significant perpendicular anisotropy in both (111)- and (001)-oriented films of $\text{Co}_x\text{Pd}_{1-x}$ ($x \approx 0.25$) alloys grown by MBE. For (001)CoPd, the only possible explanation resides in short-range ordering of the Co atoms in the Pd matrix. For the (111) films, we cannot rule out that the perpendicular anisotropy arises from a large magnetocrystalline energy intrinsic to the disordered FCC phase (with $K_1 < 0$), but, in view of our results on (001) films, we are inclined to ascribe the anisotropy in this case also to short-range atomic ordering.

¹ B. N. Engel, C. D. England, M. Nakada, R. V. Leeuwen, and C. M. Falco, in *Science and Technology of Nanostructured Magnetic Materials*, edited by G. C. Hadjipanayis and G. A. Prinz (Plenum, New York, 1991), p. 181.

² D. Weller, H. Brandt, and C. Chappert, *J. Magn. Magn. Mat.* **121**, 461 (1993).

³ S. Tsunashima, K. Nagase, K. Nakamura, and S. Uchiyama, *IEEE Trans. Magn.* **25**, 3761 (1989).

⁴ S. Hashimoto, Y. Ochiai, and K. Aso, *J. Appl. Phys.* **66**, 4909 (1989).

⁵ R. Gontarz, L. Smardz, B. Szymanski, and P. Juzikis, *J. Magn. Magn. Mat.* **120**, 278 (1993).

⁶ D. M. S. Bagguley and J. A. Robertson, *J. Phys. F* **4**, 2282 (1974).

⁷ T. Tokunaga, M. Kohri, N. Kadomatsu, and H. Fujiwara, *J. Phys. Soc. Jpn.* **50**, 1411 (1981).

⁸ Y. Matsuo, *J. Phys. Soc. Jpn.* **32**, 972 (1972).

⁹ J. M. Sanchez, J. L. Moran-Lopez, C. Leroux, and M. C. Cadeville, *J. Phys. Condensed Matter* **1**, 491 (1989).

¹⁰ R. F. C. Farrow, R. H. Geiss, G. L. Gorman, G. R. Harp, R. F. Marks, and E. E. Marinero, *J. Magn. Soc. Jpn.* **17**, Sup. S1, 140 (1993).

¹¹ C. J. Chien, R. F. C. Farrow, C. H. Lee, C. J. Lin, and E. E. Marinero, *J. Magn. Magn. Mat.* **93**, 47 (1991).

¹² J. Crangle and W. R. Scott, *J. Appl. Phys.* **36**, 921 (1965).

In situ measurement of stress and surface morphology for Co/Pd multilayer films fabricated by rf sputtering

H. Takeshita, K. Hattori, Y. Fujiwara, K. Nakagawa, and A. Itoh

Department of Electronic Engineering, College of Science and Technology, Nihon University, Funabashi, Chiba 274, Japan

In this paper, we report the results of *in situ* measurements of stress and surface morphology for Co/Pd multilayer films deposited on glass substrate by rf sputtering. For the multilayer film sputtered in low Ar gas pressure at 10 mTorr, after more than 20 periods of Co/Pd deposition, the film is subjected to compressive stress, however, during the Co layer deposition, the value of the compressive stress is decreasing. For the film sputtered in high Ar gas pressure at 40 mTorr, the film is always subjected to tensile stress, and the value of the tensile stress in the film is increasing during the deposition of the Co layer. These changes in the stress during the Co deposition can be explained qualitatively by the difference in the lattice constants of Co and Pd at the interfaces. The surface morphology of the films observed by an atomic force microscope (AFM) in air shows that the surface of both films become rougher with increasing total film thickness. The surface roughness of the films deposited at 10 mTorr is smaller than that of the films deposited at 40 mTorr.

INTRODUCTION

Co based metallic multilayer films such as Co/Pt and Co/Pd with perpendicular magnetic anisotropy are currently investigated as a magneto-optical recording media.¹⁻⁶ One of the origins of the perpendicular magnetic anisotropy is stress-induced magnetic anisotropy.⁴

In this report, the results of *in situ* measurement of stress depend on the gas pressure for Co/Pd multilayer films deposited by rf sputtering, and the surface morphology observed by an atomic force microscope (AFM) are reported.

EXPERIMENTAL PROCEDURES

Films were deposited at room temperature on 150 μm thick, 3 cm long, and 0.8 cm wide glass substrates by rf sputtering. On the backside of the substrate, a reflecting Al layer (1000 Å) was deposited and an optical noncontact displacement detector⁷ was employed to measure the bending of the substrate, as shown in Fig. 1. The following sputtering conditions were used; back pressure is 4×10^{-7} Torr, Ar pressures are 10 and 40 mTorr, and applied rf power is 100 W. The purities of Co and Pd targets are 99.9%. Deposition rates are 0.39 Å/s for Co, 0.42 Å/s for Pd at Ar gas pressure 10 mTorr, and 0.66 Å/s for Co, 0.73 Å/s for Pd at 40 mTorr, respectively.

Assuming the thickness of the glass substrate is much larger than that of the whole film, and film structure is continuous, the average internal stress $\langle \sigma_{\text{int}} \rangle$ can be expressed by the following equation:

$$\langle \sigma_{\text{int}} \rangle = \frac{E_s \times t_s^2}{3(1 - \nu_s)L^2} \frac{d}{h}, \quad (1)$$

where E_s , ν_s , and t_s are Young's modulus, Poisson's ratio, and the thickness of the substrate, respectively. L is the length of the cantilever and h is the total film thickness. The displacement d is measured by using the optical noncontact displacement detector. Positive and negative values of d/h means that the film already deposited was subjected to a tensile and compressive stress, respectively.

EXPERIMENTAL RESULTS

The changes of the bending d and $\langle \sigma_{\text{int}} \rangle$ of the Co(4 Å)/Pd(30 Å) multilayer film with total thickness for $N=55-58$ periods during fabrication in low Ar gas pressure at 10 mTorr is shown in Fig. 2, where N means the number of periods of Co/Pd. The case of the film sputtered in high Ar gas pressure at 40 mTorr are also shown in Fig. 3.

For the multilayer film sputtered at 10 mTorr, d at the beginning of the film deposition is quite different from that at $N=55-58$. At the beginning of the deposition, Co/Pd film is subjected to tensile stress. After more than 20 periods, it changed to compressive stress. Even in the case for the total average stress is compressive, the change of d during Co deposition is positive for the case $N > 20$. It means that $\langle \sigma_{\text{int}} \rangle$ tends to change toward the tensile one by an incremental deposition of the Co layer. During Pd deposition for $N > 20$, the compressive stress increases over only a monoatomic layer of Pd, and it changed to decrease over a few monoatomic layers, and then it increases again, as shown in Fig. 2(b).

For the film sputtered in high Ar gas pressure at 40 mTorr, the film is always subjected to tensile stress and the change of $\langle \sigma_{\text{int}} \rangle$ during Co deposition is always positive, which means that the tensile stress has been enhanced by the

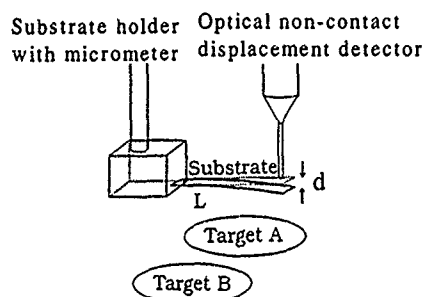


FIG. 1. Schematic representation of the cantilever method for measuring the bending of a substrate. d is the change of gap length between an optical noncontact displacement detector and a substrate.

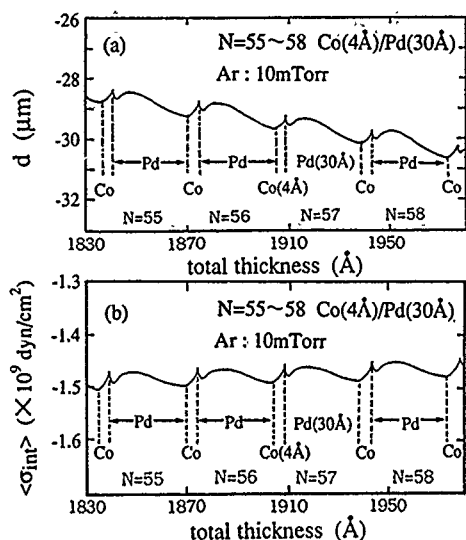


FIG. 2. (a) Substrate bending and (b) $\langle\sigma_{\text{int}}\rangle$ derived from Eq. (1), during the fabrication of $\text{Co}(4 \text{ \AA})/\text{Pd}(30 \text{ \AA})$ multilayer films at the periods $N=55-58$, by rf sputtering in low Ar gas pressure at 10 mTorr. Deposition rates: $\text{Co}=0.39, \text{Pd}=0.42 \text{ \AA/s}$.

incremental deposition of Co layers, as shown in Fig. 3(b). During the Pd deposition, $\langle\sigma_{\text{int}}\rangle$ decreases over a monoatomic layer of Pd.

The dependence of the surface morphology on the total film thickness observed by AFM in air. The results for the $\text{Co}(4 \text{ \AA})/\text{Pd}(30 \text{ \AA})$ multilayer films deposited under different Ar gas pressure (10 and 40 mTorr), are shown in Fig. 4 and Fig. 5, respectively. Structures like particles or columns can be observed at the surface of the films, and the average size of the particles is about 10 nm in diameter. The diameter becomes larger with increasing the total film thickness. These structures may be due to the influence of the initial island growth at the beginning of the deposition. It is

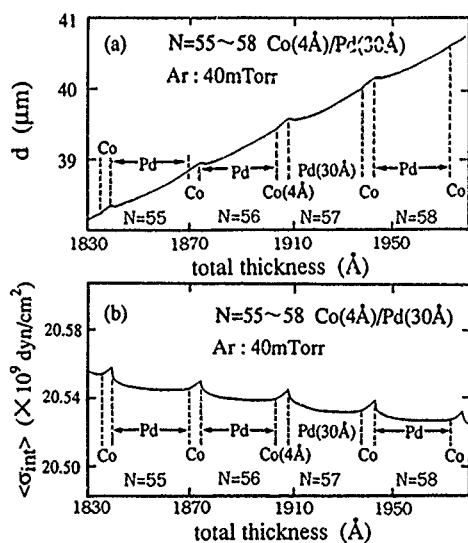


FIG. 3. (a) Substrate bending and (b) $\langle\sigma_{\text{int}}\rangle$ derived from Eq. (1), during the fabrication of $\text{Co}(4 \text{ \AA})/\text{Pd}(30 \text{ \AA})$ multilayer films at the periods $N=55-58$, by rf sputtering in high Ar gas pressure at 40 mTorr. Deposition rates: $\text{Co}=0.66, \text{Pd}=0.73 \text{ \AA/s}$.

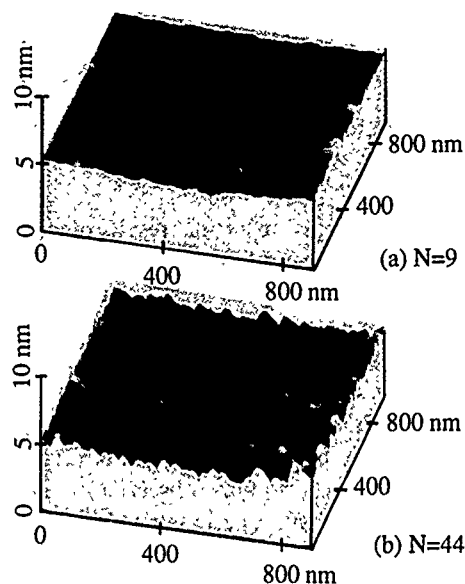


FIG. 4. AFM images for the different thickness of the $\text{Co}(4 \text{ \AA})/\text{Pd}(30 \text{ \AA})$ multilayer films deposited on glass substrate in Ar gas pressure at 10 mTorr.

observed that the surface roughness of the films deposited at 10 mTorr is smaller than that of the films at 40 mTorr. The surface of both films, however, become rougher with increasing the total film thickness.

DISCUSSION

One of the origins of the difference in the dependence of the stress on Ar gas pressure seen in Figs. 2(b) and 3(b), may be due to the structural difference caused by the energy difference of the sputtered atoms and/or the sputtering gas ions.

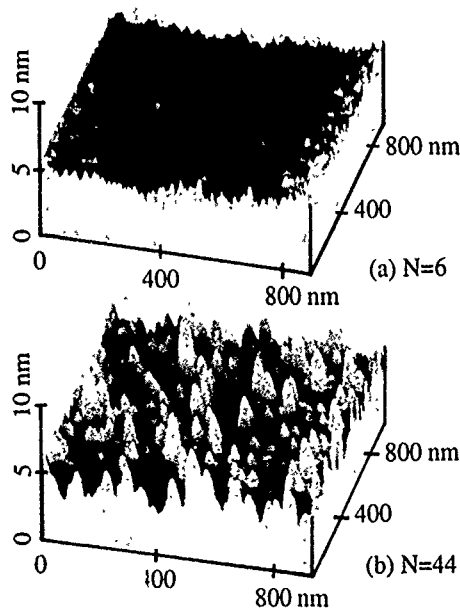


FIG. 5. AFM images for the different thickness of the $\text{Co}(4 \text{ \AA})/\text{Pd}(30 \text{ \AA})$ multilayer films deposited on a glass substrate in Ar gas pressure at 40 mTorr.

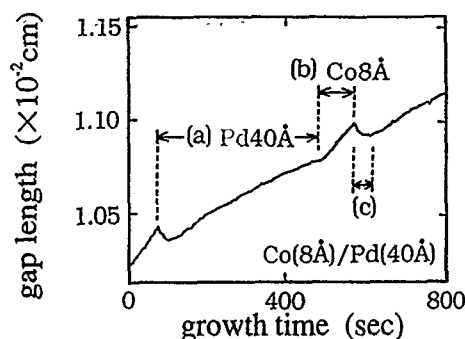


FIG. 6. Substrate bending during fabrication of the Co(8 Å)/Pd(40 Å) multilayer by ultrahigh vacuum evaporation. Deposition rates of Co and Pd are 0.1 Å/s.

In the case of the rough surface, such as the film deposited in a high Ar gas pressure at 40 mTorr, as seen in Fig. 5, surface tension is caused by the increase in the surface area compared with a perfectly flat surface. The surface tension makes tensile stress to the film. Bending of the substrate caused by the surface tension is presented by the following formula:

$$\Delta d = \frac{3L^2}{E_s \times t_s^2} \gamma \frac{\Delta S}{S}, \quad (2)$$

where γ is surface free energy of the film, S is the area of the flat surface, and ΔS is the amount of the difference in the area from the flat surface, respectively. In Eq. (2), the constriction of the substrate caused by Poisson's ratio was neglected, and it was assumed that the γ of the Co(4 Å)/Pd(30 Å) multilayer film is roughly equal to that of the Pd single crystal, because the difference in their layer thickness is large enough ($h_{Pd} \gg h_{Co}$).

The increase in the surface area compared with a perfectly flat surface, obtained from the AFM images of the films ($N=44$) deposited in Ar gas pressure at 10 and 40 mTorr, are about 0.3% and 10%, respectively. However, the values of bending estimated by Eq. (2) for the films are ten times smaller than the experimentally obtained ones.

An example of the *in situ* observation of d for the film deposited by the UHV evaporation method^{5,6} is shown in Fig. 6. The film thickness is about 1000 Å. Comparing Fig. 3(a) with Fig. 6, it is seen that the change of $\langle \sigma_{int} \rangle$ during the

fabrication by sputtering at high Ar pressure (40 mTorr) is similar to that of the case for the films deposited by UHV evaporation.

The changes of the $\langle \sigma_{int} \rangle$ during the deposition of each Co layer, and also in each one monoatomic layer of Pd just on Co deposited by using sputtering and UHV evaporation methods, are very similar to each other, as shown in Figs. 2(b), 3(b), and 6. The changes of $\langle \sigma_{int} \rangle$ by the incremental deposition of Co and Pd layers can be explained qualitatively by the difference in the lattice constants of Co and Pd at the interfaces.

CONCLUSION

By an incremental deposition of the Co layer, $\langle \sigma_{int} \rangle$ increases its tensile component for the both films deposited by sputtering and UHV evaporation, and it can be explained qualitatively by the difference in the lattice constants of Co and Pd.

The AFM observation shows that the surface of both films become rougher with increasing total film thickness. The surface roughness of the films deposited at 10 mTorr is smaller than that of the films at 40 mTorr. The difference in surface morphology should be connected to the difference of energy of atoms and may cause internal stress difference, however, the stress estimated from the surface free energy is much smaller than that obtained from this experiments.

ACKNOWLEDGMENTS

The authors thank Dr. T. Katayama and Dr. Y. Suzuki at Electrotechnical Laboratory for the useful discussions. This work was partially supported by a Grant-in-Aid for Scientific Research from the Ministry of Education, Science, and Culture, Japan.

¹P. F. Carcia, A. D. Meinhardt, and A. Suna, Appl. Phys. Lett. **47**, 178 (1985).

²H. J. C. Draaisma, F. J. A. den Broeder, and W. J. M. de Jonge, J. Magn. Magn. Mat. **66**, 351 (1987).

³S. Hashimoto, Y. Ochiai, and K. Aso, J. Appl. Phys. **66**, 4909 (1989).

⁴K. Nakamura, S. Tsunashima, S. Iwata, and S. Uchiyama, J. Magn. Soc. Jpn. **13**, 319 (1989) (in Japanese).

⁵H. Awano, Y. Suzuki, T. Yamazaki, T. Katayama, and A. Itoh, IEEE Trans. Magn. **MAG-26**, 2742 (1990).

⁶H. Awano, Y. Suzuki, T. Katayama, and A. Itoh, J. Appl. Phys. **68**, 4569 (1990).

⁷H. Akimoto, T. Sugimoto, K. Nakagawa, and A. Itoh, MORIS'92, J. Magn. Soc. Jpn. **17**, Suppl. S1, 52 (1993).

Temperature-dependent interface magnetism and magnetization reversal in Co/Pt multilayers

Z. S. Shan,^{a)} J. X. Shen, R. D. Kirby, and D. J. Sellmyer

Behlen Laboratory of Physics and Center for Materials Research and Analysis, University of Nebraska, Lincoln, Nebraska 68588-0111

Y. J. Wang

Institute of Physics, Chinese Academy of Sciences, 100080 Beijing, China

We report on the temperature dependence of the magnetic properties and interface magnetism of Co/Pt multilayers. The magnetic properties including magnetization and anisotropy change substantially as the temperature varies from 300 to 10 K for samples with Co layer thickness in the range from 3 to 7 Å. The interface anisotropy of about 0.38 erg/cm² is nearly independent of temperature. The magnetization reversal is dominated by domain wall motion for the thinner Co layers and dominated by nucleation for the thicker Co layers.

INTRODUCTION

Co/Pt multilayers have attracted much attention as possible magneto-optical recording media because of their large perpendicular anisotropy, large Kerr rotation at short wavelength, and high corrosion resistance.¹⁻⁵ However, aside from the study of magnetization by Bloemen *et al.*,⁶ very little work on the temperature dependence of the magnetic properties of this system has been presented. Recently, we have studied these properties and the magnetization reversal of Co/Pt, Co/Au, and Co/Pd multilayers. In this paper we report our studies on Co/Pt, and the results for Co/Au and Co/Pd will be published elsewhere.

EXPERIMENT

Co/Pt multilayers of the form $X \text{ ÅCo}/15 \text{ ÅPt}$ ($X=3, 4, 5, 7, 9, 12, 15$, and 20) were fabricated by sputtering on Si(111) substrates with a 200 ÅPt buffer layer. The sputtering rate and power for Co (DC gun) were $\sim 0.6 \text{ Å/s}$ and 20 W and for Pt (RF gun) were 1.1 Å/s and 40 W, respectively. The vacuum prior to sputtering was 1×10^{-7} Torr and the Ar pressure during sputtering was 5×10^{-3} Torr. All eight samples were prepared in one vacuum run to ensure the same preparation conditions.

Measurements of the hysteresis loops were carried out using an alternating gradient magnetometer (AGM) and SQUID from 300 to 10 K. The measured magnetic anisotropy was determined from the area between the perpendicular and parallel (in-plane) magnetization curves. The time decay of Kerr rotation was measured on the apparatus described in Ref. 7. Structural properties were analyzed with both small and large angle x-ray diffraction.

STRUCTURE

A small angle x-ray diffraction scan [see Fig. 1(a)] showed that the peaks corresponding to the multilayer structure appeared at the right positions and up to the fourth superlattice peak was observed for the thinnest Co layer sample ($X=3 \text{ Å}$). Therefore all samples have distinct interfaces.

Large angle x-ray diffraction [see Fig. 1(b)] showed a pronounced FCC (111) texture, with the main peak falling between the pure FCC Co(111) and Pt(111).

MAGNETIC PROPERTIES

Both perpendicular (H_{\perp} film plane) and parallel (H_{\parallel} film plane) hysteresis loops were measured from 300 to 10 K for all samples. The temperature dependences of magnetization, anisotropy, and polarization of Pt atoms are summarized as follows.

A. Temperature dependences of magnetizations

The temperature (or Co layer-thickness) dependences of saturation magnetization for $X=3, 4, 5, 7, 12$, and 20 Å (or $T=10, 100, 200$, and 300 K) are illustrated in Fig. 2(a) [or Fig. 2(b)]. The magnetization here is defined as the ratio of the measured moment to the Co mass, assuming that all the moment is from Co atoms. It is seen that (1) The samples with thinner Co layers show the stronger temperature dependence. As the temperature varies from 300 to 10 K, the saturation magnetization increases by 30, 20, 13, 6.7, and $\sim 2.4\%$ for $X=2, 4, 5, 7$, and 12 Å, respectively. We notice that the $X=12$ and 20 Å samples have essentially the same magneti-

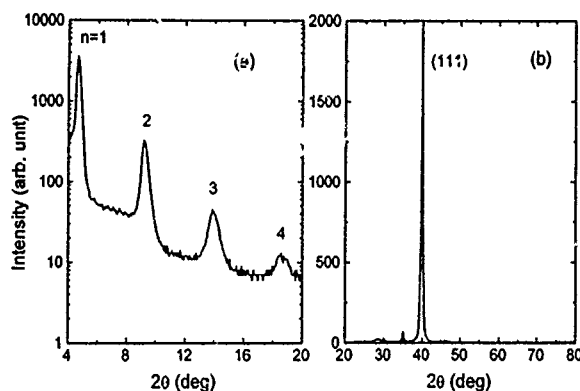


FIG. 1. CoK α (a) small-angle and (b) large-angle diffraction intensity for 3 ÅCo/15 ÅPt as a function of 2θ .

^{a)}Permanent address: Dept. of Electronic Engineering, Hangzhou University, Hangzhou, Zhejiang, People's Republic of China.

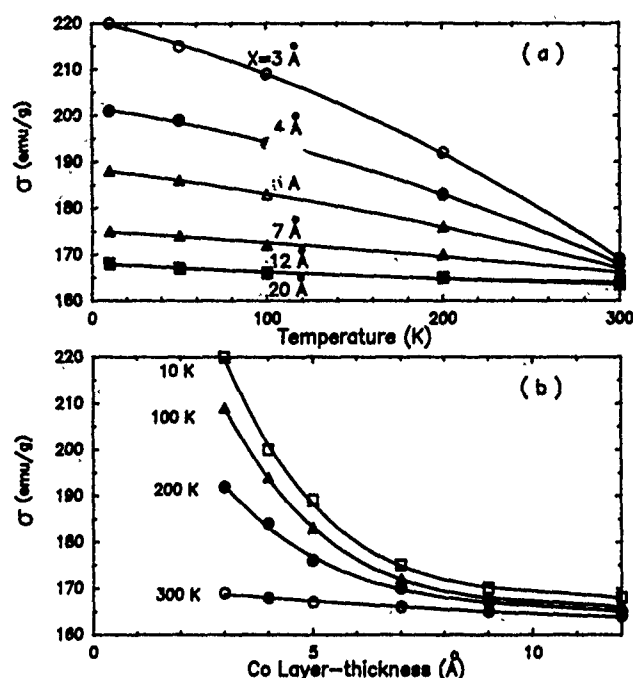


FIG. 2. Temperature dependence of Co saturation magnetization for (a) different Co layer-thickness and (b) layer-thickness dependence of Co saturation magnetization at different temperatures.

zations. (2) The Co layer-thickness dependence of magnetization becomes much stronger at the lower temperature [see Fig. 2(b)].

It is well known that the magnetization of pure Co is only weakly temperature dependent (σ_{Co} only increases $\sim 1\%$ as the temperature decreases from 300 to 4.2 K). The enhancement of magnetization in Figs. 2(a) and 2(b) thus originates from the multilayer structure and interface magnetism. Because of the interdiffusion or mixing between Co and Pt atoms at the interface region, as the Co layer becomes very thin, e.g., one to three atomic layers, the interfaces may approximately be regarded as a disordered Co-Pt alloy. Then the polarization of Pt atoms and the temperature dependence of magnetization of the interfaces can be calculated in terms of the mean-field theory, as has been done for Co-Pd and Co-Cu alloys in Refs. 8 and 9. We will not give a detailed discussion of the mean-field calculation to save space, and only point out the main result here: Co-Pt alloys with smaller Co concentration have a lower ordering temperature and show a stronger temperature dependence of magnetization. Thus one might expect that thinner Co-layer samples, whose interfaces correspond to Co-Pt alloys with smaller Co concentration, manifest the stronger temperature dependence of magnetization.

B. Temperature dependences of anisotropy

A summary of the temperature (or Co layer-thickness) dependencies of measured anisotropy for $X=3, 4, 5, 7, 12$, and 20 Å (or $T=10, 100, 200$, and 300 K) are shown in Fig. 4(a) [or 4(b)]. It is worthwhile to mention the following: (1) The measured anisotropy K_u is positive for $X \leq 9 \text{ Å}$ and negative for $X \geq 10 \text{ Å}$ over the whole temperature range [see

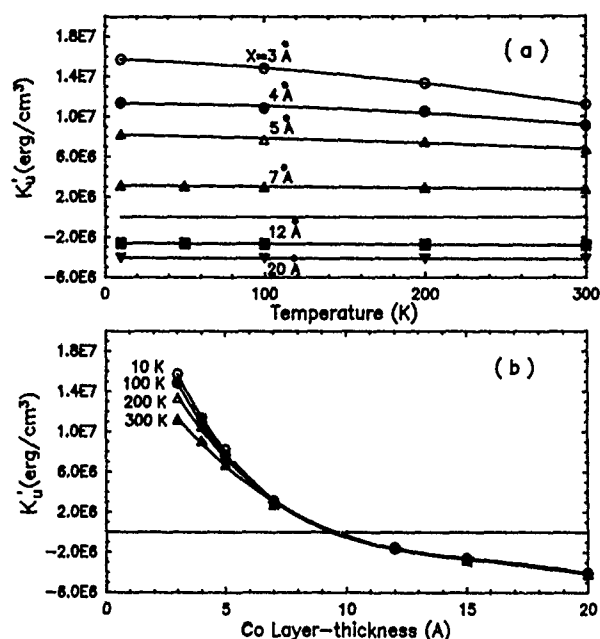


FIG. 3. Temperature dependence of measured anisotropy for (a) different Co layer thickness and (b) layer-thickness dependence of measured anisotropy at different temperatures.

Fig. 4(b)]. (2) Samples with thinner Co layers show a stronger temperature dependence of K_u [see Fig. 4(a) and 4(b)]. K_u values increase by 40%, 24%, and 22% for $X=3, 4$, and 5 Å as temperature decreases from 300 to 10 K. (3) We have determined the interface anisotropy K_i for these samples using the standard method of plotting " λK_u vs d_{Co} ," as described in Refs. 9 and 10. We found K_i to be $\sim 0.38 \text{ (erg/cm}^2\text{)}$. K_i is also nearly independent of temperature. The fact that the samples with thinner Co layers ($X=3, 4$, and 5 Å) show stronger temperature dependences of the anisotropy, while, for samples with $X \geq 7 \text{ Å}$ the anisotropy is nearly independent of temperature, implies that the interfaces give the major contribution to the temperature dependence of anisotropy.

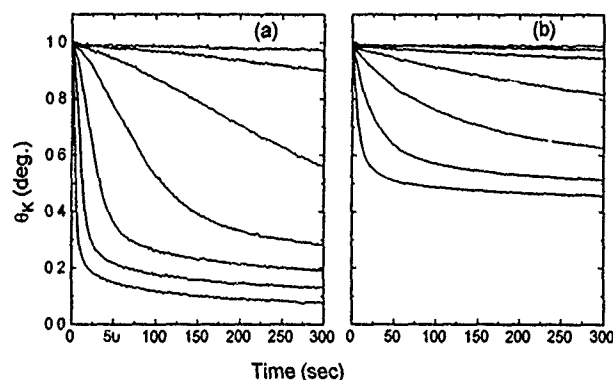


FIG. 4. Kerr rotation as a function of time after magnetization reversal for (a) $3 \text{ Å Co}/15 \text{ Å Pt}$ and (b) $5 \text{ Å Co}/15 \text{ Å Pt}$. Different curves correspond to the different reversing fields ($\leq H_c$), with the uppermost curve corresponding to the smallest field.

To study the origins of anisotropy, Co/Pt, and Co/Au multilayers were prepared, and their temperature dependencies of the anisotropy K_u have been measured. We note that the thermal expansion coefficients of Au, Co, and Pt are 14.2×10^{-6} , 12×10^{-6} , and 9×10^{-6} ($^{\circ}\text{C}^{-1}$), respectively.¹¹ Also, the expansion coefficient of Au is greater than that of Co, while the expansion coefficient of Pt is less than that of Co. Therefore, if stress anisotropy were the major source of K_u , one would expect that the anisotropy of Co/Pt and Co/Au would show opposite temperature dependences: one increasing with decreasing temperature while the other decreasing with decreasing temperature. However, our experiment shows that both for Co/Pt and Co/Au multilayers, the K_u values increase with decreasing temperature for samples with thin Co layers. This may be regarded as evidence that stress plus inverse magnetostriction is a minor contribution to the anisotropy in our (111) textured samples, in comparison with magnetocrystalline anisotropy generated by spin-orbit interaction in the highly anisotropic multilayers structure.^{12,13}

C. Magnetization reversal

Magnetization reversal can be studied by the time decay of Kerr rotation. The measurement procedure was described in Ref. 7, and results are given in Figs. 5(a) and 5(b) for $X=3$ and 5 \AA , respectively.

Several authors^{14,15} have pointed out that if the nucleation rate is small and the domain wall motion velocity is large, the decay curve will first decrease slowly by nucleation at a few isolated sites and then fall quickly through the rapid expansion of the domain walls. The decay curves in Fig. 5(a) are consistent with this behavior. On the other hand, if the nucleation rate is large and the domain wall velocity is very small, the decay curve first decreases exponentially and then decreases approximately as $\ln(t)$ (t is the time) at long times. The decay curves in Fig. 5(b) show such behavior. The $\ln(t)$ behavior can arise either as a consequence of a distribution of thermal activation energies or because part of the driving force (the demagnetizing field) for reversal is decreasing with time as the sample reverses.¹⁶ Therefore the reversal is dominated by domain wall motion for samples with thinner Co layers, while it is dominated by nucleation for thicker Co layer samples. Presumably this difference in behavior results from details of the nanostructures (defects, interface mixing, etc.), as well as differences in demagnetizing fields, both of which must be further investigated to obtain a clear understanding of the reversal behavior.

CONCLUSIONS

It is concluded that the substantial temperature dependence of the magnetic properties of the thin Co layer multilayers originates from the alloying effect at the interfaces. As the temperature decreases, the enhancement of magnetization can be understood in terms of mean-field theory and the enhancement of anisotropy results from the interfacial magnetism, however, the detailed mechanism still remains to be solved. This is a challenging problem when interfacial mixing is present, because up to the present time the theoretical calculations of magnetic anisotropy in multilayers have assumed perfect boundaries with no atomic disorder. Some experiments were performed to probe the origin of the anisotropy. It was found that stress plus magnetostriction does not appear to play a dominant role. Magnetization reversal is dominated by wall motion and nucleation for thinner and thicker Co layers, respectively.

ACKNOWLEDGMENTS

This work was supported by the National Science Foundation under Grant No. DMR-9222976, for which we are grateful. The authors would like to thank S. S. Jaswal and A. Runge for assistance and helpful discussion.

- ¹W. B. Zeper, H. W. van Kesteren, B. A. J. Jacobs, J. H. M. Spruit, and R. F. Garcia, *J. Appl. Phys.* **70**, 2264 (1991).
- ²S. Hashimoto, Y. Ochiai, and K. Aso, *J. Appl. Phys.* **67**, 2136 (1990).
- ³F. J. A. den Broeder, W. Hoving, and P. J. H. Bloemen, *J. Magn. Magn. Mat.* **93**, 562 (1991).
- ⁴T. Suzuki, H. Notarys, D. C. Dobberty, C. J. Lin, D. Weller, D. C. Miller, and G. Gorman, *IEEE Trans. MAG-28*, 2754 (1992).
- ⁵Y. J. Wang and W. Kleemann, *J. Magn. Magn. Mat.* **115**, 9 (1992).
- ⁶P. J. H. Bloemen, W. J. M. de Jonge, and F. J. A. den Broeder, *J. Magn. Magn. Mat.* **93**, 105 (1991).
- ⁷J. X. Shen, R. D. Kirby, and D. J. Sellmyer, *J. Magn. Magn. Mat.* **81**, 107 (1989).
- ⁸Z. S. Shen, P. He, C. Moore, J. Woollam, and J. Sellmyer, *J. Appl. Phys.* **73**, 6057 (1993).
- ⁹Z. S. Shen, S. Nafis, J. Woollam, S. H. Liou, and J. Sellmyer, *J. Appl. Phys.* **73**, 6347 (1993).
- ¹⁰P. F. Garcia, *Appl. Phys. Lett.* **47**, 178 (1985).
- ¹¹*Handbook of Chemistry and Physics* 52nd ed., edited by R. C. Weast (Chemical Rubber, 1971-1972), p. D-141.
- ¹²J. M. Maclaren and R. H. Victora, *IEEE Trans. Magn. MAG-29*, 3034 (1993).
- ¹³Daalderop, P. J. Kelly, and M. F. H. Schuurmans, *Phys. Rev. B* **42**, 7270 (1990).
- ¹⁴M. Labrune, S. Andrieu, F. Rio, and P. Bernstein, *J. Magn. Magn. Mat.* **80**, 211 (1989).
- ¹⁵R. D. Kirby, J. X. Shen, R. J. Hardy, and D. J. Sellmyer (unpublished).
- ¹⁶D. K. Lottis, R. White, and E. D. Dahlberg, *Phys. Rev. Lett.* **67**, 362 (1991).

Structural and magnetic properties of Co/Cr(001) superlattices

W. Donner, T. Zeidler, F. Schreiber, N. Metoki, and H. Zabel

Institut für Experimentelle Festkörperphysik, Ruhr-Universität Bochum, D-44780 Bochum, Germany

Epitaxial Co/Cr(001) superlattices were prepared by Molecular-Beam-Epitaxy (MBE). The crystal structure was determined both with Reflection High Energy Electron Diffraction (RHEED) and x-ray diffraction experiments. The Co layers grow in an hcp phase with their (11.0) planes oriented parallel to the Cr(001) planes. The magnetic anisotropy was measured using the Magneto-optical Kerr Effect (MOKE) and Ferromagnetic Resonance (FMR) technique. It is found that the easy axis of the magnetization is perpendicular to the film plane below a Co thickness of about 14 Å. The value of the interface anisotropy constant K_s is determined to $(0.85 \pm 0.1) \text{ erg/cm}^2$ assuming the bulk magnetization of hcp Co.

I. INTRODUCTION

Perpendicular anisotropy in ultrathin magnetic multilayers is a highly interesting topic for fundamental studies, as well as for applications as high-density magneto-optical storage devices.¹ Usually in thin film systems the magnetization tends to be oriented parallel to the film plane because of the demagnetization energy. In ultrathin films, however, the interfacial anisotropy that is due to the symmetry breaking at the interface² and/or hybridization effects³ plays an important role, so that perpendicular spin orientation has been observed in many systems.¹ In addition to the above mechanisms, crystal anisotropy and magnetoelastic interactions⁴ can also contribute to the perpendicular anisotropy.

In this paper we present the existence of a strong perpendicular anisotropy in high-quality MBE-grown Co/Cr(001) superlattices studied by means of the Magneto-optical Kerr effect and FMR. We believe that the observed interfacial anisotropy has an electronic origin, since we find from our intensive studies that the magnetoelastic and crystal anisotropy contributions are not large enough to force the magnetization into the perpendicular orientation.

II. STRUCTURAL PROPERTIES

The preparation of the samples is described in detail elsewhere,⁵ which is briefly summarized here: the Co/Cr(001) superlattices are grown on $\text{Al}_2\text{O}_3(1\bar{1}.2)$ substrates with Nb(001) seed layers and Cr(001) buffer layers at growth temperatures of 300 °C–350 °C. The obtained RHEED pictures (Fig. 1) show sharp streaks, implying atomically flat surfaces. We were able to observe RHEED intensity oscillations during Co growth up to a thickness of 20 atomic layers. Very small interfacial roughness (≤ 5 Å) has been derived from x-ray reflectivity measurements. From the position of the in-plane diffraction spots, we find that hcp-Co(11.0) grows epitaxially on Cr(001), with the c axis of Co being oriented parallel to the Cr[110] axis. This orientation can also be recognized from the additional streaks in the RHEED pattern in [Fig. 1(b)] resulting from the Co layers. Since the substrate has a fourfold symmetry, in most of the samples we observed two equivalent crystallographic domains, which are oriented perpendicular to each other.

This orientation is similar to the Burgers relationship,⁶ which is the orientational relation in the BCC-hcp Martensitic transition. We have obtained experimental evidence⁷ that

the Co layers in Co/Cr(001) superlattices exhibit a precursive structural transition from hcp to BCC with decreasing Co thickness. First, the shape of the in-plane unit cell changes from rectangular to nearly square, and second, the intensity of the hcp-Co $\{1\bar{1}.1\}$ spots, which are forbidden in the BCC structure, shows a continuous decrease, implying a symmetry



(a)



(b)

FIG. 1. RHEED patterns at 30 kV with the electron beam perpendicular to the Cr(130) direction. (a) (bottom): 500 Å Cr buffer layer; (b) (top): after the growth of 30 Å Co on top of Cr.

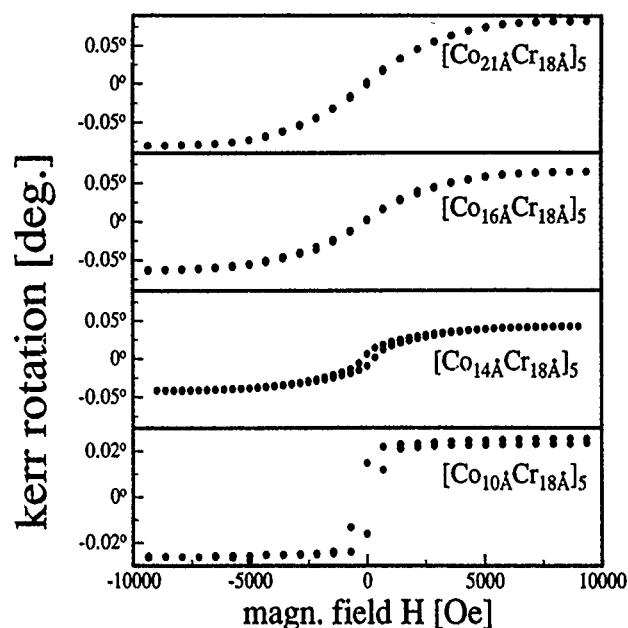


FIG. 2. Hysteresis loops obtained with an applied field perpendicular to the film plane of four Co/Cr superlattices with decreasing Co thickness.

change of the Co layers from hcp to BCC with decreasing t_{Co} . In addition, the observed anomalous out-of-plane expansion of the Co layers is an indication for a precursive BCC-hcp structural phase transition, since it can be explained by a rigid-atom-model, assuming that the structural transition takes place.

The structural coherence length of our samples reaches about 100 Å in the film plane and several hundred Angströms in the out-of-plane direction.

III. MAGNETIC ANISOTROPY

Figure 2 shows typical polar hysteresis curves of Co/Cr superlattices. For $t_{\text{Co}}=21$ Å the polar hysteresis loop exhibits a continuous change of Kerr angles θ_K as a function of the external field H without remanence. The longitudinal hysteresis curve of this sample has a perfect square shape with $H_c=250$ Oe. These two hysteresis curves indicate that the Co magnetization is parallel to the film plane. With decreasing t_{Co} the saturation field in the polar hysteresis curves decreases continuously, and nonzero remanence is observed below $t_{\text{Co}}=14$ Å. Below this critical film thickness we observed square-type hysteresis loops, indicating that the direction of the easy axis is perpendicular to the film plane. The large critical film thickness of about 14 Å is an indication of the existence of a strong perpendicular anisotropy.

The effective anisotropy energy K_{eff} can be determined by integrating the area enclosed by the polar (H_{\perp}) and longitudinal (H_{\parallel}) hysteresis curves. In this paper, however, we evaluate the effective anisotropy field $H_A=2K_{\text{eff}}/M_s$ instead of K_{eff} , because H_A can be determined⁹ by MOKE experiments without knowing the magnetization of our samples M_s :

$$H_A = \frac{2}{\theta_K} \int_0^{\theta_K} (H_{\parallel} - H_{\perp}) d\theta'_K; \quad (1)$$

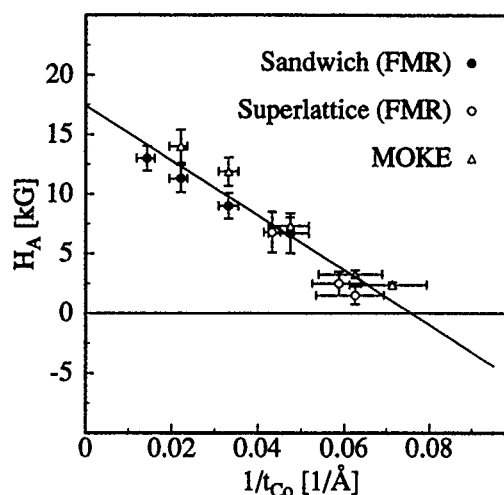


FIG. 3. Effective magnetization versus a reciprocal Co thickness of Cr/Co/Cr sandwich structures and Co/Cr superlattices measured with FMR and values calculated from longitudinal and polar MOKE measurements. The straight line is a linear fit to the data. For a definition of H_A see Eq. (3).

H_A can also be measured directly by the resonance field H_{res} in out-of-plane FMR measurements. From the resonance condition in perpendicular orientation we get

$$H_A = H_{\text{res}} - (\omega/\gamma), \quad (2)$$

where $\omega/2\pi$ is the microwave frequency (X and Q band in our experiments), and γ is the gyromagnetic ratio. The experimental results of H_A are shown in Fig. 3, both for MOKE and FMR. It can be readily seen that both data sets agree very well and that the anisotropy field H_A exhibits a $1/t_{\text{Co}}$ behavior. This behavior can be understood in terms of an interfacial anisotropy. The anisotropy in thin films can be described as a sum of interfacial and bulk contributions K_s and K_v , respectively,

$$H_A = 2 \cdot \frac{2K_s}{M_s \cdot t_{\text{Co}}} + \frac{2 \cdot K_v}{M_s}. \quad (3)$$

The slope of the least-squares fit to the experimental data with Eq. (3) yields $K_s=0.85$ erg/cm², if we assume that the magnetization of the Co layers is the same as in the bulk: $M_s=1430$ emu/cm³. This interfacial contribution is very large in comparison with other 3d systems like in Co/Cu ($K_s=0.1-0.5$ erg/cm²) or Co/Ni ($K_s=0.1$ erg/cm²), and is comparable with Co/Pt, Au ($K_s \approx 1$ erg/cm²).

The intercept of the fitting gives us $2 \cdot K_v/M_s=17$ KOe. We argue below that this anisotropy field can be explained by the demagnetization field $4\pi M_s$ and the crystal anisotropy energy F_{Ani} . By taking into account the crystallographic domain structure, the crystal anisotropy energy can be expressed as follows:

$$F_{\text{Ani}} = -\frac{1}{2}(K_1 + 2K_2)\sin^2 \theta + \frac{3}{8}K_2 \sin^4 \theta + \frac{1}{8}K_2 \sin^4 \theta \cos(4\Phi), \quad (4)$$

where θ is the polar angle from the film normal and Φ is the azimuthal angle from the c axis of the Co layers. This expression is valid when the magnetic domains are larger than the crystallographic ones, which has been confirmed by both

the MOKE (static method) and FMR (dynamic method) experiments: longitudinal hysteresis loops with the magnetic field along the hard axis yielded a $\sqrt{2}$ fraction of the remanent signal of the easy axis loops, as is expected from a fourfold symmetry. In FMR experiments we observed only one resonance (at a fixed orientation) due to the *coupled* excitation of the two domains.

For out-of-plane MOKE measurements the difference of the anisotropy energy from perpendicular to parallel spin orientation, $F_{\text{Ani.}}(\theta=90^\circ, \Phi=45^\circ) - F_{\text{Ani.}}(\theta=0^\circ, \Phi=45^\circ)$ is important for K_v ,

$$\text{MOKE: } K_v^{\text{MOKE}} = 2\pi M_s^2 + \frac{1}{2}K_1 + \frac{3}{4}K_2, \quad (5)$$

while K_v for FMR is slightly different from the one obtained from MOKE, because $\sin^4 \theta$ terms in $F_{\text{Ani.}}$ have no influence on the resonance condition in out-of-plane FMR signals:

$$\text{FMR: } K_v^{\text{FMR}} = 2\pi M_s^2 + \frac{1}{2}K_1 + K_2 \quad (6)$$

Despite the slight difference in the crystal anisotropy energy, it makes no significant difference in K_v because the demagnetization factor [the first term in Eqs. (5) and (6)] is most dominant. Assuming bulk anisotropy constants we get $2 \cdot K_v / M_s \approx 22$ KOe, which is close but not in perfect agreement with our experimental results. The reason could be a reduced anisotropy due to stepped surfaces¹⁰ or slightly tilted crystallographic directions, but this has not been investigated in detail.

The origin of the large surface anisotropy is thought to be of the Néel type (symmetry breaking at the surface). Furthermore, electronic effects at the interface of these two 3d metals should play an important role. Our calculations show that magnetoelastic (at least *linear*) effects are not sufficient to explain the magnitude of K_s . We determined the magnetoelastic energy using a model developed in Ref. 11. According to Mason, the difference in magnetoelastic energy of a hexagonal system with the spin perpendicular to the (11.0) plane and parallel to this plane (for the case of two-domain samples) can be expressed as

$$\begin{aligned} K_{ME}^\perp - K_{ME}^\parallel = & [(-\lambda_B + \frac{1}{2}\lambda_A) \cdot c_{11} + (-\lambda_A + \frac{1}{2}\lambda_B) \cdot c_{12} \\ & + (-\frac{1}{2}\lambda_C) \cdot c_{13}] \cdot e_1 [(-\lambda_B + \frac{1}{2}\lambda_A) \cdot c_{12} \\ & + (-\lambda_A + \frac{1}{2}\lambda_B) \cdot c_{11} + (-\frac{1}{2}\lambda_C) \cdot c_{13}] \cdot e_2 \\ & \times [(-\lambda_B + \frac{1}{2}\lambda_A) \cdot c_{13} + (-\lambda_A + \frac{1}{2}\lambda_B) \cdot c_{13} \\ & + (-\frac{1}{2}\lambda_C) \cdot c_{33}] \cdot e_3, \end{aligned} \quad (7)$$

where λ_i are the magnetostriction constants and c_{ij} are the elastic constants of bulk hcp Co. Substituting the measured values for the in-plane strain, $e_1 = -4\%$ and $e_3 = +0.2\%$, and the out-of-plane lattice expansion $e_2 = +7\%$ of a sample with a Co thickness of 10 Å in this equation, we find a value for $K_{ME}^\perp - K_{ME}^\parallel$ of -3.3×10^6 erg/cm³, which corresponds to a field of -4.6 kOe. This is not big enough to overcome the in-plane bulk contribution $2 \cdot K_v / M_s = 17$ kOe and not small enough to be neglected. It has to be remarked that using the

bulk constants for hcp Co in Eq. (7) could lead to a slightly different K_{ME} because of the structural transition in our Co layers.

In a previous investigation of Co/Cr superlattices with a different orientation,¹² it was argued that the observed perpendicular anisotropy was governed by the shape anisotropy resulting from the columnar growth in those samples. In our samples this mechanism can be excluded, because in the investigated sandwich structures the in-plane structural coherence lengths were larger than the Co thickness.

It is known that interface interdiffusion or roughness reduces the magnetization of Co/Cr multilayers.¹³ Since the slope of the linear fit is also determined by the "thick" samples, in which the relative fraction of the interfaces is rather small, we believe, however, that using the bulk magnetization should not alter the result in a dramatic way. As described in Ref. 7 in more detail, the interdiffusion in our samples is limited to a few atomic layers only.

IV. SUMMARY AND CONCLUSIONS

In Co/Cr(001) superlattices, hcp-Co(11.0) layers were found to be oriented parallel to Cr(001) planes, with their *c* axis aligned parallel to the Cr[110] directions. A precursive structural change to the BCC-Co phase with decreasing Co thickness is accompanied with a change of the easy axis of magnetization from in plane to the direction perpendicular to the film plane. The corresponding interface anisotropy K_s is (0.8 ± 0.1) erg/cm². The interface anisotropy may originate from broken symmetry, electronic effects at the interface, and from magnetoelastic effects. Since the magnetoelastic effects can be excluded, the first two effects must govern the observed anisotropic behavior.

ACKNOWLEDGMENTS

We would like to thank J. Podschwadek and W. Oswald for their technical assistance. This work was partly supported by the Deutsche Forschungsgemeinschaft (SFB 166) and by the Ministerium für Wissenschaft und Forschung NRW (Germany), which is gratefully acknowledged. One of us (W.D.) would like to thank the Ruth und Gert Massenberg-Stiftung for a travel grant.

¹For a recent review see "Proceedings of the 37th annual conference on magnetism and magnetic materials," J. Appl. Phys. 73(10) (1993).

²L. Néel, J. Phys. Rad. 15, 225 (1954).

³G. Schütz, R. Wienke, W. Wilhelm, W. B. Zeper, H. Ebert, and K. Spörl, J. Appl. Phys. 67, 4456 (1990).

⁴C. H. Lee, H. He, F. J. Lamelas, W. Vavra, C. Uher, and R. Clarke, Phys. Rev. B 42, 1066 (1990).

⁵W. Donner, N. Metoki, A. Abromeit, and H. Zabel, Phys. Rev. B 48, 14 745 (1993).

⁶W. G. Burgers, Physica 1, 36 (1957).

⁷N. Metoki, W. Donner, and H. Zabel, Phys. Rev. B (to be published).

⁸C. Chappert and P. Bruno, J. Appl. Phys. 64, 5736 (1988), M. Sakurai and T. Shinjo, J. Phys. Soc. Jpn. 62, 1853 (1993).

⁹If no higher-order contributions ($\sin^4 \theta$) are relevant.

¹⁰P. Bruno, J. Appl. Phys. 64, 3153 (1988).

¹¹W. P. Mason, Phys. Rev. 96, 303 (1954).

¹²N. Sato, J. Appl. Phys. 61, 1979 (1987).

¹³M. B. Stearns, C. H. Lee, and T. L. Groy, Phys. Rev. B 40, 8256 (1989).

Orientational and structural dependence of magnetic anisotropy of Cu/Ni/Cu sandwiches: Misfit interface anisotropy

R. Jungblut, M. T. Johnson, J. aan de Stegge, A. Reinders, and F. J. A. den Broeder
 Philips Research, Prof. Holstlaan 4, 5656 AA Eindhoven, The Netherlands

Magnetic anisotropies and misfit strain relaxations have been investigated in Cu/Ni-wedge/Cu (100) and (111) sandwiches deposited by molecular beam epitaxy on single-crystal Cu substrates. Our results reveal a clear distinction in the nature of the measured anisotropy at Ni thicknesses below and above the critical value t_c , where the growth becomes incoherent. Below t_c , coherent lattice strain modifies only the volume anisotropy, while interface anisotropy is Néel type; above t_c , magnetoelastic effects are found to contribute to the interface anisotropy.

In recent years, one of the most intriguing properties displayed by several magnetic ultrathin films and multilayers (MLs) has been a preferential magnetization perpendicular to the film plane, called perpendicular magnetic anisotropy (PMA).¹ Phenomenologically, it appears that this effect is associated with the interfaces between magnetic and non-magnetic layers, since the effective anisotropy constant K has been found to show the following dependence on magnetic layer thickness t :²

$$Kt = K_V t + 2K_S. \quad (1)$$

Here, K_V is a magnetic volume coefficient, largely composed of magnetostatic energy, favoring in-plane magnetization. The interface contribution K_S , which sometimes favors perpendicular magnetization, has usually been associated with Néel's surface anisotropy K_N originating in the broken symmetry of interface atoms.³ On the other hand, Chappert and Bruno⁴ have proposed that lattice misfit strain may, via magnetostriction, contribute not only to the volume anisotropy in coherent structures, but also to the surface anisotropy in incoherent structures, via the misfit interface anisotropy, K_λ .

Experimentally, the challenge has been to isolate these different contributions to K_S , but various research groups have come to quite opposite conclusions. In a pioneering experiment, Gradmann⁵ noted that tensile stresses in the Ni layers of Cu/Ni sandwich structures were responsible for the appearance of PMA at certain Ni layer thicknesses, but could not explain the reappearance of in-plane magnetization for thinner Ni layers. Recently, Lee *et al.*⁶ explained the thickness dependence of the anisotropy for Co/Au and Co/Cu MLs as being due solely to Co-layer misfit strain variation. In addition, Nakamura *et al.*⁷ also considered that, in sputtered Co/Pd MLs, PMA is caused mainly by interfacial strain anisotropy of interface alloys. On the other hand, in a series of experiments on Co/Pd MLs with various crystal orientations,⁸ the K_V values could be fully accounted for by magnetoelastic and magnetocrystalline anisotropy contributions, suggesting that K_S was only due to Néel-type anisotropy. This unclear situation regarding the role of K_N and K_λ is probably related to the large lattice misfit ($\approx 8\%$) in the Co/Pd system, and in other systems, precipitating immediate incoherent growth, which excludes distinct identification of K_N and K_λ .

In this paper, we unambiguously demonstrate that both Néel and misfit interface anisotropies are active in determin-

ing the magnetic anisotropy in Cu/Ni/Cu sandwich structures. In this system with a relatively small lattice misfit ($\approx 2.5\%$), the relaxation of misfit strain as the Ni layer changes from a coherent to an incoherent structure could be followed in samples with a Ni wedge structure and related to changes in the anisotropy. This made it possible to quantify the contribution of strain to both K_S and K_V .

The central concept in the understanding of the misfit interface anisotropy is the existence of a critical layer thickness, t_c . Below t_c , growth is coherent and the lattice misfit is absorbed by elastic strain. Above t_c , growth is incoherent and strain relaxes by misfit dislocations. The critical thickness can be derived from⁹

$$\frac{t_c}{b} = \frac{Gx}{4\pi\eta E} \ln\left(\frac{t_c}{b} + 1\right), \quad (2)$$

with b the Burgers vector, G is the shear modulus, E is the elastic constant in the film plane, and η is the lattice misfit [$= (a_s - a)/a$, with a the overlayer and a_s the substrate-lattice constants]. In practice, $x=1$ for a single layer deposited on a substrate, whereas $x=2$ if the stressed layer is sandwiched between two equivalent thick layers, which both support coherent growth. It should be noted that for the sandwich case $x=2$ is a purely thermodynamic result, implying no barriers for dislocation motion. In the incoherent region above t_c , Chappert and Bruno⁴ have shown that the residual strain ϵ can be written as $\epsilon = \eta t_c/t$. This inverse proportionality of strain to layer thickness, which has been experimentally observed in, for example, Ni overlayers on a Cu(100) substrate,¹⁰ will have important consequences for the interpretation of the anisotropy, as outlined below.

A separate interpretation of the magnetic anisotropy must be made in the regions above and below t_c . For coherent systems, the volume anisotropy K_V incorporates shape anisotropy, magnetocrystalline anisotropy (K_{MC}) and strain anisotropy (K_{ME}), with interface anisotropy being solely Néel type. Following den Broeder,¹¹ we find

$$K_S = K_N, \quad (3)$$

$$K_V = -\frac{1}{2}\mu_0 M_s^2 + K_{MC} + K_{ME}, \quad (4)$$

with

$$K_{ME} = -\frac{3}{2} \lambda \sigma = -\frac{3}{2} \lambda \left(\frac{E \eta}{1 - \nu} \right), \quad (5)$$

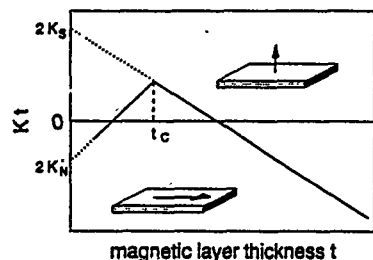


FIG. 1. Schematic dependence of Kt on layer thickness t , in the presence of negative Néel surface anisotropy K_N .

with M_s the saturation magnetization, λ the magnetostriction constant, σ the stress, and ν the Poisson ratio. In this region, the influence of misfit strain thus appears as a volume contribution to the anisotropy.

In the incoherent region above t_c , the distinctive form of volume strain has been shown⁴ to lead to an apparent interface contribution—the magnetoelastic interface anisotropy. Following Ref. 11 and Eq. (2), we find

$$K_S = K_N + K_\lambda, \quad (6)$$

with

$$K_\lambda = \pm \frac{3}{8\pi} \left(\frac{Gb\lambda}{1-\nu} \right) \ln \left(\frac{t_c}{b} + 1 \right), \quad (7)$$

and

$$K_V = -\frac{1}{2}\mu_0 M_s^2 + K_{MC}, \quad (8)$$

where the + and - signs in Eq. (7) refer to the respective cases $\eta < 0$ and $\eta > 0$. Figure 1 schematically illustrates the expected dependence of Kt on t , with a marked kink appearing at the critical thickness t_c . In the remainder of this paper, we will discuss how relevant this picture is by considering the Cu/Ni model system.

The majority of the structural and magnetic properties were determined from measurements on only two Cu/Ni/Cu samples: one for the (100) and one for the (111) crystallographic orientations. For both samples, the Ni layer was grown in the form of a wedge. The layers were deposited at room temperature by Molecular Beam Epitaxy (MBE), the final sample-composition being Cu(100)/Ni wedge (0–130 Å, slope: 15 Å/mm)/Cu(10 Å)/Au (25 Å); and Cu(111)/Ni wedge (0–40 Å, slope: 3.6 Å/mm)/Cu (12 Å)/Au (25 Å). More details concerning the substrate-preparation and growth technique can be found in Ref. 12. In addition, a small number of (111) oriented samples with uniform Ni thicknesses in the range 100–300 Å were prepared on Si(111)/2000 Å Cu substrates.

The established onset of strain relaxation in Ni layers on Cu crystals^{10,13} was confirmed using LEED. Initially, the Ni displays a 2.5% expanded fcc surface net that was within experimental error identical to that of the Cu substrate. In-plane strain relaxation manifests itself in the LEED patterns through small changes in the position of the diffraction spots and the occurrence of additional features located close to the primary diffraction spots, possibly caused by diffraction from arrays of dislocations at large repeat intervals ($\approx a/\eta$),

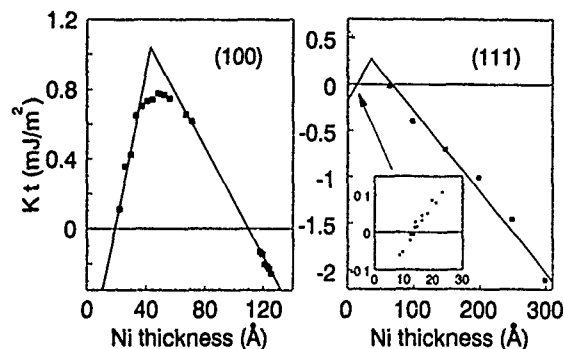


FIG. 2. The product of total anisotropy K and Ni layer thickness t , plotted as a function of t for (100) and (111) orientations.

which have recently been imaged with TEM in the Cu(100)/Ni system.¹³ In-plane relaxation starts at ≈ 13 Å Ni in the (111) orientation, and ≈ 15 Å Ni in the (100) case. The latter value agrees closely with that determined by Matthews and Crawford ($t_c = 14.6 \pm 3$ Å¹⁰).

To evaluate the agreement between these observations and theory, we consider Eq. (2) in the approximation $x=1$ (the single layer situation actually encountered in the LEED measurements). Using literature values for the (orientation-dependent) elastic and shear moduli for Ni,¹⁴ and $b=2.5$ Å ([110] slip direction), we expect $t_c(111)=11$ Å and $t_c(100)=12.5$ Å. The close agreement between predicted and observed critical thicknesses in both orientations lends validity to the considerations presented above. We now consider whether elastic strain ($t < t_c$) and strain relaxation ($t > t_c$) play a role in determining the anisotropies of the samples.

The magnetic anisotropy was determined at various positions along the Ni wedges using a Kerr Effect apparatus. Providing the magnetization rotates homogeneously, anisotropies at thicknesses where the magnetization was *in plane* could be determined by forcing the sample toward saturation in a field applied along the film-normal, whereas *perpendicular* anisotropies were derived by forcing the magnetization away from the film-normal using an external field with an in-plane component.¹⁵ The nonuniformity in magnetization rotation accounts for the absence of measurements at intermediate Ni thicknesses. For the (111) orientation, supplementary anisotropy measurements using standard vibrating sample magnetometry were carried out on the samples of uniform thickness.

The results of the study appear in Fig. 2. We immediately see that the form of both curves strongly resembles the schematic depiction in Fig. 1. Clear breaks are observed in both curves. In the spirit of Fig. 1, we can straightforwardly assert a linear dependence of Kt on t , both below and above t_c . The resulting anisotropies are also compiled in Table I. Comparing Eqs. (3) and (4) with (6) and (8), respectively, it is easy to derive values for the strain-related interface (K_λ) and volume (K_{ME}) terms, which are also compiled in Table I (assuming $K_{MC} \approx 0$ for Ni). Using the relevant magnetostriction and elastic constants in these equations ($\lambda_{111} = -24 \times 10^{-6}$ and $\lambda_{100} = -46 \times 10^{-6}$), the *theoretical* values of K_λ and K_{ME} can be determined. As shown in Table

TABLE I. Summary of Cu/Ni anisotropy data pertaining to both investigated orientations. Critical thicknesses (t_c reported for both single layers and sandwiches) and stress-induced anisotropy energies are determined both experimentally and (in parentheses) by calculation.

Orientation	t_c (Å)		K below t_c	K above t_c	Stress-induced anisotropy
	Layer	Sandwich			
(111)	13	32	$K_N = -0.08$ mJ/m ²	$K_S = +0.27$ mJ/m ²	$K_A = 0.35$ mJ/m ² (0.64)
	(11)	(35)	$K_V = +0.13$ MJ/m ³	$K_V = -0.09$ MJ/m ³	$K_{ME} = 0.22$ MJ/m ³ (0.36)
(100)	15	42	$K_N = -0.4$ mJ/m ²	$K_S = +0.9$ mJ/m ²	$K_A = 1.3$ mJ/m ² (0.8)
	(12.5)	(40)	$K_V = +0.39$ MJ/m ³	$K_V = -0.16$ MJ/m ³	$K_{ME} = 0.55$ MJ/m ³ (0.39)

I, the predicted volume and interface strain anisotropies all have the correct magnitude and sign to account for the experimental observations. Quantitatively, the uncertainty in defining magnetostriction and elastic constants for ultrathin layers, or the presence of interface Cu-Ni alloys with radically different magnetostriction may preclude closer agreement. The positions of the breaks are not in agreement with the t_c values established from LEED studies. Probably the presence of the overlayer has increased t_c for the sandwich structure, in accordance with Eq. (2). By inserting $x=2$ into Eq. (2), we expect $t_c=35$ Å for Cu(111)/Ni/Cu and $t_c=40$ Å for Cu(100)/Ni/Cu, close to the break points of Figs. 2(a) and 2(b). Previous work on Cu/Ni MLs¹⁶ has revealed respective (100) and (111) interface anisotropies of -0.23 mJ/m² and -0.12 mJ/m² on samples with rather thin individual layers, where the growth was essentially coherent. A similar situation is encountered in the present work, with a more negative K_S being found in the (100) orientation than in the (111) orientation, in the coherent region below t_c . Concerning the crossover from perpendicular to in-plane anisotropies at larger Ni thicknesses, the present results are seen to be consistent with the work of Chang.¹⁷ There, a reversal of the magnetic anisotropy was measured for Ni layers sandwiched between thick Cu(100) layers that occurred at a Ni thickness in between 50 Å (perpendicular remanence) and 100 Å (in-plane remanence). In their attempt to explain the anisotropy of Co/Pd MLs by magnetoelastic anisotropy of interface alloys, Nakamura *et al.*⁷ found similar kinks in the anisotropy of Pd₆₇Co₃₃/Au and Pd₆₇Co₃₃/Cu MLs. We suggest that this behavior is related to the mechanism proposed in this paper.

In conclusion, we summarize why the present experiment has allowed isolation of the Néel- and misfit-type anisotropies, which have previously eluded separation. Several favorable conditions are met in the present Cu/Ni/Cu samples. First, both metals are fcc, with only a small lattice

misfit. Consequently, as revealed by our LEED studies, both coherent and incoherent structures can be realized across wide ranges of Ni thicknesses accessible to anisotropy measurements. In addition, the small saturation magnetization of Ni (compared to Co or Fe) results in a domination of strain-induced anisotropies compared to shape anisotropy. Finally, magnetocrystalline anisotropies are rather small in Ni.

¹Several papers in *Symposium C on Magnetic Thin Films, Multilayers and Surfaces*, edited by A. Fert, G. Güntherodt, B. Heinrich, E. E. Marinero, and M. Maurer, Proceedings of the E-MRS Spring 1990 Meeting, Strasbourg, J. Magn. Magn. Mat. **93** (1991).

²P. F. Carcia, A. D. Meinhaldt, and A. Suna, Appl. Phys. Lett. **47**, 178 (1985).

³L. Néel, J. Phys. **15**, 225 (1954).

⁴C. Chappert and P. Bruno, J. Appl. Phys. **64**, 5736 (1988).

⁵U. Gradmann, Ann. Physik. Leipzig **17**, 91 (1966).

⁶C. H. Lee, Hui He, F. J. Lamelas, W. Vavra, C. Uher, and R. Clarke, Phys. Rev. B **42**, 1066 (1990).

⁷K. Nakamura, S. Tsunashima, M. Hasegawa, and S. Uchiyama, J. Magn. Magn. Mat. **93**, 462 (1991).

⁸B. N. Engel, C. D. England, R. A. van Leeuwen, M. H. Wiedmann, and C. M. Falco, J. Appl. Phys. **70**, 5873 (1991).

⁹J. W. Matthews and A. E. Blakeslee, J. Cryst. Growth **27**, 118 (1974); **29**, 273 (1975).

¹⁰J. W. Matthews and J. L. Crawford, Thin Solid Films **5**, 187 (1970).

¹¹F. J. A. den Broeder, W. Hoving, and P. J. H. Bloemen, J. Magn. Magn. Mat. **93**, 562 (1991).

¹²M. T. Johnson, S. T. Purcell, N. W. E. McGee, R. Coehoorn, J. aan de Stegge, and W. Hoving, Phys. Rev. Lett. **68**, 2688 (1992).

¹³H. E. Inglefield, C. A. Ballentine, G. Bochi, S. S. Bogomolov, R. C. O'Handley, and C. V. Thompson, *Proceedings of the MRS Spring 1993 Meeting*, San Francisco, CA.

¹⁴*Metals Reference Book*, edited by C. J. Smithells (Butterworths, New York, 1976), p. 978.

¹⁵S. T. Purcell, M. T. Johnson, N. W. E. McGee, W. B. Zeper, and W. Hoving, J. Magn. Magn. Mat. **113**, 257 (1992).

¹⁶G. Xiao and C. L. Chien, J. Appl. Phys. **61**, 4061 (1987); E. M. Gyorgy, J. F. Dillon, Jr., D. B. McWhan, L. W. Rupp, Jr., L. R. Testadi, and P. J. Flanders, Phys. Rev. Lett. **45**, 57 (1980).

¹⁷C.-An Chang, J. Appl. Phys. **68**, 4873 (1990).

Magnetic anisotropy in ultrathin films grown on vicinal surfaces (abstract)

D. S. Chuang, C. A. Ballentine, and R. C. O'Handley
Massachusetts Institute of Technology, Cambridge, Massachusetts 02139

Growth of thin epitaxial magnetic films on terraced substrates, such as Co/Cu(1 1 13) vicinal to (001), leads to unexpected magnetic anisotropy associated with the surface steps. This anisotropy remains largely unexplained and is of potential technological importance. We have studied the anisotropy of fcc Co/Cu(1 1 13) films of 3–20 ML thicknesses using *in situ* MOKE. The presence of monoatomic steps on the Cu(1 1 13) surface induces a uniaxial anisotropy favoring magnetization parallel to the steps. The strength of this anisotropy decreases with increasing film thickness. In this paper we focus on the interpretation of this anisotropy in terms of the Néel model.^{1,2} Vicinal surfaces are characterized by (001) terraces separated by monoatomic steps. The Néel anisotropy energy for such a surface has the form $E_{\text{total}}^N = E_{\text{bulk atoms}} + (E_{\text{surface atoms}}/t) + E_{\text{step-edge atoms}}/td$, where t and d are film thickness and terrace width, respectively. The last term includes contributions from sites at both the top and bottom of the step and is responsible for the step-induced anisotropy. For 10 ML of Co on Cu(1 1 13), the magnitude of this term is approximately 0.3 erg/cm², favoring M parallel to the steps, as we have observed. Fe/W vicinal to (001) films show a preference for in-plane magnetization perpendicular to the steps.³ The Néel model predicts this anisotropy for a bcc Fe film provided the magnetization lies in the film plane, not in the (001) plane.

¹M. Albrecht, T. Furubayashi, M. Przybylski, J. Korecki, and U. Gradmann, *J. Magn. Magn. Mater.* **113**, 207 (1992).

²R. H. Victora and J. M. MacLaren, *Phys. Rev.* **47**, 11583 (1993).

³J. Chen and J. Erskine, *Phys. Rev. Lett.* **68**, 1212 (1992).

Theoretical predictions for magnetic anisotropy of superlattice defects (abstract)

R. H. Victora

Storage Technology Research and Development Division, EIPC, Eastman Kodak Company, Rochester,
New York 14650-2017

J. M. MacLaren

Physics Department, Tulane University, New Orleans, Louisiana 70118

Most experimental superlattices contain numerous defects that substantially affect the anisotropy. Calculations based on two different theoretical approaches are presented for a variety of substitutional defects at the interface. The first method involves electronic structure calculations employing the local density approximation within the layer Korringa-Kohn-Rostoker technique. Defects are treated as periodic at a third nearest-neighbor spacing. Large in-plane contributions to the anisotropy are found for a substituted atom within the (111) Co layer of both the Co/Pd and Co/Pt systems. For example, $-203 \mu\text{Ry}$ is obtained for a single defect in the 1Co/1Pt superlattice: this is -4.2 times the interface anisotropy. This is believed to be the first *ab initio* prediction of the anisotropy energy of defects. The second method sums pair interactions using the potential $(\mathbf{M} \cdot \mathbf{R})^2$, where \mathbf{M} is the magnetization and \mathbf{R} is the vector connecting the two atoms. This method has been previously demonstrated¹ to be accurate in comparison both to electronic structure calculation and to experiment. For the fcc (111) interface, it is predicted that the anisotropy (in units of interface anisotropy) of a substitution in a monolayer is -4 , the anisotropy of an adatom is -2 , and the anisotropy of a one-atom recess that does not penetrate the magnetic layer is -2 . These predictions are found to approximately match the electronic structure theory in those cases we have tested. Finally, the summation of a variety of randomly chosen defects to form a diffuse interface yields an anisotropy equal to that of a perfect interface times the sum over all layers i of $[P(i) - P(i+1)]^2$, where $P(i)$ is the probability of a magnetic atom in layer i . This suggests that the highest anisotropy is obtained at the sharpest interface.

¹R. H. Victora and J. M. MacLaren, Phys. Rev. B 47, 11583 (1993).

Magnetoelastic coefficients at tetragonal surfaces (abstract)

Oh Sung Song, C. A. Ballentine, and R. C. O'Handley
Massachusetts Institute of Technology, Cambridge, Massachusetts 02139

Surfaces and thin films are generally highly strained relative to their bulk structures. The magnetoelastic (ME) coefficients coupling these strains to magnetic properties must be considered in lower symmetry than the bulk values. We outline a method of analyzing the ME problem at a surface in tetragonal symmetry (assuming the bulk is cubic). Five ME coefficients are required. Two methods have been developed to extract these surface ME coefficients from the M-H behavior of films subjected to different strains. One method fits the M-H behavior with that predicted by an equation of motion derived from a free energy which includes ME, magnetostatic, crystal field, and Zeeman terms. This method is useful in certain simple cases where canonical linear M-H behavior is observed. In more complicated cases, it can be shown that the ME coefficients are related to the area $A(\Delta H, \Delta e)$ between two anhysteretic M-H curves at two different strain levels and between arbitrary field limits (see Fig.). The choice of field limits allows the M-H results near the origin, $H \leq H_c$, and near saturation $H \geq H_K$ to be omitted from the analysis. The validity of the method is illustrated with measurements on thin cobalt, nickel, and permalloy films.

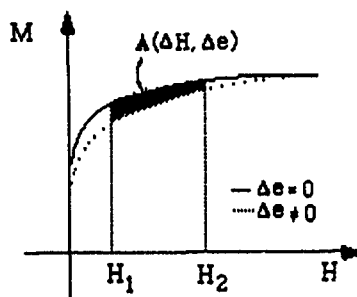


FIG. 1. ME coefficients as related to the area $A(\Delta H, \Delta e)$ between two anhysteretic M-H curves at two different strain levels and between arbitrary field units.

Magnetic anisotropy in epitaxial Ni/Cu(001) thin films: Effects of misfit strain on perpendicular magnetic anisotropy (abstract)

G. Bochi, C. A. Balentine, H. E. Inglefield, S. S. Bogomolov, C. V. Thompson, and R. C. O'Handley

Massachusetts Institute of Technology, Cambridge, Massachusetts 02139

Several epitaxial magnetic systems, notably Fe/Ag(001) and Fe/Cu(001), exhibit perpendicular magnetic anisotropy (PMA) over a relatively narrow thickness range, approximately 2–6 ML. Recently, it has been shown^{1,2} that a similar region of perpendicular anisotropy exists for Ni/Cu(001), but over a much broader range of film thicknesses extending up to approximately 40 ML. The effective anisotropy energy density can be written as $K_{\text{eff}} = -2\pi M_s^2 + 2B_1\epsilon(t) + (2K_N/t)$, which includes magnetostatic (MS), magnetoelastic (ME), and Néel (averaged over two surfaces) terms. The effective anisotropy vanishes at the perpendicular to in-plane transition thickness of about 60 Å. If we assume bulk values for M_s and B_1 , the ME coupling coefficient, and use our measured strain values $\epsilon(t)$, we find that the Néel term is an order of magnitude smaller than the ME and MS terms. These large competing terms therefore control the PMA in this system. We have extended our studies of PMA in Ni/Cu(001) to include $\text{Cu}_{1-x}\text{Ni}_x$ ($0\% < x < 50\%$) alloy substrates for which the misfit strain with the Ni film is reduced. We find that the perpendicular-to-in-plane transition, at $t \approx 40$ ML for Ni/Cu(001), shifts to thinner nickel layers as the misfit strain is decreased by deposition on $\text{Cu}_{1-x}\text{Ni}_x$ substrates. This further confirms the important role of ME energy in PMA for this system.

¹G. Bochi *et al.*, *Mater. Res. Soc. Proc.* **313**, 308 (1993).

²R. Jungblut *et al.*, *J. Appl. Phys.* (to be published).

Spin-wave study of the magnetic excitations in a layered structure with bilinear and biquadratic interlayer exchange

M. Macciò and M. G. Pini

Istituto di Elettronica Quantistica, Consiglio Nazionale delle Ricerche, Via Panciatichi 56/30, I-50127 Firenze, Italy

P. Politi and A. Rettori

Dipartimento di Fisica dell'Università di Firenze, Largo Enrico Fermi 2, I-50125 Firenze, Italy

Using a microscopic and quantum approach, we study the ground state configuration and the spin-wave excitations of a model of two ferromagnetic monolayers, interacting via both bilinear and biquadratic exchange, and subject to an easy-plane anisotropy, a quartic in-plane anisotropy, and an external field. Peculiar features are found in the field dependence of the acoustic and optical frequency gaps in correspondence to the critical fields for which the canting angle between the magnetizations of the two coupled layers presents discontinuities. In particular, we suggest that a minimum in the optical gap at the saturation field could be experimentally observed by Brillouin light scattering in real systems, like Fe/Cr/Fe trilayers.

I. INTRODUCTION

Sandwich structures consisting of two ferromagnetic films separated by a nonmagnetic spacer, like Fe/Cr/Fe trilayers, have attracted wide interest since the discovery of interlayer antiferromagnetic coupling.¹ Later on, detailed investigations of wedge shaped samples revealed the existence of long- and short-period damped oscillations of the interlayer coupling with increasing Cr thickness.^{2,3} Recently, magnetooptic and magnetometry techniques^{4,5} provided experimental evidence for a nearly perpendicular orientation of the magnetizations of the two Fe layers. It was suggested⁴ that such a configuration is due to the presence of a biquadratic interlayer exchange, in addition to the usual bilinear one. Several mechanisms were proposed for the biquadratic coupling, both of macroscopic⁶ and microscopic⁷ origin.

In this paper we study, within a microscopic and quantum approach, the ground state configuration and the spin-wave excitations for the simple model of two ferromagnetic monolayers, interacting via both bilinear and biquadratic interlayer exchange, and subject to an easy-plane single-ion anisotropy, a quartic in-plane anisotropy, and an external field. Whatever its origin, in our model the biquadratic coupling is assumed as a phenomenological parameter. Analytical results are obtained for the frequencies of the two spin-wave modes. Peculiar features are found in the field dependence of the acoustic and optical frequency gaps in correspondence to the critical fields where the canting angle between the magnetizations of the two coupled layers presents discontinuities. Finally, we discuss the relevance of our calculations with respect to real systems, like Fe/Cr/Fe trilayers, and suggest that a minimum in the optical gap at the saturation field could be experimentally observed by Brillouin light scattering (BLS).

II. SPIN-WAVE THEORY

We assume a model of spins localized on the sites of two parallel monolayers, with simple quadratic structure and lattice constant a , separated by a fixed distance c , with a registered (010) interface. The spin Hamiltonian reads

$$\begin{aligned} \mathcal{H} = \sum_{l,l'} \left\{ -\frac{J}{2} \sum_{\delta} \mathbf{S}_l(l_{||}) \cdot \mathbf{S}_{l'}(l_{||} + \delta) + D[S_l^y(l_{||})]^2 \right. \\ \left. - \frac{K}{2} ([S_l^x(l_{||})]^4 + [S_l^z(l_{||})]^4) - g\mu_B \mathbf{H} \cdot \mathbf{S}_l(l_{||}) \right\} \\ - A \sum_l \mathbf{S}_1(l_{||}) \cdot \mathbf{S}_2(l_{||}) - B \sum_l [\mathbf{S}_1(l_{||}) \cdot \mathbf{S}_2(l_{||})]^2, \quad (1) \end{aligned}$$

where $l_{||} \equiv (l_x, l_z)$ and $l (=1,2)$ denotes the plane index. We are particularly interested in the peculiar features arising from the competition between the nearest neighbor ferromagnetic intralayer exchange ($J > 0$) and the antiferromagnetic bilinear ($A < 0$) and biquadratic ($B < 0$) interlayer couplings. We also assume a single-ion anisotropy ($D > 0$), sufficiently strong to make the spins lie in the xz plane, and a quartic anisotropy (K) breaking the in-plane rotational symmetry. We take $K > 0$, so that $\{100\}$ is the easy direction, and $\{101\}$ the hard one. A magnetic field is applied within the xz plane, along a high symmetry direction.

We first perform a transformation of the spin components from the crystallographic frame of reference to a local one, then the usual Dyson-Maleev transformation from spin to bosonic operators. Using the mixed representation $(\mathbf{k}_{||}, l)$, allowed by the translational invariance in the xz plane, and retaining up to quadratic terms in the bosonic operators, the Hamiltonian (1) takes the form

$$\mathcal{H} = E(\varphi_1, \varphi_2) + \sum_{\mathbf{k}_q} \sum_{l,m=1,2} [\mathcal{A}_{lm} a_{\mathbf{k}_q,l}^\dagger a_{\mathbf{k}_q,m} + \frac{1}{2} \mathcal{E}_{lm} (a_{\mathbf{k}_q,l}^\dagger a_{-\mathbf{k}_q,m}^\dagger + a_{\mathbf{k}_q,l} a_{-\mathbf{k}_q,m})]. \quad (2)$$

Defining $h = g\mu_B H$, $\Delta = (\varphi_2 - \varphi_1)$, $\Gamma = (\varphi_1 + \varphi_2)/2$, $f_n = [1 - n/(2S)]$ (with $n=1,2,3$), and $\psi=0$ ($\pi/4$) for H applied along an easy (hard) axis, the diagonal elements are written as

$$\begin{aligned} \mathcal{E}_{ll} &= 4JS[1 - \gamma(\mathbf{k}_q)] + h \cos(\psi - \varphi_l) + DSf_1 + AS \cos \Delta \\ &\quad - \frac{1}{2} BS[2S^2 f_1^2 (1 - 3 \cos^2 \Delta) + \cos \Delta] \\ &\quad - \frac{1}{2} KSf_1[-4S^2 f_3 + S - 4 + 5S^2 f_2 f_3 \sin^2(2\varphi_l)], \\ \mathcal{E}_{ll} &= -DSf_1 - BS^2 f_1^2 \sin^2 \Delta - \frac{1}{2} KSf_1[3S - 2 \\ &\quad + 3S^2 f_2 f_3 \sin^2(2\varphi_l)], \end{aligned} \quad (3)$$

where $\gamma(\mathbf{k}_q) = [\cos(k_x a) + \cos(k_y a)]/2$, with $-\pi \leq k_x a, k_y a \leq \pi$. The off-diagonal elements ($l \neq m$) are

$$\begin{aligned} \mathcal{A}_{lm} = \mathcal{A}_{ml} &= -AS \cos^2 \frac{\Delta}{2} - BS \\ &\quad \times [2S^2 f_1^2 \cos^2 \Delta - S^2 f_2 (1 - \cos \Delta) - \frac{1}{2}], \\ \mathcal{E}_{lm} = \mathcal{E}_{ml} &= AS \sin^2 \frac{\Delta}{2} - BS \\ &\quad \times [2S^2 f_1^2 \cos^2 \Delta - (S^2 f_2 + \frac{1}{2}) \cos \Delta - S^2 f_2]. \end{aligned} \quad (4)$$

The ground state configuration is found minimizing the zero boson term

$$\begin{aligned} E(\varphi_1, \varphi_2) &= (\frac{1}{2} B - A) S^2 \cos \Delta - BS^4 f_1^2 \cos^2 \Delta \\ &\quad + \frac{1}{4} KS^4 f_1 f_2 f_3 [\sin^2(2\varphi_1) + \sin^2(2\varphi_2)] \\ &\quad - hS [\cos(\psi - \varphi_1) + \cos(\psi - \varphi_2)] \end{aligned} \quad (5)$$

with respect to φ_1 and φ_2 (i.e., the angles formed by the magnetizations of the two coupled ferromagnetic monolayers with the in-plane easy axis [100]), or equivalently with respect to Δ and Γ (i.e., the canting angle, and the angle formed by the vector sum of the two magnetizations with [100], respectively). In the classical limit $S \rightarrow \infty$ (so that $f_n \rightarrow 1 \forall n$), we recover the results previously found in Ref. 4 for the $H=0$ ground state configuration.

The frequencies of the spin-wave excitations are obtained, in the framework of a Green's function method previously developed for the study of magnetic multilayers,⁸ as the eigenvalues of the 4×4 real nonsymmetric dynamical matrix

$$\mathcal{P}(\mathbf{k}_q) = \begin{pmatrix} \mathcal{A} & \mathcal{E} \\ -\mathcal{E} & -\mathcal{A} \end{pmatrix}. \quad (6)$$

In the limiting cases with high symmetry, such that $\mathcal{A}_{11} = \mathcal{A}_{22}$ and $\mathcal{E}_{11} = \mathcal{E}_{22}$, they turn out to be⁹

$$\begin{aligned} \omega_{ac}^2(\mathbf{k}_q) &= (\mathcal{A}_{11} + \mathcal{A}_{12})^2 - (\mathcal{E}_{11} + \mathcal{E}_{12})^2 \\ \omega_{op}^2(\mathbf{k}_q) &= (\mathcal{A}_{11} - \mathcal{A}_{12})^2 - (\mathcal{E}_{11} - \mathcal{E}_{12})^2. \end{aligned} \quad (7)$$

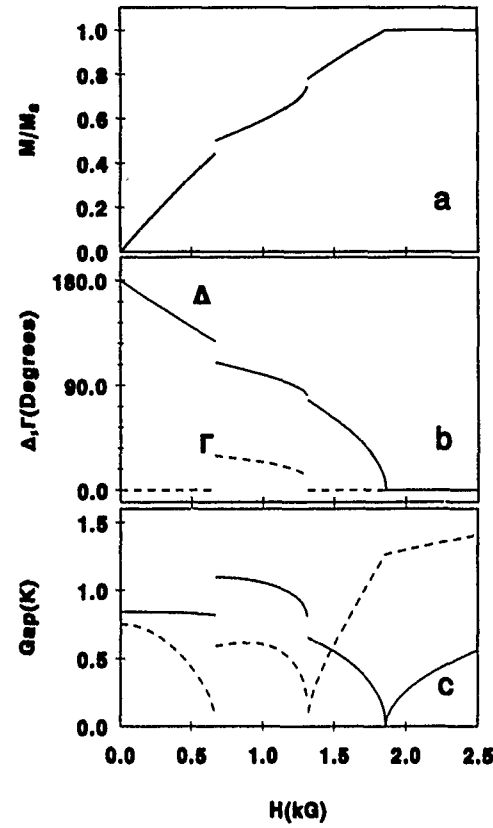


FIG. 1. (a) Mean of the $T=0$ magnetizations of the two coupled films versus the intensity of a magnetic field applied along an in-plane easy axis, [100]. (b) Field dependence of the canting angle Δ (full line), and of the angle Γ (dashed line), formed by the total magnetization with the field direction. (c) Field dependence of the optical (full line) and acoustic (dashed line) frequency gaps. The Hamiltonian parameters are fixed to $A = -0.06$ K, $B = -0.01$ K, $K = 0.1$ K, $D = 1$ K, $S = 2$, $g = 2$.

From the analysis of the eigenvectors of $\mathcal{P}(\mathbf{k}_q)$, one finds that ω_{ac} and ω_{op} can be identified with the acoustic and the optical mode, since they are associated to in-phase and out-of-phase motion of the spins, respectively.⁹

III. RESULTS AND DISCUSSION

In Fig. 1(a) we report the mean of the $T=0$ magnetizations of the two coupled films, $M/M_s = (\cos \varphi_1 + \cos \varphi_2)/2$, versus the intensity of a magnetic field applied along the in-plane easy axis [100]. We choose Hamiltonian parameters such that for $H=0$ the ground state is antiferromagnetic,¹⁰ as experimentally observed by Köbler *et al.* in Fe/Cr/Fe sandwiches.⁵ In agreement with previous calculations,⁵ four different phases are clearly distinguishable with increasing field.¹¹

From Fig. 1(b), where the field dependence of the canting angle Δ and of the angle Γ are reported, one can see that in correspondence to the two lower critical fields separating the first three phases, one has a first order transition since both angles undergo abrupt changes. Instead, at the saturation field $H_s = [B(1 - 4S^2 f_1^2) - 2A - 2KS^2 f_1 f_2 f_3]S/(g\mu_B)$, one has a second order transition.⁵ Moreover, we notice that in the second phase, characterized by an almost perpendicular mutual orientation of the magnetizations of the two

coupled layers, $\Delta \simeq 90^\circ$, the total magnetization is not directed along the field, $\Gamma \neq 0$: these two features result in an almost half-saturation value for the mean of the magnetizations [see Fig. 1(a)].

In correspondence to the critical values of H , for which the magnetization undergoes a first-order phase transition, also the acoustic and optical frequency gaps, $\omega(\mathbf{k}_\parallel=0)$, present discontinuities: see Fig. 1(c). The most interesting feature is the vanishing of the optical gap at the saturation field H_s , even in the presence of a finite in-plane anisotropy, $K \neq 0$. This can be explained, by inspection of the explicit analytic expressions for the frequency gaps,⁹ in terms of a field-induced mechanism of isotropization of the in-plane motion of the spins. In fact, we find that while the energy barrier for deviations of the spins out of the film plane is constant with respect to H , its in-plane counterpart does depend on the field. More precisely, upon H approaching H_s , the energy barrier for in-plane deviations from the canted ground state decreases (i.e., the system becomes more and more isotropic) until, when the field increases further, it constitutes itself an energy barrier.

We suggest that the peculiar features, predicted in the field dependence of the acoustic and optical frequency gaps, could be experimentally observed by BLS in sandwich structures made of ultrathin ferromagnetic films separated by a nonmagnetic spacer. However, for our theory to be applicable, two conditions have to be satisfied. First, the in-plane exchange interaction should be much greater than the interlayer ones, so that the low frequency modes measurable by BLS are determined only by the feeble bilinear and biquadratic interlayer couplings. Second, the system should be able to jump between monodomain stable configurations (with respect to which the spin-wave excitations have been

calculated) without forming domains. Both conditions seem to be satisfied in the case of Fe/Cr/Fe trilayers.¹²

In conclusion, our microscopic spin-wave study of the magnetic excitations, in sandwich structures coupled by bilinear and biquadratic exchange, provides analytical expressions for the spin-wave dispersion curves, which could be useful for the determination of the interlayer coupling constants from BLS data in real systems. In particular, by this technique one could detect the peculiar features predicted in the field dependence of the acoustic and optical frequency gaps, in correspondence to the critical fields for which the canting angle between the magnetizations of the two coupled layers presents discontinuities.

¹P. Grünberg, R. Schreiber, Y. Pang, M. B. Brodsky, and H. Sowers, Phys. Rev. Lett. **57**, 2442 (1986).

²J. Unguris, R. J. Celotta, and D. T. Pierce, Phys. Rev. Lett. **67**, 140 (1991).

³S. Demokritov, J. A. Wolf, and P. Grünberg, Europhys. Lett. **15**, 881 (1991).

⁴M. Rühlig, R. Schäfer, A. Hubert, R. Mosler, J. A. Wolf, S. Demokritov, and P. Grünberg, Phys. Status Solidi A **125**, 635 (1991).

⁵U. Köbler, K. Wagner, R. Wiechers, A. Fuss, and W. Zinn, J. Magn. Magn. Mater. **103**, 236 (1992).

⁶J. C. Slonczewski, Phys. Rev. Lett. **67**, 3172 (1991).

⁷J. Barnaś and P. Grünberg, J. Magn. Magn. Mater. **121**, 73 (1993); J. Barnaś, J. Magn. Magn. Mater. **123**, L21 (1993).

⁸P. Politi, M. G. Pini, and A. Rettori, Phys. Rev. B **46**, 8312 (1992).

⁹M. Macciò, M. G. Pini, P. Politi, and A. Rettori, Phys. Rev. B **49**, 3283 (1994).

¹⁰With an appropriate choice of the Hamiltonian parameters, one can obtain (see Refs. 4,9) a canted ground state configuration at $H=0$, as experimentally observed by Rühlig *et al.* (see Ref. 4).

¹¹Upon reducing the biquadratic exchange constant, one finds that the third phase disappears (see Refs. 5,9).

¹²In the light of the experimental results by Köbler *et al.* (see Ref. 5) the multi-domain state observed in Fe/Cr/Fe wedge shaped samples (see Ref. 4) appears to be a very unstable intermediate state between monodomain stable configurations.

Temperature dependence of interlayer exchange coupling in Co/Ru/Co trilayer structures

Z. Zhang, L. Zhou, and P. E. Wigen

Department of Physics, The Ohio State University, Columbus, Ohio 43210

K. Ounadjela

Institut de Physique et Chimie des Matériaux de Strasbourg, Groupe d'Etudes des Matériaux Metalliques, 4 rue Blaise Pascal, 67070 Strasbourg, France

The temperature dependence of the interlayer exchange coupling field H_{ex} and the effective anisotropy field H_{eff} within ferromagnetic layers was investigated for Co/Ru/Co trilayer structures using the angular dependence of ferromagnetic resonance (FMR). It was found that both H_{ex} and H_{eff} increase with decreasing temperature. The dependence of H_{ex} on temperature follows roughly the relationship $H_{ex} \propto (T/T_0) \sinh(T/T_0)$ predicted by Edwards *et al.*, and the characteristic temperature T_0 decreases with increasing Ru spacer thickness as predicted.

Since the first discovery of antiparallel exchange coupling in the Fe/Cr system,¹ a lot of work has been done to evaluate the interlayer exchange coupling strength in various magnetic multilayer systems using ferromagnetic resonance (FMR) and Brillouin light scattering (BLS).²⁻⁵ For a trilayer system consisting of two ferromagnetic layers separated by a nonmagnetic spacer, the interlayer exchange coupling energy per unit surface area is generally assumed to have the form

$$A_{12} \frac{\mathbf{M}_1 \cdot \mathbf{M}_2}{M_1 M_2}, \quad (1)$$

where A_{12} is the exchange coupling coefficient and \mathbf{M}_1 and \mathbf{M}_2 are magnetization vectors in ferromagnetic layers 1 and 2, respectively.

While many of the FMR and BLS experiments were performed at room temperature, limited research has been devoted to the temperature dependence of the magnetic properties in the magnetic multilayer system. Using a polarized one-band model and an analogy with the de Haas-van Alphen effect, Edwards *et al.*⁶ predicted that the exchange coupling coefficient A_{12} decreases with increasing temperature and follows the relationship

$$A_{12} \propto \frac{T}{T_0} \left/ \sinh\left(\frac{T}{T_0}\right) \right. \quad (2)$$

For multilayer films, the characteristic temperature given by

$$T_0 = \hbar v_F / 2 \pi k_B L, \quad (3)$$

is on the order of 100 K. Here v_F is the Fermi velocity and L is the spacer thickness. Celinski *et al.* performed FMR measurements at several low temperatures on Fe/Pd/Fe and Fe/Cu/Fe trilayer structures and found that the exchange coupling strength at 77 K is almost twice as large as the value at room temperature.⁷ However, the data are too limited to draw any systematic conclusions.

The temperature dependence of the interlayer exchange coupling is readily obtained if both the acoustic mode and the optic mode can be observed in the trilayer system.⁸ However, for the samples in which the two ferromagnetic layers are identical, only the acoustic mode can be observed. In this case, a sensitive experimental method must be developed. The angular dependence of the dispersion relation for a sym-

metrical trilayer system was calculated by adding an exchange field $H_{ex} = 2A_{12}/dM_s$, where d is the thickness of the magnetic layer to the standard single-layer model.⁹ One important result from the calculation is that for an antiparallel coupled system, even the resonance position of the acoustic mode is significantly modified from that of the noncoupled system if the magnetic layers are not saturated at resonance. Furthermore, the angular dependence of the acoustic mode in the unsaturated region is very sensitive to small changes in the exchange coupling strength or to the internal anisotropy energies for certain frequencies.⁹ This provides another way to study the temperature dependence of the interlayer exchange coupling.

Both methods were used to investigate the temperature dependence of the interlayer exchange coupling for a series of Co(32 Å)/Ru(t_{Ru})/Co(32 Å) trilayer structures, where $6 \text{ Å} < t_{Ru} < 80 \text{ Å}$. These trilayer films were prepared in ultra-high vacuum by evaporation on freshly cleaved mica substrate. Transmission electron microscopy (TEM) studies have shown that the layers are epitaxially grown with good crystalline features and relatively sharp interfaces.¹⁰ From the previous FMR and magnetization measurements,⁸ oscillations in the exchange coupling between the Co layers have been found as a function of the Ru spacer at room temperature. The magnetization vectors of the two Co layers are strongly antiparallel coupled for $t_{Ru} \leq 12 \text{ Å}$, parallel coupled for $t_{Ru} \sim 16 \text{ Å}$ and antiparallel coupled for $20 \leq t_{Ru} \leq 24 \text{ Å}$. Insignificant coupling was found for samples with a Ru thickness greater than 28 Å.

The three samples reported here have a Ru thickness of 9 Å (S1), 20 Å (S2), and 24 Å (S3). The Co layers are antiparallel coupled and have easy plane anisotropy energy. Sample S1 is in the first antiparallel coupled region while samples S2 and S3 are in the second antiparallel coupled region.⁸ FMR measurements have been performed at X-band (9.2 GHz) and K-band (23 GHz) frequencies with the temperature ranging from 50 K to 300 K. At each temperature, the external field is rotated from the orientation parallel to the film plane, $\theta_H = 90^\circ$, to the orientation perpendicular to the film plane, $\theta_H = 0^\circ$, in 10° steps.

Figure 1 shows the angular dependence of the FMR spectra for the $t_{Ru} = 9 \text{ Å}$ (S1) sample at K-band frequencies

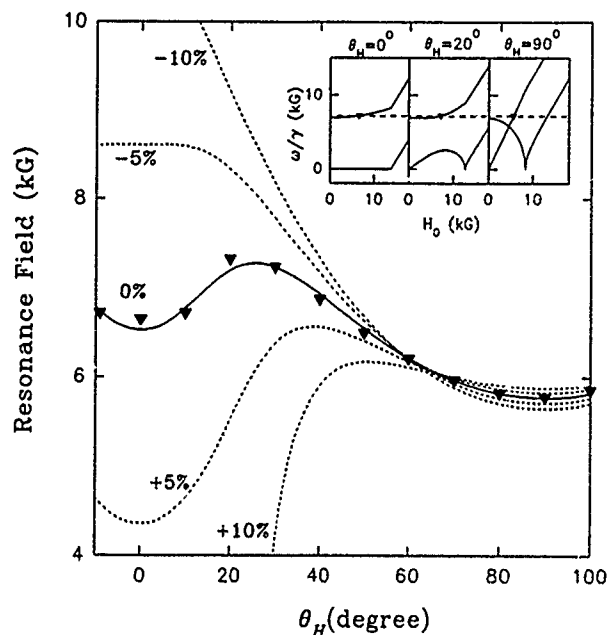


FIG. 1. The angular dependence of the resonance field at K -band frequency (23 GHz) for the Co(32 Å)/Ru(9 Å)/Co(32 Å) sample at room temperature. The solid line is the theoretical curve using the parameters. $H_{ex}=8.74$ kG, $H_{eff}=-5.80$ kG, and $g=2.22$. The dashed lines are the predictions corresponding to a 5% and 10% variation in the exchange field H_{ex} . The inset figures are the predictions of the dispersion relations for this sample at the angles $\theta_H=0^\circ$, 20° , and 90° . The dashed line in the inset figures indicate the position of the K -band frequency.

and room temperature. The resonance field increases as the external field is rotated away from the parallel orientation ($\theta_H=90^\circ$) until it reaches a maximum value at some intermediate angle. The resonance field then decreases as the applied field continues to rotate toward the perpendicular orientation ($\theta_H=0^\circ$). In contrast to the case of a single-layer system, this behavior is not due to a large higher-order anisotropy energy term, but rather related to the nonparallel orientation of the magnetization vectors in the two Co layers due to the large antiparallel interlayer exchange coupling as expected from the magnetization measurement which shows an in-plane saturation field $H_{sat,\parallel} > 8$ kG. Using the exchange coupled resonance theory,⁹ the experimental data can be fitted as shown by the solid line in Fig. 1. The same fitting parameters account for the resonance data at X -band frequencies as well.

If the internal anisotropy field is constant but the exchange coupling field H_{ex} varies by 5% or 10%, Fig. 1 shows that the angular dependence of the resonance spectra changes significantly (dotted line). The agreement between the experimental data and the theoretical calculation indicates that the uncertainty of H_{ex} and the contribution from the bi-quadratic exchange coupled term should be less than 1% for this sample. With the increase of H_{ex} , it can be seen that (1) the angle, θ_H^{max} , at which the resonance field reaches its maximum value increases; (2) the resonance field in the perpendicular orientation decreases; and (3) the change of resonance fields in the parallel orientation is insignificant.

From the temperature dependent FMR spectra for this sample at K -band frequencies, it was found that θ_H^{max} in-

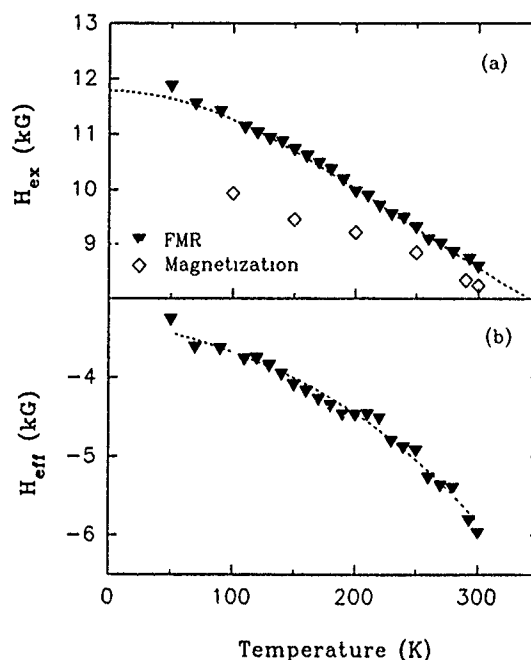


FIG. 2. (a) The interlayer exchange coupling field H_{ex} and (b) the effective anisotropy field H_{eff} as a function of temperature for the sample Co(32 Å)/Ru(9 Å)/Co(32 Å). The dashed lines are the best fit using Eq. (4).

creases from about 20° at 300 K to nearly 80° at 50 K, due to an increase of the interlayer exchange coupling with decreasing temperature. These results are consistent with the in-plane magnetization measurements which show an increase of $H_{sat,\parallel}$ from 8.3 kG at 300 K to 9.9 kG at 100 K. The resonance field in the perpendicular orientation does not change significantly over the temperature range (decreases from 6.5 kG at $T=300$ K to 6.15 kG at $T=50$ K) even though the magnetization measurement indicates a 20% increase in the exchange coupling field as the temperature decreases from 300 to 100 K. The changes in the internal anisotropy field within each Co layer over this temperature range nearly compensates for the increasing in the exchange coupling at the perpendicular orientation but gives a significant increase to the parallel resonance field, from 5.6 kG at room temperature to 6.6 kG at 50 K.

From the FMR results, the g value, H_{ex} , and the effective anisotropy field $H_{eff}=H_u-4\pi M_s$ were evaluated. The g value from this fitting is between 2.18 and 2.26 through the whole temperature range. Both H_{ex} and H_{eff} decrease with increasing temperature (as shown in Fig. 2). The variation of H_{ex} with temperature follows the relationship

$$H_{ex}=H_{ex}^0\left(\frac{T}{T_0}\right)^{\frac{1}{2}}/\sinh\left(\frac{T}{T_0}\right)+H_{ex}^\infty, \quad (4)$$

which is shown as the broken curve in Fig. 2(a). In comparison with Eq. (2) predicted by Edwards *et al.*,⁶ a temperature-independent term, H_{ex}^∞ , is added in order to get a better fit. The characteristic temperature T_0 for this sample is about 150 K. Also shown in Fig. 2(a) are the in-plane saturation fields $H_{sat,\parallel}=H_{ex}$ from the magnetization measurements. The trend of H_{ex} with temperature agrees with the FMR results; however, the values of H_{ex} are noticeably different, which is

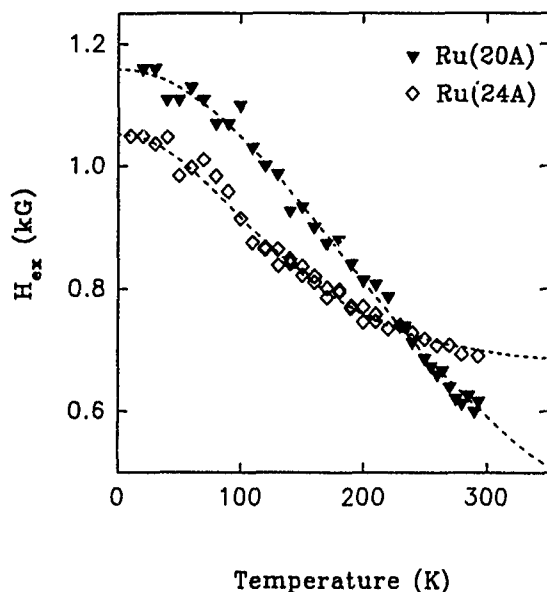


FIG. 3. H_{ex} as a function of temperature for the samples Co(32 Å)/Ru(20 Å)/Co(32 Å) and Co(32 Å)/Ru(24 Å)/Co(32 Å). The dashed lines are the best fit using Eq. (4).

probably due to the inaccurate measurement from the magnetization curve.

For the $t_{Ru}=20$ Å (S2) and 24 Å (S3) samples, the exchange coupling strength is about 0.5 kG at room temperature, much smaller than that in sample S1. Therefore, the magnetization vectors of the Co layers are saturated at resonance. There is a small difference in the internal anisotropy field between the two Co layers in these two samples due to different growth quality.⁸ As a result, both the acoustic mode and the optic mode can be observed. The field separation between the acoustic mode and the optic mode is equal to the exchange field H_{ex} plus the contribution due to the difference in the effective anisotropy field between the two Co layers, $|H_{eff,1} - H_{eff,2}|$. However, the analysis shows that the contribution of the latter term is insignificant for these two samples when the external field is applied parallel to the film plane at X-band frequencies; therefore the field separation in the parallel FMR spectra is used as the exchange coupling field H_{ex} .

Similar to sample S1, H_{ex} in samples S2 and S3 increases with decreasing temperature and can be fitted to Eq. (4) as shown by the dashed lines in Fig. 3. However, T_0 was found to be about 110 K and 60 K for samples S2 and S3, respectively, smaller than that for sample S1 as expected for the thicker Ru layers from Eq. (3).

In these two samples, the parallel resonance field of the acoustic mode increases while the perpendicular resonance field decreases with decreasing temperature, suggesting a decrease in amplitude of the effective anisotropy field H_{eff} at low temperatures. At 100 K $|H_{eff}|$ is observed to decrease by 2–3 kG from the value at room temperature, similar to the result obtained in sample S1, shown in Fig. 2(b).

From the results obtained for the three Co/Ru/Co trilayer structures, it was found that the variation of H_{ex} with temperature follows roughly the relationship predicted by Edwards *et al.*⁶ The characteristic temperature T_0 decreases with an increase of the Ru layer thickness—from 150 K at $t_{Ru}=9$ Å to 60 K at $t_{Ru}=24$ Å. However, T_0 does not seem to follow the $1/t_{Ru}$ relation predicted in the Edwards model which would give $T_0 \sim 70$ K at $t_{Ru}=20$ Å, a value much smaller than the 110 K observed in sample S2.

The authors would like to acknowledge travel support from the North Atlantic Treaty Organization through Grant No. RG.930480.

- ¹ P. Grunberg, R. Schreiber, Y. Pang, M. B. Brodsky, and H. Sowers, Phys. Rev. Lett. **57**, 2442 (1986).
- ² J. J. Krebs, P. Lubitz, A. Chaiken, and G. A. Prinz, Phys. Rev. Lett. **63**, 1645 (1989).
- ³ B. Heinrich, S. T. Purcell, J. R. Dutcher, K. B. Urquhart, J. F. Cochran, and A. S. Arrott, Phys. Rev. B **38**, 12 879 (1988).
- ⁴ J. F. Cochran, J. Rudd, W. B. Muir, B. Heinrich, and Z. Celinski, Phys. Rev. B **42**, 508 (1990).
- ⁵ B. Hillebrands, A. Boufelfel, C. M. Falco, P. Baumgart, G. Guntherodt, E. Zirngiebl, and J. D. Thompson, J. Appl. Phys. **63**, 3680 (1988).
- ⁶ D. M. Edwards, J. Mathon, R. B. Muniz, and M. S. Phan, Phys. Rev. Lett. **67**, 493 (1991).
- ⁷ Z. Celinski, B. Heinrich, J. F. Cochran, W. B. Muir, A. S. Arrott, and J. Kirschner, Phys. Rev. Lett. **65**, 1156 (1990); Z. Celinski and B. Heinrich, J. Magn. Magn. Mater. **99**, L25 (1991).
- ⁸ Z. Zhang, P. E. Wigen, and K. Ounadjela, IEEE Trans. Magn. **29**, 2717 (1993).
- ⁹ Z. Zhang, P. E. Wigen, and K. Ounadjela (unpublished).
- ¹⁰ G. Z. Pan *et al.* (unpublished).

Oscillatory exchange coupling in Fe/Au/Fe(100)

J. Unguris, R. J. Celotta, and D. T. Pierce

Electron Physics Group, National Institute of Standards and Technology, Gaithersburg, Maryland 20899

Scanning electron microscopy with polarization analysis was used to investigate the interlayer exchange coupling in Fe/Au/Fe(100) sandwich structures. The films were epitaxially grown on single-crystal Fe(100) substrates. Electron diffraction measurements revealed that the Au spacer film grew with a surface reconstruction consistent with that observed for bulk Au crystals. The exchange coupling oscillates between primarily ferromagnetic and antiferromagnetic coupling for Au spacer layers up to 65 layers (13 nm) thick, but a significant biquadratic coupling component was also observed. The oscillatory coupling exhibited two components with periods of 2.48 ± 0.05 layers (0.506 ± 0.010 nm) and 8.6 ± 0.3 layers (1.75 ± 0.06 nm). The measured periods are in excellent agreement with those calculated from spanning vectors of the Au Fermi surface.

I. INTRODUCTION

Magnetic measurements from atomically well-ordered magnetic multilayer structures are essential in order to make meaningful evaluations of various models of oscillatory exchange coupling. Thickness variations due to deviations from ideal layer-by-layer growth can obscure important features of the magnetic coupling. For example, in Fe/Cr/Fe multilayers it has been shown that a Cr spacer roughness of only a quarter layer can completely obscure the short, two-layer period, exchange coupling oscillations.¹⁻³

In this work we have investigated the interlayer exchange coupling in epitaxially grown Fe/Au/Fe(100) sandwich structures. Au(100) rotated by 45° is a very close lateral match to the Fe(100) surface and should therefore be a possible candidate for atomically well-ordered growth. In previous work, where the Fe/Au/Fe multilayer was deposited on a Ag(100) substrate, Celinski and Heinrich⁴ did not observe any well-defined oscillatory behavior of the exchange coupling through the Au(100). Using GaAs(100) substrates to grow Fe(100) and a wedge-shaped Au spacer layer, Fuss *et al.*⁵ observed oscillatory coupling consisting of a long-period component of 6.9 layers and a weaker short-period oscillation of about two layers. We have used single-crystal Fe whisker substrates in our studies and have observed very well-defined short- and long-period coupling oscillations that extended over a large Au thickness range.

II. EXPERIMENT

The experimental procedures used to investigate the exchange coupling in Fe/Au/Fe have been described in detail elsewhere.^{2,6} Briefly, the chemical composition and the structural order of the samples were measured using scanning Auger spectroscopy and reflection high-energy electron diffraction (RHEED), respectively. Scanning electron microscopy with polarization analysis (SEMPA) was used to make *in situ* measurements of the sample's magnetization during and following film growth. The films were grown on Fe(100) single-crystal substrates that were cleaned by Ar-ion sputtering followed by 750°C annealing cycles. Scanning tunneling microscope images of similar whiskers show high-quality surfaces with only about one single atomic height step per square μm .⁷ RHEED patterns from the bare whiskers showed sharp diffraction spots distributed along Laue arcs as

expected for a perfect crystal. The Auger spectra established that contamination levels were below 0.05 monolayers.

In order to measure the Au thickness dependence of the exchange coupling, wedge-shaped Au spacer layers were grown by moving a shutter in front of the Fe substrate during Au deposition. The geometry of the wedge is shown schematically in Fig. 1. The slope of the Au wedge was small, about 0.001° , which is less than the 0.01° average slope of the Fe whisker substrate. Au spacer layers were grown at Fe substrate temperatures between 80 and 100°C , and at an evaporation rate of about 8 layers/min. The direction of the interlayer exchange coupling was determined by measuring the magnetization of the top Fe film with SEMPA. Fe whisker substrates with the simple two-domain structure shown in Fig. 1 were used in order to check for and eliminate any instrumental offsets in the SEMPA measurement.

III. RESULTS

The crystalline order and thickness of the Au films were measured using spatially resolved scanning RHEED. Figure 2 shows the specular RHEED intensity as the incident electron beam was scanned along the wedge and a RHEED pattern from a 10-layer-thick Au film. The RHEED intensity oscillations were used to determine the Au thickness con-

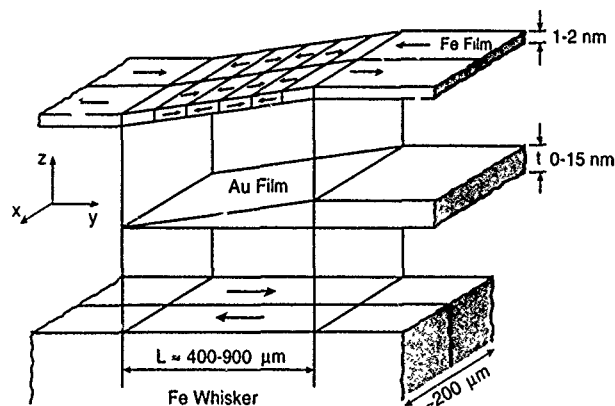


FIG. 1. An exploded schematic view of the sample structure showing the Fe(100) single-crystal whisker substrate, the evaporated Au wedge, and the Fe overlayer. Arrows in the Fe show the magnetization direction.

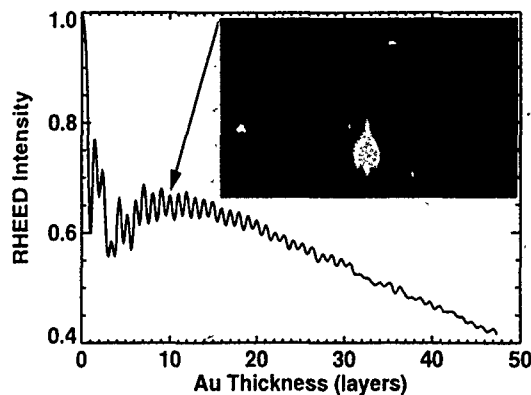


FIG. 2. The specular RHEED intensity as a function of the Au thickness obtained by scanning the electron beam along the wedge. A RHEED pattern from a 10-layer-thick film is shown in the inset.

tours along the wedge. For Au films less than three layers thick, the RHEED patterns were similar to those for clean Fe, but after three layers the diffraction spots stretched into sharp streaks and superlattice streaks began to form. The four extra streaks that appeared between the primary diffraction beams were characteristic of a fivefold surface reconstruction. Both (5×1) and (5×20) surface reconstructions have been observed for bulk Au.⁸ While the presence of streaks in the diffraction patterns indicates some disorder, the surface reconstruction suggests that the Au films have bulklike structural order. In fact the sharpness of the streaks indicates that the Au grows in patches that are internally well ordered but slightly misaligned with respect to one another.

The direction of the magnetic coupling was determined by measuring the magnetization of the top Fe film using SEMPA. A SEMPA image of a Au wedge coated with five layers of Fe is shown in Fig. 3. The component of the magnetization along the whisker direction is M_y , and the orthogonal component of the in plane magnetization is M_x . Oscillations between ferromagnetic and antiferromagnetic "bilinear" coupling are most clearly visible in the M_y component. The M_x component, on the other hand, emphasizes

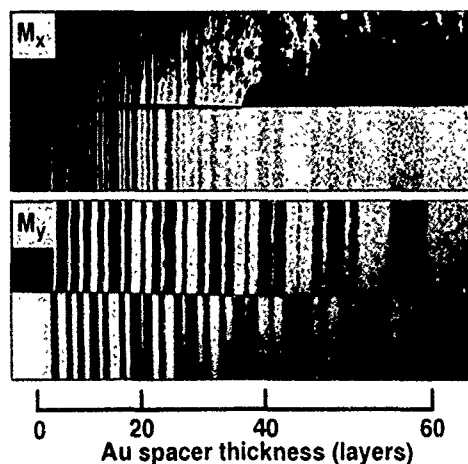


FIG. 3. SEMPA images from the five-layer-thick Fe overlayer, showing the in-plane magnetization components along the wedge, M_y , and orthogonal to the wedge, M_x .

the perpendicular "biquadratic" coupling between the Fe film and substrate. The thickness scale on these images is not linear, because of a gradual drift in the Au evaporation rate. This nonlinearity, as well as any other spatial variations in the Au thickness, was accounted for by using scanning RHEED images from the same region. The scanning RHEED images were correlated with the SEMPA images by aligning topographic features in the RHEED images with the same features in intensity images that were acquired at the same time as the magnetization images.

Averaged, linearized line scans of M_y taken from the data in Fig. 3 and from a different Fe/Au/Fe(100) wedge are shown in Fig. 4. One can see from these data that the periodicity of the coupling is very reproducible, but the amplitude of the oscillations and the thickness at which they eventually vanish vary among samples grown under slightly different conditions.

In order to measure the coupling periods precisely, we followed a previously described procedure⁶ and modeled the bilinear coupling J by the sum of two sine waves such that

$$J = A_1 \sin(2\pi t/d_1 + \phi_1) + A_2 \sin(2\pi t/d_2 + \phi_2), \quad (1)$$

where t is the Au thickness, and A , d , and ϕ are adjustable amplitudes, periods, and phases, respectively. To simulate the SEMPA data, this continuous function was first discretized with the Au lattice so that each monolayer was assigned a single coupling strength. The thicknesses at which the coupling switched sign were then determined by taking the weighted average of the coupling from adjacent layers. Finally, all positive coupling values were set to the same magnetization level and all negative coupling to the equal but opposite magnetization. Figure 4 shows the results of a calculation that gave the best fit of the model to the data. The parameter values for this model were $A_1/A_2 = 2.1$, $d_1 = 2.48$ layers, $\phi_1 = 0.44$, $d_2 = 8.60$ layers, and $\phi_2 = 3.14$.

In addition to the bilinear coupling, biquadratic coupling was also observed in these films. While SEMPA cannot directly measure the absolute strength of the magnetic coupling, the magnetization direction is roughly proportional to the ratio of the biquadratic to bilinear coupling.⁹ The M_x

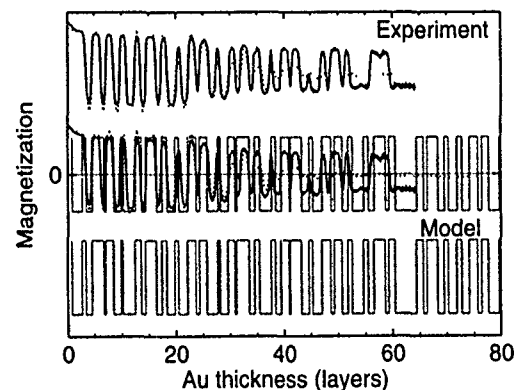


FIG. 4. The results of the model calculation described in the text are compared with an averaged, linearized line scan of the M_y data from Fig. 3 and from a SEMPA measurement from a different wedge (dotted line). For comparison, the calculated (bottom) and measured (top) curves are shown both separately and overlaid.

image in Fig. 3 shows that in the thin part of the wedge the biquadratic coupling is only significant at the transitions between the ferromagnetic and antiferromagnetic regions. As the Au thickness increases, the relative strength of the biquadratic coupling also increases, so that for thicknesses greater than about 20 layers, the biquadratic coupling is always present, and the coupling oscillations are no longer between purely ferromagnetic or antiferromagnetic states, but between some intermediate angles. For thicker Au films the coupling also tends to break up randomly into islands with different M_x magnetization components but the same M_y component. The formation of these regions is not understood, but the length scales involved suggest that it is related to the details of the Au growth.

IV. DISCUSSION

Qualitatively, the Au results are similar to SEMPA measurements of the coupling in Fe/Cr/Fe(100) (Ref. 2) and Fe/Ag/Fe(100) (Ref. 6). In each case, oscillatory coupling was observed that consisted of two periodic components, and the oscillations persisted for spacer layers greater than 10 nm thick. Another common feature of these films grown on Fe whisker substrates is that the short-period oscillations are more pronounced and the oscillations extend over a greater thickness range than in multilayers grown on more conventional substrates. Fe/Au/Fe sandwiches grown on Ag substrates show no oscillatory coupling.⁴ Fe/Au/Fe sandwiches grown on GaAs substrates only reveal weak short-period modulations in the long-period antiferromagnetic coupling.⁵

The ability to observe many coupling oscillations over a large interlayer thickness range allows the coupling periods to be measured with sufficient precision to provide a stringent test of current theories of multilayer exchange coupling. Currently, there are two quantitative predictions of Fe/Au/Fe coupling periods available. In both theories the oscillatory coupling periods are determined by wave vectors that are perpendicular to the surface and span nearly parallel faces of

the spacer layer's bulk Fermi surface. Stiles¹⁰ used a tight-binding fit to a local-density approximation of the Au band structure to compute coupling periods of 2.50 and 9.36 layers. Bruno and Chappert¹¹ used a nearly-free-electron fit to de Haas-van Alphen and cyclotron resonance measurements of Fermi surface extremals and predicted coupling periods of 2.51 and 8.60 layers for Au(100). Both calculations are in good agreement with our measured Au coupling periods of 2.48 ± 0.05 and 8.6 ± 0.3 layers, although the Bruno and Chappert calculation matches the long period better. The general agreement between our measurements and these theories further supports the hypothesis that the oscillatory exchange coupling periods in atomically well-ordered materials are determined by Fermi surface spanning vectors.

ACKNOWLEDGMENTS

We wish to thank M. D. Stiles for many helpful discussions. The whiskers were grown at Simon Fraser University under an operating grant from the National Science and Engineering Research Council of Canada. This work is supported by the Office of Technology Administration of the Department of Commerce and by the Office of Naval Research.

¹Y. Wang, P. M. Levy, and J. L. Fry, *Phys. Rev. Lett.* **65**, 2732 (1990).

²J. Unguris, R. J. Celotta, and D. T. Pierce, *Phys. Rev. Lett.* **67**, 140 (1991).

³D. T. Pierce, J. A. Strosio, J. Unguris, and R. J. Celotta (unpublished).

⁴Z. Celinski and B. Heinrich, *J. Magn. Magn. Mater.* **99**, L25 (1991).

⁵A. Fuss, S. Demokritov, P. Grünberg, and W. Zinn, *J. Magn. Magn. Mater.* **103**, L221 (1992).

⁶J. Unguris, R. J. Celotta, and D. T. Pierce, *J. Magn. Magn. Mater.* **127**, 205 (1993).

⁷J. A. Strosio, D. T. Pierce, and R. A. Dragoset, *Phys. Rev. Lett.* **70**, 3615 (1993).

⁸Y. Kuk, P. J. Silverman, and F. M. Chua, *J. Microsc.* **152**, 449 (1988).

⁹M. Ruhrig, R. Schafer, A. Hubert, R. Mosler, J. A. Wolf, S. Demokritov, and P. Grünberg, *Phys. Status Solidi A* **125**, 635 (1991).

¹⁰M. D. Stiles, *Phys. Rev. B* **48**, 7238 (1993).

¹¹P. Bruno and C. Chappert, *Phys. Rev. Lett.* **67**, 1602 (1991).

Oscillation of the interlayer coupling in Co/Au(111)/Co

J. J. de Vries and W. J. M. de Jonge

Eindhoven University of Technology, Physics Department, P.O. Box 513, 5600 MB Eindhoven, The Netherlands

M. T. Johnson, J. aan de Stegge, and A. Reinders

Philips Research Laboratories, P.O. Box 80000, 5600 JA Eindhoven, The Netherlands

An oscillatory interlayer coupling in Co/Au(111)/Co has been obtained from polar Kerr hysteresis loop measurements on a molecular-beam-epitaxy-grown 50 Å Au/2 Å Co/0–40 Å Au wedge/7 Å Co/20 Å Au sample deposited on a Cu(111) single crystal. The period of the coupling is seen to increase from 11 to 14 Å with increasing Au thickness, indicating a preasymptotic behavior. The asymptotic period of 14 ± 1 Å is larger than the theoretically expected period of 11.4 Å. The observation of coupling up to 40 Å Au will be discussed in relation to the general absence of coupling in evaporated Co/Cu(111)/Co samples.

I. INTRODUCTION

Lately, much attention has been given to the antiferromagnetic (AF) interlayer coupling and its oscillation period in evaporated Co/Cu(111)/Co samples.^{1–5} In general, experiments failed to reveal AF coupling¹ or an oscillation period,² except for recent measurements by Schreyer *et al.*³ and Howson *et al.*,⁴ who only detect a small fraction of AF-coupled Co, and Kohlhepp *et al.*,⁵ who found full AF coupling when using Co layers only one monolayer thick. The difficulty in obtaining interlayer coupling at thicknesses larger than that of the first AF maximum was suggested by Bruno and Chappert⁶ to originate from a cutoff length for the interlayer coupling, whereas others⁷ propose formation of magnetic links through a granular interlayer.

In the former suggestion, the cutoff length results from a loss of translational invariance along the interfaces between the interlayer and the magnetic layers. Consequently, destructive interference in the oscillating interlayer interaction suppresses the coupling at interlayer thicknesses typically larger than the cutoff length. Loss of translational invariance, in turn, can have various origins: mixing at the interfaces, roughness, grain boundaries, or dislocations associated with the incoherent growth present in lattice-mismatched systems. Specifically for the (111) orientation, the expected effect of suppression is dramatic, because of the large angle between the Fermi velocity and the film normal. Assuming only incoherent growth, Bruno and Chappert⁶ have evaluated the cutoff length in the case of Co/Cu(111)/Co to be 52 Å Cu; for Co/Au(111)/Co only 9 Å Au was predicted. The shorter cutoff length in the latter case follows from the large lattice mismatch of approximately 14% compared to about 2% in the case of Co/Cu, as the cutoff length originating from incoherent growth is proportional to the inverse of the lattice mismatch.⁶ If incoherent growth due to a lattice mismatch is to be responsible for the absence of interlayer coupling in various coupling experiments on evaporated Co/Cu(111)/Co samples, then certainly no interlayer coupling is expected in Co/Au(111)/Co. In this article the above hypothesis is tested.

II. EXPERIMENT

In the present experiments, the interlayer was deposited in a wedge shape by translation of a shutter along the sample

during evaporation. The Co layers were chosen to be thin, in order to be able to measure even weak antiferromagnetic coupling (2 Å Co) or to have a perpendicular anisotropy⁸ in order to obtain a large coercive field (7 Å Co). Unequal thicknesses for the two Co layers were used to obtain different coercivities.⁹ This allows measurement of both AF coupling and small ferromagnetic (F) coupling as described in the following section.

The composition of the sample, prepared by molecular beam epitaxy (MBE) in a VG Semicon V80M system, was 50 Å Au/2 Å Co/0–40 Å Au wedge/7 Å Co/20 Å Au. A Cu(111) single crystal of 1 mm thickness and 12 mm diameter was used as a substrate. All layers were deposited at room temperature, at pressures of 10^{-9} Pa and with deposition rates of typically 0.1 Å/s. Layer thicknesses were controlled by a vibrating quartz crystal monitor and checked with *in situ* Auger electron spectroscopy (AES). The wedge start was also determined with AES and its slope was obtained using the quartz crystal (4.1 Å/mm) and confirmed with AES (4.0 Å/mm). Low-energy electron diffraction (LEED) investigations revealed that incoherent growth of the Au base layer resulted in an almost complete relaxation to the bulk Au lattice spacing. Deposition of the ultrathin 2 Å Co layer decreased the sharpness of the LEED spots. The spots remained at their position, which can be interpreted as coherent growth of the Co on Au or as due to the Au layer below the ultrathin, perhaps incoherent, Co layer. Upon deposition of the Au wedge the spots became still more diffuse. Deposition of the thicker upper Co layer clearly proceeded by incoherent growth, with the Co layer assuming bulk lattice spacings. The sixfold symmetry of all LEED photos is ascribed to either a twinned fcc(111) structure or possibly hcp(0001) structure in the case of Co. The presence of incoherent growth establishes that the conditions are met for which the occurrence of the cutoff length has been predicted.

In a perpendicularly applied field, polar Kerr hysteresis loops were measured at various positions along the Au wedge and hence at various Au interlayer thicknesses.

III. RESULTS AND DISCUSSION

In Fig. 1 schematic hysteresis loops are given in case of weak and strong, F and AF coupling. A large and small arrow

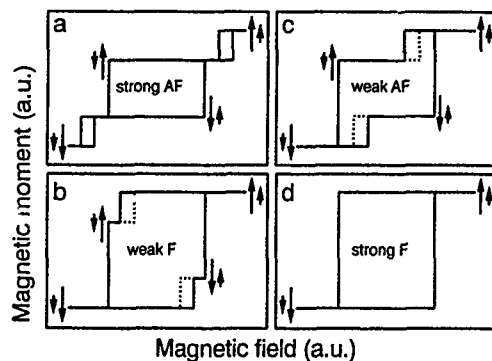


FIG. 1. Model hysteresis loops in case of (a) strong AF, (b) weak F, (c) weak AF, and (d) strong F interlayer coupling. A small and a large arrow indicate a thin and thick layer, respectively. The path indicated by the dotted lines appears if an inner loop is measured.

indicate the magnetic moment of a thick layer (layer 1) with a large coercive field and that of a thin layer (layer 2) with a smaller coercive field, respectively. Both layers are assumed to have a perpendicular easy axis, along which the external field is applied. In case of F [AF] interlayer coupling, the moment of layer 2 is oriented [anti] parallel to that of layer 1 at zero field and does not flip until the coupling is overcome by a large enough negative [positive] magnetic field, as is visible in Fig. 1(b) [1(a) and 1(c)]. As a result the hysteresis loop of layer 2 will be shifted to negative [positive] magnetic fields, although measurement of an inner loop, indicated by the dotted lines, may be required to reveal the full hysteresis loop of this layer. However, the finite coercivity of layer 1 puts an upper limit to the maximum F coupling to be measured. In the case of strong F coupling, the flipping of the moment of layer 1 at its coercive field ends the pinning of the moment of layer 2 via the F coupling against the external field. As a consequence, both moments simultaneously flip and a square hysteresis loop results as shown in Fig. 1(d). Regions of AF coupling can be identified in a straightforward way via a decrease in remanent magnetization.

A compilation of measured Kerr loops obtained at the indicated thickness of the Au interlayer is shown in Fig. 2. First, note that in the loops that show two transitions [2(e)–2(h)] one transition is large and steplike (perpendicular anisotropy), whereas the other is small and gradual (in-plane easy axis). In view of the thickness of the Co layers as well as their position below the top layer, the large steplike transition in the Kerr effect originates from a flipping of the perpendicular moment of the 7 Å Co layer, and the small gradual transition from a rotation of the in-plane moment of the 2 Å Co layer. A clear correspondence between the loops in Figs. 1 and 2 is visible. However, the steplike transition of layer 2 in Fig. 1 has become a gradual transition instead, as can be seen if one compares loop 1(c) with loop 2(h) where an inner loop was measured. An inner loop could not be measured in all cases as the AF state was not always completely reached before the transition of layer 1 took place, e.g., loop 2(f). Nevertheless, a shift of the remaining branch of the transition of layer 2 can still be seen. Comparison with Fig. 1 shows that the loops in Figs. 2(e), 2(g), and 2(h) reveal AF coupling, whereas the loop in Fig. 2(f) indicates weak F

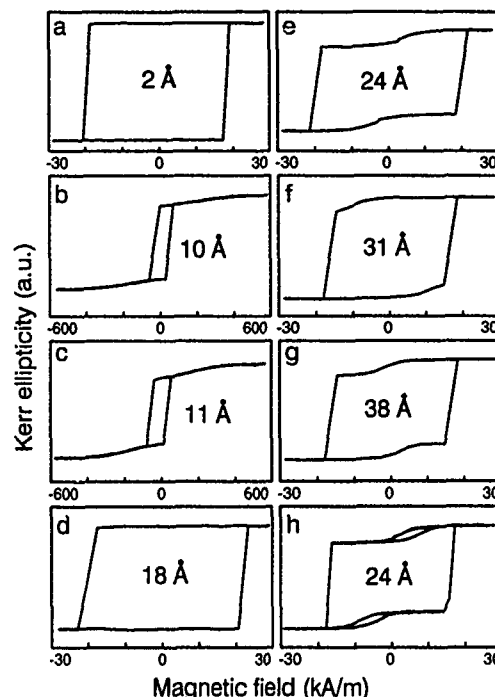


FIG. 2. Kerr hysteresis loops measured at the indicated Au interlayer thickness. Note that the magnetic field range of loops (b) and (c) is much larger than the range of the other loops.

coupling. The square loops in Figs. 2(a) and 2(d) indicate a strong F interlayer coupling. In Figs. 2(b) and 2(c) the magnetic transition of the 2 Å Co layer also indicates AF coupling, but the transition extends over a much larger field range than for example in Fig. 2(e). This can be partly understood from numerical absolute minimum energy calculations as discussed in a more extensive article,¹⁰ in which also the transition fields as observed in Fig. 2, containing the strength of the interlayer interaction, will be analyzed. However, since the main point of this article is the oscillatory behavior of the interlayer coupling, an analysis of the remanence is sufficient.

In Fig. 3, the remanence is plotted against the Au interlayer thickness. Three minima corresponding to maximum AF coupling are visible at 12.6, 23.8, and 38.0 Å Au. The period increases with increasing spacer thickness from 11.2 to 14.2 Å (with an estimated error of ± 1 Å due to wedge slope uncertainties), which indicates preasymptotic behavior. Although a decreasing period was predicted by Zlatić¹¹ an increasing period was also found by Shintaku, Daitoh, and

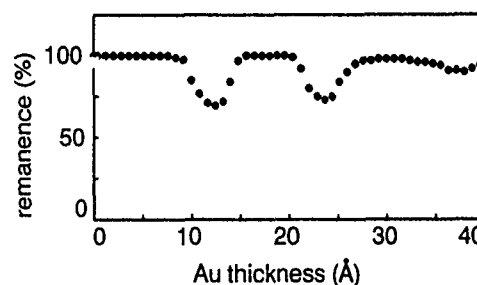


FIG. 3. Plot of the remanence against Au interlayer thickness.

Shinjo¹² for Fe/Au(100). The period at large Au thicknesses is significantly larger than the predicted¹³ asymptotic period of 11.4 Å. The origin of this discrepancy is not clear, but a similar discrepancy was observed for Co/Cu(100).¹⁴ The analysis of the transition fields¹⁰ corroborates these results.

It has thus been established that a clear oscillatory interlayer coupling across Au(111) layers separating (partly) incoherent Co layers can be observed up to 40 Å Au. This result must be confronted with the discussion of Bruno and Chappert,⁶ who argue that, in Co/Au(111)/Co, the interlayer coupling would be suppressed typically above 9 Å, being the cutoff length due to lattice mismatch. Apparently, the suppression is not strong enough to obscure the interlayer coupling at larger Au thicknesses. In view of the considerably smaller cutoff length due to lattice mismatch in the present system as compared to the cutoff length in Co/Cu(111)/Co (52 Å), one is tempted to conclude that the controversial behavior in evaporated Co/Cu(111)/Co cannot be due to this suppression. The observation of an oscillation of the coupling strength in sputtered incoherent Co/Cu(111)/Co samples¹⁵ supports this. Still, other sources of loss of translational invariance, such as interface mixing, could be responsible for the different behavior of the Co/Cu(111) and the Co/Au(111) systems.

IV. CONCLUSIONS

From magnetization remanence data the interlayer coupling oscillation period for Au(111) between Co layers is deduced and is found to increase with spacer thickness, reflecting a preasymptotic behavior. The period of 14 ± 1 Å at large Au thickness is larger than the predicted¹³ period of 11.2 Å.

Note added in proof. After completion of this work, we were informed of a similar investigation of the F and AF interlayer coupling in Co/Au(111)/Co by Grolier *et al.*¹⁶

ACKNOWLEDGMENTS

The authors would like to thank P. Bloemen for useful discussions and for a careful reading of the manuscript. Part of this research was financially supported by the Dutch Foundation for Fundamental Research (FOM).

- ¹W. F. Egelhoff, Jr., and M. T. Kief, *Phys. Rev. B* **45**, 7795 (1992).
- ²M. T. Johnson, R. Coehoorn, J. J. de Vries, N. W. E. McGee, J. aan de Stegge, and P. J. H. Bloemen, *Phys. Rev. Lett.* **69**, 969 (1992).
- ³A. Schreyer, K. Brühl, J. F. Ankner, C. F. Majkrzak, Th. Zeidler, P. Böderker, N. Metoki, and H. Zabel, *Phys. Rev. B* **47**, 15 334 (1993).
- ⁴M. A. Howson, B. J. Hickey, J. Xu, D. Grieg, and N. Wiser, *Phys. Rev. B* **48**, 1322 (1993).
- ⁵J. Kohlhepp, S. Cordes, H. J. Elmers, and U. Gradman, *J. Magn. Magn. Mater.* **111**, L231 (1992).
- ⁶P. Bruno and C. Chappert, *Phys. Rev. B* **46**, 261 (1992).
- ⁷J. de la Figuera, J. E. Prieto, C. Ocal, and R. Miranda, *Phys. Rev. B* **47**, 13 043 (1993).
- ⁸C. Chappert, K. Le Dang, P. Beauvillain, H. Hurdequint, and D. Renard, *Phys. Rev. B* **34**, 3192 (1986).
- ⁹P. Beauvillain, P. Bruno, J. P. Chauvinaeu, M. Galtier, K. Le Dang, C. Marlière, R. Mégy, D. Renard, J. Seiden, F. Trigui, P. Veillet, and E. Vélú, *J. Magn. Magn. Mater.* **94**, 319 (1991).
- ¹⁰J. J. de Vries, P. J. H. Bloemen, M. T. Johnson, J. aan de Stegge, A. Reinders, and W. J. M. de Jonge, *J. Magn. Magn. Mater.* **129**, L129 (1994).
- ¹¹V. Zlatic, *Solid State Commun.* **86**, 523 (1993).
- ¹²K. Shintaku, Y. Daitoh, and T. Shinjo, *Phys. Rev. B* **47**, 14 584 (1993).
- ¹³P. Bruno and C. Chappert, *Phys. Rev. Lett.* **67**, 1602 (1991).
- ¹⁴M. T. Johnson, S. T. Purcell, N. W. E. McGee, R. Coehoorn, J. aan de Stegge, and W. Hoving, *Phys. Rev. Lett.* **68**, 2688 (1992).
- ¹⁵S. S. P. Parkin, R. Bhadra, and K. P. Roche, *Phys. Rev. Lett.* **66**, 2152 (1991).
- ¹⁶V. Golier, D. Renard, B. Bartenlian, P. Beauvillain, C. Chappert, C. Dupas, J. Ferré, M. Galtier, E. Kolb, M. Mulloy, J. P. Renard, and P. Veillet, *Phys. Rev. Lett.* **71**, 3023 (1993).

Theory of Brillouin light scattering from dipole-exchange spin waves in magnetic double layers with interlayer exchange coupling

A. N. Slavin

Physics Department, Oakland University, Rochester, Michigan 48309

I. V. Rojdestvenski and M. G. Cottam

Physics Department, University of Western Ontario, London, Ontario N6A 3K7, Canada

The analytic theory of Brillouin light scattering from dipole-exchange spin waves (SW) in single magnetic films is extended to the case of perpendicularly magnetized exchange-coupled magnetic double layers. It is shown that the influence of the interlayer exchange coupling on the SW spectrum of a symmetric double layer can be taken into account by renormalizing the pinning parameter at the interface between the magnetic film and the spacer for the antisymmetric SW modes (the symmetric modes are unaffected). Using a Green's-function formalism for light scattering from magnetic films, we calculate the light-scattering cross sections from the dipole-exchange discrete SW branches of the double layer. Numerical examples are presented.

I. INTRODUCTION

In our previous papers^{1,2} we have developed a simple analytical formalism for Brillouin light scattering from dipole-exchange spin waves (SW) in ferromagnetic films with arbitrary surface anisotropies. The aim of the present paper is to extend this theory to the case of layered structures consisting of two ferromagnetic films separated by thin non-magnetic layers. The complete theory should account for dipole-dipole and exchange interactions within each ferromagnetic layer as well as the dipole-dipole and exchange couplings between different films (layers).

The problem of SW excitations in double-layer systems has been addressed by several authors and, although theoretical curves obtained adequately describe the existing experimental data, the theory involves lengthy numerical calculations of a rather cumbersome system of initial equations. Here we develop a more simple, analytic approach to the theoretical description of this system, and we make applications to Brillouin light scattering.

II. SPIN-WAVE SPECTRUM FOR THE DOUBLE-LAYER SYSTEM

Let us consider a perpendicularly magnetized layered structure consisting of two ferromagnetic films (labeled 1 and 2) of thicknesses L_1 and L_2 , separated by a nonmagnetic layer of thickness b . The pinning constants d_1^s and d_2^s characterize pinning on the outer surface (s) and interface (i), respectively, of each film. The z axis is taken to be perpendicular to the planar surfaces and interfaces.

We assume that the interlayer exchange interaction is characterized by a phenomenological parameter $\beta_j = A_{12}/A_j$, j and A_j being the film number and the corresponding exchange constant, respectively, and A_{12} is the interlayer exchange constant as defined in Refs. 3 and 4. The parameter β is a function of the spacer thickness b . The typical experimental behavior of β as a function of b is discussed elsewhere.^{5,6} It can be positive, negative, or oscillatory, being generally of the order of magnitude 10^6 cm^{-1} . In our theory we use β as an empirical parameter already known either from microscopic calculations or from experiment.

The procedure of obtaining the SW spectrum for the multilayered system has been developed in Ref. 7 for the case of purely dipolar coupling between the layers. It is based on the expansion of the variable part of magnetization $\mathbf{m}_j(\mathbf{r}, t)$ and the dipolar field $\mathbf{h}_j^{\text{dip}}(\mathbf{r}, t)$ of the film j into the Fourier series of the following kind:

$$\mathbf{m}_j(\mathbf{r}, t) = \sum_{\mathbf{k}} \sum_n \mathbf{m}_{kjn} \phi_{jn}(z) \exp[-i(\mathbf{k}\mathbf{r} - \omega t)], \quad (1)$$

$$\mathbf{h}_j^{\text{dip}}(\mathbf{r}, t) = \sum_{\mathbf{k}} \sum_n \mathbf{h}_{kjn}^{\text{dip}} \phi_{jn}(z) \exp[-i(\mathbf{k}\mathbf{r} - \omega t)], \quad (2)$$

where \mathbf{k} and \mathbf{r} are the in-plane wave vector and radius vector, respectively, and the functions $\phi_{jn}(z)$ for the case of two layers should be taken in the form:

$$\begin{aligned} \phi_{1n}(z) &= A_{1n} \cos \kappa_{1n} \left(z + \frac{b}{2} + L_1 \right) \\ &\quad + B_{1n} \sin \kappa_{1n} \left(z + \frac{b}{2} + L_1 \right), \\ \phi_{2n}(z) &= A_{2n} \cos \kappa_{2n} \left(z - \frac{b}{2} - L_2 \right) \\ &\quad + B_{2n} \sin \kappa_{2n} \left(z - \frac{b}{2} - L_2 \right), \end{aligned} \quad (3)$$

where κ_{jn} are the transverse discrete wave numbers. To incorporate the effects of the interlayer exchange coupling into the theory⁷ we require that the eigenfunctions (3) satisfy the linearized Hoffmann boundary conditions:⁵

$$\begin{aligned} -\frac{\partial \phi_{1n}}{\partial z} + d_1^s \phi_{1n} \Big|_{z=-(L_1+b/2)} &= 0, \\ \frac{\partial \phi_{2n}}{\partial z} + d_2^s \phi_{2n} \Big|_{z=(L_2+b/2)} &= 0, \\ \frac{\partial \phi_{1n}}{\partial z} + (d_1^i + \beta_1) \phi_{1n} \Big|_{z=-b/2} - \frac{M_{01}}{M_{02}} \beta_1 \phi_{2n} \Big|_{z=b/2} &= 0, \end{aligned} \quad (4)$$

$$-\frac{\partial \phi_{2n}}{\partial z} + (d_2^i + \beta_2) \phi_{2n} \Big|_{z=b/2} - \frac{M_{02}}{M_{01}} \beta_2 \phi_{1n} \Big|_{z=-b/2} = 0,$$

where M_{0j} is the static magnetization in the film j . In particular, for a symmetric structure with two identically magnetized layers (i.e., $L_1 = L_2 \equiv L$, $d_1^i = d_2^i \equiv d^i$, $\beta_1 = \beta_2 \equiv \beta$, $M_{01} = M_{02} \equiv M_0$, $\kappa_{1n} = \kappa_{2n} \equiv \kappa_n$), Eqs. (4) lead to

$$(\kappa_n^2 - d^s d^i) \tan \kappa_n L = \kappa_n (d^s + d^i) \quad (5)$$

for the *symmetric* modes, i.e., the modes with the variable magnetization in the both layers distributed similarly, and

$$[\kappa_n^2 - d^s (d^i + 2\beta)] \tan \kappa_n L = \kappa_n [d^s + (d^i + 2\beta)] \quad (6)$$

for the *antisymmetric* modes.

Equation (5) is the same as that for a single (uncoupled) layer of thickness L (see, e.g., Refs. 8 and 9). Equation (6) has a similar form but with a modification of the interface pinning due to the interlayer exchange β , i.e., $d^i \rightarrow d^i + 2\beta$. Thus we conclude that the interlayer coupling affects only antisymmetric modes. This conclusion is in agreement with the results of Ref. 3. In particular, in the case of unpinned surface spins ($d^i = d^s = 0$) we recover from Eq. (6) all the results for transverse wave numbers of antisymmetric modes obtained in Ref. 3. It also follows from the results of Refs. 8 and 9 that when $d^i = d^s = 0$ for $\beta > 0$ we get only real solutions for κ (bulk modes), while for $\beta < 0$ along with the infinite number of bulk solutions we obtain one (lowest) surface solution with imaginary κ_n . By making the replacement $d^i \rightarrow d^i + 2\beta$, we can apply all the conclusions of our previous papers^{1,2} to describe quantitatively the SW dispersion in exchange-coupled magnetic double layers.

Using Eqs. (5) and (6) to calculate the transverse SW wave numbers κ_n in a double layer with exchange coupling, and the formalism developed in Ref. 7 for dipolar coupling of magnetic layers we can derive an approximate dispersion relation for SW propagating in a magnetic double layer consisting of two identical magnetic films coupled by both dipole-dipole and exchange interactions. In a particular case of coupling of two identical (n th) modes in both films we get the following dispersion relation for a double layer:

$$(\omega_n^\pm)^2 = \Omega_n (\Omega_n + \omega_M P_{nn}) \pm (\omega_M \Omega_n P_{nn}^{12})^2, \quad (7)$$

where the $+$ sign corresponds to antisymmetric modes, the $-$ sign corresponds to symmetric modes, $\omega_M = 4\pi\gamma M_0$, and γ is the gyromagnetic ratio. $\Omega_n = \Omega(\kappa_n)$ is the eigenfrequency of the n th SW mode of a single film in the purely exchange limit (see Refs. 7 and 8); it depends on $\omega_H = \gamma(H_e - 4\pi M_0)$, where H_e is the external bias magnetic field. We do not reproduce here the lengthy expressions for the diagonal $P_{nn} = P_{nn}^{11} = P_{nn}^{22}$ and off-diagonal P_{nn}^{12} dipole matrix elements in coupled magnetic films as the procedure of their analytical evaluation is well developed (see, e.g., Refs. 7 and 8). We note that, as the expressions for P_{nn} and P_{nn}^{12} depend on the values of the transverse wave numbers κ_n (and therefore on the value of the exchange coupling coefficient β), so does the splitting of the spectral branches. This leads us to the conclusion that the dipole-dipole and exchange splitting of the dispersion branches should not be considered separately. Both types of splitting influence the

spectrum and, though interlayer exchange mainly affects the frequencies of antisymmetric SW modes near $k=0$ [see Eq. (6)], it will also significantly change the dipole-dipole branch repulsion in the short-wavelength ($kL \gg 1$) region.

III. BRILLOUIN LIGHT SCATTERING

The Green's-function formalism for Brillouin light scattering from multilayered magnetic structures is well established (see Ref. 10 and references therein) and can be considered as a direct generalization of our earlier work^{1,2} for thin films. Basically, the scattering cross section can be expressed in terms of a weighted summation over magnetization-dependent Green's functions $\langle\langle m_{nk}^\mu; m_{n'k'}^\nu \rangle\rangle$ with $\mu, \nu = x, y$. The weighting factors depend on the temperature, magneto-optical coupling, electric field polarizations, scattering geometry, and the optical transmission coefficients at the various surfaces and interfaces. Hence, since the appropriate Green's functions have been calculated from the formalism described earlier, it is straightforward in principle to determine the light-scattering intensities associated with the various SW modes. In the general case it is necessary to take account of the various internal multiple reflections of the incident and scattered light at the surfaces and interfaces of the sample. In the present paper we avoid this difficulty by restricting attention to the case when the optical penetration depth of the light in the sample is smaller than L (e.g., as would be typically in the case of Fe films), thereby making the multiple reflection effects negligible.

IV. DISCUSSION OF NUMERICAL RESULTS

We are interested here in surface SW modes of a double layer that correspond to the solutions of Eqs. (5)–(7) for imaginary κ_n . The numerical analysis shows, that, depending on the values of d^i , d^s , and β , there exist two, one, or no such solutions. When both of the effective pinning parameters d^i and d^s are negative and sufficiently large, there are two imaginary solutions for κ_n , while for non-negative values of one of these parameters a single solution exists only if the second parameter is negative. The same kind of analysis can be applied to the dependence of the κ values on the exchange coupling coefficient β . As the symmetric modes are not affected by the interlayer exchange, the κ_n values for the symmetric modes remain the same for all values of β . Contrary to that, for the antisymmetric modes the effective interface pinning changes with β and so do the κ_n values.

We calculated the dependence of the imaginary transverse wave numbers (corresponding to surface SW modes) on the interlayer exchange parameter β for the system Fe/spacer/Fe. We used the following set of parameters:¹ exchange parameter^{1,2} $\alpha = A/(2\pi M_0^2) = 1.15 \times 10^{-13} \text{ cm}^{-1}$, film thickness $L = 200 \text{ \AA}$, $4\pi M_0 = 21 \text{ kG}$, the external bias magnetic field $H_e = 22.5 \text{ kOe}$, and the pinning parameters $d^s = d^i = d = K_s/A = -1 \times 10^6 \text{ cm}^{-1}$. The values of β were taken to vary from -5×10^5 to $1 \times 10^5 \text{ cm}^{-1}$. The results are presented in Fig. 1. For the given set of parameters there exist one surface branch for the symmetric mode (horizontal line A) and two surface branches for the antisymmetric mode

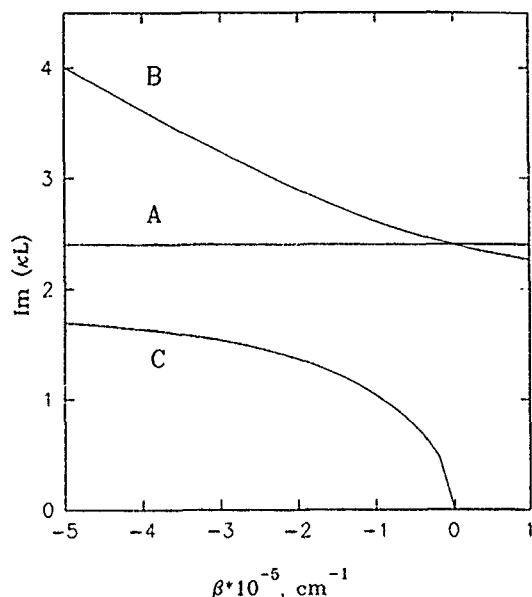


FIG. 1. The dependencies of imaginary perpendicular SW wave numbers on the interlayer exchange coefficient β for the Fe/spacer/Fe structure (see text for the parameters and details).

(curves B and C). Curve C ends at the point $\beta=0$, where the corresponding branch of the SW spectrum meets the bulk continuum.

The existence of the imaginary solutions for κ_n , however, does not guarantee the existence of the corresponding branches in the SW spectrum. This becomes clear from the analysis of the dispersion equation (7). The dipole matrix elements P_{nn}^{ik} are always positive. However, the sign of the Ω_n depends on the values of $|\mathbf{k}|$ and κ_n , sometimes be-

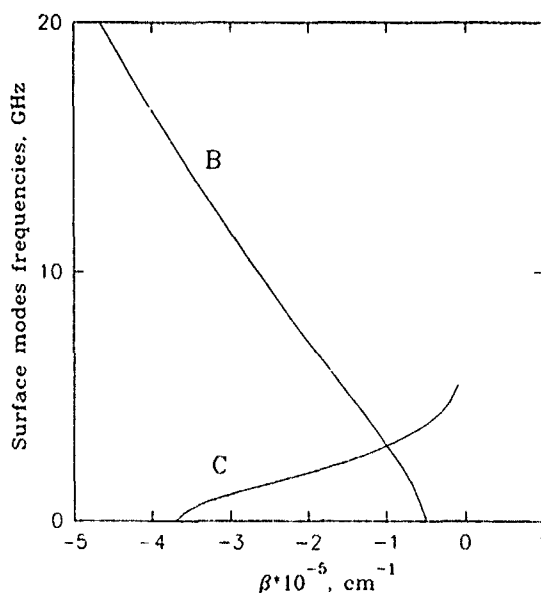


FIG. 2. The dependencies of surface SW frequencies on the interlayer exchange coefficient β for the Fe/spacer/Fe structure (see text for the parameters and details).

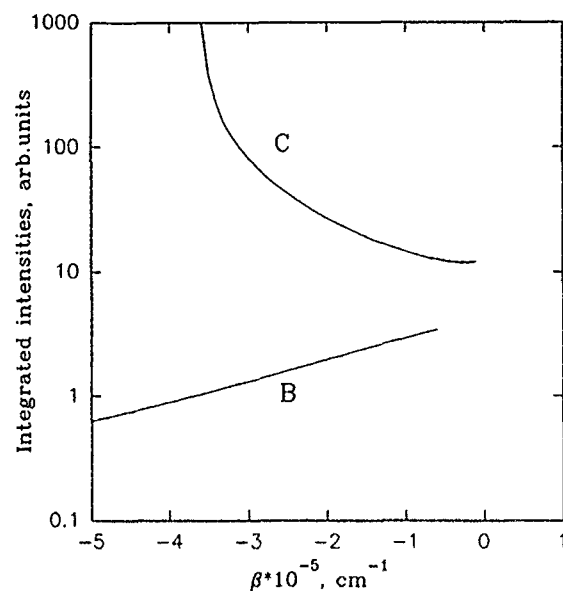


FIG. 3. The dependencies of the integrated intensities of Brillouin light scattering from the surface SW on the interlayer exchange coefficient β for the Fe/spacer/Fe structure (see text for the parameters and details).

coming negative. In this case if P_{nn}^{ik} are sufficiently large, the right-hand side of Eq. (7) becomes negative.

The above conclusions are confirmed by the results of our calculations of the SW spectrum and the integrated intensities of the light scattering from the system Fe/spacer/Fe for the given values of the parameters. We used the same 180° backscattering geometry as previously,^{1,2} taking the complex refractive index $\eta=2.72+2.86i$, incident light wavelength $\lambda=488$ nm, and the scattering angle $\Theta=\pi/4$. This provides for the in-plane wave number of the SW to be $|\mathbf{k}|\approx 1.8\times 10^5$ cm⁻¹. In Fig. 2 we display the dependencies of the surface modes frequencies on β . It can be seen that though the imaginary κ for symmetric mode exists, there is no corresponding branch in the SW spectrum. As well, branch C in Fig. 2, corresponding to curve C in Fig. 1, appears only when the β values are in the interval from about -3.6×10^5 to 0 cm⁻¹. In the same way, branch B ceases to exist when $\beta\geq -0.5\times 10^5$ cm⁻¹ while the corresponding κ dependence (curve B in Fig. 1) still shows the existence of the solution. Basically the same characteristic features can be seen in Fig. 3, where the integrated intensities of the Brillouin light scattering are depicted.

¹I. V. Rojdestvensky, M. G. Cottam, and A. N. Slavin, *J. Appl. Phys.* **73**, 7001 (1993).

²I. V. Rojdestvensky, M. G. Cottam, and A. N. Slavin, *Phys. Rev. B* **48**, 12768 (1993).

³K. Vayhinger and H. Kronmüller, *J. Magn. Magn. Mater.* **72**, 307 (1988).

⁴B. Hillebrands, *Phys. Rev. B* **41**, 530 (1990).

⁵M. Vohl, J. Barnas, and P. Grunberg, *Phys. Rev. B* **39**, 12003 (1989).

⁶B. Heinrich, Z. Celinski, J. F. Cochran, A. S. Arrott, K. Myrtle, and S. T. Purcell, *Phys. Rev. B* **47**, 5077 (1993).

⁷B. A. Kalinikos and P. A. Kolodin, *Izv. Vuzov-Radiofizika* **32**, 1290 (1989).

⁸B. A. Kalinikos and A. N. Slavin, *J. Phys. C* **19**, 7013 (1986).

⁹R. C. Moul and M. G. Cottam, *J. Phys. C* **16**, 1307 (1983).

¹⁰M. G. Cottam and D. J. Lockwood, *Light Scattering in Magnetic Solids* (Wiley, New York, 1986).

Self-stabilization of domain walls in antiferromagnetically coupled multilayered magnetic films

Hideo Fujiwara, Tomohiro Ishikawa, and W. D. Doyle

The University of Alabama, Center for Materials for Information Technology, Tuscaloosa, Alabama 35487-0209

In our previous work, it was shown that in antiferromagnetically coupled multilayered films there is the possibility of the appearance of both Bloch-type walls and Néel-type walls at the center of which the magnetizations point parallel (PB,PN) or antiparallel (AB,AN) to each other between the adjacent layers when a high field is applied in one direction and then removed. Here it is shown that the shift of the walls in each layer from their vertical alignment will give substantially lower energy for the AB walls and for the PN walls, giving rise to self-stabilization, and that the effect is greater for the latter than the former for $[\text{Co/Cu}]_N$ systems with the thickness ratio $t_{\text{Co}}/t_{\text{Cu}}=2$. This will result in a greater possibility of the PN walls formation than was expected in the previous work. In the region where the number of layers and the coupling field are of practical interest, Néel walls are favored, and AN walls have lower energy than PN walls. In this case, it is likely that the transition of the wall types from PN to AN and vice versa will occur during the magnetization process, which will cause noise in sensor applications.

INTRODUCTION

The giant magnetoresistance effect in antiferromagnetically coupled multilayered films has raised great interest both from the viewpoint of physics and from the viewpoint of its applications to magnetic sensors, such as read heads in magnetic recording. Domain wall behavior is one of several important properties that should be investigated thoroughly, especially for applications. Although there have been extensive studies on domain walls in multilayered films, they were mostly on ferromagnetically and/or magnetostatically coupled films (see, for instance, the first reference¹). Our previous work² showed that in antiferromagnetically coupled multilayered films, such as $[\text{Co/Cu}]_N$ films, when a high field is applied in one direction and then removed, both parallel and antiparallel magnetization configurations with respect to the magnetization direction at the center of the walls of adjacent layers will become stable, both for Bloch-type and for Néel-type walls, depending on the film geometry and the strength of antiferromagnetic exchange coupling between the layers. In this paper we report on the effect of the shift of the walls from their vertical alignment on the wall energy, which reveals that the formation of parallel Néel (PN) walls is more favored by the shift than parallel Bloch (PB) and antiparallel Bloch (AB) walls for some cases of multilayered films of interest. A probable occurrence of the transition from PN to AN (antiparallel Néel) walls and vice versa during the magnetization processes will also be discussed.

DOMAIN WALL MODELS

Figure 1 illustrates the magnetization configurations in parallel (PB) and antiparallel (AB) Bloch walls and parallel (PN) and antiparallel (AN) Néel walls when no external field is applied. It is evident that for AB walls and PN walls, a shift of the center of the domain walls with respect to that of the adjacent layers, as shown in the figure, gives lower energy through the reduction in magnetostatic energy, while for PB walls and AN walls, it will not. The shift will make a zig-zag configuration for AB walls, while, for PN walls, it will result in a step-type configuration, because the magnetostatic interaction between the next nearest neighbors is at-

tractive for the AB walls, while that for PN walls is repulsive.

DOMAIN WALL SHIFT

For simplicity, it is assumed that the magnetization direction in the wall changes linearly in the width direction, x , in a way, as given by

$$\phi = \pi x / \delta \quad \text{and} \quad -\pi x / \delta, \quad \text{for parallel walls,} \quad (1a)$$

$$\phi = \pi x / \delta \quad \text{and} \quad \pi x / \delta + \pi, \quad \text{for antiparallel walls.} \quad (1b)$$

Here, the origin of the x axis is set at the center of each wall, δ denotes the wall width, and the former and the latter formulas in each equation correspond to the magnetization direction of the odd and even numbered layers from the bottom, respectively.

The wall energy per unit area σ is expressed as a sum of the exchange energy σ_A , anisotropy energy σ_k , antiferromagnetic coupling energy σ_{AF} , and magnetostatic energy σ_s , as

$$\sigma = \sigma_A + \sigma_k + \sigma_{AF} + \sigma_s. \quad (2)$$

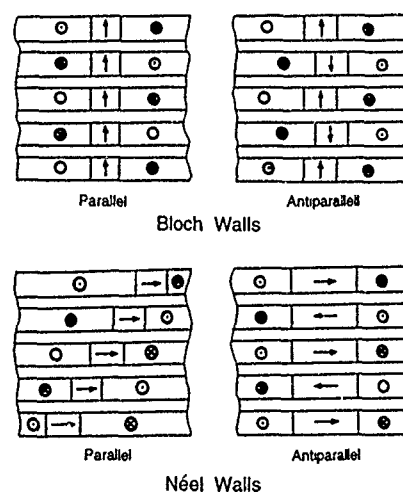


FIG. 1. Magnetization configurations in parallel and antiparallel Bloch walls and parallel and antiparallel Néel walls.

Among the above four energies, σ_{AF} , as well as σ_s , varies explicitly with the amount of the shift Δ , while the other two vary implicitly through the change of the wall width σ .

The antiferromagnetic coupling energy σ_{AF} is expressed as

$$\sigma_{AF} = \left(\frac{I_s H_s}{4} \right) \int_{-\delta/2}^{\delta/2 + \Delta} (1 + \cos \Delta \phi) dx, \quad (3)$$

where, I_s is the saturation magnetization, H_s is the effective antiferromagnetic coupling field, and $\Delta \phi$ is the difference of the angle of the magnetization between the adjacent magnetic layers. Therefore, by using (1a) and (1b), we obtain, for both AB walls and PN walls,

$$\sigma_{AF}^{AB} = (I_s H_s / 4) [(\delta + \Delta) - (\delta - \Delta) \cos(\pi \Delta / \delta)] - (2\delta / \pi) \sin(\pi \Delta / \delta), \quad \text{for } \Delta \leq \delta, \quad (4a)$$

$$= I_s H_s \Delta / 2, \quad \text{for } \Delta \geq \delta, \quad (4b)$$

and

$$\sigma_{AF}^{PN} = \left(\frac{I_s H_s}{4} \right) \left[(\delta + \Delta) - \left(\frac{\delta}{\pi} \right) \sin \left(\frac{\pi \Delta}{\delta} \right) \right], \quad \text{for } \Delta \leq \delta, \quad (5a)$$

$$= I_s H_s \Delta / 2, \quad \text{for } \Delta \geq \delta, \quad (5b)$$

respectively.

On the other hand, the calculation of the magnetostatic energies for AB walls and PN walls, σ_s^{AB} and σ_s^{PN} , are carried out according to the method described in the previous paper.² The results are as follows:

$$\sigma_s^{AB} = \left(\frac{I_s^2 t}{4N} \right) \sum_{m,n=1}^N (-1)^{n-m+1} \int_0^{\delta'} (\delta' - \xi') \cos \left(\frac{\pi \xi'}{\delta'} \right) + \left(\frac{\delta'}{\pi} \right) \sin \left(\frac{\pi \xi'}{\delta'} \right) [L(\Delta'_{mn} + \xi') + L(\Delta'_{mn} - \xi')] d\xi', \quad (6)$$

$$L(X) = \log \{ (B_{mn}^2 + X^2)^2 / [(B_{mn} + 1)^2 + X^2] \} \times [(B_{mn} - 1)^2 + X^2], \quad (7)$$

$$B_{mn} = (n - m)(1 + d'), \quad d' = d/t, \quad (8)$$

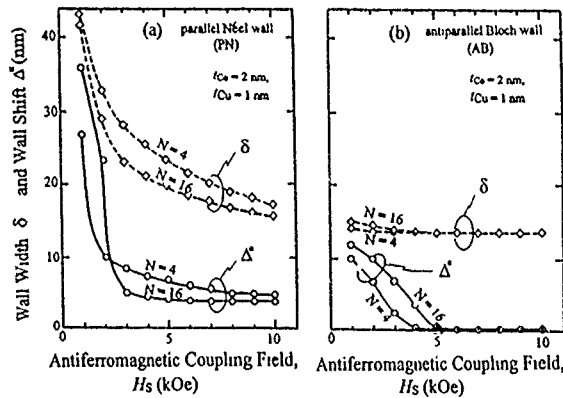


FIG. 2. Domain wall width and the amount of the wall shift at the equilibrium state estimated for [2 nm Co/1 nm Cu]_N multilayered films. (a) parallel Néel walls (PN); (b) antiparallel Bloch walls (AB).

$$\Delta'_{mn} = \Delta' = \Delta/t, \quad \text{for } (n-m): \text{odd},$$

$$= 0, \quad \text{for } (n-m): \text{even},$$

$$\sigma_s^{PN} = \left(\frac{\pi I_s^2 t}{4N} \right) \sum_{m,n=1}^N \int_0^{\delta'} \left(1 - \frac{\xi'}{\delta'} \right) \sin \left(\frac{\pi \xi'}{\delta'} \right) \{ [(n-m)\Delta' + \xi'] F[(n-m)\Delta' + \xi'] - [(n-m)\Delta' - \xi'] \times F[(n-m)\Delta' - \xi'] \} d\xi'. \quad (9)$$

The formulations for the other energies are the same as in the previous paper.²

The magnetostatic energy shown above decreases with increasing shift Δ almost monotonically, while the antiferromagnetic coupling energy increases quadratically at the beginning and linearly in the end. Therefore, at some point an equilibrium is attained.

CALCULATION OF THE EFFECT OF THE WALL SHIFT ON THE WALL ENERGY OF [Co/Cu]_N MULTILAYERED FILMS

Numerical calculations were performed for [Co/Cu]_N multilayered films having the thickness ratio $t_{Co}/t_{Cu} = 2$, using the formulas derived above. For the calculations, the saturation magnetization I_s and the exchange constant A of the cobalt were assumed to be 1.45×10^3 emu/cm³ and 1.3×10^{-6} erg/cm, respectively, and the uniaxial anisotropy was assumed to be negligible compared to the effective field H_s of the antiferromagnetic exchange coupling.

Figures 2(a) and 2(b) show how the wall shift at the equilibrium state Δ^* depends on H_s for PN walls and AB walls in [Co/Cu]_N films ($N=4, 16$), respectively. It is noticed that with the increase in H_s , Δ^* decreases rapidly. The figures also show how the wall width δ changes with H_s . For weak H_s , Δ^* is seen to approach the wall width.

Figure 3 shows the wall energy dependence on H_s for PB, AB, and PN walls with the number of Co layers, N , as a parameter. The case of AN walls is discussed in the next section. Figure 4 illustrates the critical field at which the wall type changes from one to another as a function of N . For comparison, the critical curves obtained without taking into account the effect of the wall shift are also shown by dotted lines. It is seen that the wall shift favors PN walls more than AB walls and that the area in which PN walls are stable is substantially expanded by the shift effect.

DISCUSSION

As is evident from the results described above, PN walls will be the most likely walls to appear among the three PB, AB, and PN walls, especially for the multilayered films for practical applications such as read heads for magnetic recording, where weak antiferromagnetic coupling is required in order to obtain high field sensitivity. Of course, AN walls should have lower energy than PN walls when no external field is applied. However, during the magnetization process after the multidomain splitting from the saturated state, there is a possibility of forming PN walls before they turn into AN walls. Figure 5 shows PN and AN wall energies calculated as

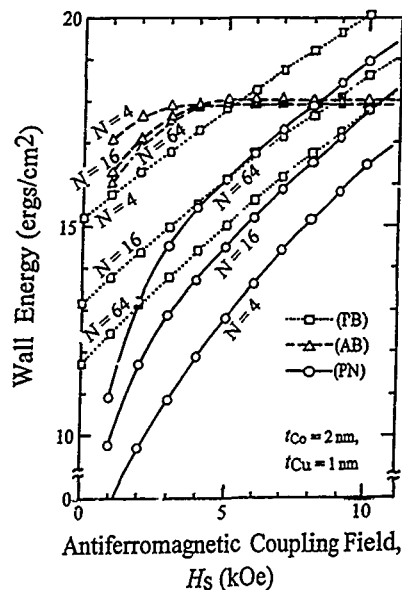


FIG. 3. Wall energy vs antiferromagnetic coupling field curves for parallel and antiparallel Bloch walls (PB and AB) and for antiparallel Néel walls (AN) in $[2 \text{ nm Co}/1 \text{ nm Cu}]_N$ multilayered films obtained by calculation.

a function of the applied field in the hard direction. The calculation was performed almost the same way as above, the detail of which will be presented elsewhere. Here, the film is assumed to be of the form $[2 \text{ nm Co}/1 \text{ nm Cu}]_4$ with an anisotropy field and an effective antiferromagnetic coupling field of 20 Oe. It is seen that at the applied field of about 10 Oe, the two curves cross each other. Therefore, in this case, the type of walls will transfer from PN to AN, and vice versa, during the ascending and descending processes. The transi-

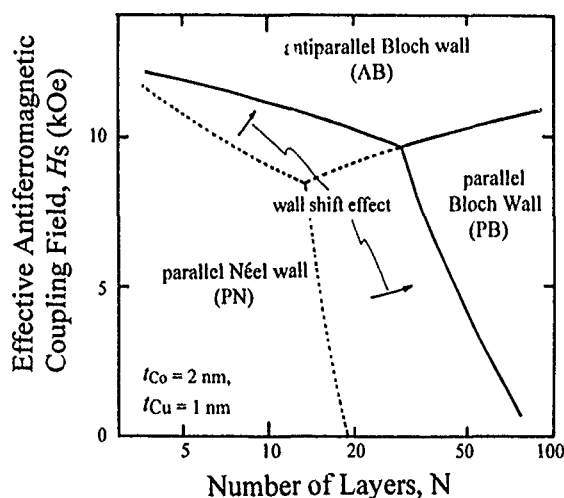


FIG. 4. Critical coupling fields for transition of the types of wall as a function of the number of layers of $[2 \text{ nm Co}/1 \text{ nm Cu}]_N$. Dotted lines are for the case where no wall shift is taken into consideration.

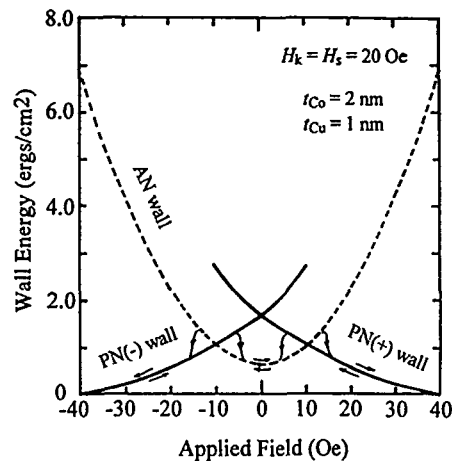


FIG. 5. PN and AN wall energies as a function of applied field calculated for $[2 \text{ nm Co}/1 \text{ nm Cu}]_4$ multilayered films. Anisotropy field H_k and the effective antiferromagnetic coupling field H_s are assumed to be 20 Oe. PN(+) and PN(-) denote the PN walls magnetization at the center of which possess + or - polarities, respectively.

tions will occur as indicated by the arrows in the figure, because some coercivity is likely to exist for the transition, and this will give rise to noise when such a film is applied to sensor devices.

CONCLUSION

It was confirmed by energy estimation that, in antiferromagnetically coupled multilayered films, the shift of the center of the walls of the adjacent layers with respect to each other reduces their magnetostatic energy substantially for PB and AN walls, resulting in self-stabilization. This effect is especially prominent when the coupling energy is small, because the smaller the coupling energy, the more shift is allowed. It was also confirmed that for $[\text{Co}/\text{Cu}]_N$ films with the thickness ratio $t_{\text{Co}}/t_{\text{Cu}}=2$, this effect favors PN walls more than AB walls, leading to more of a likelihood of the PN walls' appearance than PB or AB walls. As AN walls have lower energy than PN walls when no field is applied, it may be likely that a transition from PN to AN and vice versa will occur during the magnetization process.

ACKNOWLEDGMENTS

The authors are indebted to Dominic-savio Arokiasamy for his intensive assistance in the numerical calculations performed in this work and to Dr. J. W. Harrell for his valuable discussion and reviewing of this paper. They would also like to express their sincere thanks to Dr. I. Miyagawa of the University of Alabama and to Dr. H. Watanabe and Dr. T. Manabe of Hitachi Maxell, Ltd. for their continuing encouragement and support.

¹I. Tomas, H. Niedoba, M. Ruhrig, G. Wittmann, A. Hubert, H. O. Gupta, L. J. Heyderman, and I. B. Puchalska, *Phys. Status Solidi A* **128**, 203 (1991).

²H. Fujiwara, *IEEE Trans. Magn.* **29**, 2557 (1993).

Short period oscillation of the interlayer exchange coupling in sputtered Co-Re superlattices

J. L. Leal

*Instituto de Engenharia de Sistemas e Computadores, R. Alves Redol, 9-1, 1000 Lisbon, Portugal and
Centro de Fisica Nuclear da Universidade de Lisboa, Av. Prof. Gama Pinto 2,
1699 Lisbon, Portugal*

P. P. Freitas

*Instituto de Engenharia de Sistemas e Computadores, R. Alves Redol, 9-1, 1000 Lisbon, Portugal and
Instituto Superior Tecnico, R. Rovisco Pais, 1000 Lisbon, Portugal*

A short period oscillation was observed in the interlayer exchange coupling of *sputtered* Co-Re superlattices, superimposed on a long period oscillation. This effect is observed on hcp-textured samples with the *c* axis perpendicular to the plane of the film. The variation of the exchange coupling strength with the spacer thickness can be described using the Bruno and Chappert theory with two oscillatory terms, with periods of 2.9 ± 0.2 and 10.2 ± 0.2 Å. Both magnetization and magnetoresistance measurements reflect the influence of this multiperiodic exchange.

After the discovery of antiferromagnetic (AF) exchange coupling between ferromagnetic transition-metal layers across metallic spacers¹ and the subsequent discovery of its oscillatory behavior as a function of the interlayer thickness,² many important details of this interaction have been reported.

Large oscillation periods were found initially (10–20 Å) for most transition-metal and noble-metal spacers.³ More accurate measurements of the interlayer coupling on molecular beam epitaxy (MBE)-prepared samples with very good epitaxial growth have shown the presence of additional oscillations with a short period, down to 2 to 3 monolayers (ML).^{4–6} The modified Ruderman-Kittel-Kasuya-Yosida theory proposed by Bruno and Chappert^{7,8} provides an explanation for the occurrence of these multiperiodic oscillations. In their approach, in which the discreteness of the spacer is taken into account, the coupling is related to the topological properties of the Fermi surface of the spacer material. Quantitative predictions for the oscillation periods and relative strength in the case of noble-metal spacers could be obtained and were compared with experimental values. Good agreement was obtained for several epitaxially grown systems such as (001) Fe/Au/Fe or (001) Co/Cu/Co. The influence of structural imperfections on the coupling strength was observed experimentally, and an increase in interface roughness was shown to be detrimental for the observance of short period oscillations.⁹ This explains why sputtered systems, probably due to their less perfect interfaces, did not show until now evidence of short period oscillations.

In the present study we report the observation of a multiperiodic oscillation of the interlayer exchange coupling on *sputtered* Co-Re superlattices (SL). In a previous study we have shown that high-quality Co-Re SL's can be prepared, depending on the substrate, buffer thickness, and deposition conditions.¹⁰ Rutherford backscattering analysis indicated that chemical mixing or surface topography occurred within 2.5 Å of each side of the interface.^{10,11} Anisotropic magnetoresistance (AMR) measurements confirm up to 15% Re mixed into the Co layer, leading to negative AMR, characteristic of virtual bound-state impurities such as Re, Ru, and Ir, in a Co matrix.¹²

We decided to perform a detailed study of the coupling dependence on the Re spacer thickness on these high-quality samples in order to determine if any fine structure in the coupling could be detected, apart from the well-known long period oscillation.^{3,13}

Co-Re SL's were grown in a automated, load-locked, high-vacuum magnetron sputtering system (Nordiko 2000). The base pressure before deposition is 2×10^{-8} Torr. Ar pressure during deposition was maintained at 5 mTorr. Samples were deposited onto water-cooled substrate holders. The Co was deposited by dc magnetron sputtering at a rate of 1.9 Å/s while Re was deposited at rates of 0.6 Å/s. Care was taken in order to have a ± 0.25 -s precision control on deposition times, thus leading to an uncertainty of ± 0.15 Å on the Re thickness. We should stress, however, that these are only average values. Transmission electron microscopy (TEM) pictures of sputtered SL's show that 1- or 2-Å local variations in the thickness of the spacer layers are possible. Co and Re deposition rates were calibrated by Rutherford backscattering spectrometry (RBS) and profilometer analysis. The individual Re and Co thickness of specially prepared multilayers was directly cross-checked by RBS.

We have analyzed a set of samples with the following structure: glass/Re₂₀₀ Å/[Co₁₇ Å/Re_{*t_{Re}*}]₁₆, where *t_{Re}* varies from 2.5 to 19 Å by 0.3-Å steps. Magnetic characterization was performed at room temperature using a vibrating sample magnetometer (VSM), with a resolution of 5×10^{-6} emu. A superconducting quantum-interference device (SQUID) setup was used to perform the magnetization measurements at 20 K. Both substrate and sample holder contributions to the total magnetization were removed. Transport measurements were done at room temperature using the standard dc four-probe technique with the current flowing in the plane of the structure and perpendicular to the external applied field.

Room-temperature magnetization results for a set of [Co₁₇ Å/Re_{*t_{Re}*}]₁₆ SL's are shown in Figs. 1 and 2. Figures 1(a) and 1(b) show magnetization hysteresis loops for samples in the two main antiferromagnetic peaks (*t_{Re}*=5 Å and *t_{Re}*=16 Å). For Re thicknesses between 9.5 and 12.5 Å ferromagnetic coupling occurs. Figure 1(d) shows magneti-

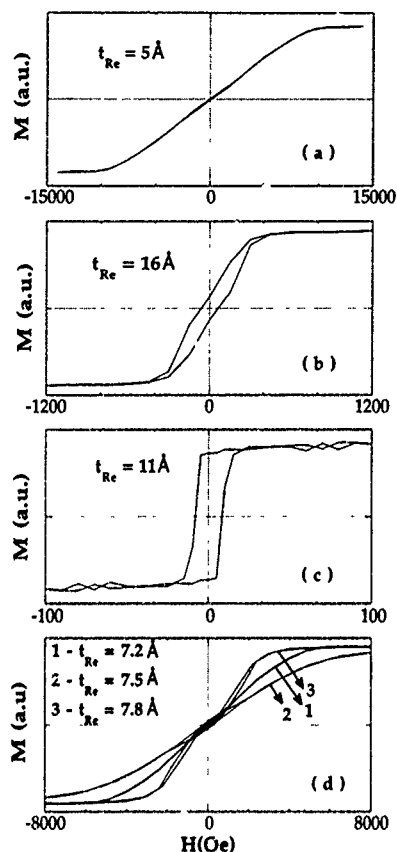


FIG. 1. Room-temperature magnetization hysteresis cycles at different Re spacer thicknesses. (a) and (b) correspond to antiferromagnetic coupling at $t_{\text{Re}}=5$ and 16 Å . (c) shows a ferromagnetically coupled sample. (d) shows magnetization curves for Re thicknesses of 7.2 , 7.5 , and 7.8 Å . Notice the peak in the saturation field at $t_{\text{Re}}=7.5 \text{ Å}$.

zation data obtained in the region of the narrow peak at $t_{\text{Re}}=7.5 \text{ Å}$.

In order to evaluate $J(t_{\text{Re}})$ as a function of the spacer thickness, we measured the saturation field H_S from magnetization curves taken at room temperature and at 20 K . H_S was defined as the field needed to reach 90% of the saturation magnetization. The saturation field and the total coupling are related by⁵

$$J(t_{\text{Re}}) = -t_{\text{Co}} M_S H_S / 4, \quad (1)$$

where M_S is the ferromagnetic layer magnetization and t_{Co} its thickness. In Figs. 2 and 3 we plot the dependence of H_S on the Re thickness at room temperature and at 20 K , respectively. Notice the fine structure observed around $t_{\text{Re}}=7.5 \text{ Å}$ and near the second antiferromagnetic peak. Consider first the peak at $t_{\text{Re}}=7.5 \text{ Å}$. It could arise due to a thickness-dependent anisotropy on top of the antiferromagnetic exchange. However, careful magnetization measurements in this region show no evidence of in-plane anisotropy on any of the antiferromagnetic coupled samples. Furthermore, as we will see later, the magnetoresistance also shows a maximum in this region, corresponding to a better defined antiparallel alignment between the Co layers due to stronger antiferromagnetic exchange coupling.

We will then analyze our data for the exchange constant in terms of a long period oscillation, by now well known in

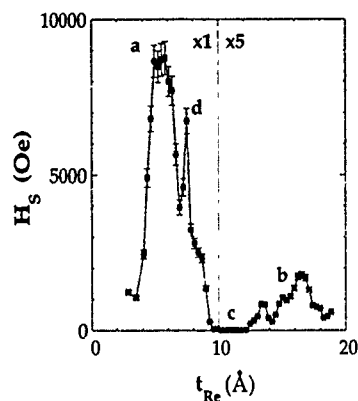


FIG. 2. Saturation field vs Re spacer thickness (t_{Re}) for the Co-Re SL's under study (300 K). The two major peaks observed at $t_{\text{Re}}=5.5$ and 16.5 Å correspond to the long period oscillation. The narrow and sharp peak observed at $t_{\text{Re}}=7.5 \text{ Å}$, as well as the peaks at 13.5 and 16.5 Å , corresponds to a short period oscillation of the coupling constant with a periodicity of $\sim 3 \text{ Å}$.

Co-Re SL's,^{3,13} $\Lambda_1 \sim 10 \text{ Å}$, and a small period oscillation, $\Lambda_2 \sim 3 \text{ Å}$, that will be responsible for the extra peaks observed. We then write $J(t_{\text{Re}}) = J_1(t_{\text{Re}}, \Lambda_1) + J_2(t_{\text{Re}}, \Lambda_2)$.

The long period component is responsible for the antiferromagnetic peaks observed at 5.5 and 16.5 Å , and the short period component is responsible for those observed at 7.5 , 13.5 , and also at 16.5 Å .

From the theory of Bruno and Chappert, the dependence of $J(t_{\text{Re}})$ on the interlayer thickness is given by:

$$J(t_{\text{Re}}) = -J_0 (1/t_{\text{Re}})^2 \sum (a_\alpha \sin(q_\alpha t_{\text{Re}} + \phi_\alpha) \times \{ [t_{\text{Re}}/L_\alpha(T)] / \sinh[t_{\text{Re}}/L_\alpha(T)] \}), \quad (2)$$

where J_0 is a constant, the a_α are weight factors, and $L(T)$ is an attenuation length inversely proportional to the temperature. The q_α are extremal spanning vectors of the Re Fermi surface, parallel to the growth direction of the system. The ϕ_α are phase shifts related to the topology of the Fermi surface.

Using this theory we have performed a fit to the experimental data shown in Figs. 2 and 3. For the room-temperature data, the results of this fit are shown in Fig. 4. The solid line was obtained using a two-period model (α

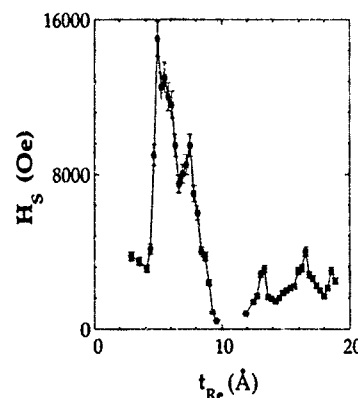


FIG. 3. Same as Fig. 2 but obtained at 20 K with a SQUID setup. Again, a multiperiodic oscillation can be observed.

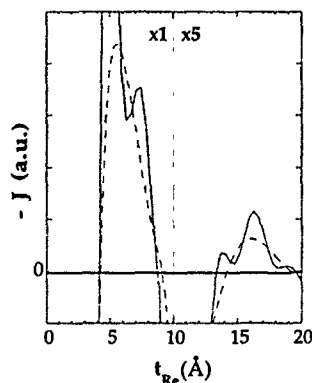


FIG. 4. Theoretical prediction for the exchange coupling constant variation with Re spacer thickness (t_{Re}), at room temperature, using Bruno and Chappert's theory. The dashed line corresponds to the long period oscillation only, while the solid line assumes two periods of 10.2 ± 0.2 and 2.9 ± 0.2 Å, respectively. Notice the good agreement between the experimental data and the theoretical fit.

$=1,2$) with $\phi_1 = \pi/6$, $\phi_2 = \pi/3$, $a_2/a_1 = 0.3$, and shows a long period oscillation, $\Lambda_1 = 2\pi/q_1 = 10.2 \pm 0.2$ Å, and a short period oscillation, $\Lambda_2 = 2\pi/q_2 = 2.9 \pm 0.2$ Å. The main temperature-dependent parameter is $L_\alpha(T)$, which is 5–6 times larger at low temperature than at room temperature. We find $L_1(300 \text{ K}) = 4.75$ Å and $L_2(300 \text{ K}) = 6$ Å. The fit is in good agreement with the experimental data. The dashed line in Fig. 4 was obtained taking into account only the long period interaction ($\alpha=1$). Notice that from our magnetization data we can only measure the coupling constant for AF coupled layers [$J(t_{\text{Re}}) < 0$].

The Bruno and Chappert model states that experimentally measured periods are equal to $2\pi/|q_\alpha|$. However, due to the discreteness of the spacer thickness, only vectors q_α for which $|q_\alpha| \leq \pi/d$ are relevant (d is the distance between lattice planes of the interlayer material). As a consequence the periods are expected to be at least 2 ML. Our Co-Re samples are mainly hcp with the $\langle 0001 \rangle$ axis perpendicular to the plane of the sample.¹⁴

It is then important to compare the observed periodicities with the Fermi surface extremal spanning vectors for the Re spacer.¹⁵ The main spanning vector found parallel to the $\langle 0001 \rangle$ direction corresponds to observed long period oscillation. No shorter periods are predicted for this direction.¹⁶ On the other hand, shorter period oscillations ($\Lambda \approx 3$ –6 Å) are predicted for spanning vectors parallel to the $\langle 1120 \rangle$ and $\langle 1100 \rangle$ directions. In the particular case of the $\langle 1120 \rangle$ direction (2 ML = 2.76 Å) a short period oscillation of ≈ 3 Å is predicted.¹⁶ The observed short period oscillation in our $\langle 0001 \rangle$ textured samples could then be associated with a small fraction of crystallites grown with the $\langle 1120 \rangle$ axis parallel to the growth direction. This hypothesis will have to be checked by growth of the appropriate single crystal films.

Figure 5 shows the room-temperature magnetoresistance (MR) for the set of samples used before, with t_{Re} varying from 3 to 9.5 Å. We define $\Delta\rho/\rho = (\rho_{H=0} - \rho_{H=H_s})/\rho_{H=0}$, where $\rho_{H=0}$ and $\rho_{H=H_s}$ are the resistivities measured at zero

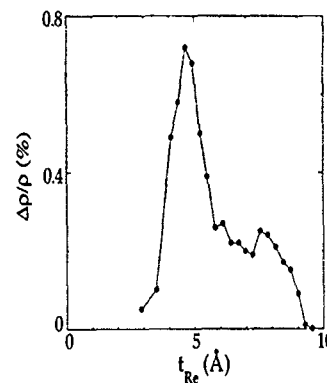


FIG. 5. Magnetoresistance vs Re thickness (t_{Re}) for Co-Re SL's with t_{Re} ranging from 3 to 9.5 Å. The magnetoresistance closely follows the exchange coupling constant dependence on Re thickness, being larger at Re thicknesses where the exchange is strongest, therefore leading to well-defined antiparallel Co layers.

field and after magnetic saturation. Notice the sharp peak in the MR at 5 Å of Re, followed by a fast decrease, and leveling between 6 and 8 Å of Re. This leveling of the $\Delta\rho/\rho$ value in a region where the coupling constant shows a peak can be understood by remembering that an extra damping factor, $\exp(-t_{\text{Re}}/\lambda)$, where λ is a quantity related to the electron mean free path in the ML, affects the magnetoresistance due to the interfacial nature of spin-dependent scattering in Co-Re superlattices.¹⁷ This damping factor balances the increase in MR due to better antiparallel alignment as the coupling constant gets stronger.

- ¹ P. Grünberg, R. Schreiber, Y. Pang, M. B. Brodsky, and H. Sowers, *Phys. Rev. Lett.* **57**, 2442 (1986).
- ² S. S. P. Parkin, N. More, and K. P. Roche, *Phys. Rev. Lett.* **64**, 2304 (1990).
- ³ S. S. P. Parkin, *Phys. Rev. Lett.* **67**, 3598 (1991).
- ⁴ J. Unguris, R. J. Celotta, and D. T. Pierce, *Phys. Rev. Lett.* **67**, 140 (1991).
- ⁵ S. T. Purcell, W. Folkerts, M. T. Johnson, N. W. E. McGee, K. Jäger, J. van de Stegge, W. B. Zeper, W. Hoving, and P. Grünberg, *Phys. Rev. Lett.* **67**, 903 (1991).
- ⁶ S. Demokritov, J. A. Wolf, and P. Grünberg, *Europhys. Lett.* **15**, 881 (1991).
- ⁷ P. Bruno and C. Chappert, *Phys. Rev. Lett.* **67**, 1602 (1991).
- ⁸ P. Bruno and C. Chappert, *Phys. Rev. B* **46**, 261 (1992).
- ⁹ P. Grünberg, S. Demokritov, A. Fuss, R. Schreiber, J. A. Wolf, and S. T. Purcell, *J. Magn. Magn. Mater.* **104-107**, 1734 (1992).
- ¹⁰ J. L. Leal, N. P. Barradas, J. C. Soares, M. F. da Silva, M. Rots, and P. P. Freitas, *Mater. Res. Soc. Symp. Proc.* **313**, 773 (1993).
- ¹¹ N. P. Barradas, J. L. Leal, J. C. Soares, M. F. da Silva, P. P. Freitas, M. Rots, S. I. Molina, and R. Garcia, in *Proceedings of the 11th International Conference on Ion Beam Analysis*, Balatonfüred, Hungary, 1993 (to be published).
- ¹² P. P. Freitas, *Bull. Am. Phys. Soc.* **32**, 527 (1987).
- ¹³ P. P. Freitas, L. V. Melo, I. Trindade, M. From, J. Ferreira, and P. Monteiro, *Phys. Rev. B* **45**, 2495 (1992).
- ¹⁴ L. V. Melo, I. Trindade, M. From, P. P. Freitas, N. Teixeira, M. F. da Silva, and J. C. Soares, *J. Appl. Phys.* **70**, 7370 (1991).
- ¹⁵ Landolt-Bornstein, New Series Group 111, Vol. 13b, edited by K. H. Hellwege (Berlin, Germany, 1983), p. 248.
- ¹⁶ M. D. Stiles, *Phys. Rev. B* **48**, 7238 (1993).
- ¹⁷ P. P. Freitas, I. G. Trindade, L. V. Melo, N. Barradas, and J. C. Soares, in *Proceedings of the NATO ARW on Structure and Magnetism in Systems of Reduced Dimensions*, Corsica, June 1992, NATO Series, edited by R. F. C. Farrow, B. Diemy, M. Domath, A. Fert, and B. D. Hermseim (Plenum, New York, 1993), p. 343.

Hot electron spin-valve effect in coupled magnetic layers

R. J. Celotta, J. Unguris, and D. T. Pierce

Electron Physics Group, National Institute of Standards and Technology, Gaithersburg, Maryland 20899

SEMPA observations of magnetic exchange coupling in the Fe/Ag/Fe, Fe/Au/Fe, and Fe/Cr/Fe systems reveal an intensity variation in the emitted secondary electron signal that depends only on whether the Fe layers are coupled in a ferromagnetic or antiferromagnetic sense. We ascribe this new effect to spin dependence in the transport of electrons between the two magnetic layers.

INTRODUCTION

The phenomena of exchange coupling of ferromagnetic layers and the related giant magnetoresistance effect (GMR) have been the subject of extensive recent research,¹ owing, in part, to the potential such effects have for application in a new class of devices called spin valves.² The GMR effect depends upon a difference in the spin-dependent transport of Fermi energy electrons between two or more ferromagnetic layers that are aligned either ferromagnetically or antiferromagnetically with each other. We have discovered a similar effect, an alignment-dependent variation in the emission of secondary electrons, in Fe/Ag/Fe, Fe/Au/Fe, and Fe/Cr/Fe sandwiches. We ascribe this new effect to spin-dependent transport of much higher energy electrons, i.e., hot electrons with energies of 5–15 eV with respect to the Fermi level.

In a series of measurements, we have applied the technique of scanning electron microscopy with polarization analysis³ (SEMPA) to the study of the Fe/Cr/Fe,⁴ Fe/Ag/Fe,⁵ and Fe/Au/Fe⁶ exchange coupled layers. The experimental arrangement we have used for our SEMPA studies of exchange coupling in Fe/Ag/Fe is shown in Fig. 1. Although we have obtained similar results for the Fe/Cr/Fe and Fe/Au/Fe systems, we will illustrate this new effect in this paper by concentrating on measurements of the Fe/Ag/Fe system.

An Fe single crystal whisker is used for the substrate because of its very high degree of crystalline perfection and surface flatness. A Ag film is grown epitaxially in the shape of a wedge with its thickness varying from 0 to 25 ML. Finally, an Fe overlayer is grown with a uniform thickness in the range of 3–12 ML. The domain structure of the Fe substrate is very simple; it consists of two oppositely oriented domains, as shown in Fig. 1. As a result of the periodic reversal of exchange coupling as a function of interlayer thickness, domains in the Fe overlayer will be oriented either parallel or antiparallel to the substrate domains depending on the sign of the coupling, and will form a pattern that directly reflects the periodicity of the coupling. The SEMPA instrument³ can directly observe this magnetization pattern by measuring the polarization of the secondary electrons produced by the incident beam of a scanning electron microscope. In this way, very accurate determinations of the periods of the exchange coupling can be made and used to test the prevailing theory, in which the oscillations are correlated with the existence of nesting vectors in the Fermi surface of the interlayer material.^{7,8}

In general, in SEMPA measurements the magnetization information is carried by the polarization of the secondary electrons, and is not reflected in the secondary electron in-

tensity. However, measurements of sandwich structures with Fe whisker substrates, Fe overlayers, and Ag, Cr, and Au interlayers, reveal a very interesting secondary intensity signal, which *depends only on the relative alignment of the substrate and overlayer magnetization*. We attribute this signal to the propagation of energetic, or "hot," electrons from the substrate experiencing spin-dependent interactions during transport. Following a discussion of the specifics of the experimental procedure and results, we discuss our model for this effect.

EXPERIMENT

Complete details of the experimental procedure exist elsewhere.^{3,4} The Fe(100) single crystal whiskers were cleaned with standard procedures,⁹ and examined using SEMPA, reflection high energy electron diffraction (RHEED); and scanning Auger microscopy. Under inspection by scanning tunneling microscopy,¹⁰ these Fe whisker surfaces are seen to be extremely flat with single atom high steps approximately every 1 μm . RHEED patterns of the Fe whiskers show a Laue arc of sharp spots after the whiskers are cleaned by Ar sputtering and annealed at 800 °C.

The interlayer wedge is grown by evaporating Ag at a rate between 0.07 and 0.8 monolayers/s while moving a shutter over the surface of the whisker. Growth at substrate temperatures between 60 °C and 100 °C produced RHEED patterns indicative of nearly perfect layer-by-layer growth. The observation of RHEED intensity oscillations indicated somewhat disordered growth for the first 3–4 layers, with much better growth for Ag thicknesses of 6–30 layers, followed by increasing disorder.

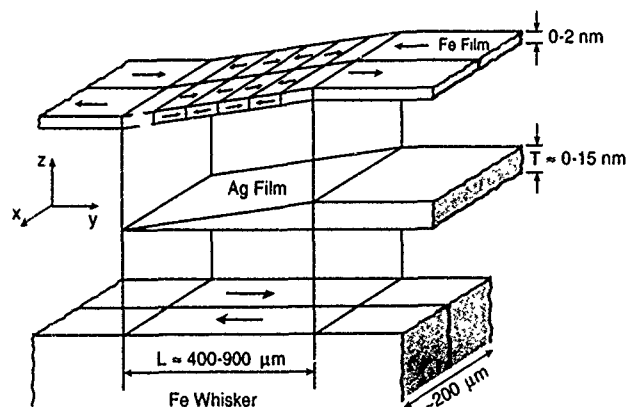


FIG. 1. Schematic diagram of Fe/Ag/Fe sandwich nanostructure showing the modulation in the sign of exchange coupling between Fe films.

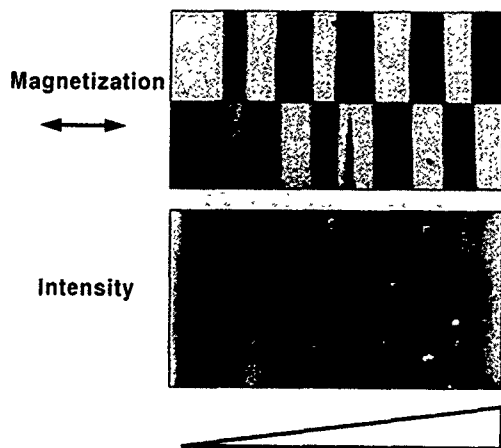


FIG. 2. Top: Magnetization image of wedge area. White (black) indicates magnetization to the right (left). Bottom: Intensity image of same region. Linear gray scale mapping with white indicating high intensity.

SEMPA images from the measurement of an Fe/Ag/Fe sandwich structure are shown in Fig. 2. The top image is the conventional SEMPA magnetization image, while the bottom image is the related secondary electron intensity image with its zero suppressed to better display the band-like intensity variations. Notice that while the two domain substrate structure creates a checkerboard pattern in the magnetization image, only bands are seen in the intensity. The secondary intensity image data can be reduced to a series of curves by computing, at each position along the wedge, i.e., each interlayer thickness, the secondary intensity averaged over the width of the wedge. The SEMPA magnetization image data is similarly reduced to curves, except the averaging is done within each of the two substrate domains and symmetry is invoked to correct for any instrumental zero offset in the magnetization measurement. The thickness scale can be determined very accurately by a method similar to the conventional method of monitoring RHEED intensity oscillations during evaporation. Instead, the microscope's electron beam is used to generate a RHEED image from a spot on the wedge portion of the sample. The intensity of a selected region of this image is used to form a "RHEED intensity image" as the incident beam scans the sample. The RHEED intensity image exhibits oscillations in intensity with the increasing thickness of the wedge. When correlated with the measured magnetization images by defect matching, the RHEED intensity image allows setting the thickness scale at every point of the magnetization or SEM intensity images to within ± 0.1 layers. The data are summarized in Fig. 3, where the lower curve shows the measured RHEED intensity oscillations for the first 20 layers of a wedge.

The topmost curves of Fig. 3 present the secondary electron intensity for Fe overlayer thicknesses of 3, 6, and 12 monolayers. Most notable is the rise in intensity in the 3 ML Fe curve as a function of Ag wedge thickness. This is presumably due to a greater secondary yield for Ag relative to Fe. When the background is subtracted from these curves by estimating it with a smoothly varying, low-order polynomial, a very interesting structure is revealed. These curves are re-plotted with their smoothly varying background subtracted in

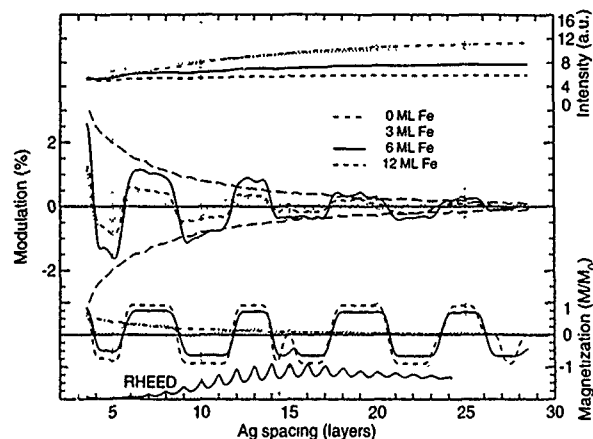


FIG. 3. Top: secondary intensity; center: modulation of secondary intensity; polarization envelope of 0 ML Fe secondaries (long dashes; see the text); bottom: normalized magnetization; RHEED intensity oscillations.

the middle of Fig. 3. The obvious modulation is presented as a percentage of the average intensity value at each Ag thickness. This modulation is seen for 3, 6, and 12 ML Fe overlayers, and closely mirrors the measured oscillation in the Fe/Ag/Fe interlayer exchange coupling. The amplitude of the modulation is greatest for a 6 ML Fe coverage, and the modulation amplitude is seen to decrease for all Fe thicknesses as the Ag thickness increases.

Below the intensity curves just discussed, we plot the magnetization measured in the positive y direction along the whisker. All magnetization values are shown normalized to the observed magnetization of bulk Fe, M_0 . There are four curves here corresponding to Fe overlayer thicknesses of 0, 3, 6, and 12 ML. The 0 ML curve reflects the polarization of the Fe substrate as a function of Ag thickness, and we see an exponential falloff as the substrate polarization is attenuated by the increasing Ag interlayer thickness. The other magnetization curves display the expected^{5,7} modulation of overlayer magnetization from exchange coupling. We note that it is not until an overlayer thickness of 12 ML that the full, bulk Fe magnetization is realized.

The correspondence between the modulation in the magnetization curves, with Ag thickness, and the modulation in the intensity curves, is obvious and striking. One might be led to the conclusion that the direction of magnetization of the Fe overlayer somehow affects the number of secondary electrons ejected. However, the Fe whisker substrate has two oppositely directed domains, as shown in Fig. 1, so the Fe overlayer domain structure is split into two halves with two oppositely directed magnetizations at each Ag thickness, also as shown in Fig. 1. If the overlayer magnetization from the other half of the Fe whisker were plotted, the curves would look as if they had been inverted with respect to the x axis. The intensity curves from this half of the whisker do not invert, however. Hence, *the intensity oscillations are correlated with the relative alignment of magnetization of the Fe films.*

DISCUSSION

The electrons used to form images in the SEMPA technique are secondary electrons. They are generated from the

cascade of incident primary electrons or backscattered electrons, and originate from a region within a few nanometers of the surface because of mean-free path considerations. The electrons that contribute to the signals displayed in Fig. 3 may originate in the Fe substrate, the Ag interlayer, or the Fe overlayer, depending on the particular situation. For example, the 0 ML Fe magnetization curve is seen to exhibit an approximately exponential decay with Ag thickness. This decrease in polarization corresponds to the increased number of unpolarized electrons originating in the Ag accompanied by the attenuation of the polarized secondary electrons from the Fe substrate. This 0 ML polarization curve has been scaled and replotted, with its mirror image, in the middle of Fig. 3. The envelope created suggests that the falloff in intensity modulation amplitude with Ag thickness is related to the relative abundance of secondary electrons from the substrate.

The explanation of the observed effect lies in the filtering of hot electrons due to spin-dependent scattering, and is directly analogous to explanations of the basis for the giant magnetoresistance in similar sandwich structures. Incident primary electrons, and other electrons in the cascade, generate polarized electrons in the substrate, some of which are directed toward the surface. These electrons are attenuated during their transport to the surface by spin-dependent as well as spin-independent interactions. Transport through the Ag interlayer may be presumed to occur in a spin-independent manner. However, there may be spin-dependent interactions within the Fe overlayer or at the Ag/Fe interface. For example, there have been both theoretical^{11,12} and experimental^{13,14} determinations of spin-dependent mean-free paths in bulk materials, as well as a discussion¹⁵ of using the difference in mean-free path as the basis of a spin detector. The spin-dependent interactions, which depend only on the relative alignment of the magnetic layers, control the number of substrate electrons that make it to the near surface region. However, since the measured electron polarization is constant for all but the smallest Ag interlayer thicknesses, the secondary electrons ejected reflect the overlayer polarization and must originate there. The experimental results can therefore be explained by spin-dependent, hot electron transport of substrate electrons to the near surface region, followed by the ejection of polarized overlayer electrons with an intensity modulation that reflects the spin dependence of the transport.

The secondary electrons from the substrate, which must have an energy nominally greater than 5 eV above the Fermi level, experience a few percent difference in transmission probability for the two cases of parallel and antiparallel ferromagnetic layer alignment. As in the GMR effect, the transport is higher for the parallel magnetization configuration. However, the GMR phenomena is related to Fermi level electrons, while those playing a role here are obviously of a much higher energy.

We have made similar measurements in the Fe/Au/Fe and Fe/Cr/Fe systems, as shown for comparison, along with the Fe/Ag/Fe data in Fig. 4. In both cases the measured secondary intensity is modulated and the modulation correlates directly with the relative alignment between the ferromagnetic layers. As was the case in Ag, aligned ferromagnetic layers produce higher secondary electron intensities.

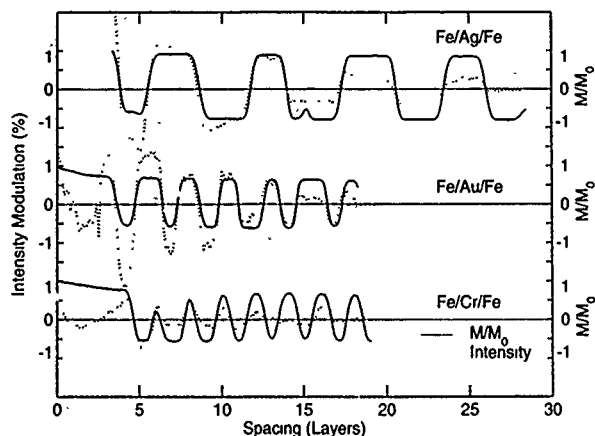


FIG. 4. Relationship between secondary intensity oscillations (dotted lines, scales to left) and magnetization direction (solid lines, scales to right).

CONCLUSION

We report a modulation in the production of near surface secondary electrons in Fe sandwich structures that depends on the relative orientation of the two Fe layers, when separated by Ag, Au, or Cr. The modulation in amplitude, of a few percent, is seen to be due to the spin-dependent transport of hot electrons between the Fe substrate and the Fe overlayer, resulting in the ejection of an overlayer electron. Parallel alignment of the Fe layers, in the cases we studied, always corresponds to a higher secondary emission current.

ACKNOWLEDGMENTS

We wish to acknowledge the support of the Technology Administration of the U.S. Department of Commerce and the Office of Naval Research. The Fe whiskers were grown at Simon Fraser University under an operating grant from the National Science and Engineering Research Council of Canada.

- ¹ See, for example, *Ultrathin Magnetic Structures*, edited by B. Heinrich and J. A. C. Bland (Springer, New York, 1993).
- ² B. Dieny, V. S. Speriosu, S. S. P. Parkin, B. A. Gurney, D. R. Wilhoit, and D. Mauri, *Phys. Rev. B* **43**, 1297 (1991).
- ³ M. R. Scheinfein, J. Unguris, M. H. Kelley, D. T. Pierce, and R. J. Celotta, *Rev. Sci. Instrum.* **61**, 2501 (1990).
- ⁴ J. Unguris, R. J. Celotta, and D. T. Pierce, *Phys. Rev. Lett.* **67**, 140-143 (1991).
- ⁵ J. Unguris, R. J. Celotta, and D. T. Pierce, *J. Magn. Magn. Mat.* **127**, 205 (1993).
- ⁶ J. Unguris, R. J. Celotta and D. T. Pierce, *J. Appl. Phys.* (these proceedings).
- ⁷ M. D. Stiles, *Phys. Rev. B* **48**, 7238 (1993).
- ⁸ K. B. Hathaway, and references therein, in Ref. 1.
- ⁹ S. T. Purcell, A. S. Arrott, and B. Heinrich, *J. Vac. Sci. Technol. B* **6**, 794 (1988).
- ¹⁰ J. A. Strosio, D. T. Pierce, and R. A. Dragoset, *Phys. Rev. Lett.* **70**, 3615 (1993); J. A. Strosio and D. T. Pierce, *Proceedings of STM'93*, Beijing, China, *J. Vac. Sci. Technol.* (in press).
- ¹¹ D. R. Penn, S. P. Apell, and S. M. Girvin, *Phys. Rev. Lett.* **55**, 518 (1985); *Phys. Rev. B* **32**, 7753 (1985).
- ¹² J. Glazer and E. Tosatti, *Solid State Commun.* **52**, 905 (1984).
- ¹³ D. P. Pappas, K.-P. Kämper, B. P. Miller, H. Hopster, D. E. Fowler, C. R. Brundle, A. C. Luntz, and Z.-X. Shen, *Phys. Rev. Lett.* **66**, 504 (1991).
- ¹⁴ H. Hopster, and references therein, in Ref. 1.
- ¹⁵ G. Schönhense and H. C. Siegmann, *Ann. Phys.* **2**, 465 (1993).

Magnetothermopower of Co/Cu_{1-x}Ni_x multilayers

Jing Shi and E. Kita
University of Illinois, Urbana, Illinois 61801

S. S. P. Parkin
IBM Almaden Research Center, San Jose, California 95120-6099

M. B. Salamon
University of Illinois, Urbana, Illinois 61801

We studied the magnetothermopower of Co/Cu_{1-x}Ni_x multilayers (with $x=0.37$ and 0.42) at various temperatures. Both systems have negative thermopower and the magnitude of the thermopower increases as the magnetic field increases. We found that as the ferromagnetic component of the magnetization becomes larger at lower temperatures, both the magnetothermopower and the magnetoresistance decrease. The inverse relationship between the thermopower and the resistance, when the field H varies, holds well at different temperatures. We interpret the results in terms of the two-current model, with an emphasis on the spin-split density of states.

The thermoelectric power has been shown to be a very useful probe of the giant magnetoresistive (GMR) mechanism in magnetic systems.¹⁻³ An unusually large field-dependent thermopower coexists⁴⁻⁶ with the giant magnetoresistance; an inverse relationship between the field-dependent diffusion thermopower and the resistance has been found to hold for GMR systems. These experimental results were interpreted in terms of the two-current model, with an emphasis on the spin-split final density of states (DOS).¹⁻³ To better understand the coupling in multilayers and the origin of giant magnetoresistance, we studied the magnetothermopower of two Co/CuNi multilayer systems with different Ni concentrations.

The Co/Cu_{1-x}Ni_x multilayers ($x=0.37$ and 0.42) used for the thermopower study were prepared by sputtering onto glass substrates. Both have the same Co-layer and CuNi-layer thicknesses and the structures can be represented as 50 Å Fe/(10 Å Co/16 Å Cu₆₃Ni₃₇)₁₅/10 Å Co/25 Å Cu₆₃Ni₃₇, and 50 Å Cu₅₈Ni₄₂/(10 Å Co/16 Å Cu₅₈Ni₄₂)₁₅/10 Å Co/25 Å Cu₅₈Ni₄₂. The magnetoresistance ratios at room temperature are 7% and 6%, respectively, and both samples are at the first antiferromagnetic peak in the exchange coupling.

Magnetic hysteresis loops were measured at various temperatures. It is found from the multilayer magnetization curves that there is a large ferromagnetic component at temperatures for which the CuNi spacer material at these compositions does not have a ferromagnetic transition. This suggests that, by introducing Ni into Cu, the coupling between the neighboring Co layers is not completely antiferromagnetic as it is in the Co/Cu case. The reduction in the antiferromagnetic coupling is responsible for lowering the saturation fields and for decreasing the magnetoresistance ratios.

Resistance and magnetization were measured conventionally at and below room temperature. Thermoelectric power measurements were carried out using the technique described previously.⁶ Narrow Pb foils were used for the electrodes, and type E differential thermocouples for detecting the temperature gradient. The field dependence of the thermopower was studied at various temperatures. The magnetoresistance decreases and the ferromagnetic component of

both samples increases as the temperature is reduced. For the higher Ni concentration sample, the magnetoresistance disappears at about 100 K while the low Ni concentration sample exhibits a finite magnetoresistance over the whole temperature range ($T>4$ K).

Figure 1 shows the field dependence of the thermopower of both samples at 300 K. The zero-field thermopower for Co/Cu₅₈Ni₄₂ is negative ($-26 \mu\text{V/K}$), and its magnitude increases with increasing magnetic field until it saturates at about 500 Oe. The field dependence of thermopower of Co/Cu₆₃Ni₃₇ is qualitatively the same as that of the higher Ni concentration sample, but the saturation field is about 400 Oe and the zero-field thermopower is about $-19 \mu\text{V/K}$. Because the determination of the absolute value of thermopower depends on the closeness of the thermal EMF leads to the type-E thermocouple leads, the absolute value has some uncertainty due to the misplacement of the leads. However, the

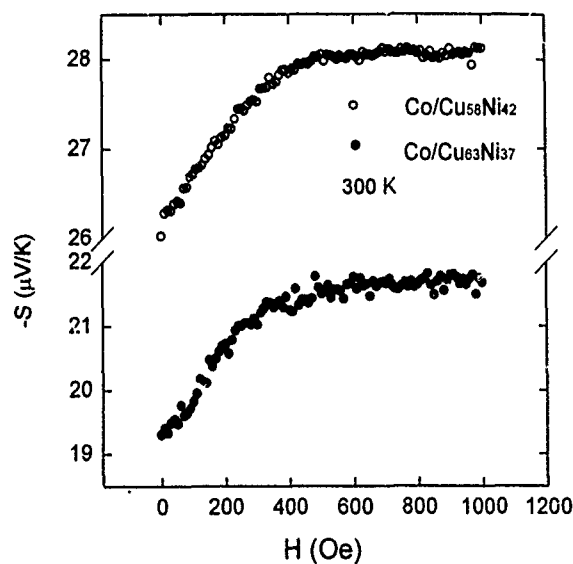


FIG. 1. Thermoelectric power as a function of magnetic field for both samples at room temperature. The open circles are for the higher Ni concentration sample, the closed circles for the lower Ni concentration sample.

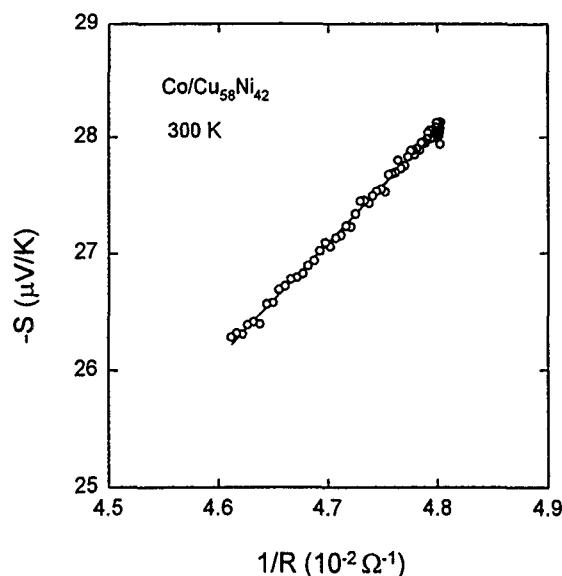


FIG. 2. $-S$ vs $1/R$ plot for the data shown in Fig. 1, in the case of the higher Ni concentration sample.

magnitude of the higher Ni concentration sample's thermopower is consistently larger than that of the lower Ni concentration sample. The difference may be caused by the Fe underlayer, which has a relatively large positive thermopower and is effectively in parallel connection to the Co/CuNi multilayer structure.

We demonstrate the inverse relationship between resistance and thermopower in variable fields in Fig. 2 (for the higher Ni concentration sample). The magnetothermopower $|S(H) - S(0)|$ decreases as the temperature is decreased, vanishing near 100 K for this sample. The magnetoresistance also vanishes at this temperature, indicating that a single underlying mechanism causes the coexistence of magnetothermopower and magnetoresistance. The inverse relationship also holds very well at various temperatures for the lower Ni concentration sample; the $-S$ vs $1/R$ plot at 150 K is shown in Fig. 3 for that sample.

The temperature dependence of the zero-field thermopower $S(0)$ was also measured for both samples. From the lowest temperature (4 K) to room temperature, $S(0)$ shows a linear temperature dependence, which means that the diffusion thermopower dominates. The temperature dependence of the thermopower for the low Ni concentration sample is shown in Fig. 4.

As pointed out previously,¹⁻³ the large field dependence of thermopower suggests that the different DOS of spin-up and spin-down d bands at the Fermi surface is essential to the scattering process. In that model, we assumed that s electrons are the main charge carriers, that the spin-flip scattering mean-free path is much longer than the spacer layer thickness, and that scattering into the d bands by the interfacial potential is the most important relaxation process. Neglecting spin-mixing scattering and applying the two-current model, we could successfully explain the following facts: the large field dependence of thermopower; the large magnitude of the thermopower and the closeness of its saturation value

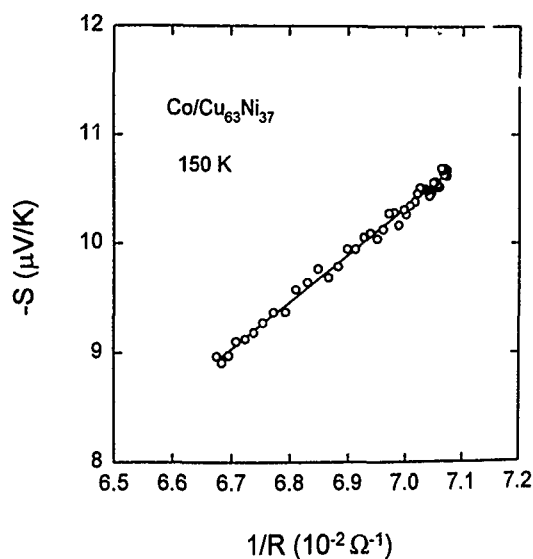


FIG. 3. $-S$ vs $1/R$ plot for the lower Ni concentration sample data at 150 K.

to the bulk thermopower of Co; the inverse relationship between the thermopower and the resistance in variable fields; and the linear temperature dependence. In applying this model to granular systems, we also included a matrix contribution because the scattering within the matrix is not negligible in that case.

There are two factors that decrease the magnetoresistance ratio, which otherwise would be determined by the magnetic layer's DOS only: scattering within the nonmagnetic layer as in the granular case,² and reduced antiferromagnetic coupling. In Co/CuNi samples, both contribute. The nonmagnetic layer is thicker and more resistive as compared with the Co/Cu case, and there is a significant ferromagnetic coupling component in zero magnetic field. Here

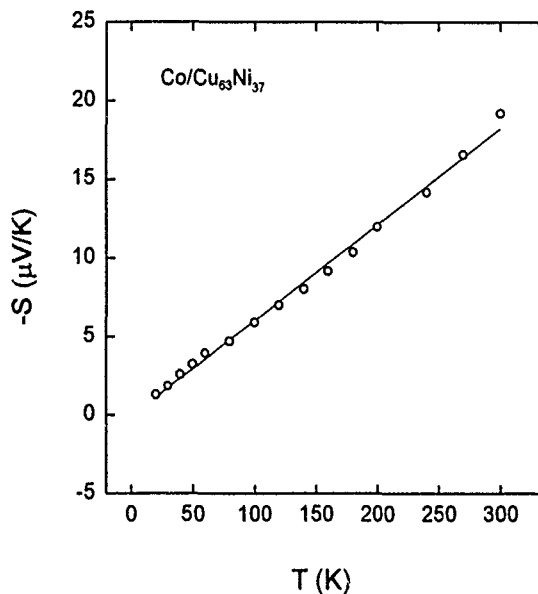


FIG. 4. Thermoelectric power as a function of temperature for the lower Ni concentration sample.

we consider only the latter. With the assumptions mentioned earlier, we can obtain an expression for the resistivity in magnetic field,

$$\rho(H) = [1 - f(H)]\rho_{af} + f(H)\rho_f, \quad (1)$$

where ρ_{af} denotes the resistivity in the fully antiferromagnetically coupled state, ρ_f the resistivity in the ferromagnetically aligned state, and $f(H) = [M(H)/M_s]^2 = \cos^2 \theta(H)$. $\theta(H)$ is the angle between the magnetization and the applied field. If we assume that θ does not start from a right angle but from an intermediate angle between 90° and 0° , i.e., that $f(H)$ starts from a nonzero value f_0 , then we will have a magnetoresistance ratio that depends on the ferromagnetic coupling parameter f_0 ,

$$r \equiv \frac{\Delta\rho}{\rho_f} = \frac{\rho_0 - \rho_f}{\rho_f} = (1 - f_0) \left(\frac{\rho_{af} - \rho_f}{\rho_f} \right). \quad (2)$$

The magnetoresistance ratio is reduced by a factor of $(1 - f_0)$ from its maximum $[(\rho_{af} - \rho_f)/\rho_f]$, which is determined by the DOS of d bands at Fermi surface. As the ferromagnetic component increases, the magnetoresistance ratio decreases until $f \rightarrow 1$, where the magnetoresistance vanishes.

From Mott's formula,⁷

$$S = \frac{\pi^2 k_B^2 T}{3|e|} \left(\frac{\partial \ln \rho}{\partial \epsilon} \right)_{E_F}, \quad (3)$$

we can obtain the inverse relationship between resistivity and thermopower. Thermopower changes from its initial value S_0 ,

$$S_0 = S_{af} - \frac{f_0}{1 + r} [S_{af} - S_f], \quad (4)$$

to S_f as H is increased, where both S_{af} and S_f are determined by the DOS of d bands. Obviously, the magnetothermopower is also reduced, by a factor $[f_0 r / (1 + r)]$, by the existence of ferromagnetic coupling.

We compare Co/CuNi samples to the Co/Cu samples with comparable spacer-layer thickness studied previously.⁶ To decrease the magnetoresistance ratio from 18% to about 7% requires that $f_0 \approx 0.61$, corresponding to an initial magnetization: $M(0) \approx 0.78M_s$. This is larger than indicated by the magnetization data, for which $M(0) \approx 0.5M_s$ at room temperature. We conclude that scattering within the more resistive nonmagnetic layer also contributes to the suppression

of both the magnetoresistance and magnetothermopower. Both possibilities still preserve the inverse relationship in magnetic field. Recently, there has been some discussion⁸ of biquadratic coupling in multilayers in the literature, which leads to values of f_0 other than 0 and 1. The results suggest the possibility that biquadratic coupling is introduced when Ni atoms are added into Cu. An entirely different picture is that some layers are coupled ferromagnetically and others coupled antiferromagnetically, with both types connected in parallel. This scenario is not consistent with the inverse relationship between thermopower and resistance, and can be ruled out.

In summary, we studied the magnetothermopower of Co/CuNi samples at different temperatures. Thermopower values are negative in both samples, and the magnitude of the thermopower increases as the resistance decreases in magnetic fields. The inverse relationship between the thermopower and the resistance holds very well at all temperatures, which is a general consequence of the two-current model. Magnetothermopower and magnetoresistance decrease as the ferromagnetic component increases, and both vanish when antiferromagnetic coupling disappears. We emphasize again here that a spin-dependent scattering matrix element will not give rise to *both* GMR and magnetothermopower effects.

We thank K. Pettit for help and discussions. The work was supported by U.S. Department of Energy Grant No. DEFG02-91ER45439 through the University of Illinois, Materials Research Laboratory. E. K. was supported by Monbusho-sponsored Japanese Overseas Research Fellowship.

¹ J. Shi, S. S. P. Parkin, L. Xing, and M. B. Salamon, *J. Magn. Magn. Mater.* **125**, L251 (1993).

² J. Shi, E. Kita, L. Xing, and M. B. Salamon, *Phys. Rev. B* **48**, 16119 (1993).

³ L. Xing, Y. C. Chang, M. B. Salamon, D. M. Frenkel, and J. Shi, *Phys. Rev. B* **48**, 6728 (1993).

⁴ J. Sakurai, M. Horie, S. Araki, H. Yamamoto and T. Shinjo, *J. Phys. Soc. Jpn.* **60**, 2522 (1991); L. Piraux, A. Fert, P. A. Schroeder, R. Loloce, and P. Etienne, *J. Magn. Magn. Mater.* **110**, L247 (1992).

⁵ M. J. Conover, M. B. Brodsky, J. E. Mattson, C. H. Sowers, and S. D. Bader, *J. Magn. Magn. Mater.* **102**, L5 (1991).

⁶ J. Shi, R. C. Yu, S. S. P. Parkin, and M. B. Salamon, *J. Appl. Phys.* **73**, 5524 (1993).

⁷ N. W. Ashcroft and N. D. Mermin, *Solid State Physics* (Saunders, Philadelphia, 1976).

⁸ J. C. Slonczewski, *J. Appl. Phys.* **73**, 5957 (1993).

High-field polar MOKE magnetometry as a probe of interlayer exchange coupling in MBE-grown Co/Cu/Co(111) and Fe/Cr/Fe(001) wedged trilayers

A. J. R. Ives, R. J. Hicken, J. A. C. Bland, C. Daboo, M. Gester, and S. J. Gray
Cavendish Laboratory, University of Cambridge, Madingley Road, Cambridge CB3 0HE, United Kingdom

We discuss the use of room temperature polar magneto-optic Kerr effect (MOKE) measurements at high field (≤ 7 T) in investigating antiferromagnetic (AFM) and ferromagnetic (FM) exchange coupling in MBE-grown wedged trilayers. In the case of Co/Cu/Co(111), the polar MOKE revealed the first AFM coupling peak at 9 Å Cu thickness and the second weaker AFM coupling peak at 20 Å. This is an important result because it helps in resolving the present controversy over whether oscillatory coupling exists in (111) oriented MBE-grown Co/Cu/Co structures. For Fe/Cr/Fe(001), polar MOKE is found to be less sensitive than in-plane MOKE for extracting the detailed form of the coupling. However, polar MOKE reveals additional variations in the perpendicular saturation fields as a function of interlayer thickness, which are not found in the in-plane MOKE saturation fields.

In-plane magneto-optic Kerr effect (MOKE) magnetometry is now a standard technique that has been used successfully to determine the antiferromagnetic (AFM) interlayer exchange coupling in a number of magnetic transition metal thin film structures. We show here that perpendicular magnetization curves obtained using polar MOKE can provide valuable information about the coupling strength and the sample homogeneity in wedged trilayer structures with a hard axis along the film normal. This information is not always obtained from in-plane MOKE measurements.

From the perpendicular magnetization curves we can measure the perpendicular saturation field H_s^\perp , and a saturation field extrapolated from the initial magnetization gradient, χ_0 , defined as $H_s^{\chi^\perp} = 1/\chi_0$, with the magnetization normalized to unity, as illustrated in Fig. 1. Our values of H_s^\perp are calculated from the intersection of the magnetization curve with $M/M_s = \alpha$, where α is the highest value of M/M_s at which H_s^\perp could be accurately determined, due to the gradual approach of the magnetization to saturation. This leads to H_s^\perp being an underestimate of the true saturation field. We consider two cubic ferromagnetic layers with thicknesses d_1 and d_2 , separated by a nonmagnetic interlayer, with uniform magnetizations M_1 and M_2 . We assume a bilinear exchange coupling energy per unit area given by $-2A_{12}\hat{M}_1 \cdot \hat{M}_2$ and ignore the generally much smaller effect of biquadratic coupling. It is possible to obtain general expressions relating H_s^\perp and $H_s^{\chi^\perp}$ to A_{12} .¹ In the case of non-identical magnetic layers with significantly different interface anisotropy fields, these expressions may be used to extract estimates of both the FM and AFM coupling strengths from the perpendicular magnetization curves, and we have used this to measure the FM coupling in an Fe/Pd/Fe(001) wedge structure.² For the samples presented here, which have identical magnetic layers, both the in-plane and perpendicular saturation fields have a contribution that depends on the AFM coupling strength, $-4A_{12}/\mu_0Md$, and a contribution H_a , which depends on magnetocrystalline and interface anisotropies, and on demagnetizing effects. Thus, for AFM coupling, A_{12} can be obtained from the in-plane and the perpendicular magnetization data using

$A_{12} = -\frac{1}{4}\mu_0Md(H_s - H_a)$. We shall assume M and d are the bulk magnetization and the nominal thickness of the magnetic layers. For easy axis in-plane magnetization curves, we can usually neglect H_a and write $A_{12} = -\frac{1}{4}\mu_0MdH_s^\parallel$, where H_s^\parallel is the easy axis in-plane saturation field. From the perpendicular saturation field we obtain $A_{12} = -\frac{1}{4}\mu_0Md \Delta H_s^\perp$, where $\Delta H_s^\perp = H_s^\perp - H_a^\perp$, and from the perpendicular saturation field extracted from χ_0 we obtain $A_{12}^{\chi^\perp} = -\frac{1}{4}\mu_0Md \Delta H_s^{\chi^\perp}$, where $\Delta H_s^{\chi^\perp} = H_s^{\chi^\perp} - H_a^{\chi^\perp}$.

The polar MOKE measurements were made with a 7 T superconducting magnet. The samples were placed at the end of an insert tube, close to the center of the magnet, at room temperature. The laser beam was focused on to the sample and moved across it using a concave mirror mounted on a micrometer stage. This geometry was designed so that the laser light did not pass through any windows or lenses in the vicinity of the field, thus eliminating problems due to Faraday rotation or birefringence.

We have made room temperature in-plane MOKE mea-

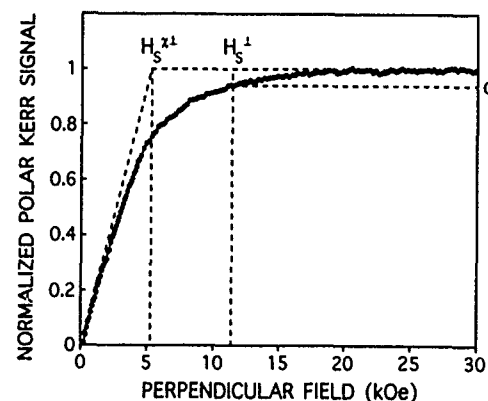


FIG. 1. A polar MOKE magnetization curve from the Co/Cu/Co(111) wedge corresponding to a Cu thickness of 7.4 Å. The dashed lines show how H_s^\perp and $H_s^{\chi^\perp}$ are defined. H_s^\perp is obtained from the intersection of the magnetization curve with $M/M_s = \alpha$, where we have taken $\alpha = 0.94$ for the Co/Cu/Co wedge and 0.96 for the Fe/Cr/Fe wedge. $H_s^{\chi^\perp}$ is obtained by applying a linear fit to the magnetization curve for $-2 \text{ kOe} < H < 2 \text{ kOe}$, and then extrapolating this fit to the intersection with $M/M_s = 1$.

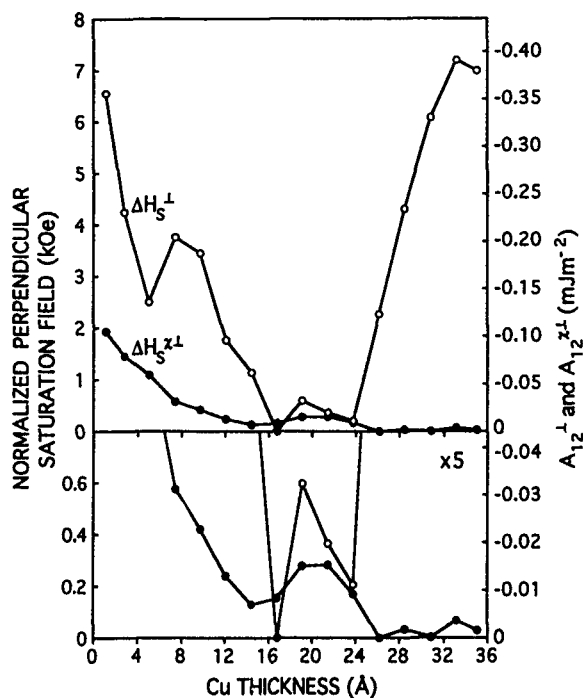


FIG. 2. ΔH_s^\perp (open circles) and $\Delta H_s^{x\perp}$ (closed circles) are plotted versus Cu thickness for the Co/Cu/Co(111) wedge sample. From the right-hand scale we obtain A_{12}^\perp and $A_{12}^{x\perp}$.

measurements in fields up to 1.2 T using a conventional electromagnet, and polar MOKE measurements up to 6 T, on a wedged MBE-grown Co(111)/Cu(111)/Co(111) trilayer with structure Au(13 Å)/Cu(15 Å)/Co(15 Å)/Cu(0–35 Å)/Co(15 Å)/Cu(15 Å)/Au(200 Å)/Co(15 Å)/Ge(500 Å)/GaAs(110). The Co seed layer contributes very little to the MOKE signal due to the limited penetration depth of the laser beam. Prior to growth, the GaAs(110) substrate was cleaned by heating to 600 °C. The Ge buffer was grown at 500 °C at a rate of 0.15 Å per second. The Au, Co, and Cu layers were deposited at 150 °C at rates of 0.067, 0.2, and 0.2 Å/s, respectively, at a growth pressure of 10^{-10} mbar. RHEED, x-ray, and NMR measurements on similar samples showed that the layer growth is (111) for the Au buffer layer and subsequent layers, and that the Co/Cu layers have very smooth interfaces.^{3,4}

The in-plane magnetization curves all have large remanence, even from parts of the wedge in which significant AFM coupling, and hence strongly reduced remanence, is expected. This suggests that large regions of the sample are either FM coupled or uncoupled.^{5–9} The approach to saturation is gradual at all Cu interlayer thicknesses, making determination of the in-plane saturation fields difficult, and so we have been unable to deduce consistent values of A_{12} from our data. Other authors have found very similar magnetization behavior in MBE-grown Co/Cu(111) trilayers and multilayers.^{6–9}

In Fig. 2 we have plotted ΔH_s^\perp and $\Delta H_s^{x\perp}$ on the left-hand scale versus Cu layer thickness, with corresponding values of A_{12}^\perp and $A_{12}^{x\perp}$ on the right-hand scale. Previous workers have found oscillatory coupling in sputtered Co/Cu/Co(111) structures with first and second AFM coupling peaks

at about 9 and 20 Å Cu, respectively.¹⁰ In contrast, it has proved to be difficult to find evidence of oscillatory coupling in similar films grown by MBE.¹¹ While a number of groups have found the first AFM peak in MBE-grown Co/Cu/Co(111) structures,^{6,8,9} only two groups have clearly seen the second peak, and conflicting values have been obtained for the coupling period.^{5,7} However, our plot of ΔH_s^\perp shows both the 9 and 20 Å peaks. The plot of $\Delta H_s^{x\perp}$ shows the peak at 20 Å, but the peak at 9 Å is obscured by a steady increase in $\Delta H_s^{x\perp}$ toward zero Cu thickness. This increase is of even greater magnitude in the plot of ΔH_s^\perp . Above 24 Å Cu thickness, $\Delta H_s^{x\perp}$ flattens out as expected, but ΔH_s^\perp increases rapidly. The increases in both ΔH_s^\perp and $\Delta H_s^{x\perp}$ toward zero Cu thickness, and the increase in ΔH_s^\perp above 24 Å Cu, may be due to variations in the interface anisotropy field along the wedge, which may occur as a result of changes in roughness and/or strain with Cu thickness. In the region 7 Å Cu–24 Å Cu, the amplitude of the oscillations in A_{12}^\perp is clearly much greater than the amplitude of those in $A_{12}^{x\perp}$. This is consistent with the sample containing both AFM-coupled and FM-/uncoupled regions. An FM-/uncoupled region should have a perpendicular saturation field below that of an AFM-coupled region. The value of ΔH_s^\perp is representative of the saturation field of the AFM-coupled regions. However, the value of $\Delta H_s^{x\perp}$, being an average over both types of region, is reduced by the presence of the FM-/uncoupled regions. Since the amplitude of $A_{12}^{x\perp}$ is seen to decrease relative to that of A_{12}^\perp with decreasing Cu thickness, this implies that the proportion of FM-/uncoupled regions increases with decreasing Cu thickness in our sample. This could be caused by increased pinhole coupling between the Co layers with decreasing Cu thickness.

An estimate of the maximum value of A_{12} is obtained from A_{12}^\perp and is $A_{12} = -0.20$ mJm⁻². However, this is likely to be less than the true value of A_{12} , because, as stated above, H_s^\perp is an underestimate of the true saturation field. It compares with maximum values of $A_{12} = -0.27$ mJm⁻² (300 K) for an MBE-grown Co/Cu(111) superlattice in Ref. 7, and $A_{12} = -0.55$ mJm⁻² (300 K) for an MBE-grown Co/Cu(111)/Co wedge in Ref. 8. The period of the coupling determined from ΔH_s^\perp is 11 ± 2 Å, which compares with periods of 17 and 9 Å in Refs. 5 and 7.

We have performed room temperature in-plane MOKE measurements in fields up to 0.3 T, and polar MOKE measurements up to 4.7 T on a wedged MBE-grown Fe(001)/Cr(001)/Fe(001) trilayer with structure Cr(20 Å)/Fe(20 Å)/Cr(0–40 Å)/Fe(20 Å)/Ag(600 Å)/Fe(15 Å)/GaAs(001). Once again, the Fe seed layer contributes very little to the MOKE signal. Prior to growth, a commercially polished GaAs(001) substrate was heated to 600 °C for one hour. The Fe, Cr, and Ag layers were then grown using *e*-beam evaporators, at rates of 1 Å/min for Fe and Cr, and 0.5 Å/min for Ag, and at a growth pressure of 10^{-9} mbar. The Fe seed layer was grown at 150 °C, and the other layers were grown at room temperature. The Ag buffer layer was post-annealed at 300 °C for two hours and the first Fe layer on the Ag buffer was post-annealed at 150 °C for half an hour. LEED patterns confirmed the good epitaxial (001) growth of all layers. The situation in Fe/Cr/Fe(001) trilayers with Ag buffer layers is

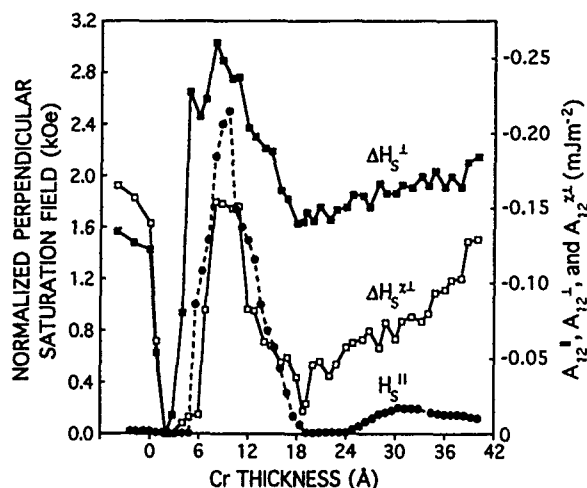


FIG. 3. ΔH_s^\perp (closed squares), $\Delta H_s^{x\perp}$ (open squares), and H_s^\parallel (closed circles) are plotted versus Cr thickness for the Fe/Cr/Fe(001) wedge sample. From the right-hand scale we obtain A_{12}^\parallel , A_{12}^\perp , and $A_{12}^{x\perp}$.

quite different from that in Co/Cu/Co(111) trilayers. At Cr thicknesses where AFM coupling is obtained, the in-plane magnetization curves have almost zero remanence. This is consistent with the sample being homogeneous so that, unlike in Co/Cu/Co(111), large FM/uncoupled regions do not occur.

In Fig. 3, we have plotted H_s^\parallel , ΔH_s^\perp , and $\Delta H_s^{x\perp}$ on the left-hand scale versus Cr layer thickness, with corresponding values of A_{12}^\parallel , A_{12}^\perp , and $A_{12}^{x\perp}$ on the right-hand scale. The plot of H_s^\parallel suggests that regions of FM coupling occur from 0–5 Å and from 19–24 Å Cr thickness, and that regions of AFM coupling occur from 5–19 Å and from 24–40 Å Cr thickness, in approximate agreement with previous work.¹² For the first three data points on the left-hand side of the plots of ΔH_s^\perp and $\Delta H_s^{x\perp}$ the Cr interlayer has zero thickness, so the effective Fe layer thickness is 40 Å. At subsequent points, the Cr interlayer has finite thickness, and the values of ΔH_s^\perp and $\Delta H_s^{x\perp}$ both fall abruptly by ~ 1.6 kOe, due to the increased interface anisotropy fields associated with the thinner separate Fe layers. In contrast, H_s^\parallel changes only slightly from 11 to 5 Oe at the point where the Cr interlayer begins. For well-separated Fe layers we expect the variations in ΔH_s^\perp and $\Delta H_s^{x\perp}$ to have the same form as the variations seen in H_s^\parallel , and the first AFM coupling peak from 5–19 Å Cr is clearly seen in the plots of ΔH_s^\perp and $\Delta H_s^{x\perp}$. The height of the peak at 10 Å in ΔH_s^\perp is unexpectedly large compared with the in-plane peak, and ΔH_s^\perp has a much higher value than H_s^\parallel in the region 19–40 Å Cr. $\Delta H_s^{x\perp}$ is smaller than H_s^\parallel at the center of the 10 Å peak, and again has a much higher value than expected in the region 19–40 Å Cr. The large values of ΔH_s^\perp and $\Delta H_s^{x\perp}$ in this region hide the second AFM peak, which is clearly observed in H_s^\parallel at 30 Å. A pos-

sible reason for the large perpendicular saturation field is a reduction in the interface anisotropy field in this region, due to a variation in strain or in interface roughness with Cr thickness.

The best estimate of the maximum value of A_{12} in the Fe/Cr/Fe(001) wedge is obtained from H_s^\parallel , giving $A_{12} = -0.22$ mJm⁻². This value is, however, much smaller than the maximum value of -0.65 mJm⁻² (300 K) from Ref. 12. The period of the coupling obtained from H_s^\parallel is 20 Å, which compares with a period of 19 Å in Ref. 12.

We cannot explain all the features in the perpendicular MOKE data for either the Co/Cu/Co(111) wedge or the Fe/Cr/Fe(001) wedge. However, our results show that, in addition to a thickness-dependent exchange coupling, there are changes in the magnetic properties of the wedges along their length, associated with possible variations in structure, which would not be found using in-plane MOKE measurements. Furthermore, in the case of the Co/Cu/Co(111) sample, the perpendicular data revealed both the first and second AFM coupling peaks, whereas our in-plane data did not. This shows the value of making perpendicular magnetization measurements in addition to performing in-plane magnetometry.

Note added in proof. Since we submitted this paper Dupas *et al.* [J. Magn. Magn. Mater. **128**, 361 (1993)] have also reported the observation of oscillatory coupling in a Co/Cu(111) multilayer.

ACKNOWLEDGMENTS

We gratefully acknowledge help from M. J. Baird. We thank M. J. Walker and D. Greig of the University of Leeds for the Co/Cu/Co wedge. The support of the Toshiba Corporation, the SERC, and the Newton Trust is gratefully acknowledged.

- ¹ A. J. R. Ives, J. A. C. Bland, R. J. Hicken, C. Daboo, M. Gester, and S. J. Gray (unpublished).
- ² R. J. Hicken, A. J. R. Ives, D. E. P. Eley, C. Daboo, J. A. C. Bland, and A. Schuhl (unpublished).
- ³ D. Greig, M. J. Hall, C. Hammond, B. J. Hickey, H. P. Ho, M. A. Howson, M. J. Walker, N. Wiser, and D. G. Wright, J. Magn. Magn. Mat. **110**, L239 (1992).
- ⁴ J. S. Lord, H. Kubo, P. C. Riedi, and M. J. Walker, J. Appl. Phys. **73**(10), 6381 (1993).
- ⁵ J. Kohlhepp, S. Cordes, H. J. Elmers, and U. Gradmann, J. Magn. Magn. Mat. **111**, L231 (1992).
- ⁶ J. P. Renard, P. Beauvillain, C. Dupas, K. Le Dang, P. Veillet, E. Velu, C. Marliere, and D. Renard, J. Magn. Magn. Mat. **115**, L147 (1993).
- ⁷ A. Schreyer, K. Brohl, J. F. Ankner, C. F. Majkrzak, Th. Zeidler, P. Bodeker, N. Metoki, and H. Zabel, Phys. Rev. B **47**, 15 334 (1993).
- ⁸ M. T. Johnson, R. Coehoorn, J. J. de Vries, N. W. E. McGee, J. aan de Stegge, and P. J. H. Bloemen, Phys. Rev. Lett. **69**(6), 969 (1992).
- ⁹ M. A. Howson, B. J. Hickey, J. Xu, D. Greig, and N. Wiser, Phys. Rev. B **48**(2), 1322 (1993).
- ¹⁰ S. S. P. Parkin, R. Bhadra, and K. P. Roche, Phys. Rev. Lett. **66**, 2152 (1991).
- ¹¹ W. F. Egelhoff, Jr. and M. T. Kief, Phys. Rev. B **45**, 7795 (1992).
- ¹² S. Demokritov, J. A. Wolf, and P. Grunberg, Europhys. Lett. **15**(8), 881 (1991).

Orientationally independent antiferromagnetic coupling in epitaxial Fe/Cr(211) and (100) superlattices

Eric E. Fullerton, M. J. Conover, J. E. Mattson, C. H. Sowers, and S. D. Bader
Materials Science Division, Argonne National Laboratory, Argonne, Illinois 60439

We present structural and magnetic characterization of epitaxial Fe/Cr(211) and Fe/Cr(100) superlattices grown simultaneously on MgO(110) and MgO(100) substrates by magnetron sputtering. The epitaxial orientation of the Fe/Cr(211) superlattice with the MgO(110) substrate is Fe/Cr[011]/MgO[001] and the orientation of Fe/Cr(100) is Fe/Cr[001]/MgO[011]. We find that for both orientations, that the interlayer coupling oscillates in sign with a period of 18 Å, and, furthermore, that the strength and phase of the magnetic coupling are also nearly identical for these two orientations.

Oscillatory interlayer coupling across nonmagnetic spacer layers in ferromagnetic/nonmagnetic transition-metal multilayers¹⁻⁴ has become a challenging theoretical problem.⁵⁻¹³ Most theories are based on a band-structure-modified RKKY treatment of the spacer layer. Within this framework, the oscillations in the coupling arise from spanning vectors normal to the layers that join extremal points of the bulk Fermi surface. A stringent test of this approach is to study the interlayer coupling along different crystallographic directions of the spacer, since different spanning vectors should be probed for each orientation. This type of experiment has been performed most extensively for the Co/Cu system.¹³⁻¹⁷ In this paper, we discuss the interlayer coupling of Fe/Cr(211) and (100) superlattices. We find that for both orientations that the interlayer coupling oscillates in sign with a period of 18 Å, and, furthermore, that the strength and phase of the magnetic coupling are also nearly identical.

The Fe/Cr superlattices were grown by dc magnetron sputtering onto single-crystal MgO(110) and MgO(100) substrates in an Ar pressure of 3 mTorr. The (110) and (100) substrates were mounted side by side onto the sample holder and codeposited. A 100 Å-Cr buffer layer was initially deposited at a substrate temperature of 600 °C.¹⁸ The substrate was then cooled to 180 °C and the samples were grown by sequential deposition of the Fe and Cr layers. A similar growth sequence has been used by Kamijo and Igarashi.¹⁹ Two series of samples were grown. The first was of [Fe(14 Å)/Cr(t_{Cr})]_N superlattices with 8 < t_{Cr} < 70 Å, and N was adjusted so that the total superlattice thickness was constant at ≈ 1200 Å.²⁰ A second series of samples based on the design of Parkin and Mauri²¹ was grown to measure the ferromagnetic interlayer coupling. The structure was characterized by x-ray diffraction using Cu-K_α radiation. Magnetic properties were measured by SQUID magnetometry and longitudinal Kerr rotation.

The high-angle x-ray spectra of [Fe(14 Å)/Cr(46 Å)]₂₀ superlattices grown on MgO(110) and MgO(100) substrates are shown in Figs. 1(a) and 1(b), respectively. Figure 1(a) contains the MgO(220) peak and the Fe/Cr(211) reflections, and Fig. 1(b) contains the MgO(200) and Fe/Cr(200) reflections. Fittings of the high-angle diffraction spectra to a general structural model²² yield Fe and Cr lattice spacings, which agree with the bulk values to better than 0.15% for both orientations.

Asymmetric diffraction scans were performed on selected samples to determine the in-plane epitaxial orientation of the superlattice. The (110) diffraction intensity was monitored as the sample was rotated by angle ϕ about the surface normal. The results of these scans are shown as the insets of Figs. 1(a) and 1(b). A two- and four-fold rotational symmetry is observed for the (211) and (100) orientations, respectively, as expected. From the position of the peaks, the following epitaxial orientations are determined: Fe/Cr[011]/MgO[001] for the Fe/Cr(211), and Fe/Cr[011]/MgO[001] for the Fe/Cr(100). The same epitaxial relation has been observed for the MBE growth of Fe(211) on MgO(110).²³

The in-plane magnetization hysteresis loops were measured for the superlattices with the applied field H parallel to the Fe[111] and Fe[011] directions for the (211) orientation and to the [011] direction for the (100) orientation. For the 14-Å Fe(211) layers, there is a strong in-plane uniaxial an-

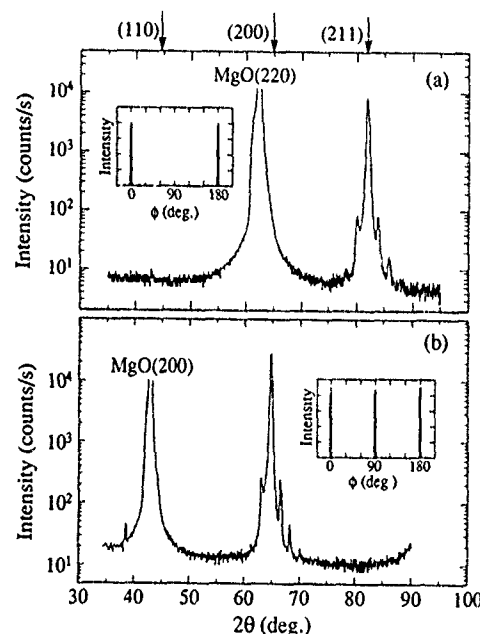


FIG. 1. X-ray diffraction results for Fe/Cr superlattices grown on MgO. High-angle spectra for [Fe(14 Å)/Cr(46 Å)]₂₀ superlattices grown on (a) MgO(110) and (b) MgO(100). Arrows at the top identify the position of possible Fe/Cr reflections. The MgO reflections are also identified. The insets show the Fe/Cr(110) intensity as a function of rotation angle ϕ about the surface normal for [Fe(14 Å)/Cr(17 Å)]₃₆ superlattices grown on (a) MgO(110) and (b) MgO(100).

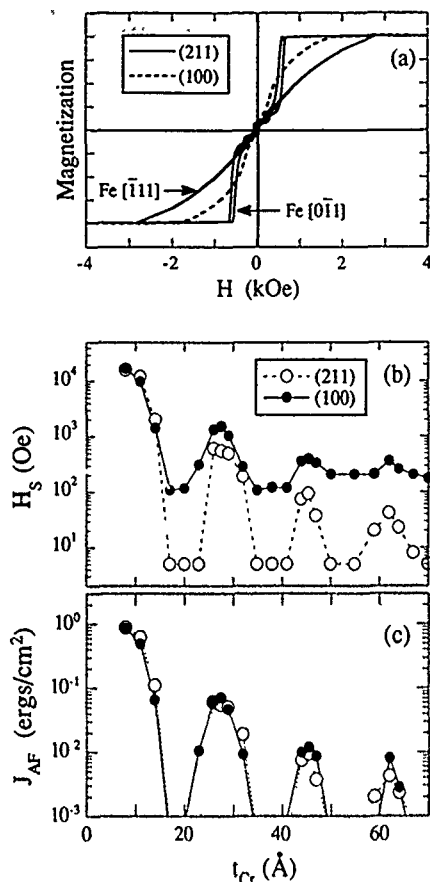


FIG. 2. (a) Room temperature magnetic hysteresis loops for (100)- and (211)-oriented $[\text{Fe}(14 \text{ Å})/\text{Cr}(26 \text{ Å})]_N$ superlattices. The applied field is along the $\text{Fe}[011]$ direction for the (100) superlattice and along the easy $\text{Fe}[011]$ and hard $\text{Fe}[111]$ directions for the (211) superlattice. (b) Switching field H_S for (211)- and (100)-oriented $\text{Fe}(14 \text{ Å})/\text{Cr}(t_{\text{Cr}})$ superlattices measured at room temperature with H parallel to the $\text{Fe}[011]$ direction. (c) Antiferromagnetic coupling strength J_{AF} vs t_{Cr} for (211)- and (100)-oriented $\text{Fe}(14 \text{ Å})/\text{Cr}(t_{\text{Cr}})$ superlattices determined from H_S values shown in (b).

isotropy along the $\text{Fe}[011]$. To quantify the anisotropy, we analyze the hysteresis loop of a ferromagnetically coupled sample with H along the hard axis ($\text{Fe}[111]$), utilizing an expression that includes a magnetocrystalline anisotropy (K_1), a uniaxial anisotropy (K_U), and a Zeeman term.^{23,24} We determined $K_U \approx 9 \times 10^5 \text{ ergs/cm}^3$ and $K_1 \approx 4 \times 10^5 \text{ ergs/cm}^3$ for the 14-Å Fe layers at room temperature, consistent with the other studies of $\text{Fe}(211)$ films.^{23,24}

Shown in Fig. 2(a) are the room-temperature hysteresis loops for AF-coupled (100)- and (211)-oriented $[\text{Fe}(14 \text{ Å})/\text{Cr}(26 \text{ Å})]_N$ superlattices. The effect of the in-plane anisotropy is evident in the shape and saturation fields along orthogonal directions of the (211) superlattice. There is a clear spin-flop transition when the field is along the easy axis ($\text{Fe}[011]$). When the field is along the hard axis ($\text{Fe}[111]$), continuous rotation to saturation is observed, which is similar to the behavior in the loop for the $\text{Fe}/\text{Cr}(100)$ sample.

The value of J_{AF} can be calculated from the saturation field H_S and the anisotropy constants for H applied along the easy and hard axis by the following equations from Refs. 25 and 26:

$$J_{\text{AF}}(211)$$

$$= \begin{cases} \frac{(H_S + H_K)M_S t_{\text{Fe}}}{4}, & \text{for } H//\text{Fe}[011] \\ & \text{and } J_{\text{AF}} > K_U t_{\text{Fe}}, \end{cases} \quad (1a)$$

$$= \begin{cases} \frac{H_S M_S t_{\text{Fe}}}{2}, & \text{for } H//\text{Fe}[011] \\ & \text{and } J_{\text{AF}} < K_U t_{\text{Fe}}, \end{cases} \quad (1b)$$

$$J_{\text{AF}}(211) = \frac{(H_S - H_K)M_S t_{\text{Fe}}}{4}, \quad \text{for } H//\text{Fe}[111], \quad (2)$$

$$J_{\text{AF}}(100) = \frac{(H_S - H_K)M_S t_{\text{Fe}}}{4}, \quad \text{for } H//\text{Fe}[011], \quad (3)$$

$$J_{\text{AF}}(100) = \frac{(H_S + H_K)M_S t_{\text{Fe}}}{4}, \quad \text{for } H//\text{Fe}[001], \quad (4)$$

where H_K is the anisotropy field given by $2K_U/M_S$ for the (211) samples, and $2K_1/M_S$ for the (100) samples. The values of H_K are estimated from the saturation fields of the ferromagnetically coupled superlattices when the field is applied along the hard axis. Applying Eqs. (1)–(3) to the loops shown in Fig. 2 yields $J_{\text{AF}}(211) = 0.061$ and 0.064 ergs/cm^2 for the hard and easy axis, respectively, and $J_{\text{AF}}(100) = 0.062 \text{ ergs/cm}^2$.

Shown in Fig. 2(b) are the measured saturation fields for the Fe/Cr superlattices as a function of Cr layer thickness for both orientations. Four oscillations are observed with the phase and period (18 Å) identical for the two orientations. To compare the interlayer coupling strengths requires converting H_S using Eqs. (1) and (3) into J_{AF} values. The calculated values for J_{AF} are shown in Fig. 2(c), where H_K for both orientations were determined from the saturation field of ferromagnetically coupled samples with neighboring Cr thicknesses. As can be seen in Fig. 2(c), in addition to the phase and period of the oscillations, the strength of the AF coupling is independent of the crystallographic orientation.

To explore the coupling of the superlattice across regions where square hysteresis loops were observed for the superlattices, we have employed the structure suggested by Parkin and Mauri shown by the lower inset in Fig. 3(a).²¹ The 9-Å Cr layer was used to strongly AF couple the middle Fe layer to the thicker bottom Fe layer. Monitoring the switching of the top Fe layers allows the determination of the ferromagnetic interlayer coupling. The measured Kerr intensity for the (211)-oriented sample in which the top and middle Fe layers are separated by a 19-Å Cr layers. There are two switching fields observed that are labeled H_{S1} and H_{S2} in Fig. 3(a). H_{S1} is related to the ferromagnetic coupling across the 19-Å Cr layer, and H_{S2} is related to the AF coupling across the 9-Å Cr layer. The relationship between H_{S2} and the AF interlayer coupling for strong coupling strengths is given by²⁷

$$J_{\text{AF}}(211) \approx \frac{(H_{S2} + H_K)M_S t_1}{(1 + t_1/t_2)}, \quad \text{for } H//\text{Fe}[011], \quad (5)$$

where t_1 and t_2 correspond to the thickness of the middle and bottom Fe layers, and H_K is estimated by measuring the

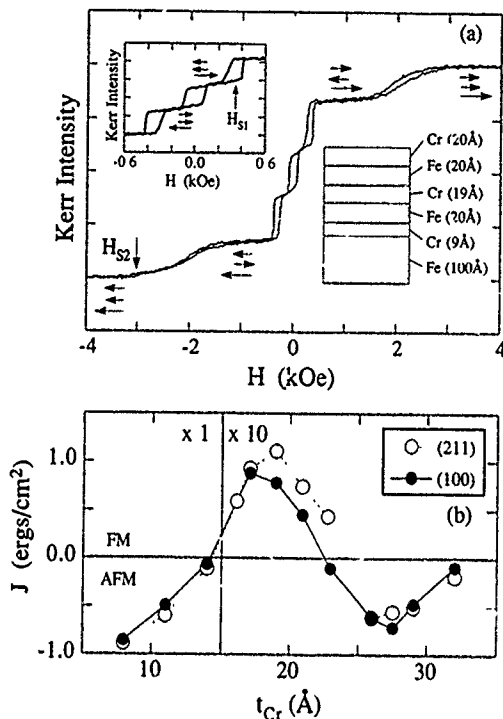


FIG. 3. (a) Room-temperature hysteresis loop measured by Kerr rotation of a (211)-oriented Fe(100 Å)/Cr(9 Å)/Fe(20 Å)/Cr(19 Å)/Fe(20 Å)/Cr(20 Å) sample. The arrows indicate the magnetization directions of the three Fe layers. The inset shows an expanded view of the low-field region. (b) Interlayer coupling J vs t_{Cr} for (211)- and (100)-oriented samples, where antiferromagnetic coupling ($J < 0$) was determined from the superlattices and ferromagnetic coupling ($J > 0$) was determined from the samples shown schematically in (a). Note the change in scale at $t_{Cr} = 15$ Å.

difference in H_S along both the easy and hard directions. The ferromagnetic coupling strength when H is along the easy axis is given by

$$J_F(211) = H_{S1} M_{SF_{Fe}}, \quad \text{for } H // \text{Fe}[011] \text{ and } J_F < 2K_U t_{Fe}. \quad (6)$$

There are equivalent expressions for the (100) orientations. For the sample shown in Fig. 3(a), J_{AF} determined from Eq. (5) is 0.09 ergs/cm², which is consistent with the superlattice results. Shown in Fig. 3(b) is the interlayer coupling measured from 8 to 32 Å Cr, showing the coupling oscillating about zero for both orientations.

The short-period (two monolayer) oscillations observed in Fe/Cr(100)/Fe wedged samples are thought to be directly related to the nested Fermi surface of Cr, which gives rise to the spin-density wave in Cr.^{3,4} The origin of the 18-Å long-period oscillation is not as easily related to the magnetic properties of Cr. Stiles⁸ has shown that there are a number of spanning vectors in Cr (100), (110), and (111) orientations, which could give rise to long-period oscillations. However, it is not understood within this theoretical framework which of the many spanning vector will give rise to the coupling. In general, it is expected that the coupling should be strongly

dependent on the crystal orientation. Given this expectation, the results in Figs. 2 and 3 showing no difference between the (100) and (211) oriented samples is surprising. In addition to the orientations studied in this paper, oscillations in the AF coupling has been observed with the same phase and period and similar coupling strengths in (110) textured multilayers.²⁸ At present, all the studies of the Fe/Cr system that show oscillatory behavior have found the same 18 Å long-period oscillation.

In conclusion, we have grown epitaxial Fe/Cr(100) and (211) superlattices on MgO(100) and (110) substrates, respectively. Both orientations show interlayer coupling, which oscillates from antiferromagnetic to ferromagnetic with a period of 18 Å. The phase, period, strength of the coupling is found to be independent of the crystallographic orientation.

The work was supported by the U.S. Department of Energy, Basic Energy Sciences—Materials Sciences, under Contract No. W-31-109-ENG-38.

- ¹ P. Grünberg, R. Schreiber, Y. Pang, M. B. Brodsky, and C. H. Sowers, Phys. Rev. Lett. **57**, 2442 (1986).
- ² S. S. P. Parkin, N. More, and K. P. Roche, Phys. Rev. Lett. **64**, 2304 (1990).
- ³ J. Unguris, R. J. Celotta, and D. T. Pierce, Phys. Rev. Lett. **67**, 140 (1991).
- ⁴ S. T. Purcell, W. Folkerts, M. T. Johnson, N. W. E. McGee, K. Jager, J. van de Stegge, W. B. Zeper, W. Hoving, and P. Grünberg, Phys. Rev. Lett. **67**, 903 (1991).
- ⁵ Y. Wang, P. M. Levy, and J. L. Fry, Phys. Rev. Lett. **65**, 2732 (1990).
- ⁶ P. Bruno and C. Chappert, Phys. Rev. Lett. **67**, 1602 (1991); Phys. Rev. B **46**, 261 (1992).
- ⁷ F. Herman and R. Schrieffer, Phys. Rev. B **46**, 5806 (1992).
- ⁸ M. D. Stiles, Phys. Rev. B **48**, 7238 (1993).
- ⁹ J. Mathon, M. Villere, and D. M. Edwards, J. Phys. Condensed Matter **4**, 9873 (1992).
- ¹⁰ R. P. Erickson, K. B. Hathaway, and J. R. Cullen, Phys. Rev. B **47**, 2626 (1993).
- ¹¹ R. Coehoorn, Phys. Rev. B **44**, 933 (1991).
- ¹² E. Bruno and B. L. Gyorffy, Phys. Rev. Lett. **71**, 181 (1993).
- ¹³ S. S. P. Parkin, R. Bhadra, and K. P. Roche, Phys. Rev. Lett. **66**, 2152 (1991).
- ¹⁴ M. T. Johnson, R. Coehoorn, J. J. de Vries, N. W. E. McGee, J. van de Stegge, and P. J. H. Bloemen, Phys. Rev. Lett. **69**, 969 (1992).
- ¹⁵ Z. Q. Qiu, J. Pearson, and S. D. Bader, Phys. Rev. B **46**, 8659 (1992).
- ¹⁶ A. Schreyer, K. Brühl, J. F. Ankner, C. F. Majkrzak, Th. Zeidler, P. Bödeker, N. Metoki, and H. Zabel, Phys. Rev. B **47**, 15 334 (1993).
- ¹⁷ S. N. Okuno and K. Inomata, Phys. Rev. Lett. **70**, 1711 (1993).
- ¹⁸ B. M. Lairson, M. R. Visokay, R. Sinclair, and B. M. Clemens, Appl. Phys. Lett. **61**, 1390 (1992).
- ¹⁹ A. Kamijo and H. Igarishi, J. Appl. Phys. **71**, 2455 (1992).
- ²⁰ E. E. Fullerton, M. J. Conover, J. E. Mattson, C. H. Sowers, and S. D. Bader, Phys. Rev. B **48**, 15755 (1993).
- ²¹ S. S. P. Parkin and D. Mauri, Phys. Rev. B **44**, 7131 (1991).
- ²² E. E. Fullerton, I. K. Schuller, H. Vanderstraeten, and Y. Bruynseraede, Phys. Rev. B **45**, 9292 (1992).
- ²³ A. Marty, B. Gilles, J. Eymery, A. Chamberod, and J. C. Joud, J. Magn. Magn. Mat. **121**, 57 (1993).
- ²⁴ Y. Ueda and M. Takahashi, J. Magn. Magn. Mat. **71**, 212 (1988).
- ²⁵ W. Folkerts, J. Magn. Magn. Mat. **94**, 302 (1991).
- ²⁶ W. Folkerts and F. Hakkens, J. Appl. Phys. **73**, 3922 (1993).
- ²⁷ W. Folkerts and S. T. Purcell, J. Magn. Magn. Mat. **111**, 306 (1992).
- ²⁸ S. S. P. Parkin, N. More, and K. P. Roche, Phys. Rev. Lett. **64**, 2304 (1990).

Oscillatory interlayer coupling through (111) oriented noble metal spacers

D. J. Keavney, D. F. Storm, J. W. Freeland, and J. C. Walker

The Johns Hopkins University, Department of Physics and Astronomy, 3400 North Charles Street, Baltimore, Maryland 21218

M. G. Pini

Istituto di Elettronica Quantistica, Consiglio Nazionale delle Ricerche, Via Panciatichi 56/30, I-50127 Firenze, Italy

P. Politi and A. Rettori

Dipartimento di Fisica dell'Università di Firenze, Largo Enrico Fermi 2, I-50125 Firenze, Italy

We use a surface-sensitive Mössbauer spectroscopy technique to examine the spin-wave spectrum, at the Fe(110)/NM(111) interface only, of a multilayer structure with a noble metal (NM) interlayer. We find that the temperature dependence of the hyperfine field follows a Bloch law $(1-BT^{3/2})$, and use spin-wave calculations to connect the surface spin-wave stiffness parameter, B , to the interlayer exchange coupling. Films grown with Ag(111) interlayers show clear oscillations with a period of 6 ML, in good agreement with recent predictions.

I. INTRODUCTION

The phenomenon of oscillatory interlayer magnetic coupling of ultrathin magnetic films¹⁻³ has generated a great deal of enthusiasm in recent years from a fundamental point of view,⁴⁻⁷ and, owing to the Giant Magneto-Resistance (GMR) effect exhibited by many of these coupled systems,^{1,8,9} from a more device-oriented point of view as well. The origin of the coupling has been attributed⁴⁻⁷ to a Ruderman-Kittel-Kasuya-Yosida (RKKY) interaction, and definite predictions of oscillation period based on Fermi surface topology are available for many interlayer materials. Experimental observations of the oscillation periods have been somewhat less forthcoming for some interlayers, in particular the (111) oriented noble metals (NM). We believe that this can be explained by the high Fermi surface curvature at the nesting Fermi wave vectors, which are responsible for the oscillations. This can result in very low-amplitude oscillations, which can be missed by traditional magnetometry techniques because of the requirement of an applied field.

In this work, we use a surface-sensitive Mössbauer spectroscopy technique to examine the spin-wave spectrum of multilayer structures Fe(110)/NM(111), with different thicknesses of the noble metal (NM) interlayer, only in the region near the Fe/NM interface. The hyperfine field due to Fe atoms in this interfacial region is found to follow a Bloch law $(1-B_s T^{3/2})$, with a surface spin-wave stiffness parameter B_s that is closely related to the interlayer exchange coupling J_1 . In order to connect the two quantities, we present model spin-wave calculations. Films grown with Ag(111) interlayers show clear oscillations with a period of 6 ML, in good agreement with the RKKY model prediction⁶ of 5.94 ML.

II. EXPERIMENT

The samples were prepared by molecular beam epitaxy (MBE) in a Perkin-Elmer PHI 430B MBE system equipped with *in situ* reflection high-energy-electron diffraction (RHEED) (vacuum during growth $<2 \times 10^{-9}$ Torr). The multilayer structures had the form $[\text{Fe}(110)_x \text{ } ^{57}\text{Fe}(110)_2 \text{ NM}(111)_y]_z + \text{Fe}(110)_x$, with the noble metal interlayer thick-

ness, y , variable between 0 and 40 ML. In this arrangement, more than 90% of the Mössbauer sensitive ^{57}Fe is segregated to the interfacial region, thus allowing us to look experimentally at the interface spin-wave spectrum.

Each multilayer structure was grown on a 5000 Å thick Ag(111) single crystal, which was grown *in situ* by MBE on a V-2 quality mica substrate. Fe layer thicknesses were measured by quartz crystal microbalance, independently calibrated by profilometry; Ag layer thicknesses were monitored by electron impact emission spectroscopy (Inficon Sentinel III). For Fe(110)/Ag(111) samples, the RHEED patterns obtained during growth of the substrate and of the multilayer structure gave evidence for high quality, flat surfaces at the atomic scale, and for a highly repeatable structure. Also, the absence of line broadening and asymmetric line intensity ratios in the transmission Mössbauer spectra indicate that the surface being probed is very flat at the atomic scale and that interdiffusion between ^{57}Fe and natural Fe is negligible.^{10,11} For Fe(110)/Cu(111) samples, the interdiffusion of Fe and Cu is more significant, but it can be reduced by decreasing the multilayer growth temperature to 150 °C (to be compared with 180 °C, for samples with Ag interlayer).

The multilayer structures described above can be considered three dimensional (3-D), since the thickness of natural Fe, x , was at least 20 ML. Indeed, the interface hyperfine field was found to follow a Bloch $(1-kBT^{3/2})$ law, similar to the temperature dependence of the magnetization,¹² where B is the bulk spin-wave stiffness parameter and k is related to the interlayer exchange interaction experienced by the Fe spins at the interface.

In Fe(110)/Ag(111) multilayers, k was found to increase to 1.83 with increasing y , with clear oscillations superimposed: see the full line through circles in Fig. 1(a). Actually, the minima occur at $y=6, 11$, and 18 ML, in close agreement with the 5.94 ML period predicted by the RKKY-like theory.⁶ To our knowledge, our measurements provide the first evidence of oscillations in exchange coupling strength through Ag(111) interlayers, experimentally detected via a thermodynamic property. As for the sign of the interlayer coupling, vibrating sample magnetometry (VSM) measure-

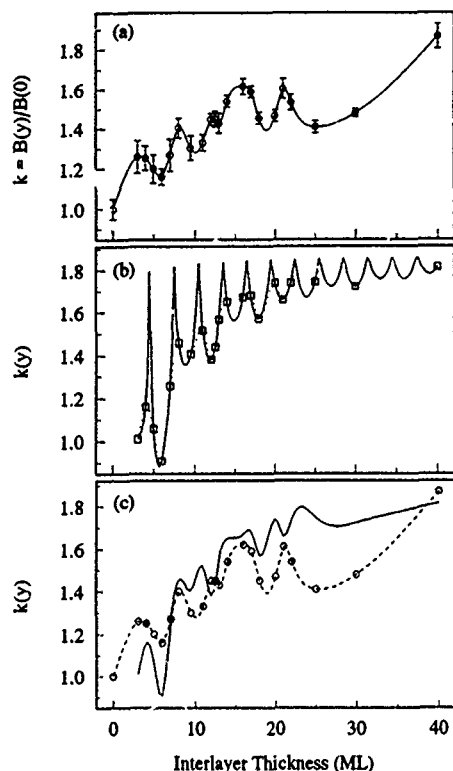


FIG. 1. Surface spin-wave stiffness parameter, $k(y)$, as a function of thickness, y , expressed in ML. (a) Circles: experimental results for Ag(111) interlayer (the full line is a guide to the eye). (b) Full line: $k(y)$ as predicted fitting RKKY theory, Eq. (4), to the data; squares: sampling of predicted $k(y)$ values at points where experimental data exist (the dotted line is a guide to the eye). (c) Comparison of a sampled fit to experimental data.

ments performed at 4.2 K suggested very weak antiferromagnetic (AF) coupling for $y=6$ ML; for all the other values of y , the hysteresis loops were found to be completely ferromagnetic (FM) in character. In Fe(110)/Cu(111) multilayers, preliminary Mössbauer data, obtained with Cu spacer thicknesses ranging between 3 and 8 ML, showed evidence for the first dip in k .

III. SPIN-WAVE THEORY

In order to connect the surface spin-wave stiffness parameter $B_s = kB$ to the interlayer exchange coupling J_1 , we perform spin-wave theory calculations for the simplified model of two semi-infinite, simple cubic, Heisenberg ferromagnets, interacting through the interfacial ($l=-1, 0$) planes via a nearest neighbor exchange J_1 , with Hamiltonian:

$$\mathcal{H} = - \sum_{\mathbf{l}, \mathbf{m}} \left(\sum_{\mathbf{l}, \mathbf{m} \leq -1} + \sum_{\mathbf{l}, \mathbf{m} \geq 0} \right) J(\mathbf{l}-\mathbf{m}) \mathbf{S}_{\mathbf{l}} \cdot \mathbf{S}_{\mathbf{m}} - 2J_1 \sum_{\mathbf{l}} \mathbf{S}_{\mathbf{l}, -1} \cdot \mathbf{S}_{\mathbf{l}, 0}. \quad (1)$$

One has $J(\mathbf{l}-\mathbf{m}) = J_0 > 0$ for nearest neighbor pairs within each semi-infinite part of the system, and zero otherwise; $\mathbf{l} = (\mathbf{l}_\parallel, l)$ are the lattice vectors.

We perform the usual Holstein-Primakoff transformation from spin to bosonic operators, and work in the mixed Bloch-Wannier representation to take care of the lack of

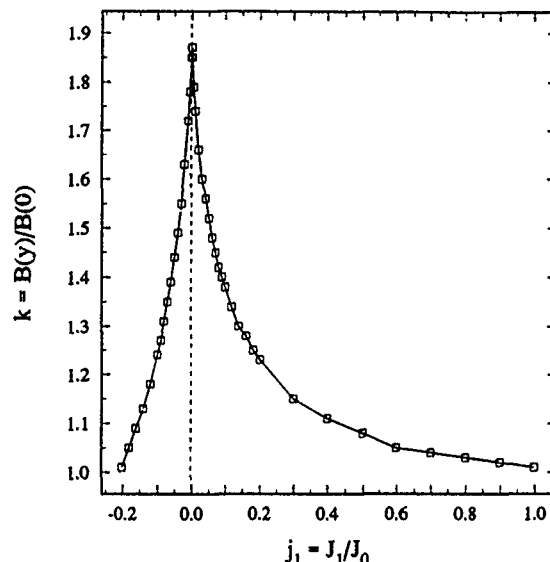


FIG. 2. Surface spin-wave stiffness parameter, $k(j_1)$, as a function of the inter-to-intralayer exchange ratio, $j_1 = J_1/J_0$. The calculation is performed for the $l=0$ and $l=1$ layers of a simple-cubic biferromagnetic interface.

translational symmetry perpendicular to the interface. For ferromagnetic interfacial exchange ($J_1 > 0$), we introduce the two-particle Green's function (GF) $G_{lm}(E, \mathbf{k}_\parallel) \equiv \langle \langle a_{\mathbf{k}_\parallel, l}; a_{\mathbf{k}_\parallel, m}^\dagger \rangle \rangle_E$. Treating the interfacial part of the quadratic bosonic Hamiltonian as a perturbation with respect to the noninteracting part, relative to the semi-infinite system, one can obtain, via Dyson's equation, the interacting GF from the noninteracting one.¹³ For antiferromagnetic interfacial interaction ($J_1 < 0$), a similar theoretical treatment can be developed. One must introduce two different families of bosonic operators, since the quantization directions are different for $l \leq -1$ and $l \geq 0$. Thus, one obtains two Green's functions, $G_{lm}(E, \mathbf{k}_\parallel)$ and $G'_{lm}(E, \mathbf{k}_\parallel) \equiv \langle \langle a_{-\mathbf{k}_\parallel, l}^\dagger; a_{\mathbf{k}_\parallel, m}^\dagger \rangle \rangle_E$, coupled via two Dyson's equations.¹⁴ In both cases, the local magnetization at the plane l can be expressed in terms of the trace of the two-particle GF

$$\langle S_l^z \rangle = S - \int_{-\infty}^{+\infty} dE f(E, T) \text{Tr Im } G_{ll}(E, \mathbf{k}_\parallel), \quad (2)$$

where $f(E, T)$ is the Bose-Einstein distribution. For ferromagnetic interfacial interaction, it turns out that the effective Bloch law,

$$\langle S_l^z \rangle / S = 1 - k(J_1/J_0) B_{sc} T^{3/2}, \quad (3)$$

is followed for any value of the ratio $j_1 = J_1/J_0$, with the limits $k(1)=1$ (bulk) and $k(0)=2$ (surface),¹⁵ in the case of a single interfacial plane ($l=0$ or $l=-1$). B_{sc} is the bulk spin-wave stiffness parameter for the simple cubic ferromagnet. For antiferromagnetic interfacial interaction, in general, we find that the local magnetization does not follow a $T^{3/2}$ law, unless the coupling is rather weak, $j_1 < 0.2$.

In Fig. 2 we report the prefactor $k(j_1)$, calculated—for the valid range of j_1 ($-0.2 \leq j_1 \leq 1.0$)—taking into account both the $l=0$ and the $l=1$ planes. We note that the inclusion of the $l=1$ plane, required by the experimental situation in

Fe/Ag multilayers, prevents $k(0)$ from reaching the value 2, pertinent to a free surface.¹⁵ Actually, in the limit of zero coupling, the value $k=1.86$ is calculated, to be compared with the value $k=1.83$, experimentally found in Fe(110)/Ag(111) multilayers for $y=40$ ML. Such close agreement confirms that interdiffusion effects are negligible.

IV. DISCUSSION

We now attempt to reproduce the observed behavior of $k(y)$ by assuming an oscillating $J_1(y)$ like the RKKY function,⁶

$$\frac{J_1(y)}{J_0} = -\frac{d^2 m^*}{y^2 m} \sin\left(\frac{2\pi y}{\Lambda} + \Phi\right) \frac{y/L(T)}{\sinh[y/L(T)]}, \quad (4)$$

where we used J_0 as the energy scale for $J_1(y)$, and took $\Phi=\pi/2$ as in Ref. 6. The oscillation period, Λ , the amplitude of the oscillations, m^* , and the temperature-dependent attenuation length, $L(T)$, have been taken as free parameters.

In Fig. 1(b) we plot $k(y)$ (full line), as obtained by performing a least square fit to our data. Owing to the steepness of k vs j_1 near $j_1=0$, $k(y)$ is very sensitive to very weak interlayer couplings: in fact, $k(y)$ must have its maximum value of 1.86 at every point where $j_1(y)$ passes through zero. It is this feature of the spin-wave stiffness that makes this surface sensitive method highly suitable for the detection of interlayer coupling in very weak ferromagnetic multilayer structures, in addition to ferromagnetic ones. The dotted line through squares in Fig. 1(b) illustrates what happens when the $k(y)$ predictions obtained from Eq. (4) are sampled at only the interlayer thicknesses where we have data: it represents a least squares fit of this sampled function to the data. One sees that, even when sampling at 1 ML intervals, it is easy to miss the sharp peaks in $k(y)$. From the comparison with the experimental results for $k(y)$ [as shown in Fig. 1(c)], it is apparent that the qualitative agreement is quite good: at all the dips in our data up to $y=22$ ML, a corresponding dip occurs in the best fit just near the same interlayer thickness. We note that, although m^* and $L(T)$ for the best fit are not close to the theoretical predictions,⁶ the

oscillation period of $j_1(y)$ is about 6 ML, in good agreement with the theoretical value⁶ of 5.94 ML for Ag(111) interlayers. The latter feature represents the critical test of the RKKY-like theory.⁶

In conclusion, using a surface-sensitive Mössbauer spectroscopy technique, we have found that the hyperfine field due to Fe atoms in the interfacial region of Fe(110)/NM multilayers follows an effective $T^{3/2}$ Bloch law. We have developed model spin-wave calculations to connect the spin-wave stiffness parameter to the interlayer exchange coupling through the noble metal interlayer. Films grown with Ag(111) interlayers show clear oscillations with a period of 6 ML, in close agreement with recent theoretical predictions.⁶

ACKNOWLEDGMENTS

We thank T. Ambrose and C. L. Chien of the Johns Hopkins University for their help in performing the VSM measurements. This work was supported in part by the National Science Foundation Grant No. DMR-9110005.

- ¹S. S. P. Parkin, N. More, and K. P. Roche, Phys. Rev. Lett. **64**, 2304 (1990).
- ²J. Unguris, R. J. Celotta, and D. T. Pierce, Phys. Rev. Lett. **67**, 140 (1991).
- ³S. Demokritov, J. A. Wolf, and P. Grünberg, Europhys. Lett. **15**, 881 (1991).
- ⁴Y. Wang, P. M. Levy, and J. L. Fry, Phys. Rev. Lett. **65**, 2732 (1990).
- ⁵D. M. Edwards, J. Mathon, R. B. Muniz, and M. S. Phan, Phys. Rev. Lett. **67**, 493 (1991); J. Phys. Condensed Matter **3**, 4941 (1991).
- ⁶P. Bruno and C. Chappert, Phys. Rev. Lett. **67**, 1602 (1991); **67**, 2592 (1991); Phys. Rev. B **46**, 261 (1992).
- ⁷R. Coehoorn, Phys. Rev. B **44**, 9331 (1991).
- ⁸G. Binash, P. Grünberg, F. Saurenbach, and W. Zinn, Phys. Rev. B **39**, 4828 (1989).
- ⁹M. N. Baibich, J. M. Broto, A. Fert, F. Nguyen Van dau, F. Petroff, P. Etienne, G. Creuzet, A. Friederich, and J. Chazelas, Phys. Rev. Lett. **61**, 2472 (1988).
- ¹⁰C. J. Gutierrez, S. H. Mayer, and J. C. Walker, J. Magn. Magn. Mat. **80**, 299 (1989).
- ¹¹C. J. Gutierrez, Z. Q. Qiu, M. D. Wiczorek, S. H. Mayer, and J. C. Walker, Phys. Rev. B **44**, 2190 (1991).
- ¹²G. Lugert and G. Bayreuther, Phys. Rev. B **38**, 11 068 (1988).
- ¹³A. Yaniv, Phys. Rev. B **28**, 402 (1983).
- ¹⁴D. J. Keavney, D. F. Storm, J. W. Freeland, J. C. Walker, M. G. Pini, P. Politi, and A. Rettori (to be published).
- ¹⁵D. L. Mills and A. A. Maradudin, J. Phys. Chem. Solids **28**, 1855 (1967).

Ab initio study of the interlayer magnetic couplings in Fe/Pd(001) superlattices and of the polarization induced in the Fe and Pd layers

D. Stoeffler, K. Ounadjela, J. Sticht,^{a)} and F. Gautier

Institut de Physique et de Chimie des Matériaux (U.M.R. 46 C.N.R.S.)—Gemme, Université Louis Pasteur, 4 rue Blaise Pascal, 67070 Strasbourg, France

In this paper we present a theoretical study of the magnetic properties of $\text{Fe}_m\text{Pd}_n(001)$ superlattices, (m and n being the number of Fe and Pd atomic layers). Our attention is mostly focused on the determination of both the interlayer magnetic couplings and the magnetic moments distributions as a function of the Fe layer's and Pd spacer's thicknesses. We use an *ab initio* LSDA method (ASW) to determine self-consistently the electronic structure, the magnetic moment distributions, and the total energies for the considered systems. For studying the role of the Pd spacer's structure, we consider two model structures for the Pd spacers (i) a fct structure for which the Pd atoms keep their bulk atomic volume, and (ii) a fcc structure for which the Pd atomic volume is expanded. For the first structure, the magnetic polarization in the palladium spacer is limited mostly to the Fe-Pd interfaces, and the couplings are similar to the ones obtained for nonmagnetic spacers. On the contrary, for the second atomic structure, the whole Pd spacer is polarized with a moment of about $0.15\mu_B/\text{atom}$ for $n \leq 14$, and the couplings are ferromagnetic in a large range of Pd thicknesses. We present a detailed study of Fe_mPd_1 and Fe_3Pd_n superlattices to determine both the couplings and the polarization induced in the Fe and Pd layers.

I. INTRODUCTION

The discovery, during the last decade, of oscillating interlayer magnetic couplings between ferromagnetic (F) layers A_m ($A = \text{Fe, Co, Ni}$) separated by a nonmagnetic or anti-ferromagnetic (AF) metallic spacer B_n (Ref. 1) (m and n correspond, respectively, to the number of atomic layers) and of the related giant magnetoresistance,² has stimulated a lot of experimental and theoretical activity. It has been shown that (i) for nonmagnetic spacers, the period of the couplings are related to the shape of the nonmagnetic metal's Fermi surface; and (ii) for AF spacers, the couplings are due to the magnetism of the spacer and related to the compatibility of the spacer's AF order and the interlayer magnetic arrangement. The case where the spacer is a nearly F metal (Pd, Pt) can be considered as intermediate between the two previous ones. Our aim is to determine the main features of the magnetic moments distributions and of the couplings in the local spin density approximation (LSDA) framework for Fe/Pd(001) superlattices.

The Fe/Pd sandwiches and multilayers have been recently studied experimentally. Fe(001)/Pd_{*n*}(001)/Fe(001) sandwiches have been first synthesized by Celinski *et al.*^{3,4} The authors found that (i) the whole Pd spacer is not entirely polarized for Pd thicknesses n larger than four monolayers (ML); (ii) for $n \leq 12$ ML, the couplings are F and show oscillations with a period of 4 ML; (iii) for $n > 12$ ML, the couplings become AF; and (iv) they are strongly sensitive to temperature variations. Fe/Pd(001) multilayers have been realized more recently in the Thomson-CSF group⁵⁻⁷ to study their magnetotransport properties. Epitaxial growth has been obtained, in agreement with the results of Celinski *et al.* The authors obtained hysteresis loops consistent with an AF coupling between the Fe layers in the same thickness range⁵ as the one observed by Celinski *et al.*⁴ However, by a more

detailed analysis of the hysteresis loops, they found no evidence for isotropic AF couplings. Moreover, by Kerr optical microscopy, they have recently obtained a strong evidence of a F coupling for $5 \leq n \leq 25$.⁷

Theoretically, the Fe/Pd interfaces have been mostly studied^{8,9} when ultrathin Pd overlayers are deposited onto a Fe substrate. However, it is not possible to split the origin of the induced Pd polarization into an Fe/Pd interfacial and a surface contribution, so that these results cannot be transposed to a multilayer situation. More recently, $\text{Fe}_5\text{Pd}_n/\text{Fe}_5(001)$ sandwiches and $\text{Fe}_5\text{Pd}_n(001)$ superlattices have been studied using a tight binding description of the electronic structure.¹⁰ The magnitudes for the couplings reported in these papers are very strong, as compared to the experimental data, to the results of similar calculations for Co_4Pd_n superlattices¹¹ and to those obtained in the present work.

II. INTERLAYER MAGNETIC COUPLINGS IN Fe_mPd_n SUPERLATTICES

We determine the couplings by calculating the difference $\Delta E_{F-AF} = E_F - E_{AF}$ between the total energies obtained for the two opposite interlayer magnetic arrangements F and AF. The F (AF) interlayer magnetic arrangement corresponds (respectively) to parallel (antiparallel) magnetizations of successive Fe layers. Here, we use the augmented spherical wave (ASW) method¹² and the LSDA formalism for treating exchange and correlation of a many electron system, which allow us to determine the electronic structure of the superlattices. More technical informations concerning the methodology used here can be found in another paper.¹³

Only the in-plane parameter is experimentally known and is found to be nearly equal to the bulk Fe one. If we assume that the (001) plane of fcc Pd when rotated by 45° matches the (001) plane of bcc Fe, a 5% in-plane expansion of the Pd parameter is obtained. Consequently, the fcc cell is

^{a)}Present address: BIOSYM Technologies, Inc., 9685 Scranton Rd., San Diego, California 92121.

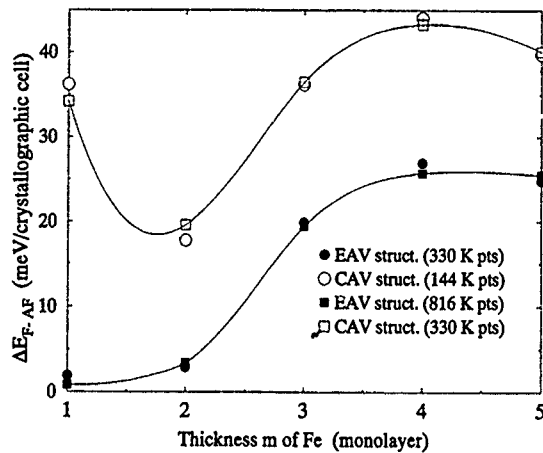


FIG. 1. Interlayer magnetic couplings $\Delta E_{F-AF} = E_F - E_{AF}$ in Fe_mPd_1 superlattices as a function of m for the CAV (full line with square symbols) and for the EAV (dashed line with circle symbols) structure obtained with the two largest number of k points used.

a priori tetragonally deformed, giving a fct structure for the Pd layers.

The precise value of the tetragonality, i.e., of the interplanar distances being unknown, we consider two extreme model structures: (i) the first one, for which the atomic volume of the Pd atoms is taken to be equal to the bulk one (noted CAV for constant atomic volume), and consequently induces a tetragonal deformation of the Pd fcc structure (fct); and (ii) the second one, for which the structure of the Pd layers is assumed to be fcc (noted EAV for expanded atomic volume). In the first structure the distance, $d_{\perp}(\text{Pd-Pd})$, between Pd planes is equal to $0.625 \times a_{\text{Fe}}$, $a_{\text{Fe}} = 5.42$; the atomic unit being the experimental value of the bcc iron lattice parameter. For the second structure, $d_{\perp}(\text{Pd-Pd})$ is equal to $(\sqrt{2}/2) \times a_{\text{Fe}}$, so that the palladium atomic volume increase $\Delta\Omega$ from its bulk value Ω , $\Delta\Omega/\Omega$ is equal to 13%. We have verified that, for these two structures, the bulk Pd crystal is not magnetic. Finally, for the distance $d_{\perp}(\text{Pd-Fe})$ between a Pd plane and a Fe plane, we use the average $[d_{\perp}(\text{Pd-Pd}) + d_{\perp}(\text{Fe-Fe})]/2$ value with $d_{\perp}(\text{Fe-Fe}) = a_{\text{Fe}}/2$.

We have first calculated the couplings for Fe_mPd_1 superlattices (Fig. 1) to determine the smallest Fe thickness for which the results can be considered as representative of the ones that would be obtained for very large Fe thicknesses. For $m=1$ and 2, the couplings are found to be very different—mainly for the EAV structure—from the ones obtained for $m=3-5$. The couplings being nearly equal for these values, we can limit our study to Fe_3Pd_n superlattices to reduce the number of inequivalent sites in the elemental cell.

Figure 2 is a plot of the couplings versus the Pd spacer's thickness n . The couplings obtained for the CAV structure oscillate from AF ($n=1,2$) to F ($n=3,4,5$) and to AF ($n=6$) values. These oscillations can be roughly assimilated to the ones obtained with the "RKKY-like" theories. On the contrary, the couplings obtained for the EAV structure are F, except for $n=1$. The couplings are positive for both structures, i.e., the AF arrangement is the most stable one. This suggests that, for the F arrangement, the polarization of the

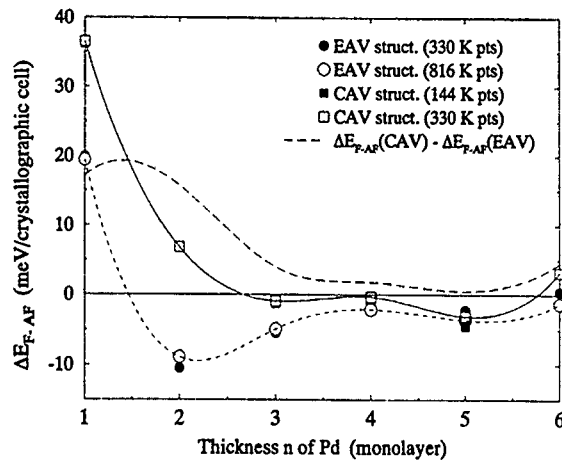


FIG. 2. Interlayer magnetic couplings $\Delta E_{F-AF} = E_F - E_{AF}$ in Fe_3Pd_n superlattices as a function of n for the CAV (full line with square symbols) and for the EAV (dashed line with circle symbols) structure obtained with the two largest number of k points used. The long dashed line corresponds to the difference $\Delta E_{F-AF}(\text{CAV}) - \Delta E_{F-AF}(\text{EAV})$ between the couplings obtained for the two structures, which is always found to be positive. The interplanar Pd expansion introduces a contribution that always stabilizes the F state. However, we deduce that this effect is short ranged (three monolayers).

Pd spacer costs some magnetic moment formation energy, which can be larger than the energy gain coming from the F interfacial coupling between Fe and Pd layers, these two contributions vanishing for the AF arrangement for which the Pd layer is nonmagnetic. This conjecture is consistent with the fact that the lowest AF couplings is obtained for the EAV structure, i.e., for large Fe-Pd distances, so that a given polarization of the Pd atoms costs less energy, the Pd atoms being closer from the Stoner instability.

III. INDUCED POLARIZATION IN THE Fe AND Pd LAYERS

The experimental F couplings, as measured by Celinski *et al.*⁴ show a nonmonotonic behavior with n . The authors have obtained local minima for $n=6,9$ and local maxima for $n=7,11$. Unfortunately, it is not possible to determine theoretically the couplings for so large Pd thicknesses because they are certainly too small to be accurately determined and would need too large a computer time. Childress *et al.*⁷ have measured the enhancement of the polarization in the superlattices, which has been found to be equal to $(3.3 \pm 1.6) \mu_B$ for each interfacial atom. Even if the couplings cannot be calculated for large spacer thicknesses, it is nevertheless possible to determine the magnetic moments distributions for larger m and n values by restricting our study to the F arrangement to reduce by symmetry the size of the cell by a factor of 2. This allows us to get information on the induced magnetic polarization. Therefore, we have determined the polarization in (i) the Fe layer for a $\text{Fe}_{15}\text{Pd}_1$ superlattice and (ii) the Pd spacer for large thicknesses (up to $n=20$).

In Fig. 3 we have plotted the magnetic moments distributions in the Fe layer for $\text{Fe}_{15}\text{Pd}_1$ and in the Pd spacer for $\text{Fe}_3\text{Pd}_{15}$ for both structures.

We have verified that the magnetic moments on the Fe atoms in Fe_3Pd_n superlattices are insensitive to the thickness

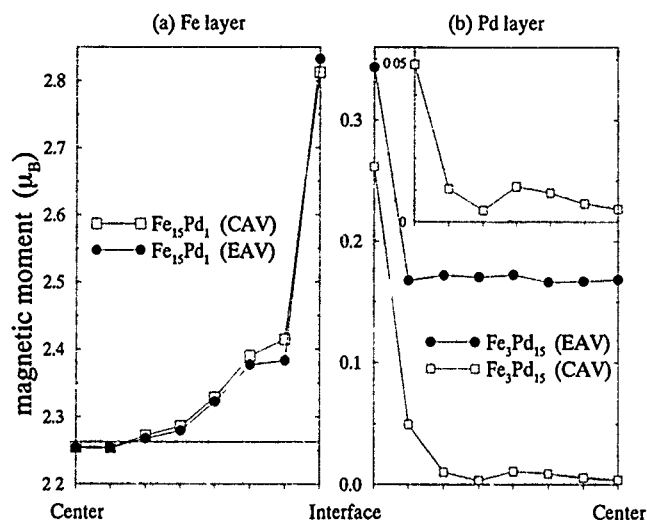


FIG. 3. (a) Polarization of the Fe layer in $\text{Fe}_{15}\text{Pd}_1$ superlattices determined with 330 k points for both the CAV and EAV structure. The horizontal line corresponds to the bulk magnetic moment. (b) Polarization of the Pd spacer in $\text{Fe}_3\text{Pd}_{15}$ superlattices determined with 330 (108) k points for the EAV (CAV) structure. The inserts represent the same values for the CAV structure at a larger scale. The values are only given for half the sites. The others can be deduced by symmetry.

of the Pd spacer. This is why we can reasonably assume that the Fe polarization obtained for $\text{Fe}_{15}\text{Pd}_1$ is representative of the polarization obtained for larger n values. Our result also shows that the Fe polarization is nearly insensitive to the structure (CAV or EAV) of the Pd spacer. Consequently, the total polarization induced in the Fe layer is at least found equal to $0.9\mu_B$ per interfacial atom.

The polarization of the Pd spacer is nearly insensitive to the thickness of the Fe layer. However, it is strongly sensitive to the structure of the Pd spacer. In the CAV structure, the magnetic polarization of the palladium layers induced by the Fe interfacial layers is limited to the first three neighboring layers, the total induced magnetic moment being equal to about $0.35\mu_B$ per interfacial atom. However, the magnetic polarization shows a nonmonotonous decay and suggest that both interfacial polarizations are interacting. A minimum is always obtained in the magnitude of the magnetic moments on the fourth Pd layers from the interface. In the EAV structure, the whole Pd spacer remains polarized with large magnetic moments on the inner layers (0.13 – $0.19\mu_B$) up to large thicknesses. This is due to the fact that, for this atomic volume, the Pd is close to the F state.

IV. DISCUSSION AND OUTLOOK

In this paper we have shown that (i) the ground states of Fe_3Pd_1 in both structures and for Fe_3Pd_2 in the CAV structure is AF. (ii) The couplings are found to oscillate in the CAV structure, whereas they are F in the EAV structure. (iii) For large Pd thicknesses values ($n > 4$), the polarization of the Pd spacer is completely different for the two structures considered here: it is limited to the interfacial atoms for the CAV structure, whereas the whole Pd spacer is polarized with a magnetic moment of approximately $0.15\mu_B$ /atom for the inner layers in the EAV structure. (iv) The induced polarization

in the Fe layer is at least equal to $0.9\mu_B$ and in the Pd spacer is approximately equal to $0.35\mu_B$ per interfacial atom for the CAV structure.

The comparison with the experimental results shows interesting features that can be summarized as follows.

(i) The mean magnetic moment per Pd atom is estimated by Celinski *et al.* to be equal to $0.25\mu_B$ in $\text{Fe}_3/\text{Pd}_4/\text{Fe}_{10}$.³ This result is in agreement with the one we obtain for the Fe_3Pd_4 superlattices in the EAV structure, the calculated mean magnetic moment being found equal to $0.265\mu_B$.¹³ This could suggest that the experimental structure is expanded for such small thicknesses.

(ii) Childress *et al.*⁷ have measured an induced polarization equal to $(3.3 \pm 1.6)\mu_B$ per interfacial atom. Our calculations give $1.25\mu_B$ per interfacial atom in the CAV structure, which is less than the experimental lower bound ($1.7\mu_B$).

(iii) Celinski *et al.* have also deduced that the maximum number of Pd atomic layers for which the whole Pd layer is ferromagnetically ordered is $n=4$.³ This is not consistent with our calculations for perfect superlattices: we have shown that the Pd polarization for the CAV structure is limited to the interfacial atomic layer, while the Pd spacer is entirely polarized up to $n=15$ for the EAV structure. The present results can be consistent with experiment only if a structural change (from the EAV to the CAV structure) occurs for $n=5$. Up to now, there is no experimental evidence of such a change.

In view to clarify this point, we have recently done preliminary calculations to determine the values of the Pd interplanar distances, which minimize the total energy of the superlattice. These results show that the ground state structure is very close to the CAV one. Consequently, in contradiction with the previous conjecture, the structural change from an EAV to a CAV structure cannot be theoretically predicted. Therefore, the disagreement between theory and experiment could only be resolved if we introduce some interfacial interdiffusion. Such a study is now under progress.

¹S. S. P. Parkin, N. More, and K. P. More, Phys. Rev. Lett. **64**, 2304 (1990).

²M. N. Baibich, J. M. Broto, A. Fert, F. Neuyen Van Dau, F. Petroff, P. Etienne, G. Creuzet, A. Friederich, and J. Chazelas, Phys. Rev. Lett. **61**, 2472 (1988).

³Z. Celinski, B. Heinrich, J. F. Cochran, W. B. Muir, A. S. Arrott, and J. Kirschner, Phys. Rev. Lett. **65**, 1156 (1990).

⁴Z. Celinski and B. Heinrich, J. Magn. Magn. Mater. **99**, L25 (1991).

⁵A. Schuhl, J. R. Childress, J.-M. George, P. Galtier, O. Durand, A. Bartheleny, and A. Fert, J. Magn. Magn. Mater. **121**, 275 (1993).

⁶J. R. Childress, A. Schuhl, J.-M. George, O. Durand, P. Galtier, V. Cros, K. Ounadjela, R. Kergoat, and A. Fert, in "Magnetism and structure in systems of reduced dimension," *Proceedings of the NATO Advanced Workshop in Corsica, France*, June 1992 (Plenum, New York, 1993).

⁷J. R. Childress, R. Kergoat, O. Durand, J.-M. George, P. Galtier, L. Miltat, and A. Schuhl (unpublished).

⁸S. Blügel, B. Drittler, R. Zeller, and P. H. Dederichs, Appl. Phys. A **49**, 547 (1989).

⁹C. Li, A. J. Freeman, H. J. Hansen, and C. L. Fu, Phys. Rev. B **42**, 5433 (1990).

¹⁰H. Nait-Laziz, S. Bouarab, C. Demangeat, A. Mokrani, and H. Dreyssé, J. Magn. Magn. Mater. **118**, 365 (1993).

¹¹D. Stoeffler and F. Gautier, Prog. Theor. Phys. Suppl. **101**, 139 (1990).

¹²A. R. Williams, J. Kübler, and C. D. Gelatt, Jr., Phys. Rev. B **19**, 6094 (1979).

¹³D. Stoeffler, K. Ounadjela, J. Sticht, and F. Gautier, Phys. Rev. B **49**, 299 (1994).

Induced spin polarization on Fe/nonmagnetic metal interfaces

J. L. Pérez-Díaz and M. C. Muñoz

Instituto de Ciencia de Materiales, C.S.I.C., Serrano, 144, E-28006 Madrid, Spain

We have investigated the Fe/Au, Ag, Pt, and Al(001) single interfaces by means of an empirical tight-binding Hamiltonian within the Green's function matching formalism. The method is exact and describes equally interface states and bulk resonances. The evolution of the layer density of states indicates a rearrangement of the electronic density at the interface in form of spin polarization of the nonmagnetic layers. The induced magnetic moments in the nonmagnetic layers are only appreciable in Pt and Al, while variations of the interface Fe magnetization are predicted for all the systems.

I. INTRODUCTION

The discovery of long-range oscillatory exchange coupling between magnetic layers separated by a nonmagnetic spacer¹ has opened new perspectives in the study of magnetic layered structures. The oscillatory and long-range character of the coupling suggests that the nature of the interaction among ferromagnetic layers is indirect and associated to the Ruderman-Kittel-Kasuya-Yosida (RKKY) indirect exchange. As is well known, the RKKY interaction stems from the spin polarization induced in the spacer material by adjoining magnetic slabs. Then, the electronic interaction at the interface determines the spin polarization of the nonmagnetic material and indirectly the role of their energy bands. In multilayers, where different interfaces are simultaneously involved, the scattering at the multiple interfaces would give rise to specific modulation of the multilayer electronic structure.² Nevertheless, the induced spin polarization of the nearly free electrons would be identical in the one-interface case. On the other hand, overlayers and sandwiches of magnetic metals have an added interest due to their remarkable two-dimensional magnetic properties. It has been shown that the interface magnetic properties of a Fe monolayer (ML) grown on Au, Ag, or Pt single crystals differ from the bulk ones.³ Besides the enhancement of the Fe magnetic moment (MM), an appreciable magnetization of the first nonmagnetic layer has also been predicted. The explanations for these effects are based on the variation of the coordination number of the overlayer atoms.⁴ However, in multilayers and consequently in the single interfaces formed by bcc Fe and a fcc metal, the coordination number holds up throughout the interface. Then, in these systems magnetic effects are only produced by the electronic interaction between the two metal energy bands. The purpose of the paper is to investigate the interface electronic structure of Fe(bcc)/X(fcc)(001) single interfaces, where X is a nonmagnetic metal.

II. MODEL AND METHOD

The electronic structure of the interfaces has been self-consistently calculated by means of an empirical tight-binding (TB) Hamiltonian within the surface Green's function matching (SGFM) approach.⁵ The method is exact and allows us to determine the electronic properties of any desired layer of the entire semi-infinite crystals. The SGFM yields the interface Green's function (GF) in terms of the Hamiltonians and GF's of the bulk constituents and the in-

teraction across the interface. It deals equally with interface states and bulk resonances. The interface GF is evaluated as a function of energy E , two-dimensional wave vector k_{\parallel} parallel to the interfaces and layer indexes n and n' . To calculate the total Layer Density of States (LDOS), a weighted sum of the Cunningham special points⁶ in the two-dimensional Brillouin zone have been used. The bcc and fcc (001) semicrystals are coupled by rotating the fcc lattice 45° around the z axis.⁷ The small lattice mismatch is neglected, since the Fe lattice constant is almost a factor of $\sqrt{2}$ smaller than the Ag, Au, Pt, and Al lattice parameters. Then, the two-dimensional lattice is square and a_{\parallel} is the same for both constituent semicrystals and equal to that of Fe, while a_{\perp} is different on each side of the geometrical interface. The distance between the Fe and the fcc metal layers is obtained averaging the interlayer distances of both sublattices.

An empirical TB Hamiltonian, with a spd orbital basis has been used to describe the bulk materials. Because the bcc third-neighbor and fcc second-neighbor distances coincide, we have taken up to third-nearest-neighbor interactions for Fe, and second-nearest-neighbor interactions for fcc metals. The orthogonal two-center TB parameters given by Papaconstantopoulos⁸ have been used. To calculate the cross-coupling matrix elements, we consider the actual Fe-X ($X = \text{Ag, Au, Pt, Al}$) bond angles, while for the TB parameters we take the arithmetic averages of the corresponding bulk ones. This is a good approximation, since the bulk parameters have either the same sign or one is much larger than the other.

To obtain charge neutrality we add a diagonal potential to the Hamiltonian of the first two layers on each side of the geometrical interface. Its main effect is to shift in energy the interface LDOS, and consequently to vary the orbital occupancies. In all the interfaces, charge neutrality, to within 0.05 electrons, has been achieved.

III. RESULTS AND DISCUSSION

A. Fe/transition metal interfaces

In the Fe/transition metal interfaces, the overlap between the fcc metal and the Fe bands increases along the Ag, Au, and Pt series, since the bulk valence band becomes wider and at higher energy. Figures 1-3 show the LDOS for the first two atomic planes and for a bulk plane on each side of the Fe/Ag, Fe/Au, and Fe/Pt interfaces. Solid and dashed lines correspond to majority and minority spin states, respectively. The energy zero is at the Fermi level. The LDOS of the three metals, Ag, Au, and Pt, exhibits spin-polarization. For Ag the

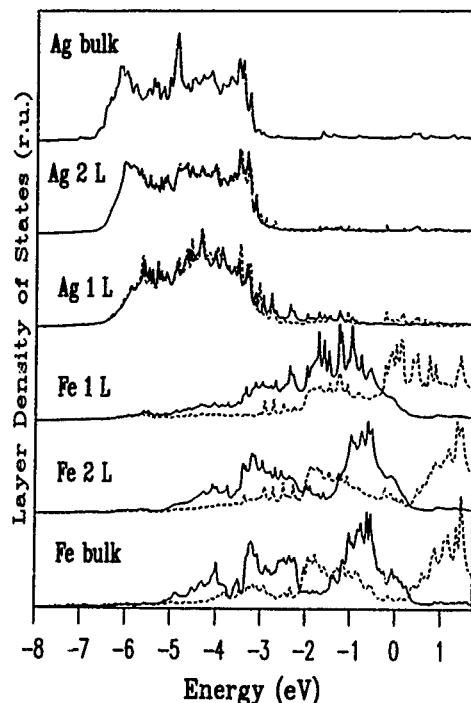


FIG. 1. Total LDOS for the first two atomic planes and a bulk plane on each side of the Fe/Ag (001) interface. Solid lines represent majority-spin states and dashed lines represent minority-spin states.

splitting is very small and almost restricted to the first layer. It is positive in the entire range of the Ag *d* band, except around -6 eV. Bulk resonances, particularly at about -4 eV, are induced by the Fe layer. The splitting of the Au band is larger and is also observable in the second Au layer. The strongest modification of the first Au LDOS is around the top

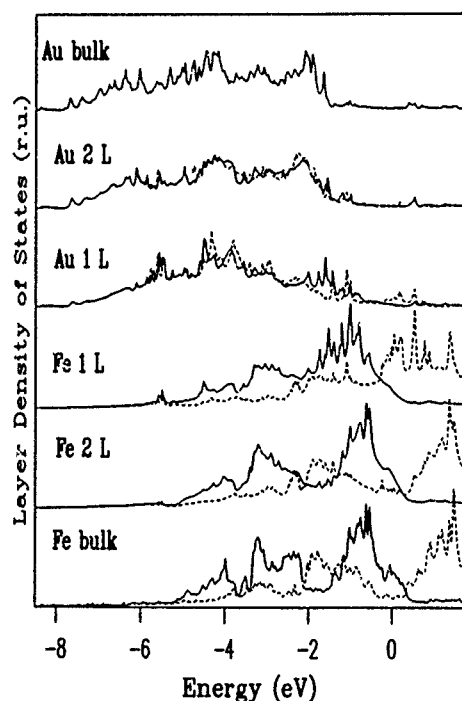


FIG. 2. As in Fig. 1, for the Fe/Au(001) interface.

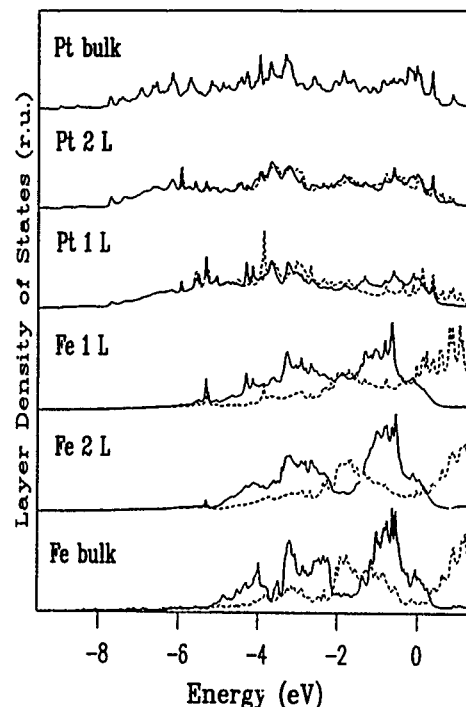


FIG. 3. As in Fig. 1, for the Fe/Pt(001) interface.

of the *d* band (-1.5 eV), where besides a decrease of the Au-like states, the appearance of Fe induced resonant states is observed. However, comparing the three interface systems, the greatest spin polarization is induced in the Pt interface layer, where hybridization of the *d* bands is noticeable along all the band extend. The MM of the nonmagnetic interface layers takes the values $0.01\mu_B$ for Ag, $0.08\mu_B$ for Au, and $0.18\mu_B$ for Pt, which agree reasonably with those calculated for overlayers and superlattices.⁹ Namely, zero and $0.05\mu_B$ for one and two MLs of Fe grown on Ag; $0.015\mu_B$ for a Fe ML on Au, and $0.3\mu_B$ for Pt/Fe superlattices. The present results indicate that the increase of the MM correlates with a stronger band hybridization at the interfaces.

The overall structure of the first Fe LDOS is similar for the three interfaces. There is a depletion of states at the bottom and an enhancement near the top of the *d* band for both majority and minority spin polarization. These effects are more appreciable in Ag, while for the Fe/Pt interface the LDOS is closer to that of a bulk Fe plane. The dominant structure is located at about -1.5 eV on the majority and at Fermi level on the minority-spin band, being larger for the Fe/Ag interface. Since the Ag *d* band is below -2 eV, this structure must be due to not only *d-d* but also *sp-d* hybridization. Furthermore, the modifications of the majority-spin LDOS are mainly in the occupied states region, while those of the minority-spin LDOS are in the empty-state area. Therefore, there is an imbalance of spin-up and spin-down states, which gives rise to the enhancement of the Fe magnetization at the interface layers.

The MM of the first and second Fe layers increases by 16% and 1% for Ag, 10% and 5% for Au, and 5% and 6% for Pt interfaces, respectively. In the Fe/Pt system, the slow decay of the Fe MM to the bulk value, besides the appre-

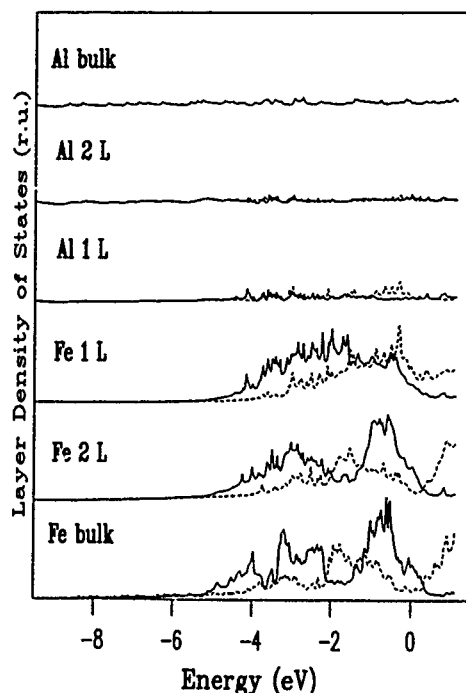


FIG. 4. As in Fig. 1, for the Fe/Al(001) interface.

ciable Pt induced MM, may explain the great magneto-optical Kerr effect observed in Fe/Pt modulated structures.¹⁰

B. Fe/Al interface

The LDOS for the Fe/Al interface is represented in Fig. 4. The planes displayed are those of Figs. 1–3. In spite of the different electron occupancy—the Al band has three *sp* electrons per spin—the large modification of the Al and Fe interface LDOS suggests a strong *sp*–*d* interaction. In fact, the interface resonances, and consequently the *sp*–*d* hybridization, extend to all the band for both majority and minority spin polarization. The Al induced MM in the first layer is $0.15\mu_B$, comparable to the Pt MM. Nevertheless, while the Pt–Fe MMs are ferromagnetically oriented, the Al–Fe MMs are antiferromagnetically coupled. This is due to the strong

sp–*d* hybridization of the minority spin band just below the Fermi level. On the other hand, the MM of the Fe interface layer diminishes by as much as 24%. The strong *sp*–*d* interaction seems to be responsible for this significant reduction.

In summary, the interaction between the Fe and the fcc metals induces spin-polarization on the interface nonmagnetic bands for all the systems studied. However, a noticeable MM is only exhibited by the Pt and Al interface layers. Enhancement of the Fe interface MM is obtained for the transition metal interfaces, while a large decrease is predicted for the Fe/Al system. In this system the coupling at the interface is antiferromagnetic.

ACKNOWLEDGMENT

This work was partly supported by the Spanish Comisión Interministerial de Ciencia y Tecnología under Grant No. MAT92-0937.

¹S. S. P. Parkin, Phys. Rev. Lett. **67**, 3598 (1991); A. Fuss, S. Demokritov, P. Grünberg, and W. Zinn, J. Magn. Magn. Mat. **103**, L221 (1992); J. J. de Miguel, and R. Miranda, Phys. Rev. Lett. **64**, 1059 (1990).

²J. L. Pérez-Díaz and M. C. Muñoz, submitted to Phys. Rev. Lett.

³M. E. McHenry, J. M. MacLaren, and D. P. Clougherty, J. Appl. Phys. **70**, 5932 (1991) and references therein. C. Li, A. J. Freeman, and C. L. Fu, J. Magn. Magn. Mat. **75**, 201 (1988).

⁴M. E. McHenry, J. M. MacLaren, and D. P. Clougherty, J. Appl. Phys. **70**, 5932 (1991), and references therein. C. Li, A. J. Freeman, and C. L. Fu, J. Magn. Magn. Mat. **75**, 201 (1988).

⁵M. C. Muñoz and M. P. López Sancho, Phys. Rev. B **41**, 8412 (1990).

⁶S. L. Cunningham, Phys. Rev. B **10**, 4988 (1974).

⁷Fe/Au: H. Kikuchi, Y. Suzuki, and T. Katayama, J. Appl. Phys. **67**, 5403 (1990); S. D. Bader and E. R. Moog, J. Appl. Phys. **61**, 3729 (1987); Fe/Ag: B. T. Jonker and G. A. Prinz, Surf. Sci. **172**, L568 (1986); A. Barthelemy and A. Fert, J. Appl. Phys. **67**, 5409 (1990); Fe/Au: R. Gernmar, W. Dürr, J. W. Krewer, D. Pescia, and W. Gudat, Appl. Phys. A **47**, 393 (1988); Fe/Al: W. Zinn, Ch. Sauer, S. Handschuh, and M. Schäfer, Phys. Scr. **T45**, 110 (1992).

⁸D. A. Papaconstantopoulos, *Handbook of the Band Structure of Elemental Solids* (Plenum, New York, 1986).

⁹C. L. Fu, A. J. Freeman, and T. Oguchi, Phys. Rev. Lett. **54**, 2700 (1985); R. Richter, J. G. Gay and J. R. Smith, Phys. Rev. Lett. **54**, 2704 (1985); M. E. McHenry, J. M. MacLaren, M. E. Eberhart, and S. Crampin, J. Magn. Magn. Mat. **88**, 134 (1990); M. E. McHenry, J. M. MacLaren, and D. P. Clougherty, J. Appl. Phys. **70**, 5932 (1991).

¹⁰See, for example, Y. B. Xu, H. R. Zhai, M. Lu, Q. Y. Jin, and Y. Z. Miao, Phys. Lett. A **168**, 213 (1992), and references therein.

The temperature dependence of the bilinear and biquadratic exchange coupling in Fe/Cu, Ag/Fe(001) structures (abstract)

Z. Celinski, B. Heinrich, and J. F. Cochran

Physics Department, Simon Fraser University, Burnaby, British Columbia V5A 1S6, Canada

The exchange coupling through nonmagnetic metallic interlayers is described by bilinear and biquadratic exchange coupling terms. In simple metals such as Cu(001) and Ag(001), the bilinear exchange coupling exhibits strong short wavelength oscillations (~ 2 ML). The exchange coupling through non ferromagnetic interlayers is strongly affected by the interface roughness. Realistic interfaces consist of finite atomic terraces that result in variations of the interlayer thickness. Slonczewski showed that in this case the biquadratic exchange term can be produced by frustration of local magnetic moments. Recent band structure calculations showed that the biquadratic exchange coupling can be intrinsic. In this case its strength is usually found to be significantly weaker than that of bilinear coupling. The temperature dependence of biquadratic exchange coupling is expected to be different for the Slonczewski and intrinsic mechanisms. The intrinsic biquadratic exchange coupling is expected to vary with temperature faster than that predicted by the Slonczewski mechanism. In the present studies using the FMR and MOKE techniques we have investigated extensively the temperature dependence of the bilinear and biquadratic exchange coupling in Fe/Cu/Fe and Fe/Ag/Fe(001) structures. The quantitative studies of the exchange coupling were carried out in the temperature range 77–400 K. By growing the first Fe layer at various substrate temperatures one can prepare samples possessing interfaces with a variable atomic terrace width at the Fe/Cu, Ag interface. That way one can control the strength of the biquadratic exchange coupling. Two limits were investigated: (a) The strength of the biquadratic term in the exchange coupling was much smaller (10%) compared to the bilinear term; (b) the strength of the biquadratic term was comparable to the bilinear exchange coupling. The results are discussed within the framework of existing theories.

Exchange coupling through ferromagnetic bridges in magnetic multilayers (abstract)

J. C. Slonczewski

IBM Research Division, Thomas J. Watson Research Center, P.O. Box 218, Yorktown Heights,
New York 10598

It has been known for 27 years¹ that ferromagnetic bridges joining two ferromagnetic films can result in a $\cos \theta$ dependence of the exchange-coupling energy W_b only under very restricted circumstances. In more natural circumstances, considered here, one expects $W_b = C \theta^2 \geq 0$ to hold in the full angular range $0 \leq \theta \leq \pi$. The principal condition for this relation to hold is that local spontaneous spin polarization actually exists at the given temperature for all sites composing complete chains of exchange-coupled local spins extending between the ferromagnetic films. One easily finds estimation formulas in special limits; e.g., for a set of thin uniform filamentary bridges, $C = A \phi / w$, where A is the exchange stiffness, ϕ is the fractional cross section of filaments, and w is the spacer thickness. Because of this peculiar angular dependence of W_b , ferromagnetic bridges are conducive to noncollinear arrangements of the sublayer moments. In particular, nearly 90° -domain arrangements are favored in epitaxial (100) multilayers which have sufficiently strong positive cubic anisotropy W_k . Observed 90° arrangements were previously attributed to biquadratic coupling.² One condition for 90° arrangements due to bridges is that the additional coupling $W_a = -J \cos \theta$ through the normal-metal spacer medium is antiferromagnetic and its strength is in the appropriate range. Let the total energy be $W = W_k + W_a + W_b$. Then, if $W(0)$ is thus made nearly equal to $W(\pi)$, the θ^2 dependence of the bridge term insures that W is minimized near $\theta = \pi/2$.

¹O. Massenet *et al.*, IEEE Trans. Magn. **MAG-2**, 553 (1966).

²M. Rührgig *et al.*, Phys. Status Solid A **125**, 635 (1991).

Exchange coupling between ferromagnetic layers: Effect of quantum well states (abstract)

James R. Cullen and Kristi B. Hathaway

Naval Surface Warfare Center, Dahlgren Division, White Oak Detachment, 10901 New Hampshire Avenue, Silver Spring, Maryland 20903-5640

It is a well-established experimental result that the exchange coupling between ferromagnetic metals Fe, Co, or Ni is an oscillatory function of the thickness of the paramagnetic spacer. Theories of this coupling are almost in complete unanimity in attributing the observed periodicity to the properties of the Fermi surface of the paramagnetic spacer. Little has been done, and no consensus reached, as to the origin of the strength of the coupling. A realistic assessment of this quantity requires the use of an itinerant picture of the ferromagnetic constituent. From a recent study based on this picture,¹ it became clear that the ratio of the spin-split band gap to the Fermi energy is important in establishing not only the strength of the coupling, but the phase of the oscillations in the nonasymptotic spacer thickness regime. Here we extend the work, which was limited to cases in which the minority-spin band of the ferromagnet was energy matched to the paramagnetic band, to cases in which the match is to that of the majority-spin band. In the latter arrangement, electrons of one spin are trapped in a well whose width equals the thickness of the spacer. We calculated the spin-flip current, and hence, the torque, exerted by one ferromagnet on the other as the magnetization direction of the former is rotated with respect to that of the latter. As in the earlier case, the torque leads to higher-order (in the cosine of the angle between the magnetizations of the ferromagnets) coupling as well as the usual linear coupling. The bound states produced by the quantum well structure are most important when the band splitting in the ferromagnet is large. The new features produced by these states will be discussed; in particular, their effects on the coupling strength and the phase shift will be discussed.

¹R. P. Erickson *et al.*, Phys. Rev. 47, 2626 (1993).

Ferromagnetic resonance studies of Py bilayers for the system (Permalloy/ Al_2O_3) (abstract)

H. Hurdequint, N. Bouterfas, and A. Vaurés

Laboratoire de Physique des Solides, Université Paris-Sud, 91405 Orsay Cédex, France

We report a detailed ferromagnetic resonance study, performed at X band and room temperature, of magnetic permalloy (Py) bilayers ($\text{Py1}/\text{Al}_2\text{O}_3/\text{Py2}$) deposited by rf sputtering on mica substrates. We will present and discuss results relative to two series of Py bilayers characterized by an ultrathin Py layer thickness and corresponding to the two following sets of spacer thickness t_s : (40;30;19 Å) and (15;12;9 Å). These films have been deposited at room temperature and subsequently annealed (at $T=220$ and 190°C , respectively, for these two sets). The resonance spectrum is studied as a function of the orientation [$\Theta_H=(N,H)$ with respect to the film normal N] of the applied dc field H in a plane perpendicular to the film. (i) For the three samples of the first series the resonance spectrum is composed of two resolved lines which can be attributed to the resonances of the individual layers (Py1 and Py2) dynamically uncoupled. As for a single¹ Py layer, the angular variation $H_{\text{res}}(\Theta_H)$ of each line observed is well accounted for in terms of a unique parameter ($4\pi M-H_A$), where H_A is a uniaxial perpendicular anisotropy field arising from the interface-induced anisotropy. The anisotropy fields H_{A1} (for Py1) and H_{A2} (for Py2) are found slightly different ($H_{A2}-H_{A1}=500$ G), reflecting some differences in the structural characteristics of the ($\text{Py}/\text{Al}_2\text{O}_3$) interfaces in the two Py layers. (ii) In the second series of lower t_s values, by contrast, the observed resonance spectrum is more complex revealing for a given orientation Θ_H two main modes (with a more intense one) and for specific geometries (around $\Theta_H=0$) the presence of other resonance modes of much weaker intensities. For these samples the angular variation $H_{\text{res}}(\Theta_H)$ of the different modes observed, by comparison to the behavior found in the Py single-layer control sample, provides clear evidence for the presence of a dynamical coupling between the magnetizations of the two Py layers. The main mechanisms, likely responsible for this intermagnetic layer coupling, will be discussed: dipolar coupling and exchange coupling (either direct through pinholes or indirect).

¹Bouterfas *et al.*, abstract on single Py layers submitted to this conference.

Exchange coupling in [Dy|Er] metallic superlattices

W. T. Lee, H. Kaiser, and J. J. Rhyne

Research Reactor Center, University of Missouri, Columbia, Missouri 65211

K. Dumesnil, C. Dufour, Ph. Mangin, and G. Marchal

Laboratoire de Physique du Solide, University of Nancy I, 54506 Vandoeuvre les Nancy Cedex, France

R. W. Erwin and J. A. Borchers

Reactor Radiation Division, National Institute of Standards and Technology, Gaithersburg, Maryland 20899

Magnetic exchange coupling in metallic superlattices of [Dy|Er], grown by molecular-beam epitaxy, has been examined by neutron diffraction. In a superlattice of 65-Å layers of Dy and 55-Å layers of Er, distinct ordering temperatures were observed for the Dy and Er layers. Basal plane helical ordering of the Dy layers was initiated at temperatures close to T_N for bulk Dy (178 K) with a long-range interaction, preserving both phase and chirality, mediated through the Er layers. At a temperature near 70 K, the helical coupling of the Dy spins is replaced by an antiferromagnetic coupling of adjacent ferromagnetically ordered Dy layers coexisting with a remanent helical order. At a temperature well below T_N of bulk Er, c -axis ordering of the Er spins occurs in the superlattice, and in measurements at 10 K there is evidence of basal plane moment ordering in the Er.

INTRODUCTION

Rare-earth superlattices, consisting of layers of a magnetic rare earth alternated with layers of a nonmagnetic rare earth,¹ have provided unique insight into the propagation of long-range magnetic order via spin density wave coupling mechanisms and on the effect of lattice strains on the occurrence of different periodic moment and ferromagnetic spin states.

In a new departure, superlattices have recently been grown at the University of Nancy that consist of alternate layers of the dissimilar magnetic elements Dy and Er. These superlattices have been grown by molecular-beam epitaxy (MBE) techniques and have been examined by x-ray and neutron diffraction and magnetization measurements. Only the neutron scattering results are presented in this article.

In bulk elemental form, Dy orders at 178 K (T_N) in a helical spin structure consisting of ferromagnetic sheets perpendicular to the c crystal axis that are rotated from plane to plane through a temperature-dependent turn angle. Below 85 K, magneto-elastic effects destroy the helical order and induce a ferromagnetic spin state. In superlattices of [Dy|Y], epitaxial clamping of the Dy to the larger basal plane lattice of Y has been shown¹ to completely suppress the ferromagnetic transition due to constraints on the magnetostatic modes that drive the transition. Conversely, [Dy|Lu] superlattices² exhibit an enhanced ferromagnetic transition temperature due to the epitaxy of the Dy to the smaller Lu lattice.

In contrast to the basal plane spin ordering of Dy, bulk Er orders initially at 85 K (T_N) into a sinusoidally modulated moment structure with spins along the c axis. At temperatures below about 56 K, a more complex structure ensues involving ordering of both c -axis and transverse (basal plane) moment components. This structure collapses into a

c -axis conical ferromagnetic state below 20 K. Superlattices of [Er|Y] again show a suppression of the ferromagnetic state¹ due to strain effects.

EXPERIMENTAL DIFFRACTION RESULTS

Neutron scattering data on [Dy|Er] superlattices were taken at the University of Missouri Research Reactor on a triple-axis spectrometer with the analyzer set for zero energy transfer and used to minimize background. The incident neutron wavelength was 2.357 Å from a Si monochromator. Soler slit collimations of 27'-10'-23'-19' were used before and after the monochromator and analyzer, respectively, yielding an elastic resolution width of 0.0136 Å⁻¹. In a superlattice consisting of 65-Å layers of Dy alternated with 55-Å layers of Er, distinct ordering temperatures were observed for the Dy basal plane and c -axis moments. Basal plane helical ordering of the Dy layers was initiated at temperatures close to T_N for bulk Dy. The occurrence of fully resolved superlattice harmonics of the magnetic satellites symmetric about the (0002) Bragg reflection (Fig. 1) confirmed that the ordering was long range, extending across multiple bilayers and preserving both phase and chirality of the Dy spin structure. This coupling was mediated through the Er layers, which are ostensibly paramagnetic.

At approximately 70 K, the Dy layers exhibit a collapse into a planar ferromagnetic state with the adjacent layers coupled in an antiferromagnetic arrangement. This is manifested by the appearance of an additional magnetic diffraction peak (and harmonics) between the principal nuclear structural peak and its first harmonic (Fig. 2). The reflections associated with the helical spin ordering of the Dy coexist with the antiferromagnetic reflection, but diminish in intensity at lower temperatures.

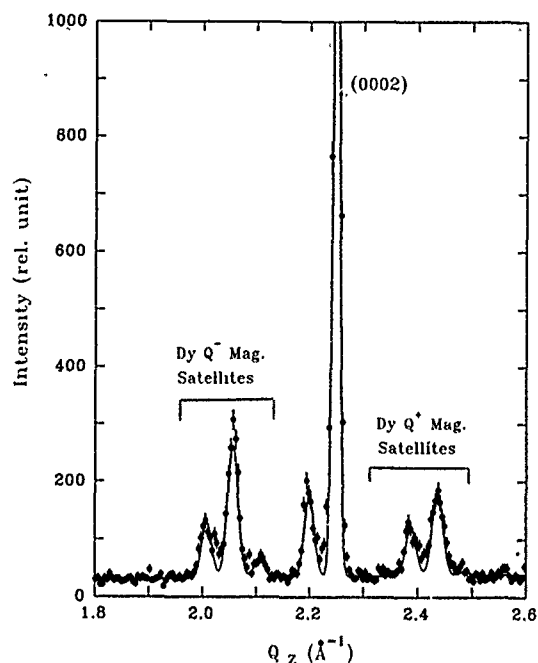


FIG. 1. Diffraction scan along (0002) of a [Dy|Er] superlattice at 110 K showing the development of long-range helical incommensurate order in the Dy planes mediated through the alternate paramagnetic Er layers.

At temperature below the T_N of bulk Er, c -axis ordering appears for the Er spins, as evidenced by the appearance of magnetic satellites about the (10 $\bar{1}$ 0) reflection. The scattering intensity from this ordering is delineated from the basal plane components by geometrical factors in the scattering

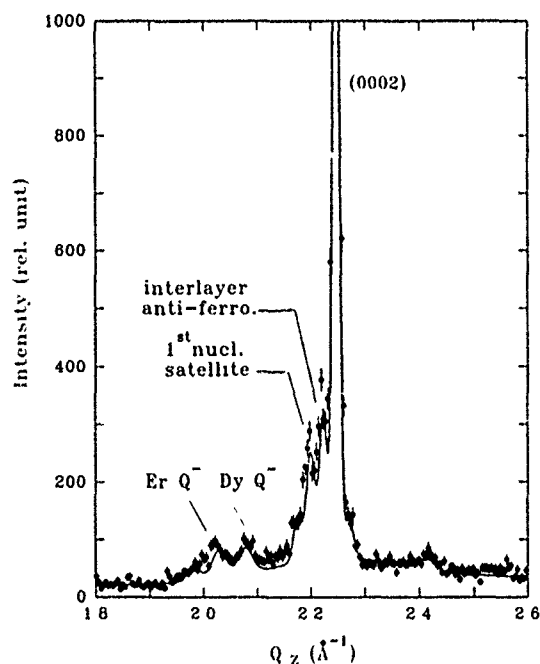


FIG. 2. Scan at 10 K along (0002) exhibiting an additional magnetic peak between the principal nuclear structure peak and its first harmonic illustrating the development of antiferromagnetic coupling of alternate Dy layers, each internally ferromagnetically ordered. The incommensurate order peaks suggest a remanent ordering of the Er and Dy spins.

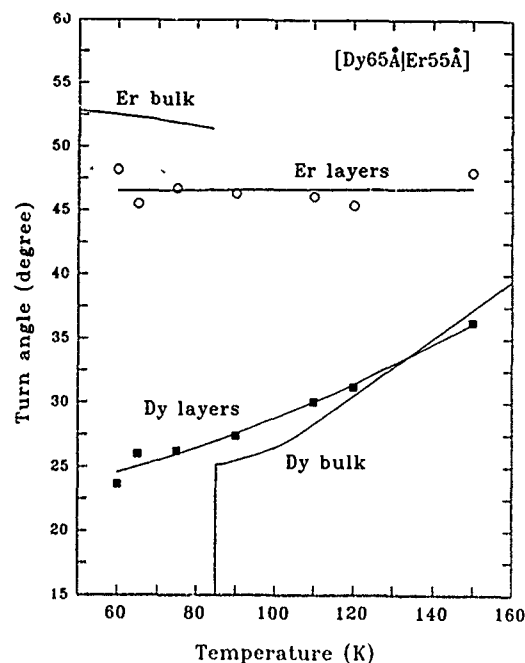


FIG. 3. Turn angles of spins in the Dy and Er layers as a function of temperature. The results for bulk Dy and Er are shown for comparison.

cross section. Because of inadequate statistics, no attempt was made to calculate magnetic moment values from these results. In the 10-K (0002) scan shown in Fig. 2, there is evidence of a shift in q of the incommensurate magnetic reflections and an increase of intensity over that observed at 30 K that suggests an ordering of the basal plane components of the Er structure in addition to the vestigial Dy helical ordering.

The low temperature data (e.g., 10 K in Fig. 2) also show evidence of a broad magnetic peak underlying the pattern and centered on the (0002) nuclear peak. This peak has a width that would correspond to short-range ferromagnetic correlations of approximately 17 Å range. Similar short-range correlations have also been observed in other rare-earth superlattices¹ at low temperature and have been ascribed to spins near the interfaces.

TURN ANGLES AND MAGNETIC MOMENTS

The neutron diffraction data have been analyzed by least-squares fitting to a structure factor containing both nuclear and magnetic scattering components to obtain the magnetic periodicity in both the Dy and Er layers. These results are shown in Fig. 3. The Dy turn angle is strongly temperature dependent and, over the range 85 K < T < 150 K, exhibits similar values to that in bulk Dy. Even though the Er is ostensibly paramagnetic, it is still possible to assign an "effective turn angle" to an Er spin density wave induced by the Dy helically ordered layer moments. The existence of a spin-density-wave-like coupling is manifested by the phase coherence of the helical order extending over several bilayers. This Er turn angle is nearly temperature independent

over the range analyzed, $60\text{ K} < T < 150\text{ K}$, with a value near $47^\circ/\text{plane}$. This is roughly comparable with that found in bulk Er.

The helical ordering peaks in the c^* -axis scans have also been analyzed to obtain the Dy moment associated with the helical ordering. The moment values range from $6.4\mu_B$ at 60 K down to $4.8\mu_B$ at 150 K. The low-temperature moment values are lower than in bulk Dy at the same temperature ($\mu_{T=0} = 10\mu_B$) and exhibit a weaker temperature dependence.

SUMMARY

These results demonstrate that long-range magnetic order occurs in superlattices of two dissimilar magnetic rare earths, Dy and Er, and that the Dy spin coupling can be propagated through Er while it is in a paramagnetic state.

The Dy and Er layers exhibit distinct ordering temperatures not far from their bulk counterpart elements, and show approximately the same magnetic periodicity. Further work is in progress with superlattices of varying Er and Dy thickness to examine thickness effects on the magnetic coherence and the role of epitaxial strain in the ordering transitions.

ACKNOWLEDGMENT

The support of the NATO under Travel Grant No. 550/87 is acknowledged.

¹For a review, see J. J. Rhyne, M. B. Salamon, C. P. Flynn, R. W. Erwin, and J. A. Borchers, *J. Magn. Magn. Mater.* **129**, 39 (1994).

²R. S. Beach, J. A. Borchers, A. Matheny, R. W. Erwin, M. B. Salamon, B. Everitt, K. Pettit, J. J. Rhyne, and C. P. Flynn, *Phys. Rev. Lett.* **70**, 3502 (1993).

Spin-valve structures exchange biased with $a\text{-Tb}_{0.23}\text{Co}_{0.77}$ layers

P. P. Freitas^{a)} J. L. Leal,^{b)} T. S. Plaskett, and L. V. Melo^{a)}
INESC, R. Alves Redol 9-1, 1000 Lisbon, Portugal

J. C. Soares
CFNUL, Av. Prof. Gama Pinto, 1010 Lisbon, Portugal

Spin-valve structures, glass/NiFeI/Cu/NiFeII/ $a\text{-TbCo}$ /Cu, were prepared where the pinned Permalloy layer is exchanged biased by a 200 to 400 Å thick $a\text{-Tb}_{0.23}\text{Co}_{0.77}$ layer. Exchange fields between 50 and 250 Oe were achieved with TbCo thicknesses below 400 Å, for a pinned Permalloy layer 150 Å thick. The exchange fields are strongly dependent on substrate bias. The magnetoresistance of these structures reaches 4.5% when thin Co layers are added at the NiFe/Cu interfaces.

INTRODUCTION

Spin-valve structures consist of two ferromagnetic layers separated by a low resistivity nonmagnetic metal spacer.^{1,2} One of the ferromagnetic layers is pinned through exchange coupling to an antiferromagnetic film, while the other ferromagnetic layer is free. This structure provides an antiparallel alignment of the ferromagnetic layers for an applied field between the coercive field of the free layer, and the exchange field at the pinned layer. Due to spin-dependent scattering in the bulk of the ferromagnetic layers, or at the noble-metal/ferromagnet interfaces, the resistivity is higher when the ferromagnetic layers are antiparallel, and lower when they are parallel. In order to be considered for magnetoresistive head applications, these structures must surpass Permalloy, with a magnetoresistance (MR) signal of 2%–3% at room temperature (RT) and coercivities below 1 Oe for films 200–400 Å thick. A typical spin valve has the following structure, substrate/NiFeI/Cu/NiFeII/FeMn/cap. NiFeI is the free Permalloy layer ($\text{Ni}_{81}\text{Fe}_{19}$), with a thickness between 100 and 200 Å in order to maximize the spin-valve MR effect. The Cu layer thickness is between 30 and 50 Å, thick enough to provide continuity, no pinholes and to avoid exchange coupling between NiFeI and NiFeII. NiFeII is pinned through exchange coupling to FeMn, and the NiFeII thickness determines the exchange field ($H_{\text{ex}} \propto 1/t_{\text{NiFeII}}$).³ Exchange fields up to 100 Oe can be obtained with NiFeII thickness ranging from 100 to 150 Å, and FeMn thickness of 150 Å. In order to achieve exchange coupling, FeMn must be in its fcc antiferromagnetic phase, which requires a fcc seed layer (NiFeII) and correct film stoichiometry (Fe48Mn52). The exchange field value can only be controlled by varying NiFeII thickness. The direction of the induced exchange field can be chosen by deposition under a small magnetic field, or by *a posteriori* field annealing.

Amorphous ferrimagnetic $\text{Tb}_x\text{Co}_{1-x}$ films have been proposed as an alternative candidate for biasing MR heads, since it was found that in a restricted composition range they would exchange couple to Permalloy.^{4–7} This material has

the advantage of allowing exchange field tuning by slight composition variations, substrate RF bias, or $\text{Tb}_x\text{Co}_{1-x}$ thickness variation.

For conventional MR Permalloy head applications, a 1500 Å thick $\text{Tb}_{0.28}\text{Co}_{0.72}$ film was exchanged coupled to a 500 Å Permalloy layer, leading to an exchange field of 100–150 Oe.³ For 250 Å thick Permalloy films, these authors quoted exchange fields ranging from 300 to 500 Oe. A drastic decrease in the exchange field was reported for a TbCo thickness of 500 Å. Considering spin-valve applications, a 60–100 Å Permalloy layer is needed to maximize the MR signal. Also, thinner TbCo layers are required for particular head designs. We were able to maintain the exchange field within the required limits (100–200 Oe), by decreasing the $\text{Tb}_x\text{Co}_{1-x}$ film thickness, and by using a different $\text{Tb}_x\text{Co}_{1-x}$ composition with a small in-plane magnetization component.

In this work we show that TbCo amorphous films with thicknesses between 200 and 400 Å can be successively used to exchange bias spin valves, leading to exchange fields up to 250 Oe, which can be tuned by RF substrate bias, or by varying the TbCo thickness. The spin valves produced so far have a MR signal close to 4.5%.

EXPERIMENTAL METHOD

The spin valves were prepared in an automated NORDIKO 2000 sputtering system with a base pressure of 2×10^{-8} Torr. A mosaic target for the $\text{Tb}_x\text{Co}_{1-x}$ alloy was prepared using Co squares 0.7 mm thick on a three inch Tb target. We aimed at a Tb content leading to a compensation temperature, close to room temperature, that is $0.23 < x < 0.28$. For these compositions the rare-earth and transition metal sublattices compensate, and exchange coupling occurs. Four mosaic targets were studied, giving rise to the following compositions $x = 0.18, 0.23, 0.24$, and 0.27 , checked by the Rutherford Backscattering Analysis. The $\text{Tb}_x\text{Co}_{1-x}$ films were RF sputtered at 100 W and 10 mTorr(Ar). The target to substrate distance was 10 cm. No field was applied during deposition apart from the residual field of the magnetron of the order of 10–20 Oe, in the plane of the substrate. RF substrate bias during deposition was used to fine tune the

^{a)}Also at IST, R. Rovisco Pais, 1000 Lisbon, Portugal.

^{b)}Also at CFNUL, Av. Prof. Gama Pinto, 1010 Lisbon, Portugal.

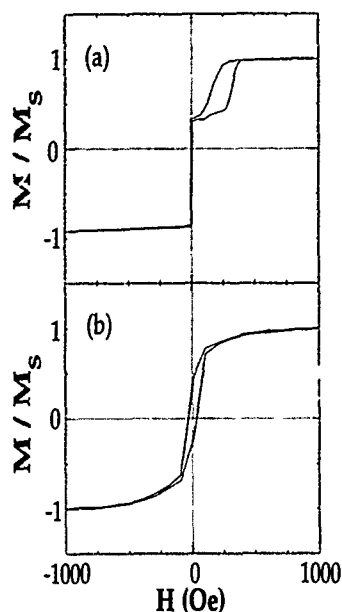


FIG. 1. Hysteresis loop for a glass/NiFe₂₅₀ Å/Cu₃₀ Å/NiFe₁₅₀ Å/TbCo₃₈₀ Å/Cu₃₀ Å spin valve with an exchange field of 230 Oe, (a) with the applied field along the induced in-plane easy axis, and (b) with the applied field perpendicular to the easy axis.

in-plane and out-of-plane magnetization components. Permalloy and Cu were dc sputtered at 3 mTorr. Room temperature resistivities for 500 Å thick Permalloy, Cu, and TbCo films are, respectively, $(27 \pm 2) \mu\Omega$ cm, $(5 \pm 2) \mu\Omega$ cm, and $(236 \pm 10) \mu\Omega$ cm, respectively. Transport measurements were done with a linear four-point dc method, on samples 10 mm long by 3 mm wide.

EXPERIMENTAL RESULTS AND DISCUSSION

From the four Tb_xCo_{1-x} compositions prepared only $x=0.23$ and $x=0.24$ gave exchange coupling. For $x=0.18$, we found in-plane magnetization, but with this composition the compensation temperature is already below room temperature, so that exchange no longer occurs at 300 K. For $x=0.27$, we found perpendicular anisotropy and no exchange coupling to the adjacent Permalloy layer. For $x=0.23$ and 0.24 , we find dominant perpendicular anisotropy in the TbCo layer, but there is a small in-plane magnetization component that is strongly bias dependent. The compensation temperature is around 120 °C. Unidirectional in-plane anisotropy is induced in the NiFeII layer, leading to well-defined easy-direction hysteresis loops.

Figure 1 shows the hysteresis loop for a glass/NiFe₂₅₀ Å/Cu₃₀ Å/NiFe₁₅₀ Å/TbCo₃₈₀ Å/Cu₃₀ Å structure, with the field applied along the induced in-plane easy axis (a), or perpendicular to the easy-axis (b). The exchange field is 230 Oe, and the coercivity of the free NiFeI layer is 8 Oe.

Figure 2(a) shows the spin-valve exchange field dependence on Tb_{0.23}Co_{0.77} thickness for a fixed NiFeII thickness of 150 Å, as well as the temperature dependence of the exchange field. Above TbCo thicknesses of 500 Å, H_{ex} is practically constant. A drastic decrease occurs below 200 Å, with the unidirectional anisotropy becoming too weak below 100

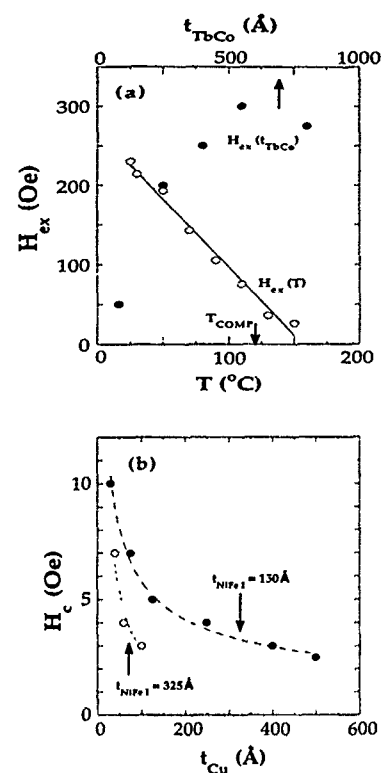


FIG. 2. (a) Exchange field dependence on the thickness of the TbCo layer for fixed NiFeII layer thickness, and exchange field dependence on temperature. (b) Dependence of the coercive field on the free Permalloy layer (NiFeI) on the Cu spacer thickness, for a TbCo exchange layer 380 Å thick. This result clearly indicates coupling across the Cu layer.

Å. This decrease could be associated to a reduction of the in-plane component of the magnetization, related to the initial stages of growth of the TbCo film on the Permalloy layer.⁴ The exchange field decreases linearly with temperature increase, vanishing slightly above the compensation temperature ($T=120$ °C).

Figure 2(b) shows the coercive field of the free Permalloy layer (NiFeI) of the spin valve, as a function of Cu spacer thickness. The coercive field of both Permalloy layers in a glass/NiFeI/Cu₃₀ Å/NiFeII structure is 1.5 Oe. When a 380 Å TbCo layer is deposited on top of the NiFeII, the coercivity of the NiFeI layer increases to 10 Oe, decreasing gradually as the Cu thickness increases, to a value of 2.5 Oe for a Cu thickness of 500 Å. This is a clear indication of coupling across the Cu layer. The coupling decreases and becomes negligible for Cu thicknesses larger than 400–500 Å.

Figure 3 shows the spin-valve hysteresis loops for different substrate bias voltages. The results were compared with hysteresis loops for a single 380 Å thick Tb_{0.23}Co_{0.77} layer grown on Si, and capped by 30 Å of Cu, at the same substrate bias voltages (see the inserts). Three regimes are found. Moderate substrate bias (from 0 up to -35 V) decreases the exchange field from 250 to 100 Oe. In this bias range, strong perpendicular anisotropy is found in the TbCo layer. For bias voltages between -40 and -60 V a symmetric hysteresis cycle is observed for the spin valve. The TbCo layer has similar in-plane and perpendicular magnetization components. The symmetric hysteresis cycle occurs because

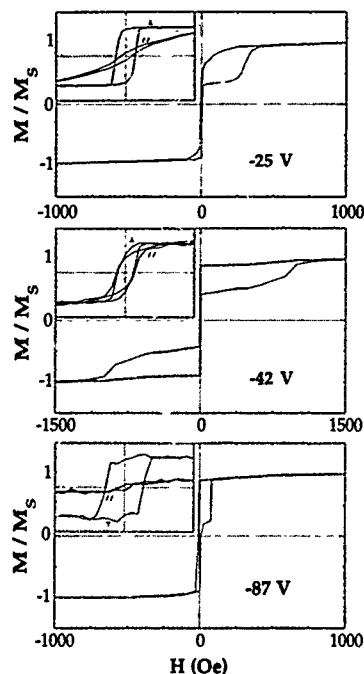


FIG. 3. Hysteresis loops for the spin valve as a function of substrate voltage bias. In the inserts we show data for a single layer TbCo film 380 Å thick on Si (data from -10 000 to 10 000 Oe). Asymmetric hysteresis cycles are observed when the TbCo layer has strong perpendicular anisotropy. For a bias voltage of -42 V, a symmetric hysteresis loop is observed, corresponding to a larger in-plane magnetization component in the TbCo layer.

the applied field is strong enough to reverse the TbCo in-plane magnetization component.⁷ For bias greater than -60 V a small unidirectional anisotropy reappears, corresponding to a return to strong perpendicular anisotropy in the TbCo layer. A RBS analysis of samples prepared under substrate bias indicate that for a bias voltage of -180 V, the Co content has decreased by almost 5 at. %, and Ar has begun to get incorporated in the sample (up to 7 at. %).

Figure 4 shows the MR signal for two spin-valves, at room temperature, one with the structure previously described, and with a MR of 2% (a), and another where a 10 Å Co layer was introduced at the NiFe/Cu interfaces,⁸ leading to a MR of 4.5% (b). This is evidence for the strong role of interface spin-dependent scattering at the Co/Cu interfaces, apart from bulk spin-dependent scattering in the NiFeI and NiFeII layers. The MR was measured with the current along the length of the sample, perpendicular to the easy axis and the applied field.

CONCLUSIONS

Spin valves have been successively prepared, where the exchange coupling layer is an amorphous ferrimagnetic

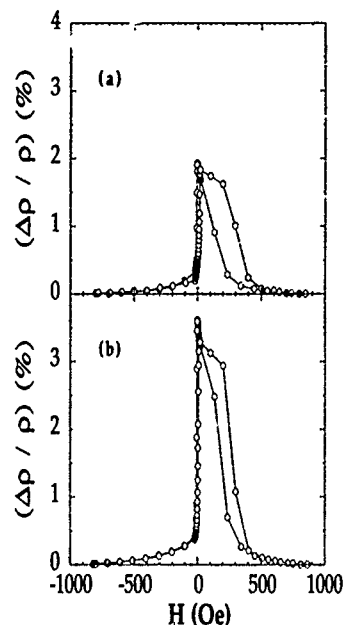


FIG. 4. Magnetoresistance signal for two spin valves: one with the conventional structure described so far (a), and another with 10 Å Co introduced at the NiFe/Cu interfaces (b).

Tb_{0.23}Co_{0.77} alloy, 200–400 Å thick. The exchange field can be varied by almost two orders of magnitude, either by changing TbCo substrate bias, or TbCo thickness. The coercivity of the unpinned Permalloy layer is slightly degraded due to coupling across the Cu layer. The substrate bias strongly affects the exchange field and the TbCo anisotropy. MR signals up to 4.5% were observed in spin valves, where a 10 Å Co layer was introduced in between the Permalloy and the Cu layers.

ACKNOWLEDGMENTS

JLL acknowledges a grant from the Junta Nacional de Investigação Científica (JNICT) under the "Ciência" program.

- ¹B. Dieny, V. S. Speriosu, S. S. Parkin, B. A. Gurney, D. R. Wilhoit, and D. Mauri, *Phys. Rev. B* **43**, 1297 (1991).
- ²B. Dieny, V. S. Speriosu, S. Metir, S. S. Parkin, B. A. Gurney, and P. Baumgart, *J. Appl. Phys.* **69**, 4774 (1991).
- ³A. P. Malozemoff, *J. Appl. Phys.* **63**, 3874 (1988).
- ⁴W. C. Cain, J. W. Lee, P. V. Koeppel, and M. Kryder, *IEEE Trans. Magn.* **MAG-24**, 2609 (1988).
- ⁵W. C. Cain, D. Markham, and M. Kryder, *IEEE Trans. Magn.* **MAG-25**, 3695 (1989).
- ⁶W. C. Cain, and M. Kryder, *IEEE Trans. Magn.* **MAG-26**, 2412 (1990).
- ⁷N. Smith and W. C. Cain, *J. Appl. Phys.* **69**, 2471 (1991).
- ⁸S. S. P. Parkin, R. F. Marks, R. F. C. Farrow, and G. Harp, in *Proceedings of the Nato Advanced Research Workshop on Magnetism and Structure in Systems of Reduced Dimension*, Nato Series (Plenum, New York, 1993).

¹⁵¹Eu Mössbauer study on Fe/Eu multilayers

E. Zaggo-Saitovitch and E. C. Passamani

Centro Brasileiro de Pesquisas Físicas, R. Dr. Xavier Sigaud 150, Rio de Janeiro, Brazil

K. Mibu and T. Shinjo

Institute for Chemical Research, Kyoto University, Uji, Kyoto-fu 611, Japan

Mössbauer spectroscopy with ¹⁵¹Eu nuclei was applied to study magnetic properties of Fe/Eu multilayers as a function of the Eu layer thickness. The Mössbauer spectra at 4.2 K for [Fe(40 Å)/Eu(x Å)] with $x=70, 100$, and 200 consist of two magnetic components: a major component with hyperfine parameters close to those of bulk Eu metal and an additional component with a smaller hyperfine field. The latter component is attributed to Eu at the interface region. The spectrum at 4.2 K for [Fe(40 Å)/Eu(30 Å)] has only a component with a reduced hyperfine field, indicating that the Eu layers lose the bulk magnetic properties.

I. INTRODUCTION

Fe/rare-earth (RE) multilayers show a variety of magnetic properties dependent on the sort of RE metals. For example, Fe/Gd multilayers, which are composed of two ferromagnetic metals with relatively small magnetocrystalline anisotropy, exhibit characteristic spin structures on account of the antiferromagnetic coupling at the interfaces.¹⁻⁴ Perpendicular magnetic anisotropy is observed in Fe/Tb,⁵⁻⁹ Fe/Dy,^{6,10,11} and Fe/Nd¹¹⁻¹³ multilayers when the Fe and RE layer thicknesses are properly controlled. From a systematic study on the Fe spin directions for all the Fe/RE systems, perpendicular magnetic anisotropy is found also in Fe/Pr multilayers.¹⁴ The RE layers are usually polycrystalline with no preferred orientation, and the magnetic structures often turn out to be complicated. It has been rare that information on the local magnetism in the RE layers is obtained; only a ¹⁶¹Dy Mössbauer study on Fe/Dy multilayers is reported so far.¹⁵ In order to study the intrinsic RE magnetism in Fe/RE multilayers, local magnetic properties should be investigated for crystallographically oriented RE layers.

In this article, magnetic properties of Fe/Eu multilayers are studied with ¹⁵¹Eu Mössbauer measurements. Eu is divalent in the bulk metal. The bulk Eu metal is antiferromagnetic below 90 K with a helical spin structure and the magnetic anisotropy is relatively small. The crystal structure is bcc, in contrast with the other trivalent RE metals with hexagonal structures. Thus, rather simple crystallographic and magnetic structures are expected to be realized in thin Eu layers. Besides, since there is no solid solution or intermetallic compound for the Fe-Eu binary system in equilibrium states, chemically sharp interfaces are expected for Fe/Eu multilayers. Information on local Eu magnetism is obtained by Mössbauer spectroscopy with ¹⁵¹Eu, which is one of the most convenient Mössbauer isotopes among RE elements.

II. EXPERIMENTAL

Fe/Eu multilayers were prepared by alternate deposition in ultrahigh vacuum. The films were deposited on polyimide films that were kept at -50 °C. The Fe layer thickness was fixed to be 40 Å, and the Eu layer thickness was changed from 30 to 200 Å. Two reference samples were also prepared: a Eu(3000 Å) film sandwiched with Fe(100 Å) layers

to examine the magnetic properties of a sufficiently thick Eu layer, and a film with the nominal thickness of [Fe(1 Å)/Eu(4 Å)] to check the possibility of forming a nonequilibrium alloy. Since Eu is one of the most reactive RE metals, the deposition was started with an Fe layer and ended with an Fe layer and a Cu protection layer was put on top of it.

¹⁵¹Eu Mössbauer spectra were measured with a ¹⁵¹SmF₃ source by a conventional absorption method. The spectra were taken at 300 K and 4.2 K with the source and absorber at the same temperature. Isomer shifts are expressed relative to the ¹⁵¹SmF₃ source.

III. SAMPLE CHARACTERIZATION

The structures of the prepared samples were checked with x-ray diffraction measurements. The multilayer samples show well-established artificial periodic structures. The Fe layers (40 Å) have a bcc polycrystalline structure and the Eu layers (from 30 to 3000 Å) have a bcc structure with (110) texture. Since the crystal parameters of Fe and Eu do not fit well, epitaxial growth is not expected in this system. There is no oxide peak or hydride peak in the x-ray patterns taken just after the preparation. However, peaks from EuO appear in several days. The Eu layers are oxidized gradually as the time passes. The ¹⁵¹Eu Mössbauer spectra also change in several weeks, so that only the spectra for nonoxidized samples are treated in this article.

The x-ray diffraction patterns for the reference sample [Fe(1 Å)/Eu(4 Å)] have strong peaks from Eu(110) and Eu(220) and a diffuse peak from Fe(110). The sample appears to be composed of segregated bcc Eu grains and amorphouslike Fe grains rather than of a nonequilibrium alloy.

According to an ⁵⁷Fe Mössbauer study on [Fe(4 Å)/RE(30 Å)], the Fe layers have an interface ferromagnetic component with reduced hyperfine fields beside a major component from inner ferromagnetic α -Fe.¹⁴ For the Fe/Eu system, the corresponding Fe thickness of the interface component is less than 3 Å, the smallest among all the Fe/RE systems. Chemically sharp interfaces are realized in this system on account of immiscibility between Fe and Eu.

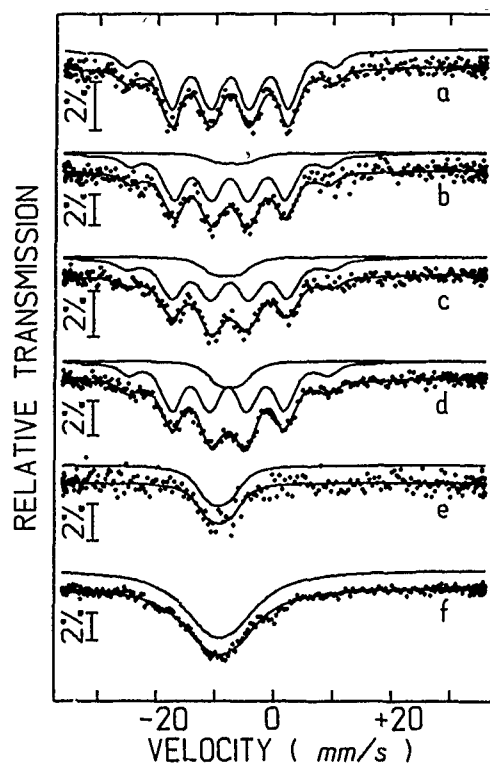


FIG. 1. ^{151}Eu Mössbauer spectra at 4.2 K for (a) Eu(3000 Å), (b) [Fe(40 Å)/Eu(200 Å)], (c) [Fe(40 Å)/Eu(100 Å)], (d) [Fe(40 Å)/Eu(70 Å)], (e) [Fe(40 Å)/Eu(30 Å)], and (f) [Fe(1 Å)/Eu(4 Å)].

IV. MÖSSBAUER RESULTS

The ^{151}Eu Mössbauer spectra of the Fe/Eu multilayers at 300 K are almost nonmagnetic. According to ^{57}Fe Mössbauer and magnetization measurements, the Fe layers are ferromagnetic at 300 K, and the Eu magnetic moments at the interface region are magnetically ordered through an exchange interaction between the interface Fe. The interface

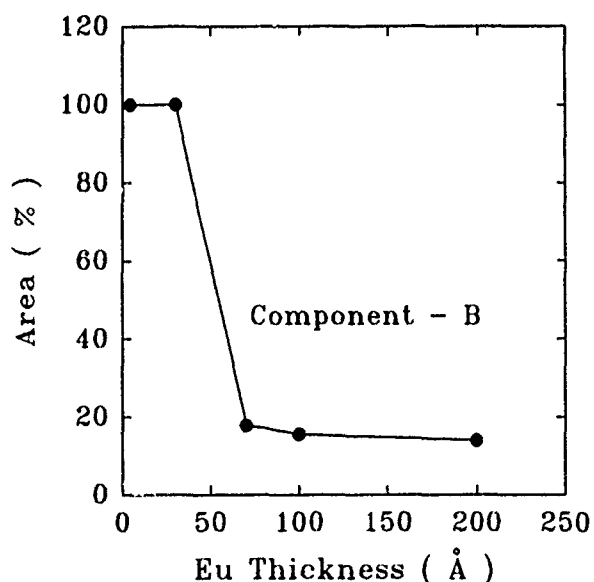


FIG. 2. Relative area of the component with a reduced hyperfine field as a function of the Eu layer thickness.

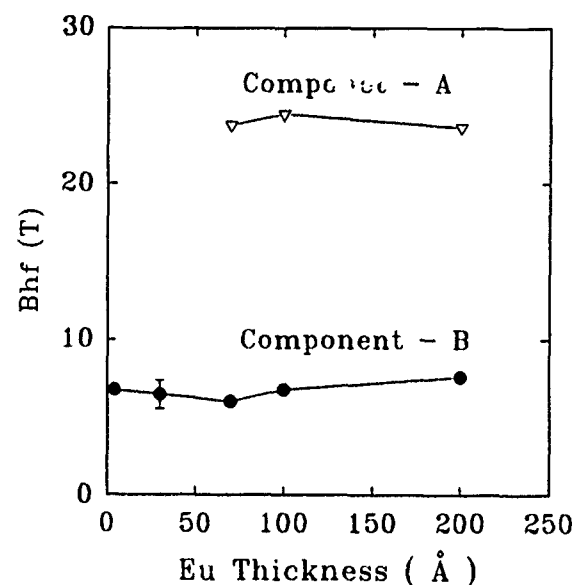
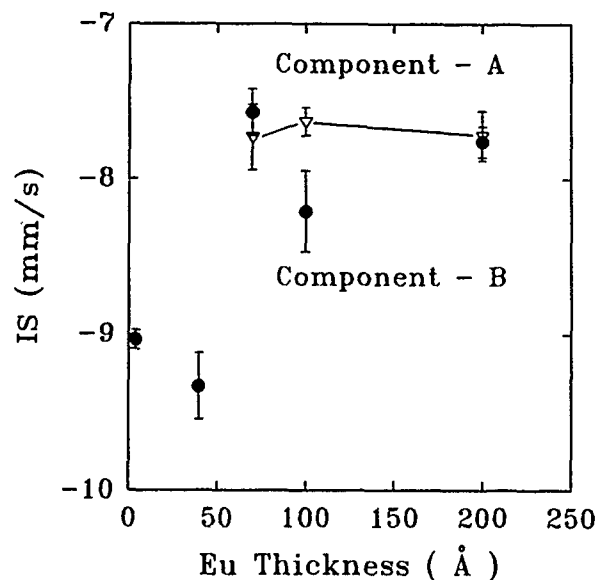


FIG. 3. (a) Isomer shifts and (b) hyperfine fields of each component of the ^{151}Eu Mössbauer spectra at 4.2 K as a function of the Eu layer thickness.

magnetic component is, however, not clearly observed in the Eu Mössbauer spectra. The time dependence of the spectra shows that the Eu layers are gradually oxidized to be EuO as the time passes.

The Mössbauer spectra for all the prepared samples at 4.2 K are shown in Fig. 1. The spectrum for the Eu(3000 Å) film is fitted with a single magnetic component with the isomer shift of -7.74 mm/s and the hyperfine field of 24.8 T. The hyperfine parameters are close to the bulk values, showing that the film is composed of metallic Eu. The spectra for [Fe(40 Å)/Eu(x Å)] with $x=70$, 100, and 200 cannot be fitted with a single component with the bulk hyperfine parameters, but an extra component with a smaller hyperfine field coexists. The spectrum for [Fe(40 Å)/Eu(30 Å)] has only a component with a reduced hyperfine field, suggesting that the Eu layers lose the bulk properties. The spectrum for [Fe(1 Å)/Eu(4 Å)] is similar to that for [Fe(40 Å)/Eu(30 Å)]. Thus, all

the spectra are fitted with two components: component A with hyperfine parameters similar to that of bulk Eu metal, and component B with a reduced hyperfine field. The relative area of the component B as a function of the Eu layer thickness is shown in Fig. 2. The isomer shifts and hyperfine fields for each component are also shown in Figs. 3(a) and 3(b).

The magnetization curve (M - H curve) for the multilayers at each temperature is explained with superposition of a ferromagnetic curve with saturation magnetization M_s , and a para(antiferro)magnetic curve with magnetic susceptibility χ : $M(H) = M_s + \chi H$. The M_s and χ are both temperature dependent. The ferromagnetic part is due to the Fe layer magnetization and antiferromagnetically coupled interface Eu magnetization. The para(antiferro)magnetic component is a contribution from the Eu magnetic moments at the inner part of the Eu layers. From the temperature dependence of χ , the Néel temperature is estimated to be about 90 K for Eu(3000 Å) and about 80 K for [Fe(40 Å)/Eu(100 Å)]. For [Fe(40 Å)/Eu(30 Å)], the magnetic transition is not observed clearly in the χ - T curve. The detail of the results on the magnetization measurements will be published elsewhere.

With the results of the magnetization measurements taken into consideration, the ^{151}Eu Mössbauer spectra of the Fe/Eu multilayers are explained as follows: the component A is attributed to the inner Eu with the magnetic properties close to the bulk properties, and the component B to the interface Eu. The corresponding Eu thickness of the interface component is estimated to be 6–14 Å per interface. As mentioned previously, the interfaces of Fe/Eu multilayers are rather chemically sharp, so that the reduction of the hyperfine field is probably due to intrinsic interface effects rather than due to a nonequilibrium alloy. The spectrum for [Fe(40 Å)/Eu(30 Å)] has only the component with a reduced hyperfine field and shows no indication of the existence of the bulk Eu component. The reduction of hyperfine fields appears not only due to the interface effect but also due to a size effect or strain effect. The hyperfine field of [Fe(1 Å)/Eu(4 Å)] may also be reduced with the same mechanism.

V. SUMMARY

Magnetic properties of Fe/Eu multilayers are studied as a function of the Eu layer thickness using ^{151}Eu Mössbauer spectroscopy for the first time. The spectra at 4.2 K for [Fe(40 Å)/Eu(x Å)] with $x=70, 100$, and 200 consist of two magnetic components: a component from the inner Eu with the hyperfine parameters close to bulk Eu, and a component from the interface Eu with a reduced hyperfine field. For [Fe(40 Å)/Eu(30 Å)], only a component with a reduced hyperfine field exists. The Eu layers appear to lose the bulk magnetic properties. A thin-film effect such as a size effect and strain effect is thought to affect the magnetic properties of the Eu layers.

¹T. Morishita, Y. Togami, and K. Tsushima, J. Phys. Soc. Jpn. **54**, 37 (1985).

²R. E. Camley and D. R. Tilley, Phys. Rev. B **37**, 3413 (1988).

³Y. Kamiguchi, Y. Hayakawa, and H. Fijimori, Appl. Phys. Lett. **55**, 1918 (1989).

⁴K. Cherifi, C. Dufour, Ph. Bauer, G. Marchal, and Ph. Mangin, Phys. Rev. B **44**, 7733 (1991).

⁵N. Sato, J. Appl. Phys. **59**, 2514 (1986).

⁶Z. S. Shan and D. J. Sellmyer, Phys. Rev. B **42**, 10433 (1990).

⁷K. Cherifi, C. Dufour, M. Piecuch, A. Bruson, Ph. Bauer, G. Marchal, and Ph. Mangin, J. Magn. Magn. Mater. **93**, 609 (1991).

⁸F. Badia, M. A. Badry, X. X. Zhang, J. Tejada, R. A. Brand, B. Scholz, and W. Keune, J. Appl. Phys. **70**, 6206 (1991).

⁹H. Hoffmann and G. Endl, J. Appl. Phys. **70**, 6230 (1991).

¹⁰K. Yoden, N. Hosoi, K. Kawaguchi, K. Mibu, and T. Shinjo, Jpn. J. Appl. Phys. **27**, 1680 (1988).

¹¹Z. S. Shan, S. Nafis, K. D. Aylesworth, and D. J. Sellmyer, J. Appl. Phys. **63**, 3218 (1988).

¹²K. Mibu, N. Hosoi, and T. Shinjo, J. Phys. Soc. Jpn. **58**, 2916 (1989).

¹³L. T. Baczewski, M. Piecuch, J. Durand, G. Marchal, and P. Delcroix, Phys. Rev. B **40**, 11237 (1989).

¹⁴K. Mibu, N. Hosoi, and T. Shinjo, J. Magn. Magn. Mater. **126**, 343 (1993).

¹⁵T. Shinjo, K. Yoden, N. Hosoi, J.-P. Sanchez, and J.-M. Friedt, J. Phys. Soc. Jpn. **58**, 4255 (1989).

Phase transitions in coupled double-layer systems

Xiao-Hu and Yoshiyuki Kawazoe

Institute for Materials Research, Tohoku University, 2-1-1 Katahira, Aoba-ku, Sendai 980, Japan

Magnetic systems consisting of a capping layer with uniaxial anisotropy and a recording layer with vertical anisotropy are studied by means of a variational method for a continuum model covering the exchange, anisotropy, and Zeeman energies. The phase transitions between different alignments of magnetization are observed when the thickness of the capping layer and/or the temperature is varied. For the capping layer with in-plane anisotropy, the phase transitions are in second order and the critical behaviors are characterized by a critical exponent $\frac{1}{2}$. For the capping layer with vertical anisotropy, the phase transitions are in first order. The analytic expressions of the critical points are presented, in terms of the relevant magnetic constants.

I. INTRODUCTION

Magnetic multilayer systems have attracted much attention recently from both fundamental and practical points of view. The magnetic double-layer systems studied in this work consist of a capping layer of uniaxial anisotropy, layer 1, and a recording layer of vertical anisotropy, layer 2, with a geometric structure shown in Fig. 1.^{1,2} The capping layer is of in-plane anisotropy in system I and of vertical anisotropy in system II. We set the z axis vertically to the layers and the origin at the interface. The direction of magnetization φ is measured from the negative direction of the z axis while an external field H_{ext} applied along the z axis is chosen to be positive. The thickness of the capping layer is denoted by a and the thickness of the recording layer is taken to be infinity as a sufficient approximation.¹

The total magnetic energy per unit area for system I is expressed as

$$\gamma = \int_0^a \left[A_1 \left(\frac{d\varphi}{dz} \right)^2 + K_1 \cos^2 \varphi + M_{s1} H_{\text{ext}} \cos \varphi \right] dz + \int_{-\infty}^0 \left[A_2 \left(\frac{d\varphi}{dz} \right)^2 + K_2 \sin^2 \varphi + M_{s2} H_{\text{ext}} \cos \varphi \right] dz. \quad (1)$$

Typical magnetic constants at room temperature are $A_1 = 1.0 \times 10^{-7}$ erg/cm, $K_1 = 0.25 \times 10^6$ erg/cm³, and $M_{s1} = 200$ emu/cm³ for the capping layer, while $A_2 = 2.0 \times 10^{-7}$ erg/cm, $K_2 = 2.0 \times 10^6$ erg/cm³, and $M_{s2} = 90$ emu/cm³ for the recording layer. The exchange coupling between the two layers is supposed to be ferromagnetic and is taken into account imposing that the direction of magnetization should be continuous at the interface.^{1,3}

II. SYSTEM I: CAPPING LAYER OF IN-PLANE ANISOTROPY

For the sake of simplicity, let us consider the case of null external field. The equation for the direction of magnetization at the top surface, φ_a , is derived by a variational method on energy (1) as

$$\frac{\text{sn}[a\sqrt{K_1/A_1}, \sin \varphi_a]}{\text{cn}[a\sqrt{K_1/A_1}, \sin \varphi_a]} \cos \varphi_a = \sqrt{\frac{A_2 K_2}{A_1 K_1}} \quad (2)$$

with Jacobian elliptic functions.¹ The total configuration of magnetization is expressed in terms of φ_a .

The left-hand side of the above equation is finite and decreases continuously with φ_a while increases uniformly with a . Therefore, for a value of $\sqrt{A_2 K_2 / A_1 K_1}$, there exists a critical thickness below which $\varphi_a = 0$ and thus $\varphi(z) = 0$ in the whole system, in spite of the fact that the magnetization is directed against the easy axis in the capping layer. A phase transition from the above trivial configuration to one with nonzero $\varphi(z)$, which is determined by Eq. (2), occurs at this critical thickness. Since the left-hand side of Eq. (2) assumes its maximum at $\varphi_a = 0$, the phase transition is in second order and the critical thickness is derived from Eq. (2) (Ref. 1):

$$a_{\text{min}} = \sqrt{\frac{A_1}{K_1}} \tan^{-1} \sqrt{\frac{A_2 K_2}{A_1 K_1}}. \quad (3)$$

It is easy to see that this critical point coincides with the minimal thickness of the capping layer that exhibits the *capping effect* in magnetic double-layer systems.^{1,4} The critical behavior for φ_a is derived analytically as^{1,5}

$$\varphi_a = \bar{\varphi}_a \times \sqrt{a/a_{\text{min}} - 1}, \quad a \geq a_{\text{min}}, \quad (4)$$

and is shown in Fig. 2(a).⁶

A phase transition between different alignments of magnetization is also observed in a system with fixed thickness when the temperature is varied.² This phenomenon can be understood from the above arguments, noting that a value of thickness larger than the critical value in Eq. (3) in a low-temperature region becomes less than that in a high-temperature region. The critical behavior is^{2,5}

$$\varphi_a = \hat{\varphi}_a \times \sqrt{T_c/T - 1}, \quad T \leq T_c, \quad (5)$$

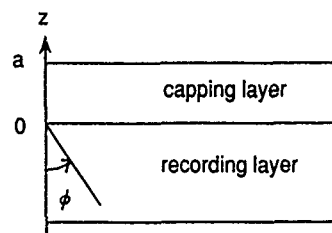


FIG. 1. Geometric structure of the double-layer system studied in the present work.

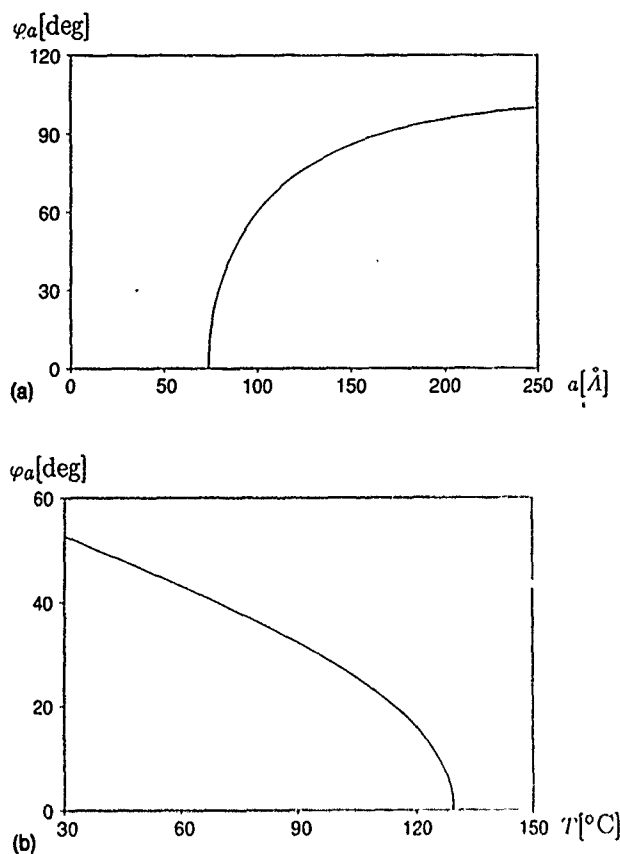


FIG. 2. (a) Thickness a dependence of the direction of magnetization at the top surface for system I. (b) Same as (a) except for temperature dependence.

and is shown in Fig. 2(b) with $T_c \approx 130$ °C.⁷ The critical temperature is also determined by Eq. (3) provided that a_{\min} is replaced by the capping film thickness of the system under study and that the temperature dependences of the relevant magnetic constants are involved.

It is worthy to point out that the phase transition according to variance of the temperature could be used as a new device for magneto-optical recording where a laser pulse adjusts the temperature.²

The mechanism of phase transitions under a finite external field is the same with that for null field and the critical thickness is given by¹

$$a_{\min} = \sqrt{\frac{A_1}{K_1 + M_{s1}H_{\text{ext}}/2}} \tan^{-1} \sqrt{\frac{A_2(K_2 - M_{s2}H_{\text{ext}}/2)}{A_1(K_1 + M_{s1}H_{\text{ext}}/2)}}. \quad (6)$$

III. SYSTEM II: CAPPING LAYER OF VERTICAL ANISOTROPY

For system II, $\cos \varphi$ in Eq. (1) is replaced by $\sin \varphi$ and a finite external field is necessary in order to observe phase transitions. For comparison, the same magnetic constants are used for numerical calculations in what follows except for that $M_{s1} = 150$ emu/cm³ is adopted since a larger magnetization will cause the easy axis to be in-plane from the geometrical effect.

For system II, Eq. (2) is replaced by

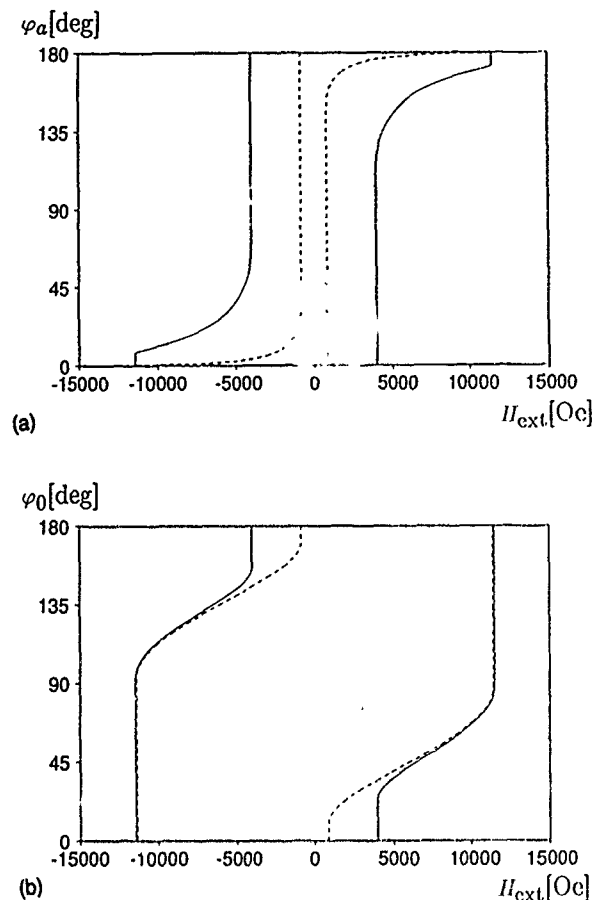


FIG. 3. (a) Hysteresis loop (solid line: $a = 100$ Å; dashed line: $a = 200$ Å) of the direction of magnetization at the top surface for system II. (b) Same as (a) except for at the interface.

$$\begin{aligned} & \frac{\text{sn}[\hat{a}, k] \text{dn}[\hat{a}, k]}{\text{cn}[\hat{a}, k]} \\ & \times \sqrt{\frac{-2 \cos \varphi_a + M_{s1}H_{\text{ext}}/K_1}{2 - (1 + \tan^2(\varphi_a/2) \text{cn}^2[\hat{a}, k])M_{s2}H_{\text{ext}}/K_2}} \\ & = \sqrt{\frac{A_2 K_2}{A_1 K_1}} \end{aligned} \quad (7)$$

with

$$\hat{a} = a \sqrt{K_1/A_1} \sqrt{-\cos \varphi_a + M_{s1}H_{\text{ext}}/2K_1}$$

and

$$k^2 = \frac{\sin^2(\varphi_a/2)(1 - \cos \varphi_a + M_{s1}H_{\text{ext}}/K_1)}{(-2 \cos \varphi_a + M_{s1}H_{\text{ext}}/K_1)}.$$

Hysteresis loops for system II are shown in Figs. 3(a) and 3(b). There are two vertical parts in each branch of the hysteresis loops. The ones for the weak fields correspond to magnetization reversals in the capping layer, while those for the strong fields are associated with the complete magnetization reversals in the whole system. The phase transitions discussed in the present section are related to the formers.

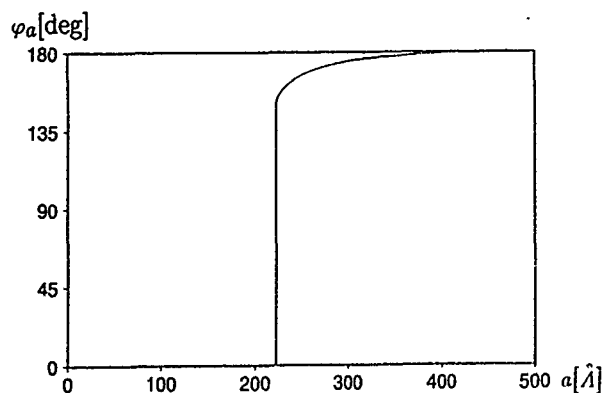


FIG. 4. Thickness a dependence of the direction of magnetization at the top surface for system II.

The phase transition between the trivial configuration $\varphi(z)=0$ and a configuration characterized by a nonzero φ_a , according to variance of the thickness a , is in first order as shown in Fig. 4. The dependence of the critical thickness on the external field is displayed in Fig. 5. We have found that the present numerical results fit satisfactorily to the following logarithmic function:

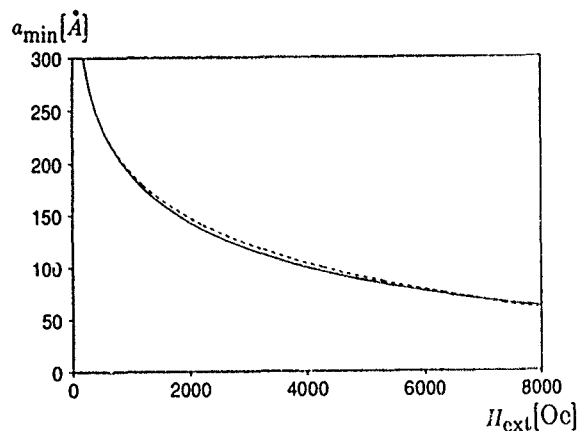


FIG. 5. Dependence of the critical thickness on the external field for system II [solid line: numerical results according to Eq. (7); dashed line: curve of Eq. (8)].

$$a_{\min} \approx \sqrt{\frac{A_1}{K_1}} \times \ln \frac{H_0}{H_{\text{ext}}} \quad (8)$$

with $H_0 \approx 20$ kOe. The divergence of a_{\min} at null external field and the slow drop with the external field show sharp contrasts with the behavior of Eq. (6).

A similar first-order phase transition can be observed in system II when the temperature is varied, provided that temperature dependences of the saturation magnetizations are given.

IV. SUMMARY

To summarize, we have studied double-layer systems with different anisotropies. Phase transitions between different magnetization configurations have been observed and the responsible mechanism is revealed. The critical point a_{\min} corresponds to the minimal thickness of the capping layer, which achieves better field sensitivity compared with that of single-magnetic-layer recording. The present study will shed light on the design of multilayer recording media.

Critical phenomena of a φ^4 model for paraferromagnetic phase transition in a system consisting of a thin layer and a semi-infinite bulk has also been studied by mean-field theory, and the renormalization group theory is used to investigate the effect of thermal fluctuations.⁵

¹ X. Hu and Y. Kawazoe, Phys. Rev. B **49**, 3294 (1994); X. Hu, T. Yoroze, Y. Kawazoe, S. Ohnuki, and N. Ohta, IEEE Trans. Magn. **29**, 3790 (1993); Y. Kawazoe, X. Hu, and S. Honma, Mater. Res. Soc. Symp. Proc. **131**, 513 (1993).

² X. Hu and Y. Kawazoe (unpublished).

³ I. M. Gelfand and S. V. Fomin, *Calculus of Variations*, translated by R. A. Silverman (Prentice-Hall, Englewood Cliffs, NJ, 1963); M. Kaneko, K. Aratani, Y. Mutoh, A. Nakaoki, K. Watanabe, and H. Makino, Jpn. J. Appl. Phys. Suppl. **28-3**, 927 (1989).

⁴ S. Ohnuki, K. Shimazaki, N. Ohta, and H. Fujiwara, J. Magn. Soc. Jpn. **15**, Suppl. S1, 399 (1991).

⁵ X. Hu and Y. Kawazoe (unpublished).

⁶ H. Wakabayashi, H. Notarys, and T. Suzuki, J. Magn. Soc. Jpn. **15**, Suppl. S1, 87 (1991). The authors studied a similar system by a numerical approach for a discrete model. A good agreement with an experiment was achieved for the critical thickness. Unfortunately, the dependence of the critical thickness on the relevant magnetic constants as that in Eq. (3) has not been revealed. No detailed discussion about the critical exponent was given, and their value of the critical exponent seems to be unit, different from the present one in Eq. (4).

⁷ Although sin decays and linear ones of stiffness constants A 's and anisotropy constants K 's, respectively, as the temperature is increased from room temperature towards the critical points ($T_{c1}=180^\circ\text{C}$ and $T_{c2}=270^\circ\text{C}$), have been assumed in order to derive numerical results shown in Fig. 2(b), we notice that these assumptions do not affect the critical behaviors.

Comparison of the electron-spin-resonance linewidth in multilayered CuMn spin glasses with insulating versus conducting interlayers

D. L. Leslie-Pelecky, F. VanWijland, C. N. Hoff, and J. A. Cowen

Department of Physics and Astronomy and Center for Fundamental Materials Research, Michigan State University, East Lansing, Michigan 48824-1116

A. Gavrin^{a)} and C.-L. Chien

Department of Physics and Astronomy, The Johns Hopkins University, Baltimore, Maryland 21218

The temperature-dependent electron-spin-resonance linewidth $\Delta H(T)$ may be used to investigate the effect of the geometry and interlayer material on the magnetic properties of multilayered systems. We compare $\Delta H(T)$ in CuMn/Al₂O₃ multilayers with previous measurements of CuMn/Cu samples. CuMn/Al₂O₃ samples with CuMn thicknesses, W_{SG} , from 40 Å to 20 000 Å obey the same form as the CuMn/Cu system, but show quantitative differences in the fitting parameters. The linewidths of the CuMn/Al₂O₃ samples, even in the bulk, are systematically larger than the linewidths for the CuMn/Cu samples, suggesting that the ESR linewidth is sensitive to differences in sample growth and structure. The value of the minimum linewidth decreases with decreasing W_{SG} in the CuMn/Al₂O₃ series, but remains constant in the CuMn/Cu series. Although susceptibility measurements of the freezing temperature T_f do not differentiate between samples with $W_{SG} \geq 5000$ Å, the ESR linewidth is sensitive to changes at larger length scales. This experiment emphasizes the importance of considering both the total sample thickness, as defined by the range of the conduction electrons, and the spin-glass layer thickness in analyzing the ESR linewidth in multilayers.

INTRODUCTION

Finite-size and dimensionality effects in multilayered spin glasses have been shown to depend on the interlayer material, especially when the spin-glass layer thickness W_{SG} becomes small.¹⁻³ We have previously demonstrated that the temperature-dependent electron-spin-resonance linewidth in multilayered CuMn/Cu systems^{4,5} provides detailed information about spin relaxation rates. In this article, we compare the temperature dependence of the electron-spin-resonance linewidth $\Delta H(T)$ in Cu_{0.92}Mn_{0.08}/Al₂O₃ multilayers with previous measurements of the Cu_{0.93}Mn_{0.07}/Cu system.

DATA AND ANALYSIS

Cu_{0.92}Mn_{0.08}/Al₂O₃ samples, with $40 \text{ Å} \leq W_{SG} \leq 20\,000 \text{ Å}$, were fabricated at the Johns Hopkins University using dc and rf sputtering. Cu_{0.93}Mn_{0.07}/Cu samples were fabricated by dc sputtering at Michigan State University. In both cases, the interlayer thicknesses are held constant at values large enough (75 Å for Al₂O₃ and 300 Å for Cu) to prevent coupling between the CuMn layers.

The depression of the spin-glass freezing temperature, T_f , with decreasing W_{SG} is described in terms of ϵ , with

$$\epsilon = \left(\frac{T_f(\infty) - T_f(W_{SG})}{T_f(\infty)} \right). \quad (1)$$

$T_f(\infty)$ is the freezing temperature of the bulk. Finite-size scaling predicts⁶ $\epsilon \propto W_{SG}^{-1/\nu}$. A crossover from three-dimensional (3D) to two-dimensional (2D) behavior has been demonstrated by frequency dependent⁷ and nonlinear susceptibility measurements.^{3,8} Figure 1 compares the depression of $T_f(W_{SG})/T_f(\infty) = 1 - \epsilon$ for insulating and conduct-

ing interlayers. Solid lines show fits to Eq. (1) with $\nu=1.3$ for CuMn/Cu samples⁴ and $\nu=1.6$ for CuMn/Al₂O₃ samples.³ The depression of T_f in CuMn/Al₂O₃ multilayers is similar to that observed in CuMn/Si.⁹

Above T_f , $\Delta H(T)$ in spin glasses is described by a superposition of two behaviors—a linear temperature dependence and a critical divergence as T_f is approached.

$$\Delta H(T) = A + BT + C \left(\frac{T - T_f}{T_f} \right)^{-\kappa}. \quad (2)$$

In Eq. (2), A is the residual linewidth, B the thermal broadening coefficient, C the divergence strength, and κ a critical exponent. The $A + BT$ behavior reflects the relative magnitudes of relaxation rates between the localized moments, conduction electrons, and lattice.^{10,11} In particular, the thermal broadening coefficient B can be modeled to include ef-

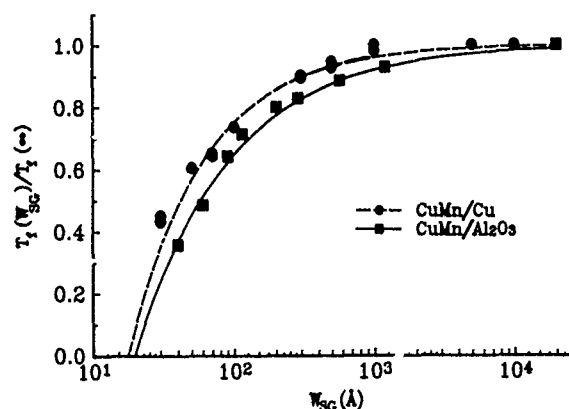


FIG. 1. The depression of the freezing temperature, $T_f(W_{SG})$, normalized to the bulk value, $T_f(\infty)$ as a function of $\log_{10}(W_{SG})$ for CuMn/Al₂O₃ (triangles) and CuMn/Cu (circles). Solid lines are fits to finite-size scaling.

^{a)}Current address: National Institute of Standards and Technology, Room B206, Building 220, Gaithersburg, MD 20899.

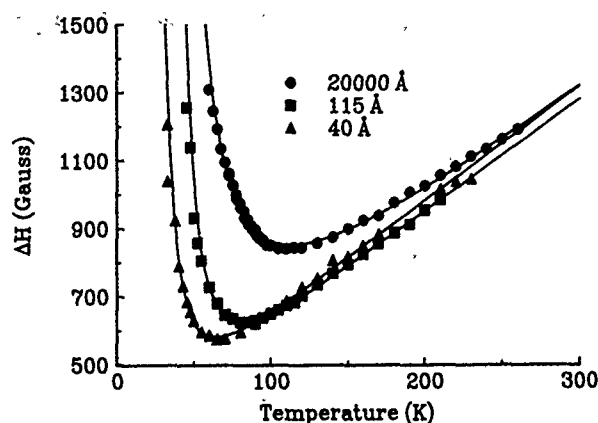


FIG. 2. Dependence of the ESR linewidth in CuMn/Al₂O₃ on temperature for CuMn layer thicknesses of 20 000 Å (circles), 115 Å (squares), and 40 Å (triangles). Solid lines represent fits to Eq. (2).

fects due to interfaces and surfaces.⁴ The linewidth diverges as T_f is approached, with $\kappa \approx 1.5$ in the bulk.⁵

Previous measurements^{4,5} of $\Delta H(T)$ in the CuMn/Cu system shows that the behavior described by Eq. (2) is obeyed for $10 \text{ Å} \leq W_{SG} \leq 10\,000 \text{ Å}$, with systematic changes in the parameters as a function of W_{SG} . Samples with $W_{SG} < \text{about } 50 \text{ Å}$ fit preferentially to a two-dimensional form ($T_f \rightarrow 0$) of Eq. (2). The data may be parametrized⁴ in terms of ϵ , with both A and B increasing linearly with ϵ . The crossover of the critical behavior from the 3D to 2D limit can be described by a continuous function of ϵ . The detailed information obtained from this study indicates that ESR is useful for studying the dependence of $\Delta H(T)$ on interlayer material.

Figure 2 shows $\Delta H(T)$ for a 20 000-Å CuMn film, and multilayered CuMn/Al₂O₃ samples with $W_{SG} = 115 \text{ Å}$ and 40 Å. The solid lines represent fits to Eq. (2), with the fitting parameters shown in Table I. The sample with $W_{SG} = 40 \text{ Å}$ fits preferentially to the $T_f = 0$ form, with the exponent from this fit shown in parenthesis in Table I.¹²

With the exception of the residual linewidth A , which remains approximately constant, all parameters obey the same general trends with decreasing W_{SG} as those from the CuMn/Cu series. The magnitudes of the thermal broadening coefficients B are comparable to those observed in the

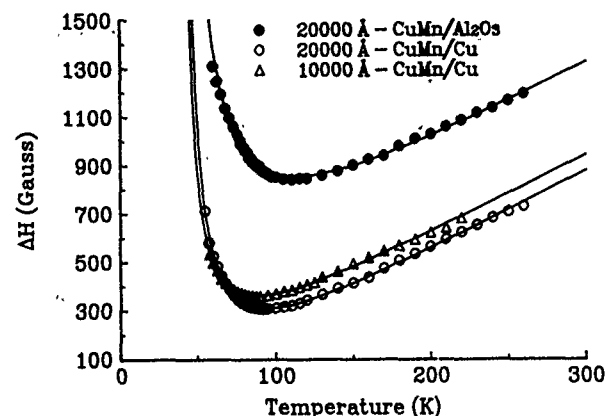


FIG. 3. Comparison of the ESR linewidth as a function of temperature for the 20 000-Å film from the CuMn/Al₂O₃ series (solid circles), and 20 000-Å (open circles) and 10 000-Å (open triangles) films from the CuMn/Cu series. Solid lines are fits to Eq. (2).

CuMn/Cu samples. The values of κ , while comparable in the bulk, are larger in the CuMn/Al₂O₃ multilayers, as are the divergence strengths. Extension of these measurements to a greater range of W_{SG} is necessary to determine if the parameters follow the same dependence on ϵ as CuMn/Cu.¹³

Distinct differences between the two sets of samples are observed. Figure 3 compares the temperature dependence of $\Delta H(T)$ for 20 000-Å films from the CuMn/Cu (Ref. 14) and the CuMn/Al₂O₃ series. The values of the parameters from fitting the CuMn/Cu sample to Eq. (1) are also shown in Table I. The linewidths for the CuMn/Al₂O₃ series are approximately 500-G larger than those of the corresponding CuMn/Cu data. The magnitude of the difference in the linewidths cannot be explained by the concentration difference, which is less than 1 at. %. Table I shows that the thermal broadening coefficients and values of κ are the same for both 20 000-Å samples, but that the residual linewidths and divergence strengths are different. Comparison of sample-growth parameters indicates no obvious differences that might explain these results.

The second significant difference between Al₂O₃ and Cu interlayers is that the CuMn/Al₂O₃ series shows a decrease in the magnitude of the minimum linewidth with decreasing W_{SG} . The minimum linewidth of the CuMn/Cu series was approximately constant for all W_{SG} .^{4,5} In the CuMn/Cu system, scattering from CuMn/Cu boundaries is negligible compared to CuMn/air boundaries and we expect surface effects due to the total sample thickness to dominate. In samples with insulating interlayers, the electrons are restricted to the CuMn layers and W_{SG} should be the dominant length. The constant values of the minimum linewidth in the CuMn/Cu series may be the result of all samples having approximately the same total thickness. This illustrates the need to consider both the total sample thickness and the spin-glass layer thickness, as the type of interlayer material will determine which length scale is dominant. Detailed conclusions are prohibited by the complicated dependence of the value of the minimum linewidth on the parameters of Eq. (2).

The dependence of $\Delta H(T)$ on the total sample thickness was studied by Nagashima and Abe¹⁵ in Cu_{1-x}Mn_x ($x=0.01$

TABLE I. Parameters obtained by fitting to Eq. (1).

W_{SG} (Å)	T_f (K)	A (G)	B (G/K)	C (G)	κ
Cu _{0.92} Mn _{0.08} /Al ₂ O ₃					
20 000	35	296	3.31	561	1.4
115	25	285	3.32	594	2.6
40	12.5	306	3.38	3601	2.9 (3.8)*
Cu _{0.93} Mn _{0.07} /Cu					
20 000	37	-133	3.31	241	1.40
10 000	37	-43	3.23	184	1.35

*The value in parenthesis for the 40-Å sample represents the exponent obtained by fitting to the 2D ($T_f=0$) form of Eq. (1). In this fit, the values of A and B remain the same and the prefactor of the divergence does not correspond directly to C . See Ref. 4 for details and the CuMn/Cu data.

and 0.055 at. %) films of thicknesses from 1000 Å to 50 000 Å. They found an increase in both the minimum value of the linewidth and in A , the residual linewidth, with decreasing W_{SG} . This is attributed to the increased importance of surface scattering relative to bulk scattering as the film thickness decreases. Nagashima and Abe did not investigate the divergence of the linewidth, so extracting reliable values for A and B for comparison to the present data is difficult.

The open triangles in Fig. 3 represent $\Delta H(T)$ for a 10 000-Å CuMn film from the CuMn/Cu series and are consistent with the behavior observed by Nagashima and Abe. Parameters from fitting to Eq. (2) are included in Table I. The values of κ are comparable for the two films, but the divergence strengths C are different. A detailed study of the dependence of these parameters on film thickness is required to determine the origin of these variances, whether the behavior is due to finite size or surface effects, and if the approach to the freezing transition is affected even on this larger length scale.

CONCLUSION

We have reported measurements of the ESR linewidth as a function of temperature in multilayered $\text{Cu}_{0.92}\text{Mn}_{0.08}/\text{Al}_2\text{O}_3$ samples with $20\,000\text{ Å} \geq W_{SG} \geq 40\text{ Å}$. We find that these data are qualitatively consistent with measurements from CuMn/Cu multilayers, but quantitatively differ. Differences between the magnitudes of the linewidths in samples fabricated at different locations suggest that this technique is sensitive to details of sample fabrication, which may include homogeneity, structure, and purity. The comparison of insulating versus conducting interlayers emphasizes the presence of two significant length scales—the total sample thickness as determined by the range of the conduction electrons and the spin-glass layer thickness. Our preliminary examination of CuMn films confirms that the electron-spin-resonance linewidth is sensitive to changes in the total thickness in samples showing no depression in T_f . We believe that study of these parameters as a function of interlayer material can provide a convenient framework within which to understand the importance of the different length scales.

Although interpretation of the temperature-dependent ESR linewidth is complicated, this technique has the poten-

tial to provide detailed information on relaxation processes not available from other types of measurements. Further effort must be given to extending the theory of electron-spin resonance in multilayered structures to fully utilize this technique.

ACKNOWLEDGMENTS

The work presented in this paper was funded by grants from the National Science Foundation and the Center for Fundamental Materials Research at Michigan State University, and the Office of Naval Research at Johns Hopkins University. F.V.W. thanks the CNRS for financial support.

- ¹ J. A. Cowen, G. G. Kenning, and J. M. Slaughter, *J. Appl. Phys.* **61**, 4080 (1987); G. G. Kenning, J. M. Slaughter, and J. A. Cowen, *Phys. Rev. Lett.* **59**, 2596 (1988).
- ² G. G. Kenning, Jack Bass, W. P. Pratt, Jr., D. Leslie-Pelecky, Lilian Hoines, W. Leach, M. L. Wilson, R. Stubi, and J. A. Cowen, *Phys. Rev. B* **42**, 2393 (1990).
- ³ A. Gavrin, J. R. Childress, C. L. Chien, B. Martinez, and M. B. Salamon, *Phys. Rev. Lett.* **64**, 2438 (1990).
- ⁴ D. L. Leslie-Pelecky and J. A. Cowen, *Phys. Rev. B* **46**, 9254 (1992).
- ⁵ D. L. Leslie-Pelecky and J. A. Cowen, *Phys. Rev. B* **48**, 7158 (1993).
- ⁶ The range of W_{SG} over which Eq. (1) is applicable has been debated in the literature. See Refs. 2 and 3 for details.
- ⁷ P. Granberg, P. Nordblad, P. Svdlinth, L. Lundgren, R. Stubi, G. G. Kenning, D. L. Leslie-Pelecky, J. Bass, and J. A. Cowen, *J. Appl. Phys.* **67**, 5252 (1990); L. Sandlund, P. Granberg, L. Lundgren, P. Nordblad, P. Svdlinth, J. A. Cowen, and G. G. Kenning, *Phys. Rev. B* **40**, 869 (1989).
- ⁸ J. Mattson, P. Granberg, L. Lundgren, P. Nordblad, G. Kenning, and J. A. Cowen, *J. Magn. Magn. Mater.* **104-107**, 1621 (1992).
- ⁹ J. Bass and J. A. Cowen, in *Recent Progress in Random Magnets*, edited by D. H. Ryan (World Scientific, Singapore, 1992).
- ¹⁰ S. E. Barnes, *Adv. Phys.* **30**, 801 (1981).
- ¹¹ R. H. Taylor, *Adv. Phys.* **24**, 681 (1975).
- ¹² For the $T=0$ fit, the values of A and B are unchanged and the prefactor for the divergence is not directly comparable with C .
- ¹³ A. Gavrin (unpublished). The values of κ in the CuMn/ Al_2O_3 increase faster with W_{SG} than the corresponding CuMn/Cu samples. One explanation may be that the Al_2O_3 interlayered samples approach 2D behavior at larger values of W_{SG} than CuMn/Cu samples.
- ¹⁴ A minor difference between the samples is that the film from the CuMn/Cu series shown in Fig. 3 is capped with 100 Å of Cu on the top and bottom of the film to protect the sample from oxidation and diffusion of silicon from the substrate. Measurements of films without the protective layer show linewidths that are slightly lower than in the sample with the protective layers.
- ¹⁵ H. Nagashima and H. Abe, *J. Phys. Soc. Jpn.* **32**, 1507 (1972).

Anisotropy studies of molecular-beam-epitaxy-grown Co(111) thin films by ferromagnetic resonance

F. Schreiber, A. Soliman, P. Bödeker, R. Meckenstock, K. Brühl, and J. Pelzl
Institut für Experimentalphysik, Ruhr-Universität Bochum, 44780 Bochum, Germany

I. A. Garifullin
Physical-Technical Institute, Kazan 420029, Russian Federation

The magnetic anisotropy of Co/Cu(111) thin films has been investigated using the ferromagnetic resonance (FMR) technique. The films were prepared by molecular-beam epitaxy in ultrahigh vacuum on sapphire substrates with niobium as a buffer layer. *In situ* RHEED investigations, *ex situ* x-ray low-angle reflectivity measurements, and high-angle Bragg scans confirm the structural quality of the films. Angular dependent FMR measurements are performed in the plane of the films and out-of-plane. The angular dependence of the line positions in-plane shows a competition between the sixfold anisotropy, which is expected for bulk Co, and a twofold anisotropy contribution. It is demonstrated that by FMR one can detect even small values of the higher-order anisotropy terms. In the analysis, we put emphasis on the relationship between magnetic and structural properties.

INTRODUCTION

Two of the main fields of interest in magnetic thin films are their exchange and anisotropy properties. Both are related to the growth process and the structure and, additionally, often connected with each other in the experimental study.^{1,2} In Co/Cu(111), the investigation of the oscillatory exchange of the Co layers via the Cu interlayer has posed problems and has not been unambiguously clarified for some time. Quite recently, the second regime of the antiferromagnetic coupling in molecular-beam-epitaxy-grown samples at $t_{\text{Cu}}^{\text{AF}}(2) \approx 19 \text{ \AA}$ [the first regime being at $t_{\text{Cu}}^{\text{AF}}(1) \approx 9 \text{ \AA}$ (Ref. 3)] has been found,^{4,5} in agreement with theoretical predictions.⁶

It has been argued⁶ that the exchange coupling in Co/Cu(111) is much more sensitive to strain and roughness effects than in Co/Cu(001), because in the (111) system the electrons that are responsible for the coupling are not propagating parallel to the interface normal. Local thinning of the Cu layers or pinholes were suggested to have a significant influence in samples grown by molecular-beam epitaxy (MBE).

A recent scanning tunneling microscopy (STM) study has shown that in fact the growth of Co on Cu(111) to some degree exhibits an island structure,⁷ an observation that explains part of the Co/Cu(111) controversy in the last few years.

In view of these peculiarities of the Co/Cu(111) system, we have studied the in-plane and out-of-plane anisotropy by FMR in connection with investigations of the structural parameters.

SAMPLE PREPARATION AND EXPERIMENT

A detailed description of the sample preparation can be found in recent publications.^{8,9} Onto the $\text{Al}_2\text{O}_3(11\bar{2}0)$ substrates we have grown by MBE a Nb(110) buffer layer ($\approx 100 \text{ \AA}$), followed by Cu(111) of about 30 \AA . Co was then grown with thicknesses t_{Co} ranging from 14 to 180 \AA . All samples were covered by a Cu layer ($\approx 30 \text{ \AA}$).

The growth was observed by RHEED. *Ex situ*, the samples were investigated by x-ray low-angle reflectivity measurements and high-angle Bragg scans, confirming the high structural quality. The values for the mosaicity are smaller than 0.1° . The interface roughness is of the order of 10 \AA as determined from x-ray low-angle scans. Remarks on the interpretation of roughness data and correlation lengths from x-ray measurements can be found in (Ref. 9).

Figure 1 shows an x-ray low-angle reflectivity and high-angle Bragg scan for the film with $t_{\text{Co}} = 85 \text{ \AA}$. The oscillations in the second half of the low-angle scan and those around 38.6° in the Bragg scan are due to the Nb buffer. In the fit of the low-angle reflectivity measurement, a partly oxidized Cu layer on top has been taken into account.

The FMR experiments were carried out at room temperature at X-band frequencies. The angular dependence of the spectra was measured in two configurations: (i) external field rotated in the plane of the sample and (ii) external field rotated to the film normal, starting in-plane from an easy direction.

To describe the angular dependence, we use a model that

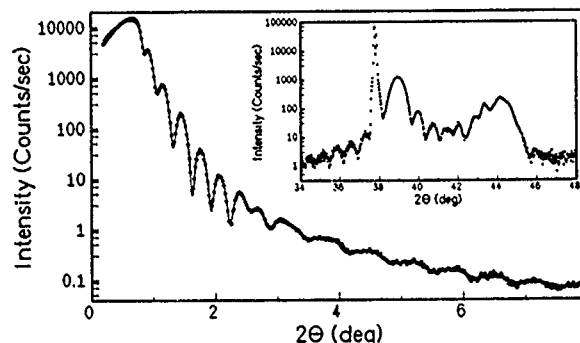


FIG. 1. X-ray low-angle reflectivity and high-angle Bragg scan (inset) of the film with $t_{\text{Co}} = 85 \text{ \AA}$. In the Bragg scan, the peak at 37.75° is due to the sapphire substrate. About four oscillations from Nb can be seen at each side of its main peak at 38.6° . The feature around 44° including its substructure is due to Co and Cu.

takes into account in the expression for the total free energy density F_{tot} , the Zeeman energy $(-\mathbf{H} \cdot \mathbf{M})$; the demagnetizing energy $(-2\pi M^2 \sin^2 \Theta)$; and anisotropy terms of the form

$$F_{\text{ani}} = K_1 \sin^2 \Theta + K_2 \sin^4 \Theta + [K_3 + K_4 \cos(6\Phi)] \sin^6 \Theta - K_u \sin^2 \Theta \cos^2(\Phi - \Phi_u), \quad (1)$$

which is appropriate for fcc(111)- and hcp(0001)-oriented films. The term K_u allows for an additional uniaxial anisotropy. Θ is measured with respect to the film normal, and Φ is the in-plane angle of the magnetization. Using standard FMR theory for the resonance condition¹⁰ yields for the case of the external field in the film plane

$$\left(\frac{\omega}{\gamma}\right)^2 = [H \cos(\Phi - \phi) + A - 6H_{A4} \cos(6\Phi) + 2H_{Au} \cos^2(\Phi - \Phi_u)] \times \{H \cos(\Phi - \phi) - 36H_{A4} \cos(6\Phi) + 2H_{Au} \cos[2(\Phi - \Phi_u)]\}. \quad (2)$$

$\gamma = g\mu_B/\hbar$ is the gyromagnetic ratio, H the external magnetic field, ϕ the in-plane external field angle, $A = 4\pi M - 2H_{A1} - 4H_{A2} - 6H_{A3}$, and $H_{Ai} = K_i/M$. As the angular derivatives of F_{tot} determine the resonance condition,¹⁰ the higher-order anisotropy term H_{A4} enters with a higher factor and therefore FMR can detect even a small sixfold in-plane anisotropy contribution.

RESULTS AND DISCUSSION

The in-plane FMR measurements show a competition between a sixfold and a uniaxial anisotropy contribution. The thicker samples are dominated by the sixfold rather than the uniaxial anisotropy and vice versa (see Fig. 2).

The origin of the uniaxial anisotropy H_{Au} that dominates in the thin samples may be explained by the evaporation process and the growth. As mentioned above, the bcc Nb buffer layer grows with its (110) plane on $\text{Al}_2\text{O}_3(11\bar{2}0)$. The (110) plane of Nb, i.e., a crystallographic plane with twofold symmetry, may be responsible for the induced twofold anisotropy of the Co layer. During the growth of the Cu layer, in the RHEED pattern the streaks characteristic for the (110) plane of Nb have been observed—in coexistence with the Cu(111) streaks. Furthermore, even after finishing the growth of the Cu layer, we could still detect considerable Auger signals from Nb. Therefore, we believe that it is possible that a small amount of Nb (probably only about one monolayer) is located upon the Cu layer, which may also contribute to H_{Au} . The rapid decrease of H_{Au} with increasing t_{Co} supports the assertion that the uniaxial anisotropy is an interface effect.

As it reflects the crystallographic symmetry, i.e., the atomic environment in the closest packed planes [fcc (111)], the sixfold anisotropy H_{A4} might be expected to have the same magnitude in all films, but the experiments show that H_{A4} is smaller in the thin films. As the dependence on t_{Co} is less pronounced than in the case of the uniaxial anisotropy, it is reasonable to assume that the intrinsic properties of Co on

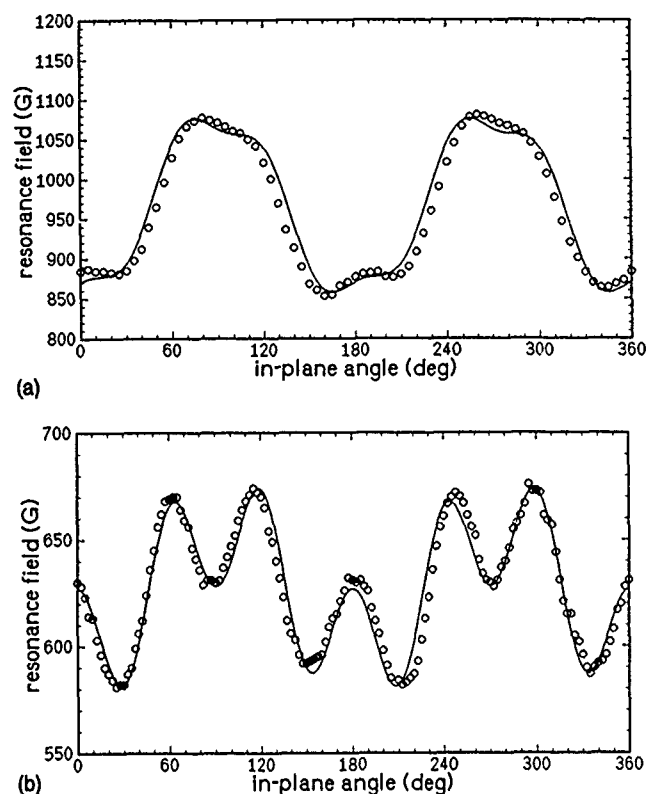


FIG. 2. In-plane angular dependence of the FMR line position for two samples. The starting angle is arbitrary. Part (a) corresponds to $t_{\text{Co}} = 14$ Å. This film is dominated by the twofold anisotropy, but the sixfold contribution is already visible, as it causes changes at the extrema of the twofold anisotropy. The film with $t_{\text{Co}} = 85$ Å (b) exhibits a stronger sixfold contribution. H_{A4} can be estimated from the difference between the maximum and the minimum of the line positions divided by 72 (see in-plane resonance condition).

Cu(111) rather than real interface effects play an important role. As pointed out by de la Figuera *et al.*,⁷ the Co layer on Cu(111) is formed by islands that do not exhibit a perfect coalescence up to seven monolayers. One can expect the sixfold anisotropy to be very sensitive to possible small in-plane crystallographic misorientations of these islands.

From the angle-dependent FMR measurements with the external field rotated with respect to the film normal we can get information on the out-of-plane anisotropy. As the K_1 term has the same angular dependence as the demagnetization energy, we can only determine the quantity $4\pi M_{\text{eff}} = 4\pi M - 2K_1/M$. In this definition, K_1 also contains the surface anisotropy contribution $2K_s/t_{\text{Co}}$. The resonance field at $\Theta = 0^\circ$ depends on $4\pi M_{\text{eff}}$ (and K_u), but not on the higher-order terms (see e.g., Ref. 11), so we can determine $4\pi M_{\text{eff}}$ directly, assuming the value of the g factor to be the bulk value of 2.18. For the thinnest film, the line positions can be fitted within the whole range of $\Theta (0^\circ \leq \Theta \leq 90^\circ)$ by using only $4\pi M_{\text{eff}}$, i.e., the higher-order contributions are very small. The analysis of the thicker films renders some difficulties as a substructure is found in the spectra around the perpendicular orientation. In an interval of about $\pm 5^\circ$ around $\Theta = 0^\circ$ often two lines appear, which partly overlap and which exhibit varying relative intensities. Therefore, we give only an estimate of $4\pi M_{\text{eff}}$ for these films. As the value of the higher-order anisotropy constants is strongly influenced by the angular dependence of the resonances close to

TABLE I. Anisotropy parameters for the four samples under investigation. $H_{A4}=K_4/M$ and $H_{Au}=K_u/M$ are obtained from a fit of the in-plane FMR measurements. $4\pi M_{\text{eff}}=4\pi M-2K_1/M$ is determined from the position of the resonance line at $\Theta=0$.

t_{Co} (Å)	H_{A4} (G)	H_{Au} (G)	$4\pi M_{\text{eff}}$ (kG)
14	0.6	60	9.7
85	0.8	15	13.5
93	0.8	13	13.3
178	1.7	9	14.0

$\Theta=0^\circ$, their determination is complicated by the above mentioned behavior.

In x-ray investigations of the stacking sequence of thin Co layers on Cu(111) grown by the same recipe (with the Nb buffer layer) only fcc stacking was found.⁹ Recent NMR experiments on our thicker films yielded a significant hcp contribution.¹² This difference in the stacking may contribute to the substructure of the out-of-plane FMR spectra. Note that an hcp stacking is expected to lead to a decrease of $4\pi M_{\text{eff}}$ compared to pure fcc, because of the higher value of K_1 in the hcp structure.

As the spectrum of the film with $t_{\text{Co}}=14$ Å shows no such irregularities, we can analyze its linewidth behavior. If the film is perfectly homogeneous, one can expect $\Delta H(\Theta=0^\circ)\approx\Delta H(\Theta=90^\circ)$. However, we observe a certain deviation from this. We introduce the inhomogeneity $\delta H_i=\delta(4\pi M-2K_1/M)$ of the first-order internal field contributions and write

$$\Delta H = \Delta H_0 + \left| \frac{\partial H_{\text{res}}}{\partial H_i} \right| \delta H_i. \quad (3)$$

Comparing the in-plane and the out-of-plane linewidth yields $\delta H_i \approx 1100$ G. We have assumed a Lorentzian shape of the absorption curve, so that the peak-to-peak linewidth measured with the field modulation technique corresponds to $(1/\sqrt{3})\Delta H$. In the case of this thin film, the inhomogeneity δH_i should be mainly caused by roughness effects. We note that measurements on polycrystalline Co on Au(111) also yielded considerable values for the inhomogeneity of the internal field in thin films.¹¹

In conclusion, we have investigated the in-plane and out-of-plane anisotropy of MBE-grown Co/Cu(111) films. In plane, the expected sixfold anisotropy is clearly visible, but for the thin films it is less pronounced, which can be taken as an indication for the nonperfect coalescence of Co on Cu(111) within the first Co layers. An additional uniaxial contribution is found that is thought to be closely related to the buffer layer.

The out-of-plane anisotropy of the film with $t_{\text{Co}}=14$ Å can be fully described by using only the lowest-order term, i.e., $4\pi M_{\text{eff}}=4\pi M-2K_1/M$. The higher-order contribution is very small. For this film, an estimate of the inhomogeneity of the internal field has been given on the basis of the FMR linewidth. The out-of-plane spectra of the thicker films exhibit some substructure and not only a single resonance line. In these samples significant hcp stacking contributions have been found.

The results confirm that the Co/Cu(111) system has its peculiarities mainly connected with the growth process and the structure.

ACKNOWLEDGMENTS

The authors wish to thank P. Riedi for providing preliminary NMR data. This work was supported by the Deutsche Forschungsgemeinschaft (SFB 166).

- ¹B. Dieny *et al.*, J. Phys. Condens. Mat. **2**, 159 (1990); B. Dieny and J. P. Gavigan, J. Phys. Condens. Mat. **2**, 178 (1990).
- ²K. Brühl *et al.*, (these proceedings).
- ³M. T. Johnson *et al.*, Phys. Rev. Lett. **69**, 969 (1992).
- ⁴A. Schreyer *et al.*, Phys. Rev. B **47**, 15334 (1993).
- ⁵C. Dupas *et al.*, J. Magn. Magn. Mater. **128**, 367 (1993).
- ⁶P. Bruno and C. Chappert, Phys. Rev. Lett. **67**, 1602 (1991); P. Bruno and C. Chappert, Phys. Rev. B **46**, 261 (1992).
- ⁷J. de la Figuera *et al.*, Phys. Rev. B **47**, 13043 (1993).
- ⁸K. Brühl *et al.*, J. Cryst. Growth **127**, 682 (1993).
- ⁹P. Bödeker *et al.*, Phys. Rev. B **47**, 2353 (1993).
- ¹⁰S. V. Vonsovskii, *Ferromagnetic Resonance* (Pergamon, New York, 1966).
- ¹¹C. Chappert *et al.*, Phys. Rev. B **34**, 3192 (1986).
- ¹²P. Riedi (private communication).

Magnetic and magneto-optic properties of sputtered Co/Ni multilayers

Y. B. Zhang, P. He, and J. A. Woollam

Center for Microelectronic and Optic Materials Research, and Department of Electrical Engineering,
University of Nebraska, Lincoln, Nebraska 68588

J. X. Shen, R. D. Kirby, and D. J. Sellmyer

Center for Materials Research and Analysis, and Department of Physics, University of Nebraska,
Lincoln, Nebraska 68588

We have investigated the magnetic and magneto-optic properties of Co/Ni multilayers deposited on Ag and Au buffer layers. The samples with Au buffer layers show perpendicular magnetic anisotropy, but those with Ag buffer layers do not. The structure and degree of crystalline alignment of the buffer layer are evidently crucial to development of perpendicular magnetic anisotropy. We also present the results of polar Kerr rotation measurements as a function of wavelength and layer thickness of the multilayers.

INTRODUCTION

Magnetic multilayers have attracted much attention¹ due to the resulting novel properties that are suitable for a variety of applications. One interesting phenomenon is the so-called perpendicular magnetic anisotropy that has been found in Co/X (X being a nonmagnetic metal such as Pt, Pd, Au, or Ir) multilayers.²⁻⁴ The large perpendicular magnetic anisotropy shown in these multilayers makes them potential candidates for MO recording media. Recently, Co/Ni multilayers were also predicted to have perpendicular magnetic anisotropy, and this was confirmed in *e-beam* evaporated multilayer samples.⁵ Magneto-optic and thermomagnetic writing tests on this *e-beam* evaporated multilayer have yielded encouraging results.⁶

In this article, the magnetic and magneto-optic properties of sputtered Co/Ni multilayers are reported. The effects of Au and Ag buffer layers on the perpendicular magnetic anisotropy of the sputtered Co/Ni multilayers are discussed, then the dependencies of the magneto-optic properties on the wavelength and the multilayer structure parameters are presented.

EXPERIMENT

Samples were prepared using both dc and rf magnetron sputtering. The system was first evacuated to below 5×10^{-7} Torr before sputtering, and Ar gas (5×10^{-3} Torr) was used in the sputtering process. In most cases, 50-nm-thick Au or Ag buffer layers were first deposited onto glass substrates. The Co thickness was varied from 0.1 to 0.4 nm and the Ni thickness from 0.2 to 1.2 nm. Multilayered structures were realized by rotating the substrates above the separate guns. The total Co/Ni thickness was varied between 5 to 30 nm.

The magnetic properties were measured using an alternating gradient force magnetometer (AGFM). Crystalline texture studies were performed using x-ray diffractometry with a Cu $K\alpha$ target in the θ - 2θ mode, and a scanning angle of 10° - 90° . The Kerr rotation (θ_k) and the Kerr ellipticity (ϵ_k) were measured at normal incidence over the wavelength range from 300 to 800 nm using apparatus previously described.⁷ All experiments are performed at room temperature.

RESULTS AND DISCUSSIONS

Figure 1(a) shows hysteresis loops obtained with the AGFM for Co(0.2 nm)/Ni(0.8 nm) on Ag for magnetic fields applied both in the plane and perpendicular to the film plane. Clearly, this sample has in-plane magnetic anisotropy, as did all other samples deposited on Ag buffer layers. In contrast, Fig. 1(b) shows perpendicular and parallel hysteresis loops for a similar multilayer deposited on a Au buffer layer. This sample clearly has perpendicular anisotropy, and the value of the uniaxial anisotropy constant (as determined by the loop-area method) is about 100 kJ/m^3 . All of our Co/Ni multilayers deposited on Au showed perpendicular anisotropy, in agreement with the results of Daalderop *et al.*⁵

While the origins of perpendicular magnetic anisotropy (PMA) are often difficult to determine, PMA can be due to tensile internal stresses.⁸ Thus the structural details of the buffer layer may be of considerable importance in determining the magnitude of the anisotropy. Figure 2 shows x-ray diffraction scans of the fcc Au and Ag buffer layers, each 50 nm thick. The dominant feature of both scans is the [111]

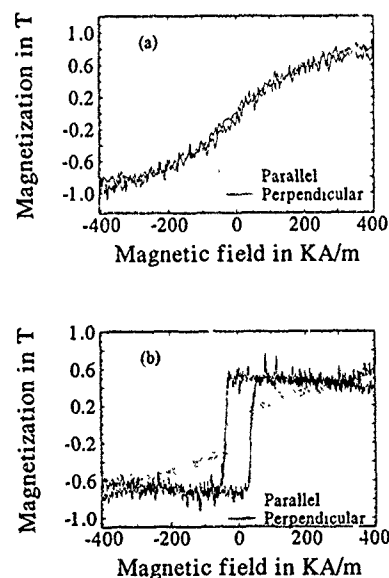


FIG. 1. Room temperature hysteresis loops for (a) Co(0.2)/Ni(0.8) \times 12 multilayers on Ag buffer layers and (b) Co(0.2)/Ni(0.8) \times 8 on Au buffer layers.

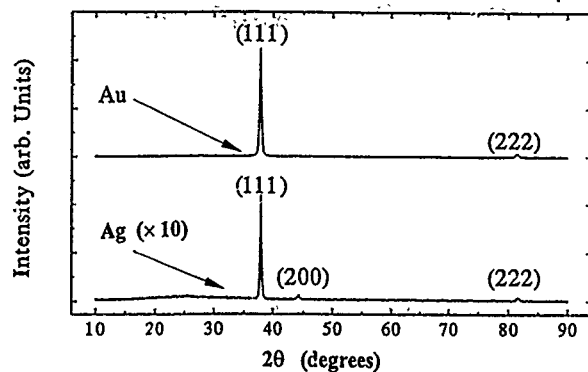


FIG. 2. 2θ x-ray diffraction patterns of Au and Ag buffer layers.

peak, indicating that the films are highly textured. The intensity of the Au peak is 10 times that of the Ag peak, whereas the ratio of the electron densities squared is only 2.8. This result suggests that the Au buffer layers exhibit either a higher degree of crystallinity or a higher degree of texture, either of which could lead to the differences in anisotropy. The presence of a weak [200] diffraction peak for the Ag buffer layer, but not for the Au buffer layer (see Fig. 2), is direct evidence that the Au buffer layer is more completely textured than the Ag buffer layer.

To further test these ideas, we carried out annealing experiments, where the buffer layer was annealed prior to deposition of the Co/Ni multilayer. Annealing the Ag buffer layer in vacuum at 400 °C for 1.5 h prior to depositing the Co/Ni multilayer resulting in significant changes in the shape of the perpendicular hysteresis loop. The remanence ratio M_r/M_s of the Co/Ni multilayers increased considerably, and the coercivity increased by a factor of nearly 5. However, the easy magnetization direction remained in the film plane. Similar annealing experiments on Au buffer layer resulted in only minor changes in the hysteresis loops. One can specu-

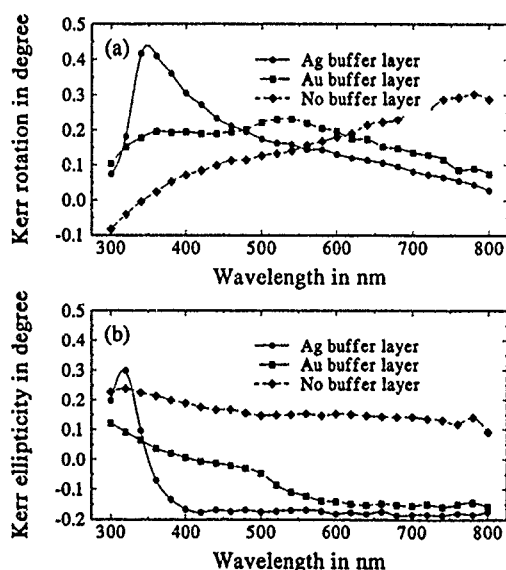


FIG. 3. Wavelength dependencies of Co(0.2)/Ni(0.8)×16 multilayers (a) polar Kerr rotation, (b) polar Kerr ellipticity.

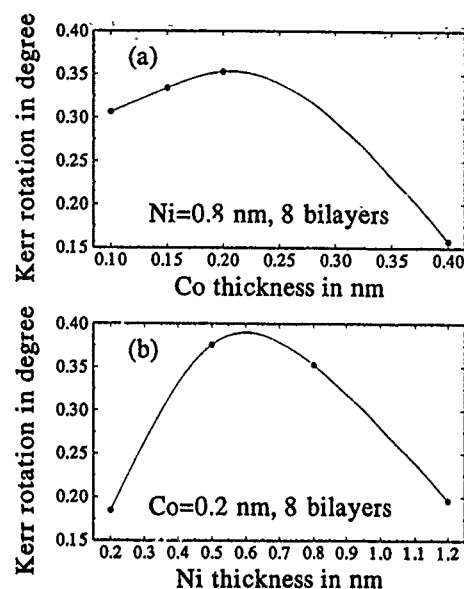


FIG. 4. Polar Kerr rotation at 350 nm as a function of (a) Co thickness and (b) Ni thickness for multilayers on Ag buffer layers.

late that if the [111] texture of the Ag buffer layer could be improved, Co/Ni multilayers deposited on Ag might also show PMA.

The wavelength dependencies of θ_k and ϵ_k for Co/Ni multilayers on both Au and Ag buffer layers are shown in

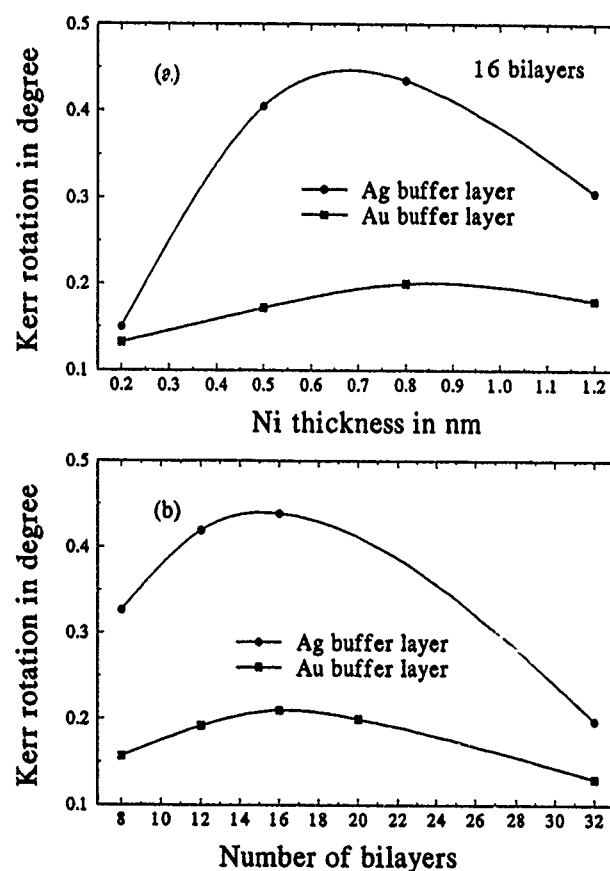


FIG. 5. Polar Kerr rotation at 350 nm as a function of (a) Ni thickness at Co=0.2 nm, (b) bilayer numbers for Co(0.2)/Ni(0.8) multilayers on Ag and Au buffer layers.

Fig. 3. For Co/Ni multilayer thickness near 10 nm, the optical effects of the buffer layer or the glass substrate is considerable,⁹ since the magnitudes of θ_k and ϵ_k are due to a combination of the magneto-optical properties of the Co/Ni multilayer and the optical properties of the buffer layer. From Fig. 3, we note that the peak of θ_k for Co/Ni on Ag falls at 350 nm, or at about the same wavelength where ϵ_k drops rapidly. These two effects occur where the optical properties of Ag are changing rapidly due to d -band transitions.¹⁰ Similar, but less dramatic, effects are noted for Co/Ni on Au. It should also be noted that the short-wavelength polar Kerr rotations of Co/Ni multilayers with Au buffer layers are considerably larger than those of rare-earth-transition-metal alloys.¹¹

We varied the individual Co and Ni layer thicknesses, and also the number of bilayers, to optimize the polar Kerr rotation, and the results are shown in Figs. 4 and 5. The maximum polar Kerr rotation is obtained for Co \approx 0.2 nm, Ni \approx 0.6 nm, at about 16 bilayers. The Kerr rotation for Co/Ni on Ag is considerably larger than that of Co/Ni on Au (see Fig. 5), primarily because the measurements were performed at $\lambda=350$ nm, where the optical properties of Ag cause a considerable enhancement of the Kerr rotation.

SUMMARY AND CONCLUSIONS

Sputtered Co/Ni multilayers show perpendicular magnetic anisotropy when deposited on a Au buffer layer, but in-plane anisotropy when deposited on a Ag buffer layer. This difference most likely arises because the Au buffer layers are more completely oriented with the [111] direction perpendicular to the film plane. The optical properties of the

buffer layer also strongly affect the magnitude of the Kerr rotation. The largest Kerr rotation measured was 0.44° for Co(0.2 nm)/Ni(0.6 nm) \times 16 bilayers on a Ag buffer layer.

ACKNOWLEDGMENTS

The authors would like to thank Z. S. Shan, D. X. Wang, and S. Nafis for assistance and helpful discussion. We are grateful to the National Science Foundation for financial support under Grant No. DMR-9222976.

¹See, for example, *Science and Technology of Nanostructured Magnetic Materials*, edited by G. C. Hadjipanayis and G. A. Prinz (Plenum, New York, 1991).

²F. J. A. den Broeder, W. Hoving, and P. J. H. Bloemen, *J. Magn. Mater.* **93**, 562 (1991).

³P. F. Carcia, A. D. Meinhaldt, and A. Suna, *Appl. Phys. Lett.* **47**, 178 (1985).

⁴B. N. Engel, C. D. England, R. A. Vanleeuwen, M. H. Wiedmann, and C. M. Falco, *Phys. Rev. Lett.* **67**, 1910 (1991).

⁵G. H. O. Daalderop, P. J. Kelly, and F. J. A. den Broeder, *Phys. Rev. Lett.* **68**, 662 (1992).

⁶F. J. A. den Broeder, H. W. van Kesteren, W. Hoving, and W. B. Zeper, *Appl. Phys. Lett.* **61**, 1468 (1992).

⁷L. Y. Chen and J. A. Woollam, in *Proceedings of the SPIE 33rd Annual International Symposium on Optical and Opto-electronic Applied Science and Engineering*, **1166**, 267 (1989).

⁸F. J. A. den Broeder, E. Janssen, W. Hoving, and W. B. Zeper, *IEEE Trans. Magn.* **28**, 2760 (1992).

⁹P. He, William A. McGahan, and J. A. Woollam, *J. Appl. Phys.* **69**, 4021 (1991).

¹⁰Frederick Wooten, *Optical Properties of Solids* (Academic, New York, 1972).

¹¹P. F. Carcia, W. B. Zeper, H. W. van Kesteren, B. A. J. Javobs, and J. H. M. Spurt, in *Proceedings of the Magneto-Optical Recording International Symposium*, 151 (1991).

Spatial modulation of the magnetic moment in Co/Pd superlattices observed by polarized neutron reflectivity

J. A. Borchers, J. F. Ankner, and C. F. Majkrzak

Reactor Radiation Division, National Institute of Standards and Technology, Gaithersburg, Maryland 20899

B. N. Engel, M. H. Wiedmann, R. A. Van Leeuwen, and C. M. Falco

Optical Sciences Center, University of Arizona, Tucson, Arizona 85721

We have measured the specular reflectivity of spin-polarized neutrons from two (111) superlattices, [Pd 80 Å/Co 60 Å]×20/Pd 300 Å/Co 10 Å/GaAs and [Pd 53 Å/Co 32 Å]×10/Pd 30 Å/Cu 354 Å/Si, grown by molecular-beam epitaxy. In a saturating field of 2300 Oe, we extract for the first superlattice a Co moment value of corresponding to 78% of the bulk Co moment. At temperatures ranging from 38 to 295 K, no excess magnetic moment from polarization of the Pd atoms is evident in the nominal Pd layer. Comparable reflectivity data from the second sample support these conclusions.

The application of controlled deposition techniques to the growth of magnetic films and multilayers has prompted novel studies of the nature of spin interactions in transition metals.¹ For example, the discovery of perpendicular magnetic anisotropy in Co/Pd superlattices^{2,3} has attracted technological interest, while a related topic of fundamental importance has been the polarization of the nonmagnetic Pd atoms²⁻⁴ arising from the proximity of Co at the superlattice interfaces. Even though its *d* band is not completely filled pure Pd is paramagnetic rather than ferromagnetic like Ni, its structural analog. A "giant moment" as large as $0.4\mu_B$ per Pd atom occurs in dilute Pd alloys with magnetic transition metals principally due to the *3d-4d* hybridization of the impurities with the Pd atoms.⁵ For a Co monolayer on a Pd substrate, a theoretical study⁶ predicts that the Co magnetization is enhanced by as much as $0.4\mu_B$ per atom and that a moment of $0.33\mu_B$ per atom is induced nearest the Pd layer. A similar calculation for Fe/Pd superlattices⁷ confirms that only the Pd atomic layer nearest the interface develops a significant moment ($>0.3\mu_B$).

Experimental measurements such as conventional magnetization²⁻⁴ provide widely varying estimates of the Pd moment in Co/Pd superlattices. In contrast with this technique, polarized-neutron reflectivity is sensitive to the depth-dependent moment distribution through the superlattice and is insensitive to sample volume. Pasyuk *et al.*⁸ have used this procedure to examine a Pd/Co/Pd trilayer structure and obtain an induced Pd moment of $0.4\mu_B$ at the Co/Pd interfaces. In this study, we have measured and modeled the specular reflectivity of x-rays and spin-polarized neutrons from two Co/Pd superlattices, [Pd 80 Å/Co 60 Å]×20/Pd 300 Å/Co 10 Å/GaAs (sample A) and [Pd 53 Å/Co 32 Å]×10/Pd 30 Å/Cu 354 Å/Si (sample B), in order to extract the average moment in each of the individual Co and Pd interlayers. These crystalline, (111)-oriented samples were prepared at the University of Arizona using molecular-beam epitaxy procedures detailed elsewhere.⁴ Because neutron reflectivity is sensitive only to those moments that lie in the sample plane, we require superlattices with thicker Co and Pd interlayers than those that typically generate perpendicular magnetic anisotropy.²⁻⁴ In neither sample do we find evidence of an excess moment in the nominal Pd interlayers at temperatures ranging from 38 K to 300 K. In addition, the Co moment in

sample A saturates to only 78% of its bulk value in an applied field of 2300 Oe. While the apparent moment depletion observed in the superlattices seems to contradict the trilayer reflectivity study by Pasyuk *et al.*,⁸ we discuss here the precision of this measurement technique for both sample geometries and place limits on the resultant Co and Pd moment values.

We performed the neutron reflectivity studies on the BT-7 reflectometer⁹ at the NIST research reactor with the samples magnetized in-plane in fields ranging from 95 Oe to 2300 Oe. Since neutrons interact with both the nuclei and electron spins of the scattering material, the refractive indices describing the reflectivity have a structural and magnetic component. For a simple ferromagnet, the refractive index can be written

$$n_{\pm} = \sqrt{1 - \frac{N\lambda^2}{\pi}} (b \pm p), \quad (1)$$

where *N* is the number density of the scatterers, *b* is the nuclear scattering length, and $p = \sigma_m \mu$ is the magnetic scattering amplitude where $\sigma_m = 0.2695 \times 10^{-4} \text{ Å}/\mu_B$ and μ is the magnetic moment per atom in the sample plane. The plus and minus subscripts designate the indices for neutrons polarized parallel and antiparallel to the sample moment. Measuring both spin states, one can, in principle, obtain a spatial profile of the distribution of structural and magnetic scatterers through the sample using a model based upon the one-dimensional wave equation for a stratified medium.¹⁰

To reduce the number of variables in the neutron data analysis, we first determine the structural characteristics of the superlattice using x-ray reflectivity. Figure 1(a) shows room-temperature data for sample A plotted as a function of the wave vector *Q*. The fitted curve was generated from the density profile shown in Fig. 1(b) and parametrized in Table I. Despite the presence of four superlattice reflections above background, the fit reveals that the superlattice interfaces are somewhat rounded. The scattering densities in the centers of the interlayers fall short of the bulk Co and Pd values [dashed lines in Fig. 1(b)], suggesting that Co atoms are present throughout the nominal Pd layer and vice versa. The structural characteristics of sample B (Table I) are comparable to those of sample A despite differences in the substrate materials and growth procedures.⁴ In both samples the ob-

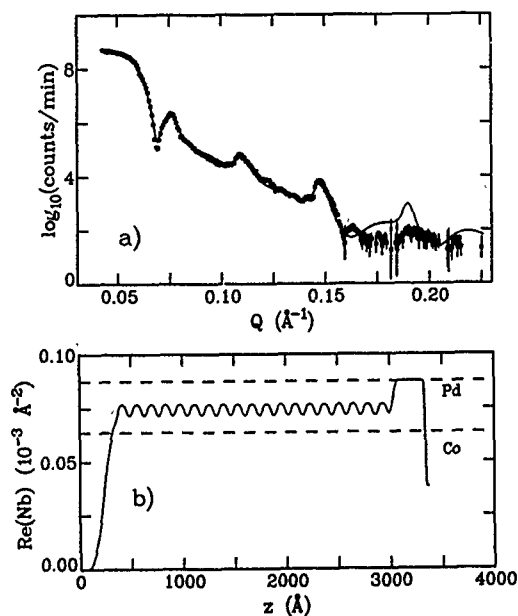


FIG. 1. (a) X-ray specular reflectivity of sample A at room temperature. The squares are the data and the solid line is the fit. (b) Scattering density profile for the x-ray reflectivity fit as a function of depth into the sample. The dashed lines mark the bulk densities of Co and Pd.

served interfacial "mixing" could originate from a combination of diffusion, atomic-scale roughness, or correlated roughness arising from substrate miscut.

Polarized-neutron scans for sample A reveal only a single superlattice reflection above the diffuse background, as demonstrated in Fig. 2(a) for measurements at 38 K in an applied field of 2300 Oe. The + and - cross sections were fit simultaneously, holding the structural parameters constant, in order to extract the moment distribution as a function of depth. The results from this analysis are summarized in Table I. The fit is guided principally by the critical angles, which are related to the square of the total bilayer moment, and by the relative intensities of the + and - superlattice peaks, which are determined by the difference between the magnetization in the nominal Co and Pd layers. Following Fourier-transform arguments, the absence of higher-order superlattice reflections limits the sensitivity of the fit to the *average* moments through the separate Co-rich and Pd-rich interlayers. Specifically, the magnetic densities of the Pd atomic planes nearest the Co/Pd interfaces cannot be distinguished.

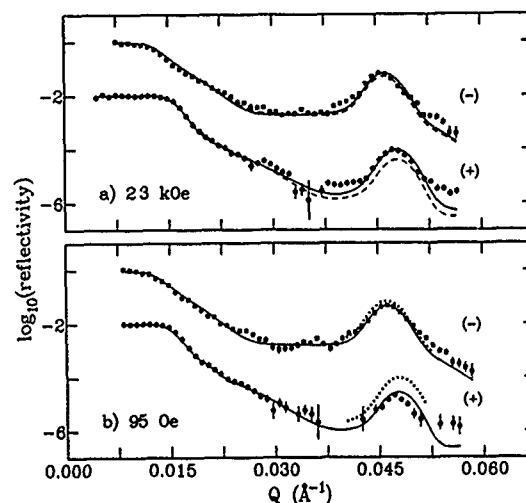


FIG. 2. (a) Polarized-neutron reflectivity of sample A at 38 K in a saturating field of 2300 Oe. The + and - cross sections are designated by circles and squares, respectively, and the former is vertically offset for clarity. The solid lines represent the fit to the data, and the dashed lines describe the reflectivities calculated assuming that the Co atoms present in both the nominal Co and Pd interlayers are magnetized with 78% of the bulk Co moment. (b) Polarized-neutron reflectivity of the same sample at 38 K in a remanent field of 95 Oe. The dotted lines here reproduce the fit to the 2300-Oe reflectivities in (a) above to enable a direct comparison of the data sets.

The magnetization profile that generates the fit (solid line) in Fig. 2(a) is shown in Fig. 3(a). The average magnetic moment in the nominal Co interlayer equals $(1.37 \pm 0.08)\mu_B$ per Co atom, corresponding to 78% of the Co bulk moment ($1.74\mu_B$). The remaining 22% of the spins elude experimental detection and are, therefore, either disordered or aligned perpendicular to the sample plane. (Complementary magnetometry measurements, normalized by the number of Co atoms in the sample, give a saturation moment of $(1.62 \pm 0.08)\mu_B$ per Co atom.) Figure 3(a) also demonstrates that the magnetic density $Re(Np)$ of the Pd-rich layer is smaller than would be expected if those Co atoms dispersed through the layer exhibited the same moment as those in the Co-rich layer. In addition, the moment in the nominal Pd interlayer decreases from $1.08\mu_B$ to $0.95\mu_B$ per Co atom upon warming the sample from 38 K to room temperature, possibly reflecting a gradient of Co Curie temperatures through the interfaces. At both temperatures we clearly observe a depletion of the magnetic moment in the nominal Pd

TABLE I. Parameters describing the fits to the x-ray and neutron reflectivity data for samples A and B. The interlayer thicknesses d and nuclear scattering densities Nb were extracted from room temperature x-ray data, while the magnetic densities Np were extracted from neutron data in a 2300-Oe applied field at 38 K for sample A and at room temperature for sample B.

Sample	X-ray reflectivity				Neutron reflectivity	
	d_{Co} (Å)	d_{Pd} (Å)	$Re(Nb)_{Co}$ (10^{-6} Å^{-2})	$Re(Nb)_{Pd}$ (10^{-6} Å^{-2})	$Re(Np)_{Co}$ (10^{-6} Å^{-2})	$Re(Np)_{Pd}$ (10^{-6} Å^{-2})
A	59.2	80.5	71.6	76.8	2.41	1.05
B	31.7	53.4	59.8	77.0	3.16	1.87
Co			13.7		4.28	
Pd				87.5		0

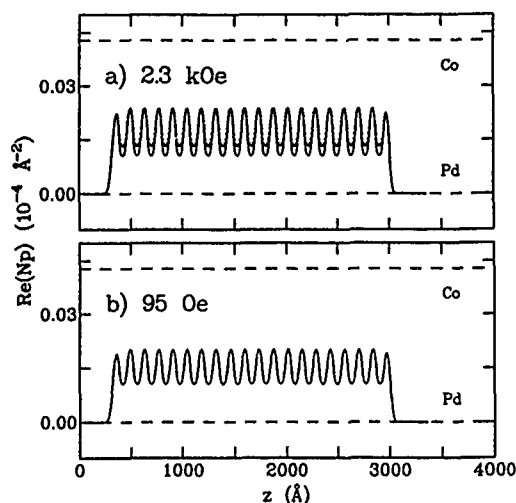


FIG. 3. (a) Magnetic scattering density profile for sample A at 38 K in a saturating field of 2300 Oe determined from the reflectivity fit in Fig. 2(a). The dashed lines mark the bulk densities of Co and Pd. The dotted line describes the density profile calculated assuming that the Co atoms present in both the nominal Co and Pd interlayers are magnetized with 78% of the bulk Co moment. (b) Magnetic scattering density profile for the same sample at 38 K in a remanent field of 95 Oe determined from the reflectivity fit in Fig. 2(b).

interlayer, rather than the predicted enhancement.

In order to place limits on our moment estimates, we have calculated reflectivity curves for sample A assuming that the Co atoms through the entire bilayer order with 78% of the bulk Co moment [dotted line in Fig. 3(a)]. As can be seen from Fig. 2(a), the differences between these curves (dashed lines) and the fitted curves (solid lines) are striking. Any enhancement of the magnetization in the nominal Pd layer would further diminish the amplitude of the + and - superlattice reflections, an effect not evident in our data.

The 38-K reflectivity for sample A does, in fact, change substantially upon lowering the applied field to 95 Oe, as shown in Fig. 2(b). The intensity of the + superlattice reflection is almost an order of magnitude smaller than that in Fig. 2(a) and the critical angles are slightly reduced. The plot of the resultant density profile in Fig. 3(b) reveals that these features originate from a decrease in the magnetic scattering contrast between the bilayer components (Table I). The moment per Co atom in the Co-rich interlayer equals $1.16\mu_B$, a reduction of $0.21\mu_B$ relative to that measured in a 2300-Oe saturating field, while the magnetization of the Pd-rich interlayer ($1.08\mu_B$ per Co atom) is identical to its high-field value. At room temperature, however, the magnetic profile extracted from 95-Oe reflectivity data approximates that shown in Fig. 3(a). The in-plane saturation field of the Co moments in the nominal Co interlayer apparently increases as the temperature decreases, an effect observed in comparable samples using conventional magnetometry techniques.¹¹ Though this behavior is generally attributed to a corresponding increase of the perpendicular magnetic anisotropy, we cannot, in this case, rule out the possible formation of ferromagnetic domains in the sample plane.

We have also measured the polarized-neutron reflectivity for sample B under comparable temperature and magnetic

field conditions, but the results are less conclusive. Unfortunately, the scattering near the critical angle is dominated by the Cu baselayer. We can thus extract for this superlattice the relative magnetization of the Co and Pd interlayers, but cannot uniquely determine the absolute magnitude of the total bilayer moment. For simplicity, we assume that the Co atoms in the Co-rich layer saturate with the full Co moment. Table I lists the magnetic densities of the Co and Pd layers obtained from a fit to the reflectivities measured at room temperature in a saturating field of 2300 Oe. The deviation of these values from their bulk counterparts directly follows from the interfacial "mixing" quantified via x-ray analysis. The splitting between the + and - first-order superlattice reflections is well defined, and we observe that the Co atoms present in both the Co-rich and Pd-rich interlayers order with identical moments. Once again, no magnetic enhancement is evident through the nominal Pd interlayer.

We have extracted the spatial profile of the magnetization through two Co/Pd superlattices using polarized-neutron reflectivity techniques. As demonstrated, this analysis is particularly sensitive to differences between the magnetic densities of the Co and Pd interlayers. For the first sample, the Co moments in the nominal Co layer saturate to 78% of the bulk Co moment. This depletion may be associated with the structural disorder revealed by x-ray characterization. In both superlattices we do not detect any excess moment in the nominal Pd layer. Either the Pd in these samples is not polarized or the effect is very small. Subtle moment enhancements in a narrow interfacial region ($<5 \text{ \AA}$) as predicted by theory^{6,7} and reported by Pasyuk *et al.*⁸ are difficult to detect using either neutron reflectivity, which requires a level of interfacial perfection difficult to achieve, or conventional techniques such as magnetometry, which depend on sample volume. Upon refinement of the structural quality, specular reflectivity provides the sensitivity to detect these small enhancements and remains a topic for future investigation.

ACKNOWLEDGMENTS

The research at the University of Arizona was supported by the University of Arizona Optical Data Storage Center and DOE Grant No. DE-FG02-87ER45297.

¹L. M. Falicov *et al.*, J. Mater. Res. 5, 1299 (1990).

²P. F. Carcia, A. D. Meinhardt, and A. Suna, Appl. Phys. Lett. 47, 178 (1985).

³F. J. A. den Broeder, H. C. Donkersloot, H. J. G. Draaisma, and W. J. M. de Jonge, J. Appl. Phys. 61, 4317 (1987).

⁴Brad N. Engel, Craig D. England, Robert A. Van Leeuwen, Michael H. Wiedmann, and Charles M. Falco, Phys. Rev. Lett. 67, 1910 (1991).

⁵J. C. Odo, J. Phys. F 13, 1291 (1983).

⁶S. Blügel, B. Drittler, R. Zeller, and P. H. Dederichs, Appl. Phys. A 49, 547 (1989).

⁷H. Nait-Laziz, S. Bouarab, C. Demangeat, A. Mokrani, and H. Dreyse, J. Magn. Magn. Mater. 118, 365 (1993).

⁸V. V. Pasyuk, H. J. Lauter, M. T. Johnson, F. J. A. den Broeder, E. Janssen, J. A. C. Bland, and A. V. Petrenko, Appl. Surf. Sci. 65, 118 (1993).

⁹C. F. Majkrzak, Physica B 173, 75 (1991).

¹⁰J. F. Ankner, A. Schreyer, Th. Zeidler, C. F. Majkrzak, H. Zabel, J. A. Wolf, and P. Grunberg, in *Neutron Optical Devices and Applications*, edited by C. F. Majkrzak and J. L. Wood (SPIE, 1992), Proc. 1738, p. 260.

¹¹Brad N. Engel (private communication).

Electron-energy-loss spectroscopy of Fe thin films on GaAs(001)

J. Yuan, E. Gu, M. Gester, J. A. C. Bland, and L. M. Brown
Cavendish Laboratory, Cambridge CB3 0HE, United Kingdom

An electron-microscopy-based technique of electron-energy-loss spectroscopy (EELS) has been used to characterize electronic and magnetic properties of ultrathin Fe films grown on GaAs(100) surface, as a function of the film thickness. Large-area electron transparent membranes for microscopic analysis are prepared by ion-beam thinning or chemical etching from the substrate side, and the top surface of the ultrathin Fe film is protected by a thin Cr layer. Analysis of the Fe 2*p*, Cr 2*p*, and O 1*s* absorption spectra confirms that only the Cr layer is oxidized. The local magnetic moments of the ultrathin Fe films are deduced from the "white line" branching ratio in the Fe 2*p* absorption spectra. For Fe films as thin as 150 Å, the magnetic moment is not different from that found in bulk α -Fe. For a 70-Å Fe film, the local magnetic moment is enhanced although the average magnetization is reduced. As doping is suspected to be the cause for the departure from bulk α -Fe properties. In the case where the 50-Å film is polycrystalline and discontinuous, spatially resolved EELS has been used to distinguish small island clusters from large crystalline particles. The large particles are α -Fe crystallites and the islands are probably also heavily affected by As doping.

I. INTRODUCTION

Epitaxially grown Fe thin films on GaAs(100) hold great promise for the integration of magnetic film technology into semiconductor and opto-electronic technologies.¹⁻³ However, many physical properties of the thin films have a strong thickness dependence and the origins of these are currently poorly understood. For example, the average magnetization per Fe atom starts to decrease from the bulk value for films as thick as 230 Å.⁴ To understand the microscopic origin of this behavior, we have to separate the intrinsic physical effects from the effect of defects, impurities, etc., associated with the growth problem. This can be achieved by studying the Fe film with a *localized magnetic probe*. In this article, we carried out such a characterization of thin and ultrathin Fe films by studying element-selective inner-shell ionization using electron-energy-loss spectroscopy (EELS).⁵ The EELS measurement is carried out using a scanning transmission electron microscope (STEM), which not only allows us to study uniformly deposited films, but also permits analysis of inhomogeneous films with high spatial resolution. All the Fe films are preserved from oxidation and degradation by encapsulation between the substrate and a top protective layer. This distinguishes us from early studies of transition metal films that are thermally evaporated with poor control for impurity and crystallinity and inevitably contains surface oxide layers. We will be able to show from the Fe 2*p* absorption, which accesses to the final states involving the Fe 3*d* conduction band, that the electronic structure of Fe films grown on the GaAs(100) surface is bulklike at 150 Å but different from the bulk for 70-Å and 50-Å ultrathin films; and that the difference is consistent with As doping.

II. EXPERIMENT

The ultrathin Fe films are deposited on a GaAs(001) substrate inside a UHV chamber with a base pressure better than 5×10^{-9} mbar during the growth. A detailed characterization of the growth process by both reflection high-energy electron diffraction (RHEED) and low-energy electron diffraction

(LEED) techniques can be found in Ref. 6. At the end of Fe deposition, the top surface is covered with a thin layer of Cr to prevent the oxidation of Fe films. To produce electron-beam-transparent samples for transmission electron microscopy and transmission electron-energy-loss analysis, the sandwich film is thinned from the substrate side only. This is achieved by either ion-beam sputtering or by chemical etching. The latter is particularly favored since a large uniform thin membrane can be produced using a thin layer (about 0.2 μ m thick) of the relatively chemically inert Ga_{0.7}Al_{0.3}As as an "etching stop" layer⁶ on top of the GaAs(100) substrate.

EELS is conducted inside a dedicated vacuum generate (VG)-HF501 STEM operating at 100 keV. The transmitted electrons are analyzed by a VG magnetic sector prism, and the spectrum is further magnified by a quadrupole lens system before being collected on a CCD (charge-coupled device)-based parallel detection system.⁷ All the spectra have been corrected for the dark current and flat-field response of the CCD camera. The convergence semiangle of the incident electron is about 7 mrad, and the collection semiangle of the spectrometer is about 8 mrad. Under such experimental conditions, inner-shell transitions of interest (O 1*s* at 530 eV, Cr 2*p* at 576 eV, and Fe 2*p* at 706 eV) all obey the dipole-selection rule. The spatial resolution of the focused electron probe is better than 5 Å and the optimal energy resolution of the EELS system is 0.3 eV.

III. RESULTS

A. Cr(25 Å)/Fe(150 Å)/GaAs(001) structure

The magnetization measurement of this 150-Å Fe film shows a pronounced fourfold anisotropy.⁸ Thin membrane of the sandwich structure is produced by chemical etching. The electron diffraction pattern is consistent with an epitaxial α -Fe film lattice-matched on a GaAs(001) substrate. The composition analysis using the theoretical cross sections⁵ for the continuum part of the Cr and Fe 2*p* absorption shows that the Fe and Cr concentrations are in the ratio 6.33, close to the expected ratio of 6.10, which is calculated from the

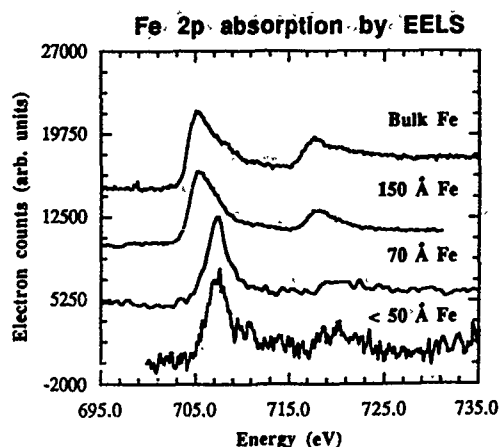


FIG. 1. The Fe 2p absorption spectra from ultrathin films of different thickness. The bulk reference spectra is taken from 2000-Å thick particles (see the text for detail).

thickness difference of the two films as measured by quartz microbalance, *in situ*. The thickness of the membrane is estimated from the low-loss spectrum to be about 300–400 Å and is very uniform. An analysis of the Cr 2p absorption spectra indicates that at least a part of Cr has been converted into oxides.⁹ The Fe 2p absorption for the thin film is shown in Fig. 1. It is similar to that for the bulk Fe absorption spectrum shown on the same figure, with the energy of the first peak at 706 eV. There is no sign of Fe oxidation since its white line would appear at much higher energies.⁹

B. Cr(25 Å)/Fe(70 Å)/GaAs(001) structure

The magnetization of this 70-Å Fe film shows a mixture of fourfold and twofold anisotropy.⁸ As there is no built-in etching stop on the GaAs substrate, ion-beam thinning was used to produce electron-beam transparent membrane. From electron diffraction analysis, the Fe film growth is again found to be epitaxial. To avoid areas where the GaAs substrate has been completely removed, we deliberately move to areas where the sandwich structure is over 700 Å thick and where signal from the GaAs substrate is unmistakable. With at least about 60 Å of the GaAs substrate still intact, the possibility of ion-beam-induced effects on the thin Fe film is very small. The Fe 2p absorption spectrum taken from this thick sample is deconvoluted to remove multiple scattering, and the result is also shown in Fig. 1. It is clear that the 70-Å Fe film is already different from the bulk and 150-Å Fe film. The first peak in the Fe 2p absorption spectrum from the 70-Å Fe film has a shoulder at 706 eV where the 2p absorption of the bulk Fe has its maximum.

C. Cr(25 Å)/Fe(50 Å)/GaAs(001) structure

This film is slightly different in its fabrication from the above two films. The GaAs wafer containing the etching-stop layer has been thinned to produce a membrane window prior to Fe deposition. The magnetization of the film is found to be isotropic⁸ and is associated with the polycrystalline nature of the film, as shown by electron diffraction. In addition, electron microscopy shows that the Fe film is discon-

tinuous and that the grains have two characteristic sizes. The Fe is mostly sparsely distributed in clusters of small islands of the order of 50 Å across. From the analysis of the ionization cross sections, using that of the Cr layer as a standard, the thickness of the Fe islands is deduced to be about 20–30 Å. The Fe 2p absorption spectrum from one of these nanometer-sized islands is shown in Fig. 1. It is similar to that of the 70-Å film, except for an additional shoulder at 710 eV. Much less numerous are the large Fe particles with diameters over several thousand angstroms. The energy-loss spectrum from the large particles has been taken as representative of the bulk Fe films and is also presented in Fig. 1 for comparison purpose.

IV. DISCUSSION

In a one-electron picture, the inner-shell transition should give information about a symmetry-projected, empty density of states localized on the excited atoms, and the result can be compared with the bandstructure calculation. In the case of Fe 2p absorption, it probes the empty density of states of the conduction band with the 3d, and to a less extent 4s character. However, strong coupling between the partially filled d band and the remaining inner-shell p electrons produce a significant distortion to the empty density of state. The spectra are dominated by two “white-line” structures separated by 12.5 eV, approximately the energy difference between the Fe 2p_{1/2} and 2p_{3/2} core levels. Information about the electronic structure of the Fe film can still be assessed in these cases. For example, the density of the conduction electrons controls the lifetime of the core hole states, hence the width of the core level transition. In bulk metal Fe (see Fig. 1), the width of the white line is quite large (3.5 eV), reflecting a large conduction electron density around Fe. It is reduced to less than 2.1 eV for the 70-Å and 50-Å films, indicating a large reduction in the density of the conduction electron. Because of this reduction in the width, the multiplet structures in the white lines becomes visible for the spectra from these two films. These are due to resonant transition from the 2p⁶3dⁿ initial states into 2p⁵3dⁿ⁺¹ final states, and are sensitive to the d-level occupancy of the Fe atom. Comparison of line shape of I₃ peak with an atomic multiplet calculation¹⁰ suggests that the average d-level occupancy (n) in the 70-Å film is 6, assuming the crystal-field effect is unimportant.

Because of the spin-orbit coupling, the branching ratio of the white lines arising from transitions from the two sub-levels of the Fe 2p state (defined as $I_3(2p_{3/2})/[I_2(2p_{1/2}) + I_3(2p_{3/2})]$) deviates from the statistical values $\frac{2}{3}$ (Ref. 11) and depends on the specific configuration of the partially filled 3d levels.⁹ Although a first-principle calculation of these effects is still not feasible for the time being, an empirical relationship has been found between the local magnetic moment per Fe atom (which depends on the 3d configuration of the Fe) and the branching ratio of the Fe 2p absorption.¹² The branching ratio of Fe 2p absorption from the bulk and 150-Å Fe is found to be 0.74 ($I_3/I_2=2.9$), in agreement with that reported from the literature.^{12,13} The corresponding branching ratio for the 70-Å Fe film is 0.83 ($I_3/I_2=5$). This indicates an enhanced magnetic moment per

atom according to the empirical relationship of Kurata and Tanaka.¹² To translate local magnetic moments into volume magnetization, we need to consider the nature of local magnetic ordering. The branching ratio of the thinner film ("50 Å") film is not available due to poor statistics of the spectrum.

The cause for the departure from the bulk Fe signal in the thin and ultrathin films is not clear. The effect of low dimensionality is unlikely in this particular case as the Fe 2*p* absorption spectra of a two monolayer and a four monolayer film on Cu(100) substrate, obtained using *in situ* x-ray absorption,¹³ is similar to that found for bulk Fe and the 150-Å film. A more likely cause maybe due to the atomic diffusion across the boundary. The Cr/Fe bilayer has been studied extensively in terms of ultrathin film, and multilayer fabrication and interdiffusion is generally not a problem. Contamination of the Fe film by more diffusive As species has been found in earlier deposition experiments,^{4,14,15} and the formation of antiferromagnetically coupled Fe₂As microcrystallites has been speculated as a possible reason for the drop of the average magnetization per atom in thin film.⁴ There are some evidence for As contamination of Fe film from *in situ* Auger spectroscopy; however, there is no electron diffraction evidence for Fe₂As microcrystalline particles in the films we have examined. On the other hand, the As-doped α -Fe is also possible in the equilibrium phase diagram of the Fe-As binary system¹⁶ and cannot be dismissed purely from our plan-view electron microscopy and EELS results. We may speculate on the electronic structure of the As-doped Fe film. Crudely speaking, the more electronegative As atom will be an electron acceptor and reduces the *d*-level occupancy in the Fe atom. This is consistent with the reduced branch ratio and decrease in the line width of the white lines in the Fe 2*p* absorption spectra from the 70- and 50-Å films. According to the empirical relationship between branch ratio and the local magnetic moment per atom, the magnetic moment per atom for the As-induced α -Fe film may actually increase (from 2.5 to 6 μ_B). This finding may not necessary be in conflict with the decrease in the average magnetization per atom, as the relationship between the two are not necessary in tandem particularly for an itinerant ferromagnetic Fe sample, since the local ordering of the atomic moments is also important and may also be affected by As doping.

V. SUMMARY

Thin Fe films grown on GaAs(100) surface have been examined by electron-microscopy-based high-energy EELS.

Special sandwich structure has been produced to prevent the oxidation of the ultrathin Fe film at ambient atmosphere. This allows, for the first time, observation of the electron-energy-loss spectrum of Fe metal films not tainted by the surface oxide. For the 150-Å film, the Fe *L*_{2,3} absorption edge is similar in shape to that obtained from the bulk. But the spectrum from the 70-Å Fe film is very different. The local magnetic moment deduced from the branching ratio of the Fe 2*p* spectrum from the 70-Å Fe film is higher than that from the bulk. For the 50-Å film examined, the magnetization behavior is isotropic because the film is polycrystalline. The film is also discontinuous and has two distinct grain sizes. The electronic structure of the small Fe islands (about 50 Å across) is similar to that of the 70-Å Fe film. The larger grains have diameters of the order of thousand angstroms and bulklike properties. The exact nature of the electronic structure of the deposited Fe films are still under investigation. It is suspected that the changes are partially caused by the proximity of the interface and the related As diffusion across the boundary, which can induce both doping as well as alloying.

¹J. M. Florczak and E. D. Dahlberg, Phys. Rev. B **44**, 9338 (1991).

²G. A. Prinz and J. J. Krebs, Appl. Phys. Lett. **39**, 397 (1981).

³K. T. Riggs, E. D. Dahlberg, and G. A. Prinz, J. Magn. Magn. Mat. **73**, 46 (1988).

⁴J. J. Krebs, B. T. Jonker, and G. A. Prinz, J. Appl. Phys. **61**, 2596 (1987).

⁵R. F. Egerton, *Electron Energy Loss Spectroscopy in the Electron Microscope* (Plenum, New York, 1986).

⁶E. Gu, C. Daboo, J. A. C. Bland, M. Gester, A. J. R. Ives, L. M. Brown, and J. N. Chapman, J. Magn. Magn. Mater. **126**, 180 (1993).

⁷D. McMullan, J. M. Rodenburg, Y. Murooka, and A. J. McGibbon, Inst. Phys. Conf. Ser. **98**, 55 (1989).

⁸C. Daboo, R. J. Hicken, D. E. P. Eley, M. Gester, S. J. Gray, A. J. R. Ives, and J. A. C. Bland (these proceedings).

⁹R. D. Leapman, L. A. Grunes, and P. Fejes, Phys. Rev. B **26**, 614 (1982).

¹⁰G. van der Laan and I. W. Kirkman, J. Phys. Condens. Mat. **4**, 4189 (1992).

¹¹R. D. Leapman and L. A. Grunes, Phys. Rev. Lett. **45**, 397 (1980).

¹²H. Kurata and N. Tanaka, Microsc. Microanal. Microstruct. **2**, 183 (1991).

¹³J. G. Tobin, G. D. Waddill, and D. P. Pappas, Phys. Rev. Lett. **68**, 3642 (1992).

¹⁴J. R. Waldrop and R. W. Grant, Appl. Phys. Lett. **34**, 630 (1979).

¹⁵S. A. Chambers, F. Xu, H. W. Chen, S. B. Komurov, S. B. Anderson, and J. H. Weaver, Phys. Rev. B **34**, 6605 (1986).

¹⁶F. A. Shunk, *Constitution of Binary Alloys*, 2nd suppl. (McGraw-Hill, New York, 1969).

Effect of interface on the properties of Ti/NiFe thin films

Shuxiang Li, Minglang Yan, Chengtao Yu, and Wuyan Lai

Institute of Physics, Chinese Academy of Sciences, P.O. Box 603, Beijing 100080, China

The microstructure, anisotropic magnetoresistance, and magnetic properties of Ti/Ni₈₁Fe₁₉ thin films have been investigated with respect to annealing temperatures (T_A) up to 450 °C as well as to anneal times (t_A). It has been shown that 120 °C is the optimum annealing temperature and that t_A has no significant influence on the properties with annealing at 270 °C. Auger depth profiling was used to study interdiffusion kinetics. The diffusivity D and activation energy ϵ have been estimated at about 2.0×10^{-17} cm²/s and 1.69 eV, respectively.

I. INTRODUCTION

The polycrystalline NiFe thin film is of technological importance because of its unique soft magnetic properties. In particular, it is a popular sensor material for magnetoresistive (MR) sensors because of its small magnetostriction and large anisotropic magnetoresistance. The reliability of MR sensors not only depends on anisotropic magnetoresistance (AMR) values (actually in the percent regime), but also on other properties, such as magnetic properties and the sensitivity to temperature or stress of the sensor material. In order to have better adhesion to gold contacts, NiFe films are often used with an overlayer of another metal such as Ti or Ta. In the photolithographic process of patterning, films are often exposed to temperatures above 200 °C. This probably changes characteristics of interface and stress, and then reduces AMR. On the other hand, a suitable annealing treatment can reduce bulk resistance, and it is beneficial to improve the AMR. Narayan *et al.*¹ have investigated the effect of annealing of Ti/NiFe composites qualitatively and pointed out that the limit of T_A for this composite is less than 300 °C. Hashim and Atwater² have studied the interdiffusion of a Ta/NiFe multilayer using x-ray diffraction and obtained D and ϵ quantitatively.

In this article, the microstructure, magnetic properties, and anisotropic magnetoresistance of Ti/Ni₈₁Fe₁₉ thin films have been studied with respect to annealing temperatures T_A up to 450 °C as well as to anneal times t_A with annealing at 270 °C. The diffusivity D and activation energy ϵ have been calculated. The AMR and magnetic properties are improved with T_A up to 120 °C. These properties, however, become slightly inferior with a further increase of T_A in the range from 120 to 450 °C. The values of D and ϵ show that the interdiffusion between Ti and NiFe is slower than that of Ta in NiFe reported in Ref. 2. Interdiffusion, elimination of stress, etc., may account for the variation of properties.

II. EXPERIMENT

A Ti(20 nm)/NiFe(100 nm) film was deposited on a glass substrate using dc magnetron sputtering. The deposition rate was about 1.5 Å/s. In order to distinguish interface effects from bulk effects, a NiFe layer was deposited on a glass substrate at a temperature of 470 °C and held at the same temperature for 1 h to homogenize the structure; then a Ti layer was deposited on the NiFe layer when the substrate was cooled to 40 °C. There were two procedures in annealing treatment: (1) t_A was fixed at 3 h, and T_A was taken as 120,

220, 290, 360, and 420 °C; (2) T_A was fixed at 270 °C, and t_A was taken as 1, 2, 4, 6, and 8 h. All annealing treatments were carried out in a vacuum annealing furnace after achieving a base pressure of 5×10^{-6} Torr. The crystal structure was determined by x-ray diffraction. The resistance was measured at room temperature with a four-point probe on unpatterned stripes cut from the glasses. The compositional profiles were obtained by Auger depth profiling. The diffusivity D and activation energy ϵ were calculated from the compositional profiles.

III. RESULTS AND DISCUSSION

The x-ray diffraction pattern of the as-deposited Ti/NiFe film is shown in Fig. 1. It indicates that the Ti/NiFe film has already developed texture in the (002) orientation of hcp Ti and the dominant (111) orientation of fcc NiFe. The lattices between NiFe and Ti match well, which results in a minimum interface stress. Narayan *et al.*¹ found that the annealed NiFe film has texture in the (111) orientation too. Figure 2 shows the dependence of the AMR and saturation field H_s on annealing temperature T_A . It demonstrates that the AMR increases with an increase of T_A and then decreases slowly with a further increase of T_A . There is a maximum AMR of 3.1% with a minimum saturation field of 7.5 Oe at 120 °C. There are no sharp changes of the AMR and magnetic properties from 120 to 450 °C. In fact, the AMR is inversely proportional to the resistivity of the polycrystalline permalloy film, ρ , which is affected by surface scattering and grain-boundary scattering.³ ρ can be significantly reduced by an annealing treatment because of grain growth and the elimi-

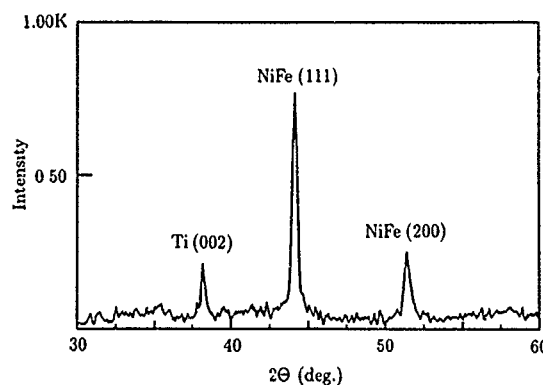


FIG. 1. X-ray diffraction pattern of an as-deposited Ti/NiFe film.

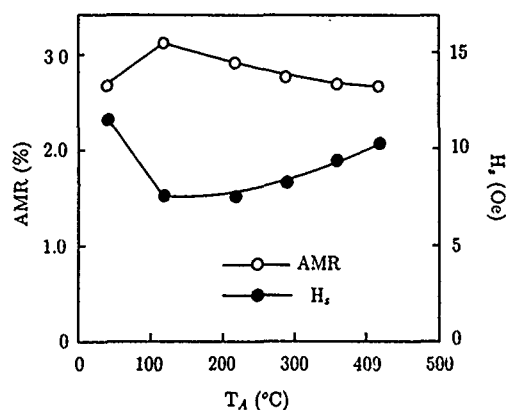


FIG. 2. The dependences of the AMR and saturation field H_s on annealing temperature T_A .

nation of crystal defects, whereas $\Delta\rho$ is almost unchanged by annealing treatment. With T_A up to 120 °C, the interface stress and crystal defects within the interface between Ti and NiFe layers are eliminated partially, so that the AMR is increased and soft magnetic properties are improved. It may be expected that the AMR should increase more with a further increase of T_A because ρ will decrease due to the consequent elimination of interface stress. The AMR, however, unexpectedly decreases with a further increase of T_A . This probably can be attributed to interdiffusion between NiFe and Ti. On the other hand, the AMR is almost unchanged with an increase of annealing time t_A with annealing at 270 °C. This result is due to the fact that the interdiffusion tends to be stable and the diffusion depth increases very slowly in this temperature range. In order to clarify the role of interdiffusion, Auger depth profiling was studied.

The Auger depth profiles (see Fig. 3) of Ti/NiFe films before and after annealing at 120 and 360 °C for 3 h show that the interface thicknesses (t_{in}) of Ti/NiFe increase about 36% and 40%, respectively, due to the annealing treatment. It is indicated that the increment of t_{in} is small when the annealing temperature T_A is above 120 °C, which is consistent with the temperature dependence of the AMR and H_s shown in Fig. 2. All these findings demonstrate that interdiffusion plays an important role in the variation of properties.

According to the Auger depth profiles of Ti/NiFe films annealed at 270 °C for 1, 2, 4, 6, and 8 h, the diffusivity D was calculated using the resolution of diffusion equation as follows:

$$C(x, t) = \frac{2}{\sqrt{4\pi Dt}} \int_0^\infty f(\xi) \exp\left(-\frac{(x-\xi)^2}{4Dt}\right) d\xi, \quad 0 \leq \xi \leq \infty \quad (1)$$

and

$$\overline{x^2} = 2Dt, \quad (2)$$

where $C(x, t)$ is the concentration, $f(\xi)$ is the distribution of the concentration before diffusion, D is diffusivity, t is time, and x is depth profile. D was calculated to be about 2.0×10^{-17} cm²/s. From the results of $D(T)$, the activation energy ϵ was estimated at 1.69 eV. Information on Ni and Fe

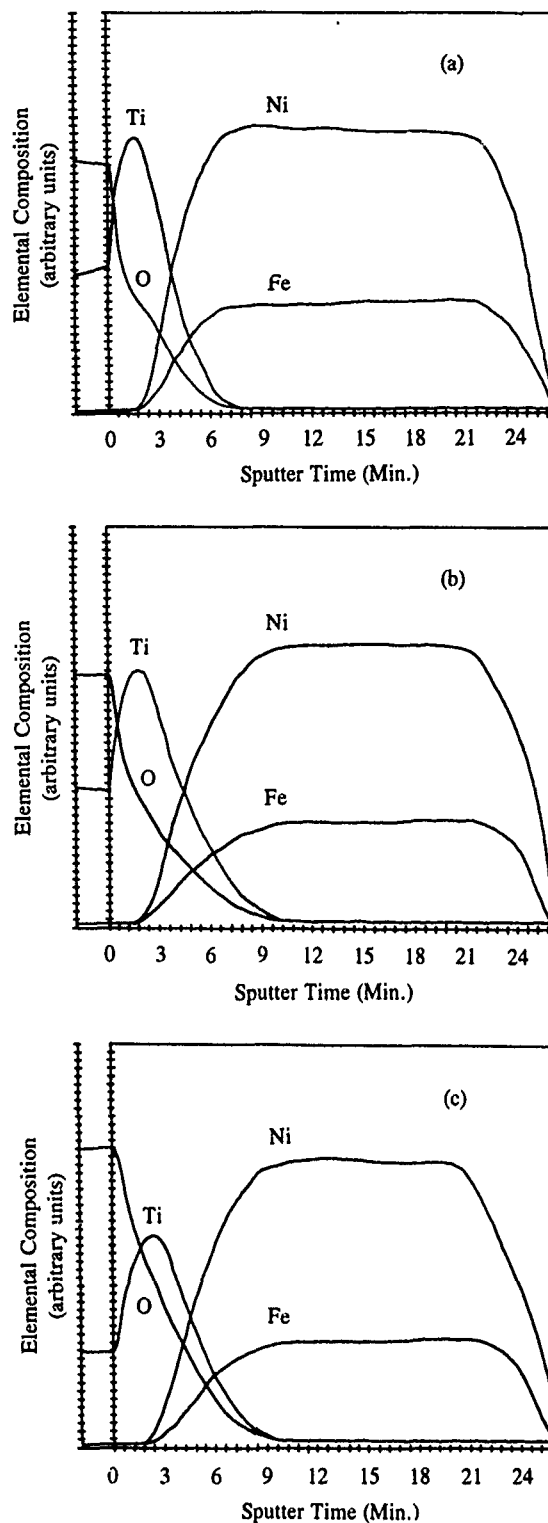


FIG. 3. Auger depth profiles of the film (a) as-deposited, and (b) and (c) annealed at 120 and 360 °C for 3 h, respectively.

lattice diffusion in Ti or vice versa is unavailable, but the activation energy for lattice self-diffusion in Ni (Ref. 4) has been reported to be 2.27 eV. Typically, the activation energy for grain-boundary diffusion is significantly less than that for lattice diffusion: $\epsilon_{gb} \approx (0.4-0.7)\epsilon_{lat}$.⁵ This suggests that grain-boundary diffusion between Ti and NiFe is dominant when T_A is below 450 °C. On the other hand, because the crystal structure is perfect enough before annealing, the

grain-boundary diffusion is restrained, so that the interdiffusion is very slow and D is small in our temperature range. It is confirmed that the AMR and H_s are not affected obviously by the anneal time t_A . Another result obtained is that the diffusion of Ti in NiFe is slower than that of Ta in NiFe reported by Hashim and Atwater.² Ti is a good material when used with sensor material NiFe magnetic layers.

In summary, our as-deposited Ti/Ni₈₁Fe₁₉ film possesses good texture, which results in high AMR and low saturation field. With annealing at 120 °C for 3 h, both maximum AMR, 3.1%, and minimum saturation field, 7.5 Oe, are obtained. The variation of AMR and H_s is small when T_A is in the 120–450 °C range. The diffusivity D and activation energy ϵ are estimated at about 2.0×10^{-17} cm²/s and 1.69 eV,

respectively. It is concluded that the interdiffusion between Ti and NiFe is very slow.

ACKNOWLEDGMENT

This research is supported by the Chinese National Laboratory of Magnetism in Beijing.

¹P. B. Narayan, R. D. Silkens, S. Bryant, and S. Dey, IEEE Trans. Magn. **28**, 2934 (1992).

²I. Hashim and H. A. Atwater, Mater. Res. Soc. Symp. Proc. **232**, 159 (1991).

³A. F. Mayadas and M. Shatzkes, Phys. Rev. B **1**, 1382 (1970).

⁴R. Hoffman, F. Pickus, and R. Wood, Trans. AIME **206**, 483 (1956).

⁵P. G. Shewmon, *Diffusion in Solids* (Williams Book Company, Jenks, 1983), p. 164.

Magnetization reversal in compositionally modulated Tb/Fe multilayers (abstract)

Roger D. Kirby, J. X. Shen, and D. J. Sellmyer

Behlen Laboratory of Physics and Center for Materials Research and Analysis, University of Nebraska, Lincoln, Nebraska 68588-0111

We have prepared compositionally modulated Tb(X Å)/Fe(5 Å) thin film multilayers with X ranging from 3.5 to 7 Å by magnetron sputtering on glass substrates. Magnetization measurements using SQUID and alternating gradient force magnetometers show that these samples have uniaxial anisotropies (K_u) up to 10^7 erg/cm³ and saturation magnetizations (M_s) between 50 and 350 emu/cm³. Constant field magnetization reversal measurements at room temperature show that these samples reverse by slow nucleation followed by relatively rapid domain wall motion. The samples with larger uniaxial anisotropies and smaller saturation magnetizations reverse completely for applied fields less than the coercivity, while those samples on the other end of the spectrum do not. The magnetization reversal curves are correlated with the shapes of the hysteresis loops, and the experimental results are interpreted using a recently developed uniaxial anisotropy model of magnetization reversal.¹

Research sponsored by the NSF under Grant No. DMR-8918889 and by the Research Corporation.

¹R. D. Kirby, J. X. Shen, R. J. Hardy, and D. J. Sellmyer, Phys. Rev. B (to be published).

Remanence and coercivity in exchange coupled amorphous R-TM/Fe bilayers and multilayers (abstract)

Hong Wan, A. Tsoukatos, and G. C. Hadjipanayis^{a)}

Department of Physics and Astronomy, University of Delaware, Newark, Delaware 19716

We have investigated the hysteresis behavior of rare-earth (R)-transition metal (TM) bilayers and multilayers consisting of a fine mixture of hard and soft phases. The films with bilayer thickness in the range of 5–100 Å were fabricated using a dc sputtering system. X-ray diffraction was used to check the crystal structure and multilayer structure. The magnetic properties were measured with a SQUID magnetometer in the temperature range of 10–300 K with fields up to 55 kOe. A strong exchange coupling between the hard magnetic phase (R-TM) and the soft phase (Fe) leads to a smooth hysteresis loop in samples with a certain thickness range. The remanent magnetization is enhanced significantly at the expense of a reduced coercivity. For example, in NdFe/Fe multilayer films, the reduced remanence increases from 0.63 to 0.92 at 10 K while the coercivity decreases from 9.3 to 1 kOe as the Fe layer thickness is varied from 0 to 10 nm. The effect of interface roughness on the exchange coupling has been investigated via different sputtering pressures and rates. The dependence of magnetic hysteresis on the layer thickness and temperature has been examined and the results will be reported.

^{a)}Work supported by NSF DMR-8917028.

Paramagnetic/ferromagnetic transition of Co/Cu(001) films during growth (abstract)

F. O. Schumann, M. E. Buckley, and J. A. C. Bland
Cavendish Laboratory, Madingley Road, Cambridge CB3 0HE, United Kingdom

We have investigated paramagnetism in epitaxial Co/Cu(001) films grown at room temperature in ultrahigh vacuum (UHV) using the transverse magneto-optical Kerr effect. These measurements are made possible by the very strong magnetic response¹ of a two-dimensional (2D) paramagnet, and in this way we have extended our previous study of the thickness dependent coercivity close to the magnetic phase transition.² The optical reflectivity was used to determine the thickness in reduced units d/d_c to better than 10% accuracy where the critical thickness d_c is determined by the onset of long-range order. In the paramagnetic region we observe a linear $M-H$ curve with a sensitively thickness dependent saturation field H_s , which decreases to zero as the critical thickness d_c is approached. At the critical point, the onset of long range order is manifested by a strongly thickness-dependent coercive field H_c , which is found to increase from zero with thickness as a power law.²

¹D. Kerkmann, D. Pescia, and R. Allenspach, Phys. Rev. Lett. 68, 686 (1992).

²F. O. Schumann and J. A. C. Bland, J. Appl. Phys. 73, 594 (1993).

Photothermally modulated ferromagnetic resonance investigations of epitaxially grown thin films (abstract)

R. Meckenstock, F. Schreiber, O. von Geisau, and J. Pelzl
Institut für Experimentalphysik III, Ruhr-Universität, 44780 Bochum, Germany

Photothermally modulated (PM) ferromagnetic resonance (FMR) is applied, for the first time, to locally investigate the magnetic anisotropy of thin epitaxially grown Fe and Co films. The PM-FMR measurements were performed at 9.2 GHz in an optical cavity. The microwave resonance absorption was thermally modulated by an intensity modulated laser beam and the change of the microwave power reflected at the cavity was synchronously detected by a lock-in amplifier. By focusing the laser beam a lateral resolution of 20 μm could be achieved. The PM-FMR signal was studied as a function of the position of the laser spot on the film, of the modulation frequency (10 Hz–10 MHz) and of the temperature. The PM-FMR measurements were complemented by temperature (5–700 K) and angle dependent conventional FMR studies. The temperature variation of the PM-FMR and its comparison with the behavior of the conventional signal yields evidence for a signal generation process of the PM-FMR that is governed by anisotropy effects. Therefore the local variation of the PM-FMR signal was used to deduce the lateral inhomogeneity of the magnetic anisotropy in the plane of the films.

Work supported partly by the Deutsche Forschungsgemeinschaft, SFB 166.

Structural and magnetic characteristics of $\text{Co}_{81}\text{Cr}_{19}/\text{Al}$ multilayers deposited by plasma-free sputtering with Kr gas (abstract)

Takakazu Takahashi

Department of Electronic and Computer Engineering, Faculty of Engineering, Toyama University, 3190, Gofuku, Toyama-shi, Toyama 930, Japan

Masahiko Naoe

Department of Physical Electronics, Faculty of Engineering, Tokyo Institute of Technology, 2-12-1, O-okayama, Meguro-ku, Tokyo 152, Japan

In multilayers deposited by sputtering, interfaces between each layer are necessary to be extremely sharp and flat. Therefore, the kinetic energy and number of sputtering gas atoms and ions recoiled from the target plane must be satisfactorily decreased. So, in this study, Kr, which is heavier than both Co and Cr in atomic weight, was used as a sputtering gas, while Ar used in conventional sputtering is lighter than them. The $\text{Co}_{81}\text{Cr}_{19}/\text{Al}$ multilayers have been prepared on plasma-free glass slide substrate at room temperature by alternately depositing $\text{Co}_{81}\text{Cr}_{19}$ and Al layers, using the facing targets sputtering (FTS) apparatus. The thickness of $\text{Co}_{81}\text{Cr}_{19}$ layer $l_{\text{Co-Cr}}$ was varied in the range of 45–140 Å, while the thicknesses of Al layer l_{Al} were approximately 7 and 14 Å. The total layer thickness was in the range of 1450–1530 Å. It has been found from the small angle x-ray diffraction diagrams and the scanning electron microscope (SEM) images that the clear periodic structure could be formed in all specimen multilayers. In the multilayers with l_{Al} of 7 Å, the $\text{Co}_{81}\text{Cr}_{19}$ layers were intrinsically composed of hcp phase crystallites with c -axis orientation $\Delta\theta_{50}$ normal to the layer plane ranging from 5.4 to 8.4. In the multilayers with l_{Al} of 14 Å, the $\text{Co}_{81}\text{Cr}_{19}$ layers seemed to be composed of hcp phase crystallites with very large $\Delta\theta_{50}$ of which value could not be estimated. However, for all specimen multilayers, the interplanar spacing between (002) planes $d_{(002)}$ were in the range of 2.033–2.038 Å. These values were nearly equal to those of $\text{Co}_{81}\text{Cr}_{19}$ single layer films (2.035 Å). M_s and H_c were significantly varied in the range of 500–1150 emu/cc and 35–260 Oe, respectively. In the multilayers with l_{Al} of 7 Å, $(Mr/Ms)_1$ was in the range of 0.28–0.36 and the perpendicular magnetic anisotropy was rather remarkable. On the other hand, in the multilayers with l_{Al} of 14 Å, $(Mr/Ms)_1$ was in the range of 0.61–0.7 and the in-plane magnetic anisotropy was significantly dominant. Co-Cr grains for l_{Al} of 14 Å were finer than those for l_{Al} of 7 Å. These results may indicate that the kinetic energy and number of atoms and ions recoiled from the target plane were significantly decreased by using Kr instead of Ar. So, the multilayers deposited by sputtering with Kr gas had excellently sharp and flat interfaces suitable for use of the apparent magnetoresistance effect.

Effects of exchange bond disorder on transport measurements

P. A. Stampe, H. Ma,^{a)} H. P. Kunkel, and G. Williams

Department of Physics, University of Manitoba, Winnipeg MB R3T 2N2, Canada

Measurements of the low field resistive anisotropy (LFRA) in amorphous $\text{Fe}_{91}\text{Zr}_9$ with and without hydrogen loading are presented. The temperature dependence of these data is compared with model calculations of the quadrupolar term $[\langle S_z^2 \rangle_T - S(S+1)/3]$, from which it is concluded that the model calculations reproduce both the temperature and the exchange bond dependence of this transport coefficient.

I. INTRODUCTION

The influence of exchange bond disorder on the magnetic properties of interacting spin systems has been studied extensively from both an experimental and a theoretical standpoint for a number of years.^{1,2} Briefly, in the frequently quoted approach³ in which the exchange bond distribution is approximated by a Gaussian with first and second moments \bar{J}_0 and \bar{J} respectively, models predict that the ground state of the system is a ferromagnet when the ratio $\eta = \bar{J}_0/\bar{J} \gg 1$, a spin-glass when $\eta < 1$, while for $1 < \eta < 2$ sequential paramagnetic to ferromagnetic to (transverse) spin-glass transitions occur on cooling. Many of these predictions are in agreement with experiment; in systems with $\eta \gg 1$ a well defined paramagnetic to ferromagnetic phase transition is observed at temperature $T_c(\propto \bar{J}_0)$, often exhibiting asymptotic critical exponents close to the values predicted by the isotropic, 3d Heisenberg model⁴ (in agreement with the Harris criterion⁵). Away from the critical point the influence of the exchange distribution can be seen in a marked temperature dependence of the effective exponent.^{2,6} Experiments on systems with $\eta < 1$ now appear to agree that a true phase transition occurs at temperature $T_{sg}(\propto \bar{J})$ marked by a divergence in the nonlinear response (reflecting a more complex order parameter/function). Experiments on sequential transitions, however, remain controversial.

By contrast much less effort has been directed towards understanding the transport properties of these systems; those few model approaches that have been investigated have focused primarily on the effects of disorder on scattering from low-lying collective excitations,^{7,8} i.e., at temperatures well below the transition temperature.

Here we report the results of the effects of exchange bond disorder on a novel transport coefficient—the low field anisotropy in the magnetoresistance—and compare the results of model calculations with measurements on amorphous $\text{Fe}_x\text{Zr}_{1-x}$ ($x \approx 0.1$) with and without hydrogen loading. Fe-Zr is a well-known system in which simple hydrogenation can convert a non-collinear ferromagnet to a uniform

ferromagnet reflecting a narrowing of the exchange bond distribution (i.e., an increase in η).

II. DESCRIPTION OF MODEL

The low field resistive anisotropy (LFRA) is given by the ratio

$$\frac{\Delta\rho(H_a)}{\rho_0} = \left\{ \frac{3[\rho_{\parallel}(H_a) - \rho_{\perp}(H_a)]}{\rho_{\parallel}(H_a) + 2\rho_{\perp}(H_a)} \right\} \quad (1)$$

for a single small applied field $\mu_0 H_a$. This ratio differs from the more well established spontaneous resistive anisotropy (SRA), defined as

$$\frac{\Delta\rho(B)}{\rho_0} = \left\{ \frac{3[\rho_{\parallel}(B) - \rho_{\perp}(B)]}{\rho_{\parallel}(B) + 2\rho_{\perp}(B)} \right\}_{B \rightarrow 0} \quad (2)$$

in which the extrapolation implicit in Eq. (2) is not only based on the induction⁹ B , but also utilizes the variation of ρ_{\parallel} and ρ_{\perp} above technical saturation in making this extrapolation¹⁰. We advocate the use of the former in characterizing the behaviour of spin systems near a potential transition where the application of a large field/induction can significantly alter the intrinsic spin configuration/polarization.

The occurrence of a magnetoresistive anisotropy requires two basic ingredients, an internal/external field to polarize the spin system and spin-orbit coupling (and hence an orbital component) at scattering centers. Both localized and itinerant models have been used to analyze the SRA, but the origin of the anisotropy is more easily understood and calculated from localized approaches. Orbital components are associated with non spherical charge distributions, and a multipole moment analysis of such a distribution indicates that the lowest order contribution to the anisotropy/asymmetry arises from the electric quadrupole moment (the electric dipole term vanishes in a central potential). The corresponding Hamiltonian \mathcal{H} for conduction electron scattering from state \mathbf{k} to \mathbf{k}' can then be written as¹¹

^{a)}Present address: Department of Electrical Engineering, University of Toronto, Toronto ON M5S 1A4, Canada.

$$\mathcal{H} = \sum_{\mathbf{k}, \mathbf{k}'} \left[V + JS \cdot \boldsymbol{\sigma} - \frac{D}{k_F^2} \{ (\mathbf{S} \cdot \mathbf{k})(\mathbf{S} \cdot \mathbf{k}') - S(S+1) \mathbf{k} \cdot \mathbf{k}' / 3 \} \right] a_{\mathbf{k}}^+ a_{\mathbf{k}} \quad (3)$$

in which V represents the screened Coulomb potential at the scattering site, $JS \cdot \boldsymbol{\sigma}$ the familiar exchange/magnetic dipole coupling between a localized spin (\mathbf{S}) and a conduction electron (spin $\boldsymbol{\sigma}$), with the final term describing scattering from the electric quadrupole moment D . In the often realized limit $V \gg J, D$ the associated anisotropy becomes¹¹

$$[\rho_{\parallel}(B) - \rho_{\perp}(B)] / \rho_0 \approx \left(\frac{D}{V} \right) [\langle S_z^2 \rangle - S(S+1)/3] \quad (4)$$

as the first two terms in \mathcal{H} are isotropic in polycrystal/amorphous systems; this anisotropy exhibits the familiar $(3 \cos^2 \theta - 1)$ angular variation expected from quadrupolar effects with axial symmetry about the field direction¹².

The localized model that we have investigated utilizes an effective field Ising approach¹³ incorporating a uniform external field h_a , random local spin-spin exchange coupling J_{ij} , and arbitrary spin quantum number S . The J_{ij} 's are assumed to be Gaussian distributed, as discussed above, leading to a set of coupled equations¹⁴ for the thermal and exchange averaged magnetization $m = \langle \langle S_z \rangle_T \rangle_J$ and the parameter $q = \langle \langle S_z^2 \rangle_T \rangle_J$:

$$m(h, T) = (2\pi)^{-1/2} \int_{-\infty}^{\infty} S B_s(x) \exp(-\alpha^2/2) d\alpha; \quad (5)$$

$$q(h, T) = (2\pi)^{-1/2} \int_{-\infty}^{\infty} S^2 B_s^2(x) \exp(-\alpha^2/2) d\alpha$$

in which the argument x of the Brillouin function $B_s(x)$ is given by $x = S(\bar{J}_0 m + \bar{J} \alpha \sqrt{q} + h_a) / k_B T$. In such a model the thermal average implicit in Eq. (4) is replaced by the double average $\langle \langle S_z^2 \rangle_T \rangle_J$. Furthermore, due to the limitations imposed by the Ising characteristics of the model,¹⁵ the ratio \bar{J}_0 / \bar{J} has been kept larger than 1.25 so that a paramagnetic to ferromagnetic transition alone occurs on cooling.

III. EXPERIMENTAL DETAILS AND RESULTS

The measurements presented here were carried out on a ribbon sample of amorphous $\text{Fe}_{91}\text{Zr}_9$ with and without hydrogen loading; details of the melt spinning¹⁶ and loading¹⁷ techniques have given previously. The specimens, of approximate dimensions $(32 \times 1 \times 0.02) \text{ mm}^3$, were mounted so that the measuring current flowed along the largest dimension, and the low field longitudinal (\parallel) and transverse (\perp) magnetoresistance measured (using an ac technique¹⁷) by rotating an electromagnet (the field was applied along the two larger sample dimensions). The remanent field of the magnet ($\mu_0 H_r \approx 5 \text{ mT}$) introduces no significant modification to either the intrinsic spin alignment or the conduction electron trajectories; basically it is used simply to render the sample single domain over distances comparable to a mean-free path.

Figure 1 summarizes measurements of the LFRA

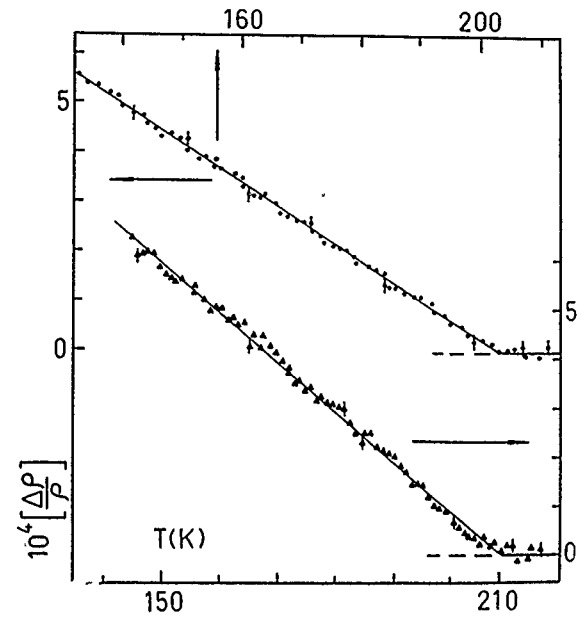


FIG. 1. The low field resistive anisotropy $\Delta\rho(H_r)/\rho_0$ plotted against temperature $T(\text{K})$ in the vicinity of the Curie temperature for amorphous $\text{Fe}_{91}\text{Zr}_9$ with (▲) and without (●) hydrogen loading. The lines drawn correspond to values of the coefficient $A(\eta)$ (see the text) of 21×10^{-4} and 16×10^{-4} respectively.

$[\rho_{\parallel}(H_r) - \rho_{\perp}(H_r)] / \rho_0$ in the temperature interval immediately below T_c . The latter temperature was estimated from the temperature at which the LFRA first vanished, and confirmed by detailed field and temperature-dependent ac susceptibility measurements.¹⁸ This agreement, incidentally, confirms that the polarizing field in the present experiment is the exchange field, which collapses at T_c . Figure 1 clearly demonstrates that immediately below T_c the LFRA $\Delta\rho(H_r)/\rho_0$ can be expressed as

$$\Delta\rho(H_r)/\rho_0 = A(\eta)(T_c - T)/T_c \quad (6)$$

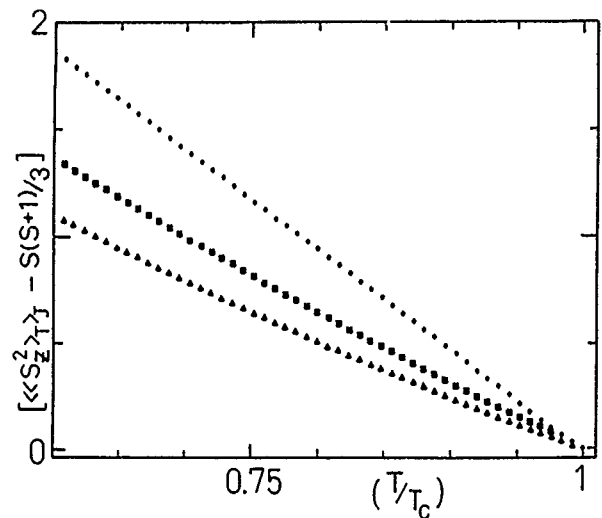


FIG. 2. The calculated variation of the quadrupolar term with reduced temperature for η values of 5 (●), 1.67 (■) and 1.25 (▲); these calculations use a local spin value of $S = 5/2$ and an applied field of 5 mT (when $T_c = 200 \text{ K}$).

with the coefficient $A(\eta)$ increasing with hydrogen loading. The introduction of hydrogen is known to not only increase T_c (and hence \bar{J}_0 —as can be seen from Fig. 1) but also to suppress the so-called reentrant transition,¹⁹ thus reducing \bar{J} . Specifically then, the coefficient $A(\eta)$ increases as the ratio $\eta = \bar{J}_0/\bar{J}$ decreases. Additional measurements support this conclusion.^{17,18}

Figure 2 reproduces calculations of the quadrupolar term $[\langle S_z^2 \rangle_T - S(S+1)/3]$ plotted as a function of reduced temperature $t = T/T_c$, a natural parameter of the model described above. A comparison of Figs. 1 and 2 indicates that these model calculations not only reproduce the essentially linear increase of the LFRA with decreasing temperature immediately below T_c , but they also replicate the increase in the coefficient $A(\eta)$ (the slope of the plots shown in Fig. 1) with decreasing bond disorder, viz. increasing η .

It is important to bear in mind in making this comparison that it is the ratio $\Delta\rho(H_r)/\rho_0$ which is compared with the quadrupolar term. As indicated in Eq. (6), by taking this ratio the details of the band structure are removed as they contribute in the same way to both $\Delta\rho(H_r)$ and ρ_0 ; however as is also clear from this equation, the ratio of the two coupling constants (D/V) is involved in the relationship between the LFRA ratio and the quadrupolar term. In making the above comparison it is assumed that the term (D/V) is basically unchanged on hydrogenation, an assumption we suggest is reasonable based on the following observations. The amount of hydrogen introduced in the present experiment was deliberately kept small—we have no direct means of measuring the hydrogen uptake, but the increase in T_c following charging in the present experiment (~ 7 K) is far less than that accompanying complete loading¹⁹ (~ 200 K). The room temperature resistivity was also monitored before and after charging, and it remained essentially unchanged between 120–125 $\mu\Omega$ cm within experimental error (typically $\leq 5\%$, due primarily to shape factor uncertainties). From this it is inferred that ρ_0 —and hence V —remains unchanged, so that the above assumptions appear to be valid provided D is not significantly altered. We know of no direct means to estimate this parameter, but naive arguments suggest at least qualitatively that the introduction of impurities of low atomic number might be expected to weaken the overall influence of spin-orbit effects—and hence reduce the anisotropy—rather than enhance them as observed.

IV. CONCLUSIONS

Measurements of the LFRA in $\text{Fe}_{91}\text{Zr}_9$ with and without hydrogen loading are compared with model calculations of the quadrupolar term $[\langle S_z^2 \rangle_T - S(S+1)/3]$. These calculations reproduce not only the linear increase in the LFRA with decreasing temperature immediately below T_c , but also the increase in magnitude of the LFRA with hydrogen loading. Such transport measurements can thus provide useful information on the extent of the exchange bond variance in disordered conductors. The full extent of this usefulness will be determined by future experiment and model calculation.

ACKNOWLEDGMENTS

Support for this work from the Natural Sciences and Engineering Research Council (NSERC) of Canada and the Board of Graduate Studies at the University of Manitoba (to P. A. Stampe and H. Ma) is gratefully acknowledged.

- ¹ K. Binder and A. P. Young, *Rev. Mod. Phys.* **58**, 801 (1986).
- ² S. N. Kaul, *J. Magn. Magn. Mater.* **53**, 5 (1985).
- ³ D. Sherrington and S. Kirkpatrick, *Phys. Rev. Lett.* **35**, 1792 (1975).
- ⁴ L. C. LeGuillou and J. Zinn-Justin, *Phys. Rev.* **B21**, 3976 (1980).
- ⁵ A. B. Harris, *J. Phys. C* **7**, 1671 (1974).
- ⁶ G. Williams, in *Magnetic Susceptibility of Superconductors and Other Spin Systems*, edited by R. A. Hein *et al.* (Plenum, New York, 1991), p. 475 *et seq.*
- ⁷ P. D. Long and R. E. Turner, *J. Phys. C (Suppl.)* **3**, S127 (1970).
- ⁸ N. Rivier and K. Adkins, *J. Phys. F* **5**, 1745 (1975).
- ⁹ J. W. F. Dorleijn, *Philips Res. Rep.* **31**, 287 (1976).
- ¹⁰ O. Jaoul, I. A. Campbell, and A. Fert, *J. Magn. Magn. Mater.* **5**, 23 (1977).
- ¹¹ A. Friederich and A. Fert, *Phys. Rev. Lett.* **33**, 1214 (1974).
- ¹² I. A. Campbell and A. Fert, in *Ferromagnetic Materials*, edited by E. P. Wohlfarth (North-Holland, Amsterdam, 1982), Vol. 3, p. 747 *et seq.*
- ¹³ B. W. Southern, *J. Phys. C* **9**, 4011 (1976); T. Kaneyoshi, *ibid.* **8**, 3415 (1975).
- ¹⁴ R. M. Roshko and G. Williams, *J. Phys. F* **14**, 703 (1984).
- ¹⁵ J. R. L. de Almeida and D. J. Thouless, *J. Phys. A* **11**, 983 (1978).
- ¹⁶ Z. Altounian, E. Batalla and J. O. Ström-Olsen, *J. Appl. Phys.* **59**, 3548 (1986).
- ¹⁷ H. Ma, Z. Wang, H. P. Kunkel and G. Williams, *J. Phys. Condensed Matter* **4**, 1993 (1992).
- ¹⁸ H. Ma, H. P. Kunkel and Gwyn Williams, *J. Phys. Condensed Matter* **3**, 5563 (1991); P. A. Stampe, H. P. Kunkel, and G. Williams, *J. Phys.: Condens. Matter* **5**, L625 (1993).
- ¹⁹ D. H. Ryan, J. M. D. Coey, E. Batalla, and J. O. Ström-Olsen, *Phys. Rev. B* **35**, 8630 (1987).

Electrical resistivity and local magnetic order in random anisotropy amorphous ferromagnets

V. S. Amaral, J. B. Sousa, and J. M. Moreira

Centro de Física da Universidade do Porto, Faculdade de Ciências, 4000 Porto, Portugal

B. Barbara and J. Filippi

Laboratoire de Magnétisme Louis Néel, CNRS, BP166X, 38042 Grenoble Cedex 9, France

In ferromagnetic systems with random anisotropy (RA), long-range magnetic order is destroyed and the correlation function of the magnetization exhibits an exponential form e^{-r/R_f} , where the correlation length R_f corresponds to the size of Imry-Ma domains. Also, the law of approach to magnetic saturation follows a $1/\sqrt{H}$ law [ferromagnet with wandering axis (FWA) regime]. We have calculated the effect of magnetic correlations on the electrical resistivity and magnetoresistance of a RA ferromagnetic system at low temperatures. We find that in zero magnetic field RA introduces a positive contribution into the electrical resistivity, which increases with the anisotropy to exchange ratio, D/\mathcal{J} . In the FWA regime the magnetoresistance has a logarithmic dependence on the magnetic field with a slope $\Delta\rho/(\rho \ln H)$ inversely proportional to R_f . These features have been observed in an experimental study of the magnetoresistance at low temperatures ($T \approx 4$ K) of the amorphous series $(\text{Dy}_x\text{Gd}_{1-x})\text{Ni}$ in which the D/\mathcal{J} ratio can be varied from near zero up to one from GdNi to DyNi. A quantitative analysis of the results enables the direct determination of the correlation length R_f and of the volume of structural correlations Ω_c . We find that R_f varies from about 12 Å in DyNi up to 300 Å in $(\text{Dy}_{0.1}\text{Gd}_{0.9})\text{Ni}$ and Ω_c is the same throughout the series ($\Omega_c \approx 500$ Å³) in excellent agreement with the values determined from magnetic measurements on the approach to saturation. These results provide an independent confirmation of the exponential decay with distance and field dependence of magnetic correlations in random anisotropy systems.

I. INTRODUCTION

Magnetic interactions make an important contribution to transport properties of metals, in particular in the vicinity of phase transitions, where magnetic correlations play a crucial role. These effects have been deeply investigated in the past,^{1,2} both experimentally and theoretically. In the case of magnetic amorphous metals, in particular rare-earth-based random anisotropy systems, in which long-range ferromagnetic order is suppressed by disorder, the situation is not so well understood. In fact, the theoretical studies of the magnetic contribution to the electrical resistivity done so far (Asomoza *et al.*,³ Bhattacharjee and Coqblin,⁴ Borch *et al.*⁵) have always used severe approximations in the description of magnetic correlations, namely mean-field approximations beyond first neighbor distances.

Recent theoretical studies of the low-temperature ($T=0$) random anisotropy magnetism by Ignatchenko and Ishakov⁶ and Chudnovsky *et al.*⁷ reached a thorough understanding of the interplay of magnetic and structural correlations in these systems, which are described by the HPZ Hamiltonian⁸

$$\mathcal{H} = -\frac{1}{2} \mathcal{J} \sum_{i \neq j} \sigma_i \cdot \sigma_j - D \sum_i (\mathbf{n}_i \cdot \sigma_i)^2 - \mathbf{H} \cdot \sum_i M_s \sigma_i. \quad (1)$$

\mathcal{J} and D are the strengths of the exchange and random anisotropy interactions. The random anisotropy directions are given by the vector \mathbf{n}_i , and σ_i is the normalized magnetic moment at each site $\sigma_i = \mathbf{M}_i/M_s$.

Using a continuous version of this Hamiltonian it was shown that in zero magnetic field the reduced magnetic correlation function decays exponentially with distance:

$$\langle \sigma(\mathbf{r}_1) \cdot \sigma(\mathbf{r}_2) \rangle = \exp(-|\mathbf{r}_1 - \mathbf{r}_2|/R_f).$$

The magnetic correlation length R_f corresponds to the size of Imry-Ma domains⁹ and is given by

$$\frac{R_f}{a} \approx \left(\frac{5\pi}{12} \right) \left(\frac{z\mathcal{J}}{D} \right)^2 \left(\frac{a^3}{\Omega_c} \right), \quad (2)$$

where a is the distance between magnetic nearest neighbors (z) and Ω_c is the volume of correlation of random anisotropy directions (structural short-range order).

On the other hand, when a magnetic field is applied ($H < H_{ex}$, see below) and the system approaches saturation [ferromagnet with wandering axes (FWA) regime], the correlations between transverse components of the magnetization [$\sigma_{\perp}(\mathbf{r})$] also decay exponentially, but with a new correlation length, R_H :

$\langle \sigma_{\perp}(\mathbf{r}_1) \cdot \sigma_{\perp}(\mathbf{r}_2) \rangle = \langle \sigma_{\perp}^2 \rangle \exp(-|\mathbf{r}_1 - \mathbf{r}_2|/R_H)$, where $\langle \sigma_{\perp}^2 \rangle$ represents the reduced deviation of magnetic moments to saturation $\langle \sigma_{\perp}^2 \rangle = 2(M_s - M)/M_s$ and varies like $1/\sqrt{H}$ in the FWA regime. The transverse correlation length is given by $R_H = R_f \langle \sigma_{\perp}^2 \rangle = R_a \sqrt{H_{ex}/H}$, where $H_{ex} = z\mathcal{J}6aM_sR_a^2$ and R_a is the structural correlation length ($\Omega_c \approx R_a^3$).

These predictions have already been confirmed experimentally, in particular with studies of the law of approach to saturation,^{10,11} concerning the $1/\sqrt{H}$ dependence of the magnetization and neutron diffraction experiments,⁷ as concerns the presence of exponential correlations and characteristic parameters, R_f and R_H .

II. THEORY

We have extended this treatment to the effects of magnetic correlations on the resistivity and magnetoresistance of

TABLE I. Characteristic parameters of the samples of the system $(\text{Dy}_x\text{Gd}_{1-x})\text{Ni}$ determined from magnetic studies: θ_p , the paramagnetic Curie temperature; D/\mathcal{F} , the ratio of anisotropy and exchange; and R_f , the ferromagnetic correlation length at $T=0$.

Sample	θ_p (K)	D/\mathcal{F}	R_f/a	R_f (Å)
DyNi	14	0.95	3.6	12
$(\text{Dy}_{0.75}\text{Gd}_{0.25})\text{Ni}$	25	0.74	5.3	17
$(\text{Dy}_{0.5}\text{Gd}_{0.5})\text{Ni}$	38.5	0.55	10.5	34
$(\text{Dy}_{0.25}\text{Gd}_{0.75})\text{Ni}$	51.5	0.32	26.9	86
$(\text{Dy}_{0.1}\text{Gd}_{0.9})\text{Ni}$	58.6	0.19	82.2	263

random anisotropy systems at low temperatures, considering the scattering of electrons by magnetic rare-earth ions of angular momentum J . For this calculation we used the approach of de Gennes and Friedel¹² for coherent magnetic scattering, which directly includes the Fourier transform of spatial magnetic correlation functions, including appropriate modifications for low temperatures.³

The magnetic contribution to the electrical resistivity at $H=0$ is given by

$$\rho_m(T=0, H=0) = \rho_M \left[c \frac{J}{J+1} + \frac{2\pi c^2}{(k_F d)^3} F(2k_F R_f) \right]. \quad (3)$$

The first part represents the single ion contribution and the second one the effect of correlations, for which we define the function $F(x) = [\ln(1+x^2) - x^2/(1+x^2)]/x$. ρ_M is the spin disorder resistivity of the rare-earth magnetic ions (scattering at high temperatures), c is their concentration, k_F is the Fermi wave vector, and d is the average interatomic distance in the alloys. Notice that the magnetic correlations in random anisotropy systems always give rise to a positive contribution.

Under an applied magnetic field the expressions are more complex. In the FWA regime, where $R_H \propto 1/H$ and as we have typically $(2k_F R_f)^2, (2k_F R_H)^2 \gg 1$, a considerable simplification can be achieved. One finally finds that the magnetoresistance $\Delta\rho/\rho$ has a logarithmic dependence on the magnetic field:

$$\Delta\rho(H) \approx \text{const} - \rho_M \frac{\pi c^2}{(k_F d)^3 k_F R_f} \ln H. \quad (4)$$

III. RESULTS

We present an experimental study of the low-temperature magnetoresistance of the random anisotropy amorphous series $(\text{Dy}_x\text{Gd}_{1-x})\text{Ni}$ in which the D/\mathcal{F} ratio can be varied from near zero (in GdNi) to about one (in DyNi) without sizeable structural and electronic changes. The characteristic magnetic parameters of these samples determined in previous studies^{10,13,14} are presented in Table I. In Figs. 1 to 3 we present the magnetoresistance measured near 4 K in the samples $x=1, 0.75$, and 0.1 . The logarithmic dependence is clearly observed, especially in the samples with larger D/\mathcal{F} ratio. Notice that the magnetoresistance diminishes by a factor 15 from DyNi to $(\text{Dy}_{0.1}\text{Gd}_{0.9})\text{Ni}$.

To make a quantitative analysis of the results we note that the slope of the logarithmic field dependence is

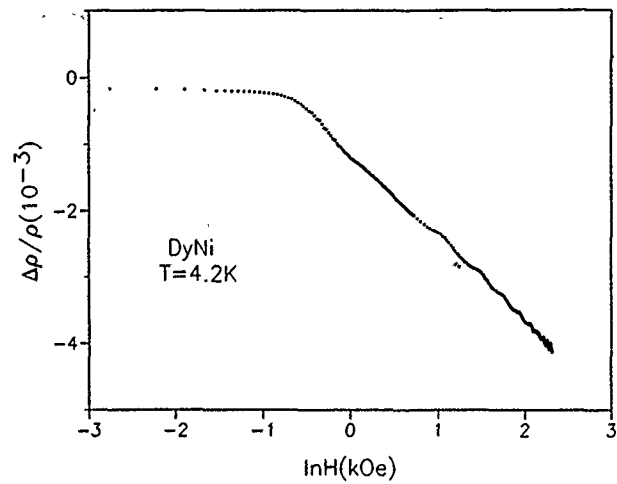


FIG. 1. Magnetoresistance of the sample DyNi as a function of the logarithm of the applied magnetic field.

$S_H = \Delta\rho/\rho \ln H = -\pi c^2 \rho_M / \rho(0) (k_F d)^3 k_F R_f$, where $\rho(0)$ is the electrical resistivity of the samples (formally at $T=0$), for which we can take the room temperature value, $200 \mu\Omega \text{ cm}$.¹³

To determine R_f we need to estimate the values of ρ_M and k_F for these alloys, and take the concentration of magnetic ions $c=0.5$. We assume that the magnetic ion contribution ρ_M varies linearly with x between the two ends of the series $\rho_M(\text{Gd})=125 \mu\Omega \text{ cm}$ and $\rho_M(\text{Dy})=71 \mu\Omega \text{ cm}$, the experimental values for polycrystalline metals.¹⁵ We use $\rho_M(x) = 71x + 125(1-x) \mu\Omega \text{ cm}$. The value of k_F is estimated in a free electron approach as $k_F^3 = 3\pi^2 z^*/d^3$, where z^* is the number of free-like electrons per atom¹⁶ and d^3 is the average atomic volume. While in simple metals (Na, Cu, etc.) one can take z^* equal to the number of s electrons in their valence atomic orbitals ($z^*=1$ for Na, Cu, $z^*=2$ for Mg), in the case of transition metals or rare-earth metals with an incomplete d band (as Ni, Gd, Dy) the estimate of z^* is more delicate. In the Friedel band model, in which the d band density of states is approximated by a constant, one

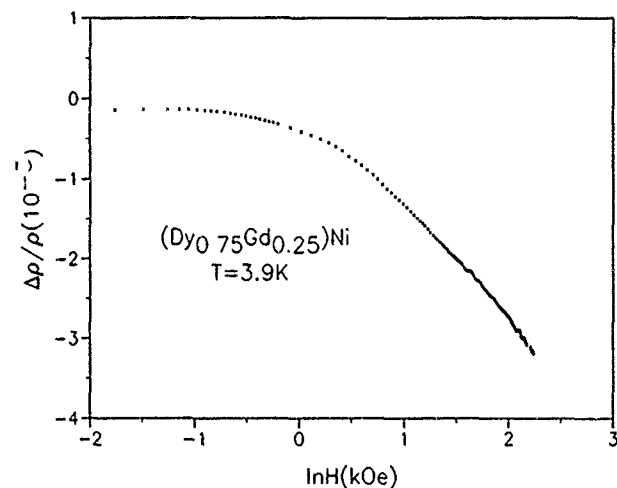


FIG. 2. Magnetoresistance of the sample $(\text{Dy}_{0.75}\text{Gd}_{0.25})\text{Ni}$ as a function of the logarithm of the applied magnetic field.

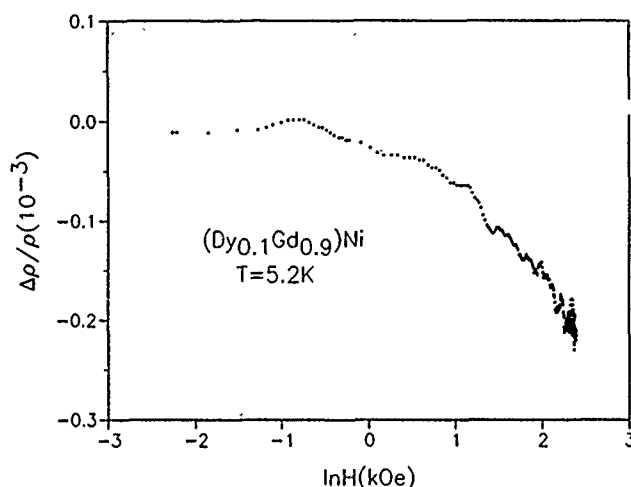


FIG. 3. Magnetoresistance of the sample $(\text{Dy}_{0.1}\text{Gd}_{0.9})\text{Ni}$ as a function of the logarithm of the applied magnetic field.

obtains the following values for the number of electrons in parabolic bands ($z^*=0.81$ for Ni and $z^*=0.54$ for La, which is adequate for Gd and Dy). Values of z^* lower than the chemical valence are experimentally confirmed by transport properties, like the Hall effect in Fe–Au and Ni–Au alloys¹⁷ which give $z^*=0.6$ for Fe and Ni. We therefore estimate $z^*=0.6$ for all the samples, and from this we obtain $k_F d = 2.6$.

The values of R_f determined from magnetoresistance are presented in Table II. The normalization R_f/a is obtained by noting that $d^3 = 0.5a^3$.

We notice a remarkable agreement between the values of the magnetic correlation lengths obtained from both procedures. This is clearly apparent in Fig. 4, where we present both values as a function of $(D/\mathcal{F})^2$. Both data sets have the best fitted straight line, $a/R_f = 0.32(D/\mathcal{F})^2$. Using Eq. (2) and number of nearest neighbors $z^*=6$, we also find that the structural correlation volume Ω_c is constant through the series $\Omega_c = 16a^3 \approx 510 \text{ \AA}^3$, in agreement with x-ray determinations.¹⁰

IV. CONCLUSIONS

We have shown that the characteristic magnetic correlations in random anisotropy alloys can also be related to electron transport properties and that the magnetic correlation

TABLE II. Results of transport studies: S_H , the slope of the magnetoresistance vs $\ln H$ and R_f ; the ferromagnetic correlation length at $T=0$, normalized by the interatomic (d) and rare-earth (a) distances.

Sample	$-S_H(10^{-3})$	R_f/d	R_f/a
DyNi	1.27	4.73	3.75
$(\text{Dy}_{0.75}\text{Gd}_{0.25})\text{Ni}$	1.28	5.59	4.42
$(\text{Dy}_{0.5}\text{Gd}_{0.5})\text{Ni}$	0.46	18.0	14.2
$(\text{Dy}_{0.1}\text{Gd}_{0.9})\text{Ni}$	0.086	118	93.2

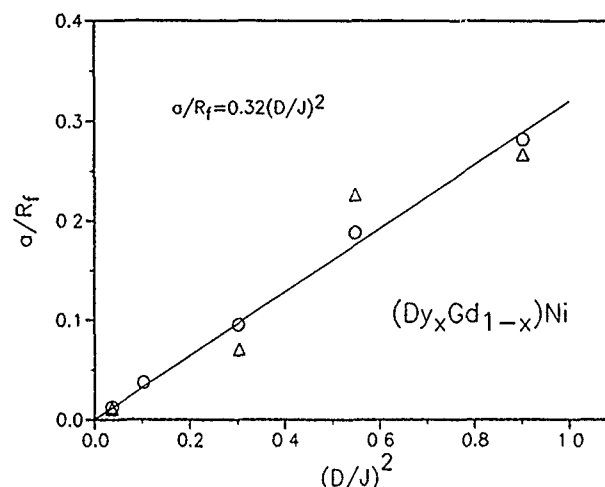


FIG. 4. Variation of the ferromagnetic correlation length R_f with D/\mathcal{F} . Circles and triangles represent the values obtained from magnetization and magnetoresistance studies, respectively. The linear dependence shows that the structural correlation volume Ω_c is the same throughout the series ($\Omega_c = 16a^3 \approx 510 \text{ \AA}^3$).

length R_f and the structural correlation volume Ω_c can be obtained directly from magnetoresistance measurements. These results give additional confirmation of the approach developed by Chudnovsky *et al.* in which transverse magnetic correlations decay exponentially with the correlation length $R_H \propto 1/\sqrt{H}$ under an applied field. Furthermore they show the relevance of transport measurements in the study of disordered magnetic systems.

This work was partially supported by the JNICT/CNRS scientific exchange program.

- ¹M. E. Fisher and J. S. Langer, Phys. Rev. Lett. **20**, 665 (1968).
- ²T. G. Richard and D. J. W. Geldart, Phys. Rev. Lett. **30**, 290 (1973).
- ³R. Asomoza, I. A. Campbell, A. Fert, A. Liénard, and J. P. Rebouillat, J. Phys. F **9**, 349 (1979).
- ⁴A. K. Bhattacharjee and B. Coqblin, J. Phys. F **8**, L221 (1978).
- ⁵E. Borch, M. Poli, and S. De Gennaro, J. Magn. Magn. Mater. **27**, 227 (1982).
- ⁶V. A. Ignatchenko and R. S. Ishakov, Sov. Phys. JETP **45**, 526 (1977); **47**, 725 (1978).
- ⁷E. M. Chudnovsky, W. Saslow, and R. A. Serota, Phys. Rev. B **33**, 251 (1986); E. M. Chudnovsky, J. Appl. Phys. **64**, 5770 (1988), and references therein.
- ⁸R. Harris, M. Plischke, and M. J. Zuckermann, Phys. Rev. Lett. **31**, 160 (1973).
- ⁹Y. Imry and S. K. Ma, Phys. Rev. Lett. **35**, 1399 (1975).
- ¹⁰J. Filippi, V. S. Amaral, and B. Barbara, Phys. Rev. B **44**, 2842 (1991).
- ¹¹D. J. Sellmeyer and M. J. O'Shea, in *Recent Progress in Random Magnets*, edited by D. H. Ryan (World Scientific, Singapore, 1992).
- ¹²P. G. de Gennes and J. Friedel, J. Phys. Chem. Solids **4**, 71 (1958).
- ¹³J. B. Sousa, J. M. Moreira, V. S. Amaral, M. M. Amado, B. Barbara, B. Dieny, and J. Filippi, J. Phys. F **17**, 2377 (1987).
- ¹⁴V. S. Amaral, B. Barbara, J. B. Sousa, and J. Filippi, Europhys. Lett. **22**, 139 (1993).
- ¹⁵B. Coqblin, *The Electronic Structure of Rare-Earth Metals and Alloys: The Magnetic Heavy Rare Earths* (Academic, New York, 1977).
- ¹⁶W. A. Harrison, *Electronic Structure and Properties of Solids* (Freeman, San Francisco, 1980).
- ¹⁷G. Bergmann, Solid State Commun. **18**, 897 (1976); Z. Phys. B **25**, 255 (1976); G. Bergmann and P. Marquardt, Phys. Rev. B **18**, 326 (1977).

***In situ* magnetic and structural analysis of epitaxial Ni₈₀Fe₂₀ thin films for spin-valve heterostructures**

I. Hashim and H. A. Atwater

Thomas J. Watson Laboratory of Applied Physics, California Institute of Technology, Pasadena, California 91125

We have investigated structural and magnetic properties of epitaxial (100) Ni₈₀Fe₂₀ films grown on relaxed Cu/Si(100) seed layers. The crystallographic texture and orientation of these films was analyzed *in situ* by reflection high energy electron diffraction (RHEED), and *ex situ* by x-ray diffraction and cross-sectional transmission electron microscopy (XTEM). In particular, RHEED intensities were recorded during epitaxial growth, and intensity profiles across Bragg rods were used to calculate the surface lattice constant, and hence the film strain. XTEM analysis indicated that the epitaxial films had atomically abrupt interfaces. The magnetic properties of these epitaxial films were measured *in situ* using magneto-optic Kerr effect magnetometry. Large H_c (10–20 Oe) was observed for epitaxial Ni₈₀Fe₂₀ (100) films less than 10.0 nm thick whereas for larger thicknesses, H_c decreased to a few Oe with the appearance of a uniaxial anisotropy. Correlations were made between magnetic properties of these epitaxial films and the strain in the film.

INTRODUCTION

Permalloy (Ni₈₀Fe₂₀) heterostructures are of great interest for magnetoresistive devices based on anomalous antiferromagnetic (AF)-coupling and giant magnetoresistance (GMR) in Ni₈₀Fe₂₀/Cu multilayers¹ and spin-valves.² To date, all investigations of such Ni₈₀Fe₂₀ heterostructures have employed polycrystalline films with atomically rough interfaces where the interface roughness is of the same order as the nonmagnetic spacer layer thickness.^{1,2} Since AF-coupling and GMR depend sensitively on Ni₈₀Fe₂₀/Cu interface structure and the film morphology, the magnetotransport properties of atomically abrupt epitaxial films should more clearly elucidate the underlying physics. With atomically abrupt film interfaces, it would be possible to fabricate thinner nonmagnetic spacer layers without the interface roughness being the limiting factor.¹ Furthermore, the growth of epitaxial single layer Ni₈₀Fe₂₀ films on silicon would be potentially of great interest for studying magnetotransport and for applications to magnetoresistive devices because of reduced interfacial and grain-boundary scattering.³ Finally, the growth of epitaxial magnetic films and the effects of coherency strain on magnetic properties especially anisotropy and magnetic moment have been the object of many previous investigations.⁴ In particular, magnetic properties of epitaxial Fe and Ni thin films on Cu(100) have been studied recently^{5,6} whereas strain relaxation in epitaxial Ni(100) films on Cu(100) has been examined in the past by Matthews and Crawford.⁷ However, unlike Ni and Fe, Ni₈₀Fe₂₀ possesses very little magnetocrystalline anisotropy ($\sim 10^3$ ergs/cm³) and the primary source of anisotropy is uniaxial anisotropy induced during deposition.

Epitaxial Ni₈₀Fe₂₀(100) films were grown on relaxed Cu(100) seed layers, 10–50 nm thick, oriented epitaxially with respect to Si(100). Because of the relatively small lattice mismatch between Ni₈₀Fe₂₀ and Cu (1.85%), the Ni₈₀Fe₂₀ layers were semicoherent with the Cu seed layer. The epitaxy of Cu(100) at room temperature on H-terminated Si(100) has been the object of earlier investigations and has been successfully demonstrated to occur in

high-vacuum and UHV conditions.^{8–10} The crystallographic orientation for this epitaxy was found to be Cu(100) || Si(100) with Cu[100] || Si[110].¹⁰ Furthermore, FeMn, which is typically used in spin valves to exchange bias one of the ferromagnetic layers,² has an epitaxial relationship with Ni₈₀Fe₂₀. Hence, epitaxial spin-valve heterostructures consisting of FeMn/Ni₈₀Fe₂₀/Cu/Ni₈₀Fe₂₀ were grown on Cu/Si(100). The magnetotransport properties of these heterostructures will be reported elsewhere.¹²

EXPERIMENTAL PROCEDURES

The basic elements of the sputtering system used for deposition, x-ray diffraction analysis, electron microscopy, magneto-optic Kerr effect (MOKE) system for magnetic *in situ* characterization, and RHEED measurements to determine the surface lattice constant and the strain in the films, are described elsewhere.^{10,11} In particular, Ni₈₀Fe₂₀ films were deposited in the presence of an external magnetic field to induce a uniaxial anisotropy.¹³

EPITAXIAL STRAIN AND MAGNETIC PROPERTIES

For growth of an overlayer B on substrate A and for small misfit f ($\leq 10\%$) between lattice constants for A and B, the lattice of B may expand or contract to form a coherent interface with that of A. However, formation of such an interface is associated with a strain energy in the overlayer B. For large enough thicknesses, it becomes energetically more favorable to relieve this coherency strain energy by generation of misfit dislocations at the interface. The critical epitaxial thickness h_c for which this transition takes place is obtained by solving the transcendental equation:¹⁴

$$h_c = \frac{b}{8\pi f \cos \alpha} \left[\frac{1 - \nu \cos^2 \beta}{1 + \nu} \right] \ln \left(\frac{4h_c}{b} \right), \quad (1)$$

where b is the misfit dislocation Burger's vector, ν is the Poisson's ratio, β and α are the angles that the Burger's vector makes with the dislocation line and the direction normal to the dislocation line lying within the plane of the in-

interface, respectively. Substituting the lattice constant of $\text{Ni}_{80}\text{Fe}_{20}$ for b , $\alpha=\beta=60^\circ$ which is often the case for fcc crystals, ν of 0.31 for Ni and misfit f for $\text{Ni}_{80}\text{Fe}_{20}/\text{Cu}$, h_c was found to be 4.1 nm from solving Eq. (1). With the onset of misfit dislocations above the critical thickness, the elastic strain in the film decreases as given by:¹⁴

$$\epsilon_{\parallel} = \frac{b^2}{8\pi h \cos \alpha} \left[\frac{1 - \nu \cos^2 \beta}{1 + \nu} \right] \ln \left(\frac{4h_c}{h} \right). \quad (2)$$

As the above equation indicates, the elastic strain falls off approximately inversely with thickness h of the film. Thus, residual strain may persist in the film for thicknesses much larger than the critical thickness h_c .

Among the effects of coherency strain on magnetic properties, it has been well known that a perpendicular anisotropy can be induced in ultrathin films due to interaction with strain.¹⁵ Furthermore, coherency strain can give rise to a biaxial in-plane stress which can couple to magnetic anisotropy via magnetostriction λ_{ij} of the thin film. However, it is well known that for Ni-Fe composition of 81% and 19%, respectively, the magnetostriction of NiFe thin films is near zero and isotropic, but nevertheless, still sensitive to the exact composition and texture of the film.¹⁶

Using linear elasticity theory, the in-plane stress due to coherency strain along $\langle 100 \rangle$ cubic axes in a coherent thin film can be expressed in terms of the elastic constants c_{ij} and the in-plane strain ϵ_{\parallel} :¹⁷

$$\sigma_{\parallel} = \left[(c_{11} + c_{12}) - \frac{2c_{12}^2}{c_{11}} \right] \epsilon_{\parallel}. \quad (3)$$

Substituting the elastic constants for Ni and the misfit f for ϵ_{\parallel} , and λ for $\text{Ni}_{80}\text{Fe}_{20}$ $\langle 100 \rangle$ -textured films obtained from that reported by Klokholm and Aboaf,¹⁶ σ_{\parallel} was calculated using Eq. (3) and substituted in:

$$E_{me} = \frac{3}{2} \lambda \sigma \sin^2 \theta \quad (4)$$

to estimate magnetoelastic energy E_{me} of $\sim 10^5$ ergs/cm³ where θ is the angle between σ and the magnetization vector. This can be compared with the induced uniaxial anisotropy energy E_k for $\text{Ni}_{80}\text{Fe}_{20}$ which is typically $\sim 10^3$ – 10^4 ergs/cm³. The fact that magnetoelastic energy associated with coherency strain is significantly higher than uniaxial anisotropy energy, suggests that for coherent films of $\text{Ni}_{80}\text{Fe}_{20}$, the former would be an important factor in governing magnetic anisotropy.

RESULTS AND DISCUSSION

Surface lattice constant measurements using RHEED shown in Fig. 1, were employed to observe the relaxation of the coherency strain in $\text{Ni}_{80}\text{Fe}_{20}$ films on Cu/Si(100). Due to the relatively small mismatch between Cu and $\text{Ni}_{80}\text{Fe}_{20}$ (1.85%) and the limited resolution of the camera used for recording RHEED images, it was difficult to accurately calculate the strain in the $\text{Ni}_{80}\text{Fe}_{20}$ film using this technique. Nevertheless, it can be observed from these studies that the $\text{Ni}_{80}\text{Fe}_{20}$ film relaxes to its bulk lattice constant after 4.5 nm.

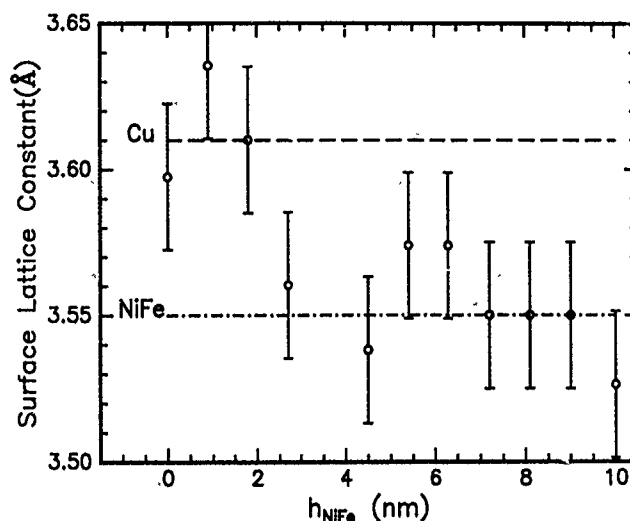


FIG. 1. Surface lattice constants as calculated from RHEED measurements of $(100) \text{Ni}_{80}\text{Fe}_{20}$ film grown on Cu/Si(100) as a function of film thickness.

No change in the RHEED intensity profiles was observed during epitaxial growth of $\text{Ni}_{80}\text{Fe}_{20}$ on Cu suggesting a layer-by-layer growth mechanism.

Figure 2 shows an x-ray scan for $\theta_i = 30^\circ$ for a $\text{Ni}_{80}\text{Fe}_{20}$ (30 nm)/Cu(30 nm)/Si(100) film which indicates that the (100) texture in the films is 2–3 orders of magnitude stronger than other fcc textures, notably (111) . Furthermore, the lattice constants calculated from the diffraction spectrum confirm that the Cu and the $\text{Ni}_{80}\text{Fe}_{20}$ films are strain-relieved; i.e., have the bulk lattice constants.

Figure 3 shows a high resolution cross-sectional transmission electron micrograph of an epitaxial $\text{Ni}_{80}\text{Fe}_{20}$ (50 nm)/Cu(50 nm)/Si(100) film along $[110]$ Si in which metal lattice fringes can be seen extending from the Cu/Si interface to $\text{Ni}_{80}\text{Fe}_{20}$ film surface. The inset shows the selected area diffraction pattern due to $(100) \text{Ni}_{80}\text{Fe}_{20}/\text{Cu}$ films and the Si substrate. The $\text{Ni}_{80}\text{Fe}_{20}/\text{Cu}$ interface cannot be clearly seen in Fig. 3 due to lack of Z-contrast between $\text{Ni}_{80}\text{Fe}_{20}$ and Cu. However, it is discernible by the presence of Moiré fringes and misfit dislocations indicating a semicoherent interface between Cu and $\text{Ni}_{80}\text{Fe}_{20}$. Furthermore, a mosaic spread of

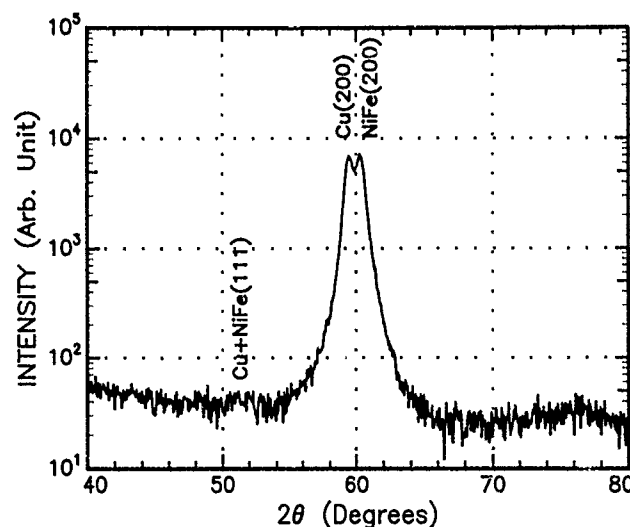


FIG. 2. Co K_α x-ray diffraction spectrum of epitaxial $(100) \text{Ni}_{80}\text{Fe}_{20}$ (30 nm)/Cu(30 nm)/Si(100).

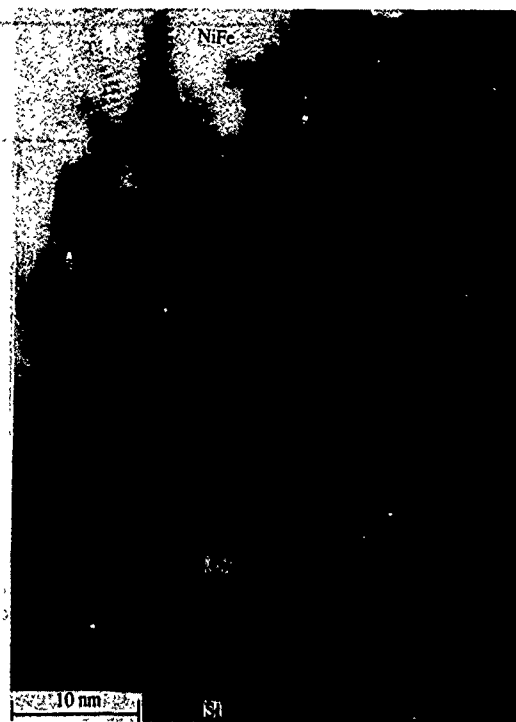


FIG. 3. High resolution cross-sectional transmission electron micrograph of epitaxial $\text{Ni}_{80}\text{Fe}_{20}/\text{Cu}/\text{Si}(100)$ film along the $\text{Si}[110]$ zone axis. The inset shows the diffraction pattern due to the film and the Si substrate.

up to $\pm 6^\circ$ in the (100) texture can be observed in the lattice fringes as well as the diffraction pattern due to the film. The smooth $\text{Ni}_{80}\text{Fe}_{20}$ film surface and the atomically abrupt Cu/Si interface suggest that the r.m.s. roughness of the epitaxial $\text{Ni}_{80}\text{Fe}_{20}/\text{Cu}$ interface is few atomic layers. However, interdiffusion of Ni or Fe into Cu or vice-versa cannot be ruled out.

Magnetic properties of the epitaxial $\text{Ni}_{80}\text{Fe}_{20}/\text{Cu}$ films, 2.0–20.0 nm thick, were measured using MOKE magnetometry. No MOKE signal could be detected for $\text{Ni}_{80}\text{Fe}_{20}$ films less than 2.0 nm thick. For films with thicknesses ≤ 10.0 nm, a biaxial anisotropy of ~ 10 Oe along the [100] crystallographic α directions of $\text{Ni}_{80}\text{Fe}_{20}$ was observed which could be due to interaction with coherency strain as discussed earlier and/or magnetocrystalline anisotropy of $\text{Ni}_{80}\text{Fe}_{20}$. The coercivity for these films was 10–20 Oe which is rather high for $\text{Ni}_{80}\text{Fe}_{20}$. For random polycrystalline films deposited under the same conditions on SiO_2/Si , it was 1–2 Oe; see Fig. 4 for variation of H_c with film thickness for $\text{Ni}_{80}\text{Fe}_{20}$ films grown on Cu/Si and SiO_2/Si . Thicker epitaxial $\text{Ni}_{80}\text{Fe}_{20}$ films (≥ 10.0 nm) had an induced uniaxial anisotropy due to the external magnetic field applied during deposition. Furthermore, these films had relatively soft magnetic properties ($H_{ce}=2.04$ Oe, $H_{ch}=0.22$ Oe, and $H_k=12.3$ Oe) which were comparable to those of random polycrystalline $\text{Ni}_{80}\text{Fe}_{20}$ films. This indicates that these films are relatively strain-free and devoid of defects or pinning sites for domain walls. It is

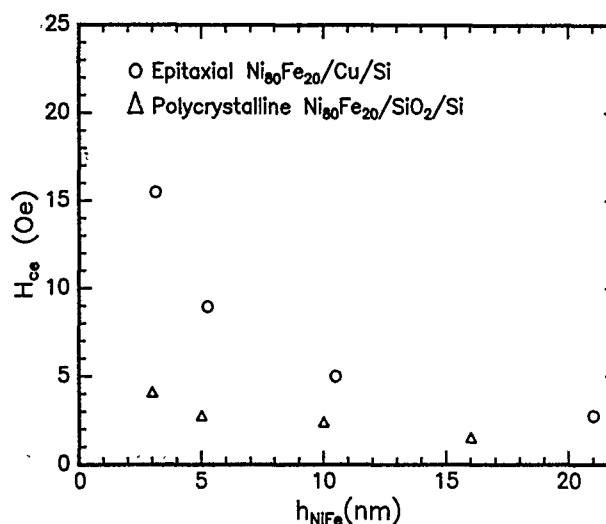


FIG. 4. Variation of H_c with $\text{Ni}_{80}\text{Fe}_{20}$ film thickness for epitaxial films on Cu/Si and polycrystalline films on SiO_2/Si .

plausible that the thinner epitaxial films have voids or sources of localized stresses due to coherency strain, which cause domain wall pinning and hence, higher H_c . Investigations are currently under way to identify the nature of these defects using atomic force microscopy.

ACKNOWLEDGMENTS

This work was supported by NSF and IBM. We would also like to acknowledge DOE grant DEFGO589ER75511 which made the use of Inel Thin Film Diffractometer possible for x-ray analysis. We thank Kirill Shcheglov and Wurzel Keir for assistance with MOKE software and hardware development, Carol Garland for assistance with electron microscopy, Bruce Gurney for helpful advice in the design of the MOKE magnetometer, and Byungwoo Park and Hyun Song Joo for help with various parts of this project.

- ¹S. S. P. Parkin, *Appl. Phys. Lett.* **60**, 512 (1992).
- ²B. Dieny, V. S. Speriosu, B. A. Gurney, S. S. P. Parkin, D. R. Wilhoit, K. P. Roche, S. Metin, D. T. Peterson, and S. Nadimi, *J. Magn. Magn. Mater.* **93**, 101 (1991).
- ³A. F. Mayadas and M. Shatzkes, *Phys. Rev. B* **1**, 1382 (1970).
- ⁴R. F. C. Farrow, S. S. P. Parkin, and V. S. Speriosu, *J. Appl. Phys.* **64**, 5315 (1988).
- ⁵L. R. Sill, M. B. Brodsky, S. Bowen, and H. C. Hamaker, *J. Appl. Phys.* **57**, 3663 (1985).
- ⁶G. Bochi, C. A. Ballentine, H. E. Inglefield, S. S. Bogomolov, C. V. Thompson, and R. C. O'Handley, *Mater. Res. Soc. Proc.* Vol. 313, (1993).
- ⁷J. W. Matthews and J. L. Crawford, *Thin Solid Films* **5**, 187 (1970).
- ⁸C. A. Chang, *Appl. Phys. Lett.* **55**, 2754 (1989).
- ⁹J. Li and Y. Shacham-Diamand, *J. Electrochem. Soc.* **139**, L37 (1992).
- ¹⁰I. Hashim, B. Park, and H. A. Atwater, *Appl. Phys. Lett.* **63**, 2833 (1993).
- ¹¹I. Hashim and H. A. Atwater, *Mater. Res. Soc. Proc.* Vol. 313, (1993).
- ¹²H. S. Joo, I. Hashim, and H. A. Atwater (unpublished).
- ¹³M. Takahashi, *J. Appl. Phys.* **33**, 1101 (1962).
- ¹⁴J. W. Matthews and A. E. Blakeslee, *J. Cryst. Growth* **27**, 118 (1974).
- ¹⁵J. G. Gay and Roy Richter, *Phys. Rev. Lett.* **56**, 2278 (1986).
- ¹⁶E. Klokholm and J. A. Aboaf, *J. Appl. Phys.* **52**, 2474 (1981).
- ¹⁷J. Y. Tsao, *Materials Fundamentals of Molecular Beam Epitaxy* (Academic, San Diego, 1993), p. 106.

Magnetic and magnetoresistive properties of inhomogeneous magnetic dual-layer films

John O. Oti, Stephen E. Russek, and Steven C. Sanders

Electromagnetic Technology Division, National Institute of Standards and Technology, Boulder, Colorado 80303

Magnetic and magnetoresistive properties of sputtered Co alloy dual-layer films are compared with micromagnetic simulations. The simulations elucidate the details of the switching behavior of the dual-layer films as a function of the interlayer exchange and magnetostatic interactions. The simulations have led to a conceptual understanding of the coercive field splitting caused by the interlayer interactions. A calculation of the anisotropic magnetoresistance (AMR) has been included in the simulations. The AMR provides a second independent macroscopic quantity (in addition to the average magnetization) which can be measured and compared with the micromagnetic simulations. The AMR is more sensitive to the micromagnetic structure perpendicular to the applied field and is a better test of the accuracy of the micromagnetic model. The simulations qualitatively describe the measured AMR data on CoNi-Cr-CoNi dual layers.

INTRODUCTION

Magnetic multilayer thin films are becoming increasingly important in the development of high coercivity media¹ and low coercivity magnetic sensors.² Magnetic interactions within and between the layers of multilayer magnetic films play an important role in determining the properties of these films.³ In this article we use our micromagnetic model^{4,5} to analyze the micromagnetics of coercive field splitting (CFS) of the major hysteresis loops and introduce magnetoresistance calculations as a tool to provide further verification of the micromagnetic model. The results of the model simulations are compared with experimental data on sputtered Co_{0.75}Ni_{0.25}-Cr-Co_{0.75}Ni_{0.25} dual-layer films.

In the micromagnetic model each magnetic layer is simulated by a rectangular array of discrete parallelepiped elements representing the grains of the layers. Each grain has a fixed magnitude magnetic moment which is allowed to dynamically relax (in three dimensions) in the presence of an external field, an effective exchange field, an effective anisotropy field, and a magnetostatic field. The magnetic layers are characterized by distributions of exchange, anisotropy, and magnetostatic parameters among the grains. The distribution of interlayer exchange coupling parameters, intralayer exchange coupling parameters, and magnetostatic interaction parameters are specified relative to certain mean values denoted, respectively, by $\langle C_e' \rangle$, $\langle C_e \rangle$, and $\langle C_{eh} \rangle$.⁶ The parameters that are assigned to the grains are selected at random from an interval centered about the mean values. Ferromagnetic interlayer exchange coupling is simulated using positive interlayer exchange parameters, and antiferromagnetic interlayer exchange coupling is simulated using negative parameters.

The films discussed in this paper are ones with moderate intragranular exchange, strong uniaxial anisotropy, and strong disorder. The disorder in these films (principally the random distribution of anisotropy axes) acts to reduce the coercive field by providing nucleation centers for the magnetization reversal. One of the most prominent features of dual-layer magnetic thin films of this type is a splitting in the coercive fields as the two layers are brought together and

allowed to interact through magnetostatic forces. At large separations, two statistically identical films will switch at approximately the same coercive field. As the films are brought closer, one film will switch first, as seen in the calculated and experimental $M-H$ curves shown in Figs. 1(a) and 1(c). We define the coercive field splitting as the difference between the top and bottom layer switching fields as determined by the distance between the peaks in the derivatives in the $M-H$ curves. The mechanism for CFS will be described in the next section.

The anisotropic magnetoresistance (AMR) can be simply modeled by assuming that each element has a change in resistance determined by the orientation of the magnetic moment relative to the current.⁷ The normalized sheet resistance of the sample is

$$R_{AMR} \approx \left[\sum_{j, \text{par}} \left(\sum_{i, \text{ser}} 1 + \delta r_{AMR} (\hat{m}_{i,j} \cdot \hat{j})^2 \right)^{-1} \right]^{-1},$$

where $\hat{m}_{i,j}$ is a unit vector along the magnetic moment of the i,j th element, \hat{j} is the direction of the current density, and δr_{AMR} is the normalized size of the anisotropic magnetoresistance. The inner summation sums the serial resistances in the direction of the current, and the outer summation sums them, reciprocally, transverse to the current. This formula does not include the effects of current redistribution and is appropriate only for systems, such as those discussed in this paper, in which the AMR is small. The average magnetization \mathbf{M} and the AMR form a set of two independent macroscopic quantities which can be computed from the micromagnetic model and compared to experimental data. Examples of computed and measured AMR for a CoNi dual-layer film are shown in Figs. 1(b) and 1(d). The AMR is quadratic in \mathbf{M} and measures the magnitude of the projection of \mathbf{M} along the current direction. In particular the AMR can probe the degree of magnetization perpendicular to the applied field and is sensitive to the details of the magnetization reversal such as the formation of vortices.

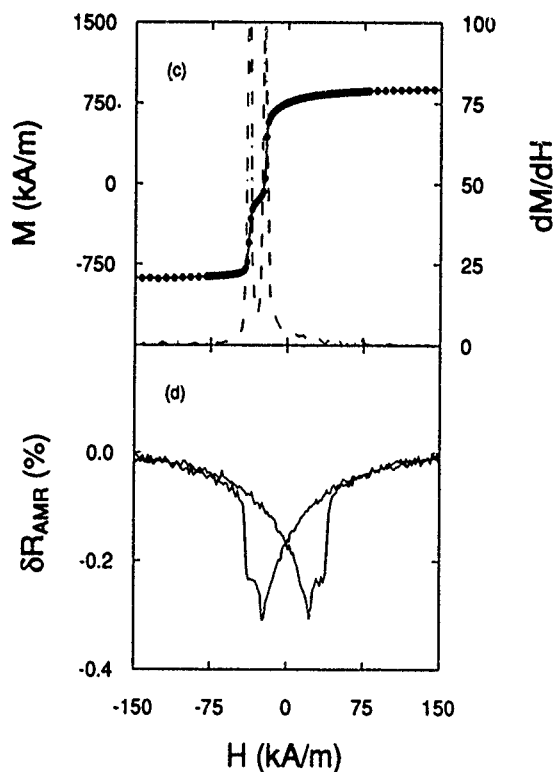
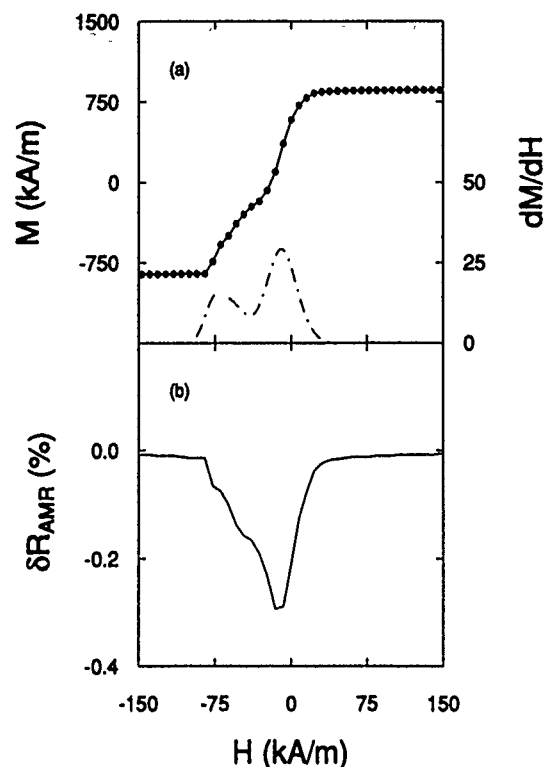


FIG. 1. (a) Calculated M - H data of CoNi dual-layer film with an 8 nm Cr separation layer showing coercive field splitting (CFS). The CFS is equal to the distance between the peaks of the derivative of the magnetization (dotted curve). (b) Calculated AMR with H parallel to J for the same film. (c) Measured M - H data for CoNi dual-layer film with 5 nm Cr separation layer showing CFS. The derivative of the magnetization is shown in the dotted curve. (d) Measured AMR with H parallel to J for the same film. Note that for clarity only one branch of the hysteresis loops are shown except for (d) which shows the full loop.

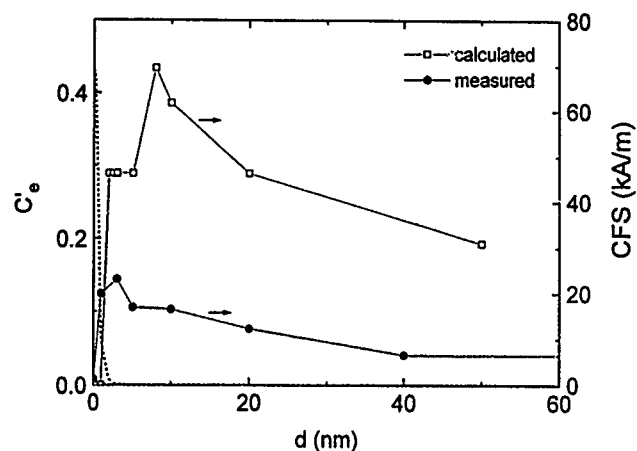


FIG. 2. Calculated and measured coercive force splitting as a function of interlayer separation d . The dotted curve on the left of the diagram represents the variation of C'_e with d .

SIMULATION AND EXPERIMENT

$\text{Co}_{0.75}\text{Ni}_{0.25}$ -Cr- $\text{Co}_{0.75}\text{Ni}_{0.25}$ dual-layer films were sputter-deposited onto silicon substrates. The magnetic layers were each 30-nm thick, and the Cr layer thickness was varied from 1 to 80 nm. Details of the film preparation and the film microstructure are described in Ref. 4. The magnetic films are simulated by assuming a random distribution of the magnetic anisotropy axes with a uniaxial anisotropy field of $H_k = 193$ kA/m (2420 Oe) and a median grain size of 22 nm. In Ref. 4, an array of 20×20 closely packed elements was used in simulating each magnetic layer of the sample. We have repeated the calculations using an array size of 50×50 elements. Periodic boundary conditions are used in the calculations to simulate the large experimental samples which have dimensions of 6×12 mm. The interlayer exchange coupling is a short-range interaction and drops off rapidly with increasing Cr spacing-layer thickness. We adopt a positive exchange constant (ferromagnetic coupling) with an exponentially decreasing form $\langle C'_e \rangle = 0.43 \exp(-2.0d)$, where d is the Cr spacing-layer thickness in nanometers. The dependence of the exchange coupling constant on spacer-layer thickness is shown in Fig. 2 (dotted curve). The same value of C'_e equal to the mean value was assigned to all the grains.

The simulations show that the magnetization reversal modes of the CoNi films are characterized by the formation and propagation of vortices in the magnetic layers. The vortices in the two layers form at different locations and different points in the hysteresis loops because of differences in their detailed microstructure. The centers of the vortices act as nucleation sites for local magnetization reversals, allowing the magnetization reversal to proceed along a low-energy path. The number of vortices in each layer initially grows with increasing externally applied field with little displacement from their original locations. Beyond a certain critical field, the vortices become extremely mobile and quickly self-annihilate, leading to complete reversal of the magnetization.

As the magnetic films are brought together they interact predominantly magnetostatically: free charges on one film attract opposite charges on the other film. The coercive fields

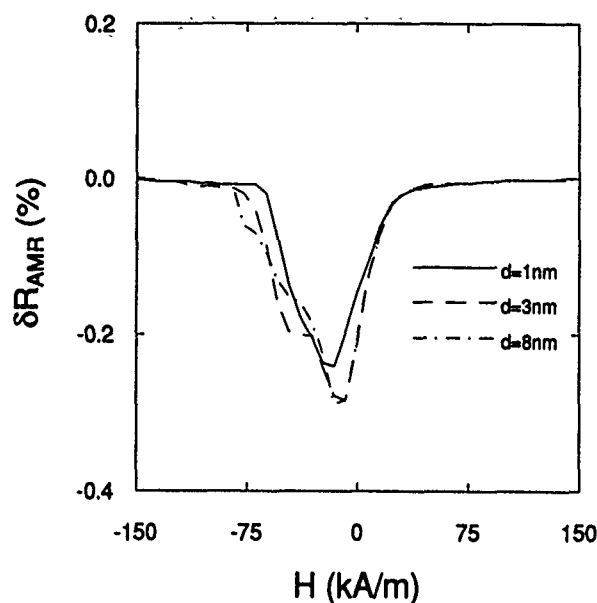


FIG. 3. Calculated AMR as a function of H for interlayer separations of 1, 3, and 8 nm (H is parallel to J).

split as shown in Figs. 1(a) and 1(c). The calculated and experimental dependence of CFS on the separation d between the magnetic layers is shown in Fig. 2. Agreement is seen in the trends of the calculated and experimental curves although magnitudes of the CFS differ. The magnitude of the CFS increases as the layers are brought together and the magnetostatic interaction increases. When the layers are sufficiently close that the exchange coupling dominates, the layers' moments are locked together and the CFS rapidly disappears.

The simulated AMR with H parallel to J is shown in Fig. 3 for different separations. The size of the AMR is directly related to the amount of magnetization perpendicular to the applied field. For smaller spacings, when the exchange interaction becomes important, the size of the AMR decreases because the layer that switches first, forces the other layer to have better registry and not have its moments lie outside the field direction.

DISCUSSION

The origin of the CFS can be understood by noting that the interlayer magnetostatic energy is a minimum in the disordered state when one of the layers has just switched and the other layer is about to switch. In this state, the disordered distribution of charges on one layer effectively compensate the disordered distribution of charges on the other layer. This magnetostatic energy minimum leads to the observed CFS, which consists of an extended stable region in which only one film has switched. An alternative approach to under-

standing the CFS is to realize that, as the layers begin to interact, they necessarily frustrate the other layer's ability to switch. When one layer begins to form a vortex in an energetically favorable location, it will cause, through the magnetostatic interaction, the other layer to reconfigure and not allow it to proceed along its lowest energy path. Therefore, when one layer switches it forces the other layer to proceed along another higher-energy path which requires a higher coercive field to switch the layer.

The coercive field splitting in the micromagnetic simulations is clearly magnetostatic in origin. The similarity of the hysteresis loops, AMR, and the dependence of the CFS on the separation layer thickness strongly suggests that the CFS seen in the experimental samples is also magnetostatic in origin. However, the interlayer exchange has not been measured in these samples, and a longer-range exchange interaction or an antiferromagnetic exchange interaction might be responsible for the observed behavior in the sputtered films. The observed splitting in the coercive fields can suggest that there is some stabilization of the antiferromagnetically aligned state and that there is antiferromagnetic exchange coupling between the layers. Often features similar to those seen in Fig. 1 have been interpreted as evidence of an antiferromagnetic exchange interaction. The results of this paper indicate that in many types of bilayer films these features can be of magnetostatic origin.

Further work needs to be done to quantify the output of the simulations (determining the correct energies and correlation functions to calculate) to obtain a better conceptual understanding of the effects of interactions in dual-layer magnetic thin films. The addition of AMR greatly improves our ability to test the accuracy of the simulations. While in the present work there is a size mismatch between the simulated sample (1 μm) and the measured sample (6 mm), this can be remedied in the future by fabricating and measuring micrometer-size samples. In this case there will be additional magnetostatic effects when the periodic boundary conditions are removed. The details of the reversal process in the range where the exchange and magnetostatic interactions are of comparable importance are still not clear, and a closer look at the micromagnetics in this range may be rewarding.

¹ S. E. Lambert, J. K. Howard, and I. L. Sanders, IEEE Trans. Magn. **MAG-25**, 2706 (1990).

² R. L. White, IEEE Trans. Magn. **MAG-28**, 2482 (1992).

³ J.-G. Zhu, IEEE Trans. Magn. **MAG-28**, 3267 (1992).

⁴ J. O. Oti and S. E. Russek, J. Appl. Phys. **73**, 5845 (1993).

⁵ J. O. Oti, IEEE Trans. Magn. **MAG-29**, 1265 (1993).

⁶ Strictly speaking, six mean parameters are necessary to fully characterize a dual-layer film when the magnetic properties of the layers are different. When the properties of the layers are the same, the number of parameters reduces to three.

⁷ P. Ciureanu, in *Thin Film Resistive Sensors*, edited by P. Ciureanu and S. Middelbrook (Institute of Physics, Bristol, 1992).

Comparison of giant magnetoresistance in multilayer systems and uranium compounds

H. Nakotte, K. Prokeš, E. Brück, P. F. de Châtel, and F. R. de Boer
Van der Waals-Zeeman Laboratory, University of Amsterdam, Valckenierstraat 65, 1018 XE Amsterdam, The Netherlands

V. Sechovsky and L. Havela
Department of Metal Physics, Charles University, Ke Karlovu 5, 121 16 Prague 2, Czech Republic

H. Fujii
Faculty of Integrated Arts and Sciences, Hiroshima University, Hiroshima 730, Japan

The enormous magnetoresistance effect at low temperatures in various uranium-based intermetallic compounds, which exceeds by far the effect found in magnetic-multilayer systems, is a consequence of the strong $5f$ conduction electron hybridization. The consequences of spin-dependent scattering for the giant magnetoresistance (GMR) effect in uranium intermetallics will be discussed and compared with the behavior in multilayer systems. Possible changes of the model parameters to achieve giant magnetoresistance (GMR) effects at higher temperatures, which are desirable for practical applications, are considered.

I. INTRODUCTION AND MOTIVATION

The occurrence of a large reduction of the electrical resistance upon application of a magnetic field in some magnetic-multilayer systems has attracted much attention in view of the possible applications (e.g., magnetic field sensor devices). As this reduction is much larger than the usual magnetoresistance effect in nonmagnetic and magnetic metals, one usually speaks about "giant magnetoresistance" (GMR) in this context. The GMR effect was originally discovered in Fe/Cr multilayers.¹ Since then, several other magnetic multilayer systems exhibiting the GMR effect have been found, which may be as large as $\Delta\rho/\rho = (\rho_{AF} - \rho_F)/\rho_F = 65\%$ at room temperature and may exceed 110% at low temperatures (e.g., in Co/Cu multilayers²). The strong dependency on the layer thickness and interface mixing (roughness, etc.) reported (for a review see Ref. 3) request several special preparative conditions for multilayer "growth" like ultrahigh vacuum, good layer thickness control, etc. This is a serious drawback with respect to possible applications, because at present such conditions can be achieved only in rather specialized laboratories, so that applications seem to be far from practice.

On the other hand, there exists a second class of materials exhibiting the GMR effect, which was hardly noticed by research groups actually dealing with the GMR in multilayers. Recently, we have reported on the GMR in various uranium-based compounds, which crystallize in layered-like structures.⁴⁻⁷ By driving these compounds through a metamagnetic transition towards an induced ferromagnetic alignment, a drastic reduction of the electrical resistivity is found, which exceeds that of multilayer systems by far and is as large as $\Delta\rho/\rho = 650\%$ at 4.2 K in the case of UNiGa.^{4,8} Although the GMR in the uranium compounds studied up to now is only present at low temperatures and (in most cases) relatively high magnetic fields, a deeper understanding of the mechanism responsible of the GMR effects in these materials could yield a considerable impetus in materials research.

In this contribution, we review the magnetoresistance effects observed in different UTX compounds (T=transition metal and X= p electron metal), which have been studied extensively on single crystals. The GMR effect found in UNiGa,^{4,8} UNiAl,^{5,8} UPdIn,^{6,8} and UNiGe^{7,8} will be compared with the effect in multilayer systems. The mechanism responsible for GMR in both types of systems and their main differences will be discussed.

II. EXPERIMENTAL RESULTS

Within an extensive research program on UTX compounds, we have studied the compounds crystallizing in the hexagonal ZrNiAl structure in most detail. The structure is built up by alternating U-T and T-X basal plane layers. For the compounds crystallizing in this structure, we find the uranium magnetic moments coupled ferromagnetically within the U-T planes, while the weaker interplane coupling is ferro- or antiferromagnetic leading to ordering with magnetic moments pointing in the c direction. In magnetic multilayers as well, ferromagnetically ordered layers are found, but in contrast to the uranium compounds here the magnetic moments are confined to the plane.

A typical example of uranium compounds is UNiGa, which orders antiferromagnetically at 40 K. Its antiferromagnetic ground state is characterized by a sequence of $(++--+-)$ orientations of equal magnetic moments. At low temperatures, UNiGa aligns ferromagnetically upon application of a magnetic field of about 1 T along the c axis. In the configuration $i\parallel B\parallel c$ axis, the metamagnetic transition toward the induced ferromagnetic alignment is accompanied by a drastic decrease of the resistivity, which exceeds $120\ \mu\Omega\text{ cm}$ at 4.2 K (Fig. 1). This means a change of the resistivity $\Delta\rho/\rho$ equal to 650%. The effect in the perpendicular configuration $i\perp B\parallel c$ axis $\Delta\rho/\rho$ is smaller, but it still amounts to 200%. In both configurations, we observe a considerable hysteresis of about 0.25 T at 4.2 K (above 10 K there is no hysteresis observed), which reflects the hysteresis seen in the magnetization curves. No metamagnetic transition is observed for the

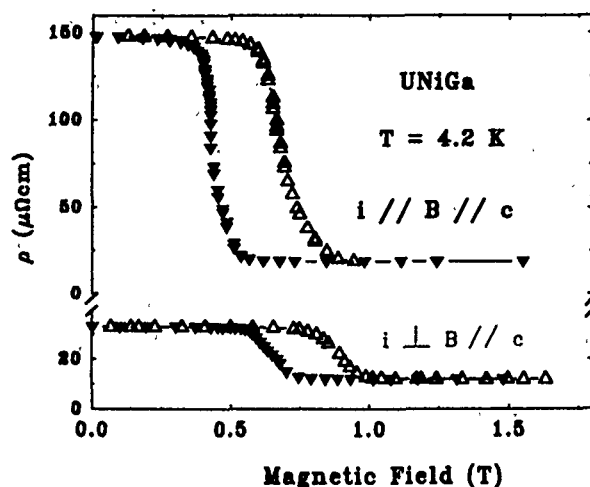


FIG. 1. Field dependence of the electrical resistivity of UNiGa at 4.2 K in the configuration $i \parallel B \parallel c$ axis and $i \perp B \parallel c$ axis. The open symbols represent the result obtained with increasing field, while the full symbols represent the one obtained with decreasing field. The lines are guides to the eye.

$B \perp c$ axis. As a consequence, there is also no comparable field effect in the electrical resistivity.

Another antiferromagnet with the ZrNiAl structure is UNiAl (Fig. 2), which orders antiferromagnetically at 18 K. At 4.2 K, the ferromagnetic alignment in this compound is achieved in fields above 11 T. Again, we find the metamagnetic transition to be accompanied by a drastic reduction of the electrical resistivity for fields applied along the c axis ($\Delta\rho/\rho=425\%$ for the $i \parallel B \parallel c$ axis and $\Delta\rho/\rho=330\%$ for the $i \perp B \parallel c$ axis). In UNiAl, the slow saturation tendency in the ferromagnetically aligned phase may originate from spin fluctuations present in this compound. In contrast to the previous compound, we do not observe any hysteresis.

Giant magnetoresistance effects in uranium intermetallics are not limited to pure antiferromagnets, which is illustrated by UPdIn, where an uncompensated antiferromagnetic structure with the stacking sequence $(++-+-)$ is found

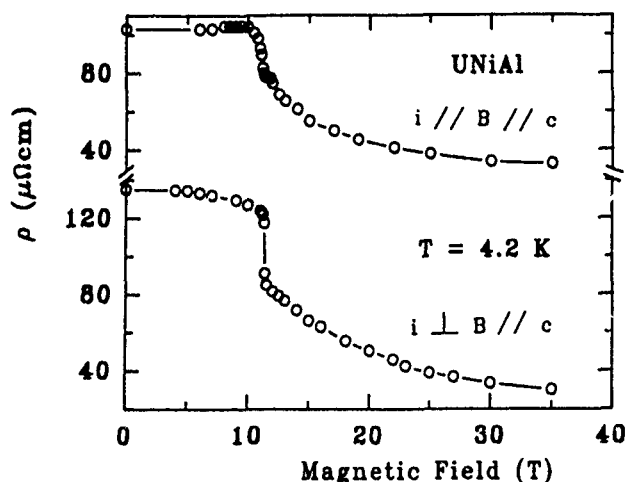


FIG. 2. Field dependence of the electrical resistivity of UNiAl at 4.2 K in the configuration $i \parallel B \parallel c$ axis and $i \perp B \parallel c$ axis. The symbols represent the data points measured in fields, which were kept constant for at least 150 ms. The lines are guides to the eye.

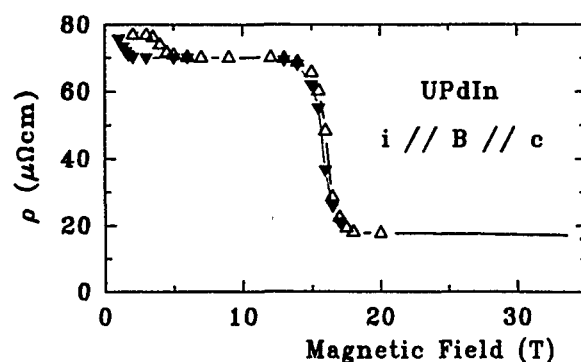


FIG. 3. Field dependence of the electrical resistivity of UPdIn at 4.2 K in the configuration $i \parallel B \parallel c$ axis. The open symbols represent the data points measured in fields, which were kept constant for at least 150 ms. Full symbols represent the measurement obtained after a preceding 20-T pulse (decreasing field). The lines are guides to the eye.

below 8.5 K. At 4.2 K, the application of a magnetic field ($B \parallel c$ axis) yields a transformation of the magnetic structure of UPdIn to a structure with a stacking sequence $(++-)$ in a field of about 3 T, which displays a hysteresis of about 1 T. The full ferromagnetic alignment is achieved above 17 T. Again, we find both metamagnetic transitions to be accompanied by a reduction of the electrical resistivity (Fig. 3). The total effect $\Delta\rho/\rho$ amounts to 350%.

The example of the antiferromagnet UNiGe, which crystallizes in the orthorhombic TiNiSi structure, shows that GMR effects are not restricted to a ZrNiAl structure-type of compounds. At 4.2 K, the destruction of the antiferromagnetic structure of UNiGe is reflected by two metamagnetic transitions at 3 and 9 T for the $B \parallel c$ axis (Fig. 4). For this compound, the total effect $\Delta\rho/\rho$ is equal to 290%. However, in contrast to the previous example an increased electrical resistivity is found for the intermediate phase between 3 and 9 T.

III. DISCUSSION AND CONCLUSIONS

In the ZrNiAl-type of compounds, the closer U-U distance and the stronger $5f-d$ hybridization within the U-T layers lead to a much stronger magnetic coupling of the ura-

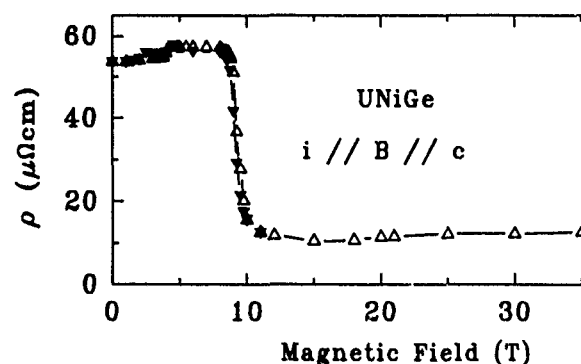


FIG. 4. Field dependence of the electrical resistivity of UNiGe at 4.2 K in the configuration $i \parallel B \parallel c$ axis. The symbols represent the results obtained with increasing (open triangles) and decreasing fields (full triangles), which were kept constant for at least 100 ms. The lines are guides to the eye.

niun magnetic moments within the basal plane than along the c axis. For these compounds, the hybridization-induced exchange yields a strong ferromagnetic coupling within the plane, while the coupling along the c axis is much weaker. For TiNiSi-type of compounds, a similar situation is found, in this case with strong coupling along the a axis. In magnetic multilayers, one also finds strong ferromagnetic intralayer coupling and "weak" interlayer coupling, although in these systems the direction of the moments is confined within the layers. On the other hand, similar to the situation in magnetic multilayers, in the uranium antiferromagnets the weak antiferromagnetic coupling can be overcome by relatively low external magnetic fields, which is a necessary prerequisite of the GMR effect. The occurrence of GMR effects in multilayer systems is usually ascribed to spin-dependent scattering (for a review see Ref. 9). This raises the question, whether the GMR effect in uranium intermetallics also may be explained by this mechanism. In an antiferromagnetically ordered compound, spin-dependent scattering is thought to occur at defects. In particular, magnetic atoms occupying sites in the nonmagnetic layers may be effective scatterers (this is the analog of surface roughness in multilayer structures). However, in view of the expected number of such atoms and the estimated value of spin-disorder scattering per atom make this an unlikely mechanism to account for the observed effects. Therefore, the origin of such a spin-dependent scattering term in the electrical resistivity remains unclear. A possible mechanism would be electron-electron interactions. In order to understand why the GMR effect is larger in uranium compounds than in the multilayers, we have to consider the differences of both systems in this context. The most obvious difference is the "layer" thickness and quality (determined by the crystal structure). In contrast to multilayers, in uranium intermetallics we are dealing with a perfect sequence of monolayers. Therefore, we cannot invoke the picture of subband conductivities, where crossing an interface is said to lead to a switching between majority and minority bands, resulting in resistance. Instead, the influence of the antiferromagnetic order on the band structure has to be considered.

In this picture, the electrical resistivity in the antiferromagnetic state in the uranium intermetallics is determined by a term involving impurity scattering and by the presence of new Brillouin zone boundaries, which eliminate parts of the Fermi surface. In the ferromagnetically aligned state, the electrical resistivity of the uranium compounds is thought to be mainly determined by the impurity term, which might be reduced with respect to its value in the antiferromagnetic state, due to the alignment of impurity spins. An analogous reduction must occur in multilayers, so that this cannot explain the large GMR effect in uranium compounds. A drastic change in the topology of the Fermi surface, in the effective number of carriers and in the Fermi velocities would be necessary to account for the spectacular effects observed. If this explanation is correct, one may doubt whether the large GMR effects discussed above can ever be achieved in multilayer systems.

With respect to possible applications, the compounds discussed in this contribution incur some problems. Quite apart from the problem of introducing uranium in the household or office environment, these compounds have low ordering temperatures and (in some cases) high magnetic fields are necessary to obtain ferromagnetic alignment. However, it may be expected that upon substitution and variation of the composition these parameters can be modified easily. A second difficulty may be that the production of good-quality single crystals is sometimes even more difficult than the production of multilayers. However, to obtain the GMR effect there is no need for single crystals, which is indicated already by the large reduction of the electrical resistivity for current both parallel and perpendicular to the magnetic field. Palstra *et al.*¹⁰ have indeed reported a reduction of the electrical resistivity of UNiGa polycrystal by 60%, which means $\Delta\rho/\rho=150\%$. Furthermore, it should be noted that neither uranium nor a layered-like structure appear to be really necessary ingredients for the occurrence of GMR effects, which was demonstrated by Schinkel *et al.* on FeRh alloys, where the electrical resistivity drops from 22 to 2 $\mu\Omega\text{ cm}$ upon application of a magnetic field.¹¹

In conclusion, the occurrence of GMR effect in uranium compounds emphasizes that there exist alternatives for application with respect to magnetic multilayers. At this stage, we try to get a deeper insight in the mechanism responsible for GMR effects in uranium systems, which could guide the search for compounds suitable for applications.

ACKNOWLEDGMENTS

This work is part of the research program of the "Stichting voor Fundamenteel Onderzoek der Materie" (FOM), which is financially supported by the "Nederlandse Organisatie voor Wetenschappelijk Onderzoek" (NWO). The work of V. S. and L. H. has been supported by Charles University under Grant No. 312.

- ¹M. N. Baibich, J. M. Broto, A. Fert, F. Nguyen Van Dau, F. Pretoff, P. Eitenne, G. Creuzet, A. Friederich, and J. Chazelas, *Phys. Rev. Lett.* **61**, 2472 (1988).
- ²S. S. P. Parkin, Z. G. Li, and D. J. Smith, *Appl. Phys. Lett.* **58**, 2710 (1991).
- ³C. F. Majkrzak, J. Kwo, M. Hong, Y. Yafet, D. Gibbs, C. L. Chien, and J. Bohr, *Adv. Phys.* **40**, 99 (1991).
- ⁴V. Sechovsky, L. Havela, L. Jirman, W. Ye, T. Takabatake, H. Fujii, E. Brück, F. R. de Boer, and H. Nakotte, *J. Appl. Phys.* **70**, 5794 (1991).
- ⁵E. Brück, H. Nakotte, F. R. de Boer, P. F. de Chatel, H. P. van der Meulen, J. J. M. Franse, A. A. Menovsky, N. H. Kim-Ngan, L. Havela, V. Sechovsky, J. A. A. J. Perenboom, N. C. Tuan, and J. Sebek, *Phys. Rev. B* (submitted).
- ⁶H. Nakotte, E. Brück, F. R. de Boer, A. J. Riemersma, L. Havela, and V. Sechovsky, *Physica B* **179**, 269 (1992).
- ⁷K. Prokeš, H. Nakotte, E. Brück, F. R. de Boer, L. Havela, V. Sechovsky, P. Svoboda, and H. Maletta, *IEEE Trans. Magn.* (to be published).
- ⁸Note, that in Refs. 4–7 there is generally used $\Delta\rho/\rho=(\rho_{AF}-\rho_F)/\rho_{AF}$, instead of the expression $\Delta\rho/\rho=(\rho_{AF}-\rho_F)/\rho_F$ commonly used in the multilayer research.
- ⁹R. E. Camley and R. L. Stamps, *J. Phys. Condensed Matter* **5**, 3727 (1993).
- ¹⁰T. T. M. Palstra, G. J. Nieuwenhuis, J. A. Mydosh, and K. H. J. Buschow, *J. Magn. Magn. Mater.* **54–57**, 549 (1986).
- ¹¹C. J. Schinkel, R. Hartog, and F. H. A. M. Hochstenbach, *J. Phys. F* **4**, 1412 (1974).

Preparation of Ni-Fe/Cu multilayers with low coercivity and GMR effect by ion beam sputtering

Masahiko Naoe, Yasuyoshi Miyamoto, and Shigeki Nakagawa

Department of Physical Electronics, Tokyo Institute of Technology, 2-12-1 O-okayama, Meguro, Tokyo 152, Japan

Multilayers composed of 30 [Ni-Fe/Cu] bilayers deposited on a 50-Å-thick Fe buffer layer were prepared by ion beam sputtering. The magnetoresistance (MR) ratio $\Delta\rho/\rho_0$ of the multilayers took high value at the Cu layer thickness δ_{Cu} of 10, 20, and 32 Å for the multilayers with Ni-Fe layer thickness $\delta_{\text{Ni-Fe}}$ of 10 Å. It was observed that (100) orientation of Ni-Fe and Cu crystallites were enhanced at δ_{Cu} of 20 and 32 Å. The multilayered film with δ_{Cu} of 10 Å exhibited $\Delta\rho/\rho_0$ as high as 12%. The multilayered film possessed good soft magnetic properties, and exhibited coercivity H_c and relative permeability μ_r of about 4 Oe and 800, respectively. The saturation magnetic field H_s was about 300 Oe. $\Delta\rho/\rho_0$, H_c , and H_s at δ_{Cu} of 20 Å, i.e., at the "second peak," were 6%, 10 Oe, and 25 Oe, respectively. The δ_{Cu} dependence of $\Delta\rho/\rho_0$ seemed to be correspondent to that of the preferential orientation of the (100) plane. Ni-Fe/Cu multilayers with the same construction but without an Fe buffer layer did not reveal apparent (100) preferential orientation and did not exhibit $\Delta\rho/\rho_0$ as high as detectable. Then, $\Delta\rho/\rho_0$ was strongly dependent not only on interlayer thickness, such as δ_{Cu} , but also (100) crystallite orientation.

I. INTRODUCTION

Giant magnetoresistance (GMR) effect has been successfully investigated for several multilayers such as Fe/Cr,¹ Co/Cu,^{2,3} and Ni-Fe/Cu.⁴⁻⁶ However, these GMR multilayers have exhibited high coercivity H_c above several hundreds Oe and saturation magnetic field H_s above 1 kOe. They should exhibit H_c and H_s as low as possible in order to apply them to MR heads and magnetic field sensors. Ni-Fe/Cu multilayers seemed to be applicable for these devices because of their soft magnetism with GMR effect. If the GMR multilayers possess soft magnetic properties applicable for the inductive recording heads, it seems to be very convenient to construct high efficient heads. Then, it is required to prepare GMR films with soft magnetic properties. There are several studies regarding low H_s in GMR multilayers.^{7,8} In this study, the multilayers composed of Ni-Fe and Cu layers were prepared by an ion beam sputtering apparatus which can deposit the Ni-Fe layer with low coercivity H_c and saturation magnetic field H_s and the Cu layer without defects on plasma-free substrate at low gas pressure.

II. EXPERIMENTAL PROCEDURE

Specimen multilayers were deposited on Si(100) wafer substrates by sputtering Ni₈₁Fe₁₉ alloy and Cu metal targets alternately by the ions extracted from a Kaufman-type of ion source. Ar gas pressure and acceleration of the ions for sputtering were set at 0.1 mTorr and 500 V, respectively. 50-Å-thick Fe buffer layers were predeposited on the substrates before preparation of the multilayers. Deposition rates of Ni-Fe and Cu layers were 14 and 23.5 Å/min, respectively. Multilayers were composed of 30 [Ni-Fe/Cu] bilayers. Crystallographic structure was analyzed by x-ray diffractometry (XRD). Magnetic characteristics, such as H_c and the saturation magnetization M_s , were evaluated by a vibrating-sample magnetometer (VSM). The relative permeability μ_r were

measured at 4 MHz by the shunt core method. The MR of the multilayers was measured by the four probe method at room temperature.

III. RESULTS AND DISCUSSION

It is well known that the GMR effect is sensitive to the thickness of the interlayer between ferromagnetic layers. Then, multilayered films were constructed with 30 bilayers composed of Ni-Fe layers with thickness $\delta_{\text{Ni-Fe}}$ of 10 Å and Cu layers with thickness of δ_{Cu} in the range of 5–34 Å. Figure 1 shows the variation of XRD patterns of multilayered films with various δ_{Cu} . These patterns implied that the preferential orientation of crystallites in Ni-Fe and Cu layers were so sensitive to δ_{Cu} for $\delta_{\text{Ni-Fe}}$ of 10 Å. It seemed that the (100) orientation of Ni-Fe and Cu crystallites were enhanced at δ_{Cu} of 20 and 32 Å. The enhancement of the (100) preferential orientation seemed to follow certain periodicity. Figure 2 shows the δ_{Cu} dependence of the ratio of the (200)

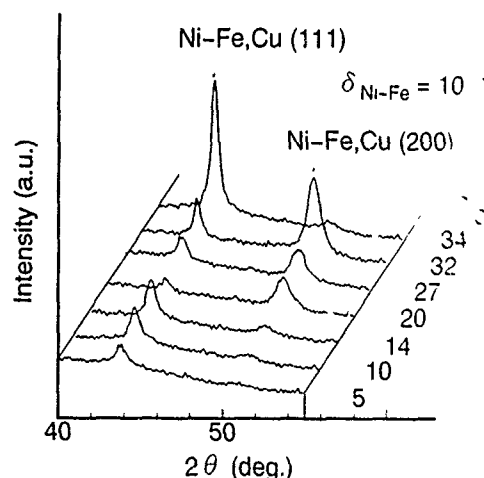


FIG. 1. Variation of XRD patterns of multilayered films for films with various δ_{Cu} .

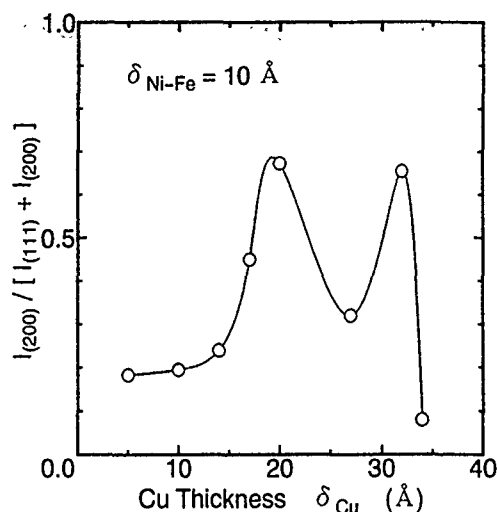


FIG. 2. δ_{Cu} dependence of the ratio of (200) diffraction intensity $I_{(200)}/[I_{(111)}+I_{(002)}]$.

diffraction intensity $I_{(200)}$ to the total of diffraction intensities of $[I_{(111)}+I_{(002)}]$. It was clearly found that the enhancement of (100) orientation occurred at δ_{Cu} of 20 and 32 Å.

Figure 3 shows the δ_{Cu} dependences of the MR ratio $\Delta\rho/\rho_0$ and the coercivity H_c . $\Delta\rho/\rho_0$ took a high value at δ_{Cu} of 10, 20, and 32 Å. Such a high $\Delta\rho/\rho_0$ seemed to be attained in the film with (100) orientation in crystallites as shown in Fig. 2. $\Delta\rho/\rho_0$ at δ_{Cu} of 10 Å, i.e., at first peak, was 12%. H_c as low as about 4 Oe at δ_{Cu} of 10 Å. The $\Delta\rho/\rho_0$ saturation magnetic field H_s was about 300 Oe. It had been confirmed that these multilayers exhibited almost the same $\Delta\rho/\rho_0$ and quite low H_c compared with other multilayers. The δ_{Cu} dependence of $\Delta\rho/\rho_0$ seemed to be correspondent to that of preferential orientation of the (100) plane as mentioned above. On the other hand, $\Delta\rho/\rho_0$, H_c , and H_s at δ_{Cu} of 20 Å, i.e., "at second peak," were 6%, 10 Oe, and 25 Oe, respectively. The films with δ_{Cu} larger than 20 Å possessed slightly semihard magnetism. Figure 4 shows the δ_{Cu} dependence of the relative permeability μ_r of the multilayers. The films with δ_{Cu} lower than 20 Å seemed to exhibit relatively high μ_r . It should be very attractive that the film

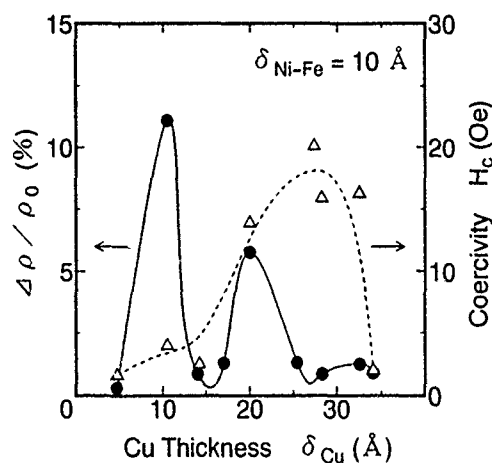


FIG. 3. δ_{Cu} dependences of the MR ratio $\Delta\rho/\rho_0$ and coercivity H_c .

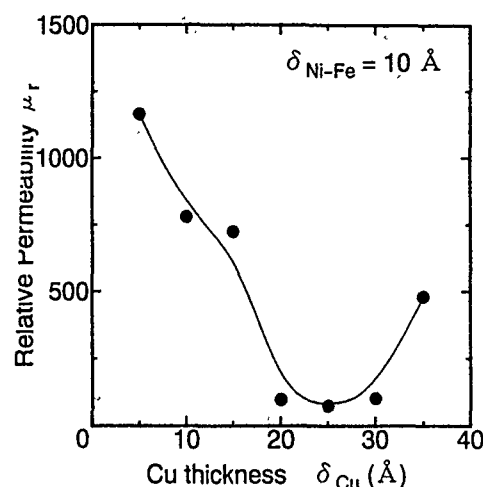


FIG. 4. δ_{Cu} dependence of μ_r multilayers.

with δ_{Cu} of 10 Å, i.e., at first peak, exhibited μ_r as sufficiently high as about 800. Figure 5 shows the typical $M-H$ hysteresis loops of the film at first peak, namely with δ_{Cu} and $\delta_{\text{Ni-Fe}}$ of 10 and 10 Å, respectively. Although a little magnetic anisotropy was detectable, the coercivities H_c were low enough in any direction. It was confirmed that the multilayers at first peak exhibited not only high $\Delta\rho/\rho_0$, but also good soft magnetism applicable for magnetic recording heads.

On the other hand, the Ni-Fe/Cu multilayers with the same construction but without an Fe buffer layer did not reveal apparent (100) preferential orientation and did not exhibit sufficiently high $\Delta\rho/\rho_0$. Then $\Delta\rho/\rho_0$ seemed to be strongly dependent not only on interlayer thickness, such as δ_{Cu} , but also on (100) orientation of both crystallites. In other words, the Fe buffer layer had played an important role for promotion of (100) orientation and enhancement of GMR effect in the multilayers. Figure 6 shows the XRD patterns for two types of films. One is a thick Ni-Fe single layer with $\delta_{\text{Ni-Fe}}$ of 1000 Å and the other is a double layer composed of a thick Ni-Fe layer with $\delta_{\text{Ni-Fe}}$ of 500 Å and an Fe buffer

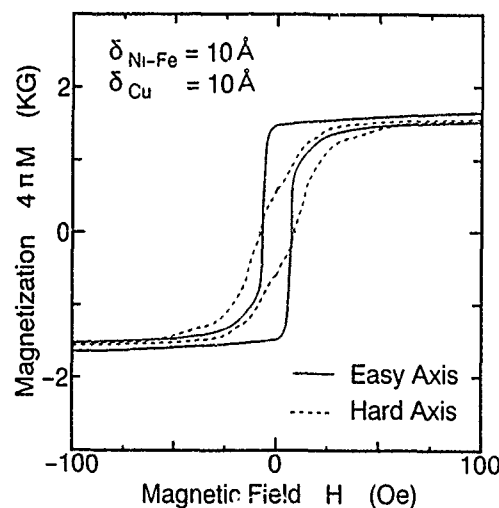


FIG. 5. Typical $M-H$ hysteresis loops of film at first peak, namely with δ_{Cu} and $\delta_{\text{Ni-Fe}}$ of 10 and 10 Å, respectively.

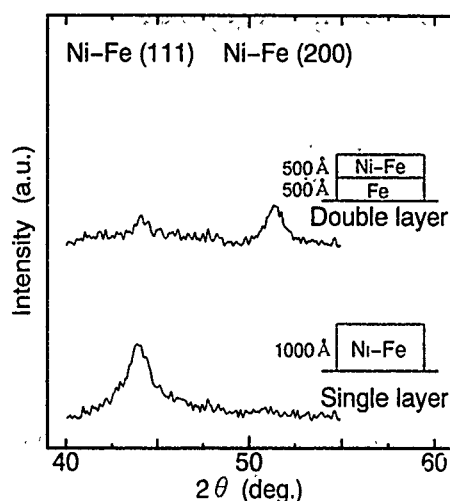


FIG. 6. XRD patterns for films of Ni-Fe single layer and Ni-Fe/Fe double layer.

layer with thickness of 500 Å. Although the Ni-Fe single layer revealed only apparent (111) orientation, the Ni-Fe layer with an Fe underlayer revealed (100) orientation. It was concluded that the Fe buffer layer promoted the (100) orientation in Ni-Fe fcc crystallites deposited on it.

IV. CONCLUSIONS

Multilayers composed of 30 [Ni-Fe/Cu] bilayers deposited on a 50-Å-thick Fe buffer layer were prepared by ion beam sputtering in order to attain a high MR ratio and possess a soft magnetism applicable to recording heads. The results obtained are as follows:

(1) (100) orientation of Ni-Fe and Cu crystallites in the multilayers were enhanced at δ_{Cu} of 20 and 32 Å. The δ_{Cu} dependence of $\Delta\rho/\rho_0$ seemed to be correspondent to that of a preferential orientation of the (100) plane.

(2) $\Delta\rho/\rho_0$ took a high value at δ_{Cu} of 10, 20, and 32 Å. For example, $\Delta\rho/\rho_0$ at δ_{Cu} of 10 Å was as high as 12%. H_c and μ_r were about 4 Oe and 800, respectively. $\Delta\rho/\rho_0$, H_c , and H_s at δ_{Cu} of 20 Å, i.e., at second peak, were 6%, 10 Oe, and 25 Oe, respectively.

(3) Ni-Fe/Cu multilayers with the same construction but without an Fe buffer layer did not reveal apparent (100) preferential orientation and did not possess $\Delta\rho/\rho_0$ as high as detectable. $\Delta\rho/\rho_0$ was strongly dependent on not only interlayer thickness, such as δ_{Cu} , but also (100) crystallites orientation.

As a result, we have succeeded in prepare, GMR multilayers with sufficiently soft magnetic properties suitable not only for detecting as a MR head but also for writing it as an inductive head. Then these multilayers seemed to be applicable for a core layer in inductive-MR hybrid type of recording heads.

¹M. N. Baibich, J. M. Broto, A. Fert, F. Nguyen Van Dau, F. Petroff, P. Etienne, G. Creuzet, A. Friedrich, and J. Chazelas, *Phys. Rev. Lett.* **61**, 2472 (1988).

²S. S. P. Parkin, R. Bhadra, and K. P. Roche, *Phys. Rev. Lett.* **66**, 2152 (1991).

³M. E. Tomlinson, R. J. Pollard, D. G. Lord, P. I. Grundy, and Z. Chun, *IEEE Trans. Magn.* **MAG-28**, 2662 (1992).

⁴S. S. Parkin, *Appl. Phys. Lett.* **60**, 512 (1992).

⁵R. Nakatani, T. Dei, T. Kobayashi, and Y. Sugita, *IEEE Trans. Magn.* **MAG-28**, 2668 (1992).

⁶R. Nakatani, T. Dei, and Y. Sugita, *J. Appl. Phys.* **73**, 6375 (1993).

⁷X. Bian, J. O. Ström-Olsen, Z. Altounian, Y. Huai, and R. W. Cochrane, *Appl. Phys. Lett.* **62**, 3525 (1993).

⁸M. Jimbo, S. Tsunashima, T. Kanda, S. Goto, and S. Uchiyama, *J. Appl. Phys.* **74**, 3341 (1993).

Novel magnetoresistance behavior in single trilayer spin valves

M. Patel, T. Fujimoto, E. Gu, C. Daboo, and J. A. C. Bland

Cavendish Laboratory, University of Cambridge, Madingley Road, Cambridge CB3 0HE, United Kingdom

Single trilayer spin valves consisting of uncapped FeNi(60 Å)/Cu(60 Å)/Co(40 Å) have been grown using ultrahigh vacuum (UHV) electron beam evaporation methods. Room temperature magnetoresistance (MR) measurements exhibit well defined plateaux corresponding to the full antiparallel alignment of the FeNi and Co magnetizations. This sharp switching behavior and precisely defined antiferromagnetic state is in contrast with the corresponding behavior reported for FeNi/Cu/Co multilayers.

INTRODUCTION

The discovery of the giant magnetoresistance (GMR) effect¹ has fuelled intense research into the properties of artificially engineered magnetic multilayers. Soft magnetic multilayers such as Fe₂₀Ni₈₀/Cu/Co² are of particular interest for their GMR behavior in low fields, in contrast with systems such as Fe/Cr and Co/Cu which saturate at high fields. In the present work we have utilized UHV electron beam evaporation growth techniques together with *in situ* magneto-optic Kerr (MOKE) magnetometry and reflection high-energy electron diffraction (RHEED) studies. We report the observation of sharp, independent magnetic switching for the two layers in the trilayer system Fe₂₀Ni₈₀/Cu/Co, corresponding to plateaux in the magnetoresistance (MR). In our samples a field of about 10 Oe aligns the layers antiparallel, and we believe this is the first direct observation of a definite antiparallel state in this system. We attribute the realization of the antiferromagnetic state to the uniaxial anisotropy induced by using MBE growth techniques. We show that the single trilayers exhibit very different properties from the work reported on multilayers. The independent switching and well defined antiferromagnetic state give rise to near ideal spin-valve³ behavior in our samples, which we investigate in detail.

The samples we have studied in all cases consist of a single trilayer of FeNi (60 Å)/Cu(60 Å)/Co(40 Å) grown on Si(100) and As-capped GaAs(001) substrates in a UHV chamber using electron beam evaporation techniques. *Ex situ* transmission electron microscopy (TEM) was used to characterize samples post growth, and revealed a polycrystalline structure with a grain size of 10 nm. In addition the MOKE measurements revealed that the first 30 Å of the FeNi was nonmagnetic, and RHEED and cross section transmission electron microscopy (XTEM) have indicated that a reaction occurs with the Si substrate to form a rough, amorphous layer consistent with other reports.^{4,5} Samples were deposited at ambient temperature (~50 °C) onto Si(100) and GaAs(001) wafers at a pressure not exceeding 5×10^{-8} mbar. Substrates were cleaned in an ultrasonic bath using IPA prior to insertion into the vacuum system. The deposition rates were typically 1, 5, and 2 Å/min for FeNi, Cu, and Co, respectively. The chamber was then vented and a CoO layer was allowed to form by oxidation of the Co surface layer. The thickness of the CoO layer was determined to be 20 Å by both SQUID magnetometry and polarized neutron reflectometry (PNR) measurements.⁶

Ex situ MR measurements were carried out using a four-point in-line geometry, at both room temperature and below using a continuous flow He cryostat. Room temperature measurements were also carried out by varying the angle between the two layer magnetizations to investigate the spin-valve effect, from which the GMR and anisotropic magnetoresistance (AMR) terms can then be isolated.

RESULTS

Figure 1 shows the *in situ* MOKE loops obtained during the growth of the sample. The loops obtained on the completed sample (a) show that the separate layers switch independently along the [100] axis, in contrast to the results of other studies on this system.² This sharp switching is realized by the presence of a uniaxial anisotropy in both layers, as evidenced by the [010] axis behavior. The anisotropy axes for the two layers are found to be rotated slightly from each other, and their directions are independent of any magnetic fields applied during growth or the substrate orientation. The abrupt switching behavior has been observed to deteriorate with increasing number of periods of the trilayer, and this suggests that the increasing waviness or roughness of the successive interfaces has a dramatic effect on the coupling between the ferromagnetic layers. This is consistent with recent reports on sputtered samples.⁷

From Fig. 1(b), the presence of a weak ferromagnetic exchange coupling between the FeNi and Co layers is also indicated by the increase of the FeNi layer coercivity upon Co deposition on the Cu interlayer. Figure 1(c) shows the effect of the CoO layer which forms almost instantaneously upon venting the chamber. The Co layer coercivity is seen to increase due to either weak exchange coupling to the paramagnetic oxide (the Néel temperature for CoO is 293 K)⁸ or pinning by structural defects formed during the oxidation process.

Figure 2(a) shows the superimposed MR and MOKE loops for a trilayer grown on Si(100). At point A, the layer magnetizations are both aligned parallel. At point B, the applied field is greater than the saturating field of the FeNi layer, but less than the coercive field of the Co layer. As a result, the layers are aligned antiparallel, and a true antiferromagnetic state is realized as has also been confirmed by SQUID and vibrating-sample (VS) magnetometry. At point C, the Co layer has also switched and so the layers are aligned parallel again. The MR behavior shows that when the layers are aligned parallel the resistance is a minimum, and that when the trilayer is in the antiferromagnetic configuration the MR exhibits plateaux. Figure 2(b) shows the sensi-

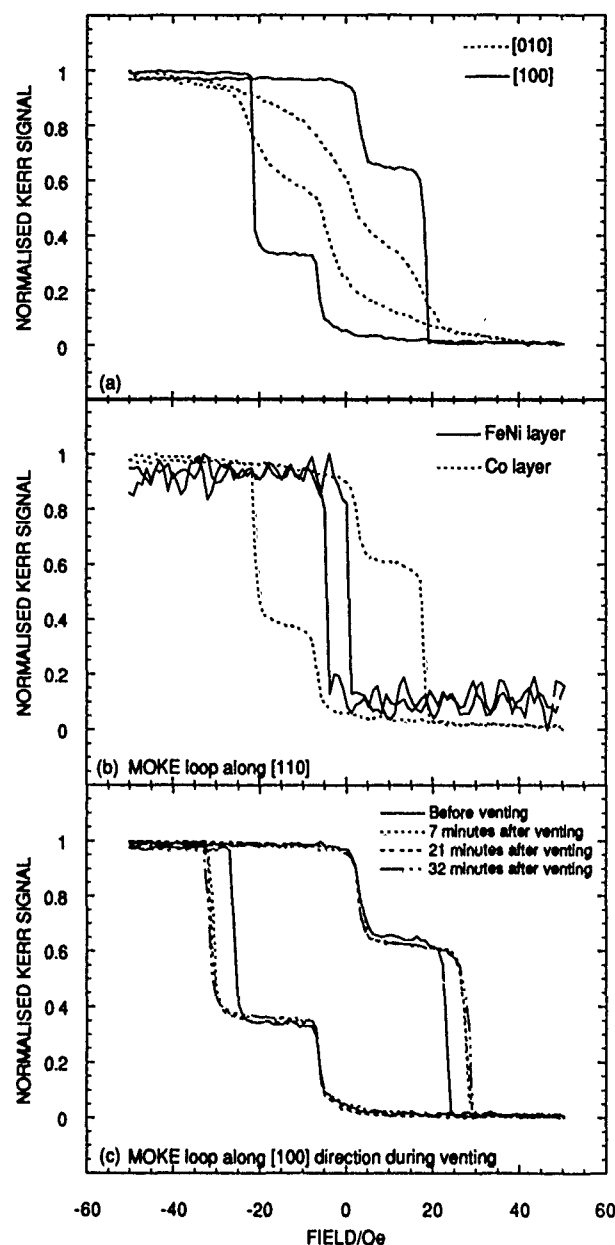


FIG. 1. *In situ* MOKE loops obtained for growth of single trilayer on a Si(100) substrate. See the main text for explanation.

tivity of a trilayer sample, which is defined as the change in MR per unit applied field. A maximum value of 0.51%/Oe is obtained for a sample with a total MR effect of 1.6%, which is larger than the sensitivity for FeNi fibers.⁹ This sample shows a slightly different MR- H characteristic due to prolonged exposure to air compared to the sample for Fig. 2(a).

Measurements were also carried out using the same method as reported by Miller¹⁰ in order to isolate the GMR and AMR terms and evaluate the spin-valve behavior of the trilayers. Samples were first saturated with an applied field of 200 Oe in the easy axis. The applied field was then reduced and rotated with respect to the sample. Figure 3 shows the resistance as a function of angle between the applied fields of 22, 28.6, and 37.4 Oe and the initial saturation direction. The resistance behavior is found to very closely follow a $\cos(\theta)$ dependence and shows one peak corresponding to antiparal-

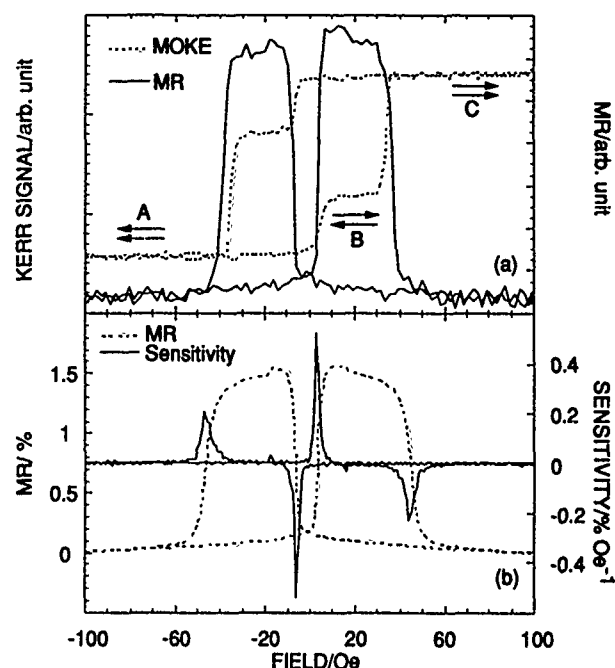


FIG. 2. *Ex situ* MOKE and MR loops for a trilayer grown on Si(100): (a) MR and MOKE loops for sample immediately after growth; (b) MR and sensitivity measured on the same sample on more sensitive equipment after 50 days.

lel layer alignment. When the field is large enough to rotate the Co layer magnetization as well, true antiparallel alignment is never achieved so the resistance change is much smaller, and two peaks are observed. The AMR term is estimated to be roughly 1/15th of the GMR term, which is consistent with previously reported values.^{3,10,11}

Figure 4 shows the temperature variation of the maximum and minimum resistance and the MR ratio with temperature. Below 50 K the samples can no longer be saturated so the minimum resistance cannot be measured. The peak in the resistance at 250 K is due to increased shunting in the Si substrate. Between 50 and 250 K the MR decreases linearly by 63%, while the FeNi layer magnetizations only decrease by 7%. The presence of the CoO layer complicates further

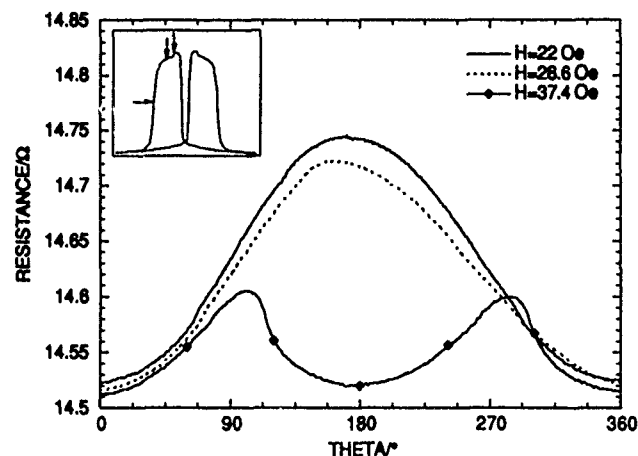


FIG. 3. Angular dependence of the MR for a trilayer grown on Si(100). The inset shows the values of the rotating applied field in relation to the MR loop along the [100] direction.

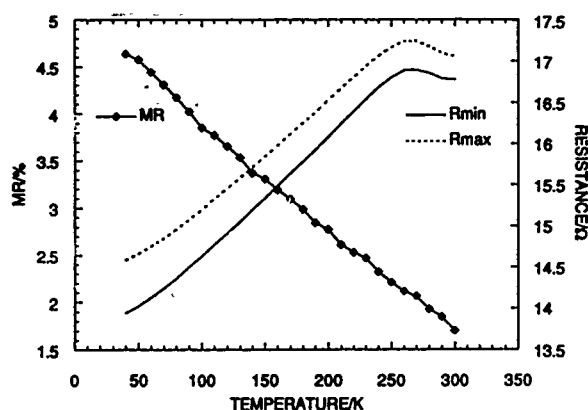


FIG. 4. Temperature dependence of the minimum resistance, the maximum resistance, and the MR ratio for a single trilayer grown on Si(100).

analysis of the data and the decrease in the Co layer magnetization cannot be measured accurately, but experiments on capped samples will be reported in a future publication.⁶ However, it can still be inferred that the change in the MR is strongly dependent on the temperature dependence of the magnon scattering, since the minimum resistance changes by only 21%.

DISCUSSION

The above results observed for the angle-dependent MR show that the samples exhibit near ideal spin-valve behavior. It is possible to simulate the MOKE response of the samples if the magnetization reversal is assumed to be a single domain coherent rotation process. The energy of the system can be expressed as

$$E = -t_1 \mathbf{M}_1 \cdot \mathbf{H} - t_2 \mathbf{M}_2 \cdot \mathbf{H} + K_{u1} \sin^2(\theta_1 - \alpha_1) + K_{u2} \sin^2(\theta_2 - \alpha_2) - 2A_{12} \cos(\theta_1 - \theta_2). \quad (1)$$

The first and second terms are the usual Zeeman terms for the interaction of a region of magnetization M and thickness t in an external field H for the two separate layers. The following two terms are the uniaxial anisotropy terms for each layer, where $(\theta - \alpha)$ is the angle between the magnetization and the easy axis. The final term is the bilinear exchange coupling term between the two magnetic layers. The calculation then gives the direction of the magnetization of each layer which can be used to approximate the hysteresis loop. Once the directions of the magnetizations are known, it is then possible to approximate the shape of the MR by using the following equation:

$$R = R_0 + R_{AMR} \cos^2 \theta_1 + R_{GMR} \cos(\theta_1 - \theta_2), \quad (2)$$

where it is assumed that the GMR and AMR terms are added in series and R_{GMR} and R_{AMR} are their amplitudes. The results for this simulation are shown with experimental results for a trilayer grown on GaAs(001) in Fig. 5. The values for the anisotropy constants used for the simulation were 3.1×10^3 and 1.4×10^5 erg/cm³ for the FeNi and Co, respectively, which are larger than the experimentally determined values from the $M-H$ loops. In addition, the switching fields for the 45° axis are less than those observed experimentally.

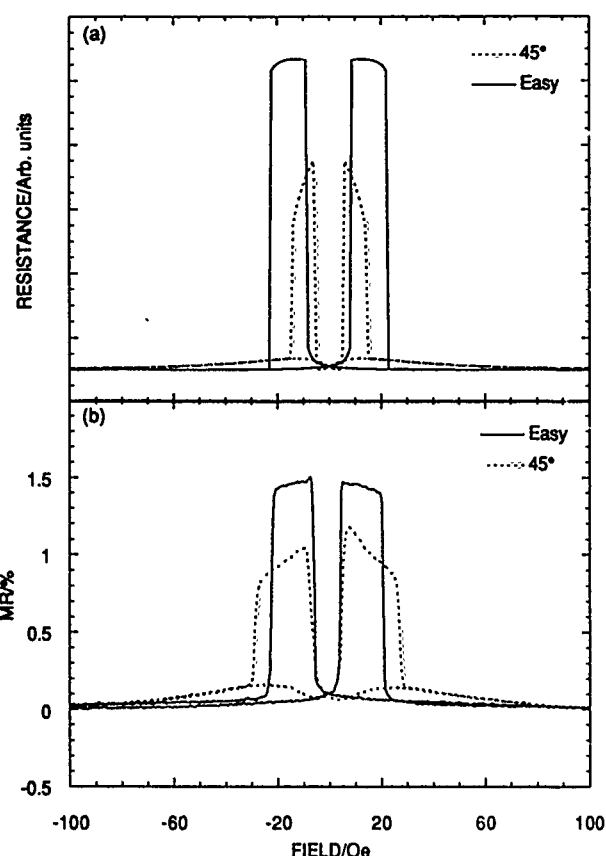


FIG. 5. MR loops for a trilayer grown on GaAs(001): (a) Simulated loops along the easy axis and the axis at 45°; (b) experimentally observed loops along the easy axis and the axis at 45°.

This indicates that domain wall sweeping rather than magnetization rotation is taking place at these fields and that there may be internal fields in our polycrystalline samples that need to be included in the calculation. However, the qualitative agreement between the simulation and the experimentally observed MR curves is still extremely good, and it can be concluded that if the field is applied along the Co easy axis, antiparallel alignment of the complete layer magnetizations can be achieved.

The financial support of the SERC and MR Sensors is gratefully acknowledged.

- ¹G. Binasch, P. Grünberg, F. Saurenbach, and W. Zinn, *Phys. Rev. B* **39**, 4828 (1989).
- ²H. Yamamoto, T. Okuyama, H. Dohnomae, and T. Shinjo, *J. Magn. Magn. Mater.* **99**, 243 (1991).
- ³B. Dieny, V. S. Speriosu, S. S. P. Parkin, B. A. Gurney, D. R. Wilhoit, and D. Mauri, *Phys. Rev. B* **43**, 1297 (1991).
- ⁴S. S. P. Parkin, *Appl. Phys. Lett.* **60**, 512 (1992).
- ⁵C. Pirri, J. C. Peruchetti, G. Gewinner, and J. Derrien, *Phys. Rev. B* **29**, 3391 (1984).
- ⁶T. Fujimoto, M. Patel, and J. A. C. Bland, *J. Appl. Phys.* (to be published).
- ⁷T. Valet, P. Galtier, J. C. Jacquet, C. Mény, and P. Panissod, *J. Magn. Magn. Mater.* **121**, 402 (1993).
- ⁸A. P. Malozemoff, *J. Appl. Phys.* **63**, 3874 (1988).
- ⁹X. Bian, J. O. Ström-Olsen, Z. Altounian, Y. Huai, and R. W. Cochrane, *Appl. Phys. Lett.* **62**, 3525 (1993).
- ¹⁰B. H. Miller, E. Y. Chen, and E. D. Dahlberg, *J. Appl. Phys.* **73**, 6384 (1993).
- ¹¹T. Okuyama, H. Yamamoto, and T. Shinjo, *J. Magn. Magn. Mater.* **113**, 79 (1992).

1/f noise in giant magnetoresistive materials

H. T. Hardner

Department of Physics, University of Illinois at Urbana-Champaign, Urbana, Illinois 61801-3080

S. S. P. Parkin

IBM Almaden Research Center, 650 Harry Road, San Jose, California 95120-6099

M. B. Weissman, M. B. Salamon, and E. Kita

Department of Physics, University of Illinois at Urbana-Champaign, Urbana, Illinois 61801-3080

The main source of 1/f resistance noise in materials exhibiting giant magnetoresistance (GMR) is the GMR effect itself. Large 1/f noise from fluctuations in the parallel vs antiparallel alignment appears when $|dR/dH|$ is large. We have studied this noise as a function of the number of Co/Cu bilayers in multilayer samples and discuss the implications for devices. Barkhausen noise in the resistance as the field is swept through the GMR transition is used to estimate coherent domain sizes between 0.1 and 10 μm^2 for a single Co layer in the multilayers. GMR noise is also seen in a Co/Ag granular system.

Materials exhibiting giant magnetoresistance (GMR) are generating great interest in part because of their potential for technical applications in magnetic recording.¹ Realization of this potential will require understanding the limits set on detector sensitivity by intrinsic noise of the materials. We have characterized a large source of 1/f noise in Co/Cu multilayers exhibiting GMR and have studied its dependence on the number of layers. In addition, measurements of the resistive noise while the magnetic field is swept allow us to characterize the effective domain size for the GMR dynamics.

We also report GMR 1/f noise in preliminary measurements on a CoAg granular system. Such measurements potentially offer information to help determine the mechanism for the GMR effect in granular systems.^{2,3}

The Co/Cu multilayers were prepared at IBM and consist of varying numbers of sputtered bilayers. Each Co layer is 10-Å thick and in the samples denoted "A" ("B") each Cu spacer layer is 19-Å (9-Å) thick. The various samples are described in Table I. Each sample is photolithographically patterned into a bridge of four parallel arms. A constant current is applied to the sample and the resulting fluctuations in voltage across the bridge are amplified with commercial low-noise amplifiers, anti-alias filtered and then digitally sampled and Fourier transformed (and squared) by a standard PC to give the noise spectrum.

All the measurements discussed employ dc currents because ac probe currents were found to completely alter the noise spectra and ac GMR response. The techniques are more fully described elsewhere.⁴ All of the multilayer measurements were made at room temperature.

The data for each noise spectrum are collected while a constant magnetic field, H , is applied in the plane of the sample. After H is changed several minutes, at least, are allowed for the magnetization to reach quasiequilibrium before taking a spectrum. For the Barkhausen measurements, on the other hand, H is ramped continuously and voltage fluctuations are recorded directly as a function of time without Fourier transforming.

Figure 1 shows the form of the noise power and resistance as a function of H . The noise is plotted in the form of the dimensionless parameter α defined by $\alpha(f) \equiv fS_R(f)N/R^2$,⁵ where $S_R(f)$ is the power spectral density of fluctuations in R and N is the number of atoms in the sample. We have previously shown that $\alpha(H)$ can be predicted, except near $H=0$, via the fluctuation dissipation theorem from the out-of-phase response of the resistance to an ac magnetic field, using the assumption that R is a function only of the magnetization M .⁴

While H is being swept, the noise power at fields with large $|dR/dH|$ is much greater than in equilibrium, as illustrated in Fig. 2. Since essentially every layer pair must rotate from antiparallel (AP) to parallel (P) alignment as H increases from zero, this nonequilibrium (Barkhausen) GMR noise allows some characterization of the domains beyond that possible from the quasiequilibrium noise, for which the fraction of the sample fluctuating is not known.

It is easy to set an upper limit to the size of any domain whose P-AP order changes significantly in a step simply by looking for the maximum step sizes in the Barkhausen noise, and applying the relation^{6,7}

TABLE I. Sample characteristics.

Sample	A39	A30	A16	A10	A5	B
Cu thickness (Å)	19	19	19	19	19	9
Number of bilayers	39	30	16	10	5	39
Zero-field R (Ω)	166	125	115	127	275	323
$\Delta R/R_p$	0.26	0.235	0.149	0.114	0.067	0.45
Peak α	17	7.1	6.7	2	0.3	0.21
ΔH_M (kOe)	5	2.7	5.3	2.5	2	1

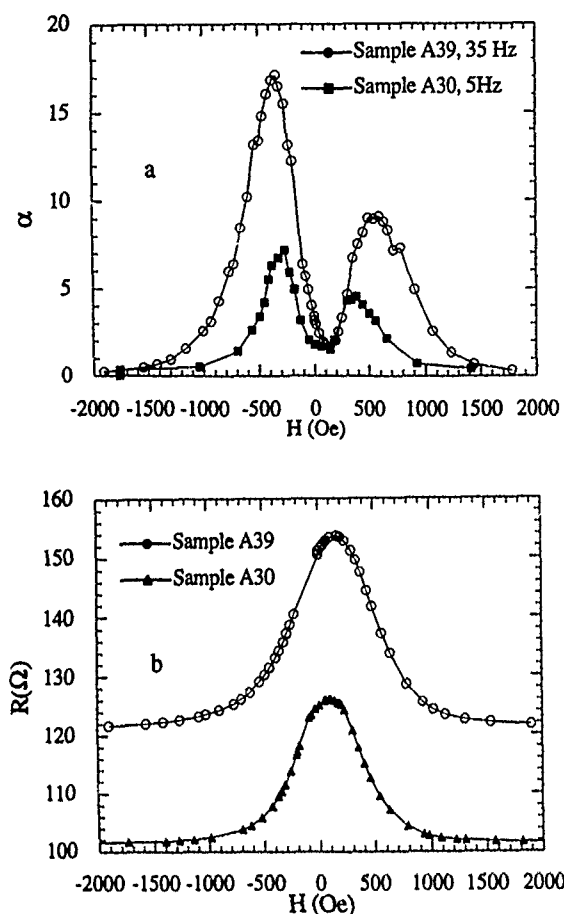


FIG. 1. (a) The dimensionless noise parameter α as a function of field, starting at large negative fields, for samples with two different numbers of bilayers. (b) Resistance as a function of field for the same two samples. Note that these resistances are measured across the sample bridges while the numbers in Table I are for a single branch of each sample.

$$R = R_{AP} - (M/M_S)^2 \Delta R, \quad (1)$$

where M_S is the saturation M and ΔR is the maximum decrease in R from R_{AP} , the antiparallel R . We find no obvious discrete domain switches, indicating that no layer pair with area greater than $10 \mu\text{m}^2$ reorders coherently.

The Barkhausen noise also lets us set a minimum typical domain size. The sweeps shown in Fig. 2 show that a finite change in H is required before one obtains a new random R , indicating that the noise signal at any field comes from domains that have rotated within about 50 Oe of that field. (This field range, like the noise amplitude, depends somewhat on field history.) Thus about 10% of the layers in the sample are involved in the Barkhausen noise at the maximum value. Then at the maximum

$$\langle (\delta R)^2 \rangle / R^2 \leq 0.1 (V_D/V) (\Delta R/R)^2 / 4 \quad (2)$$

by simple statistics, where V_D is a typical domain volume and V is the sample volume. The inequality arises because domains probably do not all switch from AP to P in single steps.

Equation (2) gives $V_D \geq 2 \times 10^{-4} \mu\text{m}^3$ or a domain area in one magnetic layer of $\geq 0.1 \mu\text{m}^2$. The number is somewhat dependent on whether $|H|$ is being increased or decreased. The limits on the domain area in sample B were

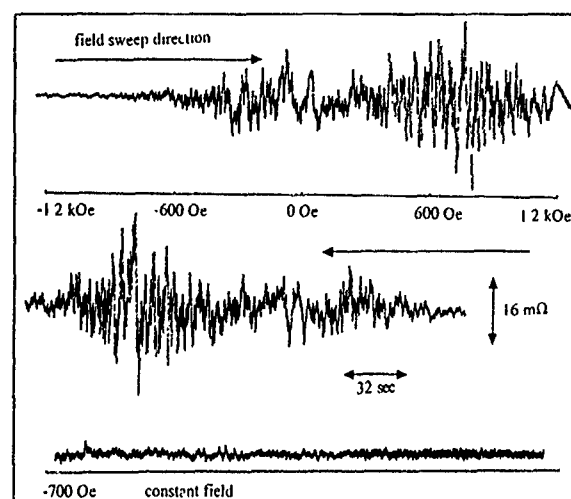


FIG. 2. Barkhausen noise in sample A39. Here the sample has 1-mA dc current in each branch. The -700-Oe constant field trace was taken after cycling to a large positive field—it corresponds to the region of largest noise when the field is continuously swept.

about an order of magnitude smaller. These rather large domains may limit the uniformity of the GMR in collections of small devices.

The size of the GMR effect ($\Delta R/R$) is well known to decrease when the number of multilayers is reduced. However, for practical applications in small devices the field sensitivity would be determined not only by the size of the GMR effect but also by the sample noise. At very high frequencies, Johnson noise rather than $1/f$ noise becomes the limiting background. However (for example), in 39-layer sensors operated at high current densities (e.g., $3 \times 10^6 \text{ A/cm}^2$) the average GMR $1/f$ noise will exceed the Johnson noise up to frequencies on the order of 10^7 Hz . In thinner samples a higher current density can be sustained, keeping the frequency below which the GMR $1/f$ noise becomes importantly high.

We have rated the samples (with various numbers of multilayers) according to the minimum field change ΔH_M , required to produce a change in R discernable above the GMR $1/f$ noise in any octave bandwidth. More precisely, we define ΔH_M by

$$(\Delta H_M)^2 = \alpha R^2 / (dR/dH)^2 N. \quad (3)$$

The results are listed in Table I.

Although both $\Delta R/R$ and N become smaller for thin samples, the reduction in the characteristic field together with the strong reduction in α give a slightly higher sensitivity (vs intrinsic $1/f$ noise) in the thinnest samples. The role of detailed sample properties, e.g., layer roughness, in determining the noise of each sample has not yet been sorted out. The deviation of sample A16 from the trend of the other samples suggests that some such individual differences may affect the comparisons of these samples. We also note that sample B, with 9-Å Cu layers has better incremental sensitivity than the samples with 19-Å layers, although at larger absolute H .

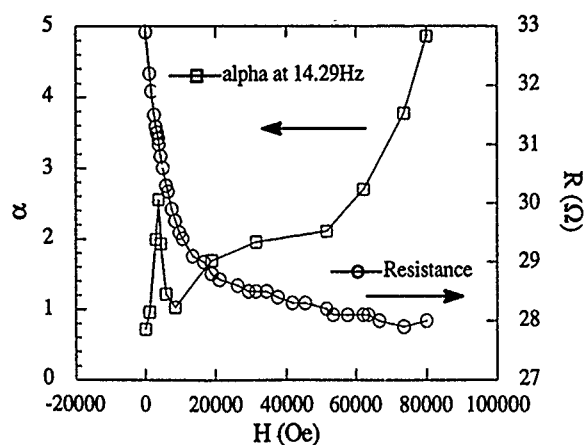


FIG. 3. α and resistance as a function of field, starting at high field, for the CoAg granular sample at 4.2 K.

Because noise measurements help characterize the couplings of the spins to R in their local environments, before averaging over the ensemble of environments, they can also be used to provide information on how the GMR itself works in inhomogeneous materials. Figure 3 shows a preliminary measurement of the $1/f$ noise and resistance in a granular Co/Ag GMR sample as a function of applied field at about 4.2 K.

The 294-nm-thick sample of Ag and (nominally 20 at. %) Co was prepared using two independent sputtering guns with rotating substrates at an Ar pressure of 5×10^{-3} Torr.⁸ α increases substantially to a peak near the maximum in $|dR/dH|$, as in the multilayers. The residual α at $H=0$ is less than 30% of the peak value. There is also a very gradual

increase in α at high H , whose origin (perhaps connected with enhancement of universal conductance fluctuations by the suppression of spin-flip scattering) remains undetermined.

This $\alpha(H)$ curve may have some implications for the GMR mechanism in an inhomogeneous material, since the noise depends on the mean square local sensitivity to magnetization, rather than the mean sensitivity. We believe that these variations in local sensitivity will prove to be different in the spin disorder scattering model³ and the d -band density-of-states model.²

In conclusion, we have shown that the GMR effect is accompanied by large $1/f$ noise, which may limit the sensitivity of GMR devices. Surprisingly, the thinner structures appear to have slightly better intrinsic field sensitivity. Preliminary experiments show that similar noise appears in a granular GMR material, for which it may provide evidence bearing on the GMR mechanism.

¹M. N. Baibich, *et al.*, Phys. Rev. Lett. **61**, 2472 (1988); G. Binach, P. Grunberg, F. Sauerbach, and W. Zinn, Phys. Rev. B **39**, 4828 (1989); J. J. Krebs, P. Lubitz, A. Chaiken, and G. A. Prinz, Phys. Rev. Lett. **63**, 1645 (1989).

²L. Xing, Y. C. Chang, M. B. Salamon, D. M. Frenkel, J. Shi, and J. P. Lu, Phys. Rev. B **48**, 6728 (1993).

³S. Zhang and P. M. Levy, Phys. Rev. B **43**, 11,048 (1991).

⁴H. T. Hardner, M. B. Weissman, M. B. Salamon, and S. S. P. Parkin, Phys. Rev. B (in press).

⁵M. B. Weissman, Rev. Mod. Phys. **60**, 537 (1988).

⁶J. Shi, S. S. P. Parkin, L. Xing, and M. B. Salamon, J. Magn. Magn. Mater. **125**, L251 (1993).

⁷S. Zhang, P. M. Levy, and A. Fert, Phys. Rev. B **45**, 8689 (1991).

⁸J. Shi, E. Kita, L. Xing, and M. B. Salamon, Phys. Rev. B **48**, 16119 (1993).

Effect of annealing on the giant magnetoresistance of sputtered Co/Cu multilayers

H. Zhang and R. W. Cochrane

*Département de Physique et Groupe de Recherche en Physique et Technologie des Couches Minces,
Université de Montréal, C.P.6128, Succ. A, Montréal, Québec H3C 3J7, Canada*

Y. Hùai

INRS-Energie et Matériaux, 1650, Montée Ste-Julie, C.P.1020, Varennes, Québec J3X 1S2, Canada

Ming Mao, X. Bian, and W. B. Muir

*Centre for the Physics of Materials and Department of Physics, McGill University, 3600 University Street,
Montréal, Québec H3A 2T8, Canada*

Co/Cu multilayers with the form of glass/Cu 50 Å[Co11.5 Å/Cu(t_{Cu})]₃₀/Cu50 Å, prepared by rf triode sputtering, exhibit oscillatory magnetoresistance (MR), as a function of the Cu layer thickness with a period of ≈ 12 Å and maximum MR values of 36.8% and 22.3% at 77 and 295 K, respectively. In order to study the effect of annealing on the structural and magnetic properties, five samples with Cu thicknesses between 9 and 34 Å were heat treated at temperatures up to 300 °C and analyzed by low- and high-angle x-ray diffraction, MR, and magneto-optic Kerr effect measurements. Annealing at moderate temperatures for the samples with Cu thicknesses around the second and third MR peaks leads to an initial increase in the MR. In contrast, annealing causes only a monotonic MR decrease for the sample at the first peak with a Cu thickness of 9 Å.

INTRODUCTION

The recent discoveries of giant magnetoresistance (GMR) and oscillatory exchange coupling in a wide variety of magnetic multilayers have stimulated a great deal of interest.^{1,2} In particular, sputtered Co/Cu multilayers exhibit the largest MR value and a well-defined oscillatory exchange coupling at room temperature.²⁻⁴ It is now generally agreed that GMR is associated with the reorientation of the magnetic moments in neighboring magnetic layers and has been interpreted on the basis of spin-dependent electron scattering at the magnetic/nonmagnetic interface and in the bulk of the magnetic layer.⁵ Studies demonstrate that in Fe/Cr^{6,7} and Co/Re⁸ multilayers the GMR is enhanced by the presence of interfacial roughness due to either changing preparation conditions⁶ or annealings^{7,8} while it decreases in some other Cu-based systems upon annealing.^{9,10}

In this paper, we report the effect of relatively low-temperature annealing up to 300 °C on the structural and magnetic properties of Co/Cu multilayers sputtered onto Cu buffer layers for a wide range of Cu thicknesses in order to follow the effect of structural modifications on the GMR.

EXPERIMENTAL DETAILS

Co/Cu multilayers with the form of glass/Cu50 Å[Co11.5 Å/Cu(t_{Cu})]₃₀/Cu50 Å were prepared using a modified single-source rf triode sputtering system¹¹ with a base pressure of less than 2×10^{-7} Torr. Depositions were carried out under 3.25 mTorr of pure argon at a rate of approximately 2 Å/s, the exact rates being calibrated by the layer thicknesses determined by low-angle x-ray diffraction. A sample shape of 8×4 mm² was chosen as suitable for both transport and x-ray measurements and was defined by a mask overlaid on the substrate during deposition. The structure of the samples was determined using low- and high-angle x-ray diffraction measurements with CuK α radiation.¹¹ The MR

was measured in magnetic fields up to 10 kOe using a high-resolution ac bridge¹² and the magnetic hysteresis loop was determined by means of the magneto-optic Kerr effect (MOKE) with the magnetic field applied in the film plane. All experiments were performed on the same samples to ensure accurate comparison of the data after each thermal treatment.

Annealing was carried out in a temperature-controlled tube furnace with the sample placed in a quartz probe which was continuously evacuated to a pressure of $\sim 5 \times 10^{-6}$ Torr. In order to follow the structural and magnetic evolution progressively, samples were annealed at each temperature step and cooled to room temperature for x-ray diffraction, MOKE, and transport measurements. This cycle was repeated at the same annealing temperature until the behavior stabilized before proceeding to a higher temperature.

RESULTS AND DISCUSSION

Figure 1 summarizes the variation of the MR magnitude as a function of the Cu thickness for the as-deposited multilayers with a 50-Å Cu buffer at 77 and 300 K. Three oscillation peaks are identified at $t_{\text{Cu}} = 9.2, 21.7,$ and 33.6 Å with a period (≈ 12 Å) and phase similar to values reported in other Co/Cu studies.²⁻⁴ The MR values at the first peak are smaller than those found for the Co/Cu multilayers grown on a 50-Å Fe buffer layer.²⁻⁴ This reduction can be ascribed partly to an incomplete antiferromagnetic coupling in our samples resulting from uneven layer growth on the Cu buffer layer^{3,13} and partly to a larger shunting effect of the 50-Å Cu buffer/cap layers which reduces the maximum MR by about 10%.³

Five samples, marked A–E in Fig. 1, were selected for annealing studies. High-angle x-ray measurements show that all our samples are polycrystalline with a (111) texture, as presented in Fig. 2 for sample D. The dominant feature is a

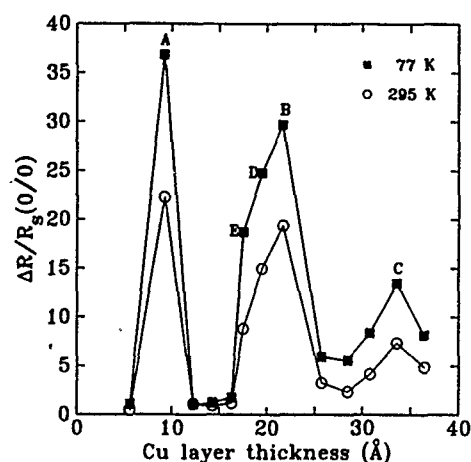


FIG. 1. Dependence of the saturation MR at 77 and 295 K on the Cu layer thickness for multilayers with the form glass/Cu50 Å[Co11.5 Å/Cu(t_{Cu})]₃₀/Cu50 Å. The five samples A, B, C, D, and E were selected for annealing studies.

strong (111) peak ($2\theta \approx 44^\circ$) situated between the fcc Cu and Co (111) Bragg peaks at 43.3° and 44.2° , respectively. A weak (200) peak (at about 51°) is also present but no evidence for interlayer coherence is apparent in these spectra. The (111) and (200) linewidths were found to decrease monotonically with each annealing step although the peak positions remain unchanged (see Table I), suggesting that the films have developed larger textured grains with no evidence for formation of phase segregated regions. This suggestion is consistent with the decrease of the zero-field resistance R_0 observed after each anneal (Table I). Low-angle x-ray reflectivity spectra for the same sample are presented in the inset of Fig. 2. Since there is no significant change in the superlattice peaks after annealing, we conclude that the composition modulation persists, consistent with the high-angle data. The slight change in the reflectivity below the 2θ value of the

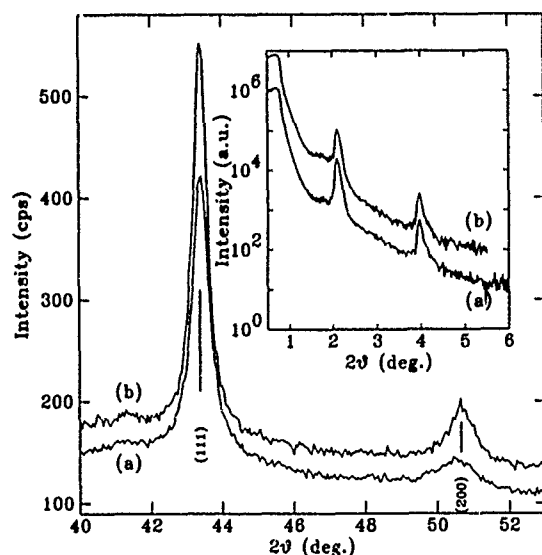


FIG. 2. High-angle diffraction spectra for sample C (a) as-deposited and (b) after an anneal at 250 °C for 2 h. The corresponded low-angle x-ray reflectivity data are shown in the inset.

TABLE I. Results measured at 295 K on the samples marked in Fig. 1 before and after annealings. T_a and t_a are the annealing temperature and time. R_0 is the resistance at zero field, $\Delta R_s = R_0 - R_s$ is the absolute change in the resistance, $\Delta R_0/R_s$ is the TMR magnitude, and $\Delta\theta$ is the linewidth of the high-angle (111) x-ray peak.

Sample (t_{Cu} Å)	T_a/t_a (°C/h)	R_0 (Ω)	ΔR_s (Ω)	$\Delta R_0/R_s$ (%)	$\Delta\theta$ (°)
A. 9.2	initial	8.13	1.48	22.3	0.80
	150/2	7.61	1.00	15.1	0.78
	150/4	7.59	0.90	13.5	0.73
	200/1	6.86	0.44	6.9	0.74
B. 21.7	initial	3.41	0.55	19.4	0.64
	250/2	3.04	0.52	20.6	0.52
	250/4	2.91	0.44	17.4	0.56
	300/1	2.48	0.20	8.5	0.46
	300/2	2.41	0.15	6.4	0.46
C. 33.6	initial	1.85	0.13	7.3	0.57
	250/2	1.54	0.14	9.8	0.46
	250/4	1.58	0.12	8.4	0.48
	300/1	1.44	0.10	7.2	0.40
	300/2	1.40	0.10	7.6	0.38
D. 19.5	initial	3.74	0.49	14.8	
	150/20	3.79	0.57	17.7	0.61
	200/20	3.60	0.55	18.0	0.60
	250/2	3.42	0.49	16.3	0.59
	250/4	3.40	0.45	15.2	0.58
E. 17.5	initial	2.87	0.16	6.0	0.54
	300/1	2.82	0.11	3.9	0.53
	initial	3.65	0.25	7.3	
	150/20	3.58	0.31	9.5	
	200/20	3.36	0.34	10.8	
	250/2	3.27	0.25	8.1	
	250/4	3.22	0.22	7.2	
	300/1	2.87	0.08	2.9	
	300/2	2.84	0.08	2.8	

first Bragg peak for the annealed film arises from the growth of an oxide overlayer during annealing. Similar behavior was observed for the other annealed samples.

Representative MR data at 295 K for samples A ($t_{Cu}=9.2$ Å), C (33.6 Å), and D (19.5 Å), as-deposited and after annealing are displayed in Fig. 3. The MR is defined here as the ratio $(R_0 - R_s)/R_s$, where R_0 is the maximum value of the resistance and R_s , the high field saturated value. The MR of sample A ($t_{Cu}=9.2$ Å) drops from 22.3% to 15.1% after annealing at only 150 °C for 2 h, whereas the MR of sample D ($t_{Cu}=19.5$ Å) increases slightly from 14.8% to 18% after the more intense treatment at 200 °C for 20 h. From the MR data in Table I it can be seen that for the samples with thicker Cu layers (B to E), the MR and ΔR_s initially pass through a maximum before decreasing. In contrast, for sample A with small $t_{Cu}=9.2$ Å, the $\Delta R_s/R_s$ and ΔR_s decrease progressively with increasing temperature and time. It appears that the atomic mixing and disorder within the very thin Cu layer of the as-deposited multilayer results in a relatively poor Co layer coupling. This conclusion is consistent with the fact that the first peak in Fig. 1 is much narrower than the second and not much higher.

The magnetic behavior of the films was also monitored after each annealing step. Figure 4 shows hysteresis loops for

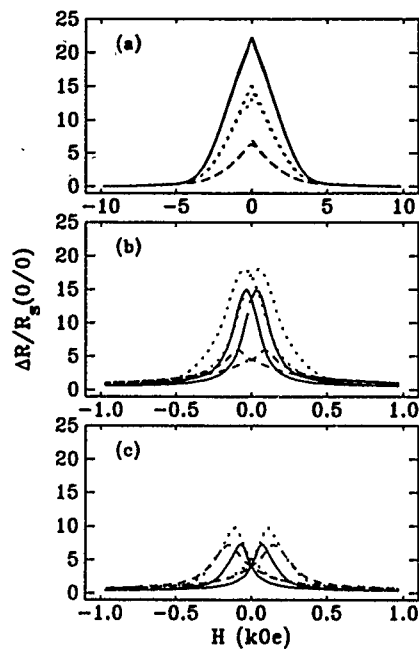


FIG. 3. Resistance vs field curves at 295 K before annealing (solid curves) and after annealing: (a) sample A, 150 °C for 2 h (dotted line), 200 °C for 1 h (dashed line); (b) sample D, 200 °C for 20 h (dotted line), 300 °C for 1 h (dashed line); (c) sample C, 250 °C for 2 h (dotted line), 300 °C for 1 h (dashed line).

sample D as-deposited and after annealing. For the as-deposited material, the Kerr rotation indicates a large remanence at zero field and a slow approach to saturation, suggesting that only a fraction of the layers is antiferromagnetically coupled. Annealing at a moderate temperature results in a nearly zero remanence and a wasp-waisted curve characteristic of a film with substantial antiferromagnetic coupling. Further annealing gives rise to an almost square loop typical of a ferromagnetic film. Samples C and D followed the same behavior. Combining the structural, transport, and magnetic results, we conclude that the initial increase in the MR can be ascribed to the larger grain size which, in turn, results in an increase of the antiferromagnetically coupled fraction of the film. On the contrary, for sample A there was only a monotonic increase in the remanence upon annealing, indicating a monotonic decrease of the interlayer antiferromagnetic coupling, as inferred from the MR results.

In summary, oscillatory MR has been observed in sputtered Co/Cu multilayers grown on glass substrates with 50-Å Cu buffer and cap layers. Annealing of samples at moderate temperatures leads to larger grain sizes with no loss in the multilayer periodicity. Annealed samples at the second and third MR peaks show an initial increase of the MR arising from an enhancement of the antiferromagnetically coupled

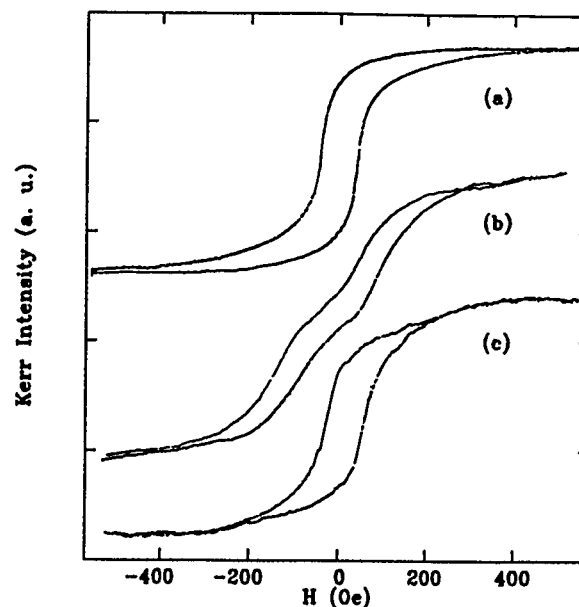


FIG. 4. MOKE hysteresis loops for sample D with $t_{\text{Cu}}=19.5$ Å: (a) as-deposited; (b) annealed at 200 °C for 20 h; (c) annealed at 300 °C for 2 h.

fraction of the films. No MR increase is observed for the sample at the first peak probably because the very thin Cu layer is initially too disordered.

ACKNOWLEDGMENTS

We thank M. Sutton and T. Gu for assistance with the low-angle x-ray measurements. We acknowledge financial support for this research from NSERC, Canada and from Fonds FCAR, Québec.

- ¹M. N. Baibich, J. M. Broto, A. Fert, F. Nguyen van Dau, F. Petroff, P. E. Etienne, G. Creuzet, A. Friederich, and J. Chazelas, *Phys. Rev. Lett.* **61**, 2472 (1988).
- ²S. S. P. Parkin, R. Bhadra, and K. P. Roche, *Phys. Rev. Lett.* **66**, 2152 (1991).
- ³S. S. P. Parkin, Z. G. Li, and D. J. Smith, *Appl. Phys. Lett.* **58**, 2710 (1991).
- ⁴D. H. Mosca, F. Petroff, A. Fert, P. A. Schroeder, W. P. Pratt, Jr., and R. Laloe, *J. Magn. Magn. Mater.* **94**, L1 (1991).
- ⁵R. E. Camley and J. Barnas, *Phys. Rev. Lett.* **63**, 664 (1989); S. Zhang, P. M. Levy, and A. Fert, *Phys. Rev. B* **45**, 8689 (1992); S. S. P. Parkin, *Phys. Rev. Lett.* **71**, 1641 (1993).
- ⁶E. E. Fullerton, D. M. Kelly, J. Guimpel, I. K. Schuller, and Y. Bruynseraede, *Phys. Rev. Lett.* **68**, 895 (1992).
- ⁷F. Petroff, A. Barthelemy, A. Hamzic, A. Fert, P. Etienne, S. Lequien, and G. Creuzet, *J. Magn. Magn. Mater.* **93**, 95 (1991).
- ⁸Y. Huai, R. W. Cochrane, and M. Sutton, *J. Appl. Phys.* **73**, 5530 (1993).
- ⁹S. S. P. Parkin, *Appl. Phys. Lett.* **60**, 512 (1992).
- ¹⁰M. J. Hall, B. J. Hickey, M. A. Howson, M. J. Walker, J. Xu, D. Greig, and N. Wiser, *Phys. Rev. B* **47**, 12 785 (1993).
- ¹¹Y. Huai, R. W. Cochrane, and M. Sutton, *Phys. Rev. B* **48**, 2568 (1993).
- ¹²R. W. Cochrane, J. Destry, and M. Trudeau, *Phys. Rev. B* **27**, 5955 (1983).
- ¹³K. Le Dang, P. Veillet, E. Vélú, S. S. P. Parkin, and C. Chappert, *Appl. Phys. Lett.* **63**, 108 (1993).

Magnetoresistance and exchange effects of NiCo/Cu sandwich films with oxide overlayer

T. R. McGuire and T. S. Plaskett^{a)}

IBM Research Division, T. J. Watson Research Center, Yorktown Heights, New York 10598

Giant magnetoresistance (GMR) of 8% at 4.2 K is found in sandwich films having the composition $\text{Ni}_{0.7}\text{Co}_{0.3}(50 \text{ \AA})/\text{Cu}(t)/\text{NiCo}(50 \text{ \AA})/\text{NiCoO}(40 \text{ \AA})$ where NiCoO is a mixed oxide overlayer that exchange couples with the NiCo alloy layer. These films show a MR temperature dependence quite similar to that previously reported for Co/Cu/Co/CoO where the MR becomes small above 200 K. When bilayers of CoO/NiO are placed on the NiCo layer, the temperature dependence of MR extends to 250 K. The magnitude of the MR at 4.2 K scales with the magnitude of the saturation magnetization in the NiCo and Co films.

I. INTRODUCTION

Giant magnetoresistance (GMR) found in multilayers^{1,2} is also found in sandwich layers^{3,4} composed of two magnetic layers, M_1 and M_2 , separated by a single layer of a nonmagnetic metal as shown in Fig. 1. Initial work by Dieny *et al.*³ described sandwiches of NiFe/Cu/NiFe with an FeMn overlay. The observed changes in resistivity with applied magnetic field was called a "spin-valve" effect because it depends on the relative angle between the directions of magnetization of the two magnetized NiFe layers. Speriosu *et al.*⁴ have also reported on Co/Cu/Co sandwiches also with an FeMn overlay that have MR of 4% at room temperature.

The importance of the FeMn alloy layer comes about because it is antiferromagnetic and exchange couples with either the FeNi or Co upper layer. This inhibits the rotation of the magnetization of the upper layer M_1 with respect to the lower magnetic layer M_2 . When the two magnetic layers in the sandwich are antiparallel at low magnetic fields (H) the sandwich film resistivity is a maximum (ρ_{\max}). For large H when M_1 and M_2 are parallel, minimum (ρ_{\min}) is measured. This resistivity effect is caused by polarized conduction electrons from one layer which are scattered by the antiparallel magnetic layer as well as any disordered magnetic moments. Magnetic saturation minimizes this scattering.

In our previous study⁵ of Co/Cu/Co we often obtained large MR (up to 12% at 4.2 K) with no special overlayers or underlayers. Subsequently it was found⁶ that consistently large values of MR could only be obtained if a CoO overlayer is deposited on the Co/Cu/Co sandwich. The antiferromagnetic CoO served the same purpose as the FeMn. Although the CoO is antiferromagnetic with a transition at 290 K, the exchange coupling was only effective to about 200 K above which the MR < 1%.

Since the antiferromagnetic transition of NiO is 520 K, in the present work sandwiches of $\text{Ni}_{0.7}\text{Co}_{0.3}(50 \text{ \AA})/\text{Cu}(t)/\text{NiCo}(50 \text{ \AA})/\text{NiCoO}$ were made in an attempt to increase the value of MR at room temperature. In addition $\text{Ni}_{0.7}\text{Co}_{0.3}$ bulk alloys are known to be magnetically soft similar to permalloy, hence NiCo films might make a more sensitive magnetic probe.

II. EXPERIMENTAL RESULTS AND DISCUSSION

The films are prepared on glass substrates by magnetron sputtering in a 3-mTorr Ar atmosphere using Cu and $\text{Ni}_{0.7}\text{Co}_{0.3}$ targets. The substrates, at ambient temperature, are moved sequentially over each gun to deposit film on the substrate. Film structure is shown in Fig. 1 and the layer thicknesses are listed in Table I. The $\text{Ni}_{0.7}\text{Co}_{0.3}\text{O}$ overlay is added by depositing additional NiCo on the upper magnetic layer M_1 and simultaneously introducing oxygen to the sputtering system. We do not know the exact composition of the oxide layer, however since the substrate temperature is $\sim 50^\circ\text{C}$, the oxide may be amorphous. The last three films listed in Table I are made with a double oxide overlay. Cobalt and nickel targets are used to first form a reactively sputtered CoO of 50 Å followed by a NiO layer of 50 Å.

Magnetization of the films was measured with a Quantum Design SQUID magnetometer. As seen in Table I values of magnetic saturation M_s at 4.2 K vary from 800 to 900 emu/cm³. Many of our films are about 10% higher than the value for bulk $\text{Ni}_{0.7}\text{Co}_{0.3}$ (812 emu/cm³). In our previous work^{5,6} with Co sandwich films, M_s was 10% to 15% lower than Co bulk values. We attribute the lower magnetization of Co to oxygen penetration of the upper Co layer, a condition which is apparently not present in the NiCo film.

Magnetoresistance is measured by the van der Pauw method on 2-cm-diam films with in-plane H and current. As listed in Table I, MR varies from 6% to 9%; also listed are ρ_{\max} , ρ_{\min} , and ΔH and these are obtained from resistivity field data as marked in Fig. 2. The MR (%) column is calculated from $(\rho_{\max} - \rho_{\min})/\rho_{\min}$.

Figure 2 shows resistivity and also M vs H for film (a) of Table I and both curves have the characteristic plateau found for sandwich films. A plateau represents some sort of

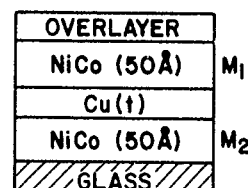


FIG. 1. Sandwich film structure of the $\text{Ni}_{0.7}\text{Co}_{0.3}$ alloy where the overlayer is either a mixed NiCoO(40 Å) or bilayer CoO(50 Å)/NiO(50 Å).

^{a)}Instituto de Engenharia de Sistemas e Computadores, 1000 Lisbon, Portugal.

TABLE I. Sandwich films $\text{Ni}_{0.7}\text{Co}_{0.3}(50 \text{ \AA})/\text{Cu}(t)/\text{NiCo}(50 \text{ \AA})/\text{NiCo oxide}$ at 4.2 K.

Film	Cu(<i>t</i>) (\AA)	Oxide (\AA)	M_s (emu/cm ³)	ρ_{max} ($\mu\Omega \text{ cm}$)	ρ_{min} ($\mu\Omega \text{ cm}$)	$\Delta\rho$ ($\mu\Omega \text{ cm}$)	ΔH (kOe)	MR (%)
NiCoO								
a	16	40	905	31.7	29.0	2.7	2.5	9.3
b	20	40	876	28.3	26.2	2.1	2.5	8.0
c	28	40	870	24.7	23.2	1.5	1.5	6.5
CoO, NiO								
d	16	50,50	765	39.5	36.6	2.9	...	7.9
e	20	50,50	828	27.8	26.1	1.7	...	6.5
f	28	50,50	820	35.5	32.7	2.8	...	8.6

stable nonparallel orientation of M_1 and M_2 . The field region ΔH of ρ_{max} extends not only over the magnetization plateau but to a portion of the magnetization curve where magnetic saturation takes place. We interpret this to mean that only a small amount of unsaturated magnetization is needed to obtain ρ_{max} . Scattering of polarized conduction electrons from a disordered magnetic layer, e.g., at an interface may be as important as bulk scattering within the magnetic layer. The relation of the scattering mechanism to the magnetic state of the sample is a complex problem.

Figure 3 shows the temperature dependence of ρ_{max} and ρ_{min} for films (a). The difference $\Delta\rho = \rho_{\text{max}} - \rho_{\text{min}}$ becomes small for $T > 200$ K. This temperature dependence is almost identical to that found for Co/Cu/Co/CoO films.⁶ The temperature dependence of MR for films (a) and (d) are plotted in Fig. 4. Film (d) which has a bi-layer CoO/NiO has a higher MR in the temperature range 125 to 250 K as compared to film (a). Possibly there is some exchange coupling between the NiO and CoO to extend the temperature range.

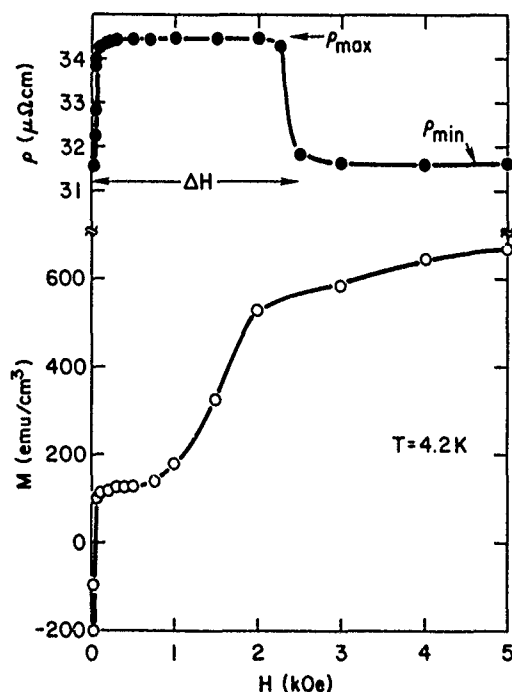


FIG. 2. Sandwich film (a) of the $\text{Ni}_{0.7}\text{Co}_{0.3}(50 \text{ \AA})$ with Cu(16 \AA) and overlayer of NiCoO(40 \AA). Upper curve is resistivity with ρ_{max} , ρ_{min} , and ΔH specified and lower curve is magnetization.

Interacting CoO–NiO superlattices with NiFe have been reported by Carey and Berkowitz.⁷ The larger MR found at 4.2 K for film (a) may be related to M_s ; M_s of film (a) is 10% greater than M_s of film (d).

A measure of the exchange coupling of the antiferromagnetic oxide overlayer to M_1 is given by the width of the plateau of ρ_{max} (Fig. 2) as listed by ΔH in Table I. The largest value of ΔH for the single layer oxide overlayer is about 2500 Oe as shown in Fig. 2. This is, however, about half that observed for Co/Cu/Co/CoO films where $\Delta H \approx 5000$ Oe.⁶ Figure 5 shows ρ vs H for film (d) which has a CoO/NiO overlayer. The shape at 4.2 K makes it difficult to specify ΔH , however it is not larger than 2500 Oe. At higher temperatures the width of the plateau narrows considerably even though MR remains large. In Fig. 3 ΔH vs T for film (a) is plotted which shows that ΔH vs T decreases more rapidly than the MR vs T decreases. This Curie-type dependence for ΔH is similar to that reported for Co/CoO. It is possible that the antiferromagnetism of the CoO or NiCoO is decreasing as $1/T$ perhaps because the oxide is off stoichiometry and also amorphous.

The magnitude of MR in the NiCo sandwich is about 7% to 8% and M is about 800 emu/cm³. This compares with 15% to 16% and 1400 emu/cm³ for Co sandwich films⁶ thus showing scaling of MR with M for these two systems. At 4.2

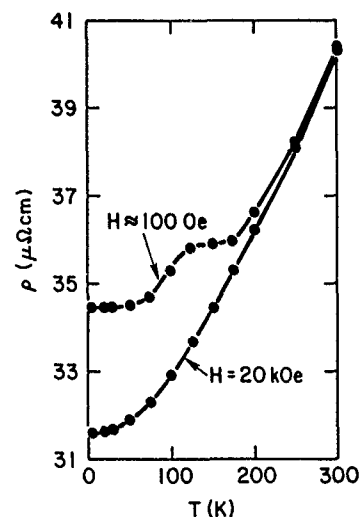


FIG. 3. Resistivity as a function of temperature for the NiCo sandwich (a) with Cu(16 \AA) and NiCoO(40 \AA) overlayer.

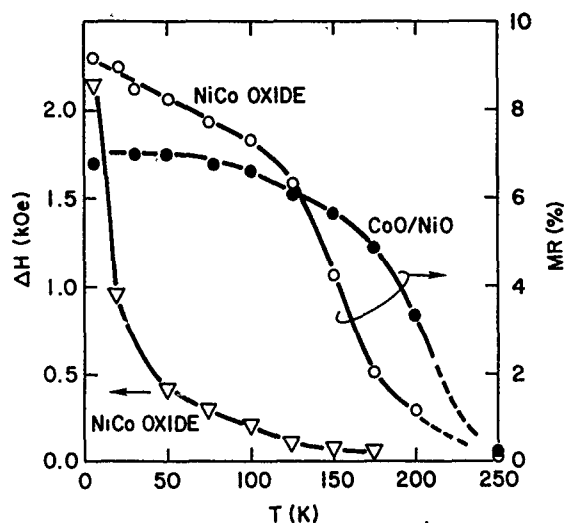


FIG. 4. Temperature dependence of MR for the NiCo sandwich (a) with NiCoO(40 Å) overlayer and film (d) CoO(50 Å)/NiO(50 Å) overlayer both with Cu(16 Å). The plateau width ΔH vs T is shown for the NiCoO overlayer film (a).

K, data for the b, c, e, and f films where the Cu thickness is 20 and 28 Å are quite similar to the Cu(16 Å). However, we do not have extensive temperature measurements on b, c, e, and f films.

III. SUMMARY

(a) Reactively sputtered overlayers of NiCoO and CoO/NiO are exchange coupled to $\text{Ni}_{0.7}\text{Co}_{0.3}$ sandwich films and cause nonparallel magnetic layers having high resistivity.

(b) The temperature dependence of magnetoresistance decreases faster for the mixed oxide NiCoO overlayer than for the bilayer CoO/NiO.

(c) The exchange coupling of the oxide to the NiCo layer decreases as $1/T$.

(d) The temperature dependence of MR and ΔH for the mixed oxide overlayer with Ni Co is almost the same as

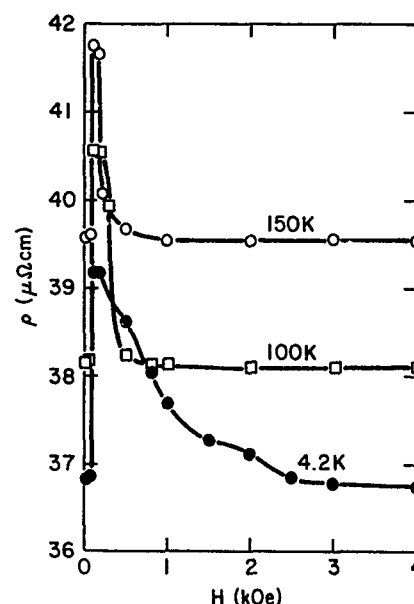


FIG. 5. Resistivity vs H for three temperatures for film (d) in Table I which has bilayer CoO(50 Å)/NiO(50 Å) overlayer and Cu(16 Å).

found previously⁶ for Co/Cu/Co/CoO sandwich films.

(e) The magnitude of MR in the NiCo and Co series scales linearly with the value of saturation magnetization in the two series.

¹M. N. Baibich, J. M. Broto, A. Fert, Nguyen van Dau, F. Petroff, P. Etienne, G. Creuzet, A. Friederich, and J. Chazelas, Phys. Rev. Lett. **61**, 2472 (1988).

²S. S. Parkin, R. Bhadra, and K. P. Rock, Phys. Rev. Lett. **66**, 2152 (1991).

³B. Dieny, V. S. Speriosu, S. S. P. Parkin, B. A. Gurney, D. R. Wilhoit, and D. Mauri, Phys. Rev. B **43**, 1297 (1991); J. Appl. Phys. **69**, 4774 (1991).

⁴V. S. Speriosu, B. Dieny, P. Humbert, B. A. Gurney, and H. Lefakis, Phys. Rev. B **44**, 5358 (1991).

⁵T. R. McGuire and T. S. Plaskett, IEEE Trans. Magn. **MAG-28**, 2748 (1992).

⁶T. R. McGuire, T. S. Plaskett, and R. J. Gambino, IEEE Trans. Magn. **MAG-29**, 2714 (1993).

⁷M. J. Carey and A. E. Berkowitz, J. Appl. Phys. **73**, 6892 (1993).

Effect of oxygen incorporation on magnetoresistance in Co/Cu multilayers

K. Kagawa, H. Kano, A. Okabe, A. Suzuki, and K. Hayashi

Sony Corporation Research Center, 174 Fujitsuka-cho, Hodogaya-ku, Yokohama 240, Japan

The background pressure dependence of magnetoresistance (MR) ratio of Co/Cu multilayer films and the effect of the Fe buffer layer were studied. Secondary ion mass spectrometry (SIMS) measurement of the films and *in situ* quadrupole mass spectrometry (QMS) analysis in conjunction with background pressure dependence of MR ratio confirmed that the oxidation of Co/Cu gives a crucial influence to the giant magnetoresistance (GMR) effect. The oxidation of Co/Cu weakens the antiferromagnetic coupling, and results in the low MR ratio. The Fe buffer layer absorbs the residual oxygen, and this leads to the increase of the MR ratio. The MR ratio of $(\text{Co}_{1 \text{ nm}}/\text{Cu}_{1 \text{ nm}})_{100}/\text{Fe}_{2.5 \text{ nm}}$ film deposited under low background pressure and high deposition rate so as to suppress oxidation reached over 80% at RT and 160% at 2 K.

INTRODUCTION

The giant magnetoresistance (GMR) of the Co/Cu multilayer has been intensively studied, from the motivation of both scientific interest and the application to magnetic sensors. But it has not been clarified yet what is the critically important condition for the GMR effect, which causes disagreement among the reported magnetoresistance (MR) ratios.^{1,2} The analysis of the Fe buffer layer effect that is known to make a large MR ratio and better reproducibility may provide clues to the question. Some groups report that an Fe buffer layer changes the texture of Co/Cu and that the crystalline orientation may play a significant role for the GMR effect.³ The increase of the small-angle x-ray diffraction peak intensity by the Fe buffer layer is also reported.⁴ However, it has not been specified yet what is the major role of the Fe buffer layer for the increase of the MR ratio.

In this work, we clarify that the oxidation of Co/Cu has a significant influence on the MR ratio by investigating the background pressure dependence of the MR ratio. The effect of the Fe buffer layer is also explained on this line.

EXPERIMENTAL PROCEDURE

Co/Cu multilayers with/without a 2.5–5-nm-thick Fe buffer layer were prepared on water-cooled⁵ glass and Si substrates by dc magnetron sputtering. Ar gas pressure during sputtering was 0.5 Pa. Substrates were moved sequentially over each gun to deposit a Co or Cu layer and the deposition rate was around 2.3 nm/s. The background pressure before deposition was varied from 9×10^{-4} to 5×10^{-5} Pa. The atmosphere during deposition was monitored by quadrupole mass spectrometry (QMS). The magnetic properties of Co/Cu multilayers were measured with a vibrating-sample magnetometer (VSM) at RT. The crystalline orientations of Co/Cu multilayers were investigated by x-ray diffraction (XRD) with $\text{CuK}\alpha$ radiation. The MR measurements were made by the dc four-terminal method at RT and 2 K with the maximum magnetic field of 15 kOe. Sample size was $5 \times 25 \text{ mm}^2$. The oxygen content of Co/Cu multilayers were investigated by secondary ion mass spectrometry (SIMS). The oxygen content was estimated as the relative oxygen ion intensity to the Cu ion intensity of the film, assuming the Cu content to be constant specified otherwise.

RESULTS AND DISCUSSION

Figure 1 shows the background pressure dependence of the MR ratio of $(\text{Co}_{1 \text{ nm}}/\text{Cu}_{1 \text{ nm}})_{100}$ multilayers with/without a 5-nm-thick Fe buffer layer. The MR ratio of Co/Cu becomes drastically larger as the background pressure is decreased below 10^{-3} Pa and then appears to saturate around 10^{-4} Pa. The Fe buffer layer works to increase the MR ratio, but the effect is relatively small for lower background pressure. The Fe buffer layered film shows six times larger MR ratio than film without a buffer for high background pressure (8.9×10^{-4} Pa), while the increase of MR ratio by Fe buffer layer is only 2%–3% for low background pressure (1.8×10^{-4} Pa). Figure 2 reveals the background pressure dependence of the x-ray diffraction intensity ratio $I_{200}/(I_{111} + I_{200})$ of $(\text{Co}_{1 \text{ nm}}/\text{Cu}_{1 \text{ nm}})_{100}$ of multilayers with/without a 5-nm-thick Fe buffer layer. The Fe buffer layer changes the texture of Co/Cu from (111) to (200) almost equally for the whole range of the background pressure. Therefore, the effect of texture change cannot account for the smaller increase of MR ratio by the Fe buffer layer for low background pressure (1.8×10^{-4} Pa). The MR ratio of Co/Cu appears to depend simply on background pressure,

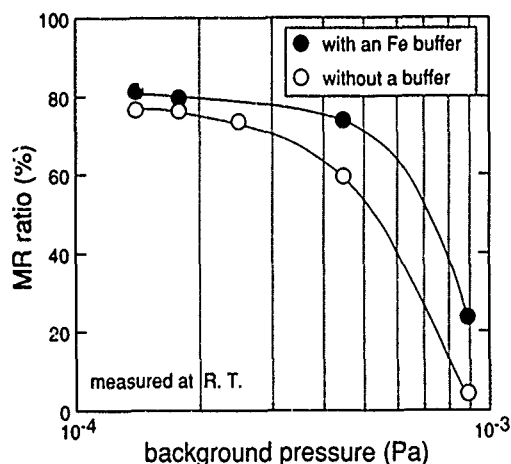


FIG. 1. Background pressure dependence of the MR ratio of $(\text{Co}_{1 \text{ nm}}/\text{Cu}_{1 \text{ nm}})_{100}$ with/without an Fe buffer layer at RT.

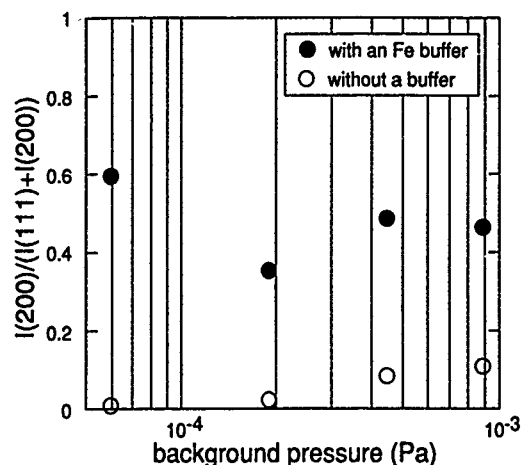


FIG. 2. Background pressure dependence of the x-ray diffraction intensity ratio $I_{200}/(I_{111}+I_{200})$ of $(\text{Co}_{1 \text{ nm}}/\text{Cu}_{1 \text{ nm}})_{100}$ with/without an Fe buffer layer.

rather than texture of the film. The background pressure is expected to have a direct relationship with the oxygen content of the film.

The relative oxygen ion intensity of Co/Cu multilayers measured by SIMS are shown in Fig. 3. The film deposition under low background pressure lowers the oxygen content of Co/Cu multilayers. The Fe buffer layered film has low oxygen content compared to the film without a buffer deposited under the same background pressure. The low oxygen content is shown to be necessary to cause the large MR change. The Fe buffer layer effect for the increase of MR ratio is attributed to reducing the oxygen content of the Co/Cu multilayers.

The oxidation of the film during deposition is monitored by *in situ* QMS analysis. As it is well-known that residual H_2O decomposes to O_2 and H_2 by sputtering, we paid attention to O_2 and H_2 partial pressure. Figures 4(a), 4(b), and 4(c) illustrate the change of residual gas partial pressure during

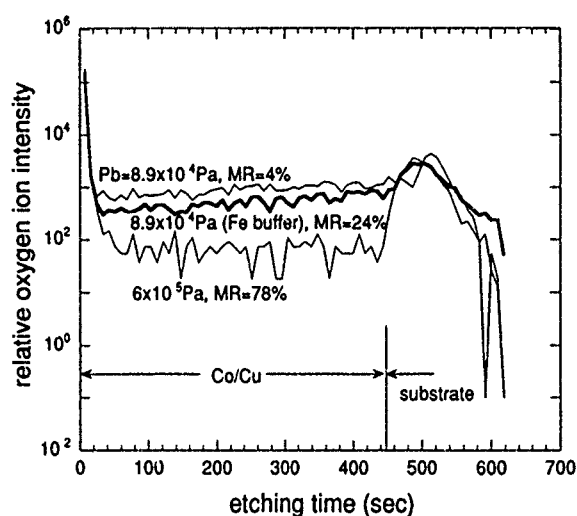


FIG. 3. Relative ion intensity of oxygen of $(\text{Co}_{1 \text{ nm}}/\text{Cu}_{1 \text{ nm}})_{100}$ films with background pressure $P_b=8.9 \times 10^{-4}$ Pa, 8.9×10^{-4} Pa with an Fe buffer layer, and 6×10^{-5} Pa.

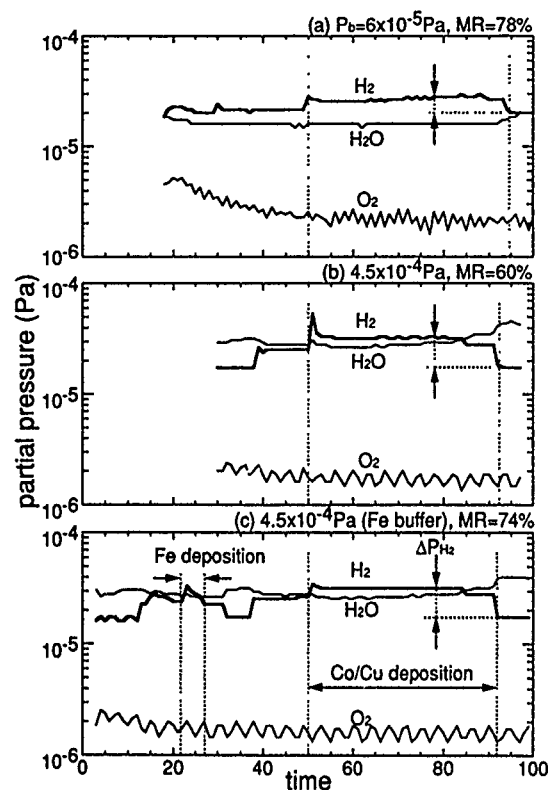


FIG. 4. Change of residual gas partial pressure during deposition of (a) $(\text{Co}_{1 \text{ nm}}/\text{Cu}_{1 \text{ nm}})_{100}$ with background pressure $P_b=6 \times 10^{-5}$ Pa, (b) 4.5×10^{-4} Pa, and (c) 4.5×10^{-4} Pa with an Fe buffer layer.

ing deposition of Co/Cu multilayers with low background pressure (6×10^{-5} Pa), with high background pressure (4.5×10^{-4} Pa), and with high background pressure (4.5×10^{-4} Pa) with an Fe buffer layer. The H_2 partial pressure increases during sputtering, while O_2 partial pressure does not increase. That implies O_2 formed by decomposition of H_2O is absorbed concurrently in the growing film. Therefore, the increase of the H_2 partial pressure ΔP_{H_2} during sputtering is the measure of the oxidation of the film. The high peak of H_2 partial pressure at the beginning of Co/Cu deposition also implies the severe oxidation of the growing film. The deposition under low background pressure reduces both ΔP_{H_2} and the peak height at the beginning of Co/Cu. The oxidation of the Co/Cu during deposition is confirmed to influence the MR ratio significantly. The deposition of an Fe buffer layer also lowers ΔP_{H_2} and the peak height. The sputtered Fe buffer layer is thought to lower the effective background pressure as an oxygen absorber. This is consistent with the smaller Fe buffer layer effect to increase the MR ratio for lower background pressure. The major role of the Fe buffer layer for the increase of MR ratio is to absorb the residual oxygen and to suppress oxidation of Co/Cu multilayers rather than texture change.

The change of magnetization behavior as the background pressure changes is measured. Figure 5 shows the $M-H$ loops of Co/Cu multilayer films grown at various background pressure. The antiparallel spin alignment of the neighboring Co layers is responsible for the spin-dependent

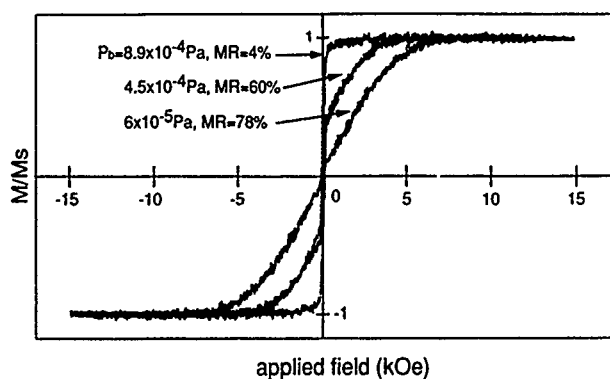


FIG. 5. M - H loop of $(\text{Co}_1 \text{ nm}/\text{Cu}_1 \text{ nm})_{100}$ with background pressure $P_b = 8.9 \times 10^{-4} \text{ Pa}$, $4.5 \times 10^{-4} \text{ Pa}$, and $6 \times 10^{-5} \text{ Pa}$.

scattering at the interfaces between Co and Cu. The antiferromagnetic (AFM) coupling reduces the remanent magnetization, and increases the saturation field. The saturation field becomes smaller and the remanent magnetization increases for higher background pressure. The oxidation of the interfaces between Co and Cu makes the antiferromagnetic (AFM) coupling incomplete. As is reported in the case of FeNi/FeMn, the suppression of oxidation of the interfaces between Co and Cu is indispensable to strengthen the AFM coupling.

It becomes clear that the suppression of Co/Cu oxidation during deposition is a significant condition to cause large MR ratio. The film deposition under lower background pressure, with an Fe buffer layer are effective to prevent oxidation. Figure 6 shows the MR curve for $(\text{Co}_1 \text{ nm}/\text{Cu}_1 \text{ nm})_{100}/\text{Fe}_{2.5} \text{ nm}$ film deposited with $5 \times 10^{-5} \text{ Pa}$ background pressure. The film exhibits an MR ratio of over 80% at RT and 160% at 2 K.

CONCLUSIONS

The effect of oxidation of Co/Cu was studied. The MR ratio is greatly improved by suppression of oxidation. The oxidation of the Co/Cu, especially the oxidation of the interfaces between Co and Cu, makes the antiferromagnetic coupling weaker, and that reduces the MR change. The Fe buffer layer effect for the large MR ratio was confirmed to be the

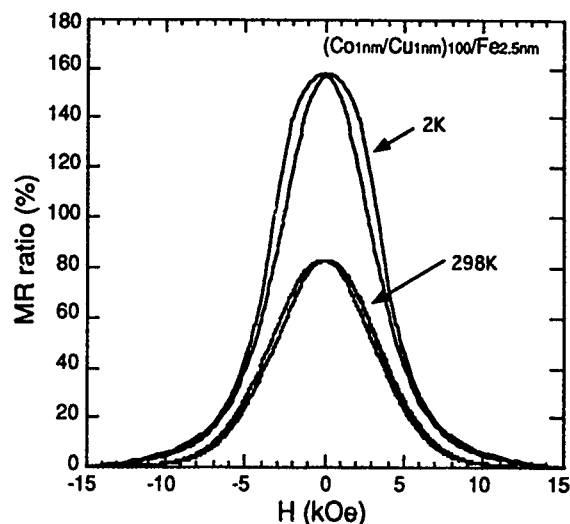


FIG. 6. MR change of $(\text{Co}_1 \text{ nm}/\text{Cu}_1 \text{ nm})_{100}/\text{Fe}_{2.5} \text{ nm}$ with $5 \times 10^{-5} \text{ Pa}$ background pressure.

residual oxygen absorption and lowering the oxygen content of Co/Cu, rather than texture change. The film deposition under low background pressure and the Fe buffer layer were confirmed to be effective to prevent oxidation. The difference of oxidation degree is thought to be one reason of the disagreement among the reported MR ratio. The MR ratio of $(\text{Co}_1 \text{ nm}/\text{Cu}_1 \text{ nm})_{100}/\text{Fe}_{2.5} \text{ nm}$ film increased to a high of over 80% at RT and 160% at 2 K by careful suppression of Co/Cu oxidation.

ACKNOWLEDGMENTS

We are grateful to S. Miwa for the skillful SIMS measurement. We would like to thank Dr. Seto and Dr. Watanabe for continuous encouragement.

- ¹ S. S. P. Parkin, Z. G. Li, and D. J. Smith, Appl. Phys. Lett. **58**, 2710 (1991).
- ² S. Honda, T. Mimura, S. Ohmoto, and M. Nawate, IEEE Trans. Magn. **MAG-28**, 2747 (1992).
- ³ W. F. Egelhoff, Jr. and M. T. Kief, Phys. Rev. **45**, 7795 (1992).
- ⁴ Z. Chun, P. J. Grundy, M. E. Tomlinson, and R. J. Pollar, Digests of the INTERMAG Conference, DQ-02 (1992).
- ⁵ H. Kano, K. Kagawa, A. Okabe, A. Suzuki, and K. Hayashi, Appl. Phys. Lett. (to be published).

Giant magnetoresistance in electrodeposited Co-Ni-Cu/Cu superlattices

M. Alper, K. Attenborough, V. Baryshev,^{a)} R. Hart, D. S. Lashmore,^{b)} and W. Schwarzacher^{c)}

H. H. Wills Physics Laboratory, Tyndall Avenue, Bristol BS8 1TL, United Kingdom

We have electrodeposited a series of Co-Ni-Cu/Cu superlattices in which the Cu layer thickness was varied between 7 and 35 Å and the Co-Ni-Cu alloy layer thickness held constant. "Giant magnetoresistance" was observed for all films, with the magnitude of the effect decreasing with increasing Cu spacer layer thickness.

Giant magnetoresistance (GMR) is one of the most interesting properties exhibited by magnetically inhomogeneous systems. It was first observed in Fe/Cr superlattices with antiferromagnetic coupling between adjacent Fe layers¹ and subsequently found in other metal/metal multilayers with or without antiferromagnetic coupling.^{2,3} Even single-layer heterogeneous alloy films can show GMR providing the magnetization varies on a length scale comparable to the conduction electron mean free path.⁴

Multilayers and single-layer heterogeneous alloy films have different perceived strengths with regard to possible technological applications of GMR. The alloy films are reasonably straightforward to fabricate, but the large fields generally required for such films to show a significant change in resistance make them less attractive than multilayers for use as magnetic field sensors. Most GMR multilayers, however, require a vacuum system (with all the attendant cost and complexity) for their fabrication.

Recently we reported the first evidence for GMR in metal/metal superlattices grown by electrodeposition.⁵ This process has the obvious advantage over techniques such as sputtering or molecular-beam epitaxy (MBE) that it does not require a vacuum system, and yet is still able to give clean multilayer films.⁶ In this paper we present more detailed data on the Cu thickness dependence of GMR in electrodeposited Co-Ni-Cu/Cu superlattices.

Our films are grown from a sulfamate electrolyte in a cell with a standard three-electrode configuration using a process similar to that described by Lashmore *et al.*⁷ Deposition was carried out with the electrolyte at $30 \pm 1^\circ\text{C}$ and $\text{pH} = 2.0 \pm 0.1$. The electrolyte contains Co^{2+} , Ni^{2+} , and Cu^{2+} ions and we can alter the composition of the electrodeposited metal by controlling the cathode (substrate) potential. For example, when the cathode potential is -0.15 V relative to the saturated calomel reference electrode only Cu will be deposited, but when the cathode is at -1.8 V all three metals will be deposited to give a ferromagnetic Co-Ni-Cu alloy. Hence we can grow a Co-Ni-Cu/Cu superlattice by switching between these two potentials. A computer is used to monitor the deposition current, and switches from one potential to the other when the charge passed reaches the value corresponding to the desired layer thickness.

The films used in this study were grown on (100) textured polycrystalline Cu plates and mounted on glass after

their Cu substrates were dissolved away by means of a chromic/sulfuric acid selective electrochemical etch. This was done to prevent the highly conductive substrates from short-circuiting the superlattice during transport measurements.

After growth, x-ray diffraction was used to measure the repeat distances Λ of our superlattices, while their compositions were measured using an electron probe fitted with wavelength dispersive x-ray spectrometers, as described in a previous paper.⁵ Some superlattices were measured by synchrotron radiation x-ray fluorescence analysis using beam line 3 on the storage ring VEPP-3 at the Institute of Nuclear Physics, Novosibirsk to determine the mass of Co, Ni, and Cu per unit area of film, and the compositions determined by this technique and using the electron probe agree quite well. The compositional measurements enable us to conclude that the ratio of Co to Ni in the ferromagnetic layers is between 3.6:1 and 3.8:1, while the Cu content of these layers could be as high as 25 at. %.⁵ From the mass of each metal per unit area of the film m_x ($x = \text{Co, Ni, Cu}$) and its bulk density ρ_x it is also possible to calculate the equivalent thickness of that metal $t_x = m_x / \rho_x$, and hence the superlattice repeat distance $\Lambda = (t_{\text{Co}} + t_{\text{Ni}} + t_{\text{Cu}}) / N$, where N is the number of repeats in the superlattice. Values of Λ obtained by this method and by x-ray diffraction agree to within $\sim 15\%$.

To measure the magnetoresistance, point-like pressure contacts are applied to the corners of a square of film as shown in Fig. 1 (van der Pauw geometry⁸) and the in-plane applied magnetic field varied between -8 and 8 kOe (the maximum field available from our electromagnet). $R_{12,34}$ is defined as the potential difference $V_4 - V_3$ between contact 4

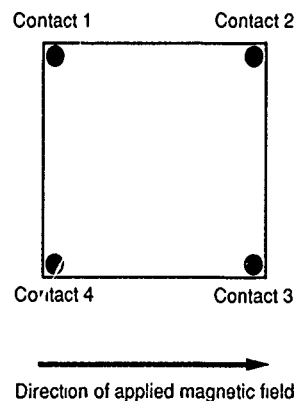


FIG. 1. Experimental geometry used for magnetoresistance measurements.

^{a)}Institute of Nuclear Physics, 630090 Novosibirsk, Russia.

^{b)}National Institute of Standards and Technology, Gaithersburg, MD 20899.

^{c)}Author to whom correspondence should be addressed.

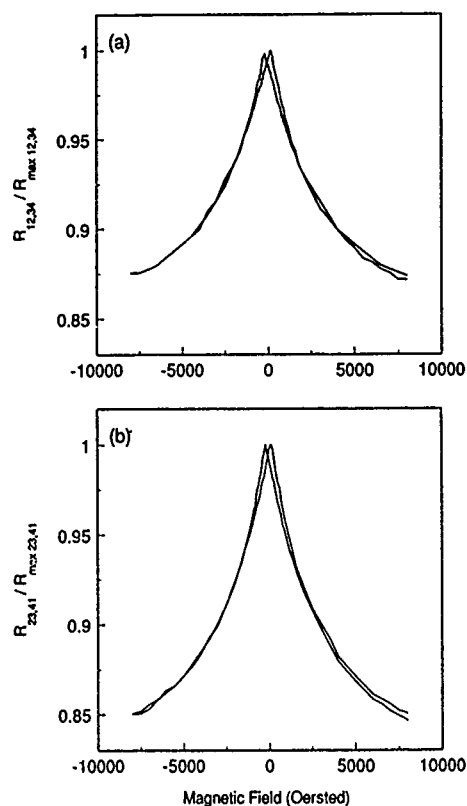


FIG. 2. Normalized magnetoresistances measured at room temperature for an electrodeposited superlattice consisting of 81 repeats of Co-Ni-Cu (~ 20 Å)/Cu (~ 7 Å). The resistance $R_{12,34}$ (a) is defined as the potential difference $V_4 - V_3$ between contact 4 and contact 3 per unit current flowing from contact 1 to contact 2, while $R_{23,41}$ (b) is defined analogously. The positions of the contacts are shown in Fig. 1. $R_{12,34}$ is predominantly a measure of the longitudinal magnetoresistance (current parallel to field) while $R_{23,41}$ is predominantly a measure of the transverse magnetoresistance (current perpendicular to field).

and contact 3 per unit current flowing from contact 1 to contact 2, and $R_{23,41}$ is defined analogously. $R_{12,34}$ is predominantly a measure of the longitudinal magnetoresistance (current parallel to field) while $R_{23,41}$ is predominantly a measure of the transverse magnetoresistance (current perpendicular to field).

Figures 2(a) and 2(b) show the results of such a measurement at room temperature on a superlattice consisting of 81 repeats of Co-Ni-Cu (~ 20 Å)/Cu (~ 7 Å). The size of the effect and the fact that both the "longitudinal" ($R_{12,34}$) and the "transverse" ($R_{23,41}$) magnetoresistance decrease when the magnitude of the applied field is increased show that we have observed GMR. Anisotropic magnetoresistance (AMR) of the kind observed in bulk alloys of the 3d transition metals⁹ also appears to make a significant contribution to the observed magnetoresistance, since the percentage change in $R_{12,34}$ is rather less than the percentage change in $R_{23,41}$ —AMR generally causes the longitudinal magnetoresistance to increase and the transverse magnetoresistance to decrease with increasing applied field.

Figure 3 shows the variation of percentage change in $R_{12,34}$ and $R_{23,41}$ as a function of the nominal Cu layer thickness (the Cu layer thickness calculated from the charge passed during deposition of each layer) for a series of superlattices with constant nominal Co-Ni-Cu thickness. The

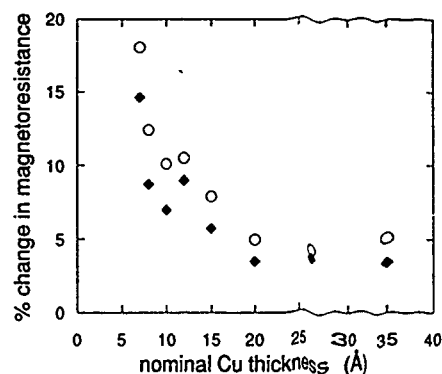


FIG. 3. Percentage change in $R_{12,34}$ ("longitudinal" magnetoresistance: \blacklozenge) and $R_{23,41}$ ("transverse" magnetoresistance: \circ) for a series of electrodeposited Co-Ni-Cu/Cu superlattices with constant nominal Co-Ni-Cu thickness and total thickness ~ 0.3 μm . The percentage change in R is calculated as $[(R_{\text{max}} - R(8 \text{ kOe})) / R(8 \text{ kOe})] \times 100$.

true layer thickness is given by the product of the nominal layer thickness and the current efficiency, which is expected to be close to 100% for Cu. In each case the percentage change in R was calculated as $[(R_{\text{max}} - R(8 \text{ kOe})) / R(8 \text{ kOe})] \times 100$, and since our maximum field of 8 kOe was insufficient to saturate the magnetoresistance (see Fig. 2), larger percentage changes in the magnetoresistance would be possible at higher fields.

A number of points of interest are apparent from Fig. 3. Firstly, the percentage change in $R_{12,34}$ is consistently less than in $R_{23,41}$, implying a contribution from AMR in the observed magnetoresistance for all films. Second, the percentage change in magnetoresistance decreases with increasing Cu layer thickness, which is expected since increasing the Cu spacer thickness decreases the probability of the spin-conserving transmission of conduction electrons between two ferromagnetic layers required for GMR.¹⁰ Third, although additional data points would be required to rule out the possibility, there is no obvious evidence of oscillations in the GMR as might be expected if it were due to oscillatory magnetic exchange coupling.¹¹ Such oscillations have been seen for sputtered Co-Ni/Cu superlattices.¹² Even so, the GMR in our samples may well be due to an antiferromagnetic exchange interaction, given the large applied fields required to saturate the magnetoresistance, although a large remanence at zero applied magnetic field measured using a vibrating-sample magnetometer (VSM) implies that only parts of the superlattice are so coupled.¹³ The lack of oscillations could be due to fluctuations in the spacer layer thickness which damp them out, though this point requires further investigation.

To summarize, we have grown a series of electrodeposited Co-Ni-Cu/Cu superlattices and characterized them by x-ray diffraction, electron probe microanalysis, and x-ray fluorescence analysis. The magnetoresistance contains both an AMR and a GMR component and its magnitude decreases with increasing Cu spacer layer thickness.

This work has been supported by the UK Science and Engineering Research Council under Grant No. GR/H08532, and by NATO under Grant No. CRG910583. Help from Dr.

S. J. Lane and Dr. C. Younes is gratefully acknowledged. One of us (W. S.) would like to thank the Institute of Nuclear Physics, Novosibirsk for its hospitality.

- ¹M. N. Baibich, J. M. Broto, A. Fert, F. Nguyen Van Dau, F. Petroff, P. Etienne, G. Creuzet, A. Friederich, and J. Chazelas, *Phys. Rev. Lett.* **61**, 2472 (1988); G. Binasch, P. Grünberg, F. Saurenbach, and W. Zinn, *Phys. Rev. B* **39**, 4828 (1989).
- ²S. S. P. Parkin, Z. G. Li, and D. J. Smith, *Appl. Phys. Lett.* **58**, 2710 (1991).
- ³B. Dieny, V. S. Speriosu, S. S. P. Parkin, B. A. Gurney, D. R. Wilhoit, and D. Mauri, *Phys. Rev. B* **43**, 1297 (1991).
- ⁴A. E. Berkowitz, J. R. Mitchell, M. J. Carey, A. P. Young, S. Zhang, F. E. Spada, F. T. Parker, A. Hutten, and G. Thomas, *Phys. Rev. Lett.* **68**, 3745 (1992); J. Q. Xiao, J. S. Jiang, and C. L. Chien, *ibid.* **68**, 3749 (1992).
- ⁵M. Alper, K. Attenborough, R. Hart, S. J. Lane, D. S. Lashmore, C. Younes, and W. Schwarzacher, *Appl. Phys. Lett.* **63**, 2144 (1993).
- ⁶M. Alper, P. S. Aplin, K. Attenborough, D. J. Dingley, R. Hart, S. J. Lane, D. S. Lashmore, and W. Schwarzacher, *J. Magn. Magn. Mater.* **126**, 8 (1993).
- ⁷D. S. Lashmore, R. Oberle, M. P. Dariel, L. H. Bennett, and L. Swartzen-druber, *Mater. Res. Soc. Symp. Proc.* **132**, 219 (1988).
- ⁸L. J. van der Pauw, *Philips Res. Rep.* **13**, 1 (1958).
- ⁹T. R. McGuire and R. I. Potter, *IEEE Trans. Magn.* **MAG-11**, 1018 (1975).
- ¹⁰A. Barthélémy, A. Fert, M. N. Baibich, S. Hadjoudj, F. Petroff, P. Etienne, R. Cabanel, S. Lequien, F. Nguyen Van Dau, and G. Creuzet, *J. Appl. Phys.* **67**, 5908 (1990).
- ¹¹S. S. P. Parkin, N. More, and K. P. Roche, *Phys. Rev. Lett.* **64**, 2304 (1990).
- ¹²H. Kubota, S. Ishio, and T. Miyazaki (to be published).
- ¹³M. A. Howson, B. J. Hickey, J. Xu, D. Greig, and N. Wiser, *Phys. Rev. B* **48**, 1322 (1993).

Giant magnetoresistance in melt-spun $\text{Cu}_{87}\text{Co}_{13}$

M. A. Howson, S. O. Musa, M. J. Walker, and B. J. Hickey
Department of Physics, University of Leeds, Leeds LS2 9JT, United Kingdom

R. Cochrane and R. Stevens
School of Materials, University of Leeds, Leeds LS2 9JT, United Kingdom

Results for the temperature and magnetic-field dependence of melt-spun $\text{Cu}_{87}\text{Co}_{13}$ are presented and discussed. The magnetoresistance of the as-spun sample exhibits superparamagnetic behavior with a magnetoresistance of 18% at 0.4 K and in a field of 80 kOe. The magnetic-field dependence of the magnetoresistance is approximately proportional to the Langevin function. The microstructure of the sample was investigated by transmission electron microscopy and it appears that the giant magnetoresistance is due to the presence of small Co precipitates with an approximate mean diameter of 12 Å and a mean separation of 35 Å.

The magnetoresistance (MR) of magnetic materials has become a subject of much interest since the discovery of giant magnetoresistance (GMR) in magnetic multilayers.^{1,2} It has recently been found that GMR is also a property of magnetic granular sputtered films.^{3,4} When the randomly oriented magnetic moments of granules are aligned by an external magnetic field, the resistivity of the film decreases dramatically—by as much as 75% in the case of CoAg.⁵ The microstructure of these films is complex, but all samples appear to have three things in common: (i) a nonmagnetic or spin-glass matrix; (ii) large precipitates of the magnetic element typically 200 Å in diameter or larger; (iii) smaller precipitates of less than 50 Å in diameter. At present it is not clear what the relative importance is of these three features determining the magnetic properties of these films.

We have studied $\text{Cu}_{87}\text{Co}_{13}$ produced by rapidly quenching the molten alloy using a melt-spinning technique. Most studies on GMR in granular systems have been based on sputtered samples^{3,4} although a few groups are now working on melt-spun samples, also.^{6,7} The alloy ingots were produced by arc melting 99.99% Co and 99.999% Cu in an argon arc furnace. Rapidly quenched ribbons were produced by means of a single copper rimmed wheel in 0.5 atm of helium gas. Part of the ribbon was used to measure the temperature and magnetic-field dependence of the resistance and part of the ribbon was thinned using a concentrated acid solution for transmission electron microscopy (TEM) studies. The TEM studies were carried out using a JEOL CX at 200 kV.

In Figs. 1(a) and 1(b) we show the TEM micrograph of the sample in bright and dark field. The grain size of the Cu matrix is about 1 μm and within the grain there are “large” Co precipitates of between 150 and 500 Å. In Fig. 1(c) we show the diffraction pattern. This shows spots consistent with the Cu matrix and twinned fcc Co precipitates, but most important we see a diffuse ring due to the presence of a high density of “small” Co precipitates. In Fig. 1(d) we show a micrograph highlighting the twinned structure within the large Co precipitates. In Fig. 1(e) we show a dark-field micrograph from the diffuse ring showing a large number of Co precipitates with a mean diameter of about 12 Å and spacing of about 35 Å. Parkin *et al.*⁸ has observed similar results

using small-angle neutron diffraction to determine the particle size distribution.

In Fig. 2 we show the magnetoresistance of the sample at various temperatures between 2 and 150 K. The maximum magnetoresistance is 18% at 0.4 K at 80 kOe, however, it is clear that at all temperatures the MR is not saturating. The MR decreases as the temperature rises and is only 2% at room temperature. In Fig. 3 we show the temperature dependence of the resistivity of the sample in zero field and in a 60 kOe field. The data in a field was the same whether the sample was zero-field cooled or field cooled.

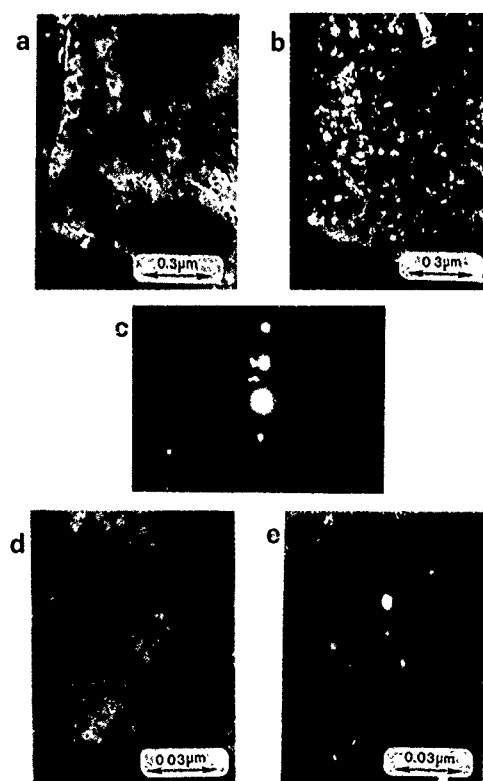


FIG. 1. (a) TEM micrograph showing the Cu-based matrix with large Co precipitates. (b) Dark-field TEM micrograph of the same area as in (a). (c) Diffraction pattern of image in (a) (d) Larger magnification micrograph showing the twinning of the large Co precipitates. (e) TEM micrograph in dark field from the diffuse ring showing the small, 15 Å Co precipitates from the diffuse ring in the diffraction pattern.

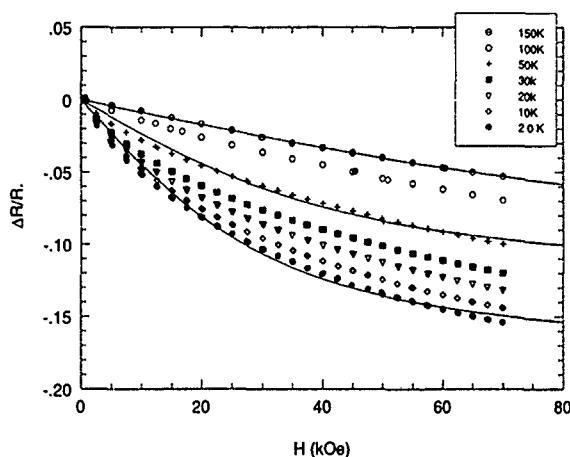


FIG. 2. The magnetoresistance of the sample at various temperatures. The solid lines are fits to the data assuming $\Delta\rho/\rho_0 \propto L(\alpha)$. For clarity the fits are only shown for 2, 50, and 150 K.

It appears that the magnetoresistance is due to the presence of the small 15 Å Co particles, and that these are superparamagnetic.⁴ If we assume that the electron scattering probability is linearly dependent on the correlation of the magnetic moments of adjacent magnetic particles, then the magnetoresistance will be proportional to the square of the magnetization.⁹ Hence, the resistivity would be proportional to the square of the Langevin function $L(\alpha)$, where $\alpha = \mu H/k_B T$ and μ is a measure of the magnitude of the moment on a particle. This assumes that the magnetic moments on each particle are uncorrelated. However, we find that we cannot fit MR data to the square of the Langevin function: The MR at low fields is very close to being proportional to $|H|$. The first point to be concerned with is the fact that if the MR is proportional to the modulus of H at low

fields then there will be a nondifferentiable point at $H=0$. This is not actually a problem; all that is required of the MR is that it is an even function of H and is continuous. In Fig. 2 we show a fit to the data using $\Delta\rho/\rho_0 \propto L(\alpha)$.

The reason the magnetoresistance is proportional to the Langevin function and not the square of the Langevin function is not clear. The result that the MR should be proportional to the square of the Langevin function is only strictly correct if the moments on the Co particles are uncorrelated. However, there are a number of ways they could become correlated: (i) the moments on the large "200 Å" Co particles will saturate at quite a low field and then the small superparamagnetic particles will interact with the field produced by the larger particles; (ii) the small particles may have a significant shape anisotropy which is oriented along the length of the ribbon; (iii) there may be some residual coupling between the particles.

A serious problem with our understanding of the field dependence of the magnetoresistance is that the value of μ extracted from the fits are temperature dependent, varying from approximately 1 to 50 μ_B as the temperature is raised from 0.4 to 200 K for the sample. Interestingly, Barlett *et al.*¹⁰ have argued that the MR in multilayer samples is also described by the Langevin function, although it is difficult to see what is the origin of the paramagnetic spins, but there is a similar problem with a temperature dependent μ . Such a temperature-dependent μ is not physically correct and this problem needs to be addressed for granular magnetic samples. However, the temperature dependence of the effective magnetic moment on a Co particle can be understood if we consider the possibility of coupling between the Co particles. Of course, the distance between the particles is of the right magnitude that there could be a residual antiferromagnetic average coupling between the particles. The possibility is being explored in depth at the moment.

We are grateful to the British Council and the Overseas Development Agency for partial funding of this project.

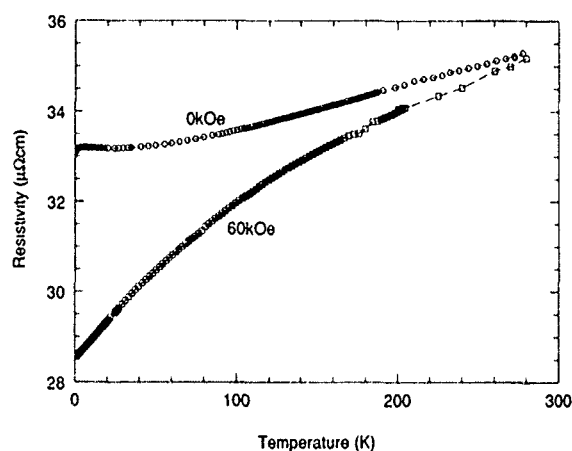


FIG. 3. The temperature dependence of the resistivity of the sample in zero field and in a 60 kOe magnetic field.

- ¹ M. N. Baibich, J. M. Broto, A. Fert, V. N. Nguyen, F. Petroff, P. Etienne, G. Creuzet, A. Freidrich, and J. Chazelas, *Phys. Rev. Lett.* **61**, 2472 (1988).
- ² S. S. P. Parkin, R. Bhadra, and K. P. Roche, *Phys. Rev. Lett.* **66**, 2152 (1991).
- ³ C. L. Chien, J. Q. Xiao, and J. S. Jiang, *J. Appl. Phys.* **73**, 5309 (1993).
- ⁴ A. E. Berkowitz, J. R. Mitchell, M. J. Carey, A. P. Young, S. Zhang, F. E. Spada, F. J. Parker, A. Hutten, and G. Thomas, *J. Appl. Phys.* **73**, 5320 (1993).
- ⁵ J. Q. Xiao, J. S. Jiang, and C. L. Chien, *Phys. Rev. B* **46**, 9266 (1992).
- ⁶ N. Katoaka, H. Endo, K. Fukamichi, and Y. Shimada, *Jpn. J. Appl. Phys.* **31**, 1969 (1993).
- ⁷ M. Rubinstein, B. N. Das, and N. C. Koon, *J. Appl. Phys.* **73**, 5540 (1993).
- ⁸ S. S. P. Parkin, R. F. C. Farrow, T. A. Rabedeau, R. F. Marks, G. R. Harp, Q. Lam, C. Chappert, M. F. Toney, R. Savoy, and R. Geiss, *Europhys. Lett.* **22**, 455 (1993).
- ⁹ M. R. Parker, J. A. Barnard, and J. Wakis, *J. Appl. Phys.* **73**, 5512 (1993); see also J. L. Gittleman, Y. Goldstein, and S. Bozowski, *Phys. Rev. B* **5**, 3609 (1972).
- ¹⁰ D. Barlett, F. Tsui, D. Gluck, L. Lauhon, C. Uher, and R. Clarke (unpublished).

Temperature effect on magnetoresistance in Co/Ru sandwiches

A. Dinia, S. Zoll, and K. Ounadjela

ULP, IPCMS-GEMME, 4 rue Blaise, Pascal, F67070 Strasbourg, France

Evidence is given of a strong dependence of magnetoresistance on temperature in Co/Ru sandwiches. This dependence while weak for thin Ru layers is much stronger for thicker Ru layers. In fact, three oscillations in saturation magnetoresistance and saturation field as a function of the thickness of the Ru layer t_{Ru} are observed at 4.2 K while only one oscillation is found at 300 K. In addition, for thin Ru layers, $t_{\text{Ru}} < 11 \text{ \AA}$, the saturation magnetoresistance is found to decrease between 4.2 and 300 K. In contrast, for Ru thickness in the range $11 \text{ \AA} < t_{\text{Ru}} < 14 \text{ \AA}$, the behavior is reversed, leading to the increase of the magnetoresistance at 300 K. This behavior is attributed to the spin disorder occurring at the interfaces at room temperature. Finally, for $t_{\text{Ru}} > 14 \text{ \AA}$ the magnetoresistance completely vanishes at 300 K while a relatively high value is still observed for large Ru thickness, $t_{\text{Ru}} = 80 \text{ \AA}$, at 4.2 K. This indicates that the mean free path of the conduction electrons in the Ru layer is strongly reduced from about 100 \AA at 4.2 K to approximately 14 \AA at room temperature.

The study of magnetic layered systems consisting of ferromagnetic layers separated by a nonmagnetic interlayer has resulted in the discovery of a variety of fascinating phenomena.¹ In particular, reports of giant magnetoresistance (GMR) in Fe/Cr multilayers² have attracted great interest for fundamental physics as well as applications. The magnetoresistance (MR) has been found to be strongly dependent on the temperature, however the comprehension of this aspect remains still lacking. The decrease of MR with temperature has been recently reported and usually explained by a decrease of the mean free path of the electrons in the nonmagnetic layers.³ Moreover, Parkin⁴ has shown that the variation of the MR with temperature is strongly enhanced when the spacer layer thickness increases, suggesting that the main contribution to the MR comes from spin diffusion within the nonmagnetic layer.

Co/Ru sandwiches were grown by UHV evaporation onto mica substrate. A 150-\AA-thick epitaxial Ru buffer layer was grown onto this substrate at 600 °C in order to provide a smooth and clean single-crystalline surface. After cooling the substrate to 120 °C, Co and Ru layers were subsequently grown and covered by 100 \AA Ru (upper layer) to protect the sample against oxidation. For this study, a series of samples was prepared with fixed Co thickness $t_{\text{Co}} = 32 \text{ \AA}$ and varied Ru thicknesses from 5 to 80 \AA. In the following, we refer to the nomenclature $(\text{Co}_x\text{Ru}_y)_n$ superlattice, where x and y indicate the thicknesses in \AA of Co and Ru sublayers and n the number of periods in which $n = 2$ corresponds to sandwiches. The reflection high-energy electron-diffraction (RHEED) patterns obtained during the samples' growth reveal high crystalline quality with a (0001) hcp stacking of the Co and Ru layers.⁵ For this series of samples in which $t_{\text{Co}} = 32 \text{ \AA}$, the magnetization lies along the film plane as reported in previous work.⁶

The resistance was measured using the conventional four-point method, at liquid-helium temperature, with the external magnetic field applied along the film plane and parallel to the electric current direction. The magnetoresistance ratio $\Delta R/R$ was defined as the ratio of the total resistivity change ΔR to the resistivity at zero field. All MR curves were cor-

rected for the classical parabolic magnetoresistance.

Figure 1 shows the MR curves obtained at 4.2 and 300 K for the strongly antiferromagnetically coupled sample $(\text{Co}_{32}\text{Ru}_5)_2$. For these two curves the maximum of resistance is observed at zero field, when the magnetizations of the two Co layers are antiparallely aligned. The resistance decreases as the magnetic field increases and becomes constant when the applied field is sufficient to overcome the antiferromagnetic (AFM) exchange coupling and to align the adjacent magnetizations in its direction. For the curve measured at room temperature, we observe a shoulder at 500 Oe which is clearly explained by the anisotropic magnetoresistance (AMR) effect.⁷ This anisotropic contribution of the MR was also deserved for all sandwiches and was taken into account for a precise determination of the spin-valve MR. The most interesting result is the temperature effect observed in this figure. In this sample, both MR and saturation field H_s obtained at 4.2 K ($\Delta R/R = 0.36\%$ and $H_s = 30 \text{ kOe}$) are much larger than those found at 300 K ($\Delta R/R = 0.11\%$ and $H_s = 20 \text{ kOe}$). This result indicates that the AFM exchange

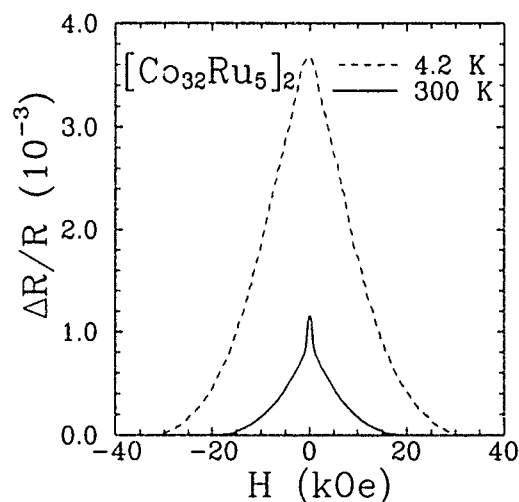


FIG. 1. Magnetoresistance curves of a $(\text{Co}_{32}\text{Ru}_5)_2$ sandwich with the applied magnetic field along the film plane and parallel to the current, respectively, at 4.2 K (dashed line) and 300 K (solid line).

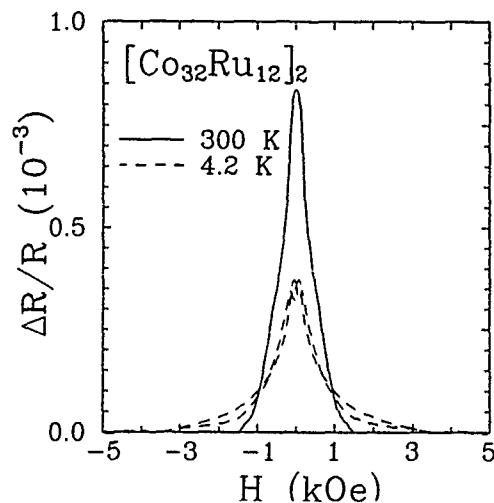


FIG. 2. Magnetoresistance curves of a $(\text{Co}_{32}\text{Ru}_{12})_2$ sandwich with the applied magnetic field along the film plane and parallel to the current, respectively, at 4.2 K (dashed line) and 300 K (solid line).

coupling strength J_{AF} decreases as the temperature increases. Its magnitude is related to the saturation field H_s by the following equation: $J_{\text{AF}} = H_s M_s t_F / 2$, where M_s and t_F are, respectively, the saturation magnetization and thickness, of the magnetic layer. Using the saturation field obtained in Fig. 1 and the saturation magnetization of the bulk Co, the J_{AF} values found for the $(\text{Co}_{32}\text{Ru}_5)_2$ bilayer are approximately equal to 6.72 erg/cm² at 4.2 K and 4.48 erg/cm² at 300 K. Such decrease of the AFM coupling by 33% between 4.2 K and room temperature is slightly higher than the reduction of 20% and 22% observed, respectively, in Fe/Cr (Ref. 3) and Co/Cu multilayers.⁸ We explain this effect as being due to the thermal spin fluctuations occurring at room temperature. On the other hand, the decrease of the MR by 60% in this sample can be attributed to the strong decrease of the mean free path in the Ru layers at room temperature.

A similar study was performed on the $(\text{Co}_{32}\text{Ru}_{12})_2$ sandwich with larger Ru thickness than the corresponding value of the sample presented above. The magnetization hysteresis loop of this sample obtained at room temperature with the field along the film plane has shown a small coercive field and a small remanent magnetization which are characteristic of a ferromagnetic (FM) canted state.⁷ This state was also confirmed by recent neutron-diffraction studies performed on the multilayer with the same Co and Ru thicknesses⁹ where only a FM peak was found with relatively smaller intensity than the one corresponding to the full ferromagnetically coupled layers. As a result the MR curves obtained at 4.2 and 300 K with H along the plane and parallel to the current I (Fig. 2) present an interesting behavior. Surprisingly the MR is found to increase at room temperature at the opposite of the other sample $(\text{Co}_{32}\text{Ru}_5)_2$ where the MR decreases at 300 K. This result was also obtained for the multilayer with the same Co and Ru thicknesses⁷ and seems to be a characteristic of Co/Ru superlattices. In these superlattices the nuclear-magnetic-resonance (NMR) study has shown the evidence of some intermixing at the interfaces along three Co monolayers.¹⁰ In these conditions the magnetization is low-

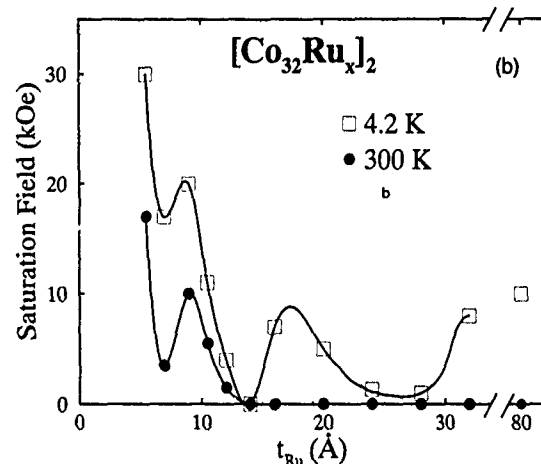
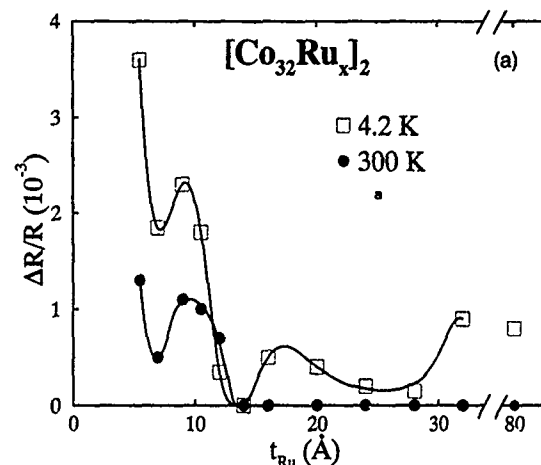


FIG. 3. Variation of the (a) magnetoresistance ratio and (b) saturation field as a function of the Ru thickness, respectively, at 4.2 K (square) and 300 K (circle). The magnetic field is applied along the film plane and parallel to the current. Solid curves are a guide to the eye.

ered at the interfaces. This suggests a gradient in Curie temperature due to the concentration gradient of the interdiffused region and the appearance of a paramagnetic zone at the top of the layer where the concentration of Ru is higher than 37 at. % for Co atoms. As a consequence, the spin disorder is maximum at the interfaces at room temperature giving a contribution to the magnetoresistance due to the scattering within the Co layers which is much larger than the one obtained at 4.2 K. This contribution is relatively important for this Ru thickness, for which the MR due to the AFM exchange coupling is small, leading to the inversion of the MR behavior at 300 K. These results indicate that the dependence of the MR on temperature gives a fine information on the nature of the magnetic state as well as the one given by neutron diffraction.

Figures 3(a) and 3(b) show the variation of the saturation field H_s and saturation magnetoresistance $\Delta R/R$ of 14 sandwiches as a function of Ru thickness t_{Ru} both at 4.2 and 300 K. Three oscillations of $\Delta R/R$ and H_s are observed at 4.2 K while only one oscillation is found at 300 K. The oscillations obtained at 4.2 K are similar to those previously reported on Co/Ru multilayers¹¹⁻¹⁴ and are indicative of an oscillation in the indirect exchange coupling from antiferromagnetic to fer-

romagnetic state as the Ru layer thickness is varied. The maximum of these oscillations corresponds to the AFM state, where the coupling is strong, particularly for thin Ru thickness, and needs high magnetic field to change the relative orientation of the two magnetic layers from antiparallel to parallel.

The more striking result obtained in this figure is the strong dependence on the temperature of the magnetoresistance and saturation field. For the MR curve three different behaviors are clearly evidenced depending on the Ru thickness, as follows.

(i) For thin Ru spacer layers, $t_{\text{Ru}} < 11 \text{ \AA}$, the MR is strongly reduced between 4.2 and 300 K. This reduction of MR is of 60% for $t_{\text{Ru}} = 5 \text{ \AA}$ and decreases as the Ru thickness is increased reaching 30% for $t_{\text{Ru}} = 10 \text{ \AA}$. To explain this effect, we have to assume that the increase of the Ru thickness is accompanied by the reduction of the AFM exchange coupling, then the corresponding MR values are also reduced. In addition, the MR due to the spin disorder is found to increase at room temperature as explained above. As a consequence, the MR due to the spin disorder becomes relatively important which gives the decrease of the MR reduction between 4.2 and 300 K.

(ii) More interestingly, for $11 \text{ \AA} < t_{\text{Ru}} < 14 \text{ \AA}$ the AFM exchange coupling is strongly decreased as confirmed by the small saturation field values. As a result, the MR due to this effect is smaller than the one due to the spin disorder at 300 K which leads to the inversion of the MR behavior where this latter is enhanced between 4.2 and 300 K.

(iii) for $t_{\text{Ru}} > 14 \text{ \AA}$ this effect is no longer observed, because the thickness becomes larger than the mean free path at 300 K and the MR completely vanishes; however, at 4.2 K two more oscillations of MR and H_s are observed for thicker Ru layers. The latter effect was also reported by Parkin⁴ on $(\text{NiFe/Cu})_n$ multilayers. The MR completely disappears for $t_{\text{Ru}} > 10 \text{ \AA}$ at room temperature while two oscillations of the MR are still observed at 4.2 K for larger Cu thicknesses. This result has been explained by the increased scattering in the Cu layers at room temperature for larger Cu thicknesses. For the variation of the saturation field with the Ru thickness reported in Fig. 3(b) the behavior is similar to the MR variation. However, the saturation field is always reduced at 300 K even for the Ru range thickness 11–14 Å where the MR was found to increase at 300 K.

Surprisingly, we find the presence of MR effect with slightly high saturation field ($H_s = 10 \text{ kOe}$) for a bilayer with Ru thickness of 80 Å, as reported in Fig. 4. This could indicate that the antiferromagnetic or ferromagnetic canted coupling persists for Ru thicknesses up to more than 80 Å and that the mean free path at this temperature is of the order of 100 Å.

In summary, we have shown that the dependence of the MR on the temperature gives fine information on the nature of the magnetic state and particularly at the interfaces. In fact, for thin Ru layers, where the AFM coupling is strong, the MR is important at 4.2 K and is sensitively reduced at 300 K due to the strong decrease of the mean free path. In contrast, for thicker Ru layers ($t_{\text{Ru}} = 12 \text{ \AA}$) the coupling is

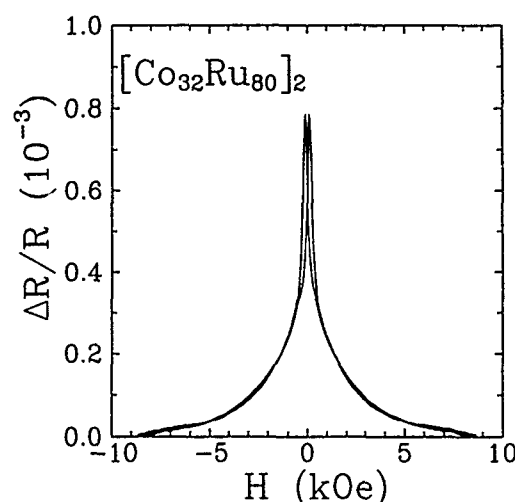


FIG. 4. Magnetoresistance curve of a $(\text{Co}_{32}\text{Ru}_{80})_2$ sandwich with the applied magnetic field along the film plane and parallel to the current at 4.2 K.

small giving a small MR, then the enhancement of MR at 300 K is mainly due to the spin disorder at the interfaces. We find well-defined oscillations in the MR and the H_s at 4.2 K. However, only one oscillation was observed at 300 K indicating the strong dependence of the temperature effect on the Ru layer thickness. Consequently, for Ru layers larger than 14 Å both the MR and H_s vanish. The observation of a significant MR for a Ru thickness of 80 Å at 4.2 K suggests that the mean free path is of the order of 100 Å at this temperature, which is much larger than the value of about 14 Å obtained at 300 K.

The authors gratefully acknowledge fruitful discussions with D. Stoeffler, E. Daniel, P. Panissod, and A. Fert. This research was supported in part by the European community Science Project: ESPRIT3 Basic Research (Smmn:S).

¹ *Metallic superlattices: Artificially Structured Materials*, edited by T. Shinjo and T. Takada, Studies in Physical and Theoretical Chemistry Vol 49 (Elsevier, Amsterdam, 1987).

² M. N. Baibich, J. M. Broto, A. Fert, F. Nguyen Van Dau, F. Petroff, P. Etienne, G. Creuset, A. Friederich, and J. Chazelas, *Phys. Rev. Lett.* **61**, 2472 (1988).

³ F. Petroff, A. Barthelemy, A. Hamzic, A. Fert, P. Etienne, S. Lequien, and G. Creuset, *J. Magn. Magn. Mater.* **93**, 95 (1991).

⁴ S. S. P. Parkin, *Appl. Phys. Lett.* **60**, 512 (1992).

⁵ D. Muller, K. Ounadjela, P. Vennegues, V. Pierron-Bohnes, A. Arbaoui, J. P. Jay, A. Dinia, and P. Panissod, *J. Magn. Magn. Mater.* **104-107**, 1873 (1992).

⁶ A. Dinia, K. Ounadjela, A. Arbaoui, G. Suran, D. Muller, and P. Panissod, *J. Magn. Magn. Mater.* **104-107**, 1871 (1992).

⁷ A. Dinia and K. Ounadjela (unpublished).

⁸ S. S. P. Parkin, Z. G. Li, and David J. Smith, *Appl. Phys. Lett.* **58**, 2710 (1991).

⁹ C. Fermon *et al.* (unpublished).

¹⁰ J. P. Schille *et al.* (unpublished).

¹¹ K. Ounadjela, D. Muller, A. Dinia, A. Arbaoui, and P. Panissod, *Phys. Rev. B* **45**, 7768 (1992).

¹² A. Arbaoui, A. Dinia, and P. Panissod, *Solid State Commun.* **85**, 475 (1993).

¹³ S. S. P. Parkin, R. Bhadra, and K. P. Roche, *Phys. Rev. Lett.* **66**, 2152 (1991).

¹⁴ P. J. H. Bloemen, H. W. van Kesteren, H. J. M. Swagten, and W. J. M. de Jonge (unpublished).

Magnetothermopower in antiferromagnetically coupled Co-Re superlattices

J. B. Sousa, R. P. Pinto, B. Almeida, and M. E. Braga

Centro de Física da Universidade do Porto and IFIMUP (IMAT), Pr.Gomes Teixeira 4000 Porto, Portugal

P. P. Freitas, L. V. Melo, and I. G. Trindade

INESC, R. Alves Redol, 9-3°, 1000 Lisboa, Portugal, and IST, R. Rovisco Pais, 1000 Lisboa, Portugal

Results are reported on the magnetothermopower of antiferromagnetically coupled Co-Re superlattices, obtained in a film of $150 \text{ Å Re}/(\text{Co } 22 \text{ Å Re } 5 \text{ Å}) \times 16/50 \text{ Å Re}$, from 10 to 300 K and in magnetic fields $0 < H < 10 \text{ kOe}$. At low temperature the magnetothermopower, $\Delta S = S(H) - S(0)$, is positive reaching a maximum around 100 K ($\Delta S/S \approx 10\%$ at saturation), and fading away when $T > 250 \text{ K}$. At each temperature, the field dependence of ΔS is rather close to that observed in the magnetoresistance. The temperature dependence of ΔS is consistent with the model of Piroux *et al.* [J. Magn. Magn. Mater. **110**, L247 (1992)] based on a two-spin-channel conduction with electron spin mixing due to magnon scattering (ρ_{11}). In this model the sign of ΔS depends on whether the parameter $\alpha = \rho_{01}/\rho_{01}$ is greater ($\Delta S < 0$) or smaller than unity ($\Delta S > 0$). The results for Co-Re superlattices, showing $\Delta S > 0$, support this prediction, since $\alpha < 1$ for Re impurities in Co, from previous studies.

I. INTRODUCTION

The two-current model, involving parallel conduction of spin-up and spin-down channels, and spin-dependent scattering at the interfaces or within the ferromagnetic layers, was successively used to explain the giant magnetoresistance in antiferromagnetically (AF) coupled Fe/Cu,¹ Co/Cr,² and Co/Re (Ref. 3) superlattices at low temperature. The observed decrease of the magnetoresistance when the temperature increases was first related to spin mixing by electron-magnon scattering.^{4,5} This idea was then generalized and used to explain the observed temperature dependence of the magnetothermopower in Fe/Cr and Co/Cu multilayers.⁶

In this work we present a detailed experimental investigation of the magnetothermopower, $\Delta S = S(H) - S(0)$, in an AF coupled Co/Re superlattice with composition Re $150 \text{ Å}/(\text{Co } 22 \text{ Å Re } 5 \text{ Å}) \times 16/\text{Re } 50 \text{ Å}$, exhibiting a large magnetoresistance at low temperature.³ The temperature dependence of ΔS is analyzed in terms of the model of Piroux *et al.*,⁶ and the field dependence of ΔS up to magnetic saturation is compared with the dependence of the magnetoresistance measured at the same temperature.

II. EXPERIMENT

The superlattice $(\text{Co } 22 \text{ Å Re } 5 \text{ Å}) \times 16$ was prepared by magnetron sputtering in a high vacuum system with a base pressure of $1 \times 10^{-7} \text{ Torr}$. The Co was deposited by rf, at a rate of 2 Å s^{-1} , and Re was deposited by dc magnetron sputtering at a rate of 0.85 Å s^{-1} . These rates were monitored by *in situ* quartz crystals and the Ar pressure during deposition was kept at 8 mTorr (for Co) and 2.5 mTorr (for Re). In order to induce [001] crystal growth perpendicular to the plane of the films, a 150-Å-thick Re buffer film was used. It also reduces spurious effects of the glass substrate on the superlattice structure. To avoid effects from external exposure, a protective layer of Re, 50 Å thick, was deposited on the top of the film. Further details on sample preparation and characterization were given elsewhere.³

The thermopower S was measured with a four-wire dynamic method (two copper and two Chromel wires attached directly to the sample), based on the application, at each experimental temperature, of a transient temperature gradient giving a small difference of temperature across the sample, $\Delta T(t)$. This induces two time-dependent thermal emf (in the copper-sample and Chromel-sample circuits) which, for small ΔT , vary linearly with each other. The small voltages are measured with nanovolt resolution, and from the corresponding slope we can obtain S relative to copper (or Chromel). Further details on the experimental method are given elsewhere.⁷

III. RESULTS AND DISCUSSION

Figure 1 shows the temperature dependence of the thermopower for the reported Co/Re superlattice, from 10 up to 300 K and in zero magnetic field. $S(T)$ is negative and its magnitude increases with T , exhibiting great similarities with the corresponding curves measured in sputtered films of pure

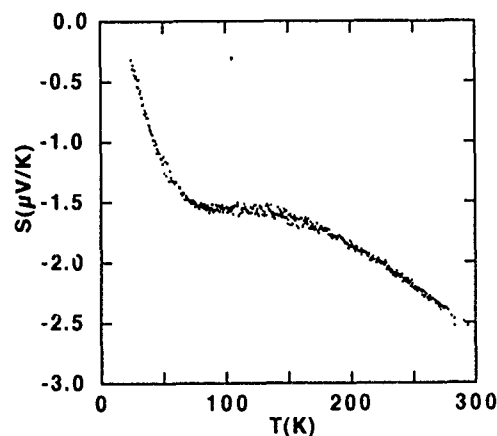


FIG. 1 Temperature dependence of the thermopower (S : Referred to copper) of the Re $150 \text{ Å}/(\text{Co } 22 \text{ Å Re } 5 \text{ Å}) \times 16/\text{Re } 50 \text{ Å}$ superlattice, measured in zero magnetic field.

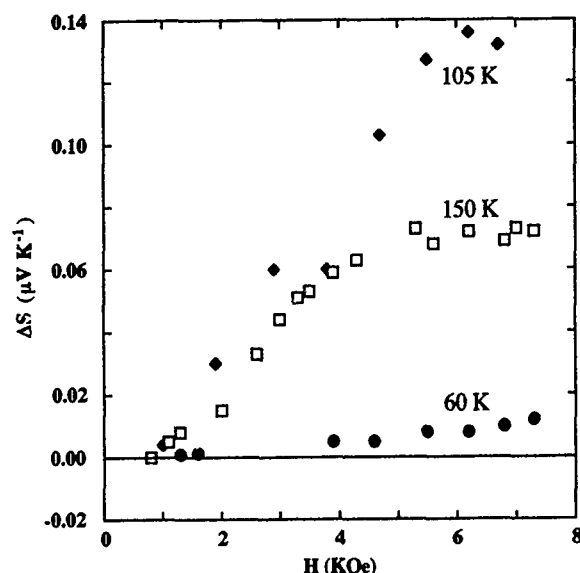


FIG. 2. Magnetic-field dependence of the thermopower, measured at three different temperatures: 60 K (●), 105 K (◆) and 150 K (○).

Co.⁸ Thus, most of the observed thermal effects reflects the dominant role of Co in the Co 22 Å/Re 5 Å superlattice.

The application of a magnetic field produces a positive contribution in the thermopower, leading ultimately to magnetic saturation as illustrated in Fig. 2 for a few measured temperatures. The corresponding saturation fields $H_s(T)$, agree with those obtained from the magnetoresistance curves measured at the same temperature. As illustrated in Fig. 3 with data obtained at $T=100$ K an approximate linear relation exists between ΔS and $\Delta\rho/\rho$.

From the experimental $S(H)$ curves obtained at different temperatures, we can construct the magnetothermopower curve in the temperature range 10–300 K, as shown in Fig. 4. Here ΔS_m is the saturation magnetothermopower, obtained at fields $H > H_s(T)$.

This curve reveals the main features predicted in the model of Piroux *et al.*⁶ based on the two-current model ($\rho_{\uparrow}, \rho_{\downarrow}$) and spin mixing due to magnon scattering ($\rho_{\uparrow\downarrow}$). It

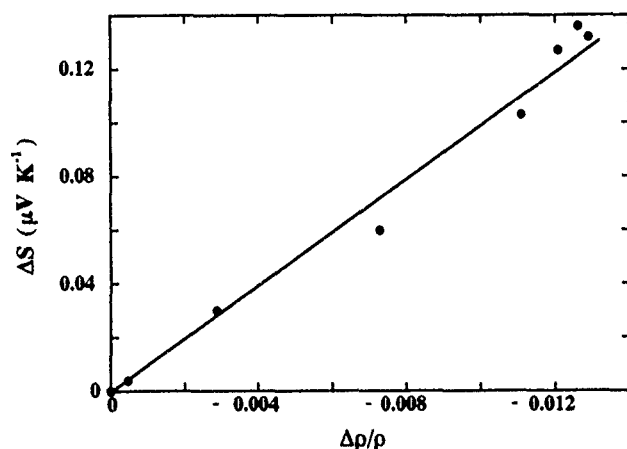


FIG. 3. An approximate linear relation exists between the changes with magnetic field of the magnetothermopower and magnetoresistance, as illustrated here for $T=100$ K.

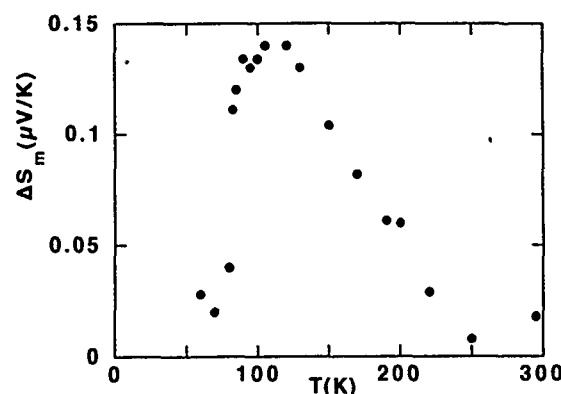


FIG. 4. Temperature dependence of the (saturation) magnetothermopower measured in the AF coupled Re 150 Å/(Co 22 Å Re 5 Å)×16/Re 50 Å superlattice.

gives a specific magnetothermopower contribution in AF coupled multilayered thin films with the form

$$\Delta S_m = \frac{\pi^2}{3} \frac{k}{|e|} R(T) \frac{\rho_{\uparrow}^2 - \rho_{\downarrow}^2}{K} \rho_{\uparrow\downarrow}, \quad (1)$$

where $R(T)$ is a positive coefficient of the order of unity which varies slowly with temperature (except at very low temperature where R vanishes exponentially) and

$$K = [\rho_{\uparrow}\rho_{\downarrow} + \rho_{\uparrow\downarrow}(\rho_{\uparrow} + \rho_{\downarrow})][\rho_{\uparrow} + \rho_{\downarrow} + 4\rho_{\uparrow\downarrow}].$$

This anomalous thermopower contribution requires asymmetric conduction ($\rho_{\uparrow} \neq \rho_{\downarrow}$) and, simultaneously, spin-mixing mechanisms originating $\rho_{\uparrow\downarrow}$ (magnon scattering in the model). The addition of 3d impurities to the ferromagnetic elements (Co, Ni, and Fe) can induce large differences in ρ_{\uparrow} and ρ_{\downarrow} . In the case of Re impurities in Co it is known that $\rho_{\downarrow} < \rho_{\uparrow}$,⁹ which could explain the positive sign of ΔS_m in our Co-Re superlattice.

As a function of temperature, according to Eq. (1), $\Delta S_m = 0$ at $T=0$ K ($\rho_{\uparrow\downarrow}=0$), increases with $\rho_{\uparrow\downarrow}$, goes through a maximum for $\rho_{\uparrow\downarrow} = 0.5(\rho_{\uparrow}\rho_{\downarrow})^{1/2}$ and decreases to zero for $\rho_{\uparrow\downarrow} \gg (\rho_{\uparrow}\rho_{\downarrow})^{1/2}$. In contrast with the cases of Fe/Cu and Co/Cu multilayers,⁶ where the expected maxima in $|\Delta S_m|$ are not observed below room temperature, in our Co/Re superlattice the maximum occurs well below room temperature. This suggests that the spin-mixing resistivity $\rho_{\uparrow\downarrow}$ in Co/Re reaches comparable values to $(\rho_{\uparrow}\rho_{\downarrow})^{1/2}$ at considerably lower temperatures. From Ref. 9 we know the values of the partial residual resistivities caused by Re impurities in a Co matrix, for spin-up and spin-down conduction electrons, $\rho_{0\uparrow} \approx 18 \mu\Omega \text{ cm}$ and $\rho_{0\downarrow} = 7.7 \mu\Omega \text{ cm}$, so $\alpha = \rho_{0\downarrow}/\rho_{0\uparrow} = 0.43$ in this case; the behavior of $\rho_{\uparrow\downarrow}(T)$ in bulk Co was found to be similar to that of Ni. The suggested enhancement in $\rho_{\uparrow\downarrow}$ in our Co/Re superlattice film could be related to a smaller value of the D constant of the magnon dispersion curve in Co ($w = Dq^2$). A similar effect has been previously reported for $\rho_{\uparrow\downarrow}$ in Fe/Co multilayers.⁶

We should now comment the small magnitude of the thermoelectric power in our Co/Re multilayers. The zero-field thermopower S of pure Co is $-30.8 \mu\text{V K}^{-1}$ at room temperature¹⁰ and similar values have been observed at satu-

ration in Co/Cu multilayers. In contrast, S in our Co/Re multilayers is about one order of magnitude smaller. The magnetothermopower in Co/Cu samples with the largest magnetoresistance is about $-6 \mu\text{V K}^{-1}$,¹¹⁻¹³ as opposed to the $+0.14 \mu\text{V K}^{-1}$ observed in our Co/Re multilayer.

These differences could be due to the distinct role played by Cu and Re impurities in cobalt. For the transition-metal impurity, the large effective impurity potential, due to its incomplete d shell, is strong enough ($\Delta Z=2$ with respect to Co) to build up a virtual bound state s_1d_1 (VBS) extending through the Fermi level, thus allowing extra conduction electron transitions, due to impurity scattering, into such VBS localized states.¹⁴ In contrast, for Cu impurities, with their $3d$ band full, such a type of impurity scattering is not possible.

In pure Co (and also Co-Cu multilayers) we expect the dominance of the usual s - d transitions induced by phonons. Due to the high density of states in the d subband which goes through E_F , $N_{d1}(E_F)$, and to its rapid decrease with energy, a large negative thermoelectric power arises, $S \sim -30 \mu\text{V K}^{-1}$ at room temperature.

As shown by Cadeville and Roussel,¹⁰ 1% Re impurities in Co is sufficient to reduce the magnitude of the room temperature thermopower from about -30 to $-2 \mu\text{V K}^{-1}$. Such dramatic reduction is due to the fact that the VBS density of states N has its maximum near E_F and so $dN/dE \sim 0$ leads to a small thermoelectric power (even to a change of sign, when we go from Os to Re).

Our results bring new information for the ongoing discussion of the physical origin of the magnetothermopower in magnetic multilayers as follows,

(i) Some authors⁶ claim that electron-magnon, spin-mixing effects, are the dominant mechanisms. In this model the magnetothermopower is negligible both at low and high temperatures, so the ΔS_m anomalies occur only at intermediate temperatures.

(ii) More recent work, mainly concerned with Co-Cu multilayers,^{11,12} emphasizes the dominant role of the phonon-induced non-spin-flip s - d transitions.

We believe that, due to the presence of the Re impurities and the high residual resistivity, s - d transition effects are not dominant in our Co-Re multilayers. It appears that the magnetothermopower essentially reflects the effects of the spin-mixing mechanisms, appropriately damped by the large residual resistivity (see below).⁶ In contrast, s - d electron transitions seem to dominate in Co-Cu originating large thermopower and magnetothermopower values.^{11,12} The temperature dependence of ΔS_m in Co/Re and Co/Cu multilayers is also consistent with the above considerations: The anomaly is concentrated at intermediate temperatures in

Co/Re (as predicted by the electron-magnon model), whereas in Co/Cu it shows no sign of fading away up to 300 K (the density-of-states model gives an increase of ΔS_m with T , as the anomaly occurs through electron-phonon scattering).

Our previous characterization of the interfacial structure of Co/Re multilayers¹⁵ indicates that interface Co-Re mixing occurs, at most, over about 5 \AA ($2.5 \text{ \AA} + 2.5 \text{ \AA}$) in each 22 \AA Co layer. Nevertheless, if we recall that just 1% Re in Co decreases S by a factor of ~ 10 , it is not surprising that atomic disorder in Co/Re multilayers may lead to a large reduction of S . Apparently this is associated with a switch from the s - d (Refs. 11-13) to the electron magnon model.⁶

ACKNOWLEDGMENTS

One of us (B. A.) gratefully acknowledges a Ph.D research grant (BD 2217/92-IC) from Junta Nacional de Investigação Científica e Tecnológica, Portugal. This work has been partially supported by Euram-Britte Project N. Breu-0153-C(TT), Stride Project N. STRDA/C/CEN/522/92 and Instituto Nacional de Investigação Científica (INIC) (Porto group).

- ¹ J. Barnas, A. Fuss, R. E. Camley, P. Grunberg, and W. Zinn, *Phys. Rev. B* **42**, 8110 (1990).
- ² A. Fert, A. Barthelemy, P. Etienne, S. Leguren, R. Loloce, D. M. Mosca, F. Petroff, W. P. Pratt, and P. A. Schroeder, *J. Magn. Mater.* **104**, 1712 (1991).
- ³ P. P. Freitas, I. G. Trindade, L. V. Melo, N. Barradas, and J. C. Soares, in *Proceedings of the NATO Advanced Research Workshop on Structure and Magnetism of Systems of Reduced Dimensions*, Corsica, June 15-20, 1992 (Plenum, New York, 1993).
- ⁴ F. Petroff, A. Barthelemy, A. Fert, P. Etienne, and S. Leguren, *J. Magn. Mater.* **93**, 95 (1991).
- ⁵ D. H. Mosca, F. Petroff, A. Fert, P. A. Schroeder, W. P. Pratt, and R. Loloce, *J. Magn. Mater.* **94**, L1 (1991).
- ⁶ L. Piraux, A. Fert, P. A. Schroeder, R. Loloce, and P. Etienne, *J. Magn. Mater.* **110**, L247 (1992).
- ⁷ J. B. Sousa, M. M. Amado, R. P. Pinto, M. Salgueiro Silva, M. E. Braga, B. Chevalier, and J. Etourneau, *J. Magn. Mater.* **111**, 239 (1992).
- ⁸ J. B. Sousa, R. P. Pinto, M. E. Braga, B. Almeida, P. P. Freitas, L. V. Melo, and I. G. Trindade (unpublished).
- ⁹ I. A. Campbell and A. Fert, in *Ferromagnetic Materials*, edited by E. P. Wohlfarth (North-Holland, Amsterdam, 1982), Vol. 3, Chap. 9, p. 768.
- ¹⁰ M. C. Cadeville and J. Roussel, *J. Phys. F* **1**, 686 (1971).
- ¹¹ J. Shi, S. S. Parkin, L. Xing, and M. B. Salamon, *J. Magn. Mater.* **125**, L 251 (1993).
- ¹² J. Shi, S. S. Parkin, L. Xing, and M. B. Salamon, *J. Appl. Phys.* **73**, 5524 (1993).
- ¹³ E. Avdi, B. J. Hickey, D. Greig, M. A. Howson, M. J. Hall, J. Xu, M. J. Walker, N. Wiser, and P. de Groot, *J. Appl. Phys.* **73**, 5521 (1993).
- ¹⁴ J. Friedel, *Nuovo Cimento*, Vol. 7, Supplement 287 (1958).
- ¹⁵ J. L. Leal, N. P. Barradas, J. C. Soares, M. F. Silva, M. Rots, and P. P. Freitas, in *Proceedings of the 1993 Spring Meeting, Materials Research Society, San Francisco, 1993*.

Structural and magnetotransport properties of Co/Re superlattices

Y. Huai and R. W. Cochrane

Département de Physique et Groupe de recherche en physique et technologie des couches minces,
Université de Montréal, C.P. 6128, Succ. A, Montréal, Québec, Canada H3C 3J7

X. Bian and M. Sutton

Department of Physics, Centre for the Physics of Materials, McGill University, 3600 University Street,
Montréal, Québec, Canada H3A 2T8

Structural properties of sputtered Si/Re 50 Å/(Co 20 Å/Re x Å)₄₀ superlattices have been investigated in detail by low- and high-angle x-ray-diffraction measurements. The low-angle x-ray reflectivity data have been analyzed using an optical model and the high-angle data have been treated on the basis of a trapezoidal model. The fitted results indicate that the films with small $x_{\text{Re}}=3, 5$, and 7 Å are essentially composed of pure Co layers and Re rich alloy (~80%) interfaces about 3–5 monolayers thick. The magnetoresistance (MR) data of the antiferromagnetically coupled films have been analyzed using a semiclassical MR model of interfacial spin-dependent scattering.

I. INTRODUCTION

Recently discovered giant magnetoresistance¹ (GMR) and oscillatory exchange coupling² in magnetic multilayers continue to attract intensive investigation because of their unusual underlying physics^{1,2} and potential applications in magnetoresistive devices.³ Since GMR has been found experimentally to be highly sensitive to the atomic structures of the individual layers as well as to the interfacial microstructures,^{4–6} detailed structural characterization is necessary for understanding the anomalous magnetotransport property. In previous articles,^{7,8} we have reported the GMR and oscillatory exchange coupling in sputtered Si/Re 50 Å/(Co 20 Å/Re x Å)₄₀ superlattices with $x_{\text{Re}}=3–32$ Å, and the annealing effect on the structure and GMR of the films. In this article, we analyze the low- and high-angle x-ray-diffraction data for the Co/Re superlattices on the basis of the structural models described in Ref. 9. In addition, the MR data of the antiferromagnetically (AF) coupled films are discussed in the light of a semiclassical MR model of interfacial spin-dependent scattering.⁴

II. EXPERIMENTAL DETAILS

The Co/Re superlattices with structures Si(oxidized)/Re 50 Å/(Co 20 Å/Re x Å)₄₀ were prepared using a modified single-source rf triode sputtering system.^{7,9} Low- and high-angle x-ray-diffraction measurements have been taken using CuK α radiation as detailed in Ref. 9. The MR was measured with the current in the film plane at temperatures from 1.5 to 325 K in magnetic fields up to 1 T, using a high-resolution ac bridge.⁷

III. RESULTS AND DISCUSSION

The reflectivity data of several films are shown in Fig. 1: Sharp superlattice peaks up to third order (except for the thinnest) are observed for all the films with Re thickness x_{Re} down to 3 Å. The reflectivity data of the films have been analyzed using an optical model⁹ which includes both interfacial mixing and discrete layer-thickness fluctuations. The fitted results (dashed lines) are also shown in Fig. 1 for films B and E and the parameters for all five films are listed in

Table I. As these values indicate, the rear and front interfaces in the small x_{Re} films extend across the entire Re layer, so that the films are essentially composed of Co layers and an alloyed interfacial region [3–5 monolayers (ML)]. For the film with the smallest $x_{\text{Re}}\sim 1$ ML, successive Co layers may not be completely separated due to interfacial roughness. For films with $x_{\text{Re}}\geq 14$ Å, the fitted results indicate an asymmetric interface configuration as found in Co/Re bilayer and equal-thickness films.⁹ Rear and front interface widths are found to be about 2 and 3 ML, respectively, somewhat smaller than found in the Co/Re equal-thickness films. This change can be understood on the basis of smaller cumulative layer roughness since the present films have only one-third the thicknesses of the previous series.

The high-angle x-ray-diffraction data for the same series of films show sharp superlattice peaks around the Bragg peaks corresponding to the Co and Re (002) average atomic spacing.⁸ The strongest superlattice peak decreases in intensity and is displaced toward the Co (002) reflection position,

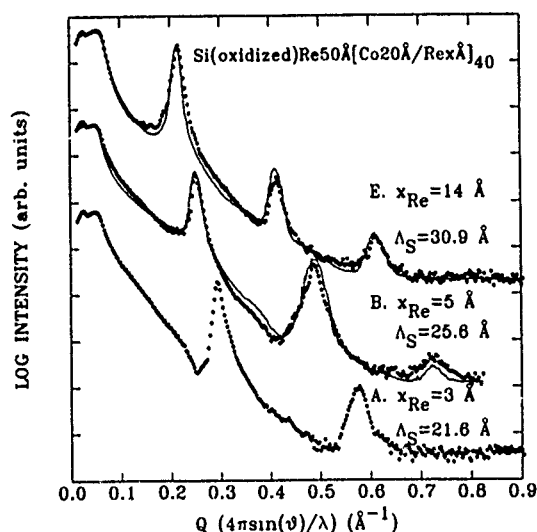


FIG. 1. Semilog plot for x-ray reflectivity data for Si/Re 50 Å (Co 20 Å/Re x Å)₄₀ films A, B, and E as a function of the scattering vector $Q=4\pi\sin\theta/\lambda$. Solid lines are fitted results.

TABLE I. Derived parameters from fits to the x-ray reflectivity data for the Si/Re 50 Å(Co 20 Å/Re x Å)₄₀ films with $x_{\text{Re}}=3-14$ Å. x_{Re} is the nominal Re layer thickness; Λ_s is the modulation wavelength; t_{Co} and t_{Re} are the Co and Re layer thicknesses; t_R and t_F are the rear (Co deposited on Re) and front (Re deposited on Co) interface widths, respectively; Δt is the layer-thickness distribution width; σ_r is the rms global interface roughness. For films A, B, and C, only Δt for the Co layer is introduced in the model calculation.

x_{Re} (Å)	Λ_s (Å)	t_R (Å)	t_{Co} (Å)	t_F (Å)	t_{Re} (Å)	Δt (Å)	σ_r (Å)
A 3	21.6	0.0±0.5	17.6±0.5	4.0±0.5	0.0±0.5	2.3±0.3	3.7±0.2
B 5	25.6	3.2	16.8	5.2	0.5	3.0	3.4
C 7	26.1	4.2	15.8	5.2	0.8	2.6	3.4
D 10	28.8	5.0	10.8	7.0	6.0	2.5	2.7
E 14	30.9	5.0	10.9	7.0	8.0	2.8	3.3

as the number of Re planes decreases. Quantitative analysis of the spectra was performed using a trapezoidal model which considers crystalline multilayers having extended interfaces with linear composition profiles.^{9,10} The fitted results for the films B and E with $x_{\text{Re}}=5$ and 14 Å are shown in Fig. 2 and the structural parameters for films B, C, D, and E are listed in Table II. Due to the appreciable fraction of independent crystallites present in film A, it was not possible to fit its spectrum with adequate precision.

For the film with $x_{\text{Re}}=14$ Å, the values of \bar{d}_{Co} and \bar{d}_{Re} are found to be comparable to those obtained in the equal-thickness Co/Re films with similar Co layer thicknesses.⁹ For films with $x_{\text{Re}} \leq 10$ Å, the \bar{d}_{Co} decreases with decreasing x_{Re} from a \bar{d}_{Co} value expanded by ~1.1% down to the Co bulk value, suggesting that the proportion of Co alloyed with the Re decreases due to the limited amount of Re available in these small x_{Re} films. On the other hand, the \bar{d}_{Re} decreases significantly (~4%) compared to the values found for larger x_{Re} films (e.g., $x_{\text{Re}}=14$ Å), and becomes even smaller than the bulk value, indicating that almost all the Re layers are involved in alloying with Co. Using Vegard's law and the \bar{d}_{Re} values listed in Table II, the average Re atomic concentration in the alloyed interfacial region is estimated to be ~80%.

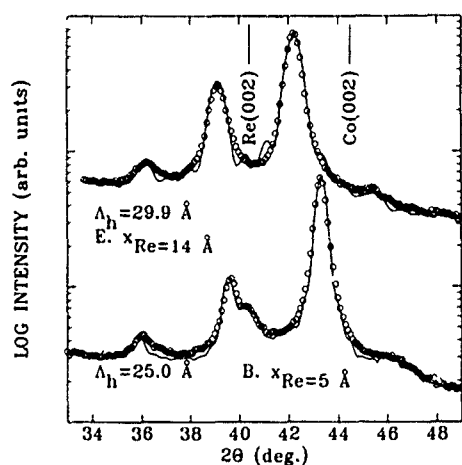


FIG. 2. High-angle x-ray-diffraction data (circles) and fitted results (solid line) for films B and E. The fitted results for film B include Re crystallites with d spacings close to that of the (002) plane. The positions corresponding to Co and Re reflections are indicated by the solid vertical lines.

TABLE II. Derived parameters from fits to the high-angle diffraction data for the same films listed in Table I. x_{Re} is the nominal Re layer thickness; Λ_h is the modulation wavelength; \bar{d}_{Co} and \bar{d}_{Re} are the average atomic interplanar distances of Co and Re (002); n_{Co} and n_{Re} the corresponding atomic plane numbers, n_R and n_F the atomic layer numbers at the rear and front interfaces; L_c is the coherence length of the multilayer crystallite along the growth direction. The values in parentheses are the corresponding layer thicknesses.

x_{Re} (Å)	Λ_h (Å)	\bar{d}_{Co} (Å)	\bar{d}_{Re} (Å)	n_R (t_R) (Å)	n_{Co} (t_{Co}) (Å)	n_F (t_F) (Å)	n_{Re} (t_{Re}) (Å)	L_c (Å)
B 5	25.0	2.048	2.190	3 (6.4)	6 (12.3)	3 (6.4)	0	143
C 7	25.2	2.056	2.200	2 (4.3)	6 (13.2)	3 (6.4)	1 (2.1)	135
D 10	27.6	2.059	2.204	2 (4.3)	6 (12.4)	3 (6.4)	2 (4.4)	129
E 14	29.9	2.051	2.232	2 (4.3)	5 (10.3)	3 (6.4)	4 (8.9)	120

Given that the trapezoidal model uses only integral monolayer thicknesses, there is good agreement between this model and the low-angle optical model as far as the individual layer thicknesses are concerned. Evidently, this conclusion also holds for the modulation wavelengths.

It is interesting to compare the MR shape,⁷ in particular in low field, for two AF coupled films with $x_{\text{Re}}=3$ and 5 Å. For $x_{\text{Re}}=3$ Å, the maximum MR is observed at $\pm B_c$ (the coercive field), suggesting that there exists a remanent magnetization in zero field for this $x_{\text{Re}}=3$ Å film. As we know, for perfect AF coupling between identical magnetic layers, one expects no remanent magnetization as seen in Fe/Cr (Ref. 1) and Co/Ru.² From the structural analysis, we know that the successive Co layers are in partial contact due to pinholes in this film, which will result in a partial ferromagnet (FM) alignment of adjacent Co layers (direct exchange) and therefore a remanent magnetization in zero field. The triangular shape of the TMR curve in low field is also indicative of incomplete AF alignment of the Co layers.² In contrast, for films with $x_{\text{Re}}=5$ Å, the TMR curve shows a plateau shape at very low field,⁷ decreases slowly as the field increases, and saturates at higher B_s , very similar to the MR behavior found in perfectly AF coupled films Fe/Cr,¹ and Co/Ru.² This form suggests that the remanent magnetization of the Co layers becomes practically zero, indicative of almost 100% AF coupling. Indeed, low- and high-angle x-ray-diffraction studies give evidence for Co layers separated by an interface region (~4 ML) with a Re atomic concentration about 80%, a nonmagnetic alloy layer. Hence, the MR properties for these two samples agree very well with the x-ray structural results.

The MR studies on these films showed oscillatory MR and interlayer magnetic coupling as a function of the Re layer thickness x_{Re} with a period of about 12 Å and a maximum MR magnitude of $\approx 1.2\%$ at 4.2 K for $x_{\text{Re}}=5$ Å. In order to analyze the MR data (at 4.2 K) more quantitatively, we have fitted the experimental data of the AF coupled films with $x_{\text{Re}}=5, 7, 16$ Å using an equation derived from the semiclassical MR model,⁴

$$\frac{\Delta R}{R(F)} = \frac{R(\text{AF}) - R(F)}{R(F)} = A \left[\mathcal{J}_3 \left(\frac{x_{\text{Re}}}{\lambda} \right) - \mathcal{J}_3 \left(\frac{x_{\text{Re}}}{\lambda} \right) \right]. \quad (1)$$

The prefactor A depends on the mean free path (MFP) λ

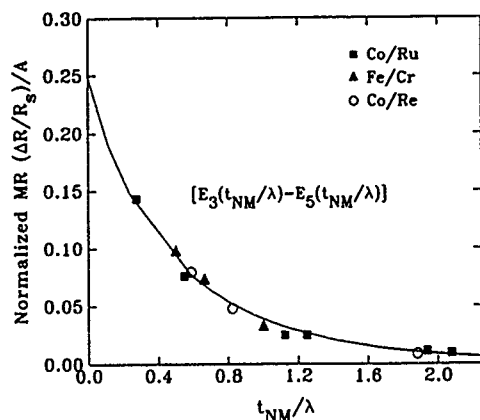


FIG. 3. Normalized MR $(\Delta R/R_F)/A$ plotted as a function of t_{NM}/λ for AF coupled multilayers: (Δ) Fe/Cr, $\lambda=20$ Å, $A=4.5$ (Ref. 4); (\square) Co/Ru, $\lambda=15$ Å, $A=0.3$, (Ref. 4); (\circ) Co/Re, $\lambda=9$ Å, $A=0.14$.

(which is assumed, for simplicity, to be the same in Co and Re layers), the coherent interface transmission coefficients for spin-down and spin-up electrons T_{\downarrow} , T_{\uparrow} , and the Co thickness x_{Co} , but not on the thickness of the nonmagnetic layer x_{Re} , \mathcal{E}_n are exponential integral functions.⁴ Figure 3 shows that the series of experimental data on Fe/Cr,⁴ Co/Ru,⁴ and Co/Re at 4.2 K can be plotted on the same curve $\mathcal{E}_3(x_{Re}/\lambda) - \mathcal{E}_5(x_{Re}/\lambda)$ when the normalized MR, $\Delta R/R$ divided by the normalization factor A , is plotted versus t_{NM}/λ ($t_{NM}=t_{Cr}$, t_{Ru} , and t_{Re}). Analysis gives $\lambda \approx 9$ Å for Co/Re, which is smaller than $\lambda(\text{Fe/Cr})=20$ Å; and $\lambda(\text{Co/Ru})=15$ Å.⁴ This smaller λ in Co/Re can be ascribed to the high resistiv-

ity of the Re spacer. The decrease in λ values is consistent with the decreasing MR found in the Fe/Cr, Co/Ru, and Co/Re systems. In addition, as indicated in Ref. 5, for x_{Re} larger than the MFP λ ($=9$ Å in Re/Co), the MR vanishes as $\exp(-x_{Re}/\lambda)$, which explains the much smaller second AF peak observed at $x_{Re} \sim 16$ Å.⁷

In summary, the results obtained from the analyses of low- and high-angle diffraction data unambiguously indicate that the films with small x_{Re} are composed of Co layers and Re-rich alloy interfaces about 3–5 ML thick. The MR data of the AF coupled films can be well described by the semiclassical MR model of interfacial spin-dependent scattering.

ACKNOWLEDGMENT

We acknowledge financial support for this research from NSERC, Canada and Fonds FCAR, Québec.

- ¹M. N. Baibich, J. M. Broto, A. Fert, F. Nguyen van Dau, F. Petroff, P. Etienne, G. Creuzet, A. Friederich, and J. Chazelas, *Phys. Rev. Lett.* **61**, 2472 (1988).
- ²S. S. P. Parkin, N. More, and K. P. Roche, *Phys. Rev. Lett.* **64**, 2304 (1990); S. S. Parkin, *ibid.* **67**, 3598 (1991).
- ³X. Bian, J. O. Ström-Olsen, Z. Altounian, Y. Huai, and R. W. Cochrane, *Appl. Phys. Lett.* **62**, 3525 (1993).
- ⁴A. Barthélémy and A. Fert, *Phys. Rev. B* **43**, 13 124 (1991).
- ⁵K. L. Dang, P. Veillet, E. Vélú, S. S. P. Parkin, and C. Chappert, *Appl. Phys. Lett.* **63**, 108 (1993).
- ⁶E. E. Fullerton, D. M. Kelly, J. Guimpel, I. K. Schuller, and Y. Bruynseraede, *Phys. Rev. Lett.* **68**, 859 (1992).
- ⁷Y. Huai and R. W. Cochrane, *J. Appl. Phys.* **72**, 2523 (1992).
- ⁸Y. Huai, R. W. Cochrane, and M. Sutton, *J. Appl. Phys.* **73**, 5530 (1993).
- ⁹Y. Huai, R. W. Cochrane, and M. Sutton, *Phys. Rev. B* **48**, 2568 (1993).
- ¹⁰M. B. Stearns, *Phys. Rev. B* **38**, 521 (1989).

Magnetic properties of an Fe/Cu granular multilayer

Mark Rubinstein

U. S. Naval Research Laboratory, Washington, D.C. 20379-5000

J. Tejada and X. X. Zhang

Dept. de Física Fonamental, Universitat de Barcelona Diagonal, 647, 08028 Barcelona, Spain

A Cu/Fe granular film, formed from a multilayer film and composed of particles of Fe imbedded in Cu, has had several of its important properties investigated. Measurements include ferromagnetic resonance, magnetoresistance, Mössbauer effect, magnetic viscosity, and magnetization. The two-phase behavior of these immiscible alloy systems, and the effect of multilayering on the shape of the magnetic precipitates, can explain some of these properties. An explanation of the ferromagnetic resonance line shape is proffered. An extraordinary macroscopic quantum tunneling effect is found to govern the magnetic relaxation at the lowest temperatures.

I. MAGNETORESISTANCE

We have manufactured a Cu/Fe multilayer, $[\text{Cu}(50 \text{ \AA})/\text{Fe}(10 \text{ \AA})] \times 50$ (and a Cu/Dy multilayer $[\text{Cu}(100 \text{ \AA})/\text{Dy}(40 \text{ \AA})]$) on Kapton. The samples were prepared by thermal evaporation in a high-vacuum system. Due, in part, to the low miscibility of Fe in Cu, this process can produce samples with small granular particles of Fe imbedded in the Cu matrix, instead of the usual layered structures. A similar process was recently used by IBM to produce their discontinuous (granular) $\text{Ni}_{80}\text{Fe}_{20}/\text{Ag}$ multilayer films which currently hold the record for the largest sensitivity in any giant magnetoresistive (GMR) structure.¹ Although our Cu/Fe has only modest GMR, and Dy/Cu has almost none, our study of granular multilayers should provide insights into the magnetic structure of $\text{Ni}_{80}\text{Fe}_{20}/\text{Ag}$.

The 4.2 K magnetoresistance of the Fe/Cu granular multilayer is plotted as a function of external applied magnetic field in Fig. 1, along with the 4.2 K magnetic moment of the sample, obtained with a superconducting quantum interference device magnetometer. The magnetoresistance is large, decreases monotonically with field, and is independent of the field direction. These are the telltale characteristics of GMR, a phenomenon often found in multilayers and granular materials. GMR is associated with magnetically inhomogeneous material, and is caused by the magnetic scattering of conduction electrons by the nonaligned magnetic entities.² At 4.2 K and 60 kOe, the fractional change of resistance $\Delta\rho/\rho = -15\%$, but neither the magnetoresistance nor the magnetic moment is completely saturated yet. This failure to saturate is not due to ordinary magnetic hardness, but is caused by the existence of a paramagnetic component, most likely Fe singlets, dimers, or trimers dissolved within the Cu matrix, which coexist with the Fe precipitates. Further evidence for the existence of a paramagnetic iron moment in the as-deposited Fe/Cu film will become apparent in the Mössbauer effect results, presented in Sec. IV.

Unlike Fe/Cu, the Dy/Cu sample showed only ordinary magnetoresistance, characterized by both a nonmonotonic field dependence and a sensitivity to the magnetic-field direction.

II. FERROMAGNETIC RESONANCE

We have obtained the ferromagnetic resonance (FMR) spectrum of the Cu/Fe granular multilayer sample at 9.55 GHz with the magnetic field both parallel and perpendicular to the film plane. (The Dy/Cu spectrum was not detected.) The spectra depend hardly at all on temperature, and the room-temperature parallel and perpendicular absorption-derivative spectra are shown in Fig. 2. The parallel resonance is centered at 1.43 kOe and has a linewidth $\Delta H_{\parallel} = 0.975$ kOe, while the perpendicular resonance is centered at 7.87 kOe with a linewidth $\Delta H_{\perp} = 1.95$ kOe. Kittel³ has derived the fields for resonance in the parallel and perpendicular configuration of thin magnetic films, H . In the absence of magnetic anisotropy they are given by the equations

$$f/\gamma = (H)^{1/2}(H + 4\pi M)^{1/2} \quad (\text{parallel resonance}),$$

$$f/\gamma = H - 4\pi M \quad (\text{perpendicular resonance}), \quad (1)$$

where f is the microwave frequency, γ is the gyromagnetic ratio, and M is the magnetization. (For a pure iron film, $\gamma = 3.2$ GHz/kOe and $4\pi M = 21.5$ kOe.)

Using the Kittel equations for the Cu/Fe sample, we obtain $g = 2.18$ and $4\pi M = 4.87$ kOe using the data shown in

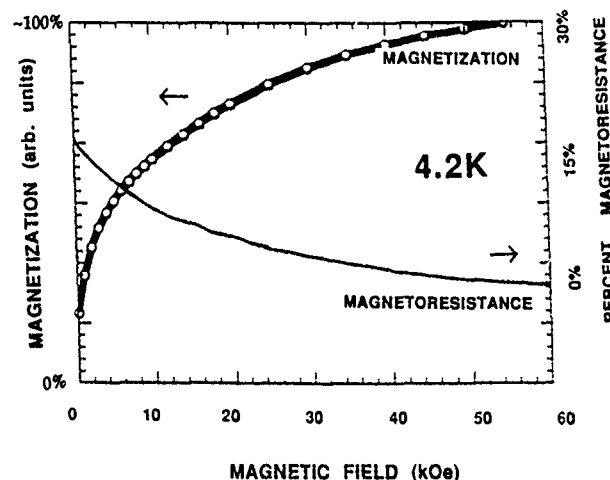


FIG. 1. Magnetization and magnetoresistance v. magnetic field at 4.2 K for $\text{Cu}(50 \text{ \AA})/\text{Fe}(10 \text{ \AA})$. An easily saturable ferromagnetic component and a hard to saturate paramagnetic component are evident.

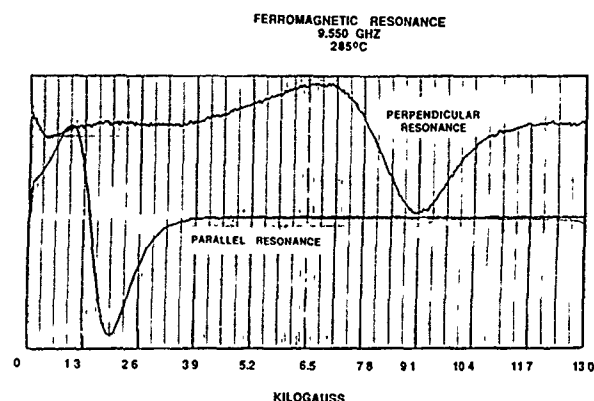


FIG. 2. 9.55 GHz FMR spectrum of Cu(50 Å)/Fe(10 Å) with applied field parallel and perpendicular to plane of film.

Fig. 2. The low value of magnetization results from the low value of the iron filling factor, $\approx 20\%$. Griscom *et al.*⁴ have shown that it is proper to use the average value of the magnetization in the Kittel equations for some granular or precipitated films. Our derived values are in agreement with this conclusion, and this result is further justified below.

In a previous publication⁵ one of the authors has shown that thin films of granular Fe₂₀Cu₈₀, made by coevaporation of the elements, with no attempt at multilayering, have larger FMR linewidths than those shown in Fig. 2. As-deposited films have linewidths of 2.5 kOe, and films annealed above 500 °C have linewidths of 4.0 kOe. The as-evaporated linewidth is attributed to a completely random distribution in the direction of the anisotropy fields⁶ of the individual single-domain iron precipitates, resulting in a powder-pattern FMR lineshape with a linewidth $\Delta H = (5/3)(2K/M)$. Iron precipitates in thin films annealed at temperature higher than 500 °C have grown into multidomain particles with a linewidth⁴ $\Delta H = (0.7)(4\pi M/3)$. The smaller linewidths of the granular multilayer—especially that of the parallel resonance—shows that the layer formation has restricted the spread in particle orientations, constraining it to be a less-than-random distribution. In the following section, we present some ideas on this matter, which also serve to explain why ΔH_{\perp} is so much larger than ΔH_{\parallel} .

III. NETZELMANN'S CONJECTURE

The underlying multilayer structure can distort the shape of the iron precipitates by (a) inducing uniaxial distortions in what, otherwise, would be a sphere, or (b) produce a collection of pancakelike magnetic particles partially aligned along the layers. These alternatives are the two extremes, neither of which may prevail in practice. The high-sensitivity NiFe-Ag granular multilayers produced by the IBM group¹ belong to group (b).

We now assume that the sample is a collection of nearly flat islandlike particles—a discontinuous multilayer. (Assuming that the particles are spheroids aligned parallel to the layer direction does not alter our quantitative conclusions, and can be treated in the same manner.) Each particle is characterized with a demagnetization tensor N_p , and the thin

TABLE I. Values for Kittel demagnetizing factors.

Effective demagnetizing factor	Prependicular resonance	Parallel resonance
N_z	$4\pi f + 4\pi(1-f)(1-2\epsilon)$	$4\pi(1-f)\epsilon$
N_x	$4\pi(1-f)\epsilon$	$4\pi f + 4\pi(1-f)(1-2\epsilon)$
N_y	$4\pi(1-f)\epsilon$	$4\pi(1-f)\epsilon$

film is characterized with a tensor N_t . Netzelmann⁷ has proposed that the effective magnetostatic energy density F_N be approximated as

$$F_N = \frac{1}{2}(1-f)\mathbf{M} \cdot \mathbf{N}_p \cdot \mathbf{M} + \frac{1}{2}f\mathbf{M} \cdot \mathbf{N}_t \cdot \mathbf{M}, \quad (2)$$

where f is the volumetric filling factor of magnetic particles and \mathbf{M} is the particle magnetization. Except for the constraint imposed by Eq. (2), each particle is assumed to precess independently during FMR. Netzelmann⁷ and Yu, Harrell, and Doyle⁸ have used this approach to determine particle orientation distributions from FMR spectra in magnetic tapes.

The generalized Kittel equation,³ applicable to an ellipsoid with demagnetizing factors designated by N_x , N_y , and N_z , is

$$f/\gamma = \{[H_0 + (N_y - N_z)M_0][H_0 + (N_x - N_z)M_0]\}^{1/2}, \quad (3)$$

where the z axis is always in the direction of the applied field H_0 , and the y and x axes are perpendicular to z . Choosing diagonal values $N_p = 4\pi(1-2\epsilon, \epsilon, \epsilon)$ and $N_t = 4\pi(1, 0, 0)$, appropriate to an ellipsoidal particle and a thin film, respectively, we obtain the following values for the Kittel demagnetizing factors, for parallel and perpendicular resonance, as shown in Table 1.

We now assume that the FMR linewidth is primarily caused by a flat distribution of particle ellipticity parameters ϵ , which vary between $\epsilon=0$ and $\epsilon=\epsilon_0$. Using Eq. (3), the perpendicular resonance linewidth is given by $\Delta H_{\perp} = 4\pi M_0 \epsilon_0(1-f)$, from which we obtain the value $\epsilon_0 = 0.12$ from the experimental value of ΔH_{\perp} . The Netzelmann-Kittel equation yields $\Delta H_{\parallel} = 0.65$ kOe for the value of the parallel resonance linewidth, compared to the experimental value of 0.97 kOe, and shows why the parallel resonance linewidth differs than from the perpendicular resonance linewidth. The equations also show that the appropriate magnetization to use in the Kittel formula is the average global magnetization for both flat and spherical precipitated particles.

Using nearly spherical particles with a distribution of ellipsoidal distortions, instead of pancake-shaped particles, yields the same quantitative conclusions. However, using nearly spherical particles results a larger discrepancy in the ratio of the two linewidths than using nearly flat particles. However, from FMR linewidths alone, we are hesitant to draw too many conclusions. Other¹ granular multilayer systems are found to have flat, islandlike precipitates.

IV. OTHER EXPERIMENTAL RESULTS

Mössbauer effect measurements were obtained at 80 K on the Cu(50 Å)/Fe(10 Å) multilayer studied here. The spec-

trum consisted of a hyperfine field sextet with splittings appropriate to ferromagnetic α -Fe and a broad zero-field "singlet" which we associate with the paramagnetic irons discussed in connection with Fig. 1. The paramagnetic component is strong, in agreement with magnetoresistance and magnetization results. The Mössbauer measurements indicate that the moments are in plane, as expected for either spheres or platelets with low magnetic anisotropy imbedded in a thin film. Details of another, more magnetically dilute, multilayer have been published elsewhere.⁹

The dynamic properties of this Fe/Cu granular multilayer has been investigated between 1.6 and 16 K by examining the time dependence of the thermoremanent magnetization, otherwise known as the magnetic aftereffect. Below $T^* \approx 4$ K the magnetic relaxation time becomes independent of temperature, which we interpret as evidence of quantum-mechanical tunneling of the single-domain magnetization of the Fe particles. Aharoni¹⁰ has shown that shape anisotropy, as well as crystalline anisotropy, alters the temperature T^* at which quantum tunneling first appears. The present study, which seeks to quantify the shape anisotropy,

may influence the interpretation of the quantum tunneling results. Further discussion of this remarkable effect can be found in Ref. 11.

Magnetic properties of similar granular-multilayer Fe/Cu and Dy/Cu films have been published elsewhere.¹²

- ¹T. L. Hylton, K. R. Coffey, M. A. Parker, and J. K. Howard, *Science* **261**, 1021 (1993).
- ²C. L. Chien, J. Q. Xiao, and J. S. Jiang, *J. Appl. Phys.* **73**, 5309 (1993).
- ³C. Kittel, *Phys. Rev.* **73**, 155 (1948).
- ⁴D. L. Griscom, J. J. Krebs, A. Perez, and M. Treilleux, *Nucl. Instrum. Methods Phys. Res. B* **32**, 272 (1988); D. L. Griscom, *J. Non-Cryst. Solids* **42**, 287 (1980).
- ⁵M. Rubinstein, *Phys. Rev. B* (to be published).
- ⁶W. A. Yager *et al.*, *Phys. Rev.* **80**, 744 (1950).
- ⁷U. Netzelmann, *J. Appl. Phys.* **68**, 1800 (1990).
- ⁸Y. Yu, J. W. Harrell, and W. D. Doyle, this conference.
- ⁹F. Badia, G. Fratucello, D. Fiorani, A. Labarta, and J. Tejada, *J. Magn. Magn. Mater.* **109**, L159 (1992).
- ¹⁰A. Aharoni (private communication).
- ¹¹J. Tejada, X. X. Zhang, and E. M. Chudnovsky, *Phys. Rev. B* **47**, 14 977 (1993).
- ¹²L. L. Balcells, X. X. Zhang, F. Badia, J. M. Ruiz, C. Ferraté, and J. Tejada, *J. Magn. Magn. Mater.* **93**, 425 (1991).

Structural and magnetoresistance studies in granular $(\text{Ni}_{81}\text{Fe}_{19}, \text{Ni}_{80}\text{Co}_{20})/\text{Ag}$ synthesized from annealed multilayers

X. Bian, Z. Altounian, J. O. Stöm-Olsen, and A. Zaluska

Centre for the Physics of Materials and Department of Physics, McGill University, 3600 University St., Montréal, Québec, Canada H3A 2T8

Y. Huai

INRS-Energie et Matériaux, 1650 montée, Ste-Julie, C. P. 1020, Varennes, Québec, Canada J3X 1S2

R. W. Cochrane

Département de physique et Groupe de recherche en physique et technologie des couches minces, Université de Montréal, C. P. 6182, Succ. A., Montréal, Québec, Canada H3C 3J7

The structural and magnetotransport properties have been studied in $(\text{Ni}_{81}\text{Fe}_{19}, \text{Ni}_{80}\text{Co}_{20})/\text{Ag}$ granular alloy films synthesized by the annealing of sputtered multilayers containing ultrathin magnetic layers. The magnetic concentration, particle size, and morphology of the precipitates can be controlled by adjusting the magnetic layer thickness during the deposition process. Magnetoresistance as large as 30% was found at 4.2 K with a rather small saturation field (<2 kOe), leading to relatively high field sensitivity. Magnetoresistance and saturation field in these alloy films essentially depend on the magnetic precipitate size, concentration, and annealing temperature. The temperature dependence of magnetization and magnetoresistance was also studied, and the correlations among the microstructure, magnetotransport, and magnetic properties are discussed.

I. INTRODUCTION

The recent observation of giant magnetoresistance (GMR) for ferromagnetic granules in a nonmagnetic metal matrix^{1,2} adds a new dimension to the phenomenon of GMR in magnetic multilayers.³ High negative MR of immiscible granular alloy systems, such as Co-Cu,^{1,2} and Co-Ag,⁴ have extended our fundamental understanding of GMR effects. It has been shown that the interface spin-dependent scattering plays a key role in granular systems due to the large surface-to-volume ratio of the magnetic ultrafine precipitates;⁵ however, to be useful as magnetoresistive sensor devices, thin-film materials with enhanced magnetoresistance in a small magnetic field are required. Identifying a proper structure of the inhomogeneous system with these characteristics still remains a key problem.

The important requirement for preparing granular magnetic films is to control the size and spacing of the magnetic precipitates. In this article, we report the synthesis of $\text{Ni}(\text{Fe}, \text{Co})/\text{Ag}$ phase-separated alloy films based on the heat treatment of multilayered samples containing ultrathin NiFe or NiCo layers. Selecting a soft magnetic alloy (e.g. $\text{Ni}_{81}\text{Fe}_{19}$ or $\text{Ni}_{80}\text{Co}_{20}$) which has an intrinsically small magnetocrystalline anisotropy and which is insoluble in Ag over a wide composition range,⁶ may result in enhanced MR and small saturation fields.

II. EXPERIMENTAL DETAILS

The $(\text{Ni}_{81}\text{Fe}_{19}, \text{Ni}_{80}\text{Co}_{20})/\text{Ag}$ multilayers with individual magnetic layers ranging from 4 to 7 Å and Ag layers of 20 to 22 Å were prepared by dc magnetron sputtering from separate targets of $\text{Ni}_{81}\text{Fe}_{19}$ or $\text{Ni}_{80}\text{Co}_{20}$ alloy and Ag onto glass substrates at room temperature. The background pressure was $<2 \times 10^{-7}$ Torr. With a sputtering pressure of 7.5 mTorr of argon, the deposition rates (determined from the measured thicknesses of single films by low-angle x-ray reflectivity

measurements) were 1.4 Å/s for $\text{Ni}_{81}\text{Fe}_{19}$ and 1.6 Å/s for Ag. The individual layer thicknesses of the magnetic alloys and Ag were adjusted to yield films of magnetic composition between 20 and 45 at. %. Total film thicknesses were 900–1200 Å. All the samples were examined as deposited and postheat treated under a vacuum of $<2 \times 10^{-6}$ Torr.

The structural characterization of the samples were performed by low- and high-angle x-ray diffraction using $\text{Cu-K}\alpha$ radiation⁷ and a high-resolution Philips 200 kV (CM20) transmission electron microscope (TEM). The film compositions, as determined by electron microprobe measurements, were found to be within 4% of the nominal values. The magnetoresistance measurements were carried out using a four-terminal geometry and a high-resolution ac bridge.⁸ The current was in the plane of the film with the magnetic field either in the film plane and perpendicular to the current (transverse ρ_T) or perpendicular to the plane (perpendicular ρ_L). Magnetization data between 4.2 and 300 K were obtained using a superconducting quantum-interference device (SQUID) magnetometer.

III. RESULTS AND DISCUSSIONS

The low angle x-ray reflectivity spectra reveal superlattice peaks for all the as-deposited samples down to a bilayer thickness of $\Lambda = 26$ Å (with a 4 Å layer of magnetic component), indicating a well-defined composition modulation along the growth direction. The corresponding high-angle x-ray diffraction and electron diffraction for these samples show that the multilayer films have coherent interfaces and a highly textured structure with (111) orientations normal to the film plane.⁹ However, after annealing the samples at 450 °C for 10 minutes, both low- and high-angle x-ray results show that the superlattice structures are washed out, indicating significant interdiffusion during the annealing stage. The NiFe particle sizes, observed from TEM images as

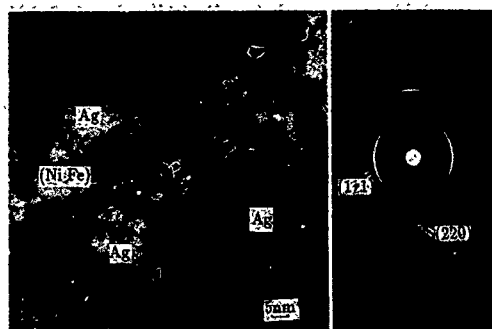


FIG. 1. TEM micrograph for the sample (NiFe 4 Å/Ag 20 Å)×30 annealed at 450 °C for 10 min. The inset is the electron diffraction pattern showing the fcc (111) textured structure.

shown in Fig. 1, have variable size up to 100 Å at this annealing temperature depending on the original thickness of the NiFe layers. The highly (111) textured structures can still be seen in the annealed samples as demonstrated by the electron diffraction in the inset of Fig. 1. As the annealing temperature is increased, the superlattice coherence is lost and, the high-angle x-ray peak intensity, which assign the (111) peak of NiFe, increases and becomes sharper, indicating the growth of NiFe particles upon the heat treatment.⁹

Magnetoresistance measurements were performed between 4.2 and 300 K in magnetic fields of up to 10 kOe. The results of the as-deposited multilayers show no apparent GMR and no evidence of antiferromagnetic coupling between the NiFe or NiCo layers across the Ag spacer, as inferred from the magnetization curves. However, the structural and magnetotransport properties are very sensitive to the heat treatment. Figure 2 shows the dependence of MR at 4.2 K on the annealing temperature T_a , for multilayers containing either ultrathin $\text{Ni}_{81}\text{Fe}_{19}$ or $\text{Ni}_{80}\text{Co}_{20}$ layers. The maximum MR is found in the samples annealed at 300 °C. In sample NiFe 4 Å/Ag 20 Å (i.e., 24 at. % NiFe), for example, an appreciable increase of $\Delta\rho$ ($=\rho_{(H=0)}-\rho_{(H=H_s)}$) up to 85% is observed upon annealing. The resistivity ρ , however, decreases by about a factor of 1.4 due to the reduced struc-

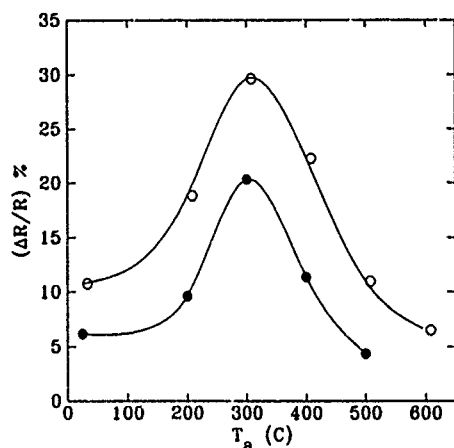


FIG. 2. Dependence of magnetoresistance, at 4.2 K, on the annealing temperature (●) (NiCo 4 Å/Ag 20 Å)×30 and (○), (NiFe 4 Å/Ag 20 Å)×30.

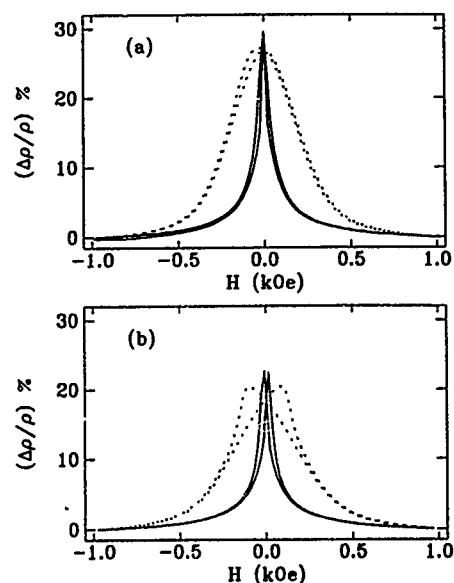


FIG. 3. GMR of the (NiFe t Å/Ag 20 Å)×30 films annealed at 300 °C, 1 h; measured at 4.2 K. Solid line: field in the film plane; dotted line: field perpendicular to the film plane; (a) $t_{\text{NiFe}}=4$ Å, or 24 at. % NiFe; (b) $t_{\text{NiFe}}=6$ Å, or 30 at. % NiFe.

tural disorder. The net result gives an enhancement of up to 30% for the value of $\Delta\rho/\rho$. The structural studies reveal that such a behavior is correlated to a structure which is layered in the film growth direction but discontinuous in the lateral direction.¹⁰ It is also noted that the high-temperature (>450 °C) annealing substantially decreased the MR, as can be ascribed to the extreme growth of NiFe grains or a decrease in surface-to-volume ratio. Upon substitution of $\text{Ni}_{81}\text{Fe}_{19}$ by $\text{Ni}_{80}\text{Co}_{20}$, the annealing effect is essentially similar, the relatively small magnitude of MR in $\text{Ni}_{80}\text{Co}_{20}/\text{Ag}$ may be ascribed to the intrinsically small magnetization in this alloy.

The important feature of our alloy films is their small saturation fields compared with those found in other heterogeneous granular systems. Figure 3 shows typical MR curves of $\text{Ni}_{81}\text{Fe}_{19}/\text{Ag}$ films annealed at 300 °C. Together with the substantial high MR magnitude, a rather small saturation field less than 2 kOe can be deduced for the sample containing a 4 Å NiFe layer (i.e., 24 at. % NiFe), as inferred from Fig. 3(a). The value is about 5–10 times smaller than those found in cosputtered Co/Cu (Refs. 1 and 2) and Co/Ag⁴ granular alloy systems. Further increase of the magnetic layer thickness (namely increasing the magnetic concentration) results in a decrease of the MR as shown in Fig. 3(b). The composition dependence of MR of these films has revealed that maximum MR is near the 24 at. % magnetic content,⁹ where the spin-dependent scattering, particularly at the interface of the magnetic particles and the metallic matrix, may be most effective according to the model of Zhang.⁵ The saturation fields H_s , as described in a previous study,⁹ are also related to the magnetic concentration. Even smaller H_s (<1 kOe) for NiFe concentrations above 35 at. % can be obtained. The MR curves, in fact, are broad for the field perpendicular to the film plane and narrow for the field in the plane of the film as can be seen from Fig. 3, implying

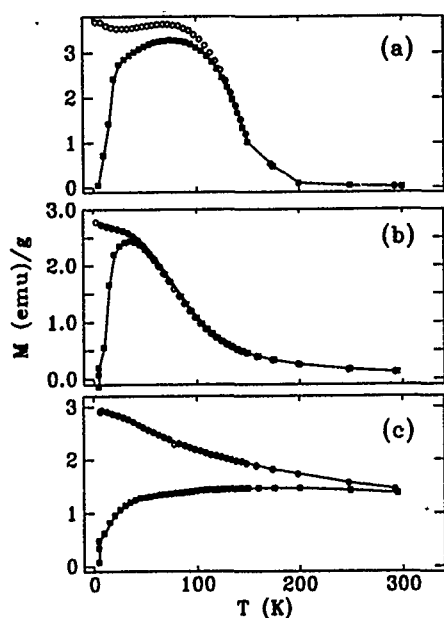


FIG. 4. Field-cooled (FC) and zero-field-cooled (ZFC) magnetization vs temperature for NiFe 4 Å/Ag 20 Å measured in an external field of 40 Oe: (a) as-deposited; (b) annealed at 300 °C, 1 h; (c) annealed at 400 °C, 1 h.

the existence of some platelike particles. The small H_s in these films may be simply ascribed to the shape of the magnetic precipitates. We also note that the maximum MR occurs at zero applied field for 24 at. % NiFe sample [Fig. 3(a)] showing this sample to be more superparamagneticlike, while it occurs at the nonzero coercive fields for the 30 at. % NiFe sample [Fig. 3(b)] reflecting in some degree the existence of more stable single-domain particles.¹¹ Selecting and controlling of the structural parameters, in order to maximize MR and minimize H_s , is an important aspect for the use of granular alloy films in magnetic sensor application.

Figure 4 shows the zero-field-cooled (ZFC) and field-cooled (FC) magnetization data of Ni₈₁Fe₁₉ 4 Å/Ag 20 Å sample measured as a function of temperature in a small external field of 40 Oe. The as-deposited sample [Fig. 4(a)] shows a quite broad peak in the ZFC curve with the onset of the irreversibility (where the FC and ZFC curves join) occurring at a slightly higher temperature. The data reveal the existence of a large size distribution of the magnetic entities in the as-deposited sample due to the possibly imperfect layered structure, and can be interpreted in the so-called reentrant magnetic behavior representing the coexisting of both spin-glass and ferromagnetic orders.¹² The sample annealed at 300 °C [Fig. 4(b)] shows clearly a narrow ZFC peak with the peak position (defined as the blocking temperature) occurring at a fairly low temperature with the irreversibility onset closer to the peak position. This behavior reflects the

possible formation of a uniform size distribution as the consequence of structural relaxation and interdiffusion after annealing. Correspondingly, M_T is maximum at 4.2 K, and dramatically decreases above the blocking temperature (>50 K) where the magnetic particles exhibit superparamagnetic behavior. Heating the sample above 400 °C [Fig. 4(c)] increases the magnetic stability with increasing the particle size, as indicated by the increase of the blocking temperature and the onset of the irreversibility. The fact that both MR and magnetization can be readily saturated in a field of less than 1 kOe, may imply the formation of multidomain particles, but we have no direct evidence for this.

IV. CONCLUSIONS

We have synthesized phase-separated (Ni₈₁Fe₁₉, Ni₈₀Co₂₀)/Ag alloy films by annealing multilayered structures containing ultrathin magnetic layers. The magnetic concentration and precipitate size can be controlled by adjusting the magnetic layer thickness in the deposition stage as well as by postheat treatment. The alloy films display giant magnetoresistance with a maximum value of 30% at 4.2 K for NiFe concentration near 24 at. %, and a rather small saturation field of less than 2 kOe. Even lower saturation fields can be obtained by increasing the magnetic concentration and annealing temperature. However, in order to achieve high performance in magnetic sensor applications, further studies of granular films will be needed to explore a variety of particle shapes and size distributions.

ACKNOWLEDGMENTS

We wish to thank Professor C. Stager of McMaster University for SQUID measurements, and we acknowledge the financial support from the Natural Sciences and Engineering Research Council of Canada and Fonds FCAR du Québec.

- ¹ A. E. Berkowitz, M. J. Carey, J. R. Mitchell, A. P. Young, S. Zhang, F. E. Spada, F. T. Parker, A. Hutten, and G. Thomas, *Phys. Rev. Lett.* **68**, 3745 (1992).
- ² J. Q. Xiao, J. S. Jiang, and C. L. Chien, *Phys. Rev. Lett.* **68**, 3749 (1992).
- ³ M. N. Baibich, J. M. Broto, A. Fert, F. Nguyen van Dau, F. Petroff, P. E. Etienne, G. Creuzet, A. Friederich, and J. Chazelas, *Phys. Rev. Lett.* **61**, 2472 (1988).
- ⁴ J. Q. Xiao, J. S. Jiang, and C. L. Chien, *Phys. Rev. B* **46**, 9266 (1992).
- ⁵ S. Zhang, *Appl. Phys. Lett.* **61**, 1855 (1992).
- ⁶ T. B. Massalski, *Binary Alloy Phase Diagrams* (Wiley, New York, 1986), Vol. 1, pp. 25 and 48.
- ⁷ Y. Huai, R. W. Cochrane, Y. Shi, H. E. Fischer, and M. Sutton, *Mater. Res. Soc. Symp. Proc.* **238**, 671 (1992).
- ⁸ Y. Huai and R. W. Cochrane, *J. Appl. Phys.* **72**, 2523 (1992).
- ⁹ X. Bian, A. Zaluska, Z. Altounian, J. O. Ström-Olsen, Y. Huai, and R. W. Cochrane, *Mater. Res. Soc. Symp.* **313**, 405 (1993).
- ¹⁰ X. Bian, A. Zaluska, Z. Altounian, J. O. Ström-Olsen, Y. Huai, and R. W. Cochrane (unpublished).
- ¹¹ A. E. Berkowitz, J. R. Mitchell, M. J. Carey, A. P. Young, D. Rao, A. Starr, S. Zhang, F. E. Spada, F. T. Parker, A. Hutten, and G. Thomas, *J. Appl. Phys.* **73**, 5320 (1993).
- ¹² J. R. Childress and C. L. Chien, *Phys. Rev. B* **43**, 8084 (1991).

Giant ac magnetoresistance in the soft ferromagnet $\text{Co}_{70.4}\text{Fe}_{4.6}\text{Si}_{15}\text{B}_{10}$

F. L. A. Machado, B. L. da Silva, S. M. Rezende, and C. S. Martins
 Departamento de Física, Universidade Federal de Pernambuco, 50732-910 Recife,
 Pernambuco, Brazil

ac magnetoresistance (MR) measurements performed in thin ribbons of the amorphous soft ferromagnet $\text{Co}_{70.4}\text{Fe}_{4.6}\text{Si}_{15}\text{B}_{10}$ are reported with a longitudinal dc applied magnetic field H varying from 0 to ± 15 Oe. The dependence of the MR with the frequency f of the measuring ac current was investigated for $0.4 \leq f \leq 100$ kHz. No significant frequency dependence in the resistivity ρ for $H=0$ and $H=\pm 15$ Oe was found. For intermediate values of H , $\rho(H)$ presents a peak in H which increases linearly in frequency. The MR peak in H at room temperature varies from typical values of 0.13% in the low-frequency range to a giant value of 27% at 100 kHz. Two possible sources for the frequency dependence of the magnetoresistance in amorphous alloys are discussed.

I. INTRODUCTION

Earlier magnetic studies showed that the amorphous alloy $\text{Co}_{70.4}\text{Fe}_{4.6}\text{Si}_{15}\text{B}_{10}$ is a soft ferromagnet with a magnetic permeability strongly dependent on the applied magnetic-field frequency and on its thermal history.¹ In addition this alloy shows spin-glass-like properties at high temperatures and low fields which can be understood within the random anisotropy model (RAM).^{2,3} More recently we observed⁴ that the magnetoresistance (MR) in this alloy presents a peak in $H=2.4$ Oe resulting from two contributions: the first one increasing with the applied magnetic field ($\text{MR} \propto H^2$) and the second one decreasing with M^2 ($\text{MR} \propto -M^2$). This behavior was observed for samples annealed in a magnetic field of 2 kOe. For samples annealed in $H=0$ the MR values are quite small compared to those observed in magnetic-field annealed samples. In Ref. 4, we reproduced quite well the MR magnetic-field dependence using the rotational model for induced transverse anisotropy (RMITA) and the measured magnetization. However, because of the strong frequency dependence of the MR in $\text{Co}_{70.4}\text{Fe}_{4.6}\text{Si}_{15}\text{B}_{10}$ reported in the present work, it seems to us that the RMITA may not be the correct model to account for the observed H^2 behavior. In this article we also discuss possible theoretical models for this new ac giant magnetoresistance effect.

II. TECHNIQUE AND EXPERIMENTAL RESULTS

The magnetoresistance was measured at room temperature using an ac four-probe technique. The frequency of the ac current was varied in the range $0.37 \leq f \leq 97.73$ kHz while its amplitude was kept constant at 10 mA. A pair of Helmholtz coils oriented to minimize the Earth's field generated the applied dc magnetic field. The electrical contacts in the sample were made with silver paint. The resistance of the contacts were of the order of few Ω . The samples were pieces of a ribbon of $\text{Co}_{70.4}\text{Fe}_{4.6}\text{Si}_{15}\text{B}_{10}$ taken from the same batch of the samples used in our earlier reported results. The sample was 50 μm thick, 1 mm wide, and 1.5 cm long. They were annealed for 15 min at 573 K in a magnetic field of 2 kOe applied transverse to the ribbon length but in the plane

of the sample. The samples were then cooled keeping the magnetic field on. The experimental setup and the data acquisition was fully automated.

The magnetoresistance $\text{MR} (=10^2[\rho(H)-\rho(H=0)]/\rho(H=0))$ is plotted in Fig. 1 for $f=9.77$, 50.77, and 97.73 kHz [curves (a), (b) and (c), respectively]. The arrows indicate the direction the magnetic field was swept. The MR curves are quite reversible. As reported earlier,⁴ the MR is positive and shows two distinct regimes which results in a peak at $H=2.4$ Oe. For small values of H , MR is dominated by a contribution which increases with the square of the applied magnetic field. For intermediate and higher H , a $-M^2$ contribution becomes dominant. The inset shows the variation of the maximum of the MR (squares) in the frequency range of the measurements. The peak in MR continuously increases with frequency with a linear dependence (solid line) for almost three decades in frequency. Strikingly, while the low-frequency MR is typical of amorphous alloys, it assumes a giant MR of 27% for $f=97.73$ kHz.

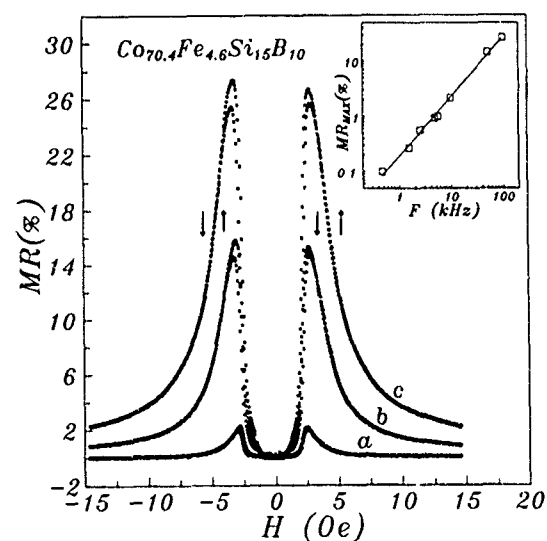


FIG. 1. Magnetoresistance $\text{MR} \{=10^2[\rho(H)-\rho(H=0)]/\rho(H=0)\}$ vs applied magnetic field H curves for three different values of measuring current frequency: (a) 9.77, (b) 50.77, and (c) 97.73 kHz. The arrows indicate the direction the magnetic field was swept. The inset shows the frequency dependence of the maximum in MR observed for $H \approx 2.4$ Oe.

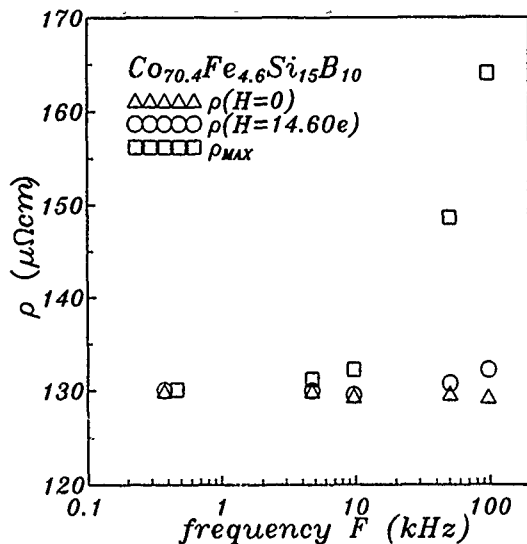


FIG. 2. Frequency dependence of the resistivity ρ for $H=0$ (triangles), $H=14.6$ Oe (circles), and for $H=2.4$ (squares) where the maximum in the resistivity is observed (ρ_{\max}).

We show in Fig. 2 the resistivity ρ in $\mu\Omega$ cm versus frequency for three different field values, $H=0$ (triangles), $H=14.6$ Oe (circles), and for $H=2.4$ Oe (squares) which is the value for the peak in $\rho(H)$ ($=\rho_{\max}$). Clearly the frequency dependence observed for $H=0$ and for $H=14.6$ Oe is very small compared to that of the peak.

In Fig. 3 we reproduced the room-temperature magnetization M versus applied magnetic field curve used to fit the data reported in Ref. 4. This curve was obtained for a sample with approximately the same dimensions of those used to measure MR.

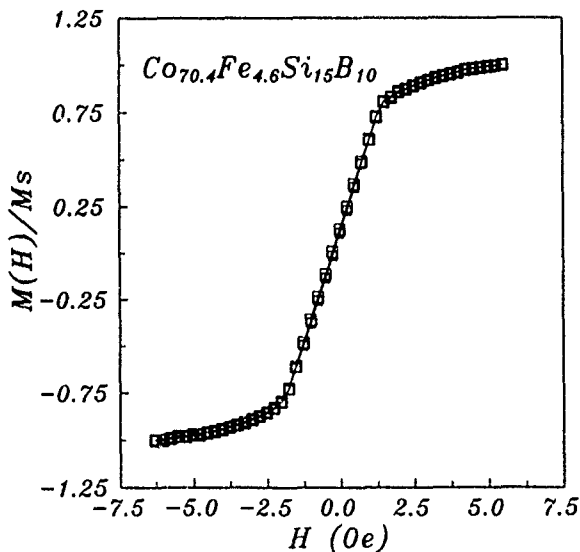


FIG. 3. Magnetization vs applied magnetic field for $\text{Co}_{70.4}\text{Fe}_{4.6}\text{Si}_{15}\text{B}_{10}$ (squares). The dimensions of the sample are about the same as those used to measure the MR. Note that the values of $M(H)$ are normalized by the magnetization measured for $H=6.27$ Oe and the coercive field is quite small (0.002 Oe). The solid line is a guide to the eyes.

III. DISCUSSIONS AND CONCLUSIONS

In an attempt to understand the frequency dependence of the magnetoresistance, we discuss a model for the transport properties of electrons in a medium with magnetic domains. This model has been extensively used by Berger⁵ for dc and for fast rising pulses, but not for ac currents. The basic assumption of the model is that the domain walls experience two forces: the Lorentz force resulting from the relative motion of the electrons through the domain wall and a pinning force associated with the coercive field H_c . We extend the model for ac currents assuming that for small enough forces the domain pinning can be replaced by a restoring force proportional to the displacement x_w of the wall away from the equilibrium position,

$$\frac{2M_s}{\mu} (\beta v_e - v_w) - kx_w = M_w \ddot{x}_w, \quad (1)$$

where β is a parameter which depends on the material, M_s is the saturation magnetization, μ is the wall mobility, v_e and v_w are the electron and wall velocities, respectively, and M_w is the wall mass. For the electron, besides the Lorentz force, the equation of motion has also a force caused by the ac applied electric field E and the Drude relaxation term,

$$\frac{2M_s}{\mu} (\beta v_e - v_w) - m \frac{v_e}{\tau} - eE e^{-i\omega t} = m \ddot{x}_e, \quad (2)$$

with τ being the electron relaxation time, m the electron mass, and x_e its displacement. Assuming that M_w is negligible and solving Eqs. (1) and (2) for v_e , one gets the current density and the resistivity ($j = -nev_e = E/\rho$),

$$\frac{\rho - \rho_0}{\rho_0} = \frac{\tau}{r_s} A \left(1 - \frac{\omega^2 A^2}{k^2 + \omega^2 A^2} \right), \quad (3)$$

where $A \equiv 2M_s/\mu$, ρ_0 is the Drude resistivity, and we used $\beta=1$.

This model does predict a frequency dependence for MR. There is an initial decrease of MR with increasing frequency f which saturates for $\omega^2 A^2 \gg k^2$, and the MR is approximately linear in some frequency range. However, the predicted frequency-dependent MR is negative, whereas our measurements indicate a positive MR. Notice that because of the logarithmic time decay of the magnetization some models also include a restoring force in the equation of motion for the domain with a time-dependent coefficient.⁶ However, this contribution does not seem to predict a linear increase of MR with ω .

Two theoretical models predict a $-M^2$ contribution to MR. The first one, which falls in the class of the model described above, is based on eddy currents due to nonuniform current in the sample.⁵ Unfortunately, such a mechanism does not account for the observed frequency-dependent MR. The second model predicts a scaling of the magnetoresistance in spin-glass-like systems^{7,8} with M^2 . Essentially, this model shows that for this kind of magnetic phase the magnetoresistance is proportional to the Edward-Anderson order parameter

$$Q = \lim_{|t_1 - t_2| \rightarrow \infty} \langle [S_i(t_1) S_i(t_2)] \rangle_{\text{avg}}$$

which is essentially given by the spin-spin correlation function at site i . The correlation function is also frequency dependent [$\sim \omega\tau/(1+\omega^2\tau^2)$] which has a linear behavior in the limit $\omega\tau \ll 1$, where τ is the spin relaxation time. Because of the spin-glass-like properties of this material² associated with its frequency-dependent magnetic permeability, it is possible that the linear dependence of MR with ω is due to the random anisotropy existing in amorphous magnetic alloys.

Giant magnetoresistance has also been observed in other nonmultilayers magnetic system.^{9,10} We note, however, that our system shows this property at room temperature and the saturation fields are quite low compared with granular materials. These characteristics makes amorphous $\text{Co}_{70.4}\text{Fe}_{4.6}\text{Si}_{15}\text{B}_{10}$ interesting for some technological applications.

ACKNOWLEDGMENTS

We thank M. V. P. Altoé and F. P. Missell for kindly providing the samples and M. A. Continentino, S. G.

Coutinho, C. L. Chien, and F. C. Montenegro for discussions. This work was partially supported by FINEP-PADCT, CNPq, FACEPE, and CAPES (Brazilian Agencies).

¹R. S. Turtelli and F. L. A. Machado, IEEE Trans. Magn. MAG-25, 3350 (1989).

²E. Montarroyos, F. L. A. Machado, S. M. Rezende, J. R. L. de Almeida, M. V. P. Altoé, and F. P. Missell, J. Appl. Phys. **70**, 6169 (1991).

³E. Montarroyos, J. R. L. de Almeida, F. L. A. Machado, and S. M. Rezende, J. Magn. Magn. Mater. **104-107**, 149 (1992).

⁴F. L. A. Machado, B. Lopes da Silva, and E. Montarroyos, J. Appl. Phys. **73**, 6387 (1993).

⁵See, for example, L. Berger, J. Appl. Phys. **49**, 2156 (1978); J. Appl. Phys. **71**, 2721 (1992), and references therein.

⁶P. Allia, C. Beatrice, and F. Vinai, in *Fundamental and Applicative Aspects of Disordered Magnetism*, edited by P. Allia, D. Fiorani, and L. Lanotte (World Scientific, Singapore, 1989).

⁷A. K. Nigam and A. K. Majumdar, Phys. Rev. B **27**, 495 (1983).

⁸A. K. Majumdar, Phys. Rev. B **28**, 2750 (1983).

⁹A. E. Berkowitz, J. R. Mitchell, M. J. Carey, A. P. Young, S. Zhang, F. E. Spada, F. T. Parker, A. Hutten, and G. Thomas, Phys. Rev. Lett. **68**, 3745 (1992).

¹⁰J. Q. Xiao, J. S. Jiang, and C. L. Chien, Phys. Rev. Lett. **68**, 3749 (1992).

On the resistivity minimum in amorphous metallic spin-glasses (abstract)

J. Koetzler and G. Thummes^{a)}

Institut für Angewandte Physik, Universität Hamburg, D-20355 Hamburg, Germany

Though the occurrence of a low-temperature resistivity minimum is a rather general feature of magnetic metallic glasses, its origin—whether magnetic or structural—is still under debate. We have performed temperature and magnetic-field-dependent measurements of the resistivity $\rho(T,B)$ and the magnetization $M(T,B)$ on amorphous $\text{Ni}_{80-x}\text{Fe}_x\text{Si}_8\text{B}_{12}$ below and above the critical concentration for ferromagnetic order ($x_c=4$). In the ferromagnetic and reentrant phases $\rho(T \rightarrow 0)$ increases as $(-T^{1/2})$, which can be related to a quantum effect from modified electron-electron interaction in the presence of structural disorder.¹ In marked contrast, in the conventional spin glass ($x=2.4$) $\rho(T \rightarrow 0, B=0)$ exhibits a linear increase below the freezing temperature $T_f=6.2$ K. A reanalysis of literature data reveals a linear upturn of $\rho(T \rightarrow 0)$ to occur in other amorphous spin glasses, too, with a quasi-universal law: $\Delta\rho/\rho \approx -4(2) 10^{-3} T/T_f$. This finding will be discussed in terms of elastic scattering from the spin-glass order parameter² and, alternatively, in terms of quantum interference on closed diffusion paths in the presence of inelastic spin-flip scattering. Recently, for the latter case, a linear T-law has been predicted to evolve from a crossover from dynamic spin scattering to the static limit at zero temperature.³

^{a)}Also at: Institut für Angewandte Physik, Justus-Liebig-Universität, D-35392 Giessen, Germany.

¹G. Thummes *et al.*, Z. Phys. B **69**, 489 (1988).

²K. H. Fischer, Z. Phys. B **34**, 45 (1979).

³V. L. Falko, JETP Lett. **53**, 342 (1991).

Dependence of the anisotropic magnetoresistance on aspect ratio in cobalt films (abstract)

Mark Tondra, B. H. Miller, and E. Dan Dahlberg

School of Physics and Astronomy, University of Minnesota, 116 Church Street S. E., Minneapolis, Minnesota 55455

High quality measurements of the anisotropic magnetoresistance, defined as the difference in the resistivities when the saturated sample magnetization is parallel and perpendicular to the current, are performing using four terminal measurements. What is occasionally not considered in these measurements is the geometry of the sample and contacts. This work reports how the anisotropic magnetoresistance (AMR), measured with four in-line point contacts attached to thin film specimens, is affected by the geometry of the films. Cobalt samples were lithographically narrowed in 2 mm steps from 10 mm \times 10 mm to 2 mm \times 10 mm. For each of the five sizes, the AMR and resistivity were measured using the four-probe-in-line technique with 3 mm from one contact to the next. The results show that the measured AMR increases by a factor of 2 from the widest to narrowest size. This width dependence of the AMR arises from spreading of the current between the voltage contacts. In order to make an accurate assessment of the AMR, the current across the entire width of the sample must be parallel to the line joining the voltage contacts. Similar work has been performed by A. Iwaide *et al.*, and published in *J. Magn. Soc. Jpn.* **16**, 197 (1992). The results reported in this abstract are in agreement with those in the above-mentioned paper.

Nonoscillatory behavior in the magnetoresistance of Cu/Ni superlattice (abstract)

W. Abdul-Razzaq

Physics Department, West Virginia University, Morgantown, West Virginia 26506-6315

It was reported that in many magnetic/nonmagnetic metallic multilayered systems, the interlayer-coupling oscillates between antiferromagnetic and ferromagnetic upon increasing the thickness of the nonmagnetic layer. This was evident by the oscillation of the magnetoresistance (MR) in these materials. Recently however, Harp, Parkin *et al.*¹ found that the MR and coupling strength change monotonically with increasing Cu thickness in Co/Cu multilayers deposited by MBE, contradicting results on similar samples made by sputtering in which the MR was oscillatory. In this study, we show that in the Cu/Ni superlattice made by sputtering, the MR varies monotonically with increasing Cu thickness. This nonoscillatory behavior was observed at room temperature and at 77 K and, regardless of the direction of the magnetic field in relation to the direction of the current. The resistivity at zero magnetic field as a function of temperature also changes systematically with reducing the Cu layer thickness. The nature of the magnetic state in Cu/Ni superlattice is discussed in light of the transport property measurements.

¹G. P. Harp, S. S. Parkin, *et al.*, *Phys. Rev.* **47**, 8721 (1993).

Preparation and magnetic properties of Mn_4N films by reactive facing targets sputtering

Shigeki Nakagawa and Masahiko Naoe

Dept. of Physical Electronics, Tokyo Institute of Technology, 2-12-1 O-okayama, Meguro, Tokyo 152, Japan

Ferrimagnetic Mn_4N films have been successfully prepared at low process temperatures using the facing targets sputtering apparatus. The mixture gas of Ar and N_2 with the ratio of N_2 in pressure to total gas R_{N_2} of 10% was optimal as the reactive working gas for depositing Mn_4N films, since the deposition at excessive R_{N_2} tended to cause the formation of Mn_3N_2 crystallites. In fact, they appeared in films deposited at R_{N_2} higher than 30%. The film deposited at the substrate temperature T_s of 200 °C exhibited saturation magnetization $4\pi M_s$ of about 300 G. The films prepared at T_s of 350 °C exhibited $4\pi M_s$ and an in-plane coercivity $H_{c\parallel}$ of 450 G and 300 Oe, respectively. The films annealed at 400 °C in vacuum furnace exhibited $4\pi M_s$ larger than about 510 G. However, the film annealed at temperature above 500 °C exhibited $4\pi M_s$ smaller than 80 G.

I. INTRODUCTION

Mn_4N is well known as a typical ferrimagnetic material with an effective moment of Bohr magnetons of 1–1.2 μ_B per unit cell.^{1–5} However, it is very difficult to synthesise bulk Mn_4N , because its process needs a gas-solid reaction at high temperatures without the inclusion of oxygen.⁴ Sputtering techniques seem to be suitable for preparing Mn_4N films even on substrates at low temperatures, because the surface mobility of adatoms may be sufficiently high. In this study, Mn_4N films have been successfully deposited on substrates at low temperatures by reactive sputtering and their magnetic properties have been investigated.

II. EXPERIMENTAL PROCEDURE

The specimen manganese nitride (Mn_xN) films were prepared using a facing targets sputtering (FTS) apparatus.⁶ They were deposited on Si wafers by sputtering a pair of targets of sintered Mn disks in a mixture of Ar and N_2 gases, with the total pressure during deposition set at 2 mTorr. The ratio in pressure of N_2 gas to the mixture R_{N_2} ranged from 0 to 40%. The substrate temperature T_s was varied from 40 to 400 °C. The deposition rate and thickness of Mn_xN films were about 150 Å/min and 2000 Å, respectively. Post-annealing processes were performed for 1 h in an evacuated furnace at residual gas pressure below 1.0×10^{-6} Torr at temperature T_A of 350, 400, and 500 °C.

III. RESULTS AND DISCUSSION

The nitridation degree and crystal structure in films deposited at T_s of 40 °C varied with increase of R_{N_2} . X-ray diffraction studies told that the increase of R_{N_2} in the range from 7.5% to 20% changed the preferential orientation of the α -Mn crystallites from (411) to (332) and caused an apparent lattice expansion in the crystallites. Mn_3N_2 crystallites with an excessive degree of nitridation were evident in films de-

posited at R_{N_2} higher than 30%. Therefore, R_{N_2} above 30% seemed to be too high for forming Mn_4N crystallites. Accordingly, it was predicted that R_{N_2} in the range between 5% and 20% was appropriate for synthesizing Mn_4N films.

Figure 1 shows the variation of x-ray diffraction patterns of films deposited at T_s of 250 °C for various R_{N_2} . Although they reveal a complicated mixture composed of α -Mn and Mn_xN crystallites, the films deposited at R_{N_2} below 10% possess Mn_4N crystallites, as clearly seen in these diffraction patterns. The increase of R_{N_2} up to 20% prevented the synthesis of Mn_4N crystallites. The deposition at R_{N_2} of about 10% seemed to be suitable for synthesizing the Mn_4N films in this reactive sputtering method.

Figure 2 shows the R_{N_2} dependence of the saturation magnetization $4\pi M_s$ for the films deposited at T_s of 250 °C.

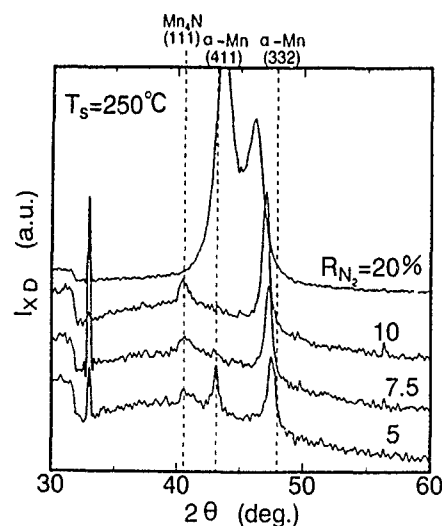


FIG. 1. Variation of x-ray diffraction patterns of the films prepared at T_s of 250 °C for various R_{N_2} .

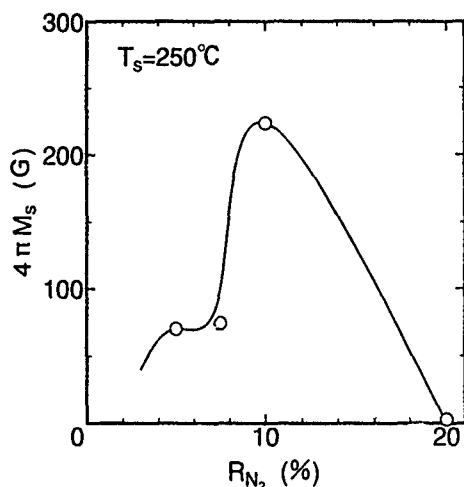


FIG. 2. R_{N_2} dependence of saturation magnetization $4\pi M_s$ for films prepared at T_s of 250 °C.

Large $4\pi M_s$ had been exhibited in the films for which the x-ray diffraction intensity $I_{X.D.}$ from Mn_4N crystallites was large, as shown in Fig. 2. It was found that films deposited at R_{N_2} of 10% have the largest amount of ferrimagnetic Mn_4N crystallites. The films deposited at T_s and R_{N_2} of 250 °C and 10%, respectively, exhibited $4\pi M_s$ of about 220 G.

Figure 3 shows the variation of x-ray diffraction patterns of films deposited at R_{N_2} of 10% for various T_s . Although the film deposited at T_s of 40 °C revealed a diffraction pattern corresponding to α -Mn crystallites, it was seen that the elevation of T_s caused the formation of Mn_4N crystallites and a decrease in $I_{X.D.}$ for α -Mn crystallites.

Figure 4 shows the T_s dependence of $4\pi M_s$, perpendicular coercivity $H_{c\perp}$, and in-plane coercivity $H_{c\parallel}$ for films deposited at R_{N_2} of 10%. It was seen that films deposited at T_s higher than 200 °C were ferrimagnetic. The elevation of T_s up to about 350 °C enhanced the formation of ferrimagnetic

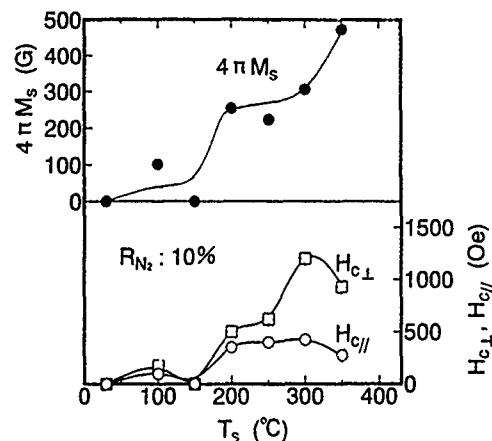


FIG. 4. T_s dependence of $4\pi M_s$, perpendicular coercivity $H_{c\perp}$ and in-plane coercivity $H_{c\parallel}$ for films deposited at R_{N_2} of 10%.

netic Mn_4N crystallites. The film deposited at T_s of 350 °C exhibited $4\pi M_s$ of about 480 G. $H_{c\perp}$ took relatively large values for films with a large amount of ferrimagnetic crystallites. It was indicated that the film with the largest $4\pi M_s$ revealed weak perpendicular magnetic anisotropy. Since the Mn_4N crystal itself owns a cubic symmetry, the perpendicular magnetic anisotropy seemed to originate from the shape anisotropy of ferrimagnetic Mn_4N grains in paramagnetic manganese nitride matrix and, in addition, stress-induced anisotropy through magnetostrictive effect. The films deposited at T_s of 350 °C exhibited $4\pi M_s$, $H_{c\perp}$, and $H_{c\parallel}$ of 450 G, 1200 Oe, and 300 Oe, respectively.

It is well known that bulk Mn_4N has been formed at a high-temperature process in a nitrogen atmosphere.⁴ A study of post-annealing the as-deposited films seemed to be useful to investigate the formation process of Mn_4N crystallites. Figure 5 shows the variation of x-ray diffraction patterns of the film deposited at T_s and R_{N_2} of 40 °C and 10%, respectively, and annealed at various annealing temperatures T_A .

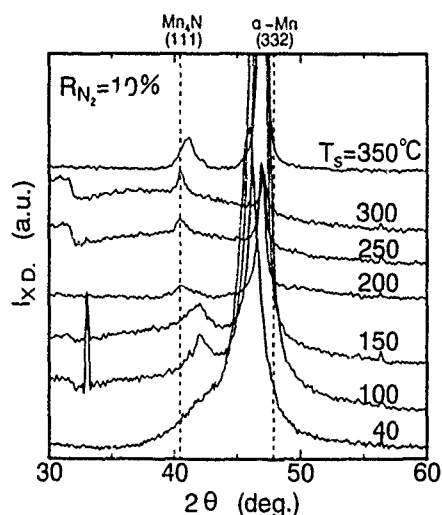


FIG. 3. Variation of x-ray diffraction patterns of the films deposited at R_{N_2} of 10% for various T_s .

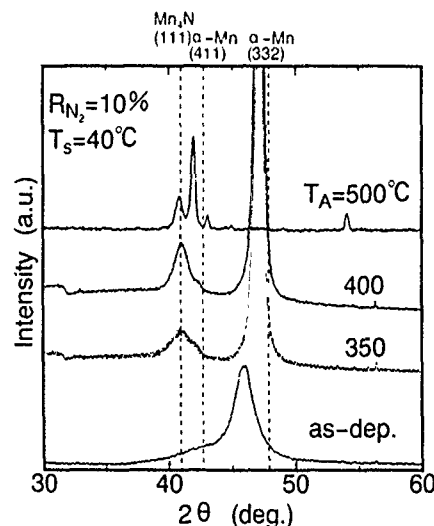


FIG. 5. Variation of x-ray diffraction patterns for films annealed at various annealing temperature T_A .

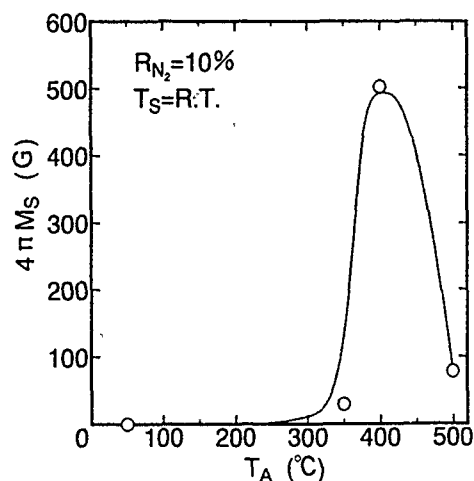


FIG. 6. Dependence of $4\pi M_s$ on annealing temperature T_A .

Although the as-deposited film did not possess Mn_4N crystallites, the film annealed at T_A higher than 300 °C was clearly found to possess those crystallites. However, the film annealed at T_A higher than 500 °C revealed a complicated diffraction pattern for 2θ between 40° and 43°. Such a complicated pattern seemed to originate from a mixture composed of several types of crystallites. The complicated structure did not show enhanced ferrimagnetism. Figure 6 shows the T_A dependence of $4\pi M_s$. The films annealed at 400 °C in vacuum exhibited $4\pi M_s$ larger than about 510 G. How-

ever, the film annealed at T_A above 500 °C exhibited smaller $4\pi M_s$ of 80 G. The nitrogen dissociation from the films and the recrystallization of other phase crystallites seemed to cause the decrease of $4\pi M_s$.

IV. CONCLUSION

The preparation of ferrimagnetic Mn_4N films has been attempted in this study using a facing targets sputtering (FTS) apparatus. R_{N_2} of 10% was appropriate for deposition of Mn_4N films at T_s higher than 200 °C. Deposition at excessive R_{N_2} tended to cause the formation of nonmagnetic Mn_3N_2 crystallites. The film prepared at T_s and R_{N_2} of 350 °C and 10%, respectively, revealed a mixed phase of Mn and Mn_4N . The film possessed $4\pi M_s$, $H_{c\parallel}$, and $H_{c\perp}$, of 450 G, 300 Oe, and 1200 Oe, respectively. The films annealed at 400 °C in vacuum exhibited $4\pi M_s$ larger than about 510 G. However, the film annealed at temperatures above 500 °C exhibited $4\pi M_s$ below 80 G. Consequently, ferrimagnetic Mn_4N films have been successfully prepared even at relatively low process temperatures using the reactive FTS apparatus.

- ¹R. Juza, H. Puff, and F. Wagenknecht, Z. Electrochem. **61**, 804 (1957).
- ²W. J. Takei, G. Shirane, and B. C. Frazer, Phys. Rev. **119**, 122 (1960).
- ³W. J. Takei, R. R. Heikes, and G. Shirane, Phys. Rev. **125**, 1893 (1962).
- ⁴M. Mekata, J. Phys. Soc. Jpn. **17**, 798 (1962).
- ⁵M. Mekata, J. Haruna, and H. Takaki, J. Phys. Soc. Jpn. **21**, 2267 (1966).
- ⁶M. Naoe, S. Yamanaka, and Y. Hoshi, IEEE Trans. Magn. **MAG-16**, 640 (1980).

Magnetovolume effects in strong paramagnets

E. G. Moroni

Department of Theoretical Physics, Royal Institute of Technology, S-10044 Stockholm, Sweden

T. Jarlborg

Département de Physique de la Matière Condensée, Université de Genève, CH-1211 Genève, Switzerland

We present calculations of magnetovolume properties for different strong paramagnetic systems such as ZrV_2 , TiBe_2 , and ZrZn_2 in the C15 structure. These materials show indications of anti-Invar behavior, i.e., enhanced magnetostriction, and thermal expansion.

We report in this paper results of calculations based on the local spin density (LSD) formalism of the magnetovolume properties of several compounds in the C15 structure such as ZrV_2 , ZrZn_2 , and TiBe_2 . These compounds are particularly interesting examples of weak itinerant ferromagnets as for ZrZn_2 or strongly exchange-enhanced systems such as TiBe_2 and ZrV_2 . The electronic structure of these paramagnetic compounds is well known and has been studied previously mainly in connection with the superconductivity, magnetism, and electron-phonon interactions.^{1,2} TiBe_2 is an example of strong exchange-enhanced paramagnetic system with a very large Stoner enhancement factor. This system becomes ferromagnetic when doped with a few percent of Cu,³ while a dilute addition of Fe is sufficient to suppress the enhanced paramagnetism.⁴ ZrZn_2 shows weak itinerant magnetism and the measured linear thermal expansion coefficient^{5,6} shows a magnetic contribution also at 260 K, much above its Curie temperature of 18 K. ZrV_2 in rhombohedral phase is superconducting below about 8 K (Ref. 6) and at a temperature much higher (about 120 K) a structural transformation into the C15 phase occurs.

The fixed-spin-moment (FSM) procedure^{8,9} has been used to determine self-consistently the total energy $E(V, M)$ at constraint magnetization M and at fixed volume V . The equilibrium properties are determined from the minimum condition of the total energy, when $P(V, M) = 0$ and $H(V, M) = 0$. For these compounds it is not trivial to fit all the nearly degenerate local minima of the total energy in the (V, M) space and to extract from the fitted total energy surface accurate information on pressure and magnetic field. Moreover, as is shown in Fig. 1 for TiBe_2 , we have found that the position of the local minima of the total energy depend sensitively on the exchange-correlation potential. More stable results can be obtained by use of the computed pressure $p(V, M)$ function given by Libermann¹⁰ and Pettifor.¹¹ Our calculations use the form of the Madelung potential derived in Ref. 12. Using the same technique we obtain also the spin-polarized electronic partial pressures.

The spin-polarized band structures and energies were determined self-consistently using the linear-muffin-tin-orbital (LMTO) method^{12,13} and for the exchange-correlation potential we use the LSD approximation with the parametrization of Vosko *et al.*¹⁴ For TiBe_2 , we also tested the effects of gradient corrections¹⁵ in describing the magnetic energy (see Fig. 1).

The computed ground-state properties for ZrV_2 , ZrZn_2 , and TiBe_2 in the C15 structure are in good agreement with

experiments. For TiBe_2 we obtain nearly degenerate low-moment (LM) and nonmagnetic (NM) total energies, with the same lattice constant of 11.95 a.u. The measured experimental value is 12.18 a.u. The computed bulk modulus of 1.38 Mbar compares also well with the experimental one of 1.32 Mbar.⁵ The calculation of the total energy for the NM state during the self-consistent procedure is unstable due to a high and structured peak of the density of states near the Fermi level. These features make it difficult to analyze the magnetic energy from total energy results. Our spin-polarized calculations show a very small magnetic moment of $0.05 \mu_B/\text{atom}$ at the Ti site for the experimental lattice. This spontaneous magnetization result is obtained using both the Vosko potential and the gradient-corrected potential.¹⁵ In Fig. 1(a) are shown at the fixed experimental volume the total energy behavior as a function of the total moment in the unit cell, for two different potentials. The position of the

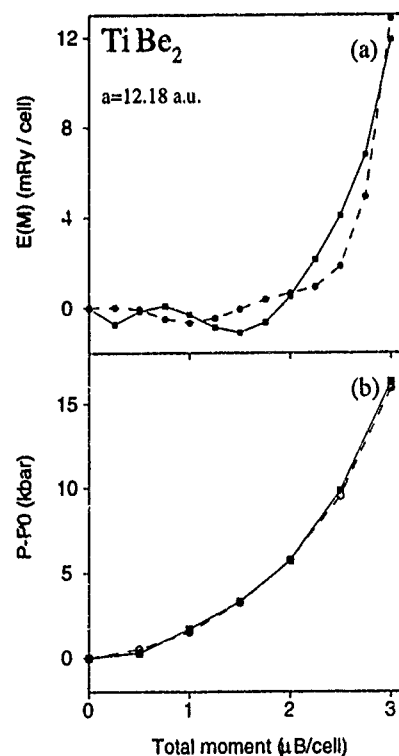


FIG. 1. (a) Computed total energy $E(M)$ curve and (b) magnetic pressure $\Delta P = P(M) - P(0)$ vs magnetic moment M . The lattice is fixed at the experimental value. The broken and full curves indicate the nonlocal and local choice for the exchange-correlation potential.

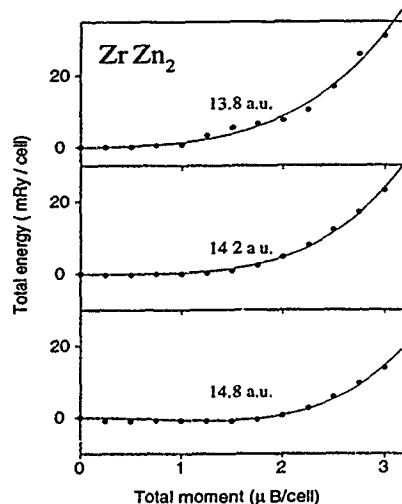


FIG. 2. Total energy vs magnetic moment for ZrZn_2 at $a=13.8$, 14.2 , and 14.8 . The reference energy E_0 is different for each curve and corresponds to the volume-dependent energy at $M=0$.

local minima of the total energy function are not the same for the two potentials. Similar results have also been obtained for iron in the fcc structure near the NM-FM instability region. However, in Fig. 1(b) is shown that the pressure behavior as a function of magnetization is almost the same also for different exchange-correlation potentials. The computed pressures differ only by a constant pressure $\Delta P = P(0)_{\text{LSD}} - P(0)_{\text{NL}} = -80$ kbar. Therefore in TiBe_2 the correction to the forced magnetostriction, using gradient-corrected potentials, comes essentially from the softer bulk modulus and larger lattice, rather than from a different magnetic pressure $\Delta P(M)$. More details can be found in Ref. 15. From Fig. 1(b) we can estimate (by numerical differentiation of the pressure curves) the magnetovolume coupling for TiBe_2 . The estimated value at very low applied magnetic field is of the order of $1 \text{ kbar}/\mu_B$. At increased field the estimated value is $5 \text{ kbar}/\mu_B$. The numerical estimation predicts a positive relative volume expansion of $\Delta V_M/V \sim 3.4 \times 10^{-6}$ for a field of 1 T. This computed magnetostriction is one to two times larger with respect to the measured experimental value.³

For ZrZn_2 the energy minimum is found at 13.64 a.u. while the experimental lattice is 13.82 a.u. At the experimental lattice we observe a very low moment of the order of $0.02\mu_B$ on Zr site, in agreement with experiments that indicate a very weak ferromagnetism in this system. In Fig. 2 we show $E(M)$ results for ZrZn_2 at different lattices constant. To analyze the $E(M)$ curves we have performed at each lattice a Landau expansion of the energy in even powers of M , of the form, $E - E_0 = \alpha M^2 + \beta M^4 + \dots$, where α and β are coefficients depending on volume. Paramagnetism requires α to be positive, and when α goes to zero, the susceptibility diverges and there occurs a transition to the low-magnetic state. In the case of ZrZn_2 this transition occurs near $a=14.2$ a.u. The calculated results for $H(V, M)$ as a function of M for two values of the lattice constant are shown in Fig. 3(a), while in Fig. 3(b) are shown the results for $p(V, M)$. The dependence on M of $H(V, M)$ is estimated

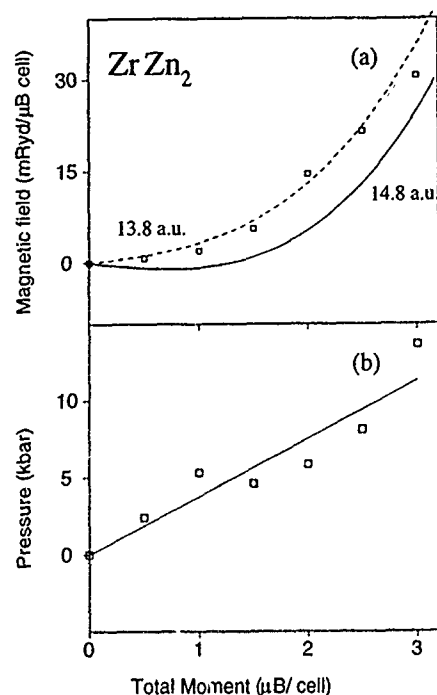


FIG. 3. (a) Magnetic field as a function of total moment for ZrZn_2 . The broken curve is obtained from the fit procedure of $E(M)$, while the open squares are calculated via the FSM definition of $H(V, M)$. The full line estimates $H(V, M)$ at $a=14.8$ a.u., where ZrZn_2 is found to be magnetic. (b) Magnetization dependence of the pressure in ZrZn_2 for $a=13.8$ including a linear fit.

by numerical differentiation of the Landau fit of the total energy, and also by the relation $H(V, M) = [E_F^1(V, M) - E_F^1(V, M)]/2\mu_B$. As is shown in Fig. 3(a) the two different procedures give the same results, which provides a supplementary control of the accuracy of the calculations. The slope $\Delta P/M$ is not constant and can change drastically depending on the volume. The magneto-volume coupling estimated by a linear interpolation is $3.7 \text{ kbar}/\mu_B$ near the experimental volume. Using $\Delta V_M/V = \Delta P_M/B$ and with a computed estimation of the bulk modulus of 1400 kbar we obtain a positive magnetostriction at a rate of the order of 0.2% per μ_B . This can also be expressed as a relative volume expansion of 2.9×10^{-6} per T. In Ref. 5 it was found that there is a magnetic contribution to the thermal expansion. This is coupled to the magnetostriction, but the admixture of excited states makes a numerical estimate of the thermal expansion more difficult.

For ZrV_2 in the C15 structure the computed ground state has a minimum at 13.7 a.u. and the total moment is zero. However, in contrast to Invar systems, such as $\text{Fe}_{65}\text{Ni}_{35}$, we find that the near degeneracy between NM and low magnetic (LM) excited configurations is extended over a wide volume range (for a between 13.7 and 14.3 a.u.). The total energy $E(V, M)$ around the local minimum shows a broad rather flat region. Within this flat region the low-moment (LM) states (with $M < 3\mu_B/\text{cell}$) have an energy smaller than 1 mRy per atom (or about 160 K) above the NM ground state. Models of thermal fluctuations between the LM to the NM state describe many Invar effects.¹⁸ Here, by choosing ZrV_2 , we search for an opposite situation in which the ground state is

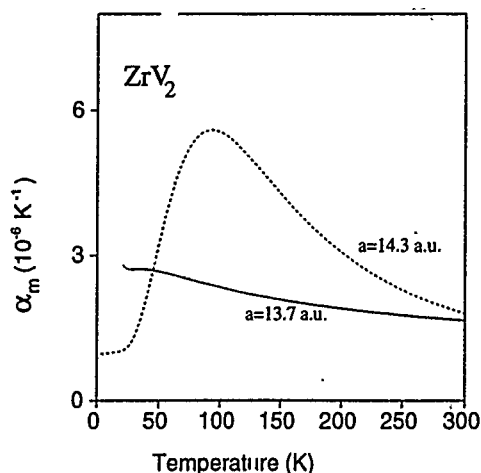


FIG. 4. Thermal behavior of the magnetic thermal expansion coefficient $\alpha_m(T)$ in ZrV_2 . $\alpha_m(T)$ is computed using Eq. (2) at two different lattices.

the small volume NM state, but where small energy fluctuations to higher-volume LM states are possible. Many strongly enhanced paramagnets or very weak ferromagnets should have a LM high-volume state very near to the NM ground state, and therefore they may be good candidates for an anti-Invar behavior provided that there is also a large difference between the equilibrium volumes. We have chosen ZrV_2 as an example of such a system, since its electronic structure is well known. Combining the total energy results with a Boltzmann model we estimate the magnetic contribution to thermal expansion in ZrV_2 . Therefore, similar to the model of Ref. 18, we perform a calculation in which only moment fluctuations occur. Contrary to the model for Invar behavior in Ref. 18 here $E(M)$ is so flat that several states have to be included in the sum, while for the situation in the Fe_3Ni Invar system the reduction to the two state model was possible. The thermal magnetic pressure is calculated as

$$\Delta P_m(T) = \frac{\sum_i \Delta P_i e^{-\Delta E_i/k_B T}}{\sum_i e^{-\Delta E_i/k_B T}} \quad (1)$$

with $\Delta P_i = P(M_i) - P(0)$ and $\Delta E_i = E(M_i) - E(0)$ and where the sum is over all states with varying moment but fixed volume. The result is that $\Delta P_m(T)$ increases linearly with T , indicating that the averaged volume will increase as well. By computing the change of magnetic pressure with the variation of temperature, we estimate the magnetic contribution to the thermal expansion, α_m as

$$\alpha_m(T) = \frac{1}{B_T} \frac{\partial \Delta P_m(T)}{\partial T} \quad (2)$$

The thermal behavior of $\alpha_m(T)$, calculated at the equilibrium volume and at an expanded lattice, is shown in Fig. 4. At room temperature the magnetic pressure is increased to about 1 kbar and with a bulk modulus of 1600 kbar, we obtain 0.06% of volume expansion up to room temperature (without phonon contribution).

The forced magnetostriction in ZrV_2 amounts to about 2.9×10^{-6} per T if computed at $a = 13.7$ a.u., while it increases to 59.0×10^{-6} per T at $a = 14.3$ a.u. Thus, when computed at the respective equilibrium lattice, we found similar forced magnetostriction, between the three studied systems. In ZrV_2 there is a large sensitivity of the forced magnetostriction on the lattice parameter and we interpret its positive value as a weak anti-Invar effect. Also in ZrZn_2 the conditions for the same mechanism are present, while experimentally, the situation is complicated by the FM ordering at low T .

The results suggest two ways of detecting the anti-Invar behavior; one by measuring the thermal expansion effect, and one by measuring the expected large volume expansion as a function of applied magnetic field. The latter method should be safer since it does not depend on thermal fluctuations. At increased temperatures the positive pressure due to the populations of the spin-polarized states enhances the lattice of the paramagnetic C15 compound. It is also possible that the competition between FM and NM states is responsible of the low-temperature structural instability of ZrV_2 . The closeness between the paramagnetic ground state and the excited low-moment (LM) states has also suggested that enhanced paramagnets, like ZrV_2 , may give quite unusual effect in spectroscopic measurements. In ZrV_2 , calculations based on final state rule predict various signature of the magnetic state in form of unusual x-ray absorption and x-ray dichroism spectra.^{16,17}

- ¹T. Jarlborg and A. J. Freeman, Phys. Rev. B **22**, 2322 (1980); T. Jarlborg, A. J. Freeman, and D. D. Koelling, J. Magn. Magn. Mater. **23**, 291 (1981); T. Jarlborg, P. Monod, and M. Peter, Solid State Commun. **47**, 889 (1983).
- ²B. M. Klein, W. E. Pickett, D. A. Papaconstantopoulos, and L. L. Boyer, Phys. Rev. B **27**, 6721 (1983); M. Huang, H. J. F. Jansen, and A. J. Freeman, *ibid.* **37**, 3489 (1988).
- ³G. Creuzet and I. A. Campbell, J. Magn. Magn. Mater. **37**, 173 (1983); W. Gerhardt, J. S. Schilling, H. Olijnyk, and J. L. Smith, Phys. Rev. B **28**, 5814 (1983).
- ⁴I. Felner, I. Nowik, and D. Shaltiel, Solid State Commun. **40**, 1073 (1981).
- ⁵S. Ogawa, Physica **119B**, 68 (1983); P. E. Brommer and J. J. M. Franse, J. Magn. Magn. Mater. **45**, 129 (1984).
- ⁶V. A. Marchenko and V. M. Polovov, Sov. Phys. JETP **51**, 535 (1980); E. S. Karpov, I. I. Papiro, E. A. Pushkarev, and V. A. Finkel, Sov. Phys. Solid State **21**, 2050 (1979).
- ⁷I. Takahashi and M. Shimizu, J. Phys. F **18**, 2081 (1988).
- ⁸P. M. Marcus and V. L. Moruzzi, J. Appl. Phys. **63**, 4045 (1988).
- ⁹P. H. Dederichs, S. Blugel, R. Zeller, and H. Akai, Phys. Rev. Lett. **53**, 2512 (1984).
- ¹⁰D. A. Libermann, Phys. Rev. B **3**, 2081 (1971).
- ¹¹D. G. Pettifor, Commun. Phys. **1**, 141 (1976); J. Phys. **7**, 613 (1977); **8**, 219 (1978).
- ¹²G. Arbman and T. Jarlborg, J. Phys. **7**, 1635 (1977).
- ¹³O. K. Andersen, Phys. Rev. B **12**, 3060 (1975).
- ¹⁴S. H. Vosko, L. Wilk, and M. Nusair, Can. J. Phys. **58**, 1200 (1980).
- ¹⁵J. P. Perdew and Y. Wang, Phys. Rev. B **33**, 8800 (1986); B. Barbiellini, E. G. Moroni, and T. Jarlborg, J. Phys. **2**, 7597 (1990).
- ¹⁶P. Lerch, E. G. Moroni, and T. Jarlborg, in *Proceedings ICPTM 92 Darmstadt*, edited by P. M. Oppeneer and J. Kubler (World Scientific, Singapore, 1992), p. 774.
- ¹⁷P. Lerch, E. G. Moroni, and T. Jarlborg, Solid State Commun. **88**, 167 (1993).
- ¹⁸E. G. Moroni and T. Jarlborg, Phys. Rev. B **41**, 9600 (1990).

Synthesis and characterization of Fe_{16}N_2 in bulk form

M. Q. Huang, W. E. Wallace, S. Simizu, A. T. Pedziwiatr,^{a)} R. T. Obermyer, and S. G. Sankar

Carnegie Mellon Research Institute, Carnegie Mellon University, Pittsburgh, Pennsylvania 15213

Using molecular-beam epitaxy and ion implantation, Japanese workers have formed Fe_{16}N_2 in thin Fe films. They report a large magnetic induction for this nitride, ≥ 2.8 T. In the present study, Fe_{16}N_2 has been prepared in bulk form by treating Fe powder with NH_3/H_2 gas mixtures at temperatures in the range 660–670 °C. The γ -phase alloy, which forms under these conditions, was quenched to room temperature to form the α' -Fe-N phase and then heat treated at 120–150 °C to form the α'' -Fe-N phase. The α' phase has been prepared in 80% purity, the other phase being nonmagnetic γ -Fe-N. The α'' phase has been prepared in 50% purity, the impurity phases being α -Fe and γ -Fe-N. Magnetic measurements give saturation magnetizations at room temperature of 250 ± 10 emu/g ($2.6 \mu_B/\text{Fe}$) for the α' phase, 285 ± 10 emu/g ($2.9 \mu_B/\text{Fe}$) for the α'' phase, and essentially zero for the γ phase. Mössbauer measurements confirm that nitrogen austenite is nonmagnetic. The anisotropy of Fe_{16}N_2 is small but detectable.

I. INTRODUCTION

It is well known that when iron is exposed at elevated temperatures to a mixture of NH_3 and H_2 , it forms several nitrides. One of these Fe nitrides is nitrogen austenite, the γ -Fe-N phase. This is a material in which Fe is in a simple fcc arrangement with N distributed randomly in the octahedral sites. Upon cooling to cryogenic temperatures, the γ phase undergoes a martensitic transformation into a phase termed α' or nitrogen martensite. When nitrogen martensite, which has the stoichiometry Fe_8N , is heat treated at low temperatures (~ 150 °C) it undergoes a structural transformation into a phase termed α'' . The α'' phase has the stoichiometry Fe_{16}N_2 . The α'' phase is currently attracting much attention because of indications that it has a giant magnetic induction.

In a series of classic papers published in the late 1940's and early 1950's, Jack structurally characterized both the α' and α'' phases (as well as several other Fe-N phases).^{1–4} He found the α' phase to be tetragonal with two atoms of Fe per unit cell and the α'' phase also to be tetragonal with one formula unit of Fe_{16}N_2 per unit cell. The axial ratio is ~ 1.1 for both phases.

Fe_{16}N_2 has been formed in thin Fe films by a variety of techniques, beginning with the work of Kim and Takahashi.⁵ This work, and later work of a generally similar nature, indicated that nitrogenation substantially increases the Fe moment.⁶ A saturation magnetic induction of 2.8–3.0 T was reported in these studies. In contrast with these findings, very recent work by Shoji *et al.*⁷ on Fe_xN_2 produced through dc sputtering of Fe films showed B_{sat} no larger than that of α Fe.

In view of the discrepancy between the results of Shoji *et al.* and those of other investigators, a reexamination of the magnetic behavior of Fe_{16}N_2 is warranted. In the present investigation, bulk quantities of Fe_{16}N_2 have been prepared and studied magnetically. (The preparation method used was essentially identical with that employed by Jack.^{1–4}) This is in contrast with all previous magnetic work on Fe_{16}N_2 which involved thin Fe films.

^{a)}On leave from the Institute of Physics, Jagiellonian University, 30-059 Cracow, Poland.

II. EXPERIMENTAL DETAILS

Nitrogen austenite (γ phase) with different nitrogen contents ($C_N = \text{N}/100 \text{ Fe} = 6.4\text{--}10.7$) was produced by treating Fe powder (6–9 μm) with a $\text{NH}_3\text{--H}_2$ gas mixture at 1 atm pressure and at temperatures in the range of 660–670 °C for 2–3 h. The alloy was then quenched to room temperature or lower by He gas and liquid N_2 or liquid He to form the martensite α' phase, followed by a low-temperature heat treatment at temperatures of 120–150 °C for 0.5–2 h in vacuum to form $\alpha''\text{-Fe}_{16}\text{N}_2$ phase.

The phases present in Fe-N samples and their lattice parameters were determined by x-ray diffraction (XRD) using Cu radiation. Quantitative analysis of the relative amounts of each phase in the Fe-N samples was established by the direct comparison method of Cullity,⁸ based on the measured intensities of XRD lines and using the calculation of the structure factor (including the multiplicity factors) and the Lorentz-Polarization factors. The nitrogen content was determined by using the equations $a = 3.575 + 0.0080 C_N$ for γ and $c/a = 1 + 0.0091 C_N$ for α' , relating lattice parameters to composition. For some samples, N content was also measured by weight increase after nitriding. The magnetic properties, M , T_c , and anisotropy, were measured using standard methods. Measurements were made in the temperature range of 10–1273 K and in fields of 500 Oe to 17 kOe. Hot XRD from room temperature to 700 °C was used to detect the phase transitions. This was supplemented by TMA in a field of 500 Oe and at temperatures of 10–1273 K.

III. RESULTS AND DISCUSSION

A. Phase transformation from γ to α' -Fe-N

A number of Fe-N austenites (γ phase) with differing N content ($\text{N}/100 \text{ Fe} = 6.4\text{--}10.7$) were synthesized. The N contents were controlled by changing the ratio of NH_3/H_2 . When the γ phase was quenched from high temperature to room temperature or lower, it partially transformed to α' (see Table I). The quantity transformed depends on N content and quenching temperature T_q . The crystal and magnetic properties of the quenched alloys are given in Table I. For sample 6.4, with lowest N content, almost 87% of the α' phase was

TABLE I. The crystal and magnetic properties of the quenched alloys.

C_N^a (at. %)	T_q (K)	Lattice parameters				$C(\%\alpha')^b$ (wt %)	M^c (emu/g)	T_I^d ($\gamma \rightarrow \alpha'$) (K)
		γ a (Å)	a (Å)	α' c (Å)	c/a			
~6.4	RT	3.615	2.857	3.022	1.057	~87	210	~RT
~8.1	RT	3.632	2.852	3.064	1.074	~72	177	~RT-110 K
	LN	3.632	2.852	3.064		~82	202	
~10.7	RT	3.652				~0	3	30-150 K
	LN	3.652	2.846	3.126	1.098	~51	133	
	LHe	3.652	2.846	3.126		~56	146	

^a C_N is the N concentration expressed as N/100 Fe.

^b $C(\%\alpha')$ is the estimated concentration of the α' phase in the quenched alloy. *Vide infra*.

^c M is the magnetic moment of the sample. It is lower than M for α' phase because of the presence of some nonmagnetic γ phase.

^d T_I gives the temperature range in which the $\gamma \rightarrow \alpha'$ transformation occurs.

formed at room temperature. This sample carries a magnetic moment of 210 emu/g. For sample 10.7, with the highest N content, a near-zero magnetic moment is observed at room temperature. The XRD pattern indicates a single- γ phase (Fig. 1). On quenching to liquid-N or liquid-He temperature, the α' phase formed and the magnetic moment of the sample increased to 133 and 146 emu/g, and the relative amounts of α' phase increased to 51 and 56 at. %, respectively. The transformation temperatures from γ to α' , T_I , in Table I were obtained by TMA measurements. It is to be noted that when the N content of the γ phase increases, T_I decreases.

B. The α' phase

As seen in Table I, the lattice parameters are compositionally dependent. The results obtained are in agreement with the results of others.^{4,9} To determine the moment of the α' phase, one must ascertain the fraction of the sample which is in the α' phase. This is done by XRD measurements of line intensities. In principle, this is straightforward, but in practice it is complicated by line overlap of the most intense diffraction lines (see Fig. 2). The procedure employed is depicted in Fig. 3, in which the measured moment is plotted against the ratio of the intensities of the two strong lines in the XRD pattern. Magnetization increases as the intensity ratio decreases, since the amount of the nonmagnetic γ phase is decreasing. Extending the lines to $I\gamma(200)=0$, magnetization reaches 248-262 emu/g, which can be taken as the

magnetic moment of the α' phase. It seems that the α' phase with higher N content exhibits a higher moment. As seen in Fig. 3, the α' samples for the lines A, B, and C with different N contents, the corresponding magnetizations [at $I\gamma(200)=0$] are ~248, 252, and 262 emu/g, respectively. We also used the XRD line intensities to calculate the mass fraction of α' for these samples and used these to estimate the concentration of α' phase (see Table I) as well as its moment. Both results are quite close, considering the ~5% error of estimating intensities.

C. α' Fe₁₆N₂ phase

A number of samples containing the α' phases were heat treated at temperatures ranging from 120 to 150 °C for 0.5-2 h to form the α'' phase. Typical and characteristic XRD lines, (213) and (004) of α'' phase, were observed on a sample with $C_N=10.0$, after treating at 150 °C for 2 h (as seen in Fig. 4). The other lines, 202, 220, 400, 224, and 422, shifted from the positions of lines of original martensite α' . The lattice constants a and c are very close to that reported by Jack, $a=5.718$ Å and $c=6.290$ Å. The magnetic moment increases from 182 to 189 emu/g when the α' phase transforms to α'' . The sample was estimated to contain 56 α'' , 12% α Fe, and 31% γ . The estimated moment is ~285 emu/g for α'' . As with the analysis of the moment of the α' phase, we plotted the measured moment of the α'' phase samples, M , versus the measuring XRD intensity ratio $I\gamma(200)/[I\gamma(111)]$

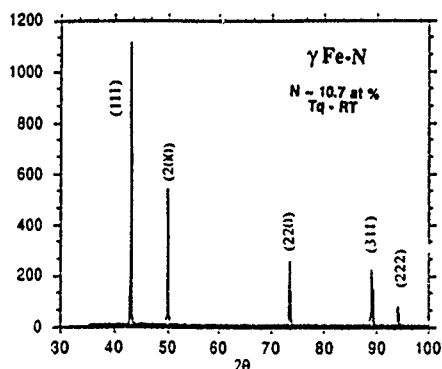


FIG. 1. XRD of sample 10.7 in Table I.

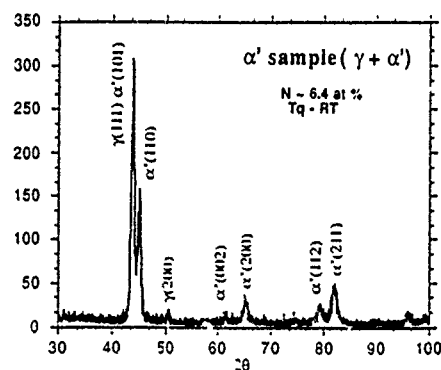


FIG. 2. XRD of sample 6.4 in Table I.

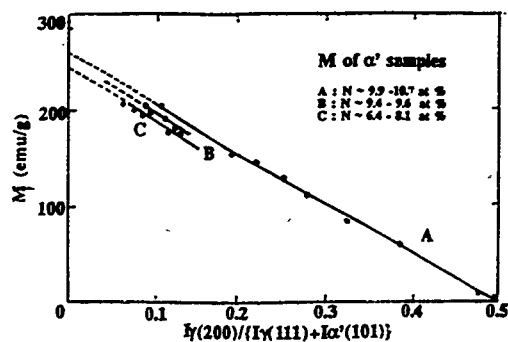


FIG. 3. $M-I\gamma(200)/[I\gamma(111)+I\alpha'(101)]$.

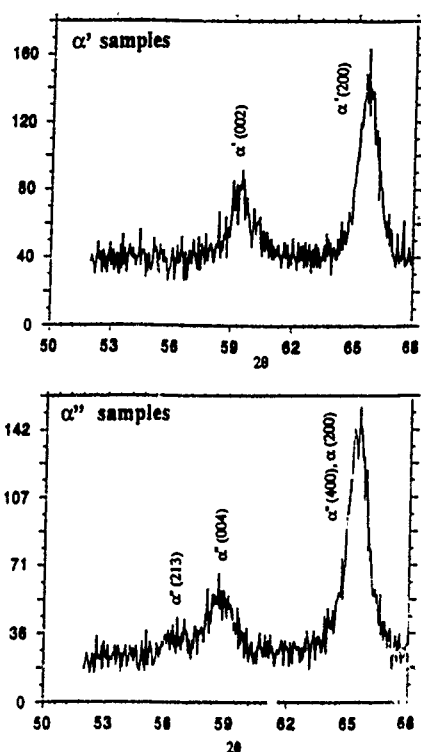


FIG. 4. (a) XRD of α' sample, (b) XRD of α'' sample.

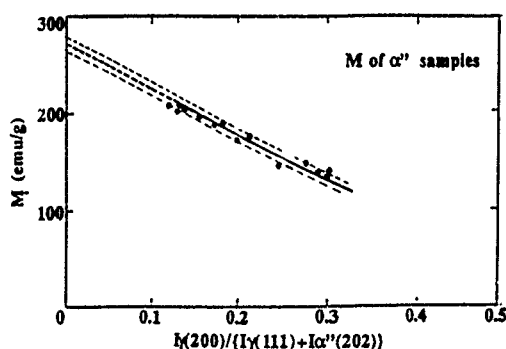


FIG. 5. $M-I\gamma(200)/[I\gamma(111)+I\alpha''(202)]$.

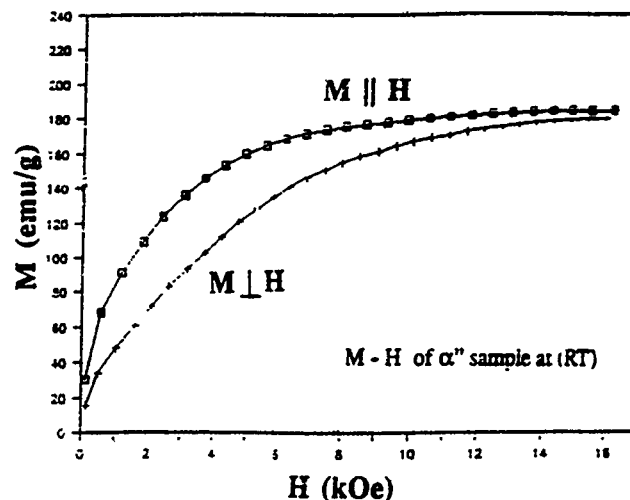


FIG. 6. $M-H$ of α'' sample at RT.

+ $I\alpha''(202)$] in Fig. 5. When extending the plot to the intersection with the y axis, i.e., where the γ phase is absent, M reaches ~ 275 emu/g. The moment is contributed by the Fe_{16}N_2 and α -Fe phases. The maximum N content in the α' phase is 10.7, which is less than that of the α'' phase, 12.5. Hence, during the formation of α'' , Fe is rejected in the form of α -Fe. Based on the known N concentration, one can estimate the amount of α -Fe formed. Knowing this, one can establish the moment of the α'' phase to be 280 ± 10 emu/g.

As reported by Drabecki,¹⁰ the α'' phase shows a weak uniaxial anisotropy with $K_0 = 78.10^4 \text{ J/M}^3$, as measured magnetically. We examined the anisotropy by observing the difference of XRD of an α'' sample random and aligned in a magnetic field of 17 kOe. The XRD intensities did show a slight change after alignment when a 17 kOe field is applied. The field dependencies of magnetization for aligned powders are shown in Fig. 6 for fields applied parallel and perpendicular to the aligning field. These confirm that there is a measurable magnetic anisotropy.

ACKNOWLEDGMENTS

The work was supported by a grant from the Army Research Office. The authors wish to acknowledge many helpful suggestions from Professor K. H. Jack. The authors wish to express appreciation to Professor Gary Long and Professor O. A. Pringle of the University of Missouri, Rolla for providing the Mössbauer measurements which confirm that the γ -Fe-N phase is nonmagnetic.

¹ K. H. Jack, *Acta Cryst.* **3**, 392 (1950).

² K. H. Jack, *Proc. R. Soc. London Ser. A* **195**, 41 (1949).

³ K. H. Jack, *Proc. R. Soc. London Ser. A* **208**, 200, 216 (1951).

⁴ K. H. Jack, *Acta Cryst.* **5**, 404 (1952).

⁵ T. K. Kim and M. Takahashi, *Appl. Phys. Lett.* **20**, 492 (1972).

⁶ See reviews by Y. Sugita and his associates, *J. Appl. Phys.* **67**, 5126 (1990); **71**, 5977 (1991).

⁷ H. Shoji, H. Takahashi, M. Tunii, Migaku Takahashi, and T. Wakiyama, *J. Jpn. Appl. Magn. Soc.* **17**, 323 (1993).

⁸ B. D. Cullity, *Elements of X-ray Diffraction* (Addison-Wesley, Reading, 1978), p. 411.

⁹ B. Rauschenbach and A. Kolitsch, *Phys. Status Solidi A* **80**, 211 (1983).

¹⁰ J. Drabecki, *Acta Physica Polonica A* **60**, 1981.

Magnetic properties of FeRhP: Influence of metallic clusters on ferromagnetism

M. Guillot, M. Artigas,^{a)} M. Bacman,^{b)} D. Fruchart,^{b)} D. Boursier,^{c)} and R. Fruchart^{c)}
Service National des Champs Intenses, C.N.R.S. B.P. 166 X, 38042 Grenoble-Cédex, France

Synthesis of compounds belonging to the FeRhP system reveal the existence of three main structures: hexagonal H_3 -Fe₂P type, orthorhombic O_{10} -NdCoB type, and hexagonal H_{12} -FePdP type described as polytypes resulting from different packings of a pseudorhombohedral FeRhP subcell. High magnetic field magnetic measurements were carried out in the 4.2–300 K temperature range in fields up to 200 kOe. Very different magnetic properties were observed for the three phases. To explain the low saturation magnetization of both O_{10} and H_{12} phases compared to that of the H_3 phase, a structural magnetic framework that leads to the formation of diamagnetic clusters within the ferromagnetic matrix is proposed.

I. INTRODUCTION

Several phosphides of the first-row transition metals, for example, Fe₃P, Fe₂P, MnP, MnAs are ferromagnetic.¹ Fe₂P has attracted attention due to its peculiar magnetic properties (a first-order transition at 214 K and giant short-range magnetic order up to temperatures three times higher than T_c), but saturation moments and Curie temperatures reported in the literature vary widely.^{2–4} These conflicting results reflect the extreme sensitivity of the magnetic properties to both chemical and physical parameters, e.g., low substitutions of Mn and Cr or nonstoichiometry, structural defects, sensibility to pressure and magnetic field. In this work, we report high magnetic field magnetization and magnetic susceptibility measurements made on ternary iron phosphides of compositions FeRhP and Fe_{1.33}Rh_{0.66}P.

First, the hexagonal structure of Fe₂P (space group $P\bar{6}2m$ with three formulae/unit cell) will be briefly described. Along the c axis, phosphorus atoms form, alternately, in tetrahedra and square-based pyramids generating channels of triangular section.⁵ Because the occupation of both tetrahedral and pyramidal sites cannot happen simultaneously inside the same channel, two kinds of channels must occur: in the first one, only the tetrahedral sites are occupied; in the second one, only Fe atoms are surrounded by five P atoms (pyramids). Channels of different types share common pyramidal square bases to form channel pairs. This pairing results in pseudorhombohedral subunits which consist of two filled sites (square-based pyramid and tetrahedron) and two empty sites (inset Fig. 1).

The preparation of the different polytypes of composition FeRhP was a delicate task.⁶ For a long time it was suggested that this compound did not exist. The difficulties resulted from the successive and unusual structural transformations required to accommodate the formation of clusters. Furthermore it should be noted that in Co_{0.8}Ni_{0.2}P, similar clusters of cobalt and nickel produce diamagnetic properties.⁷

II. EXPERIMENTAL PROCEDURE

Rhodium-iron-phosphides cannot be prepared by the diffusion of powdered rhodium in FeP at temperatures of about 1200 K as in the case for the other ternary phosphides.⁶ FeRhP and the parent Fe (Fe_xRh_{1-x})P solid solutions must be stabilized under various structural forms through a drastic control of the thermal treatment. Three main structures were identified from the magnetic susceptibility temperature dependence and analysis of powder x-ray patterns.^{8,9} The first form discovered was assigned the hexagonal Fe₂P-type structure;⁷ since it is unstable, it must be stabilized by a water quenching from 1320 K to room temperature; it is designed the H_3 polytype. On the other hand, a slow cooling of the H_3 phase from 1320 K to room temperature leads to the CoNbB-type orthorhombic structure (O_{10} polytype). Finally, a third structural type (H_{12} polytype) was stabilized by annealing of the H_3 phase near 500 K with patterns apparently similar to H_3 Fe₂P type: absence of superstructural lines indicates a low-ordering range (LOR) for this phase, designed H_{12} . After a long annealing of 72 days at 670 K, the superstructural lines which appear lead to an hexagonal structure of the FePdP type.¹⁰ All of the polytype phases can be considered as 3D networks of the rhombohedral subunit previously described: the subscript of letter H or O repre-

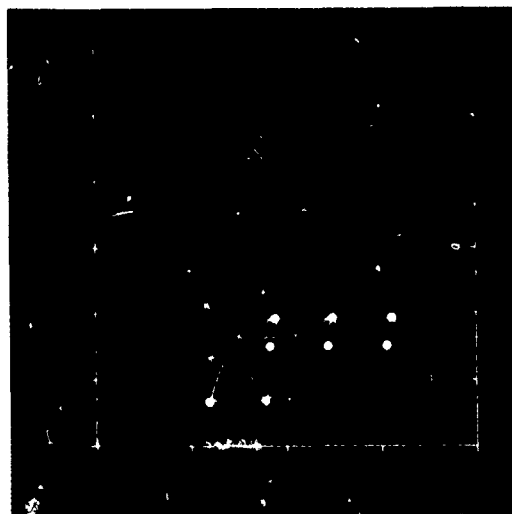


FIG. 1. Magnetization curves at 4.2 K for the three polytypes of FeRhP. Insert: rhombohedral subunit formed by pyramidal and tetrahedral sites (Ref. 1).

^{a)}Instituto de Ciencia de Materiales de Aragon, Zaragoza, Spain.

^{b)}Laboratoire de Cristallographie, C.N.R.S., B.P. 166 X, Grenoble Cédex, France.

^{c)}C.N.R.S. U-A 1109, E.N.S.P.G., B.P. 46, 38042 Saint Martin d'Hères, France.

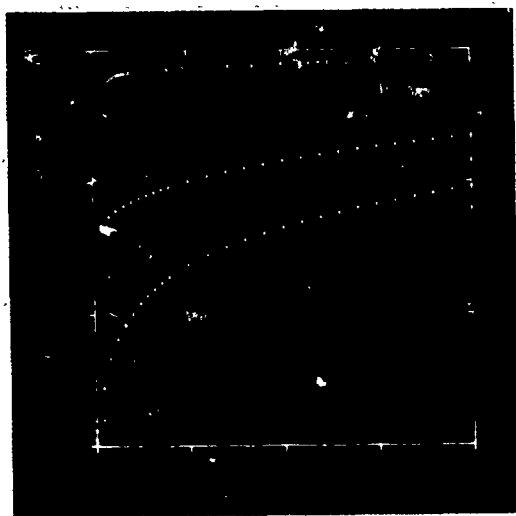


FIG. 2. Magnetization curves for a powder sample of FeRhP in O_{10} (CoNbB type) phase at different temperatures.

sents the number of rhombohedra. The phases H_{12} and O_{10} result from the cooperative displacements of $c/2$ of some chains of phosphorus atoms along the c axis. Whereas in the H_3 structure both iron and rhodium atoms are distributed over the tetrahedral and pyramidal sites with a nearly complete degree of disorder, in the two other phases the translations of the chains of P atoms result in strong variations of these characterized distributions. In FePdP an overconcentration of rhodium around some particular phosphorus atoms was observed.^{7,9} In order to determine the influence of these metallic clusters on the ferromagnetism of the FeRhP system, magnetic properties of the three polymorphic phases will be reported.

Measurements of the magnetization over the temperature range 4.2–400 K were carried out using extraction technique in dc magnetic fields up to 200 kOe produced by a water-cooled Bitter magnet (magnetometer is described in Ref. 11). On the other hand, the temperature dependence of the initial magnetic susceptibility were determined in the 300–1300 K temperature range using a homemade Faraday-type device.

III. RESULTS AND DISCUSSION

Some typical magnetic isotherm curves reported in Figs. 1 and 2 reveal significant differences between the three polytypes of the two studied phosphides. First, a large discrepancy between the magnetic moments is observed (nearly a factor of 2 between the H_3 and H_{12} phases). Second, whereas for both H_3 and O_{10} phases the general shape of the $M(H)$ curves is in accordance with a rapid saturation, for the H_{12} polytype only 90% of saturation is reached at 50 kOe. Within our experimental accuracy ($\pm 1\%$), neither hysteresis on the $M(H)$ curves nor changes on the results were observed after cooling from 300 to 4.2 K under 200 kOe. This behavior confirms the good quality of the samples which were initially checked by x-ray and neutron diffractions.⁹

For all of the samples studied, the experimental curves are well described by a law of approach to saturation which contains a b/H^2 term only¹² in a high-field domain (100–200

TABLE I. Magnetic Properties of the metallic H_3 , O_{10} , and H_{12} polytypes of iron-rhodium phosphides.

FeRhP	H_3	O_{10}	H_{12}
$M^{\text{sat}}(\mu_B \text{ mole}^{-1})$	2.02	1.46	1.09
$T_c(\text{K})$	355	235	120
$C(\text{uem})$	1.42	1.26	1.14
$n_{\text{eff}}(\mu_B)$	3.37	3.18	3.02
$m^{\text{ferro}}(\mu_B)$	2.02	1.46	1.09
$m^{\text{para}}(\mu_B)$	2.50	2.35	2.18
$\text{Fe}_{1.333}\text{Rh}_{0.666}\text{P}$	H_3	O_{10}	H_{12}
$M^{\text{sat}}(\mu_B \text{ mole}^{-1})$	2.11	1.64	1.38
$T_c(\text{K})$	360	290	230
$C(\text{uem})$	1.77	1.53	1.44
$n_{\text{eff}}(\mu_B)$	3.26	3.04	2.95
$m^{\text{ferro}}(\mu_B)$	1.58	1.24	1.04
$m^{\text{para}}(\mu_B)$	2.41	2.20	2.12

kOe). The saturation moment (M^{sat}) in Bohr magneton μ_B per mole, at 4.2 K, was determined using a least-squares procedure. The results are in Table I with the corresponding values of m^{ferro} , $\mu_B/\text{iron atom}$. For the H_3 and O_{10} polytypes, m^{ferro} decreases with the rhodium content but in the H_{12} form, m^{ferro} is practically independent of the Rh content (Table I). The first-order anisotropy constant K is determined from the coefficient b ($b = 4K^2/15M_{\text{sat}}^2$ in the hexagonal case), it is obtained: $K \sim 1.7 \times 10^7 \text{ erg cm}^{-3}$ and $K \sim 2.5 \times 10^7 \text{ erg cm}^{-3}$ for $\text{Fe}_{1.333}\text{Rh}_{0.666}\text{P}$ and FeRhP respectively in the H_{12} phase. In the H_3 phase, K is found to be $\sim 0.7 \times 10^7 \text{ erg cm}^{-3}$ and is independent of Rh content. This last value contrasts strongly with the average value of $2.5 \times 10^7 \text{ erg cm}^3$ proposed for Fe_2P .²

For all samples, the reciprocal magnetic susceptibilities follow a Curie law (see figure in Ref. 8). The experimental values of both Curie constants (C) and paramagnetic Curie temperature (T_c) are summarized in Table I where the values of n_{eff} , effective number of Bohr magnetons/Fe atom, deduced from C are also reported. As the classic plot of H/M vs M^2 provides values of T_c that are in very good agreement with the preceding determinations, we conclude that the paramagnetic and ferromagnetic Curie temperatures coincide. The values of m^{para} , magnetic moment in the paramagnetic state, given in Table I were deduced from the relation $n_{\text{eff}}^2 = m^{\text{para}}(m^{\text{para}} + 2)$.¹³ It should be noted that the ratio $m^{\text{para}}/m^{\text{ferro}}$ is always much larger than 1 as expected by a localized electron model; this result can be interpreted on the basis of a collective electron model of ferromagnetism.¹³ In addition, a strong decrease of m^{para} is observed when the structure turns from H_3 to H_{12} .

To explain the very different magnetic behaviors observed for the three phases, we shall analyze the H_{12} case. All of the atoms occupy planes perpendicular to the $[001]$ direction at $z=0$ and $z=1/2$, respectively. The structure consists of 12 pseudorhombohedral subunits which form two types of blocks. The first contains three subunits and is projected as hexagons in the (001) plane; projection in this plane of the second type, which contains six of the rhombohedral subcells, leads to the "star-shaped" arrangement (Fig. 3).⁹ In the unit cell described by the association of two "hexagon"

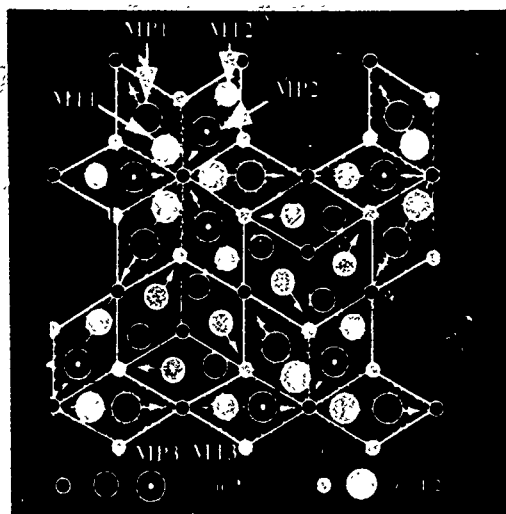


FIG. 3. FeRhP structure in the H_{12} form: projection on the (001) plane; the iron content for the six metallic sites is equal to: 0 for MT_1 and MP_1 , 54% for MP_2 , 41% for MP_3 , 91% for MT_2 ; and 82% for MT_3 , respectively (arrows on the pyramidal sites suggest the axial symmetry).

and one "star-shaped" blocks, the metallic atoms are distributed over three tetrahedra (noted MT) and three pyramids (MP): on four sites (MT_2 , MT_3 , MP_2 , and MP_3), a statistical disorder of the Fe and Rh atoms is observed (occupations are given in the caption of Fig. 3). In contrast MT_1 and MP_1 which belong to the "star-shaped" block are occupied only by rhodium atoms. It is important to emphasize the local overstoichiometry of rhodium around the P (0,0,0) atom when the structure changes from H_3 to H_{12} .

For the completely disordered H_3 phase, the magnetization of the pseudorhombohedral unit (formula FeRhP) is equal to

$$m(\text{phase } H_3) \approx (3/6)(m_T + m_P), \quad (1)$$

m_T and m_P represent the Fe atom magnetic moment in tetrahedral and pyramidal positions, respectively. In the H_{12} phase, the saturation magnetization is given by

$$m(\text{phase } H_{12}) = 0.2275m_{T2} + 0.135m_{P2} + 0.205m_{P3} + 0.41m_{T3}. \quad (2)$$

Since no values of m_T and m_P are available to explain the saturation of the H_3 form, we estimate that $m_T \approx 1\mu_B$ and $m_P \approx 3\mu_B$ based on the order of magnitude proposed for Fe_2P . In the H_{12} phase, the MP_2 site is located in the region where the overstoichiometry of rhodium occurs; on the other hand, this site contains only 54% Fe atoms. These two points

lead to the conclusion that the Fe atoms of this site are non-magnetic, and occurs as diamagnetic clusters. According to this hypothesis, m_{P2} is taken equal to zero; furthermore assuming always that $m_T = m_{T2} = m_{T3} \approx 1\mu_B$ and $m_P = m_{P3} \approx 3\mu_B$, we can roughly estimate that the saturation of the H_{12} phase is equal to $1.25\mu_B$. Although the compound contains a very large amount of iron, the presence of diamagnetic clusters can be explained by a gain of stability created by a complete filling of the $\text{Fe } d^{10}$ levels due to valence electrons transfers from neighboring rhodium and phosphorus atoms in the region of high rhodium content to form $(\text{Fe}_{1.62}\text{Rh}_{7.38}\text{P})$ groups. This hypothesis suggests more localized bondings in the clusters. It appears, therefore, that a very simple structural chemical framework can explain the

critical behavior of the magnetic properties which are strongly influenced by this metal clustering. Similar arrangement occurs in the O_{10} phase although the distribution of the iron atoms is more complex.⁹ This existence of diamagnetic clusters was previously suggested to interpret the diamagnetic properties of the system $\text{Ni}_2\text{P-Co}_2\text{P}$.⁷

In this paper quantitative data on the intrinsic properties of the FeRhP system are reported. Through the interpretation of these results and those of earlier studies, we have determined that diamagnetic clusters occur in the H_{12} and O_{10} phases. It is clear that further experiments on local properties using Mössbauer effect and neutron diffraction are needed to obtain more detailed information on diamagnetic clustering in both O_{10} and H_{12} polytypes.

ACKNOWLEDGMENT

One of us (M. A) is very grateful for the grant from the "Diputacion General de Aragon" (Spain).

- ¹ R. Fruchart, A. Roger, and J. P. Sénateur, *J. Appl. Phys.* **40**, 1250 (1969).
- ² O. Erikson, J. Sjöström, B. Johanson, L. Haggström, and H. L. Skriver, *J. Magn. Magn. Mater.* **74**, 347 (1988).
- ³ L. Lungren, G. Tarmohamed, O. Bekman, B. Carlson, and S. Rundqvist, *Phys. Scr.* **17**, 39 (1978).
- ⁴ H. Fuji, Y. Uwatoko, K. Motoya, Y. Ito, and T. Okamoto, *J. Appl. Phys.* **57**, 2143 (1988).
- ⁵ R. Fruchart, *Ann. Chim. Fr.* **7**, 563 (1982).
- ⁶ A. Roger and R. Fruchart, *C. R. Acad. Sci. Paris* **264**, 508 (1967).
- ⁷ M. Artigas, M. Bacman, D. Boursier, D. Fruchart, R. Fruchart, and J. L. Soubeyroux, *C. R. Acad. Sci. Paris*, t. **315**, série II, 29 (1992).
- ⁸ M. Artigas, D. Fruchart, D. Boursier, and R. Fruchart, *C. R. Acad. Sci. Paris* **310**, 1621 (1990).
- ⁹ M. Artigas, Ph.D. thèse, Université Grenoble, 1992.
- ¹⁰ M. Artigas, M. Bacman, D. Fruchart, P. Wolfers, and R. Fruchart, *J. Alloys Comp.* **176**, 106 (1991).
- ¹¹ J. C. Picoche, M. Guillot, and A. Marchand, *Physica B* **155**, 407 (1989).
- ¹² R. Grössinger, *Phys. Status Solidi A* **66**, 665 (1981).
- ¹³ P. Rhodes and E. P. Wohlfarth, *Proc. R. Soc. London* **273**, 247 (1963).

Magnetism in metastable bcc and fcc iron-copper alloys

P. A. Serena and N. García

Departamento de Física de la Materia Condensada, Universidad Autónoma de Madrid, Cantoblanco, E-28049 Madrid, Spain

We present linearized augmented plane-wave calculations for FeCu fcc and bcc metastable phases using the local density approximation. Curves for the density of states (without including the spin-polarization effects) at several Fe concentrations are given, noticing that the density of states at the Fermi level for determined fcc alloys suffers significant large increases in relation to the fcc Fe. This fact provides an explanation to the magnetic character found in some fcc FeCu alloys. The magnetization is calculated at different compositions by applying the Stoner criteria, assuming a simple behavior for the magnetic exchange integral, and including the effect of randomness in a simple way. We find that the magnetic moment per Fe atom is similar to that of bcc Fe for some fcc FeCu alloys.

In the last few years it has been possible to prepare metastable phases of fcc and bcc Fe-Cu alloys by mechanical alloying¹ and sputtering.^{2,3} These techniques have provided new perspectives of understanding mechanisms for producing magnetism as well as the growth of new magnetic materials. In particular, Chien *et al.*² have shown that the fcc phase can be grown by sputtering if the amount of Fe is smaller than 75%, where the fcc phase starts to coexist with bcc phase. Also, recent magnetic measurements⁴ have shown that the metastable fcc phase of Fe₅₂Cu₄₈ has a larger magnetic moment than the segregated fcc-Cu and bcc-Fe phase. However, the magnetic properties of these new metastable alloyed phases are far from being explained and represent a field in which an intensive work remains to be done.

In order to understand the magnetic behavior of these FeCu alloys we have performed all electron linearized augmented plane-wave (LAPW) calculations of band structures and density of states (DOS) for Fe_xCu_{100-x} ordered alloys in both bcc and fcc phases and for some specific Fe concentrations x . The calculations were carried out by using the Soler-Williams⁵ implementation of the APW method in its linearized version.⁶ The computations were performed within the framework of the local density approximation⁷ (LDA) and therefore they do not include the spin polarization, so that not exchange splittings are obtained. However, the LD densities of states at the Fermi level of the unpolarized systems can be approximately correlated to the exchange splittings and magnetic moments through the Stoner theory.^{8,9}

Due to the mandatory use of supercells in LAPW calculations, the representation of bcc and fcc Fe_xCu_{100-x} ordered alloys involves serious difficulties when intermediate fractions x are considered, since there are a huge number of nonequivalent atomic positions, turning a detailed description into a unaffordable task. Thus, we have restricted ourselves to the study of five concentrations ($x=0, 25, 50, 75, 100$) for which there are simple ordered representations involving few atoms. In this way, the study of bcc and fcc phases has been carried out with unit cells containing four atoms, reducing as much as possible the calculation resources. We use the same muffin-tin radius for both Fe and Cu species, taking $R_{mt}=2.30$ a.u., and a plane-wave energy cutoff of $T_{max}=10.0$ Ry has been considered in all the cases. The exchange-correlation functional was described within

the LDA by using the Hedin and Lundqvist¹⁰ parametrization. Here, we must point out that due to the absence of spin-polarization effects, there is no way of determining directly the magnetic properties (magnetic moment and exchange splitting) as in the local-spin-density¹¹ (LSD) approximation. Sampling grids ranging from 56 to 126 special points¹² in the irreducible wedge of the Brillouin zone are used for the study of bcc and fcc structures.

In order to test the validity of the parameters we have chosen for describing the FeCu alloys, we have started our investigations with pure bcc Fe, obtaining a cohesive energy of 5.8 eV per atom and a density of states at the Fermi level of DOS (E_F) = 3.4 states/eV per atom. Notice that we have used the experimental lattice constant, and no minimization of the total energy versus the unit cell volume was performed. Both quantities are in agreement with previous results of Moruzzi *et al.*¹³ After determining the DOS, we have included the polarization of the electrons using a scheme based on the Stoner model⁸ by shifting rigidly the two half bands (up and down) a relative magnetic exchange energy of 2.2 eV, previously computed¹³ within the LSD approximation. Once the rigid shift is applied, we have calculated the transferred charge from the down to the up bands, obtaining a magnetic moment of $2.25 \mu_B$ per atom which agrees well with the $2.15 \mu_B$ LSD result.¹³ Hence, this confirms that our calculated band structure describes the crucial features of the system. Now, we proceed to apply the same computational scheme to our set of periodic representants of these Fe_xCu_{100-x} alloys. All the calculations for the fcc phase compounds were done assuming that the lattice constant a is identical to that of fcc Cu ($a=6.82$ a.u.), whereas for bcc phase compounds we took the bcc Fe lattice constant ($a=5.42$ a.u.), being these values very similar to those found experimentally,² although the effect of small variations of the unit cell volume also will be discussed below.

In Fig. 1 we show the density of states (DOS) for the Fe_xCu_{100-x} alloys in bcc and fcc phases obtained from the present nonpolarized LAPW calculation. Looking at the bcc series, we can notice that when bcc Fe samples are doped with Cu, the d peak close to the Fermi level is diminishing and the bottom of the band suffers strong modifications due to the appearance of Cu deeper levels. The situation in the fcc case is rather more complicated. When the fcc Cu sample

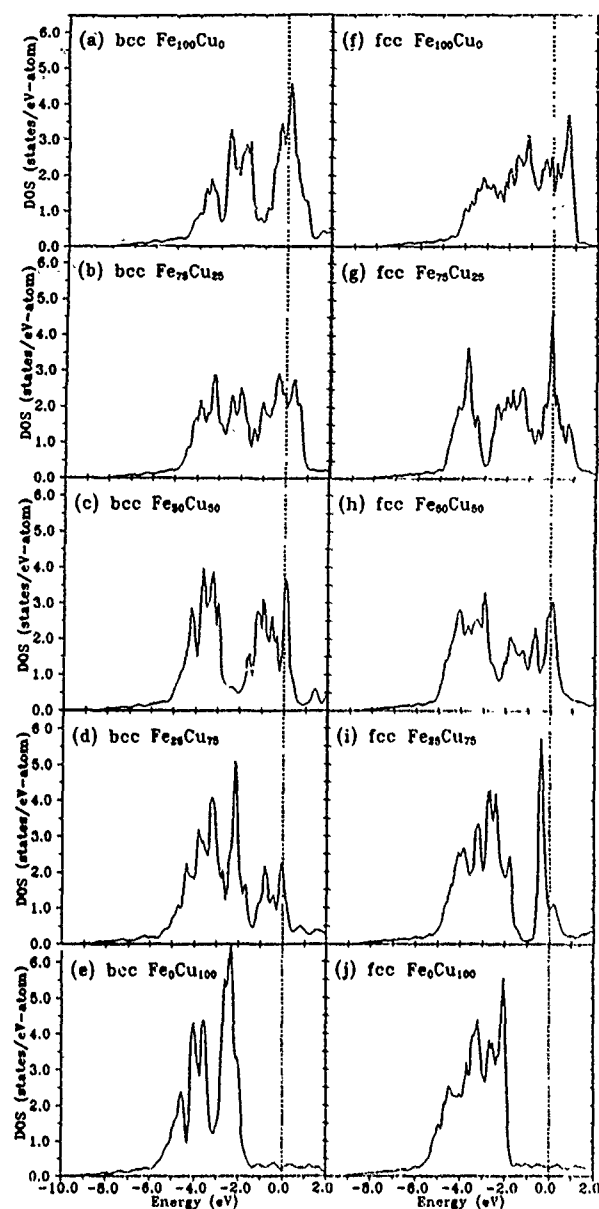


FIG. 1. Density of states (DOS) for bcc (a)-(e) and fcc (f)-(j) $\text{Fe}_x\text{Cu}_{100-x}$ alloys with Fe fractions $x=0, 25, 50, 75$, and 100.

is doped with Fe a strong peak corresponding to Fe states is developed near the Fermi level. The more surprising characteristic we can see is that for the compounds $\text{Fe}_{50}\text{Cu}_{50}$ and $\text{Fe}_{75}\text{Cu}_{25}$ the DOS at E_F presents a value higher than that found in fcc Fe. Furthermore, in the case of $\text{Fe}_{75}\text{Cu}_{25}$ the DOS at E_F is even larger than the value found for the pure bcc Fe. We have checked the influence of possible lattice constant contractions/expansions for the case $x=75$, since for such Fe content a change of 4% in the sample volume has been reported.² For the bcc $\text{Fe}_{75}\text{Cu}_{25}$ we have increased the volume per atom in a 4% noticing an increase of a 3% in the DOS at E_F . For the fcc $\text{Fe}_{75}\text{Cu}_{25}$ phase a similar change in the volume per atom lead to an increase of 1.6% in the DOS at the E_F . These results represent only a minor variation in the DOS and they do not imply any change in the magnetic behavior we will discuss below.

Figure 2 shows the density of states at the Fermi level

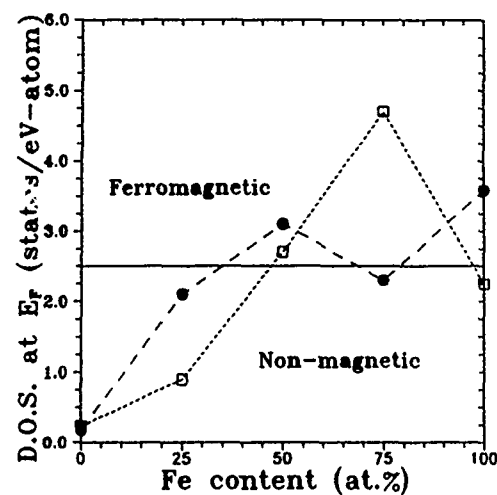


FIG. 2. DOS at the Fermi level E_F for bcc (black circles) and fcc (open squares) $\text{Fe}_x\text{Cu}_{100-x}$ metastable phases. Lines connecting points are guides for the eye. The horizontal line represents the DOS (E_F) frontier value between ferromagnetic and nonmagnetic behaviors corresponding to a molecular exchange constant of $\lambda=6000$.

for the fcc and bcc structures. Once this value is computed we have applied the Stoner model,⁸ using a molecular exchange constant $\lambda=6000$ (Ref. 14) in order to take into account the magnetic interactions in these systems containing iron. The Stoner criteria has been graphically displayed on Fig. 2 by defining a frontier line (associated to such molecular exchange constant) for the DOS (E_F) value, which permits to distinguish magnetic from nonmagnetic systems. Above this value the behavior is ferromagnetic whereas below the behavior is nonmagnetic. We notice that with this reasonable choice of λ the pure bcc Fe presents ferromagnetic properties whereas the pure fcc Fe structure corresponds to a paramagnetic system. A striking fact is that the DOS for bcc $\text{Fe}_{75}\text{Cu}_{25}$ is approximately equal to the DOS at E_F for fcc Fe, which is nonmagnetic, and therefore this could explain the diminishing of the magnetic moment in segregated phases with respect to fcc phases⁴ by assuming that a fraction of the Cu atoms enter into the bcc Fe structure, giving raise to a decrease of the magnetic moment. From these results, and after applying the Stoner criteria, we conclude that metastable alloys $\text{Fe}_{50}\text{Cu}_{50}$ and $\text{Fe}_{75}\text{Cu}_{25}$ present a well-defined ferromagnetic character despite the fcc Fe structure is not ferromagnetic.

In order to calculate the magnetic moment associated to each configuration we have assumed a magnetic exchange splitting of 2.2 eV for Fe and that such a value decreases to 1.5 eV in the limit of one isolated Fe atom in a Cu matrix,¹⁵ being these values obtained from previous LSD results. In this way we can estimate the magnetic moment for our magnetic ordered representants. For instance, the calculated magnetization for fcc $\text{Fe}_{50}\text{Cu}_{50}$ is 117 emu/g and only differs in a 7% with respect to the experimental measurement⁴ on the real alloy, which is a good result taking into account our previous hypothesis for λ or the exchange splitting. Therefore, once we have delimited the magnetic properties of these ordered configurations, we assume that the magnetization of

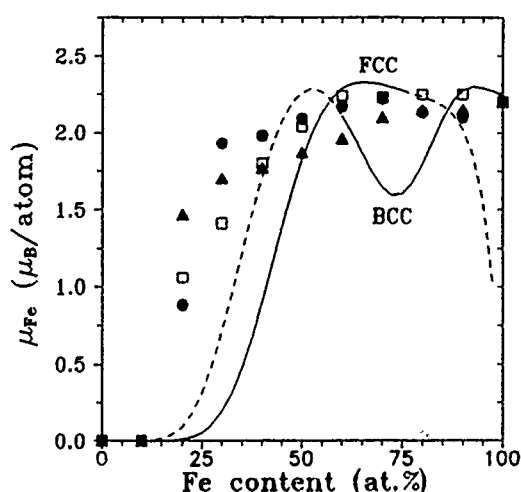


FIG. 3. Magnetic moment per Fe atom for bcc and fcc $\text{Fe}_x\text{Cu}_{100-x}$ metastable alloys. Dashed lines represent nonobserved experimentally phases. Experimental results are also shown (triangles from Ref. 2, black dots from Ref. 16, and squares from Ref. 17).

other fractional configurations (different from those here presented) can be calculated by a simple interpolation scheme. However, these calculated values do not take into account directly the alloy random character. We can incorporate the effect of randomness into the alloy composition by assuming that the lattice positions are to be occupied following a Poisson distribution which is dependent on the iron content of the alloy. This means that for a given average concentration x , it is possible to find small regions of different stoichiometric composition with a probability determined by the corresponding Poisson distribution, and, furthermore, the magnetization of these small regions can be evaluated by the interpolation scheme from the values obtained for the ordered samples. Figure 3 summarizes the results for the magnetic moment of the $\text{Fe}_x\text{Cu}_{100-x}$ alloys. Our main result is that the magnetic moment for Fe atom is almost independent of the Cu richness for a wide range of Cu content, in good agreement with experimental data^{2,16,17} up to 50% of Cu content.

In conclusion, we have shown that the fcc phase is magnetic for some configurations ($\text{Fe}_{75}\text{Cu}_{25}$ and $\text{Fe}_{50}\text{Cu}_{50}$) and why the magnetic moment per Fe atom is almost constant for a wide interval of Fe content in FeCu alloys.^{2,16,17} Although our results are based on a combination of LDA, Stoner criteria, the choice of a low number of ordered representants for the description of the alloy composition, and the mixing of the magnetic moments through a Poisson distribution, we believe that the basic ideas needed for the description of magnetism in these systems rely on the high density of states noticed for some specific cases. Furthermore, preliminary studies based on LSD calculations¹⁸ seem to confirm the present results.

This work has been partially supported by the DGICYT of Spain.

¹A. R. Yavari, P. J. Desré, and T. Benamer, *Phys. Rev. Lett.* **68**, 2235 (1992).

²C. I. Chien, S. H. Liou, D. Kofalt, W. Yu, T. Egami, and T. R. McGuire, *Phys. Rev. B* **33**, 3247 (1986).

³K. Sumiyama and Y. Nakamura, *J. Magn. Magn. Mater.* **35**, 219 (1983).

⁴A. Hernando, P. Crespo, J. M. Barandiarán, A. García Escorial, and R. Yavari, *J. Magn. Magn. Mater.* (in press).

⁵A. R. Williams and J. M. Soler, *Bull. Am. Phys. Soc.* **32**, 562 (1987); J. M. Soler and A. R. Williams, *Phys. Rev. B* **40**, 1560 (1989).

⁶O. K. Andersen, *Phys. Rev. B* **12**, 3060 (1975).

⁷P. Hohenberg and W. Kohn, *Phys. Rev. B* **136**, 864 (1964); W. Kohn and L. J. Sham, *Phys. Rev.* **140**, A1133 (1965).

⁸C. Herring, in *Magnetism*, edited by G. T. Rado and H. Suhl (Academic, New York, 1966), Vol. IV, p. 256.

⁹For an earlier application of the Stoner criteria to several alloys in the same LDA context, see, for instance, D. G. Pettifor, *J. Magn. Magn. Mater.* **15**, 847 (1980).

¹⁰L. Hedin and B. I. Lundqvist, *J. Phys. C* **4**, 2064 (1971).

¹¹U. von Barth and L. Hedin, *J. Phys. C* **5**, i629 (1972).

¹²H. J. Monkhorst and J. D. Pack, *Phys. Rev. B* **13**, 5188 (1976).

¹³V. L. Moruzzi, J. F. Janak, and A. R. Williams, *Calculated Electronic Properties of Metals* (Pergamon, New York, 1978).

¹⁴The molecular exchange constant has been determined by averaging among several values obtained from the literature.

¹⁵R. Podlocky, R. Zeller, and P. H. Dederichs, *Phys. Rev. B* **22**, 5777 (1980).

¹⁶K. Uenishi, K. F. Kobayasi, S. Nasu, H. Hatano, K. N. Ishihara, and P. H. Shingu, *Z. Metallkd.* **83**, 2 (1992).

¹⁷K. Sumiyama, T. Yoshitake, and Y. Nakamura, *Acta Metall.* **33**, 1791 (1985).

¹⁸P. A. Serena and N. García (unpublished).

On spin-canting in maghemite particles

S. Linderøth and P. V. Hendriksen

Materials Department, Risø National Laboratory, DK-4000 Roskilde, Denmark

F. Bødker, S. Wells, K. Davies, and S. W. Charles

Department of Chemistry, University of North Wales, Bangor, Gwynedd LL57 2UW, United Kingdom

S. Mørup

Department of Physics, Technical University of Denmark, DK-2800 Lyngby, Denmark

The degree of alignment of the magnetic moments of Fe^{3+} ions in ultrafine maghemite particles has been studied in samples with induced magnetic texture. The textured samples were prepared by freezing ferrofluids, containing 7.5 nm maghemite particles, in a magnetic field. Mössbauer spectroscopy studies of the textured samples in large magnetic fields demonstrate that the lack of full alignment is not an effect of large magnetic anisotropy, as suggested recently, but that the effect is rather due to canting of individual spins.

I. INTRODUCTION

The lack of full alignment of the spins in ultrafine maghemite particles in large applied fields was demonstrated by Coey¹ more than 20 years ago. He found, by using Mössbauer spectroscopy, that even a magnetic field of 5 T was insufficient to align all spins in 6 nm $\gamma\text{-Fe}_2\text{O}_3$ particles. The spin structure of the particles was suggested to be noncollinear due to competing antiferromagnetic exchange interactions, most likely at the surfaces of the particles.¹ The observations by Coey also explain why the saturation magnetization of small magnetic particle systems is smaller than that of the bulk material. The phenomenon of canting of spins in nominally ferrimagnetic particles has later been observed in other oxides²⁻⁴ as well as for thin oxide layers on metallic iron.⁵

The suggestion¹ that spin canting is a surface phenomenon has been supported by several later studies, e.g., by ^{57}Fe or ^{57}Co surface enrichment of maghemite particles.⁶⁻⁸ However, recent Mössbauer studies of maghemite particles, with and without surface enrichment with ^{57}Fe , have indicated⁹ that spin canting is not a surface effect, but rather a finite-size effect that is uniform throughout the whole volume of the particles. Also, lately, Pankhurst and Pollard¹⁰ have shown that the observation of nonzero $\Delta m = 0$ Mössbauer line intensities may be explained by the response of a randomly oriented ferrimagnetic powder to a large magnetic field when the individual particles are assumed to have a large uniaxial anisotropy, i.e., they suggest that the so-called spin canting effect is due to the lack of full alignment of all the spins in the particles. Hence, the lack of full alignment of spins is a matter of continuing dispute, despite the long history of the discussion and the great importance of maghemite particles in, for example, magnetic recording media and ferrofluids.

We have devised a simple experiment in order to clarify whether the incomplete spin alignment in ultrafine maghemite particles is an effect of specific spins being canted relative to the field direction or, as suggested by Pankhurst and Pollard,¹⁰ that it stems from the inability of the applied field to make the magnetization vector overcome the magnetic anisotropy of the particles. The idea of our

experiment is that if full alignment of the magnetic moments is hindered by the volume anisotropy of the particles, then the degree of alignment will depend on the angular distribution of the anisotropy directions with respect to the applied field. A non-random distribution of easy axes (magnetic texture) can be obtained by freezing a ferrofluid in an applied magnetic field. The degree of texture is a function of the magnetic moment of the particles, the intensity of the applied magnetic field, the magnetic anisotropy, and the freezing temperature of the ferrofluid.^{11,12} Here, we will show, results of studies of magnetically textured samples of 7.5 nm $\gamma\text{-Fe}_2\text{O}_3$ particles. Recently, we performed similar experiments on 9.0 nm maghemite particles.¹³ The advantage of studying 7.5 nm maghemite particles is, as will be shown, that the so-called spin canting effect is more prominent in the smaller particles.

II. EXPERIMENT

Magnetite particles were prepared by coprecipitation of Fe(II) and Fe(III) from an aqueous solution. Leaving the prepared ferrofluid in air resulted in oxidation of the magnetite (Fe_3O_4) into maghemite ($\gamma\text{-Fe}_2\text{O}_3$).

Magnetization measurements were carried out by using a vibrating-sample magnetometer. Mössbauer spectroscopy studies were performed by using a conventional constant acceleration spectrometer with a ^{57}Co source in rhodium. Magnetic fields between zero and 4.35 T could be applied parallel or perpendicular to the γ -ray direction. Transmission electron microscopy was performed using a Philips EM301 electron microscope.

Energy dispersive x-ray diffraction spectra were obtained by measuring the energy spectrum of scattered white x-ray radiation. From the line broadening of the diffraction peaks an estimate of the mean crystallite size could be deduced.

III. RESULTS AND DISCUSSION

Figure 1 shows the magnetization versus applied magnetic field at room temperature. The solid line is a fit, following the method of Chantrell *et al.*,¹⁴ to the magnetization curve, assuming a lognormal distribution of particle size.

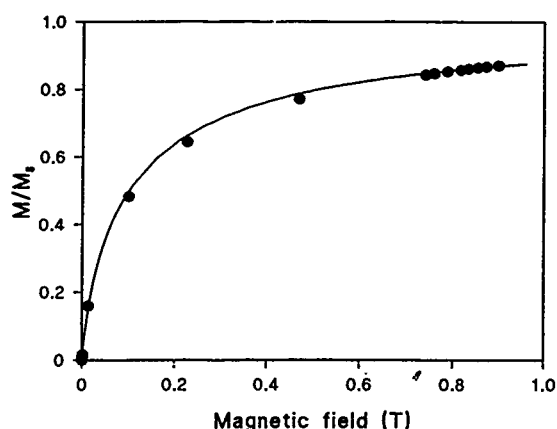


FIG. 1. The magnetization, at room temperature, as a function of applied magnetic field. The full curve is the best fit obtained using the method of Chantrell *et al.*¹⁴

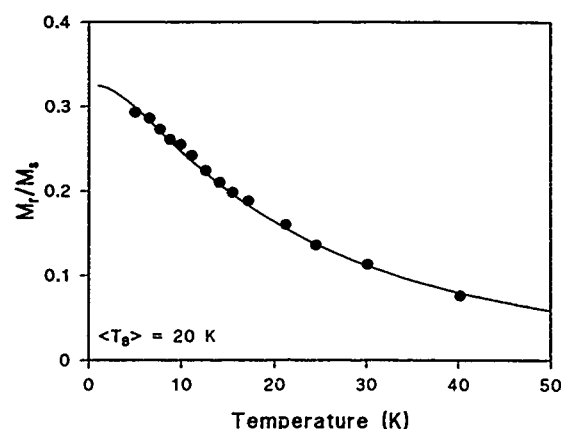


FIG. 2. The temperature dependence of the remanent magnetization. The circles are the experimental data and the solid lines are the best fits, using Eq. (1), for different chosen $\langle T_B \rangle$ values. The distribution of T_B has been assumed to be lognormal (see the text).

From electron micrographs, Mössbauer spectroscopy, x-ray diffraction, and magnetization measurements, the volume-weighted mean particle diameter was found estimated to be $\bar{D} = 7.5 \pm 1.0$ nm.

From the decay of remanence the mean superparamagnetic blocking temperature, $\langle T_B \rangle$, can be extracted by fitting with the following expression:

$$\frac{\bar{M}_r(T)}{\bar{M}_s} = \frac{\bar{M}_r(0)}{\bar{M}_s} \int_{T/(T_B)}^{\infty} f(T_r) dT_r, \quad (1)$$

where \bar{M}_r is the reduced remanence, $\bar{M}_r(0)$ is the reduced remanence at 0 K, $T_r = T_B / \langle T_B \rangle$ is the reduced blocking temperature, and $f(T_r)$ is the normalized distribution of blocking temperatures. Assuming the effective magnetic anisotropy constant, K_{eff} , to be size independent, $f(T_r)$ will follow a lognormal distribution. The best fit of Eq. (1) to the $\bar{M}_r(T)$ curve (see Fig. 2) was found for $\langle T_B \rangle \approx 20$ K. From

$$\tau_m = \tau_0 \exp(K_{\text{eff}} V / k_B T_B), \quad (2)$$

where $V = \pi/6 \bar{D}^3$, and τ_m and τ_0 are the measuring time (100 s) and the minimum relaxation time (10^{-10} – 10^{-12} s),^{15–17} respectively, K_{eff} is deduced to be $(3\text{--}4) \times 10^4$ J m⁻³.

Mössbauer spectra of the ferrofluid, frozen in a magnetic field of 4.35 T applied parallel or perpendicular to the sample plane, are shown in Fig. 3. The spectra were obtained at 5 K in a remanence field of 0.06 T perpendicular to the sample plane. The spectra are typical for ultrafine maghemite particles,¹⁸ the spectra are asymmetric with lines 1, 2, and 3 more intense than lines 4, 5, and 6, respectively, and with an inward broadening of each of the absorption lines. As evident from Fig. 3, the spectra have different absorption intensities in the line pair 2 and 5 (the spectra have been normalized to the same maximum absorption intensity in line 1). The relative intensity of the absorption lines 2 and 5 depends on the direction of the magnetic hyperfine field, acting at the absorbing Mössbauer nuclei, relative to the direction of the gamma rays. When the hyperfine field is parallel to the γ -ray direction, the intensity of lines 2 and 5 will be zero, while a spin orientation perpendicular to the γ -ray direction will re-

sult in the relative line intensities 3:4:1:1:4:3. The different intensities of lines 2 and 5 for the two sample preparation fields thus reveal different average orientations of the magnetic moments, i.e., it demonstrates the induced texture of the samples. The lower part of Fig. 3 shows the difference spectrum.

Increasing the magnitude of the magnetic field applied during the measurements results in a change of the relative areas of lines 2 and 5. Already for fields below 1 T, a saturation is found in the orientation of the magnetic moments in the direction of the applied field. Mössbauer spectra of 7.5 and 9.0 nm samples, when measured in a magnetic field of 4.35 T applied parallel with the γ -ray direction, are shown in Fig. 4. The line intensities of lines 2 and 5 were found to be independent of the direction of the induced texture. The intensities of lines 2 and 5 have decreased considerably, but

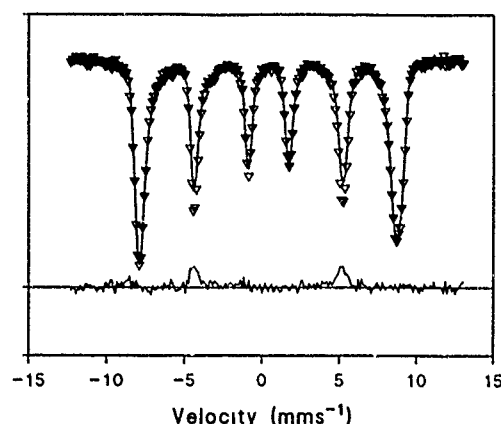


FIG. 3. Mössbauer spectra of samples with frozen-in magnetic texture. The freezing field was 4.35 T. The spectrum of the sample frozen in a field perpendicular to the sample plane is given by a solid line, while the triangles denote the sample frozen with the field applied parallel to the sample plane. The Mössbauer spectra were obtained at 5 K in a field of 0.06 T along the γ -ray direction. The spectra have been normalized to the same maximum absorption in line 1. The lower part of the figure shows the difference spectrum.

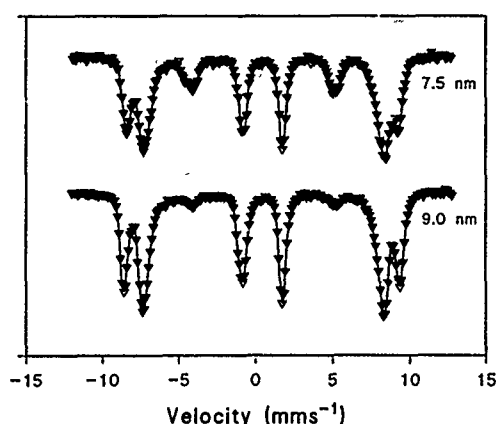


FIG. 4. Mössbauer spectra of 7.5 nm (the upper spectrum) and 9.0 nm maghemite¹³ particles in a magnetic field of 4.35 T parallel to the γ -ray direction. The spectra were obtained at 5 and 15 K, respectively.

they have not achieved the value of zero as they should if all spins were aligned by the field. This observation is similar to that made by Coey.¹ If the model of Pankhurst and Pollard (the PP model) was correct, one should expect that the degree of spin alignment in the 4.35 T field should differ for the 7.5 and the 9.0 nm samples. The fact that relatively low fields, applied during the measurements, are able to align the particle magnetic moment, but with some spins retaining an angle relative to the applied field, is consistent with the concept of spin canting.

Furthermore, the magnetic anisotropies of the studied maghemite particles are much smaller than would be necessary to account for the lack of full alignment by the model of Pankhurst and Pollard.¹⁰ We fit $K_{\text{eff}} = (3-4) \times 10^4 \text{ J m}^{-3}$, while in the PP model an effective magnetic anisotropy constant about an order of magnitude larger is needed to explain the observed incomplete alignment.

The degree of spin canting depends on the particle size. As shown in Fig. 4, the intensity of lines 2 and 5 is largest for the 7.5 nm particles. When assuming the area ratio of line pairs (2,5) and (1,6) in the Mössbauer spectra to be $\frac{2}{3}$ for canted spins and zero (in an applied field of 4–5 T) for noncanted spins, the fraction, p , of the spins being canted may be found. In Fig. 5, p is plotted for different samples as a function of the inverse particle diameter. It is clear that the degree of spin canting increases with decreasing particle size. This is expected, both when assuming the spin canting to be a surface effect and when assuming it to be a finite size effect uniform throughout the particle. If the spin canting is due to spin canting of a certain surface layer with thickness t , then the plot of p vs d^{-1} should, in a first-order approximation, follow a straight line. From the straight-line fit in Fig. 5, $t \approx 0.9 \text{ nm}$ is deduced. However, the data suggest that other parameters than the particle size influence the degree of spin canting in ultrafine maghemite particles.

When fitting the Mössbauer spectrum of the 7.5 nm particles in Fig. 4 with single lines, the deduced magnetic hyperfine field derived from the positions of lines 2 and 5 is

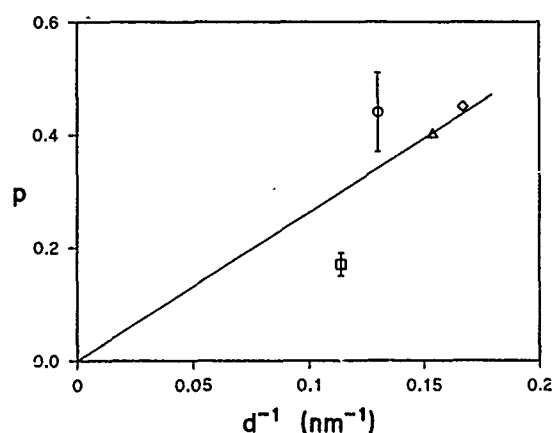


FIG. 5. The fraction of canted spins, p , versus the inverse of the particle diameter of maghemite particles (\diamond ,¹ Δ ,⁴ \square ,¹³ and \circ , present study) as found, by Mössbauer spectroscopy, at about 5 K and in an applied field of 4–5 T.

found to be about 1 T smaller than that deduced from lines 1 and 6. This observation cannot be accounted for by the PP model, because the incomplete alignment is ascribed to the incomplete alignment of all spins, whereas the observation can be understood in the model of spin canting, because the canting of the spins must originate from the surroundings of the spins being different from that of the average spin (on either the A site or the B site). A similar observation has been made for the 9.0 nm maghemite particles.¹³

ACKNOWLEDGMENTS

The work was supported by the Danish Council for Technical Research and the EEC Science Programme. The authors acknowledge Dr. M. El-Hilo and Dr. K. O'Grady for assistance with the magnetization measurements.

- ¹J. M. D. Coey, Phys. Rev. Lett. **27**, 1140 (1971).
- ²A. E. Berkowitz, J. A. Lahut, I. S. Jacobs, L. M. Levinson, and D. W. Forester, Phys. Rev. Lett. **340**, 594 (1975).
- ³K. Haneda, H. Kojima, A. H. Morrish, P. J. Picone, and K. Wakai, J. Appl. Phys. **53**, 2686 (1982).
- ⁴A. H. Morrish and K. Haneda, J. Magn. Magn. Mat. **35**, 105 (1983).
- ⁵K. Haneda and A. H. Morrish, Surf. Sci. **77**, 584 (1978).
- ⁶A. H. Morrish, K. Haneda, and P. J. Schurer, J. Phys. C **37**, 6 (1976).
- ⁷A. Ochi, K. Watanabe, M. Kiyama, T. Shinjo, Y. Bando, and T. Takada, J. Phys. Soc. Jpn. **50**, 2777 (1981).
- ⁸T. Okada, H. Sekizawa, F. Ambe, and T. Yamada, J. Magn. Magn. Mat. **31–34**, 105 (1983).
- ⁹F. T. Parker, M. W. Foster, D. T. Margulies, and A. E. Berkowitz, Phys. Rev. B **47**, 7885 (1993).
- ¹⁰Q. A. Pankhurst and R. J. Pollard, Phys. Rev. Lett. **67**, 248 (1991).
- ¹¹U. Hartmann and H. H. Mende, Philos. Mag. B **52**, 889 (1985).
- ¹²P. V. Hendriksen, F. Bødker, S. Linderroth, and S. Mørup, to be published.
- ¹³P. V. Hendriksen, S. Linderroth, C. A. Oxborrow, and S. Mørup, to be published.
- ¹⁴R. W. Chantrell, J. Popplewell, and S. W. Charles, IEEE Trans. Magn. **MAG-14**, 975 (1978).
- ¹⁵C. Johansson, M. Hanson, P. V. Hendriksen, and S. Mørup, J. Magn. Magn. Mat. **122**, 125 (1993).
- ¹⁶S. Linderroth, L. Balcells, A. Labarta, J. Tejada, P. V. Hendriksen, and S. A. Sethi, J. Magn. Magn. Mat. **1240**, 269 (1993).
- ¹⁷P. Prené, E. Tronc, J. P. Jolivet, J. Livage, R. Cherkaoui, M. Noguère, J. L. Dormann, and D. Fiorani, IEEE Trans. Mag. **29**, 2658 (1993).
- ¹⁸R. J. Pollard, Hyperfine Interface **41**, 509 (1988).

Metamagnetism and spin arrangement in $\text{Nd}_6\text{Fe}_{13}\text{Sn}$

M. Rosenberg and R. J. Zhou^{a)}

Experimentalphysik VI, Ruhr-Universität Bochum, Postfach 102148, 44721 Bochum, Germany

M. Velicescu and P. Schrey

Vacuumschmelze GmbH, Grüner Weg, 63450 Hanau, Germany

G. Filoti

Institute of Physics and Technology of Materials, PB-MG-07, 7000 Bucharest, Magurele, Romania

A magnetic and Mössbauer spectroscopy study of nonoriented and magnetically oriented samples of $\text{Nd}_6\text{Fe}_{13}\text{Sn}$ was performed. At 4.2 K a metamagnetic transition takes place in a field of 7.1 T. Strong evidence for antiferromagnetic spin arrangements in the iron magnetic sublattice and antiferromagnetism of the Nd moments with only a small contribution to the net magnetization in fields up to 14 T was found.

The preparation and some of the magnetic properties of the new ternary compounds $\text{RE}_6\text{Fe}_{13}\text{M}$ where $\text{RE}=\text{Pr, Nd, Sm}$ and $\text{M}=\text{Ge, In, Pb, Tl, Sn, Bi, Sb}$ were recently reported.^{1,2} They crystallize in the tetragonal $\text{Nd}_6\text{Fe}_{13}\text{Si}$ -type structure³ with five nonequivalent iron sites $4a$, $4d$, $16k$, $16l_1$, and $16l_2$ and two nonequivalent rare-earth sites $8f$ and $16l$. In the case of the Nd-containing compositions the magnetic critical temperatures lie between 330 and 550 K,¹ in dependence on the type of the element M. A ferrimagnetic type of ordering with the iron moments oriented antiparallel to the rare-earth moments was proposed in Ref. 1. A more detailed magnetic and Mössbauer study of $\text{Nd}_6\text{Fe}_{13}\text{Ge}$ and $\text{Pr}_6\text{Fe}_{13}\text{Ge}$ (Ref. 2) was interpreted in terms of slightly uncompensated antiferromagnetic ordering of the Fe spins which has to result in a magnetization of $1.6\mu_B/\text{f.u.}$ and an antiferromagnetic order of the rare-earth moments with no contribution to the net magnetization. In order to get a better insight in the peculiarities of the spin structure in the $\text{RE}_6\text{Fe}_{13}\text{M}$ compositional series we chose the compound $\text{Nd}_6\text{Fe}_{13}\text{Sn}$ and we combined magnetometric measurements in fields up to 14 T with a Mössbauer study on both nonoriented and magnetically oriented samples.

The $\text{Nd}_6\text{Fe}_{13}\text{Sn}$ samples were prepared by arc melting of the pure constituent elements. The crystal structure of $\text{Nd}_6\text{Fe}_{13}\text{Sn}$ was confirmed to be of the tetragonal $\text{Nd}_6\text{Fe}_{13}\text{Si}$ type³ with the space group $I4/mcm$.¹ The magnetic measurements were carried out using a vibrating sample magnetometer (VSM) in fields up to 14 T at temperatures between 4.2 K and room temperature (RT). The ^{57}Fe Mössbauer spectra were taken using a conventional Mössbauer spectrometer equipped with a ^{57}Co (Rh) source at temperatures between 4.2 K and RT. Some spectra were obtained in the presence of a magnetic field up to 8 T parallel to the direction of the gamma rays. For both the magnetic and Mössbauer measurements oriented samples were also used. The particles of $\text{Nd}_6\text{Fe}_{13}\text{Sn}$ were aligned at RT in a magnetic field of about 2.8 T. The field-oriented Mössbauer absorbers were prepared by embedding the powder in epoxy resin before applying a field perpendicular to the plane of the absorber.

The magnetization curves of an oriented $\text{Nd}_6\text{Fe}_{13}\text{Sn}$

sample measured in the first quadrant at 4.2 K and RT with a magnetic field oriented perpendicular or parallel to the direction of the orientation field are shown in Figs. 1 and 2. A sharp transition at about 7.1 T (B_{cr1}) was observed at 4.2 K for the measurement in a field perpendicular to the orientation field at a magnetization value of $14\mu_B/\text{f.u.}$ At $24.3\mu_B/\text{f.u.}$ a less sharp transition in a field of 11.3 T also takes place. For the measurement in the parallel field the magnetization increases stronger in the range 0–10 T but in a rather continuous manner, but again with a transition in the field of 11.3 T. The magnetization curve of an unaligned powder was very similar to the one of the oriented powder for the measurement in perpendicular field.

The drastic increase of the magnetization above B_{cr1} at 4.2 K reminds one of similar findings in the case of unaligned $\text{RE}_6\text{Fe}_{11}\text{Al}_3$ powder samples¹ considered as typical for metamagnetic transitions or a more general first-order magnetization process (FOMP). As can be seen from Fig. 2, the difference between the magnetization curve in perpendicular and parallel fields is strongly reduced at RT. The hysteretic character of the magnetization found at 4.2 K practically vanishes at RT. It is also worth mentioning that the value of the magnetization reached at 4.2 K in our maximum field of 14 T was $29.1\mu_B/\text{f.u.}$ The Mössbauer spectra taken at

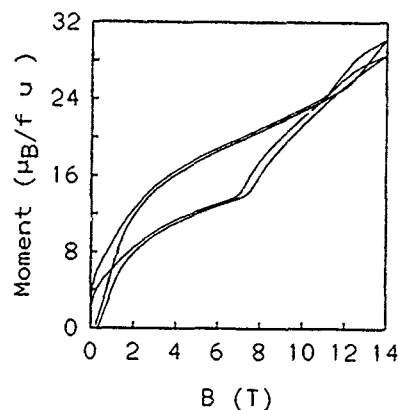


FIG. 1. Magnetization curves of a field-oriented $\text{Nd}_6\text{Fe}_{13}\text{Sn}$ sample at 4.2 K; measuring field applied parallel to (upper curve) and perpendicular (lower curve) to the orienting field.

^{a)}Present address: Department of Physics, Lanzhou University, Lanzhou, Gansu, People's Republic of China.

4.2 and 77 K and RT shown in Fig. 3 were basically fitted to four Lorentzian sextets with intensity ratio 1:4:4:4 corresponding to the population of the unequivalent four iron sites under the assumption that the Sn atoms occupy all the available $4a$ sites. The as-variable taken linewidths varied at 4.2 K between 0.32 and 0.35 mm s^{-1} . An extra sextet with a relative intensity lying between 6% and 9% and a hyperfine field of 29 T at 4.2 K was necessary in order to substantially improve the fit. A Mössbauer spectrum taken at 320 K eliminated the suspicion of the presence of some amount of $\text{Nd}_2\text{Fe}_{17}$ with $T_C=329 \text{ K}$ as a second phase. The origin of the fifth sextet still has to be determined.

The magnetic ordering temperature, the one at which the narrowing sextets collapsed giving rise to paramagnetic doublets, reached about 410 K in very good agreement with $T_N=420 \text{ K}$ obtained recently in a magnetic study of $\text{Nd}_6\text{Fe}_{13}\text{Sn}$.⁴ The values of the hyperfine (HF) field at 4.2 and 77 K and RT are given in Table I. The assignment of the HF values to the different Fe sites is based as proposed in Ref. 2 on the nearest-neighbor environment of the Fe atoms, i.e., the number of Fe and RE neighbors and distances to them. Our room-temperature HF values are similar to the ones found recently by Hu *et al.*² for $\text{Pr}_6\text{Fe}_{13}\text{Ge}$ and $\text{Nd}_6\text{Fe}_{13}\text{Ge}$. The average HF values of 31 and 30.6 T at 4.2 and 77 K, respectively, are very similar to the average hyperfine fields of 31.2 T at 4.2 K and 29.7 T at 77 K found for the intermetallic compound Y_2Fe_{17} .³ Taking $15 \text{ T}/\mu_B$ for the iron hyperfine field constant one obtains an average iron moment of $2.06\mu_B$ at 4.2 K and $1.64\mu_B$ at RT.

The 4.2 K Mössbauer spectrum of a sample prepared from a powder previously oriented in a magnetic field at RT offered strong evidence for the preferential orientation of the Fe moments close to or in the plane of the absorber. Such behavior was confirmed by taking RT Mössbauer spectra of the oriented absorber under the variable angles of 90° , 60° , 45° , and 35.3° with respect to the direction of gamma rays. From the ratios between the intensities of the third and second lines of the Mössbauer fitting sextets one derives an average angle of about 30° between the direction of the Fe spins and the plane of the absorber. Because one cannot expect a perfect orientation of the particles which already may contain several crystallites it seems reasonable to assume that

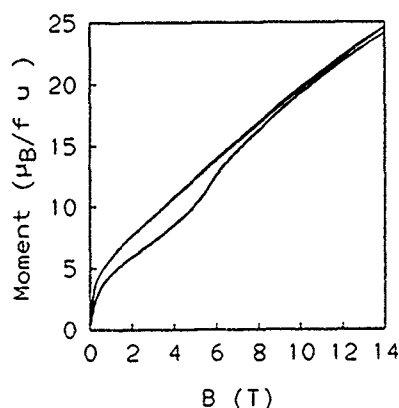


FIG. 2. The same as in Fig. 1 but at RT.

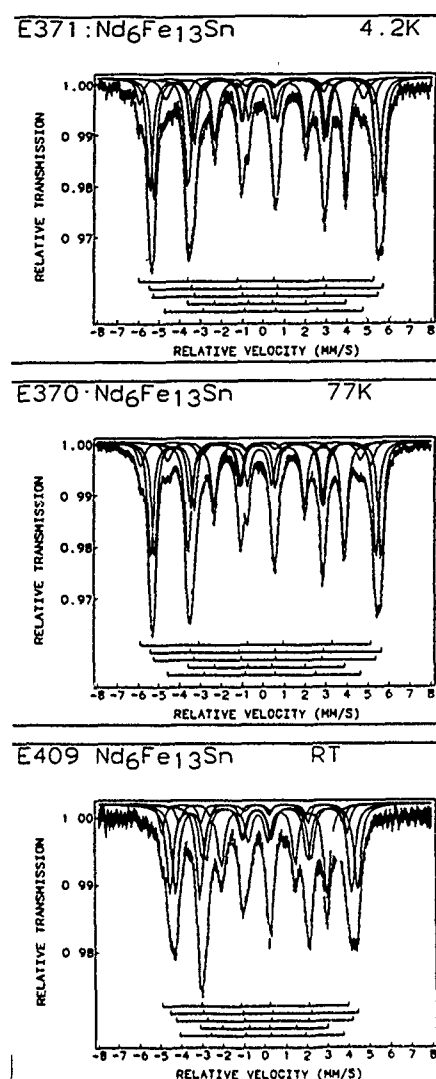


FIG. 3. Best fits to the Mössbauer spectra of $\text{Nd}_6\text{Fe}_{13}\text{Sn}$ taken at 4.2, 77, and 295 K.

Fe moments are probably oriented close to or in plane of the absorber. A parallel ferromagnetic orientation of the Fe moments has to provide at 4.2 K a contribution to the total moment of $26.8\mu_B/\text{f.u.}$ It is usual to take for the Nd moment in the rare-earth intermetallics with iron the free-ion value of $3.2\mu_B$, giving rise for the parallel alignment to a contribution of $19.2\mu_B/\text{f.u.}$ In the ferromagnetic alignment of both Fe and Nd moments one should therefore expect $46\mu_B/\text{f.u.}$ at 4.2 K, i.e., much more than the $29.1\mu_B/\text{f.u.}$ we got from the mag-

TABLE I. Hyperfine field values at 4.2, 77, and 295 K for the four crystallographically nonequivalent Fe sites in the crystal lattice of $\text{Nd}_6\text{Fe}_{13}\text{Sn}$.

Crystallographic site	Hyperfine field (T)		
	4.2 K	77 K	RT
4d	36.6	35	29.5
16k	34.7	34.4	27.8
16l ₁	33.3	33.1	26
16l ₂	23.5	23.4	19

netic measurement in 14 T at this temperature. The tendency of the Fe spins to lie in a plane perpendicular to the direction of the orientation field at room temperature and also after cooling the oriented Mössbauer absorber down to 4.2 K speaks for a type of antiferromagnetic, maybe noncolinear, spin arrangement of the Fe magnetic sublattices. In fact a ferromagnetic arrangement even with a small total magnetic moment would give rise to a Mössbauer absorber prepared under field orientation to another pattern of intensities with the tendency of the disappearance of the lines 2 and 5, which was obviously not the case. The Mössbauer spectra of an unoriented absorber taken in fields of 2, 4, and 8 T at RT also offer evidence for an antiferromagnetic spin arrangement as a ground state. In fields up to 4 T the lines of some Mössbauer subspectra shift as if the field direction would be opposite to the direction of the hyperfine field, whereas for other subspectra the shifts correspond to hyperfine fields parallel to the direction of the applied magnetic field. However, the Mössbauer spectrum taken in a field of 8 T all the line-shifts can be attributed to Fe moments oriented preferentially in the direction of the applied field, which has to be opposite to the intrinsic hyperfine field. It is worth mentioning that the field of 8 T is larger than the critical field B_{cr1} of 7.1 T in which (at 4.2 K) the more drastic increase of the magnetization already mentioned above starts (Fig. 1). For this reason we can tentatively assume that at B_{cr1} a kind of metamag-

netic transition involving the Fe magnetic sublattices of $\text{Nd}_6\text{Fe}_{13}\text{Sn}$ takes place. An interesting point is that the relative change of the average Fe hyperfine field between 4.2 K and RT coincides practically with the relative variation of the magnetization in the same temperature range. That could mean in agreement with Hu *et al.*² that at least up to our maximum field of 14 T the Nd contribution to the total magnetization is relatively small, and the Nd magnetic sublattice is basically antiferromagnetic with a strong negative coupling, the overall exchange coupling to the Fe magnetic sublattice being probably rather weak.

In conclusion it seems that the $\text{RE}_6\text{Fe}_{13}\text{M}$ intermetallics are characterized by not very strong antiferromagnetic interactions inside the Fe magnetic sublattice, whereas in the RE sublattice the antiferromagnetic exchange is much more stronger. Magnetic measurements in very high fields on both polycrystalline and single-crystal samples and magnetic scattering studies would be very useful indeed in order to better understand the complex spin structure of these compounds.

¹H. S. Li, B. P. Hu, J. M. Cadogan, J. M. D. Coey, and J. P. Gavigan, *J. Appl. Phys.* **67**, 4841 (1990).

²B. H. Hu, J. M. D. Coey, H. Klesnar, and P. Rogl, *J. Magn. Magn. Mater.* **117**, 225 (1992).

³J. Allemand, A. Letant, J. M. Moreau, J. P. Nozières, and P. Perrier de la Bâthie, *J. Less-Common Mater.* **166**, 73 (1990).

⁴P. Schrey and M. Velicescu, *J. Magn. Magn. Mater.* **101**, 417 (1991).

Temperature dependence of magnetic order in single-crystalline UPdSn

R. A. Robinson

LANSCE, Los Alamos National Laboratory, Los Alamos, New Mexico 87545

J. W. Lynn

Reactor Radiation Division, National Institute of Standards and Technology, Gaithersburg, Maryland 20899

A. C. Lawson

Materials Science and Technology Division, Los Alamos National Laboratory, Los Alamos, New Mexico 87545

H. Nakotte

Van der Waals-Zeeman Laboratory, University of Amsterdam, 1018 XE, Amsterdam, The Netherlands

The noncollinear hexagonal antiferromagnet UPdSn exhibits two magnetic phase transitions, at 35.5 and 23 K. The first transition is from a hexagonal paramagnetic state to a noncollinear antiferromagnetic state with a doubled unit cell (phase I). The second 23-K transition is to a monoclinic magnetic structure (phase II). Ever since these transitions were discovered, the question has been whether the moments simply rotate at 23 K, or whether the y and z components of the moment order at 35.5 K while the x component orders out of incipient fluctuations at the lower 23-K transition. While previous powder studies were rather inconclusive on this point, in this study new single-crystal neutron-diffraction results are presented that show the second picture to be correct. In addition, the structural distortions that accompany the change in symmetry are discussed and show that there is phase-II type magnetic short-range order between 23 and 35.5 K.

The ternary intermetallic compound UPdSn is one member of the set of 1:1:1 UTX (where T=transition metal, X= p -electron metal) compounds that has been studied for some time now¹⁻³ with a view to understanding the role of f - d hybridization in uranium magnetism, and in particular the huge magnetocrystalline anisotropies that are observed. A picture is emerging in which the f electrons hybridize in directions or planes containing nearest-neighbor U-U links, with the ordered magnetic moments perpendicular to these directions or planes. However, UPdSn does not fit the general pattern and exhibits more localized behavior, as manifested in its low electronic specific heat ($\gamma_{el}=5$ J mol⁻¹ K⁻²)⁴ and its relatively large ordered moment (2.05 μ_B at low temperature).⁵ The Pd and Sn atoms are ordered chemically in the GaGeLi structure and the uranium ions exhibit a complicated noncollinear magnetic structure with a Néel temperature of 37 K.⁵ The original powder-diffraction work⁵ on the magnetic structure assumed two magnetic phase transitions, the lower being at 25 K, with a monoclinic noncollinear magnetic structure (phase II, see Fig. 1) below 25 K, an orthorhombic noncollinear magnetic structure (phase I, in which $\theta=0$ and $\gamma=90^\circ$) between 25 and 37 K and a paramagnetic hexagonal phase above 37 K. Magnetically driven structural distortions with these symmetries have recently been observed and characterized,⁶ confirming the original magnetic structure determination. However, there have always been two different ways of regarding the 25-K transition; in a moment-rotation picture, well-defined local moments would start to rotate away from the b - c plane at 25 K, but there would be no anomalies in the temperature variation of the total uranium moment. Alternatively, the y and z components of the moment could order at 37 K, while the x component ordered at the lower temperature of 25 K. In between, μ_x would only be short-range ordered or fluctuating. In this case, there would be a discontinuity in the varia-

tion of the total moment with temperature, so the two pictures should be distinguishable by experiment. In fact a careful temperature-dependent study has already been done on a powder sample,⁷ but the results were rather inconclusive. If viewed in spherical-polar coordinates, the order parameters all seem to vary smoothly with no evidence of the 25-K transition. On the other hand, if viewed in Cartesian coordinates, it seems that μ_y orders at 37 K or so while μ_x orders at 25 K, thereby favoring the idea that μ_x condenses at the lower temperature.

Since that study single crystals have been grown and, in the course of a study of the magnetic phase diagram⁸ of UPdSn, it was shown that the 010 reflection, whose intensity is proportional to μ_x^2 , does vary much more sharply with

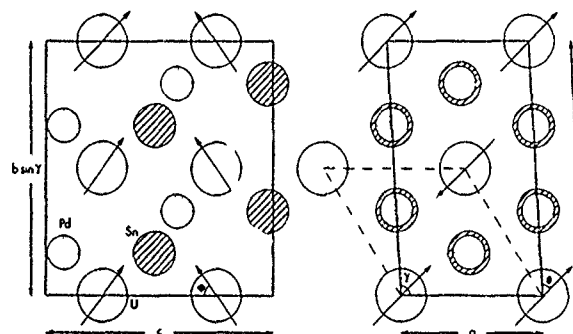


FIG. 1. The crystallographic and magnetic structures at low temperature of UPdSn, with magnetic space group P_2112_1 . The figure on the right shows the monoclinic basal plane. The primitive crystallographic unit cell (which corresponds to the parent hexagonal cell) is shown by the dashed lines, while the magnetic unit cell is shown by the solid lines. The figure on the left shows the projection onto a plane perpendicular to the a axis. Neither the atom sizes nor the lattice constants are drawn to scale and the deviation from 90° of the monoclinic angle γ has been grossly exaggerated. However, the atom coordinates within the cell are drawn to scale.

temperature than in the powder. In this article, we report new temperature-dependent single-crystal data taken on the 010, 011, 012, 100, and 120 reflections. These give definitive evidence that μ_x does indeed condense at the lower temperature of 23 K and that it is short-range ordered or fluctuating between 23 and 35.5 K.

The crystal of UPdSn is the same 1 mm-diam 5-mm-long sample used in previous studies of the magnetic phase diagram⁸ and magnetic form factor.⁹ It was grown by the tri-arc Czochralski method and for the present experiments was glued into a 1-cm-diam cylindrical aluminum block. The cylinder axis of the crystal was approximately 18° away from the $[110]_{\text{hexagonal}} (= [100]_{\text{orthorhombic}})$ axis which was aligned along the axis of the aluminum block. This was installed in a closed-cycle helium refrigerator, which was mounted on the BT-4 triple-axis spectrometer at the NIST Research Reactor. A pyrolytic graphite monochromator and filter were used with an incident neutron wavelength $\lambda = 2.35$ Å and the analyzer was removed. For most of the data presented here, the collimation was 40'/40'/40', but both coarser (40'/40'/open) and tighter (60'/20'/20' and 20'/20'/10') collimations were used in the specific instances noted in some of the figures. Two different crystal orientations were used; (a) with the $[100]_{\text{orthorhombic}}$ axis vertical, giving access to the 010, 011, and 012 reflections of one particular domain pair, and (b) the $[001]$ axis giving access to the 010, 120, and 100 reflections of the same domain pair. As the cylinder axis of the sample is close to vertical in the first geometry, corrections for self-absorption are a minimum in this case and will be similar for the 010, 011, and 012 reflections. In contrast, with the $[001]$ axis vertical such corrections will be much larger and more variable from reflection-to-reflection. We have, therefore, only used the 010, 011, and 011 reflections to determine the model parameters μ , θ , and ϕ in the magnetic structure of UPdSn.

The temperature variations of the peak intensities of all reflections measured are shown in Fig. 2. The peak widths were also measured at a limited sample of these temperatures for each reflection and, except for the case of the 100 reflection, were found to be temperature independent. There is evidence in these scans of two transitions and we extract transition temperatures of 23 and 35.5 K. These values are in reasonable agreement with previous results.

In the case of the 100 reflection, full peak scans were also made in order to measure the integrated intensities and the results are shown in Fig. 3. These results are very different from the peak intensities in Fig. 2(e) and the reason is that the peak width increases dramatically below 23 K. The inset to Fig. 3 shows peak widths of rocking curves measured with very high angular resolution. This broadening is due to the structural transformation, i.e., orthorhombic to monoclinic, that accompanies the magnetic transition from phase I to phase II.⁶ The monoclinic angle γ has previously been determined to be 90.35°, by means of high-resolution neutron powder diffraction.⁶ No splitting between the two monoclinic domains was observed, but the angular distribution is broad and flat-topped with a width of approximately 0.8° full width at half-maximum (FWHM). This is qualitatively consistent with having both monoclinic domains and

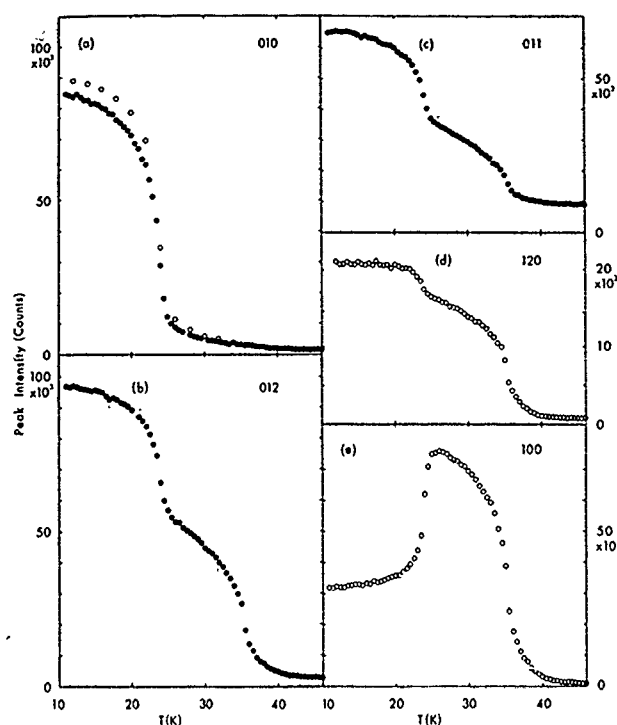


FIG. 2. The variation in peak intensity with temperature for the following magnetic Bragg reflections: (a) 010, (b) 012, (c) 011, (d) 120, and (e) 100. All data are for the magnetic domain (or pair of domains in the low-temperature monoclinic phase) and 40'/40'/40' collimation was used in all cases. The solid circles represent data taken with the $[100]_{\text{orthorhombic}}$ axis vertical, while the open circles represent data taken with the $[001]$ axis vertical. The data were counted for 5 min per point except for the solid circles in (a) which were counted for 3 min per point. These single crystal data are directly comparable with the powder results in Fig. 4 of Ref. 7.

the consequent angular spread of 0.7° between them, but with a large population of domains in each orientation and a continuous distribution of orientations to accommodate the strains that are induced by the transformation.

We therefore believe that, apart from the 100 reflection, the peak intensities are proportional to the integrated intensity that one would measure in a rocking-curve measurement. The intensity of the 010 reflection shown in Fig. 2(a) is much as reported previously, for this single crystal.⁸ There is also clear evidence of two transitions in Figs. 1(b)–(d). Indeed it is almost inconceivable that simple moment rotation could give rise to the step rise at approximately 23 K. In order to demonstrate this point definitively, the intensities of the 010, 011, and 012 reflections were fitted to the model of the magnetic structure shown in Fig. 1. The high-temperature background, derived from data points with temperatures greater than 42 K, was subtracted from the data and the intensities were corrected for the difference in counting time, the $1/\sin \theta$ Lorentz factor as is appropriate for integrated intensities of rocking curves¹⁰ and the U^{3+} magnetic form factor.⁹ The model parameters μ , θ , and ϕ were then treated as adjustable variables and the results are shown as the solid circles in Fig. 4. The rise in total moment at 23 K is clear evidence that the moments are not simply rotating. An extra component seems to be condensing at this temperature. The open circles in Fig. 4 represent simply the component of the

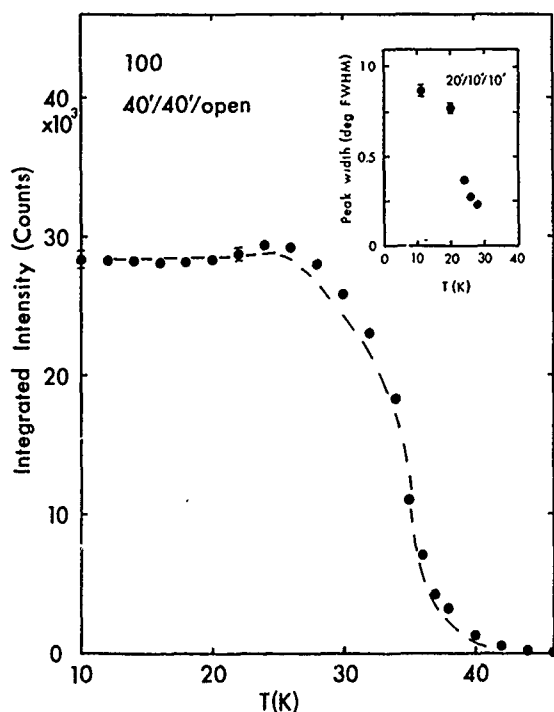


FIG. 3. The variation in integrated intensity for rocking curves through the 100 magnetic reflection, as a function of temperature. The solid circles are the raw data and the dashed line is calculated from the model parameters displayed in Fig. 4, which were in turn derived from the peak intensities of the 010, 011, and 012 reflections as displayed in Fig. 2. The inset shows the variation in peak width with temperature for the same 100 reflection measured with 20'/10'/10' collimation.

moment in the b - c plane and this is fairly well behaved at 23 K. The small glitch there may be evidence of coupling between moments in the b - c plane and those perpendicular (μ_x) to it, but the basic picture for this material is that the in-plane moments condense at 35.5 K with μ_x condensing at the lower transition. Now, the integrated intensity of the 100 reflection is simply proportional to μ_y^2 and we can, therefore, calculate the intensity of the 100 reflection at all temperatures from the values of μ_y . Suitably scaled to the lowest-temperature-measured integrated intensity, these results are shown as the dashed line in Fig. 3. The agreement between these results, which were derived from the peak intensities of the 010, 011, and 012 reflections are in very good agreement with our direct measurements of integrated intensities for the 100 reflection.

In summary, the main result of this article is shown in the lowest panel of Fig. 4, which shows definitively that the 23-K transition in UPdSn is best thought of as due to condensation of a long-range ordered μ_x out of short-range magnetic order in this coordinate between 23 and 35.5 K. In UPdSn, we are not dealing with simple rotation of local moments. In addition, we have observed a large orientational broadening in the single crystal, which is consistent with the monoclinic structural distortion previously observed by powder diffraction.

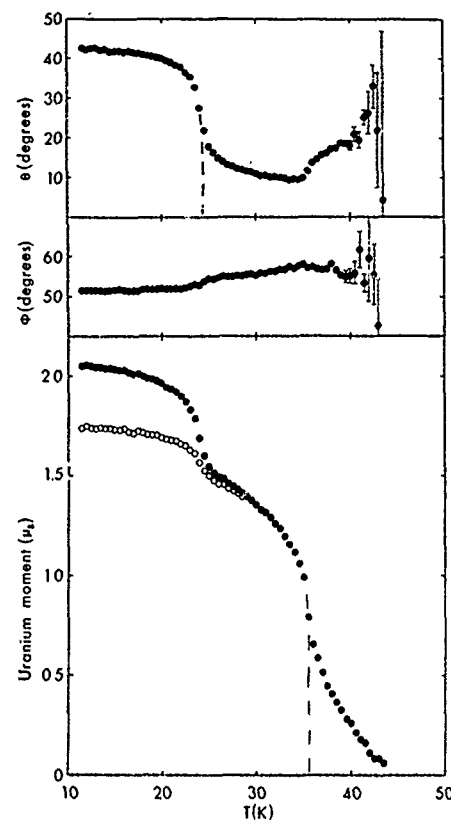


FIG. 4. The variation of model parameters μ , θ , and ϕ , with temperature as extracted from the 010, 011, and 012 peak intensities from Fig. 2. These single-crystal data are directly comparable with the powder results in Fig. 3 of Ref. 7. The dashed lines are guides to the eye and have no theoretical significance.

We are grateful to M. F. Collins, who originally suggested to us that the 25-K transition might be better thought of as due to the x -component ordering at a lower temperature than the components in the b - c plane. This work was supported in part by the division of Basic Energy Sciences of the U.S. Department of Energy.

- ¹T. T. M. Palstra, G. J. Nieuwenhuys, R. F. M. Vlastuin, J. van den Berg, J. A. Mydosh, and K. H. J. Buschow, *J. Magn. Magn. Mater.* **67**, 331 (1987).
- ²V. Sechovsky, L. Havela, H. Nakotte, F. R. de Boer, and E. Brück, *J. Alloys Compounds* (to be published).
- ³R. A. Robinson, A. C. Lawson, V. Sechovsky, L. Havela, Y. Kergadallan, and H. Nakotte, *J. Alloys Compounds* (to be published).
- ⁴F. R. de Boer, E. Brück, H. Nakotte, A. V. Andreev, V. Sechovsky, L. Havela, P. Nozar, C. J. M. Denissen, K. H. J. Buschow, B. Vaziri, P. Meissner, H. Maletta, and P. Rogl, *Physica B* **176**, 275 (1991).
- ⁵R. A. Robinson, A. C. Lawson, K. H. J. Buschow, F. R. de Boer, V. Sechovsky, and R. B. Von Dreele, *J. Magn. Magn. Mater.* **98**, 147 (1991).
- ⁶R. A. Robinson, A. C. Lawson, J. A. Goldstone, and K. H. J. Buschow, *J. Magn. Magn. Mater.* **128**, 143 (1993).
- ⁷R. A. Robinson, A. C. Lawson, J. W. Lynn, and K. H. J. Buschow, *Phys. Rev. B* **45**, 2939 (1992).
- ⁸H. Nakotte, R. A. Robinson, J. W. Lynn, E. Brück, and F. R. de Boer, *Phys. Rev. B* **47**, 831 (1993).
- ⁹S. W. Johnson, R. A. Robinson, H. Nakotte, E. Brück, F. R. de Boer, and A. C. Larson, *J. Appl. Phys.* **73**, 6072 (1993).
- ¹⁰G. L. Squires, *Introduction to the Theory of Thermal Neutron Scattering* (Cambridge University Press, Cambridge, 1978), pp. 41-42.

Magnetic properties of Dy-Lu alloys

B. A. Everitt, M. B. Salamon, C. P. Flynn, and B. J. Park
University of Illinois at Urbana-Ch., Urbana, Illinois 61801

J. A. Borchers and R. W. Erwin
National Institute of Standards and Technology, Gaithersburg, Maryland 20899

F. Tsui
University of Michigan, Ann Arbor, Michigan 48109

Although many binary heavy rare-earth alloy systems have been studied extensively, there has been little work reported on the Dy-Lu system. The properties of single-crystal $\text{Dy}_x\text{Lu}_{1-x}$ films grown by molecular beam epitaxy are reported. SQUID magnetometer and neutron diffraction measurements on samples with $x=0.4, 0.5$, and 0.6 show that the samples order helimagnetically with Néel temperatures of $T_N=90, 105$, and 120 K, respectively. The helical turn angle was mapped as a function of temperature for each of the three alloys. Magnetic x-ray scattering, the first in an alloy, was observed at the $(002)^\pm$ positions at 15 and 60 K in the $x=0.4$ sample using resonant exchange scattering of synchrotron radiation at the Dy L_{III} edge.

Due to the similarity of their chemical properties, the heavy rare earths and yttrium are almost completely mutually soluble. In binary alloys, the concentration may be varied continuously to change such properties as the ordering temperature and lattice spacings.¹ Ordering temperatures and wave vectors for the heavy rare-earth binary alloys with each other and with Y have been shown to follow universal curves.² While many rare-earth alloys have been studied in the past, little work has been reported on the Dy-Lu alloy system. This system is of interest as part of our ongoing work on Dy/Lu superlattice structures.³

We have studied three c -axis samples grown by molecular beam epitaxy (MBE) at the University of Illinois Epicenter. The $\text{Dy}_{0.4}\text{Lu}_{0.6}$, $\text{Dy}_{0.5}\text{Lu}_{0.5}$, and $\text{Dy}_{0.6}\text{Lu}_{0.4}$ alloy films are $2300, 2400$, and $20\,540$ Å thick, respectively. The films were grown on Y and Nb buffer layers upon a sapphire substrate and with Lu cap layers. Sample quality was verified by x-ray diffraction. The 2300 - and 2400 -Å films have in-plane mosaics of 0.3° and 0.4° , respectively. The thick ($2.05\text{-}\mu\text{m}$) film has an in-plane mosaic of 0.1° . The c -axis coherence lengths of the films were 760 Å for the $\text{Dy}_{0.4}\text{Lu}_{0.6}$ film, 600 Å for the $\text{Dy}_{0.5}\text{Lu}_{0.5}$ film, and 1330 Å for the thickest film ($\text{Dy}_{0.6}\text{Lu}_{0.4}$).

In bulk Dy, the moments initially order at $T_N=179$ K in a c -axis helimagnetic structure; the moments are confined to the basal plane, and their direction rotates through a turn angle $\omega(T)$ in going from layer to layer along the c axis. The initial turn angle ω_i is 43° just below T_N , decreasing to 26.5° at $T_C=89$ K. Below T_C , bulk Dy is ferromagnetic. Bulk Lu is weakly paramagnetic. We will contrast the properties of Dy-Lu alloys with bulk Dy.

The magnetic moment was measured as a function of temperature using a SQUID magnetometer in zero-field cooled (ZFC) and field-cooled (FC) configurations. Cusps in the field-cooled susceptibility indicate that the Néel temperatures occur at $90, 105$, and 120 K for the $\text{Dy}_{0.4}\text{Lu}_{0.6}$, $\text{Dy}_{0.5}\text{Lu}_{0.5}$, and $\text{Dy}_{0.6}\text{Lu}_{0.4}$ films, respectively (see Fig. 1). The Néel temperatures of the alloys follow the $2/3$ power of the effective spin parameter (de Gennes factor)

$$x = c(\lambda - 1)^2 J(J + 1), \quad (1)$$

where c is the concentration of the rare earth with angular momentum J , and λ is the Landé factor. Néel temperatures of many other rare earth-rare earth, rare earth-yttrium, and rare earth-lutetium binary alloys have been shown to follow this universal curve⁴ (see inset, Fig. 2). Consistent with previous results,⁵ which show a sharp suppression of T_C in heavy rare earths diluted with Y and Lu, no ferromagnetic transition was observed at temperatures above 10 K in any of the three Dy-Lu alloy samples.

The Néel temperatures were confirmed by neutron diffraction, and the films were shown to order helimagnetically (see Fig. 2). The magnetic coherence length along the c axes of the films is approximately the same as the structural c -axis coherence length at low temperatures. The intensity and position of the magnetic satellites were determined as a function of temperature for the three films. The separation Q of

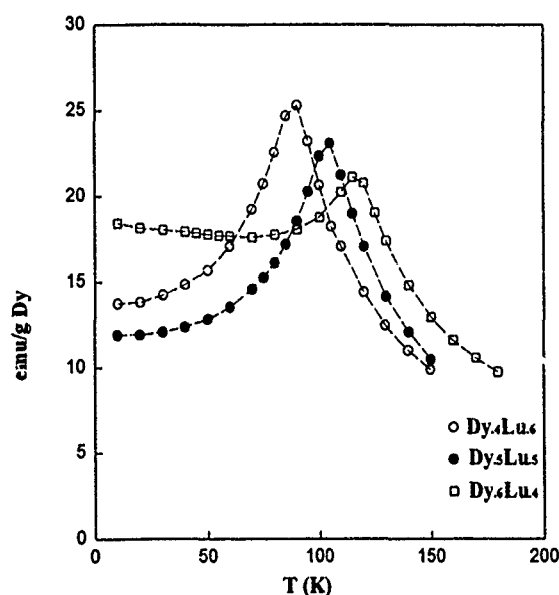


FIG. 1. Field-cooled SQUID magnetization data in a 5-kOe field. Cusps in the susceptibility indicate Néel temperatures of $90, 105$, and 120 K for the $\text{Dy}_{0.4}\text{Lu}_{0.6}$, $\text{Dy}_{0.5}\text{Lu}_{0.5}$, and $\text{Dy}_{0.6}\text{Lu}_{0.4}$ alloys, respectively.

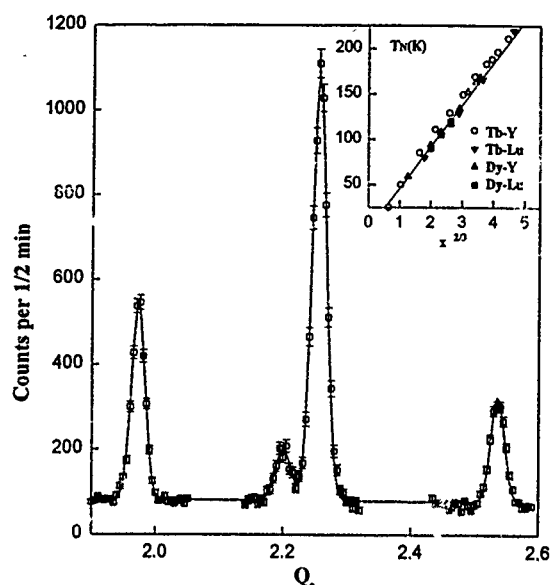


FIG. 2. Neutron scan along the c^* hcp axis of sample $\text{Dy}_{0.5}\text{Lu}_{0.5}$ at 30 K. The structural (002) Bragg peak at $Q_z = 2.26 \text{ \AA}^{-1}$ has magnetic satellites at 1.97 and 2.54 \AA^{-1} , indicating helimagnetic order. The structural peak at 2.20 \AA^{-1} is from the (002) Y buffer layer. *Inset*. Néel temperature as a function of the $2/3$ -power of the de Gennes factor for selected alloys. Tb-Y, Tb-Lu, and Dy-Y data are from Ref. 5. The data are seen to follow the curve given by $T_N = 46x^{2/3}$.

the magnetic satellites from the central (002) Bragg peak determines the turn angle per atomic layer. The turn angles $\omega = Qc/2$, where c is the lattice constant, for the $\text{Dy}_{0.4}\text{Lu}_{0.6}$ and $\text{Dy}_{0.5}\text{Lu}_{0.5}$ films varied with temperature from 47° at T_N to 45° at low temperature (see Fig. 3). The turn angle for the thicker film varied over a wider range; from 47.5° at the Néel temperature to 43.5° at low temperature. Previous work has shown similar results; Child⁵ *et al.* have found that the turn

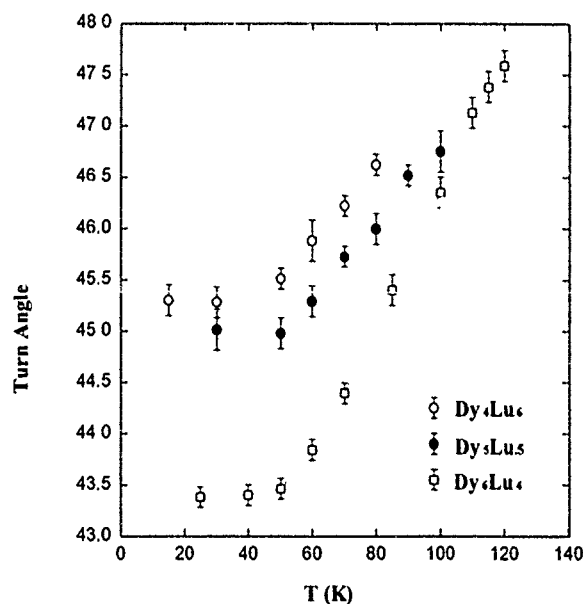


FIG. 3. Helimagnetic c -axis turn angle per atomic layer for each of the three alloys as a function of temperature. Lines through data points serve to guide the eye.

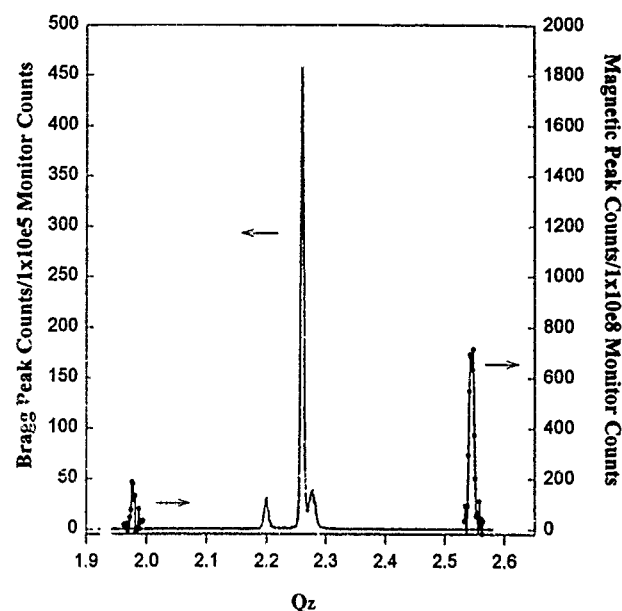


FIG. 4. Synchrotron x-ray diffraction data showing the Dy (002) Bragg peak ($Q_z = 2.26 \text{ \AA}^{-1}$) and x-ray resonant enhanced magnetic satellites ($Q_z = 1.974$ and 2.541 \AA^{-1}) of sample $\text{Dy}_{0.4}\text{Lu}_{0.6}$ at 15 K. The structural peaks at 2.20 and 2.27 \AA^{-1} are due to the Y buffer layer and Lu cap layer, respectively. Note the different scales for the nuclear and magnetic scattering.

angle initially decreased linearly with temperature from T_N in heavy rare earth-yttrium alloys, then remained constant at low temperatures. As the concentration of Y was increased, $\omega(T)$ varied over a smaller range, and at high Y concentrations approached 50° per layer at all temperatures below T_N . The Tb-Lu⁵ and Dy-Lu systems have qualitatively similar behavior to the rare earth-yttrium systems, although the limiting turn angle appears closer to 48° .

Synchrotron x-ray magnetic scattering, the first in an alloy, was observed from the $(002)^\pm$ magnetic satellites using resonant exchange scattering enhancement (XRES) at the Dy L_{III} edge.⁶ The $\text{Dy}_{0.4}\text{Lu}_{0.6}$ alloy was studied at the National Synchrotron Light Source at Brookhaven National Laboratory. The first-order harmonic was used to study the helimagnetic structure of the alloy at low temperature. A polarimeter was used to separate magnetic from charge scattering by exploiting the fact that the polarization of magnetically scattered radiation is rotated 90° relative to the incident polarization. Here, we label the major polarization component of the incident radiation (97%) σ and the orthogonal polarization π . Radiation scattered from the sample is diffracted a second time from the polarimeter analyzer crystal at a Bragg angle (θ) of 44.8° in order to select out a single polarization component.

The Dy $(002)^\pm$ magnetic satellites of the (002) Bragg peak were seen when scattering from the incident σ polarization into the detector π configuration. At 15 K, magnetic satellites are located at $Q(002)^+ = 2.541 \text{ \AA}^{-1}$ and $Q(002)^- = 1.974 \text{ \AA}^{-1}$ (Fig. 4), corresponding to a turn angle of 45.2° per atomic layer. At 60 K, the integrated intensity of the magnetic peaks has decreased by a factor of 0.7 from the 15 K data, and the turn angle is 45.7° per atomic layer. These results are consistent with the earlier neutron diffraction data

taken at NIST. At 120 K no magnetic satellites were visible. The satellites were not observed in the analyzer σ - σ scattering configuration at any temperature.

We have studied the magnetic ordering of $\text{Dy}_x\text{Lu}_{1-x}$ alloys using a variety of techniques. The Néel temperatures of the three alloys ($x=0.4, 0.5$, and 0.6) and suppression of the Dy ferromagnetic transition are consistent with the behavior of other rare-earth alloy systems. A helimagnetic structure was confirmed by neutron diffraction, and the turn angle $\omega(T)$ was shown to have a qualitatively similar temperature dependence to Tb-Y, Tb-Lu, and Dy-Y alloys.⁵ Magnetic x-ray scattering was observed at the $(002)^\pm$ positions at 15 and 60 K in the $x=0.4$ sample using resonant exchange scattering of synchrotron radiation at the Dy L_{III} edge.

This work was supported in part by the National Science Foundation Grant No. NSF DMR-91-21888. The authors gratefully acknowledge the advice and assistance of Dr. Mitch Nelson and Dr. Paul Zschack at the NSLS X14 beam-

line, and the helpful assistance of Kevin Pettit. This research was performed in part at the Oak Ridge National Laboratory PRT beamline X14 at the NSLS, BNL, and is sponsored by the U.S. DOE under Contract No. DE-AC05-84OR21400 with Martin Marietta Energy Systems, Inc.

¹J. Jensen and A. R. Mackintosh, *Rare Earth Magnetism: Structures and Excitations* (Oxford University Press, New York, 1991), p. 247.

²W. C. Koehler, *Magnetic Properties of Rare Earth Metals*, edited by R. J. Elliott (Plenum, New York, 1972), p. 94.

³R. S. Beach, J. A. Borchers, A. Matheny, R. W. Erwin, M. B. Salamon, B. Everitt, K. Pettit, J. J. Rhyne, and C. P. Flynn, *Phys. Rev. Lett.* **70**, 3502 (1993).

⁴B. Coqblin, *The Electronic Structure of Rare-Earth Metals and Alloys: The Magnetic Heavy Rare Earths* (Academic, New York, 1977), p. 83.

⁵H. R. Child, W. C. Koehler, E. O. Wollan, and J. W. Cable, *Phys. Rev. A* **138**, 1655 (1965).

⁶E. D. Isaacs, D. B. McWhan, D. P. Siddons, J. B. Hastings, and D. Gibbs, *Phys. Rev. B* **40**, 9336 (1989).

Magnetic ordering and electric polarizability of Zn-doped $\text{La}_2\text{CuO}_{4+\delta}$ single crystals

G. Cao, J. W. O'Reilly, J. E. Crow, and L. R. Testardi

National High Magnetic Field Laboratory and Center for Materials Research and Technology,
Florida State University, Tallahassee, Florida 32306

Magnetization, magnetic susceptibility, and low-frequency dielectric constant of $\text{La}_2\text{Cu}_{1-x}\text{Zn}_x\text{O}_{4+\delta}$ ($x=0$, and 0.07) single crystals were measured. Results obtained in this work show that Zn doping eliminates spins from CuO planes, thus, reducing the correlation length, ξ_{2D} . However, unlike Sr doping, magnetic dilution due to Zn doping is a very local effect, thus suppresses T_N relatively slowly and shows little impact on metamagnetic behavior. Our data marks a difference from some results previously reported which claimed a stronger effect on Zn doping on the magnetic properties. It is interesting that Zn doping shows a large influence on the dielectric properties, and resulting in a significant change in the dielectric constant K_c . Most remarkably, the simultaneous polarization and magnetization ordering, described in this study, suggests a coupling of magnetic ordering and electric polarizability in the oxides.

One of the fundamental features found in the high T_c cuprates is the dramatic disappearance of the insulating antiferromagnetic (AF) long-range order and the appearance of the superconducting state upon the introduction of mobile vacancy. The properties of the AF insulating state for La_2CuO_4 can be understood in terms of a two-dimensional (2D) $S=1/2$ Heisenberg model, and the origin of the magnetism is commonly attributed to the copper $3d^9$ configuration. However, the nature of the superconducting state remains a puzzle. A considerable attention has been focused on pairing models originating from a variety of approaches applied to the t - J , 2D Hubbard, and other related models. These models generally rely on some type of magnetic interactions to drive the charge carrier pairing responsible for the superconductivity. Thus it is critical to establish a more complete understanding of the unusual magnetic behavior displayed by La_2CuO_4 and the change of their magnetic response with change in carrier density and impurities. The dielectric constant, on the other hand, can also provide important insights. It has been observed that the near-conducting phases of $\text{YBa}_2\text{Cu}_3\text{O}_{7-\delta}$,¹ $\text{PrBa}_2\text{Cu}_3\text{O}_{7-\delta}$,² and related materials³⁻⁵ have shown the occurrence of enhanced low-frequency dielectric response approaching values reported for ferroelectrics. Recently, we have reported⁶ dielectric measurements of $\text{La}_2\text{CuO}_{4+\delta}$ which, again, show large dielectric constants and, in addition, a further enhancement of the electric polarizability in the vicinity of the magnetic ordering. Since such dielectric behavior is often the signature of ferroelectricity or incipient ferroelectricity in many perovskite oxides, such as $\text{BaBi}_{1-x}\text{Pb}_x\text{O}_3$, it has been tempting to suggest the possibility of a common origin of ferroelectricity and high T_c superconductivity in oxides.⁷⁻⁹ Bussmann-Holder *et al.*,¹⁰ in particular, have drawn attention to this point and described a lattice dynamical model for displacive-type (or soft mode) ferroelectrics which might be applied to high T_c superconductors.

With these considerations in mind, we have recently focused our attention to Zn-doped $\text{La}_2\text{CuO}_{4+\delta}$ as an extension of our study of magnetic and dielectric properties in $\text{La}_2\text{CuO}_{4+x}$. It is well known that substituting small amounts

of Zn for Cu strongly inhibits superconductivity in both $\text{La}_{2-x}\text{Sr}_x\text{CuO}_{4+\delta}$ and $\text{YBa}_2\text{Cu}_3\text{O}_{7-\delta}$. Zn ($3d^{10}$) is a unique dopant in that it has almost the same ionic radius as Cu ($3d^9$) ($r_{\text{Cu}^{2+}}=0.73$ Å and $r_{\text{Zn}^{2+}}=0.75$ Å) and the same ionic valence (+2). With a filled d^{10} shell, however, Zn is nonmagnetic. Therefore, it would be expected that Zn substitution at Cu site removes a spin from the 2D antiferromagnetic lattice with little effect on the semiconducting properties of the material except a disruption of the Cu-O hybridization in conductive samples. However, our results appear to indicate that Zn doping not only suppresses T_N but also dramatically changes the dielectric properties of the system, and, thus, suggests a possible correlation between magnetic and dielectric properties.

The magnetization was measured using a Quantum Design magnetometer (SQUID). Measurements of the impedance with E field parallel to the c axis were made at temperatures between 100 and 400 K with frequency varying from 10 kHz to 1 MHz using an HP model 4284A precision LCR meter. To make electrical contacts the two surfaces normal to the field direction were covered with silver paint. As discussed in Ref. 11, at low frequencies, contact effects, which is negligible at low temperatures, becomes significant at higher temperatures due to the decreasing resistances of the sample and contact. To ensure the true dielectric constant, we restricted our measurements to the frequency range where the dissipation factor was below 6.

Figure 1 shows $\chi(T)$ (defined as M/H) as a function of temperature T for $\text{La}_2\text{Cu}_{1-x}\text{Zn}_x\text{O}_{4+\delta}$ with $x=0$, and 0.07. The data were obtained under a magnetic field H of 0.5 T parallel to the c axis. The Néel temperature T_N decreases as Zn is doped. This is expected in that Zn doping eliminates spins from the 2D lattice, thus reducing ξ_{2D} , the 2D spin-spin correlation length and consequently suppressing magnetic ordering. It is worth noting that T_N for the doped sample with $x \approx 0.07$ is at $T=200$ K, and much higher than those ($T_N < 150$ K even for $x=0.04$) on polycrystalline samples reported previously,¹²⁻¹⁴ some investigators even claimed that 5.5% Zn would drive T_N to zero.¹³ Apparently, the depression of T_N by Zn observed in this work is much

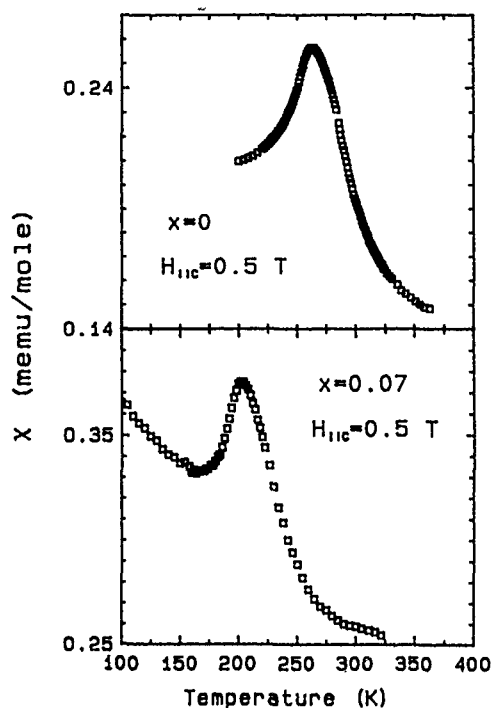


FIG. 1. Magnetic susceptibility χ (defined as M/H) vs temperature for $x=0$ (top) and $x=0.07$ (bottom) at $H_c=0.5$ T.

slower. In fact, our data are supported by results of muon-spin-rotation measurements (μ SR),¹⁵ which clearly show that AF long-range order exists up to significantly larger value of x (~ 0.11), and T_N for 7% Zn is of 180 K. The value of T_N presented here is also consistent with results published earlier by other investigators, where Néel temperatures of several Zn-doped La_2CuO_4 samples up to 8% Zn concentration was reported.¹⁶ The discrepancy for the value of T_N is likely due to quality of samples. In addition, it is remarkable that the peak for the 7% doped sample remains as sharp as the undoped one. This is, again, in variance from results on polycrystalline samples reported earlier where the width of the peak in the $\chi(T)$ increases upon Zn doping and, thus, the peak becomes less well defined.^{12,14} It is believed that within the mean-field theory the sharpness of the peak is the total 3D susceptibility is entirely controlled by the rapid variation with T of $\chi_{2D}(\sim \xi_{2D}^2/\kappa_B T$ at low temperatures), the staggered susceptibility of the CuO_2 planes. The variation of χ_{2D} thus depends on the rapid or slow variation of ξ_{2D} with T . The broadened peak observed in those measurements was accordingly attributed to the rapid reduction of the correlation length ξ_{2D} .¹⁴ The sharp peak for the doped sample displayed in the Fig. 1 suggests that the effect of the peak broadening is not intrinsic and validity of this view point is thus in question.

In Fig. 2 the magnetization M as a function of the magnetic field H parallel to the c axis was measured for the same Zn-doped sample at temperatures below and near the Néel temperature $T_N \approx 200$ K. For $T < T_N$, a sharp metamagnetic transition with $H_c \approx 4$ and 5 T is seen at $T=120$ and 160 K, respectively, whereas a nearly straight line at $T=195$ K, as expected, is found. The behavior seen here is obviously simi-

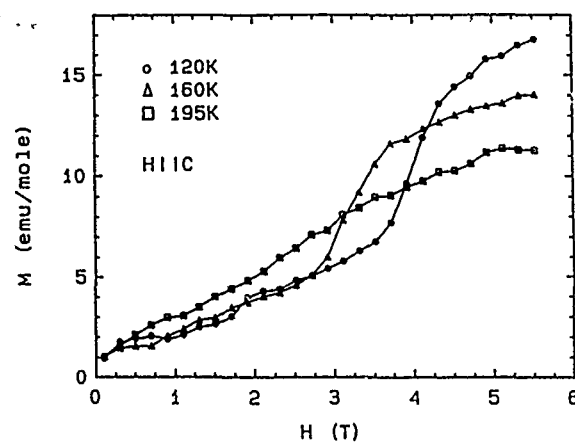


FIG. 2. Magnetization M vs H for $x=0.07$ at $T=120, 160$, and 195 K.

lar to that found in the parent compound $\text{La}_2\text{CuO}_{4+\delta}$ reported earlier except for $H_c(T)$ is corresponding to lower temperatures, suggesting little impact of Zn doping on the metamagnetism. This metamagnetic response can be well described by a Dzyaloshinskii-Moriya (DM) antisymmetric term.¹⁷ This term is allowed by certain broken crystal symmetries due to the slight rotation of the CuO_6 octahedra around the Cu sites, and can produce a canting of the spins away from the plane of staggered magnetization, thus a ferromagnetic moment pointing in the direction perpendicular to planes appear. For $T < T_N$ and $H < H_c$ the canting alternates its direction between planes. At $H = H_c$, the canting in all planes abruptly aligns with the finite external field which is the cause of the jump in Fig. 2. In earlier reported data,^{12,14} the magnetization was largely broadened and less well defined due to, at least, partially unoriented polycrystalline samples.

It becomes apparent that Zn doping has much weaker effect on both the depression of the Néel temperature and metamagnetic behavior than Sr doping, which introduces mobile holes. Our data on Sr-doped single crystals of $\text{La}_2\text{CuO}_{4+\delta}$ (not shown) confirms that roughly 2% Sr doping drives T_N to zero, which is in agreement with results already published. It has been thought that this difference is primarily a consequence of the different locations of the two types of vacancies. Zn doping, as stated above, removes the spin on the Cu site, thus reducing ξ_{2D} , but, even for x as high as 0.07, does not suppress T_N as dramatically as some other dopants. It resembles the situation of magnetic dilution. In contrast, Sr doping introduces the excess hole which resides on the oxygen site. The mobile hole couples with neighboring Cu spins effectively removing these spins from the system or frustrates the local AF order. It has been found that the hole introduced by Sr is only weakly localized before the insulator-metal transition ($x \sim 0.05$),⁹ whereas the Zn non-magnetic site is completely localized. Thus the finite mobility of the hole associated with Sr effectively or globally suppresses magnetic ordering, whereas the Zn doping inhibits magnetic ordering only by locally diluting the spin lattice.

Figure 3 shows the temperature dependence of the relative dielectric constant in the c axis, K_c , of $\text{La}_2\text{CuO}_{4+\delta}$ for three measurement frequencies. Note that values ~ 1500 at room temperature are obtained, again showing the large elec-

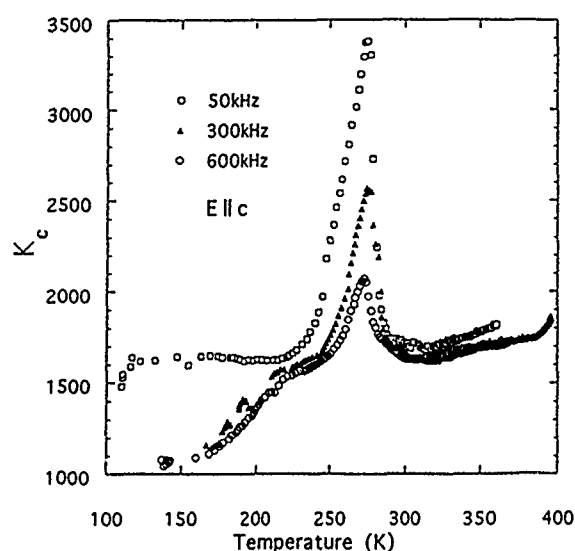


FIG. 3. Dielectric constant in the c -axis direction, K_c vs temperature for $x=0$ at three measurement frequencies.

tric polarizability of the insulating parent oxide phase. One notable difference for La_2CuO_4 compared to $\text{YBa}_2\text{Cu}_3\text{O}_{7-\delta}$ and $\text{PrBa}_2\text{Cu}_3\text{O}_{7-\delta}$ however, is the substantially smaller frequency dependence of the former's high dielectric constant in the vicinity of 300 K.

The major feature of the dielectric response is the large enhancement in K_c occurring near 270 K, Néel temperature T_N . We thus infer that the transition state for magnetic ordering is accompanied by a large additional electrical polarizability. No evidence of a shift in the temperature of the peak in K_c (i.e., thermal activation) with frequency can be discerned.

Shown in Fig. 4 is the relative dielectric constant K_c of $\text{La}_2\text{Cu}_{1-x}\text{Zn}_x\text{O}_{4+\delta}$ ($x \approx 0.07$) as a function of temperature for the six measurement frequencies. The values $K_c \sim 5000$ ob-

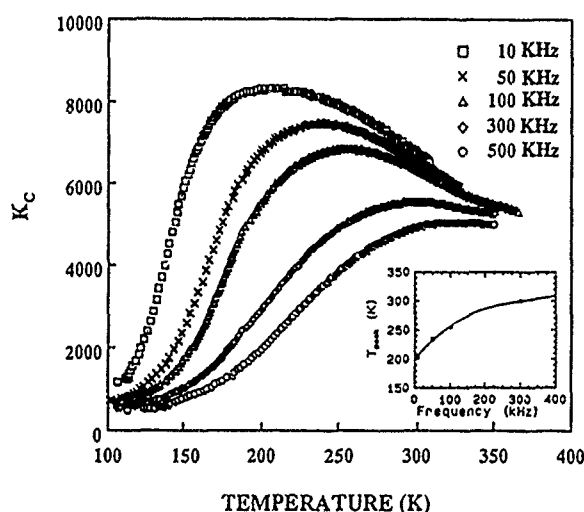


FIG. 4. Dielectric constant in the c -axis direction, K_c vs temperature for $x \approx 0.07$ at five measurement frequencies. Inset: the peak temperature T_{peak} vs frequency for $x \approx 0.07$.

tained in the temperature range $190 \leq T \leq 250$ K is larger than those (~ 1500) at room temperature for the parent compound. Additionally, unlike La_2CuO_4 , the peak of the enhancement becomes not only largely broadened but also strongly frequency dependent in the temperature range $160 \leq T \leq 300$ K. The behavior found here may suggest the possible thermal activation in the system which is not evident in the parent compound. However, there is a striking common feature of the dielectric response for both undoped and doped samples, i.e., the large enhancement in K_c tends to occur near the Néel temperature T_N . Yet, the peak of the enhancement for the doped sample is frequency dependent, but the peak appears to occur around $T \approx 200$ K, where the Néel temperature T_N is as the static limit is approached. Indeed, this point becomes more perceived in inset of Fig. 4, a plot of peak temperature, T_{peak} , as a function of frequency, where extrapolation to 0 Hz gives $T_{\text{peak}} = 200$ K.

The unusual phenomena we have observed in this study seem to imply a correlation between the antiferromagnetic ordering and the electrical polarizability in the oxides. However, no quantitative model for the strong microscopic magnetoelectric coupling indicated by these data have been published. Structural instability models of (anti)ferroelectricity driven by O atom displacements or rotations would lead to behavior similar to that observed. Although (anti)ferroelectric antiferromagnets are known to exist, the authors are unaware of a case of simultaneous polarization and magnetic ordering.

- ¹ L. R. Testardi, W. G. Moulton, H. Mathias, H. K. Ng, and C. M. Rey, Phys. Rev. B **37**, 2324 (1988); Q. X. Jia and A. Anderson, J. Appl. Phys. **66**, 452 (1989); G. A. Samara, W. F. Hammetter, and E. L. Venturin, Phys. Rev. B **41**, 8974 (1990); C. M. Rey, H. Mathias, L. R. Testardi, and S. Skirius, Phys. Rev. B **45**, 10 639 (1992).
- ² G. P. Mazzara, S. Skirius, G. Cao, G. Chern, R. J. Clark, J. E. Crow, H. Mathias, J. W. O'Reilly, and L. R. Testardi, Phys. Rev. B **47**, 8119 (1993).
- ³ K. B. R. Varma, G. N. Subbana, T. V. Ramakrishnan, and C. N. R. Rao, Appl. Phys. Lett. **55**, 75 (1989).
- ⁴ D. Reagor, E. Ahrens, S.-W. Cheong, A. Migliori, and Z. Fisk, Phys. Rev. Lett. **62**, 2048 (1990).
- ⁵ D. Emin and M. S. Hillery, Phys. Rev. B **39**, 6575 (1989).
- ⁶ G. Cao, J. W. O'Reilly, J. E. Crow, and L. R. Testardi, Phys. Rev. B **47**, 11 510 (1993).
- ⁷ S. K. Kurtz, L. E. Cross, N. Setter, D. Knight, A. Bhalla, W. W. Cao, and W. N. Lawless, Mater. Res. Lett. **6**, 317 (1988); S. K. Kurtz, J. R. Hardy, and J. W. Flocken, Ferroelectrics **87**, 29 (1988).
- ⁸ D. P. Billesbach, J. R. Hardy, and P. J. Edwardson, Phys. Rev. B **39**, 202 (1989).
- ⁹ I. Batistisc, A. R. Bishop, R. L. Martin, and Z. Tesanovic, Phys. Rev. B **40**, 6896 (1989).
- ¹⁰ A. Bussmann-Holder, A. Simon, and H. Buttner, Phys. Rev. B **39**, 207 (1989).
- ¹¹ C. Y. Chen, R. J. Birgeneau, M. A. Kastner, N. W. Preyer, and Tineke Thio, Phys. Rev. B **43**, 392 (1991).
- ¹² A. Chakraborty, A. J. Epstein, and M. Jarrell, Phys. Rev. B **40**, 5296 (1989).
- ¹³ Gang Xiao, Marta Z. Cieplak, and C. L. Chien, Phys. Rev. B **42**, 240 (1990).
- ¹⁴ S. T. Ting, P. Pernambuco-Wise, J. E. Crow, and E. Manousakis, Phys. Rev. B **46**, 11 772 (1992).
- ¹⁵ R. L. Lichti, C. Boekema, J. C. Lam, D. W. Cooke, S. F. J. Cox, S. T. Ting, and J. E. Crow, Physica C **180**, 358 (1991).
- ¹⁶ B. Keimer, A. Aharony, A. Auerback, R. J. Birgeneau, A. Cassanho, Y. Endoh, R. W. Erwin, M. A. Kastner, and G. Shirane, Phys. Rev. B **45**, 7430 (1992).
- ¹⁷ I. E. Dzyaloshinskii, J. Phys. Chem. Solids **4**, 241 (1958); T. Moriya, Phys. Rev. **120**, 91 (1960).

Two-dimensional magnetic order in $\text{Pb}_2\text{Sr}_2\text{TbCu}_3\text{O}_8$

S. Y. Wu, W. T. Hsieh, W-H. Li, and K. C. Lee

Department of Physics, National Central University, Chung-Li, Taiwan 32054

J. W. Lynn

Reactor Radiation Division, National Institute of Standards and Technology, Gaithersburg, Maryland 20899

H. D. Yang

Department of Physics, National Sun Yat-Sen University, Kaohsiung, Taiwan 80424

Neutron diffraction techniques have been used to investigate the magnetic ordering of the Tb ions in polycrystalline $\text{Pb}_2\text{Sr}_2\text{TbCu}_3\text{O}_8$. Significant magnetic correlations are found to develop below ~ 10 K, and these correlations are two dimensional in nature, representative of the strongly anisotropic magnetic interactions in these layered materials. The correlation length increases with decreasing temperature, and long-range order is observed to develop at $T_N \approx 5.5$ K. However, the sawtooth Bragg profile for the scattering demonstrates that the long-range order is two dimensional, rather than three dimensional, with a spin configuration where nearest-neighbor spins are antiparallel. The scattering profile can be explained quantitatively by assuming long-range order within the ab plane, with no significant correlations along the c axis to the lowest temperatures measured (1.36 K). Our results suggest that the system is well described by a two-dimensional Ising model. The only other (pure) system where a crossover to three-dimensional behavior is *not* observed is $\text{DyBa}_2\text{Cu}_4\text{O}_8$.

One of the most remarkable properties of the Cu and RE (RE=rare-earth elements) magnetism of the high T_c oxides is that they are two dimensional (2D) in nature. The 2D behavior of the Cu magnetism originates from the strong Cu-O bonding within the layers, which yields highly anisotropic exchange interactions between the Cu ions. On the other hand, the RE atoms form an orthorhombic sublattice where the nearest-neighbor distance along the c axis is much greater than that within the ab plane, which again leads to highly anisotropic magnetic interactions between the RE ions and generates the 2D magnetism. Such 2D behavior of the RE ions has been observed in the $\text{REBa}_2\text{Cu}_3\text{O}_7$ ^{1,2} (RE1237), $\text{REBa}_2\text{Cu}_4\text{O}_8$ ³ (RE1248), and $\text{RE}_2\text{Ba}_4\text{Cu}_7\text{O}_{15}$ ⁴ (RE24715) systems. Among them, a rod of scattering characteristic of 2D behavior has been observed² in single crystals of Er1237 and Dy1237, and their order parameters are found to obey the Onsager⁵ solution for the $S=\frac{1}{2}$, 2D Ising antiferromagnet. Moreover, for the Dy ions in the Dy1248 a geometric cancellation of the already weak interactions occurs along the c axis, which renders the system two-dimensionally ordered even at temperatures well below the Néel temperature.³

In this article we report another system which exhibits 2D magnetic order, as observed by neutron diffraction experiments. In this material we observe significant 2D magnetic correlations of the Tb spins in the $\text{Pb}_2\text{Sr}_2\text{TbCu}_3\text{O}_8$ (Tb22138) compound below $T \sim 10$ K. Long-range order is observed to develop at $T_N \approx 5.5$ K, but even at $T = 1.36$ K the magnetic correlations are still mainly two dimensional, with nearest-neighbor spins within the ab plane being aligned antiparallel.

The RE22138 systems are even more anisotropic in their physical properties than those of the RE1237 system,^{6,7} as there are more intervening layers of atoms stacked along the c axis. The rare-earth atoms in the RE22138 system form an orthorhombic unit cell where the distance between

the nearest neighbors along the c axis is more than four times that in the ab plane. It is clear that the crystallographic anisotropy naturally leads to highly anisotropic magnetic interactions. The rare-earth unit cell is related to the nuclear unit cell of the compound by rotation of the a and b axes of the nuclear unit cell by $\sim 45^\circ$ and reducing their lengths by $\sqrt{2}$. We employ the notation of (abc) and $(a'b'c')$ to represent the axes of the nuclear and rare-earth unit cells, respectively. We note that by using this system of notation, the ab plane and $a'b'$ plane are essentially the same planes.

Powder samples of $\text{Pb}_2\text{Sr}_2\text{TbCu}_3\text{O}_8$ were prepared by the standard solid-state reaction techniques, and the details of the sample preparation technique can be found elsewhere.⁸ Both x-ray and neutron diffraction were used to characterize the sample. The x-ray diffraction pattern is well described by the orthorhombic Y22138 structure,⁶ which is only slightly deviated from tetragonal symmetry, with room-temperature lattice parameters $a = 5.452(7)$ Å, $b = 5.459(9)$ Å, and $c = 15.66(2)$ Å for the chemical unit cell of the compound. The nearest-neighbor distances of the Tb ions are, therefore, $a' \approx b' = 3.856$ Å within the $a'b'$ plane and $c' = 15.66$ Å along the c' axis, respectively.

Neutron diffraction measurements were performed at the Research Reactor at the U.S. National Institute of Standards and Technology. The data were collected using the BT-9 triple-axis spectrometer which was operated in double-axis mode. A pyrolytic graphite PG(002) crystal was used as the monochromator to extract neutrons of energy 14.8 meV ($\lambda = 2.351$ Å). A PG filter was also placed after the monochromator position to suppress higher-order wavelength contaminations. The angular collimations used were $40'$ before the monochromator, and $48'-48'$ before and after the sample, respectively. The sample was mounted in a cylindrical aluminum can filled with helium exchange gas to facilitate thermal conduction at low temperatures. A pumped ^4He cryostat was used to cool the sample, and the lowest temperature

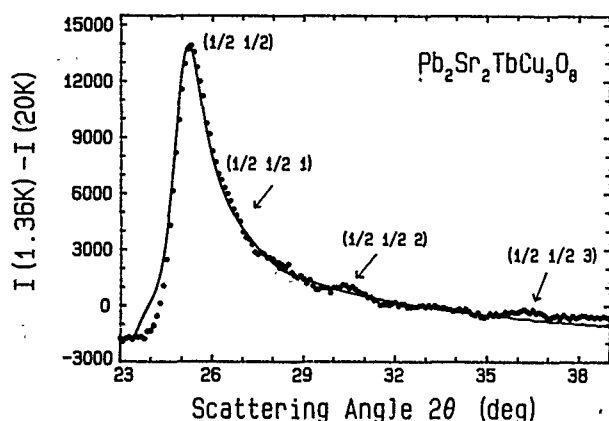


FIG. 1. Magnetic intensities observed in $\text{Pb}_2\text{Sr}_2\text{TbCu}_3\text{O}_8$ at $T=1.36$ K, which is well below the ordering temperature. The pronounced asymmetry of the observed peak is a classic profile of the two-dimensionally ordered system. The magnetic peaks may be indexed as the $(\frac{1}{2} \frac{1}{2})$ rod of scattering based on the Tb unit cell. Small 3D-like Bragg peaks, with positions that may be indexed as the $(\frac{1}{2} \frac{1}{2} 1)$, $(\frac{1}{2} \frac{1}{2} 2)$, and $(\frac{1}{2} \frac{1}{2} 3)$ reflections, are also revealed. The solid line is a fit to the 2D theoretical profile.

obtained was 1.36 K. For each temperature change, sufficient time was given to allow the sample to reach thermal equilibrium.

Three powder diffraction sets of data were collected over the range of scattering angles from $2\theta=5^\circ$ to 65° : One at a temperature well below, one just above, and the other well above the Néel temperature. The subtraction technique⁹ was used to isolate the magnetic signal from the nuclear one, where the diffraction pattern taken at a temperature well above the ordering temperature was subtracted from the one taken at low temperature.

The magnetic diffraction pattern obtained at $T=1.36$ K is shown in Fig. 1, where the diffraction pattern taken at $T=20$ K serves as the nonmagnetic "background" has been subtracted from the data. The sawtooth Bragg profile of the observed peak is a classic profile of a two-dimensionally ordered system.^{3,10} The scattering pattern is dominated by a single 2D-like peak, even though we were well below the Néel temperature ($T_N \approx 5.5$ K, see below). The solid curve in the figure is a least-squares fit to the theoretical 2D scattering profile convoluted with the Gaussian instrumental resolution function, assuming long-range order within the $a'b'$ plane and no correlations along the c' -axis direction. Based on the Tb unit cell, the observed asymmetrical peak corresponds to the $(\frac{1}{2} \frac{1}{2})$ rod of scattering. This is the same type of scattering that has been observed³ in Dy_{1248} . The magnetic correlations along the c' -axis direction are much weaker than those within the $a'b'$ plane. However, the observed intensities shown in Fig. 1 also suggest some 3D ordering character, where small 3D peaks at $2\theta=26.23^\circ$, 30.09° , and 36.23° , which would correspond to the $(\frac{1}{2} \frac{1}{2} 1)$, $(\frac{1}{2} \frac{1}{2} 2)$, and $(\frac{1}{2} \frac{1}{2} 3)$ Bragg reflections, respectively, are evident. This may indicate that a small fraction of the samples is ordered three dimensionally at low temperatures.

The presence of the $(\frac{1}{2} \frac{1}{2})$ rod of scattering demonstrates that the 2D magnetic unit cell of the Tb ions is doubled in size compared to the nuclear one along both the a' and b'

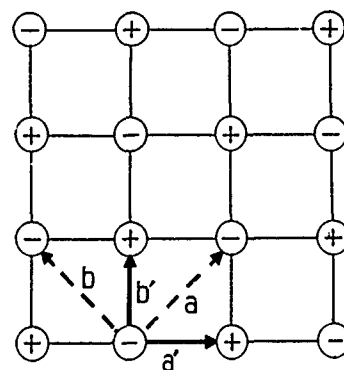


FIG. 2. The 2D spin configurations of the Tb ions within the $a'b'$ plane. The nearest-neighbor spins are aligned antiparallel, and the plus and minus signs then represent spins that are in opposite directions. a' and b' indicate the axes of the Tb unit cell, and a and b indicate the axes of the nuclear unit cell of the compound.

axes. The nearest-neighbor spins of the Tb ions are therefore aligned antiparallel. The 2D spin configuration for the Tb moments in the $a'b'$ plane is shown in Fig. 2, where the a and b axes of the nuclear unit cell of the compound are also indicated. In addition, the weak $(\frac{1}{2} \frac{1}{2} l)$ type of reflections, with $l=\text{integer}$, revealed in Fig. 1 indicate that the Tb spins have the tendency to align parallel along the c' axis. These data suggest that 3D order may set in at lower temperatures. Further work at lower temperatures is planned to clarify this point.

The low-temperature ordered moment⁴ was obtained by comparing the magnetic to nuclear intensities. For the case of 2D magnetic ordering, we need to integrate the magnetic scattering over the angular range corresponding to the first Brillouin zone. Comparing the magnetic intensity with the $\{001\}$ nuclear intensity establishes that the saturated moment for each Tb ion is $\langle \mu_z \rangle = 7.43 \pm 0.02 \mu_B$, assuming the spin direction is along the c' -axis direction. This choice of the c' -axis direction is consistent with the moment direction usually found in these materials.

The temperature dependence of the intensity at the 2D $(\frac{1}{2} \frac{1}{2})$ peak position is shown in Fig. 3. The magnetic Bragg intensity is proportional to the square of the ordered moment, which is the order parameter of the phase transition. Assuming that the magnetic peak profile remains the same for the temperature range studied, a measurement of the temperature dependence of the peak intensity then measures the square of the order parameter. The sharp drop in intensity shown in Fig. 3 is typical for a 2D magnetic phase transition, while the rounding in the vicinity of the ordering temperature is typical for the (critical) scattering observed in a powder. The Néel temperature is estimated to be $T_N \approx 5.5$ K.

Above the ordering temperature magnetic scattering was also observed, and the shape of this scattering also demonstrates the 2D magnetic character of the system. Figure 4 shows the $(\frac{1}{2} \frac{1}{2})$ rod of scattering observed at $T=6$ K, which is just above the ordering temperature. The intensity on the lower angle side of the peak does not show as sharp an increase because of the finite correlation range above the ordering temperature. The solid curve is a fit to the theoretic-

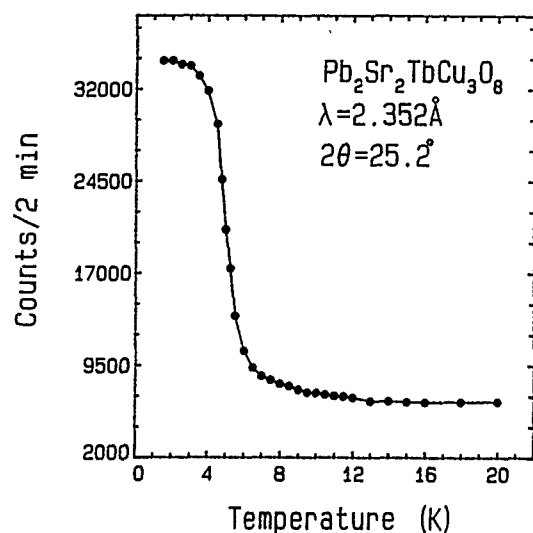


FIG. 3. Temperature dependence of the $(\frac{1}{2}, \frac{1}{2})$ peak intensity, showing the variation of the square of the staggered magnetization with temperature. The sharp drop in intensity is typical for a 2D order parameter. The ordering temperature is determined to be $T_N \approx 5.5$ K. The solid curve is a guide to the eye only.

cal 2D profile, assuming a finite correlation length within the $a'b'$ plane and no correlations along the c' -axis direction. The 2D Bragg rod gives an excellent fit to the observed data. We, hence, conclude that there are strong magnetic correlations within the $a'b'$ plane while those along the c' -axis direction are weak, and the fundamental energetics is 2D in nature. The intrinsic linewidth of this peak is related to the inverse 2D correlation length, and the correlation length that we obtained from the fit at $T = 6$ K is $\xi = 550$ Å. Further work is in progress on the temperature dependence of the 2D magnetic correlation length in this system.

The research at the NCU was supported by the National Science Council of the Republic of China under Grant No. NSC 82-0212-M-008-073, and was partially supported by

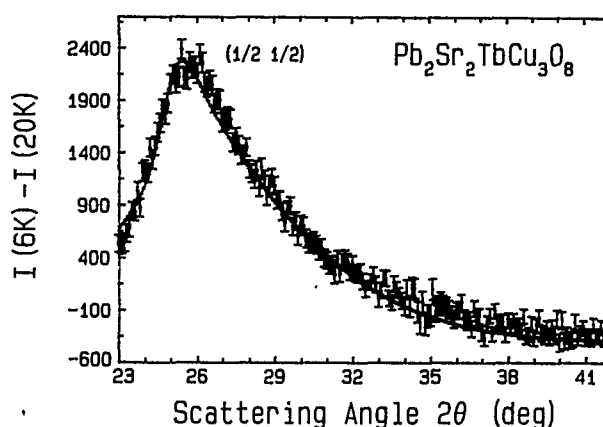


FIG. 4. The $(\frac{1}{2}, \frac{1}{2})$ rod of scattering observed at $T = 6$ K, which is just above the ordering temperature. The observation of this scattering directly demonstrates the 2D energetics of the system. The solid line is a fit to the 2D theoretical profile with a correlation length of $\xi = 550$ Å within the $a'b'$ plane and no correlations along the c' -axis direction.

the NCU Physics Department under Grant No. NCU-PD-WHLI-070.

- ¹J. W. Lynn, W.-H. Li, Q. Li, H. C. Ku, H. D. Yang, and R. N. Shelton, Phys. Rev. B **36**, 2374 (1987).
- ²J. W. Lynn, T. W. Clinton, W.-H. Li, R. W. Erwin, J. Z. Liu, K. Vandervoort, and R. N. Shelton, Phys. Rev. Lett. **63**, 2606 (1989).
- ³H. Zhang, J. W. Lynn, W.-H. Li, T. W. Clinton, and D. E. Morris, Phys. Rev. B **41**, 11 229 (1990).
- ⁴H. Zhang, J. W. Lynn, and D. E. Morris, Phys. Rev. B **45**, 10 022 (1992).
- ⁵L. Onsager, Phys. Rev. **65**, 117 (1944).
- ⁶R. J. Cava, B. Batlogg, J. J. Krajewski, L. W. Rupp, L. F. Schneemeyer, T. Siegrist, R. B. vanDover, P. Marsh, W. F. Peck, Jr., P. K. Gallagher, S. H. Glarum, J. H. Marshall, R. C. Farrow, J. V. Waszczak, R. Hull, and P. Trevor, Nature **336**, 211 (1988).
- ⁷T. Mochiku and K. Kadowaki, J. Phys. Soc. Jpn. **61**, 881 (1992).
- ⁸K.-W. Liaw, T.-H. Meen, Y.-C. Chen, W.-H. Lee, and H. D. Yang, Jpn. J. Appl. Phys. **32**, 1225 (1993).
- ⁹W.-H. Li, K. J. Chang, W. T. Hsieh, K. C. Lee, J. W. Lynn, and H. D. Yang, Phys. Rev. B **48**, 519 (1993).
- ¹⁰J. K. Kjems, L. Passell, H. Taub, J. G. Dash, and A. D. Novaco, Phys. Rev. B **13**, 1446 (1976).

Structure of the modulated magnetic phase of Mn_3Sn (abstract)

J. W. Cable

Oak Ridge National Laboratory, P. O. Box 2008, Oak Ridge, Tennessee 37831-6393

N. Wakabayashi

Keio University, Yokohama 223, Japan

P. Radhakrishna

Jawaharal Nehru Centre for Advanced Scientific Research, Bangalore 560012, India

The intermetallic compound Mn_3Sn has the hexagonal DO_{19} crystal structure with six Mn and two Sn atoms per unit cell. The triangular antiferromagnetic order that develops below $T_N=420$ K becomes modulated below 270 K in what is generally described as a helical modulation. However, magnetic excitation spectra show the presence of an energy gap of about 4 meV for both the triangular and the modulated phases, and this can occur for a helical modulation only if the period is commensurate with the lattice. This prompted us to re-examine the structure of the modulated phase by neutron diffraction. We find two distinct moment modulations, both propagating along the c axis and both of which are commensurate below 120 K with periods of $11c_0$ and $14c_0$. Above 120 K, both modulation wave vectors increase with temperature and become incommensurate. The satellite reflections exhibit quite different intensities and temperature dependencies, and this suggests coexistent modulated phases. For the predominant $11c_0$ (22 layer) phase, we observe a third harmonic with about 20% of the amplitude of the first harmonic and with no fifth harmonic to 1% in amplitude. This shows that the modulation in Mn_3Sn is definitely not that of a uniform helix. The observed intensity distributions are compared with configurational models in which multilayer blocks of the triangular order align along the easy sixfold axes in the basal plane and rotate by 60° per block in proceeding along the c axis.

The research was supported by the Division of Materials Sciences, U. S. Department of Energy under Contract Number DE-AC05-84OR21400 with Martin Marietta Energy Systems, Inc.

Magnetic structure of NdCu₂ (abstract)

R. R. Arons

*Institut für Festkörperforschung, Forschungszentrum Jülich, D-52425 Jülich, Germany and CEA,
Département de la Recherche Fondamentale sur la Matière Condensée, SPSMS/MDN, 17 Rue des Martyrs, F-
38054 Grenoble Cedex 9, France*

M. Loewenhaupt

Institut für Festkörperforschung, Forschungszentrum Jülich, D-52425 Jülich, Germany

E. Gratz

Institut für Experimentalphysik, TU Wien, A-1040 Wien, Austria

RCu₂ compounds (R =rare earth) with orthorhombic crystal structures exhibit a rich variety of magnetic structures at low temperatures, originating from a subtle interplay between RKKY-type exchange and crystal field anisotropy. Though most of the magnetic properties of NdCu₂ are well understood,¹ there are controversial proposals for the magnetic phases, as deduced from different experiments.^{1,2} Therefore we have investigated the magnetic structure of NdCu₂ by neutron diffraction as a function of temperature between 1.4 and 8 K in the zero external field. The diffraction patterns of a powdered sample were obtained on the multidetector DN5 at the SILOE reactor of CEN-G. Only two different magnetic phases were observed, in agreement with Ref. 1. For temperatures between 5.2 K and $T_N=6.5$ K, the magnetic structure can be described by a sinusoidal oscillating component along b with wave vector $\tau_2=(0.62, 0.042, 0)$. Accordingly, the structure is incommensurate with the lattice. Below 4.0 K the structure remains an oscillating component along b . However, the wave vector becomes commensurate with the lattice and is given by $\tau_1=(0.60, 0, 0)$. Additionally, a progressive squaring up from the appearance of the third harmonic 3τ in the range from 4.0 K down to 1.4 K is observed. At 1.4 K the amplitudes of the fundamental and the third harmonic are $2.4\mu_B$ and $0.9\mu_B$, respectively. Around 4.4 K, the spectra seem to be determined by a superposition of the high- and low-temperature phases. The low-temperature structure of NdCu₂ is comparable with that for TmCu₂, observed earlier in Ref. 3. Though in that work a different interpretation was chosen, the wave vector of the fundamental oscillation can be described by $(0.625, 0, 0)$, while the amplitudes for the fundamental and third harmonic are given by $8.0\mu_B$ and $2.6\mu_B$, respectively.

¹E. Gratz *et al.*, J. Phys. Condens. Matter 3, 9297 (1991).

²P. Svoboda *et al.*, J. Magn. Magn. Mat. 104-107, 1329 (1992).

³M. Heidelmann *et al.*, J. Phys. Condens. Matter 4, 8773 (1992).

Easy-axis transition in SmMn_2Ge_2 (abstract)

R. B. van Dover, E. M. Gyorgy, R. J. Cava, J. E. Krajewski, W. F. Peck, Jr.,
and R. J. Felder

AT&T Bell Labs, Murray Hill, New Jersey 07974

SmMn_2Ge_2 is a layered ferromagnet with unusual magnetic and electrical properties. In some regards it is a natural analog to artificially layered thin film materials, and its study can provide valuable insights. SmMn_2Ge_2 is ferromagnetic from 0 to 90 K, with easy axes parallel to the (110) directions (FM1 state). Between 90 and 150 K it is antiferromagnetic, and from 150 K to T_c (340 K) it is again ferromagnetic, with an easy axis parallel to the (001) direction (FM2 state). We have used a continuous recording torque magnetometer to monitor the energy surface of SmMn_2Ge_2 as a function of temperature. We have found that the moments are parallel to (110) in the AFM state, and that the anisotropy constant varies continuously, i.e., that $K \rightarrow 0$ at the easy-axis transition, which is found to be at essentially the same temperature as the zero-field AFM/FM2 transition. The FM1/AFM and AFM/FM2 transition temperatures can be varied over a wide range by substitution on the various sites. Substitution of Y or Gd on the Sm site increases $T_{\text{AFM/FM2}}$ strongly, and is found to increase the temperature of the easy axis transition, but not by precisely the same factor. Substitution of a small amount of Cr on the Mn site decreases $T_{\text{AFM/FM2}}$ but appears to have no effect on the easy-axis transition. M - H curves and M - T curves taken in a vibrating sample magnetometer and in a SQUID magnetometer provide corroborating evidence for these conclusions.

Neutron diffraction study of the magnetic ordering of BaCuO_{2+x} (abstract)

Xun-Li Wang and J. A. Fernandez-Baca

Oak Ridge National Laboratory, Oak Ridge, Tennessee 37831

Z. R. Wang, D. Vaknin, and D. C. Johnston

Department of Physics and Ames Laboratory, Iowa State University, Ames, Iowa 50011

Neutron diffraction experiments have been performed in order to study the magnetic ordering of BaCuO_{2+x} . In these measurements unpolarized neutrons and polarized neutrons with full polarization analysis have been utilized. From these measurements it has been determined that BaCuO_{2+x} orders antiferromagnetically below $T_N = 15.0 \pm 0.5$ K with a magnetic propagating vector $\mathbf{k} = [1\ 1\ 1]$. This structure is commonly referred to as a $[\pi\pi\pi]$ or a G structure. The Cu atoms in the Cu_6 ring clusters, located at the $(\frac{1}{4}, \frac{1}{4}, \frac{1}{4})$ positions, order ferromagnetically within these clusters while the clusters themselves order antiferromagnetically. The ordered magnetic moment of each of these Cu atoms is $0.89 \pm 0.05 \mu_B$ at $T = 4.2$ K. No evidence of long-range magnetic ordering of the Cu atoms in the Cu_{18} clusters, located at the $(0, 0, 0)$ and $(\frac{1}{2}, \frac{1}{2}, \frac{1}{2})$ positions, was found down to a temperature $T = 2.5$ K. The work at Oak Ridge National Laboratory (ORNL) was sponsored by the Division of Materials Sciences, U.S. Department of Energy (DOE). ORNL is managed for the U.S. DOE by Martin Marietta Energy Systems, Inc., under Contract No. DE-AC05-84OR21400. Ames Laboratory is operated for the U.S. DOE under Contract No. W-7405-Eng-82. The work at Ames was supported by the Director for Energy Research, Office of Basic Energy Sciences.

Magnetic properties of metallic Co- and Fe-based granular alloys

Gang Xiao and Jian-Qing Wang

Department of Physics, Brown University, Providence, Rhode Island 02912

We have studied the magnetic properties of Co-Ag and Fe-Ag granular alloys made using vapor-quenching techniques and thermal annealing. Magnetic coercivity (H_c) and remanence can be controlled over a large range by varying annealing temperature and particle volume fraction. A large H_c on the order of 2 kG has been obtained in the Co-Ag system. We have investigated magnetic anisotropy, the effect of particle size, and coalescence in these nanostructured materials.

Magnetic granular solids have received considerable attention in the past few years.¹⁻¹⁰ In these composite materials, ultrafine magnetic particles of a few nanometers in size are embedded in a metallic or insulating matrix by certain synthesis processes. Because of their microstructure and the tunability in materials and geometrical parameters, these materials possess different and sometimes enhanced properties when compared with their bulk counterparts. In particular, a giant magnetic coercivity (H_c) has been achieved in Fe-SiO₂ granular films,¹ with H_c enhanced by as much as three orders of magnitude over the bulk value. The large H_c and magnetization of the material make it suitable for application in magnetic recording. It has also been discovered that metallic granular alloys, such as Co-Cu, Co-Ag, and Fe-Ag, exhibit giant magnetoresistance effects (GMR),⁶⁻¹⁰ with a magnitude rivaling the best multilayers with GMR. These developments in granular solids call for more systematic studies of their magnetic properties. The understanding of the novel GMR effect also requires the exploration of the underlying magnetic state which strongly correlates with the behavior of GMR. In this work, we present a study on two transition metal granular solids, Co-Ag and Fe-Ag, both of which have been shown to have GMR effect.⁸⁻¹⁰ The main focus here is how the thermal treatment and volume fraction of the magnetic particles affect the magnetic properties.

We have fabricated Co-Ag and Fe-Ag granular films by taking advantage of the immiscibility between Co (or Fe) and Ag in alloy formation. High vacuum sputtering from a cold-pressed composite target yields a phase-separated film with magnetic particles precipitating from the Ag matrix. The particle size of an as-sputtered sample is very small, on the order of 1–2 nm. We have also fabricated samples using codeposition technique and obtained similar physical properties. Thermal annealing is an effective means to enlarge the particle size. We have prepared a series of samples with different thermal annealing as well as varying volume fraction. Phase separation has been confirmed by using a combination of analysis, i.e., transmission electron microscopy (TEM), x-ray diffraction, and magnetic susceptibility measurement. Detailed results will be presented elsewhere.¹¹ Analysis of phase separation for the Co-Ag system can also be found in Ref. 12.

We used a superconducting quantum interference device (SQUID) magnetometer to measure the magnetic hysteresis curve of our samples. Since we are interested in the ground

state properties, most of our measurements were carried out at low temperatures. The saturated magnetization of the magnetic component (Fe or Co) is approximately equal to that of the bulk. In addition to magnetic measurements, we have also performed magnetoresistance and Hall effect measurements. Both Fe-Ag and Co-Ag show GMR effect and extraordinary Hall effect.⁸⁻¹⁰ The Hall resistivity can be described by $\rho_{xy} = \rho_{xy}^0 + R_s M$. In this relation, ρ_{xy}^0 is due to the ordinary Hall effect and is linear in magnetic field. The second term, due to the extraordinary Hall effect,¹³ results from the left-right asymmetry in electron scattering in magnetic systems. Because of its linear relationship with M , the field dependence of ρ_{xy} after removing ρ_{xy}^0 shows a one-to-one correspondence with the magnetic hysteresis curve. Therefore, when the sample plane is perpendicular to the external magnetic field, we can consistently obtain remanent magnetization and coercivity from either Hall effect or magnetization measurements. It is noted that it is more efficient and economical to measure the Hall effect than the magnetization using a SQUID magnetometer.

Figure 1 shows the magnetization curves at $T=5$ K for two representative as-prepared samples, Co₂₀Ag₈₀ and Fe₂₀Ag₈₀, with H perpendicular and parallel to the sample plane (both samples are specified by volume fractions of their components). The initial susceptibility measurement indicates that the superparamagnetic transition temperature is about 20–30 K. Therefore, at 5 K, the magnetic moment vectors of the particles are fixed in random directions. As shown in Fig. 1, the Co₂₀Ag₈₀ sample has a much larger H_c than the Fe₂₀Ag₈₀ sample. Most interestingly, the easy axis tends to be out of plane for Co-Ag, whereas it is in plane for Fe-Ag.

The anisotropy in Co-Ag is most likely caused by the crystalline and shape anisotropies of the Co particles. The maximum H_c which could result from crystalline or strain anisotropy is about 2900 (fcc) or 600 G respectively.¹⁴ The large perpendicular H_c value of about 2 kG seen in Fig. 1 can be accounted for by magnetocrystalline anisotropy. The perpendicular H_c in Co-Ag is larger than the parallel H_c . To account for the observed perpendicular H_c in Co-Ag, it is reasonable to conjecture that the Co particles are slightly elongated along the growth direction. Another possible source of anisotropy is from the interface between the magnetic particles and the surrounding Ag matrix. Because of the

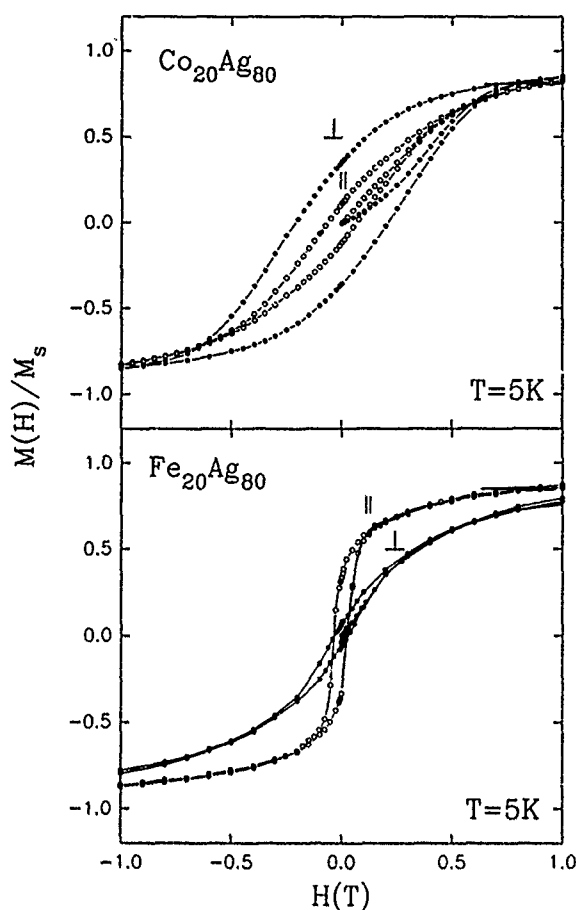


FIG. 1. Magnetic hysteresis curves in perpendicular and parallel field configurations for $\text{Co}_{20}\text{Ag}_{80}$ (upper panel) and $\text{Fe}_{20}\text{Ag}_{80}$ (lower panel) at $T=5\text{ K}$.

small size of the particles, interfacial effect could play an important role. Nevertheless, without the proposed growth texture, it is difficult to imagine how the interface anisotropy could cause the observed perpendicular anisotropy under the influence of the large demagnetization field of the thin film.

The H_c for the Fe-Ag system is of the magnitude of 300 G. While it is considerably larger than that of a polycrystalline Fe film (a few tens of G), it is much below the limit of crystalline (540 G) and strain (600 G) anisotropy for single-domain particles.¹⁴ The shape anisotropy in Fe can provide a maximum H_c of 10.7 kG,¹⁴ although experimentally such a large H_c in single-domain Fe particles has never been discovered. In Fe-SiO₂ granular films, a maximum H_c value of about 3 kG has been observed,¹ where the Fe particle size is about 50 Å. We have obtained the particle sizes in our $\text{Fe}_{20}\text{Ag}_{80}$ samples using both TEM and analysis of superparamagnetic behavior.¹¹ The $\text{Fe}_{20}\text{Ag}_{80}$ sample used for Fig. 1 has an average particle size of 29 Å. Thermal annealing at 300 °C enlarges the particle size to 51 Å, but the H_c was found to decrease to about 200 G. The comparison between Fe-Ag and Fe-SiO₂ granular systems shows convincingly that particle-matrix interface could be one of the important factors in the magnetic anisotropy of Fe-based systems.

Among the magnetic parameters of a ferromagnetic solid, the ground state magnetization is basically an intrinsic parameter, whereas H_c and remanence M_r/M_s are primarily extrinsic parameters. They are sensitive to disorder, stress,

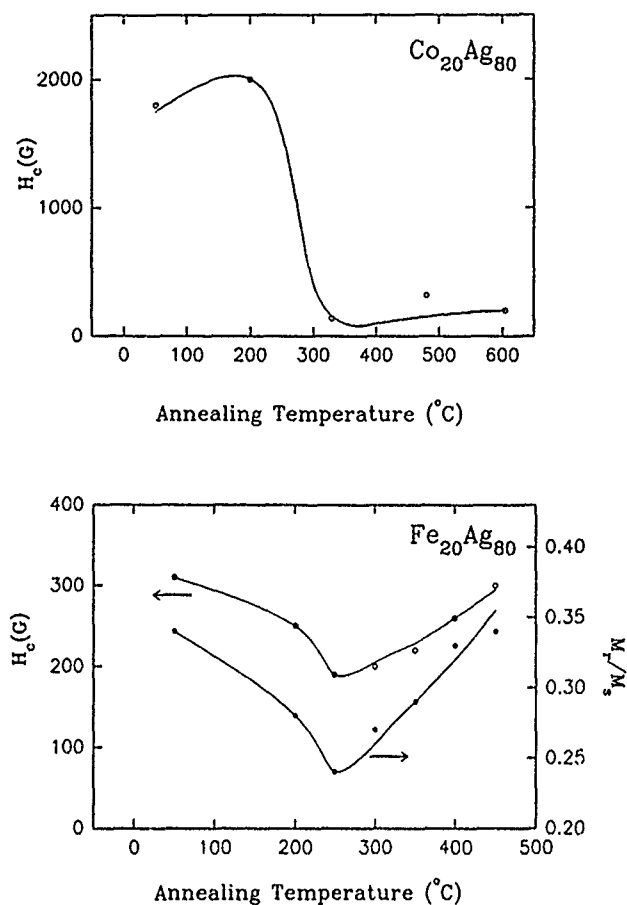


FIG. 2. Coercivity H_c vs annealing temperature T_A for $\text{Co}_{20}\text{Ag}_{80}$ (upper panel) and $\text{Fe}_{20}\text{Ag}_{80}$ (lower panel). Also shown in the lower panel is the remanence M_r/M_s for $\text{Fe}_{20}\text{Ag}_{80}$. $T=5\text{ K}$.

and particle morphology. Thermal treatment is an effective means to induce phase separation, to enlarge particle size, and to reduce crystalline disorder and stress in granular materials. In Fig. 2, we present the results of annealing on H_c for $\text{Co}_{20}\text{Ag}_{80}$ and $\text{Fe}_{20}\text{Ag}_{80}$. Also included in Fig. 2 is an annealing temperature (T_A) dependence of M_r/M_s for $\text{Fe}_{20}\text{Ag}_{80}$. Thermal annealing was done in high vacuum (1×10^{-7} Torr) at a chosen T_A for 15 min, followed by natural cooling. From the TEM micrograph, it was found that the Co particle size increases from about 20 to 130 Å as T_A reaches 605 °C. X-ray diffraction revealed that the Co particles have fcc structure and are [111] textured.⁸

As shown in Fig. 2, H_c for $\text{Co}_{20}\text{Ag}_{80}$ drops by a large amount once T_A exceeds 250 °C. This variation of H_c has been verified more than once. Such a drop in H_c is desirable because it tends to reduce the saturation field and hysteresis in GMR effect, which was indeed observed.⁸ There are a few possible causes for this drop. First of all, it is not due to the enlarged particle size which may induce multidomain formation and reduce H_c . Within our T_A range, the Co particle size is always below the critical single-domain particle size.¹⁴ Most likely, as the particle size grows, the original growth texture diminishes, which reduces the particle shape anisotropy. Another possible cause is that annealing makes phase separation more complete and tends to reduce crystalline disorder and stress. Both effects will reduce pinning force for magnetization, and, therefore, lower H_c .

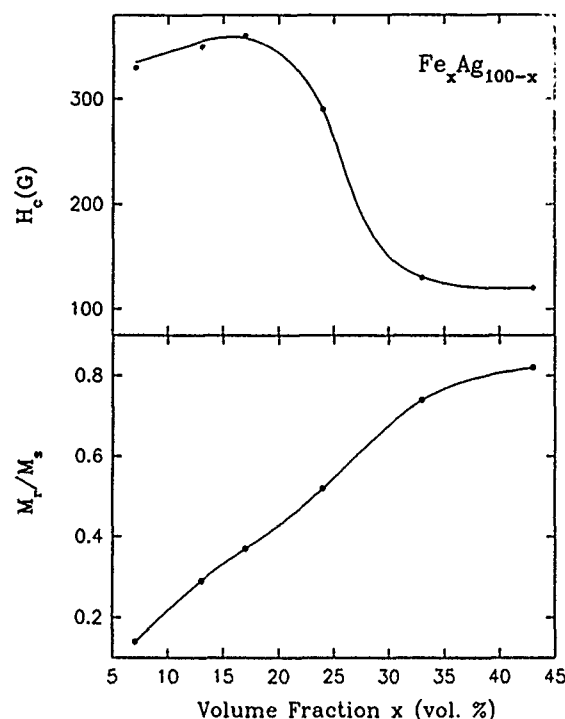


FIG. 3. Coercivity H_c (upper panel) and remanence M_r/M_s (lower panel) for $\text{Fe}_x\text{Ag}_{100-x}$ alloys as functions of volume fraction x . $T=5$ K.

The variation of H_c with T_A for $\text{Fe}_{20}\text{Ag}_{80}$ resembles the behavior in $\text{Co}_{20}\text{Ag}_{80}$, in that we see a similar drop in H_c near 250 °C. However, beyond 250 °C, H_c increases as Fe particles become larger. The remanence has a similar dip near 250 °C. Particle size analysis shows that the Fe particle size steadily increases from 21 Å in the as-sputtered sample to 71 Å at the maximum T_A of 400 °C. All are considered as single-domain particles.¹⁴

The above results reveal that thermal annealing has the universal effect of increasing particle size, however, its role on H_c is not straightforward, but is material dependent in metallic granular solids. At present, the cause for these diverse observations is not clear. However, it is important to remember that there are many sources at play for H_c , almost all are affected to varying degrees by thermal annealing.

Earlier studies have shown that thermal annealing substantially enhances H_c of various Fe-^{2,4} and Co-based^{3,4} granular solids. This is in sharp contrast with the behaviors of our Fe-Ag and Co-Ag systems, where moderate annealing depresses H_c . The difference is due to the fact that the earlier studies were performed at room temperature, whereas ours are at low temperature. At $T=300$ K, thermal relaxation reduces H_c severely for moderately annealed samples where the magnetic particles are small in size. In fact, any superparamagnetic sample has zero hysteresis. For samples annealed at high temperatures, and therefore, having large particle size, thermal agitation is less important, and H_c appears higher. In order to eliminate the effect of thermal relaxation, measurements need to be done at low temperatures.

Next we turn our attention to the effect of particle volume fraction (x) on magnetic properties. Here, x was determined from the composition and the bulk density of each component. Figure 3 shows H_c and M_r/M_s as functions of x

for the $\text{Fe}_x\text{Ag}_{100-x}$ as-sputtered system. In the low x region ($x < 0.2$), H_c remains relatively constant. Starting at $x \sim 0.2$, H_c gradually decreases, approaching the bulk value of polycrystalline Fe. M_r/M_s , on the other hand, increases smoothly with x in the whole x range studied. The evolution of H_c and M_r/M_s with x is the result of the transition from an assembly of almost independent particles to a network of connected particles. As x increases, there is an increasing coalescence of magnetic particles. In fact, above the percolation threshold x_c , cluster network of infinite extension is formed. Beyond this limit, the granular solid becomes increasingly bulk-like, and bulk polycrystalline Fe film is characterized by low H_c and large remanence.

For a random three-dimensional system, the percolation threshold x_c is near 0.2. In our granular material, H_c starts to decrease at almost the same x . We have also measured the GMR effect ($\Delta\rho/\rho$) as a function x .¹⁰ $\Delta\rho/\rho$ exhibits a peak at $x=0.2$, coinciding with the peak of H_c . This is because both GMR and H_c are sensitive to multidomain or cluster formation in a granular solid.

In summary, ground state magnetic properties have been measured for Co-Ag and Fe-Ag granular alloys which exhibit GMR. The Co-Ag films have a perpendicular magnetic anisotropy, whereas the easy axis of the magnetization of the Fe-Ag films is in-plane. The large H_c and perpendicular anisotropy in Co-Ag are attributed to the crystalline anisotropy and the elongation of Co particles in the growth direction. Thermal annealing affects H_c profoundly in both systems. This cannot be explained by the monotonical increase of magnetic particle size. Other mechanisms such as phase separation, effect of disorder, and evolution of particle shape need to be considered. It is also found that coalescence of particles reduces H_c .

We are grateful to Dr. C. L. Chien for providing some Co-Ag samples. We also thank Dr. P. Xiong for helpful discussion and technical assistance. This work was supported by National Science Foundation Grant No. DMR-9258306. G. X. wishes to thank the A. P. Sloan Foundation for a fellowship.

¹G. Xiao and C. L. Chien, Appl. Phys. Lett. **51**, 1280 (1987).

²J. R. Childress, C. L. Chien, and M. Nathan, Appl. Phys. Lett. **56**, 95 (1987).

³J. R. Childress and C. L. Chien, J. Appl. Phys. **70**, 5885 (1991).

⁴Y. X. Zhang, S. H. Liou, R. J. DeAngelis, K. W. Lee, C. P. Reed, and A. Nazareth, J. Appl. Phys. **69**, 5273 (1991).

⁵S. H. Liou, S. Malhotra, Z. S. Shan, D. J. Sellmyer, S. Nafis, J. A. Woolam, C. P. Reed, R. J. DeAngelis, and G. M. Chow, J. Appl. Phys. **70**, 5882 (1991).

⁶A. E. Berkowitz, J. R. Mitchell, M. J. Carey, A. P. Young, S. Zhang, F. E. Spada, F. T. Parker, A. Hutten, and G. Thomas, Phys. Rev. Lett. **68**, 3745 (1992).

⁷J. Q. Xiao, J. S. Jiang, and C. L. Chien, Phys. Rev. Lett. **68**, 3749 (1992).

⁸P. Xiong, G. Xiao, J. Q. Wang, J. Q. Xiao, J. S. Jiang, and C. L. Chien, Phys. Rev. Lett. **22**, 3220 (1992).

⁹G. Xiao, J. Q. Wang, and P. Xiong, Appl. Phys. Lett. **62**, 420 (1993).

¹⁰J. Q. Wang, P. Xiong, and G. Xiao, Phys. Rev. B **47**, 8341 (1993).

¹¹J. Q. Wang and G. Xiao, Phys. Rev. B **49**, 3982 (1994).

¹²J. Q. Xiao, J. S. Jiang, and C. L. Chien, Phys. Rev. B **46**, 9266 (1992).

¹³L. Berger and G. Bergmann, in *The Hall Effect and Its Applications*, edited by C. L. Chien and C. R. Westgate (Plenum, New York, 1979), p. 554.

¹⁴*The Physical Principles of Magnetism*, by A. H. Morrish (Krieger, Malabar, 1983), p. 332.

Magnetic and ferromagnetic resonance studies in Co-Cu composite films

R. Krishnan, H. Lassri, M. Seddat, and M. Tessier

Laboratoire de Magnétisme et Matériaux Magnétiques, C.N.R.S. 92195 Meudon, France

Sivaraman Guruswamy and Satyam Sahay

Department of Metallurgical Engineering, University of Utah, Salt Lake City, Utah 84112

Co_{1-x}Cu_x composite films with $0 \leq x \leq 83$ have been sputter deposited on to water-cooled glass substrates. Transmission electron microscopy and scanning tunneling microscopy studies reveal clusters whose average size is 250 Å. Magnetization when corrected to the Co volume is independent of Cu concentration and is equal to that of bulk Co. The in-plane saturation field is about 200 Oe at $x=0$, starts increasing for $x=40$, and shows a peak value of 1.2 kOe for $x=60$. Coercivity shows a similar behavior. Out-of-plane perpendicular anisotropy develops with the increase in Cu concentration. The ferromagnetic resonance studies show that (i) the linewidth increases for $x > 75$ and (ii) perpendicular anisotropy, probably induced by stress, also increases with x . Annealing up to 300 °C does not produce any noticeable changes but when annealed at 400 °C the perpendicular anisotropy decreases indicating some stress relief.

INTRODUCTION

Granular solids, consisting of metallic particles embedded in a matrix of another metal or oxide material have been studied in the past because of their interesting physical properties.^{1,2} Recently great interest has indeed been aroused in such materials following the exciting work by Berkowitz *et al.*³ and Xiao *et al.*,⁴ who observed large magnetoresistance (MR) in composite films of Co-Cu and Co-Ag. The origin of this effect is far from being well understood. Several papers which are basically devoted to the study of MR effects are appearing on these materials. Considerable effort is being devoted to the materials research of these kinds of films in order to optimize the properties for applications as sensors. We have chosen the Co-Cu system for this study and focused our attention on magnetic properties such as magnetization and anisotropy using ferromagnetic resonance (FMR) techniques. We have also carried out some structural studies using transmission electron microscopy (TEM) and scanning tunneling microscopy (STM).

EXPERIMENTAL DETAILS

The Co-Cu composite (we prefer this terminology to alloy) films were deposited on water-cooled glass substrates by rf sputtering using a 75-mm-diam disk of Co and Cu chips as target. Most of the samples were prepared under standard conditions, namely, with a rf power of 80 W, argon pressure p_{Ar} of 6 mTorr and a film thickness of 1400 ± 200 Å, monitored by quartz oscillators. Some samples were prepared with rf power of 80 and 100 W, p_{Ar} in the range $3-23 \times 10^{-3}$ Torr, and film thickness ranging from 300 to 2600 Å.

The composition of the samples was determined by electron probe microanalysis and the film thickness with a profilometer. Some selected samples were studied by TEM using a JEOL 200 CX microscope and also by STM.

Magnetization and $M-H$ loops were measured with a vibrating sample magnetometer. FMR was observed at 9.8 GHz with the dc applied field both in the film plane (H_{para}) and perpendicular (H_{perp}) to it.

RESULTS AND DISCUSSIONS

The planar TEM picture corresponding to the sample with Cu=46 at. % shown in Fig. 1, has a magnification of $308\,571\times$. One can observe clusters varying in size from about 160 to 450 Å. The average cluster size averaged over 30 clusters that are reasonably clear is about 250 Å. The clusters are separated by grain boundaries. The cluster size varies from location to location even within this micrograph. This appears to be consistent with STM studies to be described below.

Surface roughness studied by STM of several samples showed no significant differences with the film thickness or Cu content. Figure 2 shows the surface roughness of the sample with Cu=66 at. % as a typical case. The top surface appears to be wavy with the average maximum height of about 50 Å. The size of such zones is in the range 300-450 Å although one could see regions of smaller ones. Such shapes and sizes would lead to demagnetization factors which are not easy to calculate as discussed later.

The $M-H$ loops along the film normal were typical of hard axis ones with no remanence. The in-plane $M-H$ loops are rectangular and their shapes change with increasing Cu



FIG. 1. TEM planar picture of the sample with Cu=46. Magnification $\times 0.3 \times 10^6$.

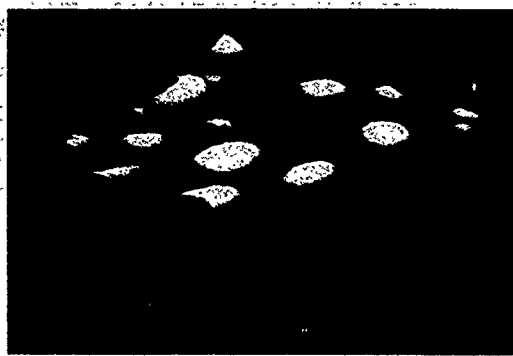


FIG. 2. STM surface image of the sample with Cu=66%. x axis 50 nm/div, z axis 15 nm/div.

content due to the appearance of perpendicular anisotropy (H_p). We will discuss the presence of H_p when describing the FMR results. No uniaxial anisotropy in the film plane could be detected. Figures 3(a) and 3(b) show two typical results for $x=20$ and 60, respectively. Figure 3(b) is typical of a loop with the presence of H_p and consequently this leads to an increase in the saturation field H_s . Figure 4 shows the Cu content dependence of H_s . It is seen that it is low and around 200 Oe for $x \leq 40$ but shows a sudden jump for $x > 40$ to reach a peak value of about 1.2 kOe for $x=60$. The Cu content dependence of the in-plane coercivity H_c is also very interesting and somewhat analogous to that of H_s , as shown in Fig. 4. H_c first increases sharply for $x > 30$ and after showing a broad peak it decreases again. The peak value of H_c is about 100 Oe. The magnetization, when expressed in terms of the total sample volume Co+Cu shows a linear decrease as x increases. But since Co and Cu do not form an alloy the magnetization should be expressed in terms of the actual Co volume. In this case the magnetization of all the samples equals that of bulk Co. A similar conclusion was also reached by Kneller⁵ on evaporated Co-Cu films. This shows that the Co moment is conserved because the Co atoms tend to cluster together. The magnetization of the samples was independent of the deposition parameters and the film thickness in the range 300–2500 Å, but not so for the FMR properties as will be discussed later.

The FMR resonance linewidth ΔH , as is well known, is a sensitive tool to check the quality of the films. We made a systematic study of ΔH as a function of the deposition parameters (rf power and p_{Ar}) and film thickness. Changing the rf power from 80 to 100 W did not sensibly affect the FMR

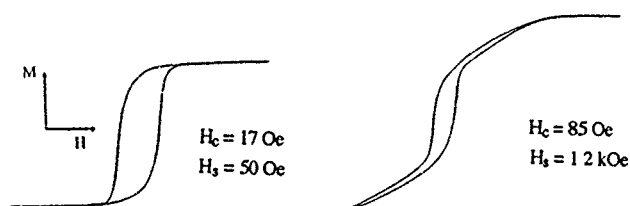


FIG. 3. The in-plane $M-H$ loops for the samples for (a) Cu=20 and (b) 60 at. %, respectively.

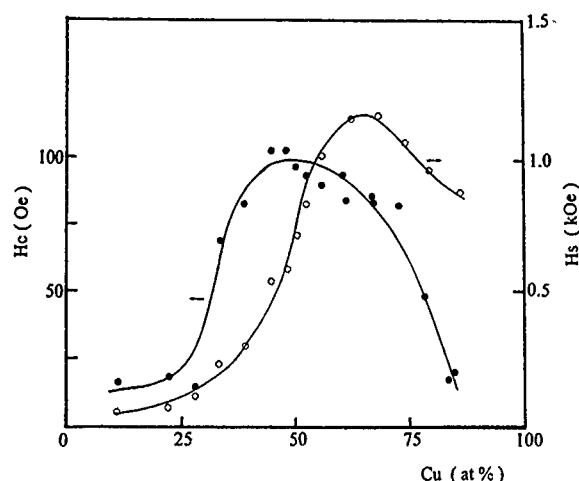


FIG. 4. The Cu content dependence of the saturation field H_s and the in-plane coercivity H_c .

properties. ΔH_{para} was generally higher than ΔH_{perp} in all the samples. This could arise from an inhomogeneous demagnetization field in the film plane due to the interspersing of Co and Cu clusters. For a given composition both ΔH_{para} and ΔH_{perp} remain almost independent of p_{Ar} in the range 6–23 mTorr but show a rapid increase by a factor of 7 for $p_{Ar}=3.5$ mTorr. This is due to inhomogeneous line broadening and it can be inferred that very low p_{Ar} leads to inhomogeneity. This cannot be due to Ar inclusion which is known to occur only for high Ar pressures. Therefore we attribute this to the inhomogeneity caused by the high kinetic energy of the adatoms resulting from lesser collisions due to a large mean free path at the fairly low Ar pressure. This leads to more mixing of Co and Cu and the resonance fields are perturbed by the presence of nonmagnetic inclusion of Cu. Also at low argon pressures, plasma instability occurs. Finally the study of the thickness dependence of ΔH_{perp} showed that it decreases from 90 to 70 Oe when the film thickness is increased from 300 to 1400 Å and then decreases only slightly for 2600-Å-thick sample. So the following standard conditions of preparation were adopted; $p_{Ar}=6$ mTorr, rf power=80 W, and film thickness=1400±200 Å. The properties of the samples with different Cu content are discussed below.

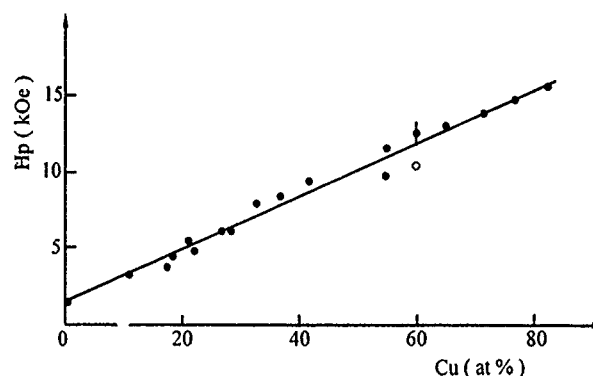


FIG. 5. The Cu content dependence of the perpendicular anisotropy H_p assuming a demagnetization field of $4\pi M$. corresponds to after annealing at 405 °C. See the text.

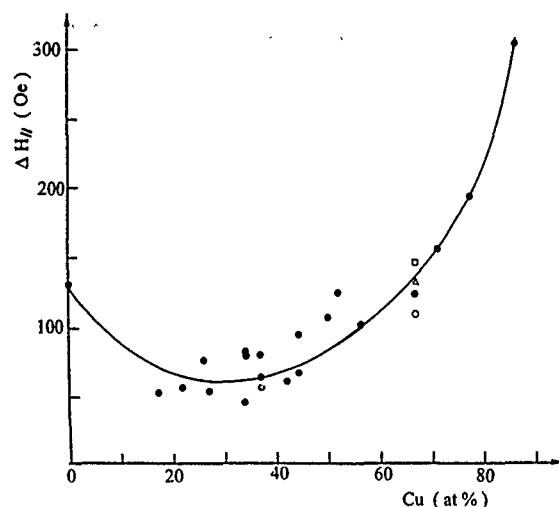


FIG. 6. The Cu content dependence of the parallel FMR line width ΔH_{para} . Also are shown data for $x=67$, for film thicknesses \square 300 Å, \triangle 720 Å, \bullet 1200 Å, \circ 2600 Å, respectively.

The FMR spectra in composite films are to be distinguished from those on multilayers where oscillatory coupling exists between the magnetic layer and where supplementary resonance modes have been observed.⁶ The FMR spectra with H in the film plane showed a single intense mode except in the very few cases where a very small shoulder could be observed at the lower field side which we have neglected for the present discussion. However, the perpendicular spectra of all the samples consisted of an intense mode followed at lower fields by two or sometimes, three satellite modes of smaller ($\sim 5\%$) intensity as compared to the first one. These modes are not standing spin waves as shown by the absence of a quadratic behavior in their field positions and the random way in which their intensities varied. No clear correlation could be established between the spacing of the modes and either the Cu content or the film thickness. Apparently the composite nature of the samples perturbs these modes which could be eigenmodes. From the parallel and perpendicular resonance fields we calculated the g factor and effective demagnetization $4\pi M' = 4\pi M - H_p$, where we have implicitly assumed that the demagnetization factor corresponds to that of a thin film. For the calculation we considered only those resonance modes which yielded the g factor close to 2.2 typical of Co. From $4\pi M'$ one can calculate H_p , provided one knows the value of $4\pi M$. If we consider only the Co clusters which are participating in the resonance then $4\pi M$ has to be taken as 17.5 kG based on the measured M values. In this case H_p increases almost linearly with the Cu content as shown in Fig. 5. These H_p values are unreasonably large because the in-plane loops study shows that the magnetization is essentially in the film plane. One might therefore ask what would be the real demagnetization factor in such composite films which consist of clusters and are not homogeneous. From TEM studies we had inferred that the average cluster size was about 240 Å. Considering the films thickness, which is 1200 ± 100 Å, the aspect ratio is not any-

more that of a thin film. Therefore the demagnetization factor N which creates the internal field $N(4\pi M)$ should be much less than one normally used for thin films. Calculation of the exact demagnetization factor is quite complex for the clusters with which we are concerned.⁷ If one assumes as a first approximation, $N=0.5$ which is reasonable then the demagnetization field becomes $2\pi M$. In this case the H_p values reported in Fig. 5 will have to be halved. These H_p values are more reasonable and consistent with the easy plane loops observed. There could be some contribution to H_p from magnetoelastic energy ($\sigma \times \lambda$) (where the first and second terms represent the stress and the magnetostriction) due to stresses arising from the Cu clusters which surround the Co ones. Of course some stress would also be created by the sputter growth process. Indeed we annealed some samples in a vacuum of about 5×10^{-6} Torr for a duration of 3 h and studied the effect on the magnetic properties. No change was observed for annealing temperatures up to 300 °C. However annealing at 405 °C produced some changes in the FMR properties. No change in the magnetization was observed as was expected because the magnetization cannot exceed that of bulk cobalt but a decrease in H_p was observed as shown in Fig. 5 for $x=60$ at. %. This reduction could be attributed to the relieving of some of the stress hence a reduction in the magnetoelastic anisotropy. Annealing at 405 °C also leads to a small increase in coercivity of about 15%. The coercivity depends on the microstructure which was possibly modified by the annealing treatment. More structural work is needed to interpret this result.

As regards the Cu concentration dependence of the linewidth, the ΔH_{perp} remains constant at 80 ± 20 Oe for $17 \leq x \leq 60$ and for $x \geq 60$ it increases rapidly to a value of 200 Oe. But ΔH_{para} shows a totally different behavior as shown in Fig. 6. It decreases initially with the Cu addition and after showing a broad minimum starts increasing rapidly for $x \geq 60$ to reach a value of 300 Oe for $x=82$. In the same figure is also shown the linewidth for samples with $x=67$, with thicknesses 300, 720, 1200, and 2600 Å, the highest linewidth being for the thinnest sample as mentioned earlier. More structural studies are needed to understand the above results and are in progress.

We wish to thank Y. Dumond for the determination of composition and Dominique Imhoff for helping with STM studies.

¹B. Abeles, in *Applied Solid State Science: Advances in Materials and Device Research*, edited by R. Wolfe (Academic, New York, 1976), p. 1, and references therein.

²M. Gadanne, P. Gadanne, M. T. Ramdou, J. P. Segaud, H. Lassri, R. Krishnan, and C. Sella, *Proceedings of the Materials Research Society Symposium*, Strasbourg, 3–6 November 1992 (to be published).

³A. E. Berkowitz, J. R. Mitchell, M. J. Carey, A. P. Young, S. Zhang, F. E. Spada, F. T. Parker, A. Hutten, and G. Thomas, *Phys. Rev. Lett.* **68**, 3745 (1992).

⁴J. Q. Xiao, J. S. Jiang, and C. L. Chien, *Phys. Rev. Lett.* **68**, 3749 (1992).

⁵E. Kneller, *J. Appl. Phys.* **33**, 1355 (1962).

⁶P. E. Wigen, Z. Zhang, L. Zhou, M. Ye, and J. A. Cowen, *J. Appl. Phys.* **73**, 6338 (1993).

⁷J. A. Osborn, *Phys. Rev.* **67**, 351 (1945).

Structure and magnetism of heat-treated nanocrystalline $\text{Cu}_{80}\text{Co}_{20}$ powders prepared via chemical means

V. G. Harris, F. H. Kaatz, V. Browning, D. J. Gillespie, R. K. Everett, A. M. Ervin, W. T. Elam, and A. S. Edelstein

U.S. Naval Research Laboratory, Washington, D.C. 20375

Nanocrystalline $\text{Cu}_{80}\text{Co}_{20}$ powders were fabricated using a chemical precipitation technique. As-prepared powders consist of metal-oxides having an average particle size of 100 Å. When appropriately heat treated, these powders reduce to form a CuCo face-centered cubic alloy; heat treatments at higher temperatures ($\geq 400^\circ\text{C}$) facilitate the phase separation of the alloy to its elemental components. Concurrent with an increase in annealing temperature, the coercive field decreases while the magnetization increases, reflecting particle coarsening and the relative amount of free cobalt in the mixture.

I. INTRODUCTION

Nanoscale particles have proven useful in a very diverse range of applications ranging from catalysts and composites to magnetic storage media. Our interest in CuCo nanoparticles is to investigate the possibility of expanding the limited miscibility region of the Cu-Co equilibrium phase diagram using chemical processing. A related interest is to investigate if such metastable alloys, after appropriate heat treatments, show an enhanced magnetoresistance effect similar to that exhibited by metastable alloys processed via vapor-quenching^{1,2} and melt-spinning techniques.^{3,4}

In this paper we report the fabrication of nanostructured metastable CuCo particles via a chemical reduction technique. In this technique, transition metal-oxides are precipitated from solution and reduced to a metallic alloy by heat treatment at 400°C under H_2 gas flow. Heat treatments at temperatures $\geq 400^\circ\text{C}$ cause this alloy to phase separate to its elemental components. Magnetoresistance (MR) measurements of compacted annealed powders show a modest MR effect of 1% at 2 K in high-porosity compacts.

II. EXPERIMENTAL

Metallic powders consisting of Cu and Co were prepared using a chemical precipitation technique. Details of the sample processing will be presented elsewhere.⁵ Samples were heat treated under flowing H_2 gas at temperatures ranging from 200 to 650°C for a period of 60 min. This heat treatment procedure was found to be effective in selectively removing the oxygen from the samples reducing them from oxides to metals. Structural, chemical, and magnetic measurements of the as-prepared and heat-treated samples were performed *ex situ* under ambient conditions. Structural characterization was performed using extended x-ray absorption fine structure (EXAFS), x-ray diffraction (XRD), and electron microscopy measurements. The magnetic properties of the samples were measured using a vibrating sample magnetometry (VSM). Cold-pressed pellets made from the heat-treated powders were measured for their MR [$\Delta\rho/\rho = (\rho - \rho_0)/\rho_0$; ρ_0 =zero field applied] properties using a collinear four point probe technique at a temperature of 2 K and an applied field strength of 5 T.

We limit our discussion here to include XRD, EXAFS, and VSM results. We find that the use of both a long-range structural probe, XRD, and a short-range structural probe, EXAFS, are needed to obtain a coherent picture of the structural evolution of these powders with heat treatment. XRD analysis was performed using a $\text{Cu}_{K\alpha}$ source operating in a θ - 2θ diffractometer while EXAFS measurements of the Co and Cu K absorption edges were performed at the National Synchrotron Light Source in transmission mode on NRL's beamline, X23B. EXAFS analysis procedures follow those outline in Ref. 6 leading to Fourier transforms of the Co and Cu EXAFS data. In this form the EXAFS data are analogous to a partial radial distribution function where the position and amplitude of Fourier peaks typically correspond to atoms in the local environment around the absorbing atom.

III. RESULTS AND DISCUSSION

A. Structural evolution with heat treatment

Figure 1 is a plot of the XRD patterns for $35^\circ \leq 2\theta \leq 55^\circ$ for the samples heat treated at 265, 330, 400, and 650°C . All features in the diffraction scans can be identified with metallic-oxides or an fcc metallic phase. Dark field transmission electron microscopy (TEM) images of the as-prepared powder show particles to be spherical in shape and range in size from 50 to 100 Å in diameter. A smaller number of larger particles, ranging in size from 200 to 400 Å, were also observed. Selected area diffraction showed broad diffuse rings characteristic of nanocrystalline structures.

After an anneal at 265°C , the XRD pattern indicates that the powder has been substantially reduced, with only weak diffraction features corresponding with the precipitate phase. The dominant phase in this annealed sample is the Cu_2O phase with evidence for small amounts of CuO and possibly free fcc Cu. It is unclear in which phase the Co atoms reside. Several stable CuCo-oxides exist and some have diffraction features which overlap those in Fig. 1. However, no match was made to the diffraction files of these phases leading us to conclude that the Co has been incorporated into the Cu_2O phase but has not formed an ordered $(\text{Cu}_x\text{Co}_{1-x})_2\text{O}$ structure.

Fourier transformed Co EXAFS data for the sample annealed at 265°C are presented as the solid curve in Fig. 2(a).

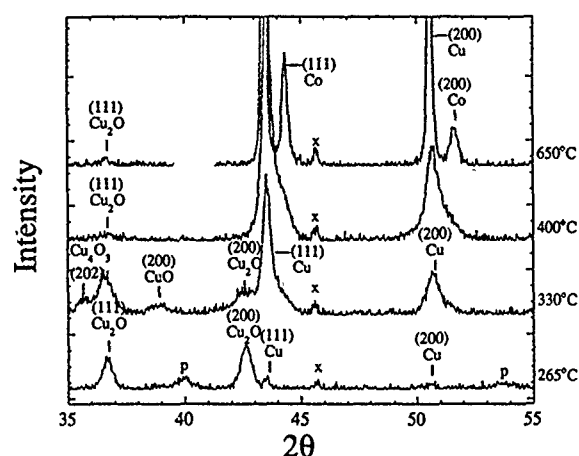


FIG. 1. X-ray θ - 2θ diffraction patterns for heat-treated powder samples. All diffraction features are identified on the plot. (x: contamination from processing; p: precipitate phase).

The dominant features of the data presented in Fig. 2 have been identified by comparison to Fourier transformed EXAFS data collected from an empirical standard. The Fourier peaks labeled with a superscript "o" correspond to neighbors in an oxide phase while those labeled with a superscript "m" correspond with neighbors in a close-packed metal phase. The subscript defines the number of the atomic shell relative the absorber. Figure 2(a) indicates that the 265 °C annealed sample has only oxide neighbors in its local environment. Although, higher order neighbors may include transition metals they appear at distances and with relative amplitude which match those of the oxide phases.

The diffraction pattern following an anneal at 330 °C is dramatically different, having strong diffraction peaks at 2θ values of 43.5° and 50.7°, corresponding with the (111) and (200) lines of the fcc-Cu phase. Concurrent with the heat treatment, the diffraction features for the Cu_2O phase are seen to decrease in intensity and those corresponding with the precipitate phase are no longer visible. Small diffraction features exist which correspond with minority phases of CuO , Cu_2O , and Cu_4O_3 . Again no evidence is seen for the presence of any Co phase. The very broad Cu lines, having a slight asymmetry on the right-hand side corresponding with a smaller d spacings, suggests that the Co may reside with the Cu in the fcc structure. The Fourier transformed Co EXAFS data for the 330 °C sample, presented as the dashed curve in Fig. 2(a), support this interpretation. In contrast to the 265 °C Fourier transformed data, these data illustrate a well-resolved, large Fourier peak centered at 2.2 Å corresponding to a transition metal near neighbor in the fcc structure (uncorrected for electron phase shifts). Peaks appearing at higher radial distances ($3 \text{ Å} \leq r \leq 5 \text{ Å}$) also correspond with fcc sites. The small peak centered near 1.5 Å and the shoulder on the left-hand side of the 2.2 Å Fourier peak indicates that not all of the Co atoms occupy fcc sites, some remain in oxide phases. Taken together, the results of the XRD and the EXAFS indicate that the Co atoms in the sample annealed at 330 °C predominantly occupy lattice po-

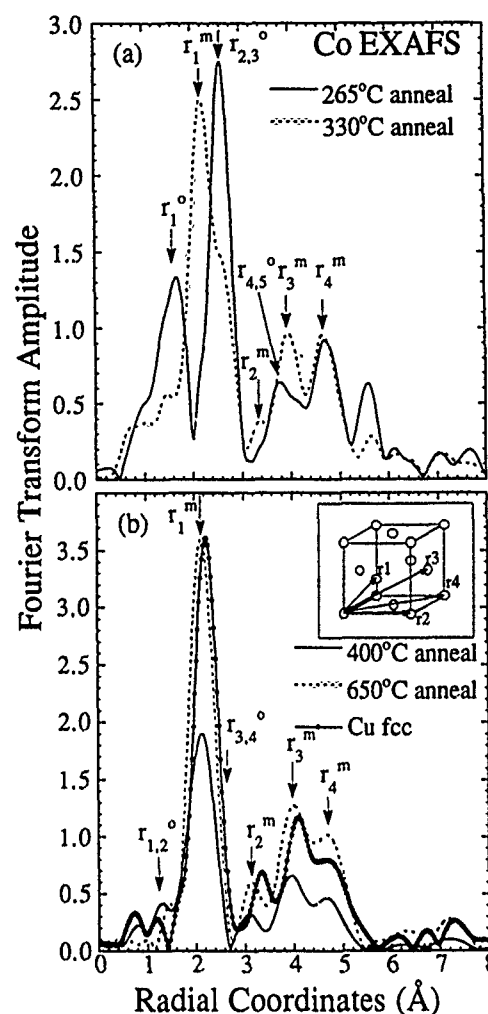


FIG. 2. Fourier transformed Co EXAFS data for samples heat treated at (a) 265 and 330 °C, and (b) 400 and 650 °C. Fourier transformed EXAFS data for a fcc Cu standard is presented in (b) to allow qualitative comparisons. Fourier transforms were performed using k ranges of 2.5–14 Å^{-1} and a k^2 weighting. Electron phase shift corrections have not been incorporated in these data therefore radial distances do not represent true bond lengths.

sitions within a metallic, close-packed, structure having a lattice parameter very close to that of fcc Cu. This suggests that the Co atoms have transformed with heat treatment from the Co-oxide to a disordered CoCu-oxide and finally to a CuCo alloy.

A heat treatment at 400 °C is seen in Fig. 1 to further reduce the oxide content of the powder; the diffraction features of the minority Cu-oxide phases have nearly been eliminated. The dominant features of these data are identified with the Cu-rich fcc phase. The asymmetry seen in the XRD data for the 330 °C annealed sample appears as a pronounced shoulder in the XRD scan of the 400 °C annealed sample suggesting that the Co in the Cu matrix has begun to chemically separate from the Cu matrix but has not yet formed fcc Co particles. The Fourier transformed Co EXAFS data for this sample are presented as the solid curve in Fig. 2(b) together with the data for the sample annealed at 650 °C and the fcc Cu data; the latter presented for qualitative comparison purposes. The inset graphic defines the relationship between the Fourier peaks and the fcc lattice sites. All Fourier

features are seen to correspond with the metallic fcc structure. The excessive broadness of the near neighbor peak hints that the structure is disordered and likely exists as small grains only a few unit cells in diameter. Supporting this interpretation, TEM analysis and selected area diffraction were insensitive to the presence of the Co fcc phase.

Annealing at a temperature of 650 °C facilitates a phase separation of the CuCo alloy to Co and Cu fcc phases. The shoulder features seen in the 400 °C XRD data now appear as resolved peaks at lower d spacings corresponding to the fcc Co phase. A small diffraction feature appears at a d spacing which matches that of the Cu₂O phase. This is the only evidence that oxidation has occurred in these powders. TEM analysis of the powders annealed at 650 °C show a slight coarsening of the particles to a mean diameter size ranging from 100 to 200 Å; a smaller number of larger particles ranging in size from 400 to 600 Å are also observed. The distances and relative amplitudes of the peaks in the Fourier transformed Co EXAFS data for this sample match closely with those of the Cu fcc standard. The shifts in the distances of the Fourier peaks over the 1–5 Å range between the Cu standard and the Co EXAFS of the annealed sample are expected due to the Co-Co and Co-Cu correlations; Co being a slightly smaller atom than Cu.

B. Magnetic properties

The magnetic properties of powders annealed at 265–650 °C are presented in Fig. 3 with the magnetization versus applied field (M vs H) curves presented as the inset plot to Fig. 3. VSM measurements of the as-prepared and 265 °C annealed samples show them to be paramagnetic with no evidence of a ferromagnetic component. The sample annealed at 400 °C illustrates a ferromagnetic behavior in its M vs H curve. This corresponds with the appearance of the metallic CuCo alloy in the XRD and EXAFS data indicating that some of the Co has chemically segregated from within the Cu lattice to form ferromagnetic particles or regions.

The M vs H curves for annealed samples appear to nearly saturate at an applied field of 8 kOe but a paramagnetic slope is clearly present. The paramagnetic slope is likely caused from those Co atoms remaining within the Cu lattice and surrounded predominately by Cu atoms. A similar paramagnetic signature was observed in vapor-quenched films and melt-spun ribbons having similar composition and heat treatment histories; this was also attributed to Co atoms stabilized in the Cu matrix.^{1–4} Figure 3 illustrates the trend in magnetic properties with annealing temperature. The coercive field decreases while the magnetization values increase reflecting the particle coarsening and the segregation of fcc Co, respectively.

In an attempt to investigate the magnetotransport properties of these samples the CuCo powder annealed at 650 °C for 60 min was compacted using an uniaxial pressure of approximately 500 MPa. The resulting compact was measured to have a density of 61% (of the theoretical bulk) and a room temperature electrical resistivity of $\approx 300 \mu\Omega \text{ cm}$ (200 $\mu\Omega \text{ cm}$ at 2 K). A modest MR of 1% was measured at 2 K. We believe the high electrical resistivity and lower than ex-

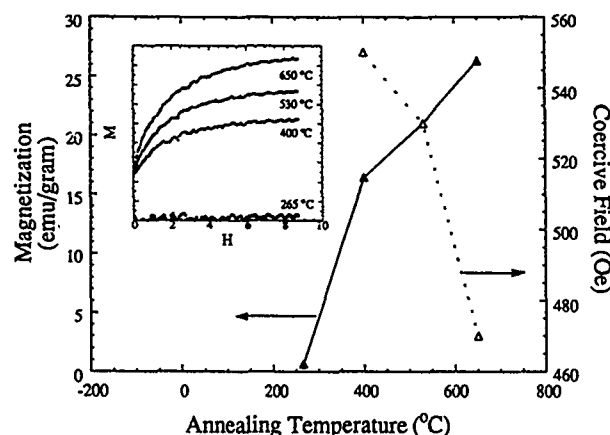


FIG. 3. Magnetization and coercive field values for annealed powders as a function of annealing temperature. Inset plotted data are M vs H curves for annealed samples illustrating the trend of increasing magnetization with annealing temperature.

pected MR effect are related to the high porosity of the compact. Following a cold-forging procedure which increased the pellets density from 61% to approximately 70% the room temperature electrical resistivity was reduced to 30 $\mu\Omega \text{ cm}$ (18 $\mu\Omega \text{ cm}$ at 2 K); an order of magnitude decrease. Hot-isostatic pressing improved the density of the compact to $\approx 95\%$ and lowered the electrical resistivity to 4.5 $\mu\Omega \text{ cm}$ (2.5 $\mu\Omega \text{ cm}$ at 2 K). However, the MR effect decreased by a factor of 2 as a result of the improved densification. The lack of a “giant” MR in this compacted Cu₈₀Co₂₀ powder can be attributed to: (1) the large field independent component of the MR arising from the scattering across the particle interface, possibly enhanced due to a thin oxide layer, or (2) the mixing of particle interfaces brought about by sample heating during forging. Investigations are underway to further explore the processing dependence of the magnetic and transport properties of these powders.

ACKNOWLEDGMENTS

We thank Dr. A. E. Erhlich for valuable discussions concerning the magnetoresistance data. This research was carried out in part at the National Synchrotron Light Source (Brookhaven National Laboratory, Upton, NY), which is sponsored by the U.S. Department of Energy (Division of Materials Science and Division of Chemical Science of the Office of Basic Energy Sciences). F. H. K. acknowledge support from the National Research Council—Naval Research Laboratory fellowship program.

¹A. E. Berkowitz, J. R. Mitchell, M. J. Carey, A. P. Young, S. Zhang, F. E. Spada, F. T. Parker, A. Hutton, and G. Thomas, *Phys. Rev. Lett.* **68**, 3745 (1992).

²J. Q. Xiao, J. S. Jiang, and C. L. Chien, *Phys. Rev. Lett.* **68**, 3749 (1992).

³B. Dieny *et al.*, *J. Magn. Magn. Mater.* (in press).

⁴V. G. Harris, B. N. Das, M. Kubinstein, J. L. Goldberg, W. T. Elam, and N. C. Koon, *IEEE Trans. Magn.* **29**, 2664 (1993).

⁵A. S. Edelstein (to be published).

⁶D. E. Sayers and B. A. Bunker, in *X-ray Absorption: Basic Principles of EXAFS, SEXAFS, and XANES*, edited by D. C. Koningsberger and R. Prins (Wiley, New York, 1988).

Relaxation measurements and particle size determination in Co-Ag heterogeneous alloy films

S. B. Slade, F. T. Parker, and A. E. Berkowitz

Center for Magnetic Recording Research, Mail Code 0401, University of California, San Diego, La Jolla, California 92093-0401

Magnetic properties of dilute Co-Ag heterogeneous alloy films are investigated to test the Néel model of magnetic relaxation. The static properties indicate a narrow particle size distribution for each sample. Dynamic susceptibility measurements indicate a frequency dependence for the susceptibility peak that is not consistent with the Néel model.

INTRODUCTION

There exists a need to test the Néel model of magnetic viscosity¹ on well-characterized samples.² An impressive body of experiments on ferrofluids,³ for example, indicates a logarithmic time dependence for the magnetization, even though the Néel model predicts an exponential decay with time. A wide distribution of relaxation times is usually cited as the cause of the logarithmic decay,⁴ with deviations from $\ln(t)$ behavior attributed to interactions or the distribution itself.⁵ Because of the wide distribution and interactions, the basic expression is not usually questioned. Our work focuses on characterizing dilute Co-Ag granular films in detail, so that a theoretical model can be developed from the data using a minimum of adjustable parameters.

SAMPLE PREPARATION

Heterogeneous Co-Ag alloy films were produced using dc magnetron sputtering from separate targets onto a rotating planetary substrate heated to 80 °C. Films approximately 1 mm thick were deposited onto 1 ml Kapton substrates after back-sputtering for 15 min. Films of pure Ag were also prepared under identical conditions to serve as references. Atomic absorption measurements indicated a film thickness of 9000 Å and a Co concentration of 5% by volume. Samples of the films were annealed in flowing hydrogen for 8 h at 200 °C. Preliminary TEM analysis indicates the films consist of FCC Co precipitates dispersed in a polycrystalline FCC Ag matrix.

dc MAGNETIC MEASUREMENTS

Static magnetic measurements as functions of field and temperature were performed using a SQUID magnetometer in order to determine the Co particle sizes and distributions. In each case the data were corrected for Kapton and Ag contributions. Figure 1 shows magnetization curves measured at 50, 100, 200, and 300 K for both samples. These temperatures are well above each sample's blocking temperature, allowing a superparamagnetic analysis to be performed. The data at each temperature were fit to a Langevin function having a lognormal distribution of particle volumes. No additional anisotropy or susceptibility terms were used in the fit. The adjustable parameters for these fits are the sample's saturation magnetization M_s , the geometric mean volume $\langle V \rangle_G$, and the distribution width parameter σ_v . In the figure the value of $\langle V \rangle_G$ is given as $\langle D \rangle_G$, the diameter of a

particle with volume $\langle V \rangle_G$. All the Co is assumed to contribute to the moment, and the magnetization of each Co cluster is fixed at 1435 emu/cm Co, a value determined by measuring the moment of the annealed sample at 1.75 K in 70 kOe. The fits were all of a high quality, as evidenced by the low uncertainties in the fit parameters, reasonable values of M_s , and low values of chi squared. The results for each sample at $T=100$ K, which are typical of the fits at all temperatures, are indicated in the figure.

Figure 2 shows the dc susceptibility measured after cooling in zero field to 6 K (ZFC), and the susceptibility measured after cooling in 50 Oe to 6 K (FC) for each sample. For both ZFC and FC the susceptibility was determined by calculating a linear fit to the moment measured in fields of 10, 20, 30, 40, and 50 Oe at each temperature. Annealing is seen to shift the peak in the ZFC susceptibility from 11 K to 8.5 K. Similar downward shifts have been reported for more concentrated Co-Ag films.⁶ The temperature of the peak in

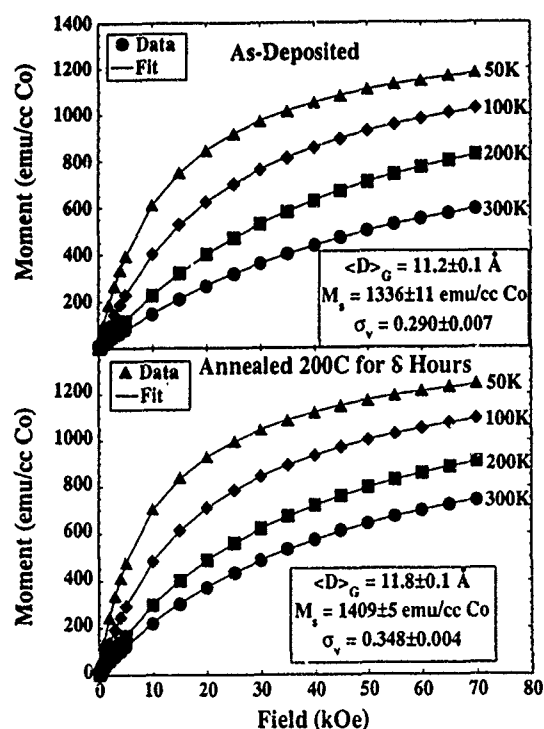


FIG. 1. Magnetization curves measured at the indicated temperatures. The solid lines are the calculated fits at each temperature. Parameters listed are for the $T=100$ K data.

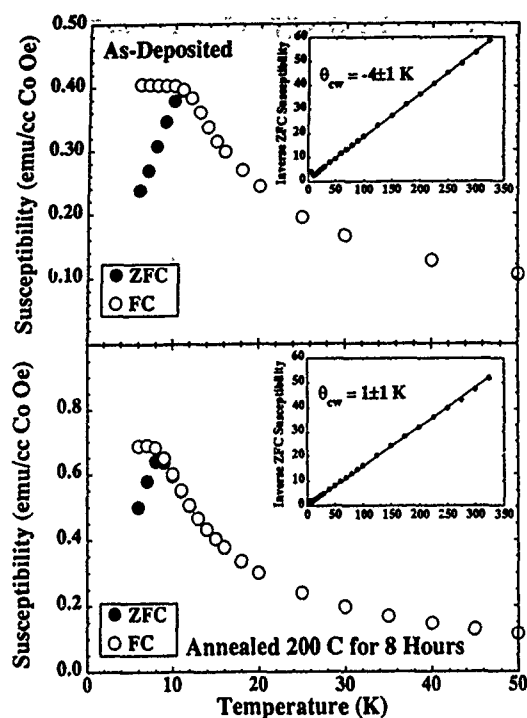


FIG. 2. ZFC and FC susceptibility. Inset: inverse of the ZFC susceptibility.

the ZFC data is identified as the blocking temperature, T_b , for the mean particle volume in the sample. No divergence is seen between the ZFC and FC data until the ZFC peak in the as-deposited film. The annealed film shows divergence between the ZFC and FC below 11 K. This divergence is small, and may not be apparent in the figure. The onset of irreversibility is indicated by the divergence of the FC and ZFC susceptibilities. The field applied during cooling partially aligns the moments of the particles, and once those particles are cooled to below their blocking temperatures they will exhibit irreversible behavior. With decreasing temperature, this irreversibility will first appear in the largest particles in the sample, and as such may help to indicate the width of the size distribution. The data from the annealed film indicate a very narrow distribution of particle sizes, with the largest particles becoming blocked at 11 K, and the majority blocked at 8.5 K. The as-deposited data indicate a still narrower distribution, with essentially all the particles blocking at 11 K. The inset of Fig. 2 shows the inverse of the ZFC susceptibility. Extrapolation to the temperature axis determines the value of the Curie-Weiss constant θ_{CW} , which is a measure of the strength of particle interactions. The as-deposited data extrapolate to $\theta_{CW} = -4 \pm 1$ K, while the annealed sample extrapolates to $\theta_{CW} = 1 \pm 1$ K. These data indicate there may be some weak net antiferromagnetic interactions in the as-deposited sample, presumably from interparticle exchange, while the annealed sample is noninteracting within the uncertainty of the extrapolation. The total anisotropy, K , assumed to be uniaxial, can be estimated from T_b and the known volume distribution using a simulation of the dc susceptibility (discussed below) and the Néel relation¹ $K = k_B T_b \ln(t_{\text{meas}}/\tau_0)/V$. Here k_B is the Boltzmann's constant, t_{meas} is the measurement time, taken to be 100 s, and τ_0 is

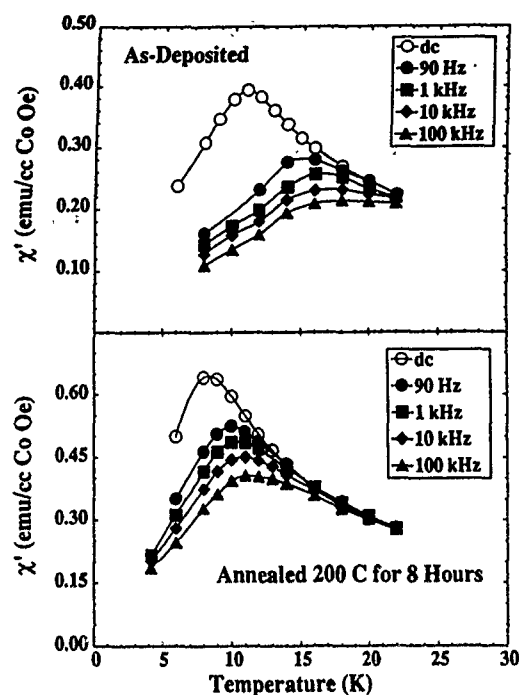


FIG. 3. In-phase ac susceptibility, χ' , measured in the 3 Oe field. Also shown is the dc ZFC susceptibility. The lines are guides for the eye.

taken to be 10^{-10} s, representing the inverse of an attempt frequency for switching over the anisotropy barrier to reversal. The anisotropy analysis assumes the peak in the ZFC susceptibility is entirely due to the blocking of superparamagnetic particles. This assumption seems reasonable, given the very small values of θ_{CW} . The value of K for each sample is determined by matching the experimental data to the simulation, with K the only adjustable parameter. The result is $K = 4.1 \times 10^7$ erg/cm³ for the as-deposited and 2.4×10^7 erg/cm³ for the annealed sample. These values are higher than the 1.2×10^6 erg/cm³ maximum cubic crystalline anisotropy reported for FCC Co⁷ or the maximum uniaxial shape anisotropy of 6×10^6 erg/cm³. Similar high anisotropy values have been reported for other granular films^{8,9} and attributed to surface anisotropy or a stress-induced anisotropy. If part of the observed anisotropy is stress related, then the lower value for the annealed sample may be due to stress relief. However, the value of M_s used will not reflect the true particle moment if some of the Co is in the Ag matrix, or if the matrix contributes a separate susceptibility due to the presence of Co in the matrix. A different M_s value would change the particle size, which, in turn, would change K .

ac SUSCEPTIBILITY

Measurements of the ac susceptibility taken after four decades of frequency in a 3 Oe (zero-to-peak) field as a function of temperature after cooling in the zero field were made using an ultrahigh sensitivity ac susceptometer.¹⁰ This instrument allows for the simultaneous measurement of the in-phase and out-of-phase signal components with a noise level below 10^{-8} emu. Figure 3 summarizes the susceptibility data for each sample. In general, the susceptibility peak

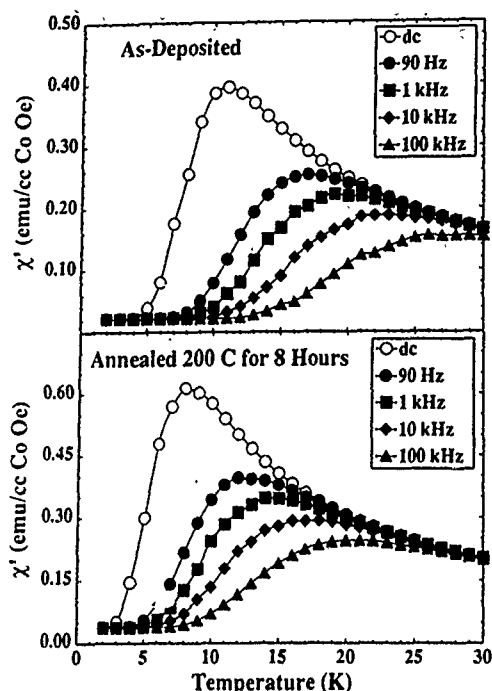


FIG. 4. Numeric simulations based on the Néel model of magnetic relaxation. The lines are a guide for the eye.

shifts to higher temperatures and broadens with increasing measurement frequency. At $T = T_b$, the relaxation time, τ , is equated to the measurement interval, t_{meas} , taken to be the half-period of the applied field. The frequency dependence of T_b can be used to investigate the relaxation time, predicted by the superparamagnetic Néel model for isolated particles as $\tau = \tau_0 \exp(KV/k_B T_b)$. The shift of T_b with increasing measurement frequency is an excellent method of verifying the functional form of this equation. However, given the highly nonlinear dependence of τ on V , and a sample having a distribution of particle volumes, it is not reasonable to expect the value of τ found from using $V = \langle V \rangle_G$ will accurately predict the relaxation time for the entire distribution.

Numeric simulations on particle assemblies having a lognormal distribution of particle volumes and the parameters found from fitting the magnetization curves were studied to determine if the Néel relaxation time expression accurately predicts the observed ac susceptibility. The simulations calculate τ for each particle in the distribution and then assign a blocked or superparamagnetic susceptibility depending on whether $\tau > t_{\text{meas}}$ or $\tau < t_{\text{meas}}$, respectively. Figure 4 shows the simulated susceptibility for each sample. The numeric simulations have a much greater frequency dependence of T_b than the experimental data. Comparison with the

experimental data clearly indicates the Néel relaxation time equation does not have the correct functional form to account for the observed frequency dependence of T_b . Assuming the functional form of the relaxation time equation involves a simple exponential, a plot of $\ln(\tau)$ vs $1/T_b$ for each frequency will provide a measure of the frequency pre-factor, τ_0 . The values calculated by this method are 3×10^{-26} s for the as-deposited film and 2×10^{-26} s for the annealed film. Both values are unphysical within the Néel model. The much smaller frequency dependence of the experimental data results in the unphysical values of τ_0 determined above. Several different models for the relaxation time equation have been proposed in the study of spin glasses.¹¹ In particular, a Vogel-Fulcher analysis is often used on ac susceptibility data which has a small frequency dependence of T_b . This type of analysis leads to an ordering temperature of $T_0 = 2.5$ K for the as-deposited sample and $T_0 = 8$ K for the annealed sample, both of which are inconsistent with our χ^{-1} data.

CONCLUSION

Static and dynamic magnetic measurements have been performed on dilute Co-Ag heterogeneous alloy films, both as-deposited and annealed. The dc data indicate a very narrow size distribution that can be fit using the basic equations of superparamagnetism for a sample having a lognormal distribution of particle volumes. The ac susceptibility data from both samples exhibit much less frequency dependence of T_b than predicted by the Néel model of magnetic relaxation, resulting in unphysical values of the exponential pre-factor, τ_0 .

ACKNOWLEDGMENT

This work was supported by the National Science Foundation Grant No. DMR-90-10908.

- ¹ L. Néel, *Ann. Geophys.* **5**, 79 (1949).
- ² A. Aharoni, *J. Appl. Phys.* **5**, 4702 (1985).
- ³ A. T. Cayless, S. R. Hoon, B. K. Tanner, R. W. Chantrell, and M. Kilner, *J. Magn. Magn. Mat.* **30**, 303 (1983).
- ⁴ A. Labarta, O. Iglesias, L. I. Balcells, and F. Badia, *Phys. Rev. B* **48**, 10 240 (1993).
- ⁵ M. El-Hilo, K. O'Grady, and R. W. Chantrell, *J. Magn. Magn. Mat.* **109**, L164 (1992).
- ⁶ A. E. Berkowitz, J. R. Mitchell, M. J. Carey, A. P. Young, D. Rao, A. Starr, Z. Zhang, F. E. Spada, F. T. Parker, A. Hutten, and G. Thomas, *J. Appl. Phys.* **73**, 5320 (1993).
- ⁷ C. P. Bean, J. D. Livingston, and D. S. Rodbell, *J. Phys. Rad.* **20**, 298 (1959).
- ⁸ C. Djega-Mariadassou, J. L. Dormann, M. Nogues, G. Villers, and S. Sayouri, *IEEE Trans. Magn.* **26**, 1819 (1990).
- ⁹ G. Xiao, S. H. Liou, A. Levy, J. N. Taylor, and C. L. Chien, *Phys. Rev. B* **34**, 7573 (1986).
- ¹⁰ S. B. Slade and A. E. Berkowitz, *IEEE Trans. Magn.* **28**, 3132 (1992).
- ¹¹ D. Fiorani and J. L. Dormann, *J. Phys. C* **19**, 5495 (1986).

Studies of magnetic interactions between Gd granules in copper matrix

J. H. Hsu and Y. H. Huang

Department of Physics, National Taiwan University, Taipei, Taiwan, China

Ultrafine Gd particles in the Cu metallic material have been obtained by rapid annealing of sputtered metastable $\text{Gd}_x\text{Cu}_{1-x}$ alloys. The particle shape and size were measured by a transmission electron microscopy. The evolution of crystal structure with annealing temperature has been investigated by x-ray diffraction and electron diffraction. It has been found that the Gd granules have formed following annealing above 300 °C and the granular size increases with rising annealing temperature. The magnetic data show that the as-sputtered metastable $\text{Gd}_{0.1}\text{Cu}_{0.9}$ and $\text{Gd}_{0.2}\text{Cu}_{0.8}$ alloys obey a Curie-Weiss law at high temperature with a negative value of θ . After annealing, the θ value varies with annealing temperature according to an oscillatory function. The evolution of the magnetic properties and microstructure during annealing are described in detail.

INTRODUCTION

Recently, the magnetic behaviors of ultrafine particles in the thin films have been investigated extensively.¹ Granular solids consist of small metal particles embedded in an immiscible medium which may be insulating or metallic. Examples of insulating medium are SiO_2 , Al_2O_3 , and MgO which are poor conductors. On the other hand, granular solids with a conducting matrix offer both good magnetic and electrical properties, e.g., high magnetization and coercivity with very low resistivity. In order to obtain such materials, however, two metal constituents must be mutually immiscible under equilibrium conditions. Gd with Cu is such an example.² From our previous studies,³ we have demonstrated that sputtering is a powerful technique for preparing metastable alloys from two mutually immiscible elements. And after post-annealing of these sputtered metastable alloys at an elevated temperature, the phase separation will occur and nanostructured composite films can thus be obtained. Besides, the granule sizes can be properly controlled by annealing conditions such as temperature and time.

The study of a copper medium containing Gd granules is also interesting from a more fundamental point of view. Single-domain particles are realized in a granular solid with low magnetic volume fraction. All moments within the particles are ferromagnetically aligned and the interactions of magnetic Gd granules in the nonmagnetic conducting material is expected to be Ruderman-Kittel-Kasuya-Yosida (RKKY) type via conduction electrons of Cu. The strengths and types of magnetic coupling strongly depend on the distance between Gd granules. By varying sputtering and annealing conditions, we can systematically study the processing effects on magnetic properties as well as microstructures. In this manner various magnetic states from these composite materials will be observed.

EXPERIMENT

The metastable $\text{Gd}_x\text{Cu}_{1-x}$ alloys ($0.4 \leq x < 1$) were prepared by dc magnetron sputtering with homogeneously mixed composite targets. The kapton foils were used as the sub-

strates which were cooled by liquid nitrogen during sputtering. The Ar pressure was maintained at 8 mTorr. Throughout this work, the $\text{Gd}_x\text{Cu}_{1-x}$ samples are denoted by their Gd relative volume fraction x .

After the alloy films were made, they have been annealed, respectively, at various temperatures in a computer-controlled furnace in a flowing argon atmosphere. Starting from 100 °C, the annealing temperature (T_A) was raised in 100 °C increments to as high as 500 °C. At each temperature, the samples were annealed for a preset time of 12 min, then cooled to room temperature. One sample was removed from oven for measurements, and other pieces were quickly heated again for annealing at the next higher temperature.

The film structures were examined by x-ray diffraction. Transmission electron microscopy (TEM) studies were used for determination of both crystal structure and microstructure of the samples. The magnetic measurements were performed on a superconducting quantum interference device in the temperature range between $5 \leq T \leq 300$ K with a maximum applied field of 5 T.

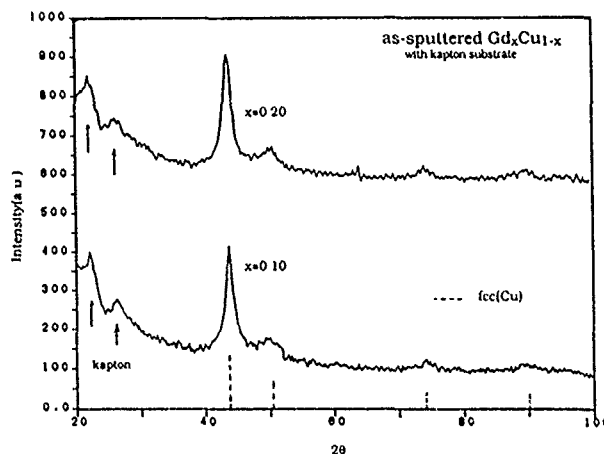


FIG. 1. X-ray diffraction patterns for as-sputtered $\text{Gd}_{0.1}\text{Cu}_{0.9}$ and $\text{Gd}_{0.2}\text{Cu}_{0.8}$ alloys with kapton substrate.

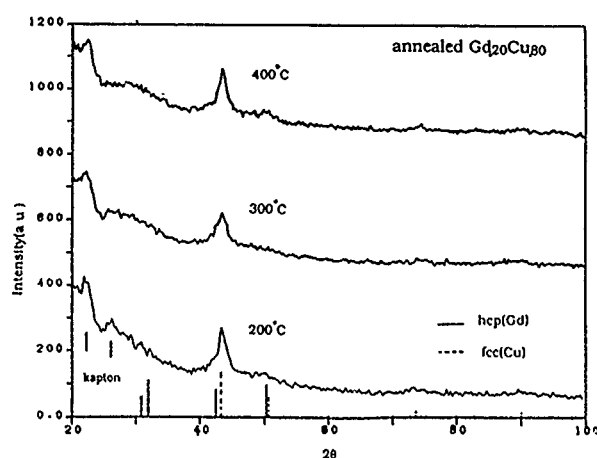


FIG. 2. X-ray diffraction patterns of $Gd_{0.2}Cu_{0.8}$ after annealing at T_A for 12 min.

RESULTS AND DISCUSSIONS

In Fig. 1 it indicates that the structures of the film with kapton substrate for as-sputtered metastable $Gd_{0.1}Cu_{0.9}$ and $Gd_{0.2}Cu_{0.8}$ contain only a face-centered cubic phase, the same as in Cu. Annealing below 300 °C does not change the microstructure appreciably as shown in Fig. 2. After annealing above 300 °C, a small broad peak at $2\theta \approx 30^\circ$ starts to appear, signaling the recrystallization of the metastable alloy into fcc Cu and hcp Gd. It is an indication that the Gd gran-

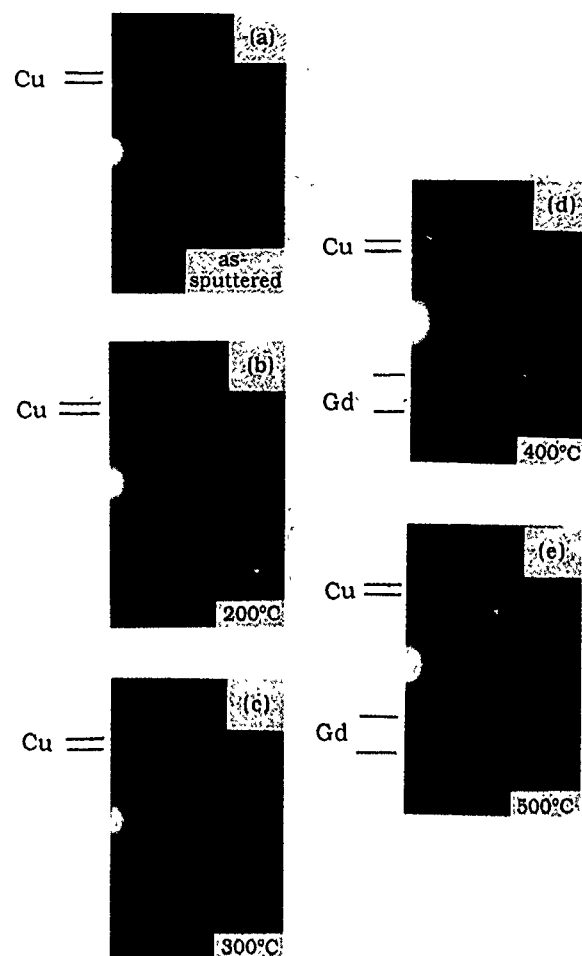


FIG. 4. Electron diffraction patterns of $Gd_{0.2}Cu_{0.8}$.

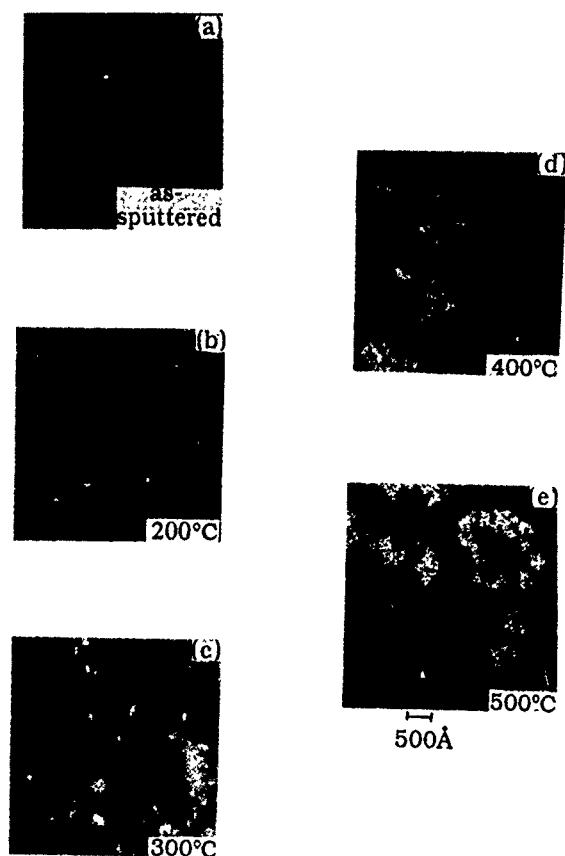


FIG. 3. TEM micrographs of $Gd_{0.2}Cu_{0.8}$.

ules have formed which can be also confirmed from TEM results as shown in Fig. 3. Furthermore, the broad peaks of Gd become more significant with increasing annealing temperature (T_A). As a result it can be determined that a rapid growth of Gd grains occurs as T_A is increased. Figure 4 illustrates the evolution of microstructure with annealing

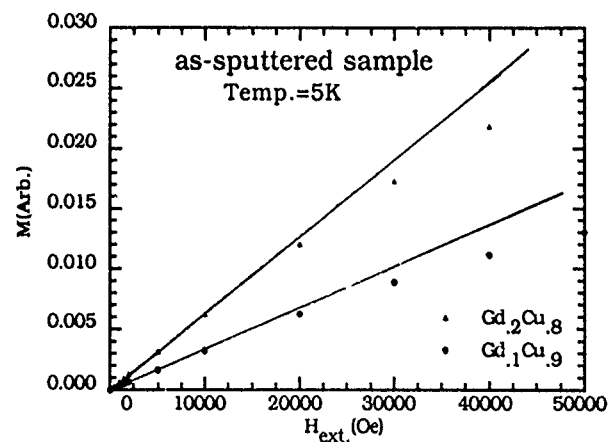


FIG. 5. Magnetization vs magnetic field for as-sputtered $Gd_{0.1}Cu_{0.9}$ and $Gd_{0.2}Cu_{0.8}$ at 5 K.

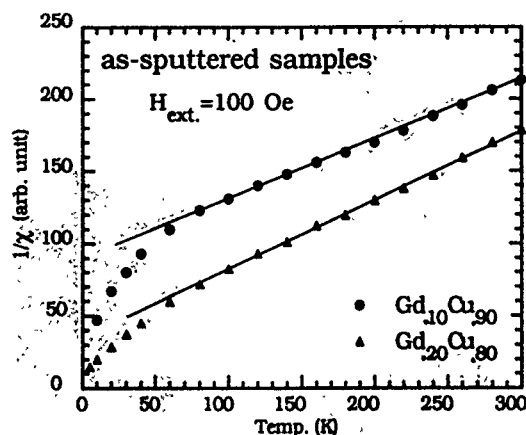


FIG. 6. Reciprocal magnetic susceptibility for as-sputtered $\text{Gd}_{0.1}\text{Cu}_{0.9}$ and $\text{Gd}_{0.2}\text{Cu}_{0.8}$ alloys as a function of temperature with an applied field of 100 Oe.

temperature. The fcc structure is preserved up to $T_A = 300^\circ\text{C}$. Following annealing above 300°C , the hcp lines of Gd suddenly appear, which continue to grow with increasing annealing temperature.

The magnetic field dependence of magnetization at 5 K for as-sputtered $\text{Gd}_{0.1}\text{Cu}_{0.9}$ and $\text{Gd}_{0.2}\text{Cu}_{0.8}$ is plotted in Fig. 5. A linear behavior has been observed for the fields smaller than 15 000 Oe and the magnetic moments of Gd atoms are not aligned even under the applied field of 5 T. Figure 6 shows the dependence of reciprocal magnetic susceptibility ($1/\chi$) on temperature for as-sputtered metastable $\text{Gd}_{0.1}\text{Cu}_{0.9}$ as well as $\text{Gd}_{0.2}\text{Cu}_{0.8}$. It indicates that there is excellent agreement with the Curie-Weiss law⁴ for both samples at temperatures above 80 K with a negative value of the constant θ which is related to parameters characterizing the mag-

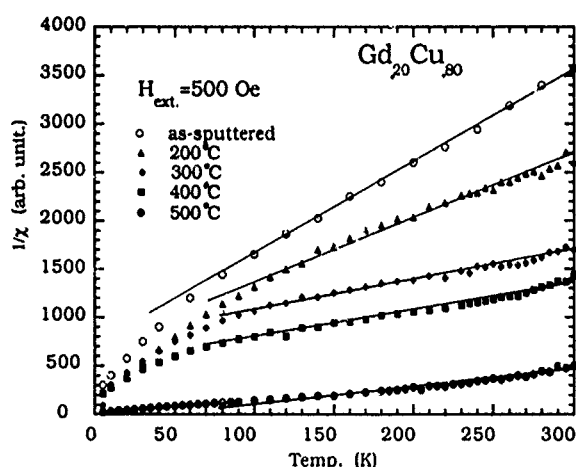


FIG. 7. Reciprocal magnetic susceptibility for as-sputtered and annealed $\text{Gd}_{0.2}\text{Cu}_{0.8}$ alloys as a function of temperature with an applied field of 100 Oe.

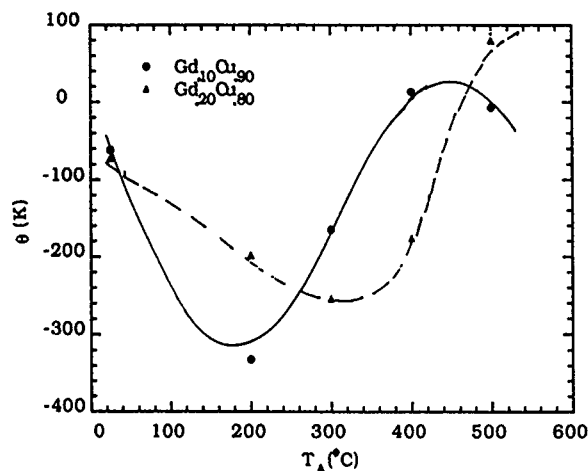


FIG. 8. Curie-Weiss temperatures for $\text{Gd}_{0.1}\text{Cu}_{0.9}$ and $\text{Gd}_{0.2}\text{Cu}_{0.8}$ as a function of annealing temperature T_A .

netic interactions in the solid. In addition, a magnetic ordering occurs below 5 K which is the lower limit of our measurement temperatures. After annealing, as indicated in Fig. 7, the annealed samples exhibit the similar behavior with the as-sputtered samples as explained above. However, the Gd granules form superparamagnetic particles.⁵ Besides, a drastic change of θ values have been found. The θ value versus T_A is plotted in Fig. 8. The θ value first becomes more negative at 200°C for both samples but does not continue to decrease further with annealing temperature. It becomes less negative at higher T_A and furthermore a positive value has been discovered at 500°C . As is known, the average granules size and distance have been found to vary with annealing conditions.⁶ It is apparent that the oscillatory behavior of θ with T_A is due to the variation of film microstructure. And the dependence of θ on T_A is related to RKKY interactions in the solids. The detailed studies of magnetic ordering below LHe-temperature are underway.

In summary, we have synthesized Gd/Cu composite metal films with nanometer sizes of Gd. The ability to control the size of Gd granules has been demonstrated. And the annealing effects on magnetic properties have been determined.

This work is supported by National Science Council of ROC under Grant No. NSC82-0208-M002-067.

¹See, for example, A. Gavrin and C. L. Chien, J. Appl. Phys. 67, 938 (1990).

²M. Hansen and K. Anderko, *Constitution of Binary Alloys* (McGraw-Hill, New York, 1958).

³See, for example, J. H. Hsu et al., J. Appl. Phys. 70, 6308 (1991).

⁴B. D. Cullity, *Introduction to Magnetic Materials* (Addison-Wesley, New York, 1972), p. 1582.

⁵C. P. Bean and J. D. Livingston, J. Appl. Phys. 30, 120S (1959).

⁶J. R. Childress and C. L. Chien, Appl. Phys. Lett. 56, 95 (1990).

Magnetic reversal in small structures

D. I. Paul

Department of Materials Science, M.I.T., Cambridge, Massachusetts 02139

A. Cresswell

Department of Physics, Gettysburg College, Gettysburg, Pennsylvania 17325

In this paper we establish a model explaining the experimentally observed anomalous enhanced coercivity of granular magnetic solids and thin films or multilayers that have pinned surface magnetic moments. We also predict a normalized critical length for the material, above which the magnetic reversal mechanism is coercive and below which it occurs by a switching mode which is non-energy dissipative. The model used assumes a dependence of the magnetization along the small dimension of the granule or the depth of the layer. The contribution of the exchange term is obtained using the Landau semi-classical formalism, and thus we do away with the mean field approximation. The coercivity is defined in such a manner as to retain its nonreversible nature. Results are presented in dimensionless units. When applied to cobalt and iron, they show coercivities larger than the theoretical maximum obtainable without pinning in accord with experimental data.

The magnetic properties of thin films and multilayers bounded by oxidizing layers and of small metal granules embedded in an immiscible medium which may be insulating (i.e., iron and cobalt in SiO_2 , Al_2O_3 , etc.), are currently active fields.¹⁻³ At sizes and packing fractions sufficiently small to exhibit single domain behavior and isolation of one granule from the other, the materials show coercivities considerably in excess of the zero temperature rotational coercivity due to crystalline anisotropy, (i.e., $2K/M$). Micromagnetic calculations⁴ and further experimental studies⁵ on passivated $\gamma\text{-Fe}_2\text{O}_3$ particles have shown that the thickness and magnetic state of the surrounding oxide surface affects the coercivity. In this paper, we show that, when the surface atoms of these granules or layers have their magnetization pinned to the strong-bonding insulating matrix either through surface stress or some form of exchange coupling, such enhanced coercivity is predictable.

We consider a ferromagnetic material of length, L , along the X axis in the presence of an external uniform magnetic field in the negative Z direction. The angle of magnetization, θ , is in the YZ plane and is assumed to vary as a function of X only. Further, we assume that the magnetic moments at the ends or surface of the material ($X=0$ and L) are rigidly pinned such that they point in the $+Z$ direction due either to very large stresses such as in the granular Fe-SiO_2 systems^{1,2} or to surface exchange pinning as in multilayers.

The exchange field is utilized in the semiclassical form originally proposed by Landau. Our calculation, being done at 0 K , we do not consider superparamagnetism in our model, and one must be careful with the interpretation of our work for lengths less than about 200 \AA . We note that we could have done a three dimensional calculation for the sphere including temperature variation using mean field theory^{6,9} for the exchange Hamiltonian. However, mean field theory tends to falsely mask the effect of spin correlations and thus fluctuations while, at the same time, giving an artificial dependence of the coercivity on the exchange energy. Although valid for the coercivity in those cases where the effect of surface pinning is small and the magnetization rotates in a coherent fashion,⁶ the mean field approximation

would clearly be in contradiction with the geometry of our problem (the average magnetization not staying parallel to the Z axis).

We note that the symmetry imposed implies that the direction of magnetization at the midpoint, $X=L/2$, is a maximum, θ_m , and it suffices to consider only the region $0 < X < L/2$. Our energy per cross sectional area is

$$E = 2 \int_0^{L/2} [A(d\theta/dx)^2 + K \sin^2(\theta - \Theta) + 2\pi NM^2 \sin^2 \theta - HM \cos \theta] dx. \quad (1)$$

The extremum energy path is determined from the Lagrange-Euler equation,

$$-2A(d^2\theta/dx^2) + K \sin 2(\theta - \Theta) + 2\pi NM^2 \sin 2\theta + MH \sin \theta = 0. \quad (2)$$

A first integral is easily obtained, which, upon imposing the boundary conditions at $x=L/2$, yields

$$L/L_0 = \int_0^{\theta_m} [\cos 2(\theta_m - \Theta') - \cos 2(\theta - \Theta')] + h'(\cos \theta_m - \cos \theta)]^{-1/2} d\theta, \quad (3)$$

where the effective anisotropy constant, normalized external field, and anisotropy angle, in the presence of demagnetization, are given by

$$K' = [(2\pi NM^2 + K \cos 2\Theta)^2 + K^2 \sin^2 2\Theta]^{1/2}, \quad (4a)$$

$$h' = 2HM/K', \quad (4b)$$

$$\tan 2\Theta' = K \sin 2\Theta / (2\pi NM^2 + K \cos 2\Theta), \quad (4c)$$

and where $L_0 = (2A/K')^{1/2}$. Note that these terms revert to unprimed parameters in the absence of such demagnetization. We shall now drop the primes, remembering that our values for K , h , and Θ can always be converted to include the demagnetization energy by use of Eq. (4). Inasmuch as, for a given material, L/L_0 and Θ have fixed values, the existence of a Lagrange-Euler path is dependent on the values

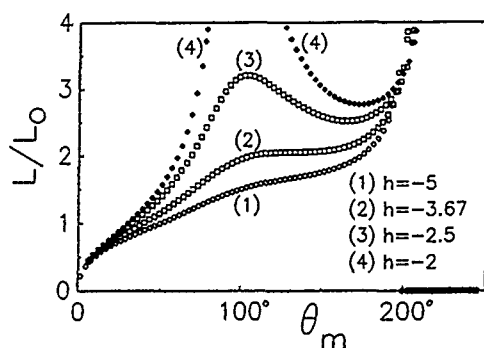


FIG. 1. Reduced sample length, L/L_0 vs θ_m , the maximum angle of magnetization. The anisotropy angle is 45° and the reduced external field $h = 2HM/K$.

of the two parameters, h and θ_m , in the integral. The integral in Eq. (3) is computed numerically, and the results are discussed in the next section.

The various behaviors of the materials under consideration can be understood from studying Fig. 1 where the anisotropy angle Θ has for illustrative purposes been placed equal to 45° . Each θ_m corresponds to a unique and well defined configuration of moments characterized by their corresponding length L/L_0 . We note that there exists regions of forbidden θ_m 's (corresponding to values of θ_m leading to negative square roots in the distance integral). For $0 > h > -2$, there exists two such regions—one for large θ_m ($\theta_m > \text{about } 240^\circ$ and indicated with zeros in Fig. 1)—and the other with θ_m centered at approximately 100° . As h increases from zero to -2 in the negative Z direction, this second forbidden region of θ_m 's yields to a local maximum which in turn disappears completely at the critical field h_c of -3.67 , [corresponding to a critical length, $(L/L_0)_c$ equal to 2.05 at a θ_m of 133°], and leaves L/L_0 as a monotonically increasing function of θ_m . Increasing h past this value does not change the general shape of the plot. Also, materials of an arbitrarily large length will always have at least one stable configuration by choosing θ_m close enough to the singularities of the integral.

(1) *Materials with lengths $L/L_0 > (L/L_0)_c$* : For these materials, Fig. 1 shows that the number of possible configurations depends on the value of the external field parameter h . For h small enough (e.g., absolute h less than 2.5 for a material whose $L/L_0 = 3.2$), there exists three Lagrange-Euler configurations that optimize the energy: these correspond to three maximum angles, θ_{m1} , θ_{m2} , and θ_{m3} (where $\theta_{m1} < \theta_{m2} < \theta_{m3}$). Of these, however, only θ_{m1} and θ_{m3} minimize the energy. (θ_{m2} maximizes the energy.) As h increases negatively, two of the configurations coalesce and disappear leaving only θ_{m3} as an allowed configuration.

Starting from a saturation of the magnetization by a strong field initially in the positive Z direction, let us consider what happens when that field is turned off and then made to increase in the negative Z direction. For h still small (but now pointing in the negative Z direction) the moments relax to the nearest minimum and occupy a configuration defined by θ_{m1} corresponding to a net positive magnetization, (e.g., for $L/L_0 = 3.2$ and $h = -2$, $\theta_{m1} = 75^\circ$). As the

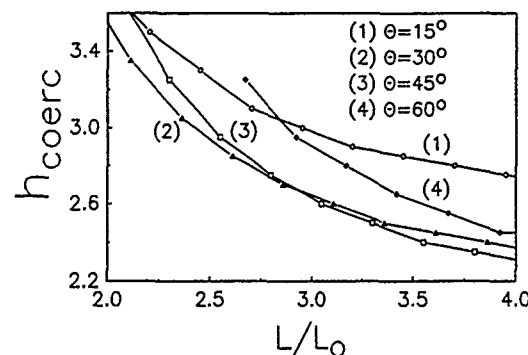


FIG. 2. Plot of reduced coercivity as a function of reduced sample length for anisotropy angles, 15° , 30° , 45° , and 60° .

field increases in the negative Z direction, the moments stay trapped initially in the θ_{m1} configuration while it remains a secondary minimum of energy. Coincidentally, the energy minimum of the θ_{m3} configuration deepens. There exists a field reached wherein θ_{m1} and θ_{m2} coalesce and the associated configuration minimum and maximum disappear. (In our example of $L/L_0 = 3.2$, this field is given in Fig. 1 as -2.5 .) Since θ_{m1} is no longer a valid maximum angle of a stable configuration, the moments are forced to rotate to the lower hemisphere in a nonreversible fashion. Thus, we are justified in calling this the coercive field, h_{coerc} . The value of h_{coerc} is determined uniquely by the value L/L_0 , the normalized length of the given material.

Depending on the material, the energy thus released could overcome the surface pinning, leading to an equilibrium configuration in the lower hemisphere, opposite from the initial configuration, with moments pinned along $-Z$. In this case, the symmetry of the problem would clearly yield a symmetrical hysteresis loop. If the energy available is not sufficient to overcome the pinning, then the moments simply rotate (still in a nonreversible way, of course) to the θ_{m3} configuration leading to a nonsymmetrical hysteresis for this particular set of boundary conditions. However, we should point out that, in actual physical situations where pinning at the surface is caused by stresses, etc., there are granules with surface spins pinned "up" and there are granules with surface spins pinned "down," and therefore on the average the hysteresis loop is symmetrical. Thus, except in special circumstances, we should not expect to see this asymmetry.

Figure 2 shows the normalized coercive field as a function of the normalized length for several different anisotropy angles. With increased length, the moments have room to rotate against the exchange and thus h_{coerc} is a decreasing function of length.

(2) *Switching behavior for materials with $L/L_0 < (L/L_0)_c$* : For this range of lengths, the combination of pinned moments at the surface and short distances prevents the existence of two minima. Thus, for a given h , there exists a unique Lagrange-Euler path of magnetization angles from 0 to θ_m , i.e., the quantity θ_m is a single valued function of h . As the h field is decreased from a positive value to zero and then increased in the negative Z direction, θ_m remains a stable configuration and increases continuously, eventually

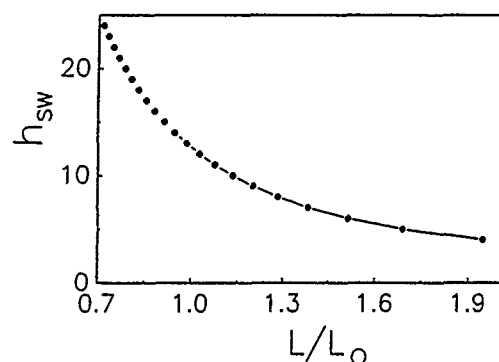


FIG. 3. Reduced switching field as a function of L/L_0 at $\Theta=45^\circ$.

bringing the average magnetization of the materials towards the negative Z axis. We define the switching field, h_{sw} , as the field necessary to bring θ_m to a value of 135° which will bring the magnetization of the material to approximately zero. Assuming that the end moments stay pinned, the process is reversible and the "hysteresis" curve has a vanishing enclosed area. This behavior justifies calling h_{sw} a switching field rather than a coercive field. (One should remark that a coercive behavior of materials with lengths in this range could be achieved by assuming a breakdown of the surface pinning of the moments.) Figure 3 is a plot of the switching fields versus the reduced length for the specific example $\Theta=45^\circ$.

To illustrate further the dependence on the anisotropy angle, we have graphed in Fig. 4 the critical length, $(L/L_0)_c$, as a function of the anisotropy angle. We note that our curve separates the space into two regions. As the anisotropy angle approaches 0° , i.e., as the anisotropy direction becomes parallel to the direction of the applied external field and that of the pinned magnetic moments at the surface, $(L/L_0)_c$ becomes very small and the coercivity mechanism dominates for practically all lengths. The reverse situation occurs as the anisotropy angle approaches 90° . Thus, in a sense, this curve

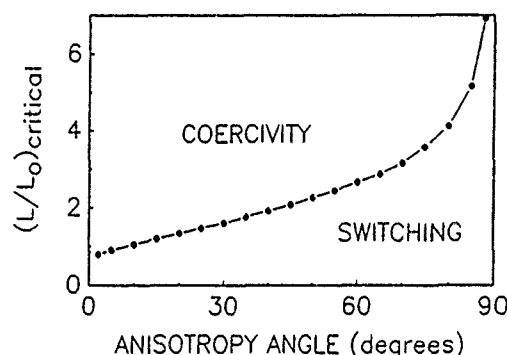


FIG. 4. Critical sample length as a function of anisotropy angle showing the regions of different magnetic reversal mechanism.

represents a "phase transition" with respect to energy dissipation, and to the best of our knowledge is the first time that any quantitative representation of this phenomenon has been given, (although the concept of a switching mode and the absence of hysteresis loops for this mode was pointed out by Gota *et al.*, in 1965⁸). Of course, one must apply caveats to our result such as that the surface moments remain pinned during the reversal process, that there are no material inhomogeneities nor acoustic emission to yield energy dissipation, etc.

We apply our results to iron and cobalt, (using $\Theta=45^\circ$). For iron they show coercivities larger than the theoretical maximum without pinning, i.e., larger than the anisotropy field. For a length of 800 Å we obtain a coercivity of ~ 400 Oe. At smaller lengths, we are in the switching field regime. At $L=500$ Å, the switching field is ~ 590 Oe, while at $L=200$ Å, the switching field increases to ~ 3500 Oe. The coercivity of cobalt gives higher values. For a length of 450 Å, the coercivity is ~ 3900 Oe, while at $L=150$ Å the switching field is $\sim 11\,000$ Oe. Fields larger than the anisotropy fields have similarly been observed experimentally in these materials though it is difficult to compare the actual values due to indefinite information regarding the particle dimensions in these experiments.¹⁻⁴

Further, we must consider the experimental dependence of the coercivity on the size of the granules. These experiments show an increase in $\text{Fe}_{75}(\text{SiO}_2)_{25}$ from 1500 to 3000 Oe as the substrate temperature is increased from about 300 to 800 K, and then a rapid drop beyond this.^{1,2} (Increasing substrate temperature is correlated with increasing granule size.) We attribute the initial increase in coercivity to the change from superparamagnetism to ferromagnetism—or, to place it in context with our work, we attribute our continued rise in coercivity, as the length continues to decrease, to the fact that our model does not contain the effect of temperature fluctuations—our calculations being done at 0 K.

The difference in our results compared to those of Schabes and Bertram⁴ is of course attributable to our restriction to a one dimensional functional dependence of the magnetization angle and thus the absence of multidimensional demagnetization effects such as flower states, etc. Another major factor is the difference in boundary conditions. We have assumed that stresses and exchange fields have pinned our surface states such that their directions of magnetization are fixed.

¹C. L. Chien, J. Appl. Phys. **69**, 5267 (1991).

²G. Xiao and C. L. Chien, J. Appl. Phys. **63**, 4253 (1988).

³S. Gangopadhyay, G. C. Hadjipanayis, S. I. Shah, C. M. Sorensen, K. J. Klabunda, V. Papaefthymiou, and A. Kostikas, J. Appl. Phys. **70**, 5888 (1991).

⁴M. E. Schabes and H. N. Bertram, J. Appl. Phys. **67**, 5149 (1990).

⁵T. Miyahara and K. Kawakami, IEEE Trans. Magn. **MAG-23**, 2877 (1987).

⁶A. Cresswell and D. I. Paul, J. Appl. Phys. **67**, 398, 5775 (1990).

⁷D. I. Paul and L. M. Pecora, Phys. Rev. B **19**, 4608 (1979).

⁸E. Gota, N. Hayashi, T. Miyashita, and K. Nakagawa, J. Appl. Phys. **36**, 2951 (1965).

Exchange interactions among ferromagnetic clusters in Cu-Co heterogeneous alloy films (abstract)

A. E. Berkowitz

Physics Department and Center for Magnetic Recording Research, University of California at San Diego, La Jolla, California 92093

F. T. Parker and D. Rao

Center for Magnetic Recording Research, University of California at San Diego, La Jolla, California 92093

Sputtered thin films of Cu-Co contain ferromagnetic clusters, even in the as-deposited condition, due to the immiscibility of Co and Cu. This structural heterogeneity is indicated by diffraction data, transport properties, and strongly temperature dependent magnetization and hysteresis behavior. In addition, these films exhibit some unusual properties that suggest the existence of both strong intercluster ferromagnetic exchange interactions and features usually associated with an exchange anisotropy coupling of ferromagnetic and antiferromagnetic materials. Some of these properties are (a) field-cooled samples exhibit strongly shifted hysteresis loops in measuring fields of 7 T, (b) coercive force depends on the magnitude of the cooling field, (c) initial susceptibility measurements given an interparticle ordering temperature >100 K, (d) Curie-Weiss analysis above the interparticle ordering temperatures indicates cluster sizes of a few nm and interparticle molecular fields ≈ 10 T, (e) fitting the magnetization curves with a Langevin analysis above the interparticle ordering temperatures yields similar cluster sizes and molecular fields. Thus, the films exhibit behavior associated with both "micromagnetism"¹ and "superferromagnetism".² We shall discuss our attempts to model this behavior in a consistent manner.

¹P. Beck, *Prog. Mater. Sci.* **23**, 1 (1978).

²S. Morup, M.B. Madsen, J. Franck, J. Villadsen, and C. J. W. Koch, *J. Magn. Mater.* **40**, 163 (1983).

Ferromagnetic resonance studies of granular materials (abstract)

Mark Rubinstein, Badri Das, D. B. Chrisey, J. Horwitz, and N. C. Koon

U. S. Naval Research Laboratory, Washington, D.C. 20375-5000

We have investigated the ferromagnetic resonance (FMR) spectra of several granular alloys displaying giant magnetoresistance (GMR). For this task, we have produced melt-spun ribbons of $\text{Fe}_{50}\text{Co}_{15}\text{Cu}_{80}$ and $\text{Co}_{20}\text{Cu}_{80}$ by rapid quenching and thin films of $\text{Co}_{80}\text{Cu}_{20}$ by pulsed laser deposition. The salient feature of the FMR spectra is the increase of the resonance linewidth as a function of increasing annealing temperature. We have deconvoluted the FMR spectra to a single-domain powder pattern and a multidomain powder pattern. As a function of annealing temperature, the GMR of these samples attains a maximum value. Near the peak of the GMR curve, the FMR spectrum reveals that the ferromagnetic particles are half mono- and half multidomain. Since the maximum size of a single-domain particle is known, this enables us to estimate the spin diffusion length of the Cu conduction electrons. We have also demonstrated, theoretically and experimentally, that the appropriate demagnetizing field to apply to the ensemble of spherical magnetic particles that comprise our granular thin film is simply the field corresponding to the average magnetization.

Complete article has been accepted in *Phys. Rev. B*.

Magnetic properties of cobalt clusters deposited on MgO substrates by molecular beam epitaxy (abstract)

R. Morel, A. Barthélémy, F. Charrière, J. R. Childress, and A. Fert
Laboratoire de Physique des Solides, Université Paris-Sud, 91405 Orsay Cédex, France

B. Bellamy and A. Masson
Laboratoire de Physico-Chimie des Surfaces, ENSCP 11, rue Pierre et Marie Curie, Paris, France

We report on the preparation and characterization of clusters of Co deposited on MgO(001) and MgO(110) substrates. The preparation is by cell evaporation in ultrahigh vacuum. The size of the clusters is controlled by the substrate temperature and deposition rate or, after deposition, by annealing. This results in clusters with diameters ≈ 100 – 1500 Å and heights ≈ 30 – 200 Å. The characterization is by Rutherford backscattering, photoemission spectroscopy, and atomic force microscopy. The magnetic properties have been investigated by SQUID magnetometry. Depending on the size of the clusters, we have observed superparamagnetic or ferromagnetic behaviors. When the cluster diameter is much smaller than its height, the magnetization is much easier for in-plane fields, due to the demagnetization energy. In some of the samples, we have combined clusters of Co and nonmagnetic Ag, with sufficient density for metallic percolation, and we present their magnetoresistance properties.

Particle interactions in granular Co films (abstract)

A. Tsoukatos, H. Wan, and G. C. Hadjipanayis
Department of Physics and Astronomy, University of Delaware, Newark, Delaware 19716

The interparticle interactions of hcp-Co particles embedded in silica (SiO_2) and boron nitride (BN) matrices have been studied via isothermal remanence curve measurements. The films were prepared by a combination of dc/rf magnetron sputtering. The strength of the interaction fields was varied as a function of metal content (x_v) and temperature. The average particle size was kept below 10 nm for all the samples investigated. The volumetric fraction of Co was varied between 0.035 and 0.66. Henkel plots¹ (normalized M_r vs M_d plots) showed that in hcp granular Co the interactions are negative, i.e., they have the tendency to destabilize the saturation state. Switching field distribution (SFD) plots showed a decreased width with increasing x_v and temperature. In the low metal volume fraction specimens, magnetizing and demagnetizing SFD curves indicate that the dominant interactions are dipolar in origin due to the fact that they nearly overlap. However, as x_v increases, the presence of exchange interactions is also evident. A detailed discussion of these studies will be presented in an effort to determine the interaction mechanisms controlling the magnetic behavior of these films as compared to existing theoretical models.^{2,3}

Work was supported by NSF DMR-8917028.

¹O. Henkel, *Phys. Status Solidi* **7**, 919 (1964).

²E. P. Wohlfarth, *J. Phys. Rad.* **20**, 295 (1959).

³R. W. Chantrell, K. O'Grady, A. Bradbury, S. W. Charles, and N. Hopkins, *IEEE Trans. Magn.* **MAG-23**, 204 (1987).

Investigation of the microstructure of granular Ag-Fe and Ag-Co thin films by TEM and STEM (abstract)

Z. G. Li

DuPont Company, P.O. Box 80356, Wilmington, Delaware 19880-0356

H. Wan

Department of Physics, University of Delaware, Newark, Delaware 19716

J. Liu

CSSS, Arizona State University, Tempe, Arizona 85287

T. Tsoukatos and G. C. Hadjipanayis

Department of Physics, University of Delaware, Newark, Delaware 19716

Giant magnetoresistance (GMR) at room temperature was found in granular thin films such as Co-Cu, Fe-Ag, Co-Ag, etc., which has stimulated intense research activity. It is still unclear whether the as-deposited Ag-rich (75%-90%) thin films are an alloy or are two separate phases. We have investigated the microstructure of granular Ag-Fe and Ag-Co thin films by atomic resolution transmission electron microscopy (TEM) and nanochemical analysis scanning transmission electron microscopy (STEM). Transition metal particles with a size of less than 1.5 nm in the as-deposited granular Ag-rich thin films were directly observed and were separated by the nanosize of Ag particles. The structure of the as-deposited thin films was metastable, and it changed by annealing. The GMR strongly depends on the nanostructure in the films, and their relationship will be discussed.

Resonant ultrasound measurements of elastic constants in melt-spun $R_2Fe_{14}B$ compounds ($R=Ce, Pr, Nd, Er$)

C. D. Fuerst and J. F. Herbst

Physics Department, General Motors NAO Research and Development Center, 30500 Mound Road,
Warren, Michigan 48090-9055

J. L. Sarrao and A. Migliori

Los Alamos National Laboratory, Los Alamos, New Mexico 87545

Measurements are reported of the longitudinal and transverse elastic moduli of the $R_2Fe_{14}B$ compounds having rare-earth component $R=Ce, Pr, Nd$, and Er . A resonant ultrasound technique was used to determine the elastic constants on hot-pressed, melt-spun samples which are essentially isotropic, polycrystalline specimens of the four compounds. The results for $Nd_2Fe_{14}B$, which agree well with previous studies, and $Er_2Fe_{14}B$ exhibit clear signatures of the spin reorientations which occur in those compounds. No such signature appears in the data for $Pr_2Fe_{14}B$, consistent with the fact that no spin reorientation occurs in that material. The ultrasonic attenuation of each sample has also been measured and it has been found that it shows features in the vicinity of spin reorientations ($Nd_2Fe_{14}B, Er_2Fe_{14}B$) and the Curie point ($Ce_2Fe_{14}B$).

Numerous scientific investigations have centered on the structural and magnetic characteristics of the tetragonal $R_2Fe_{14}B$ compounds ($R=\text{rare earth}$) since the prototypical representative, $Nd_2Fe_{14}B$, is the essential constituent of the most powerful permanent magnets yet developed.¹ The elastic properties of the $R_2Fe_{14}B$ materials have received much less attention. Dadon *et al.*² determined the Young modulus, shear modulus, and adiabatic compressibility of polycrystalline $Nd_2Fe_{14}B$ from sound velocity measurements between 77 and 300 K. Shiga *et al.*³ measured the longitudinal and transverse moduli of $Y_2Fe_{14}B$ and $Nd_2Fe_{14}B$ from 4 K to the Curie temperature T_c , employing sintered samples with highly aligned c -axes.

Using a novel resonant ultrasound spectroscopy (RUS) technique,⁴ we have determined, and here report, longitudinal and transverse elastic constants and ultrasonic attenuation coefficients as functions of temperature for polycrystalline samples of four $R_2Fe_{14}B$ compounds: $Pr_2Fe_{14}B$ and $Nd_2Fe_{14}B$ (100–200 K), $Er_2Fe_{14}B$ (300–350 K), and $Ce_2Fe_{14}B$ (400–450 K). For the Nd, Er , and Ce materials the temperature intervals were chosen to include the two types of spin reorientation observed in the $R_2Fe_{14}B$ series and a Curie point transition. As T decreases through $T_s \approx 140$ K the easy direction of magnetization in $Nd_2Fe_{14}B$ gradually cants away from the c axis toward a $\langle 110 \rangle$ basal plane direction by an angle θ which increases to a maximum of $\theta \sim 30^\circ$ at 4 K; a similar transition occurs in $Ho_2Fe_{14}B$ ($T_s \sim 58$ K). In $Er_2Fe_{14}B$ the easy direction abruptly changes from a $\langle 100 \rangle$ basal-plane direction below $T_s \approx 323$ K to a $\langle 001 \rangle$ direction above T_s ; analogous spin reorientations take place in $Tm_2Fe_{14}B$ ($T_s \sim 313$ K) and $Yb_2Fe_{14}B$ ($T_s \sim 115$ K). The Curie temperature of $Ce_2Fe_{14}B$ is $T_c \approx 424$ K.

Samples for this study were prepared by hot-pressing melt-spun $R-Fe-B$ ribbons.^{5–7} The RUS method is described elsewhere.⁴

Values of the c_L (longitudinal) and c_T (transverse, or shear) elastic constants for $Pr_2Fe_{14}B$ and $Nd_2Fe_{14}B$ in the 100–200 K temperature interval are compared in Fig. 1. It is evident that (i) $Pr_2Fe_{14}B$ is approximately 4% softer than $Nd_2Fe_{14}B$ and (ii) the moduli for the Nd compound, especially c_T , exhibit anomalous behavior in the vicinity of the

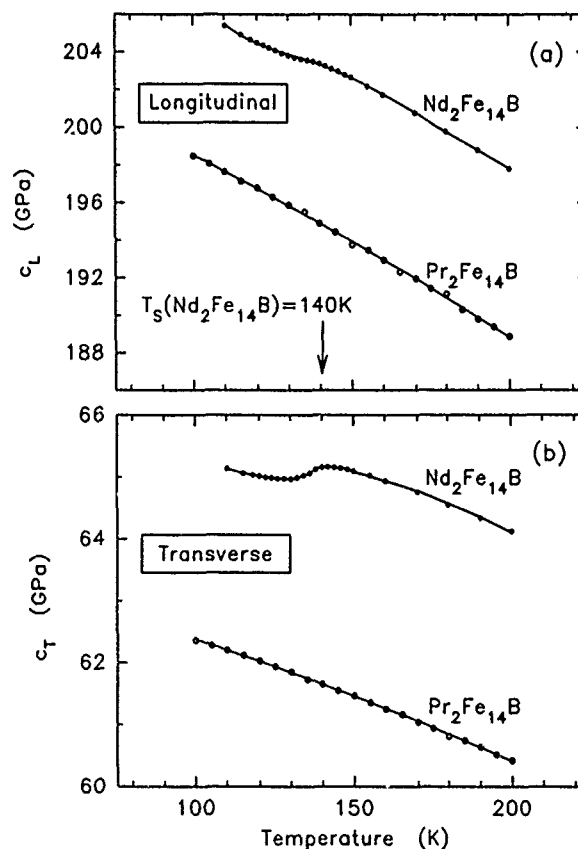


FIG. 1. (a) Longitudinal and (b) transverse elastic constants of $Pr_2Fe_{14}B$ and $Nd_2Fe_{14}B$ in the 100–200 K temperature range.

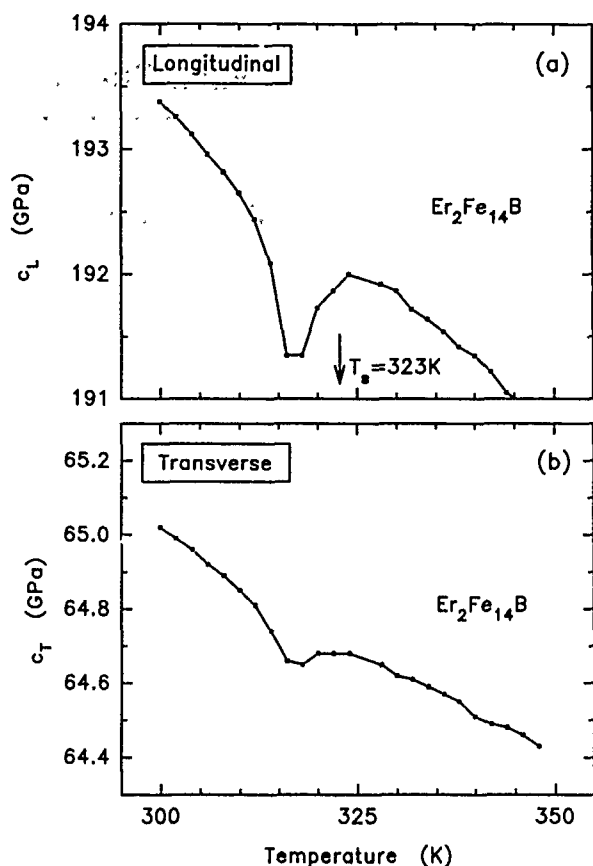


FIG. 2. (a) Longitudinal and (b) transverse elastic constants of $\text{Er}_2\text{Fe}_{14}\text{B}$ in the 300–350 K temperature range.

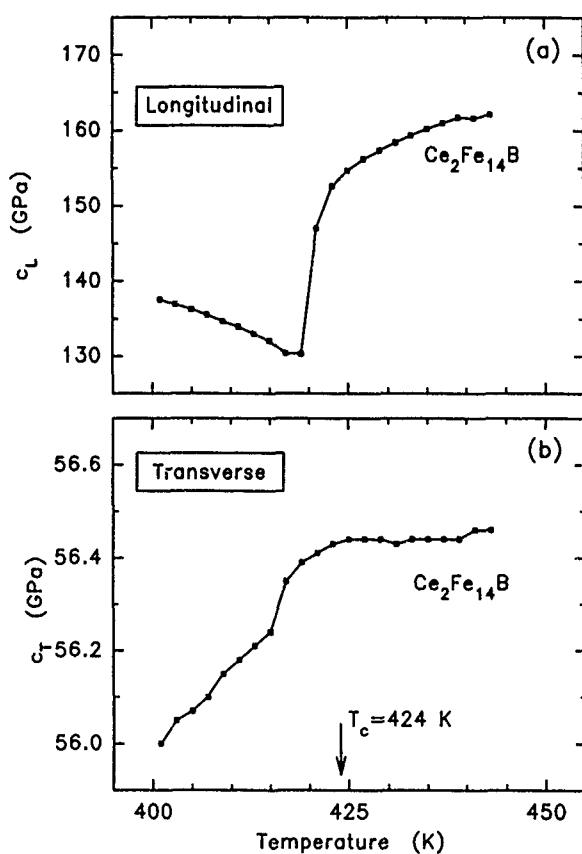


FIG. 3. (a) Longitudinal and (b) transverse elastic constants of $\text{Ce}_2\text{Fe}_{14}\text{B}$ in the 400–460 K temperature range.

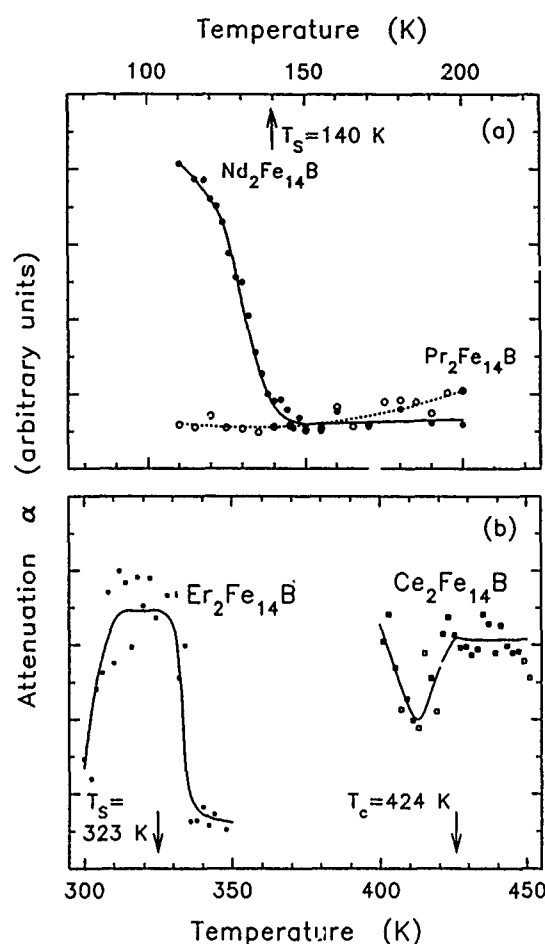


FIG. 4. Ultrasonic attenuation coefficients α of (a) $\text{Pr}_2\text{Fe}_{14}\text{B}$, $\text{Nd}_2\text{Fe}_{14}\text{B}$ and (b) $\text{Ce}_2\text{Fe}_{14}\text{B}$, $\text{Er}_2\text{Fe}_{14}\text{B}$. α is proportional to $1/Q$, where Q of a specific resonance is its center frequency divided by its full width at half-maximum.

spin reorientation temperature $T_s \approx 140$ K. Our results depart by at most 3% from previous work on $\text{Nd}_2\text{Fe}_{14}\text{B}$.^{2,3} Since $\text{Pr}_2\text{Fe}_{14}\text{B}$ and $\text{Nd}_2\text{Fe}_{14}\text{B}$ are dissimilar only insofar as the latter exhibits moment canting with an onset at T_s , we can conclude unambiguously that the anomalies in the $\text{Nd}_2\text{Fe}_{14}\text{B}$ results of Fig. 1 are associated intimately with the spin reorientation.

Detailed analysis of anomalies such as those in c_L and c_T of $\text{Nd}_2\text{Fe}_{14}\text{B}$ near T_s must await single-crystal measurements, but we can make some qualitative observations. The relatively strong feature in c_T ($\text{Nd}_2\text{Fe}_{14}\text{B}$) suggests significant magnetoelastic interaction between transverse waves and the order parameter θ for the anisotropy-driven second-order spin reorientation transition. Since $c_L = K + 4c_T/3$ for

TABLE I. Values of the elastic constants c_i , corresponding sound velocities v_i , and densities ρ of the specified $\text{R}_2\text{Fe}_{14}\text{B}$ compounds at 300 K ($c_i = \rho v_i^2$).

Compound	ρ (gm/cm^3)	c_L (GPa)	v_L (10^5 cm/s)	c_T (GPa)	v_T (10^5 cm/s)
$\text{Ce}_2\text{Fe}_{14}\text{B}$	7.60	161.1	4.60	56.3	2.72
$\text{Pr}_2\text{Fe}_{14}\text{B}$	7.36	179.2	4.93	58.4	2.82
$\text{Nd}_2\text{Fe}_{14}\text{B}$	7.57	188.5	4.99	62.0	2.86
$\text{Er}_2\text{Fe}_{14}\text{B}$	8.11	193.8	4.89	65.1	2.83

an isotropic polycrystal, where K is the bulk modulus, the smaller feature in c_L ($\text{Nd}_2\text{Fe}_{14}\text{B}$) observed here likely reflects anomalies in the longitudinal as well as the transverse single-crystal elastic constants. Analyses of single-crystal experiments on orthorhombic ferrites such as ErFeO_3 and TmFeO_3 , which are α' characterized by rotation of the moment in a plane, have demonstrated that magnetoelastic couplings quadratic in θ can generate step discontinuities and couplings linear in θ can lead to softening of elastic modes.^{8,9} We expect similar couplings for $\text{Nd}_2\text{Fe}_{14}\text{B}$ and the other $\text{R}_2\text{Fe}_{14}\text{B}$ systems exhibiting spin reorientations, but with differences introduced by the form of the anisotropy energy for tetragonal lattice symmetry and the specifics of the moment configuration. Moreover, a change in the magnitude of the iron moment μ_{Fe} may be involved; from anomalies in the linear and volume magnetostriction Andreev *et al.*¹⁰ inferred a 2%–3% decrease in μ_{Fe} of $\text{Nd}_2\text{Fe}_{14}\text{B}$ in the spin reorientation region.

In contrast to the $\text{Nd}_2\text{Fe}_{14}\text{B}$ results, c_L undergoes larger excursion than c_T in the neighborhood of T_s for the $\langle 001 \rangle \leftrightarrow \langle 100 \rangle$ spin reorientation in $\text{Er}_2\text{Fe}_{14}\text{B}$ (Fig. 2). Furthermore, with declining temperature c_L ($\text{Er}_2\text{Fe}_{14}\text{B}$) in Fig. 2 shows a decrease beginning near 325 K and a subsequent increase near 310 K with recovery to the linear contribution which is evident from extrapolation of the $T \geq 330$ K measurements; only a single peak at $T_s \approx 323$ K appears in our DSC data. These features resemble the single-crystal analogs observed by Gorodetsky and Lüthi⁸ in ErFeO_3 , whose magnetization rotates from the (orthorhombic) c -axis completely into the a direction on cooling. The elastic constants of ErFeO_3 (and TmFeO_3 , in which the rotation is from the a to the c direction on cooling) are anomalous at temperatures T_1 and T_2 corresponding to the onset and the completion of the spin reorientation,^{8,9} and on the basis of Landau-type free-energy considerations two second-order phase transitions, one at T_1 and another at T_2 are to be expected.¹¹ Our results indicate that analogous behavior occurs in $\text{Er}_2\text{Fe}_{14}\text{B}$, c_L exhibiting, over a linear background, a step down at ~ 325 K and a step up at ~ 310 K which are smeared by polycrystalline effects; i.e., two second-order phase transitions, separated by only ~ 15 K, characterize the spin reorientation. This suggestion departs from the prevailing opinion in the literature, based on magnetization and other measurements, that one transition is involved and calls strongly for further single-crystal work on $\text{Er}_2\text{Fe}_{14}\text{B}$.

Only one second-order transition takes place near T_s in $\text{Nd}_2\text{Fe}_{14}\text{B}$, whose spin reorientation is not completed in a symmetry direction. In this respect $\text{Nd}_2\text{Fe}_{14}\text{B}$ resembles elemental gadolinium, the elastic properties of which also exhibit one anomaly in the region of its similarly incomplete spin reorientation.^{11,12} It is clear from Fig. 1 that c_T ($\text{Nd}_2\text{Fe}_{14}\text{B}$) shows a single step down as T decreases through T_s and does not recover to the linear behavior for $T > T_s$.

Figure 3 displays our results for $\text{Ce}_2\text{Fe}_{14}\text{B}$ in the 400–460 K interval encompassing $T_c \approx 424$ K. A very large softening of c_L occurs as the temperature decreases through T_c , while c_T shows a much smaller decrease. Essentially identical Curie temperature anomalies were observed by Shiga *et al.*³ for $\text{Y}_2\text{Fe}_{14}\text{B}$ and $\text{Nd}_2\text{Fe}_{14}\text{B}$, although the moduli of

those compounds substantially exceed their $\text{Ce}_2\text{Fe}_{14}\text{B}$ cognates. The softening is undoubtedly associated with the enormous volume magnetostriction ($\sim 2\%$) due principally to the iron sublattice (which, together with ordinary thermal expansion in the paramagnetic range, generates a strong Invar effect in the $\text{R}_2\text{Fe}_{14}\text{B}$ compounds; see, e.g., Ref. 10). Shiga *et al.*³ have advanced a thermodynamic argument in support of this view which focuses on the difference between the bulk moduli for constant applied field and for constant magnetization.

The attenuation coefficient extracted from a given resonance can also display anomalous behavior near T_s or T_c . Figure 4 shows $\alpha(T)$ obtained from predominantly shear-type modes in each of the four samples. In the 100–200 K range α ($\text{Pr}_2\text{Fe}_{14}\text{B}$) is essentially constant, but α ($\text{Nd}_2\text{Fe}_{14}\text{B}$) increases dramatically with decreasing temperature below an onset at T_s . It is suggestive that $\alpha(T)$ for $\text{Nd}_2\text{Fe}_{14}\text{B}$ strongly resembles $\theta(T)$, the canting angle between the magnetization direction and the c axis as a function of temperature, which has been measured by, among others, Tokuhara *et al.*¹³ Somewhat less striking, although still pronounced, features are evident in the attenuation coefficients of $\text{Er}_2\text{Fe}_{14}\text{B}$ and $\text{Ce}_2\text{Fe}_{14}\text{B}$ in Fig. 4(b) near T_s and T_c , respectively.

We conclude by noting an interesting hierarchy which is obeyed by the moduli at 300 K and which we conjecture to persist except possibly in the vicinity of magnetic transitions. Table I lists c_i ($i \equiv L, T$), the corresponding sound velocities v_i , and the density for each of the compounds at 300 K. It is clear that

$$c_i(\text{Ce}_2\text{Fe}_{14}\text{B}) < c_i(\text{Pr}_2\text{Fe}_{14}\text{B}) < c_i(\text{Nd}_2\text{Fe}_{14}\text{B}) \\ < c_i(\text{Er}_2\text{Fe}_{14}\text{B}),$$

so that both the longitudinal and transverse elastic constants of these compounds have the same order as the atomic numbers of their rare-earth constituents, despite the fact that the densities and sound velocities do not.

Work at Los Alamos performed under the auspices of the U. S. DOE.

¹ For a review, see J. F. Herbst, Rev. Mod. Phys. **63**, 819 (1991).

² D. Dadon, M. P. Dariel, Y. Gefen, H. Klimker, and M. Rosen, Appl. Phys. Lett. **48**, 1444 (1986).

³ M. Shiga, Y. Kusakabe, Y. Nakamura, K. Makita, and M. Sagawa, Physica B **161**, 206 (1989).

⁴ A. Migliori, J. L. Sarrao, W. M. Visscher, T. M. Bell, M. Lei, Z. Fisk, and R. G. Leisure, Physica B **183**, 1 (1993).

⁵ R. W. Lee, E. G. Brewer, and N. A. Schaffel, IEEE Trans. Magn. **MAG-21**, 1958 (1985).

⁶ J. F. Herbst, R. W. Lee, and F. E. Pinkerton, Ann. Rev. Mater. Sci. **16**, 467 (1986).

⁷ C. D. Fuerst, J. F. Herbst, and E. A. Alson, J. Magn. Magn. Mater. **54-57**, 567 (1986).

⁸ G. Gorodetsky and B. Lüthi, Phys. Rev. B **2**, 3688 (1970).

⁹ G. Gorodetsky, S. Shaft, and B. M. Wanklyn, Phys. Rev. B **14**, 2051 (1976).

¹⁰ A. V. Andreev, A. V. Deryagin, S. M. Zadvorkin, and S. V. Terent'ev, Sov. Phys. Solid State **27**, 987 (1985).

¹¹ K. P. Belov, A. K. Zvezdin, A. M. Kadomtseva, and R. Z. Levitin, Sov. Phys. Usp. **19**, 574 (1976).

¹² M. Long, Jr., A. R. Wazzan, and R. Stern, Phys. Rev. **178**, 775 (1969).

¹³ K. Tokuhara, Y. Ohtsu, F. Ono, O. Yamada, M. Sagawa, and Y. Matsura, Solid State Commun. **56**, 333 (1985).

Comparison of the improvement of thermal stability of NdFeB sintered magnets: Intrinsic and/or microstructural

B. M. Ma, W. L. Liu, Y. L. Liang, D. W. Scott, and C. O. Bounds
Rhône-Poulenc Basic Chemicals, CN 7500, Cranbury, New Jersey 08512

Temperature-dependent magnetic properties of nine NdFeB sintered magnets with various Co-Nb, Co-V, or Co-Mo additions have been measured up to 175 °C using both closed-loop and open-circuit methods. The irreversible loss of induction, reversible temperature coefficient of induction (α), and temperature coefficient of intrinsic coercivity β have been related to the T_c , the B_r , and the H_{ci} at 25 and 175 °C. The irreversible loss of induction is strongly affected by the H_{ci} at 25 °C and the α has been found to be strongly dependent upon the T_c . Intrinsic coercivity of more than 25 and 7.5 kOe at 25 and 175 °C, respectively, are essential to bring the β to better than $-0.5\%/^{\circ}\text{C}$. A magnet with a composition of $\text{Nd}_{12}\text{Dy}_3\text{Fe}_{70}\text{Co}_5\text{Nb}_2\text{B}_8$ has been found to exhibit an outstanding thermal stability: a B_r of 8.5 kG (comparable to that of SmCo_5 sintered magnet) and a H_{ci} of 12.9 kOe when measured at 175 °C. An α of $-0.10\%/^{\circ}\text{C}$ and a β of $-0.4\%/^{\circ}\text{C}$ have been obtained.

I. INTRODUCTION

Potential means to increase the useful operating temperature of NdFeB magnets include raising the Curie temperature T_c or increasing the intrinsic coercivity at 25 °C. The former may be achieved by incorporating Co in the alloy at the cost of reduced intrinsic coercivity and the latter may be obtained by including Dy into the alloy at the cost of decreased maximum energy product BH_{max} . Recently, incorporating V or Mo into magnets containing 5 at. % Co has been reported to increase the intrinsic coercivity H_{ci} at room temperature and to improve the thermal stability.^{1,2} Additionally, the microstructure of V-Co or Mo-Co-containing sintered magnets has been drastically modified.²⁻⁵

It is of interest to compare the temperature-dependent properties of such magnets, using both open- and closed-circuit measurements, with conventional NdFeB magnets. The irreversible loss of induction, the reversible temperature coefficient of induction (conventionally known as α), and the temperature coefficient of H_{ci} (β) of NdFeB magnets are important for magnetic circuit design and are often reported in the literature. However, these values have not been cooperatively related to the more fundamental variables, for instance T_c , or readily measurable magnetic parameters, i.e., the remanence B_r or the H_{ci} of the magnets.

In this article we compare the thermal stability of nine NdFeB magnets with Co-Nb, Co-V, or Co-Mo additions and report their magnetic properties over a temperature range of 25–175 °C with an attempt to relate the irreversible loss of induction, α and β to the more readily measurable magnetic properties: T_c , B_r , or H_{ci} . Additionally, an effort was made to identify a composition which yields a B_r equivalent to that of a SmCo_5 sintered magnet at 175 °C and maintains a H_{ci} of at least 10 kOe at 175 °C without a significant irreversible loss of induction.

II. EXPERIMENT

Magnets used in this study were prepared from conventionally cast ingots using classical powder metallurgy techniques. All alloys were cast by vacuum induction melting via controlled directional solidification. The cast ingots were

then hydrogen decrepitated, evacuated to 2×10^{-2} Torr, and ground to less than 250 μm . The alloy powders were then attrition milled in toluene to an average particle size of approximately 3.0 μm , as measured by a Fisher subsieve sizer (FSSS). Vacuum evaporation was applied to remove toluene from the powder slurry. The dry powders were then packed into rubber molds, magnetized with a peak field of 60 kOe, and pressed cold isostatically to form consolidated pieces. All green compacts were sintered under vacuum in a temperature range from 1095 to 1100 °C for 3 h. A postsintering treatment over a temperature range of 550–650 °C was applied to obtain the optimum H_{ci} .

The T_c was determined by finding the inflection point of the temperature scan of induction using a vibrating sample magnetometer (VSM) under an applied magnetic field of 0.5 kOe. The closed-loop magnetic properties, B_r and H_{ci} , were measured using a Walker hysteresisgraph in conjunction with a temperature box capable of temperatures ranging from -100 to 300 °C. The open-circuit properties, namely the irreversible loss of induction and α , were determined by placing a 3 mm cube of fully magnetized magnets in a VSM under a zero applied field, cycled from 25 to 200 °C at a heating rate of 4 °C/min then cooled to room temperature at the same rate. The ratio of the difference in induction to its original value at 25 °C was determined to be the irreversible loss of induction. The α is determined by calculating the slope of the linear portion (the cooling part) of the temperature scan of induction. Unlike α , the β is determined from the H_{ci} measured at 25 and 175 °C using a closed-circuit measurement.

III. RESULTS AND DISCUSSION

Listed in Table I are the sample identification, the chemical composition in formula form, the T_c , the B_r , and the H_{ci} at 25 and 175 °C, and the irreversible loss and α and β of samples included in this study. The composition of these magnets ranges from a VCM grade with a T_c of 312 °C (sample no. 1) to a magnet containing 17 at. % Co with a T_c of 448 °C (sample no. 8).

As anticipated, incorporating Co into the magnet composition increases T_c by approximately 10 °C for each

TABLE I. Chemical composition, Curie temperature, B_r , and H_{ci} at 25 and 175 °C, irreversible loss of induction, reversible temperature coefficient of induction α , and temperature of coefficient of H_{ci} (β).

Sample no.	Formula	T_c (°C)	B_r (kG) at Temp. (°C)		H_{ci} (kOe) at Temp. (°C)		Irrev. loss (%)	α (%/°C)	β (%/°C)
			25	175	25	175			
1	(Nd ₁₄ Dy ₁) FeNb _{0.7} B ₇	312	12.5	10.4	14.7	2.2	41	-0.130	-0.57
2	(Nd ₁₂ Dy ₂) FeNb _{0.5} B ₈	312	12.0	9.6	24.7	6.6	19	-0.130	-0.49
3	(Nd ₁₂ Dy ₃) FeNb _{0.7} B ₇	312	11.1	9.3	26.3	7.6	5	-0.130	-0.47
4	(Nd ₁₃ Dy ₂) FeCo ₅ Nb _{0.7} B ₇	360	11.4	10.0	20.4	4.2	32	-0.100	-0.53
5	(Nd ₁₃ Dy ₂) FeCo ₅ Nb ₂ B ₆	363	10.4	9.1	>30	10.6	2	-0.100	-0.5
6	(Nd ₁₂ Dy ₃) FeCo ₅ Nb ₂ B ₈	364	10.3	8.5	>30	12.9	5	-0.100	-0.4
7	(Nd ₁₃ Dy ₂) FeCo ₅ V ₄ B ₇	348	10.4	9.3	24.2	6.6	8	-0.100	-0.48
8	(Nd ₁₂ Dy ₃) FeCo ₁₇ Mo ₂ B ₇	448	10.4	9.0	16.7	3.2	26	-0.064	-0.54
9	(Nd ₁₂ Dy ₃) FeCo ₅ Mo ₂ B ₈	355	10.5	8.8	25.0	8.8	3	-0.110	-0.43

atomic percentage of Co addition (from approximately 312 to 360 with 5 at. % of Co addition). However, the addition of Co has typically been limited to below 5 at. % to minimize the negative impact on H_{ci} to maintain a H_{ci} of at least 14 kOe at room temperature. The addition of Nb, V, or Mo appears to change T_c slightly suggesting that the actual Co concentration in the major magnetic phase may be less than that calculated from the alloy composition assuming random substitution of Co for Fe. It is surmised that some of the Co may appear in the grain-boundary region.

A significant loss of induction, as shown in Fig. 1, at 25 °C can be observed by exposing the magnet to a temperature of 200 °C. This loss consists of an irreversible loss that is not recoverable when the magnet is cycled again to below 200 °C, and a reversible loss which is recovered. The irreversible loss of induction of these magnets varies from the 41% of sample no. 1 to less than 5% in sample nos. 3, 5, 6, and 9. In general, magnets exhibiting low irreversible loss of induction all display a H_{ci} of at least 8 kOe at 175 °C. The H_{ci} at elevated temperatures appears to be the dominant factor affecting the irreversible loss of induction. Furthermore, the 41%, 32%, and 26% of irreversible loss of induction in

sample nos. 1, 4, and 8 (T_c of 312, 360, and 448 °C, respectively) suggest that T_c has no measurable effect on the irreversible loss of induction.

Unlike the irreversible loss of induction, the reversible temperature coefficient of induction (α) appears to be strongly dependent upon T_c and weakly determined by the intrinsic coercivity, as shown in Figs. 2(a) and 2(b), as evi-

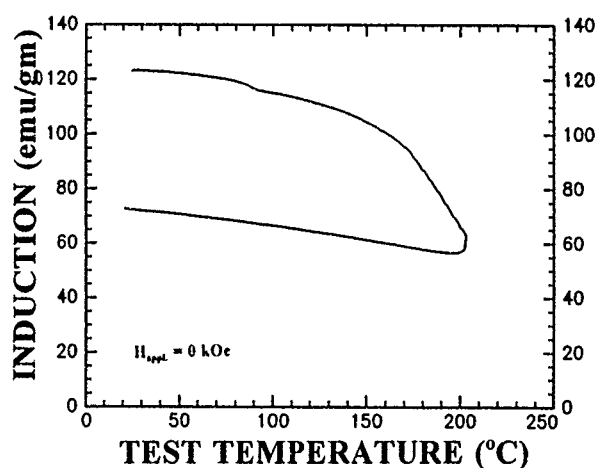


FIG. 1. A temperature scan of induction of a 3 mm cube sintered magnet under a zero applied magnetic field showing the irreversible loss of induction and the reversible induction after exposing to a temperature of 200 °C.

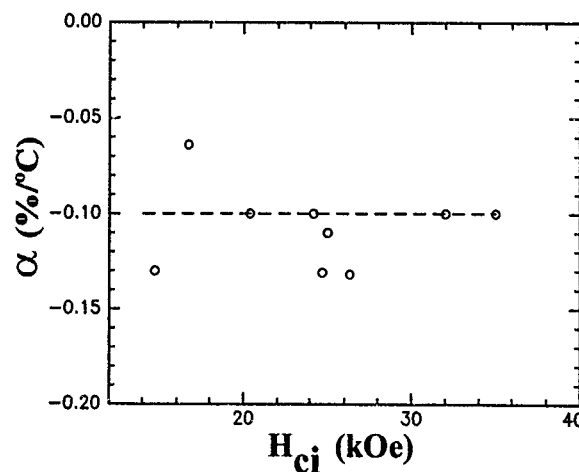
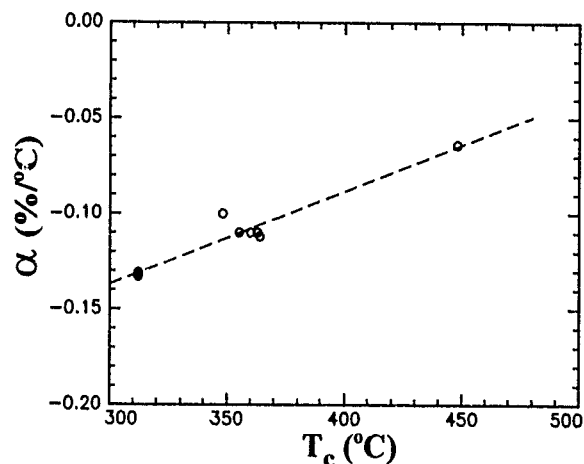


FIG. 2. The relationship of reversible temperature coefficient α to (a) a linear correlation with Curie temperature T_c and (b) a weak correlation with H_{ci} at 25 °C of NdFeB-type magnets.

denced by the α of -0.130 and -0.064 $\%/^{\circ}\text{C}$ of samples no. 1 (T_c of 312°C and H_{ci} of 2.2 kOe at 175°C) and no. 8 (T_c of 448°C and H_{ci} of 3.2 kOe at 175°C), respectively. Based on these results, it can generally be stated that magnets with a higher T_c (through Co addition) usually exhibit a lower α than those of lower T_c (without Co addition). The conventional temperature coefficients of H_{ci} (β) of samples studied are also included in Table I for comparison. They range only from -0.4 to -0.6 $\%/^{\circ}\text{C}$ regardless of the T_c . The general trend is that magnets of lower magnitude of β all exhibit a relative high H_{ci} at both 25 and 175°C . Regardless of the alloy composition, an H_{ci} of more than 25 kOe appears to be necessary to assure an H_{ci} higher than 8 kOe at 175°C . Despite the fact that V or Mo addition in the Co-containing alloys does slightly increase the H_{ci} at room temperature and even at elevated temperatures, it may not be the most effective means to raise H_{ci} at elevated temperature. Comparing the H_{ci} of 26.3 kOe at 25°C and more than 30 kOe of samples no. 3 (0% Co), no. 6 (5% Co, 2% Nb), no. 7 (5% Co, 4% V), and no. 9 (5% Co, 2% Mo), respectively, it may be deduced that Dy is even more effective in increasing the H_{ci} at room temperature and in maintaining the H_{ci} at 175°C . This is evidenced by the results that magnets exhibiting an H_{ci} of more than 8 kOe at 175°C all contain at least 3 at. % of Dy. The fact that sample no. 3 contains no Co at all suggests that V or Mo addition into Co-containing magnets is beneficial but may not be necessary for obtaining high H_{ci} (and high B_r) at elevated temperatures.

While it is desirable to have a low irreversible loss and low magnitude of α , it is more meaningful to measure the B_r and the H_{ci} values at the desired operation temperature. Instead of plotting all data obtained in this study, representative samples are selected for illustration. Shown in Figs. 3(a) and 3(b) are the variation of B_r and H_{ci} with the test temperature for four selected samples, namely, sample nos. 1, 4, 6, and 7. Conventional VCM magnets (sample no. 1) exhibit the highest B_r , but the lowest H_{ci} at 175°C while sample no. 6 exhibits an H_{ci} of more than 10 kOe with a $B_r=8.5$ kG at 175°C . The B_r of 8.5 kG at 175°C is comparable to or better than that of SmCo_5 at the corresponding temperature (B_r of 8.8 and 8.2 kG at 25 and 175°C , respectively). At 175°C , the B_r and the H_{ci} of the Co-V-containing magnet (sample no. 7) all fall in between those of sample nos. 1 and 6. This suggests that the modification of microstructure may increase the H_{ci} to a reasonable level but the key success for achieving high H_{ci} at elevated temperature may still be the fundamental (or the intrinsic) issue—increasing the H_{ci} by raising the anisotropy field through Dy addition.

IV. CONCLUSIONS

Temperature-dependent magnetic properties, namely, the irreversible loss of induction, the B_r , the H_{ci} , the α , and the β of nine NdFeB magnets with Co, Co-Nb, Co-V, or Co-Mo addition have been measured over the temperature range of 25 through 175°C . We have found that a high H_{ci} at 175°C is essential for low irreversible loss and a higher T_c is beneficial for α . For magnets of similar T_c those exhibiting higher H_{ci} (or lower B_r) usually display a higher α value.

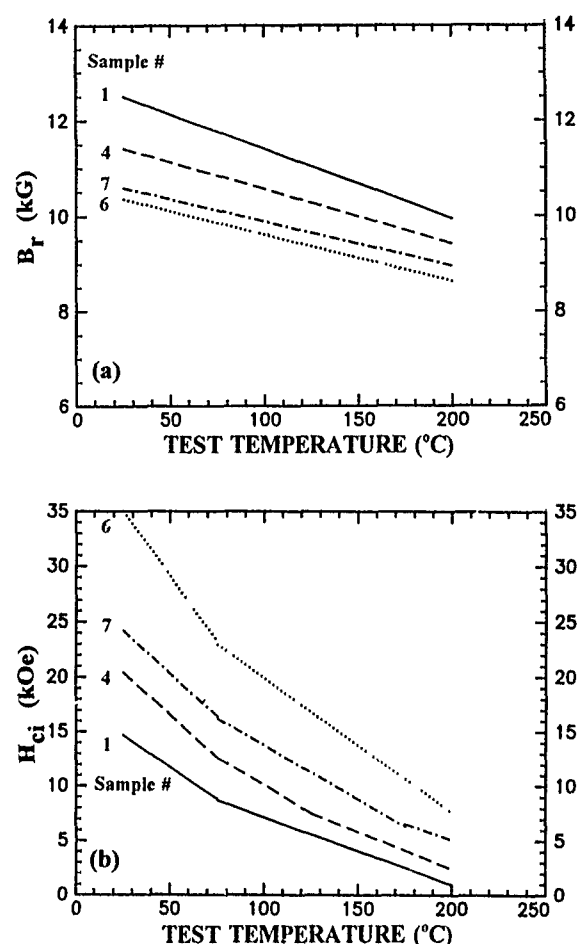


FIG. 3. Variation of (a) B_r and (b) H_{ci} of $(\text{Nd}_{14}\text{Dy}_1)\text{FeNb}_{0.7}\text{B}_7$ (sample no. 1), $(\text{Nd}_{13}\text{Dy}_2)\text{FeCo}_5\text{Nb}_{0.7}\text{B}_7$ (sample no. 4), $(\text{Nd}_{13}\text{Dy}_2)\text{FeCo}_5\text{V}_4\text{B}_7$ (sample no. 7) and $(\text{Nd}_{13}\text{Dy}_3)\text{FeCoNb}_2\text{B}_8$ (sample no. 6) with test temperature.

Regardless of alloy composition, an H_{ci} of more than 25 kOe is necessary to obtain a β of less than $-0.51\%/^{\circ}\text{C}$. A Dy content of more than 3 at. % in the final magnet is more advantageous for obtaining a high B_r and H_{ci} at elevated temperatures than additions of Co-V or Co-Mo. A magnet with a composition of $\text{Nd}_{12}\text{Dy}_8\text{Fe}_{70}\text{Co}_5\text{Nb}_2\text{B}_8$ has been found to exhibit a B_r of 8.5 kG (superior to that of SmCo_5 sintered magnets) and an H_{ci} of 12.9 kOe at 175°C .

ACKNOWLEDGMENTS

The authors wish to thank J. Riesen, R. Carleton, and B. Zell for helpful discussion. We are grateful to Rhône-Poulenc Phoenix Plant for preparing cast ingots and conducting chemical composition analysis for alloys used in this study.

¹ M. Sagawa, P. Tenaud, F. Vial, and K. Hiraga, IEEE Trans. Magn. MAG-26, 1957 (1990).

² S. Hirose, H. Tomizawa, S. Mino, and A. Hamamura, IEEE Trans. Magn. MAG-26, 1960 (1990).

³ P. Tenaud, F. Vial, and M. Sagawa, IEEE Trans. Magn. MAG-26, 1930 (1990).

⁴ J. Bernardi, J. Fidler, and F. Fodermayr, IEEE Trans. Magn. 28, 2127 (1992).

⁵ J. Fidler, in 7th International Symposium on Magnetic Anisotropy and Coercivity in Rare-Earth Transition-Metal Alloys, edited by H. Perin Laboratory, The University of Western Australia, 1992, pp. 11–22.

Mechanical properties of hot-rolled Pr-Fe-B-Cu magnets

A. Arai, O. Kobayashi, F. Takagi, K. Akioka, and T. Shimoda

Advanced Materials R&D Department, Seiko Epson Corporation, 3-3-5 Owa, Suwa-shi, Nagano-ken 392, Japan

Mechanical strength and properties of thin plates were investigated for hot-rolled Pr-Fe-B-Cu magnets. Tensile strengths of the hot-rolled magnets were more than 23.7 kg f/mm². Bending tests were also applied and the strength of 37.7 kg f/mm² was obtained. The strengths obtained are definitely higher than that of commercial Nd-based sintered magnets. It was found that the mechanical strengths were enhanced by Pr₂Fe₁₄B grain refinement caused by Cu addition. Related to high mechanical strength, hot-rolled Pr-Fe-B-Cu magnets show excellent machinability. Thin plate magnets up to 0.1 mm in thickness with fairly large surface area were produced without any cracking. Moderate energy products better than 20 MGOe were achieved by heat treatment after machining.

I. INTRODUCTION

In our previous articles^{1,2} we introduced a new method for producing high-energy Pr-Fe-B-Cu magnets by hot working cast alloys. Columnar cast structure having fine grains was determined to be important to achieve high magnetic properties.

Hot-rolled Pr-Fe-B-Cu magnets have several unique characteristics because of their manufacturing method and composition. First, hot rolling is the most suitable method for making large-sized magnets. Second, the corrosion resistance is higher than that of sintered magnets because of the lower contamination of oxygen and the absence of voids. Third, pieces of magnets can be easily joined by liquid-phase bonding.³

In addition to these characteristics, this article especially focuses on the mechanical properties such as mechanical strength and machinability, and discusses the properties as compared to those of sintered magnets.

II. EXPERIMENTAL PROCEDURE

The alloys investigated were prepared using an induction furnace. The raw materials used were Pr (99 wt % pure), Fe (99.9 wt % pure), Cu (99.9 wt % pure), and 20 wt % B-80 wt % Fe. An alloy ingot was packed into a steel capsule and then rolled at 950 °C up to 75% reduction. After rolling, the magnets were heat treated under an Ar atmosphere. For microstructural study, optical microscopy, and scanning electron microscopy (SEM) were utilized. Electron probe microanalysis (EPMA) was also used for compositional analysis of the microstructure. Tensile tests were applied using the Shimadzu model AG-2000D. In the tensile tests, the cross-head speed was 0.5 mm/min. Tensile direction was the same as the rolling direction. Three-point bending tests were also applied. The sample size was 6×6×40 mm.³ Bending direction was parallel to the press direction of the magnets. Magnetic properties were measured on a dc magnetic hysteresis loop tracer under a maximum magnetizing field of 25 kOe. Thin plate magnets were evaluated using a vibrating sample magnetometer (VSM) under a maximum field of 15 kOe.

III. RESULTS AND DISCUSSION

Figure 1 shows a SEM backscattered image of Pr_{17.0}Fe_{76.3}B_{5.2}Cu_{1.5} magnet which was subjected to a two-step heat treatment (20 h at 1025 °C and 6 h at 500 °C) after rolling. A comparatively large amount of the intergranular phases is observed.⁴ The microstructure consists of three phases labeled as (a), (b), and (c) in the figure. EPMA analysis of the phases was performed, and the phases (a), (b), and (c) appeared to be Pr₂Fe₁₄B phase, Pr₆Fe₁₃Cu phase,⁵ and Pr-Cu-rich phase, respectively. Figure 2 shows the relation between iH_c and the temperature of the second treatment (designated as T) for a two-step heat treatment such as 1025 °C for 20 h + T °C for 2 h. High coercivities were obtained in the temperature range from 450 to 650 °C, causing Pr₆Fe₁₃Cu formation and Pr₂Fe₁₄B phase separation.⁵

Tensile tests were applied to the Pr_{17.0}Fe_{76.3}B_{5.2}Cu_{1.5} magnets with tensile strengths of more than 23.7 kg f/mm² being obtained. Commercial Nd-based sintered magnets show tensile strengths of about 8 kg f/mm².^{6,7} Therefore, hot-rolled magnets are about three times as strong as the sintered magnets. A SEM micrograph of the fracture surface after a tensile test is shown in Fig. 3. The fracture surface of the

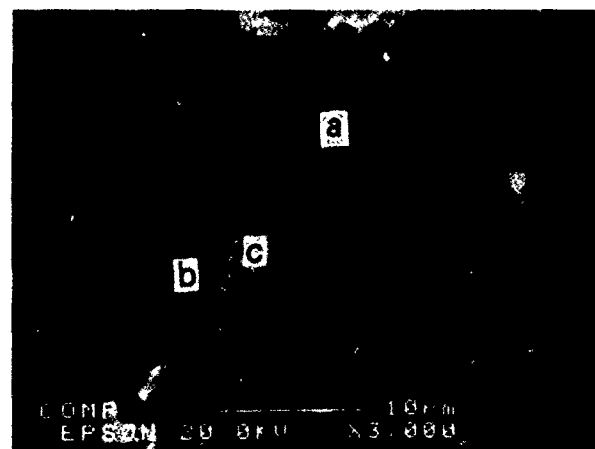


FIG. 1. SEM backscattered image of Pr_{17.0}Fe_{76.3}B_{5.2}Cu_{1.5} magnet: (a) Pr₂Fe₁₄B; (b) Pr₆Fe₁₃Cu, and (c) Pr-Cu rich.

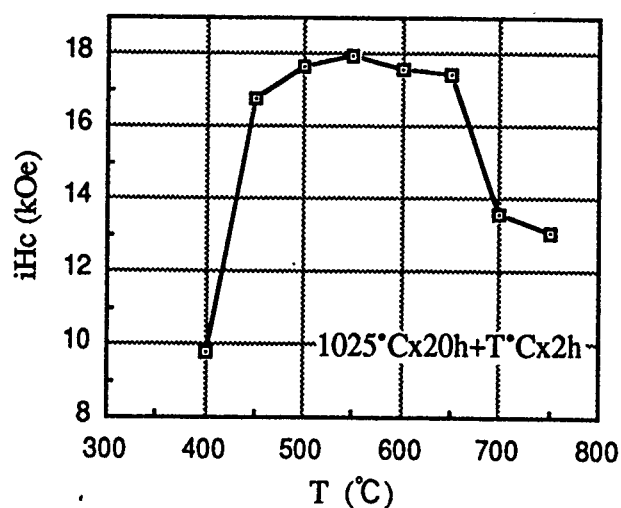


FIG. 2. Change of iH_c as a function of temperature of the second heat treatment in two-step heat-treated $\text{Pr}_{17.0}\text{Fe}_{76.3}\text{B}_{5.2}\text{Cu}_{1.5}$ magnet.

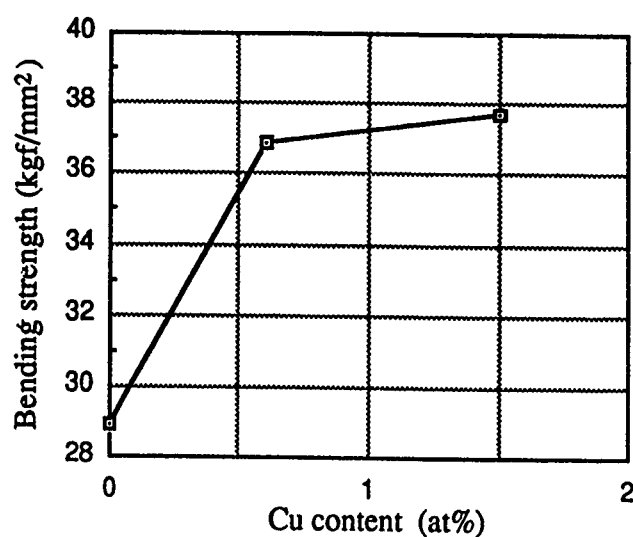


FIG. 5. Cu content dependence of bending strength.



FIG. 3. SEM micrograph of the fracture surface after tensile test.

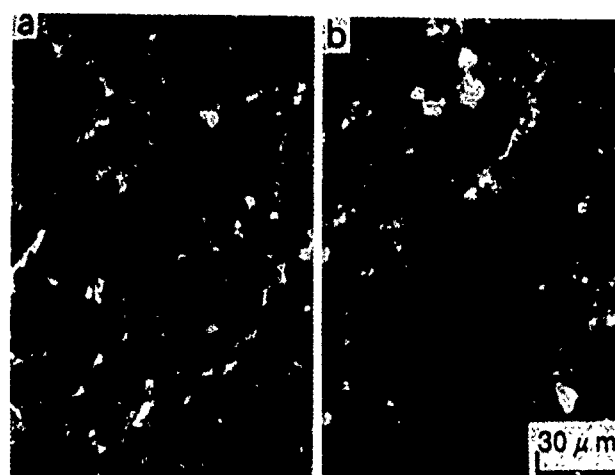


FIG. 6. Optical micrographs of magnets with and without Cu addition: (a) $\text{Pr}_{17.0}\text{Fe}_{76.3}\text{B}_{5.2}\text{Cu}_{1.5}$ and (b) $\text{Pr}_{18.0}\text{Fe}_{76.3}\text{B}_{5.2}$.

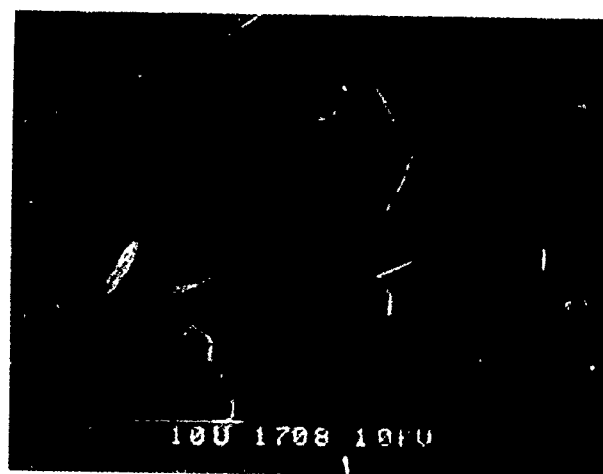


FIG. 4. SEM micrograph of the fracture surface after bending test.

TABLE I. Mechanical properties of hot-rolled $\text{Pr}_{17.0}\text{Fe}_{76.3}\text{B}_{5.2}\text{Cu}_{1.5}$ magnets and commercial Nd-based sintered magnets.

	$\text{Pr}_{17.0}\text{Fe}_{76.3}\text{B}_{5.2}\text{Cu}_{1.5}$	Nd sintered
Tensile strength	$>23.7 \text{ kg f/mm}^2$	8 kg f/mm^2 ^{a,b}
Bending strength	37.7 kg f/mm^2	25 kg f/mm^2 ^{a,b}
Compressive strength	95 kg f/mm^2	110 kg f/mm^2 ^a
Poisson's ratio	0.24	0.24 ^b

^aReference 6.

^bReference 7.

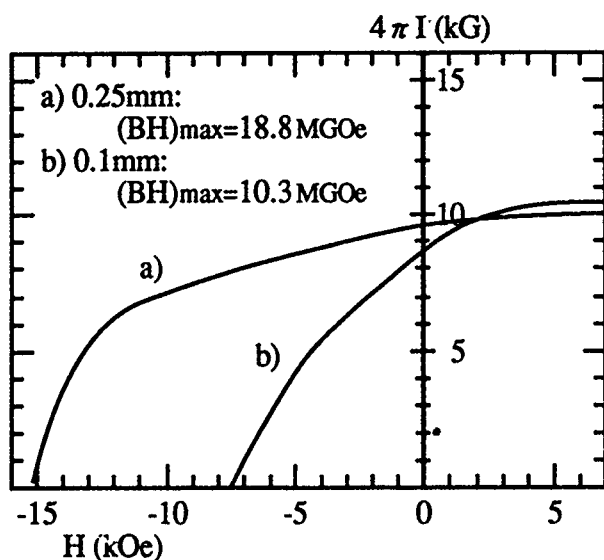


FIG. 7. Demagnetization curves of thin plate $\text{Pr}_{16.5}\text{Fe}_{77.2}\text{B}_{5.1}\text{Cu}_{1.2}$ magnets.

intergranular region forms a dimplelike fracture, suggesting that the fracture in the region was a ductile one. In view of the microstructure and the fracture surface, the Pr-Cu-rich phase seems to permit the ductile fracture, contributing to high tensile strength.

Three-point bending tests were also applied to these magnets. The bending strength obtained was 37.7 kg f/mm^2 , and is larger than that (25 kg f/mm^2) of commercial Nd-based magnets.^{6,7} Nd-based sintered magnets generally contain voids formed in the sintering process. For hot-rolled magnets, however, such voids are not observed in the microstructure as shown in Fig. 4. This is because the magnets were not produced by using any powder metallurgical process, but by hot rolling alloys having a liquid phase under high isostatic pressure.

Cu content dependence of bending strength was also investigated in $\text{Pr}_{18.5-x}\text{Fe}_{76.3}\text{B}_{5.2}\text{Cu}_x$ ($x=0, 0.6, 1.5$) magnets. Cu-free ternary $\text{Pr}_{18.5}\text{Fe}_{76}\text{B}_{5.2}$ magnet showed only 28.9 kg f/mm^2 as illustrated in Fig. 5. Figure 6 shows that the $\text{Pr}_2\text{Fe}_{14}\text{B}$ grains of the ternary magnet are larger than those of the Cu added magnet. The large grains prevent the ternary magnets from achieving high strength. In addition, the ductile Pr-Cu-rich phase, formed in Cu-added magnets, does not exist in Cu-free magnets. The low strength in Cu-free magnets is caused by the large grain size and the lack of the ductile phase.

Compressive strength and Poisson's ratio were also measured for the $\text{Pr}_{17.0}\text{Fe}_{76.3}\text{B}_{5.2}\text{Cu}_{1.5}$ magnet. The results are listed in Table I. Among these mechanical properties, tensile strength is the most remarkable in comparison with that of sintered magnets. On the other hand, compressive strength is not higher than that of the sintered magnets. It seems that the change in intergranular phases does not influence the compressive strength very much.

Hot-rolled Pr-Fe-B-Cu magnets have such excellent machinability that thin plates up to 0.1 mm in thickness are produced without cracking. Demagnetization curves of the thin plate magnets are shown in Fig. 7 (0.25 and 0.1 mm in

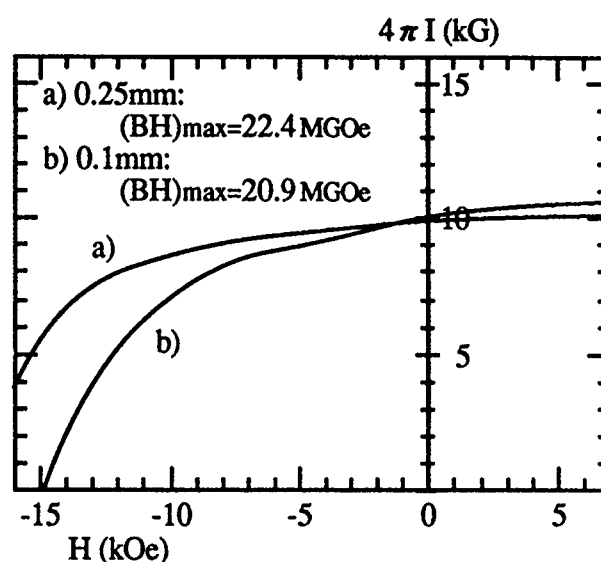


FIG. 8. Demagnetization curves of thin plate $\text{Pr}_{16.5}\text{Fe}_{77.2}\text{Be}_{5.1}\text{Cu}_{1.2}$ magnets after heat treatment.

thickness). The direction of easy magnetization is normal to the plate. Magnetic properties measured by VSM were corrected by adopting the demagnetization factor: $N=0.9$. $(BH)_{\text{max}}=18.8 \text{ MGOe}$ and $iH_c=15.0 \text{ kOe}$ were obtained for the 0.25-mm-thick magnet. The same properties of the 0.1-mm-thick magnet, however, deteriorated severely due to the damage induced during machining. In order to recover the properties, a heat treatment (2h at 600°C) was performed in vacuum. The demagnetization curves after the heat treatment are shown in Fig. 8. The magnetic properties obtained were greatly recovered. Even in the 0.1-mm-thick magnet, $(BH)_{\text{max}}=20.9 \text{ MGOe}$ was obtained, and intrinsic coercivity was also enhanced up to 14.8 kOe . SEM observations revealed that the damaged surface caused by machining turned into a relatively flat surface after the heat treatment. It seems that the Pr-Cu-rich phase, having a low melting point, became liquid during the heat treatment and removed the defects which had been formed on the $\text{Pr}_2\text{Fe}_{14}\text{B}$ grains. Therefore, high coercivities were obtained. Although a similar recovery effect in sintered magnets had been reported, the recovery was achieved up to much higher S/V (S : surface area; V : volume) in the hot-rolled magnets than in the sintered magnets.⁸

¹T. Shimoda, K. Akioka, O. Kobayashi, and T. Yamagami, IEEE Trans. Magn. MAG-25, 4099 (1989).

²T. Shimoda, K. Akioka, O. Kobayashi, T. Yamagami, and A. Arai, in Proceedings of the 11th International Workshop on RE Magnets and Their Applications, 1990, p. 17.

³F. Takagi, O. Kobayashi, A. Arai, K. Akioka, and T. Shimoda (unpublished).

⁴M. Sagawa, S. Fujimura, H. Yamamoto, and Y. Matsuura, IEEE Trans. Magn. MAG-20, xxx (1984).

⁵T. Kajitani, K. Nagayama, and T. Umeda, J. Magn. Mater. 117, 379 (1992).

⁶TDK Corp., "NEOREC" catalogue, printed in Japan, March 1991.

⁷Sumitomo Special Metals Corp., "NEOMAX" catalogue, printed in Japan, April 1993.

⁸H. Nishio, H. Yamamoto, M. Nagakura, and M. Uehara, IEEE Trans. Magn. MAG-26, 257 (1990).

Magnetocaloric dependence of magnetic viscosity measurements in NdFeB

L. Folks, R. Street, R. Woodward, and P. G. McCormick

Research Centre for Advanced Mineral and Materials Processing, The University of Western Australia,
Nedlands 6009, Australia

Measurements of the time dependence of magnetization may be analyzed by means of a constitutive equation to give information regarding the fundamental nature of magnetization reversal processes. The quantity Λ (\equiv the fluctuation field H_f) may be measured and then related to the activation volumes involved in the magnetization reversal processes. These measurements are commonly made at or near room temperature for hard permanent magnet materials, since this is the usual operating temperature, and the system is assumed to be isothermal. However, the experimental work described shows for these materials the magnetocaloric effect (MCE) cannot be neglected at these temperatures. Magnetic viscosity measurements have been made in two ways which lead to different thermal behavior in the sample. Thermometric measurements were made concurrently with the magnetic viscosity measurements in a sample of sintered NdFeB. The measurements show that the calculated value of Λ can be changed by as much as 10% when isothermal conditions do not hold. This effect is particularly evident near room temperature in NdFeB-type materials because of the strong dependence of coercivity on temperature and the proximity to the Curie point ($T_c \sim 620$ K) where reversible and irreversible components of MCE peak.

I. INTRODUCTION

Measurements of time dependence of magnetization, or magnetic viscosity, may provide useful information regarding the intrinsic magnetization reversal behavior in bulk materials. In permanent magnet materials, such as $\text{Nd}_2\text{Fe}_{14}\text{B}$, room-temperature measurements show significant time dependence of magnetization arising from the thermal activation of metastable magnetization events. Analysis and interpretation of viscosity data gives information regarding the origin of reversal events.

When a field is applied to a magnetic material under adiabatic conditions such that the magnetization changes, heat is evolved or absorbed in a reversible manner. This heat is manifested as an increase or decrease in the temperature of the sample which is known as the magnetocaloric effect (MCE). Andreenko *et al.*¹ attribute this "reversible MCE" to two effects, the changes in exchange energy and the changes in the magnetic anisotropy energy. The first effect will be greatest at temperatures close to the Curie point T_c where the changes in rotational behavior are pronounced. The second effect is in general smaller and becomes significant when the magnetocrystalline anisotropy constant changes rapidly with temperature.

In addition to these reversible effects, magnetically ordered materials will show irreversible thermal effects induced by irreversible changes in the magnetization. Events which might give rise to these changes include irreversible domain-wall movements and irreversible magnetization rotations. These effects give rise to the "irreversible MCE."

Because NdFeB-type materials have values of T_c close to room temperature it is possible to detect substantial reversible and irreversible MCE at ambient temperatures. The measurements described here, while not being strictly adiabatic, show that these effects have a substantial impact on measurements of magnetic viscosity. These results are

discussed in light of the constitutive equation developed by Estrin, McCormick, and Street² for the description of magnetic state.

II. EXPERIMENT

All magnetic measurements were made using a vibrating sample magnetometer in conjunction with a 50 kOe superconducting solenoid. A cryostat was available to maintain the ambient sample temperature during the measurements, which have all been made at or near room temperature. A variety of sintered NdFeB-type materials supplied by Sumitomo Special Metals, Japan, and Electron Energy Corp., USA, has been used in this work. The magnetic viscosity tests were performed on spherical samples (demagnetization factor of $4\pi/3$ in Gaussian units) mounted in epoxy resin. To record changes in sample temperature a copper-constantan thermocouple was spot welded to the surface of the sample.

Magnetic viscosity measurements were performed in two ways. First is the multiple step per loop measurement technique (MS): (a) sample cycled in saturating field to establish a consistent magnetic state; (b) field ramped from $+H_{\max}$ to the first measurement field, $-H_a$; (c) magnetization changes recorded at constant $|H_a|$ for a set period of time t_1 (here $\sim 10^2$ s); (d) field increased to next measurement field $|H_a + \Delta H_a|$, and the process repeated.

The second is the single step per loop measurement technique (SS): as for MS except that after (c) the field was ramped to $-H_{\max}$ and then returned to $+H_{\max}$, before establishing a new measurement field.

The results of both types of experiment have been analyzed in the manner described in Street, McCormick, and Folks³ where it is assumed that the magnetic state of the material may be described as a function of the irreversible magnetization M_{irr} , the internal field H_i , and the time rate of change of irreversible magnetization \dot{M}_{irr} ,

$$dH_i = (1/\chi_{\text{irr}}^i) dM_{\text{irr}} + \Lambda d \ln \dot{M}_{\text{irr}}, \quad (1)$$

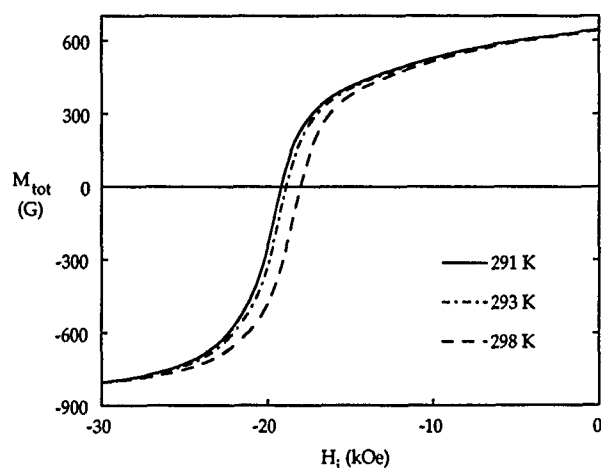


FIG. 1. M_{tot} vs H_i for $\text{Pr}_2\text{Fe}_{14}\text{B}$ at 291, 293, and 298 K, showing the large shift near H_c .

where $\chi_{\text{irr}}^i = (\partial M_{\text{irr}} / \partial H_i)_{M_{\text{irr}}}$ is the intrinsic irreversible susceptibility and $\Lambda = (\partial H_i / \partial \ln \dot{M}_{\text{irr}})_{M_{\text{irr}}}$.

The quantity Λ may be related to an activation volume v by the expression

$$\Lambda = (k_B T / v M_s), \quad (2)$$

where M_s is the spontaneous magnetization of the material, T is the temperature, and k_B is the Boltzmann factor. The determination of Λ was found to be independent of many of the experimental conditions, including the rate of change of the applied field between steps \dot{H}_a , the time over which the magnetic viscosity is recorded t_1 , and the field interval between steps ΔH_a , in the ranges available.

Hysteresis curves of NdFeB-type materials exhibit marked changes in coercivity H_c with T near room temperature. Figure 1 shows the total magnetization M_{tot} versus internal field H_i curves with $\dot{H}_a = 450$ Oe/s for a sample of $\text{Pr}_2\text{Fe}_{14}\text{B}$ ($T_c \sim 595$ K) at ambient temperatures of 291, 293, and 298 K. The value of H_c (taken as the field at which the maximum value of susceptibility occurs) decreases by 1260 Oe between 291 and 298 K ($\sim 0.87\%/K$), slightly higher than the value of $0.7\%/K$ reported by Strnat.⁴ For the determination of Λ , however, it is more appropriate to consider the change in M at a fixed value of H_i for a given change in ambient temperature. For this material at $H_i = -19.1$ kOe ($\sim H_c$), M_{tot} changes by ~ 330 G between 291 and 298 K.

However, a simple calculation to approximate the MCE for the demagnetizing curve [using the expression $\Delta T = (\rho s)^{-1} \int H dM$, where ρ is the density and s is the specific heat] suggests that the temperature of the sample increases by ~ 0.9 K over this part of the curve under adiabatic and isobaric conditions. To measure the actual effect under experimental conditions a thermocouple was attached to a sample of anisotropic sintered $\text{Nd}_2\text{Fe}_{14}\text{B}$ ($T_c \sim 620$ K) and the changes in temperature were monitored as the sample was cycled around the hysteresis loop. For this material H_c varies by $0.72\%/K$ near room temperature. Figure 2 shows the measured change in sample temperature as the field was cycled at $\dot{H}_a = 450$ Oe/s. Initially T decreases slightly between $+50$ and 0 kOe, but near coercivity there is

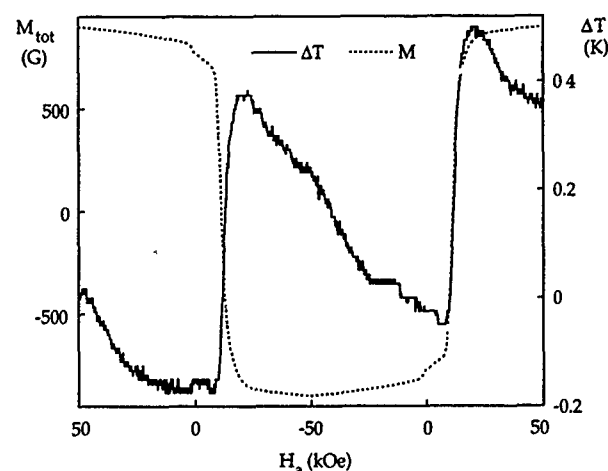


FIG. 2. Variation of M_{tot} and ΔT as H_a is cycled from $+50$ to -50 kOe at $\dot{H}_a = 450$ Oe/s for a sample of sintered $\text{Nd}_2\text{Fe}_{14}\text{B}$ at an ambient temperature of 293 K.

a sudden increase in T of ~ 0.5 K, comparable to the calculated figure, given that some heat will be lost to the environment. The total change in temperature as the specimen is taken around a loop is ~ 0.36 K.

Measurements of ΔT were made on the same sample as MS and SS experiments were conducted. Figure 3(a) illustrates the variations in T as a SS experiment was performed, with five steps at 1 kOe intervals, at $\dot{H}_a = 450$ Oe/s and an ambient temperature of 293 K. The sample was allowed to come to thermal equilibrium with the experimental environment before the measurement started. Again the initial part of each loop was accompanied by a decrease in T , followed by an increase in T in the second quadrant. During the first viscosity measurement T continued to rise, but during each of the subsequent steps T decreased. However, at the start of each loop the values of T varied only by ~ 0.3 K and at the start of each viscosity measurement T varied by only ~ 0.05 K. Figure 3(b) gives the equivalent data for a MS experiment under similar conditions, along with the corresponding changes in M . In this case T does not vary much over the duration of the viscosity measurements for steps after the first one, but the T at the beginning of each step drifts upward. For this material Λ from the SS measurement was $\sim 7\%$ smaller than from the MS measurement.

Conventional MS and SS measurements (without an attached thermocouple) were made on a variety of sintered NdFeB-type materials in spherical form mounted in epoxy resin. The values of Λ derived consistently differed, by as much as 14%, for the two methods, as shown in Fig. 4 for the sample of $\text{Pr}_2\text{Fe}_{14}\text{B}$ at an ambient temperature of 293 K. It may be seen that the form of the data is similar but that the values differ by $\sim 10\%$ near H_c . Similar results were found for a range of sintered NdFeB-type materials. However, there is no discernible difference in values of Λ derived from experiments at different ambient temperatures near room temperature where the experimental method is the same. Moreover, MS and SS tests on CrO_2 , for which $T_c \sim 390$ K, gave identical values of Λ within experimental error.

Examination of the MS and SS data for NdFeB materi-

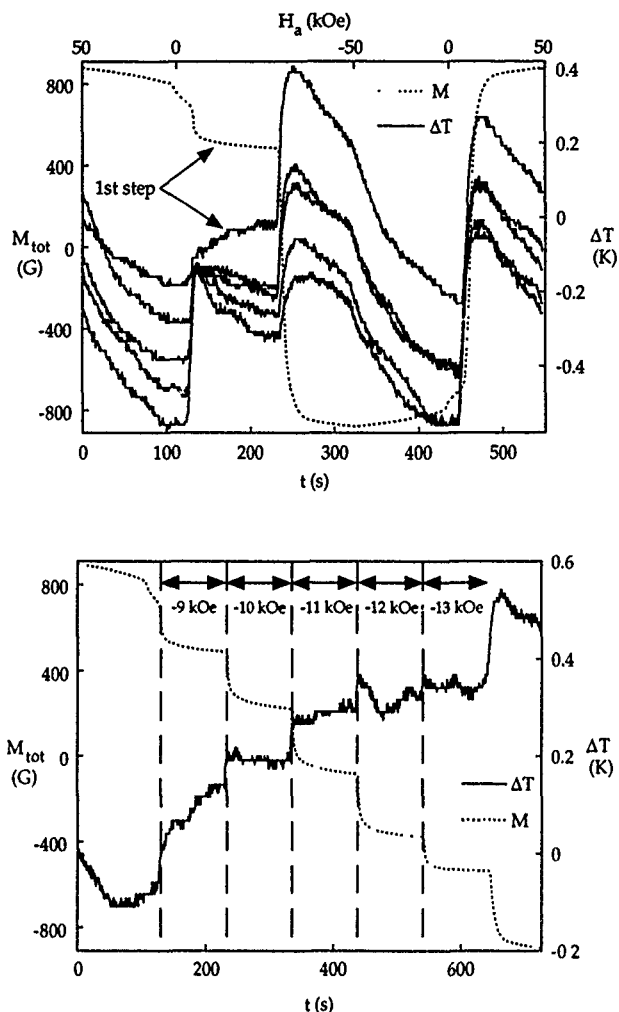


FIG. 3. Variation of M_{tot} and ΔT as a function of time t during (a) a SS experiment (M_{tot} shown for first step only) and (b) a MS experiment, on the sample of $\text{Nd}_2\text{Fe}_{14}\text{B}$ at an ambient temperature of 293 K. The period during which magnetic viscosity is measured is indicated.

als, including the portions of the loops between the steps, shows that associated with the changes in sample temperature are significant deviations from the hysteresis curve at the same ambient temperature, and these are found to be dependent on \dot{H}_a .

III. SUMMARY

The observation of changes in temperature associated with irreversible changes in magnetization is unsurprising and particularly striking measurements have been made by Otani *et al.*⁵ in NdFeB at 2.5 K, where temperature changes associated with individual Barkhausen events have been recorded. Here, the impetus for measuring changes in sample temperature as viscosity measurements were being made arose from the observation that values of Λ , while independent of most experimental conditions, were consistently different from experiments in which the sample was cycled in a saturating field between each measurement of viscosity.

For both the MS and SS experiments, measurement of T during the first magnetic viscosity measurement gives the same result, an increase of ~ 0.1 K. At the beginning of this

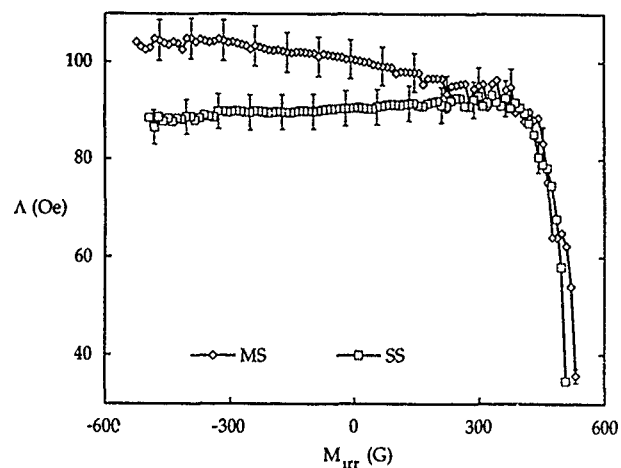


FIG. 4. Λ vs M_{irr} derived from MS and SS experiments on the sample of $\text{Pr}_2\text{Fe}_{14}\text{B}_2$. Experimental error bars are shown ($\sim 4\%$) for some of the data.

step the sample temperature is close to the ambient experimental temperature and the MCE associated with the magnetic viscosity leads to an increase in T . After the first step the thermal behavior of the sample differs between the two methods. For the MS method T does not vary by much during the viscosity measurement but for the SS method T decreases by varying amounts during each step. These differences arise from the balances between MCE, from both magnetic viscosity and changes in the applied field, and heat loss to the environment.

For all the NdFeB -type materials measured, Λ from SS measurements was $\sim 10\%$ smaller than that from MS measurements for a given ambient T . The thermometric measurements described here show that this may be accounted for by the different thermal behavior of the sample during magnetic viscosity experiments carried out under MS and SS conditions. Changing the ambient T in the range 291–298 K produced no change in Λ where the experimental method was the same. Similar experiments on a sample of CrO_2 showed no change in Λ with method, commensurate with the smaller energies associated with magnetization reversal in this material and the low T dependence of H_c near room temperature. That Λ should be critically dependent on changes in temperature during the measurement is clear from the definition [Eq. (1)]; Λ is proportional to changes in H , but for NdFeB , H is strongly dependent on T .

In order to eliminate magnetocaloric induced effects it is necessary to ensure that magnetic viscosity measurements of NdFeB -type materials are carried out under isothermal conditions. Nonisothermal results should be viewed with some caution.

¹A. S. Andreenko, K. P. Belov, S. A. Nikitin, and A. M. Tishin, *Sov. Phys. Usp.* **32**, 649 (1989).

²Y. Estrin, P. G. McCormick, and R. Street, *J. Phys. Condens. Matter* **1**, 4845 (1989).

³R. Street, P. G. McCormick, and L. Folks, *J. Magn. Magn. Mater.* **104-107**, 368 (1992).

⁴K. J. Strnat, *Proc. IEEE* **78**, 923 (1990).

⁵Y. Otani, J. M. D. Coey, B. Barbara, H. Miyajima, S. Chikazumi, and M. Uehara, *J. Appl. Phys.* **67**, 4619 (1990).

Die-upset PrCo₅-type magnets: Enhanced coercivities

C. D. Fuerst and E. G. Brewer

Physics Department, GM Research and Development Center, Warren, Michigan 48090-9055

Rare-earth-cobalt alloys have been melt spun, yielding ribbons whose major phase was the hexagonal PrCo₅ phase. Fully dense hot-pressed magnets with essentially isotropic magnetic properties have been formed by consolidating the ribbons at high temperatures and pressures. The hot-pressed precursor was then subjected to hot deformation or die upsetting, thereby inducing partial alignment of the *c* axis along the press direction. The resulting magnets had remanences approaching ~75% of the saturation magnetization of the hexagonal PrCo₅ phase. Three approaches were used to optimize the coercivity of the die-upset magnets: (i) replacing small amounts of cobalt with carbon; (ii) partially substituting samarium for the praseodymium; and (iii) high-temperature heat treatment followed by a thermal quench. Coercivities near ~20 kOe were achieved with thermally quenched die-upset (Pr_{0.6}Sm_{0.4})₁₈Co₈₁C magnets, while maintaining remanences above 8 kG.

There continues to be considerable scientific and technical interest in rare-earth-cobalt permanent magnets,^{1,2} primarily for their high Curie temperatures and high magneto-crystalline anisotropies. Although similar to SmCo₅ in many respects, PrCo₅ has not been as successfully exploited as a permanent magnet material despite reports of sintered magnets with relatively high remanences (~10.5 kG) and energy products (26.2 MGOe).³ This is largely due to the relatively low coercivity (H_{ci} ~5 kOe) of sintered PrCo₅-type magnets.⁴⁻⁶ Higher coercivities ($6 < H_{ci} < 10$ kOe) have been reported for melt-spun PrCo₅ ribbons,⁷⁻¹⁰ but like melt-spun Nd₂Fe₁₄B ribbons,¹¹ they are crystallographically isotropic with remanences (B_r ~6 kG) of about half the saturation magnetization ($4\pi M_s$ ~12 kG) of the primary phase.¹

Recently we have shown that the remanences of melt-spun PrCo₅ alloys¹² can be enhanced by thermomechanical alignment or die upsetting,¹³ using techniques first developed for melt-spun Nd₂Fe₁₄B alloys.¹⁴ In the first step of the process, the Pr-Co ribbons are confined to the cavity of a hot die and isostatically pressed, causing ribbon fragments to deform and fill the surrounding voids. This consolidates the ribbon fragments and results in a fully dense isotropic magnet. For example, hot pressing ribbons of the composition Pr₁₈Co₈₂ (see Fig. 1) yielded a magnet with a density of 8.3 g/cm³ and a remanence of just over 6 kG, both of which coincide with the values expected for an isotropic PrCo₅ magnet. The hot-pressed magnet can then be used as a precursor in the second process step (die upsetting), where the reheated sample is placed in an oversized die and plastically deformed by applying a uniaxial force. The degree of alignment produced during die upsetting depends on the level of deformation; we found that reducing the sample height by a little over 50% produced a remanence of ~8.3 kG in the Pr₁₈Co₈₂ magnet (see Fig. 1). This remanence represents a ~35% increase relative to the remanence of the hot-pressed precursor. As with die-upset Nd-Fe-B magnets, the remanence enhancement occurred parallel to the press direction (perpendicular to the direction of material flow). X-ray diffraction from the surface of the die-upset Pr-Co magnets has confirmed the crystallographic alignment of the *c* axes along the press direction.

Unfortunately, the coercivities of our binary Pr-Co melt-spun magnets, like their sintered counterparts, have remained relatively low (H_{ci} ~3 kOe). In this article we summarize our efforts to optimize the coercivities of this class of permanent magnets. For example, postpress heat treatments, particularly quenching from high temperatures, can produce varying degrees of enhancement in H_{ci} ; as Fig. 1 shows, the coercivity of the die-upset magnet increased by ~15% after quenching from 800 °C. In addition to heat treatments, adding carbon and samarium to the alloys can also enhance the coercivities of melt-spun PrCo₅-type magnets. Experimental details have been presented elsewhere.¹⁵

Improving coercivity by adding or substituting elements into the alloy is almost always accompanied by a decrease in remanence. At most concentrations the addition of carbon to Pr-Co alloys (Pr₁₈Co_{82-x}C_x) is no exception to this tradeoff.

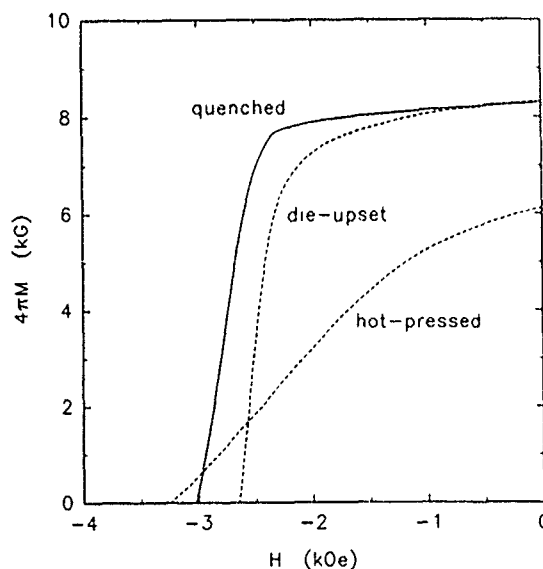


FIG. 1. Demagnetization curves for hot-pressed, die-upset, and quenched die-upset magnets having the composition Pr₁₈Co₈₂. The (dashed) curves labeled hot pressed and die upset were obtained from as-pressed magnets. The (solid) curve labeled quenched was obtained from a die-upset magnet heated to 800 °C before quenching in an oil reservoir. The die-upset (DU) level was 53%.

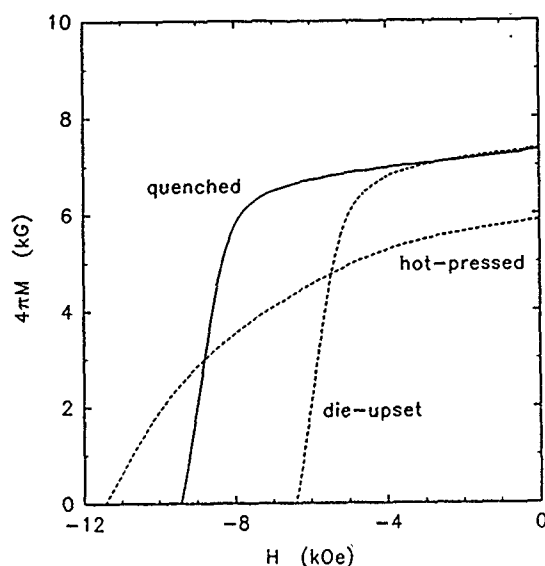


FIG. 2. Demagnetization curves for hot-pressed, die-upset, and quenched die-upset magnets having the composition $\text{Pr}_{18}\text{Co}_{78}\text{C}_4$. The (dashed) curves labeled hot pressed and die upset were obtained from as-pressed magnets. The (solid) curve labeled quenched was obtained from a die-upset magnet heated to 800°C before quenching in an oil reservoir. The die-upset (DU) level was 53%.

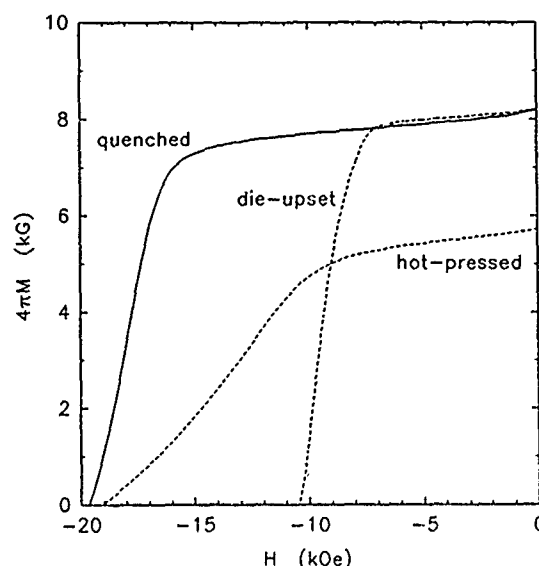


FIG. 4. Demagnetization curves for hot-pressed, die-upset, and quenched die-upset magnets having the composition $\text{R}_{18}\text{Co}_{78}\text{C}$ where $\text{R}=(\text{Pr}_{0.6}\text{Sm}_{0.4})$. The (dashed) curves labeled hot pressed and die upset were obtained from as-pressed magnets. The (solid) curve labeled quenched was obtained from a die-upset magnet heated to 800°C before quenching in an oil reservoir. The die-upset (DU) level was 53%.

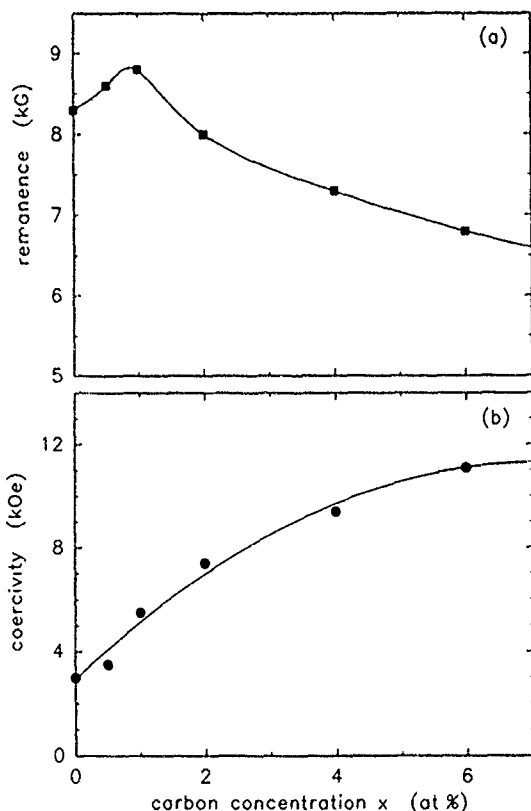


FIG. 3. (a) Remanence and (b) coercivity of die-upset $\text{Pr}_{18}\text{Co}_{82-x}\text{C}_x$ magnets vs carbon concentration x . To maximize coercivity, the die-upset magnets were first heated to 800°C before quenching in an oil reservoir. The die-upset (DU) level was 53%.

Adding 4 at. % carbon ($x=4$) to the Pr-Co alloy more than doubled the coercivity of the hot-pressed and die-upset magnets (see Fig. 2). This gain was, however, offset by a commensurate loss of remanent moment; the remanence of the die-upset magnet ($B_r=7.3$ kG) was 12% less than that of its carbon-free counterpart ($B_r=8.3$ kG). The trend to lower remanence with increasing carbon concentration (x) was observed for all magnets with $x \geq 2$ at. % [see Fig. 3(a)]. However, for a narrow range of low carbon levels, $0.5 \leq x \leq 1$, the remanence of the die-upset magnets actually increased a moderate amount ($\sim 5\%$) from the carbon-free value. This makes it possible to use low levels of carbon to increase coercivity [see Fig. 3(b)] without compromising remanence.

The coercivities in Fig. 3(b) are for quenched, rather than as-pressed, die-upset magnets. The coercivities of the as-pressed magnets were sensitive to press conditions and the efficiency with which the magnets were ejected from the die, and thus tended to be inconsistent. In some cases, thermal quenching from high temperatures ($\sim 800^\circ\text{C}$) provided substantial improvements to the coercivity. The demagnetization curve in Fig. 2 shows a $\sim 50\%$ increase in the coercivity of the $\text{Pr}_{18}\text{Co}_{78}\text{C}_4$ die-upset magnet after quenching. Increasing the heat treatment temperature (800 – 1000°C) or lengthening the soak time (10 – 100 min) did not provide any further enhancement to the coercivity. Quenching from lower temperatures produced progressively less improvement, and quenching from temperatures below 600°C produced no change in coercivity. It must be presumed that the change to the microstructure during this heat treatment were subtle since the magnetization, specifically the remanence, did not change. The quenched magnets did tend to crack and they often fractured, either upon quenching or when magnetized.

Complete substitution of samarium for praseodymium in

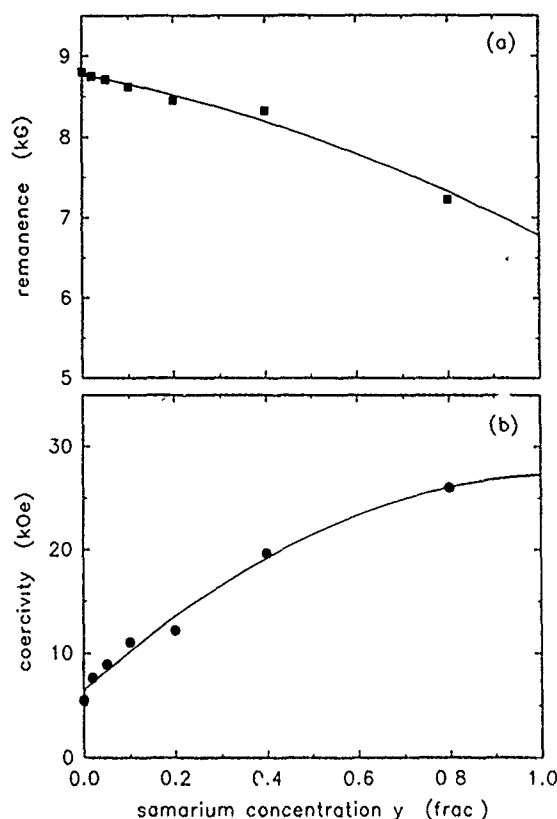


FIG. 5. (a) Remanence and (b) coercivity of die-upset $(\text{Pr}_{1-y}\text{Sm}_y)_{18}\text{Co}_{82}\text{C}$ magnets vs samarium fraction y . To maximize coercivity, the die-upset magnets were first heated to 800 °C before quenching in an oil reservoir. The die-upset (DU) level was 53%.

the hexagonal RCO_5 phase, where $\text{R}=(\text{Pr}_{1-y}\text{Sm}_y)$, can double the room-temperature magnetocrystalline anisotropy with only a small loss in saturation magnetization ($\sim 10\%$).^{16,17} Consequently, the effect of even partial substitution ($y < 1$) on the coercivity of melt-spun magnets is quite substantial. The coercivities of $(\text{Pr}_{0.6}\text{Sm}_{0.4})_{18}\text{Co}_{81}\text{C}$ (i.e., $y=0.4$) hot-pressed and die-upset magnets were 19 and 10.5 kOe, respectively (see Fig. 4). After quenching the die-upset magnet had a coercivity of 19.5 kOe, nearly twice the coercivity of the as-pressed die-upset magnet and even exceeding that of the hot-pressed precursor. The remanence of the die-upset $y=0.4$ magnet ($B_r=8.3$ kG) was slightly less than that of the samarium-free ($y=0$) magnets ($B_r=8.7$ kG), and in fact the trend to lower remanences with increasing samarium levels was nearly linear [see Fig. 5(a)]. The loss of remanence extrapolates to $\sim 20\%$ at complete samarium substitution ($y=1$), more than expected from the change in the saturation magnetization of the RCO_5 phase.¹ Without microstructural analysis of these magnets, we can only speculate that the higher samarium levels interfere with crys-

tallographic alignment during deformation, lowering the remanence. As expected, coercivities increased with increasing samarium levels [see Fig. 5(b)], with a slightly steeper increase at moderate levels ($y \leq 0.4$). Accurate coercivity measurements at high samarium levels were limited by the field of our electromagnet.

By increasing the die-upset level to 75%, we obtained remanences as high as 9.2 kG, with coercivities near 6 kOe and energy products of ~ 19 MGOe for alloys containing small amounts of both carbon ($x=1$) and samarium ($y=0.02$). Although this is a significant improvement over the remanence of the isotropic magnet ($B_r \approx 6$ kG), it is still only $\sim 76\%$ of the saturation magnetization. In comparison, die-upset Nd-Fe-B-type magnets are capable of much better alignment since the remanence can exceed 90% of the saturation magnetization of the $\text{Nd}_2\text{Fe}_{14}\text{B}$ phase.¹⁵

Melt-spun Pr-Co alloys can be hot pressed to produce fully dense magnets with remanences near that expected for isotropic magnets, i.e., half the saturation magnetization. Further processing by hot deformation or die upsetting creates crystallographic texture, with the c axes oriented preferentially along the press direction of the magnet. This enhances the remanence by over 35% relative to the isotropic precursor. Three methods have been identified to enhance the coercivity of these magnets: (i) replacing some of the cobalt with carbon; (ii) replacing some of the praseodymium with samarium; and (iii) brief high-temperature heat treatments followed by a thermal quench.

- ¹ K. J. Strnat and R. M. W. Strnat, *J. Magn. Magn. Mater.* **100**, 38 (1991).
- ² K. Kumar, *J. Appl. Phys.* **63**, R13 (1988).
- ³ W. E. Wallace, R. S. Craig, H. O. Gupta, S. Hirose, A. Pedziwiatr, E. Oswald, and E. Schwab, *IEEE Trans. Magn.* **MAG-20**, 1599 (1984).
- ⁴ E. M. T. Velu, R. T. Obermyer, S. G. Sankar, and W. E. Wallace, *IEEE Trans. Magn.* **MAG-25**, 3779 (1989).
- ⁵ E. M. T. Velu, R. T. Obermyer, S. G. Sankar, and W. E. Wallace, *J. Less-Common Met.* **148**, 67 (1989).
- ⁶ Y. Shen, D. E. Laughlin, E. M. T. Velu, and S. G. Sankar, *J. Magn. Magn. Mater.* **94**, 57 (1991).
- ⁷ K. Morimoto, M. Yagi, and T. Takeshita, *Mater. Trans.* **32**, 562 (1991).
- ⁸ S. Ishio, M. Takahashi and T. Miyazaki, *J. Magn. Magn. Mater.* **86**, 31 (1990).
- ⁹ T. Miyazaki, M. Takahashi, and X. Yang, *J. Jpn. Inst. Met.* **54**, 1408 (1990).
- ¹⁰ T. Miyazaki, M. Takahashi, S. Ishio, and M. Takahashi, *J. Jpn. Inst. Met.* **54**, 1414 (1990).
- ¹¹ F. E. Pinkerton, in *Science and Technology of Nanostructured Magnetic Materials*, edited by G. C. Hadjipanayis and G. A. Prinz (Plenum, New York, 1991), pp. 591-597.
- ¹² C. D. Fuerst, J. F. Herbst, C. B. Murphy, and D. J. Van Wingerden, *J. Appl. Phys.* (to be published).
- ¹³ C. D. Fuerst and E. G. Brewer (unpublished).
- ¹⁴ R. W. Lee, *Appl. Phys. Lett.* **46**, 790 (1985).
- ¹⁵ C. D. Fuerst and E. G. Brewer, *J. Appl. Phys.* **73**, 5751 (1993).
- ¹⁶ H. P. Klein, A. Menth, and R. S. Perkins, *Physica B* **80**, 153 (1975).
- ¹⁷ K. J. Strnat, in *Ferromagnetic Materials*, edited by E. P. Wohlfarth and K. H. J. Buschow (North-Holland, Amsterdam, 1988), pp. 131-209.

Nonepitaxial sputter synthesis of aligned strontium hexaferrite, $\text{SrO} \cdot 6(\text{Fe}_2\text{O}_3)$, films

H. Hegde, P. Samarasekara, and F. J. Cadieu

Physics Department, Queens College of CUNY, Flushing, New York 11367

Films of strontium hexaferrite were synthesized through rf diode sputter deposition, nonepitaxially onto polycrystalline Al_2O_3 substrates. So far such films for the analogous Ba phase have been synthesized mostly through epitaxial growth onto suitably chosen matching substrates. Crystallization of the strontium hexaferrite phase was achieved for deposition temperatures as low as 500 °C. For nonepitaxially synthesized 2–3- μm -thick polycrystalline films, a fairly high degree of variable and controlled *c*-axis orientation of the crystallites has been obtained. The x-ray-diffraction traces of films with a strong *c*-axis in-plane alignment showed predominantly (110)-type reflections. The film coercivities were increased by postdeposition annealing in O_2 . The remnant to saturation flux density ratio of such in-plane anisotropy films for in-plane measurements was 0.62, with an in-plane coercivity ≈ 2.3 kOe.

I. INTRODUCTION

Thin films of magnetically uniaxial barium hexaferrite and its analogue strontium hexaferrite have many applications in microwave devices;^{1–3} they also have potential applications as recording media.^{4–6} So far, the synthesis of these films has involved expensive epitaxial growth on either substrates of the structurally related spinels or through the matching of the oxygen planes of metal oxides in the film and the substrate.^{1–7} As expected from epitaxial growth, strong crystallographic orientation in the film has been achieved for such cases. Generally, in cases where the films were synthesized through sputter deposition, crystallization was achieved through postdeposition annealing of an amorphous deposit, in an oxygen atmosphere at a relatively high temperature, in excess of 800 °C. Good quality crystalline films were formed in this fashion.⁷ In recent years, there has been great progress in the nonepitaxial sputter synthesis of uniaxial, high-energy product rare-earth-transition-metal (RE-TM) permanent magnet films. The *c*-axis orientation of the crystallites in these polycrystalline metallic films could be controlled through sputter process control.⁸ Control of the *c*-axis orientation in nonepitaxial films of these uniaxial RE-TM films results only when the deposition is carried out at temperatures above the minimum crystallization temperature. Anisotropic nonepitaxial films could not be formed by crystallization of originally amorphous deposits.⁸ It would be interesting to explore the feasibility of synthesizing the dielectric hexaferrites through a similar procedure. In this article, we report the nonepitaxial synthesis of strontium hexaferrite films on polycrystalline Al_2O_3 substrates. The *c*-axis orientation of the crystallites in our polycrystalline films was controllable through sputter process control. We were successful in synthesizing crystalline hexaferrite films at temperatures as low as 500 °C. In-plane coercivities as high as 3.8 kOe were achieved.

II. EXPERIMENT

All films in this study were synthesized onto polycrystalline Al_2O_3 substrates having grain sizes in the 1–2 μm range. Films were deposited through planar diode sputter

deposition with a target-to-substrate distance of about 6 cm, with substrate temperatures from 500 to 650 °C. The strontium hexaferrite phase could not be formed from bulk sputtering targets of the same composition. For films deposited from commercially available strontium hexaferrite targets, the sputter deposition was carried out for pressure ranges 20–100 μm and gas mixtures of Ar and up to 10% O_2 . At the deposition temperatures required to crystallize these films, they were found to be extremely deficient in Sr and the hexaferrite phase could not be formed. With 100% Ar, at a pressure of 100 mTorr for deposition temperature of 500 °C, the Sr to Fe atomic ratio was about 30% of the stoichiometric value. The strontium concentration dropped monotonically with increasing substrate temperature, decreasing gas pressure, and increasing oxygen gas concentration in the sputtering gas. All of these parameters affect the exposure of the growing films to energetic bombardment of O^- ions. These results indicated there was a large preferential resputtering of Sr due to bombardment of the film by energetic O^- ions. To compensate for the loss of Sr in the film, custom-made oxide targets greatly enriched in Sr with approximate composition $\text{Sr}:\text{Fe}:\text{O} = 1:4:7$ were used. When sputtering from these targets, hexaferrite films were formed without the use of O_2 in the sputter gas. The oxygen content of the target was sufficient to directly crystallize the films in hexaferrite form.

III. RESULTS AND DISCUSSION

Hexaferrite films were synthesized for Ar gas pressures of 100 mTorr and deposition temperatures from 500 to 650 °C. While all the films were crystalline as deposited, many films were further annealed at the same temperature as their deposition temperature, in an O_2 atmosphere of 500 Torr pressure for about 30 min. All films had a deposition rate of around 0.1 $\mu\text{m}/\text{h}$, and thicknesses around 2–3 μm .

All films deposited from the Sr-rich targets at temperatures of 500 °C and above formed in the basic hexaferrite structure of $\text{PbO} \cdot 6(\text{Fe}_2\text{O}_3)$ as determined from x-ray-diffractometer traces, using $\text{CuK}\alpha$ radiation; however, the coercivities of the films increased dramatically on annealing the films in an oxygen atmosphere at a pressure of 500 Torr,

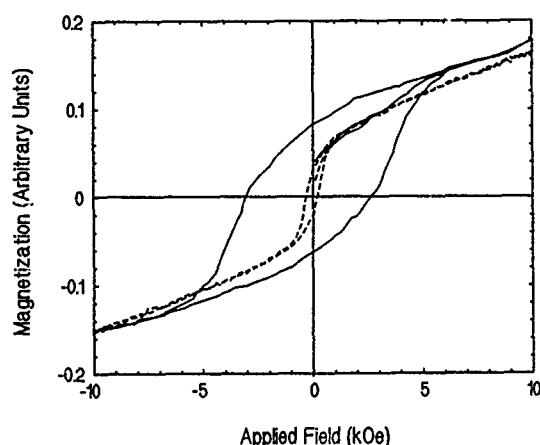


FIG. 1. Hysteresis loops of film deposited at 550 °C, before (dashed) and after (solid) annealing in 500 Torr oxygen for 30 min, at 550 °C.

for about 30 min. The in-plane hysteresis loops of films deposited at 550 °C temperature, before and after annealing, are given in Fig. 1. The in-plane coercivity increased from ≈ 0.5 to 3.8 kOe during the oxygen annealing. The typical grain size in the polycrystalline films was 2500 Å for deposition temperature near 550 °C as determined from the scanning electron microscopy (SEM) micrograph shown in Fig. 2. No change in the grain size or x-ray patterns was noticeable as a result of the postdeposition annealing in oxygen.

The film easy-axis orientation, as dictated by the average c -axis orientation of the hexaferrite crystallites in the film, was found to be strongly dependent on the deposition temperature. The x-ray-diffraction patterns of the films showed large departures from the powder diffraction pattern. As an

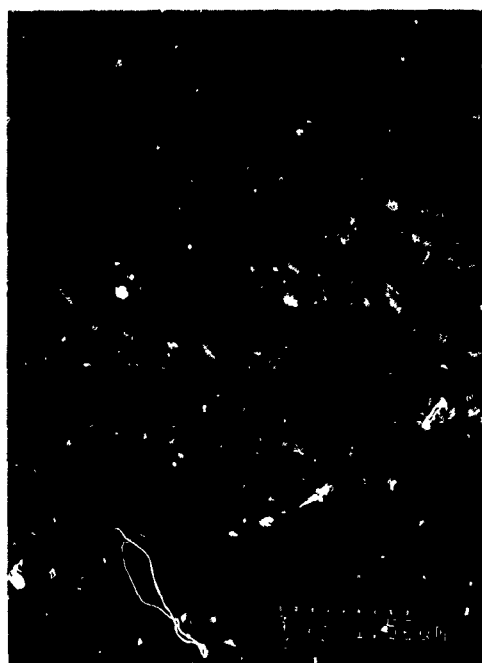


FIG. 2 SEM micrograph of the surface of a strontium hexaferrite film deposited at 550 °C. Each division of the scale given corresponds to 1500 Å.

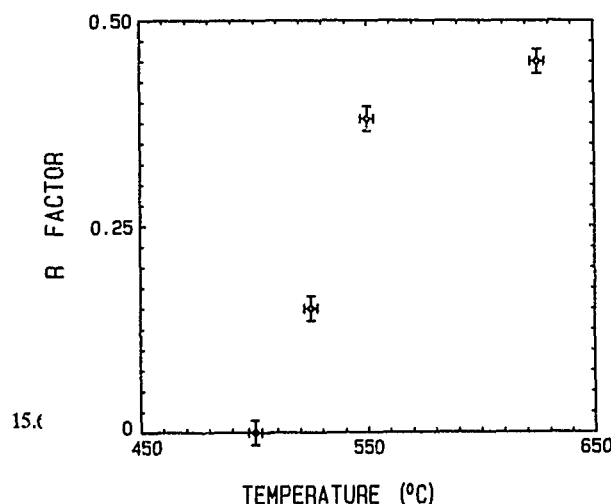


FIG. 3. Change in R value with deposition temperature.

estimate of the degree of anisotropy in the film, we define a function R given by

$$R = N \sum_i \cos \Theta_i^* (I_i / I_{0i}),$$

and

$$N = 1 \left[\sum_i \left(\frac{I_i}{I_{0i}} \right) \right]^{-1}.$$

Θ_i is the angle between the c axis of a particular crystallite and the normal to the film plane, I_i are the intensities of x-ray-diffraction lines of the film, and I_{0i} are the corresponding powder diffraction pattern intensities.

Function R gives a measure of the average c -axis orientation with respect to the film plane. The function R is unity for a pure perpendicular texture such as (00 l), zero for ($hk0$) textures, and 0.5 for random c -axis orientation as in the powder diffraction pattern. At present, we are able to synthesize the films with R ranging from close to zero to 0.5. The best parallel value was achieved for the lowest crystallization temperature, 500 °C, and on the other end, an R value of ≈ 0.5 was achieved for crystallization temperatures from 600 to 650 °C. In other words, for such temperatures, the film pattern resembled a random powder. For the intermediate temperatures the films exhibited mixed texture crystallites. The dependence of R value on the deposition temperature is given in Fig. 3.

The CuK_α x-ray-diffraction patterns of films synthesized at deposition temperatures of 500, 550, and 625 °C are given in Figs. 4(a), 4(b), and 4(c), respectively. The diffraction pattern of films at deposition temperatures exceeding 600 °C resemble the powder pattern of Sr hexaferrite as in Fig. 4(c). The dominant texture at 500 °C was in plane (110) as in Fig. 4(a), while at 550 °C it was (114) as shown in Fig. 4(b). The R values for patterns in Figs. 4(a), 4(b), and 4(c) were approximately zero, 0.38, and 0.45, respectively. These R values correspond to average c -axis orientations away from the film normal of 90°, 68°, and 63°, respectively.

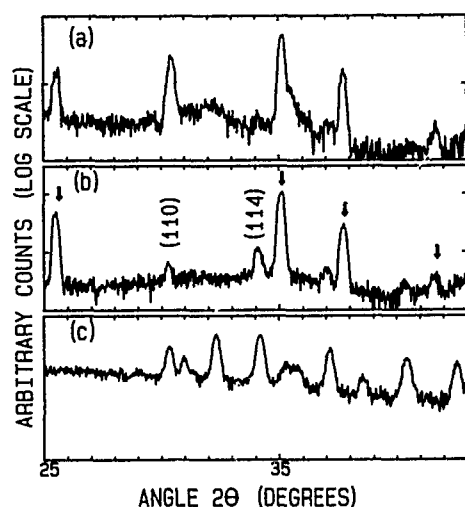


FIG. 4. $\text{CuK}\alpha$ x-ray-diffraction patterns of films synthesized at temperatures (a) 500 °C, (b) 550 °C, and (c) 625 °C. In (a) and (b) substrate lines are indicated through arrows.

Magnetic hysteresis loops measured parallel and perpendicular to the plane of a film synthesized at 525 °C are shown in Fig. 5. The diffraction trace of the film showed predominant (110) with some (114) reflections. The R value was estimated to be around 0.15, corresponding to a c -axis orientation of 81° with respect to the film normal. For the film, the remnant to saturation ratio was 0.62 in the plane, and 0.31 perpendicular to the plane direction.

IV. CONCLUSION

Crystalline films of strontium hexaferrite were synthesized nonepitaxially by rf diode sputtering in Ar onto polycrystalline Al_2O_3 substrates for substrate temperatures from 500 to 650 °C. To counter severe Sr depletion during sputtering, targets highly enriched in Sr were utilized. After deposition large increases in coercivity up to 3.8 kOe, but with no apparent changes in x-ray patterns, resulted from annealing the films in 500 Torr O_2 . The films produced in these studies exhibited crystallites with well-defined c -axes

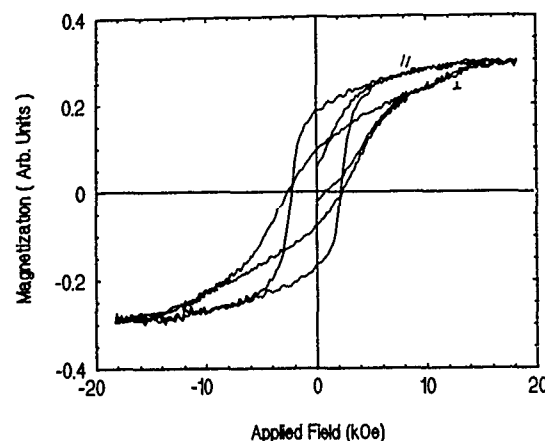


FIG. 5. Hysteresis loops parallel and perpendicular to film plane for film synthesized at 525 °C in 100 mTorr of Ar. X-ray-diffraction trace of film showed predominant (110) reflection with some (114) reflections.

orientations. For deposition temperatures near 500 °C, the films consisted of random in-plane c -axes grains. For deposition temperatures from 600 to 650 °C, the films consisted of grains with random c -axes orientations in three dimensions.

ACKNOWLEDGMENT

F. J. C. is supported by the Air Force Office of Scientific Research.

- ¹H. L. Glass and J. H. W. Liaw, *J. Appl. Phys.* **49**, 1578 (1978).
- ²I. Zaquine, H. Benazizi, and J. C. Mage, *J. Appl. Phys.* **64**, 5822 (1988).
- ³M. S. Yuan, H. L. Glass, and L. R. Adkins, *Appl. Phys. Lett.* **53**, 340 (1988).
- ⁴M. Matsuoka, Y. Hoshi, M. Naoe, and S. Yamanaka, *IEEE Trans. Magn.* **MAG-18**, 1119 (1982).
- ⁵A. Morisako, M. Matsumoto, and M. Naoe, *IEEE Trans. Magn.* **MAG-22**, 1146 (1986).
- ⁶M. Matsuoka, M. Naoe, and Y. Hoshi, *J. Appl. Phys.* **57**, 4040 (1985).
- ⁷T. L. Hylton, M. A. Parker, K. R. Coffey, and J. K. Howard, *J. Appl. Phys.* **73**, 6257 (1993).
- ⁸F. J. Cadieu, *Physics of Thin Films* (Academic, San Diego, 1992), Vol. 16, Chap. 2.

Order-disorder and magnetic exchange interactions in substituted strontium hexaferrite $\text{SrA}_x\text{Fe}_{12-x}\text{O}_{19}$ ($\text{A}=\text{Ga}, \text{In}$)

G. K. Thompson and B. J. Evans

Department of Chemistry, University of Michigan, Ann Arbor, Michigan 48109-1055

The unusual magnetic behavior of the 12k site in $\text{SrGa}_x\text{Fe}_{12-x}\text{O}_{19}$ ($0.3 \leq x \leq 6.0$) and $\text{SrIn}_x\text{Fe}_{12-x}\text{O}_{19}$ ($0.3 \leq x \leq 1.4$) has been investigated by means of ^{57}Fe Mössbauer spectroscopy at 298 K. The bifurcation of the 12k Mössbauer subspectrum into $12k_1$ and $12k_2$ components of widely differing intensities has been confirmed for both Ga^{3+} and In^{3+} . The bifurcation is apparent at x values as low as 0.3, and the less intense $12k_2$ pattern corresponds to an abrupt drop in the hyperfine magnetic field H_{eff} , of 50 and 75 kOe for Ga^{3+} and In^{3+} , respectively. H_{eff} for the more intense $12k_1$ pattern is virtually unchanged from that of pure $\text{SrFe}_{12}\text{O}_{19}$ for x values as high as 1.0. Room-temperature Mössbauer spectra confirm that the Ga^{3+} and In^{3+} ions preferentially occupy the $4f_2$ octahedral site. There are indications, however, that the dopants also enter the $2b$ trigonal-bipyramidal site. The change in H_{eff} at the 12k sites indicates that complex and competing exchange interactions are present, and that the splitting of the 12k magnetic hyperfine spectrum is not due simply to random disruptions of the exchange interactions. The intensities of the $12k_1$ and $12k_2$ subspectra have been used to model the exchange interactions at the 12k site.

I. INTRODUCTION

The magnetoplumbite structure, $\text{MFe}_{12}\text{O}_{19}$ ($\text{M}=\text{Sr}, \text{Ba}, \text{Pb}$), consists of alternating hexagonal ($R=\text{MFe}_6\text{O}_{11}^{2-}$) and spinel subunits ($S=\text{Fe}_6\text{O}_8^{2+}$) stacked along the hexagonal c axis. Within the R block are the trigonal-bipyramidal $2b$ and octahedral $4f_2$ Fe^{3+} sites, while the S layer contains the octahedral $2a$ and tetrahedral $4f_1$ Fe^{3+} ions; the 12k octahedral Fe^{3+} ions exist at the R - S interface.¹

In addition to the $2b$ Fe^{3+} site, the octahedral 12k site of the M-type hexaferrites exhibits very unusual crystal chemical and magnetic properties. It is clear that an understanding of the high magnetocrystalline anisotropy and of the rapid decrease in the bulk magnetization of the magnetoplumbite hexaferrites depend to a great extent on an understanding of the structure/property relationships for these two sites.

In previous investigations, it was reported that $\text{SrFe}_{12}\text{O}_{19}$ and $\text{BaFe}_{12}\text{O}_{19}$ substituted with Sc^{3+} , Ga^{3+} , and In^{3+} exhibited Mössbauer spectra with the 12k subpattern split into two components.^{2,3} However, there is still some question as to how low a dopant level is required to produce the 12k bifurcation. In addition, further analysis of this phenomenon could give valuable insights into the magnetic exchange in-

teractions of the octahedral 12k Fe^{3+} . We present the results of such an investigation in this article.

II. EXPERIMENT

Polycrystalline samples of $\text{SrGa}_x\text{Fe}_{12-x}\text{O}_{19}$ ($x=0.3, 0.5, 0.8, 1.0$, and 6.0) and $\text{SrIn}_x\text{Fe}_{12-x}\text{O}_{19}$ ($x=0.3, 0.4, 0.8$, and 1.4) were prepared from SrCO_3 , Fe_2O_3 , Ga_2O_3 , and In_2O_3 , using solid-state syntheses similar to those used in earlier reports.^{2,3} Electron microprobe analysis (EMPA) and x-ray powder diffractometry were employed to determine the composition, phase purity, and lattice constants of the samples. For each of the substituted hexaferrites, room-temperature ^{57}Fe Mössbauer spectra were collected and analyzed as described in detail in a previous article.⁴

III. RESULTS AND DISCUSSION

The lattice parameters of substituted $\text{SrFe}_{12}\text{O}_{19}$ are presented in Table I; as evident in Fig. 1, Vegard's law is followed by both solid solution series.⁵ As expected, increasing

TABLE I. Lattice constants of substituted $\text{SrFe}_{12}\text{O}_{19}$.

	x	a (Å) ^a	c (Å) ^a
$\text{SrGa}_x\text{Fe}_{12-x}\text{O}_{19}$	0	5.884	23.06
	0.3	5.879	23.05
	0.5	5.880	23.06
	0.8	5.877	23.06
	1.0	5.877	23.06
	6.0	5.831	23.04
$\text{SrIn}_x\text{Fe}_{12-x}\text{O}_{19}$	0	5.884	23.06
	0.4	5.893	23.09
	0.8	5.902	23.13
	1.4	5.916	23.18

^aThe error is ± 0.002 and ± 0.02 Å for a and c , respectively.

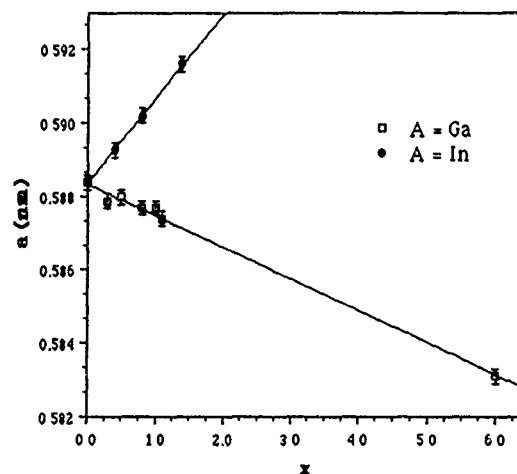


FIG. 1. Plot of lattice parameter a vs moles of dopant per formula unit for $\text{SrA}_x\text{Fe}_{12-x}\text{O}_{19}$.

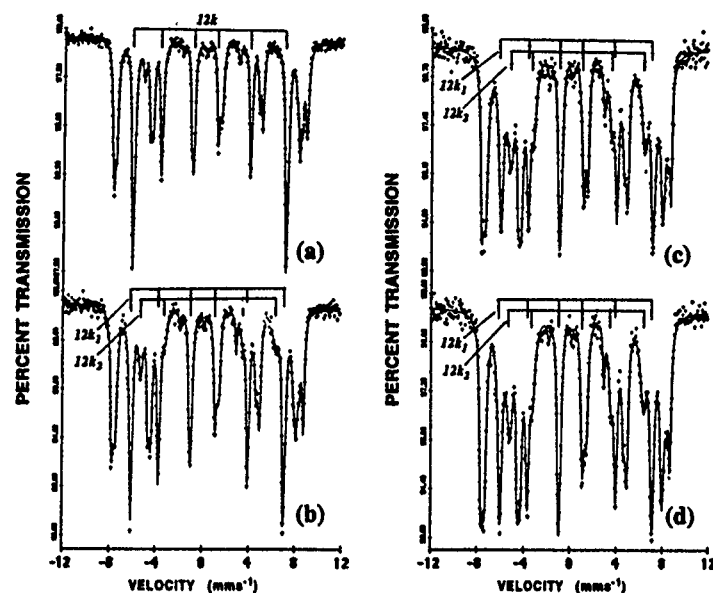


FIG. 2. ^{57}Fe Mössbauer spectra of polycrystalline $\text{SrGa}_x\text{Fe}_{12-x}\text{O}_{19}$ at 298 K: (a) $x=0$; (b) $x=0.3$; (c) $x=0.5$; (d) $x=1.0$.

substitution of Fe^{3+} by the smaller Ga^{3+} ions results in a gradual decrease in the dimensions of the unit cell, while introduction of the larger In^{3+} ions has the opposite effect.

Selected Mössbauer spectra of $\text{SrGa}_x\text{Fe}_{12-x}\text{O}_{19}$ and $\text{SrIn}_x\text{Fe}_{12-x}\text{O}_{19}$ at 298 K are shown in Figs. 2 and 3, respectively; the hyperfine interaction parameters are presented in Tables II and III. In the case of both substituted hexaferrites, the bifurcation of the $12k$ subspectrum is visible at a dopant concentration as low as 0.3 mol per formula unit. H_{eff} for $12k_1$ in $\text{SrGa}_x\text{Fe}_{12-x}\text{O}_{19}$ is essentially unchanged from that of the unsplitted $12k$ pattern in $\text{SrFe}_{12}\text{O}_{19}$. However, as the In^{3+} ion concentration increases in $\text{SrIn}_x\text{Fe}_{12-x}\text{O}_{19}$, H_{eff} for the $12k_1$ does decrease somewhat from that of the $12k$ pattern in $\text{SrFe}_{12}\text{O}_{19}$.

For the $12k_2$ subspectrum of $\text{SrGa}_x\text{Fe}_{12-x}\text{O}_{19}$ and $\text{SrIn}_x\text{Fe}_{12-x}\text{O}_{19}$, H_{eff} is roughly constant at, respectively, 50 and 75 kOe lower than that of the $12k$ pattern for $\text{SrFe}_{12}\text{O}_{19}$. Despite the near constancy of H_{eff} for the $12k_2$ subspectrum, its intensity exhibits remarkable increases as x increases. Indeed, for $x \approx 1.0$ and 0.8 for Ga^{3+} and In^{3+} , respectively, the $12k_1$ and $12k_2$ subspectra have comparable relative intensities. By the time x reaches a value of 6.0 for $\text{SrGa}_x\text{Fe}_{12-x}\text{O}_{19}$, the Mössbauer spectrum at 298 K consists only of a pair of partially resolved quadrupole doublets, indicating a significant drop in the Curie temperature T_C .

Analysis of the area ratios of the Mössbauer spectra (Tables II and III) confirms that the dopant ions are entering the octahedral $4f_2$ site. In compensation for the loss of in-

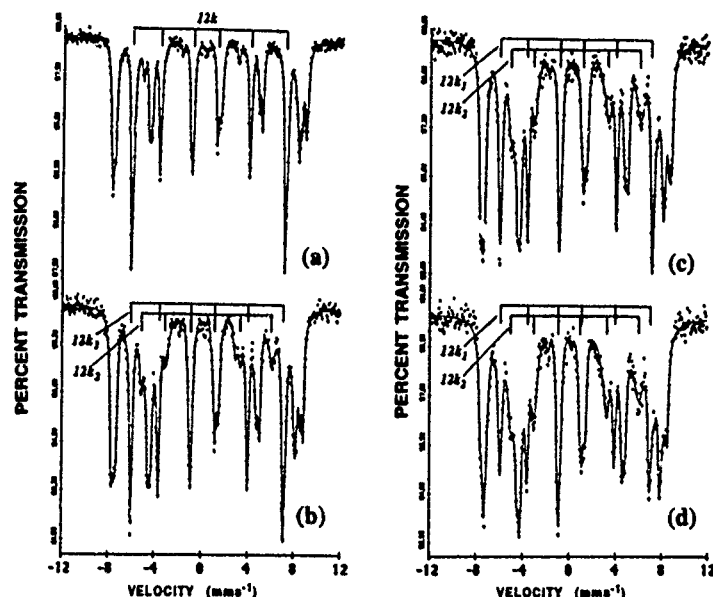


FIG. 3. ^{57}Fe Mössbauer spectra of polycrystalline $\text{SrIn}_x\text{Fe}_{12-x}\text{O}_{19}$ at 298 K: (a) $x=0$; (b) $x=0.4$; (c) $x=0.8$; (d) $x=1.4$.

TABLE II. ^{57}Fe Mössbauer parameters for $\text{SrGa}_x\text{Fe}_{12-x}\text{O}_{19}$ at 298 K.

x	Fe^{3+} site	H_{eff}^a (mm s $^{-1}$)	ΔE_Q^a (mm s $^{-1}$)	δ^a (mm s $^{-1}$)	Area %
0	2a	503	0.01	0.36	5.9(4)
0.3		499	0.10	0.36	9(1)
0.5		497	0.12	0.35	8(1)
0.8		494	0.14	0.36	9(2)
1.0		495	0.16	0.36	9(1)
0	2b	408	2.26	0.30	6.8(6)
0.3		408	2.16	0.25	5.6(7)
0.5		405	2.20	0.27	5.6(8)
0.8		402	2.21	0.27	6(1)
1.0		399	2.02	0.18	8(2)
0	4f ₁	491	0.16	0.26	18(1)
0.3		484	0.17	0.27	22(1)
0.5		482	0.15	0.27	21(1)
0.8		477	0.13	0.27	22(2)
1.0		476	0.11	0.26	25(1)
0	4f ₂	518	0.27	0.36	20(1)
0.3		514	0.26	0.37	14(1)
0.5		512	0.26	0.37	16(1)
0.8		509	0.26	0.37	12(1)
1.0		508	0.26	0.36	9.6(5)
0	12k ₁	411	0.39	0.35	49(1)
0.3		411	0.39	0.35	41(1)
0.5		411	0.39	0.35	36(1)
0.8		409	0.40	0.35	32(1)
1.0		408	0.39	0.35	28(1)
0	12k ₂
0.3		358	0.44	0.40	9(1)
0.5		362	0.40	0.36	13(1)
0.8		361	0.41	0.37	19(1)
1.0		359	0.44	0.38	20(1)

^aEstimated errors in H_{eff} , ΔE_Q , and δ (relative to Fe metal) are ± 1 kOe, ± 0.03 mm s $^{-1}$, and ± 0.02 mm s $^{-1}$, respectively.

tensity in the 4f₂ pattern, the areas of the octahedral 2a and tetrahedral 4f₁ subspectra increase with the dopant concentration; the area of the combined 12k₁ and 12k₂ subspectra remains essentially constant. There also appears to be a small decrease in the area of the trigonal-bipyramidal 2b pattern, suggesting the occurrence of some substitution in the site. The large uncertainties of the area-percent values in the various subspectra, however, do not allow for a more definitive conclusion in the case of the 2b pattern.

IV. CONCLUSION

This investigation has verified that doping $\text{SrFe}_{12}\text{O}_{19}$ with as little as 0.3 mol per formula unit of Ga^{3+} or In^{3+} ions results in the bifurcation of the 12k octahedral subspectrum. This splitting is due to a change in the magnetic exchange

TABLE III. ^{57}Fe Mössbauer parameters for $\text{SrIn}_x\text{Fe}_{12-x}\text{O}_{19}$ at 298 K.

x	Fe^{3+} site	H_{eff}^a (mm s $^{-1}$)	ΔE_Q^a (mm s $^{-1}$)	δ^a (mm s $^{-1}$)	Area %
0	2a	503	0.01	0.36	5.9(4)
0.3		492	0.24	0.43	6.9(3)
0.4		492	0.28	0.44	8.8(7)
0.8		492	0.27	0.45	15(2)
1.4		481	0.28	0.44	10(1)
0	2b	408	2.26	0.30	6.8(6)
0.3		390	1.91	0.18	7.4(1)
0.4		388	1.77	0.18	6.4(7)
0.8		392	1.98	0.18	5.7(8)
1.4		388	1.99	0.17	6.0(9)
0	4f ₁	491	0.16	0.26	18(1)
0.3		486	0.10	0.26	26(0)
0.4		486	0.07	0.25	28(1)
0.8		483	0.07	0.23	27(1)
1.4		474	0.09	0.23	22(2)
0	4f ₂	518	0.27	0.36	20(1)
0.3		514	0.28	0.37	13(0)
0.4		513	0.27	0.37	11(0)
0.8		510	0.28	0.37	7(1)
1.4		503	0.38	0.36	5.4(7)
0	12k ₁	411	0.39	0.35	49(1)
0.3		408	0.38	0.36	31(0)
0.4		409	0.38	0.36	32(1)
0.8		407	0.38	0.35	27(1)
1.4		403	0.38	0.36	21(1)
0	12k ₂
0.3		339	0.46	0.40	16(0)
0.4		338	0.50	0.42	15(1)
0.8		337	0.50	0.39	23(2)
1.4		334	0.52	0.41	30(1)

^aEstimated errors in H_{eff} , ΔE_Q , and δ (relative to Fe metal) are ± 1 kOe, ± 0.03 mm s $^{-1}$, and ± 0.02 mm s $^{-1}$, respectively.

interactions of some of the 12k Fe^{3+} ions as increasing amounts of the diamagnetic dopant enter the 4f₂ site, and possibly the 2b site. The fact that the magnitude of the hyperfine magnetic field of the 12k₁ and 12k₂ patterns remains almost constant with increasing levels of substitution implies that the 12k splitting is not due simply to random changes in the exchange interactions.

¹X. Obradors, X. Solans, A. Collomb, D. Samaras, J. Rodriguez, M. Pernet, and M. Font-Altaba, *J. Solid State Chem.* **72**, 218 (1988).

²G. Albanese, G. Asti, and P. Batti, *Nuovo Cimento*, **B 58**, 467 (1968).

³G. Albanese, A. Deriu, E. Lucchini, and G. Slokar, *Appl. Phys. A* **26**, 45 (1981).

⁴B. J. Evans, F. Grandjean, A. P. Lilot, R. H. Vogel, and A. Gérard, *J. Magn. Magn. Mater.* **67**, 123 (1987).

⁵B. D. Cullity, *Elements of X-ray Diffraction* (Addison-Wesley, Reading, MA, 1978, p. 376).

Enhanced remanence in isotropic Fe-rich melt-spun Nd-Fe-B ribbons

L. Withanawasam and G. C. Hadjipanayis

Department of Physics and Astronomy, University of Delaware, Newark, Delaware 19716

R. F. Krause

Magnetics International, Inc., 1111 North State Road 149, Burns Harbor, Indiana 46304

High isotropic remanences and energy products have been obtained in melt-spun Nd-Fe-B samples with a fine grained mixture of α -Fe and $\text{Nd}_2\text{Fe}_{14}\text{B}_1$ containing more than 50 wt % of α -Fe. Reduced remanences as high as 0.78 with high saturation magnetization (190 emu/g) led to $(BH)_{\text{max}}$ of 14 MGOe. The coercivities varied from 2–4 kOe for samples with 70–50 wt % α -Fe, respectively. Reversible demagnetization curves were observed consistent with the “exchange spring” mechanism.

I. INTRODUCTION

Anisotropic Nd-Fe-B magnets have been widely used in industry because of their excellent properties with energy products $(BH)_{\text{max}}$ exceeding 40 MGOe. In isotropic bonded magnets the maximum energy products are below 12 MGOe because of the low reduced remanent magnetization (M_r/M_s). However, in the past high remanence values were obtained in isotropic melt-spun Nd-Fe-B ribbons via additions of Si and Al.¹ It was shown that these high remanence values were the results of a uniform fine microstructure with small (18 nm) grain sizes and with exchange interaction between adjacent 2:14:1 grains.² Davis, Manaf, and Zhang³ also observed high remanence in Nd-Fe-B ribbons without any additions of Si or Al. More recently, theoretical studies have predicted high energy products in magnets consisting of a mixture of hard and soft phases which are exchange coupled through a uniform and fine-grained microstructure.⁴ Coehron, De Mooji, and De Waard⁵ obtained in $\text{Nd}_4\text{Fe}_{77}\text{B}_{19}$ a microstructure consisting of a fine mixture of $\text{Nd}_2\text{Fe}_{14}\text{B}_1$ and Fe_3B grains with a maximum energy product of 12 MGOe.

In this work we have studied the magnetic and structural properties of $\text{Nd}_2\text{Fe}_{14}\text{B}_1/\text{Fe}$ composite magnets with high Fe content. The samples studied can be grouped in three categories according to the percentage of 2:14:1 and α -Fe phases present: 50 wt % α -Fe/50 wt % 2:14:1; 70 wt % α -Fe/30 wt % 2:14:1; and α -Fe/2:14:1/ Fe_3B . Throughout the text these samples are referred to as A, B, and C, respectively.

II. EXPERIMENT

$\text{Nd}_x\text{Fe}_y\text{B}_z$ ingots with different composition ($3 \leq x \leq 8$, $80 \leq y \leq 90$, $4 \leq z \leq 15$) were prepared by arc melting the constituent elements in an argon atmosphere. Pieces of the ingot were melt spun from a quartz tube having an orifice diameter of ~ 1 mm. A wheel speed in the range of 25–35 m/s was used. The resulting ribbons were heat treated at different times and temperatures to optimize the magnetic properties. X-ray diffraction ($\text{CuK}\alpha$) was used to identify the phases present and selected samples were studied using Mössbauer spectroscopy. The hysteresis loops were measured in a vibrating sample magnetometer (VSM) with a maximum field of 20 kOe on long sample pieces to minimize demagnetization effects. Selected samples were also mea-

sured in a superconducting quantum interference device (SQUID) magnetometer with a maximum field of 55 kOe. The microstructure of samples with optimum coercivity was studied by transmission electron microscopy (TEM).

III. RESULTS AND DISCUSSION

The melt-spun ribbons were found by x ray to be amorphous (and/or microcrystalline) in structure. Annealing the ribbons at around 700 °C for 20–60 min resulted in a two-phase microstructure consisting of 2:14:1 and α -Fe for samples A and B, and a three-phase mixture of 2:14:1, Fe_3B , and α -Fe in the high-boron sample (sample C) as indicated by x-ray and thermomagnetic data (see Figs. 1 and 2). Mössbauer results on sample A showed 55% 2:14:1 and 45% α -Fe. In the same sample there is an intermediate magnetic phase, formed by a low-temperature heat treatment (600 °C/20 min), with a Curie temperature of about 200 °C. Our structural data indicate that this phase is the $\text{R}_3\text{Fe}_{62}\text{B}_{14}$ bcc phase reported by Buschow, De Mooji, and Coehron⁶ with $a = 1.235$ nm.

A TEM micrograph of sample A with optimum coercivity is shown in Fig. 3. The average size of the grains is about

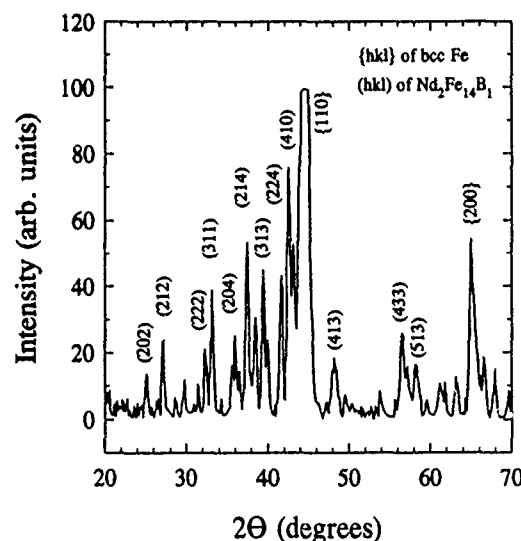


FIG. 1. X-ray diffraction ($\text{CuK}\alpha$) pattern of sample A (50 wt % α -Fe/50 wt % $\text{Nd}_2\text{Fe}_{14}\text{B}_1$) showing bcc Fe and 2.14.1 peaks. (Only part of the {110} bcc Fe reflection is shown.)

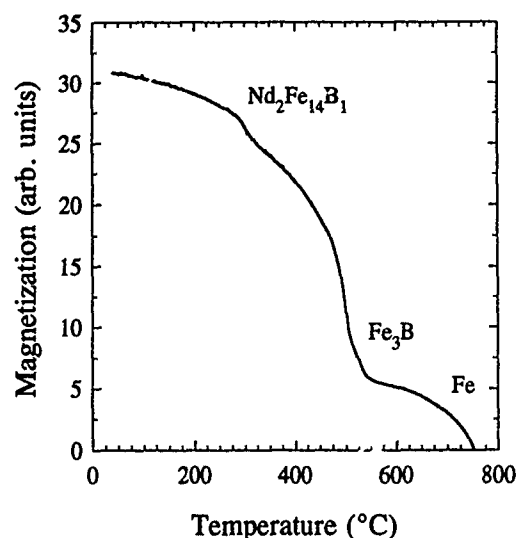


FIG. 2. Temperature dependence of magnetization for sample C (α -Fe/ $\text{Nd}_2\text{Fe}_{14}\text{B}$ / Fe_3B) showing the three magnetic phases.

50 nm in diameter. The dark-field observations show the grains of α -Fe to be uniformly distributed in the sample.

Optimally annealed sample A had a coercivity of 4 kOe along with a magnetization of 155 emu/g at 20 kOe and a remanence value of 110 emu/g. The corresponding values for sample B were $H_c=2.7$ kOe, $M_s=185$ and $M_r=145$ emu/g. The reduced remanences ($m_R=M_r/M_s$) were 0.71 and 0.78, respectively, for samples A and B (see Fig. 4). These values are much higher than the 0.50 value expected for an assembly of randomly distributed and noninteracting single-domain particles with uniaxial anisotropy. Loops measured along and transverse to the ribbon length in the plane of the ribbon showed essentially the same remanence indicating that the ribbons are isotropic. The maximum energy product $(BH)_{\max}$ was estimated using the second quadrant data on long ribbon samples with negligible demagnetization factors. Furthermore, the density of the material was taken to be 7.60 g/cm^3 (density of $\text{Nd}_2\text{Fe}_{14}\text{B}_1$), although the $\text{Nd}_2\text{Fe}_{14}\text{B}_1$ phase content is about 50 wt % or less, regardless of the sample composition. A summary of the magnetic data is shown in Table I.

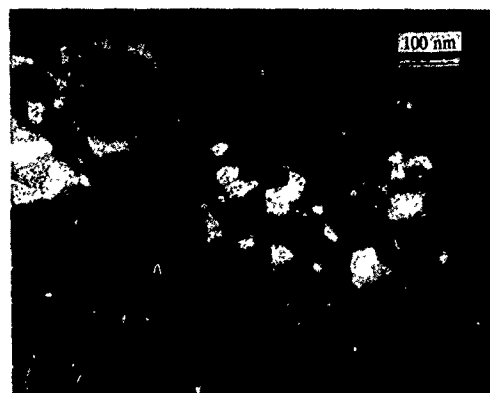


FIG. 3. A TEM micrograph of optimally annealed sample A (50 wt % α -Fe/50 wt % $\text{Nd}_2\text{Fe}_{14}\text{B}$).

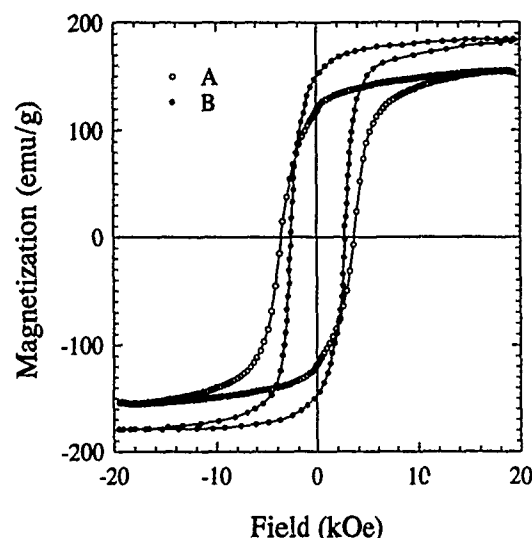


FIG. 4. Hysteresis loop showing high remanence values.

Figure 5 shows the temperature dependence of coercivity measured up to 140°C for both A and B samples. The temperature coefficients were calculated, assuming a linear dependence, according to the following formula:

$$\frac{H_c(T_2) - H_c(T_1)}{(T_2 - T_1)H_c(T_1)} 100,$$

and were found to be -0.39 and $-0.55 \text{ }^\circ\text{C}^{-1}$ for A and B, respectively.

The variation of remanence with temperature was also measured for the same samples and is shown in Fig. 6. The corresponding coefficients calculated using the same formula are -0.06 and $-0.07 \text{ }^\circ\text{C}^{-1}$. The temperature coefficients of coercivity are close to those of pure 2:14:1 ribbons while the temperature coefficients of remanence are much lower.⁷ Heating the samples above the Curie temperature of the $\text{Nd}_2\text{Fe}_{14}\text{B}_1$ phases reduces the remanent magnetization to a low but nonzero value.

The high reduced remanence values indicate an exchange coupling between the grains of the hard and soft phases. As a consequence of this coupling there is a larger degree of reversibility in the demagnetization behavior. According to Kneller and Hawig⁴ the magnetization would return to the remanent configuration reversibly for reverse fields lower than the nucleation field. We have measured the dc demagnetization curves by applying progressively increasing reverse fields and measuring the remanence values corresponding to each such field, thus obtaining $M_r(H)$. A plot of $[M_r(0) - M_r(H)]/2M_r(0)$ ($= -\Delta M_r/2M_r$) versus

TABLE I. Room-temperature coercivities (kOe), remanence (kG), and estimated maximum energy product (MGOe) for the three samples.

Sample	H_c	H_{ci}	B_r	$(BH)_{\max}$
50 wt % α -Fe/50 wt % $\text{Nd}_2\text{Fe}_{14}\text{B}$	3.10	3.80	10.4	9.78
70 wt % α -Fe/30 wt % $\text{Nd}_2\text{Fe}_{14}\text{B}$	2.60	2.70	14.5	14.45
$\text{Nd}_2\text{Fe}_{14}\text{B}/\text{Fe}_3\text{B}/\alpha$ -Fe	2.18	2.40	12.3	9.10

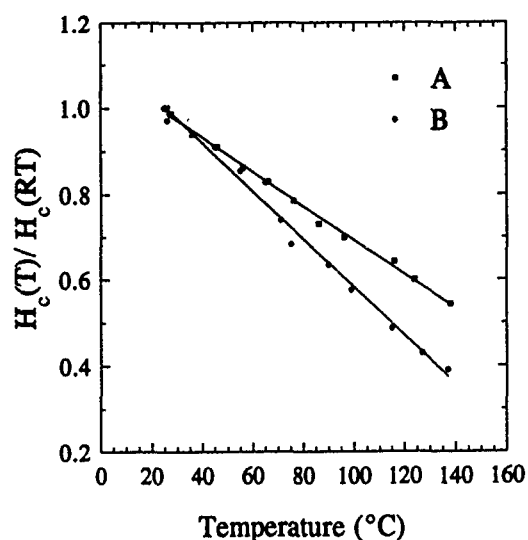


FIG. 5. The variation of coercivity (normalized by their room-temperature value) with temperature.

reverse field is shown in Fig. 7 for sample A with a coercive field of 3.6 kOe. The change in ΔM_r is very small up to fields of about 2.6 kOe which corresponds to the reversible region of the demagnetization curve. At higher reverse fields ΔM_r increases rapidly due to the irreversible rotation of magnetic moments.

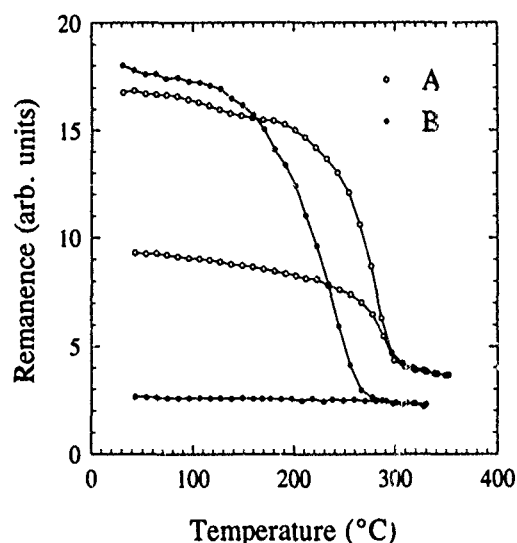


FIG. 6. Temperature dependence of remanent magnetization for samples A (50 wt % α -Fe/50 wt % $\text{Nd}_2\text{Fe}_{14}\text{B}$) and B (70 wt % α -Fe/30 wt % $\text{Nd}_2\text{Fe}_{14}\text{B}$).

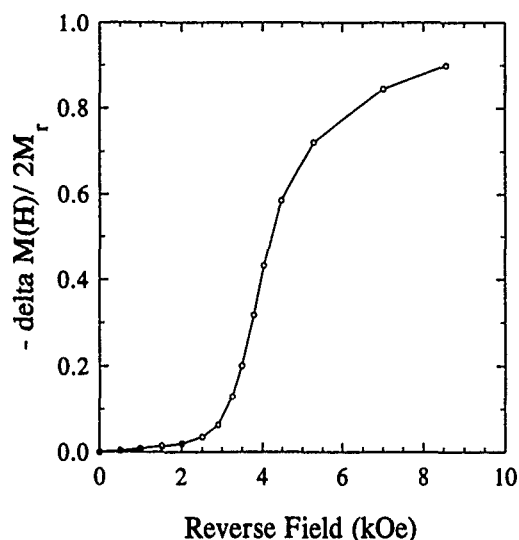


FIG. 7. A plot of $[M_r(0) - M_r(H)]/2M_r(0)$ ($= -\Delta M_r/2M_r$) vs reverse field for sample A (50 wt % α -Fe/50 wt % $\text{Nd}_2\text{Fe}_{14}\text{B}$) with a coercivity of 3.6 kOe showing reversibility in the demagnetization curves.

IV. CONCLUSIONS

High reduced remanences (up to 0.78) and energy products (up to 14 MGOe) have been obtained in Fe-rich Nd-Fe-B samples with a mixture of α -Fe and $\text{Nd}_2\text{Fe}_{14}\text{B}_1$ grains which are believed to be the result of exchange coupling across the grain boundaries.

ACKNOWLEDGMENTS

This work was supported by Magnetix International and in part by the U.S. Army Research Office. Authors thankfully acknowledge the Mössbauer studies performed by Dr. V. Pappathymiou at the University of Ioannina, Greece.

¹R. W. McCallum, A. M. Kadin, G. B. Clemente, and J. E. Keem, *J. Appl. Phys.* **61**, 3577 (1987).

²G. C. Hajipanayis and W. Gong, *J. Appl. Phys.* **64**, 5559 (1988).

³H. A. Davies, A. Manaf, and P. Z. Zhang, *J. Mater. Eng.* (to be published).

⁴E. F. Kneller and R. Hawig, *IEEE Trans. Magn.* **MAG-27**, 3588 (1991).

⁵R. Coehroon, D. B. De Mooji, and D. De Waard, *J. Magn. Magn. Mater.* **80**, 101 (1989).

⁶K. H. J. Buschow, D. B. De Mooji, and R. Coehroon, *J. Less-Common Met.* **145**, 601 (1988).

⁷R. W. Lee, E. G. Brewer, and N. A. Schaffel, *IEEE Trans. Magn.* **MAG-21**, 1958 (1985).

Mechanically alloyed nanocomposite magnets

Wei Gong and G. C. Hadjipanayis

Department of Physics and Astronomy, University of Delaware, Newark, Delaware 19716

R. F. Krause

Magnetics International, Inc., 1111 North State Road 149, Burn Harbor, Indiana 46304

The magnetic and structural properties of mechanically alloyed $\text{Nd}_2\text{Fe}_{14}\text{B} + (\text{Fe}, \text{FeCo})$ powders have been investigated over a wide range of temperatures. X-ray diffraction patterns on samples milled for 48 h showed that the powders had a two-phase structure consisting of a disordered Nd-Fe-B alloy and α -Fe with a fine grain size about 140 Å. Enhanced magnetic remanence in the range of 95–105 emu/g with reduced remanence $\alpha = M_r/M_s = 0.60$ –0.68 and a coercivity $H_c = 4$ –6 kOe have been obtained after annealing at 650–750 °C. This behavior is the result of an exchange coupling between the hard and soft phases with small grain sizes, about 500 and 200 Å, respectively.

I. INTRODUCTION

Mechanical alloying has been widely used in a number of laboratories as an attractive technique for manufacturing permanent magnets. With this process ultrafine composite particles are formed during milling in a high-energy ball mill with leads to very high coercivities after a suitable heat treatment.^{1–7} A possible way to increase the remanence in mechanically alloyed powders is to use nanocrystalline materials consisting of a mixture of hard and soft magnetic phases. The composite magnets may retain high values in both remanence and coercivity when an exchange coupling extends across the interface of the hard and soft phases.^{8,9}

In this article, the magnetic and structural properties of mechanically alloyed Nd-Fe-B nanocomposite powders have been investigated over a wide range of temperatures.

II. EXPERIMENT

Alloys of $\text{R}_x\text{Fe}_y\text{B}_z\text{M}_w$ ($\text{R}=\text{Nd}, \text{Tb}$; $\text{M}=\text{Nb}$) with $5 \leq x \leq 15$, $77 \leq y \leq 90$, $5 \leq z \leq 8$, $0 \leq w \leq 3$ and Fe-Co were prepared by arc melting using high-purity elements. The mechanically alloyed samples were prepared in a high-energy ball mill (SPEX 8000 mixer/mill) using powders with a particle size about 150 μm and pure Fe powders with a particle size of about 40 μm . The mechanically alloyed powders were heat treated in the temperature range of 600–900 °C for 15–60 min under a vacuum of 10^{-6} Torr.

The structure of the powders was determined using a Phillips x-ray diffractometer (APD3520). The mean grain size of the powders was measured from the x-ray line broadening using the Scherrer formula.¹⁰

The magnetic properties of the powders were measured with a vibrating sample magnetometer (VSM) in fields up to 20 kOe and with a superconducting quantum interference device (SQUID) magnetometer in fields up to 55 kOe. A rough estimate of the saturation magnetization M_s was made using the law of approach to saturation by plotting M as a function of $1/H^2$ and extrapolating the infinite fields with a relative error less than 5%. The remanence was measured at $H_{\text{eff}}=0$, where the effective magnetic field $H_{\text{eff}}=H_a-H_d=H_a-4\pi NM$, and N is the demagnetization factor. For the samples measured with the VSM, N was determined from the diameter/length ratios of the cylindrical

compacted samples. For the SQUID powdered samples, an $N=1/3$ was used because of the nearly spherical shape of the particles.

III. RESULTS AND DISCUSSION

A. $\text{Nd}_2\text{Fe}_{14}\text{B}$ and $\text{Nd}_2\text{Fe}_{14}\text{B}+\text{Fe}$

The $\text{Nd}_2\text{Fe}_{14}\text{B}$ system was chosen for the initial detailed study. After ball milling for 48 h the $\text{Nd}_2\text{Fe}_{14}\text{B}$ alloy powders had a mixture of an amorphous Nd-Fe-B structure and α -Fe with a fine grain size about 140 Å [see Fig. 1(A)]. The mechanically alloyed powders were heat treated in the temperature range of 600–900 °C to form the 2:14:1 phase. The diffraction pattern of powders heat treated at 800 °C for 30 min is shown in Fig. 1(B). A small amount of α -Fe was still found in the powders to coexist with the 2:14:1 phase forming a nanocomposite magnet. An addition of 10 wt % α -Fe was used to increase the amount of Fe in the nanocomposite $\text{Nd}_2\text{Fe}_{14}\text{B}+\text{Fe}$ samples. The $\text{Nd}_2\text{Fe}_{14}\text{B}$ and $\text{Nd}_2\text{Fe}_{14}\text{B}+\text{Fe}$ powders were prepared with the same milling and heat-treating conditions. The coercivity H_c and the reduced remanence $\alpha = M_r/M_s$ of the two powders after a heat treatment at 600–900 °C are shown in Fig. 2. The highest coercivity 7.4 kOe was obtained in the $\text{Nd}_2\text{Fe}_{14}\text{B}$ after a heat treatment at a

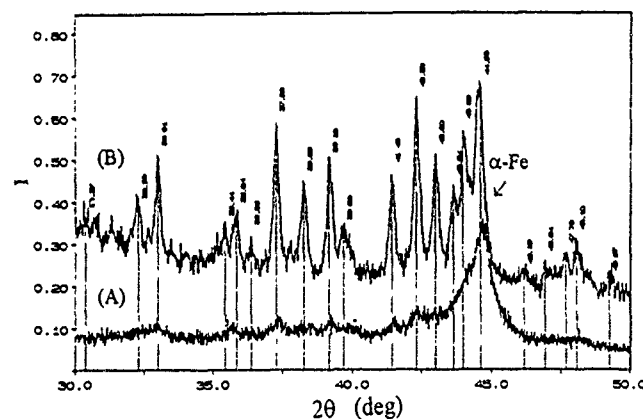


FIG. 1. X-ray-diffraction patterns of $\text{Nd}_2\text{Fe}_{14}\text{B}$ mechanically alloyed powders: (A) the powders after ball milling for 48 h; (B) after heat treating at 800 °C for 30 min.

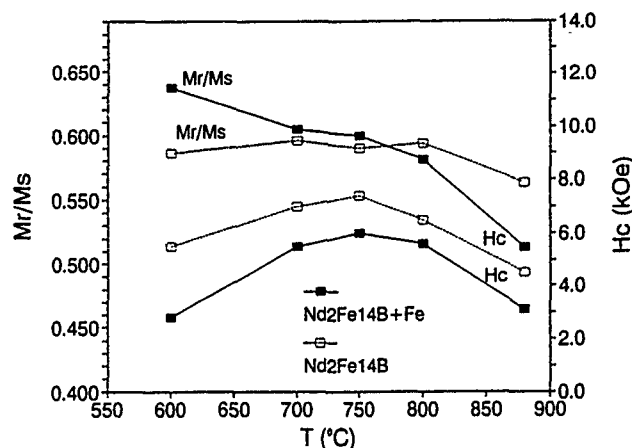


FIG. 2. The coercivity H_c and the reduced remanence $\alpha = M_r/M_s$ of the $\text{Nd}_2\text{Fe}_{14}\text{B}$ and +Fe powders heat treated at different temperatures.

temperature of 750 °C. The grain size of the $\text{Nd}_2\text{Fe}_{14}\text{B}$ phase was about 500 Å and it did not depend on the milling intensity but on the annealing temperature.¹¹ The coercivity was low in samples annealed at both lower and higher temperatures because the grain size was either too small or too large, respectively. The coercivity of $\text{Nd}_2\text{Fe}_{14}\text{B} + \text{Fe}$ powders was reduced by 1–2 kOe as compared to the $\text{Nd}_2\text{Fe}_{14}\text{B}$ powders. However, a strong exchange coupling between the hard and soft phase was observed for annealing at temperatures below 700 °C which led to an increase in remanence. The reduced remanence of the powders was very high ($\alpha = 0.64$) when the grain size of the soft phase was about 150–200 Å and it decreased drastically with annealing temperature dropping to 0.51 at 880 °C which is below that of $\text{Nd}_2\text{Fe}_{14}\text{B}$ powders (see Fig. 2). It appears that the exchange coupling decreases substantially at the higher heat-treatment temperatures because the grain size of $\alpha\text{-Fe}$ is much larger than the critical dimension for optimum coupling. For the optimum properties, it is important that the soft phase has a small grain size close to that of the magnetic hard phase. Typical magnetic properties of $\text{Nd}_2\text{Fe}_{14}\text{B}$ and $\text{Nd}_2\text{Fe}_{14}\text{B} + \text{Fe}$ samples are summarized in Table I. With the addition of 10 wt % Fe the saturation magnetization and the reduced remanence was increased from 153 to 158 emu/g and from 0.59 to 0.60, while H_c was reduced from 7.4 to 6.0 kOe.

B. $\text{Nd}_{15}\text{Fe}_{77}\text{B}_8 + x \text{ wt } \% (\text{Fe}_{70}\text{Co}_{30})$

An attempt was made to increase the coercivity of the nanocomposite magnets by using Nd-rich Nd-Fe-B alloys which have been known to have high coercivities in me-

TABLE I. Magnetic properties of the mechanically alloyed powder samples.

Samples	M_s (emu/g)	M_r (emu/g)	$\alpha (M_r/M_s)$	H_c (kOe)
$\text{Nd}_2\text{Fe}_{14}\text{B}$	153	90	0.59	7.4
$\text{Nd}_2\text{Fe}_{14}\text{B} + \text{Fe}$ (10 wt %)	158	94	0.60	6.0
$\text{Nd}_2\text{Fe}_{14}\text{B} + \text{FeNb}$ (45 wt %)	162	101	0.62	4.4
$(\text{NdTb})_2\text{Fe}_{14}\text{B} + \text{FeNb}$ (45 wt %)	154	104	0.68	6.0

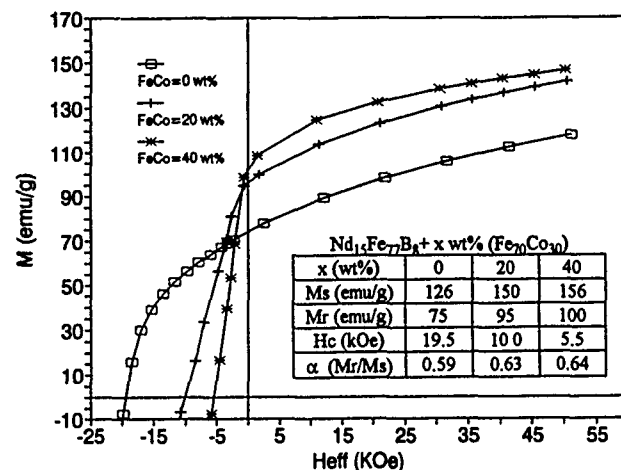


FIG. 3. Magnetization curves of the $\text{Nd}_{15}\text{Fe}_{77}\text{B}_8 + x(\text{Fe}_{70}\text{Co}_{30})$ with samples $x = 0, 20$, and 40 wt %.

chanically alloyed $\text{Nd}_{15}\text{Fe}_{77}\text{B}_8$ samples.¹² Also, a mechanically alloyed $\text{Fe}_{100-x}\text{Co}_x$ sample showed the highest saturation magnetization with x about 30 at %, which is very close to that of as-cast alloys.¹³ The magnetization curves of $\text{Nd}_{15}\text{Fe}_{77}\text{B}_8 + x(\text{Fe}_{70}\text{Co}_{30})$, $x = 0, 20$, and 40 wt %, nanocomposite magnets after optimum heat treatment are shown in Fig. 3. The saturation magnetization M_s was increased from 126 to 156 emu/g when x varied from 0 to 40 wt %, and the coercivity H_c was decreased from 19.6 to 5.5 kOe. However, an increase in the magnetic remanence has been observed in the $\text{Nd}_{15}\text{Fe}_{77}\text{B}_8 + \text{Fe}_{70}\text{Co}_{30}$ samples. In reality, the total ratio in the weight percent of transition element (Fe or FeCo) and rare-earth Nd was almost the same (Fe/Nd and FeCo/Nd 3.07) in both samples of $\text{Nd}_2\text{Fe}_{14}\text{B} + \text{Fe}$ 10 wt % and $\text{Nd}_{15}\text{Fe}_{77}\text{B}_8 + (\text{Fe}_{70}\text{Co}_{30})$ 40 wt %; but, the remanence of the $\text{Nd}_{15}\text{Fe}_{77}\text{B}_8 + (\text{Fe}_{70}\text{Co}_{30})$ 40 wt % ($M_r = 100$ emu/g) was higher than that of $\text{Nd}_2\text{Fe}_{14}\text{B} + \text{Fe}$ 10 wt % ($M_r = 95$ emu/g). This increase in M_r was accompanied by a similar increase in the reduced remanence α , $\alpha = 0.64$ for

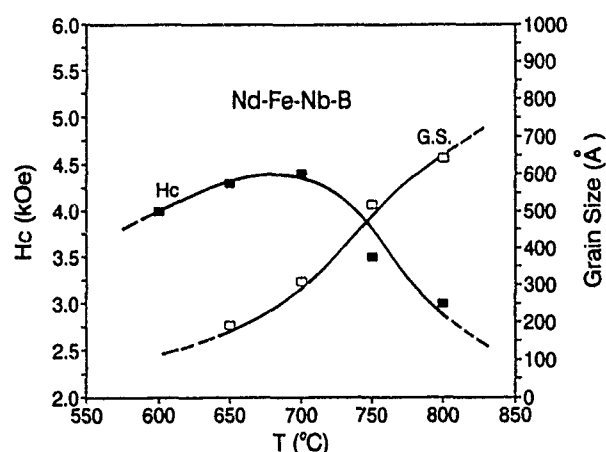


FIG. 4. The coercivity H_c and grain size of Nd-Fe-B+FeNb mechanically alloyed powders after different heat-treated temperatures.

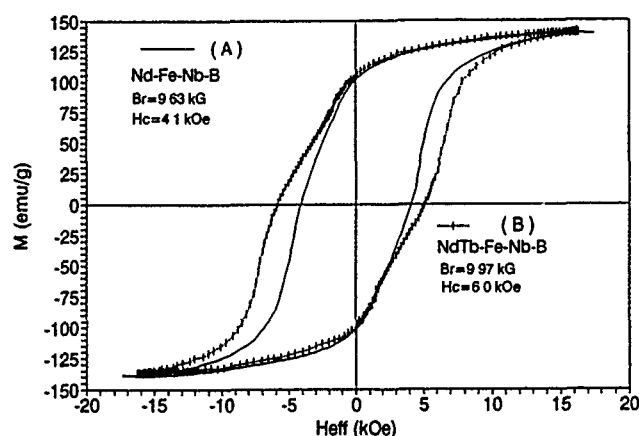


FIG. 5. Hysteresis loops of the Nd-Fe-B+FeNb and NdTb-Fe-B+FeNb mechanically alloyed powders.

$\text{Nd}_{15}\text{Fe}_{77}\text{B}_8 + (\text{Fe}_{70}\text{Co}_{30})$ 40 wt % and $\alpha=0.60$ for $\text{Nd}_2\text{Fe}_{14}\text{B} + \text{Fe}$ 10 wt % (see Detail data in Table I and Fig. 3).

C. $\text{Nd}_2\text{Fe}_{14}\text{B}$ with FeNb alloy

Nb additions in Nd-Fe-B alloys have been found to increase the crystallization temperature by about 100 °C and coercivity H_c significantly.¹⁵ The enhancement in coercivity was attributed to the presence of small precipitates within the hard magnetic phase.¹⁶ The grain size of the FeNb alloy in the amorphous Nd-Fe-B was about 140 Å after ball milling for 48 h and increased to 640 Å after a heat treatment at 800 °C for 30 min. The dependence of coercivity and grain size for $\text{Nd}_2\text{Fe}_{14}\text{B} + \text{FeNb}$ on annealing temperature is shown in Fig. 4. The annealing temperature for highest coercivity $H_c=4.4$ kOe was about 700 °C with the grain size of the FeNb alloy around 300 Å. A typical hysteresis loop of a cylindrical shape sample with demagnetization factor $N=0.23$ is shown in Fig. 5(A). The experimental data showed a saturation magnetization $M_s=162$ emu/g ($4\pi M_s=15.4$ kG), the magnetic remanence $M_r=101$ emu/g ($4\pi M_r=9.63$ kG), and $\alpha=0.62$. A partial substitution of Tb for Nd in mechanically alloyed powders led to increase in the coercivity up to 6.0 kOe at room temperature. A hysteresis

loop of the sample with demagnetization factor $N=0.295$ after annealing at 650 °C for 30 min is also shown in Fig. 5(B); here, $M_s=154$ emu/g ($4\pi M_s=14.7$ kG), $M_r=104$ emu/g ($4\pi M_r=9.97$ kG), and $\alpha=0.68$. The magnetic properties of the samples are also summarized in Table I. The enhancement in magnetic remanence for NdTb-Fe-B + FeNb powders can be attributed to both an increase in the magnetic anisotropy and coercivity of the hard phase and a reduction in grain size of the soft phase at the low annealing temperatures.

IV. CONCLUSIONS

Enhanced magnetic remanence has been obtained in mechanically alloyed Nd-Fe-B powders with a microstructure consisting of a mixture of hard and soft magnetic phases. The large reduced remanence $\alpha=0.60$ – 0.68 is the result of magnetic exchange coupling between the hard and soft phases with small grain size of about 500 and 200 Å, respectively.

ACKNOWLEDGMENTS

This work has been supported by Magnetics International, Inc. and the U. S. Army Research Office.

- ¹ L. Schultz, J. Wecker, and E. J. Hellstern, *J. Appl. Phys.* **61**, 3583 (1987).
- ² G. C. Hadjipanayis and W. Gong, *J. Appl. Phys.* **64**, 5559 (1988).
- ³ K. Schnitzke, L. Schultz, J. Wecker, and M. Katter, *Appl. Phys. Lett.* **57**, 2853 (1990).
- ⁴ P. G. McCormick, R. Street, J. Ding, Y. Liu, and P. A. I. Smoth, in 12th International Workshop on RE Magnets and their Applications, 1992, p. 329.
- ⁵ J. Ding, R. Street, and P. G. McCormick, *J. Magn. Magn. Mater.* **115**, 211 (1992).
- ⁶ W. Gong and G. C. Hadjipanayis, *IEEE Trans. Magn.* **MAG-28**, 2563 (1992).
- ⁷ W. Gong and G. C. Hadjipanayis, *J. Appl. Phys.* **73**, 6245 (1993).
- ⁸ E. F. Kneller and R. Hawig, *IEEE Trans. Magn.* **MAG-27**, 3588 (1991).
- ⁹ R. Skomski and J. M. D. Coey, *Intermag-93*, Stockholm Sweden, 1993.
- ¹⁰ A. Guinier, *X-ray Diffraction* (Freeman, San Francisco, 1963), p. 124.
- ¹¹ L. Schultz, K. Schnitzke, J. Wecker, M. Katter, and C. Kuhrt, *J. Appl. Phys.* **70**, 6339 (1991).
- ¹² L. Schultz, K. Schnitzke, and J. Wecker, *J. Appl. Phys.* **64**, 5302 (1988).
- ¹³ C. Kuhrt and L. Schultz, *J. Appl. Phys.* **71**, 1896 (1992).
- ¹⁴ G. Couderchon and J. F. Thiers, *J. Magn. Magn. Mater.* **26**, 196 (1982).
- ¹⁵ J. Wecker and L. Schultz, *J. Magn. Magn. Mater.* **83**, 189 (1990).
- ¹⁶ R. J. Pollard, S. F. H. Parker, and P. J. Grundy, *J. Magn. Magn. Mater.* **75**, 239 (1988).

Microstructure of high-remanence Nd-Fe-B alloys with low-rare-earth content

Raja K. Mishra

Physics Department, GM Research and Development Center, Warren, Michigan 48090-9055

V. Panchanathan

Magnequench—Delco Remy Division, General Motors Corporation, Anderson, Indiana 46013

The microstructure and magnetic properties of bonded and fully dense magnets produced from melt-spun ribbons of the composition $\text{RE}_{4.5}\text{TM}_{76}\text{Ga}_1\text{B}_{18.5}$ have been investigated, where RE refers to a mixture of Nd and Dy, and TM refers to a mixture of Fe and Co. Results show that annealing overquenched ribbons with about 3 wt. % Dy and 3 wt. % Co at 700 °C can produce materials with $H_{ci} \approx 4$ kOe, $B_r \approx 11.5$ kG, and $(BH)_{\max} \approx 14.5$ MGOe, the latter being comparable to those of commercial ribbons containing three times as much Nd. The microstructure of annealed ribbons consists of about 30% $\text{Nd}_2\text{Fe}_{14}\text{B}$ grains, 65% Fe_3B grains, and 5% α -Fe grains. The grains of all the phases are nearly spherical. The grain diameters are in the 30–50 nm range. Hot-pressed magnets made from overquenched ribbons are fully isotropic, with magnetic and microstructural characteristics similar to those of the annealed ribbons. The high remanence and low coercivity correlate well with the microstructure consisting of a uniform mixture of the hard $\text{Nd}_2\text{Fe}_{14}\text{B}$ phase and soft α -Fe and Fe_3B phases.

I. INTRODUCTION

Improvement of hard magnetic properties, simplification of processing, and reduction of cost, besides others, have been the principal motivating factors for much of the research on Nd-Fe-B permanent magnet materials^{1,2} since they were discovered a decade ago. Many studies of modification of chemical composition have helped improve the hard magnetic properties, Curie temperature, thermal and environmental stability, etc. Other research and studies have contributed toward streamlining preparation procedures which facilitate commercial production. There is now a sufficiently broad base of information on the $\text{Nd}_2\text{Fe}_{14}\text{B}$ magnets to help design compositions and microstructure suited for diverse applications. This article discusses the results of a study of a Nd-Fe-B magnet which is a mixture of two different ferromagnetic phases with the aim of enhancing magnetic properties while reducing overall Nd content compared to the standard $\text{Nd}_2\text{Fe}_{14}\text{B}$ magnet. Since Nd still accounts for a substantial fraction of the cost of the $\text{Nd}_2\text{Fe}_{14}\text{B}$ alloys and lower Nd content generally improves the aging behavior of the $\text{Nd}_2\text{Fe}_{14}\text{B}$ magnets, preparing viable magnets through this route is of both commercial and technological interest.

By altering the amount of Nd in the Nd-Fe-B alloy one can enter into a phase field in the Nd-Fe-B phase diagram where Fe_3B phase is one of the equilibrium phases.³ Fe_3B has a room-temperature saturation magnetization of 16 kG, comparable to that of the $\text{Nd}_2\text{Fe}_{14}\text{B}$ phase.⁴ It has planar anisotropy and it behaves as a soft magnet.⁵ The Curie temperature of Fe_3B is 513 °C, nearly 200 °C more than that of $\text{Nd}_2\text{Fe}_{14}\text{B}$. European⁴ and Japanese⁶ researchers have reported that in a $\text{Nd}_4\text{Fe}_{78}\text{B}_{18}$ alloy containing over 50% Fe_3B , B_r of 12 kG, H_{ci} of 3.8 kOe, and $(BH)_{\max}$ of 12 MGOe can be achieved. Alloying additions such as Dy, Co, and Ga are known to alter anisotropy, coercivity, and Curie temperature of $\text{Nd}_2\text{Fe}_{14}\text{B}$ magnets.¹ One of the aims in this study is to prepare and characterize an alloy utilizing the beneficial ef-

fects of both the mixing of two ferromagnetic phases as well as selective alloying modifications to improve coercivity and other characteristics. We also report here the results of microstructural characterizations of the new alloy and correlate them with the observed properties.

II. EXPERIMENT

The starting material used in this investigation was prepared from an induction melted ingot (5 pound charge) of nominal composition 13.2 wt. % Nd, 83.6 wt. % Fe, and 3.2 wt. % B ($\text{Nd}_{4.8}\text{Fe}_{77.5}\text{B}_{17.7}$), melt spun at wheel speeds between 4 and 22 m/s. The ribbons were annealed at temperatures between 680 and 720 °C for 5 min. Additional alloys were prepared by substituting 3 wt. % Co and 1 wt. % Ga for Fe and 3 wt. % Dy for Nd. Some alloys were made with B content up to 3.6 wt. % and Nd (Dy) content between 10.3 and 21.2 wt. %. Second quadrant demagnetization curves were measured from powder samples (demagnetization correction factor of 0.33) as well as from resin bonded magnets. Hot-pressed samples were prepared from the 22 m/s ribbons by standard procedure at 750 °C. Temperature coefficients of B_r and H_{ci} were calculated from demagnetization data at different temperatures. Loss characteristics were measured for bonded magnets held at elevated temperatures⁷ for up to 1000 h.

Thin foils for electron microscopy were prepared from annealed and unannealed ribbons by ion milling. The electron transparent foils were examined in a Philips 430 microscope operating at 300 kV.

III. RESULTS

Since it is possible to prepare microcrystalline ribbons of Nd-Fe-B alloys either by directly quenching from the melt at an optimum cooling rate or by annealing ribbons which were first overquenched from the melt, we have investigated both of these paths for optimum properties. For the low Nd con-

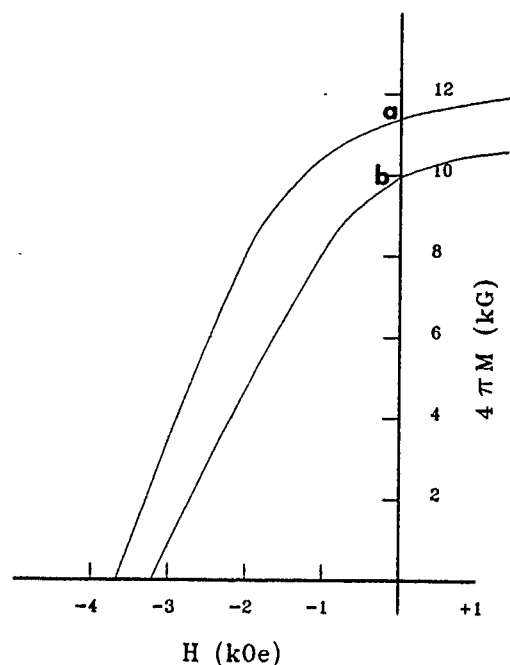


FIG. 1. Second quadrant demagnetization curve of $\text{Nd}_{3.5}\text{Dy}_1\text{Fe}_{73}\text{Co}_3\text{Ga}_1\text{B}_{18.5}$ (a) powder overquenched at 22 m/s and annealed at 700 °C with demagnetization correction factor 0.333; (b) hot-pressed magnet. The remanence to saturation magnetization ratio of 0.62 is the highest reported for any fully dense isotropic magnet.

tent compositions studied in this article, the best properties are exhibited by ribbons that are melt spun at 22 m/s and then annealed at temperatures close to 700 °C. Transmission electron microscopy results show that the ribbons of all compositions used in this study are microcrystalline for wheel speeds of 22 m/s. Figures 1(a) and 1(b) show the second quadrant demagnetization curves for overquenched ribbons of $\text{Nd}_{3.5}\text{Dy}_1\text{Fe}_{73}\text{Co}_3\text{Ga}_1\text{B}_{18.5}$, annealed for 5 min at 700 °C and hot pressed to full density, respectively. Microstructure of annealed ribbon corresponding to Fig. 1(a) is shown in Fig. 2(a). The microstructure consists of three phases, namely $\text{Nd}_2\text{Fe}_{14}\text{B}$, tetragonal Fe_3B , and $\alpha\text{-Fe}$. The grain sizes of Fe_3B and $\text{Nd}_2\text{Fe}_{14}\text{B}$ are nearly the same (average grain diameter in the 20–50 nm range) while $\alpha\text{-Fe}$ appears as isolated grains. The distribution of $\text{Nd}_2\text{Fe}_{14}\text{B}$ and Fe_3B phases is homogeneous. There is no evidence of intergranular phase at the grain boundaries.⁸ The microstructure of the hot-pressed sample is similar to that of the annealed ribbon in all respects. In contrast, the microstructure of the best directly quenched ribbon (wheel speed of 7 m/s) of the same composition, shown in Fig. 2(b), is not homogeneous. The grain diameters of the Fe_3B grains are much larger than those of the $\text{Nd}_2\text{Fe}_{14}\text{B}$ grains. There is a clearly defined intergranular phase at the $\text{Nd}_2\text{Fe}_{14}\text{B}$ grain boundaries. $\alpha\text{-Fe}$ is found as isolated particles. EDX analysis failed to detect any Nd in the Fe_3B grains. Dy, Co, and Ga additives were all detected in the $\text{Nd}_2\text{Fe}_{14}\text{B}$ phase with Ga concentrations mostly near the grain boundary. Microstructural features in ribbons of different compositions are the same except for the relative amounts of the three phases.

Table I lists the temperature coefficients of B_r and H_{ci}

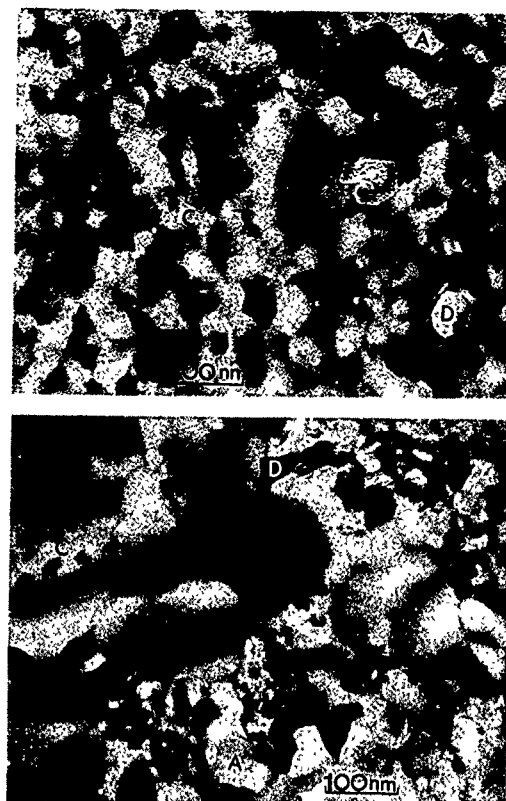


FIG. 2. Transmission electron micrographs of $\text{Nd}_{3.5}\text{Dy}_1\text{Fe}_{73}\text{Co}_3\text{Ga}_1\text{B}_{18.5}$ ribbons (a) quenched at 22 m/s and annealed at 700 °C and (b) quenched at 7 m/s. Note the nonuniform grain sizes of different phases in (b). A= Fe_3B , C= $\text{Nd}_2\text{Fe}_{14}\text{B}$, and D= $\alpha\text{-Fe}$.

between room temperature and 175 °C, measured using bonded magnets of composition $\text{Nd}_{4.8}\text{Fe}_{77.5}\text{B}_{17.7}$ and $\text{Nd}_{3.5}\text{Dy}_1\text{Fe}_{73}\text{Co}_3\text{Ga}_1\text{B}_{18.5}$. These values are essentially the same as those of commercial grade bonded Nd-Fe-B magnets. We also find that the structural and irreversible loss characteristics of these alloys are the same as commercial grade magnets. There is practically no loss in H_{ci} after aging for 1000 h at 100 °C and alloys without Co have no structural loss.

The initial magnetization and demagnetization curves of a bonded magnet premagnetized to two different field strengths are shown in Fig. 3. It is observed that while the coercivity of the material is not very high, the field needed for saturation is at least 10 times higher than the coercive

TABLE I. Temperature coefficients of B_r and H_{ci} in bonded magnets. Composition A: $\text{Nd}_{4.8}\text{Fe}_{77.5}\text{B}_{17.7}$; composition B: $\text{Nd}_{3.5}\text{Dy}_1\text{Fe}_{73}\text{Co}_3\text{Ga}_1\text{B}_{18.5}$.

Temperature (°C)	Temp. coeff. B_r (%/°C)		Temp. coeff. H_{ci} (%/°C)	
	A	B	A	B
50	-0.12		-0.43	
75	-0.10	-0.08	-0.42	-0.39
100	-0.13	-0.1	-0.39	-0.39
125	-0.14	-0.1	-0.38	-0.38
150	-0.14	-0.1	-0.38	-0.37
175		-0.11		-0.37

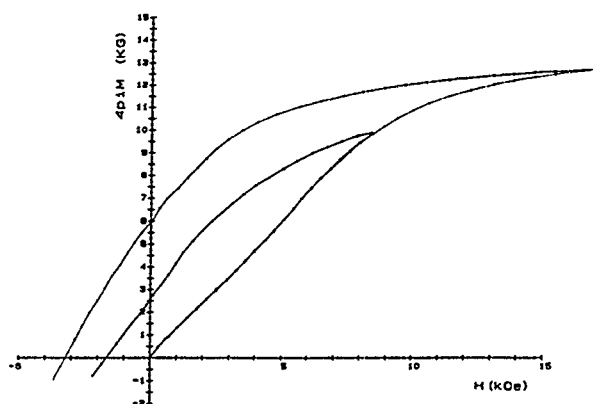


FIG. 3. Initial magnetization and second quadrant demagnetization curves for $\text{Nd}_{3.5}\text{Dy}_1\text{Fe}_{73}\text{Co}_3\text{Ga}_1\text{B}_{18.5}$ bonded magnet after magnetizing up to (a) 9 kOe and (b) 18 kOe. The kinks in (a) and (b) are characteristic of the two-phase material.

field. The initial magnetization curve is linear up to a field at least twice the coercive field. The demagnetization curves for the material magnetized up to 9 and 18 kOe are nearly parallel. The entire demagnetization curve shifts toward higher B_r and H_{ci} if the magnet is premagnetized to 45 kOe.

IV. DISCUSSION

Microstructural measurement shows that the material consists of approximately 30% $\text{Nd}_2\text{Fe}_{14}\text{B}$, 65% Fe_3B , and 5% $\alpha\text{-Fe}$ phase. These volume fractions are consistent with what one would expect from atomistic considerations if one assumes that all the Nd atoms are incorporated into the $\text{Nd}_2\text{Fe}_{14}\text{B}$ phase, the remaining B atoms are incorporated into the Fe_3B phase and the remnant transition metal atoms are left behind in elemental form. The saturation magnetization values of the three phases are roughly the same, close to 16 kG. Tetragonal Fe_3B has planar anisotropy, and the maximum contribution to remanence from isotropic distribution of the Fe_3B grains will be $\pi/4$ or 0.79 of saturation value if the basal plane of the tetragonal Fe_3B structure is assumed to contain no preferential direction for the magnetization vector.⁵ Since there are at least two grains of Fe_3B for every $\text{Nd}_2\text{Fe}_{14}\text{B}$ grain, in spite of the strong uniaxial anisotropy of the $\text{Nd}_2\text{Fe}_{14}\text{B}$ grains, the demagnetization characteristics of the material will be dominated by that of Fe_3B phase, giving a remanence close to 0.79 of the saturation value. If the $\text{Nd}_2\text{Fe}_{14}\text{B}$ phase were to determine the demagnetization behavior, the remanence would be in the range of half of the saturation magnetization value. Clearly, the high remanence in the material observed here and by others suggest the latter not to be the case.

The coercivity of the material is dominated by the crystallite distribution. Grain size plays a role in changing the value of H_{ci} . The moderate value of H_{ci} must be a result of the influence of the $\text{Nd}_2\text{Fe}_{14}\text{B}$ phase since the planar anisotropy of the Fe_3B phase makes that phase a soft ferromagnet. Application of a reverse field in this system can easily nucleate reverse domains and these domain walls can move rela-

tively freely in the Fe_3B grains while $\text{Nd}_2\text{Fe}_{14}\text{B}$ grains will act as barriers to domain-wall motion. Approach to saturation in such a material will be determined by the flipping of the magnetization vector in individual $\text{Nd}_2\text{Fe}_{14}\text{B}$ grains. The approach to zero magnetization at the coercive field will be a result of a sufficient amount of Fe_3B with reverse magnetization canceling out the contribution from the $\text{Nd}_2\text{Fe}_{14}\text{B}$ phase. Such an explanation is consistent with the large field (compared to the coercive force) needed for full saturation. This is also consistent with the observation of parallel demagnetization curves (a) and (b) in fig. 3.

The phase distribution is a result of both the chemistry and the kinetics of crystallite formation during quenching or annealing. The grain size distribution in the directly quenched alloy suggests that grain growth kinetics for Fe_3B and $\text{Nd}_2\text{Fe}_{14}\text{B}$ are different at elevated temperatures encountered during melt spinning. The grain growth kinetics of the two phases are similar at temperature and time intervals encountered during annealing of the overquenched alloy. It is also possible that nucleation of $\text{Nd}_2\text{Fe}_{14}\text{B}$ phase takes place in pockets which are saturated with Nd after Fe_3B grains have formed and grown in the directly quenched ribbons. Excess $\alpha\text{-Fe}$ is left behind in both cases at the end of solidification as a terminal phase. That no Nd atoms were detected in the Fe_3B phase contrary to the suggestion in Ref. 9 indicates that the Fe-B trigonal prism which forms the building block in Fe_3B and $\text{Nd}_2\text{Fe}_{14}\text{B}$ does not readily permit substitution of Fe by Nd. This is also consistent with the observation that various substitutions to the starting alloy do not alter the microstructure in any significant way. Most of the substituted atoms are incorporated into the $\text{Nd}_2\text{Fe}_{14}\text{B}$ phase. Fe_3B phase or boundaries between Fe_3B grains does not show any segregation of Dy, Co, or Ga. We find Ga associated with the $\text{Nd}_2\text{Fe}_{14}\text{B}$ phase, mostly at the boundary between $\text{Nd}_2\text{Fe}_{14}\text{B}$ and Fe_3B grains. The changes in the temperature coefficient of B_r and H_{ci} and the loss properties with various alloying additions are thus considered to be primarily due to changes to the $\text{Nd}_2\text{Fe}_{14}\text{B}$ phase upon alloying. Finally, these results indicate that further research on optimization of hard and soft magnet mixtures can potentially yield improved permanent magnets.

ACKNOWLEDGMENTS

The authors wish to thank J. Herbst, Fred Pinkerton, and John Croat for stimulating discussions and encouragement during this work.

- ¹ J. F. Herbst, Rev. Mod. Phys. **63**, 819 (1991).
- ² K. H. J. Buschow, Rep. Prog. Phys. **54**, 1123 (1991).
- ³ K. H. J. Buschow, D. B. de Mooij, and H. M. van Noort, J. Less-Common Met. **125**, 135 (1986).
- ⁴ R. Coehoorn, D. B. de Mooij, and C. de Waard, J. Magn. Magn. Mater. **80**, 101 (1989).
- ⁵ W. Coene, F. Hakkens, R. Coehoorn, D. B. de Mooij, C. de Waard, J. Fidler, and R. Gorssinger, J. Magn. Magn. Mater. **96**, 189 (1991).
- ⁶ S. Hirose, H. Kanekiyo, and M. Uehara, J. Appl. Phys. **73**, 6483 (1993).
- ⁷ V. Panchanathan, J. Mater. Eng. **13**, 129 (1991).
- ⁸ R. Mishra, J. Magn. Magn. Mater. **54-57**, 450 (1986).
- ⁹ M. Mao, C. Yang, Z. Cheng, Y. Zhang, B. Shen, L. Yang, and F. Li, J. Phys. Condens. Matter **4**, 9147 (1992).

Magnetic properties of sintered Alnico 5 magnet via rapid solidification technology

C. J. Yang, W. Y. Lee, and S. D. Choi

Electromagnetic Materials Laboratory, Research Institute of Industrial Science and Technology,
P.O. Box 135, 790-330 Pohang, Korea

A process for making Alnico magnets (grade 5-8) via rapid solidification technology has been developed. The process includes extractive melt spinning of alloy powders, press forming, heat treatment under a magnetic field, and aging. The Alnico 5 magnets made by this process showed superior magnetic properties to those of cast magnet of the corresponding composition. The superior magnetic properties of the sintered magnets with $B_r=13.2$ kG, $H_c=680$ Oe, and $(BH)_{\max}=6.02$ MGOe are due to the spinodal decomposition which is completely free of γ phase.

I. INTRODUCTION

The magnetic behavior of Alnico alloys is governed by two metallurgical transformations. The more important of the two is the decomposition of the bcc α matrix, which is stable at high temperature, into two phases, α_1 and α_2 , which are also bcc. The ferromagnetic α_1 phase, which is rich in Fe and Co, is finely dispersed throughout the weakly magnetic α_2 phase by spinodal decomposition.¹ The composition, orientation, and distribution of the α_1 precipitates determine the magnetic properties of the alloys. At high temperature, the second transformation occurs which has detrimental effect on the magnetic properties, i.e., the fcc γ phase precipitates from the α matrix upon cooling from about 1200 °C. Many investigations²⁻⁴ have reported the $\alpha \rightarrow \gamma$ precipitation and have pointed out that it causes a considerable decrease in the magnetic properties because it takes place at the expense of the α matrix.

In our recent investigation, the possibility of formation of γ phase was completely avoided by our proprietary extractive melt-spinning technique.⁵ In addition, the simple process based on melt-spun powders which are press formed and heat treated under a magnetic field renders these magnets economically competitive with existing magnets produced by powder metallurgy using elemental metal powders. We report the details of part of our recent investigations on the newly developed sintered Alnico 5 type magnet.

II. EXPERIMENT

Alloys of 14% Ni-24% Co-8% Al-3% Cu-51% Fe were prepared by argon plasma arc melting from each element of 99.95% purity. The arc-melted ingots were remelted three times to assure homogeneity, and extractively melt spun into powders of 60 mesh. Cooling substrate speeds of 8.5-33 m/s were used to give average grain sizes in the range 2.5-25.6 μm in the precursor powders. Magnetic measurements on the powder samples were carried out using a Toei vibrating sample magnetometer while compacted magnets were evaluated by a LDJ B-H loop tracer. A Perkin-Elmer thermomagnetic analyzer was used to study thermomagnetic behaviors and phase transitions. Electron microscopy was done using a Philips high-resolution 400 kV transmission microscope. The heat treatment under a magnetic field was carried out using

an in-laboratory assembled furnace; the magnetic fields ($H_a=5-10$ kOe) were applied using an electromagnet.

III. RESULTS AND DISCUSSION

A. Sintering, solutionizing, and magnetic properties

Figure 1 shows the variation of magnetic properties and density as a function of sintering temperature. The compact was made by pressing the melt-spun powders having an average particle size of 38 μm in a uniaxial pressure of 9.8×10^7 N/m². The grain size of the precursor powders was 10 μm . The magnet samples were prepared by sintering for 1 h, solutionizing at 1250 °C for 10 min, cooling from 900 to 600 °C at the cooling rate of 1.26 °C/s under the magnetic field of 7 kOe, and aging at 600 °C for 4 h. The magnet

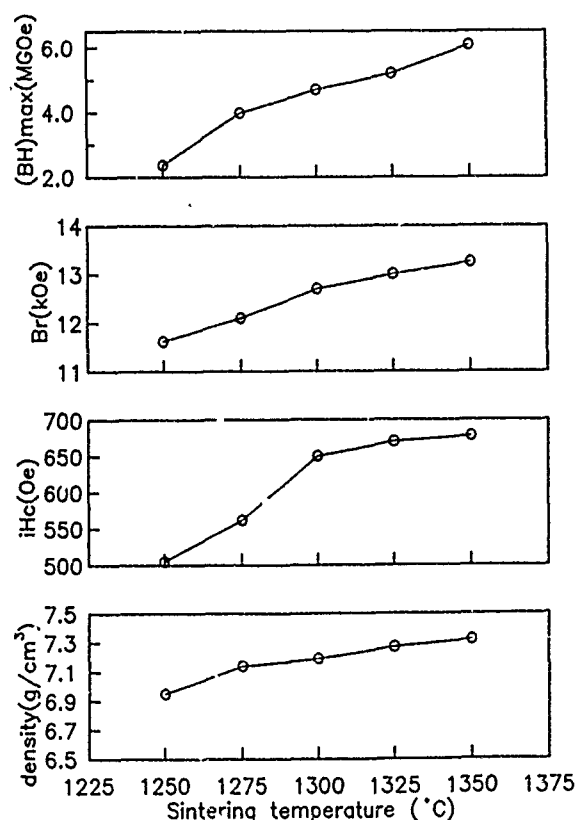


FIG. 1. Magnetic properties and density of the melt-spun-based sintered Alnico 5 magnets as a function of sintering temperature.

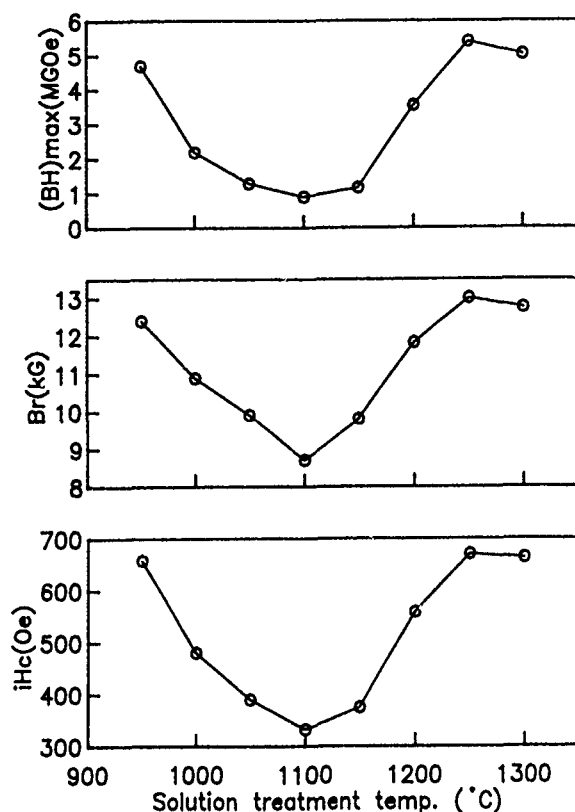


FIG. 2. Variation of magnetic properties of the sintered Alnico 5 magnets as a function of solutionizing temperature.

sintered at 1300 °C already shows properties superior to those of sintered magnets made by the existing process [$(BH)_{max}=5-5.5$ MGOe],⁶⁻⁸ and the magnet sintered at 1350 °C exhibits an energy product, $(BH)_{max}=6.0$ MGOe which is higher than that of cast-type Alnico 5 magnets [$(BH)_{max}=4.8-5.5$ MGOe].^{9,10} The superior magnetic properties were found to result from the high densities ρ of the green compacts ($\rho > 7.3$ g/cm³). In the existing process of making sintered-type Alnico magnets, a mixture of powders of elemental Ni, Co, FeAl, Cu, FeTi, Fe, and returned Alnico powders from cast magnets is used as precursor. The compactability of this mixture is inferior to that of the melt-spun powders. The microstructures of melt-spun precursors and the grain aspect of the magnet sintered at 1300 °C commonly showed uniform, equiaxed grains which were free from any observable γ phase. Only a few pores could be seen for the magnet sintered at 1300 °C.

The effect of solutionizing temperature on the magnetic properties is shown in Fig. 2. The magnet samples were prepared by sintering at 1350 °C for 1 h, solutionizing at the indicated temperature for 30 min, cooling from 900 to 600 °C at the cooling rate of 1.26 °C/s under the magnetic field of 7 kOe, and aging at 600 °C for 4 h. This figure indicates that, in spite of the rapidly solidified precursor powders, the selection of appropriate solutionizing treatment after sintering enhances the magnetic properties. The drastically poorer magnetic properties obtained for sintering temperatures in the range 1000–1200 °C are due to the martensitic transformation of (α_1) of the γ phase from the α matrix

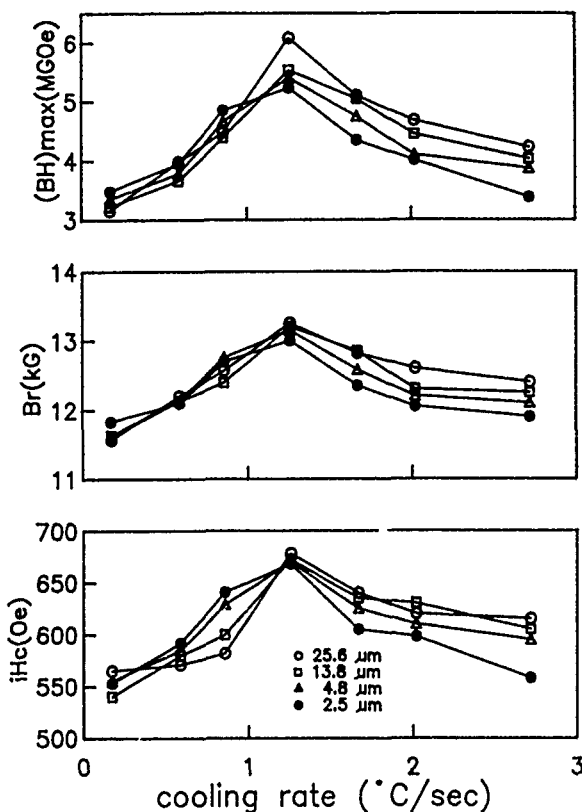


FIG. 3. Variation of magnetic properties of the sintered and aged magnets as functions of cooling rate during magnetic annealing and precursor grain size.

during cooling.³ The most appropriate solutionizing temperature for the Alnico 5 magnets made via rapid solidification process was found to be 1250 °C. No γ precipitate in α was seen in the magnets solutionized at temperature over 1250 °C.

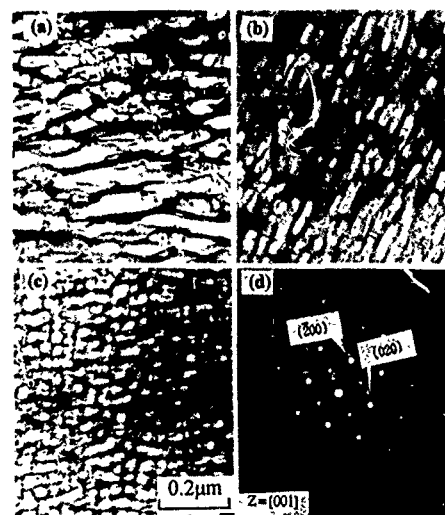


FIG. 4. TEM micrographs showing the α_1 precipitates formed during the magnetic annealing. (a), (b), and (c) are for cooling rates of 0.17 °C/s, 1.26 °C/s, and 1.67 °C/s, respectively; (d) is a selected-area-diffraction pattern from (b).

B. Magnetic annealing under an external field

The variation of magnetic properties is shown in Fig. 3 as a function of cooling rate during the magnetic annealing. The magnet samples were prepared by sintering at 1350 °C for 1 h, solutionizing at 1250 °C for 10 min, cooling from 900 to 600 °C at the rate of indicated speed in Fig. 3, and aging at 600 °C for 4 h. The initial grain sizes of the precursor powders are shown in Fig. 3(c). It can be seen that cooling rates below or above 1.26 °C/s during magnetic annealing influence the final magnetic properties in dissimilar ways. This is because the aspect ratio, distribution, and frequency of the magnetically hard, (Fe-Co)-rich α_1 precipitates are dependent upon the cooling rate. At a rate below 1.26 °C/s, the α_1 precipitation during the spinodal decomposition takes a coarse rod-type morphology with a small aspect ratio resulting in poor magnetic properties. Cooling rates faster than 1.26 °C/s, on the other hand, prevent the precipitates from growing into well-developed Co-rich particles having a high shape anisotropy. High Co concentration within the α_1 precipitates is known to enhance the magnetic properties of the Alnico-type magnets.¹¹ High cooling rates also prevented the axial alignment of the α_1 particles along the $\langle 100 \rangle$ orientations during magnetic annealing. It is of interest to note in Fig. 3 that the principle magnetic properties increase as the grain size of the precursor powders decreases for the magnets cooled at the rates below 1.26 °C/s, but that the magnetic properties (especially the coercivity) decrease as initial grain size decreases for the magnets cooled at the rates above 1.26 °C/s.

Figure 4 is the TEM micrographs showing the α_1 precipitates aligned along the $[100]$ direction. The micrographs were taken from the longitudinal section with respect to the applied field direction. The $[100]$ corresponds to the magnetic field direction during annealing. The long white islands

are the α_1 precipitates, and the grey matrix corresponds to the α_2 phase which is high in (Ni-Al). The magnet cooled at 0.17 °C/s shows α_1 precipitates that are 200 nm long and 50 nm wide. A cooling rate of 1.26 °C/s which was found to be optimal resulted in well-aligned and finely distributed precipitates [Fig. 4(b)] with an aspect ratio of (length/width) $= (200 \text{ nm}/30 \text{ nm}) = 6.7$. At a cooling rate of 1.67 °C/s, however, the α_1 precipitates took place in random orientations with malformed shapes. Figure 4(d) shows the electron-diffraction pattern obtained from the area corresponding to Fig. 4(b). The critical magnetic field above which the α_1 precipitates are aligned effectively in the melt-spun Alnico 5 type magnets was found to be 5 kOe.

IV. CONCLUSION

An economical process for producing the Alnico 5 type magnets using a rapid solidification technology has been developed. Sintered magnets made by this powder metallurgical method exhibited superior properties to those of cast magnets having corresponding compositions. The optimized process produced magnets with properties of $B_r = 12.8\text{--}13.2$ kG, $H_c = 630\text{--}680$ Oe, and $(BH)_{\text{max}} = 5\text{--}6$ MGOe.

¹B. D. Cullity, *Introduction to Magnetic Materials* (Addison-Wesley, Reading, MA, 1972), p. 574.

²C. A. Julien and F. G. Jones, *J. Appl. Phys.* **36**, 1173 (1965).

³G. Vallier, C. Bronner, and R. Pfeffer, *Cobalt* **34**, 10 (1967).

⁴C. Bronner, J. P. Harbener, E. Planchard, and J. Sauze, *Cobalt* **49**, 187 (1970).

⁵C. J. Yang, *J. Powder Rep.* **43**, 54 (1989).

⁶K. Oda, Japan Patent No. 190,338 (1984).

⁷K. Oda and I. Tahara, Japan Patent No. 100,647 (1985).

⁸K. Oda and I. Tahara, Japan Patent No. 103,150 (1985).

⁹R. K. Tenzer and K. J. Kronberg, *J. Appl. Phys.* **29**, 302 (1958).

¹⁰E. Steinort, *J. Appl. Phys.* **33**, 1310 (1962).

¹¹S. Chikazumi, *Jpn. J. Appl. Phys.* **37**, 127 (1982).

Effect of additives on thermal stability of Nd-Fe-B bonded magnets (abstract)

T. Nishio, H. Yagi, T. Furuya, and Y. Kasai

Research and Development Division, Daido Steel Co., Ltd., Nagoya 457, Japan

Effects of Zr and Nb on magnetic properties and thermal stability were studied for Nd-Fe-B bonded magnets. Bonded magnets with a composition of $\text{Nd}_x(\text{Fe}_{94-x-y})\text{B}_6\text{T}_y$, where $\text{T}=\text{Zr}$ and Nb ; $x=11.0$, 11.5 , and 12.0 ; $y=0$, 0.5 , 1.0 , 1.5 , and 2.0 ; were prepared by using melt spun ribbons. The addition of Zr up to 0.5 at. % increased the $(\text{BH})_{\text{max}}$ of the bonded magnets, and further addition of Zr decreased the $(\text{BH})_{\text{max}}$ at each Nd content level. H_{ci} increased monotonously with an increase in Zr. $(\text{BH})_{\text{max}}$ and H_{ci} of the Nb containing bonded magnets also showed similar behavior. Irreversible flux loss after exposure at 180°C for 1000 h significantly reduced with an increase in the Zr content at each Nd content level. Both the structural flux loss and the thermal fluctuation flux loss were reduced with an increase in the Zr content. An irreversible flux loss of about 5% was obtained when the Nd and Zr content were 11.5 at. % and 2.0 at. %, respectively. A similar value of irreversible flux loss was also obtained in Nb containing bonded magnets with the same composition. It was found that the oxygen pickup by the bonded magnets during the heat resistant test was well correlated to the structural loss of the bonded magnets. A structural flux loss of less than 3% was obtained when the oxygen pickup was less than 0.4 wt. % for both additives. SEM studies revealed that the grain size of the 2-14-1 phase observed in the additive-containing specimens was finer than that of the base alloy.

Coercivity in hard magnets based on $\text{Sm}_2\text{Co}_{17}$ (abstract)

Eric Lectard, Claire Maury, and Colette H. Allibert

L.T.P.C.M.-INPG, 38402 St. Martin d'Hères, France

Lew Rabenberg

University of Texas, Austin, Texas 78712-1063

Despite the research devoted to new compounds, the Sm-Co-Cu-Fe-Zr alloys with the 2:17 type are, as yet, the only hard magnets to be used above 200°C . However, these materials are not optimized because their coercivity mechanism is not clearly understood. Their typical microstructure consists of a network of 2:17 cells separated by 1:5 boundaries. Their coercivity is ascribed to the domain wall pinning by the 1:5 cell boundaries. The compositions of the 1:5, 2:17 phases during the cell microstructure genesis were recently¹ evaluated for the alloy $\text{Sm}(\text{Co}_{0.66}\text{Fe}_{0.25}\text{Cu}_{0.06}\text{Zr}_{0.03})_{7.6}$. In the present work, the coercivity behavior of this alloy is analyzed from the comparison of the domain wall energies $\gamma_{1:5}$, $\gamma_{2:17}$. Sintered samples, heat-treated in various conditions, are characterized by transmission electron microscopy and hysteresis curves. $\gamma_{2:17}$ and $\gamma_{1:5}$ are calculated from measured and published data of magnetization and anisotropy. The different treatments generate similar cell microstructures but two ranges of coercivity (about 600 and 2200 K A m^{-1}). In the two cases, $\gamma_{1:5}$ is larger than $\gamma_{2:17}$: the cell boundaries appear as repelling energy barriers rather than pinning sites. The existence of a disturbed anisotropy layer along the 1:5/2:17 interface is proposed to explain the higher coercivity state. The evaluation of H_{c} using the usual models² is attempted.

¹ C. Maury, L. Rabenberg, and C. H. Allibert, *Phys. Status Solidi* **140**, 57 (1993).

² K. D. Durst, H. Kronmüller, and W. Ervens, *Phys. Status Solidi* **108**, 705 (1988).

Orientalional dependence of the exchange biasing in molecular-beam-epitaxy-grown $\text{Ni}_{80}\text{Fe}_{20}/\text{Fe}_{50}\text{Mn}_{50}$ bilayers (invited)

R. Jungblut, R. Coehoorn, M. T. Johnson, J. aan de Stegge, and A. Reinders
Philips Research Laboratories, Prof. Holstlaan 4, 5656 AA Eindhoven, The Netherlands

The exchange biasing field (H_{cb}) and coercive field (H_c) of molecular-beam-epitaxy-grown $\text{Cu}/\text{Ni}_{80}\text{Fe}_{20}/\text{Fe}_{50}\text{Mn}_{50}$ samples in [111], [001], and [110] orientations have been investigated by longitudinal Kerr effect measurements. $\text{Ni}_{80}\text{Fe}_{20}$ and $\text{Fe}_{50}\text{Mn}_{50}$ were deposited as orthogonal wedge-shaped layers on single-crystal Cu substrates in a magnetic field, enabling the study of the thickness dependence of H_{cb} and H_c on a single sample for each orientation. A strong dependence of H_{cb} and H_c on the growth orientation is observed. The results are interpreted in terms of the observed noncollinear spin structure of the antiferromagnet and a comparison is given with the predictions from recent theoretical models.

I. INTRODUCTION

Exchange coupling at the interface between a ferromagnetic (FM) layer and an antiferromagnetic (AF) layer can cause a unidirectional anisotropy of the FM layer if the sample is grown in a magnetic field or cooled down in a magnetic field after heating above the Néel temperature of the AF layer.¹ It manifests itself by a shift of the hysteresis loop along the field axis. The size of this field shift is called the exchange biasing field, H_{cb} .

The most intensively studied systems comprise the antiferromagnetic oxidic layers CoO and NiO ² and the antiferromagnetic metallic alloy $\text{Fe}_{50}\text{Mn}_{50}$. A unidirectional anisotropy in entirely metallic systems was first found for $\text{Ni}_{80}\text{Fe}_{20}/\text{NiFeMn}$ bilayers.³ In particular, the alloy system $\text{Ni}_{80}\text{Fe}_{20}/\text{Fe}_{50}\text{Mn}_{50}$, which was found to display the biasing effect in 1978,⁴ has been studied extensively, motivated by practical industrial applications in magnetoresistive sensors based on the anisotropic magnetoresistance⁵ or giant magnetoresistance ("spin-valve") effect.⁶

Investigations on the system $\text{Ni}_{80}\text{Fe}_{20}/\text{Fe}_{50}\text{Mn}_{50}$ have revealed several interesting observations concerning the hysteresis loop shift and related phenomena. An important finding was that the coupling H_{cb} varies approximately inversely with the thickness of the FM layer, t_{FM} .⁷ This provides evidence of the interfacial nature of the interaction effect that gives rise to exchange biasing. Balancing the Zeeman energy and the unidirectional anisotropy energy results in a phenomenological expression for the loop shift

$$H_{\text{cb}} = \frac{\Delta\sigma}{2\mu_0 M_{\text{FM}} t_{\text{FM}}}, \quad (1)$$

where M_{FM} is the saturation magnetization of the ferromagnetic layer and $\Delta\sigma$ is the change of the interfacial exchange energy upon a reversal of the magnetization of the FM layer. H_{cb} has been observed to decrease linearly with increasing temperature and becomes zero at the "blocking temperature," slightly below the Néel temperature of the AF layer.⁷ Other interesting observations concern (i) the influence of

the interfacial exchange coupling on the coercive field H_c (half-width of hysteresis loop at zero net magnetization) of the FM/AF double layer, (ii) the different loop shifts of FM/AF layers grown in a magnetic field and AF/FM layers cooled through the Néel temperature of the AF layer in a magnetic field,⁸ and (iii) the initial reduction of H_{cb} and H_c with the number of hysteresis loop cycles ("magnetic training effect").⁹

In spite of the continuing interest in the exchange biasing effect, its microscopic origin has remained a subject of debate.¹⁰ In a first model¹ it was assumed that the interface magnetization of the AF layer is "uncompensated" (only one of two antiferromagnetic sublattices adjoins the interface) and remains fixed when the magnetization of the FM layer is rotated. In that case, the change of the interfacial exchange energy is given by $\Delta\sigma = 2J/a^2$, where a is the lattice parameter and J is the exchange constant. In an order of magnitude calculation we use Eq. (1) and values for J typical for exchange interactions in Fe-based alloys ($J \approx 10^{-21}$ J). Expressing the normalized value of the exchange coupling by the product $H_{\text{cb}} t_{\text{FM}}$, we obtain $\approx 1.6 \times 10^5$ kA/m Å, being much larger than the experimental values for the $\text{Ni}_{80}\text{Fe}_{20}/\text{Fe}_{50}\text{Mn}_{50}$ system, summarized in Table I. Furthermore, for cases in which the AF interface is compensated this model predicts no loop shift. As will be discussed in more detail, this is the case for $\text{Fe}_{50}\text{Mn}_{50}$ (100) and (111).

Mauri *et al.*¹¹ modified this model by showing that the energy of the reversed state can be lowered by the introduction of a domain wall into the AF layer parallel to the interface. $\Delta\sigma$ is now equal to the wall energy, $4(A_{\text{AF}}K_{\text{AF}})^{1/2}$, where A_{AF} is the exchange stiffness and K_{AF} is the uniaxial anisotropy per unit volume in the antiferromagnet. It has been remarked that this model predicts a loop shift which is in good agreement with experiments, if A_{AF} and K_{AF} are chosen comparable to the values for permalloy ($A_{\text{AF}} \approx 2 \times 10^{-11}$ J/m and $K_{\text{AF}} \approx 1.6 \times 10^3$ J/m³). However, this choice of parameters is not consistent with the observation by polarized neutron diffraction experiments¹² that the ferromagnetic exchange stiffness and anisotropy are large enough

TABLE I. Experimental values for the $\text{Ni}_{80}\text{Fe}_{20}/\text{Fe}_{50}\text{Mn}_{50}$ system.

Preparation method	Substrate	$t_{\text{Ni-Fe}}$ (Å)	$H_{\text{cb}} t_{\text{Ni-Fe}}$ (kA/m Å)	$\text{Fe}_{100-x}\text{Mn}_x$ (at. %)
MBE ^a	Cu(111)	68	1000	57
MBE ^a	Cu(110)	70	620	59
MBE ^a	Cu(001)	70	690	47
HV evap. ^b	f	400	670	57
HV evap. ^b	f	400	1160	53
HV evap. ^b	f	400	1040	47
HV evap. ^b	f	400	1300	46
HV evap. ^b	f	400	920	44
Sputtered ^c	Si(001)/Ta/Ni-Fe/Cu	60	1320	50
Sputtered ^d	Si(111)	400	1280	50
Sputtered ^e	Glass	400	360–820	50

^aThis paper.

^bReference 4.

^cReference 25.

^dReference 26.

^eReferences 7, 17, 20, 27, and 28.

^fNot reported.

to confine the domain wall to the AF layer, i.e., $(A_{\text{AF}}K_{\text{AF}})^{1/2} \ll (A_{\text{FM}}K_{\text{FM}})^{1/2}$. Consequently, this model predicts an H_{cb} which is too small. Another inconsistency with the assumed values of A_{AF} and K_{AF} is that the exchange biasing effect is usually measured for AF thicknesses much lower than the expected domain wall width $\pi(A_{\text{AF}}/K_{\text{AF}})^{1/2} \approx 0.35 \mu\text{m}$. Furthermore, the model treats only the case of a perfect and uncompensated interface.

Subsequently, Malozemoff¹³ presented a model which does not suffer from these shortcomings. He explained the biasing effect by assuming domains in the antiferromagnet, separated by domain walls perpendicular to the interface in conjunction with the presence of roughness of the AF interfaces which would otherwise be perfectly compensated. The interface roughness will give rise to a random exchange field. However, due to the finite size of the domains, with typically N atoms at the interface, these random fluctuations will not compensate each other completely. On the average $N^{1/2}$ spins (order of magnitude) at the interface will be uncompensated. Upon growth in a field or after cooling from a temperature above the blocking temperature, the resulting spin structure in each of the domains will support the same magnetization direction of the FM layer. Reversal of the FM layer will then cost $\Delta\sigma \approx N^{-1/2}J/a^2$. Malozemoff further argues that the domain diameter is approximately equal to the wall thickness $L \approx \pi(A_{\text{AF}}/K_{\text{AF}})^{1/2}$, which, with $N^{1/2} = a/L$, results in

$$H_{\text{cb}} \approx \frac{\sqrt{A_{\text{AF}}/K_{\text{AF}}}}{\pi\mu_0 M_{\text{FM}} T_{\text{FM}}} \quad (2)$$

In a later paper, Malozemoff¹⁴ predicts an enhanced H_{cb} below a characteristic thickness of the AF, corresponding with the transition between an "Ising-domain" state where the domain diameter is in the order of the wall thickness and a "Heisenberg-domain" state with the domain diameter smaller than the wall thickness.

A shortcoming of these models, when applied to the $\text{Ni}_{80}\text{Fe}_{20}/\text{FeMn}$ system, is that they do not take the details of

the spin structure of the AF layer into account. Let us consider the spin structure of $\gamma\text{-FeMn}$. The average spin structure, which does not take the detailed (random) occupation of sites with Fe and Mn atoms into account, is described by the commonly accepted $\langle 111 \rangle$ model.¹⁵ Atoms on the $(0,0,0)$, $(\frac{1}{2}, \frac{1}{2}, 0)$, $(0, \frac{1}{2}, \frac{1}{2})$, and $(\frac{1}{2}, 0, \frac{1}{2})$ positions have moments which are directed to the center of the tetrahedron that is defined by these atomic positions, i.e., along the $\langle 111 \rangle$ directions. Figure 1 shows that terminating the bulk $\text{Fe}_{50}\text{Mn}_{50}$ crystal along the (111) , (110) , and (001) planes leads to entirely different spin configurations at the surfaces. In the (111) planes the moments are directed $\pm 19.5^\circ$ and $\pm 90^\circ$ out of plane with their in-plane components compensating each other. In the (001) planes the moments are $\pm 35.3^\circ$ out-of-plane pointing along the $[110]$ and $[\bar{1}10]$ in-plane directions. The resulting in-plane moment is also compensated. For the (110) planes we have to distinguish between two different layers: One type of layer has its moments in plane whereas for the other layer $\pm 54.7^\circ$ out of plane moments are found. In contrast to the other two surfaces a resultant in-plane moment along the $[100]$ directions is found: the (110) plane is uncompensated.

It would be of fundamental interest to know whether these entirely different spin structures for FeMn result in an orientational dependence of the exchange biasing effect. Here we present results of the first investigation into this issue. We have grown $\text{Ni}_{80}\text{Fe}_{20}/\text{FeMn}$ bilayers on single crystal Cu substrates of different orientations by molecular beam epitaxy (MBE) in a magnetic field. The bilayers were grown as "double" wedges to enable the study of the dependence of H_{cb} and H_c on the thickness of the AF and FM layers on a single sample.

II. EXPERIMENTAL DETAILS

A schematic view of the samples used is given in Fig. 2. Fe and Ni, as well as Fe and Mn were coevaporated from

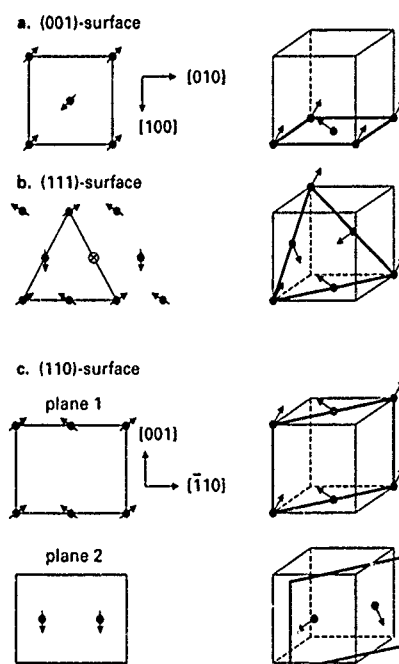


FIG. 1. Spin structure in the $\langle 111 \rangle$ model for the different orientations.

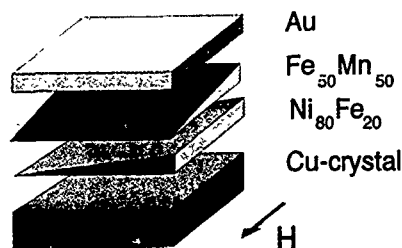


FIG. 2. Schematic view of the samples.

electron beam evaporators and Knudsen cells on [111], [110], and [001] oriented Cu single crystals held at room temperature. During growth a magnetic field of ≈ 20 kA/m was applied along several high symmetry directions in the surface plane. The wedge shape of the layers was achieved by withdrawing an eclipsing shutter. Care has to be taken that the shutter causes equal shadows for the flux from both evaporation sources forming the alloy. Evaporation rates (FeMn and $\text{Ni}_{80}\text{Fe}_{20}$: 0.8 \AA/s) and compositions were controlled by crystal thickness monitors calibrated by chemical analysis. After completion of the $\text{Ni}_{80}\text{Fe}_{20}$ wedge the sample was rotated by 90° to grow the $\text{Fe}_{50}\text{Mn}_{50}$ wedge. A thickness dependent structural study was done by low energy electron diffraction (LEED). The perpendicular and the parallel lattice spacings (d_\perp, d_\parallel) were determined kinematically by measuring the energies of the primary Bragg reflections along the [00] rod, and by analysis of LEED patterns at constant energy, respectively. The wedge starts, their slopes and finally their composition were controlled by combining secondary electron microscopy and Auger electron spectroscopy. The error in determining the composition is estimated to be ± 3 at. %. The samples to be discussed had the following composition: Cu(001)/ $\text{Ni}_{74}\text{Fe}_{26}$ (0–80 \AA)/ $\text{Fe}_{53}\text{Mn}_{47}$ (0–135 \AA)/Au (20 \AA), $H \parallel$ [001] and [011]; Cu(110)/ $\text{Ni}_{77}\text{Fe}_{23}$ (0–80 \AA)/ $\text{Fe}_{41}\text{Mn}_{59}$ (0–85 \AA)/Au (20 \AA), $H \parallel$ [110]; Cu(111)/ $\text{Ni}_{79}\text{Fe}_{21}$ (0–86 \AA)/ $\text{Fe}_{43}\text{Mn}_{57}$ (0–130 \AA)/Au (20 \AA), H in arbitrary direction.

The Au top layer was deposited to protect the sample against oxidation.

The magnetic characterization was done *ex situ* by the longitudinal magneto-optic Kerr effect employing a laser beam focussed to $\approx 100 \text{ }\mu\text{m}$. The magnetic fields applied in Kerr measurements were parallel to the fields applied during growth. By scanning the laser beam over the sample the entire AF- and FM-layer thickness dependence of H_{eb} and H_c could be studied on only one sample for each orientation. The lack of Kerr-signal restricted reliable measurements to FM layer thicknesses $\geq 20 \text{ \AA}$. Before scanning the sample the magnetic field was cycled about 10 times between its maximum values to avoid possible ambiguities related to the training effect.⁹

III. RESULTS

A. Growth and structure

When MBE-depositing $\text{Ni}_{79}\text{Fe}_{21}$ (disordered $\text{Ni}_{80}\text{Fe}_{20}$: $a = 3.5489 \text{ \AA}$) on the Cu(111) substrate (Cu: $a = 3.6150 \text{ \AA}$,

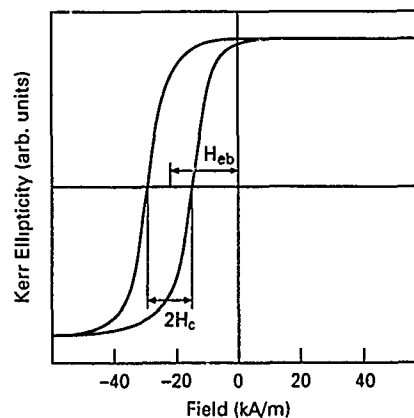


FIG. 3. Hysteresis loop of Cu(111)/68 \AA $\text{Ni}_{79}\text{Fe}_{21}$ /45 \AA $\text{Fe}_{43}\text{Mn}_{57}$ /Au.

$d_\perp = 2.09 \pm 0.01 \text{ \AA}$), we observed LEED patterns with fcc(111) symmetry over the whole investigated thickness range. On increasing the $\text{Ni}_{79}\text{Fe}_{21}$ thickness its perpendicular lattice parameter gradually increased to reach its bulk value ($d_\perp = 2.04 \pm 0.01 \text{ \AA}$) at $\approx 33 \text{ \AA}$ $\text{Ni}_{79}\text{Fe}_{21}$. Between 34 and 44 \AA $\text{Ni}_{79}\text{Fe}_{21}$ triangle-shaped diffraction spots, probably related to arrays of misfit dislocations occurred. Growing $\text{Fe}_{43}\text{Mn}_{57}$ ($\text{Fe}_{50}\text{Mn}_{50}$: $a = 3.625 \text{ \AA}$) on Cu(111)/ $\text{Ni}_{79}\text{Fe}_{21}$, no clear LEED pattern was observed for thicknesses between 19 and 46 \AA . The quality of the LEED pattern improved over the remaining thickness interval up to 130 \AA . The perpendicular lattice parameter of the $\text{Fe}_{43}\text{Mn}_{57}$ layers (on relaxed $\text{Ni}_{79}\text{Fe}_{21}$) was found to be relaxed to $d_\perp = 2.09 \pm 0.02 \text{ \AA}$ at thicknesses higher than 46 \AA .

For the $\text{Ni}_{74}\text{Fe}_{26}$ grown on Cu(001), fcc LEED patterns were observable for the investigated thickness range, indicating epitaxial growth. From the LEED [00] reflections we derived $d_\perp = 1.81 \pm 0.01 \text{ \AA}$ for the Cu substrate. For $\text{Ni}_{74}\text{Fe}_{26}$ thicknesses larger than 16 \AA $d_\perp = 1.72 \pm 0.01 \text{ \AA}$ was found, which remained unchanged over the whole investigated thickness range. When growing $\text{Fe}_{53}\text{Mn}_{47}$ on this $\text{Ni}_{74}\text{Fe}_{26}$, layer d_\perp reverted to $1.51 \pm 0.01 \text{ \AA}$. At about 21 \AA $\text{Fe}_{53}\text{Mn}_{47}$ cross-shaped LEED spots became visible possibly hinting to the presence of misfit dislocations along the [100] directions.

Growing $\text{Ni}_{77}\text{Fe}_{23}$ on a Cu(110) substrate ($d_\perp = 1.28 \pm 0.01 \text{ \AA}$), we measured $d_\perp = 1.26 \pm 0.02 \text{ \AA}$ from about 15 \AA up to a thickness of 85 \AA . The $\text{Fe}_{41}\text{Mn}_{59}$ wedge grew coherently up to $\approx 20 \text{ \AA}$. For larger thicknesses the perpendicular lattice parameter became $d_\perp = 1.30 \pm 0.02 \text{ \AA}$.

B. Exchange biasing and coercive field

For each orientation, typically 120 Kerr hysteresis loops (Fig. 3) were recorded. For the [111] oriented layer the results of the Kerr measurements are summarized in contour plots for H_{eb} and H_c (Fig. 4). For an easier interpretation intersections of these plots for different FeMn thicknesses are given in Fig. 5. The onset of the biasing was found at $\approx 25 \text{ \AA}$ FeMn reaching saturation at $\approx 55 \text{ \AA}$ FeMn independently of the $\text{Ni}_{80}\text{Fe}_{20}$ thickness. For $\approx 70 \text{ \AA}$ $\text{Ni}_{80}\text{Fe}_{20}$ H_{eb} stays almost constant at 14.7 kA/m in the investigated FeMn thickness range above 60 \AA [Fig. 5(b)]. H_c displays a sharp

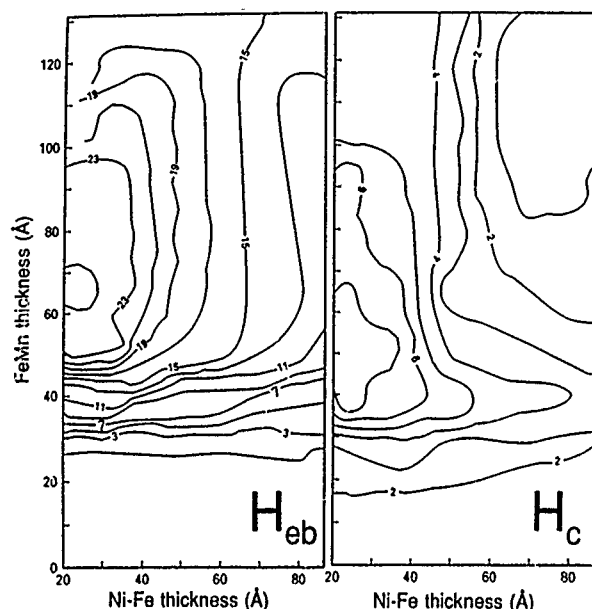


FIG. 4. Contour plots of H_{cb} and H_c for the [111] oriented sample.

maximum at the onset of the biasing effect, dropping at thicker FeMn layers. For all thickness combinations with a FeMn thickness ≥ 40 Å, H_c is smaller than H_{cb} . For $\text{Ni}_{80}\text{Fe}_{20}$ thicknesses lower than ≈ 50 Å a maximum in H_{cb} and H_c for FeMn thicknesses in the range of 60–90 Å is observed [Fig. 5(a)]. For (111) bilayers with the $\text{Ni}_{80}\text{Fe}_{20}$ thickness in the interval 20–35 Å, H_{cb} is lower than expected from the $1/t_{\text{FM}}$ behavior observed for thicker $\text{Ni}_{80}\text{Fe}_{20}$.

For the (001) orientation two different samples were grown with the field during growth and Kerr measurements applied along the [100] and [110] in-plane directions, respectively. The aim of making these two samples was to determine whether there is a correlation between the AF surface spin directions {component along the [110] in-plane directions in the (111) spin model, see Fig. 1(a)} and the strength of the biasing. Results for a $\text{Ni}_{80}\text{Fe}_{20}$ layer thickness of 65 Å are rendered in Fig. 6, where within the experimental error margins ($\pm 10\%$) the same thickness dependence of H_{cb} was found for both samples, saturating to $H_{cb} = 10$ kA/m for high FeMn thicknesses. However, a much higher H_c was measured in the sample grown with the field in the [110] direc-

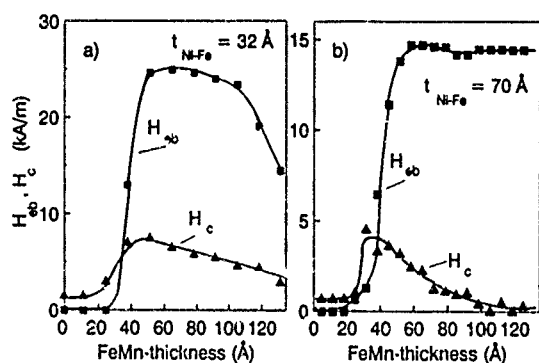


FIG. 5. $H_{cb}(t_{\text{FeMn}})$ and $H_c(t_{\text{FeMn}})$ for the [111] oriented sample for 32 and 70 Å $\text{Ni}_{80}\text{Fe}_{21}$.

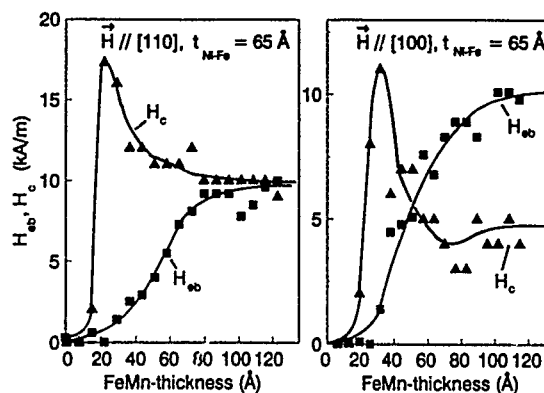


FIG. 6. $H_{cb}(t_{\text{FeMn}})$ and $H_c(t_{\text{FeMn}})$ for the [001] oriented samples grown and measured with $H \parallel [110]$ and $H \parallel [100]$.

tion. In contrast to the [111]-oriented samples, H_c stayed at a high level even for high FeMn thicknesses. The onset of the biasing, together with an increase in H_c is found at a FeMn thickness of ≈ 20 Å, whereas constant biasing is reached at ≈ 90 Å. This result was seen to be independent of the $\text{Ni}_{80}\text{Fe}_{20}$ thickness. For a given FeMn thickness, Fig. 7 shows the dependence of H_{cb} and H_c on the $\text{Ni}_{80}\text{Fe}_{20}$ thickness and the orientation of the magnetic field. Whereas for a magnetic field applied during growth and measurement along [110] H_c and H_{cb} vary in a similar manner, for a field applied along [100] H_c became smaller than H_{cb} at ≈ 40 Å $\text{Ni}_{80}\text{Fe}_{20}$. For $\text{Ni}_{80}\text{Fe}_{20}$ thicknesses smaller than ≈ 70 Å we find a larger H_{cb} for the sample with the field during growth and measurement along the [110] direction. Biasing is stronger parallel to the surface spin direction, which supports the (111) spin model.

For the (110)-oriented bilayer the onset of the biasing effect is found at ≈ 20 Å FeMn and it saturates at ≈ 50 Å independently of the $\text{Ni}_{80}\text{Fe}_{20}$ thickness [Fig. 8(a)]. A weak maximum in the biasing effect is visible for a FeMn thickness of ≈ 60 Å, reaching a H_{cb} of ≈ 8.9 kA/m at 69 Å $\text{Ni}_{80}\text{Fe}_{20}$. The coercivity again shows a sharp peak at the onset of the biasing effect and stays larger than the loop shift even for thick FeMn layers. The expected $1/t_{\text{FM}}$ dependence of H_{cb} was observed down to $t_{\text{NiFe}} \geq 20$ Å. The coupling of

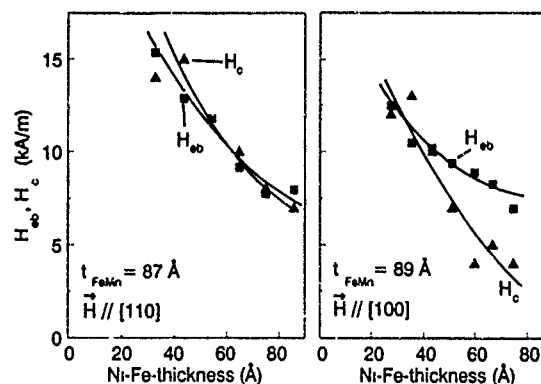


FIG. 7. $H_{cb}(t_{\text{NiFe}})$ and $H_c(t_{\text{NiFe}})$ for the [001] oriented samples for comparable FeMn thickness, but grown and measured with $H \parallel [110]$ and $H \parallel [100]$.

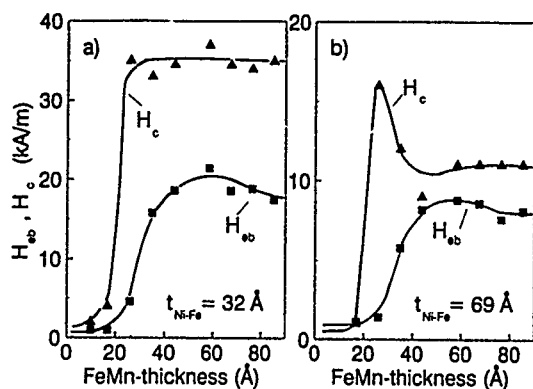


FIG. 8. $H_{cb}(t_{\text{FeMn}})$, $H_c(t_{\text{FeMn}})$ for the [011] oriented sample for 32 and 69 Å $\text{Ni}_{80}\text{Fe}_{20}$.

the $\text{Ni}_{80}\text{Fe}_{20}$ film to the FeMn introduces a remarkable in-plane anisotropy. For 30 Å $\text{Ni}_{80}\text{Fe}_{20}$ and a 70 Å FeMn layer, a field of ≈ 220 kA/m has to be applied along the [001] in-plane direction to obtain saturation. Details of this anisotropy and its possible explanations will be discussed elsewhere.

IV. DISCUSSION

To grow the substitutional disordered alloy $\text{Fe}_{50}\text{Mn}_{50}$ in the antiferromagnetic γ phase, a suitable fcc substrate is desired. The γ phase is metastable for Mn concentrations of more than 54 at. %. Even in the presence of a fcc seed layer such as $\text{Ni}_{80}\text{Fe}_{20}$ or Cu the FeMn α phase has been observed to form in sputtered samples beyond a thickness of a few hundred Å.¹⁶ Our experiments show that it is possible to stabilize γ -phase FeMn on several differently oriented permalloy layers. However, for the (111) case, the LEED studies did not convincingly show that high quality epitaxial growth was realized for all FeMn thicknesses.

The growth of $\text{Fe}_{50}\text{Mn}_{50}$ on $\text{Ni}_{80}\text{Fe}_{20}$ was investigated earlier by transmission electron microscopy (TEM) on sputtered samples,¹⁷ where an epitaxial relationship between the two layers was found. Epitaxial strain (2.4% misfit) was found to be confined locally within each grain and was accommodated by coherent strain across the interface. Therefore, we were curious whether a Cu(111) single crystal, which has a closer lattice match with $\text{Fe}_{50}\text{Mn}_{50}$ than $\text{Ni}_{80}\text{Fe}_{20}$, would be a better substrate for growing epitaxial well-oriented Fe-Mn. We found that this is not the case. MBE-evaporated layers of $\text{Fe}_{100-x}\text{Mn}_x$ alloys ($x=46-51$) on a Cu(111) substrate at 300 and 450 K still gave diffuse LEED patterns with three-fold symmetry in the 0–20 Å thickness range. For thicker layers the spots became even fuzzier and disappeared at ≈ 45 Å. This suggests a polycrystalline growth of FeMn on Cu.

To allow a comparison of the magnetic properties of our $\text{Ni}_{80}\text{Fe}_{20}/\text{Fe}_{50}\text{Mn}_{50}$ bilayers with earlier work, Table I gives a compilation of results on sputtered and evaporated substrate/ $\text{Ni}_{80}\text{Fe}_{20}/\text{Fe}_{100-x}\text{Mn}_x$ samples prepared on different substrates. The strength of the exchange biasing is expressed in terms of the product $H_{cb} \cdot t_{\text{FM}}$. It cannot be excluded that the variation of the composition of the Fe-Mn layers slightly influences the observed variation of H_{cb} with

the growth direction; this dependence is however well documented.^{4,18} Hemstead *et al.*⁴ find a maximum biasing for their HV evaporated $\text{Fe}_{47}\text{Mn}_{53}$ alloy. In our samples, even when taking possible differences in the FeMn compositions into account, the [111] oriented bilayers had the strongest exchange coupling. No correlation is found between the strength of the biasing and the compensated or uncompensated nature of the ideal interfaces illustrated in Fig. 1. Specifically, the [110] oriented sample, with uncompensated interface in the ideal case, shows the weakest biasing. Possible explanations include a different spin structure, modification of the interface spin structure or the presence of a rough interface. Since results on the (001) samples support the $\langle 111 \rangle$ spin model, it is perhaps most likely that roughness causes partially uncompensated interfaces in all orientations. Malozemoff's¹³ proposals can then account for the presence of biasing in all three orientations.

Sputtered samples on Si and Si(001)/Ta/ $\text{Ni}_{80}\text{Fe}_{20}$ /Cu "substrates," i.e., in a spin-valve magnetoresistance multilayer, display the strongest biasing. The interface coupling of sputtered bilayers on glass substrates varies strongly with the sputtering conditions. Our MBE-grown samples have a well-defined sharp interface. Interface mixing due to the higher kinetic energy of the sputter-deposited atoms could cause stronger biasing similar to the effect caused by annealing, creating a Ni-Mn-Fe alloy at the interface.¹⁹ The presence of a thin ferromagnetic layer at the interface with a magnetization different from the bulk²⁰ could result in a wrong determination of the "magnetic thickness." Results for thick t_{FM} are therefore more reliable.

For the observed dependence of the biasing field and coercivity on the thickness of the AF layer we present the following hypothesis: The stability of the AF spin configuration depends on the balance between the change of the interfacial energy when the FM layer is reversed and the stabilizing "coercivity" in the AF layer. Upon increasing the AF-film thickness the number of bulk inhomogeneities in the AF layer is increased leading to more effective pinning of the AF spin configuration and to biasing beyond a certain critical Fe-Mn thickness. Around this critical Fe-Mn thickness locally the spin configuration remains fixed, leading to biased FM "particles" in a matrix of magnetically soft unbiased material. This results in the high coercivity of such a magnetically inhomogeneous system.²¹ Upon a further increase of the Fe-Mn layer thickness, the $\text{Ni}_{80}\text{Fe}_{20}$ layer becomes more homogeneously biased, and H_c drops. The precise nature of the inhomogeneities in the AF layer (e.g., structural, thickness or compositional randomness), is unclear. If compositional randomness in the AF leads to variations of the anisotropy constant this model coincides with an earlier suggestion by Schlenker *et al.*,⁹ who proposed different types of AF regions. In some regions with large AF anisotropy the spins are blocked and responsible for the loop shift; in others with weaker anisotropy the AF moments rotate irreversibly when the FM magnetization rotates. In another interpretation, Speriosu *et al.*²² and Parkin *et al.*²³ discuss regions with locally different blocking temperatures depending on t_{AF} which contribute to the net anisotropy as independent particles.

At Fe-Mn thicknesses where biasing is saturated we observe for the [111] orientation that H_c becomes smaller toward higher FeMn thicknesses, whereas for the [100] and [110] orientations it stays almost constant for a given $\text{Ni}_{80}\text{Fe}_{20}$ thickness. We correlate this to the in-plane anisotropy of the exchange coupled $\text{Ni}_{80}\text{Fe}_{20}$ system. The anisotropy energy is isotropic in the (111) plane, whereas there are easy and hard directions in the (100) and (110) planes.

The weak maximum in H_{cb} just after the onset of the biasing for $\approx 60 \text{ \AA}$ FeMn thickness found in our [111] and [110] oriented samples (Figs. 4 and 7), was also observed for sputtered glass/Ta/NiFe/FeMn and glass/NiFe/FeMn samples,²⁴ especially after annealing the samples. In our experiments and the earlier work it is not clear if these findings have their origin in structural properties of the bilayer, or if they confirm Malozemoff's¹⁴ prediction of an increased H_{cb} in the "Heisenberg domain state."

V. CONCLUSIONS

In conclusion, for highly oriented MBE grown $\text{Ni}_{80}\text{Fe}_{20}/\text{Fe}_{50}\text{Mn}_{50}$ systems we have demonstrated that H_{cb} and H_c strongly depend on the crystal orientation. To obtain maximum biasing at a minimum coercive field a [111]-oriented layer system is favorable. No obvious relation between the strength of the biasing and the compensated or uncompensated nature of the FM/AF interface in the [111], [001], or [110] oriented bilayers was found. However, we observe that the (110) samples behave differently in that they show a high in-plane anisotropy. The observation that H_{cb} and H_c depends on the in-plane direction of the field applied during growth and measurement for the (001) samples, giving a higher H_{cb} for $H \parallel [110]$, is consistent with the <111> spin model for the antiferromagnetic layer.

¹W. H. Meiklejohn and C. P. Bean, Phys. Rev. **102**, 1413 (1956); **105**, 904 (1957).

- ²M. J. Carey and A. E. Berkowitz, J. Appl. Phys. **73**, 6892 (1993).
- ³O. Massenet and R. Montmory, C. R. Acad. Sci. Paris **258**, 1752 (1964); O. Massenet, R. Montmory, and L. Néel, IEEE Trans. Magn. **MAG-1**, 63 (1965).
- ⁴R. D. Hempstead, S. Krongelb, and D. A. Thompson, IEEE Trans. Magn. **MAG-14**, 521 (1978).
- ⁵C. Tsang and R. E. Fontana, IEEE Trans. Magn. **MAG-18**, 1149 (1982).
- ⁶B. Dieny, V. S. Speriosu, S. S. P. Parkin, B. A. Gurney, D. R. Wilhoit, and D. Mauri, Phys. Rev. B **43**, 1297 (1991).
- ⁷C. Tsang, N. Heiman, and K. Lee, J. Appl. Phys. **52**, 2471 (1981); C. Tsang and K. Lee, *ibid.* **53**, 2605 (1982).
- ⁸J. H. Greiner, J. Appl. Phys. **37**, 1474 (1966).
- ⁹C. Schlenker, S. S. P. Parkin, J. C. Scott, and J. K. Howard, J. Magn. Mater. **54-57**, 801 (1986).
- ¹⁰A. P. Malozemoff, J. Appl. Phys. **63**, 3874 (1988).
- ¹¹D. Mauri, H. C. Siegmann, P. S. Bagus, and E. Kay, J. Appl. Phys. **62**, 3047 (1987).
- ¹²S. S. P. Parkin, V. R. Deline, R. O. Hilleke, and G. P. Felcher, Phys. Rev. B **42**, 10 583 (1990).
- ¹³A. P. Malozemoff, Phys. Rev. B **35**, 3679 (1987).
- ¹⁴A. P. Malozemoff, Phys. Rev. B **37**, 7673 (1988).
- ¹⁵H. Umebayashi and Y. Ishikawa, J. Phys. Soc. Jpn. **21**, 1281 (1966), Y. Endoh, and Y. Ishikawa, *ibid.* **30**, 1614 (1971).
- ¹⁶K. T.-Y. Kung, L. K. Louie, and G. L. Gorman, J. Appl. Phys. **69**, 5634 (1991).
- ¹⁷C. Hwang, R. H. Geiss, and J. K. Howard, J. Appl. Phys. **64**, 6115 (1988).
- ¹⁸H. Fujimori, X. Lin, and H. Morita, J. Phys. C **8**, 49, 1931 (1988).
- ¹⁹M. F. Toney, Ching Tsang, and J. K. Howard, J. Appl. Phys. **70**, 6227 (1991).
- ²⁰A. Layadi, J.-W. Lee, and J. O. Artman, J. Appl. Phys. **63**, 3808 (1988).
- ²¹E.g., C. P. Bean, J. Appl. Phys. **26**, 1381 (1955), V. E. Osukhovskiy, Y. D. Vorob'ev, L. A. Chebotkevich, I. V. Lobov, and V. I. Malyutin, Phys. Met. Metall. **57**, 37 (1984).
- ²²V. S. Speriosu, D. A. Herman, I. L. Sanders, and T. Yogi, IBM J. Res. Develop. **34**, 884 (1990).
- ²³S. S. P. Parkin and V. S. Speriosu, in *Magnetic Properties of Low-Dimensional Systems II*, Springer Proceedings in Physics Vol. 50 (Springer, New York, 1990), p. 110.
- ²⁴O. Allegranza and M.-M. Chen, J. Appl. Phys. **73**, 6218 (1993).
- ²⁵T. G. S. M. Rijks *et al.* (to be published).
- ²⁶M. A. Russak, S. M. Rossmagel, S. L. Cohen, T. R. McGuire, G. J. Scilla, C. V. Jahnes, J. M. Baker, J. J. Cuomo, and C. Hwang, J. Electrochem. Soc. **136**, 1793 (1989).
- ²⁷D. Mauri, E. Kay, D. Scholl, and K. Howard, J. Appl. Phys. **62**, (1987).
- ²⁸J. K. Howard and T. C. Huang, J. Appl. Phys. **64**, 6118 (1988).

Magnetic properties of epitaxial MnAl/NiAl magnetic multilayers grown on GaAs heterostructures (invited)

T. L. Cheeks, J. P. Harbison, M. Tanaka,^{a)} D. M. Hwang, T. Sands,
and V. G. Keramidas

Bellcore, Red Bank, New Jersey 07701

New ultrathin epitaxial magnetic multilayers consisting of ferromagnetic τ MnAl and nonmagnetic NiAl have been prepared on GaAs by molecular beam epitaxy. The magnetic and magneto-optic properties of these multilayers and the effect of incorporating nonmagnetic NiAl into the structure have been investigated. Perpendicular magnetization was confirmed and the remnant magnetization and coercivity were improved compared to τ MnAl thin films. In addition, by systematically changing the thickness of the NiAl layer the magnetic properties could be controlled. We discuss these issues and compare the magnetic and magneto-optic properties of these structures with other epitaxial magnetic structures.

A variety of novel thin films and heterostructures have been made possible due to the recent progress in heteroepitaxial growth techniques. One unique combination is the epitaxial growth of ferromagnetic metals on compound semiconductors for a new class of potential devices that exploit the properties of both materials. This requires compatible materials that retain both their magnetic and semiconducting properties during growth. In recent years epitaxial growth of ferromagnetic metal films, such as Fe on GaAs have been demonstrated by Prinz.¹ This work generated a great deal of interest in the properties of single crystal ultrathin magnetic layers. Prinz² describes the potential of these materials for devices such as magnetic memory elements using magnetic sandwiches and spin injection devices. Although many applications require the magnetization to be in-plane, there are a number of applications that require the magnetization to be perpendicular to the film plane. This configuration not only allows higher density magnetic and magneto-optic recording, but also allows using the magnetic field to influence the electrons in an underlying semiconductor or to use the magneto-optic properties of the magnetic thin film to control underlying optoelectronic devices.

Recently, Sands and co-workers^{3,4} reported successful growth of epitaxial, perpendicularly magnetized, ferromagnetic τ MnAl films on {100} GaAs by molecular beam epitaxy (MBE). The τ phase of MnAl in the bulk has a Curie temperature of 380 °C, a saturation magnetization of 490 emu/cm³ and an intrinsic coercivity of 4.6 kOe.⁵ It is the only ferromagnetic phase in the bulk τ MnAl system and can be formed in the bulk by rapid cooling from the high-temperature hexagonal phase. Other techniques, such as evaporation⁶ and magnetron sputtering⁷ have been used to deposit polycrystalline τ MnAl films, but stabilizing the τ phase was difficult. It was found that heteroepitaxy helps to align the c axis of the tetragonal unit cell, which is the direction of easy magnetization, along the direction perpendicular to the substrate. The perpendicular magnetization of τ MnAl thin films was demonstrated by the extraordinary Hall effect (EHE).³ The measurements showed a hysteretic

behavior with rectangular shaped loops and 100% remnance. The remnant magnetization (M_r) of the films was 171 emu/cm³ with a coercivity (H_c) of 5.03 kOe and magneto-optic Kerr rotation of 0.16°. In addition, the integrity of the interfaces between the magnetic metal and the underlying (Al,Ga)As could be maintained as indicated by the Schottky diode characteristics.⁹

Because many applications require higher M_r (>200 emu/cm³), lower values of H_c (0.5 kOe < H_c < 3.0 kOe) and a higher magneto-optic Kerr rotation (>0.3°) in addition to a square hysteresis, we have investigated other material systems. The possibility of improving the magnetic and magneto-optic properties has been explored by growing thin films such as (Mn,Ni)Al,^{10,11} MnGa,¹² (Mn,Ni)Ga,¹³ and magnetic multilayers.^{14,15}

The addition of up to 4 at. % Ni to τ MnAl sputtered films has led to higher M_r and H_c .⁷ We have shown¹¹ that in epitaxial τ MnAl films with up to 17 at. % Ni a similar increase in magnetization was not observed most probably due to the coherency that existed between the films and the GaAs. Unlike τ MnAl, which is a metastable phase, thermodynamically stable epitaxial films of MnGa with 55%–60% Mn have been grown successfully.¹² An M_r of 225 emu/cm³ and H_c of 3.15 kOe have been measured, which represents an improvement over the magnetic properties of τ MnAl films. Similarly, the addition of Ni to MnGa thin films resulted in decreasing the perpendicular magnetization.¹³

In the past, semiconductor superlattices have had a tremendous impact on the fundamental physics of semiconductors and device applications. Ultrathin multilayers and heterostructures of dissimilar metallic compounds may also have the same potential. A new class of ultrathin epitaxial magnetic multilayers consisting of ferromagnetic metal τ MnAl and nonmagnetic metal NiAl have been grown recently by MBE.¹⁵ These new structures allow further exploitation of the accurately controlled thicknesses and abrupt interfaces obtained by MBE. Furthermore, the possibility of controlling the magnetic properties within these unique epitaxial structures opens up new opportunities for novel device applications.

In this paper, we discuss the magnetic and magneto-optic

^{a)}On leave from the Dept. of Electrical Engineering, The University of Tokyo, 7-3-1 Hongo, Bunkyo-ku Tokyo 113, Japan.

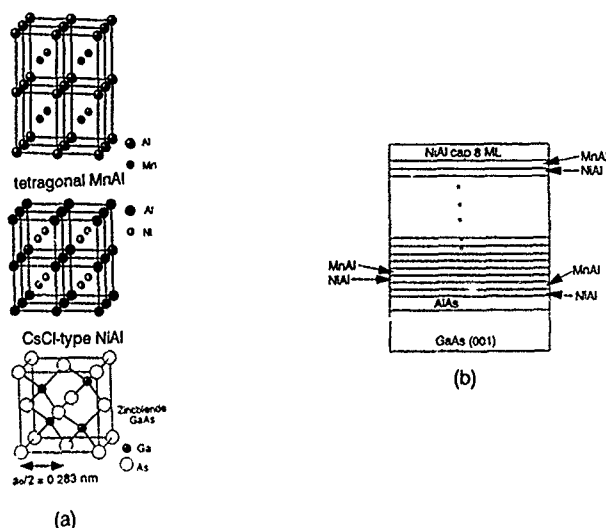


FIG. 1. Schematic of crystal structures of τ MnAl, NiAl, and GaAs, and the multilayer structure of MnAl/NiAl grown on GaAs.

properties of ultrathin τ MnAl/NiAl multilayers films. We describe these properties as a function of systematically increasing the NiAl film thickness within the multilayer structure. Furthermore, we compare the properties of the multilayer films with that of τ MnAl, (Mn,Ni)Al, and MnGa/NiGa magnetic multilayers.

The crystal structure of τ MnAl is an ordered CuAu-type tetragonal lattice with alternating planes of Mn and Al along the c axis as shown in Fig. 1(a). In bulk quenched films, the basal plane lattice parameter is $a_0=0.277$ nm and $c_0=0.354$ nm.⁵ Stoichiometric NiAl is a nonmagnetic intermetallic with a cubic CsCl-type crystal structure with a lattice constant of $a_0=0.289$ nm. The basal plane lattice parameters for both NiAl and τ MnAl are close to half of the lattice constant of GaAs ($a_0=0.283$ nm). Thus the lattice mismatch for NiAl on GaAs is +2.1% and τ MnAl on GaAs is -2.1%. The measured lattice parameters for MBE grown epitaxial τ MnAl on GaAs by x-ray diffraction show that $a_0=0.283$ nm and $c_0=0.345$ nm indicating that coherency between τ MnAl and the underlying GaAs result in a reduced tetragonality compared to bulk crystals.³

In this study, a series of multilayer samples were grown with alternating Y monolayers of τ MnAl and X monolayers of NiAl. A monolayer (ML) thickness of MnAl/NiAl is defined here as the Al-Al spacing in the ordered CuAu-type tetragonal structure (CsCl-type structure).¹⁵ The number of τ MnAl monolayers was held constant at $Y=3$ ML (1.05 nm) while the number of NiAl monolayers ranged from $X=1$ –6 ML. This corresponds to a NiAl thickness of 0.35 to 2.1 nm. The τ MnAl thickness was held constant because thicker layers would influence the magnetic properties. There were ten periods for all samples resulting in a total τ MnAl thickness of 10.5 nm.

The MnAl/NiAl multilayers were grown using a conventional MBE equipped with Mn and Ni effusion cells. The multilayer structures were grown beginning with a semi-insulating (001) GaAs substrate as shown in the schematic in Fig. 1(b). Above the substrate, a 100-nm-thick undoped

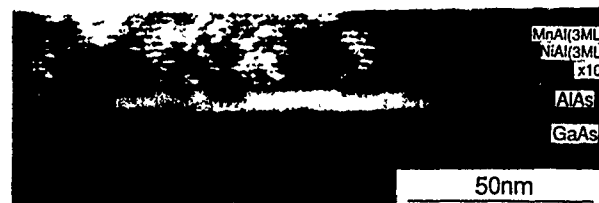


FIG. 2. Cross-sectional transmission electron microscopy taken from a MnAl(3 ML)/NiAl(3 ML) film with ten periods.

GaAs buffer layer and a 5-nm-thick AlAs layer were grown at 580 °C. Following the heterostructure growth, the substrate temperature was cooled to 250 °C and the arsenic flux eliminated. The multilayers were then grown at a substrate temperature of 250 °C in an arsenic-free ambient. The metal layers were grown using a template approach in which 1 ML of Ni was initially deposited on the AlAs surface and then Ni and Al at a 1:1 ratio were codeposited at a growth rate of 0.052 $\mu\text{m/h}$. Then, τ MnAl was grown on the CsCl-type (001) NiAl surface by codeposition of Mn and Al at a growth rate of 0.061 $\mu\text{m/h}$. The Mn/Al ratio was 60/40 in order to ensure the formation of the ferromagnetic τ phase with good magnetic properties.¹⁵ Alternating monolayers of τ MnAl and NiAl were repeated to form a structure with the desired number of periods. Finally, a 8-ML-thick NiAl cap was grown on top and a postgrowth anneal of 350 °C for 2 min was performed. The time and temperature of the postgrowth anneal was optimized in order to produce the best magnetic properties. The anneal was found to be absolutely essential to the obtaining good magnetic properties.

Additional samples, with MnAl(6 ML)/NiAl(3 ML) with five periods and a $\text{Mn}_{30}\text{Ni}_{30}\text{Al}_{40}$ alloy were grown to determine the effect of thicker MnAl multilayers and comparable alloys on the magnetic properties.

The crystalline structure was verified using *in situ* reflection high-energy electron diffraction (RHEED) along the $\langle 110 \rangle$ azimuth during growth. Streaky RHEED patterns¹⁵ were maintained throughout the growth of the multilayers indicating that monocrystalline multilayers with the desired epitaxial orientation of $[110](001)\text{MnAl/NiAl}/[110](001)\text{GaAs}$ were maintained. After the tenth period, the RHEED pattern of the NiAl surface was a little less streaky than the τ MnAl surface which showed very sharp streaks. This indicates that roughness on an atomic scale was present on the NiAl surface under the present growth conditions. The RHEED pattern did not change significantly after the postgrowth anneal. The sharp, streaky RHEED patterns were observed throughout most of the multilayer growth runs which indicates that they were all high-quality monocrystalline films with the proper epitaxial orientations. The RHEED patterns of the multilayers were better than those of τ MnAl, which may be due to the reduction in strain between these layers.

Cross-sectional transmission electron microscopy (TEM) results for a MnAl(3 ML)/NiAl(3 ML) sample is shown in Fig. 2. The figure shows a $\langle 110 \rangle$ bright field image of the multilayer with ten periods grown on AlAs/GaAs. The image shows that the interfaces were very smooth and that compo-

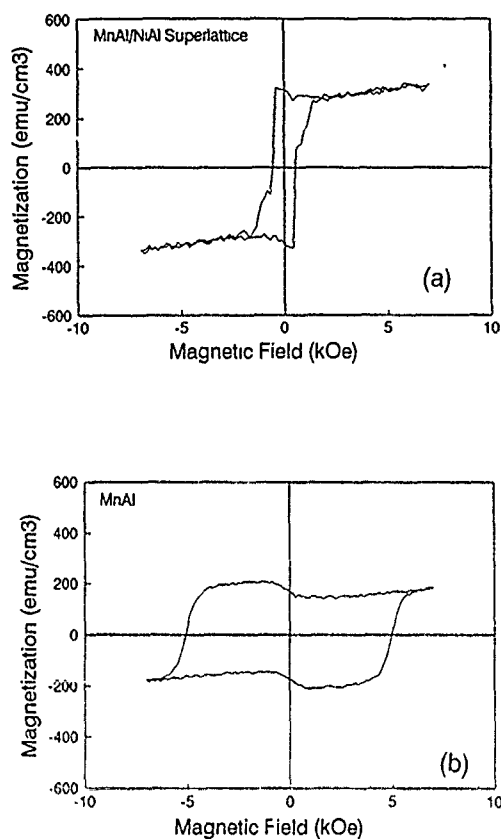


FIG. 3. Magnetization curves of (a) MnAl/NiAl multilayer and (b) π MnAl thin film.

sitional modulation was achieved in such a thin periodic structure. The extremely smooth interfaces indicated that there was little if any interfacial mixing between the π MnAl and the NiAl. Analysis of the diffraction pattern confirmed that the multilayers were stacked with the desired epitaxial orientations of $[110](001)\text{MnAl}/\text{NiAl}/[110](001)\text{GaAs}$ and that the c axis of the tetragonal π MnAl was aligned normal to the substrate. The c_0 lattice parameter of the π MnAl layers was estimated to be 0.33–0.34 nm. This value was less than the 0.354-nm bulk value and slightly less than the 0.345 value for 10-nm-thick MBE grown π MnAl films.¹⁶ This indicates that the π MnAl multilayers showed a significantly reduced tetragonality possibly due to elastic strain at the interface.

Measurements of the magnetic properties of the MnAl/NiAl multilayers were performed using vibrating sample magnetometer (VSM), magneto-optic Kerr effect (θ_k) measurements and the extraordinary Hall effect at room temperature. The multilayer samples were all measured by VSM in a magnetic field up to 10 kOe. Figure 3(a) shows a hysteresis loop from a MnAl(3 ML)/NiAl(3 ML) sample with a slightly different annealing condition. The nearly square hysteresis loop indicates perpendicular magnetization and the M_r and H_c measured 314 emu/cm³ and 0.550 kOe, respectively. For comparison, the hysteresis loop of a π MnAl thin film is shown in Fig. 3(b). The figure shows that not only was the magnetization improved, but the H_c was also dramatically reduced.

The M_r and H_c values obtained for this multi-layer film

TABLE I. Comparison of magnetic properties in MnAl(3 ML)/NiAl(3 ML), π MnAl, Mn₃₀Ni₃₀Al₄₀, and MnGa(6 ML)/NiGa(6 ML).

Sample	M_r (emu/cm ³)	H_c (kOe)	θ_k (degree)
MnAl(3 ML)/NiAl(3 ML)	314	0.550	0.1
π MnAl	171	5.029	0.16
Mn ₃₀ Ni ₃₀ Al ₄₀	57	1.215	...
MnGa(6 ML)/NiGa(6 ML)	302	2.29	...

were higher than those obtained for π MnAl, (Mn,Ni)Al films and MnGa/NiGa multilayers. Table I compares the M_r , H_c , and θ_k of these four structures. The M_r and H_c of a 10-nm-thick π MnAl film clearly differs from that of the MnAl(3 ML)/NiAl(3 ML) multilayer such that the M_r (171 emu/cm³) was lower and the H_c was higher (5.029 kOe) than the multilayer. In addition, a similar thickness Mn₃₀Ni₃₀Al₄₀ alloy of comparable composition to the multilayer also showed a somewhat reduced M_r (57 emu/cm³) and a higher H_c (1.215 kOe) than the multilayer. Also, multilayers of MnGa(6 ML)/NiGa(6 ML) showed a reduced M_r and higher H_c for even thicker magnetic (MnGa) layers.¹⁴ Thus for applications that require integration of perpendicularly magnetized materials with underlying semiconductor electronics the higher magnetization and lower coercivity measured here for MnAl/NiAl multilayers seem quite desirable.

The effect of incorporating NiAl into a multilayer structure was studied with the series of samples with the same growth and annealing conditions. Figure 4 shows the effect of increasing the NiAl thickness on the M_r and H_c in the MnAl(3 ML)/NiAl(X ML) samples. As the NiAl thickness

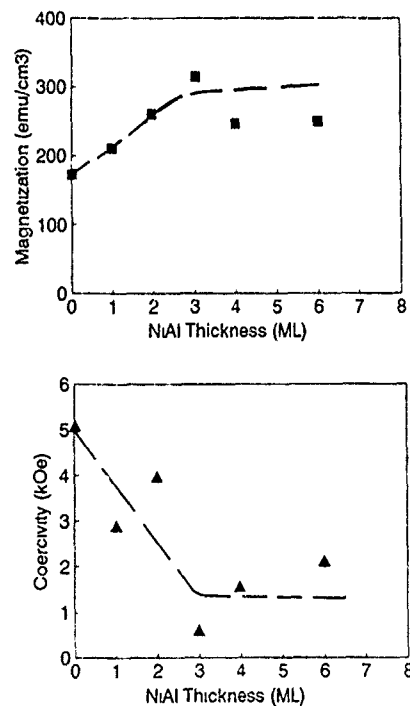


FIG. 4. Measurement of (a) remnant magnetization and (b) coercivity of MnAl(3 ML)/NiAl(X) with $X=1-6$ ML multilayers as a function of NiAl thickness.

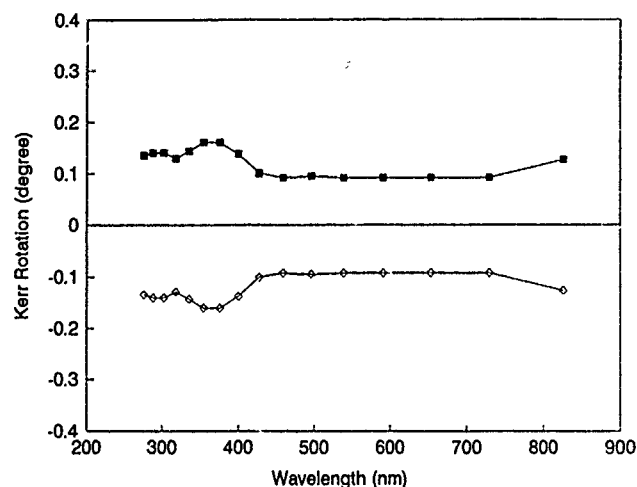


FIG. 5. Magneto-optic Kerr rotation of MnAl(3 ML)/NiAl(3 ML) as a function of wavelength.

(X) increases, the M_r increases from 171 emu/cm^3 to as high as 314 emu/cm^3 for $X=3 \text{ ML}$. Beyond 3 ML the M_r remained fairly constant. The figure also shows that the H_c decreases to a value of 0.55 kOe for $X=3 \text{ ML}$. In all cases, the M_r of the multilayer structures was higher than the πMnAl , (Mn,Ni)Al, and MnGa/NiGa samples of similar thickness. As expected, the M_r increased if the thickness of the πMnAl was increased, as indicated by measurements of a MnAl (6 ML)/NiAl(3 ML) multilayer with a M_r of 342 emu/cm^3 .

The magneto-optic Kerr rotation was measured on a MnAl (3 ML)/NiAl(3 ML) sample as a function of the wavelength from 830 to 270 nm. The rotation was measured after the samples had been poled either parallel or antiparallel to the film normal by exposure to a 8.0-kOe magnetic field. The Kerr rotation, shown in Fig. 5 was about 0.10° at 800 nm and remained fairly constant between 450 and 800 nm . The lower Kerr rotation measured for the multilayer compared to πMnAl may be attributed in part to 2.8-nm -thick nonmagnetic NiAl cap on the surface of the structure. Both rotation values are slightly lower than the 0.3° to 0.4° values reported for TbFeCo, but similar to 0.1° – 0.2° reported for Co/Pt multilayers.¹⁷ A reasonable value of the Kerr rotation is important particularly for applications such as magneto-optic recording or devices which utilize the rotation of polarization for the modulation of light.

The extraordinary Hall effect measurements performed on MnAl(3 ML)/NiAl(X ML) multilayers were all nearly square. The EHE is caused by the asymmetric scattering of electrons by magnetic species in a ferromagnetic material. A square shaped hysteresis loop therefore indicates a large component of magnetization perpendicular to the film plane and the Hall resistance is a measure of the film quality. Samples were fabricated into a Hall bar configuration by photolithography and chemical etching. Typically, a $100\text{-}\mu\text{A}$ dc current was applied to a $200\text{-}\mu\text{m}$ -wide Hall bar that was placed into a magnetic field oriented perpendicular to the film plane.

Figure 6 shows the results of a $200\text{-}\mu\text{m}$ Hall bar mea-

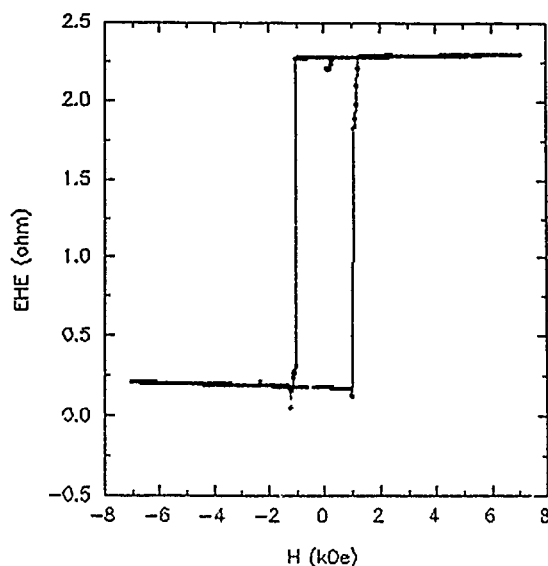


FIG. 6. Extraordinary Hall effect characteristics of a MnAl(3 ML)/NiAl(3 ML) multilayer measured at room temperature.

surement in which a rectangular hysteresis loop was obtained. Switching of the magnetization direction occurred within an increment of $200\text{--}400 \text{ kOe}$. The switching field needed to reach saturation is believed to be due to a domain wall sweeping across the intersection of the Hall bar. The saturation values of the Hall resistance were in the range of $2.0\text{--}2.5 \Omega$, which are considered large enough for electrical readout.¹⁵ Single step hysteresis loops were observed for all the measured samples. This differed from the multisteped EHE measured for MnGa/NiGa multilayers which may be applicable to multilevel signal recording.¹⁴ The reason for these steps or lack of them is not clear, but may be due to less strain energy within the πMnAl multilayers than the MnGa multilayers.

The improved magnetization with thicker NiAl layers may in part be due to the reduced tetragonality observed in these structures compared to πMnAl . The c/a ratio decreased from 1.29 in the bulk, to 1.22 in epitaxial πMnAl to about 1.18 for MnAl (3 ML)/NiAl(3 ML) multilayers. This suggests a decrease in the tetragonality which appears to be coincident with a rise in remnant magnetization. Morisako⁷ suggested that as both the c_0 and a_0 lattice constants decrease the magnetization of πMnAl should increase.⁷ It was suggested that the elongated distortion of the tetragonal lattice weakens the exchange interaction between the electrons. Therefore, if the lattice constants are reduced, a higher magnetization would be obtained. In general, this may explain the improved magnetization within an optimized MnAl (3 ML)/NiAl(3 ML) multilayer. Hence, the role of strain on both magnetization and coercivity may be an important parameter that requires further investigation in order to exploit tunable magnetic properties within epitaxially designed magnetic thin films.

In summary, we have discussed the magnetic and magneto-optic properties of ultrathin ferromagnetic πMnAl and nonmagnetic NiAl multilayers grown by MBE on (Al,Ga) As heterostructures. These structures showed per-

pendicular magnetization, improved remnant magnetization and a lower coercivity compared to thin film γ -MnAl. Both the remnant magnetization and coercivity can be adjusted and further improved by incrementally increasing the monolayer thickness of the nonmagnetic NiAl layer. The magneto-optic and magnetic properties described here may be suitable for device applications which include magnetically controlled optoelectronics and nonvolatile memory elements.

¹G. A. Prinz, *Science* **250**, 1092 (1990).

²G. A. Prinz, B. T. Jonker, J. J. Krebs, J. M. Ferrari, and F. Kovanic, *Appl. Phys. Lett.* **48**, 1756 (1986).

³T. Sands, J. P. Harbison, M. L. Leadbeater, S. J. Allen, Jr., G. W. Hull, R. Ramesh, and V. G. Keramidas, *Appl. Phys. Lett.* **57**, 2609 (1990).

⁴J. P. Harbison, T. Sands, R. Ramesh, L. T. Florez, B. J. Wilkens, and V. G. Keramidas, *J. Cryst. Growth* **111**, 978 (1991).

⁵H. Kono, *J. Phys. Soc. Jpn.* **13**, 1444 (1958).

⁶J. X. Shen, R. D. Kirby, and D. J. Sellmyer, *J. Magn. Magn. Mater.* **81**, 107 (1989).

⁷A. Morisako, N. Kohshiro, and M. Matsumoto, *J. Appl. Phys.* **61**, 4281 (1987).

⁸T. L. Cheeks, M. J. S. P. Brasil, T. Sands, J. P. Harbison, S. J. Allen, Jr., D. E. Aspnes, and V. G. Keramidas, *Appl. Phys. Lett.* **60**, 1393 (1992).

⁹T. L. Cheeks, R. E. Nahory, T. Sands, J. P. Harbison, M. J. S. P. Brasil, H. L. Gilchrist, S. A. Schwarz, M. A. Pudensi, S. J. Allen, Jr., L. T. Florez, and V. G. Keramidas, *Inst. Phys. Conf. Ser. No 120*, 101 (1992).

¹⁰J. P. Harbison, T. Sands, J. De Boeck, T. L. Cheeks, P. Miceli, M. Tanaka, L. T. Florez, B. J. Wilkens, H. L. Gilchrist, and V. G. Keramidas, *J. Cryst. Growth* **127**, 650 (1993).

¹¹T. L. Cheeks, M. J. S. P. Brasil, J. De Boeck, J. P. Harbison, T. Sands, M. Tanaka, A. Scherer, and V. G. Keramidas, *J. Appl. Phys.* **73**, 6121 (1993).

¹²M. Tanaka, J. P. Harbison, T. Sands, B. Phillips, T. L. Cheeks, J. De Boeck, L. T. Florez, and V. G. Keramidas, *Appl. Phys. Lett.* **62**, 1565 (1993).

¹³M. Tanaka, J. P. Harbison, T. Sands, B. A. Phillips, J. De Boeck, T. L. Cheeks, L. T. Florez, and V. G. Keramidas, *Mater. Res. Proc.* (to be published).

¹⁴M. Tanaka, J. P. Harbison, T. Sands, B. Phillips, T. L. Cheeks, J. De Boeck, L. T. Florez, and V. G. Keramidas, *Appl. Phys. Lett.* **63**, 696 (1993).

¹⁵M. Tanaka, J. P. Harbison, T. Sands, T. L. Cheeks, J. De Boeck, D. M. Hwang, L. T. Florez, and V. G. Keramidas, *Appl. Phys. Lett.* **63**, 839 (1993).

¹⁶T. Sands, J. De Boeck, J. P. Harbison, A. Scherer, H. L. Gilchrist, T. L. Cheeks, P. F. Miceli, R. Ramesh, and V. G. Keramidas, *J. Appl. Phys.* **73**, 6399 (1993).

¹⁷F. J. A. M. Greidanus and W. B. Weber, *Mater. Res. Bull.* **15**, 31 (1990).

Magneto-optical and structural properties of BiAlDyIG/Fe multilayers

J. X. Shen and K. W. Wierman

Behlen Laboratory of Physics and Center for Materials Research and Analysis, University of Nebraska, Lincoln, Nebraska 68588-0113

Y. B. Zhang

Department of Electrical Engineering and Center for Microelectronic and Optical Materials Research, University of Nebraska, Lincoln, Nebraska 68588-0113

R. D. Kirby

Behlen Laboratory of Physics and Center for Materials Research and Analysis, University of Nebraska, Lincoln, Nebraska 68588-0113

J. A. Woollam

Department of Electrical Engineering and Center for Microelectronic and Optical Materials Research, University of Nebraska, Lincoln, Nebraska 68588-0113

D. J. Sellmyer

Behlen Laboratory of Physics and Center for Materials Research and Analysis, University of Nebraska, Lincoln, Nebraska 68588-0113

Bi- and Al-doped DyIG(y Å)/Fe(x Å) ($y=50$ to 130 Å and $x=5$ to 15 Å) multilayer thin films were made by magnetron sputtering onto Si(111) substrates. Rapid thermal annealing was used to crystallize these garnet multilayers. The crystallized multilayer samples possess well-defined interfaces. Atomic force microscopy showed that the annealed samples had smooth surfaces, with small grain sizes (~ 30 to 80 nm). All of the samples had perpendicular magnetic anisotropy with very square hysteresis loops. The coercivity was found to vary from 600 Oe to 2 kOe, depending on Fe thickness and annealing conditions. The measured figure of merit $\sqrt{R(\theta_K^2 + \epsilon_K^2)}$ at 420 nm was bigger than 0.4 , suggesting that Bi- and Al-doped DyIG/Fe multilayers are promising candidates for blue light magneto-optical recording applications.

Bi-doped DyIG (garnet) thin films have moderate perpendicular magnetic anisotropy and large magneto-optical Faraday effect in the blue region of the spectrum. The magnetic parameters such as the coercivity H_c and the saturation magnetization M_s are easily varied through changes in the composition. These properties are the key for the materials to be used as a magneto-optical (MO) recording media at blue laser wavelengths.¹⁻⁵ Unfortunately, the garnets are polycrystalline with a large grain size and a rough surface, which will give a substantial media noise which is absent in the rare-earth-transition metal (RE-TM) amorphous MO recording media. Suzuki^{5,6} demonstrated that by using rapid thermal annealing (RTA), where the heating ramp rate can exceed 50 °C/s, the grain size can be reduced to about 40 nm and the surface morphology can also be improved. Suzuki⁶ also showed that the microstructure of the garnet films could be further improved through multilayering the garnet with Cr, Co, and SiO₂; this is because the space layer will interrupt the growth of garnet. In this paper, we will report the microstructure and the magneto-optical properties of thin films of Bi- and Al-doped DyIG multilayered with Fe.

Dy_{1.6}Bi_{1.4}Fe_{1-x}Al_xO₁₂ ($x=0.6$ to 1.0) and Fe multilayers were deposited on Si(111) and quartz room-temperature substrates by rf (for garnet) and dc (for Fe) magnetron sputtering in a pure Ar atmosphere. The Si was used for the purpose the RTA. Standard sintering techniques were used to make the ceramic garnet target. The individual garnet layer thickness was varied between 50 and 130 Å, while the Fe individual layer thickness was varied from 5 to 15 Å. We adjusted the total number of bilayers to keep the total sample thickness

roughly at 1000 Å. As-deposited films are amorphous. The samples were then crystallized in air using a home-built rapid thermal annealing system consisting of a 1 -kW halogen lamp with the light focused on the sample by an ellipsoidal mirror. The maximum heating ramp rate using this system was about 30 °C/s. The samples were typically annealed at 650 °C for 2 to 5 min. The microstructure and surface morphology of both as-deposited and annealed samples were investigated by atomic force microscopy (AFM). Both large- and small-angle x-ray diffraction were used to characterize the crystalline and multilayer structures. Kerr rotation measurements were carried out over the wavelength range 350 – 600 nm in magnetic fields up to 12 kOe.

After rapid thermal annealing, large-angle x-ray diffraction spectra shown that a single garnet phase was formed, with no trace of pure Fe diffraction peaks. The garnet grains are totally randomly oriented, with no preferred orientation in these multilayer thin films. Figure 1 shows the small-angle x-ray diffraction spectra both before and after annealing of a [BiAlDyIG(100 Å)/Fe(9 Å)] $\times 10$ sample. The two spectra both show six superlattice peaks, indicating that there are well-defined interfaces between the garnet and Fe layers even after a 650 °C RTA for 2 min. One surprising result is that the superlattice peaks of the annealed samples are slightly higher than those of the as-deposited samples, which suggests that the crystallization of the garnet improves the interface definition. However, more detailed studies are needed to fully understand this result. After crystallization, the positions of all the superlattice peaks shift toward larger angles, indicating that the crystallized garnet layers are

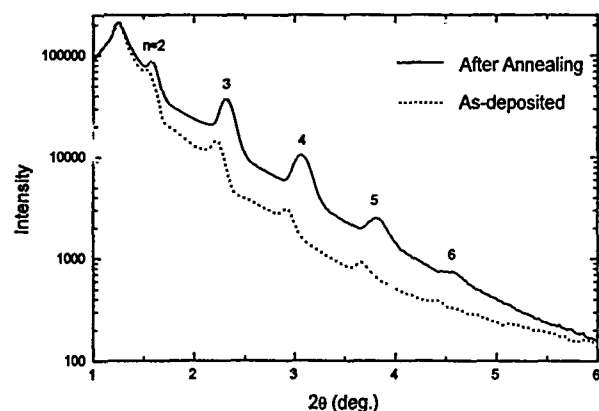


FIG. 1. Small-angle x-ray diffraction spectrum of $[\text{BiAlDyIG}(100 \text{ Å})/\text{Fe}(9 \text{ Å})] \times 10$ multilayers before (dashed line) and after (solid line) annealing.

denser than the as-deposited amorphous layers.

We characterized the microstructure of our multilayer samples using atomic force microscopy. AFM pictures show that as-deposited amorphous multilayer films have little surface structure, with a surface roughness of $\sim 1 \text{ nm}$. Figure 2 shows an AFM picture of $[\text{BiAlDyIG}(100 \text{ Å})/\text{Fe}(11 \text{ Å})] \times 9$ after 5 min RTA. From this picture we estimate the grain size to be roughly 80 nm , which is much smaller than the grain size of $1 \mu\text{m}$ typically obtained with oven-annealed single layer garnet films.⁷ The surfaces of annealed samples are considerably rougher than those of the as-deposited films. An estimate of the peak-to-peak surface roughness for the sample of Fig. 2 is about 5 nm . Although the observed 80-nm grain size is much smaller than $1 \mu\text{m}$, it is still far too large for magneto-optical recording applications. In order to further reduce the grain size and improve the surface smoothness, a shorter annealing time was used. Figures 3 and 4 show AFM pictures of a $[\text{BiAlDyIG}(100 \text{ Å})/\text{Fe}(9 \text{ Å})] \times 10$ multilayer film with different vertical scales. Assuming that the bumps observed in these figures are grains, we estimate the average grain size to be 20 to 30 nm . A $20 \mu\text{m} \times 20 \mu\text{m}$ scan (Fig. 4) shows the surface morphology of this same sample. Comparing Figs. 2 and 4, we can see clearly that shortening the annealing time is a very effective way of ob-

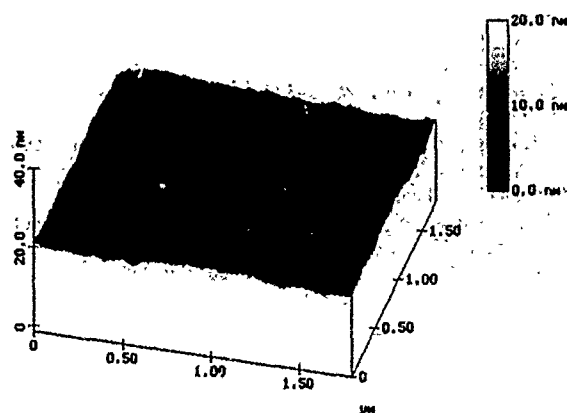


FIG. 2. AFM picture of $[\text{BiAlDyIG}(100 \text{ Å})/\text{Fe}(11 \text{ Å})] \times 11$ after 5-min rapid thermal annealing at 650 °C .

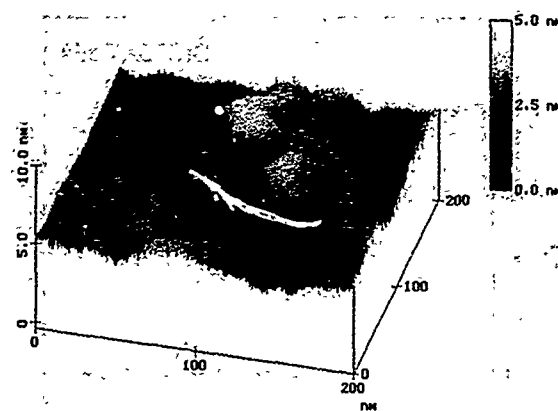


FIG. 3. AFM picture of $[\text{BiAlDyIG}(100 \text{ Å})/\text{Fe}(9 \text{ Å})] \times 10$ after 2-min rapid thermal annealing at 650 °C .

taining smooth surfaces. We estimate the peak-to-peak surface roughness to be 2 to 3 nm .

Although these results regarding the grain size must be confirmed by transmission electron microscopy (TEM) studies, we can safely conclude that rapid thermal annealing will reduce the grain size and multilayering the garnet with Fe (or other elements) will reduce the grain size further and substantially improve the surface morphology.

Figure 5 shows a Kerr hysteresis loop for a $[\text{BiAlDyIG}(75 \text{ Å})/\text{Fe}(5 \text{ Å})] \times 13$ sample which had been annealed at 650 °C for 5 min . The very square loop indicates that the sample has perpendicular magnetic anisotropy. Since our x-ray diffraction measurements show that the grains are randomly oriented, this perpendicular anisotropy must come from the stress.⁸ The measured Kerr rotation is 1.2° at a wavelength of 410 nm and this value is independent of annealing time after more than 60-s annealing. This measured value is the combination of both Kerr and Faraday rotations, and it includes the effects of optical interference in the sample. The coercivity of this particular sample is $\sim 1 \text{ kOe}$, and it sensitively depends on the annealing conditions and the individual garnet and Fe layer thicknesses. The figure of merit $\sqrt{R(\theta_K^2 + \epsilon_K^2)}$ for $[\text{BiAlDyIG}(104 \text{ Å})/\text{Fe}(5 \text{ Å})] \times 14$ with

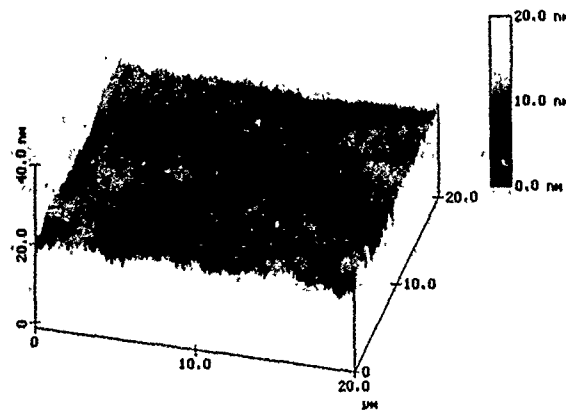


FIG. 4. Surface morphology of $[\text{BiAlDyIG}(100 \text{ Å})/\text{Fe}(9 \text{ Å})] \times 10$ after 2-min rapid thermal annealing at 650 °C .

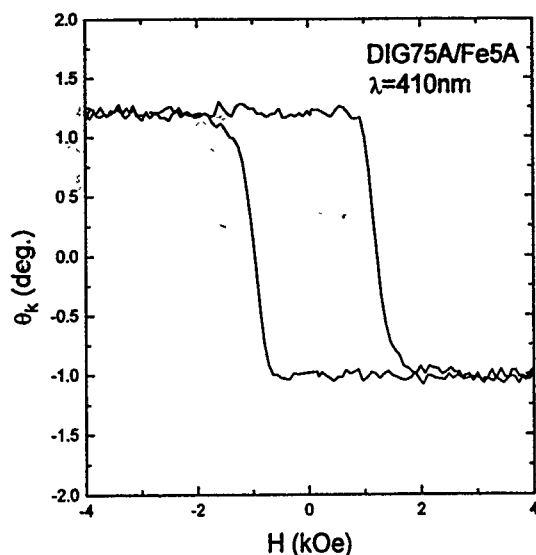


FIG. 5. Kerr hysteresis loop of $[\text{BiAlDyIG}(75 \text{ Å})/\text{Fe}(5 \text{ Å})] \times 13$ measured at a wavelength of 410 nm at room temperature. The magnitude of the rotation includes contributions from Kerr and Faraday rotations, as well as interference enhancements.

Al reflect layer is 0.4 to 0.6 between the 400- and 500-nm region. In our experiments, we have found that if the individual Fe layer thickness is held fixed at 5 Å, the coercivity oscillates between 0.6 and 1.5 kOe as the individual garnet layer thickness is varied from 50 to 130 Å. This variation is not due to the shifting of the compensation temperature as the compensation temperature is about 170 K for most of our samples and is independent of the individual garnet layer thickness. These oscillations are difficult to understand and they need further investigation. A possible explanation might be related to thickness-dependent defects or inhomogeneities of our samples.

Figure 6 shows the dependence of the coercivity on the total number of bilayers for $[\text{BiAlDyIG}(90 \text{ Å})/\text{Fe}(5 \text{ Å})] \times N$, where N is varied from 4 to 24. All these samples were annealed at 650 °C for 2 min with RTA technique. The coercivity decreases with increasing number of bilayers (that is the total thickness of the sample). It should be noted that the samples with N less than ten cannot be crystallized with the annealing condition mentioned above. To crystallize these thin samples either a higher annealing temperature or a longer annealing time is needed. The same situation was also noted for samples with individual garnet layer thicknesses less than 50 Å. This phenomenon is attributed to the increase of the surface-to-volume ratio or the surface tension of the garnet phase with decreasing particle size, as discussed by Cho *et al.*⁹ The surface energy and surface stress usually tends to hinder the nucleation and growth of the garnet

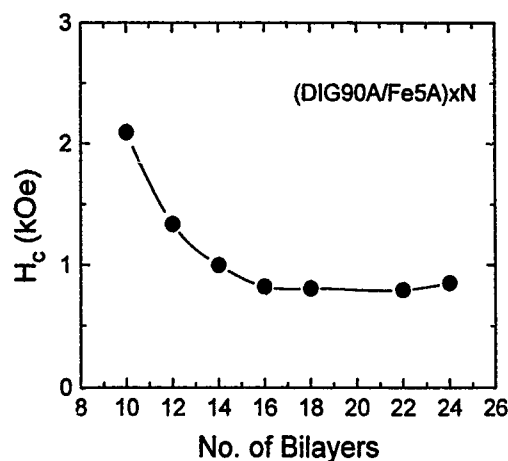


FIG. 6. Coercivity of $[\text{BiAlDyIG}(90 \text{ Å})/\text{Fe}(5 \text{ Å})] \times N$ as a function of the number of bilayers N after 650 °C 5-min annealing.

phase.¹⁰ So the increase in H_c with decreasing number of bilayers may be due to either the smaller grain size or to a mixture of the crystalline and amorphous garnet phases in the thinner samples. The observed smaller saturation magnetization in these samples also support this assumption. Once again, a detailed TEM investigation will be needed to understand these results.

We have successfully made garnet/Fe multilayers with relatively sharp interfaces. Small grains (~ 30 nm) and smooth surfaces were realized by a rapid thermal annealing technique. The multilayers of garnet/Fe have square hysteresis loops with a large coercivity and large magneto-optic activity in the blue portion of the spectrum. These results show that the garnet/Fe multilayers are promising candidates for magneto-optic recording using blue lasers. Systematic studies of how the multilayers affect the magneto-optic behavior and the sample microstructure are underway.

We are thankful to Dr. Z. S. Shan and Dr. T. Suzuki for helpful discussions and to NSF and ARPA for financial support under Grants DMR-9222976, NSF-OSR-9255225, and MDA 972-93-1-009, respectively.

¹P. Hansen, J.-P. Krumme, and D. Mergel, *J. Magn. Soc. Jpn.* **15**, 219 (1991).

²M. Gomi, K. Satoh, and M. Abe, *J. Appl. Phys.* **63**, 3642 (1988).

³A. Itoh and K. Nakagawa, *Jpn. J. Appl. Phys.* **31**, L790 (1992).

⁴K. Shono, S. Kuroda, and S. Ogawa, *IEEE Trans. Magn.* **MAG-27**, 5130 (1991).

⁵T. Suzuki, F. Sequeda, H. Do, T. Huang, and G. Gorman, *J. Appl. Phys.* **67**, 4435 (1990).

⁶T. Suzuki, *J. Appl. Phys.* **69**, 4755 (1991); Co results (private communication).

⁷J.-P. Krumme, V. Doormann, P. Hansen, H. Baumgart, J. Petruzzello, and M. P. A. Viegars, *J. Appl. Phys.* **66**, 4393 (1989).

⁸M. Abe and M. Gomi, *J. Magn. Soc. Jpn.* **11**, 299 (1987).

⁹J. Cho, M. Gomi, and M. Abe, *Jpn. J. Appl. Phys.* **27**, 2069 (1988).

¹⁰W. D. Kingery, H. K. Bowen, and D. R. Uhlmann, *Introduction to Ceramics*, 2nd ed. (Wiley, New York, 1976), Chap. 8, p. 328.

Inverted hysteresis in magnetic systems with interface exchange

M. J. O'Shea

Department of Physics, Cardwell Hall, Kansas State University, Manhattan, Kansas 66506-2601

A.-L. Al-Sharif

Department of Physics, Mu'tah University, Karak, Jordan

The effects of interface exchange on magnetic hysteresis are considered for a variety of situations in a two-phase model in which the phases are coupled antiferromagnetically. This work is motivated by studies of Co-CoO nanophase systems where inverted hysteresis loops, a phenomenon closely related to shifted hysteresis loops, are obtained. Some previous examples of systems with inverted hysteresis loops are reviewed and a two-phase model with uniaxial anisotropy and interface exchange is considered. It should be emphasized that this model cannot completely explain inverted hysteresis loops, but it does show that partially inverted loops can be obtained. Cases where H is not along an anisotropy axis are discussed; it was concluded that some alignment of H with the axis of the stronger anisotropy phase is necessary to obtain partially inverted hysteresis.

Interface exchange, identified over three decades ago,¹ can substantially influence magnetic hysteresis. These effects include (i) shifted hysteresis loops^{1,2} where one magnetic phase provides a bias field to a second magnetic phase while not itself taking part in magnetic reversal and (ii) a more general case in which the biasing phase does take part in the magnetic reversal. In this work we shall briefly review experimental examples of inverted hysteresis loops, a phenomenon in which the forward and reverse branches are shifted in opposite directions so that they completely cross over. We believe that such loops are related to case (ii) above and will consider the extent to which interface exchange models are able to explain this type of hysteresis loop.

Figures 1(a) and 1(b), respectively, show examples of inverted hysteresis loops for a nominally amorphous $Zr_{40}Cu_{50}Mn_{10}$ amorphous alloy³ prepared by rapid quenching and a layered material with a Co-based layer alternating with a Cu layer.⁴ In this latter system the Co-based layer is made up of a dispersion of pure Co and CoO and the layer thickness is less than 10 nm.⁴

The similarity of inverted hysteresis loops to shifted loops suggests that interface exchange, and in particular an antiferromagnetic interface exchange, plays an important role. In order for interface exchange to be important, there must be a large interface area between two magnetic phases present in a system. To achieve this the system must be structured on a very fine scale, usually of the order of nanometers. In the case of the Co-O/Cu system we believe that it is the granular nature of the Co-O layer that is important.⁴ In the case of the amorphous $Zr_{40}Cu_{50}Mn_{10}$ alloy,³ we speculate that a fine grain structure exists here too. The structural correlation length calculated from the x ray for this alloy using the width of the broad amorphous maximum indicates short-range order on the scale of 2.5 nm. Note also that chemical short-range order could be present in this amorphous system as has been found in other amorphous systems.⁵

In this work we report on calculations of magnetic hysteresis in a model with two nonidentical phases, both having uniaxial anisotropy, as a function of (i) anisotropy strength,

(ii) interface exchange strength, and (iii) angle between the anisotropy axes and applied field. We note that we do not expect this model (or any purely magnetic model) to produce completely inverted hysteresis behavior since the area of the loop will always be positive in such model solutions, but we will show that certain aspects of inverted hysteresis may be reproduced in this model. Calculations have been reported on a similar model and it is often assumed that the magnetization in each layer or phase may be described by a single vector M of constant magnitude. This rigid rotation assumption will be correct only in special cases. The strong ferromagnetic exchange in Co suggests that the rigid rotation assumption may have some validity here. Reference 6 has discussed the condition for the assumption of rigid rotation of the spins in a magnetic layer to be valid. We consider two phases, A and B, interacting through an interface exchange.

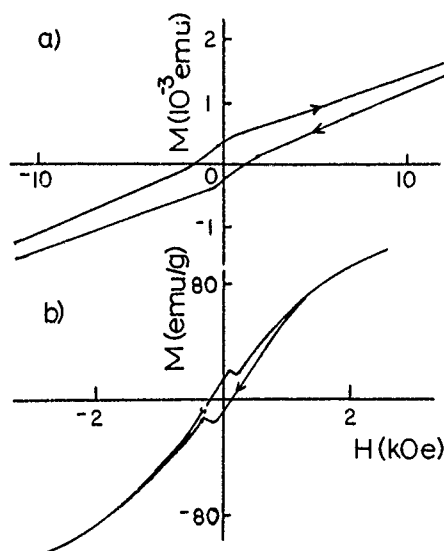


FIG. 1. Hysteresis loops for (a) amorphous $Zr_{40}Cu_{50}Mn_{10}$ (from Ref. 3), (b) a (Co-O)/Cu multilayer (from Ref. 4) with the applied field perpendicular to the film.

The macroscopic energy for this model is taken to be

$$E = -M_A H \cos \theta_A - M_B H \cos \theta_B - J \cos(\theta_B - \theta_A) + K_A \sin^2(\theta_A - \phi_A) + K_B \sin^2(\theta_B - \phi_B). \quad (1)$$

The first two terms represent Zeeman magnetic energies of the two phases of magnetizations M_A and M_B , the third term represents the interface exchange of strength J and the last two terms represent the anisotropy of each phase of strengths K_A and K_B . θ_A and θ_B are the angles that M_A and M_B , respectively make with the magnetic field direction. ϕ_A and ϕ_B are the angles that the uniaxial anisotropy axes of each phase makes with H . We have already discussed this model with reference to Co-O and associate the A phase with pure Co and the B phase with CoO.⁴ Previous calculations assuming a rigid rotation of the magnetization⁶⁻¹⁰ consider cases where H is along a high symmetry anisotropy direction for cubic or uniaxial anisotropy.

In our calculation we find that provided H is applied in a plane defined by the two anisotropy axes, then M_A and M_B remain in this plane for the range of parameters used in this work. Thus we can describe the directions of these magnetizations by one angle each (θ_A and θ_B , respectively) in Eq. (1). Values of θ_A and θ_B as a function of H are determined by following a local minimum in E of Eq. (1) by solving $\partial E / \partial \theta_A = 0$ and $\partial E / \partial \theta_B = 0$. The magnetization M is then calculated from

$$M = M_A \cos \theta_A + M_B \cos \theta_B. \quad (2)$$

We have shown previously that for selected values of the above parameters this model yields a magnetic hysteresis which produces partially inverted hysteresis. We show an example of a hysteresis loop for $M_A=2$, $M_B=1$, $K_A=1$, and $K_B=4$ with the anisotropy axes parallel to H ($\phi_A = \phi_B = 0$) in Fig. 2. Only partially inverted behavior of hysteresis loops is found in this model. There is a large normal hysteresis at high fields that is not seen in experiments which accompanies the inverted behavior seen at smaller fields.

Figure 3 shows a complete magnetic phase diagram as a function of H (decreasing) and J using the above values of M and K for the case where the anisotropy axes are parallel to H . The insert in the figure shows the four possible collinear states and a canted state. A partially inverted hysteresis loop is generated if M_A reverses before H reaches zero when H is reduced from a high positive value, i.e., when state 2 (of the insert to Fig. 3) appears above the J axis. This occurs for J values of -1.6 to -7.1 . Thus we find that if phase A has a somewhat larger M and smaller K than phase B then inverted behavior is present for a range of negative values of J .

Changing the angle between H and the anisotropy axes modifies the hysteresis loops. Figure 4 shows a series of magnetic hysteresis loops for a range of values of the anisotropy axes angles ϕ_A and ϕ_B with $J = -7$. As can be seen, the changes as a function of ϕ_A for a given value of ϕ_B are small. It appears that significant changes in the hysteresis occur when ϕ_B , the anisotropy axis angle for the more anisotropic phase, is varied. If ϕ_B is 90° then inverted behavior is not present. The small hysteresis observed for the loops corresponding to ϕ_A of 30° and 60° with $\phi_B = 90^\circ$ is normal

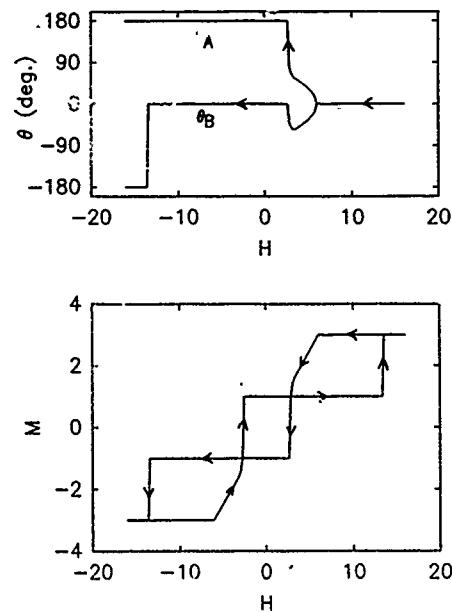


FIG. 2. Calculated magnetization (lower panel) from Eq. (2) and corresponding values of θ_A and θ_B (upper panel) determined from Eq. (1) as described in the text as a function of applied field for $M_A=2$, $M_B=1$, $K_A=1$, $K_B=4$ with $\phi_A = \phi_B = 0$. Note that values of θ are only shown for half of the hysteresis cycle.

hysteresis as indicated by the arrows on the hysteresis loops. It is not surprising that inverted hysteresis vanishes in this limit since no metastable configuration exists for the strong anisotropy phase (phase B) when $\phi_B = 90^\circ$.

Relaxation of the rigid rotation assumption modifies the above results. A number of calculations have been reported on the magnetic hysteresis of a system where rigid rotation is not assumed to study the influence of interface exchange in various circumstances.¹¹⁻¹³ We find that allowing spins in phase A and B to deform, reduces the range of H over which inverted behavior is observed. This result is also not surprising since the inverted behavior corresponds to a rather high-

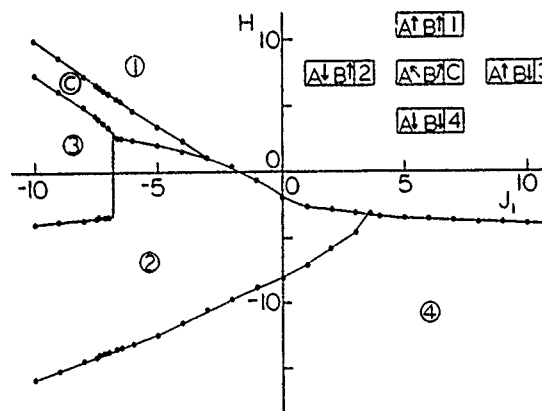


FIG. 3. Magnetic phase diagram for $M_A=2$, $M_B=1$, $K_A=1$, $K_B=4$ with $\phi_A = \phi_B = 0^\circ$ determined from Eqs. (1) and (2) as described in the text. The insert shows the four possible collinear magnetic states (numbers 1-4) and a canted state (labeled C). The range of J for which inverted hysteresis loops exist is given by the range of J for which state 2 is present above the J axis.

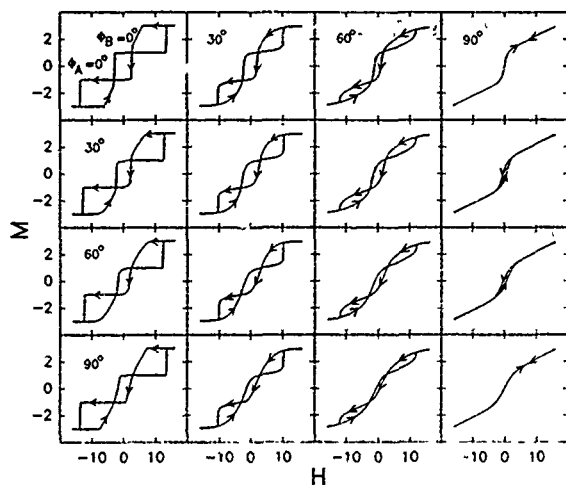


FIG. 4. Hysteresis loops for selected values of ϕ_A and ϕ_B using $M_A=2$, $M_B=1$, $K_A=1$, $K_B=4$, and $J=-7$. The values of ϕ_B and ϕ_A used are given in tabular form across the top and down the left of the diagram.

energy metastable state being occupied by M_A and M_B . Allowing the magnetization to deform allows the system to leave this metastable state for smaller reverse fields. We shall discuss these results in more detail elsewhere.¹⁴

A more complete model of inverted hysteresis should include a coupling of the magnetization to another property of the system which is able to store and release energy from the magnetic system. A possibility here is magnetoelastic ef-

fects which would have to store energy in strain fields in the material.

In summary we have shown within a simple model that partially inverted hysteresis loops may be obtained for selected values of anisotropy and selected negative (antiferromagnetic) values of interface exchange. If the assumption of rigid rotation is relaxed then the field range over which inverted behavior occurs is reduced. We are extending these calculations to include some magnetoelastic effects to determine if such effects can lead to completely inverted loops.

Work supported by NSF OSR92-55223 and NSF DMR 9123831.

¹W. H. Meiklejohn and C. P. Bean, *Phys. Rev.* **105**, 904 (1957).

²I. S. Jacobs and J. S. Kouvel, *Phys. Rev.* **122**, 412 (1961).

³G. Gruzalski, Ph.D. thesis, University of Nebraska, 1977.

⁴C. Gao and M. J. O'Shea, *J. Magn. Magn. Mater.* **127**, 181 (1993).

⁵S. G. Cornelison, D. J. Sellmyer, J. G. Zhao, and Z. D. Chen, *J. Appl. Phys.* **53**, 2330 (1982).

⁶J. Barnas and P. Grunberg, *J. Magn. Magn. Mater.* **98**, 57 (1991).

⁷M. L. Watson, W. D. Doyle, H. Fujiwara, and S. Hossain, *J. Appl. Phys.* **73**, 5518 (1993).

⁸W. Folkerts, *J. Magn. Magn. Mater.* **94**, 302 (1991).

⁹T. Kobayashi, H. Tsuji, S. Tsunashima, and S. Uchiyama, *Jpn. J. Appl. Phys.* **20**, 2089 (1981).

¹⁰Z. Q. Qui, J. Pearson, and S. D. Bader, *J. Appl. Phys.* **73**, 5765 (1993).

¹¹W. Schmidt, *J. Magn. Magn. Mater.* **84**, 119 (1990).

¹²N. Smith and W. C. Cain, *J. Appl. Phys.* **69**, 2471 (1991).

¹³B. Dieny, D. Givord, and J. M. B. Ndjaka, *J. Magn. Magn. Mater.* **93**, 503 (1991).

¹⁴D. Dimitrov, G. Wysin, and M. J. O'Shea (to be published).

Magnetic and structural properties of Co/CoO bilayers

X. Lin and G. C. Hadjipanayis

Department of Physics and Astronomy, University of Delaware, Newark, Delaware 19716

S. I. Shah

Central Research and Development, E. I. duPont, Wilmington, Delaware 19880-0356

The magnetic and structural properties of Co/CoO bilayers prepared by sputtering have been studied in films with Co thickness in the range of 65 to 250 Å. A two-phase structure consisting of hcp Co and fcc CoO was observed in the films. The coercivity was found to change inversely proportional to the Co thickness and to the sputtering rate. The highest H_c (9 kOe) was obtained in films exposed to ambient conditions for long periods of time. A shift in the hysteresis loop was found in field-cooled samples, indicating a strong exchange coupling between the Co and CoO phases.

Co/CoO films have been found to possess many novel properties, such as a perpendicular anisotropy, enhanced Kerr rotation, and exchange anisotropy.¹⁻⁵ These properties have potential applications in new perpendicular recording media. In previous studies, Co/CoO films were made by reactive sputtering in a mixture of Ar and O₂ gases²⁻⁴ or by evaporation in O₂ gas.¹ These films had a microstructure consisting of hcp Co and fcc CoO fine particles in a columnar morphology perpendicular to the film plane. The magnetic and structural properties of the films were found to depend strongly on the partial pressure of oxygen during sputtering or evaporation. The unidirectional exchange anisotropy between Co and CoO particles is believed to play an important role in inducing the perpendicular magnetic anisotropy.³

In this study, the Co/CoO films are in the form of bilayers with the CoO formed by oxidizing the surface of the single Co films. In this morphology, the interaction is confined to the film's surface so that it is easier to study the exchange coupling between Co and CoO.

A dc sputtering apparatus was used to prepare the Co/CoO bilayers. The sputtering target was a 99.9% Co disk 2 in. in diameter and 0.053 in. in thickness. The distance between the target and the water-cooled substrate was 13.5 cm. The sputtering chamber was initially pumped down to $6-7 \times 10^{-8}$ Torr by a cryopump and then the Co film was deposited onto a kapton substrate by sputtering in a 5 mT Ar

gas. The thickness range of the films was between 65 and 250 Å. Soon after the film was made, a small amount of air was introduced into the system under two different pressures (370 and 710 mTorr) to oxidize the surface of Co films for 2 h. The as-made Co/CoO films were also exposed to air for long periods of time (4 months) and the effect of additional oxidation was investigated.

The Co thickness was measured with Rutherford backscattering (RBS) and that of CoO by x-ray photoelectron spectroscopy (XPS). The crystal structure of bilayers was determined from selected area electron diffraction data and the microstructure was studied using a JEOL 100C transmission electron microscope (TEM). The magnetic properties were studied using a SQUID magnetometer.

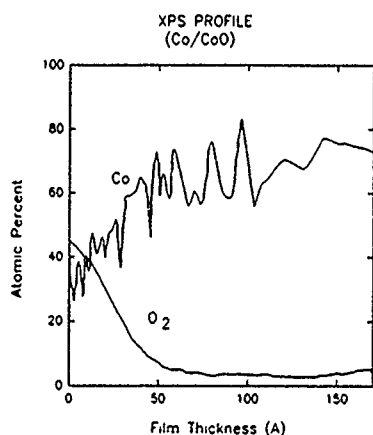


FIG. 1. A depth profile for a Co/CoO sample from XPS.

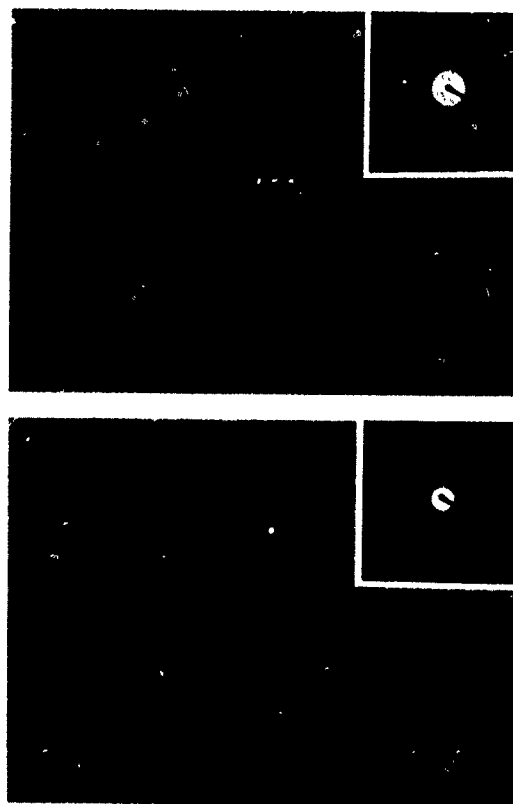


FIG. 2. TEM pictures of Co/CoO bilayers. (a) Co thickness=65 Å; (b) Co thickness=170 Å.

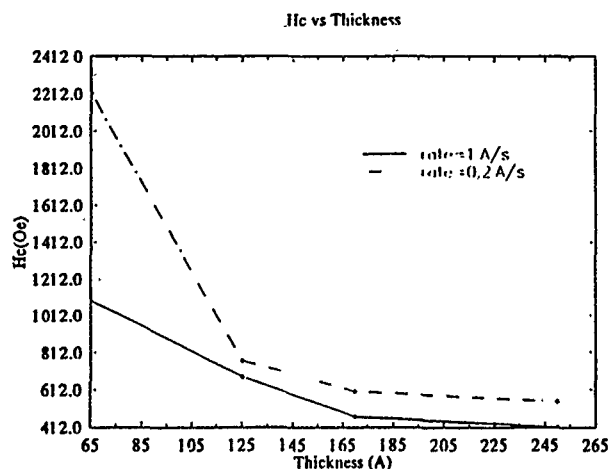


FIG. 3. Coercivity H_c vs Co thickness at 10 K for Co/CoO films.

The XPS data for the as-made and etched samples are shown in Fig. 1. The surface oxide layer was found to be CoO and its thickness varied from 26 Å in the 65 Å Co films to 64 Å in the 170 Å Co films. Selected area electron diffraction (Fig. 2) showed a mixture of hcp Co and fcc CoO phases. The grain size was found to increase with increasing film thickness from 45 to 70 Å for the 65 and 170 Å films, respectively. The bright field micrographs show that the distribution of Co particles is homogeneous.

The saturation magnetization M_s of Co/CoO bilayers exhibits a complex behavior with the Co thickness, the sputtering rate, and the oxidation conditions. The thin bilayers (<100 Å) showed a larger M_s when passivated at higher air pressures (710 mT). Co/CoO films exposed in air at ambient conditions for 4 months had a lower M_s .

The coercivity of the as-deposited films was found to increase with decreasing Co layer thickness as shown in Fig. 3. This behavior is also similar to the size dependence of H_c in Co powders.⁶ Table I also shows that the coercivity changes inversely proportional to the sputtering rate. For larger sputtering rates, the quenching rates are higher and much finer particles (below the single domain particle size of 200 Å) are formed with a lower H_c . The thinner films (<100 Å) are also more sensitive to the sputtering rate than the thicker films. A larger H_c was obtained in the films passivated at the 370 mTorr air pressure than at 710 mTorr. It may be that the passivation is not complete at 370 mTorr, so when the samples are exposed to ambient conditions a stronger oxidation takes place resulting in thicker surface oxides. This explanation is consistent with the huge coercivity obtained in films exposed to air for long periods of time. The same ar-

TABLE I. H_c vs sputtering rate and oxidation.

Co thickness (Å)	H_c (Oe) 1 Å/s	H_c (Oe) 0.6 Å/s	H_c (Oe) 0.2 Å/s
65	864, ^a 1092 ^b	1144, 1809	2082, 2217
170	340, 468	489, 607	396, 603
250	298, 412	305, 359	392, 548

^a370 mTorr.

^b710 mTorr.

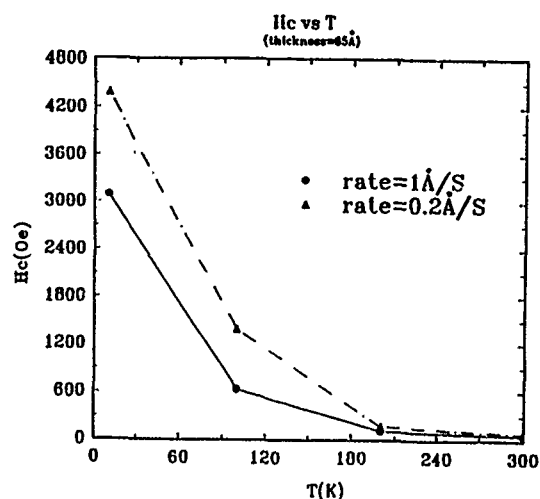


FIG. 4. Coercivity H_c vs temperature for Co/CoO films of thickness 65 Å prepared with sputtering at rates 1 Å/s and 0.2 Å/s.

gument can also be used to explain the magnetization dependence on passivation; films with proper passivation (710 mTorr) were less oxidized after exposing to ambient conditions than those with incomplete passivation (360 mTorr), and therefore they had a higher M_s . This behavior is similar to that of Fe fine particles⁷ and indicates that the thickness of the surface oxide is critical to the hysteresis properties of the bilayers. As the temperature increased from 10 to 300 K, a steep drop in H_c to less than 100 Oe (Fig. 4) was observed.

The hysteresis loops of field-cooled samples were found to be shifted (Fig. 5), indicating the presence of an exchange anisotropy.⁸⁻¹⁰ The change of coercivity between the zero-field-cooled and field-cooled samples, H_s , was used as a parameter to describe the exchange coupling between CoO and Co. Table II gives some results for H_s . For thin Co films, a larger H_s was observed, indicating a stronger influence of CoO.

No perpendicular anisotropy was observed in the films even with a Co thickness as low as 65 Å (see Fig. 6). This result is different from other studies²⁻⁴ and it is probably due

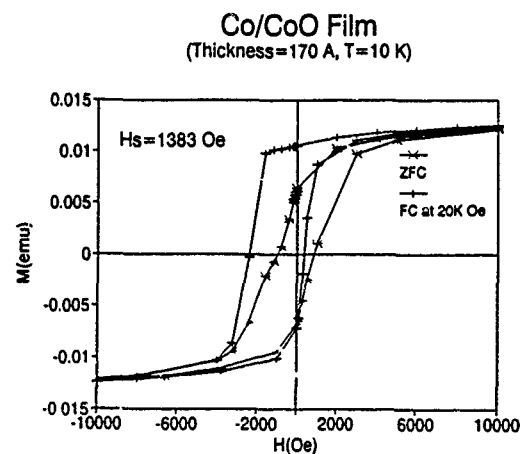


FIG. 5. The hysteresis loop of a Co/CoO bilayer with Co thickness 170 Å after field cooling at 10 K.

TABLE II. Loop shift H_s as a function of thickness and oxidation conditions in films sputtered at 1 Å/s.

Co thickness (Å)	H_s (Oe) 710 mTorr	H_s (Oe) 370 mTorr
65	4326	3050
170	961	615

to the formation of CoO films only on the surface of the films. It is well known that thin Co films have a perpendicular magnetic anisotropy, which arises from the magnetocrystalline anisotropy of hcp Co and the shape anisotropy of the columnar structure.³ If the CoO is formed as a shell around the columnar Co, the exchange anisotropy between the ferromagnetic Co and antiferromagnetic CoO will enhance the Co perpendicular anisotropy;³ but if the CoO is formed on the surface of the Co film, only the top Co particles are shelled by the CoO. In this case, the exchange anisotropy

tends to turn the easy axis to the parallel direction and must compete with the magnetocrystalline and shape anisotropy. When a continuous CoO film is formed on the surface of the Co film, a large exchange anisotropy is expected to turn the easy axis parallel to the surface of the film. This is just what we found in the Co/CoO bilayers. The quantitative relation between the exchange anisotropy, magnetocrystalline, and shape anisotropy needs further investigation.

Co/CoO bilayers were made with dc sputtering by forming the Co films first and then oxidizing their surface. The bilayers were composed of hcp Co and fcc CoO. No perpendicular anisotropy was found in the bilayers and this is probably due to the exchange coupling between CoO and Co at the film's surface which exceeds the magnetocrystalline and shape anisotropy of inner Co particles. The large coercivity and the loop shift found in field-cooled thin films (with thickness of Co at 65 Å) are the result of a strong exchange interaction between Co and CoO.

The authors wish to thank Dr. C. Swann for the RBS measurements, and J. Yuan for the TEM pictures. This work is supported by NSF DMR-8917028.

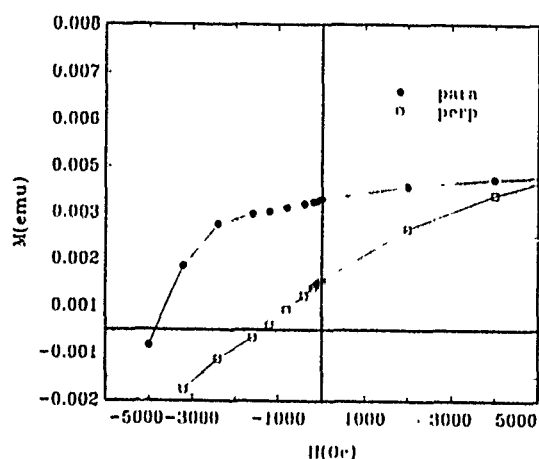


FIG. 6. Parallel and perpendicular hysteresis loops of a Co/CoO bilayer with Co thickness 65 Å at 10 K.

- ¹J. W. Schneider, A. M. Stoffel, and G. Trippel, IEEE Trans. Magn. **MAG-9**, 183 (1973).
- ²Y. Ota, T. Asaka, S. Asari, K. Nakamura, and A. Itoh, IEEE Trans. Magn. **MAG-20**, 1030 (1984).
- ³M. Ohkoshi, K. Tamari, S. Honda, and T. Kusuda, IEEE Trans. Magn. **MAG-20**, 788 (1984).
- ⁴M. Ohkoshi, K. Tamari, S. Honda, and T. Kusuda, J. Appl. Phys. **57**, 4034 (1985).
- ⁵W. H. Meiklejohn and C. P. Bean, Phys. Rev. **105**, 904 (1957).
- ⁶S. Gangopadhyay, G. C. Hadjipanayis, C. M. Sorensen, and K. J. Klabunde, IEEE Trans. Magn. **MAG-28**, 3174 (1992).
- ⁷S. Gangopadhyay, G. C. Hadjipanayis, B. Dale, C. M. Sorensen, K. J. Klabunde, V. Papaefthymiou, and A. Kostikas, Phys. Rev. B **45**, 9778 (1992).
- ⁸A. P. Malozemoff, J. Appl. Phys. **63**, 3874 (1988).
- ⁹A. Yelon, Phys. Thin Films **6**, 205 (1971).
- ¹⁰S. Gangopadhyay, G. C. Hadjipanayis, C. M. Sorensen, and K. J. Klabunde, J. Appl. Phys. **73**, 6964 (1993).

Resistivity anomaly in nonmagnetic metals with ferromagnetic insulator proximity layers

G. M. Roesler, Jr., Y. U. Idzerda, P. R. Broussard, and M. S. Ososky
Naval Research Laboratory, Code 6340, Washington, DC 20375-5343

Epitaxial bilayers and multilayers were prepared using the ferromagnetic insulator EuO and the metals V and Ag. For metal films of thickness 10 nm or less, there is a sharp change in the slope of the resistivity *versus* temperature, which occurs at 86 K for EuO/V specimens and at 50 K for EuO/Ag specimens. Soft x-ray magnetic circular dichroism measurements showed a clear dichroism for Eu but none for V. Therefore, the dR/dT discontinuity is attributed to a change in spin-dependent surface scattering at the insulator/metal interface caused by the magnetization of the surface layer of Eu^{++} ions. The difference in temperature between the dR/dT discontinuities between the two metals (and from the bulk EuO Curie temperature of 70 K) is tentatively attributed to the influence of the Ruderman-Kittel-Kasuya-Yosida (RKKY) mechanism.

Metallic multilayers involving magnetic materials are hosts to a rich variety of physical phenomena, including the recently observed giant magnetoresistance.¹ Among the physical variables affecting these phenomena may be the band structures and electron densities of the two component metals. Microscopically, the current carriers in such multilayers may experience spin-dependent scattering, specular or diffuse boundary scattering, and exchange at the interfaces, thus complicating the understanding of anomalous transport properties. Here, we report results on the transport behavior of single metals in contact with a ferromagnetic insulator. Such structures provide a physical system which is simpler than the all-metallic multilayer problem, as the magnetic moments are separate from the conduction sea (except at the interface), and the band structure of only one metal rather than two need be considered. We have observed a resistance anomaly in bilayers and multilayers of vanadium or silver in contact with the ferromagnetic insulator EuO. The anomaly may be caused by the magnetization of the layer of Eu^{++} ions at the interface. Furthermore, the Curie temperature of that layer may be affected by Ruderman-Kittel-Kasuya-Yosida (RKKY) coupling between Eu^{++} ions through the V or Ag conduction sea.

These metal/ferromagnetic insulator structures were prepared under conditions of heteroepitaxy. The V films were prepared by electron beam evaporation at typical pressures of 10^{-10} mbar, while the Ag films were prepared by thermal evaporation at typical pressures of 10^{-8} mbar. Sapphire or cubic zirconia substrates were used, and were held at 300–700 °C to obtain planar surfaces. The EuO layers were grown by thermal evaporation with the substrate held at 300 °C. Reflection high-energy electron diffraction (RHEED) from the film surface was used to monitor crystal structure and surface quality during growth of metal and insulator layers. RHEED patterns typically indicated two-dimensional films with a single crystal structure. Details of the film growth process will be published separately.² X-ray diffraction showed the presence of EuO and no other europium oxides. SQUID magnetometer studies indicated that the EuO layers became magnetic at the bulk Curie temperature (T_c) of 70 K, and the large Faraday rotation characteristic of EuO was observed.

Resistance was measured as a function of temperature using a four-terminal ac technique. A typical example of $R(T)$ for a EuO/V specimen is shown in Fig. 1. Note that the slope changes sharply at a temperature of 86 K, near but somewhat higher than the T_c of EuO. This feature occurred (always at 86 K) in the majority of EuO/V samples prepared. The feature did not appear to depend upon layer thickness of V between 1.6 and 10 nm, nor upon EuO layer thickness between 3 and 10 nm. A similar feature was observed in EuO/Ag bilayers, at 50 K rather than 86 K. In samples displaying this dR/dT discontinuity, there appeared to be no Kondo effect, as dR/dT remained positive down to the lowest temperature of measurement (4.2 K). By contrast, a minority of samples displayed Kondo-like behavior, that is, showed a resistance minimum between 20 and 50 K.

Whether a particular EuO/V sample would show the dR/dT discontinuity or Kondo behavior (which appear to be mutually exclusive) may depend sensitively on the atomic ordering at the metal/insulator interface. During some growths, the RHEED pattern did not change immediately when overlayer growth commenced, but changed to the new structure gradually over several atomic layers. Such struc-

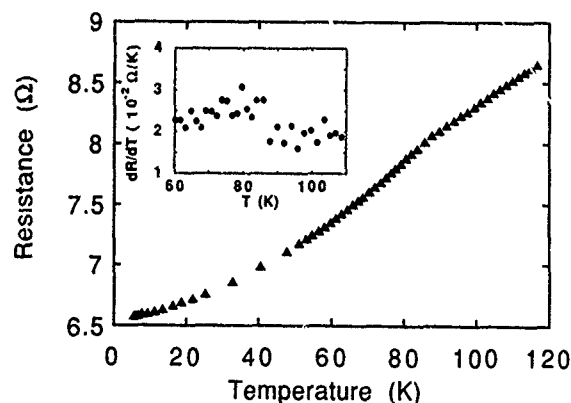


FIG. 1. The resistance of a vanadium-europium oxide multilayer as a function of temperature. The sample had the structure EuO/V/EuO/V/EuO, with 3-nm EuO layers and 2.7-nm V layers. Inset shows the temperature behavior of dR/dT . Bilayer samples show the same feature at 86 K as the multilayer samples.

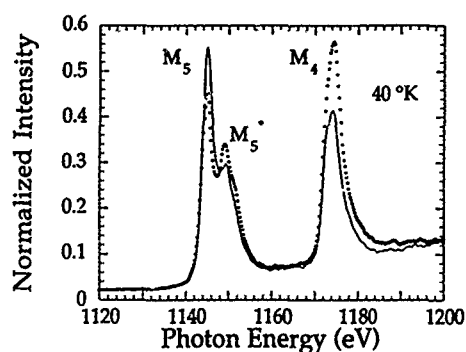


FIG. 2. XAS spectra of the M_5 and M_4 peaks of Eu in an EuO/V multilayer. The solid curve is the spectrum for negative helicity photons, and the dotted curve is for positive helicity. Pure EuO films had identical behavior.

tures displayed the dR/dT discontinuity. During other growths, the RHEED pattern disappeared immediately and a new one reappeared after several atomic overlayers were deposited. Some of the latter structures showed Kondo-like behavior.

We have considered two microscopic mechanisms by which the magnetization of the EuO might cause the observed dR/dT discontinuities. Magnetization could affect the band structure of the metal, and it could affect spin-dependent scattering at the metal/insulator interface. The band structure effect model is motivated by the similarity of the discontinuity in dR/dT to that observed in ferromagnetic metals, e.g., Ni. The effect of magnetization in producing a resistivity slope change in Ni is successfully explained by the model of Mott.³ This model requires that a large fraction of the scattering events in a metal be interband scattering events involving an unfilled d band at the Fermi energy. This picture is appropriate in V but may not apply to Ag. In the EuO/metal system, the d band of the metal must become polarized through exchange with the localized Eu f states. When the Eu^{++} ions become magnetized, the d band splits by the exchange Zeeman energy, reducing the d states available for s - d scattering. The second model explains the dR/dT discontinuity in terms of a reduction of spin-dependent surface scattering rather than a reduction of interband scattering. Here, the magnetization of the surface layer of Eu^{++} ions is supposed to greatly increase the energy required for an (inelastic) spin-flip scattering event, thus presumably reducing the resistivity below the magnetic ordering temperature.

In an effort to detect magnetization of V, which would be required in the s - d scattering picture, soft x-ray magnetic circular dichroism (SXMCD) measurements were made on a EuO/V multilayer as well as on single-layer EuO films. SXMCD is the difference between the x-ray absorption of positive and negative helicity (left- and right-circularly polarized) photons at the $3d$ metal L_3 and L_2 absorption white lines, or at the M_5 and M_4 absorption white lines of a $4f$ metal. This technique is used for element-specific determination of the presence of ferromagnetism in heteromagnetic samples.⁴ The ferromagnetism of the EuO layers is observed in the SXMCD of the Eu spectrum. Figure 2 shows a strong dichroism between the x-ray absorption spectroscopy (XAS)

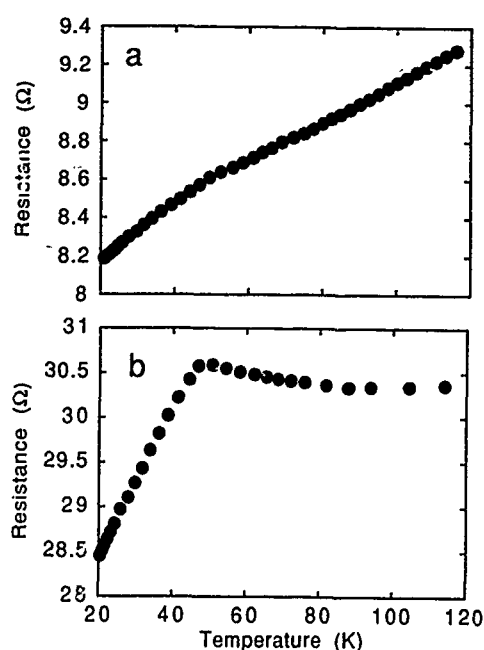


FIG. 3. The resistance of two EuO/Ag bilayers as a function of temperature. Ag thicknesses were (a) 7.6 nm and (b) 3.6 nm. EuO thickness was 10 nm.

spectra for negative-helicity (solid) and positive-helicity (dots) photons at the Eu M_5 and M_4 absorption edges. A strong and unexpected temperature dependence in the difference of these spectra, that is, in the SXMCD signal, was observed in both multilayer samples and pure EuO films.⁵ However, no dichroism was observed between the L_3 and L_2 spectra of V upon cooling below the dR/dT discontinuity.

The lack of SXMCD for V with an EuO proximity layer is difficult to reconcile with the s - d scattering model. Another difficulty with that picture is the presence of a dR/dT discontinuity in bilayers containing Ag rather than V. The resistance *versus* temperature of two such bilayers may be seen in Fig. 3. Since Ag has filled d bands, the Mott s - d scattering mechanism is not implicated. We surmised that measuring the Hall effect in the EuO/V system would help clarify the scattering mechanism. If spin-dependent scattering is occurring, one might expect to see anomalous Hall behavior. However, both above and below the dR/dT discontinuity, the measured Hall coefficient was the same in sign and magnitude as that measured⁶ in bulk V. Because the Eu^{++} ions are in an S state, however, the absence of anomalous Hall scattering might not be unusual. High-field magnetoresistance measurements are planned to help resolve the scattering mechanism question.

There is a qualitative difference in the scattering behavior near the dR/dT discontinuity between specimens with Ag and those with V. There is little thickness dependence to the absolute magnitude of the discontinuity in samples containing V; however, as seen in Fig. 3, the feature at 50 K in samples with Ag becomes much more dramatic as thickness is decreased. Furthermore, the slope dR/dT remains essentially constant above the 86-K feature in V specimens; however, in the Ag specimens, the slope decreases significantly as the 50-K feature is approached, even becoming negative

in the thinnest samples, as may be seen in Fig. 3(b). Similar behavior is predicted⁷ for critical behavior of the resistivity near magnetic transitions, assuming ferromagnetic behavior at the V/EuO interface and antiferromagnetic behavior at the Ag/EuO interface. The upward (downward) displacement of the resistivity features from the bulk EuO Curie temperature of 70 K at an interface with V(Ag) is consistent with a ferromagnetic (antiferromagnetic) interaction at the interface. A possible model of this interaction is the RKKY coupling of the *surface layer* of Eu^{++} ions through the conduction sea of V or Ag. A calculation to determine whether the RKKY mechanism is plausible would consider ions on the surface of a *semi-infinite* conduction sea rather than the usual infinite one. The tendency of the surface layer of V to magnetize⁸ may also be germane. The novel transport phenomenon described here is yet another example of the richness of the physics involved when magnetic atoms and conduction electrons interact.

We are grateful to A. Erlich, J. Krebs, M. Rubinstein, and G. A. Prinz for useful discussions, and to S. Gazdo who performed some of the measurements. One of us (GMR) acknowledges the support of the National Research Council Postdoctoral Associateship program.

¹M. N. Baibich, J. M. Broto, A. Fert, F. Nguyen Van Dau, F. Petroff, P. Eitenne, G. Creuzet, A. Friederich, and J. Chazelas, *Phys. Rev. Lett.* **61**, 2472 (1988); J. Krebs, P. Lubitz, A. Chaiken, and G. A. Prinz, *ibid.* **63**, 1645 (1989).

²G. M. Roesler, Jr. and P. R. Broussard (to be published).

³N. F. Mott, *Proc. R. Soc. London Ser. A* **156**, 368 (1936).

⁴C. T. Chen, F. Sette, Y. Ma, and S. Modesti, *Phys. Rev. B* **42**, 7262 (1990).

⁵Y. U. Idzerda, G. M. Roesler, Jr., P. R. Broussard, M. S. Osofsky, H.-J. Lin, G. H. Ho, G. Meigs, and C. T. Chen, *National Synchrotron Light Source Annual Report*, 1993.

⁶S. Foner, *Phys. Rev.* **107**, 1513 (1957).

⁷S. Alexander, J. S. Heiman, and I. Balberg, *Phys. Rev. B* **13**, 304 (1976).

⁸J. S. Moodera and R. Meservey, *Phys. Rev. B* **40**, 8541 (1989).

Complex magnetization processes of exchange coupled trilayers

S. Wüchner, J. Voiron, and D. Givord

Laboratoire Louis Néel, C.N.R.S., BP 166, 38042 Grenoble-Cedex 9, France

D. Boursier

Laboratoire de Matériaux et Génie Physique, ENSPG, BP46, 38402 St Martin d'Hères, France

J. J. Préjean

C.R.T.B.T., C.N.R.S., BP 166, 38042 Grenoble-Cedex 9, France

The magnetization processes of two series of sandwiches of compositions Sm-Co/Co/Sm-Co' and Sm-Co/Gd-Co/Sm-Co' prepared by dc bias sputtering are presented. The layers of Sm-Co and Sm-Co' have different compositions each with a different coercive field. The central layer consists of a soft magnetic material with a thickness varying from 500 to 5000 Å. In these systems, it is possible to stabilize a magnetic configuration with the magnetic moments of the external layers having opposite directions. Due to the magnetic coupling between the layers associated with the strong exchange interactions between cobalt atoms throughout the whole sample, a large planar Bloch wall is formed in the central layer. The width of this wall depends on the intrinsic properties of this central layer, but the magnetization processes vary with the relative magnitude of the wall width to the thickness of this layer. For a large thickness of the central layer, the Bloch wall is very mobile under applied field leading to a very large susceptibility.

Magnetic multilayers made from rare-earth and transition metal alloys may exhibit a wide variety of magnetic properties. Indeed, considering the numerous possibilities of chemical composition and thickness of each constituting layer, their magnetic moment, anisotropy, and coercivity can be fitted to yield specific and original magnetic properties of the sample.

Recently, Alameda *et al.*¹ reported on the magnetic properties of a (Sm-Co)/(Zr-Co)/(Sm-Co)' system: They showed that it is possible to stabilize a peculiar magnetization state with the magnetic moments in the two Sm-Co layers pointing into opposite directions and a domain wall existing in the central layer. This wall, very mobile in this amorphous material, leads to an almost reversible magnetization process, in contrast to the irreversible process observed in a single Co-Zr layer.

We have undertaken the study of such a behavior in two series of sandwiches of compositions A: (Sm-Co)/(Gd-Co)/(Sm-Co)' and B: (Sm-Co)/Co/(Sm-Co)'. All these samples are characterized by a central layer consisting of a relatively soft magnetic material (Co or Gd-Co) sandwiched between two hard magnetic Sm-Co layers with different coercivities. In Sm-Co intermetallic compounds, the Sm and Co moments are ferromagnetically coupled, while in Gd-Co compounds, the Gd and Co moments are coupled antiferromagnetically, with the Gd moment dominating the Co one for the composition used. The Co-Co exchange interactions, which are the strongest, lead in zero field to a macroscopic ferrimagnetic arrangement for the system A (the magnetization direction alternates in adjacent layers) and to a ferromagnetic one for the system B. In the ferrimagnetic Gd-Co system, a saturated state is induced under applied field, with the formation of a Bloch wall in the Co sublattice at each interface. The transition field and the creation or annihilation of such Bloch walls have been studied in more detail in (Y-Co)/(Gd-Co)/(Y-Co) sandwiches.¹⁻⁴

In this paper we discuss a variety of original magnetiza-

tion processes of a series of sandwich systems in which the layer moments, layer coercivities, and layer thicknesses are different.

The sandwiches (Sm-Co)/Co/(Sm-Co)', (Sm-Co)/(Gd-Co)/(Sm-Co)' have been prepared at the IBM Research Center in San José from targets of Sm, Co, and Gd_{0.37}Co_{0.63} by dc bias sputtering under a residual Ar pressure of 3 mTorr, the initial vacuum being 10⁻⁷ Torr. The Sm-Co layers are in fact multilayers obtained by alternate deposition of very thin Co and Sm films [respectively, (Sm₅ ÅCo₁₀ Å)₃₀ and (Sm₅ ÅCo₂₀ Å)₂₀], giving a different coercive field for each layer.

A quartz oscillator was used to control the thicknesses of ~500 Å for the external layers and between 500 and 5000 Å for the central layers. Except for the crystalline films obtained from pure Co, the materials are amorphous.

An easy direction magnetization was induced by placing a permanent magnet next to the silicon substrates and thus applying a field parallel to the film surface during deposition.

Magnetization experiments were performed using a SQUID magnetometer at 4.2 K and a vibrating-sample magnetometer at 20 and 300 K. The magnetic field was applied in the easy direction of magnetization. The magnetization curves for the different samples are shown in Figs. 1-5.

The magnetization curves of all the samples are characterized by three or two steps, when the magnetic field sweeps in the same direction. These transitions are associated with the reversal of the magnetic moment of a layer at a field value that depends on the coercivity of the layer as well as on its magnetic coupling with adjacent layers. Indeed, the strong exchange interactions between cobalt moments lead to the existence of Bloch walls in some of the magnetization states. For example, in the saturated state of the samples with Gd-Co as central layer, the Sm-Co layer moment and the Gd moments are aligned in the direction of the field, while the Co moments of the Gd-Co layer point in the opposite direction. Consequently, in the saturated state, a large planar

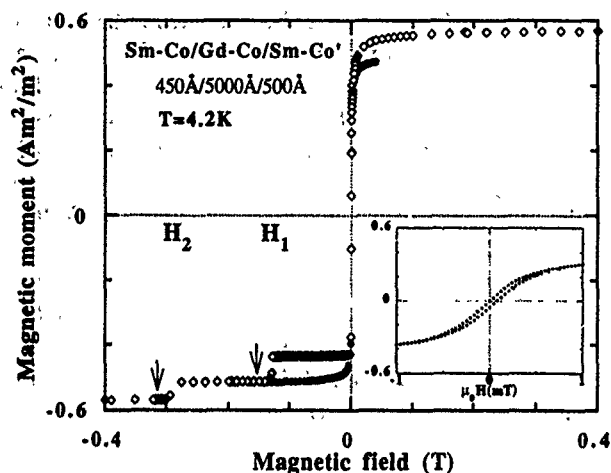


FIG. 1. Magnetization curve at 4.2 K with the applied field in the easy direction for the Sm-Co/5000 Å Gd-Co/Sm-Co' sample. The insert shows the magnetization process after application of a field between H_1 and H_2 , with a different scale.

Bloch wall lies in the vicinity of each interface, while there is none in zero field. When decreasing the field from the saturated state on, the existence of these Bloch walls explains the curvature observed at low field in the magnetization curves of the samples (Gd-Co 5000 Å) (Fig. 1) and (Gd-Co 1000 Å) (Fig. 3), as well as the transition taking place in a small positive field (H_0). In zero field, all the Co moments are aligned throughout the whole sample after suppression of the Bloch walls, minimizing the total exchange energy, in absence of Zeeman energy. At room temperature (Fig. 2), this transition appears in a larger field (~ 20 mT) than at 4.2 K (< 1 mT) (Fig. 1) in agreement with the much smaller value of the magnetic moment of the central layer (3). For the same reason, a larger transition field (~ 5 mT) is observed for the sample with the thinner central layer (Gd-Co 1000 Å) than in the (Gd-Co 5000 Å) sample, corresponding to the reversal of a smaller magnetic moment.

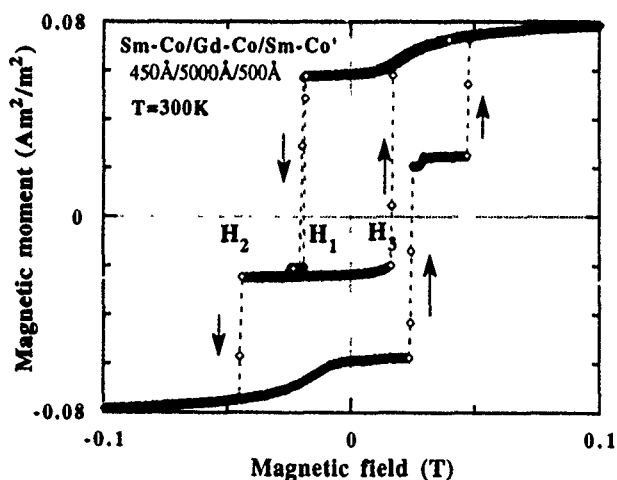


FIG. 2. Magnetization curve at 300 K with the applied field in the easy direction for the Sm-Co/5000 Å Gd-Co/Sm-Co' sample. Arrows indicate irreversible magnetization process.

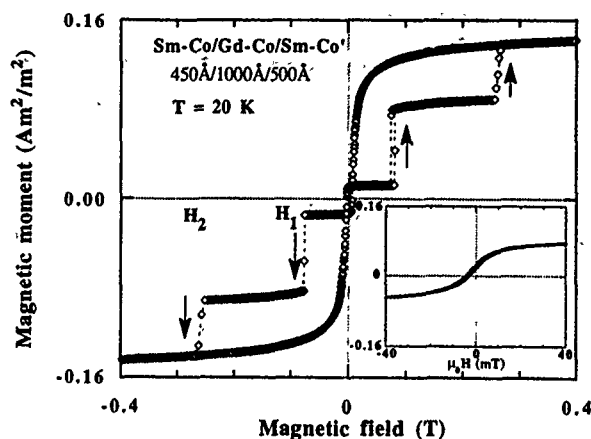


FIG. 3. Magnetization curve at 20 K with the applied field in the easy direction for the Sm-Co/1000 Å Gd-Co/Sm-Co' sample. The insert shows the magnetization process after application of a field between H_1 and H_2 . Arrows indicate irreversible magnetization process.

The subsequent application of a magnetic field in the opposite direction does not change the value of the total magnetic moment which indicates a single domain configuration in each layer. Increasing the field further in this negative direction induces a second transition at H_1 (130 mT in Gd-Co samples). This transition corresponds to magnetization reversal in the less coercive Sm-Co layer, accompanied by the creation of a Bloch wall in the Gd-Co layer minimizing the large Co-Co exchange interactions throughout the whole sandwich. Finally, a last transition occurs at a field H_2 [~ 280 mT in (Gd-Co 5000 Å) and (Gd-Co 1000 Å)], when the second layer of Sm-Co with the larger coercive field reverses with the creation of a second Bloch wall in Gd-Co at the second interface.

The observed behavior is somewhat different in the sandwiches with cobalt in the central layer (Co 1000 Å, Fig. 4 and Co 500 Å, Fig. 5): in the saturated state all the Co moments are aligned in the direction of the field and no Bloch wall exists. Decreasing the field down to zero keeps

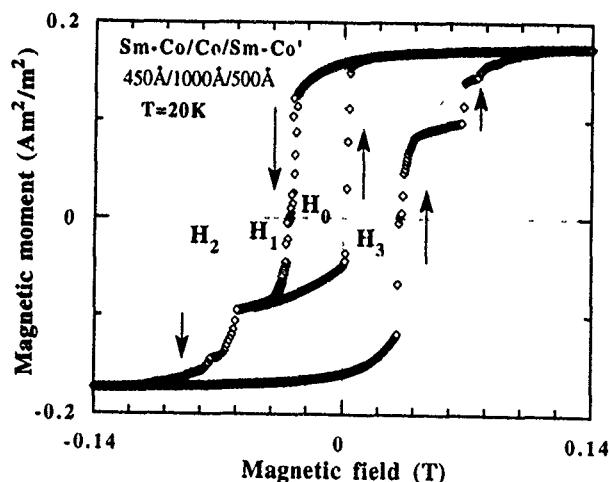


FIG. 4. Magnetization curve at 20 K with the applied field in the easy direction for the Sm-Co/1000 Å Co/Sm-Co' sample. Arrows indicate irreversible magnetization process.

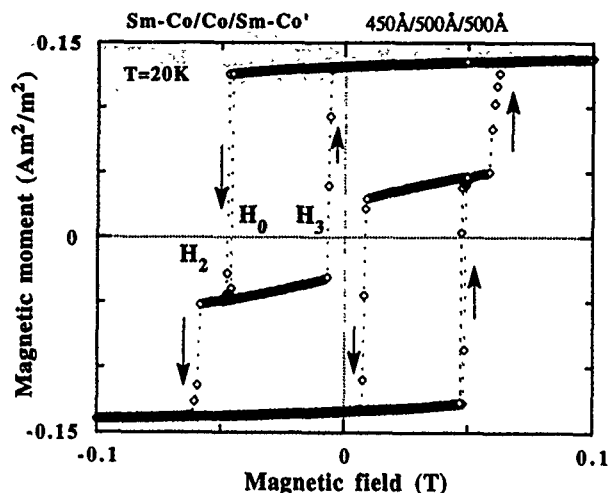


FIG. 5. Magnetization curve at 20 K with the applied field in the easy direction for the Sm-Co/500 Å Co/Sm-Co' sample. Arrows indicate irreversible magnetization process.

this state with a quite constant total magnetic moment, which is the signature of single domain configuration for each layer. Applying a field in the negative direction decreases the total magnetic moment in the (Co 1000 Å) sample (Fig. 4) but not in the thinner (Co 500 Å) sample (Fig. 5). Indeed, the decrease of the total magnetic moment necessitates to reverse some magnetic moments of cobalt and then to create at least two Bloch walls in the cobalt layer. Considering the relative thickness of the wall in comparison with the thickness of the cobalt layer, this situation is possible in the thicker layer but not in the thinner one, at least for a field smaller than the field at which the less coercive Sm-Co layer reverses its magnetization. In fact, in these two samples, the magnetic moment of the Co central layer and that of Sm-Co reverse together (H_0 and H_1 are identical) under creation of one Bloch wall, the transition being particularly sharp for the thinner sample. The next transition occurs in a nearby applied field (H_2), because it corresponds to the reversal of the second Sm-Co layer with the concurrent annihilation of the existing Bloch wall.

We now have a closer look at the magnetic state, in which the two Sm-Co layers have their magnetization in opposite directions, with a Bloch wall inside the central layer of Gd-Co or Co. This state is obtained, after saturation of the sample, by applying a magnetic field in the opposite direction, with a value between H_1 and H_2 and releasing the field afterwards. A nearly completely reversible magnetization process is obtained as reported in Fig. 1 for the (Gd-Co 5000 Å) sample. The insert in Fig. 1 shows that 1 mT is enough to reverse the major part of the magnetization of the Gd-Co layer. Around zero field, it corresponds to a susceptibility of

~ 2300 SI (or ~ 20 emu/g Oe to be compared to the value of 2.3 emu/g Oe obtained in the ZrCo system of Ref. 1). This large susceptibility is associated with a very mobile wall in the thick layer of Gd-Co. Such a behavior is also obtained for the (Gd-Co 1000 Å) sample, but with a much smaller susceptibility (insert on Fig. 3). In that case, the wall width has the same order of magnitude as the entire Gd-Co layer thickness and the wall doesn't have the same mobility.

A different behavior occurs in samples with cobalt in the central layer (Figs. 4 and 5). After application of a field ($H_1 < H < H_2$) creating the configuration with a Bloch wall in the Co layer, the decrease of the magnitude of the applied field leads to a transition (at H_3) towards the saturated state. This transition corresponds to the reversal of the magnetization of the less coercive Sm-Co layer simultaneously with the Co layer but it happens in a very small positive field ($H_3 \ll H_1$) in the (Co 1000 Å) sample, while the transition occurs in a negative field in the Co 500 Å layer. This transition is then associated with the suppression of the Bloch wall inside the cobalt layer and happens in a lower field than the coercive field of the noncoupled layer.

The reversible part, with a small susceptibility, is reduced to a small field region between H_1 and H_3 . The susceptibility is smaller for the thinner Co layer, because the wall occupies a large part of the layer width and then the magnetic moment of the layer is small. It is also possible that this Bloch wall, which has been created at the interface with the more coercive Sm-Co layer, is trapped at this interface and needs a larger field to be unpinning. A similar behavior is observed in the (GdCo 5000 Å) sample at room temperature (Fig. 2), in which the magnetic moment of the Gd-Co is small.

In conclusion, we have presented complex and original magnetization processes observed in sandwiches consisting of three layers, made of different materials and exchange coupled together. Particularly, it has been possible to stabilize a magnetic state with a large susceptibility, associated with the motion of a Bloch wall. Quantitative analyses are in progress in order to have a better understanding of the observed properties.

The authors wish to acknowledge V. S. Speriosu and D. R. Wilhoit for their kind help during the preparation of the samples.

¹J. M. Alameda, L. T. Baczewski, B. Dieny, D. Givord, J. M. Ndjaka, J. P. Nozières, J. J. Préjean, J. P. Rebouillat, and F. H. Salas, *J. Magn. Mater.* **104-107**, 1813 (1992).

²B. Dieny, D. Givord, and J. M. Ndjaka, *J. Magn. Mater.* **93**, 503 (1991).

³D. Givord, A. D. Santos, Y. Souche, J. Voiron, and S. Wüchner, *J. Magn. Mater.* **121**, 216 (1993).

⁴S. Wüchner, J. Betz, D. Givord, K. Mackay, A. D. Santos, Y. Souche, and J. Voiron, *J. Magn. Mater.* **126**, 352 (1993).

Magnetic properties of antiferromagnetic superlattices

Shufeng Zhang

Department of Physics, New York University, New York, New York 10003

Guihua Zhang

Courant Institute of Mathematical Sciences, New York University, New York, New York 10012

The temperature dependence of the magnetic properties of magnetic superlattices by using the Bethe approximation to the inhomogeneous Ising model is studied. A self-consistent equation which determines the variation of the magnetic moment for any layer thicknesses is derived. In particular, the crossover from bulk-dominated behavior for large thicknesses of layers to interface-dominated behavior for small thicknesses is discussed. The results both qualitatively and quantitatively differ from mean-field theory; the experimental observation for $\text{FeF}_2/\text{CoF}_2$ and CoO/NiO superlattices is explained.

Magnetic superlattices are new materials whose magnetic properties are readily distinguishable from those of bulk materials. For example, the specific heat of an $\text{FeF}_2/\text{CoF}_2$ superlattice cannot be obtained by the superposition of the individual bulk specific heats of FeF_2 and CoF_2 due to interfacial interaction. Many theoretical investigations^{2,3} on magnetic superlattices have been put forward with different models and approximations. While most of the attention was focused on low-temperature properties, Diep⁴ has recently studied the magnetic transition temperature of a Heisenberg model of antiferromagnetic superlattices by using a Green's function method. To explain the experimental data¹ on thermal expansion coefficient which is proportional to magnetic contribution of specific heat, a mean-field theory^{5,6} has also been developed. With this theory, one can qualitatively estimate a critical thickness of the layers above which the specific heat displays two maxima with respect to temperature. The peak at the higher temperature corresponds to the phase transition in the superlattice while the other at the lower temperature is due to the rapid increase of the moments of the material with lower bulk Néel temperature. This latter maximum may be suppressed by interfacial interaction when the layer thicknesses are reduced. Although the mean-field theory successfully describes some properties of the superlattices, it fails to explain the long magnetic coherence length observed experimentally. Borchers *et al.*⁷ have shown that for certain temperature ranges, e.g., above 400 K, the center of the CoO layers (Néel temperature of bulk CoO is 291 K) has vanishingly small moments while the magnetic coherence length is still much larger than the bilayer thickness of NiO/CoO superlattices.

We study the temperature dependence of the magnetic properties of magnetic superlattices by using the Bethe-Peierls approximation. This approximation⁸ is a useful tool for studying spin-glass systems in which both the magnitude and the sign of the interactions between neighboring magnetic spins are random.⁹ Although both the Bethe approximation and the mean-field theory give the same critical exponents near the transition temperatures, the key difference is that the former takes into account the short-range correlation which is essential in understanding the temperature dependence

of the magnetic properties. It turns out that experimental data on the magnetization, the coherence length, and the specific heat can be well explained.

The interaction we consider is of the nearest-neighbor Ising type in which a spin in the n th layer parallel to the interfaces only couples with spins in nearest layers:

$$H = - \sum_{n,i} H_n^i s_n^i - \sum_{n,(i,j)} J_{n,n+1} s_n^i s_{n+1}^j, \quad (1)$$

where s_n^i is the spin at site i in the n th layer, and H_n^i is the local external magnetic field. Here we have neglected coupling of the spins within the same layers.¹⁰ We now apply the Bethe approximation to the above Hamiltonian for spin-half, i.e., $s_n^i = \pm 1$; extension to the higher order spins will be given elsewhere.

The Bethe approximation to an Ising spin system on a regular lattice can also be taken as an exact solution of the system on a Bethe lattice.¹¹ This lattice is simply connected, i.e., for any two sites there is a unique path to connect them; each site connects with independent branches. The interaction from all branches to a given site can be represented by effective fields h_n^l , where integer l runs from 1 to the coordination number 2μ . For layered structures, translational invariance in planes parallel to the interfaces simplifies these effective fields to A_n and B_n which are the contributions from the branches connecting n th layer to $(n+1)$ -th and $(n-1)$ -th layers, respectively. Therefore, the thermodynamic average of the spin s_n^i can be written as⁹

$$s_n \equiv \langle s_n^i \rangle = \tanh(\beta H_n^i + \beta \mu A_n + \beta \mu B_n), \quad (2)$$

where $\beta = 1/kT$ and we have used uniform external fields in planes parallel to interfaces, i.e., $H_n = H_n^i$.

To find these effective fields, we focus on one branch from a site in the n th layer to one in the $(n+1)$ -th layer. For this one branch system, one can easily arrive at

$$\frac{e^{\beta A_n}}{e^{-\beta A_n}} = \frac{e^{\beta(J_{n,n+1} + h_{n+1}')} + e^{\beta(-J_{n,n+1} - h_{n+1}')}}{e^{\beta(-J_{n,n+1} + h_{n+1}')} + e^{\beta(J_{n,n+1} - h_{n+1}')}}, \quad (3)$$

where $h_{n+1}' \equiv H_{n+1} + (\mu-1)A_{n+1} + \mu B_{n+1}$. A simple algebra leads to

$$\tanh(\beta A_n) = \tanh(\beta J_{n,n+1}) \tanh[\beta H_{n+1} + \beta(\mu-1)A_{n+1} + \beta \mu B_{n+1}]. \quad (4)$$

Similarly,

$$\tanh(\beta B_n) = \tanh(\beta J_{n-1,n}) \tanh[\beta H_{n-1} + \beta(\mu-1)B_{n-1} + \beta \mu A_{n-1}]. \quad (5)$$

The above equations, Eqs. (4) and (5), with the periodic boundary conditions form a complete set of self-consistent equations for $\{A_n\}$ and $\{B_n\}$ that can be solved numerically; so can all the derivatives. Once we solve these recursion equations, the magnetization in each layer for the superlattice can be obtained by using Eq. (2). The other thermodynamic quantities can also be found numerically.

The internal energy is

$$U = - \sum_n H_n s_n - \sum_{n,\langle i,j \rangle} J_{n,n+1} \langle s_n^i s_{n+1}^j \rangle \quad (6)$$

and specific heat is $c_v = dU/dT$. To calculate these quantities, we need to find the correlation function $\langle s_n^i s_m^j \rangle$. In general, this can be done by first calculating the local susceptibility and then by using the fluctuation-dissipation relation. For a particular case where $m = n+1$, we find the correlation between two neighboring spins is

$$\langle s_n^i s_{n+1}^j \rangle = q_{n,n+1} \pm (q_{n,n+1}^2 - 2q_{n,n+1} s_n s_{n+1} + s_n^2 + s_{n+1}^2 - 1)^{1/2}, \quad (7)$$

where $q_{n,n+1} = \coth(2\beta J_{n,n+1})$, and $+$ ($-$) corresponds to $J > 0$ ($J < 0$). It is clearly seen that above the transition temperature, in which all $s_n = 0$, the correlation does not vanishes, in contrast to the mean-field theory.

We now consider an infinite antiferromagnetic superlattice which consists of material A with exchange constant $J_A < 0$ and layer thickness N_A (in units of monolayers), and material B with exchange constant $-J_B > -J_A$ and layer thickness N_B . We choose J_A and J_B such that they give the correct Néel temperatures T_A and T_B for bulk samples of A and B within the Bethe-Peierls approximation, i.e., $J_{A(B)} = 0.5kT_{A(B)} \exp[(2\mu-2)/2\mu]$.¹² The only unknown parameter is the exchange constant at an interface J_s which characterizes the coupling between materials A and B. A reasonable value for J_s is an average of J_A and J_B for an ideal superlattice. The magnetic unit cell of the superlattice is $P = N_A + N_B$ if it is even and $P = 2(N_A + N_B)$ if $N_A + N_B$ is odd. To solve Eqs. (4) and (5) efficiently, we expand their right sides in terms of $\tanh \beta A_n$ and $\tanh \beta B_n$. Rather than solve for A_n and B_n , we determine $\tanh \beta A_n$ and $\tanh \beta B_n$ because these functions are bounded between -1 to 1 and are well-behaved numerically. By giving initial random values of $\tanh \beta A_n$ and $\tanh \beta B_n$ ($n = 1, 2, \dots, P$) and by using periodic boundary conditions (e.g., $\tanh \beta A_{P+1} = \tanh \beta A_1$), one can easily achieve solutions for any given temperatures. In all the ranges of temperature we considered, the number of iterations required for convergence is typically smaller than 10^4 , even near the transition temperature.

The temperature variation of the moments in the superlattice is depicted in Fig. 1 where we show the moments of

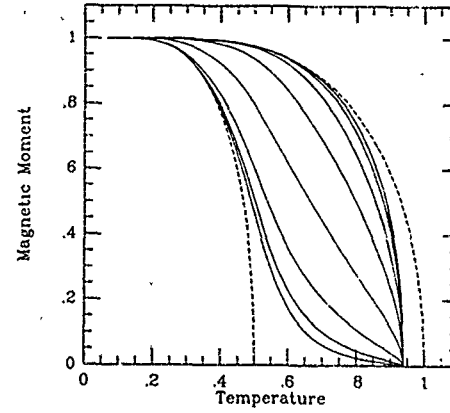


FIG. 1. Temperature dependence of the moments in a superlattice. We have chosen $N_A = N_B = 8$, $J_B = 2J_A$, $J_s = 1.5J_A$, and $2\mu = 8$. Temperature is normalized to the bulk Néel temperature T_B . The dashed curves represent the moments of bulk materials of A (lower curve) and B (upper curve). The eight moments from the center of the A layers to the center of B layers are represented by the eight solid curves (from lowest to highest).

the layers from the center of the material A to the center of the material B. When the temperature is lowered to the transition temperature, the ordering occurs in the entire superlattice simultaneously; this can be seen by nonzero values of moments for all layers below the transition temperature. When the moments are built up for layers of B, they act as an "external field" and induce moments in A layers. However, the moments in the center of A remain small until the temperature is lowered close to the bulk Néel temperature T_A —a signature of bulk feature that the moments increase rapidly near T_A . The magnetization curves in Fig. 1 are in good agreement with the neutron scattering experiment.⁷

Although mean-field theory gives the similar behavior to Fig. 1, there are significant differences in understanding other magnetic properties. Let us suppose the superlattice is divided into pieces; each piece consists of material B with thickness N_B sandwiched by A with thickness of $N_A/2$ on both sides. Since the mean-field theory neglects local correlations, these pieces are coupled through average moments of the boundaries of each piece (same as the moments in the center of A layers, see Fig. 1). These moments are quite small when the temperature is close to T_B , e.g., $T > 0.8T_B$. Therefore, the mean-field theory predicts that these pieces defined above are magnetically uncoupled for temperature $T > 0.8T_B$. Equivalently, the magnetic correlation length must be smaller than bilayer thickness at these temperatures; this is in contradiction with the experimental observations by Borchers *et al.*⁷ They have shown that the magnetic coherence length of the NiO/CoO superlattice is several times larger than the bilayer thickness at $T = 400$ K while the moments of the center of the CoO layers are practically zero. Our formulation overcomes this apparent shortcoming of the mean-field theory, because we have taken into account the short-range correlations. From Eq. (7), the correlation function is sizable even if s_n is zero. The energy, Eq. (6), depends on these correlation function and, therefore, one cannot freely flip all the spins in one piece mentioned above without changing the spins in other parts. To describe the magnetic

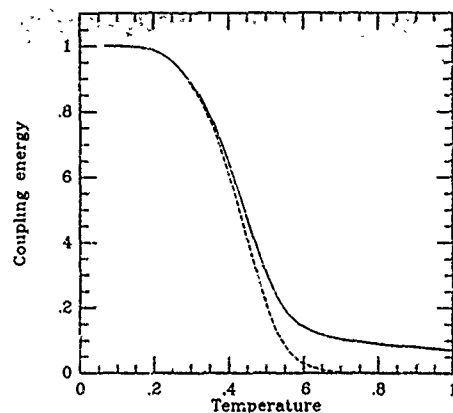


FIG. 2. Temperature dependence of the coupling energy for the same superlattice with Fig. 1. Solid and dashed curves are from our calculation and the mean-field theory, respectively.

coupling in the antiferromagnetic superlattice we define the coupling energy to be the change of energy by flipping all the spins in one piece while leaving all others unchanged. This definition of the coupling energy is similar to that for ferromagnetic superlattices, e.g., Fe/Cr.¹³ We show in Fig. 2, the coupling energy as a function of temperature. For comparison, we also show the corresponding curve from the mean-field theory. The salient feature is that the coupling energy, which is proportional to the correlation function, is considerably larger than that of mean-field theory when the temperature is above T_A . Therefore, we are able to explain why the superlattice of NiO/CoO is coherent while the moments in the center of CoO layers are vanishingly small.

To compare with experimental results on the thermal expansion of FeF₂/CoF₂ which is proportional to the specific heat, we calculate the specific heats for three samples with different combinations of layer thicknesses. For thick samples $N_A=30$ and $N_B=25$, there are two peaks shown in Fig. 3. The first peak near T_B characterizes the phase transition, while the second peak comes from rapid changes of the moments in the material A (CoF₂) near T_A . Although the second peak (to be called as quasitransition peak) does not represent a true phase transition, it reflects the bulk property of CoF₂. When the CoF₂ layer is thin as for the sample of $N_A=6$ and $N_B=19$, however, the quasitransition is completely suppressed by interfacial interactions. The presence or absence of the quasitransition peak, as well as the shape of the specific curves for FeF₂/CoF₂ superlattices, are in excellent agreement with the experimental results.¹

We should point out that the specific heats we show in Fig. 3 are different from that coming from the mean-field calculation. Since the mean-field theory sets zero correlation,

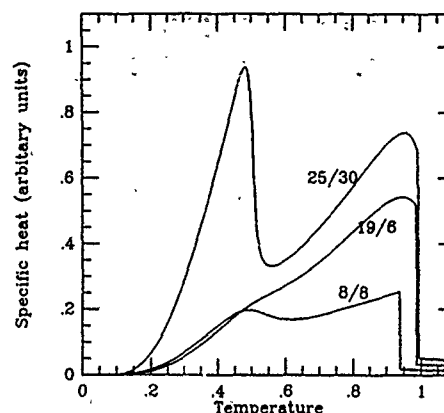


FIG. 3. Temperature dependence of specific heats per superlattice period. The three curves labeled as 25/30, 19/6, and 8/8 are for three samples with different layer thickness N_B/N_A .

the influence of the material B to the material A is underestimated. The quasitransition peaks in specific heats which characterize one of the bulk properties for material A are much higher than ours. Therefore, in order to explain the on-set of the suppression of the quasitransition peak in thin layers one must choose much larger interfacial interaction constant in the mean-field theory than in our approximation. In addition, we find the specific heat is nonzero when the temperature is higher than the transition temperature, (see Fig. 3), in contrast to the mean-field theory.

This work was supported by the Office of Naval Research Grant No. N00014-91-J-1695 (SZ), the National Science Foundation Grant No. CHE-9002146 (GZ), and NSF postdoctoral Fellowship ASC-9310295 (GZ).

¹C. A. Ramos, D. Lederman, A. R. King, and V. Jaccarino, Phys. Rev. Lett. **65**, 2913 (1990).

²B. Hillebrands, Phys. Rev. B **37**, 9885 (1988).

³L. L. Hinchey and D. L. Mills, Phys. Rev. B **34**, 1698 (1986).

⁴H. T. Diep, Phys. Rev. B **40**, 4818 (1989).

⁵A. S. Carrico and R. E. Camley, Phys. Rev. B **45**, 13 117 (1992).

⁶R. W. Wang and D. L. Mills, Phys. Rev. B **46**, 11681 (1992).

⁷J. A. Borchers, M. J. Carey, R. W. Erwin, C. F. Majkrzak, and A. E. Berkowitz, Phys. Rev. Lett. **70**, 1878 (1993).

⁸G. Zhang and J. K. Percus, J. Stat. Phys. **70**, 1365 (1992); J. K. Percus, *ibid.* **60**, 221 (1990).

⁹G. Zhang and J. K. Percus, J. Math. Stat. Phys. **32**, 2561 (1991).

¹⁰We can also introduce the interactions within the plane of the layers; this will engender an additional coupling parameter. Furthermore, for the NiO/CoO and FeF₂/CoF₂ superlattices stacked on (111) direction, the interactions within the layer planes are much smaller than those of interplanes.

¹¹R. J. Baxter, in *Exactly Solved Models in Statistical Mechanics* (Academic, New York, 1989), p. 47-49.

¹²K. Huang, in *Statistical Mechanics*, 2nd ed. (Wiley, New York, 1987), pp. 357-361.

¹³J. J. Krebs, P. Lubitz, A. Chaiken, and G. A. Prinz, Phys. Rev. Lett. **63**, 1645 (1989).

Magnetic and crystallographic properties of molecular beam epitaxially grown $\text{Fe}_3\text{O}_4/\text{NiO}$ superlattices and Fe_3O_4 films

J. J. Krebs

Naval Research Laboratory, Washington, DC 20375-5000

D. M. Lind, E. Lochner, K. A. Shaw, W. Portwine, and S. D. Berry

Department of Physics and MARTECH, Florida State University, Tallahassee, Florida 32306-3016

Ferromagnetic resonance, SQUID magnetometry, and x-ray diffraction have been used to characterize a set of $[\text{Fe}_3\text{O}_4(68 \text{ \AA})/\text{NiO}(17 \text{ \AA})]_N$ superlattices (SL) with $N=3, 10, 30$, and 100 , as well as a $1.5\text{-}\mu\text{m}$ -thick Fe_3O_4 film. For this NiO thickness, Fe_3O_4 layers are strongly coupled and the in-plane anisotropy is much less than the 330-Oe ferromagnetic resonance (FMR) linewidth at 35 GHz. Both in-plane and perpendicular FMR at 9.5 and 35 GHz have been used, with the 9.5-GHz data showing significant hysteresis associated with the sample magnetization. X-ray diffraction indicates that both the film and SL's are nearly cubic single-crystalline structures with long-range coherence. The 300 K magnetization data indicate the presence of small cubic anisotropy in the SL's, although bulklike Fe_3O_4 magnetic ordering in the thick single film. When the Fe_3O_4 film is cooled below the Verwey transition in a 10 kOe field (aligned along $\langle 100 \rangle$), the FMR shows that the sample develops a large uniaxial ($K_u=1.8$ kOe) in-plane anisotropy with its easy axis along the field direction. Decreased microwave loss also occurs abruptly at the film T_V .

The near-lattice-matched structures of Fe_3O_4 , NiO, and MgO permit one to grow superlattices (SL) of $\text{Fe}_3\text{O}_4/\text{NiO}$ on MgO(001) substrates. Recent work shows that the interplay of the interlayer exchange, the bulk and strain-induced anisotropy, and alternating ferrimagnetic and antiferromagnetic structures lead to unusual magnetic properties in this system.^{1,2} In this paper, we extend the coordinated ferromagnetic resonance (FMR), magnetometry, and x-ray diffraction study carried out earlier³ to examine the effect of temperature, field cooling and the number of bilayers on the magnetic properties of $\text{Fe}_3\text{O}_4/\text{NiO}$ superlattices and Fe_3O_4 films.

A Fe_3O_4 sample $1.5 \mu\text{m}$ thick and a series of $(\text{Fe}_3\text{O}_4/\text{NiO})_N$ superlattice samples were grown on thin MgO(001) substrates by oxygen-plasma-assisted molecular beam epitaxy using the methods described previously.⁴ For the superlattices used in the present study, the Fe_3O_4 layer thickness was held fixed at 68 \AA (eight magnetic unit cells) and the NiO thickness at 17 \AA (four magnetic unit cells). Samples were prepared with $N=3, 10, 30$, and 100 to probe the effect of the bilayer repetition number on the magnetic behavior.

Ferromagnetic resonance measurements were carried out at 35 and 9.5 GHz at various temperatures in the range 100–300 K. Both magnetic field in-plane and perpendicular data were obtained. SQUID magnetometry data were acquired on all samples in fields up to 55 kOe either parallel or normal to the thin film. The θ - 2θ x-ray diffraction patterns measured for each of these samples permitted the SL period and the in-plane and perpendicular coherence to be established. The more intense modulation satellites could be seen easily even for the $N=3$ superlattice while for the $N=100$ sample at least nine high-angle satellites were measurable. Analysis of the peak positions and linewidths of the x-ray spectra established the presence of a nearly cubic single-crystal lattice with long-range ($>2000 \text{ \AA}$) coherence in the Fe_3O_4 film, and SL's with a nearly 1% in-plane lattice distortion and coherence length that scales with the total SL thickness. X-ray

spectra of similar superlattices have been reported previously.^{1,4}

When the temperature of bulk Fe_3O_4 is cooled below the so-called Verwey transition, the conductivity abruptly decreases, caused by the atomic ordering of the Fe^{2+} ions, and the lattice distorts.⁵ Based on this behavior, the film FMR was examined as a function of temperature, and Fig. 1 shows the FMR spectra at 35 GHz after the sample has been cooled through the Verwey temperature T_V with a field of 14 kOe applied along $[100]$.

Note that the previously equivalent $[100]$ and $[010]$ spectra are very distinct after the field cooling. Most of the film gives rise to the broad FMR lines near 5.6 kOe for $\vec{H}||[100]$ and 10.9 kOe for $\vec{H}||[010]$. A small fraction of the film which did not distort produces the narrower FMR lines near 9.4 kOe in both orientations. Alternatively, one can cool with $\vec{H}||[010]$ and the roles of $[100]$ and $[010]$ are reversed. This indicates that the application of a large field along a given $\langle 100 \rangle$ during cooling selects that direction as the magnetically easy direction for all (or almost all) of the sample.

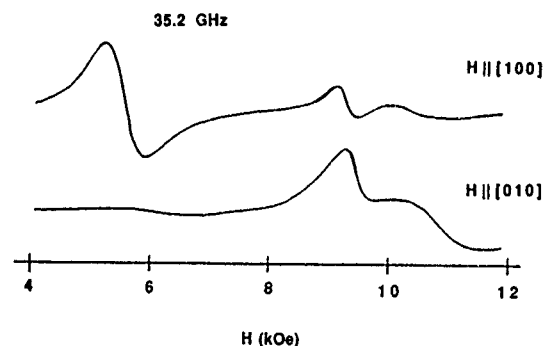


FIG. 1. Effect of cooling a Fe_3O_4 film through the Verwey transition with a field of 14 kOe along the in-plane $[100]$. The subsequent in-plane 35.2-GHz FMR spectra are shown for $\vec{H}||[100]$ and $\vec{H}||[010]$. At room temperature, a single narrow FMR line at 10.3 kOe is found for both these field directions.

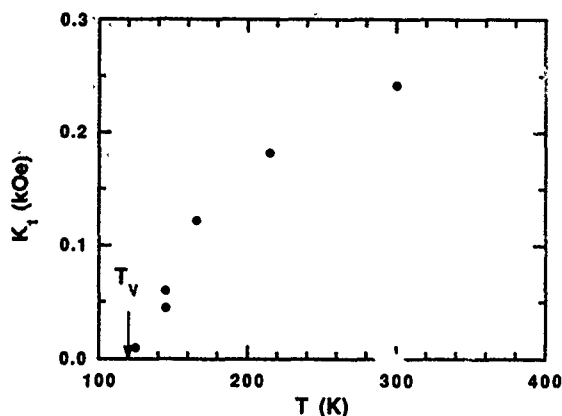


FIG. 2. Temperature dependence of the cubic anisotropy parameter K_1 for a 1.5- μm -thick Fe_3O_4 film.

We found that cooling in zero field leaves the two in-plane $\langle 100 \rangle$ directions equivalent and the spectrum a superposition of the two field-cooled cases, indicating that the film breaks up into different regions with their local distortion axes (and, hence, easy directions) along one or the other $\langle 100 \rangle$.

The in-plane angular dependence of the spectra in the distorted Verwey state can be fit fairly well with the following parameters: $4\pi M' = 7.5$ kG, $K_u/M = -1.8$ kOe, and $K_1 = 0$. Here, $K_u \cos^2 \alpha$ is a uniaxial anisotropy which favors $M \parallel \vec{H}_{\text{cool}}$, α is the angle between \vec{H}_{cool} and M , and K_1 is the usual fourth-order cubic anisotropy. The strain introduced as the film distorts introduces a significant change in the effective magnetization $4\pi M' = 4\pi M + 2K_1/M$.

We found that a large (cold) field applied 90° away from the field-cooled direction causes a decrease in intensity of the field-cooled signal. Furthermore, as the sample warms toward T_V , the field-cooled signal also decreases while the previously weak signal due to undistorted Fe_3O_4 (near 9.4 kOe in Fig. 1) increases and narrows rapidly. After the abrupt decrease in microwave cavity Q (indicating the increase in sample conductivity at T_V) occurs, only the undistorted signal remains. The temperature variation of the cubic anisotropy of the film for $T > T_V$ is shown in Fig. 2. It appears that K_1 , which decreases as the temperature is lowered below 200 K, vanishes at T_V .

Finally, we note that when one carries out similar experiments at 9.1 GHz with a 14-kOe field normal to the film during cooling below T_V , the marked hysteresis shown in Fig. 3 is found. The intense signal near 5.2 kOe (found only when H is decreasing) occurs just as the sample magnetization direction starts to deviate from being parallel to H . It is not clear why only a very weak version of this signal is observed for H increasing. Note also the decrease in $4\pi M'$ (shown by the drop in the resonance field, see trace c) when $T < T_V$. This is due to a decreased $4\pi M'$ induced by the Fe_3O_4 distortion favoring M normal to the film when \vec{H}_{cool} is along the normal. The low-field satellites seen in Fig. 3(c) are spin waves as indicated by explicit calculations.

We call attention to the fact that the FMR behavior described above is similar to that found⁶ for bulk Fe_3O_4 . This shows that the substrate-induced distortion ($\approx 0.3\%$ for this

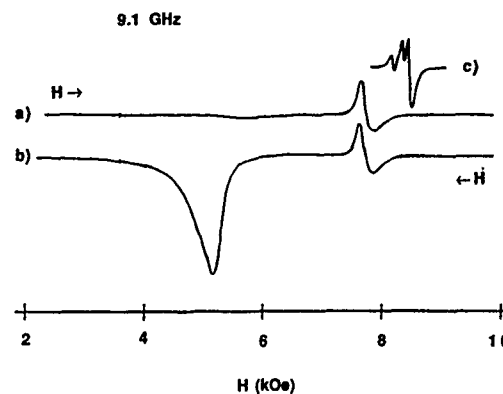


FIG. 3. Note the marked hysteresis in the 9.1-GHz FMR spectrum of a Fe_3O_4 film field-cooled with H (and \vec{H}_{cool}) along the $[001]$ film normal for (a) increasing and (b) decreasing field scans. Trace (c) shows the corresponding spectrum at 300 K.

sample) does not have any major qualitative effect on the magnetic properties of the film.

The most significant magnetic aspect of the behavior of $\text{Fe}_3\text{O}_4/\text{NiO}$ superlattices is the difficulty in saturating the magnetization even when the magnetic field is applied in plane.^{1,2} For example, our present measurements show that the magnetization of a $[\text{Fe}_3\text{O}_4(68 \text{ \AA})/\text{NiO}(17 \text{ \AA})]_{100}$ SL [shown in Fig. 4(a)] is only 65% of saturation at 20 kOe and is still not saturated at 50 kOe. The magnetization profiles of the $N=30$ and 10 SL's are qualitatively the same as the $N=100$ SL, when the total moment is normalized to the Fe_3O_4 volume, with sigmoidal hysteresis and difficulty of saturation. The profile for $[\text{Fe}_3\text{O}_4(68 \text{ \AA})/\text{NiO}(17 \text{ \AA})]_3$ [Fig.

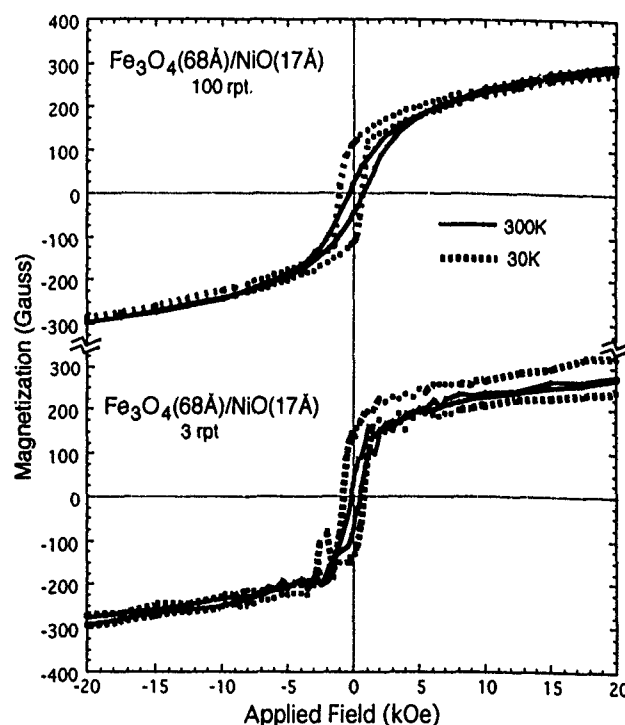


FIG. 4. Magnetization vs magnetic field behavior for two $[\text{Fe}_3\text{O}_4(68 \text{ \AA})/\text{NiO}(17 \text{ \AA})]_N$ superlattices with $H \parallel [100]$; (a) $N=100$ and (b) $N=3$.

TABLE I. FMR Parameters of $(\text{Fe}_3\text{O}_4/\text{NiO})_N$ superlattices. Based on 35-GHz data at 300 K, $g \approx 2.12$ assumed.

N	$4\pi M'$ (kG)	δH (kOe)	W_{\parallel} (kOe)	W_{\perp} (kOe)
100	2.34	0.08	0.33	0.47
30	2.12	0.08	0.33	0.44
10	2.14	0.075	0.32	0.37
3	2.34	0.06	0.34	0.44

4(b)] is somewhat narrower and squarer with a low-field shoulder and nearly linear high-field slope.

We consider this lack of saturation most likely to be due to a frustrated magnetic state in which different Fe_3O_4 regions of the SL sample have their net magnetic moments aligned in opposite directions (in zero field). This "frustration" is thought to arise from local errors in the nominal Fe_3O_4 or NiO thickness which lead to some adjacent 68-Å Fe_3O_4 layers being exchange coupled antiparallel rather than parallel as would be the case for a perfect superlattice.

Assuming this is the origin of the effect, the question arises as to whether this variation is mostly a bilayer-to-bilayer effect or if the errors are distributed randomly across the film plane. Since the likelihood of the occurrence of a layer-to-layer fluctuation increases with the number of $\text{Fe}_3\text{O}_4/\text{NiO}$ repeats, one would expect to see corresponding changes in the M vs H and FMR behavior with N if layer-to-layer effects were dominant.

The relevant FMR data are summarized in Table I for the superlattices studied. The effective magnetizations $4\pi M'$ determined from H in-plane or H perpendicular data are in

good agreement and only the average value is given. The quantity δH represents the maximum variation in the FMR field position as the direction of H is varied in-plane. As can be seen from Table I, this anisotropy variation is never more than a small fraction of the parallel or perpendicular linewidths W . We also note that the FMR positions do not show full fourfold symmetry as H is rotated in plane although weak inequivalent minima were observed at the two $\langle 100 \rangle$ directions.

The most important information in Table I, however, is the observation that none of the parameters listed show any large or systematic variation with N even though N is varied by more than a factor of 30. From this and the magnetization data of Fig. 4, we conclude that any region-to-region coupling-sign variation must be distributed primarily among areas within individual superlattice bilayers rather than mainly through the SL thickness.

The authors wish to acknowledge the support given by the Office of Naval Research and the National Science Foundation to different aspects of this work. We are also grateful to P. Lubitz and S. A. Shaheen for helpful discussions during this investigation.

¹D. M. Lind, S.-P. Tay, S. D. Berry, J. A. Borchers, and R. W. Erwin, J. Appl. Phys. **73**, 6886 (1993).

²S. D. Berry, D. M. Lind, G. Chern, and H. Mathias, J. Magn. Mater. **123**, 126 (1993).

³J. J. Krebs, D. M. Lind, and S. D. Berry, J. Appl. Phys. **73**, 6457 (1993).

⁴D. M. Lind, S. D. Berry, G. Chern, H. Mathias, and L. R. Testardi, Phys. Rev. B **45**, 1838 (1992).

⁵Z. Kalol and J. M. Hönl, Phys. Rev. B **40**, 9090 (1989); R. Aragon, R. J. Rasmussen, J. P. Shepherd, J. W. Koenitzer, and J. M. Hönl, J. Magn. Mater. **54-57**, 1335 (1986).

⁶L. R. Bickford, Phys. Rev. **78**, 499 (1950).

Studies of the Verwey transition in $\text{Fe}_3\text{O}_4/\text{NiO}$ superlattices by SQUID magnetometry and neutron diffraction techniques (abstract)

S. D. Berry

Department of Physics and MARTECH, Florida State University, Tallahassee, Florida 32306

J. A. Borchers and R. W. Erwin

Material Science and Engineering Laboratory, NIST, Gaithersburg, Maryland 20899

D. M. Lind, K. A. Shaw, and E. Lochner

Department of Physics and MARTECH, Florida State University, Tallahassee, Florida 32306

Single crystal superlattices of Fe_3O_4 and NiO , grown on $\text{MgO}(100)$, provide a means to study the competition between interfacial exchange coupling effects and epitaxial strain induced by these closely, but not perfectly, lattice matched materials. Both induce profound macroscopic magnetic effects in the superlattices, especially for films with very thin ($<80 \text{ \AA}$) modulation thicknesses. The Fe_3O_4 Verwey conductivity transition in the bulk ($\sim 120 \text{ K}$) is highly sensitive to both the exact stoichiometry of the iron oxide and the presence of strain and is accompanied by a structural and magnetic anisotropy change. X-ray diffraction measurements show that these superlattices are tetragonally distorted (up to 1%), with the increased strain associated with superlattices composed of thin bilayers. By tracking the magnetic evidence of this phase transition using SQUID magnetometry techniques, we observe attenuation of the effect in superlattice films as the iron oxide layers grow thinner and the nickel oxide layers are thickened, which suggests that the presence of strain in the iron oxide layers is highly important. The small structural distortion is observable in neutron diffraction measurements of a Fe_3O_4 film. Studies of the diffuse and critical scattering associated with this transition in strained iron oxide films and $\text{Fe}_3\text{O}_4/\text{NiO}$ superlattices and a comparison to previous work on bulk Fe_3O_4 single crystals will be discussed.

The research at FSU was supported by NSF Grant No. DMR-92-06870.

Magnetic structure determination for $\text{Fe}_3\text{O}_4/\text{NiO}$ superlattices by neutron diffraction techniques (abstract)

J. A. Borchers, R. W. Erwin, and J. F. Ankner

*Material Science and Engineering Laboratory, National Institute of Standards and Technology,
Gaithersburg, Maryland 20899*

S. D. Berry, D. M. Lind, E. Lochner, and K. A. Shaw

Department of Physics and MARTECH, Florida State University, Tallahassee, Florida 32306

Neutron diffraction measurements reveal the nature of the magnetic structure in $\text{Fe}_3\text{O}_4/\text{NiO}$ superlattices grown by molecular beam epitaxy. By taking advantage of differences between the spinel and rocksalt crystalline symmetries, we have separated the magnetic order parameters of the Fe_3O_4 and NiO bilayer components. The NiO antiferromagnetic order develops at temperatures 10–150 K greater than $T_{\text{Néel}}$ for bulk (520 K) due to exchange coupling of the Ni spins to the Fe_3O_4 ($T_{\text{Curie}}=858$ K) at the superlattice interfaces. The resultant scaling of the NiO transition temperature with the bilayer composition is consistent with expectations from mean-field treatments for a modulated magnetic material. In addition, the NiO spin order propagates coherently through several superlattice bilayers, while the magnetic coherence of the Fe_3O_4 is limited by a random stacking of the spinel unit cell at the interfaces when the NiO interlayers are thicker than ≈ 15 Å. A model for the diffraction data, based upon a Hendricks–Teller description of the interfacial disorder, demonstrates that the observed broadening of selected crystalline and magnetic reflections originates directly from these stacking faults. Combining the high angle diffraction results with those from polarized-beam reflectivity analysis, we extract specific information about the moment distribution in these superlattices and qualitatively explain the evolution of the magnetic structure with temperature.

The research at FSU was supported by Grant No. NSF DMR-92-06870.

Perpendicular magnetoresistance in magnetic multilayers: Theoretical model and discussion (invited)

Albert Fert

Laboratoire de Physique des Solides,^{a)} Université Paris-Sud, 91405 Orsay, France

Thierry Valet

Laboratoire Central de Recherches Thomson-CSF, 91404 Orsay, France

Jozef Barnas

Institute of Physics, A.M. University, 60-769 Poznan, Poland

After a general introduction describing the mechanisms of the current perpendicular to the layer plane magnetoresistance (CPP-MR), a microscopic model based on the Boltzmann equation is presented and a general expression of the magnetoresistance is derived in which the spin diffusion length appears as the unique scaling length of the problem. In the limit where the spin diffusion lengths are much larger than the layer thicknesses, the expression of the CPP-MR becomes very simple and similar to that already used at Michigan State University for the analysis of experimental results. Out of this limit, the model predicts a dramatic reduction of the CPP-MR if the spin diffusion lengths are shortened sufficiently by paramagnetic impurities or spin-orbit scatterers. Finally, a calculation is presented of the spin-dependent interface resistances involved in the model and related to interface potential steps, and experimental data are compared.

I. INTRODUCTION

The giant magnetoresistance (GMR) of the magnetic multilayers^{1,2} was first observed and studied in the so-called CIP (current-in-plane) geometry. Then, in 1991, Pratt *et al.*³ at Michigan State University could also measure GMR effects in the CPP (current perpendicular to the layer plane) geometry. We refer to Pratt *et al.*⁴ and to the invited paper of Bass *et al.* at this conference⁵ for a review of the extensive results obtained at Michigan State University on multilayer structures based on the Co/Cu and Co/Ag systems. More recently, Gijs, Lenczowski, and Giesbert⁶ have also been able to measure CPP-GMR effects on mesoscopic structures prepared by lithography (which allows them measurements at room temperature).

The several models developed for the CIP-GMR (Ref. 7 and 8) are very generally based on the different conduction properties of the spin \uparrow (majority) and spin \downarrow (minority) electrons in ferromagnetic metals.⁹ Although the CPP-MR can be also attributed to spin-dependent conduction, there are important fundamental differences between the mechanisms of the CPP- and CIP-MR. The main difference actually comes from the spin accumulation and spin relaxation effects occurring in the CPP geometry.

An illustration of the spin accumulation and relaxation effects at an interface is presented in Fig. 1. A plane boundary separates two semi-infinite ferromagnetic materials having opposite magnetizations (one can imagine a very thin nonmagnetic layer separating the two regions). We suppose that the conductivity of the majority spin channel is larger. Therefore, far from the boundary on the left-hand side, the

spin \uparrow electrons (those which are majority electrons in this region) carry a larger part of the current than the spin \downarrow electrons. On the contrary, at the right-hand side, the spin \downarrow (now minority electrons) carry a smaller part of the current. Consequently, for electrons flowing from the left- to the right-hand side, the incoming flux of spin \uparrow (spin \downarrow) electrons from the left-hand side is larger (smaller) than their outgoing flux to the right-hand side, which gives rise to accumulation (depression) of spin \uparrow (spin \downarrow). This means an out-of-equilibrium polarization and an increase (for spin \uparrow) or decrease (for spin \downarrow) of the chemical potential around the boundary. In a stationary regime, the out-of-equilibrium polarization is balanced by spin relaxation processes. However, because the spin relaxation time is very long (compared to the momentum relaxation time), the spin \uparrow accumulation (or spin \downarrow depression) diffuses far from the interface. The equations of this problem have already been written down by Johnson and Silsbee¹⁰ or van Son, van Kempen, and Wyder.¹¹ In the case of Fig. 1, with, in addition, symmetric spin \uparrow and spin \downarrow bands differing only by their scattering rates, one obtains an exponential variation of the spin polarization, that is, an exponential increase (decrease) of the chemical potentials of the spin \uparrow (spin \downarrow) electrons, $\Delta\mu_{\uparrow(\downarrow)} = \pm\Delta\mu$ with $\Delta\mu \sim \exp(z/l_{sf})$ on the left-hand side and $\Delta\mu \sim \exp(-z/l_{sf})$ on the right-hand side; l_{sf} is the spin diffusion length (SDL) that we define precisely below. $\Delta\mu$ is represented in Fig. 1(a). The variation with z of the spin-dependent chemical potentials gives rise to spin-dependent forces (pseudoelectric fields) that slow down (accelerate) the spin \uparrow (spin \downarrow) electrons at distances of the order of l_{sf} on both sides of the boundary. Consequently the currents, see Fig. 1(b), and also the electric field, see Fig. 1(c), are affected in a broad range, $-l_{sf} \leq z \leq +l_{sf}$, around the interface.

^{a)} Associé au Centre National de la Recherche Scientifique.

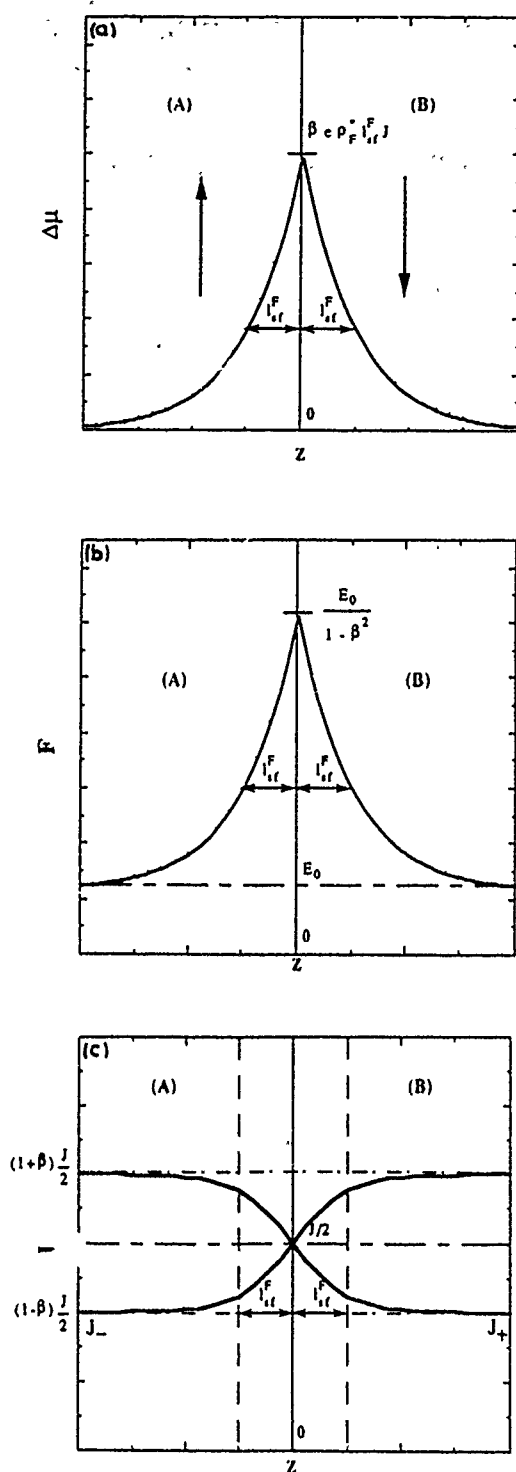


FIG. 1. Illustration of spin accumulation effects at the interface $z=0$ between two semi-infinite ferromagnetic regions with opposite magnetizations. The arrows indicate the majority spin direction in each region. The electrons flow from left- to right-hand side, and the spin + electrons are supposed to be weakly scattered at the left-hand side and strongly at the right-hand side. The change $\Delta\mu$ of the chemical potential of the spin + electrons (proportional to the out of equilibrium spin polarization), the absolute values of the current densities for spin + and spin - electrons, J_+ and J_- , respectively, and the absolute values of the electric field E are plotted vs z . See also Refs. 14 and 15.

In contrast, in the CIP geometry, the perturbation by an interface does not extend farther than the resistivity mean free path (MFP) λ . This is an important difference since, in systems such as Co/Cu or Co/Ag, l_{sf} is estimated at a few thou-

sand Å and is larger than λ by one order of magnitude.^{12,13}

This fundamental difference between CIP and CPP appears clearly also in the theoretical models: the MFP λ is the scaling length of CIP-MR,^{7,8} whereas, as shown in Sec. II, the spin diffusion length (SDL) l_{sf} becomes the unique scaling length of the CPP problem. More practically, this also means, for example, that the CIP-MR vanishes when the thicknesses exceed λ , and the CPP-MR only when they exceed l_{sf} (see Sec. IV). Another important consequence is that, with values of l_{sf} of a few thousands of Å, most experiments of CPP-MR have been performed in multilayers with individual thicknesses much shorter than l_{sf} . In this limit, the expression of the CPP-MR becomes very simple,^{12,16} in agreement with the phenomenological picture developed at Michigan State University.^{4,5} In CIP-MR, a similar simple limit is expected for individual thicknesses much shorter than the MFP λ , but this thickness range is hard to reach and never very extended.

How do these questions of spin accumulation, spin relaxation and spin diffusion length appear in the theoretical models develop for the CPP-MR up to now?

Johnson and Silsbee¹⁰ and van Son and co-workers¹¹ have treated the problem of spin accumulation at interfaces with macroscopic equations, and Johnson¹⁴ has applied the same approach to the problem of the CPP MR. The model of Valet and Fert,^{12,16} that we summarize in the first part of this article, is a microscopic model of the spin accumulation effects in CPP MR, based on the Boltzmann equation. The first result of this model is that the macroscopic equations of Johnson and Silsbee¹⁰ or van Son and co-workers¹¹ are justified if the MFP λ is much shorter than the SDL l_{sf} (in addition, in this limit, l_{sf} becomes the unique scaling length of the problem). Then, in the application of the CPP MR of the multilayers, our calculation departs from that of Johnson.¹⁴ We show that it is important to treat the interplay between spin accumulation at successive interfaces and we find a general expression¹² of the CPP MR quite different from Johnson's expression.¹⁴ In the limit of very long spin diffusion lengths (much longer than the individual thicknesses) our expression of the GMR becomes very simple and is equivalent to the expressions that Pratt *et al.*^{4,5} have found in a simple "two-channel model" and used for the interpretation of their experiments.

Besides the approach of Johnson¹⁴ or Valet and Fert^{12,16} taking into account the spin accumulation effects and their balance by spin-flip processes, several other models by Zhang, Levy, and Camblong,¹⁷ Bauer,¹⁸ or Inoue, Itoh, and Maekawa¹⁹ are based on the assumption that the current is conserved in each spin channel (no spin flip). This assumption that the electrons of a given absolute spin direction carry the same proportion of the total current in the layers where they are spin \uparrow (majority) and, say, weakly scattered, as well as in the layers where they are spin \downarrow and strongly scattered, is not so odd as it could appear at first view. As a matter of fact, in the limit of very long SDL in our model, the spin-dependent forces arising from spin accumulation accelerate and slow down the electrons in such a way that, in first approximation, the current proportion in each channel does not change when the magnetization flips. Thus, the existence

of spin accumulation effects, with the additional hypothesis of infinite SDL, is the hidden basis of the models with conserved current for each spin direction. It is therefore probable that there are many common features with the predictions of these models¹⁷⁻¹⁹ and what we predict in the long SDL limit of our calculation (in spite of the use of different formalisms, Kubo, Landauer, or Boltzmann).

II. MODEL (REFS. 14 AND 15)

We present shortly the model which is described in detail in Ref. 12. The starting point is a Boltzmann-like equation in which we introduce the following distribution function for the electrons of spin s (note that, throughout the article, we refer to $+$ or $-$ for the absolute spin directions of the conduction electrons, and to \uparrow or \downarrow for the majority and minority spin directions in the magnetic layers),

$$f_s(z, \mathbf{v}) = f^0(v) + \frac{\partial f^0}{\partial \epsilon} \{ [\mu^0 - \mu_s(z)] + g_s(z, \mathbf{v}) \}. \quad (1)$$

The term $g_s(z, \mathbf{v})$ express the displacement of the distribution in the presence of current and the term $\mu_s(z)$ accounts for the z dependence of the chemical potential related to spin accumulation effects [$f^0(v)$ is the Fermi-Dirac distribution]. We obtain for the linearized Boltzmann equation

$$v_z \frac{\partial g_s}{\partial z}(z, \mathbf{v}) + \left(\frac{1}{\tau_s} + \frac{1}{\tau_{sf}} \right) g_s(z, \mathbf{v}) = \left(v_z \frac{\partial \tilde{\mu}_s}{\partial z}(z) + \frac{\tilde{\mu}_s(z) - \tilde{\mu}_{-s}(z)}{\tau_{sf}} \right), \quad (2)$$

where $\tilde{\mu}_s(z) = \mu_s(z) - eV(z)$ is the electrochemical potential for spin s , and $(\tau_{sf}^{-1} + \tau_s^{-1}) = (\tau'_s)^{-1}$ and τ_{sf}^{-1} are the relaxation rates for the momentum in each channel and for the spin polarization, respectively. In the low-temperature limit, we neglect the momentum transfer between the two channels by coherent electron magnon scattering, that is, in the usual notation, the spin mixing term $(\tau_{sf}^{-1} \sim \rho_{\uparrow\downarrow})$.⁹ Since τ_{sf} , related to spin-flip scattering, is generally, much longer than the momentum relaxation time τ_s involved in the resistivity, τ'_s/τ_{sf} is a small number. At the lowest order in τ'_s/τ_{sf} , one obtains¹² the macroscopic equations already derived by Johnson and Silsbee¹⁰ or van Son and co-workers,¹¹

$$J_s = \frac{\sigma_s}{e} \frac{\partial \tilde{\mu}_s}{\partial z}, \quad (3)$$

$$\frac{e}{\sigma_s} \frac{\partial J_s}{\partial z} = \frac{(\tilde{\mu}_s - \tilde{\mu}_{-s})}{l_s^2}, \quad (4)$$

where J_s is the current density for spin, s , $\sigma_s = n_s e^2 \tau'_s / m$ is the conductivity for the spin s channel, l_s is the SDL for spin s defined by

$$l_s = v_F [\tau_{sf}(\tau_{sf}^{-1} + \tau_s^{-1})^{-1}/3]^{1/2} \approx v_F (\tau_{sf} \tau_s / 3)^{1/2}. \quad (5)$$

Equation (3) is a sort of Ohm law and Eq. (4) expresses the balance between spin accumulation by the current divergence and the spin relaxation by spin flip. These equations lead to a diffusion-type equation for $\Delta\mu = (\mu_+ - \mu_-)/2$,

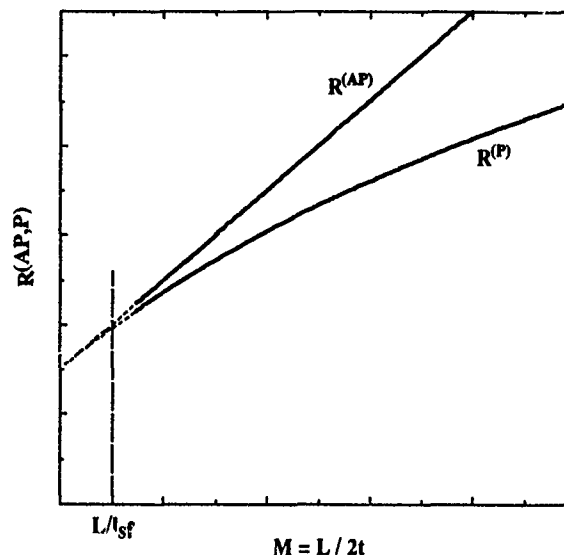


FIG. 2. Predicted variation of the CPP resistance of a multilayer as a function of the number of bilayers M for a fixed total thickness L and the same individual thickness for the ferromagnetic and normal layers, $t_F = t_N = t = L/(2M)$. The calculation is performed for interface spin dependent scattering only ($\beta=0$).

$$\frac{\partial^2 \Delta\mu}{\partial z^2} = \frac{\Delta\mu}{l_{sf}^2}, \quad (6)$$

where $l_{sf}^{-2} = l_1^{-2} + l_2^{-2}$ and to variations as $\exp(\pm z/l_{sf})$ for $\Delta\mu$, for the currents J_+ and J_- and for the electric field $F = (2e)^{-1} \partial(\tilde{\mu}_+ + \tilde{\mu}_-)/\partial z$. We have shown in Fig. 1 the variation of $\Delta\mu$, J_{\pm} , and F for an isolated interface. In multilayers, the interference between successive interfaces gives rise to combinations of $\exp(\pm z/l_{sf})$ and to oscillations with the period of the multilayered structure. Examples are given in Fig. 2 of Ref. 12. In the limit where the SDL l_{sf} is much longer than the layer thicknesses t , the amplitude of the oscillations of $(J_+ - J_-)/(J_+ + J_-)$ vanishes as $(t/l_{sf})^2$, which shows that the assumption of conserved currents in each channel is justified in this limit.

The above model has been used to calculate the CPP resistance and the CPP MR of multilayers. The notation is the following. The resistivity for the spin \uparrow or spin \downarrow electrons in the ferromagnetic layers is written as

$$\rho_{\uparrow(\downarrow)} = \frac{1}{\sigma_{\uparrow(\downarrow)}} = 2\rho_F^* [1 - (+)\beta]. \quad (7)$$

The interface resistance due to diffuse or specular scattering at interfaces (see Sec. V) and involved in the boundary conditions for $\tilde{\mu}(z)$ [i.e., $\tilde{\mu}(0^+) - \tilde{\mu}(0^-) = r_s J_s(0)/e$] is written as

$$r_{\uparrow(\downarrow)} = 2r_b^* [1 - (+)\gamma]. \quad (8)$$

The notation in Eqs. (7) and (8) is the same as in Refs. 4 and 12: $2\rho_{\uparrow(\downarrow)}(2r_b^*)$ is the mean value of the spin \uparrow and spin \downarrow resistivities (interface resistances); β and γ are the spin asymmetry parameters which give rise to the GMR. The interface resistances^{4,12} are introduced to express the enhanced scattering in an interfacial zone that is supposed to be infinitesimally thin and include also a Landauer-type condition induced by specular reflections (Ref. 20; see also Sec. IV).

For a unit area multilayer composed of M bilayers, the following resistance is finally obtained for parallel (P) and

antiparallel (AP) arrangements of the magnetization in successive layers:

$$R^{(P,AP)} = M(r_0 + 2r_{sf}^{P,AP}) \quad \text{with} \quad r_0 = (1-\beta)^2 \rho_F^* t_F + \rho_N^* t_N + 2(1-\gamma^2) r_b^*, \quad (9)$$

$$r_{sf}^{(P)} = \frac{\frac{(\beta-\gamma)^2}{\rho_N^* l_{sf}^{(N)}} \coth\left(\frac{t_N}{2l_{sf}^{(N)}}\right) + \frac{\gamma^2}{\rho_F^* l_{sf}^{(F)}} \coth\left(\frac{t_F}{2l_{sf}^{(F)}}\right) + \frac{\beta^2}{r_b^*}}{\frac{1}{\rho_N^* l_{sf}^{(N)}} \coth\left(\frac{t_N}{2l_{sf}^{(N)}}\right) + \frac{1}{\rho_F^* l_{sf}^{(F)}} \coth\left(\frac{t_F}{2l_{sf}^{(F)}}\right) + \frac{1}{r_b^*}}, \quad (10)$$

$$r_{sf}^{(AP)} = \frac{\frac{(\beta-\gamma)^2}{\rho_N^* l_{sf}^{(N)}} \tanh\left(\frac{t_N}{2l_{sf}^{(N)}}\right) + \frac{\gamma^2}{\rho_F^* l_{sf}^{(F)}} \coth\left(\frac{t_F}{2l_{sf}^{(F)}}\right) + \frac{\beta^2}{r_b^*}}{\frac{1}{\rho_N^* l_{sf}^{(N)}} \tanh\left(\frac{t_N}{2l_{sf}^{(N)}}\right) + \frac{1}{\rho_F^* l_{sf}^{(F)}} \coth\left(\frac{t_F}{2l_{sf}^{(F)}}\right) + \frac{1}{r_b^*}}. \quad (11)$$

t_F (t_N) ($l_{sf}^{(N)}$) are the thicknesses and SDL of the magnetic (nonmagnetic) layers. Before discussing the general behavior expected from Eqs. (9)–(11) in Sec. IV, we begin by considering the long SDL limit in Sec. III.

III. LONG SPIN DIFFUSION LENGTH LIMIT

In the limit $l_{sf}^{(F)} \gg t_F$, $l_{sf}^{(N)} \gg t_N$, Eqs. (9)–(11) lead to simple expressions equivalent to those derived by Pratt *et al.*^{4,5} to account for most of their experimental data on Co/Ag and Co/Cu multilayers,

$$R^{(AP)} = M(\rho_F^* t_F + \rho_N^* t_N + 2r_b^*), \quad (12)$$

$$\frac{1}{R^{(P)}} = \frac{1}{M} \left(\frac{1}{2\rho_F^*(1-\beta)t_F + 2\rho_N^*t_N + 4r_b^*(1-\gamma)} + \frac{1}{2\rho_F^*(1+\beta)t_F + 2\rho_N^*t_N + 4r_b^*(1+\gamma)} \right) \quad (13)$$

$$\sqrt{(R^{(AP)} - R^{(P)})R^{(AP)}} = \beta \frac{t_F}{t_F + t_N} \rho_F^* L + 2\gamma r_b^* M, \quad (14)$$

where L is the total thickness [$L = M(t_F + t_N)$]. Alternatively these expressions are also obtained in a two-channel scheme where the resistance of each channel (+, -) is a series sum of the resistivity times the layer thickness of the F and N metals plus the sum of the $2M$ interface resistances, as illustrated by Fig. 3 in Ref. 12 and also described in Refs. 4 and 5.

In Figs. 2 and 3, we show examples of the predicted variations of the resistance or MR with M for a fixed total length L . In Fig. 2, for $t_F = t_N = L/2M$ and with only interfacial spin-dependent scattering (i.e., $\beta = 0$), $R^{(AP)}$ is a linear function of M ; on the other hand $R^{(P)}$ is not strictly linear but its departure from a linear variation is significant only when the contribution from interfaces is much smaller than from scattering inside the layers. This behavior has been clearly characterized in extensive measurements.^{4,5} In Fig. 3, $[(R^{(AP)} - R^{(P)})R^{(AP)}]^{1/2}$ is plotted versus M , again for a fixed total thickness L and $t_F = t_N = L/2M$. Such a plot, extensively used in the analysis of experimental results,^{4,5} is quite

interesting since the intercept of the linear variation with the vertical axis yields the bulk asymmetry parameter β , while its slope gives the interface asymmetry parameter γ (γ turns out to be larger than β in Co/Ag and Co/Cu). All these linear variations with M are predicted only in the long SDL limit, that is, for $M \gg L/l_{sf}$, and for finite SDL deviations are expected at the left-hand side of the dashed vertical line in Fig. 3. In the following section we see what is predicted for shorter SDL, that is, when the dashed vertical line comes into the experimental range of M .

IV. CPR-MR FOR FINITE SPIN DIFFUSION LENGTHS

When the SDL is not much larger than the individual layer thicknesses, the simple expressions of Sec. III, Eqs. (12)–(14), are no longer valid and we must come back to the general expression of Sec. II, Eqs. (9)–(11).

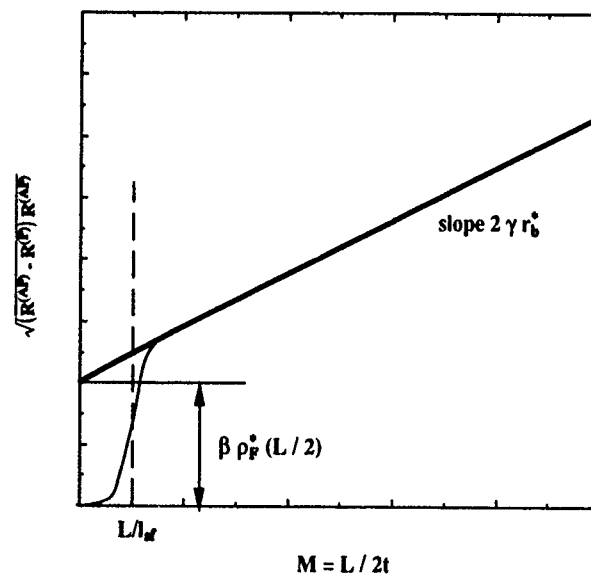


FIG. 3. $\sqrt{(R^{(AP)} - R^{(P)})R^{(AP)}}$ is plotted as a function of the number of bilayers M for a fixed total thickness L and the same individual thickness for the ferromagnetic and normal layer, $t_F = t_N = L/(2M)$. The solid line is the linear variation expected from Eq. (14) for the limit $t \ll l_{sf}$ or $M \gg L/l_{sf}$. For $M < L/l_{sf}$, Eq. (14) is no longer valid and $\sqrt{(R^{(AP)} - R^{(P)})R^{(AP)}}$ drops as $\exp(-t/4l_{sf}) \sim \exp(-L/2Mt_{sf})$ (see thin solid line).

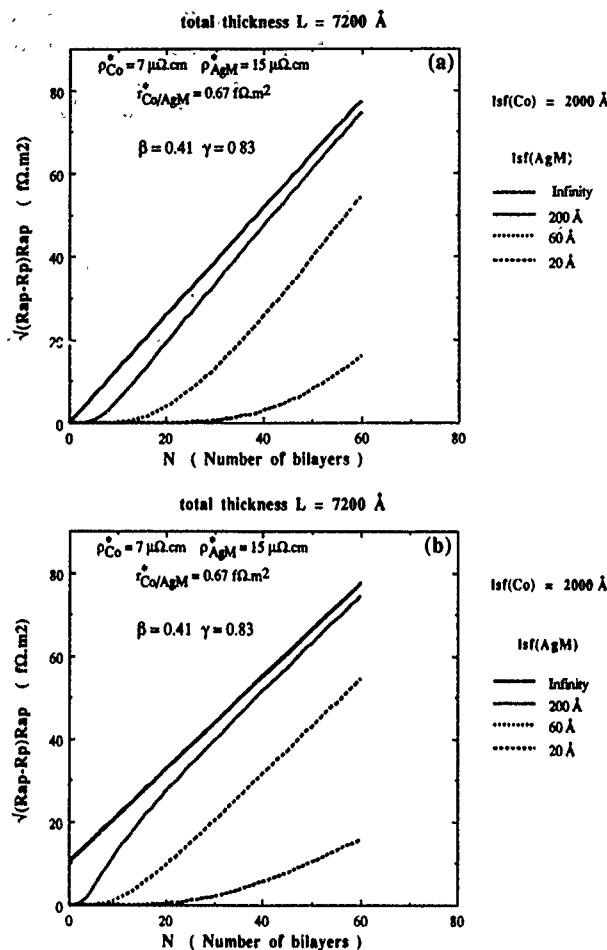


FIG. 4. $\sqrt{(R^{(AP)} - R^{(P)})R^{(AP)}}$ is plotted as a function of the number of bilayers M for several values of the SDL $l_{sf}^{(N)}$ [see values of $l_{sf}^{(N)}$ indicated in the figure] and a constant value of $l_{sf}^{(F)}$ [$l_{sf}^{(F)}(\text{Co}) = 2000 \text{ \AA}$]. The total thickness L is fixed: (a) $t_F = 60 \text{ \AA}$, $t_N = L/M - t_F$; (b) $t_F = t_N = L/2M$. The parameters of the calculations are those derived from Co/AgMn (Ref. 5), i.e., $\rho_N^* = 15 \mu\Omega \text{ cm}$, $\rho_F^* = 7 \mu\Omega \text{ cm}$, $r_b^* = 0.67 \text{ f}\Omega \text{ m}^2$, $\beta = 0.41$, $\gamma = 0.83$. For comparison with experimental results, see Bass *et al.* (Ref. 5).

In Fig. 4, for a multilayer with a fixed total thickness L , we show the curves of $[(R^{(AP)} - R^{(P)})R^{(AP)}]^{1/2}$ versus the number of bilayers M calculated for several values of $l_{sf}^{(N)}$. Figure 4(a) is for $t_F = 60 \text{ \AA}$, $t_N = L/M - t_F$, and Fig. 4(b) for $t_F = t_N = L/2M$. For the calculation from Eqs. (9)–(11), we have used the parameters ρ_N^* , ρ_F^* , r_b^* , β , γ derived by Bass *et al.*⁵ from the analysis of experimental results on Co/AgMn.

For $l_{sf}^{(N)} = \infty$, we observe the linear variation expected for this limit from Eq. (14) and already represented in Fig. 3. When $l_{sf}^{(N)}$ is shortened, the CPP-MR is dramatically reduced and departs strongly from a linear variation with M . As expected, the MR is practically reduced to zero at small values of M , that is for $t_N \gg l_{sf}^{(N)}$. It can be shown from Eqs. (9)–(11) that $[(R^{(AP)} - R^{(P)})R^{(AP)}]^{1/2}$ starts at small values of M as $\exp(-L/M l_{sf}^{(N)})$ in Fig. 4(a) and as $\exp(-L/2M l_{sf}^{(N)})$ in Fig. 4(b), and catches up with the linear variation of the long spin diffusion length limit for $M \gg L/l_{sf}^{(N)}$ (i.e., $t_N \ll l_{sf}^{(N)}$).

There are several ways to shorten the SDL in the nonmagnetic layers and test the theory [as seen easily from Eqs. (9)–(11), the SDL in the magnetic layers has less important

effects and we consider only the problem of the SDL in the normal layers]. The simplest situation is when impurities with strong spin-orbit coupling are introduced in the layers. Very efficient impurities should be $5d$ (or even $4d$) elements as, (i) their d states are strongly mixed with the conduction states, (ii) the spin orbit is strong for $5d$ states. The contribution to the spin-flip relaxation rate of the conduction electrons can be written as²¹

$$(\tau_{sf}^{-1})_{so} = N_I v_F \sigma_{sf}^{so}, \quad (15)$$

$$\sigma_{sf}^{so} = 40 \pi (\lambda_d / \Delta)^2 \sin^2(\pi Z_d / 10) / k_F^2,$$

where N_I is the impurity concentration, λ_d the spin-orbit constant of the d states, Δ the width of the d virtual bound state, and Z_d the number of d electrons on the impurity. We have estimated⁵ that 6% of Pt in Ag should reduce the SDL to about 30 \AA .

Another possibility is to induce spin relaxation by adding some paramagnetic impurities.

By adding Mn impurities in the nonmagnetic layers of Co/Ag and Co/Cu multilayers to shorten $l_{sf}^{(N)}$, Bass *et al.*⁵ have been able to observe clearly the reduction of the CPP-MR and the departure from a linear variation with the number of bilayers. We refer to Figs. 4 in Ref. 5 for a fit of our theoretical expressions with experimental data. The shortening of the SDL by Mn impurities has been calculated by one of us (A.F.).⁵ It turns out that a few at % of Mn are predicted to shorten the SDL significantly, in agreement with the experimental results.

V. SPIN-DEPENDENT INTERFACE RESISTANCES

The spin-dependent interface resistances involved in our model, see Eq. (8), can be due, either to specular reflections and refractions by perfect interfaces or, in addition, to diffuse scattering by the roughness (disorder) of the interfaces. It would be of great interest to know the relative importance of these two contributions to the interfaces resistances and also their respective spin dependencies. In addition, it happens that the specular reflections do not contribute directly to the CIP-MR,^{22,23} so that a predominant contribution from specular reflections to the CPP-MR would mean that CIP- and CPP-MR have different microscopic origins.

Two of us (J.B. and A.F.) have calculated the interface resistances induced by the electron reflection and refraction at spin-dependent potential steps (perfect interfaces) between layers.²⁴ The potential steps are of the form

$$U_\sigma(x) = \begin{cases} 0 & \text{for } x < 0 \text{ (nonmagnetic layer),} \\ U_\sigma & \text{for } x > 0 \text{ (magnetic layer),} \end{cases}$$

where U_σ ($\sigma = \uparrow, \downarrow$) are constants. The electrons are free electrons, and their Fermi energy is E_F for $x < 0$ and $E_F - U_\sigma$ for $x > 0$ and spin σ . The reflection and refraction coefficients are calculated by using the expressions given, for example, by Hood and Falicov²³ and the interfaces resistances are calculated in the Landauer formalism.²⁰ This leads²⁴ to an expression of the interface resistance that we do not reproduce here. A plot of r_σ as a function of U_σ/E_F for $U_\sigma > 0$ is shown in Fig. 5. As expected r_σ starts from zero for $U_\sigma = 0$ and diverges as U_σ tends to E_F . The experimental data

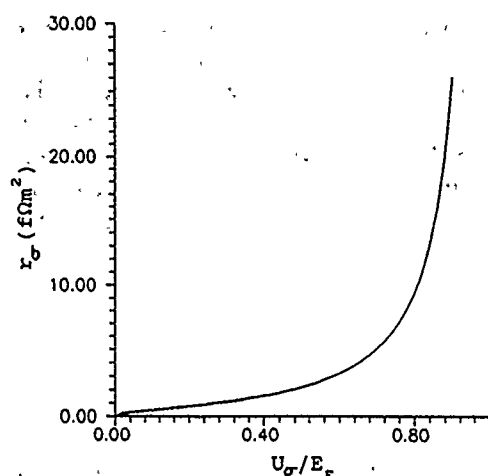


FIG. 5. Interface resistance r_σ vs U_σ/E_F [from Barnas and Fert (Ref. 22)].

found in Refs. 4¹ and 5 are $r_l=2.08 \text{ f}\Omega \text{ m}^2$ and $r_t=0.17 \text{ f}\Omega \text{ m}^2$ for Co/Ag, and $r_l=1.76 \text{ f}\Omega \text{ cm}^2$ and $r_t=0.24 \text{ f}\Omega \text{ m}^2$ for Co/Cu multilayers. As can be seen from Fig. 5, the higher resistances, $r_l=2.08 \text{ f}\Omega \text{ m}^2$ in Co/Ag and $r_l=1.76 \text{ f}\Omega \text{ m}^2$ in Co/Cu, can be accounted for by assuming reasonable values of U_l/E_F around 0.4 (in a free-electron model for s electrons in Co, Cu, and Ag, $U_l/E_F=0.4$ could be obtained, for example, by assuming 0.5 s electrons per atom and spin direction in Cu or Ag and 0.23 minority spin s in Co). The smaller values for r_t correspond to values of U_l/E_F of the order of only 0.03, i.e., to a not very different number of s electrons in Co, Cu, and Ag for this spin direction. Qualitatively, the high value of the ratio r_l/r_t can be supposed to follow from the contrast between a good fit of the s bands of Co, Cu, and Ag for one spin direction and bad mismatch of the bands for the other spin direction.

An additional contribution to the interface resistance can arise from diffusive scattering by interface disorder. Can this contribution be important? Let us consider a disordered interfacial layer of thickness 4 \AA with the typical high resistivity of an amorphous alloy of $4 \mu\Omega \text{ m}$ in each spin channel ($2 \mu\Omega \text{ m}$ is a typical value of the resistivity for amorphous alloys containing transition metals, which gives $4 \mu\Omega \text{ m}$ for each spin channel). Writing $r_\sigma = \rho_\sigma l$ with $l=4 \times 10^{-10} \text{ m}$ and $\rho_\sigma=4 \mu\Omega \text{ m}$ one obtains $r_\sigma=1.6 \text{ f}\Omega \text{ m}^2$. We thus find that scattering by interface roughness can also contribute significantly to the interface resistance.

VI. CONCLUSIONS

We have reviewed some of the main problems raised by CPP-MR experiments: the specific role of the spin accumulation and relaxation effects in the CPP geometry, the importance of the spin diffusion length as the scaling length of the problem, and the origin of the spin-dependent interface resistances. Up to now, most experiments have been performed in the long spin diffusion length limit, with the great advantage of a simple and fruitful analysis of the experimental results.³⁻⁵ The experiments on multilayers doped by Mn reported by Bass *et al.*⁵ at this conference represent certainly a

new interesting direction for the investigation of spin relaxation processes. Measurements as a function of temperature, which have been performed so far only by Gijs and co-workers⁶ should also raise interesting problems related to the scattering by spin fluctuations.

ACKNOWLEDGMENTS

We acknowledge very fruitful discussions with W. P. Pratt, P. A. Schroeder, J. Bass, M. Gijs, P. M. Levy, S. Zhang, B. Dieny, and H. Hurdequint. We also thank the Michigan State University Group for communicating unpublished data. We acknowledge support from the European Economic Community (Esprit Project B RA 6146), NATO (Grant No. 5-2-05/RG and No. 890599) and the Centre National de la Recherche Scientifique.

- ¹M. N. Baibich, J. M. Broto, A. Fert, F. Nguyen Van Dau, F. Petroff, P. Etienne, G. Creuzet, A. Friederich, and J. Chazelas, *Phys. Rev. Lett.* **61**, 2472 (1988).
- ²G. Binash, P. Grunberg, F. Saurenbach, and W. Zinn, *Phys. Rev. B* **39**, 4828 (1989).
- ³W. P. Pratt, Jr., S. F. Lee, J. M. Slaughter, R. Loloee, P. A. Schroeder, and J. Bass, *Phys. Rev. Lett.* **66**, 3060 (1991).
- ⁴W. P. Pratt, Jr., S. F. Lee, Q. Yang, P. Holody, R. Loloee, and P. A. Schroeder, *J. Appl. Phys.* **73**, 526 (1993); S. F. Lee, W. P. Pratt, Jr., Q. Yang, P. Holody, R. Loloee, P. A. Schroeder, and J. Bass, *J. Magn. Magn. Mater.* **118**, 1 (1993); P. A. Schroeder, J. Bass, P. Holody, S. F. Lee, R. Loloee, W. P. Pratt, and Q. Yang, *Magnetism and Structure in Systems of Reduced Dimension*, edited by F. R. Farrow *et al.* (NATO ASI Series, Plenum, 1993), p. 129.
- ⁵J. Bass, Q. Yang, S. F. Lee, P. Holody, R. Loloee, P. A. Schroeder, and W. P. Pratt, Jr., this conference.
- ⁶M. A. M. Gijs, S. K. J. Lenczowski, and B. Giesbert, *Phys. Rev. Lett.* **70**, 3343 (1993).
- ⁷R. E. Camley and J. Barnas, *Phys. Rev. Lett.* **63**, 664 (1989).
- ⁸P. M. Levy, S. Zhang, and A. Fert, *Phys. Rev. Lett.* **65**, 1643 (1990).
- ⁹A. Fert and I. A. Campbell, *J. Phys. B* **6**, 849 (1976); I. A. Campbell and A. Fert, in *Ferromagnetic Materials*, edited by E. P. Wohlfarth (North-Holland, Amsterdam, 1982), Vol. 3, p. 769.
- ¹⁰M. Johnson and R. H. Silsbee, *Phys. Rev. B* **35**, 4959 (1987).
- ¹¹P. C. van Son, H. van Kempen, and P. Wyder, *Phys. Rev. Lett.* **58**, 2271 (1987).
- ¹²T. Valet and A. Fert, *Phys. Rev. B* **48**, 7099 (1993).
- ¹³See Appendix A in Ref. 12.
- ¹⁴M. Johnson, *Phys. Rev. Lett.* **67**, 3594 (1991).
- ¹⁵See also an illustration of spin accumulation effects in Ref. 15 for a slightly different situation. Figure 1 of Ref. 15 is drawn for an infinite SDL in the nonmagnetic layers and in the minority spin channel of the ferromagnetic layer, and for a zero SDL in the majority spin channel. On the other hand, in our Fig. 1, we suppose nonzero density of states at E_F and finite SDL for both spin directions.
- ¹⁶T. Valet and A. Fert, *J. Magn. Magn. Mater.* **121**, 378 (1993) [note that a factor $(1-\gamma^2)$ is missing before r_σ^* in Eq. (15)]; A. Fert and T. Valet, *Magnetism and Structure in Systems of Reduced Dimension*, edited by R. F. Farrow *et al.* (NATO ASI Series, Plenum, 1993).
- ¹⁷S. Zhang and P. M. Levy, *J. Appl. Phys.* **69**, 4786 (1991); H. E. Camblong, S. Zhang, and P. Levy, *Phys. Rev. B* **47**, 4735 (1993).
- ¹⁸G. W. Bauer, *Phys. Rev. Lett.* **69**, 1676 (1992).
- ¹⁹J. Inoue, H. Itoh, and S. Maekawa (unpublished).
- ²⁰M. Buttiker, Y. Imry, R. Landauer, and S. Pinhas, *Phys. Rev. B* **31**, 6027 (1985).
- ²¹Y. Yafet, *J. Appl. Phys.* **39**, 85 (1968).
- ²²P. M. Levy, Z. P. Shi, S. Zhang, and H. E. Camblong, *J. Magn. Magn. Mater.* **121**, 357 (1993); P. M. Levy *et al.*, in 1993 MRS Spring Meeting.
- ²³R. Q. Hood and L. M. Falicov, *Phys. Rev. B* **46**, 8287 (1992).
- ²⁴J. Barnas and A. Fert (unpublished).

How to isolate effects of spin-flip scattering on giant magnetoresistance in magnetic multilayers (invited)

J. Bass, Q. Yang, S. F. Lee, P. Holody, R. Loloee, P. A. Schroeder, and W. P. Pratt, Jr.
Department of Physics and Astronomy and Center for Fundamental Materials Research, Michigan State University, East Lansing, Michigan 48824-1116

A technique is described for isolating effects of finite spin diffusion lengths on the magnetoresistance (MR) of magnetic multilayers at low temperatures by measuring the MR with the current perpendicular to the layer planes. Applying this technique to relatively concentrated Co/AgMn and Co/CuMn multilayers yields large effects, generally consistent with expectations from a theory by Valet and Fert [Phys. Rev. B 48, 7099 (1993)]. However, some complicating issues still need to be resolved.

I. INTRODUCTION

Several magnetic multilayers composed of alternating thin layers of ferromagnetic (F) and nonmagnetic (N) metals display large decreases in electrical resistance with increasing magnetic field H .¹⁻³ This phenomenon, called giant magnetoresistance (GMR), is of both scientific and technological interest.⁴ To fully understand GMR, we must understand how it depends upon all of the different kinds of scattering that electrons experience in bulk F and N metals and at F/N interfaces.⁵⁻⁷ In this article, we focus upon spin-flip scattering in the N metal at low temperatures.

At low temperatures, electron scattering in magnetic multilayers is dominated by elastic scattering at the F/N interfaces and from impurities in the F and N metals. The direction of an electron's spin then usually stays fixed as the electron traverses the multilayer. This means that the quantity of interest in the present paper, the electron spin diffusion length l_{sf} , is much longer than the structural lengths of the multilayer: F-layer thickness t_F ; N-layer thickness t_N ; and bilayer thickness, $\Lambda = t_F + t_N$.

Most GMR analyses to date have neglected spin-flip scattering. This assumption is valid at low temperatures for pure-metal-based multilayers, but becomes less valid as the temperature rises, because electron-magnon scattering, which flips spins, grows with increasing temperature. Since most technological applications of GMR will occur at room temperature, it seems clear that we need to understand effects of spin-flip scattering to fully understand GMR.

Observed T^2 variations of both the traditional MR with current flow in the layer planes (CIP MR)⁸ and the MR with current flow perpendicular to the layer planes (CPP MR)³ have been taken as evidence for scattering (including spin-flip scattering) of electrons by thermally excited magnons. However, the temperature dependence of GMR is a complex phenomenon,⁹ from which it is difficult to extract information about spin-flip scattering.

This difficulty stimulated us to look for effects of spin flip scattering on the GMR at low temperatures. We first briefly explain why we use the CPP MR instead of the more traditional CIP MR.

The CIP MR has the advantage of being much easier to measure, since the typical CIP resistance is $\approx 1 \Omega$. But the CIP MR contains several unknown parameters,¹⁰ and its behavior at low temperatures is dominated by the (elastic)

mean-free-path for momentum transfer, λ_{el} ,⁶ which is not what we wish to investigate here. The dominant effect on the CIP MR of adding impurities that flip spins is to change λ_{el} , making it difficult to isolate any effects due to spin flip scattering alone. In addition, the CIP MR is affected only by those spin-flip scattering events that transfer momentum between spin up and spin down electrons, and these events are negligible at low temperatures. The particular quantity of present interest, l_{sf} , measures the relaxation of spin accumulation at interfaces, which occurs in the CPP-MR,¹¹⁻¹⁵ but not in the CIP MR. Thus, l_{sf} does not play a role in the CIP MR and cannot be isolated by measuring the CIP MR.

The CPP MR, in contrast, is harder to measure, with either very small resistances $\approx 10^{-7} \Omega$, or the need to make very small samples by lithographic patterning.³ But it has the advantage that when l_{sf} is large, λ_{el} is not a characteristic length in the CPP MR. The only characteristic length is l_{sf} .^{14,15} The expressions for the CPP MR then become simple, as we and others have shown.^{11,13,14} In this paper we show how combining a particular set of measured quantities associated with the CPP MR lets us isolate just those effects due specifically to the reduction of l_{sf} . We could reduce l_{sf} either by adding a strong spin orbit interaction via a very heavy impurity such as Au or Pt, or by adding a strong spin-spin interaction via an impurity with a local moment, such as Mn. In this paper we examine data for both Co/AgMn and Co/CuMn.

II. SAMPLES

Each of our CPP MR samples consists of a sputtered multilayer of interest sandwiched between two ≈ 1.1 -mm-wide crossed-superconducting Nb strips with area of overlap $A \approx 1.2 \text{ mm}^2$. A known current is fed into one Nb strip and taken out of the other, and the resulting potential difference between the two Nb strips is determined. Details of our techniques for preparing samples, characterizing them, and simultaneously measuring the CPP MR and the CIP MR are given elsewhere.² We assume that our samples are best described as multilayers, although it has been suggested that sputtered metal-metal multilayers such as ours are better characterized as anisotropic inhomogeneous alloys.¹⁶

For brevity, we limit ourselves to: (a) the CPP MR; (b) samples with fixed total thickness $t_T = N\Lambda$ as close as pos-

sible to 720 nm (N is the number of bilayers in a sample); and (c) samples with fixed $t_F (=t_{Co})=6$ nm. To avoid proximity effects with the superconducting Nb current and potential leads, Co layers were sputtered on both sides of the new AgMn and CuMn multilayers, which thus consisted of N bilayers plus one extra Co layer. To avoid complications due to oscillating interactions between F layers as t_N changes, we only examine samples with $t_N \geq 6$ nm, which is beyond the range of oscillating MRs,¹ and large enough so that exchange interactions between F layers should be small. Mn was chosen because we had appropriate targets available, and experience in sputtering both AgMn and CuMn for studies of finite size effects in spin glasses.¹⁷ Fairly large Mn concentrations were chosen to maximize the chance of seeing an effect since, as we see below, the estimates for l_{sf}^N are uncertain.

III. TWO-CHANNEL MODELS

A. $l_{sf}^N \sim \infty$

We¹³ and others^{11,14} have argued that when $l_{sf} \gg l_{cl}, \Lambda$ (i.e., spin-flip scattering is negligible), the total CPP resistance times sample area AR_T can be well described by a model in which electrons are divided into two channels, up (+) and down (-) relative to the direction of the applied field H , which carry current independently. The AR_T in each channel (+, -) is simply a series sum of the resistivities times total layer thicknesses of the F and N metals plus the sum of the area times interface resistances of the F/N interfaces. Schematically, we thus have for each channel an expression of the form

$$AR^{(+,-)} = 2AR_{S/F} + (N+1)\rho_F^{(+,-)}t_F + N\rho_N t_N + 2NAR_{F/N}^{(+,-)}, \quad (1)$$

where the term $2AR_{S/F}$ accounts for the interface resistances between the superconducting (S) Nb current leads and the (F) Co boundaries at the two ends of the samples.¹⁸ We assume that this additional term is spin independent. For ease of presentation, we neglect the difference between N and $N+1$ in equations that follow.

In the standard models for the CIP MR and CPP MR of magnetic multilayers, the largest resistance occurs when the magnetizations M_i of neighboring F layers are oriented antiparallel (AP) to each other, and the smallest when they are oriented parallel (P). We thus focus upon these two limiting cases.

We define $\rho \uparrow = 2\rho_F/(1+\beta)$ to be the resistivity of a F layer when the electron spin and the local M_i are parallel to each other, and $\rho \downarrow = 2\rho_F/(1-\beta)$ to be the resistivity when they are antiparallel. Here ρ_F is the F resistivity measured on independent thin F films or sandwiches.¹⁸ Similarly, we take $R \uparrow = (2R_{F/N})/(1+\gamma)$ and $R \downarrow = (2R_{F/N})/(1-\gamma)$.

In the AP state ($M=0$) we expect, by symmetry, that $AR^{(+)} = AR^{(-)}$. Since the resistances of the (+) and (-) channels add in parallel, AR_T should be just one-half of these equal values. Continuing to neglect differences between N and $N+1$, we find¹³

$$AR_T(AP) = 2AR_{S/F} + N[(\rho_F^* t_F) + \rho_N t_N + 2AR_{F/N}^*], \quad (2a)$$

where $\rho_F^* = \rho_F/(1-\beta^2)$ and $R_{F/N}^* = R_{F/N}/(1-\gamma^2)$.

For fixed t_T and t_F , we use the relation $t_T = Nt_F + Nt_N$ to eliminate t_N from Eq. (2a),

$$AR_T(AP) = 2AR_{S/F} + \rho_N t_T + N[(\rho_F^* - \rho_N)t_F + 2AR_{F/N}^*]. \quad (2b)$$

Plotting $AR_T(AP)$ vs N should thus give a straight line with ordinate intercept $2AR_{S/F} + \rho_N t_N$ and slope $(\rho_F^* - \rho_N)t_F + 2AR_{F/N}^*$. $2AR_{Nb/Co}$ has been separately measured to be $\approx 6f\Omega \text{ m}^2$,¹⁸ and ρ_N can be calculated for a known impurity concentration¹⁹ and also directly measured on 300–500-nm-thick sputtered films. The intercept can thus be independently determined, and the only unknowns in Eq. (2b) are ρ_F^* and $R_{F/N}^*$. These two quantities can be determined by also measuring $AR_T(AP)$ for a series of samples with fixed t_T and $t_F = t_N$. We have published such measurements for Co/Ag, Co/AgSn, and Co/Cu.^{12,13,20}

In the (P) state ($H \geq H_s$, $M = M_s$), in contrast, spin + and spin - electrons behave differently. Here, we showed¹³ that adding their resistances in parallel and rearranging gives

$$AR_T(P) = AR_T(AP) - N^2(\beta\rho_F^* t_F + 2\gamma AR_{F/N}^*)^2 / [AR_T(AP)]. \quad (3)$$

Equation (3) can be rewritten to yield the important linear relationship¹³

$$A\sqrt{AR_T(AP)[R_T(AP) - R_T(P)]} = N[\beta\rho_F^* t_F + 2\gamma AR_{F/N}^*]. \quad (4)$$

The right-hand side of Eq. (4) is independent of ρ_N and also of t_T (except through N). For samples with fixed t_F , a plot of the experimentally determined left-hand-side of Eq. (4) versus N should yield a straight line through the origin. For samples with $t_F = t_N$, a similar plot should yield a straight line with slope proportional to γ and ordinate intercept proportional to β . Equation (4) thus allows independent determinations of γ and β , once ρ_F^* and $R_{F/N}^*$ have been found from Eq. (2).

For fixed t_F , if we modify ρ_N by adding only a few percent impurities to the N metal, so that the parameters on the right-hand side of Eq. (4) do not change, then the slope of the line passing through the origin should also not change. This property makes Eq. (4) ideal for testing for effects of finite l_{sf} , since simply adding elastic scattering impurities to the N metal should not move data points off this line. Reducing l_{sf} , in contrast, should decrease the difference between $AR_T(AP)$ and $AR_T(P)$, via spin relaxation,²¹ spin mixing,¹⁵ or both. The signature of a finite l_{sf} will be data that fall farther below the line from Eq. (4) as N decreases (i.e., t_N increases).

B. Finite l_{sf}^N

Formal equations for $AR(AP)$ and $AR(P)$ for finite l_{sf} were recently derived by Valet and Fert,¹⁴ and are repeated as Eqs. (9)–(11) in the preceding paper by Fert and co-workers in the present volume.²¹ Strictly, these equations contain two different spin-dependent diffusion lengths, l_{sf}^N and l_{sf}^F , for the N and F metals; but, inserting typical values for the various parameters shows that the data are insensitive to l_{sf}^F —i.e., l_{sf}^F must be ≤ 1 nm to measurably change Eq. (4). It is thus l_{sf}^N that is of primary interest, and that we try to reduce in these experiments.

TABLE I. Estimated parameters for Co/AgMn and Co/CuMn.

Alloy	Co/AgMn (9 at. %)	Co/CuMn (7 at. %)
λ_{el} (nm) ^a	5.6	2.1
λ_{sf} (nm) ^b	≈ 90	≈ 24
$l_{sf}^N = \sqrt{(\lambda_{el}\lambda_{sf})}/6$	≈ 9	≈ 3

^aThe estimates for λ_{el} were obtained by combining the free-electron equations (Ref. 25), $\lambda_{el}=836 \text{ nm}/\rho(\text{n}\Omega \text{ m})$ for Ag and $\lambda_{el}=656 \text{ nm}/\rho(\text{n}\Omega \text{ m})$ for Cu, with values for the alloy residual resistivities estimated from the intended impurity concentrations and the resistivities per at. % impurity given in Ref. 19. Independent measurements of the residual resistivities of sputtered 300- or 500-nm-thick films are consistent with these estimates for AgSn, AgMn, and CuMn.

^bThe estimates of the spin-flip mean free path λ_{sf} for AgMn and CuMn are based on calculations by Fert (Ref. 22) using available information about exchange coupling in these alloys. Interactions between the Mn impurities might lead to actual values for λ_{sf} and l_{sf} larger than these estimates.

As noted above, we chose to test our procedure by using the magnetic impurity Mn. Estimates of l_{sf}^N for scattering from noninteracting Mn impurities in AgMn and CuMn require a complex analysis, which was kindly performed by Fert.²² The actual values of l_{sf}^N for our AgMn and CuMn alloys could be larger than these estimates because, at the low temperature (4.2 K) where our measurements are made, interactions between the dilute magnetic Mn ions yield a complex coherent state called a spin glass (SG). Below its "spin-freezing temperature," this coherent state may well cause less spin-flip sputtering than for noninteracting impurities. Unfortunately, we do not understand the SG state well enough to predict how much l_{sf}^N might increase. The bulk spin-freezing temperatures in our samples are about 38 K for 7 at. % Mn in Cu and 28 K for 9 at. % Mn in Ag. Even corrected for finite size effects,¹⁷ the temperatures for our thinnest SG layers ($t_N=6 \text{ nm}$) are still well above 4.2 K.

Finally, we note that the Valet and Fert equations are strictly valid only when $l_{sf} \gg l_{el}$, whereas in our samples $l_{sf} \approx l_{el}$ (Table I). We thus do not expect detailed quantitative agreement with our AgMn and CuMn data, which would require, among other things, including an extra term,¹⁴ the magnitude of which has not yet been estimated.

IV. DATA AND ANALYSIS

We begin by showing that adding Mn does not qualitatively change the H dependence of our data. Figure 1 shows the field dependencies of $AR_T(H) - AR_T(H_s)$ for (6 nm/6 nm) multilayers of Co/Ag, Co/AgMn, and Co/AgSn, all measured in our standard CPP system, which goes only up to $H=1 \text{ kOe}$. The three data sets are similar in form: the CPP MR is largest in the initially prepared state—designated H_0 —decreases until H_s is reached, and then cycles through the curves shown, with maximum values at the peak field H_p . The values of H_p are also not much different for the three samples, suggesting similar magnetic couplings (or absence thereof) between F layers. Since the AF state is naturally associated with the largest value of $AR_T(H)$, we limited our previous analyses of Co/Ag, Co/AgSn, and Co/Cu to H_0 ,^{13,20} for similar reasons we limit ourselves here to H_0 ,

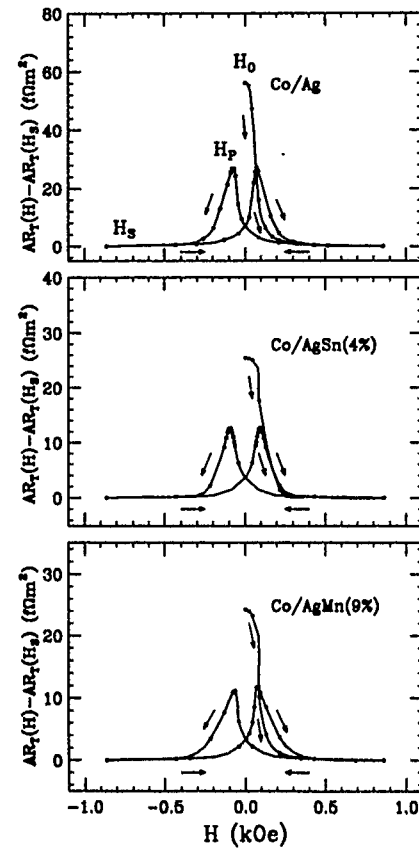


FIG. 1. $AR_T(H) - AR_T(H_s)$ vs H for (6 nm/6 nm) Co/Ag, Co/AgSn, and Co/AgMn multilayers with similar values of H_p . Values of H_p for nominally identical multilayers can vary by $\sim 50\%$. The curves through the data are simply computer drawn guides to the eye.

also. Using H_p , instead, does not change any of the conclusions we reach, but there are quantitative differences that we will discuss elsewhere.²³

We examine next whether the values of $AR_T(H_0)$ for different impurities are consistent with Eq. (2b). In Fig. 2 we plot $AR_T(H_0)$ and $AR_T(H_s)$ versus the number of bilayers N for our three Ag-based multilayers for fixed $t_{Co}=6 \text{ nm}$. The $AR_T(H_0)$ data for Co/Ag and Co/AgSn fall close to straight lines, as predicted by Eq. (2b). Within their $\approx 10\%$ scatter, the $AR_T(H_0)$ data for Co/AgMn are consistent either with the straight-line prediction in Eq. (2b) or with the slight curvature predicted by Eq. (10) from Ref. 21 (upper dashed curve in Fig. 2). With either linear or curved extrapolations, the ordinate intercepts for these and the Cu-based multilayers are all consistent to within experimental uncertainties with independently measured values of $2AR_{Nb/Co} + \rho_N t_T$.²³ As expected, the values of $AR_T(H_s)$ fall below those for $AR_T(H_0)$. As also expected, the fits to the Co/AgMn data are not as good as those to the Co/Ag and Co/AgSn data. It is not obvious from Fig. 2 alone which, if any, of the data sets involved reduced l_{sf}^N .

To isolate effects of reduced l_{sf}^N , we examine the square-root quantity of Eq. (4). As a reference against which to compare our data, Fig. 3 shows the predictions for this square root from the Valet and Fert equations for a range of values of l_{sf}^N . In Fig. 3 we have used the parameters for Co/Ag,²⁰ except that we have taken $\rho_N=15 \mu\Omega \text{ cm}$, appro-

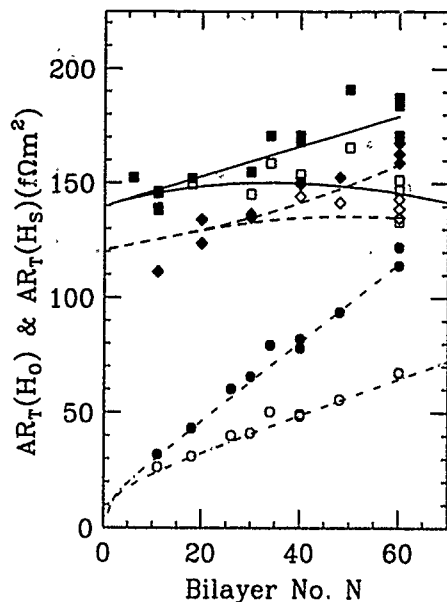


FIG. 2. $AR_T(H_0)$ (solid symbols) and $AR_T(H_s)$ (open symbols) vs bilayer number N for Co/Ag (circles), Co/AgSn (squares), and Co/AgMn (diamonds) multilayers with fixed $t_{Co}=6$ nm and $t_T=720$ nm. The broken Co/Ag curves and solid Co/AgSn curves are fits to Eqs. (2b) and (3); the downward curvature at small N for Co/Ag comes from corrections because these samples did not have a covering Co layer under the top Nb strip. The dashed Co/AgMn curves are fits to Eqs. (9)–(11) of Ref. 21. We do not expect the Co/AgMn fits to be as good as those for Co/Ag and Co/AgSn.

priate to our Ag-Mn-alloy multilayers. The fit is not sensitive to the Co/Ag parameters; an alternative set for Co/AgSn (Ref. 20) yields nearly indistinguishable predictions [e.g., compare Fig. 3 with Fig. 4(a) of Ref. 21]. Smaller values of ρ_N lead to larger deviations from the straight lines, and larger

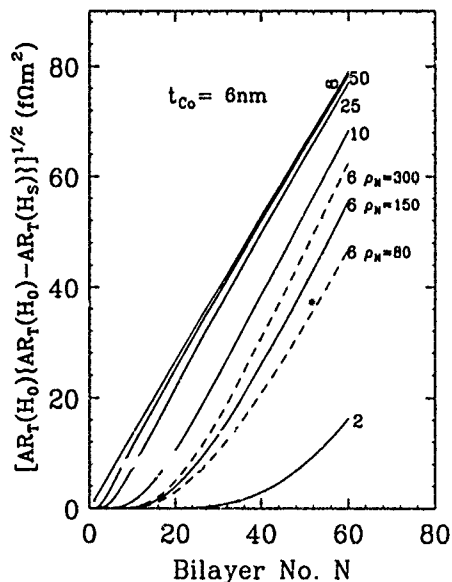


FIG. 3. $\sqrt{AR_T(H_0)[AR_T(H_0)-AR_T(H_s)]}$ vs bilayer number N calculated using Eqs. (9)–(11) from Ref. 21. The line labeled ∞ indicates the fit to Eq. (4) with the parameters for Co/Ag. The solid curves were calculated for the indicated values of l_{sf}^N using these same parameters and assuming $\rho_N=150$ nΩm. To show the effect of varying ρ_N , the dashed curves for $l_{sf}^N=6$ nm were calculated for $\rho_N=80$ and 300 nΩm as indicated.

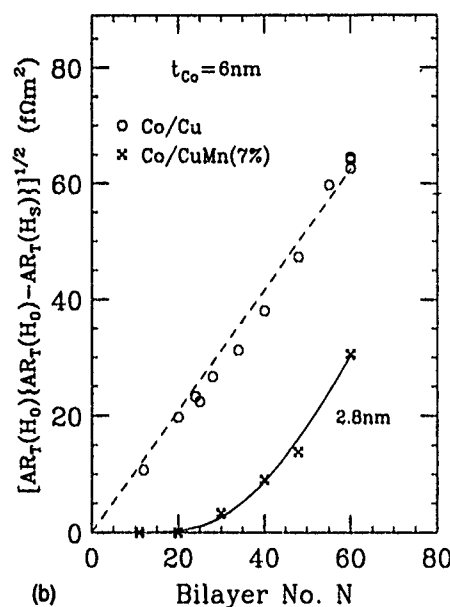
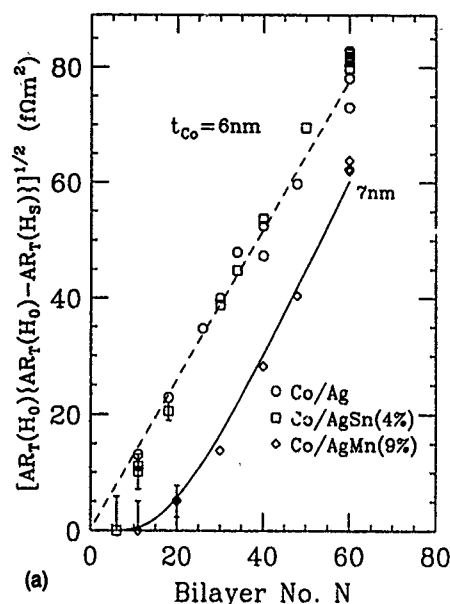


FIG. 4. (a) $\sqrt{AR_T(H_0)[AR_T(H_0)-AR_T(H_s)]}$ vs N for the data of Fig. 2. The curve through the AgMn data is for $l_{sf}^N=7$ nm. Some important error bars are shown; for larger values of the square root the uncertainties are dominated by geometric uncertainties that are $\sim \pm 4\%$ of the ordinate value. (b) $\sqrt{AR_T(H_0)[AR_T(H_0)-AR_T(H_s)]}$ vs N for Co/Cu and Co/CuMn. The curve through the CuMn data is for $l_{sf}^N=2.8$ nm.

values to somewhat smaller deviations; but, as illustrated by the alternative curves for $l_{sf}^N=6$ nm, these differences are modest, so that the curves in Fig. 3 fairly describe what we expect for our samples. If the true values of l_{sf}^N for AgMn and CuMn lie near the estimated lower bounds for l_{sf}^N given in Table I, then we expect the Co/AgMn and Co/CuMn data to fall well below the respective Co/Ag or Co/Cu lines.

Figure 4(a) shows the data for our three Ag-based multilayer sets plotted in the form of Eq. (4). As shown previously,^{13,20} to within experimental uncertainties and variations among samples from different sputtering runs, the Co/Ag and Co/AgSn data are consistent with a single straight line through the origin. The Co/AgMn data, in contrast, fall

well below the line, and display the expected larger fractional deviations from the line as $N \rightarrow 0$. Figure 4(b) shows similar data for Co/Cu and Co/CuMn. Again, the Co/Cu data fall on a straight line,²⁰ and the Co/CuMn data fall well below this line, deviating more from the line as $N \rightarrow 0$. The curves through the Co/AgMn and Co/CuMn data are calculated using the Fert and Valet equations with the values of l_{sf}^N indicated on the graphs. Given that our data do not satisfy the validity condition $l_{sf} \gg \lambda_{cl}$ for these equations, these values are surprisingly close to the estimates of Table I.

The data in Figs. 4(a) and 4(b) for Co/AgMn and Co/CuMn are consistent with the predictions from the equations of Valet and Fert with reasonable values for l_{sf}^N . We conclude by briefly examining whether these behaviors could be due to other causes.

One possibility is that the couplings between F layers might be more ferromagnetic with SG interlayers, leading to reduced values of the square root in Eq. (4). If so, we would expect to see differences in the hysteresis curves for multilayers with the different N metals. To check this possibility, we measured the saturation magnetizations and the coercive fields H_c for Co/Ag, Co/AgSn, and Co/AgMn. The results were very similar to each other.²³ This agreement for H_c was presaged by the closeness of the values of H_p in Fig. 1, since we have shown elsewhere that $H_p \approx H_c$.²

Another possibility is that the magnetic character of the SG layers causes the saturation field H_s for the CPP MR to be larger than the maximum field of 1 kOe in our standard CPP measuring system. To check this possibility, we measured selected samples in a higher field system, up to 10 kOe, limited by the H_{c2} of our Nb strips. No evidence of a higher saturation field was found for Co/Ag, Co/Cu, Co/AgSn, or Co/CuMn. However, the values of $AR_T(H)$ for Co/AgMn samples continued to decrease approximately linearly with increasing field up to 10 kOe.²³ Assuming H_s to be 10 kOe would cause the data points for AgMn in Fig. 4(a) to rise only part of the way toward the straight line for no spin-flip scattering; however, it is possible that the data continue to decrease to still higher fields. Since it is known that SGs alone can have substantial negative linear MRs at high magnetic fields,²⁴ we made some S/SG/S sandwiches of both AgMn and CuMn and measured their CPP MRs. We did not find negative MRs large enough to explain the high-field behaviors of the Co/AgMn multilayers;²³ there is thus still some question about the right explanation for the Co/AgMn data in Fig. 4(a).

V. SUMMARY

To summarize, we have shown how to isolate effects of a finite spin diffusion length l_{sf}^N , using the CPP MR of magnetic multilayers, and we have looked for such effects in multilayers containing alloys of Ag and Cu with the magnetic impurity Mn. For both Co/AgMn and Co/CuMn, the data of Fig. 4 deviate from straight-line behavior in the way expected, and the sizes of the deviations are comparable to predictions from a theory by Valet and Fert, even though the data do not satisfy the validity condition ($l_{sf} \gg \lambda_{cl}$) of this theory. The interpretation of the AgMn data is further complicated by the presence of a negative linear MR above

$H_s = 1$ kOe, the significance of which is not yet understood. To complete the case for our proposed technique, we plan to measure the CPP MR for smaller concentrations of Mn in Cu and Ag to check that the data scale with impurity concentration as predicted, and to extend measurements to the non-magnetic alloys Co/AgPt and Co/CuPt, where spin-orbit effects should shorten l_{sf}^N enough to give significant effects.

ACKNOWLEDGMENTS

This research was supported in part by the US NSF under Grant No. DMR 91-22614, by the MSU Center for Fundamental Materials Research, and by the Ford Motor Co. We are pleased to thank A. Fert for helpful advice for providing the estimates of l_{sf}^N for AgMn and CuMn and for clarifying for us the nature of l_{sf} and why it plays no role in the CIP-MR. Our collaboration with him was supported by the US NSF under Grant No. INT-92-16909 and by the companion grant AI0693 from the French CNRS. We also thank P. M. Levy and M. B. Stearns for helpful conversations and suggestions.

- ¹ See, for example, M. N. Baibich *et al.*, Phys. Rev. Lett. **61**, 2472 (1988); G. Binasch *et al.*, Phys. Rev. B **39**, 4828 (1989); C. Dupas *et al.*, J. Appl. Phys. **63**, 4300 (1988); S. S. P. Parkin *et al.*, Phys. Rev. Lett. **64**, 2304 (1990); S. S. P. Parkin *et al.*, *ibid.* **66**, 2152 (1991); D. H. Mosca *et al.*, J. Magn. Magn. Mater. **93**, 480 (1990); D. H. Mosca *et al.*, *ibid.* **94**, L1 (1991); S. Araki *et al.*, J. Phys. Soc. Jpn. **60**, 2827 (1991); S. Araki, J. Appl. Phys. (to be published).
- ² W. P. Pratt, Jr. *et al.*, Phys. Rev. Lett. **66**, 3060 (1991).
- ³ M. A. M. Gijs *et al.*, Phys. Rev. Lett. **70**, 3343 (1993).
- ⁴ See, for example, L. Falicov *et al.*, J. Mater. Res. **5**, 1299 (1990).
- ⁵ See, for example, R. E. Camley and J. Barnas, Phys. Rev. Lett. **63**, 664 (1989); S. Zhang *et al.*, *ibid.* **65**, 1643 (1990); A. Barthelemy and A. Fert, Phys. Rev. B **43**, 13 124 (1991); J.-I. Inoue *et al.*, J. Phys. Soc. Jpn. **60**, 376 (1991); D. M. Edwards *et al.*, J. Magn. Magn. Mater. **114**, 252 (1992); H. Camblong and P. M. Levy, Phys. Rev. Lett. **69**, 2835 (1992).
- ⁶ S. Zhang *et al.*, Phys. Rev. B **45**, 8689 (1992).
- ⁷ G. E. W. Bauer, Phys. Rev. Lett. **69**, 1676 (1992).
- ⁸ J. E. Mattson *et al.*, Phys. Rev. B **44**, 9378 (1991).
- ⁹ S. Zhang and P. M. Levy, Phys. Rev. B **43**, 11 048 (1991); J. J. Duvail, A. Fert, and L. G. Pereira, J. Appl. Phys. **xx** (This Volume).
- ¹⁰ L. Falicov and R. Q. Hood, J. Magn. Magn. Mater. **121**, 362 (1993).
- ¹¹ S. Zhang and P. M. Levy, J. Appl. Phys. **69**, 4786 (1991).
- ¹² S.-F. Lee *et al.*, Phys. Rev. B **46**, 548 (1992).
- ¹³ S.-F. Lee *et al.*, J. Magn. Magn. Mater. **118**, L1 (1993).
- ¹⁴ T. Valet and A. Fert, J. Magn. Magn. Mater. **121**, 378 (1993); Phys. Rev. B **48**, 7099 (1993).
- ¹⁵ H. Camblong *et al.*, Phys. Rev. B **47**, 4735 (1993); S. Zhang and P. M. Levy, *ibid.* **47**, 6776 (1993).
- ¹⁶ M. B. Stearns, J. Magn. Magn. Mater. **104-107**, 1745 (1992); J. Appl. Phys. **72**, 5354 (1992); and unpublished results.
- ¹⁷ See, for example, J. Bass and J. A. Cowen, in *Recent Progress in Random Magnets*, edited by D. H. Ryan (World Scientific, Singapore, 1992), p. 177.
- ¹⁸ C. Fierz *et al.*, J. Phys. Condensed Matter **2**, 9701 (1990).
- ¹⁹ J. Bass, in *Landolt-Börnstein New Series*, edited by K.-H. Hellwege and J. L. Olsen (Springer, Berlin, 1982), Vol. III/15a.
- ²⁰ P. A. Schroeder *et al.*, in NATO Advanced Research Workshop "Magnetism and Structure in Systems of Reduced Dimension," NATO ASI Series B **309**, 129 (1993); W. P. Pratt, Jr. *et al.*, J. Appl. Phys. **73**, 5326 (1993); W. P. Pratt, Jr. *et al.*, J. Magn. Magn. Mater. **126**, 406 (1993).
- ²¹ A. Fert, T. Valet, and J. Barnas (these proceedings).
- ²² A. Fert (unpublished).
- ²³ Q. Yang *et al.* (unpublished).
- ²⁴ See, for example, V. M. Beylin *et al.*, Phys. Met. Metall. **61**, 68 (1986), and A. K. Nigam *et al.*, J. Appl. Phys. **50**, 7361 (1979).
- ²⁵ See, for example, N. W. Ashcroft and N. D. Mermin, *Solid State Physics* (W. B. Saunders, Philadelphia, PA, 1976).

Scattering theory of perpendicular transport in metallic multilayers (invited)

Gerrit E. W. Bauer and Arne Brataas^{a)}

Faculty of Applied Physics and DIMES, Delft University of Technology, Lorentzweg 1, 2628 CJ Delft, The Netherlands

Kees M. Schep^{b)} and Paul J. Kelly

Philips Research Laboratories, P.O. Box 80.000, 5600 JA Eindhoven, The Netherlands

Electronic transport in metallic multilayers is discussed in the language of the Landauer–Büttiker scattering formalism. The semiclassical conductance through a disordered interface can be unambiguously separated into specular and diffuse scattering contributions. Analytical results are derived for the perpendicular conductance of multiple disordered interfaces. Predictions for the transport properties of interfaces with dilute but strongly scattering defects should be accessible to verification by experiments. First results of first-principles calculations of ballistic transport in magnetic multilayers are presented.

I. INTRODUCTION

The giant magnetoresistance or spin-valve effect found in antiferromagnetically coupled metallic multilayers¹ has recently been studied in the so-called CPP (current perpendicular to the interface plane) geometry, both experimentally^{2,3} and theoretically.^{4–14} One of the many advantages of this configuration compared to the more conventional CIP (current in plane) geometry is its high symmetry, which simplifies the physics and allows more insight into the electronic transport through heterointerfaces. The importance of interface scattering in many areas of metal and semiconductor physics is reflected by numerous articles since the seminal work by Fuchs,¹⁵ which are mainly concerned with transport parallel to an impenetrable rough interface, e.g., in the two-dimensional electron gas.¹⁶ In the present article interface scattering is discussed for metallic transport normal to the interfaces on the basis of the Landauer–Büttiker formalism.¹⁷ We show that in a semiclassical approximation the diffuse scattering is unequivocally connected to the impurity scattering correction to the electric field vertex. Our approach gives a simple relation between the specular and diffuse part of the transmitted wave. The conductance of a multilayer is found by a semiclassical concatenation of single interfaces. The theory can be applied to find the magnetoconductance in magnetic multilayers, where spin-dependent interface scattering is generally believed to be responsible for the spin-valve effect.

In Sec. II the Landauer–Büttiker formalism is introduced with emphasis on its relation to the conventional linear response theory. In Sec. III we review our previous results for disordered interface scattering in the semiclassical and effective mass approximations.^{6,12,13} A critical assessment of the validity of our results is given in Sec. IV, where evidence is presented for the importance of quantum interference and band-structure effects beyond the semiclassical approximation.

II. LANDAUER–BÜTTIKER FORMALISM

The Landauer conductance formula¹⁷ can be derived directly from the Kubo formula for the two-terminal configuration as sketched in Fig. 1.¹⁸ It is required that (i) the sample is connected to the contacts via two low-impedance leads and (ii) the contacts are at thermodynamic equilibrium with a small electrochemical potential difference $\Delta\mu = \mu_1 - \mu_2$. According to the Kubo linear response formalism the current can be calculated in terms of a nonlocal conductivity tensor $\sigma(\mathbf{r}, \mathbf{r}')$ and the local electric field $\mathbf{E}_{\text{loc}}(\mathbf{r})$. The total current passing through an arbitrary plane S with normal $\hat{\mathbf{n}}_S$ is given as

$$J_S = \int_S d\mathbf{r} \hat{\mathbf{n}}_S(\mathbf{r}) \cdot \mathbf{j}(\mathbf{r}) = \int_S d\mathbf{r} \int_{\Omega} d\mathbf{r}' \hat{\mathbf{n}}_S \sigma(\mathbf{r}, \mathbf{r}') \mathbf{E}_{\text{loc}}(\mathbf{r}'). \quad (1)$$

We may choose S to cut through one of the leads and to be part of the surface defining the total volume Ω which encloses the sample (see Fig. 1). The local electric field is the gradient of the electrochemical potential $\mathbf{E}_{\text{loc}}(\mathbf{r}) = \nabla\mu(\mathbf{r})/e$ which vanishes in the leads according to our assumption (i). The chemical potentials in the leads are supposed to be identical to the ones in the contacts [assumption (ii)]. The divergence theorem and the condition of local charge conserva-

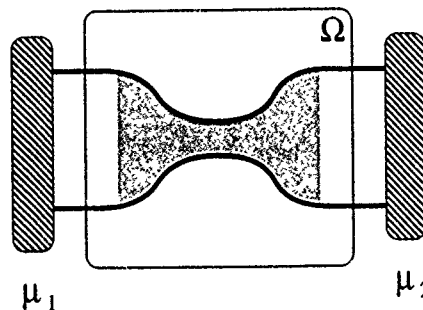


FIG. 1. Transport experiment described by Landauer's formula in the two-terminal configuration. A current flows through the sample due to an electrochemical potential difference $\mu_1 - \mu_2$ between the contacts which are indicated by heavy shading. Ω is the volume encircled by the thin line, which includes the shaded sample region and part of the low-impedance leads to the equilibrated contacts.

^{a)}Permanent address: University of Trondheim, The Norwegian Institute of Technology, Faculty of Physics and Mathematics, Division of Physics, N-7034 Trondheim, Norway.

^{b)}Also at: Faculty of Applied Physics and DIMES, Delft University of Technology, Lorentzweg 1, 2628 CJ Delft, The Netherlands.

tion, $\nabla \cdot \mathbf{j}(\mathbf{r}) = 0$, can then be employed to transform the volume integral in Eq. (1) into a surface integral,

$$J_2 = -J_1 = G \Delta \mu / e, \quad (2)$$

where J_1 and J_2 are the currents through the two leads and G is the conductance,

$$G = \int d\mathbf{r} \int d\mathbf{r}' \hat{\mathbf{n}}_1(\mathbf{r}) \underline{\sigma}(\mathbf{r}, \mathbf{r}') \hat{\mathbf{n}}_2(\mathbf{r}'). \quad (3)$$

This result shows that the current through the sample depends only on the *total* potential drop over the sample and it is not necessary to know the *local* current and electric-field distribution to obtain the transport properties. It can then be shown¹⁸ that the conductance is proportional to the sum of the transmission probabilities $|t_{m,n}|^2$ between the different modes m and n at the Fermi energy in the left- and right-hand side leads (spin-degeneracy assumed),

$$G = \frac{2e^2}{h} \sum_{m,n} |t_{m,n}|^2. \quad (4)$$

The transmission amplitude $t_{m,n}$ can be calculated via the Schrödinger equation.^{13,19}

In many experiments it is not possible to cleanly separate "contacts," "leads," and the "sample." However, the Landauer-Büttiker formalism can be applied also when the conductance is limited by a well-defined narrow sample region as sketched in Fig. 1, where the contribution of the contact/lead region, and inaccuracies of its theoretical treatment, can be safely disregarded. In macroscopic samples the effects of the contacts may be neglected anyway. One might also wonder if the formalism may be applied to the spin-valve effect. It is well known that a ferromagnetic layer causes a nonequilibrium spin polarization of the outgoing current.^{20,21} On the other hand, the equilibrated contacts are an essential ingredient in the derivation of Landauer's formula. However, this problem is of no concern as long as the spin-flip relaxation length is sufficiently longer than the length of the narrow sample section which limits the conductance. If the spin flip takes place in a wide sample section or in the contacts itself, it will not significantly contribute to the conductance. The spin-flip-induced degradation of the giant magnetoresistance with increasing temperature^{8,22} cannot be treated by our theory, however.

III. DISORDERED INTERFACE SCATTERING

We consider the configuration in Fig. 2(a), i.e., a relatively narrow pillar of metallic material which limits the current in the circuit, as fabricated by Gijs *et al.*,³ although macroscopic devices as investigated by Pratt *et al.*² can be treated as well. The de Broglie wavelength in high-density metals is only a few Å and quantum effects due to lateral confinement can be neglected for pillars wider than, say, 0.01 μm. In this regime the sample boundaries also have a negligible effect. Let us first consider scattering at a single interface. The interface roughness is modeled by short-range scatterers that are randomly distributed over the interface. The incoming and outgoing electron states are in this section ap-

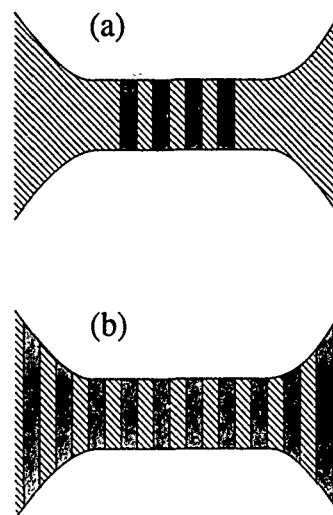


FIG. 2. (a) Sample geometry considered in the first part of the article, where the leads are made from a bulk metal, and the conductance is limited by the narrow region containing a heterostructure. (b) Pillar made from a superlattice, a configuration which is accessible to band-structure calculations.

proximated by plane waves with an effective parabolic dispersion. The wave function at an energy E is determined by the Schrödinger equation,

$$\left(-\frac{\hbar^2}{2} \nabla \frac{1}{m^*(x)} \nabla + U_C(x) + V(x, y, z) \right) \psi(x, y, z) = E \psi(x, y, z). \quad (5)$$

The conduction-band profile, $U_C(x)$, and the effective mass of the electron $m^*(x)$, are approximated by step functions at $x = 0$. The interface roughness is represented by the potential $V(x, y, z)$. Landauer's conductance formula for this situation reads (spin degeneracy assumed)

$$G = \frac{2e^2}{h} \sum_{\mathbf{k}_\parallel, \mathbf{k}'_\parallel}^{\text{prop}} |t_{\mathbf{k}_\parallel, \mathbf{k}'_\parallel}|^2. \quad (6)$$

k_\parallel and k_\perp are the transverse and longitudinal components of the wave vectors related by

$$k_\perp^L = [(2m_L^*/\hbar^2)(E_F - U_L) - k_\parallel^2]^{1/2},$$

$$k_\perp^R = [(2m_R^*/\hbar^2)(E_F - U_R) - k_\parallel^2]^{1/2}.$$

The transmission (reflection) coefficient from state \mathbf{k}_\parallel to state \mathbf{k}'_\parallel is $t_{\mathbf{k}_\parallel, \mathbf{k}'_\parallel}(r_{\mathbf{k}_\parallel, \mathbf{k}'_\parallel})$ and the summation is over propagating modes. In the following we set $\Delta U_C = 0$ and $\Delta m^* = 0$, which considerably simplifies the analytical treatment (see Ref. 13 for generalizations of the following equations). Current conservation and the continuity of the wave function relate the transmission probabilities and the transmission coefficients by an optical theorem,²³

$$\sum_{\mathbf{k}_\parallel}^{\text{prop}} |t_{\mathbf{k}_\parallel, \mathbf{k}'_\parallel}|^2 = \text{Re}(t_{\mathbf{k}'_\parallel, \mathbf{k}'_\parallel}). \quad (7)$$

The diagrams contributing to the transmission probability can be classified as crossing or non-crossing. The crossing

diagrams¹³ describe phase coherence phenomena like weak (Anderson) localization of the wave function.²⁴ Neglecting crossing diagrams, i.e., phase coherent scattering between different defects, it is possible to find the transmission probability in terms of the irreducible self-energy Σ (Ref. 13),

$$\langle |t_{k_1, k_1'}|^2 \rangle = \delta_{k_1, k_1'} \frac{k_1^2}{\left| k_1 + i \frac{m^*}{\hbar^2} \Sigma \right|^2} + \frac{k_1}{\left| k_1 + i \frac{m^*}{\hbar^2} \Sigma \right|^2} \times \frac{-m^*}{\hbar^2} \frac{\text{Im}(\Sigma)}{\Sigma_{k_1'}^{\text{prop.}}} \frac{k_1'}{\left| k_1' + i \frac{m^*}{\hbar^2} \Sigma \right|^2} \quad (8)$$

Our approximation is called semiclassical and valid for $|\Sigma|/E_F \ll 1$. Otherwise it breaks down when the distance between dephasing inelastic collisions becomes larger than the average separation between scatterers. Electrons are scattered specularly at the interface if the transverse component of the wave vector is conserved, which is the first term on the right-hand side of Eq. (8). The second term clearly represents the diffuse scattering contribution, which vanishes if the vertex correction is not taken into account.

To lowest order in the self-energy $m^* \Sigma / (\hbar^2 k_F)$ the conductance is independent of the real part of the self-energy,

$$G = G^0 (1 - 4\eta_{IR} + 2\eta_{IR}), \quad (9)$$

where $\eta_{IR} = -m^* \text{Im}(\Sigma) / (\hbar^2 k_F)$. $G^0 = (2e^2/h)(Ak_F^2)/(4\pi)$ is the Sharvin conductance which is proportional to the sample cross section A . The second term reduces the conductance due to specular scattering. The third, diffuse term *increases* the conductance by opening additional channels for electron transport.

We will now study the situation where all scatterers have equal magnitude of strength $\pm \gamma$ with an average $\bar{\gamma}$ which does not have to vanish. The self-energy is calculated in the single-site approximation, i.e., using the exact cross section for isolated defects, but neglecting crossed diagrams,

$$\Sigma^S = \frac{\eta_{IR} \bar{\gamma} - i n_{IR} (m^* / \hbar^2) \gamma^2 (k_F / 2\pi) (1 - i \sqrt{\alpha^2 - 1})}{1 + [(m^* \gamma / \hbar^2) (k_F / 2\pi)]^2 (1 - i \sqrt{\alpha^2 - 1})^2} \quad (10)$$

This result reduces to the Born result in the weak scattering limit $[m^* \gamma k_F / (\hbar^2 \pi) \ll 1]$. For strong scattering $[m^* \gamma k_F / (\hbar^2 \pi) \gg 1]$, but to lowest order in η_{IR} , we obtain the interesting result that

$$G = \frac{2e^2}{h} \left(\frac{Ak_F^2}{4\pi} - \frac{N_{IR}}{\alpha^2} \right), \quad (11)$$

where a high-momentum cutoff αk_F characterizes the spatial range of the scattering potentials. The conductance is reduced by a factor proportional to the number of defects $N_{IR} = A n_{IR}$. Each scatterer effectively blocks one channel

and the conductance becomes independent of the scattering strength. This blocking is somewhat reduced by a factor $1/\alpha^2$ via a "leak" of evanescent states. An experiment is proposed to test this expression: Insert a layer (or a multilayer, see below) with strong short-range scatterers between two low-impedance leads. Such a structure could be realized by the technique of δ -doping, which is routinely employed in semiconductor technology. By measuring the conductance and the number of impurities the theory can be checked and the leaking factor α can be determined which provides information about the range of the scattering potential. Note that a non-zero average of scatterers has no effect on the conductance in this limit.

Results for a single interface can be generalized to N interfaces, taking both interface scattering and bulk impurity scattering into account. Semiclassical concatenation of transmission probabilities¹⁹ is consistent with the neglect of crossing diagrams in the single-interface scattering. The transmission properties do not change with the distance between the interfaces in this approximation. By allowing the interfaces to be infinitesimally close to each other, one can convince oneself that the relation between the transmission probabilities and the transmission coefficients, Eq. (7), still holds for the N -interface configuration. The conductance for a multilayer is

$$\frac{G^{(N)}}{G^0} = 1 - 2x_N + 2x_N^2 \ln \left(1 + \frac{1}{x_N} \right), \quad (12)$$

where $x_N = N / (2\tilde{N}) = L / (2l)$. $\tilde{N} = l / L_p = [2\eta_{IR} + L_p / l_{BI}]^{-1}$ is the mean free number of traversed interfaces, where L is the total sample length, $L_p = L / N$, l is the global mean free path and l_{BI} is the mean free path due to bulk impurity scattering. This relation agrees with Eq. (11) in Ref. 6 for $\Delta U_C = 0$. The two-dimensional equivalent of this expression is of interest in quasiballistic transport in semiconductor nanostructures,^{25,26}

$$\frac{G_{2D}^{(N)}}{G_{2D}^0} = 1 - \frac{x_N \pi}{2} + \begin{cases} \frac{x_N^2}{\sqrt{1-x_N^2}} \ln \left(\frac{1 + \sqrt{1-x_N^2}}{x_N} \right) & \text{for } x_N < 1, \\ \frac{x_N^2}{\sqrt{x_N^2-1}} \arccos \frac{1}{x_N} & \text{for } x_N > 1, \end{cases} \quad (13)$$

where $G_{2D}^0 = (2e^2/h)(Wk_F/\pi)$ is the two-dimensional Sharvin conductance, proportional to the channel width W . For disordered homogeneous samples these expressions are similar but not identical to de Jong's solution for the Boltzmann equation.²⁶ The reason for the differences can be traced to the complete backscattering of electrons with grazing incidence in the present formalism, which in the Boltzmann approach are transmitted with probability of one-half.²⁶ In the large N limit a Drude-like (Ohm's law) expression is obtained for the conductivities,

$$\sigma_{\infty} = \begin{cases} \lim_{N \rightarrow \infty} \frac{NL_p G^{(N)}}{A} = \frac{2e^2}{h} \frac{k_F^2}{3\pi} l & \text{in three dimensions,} \\ \lim_{N \rightarrow \infty} \frac{NL_p G_{2D}^{(N)}}{W} = \frac{2e^2}{h} \frac{k_F}{2} l & \text{in two dimensions.} \end{cases} \quad (14)$$

For three-dimensional superlattices this limit has been treated before by Zhang and Levy.⁴

For a magnetic multilayer it is now straightforward to find the conductance by including spin-dependent interface and bulk scattering. The difference in the mean free number of traversed interfaces between both spin channels is $\Delta\tilde{N}$ and the spin-averaged results is \tilde{N} . The magnetoconductance of an antiparallel coupled multilayer is $\Delta G = G^P - G^{AP}$. The magnetoconductance depends on the parameters $\Delta\tilde{N}$, \tilde{N} , and the number of interfaces N . The spin-valve effect increases with the number of bilayers and saturates at the Drude limit for $N \gg \tilde{N}$ (Ref. 4). In the limit of a magnetic superlattice the relative magnetoconductance is

$$[\Delta G/G^P]_{\text{Drude}} = (\Delta\tilde{N}/2\tilde{N})^2.$$

IV. VALIDITY OF SEMICLASSICAL AND EFFECTIVE-MASS THEORY

It is important to assess the accuracy of the semiclassical and the effective-mass approximations for transition-metal multilayers, which are the most interesting class of compounds for applications of the present theory. The semiclassical approximation discards quantum interference effects which are known to be important for several other properties. The oscillatory coupling of magnetic layers is a genuine quantum interference effect since it depends on the thickness of the non-magnetic layer.²⁷ Size-quantized states have been observed by inverse photoemission and claimed to mediate the magnetic coupling.²⁸ It is therefore not clear from the outset that semiclassical approximations can be used to describe transport properties. A combined theory for coupling and transport proposed in Ref. 29 is still in a formal stage. In a numerical study on disordered multilayers Asano and co-workers^{9,10} provide evidence that quantum size effects can be very important for the transport properties. They proceed from a tight-binding approximation for the d electrons, which corresponds to a small bandwidth and large effects for a given potential discontinuity. The effect of the potential step is much smaller, however, when s electrons at the Fermi energy are considered to be responsible for the transport, especially in Cu/transition-metal multilayers. Zhang and Levy¹⁴ also found rather small quantum effects of miniband formation for the small potential step sizes seen by s electrons. In reality, free electrons and d electrons are strongly hybridized. This problem cannot be solved satisfactorily within an effective-mass approximation, revealing the need for a transport theory which takes the correct band structure of the transition metal into account. s - d hybridization has been investigated in a tight-binding approximation by Itoh, Inoue, and Maekawa³⁰ to investigate the scattering potential of a rough Cu/Ni surface. Coehoorn³¹ correlates magnetotransport with the spin-dependent occupation num-

ber differences of d orbitals at heterointerfaces obtained from first-principles band-structure calculations. Oguchi³² employs band-structure calculations of superlattices to calculate the average Fermi velocities, i.e., the gradient of the energy dispersion at the Fermi surface, parallel and perpendicular to the interfaces. The strong anisotropies are due to quantum size effects similar to those found by Asano and co-workers.^{9,10} However, transport and band structures are connected heuristically by introducing a phenomenological transport scattering time.

Here we want to emphasize that the Landauer-Büttiker formalism lends itself very well to go beyond the effective-mass and semiclassical approximations, taking into account band-structure effects rigorously. The Landauer conductance formula is easily rewritten for the case of a complicated band-structure by labeling the in- and outgoing electron states at the Fermi energy by the parallel crystal momentum q_{\parallel} inside the first Brillouin zone and band index ν (spin degeneracy assumed),

$$G = \frac{2e^2}{h} \sum_{q_{\parallel\nu}, q'_{\parallel\nu'}} |t_{q_{\parallel\nu}, q'_{\parallel\nu'}}|^2. \quad (15)$$

The calculation of the transmission probabilities is of course more difficult. In order to get a feeling for the interrelation between electronic structure and transport, we propose considering the perfectly ballistic regime of a microstructure or point contact. This regime might be realized in future devices since atomically perfect interfaces are already obtainable by molecular-beam-epitaxy crystal growth techniques. Furthermore, Asano and co-workers^{9,10} pointed out that the projected density of states of unperturbed systems is strongly correlated with the conductance affected by interface roughness scattering. The finite (Sharvin) conductance is proportional to the finite cross section A and the contact conductances in the narrow sample region due to heteroinclusions.⁶ The configuration in Fig. 2(a) is not directly accessible to band-structure calculations, however. We therefore concentrate on the configuration in Fig. 2(b), for which the Sharvin conductance comes down to the sum of the projections S of the Fermi surfaces for the different bands on the plane normal to the transport direction \hat{n} ,³³

$$\begin{aligned} G_{\hat{n}} &= \frac{2e^2}{h} \frac{A}{4\pi^2} \frac{1}{2} \sum_{\nu} S_{\nu}(\hat{n}) \\ &= \frac{2e^2}{h} \frac{A}{4\pi^2} \frac{1}{2} \sum_{\nu} \int d\mathbf{q} |\hat{n} \cdot \nabla_{\mathbf{q}} \epsilon_{\nu}(\mathbf{q})| \delta[\epsilon_{\nu}(\mathbf{q}) - E_F], \end{aligned} \quad (16)$$

which can be calculated given the band-structure energies $\epsilon_{\nu}(\mathbf{q})$ on a sufficiently fine mesh of wave vectors in the first Brillouin zone. In Fig. 3 we plot the number of conduction channels for Cu, which is proportional to the ballistic conductance through a constriction with cross section A , as calculated using first-principles band structures obtained by the linear muffin-tin orbital method (see Ref. 33 for details). To indicate the contributions from different bands the Fermi energy is varied, keeping the Cu band structure unmodified.

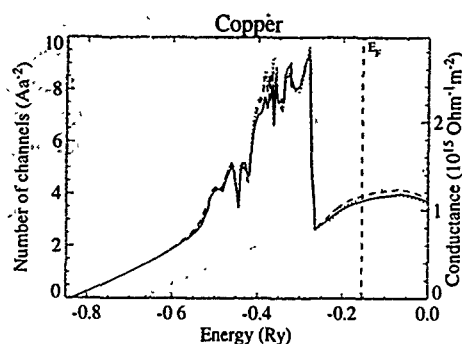


FIG. 3. Number of conducting channels in a constriction of copper with cross section A and oriented along the main crystal axes $\langle 100 \rangle$ (solid line), $\langle 110 \rangle$ (dashed line), and $\langle 111 \rangle$ (dotted line) ($a=3.61$ Å). The Fermi energy is varied for the (fixed) energy band structure calculated for Cu. The dashed straight line is the free-electron result.

Note that $G_{\hat{n}}$ is anisotropic even for cubic crystals. By calculating Eq. (16) for magnetic superlattices with \hat{n} parallel and perpendicular to the interfaces a first-principles, consistent theory of transport and magnetism can be achieved. First results have been obtained for Co_1/Cu_2 $\langle 111 \rangle$ -oriented superlattices forced into the spin-parallel (P) and spin-antiparallel (AP) configurations. The conductances are 1.14 (P) and 0.96 (AP) for the CIP geometry and 0.83 (P) and 0.64 (AP) for the CPP geometry, all in $10^{15} \Omega^{-1} \text{cm}^{-2}$. The magnetoconductance (P-AP)/AP is therefore 19% for the CIP geometry in contrast to 30% in the CPP geometry, explaining a significant fraction of the experimental value as a purely ballistic effect. A detailed analysis will be published in due course.³³

V. CONCLUSIONS

In summary, we have derived analytical semiclassical expressions for perpendicular transport through disordered interfaces. An experiment to check the theory is proposed which might lead to a deeper understanding of the scattering process and the microscopic structure of disordered interfaces. In the two-current model the expressions are easily generalized to describe the giant magnetoresistance in terms of the mean free number of traversed interfaces for the majority and minority spins. First results indicate the importance of taking realistic band structures into account.³³

ACKNOWLEDGMENTS

G.E.W.B. thanks Alexander Khaetskii, Marc de Jong, and Yuli Nazarov for helpful discussions. This work is part

of the research program of the Stichting voor Fundamenteel Onderzoek der Materie (FOM), which is financially supported by the Nederlandse Organisatie voor Wetenschappelijk Onderzoek (NWO).

- ¹M. N. Baibich, J. M. Broto, A. Fert, F. Nguyen van Dau, and F. Petroff, *Phys. Rev. Lett.* **61**, 2472 (1988); G. Binasch, P. Grünberg, F. Saurenbach, and W. Zinn, *Phys. Rev. B* **39**, 4828 (1989); for a recent review see R. Coehoorn, *Europhys. News* **24**, 43 (1993).
- ²W. P. Pratt, S. F. Lee, R. Lolee, P. A. Schroeder, and J. Bass, *Phys. Rev. Lett.* **66**, 3060 (1991); W. P. Pratt *et al.*, *J. Magn. Magn. Mater.* **126**, 406 (1993).
- ³M. A. M. Gijs, S. K. J. Lenczowski, and J. B. Giesbers, *Phys. Rev. Lett.* **70**, 3343 (1993); M. A. M. Gijs *et al.*, these proceedings.
- ⁴S. Zhang and P. M. Levy, *J. Appl. Phys.* **69**, 4786 (1991); *Phys. Rev. B* **45**, 8689 (1992).
- ⁵M. Johnson, *Phys. Rev. Lett.* **67**, 3594 (1991).
- ⁶G. E. W. Bauer, *Phys. Rev. Lett.* **69**, 1676 (1992).
- ⁷R. Q. Hood and L. M. Falicov, *Phys. Rev. B* **46**, 8287 (1992).
- ⁸T. Valet and A. Fert, *Phys. Rev. B* **48**, 8689 (1992).
- ⁹Y. Asano, A. Oguri, and S. Maekawa, *Phys. Rev. B* **48**, 6192 (1993).
- ¹⁰Y. Asano (private communication).
- ¹¹H. E. Camblong, S. Zhang, and P. M. Levy, *Phys. Rev. B* **47**, 4735 (1993).
- ¹²G. E. W. Bauer, M. A. M. Gijs, S. L. J. Lenczowski, and J. B. Giesbers, *J. Magn. Magn. Mater.* **126**, 454 (1993).
- ¹³A. Brataas and G. E. W. Bauer, *Europhys. Lett.* (in press).
- ¹⁴S. Zhang and P. M. Levy (preprint).
- ¹⁵K. Fuchs, *Proc. Philos. Camb. Soc.* **34**, 100 (1938).
- ¹⁶T. Ando, A. B. Fowler, and F. Stern, *Rev. Mod. Phys.* **54**, 437 (1982).
- ¹⁷R. Landauer, *Z. Phys. B* **68**, 217 (1987).
- ¹⁸H. U. Baranger and A. D. Stone, *Phys. Rev. B* **40**, 8169 (1989).
- ¹⁹M. Cahay, M. McLennan, and S. Datta, *Phys. Rev. B* **37**, 10 125 (1988).
- ²⁰M. Johnson and R. J. Silsbee, *Phys. Rev. Lett.* **55**, 1790 (1985).
- ²¹P. C. van Son, H. van Kempen, and P. Wyder, *Phys. Rev. Lett.* **58**, 2271 (1987).
- ²²H. Hasegawa, *Phys. Rev. B* **47**, 15 080 (1993).
- ²³Y. B. Levinson, M. I. Lubin, and E. V. Sukhorukov, *Phys. Rev. B* **45**, 11 936 (1992).
- ²⁴P. A. Lee and T. V. Ramakrishnan, *Rev. Mod. Phys.* **57**, 2 (1985).
- ²⁵S. Tarucha, T. Saku, Y. Tokura, and Y. Hirayama, *Phys. Rev. B* **47**, 4064 (1993).
- ²⁶M. J. M. de Jong, *Phys. Rev. B* (in press).
- ²⁷J. C. Slonczewski, *J. Magn. Magn. Mater.* **126**, 374 (1993).
- ²⁸J. E. Ortega and F. J. Himpsel, *Phys. Rev. Lett.* **69**, 844 (1992).
- ²⁹S. N. Molotkov, *Pis'ma Zh. Eksp. Teor. Fiz.* **57**, 103 (1993) [*JETP Lett.* **57**, 111 (1993)].
- ³⁰H. Itoh, J. Inoue, and S. Maekawa, *J. Magn. Magn. Mater.* **126**, 479 (1993).
- ³¹R. Coehoorn, *J. Magn. Magn. Mater.* **121**, 432 (1993).
- ³²T. Oguchi, *J. Magn. Magn. Mater.* **126**, 519 (1993).
- ³³C. M. Schep, P. J. Kelly, and G. E. W. Bauer (unpublished).

Perpendicular giant magnetoresistance of microstructures in Fe/Cr and Co/Cu multilayers (invited)

M. A. M. Gijs, J. B. Giesbers, M. T. Johnson, J. B. F. aan de Stegge,
and H. H. J. M. Janssen

Philips Research Laboratories Prof. Holstlaan 4, 5656 AA Eindhoven, The Netherlands

S. K. J. Lenczowski, R. J. M. van de Veerdonk, and W. J. M. de Jonge

Eindhoven University of Technology, Department of Physics, 5600 MB Eindhoven, The Netherlands.

We discuss the fabrication and microstructuring techniques of pillar structures made of high vacuum sputtered Fe/Cr multilayers and of molecular beam epitaxy evaporated Co/Cu multilayers, for which we measured the giant magnetoresistance effect with the current perpendicular to the multilayer plane from 4 K to 300 K. Using optical lithography and reactive ion etching techniques we obtained structures with a typical height of 0.5 μm and a width ranging between 3 and 10 μm . For both Fe/Cr and Co/Cu multilayers we find an enhanced magnetoresistance with respect to the in-plane case. The perpendicular magnetoresistance of the Fe/Cr pillars strongly decreases with temperature, while for the Co/Cu samples the temperature dependence is weaker, indicating electron-magnon scattering processes of different strength.

I. INTRODUCTION

Following the discovery of antiferromagnetic (AF) coupling¹ and the associated giant magnetoresistance (MR) effect in Fe/Cr magnetic multilayers,² numerous magnetoresistance studies on a variety of multilayer systems have been reported.³⁻⁹ In these experiments, the measuring current is in the plane of the multilayer, the so-called current-in-plane (CIP) geometry. The situation where the measuring current is perpendicular to the multilayer plane (the so-called CPP-geometry) has been studied more extensively theoretically¹⁰⁻¹⁵ than experimentally. Up to now only two experimental groups reported on the CPP-MR in magnetic multilayers. The first experiments were done for Co/Ag and Co/Cu multilayers at Michigan State University.¹⁶ In these experiments no microfabrication techniques were used; the multilayer was sandwiched between a superconducting Nb top and bottom contact electrode of millimeter size and the very small multilayer resistance (typically 0.01–0.1 $\mu\Omega$) was measured at 4.2 K using an ultra-sensitive SQUID-based system. This implies that measurements are only possible at liquid helium temperatures. Following another approach, we have used microstructuring techniques and fabricated Fe/Cr pillar structures, enabling us to study the CPP-MR effect from 4 K up to room temperature.¹⁷ This experiment is not at all straightforward, primarily because the perpendicular resistance of a microstructured thin film generally is much smaller than the sheet resistance R_{\square} of the contact leads. To overcome this problem, a specific contact geometry has been developed, which allows a proper measurement of the perpendicular resistance of a metal film without excessive spurious resistance contributions from the contact leads.¹⁸ Our experiments provided the first data on the temperature dependence of the CPP-MR effect, which still represents a theoretical challenge. In particular the role of spin-flip scattering on the giant MR remains to be elucidated.

Here, we will discuss experiments on the temperature dependence of the CPP-MR¹⁹ of microstructured Fe/Cr multilayers, grown by sputtering. These are compared with new experimental results on the CPP-MR of Co/Cu multilayers, grown by molecular beam epitaxy (MBE) evaporation. In

Sec. II, we will discuss the growth and characterization of the multilayers followed by an outline of the microstructuring methods to fabricate the samples. Attention will also be given to finite element calculations of the current distribution pattern in the different sample geometries. In Sec. III, we present the CPP-MR results for the Fe/Cr and Co/Cu multilayers. The CPP-MR of typically 100% at low temperatures are a factor 2 to 4 larger than the corresponding CIP-MR. For Fe/Cr the CPP-MR decreases strongly on increasing the temperature, whereas experiments on Co/Cu show a much slower decrease. The different temperature dependence of Fe/Cr and Co/Cu can be related to the role of electron-magnon scattering in the two multilayer systems. Finally, in Sec. IV, conclusions will be formulated.

II. LAYER DEPOSITION AND MICROSTRUCTURING

In this section we will first discuss the deposition, characterization, and microstructuring of the Fe/Cr multilayers; second, for the Co/Cu multilayers, the MBE deposition and characterization is explained, whereas the microstructuring is practically the same as for the Fe/Cr layers.

The processing of a Fe/Cr pillar sample is schematically shown in Figs. 1(a)–1(d). First a 0.4 μm thick Cr base layer is rf sputtered onto a SiO_2 substrate held at room temperature. Then a 0.4–0.7 μm thick Fe/Cr multilayer is deposited, using dc sputtering for the Fe and rf sputtering for the Cr, followed by a dc sputter deposition of a 0.3 μm thick Au layer. The central part of the structure consists typically of a $100 \times (3 \text{ nm Fe} + t_{\text{Cr}} \text{ Cr})$ multilayer with a variable Cr thickness t_{Cr} . All depositions were done during one vacuum run. The system pressure prior to deposition was 4×10^{-7} mbar and the Ar-pressure during sputtering was 4×10^{-3} mbar. X-ray diffraction shows predominantly (110) growth of the multilayer. For lithography the sample is covered by a 0.1 μm thick Mo layer, then by a 0.2 μm thick Al_2O_3 layer, followed by the deposition of another 0.1 μm thick Mo layer. The latter is structured using conventional lithography and using wet etching [Fig. 1(a)] and serves as a mask for the structuring of the Al_2O_3 layer, which is carried out in a CHF_3/Ar plasma (10 sccm $\text{CHF}_3/40$ sccm Ar, 25 μbar , 0.52

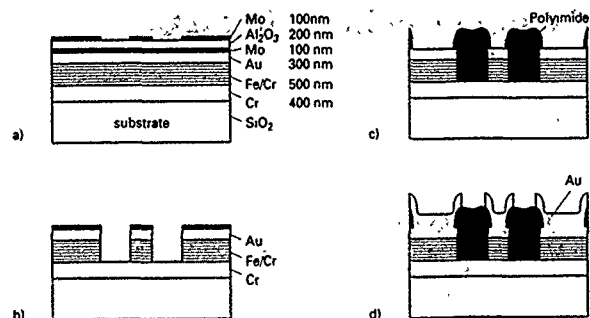


FIG. 1. Schematic diagram of different processing steps in the pillar structuring and contact fabrication.

W/cm²). The structured Al₂O₃ layer in turn is used as a mask for the etching of the Au and the Fe/Cr multilayer; this is done in an HCl plasma (40 μbar, 2.1 W/cm²) [Fig. 1(b)]. After removal of the remaining Al₂O₃, the sample is covered with an insulating polyimide layer. Contact holes in the polyimide are made using reactive ion etching, after which the remaining Mo in the hole is removed by wet etching [Fig. 1(c)]. Subsequently, the structure is covered by a 1.9 μm thick Au film, in which the contact electrode pattern is made [Fig. 1(d)]. The pillar in the middle is the actual sample; finally two Au contact leads are attached on top of it for the resistance measurement; also the side parts of the structure are contacted and serve as the lower contact leads for the pillar in the middle.

In Figs. 2(a)–2(d), microscopic images of the structure are shown. Figure 2(a) corresponds to the schematic diagram of Fig. 1(b) and shows the pillar after the structuring in the HCl-plasma. Figure 2(b) is a top view of the final structure, showing the upper Au contact structured on top of the hole in the polyimide. The upper and lower current contact is indicated by I^+ and I^- , respectively; the upper and lower voltage contact is indicated by V^+ and V^- , respectively.

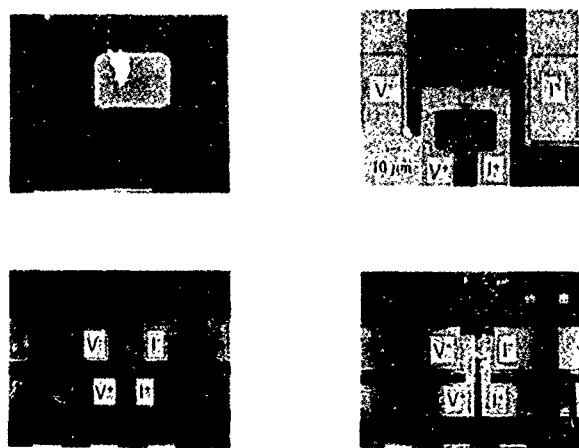


FIG. 2. (a) Micrograph of a pillar structure after the etching in the HCl plasma; (b) micrograph showing the upper Au electrode on top of the hole in the polyimide; upper and lower current contacts are indicated by I^+ and I^- , respectively; upper and lower voltage contacts are indicated by V^+ and V^- , respectively; (c) complete pillar device; (d) pillar device with additional laser trenches.

Figure 2(c) is an over-all view of the structure, as described so far, showing clearly the relative magnitude of the pillar with respect to the contact electrodes. Figure 2(d) is an improved measuring structure, which differs from Fig. 2(c) only by the presence of two trenches, etched down to the substrate using a Nd-YAG laser (532 nm). For the largest pillars fabricated on the substrate (width 10–12 μm), the trench ends at the edges of the pillar, so that the only connection between the two parts of the structure is established through the pillar. This trench plays a crucial role in the measurement of the Fe/Cr pillars, because it strongly reduces the spurious spreading resistance effect of the contact leads (particularly of the lower Cr electrode), which is necessary for a proper measurement of the very small perpendicular resistance (typically a few mΩ). The resistance of the structure without trench [Fig. 2(c)] is dominated by resistance contributions from the electrodes. The difference between the two measurement geometries can be well understood using the three dimensional simulation package TOSCA.²⁰ More specifically, electrostatic calculations, based on the finite element method, were done for a structure consisting of two 140×140 μm² square films with a thickness of 1.9 μm and 0.3 μm, respectively, centrally connected by a 4×4 μm² pillar with a height of 1 μm. This structure is schematically shown in Fig. 3(a); the location of the current and voltage contacts is indicated. The actual pillar in between the two contact layers is grey shaded. When a current is flowing from I^+ to I^- , we find equipotential lines in the 0.3 μm thick bottom electrode as shown in Fig. 3(b). Figure 3(c) is the corresponding vector plot of the electric field. The direction of the arrows corresponds to the direction of the field and their thickness to the field magnitude. It is clear that, between the voltage probes V^+ and V^- , a large spurious voltage contribution from the leads is present. For the simulated structure, we find, using contour integration, that only 3% of the totally measured voltage actually corresponds to a voltage drop over the perpendicular resistance. The structure *with* trenches is schematically shown in Fig. 3(d). Corresponding voltage and electric field plots of the lower contact electrode are given in Figs. 3(e) and 3(f), respectively. In Fig. 3(e) there is no voltage drop at all in the left voltage sensing electrode, which of course is equivalent to the locally zero electric field in Fig. 3(f). Having eliminated the electrode spreading resistance, the resistance of the multilayer pillar is still of the same order of magnitude as the residual serial contact resistance (probably located at the pillar-contact interface), which is determined experimentally by comparing different multilayer thicknesses. Also the pillar height is relatively small compared to its width w , which gives rise to a nonuniform current distribution in the pillar. Analytical calculation using Ohms law gives for the geometry with trench that $(V^+ - V^-)w^2 \propto (w/L)/\sinh(w/L)$ with L a parameter of typically 2–3 μm.²¹ This dependence w^2 checked independently by numerical simulations based on the finite element method. In the following, quoted MR values for the Fe/Cr multilayers were corrected for the serial contact resistance and are extrapolations for $w \rightarrow 0$.

The fabrication of the Co/Cu multilayer pillars is similar to that of the Fe/Cr samples. However, it is well known that

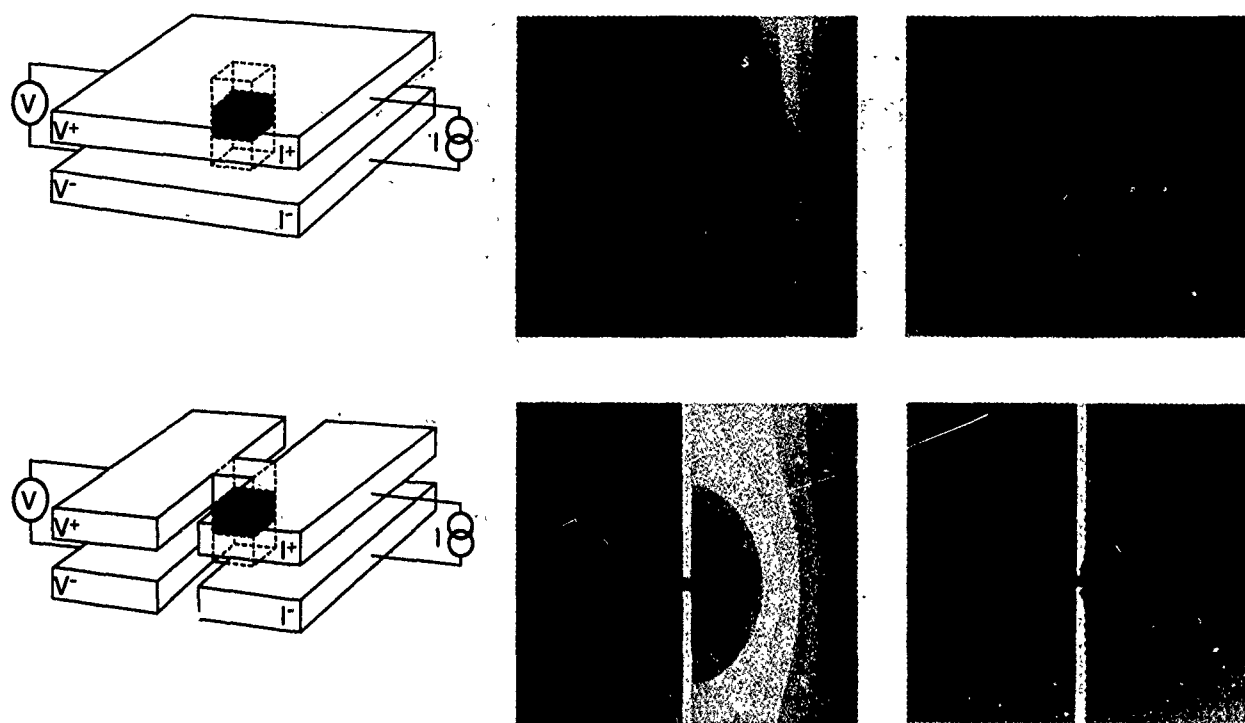


FIG. 3. (a) Schematic diagram of the simulated structure without trench. The actual pillar is grey shaded; current and voltage contacts are indicated. (b) Finite element calculation of the equipotential line distribution in the bottom electrode of a structure without trench. (c) Finite element calculation of the electric field modulus and vector plot of the electric field in the bottom electrode of a structure corresponding to a structure without trench. (d) Schematic diagram of the simulated structure with trench. The actual pillar is grey shaded; current and voltage contacts are indicated. (e) and (f): same as (b) and (c), but for a structure with laser-etched trenches. For each simulation the current drain is on the right and voltage probes are situated on the left.

the growth of AF coupled Co/Cu multilayers with large MR is very sensitive to, for instance, the choice of the substrate and the use of a buffer layer.⁵ We have investigated Co/Cu(100) oriented layers. The multilayer stacks were prepared on single crystalline Si(100) substrates in a multichamber MBE system (VG Semicon V80M). Prior to introduction into the MBE system, the substrates were IIF dipped, a procedure which resulted in a sharp low energy electron diffraction (LEED) pattern, characteristic of the Si(100) substrate. All depositions were carried out at room temperature, at a pressure of better than 10^{-10} mbar. The first stage of the multilayer stack involved deposition of a 300 nm Cu layer, later to be employed as the lower electric contact. A deposition rate of 0.053 nm/s, as registered by a calibrated quartz crystal thickness monitor, was used for the deposition. LEED analysis of the resulting Cu layer indicated that a clear (100) orientation was produced. Perpendicular and parallel lattice spacings have been determined kinematically by measuring the primary Bragg LEED reflections along the [0,0] rod, and by comparison of the LEED patterns with those of a Cu(100) single crystal. In both directions, the Cu layer displayed identical lattice spacings to that of a single crystal Cu(100). Subsequent deposition of the Co/Cu multilayer [$250 \times (1.2 \text{ nm Co} + 1.1 \text{ nm Cu})$] with identical Cu rate and a Co deposition rate of 0.05 nm/s, maintained the (100) orientation established for the Cu base layer. The in-plane lattice spacing is, within experimental error, identical to the underlying Cu base layer, establishing the presence of coherent epitaxial growth. Quantification of the perpendicular lattice spacings of thin multilayers is not reliable within the kinematic ap-

proximation (due to multiple diffraction effects); the most probable scenario however being that the growth proceeds in an equivalent manner to that established by de Miguel *et al.*,²² where Cu layers are observed to maintain their bulk perpendicular spacing (0.181 nm) and the Co layers contract in the perpendicular direction (to 0.170 nm) to accommodate the coherent in-plane expansion. X-ray diffraction studies revealed that the repeat period of the Co/Cu multilayer was $(2.27 \pm 0.04) \text{ nm}$. The multilayer stack was completed with a deposition of 300 nm of Au (deposition rate 0.03 nm/s), to be used as the top electrical contact.

The microstructuring process of the Co/Cu layers is similar to that of Fe/Cr. The only difference is that, during the pillar etching in the HCl plasma, only 180 repeats of the Co/Cu bilayer are etched through, so that the lower 70 Co/Cu bilayers become part of the lower contact electrode. The reason for this is the extremely high etching rate of pure Cu in the HCl plasma, which makes the etching down to the last Co/Cu bilayer extremely critical. The quoted MR values for the Co/Cu multilayer are as-measured; the intrinsic MR effect might be larger, as the contribution of a serial pillar contact resistance so far could not be discriminated.

Typically, a few hundred pillars with a cross section S ranging between $6 \mu\text{m}^2$ and $130 \mu\text{m}^2$ are fabricated on one substrate for each multilayer composition, 15–20 different pillar structures of the same cross-section were measured to check reproducibility. After wire bonding, the samples are mounted in a ^4He flow cryostat. Pillar resistances are measured using an ac bridge technique in the 4–300 K temperature range and in fields up to 1600 kA/m (2 T).

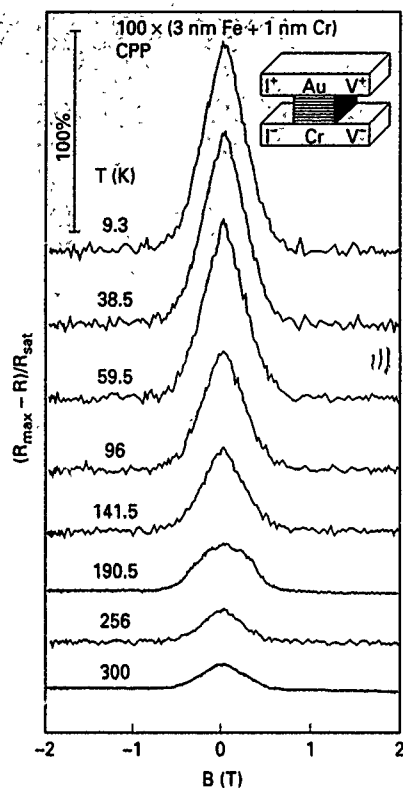


FIG. 4. Giant magnetoresistance of a microstructured pillar in a $100 \times (3 \text{ nm Fe} + 1 \text{ nm Cr})$ multilayer with the current perpendicular to the multilayer plane (CPP) and as a function of temperature. The inset shows a schematic diagram of the pillar structure with the current and voltage contacts.

III. EXPERIMENTAL RESULTS AND DISCUSSION

Figure 4 shows CIP-MR curves at different temperatures for a Fe/Cr pillar with a cross-section $S = 90 \mu\text{m}^2$ structured in a $100 \times (3 \text{ nm Fe} + 1 \text{ nm Cr})$ multilayer; for clarity the curves are displaced vertically. At 9.3 K we observe a MR effect of 108%, more than four times higher than the corresponding CIP-MR effect in unstructured films.⁸ The MR effect is weakly temperature dependent below about $T = 60 \text{ K}$; above that temperature the decrease is much stronger. At room temperature a 14% CPP-MR remains, two times larger than the corresponding CIP-MR. The saturation field B_s ($\equiv \mu_0 H_s$) is defined by the crossing point of the low field resistance decrease with the horizontal line of constant resistance at higher fields. We find that $B_s = 0.54 \text{ T}$, nearly independent of temperature. This B_s -value corresponds with an interlayer exchange coupling energy per unit surface of 1.3 mJ/m^2 (see Ref. 8). Hence, the interlayer coupling energy is orders of magnitude larger than the thermal energy for our microstructures. This implies that the strong temperature dependence of the CPP-MR cannot be attributed to incomplete AF-coupling at higher temperatures. This was verified using temperature dependent magnetization measurements. In contrast to the structure of Fig. 4 with 1 nm Cr layer, we did find a hysteretic magnetoresistance for larger thicknesses, e.g., for the $100 \times (3 \text{ nm Fe} + 4 \text{ nm Cr})$ sample. This seems very reasonable as, for this Cr-thickness, we do not expect perfect

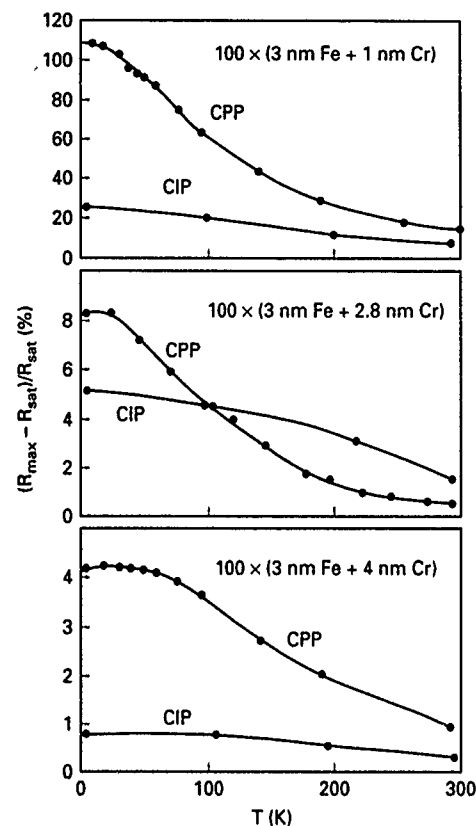


FIG. 5. Temperature dependence of the CPP-magnetoresistance of pillar structures made in $100 \times (3 \text{ nm Fe} + t_{\text{Cr}} \text{ Cr})$ multilayers with (a) $t_{\text{Cr}} = 1 \text{ nm}$, (b) $t_{\text{Cr}} = 2.8 \text{ nm}$, and (c) $t_{\text{Cr}} = 4 \text{ nm}$. Corresponding CIP-MR data are given for comparison. The full curves are a guide to the eye.

AF coupling anymore. Rather, one is in a weakly AF coupled/uncoupled situation, which is also confirmed by magnetization data for this sample.

In Figs. 5(a)–5(c) the temperature dependence of the CPP-MR is shown for multilayers with different t_{Cr} ; a comparison is made with the corresponding CIP data.⁸ Fig. 5(a) is for $t_{\text{Cr}} = 1 \text{ nm}$ and corresponds with the measurements presented in Fig. 4. The enlarged CPP-MR effect and its strong decrease with temperature is immediately clear. This decrease is also pronounced for the sample of Fig. 5(b) ($t_{\text{Cr}} = 2.8 \text{ nm}$, a Cr thickness corresponding to the second AF coupled peak, and $S = 20 \mu\text{m}^2$). Above about 100 K, the CPP-MR even becomes smaller than the CIP-MR. Presently it is hard to discriminate if this is an intrinsic effect or if this crossing of the curves arises from an excessive serial contact resistance for this CPP sample. In Fig. 5(c), the sample with $t_{\text{Cr}} = 4 \text{ nm}$ and $S = 6 \mu\text{m}^2$ is shown. Again, we observe that the CPP-MR is enhanced with respect to the CIP-MR and that the temperature dependence is markedly stronger.

In Fig. 6 we present results on the temperature dependence of the CPP-MR of a $180 \times (1.2 \text{ nm Co} + 1.1 \text{ nm Cu})$ (100) oriented multilayer grown by MBE evaporation ($S = 125 \mu\text{m}^2$), compared with a CIP-MR reference experiment. The sample used for the CIP-experiment was grown on a 30 nm thick Cu buffer layer on a Si(100) substrate. For a Cu thickness of 1.1 nm, one is in the first AF coupling peak of the Co/Cu(100) system. The latter is characterized by a

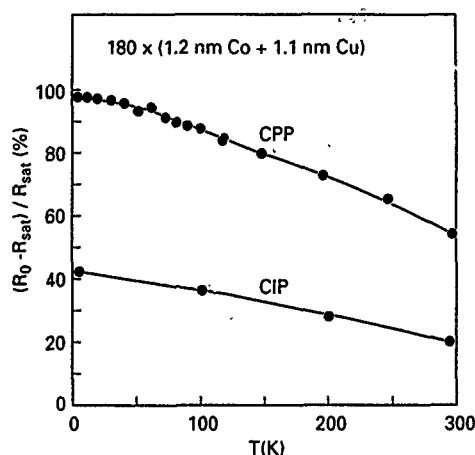


FIG. 6. Temperature dependence of the CPP-magnetoresistance of a Co/Cu(100) pillar structure made from a $180 \times (1.2 \text{ nm Co} + 1.1 \text{ nm Cu})$ multilayer. Corresponding CIP-MR data are given for comparison. The full curves are a guide to the eye.

peak with maximum at 1.0 nm Cu and a width of 0.3 nm.²³ The CIP-MR is 43% at 4 K and 21% at room temperature. This last value is one third of the maximum MR, obtained for a 100% AF coupled (100) oriented Co/Cu multilayer,²⁴ similar to the results for (111) oriented Co/Cu multilayers.^{5,25} Magnetization experiments indeed confirm that approximately one third of our CIP and CPP sample is AF coupled. Just as in the Fe/Cr case, the CPP-MR is larger than the CIP-MR: we find 98% at 4 K and 56% at room temperature. One should note again that these are as-measured numbers and hence represent minimum values for the intrinsic CPP-MR of Co/Cu(100).

The low temperature CPP-MR of Fe/Cr has been discussed elsewhere in terms of models based on spin-dependent bulk and interface scattering parameters.^{8,26} Figures 5 and 6 show that an important difference between the CPP-MR of our Fe/Cr and Co/Cu multilayers is the temperature dependence. Physically, when increasing the temperature, spin-flip scattering due to thermally excited magnons equalizes the two spin currents (the classical spin-mixing effect) and also reduces the spin-flip diffusion length l_{sf} . The strong decrease with temperature of the Fe/Cr CPP-MR (a decrease by a factor of 5–7 over the temperature range studied) is indicative for strong electron-magnon scattering.⁸ On the other hand, the Co/Cu CPP-MR decreases only by a factor 2. The weaker temperature dependence of the MR of Co/Cu multilayers with respect to that of Fe/Cr multilayers also is a general trend seen in CIP-MR experiments. The same holds for the anisotropic MR of bulk dilute alloys based on Fe or Co.^{27,28} These observations may be related to the relatively large magnon scattering for Fe, which is a weak ferromagnet [spin-up ($d\uparrow$) band not completely filled], resulting in an increased spin mixing at higher temperatures.

IV. CONCLUSIONS

We have discussed the fabrication and microstructuring of pillar-shaped structures of Fe/Cr sputtered multilayers and of Co/Cu MBE evaporated multilayers and studied the

CPP-MR effect for these systems from 4 K up to room temperature. The CPP-MR is larger than the CIP-MR of similarly prepared reference samples, certainly at low temperature where electron-magnon scattering is minimum. The temperature dependence of the CPP-MR of Fe/Cr is much stronger than that of Co/Cu, which may be attributed to the different strength of electron-magnon scattering processes in both systems.

ACKNOWLEDGMENTS

We would like to thank H. T. Munsters, H. C. Donkersloot, J. F. M. Janssen, M. M. den Dekker, H. M. M. Bakermans, and O. J. A. Buyk for their contributions to the sample preparation and G. E. W. Bauer, R. Coehoorn, A. Fert, and H. van Houten for valuable discussions.

- ¹ P. Grünberg, R. Schreiber, Y. Pang, M. B. Brodsky, and C. H. Sowers, *Phys. Rev. Lett.* **57**, 2442 (1986).
- ² M. N. Baibich, J. M. Broto, A. Fert, F. Nguyen van Dau, F. Petroff, P. Etienne, G. Creuzet, A. Friederich, and J. Chazelas, *Phys. Rev. Lett.* **61**, 2427 (1988).
- ³ G. Binasch, P. Grünberg, F. Saurenbach, and W. Zinn, *Phys. Rev. B* **39**, 4824 (1989).
- ⁴ S. S. P. Parkin, N. More, and K. P. Roche, *Phys. Rev. Lett.* **64**, 2304 (1990).
- ⁵ S. S. P. Parkin, R. Bhadra, and K. P. Roche, *Phys. Rev. Lett.* **66**, 2152 (1991); S. S. P. Parkin, Z. G. Li, and D. J. Smith, *Appl. Phys. Lett.* **58**, 2710 (1991).
- ⁶ D. H. Mosca, F. Petroff, A. Fert, P. A. Schroeder, W. P. Pratt, Jr., and R. Loloee, *J. Magn. Magn. Mater.* **94**, L1 (1991).
- ⁷ B. Dieny, V. S. Speriosu, S. S. P. Parkin, B. A. Gurney, D. R. Wilhoit, and D. Mauri, *Phys. Rev. B* **43**, 1297 (1991).
- ⁸ M. A. M. Gijs and M. Okada, *Phys. Rev. B* **46**, 2908 (1992); M. A. M. Gijs and M. Okada, *J. Magn. Magn. Mater.* **113**, 105 (1992).
- ⁹ M. Jimbo, T. Kanda, S. Goto, S. Tsunashima, and S. Uchiyama, *Jpn. J. Appl. Phys.* **31**, L1348 (1992).
- ¹⁰ S. Zhang and P. M. Levy, *J. Appl. Phys.* **69**, 4786 (1991).
- ¹¹ M. Johnson, *Phys. Rev. Lett.* **67**, 3594 (1991).
- ¹² G. E. W. Bauer, *Phys. Rev. Lett.* **69**, 1676 (1992).
- ¹³ S.-F. Lee, W. P. Pratt, Jr., Q. Yang, P. Holody, R. Loloee, P. A. Schroeder, and J. Bass, *J. Magn. Magn. Mater.* **118**, L1 (1993).
- ¹⁴ H. E. Camblong, S. Zhang, and P. M. Levy, *Phys. Rev. B* **47**, 4735 (1993).
- ¹⁵ T. Valet and A. Fert, *Phys. Rev. B* **48**, 7099 (1993).
- ¹⁶ W. P. Pratt, Jr., S.-F. Lee, J. M. Slaughter, R. Loloee, P. A. Schroeder, and J. Bass, *Phys. Rev. Lett.* **66**, 3060 (1991); S.-F. Lee, W. P. Pratt, Jr., R. Loloee, P. A. Schroeder, and J. Bass, *Phys. Rev. B* **46**, 548 (1992); P. A. Schroeder, J. Bass, P. Holody, S.-F. Lee, R. Loloee, W. P. Pratt, Jr., and Q. Yang, *Mater. Res. Soc. Symp. Proc.* Vol. **313**, 47 (1993).
- ¹⁷ M. A. M. Gijs, S. K. J. Lenczowski, and J. B. Giesbers, *Phys. Rev. Lett.* **70**, 3343 (1993).
- ¹⁸ M. A. M. Gijs, J. B. Giesbers, S. K. J. Lenczowski, and H. H. J. M. Janssen, *Appl. Phys. Lett.* **63**, 111 (1993).
- ¹⁹ We define the MR as $(R_{\max} - R_{\text{sat}})/R_{\text{sat}}$, where R_{\max} is the maximum resistance at zero field and R_{sat} the resistance value at saturation of the giant MR effect.
- ²⁰ *TOSCA Reference Manual* (Vector Fields Ltd., Oxford, U.K., 1992).
- ²¹ S. K. J. Lenczowski, M. A. M. Gijs, J. B. Giesbers, H. H. J. M. Janssen, and R. J. M. van de Veerdonk, *J. Appl. Phys.* (to be published).
- ²² J. J. de Miguel, A. Cebollada, J. M. Gallego, R. Miranda, C. M. Schneider, P. Schuster, and J. Kirschner, *J. Magn. Magn. Mater.* **93**, 1 (1991).
- ²³ P. J. H. Bloemen, R. van Dalen, W. J. M. de Jonge, M. T. Johnson, and J. aan de Stegge, *J. Appl. Phys.* **73**, 5972 (1993).
- ²⁴ S. K. J. Lenczowski, M. A. M. Gijs, R. J. M. van de Veerdonk, and J. B. Giesbers (unpublished).
- ²⁵ G. Rupp and K. Schuster, *J. Magn. Magn. Mater.* **121**, 416 (1993).
- ²⁶ G. E. W. Bauer, M. A. M. Gijs, S. K. J. Lenczowski, and J. B. Giesbers, *J. Magn. Magn. Mater.* **126**, 454 (1993).
- ²⁷ A. Fert and I. A. Campbell, *J. Phys. F* **6**, 849 (1976).
- ²⁸ B. Loegeel and F. Gautier, *J. Phys. Chem. Solids* **32**, 2723 (1971).

Spin polarization of gold films via transported (invited)

Mark Johnson.

Bellcore, 331 Newman Springs Rd., Red Bank, New Jersey 07701

The spin injection technique has been adapted to a thin-film geometry. Measurements of the spin-coupled voltage V_s as a function of film thickness d result in a determination of the spin diffusion length $\delta_s \equiv \sqrt{DT_1}$ with D the electron diffusion constant, in polycrystalline gold films. The conduction electron spin relaxation time T_1 is found to be $4.6 \pm 2.5 \times 10^{-11}$ s, for the temperature range $4 \text{ K} < T < 70 \text{ K}$. The magnitude of V_s is large enough to suggest device applications. In a three-terminal trilayer device, an electric current I_e biasing a thin permalloy film injects spin-polarized electrons into gold films of thickness $100 \text{ nm} \leq d \leq 5.1 \text{ } \mu\text{m}$, and induces a nonequilibrium magnetization \vec{M} . A second permalloy film detects the bipolar, spin-coupled voltage $eV_s = \beta M / \chi$, where β is the Bohr magneton, χ the Pauli susceptibility and e the electron charge. The sign of V_s depends on the relative orientation of the magnetizations of the permalloy films. In the thin limit, $d < \delta_s$, the magnitude of the spin-coupled impedance $Z_s = V_s / I_e$ scales inversely with d . In the thick limit, $d > \delta_s$, Z_s is exponentially diminished.

I. INTRODUCTION

The spin injection effect¹ can be thought of in two parts. The first idea is that there is a relationship, at the interface between a ferromagnetic (F) and paramagnetic (P) metal, between a current of charges (an electric current I_e) and a current of magnetic dipoles (a magnetization current I_M). For example, an electric current driven from F to P will enter the latter with a net spin polarization. After Meservey *et al.*² showed that current tunneling out of a ferromagnetic electrode was spin polarized, Aronov³ proposed the generalization that any transport current entering a nonmagnetic metal (or semiconductor) from a ferromagnetic metal would be polarized. The spin injection experiment¹ was the first empirical demonstration of this fact. Conversely and of equal importance, the presence of spin-polarized conduction electrons (equivalently a nonequilibrium magnetization \vec{M}) in P has an effect on F. Under closed-circuit conditions, \vec{M} can generate electric currents, and under open circuit conditions it can alter the chemical potential of F. Silsbee⁴ predicted this converse effect, called charge-spin coupling, and the spin injection experiment provided the first empirical proof of this as well. The second idea is that one can use charge-spin coupling to study details of conduction electron spin transport in the nonmagnetic material. For example, the experiments of Ref. 1 measured the spin relaxation time T_1 in bulk Al. Similarly, the value of T_1 reported herein for gold films is in agreement with the spin-orbit scattering time τ_{so} deduced by weak localization experiments, but is an order of magnitude longer than a theoretical estimate.

The original spin injection experiment used a four-probe, injection/detection scheme with a ferromagnetic current injector F1 and a ferromagnetic counterelectrode detector F2, fabricated on bulk samples. A constant current was driven into the sample in a steady state, and three methods were utilized to demonstrate the ideas described above: (i) The axes of magnetization \vec{M}_1 and \vec{M}_2 of F1 and F2 were independently manipulated, causing changes in the detected voltage (or current); (ii) the distance between F1 and F2 was varied, resulting in a magnitude of the detected, spin-coupled signal that decreased as the interprobe distance increased;

(iii) a transverse magnetic field was applied causing the spin-polarized electrons to precess, and resulting in a spin-coupled signal that varied as a function of external field.

In this article, the adaptation of the spin injection technique to a thin-film geometry⁵ is presented. Once again, each of the three methods listed above has been used to demonstrate the validity of the spin injection ideas in this new geometry. The observed spin-coupled signals are so large that spin dynamics dominates over charge dynamics; the large magnitude of the effect may make it appropriate for device applications.⁶ Finally, several samples have shown strong magnetic anisotropies. Because these anisotropies can affect implementation of the spin injection technique, examples are discussed.

II. CHARGE-SPIN COUPLING

The technique is conceptualized with the aid of Fig. 1.^{1,5} Figure 1(a) depicts a cross-sectional view of a pedagogical, three-terminal device. Nonmagnetic metal film P (a Pauli paramagnet) is sandwiched between two ferromagnetic films F1 and F2. Each ferromagnetic film is a single domain, and

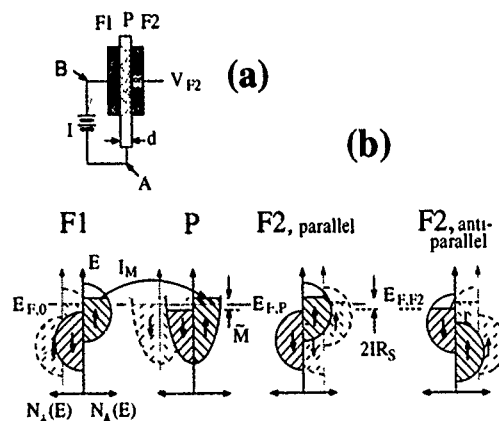


FIG. 1. (a) Pedagogical model of three-terminal device. Arrows in F1 and F2 refer to magnetization orientation as determined by majority spin sub-band. (b) Diagrams of the densities of state $N(E)$ as functions of energy E of the ferromagnet-paramagnet-ferromagnet system depicted in (a).

the axis of magnetization of each film, \hat{M}_1 and \hat{M}_2 , lies in the plane of the film. For simplicity we consider the case where \hat{M}_1 points down and \hat{M}_2 points either down or up. A battery is connected as shown, and a third wire is attached to F2 and leads to a gedanken voltmeter, one which can read the voltage V_{F2} of F2 with a single input and does not need a ground.

Details of charge and spin transport, and of the effect of current transport on V_{F2} , can be understood by using the microscopic model depicted with density-of-state diagrams in Fig. 1(b). For the sake of simplicity this model has neglected the resistance of the films and of the interface between the films,⁷ and it assumes there is no spin scattering at the interface itself. The diagrams have been drawn out of proportion to demonstrate the nonequilibrium effects. The faint diagrams in the background represent the state of the device when the switch is open. The ferromagnets are depicted in a band model where the majority spin subband lies entirely below the Fermi level. This would be appropriate, though oversimplified, for the $3d$ band, or a hybridized $s-d$ band, of transition-metal ferromagnets such as Ni, Fe, Co, or an alloy such as Permalloy $\text{Ni}_x\text{Fe}_{1-x}$. The paramagnet is represented with a free-electron model. With the switch open, the Fermi levels of the contiguous metals align with value $E_{F,0}$.

When the switch is closed, I_e is driven from F1 into P and returns back to the battery. However, current transport involves only electrons within a thermal energy range $E_F \pm k_B T$, where k_B is Boltzmann's constant and T is temperature. Since the down-spin subband is well below E_F , only the up-spin subband is available to carry the current. Thus, the electric current is spin polarized; it is a current of oriented magnetic dipoles, $I_M = \eta_1 \beta I_e / e$. Here η is a phenomenological parameter,¹ $\eta = (J_\uparrow - J_\downarrow) / (J_\uparrow + J_\downarrow)$, with $J_{\uparrow,\downarrow}$ the current densities of each spin subband, which describes the efficiency of spin transport. In the simplified model of Fig. 1(b) $\eta = 1$, but more generally the magnitude of η can be diminished by current contributions from the other spin subband and $|\eta| \leq 1$. Conceptually, the ferromagnetic film F1 acts as a spin polarizer in a manner loosely analogous to a polarizing film for light, but with the important difference that conduction electrons move diffusively, in contradistinction with photons.

The thickness d of P is chosen to be less than a spin depth δ_s , the characteristic length over which an electron can diffuse before the orientation of its spin is randomized by scattering. In the vicinity of F1, in a steady-state process, polarized spins are constantly being added to P at a rate I_M , and the polarization is being lost because of random scattering at a rate $1/T_1$. As a result, a nonequilibrium magnetization builds up in P, $\vec{M} = I_M T_1 / A d$, where A is the area of contact and $A d$ is the volume that the spins occupy in P. This is depicted in Fig. 1(b), where the net increase in occupation of the up-spin subband is offset by a decrease in occupation of the down-spin subband so that charge neutrality is preserved. In Fig. 1(a) the nonequilibrium spin magnetization is represented by the dotted "cloud" in P.

The rise in the up-spin subband chemical potential of P has an effect on F1: The chemical potential of F1 must rise so that the chemical potential of its up-spin subband aligns

with that of P. If this did not occur, there would be a backflow of spin-polarized electrons from P to F1. In more precise terms,⁷ there is a generalized thermodynamic force F_m associated with \vec{M} which acts to drive up spins back into F1. Because spin and charge are attached to the same carrier, the electron, this force also acts as an electrical impedance which appears as an interfacial resistance at the F1-P interface. Thus, a constant-current source encounters an extra, spin-coupled impedance which is labeled in the figure as Z_s and is calculated below. This can be pictured⁸ as a "spin bottleneck:" The buildup of spins acts to impede the continued flow of spins (and therefore of electrons) into the region. It is important to note that charge-spin coupling occurs at the F1-P interface, and the effect has been observed⁹ in a bilayer geometry (with F2 absent).

When \hat{M}_1 and \hat{M}_2 are parallel, the chemical potential of F2 rises so that its up-spin subband chemical potential aligns with that of P [$E_{F1,F2}$ in Fig. 1(b)]. If the floating probe to F2 were to be short circuited to ground, a current of upspins would be driven through F2 to ground. By imposing an open-circuit condition on the probe at F2, no current can flow and the chemical potential of F2 must rise by an amount eV_{F2} , where $V_{F2} = IZ_s$. Similarly, when \hat{M}_1 and \hat{M}_2 are antiparallel, the chemical potential of F2 must lower so that its down-spin chemical potential aligns with that of P. For orientations of \hat{M}_1 and \hat{M}_2 that vary between parallel and antiparallel, V_{F2} will vary as $V_{F2} = IZ_s \cos \theta$, where θ is the angle between \hat{M}_1 and \hat{M}_2 . The change of chemical potential has been derived^{1,4} to be $eV_s = \eta_2 \beta \vec{M} / \chi$. Some physical insight can be gained by noting that \vec{M} / χ has the units of magnetic field, and can be thought of as the effective magnetic field associated with the nonequilibrium spins. Then $\beta \vec{M} / \chi$ is the effective Zeeman energy of a spin-polarized electron in the presence of the effective field of all of the other nonequilibrium spins (and is the source of the thermodynamic force F_m). Combining the above expressions for I_M , \vec{M} , and V_s , and using a free-electron expression for susceptibility, $\chi = \beta^2 N(E_F) = \beta^2 3n / 2E_F$, where n is the density of conduction electrons, one finds (for the case $d \ll \delta_s$)

$$Z_s = \frac{V_s}{I_e} = \frac{\eta_1 \eta_2}{e^2} \frac{T_1 E_F}{1.5 n A d} = \eta_1 \eta_2 \frac{\rho \delta_s^2}{A d}, \quad (1)$$

where the second form has used an Einstein relation for the resistivity of the gold, $\rho = 1 / e^2 D N(E_F)$. Note that V_s is expected to be linear with I_e and should have units of impedance, and that the magnitude of Z_s is inversely proportional to the sample dimensions A and d . This follows from the fact that \vec{M} has dimensions of magnetic dipoles per unit volume, so that a constant number of nonequilibrium spins will result in a larger value of \vec{M} when the volume is diminished. In addition, recall that Eq. (1) was derived for the thin limit case, $d < \delta_s$. The density of nonequilibrium spins decreases exponentially as a function of thickness, $\vec{M} \propto e^{-d/\delta_s}$, so that a measurement of the diminished value of V_{F2} at thicknesses $d > \delta_s$ gives a direct measurement of δ_s .

In order to measure the floating voltage V_{F2} it is necessary to define a ground. A logical choice would be the base of P [point A in Fig. 1(a)]. With this choice, the bipolar voltage V_s will be superposed on top of the ohmic voltage

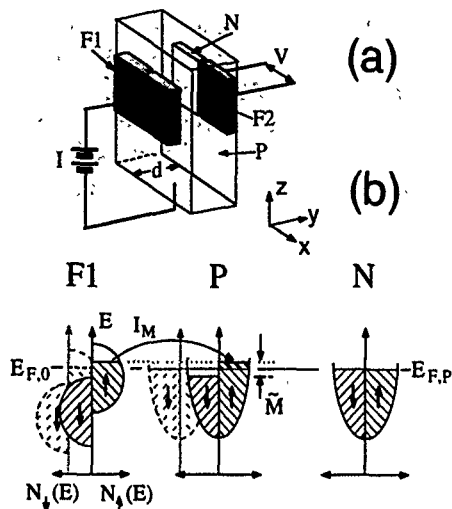


FIG. 2. (a) The geometry used to measure V_{F2} . P is depicted transparent. (b) Diagrams of the densities of state $N(E)$ showing how the chemical potential of N always aligns with the average chemical potential in P.

drop $I_e R$ from the sheet resistance R of P. Data of this kind are presented below, but it is preferable to demonstrate directly the bipolarity of V_s . Although grounding to point B would be a suitable choice, the best method of grounding is depicted in Fig. 2(a): V_{F2} is measured with respect to a normal metal counterelectrode N whose chemical potential is always aligned with the average chemical potential of P [$E_{F,P}$ in Fig. 2(b)].

Next, it is necessary to manipulate the orientations of \hat{M}_1 and \hat{M}_2 . Each film can be characterized by a coercivity $H_{c,i}$, and application of an external field H in the plane of the films will result in \hat{M}_1 and \hat{M}_2 traversing the hysteresis loops sketched in Fig. 3(a). When F1 and F2 are composed of the same material, the voltage V_{F2} is expected to be positive whenever the orientations \hat{M}_i are aligned, and negative when antialigned [Fig. 3(b)]. This effect was demonstrated in the original spin injection experiment.¹ Since antiparallel orientation occurs only over the field range $H_{c,2} - H_{c,1}$ it is necessary to maximize this difference by fabricating films with differing values $H_{c,i}$. This can be achieved by using shape anisotropies, by using different materials for F1 and F2 (with intrinsically different coercivities), or by using anisotropies associated with the substrate or with deposition conditions. The effect of anisotropies on the qualitative characteristics of the signals is discussed in Sec. V.

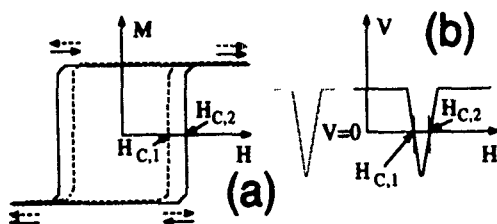


FIG. 3. (a) Hysteresis loops for F1 (dashed) and F2 (solid). Arrows represent parallel and antiparallel orientations of F1 and F2. (b) Expected shape of signal for sweeping up in field.

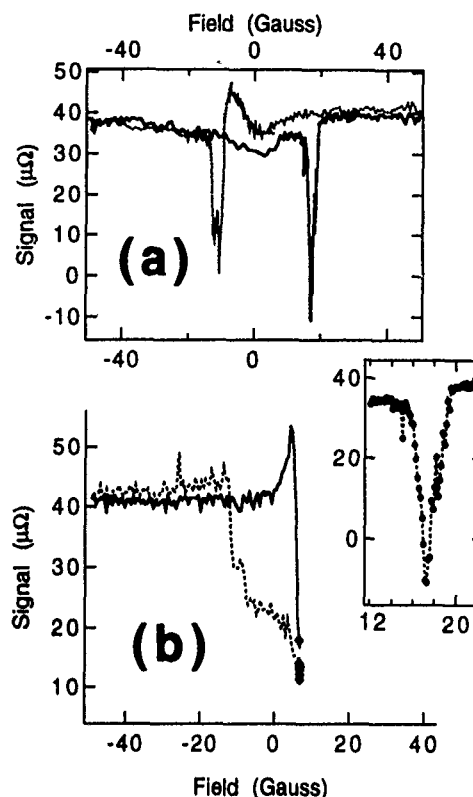


FIG. 4. Data from a sample with $d=0.098 \mu\text{m}$. Under constant bias current, the voltage is recorded as the magnetic field is changed. $I=0.2 \text{ mA}$. (a) An example of data. Solid line: sweeping up in field; dotted line: sweeping down. (b) An example of a memory effect. Solid line: sweeping up in field; dotted line: sweeping down; solid symbols: field sweep in halted; (inset): expanded view of the feature at $17 \pm 2 \text{ G}$ in (a).

III. EXPERIMENT

The samples were fabricated on sapphire substrates. The ferromagnetic films F1 and F2 of four samples were composed of Permalloy which was deposited in a vacuum of $\sim 10^{-6}$ Torr by e -beam evaporation from a single source of $\text{Ni}_{79}\text{Fe}_{21}$, and had thicknesses of 70 nm. A fifth sample used Permalloy for F1 and Co for F2. The coercivities of test films of Permalloy and Co were of order 10 G. The gold films were deposited by thermal evaporation from 5-9's gold after cleaning the Permalloy base electrode with an Ar-ion mill. The geometry was defined using photolithography and liftoff to create "windows" in insulating films of Al_2O_3 . These windows had area $A=10^{-2} \text{ mm}^2$. The voltage measurements were made with two rf superconducting quantum interference device (SQUID)¹⁰ amplifiers, and one of these was calibrated by measuring the resistance of a gold wire. This calibration also verified the polarity of the voltage measurements.

An example of data is shown in Fig. 4(a). The signals were linear with current, and the signal magnitude is given in units of impedance. Currents of typically 0.1–10 mA were used, and voltages of order 10^{-8} – 10^{-7} V were recorded; the dynamic range of the SQUID voltmeters is 10^{-7} V and this was the only limit to the voltage magnitudes observed. The shape, width, and sign of the data of Fig. 4(a) conform to the expectations of a spin injection signal [Fig. 3(b)], and similar

signals were recorded for sweeps of magnetic field along \hat{x} and \hat{z} (i.e., sweeps in the plane of the films). Note that the signal is bipolar. The nonzero median is consistent with a slight asymmetry in the placement of the "windows" F2 and N [refer to Fig. 2(a)]. Because the coercivities of F1 and F2 are so close in value, the spin-coupled signal is observed only over a small range $H_{c,1} - H_{c,2} \approx 4$ G. The observed signals must represent a lower limit of the actual value of Z_s because it is impossible to know whether the films are completely antiparallel. Despite this possible source of error, the signals were quite reproducible, typically $\pm 25\%$, and consistent from sample to sample.

An example of a memory effect is shown in Fig. 4(b). Initially the external field was negative, and both \hat{M}_1 and \hat{M}_2 were oriented along $-\hat{H}$ [refer also to Fig. 3(a)]. An increasing field sweep is halted when the voltage begins to drop due to the realignment of one of the films in the vicinity of $H = +H_{c,1}$. Reversing the field sweep results in a low voltage value until this film reorients at $H = -H_{c,1}$, and the original voltage is recovered. Note the existence of two stable voltage states, associated with two stable magnetization states, at $H = 0$. The fact that these two states differ by less than the full voltage dip $2IZ_s$ is probably because $H_{c,1}$ and $H_{c,2}$ are so close in value that F1 (or F2) had not completely flipped its orientation at the point where the external field sweep was reversed.

IV. QUANTITATIVE ANALYSIS

From Eq. (1) we see that the magnitude of Z_s is proportional to the parameters η and T_1 . While η should be temperature independent, a simple picture of spin scattering in metals suggests that any scattering event has a small, constant probability a_s of flipping a spin, and therefore $T_1^{-1} \propto \tau^{-1} = a_s \tau^{-1}$, where τ is a scattering time derived from Matthiessen's rule. It follows that $Z_s \propto \tau$, and in this approximation $Z_s(T)$ should have the same temperature dependence as the electrical conductivity σ of the gold, which also is linearly proportional to τ . Figure 5(a) demonstrates the comparable temperature dependence of $Z_s(T)$ and $\sigma(T)$ over the experimental range $4 \text{ K} < T < 70 \text{ K}$.

The expression in Eq. (1) predicts that the product $Z_s A d$ should be constant as a function of d , for thicknesses $d < \delta_s$. This scaling is demonstrated in Fig. 5(b), where the open symbols refer to comparable samples (F1 and F2 are both permalloy). It is interesting to note, in Fig. 5(b), that the resistance across the thickness of the $1.6\text{-}\mu\text{m}$ -thick film is about $1.3 \mu\Omega$, somewhat smaller than the $3.5 \pm 0.5 \mu\Omega$ spin-coupled impedance, but of the same order of magnitude. However, the resistance across the gold film decreases linearly with decreasing thickness d whereas Z_s increases in proportion to $1/d$. Thus, at a thickness of about 100 nm the spin-coupled voltage is three to four orders of magnitude larger than the resistive voltage drop; spin dynamics dominate charge dynamics in this system.

The spin depth may be determined by fitting the data of Fig. 5(b) to Eq. (1) in the thin limit, $d < 1 \mu\text{m}$, and to the thick limit form,⁵ $Z_s = (\eta_1 \eta_2 \rho \delta_s / A) e^{-d/\delta_s}$, for $d > 1 \mu\text{m}$. The best fit gives the result $\delta_s = 1.5 \pm 0.4 \mu\text{m}$. The spin relaxation time can be calculated from the expression δ_s

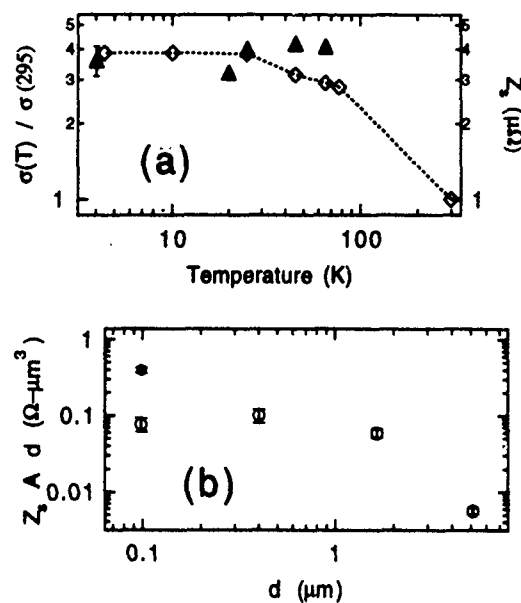


FIG. 5. (a) Comparison of $\sigma(T)$ (left-hand axis: \diamond) with $Z_s(T)$ (right-hand axis; \blacktriangle) for $d = 1.6 \mu\text{m}$ sample. (b) $Z_s A d$ as a function of d . Z_s is referred to the current through a single window. Open symbol: F1 and F2 are Permalloy; solid symbol: F2 is Co.

$= \sqrt{DT_1} \approx \sqrt{(v_F^2 \tau / 3) T_1}$, where v_F is the Fermi velocity. Using a Drude time for τ (and values of ρ measured on test strips) one finds, for the temperature range $4 \text{ K} < T < 70 \text{ K}$, $T_1 = 4.6 \pm 2.5 \times 10^{-11} \text{ s}$, and $a_{s,\text{Au}} \approx 2 \times 10^{-3}$.

A comparison can now be made between the observed magnitude of the effect and that predicted by Eq. (1). Using the above value for T_1 , the largest magnitude predicted, for the optimum value $|\eta| = 1$, is $Z_s A d \approx 3 \times 10^{-2} \Omega \mu\text{m}^3$. However, the signals in Permalloy-Au-Permalloy samples are about three times larger, and in the Permalloy-Au-Co sample it is about 12 times larger, than predicted by theory. I note that the theory has used a simplified expression for χ , and has neglected many-body effects. Furthermore, the discrepancy suggests the possible existence of a mechanism (such as Overhauser coupling to the nuclear spins or phonon trapping) that enhances the value of T_1 in the thin limit over that in the thick limit.

The theory of spin relaxation in metals implies that the spin-orbit interaction in gold should be the dominant spin scattering effect and predicts a high scattering probability¹¹ $a_{s,\text{Au}} = 5 \times 10^{-2}$. The observed probability $a_{s,\text{Au}} = 2 \times 10^{-3}$ is significantly smaller than expected, but is in good agreement with weak localization studies¹² of gold films which have measured a ratio $\tau/\tau_{so} = 8 \times 10^{-3}$, where τ_{so} is the spin-orbit scattering time. I note that τ_{so} is not identically the same as T_1 , though T_1 should approach τ_{so} in the limit of strong spin-orbit interactions.

The surprisingly long value measured for T_1 is intriguing, and experiments were performed on Nb samples in an effort to further test this result. Niobium was chosen because its resistivity is about ten times greater than gold (τ is ten times smaller), but the atomic number is smaller so the spin-orbit effect should be less important. The magnitude of the product $Z_s A d$ for Nb was two to four times larger than for

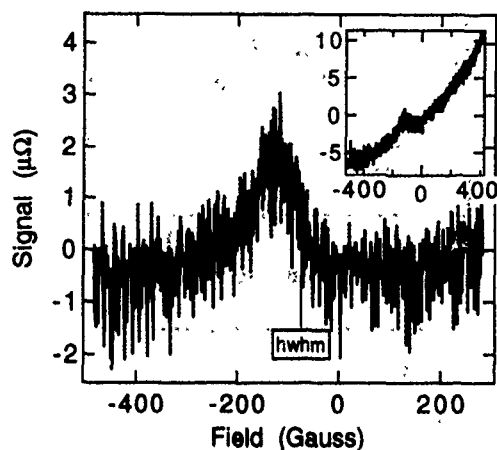


FIG. 6. Field sweep along \hat{y} axis of Nb sample with $d=940$ nm showing a feature with characteristics of a Hanle effect. The half-width at half-maximum (HWHM) is marked. Inset: raw data. The sloped baseline probably results from \hat{M}_1 and/or \hat{M}_2 tipping out of the film plane.

Au. Data for five samples were quantitatively analyzed (using $\eta=2$, as deduced herein for Permalloy-Au-Permalloy structures)¹³ to deduce T_1 , finding a value ranging from 4.8 to 6.3×10^{-10} s for four thin samples, each with residual resistivity ratio (RRR) of about 2, and $T_1=1.4 \times 10^{-9}$ s for a thick sample ($d_{\text{Nb}}=940$ nm, $\text{RRR} \approx 4$). A corroborating measurement of T_1 was made on the thick sample by applying a magnetic field along \hat{y} , transverse to the plane of the injected spin polarization. A feature appeared (Fig. 6) whose characteristics were consistent with a Hanle effect,¹ and had a half-width at half-maximum $1/\gamma T_2 \approx 70$ G corresponding to $T_2=7 \times 10^{-10}$ s, in fair agreement with the value of T_1 deduced from the amplitude.¹⁴ This value of T_1 agrees with the limit $T_1 > 10^{-11}$ s established by transmission electron-spin-resonance (TESR) studies of Cu-Nb bilayers,¹⁵ and corresponds to a spin-flip probability of about $a_{\text{Nb}} \sim 2 \times 10^{-5}$.

In summary, all deduced values of T_1 are surprisingly long but reasonable, and values of η are enhanced above their theoretically limiting value of 1 by factors of 2–6. The observations $a_{\text{Nb}} \ll a_{\text{Au}}$ is qualitatively consistent with the idea that spin-orbit interactions contribute to spin scattering, but the value of T_1 measured in Au is longer than a spin-orbit calculation predicts.

V. EFFECT OF MAGNETIC ANISOTROPIES

Many samples (particularly Nb) have exhibited strong magnetic anisotropies (easy and hard axes of magnetization of F1 and F2). Because of the importance of manipulating \hat{M}_i in implementing the spin injection technique, examples of these anisotropies, and their qualitative effect on the spin coupled signal, are briefly discussed. Data which imply that both F1 and F2 have an easy magnetization axis along \hat{z} and a hard axis along \hat{x} are shown in Fig. 7(a), and can be interpreted in the following way. The dotted trace was taken sweeping H down along the \hat{z} axis over a large field range. In these experiments the detector ground was downstream from the injector [point A in Fig. 1(a)], so the bipolar spin-coupled signal is superposed on the ohmic resistance of a portion of the Nb film, $R \approx 42.7$ mΩ. The changing orienta-

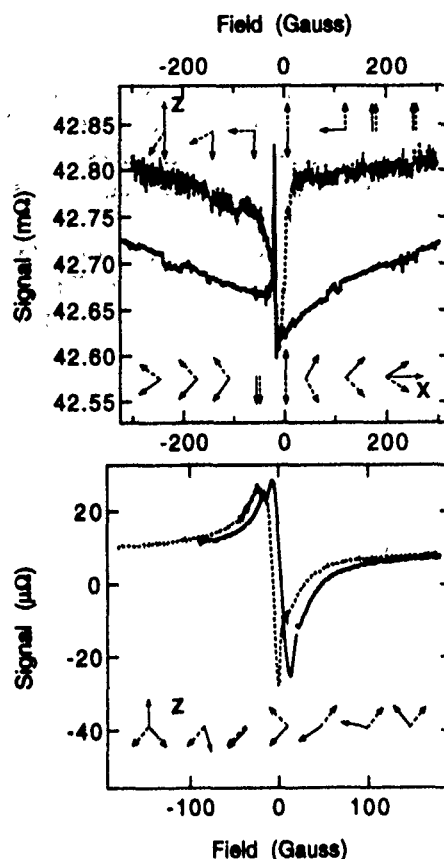


FIG. 7. Examples of magnetic anisotropies (easy and hard magnetization axes) in Nb samples. (a) Geometry with V_{F2} grounded at point A of Fig. 1(a). Dotted line: sweeping field down along \hat{z} ; solid line: sweeping field down along \hat{x} . (b) Example of anisotropy axes oriented about 45° to sample axes. Field sweeps along \hat{x} and \hat{z} had qualitatively similar shapes. Here, sweep is along \hat{z} . Geometry of Fig. 2(a). An offset of $205 \mu\Omega$ results from imperfect window alignment and has been subtracted from the baseline. Solid line: sweeping up in field; dotted line: sweeping down.

tion of \hat{M}_1 and \hat{M}_2 is modeled with the arrows at the top of the figure. These arrows correspond to the overall sequence of changes of \hat{M}_1 and \hat{M}_2 ; the location of any pair of arrows is not intended to be associated with the corresponding field value.

The solid trace was taken sweeping H down along the \hat{x} axis. Values of the baseline resistance (at ± 300 G) were confirmed using dc I - V measurements. Beginning at the right, an applied field of 300 G is insufficient to orient \hat{M}_1 and \hat{M}_2 along \hat{x} , their hard axis; \hat{M}_1 (\hat{M}_2) is oriented about $\pm 35^\circ$ relative to $+\hat{x}$ [refer to the arrows at the bottom of Fig. 7(a), which represent the sequence of changes of \hat{M}_1 and \hat{M}_2] and V_s is small. As H_x is diminished, \hat{M}_1 and \hat{M}_2 rotate further away from \hat{x} , in opposite directions, in order to align with their easy axis \hat{z} . When \hat{M}_1 and \hat{M}_2 are perpendicular $V_s=0$ (the measured signal is entirely from the spreading resistance, $R \approx 42.7$ mΩ), and as θ opens up past 90° , V_s becomes negative. At about $H_x = -20$ G, \hat{M}_1 and \hat{M}_2 are both oriented along \hat{z} , in opposite directions, and V_s reaches its full negative value (corresponding to the signal minimum, $V=IR-|V_s|$). This is verified by comparison with the full negative value of V_s as measured by sweeping H along \hat{z} , i.e., comparison with the minimum value of the dotted curve. Once oriented along \hat{z} it is easy for \hat{M}_1 and \hat{M}_2 to flip by

180°. The orientation of \hat{M}_1 flips at a slightly different value than that of \hat{M}_2 so that for a small field range, $H_x \approx -22 \pm 2$ G, \hat{M}_1 and \hat{M}_2 are parallel and V_s reaches its full positive value (compare with the signal maximum, as determined by the \hat{z} sweep). As H is further increased along $-\hat{x}$, \hat{M}_1 and \hat{M}_2 rotate away from \hat{z} to an orientation nearly perpendicular, and again the contribution to the signal provided by V_s is nearly zero. Further increasing H along $-\hat{x}$ gradually pulls \hat{M}_1 and \hat{M}_2 into closer alignment along $-\hat{x}$ and V_s gradually increases. This interpretation relies on two reasonable assumptions, as follows.

(i) The field axes are not exactly aligned with the anisotropy axes. Thus, a field H_x ($-H_x$) has a small component H_z ($-H_z$) along the easy axis of F1 causing \hat{M}_1 to flip near $H_x=0$. In one sample, the field axes were oriented about 45° with respect to the sample axes [refer to Fig. 7(b)], supporting the assumption that the field and anisotropy axes need not be well aligned.

(ii) F1 and F2 are weakly coupled by magnetostatics, so that stray fields from the edges of F1 induce the orientation of \hat{M}_2 to be antiparallel with that of F1. The effect of weak coupling will be to result in the flip of \hat{M}_2 (along \hat{z}) following that of \hat{M}_1 .

ACKNOWLEDGMENT

The author is grateful to L. H. Greene for preparing the Nb films.

- ¹M. Johnson and R. H. Silsbee, Phys. Rev. Lett. **55**, 1790 (1985); Phys. Rev. B **37**, 5312 (1988); **37**, 5326 (1988); J. Appl. Phys. **63**, 3934 (1988).
- ²P. M. Tedrow and R. Meservey, Phys. Rev. Lett. **26**, 192 (1971); Phys. Rev. B **7** (1973); R. Meservey *et al.*, Phys. Rev. Lett. **37**, 858 (1976).
- ³A. G. Aronov, Pis'ma Zh. Eksp. Teor. Fiz. **24**, 37 (1976) [Sov. Phys. JETP Lett. **24**, 32 (1976)].
- ⁴R. H. Silsbee, Bull. Magn. Res. **2**, 284 (1980).
- ⁵M. Johnson, Phys. Rev. Lett. **70**, 2142 (1993).
- ⁶M. Johnson, Science **260**, 320 (1993).
- ⁷M. Johnson and R. H. Silsbee, Phys. Rev. B **35**, 4959 (1987); see the appendix for the fully generalized solution.
- ⁸M. Johnson, Phys. Rev. Lett. **67**, 3594 (1991).
- ⁹M. Johnson, Appl. Phys. Lett. **63**, 1435 (1993).
- ¹⁰Commercial SQUID from B.T.I.
- ¹¹Y. Yafet, in *Solid State Physics*, edited by F. Seitz and D. Turnbull (Academic, New York, 1963), Vol. 14, p. 1. Use a form similar to Eq. (20.3), note that the g shift δg is first order in the spin-orbit splitting Δ_{so} , and use values of Δ_{so} and ΔE from Table II to compute T_1/r for Au relative to that for Na (which is calculated explicitly in Sec. 21).
- ¹²G. Bergmann, Z. Phys. B **48**, 5 (1982); Phys. Rep. **107**, 2 (1984).
- ¹³M. Johnson and L. H. Greene (unpublished).
- ¹⁴With $T_1 \approx 4 \times 10^{-11}$ s in the Au samples, the Hanle feature would have a half-width at half-maximum of about 1300 G, much broader than could be observed.
- ¹⁵G. W. Graham and R. H. Silsbee, Phys. Rev. B **22**, 4184 (1980).

Transport and magnetic properties of polycrystalline $\text{Sm}_{2-x}\text{Ce}_x\text{CuO}_{4-y}$

R. F. Jardim, C. H. Westphal, and C. H. Cohenca^{a)}

Instituto de Física, Universidade de São Paulo, CP 20516, 01498-970, São Paulo, SP, Brazil

L. Ben-Dor

Department of Inorganic and Analytical Chemistry, Hebrew University, Jerusalem 91904, Israel

M. B. Maple

*Department of Physics and Institute for Pure and Applied Physical Sciences,
University of California at San Diego, La Jolla, California 92093-0019*

A systematic study of transport and magnetic properties of polycrystalline $\text{Sm}_{2-x}\text{Ce}_x\text{CuO}_{4-y}$ ($0.15 \leq x \leq 0.18$) specimens obtained from a sol-gel precursor reveals a striking double resistive superconducting transition. One of the resistive transitions takes place at a temperature T_{ci} and is almost insensitive to Ce concentration, applied magnetic field, and current density, while the other transition occurs at a lower temperature T_{cj} and is very sensitive to Ce content, applied magnetic field, and current density. Alternating-current magnetic susceptibility χ_{ac} measurements reveal two interesting features. There is only one contribution to the diamagnetic signal below ~ 20 K, which is particularly evident in the resistive component χ'' of χ_{ac} where a peak at T_{cj} can be identified. The application of an applied magnetic field shifts the χ'' peak to lower temperatures and reveals a spin-glass-like behavior. All the results can be satisfactorily explained in terms of weakly linked Josephson junctions between small superconducting islands. The small islands have a superconducting transition at a higher temperature T_{ci} , and the long-range phase coherence is achieved through Josephson coupling at lower temperatures T_{cj} . All the results suggest a superconducting glass state in a disordered Josephson network.

The occurrence of the double resistive superconducting transition in polycrystalline samples of $\text{Sm}_{2-x}\text{Ce}_x\text{CuO}_{4-y}$ ($0.13 \leq x \leq 0.20$) (Refs. 1–4) opens up a wide area of investigation in these electron-doped superconductors. This behavior is easily seen in electrical resistivity $\rho(T)$ measurements which reveal two well-defined drops in $\rho(T)$ before the system attains the zero-resistance state.¹ The first drop, which occurs at an upper transition temperature T_{ci} , has been attributed to a genuine superconducting phase,⁵ and a $\sim 25\%$ drop in the magnitude of $\rho(T)$ is often observed at T_{ci} . Below this temperature, it has been suggested that the sample is comprised of small superconducting islands embedded in a nonsuperconducting host, and $\rho(T)$ exhibits a well-defined plateau down to a lower transition temperature T_{cj} .^{1,2} It is also believed that Josephson coupling develops at T_{cj} , and a second $\sim 75\%$ sharp drop in $\rho(T)$, culminating in the zero-resistance state, is frequently observed.^{1,2,5} The above explanation involving small superconducting islands embedded in a nonsuperconducting host is useful in separating contributions from inter- and intragrain properties. One important point in such a separation is that both T_{ci} and T_{cj} can be controlled by means of Ce doping^{1,2} or oxygen removal.⁶ This provides the unique opportunity to investigate properties arising from both contributions individually: the genuine

superconducting phase and the disordered Josephson-coupled network.

In this work, we will focus on additional properties of the disordered Josephson-coupled network shown in polycrystalline samples of $\text{Sm}_{2-x}\text{Ce}_x\text{CuO}_{4-y}$ ($0.15 \leq x \leq 0.18$) obtained from a sol-gel precursor. We found that all the samples exhibit a double resistive superconducting transition, suggesting an intrinsic property of these polycrystalline samples. From results of ac magnetic susceptibility measurements, the resistive χ'' component peaks only at the Josephson-coupling temperature T_{cj} , demonstrating that the superconductivity is confined to small islands within grains. In addition, a field dependence of the χ'' peak provides clear evidence that all these samples can be understood within a superconducting glass scenario.

Polycrystalline samples of $\text{Sm}_{2-x}\text{Ce}_x\text{CuO}_{4-y}$ ($0.15 \leq x \leq 0.18$) were prepared using the sol-gel route. Stoichiometric amounts of the nitrates $\text{Sm}(\text{NO}_3)_3 \cdot 6\text{H}_2\text{O}$, $(\text{NH}_4)_2\text{Ce}(\text{NO}_3)_6$, and $\text{Cu}(\text{NO}_3)_2 \cdot 3\text{H}_2\text{O}$ were dissolved in ≈ 200 ml of water. A 50 mol % excess of citric acid was added to the solution until it was completely dissolved under stirring and low heating. Afterwards, excess ethylene glycol was added to the solution. Decomposition of nitrates and evolution of NO_2 occurred when the solution was placed on a hot plate and stirred magnetically, until the solution became colloidal. Thereafter, this solution was transferred to an alumina crucible and placed in a box furnace and the tempera-

^{a)}On a RHAE/CNPq (Brazil) fellowship.

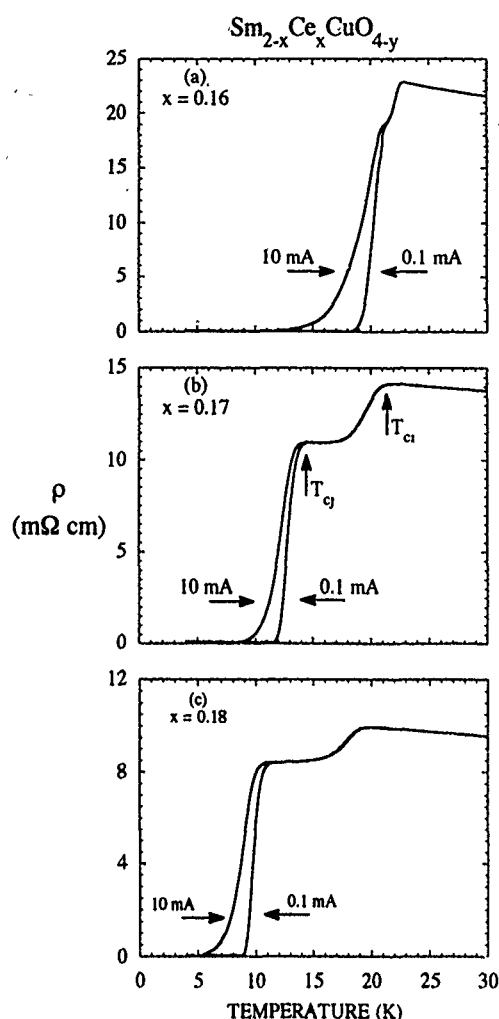


FIG. 1. Temperature dependence of electrical resistivity $\rho(T)$ for polycrystalline samples of $\text{Sm}_{2-x}\text{Ce}_x\text{CuO}_{4-y}$, (a) $x=0.16$, (b) $x=0.17$, and (c) $x=0.18$. The two transition temperature T_{ci} and T_{cj} are indicated. Excitation currents of 0.1 and 10 mA are also indicated in the figure.

ture raised to $\sim 500^\circ\text{C}$. At this temperature, the organic precursor partially decomposed into the simple oxides with consequent formation of a dark powder. The powder was sintered at 1000°C for four days with intermediate grinding. A slight reduction of the oxygen is necessary to induce superconductivity in these compounds. Sample disks were placed in a ceramic boat in a tube furnace with flowing helium gas, and heated at a constant temperature of 950°C for 20 h. The disks were split in two and then cooled to room temperature for either 1 or 2 h. Further details of this chemical route and the reduction processes employed for these samples are given elsewhere.⁴ All samples were characterized by x-ray diffraction using $\text{Cu } K_\alpha$ radiation on a Rigaku RU-200B diffractometer and had no additional phases except for the $x=0.18$ sample, which had small amounts of a $\text{Sm}_{1-x}\text{Ce}_x\text{O}_y$ spurious phase.⁷

Electrical resistivity as a function of temperature, $\rho(T)$, was measured with a Linear Research LR-400 ac bridge operating at a frequency of 16 Hz. The excitation current could be adjusted over several orders of magnitude. Alternating-current magnetic susceptibility χ_{ac} measurements, made on bar-shaped samples, were performed with a mutual-

inductance bridge operating at frequencies f in the range $17\text{ Hz} \leq f \leq 5555\text{ Hz}$ and modulation fields H_m in the range $0.01\text{ Oe} \leq H_m \leq 17\text{ Oe}$. External dc magnetic fields were produced with a NbTi superconducting coil up to 35 kOe.

It is useful to begin this discussion with Fig. 1 which shows the temperature dependence of the electrical resistivity $\rho(T)$ of polycrystalline samples of $\text{Sm}_{2-x}\text{Ce}_x\text{CuO}_{4-y}$ ($0.16 \leq x \leq 0.18$) with excitation currents of 0.1 and 10 mA. The first interesting feature of these curves is associated with the double resistive superconducting transitions where the electrical resistivity attains the zero-resistance state after two well-defined drops in $\rho(T)$. The double resistive superconducting transition persists even when samples are prepared through the sol-gel route, suggesting that it is an intrinsic property of these polycrystalline samples.^{2,4}

Another point to be stressed here concerns the first drop in $\rho(T)$ at T_{ci} . As discussed elsewhere,¹ the transition at T_{ci} appears to be associated with a genuine superconducting phase and not, for example, a structural transition. One might also imagine that such a drop in $\rho(T)$ at T_{ci} could be due to a insulator-metal ($I-M$) transition as observed, for example, in $\text{Nd}_{2-x}\text{Sr}_x\text{NiO}_{4+y}$ (Ref. 8) and PrNiO_3 (Ref. 9). However, if there was an $I-M$ transition at T_{ci} , the electrical transport data would be hysteretic due to the first-order signature of the $I-M$ transition. This is not observed in our electrical resistivity measurements, suggesting that the transition observed at T_{ci} is really associated with a genuine superconducting phase. Figure 1 also provides information regarding the transition at T_{cj} . From excitation current dependences of resistive data, a broadening and shift of T_{cj} with increasing excitation current are always observed. Such behavior strongly suggests that Josephson weak coupling develops at T_{cj} , as already proposed elsewhere.^{1,2,4,5}

Additional understanding of these polycrystalline samples can be obtained from $\chi_{ac}(T)$ data shown in Fig. 2. Here, both components of χ_{ac} for $\text{Sm}_{1.82}\text{Ce}_{0.18}\text{CuO}_{4-y}$ are plotted as a function of temperature for several applied magnetic fields. The first important feature revealed by these data is the total absence of a peak in the χ'' component at T_{ci} . There are several possible explanations for this. First, there may be an insufficient total grain volume which is consistent with a very low superconducting volume fraction.¹ It is also possible that the grain size, or more appropriately, the region where the order parameter is not depressed, may be of the order of the London penetration depth λ . On the other hand, it is also possible that all the grains have a shell-core morphology, in which the superconducting properties are confined to a thin shell that is evidently comparable to λ , as proposed elsewhere.^{3,5} Two other candidates for explaining the absence of a peak in χ'' at T_{ci} are inconsistent with previous results in these samples: (1) that in very-high-quality grains H_{c1} may be very large just below T_{ci} ; and (2) that in well-coupled systems, a small measuring field will cause the coupling peak to obscure the so-called intrinsic peak. In any event, the absence of the peak in χ'' at T_{ci} can be understood if there is a combination of insufficient total grain volume; i.e., a very low superconducting volume fraction,^{1,3} and that superconducting properties are confined to small islands with size comparable to λ .^{2,4} Thus, it is reasonable to assume that

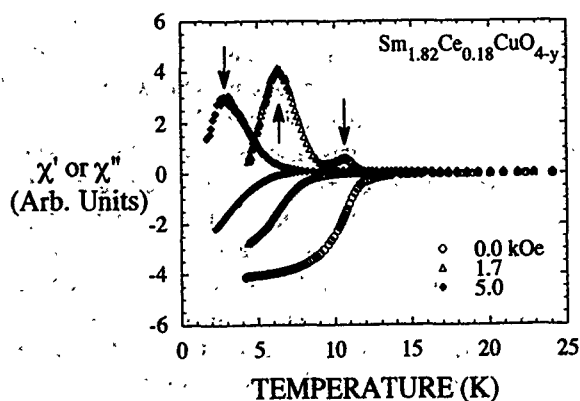


FIG. 2. Temperature dependence of the inductive and resistive components, χ' and χ'' , of the ac magnetic susceptibility χ_{ac} for different applied magnetic fields in $\text{Sm}_{1.82}\text{Ce}_{0.18}\text{CuO}_{4-y}$. The modulation field was $H_m = 4$ Oe and the frequency was $f = 15$ Hz. Arrows denote the temperatures of the peaks in χ'' .

these polycrystalline samples are comprised of small superconducting islands, which are not necessarily the physical grains, linked by Josephson coupling.

Figure 2 also shows that the application of a magnetic field shifts the peak in χ'' at T_{cj} towards lower temperatures. Such a peak has been widely attributed to the so-called irreversibility line in these cuprates and often used for constructing magnetic-field temperature phase diagrams. However, for the samples studied here, the peak in χ'' occurs at the Josephson coupling temperature T_{cj} , which is well below the intrinsic critical temperature T_{ci} . In such a scenario, it seems to be reasonable to associate the peak in χ'' with a transition in the Josephson coupling and its dependence on applied

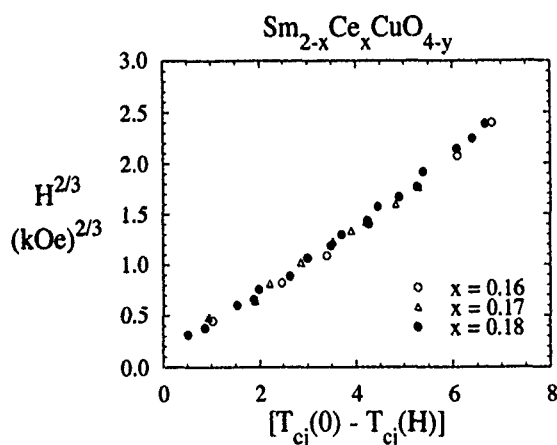


FIG. 3. Magnetic field $H^{2/3}$ against the reduced Josephson-coupling temperature $T_{cj}(0) - T_{cj}(H)$. $T_{cj}(0)$ is defined as the temperature at which χ'' peaks in zero applied magnetic field. A linear behavior suggests a quasi-de Almeida-Thouless line, characteristic of a superconducting glass state in a disordered Josephson array.

magnetic field to a phase diagram of a disordered Josephson array.^{2,5}

Values of $T_{cj}(H)$ were extracted from curves similar to those shown in Fig. 2 and used to construct the $H^{2/3}$ -vs- $[T_{cj}(0) - T_{cj}(H)]$ plots shown in Fig. 3. It can be seen that, in the low-field regime, the Josephson-coupling temperature displays the expected behavior of a disordered Josephson array, i.e., a quasi-de Almeida-Thouless behavior. This was proposed by Ebner and Stroud¹⁰ in their pioneering studies in granular superconductors and recently discussed in Ref. 11. Such an experimental result obtained in polycrystalline samples, where T_{ci} is well separated from T_{cj} , strongly suggests that contributions from the disordered array are predominant in the low-field regime, revealing the so-called superconducting glass state in a disordered Josephson array.² In this scenario, one would also expect that contributions arising from the genuine superconducting phase would dominate at higher fields. This is because with increasing field all the superconducting properties of the genuine phase are expected to be strongly field dependent, inducing a crossover in the H -vs- T phase diagram. This point is now being explored.

In summary, from the temperature dependence of the χ'' peak in polycrystalline samples of $\text{Sm}_{2-x}\text{Ce}_x\text{CuO}_{4-y}$ ($0.16 \leq x \leq 0.18$), we found evidence that these systems are comprised of small superconducting islands surrounded by Josephson junctions. The application of an applied magnetic field shifts the peak towards lower temperatures and an appropriate H -vs- T phase diagram reveals that these samples can be understood in analogy with granular superconductors. Arguments for a superconducting glass state in a disordered Josephson junction array have also been proposed.

The research of São Paulo was supported by FAPESP under Grant No. PD-EXT 91/2743-0 and at UCSD by the United States Department of Energy under Grant No. DE-FG03-86ER45230. Two of us (R.F.J. and C.H.C.) acknowledge support from the Brazilian Agency CNPq.

¹E. A. Early, C. C. Almasan, R. F. Jardim, and M. B. Maple, Phys. Rev. B **47**, 433 (1993).

²R. F. Jardim, M. C. de Andrade, E. A. Early, M. B. Maple, and D. Stroud (unpublished).

³R. F. Jardim, E. A. Early, and M. B. Maple (unpublished).

⁴R. F. Jardim, L. Ben-Dor, and M. B. Maple, J. Alloys Compounds **199**, 105 (1993).

⁵A. Gerber, Th. Grenet, M. Cyrot, and J. Beille, Phys. Rev. Lett. **65**, 3201 (1990); A. Gerber, Th. Grenet, M. Cyrot, and J. Beille, Phys. Rev. B **45**, 5099 (1992).

⁶C. Geibel, A. Vierling, P. V. Aken, R. Eichler, A. Gravel, M. Rau, S. Horn, G. Weber, and F. Steglich, Physica C **185-189**, 591 (1991).

⁷R. F. Jardim and M. B. Maple, Mater. Lett. **18**, 5 (1993).

⁸X. Granados, J. Fontcuberta, J. Alonso, M. Vallet, and J. M. Gonzalez Calbet, Physica C **191**, 371 (1992).

⁹X. Granados, J. Fontcuberta, X. Obradors, and J. B. Torrance, Phys. Rev. B **46**, 15 683 (1992).

¹⁰C. Ebner and D. Stroud, Phys. Rev. B **31**, 165 (1985).

¹¹K. A. Müller, M. Takashige, and J. G. Bednorz, Phys. Rev. Lett. **58**, 1143 (1987); I. Morgenstern, K. A. Müller, and J. G. Bednorz, Z. Phys. B **69**, 33 (1987).

Relationship between weak ferromagnetism, superconductivity, and lattice parameter in the $A_{2-x-y}B_x\text{Ce}_y\text{CuO}_4$ ($A, B \equiv \text{La, Pr, Nd, Sm, Eu, Gd, Y}$) compounds

T. Schultz, R. Smith, A. Frondado, C. Maley, T. Beacom, P. Tinklenberg, J. Gross, C. Taylor, and S. Oseroff
San Diego State University, San Diego, California 92182

Z. Fisk
Los Alamos National Laboratory, Los Alamos, New Mexico 87545

S.-W. Cheong
AT&T Bell Laboratories, Murray Hill, New Jersey 07974

T. E. Jones
NRaD, San Diego, California 92152

We report the results obtained by x-ray, dc magnetization, ac magnetic susceptibility, microwave magnetic absorption, and electron paramagnetic resonance of the magnetic and superconductive properties of a large series of compounds of the form $A_{2-x-y}B_x\text{Ce}_y\text{CuO}_4$ with $A, B \equiv \text{La, Pr, Nd, Sm, Eu, Gd, and Y}$. For $y=0$ antiferromagnetic ordering of the copper moments is present at $T_N \approx 280$ K for all the compounds formed in the tetragonal T' phase. Weak ferromagnetism (WF) associated with the canting of the copper moments is observed in all the compounds with a lattice parameter, $a < a_0$, $a_0 \approx 3.91$ Å, regardless of the rare-earth (R) ions present in the system. Superconductivity is observed only in the Ce-doped compounds with $a > a_1$, $a_1 \approx 3.92$ Å. The maximum onset temperature T_c is found for $a \approx 3.95$ Å. A phase diagram was obtained by varying the lattice parameter size as a function of A , B , and x . The correlation between the appearance of WF in the undoped compounds and the disappearance of superconductivity in the Ce-doped systems is discussed.

The $R_2\text{CuO}_4$ ($R \equiv \text{Pr, Nd, Sm, Eu, Gd}$) compounds form in the so-called T' phase, where the Cu is in a fourfold coordination, with no apical oxygen.¹ We report here detailed studies on powder samples of $A_{2-x}B_x\text{CuO}_4$ and $A_{1.85-x}B_x\text{Ce}_{0.15}\text{CuO}_4$ with $A, B \equiv \text{Pr, Nd, Sm, Eu, Gd, La, Y}$. Antiferromagnetic (AF) ordering of Cu is observed in the undoped $R_2\text{CuO}_4$ compounds below ~ 280 K.² A weak ferromagnetism (WF) component due to the canting of the Cu moments in the xy plane is present in compounds containing rare earths with smaller radii.²⁻⁴ The size boundary between WF and perfect AF in $R_2\text{CuO}_4$ compounds occurs near that of Eu_2CuO_4 .^{2,3} It has been proposed that WF is associated with displacements of the oxygen ions in the CuO_2 planes.⁴⁻⁶ These displacements lower the symmetry from tetragonal to orthorhombic at the rare-earth site for compounds with lattice parameter a smaller than ~ 3.91 Å.²⁻⁶ Thus, the existence of an antisymmetric exchange interaction of the Dzyaloshinski-Moriya type becomes possible for these compounds. Such a term is not compatible with tetragonal symmetry. Also, a critical value for the in-plane Cu—O distance seems necessary for these systems to become superconductors.⁷ In this paper we present results of x-ray powder diffraction, dc magnetization, ac susceptibility, microwave absorption, and electron paramagnetic resonance (EPR) with the purpose of finding a relationship between WF, superconductivity (SC), and Cu—O bond length.

Ceramic samples were prepared as follows: (i) The lanthanide oxides were dried in air at 900°C . (ii) Specific stoichiometric amounts of Ln_2O_3 and CuO were mixed and reacted at 900°C for about 24 h in alumina crucibles. (iii) The

mixture was ground and sintered at 1000°C for about 1 h. This process was repeated several times. (iv) The mixtures were pressed into $\frac{3}{8}$ -in. pellets at ~ 4 kbar, then placed in alumina crucibles and sintered in air for ~ 48 h at temperatures between 1050 and 1150°C depending on the compound. To promote SC it is necessary to lower the oxidation state of Cu by doping with Ce or Th as well as to anneal the sample in a reducing atmosphere.⁸ For that purpose the samples were reduced in argon or sealed in a quartz tube under a vacuum in the presence of an appropriate amount of Zr. The reducing time and temperature (T) were adjusted to obtain the best SC transition. We found that temperature was critical and it varied from ~ 800 to $\sim 1050^\circ\text{C}$ for the different compounds studied. Phase purity and lattice parameters were determined by x-ray powder diffraction. EPR was used as a more sensitive technique to determine the presence of impurity phases such as $R_2\text{CuO}_5$, $R_2\text{O}_3$, etc. Such phases were detected by EPR in $\text{Eu}_{2-x}\text{Y}_x\text{CuO}_4$ and $\text{Sm}_{2-x}\text{Y}_x\text{CuO}_4$ for $x \geq 0.4$ and 0.5 , respectively. WF and SC were measured by dc magnetization, ac susceptibility, and microwave absorption techniques.

In Fig. 1 ac susceptibility measurements for $\text{Eu}_{1.8}\text{Y}_{0.2}\text{CuO}_4$ are shown. Similar data were obtained by ac susceptibility, dc magnetization, and microwave absorption in all the systems studied with a lattice parameter $a < a_0$, $a_0 \approx 3.91$ Å. Microwave absorption is found to be the most sensitive technique to measure the onset of WF and SC in these compounds. In Fig. 2 we present a typical spectra taken with an EPR spectrometer in a WF compound. The data shown for $\text{Sm}_{2-x}\text{Y}_x\text{CuO}_4$ were taken at 9 GHz and 263 K; in

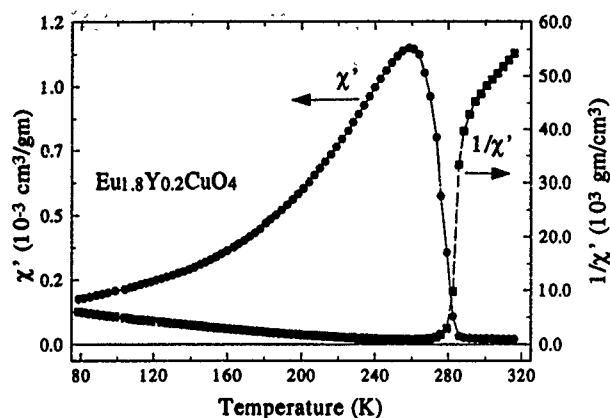


FIG. 1. ac susceptibility as a function of temperature of $\text{Eu}_{1.8}\text{Y}_{0.2}\text{CuO}_4$.

general, two signals are seen. One signal is a narrow line centered at zero field which corresponds to the rapid increase of dc magnetization and ac susceptibility for temperatures below the onset of WF.^{2,9} A second signal, which in powder samples looks like a broad shoulder, appears at a field different from zero. The second signal is always observed if WF is present.² It is the first indication of WF found in pure Eu_2CuO_4 and by adding just 1% of Y, WF is also observed in $\text{Eu}_{1.99}\text{Y}_{0.01}\text{CuO}_4$ by dc magnetization and ac susceptibility. For the last system both lines are observed in spectra similar to that shown in Fig. 2. The narrow line is not a true spin resonance but a microwave absorption signal observed because of the unbalanced EPR bridge. The second signal is a true spin resonance line which is found in all the WF compounds and is caused by a weak ferromagnetic resonance mode of the Cu moments. An analysis of this WF mode has been published already.⁹ In Fig. 3 we present the intensity of $d\chi''/dH$ as a function of temperature for $\text{Sm}_{2-x}\text{Y}_x\text{CuO}_4$ at different values of x . The onset, maximum, and general shape of the spectra do not change with x , but instead, the intensity of the signal increases with the concentration of Y. A similar behavior is observed for all the WF compounds where the average radii of the rare earth is reduced. At suf-

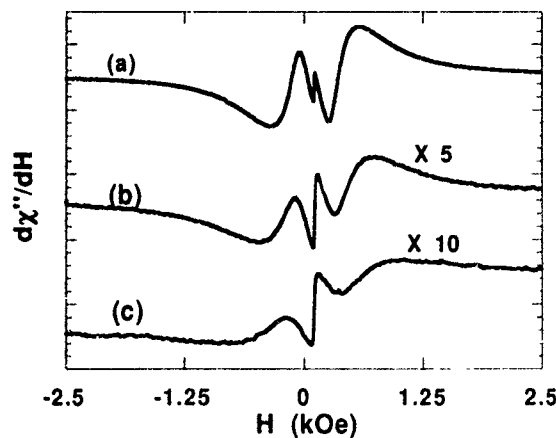


FIG. 2. Spectra for $\text{Sm}_{2-x}\text{Y}_x\text{CuO}_4$ measured at 9 GHz and 263 K, where (a), (b), and (c) correspond to $\text{Sm}_{1.4}\text{Y}_{0.6}\text{CuO}_4$, $\text{Sm}_{1.5}\text{Y}_{0.5}\text{CuO}_4$, and $\text{Sm}_{1.6}\text{Y}_{0.4}\text{CuO}_4$, respectively.

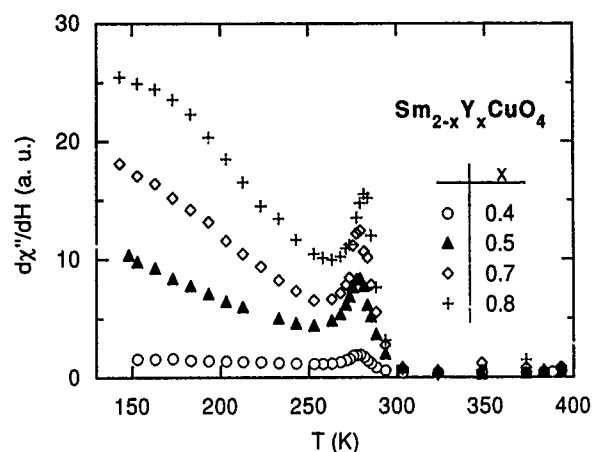


FIG. 3. Temperature dependence of $d\chi''/dH$ for $\text{Sm}_{2-x}\text{Y}_x\text{CuO}_4$ measured at 9.2 GHz.

ficiently high magnetic fields with $T < T_N$ the dc magnetization becomes linear, and when extrapolated back to zero an internal field H_i can be defined.² H_i increases with x in $\text{Eu}_{2-x}\text{Y}_x\text{CuO}_4$ and $\text{Sm}_{2-x}\text{Y}_x\text{CuO}_4$. The values obtained for H_i at the higher concentrations of Y are larger than the value measured for pure Gd_2CuO_4 .² The lattice parameter a at the boundary between WF and perfect AF for some of the compounds studied is given in Table I. Figure 4 is a phase diagram for the undoped R_2CuO_4 systems and those doped with $\text{Ce}=0.15$, $\text{R}_{1.85}\text{Ce}_{0.15}\text{CuO}_4$. As mentioned above, the onset of WF is at ~ 280 K in the undoped materials. A value of the same order has been found for T_N by neutron diffraction for the compounds which do not show WF.¹⁰ The lattice parameters given in Fig. 4 for Ce-doped compounds were measured in samples before oxygen reduction. Doping with Ce results in a contraction of the c axis and an expansion of the in-plane lattice parameter a .⁷ Thus, doping with Ce possibly reduces the distortion of the CuO_2 plane. This may explain why $\text{Eu}_{1.85}\text{Ce}_{0.15}\text{CuO}_4$ becomes a superconductor, even though Eu_2CuO_4 shows, as discussed above, indications of incipient WF. The value of the onset temperature for WF is depressed with the increase of Ce concentration. For $\text{Ce}=0.15$, the onset of WF is found at ~ 160 K for $\text{Eu}_{1.65}\text{Y}_{0.2}\text{Ce}_{0.15}\text{CuO}_4$ and $\text{Sm}_{1.45}\text{Y}_{0.4}\text{Ce}_{0.15}\text{CuO}_4$, similar to the value obtained for $\text{Gd}_{1.85}\text{Ce}_{0.15}\text{CuO}_4$.¹¹

For compounds close to the boundary, such as Gd_2CuO_4 , x-ray measurements suggest an average T' phase with some displacement of the oxygen atoms. Long-range correlation seems to occur only within each CuO_2 plane.¹² As no super-

TABLE I. Lattice parameter a for the boundary between WF and perfect AF for some of the compounds studied.

Compound	a (Å)
$\text{Eu}_{1.99}\text{Y}_{0.01}\text{CuO}_4$	3.906
$\text{Sm}_{1.65}\text{Y}_{0.35}\text{CuO}_4$	3.906
$\text{Gd}_{1.00}\text{Sm}_{1.00}\text{CuO}_4$	3.904
$\text{Gd}_{1.30}\text{Nd}_{0.70}\text{CuO}_4$	3.908
$\text{Gd}_{1.60}\text{La}_{0.40}\text{CuO}_4$	3.910
$\text{Gd}_{1.55}\text{Pr}_{0.45}\text{CuO}_4$	3.906

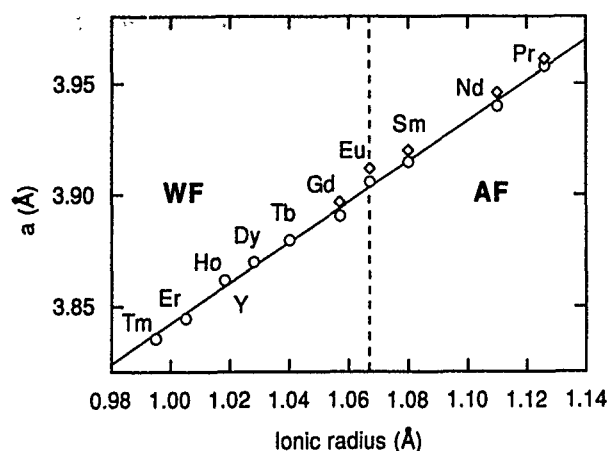


FIG. 4. In-plane lattice parameter a as a function of the ionic radius of the rare earth. The broken vertical line indicates the boundary between the WF compounds, which when doped with Ce do not show SC, and the AF compounds, which when doped become superconductors: (◊) doped, (○) undoped.

structures are observed in Gd_2CuO_4 it appears clear that only short-range interplanar correlations could exist in systems close to the boundary. For these systems the average structure remains tetragonal, and the distortions from a perfect square in the CuO_2 plane are due to displacements of the oxygen atoms along the normal to the $\text{Cu}-\text{O}$ bond. This distortion becomes larger as the size of the rare-earth ion becomes smaller. Electron paramagnetic resonance, x-ray, Mössbauer, and Raman techniques have confirmed this picture.^{4-6,12} From those results it is also possible to conclude that the local symmetry at the R site is orthorhombic.^{4-6,12} X-ray and Raman studies in systems with smaller R , such as Y_2CuO_4 and Tm_2CuO_4 which are farther from the WF-AF boundary, show extra peaks which may be associated with superstructures or a reduction in symmetry for those compounds.^{6,12}

We were not able to induce superconductivity in any of the Ce-doped compounds which showed WF measurable by dc and ac susceptibility. We attempted to induce SC in them by reducing the samples as described above. In the $\text{Ce}=0.15$ doped compounds that we studied superconductivity was observed in the compounds which had a lattice parameter a larger than ~ 3.92 Å. The maximum value of T_c , ~ 20 K, was measured for compounds with an in-plane distance between the Cu ions of ~ 3.95 Å. Away from this optimum length T_c decreases, for smaller as well as larger values of a . In Fig. 5 we present data for $\text{La}_{1.1}\text{Gd}_{0.75}\text{Ce}_{0.15}\text{CuO}_4$ with a $T_c \sim 15$ K and $a \sim 3.96$ Å. Attempts to obtain SC samples with larger concentrations of Gd and smaller values of a were unsuccessful. We do not have an explanation for this.

In summary, we found that the presence or absence of WF and SC in the T' -phase $R_2\text{CuO}_4$ compounds is independent of whether the rare-earth ion is magnetic or not. In these

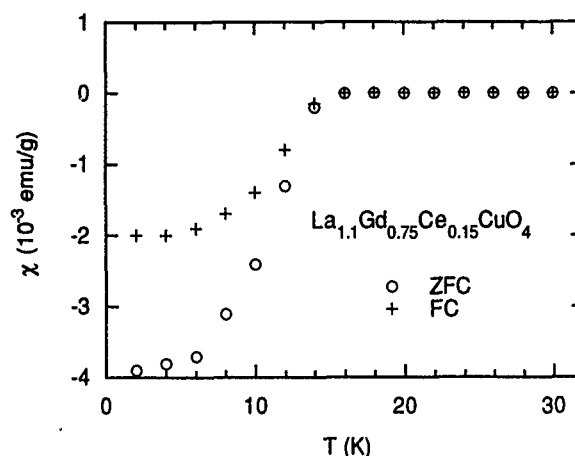


FIG. 5. dc susceptibility measured at 10 Oe on a powder sample of $\text{La}_{1.1}\text{Gd}_{0.75}\text{Ce}_{0.15}\text{CuO}_4$. The sample was reduced under vacuum in the presence of Zr.

compounds SC and WF seem to be definitively exclusive, i.e., the distortion from a perfect square in the CuO_2 plane seems to be incompatible with SC in these systems. A strong correlation between WF, SC, and the $\text{Cu}-\text{O}$ bond length is observed. Values of ~ 3.91 , ~ 3.92 , and ~ 3.95 Å are the maximum, minimum, and optimum planar lattice parameters for the presence of WF, SC, and maximum T_c , respectively.

We wish to thank Professor R. Lilly, P. Lincoln, and M. Queen for their help. This research was supported at San Diego State University by NSF-DMR-9117212 and the Research Corporation, at Los Alamos National Laboratory under the auspices of the United States Department of Energy. Additional support came from AT&T Bell Labs.

- ¹J. D. Thompson, S.-W. Cheong, S. E. Brown, Z. Fisk, S. B. Oseroff, M. Tovar, D. C. Vier, and S. Schultz, Phys. Rev. B **39**, 6660 (1989).
- ²S. B. Oseroff, D. Rao, F. Wright, D. C. Vier, S. Schultz, J. D. Thompson, Z. Fisk, S.-W. Cheong, M. F. Hundley, and M. Tovar, Phys. Rev. B **41**, 1934 (1990).
- ³L. B. Steren, M. Tovar, and S. B. Oseroff, Phys. Rev. B **46**, 2874 (1992).
- ⁴R. D. Zysler, M. Tovar, C. Rettori, D. Rao, H. Shore, S. B. Oseroff, D. C. Vier, S. Schultz, Z. Fisk, and S.-W. Cheong, Phys. Rev. B **44**, 9467 (1991).
- ⁵P. Adelmann, R. Ahrens, G. Czjzek, G. Roth, H. Schmidt, and C. Steinle-Itner, Phys. Rev. B **46**, 3619 (1992).
- ⁶M. L. Laguna, M. L. Sanjuán, A. Butera, M. Tovar, Z. Fisk, and P. Canfield, Phys. Rev. B **48**, 7565 (1993).
- ⁷E. Wang, J.-M. Tarascon, L. H. Green, G. W. Hull, and W. R. McKinnon, Phys. Rev. B **41**, 6582 (1990).
- ⁸Y. Tokura, H. Takagi, and S. Uchida, Nature **337**, 345 (1989).
- ⁹A. Fainstein, M. Tovar, and Z. Fisk, J. Phys. Cond. Matter. **4**, 1581 (1992); A. Fainstein, *ibid.* **4**, 4989 (1992).
- ¹⁰Y. Endoh, M. Matsuda, K. Yamada, K. Kakurai, Y. Hidaka, G. Shirane, and R. J. Birgeneau, Phys. Rev. B **40**, 7023 (1989); J. W. Lynn, I. W. Sumarlin, S. Skanthakumar, W.-H. Li, R. N. Shelton, J. L. Peng, Z. Fisk, and S.-W. Cheong, *ibid.* **41**, 2569 (1990); S. Skanthakumar, J. W. Lynn, J. L. Peng, and Z. Y. Li, J. Magn. Mater. **104-107**, 519 (1992).
- ¹¹A. Butera, A. Caneiro, M. T. Causa, L. B. Steren, R. Zysler, M. Tovar, and S. B. Oseroff, Physica C **160**, 341 (1989).
- ¹²Ph. Galez, P. Schweiss, G. Collin, and R. Bellissent, J. Less. Common Met. **164 & 165**, 784 (1990); P. Bordet *et al.*, Physica C **193**, 178 (1992).

Alkali metals impurities influence on the magnetic and electrical properties of YBCO

I. Nedkov and A. Veneva

Institute of Electronics, Bulgarian Academy of Sciences, 72, Tzarigradsko Chaussee, 1784 Sofia, Bulgaria

The samples were prepared using the primary batch formula $Y_{1-0.2x}Ba_{2-0.2x}Cu_{3+0.3x}(Me)_{0.4x}O_y$, where $x=0-1.20$ and Me denotes alkali metals (Na, K, Rb) introduced as carbonates. The presence of alkali carbonates during the process allows one to influence the YBCO grain size and improve the homogeneity of the structure. Despite the large concentration range of additives in the initial batch after the second treatment at temperatures higher than 900 °C, only traces of the alkali metals were revealed. The influence of Na, K, and Rb impurities in concentrations for Na about 5×10^{-1} wt %; for K to 4×10^{-2} wt %, and Rb to 2×10^{-2} wt % in polycrystalline YBCO was investigated. For Rb and K, the $R(T)$ transitions were comparable to that of pure YBCO. The microwave surface resistance R_s was least influenced by the impurities, but strongly depended on the polycrystalline microstructure. Each impurity had a specific effect on $\chi(T)$ and J_c which are related to the grain-boundary structure.

I. INTRODUCTION

Investigating the influence of the different impurities on the magnetic and electrical high-temperature superconducting (HTSC) properties is of interest, as much for the understanding of the intragranular phenomena, as for solving technological problems. However, to our knowledge, only a few isolated papers have appeared on the alkali metals impurities in YBCO^{1,2} and the data published are controversial. There have been reports on obtaining $T_c=135$ K in a YBCO system substituted with K.³ It has been assumed that the effect of adding K is due to the formation of a KCu-compound participating indirectly in the YBCO-phase formation process.² Our recent work⁴ showed that K_2CO_3 may be added to the initial batch in significant quantities without causing deterioration of the general HTSC properties; we also attributed this fact to the KCu-compound.

The aim of this work is to compare the HTSC properties of Na-, K-, and Rb-containing samples and to clarify the role of the excess of Cu when it is in quantity comparable with the alkali metal additive.

II. EXPERIMENTAL

The samples were prepared using the primary batch formula $Y_{1-0.2x}Ba_{2-0.2x}Cu_{3+0.3x}(Me)_{0.4x}O_y$, where $x=0-1.20$ which allowed us to have Cu excess in the initial batch and a comparable amount of an alkali metal ($Me=Na, K, Rb$). Attention was paid to the purity of the initial components: the basic content of Y_2O_3 was 99.99%; of $BaCO_3$, 99.99%, and CuO , 99.99%. The additives were introduced as alkali carbonates with high purity (more than 99.9 wt %). After preliminary baking of the batch at 900 °C, 1 μm grain-size powder was used to press pellets which were sintered a second time. The final temperature was different for each additive (from 900 to 980 °C for 50 h) and was selected using the differential thermal analysis (DTA) data. The single-phase YBCO ($x=0$), which we used for comparison with the doped system, was obtained via final sintering treatment consisting in baking at 980 °C for 60 h in oxygen at-

mosphere; its HTSC properties were close to the best quoted in the literature for polycrystalline untextured YBCO.

The phase content and polycrystalline microstructure were characterized using x-ray powder diffraction (XRD) and scanning electron microscopy (SEM) with x-ray microanalyzer (EPMA). The resistivity $R(T)$ transition was measured at liquid-nitrogen temperature using the standard four-probe technique (measuring current value 100 mA). The ac magnetic susceptibility $\chi(T)$ transition was followed using the contactless "pick-up coil" techniques (magnetic field 0–25 mT). To determine the critical current J_c and the surface resistance R_s (at 14.3 GHz) we developed our original equipment described in Ref. 5.

III. RESULTS AND DISCUSSION

Our investigation showed that the Na_2CO_3 , K_2CO_3 , and Rb_2CO_3 influence was well pronounced when the carbonates were in significant concentrations: for Na, $x=0.40$ (1.42 wt % Na_2CO_3) to 1.20 (4.37 wt % Na_2CO_3); for K, $x=0.40$ (2.38 wt % K_2CO_3) to 0.75 (4.49 wt % K_2CO_3), and for Rb, $x=0.20$ (2.57 wt % Rb_2CO_3) to 0.40 (5.07 wt % Rb_2CO_3). The cases of additives concentrations below these limits are well described in the literature.^{1,2} When these ranges are exceeded, it is difficult to obtain reproducible single-phase samples with HTSC properties. Our investigation was, therefore, focused on the ranges of additives concentrations mentioned.

After the first heat treatment (900 °C/24 h) the YBCO phase was about 75 wt % and the XRD data showed (and SEM and EPMA confirmed it) that in samples with Na_2CO_3 and Rb_2CO_3 additives, Na_2O , Rb_2O , and CuO phases existed in the powder, while for the case of K_2CO_3 , the analysis revealed the presence of a K_3CuO_2 phase.

Each additive had a specific influence on the final temperature of the second treatment compared with pure $Y_1Ba_2Cu_3O_y$ —generally, the sintering temperature decreased. HTSC samples for Na ($x>0.4$) were obtained at 940 °C, for K ($x>0.4$) at 950 °C and for Rb ($x>0.2$) at 930 °C. The SEM and EPMA data indicated differences in the microstructure after the second treatment. For samples

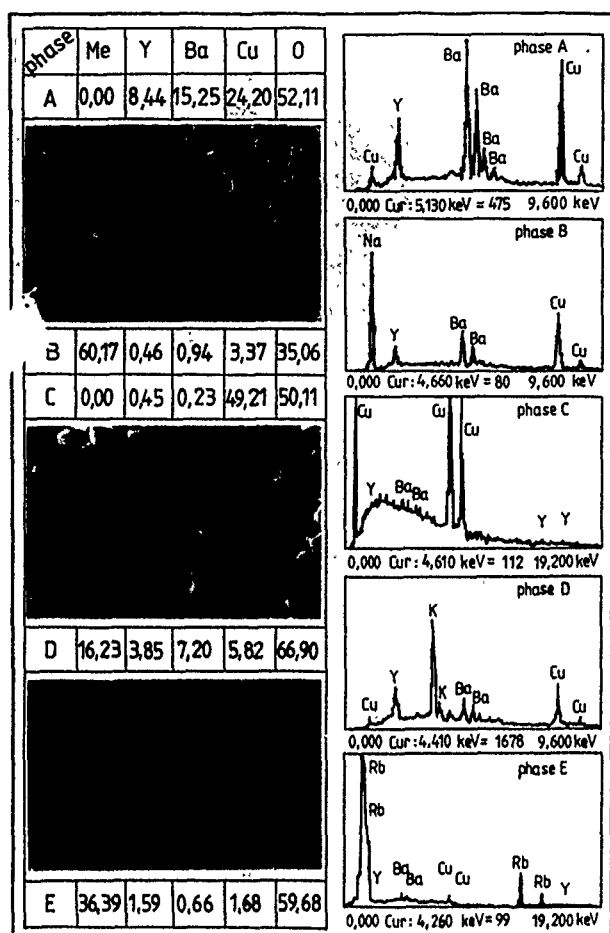


FIG. 1. SEM and EPMA data for Na-, K-, and Rb-doped samples—surface layer. The unit is at %.

with Na additive, CuO excess remained in the material as a second phase; from 2 to 5×10^{-1} wt % Na (Na_2O) was also found in the end product.

For the K_2CO_3 additive, the XRD and EPMA data revealed the existence of a K_3CuO_2 phase which evaporated above 900°C and only traces of K were revealed on the surface of the samples. To explain the disappearance of the K and Cu excess from the samples above 950°C , we analyzed our crucibles (made of Al_2O_3) after sintering. Atomic absorption spectroscopy (AAS) showed about 0.66 wt % of Cu in the crucible (as compared with 0.00024 wt % Cu in crucibles without sample) and 13.8 wt % of K in a crucible where a sample with $x=0.75$ (4.49 wt % K_2CO_3) was sintered.

The XRD, SEM, and EPMA data showed the existence of a glass-like Rb_2CO_3 phase at $840\text{--}890^\circ\text{C}$. This made us suppose that alkali-containing liquid phases participate in the polycrystalline structure formation during the second treatment by enhancing the diffusion processes thus helping the CuO excess move to the surface. On the other hand, the alkali-containing phases evaporated above 900°C . AAS study of crucible walls where the Rb doped with $x=0.4$ (5.07 wt % Rb_2CO_3) sample were baked indicated about 14.1 wt % of Rb.

Figure 1 illustrates typical surface structure and EPMA phase analysis. Five phases were identified in the specimens.

For Na-doped samples: (A) with basic structure $\text{Y}_1\text{Ba}_2\text{Cu}_3\text{O}_y$ crystals, (B) dark— Na_2O , and (C) gray— CuO . For the K- and Rb-doped samples: (D) yellow— K_3CuO_2 , (E) dark— Rb_2O , and (A) $\text{Y}_2\text{Ba}_2\text{Cu}_3\text{O}_y$ phase. The measurement accuracy of the EPMA method for metal ion analysis was 1%. The SEM studies proved that samples with K and Rb additives possessed a low-density surface layer and their thickness was about $200\text{ }\mu\text{m}$. Their chemical content depended on the alkali carbonate added: according to the EPMA data for Rb-doped samples, the layer consisted of YBCO and Rb and Cu oxides; for K, we found K_3CuO_2 (see Fig. 1). When this layer was removed, the XRD showed that the basic structure was single-phase $\text{Y}_1\text{Ba}_2\text{Cu}_3\text{O}_y$. Atomic absorption spectroscopy (AAS) revealed only traces of the alkali additives: about 4×10^{-2} wt % K and 2×10^{-2} wt % Rb. To avoid the influence of the low-density layer, we polished the sample surface before the HTSC measurements.

We accumulated a large amount of data about the Rb, Na, and K additives influence on the HTSC properties in a wide concentration range. We present here the more characteristic results for comparable concentrations of alkali carbonates (mentioned above) to illustrate the influence of different impurities on the HTSC properties. The term "impurities" was chosen because only traces of alkali metals (4×10^{-2} wt % for K and Rb and 5×10^{-4} wt % for Na) were found after the second treatment and surface layer removal. The studies allowed us to assume that the K and Rb impurities are located at the grain boundaries. Despite the fact that insignificant amounts of the additives were found in the end product, differences could be seen in the magnetic and resistive behavior of the samples as illustrated by Figs. 2(a) and 2(b). In a large concentration range, the $R(T)$ superconducting transitions were similar and better (for Rb, the initial temperature was in the order of 94.6 K and for K 93.4 K) than those of pure YBCO. In Na-containing YBCO, the impurities (Na_2O and CuO) influence on the $R(T)$ was the most significant [see Fig. 2(a)].

Each impurity had a specific influence on the $\chi(T)$ dependence [see Fig. 2(b)]. The observed worsening of the $\chi(T)$ dependence in the case of Na doping is obviously related to the presence of nonsuperconducting (Na_2O and CuO) phases in considerable amounts. In the case of K_3CuO_2 -containing boundaries ($x=0.75$ in the initial batch) we observed the best $\chi(T)$ transition with T_{end} as high as in pure YBCO, but ΔT was larger. The lower amount of Rb_2O impurities in the grain boundaries shifted the transition-onset temperature towards the lower temperatures. Rb- and K-doped samples with similar impurities concentration in the grain boundaries exhibited different $\chi(T)$ behavior. This confirmed the important role of the grain-boundary structure in influencing the $\chi(T)$.

To clarify the influence of the impurities, we investigated the parameters most sensitive to the grain structure, namely, J_c and R_s . Table I summarizes the data.

The microwave measurement showed that R_s depended weakly on the grain-boundary impurities, while being

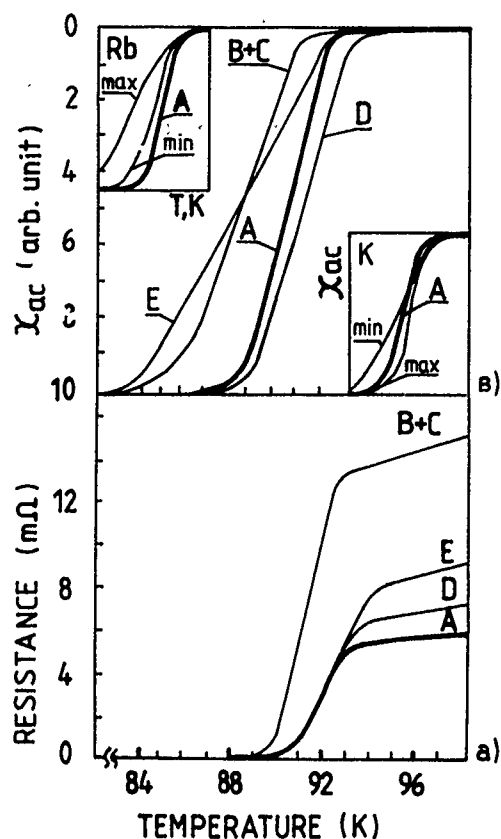


FIG. 2. (a) $R(T)$ transitions and (b) $\chi(T)$ transition for pure $Y_1Ba_2Cu_3O_y$. (A) compared with Na-, K-, and Rb-doped samples, where the basic phase is $Y_1Ba_2Cu_3O_y$ and impurity phases are (B), (C) Na_2O and CuO ; (D) K_3CuO_2 , and (E) Rb_2O are found.

strongly affected by the grain size and homogeneity. Using SEM photographs, we carried out a statistical analysis of the grain size in doped samples in comparison with pure YBCO polycrystalline structure. The YBCO grains had the specific shape of a parallelepiped. We compared the grains with different longitudinal and similar transverse dimensions and calculated the average longitudinal dimension. Figure 3 shows the grain-size distribution in doped and undoped samples. It is clear that adding Na_2CO_3 allowed us to obtain a polycrystalline structure with small average grain size and high homogeneity. These samples exhibited the best R_s , despite the low density of those with Na_2O and CuO phases, but J_c was about 40 A/cm². The K_2CO_3 additive kept the grain size relatively high which worsened R_s , but resulted in high homogeneity which was probably responsible for the good $R(T)$ transition data. We assumed, furthermore, that the

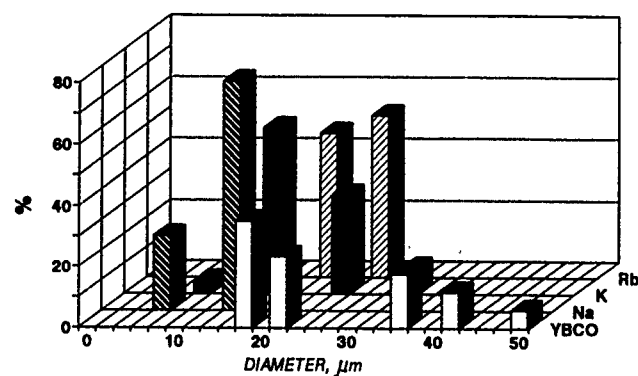


FIG. 3. The statistical analysis for grain-size distribution in polycrystalline YBCO obtained from initial batches include excesses from CuO and Na, K, and Rb carbonates in concentration about 4.5 wt %.

worse J_c in K-doped samples had to do with different grain-boundary structure.

We associated the influence of the Rb impurity on the microstructure and electrical properties with the existence of a liquid phase during the technological process which enhanced the recrystallization process. This impurity was most insignificant in the end product and only the $\chi(T)$ behavior was sensitive to its existence on the grain boundary. It is interesting to note that the samples density for Rb-containing samples was better in a larger range of concentrations and the best values of J_c and R_s were observed for this additive.

IV. CONCLUSIONS

The alkali additives react differently with CuO excess in the initial batch. Na_2CO_3 does not remove this excess; CuO and Na_2O phases remain disseminated in the entire sample. Rb_2CO_3 enhances the CuO diffusion towards the sample surface. The carbonate dissociates at 890 °C, with only traces of Rb_2O remaining as impurity at the grains boundaries after the second heat treatment. The K_2CO_3 reacts with the CuO excess and forms a KCu -compound which diffuses towards the surface and evaporates above 900 °C.

For Rb- and K-doped samples with similar impurities in the order of $2-4 \times 10^{-2}$ wt %, $R(T)$ transitions are comparable to the best one of pure YBCO. Each additive has a specific effect on $\chi(T)$ transition which is related to the grain-boundary phase structure. A lower quantity of Rb_2O leads to deterioration of the $\chi(T)$ transition and the same concentration of the KCu -compound improves T_{end} of YBCO.

The HTSC parameter most sensitive to the impurities is J_c . Only in the case of Rb, impurities at the grain boundaries in the order of 2×10^{-2} wt % virtually do not affect J_c . The experiments demonstrated that R_s is least influenced by the impurities, but strongly depends on the grains size and homogeneity.

TABLE I. Summary of the data.

General formula: $Y_{1-0.2x}Ba_{2-0.2x}Cu_{3+0.3x}(Me)_{0.4x}O_y$				
Me	undoped	Na	K	Rb
x from-to	0	0.4-1.2	0.4-0.75	0.2-0.4
wt % impurity	0	5×10^{-1}	4×10^{-2}	2×10^{-2}
J_c A/cm ²	212	40-15	100-20	261-217
R_s (mΩ) by $f = 14.3$ GHz	51	51-49	55-65	42-49
Density g/cm ³	6.0	5.3-4.6	5.9-5.4	5.9-5.9

¹ R. J. Cava, J. Krajewski, W. Peck, B. Batlogg, Jr. Rupp, R. Fleming, and A. James, *Lett. Nature* **338**, 328 (1989).

² Y. Saito, T. Noji, A. Endo, N. Higuchi, K. Fugimoto, T. Okawa, and A. Hattori, *Physica C* **148B**, 336 (1987).

³ Y. Khan, *J. Mater. Sci. Lett.* **7**, 53 (1988).

⁴ I. Dragieva and I. Nedkov, *IEEE Trans. Magn.* **26**, 1433 (1990).

⁵ I. Nedkov, A. Veneva, S. Miteva, T. Nurgaliev, and V. Lovchinov, *EMMA '93*, M2-P-18, 1993 (to be published).

Kinematical pairing and magnetism in layered systems

Valery A. Ivanov,^{a)} Michail Ye. Zhuravlev, and Pavel B. Z'ubin

N. S. Kurnakov Institute of General and Inorganic Chemistry, Academy of Science of Russia, 31, Leninsky Prospect, GSP-1, Moscow 117907, Russia

Hubbard model of two layers of strongly correlated electrons with interlayer hopping is investigated. The temperature T_c of superconducting transition and magnetic susceptibility are calculated. The external pressure dependence of T_c is discussed.

I. INTRODUCTION

Discovery of high- T_c layered perovskite compounds galvanized the theorists' interest to the role of interlayer coupling for superconductivity. In high- T_c cuprates it is noted that the influence of apical oxygen on T_c increases the throw and changes the effective interlayer hopping; the apical oxygen provides for the effective tunneling of electrons between copper cations in neighboring CuO_2 layers.

We have suggested the simplest Hubbard model of two layers of strongly correlated electrons with interlayer hopping integral τ :

$$H = - \sum_{ij\sigma} t_{ij} c_{i\sigma}^+ c_{j\sigma} + I \sum_i n_i^{\uparrow} n_i^{\downarrow} - \mu \sum_i (n_i^{\uparrow} + n_i^{\downarrow}), \quad I = \infty, \quad (1)$$

where $t_{ij} = t$ if i and j belong to the same layer, and $t_{ij} = \tau$ if i and j belong to different layers.

The interlayer hopping decreases the normal ground state energy of the system. This hopping τ gives rise to the Van Hove singularity in initial rectangular density of states in the points $\pm 2\tau$. Density of states (DOS) has the following form:

$$\rho(\epsilon) = (2/t)K \left[\sqrt{1 - \left(\frac{|\epsilon| + 2\tau}{4t} \right)^2} \right], \quad (2)$$

where K is complete elliptic integral. We have calculated the concentration dependence of the kinetic and interaction energies of the given system. The energy of interaction has the following form:

$$E_{\text{int}} = \frac{n^2(1.5n-1)w}{2(2-n)} - (1.5-1)f(n, \tau), \quad (3)$$

where $f(n, \tau) < 1$ is a positive function.

E_{int} acquires the negative sign at an electron concentration above $n = 2/3$ per site which corresponds to the sign changing of Born amplitude of mutual (σ, σ) electron scattering.

II. SUPERCONDUCTIVITY

The superconducting transition was investigated in the framework of the kinematical high- T_c mechanism.^{1,2} We have calculated the concentration dependence of superconducting transition temperature T_c . For example, when chemical potential $\mu < 2\tau(1 - n/2) - T_c$, T_c is as follows:

$$T_c = (1/2)[(2t + \tau)^2(2 - n)^2 - \mu^2] \times \exp \left(\frac{t(2 - n)\mu}{[\tau^2(2 - n)^2 - \mu^2]} \right). \quad (4)$$

For $\tau = 0$ the limiting case,¹ reproducing in Ref. 3 is obtained. Depending on the chemical potential position relative to the Van Hove singularities it is possible that the T_c increases with interlayer hopping integral τ .

We have also calculated the derivatives dT_c/dt and $dT_c/d\tau$ in connection with experimental investigations of baric derivatives of T_c .⁴ It is significant that the variation of T_c with the bandwidth is connected with electron concentration as well. Assume that the system is coupled with a reservoir of electrons: it may be Cu-O chains or BiO, TlO layers in HTSC cuprates. From the equations on electron concentration in these systems

$$\begin{cases} n = \frac{1}{3}\rho\mu + \frac{2}{3} & (\text{for correlated electrons}), \\ n_r = \rho_r\mu_r + \frac{1}{2} & (\text{for noncorrelated electrons of reservoir}), \\ \mu = \mu_r, \end{cases} \quad (5)$$

we can see that electron concentration n depends on the densities of state ρ, ρ_r , which are determined by corresponding bandwidths. In Fig. 1 are shown the calculated derivatives of T_c . We can see from Fig. 1 that derivatives of T_c , with respect to the hoppings, can be negative as well as positive. This may explain a number of experiments in which different signs of baric derivatives were observed.⁵

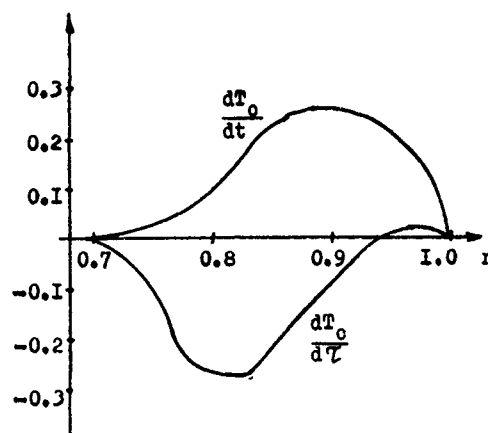


FIG. 1. The baric derivatives of T_c for $\tau/t = 1/2$.

^{a)}Institute for Molecular Science of the Okazaki National Research Institutes Center, Miodajji, Okazaki 444, Japan.

III. MAGNETIC PROPERTIES

It is interesting to calculate the static magnetic spin susceptibility with DOS (2) which rises steeply in the points $\epsilon = \pm 2\tau$. It was approximated by

$$\rho(\epsilon) = \frac{A}{2} \left(\frac{w}{(\epsilon - 2\tau)^2 + w^2} + \frac{w}{(\epsilon + 2\tau)^2 + w^2} \right) \theta(w^2 - \epsilon^2) \quad (6)$$

where $A = 2/\pi$.

We used the general formula

$$\chi(T) = \frac{-2 \int \rho(\epsilon) \frac{\delta}{\delta \epsilon} [n_F(\epsilon)] d\epsilon}{1 - \int \rho(\epsilon) \frac{\delta}{\delta \epsilon} [\epsilon n_F(\epsilon)] d\epsilon} \quad (7)$$

and obtained the following expression of Curie-Weiss type:

$$\chi(T) \sim \frac{C}{T + \theta}, \quad (8)$$

where

$$C = \frac{8(1 - n/2)^2}{3\pi^2},$$

$$\theta = \frac{\tau^2}{\pi W} (2 - n).$$

It must be emphasized that for rectangular DOS the $\chi(T)$ is essentially independent of temperature.

IV. CONCLUSION

The T_c dependence on electron concentration and magnetic spin susceptibility has been calculated for layered system of Eq. (1) type.

The calculated features of model (1) are responsive to the position of Van Hove peaks of the DOS. T_c increasing can occur for appropriate mutual positioning of the peak and chemical potential.

In relation to experiments on baric derivatives of T_c in layered high temperature superconductors we have noted also that the variation of charge carriers under pressure must be taken into account in the interpretation of these experiments. The DOS depends on external pressure and in turn

$$\frac{dT_c}{dt} = \frac{\partial T_c}{\partial t} + \frac{\partial T_c}{\partial n} \frac{\partial n}{\partial t}. \quad (9)$$

From the condition of equality of chemical potentials μ [cf. Eq. (5)] for superconducting electrons n and reservoir ones n_r it follows the dependence of electron concentration on external pressure.

¹ R. O. Zaitsev and V. A. Ivanov, Sov. Phys. Solid State **29**, 1475 (1987).

² S. Nakajima, M. Sato, and Y. Murayama, J. Phys. Soc. Jpn. **60**, 2333 (1991).

³ N. M. Plakida, V. U. Yushanhai, and P. Kaliny, Physica C **174**, 401 (1991).

⁴ U. Koch, J. Wittig, and B. Gegenheimer, Physica C **162-164** 739 (1989).

⁵ M. F. Grommie *et al.*, Phys. Rev. B **39**, 4231 (1989).

Ground-state properties and excitations of an integrable one-dimensional model with δ -function interaction involving several bands

P. Schlottmann

Department of Physics, Florida State University, Tallahassee, Florida 32306

We consider an integrable model consisting of n parabolic bands of electrons of equal mass with a δ -function exchange interaction. The interaction is attractive or repulsive depending on whether the interacting particles are in a spin-singlet or triplet state. The structure of the Bethe ansatz and the classification of states is similar to that of the n -channel Kondo problem. The attractive interaction leads to Cooper-pair-like boundstates. Some ground-state properties and the excitation spectrum are discussed for the special situation of degenerate bands.

Several multiband models^{1,2} have been proposed to explain properties of high- T_c compounds. In particular, the anomalous dependence of the Hall coefficient and T_c in $\text{La}_{2-x}\text{Sr}_x\text{CuO}_4$ and $\text{Nd}_{2-y}\text{Ce}_y\text{CuO}_4$ on doping has been attributed to an admixture of the $3d_{z^2}$ orbital.³ This admixture is consistent with polarized x-ray absorption data.³ Motivated by the possibility that both the $3d_{x^2-y^2}$ and $3d_{z^2}$ orbitals may play a role in high- T_c cuprates, we considered² an integrable model involving two one-dimensional bands separated by a crystalline field splitting, and a δ -function exchange interaction, which leads to singlet bound states of the Cooper type. In this paper we extend the results of Ref. 2 to an arbitrary number n of equal bands. The model is still integrable and the generalization to n bands changes the results of Ref. 2 only quantitatively (but not qualitatively). In addition, we discuss here the spectrum of elemental excitations. The Hamiltonian is

$$H = \sum_{m\sigma} \int dx c_{m\sigma}^\dagger(x) (-\partial^2/\partial x^2) c_{m\sigma}(x) + c \sum_{mm'\sigma\sigma'} \int dx_1 \int dx_2 \delta(x_1 - x_2) \times c_{m\sigma}^\dagger(x_1) c_{m'\sigma'}^\dagger(x_2) c_{m'\sigma}(x_2) c_{m\sigma}(x_1), \quad (1)$$

where $m=1, \dots, n$ labels the bands, and $c_{m\sigma}^\dagger(x)$ creates an electron of spin σ at the site x in the band m . Since the number of particles with up and down spin and the electrons in each band are conserved, it is straightforward to incorporate magnetic and crystalline field splittings between the bands. The interaction is an exchange, i.e., it depends on the spin and orbital indices. Electrons within the same band (and opposite spin) are attracted, while for electrons of equal spin but in different bands the interaction is repulsive. All the bands have equal mass; this is a necessary condition for the integrability of the model.

It is useful to study the two-particle problem first. The two-electron wave function can be written as a product of three factors: (i) a coordinate wave function referring to the positions and momenta, (ii) a spin wave function, and (iii) an orbital wave function involving the band labels m . The fermionic character mandates the global wave function to be antisymmetric under the exchange of the particles. Hence, if the spin and orbital wave functions have the same parity, the coordinate wavefunction has to be antisymmetric and van-

ishes if $x_1 = x_2$, and the two particles cannot interact. Interacting fermions then necessarily form a spin singlet and orbital triplet (attractive interaction) or a spin triplet and orbital singlet (repulsive potential). The scattering matrix is the product of the spin and orbital scattering matrices,²

$$\hat{S}(k) = \frac{k\hat{I}_\sigma - ic\hat{P}_\sigma}{k - ic} \times \frac{k\hat{I}_m + ic\hat{P}_m}{k + ic}, \quad (2)$$

where $\hat{I}_\sigma(\hat{I}_m)$ and $\hat{P}_\sigma(\hat{P}_m)$ are the identity and permutation operators for the spins (band indices), respectively, $k = k_1 - k_2$, and k_1 and k_2 are the wave numbers. Note that each factor just yields one, when applied to the triplet state. Hence, (2) only acts on the (orbital or spin) singlet parts of the wave function. For the case of spin and orbital singlets the two phase factors cancel and there is no effective interaction. In summary, the orbital and spin spaces factorize. Since the scattering matrix for each channel (spin and orbital) satisfies the triangular Yang-Baxter relation,⁴ their product also does and model (1) is integrable for any number of bands.

Each state of the Hamiltonian is specified by one set of N "charge" rapidities $\{k_j\}$, one set of M "spin" rapidities $\{\lambda_\alpha\}$ and $n-1$ sets of $m^{(l)}$ "orbital" rapidities $\{\xi_\alpha^{(l)}\}$, $l=1, \dots, n-1$. Imposing periodic boundary conditions we obtain the discrete Bethe ansatz equations satisfied by the rapidities^{2,4-7}

$$\begin{aligned} \exp(ik_j L) &= \prod_{\alpha=1}^M e_1(k_j - \lambda_\alpha) \prod_{\beta=1}^{m^{(1)}} e_1(k_j - \xi_\beta^{(1)}), \quad j=1, \dots, N, \\ \prod_{j=1}^N e_1(\lambda_\alpha - k_j) &= - \prod_{\beta=1}^M e_2(\lambda_\alpha - \lambda_\beta), \quad \alpha=1, \dots, M, \\ \prod_{\beta=1}^{m^{(l-1)}} e_1(\xi_\alpha^{(l)} - \xi_\beta^{(l-1)}) &\prod_{\beta=1}^{m^{(l+1)}} e_1(\xi_\alpha^{(l)} - \xi_\beta^{(l+1)}) \\ &= - \prod_{\beta=1}^{m^{(l)}} e_2(\xi_\alpha^{(l)} - \xi_\beta^{(l)}), \quad \alpha=1, \dots, m^{(l)}, \end{aligned} \quad (3)$$

where $l=1, \dots, n-1$, $\{k_j\} \equiv \{\xi_\alpha^{(0)}\}$, $m^{(n)}=0$, L is the length of the box, and $e_j(x) = (x - ijc/2)/(x + ijc/2)$. The energy, the magnetization and the number of electrons in each band are given by $E = \sum_{j=1}^N k_j^2$, $S_z = \frac{1}{2}N - M$, and $m^{(l-1)} - m^{(l)}$, respec-

tively. For $n=1$ Eqs. (3) reduce to those of the gas of electrons with attractive interaction,⁴ for $M=0$ to the multicomponent Fermi gas⁴ and for $n=2$ to the model diagonalized in Ref. 2. The Bethe ansatz Eq. (3) are also closely related to those of a variant of the two-channel Kondo problem which includes charge (valence) fluctuations, except for the impurity terms and the expression of the energy.⁵⁻⁷

In the thermodynamic limit and for the ground state the solutions to Eq. (3) can be classified in analogy to the n -channel Kondo problem:^{2,7} (i) $N-2M$ real charge rapidities k representing unpaired propagating electrons; (ii) M pairs of complex conjugated charge rapidities, $k=\lambda \pm ic/2$, corresponding to bound states of the Cooper pair type; (iii) $m_1^{(l)}$ real orbital rapidities of the set l , and $m_2^{(l)}$ two strings forming interband bound states of two electrons, $\xi^{(l)} = \xi_2^{(l)} \pm ic/2$. Here λ , and $\xi_2^{(l)}$ are real parameters representing the motion of the center of mass of the bound state. Note that necessarily $m^{(l)} = m_1^{(l)} + 2m_2^{(l)}$.

The solutions are now inserted into the Bethe ansatz Eqs. (3), which are then made logarithmic since they represent relations among phase shifts. They are defined modulo 2π and yield sets of integers (or half-integers), one for each class of states, which are the quantum numbers of the many-body problem. All integers (half-integers) within a given set have to be different, since the rapidities have to be different to guarantee the linear independence of the wave functions. A quantum number is either represented in a set (particle) or missing (hole) giving rise to Fermi statistics for all rapidities. In the thermodynamic limit the distribution of rapidities becomes dense and we introduce density functions for the particles and holes of each class of states: $\rho(k)$ and $\rho_h(k)$ are the densities for states in class (i), $\sigma(\lambda)$ and $\sigma_h(\lambda)$ the densities for class (ii), and $\phi_j^{(l)}(\xi)$ and $\phi_h^{(l)}(\xi)$ the densities for the real ξ ($j=1$) and two strings ($j=2$), $l=1, \dots, n$. Differentiating with respect to the rapidities we obtain a set of linear integral equations for the density distributions; Fourier transforming we have^{2,5-7}

$$\begin{aligned} \delta(\omega) &= \hat{\rho}_h(\omega) + \hat{\rho}(\omega) + f_1(\omega) \hat{\sigma}(\omega) - f_1(\omega) \hat{\phi}_1^{(1)}(\omega) \\ &\quad - f_2(\omega) \hat{\phi}_2^{(1)}(\omega), \\ 2\delta(\omega) &= \hat{\sigma}_h(\omega) + [1 + f_2(\omega)] \hat{\sigma}(\omega) + f_1(\omega) \hat{\rho}(\omega) \\ &\quad - f_2(\omega) \hat{\phi}_1^{(1)}(\omega) - [f_1(\omega) + f_3(\omega)] \hat{\phi}_2^{(1)}(\omega), \\ \hat{\phi}_{1h}^{(l)}(\omega) &+ [1 + f_2(\omega)] \hat{\phi}_1^{(l)}(\omega) + [f_1(\omega) + f_3(\omega)] \hat{\phi}_2^{(l)}(\omega) \\ &= [\hat{\phi}_1^{(l-1)}(\omega) + \hat{\phi}_1^{(l+1)}(\omega)] f_1(\omega) + [\hat{\phi}_2^{(l-1)}(\omega) \\ &\quad + \hat{\phi}_2^{(l+1)}(\omega)] f_2(\omega), \\ \hat{\phi}_{2h}^{(l)}(\omega) &+ [1 + 2f_2(\omega) + f_4(\omega)] \hat{\phi}_2^{(l)}(\omega) \\ &\quad + [f_1(\omega) + f_3(\omega)] \hat{\phi}_1^{(l)}(\omega) \\ &= [\hat{\phi}_1^{(l-1)}(\omega) + \hat{\phi}_1^{(l+1)}(\omega)] f_2(\omega) + [\hat{\phi}_2^{(l-1)}(\omega) \\ &\quad + \hat{\phi}_2^{(l+1)}(\omega)] [f_1(\omega) + f_3(\omega)], \end{aligned} \quad (4)$$

where the hat denotes Fourier transform, $\hat{\phi}_1^{(0)}(\omega) \equiv \hat{\rho}(\omega)$, $\hat{\phi}_2^{(0)}(\omega) \equiv \hat{\sigma}(\omega)$, $\hat{\phi}_1^{(n)}(\omega) = \hat{\phi}_2^{(n)}(\omega) = 0$, and $f_j(\omega) = \exp(-j|\omega c|/2)$.

The kinetic energy, the number of electrons, and the magnetization are given by

$$\begin{aligned} \frac{E}{L} &= \int dk k^2 \rho(k) + 2 \int d\lambda (\lambda^2 - c^2/4) \sigma(\lambda), \\ \frac{N}{L} &= \int dk \rho(k) + 2 \int d\lambda \sigma(\lambda), \quad \frac{S_z}{L} = \frac{1}{2} \int dk \rho(k). \end{aligned} \quad (5)$$

We now restrict ourselves to the situation of degenerate bands, i.e., the absence of crystalline fields. For degenerate bands the ξ rapidities (both the real rapidities and the two strings) fill the entire real axis, so that the hole functions $\phi_{1h}^{(l)}(\xi)$ and $\phi_{2h}^{(l)}(\xi)$ vanish identically. This is mathematically similar to the orbital singlet condition in the n -channel Kondo problem. The densities for the orbital rapidities can then be expressed in terms of ρ and σ and eliminated from Eqs. (4)

$$\begin{aligned} \hat{\phi}_1^{(l)}(\omega) &= \hat{F}_l(\omega) \hat{\rho}(\omega), \quad \hat{\phi}_2^{(l)}(\omega) = \hat{F}_l(\omega) \hat{\sigma}(\omega), \\ \hat{F}_l(\omega) &= \sin[(n-l)\omega c/2] / \sinh(n\omega c/2), \end{aligned} \quad (6)$$

$$\begin{aligned} \rho_h(k) + \rho(k) &= \frac{1}{2\pi} + \int_{-B}^B dk' G_1(k-k') \rho(k') \\ &\quad - \int_{-Q}^Q d\lambda D(\lambda-k) \sigma(\lambda), \end{aligned} \quad (7a)$$

$$\begin{aligned} \sigma_h(\lambda) + \sigma(\lambda) &= \frac{1}{\pi} + \int_{-Q}^Q d\lambda' G_2(\lambda-\lambda') \sigma(\lambda') \\ &\quad - \int_{-B}^B dk D(k-\lambda) \rho(k), \end{aligned} \quad (7b)$$

where $G_j(k)$ and $D(k)$ are the Fourier transforms of $\hat{G}_j(\omega) = \exp(-j|\omega c|/2) [\sinh((n-j)\omega c/2) / \sinh(n\omega c/2)]$, $\hat{D}(\omega) = \exp(-(n-2)|\omega c|/2) [\sinh(\omega c/2) / \sinh(n\omega c/2)]$.

From energy considerations we have that $\rho(k)$ and $\sigma(\lambda)$ are symmetric functions, being nonzero only in the intervals $[-B, B]$ and $[-Q, Q]$, respectively; the hole distributions are the complementary functions. B and Q are determined through Eq. (5) by the number of electrons and the magnetization.

We define energy potentials for each class of states, i.e., $\epsilon(k)$, $\psi(\lambda)$, and $\kappa_j^{(l)}(\xi)$, which are related to the density functions via

$$\begin{aligned} \rho_h(k) + \rho(k) &= -\partial \epsilon(k) / \partial (2\pi\mu), \\ \sigma_h(\lambda) + \sigma(\lambda) &= -\partial \psi(\lambda) / \partial (2\pi\mu), \\ \phi_{jh}^{(l)}(\xi) + \phi_j^{(l)}(\xi) &= -\partial \kappa_j^{(l)}(\xi) / \partial (2\pi\mu), \end{aligned}$$

where μ is the chemical potential. States for which the potential is negative (positive) correspond to particles (holes), in accordance with the Fermi statistics obeyed by the rapidities. Note that at $T=0$ $\epsilon(\pm B)=0$, $\psi(\pm Q)=0$ and for degenerate bands, $\kappa_j^{(l)}(\pm\infty)=0$ for $j=1,2$. The integral equations satisfied by $\epsilon(k)$ and $\psi(\lambda)$ are (degenerate bands)

$$\epsilon(k) = k^2 - \mu - H/2 + \int_{-B}^B dk' G_1(k-k') \epsilon(k') - \int_{-Q}^Q d\lambda D(\lambda-k) \psi(\lambda), \quad (9a)$$

$$\psi(\lambda) = 2 \left(\lambda^2 - \frac{1}{4} c^2 - \mu \right) + \int_{-Q}^Q d\lambda' G_2(\lambda-\lambda') \psi(\lambda') - \int_{-B}^B dk D(\lambda-k) \epsilon(k). \quad (9b)$$

The orbital potentials with string index $j=1,2$ are negative everywhere

$$\kappa_1^{(j)}(\xi) = \int_{-B}^B dk F_j(\xi-k) \epsilon(k),$$

$$\kappa_2^{(j)}(\xi) = \int_{-Q}^Q d\lambda F_j(\xi-\lambda) \psi(\lambda). \quad (9c)$$

Equations (9) contain the same physical information as Eqs. (6) and (7); the zeroes of $\epsilon(k)$ and $\psi(\lambda)$ provide relations between B , Q , μ , and the magnetic field H .

In zero magnetic field, $H=B=0$, the potential $\epsilon(k)$ is positive for all k . Hence, the band of unpaired electrons is empty and all electrons are spin paired in Cooper-pair-like bound states. Equations (7b) and (9b) then reduce to single Fredholm integral equations for $\sigma(\lambda)$ and $\psi(\lambda)$. A magnetic field H larger than a critical value

$$H_c = -2\mu - 2 \int_{-Q}^Q d\lambda D(\lambda) \psi(\lambda) \quad (10)$$

is needed to overcome the binding energy of the Cooper pairs, and there is no response to a field smaller than H_c . The depaired electrons for $H > H_c$ occupy the unpaired-electron band, $\epsilon(k)$, and give rise to magnetization. The critical field is a decreasing function of the band filling and increases with c . H_c vanishes as $c \rightarrow 0$. The spin-paired bound states are hard-core bosons; although bosons from the symmetry of the wave function and their spin, the Cooper pairs must have all different quantum numbers, i.e., they have a Fermi surface. They do not undergo a condensation and hence there is no long-range order.

The magnetization is proportional to $(H-H_c)^{1/2}$ if the field is only slightly above the critical one,^{2,8,9} as a consequence of the one-dimensional van Hove singularity of the empty $\epsilon(k)$ band. Hence, $H-H_c \propto B^2$ and $S_z \propto B$, while the susceptibility diverges proportionally to $(H-H_c)^{-1/2}$. The specific heat at low temperatures is obtained by a Sommerfeld expansion of the free energy and the potentials. C is proportional to T , except when the Fermi level is at a van Hove singularity, where it is proportional to $T^{1/2}$.^{2,8,9} The

Cooper-pair bound states do not cease to exist at finite temperature ($T_c=0$) and are still the dominant states if T is low. At $T \neq 0$ the system responds to a small magnetic field, but the susceptibility is exponentially small as $T \rightarrow 0$.

As $c \rightarrow 0$ the integration kernels in Eqs. (7) and (9) reduce to δ functions yielding algebraic equations. In zero field we obtain $\sigma(\lambda) = n/(2\pi)$ and $\rho_h(\lambda) = 0$ for $|\lambda| < Q$, and $\sigma_h(\lambda) = 1/\pi$ and $\rho_h(\lambda) = 1/(2\pi)$ if $|\lambda| > Q$. Similarly, we have $\psi(\lambda) = n(\lambda^2 - Q^2)$ and $\epsilon(\lambda) = 0$ for $|\lambda| < Q$, and $\psi(\lambda) = 2(\lambda^2 - Q^2)$ and $\epsilon(\lambda) = \lambda^2 - Q^2$ for $|\lambda| > Q$. The critical field vanishes in this limit. As $c \rightarrow \infty$, on the other hand, the Cooper-like bound states become strongly bound and the H_c required to depair them is very large. Another interesting limit is $n \rightarrow \infty$, where the integration kernels reduce to Lorentzians. Note that the limits $c \rightarrow 0$ and $n \rightarrow \infty$ cannot be interchanged.

Finally, we briefly discuss the excitation spectrum. There are three types of excitations: (i) charge, (ii) spin, and (iii) interband excitations. Elemental excitations are obtained by adding or removing a rapidity from the corresponding set. The energy of the excitation is given by the absolute value of the energy potential, e.g., for a charge with rapidity λ_0 we have $\Delta E_{ch}(\lambda_0) = |\psi(\lambda_0)|$. The charge excitation vanishes for $\lambda_0 = \pm Q$, which corresponds to the Fermi surface; for $|\lambda_0| < Q$ the excitations are holes and for $|\lambda_0| > Q$ they correspond to particles. The spin excitation energy $\Delta E_s(k) = |\epsilon(k)|$ is finite if $H_c > H$ [spin gap of $2(H_c - H)$]; however, if $H > H_c$ also this band has a Fermi surface given by $\pm B$. For degenerate bands the interband excitations are of the hole type; their excitation energies are $|\kappa_j^{(i)}(\xi)|$ which vanish for $\xi = \pm \infty$. The momentum of each excitation is parametrized by the added or removed rapidity, e.g., for the charges it is $p_{ch}(\lambda_0) = 2\pi \int_0^{\lambda_0} d\lambda [\sigma_h(\lambda) + \sigma(\lambda)]$ similar expressions hold for the other classes of excitations. The Fermi momentum for the charges is $p_F = (\pi/2)(N/L)$, while the one for the spin excitations ($H > H_c$) is determined by the magnetization.

The support of the Department of Energy under Grant No. DE-FG05-91ER45443 is acknowledged.

¹ C. A. Balseiro, M. Avignon, A. G. Rojo, and B. Alascio, Phys. Rev. Lett. **62**, 2626 (1989); K. A. Muttalib and V. J. Emery, *ibid.* **57**, 1370 (1986); H. Aoki and K. Kuroki, Phys. Rev. B **42**, 2125 (1990); P. Schlottmann, Phys. Rev. Lett. **69**, 2396 (1992); F. Buda, D. L. Cox, and M. Jarrell, Phys. Rev. B **49**, 1255 (1994).

² P. Schlottmann, Phys. Rev. Lett. **68**, 1916 (1992).

³ D. I. Komsikii, Physica B **171**, 44 (1971), and references therein.

⁴ M. Gaudin, Phys. Lett. A **24**, 55 (1967); C. N. Yang, Phys. Rev. Lett. **19**, 1312 (1967); B. Sutherland, *ibid.* **20**, 98 (1968).

⁵ P. B. Wiegmann and A. M. Tselik, Pis'ma Zh. Eksp. Teor. Fiz. **38**, 493 (1983) [JETP Lett. **38**, 596 (1983)]; A. M. Tselik and P. B. Wiegmann, Z. Phys. **54**, 201 (1984).

⁶ N. Andrei and C. Destri, Phys. Rev. Lett. **52**, 364 (1984).

⁷ A. M. Tselik, J. Phys. C **18**, 159 (1985).

⁸ K. Lee and P. Schlottmann, Phys. Rev. B **40**, 9104 (1989).

⁹ P. Schlottmann, Phys. Rev. B **43**, 11451 (1991).

Two-band model for Kondo insulators: Thermodynamic and scaling properties

M. A. Continentino and G. M. Japiassu

Instituto de Física, Universidade Federal Fluminense, Outeiro de S. J. Batista s/n, Niteroi 24020 RJ, Brazil

A. Tróper

Centro Brasileiro de Pesquisas Físicas, Rua Dr. Xavier Sigaud, 150, Rio de Janeiro, 22290-180 RJ, Brazil

Recently a new family of heavy fermions (e.g., $\text{Ce}_3\text{Bi}_4\text{Pt}_3$) has been discovered which is characterized by an insulating ground state. Similar behavior has been found in some transition metal compounds like FeSi. We introduce a two-band model to describe the physical properties of these systems. Coulomb correlations in the narrow band are treated beyond the mean field approach. We find that a critical value of the hybridization \tilde{V}_c is required to open a gap that produces an insulating ground state. We discuss the scaling properties of these systems close to \tilde{V}_c . The temperature-dependent magnetic susceptibility calculated in our model is in good agreement with experimental results.

Recently a new family of heavy fermions has been discovered which is characterized by an insulating ground state.¹⁻³ Similar behavior has also been found in the transition-metal-based compound FeSi. Although the general approach to the former systems is based on an Anderson lattice Hamiltonian,^{4,5} we shall introduce here a two-band model aiming for a unified description of both kinds of materials. The Hamiltonian describing our system is

$$H = \sum_{ij\sigma} t_{ij}^s c_{j\sigma}^+ c_{i\sigma} + \sum_{ij\sigma} t_{ij}^f f_{j\sigma}^+ f_{i\sigma} + \frac{U}{2} \sum_{i\sigma} n_{i\sigma}^f n_{i-\sigma}^f + V \sum_{i\sigma} (c_{i\sigma}^+ f_{i\sigma} + f_{i\sigma}^+ c_{i\sigma}), \quad (1)$$

where $t_{ij}^{s/f}$ gives the hopping probability for electrons in the large, uncorrelated s -like band and in the narrow d or f band, which from now on we refer to generally as an f band. The $c_{i\sigma}^+$, $c_{i\sigma}$ create and destroy, respectively, electrons in the wide band and $f_{i\sigma}^+$, $f_{i\sigma}$ are creation and annihilation operators for electrons in the narrow f band. The Coulomb interaction between f electrons in the same site is given by U . V is the mixing term and $n_{i\sigma}^f = f_{i\sigma}^+ f_{i\sigma}$. If it were not for the Coulomb term, the Hamiltonian above could be exactly diagonalized giving rise to two hybrid bands. However, the many body term due to the strong interaction U makes this a difficult problem for which an approximation must be introduced. Here we shall extend for the two-band problem the so-called Hubbard I approximation⁶ which goes beyond the mean-field treatment. It is very appropriate for the problem studied here where the systems we are describing have insulating ground states and no long-range magnetic order. Employing the equation of motion method,⁷ we find for the f electron propagator, in the limit $U \rightarrow \infty$,

$$G_{k\sigma}^{ff}(w) = \frac{(1 - \langle n_{-\sigma}^f \rangle)(w - \epsilon_k^s)}{2\pi \{ [w - \epsilon_k^f(1 - \langle n_{-\sigma}^f \rangle)](w - \epsilon_k^s) - V^2(1 - \langle n_{-\sigma}^f \rangle) \}} \quad (2)$$

and a similar expression is obtained for the s -electron propagator.

We can see from Eq. (2) that the main role of the interactions is to renormalize the mixing term V^2 and the f -electron propagator through the contraction factor $(1 - \langle n_{-\sigma}^f \rangle)$. The effective mass m_f defined by $\epsilon_k^f = \hbar^2 k^2 / 2m_f$ is also renormalized. Incidentally the contraction factor obtained here is different from the one which arises using the Slave-Boson^{4,5} or Gutzwiller⁸ approaches where it is given by $(1 - \langle n^f \rangle)$ with $\langle n^f \rangle = \sum_{\sigma} \langle n_{\sigma}^f \rangle$.

Since we are interested in paramagnetic solutions, $\langle n_{-\sigma}^f \rangle = \langle n_{\sigma}^f \rangle$. Besides due to a special symmetry of the bands we shall consider here and the fact that we have one electron f per unit cell, the largest value these averages can assume is $\frac{1}{2}$. In this case the contraction factor is given by $(1 - \langle n_{-\sigma}^f \rangle) = \frac{3}{4}$ and the effective hybridization \tilde{V} remains finite at all temperatures.

The new excitations of the system are given by the poles of the propagators

$$(w - \epsilon_k^s)(w - \tilde{\epsilon}_k^f) - \tilde{V}^2 = 0, \quad (3)$$

where

$$\tilde{V} = V[1 - \langle n_{-\sigma}^f \rangle]^{1/2}, \quad (4)$$

$$\tilde{\epsilon}_k^f = \epsilon_k^f(1 - \langle n_{-\sigma}^f \rangle). \quad (5)$$

Equation (3) has the following roots:

$$w_{1,2}(k) = \frac{1}{2} (\epsilon_k^s + \tilde{\epsilon}_k^f \pm \sqrt{(\epsilon_k^s - \tilde{\epsilon}_k^f)^2 + 4\tilde{V}^2}). \quad (6)$$

In order to obtain explicit results for the density of states we introduce a model of homothetic bands⁹ which consists in taking

$$\begin{aligned} \epsilon_k^s &= \epsilon_k, \\ \tilde{\epsilon}_k^f &= \alpha \epsilon_k + \beta. \end{aligned} \quad (7)$$

The quantity α may be interpreted as taking into account the different effective masses of the f and s electrons, i.e., $(m_s/m_f^*) = \alpha$. We have included in the parameter α the renormalization of the f -electron mass due to the contraction factor $(1 - \langle n_{-\sigma}^f \rangle)$ arising from the Coulomb, repulsion between

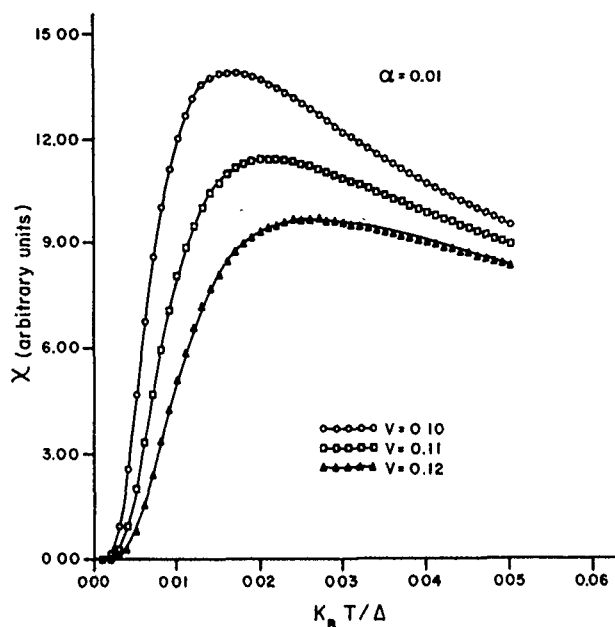


FIG. 1. The magnetic susceptibility, in arbitrary units, as a function of temperature for different parameters (see the text). Δ is the bandwidth of the large band.

electrons of opposite spins in the same site. The quantity β which gives the shift of the f band with respect to the large s band also includes the contraction factor. Introducing two new functions $g_1(w)$ and $g_2(w)$ through the equation

$$[w - w_1(k)][w - w_2(k)] = \alpha[g_1(w) - \epsilon_k][g_2(w) - \epsilon_k] \quad (8)$$

we get, in terms of these new functions, the s and f contributions to the density of states of the new hybrid bands. For the f contribution to the first hybrid band we find

$$n_{o1}^f(w) = \frac{|f'[w, g_1(w)]|}{\alpha|g_1(w) - g_2(w)|} \sum_k \delta[g_1(w) - \epsilon_k] \quad (9)$$

and for the second

$$n_{o2}^f(w) = \frac{|f'[w, g_2(w)]|}{\alpha|g_1(w) - g_2(w)|} \sum_k \delta[g_2(w) - \epsilon_k], \quad (10)$$

where

$$f_k^f(w) = (1 - \langle n_{-o}^f \rangle)(w - \epsilon_k^f) \quad (11)$$

with similar equations for the s contribution to the density of states. Now it remains to find the functions $g_{1,2}(w)$ which can be obtained from Eq. (8). We get

$$g_{1,2}(w) = \frac{1}{2\alpha} \left((1 + \alpha)w - \frac{1}{2} \Delta(1 - \alpha) \pm \left[\left[(1 - \alpha)w - \frac{1}{2} \Delta(1 - \alpha) \right]^2 + 4\alpha\tilde{V}^2 \right]^{1/2} \right). \quad (12)$$

Δ is the width of the large s band and appears in the above equation because the parameter β , which determines the position of the f band, was fixed by the condition that the center of this f band coincides with that of the large band at

the energy $\Delta/2$ for $V=0$. For symmetric bands this arrangement is particularly useful since when the hybridization is turned on and is sufficiently strong, we obtain two symmetric hybrid bands separated by a gap, each one of which can accommodate exactly two electrons. Then in the case of the 1.5 electrons per unit cell that we are considering, the Fermi level sits in the middle of the gap and does not shift with temperature. Further for symmetric hybrid bands it can be easily shown that the factors $\langle n_{\sigma}^f \rangle$ are temperature independent implying that this is also the case for the parameters α and β . Since the total number of f electrons is $\langle n^f \rangle = \frac{1}{2}$, we get $\langle n_{\sigma}^f \rangle = \frac{1}{4}$, for paramagnetic solutions and the contraction factor is given by $(1 - \langle n_{-o}^f \rangle) = \frac{3}{4}$ independent of temperature. Within a contraction solution the same ground state occurs for $\langle n_{\sigma}^f \rangle + \langle n_{-o}^f \rangle = \frac{1}{2}$ with the total number of electrons being two per unit cell.

The equation for the gap can be obtained from the difference in energy between the top of the first hybrid band and the bottom of the second. We find

$$\Delta_G = \left(\frac{\Delta^2(1 - \alpha)^2}{4} + 4\tilde{V}^2 \right)^{1/2} - (1 + \alpha) \frac{\Delta}{2}. \quad (13)$$

Consequently for a two-band system the opening of a hybridization gap, contrary to what occurs for the Anderson lattice model, requires a critical value of the hybridization which is given by

$$\tilde{V}_c = \frac{\Delta}{2} \sqrt{\alpha}. \quad (14)$$

For transition metal compounds where the ratio $\alpha_d = (m_s/m_d^*)$ is larger than that for rare-earth systems $\alpha_f = (m_s/m_f^*)$, a larger value of the hybridization is required to open a gap. A comparison of the magnitude of the critical hybridization parameter with the usual values of the hybridization for Ce , U systems and for transition metals, shows that \tilde{V}_c may be sufficiently large to make the phenomenon of hybridization gaps rather unusual especially in transition-metal-based compounds where α_d is not such a small number. Note that the many-body contraction factor, which renormalizes both V^2 and α , cancels out in Eq. (14). Consequently whenever the interacting system is insulating the same holds for the noninteracting one ($U=0$) in agreement with Luttinger's theorem. Sufficiently close to \tilde{V}_c , the gap opens as

$$\Delta_G \cong \frac{4\sqrt{\alpha}}{1 + \alpha} (\tilde{V} - \tilde{V}_c). \quad (15)$$

Consequently, the gap exponent s , defined as $\Delta_G \sim (\tilde{V} - \tilde{V}_c)^s$, assumes within our approach the value $s=1$. This gap defines a characteristic temperature $T_c \sim |\tilde{V} - \tilde{V}_c|$, which for $\tilde{V} - \tilde{V}_c$ appears in the argument of the scaling functions¹⁰ of the thermodynamic quantities as $f(T/T_c)$. The scaling form of the energy density f , close to \tilde{V}_c is given by

$$f \sim |\tilde{V} - \tilde{V}_c|^{2-\alpha} f_0(T/T_c). \quad (16)$$

The physical behavior of the system dictates the limiting form of the scaling function $f_0(x)$. We have $f_0(x \rightarrow 0) \sim e^{-1/x}$, appropriate to an insulator and at high temperatures, as expected, one has a degenerate Fermi gas. The specific heat $C = T \partial^2 f / \partial T^2$ behaves as $C \sim$

$AT^{-3}e^{-T_c/T}$ for $T_c \ll T$ and $C=AT$ for $T \gg T_c$ where $A \sim |V - \bar{V}_c|^{2-\alpha-2\nu}$. The mean field exponents $\alpha=0$, $\nu=1$ yield $A=\text{constant}$, independent of pressure for example. Since in our approach the effect of an external magnetic field is essentially to shift the bands, the scaling form of the free energy density in the pressure of such a field h is $f \sim |V - \bar{V}_c|^{2-\alpha} f_1(T/T_c, h/h_c)$, where $h_c \sim |\bar{V} - \bar{V}_c|$. From this equation the susceptibility can be easily obtained.

We can see that the effect of the interactions are solely incorporated in the parameter α in Eq. (15), its role being to reduce the gap, as compared to the noninteracting system. However, the inclusion of interactions does not modify the critical exponent s . This mean field exponent ($s=1$) may well be appropriate to describe the strongly correlated Kondo insulators due to dimensionality shifts associated with quantum phase transitions.¹⁰ In Fig. 1 we show the magnetic susceptibilities for different values of the ratio of effective masses α and effective mixing \bar{V} , with $\bar{V} > \bar{V}_c$. They show the same qualitative behavior of the experimental data and in particular that for FeSi where the susceptibility actually goes to zero exponentially after subtracting a tail due to paramagnetic impurities.¹ Other thermodynamic quantities can be readily obtained using the hybrid band density of states and the Kubo-Greenwood formula,¹¹ and will be presented in a future publication.¹²

The metal *ytterbium* has physical properties which are useful to compare with those of the materials studied here. For moderate applied pressures, Yb has a metal-insulator transition due to the opening of a hybridization gap.¹³ This material can then be considered as a typical case for which the condition $\bar{V} > \bar{V}_c$ is not fulfilled but can be reached by

applying pressure. On the other hand, the essential difference between Yb and the Kondo insulators is the strength of the many-body interaction which should be negligible in the former system. It is interesting that a large T^2 term occurs in the resistivity of metallic Yb which is enhanced as the metal-insulator transition is approached even though the f electrons are always sufficiently below the Fermi level and do not play any role in this transition.¹⁴

We would like to thank Conselho Nacional de Desenvolvimento Científico e Tecnológico-CNPq, Brazil, for partial financial support.

¹ G. Aeppli and Z. Fisk, *Comments Cond. Mat. Phys.* **16**, 155 (1992).

² M. F. Hundley, P. C. Canfield, J. D. Thompson, Z. Fisk, and J. M. Lawrence, *Phys. Rev. B* **42**, 6842 (1990).

³ J. D. Thompson, W. P. Benemann, P. C. Canfield, M. F. Hundley, G. H. Kwei, A. Laurda, Z. Fisk, R. S. Kwok, J. M. Lawrence, and A. Severing, in *Transport and Thermal Properties of f Electron Systems*, edited by H. Fujii, T. Fujita, and G. Oomi (Plenum, New York, in press).

⁴ P. Riseborough, *Phys. Rev. B* **45**, 13984 (1992).

⁵ C. Sanchez-Castro, K. Bedell, and B. R. Cooper, *Phys. Rev. B* **47**, 6879 (1993).

⁶ J. Hubbard, *Proc. R. Soc. London Ser. A* **276**, 238 (1963).

⁷ See A. L. Fetter and J. D. Walecka, *Quantum Theory of Many-Particle Systems* (McGraw-Hill, New York, 1975).

⁸ T. M. Rice and K. Ueda, *Phys. Rev. Lett.* **55**, 995 (1985).

⁹ R. Kishore and S. K. Joshi, *Phys. Rev. B* **2**, 1411 (1970).

¹⁰ M. A. Continentino, G. M. Japiassu, and A. Troper, *Phys. Rev. B* **39**, 9734 (1989).

¹¹ N. F. Mott and E. A. Davies, in *Electronic Process in Non-Crystalline Materials* (Clarendon, Oxford, 1971).

¹² M. A. Continentino, G. M. Japiassu, and A. Troper (to be published).

¹³ D. B. McWhan, T. M. Rice, and P. H. Schmidt, *Phys. Rev. B* **177**, 1063 (1969).

¹⁴ R. Jullien and D. Jerome, *J. Phys. Chem. Solids* **32**, 257 (1971).

Local magnetic moments and intermediate valence state of cerium impurities in ferromagnetic rare-earth metals

C. E. Leal

*Instituto Nacional de Pesquisas Especiais (INPE), Av. dos Astronautas 1758,
São José dos Campos, SP, Brazil*

A. Troper

*Centro Brasileiro de Pesquisas Físicas (CBPF), Rua Dr. Xavier Sigaud 150, 22290,
Rio de Janeiro, RJ, Brazil*

Using experimental data for magnetic hyperfine fields obtained through the technique of time differential perturbed γ - γ angular correlations (TDPAC) in the highly diluted system CeR (R=Gd, Tb), we theoretically discuss the formation of the local moments at the Ce impurity site, adopting an intermediate valence model. The ferromagnetic rare-earth host is considered as a transition metal in the beginning of a $5d$ series and the CeR alloys are described as strongly d - f correlated and hybridized systems. One calculates the hyperfine field which reproduces quite well the experimental data. The Ce valence in these systems is also obtained, giving values in good agreement with experimental results and theoretical claims involving Gd and Tb band calculations. Some comments about the diluted systems YbR (R=Gd, Tb) are also made.

At the present very extensive experimental data on the hyperfine fields at the sites of diluted n - d transition impurity ions ($n=3,4$) in ferromagnetic Gd are available in the literature.¹ More recently, Boysen *et al.*² reported systematic experimental hyperfine data of diluted $3d$ ions in ferromagnetic Tb and also some hyperfine data of diluted $5d$ ions in this same host were obtained.³ From the measured magnetic hyperfine fields in these locally perturbed rare-earth hosts one can estimate the local magnetic moments formed at the impurity sites. For instance, the local magnetic moments change sign when one goes from the first-half to the second-half of the $3d$ series.^{1,2,4,5}

In order to explain these data, it has been invoked^{2,4} that the main interaction between rare-earth host ions (Gd or Tb) is due to a direct d - d mechanism, thus neglecting the Ruderman-Kittel-Kasuya-Yosida (RKKY) interaction between rare-earth $4f$ moments. The proposal is based on Moriya⁶ rules: if one regards a ferromagnetic rare-earth host like Gd or Tb as a transition metal in the beginning of a $5d$ series, one always should expect a sign reversal in the local moments when one passes from the first- to second-half of the n - d series. These predictions agree qualitatively for the case of $3d$ impurities. On the other hand, all $5d$ impurities diluted in Gd have negative moments (with the possible exception of Lu)⁶ and the available data of $5d$ ions diluted in Tb (e.g., TaTb and IrTb) show a total negative magnetic hyperfine field and small negative moments.^{3,5}

So, it was suggested that an alternative theoretical approach⁵⁻⁷ based on an extended RKKY picture which can describe adequately the hyperfine field systematics of all d -transition impurities placed in the heavy ferromagnetic hosts Gd and Tb. This picture brings out the fundamental role played by the $4f$ moments in driving the ferromagnetic properties of these metals and takes into account properly the transition metal-like character of these materials, i.e., the existence of conducting s and d bands. Within this picture, we explained adequately the hyperfine field systematics of the d impurities placed in Gd and Tb.

In this work we want to discuss some available hyperfine field data on CeR and YbR (R=Gd, Tb) alloys trying to insert them in the hyperfine field systematics of $5d$ impurities placed in these rare-earth hosts. Experimental results concerning isomer shifts of the $5d$ Mössbauer element ^{193}Ir diluted in Gd and Tb show that they are nearly constant, the value of 2 mm/s being in good agreement with the systematic of isomer shifts of ^{193}Ir in $5d$ transition metal hosts.^{3,8} The same feature of almost constant isomer shifts is obtained for the $3d$ Mössbauer element Fe placed in FeR (R=Gd, Tb).^{2,9} This suggests that the host s - p and d -band occupations are quite the same for these rare-earth metals. Band calculations^{10,11} have shown indeed that Gd and Tb exhibit d bands contributing a high density of states around the Fermi level.

One can estimate⁷ from the above-mentioned band calculations the d - and s - p band occupation numbers for both metals as being, respectively, $\langle n_d \rangle = 2.2$ electrons (per host atom) and $\langle n_c \rangle = 0.8$ electrons (per host atom) giving a 3^+ configuration: $\langle n_d \rangle + \langle n_c \rangle = 3.0$ electrons (per host atom). Gd is the only rare-earth metal which goes directly from the paramagnetic phase to the ferromagnetic one with a Curie temperature T_C equal to 298 K. The saturation magnetic moment at very low temperature is $7.63\mu_B$ which is larger than the $7\mu_B$ value corresponding to the trivalent Gd^{3+} . Tb metal undergoes two magnetic transitions characterized by the Néel temperature T_N ($T_N = 229$ K) and the Curie temperature T_C ($T_C = 221$ K) and at very low temperature the saturation magnetic moment is $9.34\mu_B$, which has to be compared to the theoretical value of $9\mu_B$, expected for the trivalent ion Tb^{3+} .

The ferromagnetism of these "normal" rare-earth metals is described in a simple Stoner-type picture by two d -spin subbands split by an exchange energy, driven mainly from the exchange interaction between the effective $4f$ moment and the d electrons. Moreover, one assumes that, due to host hybridization, the s - p and d -conduction bands have antiparallel magnetizations, as occur in Fe metal.^{5,6,12}

The technique of time differential perturbed γ - γ angular correlations (TDPAC) has been widely used in the last years to obtain new information about the formation of local magnetic moments of Ce impurities in metallic elements.¹³ In particular the CeR (R=Gd, Tb) systems were studied through this technique by Thiel *et al.*,^{14,15} suggested that the single Ce ion in CeR systems (R=Gd, Tb) is in an intermediate valence (IV) state.

We assume that in an IV regime the Ce 4f level ϵ_f , which is fractionally occupied, is strongly admixed with host conduction states and lies very close to the Fermi energy of the system, i.e., $E_f - \epsilon_f < \Delta$, Δ being the 4f resonance width. The magnetic hyperfine field at rare-earth impurity nuclei placed in Gd or Tb metals is determined by a combination arising from both conduction electron polarization (CEP) and core polarization (CP) fields. The CEP field, which is due to the polarization of s - p conduction electrons, is given by

$$H_{\text{hf}}^{(sp)} = A(Z) \tilde{m}_c(0), \quad (1)$$

where $A(Z)$ is the hyperfine contact parameter¹⁶ and $\tilde{m}_c(0)$ is the s - p magnetization at the impurity site. Using Campbell's data¹⁶ for La and Lu one gets for Ce the value $A(Z) = 3.23 \times 10^3 \mu_B^{-1}$ kOe. Due to the 5d character ascribed to the anomalous rare-earth Ce impurity, a CP arises from its localized d -magnetic moment which polarizes the impurity electron core, similar to the case of a transition element impurity. It can be written as

$$H_{\text{hf}}^{(d)} = -A_{\text{CP}}^{(5d)} \tilde{m}_d(0), \quad (2)$$

where $A_{\text{CP}}^{(5d)}$ is a positive CP coupling parameter, of the order of $1200 \mu_B^{-1}$ kOe for the 5d series and $\tilde{m}_d(0)$ is the d magnetization at the impurity site. The 4f resonance in the local density of states ("impurity site") introduces an extra contribution to the CP hyperfine field. This extra CP hyperfine field is due to the occurrence of a d - f transferred local f magnetization $\tilde{m}_f(0)$.¹² One has

$$H_{\text{hf}}^{(f)} = -A_{\text{CP}}^{(4f)} \tilde{m}_f(0), \quad (3)$$

where $A_{\text{CP}}^{(4f)}$ is a positive coupling constant, the value adopted here being $1500 \mu_B^{-1}$ kOe.

The total hyperfine field is then

$$H_{\text{hf}} = A(Z) \tilde{m}_c(0) - A_{\text{CP}}^{(5d)} \tilde{m}_d(0) - A_{\text{CP}}^{(4f)} \tilde{m}_f(0). \quad (4)$$

In Ref. 12 it is shown that $\tilde{m}_f(0)$ is parallel to $\tilde{m}_d(0)$:

$$\tilde{m}_f(0) = \xi_{df} \tilde{m}_d(0) = U_{df} \rho_f(E_F) \tilde{m}_d(0), \quad (5)$$

where U_{df} is an effective d - f Coulomb type interaction and $\rho_f(E_F)$ is the density of states of the 4f resonance at the Fermi energy. Thus, the total hyperfine field is

$$H_{\text{hf}} = A(Z) \tilde{m}_c(0) - A_{\text{CP}}^{(5d)} [1 + (A_{\text{CP}}^{(4f)} / A_{\text{CP}}^{(5d)}) \xi_{df}] \tilde{m}_d(0). \quad (6)$$

The self-consistent calculation of $\tilde{m}_c(0)$ and $\tilde{m}_d(0)$, which are the solution of a Koster-Slater problem are given in detail in Refs. 5 and 6;

$$\tilde{m}_\alpha(0)$$

$$= \sum_{\sigma} \int_{-\infty}^{\mu} \frac{\rho_{\alpha\sigma}(E) f(E) dE}{[1 - V_{\alpha\sigma} F_{\alpha\sigma}(E)]^2 + [\pi V_{\alpha\sigma} \rho_{\alpha\sigma}(E)]^2}, \quad (7)$$

where $\rho_{\alpha\sigma}(E)$ is the unperturbed density of states of a α subband with spin σ ($\alpha=s$ - p or d), $F_{\alpha\sigma}(E)$ is its Hilbert transform, $f(E)$ is the Fermi Dirac function, and μ is the chemical potential. At $T=0$ K, one has $\mu=E_F$. The localized potentials are self-consistently obtained via the Friedel sum rule

$$\Delta Z_{\alpha} = \sum_{\sigma} \Delta Z_{\sigma}^{\alpha}(V_{\alpha\sigma}) = -\frac{K_{\alpha}}{\pi} \sum_{\sigma} \arctan \frac{\pi V_{\alpha\sigma} \rho_{\alpha\sigma}(E_F)}{1 - V_{\alpha\sigma} F_{\alpha\sigma}(E_F)}, \quad (8)$$

where $\Delta Z_{\sigma}^{\alpha}$ is the charge displaced by the potential $V_{\alpha\sigma}$ in the σ subband of α electrons and K_{α} accounts for degeneracy; one has $K_c=4$ and $K_d=5$.

Let us now focus our attention to the CeGd system. It is believed that the Ce valence in an IV state lies in the range (3.2-3.4). This implies in our picture that ν electrons in the range 0.2-0.4 are transferred to the d band and are screened via Eq. (8), thus fixing a local d magnetization $\tilde{m}_d(0)$ obtained through Eq. (7). Thus, the total hyperfine field is fixed when ξ_{df} is specified, since all the other terms in Eq. (6) are known if one adopts the same parameters of Refs. 5 and 6. We adopted for $\xi_{df} = U_{df} \rho_f(E_F)$ the value $\xi_{df}=3.6$. This choice yields for $T=0$ K a total negative hyperfine field $H_{\text{hf}} = -537$ kOe which is in good agreement with the value obtained by Thiel *et al.*¹⁴ which is: $|H_{\text{hf}}| = 540$ kOe and with the whole systematic of 5d impurities diluted in Gd which are always negative. The choice $\xi_{df}=3.6$ yields a valence state of 3.25 ($\nu=0.25$) and therefore the Ce configuration is $4f^{0.75} 5d^{1.25} 6s^2$, which is consistent with the results obtained in Ref. 17. The self-consistently calculated local moments are $\tilde{m}_c(0) = -0.056 \mu_B$ and $\tilde{m}_d(0) = 0.054 \mu_B$.

Let us now discuss the CeTb system. At $T=0$ K, the experimental value estimated for the total hyperfine field is:¹⁵ $H_{\text{hf}} = 550$ (80) kOe. Assuming that the Ce valence state in CeTb is the same as in CeGd, i.e., $\nu=0.25$, our calculated self-consistent local moments are $\tilde{m}_c(0) = -0.0314 \mu_B$ and $\tilde{m}_d = 0.0280 \mu_B$. In order to fit the experimental value one adopts $\xi_{df}=9.86$ and then one obtains: $H_{\text{hf}} = -543$ kOe at $T=0$ K, in good agreement with the experimental result. Notice that ξ_{df} accounts for the high density of states of the f resonance $\rho_f(E_F)$ at the Fermi level and for the strong effective d - f correlation and so one can make a comparison between the adopted values of ξ_{df} for CeGd and CeTb. One has

$$\frac{\xi_{df}(\text{CeTb})}{\xi_{df}(\text{CeGd})} = \frac{9.86}{3.60} = 2.74. \quad (9)$$

Remembering that $\xi_{df} = U_{df} \rho_f(E_F)$ and assuming that U_{df} is almost the same for both systems and that $\rho_f(E_F)$ is roughly proportional to the d peak of the density of states at the Fermi level of the hosts, one has

$$\frac{\xi_{df}(\text{CeTb})}{\xi_{df}(\text{CeGd})} \approx \frac{\rho_d^{\text{Tb}}(E_F)}{\rho_d^{\text{Gd}}(E_F)} \quad (10)$$

From band calculations^{10,11} one has $\rho_d^{\text{Tb}}(E_F) = 66$ states per atom per Rydberg whereas $\rho_d^{\text{Gd}}(E_F) = 25$ states per atom per Rydberg; thus $[\rho_d^{\text{Tb}}(E_F)]/[\rho_d^{\text{Gd}}(E_F)] = 2.64$, in a good agreement with our adopted values.

The existence of such sharp peaks near the position of the Fermi level are responsible for the steep drop with temperature of the local d magnetizations and therefore of the effective core polarization contributions to the hyperfine field [see the last term in Eq. (6)], whereas the $s-p$ contribution remains almost constant with temperature. This effect should be more dramatic in CeTb than in CeGd as is indeed experimentally verified.^{14,15}

As a final comment let us briefly discuss the YbR systems. Yb is an anomalous rare earth with a 2^+ ionic configuration: $4f^{14} 5d^0 6s^2$. The hyperfine field of Yb embedded in Gd was obtained from Mössbauer experiments yielding the value: $H_{\text{hf}}(\text{YbGd}) = -280(10)$ kOe,¹⁸ which is almost temperature independent. These authors argued that the values of the hyperfine field, together with isomer shift measurements, support the assumption that Yb in YbGd is in a 2^+ state and has no f moment. We used the same $s-p$ local magnetization calculated for CeGd, since in both the Ce and Yb cases one has the same $6s^2$ ionic configuration. From Ref. 16 one gets (interpolating between the La and Lu coefficients): $A(Z) = 4.67 \times 10^3 \mu_B^{-1}$ kOe and then $H_{\text{hf}} = H_{\text{hf}}^{\text{sp}} = -260$ kOe, which agrees quite well with the experimental value.

As far as the YbTb system is concerned there are no available experimental hyperfine field measurements. Using

the same assumptions as made for YbGd, one can predict the following value for the hyperfine field. $H_{\text{hf}} = H_{\text{hf}}^{\text{sp}} = -147$ kOe which should remain almost constant in temperature due to the flatness of the Tb $s-p$ conduction band.

¹ See, for instance, the experimental hyperfine field data tabulated by G. N. Rao, *Hyp. Int.* **24-26**, 1119 (1985).

² J. Boysen, J. Grimm, A. Ketttschan, W. D. Brewer, and G. V. H. Wilson, *Phys. Rev. B* **35**, 1500 (1987).

³ M. Forker, K. Krien, and F. Renschenbach, *Hyp. Int.* **9**, 255 (1981); M. Forker and K. Krush, *ibid.* **9**, 399 (1981).

⁴ I. A. Campbell, *J. Phys. F* **2**, L47 (1972); I. A. Campbell, W. D. Brewer, J. Floquet, A. Benoit, B. W. Mardsen, and N. J. Stone, *Solid State Commun.* **15**, 711 (1974).

⁵ C. E. Leal and A. Troper, *J. Less Common Metals* **149**, 377 (1989).

⁶ C. E. Leal O. L. T. de Menezes, and A. Troper, *Solid State Commun.* **53**, 35 (1985); *Physica B* **130**, 443 (1985).

⁷ C. E. Leal and A. Troper, *J. Appl. Phys.* **67**, 5876 (1990).

⁸ F. E. Wagner, G. Wortmann, and G. M. Kalvius, *Phys. Lett.* **42A**, 482 (1973).

⁹ W. D. Brewer and E. Wehmeier, *Phys. Rev. B* **12**, 4608 (1977); M. Forker, R. Trzcinsky, and T. Merzhauser, *Hyp. Int.* **15-16**, 273 (1973).

¹⁰ J. O. Dimmock and A. J. Freeman, *Phys. Rev. Lett.* **13**, 760 (1969); N. Harmon and A. J. Freeman, *Phys. Rev. B* **10**, 1979 (1974).

¹¹ C. Jackson, *Phys. Rev.* **178**, 949 (1969).

¹² C. E. Leal and A. Troper, *J. Appl. Phys.* **61**, 4000 (1987).

¹³ See, for instance, D. Riegel and K. D. Gross, in *Nuclear Physics Applications on Materials Science*, edited by E. Recknagel and J. C. Soares (Kluwer Academic, Dordrecht, 1988), p. 327.

¹⁴ T. A. Thiel, E. Gerdau, M. Bottcher, and G. Netz, *Hyp. Int.* **9**, 459 (1981).

¹⁵ T. A. Thiel, E. Gerdau, B. Scharnberg, and M. Botcher, *Hyp. Int.* **14**, 347 (1983).

¹⁶ I. A. Campbell, *J. Phys. C* **2**, 1338 (1969).

¹⁷ L. Pauling, *Phys. Rev. Lett.* **47**, 277 (1981); R. A. Neifeld, M. Croft, T. Mihalisin, C. V. Segre, M. S. Torikachvili, M. B. Mapple, and L. E. De Long, *Phys. Rev. B* **32**, 6928 (1985).

¹⁸ B. Perscheid, K. Krush, and M. Forker, *J. Magn. Mater.* **9**, 14 (1978).

Thermoelectric power studies of a $\text{Nd}_{1.82-x}\text{Sr}_x\text{Ce}_{0.18}\text{CuO}_y$ superconducting system (abstract)

Okram G. Singh and B. D. Padalia
Physics Department, Indian Institute of Technology, Bombay 400 076, India

Om Prakash
Materials Science Centre, Indian Institute of Technology, Bombay 400 076, India

V. N. Moorthy and Anant V. Narlikar
National Physical Laboratory, New Delhi 110012, India

We have reported recently on the revival of superconductivity in $\text{Nd}_{1.82}\text{Ce}_{0.18}\text{CuO}_y$ by doping with a divalent alkaline earth element. The doped superconductor $\text{Nd}_{1.82-x}\text{Sr}_x\text{Ce}_{0.18}\text{CuO}_y$ has a Nd_2CuO_4 (T' -type) structure. This system possesses a normal state metallic resistivity [$\rho(T)$] in polycrystalline form. The $\rho(T)$ versus temperature (T) plots are, in general, linear. We report here the results of our studies of $\rho(T)$ and thermopower $S(T)$ and their dependence on the lattice oxygen content (y) that is a function of the Sr-content x . The $d\rho(T)/dT$ improves and then deteriorates with an increase in y . However, the thermopower behavior is a more complicated function of y (or x) and its results indicate that the majority of the charge carriers are electronlike. The thermopower (in absolute value) of the superconducting $\text{Nd}_{1.73}\text{Sr}_{0.09}\text{Ce}_{0.18}\text{CuO}_{3.97}$ compound gradually decreases from 250 to 150 K, remains almost constant from 150 to 75 K, decreases very fast below 75 K, and shows negative dS/dT . The overall feature of the S vs T plot suggests that the main contribution to S is from diffusion. Unlike reduced $\text{Nd}_{1.82}\text{Ce}_{0.18}\text{CuO}_{4.01}$ and other electron-doped superconductors, we have not observed a peak near the transition temperature (T_c) on the higher temperature side of the S vs T plot of the present sample. An attempt is made to explain the salient features of the thermopower.

The magnetic and superconducting properties of $\text{Pb}_2\text{Sr}_2(\text{R}/\text{Ca})\text{Cu}_3\text{O}_8$, $\text{R}=\text{Pr}$, Ce , and Cm (abstract)

J. Simon Xue, C. W. Williams, and L. Söderholm
Argonne National Laboratory, Argonne, Illinois 60439

The series of compounds $\text{Pb}_2\text{Sr}_2(\text{R}/\text{Ca})\text{Cu}_3\text{O}_8$, ($\text{R}=\text{Ce}-\text{Tm}$) are known to superconduct at temperatures as high as $T_c=84$ K. We have studied the relationship between superconductivity and magnetism in the Ce and Pr analogs. In addition, we report the synthetic route and the magnetic properties of the actinide analog $\text{Pb}_2\text{Sr}_2(\text{Cm}/\text{Ca})\text{Cu}_3\text{O}_8$. The parent compound $\text{Pb}_2\text{Sr}_2\text{CmCu}_3\text{O}_8$ is not a superconductor, but shows evidence of long range magnetic ordering at about 18 K. This is a much higher temperature than is observed for any of the other R-ion parent compounds. These results will be discussed in terms of the different hybridization and bonding properties of the $4f$ and $5f$ electrons, and how these differences influence superconductivity. These results will be compared with the Pr and Cm analogs of the other superconducting series $\text{Ba}_2\text{Cu}_3\text{O}_7$ and $\text{R}_{2-x}\text{Th}_x\text{CuO}_4$.

This work is supported by the U.S. DOE Basic Energy Sciences-Chemical Sciences, under Contract No. W-31-109-ENG-38.

^{57}Fe and ^{119}Sn Mössbauer studies on $\text{La}_{1.25}\text{Nd}_{0.6}\text{Sr}_{0.15}\text{CuO}_4$: Evidence for local magnetic ordering below ≈ 32 K (abstract)

M. Breuer, B. Büchner, and H. Micklitz

II Physikalisches Institut, Universität zu Köln, Zùlpicher Strasse 77, 5000 Köln 41, Germany

E. Baggio-Saitovitch, I. Souza Azevedo, and R. B. Scorzelli

Centro Brasileiro de Pesquisas Físicas, Rua Xavier Sigaud 150, 22290-180 Rio de Janeiro, Brazil

M. M. Abd-Elmeguid

Experimentalphysik IV, Ruhr Universität, 4630 Bochum, Germany

^{57}Fe and ^{119}Sn Mössbauer effect studies on 0.5 at. % ^{57}Fe or ^{119}Sn doped nonsuperconducting $\text{La}_{1.25}\text{Nd}_{0.6}\text{Sr}_{0.15}\text{CuO}_4$ in the temperature region $300\text{ K} \geq T \geq 4.2\text{ K}$ reveal an onset of local magnetic ordering occurring at $T_M \approx 32\text{ K}$ for both ^{57}Fe as well as ^{119}Sn -doped samples. The local magnetic ordering shows up in the presence of a very large transferred hyperfine field of $B_{\text{hf}} \approx 11.0(5)\text{ T}$ at the ^{119}Sn nuclei. Since such a large field is present in neither antiferromagnetic La_2CuO_4 superconducting $\text{La}_{1.85}\text{Sr}_{0.15}\text{CuO}_4$ nor overdoped $\text{La}_{2-x}\text{Sr}_x\text{CuO}_4$ ($x = 0.4$), the occurrence of such local spin correlations seems to be a signature of the nonsuperconducting low temperature tetragonal phase of $\text{La}_{1.25}\text{Nd}_{0.6}\text{Sr}_{0.15}\text{CuO}_4$.

Peculiarities of inelastic neutron scattering on magnons in high- T_c materials of stoichiometrical composition Nd_2CuO_4 , La_2CuO_4 , and $\text{YBa}_2\text{Cu}_3\text{O}_6$ (abstract)

Yu. Pashkevich and M. Lariionov

Donetsk Phys.-Tech. Inst. Ukr. Acad. Sci., R. Luxemburg strasse 72, 340114 Donetsk, Ukraine

This paper focuses on the phenomenon of the "exchange amplification" of inelastic neutron scattering as compared to the elastic one around some Bragg peaks on small transferred momenta and energies. The effect is closely connected with increasing of the amplitude of uniform vibrations of some spin linear combinations. Since all the above-mentioned magnetics are multisublattice quasi-two-dimensional, those with an anomalously large intralayer exchange as compared to the interlayer one has the exchange amplification effect for the exchange and acoustic modes for all wave vectors directed perpendicularly to layers right up to the Brillouin zone edge. The same effect takes place in the region of the dispersion law being linear for small (compared with the intralayer exchange) transferred energies. The greater intensity of inelastic magnetic scattering as compared with the elastic one was observed in some experiments.^{1,2} The selection laws defining Bragg peaks around which the inelastic scattering is exchange amplified have been obtained. The peculiarities of the inelastic neutron scattering in Nd_2CuO_4 for the different magnetic structures—collinear and noncollinear—are considered.

¹N. Pyka, L. Pintschovius, and A. Yu. Rumiantsev, *Z. Phys. B-Condensed Matter* **82**, 177 (1991).

²P. Bourges, L. Boudarene, D. Petitgrand, and P. Galez, *Physica B* **180 & 181**, 447 (1992).

The sign reversal of the acoustoelectric effect in anisotropic superconductors (abstract)

A. V. Goltsev

Ioffe Physical-Technical Institute, St. Petersburg 194021, Russia

Experimental and theoretical investigations of high-temperature superconductors have revealed that the Fermi surface contains both electron- and hole-like parts, and the superconducting gap has large anisotropy in the a - b plane.¹ In the present paper we show that these two findings are sufficient to produce the sign reversal of the acoustoelectric effect observed in films of $\text{YBa}_1\text{Cu}_3\text{O}_{7-\delta}$ in transition from the normal to superconducting state.² For the purpose of studying the effect we derive a diagram method and calculate the acoustoelectric current produced by an acoustic wave in the normal state of an anisotropic metal. Then, we find that superconducting fluctuations decrease the current. Finally, we investigate the acoustoelectric effect in the mixed superconducting state. In this state the normal acoustoelectric current arises due to the quasiparticle excitation drift produced by the acoustic wave. It is compensated by the superconducting current which forces vortices to move. It is the motion that produces the acoustoelectric voltage in the superconducting state. We conclude that if the superconducting gap takes different values on the electron- and hole-like parts of the Fermi surface, then the acoustoelectric voltage can sharply change the sign near the superconducting transition. This effect is caused by the change of relative concentrations of the electron- and hole-like excitations.

¹Z.-X. Shen *et al.*, Phys. Rev. Lett. **70**, 1553 (1993).

²Yu. V. Ilisavskii *et al.*, Pis'ma Zh. Eksp. Teor. Fiz. **52**, 1138 (1990).

Four-spin exchange in Bi_2CuO_4 (abstract)

G. Petrakovskii, V. Val'kov, K. Sablina, and B. Fedoseev

Institute of Physics, SB RAS, Krasnoyarsk 660036, Russia

A. Furrer, B. Roessli, and P. Fischer

Laboratory for Neutron Scattering, ETH Zurich, CH-5232 Villigen PSI, Switzerland

Magnetic properties of Bi_2CuO_4 single crystals are of interest owing to their relationship to the high- T_c superconductor problem. Earlier^{1,2} we carried out the magnetic and neutron scattering investigations on high quality large single crystals. The Bi_2CuO_4 crystal belongs to the space group $P4/ncc$ and the magnetic group is the collinear plane antiferromagnet with a Neel temperature of 45.8 K. The three-dimensional character of the antiferromagnetic ordering is reflected by the value of the critical magnetization exponent 0.352. The sublattice magnetization depends very little on temperature up to about 15 K. The spin-wave spectrum contains two branches with energy gaps of 2.1 and 3.4 meV. The theoretical interpretation of the experimental data shows the necessity of introducing the tensor four-site exchange in the $S=\frac{1}{2}$ spin Hamiltonian with the tetragonal anisotropic bilinear exchange. This provides the gap characteristics of the acoustic branch of spin waves and the correct temperature dependence of the sublattice magnetization. This result shows the importance of the four-site exchange for the formation of Bi_2CuO_4 magnetic properties. From the similarity of magnetic subsystems, Bi_2CuO_4 , and high- T_c superconductors it is suggested that the four-site exchange is responsible for magnetic ordering of the square spin $S=\frac{1}{2}$ lattice. We also suggest a thermodynamic theory of the temperature dependence of magnetic properties of Bi_2CuO_4 .

¹G. A. Petrakovskii, K. A. Sablina *et al.*, Solid State Commun. **79**, 317 (1991).

²A. Furrer, P. Fischer *et al.*, Solid State Commun. **82**, 443 (1992).

Antiferromagnetic spin correlation suppression and superconducting characteristics improvement in $\text{YBa}_2\text{Cu}_3\text{O}_{6+\delta}$ films under light illumination (abstract)

V. Eremenko, V. Fomin, I. Kachur, V. Piryatinskaya, and O. Prikhod'ko

Institute for Low Temperature Physics and Engineering, Academy of Sciences of Ukraine, 47 Lenin Ave., 310164, Kharkov, Ukraine

Improvement of $\text{YBa}_2\text{Cu}_3\text{O}_{6+\delta}$ film superconducting characteristics that are dependent on the charge carrier concentration is possible not only by means of oxygen doping, but also by light illumination.¹ New results may be presented as follows: (i) The spectral distribution of the light absorption coefficient of Y-Ba-Cu-O films strongly depends on the index δ : there are relatively narrow bands in the spectrum at small δ and their intensity falls down as δ increases. The films with $\delta \sim 0.5-0.75$ are metallized under light illumination: the resistivity at $T < T_c$ decreases, the critical temperature T_c rises, the absorption band with an energy of $E = 2.2$ eV vanishes gradually, and the two-magnon band in the Raman spectrum also vanishes, which indicates a decrease of the antiferromagnetic spin correlation.² The above changes occur only if the photon energy is higher than that of the optical gap. The photoinduced changes are long lasting at $T < 180$ K. (ii) The charge carrier density increase is not the only effect of light illumination. We have observed an increase in the critical current density J_c (measurements were carried out in the pulse regime) of $\text{YBa}_2\text{Cu}_3\text{O}_{6.9}$ films after continuous red light illumination. Such photoinduced changes are also long lasting if $T < T_c$ and a current pulse amplitude do not exceed J_c .

¹V. I. Kudinov, A. I. Kirilyuk *et al.*, Phys. Lett. A **151**, 358 (1990).

²V. V. Eremenko, V. P. Gnezdilov *et al.*, Physica C **185-189**, 961 (1991).

ac susceptibility of $\text{Pb}_x\text{Bi}_{2-x}\text{Sr}_2\text{Ca}_2\text{Cu}_3\text{O}_{10}$ high T_c superconductors sintered for different durations (abstract)

S. C. Mathur, D. C. Dube, Urvija Sinha, and P. K. N. Raghavan

Indian Institute of Technology, Hauz Khas, New Delhi 110016, India

ac magnetic susceptibility measurements is one of the processes by which the superconducting properties of mixed oxide superconductors can be characterized. The study of the superconductors at an externally applied magnetic field predicts the existence of two superconducting transitions due to: (i) the one reflecting the intragrain properties and (ii) the other describing intergrain interactions which might be assumed as due to Josephson tunneling. In this abstract, we report our work on the ac susceptibility measurements in $\text{Pb}_x\text{Bi}_{2-x}\text{Sr}_2\text{Ca}_2\text{Cu}_3\text{O}_{10}$ superconductors to study the real part of χ' as a function of temperature, Pb concentration, and sintering time. The results have been compared with the x-ray diffraction (XRD) results. The material preparation and the characterization techniques used would be discussed. The XRD and the susceptibility measurements indicate that too high Pb concentrations and too low sintering time does not seem to improve the high T_c phase. The weak link coupling phase determined from the $\chi'-T$ dependence is strongly dependent on both the Pb concentration and the sintering time. The transition temperature for the low T_c phase decreases with sintering time and increases with the increasing Pb concentration. The results would be discussed in the light of the best superconducting properties achieved by variation of the material preparation.

Spin magnetic moment of conduction quasiparticle (abstract)

Vladimir L. Safonov

Institute of Molecular Physics, RSC "Kurchatov Institute," 123182 Moscow, Russia

A new approach for the description of charged quasiparticles (conduction electrons and holes) with the spin of $1/2$ in crystals is proposed.¹ The crystalline-field anisotropy is considered as a space-time geometry which is introduced by means of the metric tensor into the Dirac equation. In the framework of this approach both the kinetic energy and the Zeeman energy depend on the tensor of effective masses $m_j^* = G_j m_0$, where G_j is the diagonal metric tensor. Components of the g factor are $g_j = 2m_0/m_{cj}^*$, m_{cj}^* being the cyclotron mass. This relation is in good agreement with the experiment for three-dimensional (3D) anisotropic metals such as Bi. For 2D motion we have only one nonzero spin magnetic component, perpendicular to the plane. This fact can be used for an explanation of two dimensional spin confinement observed experimentally in strained quantum wells. For 1D motion the spin of the quasiparticle falls out of the Hamiltonian. The fact that the spin is a hidden coordinate in this case can originate in para-Fermi statistics in which the maximal number of quasiparticles at the same energy level is equal to two (quasiparticles with up and down spins are identical). According to the theory² of superconductivity, the system of quasiparticles with para-Fermi statistics has much greater critical temperature than the system with Fermi statistics.

¹ V. L. Safonov, *Phys. Status Solidi B* **176**, K55 (1993).

² V. L. Safonov, *Phys. Status Solidi B* **174**, 223 (1992).

Restoration of the continuous phase transition in the vortex state due to the lattice translational symmetry: Large- N limit (abstract)

Boris N. Shalaev and Sergey A. Kitorov

A. F. Ioffe Physical & Technical Institute, Russian Academy of Sciences, St. Petersburg 194021, Russia

The critical behavior of type II superconductors (SC) near the upper critical magnetic field is studied. The order parameter fluctuations in type II SC near the upper critical magnetic field were shown to destroy the off-diagonal long-range order (ODLRO) in $d < 4$ dimensions.¹ In the report this result is proved to be valid in the $1/N$ expansion. Thus, there is a serious controversy between the experimentally observed phase coherence in SC and theoretical results forbidding a spontaneous breakdown of the $U(1)$ symmetry. Lattice effects breaking the continuous translational magnetic symmetry and suppressing the dimensional reduction effect² are shown to be responsible for the existence of the ODLRO. The lattice Hamiltonian of the uniformly frustrated $O(2N)$ symmetric nonlinear sigma model³ is used to obtain the effective Ginzburg-Landau action which is analyzed in the large N limit. It is shown that the continuous phase transition does indeed occur with critical exponents being universal and identical to those of a superconductor with $H=0$.

¹ M. A. Moore, *Phys. Rev. B* **45**, 7336 (1992).

² S. A. Kitorov, Yu. V. Petrov, B. N. Shalaev, and V. S. Sherstinov, *Int. J. Mod. Phys. B* **6**, 1209 (1992).

³ M. Y. Choi and S. Doniach, *Phys. Rev. B* **31**, 4516 (1985).

Damping of spin waves in a square-lattice quantum antiferromagnet due to spin-phonon interaction (abstract)

Dirk Uwe Saenger

Institut fuer Theoretische Physik, Universitaet des Saarlandes, D-66041 Saarbruecken, Germany

The damping of spin waves due to spin-phonon interaction in a spin-1/2-Heisenberg antiferromagnet on a square lattice is calculated. The theory applies to the regimes where the sound velocities v_s are small compared with magnon velocities v_m , which is the case in antiferromagnetic high- T_c superconductor basis materials like $\text{YBa}_2\text{Cu}_3\text{O}_6$, and $k\xi \gg 1$, where \mathbf{k} and ξ are wave vector and correlation length, respectively. It is concluded that the broad spectral feature of the two-magnon line observed in layered perovskites can be explained qualitatively as a consequence of spin-phonon interaction.

The superconducting transition temperature of layered $S_I - J_{II} - S_J$ superconductors (abstract)

Valery A. Cherenkov

The Research and Development Center of Surface and Vacuum (RDCSV), The Theoretical Physical Laboratory, Andreevskay Nab. 2, 117334 Moscow, Russia

The $S_I - J_{II} - S_J$ multilayered superconductor structures containing different superconductors (S_{II}) with an isolated layer are investigated. There is a theoretical model of a tunneling Hamiltonian for the defect Josephson lattice. There are the Ising magnetic and resonance valence band models between the layers. The "saturation" of $T_c(N)$ is determined. The analogy has been present for $T_c(N)$ in the representation of a plane (high- T_c) structure and the Kosterlitz-Thouless transition.

This research was supported by the American Physical Society.

¹V. A. Cherenkov, J. Superconductivity 4, 259 (1991).

²V. A. Cherenkov, J. Superconductivity 4, 429 (1991).

Magnetism and superconductivity in heavy-fermion compounds (abstract)

A. V. Goltsev

Joffe Physical-Technical Institute, St. Petersburg 194021, Russia

The mean-field theory based on an extended high degeneracy model is derived to describe an interplay between the Kondo effect, magnetism, and superconductivity in heavy-fermion compounds. The competition and coexistence of the Kondo effect and ferro- or antiferromagnetic orders of localized moments are considered depending on the local exchange interaction. It is shown that an antiferromagnetic order arising in the coherent Kondo state can have an anomalously small antiferromagnetic moment per f atom ($\sim 0.01\mu_B$) and stimulate superconductivity with an anisotropic superconducting gap that vanishes along lines on the Fermi surface. We apply the theory for studying thermodynamic peculiarities of the antiferromagnetic and superconducting transitions, and the microscopic structure of the antiferromagnetic and superconducting states in URu_2Si_2 and UPt_3 . The theoretical estimation ($0.035\mu_B$) of the antiferromagnetic moments of U atoms in URu_2Si_2 is in good agreement with the experimental result ($0.04\mu_B$). We also study the microscopic origin of the double superconducting transition in UPt_3 . The superconducting gap in the successive superconducting states is strongly anisotropic. In the former state the gap vanishes on part of the Fermi surface, while in the following state the gap vanishes on lines only.

Magnetic properties of an isolated ferromagnetic bond embedded in Heisenberg antiferromagnets

S. T. Ting, S. Haas, and J. E. Crow

Department of Physics, Center for Material Research and Technology, and National High Magnetic Field Laboratory, Florida State University, Tallahassee, Florida 32306

The magnetic properties of an isolated ferromagnetic bond of coupling constant K embedded in a layered spin-1/2 Heisenberg antiferromagnet with interplane coupling strength $J_{\perp} = \alpha J_{\parallel}$ ($0 \leq \alpha \leq 1.0$) have been studied using linear-spin-wave (LSW) theory. In the pure lattice, the sublattice magnetization $\langle S_i^z \rangle$ is 0.304 at $\alpha=0$ and saturates to 0.422 at $\alpha=1.0$. The spin correlations $\langle S_i^x S_j^x \rangle$ decrease with increasing α within the plane and increase along the interplane direction. The introduction of an isolated ferromagnetic bond into the host lattice tends to enhance $\langle S_i^z \rangle$ at lattice sites joining the bond as K approaches zero. Increasing K will drastically suppress $\langle S_i^x S_j^x \rangle$ across the bond. Whereas, $\langle S_i^x S_j^x \rangle$ is enhanced between the neighboring sites close to the impurity link resulting in the suppression of $\langle S_i^z \rangle$. This behavior persists for all α values. The LSW theory breaks down at a certain K value. Increasing α , the critical value of K extends to a larger number.

The striking magnetic properties of high temperature superconductors have led to extensive efforts in the investigation of the spin-1/2 Heisenberg antiferromagnets.¹ The La_2CuO_4 compound, which undergoes antiferromagnetic ordering at $T_N \approx 320$ K, presents quasi-two-dimension (quasi-2D) antiferromagnetic structure with a large in-plane exchange constant $J_{\parallel} \approx 1500$ K and a very weak interplane coupling J_{\perp} between Cu-O planes. This small J_{\perp} coupling plays an important role in stabilizing the three-dimensional (3D) antiferromagnetic ordering below T_N and also gives rise to interesting metamagnetic behavior associated with the small rotation of CuO_6 octahedra in the orthorhombic phase.^{1,2}

The substitution of La with Sr, introducing extra holes into the Cu-O planes, drastically suppresses the long-range 3D antiferromagnetic ordering. Doping only 2% Sr into La site will completely destroy the Néel state. This interesting magnetic behavior leads to extensive study of a localized impurity and/or vacancy in a spin-1/2 2D Heisenberg antiferromagnet.³⁻⁷ These studies exclusively concentrate on the 2D magnetic behavior, neglecting the small interplane coupling. As mentioned earlier, the weak interplane correlations between Cu-O planes becomes an important factor in the magnetic behavior below T_N . It is interesting to investigate the magnetic behavior of impure layered 2D Heisenberg antiferromagnets with varying interplane coupling constants since the crossover effects from 2D to 3D can be observed. In addition, the layered magnets themselves present quite interesting magnetic properties.⁸ Therefore, in this paper we extend a previous calculation⁵ on an isolated bond embedded in the spin-1/2 2D Heisenberg antiferromagnet by including the interplane coupling.

We consider a simple cubic Heisenberg antiferromagnetic lattice with in-plane nearest-neighbor antiferromagnetic coupling J_{\parallel} and interplane coupling $J_{\perp} = \alpha J_{\parallel}$ ($0 \leq \alpha \leq 1.0$). An isolated ferromagnetic bond is introduced and replaces one

inplane antiferromagnetic link joining the sites 0 and 1. The Hamiltonian is given as

$$H = \frac{J_{\parallel}}{2} \sum_{\langle ij \rangle} \mathbf{S}_i \cdot \mathbf{S}_j + \frac{J_{\perp}}{2} \sum_{\langle i'j' \rangle} \mathbf{S}_{i'} \cdot \mathbf{S}_{j'} - \frac{J_{\parallel} + K}{2} \mathbf{S}_0 \cdot \mathbf{S}_1, \quad (1)$$

where the first summation is over the four nearest neighbors within the plane and the second summation involves the two nearest interplane interactions. Following standard spin-wave theory,⁹ the above Hamiltonian can be expressed as the product of bilinear bosonic operators using the Holstein-Primakoff transformation. The final Hamiltonian then can be analyzed using the Green's function method.¹⁰ The Fourier transformation of the double-time one-particle Green's function in matrix form is given as

$$\hat{G}_{k,k'}(E) \equiv \begin{pmatrix} \langle\langle a_k^+; a_{k'} \rangle\rangle & \langle\langle a_k^+; b_{k'}^+ \rangle\rangle \\ \langle\langle b_k; a_{k'} \rangle\rangle & \langle\langle b_k; b_{k'}^+ \rangle\rangle \end{pmatrix}, \quad (2)$$

where $E = \omega + i\epsilon$ with $\epsilon \rightarrow 0^+$. The exact form of $\hat{G}_{k,k'}(E)$ can be obtained from the equation of motion.^{5,6}

The sublattice magnetization $\langle S_i^z \rangle$ and the spin correlation depend on the positions of the lattice sites relative to the impurity bond and the imaginary part of the Green's function

$$\langle S_i^z \rangle = \frac{1}{2} + \frac{1}{N} \sum_{k,k'} e^{i(k-k')R_j} \int_0^{\infty} \frac{d\omega}{\pi} \text{Im} \langle\langle a_k^+; a_{k'} \rangle\rangle, \quad (3)$$

$$\langle S_i^x S_j^x \rangle = -\frac{1}{N} \sum_{k,k'} e^{i(kR_i - k'R_j)} \int_0^{\infty} \frac{d\omega}{2\pi} \text{Im} \langle\langle a_k^+; b_{k'}^+ \rangle\rangle, \quad (4)$$

where R_i or R_j represent the respective positions of spins. The sevenfold integration (two 3D k sums and one ω integration) of Eqs. (3) and (4) can be decoupled to an only twofold integration as follows:

$$\langle S_i^z \rangle^0 = \frac{1}{2} - \frac{1}{\pi} \int_0^{1+\alpha/2-\epsilon} dy \frac{y-(1+\alpha/2)}{F(y)} \int_0^\infty dt \cos[F(y)t] \left[J_0\left(\frac{t}{2}\right) \right]^2 J_0\left(\frac{\alpha t}{2}\right), \quad (5)$$

$$\langle S_i^x S_j^x \rangle^0 = -\frac{1}{2\pi} \int_0^{1+\alpha/2-\epsilon} dy F(y) \int_0^\infty dt \cos[F(y)t] \Delta(t), \quad (6)$$

$$\delta \langle S_0^z \rangle = -\frac{1+K}{4\pi} \int_0^{1+\alpha/2-\epsilon} dy \frac{2R(y)S(y)M(y) - \{[R(y)]^2 - [S(y)]^2\}N(y)}{F(y)\{[M(y)]^2 + [N(y)]^2\}}, \quad (7)$$

$$\delta \langle S_0^x S_1^x \rangle = -\frac{1+K}{8\pi} \int_0^{1+\alpha/2-\epsilon} dy \frac{[S(y)P(y) + R(y)Q(y)]M(y) - [R(y)P(y) - S(y)Q(y)]N(y)}{F(y)\{[M(y)]^2 + [N(y)]^2\}}, \quad (8)$$

where $\langle S_i^z \rangle^0$ is the sublattice magnetization, $\langle S_i^x S_j^x \rangle^0$ is the spin correlation in the pure lattice, and $J_n(t)$ is the Bessel function of the first kind. The functions $\Delta(t)$, $M(y)$, $N(y)$, $P(y)$, $Q(y)$, $F(y)$, $R(y)$, and $S(y)$ are given as

$$\Delta(t) = \frac{1}{2} \left\{ \left[J_0\left(\frac{t}{2}\right) \right]^2 J_0\left(\frac{\alpha t}{2}\right) - \frac{2}{t} J_0\left(\frac{t}{2}\right) J_1\left(\frac{t}{2}\right) J_0\left(\frac{\alpha t}{2}\right) - \left[J_1\left(\frac{t}{2}\right) \right]^2 J_0\left(\frac{\alpha t}{2}\right) - \alpha J_1\left(\frac{t}{2}\right) J_0\left(\frac{t}{2}\right) J_1\left(\frac{\alpha t}{2}\right) \right\}, \quad (9)$$

$$M(y) = 1 + \frac{(1+k)}{2F(y)} \int_0^\infty dt \sin[F(y)t] \left\{ \Delta(t) - (1+\alpha/2) \times \left[J_0\left(\frac{t}{2}\right) \right]^2 J_0\left(\frac{\alpha t}{2}\right) \right\}, \quad (10)$$

$$N(y) = \frac{(1+k)}{2F(y)} \int_0^\infty dt \cos[F(y)t] \left\{ \Delta(t) - (1+\alpha/2) \times \left[J_0\left(\frac{t}{2}\right) \right]^2 J_0\left(\frac{\alpha t}{2}\right) \right\}, \quad (11)$$

$$P(y) = \int_0^\infty dt \sin[F(y)t] \left\{ \Delta(t) - [y + (1+\alpha/2)] \times \left[J_0\left(\frac{t}{2}\right) \right]^2 J_0\left(\frac{\alpha t}{2}\right) \right\}, \quad (12)$$

$$Q(y) = \int_0^\infty dt \cos[F(y)t] \left\{ \Delta(t) - [y + (1+\alpha/2)] \times \left[J_0\left(\frac{t}{2}\right) \right]^2 J_0\left(\frac{\alpha t}{2}\right) \right\}, \quad (13)$$

$F(y) = [(1+\alpha/2)^2 - y^2]^{1/2}$, $R(y) = P(-y)$, and $S(y) = Q(-y)$. Notice that Eqs. (7) and (8) only present the variation of $\langle S_i^z \rangle$ and $\langle S_i^x S_j^x \rangle$ at the lattice sites joining the impurity link. One can easily extend them to arbitrary lattice sites.

$\langle S_i^z \rangle^0$ and $\langle S_i^x S_j^x \rangle^0$ for the pure lattice can be obtained from Eqs. (5) and (6). At $\alpha=0.0$ (2D lattice), $\langle S_i^z \rangle^0$ is 0.3034 and saturates to 0.422 at $\alpha=1.0$ (3D lattice). $\langle S_i^x S_j^x \rangle^0$ decreases in magnitude from 0.1378 at $\alpha=0.0$ to 0.0635 at

$\alpha=1.0$. These results are consistent with previous numerical calculations.¹¹⁻¹³ Since the spin correlations between nearest neighbors depend on the positions of spins, we also calculate $\langle S_i^x S_j^x \rangle^0$ along the interplane direction, which increases in magnitude from 0 at $\alpha=0.0$ to 0.0635 at $\alpha=1.0$. This result provides evidence that the interplane coupling stabilizes 3D antiferromagnetic ordering at low temperatures.

The introduction of a ferromagnetic bond into the host lattice will affect the sublattice magnetization and spin correlations surrounding the impurity. When $K=0$, the system corresponds to a missing link embedded in the host lattice. In this case, $\langle S_i^z \rangle$ is enhanced at the sites joining the impurity bond. This behavior persists for all α values as shown in Fig. 1. The enhancement of $\langle S_i^z \rangle$ becomes less evident for larger α values, e.g., 0.3034 \rightarrow 0.312 at $\alpha=0.0$ and 0.422 \rightarrow 0.4238 at $\alpha=1.0$. These results indicate that the absence of spin fluctuations is more dominant than the missing longitudinal term, especially for lattices with small interplane coupling strength. By increasing K , $\langle S_i^z \rangle$ is monotonically suppressed at the sites joining or close to the ferromagnetic bond as illustrated in Fig. 2 which shows the sublattice magnetization as a function of K/J_{\parallel} at the sites adjacent to the impurity link. The spin correlations are enhanced for almost all the lattice sites surrounding the ferromagnetic link except for

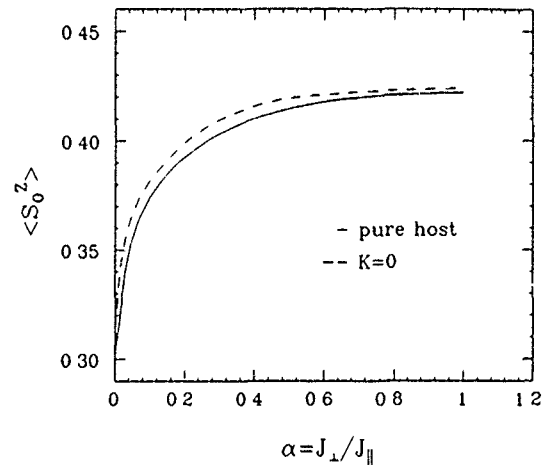


FIG. 1. The sublattice magnetization $\langle S_0^z \rangle$ at lattice site 0 joining the missing link as a function of α (dashed line), compared with that of the pure host (solid line).

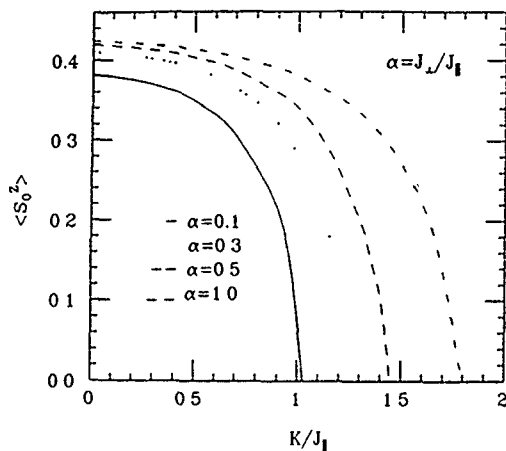


FIG. 2. The sublattice magnetization $\langle S_0^z \rangle$ at lattice site 0 adjacent to the impurity link vs K/J_{\parallel} at different α values. The LSW approximation breaks down above certain K values.

those connecting the impurity bond. These results are illustrated in Fig. 3(a) and 3(b). In Fig. 3(a), we present $\langle S_0^x S_1^x \rangle$ vs K/J_{\parallel} across the impurity bond. As expected, $\langle S_0^x S_1^x \rangle$ is strongly suppressed. Figure 3(b) shows $\langle S_0^x S_1^x \rangle$ as a function

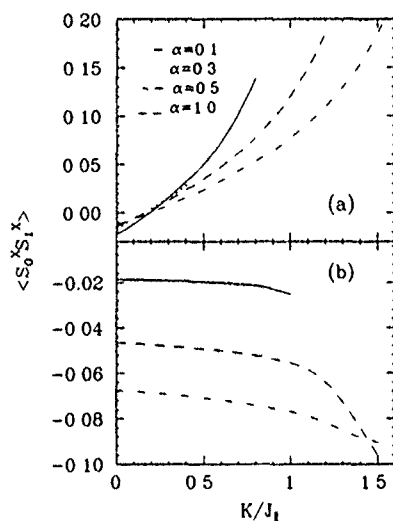


FIG. 3. The spin correlations $\langle S_0^x S_1^x \rangle$ vs K/J_{\parallel} at different α values; (a) for spins across the impurity link [i.e., (100) direction], (b) for spins along the interplane direction ((001)).

of K/J_{\parallel} along the interplane direction (001) which indicates that $\langle S_0^x S_1^x \rangle$ increases in magnitude with increasing K .

It is evident that the LSW approximation breaks down at a certain value of K , even at maximum J_{\perp} . The breakdown value extends to larger value as α is increased. As mentioned earlier, interplane interactions tend to strengthen the 3D antiferromagnetic ordering. To frustrate the spin correlations adjacent to the ferromagnetic bond, a stronger perturbation, i.e., a larger K value is necessary to overcome the exchange-coupling energy between the planes. The denominator of Eq. (7) or (8) represents the spin wave mode arising from the ferromagnetic link. This corresponds to a localized mode. As K approaches its critical value, a large number of spin waves is generated because of the strong local perturbation. In this case, one must consider higher order bosonic operators which describe the interactions between magnons, e.g., the spin operator S_j^+ for sublattice a is given as

$$S_{aj}^+ = \frac{1}{\sqrt{N}} \times \left(\sum_k e^{-ikx} a_k + \frac{1}{2N} \sum_{k,k',k''} e^{i(k-k'-k'')x} a_k^+ a_{k'} a_{k''} \right). \quad (14)$$

The complete details will be presented in a future publication.

- ¹E. Manousakis, Rev. Mod. Phys. **63**, 1 (1991).
- ²T. Thio, T. R. Thurston, N. W. Preyer, P. J. Picone, M. A. Kastner, H. P. Jenssen, D. R. Gabbe, C. Y. Chen, B. R. Birgeneau, and A. Aharony, Phys. Rev. B **38**, 905 (1988).
- ³N. Nagaosa, Y. Hatsugai, and M. Imada, J. Phys. Soc. Jpn. **58**, 978 (1989).
- ⁴N. Bulut, D. Hone, D. J. Scalapino, and E. Y. Loh, Phys. Rev. Lett. **62**, 2192 (1989).
- ⁵K. Lee and P. Schlottmann, Phys. Rev. B **42**, 4426 (1990).
- ⁶S. Haas, D. Duffy, and P. Schlottmann, Phys. Rev. B **46**, 3135 (1992).
- ⁷P. Rubin and A. Sherman, Phys. Status Solidi B **166**, 161 (1991).
- ⁸M. E. Lines, Phys. Rev. **133**, A841 (1964); J. Phys. Chem. Solids **31**, 101 (1970).
- ⁹P. W. Anderson, Phys. Rev. **86**, 694 (1952); R. Kubo, *ibid.* **87**, 568 (1952); T. Nagamiya, K. Yosida and R. Kubo, Adv. Phys. **4**, 97 (1955).
- ¹⁰D. N. Zubarev, Sov. Phys. Usp. **3**, 320 (1960); J. Callaway, *Quantum Theory of the Solid State* (Academic, New York, 1976), Chap. 2; A. S. Chakravarty, *Introduction to the Magnetic Properties of Solids* (Wiley, New York, 1980), Chaps. 17 and 18.
- ¹¹J. Carlson, Phys. Rev. B **40**, 846 (1989).
- ¹²A. Singh, Z. Tešanović, H. Tang, G. Xiao, C. L. Chien, and J. C. Walker, Phys. Rev. Lett. **64**, 2571 (1990).
- ¹³B.-G. Liu, Phys. Rev. B **41**, 9563 (1990); *ibid.* **42**, 6745 (1990); J. Phys. Condens. Matter **2**, 6007 (1990).

Spin diffusion in classical Heisenberg magnets with uniform, alternating, and random exchange

Niraj Srivastava,^{a)} Jian-Min Liu, V. S. Viswanath, and Gerhard Müller
Department of Physics, The University of Rhode Island, Kingston, Rhode Island 02881-0817

We have carried out an extensive simulation study for the spin autocorrelation function at $T=\infty$ of the one-dimensional classical Heisenberg model with four different types of isotropic bilinear nearest-neighbor coupling: uniform exchange, alternating exchange, and two kinds of random exchange. For the long-time tails of all but one case, the simulation data seem incompatible with the simple $\sim t^{-1/2}$ leading term predicted by spin diffusion phenomenology.

The anomalous character of spin diffusion in the one-dimensional (1D) classical Heisenberg model,

$$H = - \sum_i J_{i,i+1} \mathbf{S}_i \cdot \mathbf{S}_{i+1}, \quad (1)$$

with uniform exchange, $J_{i,i+1} = J$, was first proposed in 1988 on the basis of a simulation study.¹ The proposition was that the spin autocorrelation function at $T=\infty$ exhibits a distinctive power-law long-time tail,

$$C_0(t) \equiv \langle \mathbf{S}_i(t) \cdot \mathbf{S}_i \rangle \sim t^{-\alpha}, \quad (2)$$

with a characteristic exponent α that exceeds the value $\alpha_{SD}=1/2$ predicted by spin diffusion phenomenology considerably.

That conclusion was challenged by Gerling and Landau² soon after it had appeared in print. However, the consensus emerged that the slope $\tilde{\alpha}$ inferred from the simulation data (in a log-log representation) has a value $\tilde{\alpha}=0.60$ at $Jt \approx 25$ and a decrease trend for longer Jt , and that the true asymptotic behavior remained out of the reach of simulation data available at the time.^{2,3}

It was nevertheless another simulation study that yielded new insights into the anomalous transport mechanism of spin fluctuations in the classical Heisenberg chain. Having been alerted by the puzzling results for the spin autocorrelation function, Bonfim and Reiter⁴ focused their own investigation on the q -dependent spin correlation functions and the associated current correlation function. One of their conclusions was that the asymptotic behavior of the spin autocorrelation function is of the form

$$C_0(t) \sim [Jt \ln(\Omega t)]^{-\alpha} \quad (3)$$

with $\alpha \approx 0.472$. The implication is that the slope of $C_0(t)$ in a log-log plot can be described by an effective exponent,

$$\tilde{\alpha} = \alpha [1 + 1/\ln(\Omega t)]. \quad (4)$$

Böhm, Gerling, and Leschke⁵ were quick to point out that the asymptotic form of the q -dependent correlation function used in Ref. 4 is in contradiction to the non-negativity of $\langle \mathbf{S}_i(t) \cdot \mathbf{S}_{i+n} \rangle$, for which strong numerical evidence exists. They proposed an alternative asymptotic expression, which also implies an effective exponent (4), but with asymptotic value $\alpha=0.5$.

Since neither of the two conclusions was primarily based on the analysis of spin autocorrelation functions, we wish to use our own new simulation data for $C_0(t)$ as a discriminant between expressions (4) with $\alpha=0.472$ and $\alpha=0.5$, respectively. We have carried out the simulation for a system of 1024 spins with periodic boundary conditions. We have employed CM-5 machines with various numbers of processors programmed in Connection Machine FORTRAN for up to 4096 parallel time integrations. For the integration over the time interval $0 \leq Jt \leq 102.2$, we have used a fourth-order Runge-Kutta method with fixed time step $Jdt=0.005$. In this massively data-parallel programming mode we can reach previously unattained statistics with no undue effort.

For the intended analysis, we have determined the average slope $\tilde{\alpha}$ of the simulation data in a log-log representation over a time interval of length Jt_{av} as follows: each data point of $\tilde{\alpha}(t)$ is calculated by linear regression from N_{av} consecutive data points $[\ln Jt, \ln C_0(t)]$ spaced at $J\Delta t=0.2$ and assigned the Jt value at the midpoint of the interval of length $Jt_{av}=N_{av}J\Delta t$. Figure 1 shows the slope function $\tilde{\alpha}$ plotted versus $1/Jt$ for three different sizes of Jt_{av} .⁶ This representation enhances the visibility of the subtle features in the long-time tail, but it also magnifies the statistical fluctuations. The latter are kept under control by adjusting Jt_{av} .⁷

In order to facilitate a direct comparison of our simulation results with the proposed functional form (4) for the effective exponent $\tilde{\alpha}(t)$, we have subjected the asymptotic expression $\sim [Jt \ln(\Omega t)]^{-\alpha}$ to the same exponent analysis as the data. The resulting slope function $\tilde{\alpha}(t)$ still depends on the parameters α and Ω . There is no compelling reason for setting Ω equal to J in the logarithmic correction as was done in Refs. 4 and 5. Minimizing the relative rms deviation between the two slope functions $\tilde{\alpha}(t)$, namely the one representing the simulation data and the one representing the averaged exponent $\tilde{\alpha}(t)$ over the interval $5+Jt_{av}/2 \leq Jt \leq 102.2-Jt_{av}/2$, yields parameter values in the range $\alpha=0.478 \pm 0.001$, $\Omega/J=2.30 \pm 0.02$ for the three values of averaging intervals Jt_{av} used. The solid lines represent $\tilde{\alpha}$ vs $1/Jt$ for the optimal parameter values. The agreement with the simulation data is quite satisfactory. If we perform the fit for fixed $\alpha=0.5$, we obtain the optimal value $\Omega/J=9.70 \pm 0.05$ for the other parameter, and the result, represented by the dashed lines, is in clear disagreement with the simulation data.

We have repeated the analysis with more of the (evidently nonasymptotic) data at small times omitted (up to

^{a)}Present address: Thinking Machines Corporation, Cambridge, MA 02142-1264.

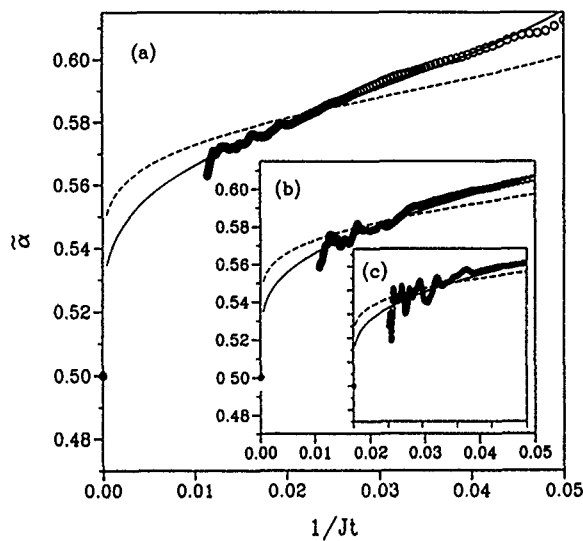


FIG. 1. Slope function $\tilde{\alpha}(t)$ for the 1D classical Heisenberg model (1) with uniform exchange, $J_{i,i+1}=J$ as determined from the slope of $C_0(t)$ in a log-log plot. The data for $C_0(t)$ represent an average over 404 484 randomly chosen initial conditions and over the 1024 sites of the lattice. Each data point $\tilde{\alpha}$ is determined by linear regression from N_{av} consecutive data points $[\ln Jt, \ln C_0(t)]$ spaced at $J\Delta t=0.2$ and plotted vs $1/Jt$ at the midpoint of the interval of length $Jt_{av}=N_{av}J\Delta t$. The simulation data are represented by the circles. The asymptotic form (3) subjected to the same procedure yields the dashed lines for $\alpha=0.5$ and the solid lines for $\alpha=0.478$. The three plots correspond to different sizes of averaging time interval: (a) $Jt_{av}=30$, (b) $Jt_{av}=20$, (c) $Jt_{av}=10$.

$15+Jt_{av}$) and found a decreasing trend of the optimal exponent value (now in the range $\alpha=0.472\pm 0.002$, in even better agreement with the value proposed in Ref. 4). Nevertheless, the problems attached to this scenario, as pointed out in Ref. 5, cannot be dismissed and suggest that the true asymptotic behavior is even more subtle.

How typical is the occurrence of anomalous long-time tails in 1D classical spin systems with isotropic exchange? It had already been noted⁴ that the anomaly disappears in the presence of uniaxial anisotropy. The question is what happens if we modify the spin coupling without altering the rotational symmetry in spin space, for example, by reducing or removing the translational symmetry along the chain.

In order to investigate that question, we have carried out simulations of comparable extent on three further variants of the classical Heisenberg model (1). In addition to model (i) with uniform exchange, $J_{i,i+1}=J$, discussed previously, we consider the model (ii) with alternating exchange, $J_{i,i+1}=(-1)^i J$, and two models with random exchange: model (iii) has $J_{i,i+1}=\pm J$ with equal probabilities and model (iv) has $|J_{i,i+1}|\leq \sqrt{3}J$ with a rectangular probability distribution.⁸ The results of this investigation are displayed in Figs. 2–4 for models (ii)–(iv) in exactly the same representation as those of model (i) exhibited in Fig. 1. The outcome is a bit surprising. It seems that long-time tails display no less individuality than, say, p_{ij} tails.⁹

Among the four models considered here, the one with alternating exchange alone appears to exhibit completely normal spin diffusive behavior. Its slope function $\tilde{\alpha}$, displayed in Fig. 2, tends to extrapolate on a fairly direct path toward $\alpha_{SD}=0.5$. The data invite no suspicion of any

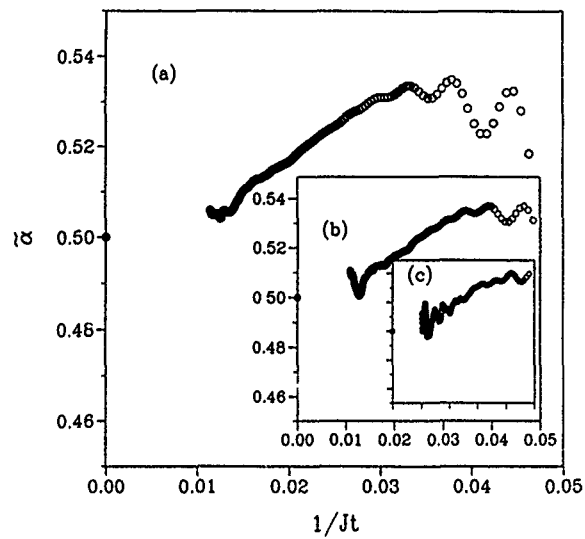


FIG. 2. Slope function $\tilde{\alpha}(t)$ for the 1D classical Heisenberg model (1) with alternating exchange, $J_{i,i+1}=(-1)^i J$, produced by the same method as that of Fig. 1. The number of integrations with randomly chosen initial conditions was 479 232 for this case.

anomaly. The strong wiggles at small t are not statistical fluctuations but originate from oscillations in $C_0(t)$, which persist to longer times in this model than in any of the other three.

The slope function $\tilde{\alpha}$ of the random-exchange model (iii) is shown in Fig. 3. Unlike in the previous two cases, it has an increasing trend for increasing t up to $\tilde{\alpha}\approx 0.53$ at the tail end of the data, where it seems to level off. While a limiting value of $\alpha_{SD}=0.5$ cannot be ruled out, the data do not show any tendency to extrapolate to that value.

Changing the distribution of random exchange constants from (iii) to (iv) produces a quite different slope function as can be observed in Fig. 4. It starts out at a much smaller

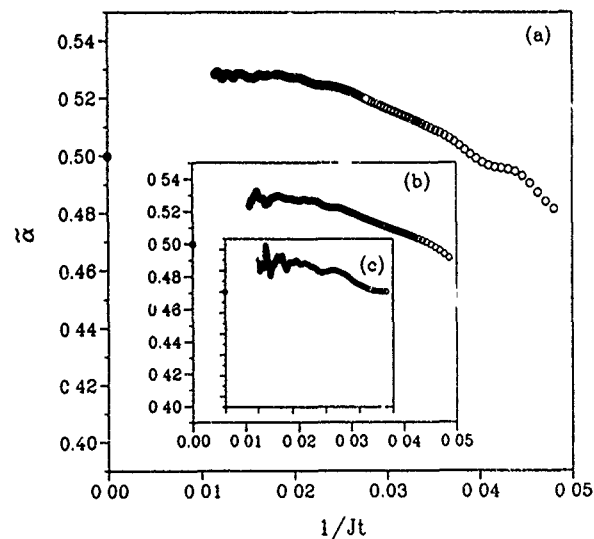


FIG. 3. Slope function $\tilde{\alpha}(t)$ for the 1D classical Heisenberg model (1) with random exchange, $J_{i,i+1}=\pm J$, produced by the same method as that of Fig. 1. The number of integrations with randomly chosen initial conditions was 409 600 for this case. For each initial configuration, the exchange constants were randomly chosen as well.

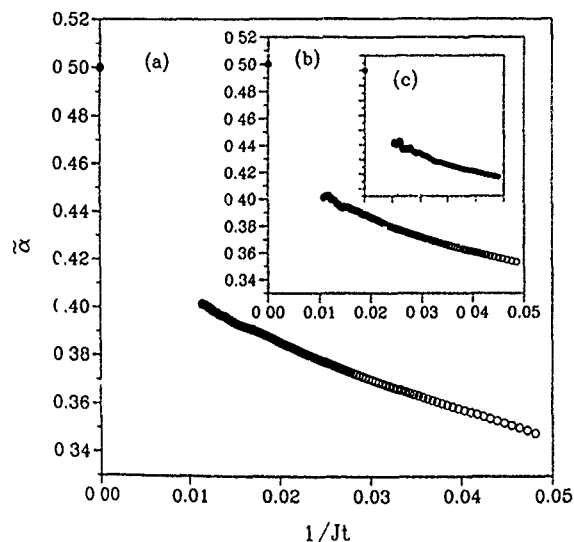


FIG. 4. Slope function $\tilde{\alpha}(t)$ for the 1D classical Heisenberg model (1) with random exchange, $|J_{i,i+1}| \leq \sqrt{3}J$, produced by the same method as that of Fig. 1. The number of integrations with randomly chosen initial condition was 424 960 in this case. For each initial configuration, the exchange constants were randomly chosen as well.

value for short t and reaches $\tilde{\alpha} \approx 0.4$ at the tail end of the data ($Jt = 102.2$). In some way this slope function looks like the mirror image of that for model (i). It may very well extrapolate to $\alpha_{SD} = 0.5$ or thereabouts by some logarithmic law—a modification of Eq. (4). But any such law would have to be motivated by an investigation of q -dependent cor-

relation functions as was done by Bonfim and Reiter⁴ for model (i). For the random-exchange model (iii), the anomaly, if it indeed exists, is much weaker than in models (i) and (iv) and will therefore be much harder to identify and analyze in q -dependent correlation functions. These are future projects.

This work was supported by the U.S. National Science Foundation, Grant No. DMR-93-12252. The simulations were run on CM-5 machines at the National Center for Supercomputing Applications, University of Illinois at Urbana-Champaign and at Thinking Machines Corporation.

¹G. Müller, Phys. Rev. Lett. **60**, 2785 (1988); **63**, 813 (1989).

²R. W. Gerling and D. P. Landau, Phys. Rev. Lett. **63**, 812 (1989); Phys. Rev. B **42**, 8214 (1990).

³J.-M. Liu, N. Srivastava, V. S. Viswanath, and G. Müller, J. Appl. Phys. **70**, 6181 (1991).

⁴O. F. de Alcantara Bonfim and G. Reiter, Phys. Rev. Lett. **69**, 367 (1992); **70**, 249 (1993).

⁵M. Böhm, R. Gerling, and H. Leschke, Phys. Rev. Lett. **70**, 248 (1993).

⁶See Fig. 2 of Ref. 2 (second paper) and Fig. 2 of Ref. 3 for previous interpretations of slope functions based on different simulation data.

⁷The price to be paid is: exchange of a smooth slope function is a systematic deviation from the true slope at a given value of Jt for all functions except pure power laws. For a given set of simulation data, if one increases Jt_{av} , one gains smoothness and along with it the ability to extrapolate. Conversely, if one decreases Jt_{av} , the systematic deviations go down, but the statistical fluctuations grow more intense. The three plots in each figure are intended to illustrate that the systematic deviations are negligible except (in some cases) for short times.

⁸The width $2\sqrt{3}J$ of the $J_{i,i+1}$ distribution has been chosen to match the initial curvature of $C_0(t)$ with those of the other three models.

⁹In Ref. 1 (second paper) we have already compared three of the four long-time tails directly and found (ii) and (iii) similar but distinct from (i). The superior statistics of our new data reveals subtle but significant differences between (ii) and (iii) as well.

Theoretical study of magnetostriction in FeTaN thin films

James C. Cates and Chester Alexander, Jr.

Center for Materials for Information Technology and Department of Physics and Astronomy, The University of Alabama, Tuscaloosa, Alabama 35487-0114

Single layer films of FeTaN have been deposited by dc magnetron sputtering, and the relationships between the magnetostriction and film composition have been studied. A linear increase in magnetostriction with nitrogen content has been explained by the dependence of λ_{100} on nitrogen concentration. The form of this dependence has been derived based on a theory developed by De Vries for describing the magnetic after effect in iron films with interstitial nitrogen. At room temperature, the best fit for the experimental magnetostriction data was found for an interstitial interaction constant of $D=4.18 \times 10^6 \text{ J/m}^3$. The total magnetic anisotropy energy per grain, U_{110} , has also been calculated as a function of the strain for FeN films with a (110) orientation under a tetragonal deformation. This calculation used the results derived for the dependence of the magnetostriction constant, λ_{100} , on nitrogen concentration. The calculated U_{110} value shows a minimum at a lattice strain value of $\epsilon_{11}=0.0029$, in close agreement with a maximum in permeability at $\Delta d_{110}/d_{110}=0.0028$ previously reported for FeN films.

I. INTRODUCTION

Recent results at The University of Alabama show that FeTaN films deposited by high-growth rate dc magnetron sputtering have suitable soft magnetic properties for use in recording heads.^{1,2} X-ray diffraction measurements of these films show a structure containing only the α -Fe phase with a (110) orientation. The addition of tantalum to the FeN films has been shown to improve the incorporation of nitrogen in the films during sputtering while suppressing the formation of iron-nitride phases, such as Fe_4N .

Wang and Kryder have examined the saturation magnetostriction in FeN films deposited by rf sputtering.³ They attributed the increase in magnetostriction found with increasing nitrogen flow rates during deposition to the existence of higher amounts of $\gamma\text{-Fe}_4\text{N}$ which exhibits a positive magnetostriction. Magnetostriction in FeN films deposited by dc magnetron sputtering has been reported by Russak *et al.* to increase linearly with the nitrogen flow rate during deposition.⁴ Similar results have been found by Nago, Sakakima, and Ihara for FeTaN films deposited by rf sputtering after annealing at 500°C .⁵

The relationship between the film composition and magnetostriction in FeN-based films has been difficult to model because the presence of additional iron-nitride phases with various orientations greatly complicates any interpretations of magnetostriction results. One important reason for examining the FeTaN system was that the structure was relatively simple, showing only the α -Fe phase with a (110) orientation. In this system the nitrogen atoms are presumed to primarily occupy interstitial sites in the iron lattice causing a deformation of the lattice from body-centered cubic to body-centered tetragonal. Increases in the nitrogen content in the film corresponded to higher occupation of the interstitial sites. The effects on the magnetostriction constants λ_{100} and λ_{111} of this nitrogen in the interstitial sites have been modeled based on a theory developed by De Vries.^{6,7} The resulting expressions have been used to predict the values of the saturation magnetostriction and the total anisotropy energy per grain, U_{110} , for comparison with experimental results.

II. EXPERIMENTAL

The FeTaN films, approximately 4000 \AA thick, were deposited on Corning 7059 glass by dc magnetron reactive sputtering in a Vac-Tec model 250 batch side sputtering system. Background pressure during deposition was 4×10^{-7} Torr with the sputtering power at 300 W. The argon flow rate was set at 60 standard cubic centimeters per minute (sccm) while the nitrogen flow rate was varied from 0 to 25 sccm. Targets used for film deposition were FeTa sintered targets with a tantalum content of 5.0 and 10.0 wt %. The composition of films deposited from these targets was measured by x-ray fluorescence and was found to contain 1.8 and 3.2 at. % tantalum, respectively. A high-precision ac magnetostriction tester, based on the design by Tam and Schroeder, was used for magnetostriction measurements.⁸

III. RESULTS AND ANALYSIS

A. Nitrogen dependence of λ_{100} and λ_{111}

The saturation magnetostriction in the FeTaN samples showed a strong dependence on the nitrogen flow rate during the film deposition. In the range of nitrogen flow rates examined in this study, the flow rate was roughly proportional to the amount of nitrogen present in the FeTaN films. Figure 1 shows the saturation magnetostriction as a function of the nitrogen concentration for films with different tantalum contents. The magnetostriction increased almost linearly with increasing nitrogen concentration. X-ray measurements showed little change in film structure with increasing nitrogen content, other than a decrease in the estimated grain size. The fact that the increase in magnetostriction with nitrogen concentration in these FeTaN samples is not due to the formation of new phases or changes in orientation of α -Fe as seen in other FeN systems should be emphasized.^{3,9} That is, in the FeTaN samples the change in magnetostriction with nitrogen content is interpreted as being mainly due to changes in the magnetostriction constants caused by the addition of nitrogen to the α -Fe lattice.

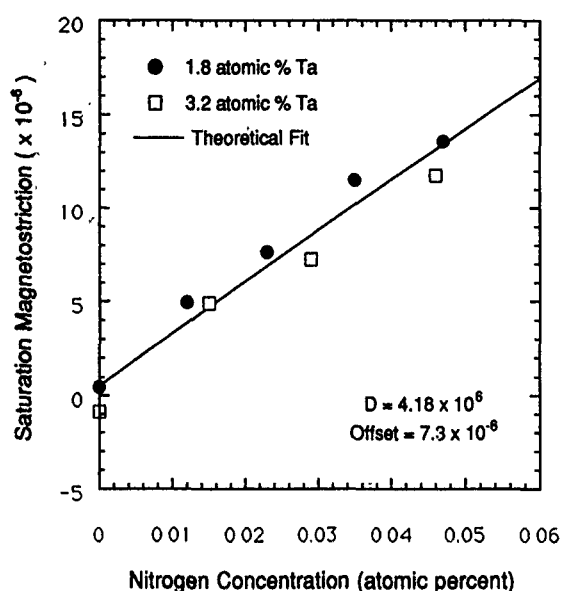


FIG. 1. Experimental values of magnetostriction for FeTaN samples for tantalum contents of 1.8 and 3.2 at. % vs nitrogen concentration. The theoretical line is calculated from Eqs. (3) and (4), using a value of $D = 4.18 \times 10^6$ J/m³.

This linear increase of the magnetostriction with nitrogen content can be modeled assuming changes in the magnetostriction constant of iron, λ_{100} , when nitrogen is added to interstitial sites in the α -Fe lattice. For this model we have extended the theory developed by De Vries for describing the magnetic after effects in iron films with interstitial nitrogen.^{6,7} Our extension included consideration of two im-

portant points: (1) the variation of the magnetoelastic constants with nitrogen concentration, and (2) the relaxation time of the distributed nitrogen.

The theory and experiments of De Vries were for iron samples with very low (<0.04 wt %) amounts of nitrogen. For these low concentrations it was assumed that the values of the magnetoelastic coupling parameters, B_1 and B_2 , did not depend on the nitrogen concentration. The FeTaN samples of the current research had a nitrogen concentration of up to 6 at. %, and it was found necessary to consider variations of the magnetoelastic coupling constants, B_1 and B_2 , with nitrogen concentration in order to have a physically meaningful theoretical description.

It was also necessary to consider the relaxation time of the interstitial nitrogen to compare the current magnetostriction results with the earlier results of De Vries on magnetic after effects. Nitrogen in interstitial sites can diffuse to alternate sites with relaxation times of a few seconds, at 300 K, when the directions of applied magnetic fields are changed. This diffusion causes temporal changes in the magnetoelastic properties of the iron samples, thus producing a magnetic after effect. In the current research the ac-magnetostriction measurements were made in a time which is 25–100 times shorter than the relaxation time of the dissolved nitrogen, and no after effects can be observed. To help make this distinction clear, the magnetostriction constants will be designated as λ^{long} and λ^{short} , depending on whether the measurement time scales were long or short compared to the nitrogen relaxation time.

De Vries modified earlier models of Polder¹⁰ and Néel¹¹ and postulated the following expression for the free energy per unit volume for a lattice containing interstitial atoms:

$$\begin{aligned}
 F - F_0 = & \frac{1}{2} c_{11}(e_{xx}^2 + e_{yy}^2 + e_{zz}^2) + \frac{1}{2} c_{44}(e_{xy}^2 + e_{yz}^2 + e_{zx}^2) + c_{12}(e_{xx}e_{yy} + e_{yy}e_{zz} + e_{zz}e_{xx}) + B'_1 \left[e_{xx} \left(\alpha_1^2 - \frac{1}{3} \right) + e_{yy} \left(\alpha_2^2 - \frac{1}{3} \right) \right. \\
 & \left. + e_{zz} \left(\alpha_3^2 - \frac{1}{3} \right) \right] + B'_2 (\alpha_1 \alpha_2 e_{xy} + \alpha_2 \alpha_3 e_{yz} + \alpha_1 \alpha_3 e_{zx}) + \epsilon (C_x e_{xx} + C_y e_{yy} + C_z e_{zz}) + \frac{RT}{2VC_0(1-C_0)} (C_x^2 + C_y^2 + C_z^2) \\
 & + D \left[\left(\alpha_1^2 - \frac{1}{3} \right) C_x + \left(\alpha_2^2 - \frac{1}{3} \right) C_y + \left(\alpha_3^2 - \frac{1}{3} \right) C_z \right] + K_1 (\alpha_1^2 \alpha_2^2 + \alpha_2^2 \alpha_3^2 + \alpha_3^2 \alpha_1^2) + K_2 \alpha_1^2 \alpha_2^2 \alpha_3^2. \quad (1)
 \end{aligned}$$

In this expression, the nitrogen concentration is $3C_0$, the c 's are elastic moduli, the e 's are lattice strains, the α 's are direction cosines of the magnetization with respect to the crystal axes, the C 's are deviations of interstitial site occupations from the mean fraction C_0 , B'_1 and B'_2 are the magnetoelastic coupling constants in a nitrogen-containing structure, the K 's are the magnetocrystalline anisotropy constants, D is the interstitial interaction constant, ϵ is a strain-interstitial coupling constant. F_0 is the free energy without any effects of strain, interstitials, or magnetization direction, T is the absolute temperature, R is the gas constant, and V is the molar volume of iron.

Equation (1) was used to calculate the effect of the interstitial nitrogen on the magnetostriction constants. The lattice equilibrium was found by minimizing the free energy of Eq. (1) with respect to the strains e_{ij} and the interstitial concentrations C_i . Compared to the De Vries treatment, we have kept higher-order terms involving the nitrogen concentration ($3C_0$), and have allowed for the dependence of B_1 and B_2 on C_0 . That is, our treatment allows for the variation of the magnetoelastic coupling constant, B , on the nitrogen concentration. With nitrogen interstitials, these constants are designated B'_1 and B'_2 , and B'_1 can be found from an expression for $\lambda_{100}^{\text{long}}$ as

$$B'_1 = -\frac{3}{2} \lambda_{100}^{\text{long}} \left(c_{11} - c_{12} - \frac{\epsilon^2 V C_0 (1 - C_0)}{RT} \right) + \frac{\epsilon D V C_0 (1 - C_0)}{RT} \quad (2)$$

The value of B'_1 corresponds to the value of the instantaneous magnetostriction constant $\lambda_{100}^{\text{short}}$, and using the well-known relationship between λ_{100} and B_1 , the magnetostriction constant, $\lambda_{100}^{\text{short}}$, can be expressed in terms of the nitrogen concentration ($3C_0$). Since the nitrogen atoms will attempt to occupy interstitial sites in planes perpendicular to the direction of the applied magnetic field, the $\lambda_{100}^{\text{long}}$ can be approximated by $\lambda_{100}^{\text{Fe}}$. The value of $\lambda_{100}^{\text{short}}$ will represent the measured value for a FeN film, which is represented as $\lambda_{100}^{\text{FeN}}$. This substitution yields

$$\lambda_{100}^{\text{FeN}} = \lambda_{100}^{\text{Fe}} \left(1 - \frac{\epsilon^2 V C_0 (1 - C_0)}{(c_{11} - c_{12}) RT} \right) - \frac{2}{3} \left(\frac{\epsilon D V C_0 (1 - C_0)}{(c_{11} - c_{12}) RT} \right) \quad (3)$$

Following the procedure indicated above for the constant λ_{111} gives the result $\lambda_{111}^{\text{FeN}} = \lambda_{111}^{\text{Fe}}$.

By proper averaging the saturation magnetostriction for a film with a (110) orientation can be shown to be

$$\lambda_s = \frac{11}{32} \lambda_{100} + \frac{21}{32} \lambda_{111} \quad (4)$$

Using this expression and Eq. (3), the theoretical value of the magnetostriction for a FeN film with a (110) orientation can be calculated, assuming that the nitrogen concentration is uniformly distributed in the film. Two sets of experimental data points and the theoretical fit are shown in Fig. 1. The values of the constants taken from the literature and used in the theoretical fit were $\epsilon = -9.2 \times 10^{10} \text{ J/m}^3$, $c_{11} = 2.41 \times 10^{11}$ and $c_{12} = 1.46 \times 10^{11} \text{ N/m}^2$, $T = 300 \text{ K}$, $\lambda_{100}^{\text{Fe}} = 20.7 \times 10^{-6}$, $\lambda_{111}^{\text{Fe}} = -21.2 \times 10^{-6}$, $R/V = 1.17 \times 10^6 \text{ J/(m}^3\text{K)}$. This fit describes the increase in magnetostriction with nitrogen content quite well. A vertical shift of the theoretical line was required to fit the experimental data. This could be caused by the presence of intercrystalline material, trace amounts of new phases, or orientations not detectable by x ray, or film contaminants. An average value of $D = 4.18 \times 10^6 \text{ J/m}^3$ gives a good fit to both sets of experimental points at room temperature. The value of D is roughly 10% less than the value reported by De Vries for his measurements conducted at 225 K.⁷ This is consistent with reports of a decrease in D with increase in temperature.¹²

B. Permeability

Measurements of other investigators have shown that the initial permeability along the hard axis of FeN films with a (110) orientation can be correlated with the magnetic anisotropy energy in each grain, calculated for a tetragonal deformation of the iron lattice under the assumption that the mag-

netocrystalline anisotropy constants, elastic moduli, and magnetostriction constants were the same as those for bulk iron.¹³⁻¹⁵ Takahashi and Shimatsu have favorably compared the location of a maximum in the initial permeability for FeN films to the minimum in the total anisotropy energy per grain, U_{110} , of iron that occurs at a lattice strain of 0.0040.¹⁶ The technique for calculating the total anisotropy per grain for an iron film has been described elsewhere.¹³⁻¹⁶

We have recalculated the total anisotropy energy per grain, U_{110} , with allowance for the dependence of λ_{100} on the nitrogen content in FeN films. The amount of lattice strain due to interstitial nitrogen was used to calculate the nitrogen concentration using an expression of Wriedt and Zwell that gives the dependence of the lattice constant of iron on the amount of interstitial nitrogen.¹⁷ The magnetostriction constant, $\lambda_{100}^{\text{FeN}}$, can then be calculated using Eq. (3). In this calculation the total nitrogen concentration was given as $3C_0$ and the experimentally determined room temperature value of $D = 4.18 \times 10^6 \text{ J/m}^3$ was used. This value of $\lambda_{100}^{\text{FeN}}$ can then be used in the calculation of the total anisotropy energy as a function of the lattice strain. We have done this calculation and find that the energy minimum occurs at a value of lattice strain $\epsilon_{11} = 0.0029$ which agrees closely with the experimental maximum in permeability previously reported at $\Delta d_{110}/d_{110} = 0.0028$.¹⁶

ACKNOWLEDGMENTS

We would like to acknowledge the assistance of IBM in the x-ray fluorescence measurements of the tantalum content of the films. The research reported here was partially supported by a grant from the Department of Commerce Advanced Technology Program administered by NSIC. J.C. also acknowledges support from a University of Alabama Graduate Council Fellowship.

- ¹ G. Ciu, E. Haftek, and J. A. Barnard, *J. Appl. Phys.* (in press).
- ² G. Ciu, E. Haftek, J. C. Cates, C. Alexander, Jr., and J. A. Barnard, *Mater. Res. Soc. Symp. Proc.* (in press).
- ³ Wang and M. H. Kryder, *J. Appl. Phys.* **67**, 5134 (1990).
- ⁴ M. A. Russak, C. V. Jahnes, E. Klokholm, J.-W. Lee, M. E. Re, and B. C. Webb, *J. Magn. Mag. Mater.* **104-107**, 185 (1992).
- ⁵ K. Nago, H. Sakakima, and K. Ihara, *J. Magn. Soc. Jpn.* **15**, 365 (1991).
- ⁶ G. De Vries, *Physica* **25**, 1211 (1959).
- ⁷ G. De Vries, D. W. Van Geest, R. Gersdorf, and G. W. Rathenau, *Physica* **25**, 1131 (1959).
- ⁸ A. Tam and H. Schroeder, *IEEE Trans. Magn.* **MAG-25**, 2629 (1989).
- ⁹ N. Ishiwata, Y. Takeshima, T. Konehara, and H. Urai, presented at the 6th International Conference on Ferrites (in press).
- ¹⁰ D. Polder, *Philips Res. Rep.* **1**, 5 (1945).
- ¹¹ L. Néel, *J. Phys. Rad.* **12**, 339 (1952).
- ¹² G. W. Rathenau, in *Magnetic Properties of Metals and Alloys*, edited by R. M. Bozorth (American Society for Metals, Cleveland, OH, 1959), p. 196.
- ¹³ M. Takahashi and T. Shimatsu, *IEEE Trans. Magn.* **MAG-26**, 1485 (1990).
- ¹⁴ M. Takahashi, H. Shoji, T. Shimatsu, H. Komaba, and T. Wakiyama, *IEEE Trans. Magn.* **MAG-26**, 1503 (1990).
- ¹⁵ T. Shimatsu, H. Shoji, M. Kyoho, M. Takahashi, and T. Wakiyama, *J. Magn. Soc. Jpn.* **15**, Suppl. No. S2, 63 (1991).
- ¹⁶ M. Takahashi, H. Shoji, T. Shimatsu, H. Komaba, and T. Wakiyama, *IEEE Trans. Magn.* **MAG-26**, 1503 (1990).
- ¹⁷ H. A. Wriedt and L. Zwell, *Trans. AIME* **224**, 1242 (1962).

Dependence of the magnetic properties $\text{Gd}_{2-x}\text{Ce}_x\text{CuO}_4$, $0 \leq x \leq 0.15$, on their particle size

J. Mahía, C. Vázquez-Vázquez, J. Mira, M. A. López-Quintela, and J. Rivas
University of Santiago de Compostela, 15706 Santiago de Compostela, Spain

T. E. Jones
NOSC, San Diego, California 92182-0325

S. B. Osseoff
San Diego State University, San Diego, California 92182-0325

$\text{Gd}_{2-x}\text{Ce}_x\text{CuO}_4$, $0 \leq x \leq 0.15$, have been synthesized by the solid state reaction, the sol-gel technique and the water-in-oil microemulsion, in order to vary the particle size. The samples have been characterized by x-ray diffraction, photon correlation spectroscopy and transmission electron microscopy. Magnetization and ac susceptibility measurements were performed between 4 and 300 K. The extrapolated linear part of the inverse magnetization shifts to lower temperatures as the particle size decreases. The internal field associated to the WF of the Cu moments diminishes with the particle diameter. Differences between the zero-field-cooling and the field-cooling magnetization curves were observed for $T < T_N$. These differences depend on the particle size.

Since the discovery of the new family of electron doped superconductors $\text{R}_{1.85}\text{M}_{0.15}\text{CuO}_4$ (with $\text{R}=\text{Pr}$, Nd , Sm , Eu , and $\text{M}=\text{Ce}$, Th)¹ much attention has been focused on the study of the properties of these materials.² Gd_2CuO_4 has been found not to be superconducting when doped with Ce or Th ,³ as contrary to the lighter rare earths compounds. This family crystallizes in the tetragonal Nd_2CuO_4 -type structure with the Cu(II) ions ordered antiferromagnetically (AF) at $T_N \approx 270$ K. The interest in Gd_2CuO_4 lies on the possible relationship between its magnetic properties and its non-superconducting behavior. The magnetic properties of this compound have been studied in detail for single crystals and powders.⁴ This compound shows a WF component below $T_N \approx 270$ K, possibly due to a distortion of the oxygens surrounding the Cu moment in the T' phase, which occurs for rare earths lighter than Eu(III) .

In the present work, we describe the synthesis of $\text{Gd}_{2-x}\text{Ce}_x\text{CuO}_4$ (with $x=0.00, 0.05, 0.10$, and 0.15) using a sol-gel technique and water-in-oil (W/O) microemulsions. Both techniques allow us to obtain polycrystalline powders of controlled size. We performed magnetization measurements in order to study the influence of particle size on the magnetic properties of these materials.

We used three different techniques to obtain particles of different sizes:

(1) Solid state reaction, using a stoichiometric mixture of Gd_2O_3 and CuO as starting materials. The mixture was ground in a ball mill and then annealed first at 800°C for 24 h with several intermediate grindings followed by a second annealing at 850°C for 48 h. The resulting powder was used as a reference.

(2) Sol-gel technique, using urea as gelificant agent. As starting materials stoichiometric amounts of nitrate salts were used, due to their high solubility in water. The solvent was evaporated directly on a hot plate with continuous stirring. When cooling a gel is formed, which is decomposed in an oven at 250°C , yielding the precursor of these samples.

After grinding the precursor, it was submitted to several annealings at different temperatures in order to obtain particles of different sizes. More details of this process had been previously reported.⁵

(3) Synthesis of Gd_2CuO_4 was done by means of a W/O microemulsion. We used *n*-heptane as organic phase, Aerosol-OT (bis-2-ethyl hexyl sodium sulfosuccinate) as surfactant and a solution of citric acid and nitrate salts as an aqueous phase. The microemulsion was heated on a hot plate to evaporate part of the organic phase. This gel was washed with *n*-heptane and acetone. The resulting powder was dried yielding to the precursor of these samples. After grinding the precursor, it was subjected to different annealings.

The polycrystalline powders were structurally characterized by x rays. The size distribution was measured by photon correlation spectroscopy (PCS) and transmission electron microscopy (TEM). The magnetic measurements were made between $4 \text{ K} \leq T \leq 300 \text{ K}$ using SQUID and VSM magnetometers in fields up to 5 kOe.

X-ray diffraction of the samples synthesized by the solid state reaction indicates a pure Gd_2CuO_4 phase. Similar data for Gd_2CuO_4 , obtained via sol-gel, show almost a pure phase for samples annealed at temperatures as low as 650°C . The time necessary to obtain this phase decreases considerably when the calcination temperature increases. For example, 72 h are needed at 650°C but only 3 h at 950°C . Seven samples between these two temperatures were obtained. $\text{Gd}_{2-x}\text{Ce}_x\text{CuO}_4$ (with $x=0.05, 0.10$, and 0.15) was also prepared via sol-gel. It was observed that when the annealing temperature decreases so does the solubility of Ce in the compound. When $x=0.05, 0.10$, and 0.15 the pure phase is obtained only for temperatures above $700, 750$, and 900°C , respectively. For samples synthesized in W/O microemulsions, the Gd_2CuO_4 phase is obtained at 700°C . X-ray diffraction shows the presence of $\approx 10\%$ of Gd_2O_3 as a secondary phase. The amount of this secondary phase is almost independent of the annealing temperature. Five samples were

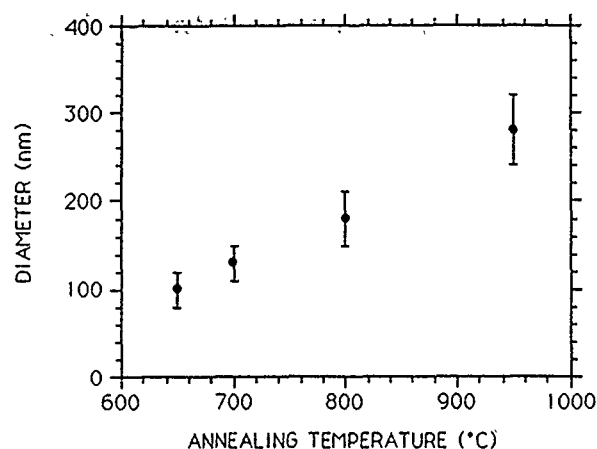


FIG. 1. Average diameter of Gd_2CuO_4 particles as a function of the annealing temperature for samples obtained via sol-gel.

prepared between 700 and 950 °C using W/O microemulsions.

The particle size of the different samples was measured by PCS. Figure 1 shows the average diameter of the particles as a function of the annealing temperature for samples obtained via sol-gel. As it can be seen the particle size increases with annealing temperature. The particles synthesized by ordinary solid state reaction present high polydispersity, contrary to the obtained by the wet methods, with sizes in the range 0.2–4 μm .

Figure 2 shows two TEM photographs, one for a sample prepared by the solid state reaction [Fig. 2(a)], and the other for a sol-gel sample annealed at 750 °C [Fig. 2(b)]. As it can

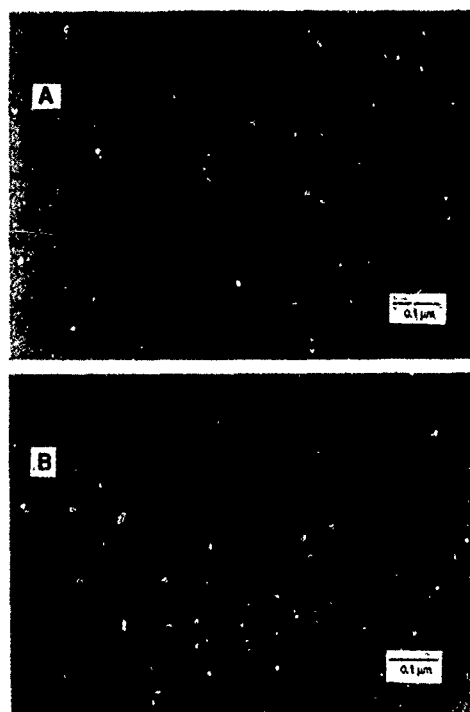


FIG. 2. TEM photographs (a) for a sample prepared by solid state reaction and (b) for a sol-gel sample annealed at 750 °C.

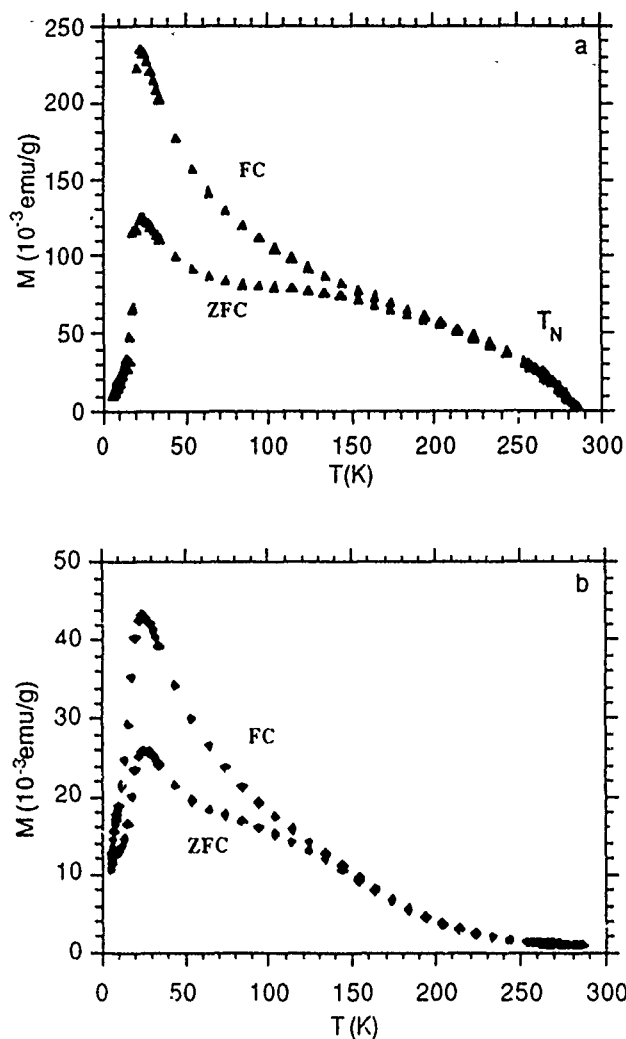


FIG. 3. (a) dc magnetization vs temperature for a ceramic Gd_2CuO_4 sample. (b) dc magnetization vs temperature for a sol-gel Gd_2CuO_4 sample annealed at 800 °C.

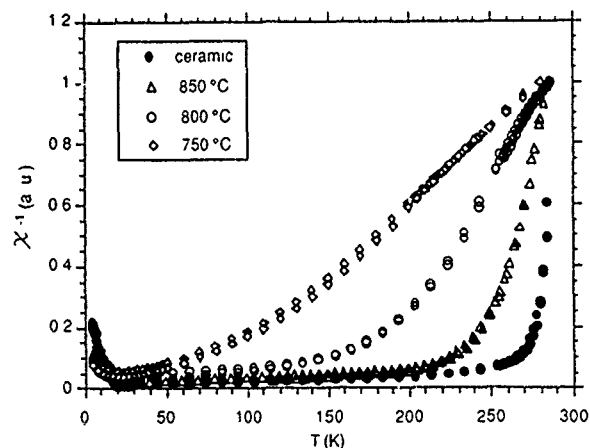


FIG. 4. Inverse of dc susceptibility curves vs temperature for sol-gel and ceramic Gd_2CuO_4 samples.

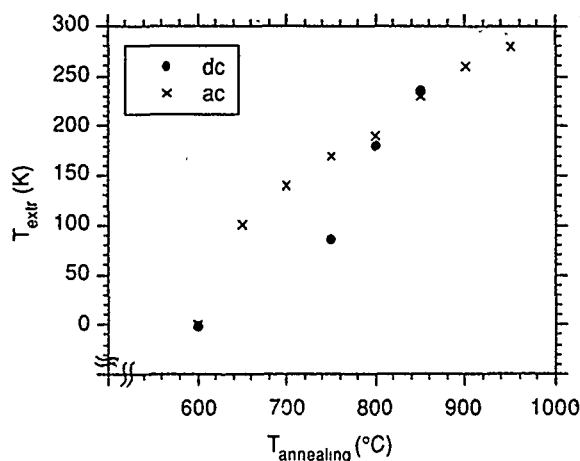


FIG. 5. Extrapolated temperatures from dc and ac susceptibilities for sol-gel Gd_2CuO_4 samples.

be seen, ceramic samples are relatively large ($\approx 1\mu\text{m}$), while the sol-gel particles are of the order of $\approx 100\text{ nm}$. The sizes measured by PCS and TEM agree well.

dc magnetization data show that the WF component found in single crystals and in polycrystalline samples of Gd_2CuO_4 below $\approx 270\text{ K}$,⁴ as shown in Fig. 3(a) for a ceramic sample, is depressed in a sample annealed at 800°C , as seen in Fig. 3(b). The WF peak in single crystals occurs at the ordering temperature of Cu(II) moments and is due to a distortion from a perfect square of the CuO_2 plane, because of the displacement of oxygen atoms along the normal to the Cu—O bond. Such a distortion results in spin-canted antiferromagnetic domains ("canted" AF ordering of the Cu moments). This property is better appreciated when plotting the χ^{-1} vs T , as done for sol-gel Gd_2CuO_4 samples in Fig. 4. If we associate the extrapolated temperature of the linear part of χ^{-1} with the onset of WF, we observe that the transition temperature seems to be reduced with the particle size. ac susceptibility measurements done in the same samples held

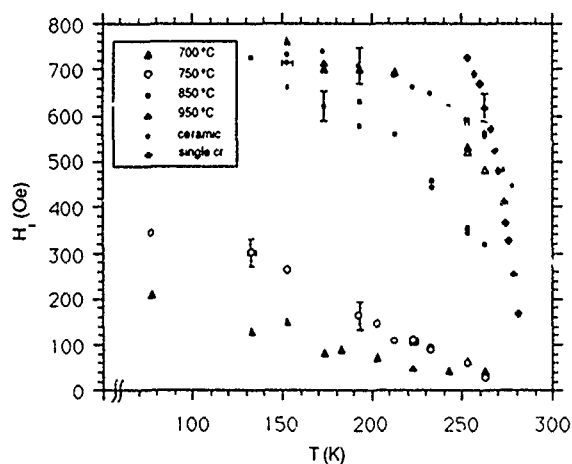


FIG. 6. Internal fields obtained from M vs H measurements for sol-gel, ceramic and single crystal Gd_2CuO_4 samples.

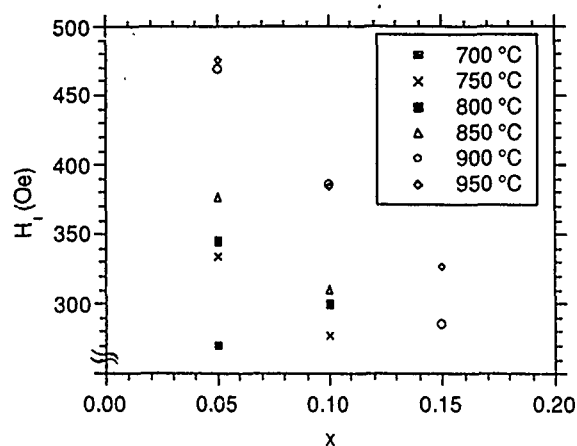


FIG. 7. Internal fields obtained from M vs H measurements for sol-gel $\text{Gd}_{2-x}\text{Ce}_x\text{CuO}_4$ samples.

similar results. In Fig. 5 it is shown the extrapolated temperature, T_{ext} , obtained by ac and dc measurements. The disappearance of the internal field could be explained if the size of the particles becomes comparable with the correlation length of the Cu(II) antiferromagnetic order. Another explanation could be due to the surface effects which become more important for smaller particles and such effects could slightly modify the lattice parameters, which are determinant in the onset of WF.² It is worth mentioning that besides the effects on this peak, other features observed are the decrease of the absolute magnetization values and differences between field cooling (FC) and zero field cooling (ZFC) magnetization curves.

In Fig. 6 the evolution of the internal field, H_i , extrapolated from the paramagnetic part of M vs H measurements at high field as a function of the temperature for sol-gel is presented. Values for ceramic and single crystal samples are also included. It is clear that the internal field diminishes with the particle size.

For the sol-gel $\text{Gd}_{2-x}\text{Ce}_x\text{CuO}_4$ samples, H_i decreases with the annealing temperature and cerium doping as seen in Fig. 7. The internal field is more sensitive to the thermal annealing than to cerium doping.

We wish to acknowledge financial support from the DGICYT, PB92-1086; Fundación Ramón Areces; NSF-DMR-91172122 and NATO, CRG920255. J. M. and C. V. also thank Fundación Segundo Gil Dávila and Xunta de Galicia, respectively.

¹ Y. Tokura, H. Takagi, and S. Uchida, *Nature (London)* **337**, 345 (1989).

² S. B. Oseroff, D. Rao, F. Wright, D. C. Vier, S. Schultz, J. D. Thompson, Z. Fisk, S. W. Cheong, M. T. Hundley, and M. Tovar, *Phys. Rev. B* **41**, 1934 (1990).

³ A. Butera, A. Caneiro, M. T. Causa, L. B. Steren, R. Zysler, M. Tovar, and S. B. Oseroff, *Physica C* **160**, 341 (1989).

⁴ J. D. Thompson, S. W. Cheong, S. E. Brown, Z. Fisk, S. B. Oseroff, M. Tovar, D. C. Vier, and S. Schultz, *Phys. Rev. B* **39**, 6660 (1989).

⁵ J. Mahía, C. Vázquez-Vázquez, M. I. Basadre-Pampín, J. Mira, J. Rivas, M. A. López-Quntela, and S. B. Oseroff, *J. Am. Ceram. Soc.* (to be published).

Magnetic properties of materials in the CaO-P₂O₅-Fe₂O₃ system

Binod Kumar and Christina H. Chen

University of Dayton Research Institute, Dayton, Ohio 45469-0170

The magnetic properties of numerous compositions in the ternary CaO-P₂O₅-Fe₂O₃ system have been studied. A relatively wide glass formation region is located around the P₂O₅ corner of the system. The Fe₂O₃-containing glasses exhibit paramagnetic behavior. The specimens inside the composition range Fe₂O₃ ≥ 30% consist of both paramagnetic and ferrimagnetic phases.

Glass formation in the CaO-P₂O₅-Fe₂O₃ system has been known and studied for over two decades.¹⁻⁴ The system provides a wide range of glass specimens for optical and magnetic studies. However, the motivation for early studies was primarily academic. The phosphate glass-forming system has recently attracted considerable attention as potential biomaterials.⁵⁻⁷ The CaO-P₂O₅-Fe₂O₃ system has also been of considerable interest in steel making.⁸

In CaO-P₂O₅-Fe₂O₃ glasses and slags, iron exists in primarily two oxidation states, the Fe²⁺ and Fe³⁺ states, which give rise to well documented characteristic optical and magnetic phenomena. The magnetic susceptibility of a few compositions in the CaO-P₂O₅-Fe₂O₃ system has been measured and reported by Sanad *et al.*⁹ However, a complete understanding of the basic mechanisms leading to variations in magnetic properties in a wide range of compositions is lacking. Thus, the purpose of this study is to conduct a limited but systematic study of the magnetic properties in the CaO-P₂O₅-Fe₂O₃ system.

The compositions used in this investigation are shown in Table I. The details for sample preparation were reported earlier.⁴ After casting, the materials were annealed at 500 °C in air. Two were further heat treated before being characterized for magnetic properties. Magnetic susceptibility was measured using a Princeton Vibrating Sample Magnetometer Model 151 from 20 to 500 °C. A few specimens were also characterized for microstructures using optical microscopy, SEM, and energy dispersive x-ray analysis.

Figure 1, a ternary diagram, shows the locations of the synthesized compositions. General observations on these compositions are presented in Table I. Based on these observations and magnetic measurements, the CaO-P₂O₅-Fe₂O₃ system is divided into three regions: glass-forming region, refractory region ($T_m > 1400$ °C), and ferrimagnetic region.

The glass-forming region has a relatively wide composition range around the P₂O₅ corner. In this region, specimens were melted easily in the temperature range of 1000–1400 °C and retained their vitreous character during the casting and heat treatment processes. Some compositions inside the ferrimagnetic region also melted with relative ease; however, they crystallized during the casting and heat treatment processes. Compositions with (CaO+Fe₂O₃) > 60% exhibited significant refractoriness, and three (Nos. 8, 11, and 12) did not melt.

Figure 2 shows magnetic susceptibility, χ , as a function of temperature for three specimens: Nos. 17, 18, and 19. These compositions are located in the glass-forming region. The calcium phosphate glass, No. 19, alone exhibits diamag-

netic behavior with a negative χ , which is relatively independent of temperature. When iron is introduced to the binary phosphate glass, it gives rise to paramagnetic behavior, the degree of which is directly related to the iron concentration. Paramagnetism originates from the presence of permanent magnetic dipole moments in the materials. Both oxidation states of iron, Fe²⁺ and Fe³⁺, lead to permanent dipole moments. The magnetic moment of Fe³⁺, with five unpaired electrons, is higher than that of Fe²⁺, which has only four. It has recently been reported that the melting atmosphere has a major influence on the relative proportion of Fe²⁺ and Fe³⁺ states in these glasses.¹⁰ In general, the oxidizing atmosphere increases the proportion of Fe³⁺. The melting atmosphere-induced redox state also affects the resulting physical and chemical properties of the glasses.⁷ The paramagnetism of Nos. 17 and 18 exhibit significant temperature dependence. Specimen No. 17 is a weaker paramagnetic material whose magnetic susceptibility is close to zero at elevated temperature. In general, paramagnetic susceptibility decreases with increasing temperature.

Paramagnetic materials show a linear relationship between applied magnetic field, H , and specific magnetization, σ . Ferrimagnetism yields a nonlinear relationship between H and σ and also results in a hysteresis effect. The bulk specimens 5, 6, 7, 9, and 10 located in the ferrimagnetic region

TABLE I. Compositions and observations in the CaO-P₂O₅-Fe₂O₃ system.

	Composition (wt %)			Observations
	CaO	P ₂ O ₅	Fe ₂ O ₃	
1	10	50	40	Good glass
2	20	50	30	Glass with a crystallized surface
3	30	50	20	Melted but could not be poured out of crucible
4	40	50	10	Very little formation of liquid phase
5	10	40	50	Good liquid but crystallized during cast
6	20	40	40	Good liquid but crystallized during cast
7	30	40	30	Melted but could not be poured out of crucible
8	40	40	20	Did not melt
9	10	30	60	Good liquid but crystallized during cast
10	20	30	50	Melted but could not be poured out of crucible
11	30	30	40	Incomplete melting
12	40	30	30	Did not melt
13–16	4–16	64–70	20–30	Good glass
17	16	79	5	Good glass
18	11	79	10	Good glass
19	28	72	0	Good glass

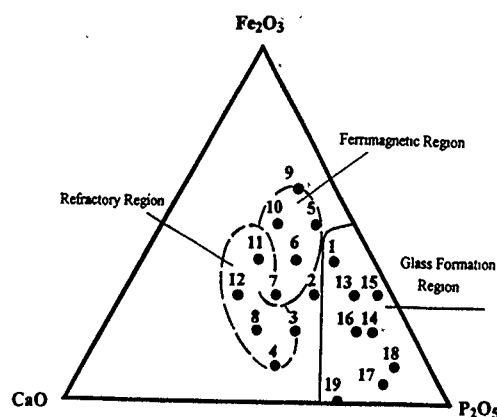


FIG. 1. Synthesized compositions in the CaO-P₂O₅-Fe₂O₃ system.

contain both paramagnetic and ferrimagnetic phases. Magnetic properties of these bulk specimens are comprised of contributions from both phases. Figure 3(a) shows a σ vs H plot of bulk No. 6 heat treated at 700 °C. The bulk magnetic response is resolved into ferrimagnetic and paramagnetic contributions as shown in Figs. 3(b) and 3(c).

Magnetic parameters MH_c , σ_s , σ_r , and χ of specimens 2, 5, 6, 7, 9, and 10 are presented in Table II. It is interesting that the paramagnetic contributions remain constant at $\sim 6 \times 10^{-5}$ emu/(g Oe) for all the specimens in the ferrimagnetic region. The paramagnetic phase is believed to be a vitreous phase containing Fe₂O₃, whereas the ferrimagnetic phase is a crystalline phase containing mostly P₂O₅ and Fe₂O₃. Specimen 10 (20CaO·40P₂O₅·50Fe₂O₃) has the highest saturation $\sigma_s \approx 26.0$ emu/g. Optical microscopy of specimen 10 revealed three phases. The volume fraction of the ferrimagnetic phase as determined from optical microscopy is about 83%. From this data, the σ_s for a single ferrimagnetic phase is estimated to be 31 emu/g which is higher than that for cubic ferrites MgO·Fe₂O₃ and CuO·Fe₂O₃.

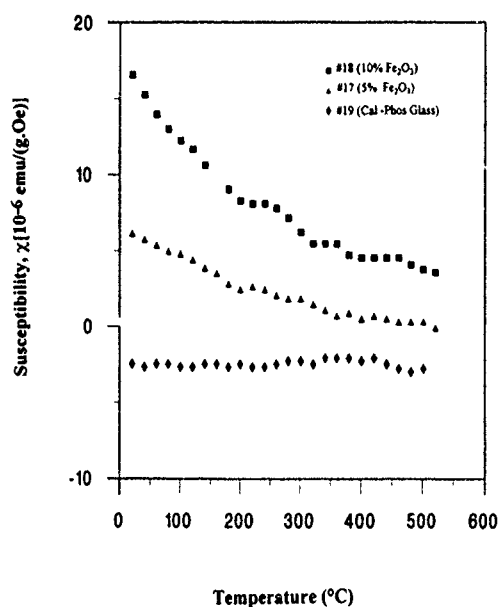


FIG. 2. Magnetic susceptibility χ vs temperature of Nos. 17, 18, and 19.

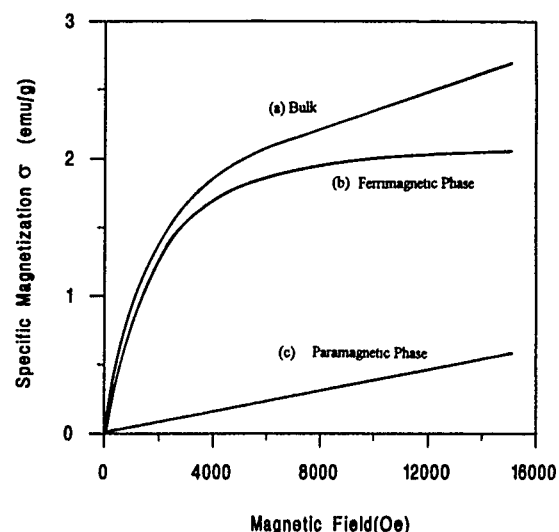


FIG. 3. Magnetization curve of No. 6 heat treated at 700 °C. (a) Bulk, (b) ferrimagnetic phase, (c) paramagnetic phase.

The magnetization curves of No. 5 are shown in Fig. 4. After annealing at 500 °C, No. 5 displays ferrimagnetic behavior with a large hysteresis loop: remanent magnetization $B_r = 29.5$ G ($\sigma_r = 0.3$ emu/g) and intrinsic coercivity $MH_c = 450$ Oe. The specimen was further heat treated at 600, 700, 750, and 850 °C for 24 h. The higher the heat treatment temperature, the lower the degree of ferrimagnetism, and it vanishes at 850 °C. Specimen No. 6 exhibited similar behavior. Table III presents a comparison of the magnetic properties of Nos. 5 and 6 for similar heat treatments. It is apparent that No. 6 possesses ferrimagnetism superior to that of No. 5, in spite of the fact that No. 6 has a lower iron concentration. However, additional heat treatments have a negative effect on the ferrimagnetic behavior of both specimens.

In an attempt to characterize the ferrimagnetic phase, specimen No. 5 was examined using scanning electron microscopy and energy dispersive x-ray analysis. The scanning electron micrographs for the 500 °C annealed and 850 °C heat-treated specimens are shown in Fig. 5. The microstructures of the specimens consist of three phases: dark gray, gray, and light gray. For the specimen after 850 °C/24 h heat treatment, its dark-gray and light-gray phases increase from 26% and 15% to 36% and 42%, respectively, and its gray

TABLE II. Ferrimagnetic paramagnetic properties of the compositions in the ferrimagnetic region at room temperature.^a

Sample No.	Ferrimagnetism of bulk specimen				Paramagnetism $\chi = M/H$ (emu/g Oe)
	MH_c (Oe)	σ_s (emu/g)	σ_r (emu/g)	Ferrimagnetic phase	
2	0%	5.0×10^{-5}
5	450	1.5	0.3		7.2×10^{-5}
6	325	2.1	0.7		6.2×10^{-5}
7	125	5.9	0.9		5.8×10^{-5}
9	~ 80	~ 0.01	< 0.01		6.2×10^{-5}
10	110	26.0	3.1	83%	6.7×10^{-5}

^aAll the specimens were heat treated at 500 °C but No. 6 was heat treated at 700 °C.

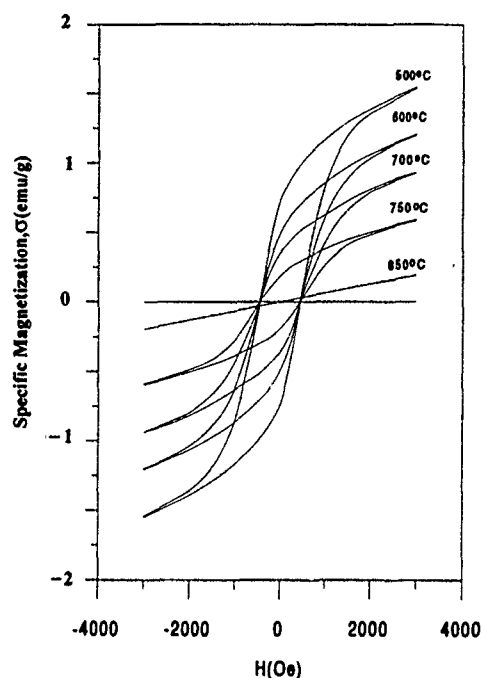


FIG. 4. Magnetization vs magnetic field of No. 5 as a function of heat treatment temperatures.

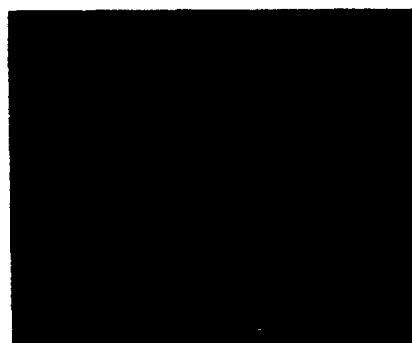
phase diminishes from 59% to 22%. Thus, we believe that this gray phase is responsible for the observed ferrimagnetism. The energy dispersive analysis reveals a composition of this phase to be approximately $3\text{Fe}_2\text{O}_3 \cdot \text{P}_2\text{O}_5$.

The lack of phase equilibrium and crystallographic data in the $\text{CaO-P}_2\text{O}_5\text{-Fe}_2\text{O}_3$ system has limited our ability to analyze and identify the ferrimagnetic phase in the system. However, it is interesting to note that a ferrimagnetic compound exists in the $\text{CaO-P}_2\text{O}_5\text{-Fe}_2\text{O}_3$ system. The phosphate-based magnetic materials may potentially have some application in the field of biomedical engineering.

Three regions have been found in the $\text{CaO-P}_2\text{O}_5\text{-Fe}_2\text{O}_3$ system. A wide glass-forming region is located around the P_2O_5 corner, in which bulk specimens could be prepared using a normal casting procedure and cooling rate. The calcium phosphate glass exhibits temperature independent diamagne-

TABLE III. Comparison of magnetic properties of Nos. 5 and 6.

Sample No.	700 °C/24 h		750 °C/24 h		850 °C/24 h	
	B_r (G)	$M H_c$ (Oe)	B_r (G)	$M H_c$ (Oe)	B_r (G)	$M H_c$ (°C)
5	14.3	450	7.5	450	0	0
6	28.9	325	8.4	370	0.9	300



(a)



(b)

FIG. 5. Microstructures of No. 5 ($10\text{CaO} \cdot 40\text{P}_2\text{O}_5 \cdot 50\text{Fe}_2\text{O}_3$, wt %). (a) After 500 °C annealing, (b) after 850 °C/24 h heat treatment.

tism. Adding iron to the calcium phosphate system leads to paramagnetic behavior. A ferrimagnetic region is located in the composition range with 10%–30% CaO , 30%–40% P_2O_5 , and $\geq 30\%$ Fe_2O_3 . Samples inside the region contain both paramagnetic and ferrimagnetic phases. Subsequent heat treatments at 600–850 °C reduces or destroys the ferrimagnetism.

¹A. Bishay and A. Kinawi, *Proceedings of the International Congress, Physics of Non-Crystalline Solids*, Delft, Netherlands, July 1964 (North-Holland, New York, 1965), p. 589.

²C. Hirayama, J. G. Castle, Jr., and M. Kuriyama, *Phys. Chem. Glasses* **9**, 109 (1968).

³R. J. Edwards, A. Paul, and R. W. Douglas, *Phys. Chem. Glasses* **13**, 137 (1972).

⁴B. Kumar, C. H. Chen, *Phys. Chem. Glasses* (to be published).

⁵B. Kumar, *Trans. Indian Ceram. Soc.* **44**, 123 (1985).

⁶G. Graves and B. Kumar, U. S. Patent No. 4,604,097, 5 August 1986.

⁷B. Kumar and S. Lin, *J. Am. Ceram. Soc.* **74**, 226 (1991).

⁸A. Muan and E. F. Osborn, *Phase Equilibria Among Oxides in Steel Making* (Addison-Wesley, Reading, MA, 1965), pp. 158–165.

⁹A. M. Sanad, I. Kashif, M. A. Khaled, S. A. Aly, and H. Farouk, *Phys. Chem. Glasses* **30**, 27 (1989).

¹⁰B. Kumar, C. H. Chen, and S. Lin, *Phys. Chem. Glasses* **33**, 45 (1992).

Magnetic properties of $Y_{3-x-y}Pr_xLu_yFe_5O_{12}$ garnet films

A. Azevedo, C. Cinbis, and M. H. Kryder

Data Storage Systems Center, Carnegie-Mellon University, Pittsburgh, Pennsylvania 15213

In this work we report on the magnetic and low-field ferromagnetic resonance properties of iron garnet films of general composition $Y_{3-x-y}Pr_xLu_yFe_5O_{12}$ for $0 \leq x \leq 0.3$ and $0 \leq y \leq 0.7$. The films were grown onto [111] gadolinium gallium garnet substrates by liquid phase epitaxy. Both growth-induced and cubic anisotropies were investigated by means of torque magnetometry and ferromagnetic resonance at room temperature. The growth-induced anisotropy constant K_u and the first order magnetocrystalline cubic constant K_1 exhibit a linear dependence with the praseodymium content. The addition of Lu with Pr enhances both K_u and K_1 dependence on the doping, yielding $\Delta K_u/x \sim -2.4 \times 10^5$ erg/cm³ and $\Delta K_1/x \sim -1.1 \times 10^5$ erg/cm³. The addition of praseodymium in the garnet films significantly improves the soft magnetic properties. In-plane coercivity is about 0.1 Oe and there is a negligible anisotropy in the plane of the film. The effect of the doping by praseodymium and lutetium on the saturation magnetization is insignificant at room temperature.

I. INTRODUCTION

Magnetic garnets exhibiting growth induced uniaxial anisotropy have been intensely studied.¹ Many epitaxially grown garnet films exhibit a positive uniaxial anisotropy, and thus the easy or preferred axis of magnetization is perpendicular to the film plane. In contrast, praseodymium-substituted iron garnet films exhibit an in-plane growth-induced anisotropy.²

The purpose of this paper is to present the magnetic and low-field ferromagnetic resonance properties of praseodymium-doped iron garnet films as a function of the doping content. Films of general composition $Y_{3-x-y}Pr_xLu_yFe_5O_{12}$ for $0 \leq x \leq 0.3$ and $0 \leq y \leq 0.7$, were grown by liquid phase epitaxy (LPE) onto [111]-oriented gadolinium gallium garnet (GGG) substrates. Lutetium was added, along with praseodymium to compensate for the lattice mismatch which would be produced due to the addition of large praseodymium ions, alone, into the garnet lattice. The uniaxial anisotropy constant K_u and the saturation magnetization $4\pi M_s$ were measured by torque and vibrating sample magnetometry respectively. The first order cubic anisotropy constant K_1 and the gyromagnetic ratio γ were obtained by low-field ferromagnetic resonance (FMR) measurements. Using a hysteresis loop tracer we have also measured the coercivity.

II. EXPERIMENTAL RESULTS

All films have been grown in super-saturated solutions using PbO-B₂O₃ based flux by the horizontal dipping technique. The films were grown isothermally using a continuous rotation rate of 100 rpm for typically 3 min. The growth rate varied between 1 and 3 μ m/min. The film thickness ranges between 1 and 12 μ m. The growth temperature ranged between 1000 and 1050 °C using supercooling ΔT between 5 and 50 °C. The initial molar fluxed melt composition used was: 333.119 g of PbO, 14.587 g of B₂O₃, 47.366 g of Fe₂O₃, and 4.927 g of Y₂O₃. The effects of praseodymium doping were then investigated by adding praseodymium and lutetium oxide in small increments.

The chemical composition and the thickness of the films were measured using a x-ray fluorescence spectrometer. The

saturation magnetization was measured with a vibrating sample magnetometer in fields up to 6 kOe at room temperature. Care was taken to extrapolate the magnetization data to zero field to avoid the large paramagnetic susceptibility of the GGG substrate. The $4\pi M_s$ values indicate that the effect of praseodymium is negligible at room temperature, in agreement with Hansen *et al.*²

The hysteresis loop traces were performed with the applied field parallel to the direction [112] at 10 Hz. There was a very small sixfold in-plane anisotropy, which only affected the rapidity of the approach to saturation, but not the coercivity of the hysteresis loops in different directions. This anisotropy is believed to be due to the magnetocrystalline anisotropy arising from the [111] orientation of the cubic garnet single crystal lattice. Two hysteresis loop traces for two different doping concentrations are shown in Fig. 1. A hysteresis loop for a pure YIG (yttrium iron garnet) film, which exhibits a coercivity of about 2.2 Oe is shown in Fig. 1(a). The hysteresis loop trace shows that the direction [112] is a hard axis with an anisotropy field of about 55 Oe. A hysteresis loop trace for a $Y_{2.25}Pr_{0.25}Lu_{0.5}Fe_5O_{12}$ film, which exhibits a coercivity of 0.094 Oe and is saturated at about 0.94 Oe is shown in Fig. 1(b). The anisotropy of the pure YIG film is completely removed as a result of the praseodymium doping. A plot of coercivity as a function of Pr content, x , is shown in Fig. 2. It is seen that for $x > 0.14$ the coercivity reaches a minimum value of about 0.1 Oe.

We used the torque curve measurements to investigate the influence of the praseodymium content on the uniaxial anisotropy constant K_u . The torque per unit volume from a (111)-growth plane with the applied field in the (110) plane is given by, $L = -\partial E / \partial \alpha = -(K_u - 2\pi M^2) \sin 2\alpha$. Where E is the free energy per unit volume and α is the angle between the magnetization and the easy direction. Here we have neglected the contribution from K_1 and from the Zeeman energy, since the applied field was sufficiently high ($H = 11.5$ kOe) to suppose that \mathbf{M} and \mathbf{H} were essentially parallel. The concentration dependence of the uniaxial anisotropy constant K_u is shown in Fig. 3(a). The plot indicates a strong negative contribution to K_u from the praseodymium content. An approximately linear dependence of K_u on x of the form $\Delta K_u/x \sim -2.4 \times 10^5$ erg/cm³, was found.

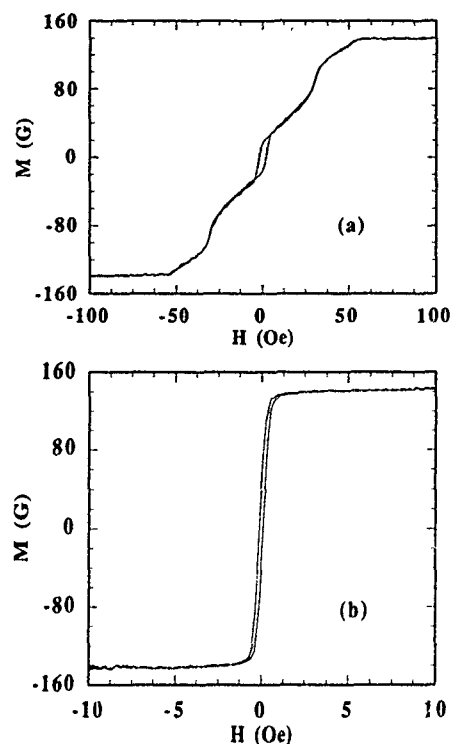


FIG. 1. In-plane hysteresis loop traces (a) for a pure YIG film and (b) for the film $Y_{2.25}Pr_{0.25}Lu_{0.5}Fe_5O_{12}$. The praseodymium-doped iron garnet film has a coercivity of 0.094 Oe and is saturated for fields around 1.0 Oe. The anisotropy of the pure YIG was eliminated, as seen in (a).

Low-field FMR measurements were performed on the films using a microwave microstrip transmission line, with the in-plane dc field parallel to the $[11\bar{2}]$ direction. The FMR spectra, for low magnetic in-plane fields ($H < 20$ Oe) present a strong single mode absorption peak. The dc magnetic field was varied from 20 to 1000 Oe and the FMR frequency was measured for each value of H . Thus, the FMR frequency was plotted as a function of H for each sample. To interpret the low-field FMR measurements, we have derived an equation taking into account the noncollinearity between \mathbf{H} and \mathbf{M} on the (110) plane.³ The resonance condition is given by

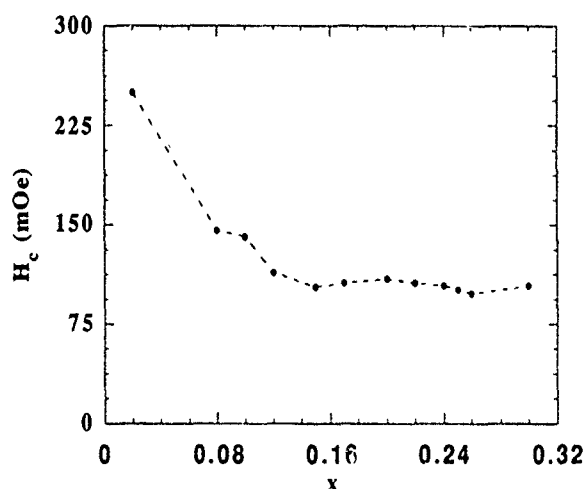


FIG. 2. Dependence of the coercivity on the praseodymium doping. The magnetic field was applied along the direction $[11\bar{2}]$.

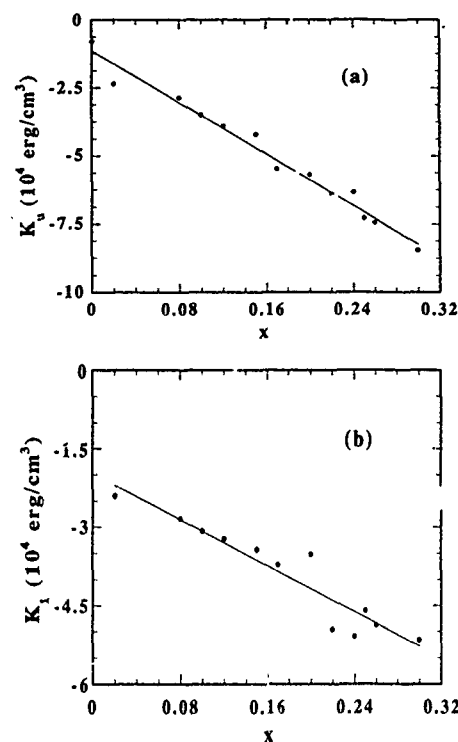


FIG. 3. Concentration dependence of the growth-induced anisotropy constant K_u (a) and the first order magnetocrystalline cubic constant K_1 (b) as a function of the praseodymium content. The negative linear dependences are given approximately by $\Delta K_u/x \sim -2.4 \times 10^5$ erg/cm³ and $\Delta K_1/x \sim -1.1 \times 10^5$ erg/cm³.

$$\left(\frac{\omega}{\gamma}\right)^2 = \frac{1}{M^2} \left[HM - 2K' + K_1 \left(-1 + \frac{10\sqrt{2}}{3} \epsilon \right) \right] \times (HM + 3\sqrt{2}K_1\epsilon) \quad (1)$$

where, $\epsilon = -\sqrt{2}K_1/6K'$ is the small angle between \bar{H} and \bar{M} , $K' = K_u - 2\pi M^2$, K_1 is the first order magnetocrystalline cubic anisotropy constant, γ is the gyromagnetic ratio, and ω is the resonance frequency. The equation above is corrected to second order in K_1 . For $\epsilon=0$, it reduces to the usual equation given by Sturge *et al.*⁴

Using the measured values of K_u and $4\pi M_s$, Eq. (1) was fitted to the FMR data, yielding the values of K_1 and γ . The dependence of the first order magnetocrystalline cubic anisotropy constant K_1 on the praseodymium content obtained in this manner is shown in Fig. 3(b). The linear dependence of K_1 with x yields, $\Delta K_1/x \sim -1.1 \times 10^5$ erg/cm³. Negative values of K_1 were already reported for bulk praseodymium-substituted garnet materials.⁵

III. CONCLUSION

We have investigated the influence of praseodymium and lutetium on the properties of garnet films. The praseodymium and lutetium doping give rise to a strong in-plane anisotropy and improves the soft-magnetic properties of the films. The microwave absorption spectra, for low magnetic in-plane fields ($H < 20$ Oe) present a strong single mode resonance line characteristic of single-domain samples. The results reveal a strong dependence of both the first order

magnetocrystalline anisotropy constant K_1 and the uniaxial anisotropy constant K_u on the doping content. The linear dependence of K_u and K_1 on x is approximately $\Delta K_u/x \sim -2.4 \times 10^5$ erg/cm³ and $\Delta K_1/x \sim -1.1 \times 10^5$ erg/cm³. The influence of the doping on the saturation magnetization is negligible at room temperature, in agreement with prior results.²

- ¹A. H. Eschenfelder, *Magnetic Bubble Technology* (Springer, New York, 1980).
- ²P. Hansen, C.-P. Klages, and K. Witter, *J. Appl. Phys.* **60**, 721 (1986).
- ³A. Azevedo, C. Cinbis, and M. H. Kryder, *J. Appl. Phys.* **74**, 7450 (1993).
- ⁴M. D. Sturge, R. C. LeCraw, R. D. Pierce, S. J. Licht, and L. K. Shick, *Phys. Rev. B* **7**, 1070 (1973).
- ⁵J. Ostorero, A. Marais, H. Makran, G. Villers, M. Port, and M. Tighezza, *J. Appl. Phys.* **53**, 2716 (1982).

Magnetic properties of amorphous Cr-Fe alloys prepared by thermal evaporation and mechanical milling

S. K. Xia, E. Baggio-Saitovitch, C. Lariça, B. V. B. Sarkissian, and S. F. Cunha
Centro Brasileiro de Pesquisas Físicas, Rua Dr. Xavier Sigaud 150, 22290, Rio de Janeiro, RJ, Brazil

J. L. Tholence
Centre de Recherches sur les Très Basses Températures, C. N. R. S., BP 166 X, 38042 Grenoble-Cedex, France

$\text{Cr}_{100-x}\text{Fe}_x$ amorphous alloys have been prepared through two different routes: thermal coevaporation and mechanical milling. The Mössbauer measurements on the materials show that the amorphization leads to a dramatic reduction of Fe magnetic moment as compared to the crystalline bulk samples. On the other hand, the magnetic ac susceptibility and the magnetization measurements indicate a dominant ferromagnetic intracluster interaction with a competing intercluster interaction. Such a competition could give rise to a spin-glass-like behavior.

I. INTRODUCTION

To obtain an amorphous binary alloy by the melt-quenching technique, either the constituents of the alloy should have a considerable difference in atomic sizes (usually larger than 15%) or some metalloid elements must be included. Therefore binary alloy systems composed of constituents with similar atomic radii are considered to be difficult for amorphization. Recently, we have succeeded in obtaining amorphous Fe-Cr alloys through mechanical milling¹ and thermal evaporation.²

The magnetism of the crystalline Cr-Fe alloys and Fe-Cr-M amorphous state stabilized by the addition of some amount of metalloid metal *M* have been a subject of intensive study in the past decades.³⁻⁸ Differing from the crystalline alloys, the Curie temperature, and the magnetic moment of the glassy $\text{Fe}_{100-x}\text{Cr}_x\text{M}_y$ alloys have been found to fall much more rapidly with increasing *x*. The magnetic order disappears around *x* = 30.

It would be interesting to know if the amorphous Cr-Fe alloys maintain the same magnetic properties as the Cr-Fe-M amorphous alloys and how the magnetism behaves. In this work, the magnetic behaviors of the Cr-Fe amorphous state are investigated through the analyses of the Mössbauer spectra, the ac susceptibility, and the magnetization measurements.

II. EXPERIMENTAL DETAILS

$\text{Cr}_{100-x}\text{Fe}_x$ films were prepared by thermal coevaporation from pure Cr and Fe metals, deposited onto kapton substrates held at room temperature (RT). During the depositions, the vacuum was about 3×10^{-7} Torr. A quartz crystal oscillator was used to control the deposition rate, which was about 25 Å/min for all the films and also to monitor the compositions, which were conformed by energy dispersive analysis (EDS). All the films have a thickness of about 3000 Å. The x-ray diffraction (XRD) patterns of the obtained films show a prominent amorphous phase in the range $25 < x < 60$, and a BCC phase appears out of this range.

The mechanically milled powder was obtained through ball milling of $\text{Cr}_{72}\text{Fe}_{28}$ solid solution at RT performed in a vibrating frame using a hardened steel vial and 16 balls, 5

with a diameter of 1.5 cm and 11 with a diameter of 1 cm. During the milling process, the sample was sealed in a vial filled with argon gas. The XRD patterns indicate a formation of an amorphous phase after 200 h milling. The compositions analysis by EDS for the powder milled for 200 h shows an increase of Fe concentration from 28% to 35%, and little amount of Ni (less than 0.4%), which was due to the contamination from the milling tools.

The Mössbauer effect was measured at 4.2 K for all the samples, using a ⁵⁷Co source in the Rh matrix. ac susceptibility was measured in a cryostat by a mutual inductance method operating at 128 Hz. The magnetization measurements were performed by a vibration sample magnetometer.

III. RESULTS AND DISCUSSION

Figures 1(a) and 1(b), respectively, show the RT and 4.2 K Mössbauer spectra of the $\text{Cr}_{72}\text{Fe}_{28}$ BCC bulk alloy, $\text{Cr}_{65}\text{Fe}_{35}$ amorphous powder and $\text{Cr}_{50}\text{Fe}_{50}$ amorphous alloy film. Due to the disordered structure, which leads a quadrupole splitting distribution, the RT Mössbauer spectra of the

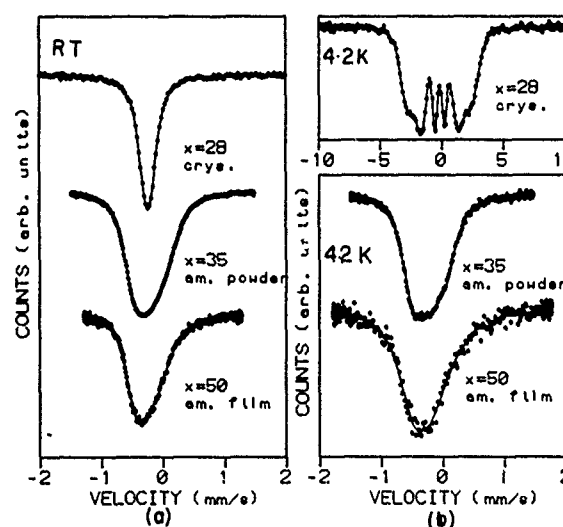


FIG. 1. (a) RT and (b) 4.2 K Mössbauer spectra of $\text{Cr}_{72}\text{Fe}_{28}$ crystalline bulk alloy, $\text{Cr}_{65}\text{Fe}_{35}$ mechanically milled amorphous alloy, and $\text{Cr}_{50}\text{Fe}_{50}$ thermal evaporated amorphous alloy.

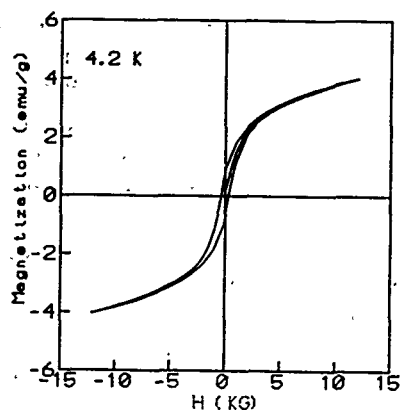


FIG. 2. Magnetization curve of $\text{Cr}_{65}\text{Fe}_{35}$ mechanically milled amorphous alloy measured at 4.2 K.

two amorphous alloys exhibit a broad absorption line and the more negative isomer shifts, as compared with the crystalline one. As the samples are cooled down to 4.2 K, unlike the crystalline alloy, the amorphous samples still maintain the unsplitted spectra, although they are more concentrated in Fe. Such behavior looks like $\text{Fe}_{85-x}\text{Cr}_x\text{B}_{15}$ amorphous alloys with $x > 30$, above which the alloys were considered to be paramagnetic.⁷ However, one does see a magnetic broadening for the film sample by comparing the 4.2 K spectrum with the RT one. For the amorphous powder, on the other hand, the spectrum broadening is not as pronounced as that of the film, therefore, the Fe may not have or carry a very small magnetic moment. The magnetization curve measured at 4.2 K in Fig. 2 for the powder, however, indeed shows a magnetic order. Taking into account the magnitude of the saturation magnetization (Fig. 2), it may be clear that the Cr in the sample carries the magnetic moment, which cannot be detected by Mössbauer spectroscopy.

The ac susceptibilities χ'_{ac} and $1/\chi'_{ac}$ [Figs. 3(a) and 3(b)] exhibit an interesting magnetic feature. Differing from Cr-Fe BCC crystalline samples, the results for both of the amorphous alloys indicate the absence of a long range ferromagnetic ordering. The results show a Curie-Weiss paramagnetic behavior above about $T=100$ K for an amorphous $\text{Cr}_{65}\text{Fe}_{35}$ powder alloy and 230 K for a $\text{Cr}_{50}\text{Fe}_{50}$ film alloy [the arrows in Fig. 3(b)], with positive Curie-Weiss temperatures. Below these temperatures, a competing interaction between ferromagnetism and antiferromagnetism is suggested by the maximums [Fig. 3(a)]. The temperature at which $\partial\chi'_{ac}/\partial T$ reaches the maximum is found to be $T=33$ K for the powder and 50 K for the film [the arrows in Fig. 3(a)], which coincide with the maximum values of χ'_{ac} .

The above magnetic behavior may be related to the feature that is similar to the systems where the magnetic properties are dominated by finite cluster effects. The ferromagnetic intracuster ordering occurs at higher temperature, while the competing intercluster interaction leads to a spin-glass-like behavior, and the clusters are frozen at the temperatures (defined as the maximum of $\partial\chi'_{ac}/\partial T$) of 33 K for the powder and 50 K for the film.

The temperature dependence of magnetization for $\text{Cr}_{35}\text{Fe}_{65}$ amorphous powder was measured with an applied

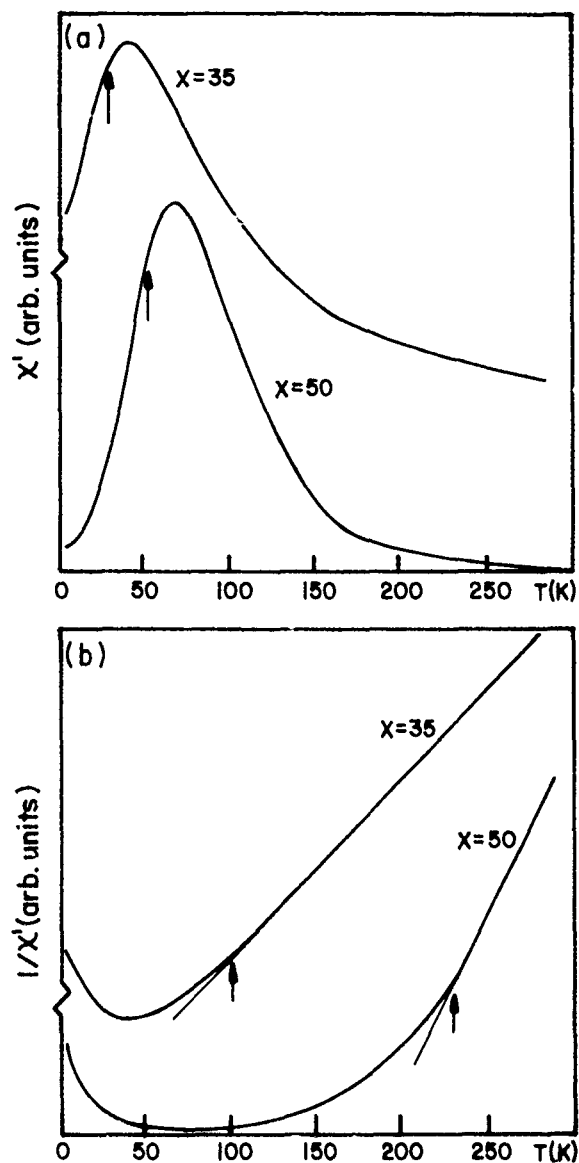


FIG. 3. (a) ac susceptibilities, χ' , of $\text{Cr}_{65}\text{Fe}_{35}$ mechanically milled amorphous powder and $\text{Cr}_{50}\text{Fe}_{50}$ thermal evaporated amorphous film and (b) the $1/\chi'$ curves for these two samples.

field of 100 G, as shown in Fig. 4. By comparing with the result of ac susceptibility, the maximum on the zero field cooled (ZFC) curve can be related to the cluster freezing. Since the ZFC curve (in Fig. 4) can be taken as a zero frequency susceptibility, one expects a lower blocking temperature than that obtained by ac susceptibility, which can be seen by comparing the two corresponding curves. Figure 4 also shows that the field cooled (FC) magnetization curve deviates from the ZFC values, even above the maximum of the ZFC curve. This may be explained by a distribution of cluster size, which may, in turn, lead to distribution of blocking temperature. The maximum on the ZFC curve may be related to the most probable blocking temperature.

The cluster-like magnetic character for both of the amorphous materials may be associated with the formation of finite size granular structure in our specimens. In an earlier work, we observed a cluster-like behavior by using Möss-

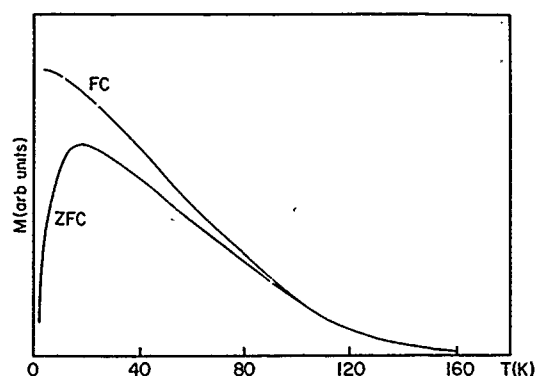


FIG. 4. Temperature dependence of zero field cooled (ZFC) and field cooled (FC) magnetization with applied field of 100 G for $\text{Cr}_{65}\text{Fe}_{35}$ mechanically milled amorphous powder.

bauer spectroscopy and ac susceptibility on Fe–Ag and Fe–Au film alloys prepared by the same evaporator, and the results suggested that the formation of the clusters is due to the inhomogeneity in atomic density in the films rather than the inhomogeneity in composition.^{9,10} Therefore, a similar structural character may also be present in the studied Cr–Fe films. The x-ray diffraction patterns of these films indeed showed a broad diffracted linewidth, even for the films with crystalline structure,² which indicates the formation of small size particles. The Mössbauer spectrum of the film shown in Fig. 1 ruled out the possibility of the formation of Fe-rich and Cr-rich two-phase, α - α' . While for the powder, the mechanical milling leads to a continuous reduction of particle size, and a granular system is finally formed. Because of the finite size of the granular system, the spin correlation length is strictly limited by the size of these granules, and therefore long range ferromagnetic ordering cannot be sustained, even in the samples with high Fe concentration.

The above results reveal a dissimilar behavior in magnetism between Fe–Cr–M and the present Fe–Cr amorphous alloys. For example, in $\text{Fe}_{100-x}\text{Cr}_x\text{B}_{15}$ amorphous, the alloys became nonmagnetic when $x > 30$, while in the present work, one sees that the Cr–Fe amorphous materials exhibit magnetic order, even for the samples with high Cr concentration. Since the metalloid element, boron, plays no crucial

part in destroying the Fe moment,¹¹ we are forced to conclude that the difference in microstructure between the present Cr–Fe and the melt-spun Fe–Cr–B amorphous alloys may lead to different magnetism. This may be attributed to the more loose-packed structure in the present amorphous samples¹² as compared with metallic glass obtained by melt spinning.

In conclusion, the magnetic properties have been studied on the amorphous Cr–Fe film and powder alloys obtained by thermal evaporation and mechanical milling, respectively. The amorphization dramatically reduces the local Fe magnetic moment in the alloys. Differing from the metalloid contained Cr–Fe amorphous alloys, the studied amorphous materials show magnetic orders, even in the samples with higher Cr concentration. Both of the film and powder amorphous alloys exhibit a cluster-type magnetic behavior, which can be attributed to the granular structure of the materials. The magnetic interaction can be described by spin-glass-type intercluster interaction with a dominated ferromagnetic intra-cluster interaction.

ACKNOWLEDGMENTS

We thank Dr. M. Elmsassalami for his helpful discussion and critical reading of the manuscript. This work was partially supported by the CNPq-SCT Grant No. 500117/90-01.

¹ S. K. Xia, E. B. Saitovitch, and F. C. R. Assunção, *J. Phys. Condens. Matter* **5**, 2729 (1993).

² S. K. Xia, E. B. Saitovitch, and C. Larica, *Phys. Rev. B* **49** (in press).

³ A. T. Aldred, B. D. Rainford, J. K. Kouvel, and T. J. Hicks, *Phys. Rev. B* **14**, 229 (1976).

⁴ S. K. Burke, R. Cywinski, J. F. Davies, and B. D. Rainford, *J. Phys. F* **13**, 451 (1983).

⁵ H. Kuwano and K. Ono, *J. Phys. Soc. Jpn.* **42**, 72 (1977).

⁶ M. Olivier, J. O. Strom-Olsen, Z. Altounian, and G. Williams, *J. Appl. Phys.* **53**, 7696 (1982).

⁷ G. L. Whittle, A. M. Stewart, and A. B. Kaiser, *Phys. Status Solidi A* **97**, 199 (1986).

⁸ U. Guntzel and K. Westerholt, *Phys. Rev. B* **41**, 740 (1990).

⁹ B. V. B. Sarkissain, C. Larica, E. Baggio-Saitovitch, and S. K. Xia, Communication on ICM, Edinburgh, 1991.

¹⁰ C. Larica, E. Baggio-Saitovitch, B. V. B. Sarkissain, and S. K. Xia (to be published).

¹¹ C. L. Chien and K. M. Unruh, *Phys. Rev. B* **24**, 1556 (1981).

¹² S. K. Xia, E. Baggio-Saitovitch, and F. C. R. Assunção, *J. Alloys Compounds* **196**, 177 (1993).

Magnetostriction in RE-Co amorphous alloy films (abstract)

S. Uchiyama, S. Yoshino, H. Takahashi, K. Tomi-ita, T. Mori, A. Itakura, S. Iwata, and S. Tsunashima

School of Engineering, Nagoya University, Nagoya 464-01, Japan

Rare earth-transition metal (RE-TM) amorphous films have been used as magneto-optical recording media. One of the most important properties is the perpendicular magnetic anisotropy, the main origin of which is explained by one ion anisotropy of rare earth ion. However, it is also noted that the anisotropy contribution due to the magnetostriction depends in a very similar manner on the RE species as in the case of the main anisotropy. Thus it was suggested that the main origin of the magnetostriction might be the one ion anisotropy of RE.¹ The present work reports the saturation magnetostriction constant λ_s of various RE-Co amorphous alloy films with RE=Y, La, Ce, Pr, Nd, Sm, Gd, Tb, Dy, Ho, Er in the range of RE concentration of 0%–40%. In most cases, λ_s increases with RE concentration, then decreases after showing a peak and disappears altogether with ferromagnetism. For an RE species with a small one ion anisotropy, λ_s is small with a value of less than 2×10^{-5} , and is found to be contributed primarily from Co. For RE with larger one ion anisotropy, namely for RE=Sm, Pr, Tb, and Dy, λ_s has values of the order of 10^{-4} and is estimated to be contributed mainly from RE one ion anisotropy.

¹Y. Suzuki, S. Takayama, F. Kirino, and N. Ohta, IEEE Trans. Magn. MAG-23, 2275 (1987).

A model for the Barkhausen noise power as a function of applied field and stress (abstract)

M. J. Sablik

Southwest Research Institute, P. O. Drawer 28510, San Antonio, Texas 78228-0510

The model of Alessandro *et al.*¹ is used to derive the Barkhausen noise power in terms of permeability μ , which is really the irreversible permeability, since the Barkhausen noise is produced by the irreversible motion of domain walls. From the model expression, it is shown that the peak in the Barkhausen noise power as a function of applied field coincides with the peak in the irreversible permeability. From the magnetomechanical hysteresis model,² an expression for the irreversible permeability is found and shown to peak at a higher magnetic field than the total permeability. Using the magnetomechanical hysteresis model and the derived expression from the Alessandro model, the Barkhausen noise power peak value is computed and found to increase almost linearly from negative (compressive) to positive (tensile) stress, with slightly decreased slope at high positive and negative values of stress, in agreement with trends in experimental observations.^{3,4} Dependence of the Barkhausen noise power on \dot{H} , the time rate of increase in the linearly increasing ramp function used for H , is also investigated and found to increase moderately sharply for intermediate ranges of \dot{H} and to saturate at larger \dot{H} .

Work supported by DOE Contract No. DCE/ER/14180.B. Alessandro, C.

¹Beatrice, G. Berotti, and A. Montorsi, J. Appl. Phys. **68**, 2901 (1990); **68**, 2908 (1990).

²M. J. Sablik and D. C. Jiles, IEEE Trans. Magn. **29**, 2113 (1993).

³R. L. Pasley, Mater. Eval. **24**, 137 (1970).

⁴C. Jagadish, L. Clapham, and D. L. Atherton, IEEE Trans. Magn. **26**, 1160 (1990).

The effects of closure domains on flux conduction in thin film recording head

Zhenzhou Guo and Edward Della Torre

Institute for Magnetism Research, George Washington University, Washington, DC 20052

The magnetic flux conductivity in the tip of a recording head was examined for various applied field and closure domain configurations using a two-dimensional micromagnetic model developed to obtain the domain patterns in soft magnetic thin films. A permalloy thin film sample was selected to simulate a monopole head configuration, and an external field was applied to various closure domain ground states that had zero net remanence magnetization. It was found that for small fields the magnetization process is linear and reversible, and both the susceptibility and the effective track width increase as the size of the closure domains is reduced. For large fields, however, the variation of the flux conduction is much less sensitive to the size of the zero-field closure domains, since the sample is nearly saturated. Small jumps were observed in the magnetization curves corresponding to the domain wall nucleation and annihilation, which can be a source of head noise. It was also observed that the effective center of magnetic pole shifts with increasing field.

The magnetization of a thin film of permalloy with an in-plane magnetic easy axis generally has 90° domain walls. Such a patterned structure is widely used in thin film recording heads. Magnetic flux along the hard axis is conducted by both magnetization rotations and domain wall motions. This wall motion besides being slow, and a source of noise due to Barkhausen jumps, destroys the symmetry of the ground state and introduces a unidirectional shift that is a source of overwrite problems in high-density recording head system which has relatively larger side domains. In other words, when one is trying to magnetize the media, the center of the flux shifts one direction when one is trying to magnetize the medium in one direction, and in the other direction when one is trying to magnetize it the other way. In order to reduce these effects, it is necessary to understand how the domain

patterns behave in the recording process. In the past, domain level calculations have analyzed both the domain rotation and the wall-displacement modes of magnetic response.^{1,2} Using our two-dimensional micromagnetic model³ that obtains the domain patterns in thin films, this paper attempts to address these questions.

In this paper, using this micromagnetic model, we tracked the magnetization and domain wall motion for various applied fields and for various ground-state configurations to observe their influence on the magnetic flux. It was seen that the expansion and contraction of the oppositely directed closure domains destroys the symmetry of the ground state and thus application of a field shifts the magnetic center of the flux from the physical center of the head. For high-density recording this could cause serious overwrite prob-

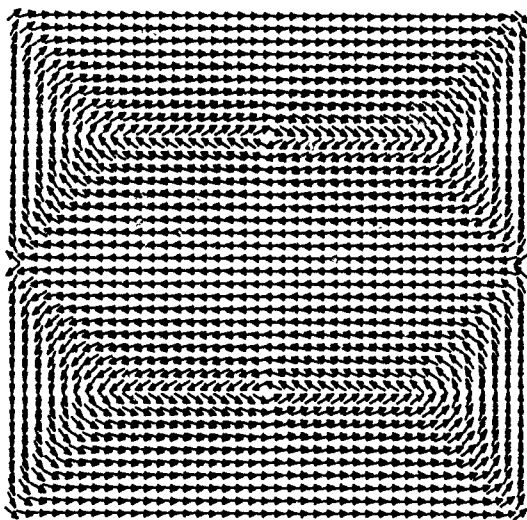


FIG. 1. The 7-domain ground state of a $4\ \mu\text{m} \times 4\ \mu\text{m} \times 100\ \text{\AA}$ permalloy film.

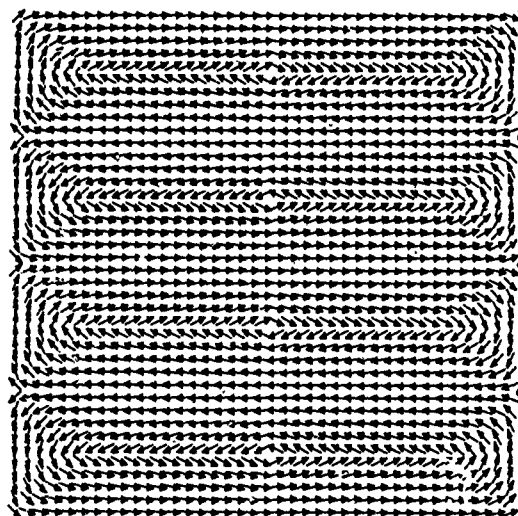


FIG. 2. The 13-domain ground state. The side domains become relatively smaller comparing with the 7-domain ground state.

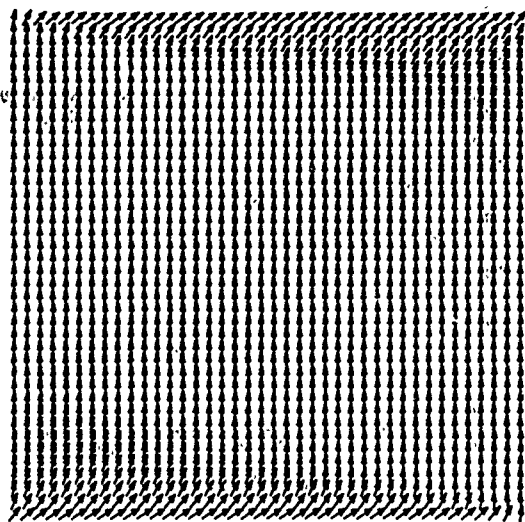


FIG. 3. Near-saturation state.

lems, since the tracks are narrow and the shift is unidirectional.

A laminated head structure with hollow cross section has been suggested as a means of eliminating the closure domain.⁴ In that case, the magnetization flux can close itself around the hollow center so that no free poles exist. Such a structure would then have no domain walls and magnetic flux conduction occurs entirely through magnetization rotation. Since unlaminated heads are easier to fabricate they continue to dominate the market. The use of a single-layer head whose sides are serrated has been suggested as a means of reducing this problem in an unlaminated head. It will be shown that this new geometry does reduce the effects of closure domains. The track shifting problem is also reduced and the available flux is less dependent upon the ground-state domain configuration.

A square piece of permalloy thin film with $4\ \mu\text{m} \times 4\ \mu\text{m} \times 10\ \text{nm}$ dimensions is selected to simulate the head tip. The geometry chosen is corresponding to the high-density recording head that is being considered for heads to reach densities of $10^9\ \text{bits/in.}^2$. This head is discretized into an array of 40×40 square elements with the following parameters: the saturation magnetization is $800\ \text{kA/m}$, the uniaxial anisotropy constant is $160\ \text{J/m}^3$ with its easy axis along the

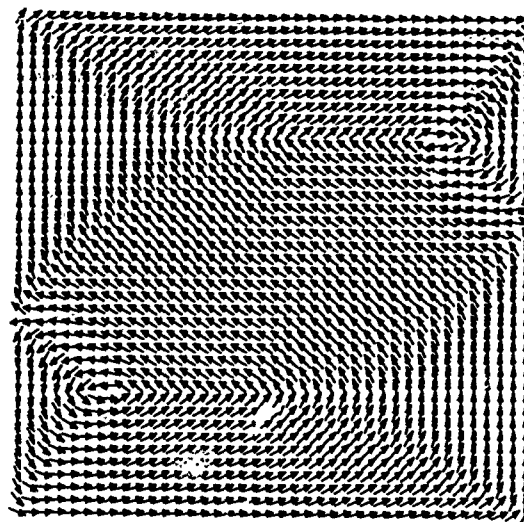


FIG. 5. Corresponding domain pattern when 1200-A/m magnetic field is applied to the 7-domain state along the vertical direction.

transverse direction, and the exchange constant is $10\ \text{pJ/m}$. The termination criterion for the program is set at a maximum rotation in all elements of less than 0.01° .

Two ground states are considered as shown in Fig. 1, a seven-domain state, and Fig. 2, a 13-domain state. Both patterns are equilibrium states relaxed from different initial guess.³ The seven-domain state has larger closure domains and narrower transverse domains than the 13-domain state. External fields are then applied to both pattern in increments of $250\ \text{A/m}$. The samples respond with both magnetization rotation and domain wall motion. With external field of $3500\ \text{A/m}$, they both approach the same near-saturation state shown in Fig. 3. It is seen that the top and bottom of the sample are still not saturated due to the demagnetizing field even when the external field is as much as an order of magnitude larger than the anisotropy field. The components of the magnetization along the external field are integrated throughout the sample to obtain the average susceptibility for each field. In Fig. 4, it is shown that for small fields, even though the magnetizing process is linear and reversible, the 13-domain state will have more flux than 7-domain state due to the latter's larger closure domains. As the fields become

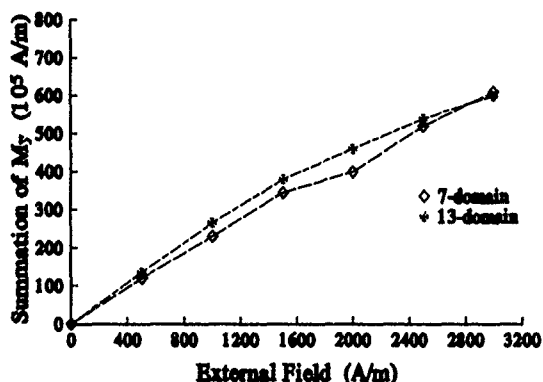


FIG. 4. M - H_0 curves of different domain patterns on the same sample.

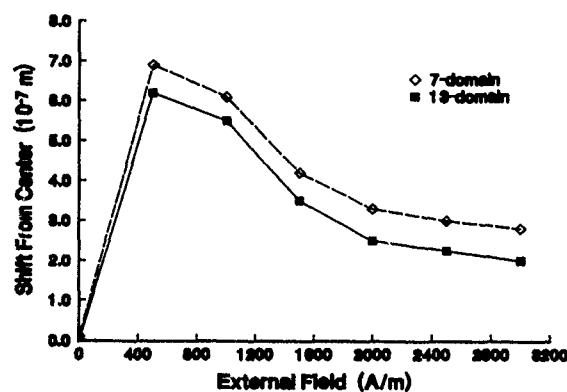


FIG. 6. Magnetic pole shift under external field.

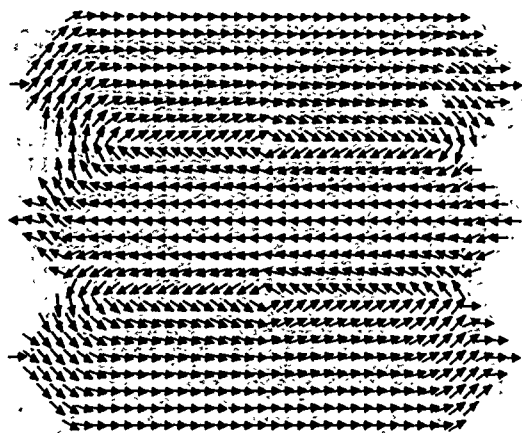


FIG. 7. Head tip with serrated sides.

larger, when the domain walls disappear only some local magnetization variations exist, which eventually go to zero. Certain jumps in the curve occurred at the moment when some closure domain walls were annihilated.

When domain wall motion is responsible for the change in the magnetization of the head, the field of the head causes one closure domain to grow at the expense of the other, as shown in Fig. 5. This causes a deviation in the flux stream from the center of the head. The deviation of the average position of the flux can be calculated as follows:

$$\delta x = \frac{\int x |M_y| dx}{\int |M_y| dx}. \quad (1)$$

The integration is carried out along the bottom edge of the sample. A plot of δx as a function of H_0 is given in Fig. 6 for the two domain patterns. As the field increases, the shift increases, reaches a maximum, and then decreases as the sample saturates. With the applied field at 800 A/m, the shift for the seven-domain state gets the maximum of 30%. Although there is no flux shift for a saturated head, it is undesirable to record at this point since, among other things, the effective gap length increases at saturation. Thus even at 75% saturation state (i.e., for a field of about 2500 A/m), this

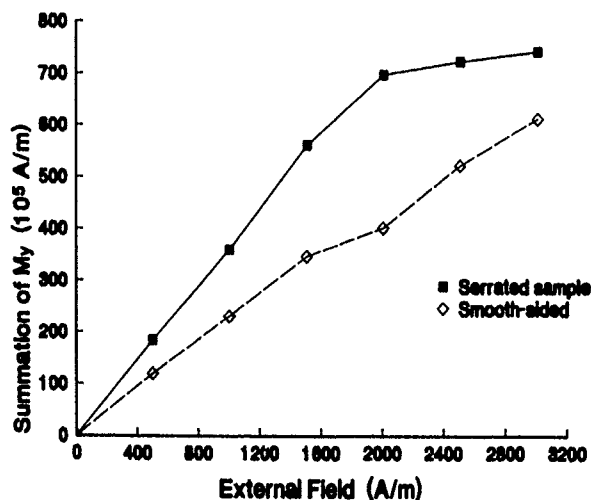


FIG. 8. Flux conduction for sample with smoothed and serrated sides.

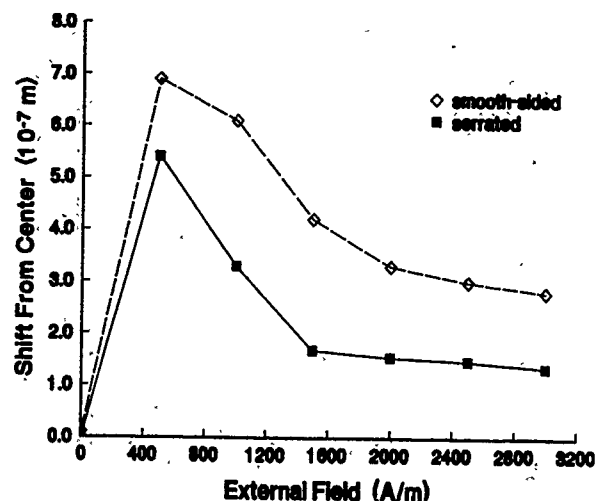


FIG. 9. Pole shift for samples with smoothed and serrated sides.

shift can still be as large as 15%. During the read process the fields involved are rather small, so this effect may be negligible in some cases.

The 13-domain state always has smaller deviations than the 7-domain state. Thus when one is trying to magnetize the media in one direction, the track effectively moves one direction, and in the opposite direction as the magnetization is reversed. This effect depends upon the magnetization history of the sample.

To try to reduce this effect, a head with serrated sides was analyzed, as shown in Fig. 7 in the ground state. This new geometry effectively reduces the closure domain due to the boundary restrictions. Figures 8 and 9, illustrate the flux conductivity and pole shift, respectively, with that for a head with smooth sides. It is seen that the flux conduction is dramatically increased for the new geometry in the linear region. The $M-H$ curve for serrated head is also smoother. The pole shift is also reduced, but not as significantly as the flux. The asymmetry still exists. Overall, we expect that the serrated head will have a slightly better performance. Although a laminated head should be superior from these points of view, from manufacturing point of view, this serration is easier to make. Thus this could be a compromise solution. Besides the shape effects, there are other ways to stabilize the domains such as using the inclusions to pin the domain walls.⁵ However, these aspects are beyond the goal of this paper.

The authors would like to acknowledge the use of the CRAY Y-MP2 supercomputer of the National Institute of Standards and Technology, Gaithersburg, Maryland, and would particularly like to thank Dr. L. H. Bennett and Dr. R. D. McMichael for their assistance. We would also like to thank F. Vajda and J. Jatau for helpful discussions. This work was supported by an ATP grant through the National Storage Industries Consortium.

¹ N. Smith, IEEE Trans. Magn. MAG-24, 2380 (1988).

² R. F. Soohoo, J. Appl. Phys. 57, 3949 (1985).

³ Z. Guo and E. Della Torre, IEEE Trans. Magn. (to be published).

⁴ J. C. Slonczewski *et al.*, IEEE Trans. MAG-24, 2045 (1988).

⁵ J. Jatau and E. Della Torre, "A study of the effect of defect sizes and their distribution on the coercivity of TbFeCo media" (these proceedings).

Effect of recorded transition shape on spatial noise distributions and correlations

T. C. Arnoldussen
IBM Corporation, SSD, San Jose, California 95193

J. G. Zhu
University of Minnesota, EE Department, Minneapolis, Minnesota 55455

Improved error rate models require better understanding of noise distributions and correlations in magnetization reversals. An analytical model is described for micromagnetic transition noise. Magnetic charge conservation is the basis for the model. The noise distribution is shown to be dependent primarily on the average transition shape. While magnetic charge variance is always peaked at the center of the transition, readback voltage noise may peak at the center for arctangent transitions or may show leading and trailing edge peaks for hyperbolic tangent or error-function transitions. Moreover, noise in the voltage derivative shows yet different distributions. Principal noise eigenfunction modes are determined for the contrasting transition shapes studied. Analytical and full micromagnetic modeling results are compared.

I. NOISE MODEL

Noise associated with thin-film magnetic recording media is concentrated in the written magnetic transitions. Error-rate modeling often treats all noise as additive, Gaussian, white, and stationary. Transition noise does not fit this picture and one desires better characterization of spatial noise distributions and correlations. Bertram and Che presented an analytical model for noise correlation in a longitudinally oriented medium.¹ Here we present a similar model which is based on magnetic charge distribution and conservation of charge in a magnetization reversal. This formulation need not assume a specific orientation of the medium.

The readback voltage for an inductive head is

$$e(x) = K \int_{-\infty}^{\infty} dx' \int_d^{d+\delta} dy' \int_{-W/2}^{W/2} dz' h_x(x', y') \times [-\nabla \cdot \mathbf{M}(x' - x, y', z')], \quad (1)$$

where $K = N\epsilon v \mu_0$, the product of the number of turns on the head, its efficiency, the disk/head relative velocity, and free space permeability. \mathbf{M} is the vector magnetization pattern written on the disk and h_x is the longitudinal component of head read sensitivity. Although this derivation assumes inductive readback, analogous equations and similar results could be written for a magnetoresistive read head. The negative divergence of \mathbf{M} is the magnetic charge density, $\rho(x, y, z)$. W is the track width, d the head-to-medium spacing, and δ the recording film thickness. Track edge effects are ignored and therefore h_x is assumed to be independent of transverse position z . The charge density can include full three-dimensional divergence \mathbf{M} effects. We only assume that for an isolated transition in "saturation" recording the integral of ρ over all x is $2M_r$, twice the longitudinal remanent magnetization. Noise between transitions caused by magnetization ripple (nonsaturation) is neglected. Thus the charge associated with a transition is constant. Media noise redistributes the charge in a transition, but total charge is conserved. Within a transition, average charge is distributed according to a probability density function²

$$p(x) = \langle \rho(x, y, z) \rangle / 2M_r = \langle \rho(x) \rangle / 2M_r,$$

where $\langle \dots \rangle$ denotes an ensemble average. The integral of $p(x)$ from $-\infty$ to ∞ is unity.

Building on Eq. (1), the voltage noise may be expressed in terms of $[\rho(x, y, z) - \langle \rho(x) \rangle]$ as in

$$e_n(x) = K \int_{-\infty}^{\infty} dx' \int_d^{d+\delta} dy' \int_{-W/2}^{W/2} dz' h_x(x', y') \times [\rho(x' - x, y', z') - \langle \rho(x' - x) \rangle]. \quad (2)$$

To simplify we assume that the media film is thin and that magnetization and magnetic charge density are uniform throughout its thickness. The integration over y' is effectively replaced by δ , the media thickness, and $h_x(x', y')$ is evaluated at an effective y spacing d_f , $h_x(x', d_f)$. The autocovariance of the noise voltage is defined by $ac(x_a, x_b) = e_n(x_a) e_n(x_b)$ and is written out in

$$ac(x_a, x_b) = K^2 \delta^2 \int_{-\infty}^{\infty} dx' \int_{-W/2}^{W/2} dz' h_x(x', d_f) [\rho(x' - x_a, z') - \langle \rho(x' - x_a) \rangle] \int_{-\infty}^{\infty} dx'' \int_{-W/2}^{W/2} dz'' h_x(x'', d_f) \times [\rho(x'' - x_b, z'') - \langle \rho(x'' - x_b) \rangle]. \quad (3)$$

Because the terms in square brackets represent noise, the two integrations over the transverse position parameter z', z'' are replaced by the factors W and W_c , where W_c is the transverse noise correlation width.³ The result is

$$ac(x_a, x_b) = K^2 \delta^2 W W_c \int_{-\infty}^{\infty} dx' h_x(x', d_f) [\rho(x' - x_a) - \langle \rho(x' - x_a) \rangle] \int_{-\infty}^{\infty} dx'' h_x(x'', d_f) \times [\rho(x'' - x_b) - \langle \rho(x'' - x_b) \rangle]. \quad (4)$$

Note: $\rho(x' - x_a)$ and $\rho(x'' - x_b)$ are values averaged over track width on a particular transition, not ensemble averages.

Charge conservation implies that noise may be introduced by adding excess positive and negative charges (in equal numbers) to the ensemble average charge distribution, provided the variance of these excess charges, at any value of x , is the same as the population variance at the same point. The excess positive and negative charges individually must be distributed according to the same probability density function $p(x)$ as the ensemble average. This is like ping-pong balls dropped into bins to form a distribution. Even if some balls are colored green (+) and some red (-), they follow the same distribution statistics, but carry different labels. Zero-sum excess charge means the independent noise sources³ are dipoles, correlated pairs of charges.

We can evaluate the voltage noise autocovariance for a single dipole pair of charges of strength q with charges located at generalized locations x_1 and x_2 . For accounting convenience we assume the positive pole is located at the smaller of x_1 and x_2 , and the negative pole at the larger value. The opposite convention could as well be used, but not both simultaneously, because a positive and negative dipole with identical x_1, x_2 values are correlated and therefore cancel. Thus, the single noise dipole is given by $q[\delta(x-x_1) - \delta(x-x_2)]$ for $x_1 < x_2$, and $q[\delta(x-x_2) - \delta(x-x_1)]$ for $x_2 < x_1$. $\delta(x)$ is a Dirac delta function. When these charge dipoles are substituted for the square-bracketed terms in Eq. (4), the dipole response is

$$ac(x_a, x_b, x_1, x_2) = K^2 \delta^2 W W_c q^2 [h_x(x_1 + x_a, d_f) - h_x(x_2 + x_a, d_f)][h_x(x_1 + x_b, d_f) - h_x(x_2 + x_b, d_f)] \quad \text{for } x_1 < x_2, \quad (5)$$

$$ac(x_a, x_b, x_1, x_2) = K^2 \delta^2 W W_c q^2 [h_x(x_2 + x_a, d_f) - h_x(x_1 + x_a, d_f)][h_x(x_2 + x_b, d_f) - h_x(x_1 + x_b, d_f)] \quad \text{for } x_2 < x_1.$$

The ensemble average charge in any incremental region Δx is $(2M_r)p(x)\Delta x$. The variance is $(q^2 N_T)p(x)\Delta x$, where the total charge is composed of N_T incremental charge units $q = 2M_r/N_T$, distributed according to $p(x)$. The total number of excess (noise) positive charges equals the number of excess negative charges, N_q . The average of the excess charge is zero, but the variance is the sum of variances of excess positive and negative charges, i.e., $2q^2 N_q p(x)\Delta x$. Therefore, $N_q = N_T/2$, and $N_q q = M_r$. The total voltage noise autocovariance is obtained by multiplying Eq. (5) by $N_q^2 p(x_1)dx_1 p(x_2)dx_2$ and integrating over all x_1 and x_2 . The final result is given in Eq. (6), which is equivalent to the Bertram and Che expression,¹ but simpler because of the charge conservation formulation:

$$\frac{ac(x_a, x_b)}{K^2 \delta^2 W W_c M_r^2} = \left\{ \begin{aligned} &\int_{-\infty}^{\infty} dx' [-m'(x')] h_x(x' + x_a, d_f) h_x(x' + x_b, d_f) \\ &- \frac{1}{2} \int_{-\infty}^{\infty} dx' [-m'(x')] h_x(x' + x_a) \int_{-\infty}^{\infty} dx'' [-m'(x'')] h_x(x'' + x_b) \end{aligned} \right\} \quad (6)$$

where

$$[-m'(x)] = -(1/M_r) \langle dM/dx \rangle = \langle \rho(x) \rangle / M_r = 2p(x).$$

Equation (6) represents the autocovariance of noise in the readback voltage. This is the form of interest for sampled-voltage detection. For peak detection, the readback voltage is differentiated and fed into a zero-crossing detector. In this case, the autocovariance of noise in the derivative of the readback voltage is of interest, and may be calculated by replacing the $h(x, d_f)$ functions in Eq. (6) by their derivatives $h'(x, d_f)$. When $x = x_a = x_b$ Eq. (6) is simply the voltage noise variance distribution.

II. RESULTS AND DISCUSSION

We assume the same set of conditions used in Bertram and Che,¹ namely $[-m(x)] = \tanh(2x/\pi a)$, $a = 1.5d_f$, and $d_f = g/2, g/4$, and $g/8$. An inductive readback head (Karlqvist form), with gap length g , was assumed. The resulting voltage variance distribution, normalized by the factor $(NEv_0 M_r \delta/g)^2 W W_c$, is shown in Fig. 1(a). Apart from an apparent difference in normalizing constant, the noise distribution is identical to that shown in Ref. 1. Notably, the voltage variance peaks just to either side of the transition center.

However, assuming the same conditions except that $[-m(x)] = (2/\pi) \tan^{-1}(x/a)$, which has the same central

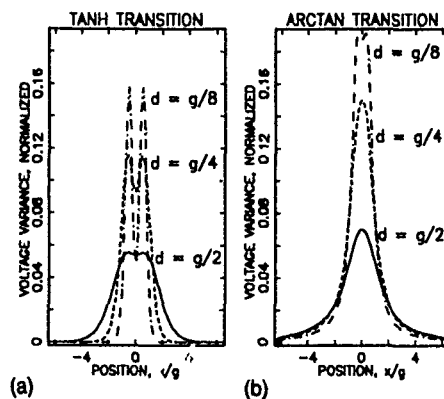


FIG. 1. Voltage variance for (a) tanh and (b) arctan transitions. Head/media spacings and longitudinal position normalized by gap.

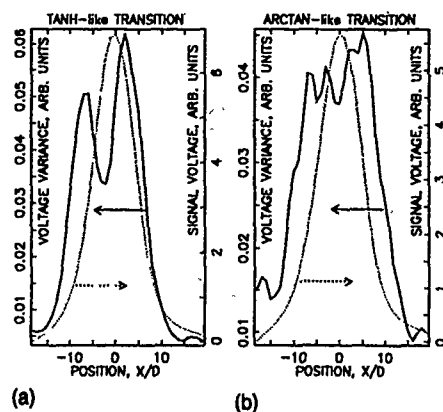


FIG. 2. Voltage variance and average readback pulses for (a) tanh-like and (b) arctan-like transitions. Longitudinal position x is normalized by crystal-lite diameter D . $g = 12D$, $d_f = 2D$, $\delta = D$.

slope as the tanh form, Fig. 1(b) gives a quite different voltage noise variance distribution. For an arctangent transition, the side noise peaks do not occur except at the very closest head/media spacing: Figure 1 indicates that the presence or absence of side noise peaks is due mainly to the functional shape of the magnetization transition, not the derivative of the head sensitivity function.¹

To verify this analytical result, the readback voltage noise variance was computed for two magnetization transitions simulated by micromagnetic modeling.⁴ One of these showed a more arctangentlike behavior while the other a more hyperbolic tangent form (error-function forms behave much like hyperbolic tangents). Figures 2(a) and 2(b) show the voltage noise variance of these two micromagnetically computed transitions. Like the analytical calculation, we see that the tanh-like transition shows noise peaks to either side of the transition center, while the arctan-like transition does not. Again, the same head was assumed for both.

We also used the analytical formulation to explore the variance of the readback voltage derivative. Figures 3(a) and 3(b) show this variance, using the same set of conditions as

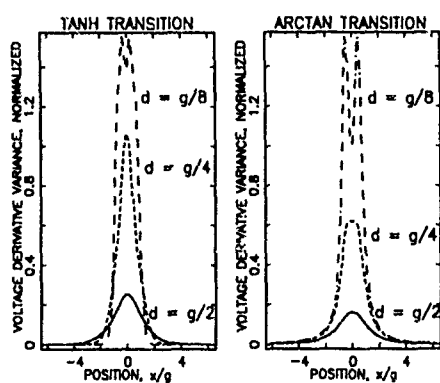


FIG. 3. Voltage derivative variance corresponding to Fig. 1 conditions.

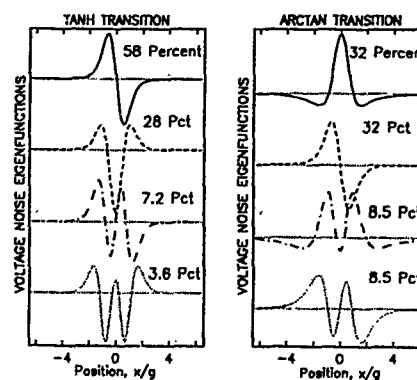


FIG. 4. First four noise voltage eigenfunction modes corresponding to conditions of Fig. 1, with $d = g/4$. Percent contributions are indicated.

in Fig. 1. For this type of noise, the arctangent transition shows a greater tendency than the tanh transition to exhibit noise peaks on either side of the transition center. As is the case for the voltage variance, side peaks become visible or prominent as head/media spacing decreases.

Equation (6), viewed as a square matrix with elements $AC_{mn} = ac(x_m, x_n)$, can be diagonalized to obtain the noise eigenfunctions and eigenvalues in order of descending contribution using the Karhunen-Loeve theorem outlined and applied by Yuan and Bertram.⁵ The first four eigenfunctions and percent contribution to total voltage noise variance are shown in Figs. 4(a) and 4(b), for the tanh and arctan transitions treated above using $a = 1.5d_f$ and $d_f = g/4$. We see that the eigenfunctions are qualitatively the same for the tanh and the arctan transitions (and this similarity remains true for the additional, less-important eigenfunctions not shown here). However, the relative contributions of corresponding eigenmodes are different for the tanh and arctan transitions. For the arctan, the eigenmodes occur in pairs of equal weight modes—one symmetric and one antisymmetric. For the tanh, the modes monotonically decrease in weight. In both cases the first two modes resemble pulse shifting (antisymmetric) and a pulsewidth-amplitude fluctuation (symmetric). While not explicitly shown here, the noise at the leading and trailing edges of a transition is negatively correlated, regardless of the transition shape or whether the noise variance exhibits leading and trailing peaks. This is a fundamental result of magnetic charge conservation.

¹H. N. Bertram and X. Che, IEEE Trans. Magn. **MAG-29**, 201 (1993).

²T. C. Arnoldussen, in *Noise in Digital Magnetic Recording*, edited by T. C. Arnoldussen and L. L. Nunnelley (World Scientific, Singapore, 1992), p. 132.

³L. L. Nunnelley, D. E. Heim, and T. C. Arnoldussen, IEEE Trans. Magn. **MAG-23**, 1767 (1987).

⁴J. G. Zhu, in *Noise in Digital Magnetic Recording*, edited by T. C. Arnoldussen and L. L. Nunnelley (World Scientific, Singapore, 1992), p. 181.

⁵S. W. Yuan and H. N. Bertram, IEEE Trans. Magn. **MAG-28**, 84 (1992).

Mean interaction field in magnetic recording media

Ikuya Tagawa, Akihiko Takeo, and Yoshihisa Nakamura

Research Institute of Electrical Communication, Tohoku University, 2-1-1 Katahira, Aoba-ku, Sendai 980, Japan

The mean interaction field was calculated for geometrical arrangements of isolated particles representing a longitudinally oriented Ba-ferrite and metal particulate medium. The effective demagnetizing factor was also calculated for a perpendicular Co-Cr recording medium. A positive mean field was obtained for the Ba-ferrite medium because the distance between particles placed in series to the magnetization direction is much shorter than that between parallel particles. When the orientation distribution became broad, the mean interaction field decreased because the location of magnetic particles changed. On the other hand, a negative mean field was obtained for the metal particulate medium. The results suggested that a positive mean field may act in the perpendicular Co-Cr medium.

I. INTRODUCTION

In magnetic recording media, the magnetic interaction between magnetic crystalline particles influences the recording and the reproducing performances.^{1,2} The Henkel plots and delta M plots are also changed by the interparticle interaction. A new medium model based on magnetization curling and a mean-field interaction theory³ was developed to analyze the interparticle interaction. By using a computer simulation of this medium model, the relationship between the Henkel plot and the mean field became clear. It was also shown that the high-density recording characteristics is influenced strongly by the mean interaction field in perpendicular magnetic recording.⁴

In this article we have investigated the relationship between the mean interaction field and both the packing density of crystalline particles and the particle orientation distribution in the medium.

II. INFLUENCE OF PACKING DENSITY

In particulate media in which magnetic crystalline grains are segregated, the magnetostatic interaction is much larger than the exchange interaction between magnetic particles. Therefore, we have investigated the magnetostatic interaction field which is the mean interaction field.

We have assumed a particulate medium model in which rectangular prismatic particles were arranged in a three-dimensional lattice shape with proper separations as shown in Fig. 1. To remove the effect of the demagnetizing field, the particles were arranged so that the arrangement configuration became a rectangular column whose aspect ratio was 1:10. The magnetization in each prismatic particle was replaced by magnetic charges at the particle surface to calculate the magnetic field. When all of the magnetizations were in the easy-axis direction such as the up direction, the magnetic field at the center particle of the particle arrangement, that is the mean interaction field, was calculated. The separation spaces between particles were decreased to decrease the packing density. The spaces were the same in the x , y , and z directions. The total number of particles was over 1 000 000.

Figure 1 shows the mean-field constant calculated for Ba-ferrite particulate media with the various packing densities. The mean field constant α was obtained by dividing the

mean interaction field (Oe) by $4\pi M$, where M is the mean magnetization (emu/cm^3) of the medium. Here the flat rectangular prisms with aspect ratio of 3.5:1 were used for the Ba-ferrite particles. We have obtained a positive mean field and it became larger as the packing density increased. Since the packing density of actual media is about 30%, the mean-field constant is estimated at around 0.43.

Figure 2 shows the mean-field constant characteristics for metal particulate media. The aspect ratio was assumed at 1:7 for the metal elongated particles. The mean field at a packing density of 100% was slightly positive because the Lorentz field never becomes negative. However, a negative mean field was obtained when the packing density was under 90%, and a minimum value was observed at a packing density of around 5%. This result is because the distance between magnetic particles placed in parallel to the magnetization direction is much shorter than that between particles in series, and so the negative interaction field brought by particles in parallel is stronger than the positive field from particles in series. The mean-field constant is estimated to be around -0.07 for the metal particulate medium when the packing density is about 30%.

III. INFLUENCE OF ORIENTATION DISTRIBUTION

The Henkel plots were measured for longitudinally oriented Ba-ferrite particulate media with various particle ori-

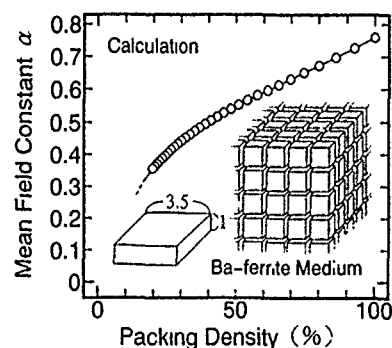


FIG. 1. Mean-field constant vs the packing density characteristics, calculated for a Ba-ferrite medium model composed of flat rectangular prismatic particles.

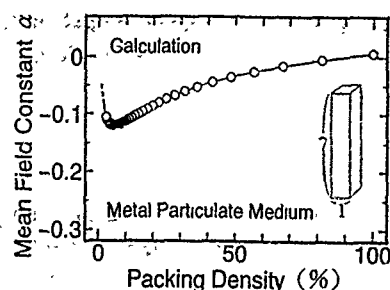


FIG. 2. Mean-field constant vs the packing density characteristics for a metal particulate medium with elongated particles.

entation distributions. The saturation magnetization and the coercive force were 145 emu/cm^3 and 1300 Oe , respectively. If there is no interaction between magnetic particles, the Henkel plot will become a straight line from an upper-left-hand corner to a lower-right-hand corner. However, the measured Henkel plots exhibited a positive interaction as shown in Fig. 3, and it was also suggested that the interparticle interaction became larger as the squareness increased.

If a compensating field to cancel the interaction field is applied in an opposite direction to external field, the Henkel plot will become straight. To estimate the mean interaction field in these Ba-ferrite media, we have measured many Henkel plots with applying various compensating fields which are changed in proportion to the mean magnetization in the medium. When a proportional constant was adjusted to 0.12 for the sample whose squareness was 0.8, the Henkel plot became almost straight as shown by open circles in Fig. 3. Therefore, the mean-field constant α was estimated at 0.12 for this Ba-ferrite medium. By this method using the linearization of the Henkel plot,⁵ the mean-field constants were also estimated at 0.10 and -0.05 for the other two samples with the squareness of 0.75 and 0.5, respectively. The measured mean-field constants were much smaller than those calculated by the particle arrangement model and they changed with the squareness. This result suggests that the mean field is diminished by the particle orientation distribution.

Figure 4 shows the influence of the orientation distribu-

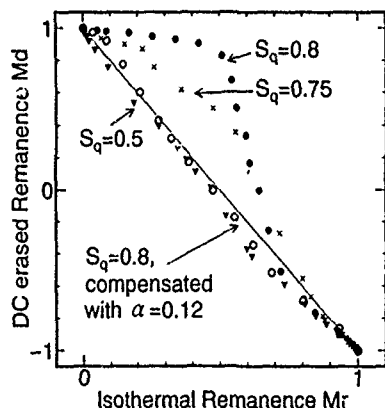


FIG. 3. Henkel plots measured for longitudinally oriented Ba-ferrite particulate media with the various orientations, and the linearization of the Henkel plot.

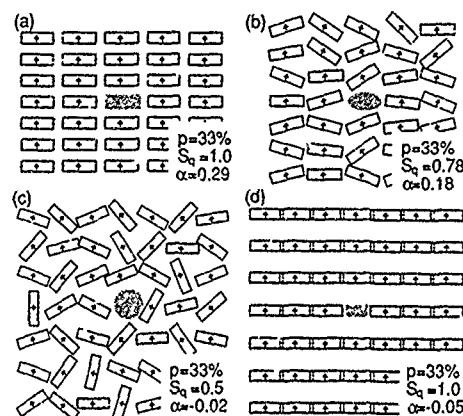


FIG. 4. Influence of the orientation distribution in the Ba-ferrite medium, calculated for (a) the perfect orientation, (b) the orientation with the squareness 0.78, (c) the random orientation, and (d) the uniform orientation but the centers of particles are located at the same positions as (c).

tion on the mean interaction field, calculated by the three-dimensional particle arrangement model for the Ba-ferrite medium. Here we have assumed the configuration of the particle arrangement as a cubic so that the demagnetizing factor became the same in the x , y , and z directions. The easy axes of particles were given using random numbers and the mean-field constant was decided by taking an average of 100 time calculations. In the case of the perfectly oriented model as shown in Fig. 4(a), the distance between the centers of particles placed in a horizontal direction is much longer than that of particles arrayed vertically. However, for the random orientation of Fig. 4(c), the particles were arranged so that the distances between the particle centers were identical in the horizontal and the vertical directions. The squareness was calculated by the medium magnetization model including the mean-field interaction.^{4,6}

The calculated mean-field constant was 0.29 for the perfect orientation of Fig. 4(a) but it decreased as the orientation became poor. The tendency to change by the orientation distribution corresponds very well with the squareness dependency of the Henkel plot as described in Fig. 3. On the other hand, as shown in Fig. 4(d), we have assumed another model in which the easy axes of particles were given uniformly but the centers of particles were located at the same positions as in the random orientation of Fig. 4(c). The mean-field constant for the model of Fig. 4(d) was -0.05 which was nearly equal to the random orientation model of Fig. 4(c). Consequently we can conclude that the mean interaction field is influenced mainly by the location of magnetic particles and not by the particle orientation.

IV. PERPENDICULAR Co-Cr MEDIUM

A perpendicularly anisotropic Co-Cr film medium is considered to be particulate from its noise characteristics⁷ and a columnar structure is proposed.⁸ Moreover, it is well known that the demagnetizing factor in the perpendicular direction is smaller than 1 mks and is roughly 0.8, in general.

The effective demagnetizing factor was investigated by the particle arrangement model. As shown in Fig. 5, many

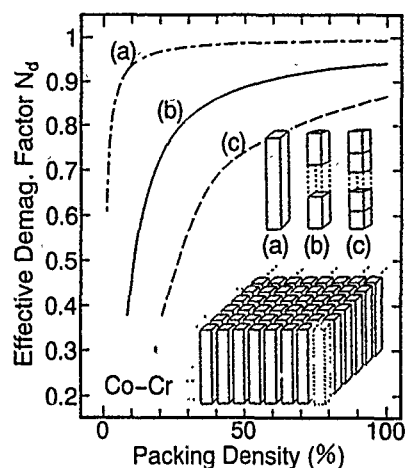


FIG. 5. Effective demagnetizing factor for a Co-Cr film medium, calculated when each column is (a) a single domain, and divided into (b) three and (c) five grains.

rectangular columnar particles whose aspect ratio was 1:10 were arrayed in rows, and the spaces between particles were changed according to the packing density. When each columnar particle was supposed as a single domain, that is by model 5(a), the effective demagnetizing factor decreased suddenly as the packing density became smaller than 10%. However, when the packing density was larger than 20%, the demagnetizing factor was larger than 0.96. Consequently, the effective demagnetizing factor is regarded as about 1 in a Co-Cr perpendicular medium with a columnar structure.

Since it is not clear why the demagnetizing factor is smaller than 1, we have assumed that a positive mean interaction field acted in the perpendicular direction of a medium and it diminished the demagnetizing field effectively. The mean field was calculated by the two different models in which each columnar particle was divided into (b) three and (c) five smaller crystalline grains as shown in Fig. 5. The effective demagnetizing factor was obtained by subtracting the mean field constant from 1. From Fig. 5, if the packing density of the magnetic grains was about 30%, each colum-

nar crystal is supposed to be composed of about three grains separated magnetically because the effective demagnetizing factor is roughly 0.8.

V. CONCLUSIONS

A positive mean field was obtained for a longitudinally oriented Ba-ferrite medium and it increased according to the increase of the packing density. On the other hand, a negative mean field was obtained for the metal particulate medium. This result is because the distance between magnetic particles placed in parallel to the magnetization direction is much shorter than that between particles in series, and so the negative interaction field brought by parallel particles is stronger than the positive field from series particles.

By the linearization of the Henkel plot and by calculation, it was shown that the mean field was changed by the squareness of the Ba-ferrite media. This result is because the distance between particles in series increased and decreased in parallel particles. In the case of a Co-Cr perpendicular medium, each columnar particle was supposed to be composed of three or four grains separated magnetically when the positive mean field acted in the medium.

The interparticle magnetic interaction is strongly influenced by the stacking of particles which was neglected in this article. The relationship between the interaction and the stacking have to be studied as well as the influence of interparticle interaction on recording density and noise characteristics.

¹P. I. Mayo, K. O'Grady, R. W. Chantrell, J. A. Cambridge, I. L. Sanders, T. Yogi, and J. K. Howard, *J. Magn. Magn. Mater.* **95**, 109 (1991).

²D. E. Spiliotis and W. Lynch, *J. Appl. Phys.* **69**, 4496 (1991).

³D. L. Atherton and J. R. Beattie, *IEEE Trans. Magn.* **MAG-26**, 3059 (1990).

⁴I. Tagawa and Y. Nakamura, *IEEE Trans. Magn.* **MAG-29**, 3981 (1994).

⁵X. He, C. Alexander, Jr., and M. R. Parker, *IEEE Trans. Magn.* **MAG-28**, 2683 (1992).

⁶Y. Nakamura and S. Iwasaki, *IEEE Trans. Magn.* **MAG-23**, 153 (1987).

⁷H. Muraoka, S. Yamamoto, and Y. Nakamura, *J. Magn. Magn. Mater.* **120**, 323 (1993).

⁸S. Iwasaki and K. Ouchi, *IEEE Trans. Magn.* **MAG-14**, 849 (1978).

Micromagnetic studies of medium noise mechanisms

Xiaodong Che

Quantum Corporation, 500 McCarthy Boulevard, Milpitas, California 95035

H. Neal Bertram

Center for Magnetic Recording Research, U.C. San Diego, La Jolla, California 92093

For a granular thin-film medium, the total noise is determined by intergranular interactions and local anisotropy fields. Among these two factors, the effect of local anisotropy on medium noise is relatively less clear. A micromagnetic model is used to study four kinds of media with different anisotropy distributions. Perpendicular anisotropy is examined in two of the four media: One has a uniform perpendicular component for all grains, the other has some perpendicular grains randomly distributed. It is found that if exchange coupling is absent, the medium with the most uniformly distributed crystalline anisotropy has the lowest noise. Otherwise, the medium with the most nonuniformly distributed anisotropy yields the lowest noise.

I. INTRODUCTION

Medium noise originates from local magnetic-field (anisotropy) fluctuations and interactions between grains that include exchange coupling and magnetostatic interactions. The effect of exchange coupling on the medium noise was studied numerically indicating that a strong intergranular exchange enhances medium noise significantly due to collective magnetic behavior.¹ Therefore, to achieve a medium with the lowest noise, exchange coupling must be eliminated. Medium noise with different anisotropy distributions was studied experimentally by using torque measurement.² Based on this experiment, media with perpendicular anisotropy component have lower noise than those without a perpendicular component. Since the torque measurement cannot reveal the micromagnetic structure, a numerical model comparing media with a 2D and a 3D distribution of anisotropy was utilized to understand the noise reduction mechanism.³ The numerical model found that these two kinds of media had a similar medium noise level. Therefore, the reason for this noise reduction observed in the experiment is still not fully understood.

In this article, a micromagnetic model is utilized to systematically study media noise with different anisotropy distributions. The purpose of this study is to further understand noise mechanisms and to explore optimal anisotropy distributions that offer very low media noise even when exchange coupling exists.

II. MODEL AND MEDIA SELECTION

The model used for this study is a standard micromagnetic model in which a portion of magnetic thin film medium is represented by a 64×64 hexagonal grains.⁴ The magnetostatic and exchange interactions between these grains are characterized by two normalized parameters hm and he defined as $hm = M_s/H_k$, $he = A^*/KD^2$, where M_s is the saturation magnetization, H_k is the crystalline anisotropy field, A^* is a phenomenological intergranular exchange coupling, D is the grain size, and K is the granular crystalline anisotropy energy.

Four media with different anisotropy distribution are investigated. The anisotropy distributions of these media are listed in Table I.

For each type of medium, 20 different 64×64 arrays are generated to obtain track average fluctuations. For each array, the magnetization is first saturated in one direction and then an isolated transition is recorded by a Karlquist head field. By obtaining 20 different magnetic transition patterns from these arrays, the magnetic fluctuation at down-track position x , $dm(x)$, is calculated by the following formula:

$$dm(x)^2 = \frac{1}{20-1} \sum_{i=1}^{20} [m_i(x) - \bar{m}(x)]^2 \quad (1)$$

where $m_i(x)$ is the cross-track magnetization average of the i th medium, and $\bar{m}(x)$ is the average of $m_i(x)$. In the following discussion, $dm(x)$ is treated as the medium noise at position x , although in a practical point of view, it is the medium noise deconvolved with the playback head function.

III. FLUCTUATIONS IN CRYSTALLINE ANISOTROPY AMPLITUDE

Medium A and medium B have the same angular distribution in the crystalline anisotropy, but medium A has a constant H_k value, and medium B has a uniform distribution in H_k from 0.5 to 1.5. In Fig. 1(a) magnetization cross track averages $\bar{m}(x)$ for medium A and medium B with $hm=0.2$, $he=0.05$ are plotted. In Fig. 1(b), the fluctuation function $dm(x)^2$ is also plotted. It is noticed that the medium fluctuation always reaches a maximum at the transition center. This

TABLE I. The anisotropy distributions of these media.

ID	Amplitude of anisotropy	Direction of anisotropy
Medium A	$H_k = 1.0$	2D random (planar)
Medium B	H_k varies from 0.5 to 1.5	2D random (planar)
Medium C	$H_k = 1.0$	2D random but with 10% grains having perpendicular crystalline anisotropy.
Medium D	$H_k = 1.0$	Almost 2D random but with a small vertical component which varies from 0 to 0.2.

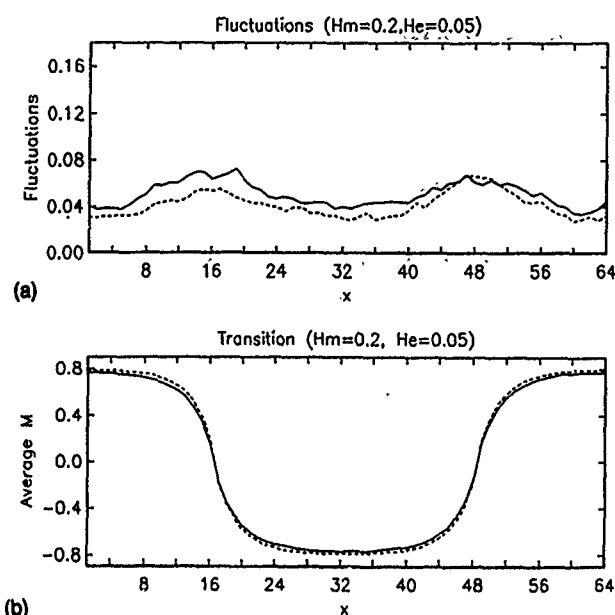


FIG. 1. (a) Magnetization transition profiles and (b) medium fluctuation for medium A (solid lines) and medium B (dashed lines) with $hm=0.2$ and $he=0.05$.

can be qualitatively understood based on a simple statistic argument: Assuming that the magnetization in each grain can only have two values: m_r or $-m_r$, it can be proven that the cross track average fluctuation is proportional to $(m_r^2 - \bar{m}^2)^{1/2}$ where \bar{m} is the magnetization average. By comparing the noise levels of these two media, one can find that the medium with a constant H_k has a higher noise level than the other in both transition region and saturation region. This indicates that the cross-track coupling in grains is reduced with a fluctuation in H_k .

In Fig. 2, the total medium fluctuation by taking the summation of $dm(x)^2$ over x is plotted versus magnetostatic interaction parameter hm with zero exchange coupling. The hm value varies from zero to 0.2 and he is equal to 0.0. When $hm=0.0$, grains in both medium A and medium B have no interactions. Therefore, the two media have the same total

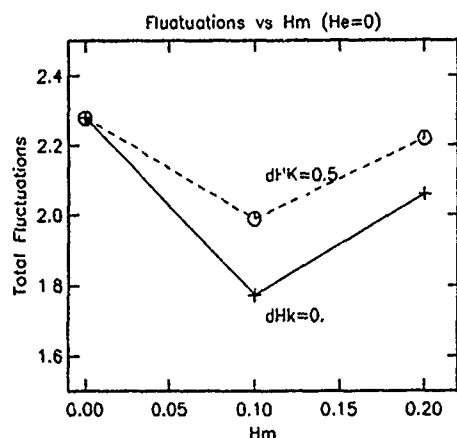


FIG. 2. The total medium fluctuation vs hm at $he=0.0$ for medium A (solid line) and medium B (dashed line).

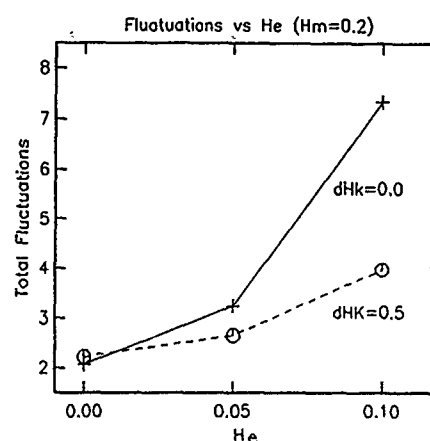


FIG. 3. The total medium fluctuation vs he at $hm=0.2$, for medium A (solid line) and medium B (dashed line).

medium fluctuation value. As hm increases, the total fluctuation first decreases and then increases. The reduction of the total fluctuation initially is due to magnetostatic interaction which offers an antiparallel interaction across the track. This reduces cross-track coupling. On the other hand, the magnetostatic interaction also lines up magnetization of each grain in the down-track direction. This reduces medium noise in the saturation region. As hm increases even further, medium fluctuations increase significantly in the transition region due to a broader transition. This results in a higher total noise. Both medium A and medium B show the same trend for the total medium noise; however, medium A always has a lower fluctuation value than medium B due to its constant H_k value.

In Fig. 3, the total medium fluctuation versus exchange coupling parameter he is plotted with $hm=0.2$. For both medium A and medium B, the total medium fluctuation increases monotonically with he . However, for medium B the noise fluctuation increases much more slowly than that for medium A. This can be explained by the following argument: Analytically, it can be proven that the total fluctuation is proportional to the cross track correlation length.⁶ Exchange coupling links the magnetization between adjacent grains and makes the correlation length longer. Medium B which has a fluctuation in the local anisotropy amplitude reduces the cross-track correlation that is developed by the exchange. This argument will also be used to explain the noise reduction in medium C.

Although medium B has slightly more noise than medium A without exchange coupling, its noise increases very slowly with increasing exchange coupling. This is a significant advantage when exchange coupling cannot be fully eliminated.

IV. PERPENDICULAR CRYSTALLINE ANISOTROPY

Both medium C and medium D have a perpendicular anisotropy component either from individual grains (medium C) or from all grains (medium D). In our study, 10% of the grains of medium C have their crystalline anisotropy directed perpendicularly. In medium D, the crystalline anisotropy in

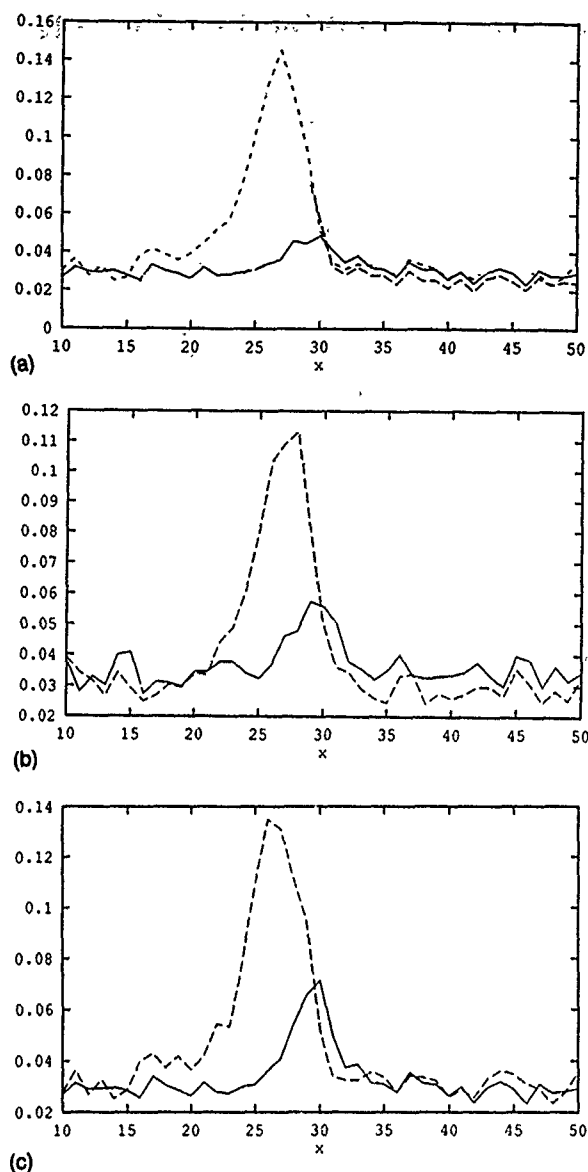


FIG. 4. (a) medium fluctuations for medium A, (b) medium fluctuations for medium C, (c) medium fluctuations for medium D. The solid lines are for $hm=0.1$, $he=0.0$, the dashed lines are for $hm=0.1$, $he=0.1$.

each grain has a perpendicular component varying from 0 to 0.2. Therefore, medium C and medium D have the same perpendicular anisotropy component with an average of 0.10.

In Figs. 4(a), 4(b), and 4(c), $dm(x)^2$ curves for medium A, C, and D are plotted, respectively. The solid curves are for $hm=0.1$ and $he=0.0$ and the dashed lines are for $hm=0.1$, and $he=0.1$. When the exchange coupling is small, the fluctuation is very small for all three media. In the transition region, medium D has the highest medium fluctuation followed by medium C. When the exchange coupling exists ($he=0.1$), the fluctuation increases significantly in the transition region, however no fluctuation increase is observed in

the saturation region. By comparing these three media, we find that medium A and medium D have a similar fluctuation level. Medium C has a lower fluctuation level than that of the other media. This indicates that medium D in which crystalline anisotropy is tilted perpendicularly slightly has the same cross-track correlation length as that of medium A. This result agrees with the previous micromagnetic study discussed in Sec. I.³ Only the perpendicular grains in medium C have sufficient strength to reduce the correlation length developed by exchange coupling. Therefore, in order to reduce exchange coupling effect, fluctuations in anisotropy fields have to be sufficiently large especially between adjacent grains.

It is more likely that the experimental results were obtained on media which have a structure similar to medium C. Since medium C and medium D have the same average perpendicular anisotropy component, the torque measurement cannot distinguish one from the other. As discussed, medium D has a lower medium noise than medium C and A. Therefore, torque measurement can not always be directly correlated with medium noise.

V. CONCLUSIONS

By utilizing a micromagnetic simulation, four idealized media with different crystalline anisotropy distributions are investigated. It is found that, when exchange coupling is absent, medium noise is determined by the local crystalline anisotropy fluctuation. The total medium noise power is low for all four media. Relatively, medium A, with the most uniform anisotropy distribution, has the lowest noise. When exchange coupling is strong, medium noise is determined by the collective magnetization behavior. Under this circumstance, a medium with a structure eliminating the exchange coupling effect has a low noise level. To achieve this kind of structure, fluctuations in the crystalline anisotropy have to be sufficiently large. In the four medium structures we tested, medium B and medium C yield a slower noise increase as exchange coupling rising. Therefore, when exchange coupling cannot be totally eliminated, a medium with a structure similar to medium B or medium C is recommended.

ACKNOWLEDGMENTS

The authors would like to thank Tadashi Yogi for his suggestion of modeling sprinkling perpendicular granular medium (medium C). This work was supported in part by the Center for Magnetic Recording Research, an IBM research grant, and NSF Grant No. DMR90-10908.

¹J.-G. Zhu and H. N. Bertram, IEEE Trans. Magn. **MAG-24**, 2707 (1988).

²D. E. Spiliotis, IEEE Trans. Magn. **MAG-26**, 2721 (1990).

³H. N. Bertram and J.-G. Zhu, IEEE Trans. Magn. **MAG-27**, 5043 (1991).

⁴X. Che and H. N. Bertram, IEEE Trans. Magn. **MAG-29**, 317 (1993).

⁵J.-G. Zhu and H. N. Bertram, J. Appl. Phys. **63**, 3248 (1988).

⁶H. N. Bertram and X. Che, IEEE Trans. Magn. **MAG-29**, 201 (1993).

Improving ferrite MiG head read-back distortions caused by domain walls and granularity (abstract)

B. E. Argyle, R. Schäfer,^{a)} P. L. Trouilloud, M. E. Re,^{b)} A. P. Praino, S. Takayama,^{c)} and D. Dingley^{d)}

IBM Research Division, T. J. Watson Research Center, Box 218, Yorktown Heights, New York 10598

Ferrite MiG heads intended for narrow track ($\leq 10 \mu\text{m}$) digital recording were recently investigated in the critical pole-tip region at the air-bearing-surface using micro-ellipsometry, Kerr microscopy, and electron back-scatter diffraction from individual grains,¹ and using magnetic force microscopy to detect air-gap remanent fields.² Comparison of these direct observations with readback-after-write waveforms from written test tracks, and consideration of granularity influences on bulk permeability and domain size, indicate that waveform instability and asymmetry from *polycrystalline* ferrite (PCF) heads would be diminished by suitable size and orientation of the grains.¹ The use of *single-crystal* ferrite³ (SCF) for advanced laser enhanced etch definition³ of narrow pole MiGs can avoid this type of distortion. However, secondary signals⁴ often appear as weak pulses separated in time from the main gap pulse. We have associated this effect with a zig-zag shaped wall seen nucleated and propagated from the pole tips by a write pulse.⁴ This wall and its underlying domains lie remanent in the stressed ABS material and evidently react to the bit fields during the read cycle. The secondary read-back response, though similar to the pseudo-gap effect, differs in origin. Its timing depends on the distance of the zig-zag wall to the gap, not the fixed position of the sendust-ferrite interface. Our results indicate that suitable grain oriented ferrite would reduce PCF MiG head read-back asymmetry and instability. For SCF heads, a method for *electrically* removing zig-zag walls is possible and secondary pulse removal has now been demonstrated on a spin test strand.

^{a)}Now at Forschungszentrum IFW, Inst. f. Metallic Materials, Helmholtzstrasse 20, D-01069 Dresden, Germany.

^{b)}Now at IBM Adstar, Cottle Rd., San Jose, CA.

^{c)}IBM Tokyo Research Laboratory, IBM Japan Ltd., Tokyo, Japan.

^{d)}University of Bristol, Royal Fort, Tyndall Ave., Bristol, England.

¹R. Schäfer, B. E. Argyle *et al.*, paper GP-07 IN'ERMAG '93 (Stockholm).

²S. Takayama *et al.*, IEEE Trans. Magn. **28**, 2647 (1992).

³M. Ichinose and M. Aronoff, IEEE Trans. Magn. **26**, 2972 (1990).

⁴R. Schäfer *et al.*, IEEE Trans. Magn. **28**, 2644 (1992).

MO polar Kerr studies of Co rich molecular beam epitaxy grown Au/Co multilayers

S. Višňovský, M. Nývlt, and V. Prosser

Department of Mathematics and Physics, Charles University, Ke Karlovu 5, CZ-121 16 Prague 2, Czech Republic

R. Atkinson, W. R. Hendren, and I. W. Salter

Department of Pure and Applied Physics, The Queen's University of Belfast, Belfast BT7 1NN, Northern Ireland, United Kingdom

M. J. Walker

Department of Physics, University of Leeds, Leeds LS2 9JT, United Kingdom

Magneto-optical (MO) polar Kerr rotation and ellipticity (PKR and PKE, respectively) of Co rich Au(111)/Co(0001) multilayers grown by molecular beam epitaxy on GaAs(110) substrates are reported. The individual layer thicknesses, t_{Au} and t_{Co} were $t_{\text{Au}}/t_{\text{Co}} = 2.6/3.2$, $1.0/1.5$, and $0.65/0.8$ nm. The samples displayed perpendicular magnetic anisotropy smaller than demagnetization energy. PKR and PKE were measured at photon energies between 1.5 and 5.2 eV. In the multilayer with $t_{\text{Co}} = 1.5$ nm, PKR at 3.1 eV reached a value of -0.34° , remarkably higher than that reported on Au rich multilayers. The spectra were compared with theory. A satisfactory agreement was obtained only for the sample with the largest bilayer thickness, $t_{\text{Au}} + t_{\text{Co}} = 5.8$ nm. This indicates that when t_{Au} and t_{Co} are reduced to a few atomic monolayers the role of interfaces is increased. The effects of strain, defects, and atomic mixing at Au-Co interfaces become more important. Both the magnetic and optical properties are modified.

I. INTRODUCTION

Several interesting phenomena have been demonstrated in ultrathin 3D ferromagnetic metal/noble metal film structures, among them perpendicular magnetic anisotropy (PMA), enhancement of magneto-optical (MO) effects, oscillating interlayer exchange coupling, etc.¹⁻⁵ This article reports on MO polar Kerr rotation and ellipticity (PKR and PKE) in molecular beam epitaxy (MBE) grown Au/Co multilayers in which the individual layer thicknesses of t_{Au} were chosen smaller than those of t_{Co} . The previous MO studies²⁻⁴ were all focused on the multilayers characterized by $t_{\text{Au}} > t_{\text{Co}}$.

II. SAMPLES AND EXPERIMENTAL METHODS

The Au/Co multilayers were grown by MBE onto (110) oriented GaAs substrates.⁶ First, a 50-nm-thick buffer layer of Ge(110) and a (110) Co layer, followed by the first Au(111) layer, were deposited and on which the Au(111)/Co(0001) multilayer structure was grown. In this way, the first and topmost layers in the multilayer systems were always gold. Three samples with individual Au and Co layer thicknesses, $(t_{\text{Au}}/t_{\text{Co}})^n = (2.6/3.2)^{20}$, $(1.0/1.5)^{40}$, and $(0.65/0.8)^{80}$ were selected for the present study. Here n denotes the number of Au-Co bilayers grown on the Au(111)/Co(110)/Ge(110) buffer system. The sample periodicity was checked by x-ray diffraction (XRD) PKR and PKE were measured at 300 K in a photon energy range from 1.5 to 5.2 eV. Use was made of the azimuth modulation and self-compensation technique.⁷ The angle of incidence was 6° . As

a first step, the PKR hysteresis loops were taken at a photon energy of 3.1 eV, which provided a value of the saturation magnetic field.

III. RESULTS AND DISCUSSION

The XRD pattern indicated a good periodicity and sharp interfaces in the $(2.6/3.2)^{20}$ and $(1.0/1.5)^{40}$ multilayers, as illustrated in Fig. 1 for the latter sample. In the $(0.65/0.8)^{80}$ sample broader peaks revealed a large amount of Au-Co mixing. The results of the PKR magnetometry are shown in Fig. 2. The saturation of PKR below 0.8 T in the $(2.6/3.2)^{20}$

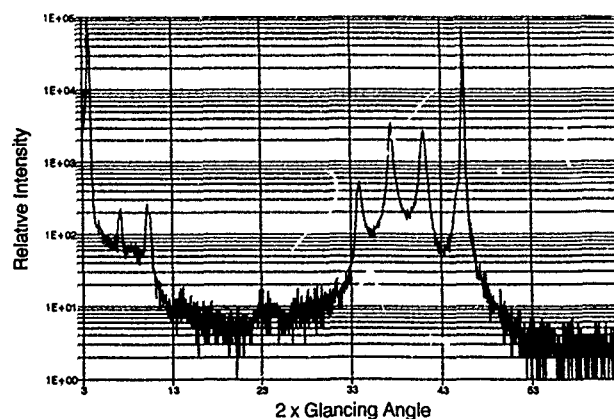


FIG. 1. X-ray diffraction ($\text{Cu K}\alpha$) from $[\text{Au}(1.0 \text{ nm})/\text{Co}(1.5 \text{ nm})]^{40}$ multilayer.

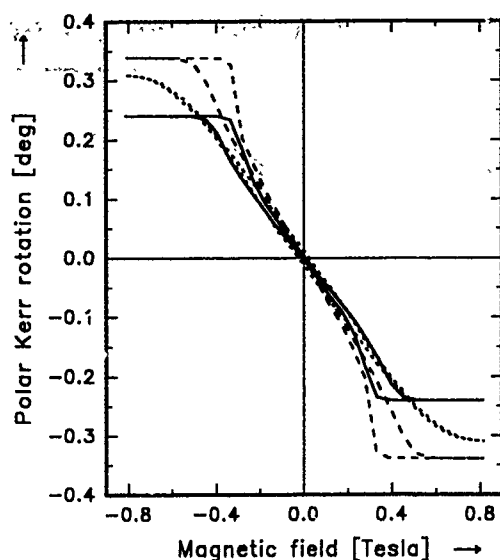
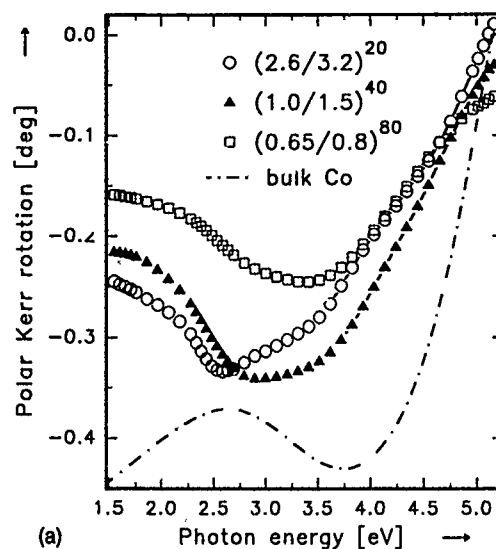


FIG. 2. Magneto-optical polar Kerr rotation hysteresis loops measured at a photon energy of 3.1 eV in [Au(2.6 nm)/Co(3.2 nm)]²⁰ (short dash), [Au(1.0 nm)/Co(1.5 nm)]⁴⁰ (long dash), and [Au(0.65 nm)/Co(0.8 nm)]⁸⁰ (solid line) multilayers.

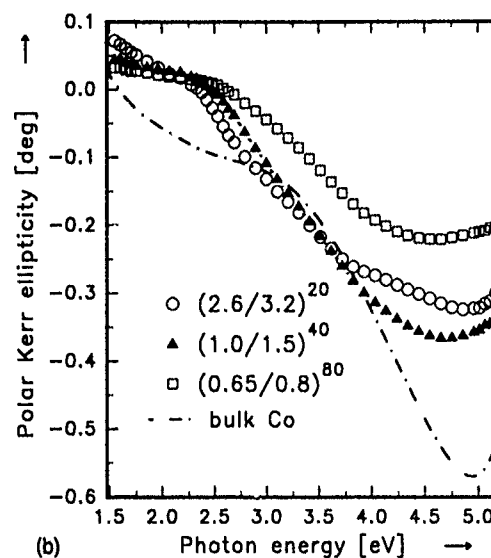
multilayer and the MO hysteresis loops, displaying low remanence and constriction in the other samples, are typical for the case when the PMA is smaller than demagnetization energy.⁸ The anisotropy is due to the magnetoelastic effect originating from larger lattice spacing in gold than in cobalt and its magnitude is sensitive to the distribution of Au and Co atoms at the interface,⁹ void concentration in Au and, possibly, to Au layer thickness when t_{Au} is reduced to a few atomic monolayers (a reduced strain effect of the Au layer in Co rich Au/Co multilayers). Note that, in Au(5 nm)/Co(t_{Co})/Au(25 nm) sandwiches, the energy of the perpendicular magnetic anisotropy dominates the demagnetization energy up to about $t_{\text{Co}}=1.5$ nm.^{10,11} This critical thickness is generally smaller in multilayers where sharp, steplike Au-Co interfaces are more difficult to achieve.^{12,13}

Figure 3 displays PKR and PKE spectra of the multilayers. In thicker samples the splitting of the major peak is observed. The structure is mainly of Au origin. Particularly, the peak arising from the plasma edge in gold situated near 2.5 eV is clearly discernible in the (2.6/3.2)²⁰ multilayer. Here PKR reaches -0.33° . This value is considerably higher than that observed in Au rich multilayers.²⁻⁴ In the (1.0/1.5)⁴⁰ multilayer the PKR amplitude is even higher (-0.34°), while the peak broadens and shifts to 3 eV. The peak is remarkably reduced in the (0.65/0.8)⁸⁰ where the nominal t_{Au} and t_{Co} are less than 3 and 4 ML, respectively, and large Au-Co mixing at the interfaces was difficult to avoid.

Several formalisms based on Maxwell's theory have been developed to describe the optical interactions in magnetic multilayers.¹⁴⁻¹⁸ We modeled the spectra using the model given elsewhere¹⁴ and the bulk optical (for Au and Co) and MO (for Co) data.¹⁹⁻²⁵ This approach was shown to be successful in the case of Au/Co/Au sandwiches where the composition profile can be made nearly ideally rectangular.¹⁹ The computed spectra in the multilayers are all similar in



(a)



(b)

FIG. 3. Magneto-optical polar Kerr effect in Au/Co multilayers and bulk Co of (a) rotations and (b) ellipticities.

shape, displaying a moderate increase in amplitude as $t_{\text{Au}}+t_{\text{Co}}$ and the thickness of the topmost layer simultaneously decrease. However, the experimentally observed spectra do not follow this simple trend. A satisfactory agreement between the measured and computed spectra is obtained only for the thickest $t_{\text{Co}}+t_{\text{Au}}$ bilayer (Fig. 4). In this case all structures in the computed spectra can be correlated with the experiment. Nevertheless, the measured spectra show broader linewidths and the peak assigned to the plasma edge in gold² occurs at slightly higher photon energy.

To explain the observed differences we have to consider the following effects: (1) Amplitude reduction of the interband transition contributing to the absorption edge in gold^{20,25} due to structural defects (e.g., voids) and the lack of long range order. These defects are likely to occur in our Au ultrathin films which were grown under a compressive stress induced by adjacent Co. (2) Increase of the Au-Co mixing at the interfaces with number of bilayers. This reduces not only the interface perpendicular anisotropy but also the magnetization and, consequently, the PKR and PKE because a part of

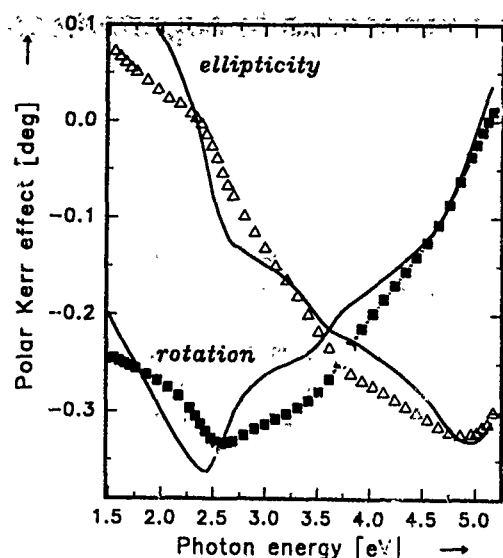


FIG. 4. Polar Kerr effect in $[\text{Au}(2.6 \text{ nm})/\text{Co}(3.2 \text{ nm})]^{20}$ multilayer. Experimental data of rotation (squares) and ellipticity (triangles); computed using the optical constants of the bulk Au (solid lines).

the Co atoms at the interfaces are not ferromagnetically coupled to each other. (3) Larger Drude (free carrier) linewidth in ultrathin gold is produced by the scattering at Au-Co interfaces. (4) Effect of electronic coupling between spin-polarized Co and Au.^{5,11,13} As a result, a contribution from spin-polarized Au to the total magneto-optical activity, especially in the region of the Au plasma edge,²⁶ cannot completely be ruled out.

An inspection of the XRD pattern in Fig. 2 proves a high degree of perfection of the $[\text{Au}(1.0 \text{ nm})/\text{Co}(1.5 \text{ nm})]^{40}$ multilayer. The sample displays a rather high PKR and PKE. The thickness of the Au spacer, t_{Au} , is smaller than 5 ML and the adjacent Co layers can be considered as coupled.¹³ The shift of the main peak towards higher photon energies is due to the changes of Au permittivity in the ultrathin film limit and partially due to a weak MO contribution of the spin-polarized gold monolayer at Au-Co interface.¹¹ The effect of Au-Co mixing at the interfaces dominates the spectra of the $[\text{Au}(0.65 \text{ nm})/\text{Co}(0.8 \text{ nm})]^{80}$ multilayer. This makes the ferromagnetically ordered Co layer thinner by about 1 ML per period¹² and, consequently, attenuates MO amplitudes in this sample.

IV. SUMMARY

In conclusion, we have presented polar Kerr effect spectra in Co rich MBE grown Au/Co multilayers. In the multilayer with $t_{\text{Co}}=1.5 \text{ nm}$ PKR at 3.1 eV reached a value of -0.34° , remarkably higher than that reported in Au rich multilayers. The spectra were compared with theory. The modeling has shown that magneto-optical Kerr spectra in Au/Co multilayers, especially in the Au plasma edge region near 2.5 eV, strongly depend on the optical constants of gold.¹⁹ In this spectral region the constants are very sensitive to Au layer perfection.^{20,25} A satisfactory agreement using bulk Au optical constants was obtained only for the sample with the thickest bilayer, $t_{\text{Au}}+t_{\text{Co}}=5.8 \text{ nm}$. This indicates

that at t_{Au} and t_{Co} reduced to a few atomic monolayers, the role of interfaces is increased. The effect of strain and defects as well as that of atomic mixing at Au-Co interfaces become more important. Both the magnetic and optical properties are modified: surface perpendicular magnetic anisotropy induced by the mismatch between the lattice parameters of Au and Co, oscillator strengths for the Au interband electronic transitions, free electron scattering in Au, etc. Also, spin polarization in Au induced by exchange coupled Co atoms at Au-Co interfaces should be taken into account.

ACKNOWLEDGMENTS

The authors are grateful to Professor D. Greig of Leeds University for the preparation of the samples. The helpful discussions with Dr. P. Šíroky are acknowledged. This research has been partially sponsored by KONSTRUKTIS Praha, Ltd. and a Grant Agency of the Czech Republic (Grant No. 202/93/2427).

- ¹C. Chappert, K. Le Dang, P. Beauvillain, H. Hurdequint, and D. Renard, *Phys. Rev. B* **34**, 3192 (1986).
- ²T. Katayama, H. Awano, and Y. Nishikazu, *J. Phys. Soc. Jpn.* **55**, 2539 (1986).
- ³D. Weller, W. Reim, and H. Braendle, *J. Magn. Magn. Mater.* **93**, 183 (1991).
- ⁴W. B. Zeper, Ph.D. thesis, Eindhoven University, The Netherlands, 1991.
- ⁵Y. Suzuki, T. Katayama, K. Tanaka, S. Yoshida, and K. Sato, *Phys. Rev. Lett.* **68**, 3355 (1992); Y. Suzuki and T. Katayama, *MRS '93 Spring Meeting*, San Francisco, CA, paper Q1-6.2, *Mater. Res. Soc. Symp. Proc.* (in press); T. Katayama, Y. Suzuki, M. Hayashi, and A. Thiaville, *Proc. of the 1st International Symposium on Magnetic Multilayers*, '93, *J. Magn. Magn. Mater.* **126**, 527 (1993).
- ⁶D. Greig, M. J. Hall, C. Hammond, B. J. Hickey, H. P. Ho, M. A. Howson, M. J. Walker, N. Wissner, and D. G. Wright, *J. Magn. Magn. Mater.* **110**, L239 (1992).
- ⁷O. Čermáková and Š. Višňovský, *Czech. J. Phys. B* **36**, 537 (1986).
- ⁸R. Krishnan, M. Porte, and M. Tessier, *IEEE Trans. Magn.* **26**, 2727 (1990).
- ⁹C. Chappert and P. Bruno, *J. Appl. Phys.* **64**, 5736 (1988).
- ¹⁰V. Grolier, J. Ferré, A. Maziewski, E. Stefanowicz, and D. Renard, *J. Appl. Phys.* **73**, 5942 (1993).
- ¹¹S. Ould-Mahfoud, R. Megy, N. Bardou, B. Bartenlian, P. Beauvillain, C. Chappert, J. Corno, B. Lecuyer, G. Sczigel, P. Veillet, and D. Weller, *Proc. of the MRS 1993 Spring Meeting*, San Francisco.
- ¹²F. J. A. den Broeder, D. Kuiper, A. P. van Mosselaer, and W. Hoving, *Phys. Rev. Lett.* **60**, 2769 (1988).
- ¹³J. P. Renard, NATO Advanced Research Workshop on Magnetism and Structure in Systems of Reduced Dimension, Institut d'Etudes Scientifique de Cargese, France, June 15-19, 1992.
- ¹⁴Š. Višňovský, *Czech. J. Phys. B* **36**, 625 (1986).
- ¹⁵R. Atkinson, *J. Magn. Magn. Mater.* **124**, 178 (1993).
- ¹⁶M. Mansuripur, *J. Appl. Phys.* **67**, 6466 (1990).
- ¹⁷K. Balasubramanian, A. S. Marathay, and H. A. MacLeod, *Proceedings of the 7th International Conference on Thin Films*, New Delhi, India, 1987.
- ¹⁸J. Zak, E. R. Moog, C. Liu, and S. D. Bader, *J. Magn. Magn. Mater.* **89**, 107 (1990).
- ¹⁹Š. Višňovský, M. Nývlt, V. Prosser, J. Ferré, G. Pénissard, D. Renard, and G. Sczigel, *J. Magn. Magn. Mater.* **128**, 179 (1993).
- ²⁰D. E. Aspnes, E. Kinsbron, and D. D. Bacon, *Phys. Rev. B* **21**, 3290 (1980).
- ²¹P. B. Johnson and R. W. Christy, *Phys. Rev. B* **9**, 5056 (1974).
- ²²H. Braendle, D. Weller, J. C. Scott, S. S. P. Parkin, and C. J. Lin, *IEEE Trans. Magn.* **28**, 2968 (1992).
- ²³P. G. van Engen, K. H. J. Buschow, and M. Erman, *J. Magn. Magn. Mater.* **30**, 374 (1983).
- ²⁴Š. Višňovský, M. Nývlt, V. Pařízek, P. Kielar, V. Prosser, and R. Krishnan, *IEEE Trans. Magn.* **29** (in press).
- ²⁵M.-L. Théye, *Phys. Rev. B* **2**, 3060 (1970).
- ²⁶S. E. Schnatterly, *Phys. Rev.* **183**, 664 (1969).

Magneto-optical properties and magnetization processes in superlattices

Ron Atkinson and Nikolai F. Kubrakov

Department of Pure and Applied Physics, The Queen's University of Belfast, Belfast BT7 1NN, United Kingdom

Sergey N. Utochkin and Anatoley K. Zvezdin

General Physics Institute, Moscow 117942, Russia

Spin-reorientation processes in anisotropic magnetic superlattices (SLs) with antiferromagnetic interfacial coupling are theoretically analyzed. Results provide magnetic phase diagrams of the kind "external field—relative magnetic moment," as well as equations for the lines of the phase transitions. The influence of possible inhomogeneous magnetization in SLs is considered phenomenologically for the normal-incidence polar Kerr magneto-optical effect assuming the Q parameter to be a function of distance along the normal to the interface. A simple approach to the solution of this problem is outlined.

INTRODUCTION

Studying magnetic superlattices (SLs) is of great importance with regard to our understanding of the influence of surfaces and interfaces on their physical properties. This is particularly true for MO media. Magnetization processes in SLs are now under comprehensive investigation.^{1,2} However, the existing theoretical models of SLs either operate with an infinite medium or involve numerical methods and thus do not explain completely the behavior of the magnetic structures in an external magnetic field. In particular, there has been little research into how bulk or surface magnetic anisotropy and the outer surfaces affect the magnetic phase transitions and the reorientation processes. Inhomogeneous magnetization can presumably occur. To ascertain whether this may affect the MO properties of SLs the normal incidence polar Kerr effect, being important for applications, should be studied for the case where the inhomogeneity is along the normal to the plane of the medium. Consequently, the MO Q parameter becomes a function of the distance z from the surface. As far as we are aware this problem has not been solved before except for the special case of homogeneous multilayered thick films.³ Although we have treated rigorously the most general case, which will be reported on in due course, the solution here is, for brevity, given in terms of the differential reflectance approach.⁴

FIELD INDUCED SPIN-REORIENTATION PROCESSES IN SLs

We consider SLs with the two layers periodically repeated. One of them is to be isotropic and the other to possess uniaxial anisotropy (e.g., Gd/Co). The SL is subjected to an external field H in the plane of the films. In the first instance the magnetization is assumed to be homogeneous in each layer. Their total number $N+1$ is odd, so the first and last layer are identical. To find the phase diagrams at the temperatures far below the Curie point we use the thermodynamic potential

$$F = - \sum_{i=1}^{N/2+1} h \cos \theta_{2i-1} - \sum_{i=1}^{N/2} (h/\mu - K/2 \cos \theta_{2i}) \times \cos \theta_2 + \sum_{i=1}^N \cos(\theta_i - \theta_{i+1}), \quad (1)$$

where θ_i is the angle between H and the magnetization in the i th layer. In (1) $\mu = d_1 M_1 / d_2 M_2$, $h = H d_1 / \lambda M_2$, $K = \tilde{K} / \lambda M_1 M_2$ are, respectively, the relative magnetic moment of the SL unit cell, the reduced external field, and the anisotropy constant. All these are defined through the thicknesses d_1, d_2 , the magnitudes of the magnetization M_1, M_2 of the layers, the positive quantity λ proportional to the interface exchange constant, and the second-order anisotropy constant \tilde{K} . The potential (1) has been written as if the isotropic layer is the first one of the SL. That for the anisotropic layer has been considered in Ref. 5. The equilibrium magnetic phases are found from the conditions: $\partial F / \partial \theta_i = 0$ and the matrix $\|\partial^2 F / \partial \theta_i \partial \theta_j\|$ is positive-definite.⁵ To simplify the analysis and gain analytical results we put $N \rightarrow \infty$. Since the sign of K essentially changes the phase diagrams, they will be considered separately for both signs.

For $K > 0$ and H perpendicular to the anisotropy axis the phase diagram of Fig. 1 consists of the following five phases:

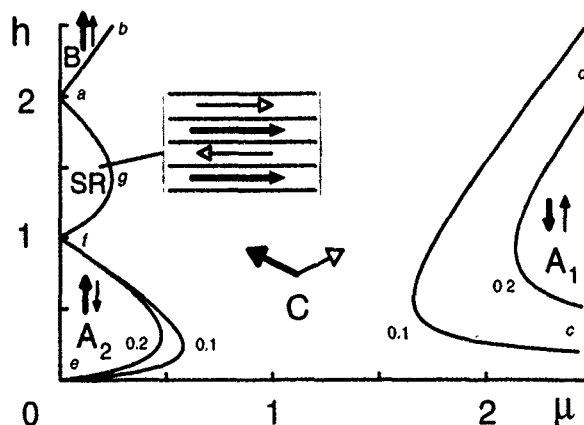


FIG. 1. Phase diagram of the ferrimagnetic SL for $K=0.1$ and 0.2 . The field H is perpendicular to the easy axis.

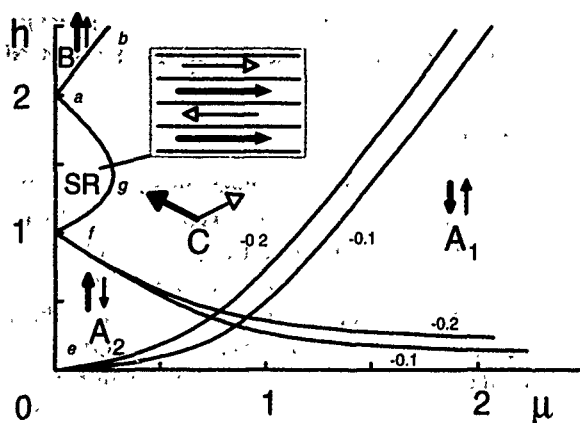


FIG. 2. Phase diagram of the ferrimagnetic SL for $K = -0.1$ and -0.2 . The field H is parallel to the easy axis.

(1) "Ferromagnetic" B , above the line ab ($\theta_1 = 0$),

$$h > 2, \quad \mu < \frac{h(h-2)}{h(2+K)-2K}. \quad (2)$$

(2) "Ferrimagnetic" A_1 , at the right of the line cd ($\theta_1 = \theta_3 = \dots = 0, \theta_2 = \theta_4 = \dots = \pi$),

$$h > \frac{2K}{2-K}, \quad \mu < \frac{h(h+2)}{h(2-K)-2K}. \quad (3)$$

(3) "Ferrimagnetic" A_2 , at the left of the line fe ($\theta_1 = \theta_3 = \dots = \pi, \theta_2 = \theta_4 = \dots = 0$),

$$h < 1, \quad \mu < \frac{h(1-h)}{h(1-K)+K}. \quad (4)$$

(4) "Surface-reoriented" (SR), at the left of the line af ($\theta_1 = 0, \theta_3 = \theta_5 = \dots = \pi, \theta_2 = \theta_4 = \dots = 0$)

$$h > 3/2, \quad \mu < \frac{h(2-h)}{h(2-K)+2K}, \quad (5)$$

$$h < 3/2, \quad \mu < \frac{h(h-1)[1-2(h-1)^2]}{h+K(h-1)(2-h)}. \quad (6)$$

The magnetization in the boundary layers is oriented parallel to H while the structure of the ferrimagnetic phase A_2 persists in the interior of the SL.

(5) "Canted" (C) between ab , af , fe , and cd lines. The magnetic moments make various angles with H . The "surface-twist" phase⁶ exists in C for small μ in the area limited by the lines eg , fe and it turns into C phase on the line defined from (5). In this phase the maximum deviation from the collinear orientation (being inherent to the both phases A_1 and A_2) takes place near the surface. This deviation vanishes with distance into the interior of SL. So the magnetization process in the SL is seen to be sophisticated if $\mu < 1$. For even $N+1$, surface phases arise though these exist near either the top surface or the bottom one.

For $K < 0$ and H directed along the anisotropy axis the second phase diagram, shown in Fig. 2, includes the same phases as in Fig. 1 although there are some important differences in the critical field lines. The stability conditions are given by Eqs. (2)–(6) with changing K to $-K$. The phases

A_1 and A_2 overlap each other. This means the existence of the first kind of phase transition between A_1 and A_2 . The equation of its line is $\mu = 1$ at $h \rightarrow 0$. At the point where the instability lines of the collinear phases A_1 and A_2 intersect each other the first order transitions between the phases C and $A_{1,2}$ take place. The region of such transitions expands with increasing value of K . Similar behavior occurs in bulk ferrimagnets.⁷

The magnetization in the layers can be inhomogeneous. This is expected to be valid particularly for SLs including rare-earth elements and transition metals. From our recent investigation of how the inhomogeneities change the critical fields we can conclude that the critical fields of the transitions $B \leftrightarrow C$, $A_1 \leftrightarrow C$ (the lines ab and cd in Figs. 1 and 2) increase but those of $A_2 \leftrightarrow C$ decrease (the line ef), that is, the region of the phase C expands.

MO POLAR KERR EFFECT OF INHOMOGENEOUS SLs

It is clear from the forgoing work that inhomogeneities in magnetization can occur in SL structures. Consequently we turn to the problem of how much inhomogeneities affect MO properties of SLs. Though the above analysis is applicable to in-plane magnetization we present, in the first instance, a consideration of the polar Kerr effect, since this is of particular interest for magneto-optic recording and can be dealt with rather easily in certain situations.

The simple differential reflectance approach for dealing with this can be applied in the specific case where the isotropic refractive index n is constant throughout the whole SL, having a total thickness d , but the MO parameter $Q(z)$ varies arbitrarily with z . Our aim is to find the Kerr rotation θ and ellipticity η (state of polarization of reflected plane wave) provided the incident wave is linearly polarized. To begin with, one considers an elemental layer of thickness δz ($\ll \lambda/2\pi|n|$), buried to a depth z in the SL. In the first instance we need only consider the MO effect of this element and do so by assuming that the rest of the medium is nonmagnetic.⁸ It may be shown that the elemental Kerr component δk resulting from this buried layer is given by

$$\delta k = B_0 \alpha Q(z) (e^{\alpha z} + B_1 e^{-\alpha z} + B_2) \delta z, \quad (7)$$

where $\alpha = 2ik_0 n$, $k_0 = 2\pi/\lambda$, $B_1 = r_s^2 e^{2\alpha d}$, $B_2 = 2r_s e^{\alpha d}$, $B_0 = in[(1+n)(1+r_0 r_s e^{\alpha d})]^{-2}$, r_0 and r_s are the isotropic Fresnel amplitude reflection coefficients at the air/film and film/substrate interfaces, respectively. At this point we invoke the general principle of superposition which applies to first-order MO effects.⁸ This principle states that the magneto-optically induced electric field components resulting from an interaction of the wave with a magnetic multilayered system are a linear superposition of the complex MO electromagnetic field components due to individual magnetic elements in the system, where the fields associated with each element are calculated on the basis that the rest of the system is non-magnetic. It therefore follows that the Kerr component for the whole SL is given by

$$k = \alpha B_0 \int_0^d Q(z) (e^{\alpha z} + B_1 e^{-\alpha z} + B_2) dz. \quad (8)$$

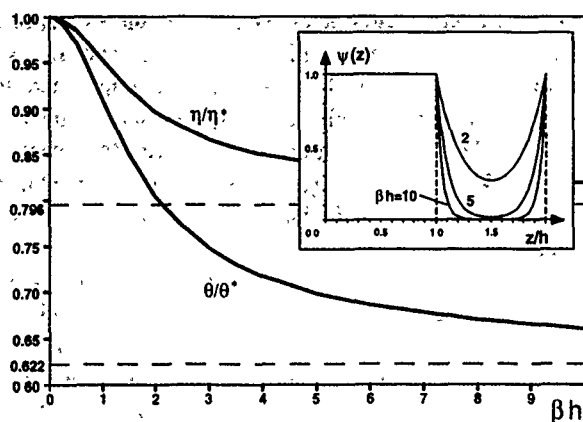


FIG. 3. Normalized Kerr angle θ/θ^* and ellipticity η/η^* vs the parameter βh of the inhomogeneity whose distribution over a period is shown in the inset.

For many functions, $Q(z)$, analytical expressions for k can be easily obtained from (8). Moreover, since $\theta + i\eta = k/r$ ($k \ll r$), where r is the amplitude reflectance of the whole SL and is given by the reiterative reflectance formula,⁹ the complex Kerr rotation can be determined.

As an illustration we consider an infinite periodic SL ($d \rightarrow \infty$). Each period is a bilayer. Its first layer is homogeneous with $Q_1 = Q_0$ and the second is inhomogeneous with $Q_2 = Q_0 \psi(z)$, where $\psi(z) = \cosh \beta(h - 2z) / \cosh \beta h$. The thicknesses are both equal to h and the inhomogeneity factor β determines how rapidly Q_2 varies with distance from the interface. The variation of Q over a period is shown in the inset in Fig. 3. For $\lambda = 633$ nm, $h = 10$ nm, $n = 2 + i4$, and $Q_0 = -0.008 + i0.017$, Fig. 3 shows that the Kerr angle and the ellipticity, normalized respectively to those at $\beta = 0$ ($\theta^* + i\eta^* = -0.178 + i0.152^\circ$), are sensitive to the inhomogeneity. For $\beta \rightarrow \infty$ the second layer becomes homogeneous and the state of polarization tends to $\theta + i\eta = -0.111 + i0.121^\circ$, being equivalent to the case where $Q_2 = 0$. If the latter is assumed beforehand then, for instance, at $\beta h = 5$ relative errors in θ and η are seen, from Fig. 3, to be $\sim 11\%$ and $\sim 5\%$, respectively. At $\beta h = 10$, its influence being less, the errors are only $\sim 6\%$ and $\sim 3\%$. The example given serves as a preliminary illustration to the more general statement that the inhomogeneities may not always be neglected

in the study of the polar Kerr effect. This may be particularly important when determining the optical constants of SLs from experimental data.

CONCLUSION

Spin-reorientation phase transitions in anisotropic magnetic superlattices have been studied theoretically within the framework of the new approach. The presence of an outer surface is shown to change magnetization processes and phase diagrams considerably. New surface spin configurations have been found. An anisotropy of the surface layer determines the type of phase transitions into the surface magnetic phases (first or second order). If the external field is applied along the hard axis then these phases are observed only for certain values of the relative magnetic moment μ . For the field applied along the easy axes the surface-twist phase arises in the magnetization process at any μ . Spatial inhomogeneities in the magnetization distribution can influence MO properties of SLs. To show this, the polar Kerr effect has been considered phenomenologically at normal incidence assuming the MO Q parameter is an arbitrary function of the distance from the interface. A simple procedure of computing the state of polarization of the reflected wave has been developed. The results presented allow us to take into account inhomogeneous systems and therefore we have the potential to explain important features in the magnetic and MO properties of superlattices.

ACKNOWLEDGMENTS

This work was partially supported by The Royal Society and NATO through the linkage scheme, reference No. 930126. Two of us, S. N. Utochkin and A. K. Zvezdin, are also greatly indebted to the Russian Fundamental Research Foundation for financial support.

¹ M. Nawate, H. Kiriake, K. Doi, S. Honda, and T. Kusuda, *J. Magn. Magn. Mater.* **104-107**, 1861 (1992).

² K. Sherifi, C. Dufour, G. Marchal, P. Mangin, and J. Hubsch, *J. Magn. Magn. Mater.* **104-107**, 1983 (1992).

³ R. P. Hunt, *J. Appl. Phys.* **38**, 1652 (1967).

⁴ R. Atkinson, *J. Magn. Magn. Mater.* **115**, 353 (1992).

⁵ A. K. Zvezdin, and S. N. Utochkin, *JETP Lett.* **57**, 439 (1993).

⁶ J. G. LePage and R. E. Camley, *Phys. Rev. Lett.* **65**, 1152 (1990).

⁷ A. K. Zvezdin and V. M. Matveev, *Sov. Phys. JETP* **35**, 140 (1992).

⁸ R. Atkinson and P. H. Lissberger, *J. Magn. Magn. Mater.* **118**, 271 (1993).

⁹ P. H. Lissberger, *Rep. Prog. Phys.* **33**, 197 (1970).

The magnetic and magneto-optical properties of Co, Cr, Mn, and Ni substituted barium ferrite films

R. Carey, P. A. Gago-Sandoval, D. M. Newman, and B. W. J. Thomas

Centre for Data Storage Materials, Coventry University, Coventry CV1 5FB, United Kingdom

Using rapid thermal processing (RTP) we recently demonstrated the production of high quality well ordered barium ferrite films in times much shorter than those required by a conventional annealing process. Influence over the magnetic and structural properties developed in annealed samples was also achieved by variation of the RTP heating profile (R. Carey, P. A. Gago-Sandoval, D. M. Newman, and B. W. J. Thomas, presented at Intermag-93, Stockholm, April 13–16, 1993). It is known that the magneto-optic properties of barium ferrite can be enhanced by selective substitution of some of the Fe by Co^{2+} and Ti^{4+} albeit at the expense of reducing the magnetic anisotropy. A multitarget scanning cosputtering process has been used in conjunction with rapid thermal processing to produce a series of barium ferrite films in which Co, Cr, Mn, Ni are selectively introduced to substitute for between 5 and 20 at. % of the Fe. A corresponding percentage of Ti is also added to maintain charge compensation. The magnetic and magneto-optic properties of these films are presented and discussed with reference to their composition and treatment respect to the properties of barium ferrite.

INTRODUCTION

Following a long development period, first generation optical data storage systems using erasable magneto-optic materials based on the rare-earth transition-metal alloys are now available. They have been well tailored with respect to their magnetic, magneto-optical, and recording properties at laser wavelengths around 800 nm. However, both the figure of merit¹ at shorter wavelengths and the long term stability of these materials is less than satisfactory.

With new techniques developed to prepare garnets and ferrite thin films,^{2–5} magnetic oxides again become potential candidates for the magneto-optical recording material. While oxide thin films are able to overcome some of the major deficiencies of the rare-earth transition metal alloy films, some properties of these materials, e.g., the uniaxial anisotropy, the coercivity, the grain size, and the high crystallization temperature, require further improvement for the optical recording application.

Our investigation indicates that barium ferrite films have a marked uniaxial anisotropy and good squareness of the in-plane hysteresis loop but the magneto-optical response remains quite poor, especially at laser wavelengths around 650 nm. The use of RTP has already reduced both the grain size and the annealing times to acceptable levels.

It is known that magneto-optical (MO) effects in garnets and ferrite materials for optical recording⁶ may be substantially enhanced by ion substitution. In barium ferrite, substitution using Co^{2+} ions has already been the subject of many reports,^{7–10} but, so far, non has considered other substitutions using elements with similar ionic radii to iron and the resultant effect on both the magnetic and the magneto-optic properties.

In this paper we present an investigation of the magnetic and magneto-optical properties of barium ferrite with some iron substitution by Co, Cr, Mn, and Ni.

EXPERIMENTAL TECHNIQUES

Films of Co, Cr, Mn, and Ni substituted barium ferrite were prepared by a combination of dc and rf magnetron cosputtering in a multitarget Nordiko 2000 system onto unheated Vycor glass substrates. Each deposition utilized three separate targets: (1) barium ferrite (rf), (2) the substitution ion (Co, Cr, Mn, Ni) (dc), and (3) titanium for charge compensation (dc). The sputtering parameters used followed those already published¹¹ (see Table I) and depositions were arranged to provide all samples with a thickness close to 200 nm, with the concentration of the substitution element Co, Cr, Mn, or Ni varying between 5 and 20 at. %. The compositions, shown in Table II, were determined using energy dispersive x-ray analysis (PV9160) in a Philips SEM505 scanning electron microscope. A vibrating sample magnetometer and a polar Kerr loop plotter were used to provide the ferrimagnetic and magneto-optical properties.

All the as-deposited samples were essentially nonmagnetic and amorphous. A post deposition heat treatment, using the RTP system,¹¹ was necessary to develop any ferrimagnetic or magneto-optical properties. Samples were therefore annealed in vacuum, for 3 min and 30 s at 810 °C achieved using a linear heating rate of 35 °C s⁻¹ and a constant predetermined duty cycle, intended to avoid any differences in microstructure between samples that might be produced by different heat treatment,¹¹ followed by slow cooling.

TABLE I. Sputtering conditions.

Sputtering parameter	Range
Background pressure	$<4 \times 10^{-7}$ Torr
Sputtering pressure	12×10^{-3} Torr
Argon: oxygen ratio	2.3:1
Substrate temperature	20 °C
Target power densities	0.2 W cm ⁻² –1.5 W cm ⁻²
Scanning speed	7 r.p.m.

TABLE II. Comparative results for barium ferrite substitution.

Ion	Comp (at. %)	Saturation polar rotation		H_c (Oe)		M_r (%)	
		670	825	Perp	Parallel	Perp	Parallel
Co	5.0	0.140	-0.058	627.0	600.0	17.0	45.0
	10.0	-0.071	-0.063	909.1	675.8	22.2	50.0
	15.0	0.021	-0.050	450.0	550.0	10.0	40.0
Ni	5.0	0.076	-0.043	696.3	667.5	15.5	37.0
	10.0	0.021	-0.021	174.1	379.3	15.0	40.0
	15.0	...	-0.059	302.0	414.8	15.0	25.0
	20.0	0.035	0.048	nil	nil
Mn	5.0	-0.121	0.090	294.5	978.6	5.0	40.0
	10.0	...	0.083	481.6	491.6	22.5	31.5
Cr	1.0	0.056	0.034	754.2	467.7	17.0	35.0
	30.0	0.087	0.033	105.5	1269.5	<5.0	60.0
BaFe	99.9	0.010	-0.070	714.3	785.4	34.0	62.0

RESULTS

The results of this study are shown in Table II. In general it can be seen that, for most samples, the saturation Kerr rotation at 670 nm is enhanced compared with the rotation produced by a barium ferrite film¹² but that there is only a slight improvement at 825 nm for Mn substitution.

A 5 at. % Co substitution provides the maximum saturation polar Kerr rotation at 670 nm of 0.14°, in good agreement with other authors,⁸ while at 825 nm the measured rotation is less than that for the barium ferrite film. When the Co content is increased to 10 at. % the saturation rotation at 670 nm is reduced to -0.071° and becomes -0.063° at 825 nm. Further increase in the Co content leads to a magneto-optic response close to that for a pure cobalt film.

The magnetic properties, as measured by the vibrating sample magnetometer, follow a similar pattern so that a hysteresis loop for the high concentration Co substitution film is very similar to that for a pure cobalt film of similar thickness. For the smaller Co concentrations, hysteresis loops are generally S-shaped with similar loops (and coercivities) being obtained for directions both perpendicular and parallel to the film plane.

There have been several studies of the magnetic properties barium ferrite films with Ni substitution.¹³ The magneto-optical results in Table II show a similar behavior to that for Co substitution but with a smaller Kerr rotation at 825 nm compared with that for the pure barium ferrite film. For the 5 at. % Ni substitution the Kerr rotation at 670 nm is again enhanced. The hysteresis loop, and particularly the remanence, seems to be more sensitive to Ni substitution than Co substitution going to a reduced remanence of 15% of the saturation value for only 5 at. % Ni and eventually vanishing at 20 at. % Ni.

For Mn substitution, the saturation Kerr rotations produced are in a similar range to those for Co substitution, but the magnetic hysteresis loops for these samples became quite irregular.

For Cr substitution the saturation Kerr rotation is again small, but the in-plane hysteresis loop showed a surprisingly large remanence and coercivity when the Cr concentration approached 30 at. %.

CONCLUSION

The results presented in this paper indicate that substitution of some of the Fe in barium ferrite thin films by small concentrations (generally about 5 at. %) of elements of the same periodic family can provide a significant enhancement of the saturation polar Kerr rotation at shorter wavelengths. Unfortunately, there is no associated improvement in the magnetic properties of the films and only in those cases where the substitution element has similar magnetic characteristics to iron (e.g., Co, Ni) are the hysteretic properties easily measured. For the cases of Mn and Cr substitution, the smaller magnetic moments produced a generally small signal and therefore noisy hysteresis loops.

With the higher concentrations of Co and Ni, the magnetic properties of the substituted samples became similar to those of thin films of the pure elements.

ACKNOWLEDGMENTS

This work was supported by Servicio F.P.I., Ministerio de Educación y Ciencia, Madrid, Spain.

¹R. Gamble, P. H. Lissberger, and M. R. Parker, IEEE Trans. Magn. **25**, 1651 (1985).

²M. Naoe, S. Hasunuma, Y. Hoshi, and S. Yamanaka, IEEE Trans. Magn. **17**, 3184 (1981).

³M. Matsumoto, A. Morisako, T. Haeiwa, K. Naruse, and T. Karasawa, IEEE Trans. J. Mag. Jap. **6**, 648 (1991).

⁴H. Machida, F. Ohmi, Y. Sawadw, Y. Kaneko, A. Watada, and H. Nakamura, J. Mag. Mag. Mater. **54-57**, 1399 (1986).

⁵E. Lacroix, P. Gerard, D. Challeton, B. Rolland, and B. Bechevet, J. Phys. (Paris) Colloq. **C8**, 941 (1988).

⁶P. Hansen, J.-P. Krumme, and D. Mergel, MORIS-91, Paper 17-G-02.

⁷R. Atkinson, R. Gerber, P. Papakonstantinou, I. W. Salter, and Z. Šimša, J. Mag. Mag. Mater. **104-107**, 1005 (1992).

- ⁸Z. Šimša, P. Görnet, A. J. Pointon, and R. Gerber, *IEEE Trans. Magn. MAG-26*, 2789 (1990).
- ⁹Z. Šimša, J. Koláček, J. Šimšová, P. Görnet, K. Fisher, and R. Gerber, *J. Mag. Mag. Mater.* **104-107**, 403 (1992).
- ¹⁰H. Nakamura, F. Ohmi, Y. Kaneko, Y. Sawada, A. Watada, and H. Machida, *J. Appl. Phys.* **61**, 3346 (1987).
- ¹¹R. Carey, P. A. Gago-Sandoval, D. M. Newman, and B. W. J. Thomas, presented at InterMag-93, Stockholm, April 13-16, 1993, paper HR-01.
- ¹²H. Kojima, in *Ferromagnetic Materials*, edited by E. P. Wohlfarth (North Holland, Amsterdam, 1982), Vol. 3.
- ¹³J. G. Rensen, J. A. Schulkes, and J. S. VanWienirgen, *J. Phys. (Paris) Colloque* **32**, C1-924 (1971).

Anisotropy of the magnetic and magnetooptic properties of HoG:Al single crystals (low and high magnetic field)

J. Ostoréro

Laboratoire de Chimie Métallurgique et Spectroscopie des Terres Rares, CNRS, 92195 Meudon Cedex, France

M. Guillot

Laboratoire de Chimie Métallurgique et Spectroscopie des Terres Rares, CNRS, 92195 Meudon Cedex, France and Service National des Champs Intenses-Max Planck Institut, CNRS, 38042 Grenoble Cedex, France

Magnetization and Faraday rotation measurements at 1152 nm have been performed on $\text{Ho}_3\text{Fe}_{5-z}\text{Al}_z\text{O}_{12}$ ($z=0.45$) single crystals as a function of temperature and magnetic field oriented along the 3 crystallographic axes [100], [110], and [111] in both experiments. A strong anisotropy is observed at low temperature ($T < 100$ K), although the Faraday susceptibility remains anisotropic until $T_{\text{comp}} = 185$ K. High field magnetization measurements (H up to 200 kOe) show that the FR anisotropy is mainly of magnetic origin. The results are interpreted on the basis of the Dionne-refined Néel model of ferrimagnetic garnets using a field dependent canting angle.

I. INTRODUCTION

In ferrimagnetic rare earth iron garnet of formula $\text{RE}_3\text{Fe}_5\text{O}_{12}$ (REIG), the magnetic ions are distributed over three crystallographic sites with sublattice magnetizations M_a (octahedral site 16a: $[\text{Fe}^{3+}]$), M_d (tetrahedral site 24d: $[\text{Fe}^{3+}]$) and M_c (dodecahedral site 24c: $\{\text{RE}^{3+}\})$.¹⁻³ The $\text{Fe}[a]-\text{Fe}(d)$ superexchange interactions determine the Néel temperature ($T_N = 560$ K) for all REIGs. Furthermore, in heavier rare earth garnets, there exists a compensation temperature T_{comp} at which the bulk magnetization vanishes. In pure HoIG, $T_{\text{comp}} = 137$ K. At low temperatures, when both crystal field and exchange anisotropies become of the same order of magnitude, an onset of noncollinear ordering takes place in the $\{c\}$ sublattice as shown by neutron diffraction experiments.^{4,5}

In REIGs, the near IR Faraday rotation (FR) is the sum of the gyroelectric and gyromagnetic contributions proportional to the three magnetic sublattices magnetizations.⁶ As M_c is mainly determined by the molecular field created by the two Fe^{3+} sublattices and the applied magnetic field H , the substitution of Al^{3+} for Fe^{3+} ions allows for the decrease of their contribution to the molecular field on the RE sublattice, thus increasing the influence of the external field on the properties of the compound. The different molecular field coefficients N_{ad} , N_{aa} , and N_{dd} originally determined for YIG are equally suitable for all other REIGs.⁷⁻⁹ Furthermore, for heavier RE garnets, fits of good quality were obtained by reduction of the net moment in the $\{c\}$ sublattice using a canting angle φ .⁸⁻¹⁰

In this work we investigated the magnetic and magnetooptic properties of $\text{Ho}_3\text{Fe}_{5-z}\text{Al}_z\text{O}_{12}$ ($z=0.45$) single crystals as a function of temperature and magnetic field oriented along the 3 crystallographic axes [100], [110], and [111] in both experiments. Al^{3+} ions are distributed over the $\{a\}$ and $\{d\}$ sites and the formula of the garnet can be written: $\{\text{Ho}_3\}[\text{Fe}_{2-x}\text{Al}_x][\text{Fe}_{3-y}\text{Al}_y]\text{O}_{12}$ with $z=x+y$ and $y \gg x$.³

II. EXPERIMENT

Single crystals of composition $\text{Ho}_3\text{Fe}_{5-z}\text{Al}_z\text{O}_{12}$ were grown by our method of flux growth under 10 bar of oxygen pressure.¹¹ Three [100], [110], and [111] oriented platelets ~ 2 mm thick were cut from the same crystal in order to minimize chemical composition differences. They were used "as grown" both for magnetic and FR experiments. Electron microprobe analysis carried out on the platelets gives $z=0.45$ ($\pm 1\%-2\%$).

Magnetization (M) measurements were performed from 4.2 to 300 K in a magnetic field up to 200 kOe. Data are expressed in Bohr magnetons, for one formula unit $\text{Ho}_3\text{Fe}_{5-z}\text{Al}_z\text{O}_{12}$. FR measurements were obtained at 1152 nm wavelength from 6 K to Curie temperature, with H up to 20 kOe. This wavelength is located on the rise at 300 K, and outside of low temperature, of the $^5I_8 \rightarrow ^5I_6$ transition¹² indicating that the FR measurements correspond mainly to a dis-

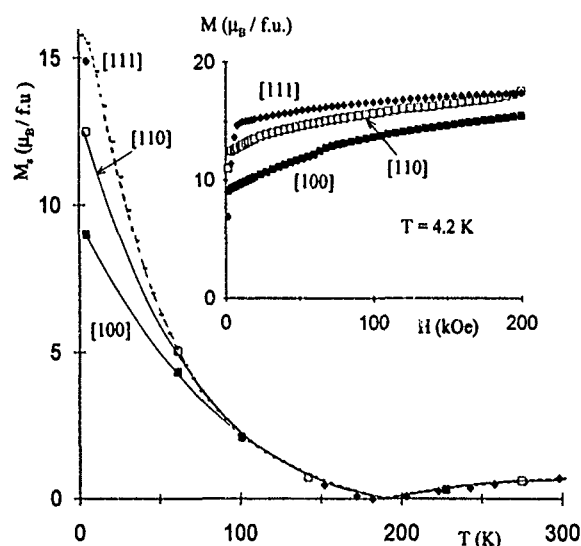


FIG. 1. Temperature dependence of the spontaneous magnetization M_s . Broken line: calculated curve. Inset: low temperature magnetization isotherms $M(H)$ (0–200 kOe).

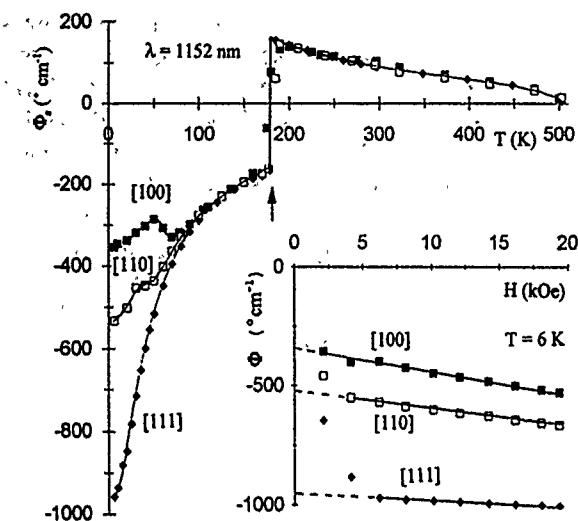


FIG. 2. Temperature dependence of the spontaneous Faraday rotation Φ_s . Arrow indicates T_{comp} . Inset: low temperature FR isotherms $\Phi(H)$ (0–20 kOe).

persive effect. In both cases, H was applied parallel to the normal of the platelets. The estimated precision of the magnetization and FR results is $\pm 2\%$.

III. RESULTS AND DISCUSSION

Low temperature isotherms of magnetization and FR are plotted in Figs. 1 and 2 for the three main crystallographic orientations. For $6 < H < 20$ kOe, they present a linear variation according to $M = M_s + \chi_M H$ and $\Phi = \Phi_s + \chi_F H$. The spontaneous magnetization M_s and spontaneous FR Φ_s of the crystals and their corresponding susceptibilities χ_M and χ_F are obtained by extrapolating this linear part to $H = 0$. The temperature dependencies of $M_s(T)$ and $\Phi_s(T)$ are reported in Figs. 1 and 2, respectively.

We observed that [111] is the easy axis of magnetization and [100] the hard axis as in pure HoIG. At 4.2 K saturation along the [110] axis is attained at $H \sim 200$ kOe (Fig. 1) which confirms that it is an intermediate direction. A similar situation is found concerning the FR isotherms. However, below 100 K, the limited magnetic field range does not permit to observe the saturation for [110] and [100] direction. Both properties lead to a compensation temperature $T_{\text{comp}} = 185$ K (± 3 K), whereas $T_N = 500$ K (Fig. 2). In the spontaneous state, the anisotropic character of both magnetic and MO properties decreases rapidly with temperature and disappears at about 100 K. However the FR susceptibility is isotropic above T_{comp} only (Fig. 3). It is to be noted that, in comparison to pure HoIG,¹³ in a large temperature range, with the exception of the T_{comp} shift, the spontaneous FR values are less affected than the magnetization values by Al substitution: e.g., at 300 K the Φ_s value shows a variation of 60%, whereas M_s value is divided by 2.7.

On the basis of the Dionne refined Néel model,⁹ the ferrite magnetization is simply written: $M_{\text{REIG}} = |M_d - M_a - M_c|$. The respective sublattice magnetizations are represented by Brillouin functions [Eq. (1) of Ref. 7]. It is noticeable that to reproduce the experimental values of

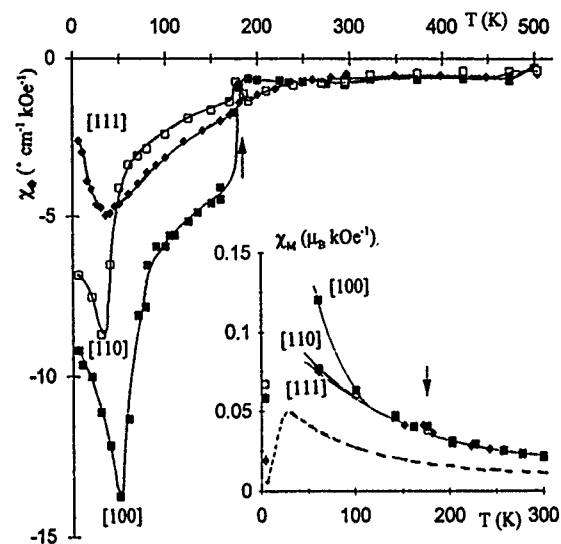


FIG. 3. Temperature dependence of the FR susceptibility χ_F . Arrow indicates T_{comp} . Inset: temperature dependence of the magnetization susceptibility χ_M (6–20 kOe).

both Fe^{3+} sublattice moments at 0 K, a correction which originates from local canting was introduced [Eq. (6) of Ref 7]. The inter and intra sublattices interactions are represented by the molecular field coefficients previously determined in YIG:Al:

$$N_{aa} = -65(1 - 0.42y) \quad (\text{mole cm}^{-3}), \quad (1)$$

$$N_{dd} = -30.4(1 - 0.43x), \quad (2)$$

$$N_{ad} = N_{da} = 97(1 - 0.125x - 0.127y). \quad (3)$$

Using Van Erk's thermodynamic model¹⁴ and assuming that the "as grown" samples correspond to a quenching temperature of ~ 1173 K, $x = 0.02$ and $y = 0.43$. The $\text{Ho}^{3+} - \text{Fe}^{3+}$ exchange interactions for $z = 0.45$ can be described, in a first approximation, by the molecular field coefficients of pure HoIG:⁹ $N_{ac} = N_{ca} = -2.1$; $N_{cd} = N_{dc} = 4$; $N_{cc} = 0$.

To complete the review of our hypotheses it is important to remark that to take into account the spin canting in the $\{c\}$ sublattice, first the "effective" quantum number of the Brillouin function was chosen equal to $J_c \cos(\varphi)$, second the magnetic moment at 0 K was written:⁸

$$M_c(0) = 3g_c\mu_B J_c \cos(\varphi), \quad (4)$$

with $J_c = 8$, $\varphi = 51.5^\circ$, and $g_c = 5/4$ as in pure HoIG.⁹

φ is considered temperature independent.⁸ Using this model, the temperature dependencies of the magnetic properties of HoIG:Al were calculated using an iterative procedure.^{15,16} As shown in Fig. 1, in the spontaneous state, there is a good agreement (maximum difference of 4% at 4.2 K) between theory and our [111] experimental data in the 4.2–300 K temperature range. In contrast, attempts to fit the magnetization curves $M(H)$ for any temperature reveals a large discrepancy with the experimental isotherms. More precisely, the calculated susceptibilities are twice the observed values (Fig. 3). Above T_{comp} , a very reasonable order of magnitude of M_c can be simply deduced from the difference between $M(\text{HoIG:Al})$ and $M(\text{YIG:Al})$ for the same z ,

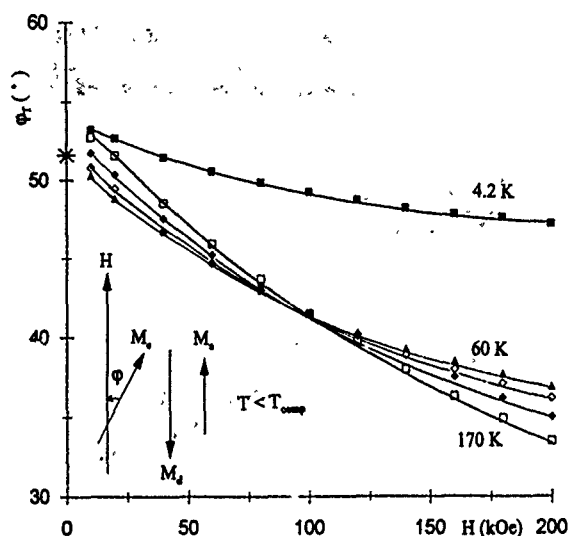


FIG. 4. Isotherms of the field dependence of the canting angle $\varphi_T(H)$ (1°-200 kOe) for $T < T_{\text{comp}}$. Temperature independent $\varphi(H=0)$ of Dionne's model (see Ref. 9) is represented by *.

T , and H conditions. In the 190–300 K temperature range, the M_c contribution tends to zero when H lies within the 75 kOe range. This situation suggests that a canting angle of 90° within the $\{c\}$ sublattice accounts for the zero M_c moment; the extension of this conclusion leads to a field and temperature dependent canting angle $\varphi_T(H)$.

Using the set of molecular field coefficients [Eqs. (1)–(4)], the spin canting angle $\varphi_T(H)$ needed to fit within experimental accuracy any isothermal magnetization curve of the HoIG:Al ferrite was determined. The main role of φ on

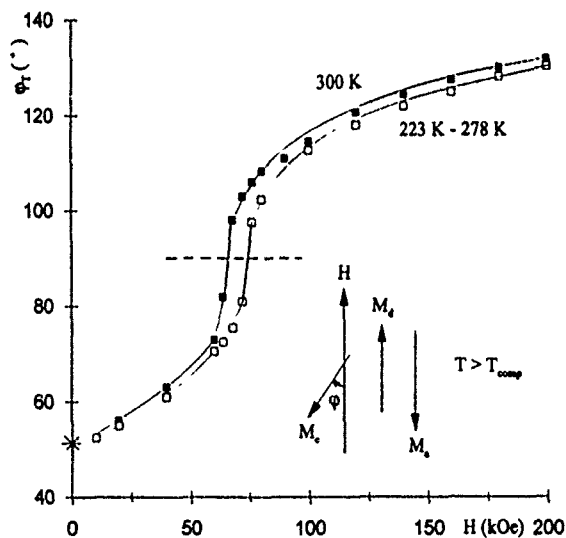


FIG. 5. Isotherms of the field dependence $\varphi_T(H)$ (10–200 kOe) for $T > T_{\text{comp}}$.

the calculation of M_c is underscored in the precedent lines. The so-obtained $\varphi_T(H)$ curves shown in Figs. 4 and 5 confirm the strong influence of the applied magnetic field with two different behaviors below and above T_{comp} . Below 185 K, the decrease of φ_T when H increases represents the tendency of M_c to align parallel to the external field. However, even for $H=200$ kOe the φ_T change remains relatively limited (30%). On the contrary, above T_{comp} , an important variation of φ_T which illustrates a progressive rotation of M_c from 51.5° to 130° is evidenced. In both cases when H vanishes towards 0, $\varphi_T \rightarrow \sim 51.5^\circ$ of pure HoIG.⁹

IV. CONCLUSION

In this paper, the magnetic and FR properties of Al substituted Holmium garnet were studied. At low temperature ($T < 100$ K) the spontaneous state of the studied garnet presents a very pronounced anisotropic character. This anisotropy, attributed to Ho^{3+} , persists until $T_{\text{comp}} = 185$ K for FR susceptibility. Similar results were previously observed for other heavier rare earth garnets like DyIG and ErIG.¹⁷

To describe the HoIG:Al ferrite magnetization, the Dionne's model was used, with the Ho^{3+} - Fe^{3+} molecular field coefficients of pure HoIG. In the spontaneous state, the properties are explained with a Brillouin function modulated by a spin angle of 51.5° independent of temperature as proposed by Dionne. On the contrary, a field dependent canting angle $\varphi_T(H)$ has to be used to interpret the high field $M(H)$ curves. Two different behaviors of $\varphi_T(H)$ were observed below and above T_{comp} .

¹S. Geller, J. P. Remeika, R. C. Sherwood, M. J. Williams, and G. P. Espinosa, Phys. Rev. A **137**, 1034 (1965).

²R. Pauthenet, Ann. Phys. (Paris) **3**, 424 (1958).

³Physics of Magnetic Garnets, edited by A. Paoletti (North Holland, Amsterdam, 1978).

⁴A. Herpin, W. C. Koehler, and P. Meriel, C. R. Acad. Sciences (Paris) **251**, 1359 (1960).

⁵M. Guillot, F. Tch  ou, A. Marchand, and P. Feldman, J. Magn. Magn. Mater. **31–34**, 631 (1983).

⁶W. A. Crossley, R. W. Cooper, J. L. Page, and R. P. Van Staple, Phys. Rev. **181**, 896 (1969).

⁷G. F. Dionne, J. Appl. Phys. **41**, 4874 (1970).

⁸G. F. Dionne, J. Appl. Phys. **47**, 4220 (1976).

⁹G. F. Dionne and P. F. Tumelty, J. Appl. Phys. **50**, 8257 (1979).

¹⁰A. Budkowski, A. Szytula, D. Rodic, R. Duraj, J. Mayer, J. Sciesinski, and V. Spasojevic, J. Magn. Magn. Mater. **78**, 226 (1989).

¹¹J. Ostor  ro, H. Le Gall, M. Guillot, and A. Barlet, IEEE Trans. Magn. **MAG-23**, 1789 (1987).

¹²M. Guillot, A. Marchand, F. Tch  ou, and H. Le Gall, Z. Phys. B **49**, 221 (1982).

¹³M. Fadly, M. Guillot, P. Feldman, H. Le Gall, and H. Makram, J. Appl. Phys. **50**, 2109 (1979).

¹⁴W. Van Erk, J. Cryst. Growth **46**, 539 (1979).

¹⁵J. Ostor  ro, H. Le Gall, H. Makram, and M. Escorne, Adv. Ceram. **15**, 265 (1985).

¹⁶J. Ostor  ro and F. Soulette, J. Appl. Phys. **69**, 5981 (1991).

¹⁷M. Guillot, A. Marchand, H. Le Gall, P. Feldman, and J. M. Desvignes, J. Magn. Magn. Mater. **15–18**, 835 (1980).

Measurement of the Faraday effect of garnet film in alternating magnetic fields

Jia Ouyang, Ying Zhang, and Huahui He

Department of Solid State Electronics, Huazhong University of Science and Technology, Wuhan, Hubei 430074, China

A method of measuring the peak value of the Faraday rotation Φ_F (hereafter referred to as the dynamic Faraday rotation) induced by an alternating magnetic field is described. It requires accurate measurement of the fundamental and the second harmonics of the photodetector currents. The sample is a $(\text{BiPrGdYb})_3(\text{FeAl})_5\text{O}_{12}$ magneto-optic garnet film prepared by liquid phase epitaxy. Using the presented method, we successfully measured the dynamic Faraday rotation in the garnet film at the near infrared wavelength $1.55 \mu\text{m}$ of the light beam. The result shows that Faraday rotation induced by an alternating magnetic field is proportional to ac current and decreases with increasing ac frequency. The method is simple, general, accurate, and can be used at any ac frequency. Experimental errors in our measurement are analyzed and an accuracy better than 2% can be obtained. Finally, some of the factors which may influence the measurement results are discussed.

INTRODUCTION

In recent years, the magneto-optical devices based on magneto-optic garnet film have found wide applications in optical communication and optical processing.¹ When magneto-optic garnet film is placed in an alternating magnetic field, its magnetization varies correspondingly to result in a dynamic Faraday rotation. The Faraday effect in alternating magnetic fields is the basis for modulator² and magnetic field sensors.³ Therefore, it is of great importance to know and understand the magneto-optical characteristics of garnet film in an alternating magnetic field. Although the research on the frequency characteristic of the Faraday rotation in some materials such as FR-5 glass and CdMnTe have been reported,^{4,5} few of the research efforts have been focused on garnet films. In this paper, we present a technique for measuring the peak value of Faraday rotation in an alternating magnetic field. The dependence of dynamic Faraday rotation on frequency and current is measured at the near infrared wavelength of the light beam. Finally, the factors influencing the measuring precision are discussed and an approximate formula for evaluating the measurement error is given.

PRINCIPLE OF MEASUREMENT

The configuration of measuring cell is shown in Fig. 1. The magneto-optic garnet film is placed in the coil which provides an alternating magnetic field. Let 0° (reference) and $(90^\circ + \Phi)$ be the polarization directions of the polarizer P and the analyzer A respectively. Neglecting the nonlinear response of dynamic Faraday rotation with respect to the ac field, the polarization rotation induced by the sample in field $H \sin \omega t$ is $\Phi_F \sin \omega t$. According to Malus law, after the light has passed through P, A , the light intensity is given by

$$I = I_0 [\cos^2(90^\circ + \Phi + \Phi_F \sin \omega t)], \quad (1)$$

where I_0 is the intensity of input laser beam and Φ_F is the

peak value of the dynamic Faraday rotation. When $\theta = 2\Phi_F \sin \omega t$, $\sin \theta$ and $\cos \theta$ can be expanded into sums of Bessel function J_n of the first kind⁶

$$\sin \theta = 2 \sum_{n:\text{odd}} J_n(2\Phi_F) \sin n\omega t, \quad (2)$$

$$\cos \theta = J_0(2\Phi_F) + 2 \sum_{n:\text{even}} J_n(2\Phi_F) \cos n\omega t. \quad (3)$$

Using Eqs. (2) and (3), it is easy to see that Eq. (1) can be rewritten as

$$\begin{aligned} 2I/I_0 = & 1 - J_0(2\Phi_F) \cos 2\Phi + 2J_1(2\Phi_F) \sin 2\Phi \sin \omega t \\ & - 2J_2(2\Phi_F) \cos 2\Phi \cos 2\omega t \\ & + J_3(2\Phi_F) \sin 2\Phi \sin 3\omega t \dots \end{aligned} \quad (4)$$

When $\Phi = 0^\circ$, i.e., P and A perpendicular to each other, the first harmonic I_f becomes zero, but the second harmonic I_{2f} reaches maximum. Let λ be the ratio between I_{2f} and I_f . When P and A deviate from perpendicular position,

$$\lambda = I_{2f}/I_f = J_2(2\Phi_F) \cos 2\Phi / J_1(2\Phi_F) \sin 2\Phi. \quad (5)$$

If we measure λ and Φ , Φ_F can be calculated.

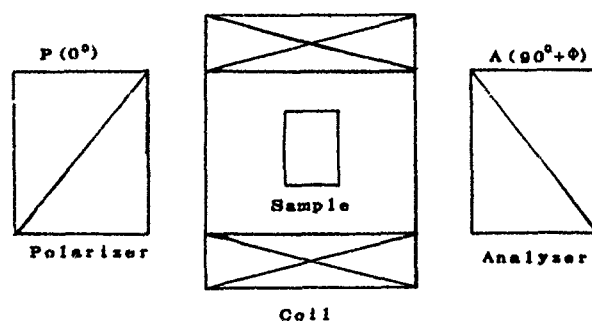


FIG. 1. Configuration of measuring cell.

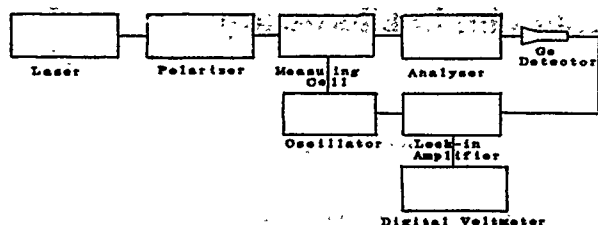


FIG. 2. The experimental apparatus for measuring the dynamic Faraday effect in the $(\text{BiPrGdYb})_3(\text{FeAl})_5\text{O}_{12}$ magneto-optic garnet film.

MEASUREMENT AND RESULT

In our experiment, the sample was a magneto-optic garnet film with a $(\text{BiPrGdYb})_3(\text{FeAl})_5\text{O}_{12}$ composition grown on (111) oriented gadolinium gallium garnet (GGG) substrate by liquid phase epitaxy (LPE). The coercivity H_a is 3 Oe, and the saturation magnetic field H_s is 320 Oe. The hysteresis loop is close to a straight line.⁷ Therefore, only the fundamental harmonic component of dynamic Faraday rotation need be considered. The measurement system is shown in Fig. 2. The light source used for the measurement was a 3 mW stabilized He-Ne laser operating at $1.55 \mu\text{m}$. For both the polarizer (P) and the analyzer (A), we chose a Glan-Thompson prism with an extinction ratio $<10^{-6}$. The transmitted light after the analyzer was detected by the Ge detector. The output of the detector was connected to the input of EG&G 128A lock-in amplifier. The reference signal came from the oscillator which also provided the ac current for the coil. The oscillator current and the dc output voltage of the lock-in amplifier were both measured using accurate digital meters. The analyzer is mounted on a rotatable table with a precision of 0.005° for the measurement of Φ .

When the lock-in amplifier reference frequency is set to f by rotating analyzer A until the amplitude of the fundamental component I_f of the transmitted light intensity became zero as indicated by the zero output of the lock-in amplifier, we can determine accurately that P and A are perpendicular to each other. Turning the lock-in amplifier reference frequency to f and $2f$ and measuring the output voltage of the lock-in amplifier, respectively, we could determine the fundamental and the second component I_f , I_{2f} of the transmitted light intensity at different angles between P and A away from the perpendicular position. When the frequency and intensity of ac current were kept at 1 kHz and 0.2 A, respectively, and the angle Φ was changed, the results of Φ_F for the $(\text{BiPrGdYb})_3(\text{FeAl})_5\text{O}_{12}$ film with a thickness of $20 \mu\text{m}$ are listed in Table I. These results show good consistency for several values of Φ and suggested the validity of our method. Keeping the current intensity constant and

TABLE I. Measurement result of dynamic Faraday rotation in $(\text{BiPrGdYb})_3(\text{FeAl})_5\text{O}_{12}$ film at different values of Φ .

Φ (deg)	1°	2°	3°	4°
V_f (mV)	1.002	2.017	2.970	4.311
V_{2f} (mV)	0.074	0.076	0.075	0.079
Φ_F (deg)	0.298	0.305	0.303	0.295

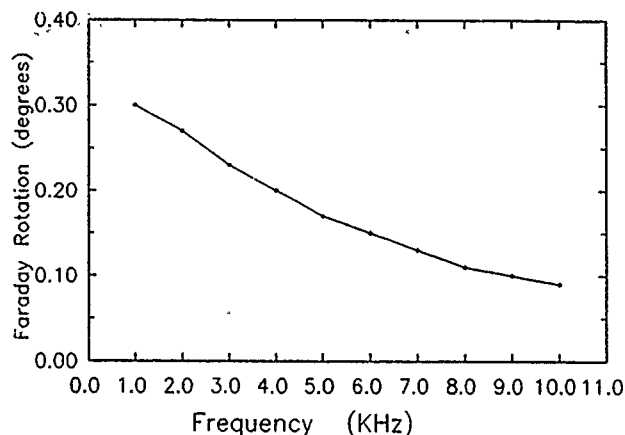


FIG. 3. The dynamic Faraday rotation vs the frequency of an alternating field.

changing the frequency, we measured the dependence of the dynamic Faraday rotation Φ_F on frequency of the ac current and the result is shown in Fig. 3. As the frequency response of dynamic Faraday effect depends on the ability of the induced magnetization to follow the applied alternating field, the relaxation of the magnetization of the garnet film leads to a decrease of the dynamic Faraday rotation when frequency of the ac current increases. This may result from defects impeding the domain-wall motion. The dependence of dynamic Faraday rotation Φ_F on the intensity of the ac current is shown in Fig. 4.

Dynamic Faraday rotation Φ_F is calculated from the given experimental values of λ and Φ . For our sample, the dynamic Faraday rotation Φ_F is much less than 1. By the approximation of the Bessel function, we have

$$J_2(2\Phi_F)/J_1(2\Phi_F) = \Phi_F/2. \quad (6)$$

From Eqs. (5) and (6) we obtain

$$\Phi_F = 2\lambda \tan 2\Phi. \quad (7)$$

Therefore, the relative measurement error of Φ_F is

$$\Delta\Phi_F/\Phi_F = \Delta\lambda/\lambda + 4\Delta\Phi/\sin 4\Phi. \quad (8)$$

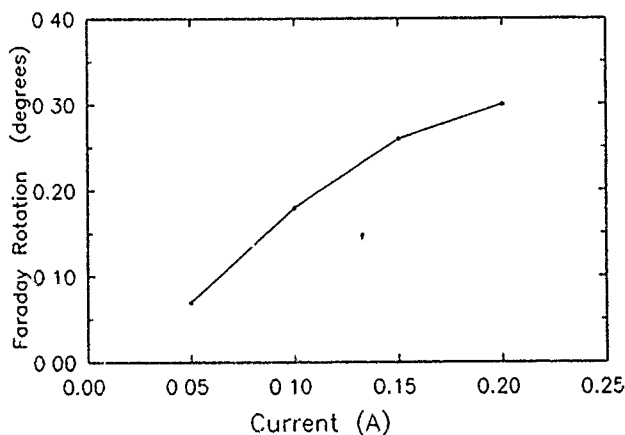


FIG. 4. The dynamic Faraday rotation vs the current intensity.

As the above equation indicates, the accuracy of measurement depends on the accuracy at which λ and Φ can be individually measured. To obtain a high accuracy, we must maintain the ac current stability better than 10^{-4} ; I_f and I_{2f} should be measured under the same sensitivities in the f and $2f$ detector channel and a high precision digital voltmeter should be used. Equation (8) also indicates that when $\Phi=22.5^\circ$, the measurement error becomes minimum, but in fact we measured λ at smaller values of Φ to avoid the shot noise. In our measurement, the accuracy of Φ is 0.005° . The I_f and I_{2f} are read on a high precision digital voltmeter which allows the relative error of measurement of λ lower than 10^{-2} . A relative precision better than 2% for Φ_F can be estimated from Eq. (8).

When the hysteresis loop of samples cannot approximate to a straight line, two factors may deteriorate the measurement result, namely the possible nonlinear response of the dynamic Faraday rotation with respect to the ac field and the possible hysteresis to the dynamic Faraday rotation. The first factor will introduce higher harmonics to the dynamic Faraday rotation. The second factor, on the other hand, will introduce retardation of the phase between the dynamic Faraday rotation and the applied field. Therefore, the dynamic Faraday rotation cannot be simply calculated from Eq. (5), and a more complicated analysis is required.

CONCLUSION

In summary, the experimental apparatus for measuring the dynamic Faraday effect is set up. By using the apparatus, we have measured the peak value of the Faraday rotation of the magneto-optic garnet induced by an alternating magnetic field. The dependence of the dynamic Faraday on the frequency and ac current is investigated. The apparatus is simple, accurate, general, and can be used to measure the dynamic magneto-optical characteristic of magneto-optic materials by observing the frequency response of the Faraday rotation.

¹R. Wolfe, *Thin Solid Film* **216**, 184 (1992).

²W. E. Ross, D. Psaltis, and R. H. Anderson, *Opt. Eng.* **22**, 485 (1983).

³R. E. Hebnner, R. A. Malweski, and E. C. Cassidy, *Proc. IEEE* **65**, 1524 (1977).

⁴M. A. Butler and E. L. Venturini, *Appl. Opt.* **26**, 1581 (1987).

⁵M. A. Butler, S. J. Martin, and R. J. Baughman, *Appl. Phys. Lett.* **49**, 1053 (1986).

⁶M. Abramowitz and I. A. Stegun, *Handbook of Mathematical Functions* (Dever, New York, 1965), p. 361.

⁷X. L. Liu and H. X. Hong, *Chin. J. Laser* **10**, 723 (1983).

An investigation on the magneto-optic and magnetic properties of Tb:YIG

Jie-Hui Yang^{a)}

Department of Physics, Nanjing University, Nanjing 210008, China

You Xu

CCAST (World Laboratory), P.O. Box 8730, Beijing 100080 and Department of Physics, Nanjing University, Nanjing 210008, China^{b)}

Guo Ying Zhang

Department of Physics, Zaozhuang Teacher's College, Zaozhuang 277160, China

The calculations of the spontaneous electric Faraday rotation (FR) and the magnetization contributed by Tb³⁺ ions in Tb substituted iron garnets based on the quantum theory are presented. The crystal field (CF) and the superexchange interaction are two crucial factors in determining FR and the magnetization. Every CF splitting level is nondegenerate. But the energy differences between the lowest seven CF split levels of the ground configuration are not very large comparing with the superexchange interaction upon the Tb³⁺ ions, so the strong admixing of these levels by the high-order perturbation of the exchange interaction makes FR and the magnetization not small. Except FR below 150 K, the calculated results are in good agreement with experiments.

I. INTRODUCTION

Many experimental investigations about the magneto-optic (MO) and magnetic properties of various rare-earth substituted garnets (RE:YIG) have been carried out. It has been found that the MO behavior of some RE:YIG is excellent, but the origin of the MO effect induced by the RE ions in such compounds is not well known. In a previous paper we have reported the calculations of the Faraday rotation (FR) at room temperature in some RE:YIG.¹ In this paper, the temperature dependence of the magnetization contributed by the Tb³⁺ ions and that of FR caused by the intra-ionic electric dipole (ED) transitions between the 4f⁸ and 4f⁷5d configurations of the Tb³⁺ ions in terbium substituted garnets (Tb:YIG) has been calculated based on the quantum theory. Except FR below 150 K, the calculated results are in good agreement with experiments.

The temperature dependence of the magnetization depends on the splitting of the ground configuration due to the crystal field (CF) and superexchange interaction upon the Tb ions. While the FR depends not only on the splitting of the ground configuration but also on the splitting of the excited configuration. Therefore, calculating the magnetization and FR at the same time is helpful for studying the origin of the MO effect and the magnetization of the RE ions in such compounds.

II. THE CALCULATION OF THE MAGNETIZATION

To calculate the magnetization contributed by the Tb³⁺ ions, it is necessary to calculate the splitting of the ground configuration of the Tb³⁺ ions. The perturbation Hamiltonian of a Tb³⁺ ion in the crystal is

$$H' = H_{SO} + H_C + H_{ex}, \quad (1)$$

^{a)}Permanent address: Department of Physics, Luoyang Teacher's College, Luoyang, China.

^{b)}Mailing address.

here H_{SO} is the spin-orbit coupling, H_C the CF Hamiltonian, and H_{ex} the superexchange interaction

$$H_{SO} = \lambda \mathbf{L} \cdot \mathbf{S}, \quad (2)$$

$$H_C = \sum_i \sum_{kq} A_{kq} r_i^k Y_{kq}(\theta_i, \varphi_i), \quad (3)$$

$$H_{ex} = 2\mu_B \mathbf{H}_m \cdot \mathbf{S}. \quad (4)$$

Here L and S are the total orbit and the total spin angular momentum operators, respectively, H_m the molecular field, and μ_B the Bohr magneton. The superexchange interaction is less than the spin-orbit coupling and CF, so we carry out the perturbation calculation in the order of priorities: $H_{SO} + H_C$ and H_{ex} . For a free Tb³⁺ ion, the lowest multiplet of the 4f⁸ configuration is ⁷F₆, the first excited multiplet is ⁷F₅. The energy difference between these two multiplets is not very large, so we take these two multiplets together for perturbation calculation. Solving the following secular equation

$$\langle JJ_z | H_{SO} + H_C | J'J'_z \rangle - E \delta_{JJ', J_z J'_z} = 0 \quad (5)$$

we have obtained the CF split energy levels and wavefunctions. The values of the matrix elements $\langle JJ_z | H_{SO} | J'J'_z \rangle \delta_{JJ', J_z J'_z}$ are taken from the book by Martin *et al.*² The choice of the proper set of the parameters of the CF upon the Tb³⁺ ions is a crucial step. The values obtained with a point charge model are too small to obtain correct results. A similar situation was also found when studying the magnetic properties of some other RE substituted garnets. Nekvasil *et al.*³ have determined a set of parameters for the CF upon the Sm³⁺ ions in SmIG by fitting the experimental results about the magnetic phase transition in SmIG. In this paper, it is supposed that the CF parameters A_{kq} are the same for the Sm³⁺ ions in SmIG and the Tb³⁺ ions in Tb:YIG. That is, the values of $\langle r^k \rangle A_{kq}$ are determined by the values of the CF parameters for the Sm³⁺ ions in SmIG and the ratio of the values of $\langle r^2 \rangle$, $\langle r^4 \rangle$, and $\langle r^6 \rangle$ of the Sm³⁺ and Tb³⁺ ions. The nonzero parameters are shown in Table I. The energies of the lowest ten CF split levels are -367.5, -355.2,

TABLE I. The values of the parameters of the CF upon the Tb ions (in cm⁻¹).

	$\langle r^2 \rangle A_{20}$	$\langle r^2 \rangle A_{2\pm 2}$	$\langle r^4 \rangle A_{40}$	$\langle r^4 \rangle A_{4\pm 2}$	$\langle r^4 \rangle A_{4\pm 4}$
4f	-638	246	-4229	214	980
5d	-3063	1180	-67567	3416	14245
	$\langle r^6 \rangle A_{60}$	$\langle r^6 \rangle A_{6\pm 2}$	$\langle r^6 \rangle A_{6\pm 4}$	$\langle r^6 \rangle A_{6\pm 6}$	
4f	1110	-109	500	49	

-294.5, -254.9, -208.9, -198.4, -108.0, 39.8, 79.2, 191.8 cm⁻¹. Here the energy of the multiplet (4f⁸)⁷F₆ of a free Tb³⁺ ion is taken to be zero. Because the environment of the Tb³⁺ ions in Tb:YIG has D₂ symmetry, every level is nondegenerate.

The nondegenerate states have no contribution to FR. But the energy differences between the lowest seven levels are not very large comparing with the superexchange interaction. So the admixing of these states due to the superexchange interaction is large and the admixed states have contribution to the magnetization and FR. Such admixing is calculated by solving the following secular equation:

$$\|(\langle \psi_i | H_{SO} + H_C + H_{ex} | \psi_j \rangle - E_g \delta_{ij})\| = 0. \quad (6)$$

In the calculation, the bras and kets include the wavefunctions of the lowest seven CF levels. The values of the matrix elements $\langle \psi_i | H_{SO} + H_C | \psi_j \rangle \delta_{ij}$ are the energy values of these states.

The Zeeman effect of the Tb³⁺ ions depends mainly on the superexchange interaction between the Fe and Tb ions. The resultant magnetization of two Fe sublattices in Tb:YIG is well represented by the magnetization of YIG (M_{YIG}). So, the molecular field H_m acting upon the Tb³⁺ ions can be expressed as

$$H_m = n M_{YIG}. \quad (7)$$

According to the idea of Neel,⁴ n is a linear decreasing function of temperature. In a first order it has the form:

$$n = n_0(1 + \gamma T). \quad (8)$$

The values of the average magnetic moment of a Tb³⁺ ion at various temperatures have been calculated with the following formula:

$$\bar{m} = -\mu_B \sum_g \langle g | (L_z + 2S_z) | g \rangle \rho_g. \quad (9)$$

Here ρ_g is the occupation probability of the state $|g\rangle$,

$$\rho_g = e^{-E_g/kT} / \left(\sum_g e^{-E_g/kT} \right) = \rho_0 e^{-E_g/kT}, \quad (10)$$

where E_g is the energy of the state $|g\rangle$. They are obtained by solving Eq. (6). The values of M_{YIG} at various temperatures have been obtained by Gonano.⁵ n_0 and γ are determined by the self-consistent calculation of \bar{m} .

The optimum value of γ is $-1.5 \times 10^{-3} \text{ K}^{-1}$. It is near the value obtained by Leycuras *et al.*⁶ for Ce³⁺ ions in Ce:YIG. The optimum value of n_0 is $8.0 \times 10^4 \text{ Oe}/(\mu_B/\text{two formula of YIG})$. The calculated values of \bar{m} are given in

Table II. In the table, the measured values obtained by Guillot *et al.*⁷ are also given as comparison. It is seen that the calculated values are in good agreement with the measured values.

III. THE CALCULATION OF THE FARADAY ROTATION

The FR per unit length of the medium caused by the intraionic ED transitions is⁸

$$\theta_F = \frac{N\pi}{9\hbar c} \frac{(\bar{n}^2 + 2)^2}{\bar{n}} \sum_{g,n} \frac{\omega^2}{\omega_{ng}^2 - \omega^2} \{ |\langle n | V_- | g \rangle|^2 - |\langle n | V_+ | g \rangle|^2 \} \rho_g \quad (11)$$

for each type of ion present in the material, where c is the velocity of the light in vacuum, N the number of ions per unit volume, \bar{n} an average refractive index, ω the angular frequency of the light wave, g runs over the CF and exchange interaction split 4f⁸ states with occupation probability ρ_g , and n runs over the CF split 4f⁷5d states at energy $\hbar\omega_{ng}$ above the ground states. V_{\pm} are the ED moment operators for right- and left-handed circularly polarized light,

$$V_{\pm} = \sum_i e[x(i) \pm jy(i)], \quad (12)$$

where Σ_i indicates summing over the ED moments of all 4f electrons.

The following formula⁹ has been used to calculate transitional matrix elements:

TABLE II. The calculated and measured values of the magnetic moment \bar{m} of the Tb³⁺ ion and the FR θ_F per unit length at 1150 nm wavelength contributed by the intra-ionic electric dipole transitions of the Tb³⁺ ions. \bar{m} in μ_B/ion , θ_F in deg/cm⁻¹ per Tb ion, T in K.

T	\bar{m} (cal.)	\bar{m} (meas.) ^a	θ_F (cal.)	θ_F (meas.) ^b
294	1.01	1.09	-81.3	-80
255	1.32	1.30	-105.5	-102
200	1.87	1.85	-149.4	-145
150	2.55	2.45	-203.3	-218
100	3.50	3.43	-285	-370
50	5.60	5.70	-464	-705

^aM. Guillot and H. Le Gall, J. Physique 38, 871 (1977).

^bM. Guillot, H. Le Gall, A. Marchand, J. M. Desvignes, and M. Artinian, J. Magn. Magn. Mater. 83, 25 (1990).

$$\begin{aligned}
& \langle l_1^n \alpha L S J M_J | r^k Y_{kq} | l_1^{n-1} l_2 (\alpha' L_1 S_1 L_2) L' S' J' M_J' \rangle \\
& = (-1)^{J+J'+L_1+S+l_1+l_2-M_J} \delta_{SS'} \left(\frac{n}{4\pi} [J, J', L, L', l_1, l_2, k] \right)^{1/2} \begin{pmatrix} J & k & J' \\ -M_J & q & M_J' \end{pmatrix} \begin{pmatrix} l_1 & k & l_2 \\ 0 & 0 & 0 \end{pmatrix} \begin{pmatrix} L & S & J \\ J' & k & L' \end{pmatrix} \\
& \times \begin{Bmatrix} l_1 & L_1 & L \\ L' & k & l_2 \end{Bmatrix} \langle l_1^n \alpha L S \{ | l_1^{n-1} \alpha' S_1 L_1 \rangle \langle l_1 | r^k | l_2 \rangle, \rangle
\end{aligned} \tag{13}$$

where $[J] = 2J + 1$.

According to Ref. 2, the lowest term of the $4f^7 5d$ configuration of the Tb^{3+} ions is 9D , the second term is 7D . The ED transition from the $(4f^8)^7F$ term to $(4f^7 5d)^9D$ term is forbidden. Furthermore, this term cannot be admixed with the 7D term by CF. The $4f^7 5d$ configuration has many higher energy terms. The transitions from them to the $(4f^8)^7F$ states are allowed. But the values of the energy of these terms are not found. Therefore, when we solve Eq. (5) to calculate the splitting of the $4f^7 5d$ configuration due to FR, only the multiplets 7D_5 and 7D_4 have been included. In calculating FR, the energies of all other terms are supposed to be equal to the average energy of the $4f^7 5d$ configuration, i.e., 64400 cm^{-1} .^{2,10} According to our calculation, the ED transition probabilities between the $(4f^8)^7F_6$ and 7F_5 multiplets and these terms are much less than the transition probabilities between the 7F_6 and 7F_5 multiplets and the $(4f^7 5d)^7D_5$ and 7D_4 multiplets. So the error due to the above approximation is small. The effect of the superexchange interaction on the $4f^7 5d$ configuration is neglected. The accurate value of $\langle r \rangle_{4f^7 5d}$ of the Tb^{3+} ion is not found, so it is determined by fitting the measured values of FR and by comparing with the similar values of other RE ions. The value used is 0.187 \AA .

The calculated values of FR per unit length per Tb ion are shown in Table II, in which the measured values obtained by Guillot *et al.*¹¹ are shown as well. It is seen that the calculated values agree with experiments in the temperature range from 150 to 300 K.

IV. DISCUSSION

From the above results, it is seen that except FR below 150 K, the behavior of the magnetization and FR contributed by the Tb^{3+} ions in the garnets is well explained. The CF and superexchange interaction are the two most important factors in determining the magnetic and MO behavior of the Tb^{3+} ions in the garnets. As the splitting of the states due to CF is not large enough, the FR at the near infrared region and the FR at the visible region have the same sign. The admixing of different CF levels of the $4f^8$ configuration by the high-order perturbation of the exchange interaction is large; otherwise, the magnetization and FR contributed by the Tb^{3+} ions will be very small.

The cause of the difference between the calculated and measured values of FR at low temperature is not clear. It can be seen from Table II, the calculated MO coefficient, which equals the ratio of θ_F to \bar{m} , is nearly a constant in the whole temperature range studied, in accord with the theory of Crossley *et al.*⁸ According to Refs. 12 and 13, the covalency of the $5d$ states with the neighboring ions is large and depends on the electronic structure of the RE ions. Therefore, the assumption that the values of the parameters $\langle \langle r^2 \rangle A_{20} \rangle$ etc.) of CF upon the $5d$ electrons are proportional to the values of $\langle r^2 \rangle$ and $\langle r^4 \rangle$ of the $5d$ shells of different RE ions may be not good. According to our work for Ce:YIG, if the CF splitting of the $4f^{n-1} 5d$ configuration is large enough, the MO coefficient will be dependent on the temperature.¹⁴ Therefore, we think that the simple assumption about the CF upon the $5d$ electrons may be one cause for making the theoretical values of FR deviate from the true values at low temperature.

ACKNOWLEDGMENTS

This work is supported by the State Key Laboratory of Magnetism, Institute of Physics, Chinese Academy of Sciences, and the National Natural Science Foundation in China.

¹ You Xu, Guoying Zhang, and Mingqian Duan, J. Appl. Phys. **73**, 6133 (1993).

² W. C. Martin, R. Zalubas, and L. Hagan, *Atomic Energy Levels-The Rare Earth Elements* (National Bureau of Standards, Washington, DC, 1987).

³ V. Nekvasil, M. Guillot, A. Marchand, and F. Tcheou, J. Phys. C **18**, 3551 (1985).

⁴ L. Neel, Ann. Phys. **3**, 127 (1948).

⁵ R. L. Ganano, Phys. Rev. **156**, 521 (1967).

⁶ C. Leycuras, H. Le Gall, J. M. Desvignes, M. Guillot, and A. Marchand, IEEE Trans. Magn. **MAG-21**, 1660 (1985).

⁷ M. Guillot and H. Le Gall, J. Physique **38**, 871 (1977).

⁸ W. A. Crossley, R. W. Cooper, J. L. Page, and R. P. Van Staple, Phys. Rev. **181**, 896 (1969).

⁹ G. S. Ofelt, J. Chem. Phys. **37**, 511 (1963).

¹⁰ John G. Conway, in *Rare Earths Spectroscopy*, edited by B. Jezowska-Trzebiatowska, J. Legendziewicz, and W. Strek (World Scientific Ltd., Singapore, 1985).

¹¹ M. Guillot, H. Le Gall, A. Marchand, J. M. Desvignes, and M. Artinian, J. Magn. Mater. **83**, 25 (1990).

¹² M. Kucera, J. Magn. Mater. **101**, 242 (1991).

¹³ R. R. Jacobs, W. F. Krupke, and M. J. Weber, Appl. Phys. Lett. **35**, 410 (1978).

¹⁴ You Xu and Jie Hui Yang (to be published).

Magneto-optical properties of $(\text{BiGdY})_3\text{Fe}_5\text{O}_{12}$ for optical magnetic field sensors

O. Kamada

Department of Electronics, Polytechnic University, 4-1-1 Hashimoto-dai, Sagami-hara, Kanagawa 229, Japan

H. Minemoto

Central Research Laboratory, Matsushita Electric Industrial Co., Ltd., Moriguchi, Osaka 570, Japan

N. Itoh

Networks Development Promotion Center, Matsushita Electric Industrial Co., Ltd., Moriguchi, Osaka 570, Japan

The temperature-dependent sensitivity characteristic in the zeroth-order diffraction beam from the multidomain materials of $\text{Bi}_x\text{Gd}_y\text{Y}_{3-(x+y)}\text{Fe}_5\text{O}_{12}$ films grown by a conventional liquid-phase-epitaxial method are studied. By measuring the variation of the sensitivity with temperature, it was found that films with $X=1.3$ and $Y=0.43$ show the minimum value of $\pm 0.5\%$ between 253 and 353 K. The contribution of the Gd substitution on the improvement of the temperature dependence of the sensitivity was explained by a simple theoretical calculation.

I. INTRODUCTION

With recent developments in optical magnetic field (current) sensors based on Faraday effect, there has been considerable demand for applying these sensors to electric power systems such as power delivery systems to measure current, and to monitor the condition of these lines.¹ Hence high sensitivity, high accuracy in the operating temperature range and high reliability are required for such sensors. It is expected that rare-earth iron garnets, especially Bi-substituted iron garnets [hereafter referred as (BiR)IG] have high sensitivity constants because of a large Faraday rotation angle. But recently the attribution of Faraday loops to both the magnetization process (the domain wall displacement or the magnetization rotation) and the light beam diffraction by the stripe magnetic domain structure of garnet films has been made clear.²

In this paper we report the experimental results on the sensitivity temperature dependence in detecting only the zeroth-order diffraction beam from (BiR)IG, which takes the boundary displacement process for magnetization reversal. And we also report on Gd-substituted (BiY)IG films with the minimum temperature dependence of the sensitivity and on the available calculation results on the temperature dependence.

II. EXPERIMENTS

(BiR)IG films were grown on (111)-oriented $(\text{GdCa})_3(\text{MgZrGa})_5\text{O}_{12}$ substrates by means of a liquid-phase-epitaxial (LPE) dipping technique with a horizontal rotation mode. A $\text{PbO-Bi}_2\text{O}_3\text{-B}_2\text{O}_3$ system was employed as a solvent and B_2O_3 rich melts were used to obtain highly Bi substituted films.³ The chemical composition of the prepared films was determined by electron probe micro-analysis.

Sensitivity constants measurements were made in the temperature range of 223–393 K using 850 nm GaAlAs-light-emitting-diode (LED) light which propagates parallel to the external field as shown in Fig. 1. Two Glan-Thompson prisms were used for the polarizer and analyzer and the analyzer is at an angle of 45° with respect to the polarizer.

Figure 2 shows the film thickness dependence of the magnetic domain width measured from Faraday effect patterns and the first-order diffraction angle of the He-Ne laser beam. From these results the first-order diffraction angle of 4.7° was obtained by the calculation at the wavelength of a light source (850 nm). This is too large to condense all of the diffracted beams by a lens (for example the rod lens of $\text{NA}=0.37$ and 2 mm ϕ used to realize compact sensor modules). So the Faraday output signal only in the zeroth-order diffraction beam throughout a pin-hole was measured by a single-ended fixed analyzer method² as shown in Fig. 1.

III. RESULTS AND DISCUSSION

Figure 3 shows the measured result of the Faraday output signal and the obvious hysteresis loop was not observed in this measurement. The normalized Faraday output intensity according to the domain wall movement magnetization is given by

$$P = [1 + (H/H_s)\tan(\theta_F d)]^2, \quad (1)$$

where, H , H_s , θ_F , and d are external magnetic field, the magnetic saturation field, the Faraday rotation angle, and the film thickness, respectively. The calculated result by Eq. (1) is represented by a solid line in Fig. 3. The measured results are in good agreement with the calculated result and it is confirmed that the boundary displacement is the dominant magnetization process in the (111)-LPE-(BiR)IG film.

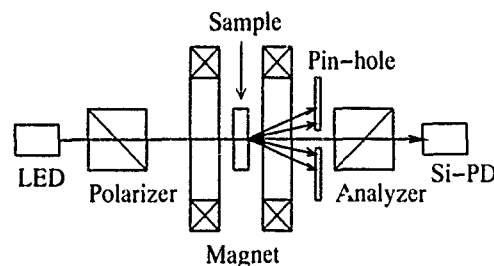


FIG. 1. A schematic diagram of the measuring system for the present study.

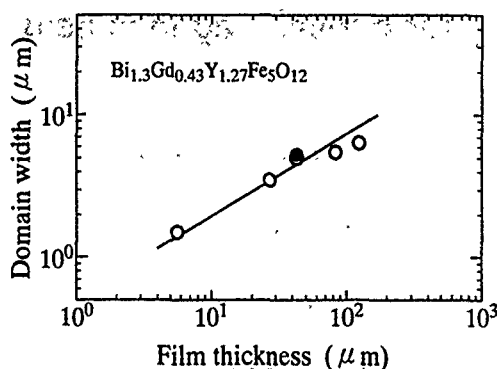


FIG. 2. The film thickness dependence of the domain width: ○ and ● show measured results from Faraday effect patterns and first-order diffraction angle, respectively.

The temperature dependence of the sensitivity deviation from the value of 300 K in four kinds of compositions is shown in Fig. 4. The results on (BiY)IG ($Y=0$), which are plotted (●), show a positive dependence and substitution with Gd decreases the gradients of the dependence and the sign of the dependence changes to minus for Y larger than 0.43. The sample of $X=1.3$ and $Y=0.43$ shows a minimum of $\pm 0.5\%$ between 253 and 353 K.

Equation (1), which gives the Faraday output intensity characteristics, contains two temperature dependent physical constants of θ_F and H_s . Hence when the term of $\tan[\theta_F(T)d]/H_s(T)$ in Eq. (1) have no temperature dependence, the sensitivity is unchanged with temperature. And by this consideration the contribution of Gd substitution to the improvement of the temperature dependence of the sensitivity can be explained as follows.

The saturation magnetization and its temperature dependence $M_s(T)$ corresponding to $H_s(T)$ of ferrimagnetic garnets can be well described in terms of the molecular field theory.⁴⁻⁶ The net magnetic moment per mole is given by

$$M_s(T) = |M_d(T) - M_a(T) - M_c(T)|, \quad (2)$$

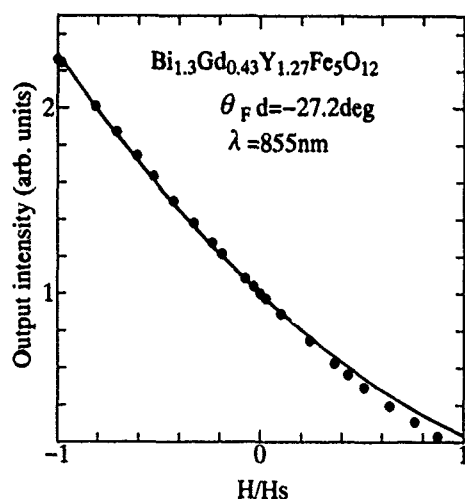


FIG. 3. Sensor output intensity vs applied magnetic field. ● show measured results and solid line show the calculated result by Eq. (1).

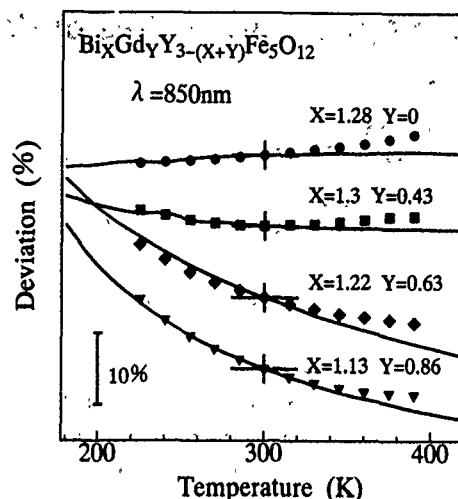


FIG. 4. Temperature dependence of sensitivity for various Gd concentrations. Plotted points show measured results and solid lines show calculated results by Eqs. (1), (2), and (3).

where the subscript refers to the particular sublattice. In calculating $M_s(T)$ of (BiGdY)IG modified molecular field coefficients^{7,8} were used to account for the linear dependence of T_{comp} and T_c with Bi concentration X . Figure 5 shows the calculated results for various Bi and Gd concentrations. It is obvious that the gradients of the temperature dependence around room temperature decreased steadily with an increase in the Gd concentration.

Figure 6 shows the measured temperature dependence of Faraday rotation angle for various Bi and Gd concentrations and over the temperature range from 300 to 600 K. From these results it is found that the Faraday rotation angle increases in proportion to the Bi concentration and does not depend on the Gd concentration. The gradients of $\theta_F(T)$ around room temperature also do not depend on the Gd concentration. According Crossley model,⁹ the value of $\theta_F(T)$ can be calculated in terms of the sublattice magnetization^{10,11} and are given as

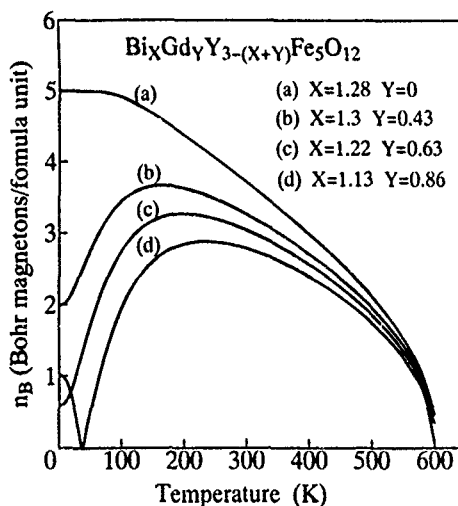


FIG. 5. Calculated results of temperature dependence of magnetization for various Gd concentrations by the molecular field theory (see Refs. 4-6).

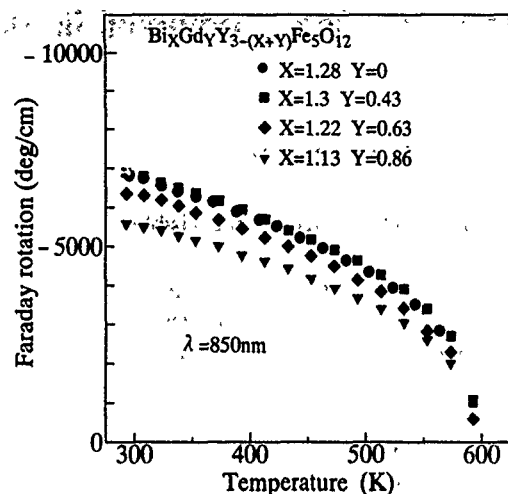


FIG. 6. Temperature dependence of Faraday rotation for various Bi and Gd concentrations.

$$\theta_F(T) = AM_a(T) + DM_d(T) + CM_c(T), \quad (3)$$

where A , D , and C are the magneto-optical coefficients for each site. From the measured results shown in Fig. 6 values of A , D , and C for (BiGdY)IG with five different compositions were determined by the fitting method and $\theta_F(T)$ over the temperature range 180–420 K were calculated by Eq. (3).

Using these calculated results on $M_s(T)$ and $\theta_F(T)$, the temperature dependence of the sensitivity was obtained by Eq. (1) for various Bi and Gd concentrations. The results

were shown in Fig. 4 with a solid line. They show good agreement with the experimental results.

IV. CONCLUSION

Bi-substituted rare-earth iron garnet films, $\text{Bi}_x\text{Gd}_y\text{Y}_{3-(x+y)}\text{Fe}_5\text{O}_{12}$ for optical magnetic field sensors were prepared by the LPE method. From sensitivity measurements it was found that in the case of the zeroth-order diffraction detection $\text{Bi}_{1.3}\text{Gd}_{0.43}\text{Y}_{1.27}\text{Fe}_5\text{O}_{12}$ has the minimum temperature dependence within $\pm 0.5\%$ over the temperature range of 253–353 K. By the calculated results on $\theta_F(T)$, which was calculated in terms of the sublattice magnetizations, and $M_s(T)$ by the molecular field theory, the contribution of the Gd substitution on the improvement of the temperature dependence of the sensitivity can be explained.

Calculated results agree well with the experimental results of the temperature dependence of sensitivity.

¹K. Kurosawa, Proceedings of the 7th International Conference on Optical Fiber Sensors, 1990, p. 67.

²T. Numata, H. Tanaike, S. Iguchi, and Y. Sakurai, J. Magn. Soc. Jpn. **14**, 642 (1990).

³C. P. Clages, J. Cryst. Growth **64**, 275 (1983).

⁴G. F. Dionne, J. Appl. Phys. **41**, 4874 (1970).

⁵C. D. Brandle and S. L. Blank, IEEE Trans. Magn. **MAG-12**, 14 (1976).

⁶G. F. Dionne and P. F. Tumelty, J. Appl. Phys. **50**, 8257 (1979).

⁷P. Hansen, K. Witter, and W. Tolksdorf, Phys. Rev. **27**, 4375 (1983).

⁸P. Hansen, K. Witter, and W. Tolksdorf, Phys. Rev. **27**, 6608 (1983).

⁹W. A. Crossley, R. W. Cooper, J. L. Page, and R. P. van Staele, Phys. Rev. **181**, 896 (1969).

¹⁰G. Abulafya and H. Le. Gall, Solid State Commun. **11**, 692 (1972).

¹¹E. V. Berdennikova and R. V. Pisarev, Sov. Phys. Solid State **18**, 45 (1976).

Magneto-optical properties of Al and In-substituted CeYIG epitaxial films grown by sputtering (abstract)

M. Gomi and M. Abe^{a)}

Department of Materials Science, Japan Advanced Institute of Science and Technology, Asahidai 15, Tatsunokuchi, Ishikawa 923-12, Japan

Cerium substitution to iron garnet strongly enhances magneto-optical (MO) effect in the visible region around $h\nu = 1.4$ and 3.1 eV. We have previously proposed a $\text{Ce}^{3+}(4f)\text{-Fe}^{3+}(\text{tet.})$ charge transfer model as an electronic transition inducing the strong MO effect.¹ In this study, we have measured Faraday spectra of CeYIG films in which Fe ions were diluted with Al or In ions. These ions, respectively, are known to preferentially occupy tetrahedral and octahedral iron sites in the garnet structure, giving us some information on the role of Fe^{3+} in the MO enhancement. The $\text{Y}_2\text{Ce}_1\text{Fe}_{5-x}\text{M}_x\text{O}_{12}$ ($\text{M}=\text{Al}, \text{In}; x=0-5$) films were epitaxially grown *in situ* on (111)-oriented $\text{Gd}_3\text{Ga}_5\text{O}_{12}$ (GGG) single crystal substrates by conventional rf diode sputtering. With the amounts of substitutions increasing, Faraday rotation and ellipticity of the films at $h\nu = 1.4$ eV reduced at nearly the same rates for both ions of Al and In. We found from the analysis using molecular field theory that these reductions are in proportion to the magnetic moment of the tetrahedral iron sublattice. This indicates that the tetrahedral Fe^{3+} contributes to the electronic transition at 1.4 eV, supporting the proposed charge transfer model.

^{a)}Dept. of Phys. Electr., Tokyo Institute of Technology, Ookayama, Meguro-ku, Tokyo 152, Japan.

¹M. Gomi, H. Furuyama, and M. Abe, J. Appl. Phys. **70**, 7065 (1991).

Enhancement of the magneto-optical quality of YIG films in a structure containing a thin metal film (abstract)

A. D. Boardman

Joule Laboratory, Department of Physics, University of Salford, Salford M5 4WT, United Kingdom

A. I. Voronko, P. M. Vetoshko, V. B. Volkovoy, and A. Yu. Toporov

IMC Ltd., Technology House, Lissadel Street, Salford M6 6AP, United Kingdom

TE/TM polarized light reflection from a multilayer structure containing a magneto-optic (MO) and a metal film is investigated theoretically and experimentally. A metal film is used whose thickness is chosen to support long-range surface polaritons (SP). This is to use their sharp resonance for tuning the whole structure. It was shown that if the MO layer is placed in a multilayer structure consisting of a thin metal film that supports a long-range surface polariton, the resonance couples to the off-diagonal element of the YIG-film dielectric tensor. This means that this process exhibits a nonreciprocal property, as well as a Faraday rotation in the MO film. A combination of these two effects enhances the value of the magneto-optic quality (Faraday rotation divided by the losses incurred by the light) and the nonreciprocity of the light reflection from the structure. Theoretical and experimental optimization of these effects at a wavelength equal to $0.5 \mu\text{m}$ has been carried out for thin monodomain single crystal YIG films, saturated by a magnetic field of the order 1 Oe. It has enabled the design of a high frequency operation circulator to be developed. These results will be reported in this paper.

Magnetic Davydov splitting in 2D AFM $(\text{CH}_2)_2(\text{NH}_3)_2\text{MnCl}_4$ (abstract)

V. Eremenko, I. Kachur, V. Piryatinskaya, and V. Shapiro

Institute for Low Temperature Physics and Engineering, Academy of Sciences of Ukraine, 47 Lenin Avenue, 310164 Kharkov, Ukraine

Recently it was shown¹ that the light absorption spectrum of $(\text{CH}_2)_2(\text{NH}_3)_2\text{MnCl}_4$ (EDAMnCl₄) differs strongly from those of other compounds of this family $(\text{CH}_2)_n(\text{NH}_3)_2\text{MnCl}_4$. Additional peculiarities in the spectral distributions of two-magnon Raman scattering and the coefficient of exciton-magnon absorption were found.² It was also determined that the pure exciton band in the absorption spectrum is of the electric dipole type of polarization. All these peculiarities are out of the framework of the usual tetragonal two-sublattice antiferromagnet model and indicate the inverse center loss and magnetic cell doubling. Results of studying the absorption spectrum of EDAMnCl₄ presented in the report show that not less than three Davydov components of the exciton band ${}^{\sigma}A_{1g}({}^{\sigma}S) \rightarrow {}^4E_g({}^4G)$ optical transition may be detected with confidence in magnetic fields oriented along the *c* axis. It confirms the four-sublattice magnetic structure of EDAMnCl₄. The presence of exciton line splitting at $H=0$ and its nonlinear character at $\mathbf{H} \parallel \boldsymbol{\alpha}$ (that is practically parallel to \mathbf{l}) allows us to make a conclusion about the resonance interaction between ions with antiparallel spins and, probably, about the initial noncollinearity of magnetic structure. Parameters characterizing the magnetic Davydov splitting are determined using comparison of the experimental data and theoretical analysis.

¹N. Watanabe, N. Kojima *et al.*, J. Phys. C **21**, 4795 (1988).

²V. V. Eremenko, I. S. Kachur *et al.*, Ukrainskii fiz. Z. **37**, 1806 (1992).

Magnetic neutron scattering (invited)

J. W. Lynn

Reactor Radiation Division, National Institute of Standards and Technology, Gaithersburg, Maryland 20899

The application of neutron scattering techniques to magnetic problems is reviewed. We will first discuss diffraction techniques used to solve magnetic structures, as well as to measure magnetic form factors, order parameters, critical phenomena, and the scattering from low-dimensional systems. We will also discuss inelastic scattering techniques, including polarized beam methods, utilized to determine the spin dynamics of various materials. Information will be provided about the types of spectrometers available at the user-oriented national facilities located at Argonne National Laboratory, Brookhaven National Laboratory, Los Alamos National Laboratory, The National Institute of Standards and Technology, and Oak Ridge National Laboratory, as well as the spectrometers at the Missouri University Research Reactor.

I. INTRODUCTION

Magnetic neutron scattering plays a central role in determining and understanding the microscopic properties of a vast variety of magnetic systems, from the fundamental nature and symmetry of magnetically ordered materials to elucidating the magnetic characteristics essential in applications. One traditional role has been the measurement of magnetic Bragg intensities in the magnetically ordered regime, which can be used to determine not only the spatial arrangement and atomic magnetization density of the magnetic moments, but also the value of the ordered moments as a function of temperature, pressure, and applied magnetic field. These types of measurements can be carried out on single crystals, powders, thin films, and multilayers, and often the information collected can be obtained by no other experimental technique. Small angle neutron scattering (SANS) is a technique to explore the magnetism over longer distances than conventional diffraction, and is ideal to study domain structures and other spatial variations of the magnetization density on length scales from 1–1000 nm. The relatively new technique of neutron reflectometry can be used to explore the magnetization distribution in the near-surface regime of thin films, multilayers, and crystals. In the investigation of the spin dynamics of systems, though, neutrons play a truly unique role. Neutron scattering is the only technique that can directly determine the complete magnetic excitation spectrum, whether it is in the form of the dispersion relations for spin wave excitations, wave vector and energy dependence of critical fluctuations, crystal field excitations, moment fluctuations, etc. In the present article we will briefly discuss some of these possibilities, and present a few examples taken from recent work at NIST. We will also discuss the neutron instrumentation presently available to the magnetism community, and plans for new instrumentation which will take the field into the next decade and beyond.

There are a number of very good sources of detailed information about neutron scattering. The textbook by Lovesey¹ treats the theory of neutron scattering in depth, and the more recent work of Balcar and Lovesey² specifically

addresses the theory for the case of magnetic neutron as well as x-ray scattering. Bacon's text³ is more for the experimentalist, treating experimental procedures and the practicalities of taking and analyzing data. Williams' text⁴ focuses on the use of polarized neutrons, while Squires' book⁵ is more of a graduate introductory text to the subject. An alternative reference is the recent compendium by Price and Sköld,⁶ which covers a variety of topics in neutron scattering in the form of chapters by various experts.

II. MAGNETIC DIFFRACTION

The integrated intensity for a magnetic Bragg reflection is given (for a simple collinear magnetic structure) by¹

$$I_M = C \mathcal{N}_\tau A(\theta_B) \left(\frac{\gamma e^2}{2mc^2} \right)^2 \langle 1 - (\hat{\tau} \cdot \hat{M})^2 \rangle |F_M|^2, \quad (1)$$

where the neutron-electron coupling constant in parenthesis is -0.27×10^{-12} cm, $\hat{\tau}$ and \hat{M} are unit vectors in the direction of the reciprocal lattice vector τ and the spin direction, respectively, and the orientation factor $\langle 1 - (\hat{\tau} \cdot \hat{M})^2 \rangle$ must be calculated for all possible domains. C is an instrumental constant which includes the resolution of the measurement, $A(\theta_B)$ is an angular factor which depends on the method of measurement, and \mathcal{N}_τ is the multiplicity of the reflection (for powders). The magnetic structure factor F_M is given by

$$F_M = \sum_{j=1}^N \langle \mu_z \rangle_j f_j(\tau) e^{-W_j} e^{i\tau \cdot r_j}, \quad (2)$$

where $\langle \mu_z \rangle_j$ is the thermal average of the aligned magnetic moment of the magnetic ion at the j th site at position r_j , W_j is the Debye Waller factor for the j th atom, $f(\tau)$ is the magnetic form factor (Fourier transform of the magnetization density), and the sum extends over all magnetic atoms in the unit cell. We see from these expressions that neutrons can be used to determine several important quantities; the location of magnetic atoms and the spatial distribution of their magnetic electrons; the temperature, field,... dependence of $\langle \mu_z \rangle$, which is directly related to the order parameter for the phase

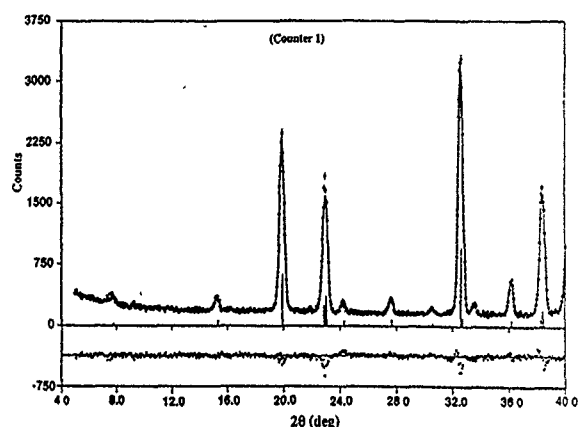


FIG. 1. Calculated (solid curve) and observed intensities for a powder of $\text{YBa}_2\text{Fe}_3\text{O}_8$. The differences between calculated and observed are shown at the bottom (Ref. 7).

transition (e.g., sublattice magnetization). The preferred magnetic axis (\hat{M}) also can often be determined from the relative intensities. Finally, the scattering can be put on an absolute scale by internal comparison with the nuclear Bragg intensities from the same sample, whereby the saturated value of the magnetic moment can be obtained.

As an example, a portion of the powder diffraction pattern from a sample of $\text{YBa}_2\text{Fe}_3\text{O}_8$ is shown in Fig. 1.⁷ The solid curve is a profile refinement of both the antiferromagnetic and crystallographic structure for the sample. From this type of data we can determine the crystal structure, lattice parameters, site occupancies, etc., as well as the magnetic structure and value of the ordered moment. The results of the analysis are shown in Fig. 2; the crystal structure is identical to the structure for the 1-2-3 superconductor with the Fe replacing the Cu, and the magnetic structure is also the same as has been observed for the Cu spins in the oxygen-reduced (semiconducting) material.

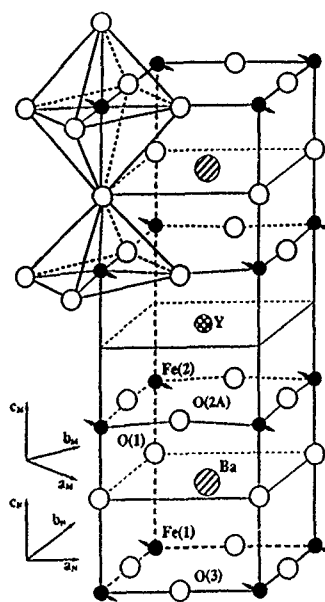


FIG. 2. Crystal and magnetic structure for $\text{YBa}_2\text{Fe}_3\text{O}_8$ (Ref. 7).

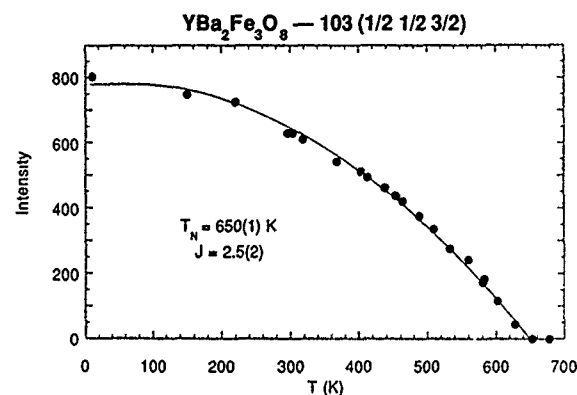


FIG. 3. Temperature dependence of the intensity of the magnetic reflection.

Experimentally we can recognize the magnetic scattering by several characteristics. First, it should be temperature dependent, and the Bragg peaks will vanish above the ordering temperature. Figure 3 shows the temperature dependence of the intensity of the peak at 19.5° , which clearly reveals a phase transition at 650 K. A second characteristic is that the magnetic intensities become weak at high scattering angles (not shown), as $f(\tau)$ typically falls off strongly with increasing angle. A third, more elegant, technique is to use polarized neutrons. The polarization technique can be used at any temperature, and for any material regardless of whether or not it has a crystallographic distortion (e.g., via magnetoelastic interactions) associated with the magnetic transition. It is more involved and time-consuming experimentally, but yields an unambiguous identification and separation of magnetic and nuclear Bragg peaks.

The polarization analysis technique as applied to this problem is in principle straightforward.⁸ Nuclear coherent Bragg scattering never causes a reversal, or spin-flip, of the neutron spin direction upon scattering. Thus the nuclear peaks will only be seen in the non-spin-flip [denoted by $(++)$] scattering geometry. The magnetic cross sections depend on the relative orientation of the neutron polarization \mathbf{P} and the reciprocal lattice vector transfer $\boldsymbol{\tau}$. In the configuration where $\mathbf{P} \perp \boldsymbol{\tau}$, half the magnetic Bragg scattering involves a reversal of the neutron spin [denoted by the $(-+)$ configuration], and half does not. Thus for the case of a purely magnetic reflection the spin-flip $(-+)$ and non-spin-flip $(++)$ intensities should be equal in intensity. For the case where $\mathbf{P} \parallel \boldsymbol{\tau}$, all the magnetic scattering is spin-flip. Hence for a magnetic Bragg peak the spin-flip scattering should be twice as strong as for the $\mathbf{P} \perp \boldsymbol{\tau}$ configuration, while ideally no non-spin-flip scattering will be observed. Figure 4 shows the polarized beam results for the same two peaks, at scattering angles (for this wavelength) of 30° and 35° ; these correspond to the peaks at 19.5° and 23° in Fig. 1. The top section of the figure shows the data for the $\mathbf{P} \perp \boldsymbol{\tau}$ configuration. The peak at 30° has the identical intensity for both spin-flip and non-spin-flip scattering, and hence we conclude that this scattering is purely magnetic in origin as inferred from Fig. 3. The peak at 35° , on the other hand, has strong intensity for $(++)$, while the intensity for $(-+)$ is smaller by a factor of 1/11, the instrumental flipping ratio. Hence this peak is a pure

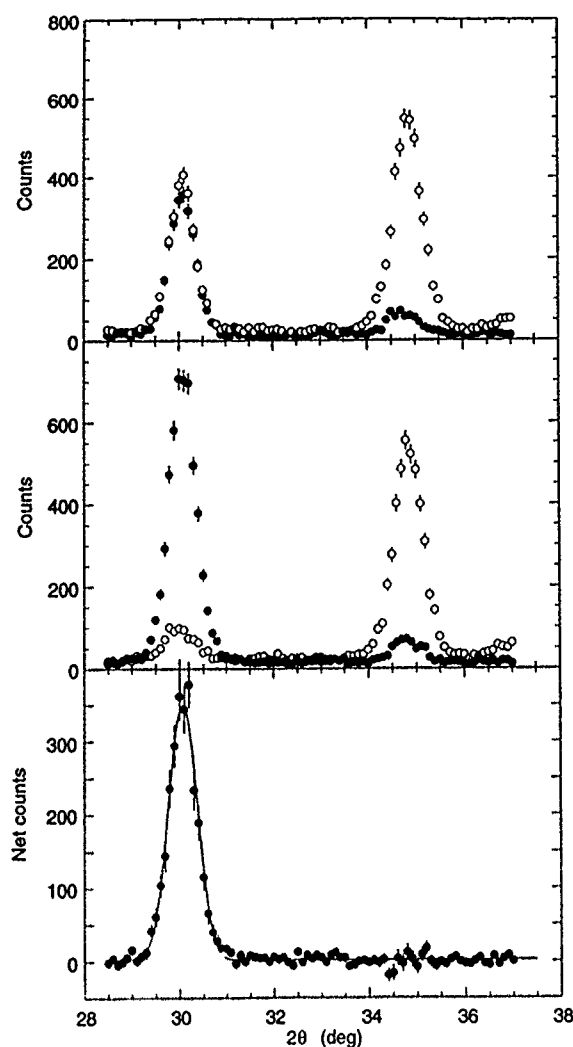


FIG. 4. Polarized neutron scattering. The top portion of the figure is for $P \perp \tau$, where the open circles \circ show the non-spin-flip scattering and the filled circles \bullet are the observed scattering in the spin-flip configuration. The low angle peak has equal intensity for both cross sections, and thus is identified as a pure magnetic reflection, while the ratio of the $(++)$ to $(-+)$ scattering for the high angle peak is 11, the instrumental flipping ratio. Hence this is a pure nuclear reflection. The center portion of the figure is for $P \parallel \tau$, and the bottom portion is the subtraction of the $P \parallel \tau$ spin-flip from the data for $P \perp \tau$. Note that in the subtraction procedure all background and nuclear cross sections cancel, isolating the magnetic scattering (Ref. 7).

nuclear reflection. The center row shows the same peaks for the $P \parallel \tau$ configuration, while the bottom row shows the subtraction of the $P \perp \tau$ spin-flip scattering from the $P \parallel \tau$ spin-flip scattering. In this subtraction procedure instrumental background, as well as all nuclear scattering cross sections, cancel, isolating the magnetic scattering. We see that there is magnetic intensity only for the low angle position, while no intensity survives the subtraction at the 35° peak position. These data unambiguously establish that the 30° peak is purely magnetic, while the 35° peak is purely nuclear. This simple example demonstrates how the technique works; obviously it would play a much more critical role in cases where it is not clear from other means what is the origin of the peaks, such as in regimes where the magnetic and nuclear

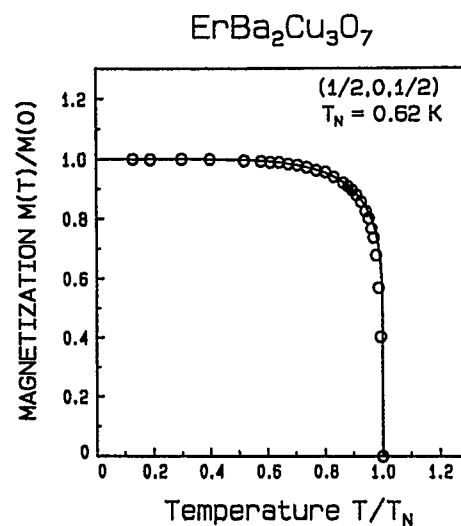


FIG. 5. Temperature dependence of the sublattice magnetization for the Er spins in superconducting $\text{ErBa}_2\text{Cu}_3\text{O}_7$, measured on a single crystal weighing 31 mg. The solid curve is Onsager's exact theory for the two-dimensional, $S = \frac{1}{2}$, Ising model (Ref. 9).

peaks overlap,⁷ or in situations where the magnetic transition is accompanied by a structural distortion.

Another example of magnetic diffraction⁹ is shown in Fig. 5. Here we show the intensity of a Bragg peak as a function of temperature for the Er ordering in $\text{ErBa}_2\text{Cu}_3\text{O}_7$. The magnetic interactions in this material are highly anisotropic, and this system turns out to be an ideal two-dimensional (planar) Ising antiferromagnet; the solid curve is Onsager's exact solution to the $S = \frac{1}{2}$, 2-D Ising model, and we see that it provides an excellent representation of the experimental data.

A final diffraction example is shown in Fig. 6, where the data for a series of molecular beam epitaxy $\text{Fe}_3\text{O}_4/\text{NiO}$ superlattices are shown.¹⁰ These scans are along the growth direction (Q_z), and we see the (222) fundamental peak (to-

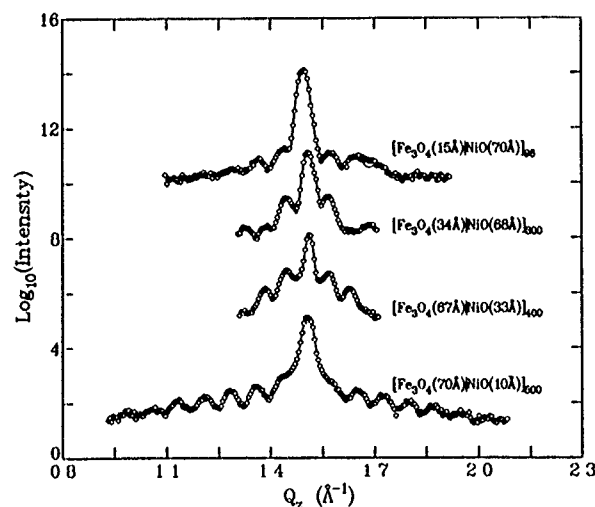


FIG. 6. Observed scattering from a series of $\text{Fe}_3\text{O}_4/\text{NiO}$ multilayers with different layer depths and total thickness. The satellites observed about the fundamental (222) reflection in the center originate from both nuclear and magnetic scattering. The typical weight of these samples is 1 mg (Ref. 10).

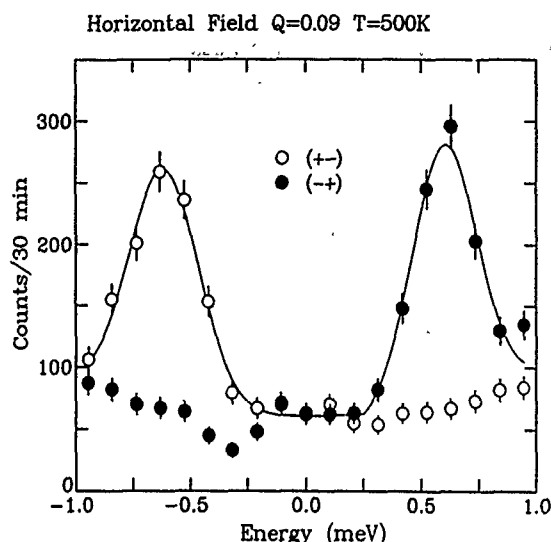


FIG. 7. Spin-flip scattering observed for the amorphous Invar $\text{Fe}_{86}\text{B}_{14}$ system in the $\hat{P}||\mathbf{Q}$ configuration. Spin waves are observed for neutron energy gain ($E < 0$) in the $(+-)$ cross section, and for neutron energy loss ($E > 0$) in the $(-+)$ configuration (Ref. 11).

gether with a peak from the MgO substrate) along with a series of satellite peaks on either side. The satellite peaks have both nuclear and magnetic contributions, and from such data the crystallographic and magnetic coherence lengths both in and between the layers can be followed as a function of temperature, field, thickness, etc.

It is interesting to compare the type and quality of data that are represented by these three examples. The powder diffraction technique is quite straightforward, both to obtain and analyze data. In this case typical sample sizes are ~ 5 g, and important and detailed information can be readily obtained with such sample sizes in a few hours of spectrometer time. The temperature dependence of the order parameter in $\text{ErBa}_2\text{Cu}_3\text{O}_7$, on the other hand, was obtained on a single crystal weighing only 31 mg. Note that the quality of the data is much better than for the powder sample even though the sample is more than two orders-of-magnitude smaller. The final example was for $\text{Fe}_3\text{O}_4/\text{NiO}$ multilayers, where the weight of the superlattices that contributes to the scattering ranges from 0.3–1.5 mg. Thus it is clear that interesting and successful diffraction experiments can be carried out on quite small samples.

III. MAGNETIC EXCITATIONS

Inelastic neutron scattering plays a unique role in determining the magnetic excitation spectra in magnetic systems, as it is the only probe that can directly measure the complete magnetic excitation spectrum. Typical examples are spin wave dispersion relations, critical fluctuations, crystal field excitations, and moment/valence fluctuations. Here we give an example of some spin wave measurements utilizing inelastic polarized beam techniques, which is a technique that is finding increasing use. In the long wavelength (small q) regime the spin wave dispersion relation for an isotropic ferromagnet is given by $E_{sw} = D(T)q^2$, where D is the spin wave "stiffness" constant. The general form of the spin

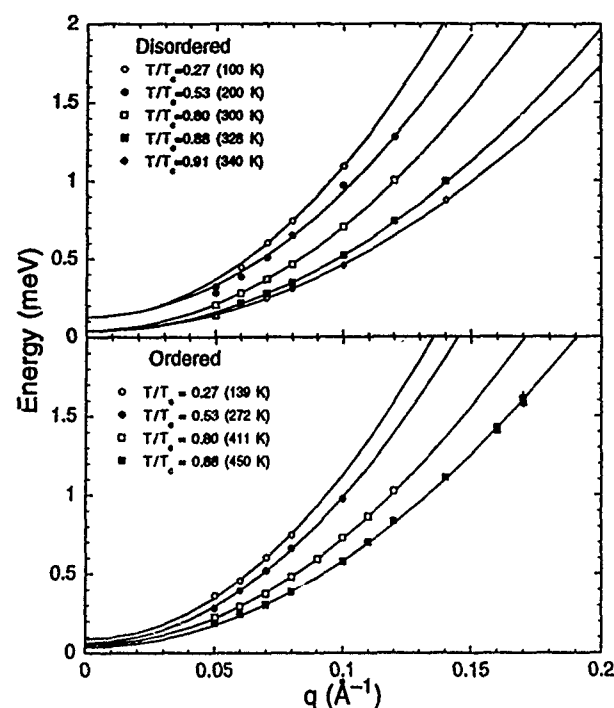


FIG. 8. Measured spin wave dispersion relations for chemically disordered (top) and ordered (bottom) Fe_3Pt (Ref. 12).

wave dispersion relation is the same for all isotropic ferromagnets, while the numerical value of D depends on the details of the magnetic interactions and the nature of the magnetism. One example of a prototypical isotropic ferromagnet is amorphous $\text{Fe}_{86}\text{B}_{14}$. Figure 7 shows an example of polarized beam inelastic neutron scattering data taken on this system.¹¹ To understand these data we note that spin wave scattering, represented in the Hamiltonian by the raising and lowering operators $S^\pm = S^x \pm iS^y$, causes a reversal of the neutron spin. These spin-flip cross sections are denoted by $(+-)$ and $(-+)$. If the neutron polarization \hat{P} is parallel to the momentum transfer \mathbf{Q} , $\hat{P}||\mathbf{Q}$, then we should be able to create a spin wave only in the $(-+)$ configuration, or destroy a spin wave only in the $(+-)$. This is precisely what we see in the data; for the $(-+)$ configuration the spin waves can only be observed for neutron energy loss scattering ($E > 0$), while for the $(+-)$ configuration spin waves can only be observed in neutron energy gain ($E < 0$). We remark that the cross sections for inelastic scattering are typically several orders-of-magnitude smaller than for elastic Bragg scattering, and thus large samples are required for these types of measurements; the sample in this case weighed ~ 10 g.

Data like these can be used to measure the renormalization of the spin waves as a function of temperature, as well as determine the lifetimes as a function of wave vector and temperature. An example for the crystalline Invar-type ferromagnet Fe_3Pt is shown¹² in Fig. 8. Here we have determined the wave vector dependence of the dispersion relation at a series of temperatures, both for the chemically ordered and disordered single crystals. These measurements can then be compared with theory as well as other experimental observa-

TABLE I. Neutron scattering spectrometers available for materials research in magnetism at the various neutron scattering centers in the U.S. Brookhaven National Laboratory (BNL) and the National Institute of Standards and Technology (NIST) operate heavy water reactors, while Oak Ridge National Laboratory (ORNL) and the University of Missouri (UM) operate light water reactors. The neutron sources at Argonne National Laboratory (ANL) and Los Alamos National Laboratory (LANL) are pulsed spallation facilities. NA=not applicable; C signifies under construction/development. At ORNL some spectrometers share a beam port and are therefore only available part time.

Spectrometer	ANL	BNL	LANL	NIST	ORNL	UM
SANS	1+1C	2	1	3	2	1C
Triple axis	NA	5	NA	5+1C	4	1
Inelastic TOF	4	0	2	1+1C	1	0
High res. powder	2	1	1	1	1	1
High intensity powder	1	1+1C	1	0	1	0
Diffraction	2	3+1C	1	1C	2	2
Spin echo	0	0	0	1C	0	0
Backscattering	0	0	1C	1C	0	0
Reflectometer	2	1	1	2+1C	1	1
User contact	T. Worlton R. Greenberg M. DiStavolo W. Kamitakahara R. Nicklow J. Rhyne ^a					

^aUM has no formal user program, and research there is accommodated on a collaborative basis only.

tions (such as magnetization measurements) which are controlled by such spin wave excitations.

IV. NEUTRON FACILITIES

The neutron scattering facilities available in the U.S. are shown in Table I. The National Laboratories all have ongoing user programs to acquire beam time, while the research at the University of Missouri reactor is done on a collaborative basis only. Brookhaven National Laboratory, Oak Ridge National Laboratory, and the National Institute of Standards and Technology operate research reactors, which provide steady beams of thermal, and in the case of NIST and BNL, cold neutrons. The NIST cold source supports a guide hall facility which can accommodate 15 or more instrumental stations when completed; it is the only project presently under construction. Argonne National Laboratory and Los Alamos National Laboratory have pulsed spallation neutron sources. This technique for producing neutrons in general is complementary to steady-state reactor sources, and the pulsed nature of the sources means that all instruments operate on the time-of-flight principle. The person to contact for more information about these facilities is provided at the bottom of the table.

Neutrons provide a unique tool not only for magnetism, but for broad areas of materials science, physics, chemistry, biology, and nuclear medicine. The reactors that are presently in use have already been operating for a quarter of a century, and there is a detailed plan to build a new research reactor, the advanced neutron source, to replace some of these facilities. The ANS would provide an order-of-magnitude more raw flux, and would also allow dramatic improvements in beam optics for many instruments; a great deal has been learned (and invented) in the last 25 years

about how to optimize neutron scattering instrumentation. If authorized for construction next year, the ANS would come on line early next decade, and would allow the U.S. to recapture the lead in the neutron scattering field. There are also plans to develop a design for a new, higher intensity spallation source. If these new facilities become a reality, then neutron scattering in the U.S. will continue to play a vital role in magnetism in particular and condensed matter physics in general, well into the next century.

ACKNOWLEDGMENTS

I would like to thank my NIST colleagues, J. A. Borchers, N. Rosov, Q. Huang, and P. Gehring, for their assistance. I would also like to thank J. D. Axe, R. M. Nicklow, J. J. Rhyne, R. A. Robinson, and T. Worlton for the information they provided.

¹S. W. Lovesey, *Theory of Neutron Scattering from Condensed Matter* (Oxford, New York, 1984), Vol. 2.

²E. Balcar and S. W. Lovesey, *Theory of Magnetic Neutron and Photon Scattering* (Oxford, New York, 1989).

³G. E. Bacon, *Neutron Diffraction* (Oxford U.P., Oxford, 1975), 3rd ed.

⁴W. Gavin Williams, *Polarized Neutrons* (Oxford, New York, 1988).

⁵G. L. Squires, *Thermal Neutron Scattering* (Cambridge, New York, 1978).

⁶*Methods of Experimental Physics: Neutron Scattering*, edited by D. L. Price and K. Sköld (Academic, Orlando, 1987), Parts C, A, and B.

⁷Q. Huang, P. Karen, V. L. Karen, A. Kjekshus, J. W. Lynn, A. D. Mighell, N. Rosov, and A. Santoro, *Phys. Rev. B* **45**, 9611 (1992).

⁸R. M. Moon, T. Riste, and W. C. Koehler, *Phys. Rev.* **181**, 920 (1969).

⁹J. W. Lynn, T. W. Clinton, W.-H. Li, R. W. Erwin, J. Z. Liu, K. Vandervoort, and R. N. Shelton, *Phys. Rev. Lett.* **63**, 2606 (1989).

¹⁰J. A. Borchers, R. W. Erwin, S. D. Berry, D. M. Lind, E. Lochner, K. A. Shaw, and D. Hilton, *Appl. Phys. Lett.* **64**, 381 (1994).

¹¹J. W. Lynn, N. Rosov, and G. Fish, *J. Appl. Phys.* **73**, 5369 (1993).

¹²N. Rosov, J. W. Lynn, J. Kästner, E. F. Wassermann, T. Chattopadhyay, and H. Bach (these proceedings).

Soft x-ray synchrotron radiation facilities for the study of magnetic materials (invited) (abstract)

Brian Tonner, W. O'Brien, M. A. Green, H. Höchst, and R. Reininger
*Synchrotron Radiation Center, University of Wisconsin-Madison, 3731 Schneider Drive, Stoughton,
Wisconsin 53589*

Synchrotron radiation sources are used for a variety of measurements of magnetic materials, including photoemission spectroscopy of band-structure (both with and without spin polarization), photoabsorption spectroscopy, and x-ray scattering. Recently, considerable attention has been paid to applications of circularly polarized monochromatic synchrotron radiation to spectroscopy and scattering of magnetic materials. Magnetic x-ray circular dichroism (MXCD), present in both x-ray absorption¹⁻³ and x-ray photoemission spectra,^{4,5} can be used as a site- and element-specific probe of local magnetic moment. With suitable instrumentation, the MXCD effect can be used to image magnetic domain structure of surfaces and buried layers, with element (and potentially chemical-state) specificity.⁶ Examples of studies using MXCD with an existing bending-magnet light source will be shown, and used to introduce the performance of a new, undulator-based variable polarization beamline under construction at SRC.

The Synchrotron Radiation Center is supported by the National Science Foundation, Division of Materials Research.

¹B. T. Thole, G. van der Laan, and G. A. Sawatzky, *Phys. Rev. Lett.* **55**, 2086 (1985).

²C. T. Chen, F. Sette, Y. Ma, and S. Modesti, *Phys. Rev. B* **42**, 7262 (1990).

³P. Carra and M. Altarelli, *Phys. Rev. Lett.* **64**, 1286 (1990).

⁴G. van der Laan, *Phys. Rev. Lett.* **66**, 2527 (1991).

⁵D. P. Pappas, G. D. Waddill, and J. G. Tobin, *J. Appl. Phys.* **73**, 5936 (1993).

⁶J. Stöhr, Y. Wu, B. D. Hermsmeier, M. G. Samant, G. R. Harp, S. Korranda, D. Dunham, and B. P. Tonner, *Science* **259**, 658 (1993).

High magnetic field research: Overview of facilities and science and technology opportunities (invited) (abstract)

J. E. Crow and H. J. Schneider-Muntau

National High Magnetic Field Laboratory, Florida State University, Tallahassee, Florida 32306

D. M. Parkin

Center for Materials Science, Los Alamos National Laboratory, Los Alamos, New Mexico 87545

N. Sullivan

Department of Physics, University of Florida, Gainesville, Florida 32611

A number of specialized facilities have been developed or are under development throughout the world to support research at high magnetic fields in a broad range of science and technology areas. These facilities provide continuous magnetic fields up to 32–35 T and pulsed fields up to 50–70 T for tens of ms periods with fields beyond 100 T for several μ s. During the last several years, new laboratories have been planned and are being developed within the United States and Japan with major expansions of facilities occurring in France, The Netherlands, and other countries. The National High Magnetic Field Laboratory, presently under construction in the United States, will include superconducting magnets ($B \leq 20$ T), resistive magnets ($B \leq 25$ –35 T depending on bore and power), hybrid magnet ($B \leq 45$ –50 T), and pulsed fields ($B \leq 60$ –70 T for 100 ms, $B \leq 50$ –70 T for 10–20 ms and $B \leq 250$ T for about 10 μ s). These new facilities within the United States and elsewhere will expand the research opportunities at the extremes of parameter space, i.e., magnetic field, ultralow temperatures, and high pressures, for researchers in the life and condensed matter science areas. An overview of the facilities throughout the world will be presented along with a brief discussion of the science opportunities and recent results at the extremes of high magnetic field.

Supported by the National Science Foundation through NSF Cooperative Agreement No. DMR 9016241 and the State of Florida.

LiNiO₂: Quantum liquid or concentrated spin glass?

M. Rosenberg and P. Stelmaszyk

Experimentalphysik VI, Ruhr-Universität Bochum, 44780 Bochum, Bundesrepublik Deutschland

V. Klein and S. Kemmler-Sack

Institut für Anorganische Chemie der Universität, Auf der Morgenstelle 18, 72076 Tübingen, Bundesrepublik Deutschland

G. Filoti

Institute of Physics and Technology of Materials, PB-MG-07, 7000 Bucharest, Magurele, Romania

From the magnetic and Mössbauer spectroscopy study of LiNi_{1-x}Fe_xO₂ with $x=0, 0.01, 0.05$, and 0.10 evidence for strong ferromagnetic correlations and spin freezing at low temperatures was found, reminding many characteristic features of spin glass behavior in variance with models describing the ground state of LiNiO₂ as a quantum liquid.

The ternary oxide LiNiO₂ was widely accepted to be a model compound for the two-dimensional (2D) antiferromagnetic triangular lattice (AFTL) with $S=1/2$ and an Ising-like anisotropy. This material has acquired special interest, since it was suggested that it may have a resonance valence bond (RVB) ground state, and so probably can contribute to the understanding of the mechanism of the high T_c superconductivity.¹ According to the RVB model the ground state has to behave as a quantum liquid with no long-range magnetic order, energetically more favorable as a classical antiferromagnetic type of order. Parallel to the theoretical development, a lot of experimental work, including mainly magnetic and specific heat measurements, electron spin resonance (ESR), nuclear magnetic resonance (NMR), neutron scattering, and magnetic relaxation studies, was invested in order to elucidate the main point, namely, the nature of the ground state of LiNiO₂ (see for instance the references mentioned in the papers by Kemp *et al.*² and Hirota *et al.*³).

Because of the still controversial character of many experimental results and their interpretation we decided to extend the study of LiNiO₂ especially in order to better understand the influence of the stoichiometry on the magnetic properties and to define the type of magnetic state occurring at lower temperatures. For the latter purpose we used the Mössbauer spectroscopy of LiNiO₂ samples doped with ⁵⁷Fe.

The samples A–F with the intended composition LiNi_{1-x}Fe_xO₂ (first column of Table I) were prepared from the intimately mixed (agate mortar) starting materials; LiOH H₂O (alpha), NiO (puratronic, Johnson–Matthey), and ⁵⁷Fe (medgenix) by firing in corundum crucibles (degussit Al 23) in air at 800 °C (3×28h with intermediate regrindings for samples with $x=0$) or at 750 °C (20h with several regrindings for the samples with $x=0.01$). X-ray checks (Philips powder diffractometer, Cu K α radiation, Au standard) showed all Ni containing materials to crystallize in the α -NaFeO₂ structure (space group R3m). The average oxidation state of Ni, determined by redox titration with Fe²⁺/Cr₂O₇¹⁻ is given in Table I. The extremely large value of 3.70 for the degree of oxidation of sample C was reached

after an extra 24-h-long treatment of sample A in SO₄H₂.

The temperature dependence of the magnetic susceptibility measured in a field of 1.5 T and of the reciprocal susceptibility for the samples A, B, and C is shown in Fig. 1. In all cases a behavior similar to that of a spin system which orders or freezes at low temperatures and with strong ferromagnetic correlations was observed. A Curie–Weiss dependence was found above temperatures which depend on composition, starting with about 150 K for sample A. The values of the Curie constants corrected for the core diamagnetism and of the derived values of the asymptotic Curie temperature θ_p and of the effective number of Bohr magnetons P_{eff} are given in Table I. One can see that θ_p increases with the degree of oxidation and with the Fe content.

A good agreement between the experimental values of the Curie constants and the expectations based on the degree of oxidation of the samples A and C and of the amount of Fe in the samples D, E, and F can be found under the assumption that the Ni³⁺ and Ni⁴⁺ ions are in the low spin states (t_{2g})⁶(e_g)¹ and (t_{2g})⁶ with the spin numbers 1/2 and 0, respectively, and the Fe atoms are present in the Fe³⁺ high spin state (t_{2g})³(e_g)² with the spin $S=5/2$. The agreement is ex-

TABLE I. Intended composition, average Ni value determined from the degree of oxidation \bar{O}_x , molar Curie constant, asymptotic Curie temperature θ_p , effective number of Bohr magnetons P_{eff} per transition metal atom of the intended composition and magnetic transition temperature T_c .

Intended composition	\bar{O}_x	C_m (cm ³ K mol ⁻¹)	θ_p (K)	P_{eff} (μ_B)	T_c (K)
A LiNiO ₂	+2.85	0.51	12	1.96	81.2
B LiNiO ₂	+2.66	0.33	182	1.62	82
C Li _{1-x} NiO ₂	+3.70	0.16	159	1.09	110
D LiNi _{0.99} Fe _{0.01} O ₂	+2.93	0.48	114	1.96	81
E LiNi _{0.95} Fe _{0.05} O ₂	...	0.62	123	2.23	94
F LiNi _{0.90} Fe _{0.10} O ₂	...	0.75	138	2.45	104.5

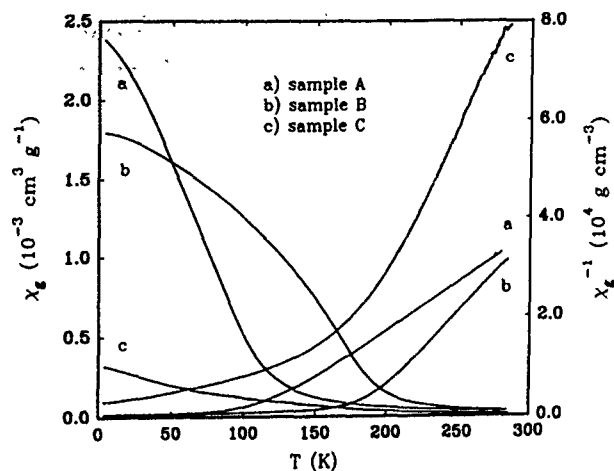


FIG. 1. Magnetic susceptibility and its inverse value vs temperature for the samples A, B, and C.

cellent for the samples A and F. The slightly larger experimental values found for samples D and E can result from the presence of a small amount of the Ni atoms in form of Ni^{2+} ions with $S=1$. An interesting point is the behavior in low magnetic fields where different temperature dependencies for the zero-field-cooled (ZFC) and field-cooled (FC) regimes were observed as can be seen in Fig. 2 for sample A and Fig. 3 for the sample D. In weak fields at temperatures between 4.2 and 20 K the susceptibility has very low values. Above 20 K the susceptibility starts to rise in a way similar to that occurring in the case of reentrant spin glass behavior. The ZFC curves are below the FC ones and their maximum shifts to higher temperatures when decreasing the field. Above a given temperature which depends on the field strength there is no more any difference between ZFC and FC curves. Using the kink point method one can determine the magnetic ordering or freezing temperatures T_c given in the last column of Table I. One can see that as was the case with the magnetic susceptibility the T_c values increase with the Fe concentration.

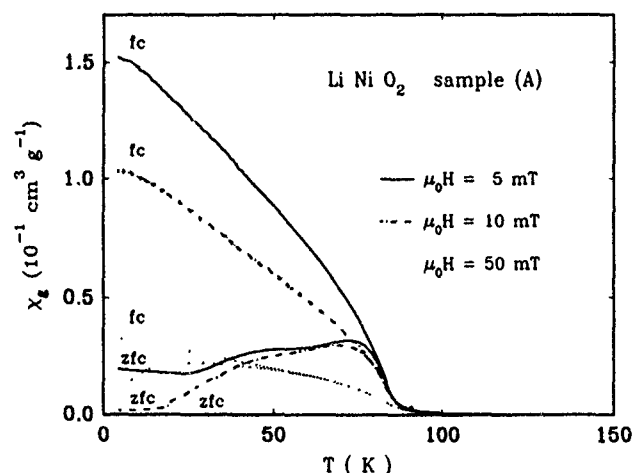


FIG. 2. Temperature dependence of the zero-field-cooled and field-cooled susceptibility of sample A.

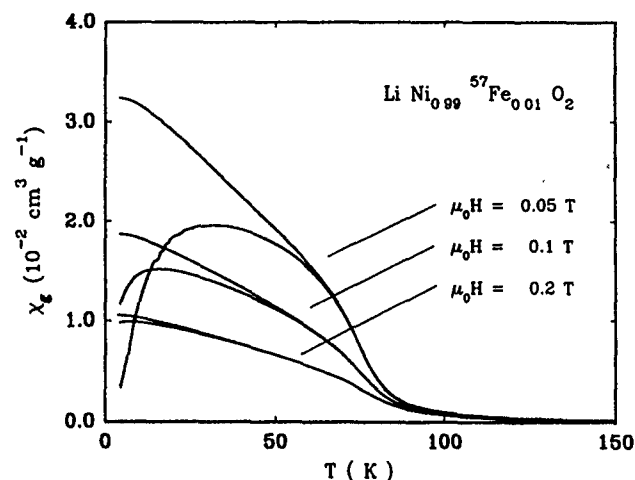


FIG. 3. Temperature dependence of the zero-field-cooled and field-cooled susceptibility of sample D.

At not too high values of the applied field the ZFC and FC values of the magnetization become identical. At any temperature below T_c the magnetization process in increasing fields has a hysteretic character as can be seen for the sample A in Fig. 4. The magnetization curve measured in fields up to 14 T is shown in the inset of the same figure. From this high-field measurement one obtains a value of the magnetization $M_S = 56, 9 \text{ A m}^2 \text{ kg}^{-1}$ corresponding to an average moment per Ni atom of $1 \mu_B$. This value confirms again the assumption of the low spin state of Ni^{3+} . But in view of the presence of 15% Ni^{2+} ions in this sample according to the measured degree of oxidation we would expect a slightly higher value of the magnetization for a parallel alignment of all the Ni spins but the field of 14 T is not strong enough in order to reach the saturation.

When considering the magnetic properties of our samples the strong analogy with the behavior of spin glasses as we already mentioned in a previous paper⁴ cannot be overlooked. The presence of strong ferromagnetic correlations

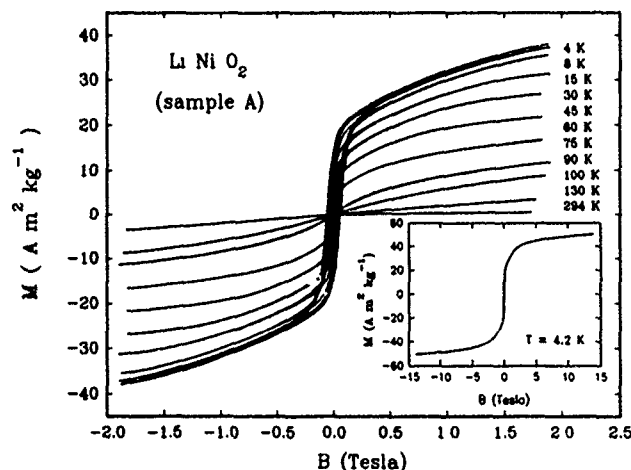


FIG. 4. Hysteresis loops of sample A taken at different temperatures. Inset: Magnetization curve at 4.2 K in fields up to 14 T.

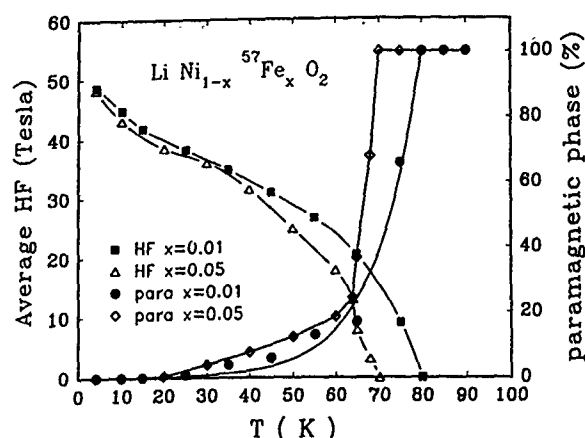


FIG. 5. Average Fe hyperfine field and amount of the paramagnetic phase in dependence on temperature for the samples D and E.

and spin glass behavior was also reported for LiNiO_2 by Kemp *et al.*² and spin glass behavior was mentioned very recently by Reimers *et al.*⁵

A deeper insight into the understanding of the magnetic properties of LiNiO_2 was gained from the Mössbauer spectroscopy study of the $\text{LiNi}_{1-x}^{57}\text{Fe}_x\text{O}_2$ samples. For all three compositions studied, the Mössbauer spectra were magnetically split below T_c . A distribution of hyperfine fields is always present, ranging for $x=0.01$ between 52.8 and 40.2 T for instance. Two main features characterize the Mössbauer spectra below T_c : (1) a strong Ising relaxation, and (2) the presence of a paramagnetic doublet above about 20 K with gradually increasing intensity up to about 60 K followed by a drastic change up to 100% over a 10–15 K temperature interval.

The temperature dependence of the average hyperfine field HF and of the concentration of the paramagnetic component for $x=0.01$ and 0.05 are shown in Fig. 5. The relatively sharp increase of HF between 20 and 4.2 K evidences the possible occurrence of a peculiar change in the magnetic properties around 20 K reminding again a reentrant spin glass behavior as was the case with the temperature dependence of the susceptibility in low fields.

The presence of a temperature-dependent HF is clear evidence for spin freezing below T_c involving obviously both Fe and Ni spins. This result is in excellent agreement with the recent results of the neutron scattering studies of

LiNiO_2 , where strong inelastic diffuse scattering has been observed, instead of the antiferromagnetic Bragg scattering⁶ together with an evidence for ferromagnetic short-range correlations increasing in intensity below 240 K and exhibiting a divergency at 35 K.⁷

A point which requires an explanation is the presence of the paramagnetic phase appearing around 20 K and increasing in intensity with temperature already mentioned above (Fig. 5). Matsubara and Inawashiro for instance analyzed the spin structure for a hexagonal close-packed (hcp) lattice with interlayer and intralayer next-neighbor interactions.⁸ They could show that for the Ising-like case with strong frustration, their model exhibited at intermediate temperatures, a special paramagnetic phase with a short-range order of the z component of the spin characterized by an incommensurate period. At higher temperatures this phase transforms in the "pure" paramagnetic one, whereas at lower temperatures a so-called nonperiodic frozen spin phase will occur.

Is the above-mentioned paramagnetic component, which develops in the Mössbauer spectra of Fe-doped LiNiO_2 above 20 K, the phase predicted in Ref. 8? Or is the paramagnetic component the result of a distribution of spin freezing temperatures occurring owing to the frustration conditions arising in the triangular lattice and to the presence of such defects as for instance intersite exchanged Ni and Li ions? There is no definite answer to these questions at the present time.

In conclusion one can only say that the LiNiO_2 samples we studied as well as the other ones studied by other groups behave magnetically at low temperatures as concentrated spin glasses and in some respects they remind a reentrant spin glass behavior.

¹ P. W. Anderson *Mater. Res. Bull.* **8**, 153 (1973).

² J. P. Kemp, P. A. Cox, and J. W. Hodby, *J. Phys.: Condens. Matter*, **6**, 699 (1990).

³ K. Hirota, Y. Nakazawa, and M. Ishikawa, *J. Phys.: Condens. Matter* **3**, 4721 (1991).

⁴ G. Filoti, M. Rosenberg, R. J. Zhou, S. Kemmler-Sack, and V. Klein, *Hyperfine Interact.* **85**, 548 (1994).

⁵ J. N. Reimers, J. R. Dahn, J. E. Greedan, C. V. Stager, G. Liu, I. Davidson, and U. Von Sacken, *J. Solid State Chem.* **102**, 542 (1993).

⁶ K. Hirakawa, R. Osborne, A. D. Taylor, and K. Takeda, *J. Phys. Soc. Jpn.* **59**, 3081 (1990).

⁷ H. Yoshizawa, H. Mori, K. Hirota, and M. Yshikawa, *J. Phys. Soc. Jpn.* **59**, 2631 (1990).

⁸ F. Matsubara and S. Inawashiro, *J. Phys. Soc. Jpn.* **56**, 4087 (1987).

Disappearance of three-dimensional magnetic ordering in Gd_2CuO_4

T. Chattopadhyay and P. J. Brown
Institut Laue-Langevin, B.P. 156X, 38042 Grenoble Cedex, France

B. Roessli
Labor für Neutronenstreuung, ETHZ, CH-5232 Villigen PSI, Switzerland

The magnetic ordering of an isotope (^{158}Gd) enriched Gd_2CuO_4 single crystal has been investigated by neutron diffraction in the temperature range 1.5–50 K. The three-dimensional magnetic order of the Cu sublattice is found to disappear abruptly in a narrow temperature range close to 7 K which is just above the ordering temperature of the Gd sublattice [$T_N(\text{Gd})=6.4$ K]. This result is thought to be intimately related to the structural distortion of the CuO planes which gives rise to weak ferromagnetism. The lack of three-dimensional order in the structural distortion imposes itself on the antiferromagnetic arrangement of the Cu sublattice through the Cu-Gd and Gd-Gd interactions and the different and incompatible wave vectors of the Cu and Gd magnetic sublattices.

The class of superconducting materials $\text{R}_{2-x}\text{M}_x\text{CuO}_4$ ($\text{R}=\text{Pr, Nd, Sm, and Eu}$; $\text{M}=\text{Ce, Th}$), for which electrons, rather than holes, in the CuO_2 planes are the charge carriers have been investigated quite intensively.^{1–4} The magnetic properties of these materials have also been studied in order to discover whether the magnetic interaction plays any role in Cooper pair formation. The Cu magnetic moments in the parent compounds R_2CuO_4 of the electron-doped superconductors order at temperatures in the range 245–285 K whereas the rare-earth moments, when they are nonzero, order only at much lower temperatures (1–6 K). Three types of magnetic interactions: Cu-Cu, Cu-R, and R-R, govern the magnetic properties of these materials of which the Cu-Cu interaction is by far the strongest. These magnetic interactions are presumably superexchange interactions via oxygen. The R-R magnetic interaction is weak being of the order of a few degrees K. The magnitude of the Cu-R interaction is not known definitely but cannot be much greater than that of R-R. For temperatures above about 50 K the magnetic properties of these compounds are essentially governed by the strong Cu-Cu interaction; but at lower temperatures Cu-R and R-R magnetic interactions become increasingly important. Interplay amongst these three types of interactions leads to interesting magnetic properties at lower temperatures. The inherent frustration of the structure with respect to antiferromagnetic ordering is also expected to play an important role in the magnetic properties of these classes of compounds.

Gd_2CuO_4 behaves rather differently from the rest of the R_2CuO_4 series. Although Gd_2CuO_4 is as easily doped with Ce or Th as the other members of the R_2CuO_4 ($\text{R}=\text{Pr, Nd, Sm, and Eu}$) family, it does not, as they do, become superconducting.⁴ Gd_2CuO_4 along with other heavy rare-earth compounds (Eu through Yb) also shows weak ferromagnetism below the copper ordering temperature.⁵ The antiferromagnetic ordering of both Gd and Cu sublattices has been investigated by neutron diffraction on isotope (^{158}Gd) enriched Gd_2CuO_4 single crystals.^{6,7} Below $T=6.4$ K Gd moments order antiferromagnetically with the wave vector $\mathbf{k}=(0,0,0)$. Ferromagnetic Gd layers parallel to the a - b plane are antiferromagnetically stacked along $[001]$. Cu^{2+} ions in Gd_2CuO_4 orders at $T_N=285$ K to the La_2NiO_4 type antifer-

romagnetic structure with the propagation vector $\mathbf{k}=(\frac{1}{2}, \frac{1}{2}, 0)$. However, the previous neutron diffraction investigation⁷ of the magnetic ordering of the Cu sublattice was restricted to temperatures above 40 K. In the present paper we report the investigation of the magnetic ordering of the Cu sublattice down to 1.5 K.

The neutron diffraction experiments were performed on the same isotope (^{158}Gd) enriched Gd_2CuO_4 plate shaped single crystal of Ref. 7 of size $20 \times 10 \times 2$ mm³ on the two-axis diffractometer P2AX of the Saphir reactor of the Labor für Neutronenstreuung, ETH Zürich. The crystal was mounted inside a helium cryostat on the diffractometer with the $[1\bar{1}0]$ crystallographic direction parallel to the ω axis of the diffractometer. We have used both pyrolytic graphite (PG 002) and $\text{Cu}(220)$ monochromators to get incident neutron wavelengths of 1.05 and 0.84 Å, respectively. To cut off higher order harmonics of the incident wavelengths we used Pu-Al alloy and Er filters for 1.05 and 0.84 Å, respectively.

Gd_2CuO_4 crystallizes in the tetragonal space group $I4/mmm$ (T' -phase). The lattice parameters at room temperatures are $a=3.892$ Å, $c=11.878$ Å. Figure 1 shows the magnetic structure of Gd_2CuO_4 below 6.4 K. This magnetic

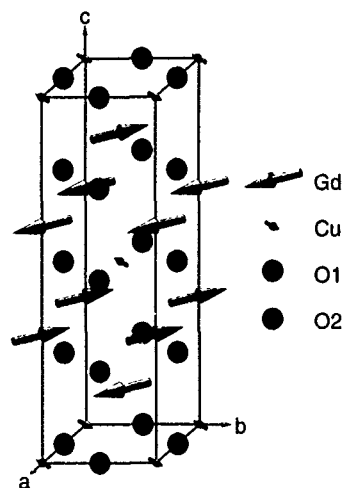


FIG. 1. Magnetic structure of Gd_2CuO_4 below $T_N(\text{Gd})$. Note that the spin directions of the Cu and Gd sublattices are at right angles. The structure model assumes a single- \mathbf{k} ordering of the Cu sublattice.

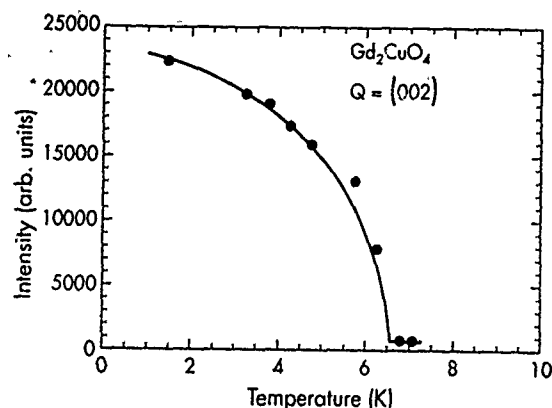


FIG. 2. Temperature variation of the integrated intensity of the 002 reflection. Below $T_N(\text{Gd})$ this reflection consists of nuclear and magnetic contributions of which the latter decreases continuously and disappears at $T_N(\text{Gd})=6.4$ K. Above $T_N(\text{Gd})$ the 002 reflection is purely of nuclear origin. The presence of magnetic contribution to the 002 reflection excludes the possibility that the Gd magnetic moments are parallel to the c axis.

structure model of Gd_2CuO_4 below the ordering temperature of Gd sublattice has been derived from the neutron diffraction results of Refs. 6 and 7. Note that the order in the Cu sublattice is given by a single- k model and we have assumed that the Gd and Cu spin directions are perpendicular so that they are independent of one another. A noncollinear double- k magnetic structure of Cu sublattice can not be ruled out on the basis of the neutron diffraction measurements,⁷ since it cannot be distinguished from the single- k model without applying either magnetic field or uniaxial stress. The magnetic structure of Gd_2CuO_4 in the temperature range $40 \text{ K} < T < 285 \text{ K}$ is basically the structure of just the Cu sublattice in Fig. 1. The Gd sublattice is paramagnetic except for a small ordered magnetic moment aligned by interaction with the antiferromagnetic Cu sublattice.

In the present neutron diffraction investigations we have measured the temperature variation of the integrated intensities of 002, $\frac{1}{2}, \frac{1}{2}, 1$ and $\frac{1}{2}, \frac{1}{2}, 3$ reflections in the temperature range 1.5 to 50 K. The intensity of the 002 reflection was used to monitor the spontaneous ordering of the Gd sublattices. Figure 2 shows the temperature variation of this reflection. It showed no significant variation between 6.4 and 40 K indicating that in this temperature range it contains no appreciable magnetic contribution. The intensity of this reflection increases strongly with decreasing temperature below $T_N(\text{Gd})=6.4$ K proving conclusively that the magnetic moment of Gd atoms cannot be oriented parallel to $[001]$.⁶ The integrated intensity of the $\frac{1}{2}, \frac{1}{2}, 1$ magnetic reflection increases continuously with decreasing temperature below $T_N(\text{Cu})=285$ K down to 45 K as was shown in Ref. 7. In Fig. 3 we show the temperature dependence of the integrated intensity of this reflection at lower temperatures. At about 45 K it starts to decrease and shows a minimum at about 20 K before it regains its previous maximum value at about 8 K. This broad minimum in intensity at about 20 K suggests some kind of phase transition also shown by magnetization and electron paramagnetic resonance (EPR) measurements.⁸ The most unexpected feature of the data is the sudden and

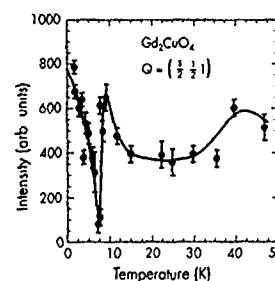


FIG. 3. Temperature variation of the integrated intensity of the $\frac{1}{2}, \frac{1}{2}, 1$ reflection in the temperature range 1.5–45 K showing a broad minimum at about 20 K and a further sharp minimum at about 7 K. The first anomaly is associated with the weak ferromagnetism, whereas the second anomaly is interpreted to be due to the disappearance of the three-dimensional ordering of the Cu magnetic moments.

complete disappearance of the $\frac{1}{2}, \frac{1}{2}, 1$ reflection at $T=7$ K. Below $T_N(\text{Gd})$ intensity of this reflection increases again in much the same way as the 002 reflection. The anomalies observed in the temperature dependence of the $\frac{1}{2}, \frac{1}{2}, 1$ reflection probably have the same origin as those observed around the same temperatures in the magnetic susceptibility.⁹ The $\frac{1}{2}, \frac{1}{2}, 3$ reflection was found to be very weak and was difficult to measure because of $\lambda/2$ contamination from 116 which is a strong nuclear reflection. However, by using a neutron wavelength of 0.84 \AA and a 0.5-mm Er filter it was possible to almost completely eliminate $\lambda/2$ and to show that the $\frac{1}{2}, \frac{1}{2}, 3$ intensity remains close to zero in the whole temperature range. The scattering amplitude in this reflection due to the induced antiferromagnetic component of the moment on the Gd sublattice must therefore be of opposite sign and almost equal in magnitude to that contributed by the Cu sublattice. This implies that the susceptibility of the Gd sublattice is almost independent of temperature and that $\mu_{\text{Gd}} = \chi \mu_{\text{Cu}}$ with $\chi = 0.9 \pm 0.3$. Search for magnetic reflections at $Q = (\frac{1}{2}, \frac{1}{2}, 0)$, $(\frac{1}{2}, \frac{1}{2}, 2)$, and $(\frac{1}{2}, \frac{1}{2}, 3)$ and other incommensurate positions in the Brillouin zone at the temperature (7 K) at which the $\frac{1}{2}, \frac{1}{2}, 1$ disappeared did not reveal any magnetic intensity. The directions scanned are shown in Fig. 4. This result suggests that at this temperature the three-dimensional magnetic ordering of the copper sublattice temporarily disappears.

The disappearance of three-dimensional magnetic ordering of the Cu sublattice just above the ordering temperature of the Gd sublattice is intimately connected with the weak ferromagnetism of Gd_2CuO_4 . Since weak ferromagnetism is forbidden both for nonzero propagation vectors and in the tetragonal space group $I4/mmm$ of Gd_2CuO_4 some structural distortion which changes the periodicity and lowers the symmetry must be present. It has been suggested⁸ that it is oxygen displacements in the CuO_2 planes which allow weak ferromagnetism in Gd_2CuO_4 . In a recent paper⁸ we have proposed a model in which oxygen atoms are displaced perpendicular to the ideal Cu–O–Cu bond direction in accordance with the x-ray measurements. Of the two possible displacement patterns we chose the one for which there is a real antisymmetric exchange interaction of the Dzyaloshinski–Moriya type between the nearest neighbors within the CuO_2 planes. For macroscopic weak ferromagnetism to occur the

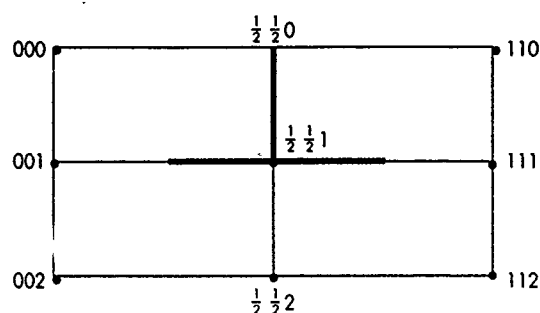


FIG. 4. The reciprocal lattice of Gd_2CuO_4 corresponding to the scattering plane. The directions scanned for detecting possible magnetic intensity are marked by thick lines. No magnetic Bragg intensity has been detected in the reciprocal scans indicated by the thick lines.

oxygen displacements within a plane must be coherent over relatively long distances. However, since there is no evidence for the superlattice reflections which would characterize three-dimensional order, there can be no appreciable correlation between the signs of the oxygen displacements in neighboring CuO_2 planes along the c direction. In the temperature range $T_N(\text{Cu})$ to about 20 K the overall magnetic structure of Gd_2CuO_4 is built up of weakly interacting sandwich layers stacked along c . Each such layer consists of a CuO_2 plane sandwiched between two Gd planes and possesses a spontaneous weak ferromagnetic moment. This model provides a possible explanation of the nature of the further transformations of the magnetic structure which occur at temperatures below 50 K. It seems probable that the driving mechanism for these structural changes is the antiferromagnetic interaction between neighboring Gd layers along c . Because of the large Gd moment this interaction becomes dominant at low temperature. At temperatures between $T_N(\text{Cu})$ and about 50 K the exchange between neighboring CuO_2 planes leads to three-dimensional antiferromagnetic ordering of the Cu sublattice in which the relative orientations of the antiferromagnetic vector \mathbf{L} in neighboring CuO_2 planes are strongly correlated. Under these circumstances the random nature of the signs of structural distortions in different CuO_2 planes imposes a frustrated random arrangement of the weak ferromagnetic vector \mathbf{M} . There are two distinct antiferromagnetic Gd-Gd interactions which are important:

that between the Gd planes in adjacent sandwich layers and that between the two Gd planes in the same sandwich layer. Satisfying the former, forces the \mathbf{M} vectors in adjacent layers to be antiparallel, and thus transfers the effects of randomness in the structural distortion to the antiferromagnetic vectors \mathbf{L} . Satisfying the latter, on the other hand, destroys the weak ferromagnetic moment \mathbf{M} of the layers themselves. The intensity variation of the $\frac{1}{2}, \frac{1}{2}, 1$ reflection shown in Fig. 3 can be explained if the effects of interlayer Gd-Gd interactions start to be manifest at a higher temperature than those of intralayer interactions. Below 50 K the appearance of some correlation between the \mathbf{M} vectors in adjacent sandwich layers leads to partial disorder of the \mathbf{L} vectors and a consequent reduction of the intensity of the $\frac{1}{2}, \frac{1}{2}, 1$ magnetic reflection. However, when the temperature falls to about 20 K, Gd-Gd antiferromagnetic correlation inside each sandwich layer starts to be important and to reduce the magnitude of the \mathbf{M} vectors of the layers themselves. This effect not only lowers and finally eliminates the weak ferromagnetic moment, but also reduces the exchange field leading to the disorder of the \mathbf{L} vectors. Hence, the recovery of the intensity of the $\frac{1}{2}, \frac{1}{2}, 1$ reflection. The disappearance of the $\frac{1}{2}, \frac{1}{2}, 1$ reflection just above $T_N(\text{Gd})$ indicates a temporary breakdown of the three-dimensional magnetic order of the Cu sublattice during the total reorganization of the magnetic structure required to satisfy the strong antiferromagnetic correlations in both the Cu and Gd sublattices.

¹ Y. Tokura, H. Takagi, and S. Uchida, *Nature* **337**, 345 (1989).

² H. Takagi, S. Uchida, and Y. Tokura, *Phys. Rev. Lett.* **62**, 1197 (1989).

³ J. T. Markert and M. B. Maple, *Solid State Commun.* **70**, 145 (1989).

⁴ J. T. Markert, E. A. Early, T. Bjornholm, G. Ghamaty, W. B. Lee, J. Neumier, R. D. Price, C. L. Seeman, and M. B. Maple, *Physica C* **158**, 178 (1989).

⁵ S. B. Oseroff, D. Rao, F. Wright, D. C. Vier, S. Schultz, J. D. Thompson, Z. Fisk, S.-W. Cheong, M. F. Hundley, and M. Tovar, *Phys. Rev. B* **41**, 1934 (1990).

⁶ T. Chattopadhyay, P. J. Brown, A. A. Stepanov, P. Wyder, J. Voiron, A. I. Zoyagin, S. N. Barilo, and D. I. Zhigunov, *Phys. Rev. B* **44**, 9486 (1991).

⁷ T. Chattopadhyay, P. J. Brown, B. Roessli, A. A. Stepanov, S. N. Barilo, and D. I. Zhigunov, *Phys. Rev. B* **46**, 5731 (1992).

⁸ A. A. Stepanov, P. Wyder, T. Chattopadhyay, P. J. Brown, G. Fillard, I. M. Vitebsky, A. Deville, B. Gaillard, S. N. Barilo, and D. I. Zhigunov, *Phys. Rev. B* **48**, 12979 (1993).

⁹ J. D. Thompson, S.-W. Cheong, S. E. Brown, Z. Fisk, S. B. Oseroff, M. Tovar, D. C. Vier, and S. Schultz, *Phys. Rev. B* **39**, 6660 (1989); T. Ishii and A. Matsuda, *Solid State Commun.* **75**, 765 (1990).

Spin-Peierls transition in CuGeO_3 : Electron paramagnetic resonance study

S. Oseroff

San Diego State University, San Diego, California 92182

S.-W. Cheong

AT&T Bell Laboratories, Murray Hill, New Jersey 07974

A. Fondado

Universidad Santiago de Compostela, Spain

B. Aktas

University of California, San Diego, California 92093

Z. Fisk

Los Alamos National Laboratories, Los Alamos, New Mexico 87545

Measurements of electron paramagnetic resonance (EPR) at 9 and 35 GHz between 2 and 300 K in single crystals and powder samples of CuGeO_3 are presented. Below 14 K a large decrease in the intensity of the Cu^{2+} EPR signal is observed. The data can be interpreted as due to a spin-Peierls transition. However, an alternative interpretation in terms of a simple structural transition cannot be ruled out. An opening of an energy gap of ~ 25 K is calculated from the analysis.

It is now well established that, as the temperature is reduced, a one-dimensional (1D) metallic lattice of uniformly spaced atoms with a half-filled conduction band can exhibit a Peierls transition.¹ Such a transition results from a distortion of the lattice in which alternate atoms are displaced in opposite directions. A splitting of the conduction band and a reduction in the energy of the electrons occupying the lower band is observed. There is a magnetic analog to the electronic Peierls instability, the so-called spin-Peierls (SP) transition.² A uniform antiferromagnetic (AF) quantum chain becomes unstable with respect to an underlying lattice distortion which dimerizes into AF chains.^{2,3} It has been argued that for the SP transition to occur, the 3D lattice, where the 1D magnetic chains are embedded, needs first to undergo a strong softening. A softening of the phonons at high temperature in the undimerized state has been found in the few 1D organic materials where, at much lower temperature, a SP transition has been observed.⁴

The AF chains are characterized below the SP transition by an energy gap between a nondegenerate singlet ground state and a band of triple excited states. The energy gap is dependent on the degree of alternation and goes to zero in the uniform chain limit. In zero magnetic field the transition is second order and the degree of alternation increases as the temperature, T , is lowered, reaching its maximum at $T=0$ K.²⁻⁴ The first experimental evidence confirming the existence of such compounds followed the discovery of the 1D organic materials TTF-CuBDT, TTF-AuBDT, and MUM(TCNQ)₂. Their properties can be satisfactorily explained within the framework of the theory of a SP transition.⁵ In many instances the spin-Peierls nature has been disputed, questioning if the doubling of the period of the 1D unit cell is due to a SP instability. The observed alternation of the AF coupling between the spins can be just a consequence of a simple structural transition which results in the doubling of the lattice period. It is then important to find whether or not the AF interaction is essential to the phase transition.

Recently the presence of a SP transition has been reported in an inorganic compound, CuGeO_3 .⁶ That study showed that the susceptibility, χ , in all the directions of the crystal rapidly decreases to zero below 14 K. Besides, the magnetic field dependence of the transition temperature, T_{sp} , agrees well with the theoretical predictions and experimental results reported previously for the organic SP systems. Electron paramagnetic resonance (EPR) is an ideal technique to study CuGeO_3 , as Cu^{2+} is one of the easiest ions to detect by EPR. This technique has been shown to be extremely sensitive for studying the dynamics of low-dimensional spin systems, which includes the already well characterized SP systems.^{5,7,8} If an energy gap opens in this compound, with a nonmagnetic singlet ground state, a rapid decrease of the intensity of the Cu^{2+} ($S=1/2$) EPR signal is expected.

In this paper we present measurements of EPR at 9 and 35 GHz between 2 and 300 K on single crystals and powder samples of CuGeO_3 . Single crystals of about $0.1 \times 0.5 \times 3$ mm³ parallel to the \bar{a} , \bar{b} , and \bar{c} axes, respectively, were obtained. Powder samples were prepared by the usual sintering method. X-ray studies shows no trace of impurity phases and the data are in good agreement with previous reports on this compound.⁹ Previous EPR has been reported in CuGeO_3 .¹⁰ However, the authors did not observe a decrease in the intensity of the EPR signal or at least did not report it. Instead, they observed for $T \leq 7$ K an increase of the magnetization and a broadening of the EPR linewidth which they attributed to long-range magnetic ordering.

Magnetization data on our samples are similar to the data reported by Hase *et al.*⁶ That is, a rapid decrease of the susceptibility is observed below 14 K, with no significant increase below 7 K, contrary to the measurements reported by Petrakovskii *et al.*¹⁰ A strong EPR signal of Cu^{2+} was measured for the single crystal as for the powder samples for $T \geq 14$ K. The intensity, I , of the signal diminishes rapidly below this temperature. In Fig. 1 we show the linewidth, ΔH , as a function of T for a single crystal measured at 35 GHz. Similar data for ΔH are obtained at 9 GHz. The inten-

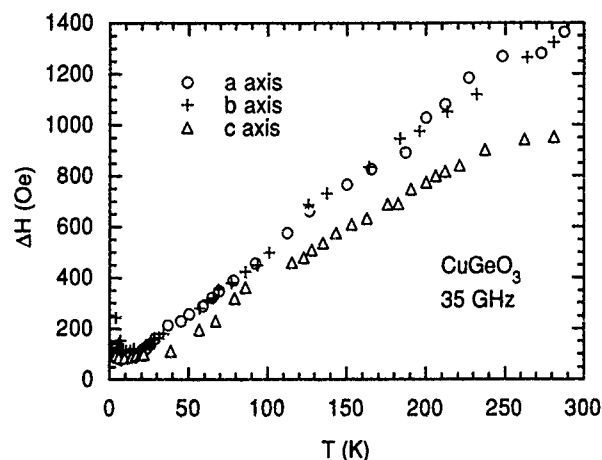


FIG. 1. EPR linewidth as a function of T for a CuGeO_3 single crystal measured at 35 GHz.

sity was estimated by finding the area of the EPR signal. We present I vs T for a single crystal measured at 35 and 9 GHz, and susceptibility data in Figs. 2–4, respectively.

The angular dependence of the Cu^{2+} line can be described by the spin-Hamiltonian:

$$H = \mu_B \mathbf{S} \cdot \mathbf{g} \cdot \mathbf{H}, \quad (1)$$

where $S = 1/2$, \mathbf{g} is the gyromagnetic tensor, μ_B is the Bohr magneton, and \mathbf{H} the external magnetic field. In Fig. 5 the angular variation of the gyromagnetic factor measured at 35 GHz for the three principal lattice planes is given. The g values for the principal axes, obtained from the best fit of the data, are listed in Table I for three temperatures.

The first question to ask is if CuGeO_3 is well described by 1D Heisenberg AF. If anisotropic components would be present in the coupling between the Cu spins, shifts in the g values as a function of T would be observed. As seen in Table I these shifts are small, so the principal exchange mechanism may be assumed to be isotropic.

In Fig. 1 we see that ΔH increases with T between ~ 40 and 300 K. It has been suggested that at high temperatures

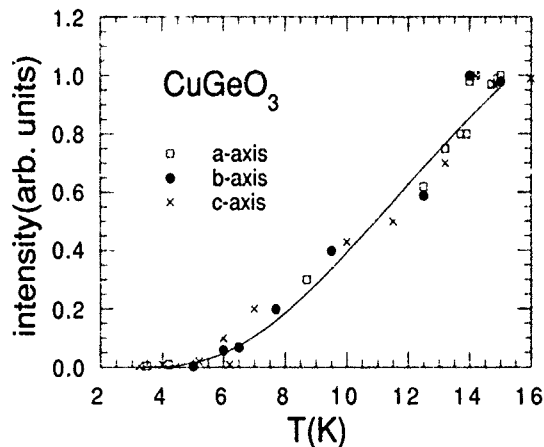


FIG. 2. Intensity of the Cu^{2+} EPR signal vs T , for a single crystal of CuGeO_3 measured at 35 GHz and $T \leq T_{sp}$. The solid curve corresponds to the fitting of Eq. (2) with $m = 42$ K.

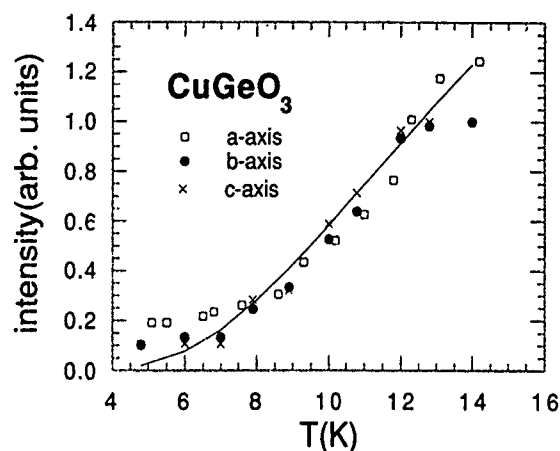


FIG. 3. Intensity vs T for a single crystal measured at 9 GHz. The solid curve corresponds to the best fitting to Eq. (2) with $m = 40$ K.

the long wavelength modes, $q \sim 0$, constitute the dominant contribution to ΔH for a 1D AF chain, with ΔH predicted to be proportional to χT .^{11,12} In our case the agreement is good. The increase in ΔH observed in single crystals for $T \leq T_{sp}$ shown in Fig. 1 can be explained as follows: The number of nonmagnetic singlet pairs increases as we lower the temperature. Then, the exchange narrowing becomes less effective and ΔH broadens. However, no broadening below T_{sp} has been found in powder samples. We do not have an explanation for this behavior. Other mechanisms such as the interaction between chains, short-range ordering, etc., may also contribute to ΔH at lower temperatures. Finally, the broadening observed in our single crystals may be due to the presence of impurities or defects in them.

For $T \leq T_{sp}$ we have fitted the intensity of the electron spin resonance (ESR) line to

$$I(T) = \frac{A}{T} \exp\left(\frac{-m}{T}\right), \quad (2)$$

this expression was obtained by Bulaevskii for an alternating chain of spins in the Hartree-Fock approximation.¹³ This approximation is expected to be accurate for temperatures

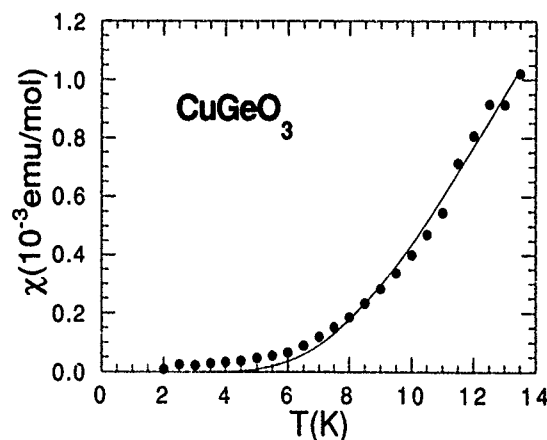


FIG. 4. Susceptibility data taken at 2 kOe in a powder sample. The solid curve is the best fitting to Eq. (2) with $m = 45$ K.

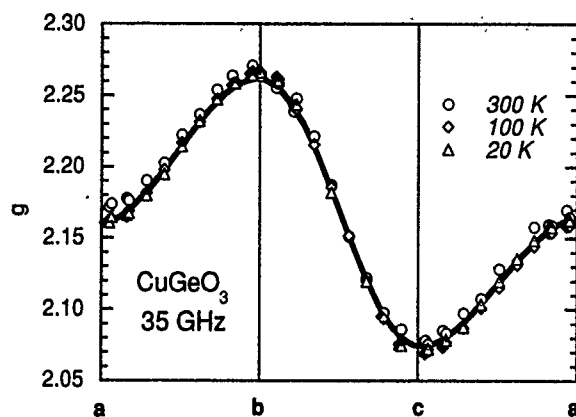


FIG. 5. Angular variation of the gyromagnetic factor at 300, 100, and 20 K. The solid curve corresponds to the best fitting to Eq. (1) for data taken at 20 K.

much smaller than the exchange interaction, $T \ll J$. As a value of $J \sim 90$ K is derived for CuGeO_3 from data,⁶ Eq. (2) should be a good approximation for $T \leq T_{sp}$. The best fitting to the data taken in a single crystal measured at 9 and 35 GHz, on powder samples measured at 9 GHz, and susceptibility data give values of $m = 40, 42, 46$, and 45 K, respectively. In Figs. 2–4 the solid curve shows the fitting of the data to Eq. (2) for those values of m .

For $T \leq T_{sp}$ the Heisenberg Hamiltonian for a 1D chain may be written as¹³

$$H = \sum_{i=1}^{N/2} J_1 \mathbf{S}_{2i} \cdot \mathbf{S}_{2i-1} + J_2 \mathbf{S}_{2i} \cdot \mathbf{S}_{2i+1}, \quad (3)$$

where the relation between the two alternating J 's of the chain are given by^{5,14}

$$J_{1,2}(T) = J\{1 + \delta(T)\}, \quad (4)$$

according to mean-field theory the energy gap $\Delta(T)$ is given by

$$\Delta(T) = pJ\delta(T), \quad (5)$$

using values of $J = 90$ K,⁶ $p = 1.637$,³⁻⁵ and $m \approx 43$ K from our measurements, we obtained $J_2/J_1 \sim 0.7$, $\delta(0) \sim 0.17$, and $\Delta(0) \sim 25$ K in agreement with Hase *et al.*⁶

Preliminary specific heat measurements show a λ -shaped anomaly at ~ 14 K, similar to that observed in organic SP

TABLE I. Gyromagnetic factors for the three principal axes. The data were taken at 35 GHz.

$T(K)$	g_a	g_b	g_c
300	2.170 ± 0.004	2.267 ± 0.005	2.078 ± 0.002
100	2.160 ± 0.002	2.266 ± 0.002	2.070 ± 0.002
20	2.162 ± 0.002	2.266 ± 0.002	2.070 ± 0.002

systems.¹⁵ Measurements of the dc magnetization at high magnetic field, up to 26 T, show a rapid increase of M at ~ 12 T at low temperature.¹⁶ In summary, our EPR results, preliminary specific heat and high-field dc magnetization could be interpreted as due to an SP transition in CuGeO_3 . However, a careful analysis of the data is needed before we can rule out a structural transition with the doubling of the lattice period as the origin of the alternation of the exchange interaction in the spin chain.

We wish to thank Professor R. Lilly, P. Lincoln, and M. Quisenberry for their help. This research was supported at San Diego State University by Grant No. NSF-DMR-9117212, by AT&T Bell Laboratories and at Los Alamos National Laboratory under the auspices of the United States Department of Energy. One of us (BA) was supported by TUBITAK and the Islamic Development Bank.

¹ R. E. Peierls, *Quantum Theory of Solids* (Oxford University Press, London, 1955), p. 108.

² G. Beni and P. Pincus, *J. Chem. Phys.* **57**, 3531 (1972); G. Beni, *ibid.* **58**, 3200 (1973); E. Pytte, *Phys. Rev. B* **10**, 2039 (1974).

³ M. C. Cross and D. S. Fisher, *Phys. Rev. B* **19**, 402 (1979).

⁴ A. I. Buzdin and L. N. Bulaevskii, *Sov. Phys. Usp.* **23**, 409 (1980).

⁵ I. S. Jacobs, J. W. Bray, H. R. Hart, Jr., L. V. Interrante, J. S. Kasper, G. D. Watkins, D. E. Prober, and J. C. Bonner, *Phys. Rev. B* **14**, 3036 (1976).

⁶ M. Hase, I. Terasaki, and K. Uchinora, *Phys. Rev. Lett.* **70**, 3651 (1993).

⁷ T. W. Hijmans and W. P. Beyermann, *Phys. Rev. Lett.* **58**, 2351 (1987).

⁸ C. F. Schwerdtfeger, S. Ostra, and G. A. Sawatzky, *Phys. Rev. B* **25**, 1786 (1982).

⁹ Y. Ginetti, *Bull. Soc. Chim. Belg.* **63**, 209 (1954).

¹⁰ G. A. Petrakovskii, K. A. Sabina, A. M. Vorotynov, A. I. Kruglik, A. G. Klimenko, A. D. Balayev, and S. S. Aplesnin, *Sov. Phys. JETP* **71**, 772 (1990).

¹¹ P. M. Richards and M. B. Salamon, *Phys. Rev. B* **9**, 32 (1972).

¹² Y. Ajiro, S. Matsukawa, T. Yamada, and T. Haseda, *J. Phys. Soc. Jpn.* **39**, 259 (1975).

¹³ L. N. Bulaevskii, *Sov. Phys. Solid State* **11**, 921 (1969).

¹⁴ E. Pytte, *Phys. Rev. B* **10**, 4637 (1974).

¹⁵ M. Hundley (private communication).

¹⁶ P. Liu (private communication).

Observations of magnetization reversal and magnetic clusters in copper ferrite films

M. M. Ibrahim and M. S. Seehra

Physics Department, West Virginia University, P.O. Box 6315, Morgantown, West Virginia 26506-6315

G. Srinivasan

Physics Department, Oakland University, Rochester, Michigan 48309

The observation of a magnetization reversal and a superparamagnetic behavior are reported for films of copper ferrite sputtered in an oxygen atmosphere. X-ray diffraction studies indicate the presence of 14-nm nanoscale crystals of CuFe_2O_4 in the films. Data on the temperature dependence of the film magnetization M for zero-field-cooled (ZFC) and field-cooled (FC) show that ZFC and FC curves separate at a temperature T_f and that T_f decreases with increasing static field strength. For $T < T_f$, M vs T data for low fields indicate the presence of a compensation point in virgin samples. For $T > T_f$, a superparamagnetic character is evident from the high-field magnetization data. An average cluster size of 16 nm obtained from such data is in excellent agreement with the results of x-ray diffraction studies.

A series of magnetically ordered amorphous oxides have been synthesized by radio-frequency (rf) sputtering in the past few years.¹⁻⁷ In a recent article, we reported on the evidence for a long-range magnetic order in amorphous copper ferrite films prepared by rf sputtering in a mixed O_2 -Ar atmosphere.⁷ For such films, the magnetization, Curie temperature, and gyromagnetic ratio are in agreement with the values expected for the crystalline copper ferrite. Therefore, the spontaneous moment in the amorphous films is suggested to arise from ordered clusters with a magnetic structure similar to that of ferrimagnetic copper ferrite.

This paper deals with the magnetic properties of similar films sputtered in a pure O_2 atmosphere. The important results of this work are as follows: (i) Unlike the films sputtered in a mixed O_2 -Ar atmosphere which are amorphous, x-ray diffraction (XRD) data for oxygen sputtered samples reveal the presence of nanoscale crystals of copper ferrite. (ii) Low-field magnetization (M) data for virgin samples show a sign reversal, i.e., a compensation point. However, the sign reversal does not occur in samples exposed to static fields (up to 50 kOe). (iii) Above the spin freezing temperature T_f (or blocking temperature), the films exhibit a superparamagnetic character. (iv) The cluster size estimated from the magnetization data agrees with the results of XRD data. Some details of these results are given below.

Samples of CuFe_2O_4 were sputtered from a target of polycrystalline copper ferrite prepared by the conventional ceramic technique. The target was mounted in a magnetron gun and the system was evacuated to a base pressure of 0.01 mTorr. The deposition was carried out in a sputter-down configuration in pure oxygen at a pressure of 1 mTorr and an rf power of 200 W at 13.6 MHz, 1- μm -thick films were obtained for a sputtering duration of 2 h on Corning 7059 glass and silicon substrates. The film composition was determined by energy dispersive x-ray spectroscopy. The films were rich in Fe and deficient in Cu, and the maximum deviation in the metal ion content was $\pm 10\%$. A Rigaku/DMax diffractometer was used for XRD studies. For magnetic measurements, a SQUID magnetometer (Quantum Design, model

MPMS) was used over the temperature range of 5–300 K and static fields up to 50 kOe.

There is considerable evidence that the samples contain clusters (or nanoscale crystals) of CuFe_2O_4 . Consider first the XRD data in Fig. 1 in which the diffraction patterns are shown for Corning 7059 substrates with and without the film. The sample spectra, obtained by subtracting the substrate background, show lines at angles corresponding to crystalline CuFe_2O_4 . The lines are considerably broadened due to small particle size and nearby lines overlap. Using the most intense line near $2\theta = 35^\circ$ (combination of 220 and 311 lines) and using the Scherrer equation for the particle diameter $L = 0.9\lambda/(\beta \cos \theta)$, where $\lambda = 1.542 \text{ \AA}$ is the x-ray wavelength and β is the corrected linewidth,⁸ we obtain an average particle diameter of 14 nm. Additional evidence for clustering comes from magnetization data discussed in later sections.

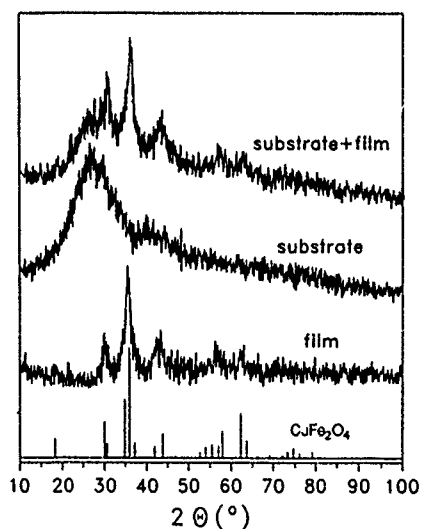


FIG. 1. X-ray powder diffractograms for an rf sputtered film of CuFe_2O_4 on a Corning 7059 glass substrate and for the substrate. The film was deposited in a pure oxygen atmosphere. The subtracted diffractogram for the film is also shown. The stick diagram is for single crystal CuFe_2O_4 .

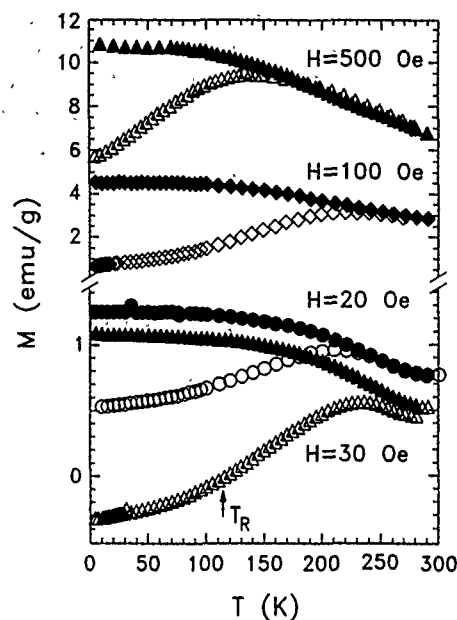


FIG. 2. Variation of magnetization M with temperature T for rf sputtered CuFe_2O_4 films. The data are for zero-field-cooled (open symbols) and field-cooled (while cooling) cases (filled symbols). Data for $H=30, 100$, and 500 Oe were taken on a virgin sample whereas data at $H=20$ Oe were obtained after subjecting the sample to high static magnetic fields. Notice that the ZFC and FC curves separate at the spin freezing temperature T_f .

Data on temperature and magnetic field dependence of M are shown in Fig. 2 for a "virgin" sample. Our measurements at $H=30$ Oe show that there is a sign reversal in M at $T_R \approx 115$ K in a ZFC (zero-field-cooled) sample in that M is negative at low temperatures, crossing zero near 115 K and then continues to increase smoothly reaching a maximum near 240 K. After reaching 300 K, we cooled the sample, at the same time taking the data (FC) as the sample cooled back to 5 K. The sign reversal in ZFC data is reminiscent of the compensation point observed in rare-earth substituted yttrium iron garnets and in rare-earth-transition metal alloys.^{9,10}

Kaneyoshi and Jascur¹¹ have predicted a similar sign reversal in M for two-dimensional amorphous structures containing spin-1/2 and spin-1 ions. The theory also predicts a decrease in T_R with increasing H . However, it is not clear at present whether the present system could behave like an amorphous structure with spins frozen in a random direction even though M data, discussed later, show spin freezing at temperatures below 250 K. Further, we obtained M vs T data under ZFC conditions for $H=20$ Oe in order to examine the predicted field dependence of T_R . The data shown in Fig. 2 for a sample which was subjected previously to high static fields, on the order of 50 kOe, reveal that a sign reversal is no longer present. Thus it may be necessary to study the possible variation of T_R with H on virgin samples unexposed to large fields. The important inference here is that the observation of a compensation pointlike effect in the present system merits further investigation.

Similar measurements for the ZFC and FC cases were carried out for $H=100$ to 700 Oe. Representative data at 100 and 500 Oe are shown in Fig. 2. At these higher fields, there

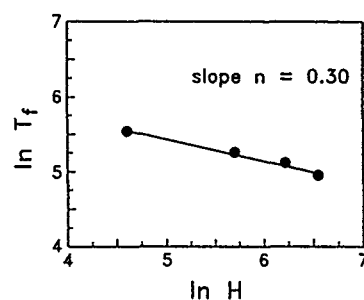


FIG. 3. Logarithmic (natural) plot of spin freezing temperature T_f vs static magnetic field H , yielding a slope of 0.30 with a correlation factor of 0.99. T_f values were obtained from data as in Fig. 2 for ZFC and FC samples.

is no sign reversal in M as it remains positive for all T values. The ZFC and FC curves separate at a temperature T_f , and T_f decreases with H according to the equation $T_f = AH^{-n}$, where A is a constant. The exponent n can be determined from a plot of $\ln T_f$ vs $\ln H$, as in Fig. 3, and we obtain $n=0.30$ with a correlation factor $R=0.99$. Such a decrease in T_f with H , with $n=0.25$, has been reported for Bi-Fe-Cu oxide samples.¹²

A superparamagnetic behavior for the sputtered films was inferred from M vs H data at a series of temperatures. The two criteria for such a behavior are (i) the magnetization above the spin freezing (or blocking) temperature must scale as H/T ; and (ii) M vs H data should show no hysteresis above the blocking temperature.¹³ Figure 4 shows the variation of M/M_∞ with H/T at three temperatures, viz., 200, 250, and 300 K. Here, M_∞ represents the M value at an applied static field of 30 kOe. It is obvious from the figure that the magnetization curves at different temperatures collapse on to the same curve.

Figure 5 shows M vs H data at 5 and 300 K, i.e., for T values above and below the spin freezing temperatures of 150 to 250 K. The data were obtained by varying H in steps from zero to 25 kOe and back to zero. The data at 5 K show hysteresis and a remanence of 11.5 emu/g whereas the data at 300 K do not show any hysteresis. Thus data in Figs. 4 and 5 lead to the conclusion that copper ferrite nanocrystals in the films are superparamagnetic.

Data on H dependence of M at 300 K can then be used to estimate the distribution $f(D)$ in the size of clusters,

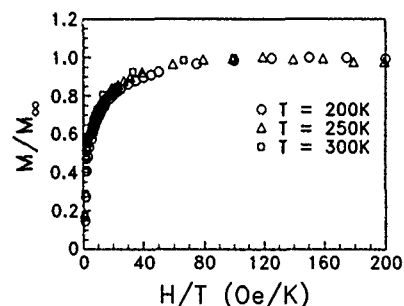


FIG. 4. Variation of the relative magnetization M/M_∞ with H/T for $T=200, 250$, and 300 K. M_∞ corresponds to the magnetization at a static field of 30 kOe. The data indicate a superparamagnetic character for CuFe_2O_4 films.

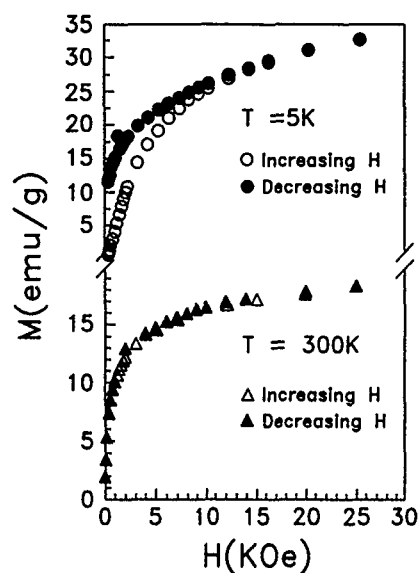


FIG. 5. Static magnetic field dependence of the magnetization for CuFe_2O_4 films at 5 and 300 K. The data indicate hysteresis at 5 K and no hysteresis at 300 K.

where D is the size (diameter) of the clusters, assuming a log normal distribution.¹⁴ We determined a cluster size distribution centered around 16 nm with the particle size ranging from 9 to 24 nm.

In conclusion, structural and magnetic characterization of copper ferrite films sputtered in oxygen atmospheres show that the films contain nanoscale crystals of CuFe_2O_4 .

The research at Oakland University was supported by a grant from the Petroleum Research Fund, administered by the American Chemical Society.

- ¹T. Fujii, S. Jinzenji, Y. Asahara, A. Kajima, and T. Shinjo, *J. Appl. Phys.* **64**, 5434 (1988).
- ²B. Uma Maheshwar Rao and G. Srinivasan, *Appl. Phys. Lett.* **58**, 2441 (1991).
- ³B. Uma Maheshwar Rao and G. Srinivasan, *Phys. Rev. B* **44**, 395 (1991).
- ⁴B. Uma Maheshwar Rao, G. Srinivasan, V. Suresh Babu, and M. S. Seehra, *J. Appl. Phys.* **69**, 5463 (1991).
- ⁵B. Uma Maheshwar Rao and G. Srinivasan, *IEEE Trans. Magn.* **MAG-28**, 2443 (1992).
- ⁶B. Uma Maheshwar Rao and G. Srinivasan, *J. Magn. Magn. Mater.* **111**, 249 (1992).
- ⁷G. Srinivasan, B. Uma Maheshwar Rao, J. Zhao, and M. S. Seehra, *Appl. Phys. Lett.* **59**, 372 (1991).
- ⁸H. P. Klug and L. E. Alexander, *X-Ray Diffraction Procedures* (Wiley, New York, 1974).
- ⁹W. H. von Aulock, *Handbook of Microwave Ferrite Materials* (Academic, New York, 1965).
- ¹⁰P. Chaudhari, J. J. Cuomo, and R. J. Gambino, *Appl. Phys. Lett.* **22**, 337 (1973).
- ¹¹T. Kaneyoshi and M. Jascur, *J. Phys.: Condens. Matter* **4**, L281 (1992).
- ¹²S. Soeya, S. Nakamura, and N. Ichinose, *J. Appl. Phys.* **68**, 2875 (1990).
- ¹³C. P. Bean and I. S. Jacobs, *J. Appl. Phys.* **27**, 1448 (1956).
- ¹⁴M. M. Ibrahim, J. Zhao, and M. S. Seehra, *J. Mater. Res.* **7**, 1856 (1992).

The structure and spin dynamics of lanthanide-bearing silicate glasses

A. J. G. Ellison, C.-K. Loong, and J. Wagner
Argonne National Laboratory, Argonne, Illinois 60439

The structure of $3\text{Na}_2\text{O} \cdot \text{R}_2\text{O}_3 \cdot 6\text{SiO}_2$ ($\text{R}=\text{Nd}$, Yb and Lu) glasses has been studied by time-of-flight neutron diffraction. The average Si-O and O-O nearest-neighbor coordination is found to be similar to those of the SiO_4 tetrahedral units in vitreous SiO_2 and other silicate glasses. The rare-earth (RE) ions coordinate with no more than seven nearest-neighbor oxygen atoms. The dynamic and static response of these glasses and their isochemical crystalline analogs has been investigated by inelastic neutron scattering and magnetic susceptibility measurements. The magnetic excitation spectra were analyzed by a ligand-field model using a method of descending symmetry. The correlation between short-range atomic order in a network glass and magnetic interactions of the RE ions with the local environment is discussed.

Oxide glasses containing rare-earth (RE) elements serve a wide range of technological functions, ranging from glass lasers to optical components with exceptionally high indices of refraction. Addition of RE elements to glasses influences the behavior of other components, such as the principal glass-forming components, and mobile charge-carrying species in ionically conducting glasses. RE elements are also important components in high-level radioactive waste, which in the United States is expected to be permanently stored in borosilicate glass. Thus there has been considerable interest in probing the environments of the RE elements in oxide glasses and the impact they have upon the chemistry of other components.

In the $(\text{M}_2\text{O})_x \cdot (\text{R}_2\text{O}_3)_y \cdot (\text{SiO}_2)_{1-x-y}$ glasses ($\text{M}=\text{Na}$, K ; $\text{R}=\text{RE}$ element) glasses, Raman spectroscopy implies that the chemistry of oxygen is significantly affected by changes in the concentration of M^+ and R^{3+} .¹ However, little is known about the effect that changes in the concentration of M^+ or R^{3+} might have upon the chemistry of each other. Inelastic neutron scattering from glasses containing lanthanides with no magnetic moment, such as La^{3+} or Lu^{3+} , can be used to obtain an average neutron-weighted vibrational density of states, which can be used to develop a more comprehensive model of contributions to various vibrational modes in the glasses. The interaction between the neutron magnetic moment and the partially filled f orbitals of a RE element produces an additional magnetic scattering component which reflects the average coordination environment in the glass. When combined with data from neutron total diffraction data for the coordination number of the RE, it is possible to model the average coordination environment of RE elements in the glass.

$3\text{Na}_2\text{O} \cdot \text{Nd}_2\text{O}_3 \cdot 6\text{SiO}_2$, $3\text{Na}_2\text{O} \cdot \text{Yb}_2\text{O}_3 \cdot 6\text{SiO}_2$, and $3\text{Na}_2\text{O} \cdot \text{Lu}_2\text{O}_3 \cdot 6\text{SiO}_2$ glasses were prepared in 100-g batches by combining appropriate amounts of reagent-grade Na_2CO_3 , Nd_2O_3 , (Yb_2O_3 or Lu_2O_3) and SiO_2 in a ball mill. The mixture was placed in a Pt crucible and fired at 1000 °C for 1 h to drive off CO_2 from the carbonate, then at 1400 °C for 8–12 h. The mixture was stirred several times to ensure homogeneity. The furnace temperature was then increased to 1500 °C, and after equilibration the sample was removed and quenched by pouring it onto a massive copper block. Polycrystalline $\text{Na}_3\text{YbSi}_3\text{O}_9$ was prepared by direct crystalliza-

tion of the $3\text{Na}_2\text{O} \cdot \text{Yb}_2\text{O}_3 \cdot 6\text{SiO}_2$ glass at 1250 °C.

Neutron time-of-flight diffraction experiments for the glasses and a $\text{Na}_3\text{YbSi}_3\text{O}_9$ crystal were performed using the glass, liquid, and amorphous diffractometer (GLAD) and the general purpose powder diffractometer (GPPD), respectively, at the Argonne Intense Pulsed Neutron Source, IPNS. Diffraction data indicated that while all glasses were homogeneous, the $\text{Na}_3\text{YbSi}_3\text{O}_9$ crystal contained a minor amorphous component. Inelastic neutron-scattering measurements were performed using the high-resolution medium-energy chopper spectrometer (HRMECS). The magnetic contribution to the total scattering in the Yb- and Nd-bearing compounds was identified by an examination of the momentum-transfer dependence of the observed intensities and by a comparison with the spectra of the nonmagnetic $3\text{Na}_2\text{O} \cdot \text{Lu}_2\text{O}_3 \cdot 6\text{SiO}_2$ glass. The data were corrected for background scattering and the effect of sample self-shielding by subtracting the combined empty-container and neutron-absorber (i.e., cadmium) runs. Measurements of the elastic incoherent scattering from a vanadium standard provided detector calibration and intensity normalization.

Since glasses lack long-range order, their structures in real space are generally expressed in terms of distribution functions obtained from the Fourier transform of their structure factors $S(Q)$. The best known of these are the pair correlation function $G(r)$, the total distribution function $T(r)$, and the radial distribution function $N(r)$:

$$G(r) = \frac{1}{2\pi^2\rho_0} \int_0^\infty [S(Q) - 1] Q^2 \frac{\sin Qr}{Qr} dQ, \quad (1)$$

$$T(r) = 4\pi r \rho_0 G(r), \quad (2)$$

and

$$N(r) = 4\pi r^2 \rho_0 G(r). \quad (3)$$

$N(r) dr$ has a direct physical interpretation as the number of atoms lying within a range $(r, r+dr)$ from any given atom. Figure 1 shows $T(r)$ obtained from the diffraction measurement of $3\text{Na}_2\text{O} \cdot \text{Yb}_2\text{O}_3 \cdot 6\text{SiO}_2$ glass. Peaks in $T(r)$ represent the most probable (average) bond distances for element pairs. The peaks at 1.63, 2.23, 2.33, and 2.65 Å correspond to the Si-O, Yb-O, Na-O, and O-O nearest-neighbor distances, respectively. The Si-O and O-O distances are typical

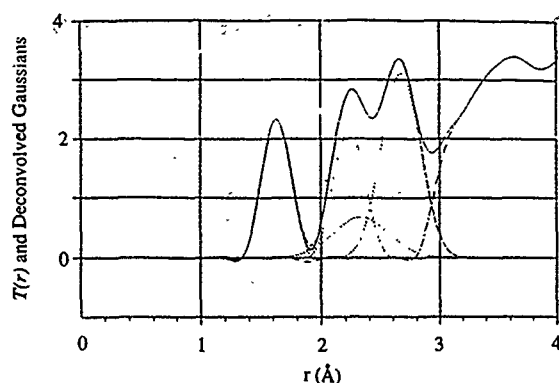


FIG. 1. The total distribution function $T(r)$, solid line, and the deconvolved Gaussian components, dotted and dot-dashed lines, of $3\text{Na}_2\text{O} \cdot \text{Yb}_2\text{O}_3 \cdot 6\text{SiO}_2$ glass.

of those found in other silicate glasses.² The area under a peak in a plot of $N(r) = rT(r)$ vs r is directly proportional to the coordination number of the atoms. Such an area under the Si-O peak gives a coordination number of 3.85, which is less than the expected value of 4 due to instrument resolution. The $N(r)$ vs r area under the Yb-O peak implies a coordination number for Yb of 5.5 ± 0.5 .

For inelastic neutron magnetic scattering the magnetic intensity of a transition between two states (e.g., $\langle i|$ and $\langle j|$) for a single ion is proportional to the square of the matrix element $\langle i|J_{\perp}|j\rangle$ (where J_{\perp} is the component of the total angular momentum operator perpendicular to the neutron wave vector) and the observed peak position is equal to the energy separation of the two states. Since the local symmetry of the RE ions in a glass varies from one site to another, the spectrum is expected to be broad. Therefore, it is instructive to compare the excitation spectra of a glass with those of an isochemical crystalline compound where better defined crystal-field spectra peaks can be identified.

We used the spectra of the $3\text{Na}_2\text{O} \cdot \text{Lu}_2\text{O}_3 \cdot 6\text{SiO}_2$ glass as the base to estimate the nuclear-scattering component for all the Yb and Nd materials. Lu has a complete $4f$ orbital thereby giving no magnetic scattering, and the small difference in the mass only affects the very low-energy phonon modes. Consequently, the magnetic intensities of the Yb and Nd materials were obtained by subtracting off from the total (nuclear and magnetic) excitation spectra the $3\text{Na}_2\text{O} \cdot \text{Lu}_2\text{O}_3 \cdot 6\text{SiO}_2$ spectrum weighted by the average nuclear-scattering cross section of its components. The resulting magnetic spectra of crystalline $\text{Na}_3\text{YbSi}_3\text{O}_9$ are shown in Fig. 2(a). According to the Kramers theorem the lowest symmetry of a state affected by a ligand electrostatic field for an odd-number electron system is a twofold degeneracy. Thus the Yb^{3+} Russell-Saunders ground multiplet is at most split into $2\Gamma_6$ and $2\Gamma_7$ doublets. If all the Yb sites in a crystal are equivalent and have a local point-symmetry less than a cubic symmetry, one expects a low-temperature magnetic excitation spectrum containing a peak at zero energy corresponding to elastic scattering within the ground-state doublet and three sharp inelastic lines corresponding to excitations from the ground state to the excited states. The excitation spectrum of crystalline $\text{Na}_3\text{YbSi}_3\text{O}_9$ can be ana-

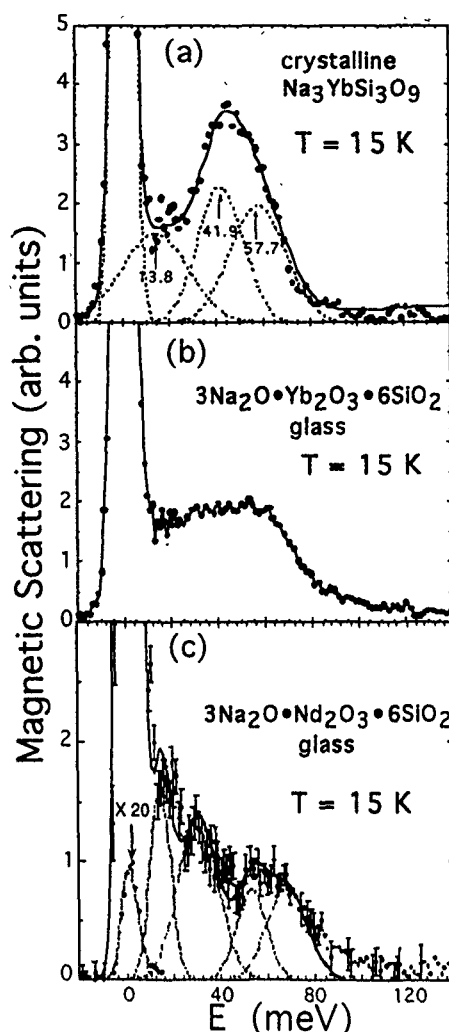


FIG. 2. (a) The magnetic excitation spectrum of crystalline $\text{Na}_3\text{YbSi}_3\text{O}_9$ (circles) and a fit to the data (solid line) by a sum of four Gaussian functions (dotted lines). (b) The magnetic excitation spectrum of the $3\text{Na}_2\text{O} \cdot \text{Yb}_2\text{O}_3 \cdot 6\text{SiO}_2$ glass (circles). The line is a guide to the eye. (c) The magnetic excitation spectrum of $3\text{Na}_2\text{O} \cdot \text{Nd}_2\text{O}_3 \cdot 6\text{SiO}_2$ glass (circles) and a fit to the data (solid line) by a sum of five Gaussian functions (dotted lines).

lyzed in terms of three broad components centered at 13.8, 41.9, and 57.7 meV, as shown in Fig. 2(a). The large widths of these excitations are probably caused by multiple Yb sites in the crystal and by the effect of chemical disorder from the minor glassy component in the material. The magnetic spectrum of the $3\text{Na}_2\text{O} \cdot \text{Yb}_2\text{O}_3 \cdot 6\text{SiO}_2$ glass [see Fig. 2(b)] shows a strong and sharp elastic peak as in the crystalline analog but the inelastic intensity is flat up to about 70 meV with a long tail extended to over 100 meV.

To assess the extent to which the local environments of the RE ions may affect the energy scale of the magnetic excitations in the crystalline and vitreous states, we analyzed the spectra using a single-ion crystal-field model. The Hamiltonian includes the atomic free-ion and crystal-field interactions for an f^N configuration ($N=3$ and 13 for Nd^{3+} and Yb^{3+} ions, respectively), formulated under the scheme of intermediate coupling using spherical tensor techniques.³ We compared the $\text{Na}_3\text{YbSi}_3\text{O}_9$ spectrum with the model first assuming octahedral coordination corresponding to six equidis-

tant O ligands for the Yb ions. After reasonable agreement with the data was achieved, the cubic environment was relaxed to allow for lower symmetries. This approach is supported by the diffraction results which indicate an average 5.6 coordination of the Yb-O atoms and the satisfactory description of a distorted octahedral environment for Yb³⁺ in oxide glasses given previously by optical spectroscopy.^{4,5} In this cubic approximation, the Yb ground multiplet splits into two doublets, Γ_6 and Γ_7 , and a quartet Γ_8 , and transitions between Γ_6 and Γ_7 are forbidden. Therefore, we fitted the Na₃YbSi₃O₉ spectrum by assigning the 45-meV band to excitation from the ground state to Γ_8 and obtained the ratio between the fourth- and sixth-order crystal-field parameters. Next, a B_0^2 term was added to fit the 0-, 13.8-, 41.9-, and 57.7-meV peaks as Γ_7 , Γ_6 , Γ_7 , and Γ_6 , respectively. The final parameters are $B_0^2=54$, $B_4^4=-57.8$, $B_6^6=86.5$ meV, $B_4^4 = -\sqrt{5/14}B_0^4$, and $B_6^6 = \sqrt{7/2}B_0^6$. The calculated energies and intensities for the three transitions agree well the observed spectrum of Na₃YbSi₃O₉.

Next we examine whether small changes in the crystal-field parameters calculated for the crystal, such as relaxing the constraints of cubic symmetry for the parameters B_4^4 and B_6^6 , can produce a magnetic spectrum similar to what are obtained for the glass. We find that varying B_4^4 between -5 to 200 meV produced shifts of the calculated magnetic spectrum to lower and higher energies, respectively, to simulate the filling of observed intensities in the 10-30 and 80-120 meV regions. Furthermore, the calculated paramagnetic susceptibility obtained using crystal-field parameters discussed above agree well with the measured susceptibility of 3Na₂O·Yb₂O₃·6SiO₂ glass.⁶ Therefore, the observed scattering is probably best explained as a superposition of the ligand-field strengths given by small variations in the crystal-field parameters away from the nominal values obtained for the crystal.

A similar approach can be taken to interpret the observed magnetic excitation spectrum for the 3Na₂O·Nd₂O₃·6SiO₂ glass as shown in Fig. 2(c). The five-peak structure between 0 and 80 meV resembles the splitting of the Nd³⁺ $^4I_{9/2}$ ground multiplet into five Kramers doublets. Under a sixfold octahedral environment of cubic symmetry, the $^4I_{9/2}$ multiplet is split into two Γ_8 quartets and one Γ_6 doublets. Therefore, if the two peaks at 0 and 15 meV and at 53 and 68 meV are assigned as splittings of the Γ_8 quartets into doublets, the observed magnetic spectrum of the 3Na₂O·Nd₂O₃·6SiO₂ glass is consistent with a nominal sixfold coordinated Nd-O environment with a distorted octahedral symmetry.

RE environments in alkali silicate glasses have been investigated using numerous techniques. Robinson and Fournier^{4,7} analyzed the optical data of Nd- and Yb-bearing alkali barium silicate glasses using a crystal-field scheme and found evidence of sixfold coordination of the RE ions. An

extended x-ray absorption fine structure measurement of an Er-bearing sodium silicate glass by Marcus and Polman showed that the Er ions have about six O first neighbors at a mean distance of 2.26 Å,⁸ and Ponader and Brown⁹ and Barber and Obermyer⁵ obtained similar results for Yb³⁺. The present neutron diffraction and magnetic-scattering studies show that Yb and Lu ions in 3Na₂O·R₂O₃·6SiO₂ glasses have average coordination numbers about 6.0 and mean R-O bond lengths of 2.23 Å, which are consistent with the above findings.

Larson and co-workers¹⁰ and Ponader and Brown⁹ studied the coordination environments of La³⁺ in alkali silicate glasses using x-ray absorption spectroscopy and report coordination numbers of seven or less and a mean La-O bond length of 2.42±0.03 Å. Mockovciak and co-workers¹¹ and Mann and DeShazer¹² studied the optical absorption and fluorescence spectra of different Nd doped silicate glasses and concluded an average sevenfold coordination of Nd-O atoms similar to the crystalline environment in Nd₂O₃. In the case of the 3Na₂O·Nd₂O₃·6SiO₂ glass, although our crystal-field analysis supports a nominal distorted octahedral coordination, a larger than six coordination number cannot be ruled out because such local environments also split the Nd³⁺ ground multiplet into five doublet states. Since the RE ionic radii decrease with increasing atomic number, Nd³⁺ and La³⁺ are expected to have coordination numbers at least as large as Yb³⁺, a result consistent with the magnetic scattering data.

We thank S. Skanthakumar and J. W. Richardson, Jr. for their assistance in the GPPD diffraction experiment. Work performed at Argonne National Laboratories is supported by the U.S. DOE, Basic Energy Sciences under Contract No. W-31-109-ENG-38.

¹D. M. Krol and B. M. J. Smets, *Phys. Chem. Glasses* **25**, 113 (1984); A. I. G. Ellison and P. C. Hess, *J. Geophys. Res.* **B 95**, 15 717 (1990); A. J. G. Ellison and P. C. Hess, *J. Non-Cryst. Solids* **127**, 247 (1991).

²E. H. Henninger, R. C. Buschert, and L. Heaton, *J. Phys. Chem. Solids* **28**, 423 (1967); and E. Lorch, *J. Phys. C* **2**, 229 (1969).

³H. M. Crosswhite and H. Crosswhite, *J. Opt. Soc. Am. B* **1**, 246 (1984).

⁴C. C. Robinson and J. T. Fournier, *Chem. Phys. Lett.* **3**, 517 (1969), and C. C. Robinson, *J. Chem. Phys.* **54**, 3572 (1971).

⁵S. W. Barber and R. T. Obermyer, *Trivalent Ytterbium as a Microprobe in Oxide Glasses* (Owens-Illinois, Toledo, OH).

⁶A. J. G. Ellison, C.-K. Loong, and J. Wagner, *J. Alloys and Compounds* (to be published).

⁷C. C. Robinson and J. T. Fournier, *J. Phys. Chem. Solids* **31**, 895 (1970).

⁸M. A. Marcus and A. Polman, *J. Non-Cryst. Solids* **136**, 260 (1991).

⁹C. W. Ponader and G. E. Brown, Jr., *Geochim. Cosmochim. Acta* **53**, 2893 (1989).

¹⁰E. M. Larson, A. J. G. Ellison, F. W. Lytle, A. Navrotsky, R. B. Gregor, and J. Wong, *J. Non-Cryst. Solids* **130**, 260 (1991).

¹¹S. Mockovciak, J. Pantoficek, and K. Pátek, *Phys. Status Solidi* **11**, 401 (1965).

¹²M. M. Mann and L. G. DeShazer, *J. Appl. Phys.* **41**, 2951 (1970).

Magnetization and ferromagnetic resonance studies on amorphous films of $\text{Fe}_2\text{O}_3\text{-Bi}_2\text{O}_3\text{-Li}_2\text{O}$

J. Chien, S. Cheney, and G. Srinivasan
Physics Department, Oakland University, Rochester, Michigan 48309

This report is on magnetic properties of samples of $0.5 \text{Fe}_2\text{O}_3\text{-(}0.5-x\text{)Bi}_2\text{O}_3\text{-}x\text{Li}_2\text{O}$ ($x=0.1\text{--}0.4$) prepared in oxygen atmospheres by rf sputtering techniques. The films develop a spontaneous moment M only when annealed in air at temperatures $T_a \geq 675$ K. The room-temperature M vs T_a data show a maximum in M for $T_a = 775\text{--}875$ K even though x-ray diffraction data do not show the precipitation of any crystalline ferromagnetic or ferrimagnetic phases. The spontaneous moment could be attributed to the presence of ordered clusters in the amorphous film. The magnetization is found to be dependent on the concentration of nonmagnetic Li_2O : M increases with increase in x . An in-plane anisotropy in the films is evident from ferromagnetic resonance studies (FMR) at x-band frequencies. The anisotropy field increases with increasing x . The room-temperature in-plane FMR linewidth decreases with increasing x .

Nakamura and others investigated the structural and magnetic properties of ternary oxides in the system $\text{Fe}_2\text{O}_3\text{-Bi}_2\text{O}_3\text{-Li}_2\text{O}$.^{1,2} The samples prepared by rapid quenching turned out to be x-ray amorphous and high-resolution electron microscopy studies revealed the formation of dense microcrystalline domains.² Magnetic characterization of the ribbons indicated a spontaneous moment. An irreversible thermomagnetization process, indicative of magnetic frustration, was observed below 200 K. Mössbauer studies provided evidence for two types of magnetic phases in the samples; a short-range antiferromagnetic phase and a ferrimagnetic phase associated with the microcrystalline phase.¹ Studies on rapidly quenched $\text{Fe}_2\text{O}_3\text{-Bi}_2\text{O}_3$ containing ZnO , CuO , or CaO showed a similar ferrimagnetic character.²⁻⁵

Here, we report on the magnetic characterization of films of $\text{Fe}_2\text{O}_3\text{-Bi}_2\text{O}_3\text{-Li}_2\text{O}$ prepared in an oxygen atmosphere by rf sputtering techniques. Data on magnetization and ferromagnetic resonance (FMR) parameters such as the effective magnetization, linewidth, and gyromagnetic ratio have been obtained as functions of Li_2O concentration and annealing temperature. A long-range magnetic order in the films is evident from such studies.

Films of $0.5 \text{Fe}_2\text{O}_3\text{-(}0.5-x\text{)Bi}_2\text{O}_3\text{-}x\text{Li}_2\text{O}$ ($x=0.1\text{--}0.4$) were prepared. A 2-in.-diam polycrystalline sintered target prepared by standard ceramic techniques was mounted in a magnetron gun. The system was evacuated to a pressure of 0.01 mTorr. The sputtering was carried out in pure oxygen atmospheres at 1 mTorr and an rf power of 200 W at 13.6 MHz. Films were deposited on Corning 7059 glass substrates mounted on a rotating unheated platform placed below the target. Samples with a thickness on the order of 1 μm are obtained for a sputtering duration of 120 min.

Techniques used for structural characterization of the films were x-ray diffraction and scanning electron microscopy. As-sputtered samples were found to be x-ray amorphous. Energy dispersive x-ray spectroscopy studies were done for chemical analysis of the samples. For magnetic characterization, a Faraday susceptibility balance and an x-band FMR spectrometer were used.

As-deposited samples of Fe-Bi-Li oxides with $x=0.1\text{--}0.4$ show a paramagnetic susceptibility χ of about 2×10^{-5}

emu/g at room temperature. We did not observe any systematic variation in χ with the concentration x of Li_2O . The films were then annealed for 60 min in air at temperatures T_a ranging from 500 to 1075 K, in steps of 50 K. Figure 1 shows the variation of the room-temperature magnetization M with T_a . Data for films with $x=0.1$ to 0.4 are given in the figure. For $T_a < 625$ K, M remains small and constant. A substantial increase in M is seen for $T_a \geq 675$ K. The data show a broad maximum in M extending from 725 to 1025 K for all x values. A constant M for high T_a values implies that any crystalline phases precipitated at high temperatures during the annealing process does not involve Fe from the amorphous structure. The magnetization could not be obtained for higher T_a values since the glass substrates melted and reacted with the films. Since the Fe_2O_3 content in the films is independent of x , the data in Fig. 1 indicate a dependence of M on the concentration of nonmagnetic Li_2O . One observes a general increase in M with x . The highest magnetization, about 27 emu/g, is achieved for $x=0.4$.

Effects of annealing on the crystal structure of the films were investigated with x-ray diffraction (XRD). Such data

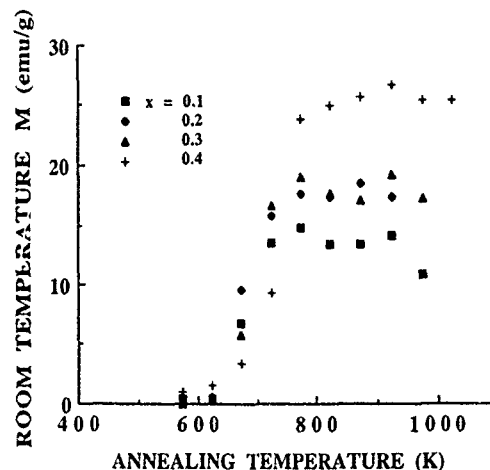


FIG. 1. Magnetization M at room temperature as a function of annealing temperature T_a for samples of $0.5 \text{Fe}_2\text{O}_3\text{-(}0.5-x\text{)Bi}_2\text{O}_3\text{-}x\text{Li}_2\text{O}$. The films prepared by rf sputtering in pure oxygen were annealed at T_a for 60 min. M was measured with a static field $H = 5$ kOe applied parallel to the film plane.

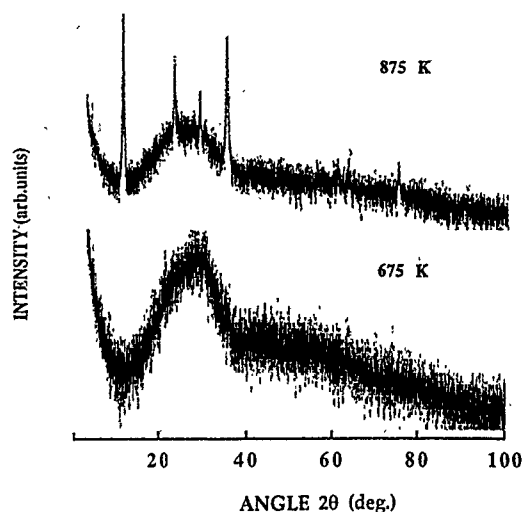


FIG. 2. X-ray diffraction pattern for films of $0.5 \text{ Fe}_2\text{O}_3\text{-}0.3 \text{ Bi}_2\text{O}_3\text{-}0.2 \text{ Li}_2\text{O}$ annealed at 675 and 875 K. Peaks in intensity for the film annealed at 875 K are due to crystalline nonmagnetic Bi_2SiO_5 .

for a film with $x=0.2$ annealed at 675 and 875 K are shown in Fig. 2. A broad peak centered at $2\theta=30^\circ$ appears due to the glass substrate. The film annealed at 675 K which shows a room-temperature M of 15 emu/g (refer to Fig. 1) is amorphous. The XRD pattern for the film annealed at 875 K shows peaks corresponding to crystalline nonmagnetic Bi_2SiO_5 . Such an impurity phase is formed most likely due to reaction with Si in the glass substrate. The most important result from XRD studies is that the sample is free of any crystalline ferrimagnetic compounds such as $\gamma\text{-Fe}_2\text{O}_3$, Fe_3O_4 , $\text{Li}_{0.5}\text{Fe}_{2.5}\text{O}_4$, or $\text{Bi}_3\text{Fe}_5\text{O}_{12}$. The observed M of 15 emu/g corresponds to a substantial volume fraction of any of the above phases, well above the limit of at least 5%–10% required for detection by XRD. Since the data in Fig. 2 do not show any peaks at positions corresponding to crystalline phases, the presence of microcrystals of any of the ferrimagnetic oxides can be ruled out.

The spontaneous moment is possibly due to ordered clusters in the film. A similar appearance of a spontaneous magnetic moment due to annealing at high temperatures has been reported in $\text{Fe}_2\text{O}_3\text{-Bi}_2\text{O}_3$ containing ABO_3 -type compounds ($\text{AB}=\text{BaTi}$, PbTi , PbZr), CuO , ZnO , or CaO .^{6–12} The moment has been suggested to arise from the formation of ferrimagnetically ordered clusters during the annealing process.

Figure 3 shows data on the temperature dependence of magnetization for a series of x values. These results are for films annealed at 600–650 °C. Data could not be obtained for temperatures above 700 K due to limitations on our system. The data show an increase in M value with x for all temperatures. The Curie temperature T_c determined from linear extrapolation of high-temperature magnetization ranges from 700 to 750 K. The T_c values do not agree with T_c for any of the crystalline ferrimagnetic phases mentioned earlier.¹³ The magnetic anisotropy field H_u for the films were determined from data on the effective magnetization $4\pi M_{\text{eff}}=4\pi M-H_u$ obtained from FMR studies at 9.2 GHz.

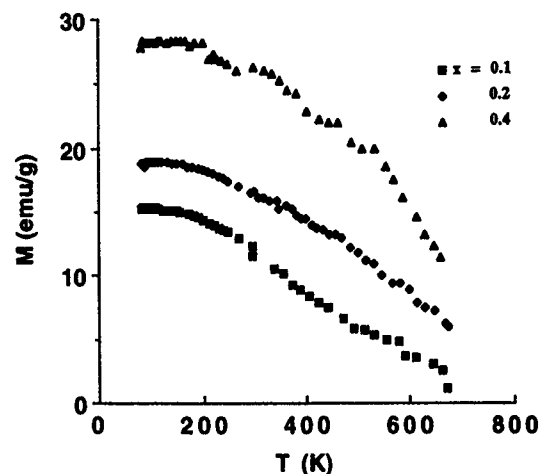


FIG. 3. Magnetization as a function of temperature for an annealed sample of $0.5 \text{ Fe}_2\text{O}_3\text{-(}0.5\text{-}x\text{)Bi}_2\text{O}_3\text{-}x \text{ Li}_2\text{O}$. The films were cooled to 77 K in zero field and M was measured at 5 kOe as T was increased.

Figure 4 shows H_u vs T data for annealed films. The anisotropy fields are negative, indicating a planar anisotropy character for the films. The magnitude of H_u increases with the concentration of nonmagnetic Li_2O in the films. As T increases, the magnitude of H_u decreases for all x values.

We also studied the composition and temperature dependence of the gyromagnetic ratio γ and the linewidth ΔH . The linewidth is found to decrease with increasing x . Figure 5 shows data on γ and ΔH vs T measured at 9.2 GHz for an annealed film with $x=0.3$. Data on ΔH are for static magnetic fields parallel and perpendicular to the film plane. Both γ and ΔH decrease with increasing T .

As mentioned earlier, Fe-Bi-Li oxides prepared by rapid quenching also show evidence for magnetic order. The largest room-temperature M of 4.5 emu/g was obtained for the sample with $x=0.25$.^{1,2} A Curie temperature of 800 K was measured for the samples. High-resolution transmission microscopy studies provided evidence for the presence of microcrystals with an average size of about 10 nm.² Films prepared by rf sputtering in the present study show a much

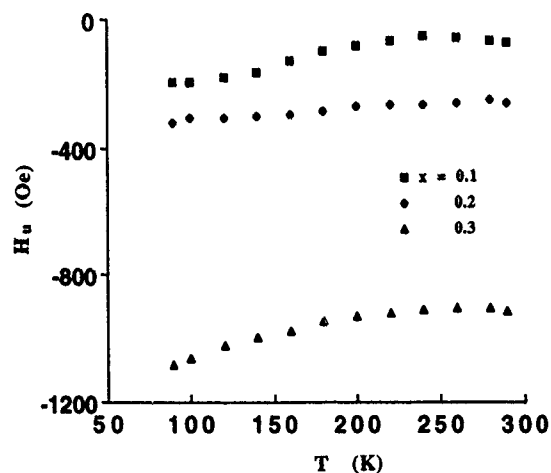


FIG. 4. The in-plane anisotropy field H_u vs temperature data for annealed films of $0.5 \text{ Fe}_2\text{O}_3\text{-(}0.5\text{-}x\text{)Bi}_2\text{O}_3\text{-}x \text{ Li}_2\text{O}$.

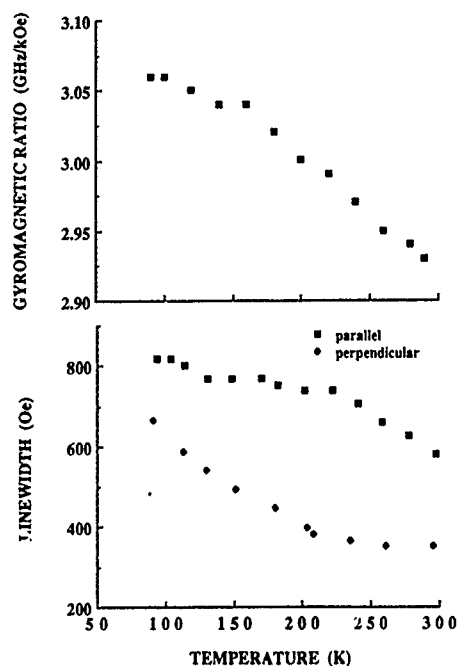


FIG. 5. Temperature dependence of the gyromagnetic ratio γ and FMR line width ΔH (for parallel and perpendicular orientation of H) for an annealed sample of $0.5 \text{ Fe}_2\text{O}_3\text{-}0.2 \text{ Bi}_2\text{O}_3\text{-}0.3 \text{ Li}_2\text{O}$.

higher magnetization, about a factor of 6 larger than for rapidly quenched samples, and a slightly smaller T_c value. The magnetization for the sputtered sample is comparable to room-temperature M for several crystalline spinel ferrites

and is larger than M values for yttrium and rare-earth iron garnets. Further studies such as Mössbauer spectroscopy and neutron diffraction on sputtered samples are important for an understanding of the origin of magnetism in the oxides.

Acknowledgment is made to the Donors of The Petroleum Research Fund, administered by the American Chemical Society, for the support of this research.

- ¹S. Nakamura and N. Ichinose, Jpn. J. Appl. Phys. **28**, 984 (1989).
- ²S. Nakamura, Y. Hiratsu, and N. Ichinose, Jpn. J. Appl. Phys. **30**, L844 (1991).
- ³N. Ota, M. Okubo, S. Masuda, and K. Suzuki, J. Magn. Magn. Mater. **54-57**, 293 (1986).
- ⁴K. Suzuki, H. Onodera, M. Sakurai, S. Masuda, A. Matsumoto, and H. Sadamura, IEEE Trans. Magn. **MAG-22**, 1090 (1986).
- ⁵S. Soeya, S. Nakamura, and N. Ichinose, J. Appl. Phys. **68**, 2875 (1990).
- ⁶T. Fujii, S. Jinzenji, Y. Asahara, A. Kajima, and T. Shinjo, J. Appl. Phys. **64**, 5434 (1988).
- ⁷A. Kajima, T. Kaneda, H. Ito, T. Fujii, I. Okamoto, T. Kimura, and K. Ohdan, J. Appl. Phys. **69**, 3663 (1991).
- ⁸B. Uma Maheshwar Rao and G. Srinivasan, Appl. Phys. Lett. **58**, 2441 (1991).
- ⁹B. Uma Maheshwar Rao and G. Srinivasan, Phys. Rev. B **44**, 395 (1991).
- ¹⁰B. Uma Maheshwar Rao, G. Srinivasan, V. Suresh Babu, and M. S. Seehra, J. Appl. Phys. **69**, 5463 (1991).
- ¹¹B. Uma Maheshwar Rao and G. Srinivasan, J. Magn. Magn. Mater. **111**, 249 (1992).
- ¹²B. Uma Maheshwar Rao and G. Srinivasan, IEEE Trans. Magn. **MAG-28**, 2443 (1992).
- ¹³W. H. von Aulock, *Handbook of Microwave Ferrite Materials* (Academic, New York, 1965).

Hysteresis and magnetic aftereffect in amorphous CoZrDy films: Trends and variations versus Dy content

G. Suran and K. Roky

Laboratoire de Magnétisme et Matériaux Magnétiques, CNRS, 92195 Meudon Cedex, France

The magnetization process was studied in amorphous $(\text{Co}_{95}\text{Zr}_5)_{100-x}\text{Dy}_x$ thin films, where $4 \leq x \leq 26$, between 6 and 300 K. The films exhibit a well-defined in-plane uniaxial anisotropy K_u . The temperature dependence of the coercive field H_c could be related to the variations of the local anisotropy K_{loc} , K_u and local defects. The thermally activated magnetic relaxation was detected for $T \leq 40$ K, and it follows with time the law $\ln(M/M_s) = at$. The constant a changes rapidly with the applied field H . The results are explained by the sharp distribution of the energy barriers. The as deduced activation volume is about the order of the ferromagnetically correlated volume.

The study of the magnetic aftereffect in magnetically disordered media is actually an active field, because theoretical computations,¹ predict that a magnetic quantum tunneling (MQT) could be observed if these systems possess some specific magnetic parameters. Very recently several experimental studies were reported,²⁻⁴ performed on various magnetically disordered compounds, where the magnetization process occurred by rotation of magnetization or tunneling of domain walls. Several of these systems exhibited a more or less well identified MQT, in the temperature range $1 \text{ K} < T < 5 \text{ K}$.

The aim of the present paper is to report a first systematic investigation of the magnetization process and of the magnetic aftereffect on a somewhat magnetically new system: $(\text{Co}_{95}\text{Zr}_5)_{100-x}\text{Dy}_x$ amorphous thin films. The as-prepared layers exhibit a very well-defined in-plane uniaxial anisotropy K_u , which should assign a particularly simple mechanism for the magnetization process: It ought to occur essentially by pure wall displacement. The films possess also a random local anisotropy K_{loc} related to the single-ion anisotropy mechanism. Consequently, the magnetization process is believed to be determined by the respective magnitude of these two terms, assumption verified by the investigations performed on films with various Dy concentrations.

The amorphous $(\text{Co}_{95}\text{Zr}_5)_{100-x}\text{Dy}_x$ thin films of thickness $0.3 \pm 0.05 \mu\text{m}$ were prepared by rf cosputtering. The concentration range investigated is $4 \leq x \leq 26$. The in-plane uniaxial anisotropy was formed by applying a dc magnetic field of 700 Oe along the film plane during deposition. The substrate temperature was held at 20°C . The Ar sputtering pressure P_{Ar} was 2 mTorr. Other details on the sample preparation are reported in Refs. 5 and 6.

The magnetization measurements were performed by a vibrating sample magnetometer (VSM). Some limitations of the present investigations were imposed by the characteristics of our VSM. The lowest temperature at which measurements could be made is about 6–7 K. Another problem was the overall sensitivity and long-term stability. Consequently, no sufficiently precise measurements could be performed when the magnetization change with time is really small. So the aftereffect could not be studied in the Rayleigh region and at very low temperatures, conditions for which the probability to detect a MQT is the highest. K_u and its temperature

dependence was measured by an automatic torque magnetometer.

The magnetization process was studied by applying the external magnetic field in the film plane along the easy axis. At room temperature and for x up to $x=22$ a rectangular hysteresis loop is detected.⁶ On films with compositions close to room-temperature compensation ($x \approx 20$) the rectangularity was verified at temperatures somewhat lower than 300 K.

The measurements revealed a strong temperature dependence of the coercive field H_c accompanied by an evolution of the loop's shape. The trends are the same whatever the composition of the deposits: H_c increases slowly as a function of decreasing temperature down to 50–40 K and exponentially for $T < 40$ K (Fig. 1). These outcomes can be discussed by considering the expression for H_c valid for pure wall displacement⁷

$$H_c = \frac{1}{4\pi} \frac{K_{\text{loc}}^2}{K_u M_s} \frac{a^3}{d^3}, \quad (1)$$

where a is the structural correlation length ($\approx 10 \text{ \AA}$) and d is the wall width $d = 5 \sqrt{A/K_u}$.

Equation (1) shows that the as observed variations are essentially related to that of K_{loc} and to the domain wall

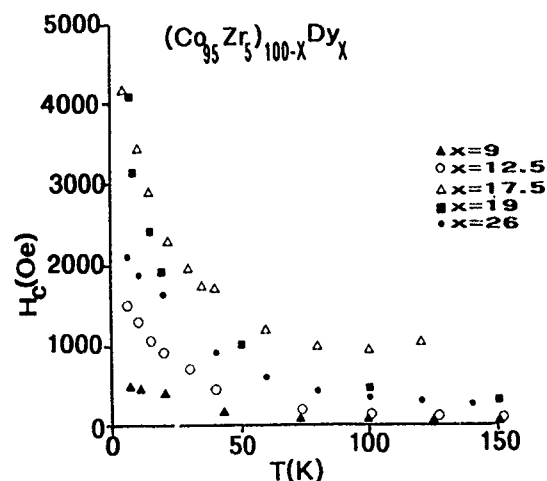


FIG. 1. Variation with temperature of the coercive field H_c for $(\text{Co}_{95}\text{Zr}_5)_{100-x}\text{Dy}_x$ films with various Dy concentration.

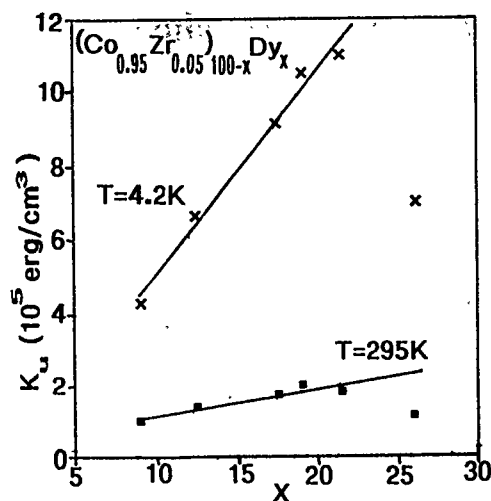


FIG. 2. The in-plane uniaxial anisotropy K_u as a function of Dy concentration as determined at $T=295$ K and 4 K.

width via K_u . The concentration and temperature dependence of K_u , measured, respectively, at 295 and 4 K are reported on Fig. 2. At both temperatures K_u varies linearly as a function of x and its value at 4 K is roughly an order of magnitude higher than that obtained at room temperature. A detailed numerical analysis,⁵ shows that its origin is related to a single-ion anisotropy mechanism.

We propose the following model for the variations of H_c : K_u results from a more or less close alignment of the local easy axis, corresponding to sites containing Dy^{3+} ions, along the field applied during deposition. At room temperature K_u is relatively small, and the width of the domain wall is broad, so even for small applied field the sample is in an aligned state. Now the value of H_c is characteristic of soft or quasisoft ferromagnets.¹

With decreasing temperature both K_{loc} and K_u increases largely, the variations of K_u being particularly marked down to 40 K. K_{loc} affect the absolute value of H_c [see Eq. (1)] and the local magnetic structure, a ferromagnet with a wandering axis forms progressively, characterized by a fluctuation of the direction of local magnetization. This process is governed by H_r^4/H_{ex}^3 , where H_r and H_{ex} are the local anisotropy and the exchange field, respectively. Here, H_r increases strongly, while the variations of H_{ex} is of the second order with decreasing T , which explains the as formed magnetic structure. The large increases of K_u affect essentially the width of the wall which becomes fairly narrow at low T . The magnitude and the local directional fluctuation of the anisotropy is much stronger at low than at room temperature and the domain walls are much narrower so more easily pinned. This wandering structure modifies probably the magnetization process (MP), which does not occur anymore by pure wall displacement but also partly by rotation of magnetization, because the local direction of M_s fluctuates even within the domains.

The evolution of the shape of the loops with temperature is also in favor of this mechanism. The high rectangularity is conserved down to 40–50 K. For lower T the loops are slightly distorted. The remanent magnetization M_R remains

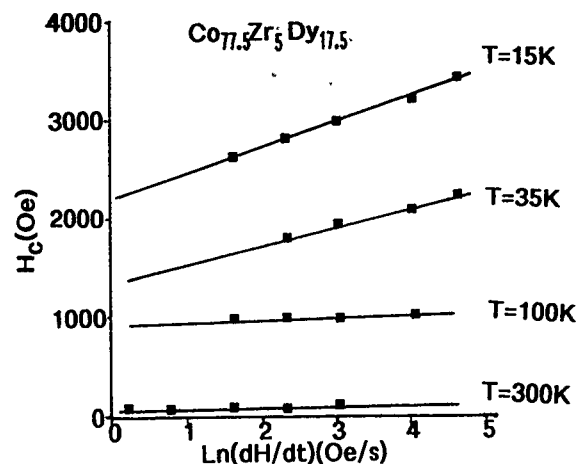


FIG. 3. Relaxation of the magnetization of the film with $x=22$. In the inset normalized variation $\ln[M(t)+M_s]/2M_s$ as a function of time.

equal to M_s within experimental uncertainties, but the loops are rounded up near $H=H_c$. It is well known that for $H \approx H_c$ the shape of the loop is very sensitive to the local magnetic structure so indicates a broader distribution of the energy barriers. Now the influence of preparation related local defects, the effect of which could be much more marked at low T , cannot be discarded.

H_c and the shape of the loops are practically independent from the field variation rate down to 100 K. The magnetic aftereffect could be observed whatever the composition of the layers for temperatures lower than 50–40 K. The time dependence of the magnetization process was measured as follows: The films were saturated along the in-plane easy axis in a positive field. Then H was reversed, decreased and stopped at a negative value $|H| < |H_c|$ and $M_s(t)$ recorded at this constant field.

Here, dM/dt at a given T varies as a function of the applied field, behavior in favor of a thermally activated magnetization reversal. Its rate is determined by $\epsilon = |H - H_c|/H_c$ and increases for smaller ϵ . The variation of $M(t)$ with time (Fig. 3) is determined by the distribution δE_a of the energy barrier E_a . It should follow an exponential $M(t)/M_s = \exp(-t/\tau)$ or logarithmic $M(t)/M_s = \ln(t/\tau)$ law, where $\tau = \tau_0 \exp(E_a/k_B T)$, following that the distribution δE_a is sharp ($\delta E_a \ll k_B T$) or broad ($\delta E_a \gg k_B T$).

In most of the magnetic systems investigated previously²⁻⁴ $M(t)/M_s$ follows a logarithmic law. Our experimental data differ markedly from the previously reported ones. We found effectively that presently an exponential law i.e., $\ln[M(t)/M_s] = at$ ($a = \text{constant}$) is generally well obeyed whatever the composition, and for the applied field range (with $\epsilon < 25\%$) used. This result shows that the apparent distribution of E_a is fairly sharp. It is believed to be related to the intrinsic magnetic properties of the films and the experimental conditions used. As a result of the quasisalignment of the local easy axis along the direction of K_u the distribution of the anisotropy energy barriers are obviously much smaller than in previously studied systems. The amplitude of the as used applied field could also favor the observed results. A model of hysteresis based upon wall dis-

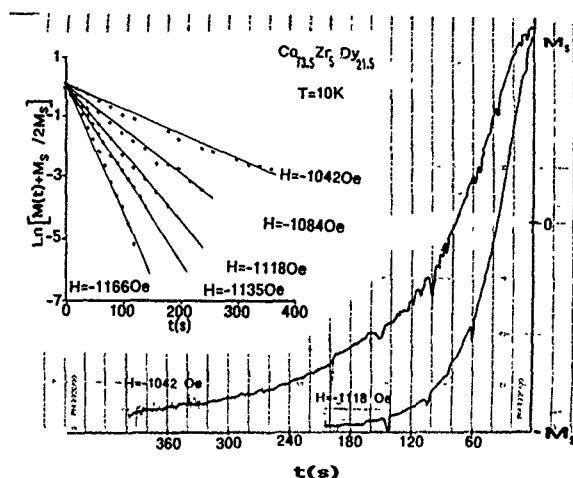


FIG. 4. Typical viscosity rate at $T=20$ K and for $\epsilon=19\%$ in film with various Dy concentration.

placement process states that getting over an obstacle requires the application of a field H at least equal to a critical one H_{crit} characterizing the obstacle. Obviously when H so $H-H_{crit}$ is large, the domain wall displacement process will be, only scarcely perturbed. Consequently, if the anisotropy barriers are distributed around a mean value K_u , the contribution of obstacles with $H_{crit} \ll H$ should be small or negligible.

We established the correlation between the magnetic viscosity and the Dy concentration in the films, by comparing dM/dt measured on the various samples at different T and for the same value of ϵ . When T is sufficiently high (see Fig. 4) the viscosity increases continuously with increasing Dy content. This result confirms that the relaxation rate is governed by K_{loc} . However, for lower temperatures ($T \leq 10$ K) this experimental rule is no more followed so regularly. These last results are related probably to the much smaller variations of K_{loc} from sample-to-sample as shown by the temperature and concentration dependence of activation volume V .

One can determine V when the distribution of the activation energy is sharp. Now at a given T a single relaxation time τ should exist and E_a is related to V by

$$E_a = VM_s(I_c - H). \quad (2)$$

It can shown easily that $\ln \tau$ should vary linearly as a function of the applied field, in agreement with the experi-

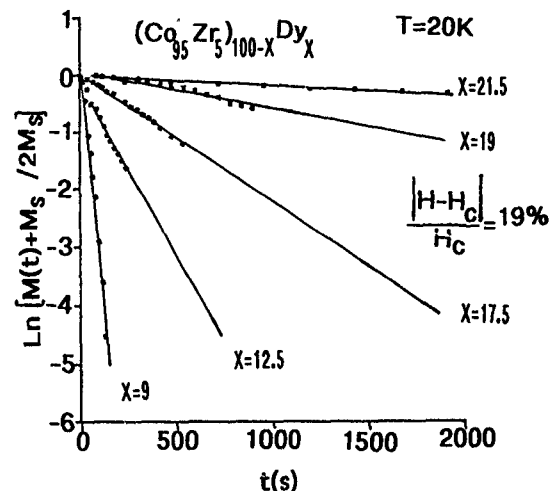


FIG. 5. Thermal variation of the average activation volume in films with various Dy concentration.

mental data, and $VM_s/k_B T$ correspond to the slope of this line. The values of V varies (Fig. 5) from $5 \times 10^3 \text{ \AA}^3$ to $9 \times 10^4 \text{ \AA}^3$ at 6 K and 10^5 \AA^3 to $13 \times 10^5 \text{ \AA}^3$ at 40 K. A numerical computation, the details being reported elsewhere, shows that if one estimates K_{loc} from H_c and evaluate the ferromagnetic correlation length r_f using formula proposed by Chudnovsky⁹ we find effectively $r_f \approx V^{1/0.3}$.

In conclusion the magnetization process and magnetic aftereffect were studied in CoZrDy amorphous thin films. The magnetization relaxation mechanism $\ln[M(t)/M_s]$ follow a linear time dependence result related to the well-defined K_u . The other characteristics of the relaxation process appears to be controlled by K_{loc} , similarly to other highly anisotropic materials.²⁻⁴ Further experiments performed at sufficiently small T and/or low applied field is necessary to find out if these films exhibit a MQT.

¹E. M. Chudnovsky and L. Gunther, Phys. Rev. Lett. **60**, 661 (1988).

²B. Barbara *et al.*, J. Appl. Phys. **73**, 6703 (1993).

³J. I. Arnaudas, A. del Moral, C. de la Fuente, and P. A. J. Groot, Phys. Rev. B **47**, 11 924 (1993).

⁴J. Tejada, X. X. Thang, and L. I. Balcells, J. Appl. Phys. **73**, 6709 (1993).

⁵G. Suran, J. Sztern, and B. Barbara, Appl. Phys. Lett. **58**, 1338 (1991).

⁶G. Suran, K. Roky, J. Sztern, and M. Porte, J. Appl. Phys. **73**, 5724 (1993).

⁷R. Alben, J. J. Becker, and M. C. Chi, J. Appl. Phys. **49**, 1653 (1978).

⁸K. Roky, G. Suran, M. Porte, and J. Sztern, EMMA '93, IEEE Trans. Mag. (to be published).

⁹E. M. Chudnovsky, J. Appl. Phys. **64**, 5770 (1988).

First-principles calculation of orbital moment distribution in amorphous Fe

Xue-Fu Zhong and W. Y. Ching

Department of Physics, University of Missouri-Kansas City, Kansas City, Missouri 64110

A model calculation on a large periodic unit cell of amorphous Fe containing 200 atoms is carried out to determine the distribution of its local orbital moments. A spin-polarized orthogonalized linear combination of atomic orbitals method including spin-orbit coupling is used for the calculation of the electronic structure. It is shown that spin-orbit coupling brings about a small change in the density of states for amorphous Fe. The average orbital moment in amorphous Fe is found to be $0.01 \mu_B$, which is much smaller than the value of $0.09 \mu_B$ for crystalline fcc Fe. The distribution of orbital moments over various sites is rather broad, indicating a strong quenching effect as a result of variation in the local structure in the amorphous case. It is speculated that such ground-state properties are favorable to the formation of the spin glass phase.

It has been speculated that structural disorder in magnetic materials may or may not lead to different types of magnetic ordering. There were many past investigations on this subject yet controversies remain.¹⁻³ In general, a spin glass (SG) phase is characterized by the random distribution of the local moments (LM) of the magnetic ions, both in magnitude and in direction. From the study of Fe-rich alloys (90% or more), it is found that the SG phase is most likely caused by the structural disorder rather than chemical disorder.⁴ Theoretical investigations on this subject^{1,2,5} indicate that the local environment effect is responsible for the magnetic properties of many amorphous transition metals. For example, it is found that in amorphous Fe, Fe atoms with large LM usually couple ferromagnetically with the neighbors, while those with small LM couple antiferromagnetically.¹ It is obvious that LM on magnetic ions are strongly influenced by their local structural environments.

In the classical theory of magnetic anisotropy for a crystalline solid, it is assumed that the local moment orientation is controlled by spin-orbit interaction, because spin itself is not related to any spatial direction. This is true in the single-ion anisotropy theory, which attributes this orientation to the orbital moments of some dominating ions (usually rare-earth ions), and also in the "pair model," in which the orbital moment may eventually lead to anisotropic exchange.⁶ In fact, the local orbital moment that remains after quenching by the neighboring atoms is of crucial importance. If a small amount of orbital moment remains unquenched, a part of the d electron orbit may rotate, carrying with it the spin magnetic moment through spin-orbit coupling. The rotation of the orbit will, in turn, change the overlap of the wave functions between the neighboring atoms, thus affect the electrostatic and exchange interactions. A process of orientation of the spin moment in the real space is thus realized. Recent work by Jansen⁷ on magnetic anisotropy theory which takes the relativistic effect into account also emphasized the influence from local orbital moment. It is shown that not only the spin-orbit coupling in the same atom is important, the coupling between the orbitals moments of the neighboring atoms is equally essential in determining the local anisotropy. It is, therefore, important to study the distribution of local orbital

moments in disordered system by means of realistic first-principles calculation.

In order to separate the influence of chemical disorder that is present in a multicomponent system from the topological disorder, we choose the pure amorphous Fe (α -Fe) system represented by a periodic model containing 200 atoms for our calculation. The electronic structure and the distribution of local spin moment for this model have been reported in an earlier paper by Xu, He, and Ching.⁸ The site-specific distribution of the Fe spin moment in an amorphous environment is analyzed as a function of local short-range order, such as the number of nearest-neighbor atoms and the average nearest-neighbor distances. The present calculation is an extension of that study to explore the distribution of the orbital moments and includes the spin-orbital coupling in the electronic structure calculation.

We use the spin-polarized version of the orthogonalized linear combination of atomic orbitals (OLCAO) method⁹ to calculate the electronic structure of the 200-atom α -Fe model. The model was constructed by a Monte Carlo relaxation method using a pairwise Lennard-Jones type of interatomic potential. The calculated radial distribution function of the model is in close agreement with experiment.⁸ We thus consider the model to be a fairly realistic representation of the α -Fe structure. In order to extract the information about the orbital moment, the spin-orbit coupling term

$$H_{sl} = \xi \mathbf{l} \cdot \mathbf{s} = \xi/2 (J^2 - l^2 - s^2) \quad (1)$$

is added to the Hamiltonian so that the spin-up and spin-down energy bands are mixed.¹⁰ The eigenvalue for the operator in Eq. (1) is simply $\xi [j(j+1) - l(l+1) - 3/4]/2$. The secular equation to be solved is, therefore, twice as large as in the spin moment calculation in which the spin-up and spin-down Hamiltonians were diagonalized separately.⁸ The spin-orbit coupling constant $\xi = 0.0137$ a.u. is taken from the corresponding atomic value for Fe.¹¹ This may lead to about 10% deviation from the corresponding value of ξ in crystalline Fe.¹⁰ Since we are mainly interested in the distribution of orbital moments, not the fine structures in the energy spectrum, this approximation will not cause any significant error in our result.

The site decomposed local orbital momentum is calculated according to

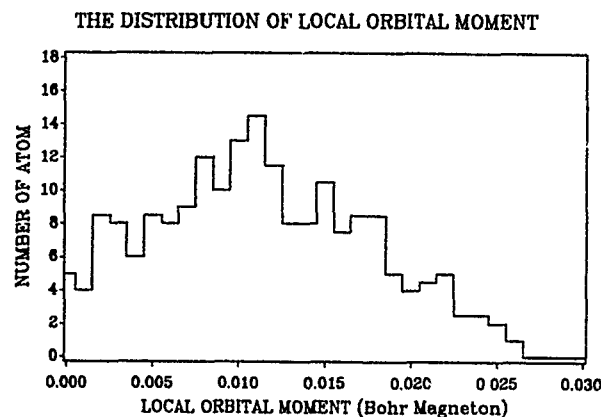


FIG. 1. The distribution of local orbital moments in the 200-atom *a*-Fe model.

$$M_1 = g \sum_{n,k}^{E_F} \langle \Psi_{n,k} | L_z | \Psi_{n,k} \rangle$$

$$= g \sum_{n,k}^{E_F} \sum_{\alpha i} \sum_{\beta j} C_{nk,\alpha i}^* C_{nk,\beta j} \int b_{\alpha i}^*(\mathbf{k}) L_z b_{\beta j}(\mathbf{k}) d\tau, \quad (2)$$

where $|\Psi_{n,k}\rangle$ are the band wave functions, $C_{nk,\alpha i}^*$, the eigenvector coefficients, $b_{\alpha i}(\mathbf{k})$, the Bloch bases, and the summation runs over all the occupied states. Because the unit cell is sufficiently large, the $\mathbf{k}=0$ solution is sufficient. Test calculations on the density of states DOS at $\mathbf{k}=0$ and at $\mathbf{k}=2\pi/a(1,1,1)$ show no discernable difference. Due to spin-orbit coupling, the eigenstates $|\Psi_{n,k}\rangle$ are characteristic of the total angular momentum j rather than the spin or the orbital momentum separately.

The integral in Eq. (2) can be evaluated rather straightforwardly,

$$\int b_{\alpha i}^*(\mathbf{k}) L_z b_{\beta j}(\mathbf{k}) d\tau$$

$$= \frac{1}{N} \sum_{m,n} \exp[i\mathbf{k} \cdot (\mathbf{R}_n - \mathbf{R}_m)] \int u_i^*(\mathbf{r} - \mathbf{R}_m - \tau_\alpha) L_z u_j$$

$$\times (\mathbf{r} - \mathbf{R}_n - \tau_\beta) d\tau$$

$$= \sum_{\mu} \exp(i\mathbf{k} \cdot \mathbf{R}_\mu) \int u_i^*(\mathbf{r} - \tau_\alpha)$$

$$\times L_z u_j(\mathbf{r} - \mathbf{R}_\mu - \tau_\beta) d\tau, \quad (3)$$

where \mathbf{R}_μ labels the lattice translational vector, α, β atoms in the model, and i, j the orbital states of the atom. Since atomic wave function u_i in the OLCAO method is classified by the angular momentum quantum number, the calculation of integrals in Eq. (3) amounts to a rearrangement of the matrix elements of the overlap integrals, which have already been calculated in forming the secular equation.

Our calculated distribution of the local orbital moments in the 200-atom *a*-Fe model is shown in Fig. 1. The outstanding feature of this distribution is the large spread of its magnitude, from near 0 to a maximum of $0.026 \mu_B$. The

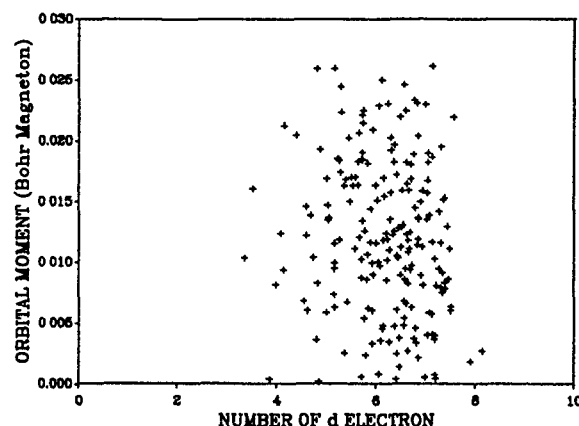


FIG. 2. Correlation plot of local orbital moment vs the number of *d* electrons on the Fe atom in the 200-atom *a*-Fe model. No obvious correlation can be established.

central position of the distribution is around $0.01 \mu_B$, which can be taken as the average local orbital moment for the system. This low value of the orbital moment in *a*-Fe indicates a strong quenching effect in the amorphous case. The local orbital moment for the crystalline fcc Fe is about $0.09 \mu_B$.¹² At first sight, it appears that a small value for the orbital moment implies almost no obvious preferential direction for the LM in *a*-Fe, since the orbital planes of the conduction electrons rotate almost equally around all directions. However, the nonvanishing values for the remaining orbital moments in ground state may be important for the formation of the SG structure. In fact, a large local orbital moment implies a preferential direction for the local moment through spin-orbit coupling (in the same atom), resulting in either ferromagnetic or antiferromagnetic ordering. In a SG phase, local moments are easy to reorient under the influence of a small field. Only a weak driving force for the orientation of local moment is favorable for the formation of this structure. Moreover, the randomness in the orientation of the local moments in a SG structure requires a rather wide distribution of local orbital moments. The deviation of the orbital moment from the average value in our calculation is actually larger than the average value itself (both the deviation and the average are around $0.01 \mu_B$). Therefore, our result is consistent with the notion that a SG structure is possible for an amorphous transition metal system.

We hope our first-principles approach to the study of orbital moments in *a*-Fe will lead to a more refined theory such that a quantitative use of the distribution of local orbital moments is possible. Kakehashi has pointed out¹ that the main-peak position in the noninteracting densities of states (without the interaction between local moments in the calculation of electronic structure) is important in determining the ferromagnetic properties of amorphous alloys. This is because the nature of magnetic coupling (exchange interaction) depends on the charge density, or the *d*-electron number. However, this by itself is not sufficient to explain some salient features of amorphous magnetism in transition metal systems. For example, there is no obvious correlation be-

tween the local orbital moment and the number of d electron on each Fe atom. This is illustrated in Fig. 2 in which we plot the orbital moment on each Fe atom versus the effective d -electron number as determined by the Mullikan population analysis of the wave function. This is because the orbital moment is more sensitive to the geometry of the local environment than the charge density. The orientation of local moments in a SG structure is a different problem from the simple magnetic coupling. The randomness in the local moments is intimately related to the local orbital moment which also determines the spatial orientation. Its average value determines the strength of the driving force in the orientation of the local moments, while the deviation from the mean is related to the randomness of the orientation. Both are necessary in the study of the magnetic properties of amorphous transition metal systems.

In summary, our calculation of the distribution of orbital moments in the amorphous Fe system provides a direct evidence for a strong quenching effect in such a disorder system. It may shed some light on the microscopic origin of the formation for the SG structure.

This work was supported by the U. S. Department of Energy under the Grant No. DE-FG002-84ER-45170.

- ¹Y. Kakehashi, Phys. Rev. B **43**, 10 820 (1991).
- ²Y. Kakehashi, Phys. Rev. B **47**, 3185 (1993).
- ³E. P. Elsukov, G. N. Konygin, V. A. Barinov, and E. V. Voronina, J. Phys.: Condens. Matter, **4**, 7597 (1992).
- ⁴K. Fukamichi, T. Goto, H. Komatsu, and H. Wakabayashi, in *Proceedings of Fourth International Conference on the Physics of Magnetic Materials*, edited by W. Gorkowski, K. Lachowicz, and H. Seymczak (World Scientific, Singapore, 1989), p. 354.
- ⁵Y. Kakehashi, Phys. Rev. B **41**, 9207 (1990).
- ⁶S. Chikazumi, *Physics of Magnetism*, English translation by S. H. Charap (Wiley, New York, 1964), pp. 147-153.
- ⁷H. J. F. Jansen, Phys. Rev. B **38**, 8022 (1988).
- ⁸Y.-N. Xu, Y. He, and W. Y. Ching, J. Appl. Phys. **69**, 5460 (1990).
- ⁹W. Y. Ching, J. Am. Ceram. Soc. **73**, 3135 (1990).
- ¹⁰X.-F. Zhong, Y.-N. Xu, and W. Y. Ching, Phys. Rev. B **41**, 10 545 (1990).
- ¹¹F. Herman and S. Skillman, *Atomic Structure Calculation* (Prentice-Hall, Englewood Cliffs, NJ, 1963).
- ¹²R. A. Reck and D. L. Fry, Phys. Rev. **184**, 492 (1969).

A magnetocalorimetric study of spin fluctuations in amorphous $\text{Fe}_x\text{Zr}_{100-x}$

A. LeR. Dawson and D. H. Ryan

Centre for the Physics of Materials Department of Physics, McGill University, 3600 University St., Montreal, Quebec, H3A 2T8, Canada

Low temperature calorimetry data on amorphous $\text{Fe}_x\text{Zr}_{100-x}$ samples near the ferromagnetic/paramagnetic phase boundary at $x=37.5$ are reported, as well as some magnetocalorimetry data in magnetic fields of up to 5 T. The data are analyzed in terms of two models, one describing the effect of spin fluctuations (SF) and the other the effect of superparamagnetic clusters. The data are shown to favor the SF model and taken with earlier resistivity work, provides convincing evidence for the existence of SF in $a\text{-Fe}_x\text{Zr}_{100-x}$.

Spin fluctuations (SF) are nonmonodispersive long wavelength magnetic excitations of characteristic energy T_{SF} , not accounted for by mean-field theories, which were predicted to apply to nearly ferromagnetic Fermi liquids and explained the specific heat capacity (C_P) of liquid ^3He .¹ Ikeda *et al.*² have given an extensive review of the quenching by high (~ 10 T) magnetic fields of the SF contribution to the low-temperature C_P . Their study surveyed several highly exchange-enhanced d - and f -band magnets for which the Stoner enhancement factor, S , is greater than 10. $\text{Ni}_{3+x}\text{Al}_{1-x}$, for example, exhibits a transition from an exchange-enhanced paramagnet to a weak ferromagnet for small values of x . SF models have been shown to be necessary to explain the values of both the Curie temperature and the ordered moment in Ni_3Al .³ A recent magnetocalorimetry study of $\text{Ni}_{3+x}\text{Al}_{1-x}$ ^{4,5} used elastic constant measurements to separate the phonon contribution to C_P and detected a small SF enhancement, which was greatest at the critical composition. Field quenching of this enhancement was found to be in agreement with predictions from T_{SF} measured in zero field. The effect of a magnetic field also ruled out the presence of superparamagnetic clusters due to possible compositional inhomogeneities in their samples, which could also have accounted for the zero-field data.

Amorphous d -band metals offer many advantages for the study of SF. The rapid quenching from the liquid state leads to a high degree of compositional homogeneity and inhibits magnetic cluster formation. Furthermore, slightly varying the sample composition should not significantly change the phonon C_P , a complication which can occur in crystalline systems. $a\text{-Fe}_x\text{Zr}_{100-x}$ is an ideal candidate system for the study of SF. It is a good glass former⁶ in the range $20 < x < 43$, where it exhibits three distinct phases, superconductivity for $x < 30$, ferromagnetism for $x > 37.5$ and paramagnetism for intermediate compositions. The susceptibility of the paramagnetic alloys suggests that they are strongly exchange-enhanced paramagnets with Stoner factors approaching 10, and the superconducting alloys exhibit a mass enhancement factor possibly arising from SF.⁷ A low-temperature resistivity study of alloys near $x=37.5$ showed a strong temperature dependence which could be analyzed using a model including scattering by SF.⁸ This analysis yielded rough estimates for T_{SF} which were as low as 20 K.

Previous C_P studies of $a\text{-Fe}_x\text{Zr}_{100-x}$ at broadly spaced compositions have been discussed in terms of a cluster model.^{9,10} In this preliminary work, we report on the low-

temperature C_P of several closely spaced $a\text{-Fe}_x\text{Zr}_{100-x}$ alloys near the ferromagnetic phase boundary at $x=37.5$. We have analyzed our data in terms of both a magnetic cluster model and a SF-model.

Appropriate amounts of Fe (99.98%) and Zr (99.9%) were induction melted on a water-cooled copper boat in a Ti-gettered argon atmosphere. The boules were twice remelted to ensure homogeneity. The alloys were then rapidly quenched by melt spinning in a He atmosphere with a tangential wheel speed of around 50 m/s, yielding meter length ribbons 1 mm wide and ~ 20 μm thick. Cu K_α x-ray diffraction using an automated Nicolet-Stoe powder diffractometer showed the samples to be amorphous. Some samples near $x=30\%$ showed small crystal peaks which did not appear on the wheel side of the ribbon and could be easily removed from the free side by a very light sanding. Sample compositions were determined by electron microprobe analysis.

Absolute C_P data were measured between 2 and 25 K using a time relaxation technique¹¹ modified by the use of an ac chopped¹² Au-0.07% Fe thermocouple and a thick film ruthenium oxide resistance thermometer.¹³ The microcalorimeter was checked for accuracy by measuring gold and copper standards¹⁴ and the overall accuracy and precision were each found to be 2%. Approximately 40 mg of ribbon were wound into a ~ 7 -mm-diam coil and silver pasted to the addenda. This mounting technique allows large sample loading with a fast internal relaxation time. The calorimeter could be placed in the bore of a 5 T superconducting solenoid with the field axis parallel to that of the sample coil to minimize demagnetization effects. The small magnetoresistance of the carbon glass thermometer was corrected for using a field-independent capacitance thermometer.

Figure 1 shows the specific heat of several of our $a\text{-Fe}_x\text{Zr}_{100-x}$ samples. Normally, for $T < \Theta_D/40$, C_P can be written as

$$C_P = \gamma T + \beta T^3, \quad (1)$$

where

$$\gamma = \frac{1}{3} \pi^2 k_B^2 (1 + \lambda_{e-p}) N_0(E_F) \equiv (1 + \lambda_{e-p}) \gamma_0$$

and

$$\beta = \frac{(1.944 \times 10^6 \text{ mJ/mol K})}{\Theta_D^3}$$

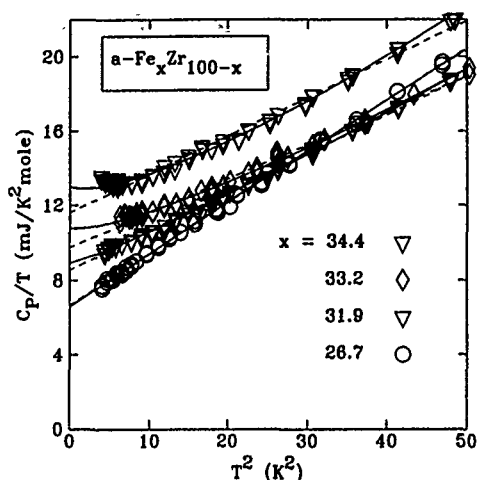


FIG. 1. C_p/T vs T^2 for $a\text{-Fe}_x\text{Zr}_{100-x}$. The dashed and solid lines are fits to Eqs. (1) and (3), respectively.

Since $\Theta_D \sim 200$ K,⁹ we expect plots of C_p/T vs T^2 to yield straight lines. This is clearly not the case, as Fig. 1 shows definite upturns for some alloys below $T^2 = 10$ K².

In the presence of SF, Eq. (1) becomes⁴

$$C_p = \gamma_0 T \left(\frac{m^*}{m} \right) + \beta T^3 + DT^3 \ln \left(\frac{T}{T_{SF}} \right). \quad (2)$$

This may be more conveniently rewritten as

$$C_p = AT + BT^3 + DT^3 \ln T, \quad (3)$$

where

$$B = \beta - D \ln T_{SF}$$

and

$$A = \gamma_0 m^*/m = \gamma_0 (1 + \lambda_{e-p} + \lambda_{spin}),$$

λ_{spin} is the the SF electron mass enhancement.

The theory also predicts that both A and D increase with the Stoner factor S . This is not surprising since a large electronic specific heat γ and the existence of magnetic order in itinerant systems are both associated with a high density of states at the Fermi level. Plotted as C_p/T vs T^2 , Eq. (2) shows a characteristic upturn at temperatures below T_{SF} . Since Eq. (2) is only valid for $T \ll T_{SF}$, in fitting to it, the range of data must be restricted to temperatures not too far above the upturn.

The parameters derived from fits of Eq. (3) to the data in Fig. 1 are shown as a function of iron content in Fig. 2. The composition dependences of the coefficients of the linear term, A , and the $T^3 \ln T$ term, D , are very similar as expected from their dependence on S . We take this similarity as support for the SF model. Assuming $\lambda_{spin} = 0$ for $a\text{-Fe}_{26.7}\text{Zr}_{73.3}$, and using $\lambda_{e-p} = 0.4$ ⁹ we can calculate γ_0 for $x = 26.7$. Assuming γ_0 and λ_{e-p} remain unchanged for $x = 34.4$, we obtain $\lambda_{spin} = 1.4$ for $a\text{-Fe}_{34.4}\text{Zr}_{65.6}$.

We have also fitted Eq. (1) to the data between 7 and 10 K, where the SF term is expected to be small. The β resulting from these fits is shown in Fig. 3. Analysis of the $a\text{-Fe}_{26.7}\text{Zr}_{73.3}$ data, which exhibits normal metallic behavior at low temperatures, shows that the specific heat drops below

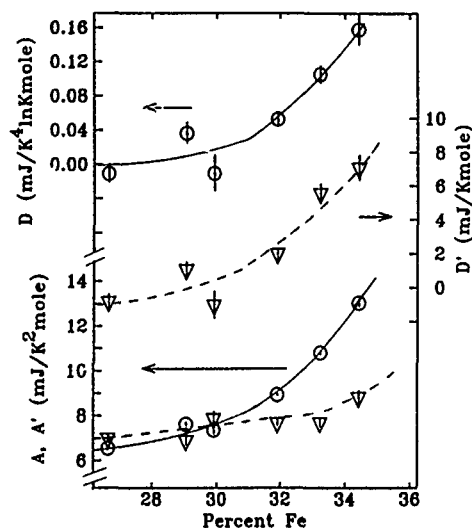


FIG. 2. Some of the parameters resulting from fits of the C_p data below 7 K: (○) A and D from Eq. (3) and (▽) A' and D' from Eq. (4). The solid and dashed lines are guides for the fits to Eqs. (3) and (4), respectively. Error bars are also calculated by the fitting program.

that predicted by a Debye function even below 7 K. Therefore, we cannot exactly determine the phonon contribution to B in Eq. (3) by extrapolation from the high-temperature fits. The departure from T^3 behavior appears as a slight downturn in a C_p/T vs T^2 plot and leads us to underestimate D , and results in slightly negative values in some cases.

Nonetheless, using the high-temperature β value and the definition of B in Eq. (3) we estimate T_{SF} for our samples which show a clear deviation from normal behavior [Eq. (1)]. These are shown in Fig. 3 together with the approximate curve obtained from the resistivity of $a\text{-Fe}_x\text{Zr}_{100-x}$.⁸ Altounian *et al.*¹⁵ have done a more detailed determination of T_{SF} through a study of the isostructural system

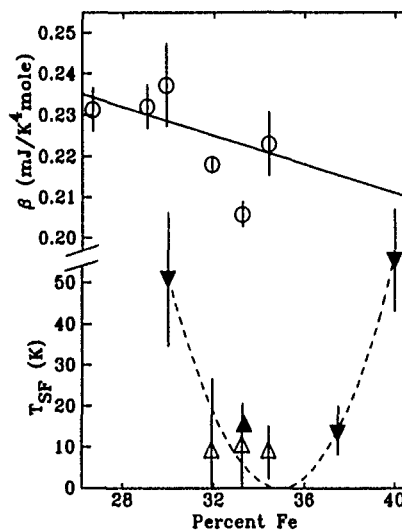


FIG. 3. (○) Phonon C_p coefficient, β , resulting from fits of the data between 7 and 10 K to Eq. (1). The straight solid line is a guide to the eye. Displayed in the lower section are approximate values of T_{SF} whose derivation is discussed in the text (△). Data taken from resistivity studies of Ref. 8 (▽ and dashed line) and Ref. 15 (▲) are also shown for comparison.

$a\text{-(Fe}_y\text{Ni}_{100-y})_{33.3}\text{Zr}_{66.7}$. Substitution of Fe by Ni allowed separation of the resistivity due to SF from that due to electron-phonon scattering since for $y < 0.4$, the latter process dominates. They find $T_{\text{SF}} = 15$ K for $y = 100$ which is also shown in Fig. 3. We take the good agreement between the T_{SF} derived from two very different measurements as further support for the SF model. The values of T_{SF} and that of λ_{spin} discussed earlier are similar to those for $\text{Ni}_{3+x}\text{Al}_{1-x}$ and so $a\text{-Fe}_x\text{Zr}_{100-x}$ can probably be classed as the same type of spin fluctuator.²

We now turn our attention to the only other plausible explanation for the data. Upturns similar to those of Fig. 1 have been seen the C_P of $\text{Cu}_{60}\text{Ni}_{40}\text{Fe}_{0.02}$ ¹⁶ and result from superparamagnetic moment clusters which form about the Fe atoms and extend for several lattice spacings. The clusters contribute an extra component to C_P as they are small enough that their energy in the local crystal field is comparable with $k_B T$. This contribution to C_P can be described as a Schottky-like function which we have approximated by a constant to yield the expression:

$$C_P = A'T + \beta'T^3 + D'. \quad (4)$$

The fits are as good as those to Eq. (3) and the results are also shown in Fig. 2. The size and composition dependence of the D' term resembles that of an earlier study¹⁰ however we do not observe a divergence in Θ_D . Identifying D' with k_B times the number of magnetic clusters per mole, we can derive a lower bound of order 10^{-3} clusters per mole. Such a small number of clusters seems unlikely in the presence of so much iron. While SF and magnetic clusters both yield an enhanced susceptibility, a more complete study of the high-field magnetization could rule out the magnetic cluster picture.

Finally, we discuss the magnetocalorimetry results. In a sample with magnetic clusters, the applied field adds to the local field felt by the clusters so that when the two are of the same order, the magnetic C_P component, D' , should increase significantly since we are on the high-temperature side of the Schottky anomaly.¹⁶ These local fields must be less than 1 T, since we know that the Schottky peak is at $T \approx 1 \text{ K} \sim \mu_B \times (1 \text{ T})$, so that we would expect a significant change in the magnetic C_P at 5 T. For SF, the effect of a magnetic field appears as a change in the linear C_P .²

$$\frac{\gamma(B=0) - \gamma(B)}{\gamma(B=0)} = 0.1 \frac{S}{\ln S} \left(\frac{\mu_B B}{k_B T_{\text{SF}}} \right)^2. \quad (5)$$

With $T_{\text{SF}} = 10$ K and $S = 10$, we would expect a decrease in γ of order 3% in a field of 5 T. The C_P of $x = 31.6$ and $x = 30.3$ samples were measured in fields of 0, 3.5, and 5 T. No change was found to within 3%. Our results, therefore, support the SF picture.

In conclusion, we have presented observations of a spin fluctuation contribution to C_P in a nearly ferromagnetic amorphous alloy. While fits to the data cannot unequivocally distinguish between a SF model and a magnetic cluster model, interpretation of the fit parameters favors the SF model, as does the preliminary field work. Taken together with earlier results on the low-temperature resistivity^{8,15} and susceptibility,⁷ this is strong evidence of spin fluctuations in this system.

This work was supported by grants from the Graduate Faculty of McGill University, the Walter C. Sumner Foundation, Nova Scotia, the Natural Sciences and Engineering Research Council of Canada and Fonds pour la formation de chercheurs et l'aide à la recherche, Québec.

¹ S. Doniach and S. Engelsberg, *Phys. Rev. Lett.* **17**, 750 (1966).

² K. Ikeda, S. K. Dhar, M. Yoshizawa, and K. A. Gscheidner, Jr., *J. Magn. Mater.* **100**, 292 (1991).

³ G. G. Lonzarich and L. Taillefer, *J. Phys. C* **18**, 1 (1985).

⁴ S. K. Dhar and K. A. Gscheidner, Jr., *Phys. Rev. B* **39**, 7453 (1989).

⁵ S. K. Dhar, K. A. Gscheidner, Jr., L. L. Miller, and D. C. Johnston, *Phys. Rev. B* **40**, 11 488 (1989).

⁶ Z. Altounian, T. Guo-hua, and J. O. Ström-Olsen, *J. Appl. Phys.* **57**, 1777 (1985).

⁷ E. Batalla, Z. Altounian, and J. O. Ström-Olsen, *Phys. Rev. B* **31**, 577 (1985).

⁸ J. Ström-Olsen, Z. Altounian, R. W. Cochrane, and A. B. Kaiser, *Phys. Rev. B* **31**, 6116 (1985).

⁹ D. G. Onn, L. Q. Wang, Y. Obi, and K. Fukamichi, *J. Non-Cryst. Solids* **61**, 1149 (1984).

¹⁰ M. Matsuura, U. Mizutani, and K. Fukamichi, in *Proceedings of the Fifth International Conference on Rapidly Quenched Metals*, edited by S. Steeb and H. Warlimont (North-Holland, Amsterdam), Vol. 1, p. 1019.

¹¹ R. Bachman, F. J. diSalvo, T. M. Geballe, R. L. Greene, R. E. Howard, C. N. King, M. C. Kisch, K. N. Lee, R. E. Schwall, H. U. Thomas, and R. B. Zubeck, *Rev. Sci. Instrum.* **43**, 205 (1972).

¹² J. R. Anderson and D. R. Zrudsky, *Rev. Sci. Instrum.* **44**, 316 (1971).

¹³ Q. Li, C. H. Watson, R. G. Goodrich, D. G. Haase, and H. Lukefahr, *Cryogenics* **26**, 467 (1986).

¹⁴ D. L. Martin, *Can. J. Phys.* **65**, 1104 (1987).

¹⁵ Z. Altounian, S. Dantu, and M. Dikeakos (unpublished).

¹⁶ R. L. Falge, Jr. and N. M. Wolcott, *J. Low Temp. Phys.* **5**, 617 (1971).

Magnetic properties of colloidal silica: Potassium silicate gel/iron nanocomposites

R. D. Shull, H. M. Kerch, and J. J. Ritter

Materials Science and Engineering Laboratory, National Institute of Standards and Technology,
Gaithersburg, Maryland 20899

Homogeneous composites of Fe and silica containing 5–40 wt % Fe have been prepared by infiltration of ferric nitrate solution into a colloidal silica: potassium silicate gel at room temperature. Previous electron microscopy, small angle neutron scattering, and nitrogen sorption (BET) measurements on such gels have shown they are comprised of an interconnected silica matrix, having pores ranging from 2–800 nm in size. Mössbauer effect and magnetization data show the Fe is in a paramagnetic environment with weak antiferromagnetic interactions. Curie–Weiss analysis indicated negative intercepts of the temperature axis for all the samples and that the magnetic moment per Fe atom (μ_{Fe}) decreased as the Fe content increased at a rate of $\sim 0.0058 \mu_B/\%$ Fe. For most of the samples $\mu_{Fe} \approx 2.1 \mu_B$. By contrast, in silica gel/Fe nanocomposites formed by the polymerization of an aqueous solution of tetraethoxysilane and iron nitrate, the Fe possessed magnetic moments varying from 3.9 to 2.9 μ_B . It is suggested that the difference is a result of the different pore structures of the gels, and not due to the different methods (e.g., postmatrix infiltration as compared to premixing prior to matrix polymerization) used to introduce the Fe.

Fine dispersions of magnetic particles in nonmagnetic matrices have been found to possess different magnetic characteristics that the same particles compacted together into a bulk material without the nonmagnetic constituent.¹ In fact, the properties may be tailored by proper adjustment of the relative composition of the two species (an easy variable to control) and the thermal-magnetic treatment given the material. Applications of such materials to recording heads,² high-density recording media,³ color reproduction,⁴ and magnetic refrigeration⁵ have been suggested. For the creation of bulk solids containing such fine particle dispersions, sol-gel methods have been found to be particularly effective.^{6,7} After preparation, their magnetic character can even be changed on demand by treatment in various gases at about 350 °C. Many magnetic phenomena have been found in materials prepared via the sol-gel route, including paramagnetism, ferromagnetism, superparamagnetism, and spin-glass behavior. Initially, it was thought that the matrix gel provided only a support for the fine Fe particles.⁶ However, subsequent studies of silica gel/Fe (SG/Fe)⁸ and alumina gel/Fe (AG/Fe)⁷ systems showed that the matrix played an active role in determining the magnitude and concentration dependence of the magnetic moment of the Fe. Recently, another type of gel, colloidal silica: potassium silicate gel (CSPS),⁹ came to our attention. This material possessed a much larger pore volume but with a combination of pore sizes varying down to a few nanometers. Fe loading in the new gel is accomplished by infiltration after formation of the gel. This process is in contrast to that followed in the previous studies of the SG/Fe and AG/Fe nanocomposites wherein the matrix gel and Fe clusters were formed simultaneously. As a test of the effect of infiltration on the magnetic character of the composite and as an attempt to increase the Fe loading without a concomitant increase in Fe cluster size, the present study was initiated.

A colloidal gel (CSPS) was made by a process devel-

oped by Shoup⁹ wherein an electrostatically stabilized sol of colloidal silica [Ludox HS-40]^{10,11} in a 90 wt % potassium silicate solution [Kasil No. 1]¹² is gelled using an aqueous formamide gelling agent at a pH of 10.8. After curing for 2–3 h at 80 °C, the alkali species were removed by ionic exchange in a 1N solution of NH_4NO_3 (90 °C) followed by immersion in a 1N solution of nitric acid (90 °C) and a wash in distilled water.¹³ Previous electron microscopy, small angle neutron scattering, and nitrogen sorption (BET) measurements on such gels have shown they are comprised of an interconnected silica matrix with extremely high surface area, having intracuster pores ranging from 2–10 nm in size and a bimodal distribution of intercluster voids with diameters centered around 200 and 800 nm.¹³ The infiltration of magnetic species into these gels was accomplished by placing carefully weighed drops of aqueous solutions of $Fe(NO_3)_3$ on top of 3-mm-thick (25-mm-diam) slices of the dried gel. Within an hour the liquid was absorbed into the solid, and the gel changed from a white to a light brownish color homogeneously throughout the sample. Magnetic measurements were performed on this material after drying in air at 300 K for two weeks. In this study nanocomposites of CSPS/Fe containing 5.7%, 10.6%, 20.3%, 30.0%, and 40.3% iron were prepared. All Fe contents herein are quoted in weight percent of the final composite, consistent with the labeling convention used for the SG/Fe and AG/Fe gels of the earlier studies. Mössbauer effect measurements were performed using the sample as the absorber and a 20 mCi ^{57}Co in Rh source. Velocity calibration of the Mössbauer equipment was performed using Fe_2O_3 , and zero velocity is the center of a pure Fe spectrum. The magnetization measurements were performed between 300 and 5 K in a SQUID magnetometer. Magnetic hysteresis measurements were performed by measuring the sample's magnetization as the magnetic field was cycled in steps from positive to negative and back to positive values after first cooling the material to the

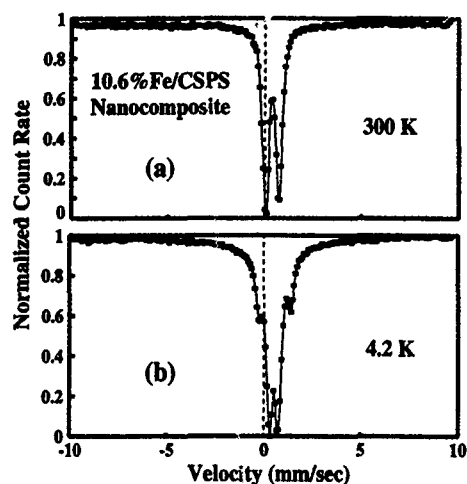


FIG. 1. Mössbauer effect spectra measured for a 10.6% Fe/CSPS nanocomposite measured at (a) 300 K and (b) 4.2 K.

measurement temperature in an 800-kA/m field.

Figure 1(a) shows an example of the Mössbauer effect spectra obtained for the CSPS/Fe nanocomposites at 300 K. The data are characterized by an absorption doublet (0.67-mm/s electric quadrupole splitting) having a small isomer shift of 0.4 mm/s. This is very similar to that which was observed at room temperature for the SG/Fe and AG/Fe nanocomposites formed by the polymerization of either tetraethoxysilane (TEOS) or aluminum triisopropoxide, respectively, in the presence of aqueous Fe nitrate.^{7,8} Those materials possessed an interconnected network of pores inside which the iron complexes formed, but those pores exhibited only a single size distribution centered about 30 nm.⁷ On cooling the 10.6% Fe CSPS/Fe sample to 4.2 K, however, the room-temperature Mössbauer effect doublet does not broaden or decompose into a six-line spectra indicative of fine Fe-containing particles slowing down their magnetic spin-flipping rate, as was observed in the previously studied SG/Fe and AG/Fe nanocomposites. Instead, for the CSPS/Fe composite of the present investigation, there is a sharpening of the room-temperature doublet (isomer shift remains at 0.4 mm/s, but the quadrupole splitting decreases to 0.52 mm/s), see Fig. 1(b). In addition, at 4.2 K there is the appearance of a second absorption doublet having a larger 0.62-mm/s isomer shift and a larger 1.56-mm/s quadrupole splitting. One possible explanation for this result is that the iron atoms in the infiltrated CSPS/Fe sample are located in two different local environments in either one or two *paramagnetic* lattices in the pores, each type of Fe atom having a different electric quadrupole temperature dependence. By contrast, the iron atoms in the SG/Fe and AG/Fe nanocomposites are located in nanometer-sized clusters of a *ferromagnetic* lattice.^{6,7} This difference is surprising, even if one realizes the matrix plays a role other than support for the iron. In the previous SG/Fe and AG/Fe studies, a difference in the nature of the iron had been discovered when the matrix was chemically different, as in a silica-gel compared to an alumina-gel matrix. However, in the present case both the CSPS/Fe and SG/Fe nanocomposites possess a silica matrix, and would

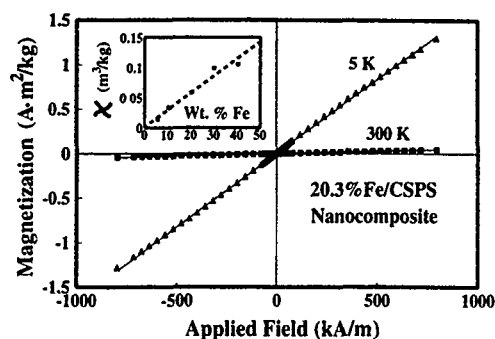


FIG. 2. Magnetization vs temperature data measured at the indicated temperatures for a 20.3% Fe/CSPS nanocomposite, and the room-temperature magnetic susceptibility (χ) vs wt % Fe (W_{Fe}) for a series of CSPS/Fe nanocomposites (inset). The dashed line ($\chi=0.00285W_{Fe}$) is a linear least-squares fit of the data.

therefore still have been expected to be magnetically similar. Since the major differences between these two silica gel/Fe nanocomposites are their vastly different morphologies and the different methods used to introduce the iron, it is attractive to conclude that either of these factors led to the different magnetic character of the nanocomposites.

Magnetic hysteresis measurements on the CSPS/Fe nanocomposites also showed that all the materials containing less than 30% Fe are paramagnetic at both room temperature and 5 K, consistent with the Mössbauer experiments. A typical example of these data is shown in Fig. 2. Note the linear relationship between field and magnetization indicative of this type of magnetic state. At room temperature the magnetic susceptibility for these materials increased linearly with Fe content from $1.36 \times 10^{-2} \text{ m}^3/\text{kg}$ for the 5.7% Fe sample at a rate of $2.85 \times 10^{-3} \text{ m}^3/\text{kg}$ per percent Fe (see inset of Fig. 2), thereby providing confidence in the quoted concentrations. Typically, a 40-fold increase in susceptibility was found for all these samples on cooling from 300 to 5 K (e.g., see Fig. 2), typical of that expected for a paramagnet. For the 40% Fe sample, there is a slight curvature toward the field axis (with essentially zero remanence) in the initial part of the hysteresis loop at both 300 and 5 K. Since the higher field data ($|H| > 15 \text{ kA/m}$) possess a linear $M-H$ behavior, these data suggest a small admixture of either a superparamagnetic or ferromagnetic component with the majority paramagnetic phase. The magnetic susceptibility values are about one-tenth that measured for the SG/Fe nanocomposites studied earlier,⁸ indicating a lower magnetic moment per Fe atom in the present samples. In order to determine this more quantitatively, the temperature dependence of the susceptibility was measured for the CSPS/Fe material. Figure 3 is representative of this data. Note, there are no discontinuities in the susceptibility data indicating the lack of magnetic transitions between 300 and 5 K. The dashed line in this figure is a least-squares fit of the high-temperature inverse susceptibility data to a straight line. All the samples in this study exhibited this Curie-Weiss behavior with significant deviations at low temperatures. The slopes of the high-temperature $1/\chi$ vs T fits were analyzed as in Ref. 8 to obtain the magnetic moment per Fe atom, and these results are shown in

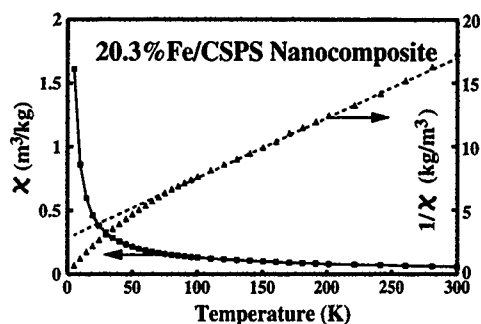


FIG. 3. Magnetic susceptibility, χ , (filled squares) and inverse susceptibility (triangles) vs temperature for a 20.3% Fe/CSPS nanocomposite showing Curie-Weiss behavior. The arrows indicate the appropriate axes. The dashed line is a least-squares fit of the high-temperature $1/\chi$ data.

Fig. 4. In the SG/Fe cluster materials of the earlier studies, the magnetic moments were above $3 \mu_B/\text{Fe}$ atom and they decreased with increasing Fe content at a rate of $0.038 \mu_B/\%$ Fe. The situation is much different for the present infiltrated CSPS/Fe nanocomposites. The present materials possess much smaller values near $2.1 \mu_B/\text{Fe}$ atom. Similar to the SG/Fe nanocomposites,⁸ the magnetic moment per Fe atom in the CSPS/Fe materials also decreases with increasing Fe content, although at the much lower rate of $0.0058 \mu_B/\%$ Fe. This decrease can be explained by the presence of weak antiferromagnetic interactions between the Fe atoms similar to that reported for ferrites via intermediary oxygen atoms.¹⁴ This interpretation is also consistent with the "negative" temperature-axis intercept found for the extrapolated high-temperature behavior for all the CSPS/Fe samples (see Fig. 3). Iron is present during the formation of the gel in the SG/Fe material and may, therefore, participate in the gelation chemistry. However, in the CSPS/Fe material the Fe is added after the formation of the CSPS matrix. Thus the interaction of the Fe with the matrices may be quite different in the two systems. In order to check this possibility, a pure

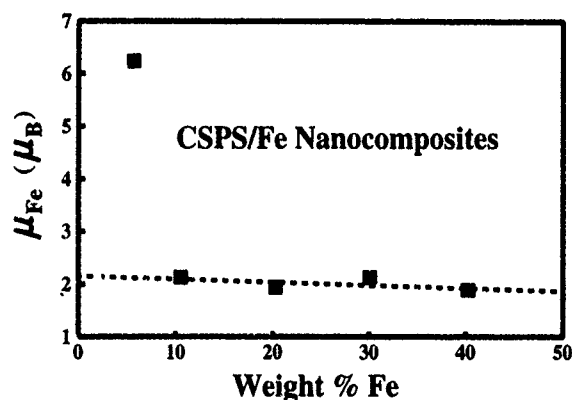


FIG. 4. Magnetic moment per Fe atom (μ_{Fe}), in Bohr magnetons (μ_B), vs wt % Fe (W_{Fe}) for a series of CSPS/Fe nanocomposites. The dashed line ($\mu_{Fe} = 2.15 - 0.00575 W_{Fe}$) is a linear least-squares fit of the data for the four most concentrated materials.

silica gel sample was prepared using the preparation technique of the SG/Fe nanocomposites. Iron was subsequently introduced into the gel to a concentration of 16% using the infiltration technique of the CSPS/Fe nanocomposites. At room temperature, the Mössbauer spectra was similar to that shown in Fig. 1(a) (isomer shift of 0.5 mm/s and an electric quadrupole splitting of 0.68 mm/s), but at 4.2 K the spectra consisted of an admixture of the room temperature central doublet and a prominent six-line hyperfine field pattern (isomer shift of 0.37 mm/s and hyperfine field of 40.3 kA/m). This result indicates the iron is in nanometer-sized ferromagnetic clusters. This result is also identical to that observed earlier for the SG/Fe nanocomposites wherein the iron was introduced *before* the solution polymerization.⁶ Consequently, we suggest the different magnetic behavior of the CSPS/Fe nanocomposites is due to different Fe-matrix interactions caused by the material's much different morphology, including the very fine 2–10 nm intracluster pores and the 200–800 nm intercluster voids,¹³ and pore chemistry. A similar phenomena was observed earlier in ion-exchange resins.⁴ In that case, the pore structures were found to be responsible for the *in situ* formation of metastable $\gamma\text{-Fe}_2\text{O}_3$ (maghemite) at room temperature.

In conclusion, the form of the Fe in the CSPS/Fe nanocomposites was found to be different from that in the SG/Fe nanocomposites, even though the source of the Fe was the same in both cases and the matrix in both cases was silica. It is suggested that the difference is a result of the different morphology and pore chemistry of the materials rather than the methods (e.g., postmatrix infiltration as compared to premixing prior to matrix polymerization) used to introduce the Fe.

The authors express their appreciation to L. Swartzendruber and W. Haller for helpful discussions of the data. Special appreciation is expressed to H. Brown for performing the magnetization measurements of this study.

¹ *Magnetic Properties of Fine Particles*, edited by J. L. Dormann and D. Fiorani (Elsevier Science, Amsterdam, The Netherlands, 1992).

² J. Q. Xiao, J. S. Jiang, and C. L. Chien, *Mater. Res. Soc. Symp. Proc.* **286**, 197 (1993).

³ R. D. Shull, U. Atzmony, A. J. Shapiro, L. J. Swartzendruber, L. H. Bennett, W. J. Green, and K. Moorjani, *J. Appl. Phys.* **63**, 4261 (1988).

⁴ J. K. Vassiliou, V. Mehrotra, M. W. Russell, E. P. Giannelis, R. D. McMichael, R. D. Shull, and R. F. Ziolo, *J. Appl. Phys.* **73**, 5109 (1993).

⁵ R. D. McMichael, R. D. Shull, L. J. Swartzendruber, L. H. Bennett, and R. E. Watson, *J. Magn. Magn. Mater.* **111**, 29 (1992).

⁶ R. D. Shull, J. J. Ritter, A. J. Shapiro, L. J. Swartzendruber, and L. H. Bennett, *Mater. Res. Soc. Symp. Proc.* **132**, 179 (1989).

⁷ R. D. Shull, J. J. Ritter, A. J. Shapiro, L. J. Swartzendruber, and L. H. Bennett, *Mater. Res. Soc. Symp. Proc.* **206**, 455 (1991).

⁸ R. D. Shull, J. J. Ritter, A. J. Shapiro, L. J. Swartzendruber, and L. H. Bennett, *J. Appl. Phys.* **67**, 4490 (1990).

⁹ R. D. Shoup, *Colloid and Interface Science* (Academic, New York, 1976), Vol. 3, p. 63.

¹⁰ Ludox HS-40, E. I. du Pont de Nemours and Co., Wilmington, DE.

¹¹ The use of tradenames in this paper is for informational purposes only, and does not constitute an endorsement by NIST or the U.S. Government.

¹² Kasil-1, Philadelphia Quartz Co., Lafayette Hill, PA.

¹³ H. M. Kerch, F. Cosandey, and R. A. Gerhardt, *J. Non-Cryst. Solids* **152**, 18 (1993).

¹⁴ C. G. Shull, E. O. Wollan, and W. C. Koehler, *Phys. Rev.* **84**, 912 (1951).

Origin of high coercive force in rare-earth–transmission-metal thin film

D. Roy Callaby, Robert D. Lorentz, and Shigeki Yatsuya
3M Company, St. Paul, Minnesota 55144

A sequence of rare-earth/transmission-metal (RE-TM) films have been sputter coated and an increase in the coercive force of over six times has been measured for a change in argon pressure from 2 to 10 mTorr. By using small-angle x-ray scattering measurements, a strong correlation has been found between the number or volume of voids and the coercive force in sputtered coatings of RE-TM materials, especially Tb-Fe-Co. A transmission electron microscopy technique has shown that the majority of these voids accumulate in the observed gaps between columns.

I. INTRODUCTION

The majority of rare-earth/transition-metal (RE-TM) magneto-optic (MO) materials used for information storage are made by sputtering, usually under argon, with a pressure above 1 mTorr. Calculations indicate that the coercive force H_c depends very much not only on the composition but also upon the sizes of voids.¹ In addition, it has been reported that the coercive force is very dependant on the argon pressure used for sputtering.² In this article we report on the effects of argon pressure on the value of H_c and on the number and sizes of voids in the MO coatings. We have also determined the position of these voids. The effects of different dielectrics and of different coating thicknesses are also discussed.

II. EXPERIMENT

The MO and SiC dielectric layers were prepared by dc sputtering, while for the SiN dielectric, rf sputtering was used. The samples were made either as an alloy or as a nanolayered structure of iron cobalt and terbium using a separate terbium target. The magnetic properties were measured with a vibrating sample magnetometer and the microstructural imaging of the films was performed with an electron microscope. The sizes and volume fractions of the voids were determined using small-angle x-ray scattering (SAXS).

III. RESULTS

A. Magnetic measurements

Measurements of the composition of the deposited films showed small variations around the average terbium content (21 at. %), resulting from the different argon deposition pressures used in this study. These compositional variations correspondingly cause slight changes in the compensation temperature T_c and this changes both H_c and M_r , but not $M_r H_c$. Figure 1 shows a comparison between coatings made at 5000 (for the SAXS measurements), 700, and 200 Å. It can be seen that there is a significant rise in H_c (or $M_r H_c$) as the thickness is reduced but the slope of $M_r H_c$ versus pressure increases as the thickness is reduced. Also shown in Fig. 1 is the effect of different dielectrics (SiC and SiN). Exami-

nation of the separate contributions of M_r and H_c show that the value of M_r changed very little, probably because of the low value of the compensation temperature used; most of the measured change with pressure was caused by changes in H_c . For these measurements, we used a nanolayered structure consisting of one layer of terbium for each layer of iron cobalt, as this gave the highest values of H_c .³ Measurements made using alloy coatings showed smaller values of H_c but the same percent increase of H_c with coating pressure.

B. Small-angle x-ray scattering measurements

Small-angle x-ray scattering (SAXS) was used to investigate the void densities contained in sputtered amorphous Tb-Fe-Co films. SAXS is sensitive to long-range (>10 Å) electron density fluctuations. These fluctuations might arise from voids or from other composition fluctuations. In this experiment, modeling was used to determine that the only reasonable explanation of the observed SAXS is that it originates from voids, rather than from phase-separated materials.

The small-angle x-ray scattering experiments were performed using $\text{CuK}\alpha$ radiation over a k range of $0.006 < k < 0.304 \text{ \AA}^{-1}$, where $k = (4\pi \sin \theta)/\lambda$. A transmission geometry was used, thereby sampling correlations in the plane of

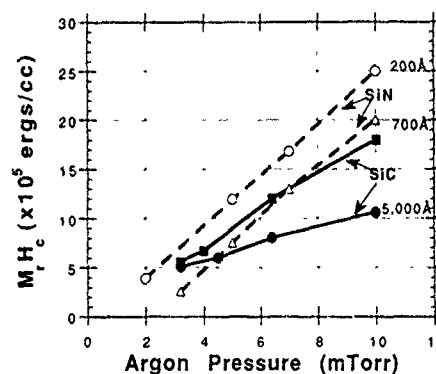


FIG. 1. $M_r H_c$ of MO layers of thicknesses 200, 700, and 5000 Å coated onto SiC and SiN dielectric layers plotted against argon coating pressure. The $M_r H_c$ values were measured at 30 °C or (for high H_c values) were obtained by extrapolation from values measured at higher temperatures.

the films. Some anisotropy in the void structures in the plane of the film and normal to it must be expected. The sizes of the voids in the plane are of interest to determine since they are relevant to the movement of domain walls.¹ The contribution to the total sample SAXS signal from the substrate was measured and removed and the resulting scattering was put on an absolute scale by referencing a standard to determine the scattering efficiency per unit thickness. The scattered efficiency is then on an absolute scale with units of inverse length and can then be compared directly to the results of calculations for various models.

SAXS can arise from many sources, including phase separation, voids, etc. To determine which of these are, and are not, consistent with the experimentally observed patterns, the scattering from several simple models was calculated. All modeling was done assuming spherically symmetric particles of a given radius in a homogeneous matrix. The scattered efficiency per unit sample thickness for closely packed spherical particles⁴ as an approximate solution for a fluid of noninteracting hard spheres was calculated. This calculation then also has units of inverse length. This method for generating the calculated data cannot be expected to reflect the actual arrangements in the alloys to a high degree. It can be, at best, only a reasonable approximation due, in part, to the assumption of spherical particles of a uniform size. It has proven sufficient, however, to eliminate potential models and to determine the approximate size of inhomogeneities in the materials.

Modeling of the SAXS from these samples was attempted with two distinct types of physical structures. In one case, we calculated the SAXS for phase separation models, in which the samples consisted of two compositionally distinct amorphous phases. No compositionally consistent models were able to simultaneously reproduce the amplitudes and shapes of the experimentally observed SAXS patterns.

Calculations were also made of the scattering expected for a Tb-Fe-Co matrix and spherical voids in that matrix. Models with large voids were chosen to represent the low-angle scattering and smaller voids were used for the higher angles. With the appropriate selection of void sizes and densities, the main features of the observed SAXS patterns were easy to fit.

The observed SAXS varies with changes in deposition pressure and period. Figure 2 shows the SAXS patterns for four films deposited at different sputtering pressures. As the pressure is increased from 3.2 to 4.5, and then to 6.4 mTorr, the amplitude of the low-angle scattering, which represents large voids, increases. Modeling indicates that the large void size drops from approximately 165 to 120 to 100 Å in these films, while the large void density increases from 1.4×10^{13} to 2×10^{14} to 3×10^{15} voids/cm³, respectively. These void densities can also be expressed as void volumes. Then, the corresponding void volumes would be 0.026%, 0.15%, and 1.3%. At 10 mTorr, a shoulder has appeared in this low-angle region. This hump is due to a higher density (6.5×10^{17} voids/cm³, 7.4% void volume) of smaller voids, about 30 Å in radius. The large voids increase in size to 165 Å, and the corresponding void density, as described above, is 4.5×10^{13} voids/cm³ (0.095% void volume). Hence, in the 10 mTorr

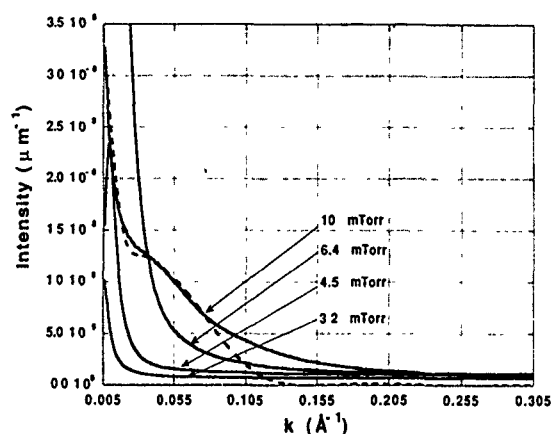


FIG. 2. Small-angle x-ray scattering from Tb-Fe-Co films deposited at 3.2, 4.5, 6.4, and 10 mTorr. The dotted line is the sum of separate calculations using models with an amorphous Tb-Fe-Co matrix plus voids of 165 Å radius and with 30 Å voids and shows a good fit to the scattering from the 10 mTorr sample.

film, the total void volume has increased substantially. Figure 2 shows the sum of the calculated scattering from the large and small void models as a dotted line. This sum fits the experimental data remarkably well, considering that there is expected to be a distribution in void size and number in the films.

C. Electron microscopy measurements

The microstructural imaging of the films was carried out using a JEOL 200CX operated at 200 kV. Two kinds of transmission electron microscopy (TEM) samples were prepared. One is a plane-view sample and the other is a cross-sectional view sample. For the plane-view samples, film stacks of SiC(150 Å)/RE-TM(~300 Å)/SiC(150 Å) were deposited on NaCl (100) crystal substrates and on SiO substrates. Films grown on NaCl substrates were floated off the NaCl substrates in water and placed on TEM grids. For the cross-sectional view samples, the same film stack was deposited on Si (100) wafers. The cross-section samples were prepared by first mechanically polishing, followed by dimpling, and finally ion milling.

Figure 3 shows a cross-sectional view of the Gd-Co thin film. The film stack of SiC/Gd-Co/SiC/Si(100) is shown in the direction of Si (110). The Si substrate shows the structure image and there is a Si oxide layer 10–20 Å thick on the Si substrate. The SiC grown on the Si substrate is amorphous and its surface is as smooth as the Si substrate. The Gd-Co layer is also amorphous and has a columnar structure, with the top of the columns being hemispherical in shape. The diameter of the columns is around 10 nm, which is consistent with the data obtained from a plane-view image.

The second SiC layer on the Gd-Co layer is amorphous, while its surface has ripples as if it followed the Gd-Co film surface. The thickness of the SiC layer t_2 on the Gd-Co film is smaller than that of the SiC layer t_1 on the Si crystal, although the same amount of SiC was deposited for both SiC layers. Assuming the sticking coefficient of SiC on the

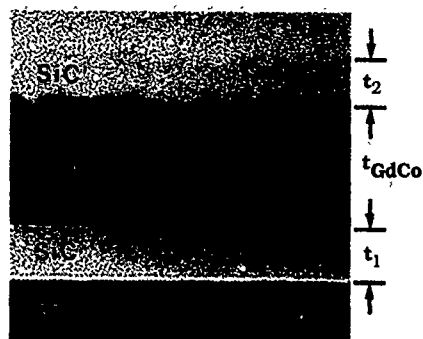


FIG. 3. Cross-sectional view of the SiC/Gd-Co/SiC film stack on a Si wafer (100). t_1 is the thickness of the SiC layer on the Si substrate, t_2 is the thickness of the SiC layer on the Gd-Co layer, and $t_{\text{Gd-Co}}$ is the thickness of the Gd-Co layer.

Gd-Co layer is similar to that on the Si substrate, SiC material corresponding to the amount of $t_1 - t_2$ per unit area entered into the gaps between columns. The value of $(t_1 - t_2)/(t_{\text{Gd-Co}})$ is equal to the gap density between columns, where $t_{\text{Gd-Co}}$ is the thickness of the Gd-Co layer. This gap density was measured to be approximately 8.5%.⁵

The columnar structures of Tb-Fe-Co films become more distinctive as the pressure increases.² The gap densities of the films sputtered at 3.2 and 6.4 mTorr were also measured from the cross-sectional views in the same manner described above. The gap densities are plotted against pressure in Fig. 4. The gap density at 10 mTorr was obtained from the Gd-Co film and the other two points were measured from the Tb-Fe-Co films. In this study, we assume that the data obtained from Tb-Fe-Co at 10 mTorr is similar to that from Gd-Co at 10 mTorr, because the plane view of the Tb-Fe-Co film resembles that of the Gd-Co film. Tb-Fe-Co has been seen to have similar physical properties to Gd-Co. It can be concluded that the gap density increases with pressure. This relationship resembles that between $M_r H_c$ (mainly H_c) and pressure as shown in Fig. 1.

IV. DISCUSSION

The void volumes in the 5000-Å-thick films, with 10 Å period, were determined by this modeling. The numbers of voids increased substantially as the deposition pressure was increased, as discussed above. When void volumes and

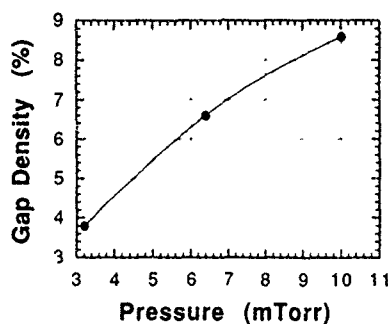


FIG. 4. Measured gap densities plotted against argon coating pressure.

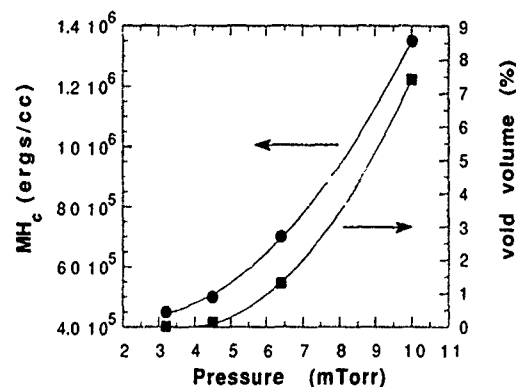


FIG. 5. $M_r H_c$ and void volume determined by SAXS vs sputtering pressure for 5000-Å-thick Tb-Fe-Co films with 10 Å period.

$M_r H_c$ values are plotted versus deposition pressure, remarkably similar dependencies are seen (Fig. 5). This strongly suggests that the volume of sizeable voids, like those expected between columns, is a determinant of the H_c values in MO films. The measured relationship between void volume and H_c is in good agreement with the modeling results obtained by Mansuripur.¹

The gap volume measured by the TEM technique described in this article also shows that this increases as the argon pressure is increased. While the measured volumes obtained from both techniques seem to agree at 10 mTorr pressure (see Figs. 4 and 5), it should be noted that the SAXS results were obtained using 5000-Å-thick samples and the TEM results were measured from 200–300-Å-thick samples, so exact agreement should not be expected. Of more importance is the fact that both void volume, gap density, and H_c increase with increase of argon sputtering pressure. The anisotropy K_u can influence H_c but measurements by Merchant and Kryder⁶ have shown that increasing the argon pressure over the range used here results in a small reduction of K_u rather than any increase.

V. CONCLUSIONS

The SAXS and VSM results show that both the void volumes and the values of H_c increase with coating pressure. The electron microscope results have shown the presence of gaps between the columns of the RE/TM coatings. It follows that there is a significant contribution to the increase of H_c with coating pressure by the increasing volume fraction of these voids located in the gaps between the columns of the MO films.

¹M. Mansuripur, R. C. Giles, and G. Patterson, *J. Magn. Soc. Jpn.* **15**, 17 (1991).

²J. W. Lee, H.-P. D. Sheih, M. H. Kryder, and D. E. Laughlin, *J. Appl. Phys.* **63**, 3624 (1988).

³N. Sato, *J. Appl. Phys.* **59**, 2541 (1986).

⁴A. Guiner and G. Fournet, *Small Angle Scattering of X-rays* (Wiley, New York, 1955), p. 48.

⁵S. Yatsuya and D. R. Callaby (unpublished).

⁶A. A. Merchant and M. H. Kryder, *IEEE Trans. Magn.* **MAG-27**, 3690 (1991).

Study of the effect of defect sizes and their distribution on the coercivity of magnetic media

James A. Jataw and Edward Della Torre

Institute for Magnetism Research, George Washington University, Washington, DC 20052

The nature of domain-wall motion coercivity in magnetic media is studied using a two-dimensional numerical micromagnetic model. It is necessarily assumed that the source of the coercivity is cylindrical anomalies in the material that have anisotropy or exchange parameters which are either larger or smaller than that of the surrounding media. Varying these parameters from those required to obtain the observed coercivity shows that a larger decrease in either parameter is required to obtain the same change in coercivity as a given increase. Thus, the dependence of coercivity on these parameters is nonlinear. It was also found that the computed coercivity decreases with an increase in the separation of the defects, and increases with an increase in defect size. It is shown that a correction for the calculated coercivity is required to account for the statistical distribution in defect sizes and locations. Finally, a suitable variation in the defect parameters can accurately characterize the temperature behavior of the coercivity.

I. INTRODUCTION

This article extends the work described in Ref. 1 by carrying out detailed calculations in the study of the nature of coercivity in media in which the magnetization reversal mechanism is domain-wall motion. In these media coercivity is introduced by defects imbedded in the lattice. Soft magnetic materials and magneto-optic media have this property. Due to the stiffness of the equations which describe the micromagnetic problem, we developed an efficient mode-pushing technique to accelerate the convergence of the numerical calculations.² Cylindrical defects in a regular periodic array are introduced in an otherwise perfect material. The problem then reduces to solving for the shape of a domain wall pinned at its ends by the defects. On the application of a magnetic field the wall bends, and at the critical field is pulled away from the defects.

Computer simulations were performed on a rectangular region measuring 15 nm in the y direction and 60 nm in the x direction. The choice of the size of this region ensured that the region included approximately two domain wall widths in the x direction, while the average distance between defects was used in the y direction. Due to the symmetry, calculations only had to be carried out over half of that region. This region was then discretized into a 60×240 square mesh. Thus, the lattice constant was 0.25 nm.

II. TYPES OF DEFECTS

In Ref. 3 the coercivity of magneto-optic media was studied using a one-dimensional energy well model. In that model it was assumed that magnetic parameters such as anisotropy and exchange are locally decreased within the defects. On the other hand, in Ref. 4 we implemented a one-dimensional case where the material parameters are assumed to be larger within the defects compared to that of the surrounding media. The implementation in Ref. 4 was based on the observation that for epitaxial garnet crystals with negative magnetostriction, localized compressive stresses resulted in an increase in the uniaxial anisotropy. The result of these observations is reported in Ref. 5. While the present study is

not carried out for garnet materials, it is noted that at present the actual sources of coercivity in the media studied is not completely understood, although our models are able to predict the coercivity observed in practice. In using this model, it is noted that in the case of the energy well the domain wall is centered on the depression, since this corresponds to the lowest-energy position. The application of a magnetic field pulls the wall away from this position until a Barkhausen jump occurs when the wall is freed from the well. In the case of the energy barrier, on the other hand, the domain wall is pinned at a location in front of the barrier, and this repulsive action is gradually overcome as the wall climbs toward the barrier with increasing magnetic field. At the critical field the wall is able to push past the defects. Coercivity was determined by tracking both the 90° and 30° loci on the domain wall. Calculations were continued until the 30° locus of the domain wall went past the pinning points.

In the following calculations, the magnetic parameters used were: an anisotropy constant of 3.2×10^{-4} J/m³, an exchange constant of 3.6×10^{-12} J/m, and a saturation magnetization of 4.2×10^4 A/m. Experimental evidence suggests, that for the material studied, the average defect size is 3 nm and the average distance between defects is 15 nm. Using this data we computed the coercivity as a function of the magnetic parameters within the defect. The magnetic properties of the defects will henceforth be expressed as a percentage relative to the nominal values above. Figure 1 shows this variation for the energy well model, while Fig. 2 shows this variation for the energy barrier model. It should be noted that only one material parameter is varied at a time in the above simulations. Thus, the exchange constant is kept at its nominal value when the anisotropy is varied, and vice versa. A comparison between Figs. 1 and 2 shows that for the same percentage change in the parameters, higher values of coercivity are obtained for the energy barrier model than for the well model. For example, a 20% change in anisotropy and exchange gives a coercivity of about 75 kA/m for the barrier model while for the well model the coercivity is about 22 and 30 kA/m for the same 20% change in anisotropy and exchange, respectively. It is seen in both cases, however, that

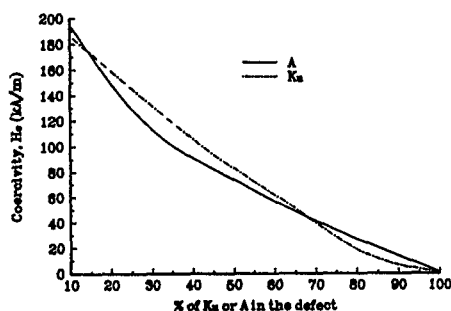


FIG. 1. Variation of coercivity as a function of the percentage of exchange or anisotropy in the defect for energy well model.

the relationship between the coercivity and the change in the magnetic parameters is nonlinear.

III. EFFECT OF DEFECT SIZE AND SEPARATION

We just discussed the fact that both the energy well and energy barrier models can be used to model the coercivity. In these calculations the average defect size and the average distance between defects was used. In order to determine the effect of a distribution in defect size and separation, the coercivity was calculated for defect sizes from 2 to 4 nm, and for distances between defects from 10 to 30 nm. It was observed, as shown in Fig. 3, that as the distance between the defects increased, the coercivity decreased nonlinearly. Figure 4 gives a plot of coercivity as function of defect sizes, for values of defect sizes less than the domain-wall thickness. A nonlinear relationship is observed, where the coercivity increases with increasing defect size. This observation agrees with the one-dimensional model calculations where the coercivity was found to increase with increase in the size of the defect and peaked when the size was of the same order of magnitude as the domain-wall thickness. This observation also agrees with the results of Ref. 6, where in their two-dimensional simulation of nucleation coercivity they observed a similar trend. The results of Figs. 3 and 4 were obtained using the anisotropy energy well model, however, the value of the anisotropy was kept at arbitrary values of 50% and 75%, respectively. A similar trend was observed when the energy well model was replaced by the barrier model. We noticed, however, that unlike our models which

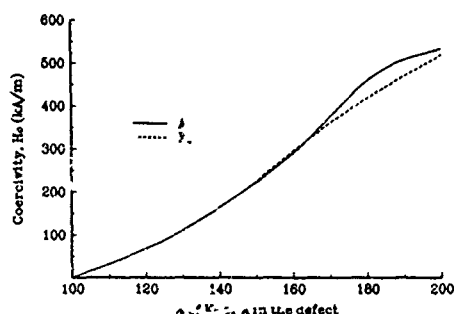


FIG. 2. Variation of coercivity as a function of the percentage of exchange or anisotropy in the defect for energy barrier model.

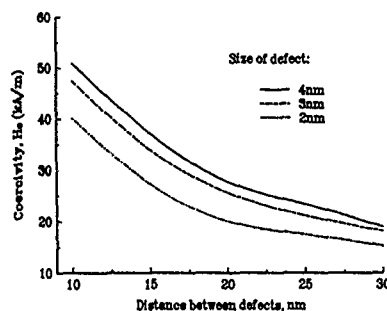


FIG. 3. Coercivity as a function of the distance between defects for anisotropy energy well model.

are able to calculate the observed coercivity, the barrier-type model of Ref. 6 calculated a much lower coercivity than that which was observed. Since this model is able to account for the bowing of the domain wall, a consequence of this is to make the wall more rigid when the defects are closer together than when they are further apart, thus resulting in a stronger field being needed to initiate the bowing of the domain wall. It is also expected that the two-dimensional model would exhibit the same trend as the one-dimensional model⁴ where the coercivity attains a maximum when the defect size is on the same order of magnitude as the domain-wall thickness.

The foregoing discussion assumed that the defects are all identical and distributed in a regular array. However, in practice, the defects are randomly distributed throughout the medium, thus a domain wall in any position will be pinned by a distribution of defects. Equally important is the fact that the sizes and therefore the pinning strength of these defects is not the same. Since the expected value of a function of a random variable is equal to the function of the expected value of the random variable only if the function is linear, and since our results show that the relationship between the coercivity and both the defect sizes and defect separation is nonlinear, it is necessary to correct the coercivity computed using the average values for the distribution in defect size and separation.

For a distribution of identical defects the calculated coercivity is found to exhibit approximately the following relationship:

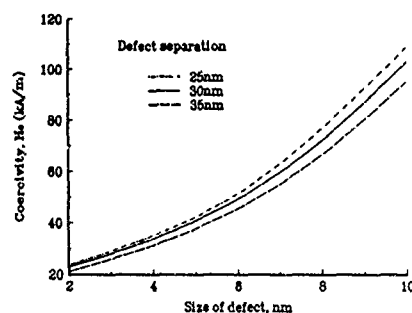


FIG. 4. Coercivity as a function of defect size for anisotropy energy well model.

$$\langle H_c \rangle \propto d^2, \quad (1)$$

where d is the average defect size. In order to assess the effect of a distribution in the defect size, a knowledge of the form of this distribution must be available or assumed. Thus, if we assume it is a normal distribution, the probability density function is given by

$$f(d) = \frac{1}{\sqrt{2\pi}\sigma_d} \exp\left(-\frac{(d-\langle d \rangle)^2}{2\sigma_d^2}\right), \quad (2)$$

where $\langle d \rangle$ is the average defect size and σ_d is the standard deviation in the size of the defect. Thus for this distribution function, we have

$$\langle d^2 \rangle = \langle d \rangle^2 \left(1 + \frac{\sigma_d^2}{\langle d \rangle^2}\right), \quad (3)$$

and the expected value of the coercivity is given by

$$\langle H_c \rangle = H_c(\langle d \rangle) \frac{\langle d^2 \rangle}{\langle d \rangle^2}. \quad (4)$$

If we assume five different defect sizes of 2, 4, 6, 8, and 10 nm, and uniformly distributed, then we will expect an increase in the coercivity of almost 30%.

In a similar way, it is seen that the coercivity varies approximately as the square of the reciprocal of the distance between defects. Thus the coercivity calculated using the average distance between defects must be corrected in the same way that the defect size was corrected. Thus, following Eq. (3) and (4), we have

$$\langle \lambda^2 \rangle = \langle \lambda \rangle^2 \left(1 + \frac{\sigma_\lambda^2}{\langle \lambda \rangle^2}\right) \quad (5)$$

and

$$\langle H_c \rangle = H_c(\langle \lambda \rangle) \frac{\langle \lambda^2 \rangle}{\langle \lambda \rangle^2}, \quad (6)$$

where $\langle \lambda \rangle$ is the average distance between defects. If we assume five different defect separations of 10, 15, 20, 25, and 30 nm of uniform defect sizes, then the coercivity calculated using the average distance between the defects must be corrected by multiplying by a factor of approximately 1.156.

IV. TEMPERATURE DEPENDENCE OF COERCIVITY

We have used our models to simulate the temperature dependence of coercivity of TbFeCo material (see Fig. 5) Using the data given in Ref. 7, where the magnetic parameters were measured at the temperatures specified, we computed the coercivity of the medium using both the well and barrier models. In this simulation, the average defect size and the average distance between defect were used. However, the percentage of anisotropy or exchange for the well model was

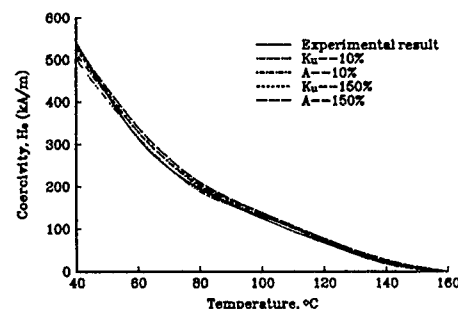


FIG. 5. Coercivity as a function of temperature for experimental and computed values.

set at 10%, while for the energy barrier model these were set to 150%. While both models are able to predict the general trend in the variation of coercivity with temperature, it is seen that a much larger decrease in the magnetic parameters is required in the well to achieve the same coercivity for a given increase of these parameters.

V. CONCLUSIONS

Two models of wall motion coercivity have been implemented by assuming a change from the surrounding medium of either the anisotropy or exchange, using a two-dimensional numerical micromagnetic model. It has been shown that both the barrier and well models for either the anisotropy or exchange can predict the values of the coercive field obtained in practice, as demonstrated using experimental results given at various temperatures. It has also been shown that due to the nonlinear variation of coercivity with defect sizes and their separation a correction is required in the calculated value of the coercivity to account for the different defect sizes and their random distribution.

ACKNOWLEDGMENTS

The authors would like to acknowledge the use of the CRAY Y-MP2 Supercomputer of the National Institute of Standards and Technology, Gaithersburg, MD, and would particularly like to thank Dr. L. H. Bennett and Dr. R. D. McMichael for their assistance. The useful discussions with members of the Institute for Magnetism Research are gratefully appreciated. This work was supported by an ATP grant through the National Storage Industries Consortium.

¹J. A. Jatau and E. Della Torre, IEEE Trans. Magn. **29**, 2374 (1993).

²E. Della Torre, IEEE Trans. Magn. **29**, 2371 (1993).

³E. Della Torre and C. M. Perlov, J. Appl. Phys. **69**, 4596 (1991).

⁴J. A. Jatau and E. Della Torre, J. Appl. Phys. **73**, 6829 (1993).

⁵J. A. Jatau, M. Pardavi-Horvath, and E. Della Torre (unpublished).

⁶R. Giles and M. Mansuripur, Comp. Phys. **5**, 204 (1991).

⁷E. Della Torre, C. M. Perlov, and M. Pardavi-Horvath, J. Magn. Magn. Mater. **104-107**, 303 (1992).

Reversal mechanisms in Tb/Fe multilayers

K. O'Grady, T. Thomson, and S. J. Greaves

Magnetic Materials Research Group, SEECs, UCNW, Bangor, Gwynedd, LL57 1UT, United Kingdom

G. Bayreuther

Institut für Angewandte Physik, Universität Regensburg, 93040 Regensburg, Germany

Reversal processes in Tb/Fe multilayer films are reported. The form of the hysteresis is explained as a function of the number of bilayers in terms of a two-coercivity model. Remanence measurements have been made which provide an insight into the distribution of the energy barriers for the two coercive processes associated with nucleation or domain-wall motion. The time dependence of magnetization has also been measured and this has been used to evaluate fluctuation fields and activation volumes for the series of films. The variation of the fluctuation field with applied field indicates that the two-coercivity model proposed is consistent with the time dependence. An increase is seen in the average activation volume with the number of bilayers.

I. INTRODUCTION

Tb/Fe multilayers are potential magneto-optic recording media. These films possess large perpendicular anisotropy, the main requirement for such media. Also of importance is the signal-to-noise ratio (SNR) which may be affected by the uniformity of written domains and their stability over time. A material is required in which domain-wall creep is a minimum to get the maximum lifetime from a medium.

Reversal processes in magneto-optic thin films may be described by a two-coercivity model in which there are two fields H_N and H_{DW} , representing the nucleation and domain-wall critical fields, respectively.¹ If we have a film in which H_N is greater than H_{DW} then the corresponding hysteresis loop will be square since as soon as reverse domains are nucleated they will immediately overcome the domain-wall critical fields. If, however $H_{DW} > H_N$ then reverse domains will be formed and be subject to pinning of their walls causing a rounding of the hysteresis loop. In a separate study on Pt/Co multilayers² we have found that this leads to the formation of smaller domains, which would be a potential advantage for magneto-optic recording.

We have examined magnetization reversal via a study of the two primary remanence curves. The isothermal remanence magnetisation (IRM) curve is a measurement of the remanence acquired as a function of the magnetizing field applied to an originally demagnetized sample and thus determines the distribution of H_{DW} since it begins from a state in which domains are present in both directions. The demagnetizing remanence (DCD) curve is a measurement of the remanence after the application of a demagnetizing field to a previously saturated sample and thus determines the distribution of either process depending on the mean activation energy.

II. EXPERIMENT

The multilayers were fabricated by sputtering. The layer thicknesses were 14.3 Å Tb/−8.5 Å Fe. Multilayers were produced with varying numbers of bilayers from 6 to 32 and were capped with a 100 Å aluminum protection layer. Magnetic measurements were made at room temperature using an automated AGFM. Hysteresis loops, IRM, and DCD curves

were measured perpendicular to the film plane. The hysteresis loops were measured with a sweep time of about 2 min and switching of the magnetization from saturation to zero took much less than 1 s. During the DCD measurements the applied field was removed from the sample in a fraction of a second keeping time-dependent effects to a minimum.

The time dependence was measured by first saturating the film in one direction then applying a reverse field and monitoring the magnetization over a 12 min period. This process was continued using increasingly larger reverse fields until the nucleation field, measured from the hysteresis loop, was approached at which point reversal of the magnetization took place in less than 1 s.

Analysis of the time-dependence data was made using the method proposed by Street, McCormick, and Folks,³ in which the Arrhenius relation is differentiated to give

$$\frac{dH}{d \ln[\dot{M}(H)/\dot{M}(0)]} = -\frac{kT}{vM_s} = -H_f, \quad (1)$$

where v is the activation volume, $\dot{M}(H)$ the change of magnetization with time, and H_f the fluctuation field. If we consider two time-dependence measurements of M , separated by an interval of applied field ΔH , then Eq. (1) may be rewritten as

$$H_f = \frac{\Delta H}{\ln \dot{M}_1 - \ln \dot{M}_2} \bigg|_M, \quad (2)$$

where \dot{M}_1 and \dot{M}_2 are the slopes of the time-dependent magnetization at some constant value of magnetization M . It can be seen from Eq. (2) that if there is a large change in the time-dependent behavior induced by the change in applied field ΔH , then the fluctuation field will decrease, conversely small changes in the time dependence with increasing H will be reflected in an increase in the fluctuation field. Measurements were made with ΔH in the range 10–15 Oe and the slopes of the curves were evaluated at $M=0$, i.e., the coercive point, so as to negate the effects of demagnetizing fields.

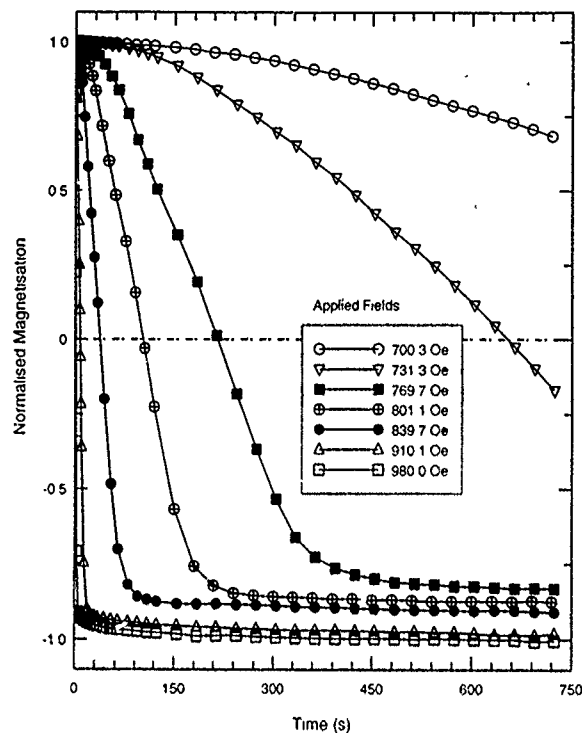


FIG. 1. Time-dependence data from the 32 bilayer film obtained at various applied fields.

III. RESULTS

The coercivity is found to decrease as the number of bilayers increases. Conversely, the magnetization increases with the number of bilayers although it is fairly constant for 14 or more bilayers. The hysteresis loops for these films are square for the samples with less than 20 bilayers. As the number of bilayers increases above 20 the hysteresis loop becomes rounded and the switching field distribution increases. This behavior is attributed to the existence of the two critical fields discussed above.

Time-dependence measurements were made at fields below the coercivity values obtained from the hysteresis loops. As the hysteresis loop coercivity was approached the time dependence became too rapid to measure accurately. Over the measuring period a wide range of applied fields below the hysteresis loop coercivity was found to produce reversal of the magnetisation. Figure 1 shows some of the data collected from the 32 bilayer film; there is an applied field range of 250 Oe in which the magnetization reaches zero. The time dependence is approximately linear with time around $M=0$, which is where the slopes used to calculate the fluctuation fields were evaluated. Also, at this point the overall demagnetizing field is zero, the thin nature of these films means that at any other value of M the demagnetizing field is large and changing as M changes with time.

Upon evaluation of the fluctuation fields two trends become apparent. For films with less than 20 bilayers the fluctuation field decreases with increasing applied field. This implies that as the field is increased and reverse domains are nucleated, they quickly expand, causing an increase in the slope of the time-dependence curve. This arises because the

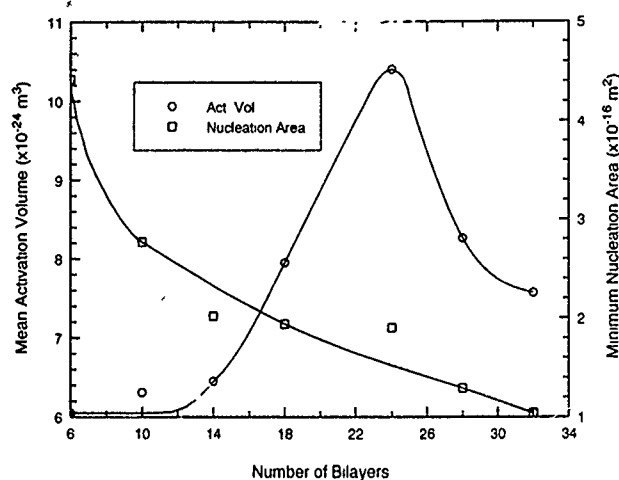


FIG. 2. Activation volumes and nucleation areas for the series of films.

nucleation field is greater than the domain-wall critical field. Where we have films with more than 20 bilayers the fluctuation field increases with applied field. This kind of behavior may be associated with pinning of the movement of the nucleated domain walls, slowing down the time-dependent change of M which is due to thermal activation of the domain walls allowing them to pass the pinning sites.

From Eq. (1) the activation volume is inversely proportional to the fluctuation field so the activation volume increases with applied field for films with less than 20 bilayers and decreases with applied field for thicker films. The average values of the activation volumes show an increase as the films become thicker. This data is shown in Fig. 2 along with the calculated values of the minimum domain nucleation area for each multilayer. We see that the minimum area decreases with increasing number of bilayers. If we assume that these volumes and areas may be related to the physical sizes of domains in these films then we can say that the average diameter of a circular domain in a film with 6 bilayers will be 24 nm and in a film with 32 bilayers it will be 12 nm.

The differentials of the IRM curves show the irreversible susceptibility $\chi_{ir}^i(H)$ which is the energy barrier distribution of the pinning sites while the DCD differentials $\chi_{ir}^d(H)$ show where nucleation from the saturated state occurs. These curves represent the energy barrier distribution and show that for films with less than 20 bilayers the IRM differential curve falls almost entirely to the left-hand side of the DCD differential, i.e., the domain-wall energy barrier distribution falls at field values less than the nucleation field distribution. Hence, once domains nucleate they can sweep unimpeded through the sample resulting in a very square hysteresis loop. Figure 3 shows the two differentials for a sample with 14 bilayers. Shown in Fig. 4 are the same two curves but for a sample with 28 bilayers from which it is clear that not all of the barriers to domain-wall motion have been passed by the time reverse domains begin to appear; this results in pinning of the domain walls and a reduction in hysteresis loop squareness. This also leads to the production of smaller domains as we reported previously.¹

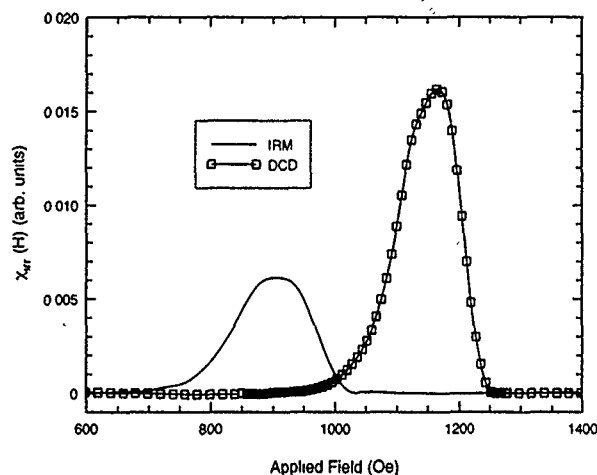


FIG. 3. IRM and DCD differentials for the 14 bilayer sample.

The behavior we have observed here is similar to that seen in MnBi films by Dekker and Huijter.⁴ As the film thickness decreases the nucleation field increases. This may be explained by assuming that domain walls are always present in the film, even in the saturated state. These are known as

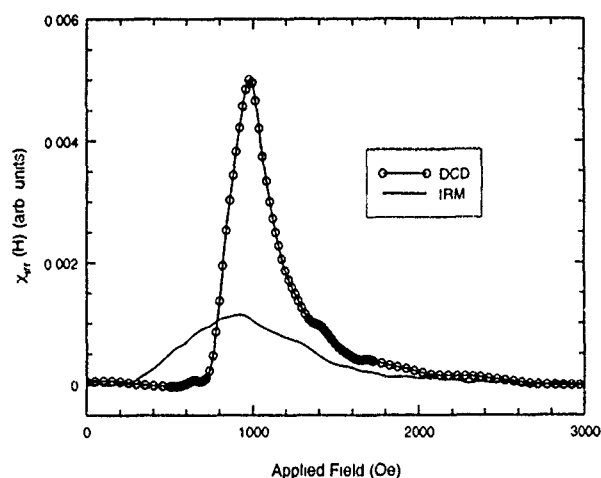


FIG. 4. IRM and DCD differentials for the 28 bilayer sample.

vestigial domains. As the film thickness increases the magnetostatic pressure on the domain walls increases. The nucleation field may now be defined as the field at which the domain walls become unstable and run out to form observable domains. Calculations by Cape and Lehman⁵ suggest that the abrupt reversal of magnetization seen here could be attributed to cylindrical vestigial domains as opposed to vestigial stripe domains. The calculations of Dekker and Huijter predict that below a certain film thickness the nucleation field will exceed the coercive field.

IV. DISCUSSION AND CONCLUSIONS

In this article we have shown that the reversal process in Tb/Fe multilayers is controlled by the relative values of the domain-wall and nucleation critical fields. We have also shown that remanence curves may be used to examine the distribution of these fields. The decrease of the nucleation critical field with increasing number of bilayers could be a consequence of the minimum area which nucleates a reverse domain also decreasing with increased film thickness thus increasing the number of possible nucleation sites. We have seen that the minimum area which may nucleate a reverse domain is about 1/3 the size, at 32 bilayers, of the area at 10 bilayers. However, those domains which do nucleate at lower reverse fields do not have sufficient energy, during the time scale of the measurements, to pass the pinning sites.

For magneto-optic recording applications it should be advantageous to have stable domains (i.e., with pinned walls) which increase the SNR performance of the films. Domains nucleated in a film with a highly square hysteresis loop may run out over a large area due to the lack of impediments to wall motion. Also, the potential storage density should be increased in films with more than 20 bilayers since we have shown that reverse domains may be smaller than in thinner films. Thus, despite the reduced coercivity of the thicker films they are the more suitable for long-term data storage.

¹A. A. Thiele, *J. Appl. Phys.* **41**, 1139 (1970).

²D. M. Donnet, V. G. Lewis, J. N. Chapman, K. O'Grady, and H. W. van Kesteren, *J. Phys. D* **26**, 1741 (1993).

³R. Street, P. G. McCormick, and L. Folks, *J. Magn. Magn. Mater.* **104-107**, 368 (1992).

⁴P. Dekker and E. Huijter, *IEEE Trans. Magn.* **MAG-11**, 1382 (1975).

⁵J. A. Cape and G. W. Lehman, *J. Appl. Phys.* **42**, 5732 (1971).

Write/erase cyclability of TbFeCo for mark edge recording

Hiroyuki Awano and Masahiro Ojima
Central Research Lab., Hitachi Ltd., Tokyo Japan

Katsusuke Shimazaki, Satoru Ohnuki, and Norio Ohta
Opto-electronics Lab., Hitachi Maxell Ltd., Ibaraki Japan

Domain size changes due to thermal relaxation after high laser power irradiation on amorphous TbFeCo films were studied. In order to achieve mark edge recording for high-density magneto-optical memory, accurate domain size recording is required even after a million erase/write cycles. Highly accelerated erase/write test was performed on typical recording media, rare-earth (RE)-rich and transition-metal (TM)-rich disks. The elongation of the domain size written on the TM-rich film after erase/write cycles was clearly evident; however, the change in the domain size of RE-rich films was small. The small domain size change of the RE-rich disk can be explained in terms of the rapid increase in the coercive force with decreasing temperature and the smaller domain-wall driving force at recording temperature than those for the TM-rich disk, even though both have the same level of structural relaxation.

I. INTRODUCTION

Mark edge recording can achieve significantly higher magneto-optical (MO) recording densities than the conventional mark position recording.¹ In this method, precise control of the recording mark shape on a magneto-optical disk must be achieved even after a million cycles of data writing and erasing. However, it is expected that the domain size expands with increasing erase/write cycles, because erase/write cycles cause reduction of the perpendicular anisotropy energy of the amorphous TbFeCo due to structural relaxation.² In order to successfully achieve mark edge recording, a material with minimal change in mark edge and width must be explored.

In this article two typical MO media, such as rare-earth (RE)-rich and transition-metal (TM)-rich TbFeCo disks, were studied in terms of erase/write cyclability for mark edge recording.

II. EXPERIMENTAL PROCEDURE AND RESULTS

RE- and TM-rich disk having the same thermal structure (identical layer thickness and structure) were prepared by magnetron sputtering. The construction of the disks is included in Fig. 1(a). Details of the erase/write cycle test are summarized in Table I. To carry out the erase/write cycles in a shorter amount of time, a higher laser power (11.0 mW) and reduced number of cycles (max 10^4) than normal (6.5 mW, 10^6 cycles) were used.

The temperature dependence of saturation magnetization M_s and coercive force H_c of RE-rich and TM-rich films is shown in Figs. 1(a) and 1(b). These data show typical magnetic properties of the RE- and TM-rich film. The Curie temperature T_c of the TM-rich disk is higher than that of the RE-rich disk. It is known that if RE- and TM-rich disks have the same T_c and thermal structure, the domain size of the RE-rich disk is smaller than that of the TM-rich disk under the same writing condition.³ From this result, it is expected that domains of the same size can be written on both TM- and RE-rich disks provided that T_c is higher for the TM-rich

film. RE- and TM-rich disks shown in Fig. 1 were found to provide the same domain size under the same writing condition.

The most dense recording pattern before and after erase/write cycles must be investigated because these patterns are most severe for mark edge recording. Here, the writing domain length and the gap length are both $0.75 \mu\text{m}$. After 2000 erase/write cycles by using a highly accelerated erase power of 11.0 mW, the carrier-to-noise ratio (C/N) of the RE-rich disk did not decrease; however, that of the TM-rich disk decreased rapidly, i.e., the C/N value reduces to 43 dB from an initial value of 53 dB.

In order to investigate this difference in the change of C/N, the recorded domain size of both disks before and after

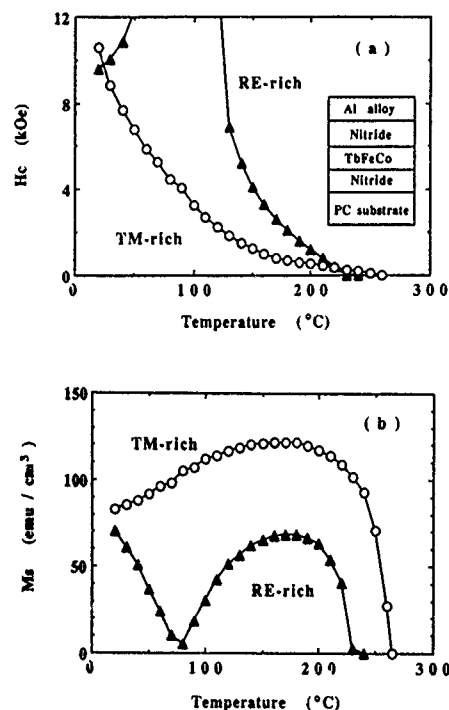


FIG. 1. Temperature dependence of (a) H_c and (b) M_s of RE- and TM-rich films. Details of the construction of the disks is included in (a).

TABLE I. Detail of the erase/write cycle test.

Accelerated erase power (nominal erase power)	11.0 mW (6.5 mW)
Applied field	600 Oe
Linear velocity of the disk	9.4 m/s
Laser wavelength	780 nm
Lens numerical aperture	0.55
Reading power	1.5 mW

2000 erase/write cycles was observed by polarized microscopy. To facilitate the observation of the change in domain size after erase/write cycles, larger domain length ($2.8 \mu\text{m}$) and gap ($2.1 \mu\text{m}$) were prepared. The results are shown in Fig. 2. The domain position of both disks does not change before and after erase/write cycles. The domain size of the TM-rich film is elongated compared with that of the RE-rich film after 2000 erase/write cycles. It is found that the degradation of C/N in the TM-rich disk can be explained by wave-form interference due to the elongated domain.

The domain length after erase/write cycles was evaluated by the half-width of the wave form of the readout signal (Fig. 3). Here, the interval between the most dense recording marks was long enough to prevent from wave-form interference. The domain length of the TM-rich film increases with increasing erase/write cycles. On the other hand, the domain length of the RE-rich film does not so change.

When a domain size (length and width) changes along with erase/write cycles, the center of the domain does not move so that influence of the domain size change is small in the case of mark position recording. However, in case of mark edge recording, domain size change directly causes edge shift in the readout wave form. Therefore, mark edge recording is more severe than mark position recording in terms of erase/write cycles.

As shown in Fig. 2(a) with the TM-rich disk, the domain edge at the central part of the track is particularly elongated, because the temperature of the film at the central part of the laser spot tends to be high. The ratio of the power change to write a stripe domain of $0.4 \mu\text{m}$ width is shown in Fig. 4. This figure shows writing sensitivity change at the central

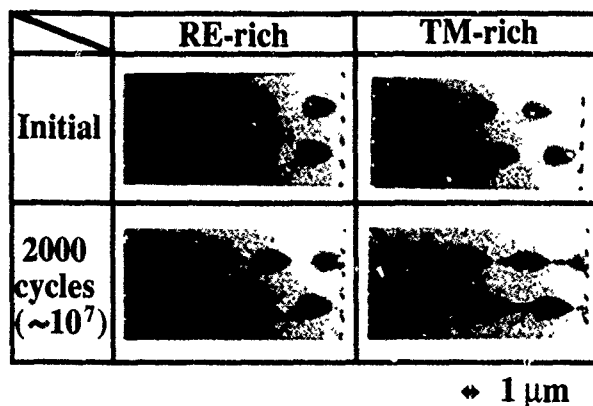


FIG. 2. Recorded domain shape for (a) RE- and (b) TM-rich disks before and after 2000 erase/write cycles.

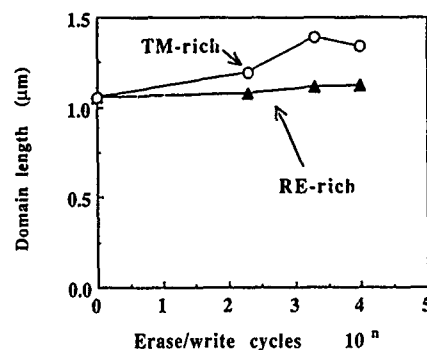


FIG. 3. Dependence of the domain length of RE- and TM-rich disks as a function of the number of erase/write cycles.

part of the track. It was found that the ratio $\Delta P_w/P_w$ of the writing power change ΔP_w of the RE-rich disk is smaller than that of the TM-rich disk. For example, after 2000 erase/write cycles, $\Delta P_w/P_w$ of RE- and TM-rich disks decreased by 12% and 37%, respectively.

Compared with TM-rich disks, the domain length and width of the RE-rich disk is very stable even after erase/write cycles. Therefore, in terms of write/erase cyclability, the RE-rich TbFeCo recording material is suitable for mark edge recording. These results are consistent with the earlier measurements confirming the ability of RE-rich media to withstand 10^6 erase/write cycles.⁴ 2 Gbit capacity in a 5.25-in.-diam disk was achieved with mark edge recording MO by using the RE-rich film.⁴

III. DISCUSSION

The stability of domain size was expressed by Huth,⁵

$$H_c = H_a + H_d - \frac{\sigma_w}{2rM_s} - \frac{1}{2M_s} \frac{\partial \sigma_w}{\partial r}, \quad (1)$$

where H_c , H_a , and H_d are the coercive force, applied field, and demagnetization field, respectively. M_s is the saturation magnetization, σ_w is the domain-wall energy, r is the domain radius. The entire right-hand side of Eq. (1) corresponds to the wall driving force and is called H_{total} . Domain size is determined at the point where H_c balances H_{total} .

Degradation of H_c and σ_w with erase cycles has been thought to originate from structural relaxation in amorphous

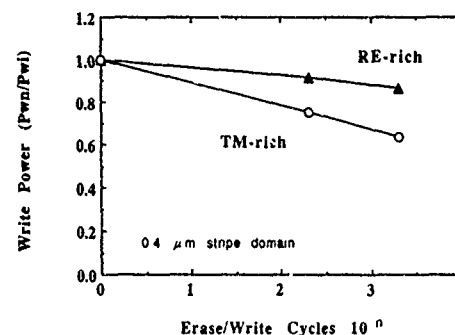


FIG. 4. Dependence of the normalized writing power vs erase/write cycles.

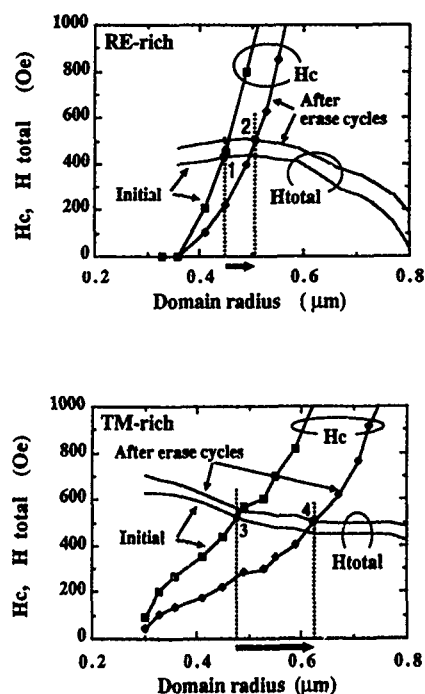


FIG. 5. Functional dependence of H_c and H_{total} on the domain radius calculated on the basis of Eq. (1). Initial and final (after erase/write cycles) curves are shown. Here, film temperature increases with decreasing radius.

TbFeCo.^{2,6} On the other hand, M_s is independent of the structural relaxation.⁶ Based on the initial dependence of H_c and H_{total} of the film on the domain radius,³ a semiquantitative discussion of the force balance of H_c and H_{total} after erase/write cycles can be constructed (Fig. 5). Here H_c and σ_w were assumed to degrade by 50% and 30%, respectively, because σ_w is proportional to square root of H_c . Moreover, it was assumed that RE- and TM-rich films have the same level of structural relaxation. The intersection points, 1 (RE-rich film) and 3 (TM-rich film), correspond to the initial domain size. After erase/write cycles, H_c decreases and H_{total} increases and then the intersection points, 1 in RE-rich and 3 in

TM-rich films, move to 2 and 4, respectively. The elongated domain length is shown by the hatched area. The area of RE-rich film is much smaller than that of the TM-rich one. This is due to the rapid increase in H_c with decreasing temperature and the smaller domain-wall driving force at the recording temperature for the TM-rich film. Thus, better cyclability of the RE-rich disk can be explained.

IV. CONCLUSIONS

Domain size change of typical two different TbFeCo media, RE and TM rich, before and after erase/write cycles was studied for mark edge recording. The domain length and width of the TM-rich disk were found to be elongated with increasing erase/write cycles, while that of the RE-rich film does not change that much. The small domain size change of the RE-rich disk can be explained in terms of the rapid increase in the coercive force with decreasing temperature and smaller domain-wall driving force at recording temperature than those for the TM-rich film, even though both have the same level of structural relaxation. 2 Gbit capacity on a 5.25-in.-diam disk was achieved with mark edge MO recording by using the RE-rich film. A RE-rich film is the key to achieving much higher-density MO than with a 2 Gbit/5.25 in. disk with mark edge recording in the future as well.

ACKNOWLEDGMENTS

We would like to thank Dr. M. Takahashi, Dr. T. Niihara, and Dr. F. Kirino (Central research Lab. Hitachi, Ltd.), and Dr. M. Yoshihiro, Dr. N. Ogihara, and Dr. T. Yoroze (Optoelectronics Lab. Hitachi Maxell, Ltd.) for useful discussions.

¹T. Maeda, F. Kirino, T. Toda, H. Ide, S. Mita, and K. Shigematsu, in Digest of Intermag'93, Stockholm, DD-06.

²F. E. Luborsky, *et al.*, IEEE Trans. Magn. **MAG-21**, 1618 (1985).

³M. Takahashi, T. Niihara, and N. Ohta, J. Appl. Phys. **64**, 262 (1988).

⁴M. Yoshihiro, K. Shimazaki, N. Ohta, T. Toda, H. Awano, and M. Ojima, in Digest of ISOM and ODS Joint Conf'93, Hawaii.

⁵B. G. Huth, IBM J. Res. Dev. **18**, 100 (1974).

⁶N. Ogihara, K. Simazaki, Y. Yamada, M. Yoshihiro, A. Gotho, H. Fujiwara, F. Kirino, and N. Ohta, Jpn. J. Appl. Phys. **28**, 61 (1989).

Recording characteristics of Kr-sputtered Tb/FeCo multilayer magneto-optical disks

Hiro Karube, Kunihiro Matsumura, Masafumi Nakada, and Osamu Okada
Functional Devices Research Laboratories, NEC Corp., Kawasaki 216 Japan

Recording magnetic-field sensitivity and readout stability for Tb/FeCo multilayer magneto-optical (MO) disks, made by sputtering with Kr and Ar gas, were studied. The 100 Oe recording magnetic-field sensitivity for Kr disks was obtained. The readout stability for Kr disk is superior to that for Ar disk. It seems that high readout stability for Kr disks is caused by the large wall coercivity and the large ratio of wall coercivity to nucleation coercivity.

High recording magnetic-field sensitivity is necessary for a magnetic-field modulation method. There are many ways improving the recording magnetic-field sensitivity, such as adding a capping layer (a capping layer disk),¹ adding a GdFeCo layer (a five-layer disk),² and varying a disk preparation condition.³⁻⁵ However, a disk structure for the capping layer disk or the five-layer disk is more complex than conventional disks. Readout stability is important for a disk reliability. The readout stability is concerned with the high recording magnetic-field sensitivity. The readout stability is inferior when the SiN underlayer etching is carried out in order to improve the magnetic-field sensitivity.³ It is important to find an appropriate method with both high magnetic-field sensitivity and high readout stability.

It is considered that wall coercivity and nucleation coercivity affect the recording magnetic-field sensitivity and readout stability. These characteristics are influenced by the microstructure of a magnetic film.⁶ The authors reported that perpendicular magnetic anisotropy of Tb/FeCo multilayers (Kr film), prepared by cosputtering with Kr gas, was larger than that of Tb/FeCo multilayers, prepared by cosputtering with Ar gas (Ar film)⁷ and that the magnetic anisotropy improvement for Kr film originates from a low-anisotropy dispersion.⁸ It is shown that the microstructure for Kr film is different from that for Ar film. In this article recording characteristics of Kr disks are studied from the recording magnetic-field sensitivity and readout stability viewpoint.

Magneto-optical (MO) disks utilized a four-layer structure that comprised a first SiN layer (1000 Å thick), a Tb/FeCo magnetic multilayer (200 Å thick), a second SiN layer (400 Å thick), and an Al layer (400 Å thick). A polycarbonate (PC) substrate (1.6 μm track pitch) was used. SiN layers were prepared by reactive rf sputtering with Ar+N₂ gas. The Al layer was prepared by vapor deposition. Tb/FeCo multilayers were prepared by dc magnetron cosputtering alternately from Tb and Fe₉₀Co₁₀ alloy targets. Two series of disks with different sputtering gases were prepared. One had a Tb/FeCo multilayer prepared by dc cosputtering with Kr gas (Kr disks). The others had a Tb/FeCo multilayer prepared by dc cosputtering with Ar gas (Ar disks). Ar disks were prepared in order to compare with Kr disks. The layer thickness of Tb was 6.4 Å and that of FeCo was varied from 8.3 to 10 Å. The substrate table was rotated at 20 rpm and the sputtering rate was selected to keep the same value at Ar

and Kr sputtering. During deposition, the sputtering gas pressure was kept constant at 8×10^{-2} Pa. Recording characteristics were measured with the read/write tester ($\lambda=830$ nm, numerical aperture=0.50) at 3.7 MHz (duty 50%) recording frequency and 11.1 m/s linear velocity. Wall coercivity and nucleation coercivity (coercive force) were determined from the Kerr hysteresis loop for the as-deposited film onto PC substrates at room temperature.³

Figure 1 shows the recording magnetic-field dependence of carrier and noise level on the Kr disks. Both "land" and "groove" were erased to the same direction, before the recording had been carried out. The recording power, minimizing the ratio of second-harmonics level to carrier level, was ranged from 8.5 to 9.0 mW. The erasing magnetic field was -400 Oe and the readout power was 1.0 mW. Over 400 and over 100 Oe recording magnetic field were required for noise saturation in the Kr disk with 8.3-Å-layer FeCo thick and in Kr disk with 9.6-Å-thick FeCo layer, respectively. That is, the FeCo layer thickness affected the recording magnetic-field saturated noise level.

Figure 2 shows the recording magnetic-field dependence of carrier and noise level on the Ar disks. The recording power, minimizing the ratio of the second-harmonics level to carrier level, was ranged from 7.5 to 8.0 mW. The other

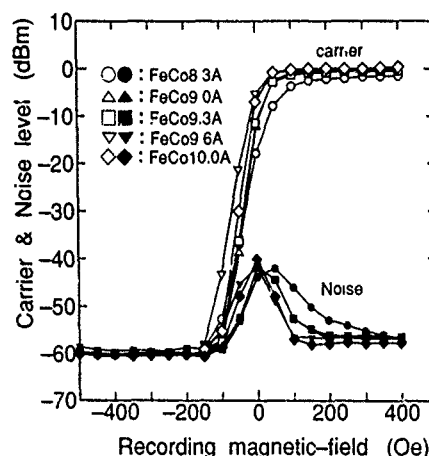


FIG. 1. Recording magnetic-field dependence of carrier and noise level on Kr disks. Open symbols indicate carrier level, and solid ones indicate noise level. Read power=1.0 mW, resolution bandwidth=30 kHz.

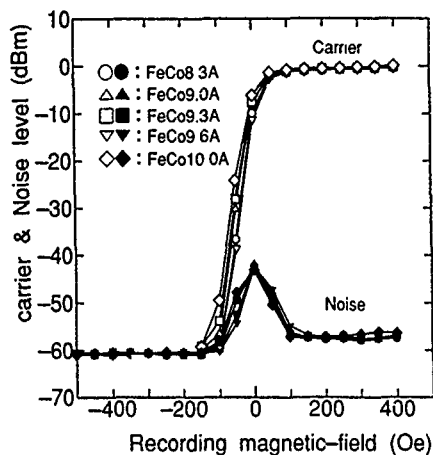


FIG. 2. Recording magnetic-field dependence of carrier and noise level on Ar disks. Open symbols indicate carrier level, and solid ones indicate noise level. Read power=1.0 mW, resolution bandwidth=30 kHz.

measurement condition was the same as the Kr-disk measurement. Recording magnetic-field values, required for noise saturation, were similar for all Ar disks.

We defined recording magnetic-field sensitivity as a minimum magnetic-field saturating both carrier and noise level. Figure 3 shows the FeCo layer thickness dependence of the recording magnetic-field sensitivity for Kr and Ar disks. High recording magnetic-field sensitivity of 100 Oe was obtained at the 9.6 Å FeCo layer thickness for Kr disks. The recording magnetic-field sensitivities for the Ar disks were higher than those for the Kr disks. However, the highest recording magnetic-field sensitivity for the Kr disk was 100 Oe and was the same as that for the Ar disks. The Ar disks had a large margin for high recording magnetic-field sensitivity as compared with Kr disks. It was found that sputtering gas preparation for the magnetic layer affects the magnetic-field sensitivity.

Satoh *et al.* reported that the recording magnetic-field sensitivity had a tradeoff with relevance to readout stability.³ Readout stability for Ar and Kr-disks was measured. Figure 4

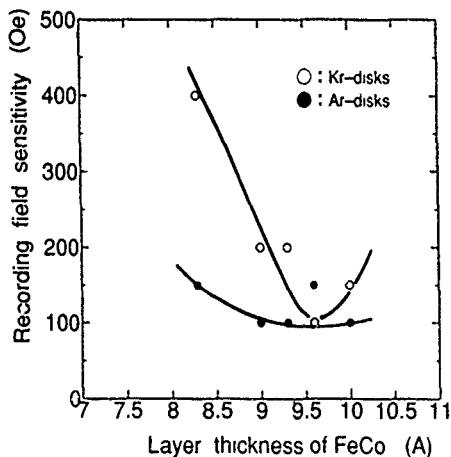


FIG. 3. FeCo layer thickness dependence of recording magnetic-field sensitivity.

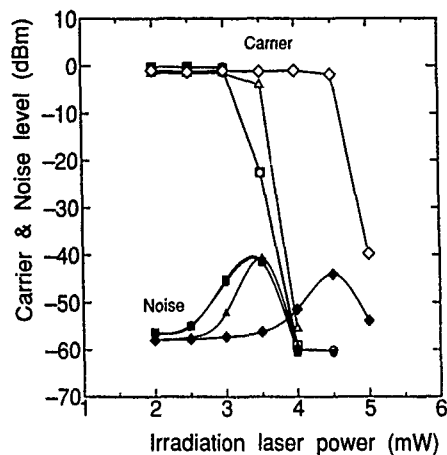


FIG. 4. Irradiation laser power dependence of carrier and noise level on Ar and Kr disks. \circ : $d\text{FeCo}=9.0$ Å; \triangle : $d\text{FeCo}=9.3$ Å; \square : $d\text{FeCo}=10.0$ Å; \diamond : Kr disk, $d\text{FeCo}=9.6$ Å. Read power=1.0 mW, resolution bandwidth=30 kHz.

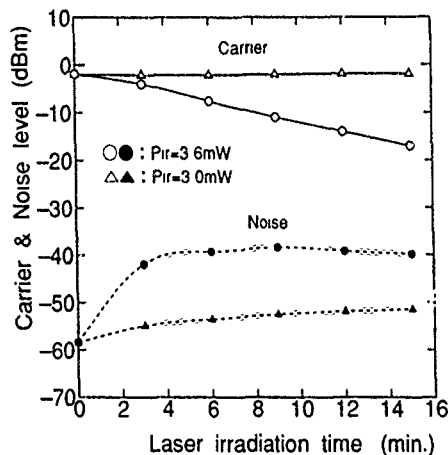
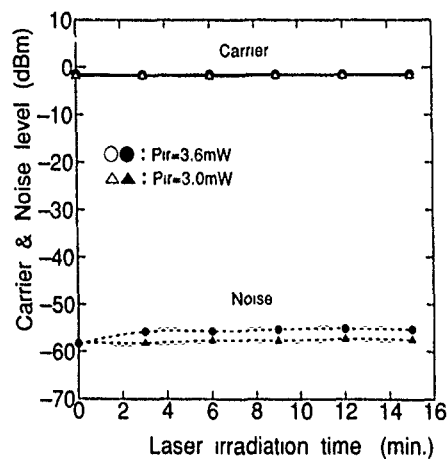


FIG. 5. Irradiation time dependence of carrier and noise level: (a) Kr disk, $d\text{FeCo}=9.6$ Å; (b) Ar disk, $d\text{FeCo}=9.3$ Å.

TABLE I. Wall coercivity for Kr and Ar disks at room temperature.

FeCo layer thickness (Å)	8.3	9.0	9.3	9.6	10.0
Kr disk (kOe)	>20	9.0	9.6	9.6	5.4
Ar disk (kOe)	6.9	3.0	10.8	6.0	4.8

shows the irradiation laser power dependence of carrier and noise level on Ar disks having 100 Oe recording magnetic-field sensitivity, whose FeCo layer thicknesses were 9.0 Å (disk no. 1), 9.3 Å (disk no. 2), and 10.0 Å (disk no. 3). Furthermore, Fig. 4 shows the irradiation laser power dependence of carrier and noise level for the Kr disk with 9.6 Å FeCo layer (disk no. 4). The recording was carried out at 400 Oe. The recording laser power was 7.5 mW. Then, the laser beam was irradiated with the 400 Oe magnetic-field applied in the erasing direction for 3 min. The readout laser power was 1.0 mW. Carrier levels did not change for less than 3.0 mW irradiation laser power. The carrier levels drastically decreased over 3.0 mW irradiation for disks no. 1 and no. 3. Over 4.0 mW power was required for complete erasure. On the other hand, carrier level for disk no. 2 did not change at 3.0 mW irradiation power. Increase in noise level for disk no. 2 was smaller than that for the other. Therefore, disk no. 2 had the highest readout stability in these three Ar disks. A comparison of readout stability between Kr and Ar disks was carried out. The recording magnetic-field sensitivity for disk no. 4 had the highest recording magnetic-field sensitivity and its value was 100 Oe. Recording laser power was 9.0 mW. The other measurement conditions were the same as for the above measurement. The Carrier level was constant up to 4.5 mW irradiation power. The readout stability for disk no. 4 (Kr disk) was more stable than that for disk no. 2 (Ar disk).

Figures 5(a) and 5(b) show the irradiation time dependence of carrier and noise levels for disk no. 4 (Kr disk) and disk no. 2 (Ar disk), respectively. The laser beam was irradiated with the 400 Oe magnetic field applied in the erasing direction. Irradiation laser power was 3.0 and 3.6 mW. The readout laser power was 1.0 mW. The noise level increased greatly through increasing the irradiation power and the irradiation time. Increase in noise level occurred at an initial irradiation time. Carrier level for disk no. 2 was decreased with increasing the irradiation stage, only when the irradiation power was 3.6 mW. Decrease in carrier level for disk no. 4 was not observed. Increase in noise level for Kr disk at the 3.6 mW irradiation power was smaller than that for disk no. 2 at the 3.0 mW irradiation power. Therefore, readout stability for disk no. 4 (Kr disk) is superior to that for disk no. 2 (Ar disk). Both high recording magnetic-field sensitivity and high-readout stability were obtained by Kr gas sputtering.

It was reported that large wall coercivity H_w was the key factor in achieving stable domains.³ H_w and nucleation coer-

TABLE II. The ratio of wall coercivity to nucleation coercivity.

FeCo layer thickness (Å)	8.3	9.0	9.3	9.6	10.0
Kr disk	...	0.67	0.70	0.63	0.61
Ar disk	0.39	0.57	0.53	0.65	0.54

civity H_n were examined in order to clarify a relationship among the readout stability, H_w value, and H_n value. Table I shows H_w at room temperature for Kr and Ar disks. Table II shows the ratio of H_w to H_n , H_w/H_n . The authors find that high-readout stability for Kr disk cannot be explained by "only" the H_w value. The H_w value for the Ar disk with 9.3 Å FeCo layer thick (disk no. 2) was the largest in all Ar disks. However, the readout stability for the Ar disk with an 8.3 Å FeCo layer (disk no. 5) was almost the same as that for the Ar disk with a 9.0 Å FeCo layer (disk no. 1) in spite of the large difference of H_w . Furthermore, the H_w value for the Kr disk with 9.6-Å-thick FeCo layer (disk no. 4), whose read stability is superior to that for Ar disk, was smaller than that for disk no. 2.

The H_w/H_n value for disk no. 4 (Kr disks) was larger than for Ar disks (disks no. 1, no. 2, no. 3, and no. 5), except 9.6-Å-thick FeCo layer samples. Moreover, the H_w/H_n value for disk no. 1 was larger than that for disk no. 5. Thus, it seems that high readout stability for Kr disks is caused by the large wall coercivity and the large ratio of wall coercivity to nucleation coercivity.

In conclusion, recording magnetic-field sensitivity for Tb/FeCo multilayer MO disks by sputtering with Kr and Ar gas was studied. It was found that sputtering gas preparation for the magnetic layer affects the magnetic-field sensitivity. The 100 Oe recording magnetic-field sensitivity for Kr disks was obtained. Readout stability for the Kr disk was superior to that for the Ar disk. Both high recording magnetic-field sensitivity and high-readout stability were achieved by Kr gas sputtering. It seems that high-readout stability for Kr disks is caused by the large wall coercivity and the large ratio of wall coercivity to nucleation coercivity.

¹S. Ohnuki, K. Simazaki, N. Ohta, and H. Fujiwara, J. Magn. Soc. Jpn. **15**, S1, 399 (1991).

²K. Ichitani, S. Tsunashima, and S. Uchiyama, J. Magn. Soc. Jpn. **17**, S1, 196 (1992).

³T. Satoh, Y. Takatsuka, H. Yokoyama, S. Tatsukawa, T. Mori, and T. Yoroze, IEEE Trans. Magn. **MAG-27**, 5115 (1991).

⁴S. Kawasaki, K. Ishizuka, S. Katsuta, and M. Solimuta, Jpn. J. Appl. Phys. **32**, 3163 (1993).

⁵E. Ikeda, T. Tanaka, T. Chiba, and H. Yoshimura, J. Magn. Soc. Jpn. **17**, S1, 335 (1992).

⁶H. Fu, R. Giles, M. Mansuripur, and G. Patterson, Comput. Phys. **6**, 610 (1992).

⁷H. Karube, K. Matsumura, and O. Okada, J. Magn. Soc. Jpn. **17**, S1, 123 (1992).

⁸H. Karube, K. Matsumura, M. Nakada, and O. Okada, Tech. Rep. IEICE **MR92-85**, 15 (1993) (in Japanese).

Double compensation point media for direct overwrite

T. K. Hatwar, D. J. Genova, and R. H. Victora

Imaging Research and Advanced Development, Eastman Kodak Company, Rochester, New York 14650-2017

Two magneto-optic media configurations are discussed that are suitable for direct overwrite by light intensity modulation using only one conventional bias magnet. One configuration consists of two magnetic layers (memory and reference having perpendicular anisotropy) exchange coupled through an intermediate soft magnetic layer. The second media configuration consists of only a memory layer and an intermediate layer. This scheme produced a respectable direct overwrite performance of 48 dB using a 3.5 μm mark size, 30 kHz bandwidth, and 7 m/s disk velocity. The major advantages of this scheme are simpler disk structures relative to a previously proposed quadrilayer scheme, and a wide range for Curie temperatures, thicknesses, and coercivities of the individual layers.

Direct overwrite (DOW) is vital for the new generation magneto-optic (MO) disk drives to achieve shorter access time and higher data rate. In recent years, substantial efforts have been directed to the development of an efficient and practical method for achieving direct overwrite on MO media. Following the limited success of DOW in a single-layer medium, schemes have been investigated based on both magnetic-field modulation and light intensity modulation.¹⁻⁷ Schemes based on light intensity modulation of the laser beam utilize multilayer media configurations and eliminate the field switching required in magnetic-field modulation. Some of these schemes have shown great promise, however, a large initializing magnetic field increases the complexity of the drive design and affects the stability of the written marks. The initializing field has been eliminated in recent direct overwrite schemes;⁴⁻⁷ however, only the quadrilayer scheme proposed by Fukami *et al.* produced a respectable performance.⁶ However, it is difficult to produce this scheme in large-scale manufacturing due to extreme constraints imposed on the large number of parameters of each layer. Further, defect density as well as the bit error rate increase tremendously as the number of layers increases in a disk structure. Therefore, a most desirable scheme that is manufacturable should have a simple disk structure, wide power margins, high writing sensitivity, and not require an IM. In this article we report a new type of direct overwrite scheme that eliminates some of the problems mentioned above. The static and dynamic performance, the underlying operational principle, and the future possibilities for this scheme are presented.

One configuration of this scheme is shown in Fig. 1 and consists of two magnetic layers (memory and reference) exchange coupled through an intermediate magnetic layer. The memory and the reference layers have a relatively large perpendicular anisotropy while the intermediate layer is magnetically soft. The memory layer has a Curie temperature T_{cm} that is greater than or approximately equal to the reference layer Curie temperature T_{cr} . The intermediate layer has a higher Curie temperature than either the memory layer or the reference layer. The room-temperature coercivity of the memory layer is higher than the room-temperature coercivity of the reference layer. The combined magnetization of the coupled layers exhibits two compensation points: This requires antiferromagnetic coupling between the memory and

reference layers over at least part of the temperature range. The thickness and composition of the reference layer is chosen so that the combined system has a compensation temperature above the ambient temperature but below the write temperature.

Figure 2(a) shows the magnetization of the three layers of the trilayer scheme as a function of temperature, whereas Fig. 2(b) shows the magnetization for the combined system. The square symbol curve in Fig. 2(b) is obtained by considering the antiferromagnetic (AF) coupling between the memory and reference layers mediated through the control layer, whereas the other curve shows the experimental values of the remnant magnetization measured using the vibrating sample magnetometer. The combined magnetization curve has lower and upper combined compensation temperature T_{clc} and T_{cuc} , which are essential for the operation of this DOW scheme. An approximate location of the write temperature T_w is also indicated in Fig. 2(b). As shown below, T_w must exceed the highest temperature at which the coercivity for the domain-wall motion is above the bias field.

When such a medium is irradiated with the low- and high-power laser beam, the magnetization of the memory and reference layers change as shown in Fig. 3. The magnetization of the medium as it comes out of the vacuum coater points in random directions. As is common for conventional media, it is initialized once (presumably at the factory) using either a high dc field or a dynamic tester.

Writing at high power is aided by the applied field and the demagnetizing field; it is opposed by the energy of creating a domain wall and by the gradient in domain-wall energy caused by the Gaussian-shaped thermal profile. This

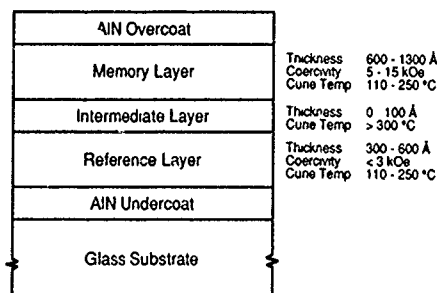


FIG. 1. Schematic of the three-layer media structure.

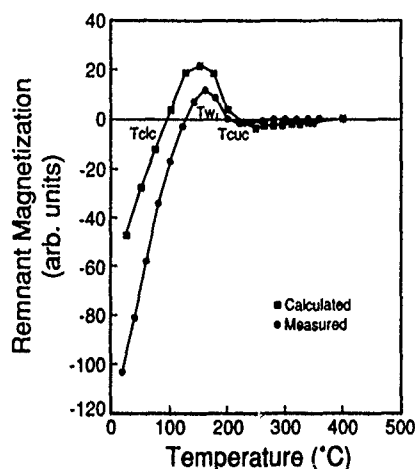
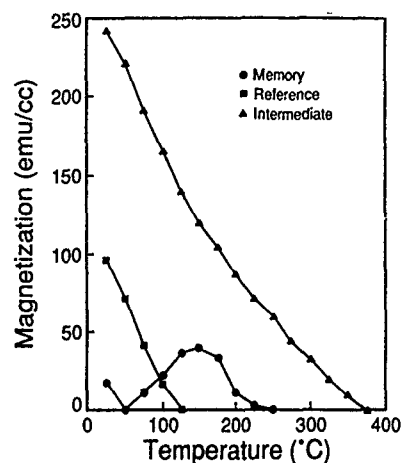


FIG. 2. (a) M_s vs temperature for the individual layer of the three-layer scheme; (b) M_s vs temperature for combined system.

profile makes a wall at small radius having a higher temperature and thus lower wall energy per unit area than a wall at a large radius. However, this profile dissipates rapidly and apparently leaves the domain wall pinned in place before the domain can vanish. Assuming that the memory layer has a larger magnetic moment at the write temperature (owing to greater thickness or other causes), the reference layer will be left with magnetization opposing the bias field, as illustrated in Fig. 3.

Erasing at low power is opposed by the applied field and the demagnetization field; it is aided by the domain-wall energy and particularly by the thermal gradient, which does not

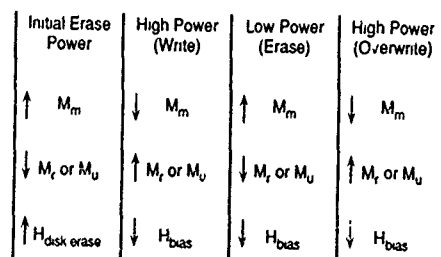


FIG. 3 Arrow diagram showing the write erase mechanism for a disk in which the memory and reference layers are antiferromagnetically coupled.

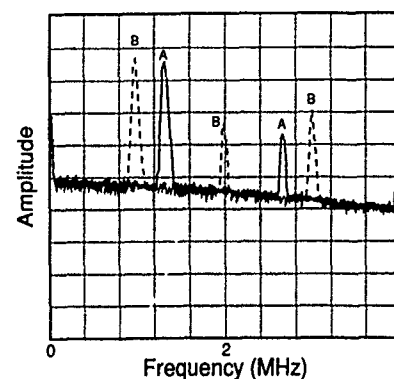


FIG. 4. Spectrum analyzer plot of the direct overwrite of the three-layer scheme. A and B correspond to original and overwritten signal, respectively.

dissipate until a much lower temperature than in the high-power case. Evidence for the proposed importance of the thermal gradient during erase is provided by the absence of a linear relationship between the measured erase power and the ambient temperature. The presence of such a relationship would allow the extrapolation of the erase temperature from the point where it crosses the temperature axis. (Such an extrapolation could be performed for the write temperature.) Its absence means that there is no one temperature at which erase occurs; erasure must depend on other variables such as the temperature gradient.

Samples containing the memory, reference, and intermediate layers were prepared on glass substrates. In one example, the memory layer comprised of $\text{Tb}_{24}\text{Fe}_{62}\text{Co}_9$ had a Curie temperature of 250 °C, compensation temperature of 30 °C, and room-temperature coercivity >13 kOe. The reference layer comprised of $\text{Tb}_{27}\text{Fe}_{64}\text{Co}_9\text{Zr}_{10}$ had a Curie temperature of 120 °C, and room-temperature coercivity <3 kOe. This layer did not have a compensation point below the Curie temperature. The intermediate layer, comprised of $\text{Gd}_{85}\text{Fe}_{22}\text{Co}_{43}$, had a Curie temperature of 400 °C. A trilayer disk was prepared using a 1300-Å-thick memory layer, 100-Å-thick intermediate layer, and 400 Å reference layer deposited sequentially on a 130-mm-diam glass substrate without breaking the vacuum in the sputtering chamber. A 5 mm band was erased dynamically using high power and an erase field of 600 Oe, thus initializing all the layers. A track was written by modulating the laser power at 6 mW (P_{low}) and 16 mW (P_{high}) levels, a frequency of 1.33 MHz (50% duty cycle), and using -400 Oe write bias field in the opposite sense to that of the erase bias field. The spectrum of the recovered signal is shown as curve A in Fig. 4 and shows the peaks at 1.33 MHz and higher harmonics as expected. The track was then overwritten while modulating the laser at 1.0 MHz. The spectrum of the recovered signal is shown as curve B in Fig. 4. The original signal at 1.33 MHz is completely overwritten with the 1.0 MHz signal and the new peaks appear corresponding to 1.0 MHz frequency.

The overwriting mechanism described earlier will become clearer from the Kerr hysteresis loop of the memory and reference layers measured at ambient and elevated temperatures. In this case memory and reference layers have

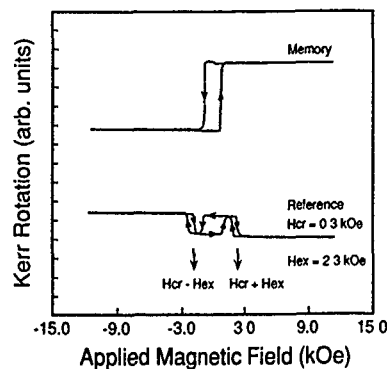


FIG. 5. Kerr hysteresis loops for the direct overwrite trilayer disk at 140 °C measured from both memory and reference layer side. Arrows on the hysteresis line indicate the direction for sweep of magnetic field.

composition of $\text{Tb}_{24}\text{Fe}_{62}\text{Co}_9\text{Zr}_5$ and $\text{Tb}_{30}\text{Fe}_{60}\text{Co}_{10}$, respectively, and the same Curie temperatures of 175 °C. The two layers are exchange coupled (exchange field ~ 1.7 kOe) to each other at room temperature. The coercivity of the memory layer was high (>12 kOe) as in a single-layer sample. The high-temperature Kerr loops show interesting features. The coercivity of the memory layer has decreased to about 1000 Oe. The reference layer indicated three separate transitions in the magnetization as shown in Fig. 5. It is interesting to note that when the applied field is small (less than 1500 Oe), the magnetization of the memory and reference layers are always oppositely aligned and, in fact, switched simultaneously. This means both of the layers are written simultaneously. We found the exchange field between the memory and reference layers at this temperature to be 2.3 kOe.

To confirm our earlier observation that the reference layer is written along with the memory layer, we wrote tracks from the memory side but read from the reference side of the disk through the substrate. In fact, a large signal was recovered on the spectrum analyzer, indicating that reference layer and memory layer are written simultaneously.

The DOW performance was found to depend on the power levels, bias field, and disk velocity. By using suitable power levels we were able to obtain DOW CNR of about 48 dB at $3.5 \mu\text{m}$ mark lengths. We also investigated several combinations of disk structures to find the operating range for bias field and power levels of the direct overwrite process. DOW performance was similar as long as the combined system compensation point was 70–110 °C. Long-term reliability has not yet been evaluated: Limited testing (ten overwrites) shows no degradation in performance with repeated cycling.

The other configuration of this scheme consists of only a memory layer and a soft magnetic underlayer exchange coupled to each other. The Curie temperature of the underlayer is higher than the Curie temperature of the memory layer. This underlayer is the same as the control layer of the three-layer scheme of Fig. 1. Figure 6 shows the calculated and measured combined magnetization of the memory layer and underlayer. The combined magnetization curve has

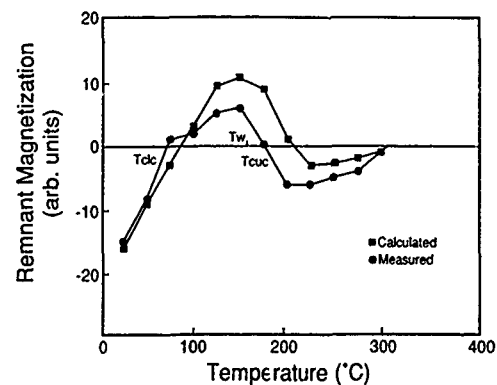


FIG. 6. Magnetization vs temperature for the two-layer scheme.

lower T_{clc} and upper compensation T_{cuc} temperatures that determine operation of the medium. This scheme also gave good dynamic performance but was about 2 dB lower than the first configuration. The mechanism of this structure is thought to be similar to that of the earlier configuration.

The CNR offered by either of the media configurations is below the desired value of 55 dB. Kerr microscopy has been used to examine the written and erased marks. It is found that if full width marks are written, then the erase power only thins the marks but does not completely remove them. This leaves a long chain of marks, modulated in width, and does not provide the desired CNR. If a lower write power is used, then marks can be fully erased, but the written areas do not have sufficient width to generate a full signal. Again, CNR is reduced. However, this scheme offers several possibilities for future improvements and exploitation. It has been found that relatively large marks can be erased if the marks occur in well-defined locations; this suggests use for fixed bit cell recording. More extensive optimization of media, particularly the domain-wall mobility, may allow larger areas to be erased and thus increase the CNR. Furthermore, the trend in MO recording is toward the smaller marks that we have no difficulty in erasing. Preliminary measurements indicate small mark ($0.7 \mu\text{m}$) performance only 4 dB lower than large mark performance. Finally, our measurements were made on a dynamic tester without high-frequency injection. This may have underestimated our performance by several dB.

We would like to acknowledge the help of A. C. Palumbo for Kerr microscopy, C. Brucker and J. Farruggia for vibrating sample magnetometer measurements, and Y. S. Tyan for several useful discussions and numerous suggestions.

- ¹H. P. D. Shieh and M. H. Kryder, *Appl. Phys. Lett.* **49**, 473 (1986).
- ²J. Saito, M. Sato, H. Matsumoto, and H. Akasaka, *Jpn. J. Appl. Phys.* **26**, Suppl. 26-4, 155 (1987).
- ³K. Aratani, M. Kaneko, Y. Mutoh, K. Watanabe, and H. Makino, *Proc. SPIE* **1078**, 258 (1989).
- ⁴F. Tanaka, S. Tanaka, and N. Imamura, *Jpn. J. Appl. Phys.* **26**, 231 (1987).
- ⁵T. Fukami, Y. Nakaki, T. Tokunaga, M. Taguchi, K. Tsutsumi, and H. Sugahara, *Jpn. J. Appl. Phys.* **28**, Suppl. 28-3, 371 (1989).
- ⁶T. Fukami, Y. Nakaki, T. Tokunaga, M. Taguchi, and K. Tsutsumi, *J. Appl. Phys.* **67**, 4415 (1990).
- ⁷T. Ohtsuki, C. J. Lin, and F. Yamada, *IEEE Trans. Magn.* **MAG-27**, 5109 (1991).

Design and performance of magneto-optic enhanced Co/Pt-based trilayers having zero Kerr ellipticity

R. Atkinson

Department of Pure and Applied Physics, The Queen's University of Belfast, Belfast, BT7 1NN, United Kingdom

P. J. Grundy

Department of Pure and Applied Physics, The University of Salford, Salford, M5 4WT, United Kingdom

C. M. Hanratty

Department of Pure and Applied Physics, The Queen's University of Belfast, Belfast, BT7 1NN, United Kingdom

R. J. Pollard

Department of Pure and Applied Physics, The University of Salford, Salford, M5 4WT, United Kingdom

I. W. Salter

Department of Pure and Applied Physics, The Queen's University of Belfast, Belfast, BT7 1NN, United Kingdom

The design philosophy and objectives for producing phase-optimized trilayer structures for magneto-optic enhancement of the polar Kerr effect is outlined. A number of alternative designs is presented based on glass/Co-Pt/SiO₂/Al. The performance of an actual device, as a function of the wavelength of the incident radiation, and of angle of incidence, for both of the principal polarization states, has been evaluated experimentally and theoretically. Results indicate excellent agreement and demonstrate the ease with which devices can be designed and fabricated.

I. INTRODUCTION

The magneto-optic (MO) Kerr effect in an absorbing medium can be enhanced by its incorporation into a suitable thin-film optical environment, usually a quadrilayer¹ or a trilayer system² which is designed to maximize the Kerr rotation for a given system reflectance. This has the effect of maximizing the signal-to-noise ratio (SNR) associated with the differential detection of the normal incidence polar Kerr effect and therefore with the readout of stored information in the MO storage disk system. Although improvements are significant, an additional and most desirable feature is the total elimination of parasitic Kerr ellipticity.³ This has the effect of producing the maximum Kerr rotation while, at the same time, effectively dispensing with the need for MO phase correcting optics in the optical readout head.

In this article we report on the optical and magneto-optical performance of a trilayer structure designed around the use of Co-Pt multilayers (MLs) as the magnetic medium. We outline briefly the design philosophy² for MO phase correction and demonstrate the ease with which these systems may be fabricated. The performance of an actual device is demonstrated by a series of comprehensive measurements which demonstrate the dispersion and angular dependence of the most important properties compared with theoretical calculations.

II. EXPERIMENT

The trilayer structures consisted of Co-Pt MLs, as the magnetic component, together with a silicon dioxide dielectric spacer layer followed by an aluminium reflector as shown in Fig. 1. All layers were prepared by magnetron sputtering in a computer-controlled, UHV-compatible ($<10^{-8}$ mbar) multisource deposition system. Depositions of all ma-

terials were made at 3 mbar of argon onto glass substrates without breaking the vacuum. Individual layer thicknesses were determined from calibrated deposition times and in the case of the Co-Pt MLs, sublayer film thicknesses and bilayer periodicity were confirmed from low-angle x-ray diffraction. The Co-Pt consisted of 1.1 nm Pt/6(0.4 nm Co-1.1 nm Pt) giving a total thickness of 10.1 nm. The optical and MO properties were obtained using a variable-angle, spectroscopic Kerr polarimeter, operating with a rotating analyzer.

III. TRILAYER DESIGN

To maximize the SNR associated with the differential readout of the Kerr effect⁴ it is necessary to satisfy three criteria. First, the MO disk reflectance R should be a specific value related to the magnitudes of the various noise sources of the detection system.¹ Typically this is likely to be within the range 0% to 33%. Second, the Kerr rotation θ_k should be a maximum. Third, the MO phase difference δ_k between the

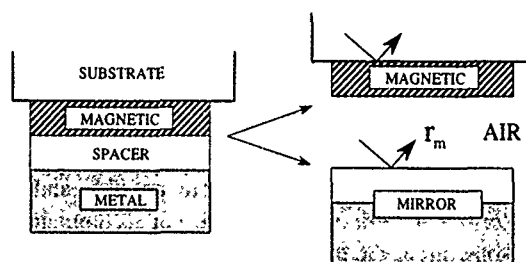


FIG. 1. The trilayer structure showing the reflectance r_m of the mirror system into a fictitious air gap.

TABLE I. Normal-incidence trilayer designs for glass/Co-Pt/SiO₂/Al $n=2.221+i4.532$ and $Q=-0.0103+i0.0104$ at a wavelength of 633 nm for Co-Pt.

R	$\cos \delta_k$	d_m (nm)	d_D (nm)	θ_k (deg)	η (%)
0.1	+1	7.3	162	1.35	90
0.2	+1	8.3	170	0.82	87
0.3	+1	9.4	176	0.56	83
0.1	-1	9.6	119	1.46	97
0.2	-1	12.1	110	0.93	98
0.3	-1	15.4	104	0.66	98

Kerr component and the isotropic amplitude reflectance vector must be either 0 or π . This gives rise to zero Kerr ellipticity ϵ_k .

The principle of the design may be understood by reference to the structure of the trilayer shown in Fig. 1. Given that the materials available for constructing the system are predetermined, there are essentially two variable parameters for satisfying the above three requirements: These are the thicknesses of the magnetic d_m and spacer layers d_D . At first sight the problem appears insoluble; however, it is important to realize that the maximization of the Kerr component is essentially determined by two factors. One is the need for d_m to be less than the optical skin depth. The other is that the complex amplitude reflectance of the underlying mirror system, into air, $r_m (=|r_m|e^{i\rho m})$ (Ref. 5) be such that $|r_m|>90\%$ and ρm is within $\pm 0.7\pi$. Satisfying this rather loose condition almost certainly guarantees that the Kerr component will be very close to its maximum value. Consequently, one may adjust d_m and d_D until R and δ_k attain desired values. The corresponding value of r_m usually ensures that the Kerr rotation is very close to its maximum value. The degree to which this is achieved is indicated by the efficiency parameter $\eta = \theta_k/\theta_{k \max}$.

Using this procedure we have designed a number of systems for $R=0.1, 0.2$ and 0.3 , and for $\delta_k=0$ and π . The dielectric spacer layer was SiO₂ and the metal mirror was semi-infinite Al. The complex refractive index n and MO parameter Q for Co-Pt were deduced from Ref. 6 and the optical constants of SiO₂ and Al were taken from Ref. 7. The incident medium was assumed to be glass of refractive index 1.52.

IV. THEORETICAL RESULTS

As can be seen from Table I there are two designs for each reflectance value which will lead to zero Kerr ellipticity. The thickness of the Co-Pt layer is typically of the order of 10–15 nm, which is below the skin depth at this wavelength, and the SiO₂ layers are all less than 180 nm. Although the first three designs for $\cos \delta_k=+1$ are possible and would lead to zero Kerr ellipticity, they are not recommended for two reasons. First, the efficiency parameter η is not particularly high ($\approx 85\%$). Second, the reflectance of the system is five times more sensitive to errors in the thickness of the magnetic layer than in the cases where $\cos \delta_k=-1$. For these reasons phase compensation with $\delta_k=\pi$ must be considered

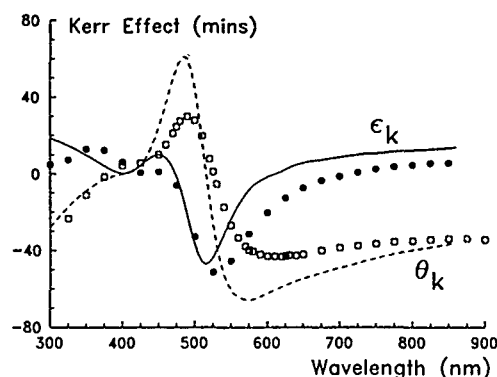


FIG. 2. Dispersion of the complex Kerr rotation ($\theta_k + i\epsilon_k$) for a trilayer.

the most expedient design choice, since this will lead to systems whose reflectances are relatively insensitive to errors in film thicknesses and which have Kerr rotations that are within 97% of their absolute maximum values.

V. PRACTICAL PERFORMANCE

To demonstrate the feasibility of producing a trilayer of this type we have fabricated a structure based on the design for $R=0.1$ and $\delta_k=\pi$. In practice the Co-Pt had a total thickness of 10.1 nm which is slightly in excess of the design value of 9.6 nm. The SiO₂ layer thickness was 119 nm and that of the aluminium was greater than 200 nm. Measurements were made of θ_k , ϵ_k , and R over the spectral range 300–900 nm and the results are shown in Figs. 2 and 3 together with theoretical calculations based on the use of optical and MO constants for Co-Pt (0.65/1.8 nm) MLs.⁸ Although these layer thicknesses are not exactly the same as those corresponding to the Co-Pt in the trilayer system they provide a useful means of assessing its performance. In addition, and because all practical MO disk systems will operate with a focused and therefore highly convergent light beam, we report on the variation of θ_k , ϵ_k , and $\cos \delta_k$ with angle of incidence. These are shown in Figs. 4 and 5 and are compared with theoretical calculations using the values of n and Q given in Table I.

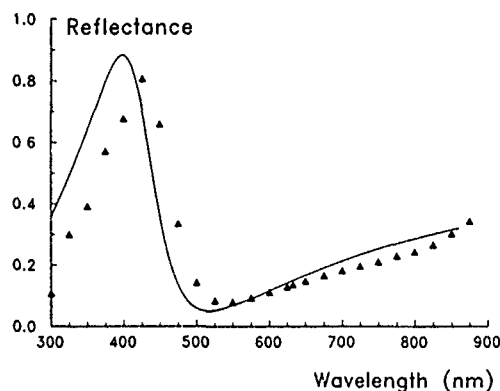


FIG. 3. Dispersion of the reflectance of a trilayer.

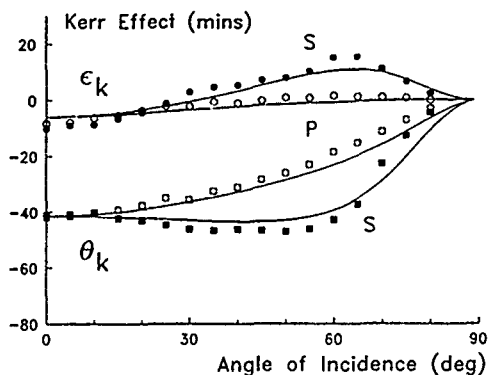


FIG. 4. Angular dependence of the complex Kerr rotation ($\theta_k + i\epsilon_k$) of a trilayer for the principal states of polarization.

When reading these figures it should be remembered that the design details were determined for a semi-infinite incident medium. In practice, measurements were taken through the substrate and as a consequence suffer from the complications of multiple incoherent reflections within the glass substrate. The theoretical curves shown in Figs. 2–5 have therefore been determined taking into account these extra reflections and should not be compared with data for R and θ_k in Table I.

At normal incidence, the rapid variation of θ_k and ϵ_k around 500 nm is associated with an antireflection condition which occurs for three-layer systems of the type being considered here. This reflectance minimum can be seen in Fig. 3. In fact, the reflectance minimum is very close to zero at the trilayer/glass interface and the corresponding Kerr rotation is very large indeed. However, the reflectance from the air/glass

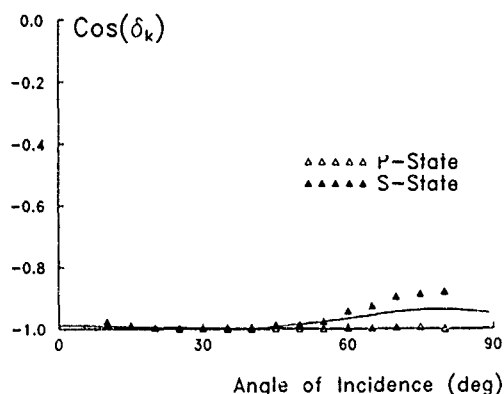


FIG. 5. Angular dependence of the MO phase function $\cos \delta_k$ for the principal states of polarization.

interface remains finite and limits the measurable rotations to those values seen in the theoretical curves. Bearing in mind the uncertainties in the basic constants of the Co-Pt and in the actual layer thicknesses, the agreement between the theoretical and experimental curves is very good indeed. It may be noted that changing the value of d_m to about 14 nm produces even better agreement. The variation in the Kerr ellipticity is also as expected and can be seen to attain very small values in the vicinity of the design wavelength and is zero at about 700 nm.

The angular variations of θ_k , ϵ_k , and $\cos \delta_k$ were measured in air and are labeled P and S corresponding to the MO component being polarized parallel or perpendicular to the plane of incidence, respectively. Theoretical curves have been calculated in the same way as before except that in this case the larger film thickness for the Co-Pt was used. This gives better agreement at normal incidence, by compensating for slight errors in actual film thickness or in the optical constants. It can be seen from these figures that the experimental behavior of the device is in accordance with expectations and that for angles of incidence up to about 30°–40° there will be little deterioration of performance resulting from the convergent nature of an optical readout beam. The effect which angle of incidence has on the MO phase term is illustrated dramatically in Fig. 5 where it can be seen that, for both polarization states, $\cos \delta_k$ remains very close to unity up to nearly 60°. This confirms the achievement of the original design goal of producing a MO phase-corrected device.

VI. CONCLUSIONS

The design philosophy and objectives for producing trilayer structures for MO enhancement have been outlined. A number of alternative designs, giving $\epsilon_k=0$, have been presented and actual structures based on glass/Co-Pt/SiO₂/Al have been fabricated successfully. The performance of one of these as a function of the wavelength of the incident radiation and as a function of angle of incidence for the principal polarization states has been evaluated experimentally and theoretically. Results indicate excellent agreement and demonstrate the ease with which devices such as this can be designed and fabricated.

¹R. Atkinson, I. W. Salter, and J. Xu, *J. Magn. Mater.* **102**, 357 (1991).

²R. Atkinson, *J. Magn. Mater.* **124**, 178 (1993).

³R. Atkinson, I. W. Salter, and J. Xu, *Appl. Opt.* **31**, 6076 (1992).

⁴M. Mansuripur and G. A. N. Connell, *J. Appl. Phys.* **53**, 4485 (1982).

⁵R. Gamble, P. H. Lissberger, and M. R. Parker, *IEEE Trans. Magn.* **MAG-21**, 1651 (1985).

⁶S. Hashimoto, Y. Ochiai, and K. Aso, *J. Appl. Phys.* **67**, 2136 (1990).

⁷E. D. Palik, *Handbook of Optical Constants of Solids* (Academic, Orlando, FL, 1985).

⁸J. Xu, Ph.D. thesis, Queen's University of Belfast, 1991.

Effect of substrate roughness on microstructure, uniaxial anisotropy, and coercivity of Co/Pt multilayer thin films

Chung-Hee Chang and Mark H. Kryder

Data Storage Systems Center, Carnegie Mellon University, Pittsburgh, Pennsylvania 15213-3890

We studied the microstructure and magnetic properties of Co/Pt multilayer thin films sputtered onto glass and Si substrates with different surface roughness caused by different methods of substrate preparation. The microstructure determined by high-resolution electron microscopy and x-ray scattering could be correlated to the observed magnetic properties. Better (111) texture and smoother layer structures produced on smoother glass substrate surfaces produced higher uniaxial anisotropy. Coercivity, on the other hand, was enhanced by either pinning of the domain walls caused by substrate surface roughness or stronger columnar structure. Although Si substrates exhibited slightly different roughness under the same preparation conditions, the dependence of magnetic properties on the substrate surface was consistent with the trends using glass substrates.

I. INTRODUCTION

Due to their intrinsic resistance to corrosion and a Kerr rotation which increases at short wavelength, Co/Pt multilayer films (MLF) are promising candidates for future high density recording.^{1,2} Extensive studies of the film characteristics as a function of film fabrication parameters have been made of this multilayer system. It has been found that the magnetic properties such as uniaxial anisotropy and coercivity of these MLF are strongly dependent on the film fabrication method.

Since the layer thicknesses and total film thickness of Co/Pt MLF suitable for magneto-optical (MO) recording are ultrathin, it was expected that roughness of the interface and layer structure induced by substrate roughness would play an important role in determining the magnetic and magneto-optical properties. In this study, we investigated the effect of substrate roughness, introduced by various substrate preparation techniques, on the microstructure and correlated it to the magnetic properties.

II. EXPERIMENTAL DETAILS

Co/Pt MLF were fabricated by dc magnetron sputtering. A Leybold-Heraeus Z-650 system was configured so that two magnetron targets of 75-mm diameter could sputter simultaneously while substrates rotated underneath from one target to the other. A series of Co/Pt MLF consisting of ten bilayers with constant Pt layer thickness of 1 nm were deposited by sputtering with Xe onto 0211 Corning glass and oxidized (002) Si substrates. The substrate temperature during the deposition was ambient. The deposition rate of the Pt layer was 0.35 nm/s. The Co layer thicknesses were varied from 0.26 to 1.5 nm by changing the deposition rate from 0.12 to 0.6 nm/s. The base pressure of the chamber was less than 4×10^{-7} Torr and gas pressure during deposition was kept constant at 10 mTorr. Both glass and Si substrates were subjected to three different preparation procedures prior to film deposition as outlined below:

- Procedure (A): (i) soaked in warm water 10 min;
(ii) cleaned with oxygen plasma 10 min.
- Procedure (B): (i) ultrasonic cleaning for 10 min each with warm water, acetone, 2-propanol, and warm water sequentially;
(ii) cleaned with oxygen plasma 10 min.
- Procedure (C): (i) Type (B) procedure;
(ii) sputter-etched at 500 V in 10-mTorr Xe 5 min.

Cross-sectional transmission electron microscopy (TEM) specimens were prepared following a method similar to that described by Bravman and Sinclair.^{3,4} The specimens were prepared so that the layers and substrate-MLF interfaces could be viewed edge-on. A specimen consisted of two pieces of MLF on both glass and Si substrates glued face-to-face by epoxy thinner than 0.1 μm . The (111)-type fringes in the Si substrate were used to align the interfaces parallel to the electron beam direction.

The magnetic properties were measured with a DMS model 800 torque and vibrating sample magnetometer (VSM). The structure of the films was characterized by large and small angle x-ray scattering (LAXS and SAXS) using a Rigaku x-ray diffractometer. A JEOL 4000EX high-resolution electron microscope (HRTEM) operated at 400 kV was used to obtain images of the films and selected area electron diffraction (SAED) patterns.

III. RESULTS AND DISCUSSION

The effective anisotropy energy per unit volume K_{eff} , multiplied by the Co layer thickness t_{Co} , is plotted as a function of t_{Co} in Fig. 1 for the multilayers deposited on glass substrates prepared using the three different methods. The data follows the linear relation⁵ $K_{\text{eff}}t_{\text{Co}} = 2K_s + t_{\text{Co}}K_v$, where K_s is the interfacial anisotropy energy density and K_v is the volume anisotropy energy density of the cobalt. It is seen that the anisotropies of multilayers on sputter-etched substrates are the largest, and that the larger anisotropy for (A)- and (C)-type samples are due to the larger interfacial anisotropy.

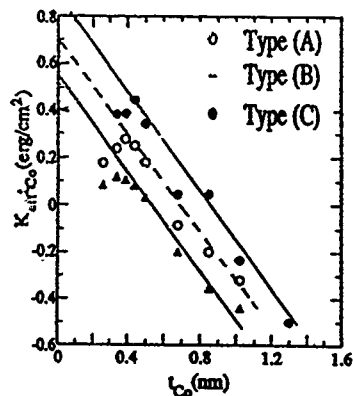


FIG. 1. Effective uniaxial anisotropy K_{eff} times the Co layer thickness as a function of Co layer thickness for Co/Pt MLF deposited on the glass substrates prepared using the three different cleaning procedures.

ropy while the volume anisotropy is constant. The larger anisotropy is attributed to a better-defined interface induced by a smoother substrate surface which agrees with a reported study made on MLF deposited on ZnO underlayers grown at different temperatures.⁶ TEM micrographs in Fig. 2 show that the layer structure of the type (C) sample is the smoothest and most continuous, and that of type (B) is rough and discontinuous. The smoothness of the layers observed by TEM is found to be consistent with SAXS patterns shown in Fig. 3(a). It is seen that type (C) exhibits the most well-defined periodic structure and type (B) the worst. SAXS patterns for thicker t_{Co} showed a systematic increase in the number of diffraction orders for type (A) and (C).

High magnification HRTEM micrographs for the three different samples on glass are shown in Fig. 4. The surface of the type (B) substrate is the roughest. Although the depth of the roughness of type (A) and (C) samples were about the same, 0.8 nm, the wavelength of the roughnesses were quite different (10 and 1.5 nm, respectively). It is noticeable from the micrograph that the substrate surface region (~ 1.7 nm) of the film is amorphous for type (A) sample. On top of this amorphous layer, the multilayer was grown with less (111) texture. However, the grains in the type (C) sample start growing right from the substrate surface. This is probably due to increased nucleation sites for crystal growth helping to form the good lattice coherency as indicated by the satellite peak at $2\theta = 34^\circ$ in the LAXS pattern shown in Fig. 3(b).

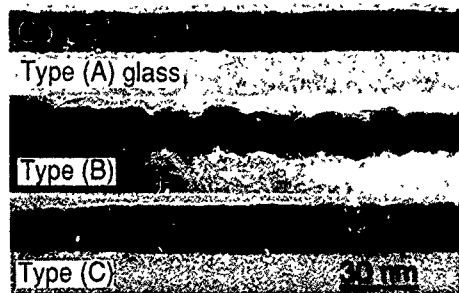


FIG. 2. Low-magnification cross-sectional HRTEM images of $10 \times (0.5\text{-nm Co}/1.0\text{-nm Pt})$ MLF deposited on the three types of glass substrates. The type (C) sample has 11 Pt layers.

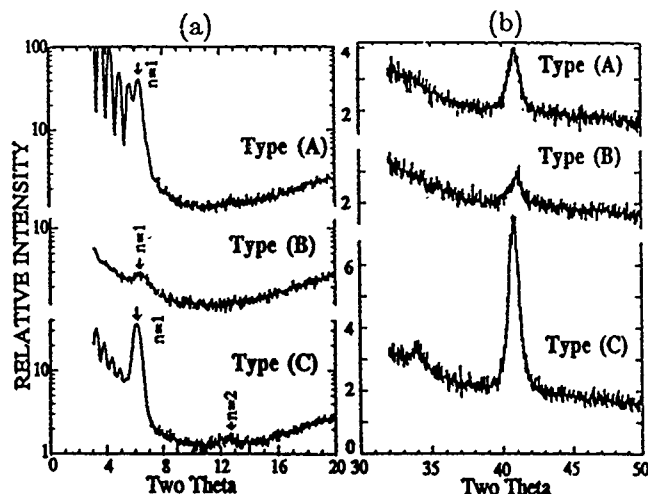


FIG. 3. (a) Small- and (b) large-angle x-ray scattering ($\lambda = 0.154$ nm) measured from nominal $(0.4/1.0)\text{-nm}$ Co/Pt MLF deposited on three types of glass substrates.

SAED patterns shown in Fig. 5 indicate that the (111) textured grains in type (C) samples are better oriented than those in type (A) and (B) samples. The relative intensity of the ring patterns from (111) textured crystallites are the strongest in the direction of film growth for type (C) and weakest for type (B) samples.

Magnetization hysteresis loops for the three types of samples are shown in Fig. 6. The squareness of the type (B)

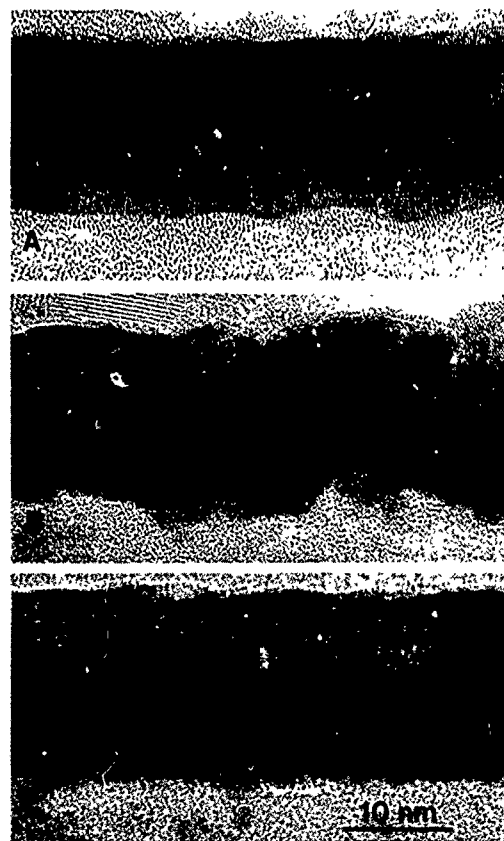


FIG. 4. High-magnification cross-sectional HRTEM images of the Co/Pt samples shown in Fig. 2

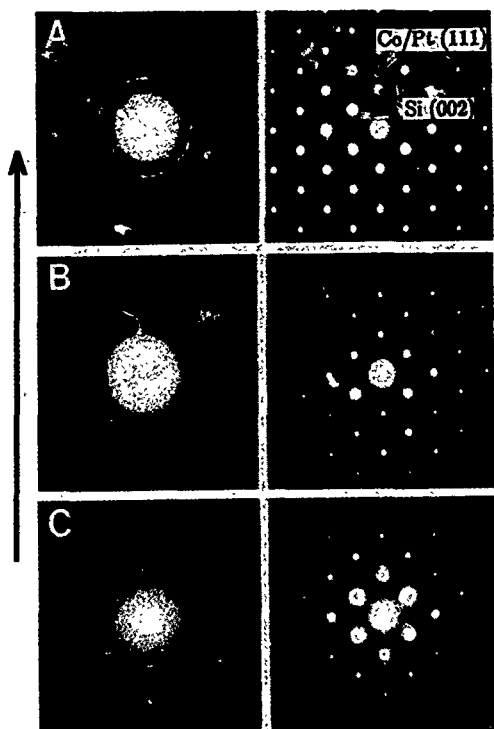


FIG. 5. Selected area electron diffraction patterns of the Co/Pt MLF samples shown in Fig. 4 and corresponding MLF deposited on Si substrates. The direction of film growth is indicated by the arrow.

sample is slightly lower than the others, but the coercivity is the largest. The large coercivity of the type (B) sample is attributed to the pinning of the domain walls caused by the surface roughness and thus by defects at the interfaces. This kind of coercivity enhancement was also observed in Co/Pt MLF deposited on a Si nitride underlayer.⁷ Poorer squareness suggests that domain reversal in this sample is nucleation dominated.^{8,9} The larger coercivity of sample type (C) as compared to sample type (A) can be attributed to more well defined grains (or columns) in type (C) samples. This may be seen in Fig. 4. Such isolated grains or columns were also reported to enhance coercivity in samples grown on a Pt underlayer.¹⁰ Increased coercivity by sputter-etching were reported elsewhere.^{11,12}

The microstructure and magnetic properties of samples prepared on Si with the same preparation procedure were

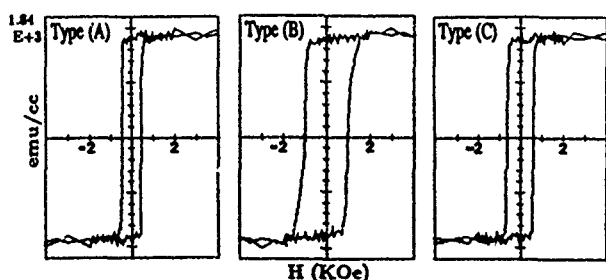


FIG. 6. Hysteresis loops of nominal (0.34/1.0)-nm Co/Pt MLF deposited on three types of glass substrates.

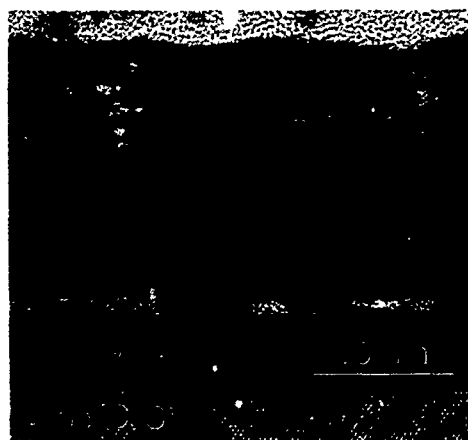


FIG. 7. HRTEM image of nominal (0.5/1.0)-nm Co/Pt MLF deposited on type (C) Si substrate.

approximately the same as those of glass samples. However, sputter-etching produced an amorphous layer about 5-nm thick on Si, which seems to further promote grain growth by providing a smooth surface underneath the 1-nm oxidized surface. Large grains measuring about 17.5 nm in the lateral dimension may be observed in Fig. 7, which is a HRTEM micrograph of a MLF grown on a type (C) Si substrate.

IV. CONCLUSIONS

The correlations between microstructure and magnetic properties of Co/Pt MLF deposited on substrates with different roughness were made. It was confirmed that the magnetic properties were very sensitive to substrate roughness. The roughness lowered the uniaxial anisotropy and raised the coercivity. The coercivity was also raised by stronger columnar structure produced by a smoother substrate surface.

ACKNOWLEDGMENTS

This work was supported in part by the National Science Foundation under Grant No. ECD-8907068. The platinum used for fabricating the majority of the Co/Pt MLF used in this study was donated by Johnson Matthey.

- ¹W. B. Zeper, F. J. A. M. Greidanus, P. F. Carcia, and C. R. Fincher, *J. Appl. Phys.* **65**, 4971 (1989).
- ²S. Hashimoto and Y. Ochiai, *J. Magn. Magn. Mater.* **88**, 211 (1990).
- ³J. Bravman and R. Sinclair, *J. Electron. Microsc. Technol.* **1**, 53 (1984).
- ⁴C.-H. Chang, Ph.D. thesis, Arizona State University (1989).
- ⁵H. J. G. Draaisma, W. J. M. deJonge, and F. J. A. denBroeder, *J. Magn. Magn. Mater.* **66**, 351 (1987).
- ⁶P. F. Carcia, Z. G. Li, and M. Reilly, *J. Appl. Phys.* **73**, 6424 (1993).
- ⁷C.-H. Chang and M. H. Kryder (unpublished).
- ⁸J. Pommier, P. Meyer, G. Penissard, and J. Ferre, *Phys. Rev. Lett.* **65**, 2054 (1990).
- ⁹J. X. Shen, R. D. Kirby, K. Wierman, Z. S. Shan, and D. J. Sellmyer, *J. Appl. Phys.* **73**, 6418 (1993).
- ¹⁰G. A. Berteio and R. Sinclair, *Proc. 51st AMMSA* (1993), p. 1038.
- ¹¹P. F. Carcia, M. Reilly, W. B. Zeper, and H. V. van Kesteren, *Appl. Phys. Lett.* **58**, 191 (1991).
- ¹²T. Suzuki, H. Notarys, D. C. Dobbertin, C.-J. Lin, D. Weller, D. C. Miller, and G. Gorman, *IEEE Trans. Mag.* **28**, 2754 (1992).

Depth distribution of birefringence in magneto-optical recording disk substrates

Raymond-Noel Kono and Myung S. Jhon

Department of Chemical Engineering, Carnegie Mellon University, Pittsburgh, Pennsylvania 15213

Thomas E. Karis

IBM Research Division, Almaden Research Center, 650 Harry Road, San Jose, California 95120

Polycarbonate substrates are the industry standard for optical storage. Optical anisotropy is frozen into the substrate as polymer orientation during mold flow and thermal stress during cooling. The substrate optical anisotropy degrades the readback of the data [carrier-to-noise ratio (CNR)] by increasing the noise level on Kerr rotation measurement. There are also synergistic effects of the disk optical properties with focus and tracking optics. For optimum CNR, the beam is focused on the magneto-optical (MO) film. For optimum tracking, the beam is focused to maximize track error signal (TES). For the disks considered the difference between the offset for optimum CNR and that for optimum TES was between 300 and 600 μm . This results in a compromise between optimum CNR and TES, which could limit MO storage density and performance. Conventional methods of bulk optical anisotropy measurement are unsuccessful in explaining this variance. These give an average or effective optical property. The optical properties are also known to vary with the depth in the substrate and especially near the mold walls as determined by optical polarizing microscope. A scanning micropolarimeter instrument is presented to rapidly measure the depth distribution of the optical properties. The interaction between the obliquely incident polarized beam with the microscopic variation in the index of refraction throughout the depth of the substrate is proposed as the source of the difference between the optimum focus offsets.

Polycarbonate (PC) substrates are the industry standard in magneto-optical (MO) recording from the mechanical, physical-chemical, as well as productivity and cost points of view. However, optical anisotropy which causes birefringence is frozen in the substrate as: polymer orientation during mold flow and thermal stress during cooling. Although injection molding techniques which minimize the in-plane birefringence in PC have been demonstrated, vertical birefringence which causes large retardation for marginal rays is an unsolved problem. Fluctuation around the average intensity distribution on the photodetector is attributed to vertical birefringence.¹ The substrate birefringence for an obliquely incident beam is very high, leading to degradation of the carrier-to-noise ratio (CNR).² Birefringence measurements are typically done by passing a beam through the substrate, for uncoated substrates,^{3,4} or by reflecting the beam from a layer on one side of the substrate, for coated substrates.⁵ These provide an average value for the optical property. A recent phenomenon observed with MO substrates that is attributed to birefringence but cannot be adequately explained in terms of the bulk average measurements is described. We developed an apparatus for rapidly measuring the microscopic variations of the index of refraction throughout the depth of the substrate in an effort to investigate this phenomenon.

When a MO disk is inserted into a drive, the focus servo-optics adjust the lens position vertically with respect to the disk substrate. In the case of an astigmatic focus servo system, the adjustment is done until the reflected spot is circular on the detector. This is considered to be focused through the substrate on the grooved surface covered by the reflective MO film structure. This is the point of zero focus offset. At this lens position both the track error signal (TES) and the signals of Kerr rotation of the data bits should be optimum,

as the servo maintains the lens in focus by translating in response to disk vertical runout. The TES should be as large as possible to provide input to the radial positioning servo. Alternatively, if the track error signal is too low, the radial positioning servo system loses its ability to follow the runout of the tracking grooves. As the track pitch is decreased from 1.6 to 1 μm or less, the importance of obtaining the maximum TES increases. However, it is found that the maximum TES usually does not coincide with the optimum focus point. Some preliminary data are shown to illustrate this phenomenon. Typical data are shown in Fig. 1. The solid circles show the TES amplitude as a function of focus offset in nanometers. Here, the in-focus point determined by the servo system is the zero focus offset. The solid curve is the regression fit of the data which is employed to analytically determine the location of the maximum or minimum from the data. The data shown in Fig. 1(a) were measured on an amorphous polyolefin (APO) substrate. In this case, the optimum focus point nearly coincides with that for maximum TES. Figure 1(b) shows a larger focus offset measured on a PC substrate. From these data alone, it may appear sufficient to adjust the focus offset to obtain the maximum TES for the disk drive operating point.

The focus position for the best ability to read the MO data shows an offset which is different from that which provides the optimum TES. The best focus point for tracking is that which gives the maximum TES, while the best focus for data readback performance is that which gives minimum jitter. The jitter is a time-domain measurement of channel noise. In this example, the jitter of a square wave was used as a measure of data readback performance rather than CNR. The jitter is shown as a function of focus offset by the open squares in Fig. 1. The offsets for optimum TES and minimum jitter do not coincide. In fact, they are significantly

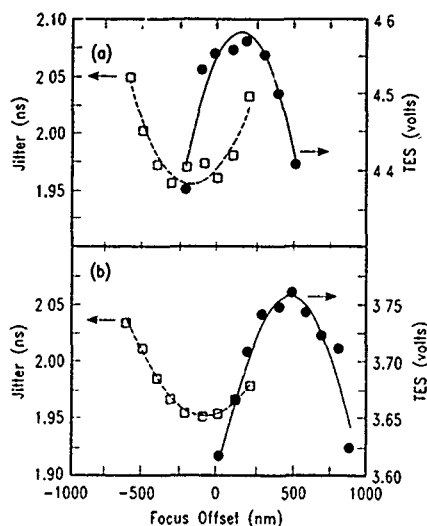


FIG. 1. The jitter (\square) and the track error signal TES (\bullet) for (a) an APO substrate and (b) a PC substrate.

different, more so for the PC substrate in Fig. 1(b) than for the APO substrate in Fig. 1(a). This difference between the focus offset for maximum TES and minimum jitter represents a fundamental limitation in the ability to increase the data storage density on MO media by narrowing the track pitch and increasing the linear density. The difference between the offset for maximum TES and minimum jitter is defined as Δ . Ideally $\Delta=0$. The nonzero Δ is the subject of the present investigation. Measurements attempting to relate the nonzero Δ with bulk and surface birefringence measurements are described below.

Several methods are available to characterize the vertical birefringence Δn_{rz} . Here subscript r denotes radial direction and z the vertical direction in the disk substrate. One technique is the transmission method.^{3,4} Here, the birefringence is measured over a range of incident angles, and the data are extrapolated to a 90° angle of incidence. Another technique is called the prism method.⁶ This approach utilizes the principle of total internal reflection. One feature of the prism method is that it is most sensitive to the optical properties near the surface of the disk substrate. There is also a novel reflection measurement method. The apparatus resembles that described in Otsuka *et al.*⁷ The geometry of this method is closer to that found in the actual optical head of the disk drive than the transmission or prism methods.

Values of Δn_{rz} measured by the transmission and prism techniques are plotted as a function of that measured by the reflection method and shown in Fig. 2(a) for various MO disk substrates. Although the magnitudes differ, the trends are in qualitative agreement. The prism method is probably higher for PC because of the high surface layer optical anisotropy. In the APO, the surface layer contribution may be small due to the lower-stress optical constant. The glass is likely to have higher stress in the surface layer due to the chemical hardening which extends several microns into the bulk.⁸

The Δn_{rz} measured by each of these methods was examined to determine which correlates with the measured focus offsets. Among the three methods, the one most corre-

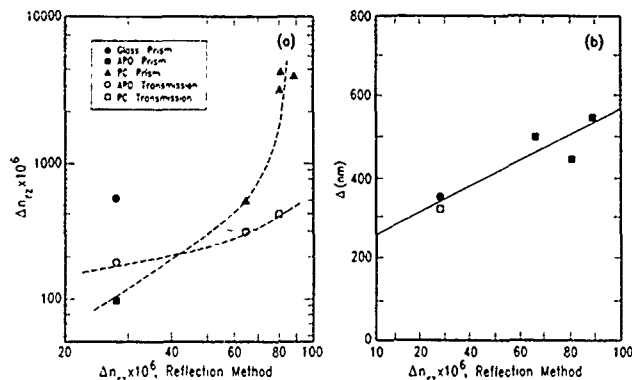


FIG. 2. A comparison of the vertical birefringence of MO disk substrates using three different types of measurement techniques. (a) The lines are drawn as an aid to the eye and (b) the distance between the two offsets Δ .

lated with Δ was Δn_{rz} from the reflection method. Δ is plotted as a function of Δn_{rz} from the reflection method in Fig. 2(b). Δ increased with increasing Δn_{rz} . This suggests that overall it is preferable to have lower Δn_{rz} for lower Δ , although there is an additional contribution to the variation of Δ .

More detailed measurement of birefringence with respect to depth in an optical disk substrate has been done by counting fringes as a function of depth in a strip cut from the substrate using an optical polarizing microscope.⁹ Since these measurements are manual and time consuming, they are impractical for studying large numbers of substrates.

In order to automate measuring the depth variation of the microscopic optical anisotropy, we have begun to develop a scanning micropolarimeter instrument. The polarimeter setup is similar to the conventional flow birefringence experiment. This apparatus is a modification of that used by Frattini and Fuller.¹⁰ A schematic of the apparatus is shown in Fig. 3. The modifications in our apparatus are the focusing and collector lenses, and the translation stage which allows stepping the sample across the beam. Monochromatic light incident on a photoelastic modulator (PEM) perpendicular to the strain axis is modulated and experiences a time varying retardance given by $\delta_m = A_c \sin(\omega t)$. Here A_c is a function of the wavelength of light and the maximum voltage applied to the crystal, and ω is the resonant frequency of the optical element. The intensity of the light at the detector then contains a fundamental frequency ω , typically 50 kHz. Fourier decomposition of the voltage from the detector facilitates simultaneous determination of the birefringence Δn_{rz} and the extinction angle χ of the sample. The beam diameter was measured with the aid of the knife-edge technique. The knife-edge technique provides an accurate means to measure the diameter of a Gaussian beam. The beam diameter without the lens is $795 \mu\text{m}$ and the focused beam is $23 \mu\text{m}$ in diameter.

The micropolarimetry experiment is interpreted using Jones matrix algebra.¹⁰ Taking the radial direction (flow field) as a reference, the incident polarizer is set at 90° , the PEM at 45° , and the analyzer at -45° . If δ is the unknown retardation of the sample, the intensity of the light at the detector is given by

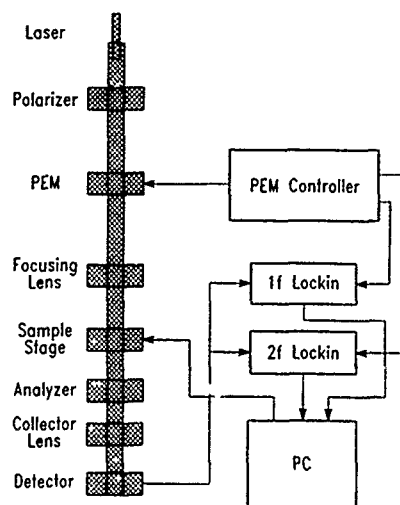


FIG. 3. A schematic of the scanning micropolarimeter apparatus using one PEM.

$$I = 2I_{dc} [1 + \cos 2\chi \sin 2\chi (1 - \cos \delta) \cos \delta_m + \cos 2\chi \sin \delta \sin \delta_m]. \quad (1)$$

Here, $2I_{dc}$ is the light intensity emerging from the polarizer, and the birefringence is related to the retardation by $\Delta n_{rz} = -\lambda \delta / 2\pi d$, with λ being the wavelength of the incident light and d the sample thickness. Equation (1) can be rearranged by recognizing that $\cos \delta_m = \cos[A_c \sin(\omega t)]$ to obtain

$$I = I_{dc} + I_{\omega} \sin(\omega t) + I_{2\omega} \cos(2\omega t) + \dots \quad (2)$$

Here, Fourier components I_{ω} and $I_{2\omega}$ are explicitly written as

$$I_{\omega} = 2J_1(A_c) \cos(2\chi) \sin(\delta) I_{dc}$$

and

$$I_{2\omega} = 2J_2(A_c) \cos(2\chi) \sin(2\chi) [1 - \cos(\delta)] I_{dc}. \quad (3)$$

$J_m(A_c)$ is the Bessel function of the first kind with order m , and we set $J_0(A_c) = 0$. The coefficients I_{ω} and $I_{2\omega}$ are measured in real time by two lock-in amplifiers tuned respectively to ω and 2ω . A phase-locked reference signal is provided to the amplifiers by the PEM control unit. I_{dc} is measured using a low-pass filter. The ratios I_{ω}/I_{dc} and $I_{2\omega}/I_{dc}$ are calculated in an IBM PC.

Defining $R_{\omega} = (I_{\omega}/I_{dc})/2J_1(A_c)$ and $R_{2\omega} = (I_{2\omega}/I_{dc})/2J_2(A_c)$, two equations with two unknowns δ and χ are obtained,

$$\cos 2\chi \sin \delta = R_{\omega}, \quad \sin 4\chi (1 - \cos \delta) = R_{2\omega}. \quad (4)$$

Therefore, by measuring R_{ω} and $R_{2\omega}$, we can, in principle, obtain χ and δ .

Figure 4 shows the R_{ω} and $R_{2\omega}$ plots for a diamond-milled section cut from a PC disk substrate. These profiles reflect the variation of the optical anisotropy with depth in the substrate. Although R_{ω} and $R_{2\omega}$ are a function of depth, careful analysis is required to convert the R_{ω} and $R_{2\omega}$ plots into Δn (or δ) and χ profiles. Note that δ and χ cannot be uniquely determined from Eq. (4) due to the multiple solu-

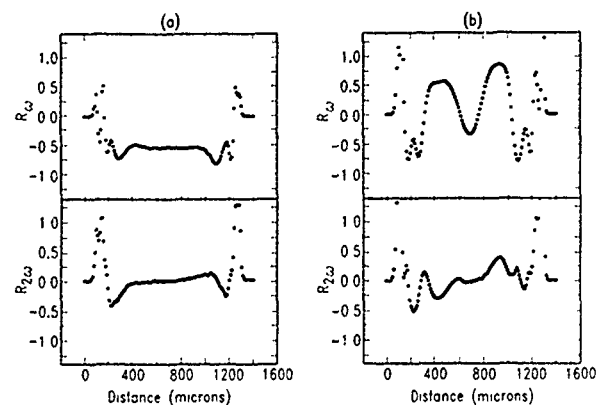


FIG. 4. The measured R_{ω} and $R_{2\omega}$ in scanning across a 1-mm-thick strip cut radially from a PC substrate that was diamond milled; (a) 10 mm and (b) 25 mm.

tions for the angles. Observation of the R_{ω} profiles as a function of depth, Fig. 4, shows considerable variation in R_{ω} as the beam is traversed across the depth of the substrate. The extinction angle ($\sim R_{2\omega}$) also varies considerably, indicating that the commonly used assumption of uniform Δn_{rz} and $\chi = 0$ throughout the depth of the substrate is clearly invalid.

The differential propagation Mueller matrix^{11,12} can be employed to calculate the actual integrated optical matrix for the disk in response to the convergent Gaussian beam used in the optical disk drive. Rigorously, $dS/dz = mS$ where S is the Stokes vector, z is the depth in the substrate, and m is a 4×4 real matrix containing the optical properties of the medium at depth z .

Depth variation in the MO substrate optical anisotropy is believed to cause focus offset differences so that both the MO signal and the TES cannot be simultaneously optimized. Automated measurement of the depth profiles of Δn_{rz} can be done using the scanning micropolarimeter instrument. The geometry using one PEM does not provide a unique value of birefringence and extinction angle for PC substrates. Future apparatus for determining Δn to within one wavelength of the retardation should include an additional PEM below the sample to act as a programmable quarter-wave plate.

The authors are grateful to R. Wimberger-Friedl of Philips Research Laboratories for providing the diamond-milled section from the PC substrate. We thank T. McDaniel of the IBM Optical Storage Laboratory for technical guidance. This work was supported in part by the IBM Storage Systems Division, and by the National Science Foundation under Grant No. ECD-8907068.

¹ A. B. Marchant, Proc. SPIE **695**, 270 (1986).

² E. Treves, and D. S. Bloomberg, Proc. SPIE **695**, 262 (1986).

³ H. Kramer, and N. Dietz, Colloid Polym. Sci. **260**, 685 (1982).

⁴ G. Kaempfer, W. Siebourg, H. Loewer, and N. Lazear, in *Polymers in Information Storage Technology*, edited by K. L. Mittal (Plenum, New York, 1990), pp. 77-104.

⁵ A. Skumanich, Opt. Lett. **18**, 155 (1993).

⁶ A. Skumanich (unpublished).

⁷ Y. Otsuka, Y. Fukui, N. Katase, and T. Sasaki, in ISOM87, Technical Digest, 1987, pp. 117-120.

⁸ D. Connolly, J. Am. Ceram. Soc., **72**, 1162 (1989).

⁹ R. Wimberger-Friedl, Polym. Eng. Sci. **30**, 813 (1990).

¹⁰ P. L. Frattini and G. G. Fuller, J. Rheol. **28**, 61 (1984).

¹¹ R. M. A. Azzam, J. Opt. Soc. Am. **68**, 1756 (1978).

¹² S. R. Galante and P. L. Frattini, J. Rheol. **35**, 1551 (1991).

Growth and subsequent relaxation of the anisotropic structure of amorphous Tb-Fe (abstract)

F. Hellman, M. C. Robson, and M. T. Messer

Physics Department, University of California, San Diego, 0319 La Jolla, California 92093-0319

The large, growth-induced magnetic anisotropy in amorphous rare earth-transition metal alloys such as Tb-Fe are shown to depend strongly on the deposition temperature and only weakly on deposition rate or deposition technique (e.g., sputtering versus electron beam co-evaporation). These dependencies can be well fit with a thermally activated form involving minimization of surface energy *during the growth* by a re-orienting of adatom configurations over potential energy barriers. In this model, the growing film lowers its surface energy by a partial alignment of local clusters, presumably such as to maximize the number of in-plane bonds, although chemical effects undoubtedly also play an important role. These effects are somewhat analogous to a surface reconstruction which becomes trapped into the growing film by low bulk diffusion rates. In particular, a two-level model with a flat distribution of energy barriers is here shown to provide an excellent fit to the observations. Such a model leads to a $\ln(t)$ dependence on deposition rate and an exponential dependence on deposition temperature. We have also studied the subsequent irreversible relaxation of the anisotropy upon annealing. This relaxation is *strongly* influenced by the original growth temperature. In particular, the higher the original growth temperature, the more resistant the film is to subsequent relaxation. This result has important technological implications. As is commonly observed, the relaxation is well fit by a two-level model, again with a flat distribution of energy barriers over a range of energies, producing a $\ln(t)$ dependence on annealing time and a thermally activated dependence on annealing temperature. In annealing, of course, the lower energy state is isotropic, unlike the surface-induced anisotropic state produced during growth. The influence of the growth temperature on this relaxation implies that the actual *process* of creating the anisotropic state during the growth has the consequence of eliminating free volume in the sample, thereby raising the energy barriers to subsequent relaxation.

This work was supported by the AFOSR Grant No. 89-0432.

Macroscopic ferrimagnets as magneto-optic media (abstract)

Richard J. Gambino,^{a)} Ralph R. Ruf, and Nestor Bojarczuk
IBM, T. J. Watson Research Center, Yorktown Heights, New York 10598

We have discovered a class of phase separated materials in which the two phases couple antiferromagnetically across the phase boundary. A prototypical example is cobalt containing ≈ 100 -Å-diam precipitate particles of EuS with the NaCl structure. These materials show many of the properties of ferrimagnets such as compensation points so we have adopted the term "macroscopic ferrimagnet" to distinguish them from ferrimagnets in which the antiferromagnetic exchange couples individual atoms. As a result of the ferrimagnetic exchange between the Co and the EuS the net magnetization of the composite is low in the vicinity of compensation so the anisotropy field is high. Electron beam evaporated thin films have a perpendicular easy axis as a result of growth induced anisotropy. Another effect of the exchange between the Co and EuS is to order the EuS well above its normal Curie point of 16 K. A film with 80 mole % Co and 20 mole % EuS has a compensation point of 55 K showing that the Eu^{2+} has essentially its full moment of $7\mu_B$ at this temperature in order to compensate the $1.65\mu_B$ of Co. The EuS even shows evidence of magnetic order at room temperature. The wavelength dependence of the sign of the magneto-optic Kerr effect can only be explained if the EuS has sufficient rotation at high photon energies to be larger than the rotation of the Co. We have prepared more complex alloys that show square loop properties at room temperature, for example, Tb-Co-EuS and Tb-FeCo-EuO. X-ray diffraction analysis shows that these films consist of an amorphous matrix (Tb-Co or Tb-FeCo) with precipitates of a NaCl structure phase (e.g., defect solid solutions¹ like $\text{Eu}_{1-x}\text{Tb}_x\text{S}_{1-x}\square_x$). Both atomic and macroscopic ferrimagnetism are operating in these compositions. Films with high remanence and coercivities over 4 kOe at room temperature have been obtained. Some of these compositions may be useful as magneto-optic storage media.

^{a)}Present address: Department of Materials Science & Engineering, State University of New York at Stony Brook, Stony Brook, NY 11794-2275.

¹R. J. Gambino, P. Fumagalli, R. R. Ruf, T. R. McGuire, and N. Bojarczuk, IEEE Trans. Mag. 28, 2973 (1992).

High-resolution magneto-optic measurements with a Sagnac interferometer (invited)

A. Kapitulnik, J. S. Dodge, and M. M. Fejer

Department of Applied Physics, Stanford University, Stanford, California 94305

A technique for measuring the Faraday effect and the magneto-optic Kerr effect has been developed. In a Sagnac interferometer, two optical beams follow identical paths in opposite directions. Effects which break time-reversal symmetry, such as magneto-optic effects, will cause destructive interference between the two beams. By measuring the phase shift between circular polarization states reflected from a magnetized sample, the polar magneto-optic Kerr effect is measured to an accuracy of $3 \mu\text{rad}$, with a spatial resolution of $2 \mu\text{m}$. The interferometric technique provides a number of advantages over conventional polarizer methods, including insensitivity to linear birefringence, the ability to completely determine the magnetization vector in a region, and the ability to sensitively measure magneto-optic effects without an external field. It is also shown that this device has great potential if incorporated into a near-field optical device. Some of the considerations for the design of a near-field Sagnac magneto-optic sensor are introduced and the advantages of the device are discussed. Some preliminary experiments are shown.

I. INTRODUCTION

Magneto-optic studies of magnetic films and of surface magnetism in bulk materials is very common.¹ In particular the surface magneto-optic Kerr effect (SMOKE)² has recently been refined to a state where selected systems can be studied to a submonolayer level. The Kerr effect, like all other magneto-optic effects,³ originates from spin-orbit coupling. Its net effect is to produce a rotation of the polarization axes as well as a slight ellipticity in linearly polarized light reflected from a magnetized surface. The amount of Kerr rotation is directly proportional to the magnetization in the film, and thus provides an excellent method to study magnetism. In bulk materials, Kerr rotation and ellipticities can be as high as 10^{-2} rad (for a measurement of a metal using visible light with an optical penetration depth of $\sim 100 \text{ \AA}$, this implies a specific rotation of $\sim 10^4 \text{ rad/cm}$). For very thin films, the effect can be reduced substantially, hence restricting the materials and configurations that can be studied.

Magneto-optics is also discussed in the context of high-density data storage, where bits are represented as domains in a magnetic film which has strong perpendicular anisotropy. Data are written optically by locally heating the film above its Curie temperature with a laser, and aligning a domain with an applied magnetic field. The data are then read by means of the polar Kerr effect. A diffraction-limited optical device is capable of handling cell sizes as low as $(1 \mu\text{m})^2$. In this limit, detailed imaging of the domain structure is beyond the capabilities of conventional polarized light microscopy, and currently we must turn to electron microscopes for high-resolution images. Near-field optical microscopy, operating in reflection with magneto-optic contrast, may be particularly useful in guiding the engineering of such storage materials. We might further imagine a near-field magneto-

optic read-write system, which could push the minimum cell size down to the order of $\sim (500 \text{ \AA})^2$, hence increasing the storage density to more than 10^{10} bits/in.²; however, to date there are no magneto-optic devices which are working both in reflection and in the near-field region.

Recently we have demonstrated⁴⁻⁷ the use of a Sagnac interferometer for the measurement of Faraday and Kerr effects. Three instruments were built to operate at 1060, 672, and 840 nm. One important advantage of these instruments over conventional SMOKE is that they are sensitive only to broken time-reversal symmetry effects while completely rejecting linear birefringence and optical activity. Our first instrument was built using an existing fiber-optic gyroscope ($\lambda = 1060 \text{ nm}$). For measurements of the Faraday rotation angle, the sensitivity achieved was $3 \mu\text{rad}/\sqrt{\text{Hz}}$. We have since built instruments ($\lambda = 672$ and 840 nm), designed more specifically for magneto-optic studies, which are slightly modified from the original with a shorter Sagnac loop. These instruments work in both transmission and reflection to measure both the Faraday and Kerr effects. The sensitivity achieved has been $2 \mu\text{rad}/\sqrt{\text{Hz}}$. The Sagnac magneto-optic sensor (SMOS) was first developed in the search for anyon superconductivity in high-temperature superconductors;⁴ we are currently giving more attention to its use for characterization of magnetic materials. An important measurement was the observation of free radicals in biological molecules.⁷ In this experiment we showed the versatility of SMOS. The sensitivity found was comparable to electron-spin resonance (ESR), the only other technique used to look for free radicals; however, the sensitivity is not the only advantage of SMOS. As we explain below, SMOS is able to measure absolute magnetization, hence avoiding the need for external field modulation. Moreover, we show that SMOS is capable

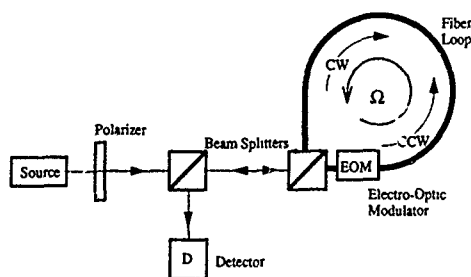


FIG. 1. Basic configuration of a Sagnac interferometer. Ω is the angular frequency of rotation of the loop.

of fully determining the state of magnetization in a sample region, and should provide a unique way to probe surface anisotropies.

II. SAGNAC INTERFEROMETER

Figure 1 shows a schematic of a basic Sagnac interferometer. The beam of light from the source enters a beam splitter, which sends half of the light clockwise (CW) and the other half counterclockwise (CCW) around a fiber loop. The two beams will come to the beam splitter after one turn and combine to constructively interfere at the detector. This is the Sagnac loop at rest and if we assume that the fiber allows one and only one path through the loop, it is completely reciprocal. If the loop is now rotated at a constant angular velocity Ω , reciprocity is no longer preserved. The rotation creates a difference in path length between the two counterpropagating beams, so that there will be a slight phase shift, the so-called Sagnac effect, introduced between them. This phase shift is translated into an intensity change when the two beams interfere at the detector. The phase shift will be proportional to the area enclosed by the loop, so with a fiber-optic loop the sensitivity to mechanical rotation can be increased by adding more windings.⁸

As described above, small changes in path length will lead to intensity changes proportional to the phase difference squared, which will in turn lead to poor sensitivity to small phase shifts. Typically the interferometer will be biased onto the linear portion of the interference curve to increase the sensitivity. In principle, this can be done by introducing a nonreciprocal element into the loop which creates a stable $\pi/4$ phase shift between the two beams. However, in practice, a dynamic biasing system is easier to engineer. In Fig. 1 we show one common bias technique, in which an electro-optic phase modulator is placed at one end of the loop. Although the phase modulator is a reciprocal device, we take advantage of the finite time it takes light to travel around the loop to create a nonreciprocal phase shift between beams which pass through the modulator at different times. With a sinusoidal phase modulation, the first-harmonic component of the detected intensity may be measured with a lock-in amplifier. For a small nonreciprocal phase shift $\Delta\phi$, and an average detected intensity I_c , the first harmonic is proportional to $k_1 I_0 \sin(\Delta\phi)$, where k_1 is a constant which depends on the phase modulation amplitude. Maximum sensitivity is achieved for a modulation frequency of $f = c/2L$, where L is

the path length of the loop. Additionally, parasitic effects due to imperfections in the phase modulator will be significantly reduced near this frequency. Consequently, although the SMOS is not designed for mechanical rotation measurements, we must maintain a finite loop length of about 30 m in order to keep the modulation frequency in the MHz range.

To achieve sensitivity to magnetic substances, one would like to measure the asymmetry between the CW and the CCW beams induced by the nonreciprocity (broken time-reversal symmetry) resulting from magnetism. To do this, we "break" a (completely reciprocal) Sagnac loop, then introduce bulk optics into the optical path to allow us to probe a sample. More specifically, we use wave plates to create two polarization states which will lead to the maximum nonreciprocal phase shift upon interaction with a magnetized sample. The simplest geometries for describing the operation of the SMOS are those in which the sample exhibits no linear birefringence, and the direction of beam propagation is both collinear with the magnetization and normal to the sample surface. This corresponds to the polar Kerr effect in reflection and the Faraday effect in transmission. Choosing the z axis as the direction of beam propagation, the conductivity tensor for the material may be written in the form

$$\sigma(\mathbf{M} \parallel \hat{z}) = \begin{pmatrix} \sigma_{xx} & \sigma_{xy} & 0 \\ -\sigma_{xy} & \sigma_{xx} & 0 \\ 0 & 0 & \sigma_{zz} \end{pmatrix}. \quad (1)$$

For both of these geometries, circular polarization states are the appropriate basis for describing magneto-optic effects.⁹ Transforming the electric-field vector to a circular basis diagonalizes the conductivity tensor and gives slightly different diagonal elements $\sigma_{\pm} = \sigma_{xx} \pm i\sigma_{xy}$ for the two basis states. The reflectance and the transmittance of the material is affected similarly, so that we may measure a difference in both the relative phase shift and the absorption between the two states. It is important to note here that this phase shift is nonreciprocal, unlike the phase shifts induced by linear birefringence or optical activity, since the magnetization breaks time reversal symmetry. It is precisely this nonreciprocity which allows us to measure magneto-optic effects using SMOS.

The most common way to measure these effects is to direct linearly polarized light at the sample and measure the polarization state of the returning light, so the literature commonly refers to the phase shift as "rotation," denoted by θ , and the differential absorption as "ellipticity," denoted by ϵ . We refer to the nonreciprocal phase shift (NRPS) throughout this article, and denote it by $\Delta\phi$. In the perpendicular geometries described above, $\Delta\phi = 2\theta$, but in general the phase shift is a function of both the rotation and the ellipticity. To measure the NRPS, we compare two states with opposing angular momentum vectors, so that one is parallel to the magnetization and the other antiparallel. In transmission, this corresponds to states of the same handedness, and in reflection the appropriate states have opposite handednesses, where handedness is defined with respect to the direction of propagation [Fig. 2(a)]. When configured in this way, the SMOS is sensitive only to Faraday or Kerr rotation, not el-

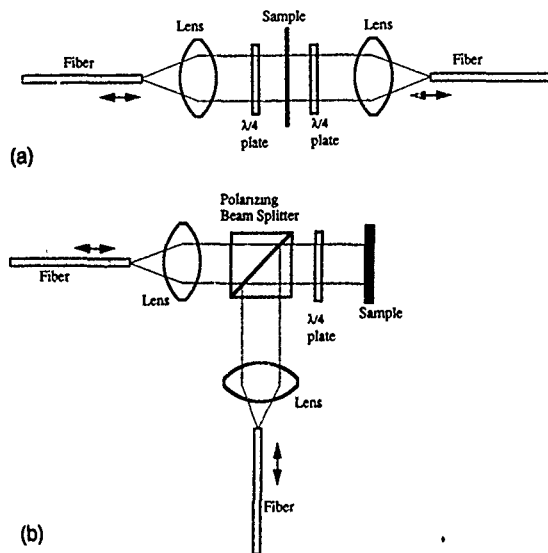


FIG. 2. Bulk optics inserted in the loop for (a) transmission and (b) reflection measurements.

lipticity, because magneto-optically induced ellipticity arises from nonreciprocal absorption, and consequently does not lead to a NRPS but to a small asymmetry in the absorption for the two polarization states.

We first describe the configuration which is used to measure the Faraday effect.⁴ As explained above, we add in succession [see Fig. 2(a)] a quarter-wave ($\lambda/4$) plate, the sample holder, and another $\lambda/4$ plate, which comprise the bulk optics. Lenses are also added to focus the beams into the fiber. The polarization state in the fiber is linear, and the two $\lambda/4$ plates are arranged such that both beams are given circular polarization of the same handedness. We choose right-handed polarization states for the sake of discussion. With no sample, the clockwise propagating light is converted into right-handed circularly polarized light by the first $\lambda/4$ plate and converted back to the original linear state of polarization by the second $\lambda/4$ plate, and the counterclockwise propagating light will do the same, in the reverse direction. Assuming that no nonreciprocal phase shift occurs in the central portion of the bulk optics, then both clockwise and counterclockwise beams will emerge with no relative phase shift. If, however, a nonreciprocal phase shift occurs in the central portion of the bulk optics, one beam will be advanced in phase while the other will be retarded in phase, and the phase difference will be detected as an intensity change at the output of the interferometer.

To modify the apparatus for reflectance measurements, only one quarter-wave plate is needed, together with a polarizing cube beam splitter [Fig. 2(b)]. We set the linear polarization state in one fiber end to be parallel to the optical table, with the other orthogonal to it, and we use the beam splitter to selectively redirect one beam to overlap with the other. Each beam is given a different handedness upon passing through the $\lambda/4$ plate, which again is set to produce circular polarization states at the sample. If a perfect mirror is used as a sample, the handedness of each polarization state is switched upon reflection and the linear polarization which results from passing through the $\lambda/4$ plate a second time will

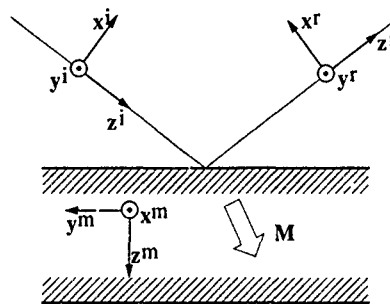


FIG. 3. Basic notations for components of incident and reflected beams from a magnetized surface.

be orthogonal to the original. Thus, the incident beam which is transmitted by the beam splitter is reflected by the beam splitter upon return, and vice versa, and a complete loop is established.

For the more general problem of measuring magneto-optic effects in the presence of linear birefringence, for arbitrary magnetization directions, and away from normal incidence, circular polarization states will no longer be eigenstates of the optical system, and we must search for the two polarization states which will lead to the largest signal. We describe the electric field of a plane wave as

$$\mathbf{E}(z, t) = \text{Re}\{E_0 \exp[i(\omega t - \phi)] \exp(-ikz)\}, \quad (2)$$

where $\mathbf{E}_0 = E_x \hat{x} + E_y \hat{y}$ is the complex vector amplitude, and E_x and E_y are complex. We may then define the Cartesian Jones vector \mathbf{E} as¹⁰

$$\mathbf{E} = \begin{bmatrix} E_x \\ E_y \end{bmatrix}. \quad (3)$$

The action of optical elements on the polarization state may be described by complex 2×2 matrices acting on this vector, assuming that the wave retains its planar character. In Fig. 3 we define the coordinate systems which we shall use to describe the reflection of a plane wave from a magnetic surface. One of these, denoted by the superscript m , refers to the orientation of the magnetization vector in the medium, and the other two refer to the incident and reflected waves, \mathbf{E}_i and \mathbf{E}_r .

The reflectivity matrix for a magnetized reflector, defined by the equation $\mathbf{E}^r = \mathbf{r}(\mathbf{M})\mathbf{E}^i$, is

$$\mathbf{r}(\mathbf{M}) = \begin{pmatrix} r_{pp} + a\mathbf{M} \cdot \mathbf{x}^m & b\mathbf{M} \cdot \mathbf{y}^m + c\mathbf{M} \cdot \mathbf{z}^m \\ -b\mathbf{M} \cdot \mathbf{y}^m + c\mathbf{M} \cdot \mathbf{z}^m & r_{ss} \end{pmatrix}, \quad (4)$$

where a , b , and c are complex coefficients which depend on the optical properties of the material and the experimental geometry, and are generally of order 10^{-3} or less, r_{ss} and r_{pp} are the diagonal elements of the reflectivity matrix for an unmagnetized material, and s and p refer to the usual s - and p -polarization convention. When the magnetization is oriented normal to the plane of incidence, which is the geometry of the transverse Kerr effect, we see that this matrix is diagonal and that the magnetization induces a small linear birefringence. This birefringence is linear in the magnetization, and is a truly nonreciprocal effect. For an appropriate choice of counterpropagating polarization states, the trans-

verse Kerr effect will lead to a nonreciprocal phase shift. Magnetization in the plane of incidence leads to nonzero off-diagonal terms, which are responsible for the well-known longitudinal and polar Kerr effects. In particular, the reflectivity matrix will be antisymmetric for magnetization oriented in the plane of the sample surface, and symmetric for magnetization oriented normal to the surface. Again, with the proper choice of polarization states, the nonreciprocal phase shift due to either one of these effects can be maximized. In fact, the symmetry properties of the reflectivity matrix are such that a measurement which is sensitive to the longitudinal effect is completely insensitive to the polar effect, and vice versa, whereas the transverse effect appears in both. By making measurements with three different sets of polarization states, we can completely determine the phase shift associated with each of these effects. In this way we may completely determine the magnetization vector, with no modification of the experimental geometry other than changing the orientations of the wave plates. Detailed analysis of the measurements required to make such a determination will appear in a subsequent publication.

III. NEAR-FIELD SAGNAC MAGNETO-OPTIC SENSOR

Resolution beyond the diffraction limit can be achieved with optical microscopy by operating in the near-field regime, where the evanescent components of the electromagnetic field strongly depend on the environment, i.e., the boundary conditions set by the sample with respect to the source.¹¹ In this near-field scanning optical microscopy mode (NSOM),¹² a subwavelength source and/or detector of visible light is placed in close proximity (of order of the size of d , the source) to a sample and raster scanned to generate images. The coupling of the near-field radiation to the far field is typically quite weak; the transmission coefficient at normal incidence has been calculated to be¹¹

$$T = \frac{P_{\text{trans}}}{P_{\text{inc}}} \approx 10 \left(\frac{d}{\lambda} \right)^6. \quad (5)$$

This is for the ideal case of a circular aperture in a perfectly conducting, infinitely thin screen, with diffraction-limited focusing of the radiation illuminating the pinhole; the problem is analogous to Rayleigh scattering (the additional factor of λ^{-2} comes from the illumination spot size). In general, the finite conductivity and thickness of the screen, as well as inefficiencies in the method used to deliver the incident light to the aperture, will lead to a reduction in this value. Recently, Betzig *et al.*¹² have demonstrated such a microscope with a spatial resolution of 120 Å, using as a light source a tapered optical fiber coated with aluminum. Polarization contrast has also been achieved by creating a polarized source and introducing a polarizer between the sample and the detector.¹³ By orienting the polarizer near the extinction position, magneto-optic contrast with a resolution of 30–50 nm was observed in thin, transparent magnetic films.¹⁴ Although some progress has been made in imaging opaque materials by using NSOM in reflection,^{15–18} serious technical barriers impede similar studies of opaque magnetic samples, and to our knowledge none have been made.

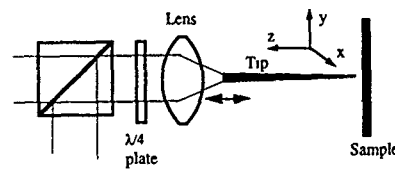


FIG. 4. Arrangement for near-field scanning in conjunction with reflection mode [Fig. 2(b)].

Many of the difficulties in achieving magneto-optic contrast NSOM in reflection are related to the crossed polarizer method for creating the contrast. Moreover, analysis of light scattered away from the normal of the sample is complicated by polarization state changes which are generally dominated by effects which have nothing to do with its magnetic state, such as the shape of the aperture, the direction of radiation in the far field, and the conductivities of both the sample and the tip. Light which reflects back through the aperture from which it came might carry fewer of these spurious polarization effects, but the problem of distinguishing the signal from an overwhelmingly large background becomes significant, since most of the light incident on the aperture is reflected without ever interacting with the sample. In other words, a large amount of "reciprocal" light is expected that will completely mask the real signal. We may expect the intensity which carries the signal to be a factor of 10^{-6} smaller than the incident intensity, and if we are to measure magneto-optic effects by analyzing this light with a crossed polarizer, we may expect a further reduction of 10^{-2} , so this is a formidable problem. One group^{16,17} has succeeded in modulating the distance between the tip and the sample and using synchronous detection to attempt to solve this problem, but their resolution is not yet better than the diffraction limit and they have not yet addressed polarization effects.

The selective sensitivity of SMOS to nonreciprocal effects has led us to explore the possibility of using it as a detection scheme for NSOM with magneto-optic contrast in reflection. If we introduce an aperture between the focusing optics and the sample in Fig. 4 only the light generated in the near field of the magnetic sample will receive a nonreciprocal phase shift, and the enormous amount of background light which passes through reciprocal optics will go undetected. In fact, the presence of this more intense reciprocal radiation can actually serve to amplify the intensity change due to the small magneto-optic phase shift by means of an optical homodyne effect. Let us decompose the fields in the fiber loop into two components for each of the two counterpropagating waves,

$$E_1 = A \exp(i\theta) + \alpha_+ \exp(i\phi_+) \quad (6a)$$

and

$$E_2 = A \exp(i\theta) + \alpha_- \exp(i\phi_-), \quad (6b)$$

where A and θ are the amplitude and phase of the reciprocal part of the fields, and α_{\pm} and ϕ_{\pm} are the amplitudes and phases of the nonreciprocal part. The nonreciprocal phase shift which we measure upon interfering these two waves will be

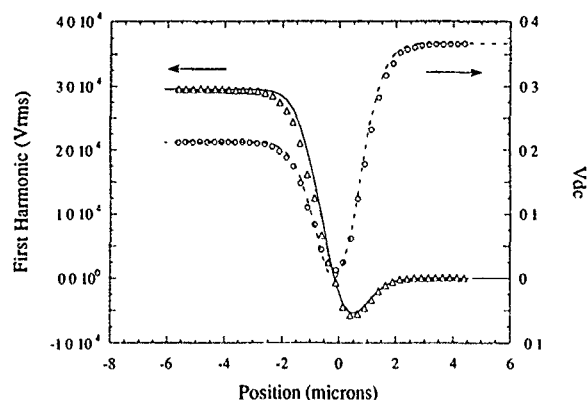


FIG. 5. First-harmonic and dc components of the detector voltage as the edge is traversed with the beam. The edge is at the center of the beam at a position of 0 and the beam is centered on the gold for positive values of the position. Solid and dashed lines represent the fit using Fourier optics analysis.

$$\Delta\phi = \arg\left(\frac{E_1}{E_2}\right) \cong \frac{2\alpha_{\text{avg}}}{A} \sin(\phi_+ - \phi_-) \cos(\phi_{\text{avg}} - \theta), \quad (7)$$

where $\alpha_{\text{avg}} \equiv (\alpha_+ + \alpha_-)/2$, $\phi_{\text{avg}} \equiv (\phi_+ + \phi_-)/2$, and we have neglected higher-order terms. The signal which we measure is then

$$I_{\omega} \propto A^2 \Delta\phi = 2\alpha_{\text{avg}} A \sin(\phi_+ - \phi_-) \cos(\phi_{\text{avg}} - \theta), \quad (8)$$

which is proportional to the field amplitude of the light reflected from the aperture, not the intensity. As a consequence, we may expect our signal to be orders of magnitude larger than NSOM in transmission, where the magneto-optic signal is proportional to the square of both the transmitted field amplitude and the magneto-optic phase shift, both small numbers. For a system which is limited by shot noise, this increase in signal will naturally be accompanied by a corresponding increase in noise, so that the signal-to-noise ratio will not change. However, the dramatic increase in signal strength allows us to move away from photomultiplier tubes to noisier but more convenient photodiode detection schemes.

To verify our analysis, we have deposited 2400 Å of TbFeCo on a silicon wafer, capped it with 200 Å of silicon nitride, then deposited 2000 Å of gold on top as a reflecting layer. We then etched 25 μm lines in the gold to expose the magneto-optic (MO) material, and scanned our beam across the edge dividing the gold from the MO material. The results of this scan are shown in Fig. 5, together with the response which we have calculated using standard Fourier optics techniques.¹⁹ The first-harmonic signal, proportional to the NRPS, as well as the dc detector voltage, proportional to the average intensity, are plotted as a function of beam position on the sample, with the edge at zero. Note that as the edge approaches the center of the beam, both signals drop to zero. This is because the thickness of the gold plus the optical thickness of the nitride cap sum to almost exactly a quarter of one wavelength, so that there is a 180° phase shift between light reflected from the gold and light reflected from the MO material. When the edge is near the center of the beam, the reflected mode is almost fully antisymmetric about

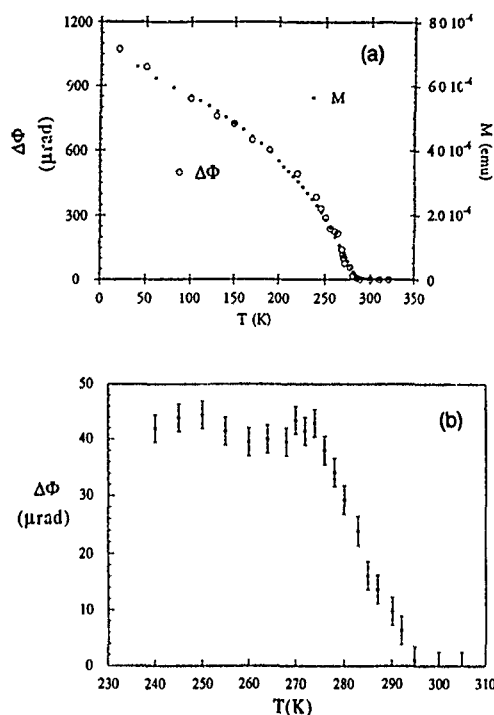


FIG. 6. (a) Transmission (Faraday) measurements and SQUID magnetometry on 480-Å-thick Gd film in an applied field of 30 Oe as a function of temperature. (b) Reflection phase shift using an applied field of 70 Oe.

the plane of the edge and the optical axis, and the single-mode fiber rejects it. As the beam is moved onto the gold, the average intensity increases with the symmetric part of the reflected mode, and the first-harmonic signal crosses zero to become negative. This is exactly the optical homodyning effect described above: Although the bare MO signal is positive, when the wave reflected from the MO material is mixed with the stronger field reflected by the gold, the sign changes because the two waves are shifted relative to each other. In the theoretical fit, we have neglected aberrations in the focusing lens as well as the finite aperture of the lens. There is only one free parameter in the model, the beam radius, which takes a value of 2.2 μm in the curves shown; by simply calculating the magnification of our optics and assuming perfect lenses we obtain a radius of 1.7 μm. The agreement between theory and experiment is quite good, especially considering the limitations of a scalar theory in treating polarization properly.

IV. ADVANTAGES OF SMOS

As explained above, SMOS may achieve high sensitivity and high common-mode rejection for reciprocal effects. The ultimate limit on our sensitivity will be set by the shot noise of the laser. For optical powers of ~1 mW at the detector, the shot-noise-limited sensitivity is ~50 nrad/√Hz. In Fig. 6(a) we show Faraday and superconducting quantum interference device (SQUID) magnetization measurements from 400 Å Gd film. The magnetization lies in the plane, and the Faraday effect measurements have been made in zero field with the sample oriented at 45° to the optical beam. However, the most striking example of the current sensitivity of the appa-

ratus is shown in Fig. 6(b), where the Kerr effect of this 400 Å Gd film is measured through the ferromagnetic transition ($T_c = 270$ K) with only a 70 Oe applied field, with a measurement time of 10 s per point. Currently, we have achieved a NRPS sensitivity of $2 \mu\text{rad}/\sqrt{\text{Hz}}$ in transmission and $4 \mu\text{rad}/\sqrt{\text{Hz}}$ in reflection. The sensitivity may be increased toward the shot-noise limit with some improvements in the construction of the apparatus and in particular the power and spectral characteristics of the source.

An important feature of the Sagnac loop is its immunity to reciprocal effects such as linear birefringence or optical activity. This immunity comes from the fact that two beams are experiencing the same optical path, and phase shifts that do not come from broken time-reversal symmetry will exactly cancel each other. This immunity may be particularly important for evaluation of anisotropic materials where birefringence may be difficult to differentiate from Kerr or Faraday effects if not analyzed properly.

Based on the advantages of the SMOS, it is clear that many of the difficulties with doing magneto-optic contrast NSOM in reflection may be eliminated. If SMOS is used, the background light, as much distorted as it may be, will not lead to a background signal. On the contrary, this light serves to amplify the magneto-optically induced signal by orders of magnitude. Moreover, the high sensitivity allows for relatively easier detection of the very small signals. We believe that this method provides an excellent scheme for expanding the potential applications of NSOM.

The advantages of the near-field SMOS (NFSMOS) microscope over other spin-polarized devices are evident. First is the possible high sensitivity, in particular for materials with large magneto-optic coefficient. The second is the spatial resolution. Current near-field optical microscopes reach a spatial resolution of 120 Å . This is smaller than a typical superparamagnetic size and thus extremely useful for the detection of magnetism. Moreover, since the detection is made with light, the relevant probing thickness is of order of optical penetration depth, hence information from deeper than the first few atomic layers can be obtained. Finally, the accumulation of data can be obtained much faster with improvements in efficiency. Thus, one may envision using this method for high-frequency measurements.

V. SUMMARY

The above instrument opens for us new avenues in the research of magnetic materials. In particular we believe that because of the complete rejection of any reciprocal optical effects, the instrument is ideal for use in reflection mode in a near-field configuration. In this way, it may be possible to do

magneto-optics on a scale of $\sim 200 \text{ Å}$ (current near-field microscopy using tips that preserve polarization may go to a length scale of $\sim 120 \text{ Å}$). This could potentially lead to new opportunities in high-density magnetic recording and magneto-optic readout.

ACKNOWLEDGMENTS

We would like to thank Michael Farle for equipment and useful discussion, as well as Federico Sequeda for fabricating the TbFeCo wafer. We would also like to acknowledge the fruitful collaborations along many phases of this work, in particular with S. Spielman and T. Geballe. Parts of this work were supported by AFOSR, by NSF through the Center for Materials Research at Stanford University, by a special grant from IBM, and by a grant from Stanford Office for Technology Licensing.

- ¹L. M. Falicov, D. T. Pierce, S. D. Bader, R. Gronsky, K. B. Hathaway, H. J. Hopster, D. N. Lambeth, S. S. P. Parkin, G. Prinz, M. Salamon, I. K. Schuller, and R. H. Victora, *J. Mater. Res.* **5**, 1299 (1990); S. D. Bader, *Proc.* **78**, 909 (1990).
- ²See, for example, C. A. Ballentine, R. L. Fink, J. Araya-Pochet, and J. L. Erskine, *Appl. Phys. A* **49**, 459 (1989); S. D. Bader and E. R. Moog, *J. Appl. Phys.* **61**, 3729 (1987).
- ³See, for example, M. J. Freiser, *IEEE Trans. Magn.* **MAG-4**, 152 (1968).
- ⁴S. Spielman, K. Fesler, C. B. Eom, T. H. Geballe, M. M. Fejer, and A. Kapitulnik, *Phys. Rev. Lett.* **65**, 123 (1990).
- ⁵S. Spielman, J. S. Dodge, K. Fesler, L. W. Lombardo, M. M. Fejer, T. H. Geballe, and A. Kapitulnik, *Phys. Rev. B* **45**, 3149 (1992).
- ⁶S. Spielman, J. S. Dodge, L. W. Lombardo, C. B. Eom, M. M. Fejer, T. H. Geballe, and A. Kapitulnik, *Phys. Rev. Lett.* **68**, 3472 (1992).
- ⁷S. Doniach, A. Kapitulnik, P. Frank, M. M. Fejer, S. Spielman and S. Dodge, in *Physical Phenomena at High Magnetic Fields*, edited by E. Manousakis, P. Schlottmann, P. Kumar, K. S. Bedell, and F. M. Mueller (Addison-Wesley, Reading, MA, 1992).
- ⁸See, for example, papers in *Fiber-Optic Rotation Sensors and Related Technologies*, edited by S. Ezekiel and H. J. Arditty (Springer, Berlin, 1982).
- ⁹L. D. Landau, E. M. Lifshitz, and L. P. Pitaevskii, *Electrodynamics of Continuous Media*, 2nd ed. (Pergamon, Oxford, 1984), p. 347.
- ¹⁰R. M. A. Azzam and N. M. Bashara, *Ellipsometry and Polarized Light* (North-Holland, Amsterdam, 1989).
- ¹¹H. A. Bethe, *Phys. Rev.* **66**, 163 (1944).
- ¹²E. Betzig, J. K. Trautman, T. D. Harris, and J. S. Weiner, and R. L. Kostelak, *Science* **251**, 1468 (1991).
- ¹³E. Betzig, J. K. Trautman, J. S. Weiner, T. D. Harris, and R. Wolfe, *Appl. Opt.* **31**, 4563 (1992).
- ¹⁴E. Betzig, J. K. Trautman, R. Wolfe, E. M. Gyorgy, P. L. Finn, M. H. Kryder, and C.-H. Chang, *Appl. Phys. Lett.* **61**, 142 (1992).
- ¹⁵J. K. Trautman, E. Betzig, J. S. Weiner, D. J. DiGiovanni, T. D. Harris, F. Hellman, and E. M. Gyorgy, *J. Appl. Phys.* **71**, 4659 (1992).
- ¹⁶D. Courjon, J.-M. Vigoureux, M. Spajer, K. Sarayeddine, and S. Leblanc, *Appl. Opt.* **29**, 3734 (1990).
- ¹⁷M. Spajer, D. Courjon, K. Sarayeddine, A. Jalocha, and J.-M. Vigoureux, *J. Phys. (Paris) III* **1**, 1 (1991).
- ¹⁸U. C. Fischer, *J. Vac. Sci. Technol. B* **3**, 386 (1985).
- ¹⁹S. Spielman, Ph.D. thesis, Stanford University, 1992.

dc magnetic force microscopy imaging of thin-film recording head

Paul Rice, John Moreland, and Andrzej Wadas

Electromagnetic Technology Division, National Institute of Standards and Technology, Boulder, Colorado 80303

Using a new form of magnetic force microscope (dc MFM) magnetic force images of a thin-film recording head have been made. Using dc MFM, atomic force microscope images are presented of the surface topography and magnetic forces taken simultaneously, allowing direct correlation of magnetic fields to the pole pieces. Magnetic force images of the head at typical head-to-disk spacings are presented. The tips used for these images had two different magnetic coatings.

I. INTRODUCTION

Recently magnetic force microscopy (MFM) has been used to study the field patterns of thin-film recording heads.¹⁻⁵ There are two fundamental modes of MFM. In one method, a vibrating cantilever is used to detect the force gradient between the sample and sensing tip attached to the cantilever. This method referred to in this article as ac MFM, in principal, has high sensitivity.⁶ The ac-MFM data can be integrated to obtain the force profile. The other type of MFM detects the deflection of a nonvibrating cantilever due to the magnetic interaction between the tip and the sample. We refer to this as dc MFM. In dc MFM the force profile can be directly obtained by multiplying the tip displacement by the cantilever spring constant. This article describes our results for applying a new form of dc MFM to thin-film recording heads.

II. EXPERIMENT

Traditionally dc MFM was difficult to apply, because there was no sensing mechanism to position the tip from the sample. Early dc-MFM attempts would scan the entire section of the sample to be imaged, saving slope information or manually adjusting the sample slope, then scan the sample again with the tip raised off the sample.⁷ There were problems with the tip-to-sample distance varying due to piezopositioner creep or hysteresis, and also surface roughness. Since the force profile is dependent on distance, the magnetic force map was not uniform and there were problems preserving the tip-sample separation.

Recently a new dc-MFM operating technique that is based on these previous efforts was developed, although with one major modification:⁸ instead of scanning the entire image and storing the slope, the sample is scanned one line at a time. First a line scan is performed using atomic force microscopy (AFM) contact mode. The topographical and slope information is stored. The tip is then lifted and scanned using the stored topography and slope information to position the tip from the surface. On this second scan the deflection of the tip is recorded as the magnetic signal. This allows for accurate tracking of the sample surface during the magnetic scan since the tip is away from the surface for only one scan line, thus minimizing error due to piezo drift. This also allows for simultaneous imaging of topography and magnetic force. While holding the tip steady, we estimate our cantilever vibration noise to be less than 0.1 nm and therefore conclude that we can detect forces less than 1×10^{-10} N when using

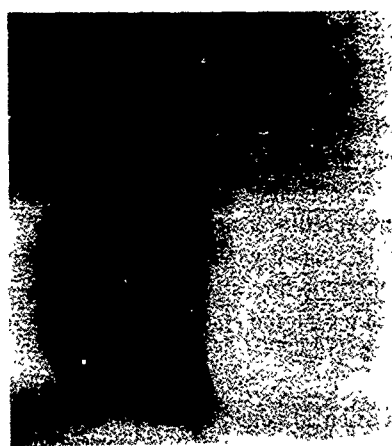
tips with less than 1 N/m spring constant. Also, lateral resolution in many cases is not limited by force sensitivity, but more often limited by the shape and magnetic domain structure at the end of the MFM tip.

Two thin-film heads were measured. These were standard thin-film heads with two pole pieces that were approximately $9 \times 3 \mu\text{m}^2$ as measured by the AFM. The separation of the poles (gap length), also measured with the AFM, varies from 300 to 500 nm. The nonuniform gap length can be attributed to polishing. On one of the heads imaged, the pole pieces were vertically offset by 200 nm. This was visible in the optical microscope and appeared to be a fracture. Although apparently flawed, the head still wrote magnetic bit patterns and produced a strong magnetic field as measured by the MFM. Separation between disk and head, or flying height, is typically between 50 and 100 nm. Saturation current for these heads was reportedly 40 mA.

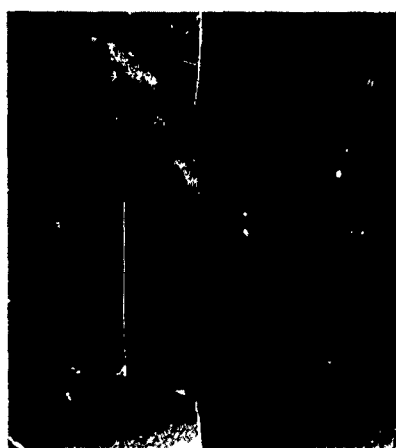
The heads were removed from the flexures and mounted in the MFM with the trailing edge of the slider to the left-hand side relative to the images presented. The head was driven with a dc current source. The tips for these measurements were standard $100 \mu\text{m}$ Si_3N_4 microfabricated cantilevers. The images presented were from two tips. One was coated with 20 nm Fe base layer and a 5 nm Au cap layer. The spring constant for this tip was 0.38 N/m as reported by the supplier. The second tip was coated with 10 nm Fe base layer and a 10 nm Au cap layer with a spring constant of 0.58 N/m. The Au coating was to minimize oxidation of the Fe. It was calculated that the change in spring constant due to these coatings was less than 5%.

III. RESULTS

Figures 1(a) and 1(b) are top-view images of the unfractured head. The second tip as described above was used for this measurement. Figure 1(a) is magnetic and Fig. 1(b) is topographic. In the magnetic image, attractive forces are indicated by dark contrast. The tip is constrained to flexing vertically, so the forces imaged are primarily vertical. The current to the head was 10 mA dc. The gap in the magnetic image can be seen as a bright line accented by the dark contrast of the pole pieces. For the magnetic image, the tip was scanned 100 nm above the surface. The maximum tip deflection is 30 nm. Multiplying this by 0.58 N/m gives a force of 17.4×10^{-9} N. Decreasing the tip height above the sample increases the magnetic contrast due to the increasing field gradient, but no additional magnetic microstructure ap-



(a)



(b)

FIG. 1. (a) Magnetic force image of the air bearing surface of a thin-film head, taken as it was driven with a current of 10 mA, with a tip-to-head separation of 100 nm. The head is oriented with the trailing edge of the slider to the left-hand side. The arrow indicates the magnetic gap. (b) Corresponding topography of the thin-film head taken simultaneously with the magnetic force image. The dark rhombus is the leading pole piece, which is recessed 20 nm due to polishing effects. The arrow indicates the gap between the pole pieces.

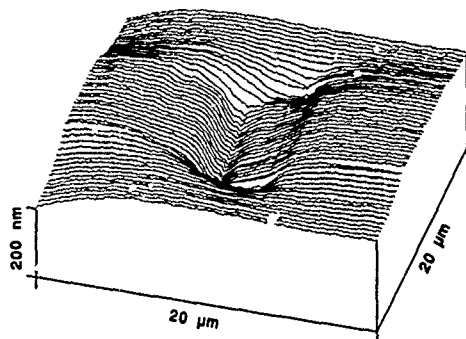


FIG. 2. Magnetic force image line scan taken of the head as it was driven with a current of 30 mA, with a tip-to-head separation of 100 nm. The gap is located at the lowest area on the scan. In the bottom of this depression, the gap can be distinguished as small rise in the scan lines. The attraction of the pole pieces is evident on both sides of the gap.

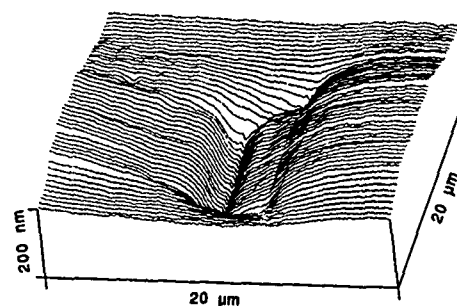


FIG. 3. Magnetic force image line scan taken of the head as it was driven with a current of 30 mA, with a tip-to-head separation of 50 nm. Notice the increase of the depression due to the increased magnetic force.

pears. Pole recession of 20 nm caused by polishing can be seen in Fig. 1(b) (topographical image of the head). Comparing the magnetic image to the topographical image shows that the magnetic contrast trails off, shadowing the edge of the pole piece. These fields compare closely with calculations of thin-film head field profiles by Zhu, Ye, and Arnoldussen.⁹ Figure 2 is a line scan of the magnetic image taken with the tip height at 100 nm and a head drive current of 30 mA. The magnetic gap is more clearly visible in the line scan image, as is the attraction due to the pole pieces. Varying the head drive current increased tip deflection linearly with current. Tip displacement for this image is 85 nm with a corresponding force of 5×10^{-8} N. With the tip-to-head spacing again at 100 nm and the head current increased to 100 mA, the tip continually snapped onto the sample. This is attributed to the soft spring constant of the cantilever.

Figure 3 is taken with the tip height at 50 nm and a head drive current of 30 mA; this technique can explore the head field at heights comparable to typical head-to-disk separations. For this image, a tip displacement of 120 nm corresponds to a magnetic force of 7×10^{-8} N.

The arrows in Fig. 4 point to two small depressions. These are the edges of the pole pieces where the field diverges most rapidly. Below the scan line, the pole pieces are indicated as blocks. This image shows that the tip is magnetically soft, since it is attracted to the pole pieces regardless of polarity. A magnetically soft tip minimizes force variations due to domain switching that can occur in high-

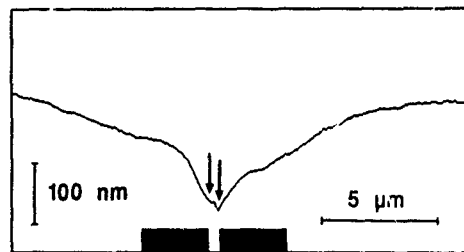


FIG. 4. An individual magnetic scan taken through the center of the head. The head was driven with a current of 30 mA and imaged with a tip-to-head separation of 100 nm. The pole piece positions are indicated as blocks below the magnetic scan line. As seen here both pole pieces attract the tip which indicates that the tip is magnetically soft.

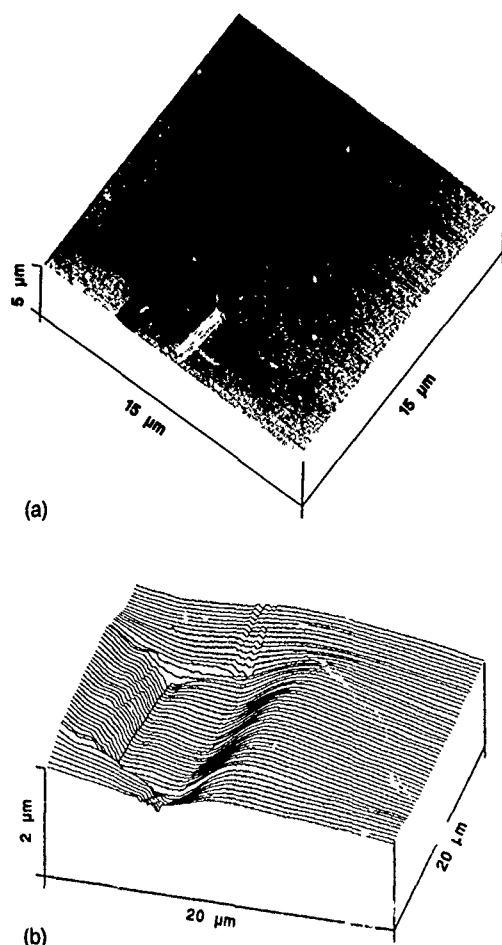


FIG. 5. (a) Topographic image of a flawed thin-film head. The step height is 200 nm. Notice the depression at the base of the step, this appears to be a crack in the head. (b) The corresponding magnetic force image, displayed as a line scan, demonstrates the ability of this MFM to image even very rough magnetic samples. For this image the head was driven with a current of 30 mA and tip-to-head separation was 187 nm. The tip used had a 20 nm coating of Fe.

coercivity (magnetically hard) tips. In the gap the magnetic field gradient is low and deflects the tip less. The asymmetry of the image is likely due to the pole recession. Scanning direction and tip angle can also make the image asymmetrical. In this case the offset seems to be comparable to the pole recession height.

As measured in air, the tip-to-head spacing for good magnetic imaging appears to be a function of surface roughness and tip spring constant. If the surface is rough or the cantilever is very flexible, the tip snaps onto the surface often. This is attributed to the difficulty of maintaining the head-to-tip separation as force deflections cannot be anticipated during the AFM scan. With proper selection of cantilever spring constants and magnetic tip coatings, rough surfaces with large magnetic fields can be imaged. Figure 5(a)

shows a topographical surface view of the head with the 200 nm vertical offset defect. The trailing pole piece is 200 nm higher than the leading one, as measured by the AFM. There is what looks like a crack at the gap making it difficult to measure the gap length. Figure 5(b) is a line scan display of the magnetic force image. The magnetic image presented was taken with a tip-to-head separation of 187 nm. When the tip was closer than this it would contact the surface and van der Waals or meniscus forces would keep the tip in contact with the surface during the rest of the scanline.

IV. SUMMARY

We have presented magnetic force images of dc current driven thin-film heads that were taken with a dc-operated magnetic force microscope. This has allowed us to study the fringing fields above thin-film heads at different driving currents and tip-to-head separations. Comparison of surface topography and magnetic forces has shown that there are magnetic fields associated with the ends of the pole pieces. These fields could possibly contribute to off-track failures of the drive if they are strong enough. With coatings of 10 or 20 nm Fe the tips are magnetically soft, while they scan the head with currents of 10–30 mA. Simultaneous imaging of surface topography and magnetic force is an advantage of this newly developed dc-MFM technique. A further advantage is that the tip-to-sample separation can be more accurately monitored, allowing much rougher samples to be imaged. In contrast, ac MFM measures the magnetic force gradient whereas dc MFM measures the magnetic force which is obtained by simply multiplying the tip deflection by the spring constant. Also, the sensitivity of dc MFM is comparable to ac MFM (in air) and detection of tip deflection is less complicated than phase shifts or amplitude changes of a vibrating tip.

ACKNOWLEDGMENT

We thank Jim Brug of Hewlett-Packard Corp. for providing the thin-film heads and for helpful discussions.

- ¹C. Schonenberger, S. F. Alvarado, S. E. Lambert, and I. L. Sanders, *J. Appl. Phys.* **67**, 7278 (1990).
- ²K. Wago, K. Sueoka, and F. Sai, *IEEE Trans. Magn.* **MAG-27**, 5178 (1991).
- ³O. Watanuki, F. Sai, and K. Sueoka, *Ultramicroscopy* **42-44**, 315 (1992).
- ⁴K. Sueoka, K. Wago, and F. Sai, *IEEE Trans. Magn.* **MAG-28**, 2307 (1992).
- ⁵S. Takayama, K. Sueoka, and H. Setoh, *IEEE Trans. Magn.* **MAG-28**, 2647 (1992).
- ⁶Y. Martin and H. K. Wickramasinghe, *Appl. Phys. Lett.* **50**, 1455 (1987).
- ⁷J. J. Saenz, N. Garcia, P. Grutter, E. Meyer, H. Heinzelmann, R. Wiesendanger, L. Rosenthaler, H. R. Hiber, and H. J. Guntherodt, *J. Appl. Phys.* **62**, 4293 (1987).
- ⁸R. Giles, J. P. Cleveland, S. Manne, P. K. Hansma, B. Drake, P. Maivald, C. Boles, J. Gurley, and V. Elings, *Appl. Phys. Lett.* **63**, 617 (1993).
- ⁹J. Zhu, X. Ye, and T. C. Arnoldussen, *IEEE Trans. Magn.* **MAG-28**, 2716 (1992).

Proposed antiferromagnetically coupled dual-layer magnetic force microscope tips

John O. Oti, Paul Rice, and Stephen E. Russek
Electromagnetic Technology Division, National Institute of Standards and Technology, Boulder,
Colorado 80303

A magnetic force microscope tip designed from dual-layer magnetic films of antiferromagnetically coupled magnetic layers is proposed. A theoretical analysis of the possible advantages of such a tip over conventional single-layer tips is given, using an extension to dual layers of a previously described micromagnetic model of single-layer tips. In contrast to single-layer tips, the magnetic domains of dual-layer tips are less sensitive to the fringing fields of the specimen, and the tips' stray fields are greatly reduced, thus minimizing the likelihood of erasure of the sample magnetization. These properties of dual-layer tips should lead to improved resolution of magnetic force microscopy images.

I. INTRODUCTION

The imaging component of a magnetic force microscope (MFM) system is a probe in the form of a sharp tip mounted at the end of a soft cantilevered spring and positioned near the surface of the specimen. The MFM image is obtained from the force interactions between the tip and specimen. Traditionally, MFM tips have been made from a single magnetic material, and a variety of tip shapes and materials have found practical application.

A MFM tip should remain uniformly magnetized as it interacts with a specimen and not generate large stray fields that inadvertently alter the magnetization pattern of the specimen. The first property helps the interpretation of images, while a contravention of the second property defeats the aim of the imaging process, which is to obtain an image of the magnetization of the specimen without destroying it. In this regard, traditional MFM tips have limited capabilities. Traditional soft magnetic tips, such as nickel with a coercivity H_c of about 40 A/m and a saturation magnetization M_s of about 500 kA/m, are, by virtue of their low coercivities, unsuitable for imaging high-moment films. Their magnetization is usually rendered unstable by the large fringing field of the film surfaces. A hard magnetic tip such as iron ($H_c \approx 160$ kA/m, $M_s \approx 1700$ kA/m), although largely immune to effects of fringing field, can itself generate high enough stray fields to alter the magnetization of soft magnetic films. All this limits the range of applicability of the tips.

We propose a new MFM tip that overcomes these limitations. The new tip is a dual-layer magnetic film, with strongly antiferromagnetically coupled ferromagnetic layers separated by a nonmagnetic layer. Each magnetic layer and the separation layer are a few nanometers thick. Strong antiferromagnetic coupling maintains the stability of oppositely directed domains in the magnetic layers. The resulting magnetic-field-flux closure at the tip edges reduces the tip's stray fields. The tip's stray field pattern leads to improved resolution of MFM images.

We have developed a micromagnetic MFM model to analyze the dual-layer tips. An analysis of the effects of the antiferromagnetic coupling on the response of dual-layer tips is presented in this article. Traditional MFM tips are called simply single-layer tips in the article.

II. MICROMAGNETIC MODEL

The micromagnetic model of the proposed tip is an extension of our previously described single-layer model.¹ The geometry of the dual-layer model for a triangular tip is shown in Fig. 1(a). The tip is scanned at a fixed distance d_0 above the sample from point A to point B. Other tip shapes

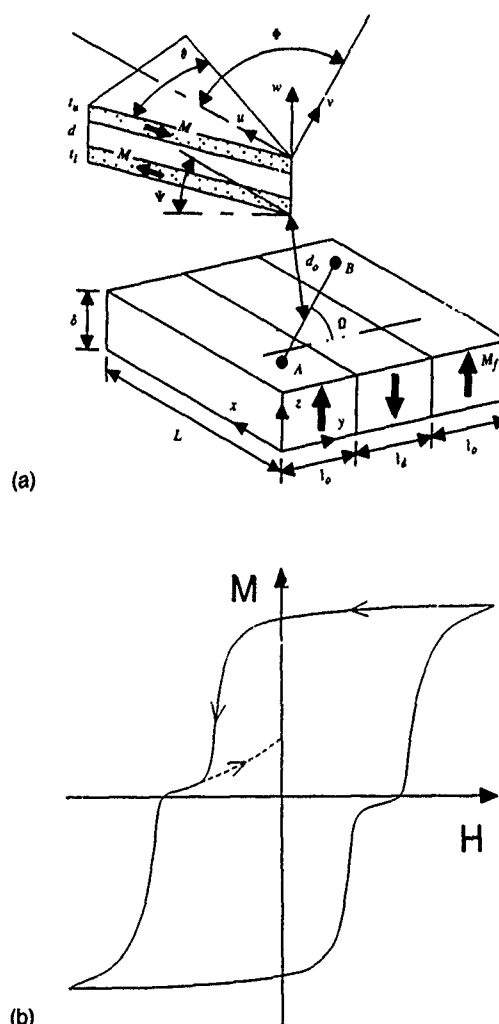


FIG. 1. (a) Geometry of micromagnetic model, showing defining dimensions and two abrupt Bloch walls. (b) Illustration of the field sequence for obtaining antiferromagnetic coupled bilayers. Arrows indicate the path traversed in the major hysteresis curve of the tip in the v direction.

such as bars are possible. A way of traversing the major hysteresis loop which results in the antiparallel orientation of magnetization in the ferromagnetic layers is illustrated in Fig. 1(b). The humps that are formed in the branches of the hysteresis loop are due to the difference in the switching fields of the magnetic layers that is enhanced by the antiferromagnetic coupling between them. Subscripts u and l are used to distinguish between quantities of the upper and lower magnetic layers of the tip in Fig. 1(a). The upper and lower magnetic layers have thicknesses of t_u and t_l , and are separated by a nonmagnetic layer of thickness d . Each magnetic layer is modeled using closely packed discrete elements with rectangular parallelepiped shapes that have square cross sections in the plane of the probe [the u - v plane of Fig. 1(a)]. The elements represent the grains of the tip medium. The grains interact with each other by nearest-neighbor exchange and long-range magnetostatic interactions. The magnetization of the tip can vary, but that of the film is assumed unaffected by its interaction with the tip. A detailed account of modeling the magnetic layers and calculating forces acting on the tip is given in Ref. 1. Antiferromagnetic coupling between the magnetic layers is simulated by introducing a negative interlayer exchange-interaction parameter. The effective exchange interaction field acting on a grain of the upper layer is given by^{1,2}

$$H_u = \frac{2A_u}{(M_u D)^2} \sum M_u + \frac{2A'}{(M_u D)^2} M_l, \quad (1)$$

where $A_u \geq 0$ is a phenomenological ferromagnetic exchange parameter for the top layer, $A' \leq 0$ is a phenomenological interlayer antiferromagnetic-exchange parameter, D is grain size, and M_u , M_l are the magnetization of grains of the upper and lower layers. The first term on the right-hand side of Eq. (1) represents the exchange interactions among grains of the upper layer; the summation is over the nearest neighbors of the grains. The second term of Eq. (1) represents exchange interactions of the upper layer with grains of the lower layer. Interlayer exchange interactions are assumed to occur between grains in corresponding positions in the layers. Positive values of A' could be used when ferromagnetic exchange coupling between the layers is intended. For simplicity it is assumed that the magnetocrystalline anisotropic properties, the magnetization and grain size D are identical for both magnetic layers. The expression for the exchange interaction field in the lower layer is obtained from Eq. (1) by interchanging the roles of the subscripts u and l .

III. SIMULATION RESULTS

The stray field patterns of the dual-layer and single-layer tips, in the active regions of the tips, are compared in Fig. 2. The stray field of the single-layer tip radiates outwardly from the tip toward the sample surface and thus is more likely to affect the magnetization of the sample. The stray field of the dual-layer tip, on the other hand, is localized about the active region due to magnetization flux closure stemming from the proximity of the opposite magnetic poles in the magnetic layers. The force sensitivity of the dual-layer tip is affected by the choice of the layer thicknesses t_u and t_l . In a region of

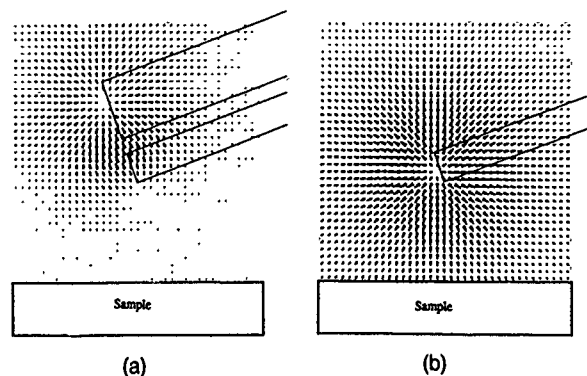


FIG. 2. Longitudinal section (in the u - w plane of Fig. 1) of stray fields for triangular tips for (a) dual-layer tip and (b) single-layer tip.

constant fringing field of the sample, the force acting on a tip of equally thick magnetic layers with a small separation between them is vanishingly small; however, when the layers have the same thicknesses, the tip is sensitive to field gradients. When the tip distance d_0 is less than the layer spacing d , these gradient forces can be nearly as large as the forces acting on a single-layer tip in a uniform field.

Force profiles from a single scan of two abrupt Bloch walls [Fig. 1(a)], for three different antiferromagnetic exchange parameters A' , are plotted in Fig. 3. A tip magnetization of $M = 1430$ kA/m and first-order anisotropy constant of $K = 4.3 \times 10^5$ J/m³, corresponding to those of cobalt,³ were used in the calculations; magnetic layer thicknesses $t_u = 10$ nm and $t_l = 15$ nm and an interlayer separation $d = 2$ nm were used. An intralayer exchange constant $A = 4 \times 10^{-10}$ J/m, corresponding to a maximum exchange field of 2343 kA/m, was used. The tip was inclined at an angle $\psi = 30^\circ$ to the sample and separated from it by $d_0 = 5$ nm. The tip was scanned normal to the domain wall [$\Omega = 0^\circ$ in Fig. 1(a)]. The same grain sizes, linear dimensions of the tips, and gyromagnetic parameters as in Ref. 1 were used. Each cobalt grain is characterized by a uniaxial magnetocrystalline anisotropy; the anisotropy directions were assigned randomly among the grains in the calculation. The sample

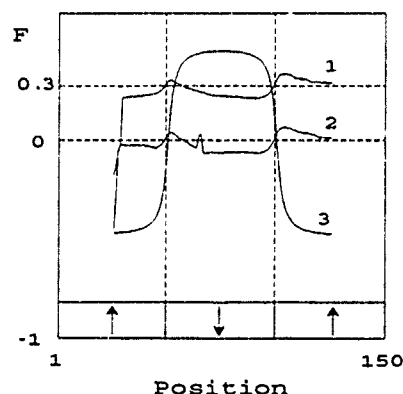


FIG. 3. Profiles of reduced force F as functions of interlayer antiferromagnetic coupling A' for $A' = -4 \times 10^{-11}$ J/m equivalent to an antiferromagnetic coupling field $H_{AF} = 468.5$ kA/m (curve 1), $A' = 0$, $H_{AF} = 0$ (curve 2), and $A' = -2 \times 10^{-10}$ J/m, $H_{AF} = 2343$ kA/m (curve 3). Curve 1 is displaced vertically by 0.3 for clarity.

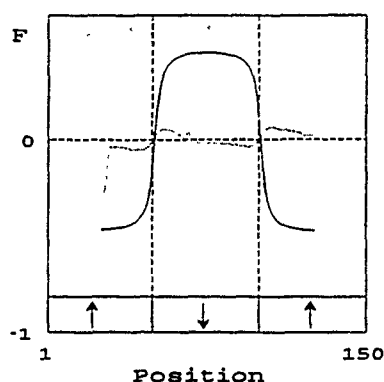


FIG. 4. Force profiles of dual-layer tip with $A' = -2 \times 10^{-10}$ J/m (solid curve) and single-layer tip (dotted curve).

properties were chosen to correspond to those of a magnetic garnet film described in Ref. 1. The following linear dimensions of the sample were used in the calculations [see Fig. 1(a)]: $\delta = 2000$ nm, $l_d = l_0 = 500$ nm, and $L = 1000$ nm.

The antiferromagnetic-coupled state of the magnetic layers is a low-energy state, which requires an external field greater than the antiferromagnetic coupling field to move it away from this state. The force profile is greatly distorted for $A' = 0$ and -4×10^{-11} J/m (curves 1 and 2) because the fringing field surpasses the antiferromagnetic coupling field and leads to instability of the magnetic domains. With increasing A' the magnetic domains of the tip gradually stabilize, the force increases, and the force transition regions sharpen (curve 3). Stable tip domains also lead to larger force amplitudes. The calculation was repeated for a single-layer tip using the same shape and mutual orientation of the tip and sample as for the dual-layer tips. The single-layer tip had a thickness equal to the combined thickness of the magnetic layers of the dual-layer tips, and the magnetic properties were the same as those of the magnetic layers of the dual-layer tips. The calculated force profile of the single

layer tip is compared with that of a dual-layer tip having $A' = -2 \times 10^{-10}$ J/m in Fig. 4; the dual-layer tip produces a larger force with a sharper transition region which is better centered and more nearly symmetrical relative to the domain walls. These properties, due to the stability of domains, in the magnetic layers lead to a better spatial resolution of the final MFM image.

IV. DISCUSSION

Strongly antiferromagnetically coupled multilayer magnetic films that are currently receiving a lot of attention in the literature in connection with their giant magnetoresistance properties would make good candidate materials for constructing the dual-layer tips.⁴ The range of interlayer separation d corresponding to antiferromagnetic coupling between the magnetic layers is material dependent. An Fe-Cr-Fe system reported in Ref. 4 has a coupling field of 1600 kA/m. The magnitude of the fringing field close to the surface of the film is bounded by the value of the saturation remanent magnetization. The saturation remanent magnetization of metallic recording films,³ for example, ranges from 400 to 1000 kA/m, which is smaller than the coupling field of the Fe-Cr-Fe system. Thus, a Fe-Cr-Fe probe is expected to remain stable while imaging such films or films with lesser saturation magnetization values. Other coupled multilayers such as Co-Cr-Co, Co-Ru-Co, and Co-Cu-Co multilayers with coupling fields of comparable magnitudes to the Fe-Cr-Fe system have also been reported.^{5,6}

¹J. O. Oti and P. Rice, J. Appl. Phys. **73**, 5802 (1993).

²J. O. Oti, IEEE Trans. Magn. **MAG-29**, 1265 (1993).

³E. Koster and T. C. Arnoldussen, in *Magnetic Recording I: Technology*, edited by C. D. Mee and E. D. Daniels (McGraw-Hill, New York, 1982), Chap. 3.

⁴R. L. White, IEEE Trans. Magn. **MAG-28**, 2482 (1992).

⁵S. S. S. Parkin, N. More, and K. P. Roche, Phys. Rev. Lett. **64**, 2304 (1990).

⁶M. A. Howson, B. J. Hickey, J. Xu, and D. Grieg, Phys. Rev. B **48**, 1322 (1993).

Anisotropy and magnetostriction measurement by interferometry

Peter S. Harlee III, George H. Bellesis, and David N. Lambeth
ECE Department, Data Storage Systems Center, Carnegie Mellon University, Pittsburgh,
Pennsylvania 15213

Extending the use of a laser-Doppler interferometer that measures magnetostriction by measuring the deflection of a thin-film cantilever sample to also measure the anisotropy is reported. When the sample is driven with a rotating magnetic field of constant magnitude, a number of harmonics of twice the rotating field frequency are evidence of the magnetization vector lagging and leading the drive field around the sample. Altering the magnitude of the drive field so that the H vector traces out an ellipse is found to null the harmonic signals. This ellipse has its major axis aligned with the hard axis. Using the Stoner-Wohlfarth single-domain-particle model, it is shown that a rotating field will cause the magnetization to rotate around the particle uniformly only if the difference in magnitude between the fields along the major and minor axes is equal to the anisotropy field. Measurements on isotropic and anisotropic samples confirm the theory.

I. INTRODUCTION

In the beam deflection method of measuring saturation magnetostriction λ_s , a magnetically soft thin-film material deposited on a nonmagnetic substrate is subjected to a rotating magnetic field.¹⁻³ As the magnetization rotates, the thin film expands (or contracts for $\lambda_s < 0$), creating a stress on the substrate, which causes the substrate and film to bend. Typically, a rectangular cantilever sample is clamped on one end and the deflection of the free end is measured. This deflection is measured using a laser Doppler interferometer.³ A laser beam is reflected off the sample and off a nearby stationary mirror, and is interfered with a second beam whose frequency is shifted by 50 kHz. This produces two sinusoidal signals that differ in phase by 2π times twice the distance between the sample and the nearby mirror divided by the laser wavelength. An inplane rotating field is used to avoid the ambiguity of the demagnetized state; only the difference in deflection is measured as the saturation magnetization is rotated from alignment along the length of the cantilever to alignment perpendicular to the cantilever.

As no difference in the field-induced strain along the cantilever occurs for a 180° change in magnetization direction, magnetization rotating at a frequency f will produce a deflection that oscillates at a frequency $2f$. However, a number of higher harmonics have been observed,³ which were partly attributed to the magnetization not rotating uniformly with the applied field. Here we describe how the elimination of these harmonics can be used to determine the anisotropy field of the sample.

II. PHYSICAL MODEL

Even though the sample is polycrystalline, for analysis purposes the magnetization of the thin-film sample is assumed to behave as that of a Stoner-Wohlfarth single-domain particle, as illustrated in Fig. 1.

The total energy of this particle when saturated is

$$E_t = K_u \sin^2 \theta - HM_s \cos(\alpha - \theta), \quad (1)$$

where θ is the angle between the magnetization and the easy axis, α is the angle between the applied magnetic field and the easy axis, M_s is the saturation magnetization, H is the

magnitude of the applied field, and K_u is the anisotropy constant. An expression for the magnetization direction θ is found by minimizing this energy,

$$\frac{\sin(\alpha - \theta)}{\sin(\theta)\cos(\theta)} = \frac{2K_u}{HM_s}. \quad (2)$$

Straightforward algebraic manipulation yields the following equation for the position of the magnetization for a given applied magnetic field:

$$\frac{\sin(\alpha)}{\sin(\theta)} - \frac{\cos(\alpha)}{\cos(\theta)} = \frac{H_k}{H}, \quad (3)$$

where $H_k = 2K_u/M_s$.

If two sets of Helmholtz coils orthogonal to each other generate the rotating field, an expression for the applied field is

$$H(t) = h_x \cos(\omega t) \hat{x} + h_y \sin(\omega t) \hat{y}, \quad (4)$$

where the first term is generated by one coil pair and the second term is generated by the other, and where x is along the easy axis as shown in Fig. 1. We refer to the case where $h_x = h_y$ as a "circular field," and the case $h_x \neq h_y$ as an "elliptic field."

Substituting Eq. (4) into Eq. (3) gives an expression for the time-dependent magnetization position,

$$\frac{h_y \sin(\omega t)}{\sin(\theta)} - \frac{h_x \cos(\omega t)}{\cos(\theta)} = H_k. \quad (5)$$

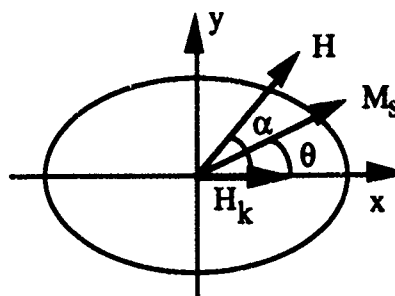


FIG. 1. Stoner-Wohlfarth single-domain particle.

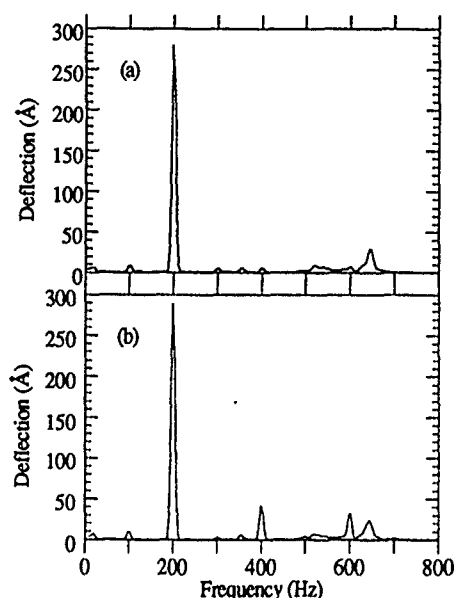


FIG. 2. Round, isotropic sample subjected to (a) a 28.3 Oe circular rotating field, and (b) an elliptic field with $h_y = 35.4$ Oe and $h_x = 28.3$ Oe.

In order for the magnetization to rotate uniformly around the sample, θ must equal ωt , yielding

$$h_y - h_x = H_k. \quad (b)$$

This means that when the deflection of the sample occurs at a single frequency, the difference between the field along the hard axis and the field along the easy axis is equal to the anisotropy field of the sample.

The cantilever deflection frequency ϑ (Hz) will be twice the frequency of the magnetization. In a circular field, an isotropic, round sample would have a uniform demagnetization and hence the magnetization would rotate at the field angular frequency ω and the cantilever deflection frequency would be $\vartheta = 2\omega/2\pi$. A sample with crystalline anisotropy or a noncircular shape would produce higher harmonics of ϑ . Hence, by Eq. (6), obtaining the h_y and h_x values required to eliminate the higher harmonics yields the sample anisotropy.

III. RESULTS ON PERMALLOY FILMS

The signal spectrum of a 21-mm-diam, 0.5- μ m-thick, isotropic FeNiZr film subjected to a 28.3 Oe field rotating at 100 Hz is shown in Fig. 2(a). The peak at 100 Hz is due to a number of causes, including mechanical vibration and metal in the sample holder.³ A number of harmonics of 60 Hz is observed, and the signal from 580 to 640 Hz is due to the mechanical resonances of the sample. The 200 Hz peak is the magnetostrictive signal ($\lambda_s = 2.68 \times 10^{-6}$). This value is determined from the deflection and the physical properties of the sample: glass substrate thickness is 229 μ m, film thickness is 0.5 μ m, cantilever length is 0.495 in., and the ratios of the Young's modulus and Poisson's ratio of the substrate and film are 1.611.³ This spectrum closely matches what the theory predicts, namely for the circular field the only significant deflection due to the sample magnetostriction is at 200 Hz. Only a very weak 400 Hz peak of 5.5 \AA is observed.

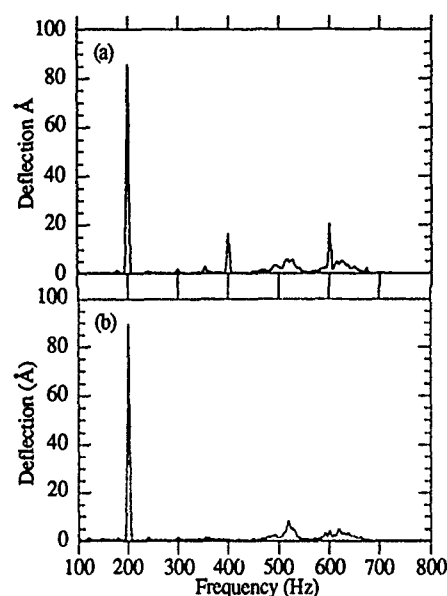


FIG. 3. Round, anisotropic sample subjected to (a) a 28.3 Oe circular field, and (b) an elliptic field with $h_y = 36.2$ Oe and $h_x = 28.3$ Oe.

Figure 2(b) shows the signal spectrum of the same sample when the applied field is changed from circular to an elliptic field with a major axis magnitude of 35.4 Oe and a minor axis magnitude of 28.3 Oe. The 200 Hz peak has risen from 280 to 289 \AA because the average field applied to the sample has risen and the sample is not fully saturated at 28.3 Oe. The 400 Hz peak has jumped from 5.5 to 38.1 \AA . A 600 Hz term is also apparent, but its magnitude is nonlinearly amplified by the mechanical resonance of the cantilever.

The signal spectrum of a 21-mm-diam, 0.5- μ m-thick, anisotropic Permalloy film on a 229 μ m glass substrate subjected to a 28.3 Oe field, rotating at 100 Hz, is shown in Fig. 3(a) ($\lambda_s = 7.72 \times 10^{-7}$). It is apparent that this spectrum is very similar to that of the isotropic sample subjected to the elliptic field. Figure 3(b) shows the signal spectrum of the sample when subjected to an elliptic field with a major axis magnitude of 36.2 Oe and a minor axis magnitude of 28.3 Oe. The 400 Hz term has almost vanished, dropping from 16.4 to 0.7 \AA . The difference in the fields along the two axes, 7.9 Oe, is equal to the anisotropy field. Figure 4 is a plot of

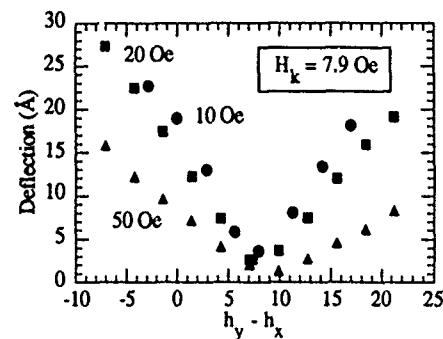


FIG. 4. 400 Hz deflection vs difference in field for several values of easy-axis field.

the 400 Hz deflection as the field along the hard axis is varied for various constant values of field applied along the easy axis. The point at which the 400 Hz term is minimized is the value of the anisotropy field. For this sample the anisotropy field is approximately 7.9 Oe. The uncertainty in the value arises from misalignment of the easy axis of the sample and the axis of the coils, and the value of the field can only be resolved to 0.2 Oe. It is worth noting that as the average field is increased the harmonic strength decreases since the magnetization more closely follows the applied field.

The anisotropy of this sample was also measured using a *M-H* loop er built by SHB industries. The value obtained by the *M-H* loop er was 7.1 Oe. This value differs from that measured using the magnetostriction instrument because in the *M-H* loop er, the film is driven with a field much lower than that needed for saturation, therefore the value of H_k obtained by this method is suspect.⁴

The round isotropic film used to obtain Fig. 2 was cut into a rectangular shape and measured in the instrument. The anisotropy of this sample is almost totally due to shape demagnetization effects. Strictly speaking, the demagnetizing field is nonuniform in the rectangular sample; however, its effect was estimated by considering the sample to be a general ellipsoid with the same axial dimensions as the rectangle. From this approximation the anisotropy due to demagnetization effects was estimated to be 0.5 Oe. The measured value of anisotropy was 1.4 Oe. The difference between the

measured and estimated values is most likely due to the difference in the actual demagnetization of a rectangle as opposed to an ellipse.

IV. CONCLUSION

The high sensitivity of the rotating field interferometric magnetostriction instrument has allowed multiple harmonics of the deflection of magnetostrictive cantilevers to be measured. By employing a Stoner-Wohlfarth model it has been shown that these harmonics are directly related to the sample's anisotropy. By creating an elliptical rotating field the harmonics are eliminated and the anisotropy field determined. Measurement of the anisotropy field of a permalloy sample was demonstrated.

ACKNOWLEDGMENTS

This material is based (in part) upon work supported by the National Science Foundation under Grant No. ECD8907068. The government has certain rights in this material. We would like to thank Shan Wang and Min Xiao of the DSSC for providing the samples.

¹E. Klokholm, IEEE Trans. Magn. **MAG-12**, 819 (1976).

²A. C. Tam and H. Schroeder, IEEE Trans. Magn. **MAG-25**, 2629 (1989).

³G. H. Bellesis, P. S. Harlee III, and D. N. Lambeth, IEEE Trans. Magn. **MAG-29**, 2989 (1993).

⁴W. C. Cam, M.S. thesis, Carnegie Mellon University, 1986.

New complex permeability measurement device for thin magnetic films

S. Hayano, I. Marinova, and Y. Saito

College of Engineering, Hosei University, Kajino, Koganei, Tokyo 184, Japan

Previously, we have proposed a strategic dual image (SDI) method to obtain the finite element solution of open boundary magnetic field problems. Also, we have derived a complex permeability from a Chua-type magnetization model. Combination of this complex permeability with the SDI method is now applied to exploit a new high frequency characteristic measurement device for thin magnetic films. Numerical simulation suggests that our new measurement method yields far superior results compared with those of the conventional one.

I. INTRODUCTION

At high frequency, the peak flux density in the magnetic materials is sufficiently small that both the flux density and field intensity are sinusoidally time varying. This makes it possible to employ a complex permeability representing the magnetization characteristics. Previously, we proposed a Chua-type magnetization model based on the magnetic domain theory.¹⁻⁵ Also, this Chua-type model was successfully applied to derive a complex permeability.⁶

In the present paper, we propose one of the novel methods for measuring the complex permeability of thin magnetic films. The measurement principle of the conventional method is that the mean flux density B in a specimen is obtained from a difference linkage flux between the detection and correction coils; and the field H is obtained from linkage flux of the detection coil. Each of the coils of the conventional measurement method is that the detection and correction coils are arranged in parallel in the exciting coil. In the new method, the detection, correction, and exciting coils are coaxially arranged in each other, and the flux density B is similarly obtained as those of the conventional one, but field intensity H in a specimen can be obtained by extrapolating the field intensities in the outer and inner detection coils. According to the simulation in the two-dimensional (2D) as well as axisymmetric coordinate systems, it is suggested that the new method yields the extremely higher accurate results compared with those of the conventional one.

II. FINITE ELEMENT SOLUTION OF OPEN BOUNDARY HYSTERETIC FIELDS

A. Complex permeability

At high frequency, it is possible to assume that both the flux density and field intensity are sinusoidally time varying. This is because the peak flux density in the magnetic materials is sufficiently small. Thus, it is possible to employ a complex permeability representing the magnetization characteristics. Previously, we proposed a Chua-type magnetization model based on the magnetic domain theory.¹⁻⁵ Also this Chua-type model was successfully applied to derive a complex permeability.⁶ A Chua-type magnetization model is given by

$$H + (\mu_r/s) dH/dt = (1/\mu) B + (1/s) dB/dt, \quad (1)$$

where H , B , μ , μ_r , and s are the field intensity, flux density, permeability, reversible permeability, and hysteresis coefficient, respectively.¹⁻⁵ These parameters can be assumed to take the constant values when the flux density B as well as the field intensity H are sinusoidally time varying. When we employ a complex notation $d/dt = j\omega$, the complex permeability $\mu(\omega)$ is derived from Eq. (1) as

$$\mu(\omega) = B/H = \mu_R(\omega) - j\mu_I(\omega) = \mu[(s^2 + \omega^2\mu\mu_r)/(s^2 + \omega^2\mu^2)] - j\mu\omega s[(\mu - \mu_r)/(s^2 + \omega^2\mu^2)], \quad (2)$$

where $j = \sqrt{-1}$; $\omega = 2\pi f$ (f : frequency). Figure 1 shows an example of the frequency characteristics of the complex permeability.

B. Strategic dual image method

For simplicity, let us consider a 2D magnetic field problem having an open boundary. The key idea of the strategic dual image (SDI) method is that any vector fields and their field sources, respectively, can be divided into two components: rotational and divergent.⁷⁻¹⁰ Thereby, it is possible to exploit a method by which the rotational and divergent components can be obtained by imposing the rotational and divergent field source images, respectively. In magnetic field problems, the rotational and divergent field sources correspond to the current i and magnetic charge m so that the rotational field component can be obtained by imposing the corresponding image current as shown in Fig. 2(a). In this case, the condition

$$\sum_{p=1}^q (i_p/r_p) = 0 \quad (3)$$

must be satisfied at the center of a circular hypothetical boundary to reduce the net image to zero. In Eq. (3), q and r_p denote the number of source currents and the distance from a center of the hypothetical boundary to the current i_p , respectively. Equation (3) and the image in Fig. 2(a) mean that the total currents in the problem region must be zero, and the vector potentials at the center as well as on the circular hypothetical boundary must be zero. Therefore, the calculation of the rotational field component can be reduced to the solution of a vector potential problem having zero boundary conditions at the circular hypothetical boundary and the center of its

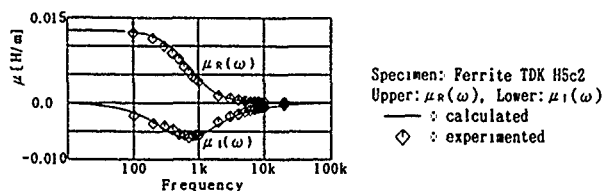


FIG. 1. Frequency characteristics of $\mu_R(\omega)$ and $\mu_I(\omega)$.

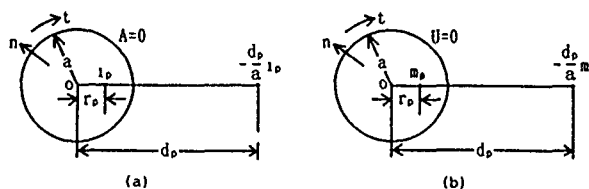


FIG. 2. (a) The rotational field source image $-(d_p/a)i_p$. (b) The divergent field source image $-(d_p/a)m_p$.

hypothetic boundary. Similarly, it is possible to show that the calculation of the divergent field component can be reduced to the solution of a scalar potential problem having zero boundary conditions at the circular hypothetic boundary and the center of the hypothetic boundary, as shown in Fig. 2(b). Obviously, the zero boundary condition of scalar potential U at the hypothetic boundary corresponds to the symmetrical boundary condition of vector potential A . This means, if we employ the vector potential A to represent the open field, then the calculation of the divergent field component may be reduced to the solution of a vector potential problem having the symmetrical boundary condition at the circular hypothetic boundary and the zero boundary condition at the center of the hypothetical boundary. Thus, the open boundary field calculation can be reduced to the solution of zero and the symmetrical boundary problems having the circular hypothetic boundary for two dimensions and the elliptic hypothetic boundary having an axial ratio of 1.8 for axisymmetrical dimensions.⁷⁻¹¹ According to Ref. 11, the axial ratio 1.8 in axisymmetrical dimensions could be determined by considering the demagnetization factor of the elliptic solid. Further, the zero condition must be set at the center of the hypothetic boundary by Eq. (3) for both zero and symmetrical boundary problems.

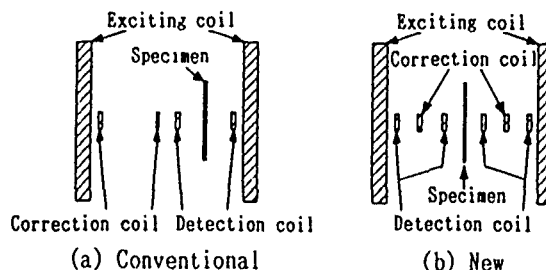


FIG. 3. The 2D models of the measurement devices.

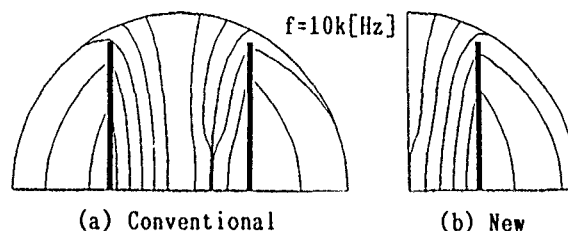


FIG. 4. Field distributions in 2D models. Specimen: TDK H5c2, thickness: 10 (μm), length: 10 (mm), frequency $f=10\text{ k}$ (Hz).

C. The high frequency measurements for the thin magnetic films

Figure 3 shows the 2D models of a high frequency characteristic measurement device for the thin magnetic films. The measurement principle of the conventional method is that the mean flux density B in a specimen is obtained from a linkage flux difference between the detection and correction coils; and the field H is obtained from the linkage flux in the detection coil. The principle may be correct if the fields in the correction and detection coils distribute in parallel to each of the correction and detection coil axes. However, this condition is not always held but the reasonable field distribution is distorted by the specimen in the detection coil. In order to overcome this difficulty, we propose here a new method. In this new method, the flux density B is similarly obtained as in the conventional one, but the field intensity H in a specimen can be obtained by extrapolating the field intensities in outer and inner detection coils.

Figure 4 shows the examples of the field distribution in 2D models. Obviously, a field of the conventional measurement method becomes asymmetrically distributed, caused by

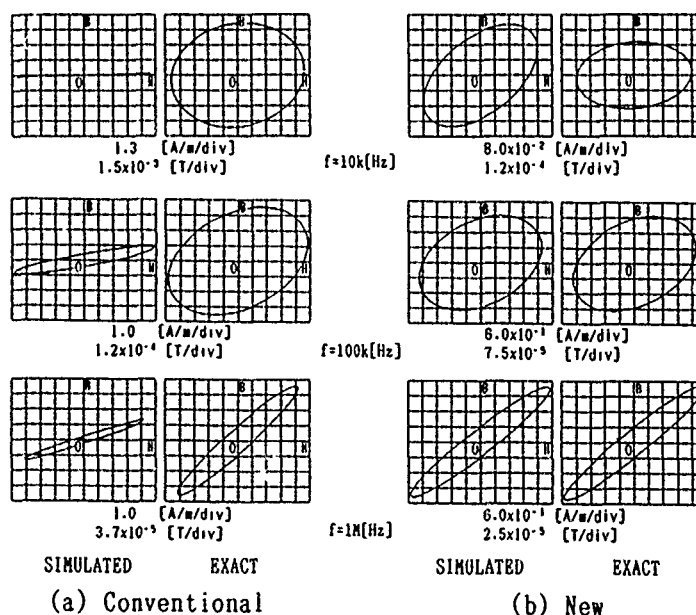


FIG. 5. Hysteresis loops of a thin magnetic film in two dimensions. Specimen: TDK H5c2, thickness: 10 (μm), length: 12 (mm).

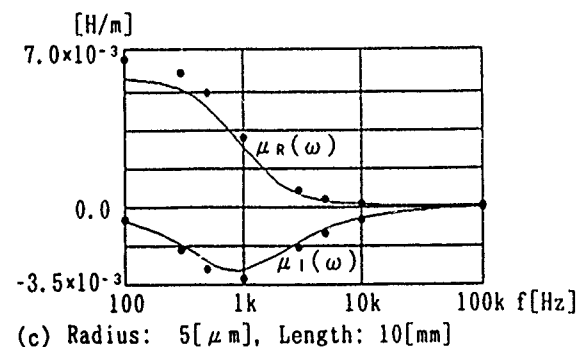
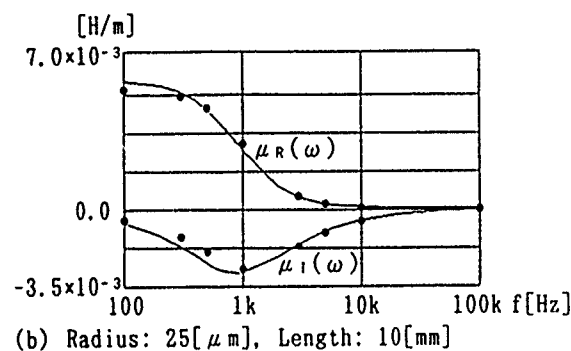
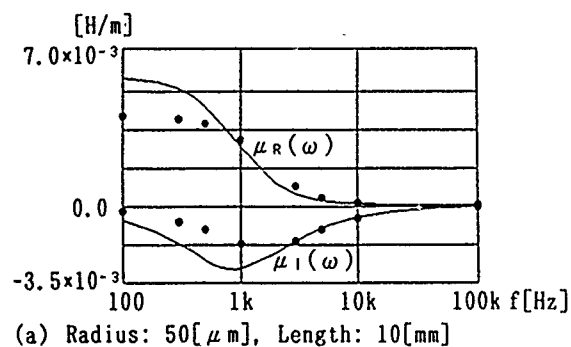


FIG. 6. Frequency characteristics of the complex permeability. Solid lines: exact, solid dots: simulated in the axisymmetrical dimensions assuming the slender magnetic bars instead of thin magnetic films. Specimen: TDK H5c2.

the specimen in the detection coil. On the contrary, a field of the new method becomes symmetrically distributed. This means that it is possible to extrapolate the field intensity H in the material with fairly good accuracy.

Figure 5 shows the comparison between the simulated and exact hysteresis loops in two dimension. The results in Fig. 5 suggest that the new method makes it possible to measure the high and low frequency characteristics of the thin films with higher accuracy.

As shown in Fig. 6, even if the axisymmetrical coordinate system assumes the slender magnetic bars instead of thin magnetic films, it is obvious that the new method provides fairly good results. Also, it is revealed that the measured accuracy becomes higher for slender magnetic bars. This is because the magnetic field distribution in the specimen becomes not uniform for thicker magnetic bars due to the skin effect.

III. CONCLUSION

As shown above, we have shown that the finite element solutions of open boundary hysteretic field problems could be evaluated by combining the SDI method with complex permeability. As an application of our method, the new high frequency characteristic measurement device for the thin magnetic films has been developed to get more accurate results compared with those of the conventional one.

ACKNOWLEDGMENT

The authors gratefully acknowledge A. Miyazaki of the IWATSU Co. LTD. for his practical coding works.

- ¹Y. Saito, S. Hayano, Y. Kishino, K. Fukushima, H. Nakamura, and N. Tsuya, IEEE Trans. Magn. **MAG-22**, 647 (1986).
- ²Y. Saito, K. Fukushima, S. Hayano, and N. Tsuya, IEEE Trans. Magn. **MAG-23**, 2227 (1987).
- ³Y. Saito, S. Hayano, and Y. Sakaki, J. Appl. Phys. **64**, 5684 (1988).
- ⁴Y. Saito, M. Namiki, S. Hayano, and N. Tsuya, IEEE Trans. Magn. **MAG-25**, 2986 (1989).
- ⁵Y. Saito, M. Namiki, and S. Hayano, J. Appl. Phys. **67**, 4738 (1990).
- ⁶S. Hayano, A. Miyazaki, and Y. Saito, J. Appl. Phys. **69**, 4838 (1991).
- ⁷Y. Saito, K. Takahashi, and S. Hayano, IEEE Trans. Magn. **MAG-23**, 3569 (1987).
- ⁸Y. Saito, K. Takahashi, and S. Hayano, J. Appl. Phys. **63**, 3366 (1988).
- ⁹Y. Saito, K. Takahashi, and S. Hayano, IEEE Trans. Magn. **MAG-24**, 2946 (1988).
- ¹⁰Y. Saito, K. Takahashi, and S. Hayano, *Proceedings of First International Symposium on Applied Electromagnetics in Materials* (Pergamon, New York, 1989), p. 237.
- ¹¹K. Takahashi, Y. Saito, and S. Hayano, *International Journal of Applied Electromagnetics in Materials* (Elsevier, Amsterdam, 1993), p. 179.

Element specific magnetic microscopy with x rays (invited) (abstract)

B. Hermsmeier

IBM Corporation, San Jose, California 95193

J. Stöhr, Y. Wu, M. Samant, and G. Harp

IBM Almaden Research Center, 650 Harry Road, San Jose, California 95120

S. Koranda, D. Dunham, and B. P. Tonner

Synchrotron Radiation Center, University of Wisconsin-Madison, Stoughton, Wisconsin 53589

We have used the magnetic circular x-ray dichroism (MCXD) technique to image magnetic domains with a spatial resolution of $1\ \mu\text{m}$. The experiments employed circularly polarized soft x rays near the edges of the three-dimensional (3d) transition metals Co ($\approx 780\ \text{eV}$) and Ni ($\approx 850\ \text{eV}$) and a photoemission microscope based on an electrostatically imaging lens system. Element specific contrast is obtained by tuning to a specific L edge resonance ("white line") and imaging the number of secondary electrons created locally near the surface of the sample. The magnetic contrast arises from the fact that the white line intensity depends on the relative orientation of the photon spin and the local magnetization direction. The obtained contrast is remarkably large ($\approx 20\%$) such that images can be recorded without background subtraction. Images taken at the L_3 and L_2 resonance energies give reversed contrast, as expected. Because of the long x-ray and secondary electron mean free paths, images can be recorded for buried magnetic layers which makes this new technique especially valuable for technological applications.

High spatial resolution spin-polarized scanning electron microscopy (abstract)

H. Matsuyama and K. Koike

Advanced Research Lab., Hitachi Ltd., Hatoyama, Saitama 350-03, Japan

F. Tomiyama, H. Aoi, Y. Shiroishi, and A. Ishikawa

Central Research Lab., Hitachi, Ltd., Kokubunji, Tokyo 185, Japan

Spin-polarized scanning electron microscopy (spin SEM) to observe magnetic domains has the potential for spatial resolution as high as $10\ \text{nm}$. The best resolution from spin SEMs attained so far, however, is around $50\ \text{nm}$. In this talk, we report a newly developed spin SEM with $20\ \text{nm}$ resolution. The major factor determining the resolution of a spin SEM is probe diameter. A smaller probe diameter, however, results in lower probe current. This is a serious issue in spin SEM because the efficiency of a spin detector is very low. Thus, to get high resolution with a reasonable signal/noise (S/N) image, higher efficiency in the spin detector and/or higher probe current are needed in addition to get a smaller probe diameter. The higher probe current has been attained by using a thermal assisted field emission cathode in an electron gun. The higher efficiency in the spin detector was achieved by increasing the acceptance angle of electron detectors inside the spin detector and optimizing both a secondary collector and transport optics. Obtaining a smaller probe diameter required a low aberration objective lens and a short working distance. Those were achieved by computer calculation so that there was no interference between the objective lens and the secondary collector. This achieved both a short working distance of $20\ \text{mm}$ and high secondary collection efficiency. As a result, magnetic images of $20\ \text{nm}$ resolution with a $25\ \text{keV}$ and $1\ \text{nA}$ probe beam have been attained. We have applied this spin SEM to observing recorded bits of longitudinal thin film media at high recording densities.

An analysis of magnetization patterns measured using a magnetic force scanning tunneling microscope (abstract)

E. R. Burke

Laboratory for Physical Science, College Park, Maryland 20740

R. D. Gomez and I. D. Mayergoyz

Department of Electrical Engineering, Institute for Advanced Computer Studies, University of Maryland, College Park, Maryland 20742

In a previous paper,¹ we made a complete analysis of the interaction between the probe tip of a magnetic force scanning tunneling microscope (MFSTM) and the magnetic fields emanating from a typical recorded pattern. In this paper we show how the magnetization distribution in the recorded media can be determined from the measurements by obtaining expressions for the magnetic fields from a Fourier series expansion for the recorded magnetizations. We have used these techniques to find the magnetic fields from many different distributions, including all those we could find in the literature. The probe tip displacement, which is the quantity measured using the MFSTM, can be calculated using these magnetic fields. The results can then be compared to the experimental data. For one set of experiments on high density recording we have found that the best fit is with a magnetization that has a modified arctan transition. The modification eliminates the discontinuity in the slope of the transitions as they are joined together, giving a more realistic representation of the magnetic distribution. The transition width can then be used as an adjustable parameter to find the best fit to the data. The MFSTM can, therefore, be used as a quantitative tool to find the magnetic recording transition widths. These theoretical techniques are not necessarily restricted to the use of a MFSTM, but can be applied to other problems in magnetic recording. For instance, we show how the probe tip displacement corresponds to the flux picked up by a conventional read head. The response of the head as a function of different magnetization patterns can then be studied and compared to experimental results. The measurable quantities are expressed in Fourier series but we show how these series can be easily evaluated with a PC and the appropriate software.

¹E. R. Burke, R.D. Gomez, A. A. Adly, and I. D. Mayergoyz, "Analysis of Tunneling Magnetic Force Microscopy Using a Flexible Triangular Probe," *IEEE Trans. Magn.* **28**, 3135 (1992).

Magnetic force microscopy of single crystal magnetite (Fe_3O_4)(abstract)

R. Proksch^{a)} and S. Foss^{a)}

School of Physics and Astronomy, University of Minnesota, Minneapolis, Minnesota 55455

C. Orme

Department of Physics, University of Michigan, Ann Arbor, Michigan

S. Sahu and B. Moskowitz

Institute for Rock Magnetism, University of Minnesota, Minneapolis, Minnesota 55455

The micromagnetic domain structure of a magnetite (Fe_3O_4) single crystal has been studied using a magnetic force microscope (MFM). The MFM responds to the perpendicular component of the stray field above the magnetite surface. The sample was polished in the (011) plane. In this case, there are two easy magnetic axes parallel to the surface. Surface domains observed near cracks and edges have a complex closure structure (see Fig. 1), while walls seen far from such boundaries have a sinusoidal structure. Of particular interest is the presence of walls with either even or odd symmetry of the perpendicular stray field component across the transition. These can be conventionally modeled as Bloch or Neel walls, respectively. Both types of walls have been modeled and compared with the experimentally observed structures. We find the Bloch domain walls to be about 300 nm wide, nearly twice the value expected from bulk wall calculations. This distinction is consistent with a surface broadening of the domain wall due to magnetostatic effects.¹

^{a)}Work sponsored by ONR Grant No. N00014-89-J-1355.

¹M. R. Scheinfein, J. Unguris, R. J. Celotta, and D. T. Pierce, Phys. Rev. Lett. **63**, 668 (1989).

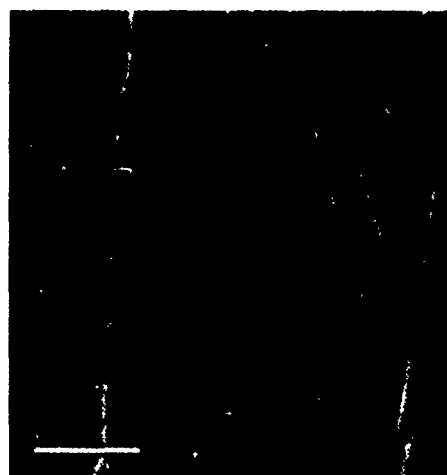


FIG. 1. MFM image of domain walls in a single crystal of magnetite. Bloch walls around closure structures are clearly visible. The domain walls are an average of 300 nm wide. The white scale bar in the lower left is 12 μm .

Interpretation of magnetic force microscopic images (abstract)

Atsushi Kikukawa, Hiroyuki Awano, Sumio Hosaka, Yukio Honda, and Ryo Imura
Central Research Laboratory, Hitachi, Ltd., 1-280 Higashi-koigakubo, Kokubunjishi, Tokyo 185, Japan

The authors have developed a magnetic force microscope (MFM) which works in a vacuum. By detecting the cantilever resonance frequency directly, it takes full advantage of the improved cantilever resonance quality, lowered noise level, and improved resolution, due to reduction of the air resistance that the cantilever suffers. Detailed observations on various magnetic recording media were made employing this instrument. An obstacle in interpreting the MFM images is that they contain both the magnetic image and the surface corrugation (directly related to the atomic force) since the cantilever detects both magnetic and atomic force at the same time. One solution for this is to compare the images of the same region observed at different tip to sample spacings because the contrast due to the magnetic force decreases as the tip to sample spacing reduces. We confirmed that this decrement in magnetic contrast occurs due to the effects of the atomic force by predicting the MFM image theoretically, utilizing a model which has taken in the effect of the atomic force estimated by an experiment. An example among the analyses on various magnetic recording media is the analysis of the magneto-optical (MO) disks which have undergone the heat cycle test. The MFM revealed the existence of irregular shaped domains, which were not observed with the conventional methods (Kerr effect microscopes) in the badly damaged regions. This information was helpful in detecting the deterioration that occurred to the magnetic layer. The authors are convinced that MFM would become a powerful and convenient tool for analyzing magnetic recording media.

The research of R. Imura was supported by the Japan Key Technology Center.

Determination of para- and ferromagnetic components of magnetization and magnetoresistance of granular Co/Ag films (invited)

Mary Beth Stearns and Yuanda Cheng^{a)}

Department of Physics and Astronomy, Arizona State University, Tempe, Arizona 85287

Several series of thin films (~ 3000 Å) were fabricated by coevaporation of Co and Ag in a dual *e*-beam UHV system at substrate temperatures, T_s , between 300 and 500 K. The composition was varied between 23 and 54 at. % Co. The maximum measured magnetoresistance was 31% at room and 67% at nitrogen temperature. Magnetization and Rutherford backscattering measurements showed that the Co and Ag atoms are completely segregated for films deposited at $T_s \geq 400$ K. The magnetoresistance (MR) and magnetization curves have been analyzed taking into account both the paramagnetic (PM) and ferromagnetic (FM) contributions that are observed to be present. The films having ≤ 32 at. % Co are entirely paramagnetic. The fraction of Co atoms in the ferromagnetic component increases monotonically with increasing T_s and/or at. % Co. The average radii of the PM granules in the films having an MR effect of 25%–31% are ~ 20 – 22 Å with a minimum average separation of ~ 10 Å. The large MR values attained in both the PM and FM components are attributed to the small effective domain sizes, ~ 40 – 50 Å. The MR values are large because the MR effect varies inversely as the mean-free-path for magnetic boundary scattering which is the average distance between domain boundaries. The variation of the resistive and magnetic behavior of the films was also studied as a function of the annealing time for an annealing temperature of 300 °C. A striking behavior seen in these films is the long relaxation times when a FM component is present.

INTRODUCTION

The $\text{Co}_x\text{Ag}_{1-x}$ system has been found to be an ideal prototypical system to study in order to examine the origin of the “giant” room temperature magnetoresistance (GMR) effect which has been seen to occur in a wide variety of multilayer and granular nanostructures. The feature that makes this system ideal is that the Co and Ag segregate essentially completely under the proper fabrication conditions. This segregation occurs because the surface free energy¹ of Co (2.71 J/m^2) is more than twice that of Ag (1.30 J/m^2) causing the Co to cluster. There is a very poor lattice match since fcc Ag has a lattice parameter that is 15% larger than that of fcc Co. The heat of formation between Co and Ag is positive ($+26 \text{ kJ/g atom}$) so that there is no tendency for formation of the compound CoAg or for alloying.²

The $\text{Co}_x\text{Cu}_{1-x}$ system is less favorable for complete segregation since all three of these effects are smaller; the surface free energy of Cu (1.93 J/m^2) is closer to that of Co, the lattice mismatch is only 2%, and the heat of formation CoCu is $+13 \text{ kJ/g atom}$.

We have found that the Co/Ag evaporated films that are codeposited at substrate temperatures that are high enough so that the adatoms have appreciable mobility are completely segregated³ as Co globules embedded in a Ag matrix.

Ironically, the granular structures are simpler and more amenable to modeling than the complex structures obtained when alternately depositing layers of nonlattice-matched materials. TEM micrographs of many such multilayer systems

have shown that usually only the first few bilayers are layered and that strong columnar growth and severe intermixing occurs farther from the substrate. Thus, in general, multilayer structures are intermediate between layered and granular structures which causes them to be difficult to model in a credible manner.

At concentrations of less than ~ 35 at. % Co the Co/Ag granular structures can be thought of as pure superparamagnet single domain Co globules embedded in a Ag matrix. The large magnetoresistance values (31% at room temperature and 67% at 77 K) are due to the same mechanism responsible for the low field ($< 20 \text{ kOe}$) magnetoresistance in pure ferromagnets.⁴ Namely, the conduction electrons of Co are predominately highly polarized itinerant *d* electrons that are strongly scattered at the magnetic boundaries between regions of different magnetization directions. In the granular and layered structures the room temperature MR is much larger than that of the pure ferromagnets because the domain size has been greatly reduced from the micrometer range, typical of pure ferromagnets, into the nanometer range.

The other proposed mechanism for the origin of the GMR, spin-dependent scattering from solutes of the non-magnetic material in the magnetic component,⁵ is inapplicable to the Co/Ag system, since there is a negligible concentration of Ag atoms in the Co globules. Moreover, since the spin-dependent resistivities of the transition metals are similar for Fe, Co, and Ni hosts,⁶ the spin-dependent scattering rates of Ag solutes are likely to be about the same as for Cu solutes in Ni. When properly analyzed by taking into account that the conduction electrons of the FM transition metals are predominately highly polarized *d* electrons it is

^{a)}Presently at Akashic Memories Corporation, San Jose, CA 95134.

found that for Cu the spin-up and -down scattering rates are essentially the same.⁷

We have previously analyzed the magnetization and MR behavior of the Co/Ag system in terms of the Co globules being mainly superparamagnetic.³ However, at Co concentrations >35 at. % this system also clearly has a ferromagnetic component. The maximum room temperature MR values are found at Co concentrations where the films are just beginning to exhibit a ferromagnetic component. In this paper we determine and take into account the ferromagnetic component in the films.

A striking effect seen in the MR behavior when a ferromagnetic component is present is very long relaxation times; sometimes several minutes. This is due to the many different energy states available by connecting the globules through different paths. Therefore, upon changing the applied field the time needed to establish the minimum energy configuration becomes very long.

II. EXPERIMENTAL DETAILS

Several series of $\text{Co}_x\text{Ag}_{1-x}$ and pure element films were prepared by coevaporation of Co and Ag in a dual *e*-beam gun UHV deposition system. The nominal thickness of the films was ~ 3000 Å. High purity single crystal Si wafers with an oxidized surface layer were used as the substrates. The deposited samples consisted of a square of ~ 2 cm on a side and a dumbbell pattern with a small neck of ~ 0.2 mm \times 5 mm for resistance measurements. The exact dimensions were determined by profilometer measurements. In order to study changes in the microstructure the substrate temperature, T_s , was varied from room temperature (RT) to 500 K. The deposition rate of Co was kept constant at 0.6 Å/s while the Ag rate was varied from 0.5 to 2 Å/s in order to change the composition of the films.

A Rigaku D/Max-IIB x-ray diffractometer with $\text{Cu K}\alpha$ radiation was used to study the grain size and crystal orientation of the films. The Co and Ag were found to be fcc with preferential growth in the $\langle 111 \rangle$ direction. The atomic compositions were deduced from the evaporation rates and were further confirmed by Rutherford backscattering (RBS). RBS also measures the areal densities, which when combined with the measured film thickness (from profilometer measurements), allowed an evaluation of the fraction of voids in the films. Studies of the morphology of the films were made using cross-sectional electron microscopy. Irregular globular structures containing many voids (consistent with the conclusions from the magnetic, resistance, and RBS measurements) were observed but in general the images were not very informative because of the random nature of granular structures.

The magnetization curves were measured on small rectangles using a vibrating sample magnetometer whose maximum field was 10 kOe. The magnetoresistance was measured on the dumbbell shaped samples using the four-probe method in a field varying up to 14 kOe. The four probes were gold plated stop balls which were connected to a digital voltmeter supplying a constant current of 10 mA. The resistivity was found to be independent of the size of the current. Resistance measurements were made at both room and liquid

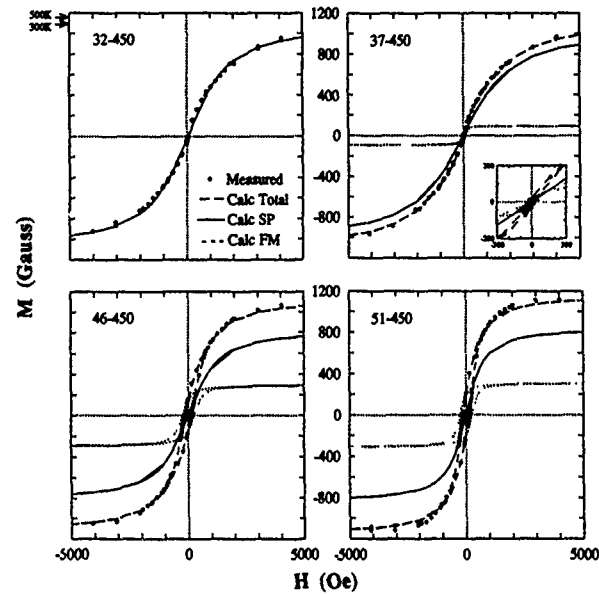


FIG. 1. Deconvolution of the measured total magnetization curves into their ferromagnetic and superparamagnetic components for the series deposited at 450 K. The insets show total and FM magnetizations near $H=0$. Note that the H_c values of the ferromagnetic components are larger than those of the total curves.

N_2 temperatures (NT). The magnetoresistance (MR) measurements were made for the applied field, H , in-plane and perpendicular to the film and with the current both transverse (TMR) and parallel (LMR) to the field.

III. MAGNETIZATION BEHAVIOR

At room temperature a ferromagnetic (FM) component began to appear in the magnetization curves of the films with ≥ 35 at. % Co. With increasing Co concentration the FM component and the coercive field, H_c , increased. Excellent fits were made to the magnetization curves, $M_T(H)$, using the general fit procedure of Kaleidagraph with a function made up of a FM and a superparamagnetic (SP) part as follows:

$$M_T(H) = \frac{2M_F^S}{\pi} \tan^{-1} \left[\frac{(H \pm H_c)}{H_c} \tan \left(\frac{\pi S}{2} \right) \right] + N_g \bar{\mu} \left[\text{ctnh} \left(\frac{\bar{\mu} H}{kT} \right) - \left(\frac{\bar{\mu} H}{kT} \right)^{-1} \right]. \quad (1)$$

The first term is the usual function used to represent a FM hysteresis curve. The second term is the usual expression for an SP component. M_{FM}^S and $M_{SP}^S = N_g \bar{\mu}$ are the saturation magnetization of the FM and SP parts. S is the squareness of the ferromagnetic loop, i.e., the ratio of the remanent magnetization, M_R , to M_{FM}^S . The average moment per globule, $\bar{\mu}$, and number of Co globules/cm³, N_g , in the SP fraction are obtained from the second term. Typical fits to the magnetization curves are shown in Fig. 1 for the series deposited at a substrate temperature of 450 K. The films are identified by the notation at. % Co-substrate temperature.

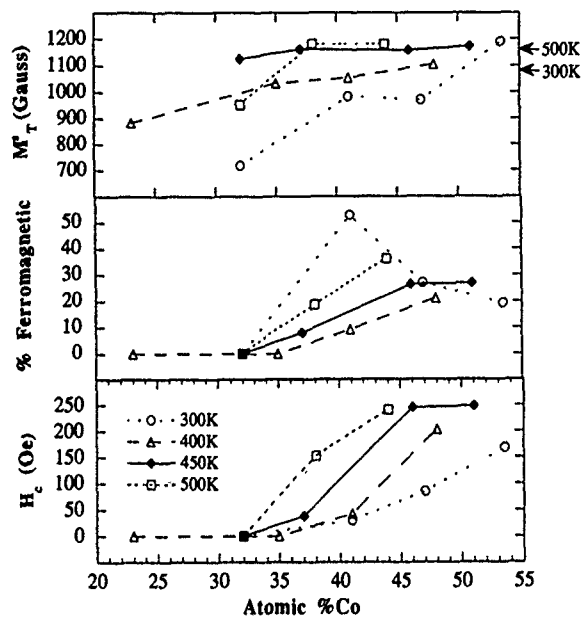


FIG. 2. Variation of total saturation moment, M_T^s , the ferromagnetic fraction of the total moment in %, M_{FM}^s/M_T^s , and the coercive field, H_c , with at. % Co. The saturation magnetization values for pure Co films deposited at 300 and 500 K are indicated on the upper right side of the graph.

A. As-prepared films

The variation of the total saturation magnetization M_T^s , the ferromagnetic fraction in %, and H_c with at. % Co are shown for each of the substrate temperatures in Fig. 2. From high resolution TEM images of many metallic multilayer systems we have found that evaporated films deposited at a substrate temperature of 300 K are composed of small, jumbled crystallites giving rise to very poorly defined structures.⁸ This is due to the adatoms not having sufficient mobility to form well-ordered structures. We see here that this causes low M_T^s values and erratic behavior in the FM fraction. The M^s values for pure Co films of the same thickness as the granular films deposited at 300 and 500 K are indicated on the right-hand side. As has been discussed previously³ all of these evaporated films contain about 20% voids. This was determined from magnetization saturation measurements, Rutherford backscattering measurements, profilometer film thickness measurements, and the known deposition rates. Such a void fraction is not unusual for evaporated films of a thickness of ~ 3000 Å. From such considerations we conclude that for films with sufficient mobility of the adatoms ($T_S \geq 450$ K) essentially all the Co is in the globules with each Co atom having a full bulk moment of $1.72\mu_B$. Discounting the anomalous behavior of the films deposited at 300 K we see that the ferromagnetic fraction of the films increases with increasing Co content. The H_c values also increase with increasing Co content with the values obtained from the deconvolution of the magnetization curves naturally being larger than the $M=0$ values of the raw data.

The number of Co atoms per globule, N_{Co} , in the SP fraction is given by $N_{Co} = \bar{\mu}/\mu_{Co}$. Typical values for the films showing the larger MR values were 3000–4000 Co atoms per globule. The average volume per globule, V_g , is given by

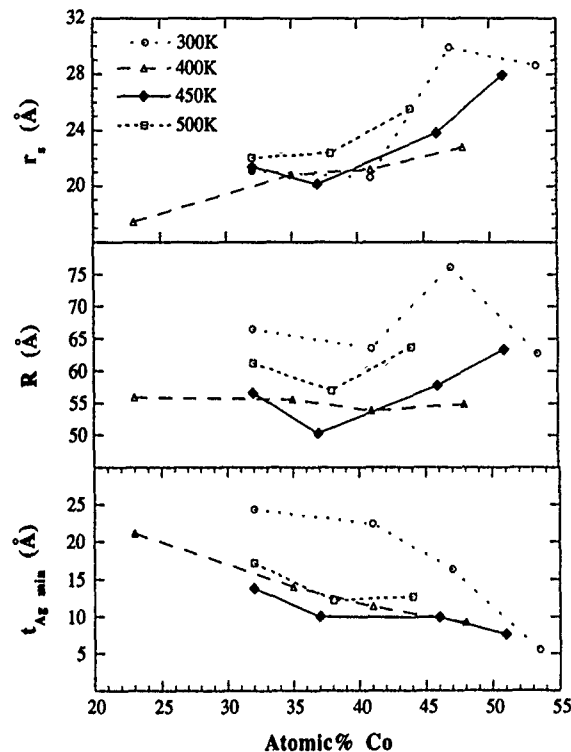


FIG. 3. Variation with Co concentration of the average globule radii r_s ; side R of a cubical volume containing the globule and the average minimum distance between globules, $t_{Ag\ min}$, for films coevaporated at various substrate temperatures.

$V_g = N_{Co}V_{Co}$. We use the bulk volume per Co atom (11.1 Å^3) for V_{Co} since, although the voids alter the average density of the films, the Co globules and Ag matrix are assumed to have essentially their bulk densities. As a first approximation let us model the system by assuming that the globules are spherical. We can then obtain the average radius of the globules, r_s , from V_g . The average number of globules per cm^3 is given by $N_g = M_{SP}^s/\bar{\mu}$. Since the Co and Ag only occupy $\sim 80\%$ of the volume of the films the average volume that a globule occupies is $0.80/N_g$. Assuming a cubic shape for this volume we obtain an average value for a side of this cube, R . A quantity of interest is the average minimum thickness of Ag between the globules; given by $t_{Ag\ min} = R - 2r_s$. We show the variations of r_s , R , and $t_{Ag\ min}$ with Co concentration in Fig. 3. We see that r_s tends to increase with increasing Co content while R is quite constant. This results in $t_{Ag\ min}$ decreasing as the fraction of Co increases. Whereas the films deposited at $T_S \geq 400$ K are quite similar in their $t_{Ag\ min}$ variation the films deposited at 300 K are again anomalous. Since the globules are more likely to touch as the at. % Co increases the FM component also increases. Thus, the observed behavior of the FM component agrees well with the globular sizes and separation which are derived from the SP parameters.

In order to investigate the assumption that the globules are spherical we considered the effect of the globules being ellipsoids of revolution with a eccentricity of 10%; i.e., the minor axes are 0.9 of the major axis. For this case the variation of the major axis is only 7% greater than the radius of a

TABLE I. Parameters obtained from fitting the magnetization curves of the annealed films. The last column is the ratio of the ferromagnetic volume of the film to the total volume.

	M_T^s (G)	M_{FM}^s/M_T^s	H_c (Oe)	N_{Co}	r_s (Å)	R (Å)	V_{Co}^{FM}/V_T
32-300							
As-prepared	720	0.0	0	3520	21.0	66.5	0.00
1st anneal	740	0.23	32	4720	23.2	82.6	0.05
2nd anneal	960	0.42	38	3650	21.0	76.7	0.10
41-300							
As-prepared	980	0.53	30	3300	20.6	66.7	0.16
1st anneal	1000	0.26	122	9810	29.4	89.2	0.08
2nd anneal	1300	0.30	98	8400	28	80.0	0.10
37-450							
As-prepared	1160	0.08	38	3040	20.1	50.6	0.02
1st anneal	1200	0.20	137	3890	24	61.2	0.06

sphere. This would cause little difference to the average distance between globules. However, in the ellipsoidal case there may be geometric effects due to the ellipsoids aligning as flat discs parallel to the plane of the film.

B. Annealed films

The effects of annealing were studied by heating a few selected films at 300 °C for one-half hour intervals. We chose two films deposited at 300 K (32-300 and 41-300) which we knew were composed of small jumbled crystallites. Thus, for these the annealing should markedly improve the structure and segregation of the Co and Ag. For comparison we also annealed the film showing the largest MR effect, 37-450. The results are listed in Table I. It can be seen that in general for the films prepared at 300 K all the parameters listed tend to increase with annealing. This indicates that the main effect of annealing is to better segregate the Co and Ag. The annealing of the optimum film 37-450 causes little change in M_T^s but an increase in the FM fraction and all the other parameters. However, as is seen in the next section, there is little change in the MR value of this film with annealing.

IV. MAGNETORESISTANCE BEHAVIOR

The variation of the resistance with applied field, H , was measured at RT and NT with H in-plane and perpendicular to the films. For the superparamagnetic films the transverse magnetoresistance (current $\perp H$, TMR) was of the same magnitude but slightly broader for H perpendicular to the film. For an in-plane field the longitudinal magnetoresistance, LMR (current $\parallel H$) was slightly different than that of the TMR. This difference, the anisotropic magnetoresistance $AMR = LMR - TMR$, was essentially the same for all films and had a maximum value of about the same magnitude as for pure Co films; i.e., $\sim 1\%$. The behavior of this difference is in agreement with the proposed mechanism for its origin, namely, that it arises because of the anisotropic shape of the electronic density of the d electrons due to the spin-orbit

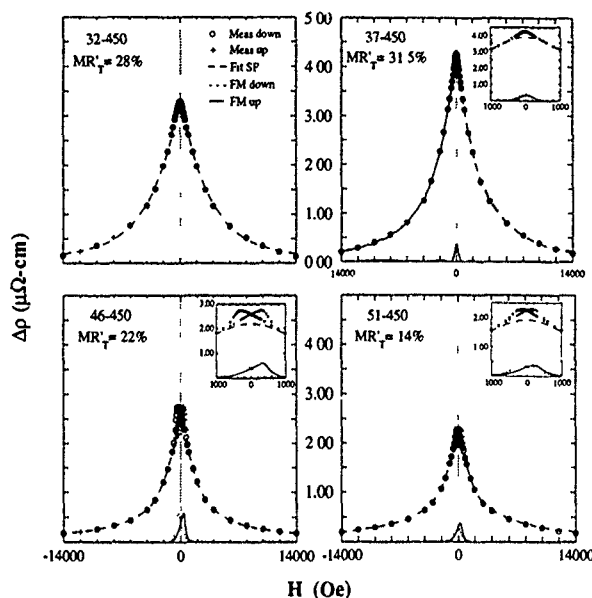


FIG. 4. Typical deconvolutions of the TMR curves into their FM and SP components for the 450 K series. The insets show the FM components near $H=0$.

coupling.^{9,10} This causes the cross-sectional area for scattering at high H to be larger for the LMR geometry than for the TMR geometry.

The magnetoresistance is here defined to be $MR = [R(H) - R_{min}] / R_{min} = [\rho(H) - \rho_{min}] / \rho_{min} = \Delta\rho / \rho_{min}$. Since our maximum field of 14 kOe was not sufficient to reach R_{min} for these granular films we determined its value in the following manner: For films that were entirely superparamagnetic the whole curve was fit with the sum of two Lorentzian functions using KaleidaGraph. Only the part of the wings that had no hysteresis was fit in the same manner for MR curves having an FM component. The entire SP component was then calculated using the parameters determined from the wings and the FM component obtained by subtracting the SP component from the total measured MR curve. It was required that the FM component be positive. Deconvolutions of the 450 K series TMR curves into their FM and SP components are shown in Fig. 4. Also shown are insets of the FM components.

It was found that all the films that had a FM component in the magnetization curves also had a FM component in the MR curves. Some of the parameters characterizing the MR curves are listed in Table II. In order to compare the various films we have converted the R values into resistivities, ρ . In Table II we list ρ_{min} , the $\Delta\rho$'s ($\Delta\rho_{(T,FM,SP)} = \rho_{max}^{(T,FM,SP)} - \rho_{min}$), the maximum MR values $MR_T' = \Delta\rho_T / \rho_{min}$, and the fields corresponding to the peak of the total TMR curve H_p^T and the ferromagnetic component H_p^{FM} . Unless otherwise noted the data are for room temperature measurements and the SP contributions are fit to the portion of the data for $H \geq |2000|$ Oe.

The full-width at half-maximum of the total MR curves for films deposited at ≥ 400 K were ~ 6000 Gauss for 30-35 at. % Co and decreased with increasing Co content. The largest decreases were seen in the films deposited at higher tem-

TABLE II. The resistivities, MR_T' values and peak positions, H_p^T and H_p^{FM} for the deconvoluted MR curves. The resistivity values are in $\mu\Omega$ cm. In the sample labels T indicates TMR and L indicates LMR geometries.

Sample	ρ_{min}	$\Delta\rho_T$	$\Delta\rho_{FM}$	$\Delta\rho_{SP}$	MR_T' (%)	H_p^T (Oe)	H_p^{FM} (Oe)
300 K							
32T	26.46	4.70	0.0	4.70	17.8	0	
32T 1 ann ^a	12.61	3.33	0.40	2.93	20.9	10	10
32T 2 ann ^a	11.91	2.75	0.31	2.43	23.0	10	10
41T	23.64	3.78	0.33	3.25	15.1	130,210	160,250
41T 1 ann ^b	12.82	2.49	0.19	2.30	19.4	~0	~0
41T 2 ann ^b	12.13	2.27	0.52	1.73	18.7	30	35
47T ^c	27.20	2.93	0.22	2.74	10.8	350,550	400,575
47L ^{c,d}	27.50	2.86	0.10	2.82	10.4	500,600	700,800
47T 1 ann	12.36	1.43	0.49	1.00	11.6	20	20
47L NT ^{c,d,e}	20.68	3.42	0.51	2.98	16.6	500,900	600,1150
53.5T ^{e,f}	26.51	1.40	0.27	1.13	5.3	80	80
400 K							
23T	14.57	3.34	0.0	3.34	22.9	0	
35T	15.69	4.26	0.0	4.26	27.1	0	
41T ^g	15.45	4.50	0.53	3.98	29.1	60	70
48T	15.67	3.44	0.56	2.91	22.0	210	210
48T 1 ann	12.07	2.10	0.38	1.76	17.4	270	320
48T NT ^h	12.28	5.27	1.38	4.40	43.0	780	850
48T NT 1 ann ⁱ	7.93	3.71	0.74	3.20	46.7	790	850
450 K							
32T	11.80	3.30	0.0	3.30	28.0	0	
32T NT ^k	8.66	5.81	1.88	4.00	67.1	0	1500
37T ^m	13.49	4.25	0.35	3.90	31.5	40	60
37T 1 ann	10.94	3.26	0.67	2.59	29.8	100	110
37T NT ⁿ	10.17	6.79	1.18	6.30	66.8	700	1000
46T	12.32	2.74	0.58	2.29	22.2	290	340
51T	16.52	2.28	0.37	2.06	13.8	170	200
51T NT ^l	11.00	2.82	0.52	2.44	25.6	240	600
500 K							
33T	12.35	3.08	0.0	3.08	25.0	0	
38T	11.58	3.20	0.59	2.62	27.6	160	200
44T	10.25	1.94	0.69	1.38	19.0	250	290
44T NT ^l	6.93	3.02	0.93	2.17	43.5	340	410

^aDimensions of the sample changed less than 1%.

^bDimensions of the sample changed less than 3%.

^cDouble peak at low fields.

^dFM has a negative dip due to AMR contribution.

^eSP curve fit for $H \geq |4000|$ Oe.

^fTwo shoulders surrounding the main peak in FM component.

^gSP curve fit for $H \geq |1000|$ Oe.

^hSP curve fit with only one Lorentzian.

ⁱSP curve fit for $H \geq |3000|$ Oe.

^jSP curve fit with one Lorentzian and $H \geq |6000|$ Oe, FM is double peaked.

^kSP curve fit for $H \geq |500|$ Oe.

^lSP curve fit with one Lorentzian and $H \geq |4000|$ Oe.

peratures, e.g., the 44–500 film had a half-width of ~ 3000 Gauss. As seen in Fig. 4 the half-widths of the FM components are much smaller, ~ 400 – 1000 Gauss, and decrease as the fraction of FM component (or at. % Co) decreases.

The poor, ill-defined structure of the films prepared at a substrate temperature of 300 K is evident in the low MR' values of these films. All the MR curves for as-prepared films for $T_S = 300$ K that did not peak at $H = 0$ (i.e., had a non-SP component) had a double-peaked behavior. Upon annealing them for $\frac{1}{2}$ h at 300°C the MR curves became single peaked and the segregation increased causing higher M_S and

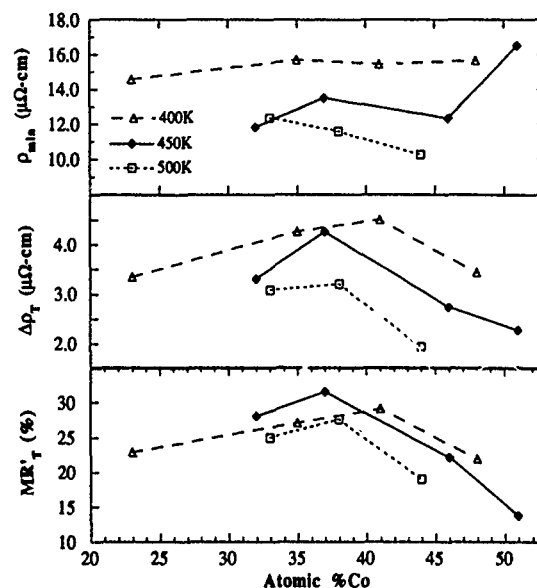


FIG. 5. Variations of ρ_{min} , $\Delta\rho_T$, and MR_T' with at. % Co for the as-prepared films deposited at $T_S \geq 400$ K.

MR' values. The magnetization curve for the 53.5–300 film also had a peculiar shape that could not be fit well with Eq. (1). Thus, the 300 K films give quite anomalous MR behavior that is attributed to their poor structure and we will not consider these films further.

V. DISCUSSION AND CONCLUSIONS

It was found that for the as-prepared films that were deposited at $T_S \geq 400$ K, the ratios of MR_{FM}'/MR_T' were very similar to the fractions of the FM component, M_{FM}^s/M_T^s .

In Fig. 5 we show the variations of ρ_{min} , $\Delta\rho_T$, and MR_T' for the as-prepared films deposited at $T_S \geq 400$ K. We see that with the exception of the 51–450 film ρ_{min} is quite constant for each value of T_S . However, $\Delta\rho_T$ is seen to have a maximum between 37–41 at. % Co which gives rise to the maximum in the MR_T' values. From Fig. 3 we see that the maximum MR' values are obtained when the globular diameter is near its minimum of ~ 40 Å and the minimum separation between the globules is ~ 10 Å. It was shown⁴ that for a pure ferromagnet the resistivity due to magnetic boundary scattering, $\Delta\rho_{MB}$, has the form

$$\Delta\rho_{MB} = A(K/\eta D), \quad (2)$$

where A is a factor depending on the magnetic alignment of the domains in the magnetic material. A sample with a net magnetization of zero has $A = 1$ for domains that are only aligned antiparallel and $A = \frac{1}{2}$ for randomly oriented domains. K is a constant that depends on the band structure of the magnetic material. For fcc Co we estimate K to be $\sim 0.6 \mu\Omega$ cm when the average domain size D is given in μm . ηD is the mean free path for the magnetic scattering causing the magnetoresistance. For fcc Co $\eta \sim 2$. For pure ferromagnets D is a few micrometers, while for granular films, $D \sim R$, the linear size of the box occupied by the granule, which is seen to be a few nm. These values lead to an estimate for $\Delta\rho_{MB} \sim 30 \mu\Omega$ cm for a pure ferromagnetic with domains of

TABLE III. Room-temperature contribution of the resistivity $\rho_{p,m}$ due to scattering by phonons and magnons.

Sample	32-450	37-450	44-500	48-400	48-400 (1 ann)	51-450
$\rho_{p,m}$ ($\mu\Omega$ cm)	4.2	4.5	4.5	4.6	5.6	7.5

5 nm. However, in materials containing a nonmagnetic material, $\Delta\rho_{MB}$ is reduced because the memory of the spin direction in the magnetic region from which the conduction electrons emerge is lost as the electrons traverse the nonmagnetic region. Thus, for granular films we multiply Eq. (2) by an attenuating factor and obtain

$$\Delta\rho_{MB}=A(K/\eta R)F \exp(-t_{Ag}/l_0). \quad (3)$$

F is a factor decreasing the magnetic resistivity due to the scattering caused by the variation in the potentials at the interfaces between the magnetic and nonmagnetic regions. Since a conduction electron must traverse two such interfaces we estimate³ that $F \sim \frac{1}{2}$. The factor $\exp(-t_{Ag}/l_0)$ is the reduction of the magnetic resistivity caused by the loss of polarization of the conduction electrons in passing through the nonmagnetic region. t_{Ag} is the average thickness of nonmagnetic material that a conduction electron travels between two sequential magnetic regions and l_0 is the mean free path or spin diffusion length for the d -conduction electrons to lose their spin memory in the nonmagnetic region. For the 37-450 film we found that $R \sim 50 \text{ \AA}$ and we take l_0 to be $\sim 35 \text{ \AA}$ at RT¹¹ and t_{Ag} to be $\sim 30 \text{ \AA}$ (between the maximum Ag distance, $\sqrt{3}R - 2r_S$ and $t_{Ag \text{ min}}$). Putting in these values we obtain that $\Delta\rho_{MB} \sim 6 \mu\Omega \text{ cm}$; in good agreement with the measured value of $\sim 4.2 \mu\Omega \text{ cm}$. From Eq. (2) we see that the highest MR' values are obtained when R is a minimum and $t_{Ag \text{ min}}$ is small but not so small that the globules are ferromagnetically coupled. When they touch or are close enough to couple indirectly via the RKKY exchange interaction an FM component occurs that then effectively increases the value of D . We see that indeed these are just the condition under which we obtain the maximum MR' values in the granular structures. As can be seen from Eq. (3), $\Delta\rho_{MB}$ is sensitive to both the magnetic and physical structure of a film.

From Table II and Fig. 5 we see that ρ_{min} is quite independent of the Co content and decreases slightly with increasing T_S . This is expected because of the higher mobility of the adatoms in the films deposited at higher T_S . ρ_{min} is composed of all the nonmagnetic scattering contributions. We separate these contributions into two categories depending on their temperature dependence: (1) Scattering from phonons and magnons, $\rho_{p,m}$, which varies as $1/T$; (2) scattering from structural imperfections and voids, ρ_i , which should be independent of T and decrease with annealing. Interfacial scattering, ρ_{if} , at the step potential between the Co and Ag interfaces. The measured decreases in ρ_{min} at NT for the as-prepared films are thus attributed to the decrease in $\rho_{p,m}$ with temperature. Using the RT and NT values of ρ_{min}

and a $1/T$ dependence for $\rho_{p,m}$ we evaluate $\rho_{p,m}$ and $\rho_i + \rho_{if}$, for the films deposited at $T_S \geq 400 \text{ K}$. The RT values obtained for $\rho_{p,m}$ are listed in Table III. We see that the values tend to increase slightly with at. % Co and vary from 4.2 to $7.5 \mu\Omega \text{ cm}$. These are very reasonable values since these thin films are expected to have somewhat larger resistivities than an intermediate value between the bulk RT resistivities of 1.6 and $5.8 \mu\Omega \text{ cm}$ of pure Ag and Co, respectively. The decrease in ρ_{min} with annealing is mainly due to a decrease in ρ_i .

In Table II it can be seen that the FM component of the films is considerably larger at NT than at RT. This occurs because in order to obtain magnetic alignment between the Co globules the effective coupling between them must be $\geq kT$. Thus the requirement of weaker coupling at NT gives rise to a greater fraction of the sample being FM.

The relaxation effects observed in these films deserve more study. In the region of the MR curves that had an FM component an appreciable time was required to reach equilibrium after changing field, from a few seconds to several minutes in various parts of the MR curve. These relaxation effects likely occur because when an appreciable fraction of the globules are close enough to couple there are numerous closely spaced energies states available to the system so it takes considerable time for the system to reach the ground state.

The authors wish to thank C.-H. Lee for measuring the hysteresis curves of the samples.

¹J. Z. Mezey and J. Giber, Jpn. J. Appl. Phys. **21**, 1569 (1982).

²A. R. Miedema, Philips Tech. Rev. **36**, 217 (1976).

³M. B. Stearns and Y. Cheng, Proc. Spring MRS Meeting, San Francisco (1993), Vol. 297.

⁴M. B. Stearns, International Conference on Magnetism, Edinburgh, Scotland, September, 1991; J. Magn. Magn. Mater. **104-107**, 1745 (1992) and Proc. Spring MRS Meeting, San Francisco (1993), Vol. 297.

⁵M. N. Baibich, M. M. Broto, A. Fert, Nguyen Van Dau, F. Petroff, P. Etienne, G. Creuzet, A. Friederich, and J. Chazelas, Phys. Rev. Lett. **61**, 2472 (1988); R. E. Camley and J. Barnas, Phys. Rev. Lett. **63**, 664 (1989); P. M. Levy, K. Ounadjela, S. Zhang, Y. Wang, C. B. Sommers, and A. Fert, J. Appl. Phys. **67**, 5914 (1990).

⁶I. A. Campbell and A. Fert, *Ferromagnetic Materials*, edited by E. P. Wohlfarth (North-Holland, Amsterdam, 1982), Vol. III, p. 747.

⁷M. B. Stearns, J. Appl. Phys. **72**, 5354 (1992).

⁸M. B. Stearns, C. H. Lee, C.-H. Chang, and A. L. Pettford-Long, *Metallic Multilayers and Epitaxy*, edited by M. Hong, S. Wolf and D. C. Gubser, (The Metallurgical Society, 1988), p. 55; M. B. Stearns, C. H. Chang, and D. G. Stearns, J. Appl. Phys. **71**, 187 (1992); G. D. Lewen and M. B. Stearns, Spring MRS Symp., Anaheim, CA, April (1991).

⁹M. B. Stearns, APS March Meeting, Seattle, WA (1993).

¹⁰R. M. Bozorth, *Ferromagnetism* (Van Nostrand, Princeton, NJ, 1961), p. 745.

¹¹B. Dieny, V. S. Speriosu, S. Metin, S. S. P. Parkin, P. Baumgart, and D. R. Wilhoit, J. Appl. Phys. **69**, 4774 (1991).

Giant magnetoresistance and microstructural characteristics of epitaxial Fe-Ag and Co-Ag granular thin films

N. Thangaraj, C. Echer, and Kannan M. Krishnan
*Materials Sciences Division, Lawrence Berkeley Laboratory, University of California,
Berkeley, California 94720*

R. F. C. Farrow, R. F. Marks, and S. S. P. Parkin
IBM Research Division, Almaden Research Center, 650 Harry Road, San Jose, California 95120-6099

The microstructure and magnetic properties of phase-separated Fe-Ag and Co-Ag granular alloy films, grown epitaxially on (001) NaCl substrates and exhibiting giant magnetoresistance (GMR), have been investigated. Surprisingly, two Fe-Ag films of similar composition grown under identical conditions are found to have substantially different microstructures yet display similar GMR. The microstructure of the films is characterized by Fe-rich or Co-rich regions, respectively, 350–700 nm in extent, surrounded by a Ag-rich matrix. Within the Ag-rich regions, the Fe concentration varies from 20 to 25 at % and the Co concentration is ≈ 16 at %. Within these regions essentially pure fcc Co particles and bcc Fe particles are in parallel and rotated epitaxial alignment respectively with the fcc silver matrix. The Co and Fe particles are ≈ 15 –25 Å in diameter. It is these small particles which most likely account for the giant magnetoresistance exhibited by these alloys. This suggests that a size distribution of magnetic particles, sharply peaked at the optimum size with limited bulk segregation, might give rise to larger GMR values.

I. INTRODUCTION

Enhanced or giant magnetoresistance (GMR), is exhibited by a variety of different inhomogeneous metallic magnetic systems comprising of magnetic layers or particles separated by nonferromagnetic material. In magnetic multilayers the largest GMR has been found in systems comprised of thin ≈ 8 Å-thick Co layers separated by thin (≈ 8 Å) Cu layers.^{1,2} In magnetic granular alloys the largest GMR has been reported in $\text{Co}_x\text{Ag}_{1-x}$ ($x \approx 0.2$).³⁻⁵ A variety of models have been proposed to account for the origin of the GMR effect.⁶⁻⁸ Of particular interest is the relationship of GMR to the detailed microstructure of the magnetic multilayer or alloy. The basic assumption of most models of GMR is the existence of spin-dependent scattering of the conduction electron either within the interior (bulk) of the magnetic particles or layers or at the interfaces between the magnetic and nonmagnetic entities. Recent experiments strongly suggest the predominant role of interfacial scattering in accounting for the GMR of both multilayers⁹⁻¹¹ and granular alloys.^{3,5,12} For the latter this means that the size of the magnetic particles is a key parameter in determining the magnitude of GMR.

Typically magnetic granular films deposited by sputtering techniques at room temperature display little GMR. However, GMR is obtained with appropriate post-growth annealing. In contrast, it has been shown recently that slow coevaporation using electron beam or thermal evaporation sources under ultrahigh vacuum (UHV) conditions at moderate substrate temperatures of ≈ 250 °C (less than required for post-growth annealing of sputtered films, i.e., ≈ 400 °C) yields GMR in the as-grown films in Co-Ag, Co-Cu, and Fe-Ag.^{5,12,13} In this paper, we report observations of the microstructure of Fe-Ag and Co-Ag thin films grown epitaxially on NaCl(001) substrates from transmission electron microscopy (TEM) studies.

II. EXPERIMENTAL PROCEDURES

Fe-Ag and Co-Ag films were grown by slow coevaporation of Fe or Co, respectively, and Ag in a molecular beam epitaxy (MBE) system. The nominal compositions of Fe-Ag and Co-Ag thin films were ≈ 29 at % Fe and ≈ 21 at % Co, respectively. The NaCl substrates were cleaved in air and cleaned *in situ* at 300 °C in ultrahigh vacuum (UHV) before growth. Thin films (≈ 500 Å thick) highly oriented in the (001) direction were then grown at a substrate temperature of 250 °C. No post-growth annealing was required to observe the GMR effect. Details of the growth and the magnetoresistance measurements of these and similar films grown on sapphire (0001) substrates are reported elsewhere.⁵ For TEM studies, the films were lifted onto Cu grids by dissolving the NaCl substrate in water and the Pt cap layer was then removed by gentle ion milling. Energy-dispersive x-ray microanalysis, and standard bright-field and dark-field TEM imaging techniques were used to analyze the microstructure of the films.

III. MICROSTRUCTURE OF Fe-Ag AND Co-Ag GRANULAR ALLOY FILMS

A typical low-magnification through-foil bright-field TEM image of the microstructure of a $\text{Fe}_{29}\text{Ag}_{71}$ film is shown in Fig. 1(a). Also included in the inset to the figure is the corresponding diffraction pattern which demonstrates the epitaxial growth of the film. The composition of the film was analyzed locally using energy-dispersive x-ray microanalysis. Electron probe sizes of 100 and 200 Å were used. The film microstructure is clearly inhomogeneous. The micrograph shows a distribution of dark (pure Ag, 350–500 nm), gray (25 at % Fe, matrix), and light (88 at % Fe, 350–700 nm) regions. The microstructure also varies locally, indicating variations in metal film nucleation on the NaCl surface. Where the NaCl surface has a large local density of (001) steps, the microstructure contains about equal amounts of

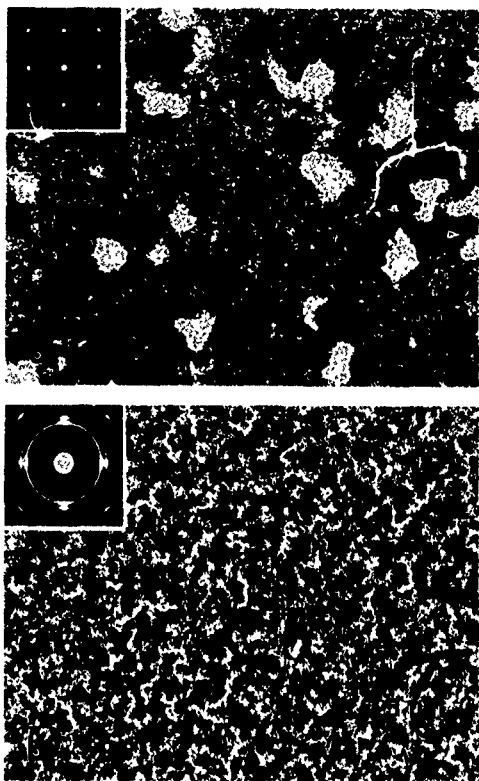


FIG. 1. (a) Microstructure of an as-deposited $\text{Fe}_{29}\text{Ag}_{71}$ grown on $\text{NaCl}(001)$. The micrograph shows bulk segregation of Fe in the light region, pure silver particles in dark contrast, and the gray region with 25 at % Fe. The diffraction pattern shown in the inset indicates the (001) epitaxy of the film with the (001) NaCl substrate. (b) A second Fe-Ag film prepared under almost identical growth conditions shows a more uniform microstructure with a polycrystalline structure.

Ag-rich (gray) and Fe-rich (light) regions. The orientation relationship is clearly $(100)\text{Fe}|| (100)\text{Ag}$ and $[01\bar{1}]\text{Fe}|| [00\bar{1}]\text{Ag}$, i.e., the reflections from the bcc Fe and the fcc Ag are in exact coincidence but rotated 45° (the lattices have only 0.8% mismatch in this arrangement). The presence of the fcc (γ) phase of Fe in the post-annealed Fe-Ag sample, as reported by Tsoukatos *et al.*¹⁴ was not found in our Fe-Ag samples. Another $\text{Fe}_{25}\text{Ag}_{75}$ deposition on NaCl under similar conditions unexpectedly resulted in a fine-grained polycrystalline film with slight (001) texture [Fig. 1(b)]. For this film the particle size distribution is highly uniform with the Fe concentration varying locally from 10 to 20 at %. However, a few isolated grains have a higher (30 at %) Fe concentration. For both samples, dark-field imaging obtained from (200) Ag did not yield any information about the distribution and size of the phase-separated Fe particles because of the overlapping of Fe and Ag reflections.

The microstructure of the $\text{Co}_{21}\text{Ag}_{79}$ films [Fig. 2(a)] is similar to the epitaxial $\text{Fe}_{29}\text{Ag}_{71}$ film [Fig. 1(a)] and consists of about 10% "Co-rich" light regions where the concentration varies from 32 to 64 at % Co. In contrast, the gray regions contain about 16 at % Co and these regions dominate the microstructure. However, where the Co-Ag film nucleates near steps on the (001) NaCl, the volume fraction of Co-rich light regions increases and reaches about 50% [Fig. 2(b)]. The (001) electron diffraction pattern obtained from

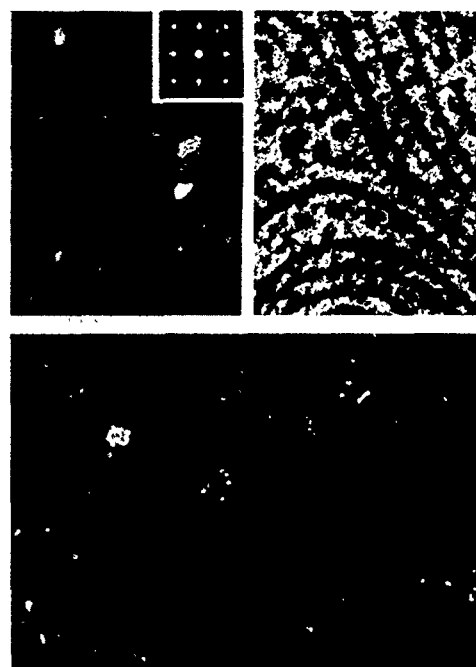


FIG. 2. Microstructure of a $\text{Co}_{21}\text{Ag}_{79}$ sample showing (a) segregated Co-rich light regions grown on the flat NaCl surface and (b) regions of the film grown on the (001) NaCl steps. The inset in Fig. 1(a) is the electron diffraction pattern showing spot-splitting (arrow) due to Co-phase segregation and parallel epitaxial alignment of Co particles with Ag. (c) Dark-field micrograph obtained using (220) Co reflection showing distribution of 20 Å Co particles in the gray region.

the same area [Fig. 2(a), inset] confirms epitaxial growth of the Co-Ag films on $\text{NaCl}(001)$. This pattern also shows distinct spots corresponding to phase separated fcc Co. Even though the Co_{fcc} and Ag_{fcc} have 13% lattice mismatch in the cube-cube orientation, the Co grows in epitaxial alignment with the Ag presumably due to high adatom mobility in this growth mode. Co particles within the Ag matrix retain their bulk lattice parameter and thus the 13% lattice mismatch between the Co and the Ag must be mostly accommodated at the interfaces. Dark-field imaging using the (220) Co reflection clearly shows the Co particle distribution and size [Fig. 2(c)]. The Co particle size varies from 15 to 25 Å, the mean "diameter" being 20 Å. The inter-particle distance [Fig. 2(c)] appears similar to the particle size but this is not conclusive since the particles contained in the 500 Å-thick film are in projection. This measurement agrees with earlier studies⁵ using grazing incidence small-angle x-ray scattering (GISAXS) for a Co-Ag film grown on sapphire (0001) which showed comparable mean Co particle size (≈ 25 Å) but a different mean interparticle distance (≈ 76 Å).

IV. MAGNETIC CHARACTERIZATION OF Fe-Ag AND Co-Ag GRANULAR ALLOY FILMS

Although the microstructures of the two Fe-Ag films shown in Figs. 1(a) and 1(b) are quite different, the films exhibit similar MR (Fig. 3). Both films show decreases in resistance (for applied fields of up to 16 kOe) of about 4%–5% at room temperature and 15% at 4.2 K. Similar values have also been reported for post-annealed sputtered

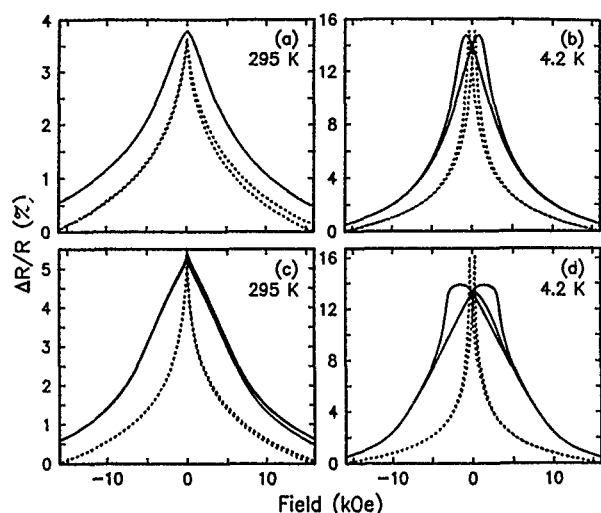


FIG. 3. (a) and (b) magnetoresistance data at 295 and at 4.2 K for the Fe-Ag film shown in Fig. 1(b). (c) and (d) show the magnetoresistance data for the Fe-Ag film shown in Fig. 1(a). The dashed lines are for the field aligned in the plane of the film and the solid lines are for the field perpendicular to the film plane. The data show significant perpendicular magnetic anisotropy.

Fe-Ag samples.¹⁴ However, the GMR reveals distinct magnetic anisotropy for field applied perpendicular and parallel to the film as shown by the solid and dashed curves respectively in Fig. 3. A similar result has previously been found in MBE-deposited Co-Ag alloy films for which various possible mechanisms were discussed.⁵ The magnetoresistance data for the Co-Ag film measured at room temperature are given in Fig. 4. A resistance change of 22% under a field of 60 kOe was observed. By varying Co composition, GMR of 40% at room temperature and 71% at 4.2 K has been observed for similar films grown on sapphire substrates.⁵

V. DISCUSSIONS AND CONCLUSIONS

If spin-dependent electron scattering at the interfaces between the magnetic particles and the host nonferromagnetic

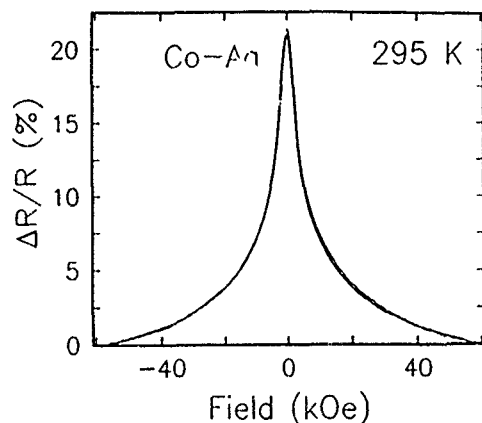


FIG. 4. Magnetoresistance data measured at room temperature for the $\text{Co}_{21}\text{Ag}_{79}$ sample.

metal is the dominant scattering mechanism for GMR, then it follows that the magnitude of the GMR will scale approximately as the inverse particle size. Thus, maximum GMR is expected for small magnetic particles. Annealing studies on MBE-grown Co-Cu granular alloys show that the GMR is significantly reduced by annealing resulting from growth of the Co particles.¹² The TEM studies presented here show that a significant fraction, $\approx 50\%$ – 90% , of the Co-Ag alloy sample is comprised of small Co particles, ≈ 20 Å in diameter, in a Ag matrix. Larger GMR is likely to be obtained by the preparation of alloys containing uniformly small Co particles. Moreover, any dissolution of the Co in the Ag matrix is likely to lead to reduced GMR.¹⁵

A surprising result of these studies is the similarity of the GMR exhibited by crystalline and polycrystalline Fe-Ag alloys grown on NaCl substrates. The microstructure of these films is quite distinct. Moreover, the GMR of these films is also similar to $\langle 111 \rangle$ oriented Fe-Ag films of the same composition grown on a Pt buffer layer on (0001) sapphire. This suggests that crystalline orientation is not a very significant factor in influencing the GMR of Fe-Ag granular films. Note that the magnitude of the GMR exhibited by magnetic multilayers is often very sensitive to small variations in growth conditions. However, for magnetic multilayers the magnitude of GMR is directly connected to the degree of antiferromagnetic alignment of the magnetic layers. This can be very sensitive to structural defects, especially for multilayers containing thin spacer layers. This means that the GMR exhibited by multilayers is often more sensitive to structural defects than that found in granular alloys.

ACKNOWLEDGMENT

This research is supported by the Director, Office of Energy Research, Office of Basic Energy sciences, Materials Sciences Division of the U.S. Department of Energy under Contract No. DE-AC03-76SF00098.

- ¹S. S. P. Parkin, R. Bhadra, and K. P. Roche, *Phys. Rev. Lett.* **66**, 2152 (1991).
- ²S. S. P. Parkin, Z. G. Li, and D. J. Smith, *Appl. Phys. Lett.* **58**, 2710 (1991).
- ³A. E. Berkowitz, J. R. Mitchell, M. J. Carey, A. P. Young, S. Zhang, F. E. Spada, F. T. Parker, A. Hutten, and G. Thomas, *Phys. Rev. Lett.* **68**, 3745 (1992).
- ⁴J. Q. Xiao, J. S. Jiang, and C. L. Chien, *Phys. Rev. Lett.* **68**, 3749 (1992).
- ⁵S. S. P. Parkin, R. F. C. Farrow, T. A. Rabedeau, R. F. Marks, G. R. Harp, Q. H. Lam, M. Toney, R. Savoy, and R. Geiss, *Euro. Phys. Lett.* **22**, 455 (1993).
- ⁶R. E. Camley and J. Barnas, *Phys. Rev. Lett.* **63**, 664 (1989).
- ⁷P. M. Levy, S. Zhang, and A. Fert, *Phys. Rev. Lett.* **65**, 1643 (1990).
- ⁸D. M. Edwards, R. B. Muniz, and J. Mathon, *IEEE, Trans. Magn.* **MAG-27**, 3548 (1991).
- ⁹E. E. Fullerton, D. M. Kelly, J. Guimpel, I. K. Schuller, and Y. Bruynseraede, *Phys. Rev. Lett.* **68**, 859 (1992).
- ¹⁰S. S. P. Parkin, *Appl. Phys. Lett.* **61**, 1358 (1992).
- ¹¹S. S. P. Parkin, *Phys. Rev. Lett.* **71**, 1641 (1993).
- ¹²T. A. Rabedeau, M. Toney, R. F. Marks, S. S. P. Parkin, R. F. C. Farrow, and G. Harp, *Phys. Rev. B* **48**, 17538 (1993).
- ¹³R. F. Marks, R. F. C. Farrow, G. R. Harp, S. S. P. Parkin, T. A. Rabedeau, M. F. Toney, A. Cebollada, N. Thangaraj, and K. M. Krishnan, *Mater. Res. Soc. Symp. Proc.* **313**, 411 (1993).
- ¹⁴A. Tsoukatos, H. Wan, G. C. Hadjipanayis, and Z. G. Li, *Appl. Phys. Lett.* **61**, 3059 (1992).
- ¹⁵S. S. P. Parkin, A. Modak, and D. J. Smith, *Phys. Rev. B* **47**, 9136 (1993).

Giant magnetoresistance and its dependence on processing conditions in magnetic granular alloys

Jian-Qing Wang, Edward Price, and Gang Xiao

Department of Physics, Brown University, Providence, Rhode Island 02912

We have studied giant magnetoresistance (GMR) effect and its dependence on processing conditions in Fe-Ag and Co-Ag alloys made by magnetron sputtering. The effect of elevated substrate temperature on GMR has been investigated and compared with the results of post-deposition annealing. As a unique feature, *in situ* annealing yields a second GMR peak at high deposition temperatures, which is associated with a substantially reduced saturation field for GMR. Deposition rate was found to be another crucial parameter in affecting GMR, whereas little effect was observed in varying the sputtering gas pressure.

Since its discovery in magnetic multilayers¹⁻³ and granular materials,^{4,5} the giant magnetoresistance (GMR) effect has been found to depend sensitively on material parameters and processing conditions. Studying the correlation between GMR and processing conditions is crucial not only in the application aspect, but also in the understanding of the underlying mechanism of GMR. It has been commonly agreed that GMR arises from spin-dependent scattering due to exchange interaction between conduction electrons and magnetic scattering centers. The magnitude of GMR directly depends on the strength of exchange interaction which in turn depends on the choice of constituents. The dimensional constraints and interface roughness of the magnetic component are also determining factors in the behavior of GMR. These factors are influenced by material growth processes, conditions, and post-deposition thermal annealing.

In this work we studied how the processing conditions affect the magnetotransport properties in two metallic granular systems, Fe-Ag and Co-Ag. The processing conditions include such factors as deposition rate, sputtering gas pressure, substrate temperature, and post-deposition annealing. We found that GMR is very sensitive to some fabrication parameters, in particular, to the deposition rate and annealing temperature. We investigated the effect of *in situ* annealing and compared it to post-deposition annealing results.

The Co-Ag samples were deposited on Si substrates by a single magnetron sputtering gun loaded with a composite target. The Fe-Ag samples were made by codeposition using cluster guns loaded with pure targets (>99.9%) of Fe and Ag. Typical samples were 5000 Å (Co-Ag) and 2500 Å (Fe-Ag) in thickness. For *in situ* annealing, the duration of heating and sputtering was about 15 min, about the same as the time of post-deposition annealing. Samples were deposited at ambient temperature (~50 °C), 200, 250, 300, 350, and 400 °C, with the same sputtering rate and gas pressure. For rate-dependence study sample depositions were done at ambient temperature (RT). All sample processing was carried out under a base vacuum of better than 1.0×10^{-7} Torr.

The standard photolithography and wet-etching technique was used to pattern the samples into a Hall bar configuration. This allowed us to simultaneously measure the resistivity and Hall resistivity. The Hall-effect measurement provides us with information of carrier density and type, as well as effective mean-free path.⁶ In the transport measure-

ments, the magnetic field was swept in a full circle ($-8 \text{ T} \leftrightarrow +8 \text{ T}$) to account for magnetic hysteresis effects. The hysteresis measured agrees with that determined by magnetic measurements, which were carried out in a superconducting quantum interference device (SQUID) magnetometer. Structural information was obtained by x-ray diffraction, transmission electron microscopy (TEM), and magnetic measurement. Detailed results are presented elsewhere.⁷

Figure 1 shows a typical measurement of magnetoresistance (MR) $\rho_{xx}(H)$ for a RT sample of $\text{Co}_{20}\text{Ag}_{80}$. Hysteresis is clearly observable with the MR maxima located at the coercive field H_c , where the magnetization of the sample reaches zero. There exist different definitions of GMR. In this work the GMR is defined as

$$\text{GMR} = \Delta\rho/\rho = [\rho_{xx}(0 \text{ T}) - \rho_{xx}(8 \text{ T})]/\rho_{xx}(8 \text{ T}), \quad (1)$$

since at $H=8 \text{ T}$ the MR is almost saturated.

Let us first pay attention to the effects of annealing. Under equilibrium Co or Fe is immiscible with Ag.⁸ For the as-sputtered samples deposited at a moderate rate ($\sim 4.0 \text{ Å/s}$), the size of the magnetic particles is about $\sim 20 \text{ Å}$ as determined by TEM and magnetic measurements. Annealing

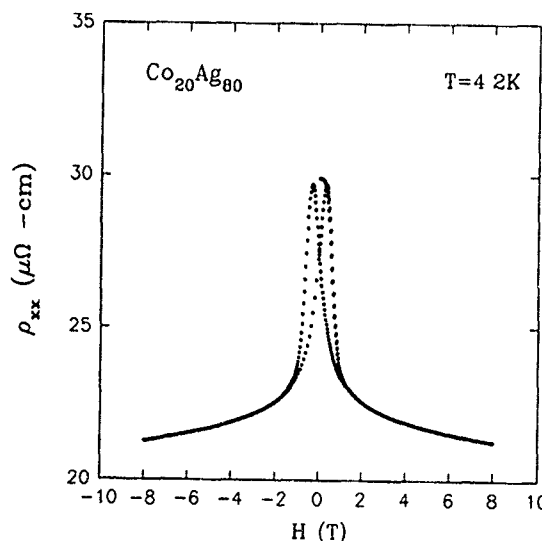


FIG. 1. Magnetoresistivity $\rho_{xx}(H)$ for $\text{Co}_{20}\text{Ag}_{80}$ deposited at ambient temperature with a rate of $R=4.0 \text{ Å/s}$ and $P_{\text{Ar}}=4.0 \text{ mTorr}$. $T=4.2 \text{ K}$.

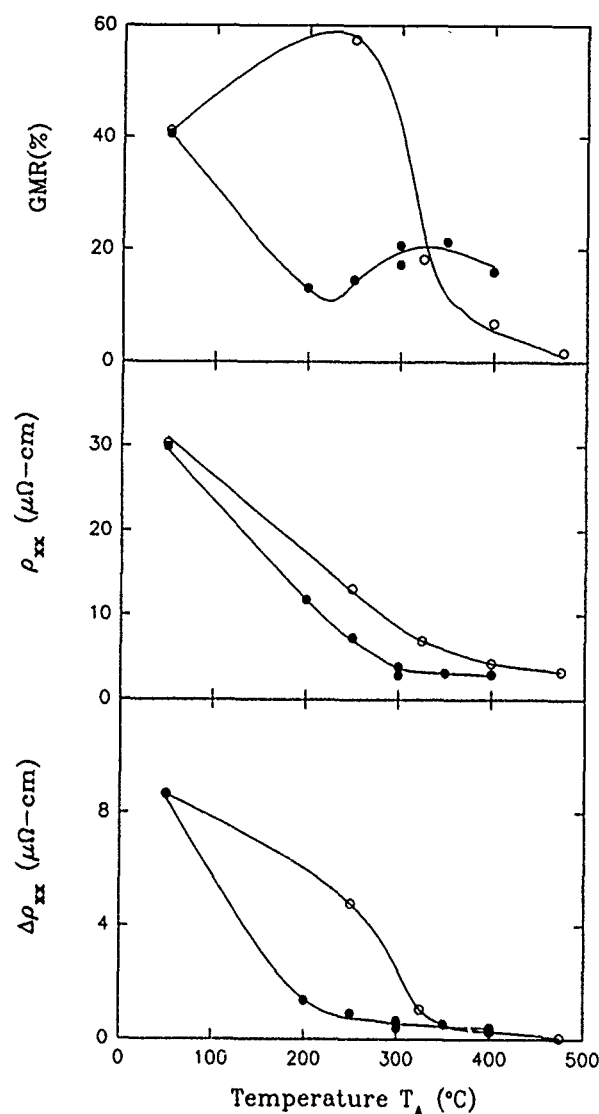


FIG. 2. GMR (upper), ρ_{xx} (middle), and $\Delta\rho_{xx}$ (lower) for $\text{Co}_{20}\text{Ag}_{80}$ samples (filled circles) deposited at various substrate temperatures, and for $\text{Fe}_{13}\text{Ag}_{87}$ samples (open circles) after post-deposition annealing at different T_A . Solid lines are guides to the eye. $T = 4.2$ K.

increases the magnetic particle size and reduces disorder. For example, after post-deposition annealing for 15 min at 400 °C, the magnetic particle size increased to ~ 70 Å, whereas the zero-field resistivity ρ_{xx} decreased by one order of magnitude. ρ_{xx} contains contributions from magnetic and nonmagnetic scattering. Both are reduced by annealing. In granular materials, the magnetic spin-dependent scattering occurs primarily at the interface.⁹ Thus if the magnetic scattering were dominant in ρ_{xx} , the decrease in ρ_{xx} would be much smaller (by about a factor of ~ 3) as a result of the reduced surface-to-volume ratio.

The effects of post-deposition annealing are demonstrated in Fig. 2. The measured GMR (upper panel), zero-field resistivity ρ_{xx} (middle), and the net change in resistivity $\Delta\rho_{xx}$ (lower) versus post-deposition annealing temperature T_A are presented for $\text{Fe}_{13}\text{Ag}_{87}$ samples as open circles. The results for $\text{Co}_{20}\text{Ag}_{80}$ and other granular systems are very similar.^{6,10} GMR initially increases with annealing tempera-

ture T_A and subsequently decreases at higher T_A . But if ρ_{xx} and $\Delta\rho_{xx}$ are examined separately, both are found to monotonically decrease as T_A increases. The variation of GMR with T_A results from the difference in the rates of change of $\Delta\rho_{xx}$ and ρ_{xx} . In the low T_A region ($T_A < 250$ °C), $\Delta\rho_{xx}$ decreases slowly, whereas ρ_{xx} decreases relatively quickly. This results in an initial increase in GMR. In the high T_A region, $\Delta\rho_{xx}$ drops very quickly over a narrow T_A range, and then monotonically approaches zero at 500 °C. The decrease in ρ_{xx} is, on the other hand, slow over the same T_A range. Hence the GMR shows the subsequent decrease in the high T_A region.

The observed variation in MR can be qualitatively explained as follows. $\Delta\rho_{xx}$ reflects the strength of the magnetic scattering. The structural characterization shows that the magnetic particle size increases slowly with T_A in the low T_A region. This results in a slow variation in magnetic scattering, and therefore in $\Delta\rho_{xx}$. The initial fast decrease in ρ_{xx} is mainly due to a decrease in the contribution of disorder and, to a lesser extent, magnetic scattering. In the high T_A region, magnetic particle size increases more rapidly with T_A . Other changes, e.g., interface roughness and particle shape, may also occur. The partial resistivity due to magnetic scattering is affected more strongly, resulting in a steeper decrease in $\Delta\rho_{xx}$ in the high T_A region. Disorder, being much reduced, becomes less sensitive to annealing.

Most studies so far have focused on the influence of post-deposition annealing on GMR. Little attention has been paid to the effects of growth temperature during thin-film deposition, i.e., *in situ* annealing, which affects the microstructure differently from post-deposition annealing. In Fig. 2, the filled circles represent the data of GMR, ρ_{xx} , and $\Delta\rho_{xx}$ for $\text{Co}_{20}\text{Ag}_{80}$ samples deposited at different substrate temperatures. It is seen that GMR suffers a large drop even at low T_A . At about $T_A \approx 200$ °C, GMR reaches a minimum and then starts to develop a peak at $T_A \approx 320$ °C. This behavior is substantially different from that of post-deposition annealing.

The cause for the above GMR behavior is again due to the rate of change of $\Delta\rho_{xx}$ and ρ_{xx} . Under *in situ* annealing, $\Delta\rho_{xx}$ decreases much faster with T_A than ρ_{xx} does below $T_A \sim 200$ °C, resulting in the initial drop of GMR. However, between 200–300 °C, the rate of change of $\Delta\rho_{xx}$ slows down substantially, while the rate of change of ρ_{xx} remains about the same. This causes a temporary increase in GMR. Figure 2 shows that at low T_A , *in situ* annealing suppresses $\Delta\rho_{xx}$ much more efficiently than post-deposition annealing. This reveals the susceptibility of microstructural changes to *in situ* thermal annealing.

The appearance of a GMR peak at high T_A is very desirable from an application point of view. Samples made at higher T_A have substantially lower saturation field for GMR. The GMR value at the second peak is about a factor of 2 smaller than that of the as-sputtered sample. But the saturation field H_s has decreased by a factor of 5. We define H_s as the field at which 90% saturation has been achieved. We found that $H_s \approx 3.1$ T for the RT sample, and $H_s \approx 0.59$ T for samples annealed at 300–400 °C. Our study opens a new route in the search for the optimal condition for GMR effect.

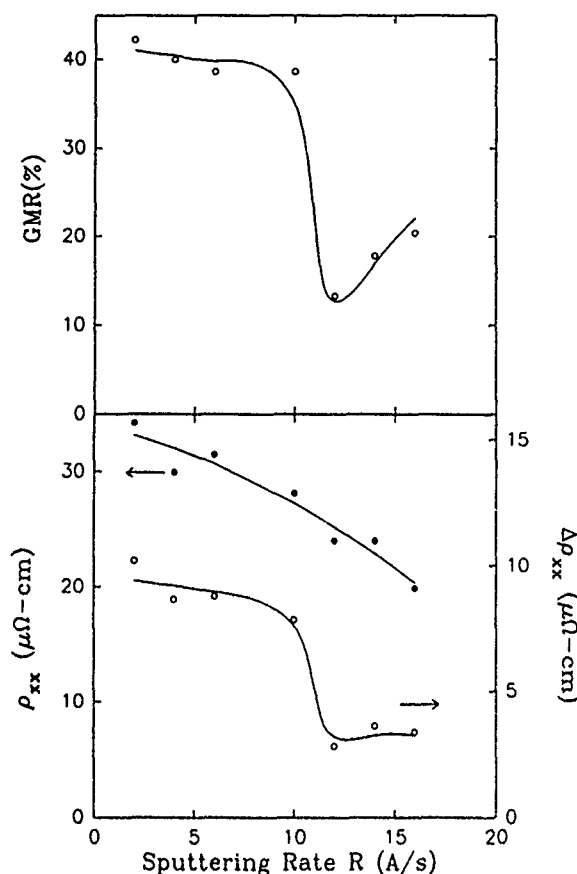


FIG. 3. GMR (top), ρ_{xx} and $\Delta\rho_{xx}$ (bottom) for $\text{Co}_{20}\text{Ag}_{80}$ samples obtained at different sputtering rates. Solid lines are guides to the eye. $T=4.2$ K.

In situ annealing could be more advantageous than post-deposition annealing.

Next we turn our attention to another processing parameter, i.e., deposition rate R . Different energies are carried by the deposited materials at various rates R . Thus different kinetics are involved in different rate regions. The measured GMR, ρ_{xx} , and $\Delta\rho_{xx}$ for $\text{Co}_{20}\text{Ag}_{80}$ as a function of R are presented in Fig. 3. GMR has its highest values ($\sim 40\%$) in the low R region ($0 < R < 10$ Å/s) and is only weakly dependent on R . But there is a sudden transition in GMR to a much lower value ($\sim 15\%$ – 20%) at $R \sim 10$ Å/s. This transition marks the onset of microstructural change occurring in the high rate region.

Examining the variations of ρ_{xx} and $\Delta\rho_{xx}$ with R independently, we observe that the transition in GMR at $R \sim 10$ Å/s is due to a large drop in $\Delta\rho_{xx}$. On the other hand, ρ_{xx} varies with R gradually, slightly decreasing as R increases. Thus the transition observed here is due to changes in magnetic arrangement in the samples deposited at high rates.

This is presumably due to the higher kinetic energy carried by the deposited materials. Structural characterization showed that the Co particle sizes increased only slightly in the high R region, indicating that the particle size effect is unlikely to be the cause for the transition in GMR at $R \sim 10$ Å/s. It is most likely due to changes occurred at the interface between the magnetic particles and Ag matrix.

It has been found that sputtering gas pressure induces changes in interface roughness and hence changes the size of GMR in multilayers.¹¹ We have investigated this possibility in our granular systems by varying the Ar gas pressure P_{Ar} from 2 to 8 mTorr. We found that the gas pressure has little effect on GMR and other magnetotransport properties in this pressure range.

In summary, processing conditions are very important in controlling the magnetotransport properties and GMR effect of metallic granular materials. A second peak in GMR at high annealing temperature is a unique feature to the *in situ* annealing. A substantially reduced saturation field coincides with this peak in GMR. We have also found a threshold in deposition rate, beyond which the strength of magnetic scattering, and hence GMR, suffers a precipitous drop. The different GMR behaviors between high substrate temperature and high sputtering rates are due to different microstructural changes in the systems. The former is mainly caused by an increase in particle size, whereas the latter is mainly due to changes in the magnetic structure at the granular interface. Among many processing parameters, only the sputtering gas pressure hardly affects GMR, ρ_{xx} , and $\Delta\rho_{xx}$.

We wish to thank Peng Xiong and Kent Ibsen for helpful technical assistance. This work was supported by National Science Foundation Grant No. DMR-9121747. G. X. wishes to thank the A. P. Sloan Foundation for a fellowship.

- ¹M. N. Baibich, J. M. Broto, A. Fert, F. Nguyen Van Dau, F. Petroff, P. Eitenne, G. Creuzet, A. Friederich, and J. Chazelas, Phys. Rev. Lett. **61**, 2472 (1988).
- ²J. J. Krebs, P. Lubitz, A. Chaiken, and G. A. Prinz, Phys. Rev. Lett. **63**, 1645 (1989).
- ³S. S. P. Parkin, N. More, and K. P. Roche, Phys. Rev. Lett. **64**, 2304 (1990).
- ⁴A. E. Berkowitz, J. R. Mitchell, M. J. Carey, A. P. Young, S. Zhang, F. E. Spada, F. T. Parker, A. Hutten, and G. Thomas, Phys. Rev. Lett. **68**, 3745 (1992).
- ⁵J. Q. Xiao, J. S. Jiang, and C. L. Chien, Phys. Rev. Lett. **68**, 3749 (1992).
- ⁶J.-Q. Wang, P. Xiong, and Gang Xiao, Phys. Rev. B **47**, 8341 (1993).
- ⁷J.-Q. Wang and Gang Xiao, J. Phys. Rev. B **49**, 3982 (1994).
- ⁸*Iron-Binary Phase Diagrams*, edited by Kubaschewski (Springer, Berlin, 1982), p. 3.
- ⁹P. Xiong, Gang Xiao, J.-Q. Wang, J. Q. Xiao, J. S. Jiang, and C. L. Chien, Phys. Rev. Lett. **69**, 3220 (1992).
- ¹⁰J. Q. Xiao, J. S. Jiang, and C. L. Chien, Phys. Rev. B **46**, 9266 (1992).
- ¹¹E. E. Fullerton, D. M. Kelly, J. Guimpel, and I. K. Schuller, Phys. Rev. Lett. **68**, 859 (1992).

Theory of magnetotransport in inhomogeneous magnetic structures

Horacio E. Camblong,^{a)} Shufeng Zhang, and Peter M. Levy
Department of Physics, New York University, New York, New York 10003

The origin of the giant magnetoresistance of magnetic multilayers and magnetic granular solids is investigated through a unified spin-dependent linear transport theory, in which the primary source of electrical resistivity is short-range scattering by impurities in the different magnetic or nonmagnetic regions and at the interfaces. Our theory predicts that magnetotransport in granular solids is similar to that for currents perpendicular to the plane of the layers in multilayers in that their magnetoresistance is independent of the average distance between adjacent magnetic regions.

Magnetotransport in inhomogeneous magnetic structures has been experimentally studied in both multilayers¹ and granular solids.² The main focus of these investigations has been the phenomenon of giant magnetoresistance, which holds promise for technological breakthroughs.

The theory of magnetotransport in multilayers with collinear magnetizations has been discussed in Refs. 3–8. Instead, magnetotransport through noncollinear magnetizations is not so well understood, either for multilayers or for granular solids.

In this paper we consider the problem of magnetotransport in inhomogeneous magnetic structures with arbitrary magnetization configurations via the introduction of a linear transport theory in the presence of effective spin-dependent fields, and we apply the formalism to three cases of experimental relevance: multilayers with currents in the plane of the layers (CIP), multilayers with currents perpendicular to the plane of the layers (CPP), and granular solids. Our model is based on scattering by impurities in the different regions of the system (layers for multilayers and granules or matrix for granular solids) as well as at the interfaces, rather than on scattering by entire regions of the inhomogeneous structure (multilayer or granular solid). We find that the characteristic exponential dependence of the magnetoresistance of CIP with respect to the thickness of the nonmagnetic spacer layer has no counterpart in either CPP or granular solids, a behavior that places them in a new class of magnetically self-averaging systems.

Our theory generalizes the real space Kubo approach of Ref. 4 and it starts from the model Hamiltonian³

$$H = H_0 + \sum_a (v_a + j_a \hat{\mathbf{M}}_a \cdot \hat{\sigma}) \delta(\mathbf{r} - \mathbf{r}_a), \quad (1)$$

where H_0 describes free electrons, $\hat{\sigma}$ is the one-electron spin vector operator, \mathbf{r}_a is the position vector of a particular impurity, $\hat{\mathbf{M}}_a$ represents the direction of magnetization of a magnetic region, and v_a and j_a are phenomenological constants. As in Ref. 4, when the reduced Fermi wavelength $\lambda_F = k_F^{-1} \approx 1 \text{ \AA}$ is much smaller than the other length scales (mean-free paths and inhomogeneity lengths), the one-particle propagator satisfies the Dyson's equation, which in real space reads

$$\left[\epsilon_F + \frac{\hbar^2}{2m} \nabla_r^2 - \Sigma(\mathbf{r}) \right] G^{\text{ret}}(\mathbf{r}, \mathbf{r}') = \delta(\mathbf{r} - \mathbf{r}'), \quad (2)$$

where $\Sigma(\mathbf{r})$ is the local self-energy due to scattering in the bulk and at the interfaces. In order to analyze transport properties we look at the imaginary part

$$\Delta(\mathbf{r}) = -\text{Im}[\Sigma(\mathbf{r})], \quad (3)$$

which we will refer to as the scattering strength.

The main difficulty posed by the existence of noncollinear magnetization is that the independence of physical properties with respect to arbitrary choices of the quantization axis requires a theory that is covariant under changes of that axis. The ensuing implication is that if the current is to be viewed as arising from different channels (two-current model), the only possible description is one in terms of the spin-dependent current densities, $\mathbf{j}_{\alpha\beta}(\mathbf{r}) = \langle \hat{\mathbf{j}}_{\alpha\beta}(\mathbf{r}) \rangle$, defined as the expectation values of the spinor current operators

$$\hat{\mathbf{j}}_{\alpha\beta}(\mathbf{r}) = \frac{e\hbar}{mi} \Psi_{\alpha}^{\dagger}(\mathbf{r}) \vec{\nabla}_{\beta}(\mathbf{r}), \quad (4)$$

where $\vec{\nabla}_r = (\vec{\nabla}_r - \vec{\nabla}_{r'})/2$ is the antisymmetric gradient operator, $\Psi_{\alpha}(\mathbf{r})$ is the real space one-electron field operator, and greek indicates label the two spin channels. Similarly, the spin-dependent constitutive relation

$$\mathbf{j}_{\alpha\beta}(\mathbf{r}) = \sum_{\gamma, \delta} \int d^3r' \sigma_{\alpha\beta, \gamma\delta}(\mathbf{r}, \mathbf{r}') \cdot \mathbf{E}_{\gamma\delta}(\mathbf{r}'), \quad (5)$$

follows by absorbing the vertex corrections via a redefinition of the internal fields $\mathbf{E}_{\gamma\delta}(\mathbf{r}')$. As a result, the fourth-rank spinor two-point conductivity $\sigma_{\alpha\beta, \gamma\delta}(\mathbf{r}, \mathbf{r}')$, which contains only the contribution from the bubble diagram in the real space Kubo formula,

$$\sigma_{\alpha\beta, \gamma\delta}(\mathbf{r}, \mathbf{r}') = -\frac{2}{\pi} \frac{e^2}{\hbar} \left(\frac{\hbar^2}{2m} \right)^2 \times A_{\beta\gamma}(\mathbf{r}, \mathbf{r}') \vec{\nabla}_r \vec{\nabla}_{r'} A_{\delta\alpha}(\mathbf{r}', \mathbf{r}), \quad (6)$$

[where $A_{\alpha\beta}(\mathbf{r}, \mathbf{r}') = (G_{\alpha\beta}^{\text{ret}}(\mathbf{r}, \mathbf{r}') - G_{\alpha\beta}^{\text{adv}}(\mathbf{r}, \mathbf{r}')/2$ is the density of states function] is proportional to the bubble part of the current-current correlation of the spinor currents, i.e., $\sigma_{\alpha\beta, \gamma\delta}(\mathbf{r}, \mathbf{r}') \propto \langle [\hat{\mathbf{j}}_{\alpha\beta}(\mathbf{r}) \hat{\mathbf{j}}_{\gamma\delta}(\mathbf{r}')] \rangle$.

In the quasiclassical regime, Eq. (2) can be solved via a global WKB integration. The corresponding reduced Green's function, $\mathcal{G}(\mathbf{r}, \mathbf{r}') = (\hbar^2/2m)G(\mathbf{r}, \mathbf{r}')$, is

^{a)}Present address. Department of Physics, University of San Francisco, San Francisco, CA 94117.

$$g(\mathbf{r}, \mathbf{r}') \approx -\frac{1}{4\pi|\mathbf{r}-\mathbf{r}'|} \exp[ik_F|\mathbf{r}-\mathbf{r}'|] \times P_{\mathbf{r}' \rightarrow \mathbf{r}} \exp\left[-\frac{1}{2}\xi(\mathbf{r}, \mathbf{r}')|\mathbf{r}-\mathbf{r}'|\right]. \quad (7)$$

Equation (7) has a very simple physical interpretation: it represents a propagating electron with a complex wave number $k(\mathbf{r}) = [k_F^2 + i2m\Delta(\mathbf{r}/\hbar^2)]^{1/2}$. In Eq. (7) the two-point exponent $\xi(\mathbf{r}, \mathbf{r}')$

$$\xi(\mathbf{r}, \mathbf{r}') = \left(\frac{2m}{\hbar^2 k_F}\right) \frac{1}{|\mathbf{r}-\mathbf{r}'|} \int_{\Gamma[\mathbf{r}, \mathbf{r}']} ds'' \Delta(\mathbf{r}''), \quad (8)$$

describes the damping of the electron's wave function (loss of momentum) as it propagates along the straight path $\Gamma[\mathbf{r}, \mathbf{r}']$ connecting the points \mathbf{r} and \mathbf{r}' , and it is essentially the average scattering encountered by the electron between \mathbf{r} and \mathbf{r}' . In the presence of spin-dependent scattering, the one-particle propagator $G^{\text{ret}}(\mathbf{r}, \mathbf{r}')$, the self-energy $\Sigma(\mathbf{r})$, the scattering matrix $\Delta(\mathbf{r})$, and the two-point exponent $\xi(\mathbf{r}, \mathbf{r}')$ are 2×2 spin matrices; thus, a path-ordering operator is required in Eq. (7), to reorder the noncommuting 2×2 scattering matrices in the exponential series from the point \mathbf{r}' to the point \mathbf{r} (from right to left). The corresponding WKB results for the two-point conductivity are [from Eq. (6)]

$$\sigma_{\alpha\beta, \gamma\delta}(\mathbf{r}, \mathbf{r}') = \frac{3C_D}{4\pi} \frac{\mathbf{n}\mathbf{n}}{|\mathbf{r}-\mathbf{r}'|^2} \{P_{\mathbf{r}' \rightarrow \mathbf{r}} \exp[-\frac{1}{2}\xi(\mathbf{r}, \mathbf{r}')|\mathbf{r}-\mathbf{r}'|] \beta\gamma \{P_{\mathbf{r} \rightarrow \mathbf{r}'} \exp[\frac{1}{2}\xi(\mathbf{r}, \mathbf{r}')|\mathbf{r}-\mathbf{r}'|] \}_{\delta\alpha}, \quad (9)$$

where $C_D = e^2 k_F^2 / (6\pi^2 \hbar)$ and \mathbf{n} is a unit vector from \mathbf{r} to \mathbf{r}' .

The computation of global or measurable transport properties requires further work, as they do not follow straightforwardly from Eq. (9). In view of this complication we will start by analyzing global properties in multilayers, and only at a later stage we will consider transport in granular solids.

For the particular case of multilayers, which are characterized by in-plane translational invariance, a Fourier transform with respect to the in-plane relative positions yields two-point conductivities $\sigma(z, z') = \sigma(k_{\parallel} = 0; z, z')$, given by

$$\sigma(z, z') = \frac{3C_D}{2} \int_1^{\infty} dt \frac{1}{t} \left[\frac{1}{2} \left(1 - \frac{1}{t^2} \right) l_{\parallel} + \frac{1}{t^2} \mathbf{e}_z \mathbf{e}_z \right] \times \exp \left[-t \int_z^{z'} \frac{dz''}{l(z'')} \right], \quad (10)$$

where l_{\parallel} is the unit tensor in the plane of the layers, the substitution $t = R/|z|$ has been made, and integration with respect to the in-plane azimuthal angle has rendered the tensor diagonal. Equation (10) describes electrical conduction in multilayers.⁴ For the CIP case, the internal electric field induced by an external uniform field is uniform, due to the in-plane symmetry of the multilayers; then the global CIP conductivity can be found by integrating the two-point conductivity of Eq. (10) twice, with respect to both arguments, z and z' , as has been explicitly derived in Ref. 4; the ensuing CIP conductivity and magnetoresistance exhibit a characteristic exponential dependence with respect to the thicknesses

of the different layers^{3,4} and the magnetoresistance vanishes exponentially in the local limit. On the other hand, for CPP the current for each spin channel is a constant⁷ as seen from Eq. (14); then, we find from Eqs. (5) and (9) that the internal field $E(z)$ is proportional to the local scattering rate $\Delta(z)$. Then, for the CPP geometry, the corresponding global resistivity is proportional to the average scattering encountered in each spin channel; thus, the CPP geometry for multilayers exhibits a self-averaging behavior (all transport properties are determined by the average scattering) not only in the homogeneous limit, but for all length scales, and the magnetoresistance is scale independent and does not vanish in the local limit, a result that had been predicted in Ref. 6 and was later experimentally confirmed.⁹ This result leads to a current line picture, according to which transport properties are determined by the scattering sampled by current lines in the whole system, provided that all current lines be essentially equivalent.

Our analysis for multilayers suggests that there exist two categories of inhomogeneous magnetic structures (according to the behavior exhibited by their magnetoresistance): (i) magnetically self-averaging, when their magnetoresistance does not vanish exponentially and is independent of the average distance between magnetic regions (like for the CPP geometry of multilayers); (ii) magnetically non-self-averaging, when their magnetoresistance vanishes exponentially with respect to the average distance between magnetic regions (like for the CIP geometry of multilayers).

The case of granular solids requires considering limiting cases. We will first analyze the homogeneous limit, which is characterized by all mean-free paths being much larger than all inhomogeneity lengths.

In the homogeneous limit the two-point function $\xi(\mathbf{r}, \mathbf{r}')$ [Eq. (8)] has a *unique limit*, as when $R = |\mathbf{r}-\mathbf{r}'| \rightarrow \infty$; in particular, this is independent of \mathbf{r} and \mathbf{r}' , and applies to both granular solids and multilayers. For multilayers the caveat is that such a unique limit holds for almost all paths, and the exception are those paths in the plane of the layers for multilayers. For magnetic systems, the function $\xi(\mathbf{r}, \mathbf{r}')$ is a spin matrix and its self-averaging limit is of the form $\bar{\xi} = \bar{\xi}_0 + \bar{\xi} \cdot \hat{\sigma}$. Thus, for both granular solids and multilayers, the "average scattering in the medium"

$$\bar{\Delta} = \frac{1}{V[\mathcal{R}]} \int_{\mathcal{R}} d^3r \Delta(\mathbf{r}) \quad (11)$$

is well defined and coincides with the asymptotic form (large R) of $\xi(\mathbf{r}, \mathbf{r}')$, provided that the size of the region \mathcal{R} be sufficiently large. In Eq. (11) $V[\mathcal{R}]$ is the volume of the corresponding region. The size of \mathcal{R} is essentially restricted by the condition that the function $\xi(\mathbf{r}, \mathbf{r}')$ become asymptotically a constant, i.e., R has to be restricted by the linear dimensions L of the sample; whence, these systems have a length scale D_{sa} , such that for $D_{sa} \lesssim R \ll L$, and the volume integral in Eq. (11) is independent of \mathcal{R} . We will naturally refer to D_{sa} as the self-averaging length scale. Therefore, the homogeneous limit yields a two-point conductivity, Eq. (9) that is effectively a function of only $R = |\mathbf{r}-\mathbf{r}'|$. Then, choosing a quantization axis that diagonalizes $\bar{\Delta}$ Eq. (5) is simplified to

$$\mathbf{j}_{\alpha\beta} = \delta_{\alpha\beta} \sum_{\gamma} \left[\int d^3r' \sigma_{\alpha\gamma, \gamma\alpha}(\mathbf{r}, \mathbf{r}') \right] \cdot \bar{\mathbf{E}} = \delta_{\alpha\beta} (\bar{\rho}_{\alpha})^{-1} \bar{\mathbf{E}}, \quad (12)$$

where $\bar{\mathbf{E}}$ stands for the average field, and it follows that the electrical resistance in each spin channel is essentially given by the average scattering $\bar{\Delta}$ sampled by the electron in the medium, i.e.,

$$\bar{\rho}_{\alpha} = \left(\frac{2m}{\hbar^2 k_F} \right) ([\bar{\Delta}^{-1}]_{\alpha\alpha})^{-1}. \quad (13)$$

This conclusion is achieved if it is assumed that the spin diffusion length is much larger than both the elastic mean-free paths and the inhomogeneity length scales, in which case the continuity equation for each spin component of the current density,

$$\nabla \cdot \mathbf{j}_{\alpha\beta}(\mathbf{r}) = 0, \quad (14)$$

is satisfied.

On the other hand, in the local limit, defined as the limiting scenario when all local mean-free paths are much smaller than the inhomogeneity lengths, the constitutive relation (5) becomes local; more precisely, the local conductivity becomes the produce of a one point conductivity function and the delta function $\delta(\mathbf{r}-\mathbf{r}')$. The electric field is then the product of the local resistivity and the current density, where the global resistivity is also $\bar{\rho}_{\alpha}$ along a typical current line, with the current constrained via Eq. (14).

From our analysis of limiting cases we conclude that our theory predicts that granular solids are magnetically self-averaging, due to *randomness* in the distribution of granules. In effect, the current line picture suggests that the global resistivity is proportional to the average scattering $\bar{\Delta}_{\alpha}$ in each spin channel, for all length scales, like for the CPP case. On the other hand, in the local limit for granular solids, current lines do *not* necessarily sample all the scattering in the medium but they only partially sample the scattering in the granules. Of course, the interfaces are probed regardless of the relative values of the local resistivities. This shows

that the local resistivity and the current cannot be completely disentangled. In conclusion, we see that the only difference between the two limiting cases is at most the contribution from the granules. Thus, the scale dependence of the magnetoresistance will show up exponentially with respect to the size of the granules but not with respect to the average distance between adjacent granules. In this sense, granular solids are magnetically self-averaging. It should be noticed that these conclusions are based on our choice of a model in which the electrical resistivity arises from short-range impurity scattering within each region of the system rather from scattering by entire regions.

In summary, we have derived the two-point conductivity of inhomogeneous magnetic structures, as well as the global resistance and magnetoresistance of magnetically self-averaging systems, for which we have shown that they are independent of the average distance between adjacent magnetic regions.

This work was supported in part by the Office of Naval Research Grant No. N00014-91-J-1695 and the New York University Technology Transfer Fund.

¹M. N. Baibich, J. M. Broto, A. Fert, F. Nguyen Van Dau, F. Petroff, P. Etienne, G. Creuzet, A. Friederich, and J. Chazelas, *Phys. Rev. Lett.* **61**, 2472 (1988).

²A. E. Berkowitz, J. R. Mitchell, M. J. Carey, A. P. Young, S. Zhang, F. E. Spada, F. T. Parker, A. Hutten, and G. Thomas, *Phys. Rev. Lett.* **68**, 3745 (1992); J. Q. Xiao, J. S. Jiang, and C. L. Chien, *ibid.* **68**, 3749 (1992).

³P. M. Levy, S. Zhang, and A. Fert, *Phys. Rev. Lett.* **65**, 1643 (1990); S. Zhang, P. M. Levy, and A. Fert, *Phys. Rev. B* **45**, 8689 (1992).

⁴H. E. Camblong and P. M. Levy, *Phys. Rev. Lett.* **69**, 2835 (1992); *J. Magn. Magn. Mater.* **121**, 446 (1993).

⁵A. Vedyaye, B. Dieny, and N. Ryzhanova, *Europhys. Lett.* **19**, 329 (1992).

⁶S. Zhang and P. M. Levy, *J. Appl. Phys.* **69**, 4786 (1991).

⁷For the particular case of collinear magnetizations, general features of the CPP geometry are discussed in H. E. Camblong, S. Zhang, and P. M. Levy, *Phys. Rev. B* **47**, 4735 (1993).

⁸T. Valet and A. Fert, *J. Magn. Magn. Mater.* **121**, 378 (1993).

⁹W. P. Pratt, Jr., S. -F. Lee, J. M. Slaughter, R. Loloee, P. A. Schroeder, and J. Bass, *Phys. Rev. Lett.* **66**, 3060 (1991); S. -F. Lee, W. P. Pratt, Jr., R. Loloee, P. A. Schroeder, and J. Bass, *Phys. Rev. B* **46**, 548 (1992).

Giant magnetoresistance of dilute Cu(Co) granular films

R. J. Gambino,^{a)} T. R. McGuire, J. M. E. Harper, and Cyril Cabral, Jr.
IBM Research Division, T. J. Watson Research Center, Yorktown Heights, New York 10598

Granular films of Cu (Co) with Co concentrations from 5.4% to 12% in the as-deposited form had magnetization showing about 60% of the Co as ferromagnetic particles and exhibited giant magnetoresistance (MR) of about 20% at 4.2 K. Annealing at $\sim 310^\circ\text{C}$ increased the MR to 40% and also increased the saturation magnetization indicating additional Co precipitation. At higher annealing temperatures MR decreased to 1%. The Zhang theoretical model involving polarized conduction electron scattering at particle interfaces seems to give a reasonable description of our results including the quadratic behavior of MR vs $[M(H)]^2$ and MR vs $[M_s(T)]^2$.

I. INTRODUCTION

Giant magnetoresistance discovered by Xiao *et al.*¹ and Berkowitz *et al.*² in granular Cu(Co) alloys represents a new approach to the large magnetoresistance (MR) found originally in multilayer films.^{3,4} The granular films consisting of a copper matrix with precipitated Co particles which have random position, random size, and random easy axis have magnetoresistive changes of up to 60% at 4.2 K. Both the magnitude and actual shape of the MR as a function of applied magnetic field are similar for both the granular and multilayer systems. Granular films, however, have substantial changes in MR when they are annealed.^{1,2} The magnetic and transport properties are found to be sensitive to both fabrication conditions and annealing procedures because cobalt particle concentration and particle size are changed.^{5,6}

Recently Zhang and Levy^{7,8} have considered the origin of MR in granular films. The giant MR is attributed mainly to the conduction electron spin-dependent scattering at the interface of the Co particle with the Cu matrix. Expressions are given for MR in terms of particle concentration (c), average particle radius (r_m), and normalized magnetization (M/M_s). It is the objective of the present work to examine a series of films where c , r_m , and M_s are varied to compare with theory and to increase our understanding of these complex systems.

II. EXPERIMENTAL PROCEDURES AND RESULTS

Film samples are prepared by coevaporation onto 12-cm-diam oxidized silicon substrates at ambient temperatures of about 50°C . The films varied in thickness from ~ 0.6 to $1.5\ \mu\text{m}$ and Co concentrations from 5.4 to 12 at %. The as-deposited films are listed in Table I. Part of each film disc is annealed and these samples are listed in Table II.

Magnetization measurements are made using a Quantum Design superconducting quantum interference device (SQUID) magnetometer with applied fields (H) up to 50 kOe. In most cases films are peeled off the silicon substrate and weighed thus the saturation magnetization M_s is given in emu/g. Resistivity (ρ) is determined by the van der Pauw method and is given in $\mu\Omega\text{ cm}$. The values ρ_{max} and ρ_{min} refer to resistivities at $H \approx 0$ and H at 40 kOe as illustrated in

Fig. 1, where $\Delta\rho = \rho_{\text{max}} - \rho_{\text{min}}$ and MR is $\Delta\rho/\rho_{\text{min}}$. Vacuum oven annealing temperatures are given in the last column of Table II. Data on M and ρ in the tables are for $T = 4.2\text{ K}$.

Figure 1 shows details of both MR and M data as a function of H for our film with the largest MR which is Co 12% (No. 13 in Table II). In this film the M_s at 124 emu/g is based on 12 at. % cobalt in particle form. If the Co is completely precipitated from the Cu matrix, the value should be $\approx 160\text{ emu/g}$ meaning that this film has about 78% precipitation of ferromagnetic Co particles and represents a value about 25% higher than the as-deposited 12% (No. 5). We note that all the 12% Co listed in the tables have low values of M_s compared to the 8% film. A second consideration is that the resistivity drops from values of $\sim 20\ \mu\Omega\text{ cm}$ and higher for as-deposited films to $\sim 4\ \mu\Omega\text{ cm}$ or less for annealed films for all Co concentrations. This decrease in ρ is evidently caused by the increased purity of the Cu matrix as the Co precipitates into particles. In the as-deposited state the matrix is a Co-Cu alloy with a high resistivity due to impurity scattering.

The MR at 4.2 K for the as-deposited films listed in Table I is around 20%. When the film is annealed two things occur. At a high annealing temperature, the MR drops to $\sim 1\%$, while at $T = 311^\circ\text{C}$, MR can increase up to 40%. Evidently a delicate balance of particle size and Cu purity is needed to obtain the highest value of MR. The Co particle size can be determined by analyzing the superparamagnetic properties of the films. The blocking temperature was found from the temperature dependence of the coercivity. The particle diameter ($2r_m$) was calculated using the relation for the particle volume (V_p): $V_p = 25kT_B/K$. Using the anisotropy energy K of Co ($K = 4.5 \times 10^6\text{ erg/cm}^3$) and assuming spherical particles we find that the Co particles are about 50 Å in diameter in all the as-deposited films. The same analysis

TABLE I. As-deposited Cu(Co) granular films. (Data for 4.2 K.)

No.	Co (%)	t (μm)	M_s (emu/g)	ρ_{max} ($\mu\Omega\text{ cm}$)	ρ_{min} ($\mu\Omega\text{ cm}$)	$\Delta\rho$ ($\mu\Omega\text{ cm}$)	MR (%)
2	5.4	1.5	140	13.17	10.50	2.67	25.4 ^a
3	8.3	1.5	116	28.21	25.45	2.76	10.8
4	8.5	0.6	86	15.57	13.41	2.16	16.1
5	12.0	0.6	100	24.29	20.00	4.29	21.5

^aMR extrapolated to $1/H \rightarrow 0$.

^{a)}State University of NY at Stony Brook, Department of Materials Science and Engineering, Stony Brook, NY 11794-2275.

TABLE II. Annealed Cu(CO) granular film. (Data for 4.2 K.)

No.	Co (%)	<i>t</i> (μm)	<i>M_s</i> (emu/g)	<i>ρ_{max}</i> (μΩ cm)	<i>ρ_{min}</i> (μΩ cm)	<i>Δρ</i> (μΩ cm)	MR (%)	Anneal (h) (°C)
6	5.4	1.5	73	14.50	11.49	3.01	26.2	1.0@325
7	8.3	1.5	163	6.83	5.04	1.79	35.6	^b
8	8.3	1.5	153	3.08	3.04	0.04	1.3	1.5@350
9	8.3	1.5	185	3.90	3.26	0.64	19.6	1.0@311
10	8.5	0.6	170	*	*	*	18.6	1.0@325
11	12.0	0.6	130	3.10	2.80	0.30	10.7	1.0@340
12	12.0	0.6	122	4.17	4.14	0.03	0.8	1.5@350
13	12.0	0.6	124	5.65	4.03	1.62	40.2	1.0@311

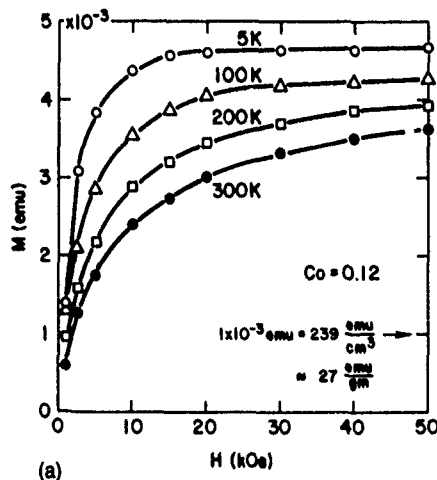
**ρ* in μΩ cm not measured.^bDone *in situ* at 300 °C.

gives a particle diameter of 90 Å in the fully annealed samples.

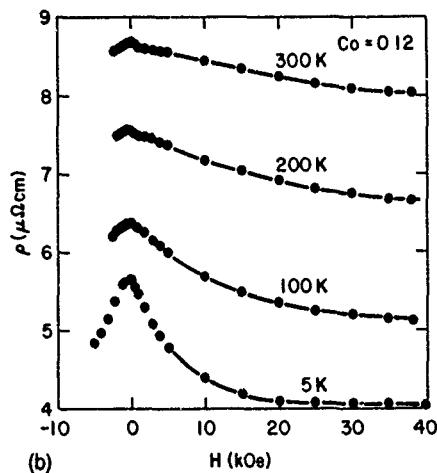
III. DISCUSSION

Zhang gives the following equation for the MR in granular films with single-domain particles:

$$\frac{\Delta\rho}{\rho} = \frac{\rho_2^2}{\rho_1^2 - \rho_2^2} \left[1 - \left(\frac{M(H)}{M_s} \right)^2 \right], \quad (1)$$



(a)



(b)

FIG. 1. (a) Magnetization and (b) resistivity as a function of applied field for various temperatures. This is the annealed 12% sample No. 13 Table II.

where ρ_1 and ρ_2 are functions of c , r_m and includes also a ratio p_s (p_b), of the electron spin-dependent to spin-independent scattering potential at the particle surface (bulk), as well as the conduction electron mean-free path at the surface λ_s and in the bulk λ_m of the particles and the mean-free path λ_{nm} in the nonmagnetic matrix. If we accept the simplification that the bulk and the interface-surface scattering of small magnetic particles are the same so that $p_b = p_s$ and $\lambda_m = \lambda_s$, Eq. (1) then reduces to

$$\frac{\Delta\rho}{\rho_s} = \frac{[2p_s(r_m+3)]^2}{\left((1+p_s^2)(r_m+3) + \frac{1-c}{c} \frac{r_m\lambda_s}{\lambda_{nm}} \right)^2 - [2p_s(r_m+3)]^2} \times \left[1 - \left(\frac{M(H)}{M_s} \right)^2 \right]. \quad (2)$$

Large $\Delta\rho/\rho_s$ (MR) is thus predicted for long mean-free path λ_{nm} and small λ_s . The MR also increases with particle concentration c . In addition MR is quadratic in magnetization as a function of field and is largest for small M . At zero field where $M/M_s \approx 0$, the point of maximum MR with respect to saturation, Eq. (2) can be written

$$\left(1 + \frac{1}{\Delta\rho/\rho_s} \right)^{1/2} = \frac{1}{2p_s} \frac{\lambda_s}{\lambda_{nm}} \frac{r_m(1-c)}{(r_m+3)c} + \frac{1+p_s^2}{2p_s}. \quad (3)$$

We wish to know how well our data fit the Zhang model as given by Eqs. (2) and (3). From Table I for as-deposited films MR seems to be large in the film having the highest Co concentrations No. 5. The large value of MR for No. 2 (5.4% Co) does not follow this trend. In addition, this film (No. 2) has the lowest value of resistivity meaning λ_{nm} is large and the largest M_s of all the as-deposited samples indicating a larger fraction of the Co is precipitated.

The quadratic behavior given by the proportionality $\Delta\rho/\rho_s \propto [1 - (M(H)/M_s)^2]$ fits quite well for M vs H dependence as shown in Fig. 2 for films No. 3, 8.3% Co. The quadratic proportionality holds best for the as-deposited samples and when M is close to saturation at high applied fields. At low fields in the annealed samples the magnetization may increase primarily by wall motion within large particles with only a small change in magnetic interface scattering. Consider also the affect of annealing at high temperatures which causes low MR. If the annealing causes a pre-

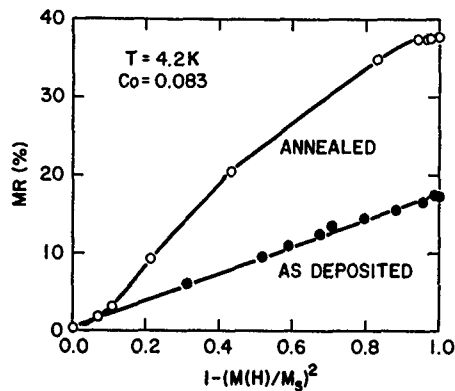


FIG. 2. Field dependence of MR at 4.2 K as a function of $1-[M(H)/M_s]^2$ for No. 3, 8.3% Co. Note the linearity of the as-deposited sample. Similar behavior is observed in the 5.4% and 12% samples.

ponderance of large Co particles without smaller particles which take large fields to saturate, then, MR is low as observed.

The quadratic dependence is also observed for M as a function of T as shown in the plots of Fig. 3. However, Eq. (2) has a positive linear slope; this slope may be from the temperature dependence of the mean-free paths.

A final consideration is to use Eq. (3) to determine the value of p_s or the ratio λ_s/λ_{nm} by plotting $\{1+[1/(\Delta\rho/\rho)]\}^{1/2}$ vs $(1-c)/c$, where c is the starting Co concentration. The particle size is assumed constant for each group of samples in the respective tables. Data points plotted on Fig. 4 for the as-deposited samples are scattered sufficiently so that a quantitative fit is not possible. We assume the annealed samples with the highest values of MR are the most like the Zhang

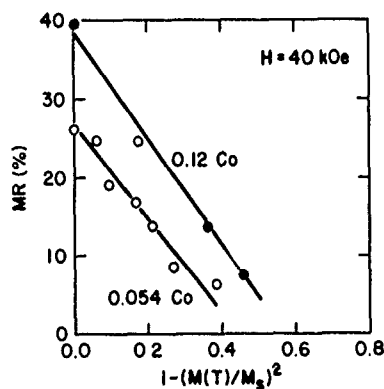


FIG. 3. Temperature dependence of MR as a function of $1-[M(T)/M_s]^2$ for film No. 2, 5.4% Co as deposited, as No. 13, 12% Co annealed.

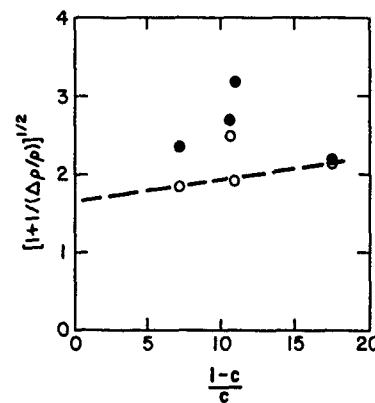


FIG. 4. Plot of $[1+(1/MR)]^{1/2}$ and $(1-c)/c$ parameters associated with Eq. (3) in text.

model, i.e., isolated single-domain particles in a pure copper matrix. These data give a small positive slope with an intercept of 1.65. From the intercept value we find p_s , the ratio of the spin-dependent to spin-independent scattering potential is about 3. From the slope and assuming r_m is 50 Å we find $\lambda_s/\lambda_{nm}=0.16$. In other words, the mean-free path in the non-magnetic matrix λ_{nm} is about six times the mean-free path in and near the surface of the magnetic particles, a reasonable number.

The origin of the MR in the granular alloys fits a model that polarized conduction electrons from random easy axis single-domain Co particles are scattered by particles that have not fully rotated in the direction of the applied field. Application of a large field fully magnetizes most of the Co particles and the resistivity decreases. If the particles are of sufficient size, they all rotate together during magnetization and no differential spin-dependent scattering is found and MR is small.

¹J. Q. Xiao, J. S. Jiang, and C. L. Chien, Phys. Rev. Lett. **68**, 3749 (1992).

²A. E. Berkowitz, M. J. Carey, J. R. Mitchell, A. P. Young, S. Zhang, F. E. Spada, F. T. Parker, A. Hutten, and G. Thomas, Phys. Rev. Lett. **68**, 3745 (1992).

³M. N. Baibich, J. M. Broto, A. Fert, Nguyen van Dau, F. Petroff, P. Etienne, G. Cruezet, A. Friederich, and J. Chazelas, Phys. Rev. Lett. **61**, 2472 (1988).

⁴S. S. Parkin, R. Bhadra, and K. P. Rock, Phys. Rev. Lett. **66**, 2152 (1991).

⁵C. L. Chien, John Q. Xiao, and J. S. Jiang, J. Appl. Phys. **73**, 5309 (1993).

⁶A. E. Berkowitz, J. R. Mitchell, M. J. Carey, A. P. Young, D. Rao, A. Starr, S. Zhang, F. E. Spada, F. T. Parker, A. Hutten, and G. Thomas, J. Appl. Phys. **73**, 5320 (1993).

⁷S. Zhang, Appl. Phys. Lett. **61**, 1855 (1992).

⁸S. Zhang and P. M. Levy, J. Appl. Phys. **73**, 5315 (1993).

Dependence of giant magnetoresistance on film thickness in heterogeneous Co-Ag alloys

J. R. Mitchell and A. E. Berkowitz

Physics Department and Center for Magnetic Recording Research, University of California, San Diego, California 92093

The dependence of magnetic properties on film thickness in as-deposited Co-Ag alloys is discussed. Films ranging in Co concentration from 0 to 100 vol % Co and thicknesses between 100 Å and 1 μm were deposited by sputtering onto Si(100) substrates. It was found that both magnetoresistance (MR, $\Delta\rho$) and MR ratio ($\Delta\rho/\rho$) increase with thickness. Resistivity (ρ) decreases with increasing thickness. The dependence of MR ratio on concentration of Co is not markedly different for 200 and 2000-Å-thick samples. Saturation magnetization is roughly constant for thicknesses greater than ~200 Å, decreasing rapidly below this cutoff. However, most of both the thin (200 Å) and thick (2000 Å) films begin showing magnetic hysteresis between 10 and 100 K. The differences in transport and magnetization properties may be ascribed to differences in film growth for thin versus thick films.

I. INTRODUCTION

Much interest is evident in the giant magnetoresistance (MR) of alloy films.¹⁻⁵ Most of the work in this field, however, uses samples at least 2000 Å thick. The properties of thinner alloy films are technologically and scientifically interesting. We report the effects of varying layer thickness for Co-Ag alloy films.

II. EXPERIMENT

Two series of Co-Ag films were produced by co-sputtering. The first series consists of films varying from 0 to 100 vol % Co. In one set, at each concentration, films 200 Å (thin) and 2000 Å (thick) were grown. The second set was comprised of films 27 vol % Co, with thicknesses ranging from 120 Å to 1 μm. All films were sputtered onto Si(100) substrates at room temperature as previously described.³ Data are reported for as-deposited samples only. Magnetoresistance data were taken using a four-point probe. Magnetization measurements were made on a superconducting quantum interference device (SQUID) magnetometer. Volume

concentrations are deduced from atomic absorption spectroscopy measurements of Co concentration, assuming all Co appears as precipitates.

III. RESULTS

The x-ray data are for films whose thicknesses are nominally 2000 Å or greater. In general, the films were fcc and (111) oriented. However, the pure Ag film was fcc but not oriented. The pure Co film was hcp. For Co concentrations greater than 14 vol %, separate Co and Ag lines are clearly visible. A typical diffraction pattern is shown in Fig. 1. As expected, the Co(111) line is shifted from the bulk value towards the Ag(111) line, and vice versa. Figure 2 summarizes the variation in lattice parameter with vol % Co. As the Co concentration increases, the difference between the calculated and the bulk lattice parameter increases for Ag and decreases for Co. In addition, the intensity of the Co(111) line increases with the concentration of Co.

Initial analysis of finite size broadening of the Co line indicates that the Co crystallite size varies as the volume fraction of Co is increased. Assuming that the Co grains are close-packed throughout the film, one can also calculate an

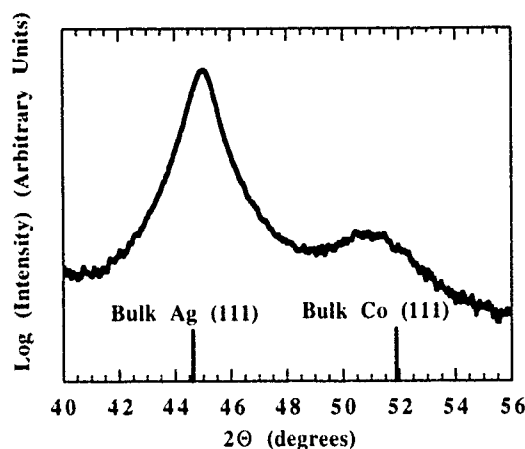


FIG. 1. X-ray diffraction spectrum using Co radiation ($\lambda = 1.79$ Å) for a 26.5 vol % Co alloy, as-deposited.

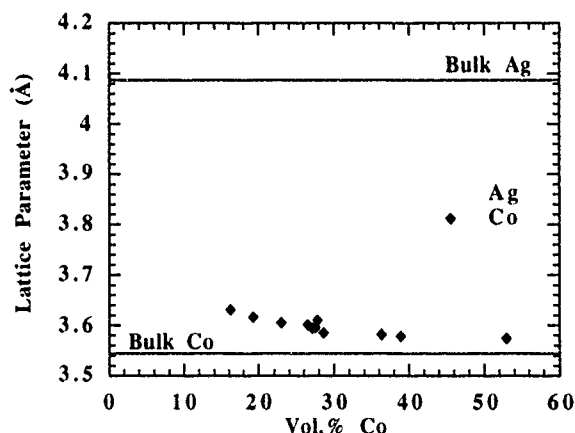


FIG. 2. Variation of Co and Ag lattice parameters with Co concentration.

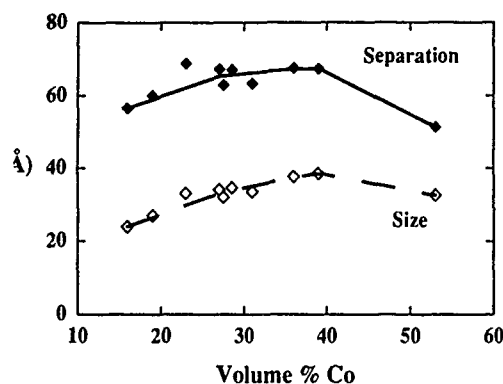


FIG. 3. Variation of Co grain size and separation for 2000-Å-thick films with Co concentration (vol %), assuming a close-packed array of particles.

average intergranular separation, i.e., the spacing between the centers of neighboring particles. Figure 3 summarizes these results. The lines in Fig. 3 are drawn to guide the eye. The grain size increases until a concentration of 39 vol % Co is reached. The Co line broadening indicates that the 53 vol % film has smaller Co grains. However, magnetic hysteresis data indicates that there may be a bimodal distribution of Co grain sizes. The smaller set of grains is responsible for the broadening that gives the 32 Å grain size. The size and separation of the grains for the sample with the maximum magnetoresistance are 33 and 40 Å, respectively. Similar analysis on the Ag line gives a grain size of roughly 150 Å for all samples. This is supported by results of dark-field transmission electron microscopy (TEM). Analysis of the x-ray data for thinner films is ongoing. Initial results indicate that, at the same concentration of Co, the Co grains are smaller and more densely packed for thinner films.

The variation of MR ratio ($\Delta\rho/\rho_{\min}$), where $\Delta\rho = \rho_{\max} - \rho_{\min}$ and $\rho_{\min} = \rho(H=20 \text{ kOe})$, with Co concentration is shown in Fig. 4. All MR data reported herein were taken at 10 K. The MR ($\Delta\rho$) displays a similar dependence on volume fraction of Co. The MR ratios of the thin (200 Å) and thick (2000 Å) films peak at similar volume fractions of Co. In the thin films, however, the MR ratio peaks at a

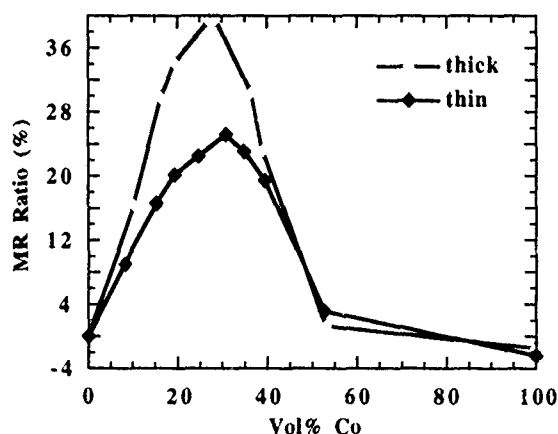


FIG. 4. Variation of magnetoresistance ratio with volume concentration of Co at $T=10 \text{ K}$ for both thick (2000 Å) and thin (200 Å) films.

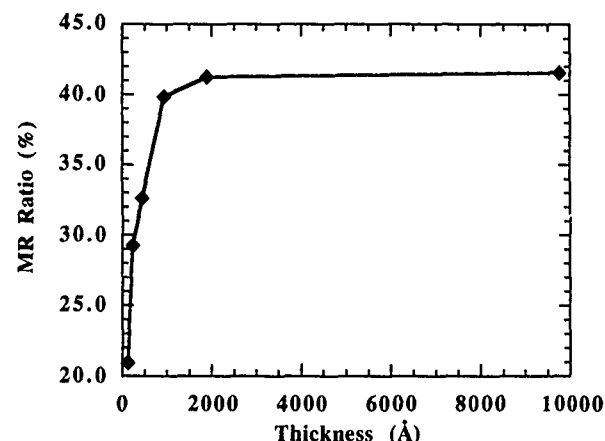


FIG. 5. Dependence of MR ratio at $T=10 \text{ K}$ on thickness. All samples have 27 vol % Co.

slightly higher concentration and does not fall off quite as rapidly with increasing volume fraction Co. Since one expects both the size and packing of Co particles to affect the MR ratio, the differences in the MR ratio between thick and thin films indicates variations in the microstructure with thickness. Figure 5 displays the dependence of MR ratio at 10 K on layer thickness for 27 vol % Co. At thicknesses $<2000 \text{ Å}$, the MR ratio falls off quite rapidly. The MR displays a similar variation.

For both thick (2000 Å) and thin (200 Å) films, the high-field (20 kOe) resistivity peaks at 53 vol % Co. This is shown (for $T=10 \text{ K}$) in Fig. 6. The peak in resistivity is probably due to impurity scattering. In other words, the electrons traveling through an Ag-rich matrix are more strongly scattered by the "impurity" (dissolved Co) than by defects in the matrix. The difference in resistivity between the thick films and the thin films also varies with Co concentration. The percent difference in high-field resistivity for the thick and thin films is smallest at the peak in the resistivity. In addition, at a fixed concentration, the relative resistivity increases with decreasing thickness as shown in Fig. 7. The data shown are for a 27 vol % Co alloy and pure Ag. The small variation in resistivity for the alloy cannot be ac-

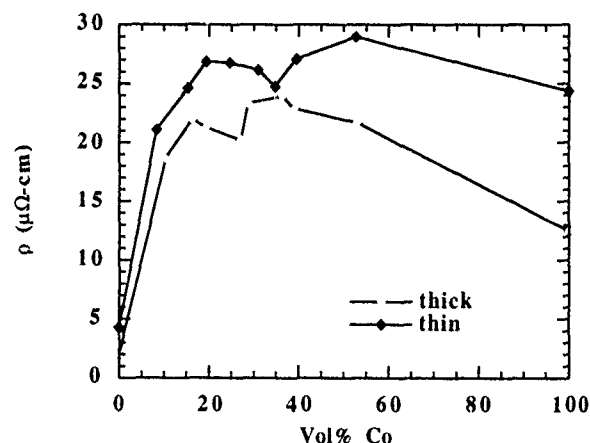


FIG. 6. Variation of high-field (20 kOe) resistivity at $T=10 \text{ K}$ with Co concentration for both thick (2000 Å) and thin (200 Å) films.

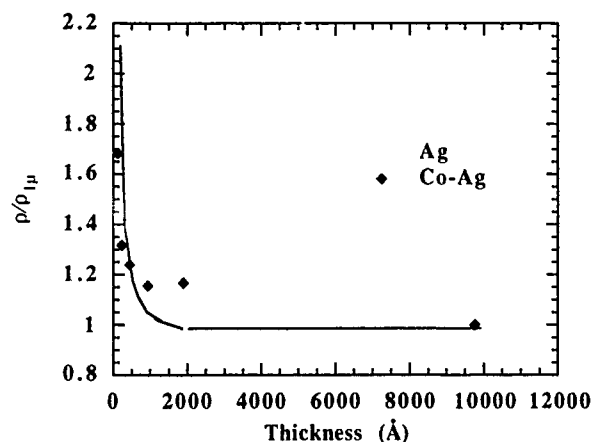


FIG. 7. Normalized resistivity (normalized to 1- μm -thick film) vs thickness for both pure Ag and a nominally 27 vol % Co-Ag alloy. The line for the pure Ag data is drawn to guide the eye.

counted for by considering the contribution of scattering at the air-film and substrate-film interfaces.^{6,7} It is probable that the difference in microstructure between the thick and thin films mentioned earlier plays a role in the variation of resistivity with thickness seen here.

For Co concentrations greater than 10 vol %, the saturation magnetization is not highly dependent on fraction of Co present. It does, however, depend on layer thickness. At a thickness of ~ 200 Å, the saturation magnetization falls off, as shown in Fig. 8. Thick samples with concentrations less than 35 vol % Co do not exhibit hysteresis until the temperature is less than 100 K. Thin samples with less than 50 vol % Co show no hysteresis at temperatures above 100 K. Again, these data indicate differences in the films' microstructure, i.e., the size and separation of the Co grains.

IV. DISCUSSION AND SUMMARY

Although a decrease in resistivity with increasing thickness is expected, the large variation in the magnetoresistance is not. The variation of magnetoresistance cannot be accounted for simply by the increased importance of scattering at the film surfaces. In addition, the dependence of the magnetization on thickness indicates that the microstructure of the thin films differ from that of the thick films. In particular, the size of the Co particles and degree of percolation in the thin films is less than that of the thick films. In other words, for the same Co concentration, the Co particles are smaller

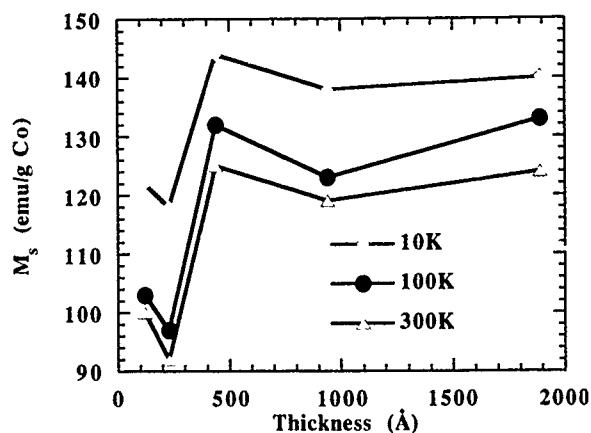


FIG. 8. Variation of saturation magnetization with thickness for 27 vol % Co.

and, therefore, closer together in the thin films than in the thick films. However, transport and magnetic measurements alone are insufficient to determine this. Other methods of structural characterization are, therefore, being used to determine the films' microstructure.

In summary, Co-Ag alloys have been produced over a range of concentrations and thicknesses. The variation of MR and magnetization with concentration is similar in both the thin and thick films. However, there are differences between the properties of thick and thin films. These variations indicate differences in microstructure between the films. Work is ongoing to determine the exact nature of the microstructure of the thin and thick films.

ACKNOWLEDGMENTS

We would like to thank Matthew Carey, Fred Parker, and Fred Spada for valuable contributions. This work was supported by NSF Grant No. DMR-90-10908 and by a grant from the Commerce Department under the Advanced Technology program administered by NSIC.

- ¹ C. L. Chien, J. Q. Xiao, and J. S. Jiang, *J. Appl. Phys.* **73**, 5309 (1993).
- ² S. Zhang and P. M. Levy, *J. Appl. Phys.* **73**, 5315 (1993).
- ³ A. E. Berkowitz, J. R. Mitchell, M. J. Carey, A. P. Young, D. Rao, A. Starr, S. Zhang, F. E. Spada, F. T. Parker, A. Hutten, and G. Thomas, *J. Appl. Phys.* **73**, 5320 (1993).
- ⁴ Barnard *et al.*, *J.M.M.M.* **114**, L230 (1992).
- ⁵ Barnard *et al.*, *J. Appl. Phys.* **73**, 6372 (1993).
- ⁶ K. Fuchs, *Proc. Camb. Philos. Soc.* **34**, 100 (1938).
- ⁷ E. H. Sondheimer, *Adv. Phys.* **1**, 1 (1952).

Modulation-induced giant magnetoresistance in a spinodally decomposed Cu-Ni-Fe alloy

S. Jin, L. H. Chen, T. H. Tiefel, and M. Eibschutz^{a)}
AT&T Bell Laboratories, Murray Hill, New Jersey 07974

R. R. Esh
Bellcore, Red Bank, New Jersey 07701

Giant magnetoresistance in a spinodally decomposed, bulk 60 Cu-20 Ni-20 Fe alloy is reported. An annealed, quenched, and heat-treated sample with a compositional modulation of $\lesssim 50$ Å size exhibits a $\Delta R/R$ value as high as 9% at 4.2 K. Optimization of the ferromagnetic phase particle geometry through a combination of spinodal decomposition and uniaxial deformation led to a locally multilayered, superlattice-like structure and a dramatic increase in room-temperature magnetoresistance from ~ 0.6 to $\sim 5\%$. This improvement in magnetoresistance is accompanied by a decrease in coercivity from ~ 620 Oe in the fully decomposed material to ~ 45 Oe in the optimized structure. Interestingly, this structure no longer exhibits the commonly observed temperature-dependent behavior of $\Delta R/R$ increasing at low temperatures, but rather shows a decrease at 4.2 K.

I. INTRODUCTION

The giant magnetoresistance (GMR) phenomenon has been discovered in recent years in Fe/Cr, Co/Cu, and various other multilayer superlattice films¹⁻⁷ as well as in heterogeneous (granular) Co-Cu thin films^{8,9}. These multilayer films exhibit electrical resistivity which decreases with magnetic field (negative magnetoresistance). The resistivity change is typically in the range of 5%–50%. The GMR effect offers a possibility of convenient magnetic sensing, e.g., as a high-resolution transducer (read head) for magnetic information storage systems.

In the present paper, we demonstrate that the GMR effect is not restricted to thin-film structures but can easily be obtained in bulk materials if a proper microstructure is introduced, for example, by spinodal decomposition and deformation in a Cu-Ni-Fe alloy.

II. EXPERIMENTAL

A 60 Cu-20 Ni-20 Fe (wt %) alloy (Cunife I, commonly used as a permanent magnet), in the form of ~ 5.0 -mm-diam rod, was procured from UGIMAG Inc., Valparaiso, Indiana. The as-received material has the coercivity (H_c) of ~ 620 Oe and the remanent induction (B_r) of ~ 2400 G at room temperature. A typical aging heat treatment to obtain these properties is an isothermal decomposition at 650 – 700 °C for several hours. The decomposed alloy was then either annealed (950 °C/30 min), water cooled, and heat treated to obtain fine spinodally decomposed precipitates or uniaxially deformed by swaging, wire drawing, and cold rolling to various diameters and thicknesses. The evaluation of magnetoresistance was carried out by four-point measurements (typical sample length ~ 2 cm) in the presence of an in-plane magnetic field up to 6 T. M - H hysteresis loops were obtained by using a vibrating sample magnetometer and a hysteresigraph ma-

chine. The microstructures of the alloys were obtained by high-resolution transmission electron microscopy using a JEOL 4000 microscope operated at 400 kV.

III. RESULTS AND DISCUSSION

Shown in Fig. 1 are the magnetoresistance (MR) ratio versus H curves at 4.2 K for the annealed and quenched sample as well as post-heat-treated samples. The MR ratio $\Delta\rho_M/\rho_S$ is defined here as $(\rho - \rho_S)/\rho_S$, where ρ_S is the resistivity at the near-saturation field and ρ is the resistivity at a magnetic field H . The electrical resistivity of the alloy samples at $H=0$ is about 20 – 25 $\mu\Omega$ cm at 4.2 K, which decreases when the field is applied. The as-quench sample shows a high magnetoresistance value of $\sim 7.2\%$. This is further increased to $\sim 9\%$ after a brief heat treatment at 450 °C/3 min as the compositional amplitude of the modulation is increased without much particle coarsening. More ex-

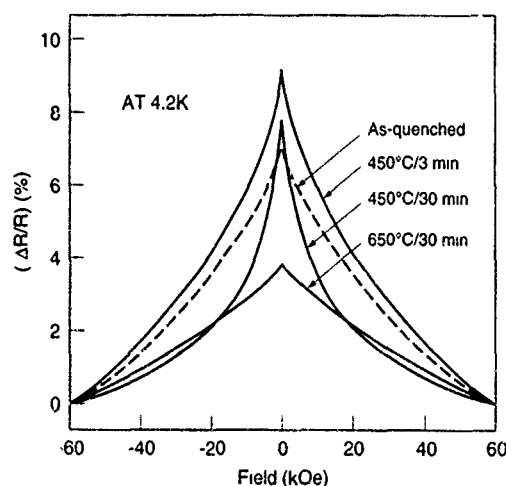


FIG. 1. MR ratio vs H at 4.2 K for the annealed and quenched or heat treated alloy.

^{a)}Formally with AT&T Bell Laboratories, is now with Physics Department, Polytechnique Univ., Brooklyn, NY 11202.

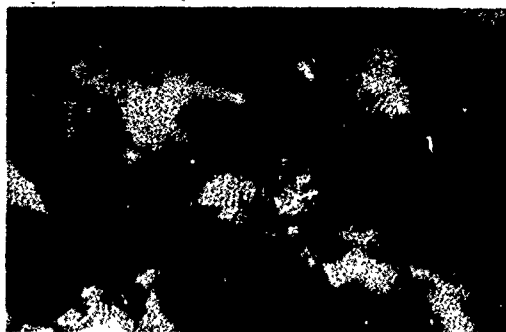


FIG. 2. TEM micrograph for the annealed and quenched alloy showing a ~ 30 Å sized modulated structure of the Ni, Fe-rich phase.

tensive heat treatment only reduces the MR effect presumably due to the coarsening of the particles and reduced surface scattering.

The Cu-Ni-Fe alloy is known to decompose spinodally into a uniformly distributed, modulated two-phase structure consisting of Ni, Fe-rich ferromagnetic phase, and Cu-rich nonmagnetic or weakly magnetic phase.¹⁰⁻¹² The observed giant magnetoresistance in the alloy is attributed to the formation of extremely fine-scale spinodally decomposed structure (Fig. 2), which shows the Ni, Fe-rich phase, ~ 30 Å in size and marked by circles (Moiré fringes), dispersed in the Cu-rich matrix. The size scale of the particles is comparable to the thickness or diameter of ferromagnetic phase in other GMR materials.¹⁻⁹ The spin-dependent scattering of electrons at the two-phase interfaces and in the strongly ferromagnetic phase is expected to influence the magnetoresistance behavior, similarly as in the multilayer films¹⁻⁷ and granular materials.^{8,9}

The samples in Fig. 1, however, exhibit much smaller values of MR ratio at room temperature, less than about one eighth of those at 4.2 K. The exact reason for this severe temperature dependence of MR ratio is not clearly understood. In order to achieve improved MR effect at room temperature, an alternative route of microstructural control was employed as described below.

The initial, as-received (as-decomposed) structure containing the oversized (~ 500 Å diameter) ferromagnetic phase particles, Fig. 3(a), was subjected to a uniaxial deformation to produce a locally multilayer-like structure with a very small layer thickness. (Wire drawing from 5.0 to 0.25 mm in diameter followed by cold rolling to about 0.052 and 0.015 mm thickness to produce three different thicknesses of the ferromagnetic phase measured or estimated to be about 60, 15, and 5 Å, respectively) Shown in Fig. 3(b) is the deformation-induced, superlattice-like structure with a 15-Å-thick ferromagnetic layers separated by nonmagnetic layers.

Shown in Fig. 4 are the room-temperature magnetoresistance (MR) ratio (given in %) versus H curve for the alloy samples with different particle thicknesses. As shown in the figure, the MR ratio increased from $\sim 0.6\%$ to $\sim 3.8\%$ after the diameter of the alloy rod was reduced by wire drawing from ~ 5.0 mm in the as-received condition to ~ 0.25 mm (99.75% reduction in cross-sectional area). The particle thickness of the ferromagnetic phase was reduced from

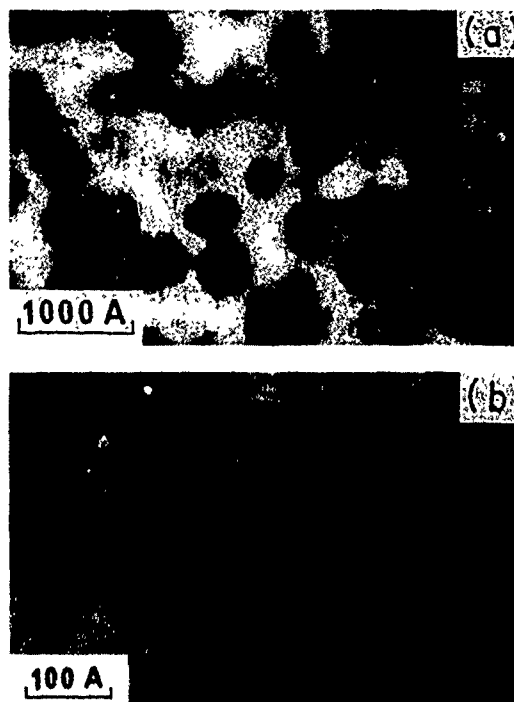


FIG. 3. Sectional TEM micrographs of the Cu-20Ni-20Fe alloy, (a) as-received, (b) after 99.94% deformation. The darker phase is the Fe, Ni-rich ferromagnetic phase.

~ 500 Å to an approximate size of ~ 60 Å (roughly estimated using the particle thickness in the similarly but more extensively deformed sample of Fig. 3(b), which was given $\sim 99.94\%$ reduction in area). The reason why the particle diameter was not reduced in exact proportional to the change in the alloy sample diameter is probably because of the difference in the mechanical properties of the two phases involved. The observed improvement in MR ratio is attributed to the much enhanced spin-dependent scattering in the ultrafine structure, similarly as in the multilayer films. Cold rolling process was subsequently applied to further reduce the dimension of the ferromagnetic phase in the Cu-Ni-Fe alloy. At the ribbon thickness of 0.052 mm [99.94% reduction in area with the measured particle thickness of ~ 15 Å, Fig. 3(b)], the MR ratio was measured to be as high as 5% as

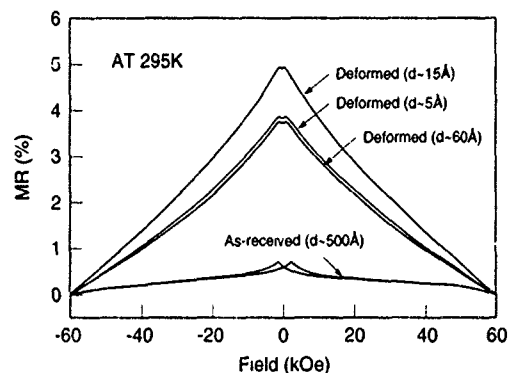


FIG. 4. MR ratio vs H at room temperature of the deformed Cu-Ni-Fe samples. The measured or estimated particle thicknesses of the ferromagnetic phase are indicated

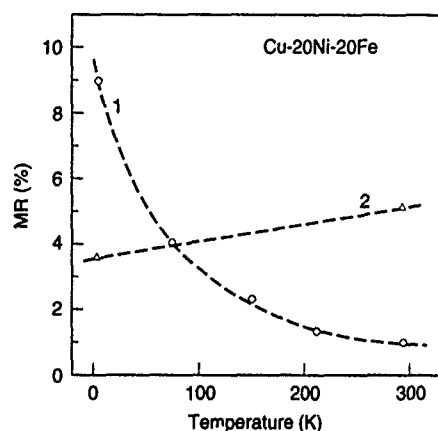


FIG. 5. Temperature dependence of the MR ratio for the sample of Fig. 2 (curve 1) and that of Fig. 3(b) (curve 2).

shown in Fig. 4. After additional rolling to a 0.015-mm-thick ribbon (99.984% reduction in area with an estimated particle thickness of ~ 5 Å), however, the MR ratio decreased to $\sim 3.9\%$. There appears to be an optimal particle thickness of the ferromagnetic phase for the largest MR ratio in the Cu-Ni-Fe alloy.

Shown in Fig. 5 are the MR ratio versus temperature curves for both the modulated sample of Fig. 2 and the deformed sample of Fig. 3(b). It is interesting to note that the MR ratio for the deformed Cu-Ni-Fe alloy sample (curve 2) at 4.2 K is not significantly different from that at room temperature and in fact smaller than the room-temperature value for the 0.052-mm-thick sample. This is a rather unusual behavior when compared to the annealed, quenched, and heat-treated (450 °C/3 min) Cu-Ni-Fe alloy (curve 1) in which the MR ratio increases significantly (by a factor of ~ 8) when cooled from room temperature to 4.2 K. Many multilayer thin films with GMR effect also exhibit a two to three times increase in the MR ratio upon cooling to 4.2 K, which is generally interpreted in terms of relatively strong temperature-dependent decrease in resistivity combined with a rather weak temperature variation of $\Delta\rho_M$.

The M - H hysteresis behavior of the Cu-Ni-Fe alloy samples is significantly affected by the material processing employed in this study. As the deformation reduced the particle thickness of the ferromagnetic phases from ~ 500 to

~ 15 Å, almost close to the superparamagnetic regime, much of the original permanent magnet properties were lost. The coercivity is reduced from ~ 620 to ~ 45 Oe, and the remanence ratio (M_r/M_s) from 0.87 to 0.21. The near-saturation magnetization at $H=3$ T of the deformed sample is ~ 175 emu/cc but the observed 10% increase in magnetization from 1 to 3 T field indicates that the ribbon sample is not fully saturated at $H=3$ T (and even at 6 T from the MR ratio versus H curves). This is different from the as-received sample, the magnetization of which appears to saturate at a field well below 5 kOe. Essentially a similar M - H behavior is observed at 4.2 K except that the remanence ratio is even further reduced to ~ 0.05 .

IV. SUMMARY

The giant magnetoresistance effect has been created in a bulk, spinodally decomposed or deformed Cu-20Ni-20Fe alloy containing an ultrafine ferromagnetic phase, either as dispersed particles or as a locally layered superlattice-like structure. The optimization of particle geometry through a combination of heat treatment and uniaxial plastic deformation led to a drastic increase in the room-temperature MR ratio from ~ 0.6 to $\sim 5\%$. The material exhibits a rather unusual temperature dependence of magnetoresistance, with the MR ratio being actually higher at room temperature than at 4.2 K.

¹M. N. Baibich, J. M. Broto, A. Fert, F. Nguyen Van Dau, F. Petroff, P. Etienne, G. Greuzet, A. Friederichand, and J. Chazelas, *Phys. Rev. Lett.* **61**, 2472 (1988).

²G. Binasch, P. Grunberg, F. Saurenbach, and W. Zinn, *Phys. Rev. B* **39**, 4828 (1989).

³S. S. P. Parkin, R. Bhadra, and K. P. Roche, *Phys. Rev. Lett.* **66**, 2152 (1991).

⁴B. Heinrich, Z. Celinski, J. F. Cochran, W. B. Wuir, J. Rudd, Q. M. Zhong, A. S. Arrot, K. Myrtle, and J. Kirschner, *Phys. Rev. Lett.* **64**, 373 (1990).

⁵S. S. P. Parkin, N. More, and K. P. Roche, *Phys. Rev. Lett.* **64**, 2304 (1990).

⁶M. E. Brubaker, J. E. Mattson, C. H. Sowers, and S. O. Bader, *Appl. Phys. Lett.* **58**, 2306 (1991).

⁷L. H. Chen, T. H. Tiefel, S. Jin, R. B. van Dover, E. M. Gyorgy, and R. M. Fleming, *Appl. Phys. Lett.* (in press).

⁸J. Q. Xiao, J. S. Jiang, and C. L. Chien, *Phys. Rev. Lett.* **68**, 3749 (1992).

⁹A. E. Berkowitz, J. R. Mitchell, M. J. Carey, A. P. Young, S. Zhang, F. E. Spada, F. T. Parker, A. Hutten, and G. Thomas, *Phys. Rev. Lett.* **68**, 3744 (1992).

¹⁰R. M. Bozorth, *Ferromagnetism* (Van Nostrand, New York, 1951), p. 402.

¹¹E. P. Butler and G. Thomas, *Acta Metall.* **18**, 347 (1970).

¹²R. J. Livak and G. Thomas, *Acta Metall.* **19**, 497 (1971).

Magnetoresistance in a granular Fe-Mg system

Kevin Pettit

Department of Physics, University of Illinois, Urbana, Illinois 61801

E. Kita, K. Araga, and A. Tasaki

Institute of Applied Physics, University of Tsukuba, Tsukuba, Ibaraki, 305, Japan

M. B. Salamon

Department of Physics, University of Illinois, Urbana, Illinois 61801

We have prepared granular films of Fe (36 at. %)-Mg (64 at. %) and measured the magnetization, resistance, and thermopower as a function of the applied magnetic field at temperatures between 300 and 6 K. The as-prepared sample has a magnetoresistance ratio ($\Delta R/R_{\max}$) of -6.3% in a field of 5.5 T at 6 K. The samples were annealed at temperatures between 150 °C and 228 °C for one hour. The MR does not vary as the square of the magnetization, as predicted by theory. We attribute this to a particle size distribution effect.

INTRODUCTION

In recent years, considerable interest has developed in the magnetoresistance (MR) of bimetallic magnetic/nonmagnetic multilayers and granular systems. The systems that have been studied most thoroughly are Co/Cu, Co/Ag, and Fe/Cr.¹⁻⁵ Most of the early theoretical work attributed the MR to the spin-dependent scattering at the magnetic/nonmagnetic interfaces.⁶⁻⁹ More recently, the role of the spin-dependent density of states (DOS) in the magnetic medium has been investigated.¹⁰⁻¹² Measurements of the MR and magnetothermopower (MTP) in Co/Cu multilayers¹¹ and Co/Ag granular systems¹³ suggest that the spin dependent DOS must be accounted for in any theoretical explanation of so-called giant magnetoresistance. We were interested in measuring the magnetization, MR, and MTP in a new system, and chose Fe-Mg because the constituents are immiscible and because we wanted to test the DOS argument in a system with a positive thermoelectric power.

EXPERIMENT

The 5800 Å thick Fe-Mg films were grown by coevaporation under ultrahigh vacuum onto Si and thin glass substrates. The concentrations were measured using inductively coupled plasma photoemission spectroscopy. The samples contained Fe (36 at. %) and Mg (64 at. %). The volume ratio is roughly 20%. A more complete description of the growth process, as well as an analysis of the as-prepared sample, can be found in an article by Araga, Kita, and Tasaki.¹⁴

Four samples were sealed in small evacuated quartz tubes and annealed at temperatures of 150 °C, 204 °C, 210 °C, and 228 °C for one hour. The temperature of the quartz tube containing the sample was monitored *in situ* and fluctuated less than 2 °C. We measured the magnetization of the samples using a SQUID magnetometer in fields of up to 5.5 T and at temperatures from 6 to 300 K. The resistance was determined using a conventional four-lead DC measurement in fields of up to 7 T. The temperature of the samples could be varied from 4.2 to 300 K. At around 6 K, the lowest temperature at which measurements were taken, the fluctuation in the sample temperature was relatively large, about ± 2 K; however, the measured temperature dependence of the

resistance was small. The uncertainty associated with the resistance measurements is $\pm 0.05\%$. We measured the thermoelectric power of the as-prepared sample in fields of up to 8 T at 100, 200, and 300 K. This was done by varnishing one end of the sample to the copper sample holder and a chip-resistor heater to the other end. The voltage leads were made of thin (0.002 in.) lead wires that were attached to the sample with silver paint. The contribution of the lead leads to the measured thermoelectric power was subtracted out using the recommended values for the absolute thermoelectric power of lead.¹⁵ The temperature gradient was monitored with a type-E differential thermocouple that was varnished to the sample. A temperature difference of 0.5 K was used in the measurements. The applied field was in the plane of the sample, parallel to the thermal gradient.

RESULTS

The as-prepared sample was studied by Araga, Kita, and Tasaki.¹⁴ Their work is summarized here. High angle x-ray diffraction scans showed no Fe peaks, indicating that the Fe is amorphous. Magnetization curves for the as-prepared sample did not fit to a single Langevin function, which indicates that the Fe particles vary in size. The curves could not be represented by a single function of H/T . This suggests that the Fe particles are weakly coupled. Using a mean field model with a discrete distribution of particle sizes, they have determined that the average Fe-particle moment is $220\mu_B$.

Magnetization curves taken at 6 K are shown in Fig. 1(a) for all the samples. Clearly, the initial susceptibility increases rapidly as the annealing temperature is increased. At this temperature the samples are hysteretic, but with coercive fields too small to be observable at this scale. The samples annealed at higher temperatures (210 °C and 228 °C) have a ferromagnetic contribution that can be readily observed in the 300 K magnetization curves shown in Fig. 1(b).

In order to quantify the magnetization curves, we make the simplifying assumption that the system consists of three components: a ferromagnetic cluster, smaller, and larger particles. Implicit here is the assumption that the annealing process ripens the system, producing a connected region that remains ferromagnetic at 300 K. We approximate the distri-

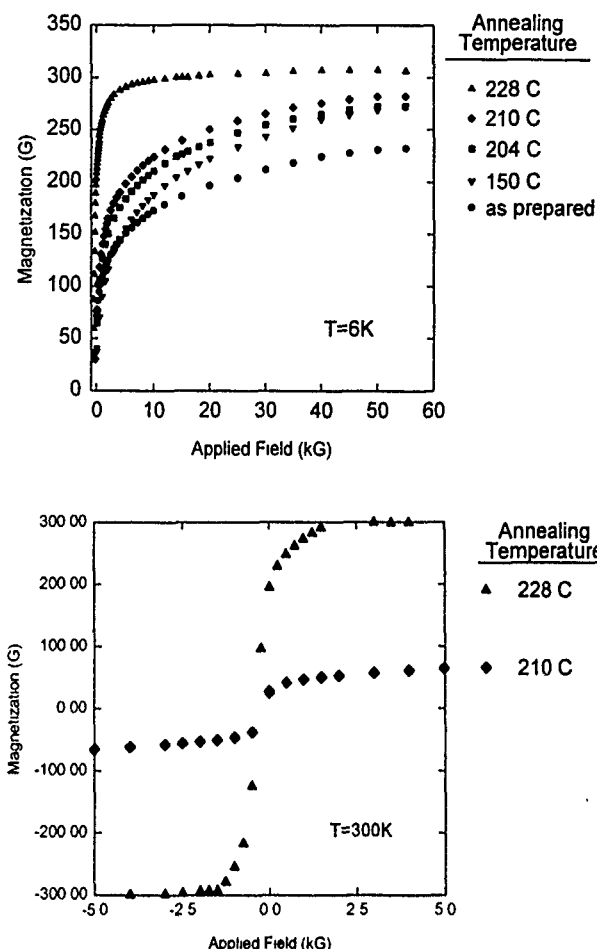


FIG. 1. (a) The 6 K magnetization curves for the Fe-Mg as-prepared sample and the samples annealed at the temperatures indicated. (b) The 300 K magnetization curves for the Fe-Mg samples annealed at 210 °C and 228 °C

bution of smaller clusters as bimodal. We can fit the data to the sum of a ferromagnetic and two Langevin contributions, for which the smaller particles have a magnetic moment of approximately $10\mu_B$, independent of annealing temperature, and the larger particles have a moment that depends on the annealing temperature. In the as-prepared sample, there is no ferromagnetic contribution, and the smaller and larger particles (whose moment is about $150\mu_B$) contribute equally to the total magnetization. As the annealing temperature is increased, the larger particles grow in size to about $250\mu_B$, their contribution to the magnetization increases, and a ferromagnetic component appears, all at the expense of the smaller-particle contribution. After annealing at 228 °C, the ripening process is apparently complete, and essentially all the Fe atoms are part of the ferromagnetic cluster.

The MR ratio, $\Delta R(H)/R_{\max} = [R(H) - R_{\max}]/R_{\max}$, at 6 K is plotted in Fig. 2 for all the samples. (Since the resistance does not saturate, we divide by the maximum resistance, which, like the magnetization, shows a slight hysteresis and occurs at fields very close to zero.) The MR and resistivity data are summarized in Table I. In all samples annealed at 210 °C or less, the resistance shows no sign of saturation in fields of less than 7 T, and the resistivities are quite high, 80–130 $\mu\Omega$ cm. In contrast, the sample annealed

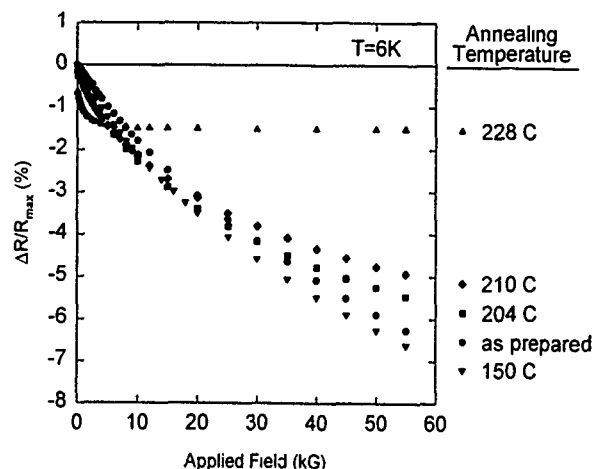


FIG. 2. The magnetoresistance ratio $\Delta R/R_{\max}$ at 6 K for the Fe-Mg granular samples annealed at the indicated temperatures.

at 228 °C saturates in a field of less than 1 T, and its resistivity is much lower, $\sim 18 \mu\Omega$ cm.

The magnetization, MR, and resistivity measurements suggest that the system ripens. In the as-prepared state, the amorphous Fe granules have a broad size distribution. Upon annealing, the small Fe particles migrate into the larger clusters, and, since the Fe concentration is above the percolation threshold, the Fe clusters may form a ferromagnetic infinite percolating cluster. The resistivity and MR drop because the infinite cluster provides a channel through which the electrons may flow, uninterrupted by strong interfacial or spin-dependent scattering.

In Fig. 3 we plot the MR ratio versus the square of the magnetization for all samples at 6 K. The MR does not depend upon the square of the magnetization, as predicted.¹² We argue that this is due to the particle size distribution.

If the electrons scatter primarily from defects in the bulk of the granules, the granules will contribute to the resistance according to their volume. In this case the MR will vary as M^2 . If, however, the electrons scatter primarily at the surface of the granules, the granules will contribute to the resistance, according to their surface area. Because the magnetization depends on the volume, the MR will not vary as M^2 in this case if the granules vary in size. This is because at low fields the larger particles magnetize easily but reduce the resistance rather feebly. As the field is increased, the smaller particles

TABLE I. A summary of the magnetoresistance and resistivity data for the Fe-Mg granular samples.

Annealing temperature (°C)	$\Delta R/R_{\max}$ (%) at $H=5.5$ T, $T=300$ K	$\Delta R/R_{\max}$ (%) at $H=5.5$ T, $T=6$ K	ρ ($\mu\Omega$ cm) $\pm 10\%$ at 300 K
As-prepared	-0.78	-6.3	130
150	-0.90	-6.6	120
204	-0.70	-5.3	86
210	-0.77	-4.9	90
228	-0.39	-1.5	18

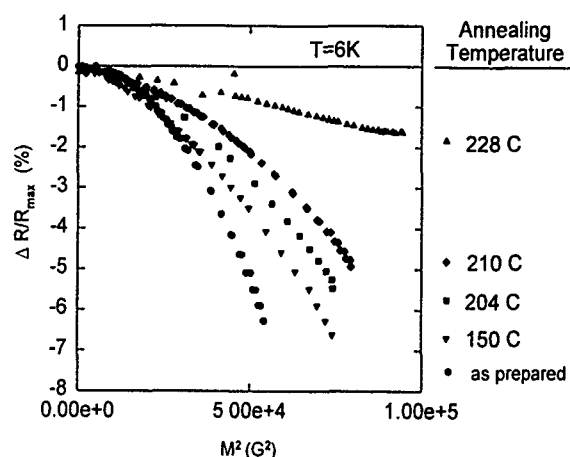


FIG. 3. The magnetoresistance ratio $\Delta R/R_{\max}$ plotted against the square of the magnetization for the Fe-Mg granular samples annealed at the indicated temperatures.

begin to align, and, because of their larger surface to volume ratio, reduce the resistance more strongly.

The zero field thermoelectric power at 300 K of the as-prepared sample was $-9.7 \mu\text{V/K} \pm 0.3 \mu\text{V/K}$. This value is below the values of both Mg ($-0.97 \mu\text{V/K}$) and Fe ($+15 \mu\text{V/K}$). We measured the MTP of the sample to determine if the TEP varied as the inverse of the resistance as has been reported in other systems.^{11,13} It has been shown that such a scaling relationship holds only when the electrons are strongly scattered into the spin-split d bands of the magnetic granules.¹³ Spin-dependent scattering alone will not produce such behavior. We measured a change in the TEP from $-9.7 \mu\text{V/K}$ in the zero field to $-10.5 \mu\text{V/K}$ in a field of 8 T, and, as predicted, the TEP varied as $1/R$. This suggests that the spin-dependent density of states of the d bands plays an important role in the magnetotransport in this system. A more complete description of the TEP measurements will be presented elsewhere.

SUMMARY

We have measured the magnetization, MR, and TEP of Fe-Mg granular samples annealed at 228 °C and below. The

magnetization data suggest that as the annealing temperature is increased, the Fe particles grow larger, and a ferromagnetic contribution emerges. The $\Delta R(H)/R_{\max}$ data does not have an M^2 dependence, as predicted by theory. We attribute this to a particle size distribution coupled with strong interfacial scattering. The as-prepared sample has a zero field thermopower of $-9.7 \mu\text{V/K}$ at 300 K. A relatively large MTP effect was measured in fields of up to 8 T, and the TEP varied as the inverse of the resistance as predicted by the spin split density of states model.

ACKNOWLEDGMENTS

We would like to thank Jing Shi for his assistance. This research was sponsored by National Science Foundation Contract No. DMR 91-21888 with facility support from the University of Illinois Materials Research Laboratory. The samples were prepared at the University of Tsukuba under partial support from the Grant-in-Aid #02254101 for Scientific Research on Primary Areas from the Japanese Ministry of Education, Science, and Culture.

- ¹W. P. Pratt, S. F. Lee, J. M. Slaughter, R. Loloce, P. A. Schroeder, and J. Bass, Phys. Rev. Lett. **66**, 3060 (1991).
- ²S. S. P. Parkin, R. Bhadra, and K. P. Roche, Phys. Rev. Lett. **66**, 2152 (1991).
- ³A. E. Berkowitz, J. R. Mitchell, M. J. Carey, A. P. Young, S. Zhang, F. E. Spada, F. T. Parker, A. Hutten, and G. Thomas, Phys. Rev. Lett. **68**, 3745 (1992).
- ⁴J. Q. Xiao, J. S. Jiang, and C. L. Chien, Phys. Rev. Lett. **68**, 3749 (1992).
- ⁵M. N. Baibich, J. M. Broto, A. Fert, F. Nguyen van Dau, F. Petroff, P. Eitenne, G. Creuzet, A. Friederich, and J. Chazelas, Phys. Rev. Lett. **61**, 2472 (1988).
- ⁶J. Inoue, and S. Maekawa, Prog. Theor. Phys. Suppl. No. 106, 187 (1991).
- ⁷P. M. Levy, S. Zhang, and A. Fert, Phys. Rev. Lett. **65**, 1643 (1990).
- ⁸R. E. Camley and J. Barnas, Phys. Rev. Lett. **63**, 664 (1989).
- ⁹B. L. Johnson and R. E. Camley, Phys. Rev. B **44**, 9997 (1991).
- ¹⁰J. Inoue, H. Itoh, and S. Maekawa, J. Phys. Soc. Jpn. **61**, 1149 (1992).
- ¹¹J. Shi, R. C. Yu, S. S. P. Parkin, and M. B. Salamon, J. Appl. Phys. **73**, 5524 (1993).
- ¹²L. Xing, Y. C. Chang, M. B. Salamon, D. M. Frenkel, J. Shi, and J. P. Lu, Phys. Rev. B **48**, 6728 (1993).
- ¹³J. Shi, E. Kita, I. Xing, and M. B. Salamon, Phys. Rev. B **48**, 16119 (1993).
- ¹⁴K. Araga, E. Kita, and A. Tasaki, preprint, 1993.
- ¹⁵R. B. Roberts, Philos. Mag. **36**, 91 (1977).

Giant magnetoresistance and induced exchange anisotropy in mechanically alloyed $\text{Co}_{30}\text{Ag}_{70}$

K. Ounadjela, A. Herr, and R. Poinot
IPCMS, 4 rue Blaise Pascal, 67070 Strasbourg, France

J. M. D. Coey and A. Fagan
Department of Physics, Trinity College, Dublin, Ireland

C. R. Staddon, D. Daniel, and J. F. Gregg
Clarendon Laboratory, University of Oxford, Oxford, OX1 3PU, United Kingdom

S. M. Thompson
Department of Physics, University of York, York, YO1 5DD, United Kingdom

K. O'Grady and S. Gieves
SEES, University College North Wales, Bangor, Gwynedd, Wales

Giant magnetoresistance of 7.7% at 5 K is observed in bulk mechanically alloyed $\text{Co}_{30}\text{Ag}_{70}$. Our recently defined $\delta(\Delta\rho/\rho)$ technique used to determine the predominant interactions within the system indicated that negative interactions dominate between the particles. Exchange anisotropy and metastable magnetization processes characterized by large Barkhausen jumps are observed at low temperatures on a small volume of the sample.

I. INTRODUCTION

The giant magnetoresistive properties exhibited by anti-ferromagnetically coupled multilayered films^{1,2} has led to extensive interest in their electrical transport and spin-dependent scattering properties—stimulated by their potential applications as magnetoresistive sensors. The different scattering probabilities of spin-up and spin-down electrons are exploited in multilayered films, in which the mean-free path of the electrons is greater than the thickness of the layers, with the result that there is no low resistance channel when the alternate magnetic layers are antiparallel. These same requirements are satisfied in granular magnetic materials,³ in which small volumes of single domain magnetic material are dispersed in a nonmagnetic matrix. Spin-dependent scattering now originates from the randomly aligned single domain regions, and is a maximum when there is the greatest degree of magnetic misalignment—usually close to the zero magnetization points on the hysteresis curve. In the as-prepared state, the material may tend to a single phase metastable alloy, however, annealing increases local fluctuations in the concentration of the magnetic species, eventually leading to phase segregation and magnetically rich clusters. The two metals used in this study are Co and Ag, in which most of the spin-dependent scattering is thought to arise from the interfacial regions between the Co and Ag, leading to a particle size dependence of magnetoresistance.⁴ The discovery that multilayered materials are not a prerequisite for giant magnetoresistance has encouraged the exploitation of different, relatively inexpensive, preparation techniques capable of producing metastable alloys of immiscible materials such as cosputtering^{3,5} and melt spinning.⁶ In this study, mechanical alloying^{7,8} has been used to produce bulk material as opposed to a thin film.

II. SAMPLE DETAILS

The starting material for the mechanical alloying consisted of a 10 g fine powder mixture of Co (99.8%, $<2\ \mu\text{m}$)

and Ag (99.9%, $2\text{--}3\ \mu\text{m}$) in a 3:7 atomic ratio. This mixture was ball milled in a Fritsch PM5 ball mill for 42 h with 170 g of 10 mm stainless steel balls. The grain size of the resulting free coarse powder was approximately $100\ \mu\text{m}$. Chemical analysis of energy-dispersive x rays in a scanning electron microscope indicated that the $\text{Co}_{30}\text{Ag}_{70}$ atomic composition was consistent on a micron scale, and that iron impurities were less than 1%. Structural analysis using x-ray diffraction showed broad diffraction peaks corresponding to those expected for small FCC cobalt particles ($a_0=0.358\ \text{nm}$) embedded in a FCC silver matrix ($a_0=0.408\ \text{nm}$), with the width of the peaks indicating particle size and strain broadening. All measurements were made on the as-prepared material without any heat treatment.

Magnetization measurements as a function of temperature were made on just a few grains of the powder in a SQUID magnetometer, on a larger volume pellet in a vibrating sample magnetometer and at room temperature using an alternating gradient force magnetometer. For magnetoresistance measurements, a pellet of 2-mm diam, 5 mm final length was made by compressing the powder under an isotatic force of two tonnes at room temperature. Magnetoresistance measurements were made in fields up to $\pm 1.4\ \text{T}$, with the current both parallel and perpendicular to the applied field by ball bonding aluminium wires onto the ends of the cylinder.

III. EXPERIMENTAL RESULTS

The magnetization loop of the pellet containing a relatively large volume of material was at all temperatures smooth, symmetric, and hysteretic, as shown at 6 K in Fig. 1. This corresponded well with the magnetoresistance, whose peak positions coincided with the coercive field. As the measurement temperature was reduced, the hysteresis in both the magnetization and magnetoresistance curves increased, with the maximum value of the latter increasing from 2.2% at room temperature to 7.7% at 5 K (Fig. 2). In complementary

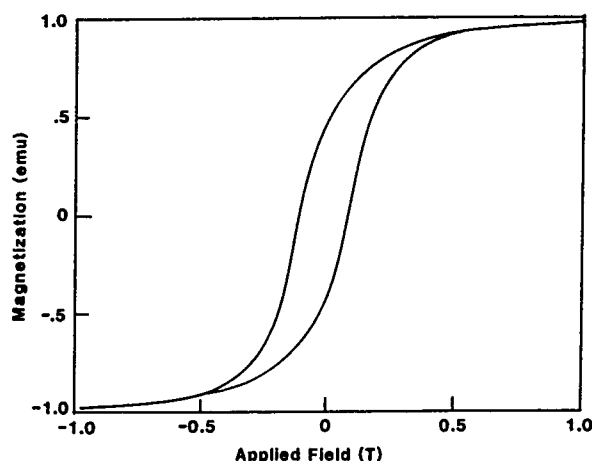


FIG. 1. Magnetization curve at $T=6$ K for a pellet of mechanically alloyed $\text{Co}_{30}\text{Ag}_{70}$.

experiments⁸ on a compressed single grain, in which the effects of compacting the powder are removed; the magnetoresistance at 5 K was found to be 9.5% compared to 7.7% in the pellet, thus indicating that the increased spin-independent scattering due to the compaction process was insignificant compared to the change in magnetoresistance. The resistance measured at 5 K immediately after cooling in the zero applied field was 0.85% higher than at any time during subsequent field sweeping. This difference is defined as $\delta(\Delta\rho/\rho)^5$ and can be correlated with the magnetic interactions within the sample.

Magnetic measurements on the SQUID magnetometer, however, gave evidence of metastable magnetization characterized by large Barkhausen jumps corresponding in some cases to nearly half the magnetization reversing in one movement. Further, the actual magnitudes and positions of the jumps were not reproducible. This is illustrated in Fig. 3, in which two magnetization curves measured in nominally identical conditions are plotted. In both cases, the sample was cooled from room temperature to 2 K in an applied field of -8 T, and then field cycled to ± 8 T. The saturation value of magnetization was 4.0 nemu, as indicated in the figure. In

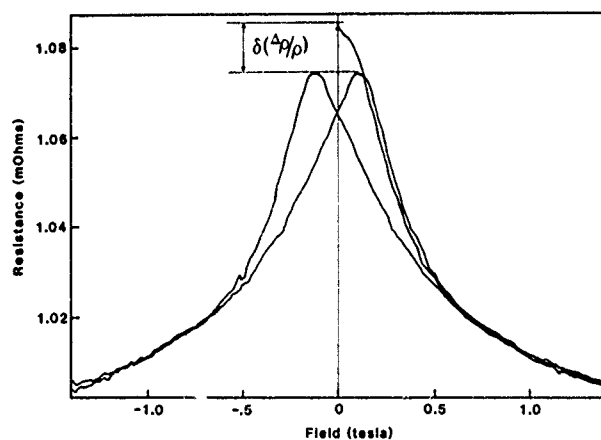


FIG. 2. Magnetoresistance of a pellet of $\text{Co}_{30}\text{Ag}_{70}$ after cooling in the zero field to $T=5$ K.

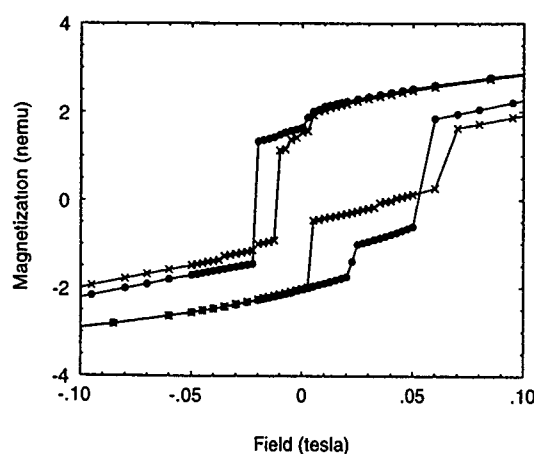


FIG. 3. Magnetization curves for a few grains of $\text{Co}_{30}\text{Ag}_{70}$ after cooling in an applied field of -8 T to $T=2$ K. The two curves were measured in nominally identical conditions.

addition to the metastability, when cooled in an applied field, the hysteresis loop was consistently asymmetric, with the loop shifted toward the direction of the field applied during cooling. This is illustrated in the sequence of Figs. 3, 4, and 5 in which the sample was cooled in -8 T, $+8$ T, and the zero field respectively. Both effects of exchange anisotropy and metastability increased as the temperature was lowered, a much reduced effect was observed at 175 K, as shown in Fig. 6, where the zero field cooled and field cooled in -8 T graphs are plotted together.

IV. DISCUSSION

The large hysteresis present in the magnetization curves of the pellet, even at room temperature, indicates that many of the particles are large enough to be blocked at room temperature. However, the remanence at 5 K is still only 30%, less than the 50% expected for a fully blocked system, indicating that there is a broad particle size distribution. The presence of giant magnetoresistance in the sample shows that in this temperature region there are active single domain

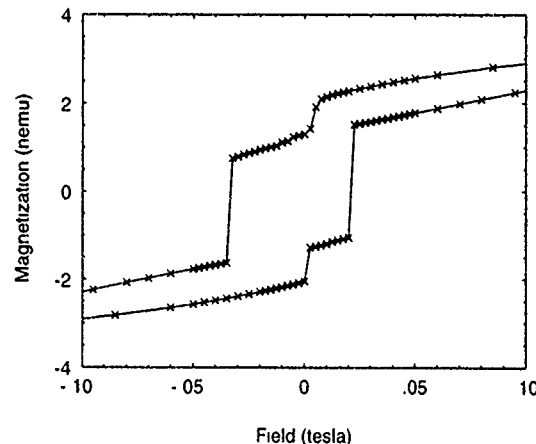


FIG. 4. Magnetization curve of a few grains of $\text{Co}_{30}\text{Ag}_{70}$ after cooling in an applied field of $+8$ T to $T=2$ K.

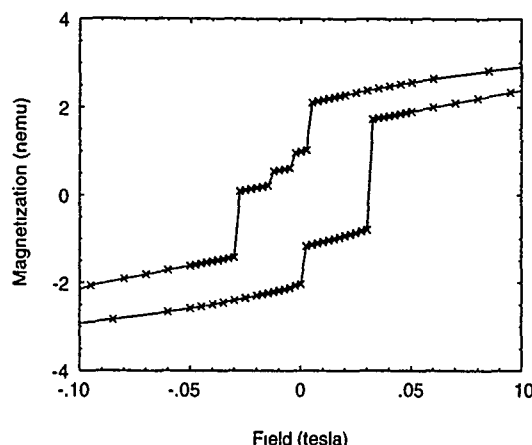


FIG. 5. Magnetization curve of a few grains of $\text{Co}_{30}\text{Ag}_{70}$ after cooling in a zero applied field to $T=2$ K.

magnetic regions of a size conducive to efficient spin-dependent scattering. The positive value of $\delta(\Delta\rho/\rho)$ indicates that negative interactions dominate within this sample.

As neither the size or position of the Barkhausen jumps is repeatable, they cannot correspond to the reversal of whole particles of Co. The situation can be compared to that of an asperomagnet, such as has been observed at extremely low temperatures in DyCu.⁹ The system experiences interactions between the particles—these may be both exchange and dipolar, leading to coupling of both signs. The particles are, however, constrained by the strong anisotropy axes of the individual particles. As the temperature is lowered, reducing their thermal energy, the effect of the anisotropy is increased. Magnetization reversal then occurs by cooperative inversion of a group of interacting particles, conserving both the an-

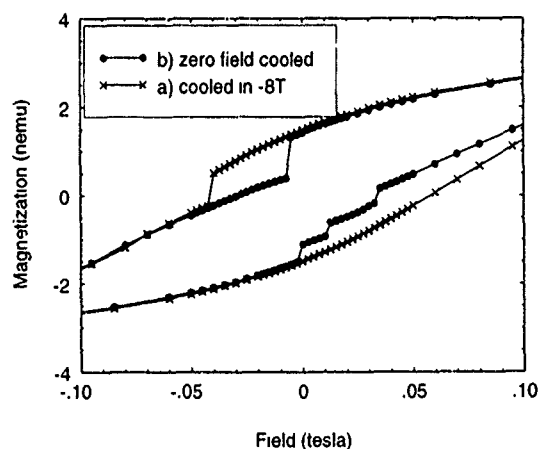


FIG. 6. Magnetization curves for a few grains of $\text{Co}_{30}\text{Ag}_{70}$ after cooling to $T=175$ K in (a) an applied field of -8 T and (b) the zero applied field.

isotropy axes and the relative orientations of the coupled particles.

The observation of exchange anisotropy suggests the presence of antiferromagnetic regions within the sample.¹⁰ It is possible that some antiferromagnetic CoO has formed at the interfacial regions between the Co and Ag x-ray photoelectron spectroscopy has indicated the presence of a small amount of oxygen in the sample. There might also be Co particles experiencing very strong antiferromagnetic coupling—consistent with the positive value of $\delta(\Delta\rho/\rho)$ observed in the large pellet.

V. CONCLUSION

This study has provided the first observation of giant magnetoresistance (7.7% at 5 K) in a bulk material prepared by mechanical alloying. Measurements on a pellet of the material indicated a broad particle size distribution and net negative interactions between the active magnetic regions. The ability to measure just a few grains of the material enabled us to observe the micromagnetic behavior of this material, which is normally averaged out in a larger sample. Both metastable magnetization processes and exchange anisotropy were observed at low temperature. The hysteresis curve was characterized by large Barkhausen jumps corresponding to cooperative reversal of a number of interacting particles, whose direction of magnetization is increasingly constrained by their anisotropy axes as the temperature was lowered.

ACKNOWLEDGMENT

The financial support of the SERC and the Royal Society is gratefully acknowledged.

- ¹ M. N. Baibich, J. M. Broto, A. Fert, F. Nguyen Van Dau, F. Petroff, P. Etienne, G. Creuzet, A. Friederich, and J. Chazelas, *Phys. Rev. Lett.* **61**, 2472 (1988).
- ² S. S. P. Parkin, N. More, and K. P. Roche, *Phys. Rev. Lett.* **64**, 2304 (1990).
- ³ J. Q. Xiao, J. S. Jiang, and C. L. Chien, *Phys. Rev. Lett.* **68**, 3749 (1992); A. E. Berkowitz, J. R. Mitchell, M. J. Carey, A. P. Young, S. Zhang, F. E. Spada, F. T. Parker, A. Hutten, and G. Thomas, *Phys. Rev. Lett.* **68**, 3745 (1992); J. A. Barnard, A. Wakis, M. Tan, E. Hafeek, M. R. Parker, and M. L. Watson, *J. Magn. Magn. Mat.* **114**, L230 (1992).
- ⁴ S. Zhang and P. M. Levey, *J. Appl. Phys.* **73**, 5315 (1993).
- ⁵ J. F. Gregg, S. M. Thompson, S. J. Dawson, K. Ounadjela, C. R. Staddon, J. Hamman, C. Fermon, G. Saux, and K. O'Grady, *Phys. Rev. B* **49**, 1064 (1994).
- ⁶ R. Ferrer, B. Barbara, B. Dieny, A. Chamberod, C. Cowache, S. Auffret, O. Redon, and J. Pierre, submitted to *Appl. Phys. Lett.*; N. Kataoka, H. Endo, K. Fukamichi, and Y. Shimada, *Jpn. J. Appl. Phys.* **32**, 1969 (1993); J. Wecker, R. von Helmholtz, L. Schultz, and K. Samwer, *Appl. Phys. Lett.* **62**, 1985 (1993).
- ⁷ S. M. Thompson, J. F. Gregg, C. R. Staddon, D. Daniel, S. J. Dawson, K. Ounadjela, J. Hamman, C. Fermon, G. Saux, K. O'Grady, and S. Grievies, *Philos. Mag.* **68**, 923 (1993).
- ⁸ J. M. D. Coey, A. J. Fagan, R. Skomski, J. Gregg, K. Ounadjela, and S. M. Thompson, *IEEE Trans. Mag. Proceedings of EMMA'93*.
- ⁹ J. M. D. Coey, T. R. McGuire, and B. Tissier, *Phys. Rev. B* **24**, 1261 (1981); B. Tissier, R. Buder, and J. M. D. Coey, *J. Magn. Magn. Mat.* **15-18**, L393 (1980).
- ¹⁰ J. S. Kouvel, *J. Phys. Chem. Solids* **24**, 795 (1963).

Correlation of x-ray diffraction and Mössbauer effect measurements with magnetic properties of heat-treated $\text{Cu}_{80}\text{Co}_{15}\text{Fe}_5$ ribbons

V. G. Harris, M. Rubinstein, B. N. Das, and N. C. Koon
U.S. Naval Research Laboratory, Washington, DC 20375

X-ray diffraction (XRD) and Mössbauer Effect (ME) measurements were performed on heat-treated $\text{Cu}_{80}\text{Co}_{15}\text{Fe}_5$ melt-spun ribbons in an attempt to understand the trends in magnetic properties with heat treatment. ME measurements indicate that the majority of Fe atoms (86%) occupy sites in ferromagnetic FCC CoFe clusters after the initial quench. A heat treatment at 900 °C acts to complete the chemical separation of Fe from the Cu matrix. The presence of Co in the Cu matrix, even after high temperature anneals, provides a paramagnetic component that prohibits saturation even at high fields.

Spurred by the recent discovery of a giant magnetoresistance (GMR) effect in granular vapor-quenched films of Cu-Co alloys,^{1,2} melt-spun ribbons of similar compositions have been investigated to determine if a GMR effect is attainable in bulk materials.^{3,4} The ribbon samples are found to display a GMR effect very near the magnitude of the vapor-quenched films. Like the films, a maximum in MR is attained after a heat treatment near 500 °C, presumably due to precipitate coarsening to a critical size and spacing. However, both bulk and film samples require high fields to saturate, a characteristic that limits their technological usefulness. In order to explore the role of structure and chemistry in the magnetic behavior of these samples, we have substituted Fe for 25% of the Co in $\text{Cu}_{80}\text{Co}_{20}$ (creating the ternary alloy: $\text{Cu}_{80}\text{Co}_{15}\text{Fe}_5$) to allow Mössbauer Effect (ME) measurements. ME investigations of dilute Fe and Co in Cu were performed by Gonser⁵ and Nasu *et al.*⁶ in the mid-1960s in pursuit of alternative Mössbauer source matrices. The results of those previous studies will be used here as a guide in understanding the ME results of this ternary alloy.

In an earlier paper³ we established the structural response and magnetoresistance properties of this alloy to heat treatment procedures. In this paper, we present new results from a more extensive x-ray diffraction analysis, including line profile modeling. These results are correlated with the Mössbauer effect measurements to explain trends in magnetic properties with heat treatments. ME measurements indicate that most ($\approx 86\%$) of the Fe atoms separate in the form of FCC CoFe particles from the Cu matrix upon the alloy's initial quench. A heat treatment at 900 °C acts to complete the chemical separation of Fe from Cu, while a significant amount of the Co remains in the Cu matrix. This dilute Co provides a paramagnetic component to the alloy's magnetization, which increases the field required to saturate the sample.

Ribbon samples having a composition of $\text{Cu}_{80}\text{Co}_{15}\text{Fe}_5$ were fabricated via a traditional melt-spinning technique, where the molten alloy is ejected through a small orifice onto a rotating Cu wheel. Additional details of the melt-spinning operation are presented in Ref. 3. The as-spun ribbons are approximately 2 mm in width, 20 μm thick, and up to several meters long. They are reflective on both the free standing side and the Cu wheel side, with small pinholes visible to the unassisted eye. Several lengths of the melt-spun ribbon were annealed at temperatures ranging from 200 °C–900 °C for 15 min under flowing H_2 gas.

X-ray diffraction measurements were performed on all samples using a θ - 2θ diffractometer equipped with a $\text{Cu}_{K\alpha}$ rotating anode source operating at 10 kW. Preliminary XRD results have been presented in Ref. 3. Here we present a more detailed analysis of the diffraction patterns, where all diffraction features are identified and indexed, and lattice parameters for each phase are calculated by plotting against the Nelson-Riley function.⁷ The area under the (111) FCC diffraction peaks and the (110) BCC diffraction peak (when available) were calculated by least-squares fitting of Lorentzian curves. These areas were converted to volume fractions by applying the appropriate corrections for a structure factor and diffraction geometry.⁸

⁵⁷Fe Mössbauer Effect (ME) measurements were made on all samples at room temperature in the transmission mode. Because these samples were not enriched in ⁵⁷Fe, multiple lengths of ribbon were overlaid to enhance the signal. The resulting ME spectra were analyzed by least-squares fitting of multiple Lorentzian curves. For most samples the ME profile consists of a well-defined sextet and a central broad line. The sextet is associated with a high-spin magnetic site common to ferromagnetic α -Fe and the central resonance line was established by Gonser⁵ to arise from paramagnetic Fe; that is, from dilute Fe atoms having 12 Cu near neighbors. Quadrupole splitting of the central resonance line from the presence of Fe-Fe dimers, trimers, and clusters are not resolved in our data, which are limited by the signal to noise ratio. The ratio of the area under the sextet to the central line provides a measure of the fraction of Fe atoms occupying magnetic sites to those occupying paramagnetic sites.

Figure 1 is a plot of the (111) diffraction peak for the as-spun $\text{Cu}_{80}\text{Co}_{15}\text{Fe}_5$ ribbon sample and those heat treated at 400 °C, 500 °C, 650 °C, and 800 °C. The solid curves in this figure represent fits to the data using four Lorentzian curves: two curves for each phases' α_1 and α_2 peaks. To simplify the modeling procedure the parameters used to fit the α_2 peaks were defined in terms of the α_1 position and amplitude using theoretical relationships. A summary of the fitting analysis is presented in Table I. X-ray diffraction measurements of the as-spun sample illustrate a family of FCC diffraction lines having a lattice parameter of 3.6104 Å. The smaller diffraction feature, appearing near $2\theta = 43.7^\circ$, corresponding with the (111) diffraction peak of a precipitate FCC phase having a lattice parameter of 3.5848 Å. Approximately 11.6 vol % of the as-spun sample exists in this precipitate phase. The ME

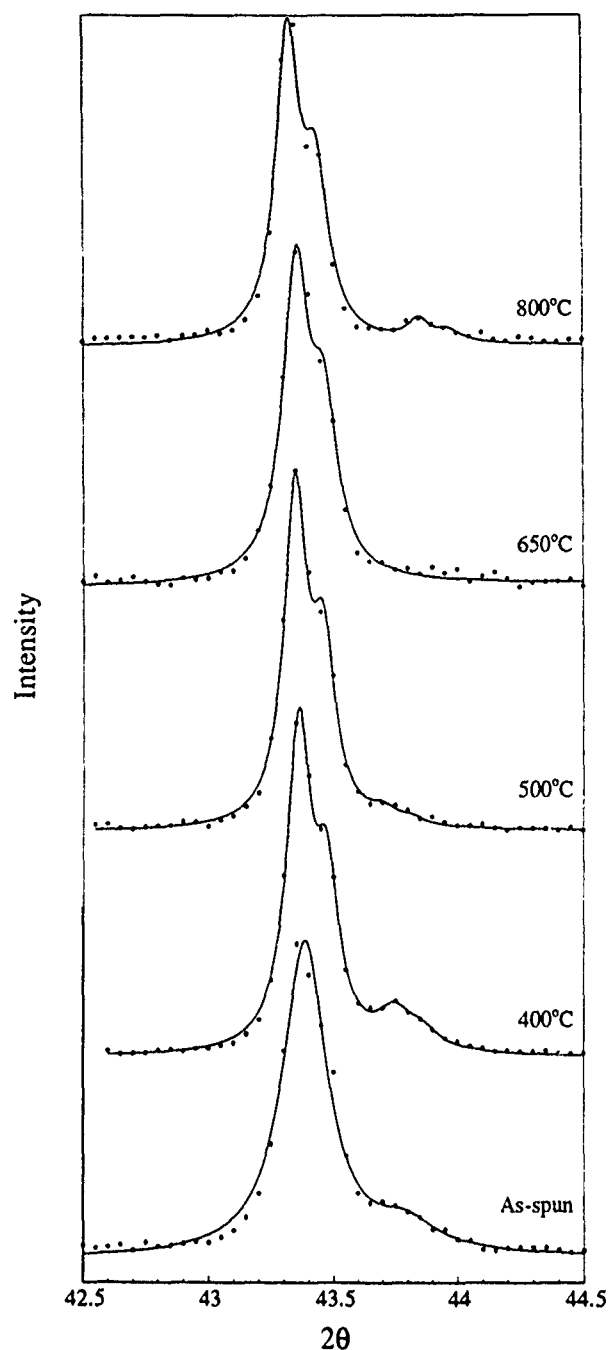


FIG. 1. X-ray diffraction data for the range $42.5^\circ \leq 2\theta \leq 44.5^\circ$ for as-spun and heat-treated $\text{Cu}_{80}\text{Co}_{15}\text{Fe}_5$ ribbon samples. Annealing temperatures are listed in the figure. The large central peak at $2\theta=43.4^\circ$ is the (111) diffraction peak of the FCC Cu-rich phase. The solid curve represents the least-squares fit to the experimental data using Lorentzian curves. A summary of the fitting results is presented in Table I.

spectrum for this sample and samples annealed at 200 °C, 500 °C, and 900 °C are presented in Fig. 2. The spectrum for the as-spun sample illustrates a well-resolved sextet with a broad central resonance line. Modeling measurements indicate that 86% of the Fe atoms occupy magnetic sites, likely within the FCC CoFe precipitate phase. The phase separation in the alloy may have occurred either during the quenching process or prior to quenching when the alloy existed in the liquid phase. This is not unexpected, because the solubility of both Fe and Co in Cu is well below a percent under equilibrium conditions and a few percent at 500 °C.⁹

TABLE I. Summary of x-ray diffraction analysis of as-spun and heat-treated ribbons. Notes: FCC': Cu-rich phase, FCC'': Co-rich phase; and BCC: CoFe-rich phase.

T_{ann}	(111)FCC'	(111)FCC''	(110)BCC
As-spun			
vol. %	88.4	11.6	∞
a_0 (Å)	3.6104 ± 0.0025	3.5848 ± 0.0017	
200 °C			
vol. %	87.6	12.4	∞
a_0 (Å)	3.6112 ± 0.0015	3.5845 ± 0.0041	
300 °C			
vol. %	86.2	13.8	∞
a_0 (Å)	$3.61130.0010$	3.5830 ± 0.0014	
400 °C			
vol. %	85.5	14.5	∞
a_0 (Å)	3.6103 ± 0.0009	3.5833 ± 0.0012	
500 °C			
vol. %	70.9	3.7	25.4
a_0 (Å)	3.6103 ± 0.0001	3.5819 ± 0.0028	2.8347 ± 0.0045
650 °C			
vol. %	preferential alignment of FCC crystals		
a_0 (Å)	3.6141 ± 0.0002	∞	2.8413 ± 0.0005
800 °C			
vol. %	preferential alignment of FCC crystals		
a_0 (Å)	3.6143 ± 0.0003	3.5743 ± 0.0002	2.8425 ± 0.0005

Heat treatments at temperatures ranging from 200 °C–400 °C serve to (i) increase the amount of the secondary FCC phase from 11.8% to 14.5%; (ii) increase the lattice parameter of the Cu-rich phase toward the FCC Cu value; (iii) decrease the lattice parameter of the CoFe-rich FCC phase; and (iv) increase the size of the CoFe particles, as evidenced from the sharpening of the (111) diffraction peak at $2\theta=43.7^\circ$ in Fig. 1. A BCC phase forms in the alloy after an anneal at 500 °C. Dark field TEM analysis of this sample illustrates uniformly dispersed spherical particles, ranging in size from less than 100 Å up to 250 Å in diameter, with a mean size of ≈ 150 Å. The diffraction peaks from the precipitate FCC CoFe phase are significantly reduced as a result of this heat treatment, suggesting that the precipitate FCC phase has transformed to a BCC structure. Inspection of the CoFe equilibrium phase diagram indicates that a BCC CoFe phase is stable over a composition range of $\text{Fe}_x\text{Co}_{1-x}$, where $0 \leq x \leq 0.725$. ME measurements indicate that approximately 10% of the Fe atoms remain in the Cu matrix in this sample. An anneal at 650 °C completes the transition from CoFe FCC to CoFe BCC as the FCC peak at $2\theta=43.7^\circ$ is seen in Fig. 1 to completely disappear. In this sample the lattice parameter of the Cu-rich FCC phase is very nearly equal to FCC Cu and the lattice parameter of the CoFe BCC phase is equal to 2.841 Å, the value reported to correspond with the $\text{Co}_{72.5}\text{Fe}_{27.5}$ alloy.⁹

Heat treatments at temperatures ≥ 650 °C facilitate the formation of another FCC phase, having a lattice parameter of 3.574 Å. In Fig. 1, the (111) peak of this phase appears at $2\theta=43.85^\circ$. The BCC CoFe phase that formed in samples annealed at 500 °C and 650 °C has undergone a BCC \rightarrow BCC + FCC phase transition. This transition is inconsistent with the CoFe binary phase diagram, which indicates that a binary alloy of $\text{Co}_{75}\text{Fe}_{25}$ quenched from 800 °C should consist of a

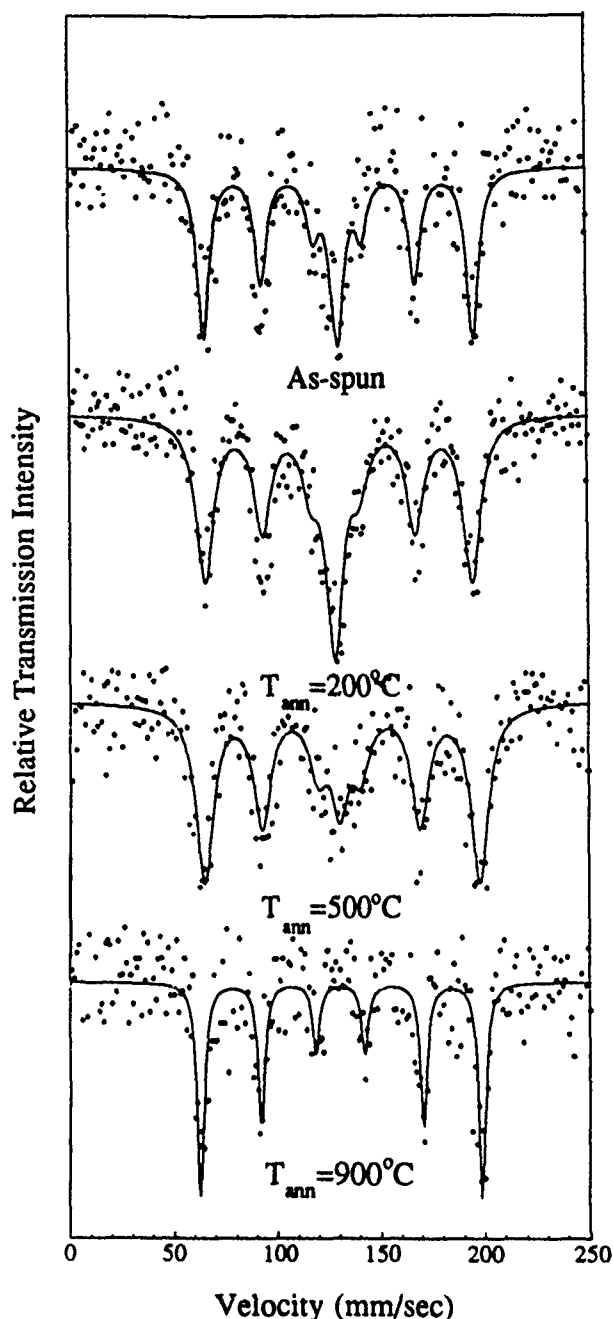


FIG 2. Mossbauer effect spectra for as-spun and heat-treated $\text{Cu}_{80}\text{Co}_{15}\text{Fe}_5$ ribbon samples. The solid curve represents the least-squares fits to the experimental data using Lorentzian curves.

mixed phase of 70% BCC $\text{Co}_{72.5}\text{Fe}_{27.5}$ ($a_0 = 2.8410 \text{ \AA}$) and 30% HCP $\text{Co}_{81}\text{Fe}_{19}$.⁹ The presence of a small amount of Cu in the precipitate may have stabilized the FCC structure in favor of the HCP structure. Because the alloy experiences a slight preferential alignment of close-packed crystallites, we are unable to accurately measure the volume fraction of these phases in samples annealed at temperatures $\geq 650^\circ\text{C}$. The ME spectrum of a sample annealed at 900°C shows that the central line has been eliminated, indicating that 100% of the Fe atoms occupy magnetic sites, signaling the complete chemical segregation of Fe atoms to high spin magnetic sites.

These $\text{Cu}_{80}\text{Co}_{15}\text{Fe}_5$ ribbons, similar to the vapor-

quenched Cu-Co films, experience a maximum MR effect after a 15 min anneal near 500°C , presumably due to precipitate coarsening to a critical size and spacing. The magnitude of the MR for these samples³ is comparable to values reported for Cu-Co films.^{1,2} Measured values decrease rapidly in samples annealed at higher temperatures.

The decrease in MR after heat treatments at temperatures $\geq 650^\circ\text{C}$ can be attributed to two mechanisms. The first involves particle clustering which we have observed directly via dark field TEM analysis of annealed samples.³ The clustering of magnetic particles will act to reduce the spin-dependent scattering by reducing the interfaces between magnetic and nonmagnetic regions. The second mechanism is associated with the structural transition of the magnetic precipitate from FCC to BCC over the annealing range of 500°C – 650°C . The BCC particles, being incoherent in the FCC matrix, will act to increase the spin-independent scattering component of the MR, because of the large strain fields that exist at the particle/matrix interface. It remains unclear as to which mechanism is dominant in reducing the MR in these samples.

SQUID magnetometry measurements performed on samples at room temperature show them how to saturate at a field strength near 8–10 kOe. However, at 4.2 K the magnetization curves have a slight positive slope over the saturation region, and do not saturate at fields up to 6 T, the limit of the SQUID magnetometer used here. This high field positive slope is evidence of a paramagnetic component to the sample's magnetization, and is present in all samples, including the sample annealed at 900°C . ME measurements indicate that 100% of Fe atoms segregate to high spin magnetic sites after a heat treatment at 900°C . In order to account for the paramagnetic signal, some of the Co must either remain in the Cu matrix or rediffuse during high temperature anneals and subsequent quenching operations. Energy dispersive x-ray spectroscopy performed during scanning electron microscopy indicates that a significant amount of Co, with very little Fe, remains in the Cu grains after high-temperature anneals.⁹ The Cu-Co equilibrium phase diagram indicates that $\approx 5 \text{ at. \%}$ of Co can be stabilized in the Cu matrix upon quenching from 800°C .

¹A. E. Berkowitz, J. R. Mitchell, M. J. Carey, A. P. Young, S. Zhang, F. E. Spada, F. T. Parker, A. Hutton, and G. Thomas, *Phys. Rev. Lett.* **68**, 3745 (1992).

²J. Q. Xiao, J. S. Jiang, and C. L. Chien, *Phys. Rev. Lett.* **68**, 3749 (1992).

³M. Rubinstein, B. N. Das, and N. C. Koon (these proceedings); also presented at MMM '92, Houston, TX, Nov. 1992; also see V. G. Harris, B. N. Das, M. Rubinstein, J. L. Goldberg, W. T. Elam, and N. C. Koon, *IEEE Trans. Magn.* **26**, 2664 (1993).

⁴B. Dieny *et al.*, *J. Magn. Magn. Mater.* (in press).

⁵U. Gonser, *Z. Metallkd.* **57**, 85 (1966), and references within.

⁶S. Nasu, Y. Murakami, and T. Shinjo, *Scr. Metall.* **2**, 648 (1968).

⁷J. B. Nelson and D. P. Riley, *Proc. Phys. Soc.* **57**, 160 (1945).

⁸*International Tables for x-ray Crystallography, Vol. III: Physical and Chemical Tables* (Kynoch, Birmingham, England, 1968).

⁹For Cu-Co and Co-Fe phase diagrams, see T. Nishizawa and K. Ishida, *Bull. Alloy Phase Diag.* **5**, 250 (1984); and T. Nishizawa and K. Ishida, *Bull. Alloy Phase Diag.* **5**, 758 (1984); for the Cu-Fe phase diagram, see M. Hansen and K. Anderko, *Constitution of Binary Alloys* (McGraw-Hill, New York, 1958).

¹⁰B. N. Das *et al.* (to be published).

Giant magnetoresistance in $\text{Ag}_{1-x}\text{Ni}_x\text{-yFe}_y$ heterogeneous alloy films

M. L. Watson

Centre for Data Storage Materials, Coventry University, Priory Street, Coventry CV1 5FB, United Kingdom

V. G. Lewis and K. O'Grady

Magnetic Materials Research Group, SEECs, University of Wales, Bangor, Gwynedd LL57 1UT, United Kingdom

We have investigated the effects of phase segregation and compositional variation on the giant magnetoresistance (GMR) observed in heterogeneous AgNiFe alloy films. The films were sputtered from a mosaic Ag/NiFe/Fe target onto glass substrates at the system ambient temperature. They had a thickness of 200–300 nm, and were rapidly thermally annealed (RTA) under vacuum in order to promote phase segregation. By altering the amount of Fe in the target mosaic, the Ni:Fe ratio was systematically varied from 80:20 to 34:66 atomic percent. The Ag concentration for all films was fixed at 78 ± 5 atomic percent. The GMR was maximized using a RTA temperature of 650 °C. Annealing at higher temperatures decreased the saturation field of the GMR, but also lowered its size. Changing the film composition had little effect on the saturation field of the GMR, but for both as-deposited and optimally annealed samples the magnetoresistance was found to decrease as the Ni concentration decreased.

INTRODUCTION

The recent discovery of giant magnetoresistance (GMR) effects in heterogeneous alloys has greatly stimulated interest in such materials. This is based in part on the possibility of their use in magnetoresistive heads, magnetometry, or as sensors. The effect has been observed in cosputtered thin films of Co–Cu,¹ Co–Ag,² Fe–Ag,³ NiFe–Ag,⁴ Co–Au,⁵ Ag–Co–Ni,⁶ and Co–Fe–Ag,⁷ in melt spun ribbons of Co–Cu⁸ and mechanically alloyed Co–Ag.⁹ It is assumed to originate from the spin-dependent scattering of electrons, either within or at the interfaces of phase segregated magnetic particles embedded in a nonmagnetic matrix.¹⁰ When the moments of the particles are randomly oriented, the resistivity is higher than when the moments are aligned by the application of an external magnetic field. Although potential use of these materials in magnetic recording may be possible, it has recently been shown to be greatly limited by both the size and anisotropy of the magnetic particles.¹¹

In order to investigate the effect of varying both the size and anisotropy of the magnetic particles on the GMR, we have deposited Ag–Ni–Fe films, having a fixed Ag concentration and varying Fe and Ni concentrations. In bulk Ni–Fe alloys, such variations result in the K_1 value of the alloy changing sign,¹² and for Ni concentrations $>31\%$ and the magnetization increasing with Fe concentration.¹³

EXPERIMENTAL METHOD

Ag–Ni–Fe films of thickness 200–300 nm were RF sputtered onto glass microscope slides at the system ambient temperature using a Nordico 2000 sputtering system. The target consisted of a 4 in. Ag (99.999%) disk, onto which $\text{Ni}_{80}\text{Fe}_{20}$ and Fe 0.25 cm² squares were placed in a mosaic pattern. The base pressure was $<2 \times 10^{-7}$ Torr, the sputtering pressure was 8 mTorr of argon and the sputtering power was 300 W. At this power the deposition rate was found to be ≈ 3 nm/s, depending on the target mosaic composition, and the deposition times were fixed at 1 min. The film thicknesses

were measured using a Tolansky multiple beam interferometer and the composition determined using EDAX on a Philips electron microscope. As the sputtering rate from $\text{Ni}_{80}\text{Fe}_{20}$ and Fe are very similar the film composition could be controlled by adding or removing squares of either of the two magnetic materials. In all cases the Ag content of the films was fixed at 78 ± 5 atomic percent.

To promote post deposition phase segregation and magnetic particle growth, strips ≈ 7 mm wide diced from the substrate were rapidly thermally annealed (RTA) under vacuum. The system uses two 6 in. 2 kW halogen bulbs which, produce a power density at the substrate of ≈ 80 W/cm². The bulb illumination is controlled by a signal generator and the temperature of the strips is measured using a thermocouple mounted directly onto the sample holder. Three maximum annealing temperatures were investigated: 600, 650, and 750 °C, and these were reached in ≈ 20 s, 2 min, and 3 min, respectively. Due to the walls of the annealing chamber being radiatively heated during the annealing process, the cooling times for the maximum annealing temperature varied for each of the temperatures used. Thus the sample temperature fell to <200 °C in 1.5 min and 6.5 min for the samples heated to a maximum temperature of 600 and 650 °C, respectively, and to <250 °C in 6 min for the sample heated to a maximum temperature of 750 °C.

The resistivity and magnetoresistance of the films were measured at room temperature using a computer controlled four point probe system based on a Keithley 196 digital voltmeter. The maximum field that could be applied was ≈ 9 kG, and thus the magnetoresistance is underestimated due to it not being fully saturated. Hysteresis loops of the films were measured at room temperature in fields up to 40 kG using an Oxford Instruments VSM and in fields up to 8 kG using a VSM constructed at the Centre for Data Storage Materials at Coventry University. The as-deposited samples were investigated by XRD using a Philips XRD system.

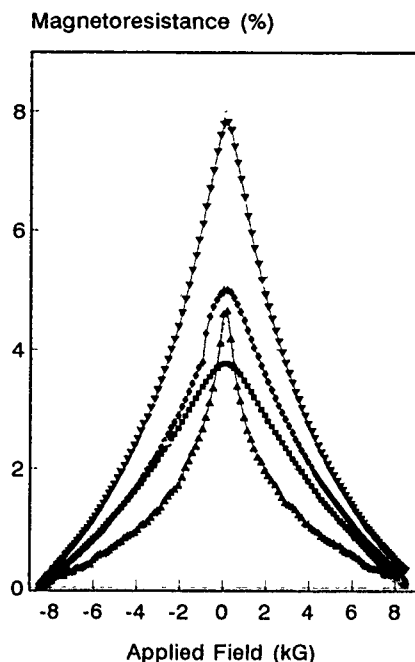


FIG. 1. Plot of the magnetoresistance of a film of composition $\text{Ag}_{72.8}\text{Fe}_{5.5}\text{Ni}_{21.7}$ for four different rapid thermal annealing temperatures. ■, as-deposited; ♦, annealed at 600 °C; ▲, annealed at 650 °C; and ▼, annealed at 750 °C.

RESULTS

It was found that for all film compositions the annealing temperature of 650 °C produced the largest GMR (calculated using $[R(H_0) - R(H_{\text{max}})]/R(H_{\text{max}})$). This is illustrated in Fig. 1, which shows the effect of annealing a film having the composition $\text{Ag}_{72.8}\text{Fe}_{5.5}\text{Ni}_{21.7}$ atomic percent. Such behavior has previously been attributed to the formation of ferromagnetic particles in the heterogeneous film. These grow to an optimum size, dependent on the electron mean-free path, after which any increase in size results in a decrease in the GMR due to the decrease in particle surface to volume ratio.¹⁴ Although the largest GMR was found for an annealing temperature of 650 °C, a more extensive study of the effect of annealing this type of material would be required to identify the optimum annealing cycle.

Annealing at the lower temperature (600 °C) was found to increase the film resistivity by $\approx 5\%$ – 10% . However, the magnetoresistance of most films was unaffected by their being annealed at this temperature. It is postulated that the increase in resistivity observed is due to increased phase segregation of the alloy materials, leading to an increase in film disorder, but without well-defined ferromagnetic particles being formed. When the films were annealed at a higher temperature (650 °C) their resistivity decreased (from typically 30–40 $\mu\text{Ohm cm}$ to 10–15 $\mu\text{Ohm cm}$), and magnetoresistance increased markedly. This is consistent with an increase in both grain and magnetic particle size. Annealing at a still higher temperature (750 °C) lowered the saturation field of the magnetoresistance, but also decreased its size.

The effect of annealing at the highest temperature investigated (750 °C) on the hysteresis of the films is shown in Figs. 2 and 3. These figures show hysteresis loops for

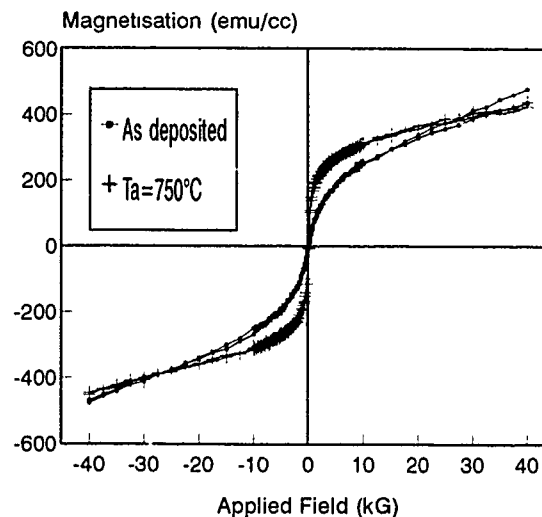


FIG. 2. Hysteresis loop of a film having the composition $\text{Ag}_{72.8}\text{Fe}_{5.5}\text{Ni}_{21.7}$ as-deposited and annealed at a maximum temperature of 750 °C.

samples having the composition $\text{Ag}_{72.8}\text{Fe}_{5.5}\text{Ni}_{21.7}$ atomic percent (Fig. 2) and $\text{Ag}_{75.98}\text{Fe}_{7.32}\text{Ni}_{16.40}$ atomic percent (Fig. 3). Note that no attempt has been made to correct this data for the diamagnetism of the Ag matrix or the substrate. As can be seen from these figures, the approach to saturation is much more rapid in the annealed samples. This is consistent with an increase in the size of the magnetic particles on annealing, rather than thermodynamically driven dilution.

Figure 4 shows the GMR of both the as-deposited and annealed at 650 °C samples in maximum applied fields of 6.4 kG. As can be seen from the figure, the GMR of the annealed samples is reduced as the Ni:Fe ratio in the film is decreased below 0.4. A similar decrease was also found for the samples annealed at a maximum temperature of 750 °C. Although the possibility exists that this decrease is related to the formation of Ni/Fe particles having the Invar composition and therefore greatly reduced magnetizations, it was not possible to obtain any corroborating structural information using the XRD sys-

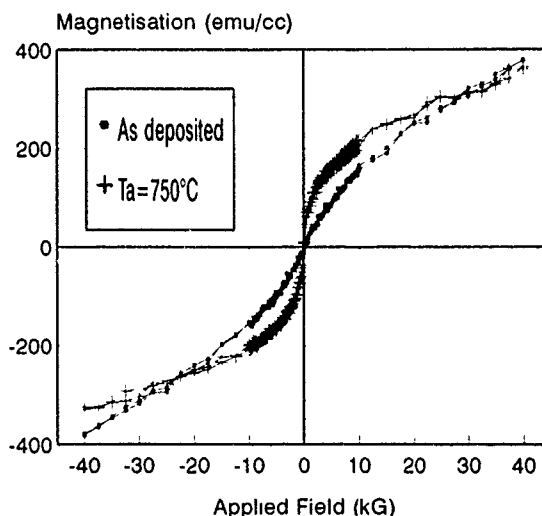


FIG. 3. Hysteresis loop of a film having the composition $\text{Ag}_{75.98}\text{Fe}_{7.32}\text{Ni}_{16.40}$ as-deposited and annealed at a maximum temperature of 750 °C.

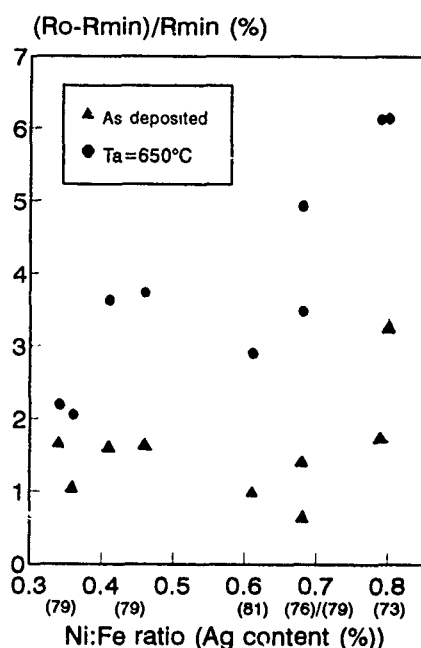


FIG. 4. Graph of the magnetoresistance of the as-deposited and annealed at 650 °C samples, plotted as a function of the Ni:Fe ratio. Note the magnetoresistance has been calculated using $[R(H_0) - R(H_{max})/R(H_{max})]$, and that the maximum applied field was 6 kG.

tem available. However, the GMR of the as-deposited films (which were investigated using XRD and found to be metastable AgNiFe alloys) is little changed as the Ni concentration is reduced. Additionally, the decrease observed may be related to small changes in the Ag(Ni/Fe) ratio. Despite the change in the Ni:Fe ratio, the saturation field of the GMR was found to be broadly constant, for a given annealing temperature, for all film compositions.

The film resistivity as a function of composition is shown in Fig. 5 for each annealing temperature. As can be seen in this figure, the resistivity of the samples annealed at an elevated temperature (650 °C and 750 °C) is broadly constant as a function of the Ni:Fe ratio. However, the resistivities of the as-deposited and annealed at 650 °C samples exhibit a shallow minima for the Ni:Fe ratios of ≈ 0.60 . It is possible that this difference in behavior reflects differences in the spin-independent electron scattering processes, occurring in the two groups of films. In the former case the ferromagnetic atoms have formed particles, while in the later case well-dispersed magnetic atoms are present.

CONCLUSIONS

Little effect of changing the composition of the ferromagnetic particles formed by phase segregation on the GMR saturation field was observed. It is postulated that this is due to shape and/or stress anisotropy dominating the magnetization process. The size of the GMR was found to depend on the film composition, decreasing with increased Fe concentration. It is postulated that this is related to changes in the magnetic particles' magnetization, resulting from the varia-

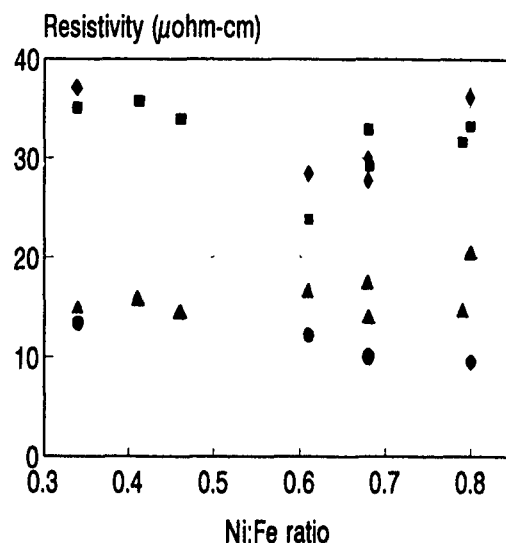


FIG. 5. Graph of the as-deposited and annealed samples resistivity plotted against their Ni:Fe ratio. ■, as-deposited; ♦, annealed at 600 °C; ▲, annealed at 650 °C; and ●, annealed at 750 °C.

tion in their Ni:Fe concentration ratios, altering the spin-dependent scattering of electrons by these particles.

ACKNOWLEDGMENT

Acknowledgment is made of the benefit gained from the comments made by the referee of this paper in its final preparation.

- ¹A. E. Berkowitz, J. R. Mitchell, M. J. Carey, A. P. Young, S. Zhang, F. E. Spada, F. T. Parker, H. Hutten, and G. Thomas, *Phys. Rev. Lett.* **68**, 3745 (1992); J. Q. Xiao, J. S. Jiang, and C. L. Chien, *ibid.*, 3749 (1992).
- ²J. A. Barnard, A. Wakis, M. Tan, E. Haftek, M. R. Parker, and M. L. Watson *J. Magn. Magn. Mat.* **114**, L230 (1992); M. J. Carey, A. P. Young, A. Starr, D. Rao, and A. E. Berkowitz, *Appl. Phys. Lett.* **61**, 2935 (1992); P. Xiong, G. Xiao, J. Q. Wang, J. Q. Xiao, J. S. Jiang, and C. L. Chien, *Phys. Rev. Lett.* **69**, 3220 (1992); A. Tsoukatos, H. Wan, G. C. Hadjipanayis, and Z. G. Li, *Appl. Phys. Lett.* **61**, 3059 (1992).
- ³A. Tsoukatos, H. Wan, G. C. Hadjipanayis, K. M. Unruh, and Z. G. Li, *J. Appl. Phys.* **73**, 5509 (1993); G. Xiao, J. Q. Wang, and P. Xiong, *Appl. Phys. Lett.* **62**, 420 (1993).
- ⁴J. S. Jiang, J. Q. Xiao, and C. L. Chien, *Appl. Phys. Lett.* **61**, 2362 (1992); M. L. Watson, J. A. Barnard, S. Hossain, and M. R. Parker, *J. Appl. Phys.* **73**, 5506 (1993); B. Dieny, S. R. Teixeira, B. Rodmacq, C. Cowache, S. Auffret, O. Redon, and J. Pierre (unpublished).
- ⁵J. A. Barnard, M. R. Parker, D. Seale, and G. Yang, *IEEE Trans. Mag. MAG-29*, 2711 (1994).
- ⁶M. Kitada, K. Yamamoto, and N. Shimizu, *J. Magn. Magn. Mat.* **124**, 243 (1993).
- ⁷B. Dieny, A. Chamberod, J. B. Genin, B. Rodmacq, S. R. Teixeira, S. Auffret, P. Gerard, O. Redon, J. Pierre, R. Ferrer, and B. Barbara (unpublished).
- ⁸J. Wecker, R. von Helmolt, L. Schultz, and K. Samwer, *Appl. Phys. Lett.* **62**, 1985 (1993).
- ⁹S. M. Thompson, J. F. Gregg, C. R. Staddon, D. Daniel, S. J. Dawson, K. Ounadjela, J. Hamman, C. Fermon, G. Saux, K. O'Grady, J. M. D. Coey, and A. Fagan, *Philos. Mag.* **68**, 923 (1994).
- ¹⁰S. Zhang, *Appl. Phys. Lett.* **61**, 1855 (1992).
- ¹¹T. L. Hylton, *Appl. Phys. Lett.* **62**, 2431 (1993).
- ¹²J. D. Kleis, *Phys. Rev.* **50**, 1178 (1936).
- ¹³J. Crangle and G. C. Hallam, *Proc. R. Soc. London Ser. A* **272**, 119 (1963).
- ¹⁴J.-Q. Wang, P. Xiong, and G. Xiao, *Phys. Rev. B* **47**, 8341 (1993).

Giant and anisotropic magnetoresistance in single layer $\text{Ni}_{66}\text{Fe}_{16}\text{Co}_{18}\text{-Ag}$ films

A. Wakis, J. A. Barnard, and M. R. Parker^{a)}

The Center for Materials for Information Technology and Department of Metallurgical and Materials Engineering, The University of Alabama, Tuscaloosa, Alabama 35487-0202

Single layer $\text{Ni}_{66}\text{Fe}_{16}\text{Co}_{18}\text{-Ag}$ thin films were made by cosputtering from a composite $\text{Ni}_{66}\text{Fe}_{16}\text{Co}_{18}\text{-Ag}$ target. At the silver rich end of the composition range ($\approx 57\%$ – 80 at. % Ag) we have found “giant” magnetoresistance (a maximum of $\approx 9\%$ at room temperature at ≈ 72 at. % Ag after annealing at 300°C for $\frac{1}{2}$ h), while in the midcomposition range ($\approx 42\%$ – ≈ 57 at. % Ag), we have observed anisotropic magnetoresistance.

I. INTRODUCTION

In the last two years, remarkably large room temperature GMR ratios have been observed in a variety of single layer film systems,^{1–4} prepared by codeposition of a ferromagnet and nonmagnet, which strongly phase separate at equilibrium. Single layer “granular” GMR appears to be restricted to alloy systems which exhibit extremely small mutual solubilities. Ni, Fe, and Co are all essentially immiscible in Ag. $\text{Ni}_{66}\text{Fe}_{16}\text{Co}_{18}$ is a zero magnetostriction and near zero magnetocrystalline anisotropy material.^{5,6} In multilayer geometries this alloy has yielded promisingly field-sensitive GMR.⁷

In this study, $\text{Ni}_{66}\text{Fe}_{16}\text{Co}_{18}\text{-Ag}$ single layer films were made over a broad composition range ($\approx 42\%$ – 80 at. % Ag). Ag-rich samples (≥ 57 at. % Ag) exhibit familiar granular GMR behavior. Samples in the midcomposition range (from $\approx 42\%$ – ≈ 57 at. % Ag) exhibit classical AMR. A maximum GMR of $\approx 9\%$ at room temperature at ≈ 72 at. % Ag has been found after annealing at 300°C for $\frac{1}{2}$ h. The magnitude of AMR observed is of the order of 1%.

II. EXPERIMENTAL METHODS AND MATERIALS

A series of $(\text{Ni}_{66}\text{Fe}_{16}\text{Co}_{18})_{100-x}\text{Ag}_x$ (x varying between ≈ 42 at. % and 80 at. %) films were grown on 7059 Corning glass substrates (2 in. \times 1 in.) from a 4 in. split target using different sputtering conditions ($p_{\text{Ar}} \approx 5, 10$, and 15 mTorr; power = 100 W and 200 W). The background pressure was 5×10^{-7} Torr. A good combination of high GMR at the silver-rich end of the composition spectrum and sharp AMR peaks at the midcomposition range of the spectrum were found for $p_{\text{Ar}} = 15$ mTorr and 100 W; that set of films is discussed in this paper. The films were characterized for their magnetic properties and structure. The characterization techniques used are explained elsewhere.² They were then subjected to a series of annealing treatments (first and second anneals were carried out each at 300°C for $\frac{1}{2}$ h, while a third anneal was carried out for samples exhibiting AMR at 400°C for $\frac{1}{2}$ h) in a high vacuum annealing chamber.

III. EXPERIMENTAL RESULTS AND DISCUSSION

A. Results on films exhibiting GMR

Figure 1 shows the plot of magnetoresistance (MR) versus composition (at. % Ag) for both as-deposited and annealed films at the Ag-rich end of the composition spectrum. There is a gradual rise in MR values with increasing Ag, with a maximum of about 9% at approximately 72 at. % Ag (following the anneal), after which the MR value begins to decline. A broad maximum in GMR versus composition in the range 30–40 at. % ferromagnetic component has been observed in other granular systems.^{2,8} There is not much difference in the MR values in the as-deposited and annealed states for the three low Ag samples (60, 64, and 68 at. % Ag), but a considerable improvement in the MR value is noted in the annealed state for the two most Ag-rich samples. A plot of MR as a function of applied field for the sample with 75.6 at. % Ag appears in Fig. 2. The MR magnitude increases from 4.5% to 7.5% on annealing. Annealing also sharpens the MR curve at low fields. This sharpening is related to ferromagnetic particle growth.

Figure 3 reveals the variation in the lattice spacing of Ag (111) as a function of at. % Ag at the Ag-rich end. In the as-deposited state there is a marked increase in the lattice spacing of Ag, as the composition of the films become more Ag rich. In the annealed state, the lattice spacing values are independent of the composition and close to (but slightly less than) the bulk Ag (111) value of 2.355 \AA . This is an indication that, on annealing, the Ag more completely phase separates from the magnetic particles. Figure 4 shows the x-ray diffraction scans in the θ – 2θ mode for a sample with ≈ 63 at. % Ag in the as-deposited and annealed states. The dashed lines in the figure are drawn at the pure, bulk positions of the Ag (111), Ni (111), and Ag (222) peaks. The observation of a sharp Ag (111) peak and the suppression of the Ag (200) peak is evidence for a (111) growth texture. The Ag (111) peak sharpens and moves to a slightly lower angle on annealing [toward bulk Ag (111)]. The positions of bulk Ni (111), Ag (200), and Co (111) are located at $2\theta = 44.49^\circ$, $2\theta = 44.27^\circ$, and $2\theta = 44.21^\circ$, respectively. The peak observed next to the Ag (111) can be due to the partial overlap of these three peaks.

^{a)}Department of Electrical Engineering.

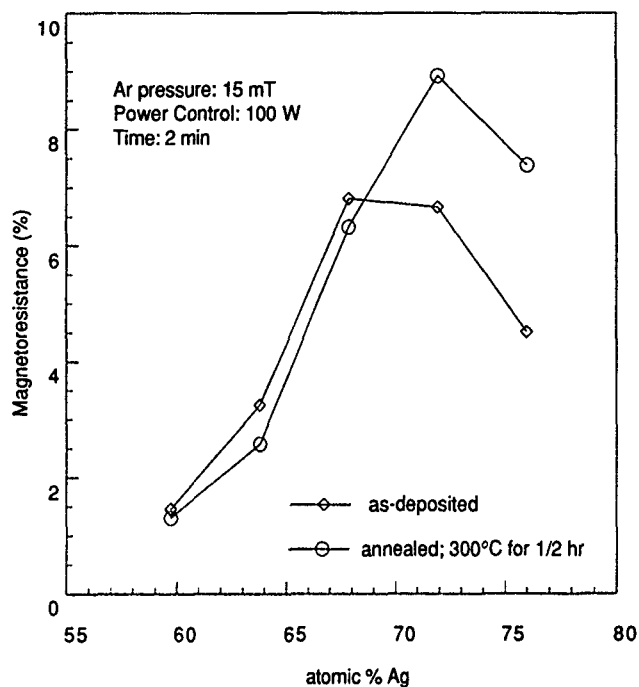


FIG. 1. Giant magnetoresistance (%) versus composition (at. % Ag) for films in the as-deposited state and after the first anneal.

B. Results on films exhibiting transverse AMR

Samples richer in the magnetic phase exhibited anisotropic MR in both the as-deposited state as well as after annealing. However, these samples did not show any appreciable improvement in MR after annealing. Figure 5 shows the MR plot in the as-deposited state, as well as after annealing, for a sample with ≈ 46 at. % Ag. The MR curves in the

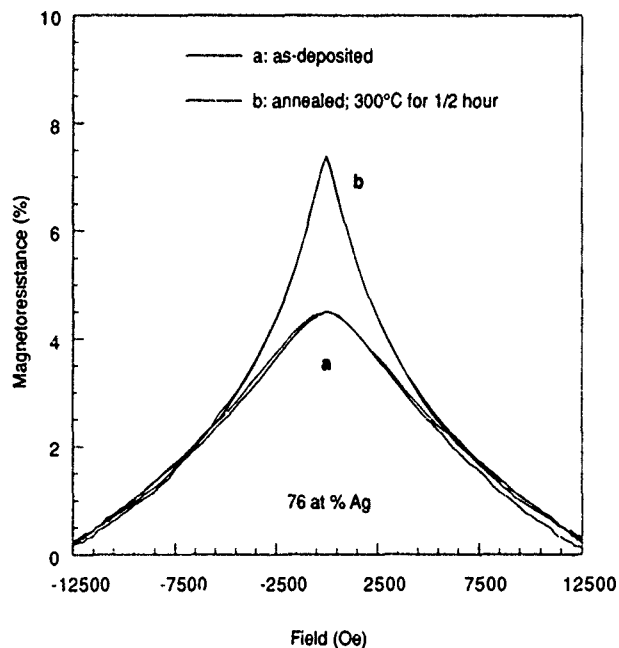


FIG. 2. Giant magnetoresistance (%) versus applied magnetic field (Oe) for films with 76 at. % Ag.

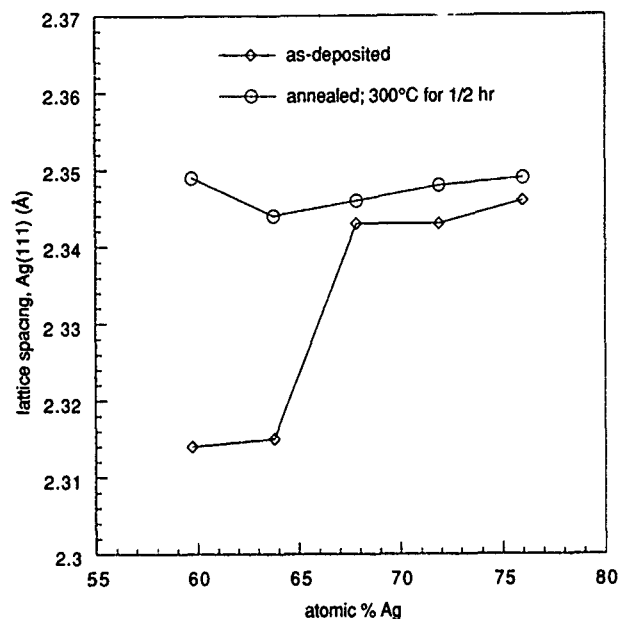


FIG. 3. Lattice spacing (Å) versus composition for samples showing GMR both in the as-deposited state and after the first anneal.

as-deposited state and after the first anneal are weakly hysteretic over an applied field range of ± 25 Oe, but become strongly hysteretic (over ± 175 Oe) after the third anneal (at 400°C for $\frac{1}{2}$ h). These hysteretic curves closely correlate with the coercivity of the samples, as observed from the VSM loops (not reproduced in this paper). The increase in coercivity on the third anneal may be associated with the growth of the single domain NiFeCo particles.

The variation of lattice spacing with at. % Ag in the Ag-poor samples appears in Fig. 6. There is a marked variation in the lattice spacing of Ag in the as-deposited state, as

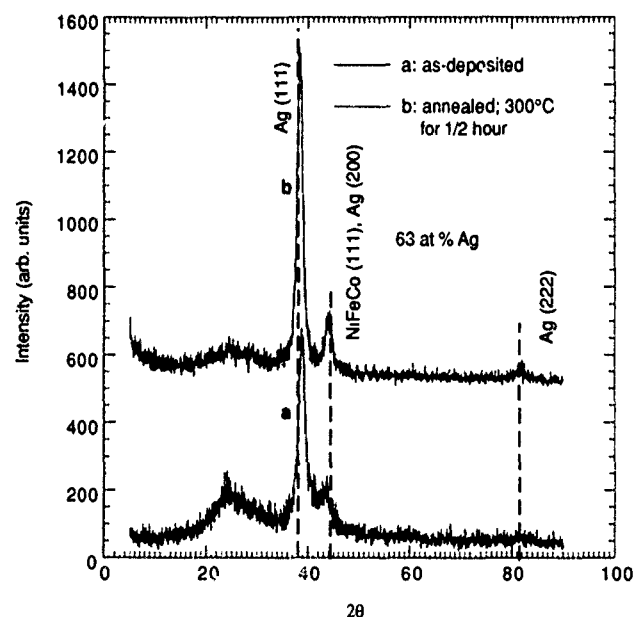


FIG. 4. Typical x-ray diffraction scans of samples showing GMR.

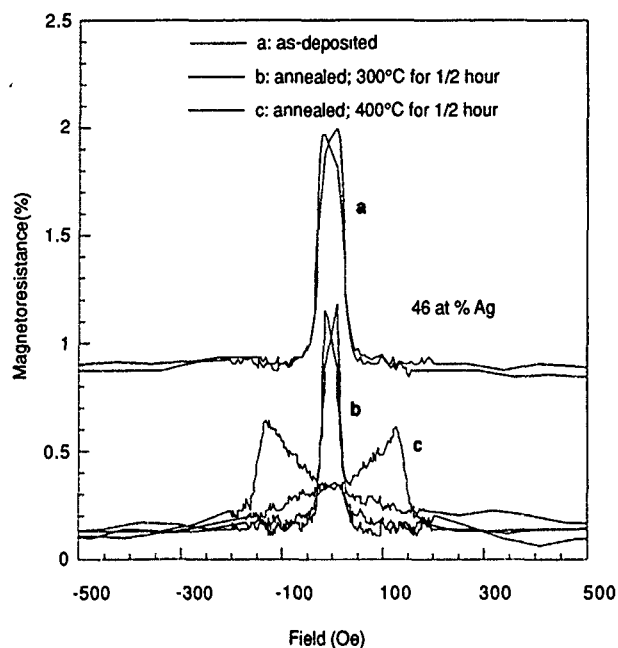


FIG. 5. Anisotropic magnetoresistance (%) versus applied magnetic field (Oe) for films with 46 at. % Ag.

well as after the first annealing. But after the second annealing the lattice spacing does not vary much with the composition of Ag and is near (but again slightly less than) the bulk Ag (111) lattice spacing of 2.355 Å. Figure 7 illustrates the effect of annealing on the evolution of Ag (111) and NiFeCo alloy (111) peaks for the sample with 46 at. % Ag. The

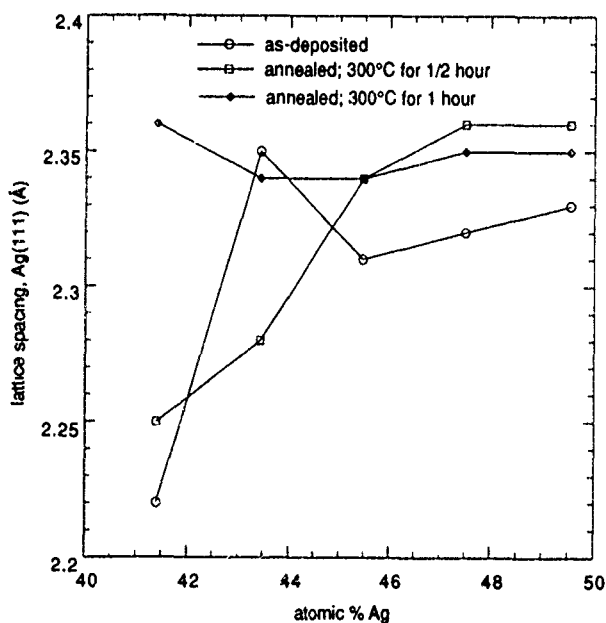


FIG. 6. Lattice spacing (Å) versus composition for samples showing AMR

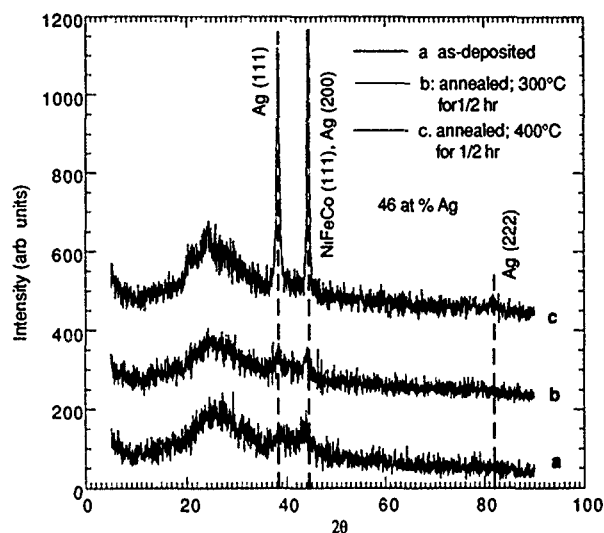


FIG. 7. X-ray diffraction scans of samples showing the evolution of Ag (111) and NiFeCo alloy (111) peaks on annealing

dashed lines represent the positions of pure, bulk Ag (111), Ni (111), and Ag (222) peaks. Ag (111) and NiFeCo alloy (111) peaks are seen as very weak peaks in the as-deposited state, and after the first anneal (at 300 °C for ½ hour), but show a significant increase in magnitude and sharpness after the third anneal (at 400 °C for ½ h). This is evidence for a sharp increase in particle size during the third annealing cycle. The lattice parameter of Ag (111) shifts toward its bulk value on annealing.

ACKNOWLEDGMENTS

Acknowledgment is made to the National Science Foundation (Grants No. DMR-9157402 and DMR-9301648), the National Storage Industry Consortium-Advanced Technology Program (funded by the Department of Commerce) and the Center for Materials for Information Technology at The University of Alabama for support of this research.

- ¹ A. E. Berkowitz, J. R. Mitchell, M. J. Carey, A. P. Young, S. Zhang, F. E. Spada, F. T. Spada, A. Hutten, and G. Thomas, *Phys. Rev. Lett.* **68**, 3749 (1992).
- ² J. A. Barnard, A. Wakis, M. Tan, E. Haftek, M. R. Parker, and M. L. Watson, *J. Magn. Magn. Mat.* **114**, 230 (1992).
- ³ M. L. Watson, J. A. Barnard, S. Hossain, and M. R. Parker, *J. Appl. Phys.* **73**, 5506 (1993).
- ⁴ J. Q. Xiao, J. S. Jiang, and C. L. Chien, *Phys. Rev. Lett.* **68**, 3749 (1992).
- ⁵ C. H. Tolman, *J. Appl. Phys.* **38**, 3409 (1967).
- ⁶ L. W. McKeenhan, *Phys. Rev.* **51**, 136 (1937).
- ⁷ M. Jimbo, T. Kanda, S. Goto, S. Tsunushima, and S. Uchiyama, *Jpn. J. Appl. Phys.* **31**, L1348 (1992).
- ⁸ S. S. Parkin, R. F. C. Farrow, T. A. Rabedeau, R. F. Marks, G. R. Harp, Q. Lam, C. Chappert, M. Toney, R. Savoy, and R. Geiss, Research Report published by IBM, 1992.

Giant magnetoresistance in heterogeneous $(\text{CoFe})_x\text{Ag}_{1-x}$ films (abstract)

R. S. Beach, D. Rao, M. J. Carey, F. T. Parker, and A. E. Berkowitz

Center for Magnetic Recording Research, Mail Code 0401, University of California, San Diego, La Jolla, California 92093-0401

The soft magnetic properties of CoFe prompted an investigation of magnetoresistance in Co-Fe-Ag alloys. A series of $(\text{FeCo})_x\text{Ag}_{1-x}$ ($10 < x < 30$) films were prepared by dc magnetron sputtering, followed by annealing in H_2 at a variety of temperatures $T_A \leq 400^\circ\text{C}$. The samples exhibit giant magnetoresistance (GMR) ratios which exceed 25% at a temperature of $T=10\text{ K}$, and 17% at $T=300\text{ K}$. The results of magnetization and x-ray scattering experiments indicate that FeCo alloy particles precipitate from the Ag matrix upon annealing. We note in particular that the full width at half maximum (FWHM) of the MR curves (approximately 2 kOe) is significantly less than that of Fe-Ag or Co-Ag sputtered films having comparable GMR ratios. We compare the sharp MR response of the $(\text{FeCo})_x\text{Ag}_{1-x}$ system to that of heterogeneous $(\text{Ni}_{80}\text{Fe}_{20})_x\text{Ag}_{1-x}$ films.

The effects of film geometry on the properties of FeTaN films

Gan Qiu and J. A. Barnard

The Department of Metallurgical and Materials Engineering, The University of Alabama, Tuscaloosa, Alabama 35487-0202

FeTaN single layer and FeTaN/SiO₂ multilayer films were grown by high rate reactive dc magnetron sputtering. The film geometry (FeTaN layer thickness, SiO₂ spacer thickness, and number of bilayer units) dependence of the structure, magnetic properties and high-frequency permeability characteristics were investigated.

I. INTRODUCTION

High performance magnetic heads for high density and high data transfer rate recording require new thin film materials with high magnetizations, low coercivities, high permeability, and near zero magnetostriction. Additionally, high-frequency response of permeability is also needed for heads used at high relative speed. In this context, FeN-based single layer films with high magnetization have received considerable recent attention.¹⁻⁴ Lamination of high moment metal films can lead to good frequency characteristics of permeability if dielectric spacers are used to suppress the eddy current loss.⁴⁻⁷ We have previously grown high moment FeTaN single layer films with soft magnetic properties and good thermal stability by high rate dc magnetron sputtering.⁸

II. EXPERIMENTAL METHODS

The FeTaN films were made by dc reactive magnetron sputtering at a fixed power of 300 W, fixed Ar pressure of 3 mTorr, and fixed N₂ flow rate of 5 sccm, where good film characteristics were obtained. These conditions produce growth rates of ~900 Å/min. A vacuum melted Fe-Ta target with nominal composition 10 w/o Ta was used. The SiO₂ spacer was deposited by rf magnetron sputtering from an SiO₂ target. Si(111) is used as the substrate with a base layer of ~92 Å of sputtered SiO₂. The films were grown in an aligning field of ~90 Oe. Three sets of films were prepared. In set A the properties of single layer FeTaN films as a function of layer thickness (from 0.19 to 1.8 μm) are studied. In set B the properties of bilayer films are studied as a function of the single spacer layer thickness. In set C the properties of multilayer films are studied as a function of number (from 1 to 5) of 0.9-μm-thick FeTaN layers for two different SiO₂ spacer thicknesses. The overall average M_s for these films is ~1570 emu/cm³.

III. EXPERIMENTAL RESULTS AND DISCUSSION

A. Set A: Single layer films

Uniaxial anisotropy induced by the external field was obtained in all the films. Typical $B-H$ curves of the films with ~4800 Å in both hard and easy directions are shown in Fig. 1. Figures 2(a) and 2(b) show the dependence of the coercivity (H_{ce} , H_{ch}) and initial permeability (μ' at 10

MHz) on film thickness. Films with thickness greater than ~4800 Å have good soft magnetic properties ($H_c < 1$ Oe and $\mu' > 2000$), which exhibit little thickness dependence. Initial permeability increases with film thickness which is consistent with the decrease of H_c . H_c of 0.6 Oe and μ' (at 10 MHz) of 2300 are obtained for the 1.8-μm-thick films. For films with thickness of 2500 and 3300 Å, μ' is independent of frequency up to 100 MHz and f_{50} (the frequency at which initial permeability drops to 50% of its low-frequency value) is higher than 250 MHz. A permeability spectrum for a single layer 1-μm film is shown in Fig. 3. μ' begins to roll off at 60 MHz and μ' decreases faster at high-frequency compared with thinner films due to the eddy current effect. The film thickness dependence of magnetostriction (λ_s) is shown in Fig. 4(a). λ_s systematically declines from $+9 \times 10^{-6}$ to $+6 \times 10^{-6}$ with an increase in film thickness. The lattice spacing derived from the expanded α -Fe (110) peak decreases with increasing film thickness, as shown in Fig. 4(b), which could be due to decreased incorporation of N₂ during the later stages of film growth.⁴ The full width at half-maximum (FWHM) of the (110) peak [Fig. 4(b)] decreases with film thickness indicating a stronger (110) film texture. The increasing amount of {110} oriented grains in the films

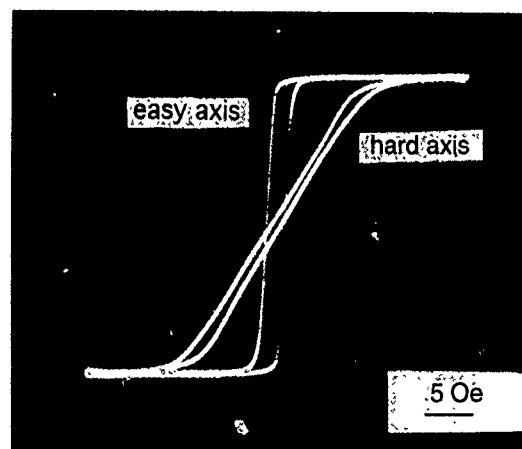


FIG. 1. $B-H$ hysteresis loop of 4800-Å-thick single layer FeTaN film.

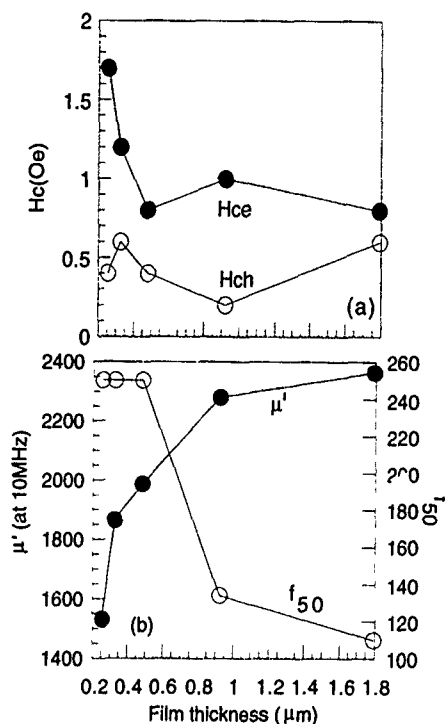


FIG. 2. Magnetic properties of FeTaN films as a function of film thickness; (a) H_c and (b) μ and f_{50} .

may account for the decrease of λ_s with increasing thickness [λ_s values for pure α -Fe films with (110) plane preferred orientation are negative].

Set B: Bilayer films

In this set two 0.9- μm FeTaN layers are separated by a sputtered SiO_2 layer of variable thickness. The SiO_2 thickness dependence of coercivity is shown in Fig. 5(a). H_{ch} which reflects anisotropy dispersion decreases up to a spacer thickness of 200 \AA , and then begins to increase at a spacer thickness of 400 \AA . The increases of coercivity with an increase in SiO_2 spacer layer thickness may be caused by weaker magnetostatic coupling between magnetic layers. When the spacer thickness reached 400 \AA , the two films switched independently giving rise to two values of H_c in a

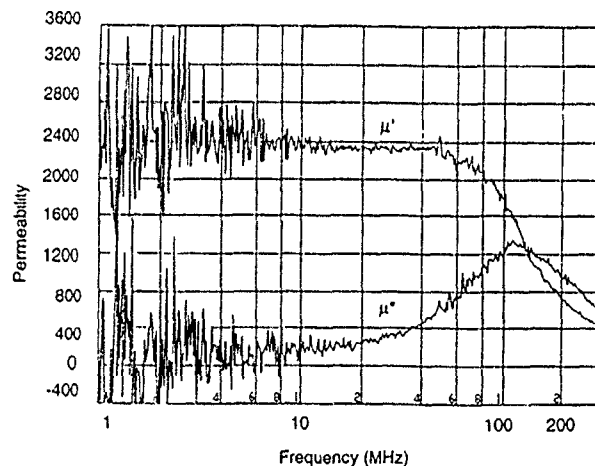


FIG. 3. Frequency dependence of permeability for 1- μm FeTaN films.

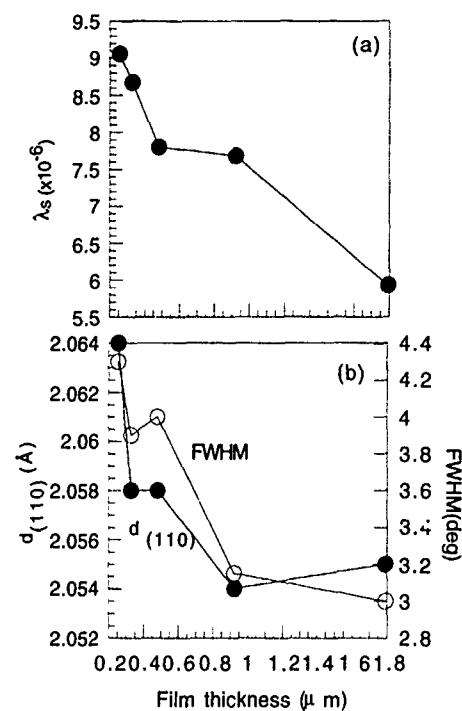


FIG. 4. Saturation magnetostriction (λ_s) (a) and d_{110} and FWHM (b) vs film thickness for single layer FeTaN films

hysteresis loop shown in the inset of Fig. 5(a). The SiO_2 thickness dependence of initial permeability μ' (at 10 MHz) and frequency at 50% of initial permeability (f_{50}) appear in Fig. 5(b). Initial permeability shows a declining trend with increasing spacer thickness, which agrees with the increase

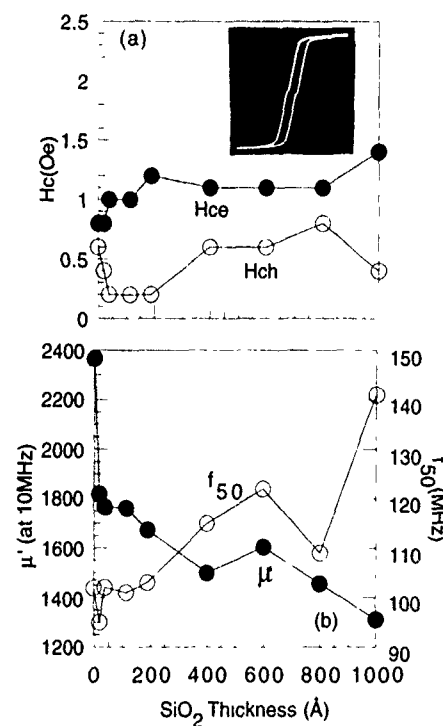


FIG. 5. Magnetic properties of 2×1 - μm double layered FeTaN films as a function of SiO_2 spacer thickness, (a) H_c and (b) μ and f_{50} . Inset of (a) shows a two-valued H_c B-H loop.

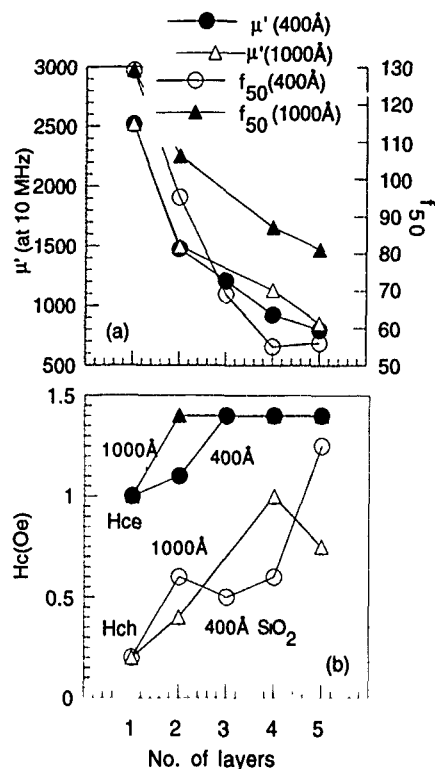


FIG. 6. Magnetic properties of multilayer FeTaN films as a function of number of layers for SiO_2 spacer thickness of 400 and 1000 Å; (a) μ and f_{50} and (b) H_c .

of H_c in the films. f_{50} appears to increase with increasing SiO_2 thickness due to more complete separation of the films resulting in increasing resistivity. Magnetostriction is essentially independent of spacer layer thickness in the bilayer films (λ_s is $\sim +6.25 \times 10^{-6}$).

C. Set C: Multilayer films

In set C the dependence of magnetic properties on number of layers, n , in a multilayer is studied for FeTaN layer thicknesses of $0.9 \mu\text{m}$ and two different SiO_2 spacer layer thicknesses, 40 and 100 nm. Hard axis coercivity increases with number of layers for both spacer layer thicknesses from ~ 0.2 to 1.25 Oe, which may again be caused by the reduced magnetostatic coupling between the magnetic layers for thicker spacers [Fig. 6(b)]. The initial permeability and f_{50} for set C is plotted in Fig. 6(a). The decrease of the initial permeability with the increase of the number of layers corresponds to the increase of the coercivity. Unexpectedly, f_{50} shows a systematic decrease with increasing number of lay-

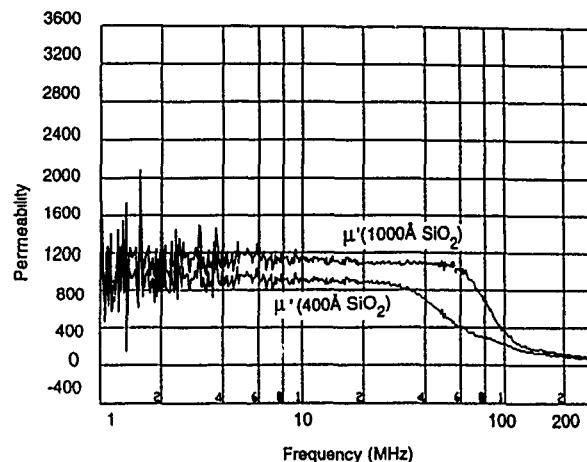


FIG. 7. Permeability as a function of frequency for $4 \times 1\text{-}\mu\text{m}$ four-layered films with SiO_2 spacer thickness of 400 and 1000 Å.

ers, which could be caused by a poorly grown insulator, weaker coupling between the magnetic layers and film stress. Permeability spectra of two $4 \times 1\text{-}\mu\text{m}$ four-layered films (SiO_2 spacer thicknesses = 40, 100 nm) are shown in Fig. 7. The high-frequency response of the multilayer is improved by increasing SiO_2 spacer thickness. μ' is maintained till 60 MHz for the films with spacer thickness of 1000 Å whereas μ' started to roll off at 35 MHz for the films with 400-Å spacer. Interestingly, the magnetostriction exhibits a significant and systematic decrease with increasing number of layers, dropping from $\sim +7.7 \times 10^{-6}$ to $+3.8 \times 10^{-6}$.

ACKNOWLEDGMENTS

Acknowledgment is made to the NSIC-ATP (funded by the Department of Commerce) and the MINT Center for support of this work.

- ¹Y. Watanabe, H. Oura, and N. Onozato, *IEEE Trans. Magn.* **Mag-26**, 1500 (1990).
- ²S. Wang, and M. H. Kryder, *J. Appl. Phys.* **67**, 5134 (1990).
- ³N. Ishiwata, C. Wakabayashi, and H. Urai, *J. Appl. Phys.* **69**, 5616 (1991).
- ⁴M. A. Russak, C. V. Jahnes, E. Klokholm, J.-W. Lee, M. Re, and B. C. Webb, *J. Magn. Magn. Mater.* **104-107**, 1851 (1992).
- ⁵K. P. Ash, D. Wachenschwanz, C. Brucker, J. Olson, M. Trcka, and T. Jagielinski, *IEEE Trans. Magn.* **Mag-26**, 2960 (1990).
- ⁶S. Wang, K. E. Obermyer, and M. H. Kryder, *IEEE Trans. Magn.* **Mag-27**, 4897 (1991).
- ⁷T. Okumura, A. Osaka, N. Ishiwata, M. Kitamura, and H. Urai, *IEEE Trans. Magn.* **Mag-28**, 2121 (1991).
- ⁸G. Qiu, J. C. Cates, E. Haftek, C. Alexander, Jr., and J. A. Barnard, In *Magnetic Ultrathin Films*, edited by B. T. Jonker, S. A. Chambers, R. F. C. Farrow, C. Chappert, R. Clarke, W. J. M. de Jonge, T. Egami, P. Grünberg, K. M. Krishnan, E. E. Marinero, C. Rau, and S. Tsunashima (Materials Research Society Pittsburgh, PA, 1993), pp. 339-344.

Relationship between ac and dc magnetic properties of a Co-based amorphous alloy

S. H. Lim

Magnetic Materials Laboratory, Korea Institute of Science and Technology, 136-791 Seoul, Korea

Y. S. Choi

R&D Division, Hankook Core Co. Ltd., Suwon, 445-970 Kyungki-do, Korea

T. H. Noh and I. K. Kang

Magnetic Materials Laboratory, Korea Institute of Science and Technology, 136-791 Seoul, Korea

How the ac effective permeability (μ_e) correlates with dc magnetic properties over a wide frequency range of 1 to 1000 kHz was studied, in an effort to understand the magnetization behavior of the Co-based amorphous alloy of Metglas 2714A subject to an ac magnetic field. In the low-frequency range up to 50 kHz, the correlations between μ_e and the dc initial permeability, and between μ_e and the coercivity are found to be good, the correlation coefficient being positive and negative, respectively. No definite correlation is observed with the dc maximum permeability. At high frequencies ranging from about 200 to 1000 kHz, the correlations between μ_e and the dc maximum permeability, and between μ_e and the coercivity are observed to be good, the correlation coefficient being negative and positive, respectively. The correlation of μ_e with the dc initial permeability is poor in this high-frequency range. The correlation with the remanence ratio is found to be rather different from the other three; the ac permeability exhibits a maximum at the value of remanence ratio of 0.5–0.6 at frequencies up to 200 kHz but, at frequencies higher than 500 kHz, it decreases linearly with the remanence ratio. From the correlation results it is considered that the dominant magnetization mechanism is the domain wall motion at frequencies up to 50 kHz and it is spin rotation at frequencies higher than 500 kHz.

Zero-magnetostrictive Co-based amorphous alloys exhibit excellent soft magnetic properties, and, hence, are of great commercial importance.¹ These alloys are mainly used in high-frequency electromagnetic devices. Therefore, it is necessary to clearly understand magnetization behavior at high frequencies, in order to use soft magnetic alloys more efficiently, and improve their magnetic properties. However, this does not appear to be easy, since magnetization behavior under an ac field is much more complex than under a dc field. Whilst dc magnetization behavior is mainly affected by domain wall motion, ac magnetization behavior is affected by numerous factors including eddy currents (both classical and anomalous) and spin rotation as well as domain wall motion.²

In an effort to understand magnetization behavior at high frequencies, we investigate how an ac magnetic property correlates with dc magnetic properties. The ac magnetic property considered in this study was the effective permeability (μ_e). Four dc magnetic properties were considered; the initial permeability (μ_i), the maximum permeability (μ_m), the coercivity (H_c), and the remanence ratio (B_r/B_{10} , where B_r is the remanent flux density and B_{10} the flux density at a field of 10 Oe). The alloy used in this investigation was the Co-based alloy of Metglas 2714 A which was supplied by Allied Signal Corp., U. S.

Two ribbons of different widths (4.5 and 6.0 mm), which were slit from wider ones, were used in the investigation. The ribbon thickness was 17 μm . The ribbons were wound onto a torodial core with inner diameter of 19 mm.

In order to examine the relationships between the magnetic properties more clearly, varying values of the magnetic properties were intentionally obtained by annealing over a

wide temperature range and carrying out different cooling methods immediately after annealing; the annealing temperatures selected were 300, 350, 400, and 500 °C, and the cooling methods included water quenching, air cooling, and furnace cooling. The annealing time was 60 min; however, at the temperatures of 350 and 400 °C, four different annealing times of 15, 30, 60, and 120 min were also used.

The ac effective permeability of annealed samples was measured by using an impedance analyzer. The dc magnetic properties were measured with a hysteresis loop tracer. The ac permeability was measured at an applied field of 5 mOe and over a wide frequency range of 1 to 1000 kHz. Each datum point presented in this work was obtained by averaging about ten separate results.

In Figs. 1(a)–1(c) are shown the results for the relationship between μ_e and μ_i . Although the results were obtained at many frequencies ranging from 1 to 1000 kHz, only the results obtained at frequencies of 1, 100, and 1000 kHz are displayed in Figs. 1(a)–1(c), respectively. (Also in the figures to be shown later, only the results from these three frequencies will be presented due to space limitation.) The present results show that μ_e is correlated well with μ_i at low frequencies below 50 kHz. The correlation coefficient between the two properties is positive, viz., μ_e increases with increasing μ_i . Although results are not shown in the figures, the degree of correlation decreases progressively as the frequency (f) increases in this range. However, at frequencies above 100 kHz, no obvious correlation is observed. The present results for the correlation between μ_e and μ_i (good correlation at low frequencies and poor one at high frequencies) can be well understood; at low frequencies, dynamic magnetization behavior is expected to be similar to static

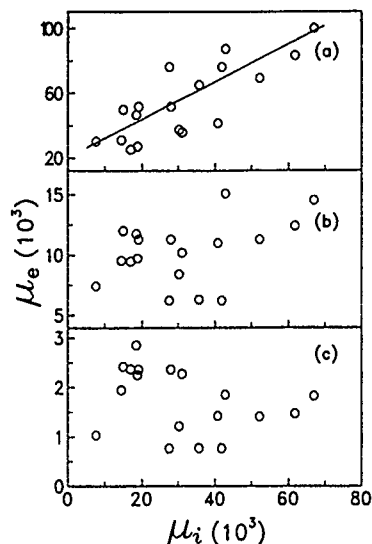


FIG. 1. The dependence of μ_e on μ_i : (a) 1 kHz, (b) 100 kHz, and (c) 1000 kHz. The line guides the eyes only.

magnetization behavior, but is expected to deviate as f increases.

The dependences of μ_e on μ_m are shown in Figs. 2(a)–2(c). At frequencies up to 100 kHz, it is observed that the correlation between μ_e and μ_m is rather poor compared to the correlation between μ_e and μ_i . This poor correlation between μ_e and μ_m even in the low-frequency range is believed to result from the fact that large magnetization including Barkhausen jumps is usually involved with the measurement of μ_m ; however, magnetization is small in the measurement of both μ_e and μ_i . It is noted that values of μ_i were measured at the (dc) magnetic field ranging from 1 to 2.6 mOe, whilst μ_m at the (dc) magnetic field ranging from 5 to 15 mOe. It is recalled that μ_e was measured at the (ac) field of 5 mOe. At high frequencies above 200 kHz, μ_e is

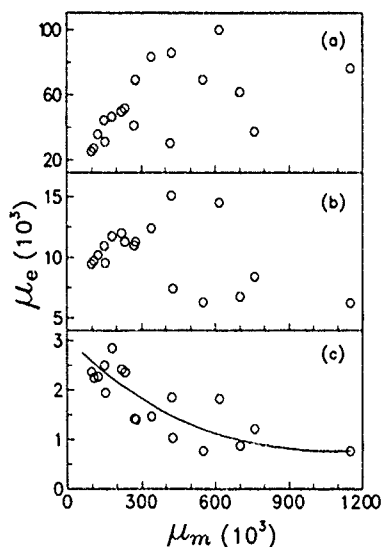


FIG. 2. The dependence of μ_e on μ_m : (a) 1 kHz, (b) 100 kHz, and (c) 1000 kHz. The line guides the eyes only.

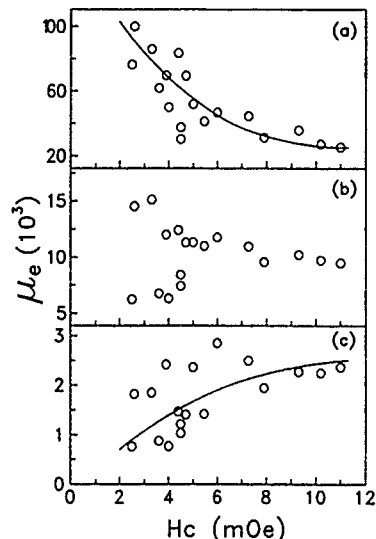


FIG. 3. The dependence of μ_e on H_c : (a) 1 kHz, (b) 100 kHz, and (c) 1000 kHz. The lines guide the eyes only.

rather well correlated with μ_m and the correlation coefficient between the two properties is negative.

The correlation results between μ_e and H_c are shown in Figs. 3(a)–3(c). In the low-frequency range, the well-known reciprocal relationship between μ_e and H_c is observed to exist. However, at intermediate frequencies of 100 and 200 kHz, there appears no definite correlation between the two properties. At high frequencies between 500 and 1000 kHz, there is a surprising good correlation between μ_e and H_c with positive correlation coefficient; this is the opposite of the low-frequency correlation behavior.

The plots of μ_e vs B_r/B_{10} are shown in Figs. 4(a)–4(c). At frequencies up to 200 kHz, μ_e increases with B_r/B_{10} , reaches a maximum value at $B_r/B_{10}=0.5-0.6$, and then decreases with a further increase of B_r/B_{10} . The remanence

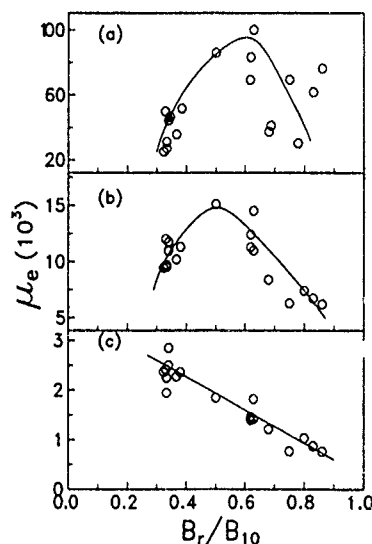


FIG. 4. The dependence of μ_e on B_r/B_{10} : (a) 1 kHz, (b) 100 kHz, and (c) 1000 kHz. The lines guide the eyes only.

ratio is known to be a measure of the distribution of the magnetization direction of domains; thus it is mainly determined by the magnitudes and directions of the anisotropies present in a given material. For a Co-based alloy where magnetization is governed by domain wall motion of 180°-type domains, the remanence ratio is estimated to be 0.5 if domain orientation is completely random.³ If more domains are in the length (transverse) direction, the remanence ratio is greater (less) than 0.5. The present results for the variation of μ_e with B_r/B_{10} in the low-frequency range may indicate that high values of μ_e are achieved when domain orientation is random, or more domains are slightly in the length direction. A similar result was previously reported by Luborsky *et al.* for Fe₄₀Ni₄₀P₁₄B₆ amorphous alloy ribbons.⁴

The value of μ_e for a sample with a small remanence ratio decreases more slowly with increasing f than that for a sample with a high remanence ratio does, as can be understood from Figs. 4(a)–4(c). As a result, at very high frequencies between 500 and 1000 kHz, the correlation behavior changes; a clear correlation between the two properties emerges, the correlation coefficient being negative.

A feature to be noted from the present results is that correlation behavior begins to change rather sharply at frequencies of 50–100 kHz for the dc properties μ_i and H_c which are mainly determined by domain wall motion. This may indicate that the dominant magnetization mechanism below 50–100 kHz is the motion of domain walls. The dominant magnetization mechanism at high frequencies may be understood from the correlation results between μ_e and B_r/B_{10} . At frequencies higher than 500 kHz, μ_e increases with decreasing remanence ratio, indicating that the ac permeability is high when more domains are distributed in the

transverse direction. It is noted here that, since the magnetic field is applied in the length direction during the measurement of all the magnetic properties, more domains are in the perpendicular direction with respect to the applied field when the remanence ratio is low. Since it is known that dynamic magnetization by spin rotation occurs easily, viz., ac permeability is high, when directions of applied field and domain are perpendicular to each other rather than parallel,⁵ the present correlation results between μ_e and B_r/B_{10} may indicate that the dominant magnetization mechanism at frequencies higher than 500 kHz is spin rotation.

In summary, we have investigated how the ac effective permeability is correlated, over a wide frequency range of 1 to 1000 kHz, with the dc initial permeability, dc maximum permeability, coercivity, and remanence ratio for the Co-based amorphous alloy of Metglas 2714A. From the correlation results it is considered that the dominant magnetization mechanism is the domain wall motion at frequencies up to 50 kHz and it is spin rotation at frequencies higher than 500 kHz.

The authors thank the Korean Ministry of Science and Technology and Hankook Core Co., Ltd. for their financial support of this work.

¹M. Kikuchi, H. Fujimori, Y. Obi, and T. Masumoto, *Jpn. J. Appl. Phys.* **14**, 1077 (1975).

²B. D. Cullity, *Introduction to Magnetic Materials* (Addison-Wesley, Reading, MA, 1972), Chap. 12.

³S. Chikazumi, *Physics of Magnetism* (Wiley, New York, 1964), Chap. 12.

⁴F. E. Luborsky, R. O. McCary, and J. J. Becker, in *Rapidly Quenched Metals*, edited by N. J. Grant and B. C. Giessen (MIT Press, Cambridge, MA, 1976), p. 467.

⁵H. Fujimori, H. Morita, M. Yamamoto, and J. Zhang, *IEEE Trans. Magn.* **22**, 1101 (1986).

Effects of nanocrystallization upon the soft magnetic properties of Co-based amorphous alloys

P. Quintana

Faculty of Chemistry, National University of Mexico, 04510 Mexico D.F., Mexico

E. Amano and R. Valenzuela

Institute for Materials Research, National University of Mexico, Apartado Postal 70-360, 04510 Mexico D.F., Mexico

J. T. S. Irvine

Department of Chemistry, University of Aberdeen Meston Walk, Old Aberdeen, AB9 2UE, Scotland, United Kingdom

Amorphous samples of Vitrovac® 6025 metallic alloys were nanocrystallized by thermal annealing at temperatures in the range 576–716 K, well below the crystallization temperature (831 K, as obtained by differential scanning calorimetry at 20 K/min) and times in the range 10–90 min. Initial magnetic permeability exhibited a maximum of $\sim 109\,000$ (from $\sim 20\,000$ for the as-quenched state) for annealing times of ~ 15 min, and then a decrease toward a plateau value (30 000–40 000) for longer times. Domain wall relaxation frequency showed the opposite behavior, a minimum of ~ 9 kHz (from 40 kHz for the as-quenched value) for the permeability maximum, and then a stabilization at ~ 15 kHz. Transmission electron microscopy observations confirmed that for annealing times up to 60 min., crystallite size is smaller than 30 nm. Permeability and relaxation frequency results are interpreted in terms of the dependence of wall bulging on anisotropy and free-wall surface area between pinning sites.

Systems with particles in the nanometer range, which are also known as nanocrystals, show unusual magnetic properties.^{1,2} Amorphous alloys provide an extremely convenient material to produce nanocrystals since the crystallization process from these phases can be controlled by thermal treatments to obtain crystals in a variety of dimensions.³

In this paper, we present an investigation of the initial magnetic permeability as a function of frequency of nanocrystallized Co-based amorphous alloys. The dynamic properties of domain walls^{4,5} provide additional information about the effects of nanocrystals on the magnetization processes.

Samples of Vitrovac® 6025 amorphous ribbons with the nominal composition $\text{Co}_{66}\text{Fe}_4\text{Mo}_2\text{Si}_{16}\text{B}_{12}$, obtained by melt spinning were crystallized in an electric furnace (stability: ± 3 K) at temperatures in the range 570–710 K, for times from 10 min up to 90 min. Since crystallization rates at these temperatures were considerably slow (the crystallization temperature is 831 K as determined by differential scanning calorimetry at a 20 K/min rate), a good control of the extent of crystallization was possible. The sample was mounted in a holder inside a silica glass with an inert (argon) atmosphere. A thermocouple close to the sample was used to monitor temperature. To avoid the effects of slow heating and cooling, the holder and sample were inserted into the silica glass tube in a preheated furnace at the beginning of the experiment, and removed from the furnace at the end of the annealing time without altering the furnace setting. Heating and cooling rates in excess of 80 K/min were achieved.

Magnetic permeability measurements were made on samples made of ~ 1 -m ribbon wound as a toroid. To apply a magnetic field, a copper wire was wound around the toroid as a coil. Usually, the toroidal shape was conserved during several consecutive thermal treatments since after the first

annealing, samples became brittle. Frequency measurements were performed at room temperature on a system that includes a HP 4192A Impedance Analyzer controlled by a HP 85 microcomputer with all the peripherals. Our software allows the measurement of 94 frequencies in the range 5 Hz–13 MHz.

The crystallization temperature was determined in a 2100 Thermal Analyst System with a differential scanning calorimetry (DSC) cell at a heating rate of 20 K/min. Transmission electron microscopy (TEM) observations were made in a JEOL JEM-1200 microscope under 200-kV accelerating voltage. Samples were thinned by electropolishing in a solution of nitric acid and alcohol.⁶ Thinning of samples annealed for long times became difficult because of their brittleness; an alternative method was to electropolish them in the as-quenched state, and perform the same thermal treat-

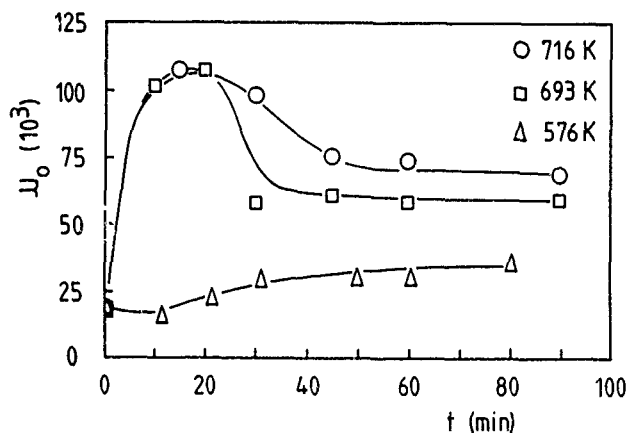


FIG. 1. Initial permeability as a function of time for three annealing temperatures.

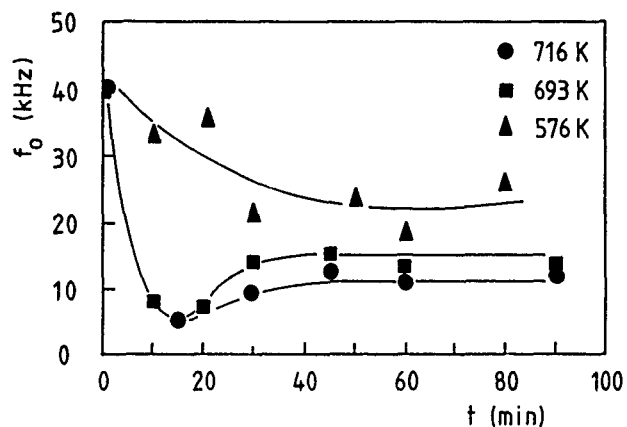


FIG. 2. Domain wall relaxation frequency as a function of time for three annealing temperatures.

ments in the DSC cell as in the toroidal sample. No substantial differences were observed between the two methods.

The resolution of initial permeability from hysteresis phenomena by impedance measurements as a function of frequency has been discussed elsewhere.^{4,5} In this paper, initial permeability, μ_0 , and domain wall relaxation frequency, ω_0 are investigated. The former corresponds therefore to the reversible magnetization variations at low fields [at a field lower than the pinning or propagation field (Ref. 5)], and the latter, to the frequency above which the domain walls are unable to follow the cyclic, driving field. Initial permeability as a function of time for three annealing temperatures is shown in Fig. 1, and for the same times and temperatures, domain wall relaxation frequency appears in Fig. 2. For 693 K, initial permeability goes through a maximum (~ 5 times the as-quenched value) for $t \sim 15$ min and then decreases toward a plateau for times larger than 30 min. Similar behavior is observed for $T = 716$ K, with a decrease to the plateau occurring for longer times but practically the with the same maximum permeability value. The results for the 576-K annealing exhibit a difference, since the tendency toward a constant value occurs without the passage through a maximum.

The relaxation frequency shows the opposite behavior from permeability; for 716 and 693 K, ω_0 goes through a minimum; from ~ 40 kHz for the as-quenched state to ~ 9

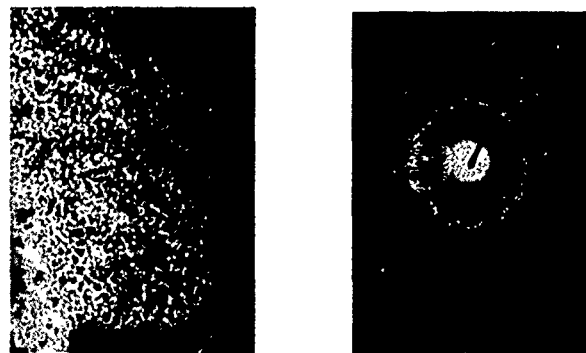


FIG. 4. TEM image and EDP for annealing 40 min at 693 K.

kHz for the permeability maximum, and then stabilizing at about 15 kHz for times longer than 30 min.

The microstructures and their corresponding electron diffraction patterns (EDP) appear in Figs. 3, 4, and 5 for 20, 40, and 60 min, respectively, at 693 K. The nucleation of crystallites takes place between 0 and 20 min; electron diffraction pattern changes from the characteristic, diffuse ring in the amorphous phase to diffraction rings formed by discrete spots. An increase in crystallite number is observed between 40 and 60 min, with a small growth in size (note the difference in magnification). Electron diffraction pattern show an increase in intensity of rings. In these annealings, however, crystallite size remains smaller than 30 nm.

The initial permeability mechanism is the result of a reversible bulging of pinned domain walls,⁷ under the "pressure" of the external field. An increase in permeability can therefore be expected to be associated with an increase in the free-bulging area, which can occur essentially by two factors, a coarsening in the domain structure and a decrease in anisotropy. The latter results in a "softer" domain wall, easier to deform under the field. A coarsening in the domain structure can be produced by factors such as stress relief, or a decrease in the pinning site concentration.

The domain wall relaxation frequency depends on an inverse manner on the above factors. A "softer" domain wall relaxes at lower frequencies than a "stiff" wall: also, an increase in pinning sites leads to a smaller bulging area, and in a similar way to the string of a musical instrument, this results in a higher vibration frequency.

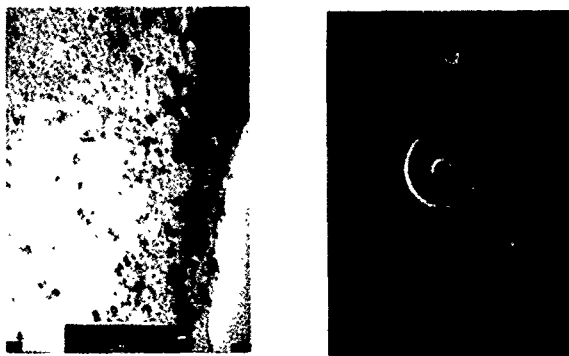


FIG. 3. Transmission electron microscopy image and electron diffraction pattern for annealing 20 min at 693 K.

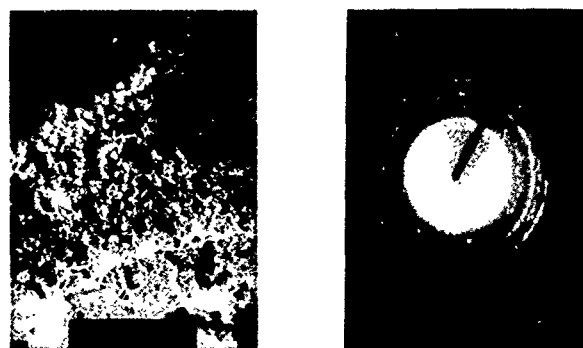


FIG. 5. TEM image and EDP for $t = 60$ min and $T = 693$ K.

Similar results, i.e., the tendency of the $\mu_0 f_0$ product to a constant value, have been reported in amorphous materials as a result of thermal annealings involving stress relief,⁸ *in situ* diffusion to directional order⁹ and "macrocrystallization."¹⁰ It seems therefore a general phenomenon associated with initial permeability. In the present case, results can be interpreted on the basis of a decrease in anisotropy and/or a coarsening of the domain structure leading to longer, unpinned walls of the amorphous phase. The same maximum permeability value for the two high annealing temperatures suggests that pinning of the walls occurs only at the external surfaces of the sample.

It has been shown in many studies¹¹ that the presence of crystallites in ferromagnetic amorphous phase leads to wall pinning. In the case of magnetic nanometer-range crystallites, however, a preferential orientation of the magnetic axis of these crystallites can lead to a cooperative effect with the domain structure of the amorphous matrix, resulting¹² in an in-plane induced anisotropy. As annealing progresses, the growth in crystallite size seems to destroy the cooperative effect, leads to a decrease in free-bulging area and therefore to a decrease¹⁰ in permeability. The fact that annealings at 576 K result in an increase in permeability with no maximum in this property seems to be due to a coarsening of the domain structure (by simple elimination of stress), but involving no decrease in anisotropy.

Finally, it has been shown that nanocrystallized structures can also be obtained in commercially available materials, by using annealing temperatures well below the conventionally measured crystallization temperature.

Authors thank Dr. H. R. Hilzinger for providing the amorphous samples. S. Jiménez-Cortés, J. Guzman, C. Vazquez, and A. Caballero for technical assistance, as well as partial funding from DGAPA-UNAM (Mexico), the CONACyT-British Council collaboration scheme and the European Commission.

¹G. Herzer, *Mater. Sci. Eng. A* **133**, 1 (1991).

²Y. Yoshizawa, S. Oguma, and K. Yamauchi, *J. Appl. Phys.* **64**, 6044 (1988).

³H. Y. Tong, B. Z. Ding, H. G. Jiang, Z. Q. Hu, L. Dong, and Q. Zhou, *Mater. Lett.* **16**, 260 (1993).

⁴J. T. S. Irvine, E. Amano, and R. Valenzuela, *Mater. Sci. Eng. A* **133**, 140 (1991).

⁵G. Aguilar, P. Quintana, E. Amano, R. Valenzuela, and J. T. S. Irvine (these proceedings).

⁶M. Blank-Bewersdorff and U. Koster, *Mater. Sci. Eng.* **97**, 313 (1988).

⁷M. Celasco, A. Maosero, P. Mazzetti, and A. Stepanescu, *J. Magn. Magn. Mater.* **54-57**, 859 (1986).

⁸R. Valenzuela and J. T. S. Irvine, *J. Appl. Phys.* **72**, 1486 (1992).

⁹R. Valenzuela and J. T. S. Irvine, *J. Non-Cryst. Solids* **156-158**, 315 (1993).

¹⁰P. Quintana, E. Amano, and R. Valenzuela, *Mater. Sci. Eng.* (to be published).

¹¹A. R. Bhatti, *Mater. Sci. Eng. A* **133**, 188 (1991).

¹²G. Herzer, *Mater. Sci. Eng.* (to be published).

Magnetic properties behaviors in $\text{Fe}_{88}\text{Zr}_7\text{B}_4\text{Cu}_1$ nanocrystalline alloy prepared by different postanneal cooling rates

K. Y. Kim

Division of Metals, Korea Institute of Science and Technology, Seoul 136-791, Korea

J. S. Lee

Department of Metallurgical Engineering, Inha University, Incheon 402-751, Korea

T. H. Noh and I. K. Kang

Division of Metals, Korea Institute of Science and Technology, Seoul 136-791, Korea

T. Kang

Department of Metallurgical Engineering, Seoul National University, Seoul 151-742, Korea

Effects of cooling rate after annealing on the soft magnetic properties were investigated for an $\text{Fe}_{88}\text{Zr}_7\text{B}_4\text{Cu}_1$ alloy with nanoscale grain structure, which was prepared by melt quenching. As the cooling rate increased, the effective permeability improved and the remanence ratio, which indicates the orientation of magnetic anisotropy (degree of pair ordering), decreased. The increase of permeability and decrease of remanence ratio were considered to result from the suppression of the induced magnetic anisotropy. Furthermore, the variation of disaccommodation behaviors with cooling rate was investigated in the $\text{Fe}_{88}\text{Zr}_7\text{B}_4\text{Cu}_1$ nanocrystalline alloy. It was found that the value of D (intensity of disaccommodation) was a little higher for the samples obtained from the high cooling rate than that for the low cooling rate. This result can be explained by domain structure stabilization due to local induced magnetic anisotropy.

Nanocrystalline magnets are promising materials for future soft magnetic applications.^{1,2} Among these materials, Fe-Zr-B-Cu based nanocrystalline alloys were reported to exhibit excellent soft magnetic properties with a high saturation magnetization and a high permeability.³ The reason for the good soft magnetic properties is rather well understood to be the reduction of the effective magnetocrystalline anisotropy by forming ultrafine grains. Although the formation of nanocrystalline grains, which are obtained by annealing at temperatures above crystallization temperature, play a dominant role in soft magnetic properties, it is important from the application point of view to know how the cooling rate after annealing influences the soft magnetic properties of these alloys. Generally, it has been known that induced magnetic anisotropy can be effectively suppressed by controlling the quenching rate or annealing in a rotating magnetic field in the case of amorphous alloys.⁴ However, not much work has been done on the effects of the cooling rate after annealing in nanocrystalline alloys. In this study the effect of the cooling rate was investigated for the $\text{Fe}_{88}\text{Zr}_7\text{B}_4\text{Cu}_1$ nanocrystalline alloy.

Ribbon samples of amorphous $\text{Fe}_{88}\text{Zr}_7\text{B}_4\text{Cu}_1$ alloy were prepared in an argon atmosphere by the single roll melt spinning technique. The ribbons were, typically, 1–2 mm wide and about 20 μm thick. They were confirmed to be amorphous by x-ray diffractometer using $\text{Cu } K_\alpha$ radiation. The as-quenched ribbons were wound onto a toroidal core with 21-mm inner diameter, and subsequently annealed in the temperature range of 500 to 650 °C for 1 h in a vacuum of about 10^{-3} Torr. The cooling rate was varied by carrying out two different cooling methods, the first is water quenching of the vacuum-sealed specimen (conventional method); and the second is water quenching with Ar gas introduction after vacuum annealing (our new method). It is considered that the

latter gives a much higher cooling rate than the former, because Ar atmosphere is more thermally conductive than the vacuum. It is noted that direct water quenching without protection is very harmful due to surface oxidation. The effective permeability (μ_e) was measured at 1 kHz under 10 mOe with an impedance analyzer. The magnetic induction at 10 Oe (B_{10}) and coercive force (H_c) were measured with a dc hysteresis loop tracer.

Figure 1 shows the effective permeability (μ_e) of $\text{Fe}_{88}\text{Zr}_7\text{B}_4\text{Cu}_1$ alloy as a function of annealing temperature (T_a). The ranges of maximum and minimum values (the bars indicate data scattering range) are shown in Fig. 1. With

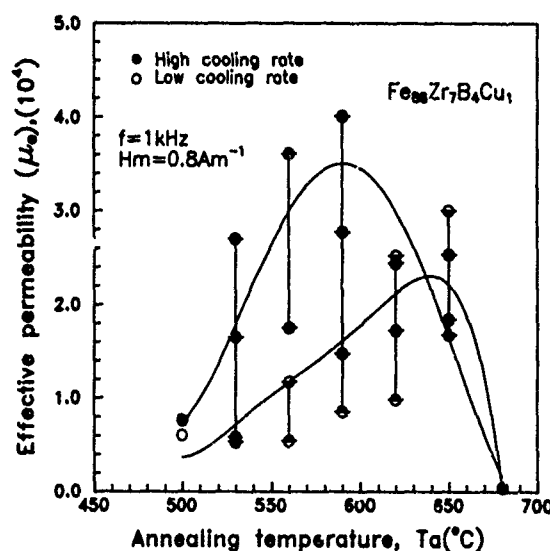


FIG. 1. The effective permeability (μ_e) at 1 kHz as a function of annealing temperature for $\text{Fe}_{88}\text{Zr}_7\text{B}_4\text{Cu}_1$ alloy annealed for 1 h. (The lines guide the eyes only.)

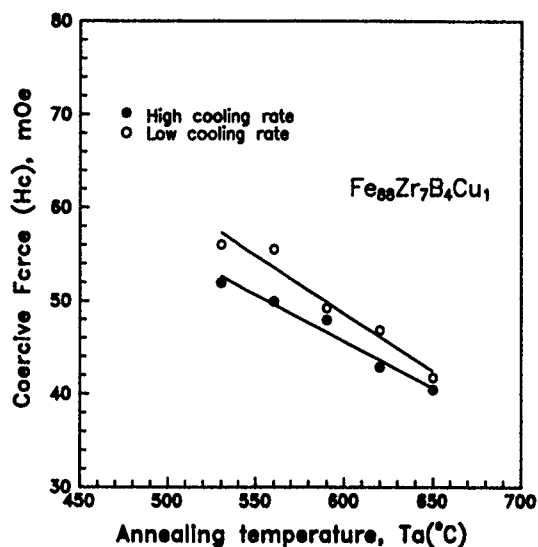


FIG. 2. The coercive force as a function of annealing temperature for $\text{Fe}_{88}\text{Zr}_7\text{B}_4\text{Cu}_1$ alloy annealed for 1 h. (The data points were obtained by averaging more than five results.)

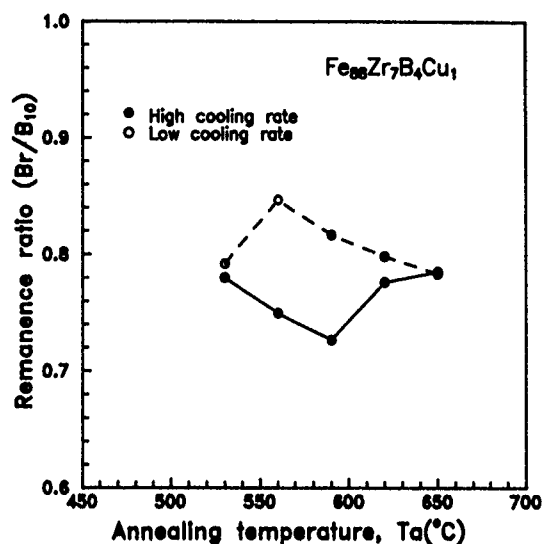


FIG. 3. The remanence ratio as a function of annealing temperature for $\text{Fe}_{88}\text{Zr}_7\text{B}_4\text{Cu}_1$ alloy annealed for 1 h. (The data points were obtained by averaging more than five results.)

onset of crystallization the effective permeability of the alloys from the higher cooling rate after annealing increases to about 4×10^4 . It is notable from Fig. 1 that this value is much higher than that of the alloys from the lower cooling rate (conventional method). The substantial improvement of μ_e can be explained by the decrease of induced magnetic anisotropy due to fast cooling rate. In the case of the higher cooling rate, the optimum annealing temperature is observed to be low compared to the lower cooling rate. μ_e begins to decrease with T_a above $T_a = 590^\circ\text{C}$. This may be caused by generation of internal stress due to very fast cooling after annealing.

Figure 2 shows the results for H_c as a function of T_a for the two different cooling rates. The coercive force decreases continuously with T_a regardless of the cooling rate. This indicates that the reciprocal relation between coercive force and permeability does not hold well for fast cooling where thermal stress is reintroduced at high T_a . As shown in Fig. 2, lower coercive force is obtained at all annealing temperatures for the higher cooling rate.

Figure 3 shows the remanence ratio (B_r/B_{10}) as a function of annealing temperature. The remanence ratio is a measure of the distribution of domain orientation and is strongly correlated with induced magnetic anisotropy.⁵ In ribbon-type amorphous and nanocrystalline soft magnets most of spontaneous magnetization is aligned to the direction of the ribbon axis. Therefore the self-induced magnetic anisotropy is considered to form along this direction. As shown in Fig. 3, the values of the remanence ratio in the higher cooling rate are low, indicating that the small induced magnetic anisotropy is formed during cooling. From this result, it is considered that induced magnetic anisotropy can be effectively suppressed by fast cooling after annealing. We examined the relationship between the effective permeability and the remanence ratio at all the temperatures investigated in this work and the result is shown in Fig. 4. Some kind of correlation between

these two quantities seems to exist. The increase of the remanence ratio is associated with the decrease of μ_e . In the case of the lower cooling rate, the values of remanence ratio are higher in most cases. This indicates induced magnetic anisotropy can be formed easily in the case of slow cooling.

From the above results it is found that a higher cooling rate has an advantage in obtaining higher permeability within the limit of creating no internal stress. The present result is in accord with that of Co-based amorphous alloys.⁶ As shown in Fig. 4, the remanence ratio which gives the maximum effective permeability is about 0.6. This value agrees well with the result of Yoshizawa *et al.*⁷ and Lim *et al.*⁸

The disaccommodation is of significant practical importance and is known to be affected by cooling rate. Therefore, we also investigated the time dependence of permeability in

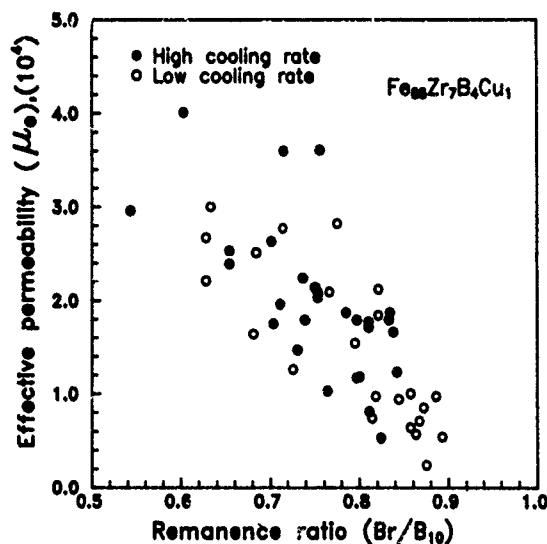


FIG. 4. The relationship between effective permeability at 1 kHz and the remanence ratio for $\text{Fe}_{88}\text{Zr}_7\text{B}_4\text{Cu}_1$ alloy annealed for 1 h.

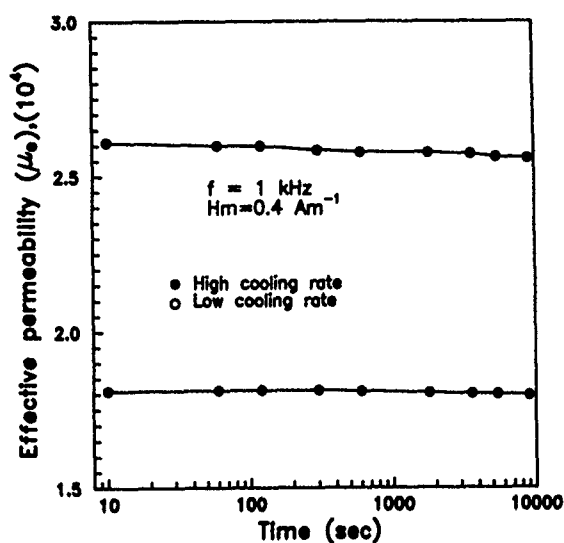


FIG. 5. The dependence of the permeability at 1 kHz on the time for $\text{Fe}_{88}\text{Zr}_7\text{B}_4\text{Cu}_1$ alloy annealed for 1 h.

the alloys obtained from different cooling rates. The result is given in Fig. 5. For the lower cooling rate little change in permeability is observed while for the higher cooling rate the permeability decreases slightly with time. Figure 6 shows the

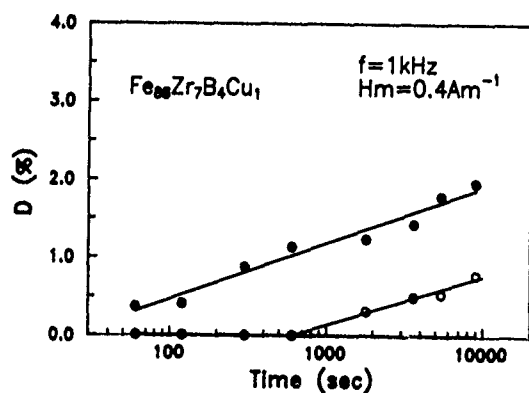


FIG. 6. Change in the intensity of disaccommodation as a function of time for $\text{Fe}_{88}\text{Zr}_7\text{B}_4\text{Cu}_1$ alloy annealed for 1 h.

intensity of disaccommodation (D) as a function of measured time. Here, D is defined by

$$D = \frac{\mu_e(10) - \mu_e(t_1)}{\mu_e(10)} \times 100(\%),$$

where $\mu_e(10)$ and $\mu_e(t_1)$ are the values of effective permeability measured at $t=10$ and $t=t_1$ s after demagnetization, respectively. In the case of $t=10$ and $t=9000$ s, the values of D are 1.9% and 0.8% for the alloys with higher and lower cooling rates, respectively. From this result, it can be seen that the higher μ_e which is obtained using a high cooling rate is related to the larger disaccommodation. This can be explained by the fast recovery rate of the frozen atoms, because free energy in the fast quenched state is high. In the case of slow cooling after annealing domain wall stabilization due to induced local magnetic anisotropy occurs during cooling, and lower permeability and lower disaccommodation are obtained.

We have investigated the effect of the cooling rate after annealing on the soft magnetic properties of an $\text{Fe}_{88}\text{Zr}_7\text{B}_4\text{Cu}_1$ alloy with nanoscale grain structure, which was prepared by melt quenching. Enhanced effective permeabilities are obtained for the alloys prepared by high cooling rates. The remanence ratio decreases with the cooling rate. The increase of permeability and decrease of remanence ratio are considered to result from the suppression of the induced magnetic anisotropy.

We have also investigated relationship between disaccommodation and cooling rate. In the higher cooling rate, the value of D is a little higher than that in the lower cooling rate. The low value of D in the slow cooling can be explained by domain structure stabilization due to local induced magnetic anisotropy.

¹Y. Yoshizawa, S. Oguma, and K. Yamauchi, *J. Appl. Phys.* **64**, 6044 (1988).

²K. Suzuki, A. Makino, N. Kataoka, A. Inoue, and T. Masumoto, *Mater. Trans. JIM* **32**, 93 (1991).

³K. Suzuki, M. Kikuchi, A. Makino, A. Inoue, and T. Masumoto, *Mater. Trans. JIM* **32**, 961 (1991).

⁴H. Sakakima, H. Senno, Y. Yanagiuchi, and E. Hirota, *J. Appl. Phys.* **52**, 2480 (1981).

⁵S. Chikazumi, *Physics of Magnetism* (Wiley, New York, 1964).

⁶T. Kulik and J. Lisiecki, *J. Magn. Magn. Mater.* **109**, 228 (1992).

⁷Y. Yoshizawa and K. Yamauchi, *J. Jpn. Inst. Met.* **63**, 241 (1989).

⁸S. H. Lim, W. K. Pi, T. H. Noh, H. J. Kim, and I. K. Kang, *J. Appl. Phys.* **73**, 865 (1993).

Soft-magnetic properties of amorphous tapes after dynamic current annealing

M. A. Escobar

Instituto de Investigaciones en Materiales, UNAM, A.P. 70-360, 04510 México, D. F., Mexico

J. C. Perron

Laboratoire de Génie Electrique de Paris (CNRS-UA127), ESE, 91192 Gif Sur Yvette, France

R. Barrué

LESIR-ENS de Cachan, 61 Avenue Président Wilson, 94235 Cachan, France

A. R. Yavari

LTPCM (CNRS-UA29), Institut National Polytechnique de Grenoble, B.P. 75, 38402 St. Martin d'Hères, France

The magnetic properties of amorphous FeSiB (2605-S2) and CoFeMoSiB (6025-Vac) tapes have been measured after conventional furnace annealing and dynamic current annealing, which takes place in air and during the winding process of tapes using Joule heating. The measurements showed a significant improvement of the magnetic properties when dynamic annealing temperatures are far below the crystallization temperatures but above the Curie temperature. Magnetic properties and domain patterns are presented and we find that our method of about 10 s of annealing gives a similar magnetic quality to that obtained by classical techniques.

The improvement of soft-magnetic properties of metallic glasses is attained after heat treatments destined to induce relaxation of both internal stresses to zones of quenched-in density fluctuation and external stresses due to imposed shapes, such as those imposed by a curved shape of a transformer toroid manufactured with magnetostrictive materials, as for example, FeSiB tapes. The relaxation of these stresses requires diffusive motion especially of structural defects, whose kinetics also control structural relaxation in general.¹⁻³

Relaxation for improvement of magnetic properties of amorphous tapes is usually induced by ≈ 2 h of furnace annealing at temperatures lower than the Curie temperature under inert gas. Joule heating was also shown to have a strong effect on structure and magnetic properties of metallic glasses after current-annealing times of the order of milliseconds (flash annealing) to several minutes.⁴⁻⁶ It had also been shown⁷ that rapid Joule heating for about 20 s just below the crystallization temperature of FeSiB glassy tapes resulted in improvement of all measured magnetic properties which were then better than those of tapes classically relaxed by furnace annealing.

We have conceived and used a new dynamic relaxation process, hereafter referred to as dynamic current annealing (DCA), which can use continuous Joule heating during the winding process of tapes as they slide on a cylindrical surface of a chosen curvature at which the tape will be used. The setup, which also quenches the tapes down to room temperature before they leave the cylinder, allows dynamic current annealing times of amorphous tapes of the order of seconds, at temperatures near crystallization, $T \approx T_x$, in air. The winding speed of the tapes can be fixed. Application of this technique during winding of transformer toroids with FeSiB amorphous tapes was found to give very good magnetic properties.⁸ The procedure, which also raises some interesting questions concerning stress and structural relaxation in

amorphous alloys, is described in more detail in a previous paper.⁹

The aim of this work was to assess the effect on magnetic properties of amorphous tapes of different thermal relaxation techniques, namely, classical furnace annealing versus dynamic current annealing using Joule heating.

The amorphous $\text{Fe}_{78}\text{Si}_9\text{B}_{13}$ and $\text{Co}_{66}\text{Fe}_4\text{Mo}_2\text{Si}_{16}\text{B}_{12}$ samples used in this study were purchased batches from Allied Signal and Vacuumschmelze, respectively, in lengths of several hundred meters. Table I gives some characteristics of the samples used. FeSiB was chosen for its highly positive magnetostriction and the CoFeMoSiB for its almost zero magnetostriction.

We have carried out on these tapes three different thermal relaxation treatments:

- (1) A furnace annealing (FA) under inert gas to 380 °C during 2 h for the FeSiB tape, and 430 and 240 °C for 1-h periods for the CoFeMoSiB tape.
- (2) A furnace field annealing (FFA) on FeSiB sample, similar to the previous one but with an applied magnetic field (800 A/m) directed along the tape axis.
- (3) Our dynamic current annealing process,⁹ which had been used to relax FeSiB and CoFeMoSiB amorphous tapes at temperatures above T_c for times of the order of 2 s.

The temperature profiles and maximum temperatures were determined from thermocouples and pyrometric readings. A radius of curvature $r=4$ cm was chosen with tape rolling

TABLE I. Sample characteristics (approximate values).

	FeSiB	CoFeMoSiB
Curie temperature, T_c	415 °C	250 °C
Crystallization temperature, T_x	550 °C	500 °C
Width	25 mm	10 mm
Thickness	19 μm	28 μm

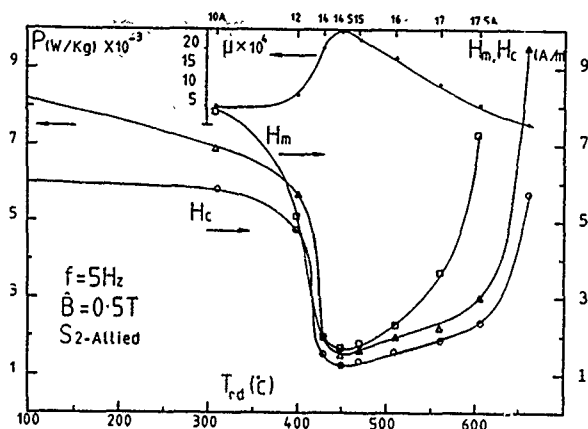


FIG. 1. Evolution of magnetic power losses P , coercive field H_c , relative permeability μ , and maximum field H_m at $B=0.5\text{ T}$ and $f=5\text{ Hz}$, of the FeSiB alloy vs maximum dynamic current annealing temperature T_{rd} (°C) and dynamic annealing current I (A).

speed of $v=1\text{ cm/s}$. To assure good contact between the tape and the current leads, the moving tape was maintained under a measured tensile stress of $\approx 50\text{ MPa}$. The strength of electric currents used in our dynamic treatment of FeSiB and CoFe-based tapes were between 9 and 18 A.

Three techniques for magnetic characterization were used to assess the effect on magnetic properties of amorphous tapes annealed with the various treatments given previously. (1) Magnetic measurements under sinusoidal flux on transformer toroid. Magnetic properties data were obtained by numerical integration of digitized hysteresis loops. Magnetic power losses P (W/kg), relative permeability μ , coercive field H_c (A/m), and maximum field H_m (A/m) at peak induction value B (T), were measured as a function of frequency f and of temperature of dynamic current annealing T_{DCA} (or T_{rd}). (2) Observation of domain structures using the magneto-optic Kerr effect. (3) Determination of the saturation magnetostriction λ_s , using a linear capacitive high precision dilatometer.^{10,11} At each stage the samples were usually checked for appearance of crystallinity by x-ray diffraction and differential scanning calorimetry (DSC).

Figure 1 shows the evolution of the magnetic properties (P , H_c , μ , and H_m), of the FeSiB alloy annealed by our dynamic process as a function of the current strength I (A) and maximum temperature T_{rd} ($\pm 10^\circ\text{C}$) reached during dynamic current annealing, at peak induction value $B=0.5\text{ T}$ and $f=5\text{ Hz}$. The most remarkable result is that the magnetic properties improve very rapidly in the T range $410 < T < 450^\circ\text{C}$, close to the Curie temperature. The optimum magnetic properties, that is minimal P and H_c and maximum μ , were found at $T_{rd} \approx 450^\circ\text{C}$ and $I=14.5\text{ A}$, respectively. The x-ray patterns and DSC experiments⁹ show that the degradation of the magnetic properties for currents $I \geq 17\text{ A}$ can indeed be attributed to the onset of crystallization and that for $I=16\text{ A}$ no significant crystallization is occurring.

Figure 2 compares the magnetic power losses at 50 Hz, of FeSiB amorphous tapes annealed in different conditions. Results are presented for the as-quenched (AQ) sample before and after FA, FFA, and DCA for $I=14.5\text{ A}$. For all

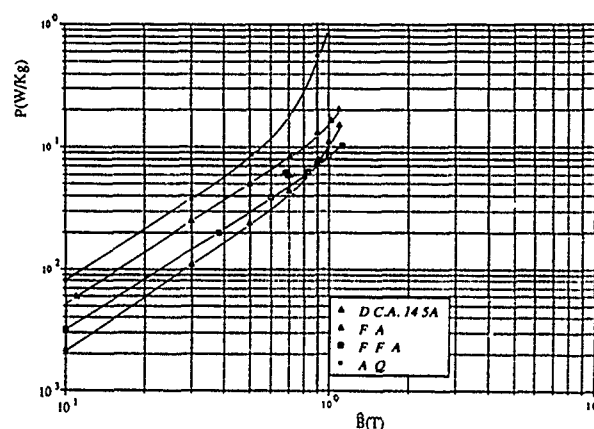


FIG. 2. Magnetic power losses P vs peak induction value B at $f=50\text{ Hz}$ for FeSiB tapes annealed by different techniques.

induction levels we observe that the magnetic losses of the DCA sample are less than the FA sample. They are also smaller than the FFA sample if the peak induction is smaller than 1 T. Figure 3 shows the peak induction B versus applied field H for the same samples at $f=50\text{ Hz}$. For all applied field levels, the magnetization curve $B(H)$ of the DCA sample is better than the FA sample one. It is also better than the FFA sample one if the peak induction is smaller than about 0.7 T. Figure 4 shows the magnetization curve $B(H)$ for the CoFe-base sample, after FA and DCA for $I=9\text{ A}$, at $f=5\text{ Hz}$ and 50 kHz, respectively. The absence of any significant difference between the magnetization curves at 5 Hz and 50 kHz for the DCA sample indicates no significant dependence of the frequency in this range.

To obtain information on the magnetic moment distributions of our samples, we have performed observations of domain structures using the magneto-optic Kerr effect. Figure 5 shows the domain patterns of FeSiB samples in the middle of the tapes. In Fig. 5(a) we observe the complex pattern of domains in the AQ sample. In Fig. 5(b) we observe that the FA sample exhibits relatively large domains whose orientation is ill defined. The FFA and DCA samples present similar magnetic structures with domains oriented along the

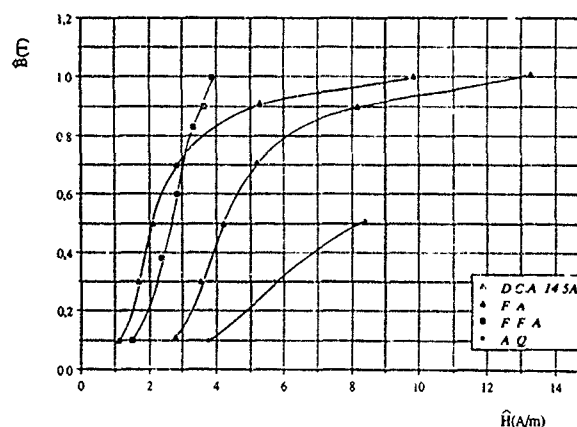


FIG. 3. Magnetization curves; peak induction value B vs applied field H at $f=50\text{ Hz}$ for FeSiB tapes annealed by different techniques.

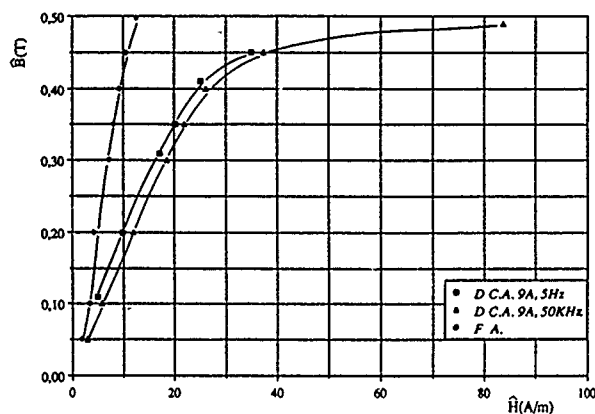


FIG. 4. Peak induction value B vs applied field H at 5 Hz and 50 kHz for CoFeMoSiB tapes annealed in different conditions.

ribbon axis [Figs. 5(c) and 5(d)]. Figure 6 shows the domains of the CoFe-base amorphous tapes for the AQ sample and the DCA sample to $I=9$ A. It was found that the DCA sample presents a narrow domain structure perpendicular to the ribbon axis.

We have measured and examined the evolution of the saturation magnetostriction λ_s of Fe- and CoFe-base amorphous tapes after FA and DCA. It was found that although very different in all respects, the two types of annealing can produce the same results, including the same optimum values of magnetostriction, indicating equivalent structural relaxation and chemical short range order states.¹⁰

The effects responsible for the improvement of the magnetic properties and in particular the magnetic anisotropy induced by our DCA, are probably due to plastic deformation and to the thin surface oxide layer that forms during the DCA in air and that puts the plane of the tapes under tension. These beneficial effects and the effect of T_c on the relaxation kinetics of amorphous tapes can only be speculative at this point and further experiments are needed and planned.

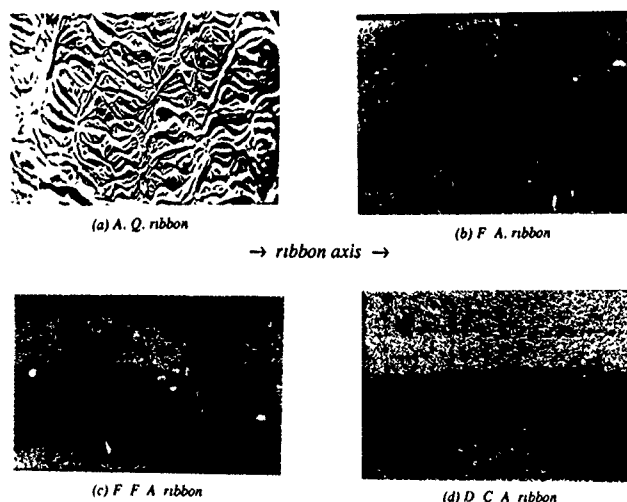
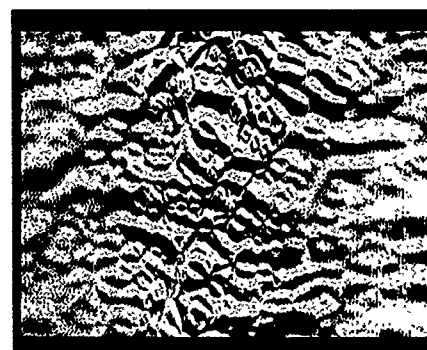
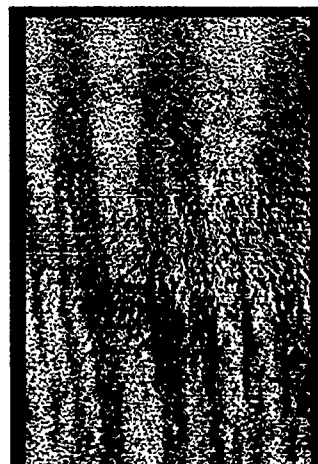


FIG. 5. Domain structure observed by Kerr effect for the FeSiB samples. We observe the magnetic anisotropy induced by our DCA at 14.5 A.



A. Q.

→ ribbon axis →



D. C. A., 9A

FIG. 6. Domain structure observed by Kerr effect for the CoFeMoSiB sample. We observe the magnetic anisotropy induced by our DCA at 9 A.

The dynamic current annealing process yields excellent magnetic properties of ferromagnetic amorphous tapes compared with those obtained by classical furnace annealing and close to those of furnace field annealed tapes. The best magnetic properties of commercial FeSiB and CoFeMoSiB tapes were attained after only about 10 s of annealing in air far below the crystallization temperatures but above the T_c . For industrial purposes it is possible to render this process continuous.

- ¹ A. I. Taub and F. Spaepen, *Acta Metall.* **28**, 1781 (1980).
- ² A. I. Taub and F. Luborsky, *Acta Metall.* **29**, 1939 (1981).
- ³ A. R. Yavari, *J. Mater. Res.* **1**, 745 (1986).
- ⁴ T. Jagielinski, *IEEE Trans. Magn.* **19**, 1925 (1983).
- ⁵ A. Zaluska and H. Matyja, *J. Mater. Sci. Lett.* **2**, 729 (1983).
- ⁶ J. González, M. Vázquez, J. M. Barandiaran, and A. Hernando, *J. Phys. D* **21**, 162 (1988).
- ⁷ A. R. Yavari, R. Barrué, M. Harmelin, and J. C. Perron, *J. Magn. Mater.* **69**, 43 (1987).
- ⁸ M. A. Escobar, R. Barrué, A. T. Tabarsi, J. C. Perron, and A. R. Yavari, *An. de Fis.* **86-B**, 178 (1990).
- ⁹ M. A. Escobar, A. R. Yavari, R. Barrué, and J. C. Perron, *IEEE Trans. Magn.* **28**, 1911 (1992).
- ¹⁰ M. A. Escobar, A. R. Yavari, E. T. de Lacheisserie, and J. González, *Mater. Sci. Eng. A* **133**, 184 (1991).
- ¹¹ E. T. de Lacheisserie, *Rev. Fr. Méc.* **64**, 19 (1977).

Magnetic behavior of the amorphous wires covered by glass

Horia Chiriac, Gheorghe Pop, and Firuta Barariu
Institute of Technical Physics, Str. Splai Bahlui 47, P.O. Box 2027, 6600 Iasi, Romania

Manuel Vázquez
Institute of Applied Magnetism, P.O. Box 155, 28230 Las Rozas, Madrid, Spain

Magnetic properties are presented of amorphous wires covered by glass, with the compositions $\text{Fe}_{65}\text{B}_{15}\text{Si}_{15}\text{C}_5$, $\text{Fe}_{60}\text{B}_{15}\text{Si}_{15}\text{Cr}_{10}$, and $\text{Fe}_{40}\text{Ni}_{40}\text{P}_{14}\text{B}_6$, which were prepared by melting the alloy in glass tubes and drawing fibers from the softened glass. The magnetization, the remanence, and the coercive force of the samples covered by glass, and of those obtained after removing the glass cover, were measured at a field of 2054 A/m. These amorphous wires have a square-shaped hysteresis loop, a value of the coercive force ranging between 255 and 462 A/m and an axial magnetization of 0.21–0.32 T for different compositions. The glass removal leads to an increase in magnetization and a decrease in the coercive force. The influence of a passing dc current through the wire during measurements has also been studied, influence that is much pronounced in the case of the wires obtained after removing the glass cover. The observed different magnetic properties of the amorphous magnetostrictive wires are attributed to the difference in internal stress distribution produced during preparation of the samples.

I. INTRODUCTION

Amorphous ferromagnetic wires present a special interest due to their magnetic properties that make them useful in sensor devices. Usually they are studied as as-quenched amorphous wires of about 125 μm in diameter,¹ obtained by the "in-rotating-water spinning method" and cold drawn in several steps down to 50 μm or lower from the 125 μm one.² The aim of this article is the study of the behavior of the amorphous wires in glass cover, having the compositions FeBSiC, FeBSiCr, and FeNiPB, with diameters ranging from 10 to 26 μm . Based on our knowledge this is the first work on the magnetic properties of the amorphous wires covered by glass.

These wires were obtained by an improved variant of the Taylor method, which consists of sealing one end of the glass tube in which the master alloy was introduced, heating the end of the tube to a temperature at which the glass is soft and the alloy molten, and drawing a fiber from the heated end. In this way metallic amorphous wires were obtained in glass cover with diameters ranging between 5 and 30 μm . The amorphous state was checked by x-ray diffraction, differential thermal analysis and thermomagnetic measurements.

II. EXPERIMENTAL PROCEDURE

The magnetization value of the above-mentioned alloys was measured by the fluxmeter method³ at 500 Hz in an alternating sinusoidal field having a maximum value of 2054 A/m, on samples 10 cm in length. The remanence and the coercive force were determined from the hysteresis loops plotted on an X-Y digital oscilloscope. We measured the saturation magnetization of these alloys using a vibrating sample magnetometer. We also studied the influence of a direct current passing through the wires during measurements. The magnetic field H_p created by this current corresponds to the maximum circular field at the surface of the wire, given by the following expression:

$$H_p = \frac{I}{2\pi R_w},$$

where I is the value of the direct current which passes through the wire and R_w is the radius of the metallic wire. In order to avoid a significant heating of the wires, the current passes through them just for a few seconds.

The magnetic measurements were made on as-quenched samples (wires covered by glass) and after the glass removal. The glass was removed by chemical etching. We used successively different concentration solutions based on hydrofluoric acid (38% and lower). Optical and electrical methods were used to have a careful control of the removing process, in order to avoid any reactions between the chemical solutions and the metallic wire.

III. RESULTS AND DISCUSSION

The values of the saturation magnetization for the studied alloys are: 1.50, 0.80, and 0.79 T for FeBSiC, FeBSiCr, and FeNiPB, respectively.

Table I illustrates the results of the measurements on the amorphous wires covered by glass with diameters ranging from 18 to 26 μm . All these samples present a square-shaped hysteresis loop, a high value of the coercive force ($H_c = 250$ –450 A/m) as compared with that of the amorphous ribbons or amorphous wires obtained by the in-

TABLE I. Magnetic properties of amorphous wires in glass cover, at a measuring field of 2054 A/m.

Composition	M (T)	H_c (A/m)	M_r/M_s	$10(R_c/R_w)$	H_p (A/m)
$\text{Fe}_{65}\text{B}_{15}\text{Si}_{15}\text{C}_5$	0.32	462	0.21	0.44	0
$\text{Fe}_{65}\text{B}_{15}\text{Si}_{15}\text{C}_5$	0.32	414	0.21	0.44	318
$\text{Fe}_{60}\text{B}_{15}\text{Si}_{15}\text{Cr}_{10}$	0.21	358	0.26	0.68	0
$\text{Fe}_{60}\text{B}_{15}\text{Si}_{15}\text{Cr}_{10}$	0.16	287	0.20	0.4	350
$\text{Fe}_{40}\text{Ni}_{40}\text{P}_{14}\text{B}_6$	0.31	255	0.36	1.3	0
$\text{Fe}_{40}\text{Ni}_{40}\text{P}_{14}\text{B}_6$	0.29	239	0.33	1.09	245

TABLE II. Magnetic properties of amorphous wires after removing the glass, at a measuring field of 2054 A/m.

Composition	M (T)	H_c (A/m)	M_r/M_s	$10(R_c/R_w)$	H_p (A/m)
Fe ₆₅ B ₁₅ Si ₁₅ C ₅	0.65	207	0.37	1.37	0
Fe ₆₅ B ₁₅ Si ₁₅ C ₅	0.65	167	0.33	1.09	245
Fe ₆₅ B ₁₅ Si ₁₅ O ₅	0.65	151	0.23	0.53	490
Fe ₆₀ B ₁₅ Si ₁₅ Cr ₁₀	0.49	119	0.61	3.72	0
Fe ₆₀ B ₁₅ Si ₁₅ Cr ₁₀	0.35	88	0.35	1.23	290
Fe ₆₀ B ₁₅ Si ₁₅ Cr ₁₀	0.28	88	0.18	0.32	579
Fe ₄₀ Ni ₄₀ P ₁₄ B ₆	0.80	127	0.82	6.72	0
Fe ₄₀ Ni ₄₀ P ₁₄ B ₆	0.73	111	0.65	4.23	490

rotating-water spinning method having the same composition. When a dc current passes through the wire, a significant change in the squareness of the hysteresis loop cannot be observed, but a decrease in the coercive force is observed. A decrease in the axial magnetization of all samples can also be observed. After removing the glass from the amorphous wires, the measurements show an increase in magnetization and a pregnant decrease in the coercive force. These results are illustrated in Table II. For these samples, the most pronounced increase in the value of the magnetization is observed for the FeNiPB alloy, at the maximal value of the measuring field. The most pronounced decrease in the coercive force is observed for the FeBSiCr samples.

Covered wires have strong transverse anisotropy as supported by the small values of M_r/M_s . After removing the glass cover, transverse anisotropy partially relaxes (M_r/M_s increases). Because of bistability, the wires (covered and after removing the glass) have a domain structure with an inner core (axially magnetized) and an outer shell (with transverse anisotropy). The radius of the core R_c can be estimated as

$$R_c = \left(\frac{M_r}{M_s} \right)^2 R_w,$$

where R_w is the radius of the metallic wire. The ratio R_c/R_w increases after removing the glass cover because the transverse anisotropy, induced by the glass cover, relaxes.⁴ Reduction of coercivity after glass removal is a consequence of removing the stresses induced by the cover.

When a direct current passes through these samples, a decrease in the magnetization and in the coercive force can be observed. Figure 1 shows the hysteresis loops for the samples covered by glass [Fig. 1(a)] and after removing the glass [Fig. 1(b)]. Figures 2(a) and 2(b) show the hysteresis loops for a FeBSiCr sample covered by glass and after removing the glass cover, respectively. At the same time, these figures illustrate the influence of a direct current that passes through the samples during measurements. Asymmetry of the hysteresis loop produced by the current through the wire is observed. It is much more pronounced when the current increases. The observed shift in the loop is found to follow the direction of the current. The bistable behavior of the amorphous wires has been explained by the fact that the macroscopic magnetization processes in these materials are especially determined by the magnetoelastic anisotropy, due to the coupling between the internal stresses induced by the fabrication process and the magnetostriction constant of the

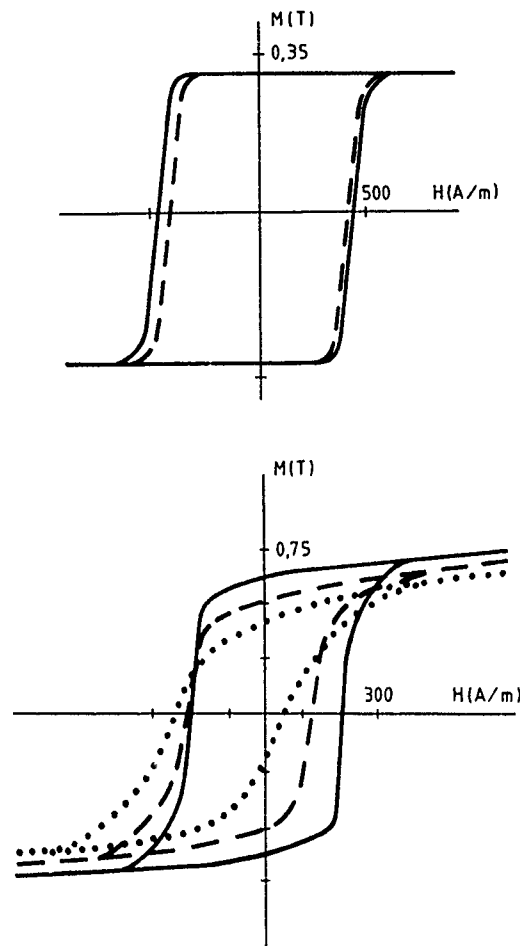


FIG. 1. M - H loops of Fe₆₅B₁₅Si₁₅C₅ amorphous wires: (a) in glass cover, $H_p=0$ A/m (solid line), $H_p=318$ A/m (dashed line), (b) after removing the glass cover, $H_p=0$ A/m (solid line), $H_p=245$ A/m (dashed line), $H_p=490$ A/m (dotted line).

material. This behavior is in accord with the model proposed by Humphrey *et al.*,⁵ Kinoshita,⁶ and Mitra and Vázquez.⁷ These wires have high positive magnetostriction constants ($\lambda \approx 10^{-5}$) and they behave as if they were made of two distinct regions, an axially magnetized inner core and a radially magnetized outer shell. The differences in magnetic behavior of the amorphous wires covered by glass and that of the same wires after removing the glass indicate a transverse anisotropy induced by the glass cover, as mentioned before. For the samples covered by glass, at the maximal value of the measuring field, the square-shaped hysteresis loops and the small value of the axial magnetization show a high value of the induced transverse anisotropy and it stretches on a large region as compared with that occupied by the axially magnetized inner core.

The shape of the hysteresis loops after removing the glass cover, the magnitude of the measured magnetic parameters, and their changes produced by the dc current through the wires agree with the above-mentioned model. At the same measuring field the magnetization of these samples after removing the glass cover is, however, lower than that of the samples with the same compositions, obtained by the in-rotating-water spinning method⁸ or by cold-drawing process; the FeNiPB alloy is an exception.⁹ This behavior sug-

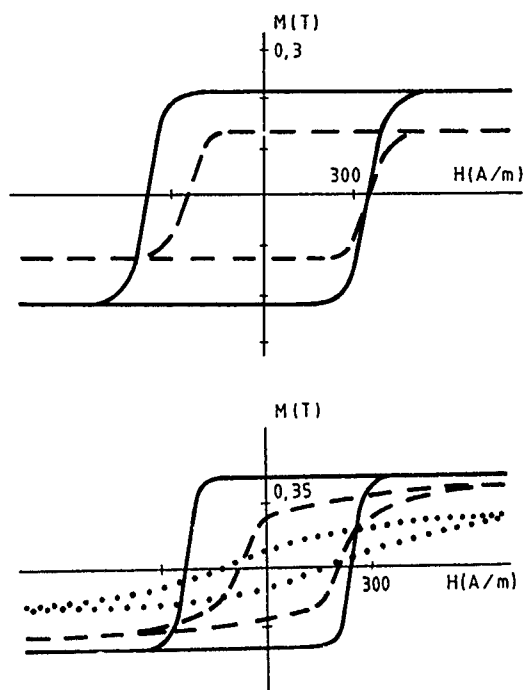


FIG. 2. M - H loops of $\text{Fe}_{60}\text{B}_{15}\text{Si}_{15}\text{Cr}_{10}$ amorphous wires: (a) in glass cover, $H_p = 0$ A/m (solid line), $H_p = 350$ A/m (dashed line); (b) after removing the glass cover, $H_p = 0$ A/m (solid line), $H_p = 290$ A/m (dashed line), $H_p = 579$ A/m (dotted line).

gests the existence of another ratio between the dimensions of the axially and radially magnetized regions, namely, the increase of the radially magnetized outer shell due to the internal stresses induced by the presence of the glass cover during the fabrication process. The thickness of the radially magnetized outer shell is reduced after removing the glass cover.

IV. CONCLUSION

The metallic amorphous wires obtained by a variant of the Taylor method¹⁰ exhibit a square-shaped hysteresis loop and a high value of the coercive force. This behavior makes them useful to generate sharp voltage pulses. Passing a dc current through these wires does not change the squareness of the hysteresis loops. It produces only a decrease of the coercive force with maximum 20%. The removal of the glass cover leads to a change in the shape of the hysteresis loop, a decrease in the value of the coercive force of about 50%, accompanied by an increase in the magnetization value, at the same value of the measuring field. It also leads to a higher variation of the magnetic parameters versus the value of the passing current through the sample. We also observed the influence of passing the dc current through the wires on these parameters, during measurements. Comparative measurements between the samples covered by glass and those obtained after glass removal were performed.

- ¹M. Hagiwara, A. Inoue and T. Masumoto, *Metall. Trans. A* **13**, 373 (1982).
- ²I. Ogasawara and K. Mohri, *IEEE Trans. Magn.* **MAG-26**, 1795 (1990).
- ³K. Mandal and S. K. Ghatak, *J. Magn. Magn. Mater.* **118**, 315 (1993).
- ⁴A. M. Severino, C. Gomez-Polo, P. Marin, and M. Vázquez, *J. Magn. Magn. Mater.* **103**, 117 (1992).
- ⁵F. B. Humphrey, K. Mohri, J. Yamasaki, H. Kawamura, R. Malmhall, and I. Ogasawara, in *Proceedings of the Symposium on Magnetic Properties of Amorphous Metals*, edited by A. Hernando, V. Madurga, M. C. Sánchez-Trujillo, and M. Vázquez (North-Holland, Amsterdam, 1987), p. 110.
- ⁶F. Kinoshita, *IEEE Trans. Magn.* **MAG-20**, 1786 (1990).
- ⁷A. Mitra and M. Vázquez, *J. Magn. Magn. Mater.* **87**, 130 (1990).
- ⁸H. Chiriac, F. Barariu and Gh. Pop, Paper S3-30 at SMM11, Venezia, Sept. 1993 (to appear in *J. Magn. Magn. Mater.* **133**, 1994).
- ⁹H. H. Liebermann, *IEEE Trans. Magn.* **MAG-17**, 1286 (1981).
- ¹⁰G. F. Taylor, *Phys. Rev.* **24**, 655 (1924).

Tensor components of the magnetization in a twisted Fe-rich amorphous wire

L. Kraus,^{a)} S. N. Kane, M. Vázquez,^{b)} G. Rivero, E. Fraga, and A. Hernando
Instituto de Magnetismo Aplicado, Laboratorio "Salvador Velayos," Apdo. Correos 155, 28230 Las Rozas, Madrid, Spain

J. M. Barandiarán

Dpto de Electricidad y Electronica, Universidad del Pais Vasco, Apartado 644, 48080 Bilbao, Spain

Four components of the susceptibility tensor of a high magnetostrictive amorphous $\text{Fe}_{77.5}\text{Si}_{7.5}\text{B}_{15}$ wire are investigated by means of ac hysteresis loop measurements. The samples have been carefully annealed in order to eliminate the internal stresses produced during the quenching. When tensile stress and/or torsion are applied bistable magnetic behavior with a large Barkhausen jump is observed. The effect of applied torque on the longitudinal and circular components of remanence magnetization and on the longitudinal and circular coercive fields is studied for different constant values of tensile stress. With increasing torque the axial and circular components of remanence decrease and increase, respectively, approaching the limit value of $0.71 M_s$. The axial coercive fields for the axial and radial magnetization components coincide. They are nearly constant at low torsion and above same threshold value, depending on applied stress, follow approximately a square-root dependence on applied torque. When tensile stress is applied the circular coercive fields show a well pronounced minimum at the same threshold torque. The experimental results are interpreted by taking into account the axial and helical components of magnetic anisotropy induced by magnetoelastic coupling.

The most outstanding property of Fe-rich amorphous wires—magnetic bistability—is a consequence of the particular distribution of internal stresses introduced by the rapid quenching process.¹ The magnetic bistability can be excited by axial H_z or circular H_ϕ magnetic fields and can be observed for both the axial M_z and circular M_ϕ magnetization components. In general, the relation between the two components of magnetization and the two components of magnetic field are described by the susceptibility tensor χ

$$\begin{pmatrix} M_z \\ M_\phi \end{pmatrix} = \begin{pmatrix} \chi_{zz} & \chi_{z\phi} \\ \chi_{\phi z} & \chi_{\phi\phi} \end{pmatrix} \begin{pmatrix} H_z \\ H_\phi \end{pmatrix}. \quad (1)$$

The diagonal components of χ correspond to the axial (M_z - H_z) loop and so called magnetoinductive (M_ϕ - H_ϕ) effect,² respectively. The nondiagonal terms are related to inverse Wiedemann (M_z - H_ϕ) and Matteucci (M_ϕ - H_z) effects.^{3,4} For the appearance of inverse Wiedemann and Matteucci effects the presence of helical magnetic anisotropy is required. This can be introduced by applied torque or by torsion annealing.

Most of the previous works deal with the conventional M_z - H_z magnetization process where the bistability is interpreted by magnetization reversal in the inner core of the wire. More complex interpretation is needed when studying the nondiagonal magnetization process or the circular magnetization process in the magnetoinductive effect. In some previous papers²⁻⁴ also the other types of hysteresis loops have been separately studied.

The aim of the present work is to measure and analyze all four components of the susceptibility tensor. In this way, a deeper information about magnetization distribution and magnetizing process can be obtained. In order to start from a more homogeneous anisotropy distribution, the internal stresses were relieved by preannealing treatment. The effect of axial and helical anisotropies was then studied by applying tensile stress and torque.

Amorphous wire $\text{Fe}_{77.5}\text{Si}_{7.5}\text{B}_{15}$ (diameter 131 μm) was kindly supplied by Unitika Co., Japan. Alternating current hysteresis loops M_z - H_z , M_z - H_ϕ , M_ϕ - H_z , and M_ϕ - H_ϕ of a 31.2-cm-long sample were measured under various applied torque and/or tensile stress. Alternating current magnetic field of frequency 11 Hz to 5.5 kHz was provided by passing triangular-wave current through either the magnetizing solenoid (H_z) or the wire (H_ϕ). The output voltage taken either from a 4-cm-long pickup coil (at the center of the sample) or between the ends of the wire was electronically integrated and supplied to one channel of a digital oscilloscope. To the other channel a voltage proportional to the driving current was supplied. The ohmic component of the output voltage produced by the driving current through the wire (in case of M_ϕ - H_ϕ measurements) was subtracted by means of a resistance Wheatstone bridge. The wire was current annealed for 2 min with a dc current of 605 mA in order to eliminate the internal stresses produced by the quenching.

The influence of applied torque ξ on the hysteresis properties was investigated at the frequency of 110 Hz. The example of a set of four hysteresis loops is shown in Fig. 1. In the case of M_z - H_ϕ and M_ϕ - H_ϕ measurements the circular magnetic field h_ϕ produced by electric current through the wire is nonuniform so we use the "ballistic" average of the field $H_\phi = (1/R) \int h_\phi dr = jR/4$, where j is the current density and R the radius of the wire.

^{a)}On leave from Institute of Physics, Academy of Sciences of Czech Republic, Na Slovance 2, 18040 Prague 8, The Czech Republic.

^{b)}On leave from Instituto de Ciencia de Materiales, Serrano 144, 28006 Madrid, Spain.

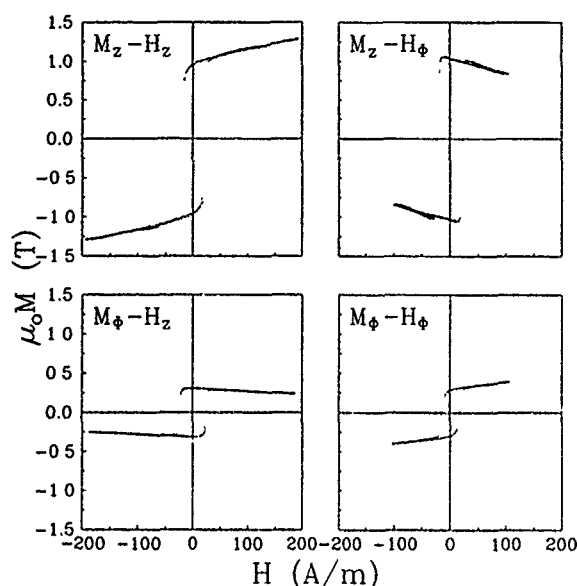


FIG. 1. Hysteresis loops of the stress-relieved amorphous $\text{Fe}_{77}\text{Si}_{15}\text{B}_{15}$ wire (frequency=110 Hz, torque $\xi=1.67$ rad/m, tensile stress $\sigma=0$).

All four hysteresis loops are sensitive to applied stress and torque. For $M_\phi-H_z$ and M_z-H_ϕ no hysteresis is observed at zero torque which indicates that there is no spontaneous helical anisotropy in the stress-relieved wire. In the strain-free state ($\sigma, \xi=0$) the M_r/M_s ratios of the M_z-H_z and $M_\phi-H_\phi$ loops are 0.56 and 0.40, respectively, which can be accounted for the presence of domain structure and the usual magnetization reversal by domain wall movement and rotational processes. With a small tensile stress and/or torque all the loops became rectangular and the magnetization reversal takes place by a large Barkhausen jump between two nearly saturated states.

The effect of applied strain on magnetic properties is related to magnetic anisotropy induced by magnetoelastic coupling. In an amorphous wire under simultaneous action of tensile stress σ and torsional strain ξ the magnetoelastic free energy is given by

$$E_a(r) = -(3/2)\lambda_s(\sigma\alpha_z^2 + 2\mu\xi r\alpha_\phi\alpha_z), \quad (2)$$

where μ is the shear modulus, r the distance from the axis of the wire, and α_ϕ, α_z are the circular and axial components of the vector M/M_s , respectively. Provided there is no intrinsic stress one obtains for $\lambda_s > 0$ an orthorhombic anisotropy with the local easy direction along the helical path at the angle

$$\Theta = (1/2)\arctan(2\mu\xi r/\sigma) \quad (3)$$

with respect to the wire axis. For $\sigma=0$ one has $\Theta=45^\circ$ in the whole volume. For $\sigma>0$ the angle Θ continuously increases from zero at the axis to $\Theta_0<45^\circ$ at the surface of the wire. Using Eq. (3) most of the experimental results can be explained.

In Fig. 2 the dependencies of M_r/M_s vs applied torque ξ are shown for three different levels of tensile stress σ . The experimental data are compared with the theoretical curves calculated with the assumption that there are no magnetic domains and the local magnetization is parallel to the local

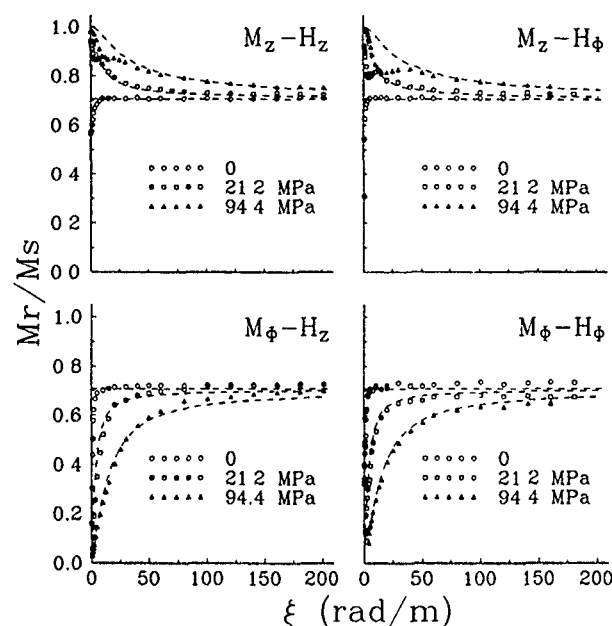


FIG. 2. Remanence-to-saturation ratio vs applied torque.

easy direction. The axial and circular remanences are obtained by averaging $M_s \cos \Theta$ and $M_s \sin \Theta$, respectively, over the appropriate cross sections of the wire. ($\mu=6 \times 10^{10}$ Pa and $\mu_0 M_s=1.55$ T were used for the calculations). It can be seen that except for low torsion the experimental data agree well with the theoretical curves. For $\sigma=0$ the remanence rapidly approaches the value $0.71 M_s$, expected for helical saturation at 45° . The approach to this limit value is much slower when tensile stress is applied because of the competition between the axial and helical anisotropies induced by stress and torque, respectively. Discrepancies between experimental and calculated behavior for the range of small applied torques should be related to the presence of some closure domains at the surface of the wire. This explanation is supported by the shape of M_z-H_z and M_z-H_ϕ loops in this range of ξ . The loops are curved before the Barkhausen jumps occur. No such anomaly is observed for the circular remanence.

The coercive force is shown in Fig. 3 as a function of square root of torsion. For $\sigma=0$ all four coercive fields are nearly equal and follow quite well the linear dependence on $\xi^{1/2}$ in agreement with the previously reported data.⁴ With applied axial stress the nature of these dependencies substantially changes. The axial coercive fields H_{cz} and $H_{c\phi}$ are nearly constant at low applied torsion but above some critical value of ξ they also roughly follow the $\xi^{1/2}$ dependence with higher slope than in case $\sigma=0$. The circular coercive fields $H_{cz\phi}$ and $H_{c\phi\phi}$ are large at low ξ , then decrease and show minima at approximately the same critical values of torsion. With further increasing ξ they again roughly follow the dependence obtained for $\sigma=0$. The observed behavior of coercive fields can be explained by the model proposed for bistable behavior of as-quenched wires.⁵ According to this model the magnetization reversal is caused by depinning of a residual oppositely polarized domain from the end of the wire. When the switching field is achieved the domain wall

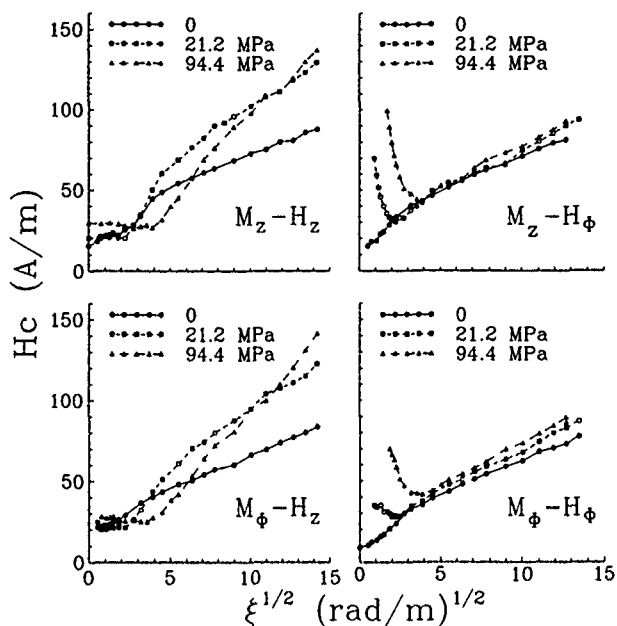


FIG. 3. Coercive fields vs square root of torque.

becomes free and rapidly moves to the opposite end of the wire. It has been shown that in wires with predominantly axial anisotropy the switching field is proportional to domain wall energy γ_w .⁶ When the applied magnetic field is not parallel to the easy direction the pressure exerted by the wall is proportional to $\cos \omega$, where ω is the angle between magnetization and magnetic field. One can thus introduce a more general equation for the switching field

$$H^* = \alpha \gamma_w / \cos \omega, \quad (4)$$

where α is a parameter accounting for the depinning process. In case of orthorhombic anisotropy the domain wall energy $\gamma_w = 4(AK_{\text{eff}})^{1/2}$ depends on the orientation of the wall.⁷ Using Eq. (2) one finds the minimum γ_w for the wall perpendicular to the surface of the wire with

$$K_{\text{eff}} = (3/4)\lambda_s \{ \sigma + [\sigma^2 + (2\mu\xi r)^2]^{1/2} \}. \quad (5)$$

Using Eq. (4) for axial (H_z^*) and circular (H_ϕ^*) switching fields one obtains

$$H_z^* = \alpha \gamma_w / \cos \Theta, \quad H_\phi^* = \alpha \gamma_w / \sin \Theta. \quad (6)$$

These formulas cannot be directly applied to the measured coercive fields because at the frequency of 110 Hz, which we

have used, there is a large contribution of anomalous eddy current losses to H_c . Some qualitative conclusions, however, can be made.

The local domain wall energy and consequently the local switching fields depend on the distance r from the axis of the wire. It is obvious from Eq. (5) that the depinning of the wall does not take place at $r=0$ because then the switching fields are independent of torque. For zero axial stress one has $\Theta=45^\circ$ and $\gamma_w \propto \xi^{1/2}$ which explains well the linear dependence of H_c on $\xi^{1/2}$. For $\sigma>0$ and low applied torque the helical easy axis is close to the wire axis (Θ is small) and the domain wall energy is predominantly determined by the tensile stress σ . This can explain the nearly constant axial coercive fields at low ξ and the high values of circular coercivities. With increasing torque $\sin \Theta$ increases and the circular coercive fields decreases. At high levels of torque, where the helical anisotropy dominates, similar behavior to $\sigma=0$ can be expected.

The observation of all four components of the "hysteresis-loop tensor" in the stress-relieved Fe-rich amorphous wire have shown that the bistable switching behavior observed with applied torque and/or tensile stress can be qualitatively explained by a simple model based on the superposition of helical and axial magnetic anisotropies. For the quantitative comparison of experimental data with the model the quasistatic measurements of the switching fields are needed. These experiments are now in progress.

One of the authors (LK) carried out the work as part of the mobility action for Cooperation in Science and Technology with Central and Eastern European Countries financed by the Commission of the European Communities under Project No. ERB-CIPA-CT-92-0127. Financial support to one of the authors (SNK), from Ministerio de Educación y Ciencia (Spain) is gratefully acknowledged.

¹F. B. Humphrey, K. Mohri, J. Yamasaki, H. Kawamura, R. Malmhall, and I. Ogasawara, in *Magnetic Properties of Amorphous Metals*, edited by A. Hernando *et al.* (North-Holland, Amsterdam, 1987), p. 110.

²K. Mohri, T. Kohzawa, K. Kawashima, H. Yoshida, and L. V. Panina, *IEEE Trans. Magn.* **MAG-28**, 3150 (1992).

³J. González, J. M. Blanco, M. Vázquez, J. M. Barandiarán, G. Rivero, and A. Hernando, *J. Appl. Phys.* **70**, 6522 (1991).

⁴M. Vázquez, J. González, J. M. Blanco, J. M. Barandiarán, G. Rivero, and A. Hernando, *J. Magn. Magn. Mater.* **96**, 321 (1991).

⁵C. Gómez-Polo, M. Vázquez, and D. X. Chen, *Appl. Phys. Lett.* **62**, 108 (1993).

⁶K. Mohri, F. B. Humphrey, Y. Konno, K. Kawashima, K. Kimura, and M. Mizutani, *IEEE Trans. Magn.* **MAG-26**, 1789 (1990).

⁷L. Kraus, *Phys. Status Solidi B* **161**, 853 (1990).

A metastable ternary Nd-Fe-B compound

B. X. Gu, B. G. Shen,^{a)} and H. R. Zhai

Department of Physics, Nanjing University, Nanjing 210008, China, and CCAST (World Laboratory),
P.O. Box 8730, Beijing 100080, China

The metastable compound $\text{Nd}_6\text{Fe}_{77}\text{B}_{17}$ has been obtained by the crystallization from the amorphous phase in the Nd-Fe-B system. Its crystal structure is similar to that of the compound $\text{Nd}_2\text{Fe}_{23}\text{B}_3$. At high temperature this metastable compound decomposes into α -Fe and $\text{Nd}_{11}\text{Fe}_4\text{B}_4$ phases. The room temperature magnetization and coercivity are $154 \text{ A m}^2/\text{kg}$ and 12 kA/m , respectively.

I. INTRODUCTION

Metastable phases have an important influence on the hard magnetic properties of a permanent magnet. The study of the structure, magnetic properties, and stability of metastable phases has attracted attention. However the metastable compounds with a single phase cannot be obtained in the cast alloys. The advent of amorphous alloys offers the possibility of preparing metastable compounds which are not observed in the corresponding phase diagrams. Boschow *et al.*¹ have found the metastable compounds $\text{Nd}_2\text{Fe}_{23}\text{B}_3$, $\text{NdFe}_{12}\text{B}_6$, and $\text{Y}_3\text{Fe}_{62}\text{B}_{14}$. We reported the structure, magnetic properties, and the stability of metastable compound $\text{Nd}_7\text{Fe}_{81}\text{B}_{16}$.^{2,3} These metastable intermetallic compounds are prepared by the crystallization of suitable amorphous alloys at lower temperatures. Recently during the investigation of the crystallization of amorphous $\text{Nd}_x\text{Fe}_{83-x}\text{B}_{17}$ alloys we obtained a metastable compound $\text{Nd}_6\text{Fe}_{77}\text{B}_{17}$. Its structure is similar to that of the compound $\text{Nd}_2\text{Fe}_{23}\text{B}_3$. In this article the structure and magnetic properties of the metastable compound $\text{Nd}_6\text{Fe}_{77}\text{B}_{17}$ are reported.

II. EXPERIMENT

The alloys with composition $\text{Nd}_6\text{Fe}_{77}\text{B}_{17}$ were prepared by induction under argon atmosphere using raw material of 99.9% purity. The homogenized alloys were rapidly quenched by ejection from a quartz crucible on to a copper wheel rapidly rotating at a speed of about 37 m/s under argon atmosphere. The samples were annealed in the temperature range of 773 to 1200 K for 10 min in a quartz tube which was evacuated to 7.5×10^{-6} Torr and backfilled with flowing high purity helium evaporated from liquid He. X-ray microanalysis was used to determine the chemical composition of the samples. The structure of as-quenched samples and phase composition of annealed samples were identified by x-ray diffraction with Co $K\alpha$ radiation. Differential thermal analysis (DTA) measurement was performed under an argon atmosphere at a heating rate of 20 K/min. Magnetic properties were measured by vibrating sample magnetometer at a maximum applied magnetic field of 800 kA/m.

III. RESULTS AND DISCUSSION

A. Structure

X-ray diffraction spectra of the as-quenched and annealed $\text{Nd}_6\text{Fe}_{77}\text{B}_{17}$ alloys are shown in Fig. 1. It can be seen that the x-ray diagram of as-quenched samples exhibits a diffused broad maximum. No contribution from the crystalline phases is seen, suggesting the amorphous nature. The x-ray spectrum of the samples annealed at 900 K shows sharp peaks. The observed values of the diffraction angle θ and relative diffraction intensity I of the compound $\text{Nd}_6\text{Fe}_{77}\text{B}_{17}$ are shown in Table I. For comparison the values of θ and I of the compound $\text{Nd}_2\text{Fe}_{23}\text{B}_3$ (Ref. 4) are given in Table I too. It can be seen that the angles and intensities of all diffraction lines are almost in agreement with that of the compound $\text{Nd}_2\text{Fe}_{23}\text{B}_3$. This result shows that the compound $\text{Nd}_6\text{Fe}_{77}\text{B}_{17}$ annealed at 900 K is single phase. It has the same crystal structure as the compound $\text{Nd}_2\text{Fe}_{23}\text{B}_3$. Mooij *et al.*⁴ have reported that the crystal structure of the compound $\text{Nd}_2\text{Fe}_{23}\text{B}_3$ is a body-centered cubic and belongs to space group $I43d$. The small difference of the values of the diffraction angles between the compounds $\text{Nd}_6\text{Fe}_{77}\text{B}_{17}$ and $\text{Nd}_2\text{Fe}_{23}\text{B}_3$ shown in Table I may originate from a slight change of the lattice constant due to the difference in the composition.

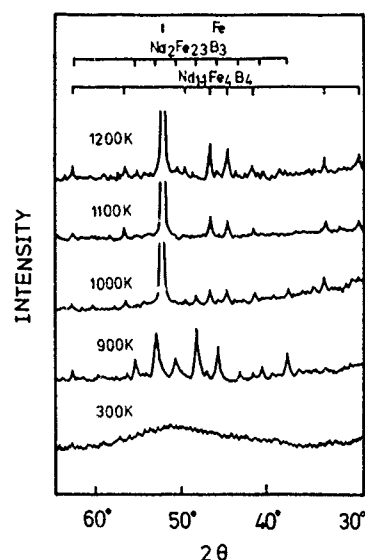


FIG. 1 X-ray (Co $K\alpha$) diffraction spectra of the annealed $\text{Nd}_6\text{Fe}_{77}\text{B}_{17}$ alloys

^{a)}Institute of Physics, Academia Sinica, Beijing 100080, China.

TABLE I. The observed values of θ and I of the metastable compound $\text{Nd}_6\text{Fe}_{77}\text{B}_{17}$ (Cu K α); (s=strong, m=medium, w=weak, v=very).

$\text{Nd}_6\text{Fe}_{77}\text{B}_{17}$		$\text{Nd}_2\text{Fe}_{23}\text{B}_3$ (Ref. 4)	
θ	I	θ	I
16.2	m	16.06	71.3
17.4	m	17.30	27.5
19.7	vs	19.54	121.1
20.7	vs	20.59	155.2
21.7	m	21.60	52.5
22.2	m	22.10	31.9
22.7	s	22.57	109.4
23.6	m	23.57	55.8
26.8	w	26.59	18.1
28.0	m	27.83	33.2

In the x-ray diffraction spectra of the sample annealed at temperatures higher than 1000 K the diffraction peaks of this phase have almost disappeared. Instead the x-ray spectra are composed of the diffraction peaks due to α -Fe and the $\text{Nd}_{11}\text{Fe}_4\text{B}_4$ phase. The amount of the $\text{Nd}_{11}\text{Fe}_4\text{B}_4$ phase increases with increasing annealing temperature. This result shows that the compound $\text{Nd}_6\text{Fe}_{77}\text{B}_{17}$ is metastable. At high temperature it decomposes into α -Fe and $\text{Nd}_{11}\text{Fe}_4\text{B}_4$ phases.

The metastable compound $\text{Nd}_6\text{Fe}_{77}\text{B}_{17}$ has not been obtained in cast alloys of the corresponding composition. It is well known that in the cast alloys crystalline phases have low free energy and thus they are stable. An amorphous alloy is not an equilibrium compound. They have high free energy. Stadelmayer *et al.*⁵ have shown that diffusion of atoms in alloys of this composition range is slow at annealing temperatures below about 1000 K. Therefore when the amorphous $\text{Nd}_6\text{Fe}_{77}\text{B}_{17}$ alloy is annealed at a temperature below 1000 K, the free energy of the amorphous alloys cannot be rapidly decreased due to the slow diffusion of atoms. So stable crystal compounds are not formed. Amorphous alloys crystallize into the metastable phase. At some higher temperature the metastable compound transforms into the equilibrium phase.

Figure 2 shows the DTA trace of the amorphous $\text{Nd}_6\text{Fe}_{77}\text{B}_{17}$ alloy. Two exotherms are observed. The sharp exothermal peak at 904 K shows the crystallization from the amorphous state into the metastable $\text{Nd}_6\text{Fe}_{77}\text{B}_{17}$ phase. Thus the crystallization temperature of amorphous $\text{Nd}_6\text{Fe}_{77}\text{B}_{17}$ al-

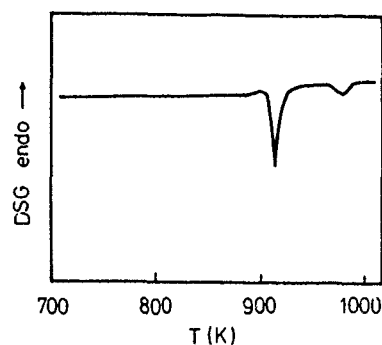


FIG. 2. The DTA trace of the amorphous $\text{Nd}_6\text{Fe}_{77}\text{B}_{17}$ alloy.

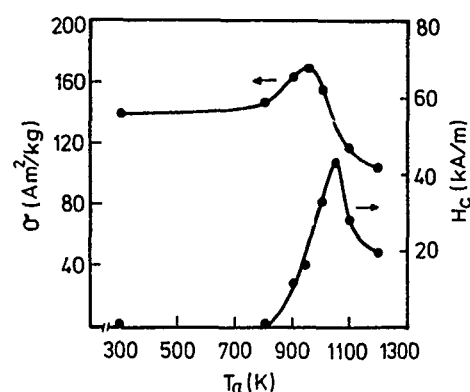


FIG. 3. The room temperature magnetization σ and coercivity H_c as a function of annealing temperature T_a .

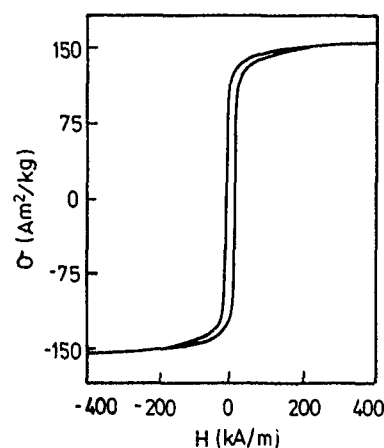


FIG. 4. Hysteresis loop of the 900 K annealed sample.

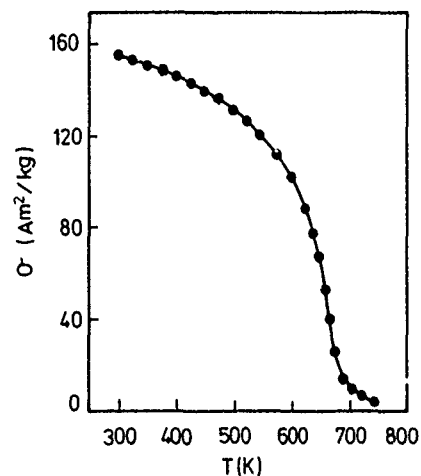


FIG. 5. Temperature dependence of the magnetization of the 900 K annealed sample.

loys is 904 K. The weak exothermal peak at about 970 K originates from the transformation from the metastable phase into the stable phases. This is in agreement with the results of x-ray diffraction.

B. Magnetic properties

Figure 3 shows the dependence of room temperature magnetization and coercivity H_c on the annealing temperature T_a . When $T_a < 950$ K the magnetization increases with increasing annealing temperature. It indicates that the magnetization of the early crystallized metastable phase is larger than that of amorphous alloys. When $T_a > 950$ K the magnetization decreases with increasing T_a . It originates from the increase of the content of the paramagnetic phase $Nd_{1.1}Fe_4B_4$ which is obtained by the decomposition of the metastable phase. The coercivity of the $Nd_6Fe_{77}B_{17}$ alloy increases with increasing annealing temperature, goes to a maximum of 44 kA/m at 1050 K, and then decreases. The room temperature magnetization and coercivity of the metastable compound $Nd_6Fe_{77}B_{17}$ are $154 \text{ A m}^2/\text{kg}$ and 12 kA/m.

The hysteresis loop and thermomagnetic curve of the 900 K annealed sample measured at a magnetic field of 800

kA/m are shown in Figs. 4 and 5, respectively. As seen in the two figures, the magnetization changes monotonously. No kink is observed. These results show that there is only a single magnetic phase in the 900 K annealed sample. It is in agreement with the result of x-ray diffraction analysis. This confirms further that the metastable compound $Nd_6Fe_{77}B_{17}$ obtained by annealing at 900 K is single phase.

ACKNOWLEDGMENT

This work was supported by State Key Laboratory of Magnetism, Institute of Physics, Chinese Academia of Sciences.

¹K. H. J. Buschow, D. B. De Mooij, and R. Coehoorn, *J. Less-Common Metals* **145**, 601 (1988).

²B. X. Gu, G. B. Shen, S. Methfessel, and H. R. Zhai, *Phys. Rev. B* **42**, 10648 (1990).

³B. X. Gu, B. G. Shen, S. Methfessel, and H. R. Zhai, *Chin. Phys. Lett.* **6**, 221 (1989).

⁴D. B. De Mooij and K. H. J. Buschow, *Philips J. Res.* **41**, 41 (1986).

⁵H. H. Stadelmater, N. C. Lin, and N. A. Eimasry, *Mater. Lett.* **3**, 130 (1985).

Helical anisotropy and Matteucci effect in Co-Si-B amorphous wires with negative magnetostriction (abstract)

J. Yamasaki and M. Takajo

Department of Electrical Engineering, Kyushu Institute of Technology, Tobata, Kitakyushu 804, Japan

F. B. Humphrey

Department of ECS, Boston University, 44 Cummington Street, Massachusetts 02215

The Co-Si-B amorphous wires having the negative magnetostriction comprises shell and core domains and exhibits the re-entrant flux reversal as the Fe-Si-B wire with positive magnetostriction.¹ One of the characteristic features of Co based wires is that a sharp pulse voltage generation between two wire ends (Matteucci effect) is accompanied with re-entrant flux reversal,² which is useful for sensor application because of no need for sense windings. In this work, we studied the origin of the large Matteucci effect of Co-Si-B wires by domain observation with a Kerr microscope and by Sixtus-Tonks experiments by driving the reverse domain propagation with the circular fields generated by the current through wires. We also tried to measure the hysteresis loop in the circular direction by integrating the Matteucci voltage. It was found that the domain patterns of the Co-Si-B wire surface is not the previously reported bamboo configuration¹ but the helical configuration. Most of the anisotropy of the amorphous materials is magnetostrictive in origin. The helical anisotropy of Co based wire seems consistent, if we assume the same residual stress distribution as in the steel rod quenched into the water.³ Because of the helical anisotropy, the Co wire has the big circular component of magnetization in the core domain as well as in the shell domain, and both domain can interact near the interface region. It was found that reverse domain propagation along the wire axis can be caused by application of the circular field and that the shell domain moves discontinuously during the re-entrant flux reversal in the core domain. These circular magnetization components in both core and shell domains due to helical anisotropy and their interaction seems responsible for the large Matteucci effect in the Co-Si-B wires.

¹J. Yamasaki, F. B. Humphrey, K. Mohri, H. Kawamura, H. Takamure, and R. Malmhall, *J. Appl. Phys.* **63**, 3949 (1988).

²H. Takamure *et al.*, *J. Mag. Soc. Jpn.* **13**, 265 (1989) (in Japanese).

³R. Isomura *et al.*, *J. Jpn. Inst. Metal.* **26**, 745 (1962) (in Japanese).

The rf permeability of dc planar magnetron sputtered FeNi multilayer films (abstract)

Craig A. Grimes and Catherine C. Ballantyne

Southwall Technologies, 1029 Corporation Way, Palo Alto, California 94303

Recording heads are commonly built in a multilayer stack to eliminate or reduce domain walls by allowing flux closure, or magnetostatic coupling, between the magnetic layers across nonmagnetic spacers. Use of an electrically insulating spacer material will reduce eddy current shielding increasing the high frequency performance of the head. As magnetic recording systems continue their trend to higher operating frequencies knowledge of the rf permeability of head-like multilayer materials becomes quite important. We examine the complex, rf permeability spectra of dc planar magnetron sputtered FeNi multilayer films as a function of spacer material, number of layers, and thickness of the spacer and magnetic layer. The permeability spectra are measured using a permeameter¹ over the frequency range 3–300 MHz. The spacer materials examined include several metals and metal alloys, the corresponding oxides, silicon, and silicon nitride. The magnetic layer is, by weight, 81.8% Ni and 18.2% Fe. We have found that for a constant magnetic layer thickness, as the nonmagnetic spacer thickness decreases from 30 to 10 nm the permeability magnitude of the multilayer stack increases and the resonance frequency shifts to lower values. As the spacer thickness increases above 30 nm the permeability response remains constant with a negligible value of μ'' . The permeability spectra are approximately the same for spacer layers made of metal or their corresponding oxides. Spacer layers made of Si_3N_4 result in permeability spectra with the highest permeability magnitudes. For example, the permeability magnitude of a multilayer stack composed of four 120 nm FeNi layers separated by 10 nm spacers is approximately 2000 for metal spacers, 2300 for Si spacers, and 4200 for Si_3N_4 spacers. For a fixed number of multilayer pairs and constant spacer layer thickness making the FeNi layer thicker tends to increase the permeability magnitude, reduce the resonance frequency, and lower the low frequency coercive force.

¹C. A. Grimes, P. L. Trouilloud, and R. M. Walser, *Trans. Mag.* 24, 603 (1988).

Phase transitions in the one-dimensional frustrated quantum XY model and Josephson-junction ladders

Enzo Granato

Laboratório Associado de Sensores e Materiais, Instituto Nacional de Pesquisas Espaciais,
12225 São José dos Campos, São Paulo, Brazil

A one-dimensional quantum version of the frustrated XY (planar rotor) model is considered which can be physically realized as a ladder of Josephson junctions at half a flux quantum per plaquette. This system undergoes a superconductor to insulator transition at zero temperature as a function of charging energy. The critical behavior is studied using a Monte Carlo transfer matrix applied to the path-integral representation of the model and a finite-size-scaling analysis of data on small system sizes. Depending on the ratio between the interchain and intrachain couplings the system can have single or double transitions which is consistent with the prediction that its critical behavior should be described by the two-dimensional classical XY-Ising model.

The two-dimensional frustrated classical XY model has attracted considerable attention recently.¹⁻⁸ It can be related to Josephson-junction arrays in a magnetic field, where it is expected to describe the finite-temperature superconductor to normal transition in arrays with half a flux quantum per plaquette.⁹ At low temperatures where capacitive effects dominate, the array undergoes a superconductor to insulator transition as a function of charging energy.¹⁰⁻¹³ These charging effects arise from the small capacitance of the grains making up the array and leads to strong quantum fluctuations of the phase of the superconducting order parameter. The critical behavior is now described by a two-dimensional frustrated quantum XY model with a Hamiltonian¹²

$$H = -\frac{E_c}{2} \sum_r \left(\frac{d}{d\theta_r} \right)^2 - \sum_{\langle rr' \rangle} E_{rr'} \cos(\theta_r - \theta_{r'}) \quad (1)$$

The first term in Eq. (1) describes quantum fluctuations induced by the charging energy $E_c = 4e^2/C$ of a non-neutral superconducting grain located at site r , where e is the electronic charge and C is the effective capacitance of the grain. The second term is the usual Josephson-junction coupling between nearest-neighbor grains. θ_r represents the phase of the superconducting order parameter and the couplings $E_{rr'}$ satisfy the Villain's "odd rule" in which the number of negative bonds in an elementary cell is odd.¹⁴ In a square lattice this can be satisfied, for example, by ferromagnetic horizontal rows and alternating ferromagnetic and antiferromagnetic columns of bonds. This rule is a direct consequence of the constraint that, for the half-flux case, the line integral of the vector potential due to the applied magnetic field should be equal to π in units of the flux quantum.

In this work we consider a one-dimensional frustrated quantum XY (1D FQXY) model¹⁵ which can be regarded as the simplest 1D version of the model (1) consisting just of a single column of frustrated plaquettes as indicated in Fig. 1. This can be physically realized as a periodic Josephson-junction ladder at half a flux quantum per plaquette.^{16,17} In

the classical limit ($E_c = 0$), the ground state of the 1D FQXY model has a discrete Z_2 symmetry associated with an antiferromagnetic pattern of plaquette chiralities $\chi_p = \pm 1$, as indicated in Fig. 1, measuring the two opposite directions of the supercurrent circulating in each plaquette. For small E_c , there is a gap for creation of kinks in the antiferromagnetic pattern of χ_p , and the ground state has long-range chiral order.

Within a path-integral approach,¹⁶ it can be shown that the effective action describing quantum fluctuations in the

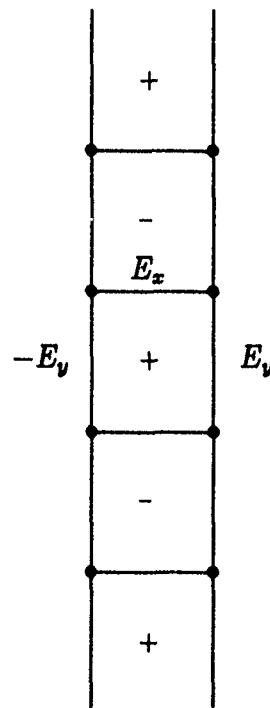


FIG. 1. Schematic representation of the one-dimensional frustrated quantum XY model with inter- (E_x) and intrachain ($\pm E_y$) coupling constants. The antiferromagnetic ordering of chiralities $\chi_p = \pm 1$ is also indicated.

1D-FQXY model leads to two coupled XY models in two (space-time) dimensions which is expected to have a critical behavior in the universality class of the 2D XY-Ising model¹⁸ defined by the classical Hamiltonian

$$BH = - \sum_{\langle rr' \rangle} [A(1 + \sigma_r \sigma_{r'} \cos(\theta_r - \theta_{r'}) + C \sigma_r \sigma_{r'})] . \quad (2)$$

The phase diagram of this model consists of three branches, in the ferromagnetic region. One of them corresponds to single transitions with simultaneous loss of XY and Ising order. Further away from the branch point, this line of single transitions becomes first order. The other two lines correspond to separate XY and Ising transitions. The 1D FQXY model is represented by a particular path through this phase diagram which will depend on the ratio E_x/E_y between the interchain and intrachain couplings of the model. In this work we describe the results of a finite-size scaling analysis of extensive calculations on the 1D FQXY model^{15,19} which shows that, in fact, the XY and Ising-like excitations of the quantum model decouple for large interchain couplings, giving rise to pure Ising model critical behavior for the chirality order parameter. As a consequence, the universality class of the superconductor-insulator transition in the related Josephson-junction ladder should then depend on the ratio between interchain and intrachain Josephson couplings.

To study the critical behavior of the 1D FQXY model, we find it convenient to use an imaginary-time path-integral formulation of the model.²⁰ In this formulation, the one-dimensional quantum problem maps into a 2D classical statistical mechanics problem where the ground state energy of the quantum model of finite size L corresponds to the reduced free energy per unit length of the classical model defined on an infinite strip of width L along the imaginary time direction, where the time axis τ is discretized in slices $\Delta\tau$. After scaling the time slices appropriately in order to get a space-time isotropic model one obtains a classical partition function where the parameter $\alpha = (E_y/E_x)^{1/2}$ plays the role of an inverse temperature in the 2D classical model. The scaling behavior of the energy gap for kink excitations (chiral domain walls) of the 1D FQXY corresponds to the interface free energy of an infinite strip in this classical model. For large α (small charging energy E_c), there is a gap for creation of kinks in the antiferromagnetic pattern of χ_p and the ground state has long-range chiral order. At some critical value of α , chiral order is destroyed by kink excitations, with an energy gap vanishing as $|\alpha - \alpha_c|^\nu$, which defines the correlation length exponent ν . Right at this critical point, the correlation function decays as a power law $\langle \chi_p \chi_{p'} \rangle = |p - p'|^{-\eta}$ with a critical exponent η . The free energy per unit length $f(\alpha)$ of the Hamiltonian on the infinite strip can be obtained from the largest eigenvalue λ_0 of the transfer matrix between different time slices as $f = -\ln \lambda_0$. To obtain λ_0 , we used a Monte Carlo transfer-matrix method²¹ which has been shown to lead to accurate estimates of the largest eigenvalue even for models with continuous symmetry. The implementation of this method is similar to the case of the 2D frustrated classical XY model⁸ and further details can be found in that work.

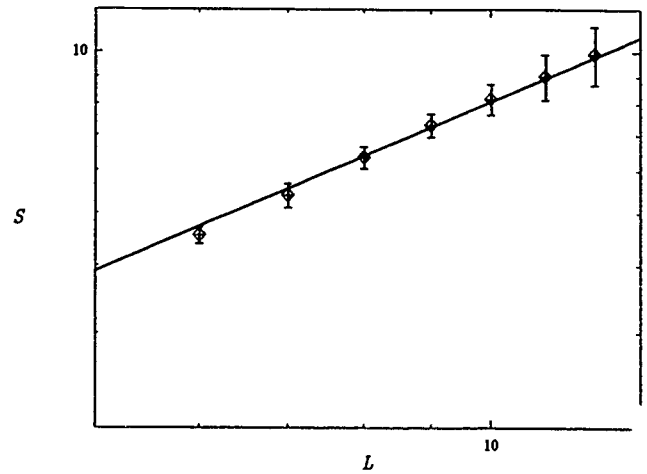


FIG. 2. $S = \partial \Delta F(\alpha, L) / \partial \alpha$ evaluated near the critical coupling α_c . The slope of the straight line gives an estimate of $1/\nu$.

The interfacial free energy for domain walls can be obtained from the differences between the free energies for the infinite strip with and without a wall. To obtain the critical exponents and critical coupling we employ the finite-size scaling $\Delta F(\alpha, L) = A(L^{1/\nu} \delta \alpha)$ where A is a scaling function and $\delta \alpha = \alpha - \alpha_c$. In a linear approximation for the argument of A , we have

$$\Delta F(\alpha, L) = a + b L^{1/\nu} \delta \alpha \quad (3)$$

which can be used to determine the critical coupling α_c and the exponent ν independently.¹⁶ The change from an increasing trend with L to a decreasing trend provides an estimate of α_c . Once the critical coupling is known, the correlation function exponent η can be obtained from the universal amplitude a in Eq. (3) through a result from conformal invariance,²² $a = \pi \eta$. To estimate the correlation length exponent ν we first obtain the derivative $S = \partial \Delta F / \partial \alpha$ near α_c , then it can easily be seen that a log-log plot of S vs L gives an estimate of $1/\nu$ without requiring a precise determination of α_c . In Fig. 2 we show this kind of plot for $E_x/E_y = 3$ from where we get the estimate $\nu = 1.05(6)$. Of course, this is only valid in the linear approximation of Eq. (3). To ensure that higher-order terms can safely be neglected, the data for $\Delta F(\alpha, L)$ must be obtained in a sufficiently small range near α_c . We also checked, using a more general finite-size scaling analysis,⁸ that allowing for higher-order terms gives results agreeing within the errors. The results for the critical coupling α_c and critical exponents ν and η for two different values of the ratio $E_x/E_y = 1$ and 3 are indicated in Table I.

For equal couplings $E_x = E_y$, the results for the critical exponents η and ν differ significantly from pure 2D Ising

TABLE I. Critical couplings [$\alpha_c = (E_y/E_x)^{1/2}$] and critical exponents (ν, η), obtained from finite-size scaling analysis of interfacial free energies for two values of the ratio between interchain and intrachain couplings (E_x/E_y).

E_x/E_y	α_c	ν	η
1	1.04(1)	0.81(4)	0.47(4)
3	1.16(2)	1.05(6)	0.27(3)

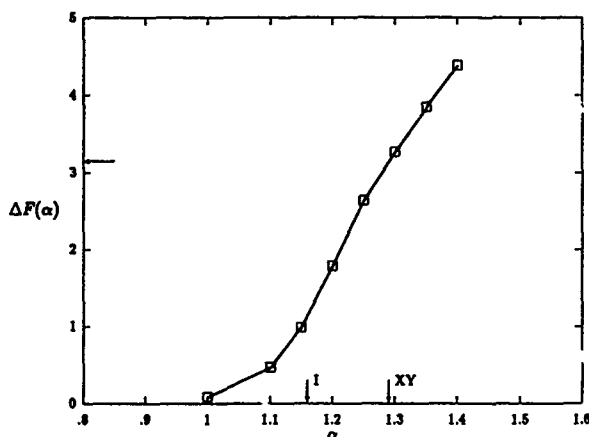


FIG. 3. Behavior of the interfacial free energy $\Delta F = L^2 \Delta f$ for a system of size $L=12$ resulting from an imposed phase twist of π . Vertical arrows indicate the locations of the Ising and XY transitions and the horizontal arrow the value $\Delta F = \pi$ from where the XY transition is located.

exponents ($\nu=1$, $\eta=0.25$). This result points to a single transition scenario. In fact, they are consistent with a point along the line of single transitions in the XY-Ising model.¹⁸ It is interesting to note that this result is also consistent with similar calculations for the 2D frustrated classical XY model.⁸ In general, the critical behavior of a d dimensional quantum model is in the same universality class of the $d+1$ dimensional classical version. However, the 1D FQXY model, apparently, is not the Hamiltonian limit of the 2D classical model. Yet, their critical behavior appears to be in the same universality class.

For the case of unequal couplings $E_x/E_y=3$, the results indicated in Table I are in good agreement with pure 2D Ising values. From the relation between the 1D FQXY model and the 2D XY-Ising model this then implies that the XY and Ising-like excitations have decoupled in this region of parameters. To show that in fact one has two decoupled and, at the same time, separated transitions we show in Fig. 3 the results for the helicity modulus which measures the response of the system to an imposed twist. The helicity modulus is related to the free-energy differences ΔF between strips with and without any additional phase mismatch of π along the strip and is given by $\gamma = 2\Delta F/\pi^2$ for large system sizes. If the model is decoupled then the transition should be in the universality class of the 2D classical XY model, where one knows that the transition is associated with a universal jump of $2/\pi$ in the helicity modulus.²³ The critical coupling can be estimated as the value of α at which $\Delta F = \pi$ which gives

$\alpha_c = 1.29$. This is to be compared with the critical coupling for the destruction of chiral order in Table I, $\alpha_c = 1.16$. This clearly indicates the transitions are well separated and thus one expects they are decoupled. We have also performed less detailed calculations at other values of the ratio E_x/E_y from which we can estimate that the Ising and XY transitions merge into a single transition roughly at $E_x/E_y \sim 2$. Since, the superconductor to insulator transition is to be identified with the loss of phase coherence²⁴ we reach the interesting result that in the 1D FQXY, or alternatively, a Josephson-junction ladder, the universality class of the superconductor-insulator transition depends on the ratio between inter- and intrachain couplings.

This work has been supported by Fundação de Amparo à Pesquisa do Estado de São Paulo (FAPESP), Proc. No. 92/0963-5 and Conselho Nacional de Desenvolvimento Científico e Tecnológico (CNPq).

- ¹S. Teitel and C. Jayaprakash, Phys. Rev. B **27**, 598 (1983); T. C. Halsey, J. Phys. C **18**, 2437 (1985).
- ²B. Berge, H. T. Diep, A. Ghazali, and P. Lallemand, Phys. Rev. B **34**, 3177 (1986).
- ³M. Gabay, T. Garel, G. N. Parker, and W. M. Saslow, Phys. Rev. B **40**, 264 (1989).
- ⁴E. Granato and J. M. Kosterlitz, J. Phys. C **19**, L59 (1986); J. Appl. Phys. **64**, 5636 (1988).
- ⁵J. M. Thijssen and H. J. F. Knops, Phys. Rev. B **42**, 2438 (1990).
- ⁶J. Lee, J. M. Kosterlitz, and E. Granato, Phys. Rev. B **43**, 11531 (1991).
- ⁷G. Ramirez-Santiago and J. José, Phys. Rev. Lett. **68**, 1224 (1992).
- ⁸E. Granato and M. P. Nightingale, Phys. Rev. B **48**, 7438 (1993).
- ⁹See articles in Proceedings of the NATO Advanced Research Workshop on Coherence in Superconducting Networks, Delft, 1987 [Physica B **152**, 1 (1988)].
- ¹⁰L. J. Geerligs, M. Peters, L. E. M. de Groot, A. Verbruggen, and J. E. Mooij, Phys. Rev. Lett. **63**, 326 (1989).
- ¹¹H. S. J. van der Zant, L. J. Geerligs, and J. E. Mooij, Europhys. Lett. **119**, 541 (1992).
- ¹²E. Granato and J. M. Kosterlitz, Phys. Rev. Lett. **65**, 1267 (1990).
- ¹³E. Granato and M. A. Continentino, Phys. Rev. B **48**, 15977 (1993).
- ¹⁴J. Villain, J. Phys. C **10**, 4793 (1977).
- ¹⁵E. Granato, Phys. Rev. B **45**, 2557 (1992).
- ¹⁶E. Granato, Phys. Rev. B **42**, 4797 (1990).
- ¹⁷M. Kardar, Phys. Rev. B **33**, 3125 (1986).
- ¹⁸E. Granato, J. M. Kosterlitz, J. Lee, and M. P. Nightingale, Phys. Rev. Lett. **66**, 1090 (1991); J. Lee, E. Granato, and J. M. Kosterlitz, Phys. Rev. B **44**, 4819 (1991); M. P. Nightingale, E. Granato, and J. M. Kosterlitz (unpublished).
- ¹⁹E. Granato, Phys. Rev. B **48**, 7727 (1993).
- ²⁰J. Zinn-Justin, *Quantum Field Theory and Critical Phenomena* (Oxford Science, Oxford, 1989).
- ²¹M. P. Nightingale and H. W. J. Blöte, Phys. Rev. Lett. **60**, 1562 (1988); M. P. Nightingale, in *Finite Size Scaling and Numerical Simulations of Statistical Systems*, edited by V. Privman (World Scientific, Singapore, 1990).
- ²²J. L. Cardy, J. Phys. A **17**, L961 (1984).
- ²³D. Nelson and J. M. Kosterlitz, Phys. Rev. Lett. **39**, 1201 (1977).
- ²⁴R. M. Bradley and S. Doniach, Phys. Rev. B **30**, 1138 (1984).

Penetration of circularly polarized electromagnetic fields into superconductors with gradual resistive transitions

I. D. Mayergoyz

Electrical Engineering Department and Institute for Advanced Computer Studies, University of Maryland, College Park, Maryland 20742

Critical state-type models of superconducting hysteresis are based on analytical study of penetration of electromagnetic fields into hard superconductors. This study has been carried out under the assumption of ideal (sharp) resistive transition. In the paper, the attempt is made to study the penetration of electromagnetic fields into hard superconductors for gradual resistive transitions described by the "power law." This requires the solution of nonlinear partial differential equations. It is shown that the exact analytical solution can be found in the case of circular polarization of electromagnetic fields due to the high degree of symmetry of the posed problem. In the limiting case of sharp transition, the obtained solutions are reduced to the solution previously asserted by Bean.

Models of superconducting hysteresis are based on analytical study of penetration of electromagnetic fields into hard superconductors. In critical state-type models,¹⁻³ this study has been carried out under the assumption of ideal (sharp) resistive transition. However, actual resistive transitions are gradual and they are usually described by the following "power law"

$$E = (j/k)^n, \quad (n > 1), \quad (1)$$

where E is an electric field, j is a current density, and k is the parameter which coordinates the dimensions of both sides of Eq. (1).

The exponent " n " is a measure of the sharpness of the resistive transition and it may vary in the range 4–1000. At first, the power law was regarded only as a reasonable empirical description of the resistive transition. However, recently there has been a considerable research effort focused on the theoretical justification of power law (1). As a result, models based on flux creep,⁴ Josephson-junction coupling between grains,⁵ sausing,⁶ and spatial distribution of critical current⁷ have been proposed. In the paper, power law (1) is used as a constitutive equation for superconductors. By using this equation, the penetration of electromagnetic fields into superconductors with gradual resistive transition is analytically investigated. This investigation requires the solution of nonlinear partial differential equations of parabolic type. It is shown below that the exact analytical solutions can be found in the case of circular polarization of electromagnetic fields due to the high degree of symmetry of the problem under consideration. In the limiting case of sharp (ideal) transition, these solutions are reduced to those previously asserted by Bean.⁸ The discussion presented below closely parallels the analytical technique developed for the calculation of eddy currents in magnetically nonlinear media.⁹

To start the discussion, consider a plane circularly polarized electromagnetic wave penetrating superconducting half-space $z > 0$ (see Fig. 1). This implies the following boundary conditions:

$$E_x(0, t) = E_m \cos(\omega t + \varphi), \quad E_y(0, t) = E_m \sin(\omega t + \varphi), \quad (2)$$

$$E_x(\infty, t) = E_y(\infty, t) = 0. \quad (3)$$

The distribution of electric field E in half-space $z > 0$ is governed by the equations

$$\frac{\partial^2 E_x}{\partial z^2} = \mu_0 \frac{\partial}{\partial t} [\sigma(\sqrt{E_x^2 + E_y^2}) E_x], \quad (4)$$

$$\frac{\partial^2 E_y}{\partial z^2} = \mu_0 \frac{\partial}{\partial t} [\sigma(\sqrt{E_x^2 + E_y^2}) E_y], \quad (5)$$

where according to (1)

$$\sigma(\sqrt{E_x^2 + E_y^2}) = \sigma(E) = kE^{1/n-1}. \quad (6)$$

We next prove that the electromagnetic field is circularly polarized everywhere in the superconducting half space. Indeed, by assuming that the solution of the boundary value problem (2)–(5) is in the form

$$E_x(z, t) = E(z) \cos[\omega t + \theta(z)], \quad (7)$$

$$E_y(z, t) = E(z) \sin[\omega t + \theta(z)], \quad (8)$$

and by introducing the phasors

$$\mathcal{E}_x(z) = E(z)e^{i\theta(z)}, \quad \mathcal{E}_y(z) = -iE(z)e^{i\theta(z)}, \quad (9)$$

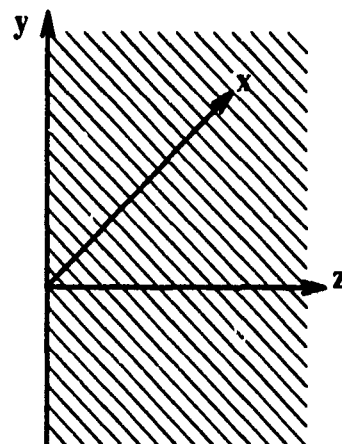


FIG. 1. Superconducting half-space.

we can exactly transform the above boundary value problem into two decoupled and mathematically identical boundary value problems for ordinary differential equations with respect to phasors $\mathcal{E}_x(z)$ and $\mathcal{E}_y(z)$:

$$\frac{d^2 \mathcal{E}_x(z)}{dz^2} = i\omega\mu_0\sigma(|\mathcal{E}_x(z)|)\mathcal{E}_x(z), \quad (10)$$

$$\mathcal{E}_x(0) = \mathcal{E}_m, \quad \mathcal{E}_x(\infty) = 0, \quad (11)$$

and

$$\frac{d^2 \mathcal{E}_y(z)}{dz^2} = i\omega\mu_0\sigma(|\mathcal{E}_y(z)|)\mathcal{E}_y(z), \quad (12)$$

$$\mathcal{E}_y(0) = -i\mathcal{E}_m, \quad \mathcal{E}_y(\infty) = 0, \quad (13)$$

where $\mathcal{E}_m = E_m e^{i\varphi}$.

The above exact transformation is possible because in the case of the circularly polarized electromagnetic fields $E = \sqrt{E_x^2 + E_y^2}$ and $\sigma(E) = \sigma(\sqrt{E_x^2 + E_y^2})$ do not change with time. Such an exact transformation can be construed as a mathematical proof that the circular polarization is preserved everywhere within the superconducting medium. As a result, there are no higher order harmonics of the electromagnetic field anywhere within the medium despite its nonlinear properties. This fact can be easily understood on the physical grounds if we take into account the circular symmetry of the posed problem.

From (6) and (9) we derive

$$\begin{aligned} \sigma(|\mathcal{E}_x(z)|) &= \sigma(|\mathcal{E}_y(z)|) = \sigma_m \left| \frac{\mathcal{E}_x(z)}{\mathcal{E}_m} \right|^{1/n-1} \\ &= \sigma_m \left| \frac{\mathcal{E}_y(z)}{\mathcal{E}_m} \right|^{1/n-1}, \end{aligned} \quad (14)$$

where $\sigma_m = kE_m^{1/n-1}$ is the value of σ on the boundary. By using (14) in (10), we find

$$\frac{d^2 \mathcal{E}_x(z)}{dz^2} = i\omega\mu_0\sigma_m \left| \frac{\mathcal{E}_x(z)}{\mathcal{E}_m} \right|^{1/n-1} \mathcal{E}_x(z). \quad (15)$$

We shall employ the following trick to solve Eq. (15). Consider the equation

$$\frac{d^2 \mathcal{E}_x(z)}{dz^2} = i\omega\mu_0\sigma_m \left(1 - \frac{z}{z_0}\right)^{-2} \mathcal{E}_x(z), \quad (16)$$

where z_0 is a parameter which will be chosen later in such a way that the solution of Eq. (16) will also be the solution of Eq. (15). The solution of Eq. (16) which satisfies the boundary conditions (11) is given by

$$\mathcal{E}_x(z) = \mathcal{E}_m \left(1 - \frac{z}{z_0}\right)^\alpha, \quad (17)$$

where $\alpha = \alpha' + i\alpha''$ is a root of the characteristic equation

$$\alpha(\alpha-1) = i\omega\mu_0\sigma_m z_0^2. \quad (18)$$

From (17) we find

$$\left| \frac{\mathcal{E}_x(z)}{\mathcal{E}_m} \right| = \left(1 - \frac{z}{z_0}\right)^{\alpha'}, \quad (\alpha' = \text{Re } \alpha). \quad (19)$$

This leads to

$$\left(1 - \frac{z}{z_0}\right)^{-2} = \left| \frac{\mathcal{E}_x(z)}{\mathcal{E}_m} \right|^{-2/\alpha'} \quad (20)$$

Now, it is evident that the solution (17) to Eq. (16) will be also the solution to Eq. (15), if

$$\alpha' = \frac{2n}{n-1}. \quad (21)$$

Next, we represent characteristic Eq. (18) as two equations (for real and imaginary parts, respectively)

$$\alpha'(\alpha'-1) - (\alpha'')^2 = 0 \quad (22)$$

$$\alpha''(2\alpha'-1) = \omega\mu_0\sigma_m z_0^2. \quad (23)$$

By substituting (21) into (22), we find

$$\alpha'' = \frac{\sqrt{2n(n+1)}}{n-1}, \quad (24)$$

which then, according to (23), leads to

$$z_0 = \frac{4\sqrt{2n(n+1)}(3n+1)^2}{\sqrt{\omega\mu_0\sigma_m}(n-1)}. \quad (25)$$

Formulas (17), (21), (24), and (25) completely define the solution of the boundary value problem (10), (11). The solution of the boundary value problem (12), (13) has a similar form:

$$\mathcal{E}_y(z) = -i\mathcal{E}_m \left(1 - \frac{z}{z_0}\right)^\alpha. \quad (26)$$

By using equations

$$\frac{d\mathcal{E}_x}{dz} = -i\omega\mu_0\mathcal{H}_y, \quad \frac{d\mathcal{E}_y}{dz} = i\omega\mu_0\mathcal{H}_x, \quad (27)$$

from (17) and (26) we derive

$$\mathcal{H}_x(z) = \mathcal{H}_m \left(1 - \frac{z}{z_0}\right)^{\alpha-1}, \quad \mathcal{H}_y(z) = i\mathcal{H}_m \left(1 - \frac{z}{z_0}\right)^{\alpha-1}, \quad (28)$$

where

$$\mathcal{H}_m = \mathcal{H}_x(0) = \frac{\alpha}{\omega\mu_0 z_0} \mathcal{E}_m. \quad (29)$$

Since z_0 depends on σ_m [see Eq. (25)] and $\sigma_m = k|\mathcal{E}_m|^{1/n-1}$, expression (29) can be construed as nonlinear impedance boundary condition for circularly polarized waves. This nonlinear relationship can also be used to determine \mathcal{E}_m when \mathcal{H}_m is given. For this reason, we can always choose such \mathcal{E}_m that $\mathcal{H}_m = H_0$ is real. Then from (28), (21), and (24) we derive

$$\begin{aligned} H_x(z, t) &= H_0 \left(1 - \frac{z}{z_0}\right)^{(n+1)/(n-1)} \cos \left[\omega t + \frac{\sqrt{2n(n+1)}}{n-1} \ln \left(1 - \frac{z}{z_0}\right) \right], \end{aligned} \quad (30)$$

$$H_y(z,t) = H_0 \left(1 - \frac{z}{z_0}\right)^{(n+1)/(n-1)} \sin \left[\omega t + \frac{\sqrt{2n(n+1)}}{n-1} \ln \left(1 - \frac{z}{z_0}\right) \right]. \quad (31)$$

Next, we shall show that, in the limiting case of sharp transition ($n \rightarrow \infty$), the above expressions are reduced to those which were asserted (rather than derived) by Bean.⁸ To this end, from (29) we find the following expression for the peak value j_0 of superconducting current on the boundary $z=0$:

$$j_0 = \frac{\omega \mu_0 \sigma_m z_0}{|\alpha|} H_0. \quad (32)$$

By substituting (25) into (32), we obtain

$$\sqrt{\omega \mu_0 \sigma_m} = \frac{|\alpha|(n-1)}{\sqrt{2n(3n+1)^2(n+1)}} \frac{j_0}{H_0}. \quad (33)$$

By substituting (33) back into (25), we arrive at the expression

$$z_0 = \frac{(3n+1)\sqrt{2n(n+1)}}{(n-1)^2|\alpha|} \frac{H_0}{j_0}. \quad (34)$$

It is well known that

$$\delta = \frac{H_0}{j_0} \quad (35)$$

is the field-dependent penetration depth is the case of ideal resistive transition and linearly polarized electromagnetic field. It is also clear that

$$\lim_{n \uparrow \infty} \frac{(3n+1)\sqrt{2n(n+1)}}{(n-1)^2} = 3\sqrt{2}, \quad \lim_{n \uparrow \infty} |\alpha| = \sqrt{6}. \quad (36)$$

From (34), (35), and (36), we find

$$\lim_{n \uparrow \infty} z_0 = \sqrt{3} \delta. \quad (37)$$

By using (37), we find that, in the limiting case of $n \rightarrow \infty$, expressions (30) and (31) can be written as follows:

$$H_x(z,t) = H_0 \left(1 - \frac{z}{\sqrt{3}\delta}\right) \cos \left[\omega t + \sqrt{2} \ln \left(1 - \frac{z}{\sqrt{3}\delta}\right) \right]. \quad (38)$$

$$H_y(z,t) = H_0 \left(1 - \frac{z}{\sqrt{3}\delta}\right) \sin \left[\omega t + \sqrt{2} \ln \left(1 - \frac{z}{\sqrt{3}\delta}\right) \right]. \quad (39)$$

The last expressions are identical to those published in Ref. 8.

The reported research is supported by the U.S. Department of Energy, Engineering Research Program.

¹C. P. Bean, Phys. Rev. Lett. 8, 250 (1962).

²H. London, Phys. Lett. 6, 162 (1963).

³Y. B. Kim, C. F. Hempstead, and A. R. Strand, Phys. Rev. Lett. 9, 306 (1962).

⁴R. J. Soulen, Jr., IEEE Trans. Magn. (to be published).

⁵C. S. Nichols and D. R. Clarke, Acta Metall. Mater. 39, 995 (1991).

⁶J. W. Ekin, Cryogenics 2, 603 (1987).

⁷C. J. G. Plummer and J. E. Evetts, IEEE Trans. Magn. 23, 1179 (1987).

⁸C. P. Bean, J. Appl. Phys. 41, 2482 (1970).

⁹I. D. Mayergoyz, F. M. Abdel-Kader, and F. P. Emad, J. Appl. Phys. 55, 618 (1984).

Magnetic shielding from alternating magnetic field by NbTi/Nb/Cu superconducting multilayer composite cylinder

Hiroaki Otsuka and Ikuo Itoh

Advanced Materials & Technology Research Laboratories, Nippon Steel Corporation, 1618 Ida, Nakahara-ku, Kawasaki 211, Japan

Magnetic shielding from alternating magnetic field by a NbTi/Nb/Cu superconducting multilayer composite cylinder was investigated at liquid-helium temperatures. The specimen employed in this study was a slender seamless cylinder about 15 mm in diameter and having an aspect ratio of 6. The frequency of the alternating magnetic field was in the range of 40–500 Hz, and the maximum amplitude was 1060 G rms at 40 and 50 Hz owing to the capacity of the ac generator. The magnetic shielding efficiency of the cylinder, defined as the ratio of the magnetic field strength with and without the cylinder, was found to be of the order of 10^{-4} . It was also found that the magnetic shielding effect depends upon the frequency investigated in this study. These shielding effects were mainly due to the shielding current originating from the superconductivity, which turned out to give superior shielding effect than that of a Cu cylinder.

I. INTRODUCTION

In our previous paper,¹ we reported that dc magnetic field as strong as 3 T can be effectively shielded by a NbTi/Nb/Cu superconducting multilayer composite cylinder. This shielding material has an advantage of shielding higher magnetic field and having a lower ac loss because of its cryogenic stabilization due to its multilayer structure in comparison with the conventional one made of only superconductor.

In this paper, we report the ac magnetic shielding properties of this multilayer composite cylinder, since the ac component of the applied magnetic field plays an important role in real applications such as magnetic levitation (Maglev). Many investigators reported the ac shielding of only weak magnetic field mainly for superconducting quantum interference device (SQUID) system.^{2,3} However, only a few reports are available for strong ac magnetic field shielding.⁴ In a Maglev system it is essential to protect the superconducting coil from the ac magnetic field originating from the propulsion coil. The strength of this magnetic field is about several hundred gauss and the frequency is in the range of 50–400 Hz. Taking this application into consideration, we investigated the basic ac magnetic shielding property using our superconducting multilayer composite cylinder.

II. EXPERIMENT

The NbTi/Nb/Cu superconducting multilayer composite cylinder was fabricated by the following processes. First, 30 NbTi sheets and 29 Cu sheets were alternately stacked and were interleaved with Nb sheets in a box made of Cu, and the box was sealed by electron beam welding in a vacuum. Next, the box was hot rolled and subsequently cold rolled to a sheet of 1 mm in thickness. The Nb layers prevent the generation of an intermetallic compound comprising Cu and Ti while the box is hot rolled.⁵ This intermetallic compound has an influence on workability of cold rolling. Welding cannot be used for fabricating the cylinder since the weld would impair the shielding properties of the cylinder. In order to overcome the above difficulty, a deep-drawing process and a

spinning process were employed in this study, and a seamless slender cylinder was successfully fabricated as shown in Fig. 1. The cylinder was 15.3 mm in inside diameter, 90.0 mm in length, and 0.5 mm in wall thickness. The magnetic shielding property of Cu (purity was 99.9%) cylinder manufactured by the same method was also measured as a reference and was compared with that of NbTi/Nb/Cu.

The solenoid coil to generate ac magnetic field was made of an NbTi multiple wire, and was 25.0 mm in average diameter and 72.0 mm in length. The above coil was wound on to a fiber reinforced plastic cylinder, which also served as a sample holder. The experimental arrangement is shown in Fig. 2. The cross marks indicate the positions of the magnetic field measured by the search coil, and 0, ± 13 , ± 23 , ± 31 , and ± 39 mm distances from the axial center of the cylinder, respectively. The number of turns of wire for the solenoid coil was 484 and that of the search coil was 94. The source of magnet current was an ac voltage and current standard (YEW, type 2558). A digital multimeter (Takeda Riken TR6861) was used to measure the voltage generated by the

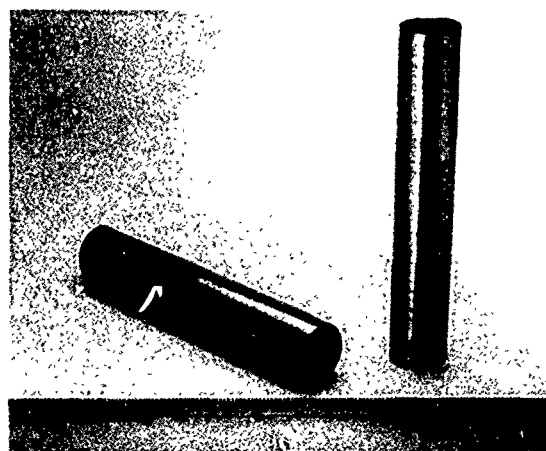


FIG. 1. The NbTi/Nb/Cu cylinder and cup fabricated by a deep-drawing and a spinning method. They are 0.5 mm in thickness, 15.3 mm in inside diameter, and 90.0 mm in length.

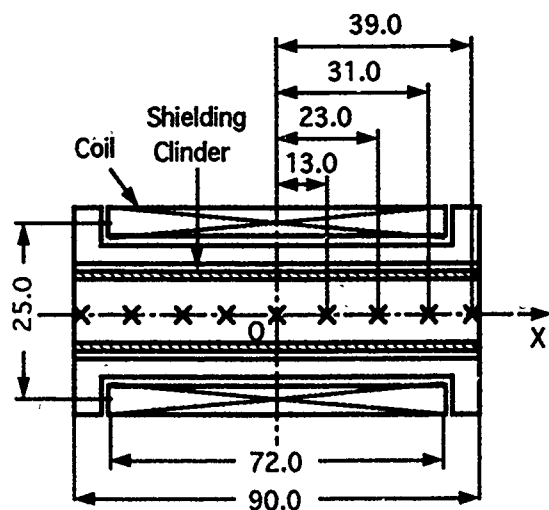


FIG. 2. Sample holder and solenoid coil generating ac magnetic field. The cross marks are the points of measurement.

search coil. The maximum amplitudes and frequencies of the applied ac magnetic field were 1000 G rms at 40 and 50 Hz, 600 G rms at 100 Hz, 200 G rms at 300 Hz, and 150 G rms at 500 Hz. The maximum amplitude, which depends upon the frequency, is limited due to the capacity of the ac generator used in this study. The precision of the voltage measurement was ± 0.001 mV, which is accurate enough for this study and the contribution from the thermal noise could be completely ignored.⁶

III. RESULT AND DISCUSSION

A. Structure of the stacked layers

Figure 3 shows the cross section of the middle part of the cylinder in the length direction. Cu layers can be seen as white and NbTi layers as black. The thickness of both layers is about 5 mm. Nb layers cannot be seen in this figure as the thickness is so thin. From this figure it can be seen that both layers are almost straight, indicating that the process of working was successful.

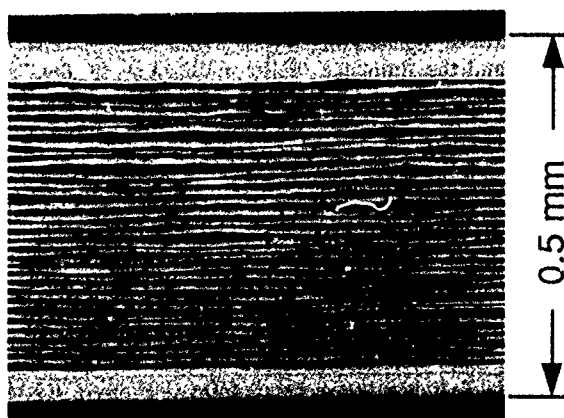


FIG. 3. Cross section of middle part of NbTi/Nb/Cu cylinder in length direction.

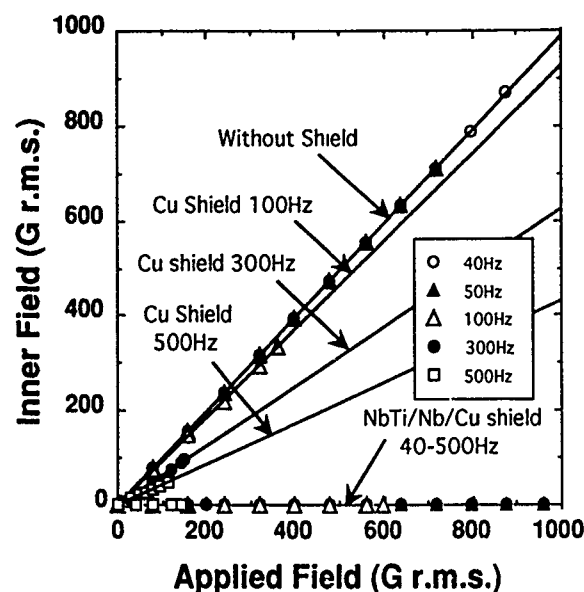


FIG. 4. Shielding properties of NbTi/Nb/Cu cylinder, Cu cylinder, and without shielding.

B. Measurement of magnetic field by the search coil

First, the ac magnetic field without shielding cylinders was measured at liquid-helium temperature (4.2 K) by the search coil. The inner magnetic field was estimated by the voltage of the search coil according to Faraday's law of induction. In the range of frequency from 40 to 500 Hz, an agreement within 1% was obtained between the calculated values and the measured ones.

C. Basic property

The shielding property of the NbTi/Nb/Cu cylinder 90 mm in length at its axial center is shown in Fig. 4. The inner magnetic fields of the cylinder are plotted as a function of the applied magnetic fields in this figure. They are also plotted in the cases with shielding cylinder and with Cu one. The lines through the Cu data were fitted by the method of the least squares. It is known that Cu shows a shielding effect against ac magnetic field due to an eddy current. However, from Fig. 4 it was observed that the Cu cylinder shows only 8% reduction at 100 Hz and 50% at 500 Hz. From these shielding effects of Cu, it can be said that the Cu cylinder cannot be used at the relatively low-frequency range such as considered in this study.

The inner magnetic field was carefully checked to evaluate the precise shielding efficiency. In Fig. 5, the scale of the inner field is more magnified than that in Fig. 4. It can be clearly seen that the inner field is less than 0.1 G until the applied field reaches about 1000 G rms. The inner field increases with increasing applied field. There is a frequency dependence of the alternating magnetic shielding. The inner magnetic field increases with applied field more steeply at higher frequencies. According to Thomasson and Ginsberg⁷ the increase of inner magnetic field accompanying the increase of the applied uniform dc magnetic field takes place because of the leakage of field from both open ends of the

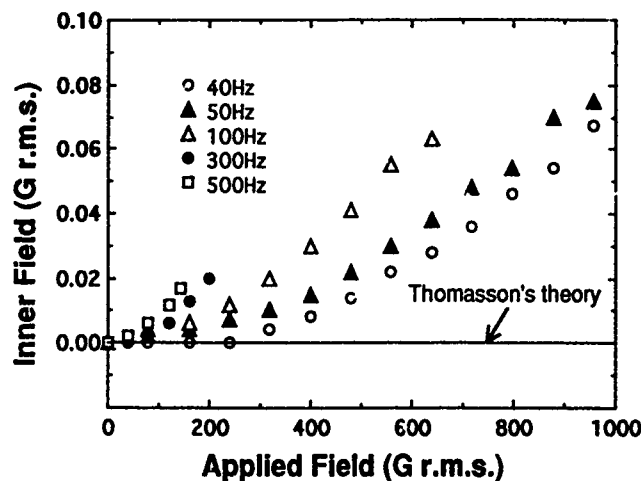


FIG. 5. Inner magnetic field at center of NbTi/Nb/Cu cylinder. Straight line is expressed by Thomasson's theory.

type 1 superconducting cylinder. The ratio of the inner magnetic field B_{in} to the outer one B_{ex} at the center of a cylinder is expressed by the following equation:

$$B_{in}/B_{ex} = 1.13 \times 10^{-(5L/3D)}, \quad (1)$$

L is the length of cylinder and D is the diameter in this equation. Supposing the alternating magnetic field is uniform and parallel to the cylinder axis at the center of the shielding cylinder, this theory can be applied to the alternating magnetic field measurement. The inner magnetic fields are calculated based on this theory, and shown in Fig. 5 as straight line since the aspect ratio of the cylinder is as large as 6. From Fig. 5 it can be seen that the measured leakage of the external magnetic field cannot be explained only by the leakage from the open ends. There must be some reason for the larger leakage than the theoretical estimation. One of the reasons is that magnetic flux lines go through the portion of the cylinder since this material is type 2 superconductor. The other possibility is that the magnetic field penetrates into the cylinder from a position somewhere on it. In order to clarify the above issue, the following experiments were carried out.

D. Influence of position in the cylinder on shielding effect

Shielding effect (SE) is defined here as follows:

$$SE = V_s/V_0. \quad (2)$$

The voltage of the search coil without shielding cylinder is expressed as V_0 and that with shielding cylinder as V_s . Figure 6 shows the SEs at positions where the distances from the axial center of the cylinder are 0, ± 13 , ± 23 , ± 31 , ± 39 mm. The SEs shown in Fig. 6 are of maximum ac external magnetic field at each frequency. From the figure, the SEs around the positions a quarter of the length of the cylinder are a little inferior to those at the center and the ends. The reason for this is considered that the magnetic field penetrates into the cylinder bore from those positions. We are going to investigate the relation between the internal struc-

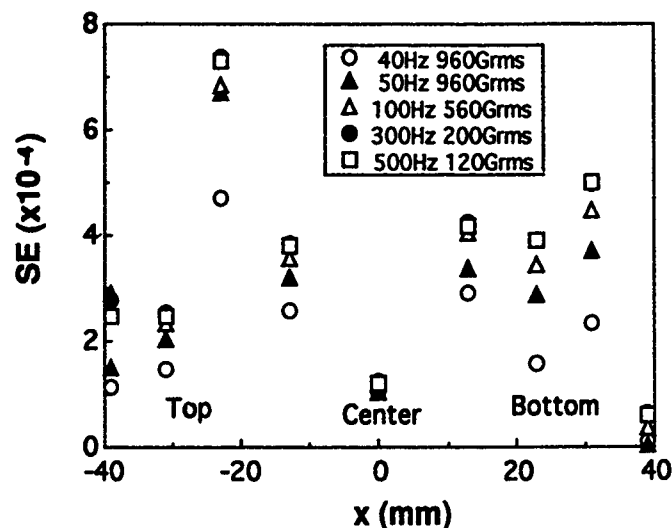


FIG. 6. Difference of shielding effect (SE) due to position in NbTi/Nb/Cu cylinder.

ture and SE after this study. Although the SE at each position is various in detail, it can be said that the shielding effect is good enough to shield from ac magnetic field of the order of several hundred gauss since all SEs are in the order of 10^{-4} .

IV. CONCLUSION

The slender cylinder with an aspect ratio of 6 can be manufactured by a deep-drawing and a spinning method from NbTi/Nb/Cu sheet of multilayer structure. Although there are slight variations in shielding effect at several positions in the cylinder, they are all of the order of 10^{-4} in the range of frequency from 40 to 500 Hz when the applied field is less than 1000 G rms. These shielding effects are superior to those of the Cu cylinder. There is a frequency dependence of alternating magnetic shielding. The magnetic field inside the superconducting cylinder increases more steeply with applied magnetic field at higher frequencies. In this study, we investigated the shielding effect of our material in the extent of magnitude of magnetic field and frequency demanded in the shielding of external alternating magnetic field of Maglev system. However, there remain some interesting points, for example, frequency dependence of the limit of magnetic shielding and the influence of the addition of dc magnetic field to ac magnetic field. We will study these points from now on.

¹ I. Itoh, T. Sasaki, S. Minamino, and T. Shimizu, IEEE Trans Appl. Supercond. 3, 177 (1993).

² J. Karthikeyan, A. S. Paithankar, K. P. Sreekumar, N. Venkatramani, and V. K. Rohatgi, Cryogenics 29, 915 (1989).

³ J. Wang and M. Sayer, IEEE Trans. Appl. Supercond. 3, 185 (1993).

⁴ B. Cabrera and W. O. Hamilton, in *The Science and Technology of Superconductors*, edited by W. D. Gregory et al. (Plenum, New York, 1973).

⁵ B. P. Strauss, R. H. Remsbottom, P. J. Reardon, C. W. Curtis, and W. K. McDonald, IEEE Trans. Magn. MAG-13, 487 (1977).

⁶ R. Boll and K. J. Overshott, *Sensors Vol. 5, Magnetic Sensors* (VCH, Weinheim, 1989).

⁷ J. M. Thomasson and D. M. Ginsberg, Rev. Sci. Instrum. 47, 387 (1976).

A method of increasing magnetic energy of superconducting magnetic energy storage

T. Morisue and T. Yajima

Nagoya University, Chikusa-ku, Nagoya 464-01, Japan

A solenoidal-type superconducting magnetic energy storage (SMES) using ferromagnetic material as an exterior magnetic circuit can store about 30% more magnetic energy than that using no ferromagnetic material. The amount of pure iron needed is 3.4 ton/MJ or 12 000 ton/MWH for the operating magnetic flux density of the solenoid between 4 and 5 T. Low grade ferromagnetic material containing more than 50% pure iron may be available for the SMES.

I. INTRODUCTION

The operating magnetic flux density of a solenoidal-type superconducting magnetic energy storage (SMES) will be greater than 4 T, and consequently the use of ferromagnetic material as the core of the magnetic circuit of the SMES is meaningless since its saturation magnetic flux density is below 2 T. However, the SMES using ferromagnetic material as an external magnetic circuit as shown in Fig. 1 will increase stored magnetic energy.

In this paper, the energy amplification by using ferromagnetic material is studied theoretically and by the computer simulation for various permeabilities and shapes of ferromagnetic material. A design example of the SMES using ferromagnetic material is presented.

II. SMES USING NO FERROMAGNETIC MATERIAL

The stored magnetic energy of a single layer solenoidal-type SMES is expressed as

$$E = LI^2/2, \quad (1)$$

where L and I are the inductance and the superconducting current of the solenoid, respectively. The inductance L is written as

$$L = F(a/h) \mu_0 \pi a^2 N^2 / h, \quad (2)$$

where a and h are the radius and the height of the solenoid, respectively, μ_0 is the permeability of free space, N is the number of the windings of the solenoid, and $F(a/h)$ is Nagoka's coefficient¹ and is written as

$$F(a/h) = \frac{4}{3\pi} \frac{1}{k'} \left[\frac{k'^2}{k^2} [K(k) - E(k)] + E(k) - k \right], \quad (3)$$

where $k = 4(a/h)^2 / [4(a/h)^2 + 1]$, $k' = \sqrt{1 - k^2}$, and K and E are the complete elliptic integral of the first kind and the second kind, respectively.

Under the constraint that the ampere-turn per unit height and the total length of the superconducting wire are constant:

$$NI/h = c_1 \quad \text{and} \quad 2\pi ah = c_2 \quad (4)$$

(c_1 and c_2 are constants), the stored magnetic energy for a thin layer solenoid is written from (1), (2), and (4) as

$$E = c_3 F(2\pi a^2/c_2) a \quad (c_3 = \mu_0 c_1^2 c_2 / 4). \quad (5)$$

Equation (5) has a maximum at $a/h \doteq 1$. [Note that $F(x)$ is a decreasing function of x .] Therefore, the optimum solenoid has the radius which is nearly equal to the height.

III. SMES USING FERROMAGNETIC MATERIAL

First, we consider the case that ferromagnetic material fills the unbounded region: $r \geq a$, $-\infty < z < +\infty$. For this case, an analytical solution is obtained by using the Fourier transform method² and the inductance is given as,³

$$L(\mu) = c \int_0^\infty \left[\frac{I_0(\omega)}{I_1(\omega)} + \frac{\mu_0 K_0(\omega)}{\mu K_1(\omega)} \right]^{-1} \times \frac{\sin^2[\omega/(2a/h)]}{\omega^3} d\omega, \quad (6)$$

where $c = 4\mu_0 a^2 N^2 / h$, μ is the permeability of ferromagnetic material, and I_n and K_n are the n th-order modified Bessel function of the first kind and the second kind, respectively.

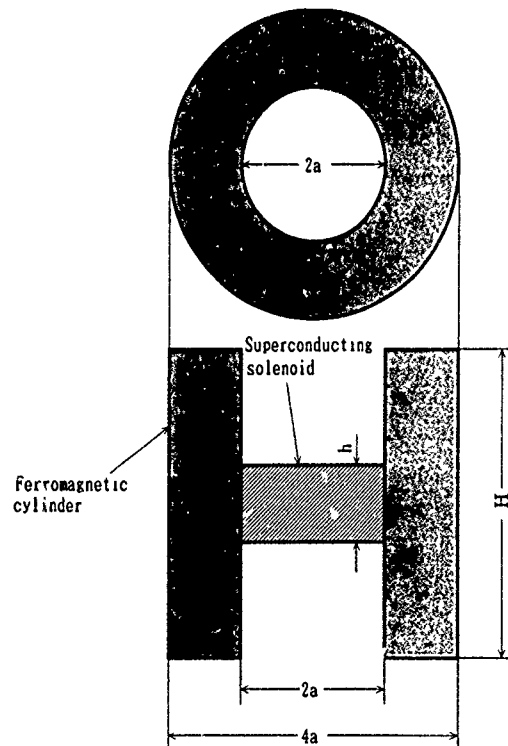


FIG. 1. SMES using ferromagnetic material as an exterior magnetic circuit.

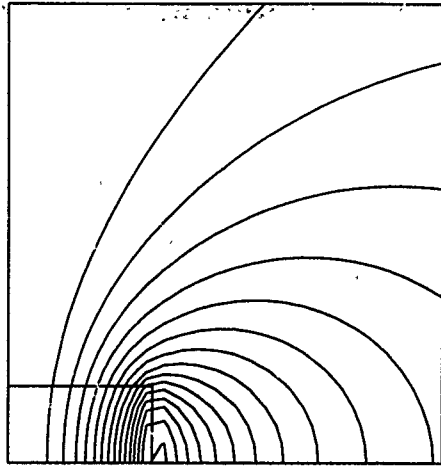


FIG. 2. Magnetic lines of force for the relative permeability of 1, $a/h=1$ and $H/h=3$.

From Eq. (6) it follows that $L(\mu)/L(\mu_0)=1.33$ for $a=h$ and $\mu \geq 1000\mu_0$, where $L(\mu)$ and $L(\mu_0)$ represent the inductance of the solenoid with and without ferromagnetic material, respectively. The energy storage amplification is, therefore, greater than 30%.

Second, we consider the case that ferromagnetic material fills the bounded region: $a \leq r \leq 2a$, $-H/2 \leq z \leq H/2$ (see Fig. 1). We assume that the operating magnetic flux density of the solenoid is between 4 and 5 T, and the saturation magnetic flux density of ferromagnetic material is between 1.6 and 1.8 T. From Fig. 1 the area of the cross section of the solenoid is πa^2 and that of the ferromagnetic material is $3\pi a^2$. Consequently, the magnetic flux density inside the ferromagnetic material is below the saturation almost everywhere.

The magnetic fields in the solenoid and ferromagnetic material are calculated by using the boundary integral equation method. The boundary integral equation in terms of the magnetic vector potential is written as⁴

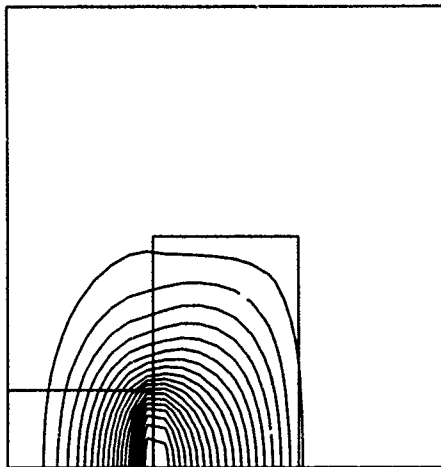


FIG. 3. Magnetic lines of force for the relative permeability of 1000, $a/h=1$ and $H/h=3$.

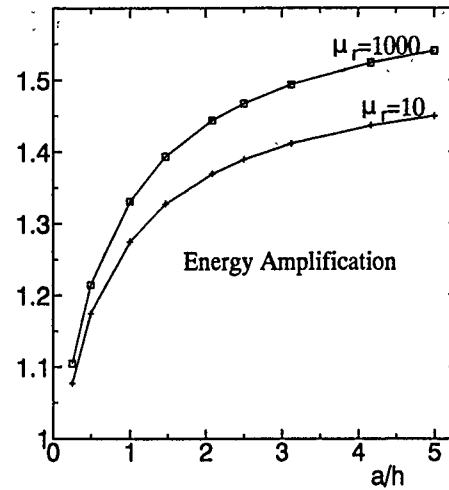


FIG. 4. Energy storage amplification with respect to a/h for the relative permeability of 10 and 1000.

$$cA(\mathbf{r}) = \int_{\Omega} \frac{\mu_0 \mathbf{j}_0(\mathbf{r}')}{4\pi|\mathbf{r}-\mathbf{r}'|} d\Omega' - \int_{\Gamma} A(\mathbf{r}') \frac{\partial}{\partial n'} \left(\frac{1}{4\pi|\mathbf{r}-\mathbf{r}'|} \right) d\Gamma' + \int_{\Gamma} \frac{\partial}{\partial n'} A(\mathbf{r}') \frac{1}{4\pi|\mathbf{r}-\mathbf{r}'|} d\Gamma', \quad (7)$$

where $c=1$, \mathbf{r} in the domain; $=1/2$, \mathbf{r} on the boundary, \mathbf{j}_0 is the exciting current density, Ω is free space, and Γ is the boundary (interface) between the ferromagnetic material and free space.

The computed magnetic lines of force are shown in Figs. 2 and 3 for the relative permeability of 1 and 1000, respectively (for $a=h$ and $H=3h$). The energy storage amplification with respect to a/h is shown in Fig. 4 for the relative permeability of 10 and 1000. The energy storage amplification with respect to various shapes of the ferromagnetic cylinder is shown in Fig. 5 for the relative permeability of 10.

We obtain from Fig. 5 that, for $a/h=1$ and $H/h=2$,

$$L(10\mu_0)/L(\mu_0) = 1.28. \quad (8)$$

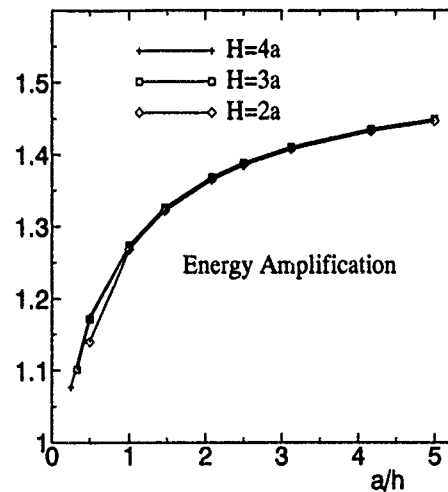


FIG. 5. Energy storage amplification with respect to various shapes of the ferromagnetic cylinder with outer diameter $4a$ and a relative permeability of 10.

TABLE I. Design example of SMES using ferromagnetic material as an exterior magnetic circuit (see Fig. 1). The saturation magnetic flux density of pure iron is assumed to be 1.7 T.

Superconducting solenoid:

radius $a=0.4$ m, height $h=0.4$ m,
ampere-turn per meter $=5 \times 10^6$ A/m,
magnetic flux density $=4.2$ T.

Ferromagnetic cylinder:

inner radius $a=0.4$ m, outer radius $2a=0.8$ m,
height $H=2h=0.8$ m, volume $=1.2$ m³,
relative permeability $=10$ (volume concentration of iron $=0.75$),
amount of iron $=7.1$ ton.

Stored magnetic energy $=2.1 \times 10^6$ J.
(energy storage amplification $=1.28$).

According to the Clausius-Mossotti equations,⁵ the permeability is related to the polarizability per sphere iron particle as

$$(\mu - \mu_0)/(\mu + 2\mu_0) = 4\pi n \rho^3/3, \quad (9)$$

where ρ is the radius of the sphere iron particle and n is the number of the particles in a unit volume. It follows from Eq. (9) that the relative permeability of 10 corresponds to the volume concentration of 75% of pure iron. (This fact agrees well with the result obtained by a computer simulation.)

A design example is shown in Table I. The amount of

ferromagnetic material is exactly proportional to stored magnetic energy under the constant ampere-turn per meter and the constant aspect ratio a/h .

IV. CONCLUSIONS

A solenoidal-type SMES using ferromagnetic material as an exterior magnetic circuit can store about 30% more magnetic energy than that using no ferromagnetic material. The amount of pure iron needed is 3.4 ton/MJ or 12 000 ton/MWH for an operating magnetic flux density between 4 and 5 T. Low grade ferromagnetic material containing more than 50% iron may be available for SMES.

A SMES using ferromagnetic material will require more space than a conventional SMES. However, this drawback may be compensated by the cost performance.

A 30% increase in the inductance or stored energy means a 30% increase in the operating magnetic flux density (for example, from 4 to 5.2 T), and the superconducting wire will be loaded heavier. Such an increase should lead to progress in SMES technology.

¹H. Nagaoka, Scientific papers (Institute of Physical and Chemical Research, Tokyo); Table No. 2, 69 (1927).

²T. Morisue, IEEE Trans. Magn. **MAG-28**, 1324 (1992).

³T. Morisue (unpublished).

⁴T. Morisue and M. Fukumi, IEEE Trans. Magn. **MAG-23**, 3311 (1987).

⁵P. J. W. Debye, *Topics in Chemical Physics* (Elsevier, Amsterdam, New York, 1962), p. 90.

Synthesis of high-temperature superconducting thin films in microwave field

Victor I. Kojuharoff

Institute of Electronics, Bulgarian Academy of Sciences, 72 Tsarigradsko Shosse Boulevard, Sofia 1784, Bulgaria

The most widely used technique to obtain high-temperature superconducting (HTSC) thin films at present, i.e., the *in situ* method, has the disadvantage of heating the substrate up to 700–800 °C. This paper proposes a novel, low-temperature method for HTSC synthesis that is capable of producing new types of multilayer structures. The technique is based on the use of microwave (MW) field to treat a thin film deposited on a single-crystal substrate. The process of superconductor formation depends on the MW power, the sample volume, and the dielectric constant. The nature of the synthesis in MW field differs significantly from the ordinary high-temperature baking, since the solid-state reaction is initiated simultaneously in the entire volume and runs at a relatively high rate. Aerosol deposition proved to be the most suitable technique, especially when combined with ultrasonic aerosol homogenization. Scanning electron microscopy observations show that the film surface consists of comparatively densely ordered, almost round grains with sizes between 100 and 130 nm. X-ray diffraction analysis clearly demonstrates that no admixtures from the substrate have penetrated the layer. The resistance versus temperature characteristic is measured by four-probe technique and the critical current densities were 2×10^5 and 0.8×10^5 A/cm² at 77 and 4.2 K, respectively.

I. INTRODUCTION

The most promising applications of high-temperature superconducting (HTSC) structures appear to be in hybrid electronic circuits, microwave (MW) linear switches, and frequency mixers and detectors.^{1–3} The most widely used technique at present is the *in situ* method, allowing a substantial lowering of the final synthesis temperature without removing the sample from the technological equipment. A disadvantage of this technique is the necessity of heating the substrate up to 700–800 °C during the film deposition. This temperature is sufficiently high to make the *in situ* method almost inapplicable to the production of sandwich-type structures. On the other hand, the HTSC film structure is strongly influenced by the changes occurring in the substrate, such as thermal expansion, polymorphic transformations, as well as other heat-induced phenomena. A typical example is LaAlO₃, which is characterized by low thermal expansion and lattice parameters close to those of the superconductor (the difference does not exceed 1.5%). A drawback of the LaAlO₃ substrates is the existence of various temperature transitions accompanied by lattice parameter changes.⁴ In view of these disadvantages of the *in situ* technique, a novel low-temperature method for HTSC film synthesis is proposed in the present paper allowing varieties of new multilayer structures to be obtained.

II. EXPERIMENT

The experimental technique is based on the use of MW field for treating the thin film deposited on a single-crystal substrate. A necessary condition for carrying out such synthesis is to have a substrate material with suitable dielectric loss. For instance, LaAlO₃, SrTiO₃, and YSZ substrates have $\tan \delta \leq 10^{-4}$ at $\epsilon' \approx 15$ –20, considerably differing from those of the HTSC film formed through “cold” deposition. The

process of superconductor formation is proportional to the MW field power W and the function $f(\rho/\nu\tau)$, where ν is the thin-film sample volume, τ is the exposure time, and $\rho = \epsilon''/\epsilon'$ is the dielectric loss tangent.

The nature of the synthesis in MW field differs significantly from the ordinary high-temperature baking. In the former, the solid-state reaction of superconducting compound formation is initiated simultaneously in the entire volume and runs at a relatively high rate. This means that the kinetic energy of the effective collision between the molecules participating in the oxides exceeds considerably that of the ordinary thermal process. Therefore the second necessary condition for obtaining high-quality HTSC compounds is high degree of layer homogeneity ensuring a homogeneous medium for the MW field. The experiments showed that the absence of such medium leads to local overheating resulting in multiphase structures. Therefore, the formation of HTSC compounds with the use of MW field is volume limited, i.e., depends strongly on the film thickness. The experiments performed showed satisfactory results with thicknesses less than 3 μm . During the tests we used different deposition techniques: screen printing,⁵ paint on,⁶ and aerosol deposition⁷ of salts of organic and inorganic acids. Aerosol deposition proved to be the most suitable method, especially when ultrasonic aerosol homogenization was used. The latter made it possible to control accurately the size of the aerosol particles and, therefore, determined to a large extent the high homogeneity of the film produced. The equipment is shown schematically in Fig. 1. In the experiments we used (110)- and (001)-oriented LaAlO₃ substrates. The solution was sprayed through a 0.04- μm -diam nozzle; 10–15 ml of solution with a concentration of 0.27 m mol/ml was needed to form one layer. The solution was made up of oxalates of Bi, Sr, Ca, Cu, Pb, or Sn in deionized water in a ratio corresponding to the formula $\text{Bi}_2\text{Me}_{0.5}\text{Sr}_{1.5}\text{CaCu}_3\text{O}_8$, where Me

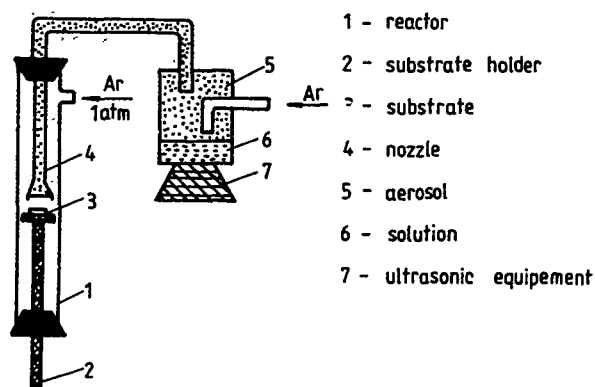


FIG. 1. The experimental equipment.

=Pb or Sn. The films thus obtained were placed in a drier for 30 min at a temperature of 60 °C. After drying, the samples were placed on a holder made of aluminum ceramics in a "Linn High Therm" type MW furnace.

In order to establish the best MW film treating mode, a series of experiments was carried out on layers with thicknesses from 0.5 to 5 μm treated for different exposure times and different MW field powers. In general, the experiments showed best results in terms of T_c and film morphology for (a) MW field power 0.6 kW, (b) exposure time 15 min, (c) frequency 2500 MHz, and (d) oxygen atmosphere $P_{\text{O}}=1.5$ atm.

III. RESULTS AND DISCUSSION

The investigation of the structure and morphology of the HTSC thin films (1 $\mu\text{m} \times 1$ mm) obtained on LaAlO_3 substrates were carried out using well-known surface analysis techniques. The scanning electron microscopy (SEM) observation showed that the sample surface consisted of comparatively densely ordered, almost round grains with sizes between 100 and 130 nm. These films were dense and uniform, the surface was not mirror like, and the gaps existing between the grains were smaller than the grains themselves (30–50 nm).

X-ray diffraction analysis was used to identify the different crystal phases present in the thin film (Fig. 2). The diffraction pattern shown corresponds to a single-phase superconductor $\text{Bi}_2\text{Pb}_{0.5}\text{Sr}_{1.5}\text{CaCu}_3\text{O}_{8+}$ with $T_c=85$ K. The diagram clearly demonstrates that no admixtures from the substrate have penetrated the layer. We should also point out that, in microscopic volumes, the film is predominantly oriented along the "c" axis indicating the presence of a texture. This is a rather unexpected result, bearing in mind that the substrate is not heated and does not interact with the film. Most probably, the thermal energy released during the synthesis as a result of the MW field interaction with the film molecules affects the substrate surface crystal field and gives rise to certain crystalline orientation.

A standard four-probe technique with mechanically pressed silver contacts was used to obtain the $R=f(T)$ function. The results from the measurement of a $\text{Bi}_2\text{Pb}_{0.5}\text{Sr}_{1.5}\text{CaCu}_3\text{O}_{8+}$ thin film are shown on Fig. 3. The

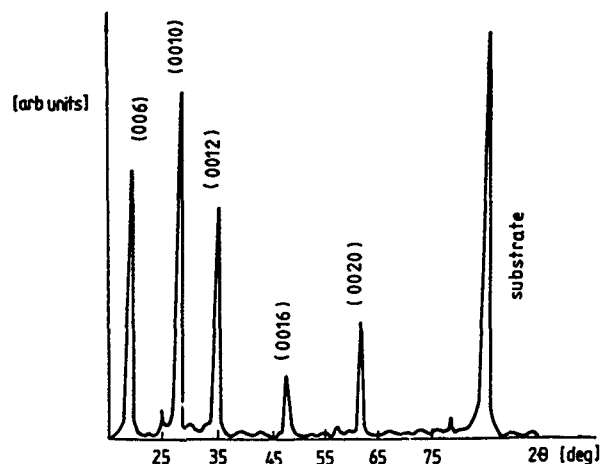


FIG. 2. The data from the x-ray diffraction analysis of the $\text{Bi}_2\text{Pb}_{0.5}\text{Sr}_{1.5}\text{CaCu}_3\text{O}_{8+}$ film.

R_{300}/R_{100} ratio was ~ 1.5 . The critical current density of the film studied was 2×10^5 A/cm², measured at 77 K, while at 4.2 K the critical current density was 0.8×10^5 A/cm².

IV. CONCLUSIONS

This work demonstrates the possibility of using a MW field in the synthesis of superconducting materials. This technique, combined with the "cold" methods of HTSC thin-film deposition, makes it possible to produce a homogeneous single-phase superconductors characterized by high accuracy of the dosage of participating components. The time needed for the superconductor synthesis is significantly shorter than times cited in the literature.

The basic advantage of the MW synthesis is the absence of substrate heating. The film is not contaminated through diffusion of substrates components, the substrate is not subjected to any morphological transformations, and the thermal expansion is close to zero. The choice of substrates for HTSC films growth is limited only by the dielectric properties of the substrate.

In order to obtain a uniform, dense, and single-phase film, one should create conditions for uniform MW field dis-

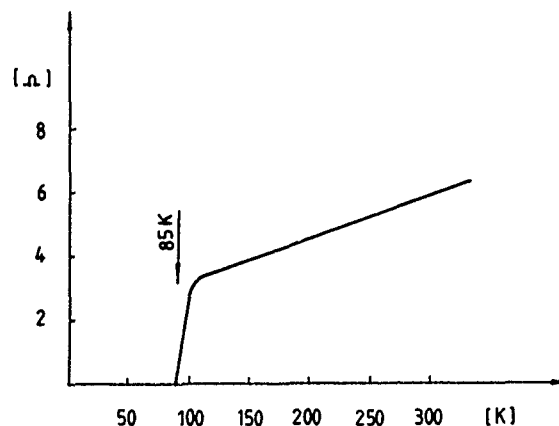


FIG. 3. Results from the measurement of the resistance of the $\text{Bi}_2\text{Pb}_{0.5}\text{Sr}_{1.5}\text{CaCu}_3\text{O}_{8+}$ film as a function of temperature.

tribution along all directions in the sample, i.e., the film deposited should exhibit uniform impedance and density over its entire volume. Therefore, the medium homogeneity is in practice inversely proportional to the film thickness.

All studies performed on bulk samples (thickness ≤ 1 mm) showed that they are predominantly multiphase systems, although some of them exhibited superconducting properties.

¹M. Adams, S. Hedges, and B. Nicholson, *GES J. Res.* **8**, 105 (1990).

²T. Konaka, M. Sato, H. Asano, and S. Kubo, *J. Supercond.* **4**, 283 (1991).

³O. Vendik, T. Samoilova, and S. Karmanenko, *J. Less Common Metals* **164-165**, 1240 (1990).

⁴Y. Hsieh, M. Siegal, R. Hill, and J. Phillips, *Appl. Phys. Lett.* **57**, 2268 (1990).

⁵S. Lee, S. Chou, and L. Hung, *J. Appl. Phys. Lett.* **55**, 286 (1989).

⁶P. Ram *et al.*, *Supercond. Sci. Technol.* **1**, 340 (1989).

⁷H. Nobumasa *et al.*, *Jpn. J. Appl. Phys.* **27**, L1669 (1988).

Estimation of fatigue exposure from magnetic coercivity

Z. J. Chen, D. C. Jiles, and J. Kameda

Ames Laboratory and Center for NDE, Iowa State University, Ames, Iowa 50011

An investigation of the effects of fatigue on A533B steel under constant load amplitude is reported in this paper. It was found that the plastic strain of the sample accumulated logarithmically with the number of stress cycles after initial fatigue softening. Based on the fact that plastic strain is often linearly related to the coercivity of material, at least for small changes of H_c , a phenomenological relationship has been developed and tested to correlate the number of stress cycles to this magnetic parameter. This result represents the first successful attempt to relate the fatigue exposure directly to a magnetic parameter.

I. INTRODUCTION

Metallic fatigue failure is a very difficult and serious problem due to its insidious nature. It has been estimated that fatigue failure is the primary cause of at least 90% of all service failures due to mechanical causes. Magnetic nondestructive evaluation techniques, such as magnetic hysteresis measurements and Barkhausen effect measurements have been proven to be powerful methods of detecting changes in mechanical properties.^{1,2} However, due to the fact that so many external factors can influence the magnetic properties, quantitative characterization of fatigue damage remains a very difficult problem.

In this paper, a phenomenological relationship relating coercivity to the number of stress cycles has been developed through the study of the results of fatigue tests under constant load amplitude. One of the significant results of this relationship is that, for the first time, the number of stress cycles was shown to be related directly to the magnetic parameter of coercivity and therefore the measurement of coercivity provides a way to estimate fatigue damage.

II. EXPERIMENTAL PROCEDURE

The material used in this investigation was a medium strength structural steel alloy (ASTM code A533B) whose mechanical properties are given in Table I. Fatigue tests were carried out on smooth tensile specimens with constant load amplitude, using a computer controlled, 10 kN, servo-hydraulic MTS system. Magnetic hysteresis parameters, such as coercivity, remanence, and initial permeability were measured by the Magnescope, a computer controlled magnetic

inspection system.³ These measurements were made at predetermined intervals throughout the fatigue life under zero load.

III. TEST RESULTS AND PREDICTIONS

Fatigue damage is a progressive effect, during which the microstructures of material, such as dislocation density, plasticity, and density of vacancy undergo continuous change before final catastrophic failure. Under cyclic stress at constant load amplitude, it was found that the maximum tensile and compressive strain increased continuously throughout the whole fatigue life, after the initial few hundred stress cycles which caused fatigue softening. A linear relationship between the magnitude of the strain amplitude and number of stress cycles was observed on a semilog graph, as shown in Figs. 1 and 2. This result indicated that the plastic strain accumulated logarithmically with the number of stress cycles.

Correlations between mechanical properties and magnetic properties have been studied previously.^{4,5} It was found for example that the coercivity H_c was generally linearly

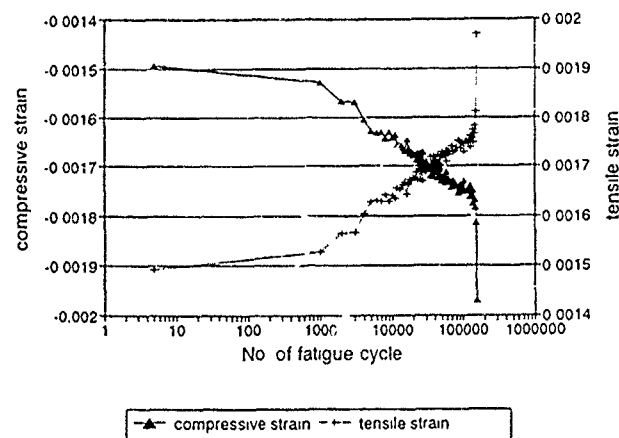


FIG. 1. Maximum tensile and compressive strain as a function of number of stress cycles at a fixed stress amplitude of 272 MPa.

TABLE I. Mechanical properties of ASTM A533B steel.

Young's modulus	0.2% Yield stress	UTS	Hardness, R_b
170 GPa	369 MPa	536 MPa	88.0

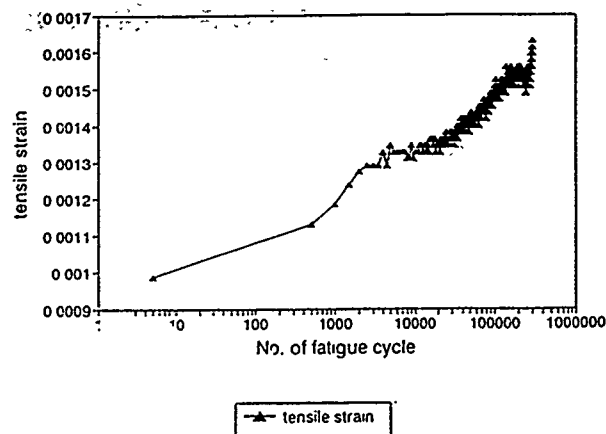


FIG. 2. Maximum tensile strain as a function of number of stress cycles at a fixed stress amplitude of 243 MPa.

related to the plastic strain of a material, and this relationship can be understood theoretically because increased plastic strain results in a linear increase in dislocation density, which increases the pinning term k in the theory of hysteresis.⁶ If this relation also holds in the fatigue process, then according to the experimental discovery of the logarithmic relationship between plastic strain and number of stress cycles, the same logarithmic relation between coercivity and number of stress cycles should be expected.

From Figs. 1 and 2, the strain amplitude and the number of stress cycles N can be related by following equation:

$$\epsilon - \epsilon_0 = a \ln(N), \quad (1)$$

where ϵ_0 is the intercept along the strain axis and a is the slope of the line. Assuming the linear relationship between the coercivity and the plastic strain, the following equation is obtained:

$$H_c - H_{c0} = b \ln(N), \quad (2)$$

where H_{c0} and b are constants under the specific test condition. Equation (2) can also be expressed as

$$N = c_1 \exp(c_2 H_c), \quad (3)$$

where C_1 and C_2 are determined by H_{c0} and b .

Magnetic measurements were performed under the same test conditions. Results are shown in Figs. 3 and 4. A linear

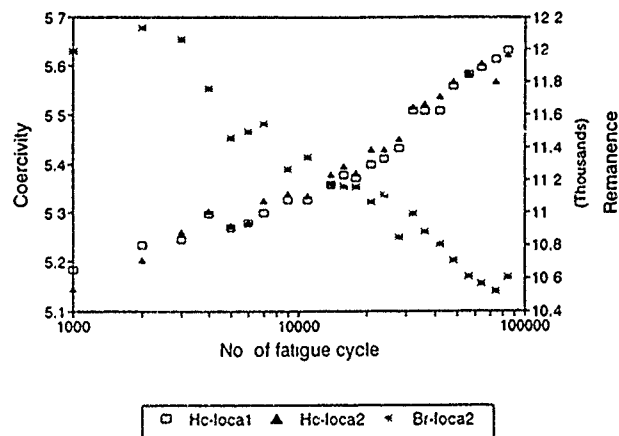


FIG. 3. Magnetic properties as a function of the number of stress cycles.

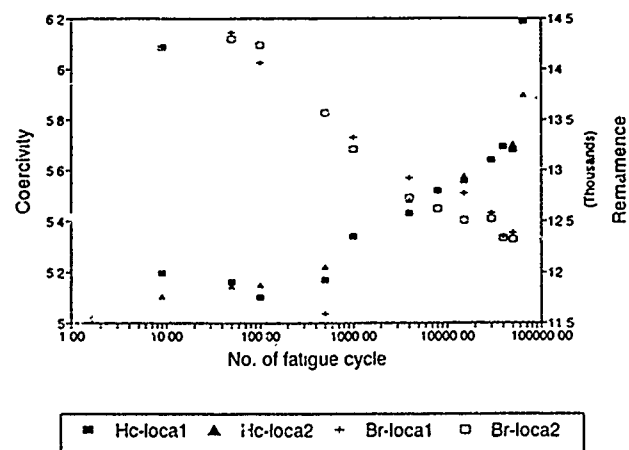


FIG. 4. Magnetic properties as a function of the number of stress cycles.

relation between coercivity and number of stress cycles is quite apparent on the semilog graph after the initial few hundred cycles of fatigue softening. This relation matches the prediction described by Eq. (2). Similar results were also found on the fatigue test at different stress amplitudes in the high cycle fatigue regions under constant stress amplitude.

IV. DISCUSSION

The relationship expressed in Eq. (1) was determined from the fatigue tests under load control. It applies to high cycle fatigue on A533B material. However, the generality of this relation between the accumulated plastic strain and the number of stress cycles should be tested on different materials, and furthermore the dependence of the parameters on the test conditions should also be investigated.

The assumption of a linear relation between plastic strain and coercivity through the theory of hysteresis leads from Eq. (1) to Eq. (2). The linear relationship between plastic strain and coercivity has been observed previously and can be explained by the fact that plastic strain introduces extra dislocations which pin domain walls and therefore increase the hysteresis loss parameter k . In our A533B material, fatigue softening was observed which indicated that there was a decrease in dislocation density. However, the fatigue induced local yielding (and therefore residue stress), and the resulting extra density of vacancies acted as additional wall pinning sites. The overall effect of fatigue can therefore still increase the hysteresis loss parameter k .

The parameters C_1 and C_2 in Eq. (3) can be experimentally determined by three measurements of (N_0, H_{c1}) , $(N_0 + \Delta N, H_{c2})$, $(N_0 + \Delta N', H_{c3})$, where ΔN and $\Delta N'$ are two intervals of the number of stress cycles between successive measurement. N_0 is the number of accumulated stress cycles when the first measurement is taken. Practically, N_0 is also an unknown number. Although Eq. (3) does not indicate the final value of fatigue life, it does show how to estimate accumulated fatigue damage by measuring coercivity. If the total fatigue life can be predetermined by an alternative method, then this relationship can be used to monitor fatigue damage.

V. CONCLUSIONS

A relationship for determining the number of stress cycles under constant stress amplitude by magnetic measurement of the coercivity has been presented. This relationship is based on experimental evidence. According to the relationship, the number of stress cycles is logarithmically related to the coercivity of the material. Although the sensitivity of the result so far is not completely satisfactory for practical applications especially during the later stages of fatigue life, the relationship demonstrated in this paper gives a connection between the magnetic properties and fatigue damage. It therefore provides a clue for further development of models for validation of nondestructive evaluation techniques for fatigue based on magnetic property measurements.

ACKNOWLEDGMENT

This work was supported by the U.S. Nuclear Regulatory Commission through the Center for NDE at Iowa State University, under Grant No. NRC-04-91-098.

¹M. K. Devine, S. Hariharan, L. J. H. Brasche, and D. C. Jiles, *Rev. Prog. QNDE* **10**, 2021 (1991).

²S. Titto, M. Ojala, and S. Saynajakangas, *NDT Int.* **9**, 177 (1976).

³D. C. Jiles, S. Hariharan, and M. K. Devine, *IEEE Trans. Magn.* **MAG-26**, 2577 (1990).

⁴D. C. Jiles, *Phys. Status Solidi, A* **108**, 147 (1988).

⁵D. C. Jiles and D. Utrata, *Rev. Prog. QNDE* **7**, 1255 (1988).

⁶D. C. Jiles, *J. Magn. Magn. Mater.* **61**, 48 (1986).

Overview of applications of micromagnetic Barkhausen emissions as noninvasive material characterization technique

L. B. Sipahi

Institute for Physical Research and Technology, Center for Nondestructive Evaluation, Iowa State University, Ames, Iowa 50011

In this concise overview, the physical principles of magnetic Barkhausen effect will be briefly discussed and its recent applications in material characterization will be considered. There are new trends in micromagnetic Barkhausen effect emissions and its applications in the material characterization area. These emissions take place in magnetic materials subjected to changing applied magnetic field, and can be used, for instance, to study noninvasively surface characterization of materials. Since these emissions are quite sensitive to changes in the microstructure and subsurface stress states in magnetic materials, various applications of these of micromagnetic emissions have been found in areas such as nuclear, aerospace, and automotive technologies which use magnetic materials.

I. INTRODUCTION

The Barkhausen effect is now being widely employed as a material characterization technique for magnetic materials. The micromagnetic emissions can be detected as voltage pulses caused by discontinuous changes in magnetization in the material, and are the result of spontaneous motion of domain walls or rotation of magnetization within domains. Since pinning of domain walls is the principal cause of hysteresis, one may easily comprehend how magnetic materials which show hysteresis also display micromagnetic Barkhausen emissions as the external magnetic field is varied.

A. Importance and applicability of micromagnetic Barkhausen emissions in material characterization

The magnetization process in magnetic materials has been an important and difficult research subject for many years because of the many factors contributing to the process. This process, which can be described on both macroscopic and microscopic scales, can be analyzed by different techniques. The magnetic hysteresis loop, Fig. 1, is mainly representative of averaged macroscopic dependence of magnetization M on field H . The micromagnetic Barkhausen effect, Fig. 1, is indicative of microscopic changes in magnetization on the domain scale. Magnetic domains, which are the regions of parallel aligned atomic magnetic moments, form the entire volume of the material. The boundary between domains is not a sharply defined geometric surface but consists of an intermediate zone with a continuous variation of the spin magnetic moment orientations with position. This width is nearly in the order of 10^2 – 10^3 Å.

As the magnetization is increased towards saturation more complicated processes play a role such as movements of 90° Bloch walls, the nucleation of new domain walls, the mutual annihilation of pairs of walls, and disappearance of walls swept to the surface of the specimen. When the magnetization reaches saturation, the domain structure becomes simpler because the material becomes a single domain. If magnetization is increased further, change in magnetization occurs essentially through the rotation of the magnetization vector within a domain against the internal anisotropy forces.

The mobility of the Bloch walls is related to the total magnetostatic energy which varies with the size and shape of specimen, and its microstructure. Irreversible domain wall motion is strongly influenced by the defect structure such as voids, second phase inclusions, dislocations, clusters of point imperfections, and also stresses.

B. Applications of Barkhausen effect in material characterization

Polycrystalline ferromagnetic materials such as steels are the most crucial of industrial commodities. For instance more steel is produced than any other metal. When alloyed with silicon it is used for electronic applications such as transformers, inductors, and motors. It is also alloyed with carbon and other metals for use as a constructional material on large-scale projects such as pipelines, railroads, and bridges. It is desirable to inspect these structures because of the likely high cost of failures which could be avoided through appropriate nondestructive evaluation methods. The detection of corrosion cracks and other defects and the evaluation of stresses, elastic and plastic deformation, and the likelihood of failure due to creep or fatigue are all important

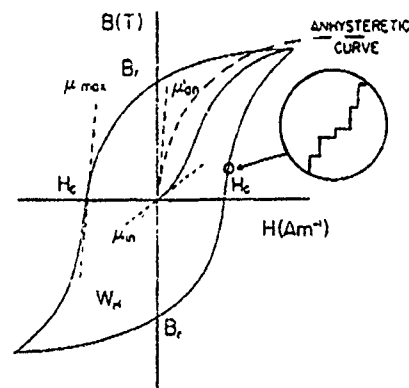


FIG. 1. The essential parameters of a BH loop with steplike Barkhausen discontinuities along the hysteresis curve by amplifying the magnetization.

reasons for developing these inspection techniques. Thus the potential catastrophic failures may be preventable by monitoring the condition of structures.

The Barkhausen effect can be used for indirect measurement of fundamental properties of magnetic materials, such as the coercive force and the demagnetizing field, and also for determining the elastic limit in ferromagnets. In the present work, applications are considered in two different categories: microstructure and stress analysis.

1. Microstructure analysis

A primary concern of the steel industry is to consistently produce large quantities of steel with well controlled and uniform mechanical or electrical properties. If calibration is possible, the magnetic Barkhausen effect can be used for assessing changes in these properties as a result of processing and service.¹⁻⁵

The mechanical properties of steel are determined by microstructural parameters such as the concentration, shape, chemical composition, and dispersion characteristics of precipitates, grain boundaries, dislocations, point defects such as interstitial or substitutional impurities, and vacancies. The dependence of the magnetic Barkhausen effect emissions on distribution of grain sizes can be explained since polycrystalline iron and steel consist of a number of inhomogeneities and pinning points such as cavities, inclusions, precipitates, dislocations, and other lattice defects which impede the motion of domain walls.^{6,7} In electrical steels, the most significant pinning points are located at grain boundaries. In electrical steel sheets the influence of grain orientation on the texture can be determined using the magnetic Barkhausen effect measurements.

Recent work has indicated that this technique has the potential to be employed in noninvasive monitoring of neutron-irradiation-induced changes in ferritic alloys in order to ensure safe operation of nuclear reactor pressure vessels by means of magnetic inspection techniques.⁸⁻¹⁰ The magnetic Barkhausen effect has been already used for flaw detection in steel plates.¹¹ By generating magnetic Barkhausen emissions at different frequencies and combining them with hysteresis measurements, the determination of the surface decarburization in steels has been studied.¹² The dependence of Barkhausen emissions on micromagnetic hardness, hardening depth for production of critical components in the automotive industry, has been also investigated.¹³ The results showed that an increase in hardness resulted in a decrease in the micromagnetic emissions.

Another important application for the magnetic Barkhausen effect is fatigue testing. If magnetic parameters at the surface are measured, information on the fatigue damage can be predicted. This technique to detect fatigue damage during cyclic loading or after a single overloading cycle has been reviewed.¹⁴

In advanced magnetic materials, such as the ternary alloy $Tb_{0.3}Dy_{0.7}Fe_2$, Terfenol-D, magnetic Barkhausen effect measurements have been carried out to locate the onset of discontinuous rotation of domain magnetizations before¹⁵ and after¹⁶ applying stress.

Using the Barkhausen effect to determine the easy axis of magnetization in steels¹⁷ was studied. Since there are several factors which affect the magnetic Barkhausen emissions, the magnetizing parameters to generate these emissions were also investigated.¹⁸ This investigation revealed that not only the choice of wave form and frequency of magnetic field excitation to generate the micromagnetic emissions within material but also the choice of detecting method were quite crucial. Further, the new analysis techniques of these emissions were discussed.

2. Stress analysis

As is well known, the magnetization of ferromagnets is influenced by stress states of material through magnetostriction because plastic deformation gives rise to regions of high dislocation density which impede domain wall motion.

Elastic stresses also affect the magnetic Barkhausen effect emissions because of the effect of elastic deformation. This deformation in material leads one to arrange the energetically favorable domain configuration due to magnetoelastic energy minimization when the domain magnetization aligns with respect to the principal axes of lattice strain.

The stress axis in a polycrystalline material is rarely along one of the crystallographic axes of a grain. Therefore, in materials with positive $d\lambda/dM$, where λ and M are the magnetostriction and magnetization, respectively, tension causes alignment of the domains with directions along the crystallographic axis nearest the stress axis, but compression makes domain directions along these same axes less favorable. Thus, when the magnetizing field is applied along the stress axis, tensile stress will increase the number of magnetic Barkhausen emissions while the compressive stress has the converse effect. But if the magnetizing field is perpendicular to the stress axis, the effects of stress on hysteresis and Barkhausen effect are reversed. Investigation of the dependence of the magnetic Barkhausen emissions on the stress and the angle between the stress and the magnetization directions¹⁹ and angular dependence of magnetic properties of polycrystalline iron under the action of uniaxial stress²⁰ were conducted. These investigations concluded that the amplitude of these emissions was nearly isotropic and independent of the direction of the applied magnetic field. On the other hand, this amplitude showed an anisotropic trend and was dependent on the angle between the stress and applied magnetic field when stress was applied. Brief coverages of the effect of stress on the magnetic Barkhausen effect emissions^{21,22} were reported. These studies were mainly investigations of the influence of shot peening, which introduces a compressive stress on surface, and tensile stress on the emissions. The results indicated that the shot peening process as a cold surface treatment decreased the amplitude of the micromagnetic emissions.

It has been observed that the number of magnetic Barkhausen emissions increases when tensile stress is applied up to the elastic limit. Then these emissions at the elastic limit will either increase or decrease according to whether the magnetostriction is positive or negative. Figures 2 and 3 show how compressive and tensile stresses affect the domains and amplitude of the magnetic Barkhausen emis-

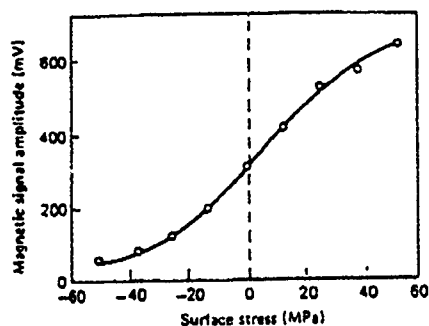


FIG. 2. Magnetic Barkhausen signal amplitude against surface stress (Ref. 23).

sions in an AISI 4340 steel²³ and bearing races.²⁴ This technique has been utilized for residual stress measurement and magnetic material characterization. Moreover, automated control of the camshaft grinding process by means of the magnetic Barkhausen effect was proposed, and it was found that fatigue strength is decreased with tensile grinding stress and increased with compressive stress.²⁵

On the other hand, there are some difficulties which researchers experience to study the micromagnetic Barkhausen emissions. These are mainly related to the very sensitive nature of the emissions to microstructural changes in specimen. A small change not only in one of the microstructural parameters but also in one of the generating or detecting parameters of these emissions of an experimental system may re-

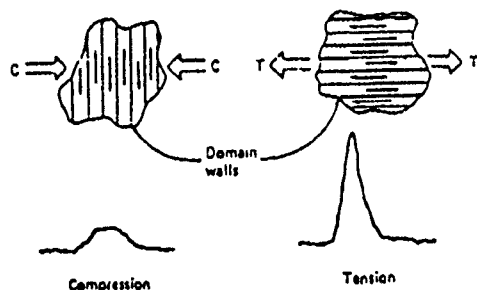


FIG. 3. Influence of compression and tension on Barkhausen effect signals in bearing races. These signatures were obtained after processing the Barkhausen emission pulses as explained by Barton *et al.* (Ref. 24).

sult in additional challenges to interpret the results. Moreover, the calibration curves of each specific case are necessary.

II. CONCLUSIONS

Due to the strong dependence of the magnetic Barkhausen emissions on microstructure and stress conditions of magnetic materials and due to its ease of measurement, the magnetic Barkhausen effect will continue being an important noninvasive magnetic material characterization method. As discussed above, this technique has been employed in many different technologies. Moreover, new potential application areas have yet to be exploited.

¹J. F. Bussiere, *Mater. Eval.* **44**, 560 (1986).

²L. B. Sipahi and D. C. Jiles, *J. Magn. Magn. Mater.* **104-107**, 385 (1992).

³S. Titto, M. Ojala, and S. Sänjäläkangas, *Non-Destr. Testing* **9**, 117 (1976).

⁴L. B. Sipahi and D. C. Jiles, in *Review of Progress in Quantitative NDE*, edited by D. O. Thompson and D. E. Chimenti (Plenum, New York, 1992), Vol. 11B, p. 1791.

⁵B. K. Tanner, *Nondestr. Test. Eval.* **5**, 9 (1989).

⁶L. B. Sipahi and D. C. Jiles, *Nondestr. Test. Eval.* **10**, 183 (1993).

⁷J. Kameda and R. Ranjan, *Acta Metall.* **35**, 1515 (1987).

⁸E. A. Little, D. J. Buttle, and C. B. Scruby, in *Effects of Radiations on Materials II* (ASTM, Philadelphia, 1990).

⁹M. I. Sablik, H. Kwun, G. L. Burkhardt, and D. G. Cadena, in *Review of Progress in Quantitative NDE*, edited by D. O. Thompson and D. Chimenti (Plenum, New York, 1993), Vol. 12, p. 1823.

¹⁰L. B. Sipahi, M. R. Govindaraju, and D. C. Jiles (these proceedings).

¹¹Y. Kagawa and T. Nakamura, *Electron. Eng. Jpn.* **110**, 82 (1990).

¹²M. Mayos, M. Putignani, and S. Segalini, IRSID Report No. 1203, 1985.

¹³G. Bach, K. Goebbels, and W. A. Theiner, *Mater. Eval.* **41**, 1576 (1988).

¹⁴K. Tiitto, *Nondestr. Test. Eval.* **5**, 27 (1989).

¹⁵L. B. Sipahi, M. P. Schulze, D. C. Jiles, and R. D. Greenough, *IEEE Trans. Magn. MAG-28*, 3153 (1992).

¹⁶L. B. Sipahi, M. P. Schulze, R. D. Greenough, D. C. Jiles, and A. G. Jenner (unpublished data).

¹⁷A. Dhar, C. Jagadish, and D. L. Atherton, *Mater. Eval.* **50**, 1139 (1992).

¹⁸L. B. Sipahi, D. C. Jiles, and D. Chandler, *J. Appl. Phys.* **73**, 5623 (1993).

¹⁹H. Kwun, *J. Magn. Magn. Mater.* **49**, 235 (1985).

²⁰D. A. Kaminski, D. C. Jiles, and M. J. Sablik, *J. Magn. Magn. Mater.* **104-107**, 382 (1992).

²¹L. B. Sipahi, M. K. Devine, D. C. Jiles, and D. D. Palmer, in Ref. 9, p. 1847.

²²C. Jagadish, L. Clapham, and D. L. Atherton, *Nondestr. Test. Eval.* **5**, 271 (1990).

²³C. G. Gardner, G. A. Matzkanin, and D. L. Davidson, *Int. J. NDT* **3**, 131 (1971).

²⁴J. R. Barton, F. N. Kusenberg, R. E. Beissner, and G. A. Matzkanin, in *Nondestructive Evaluation of Materials* (Plenum, New York, 1979).

²⁵R. M. Fix, K. Tiitto, and S. Tiitto, *Mater. Eval.* **48**, 904 (1990).

Monitoring neutron embrittlement in nuclear pressure vessel steels using micromagnetic Barkhausen emissions

L. B. Sipahi, M. R. Govindaraju, and D. C. Jiles

Center for Nondestructive Evaluation, Iowa State University, Institute for Physical Research and Technology, Ames, Iowa 50011

In nuclear power plants, neutron embrittlement of pressure vessel steels has been one of the main concerns. The use of micromagnetic Barkhausen emissions is a promising method to monitor the variations in microstructural and subsurface stress states due to their influence on these emissions. Measurements of these emissions can reveal neutron irradiation degradation in nuclear power plant components. Samples which were irradiated at different neutron fluences and annealed at different temperatures were obtained from three reactor surveillance programs. The results of different neutron fluences and annealing procedures showed noticeable fractional changes in the magnetic Barkhausen effect signal parameter, $\Delta\text{MBE}/\text{MBE}$, and in the mechanical properties of these specimens. For example, increased intensity of neutron fluence decreased the $\Delta\text{MBE}/\text{MBE}$ as well as impact energy and upper-shelf energy, but increased Rockwell hardness and yield strength. Typical changes in this parameter were in the range from -20% to -45% for fluences of up to $25 \times 10^{18} \text{ n cm}^{-2}$.

INTRODUCTION

The nuclear industry has been investigating inspection methods to ensure safe operation of nuclear reactors beyond their projected life span. Previous work has concentrated not only on destructive techniques such as Charpy tests but also on noninvasive methods such as x-ray, eddy current, hysteresis, positron annihilation, and magnetoacoustic emission measurements.¹⁻³ Neutron bombardment creates point defects distributed throughout the irradiated material. Magnetic properties such as remanence, coercivity, maximum differential permeability, and hysteresis loss are sensitive to the presence of these defects,⁴ as are Barkhausen emission spectra which were employed to characterize microstructure and subsurface stress states of the materials.⁵⁻⁷

EXPERIMENTAL

The samples investigated were mainly broken Charpy specimens of A533 grade B class 1 pressure steels. Some measurements also were taken on unbroken Charpy samples ($27.5 \times 10 \times 10 \text{ mm}^3$). Classification of the samples was made on the basis of the original surveillance program data at three different nuclear reactor plants. All the magnetic hysteresis⁸ and magnetic Barkhausen measurements on base or weldment portions of the irradiated samples were taken in the radioactive "hot cell" using a commercial Barkhausen effect device, which has been described elsewhere.⁹

RESULTS AND DISCUSSION

Measurements at Westinghouse Electric Corp., Pittsburgh, PA were conducted on the specimens from the first surveillance program where they had been irradiated to three different levels of neutron fluences: 3.9×10^{18} , 17.7×10^{18} ,

and 23.7 n cm^{-2} . The analysis showed that magnetic Barkhausen signals at each measurement depth were influenced by neutrons.

To investigate the response of Barkhausen emissions to the changes in the mechanical properties of the samples as a result of neutron embrittlement, the fractional change in the magnetic Barkhausen signal was compared to change in Rockwell hardness, upper-shelf energy, yield strength, and impact energy over the range of neutron irradiation fluence. On these same specimens, the effect of sample orientation with respect to rolling direction was also studied. The samples were denoted as transverse and longitudinal. Weldment specimens from the first surveillance program were also measured.

Similar measurements were carried out on the samples from the second surveillance program where fluence of neutrons was $13.3 \times 10^{18} \text{ n cm}^{-2}$. As summarized in Table I, the Barkhausen signal as well as the impact energy and upper-shelf energy decreased with neutron influence, whereas Rockwell hardness and yield strength were found to increase with neutron fluence over the range 0 – $25 \times 10^{18} \text{ n cm}^{-2}$. It was expected that higher hardness would result in lower magnetic Barkhausen emissions due to the increased number of defect pinning centers which impede both the movement of dislocations and magnetic domain walls.

The second part of investigation was to study the influence of successive neutron irradiation and annealing processes on magnetic Barkhausen signals from the samples from the third surveillance program. Barkhausen voltage wave forms from the unirradiated sample, [Fig. 1(a)], from the sample irradiated at $8.4 \times 10^{18} \text{ n cm}^{-2}$, [Fig. 1(b)], and from the sample annealed at 850 F for 168 h, [Fig. 1(c)] correspond to changes in micromagnetic emissions in the materials of interest. Before irradiation, the rms Barkhausen voltage was 6 V while after irradiation it was 2.5 V. Anneal-

TABLE I. The changes in magnetic Barkhausen signal parameter and mechanical properties.

	Change in magnetic Barkhausen signal	Change in Rockwell hardness	Change in yield strength	Change in impact energy	Change in upper-shelf energy
Transverse samples from the 1st surveillance program	-45%	48%	18.5%	-26%	-16.5%
Longitudinal samples from the 1st surveillance program	-19%	41%	19.5%	37%	-13%
Weldment samples from the 1st surveillance program	-42%	40%	9.5%	-52%	-26%
Samples from the 2nd surveillance program	-21%	37%	7%	-64%	-16%

ing resulted in a signal of 5 V. It was also found that the magnetic Barkhausen signal parameter decreased as a result of the first irradiation at $8.4 \times 10^{18} \text{ n cm}^{-2}$ at all measurement frequencies and hence at all depths. The first anneal, 168 h at 850 °F, restored the Barkhausen parameter. On the other hand, the second irradiation, an additional $6.6 \times 10^{18} \text{ n/cm}^2$, did not cause noticeable change in the Barkhausen signal. However, the second annealing step with some experimental conditions, as in the first annealing, further restored the mag-

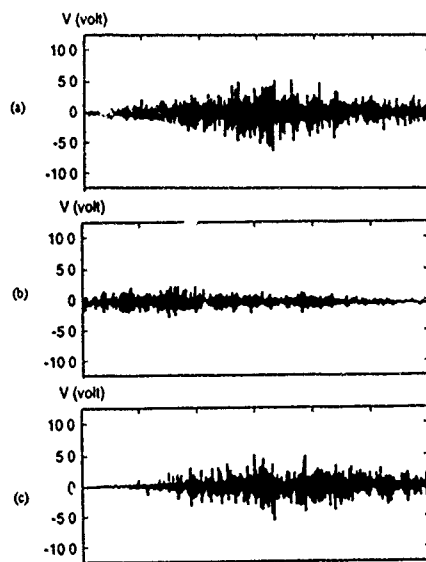


FIG. 1. Barkhausen voltage wave forms from (a) unirradiated, (b) irradiated, $8.4 \times 10^{18} \text{ n/cm}^2$, (c) annealed, 168 h at 850 °F; specimens from the third surveillance program

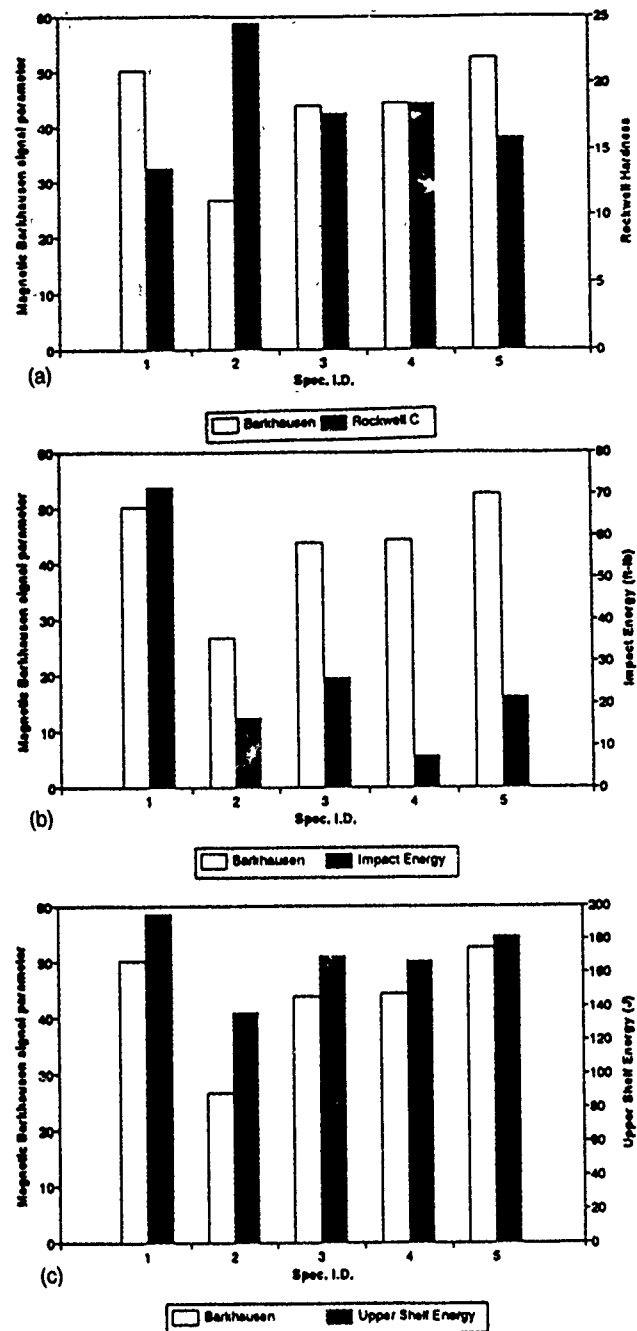


FIG. 2. The influence of successive irradiation and annealing procedures on the magnetic Barkhausen signal parameter and (a) Rockwell hardness, (b) impact energy, (c) upper shelf energy. Identification of radiation and heat treatments as follows: Spec. Id. 1: unirradiated; spec. Id. 2: 1st irradiation, $8.4 \times 10^{18} \text{ n/cm}^2$; spec. Id. 3: 1st annealing, 168 h at 850 °F; spec. Id. 4: 2nd irradiation, $6.6 \times 10^{18} \text{ n/cm}^2$; spec. Id. 5: 2nd annealing, same as the 1st annealing conditions.

netic Barkhausen signal as seen in Fig. 2. The magnetic Barkhausen signal together with the Rockwell hardness, impact energy, and upper-shelf energy have been plotted for each case in Fig. 2. As can be seen in Fig. 2(a), the first irradiation led to a decrease in magnetic Barkhausen signal while Rockwell hardness increased. On the other hand, the first annealing process decreased the Rockwell hardness but increased the magnetic Barkhausen signal. The impact energy, Fig. 2(b), and the upper-shelf energy, Fig. 2(c), in every

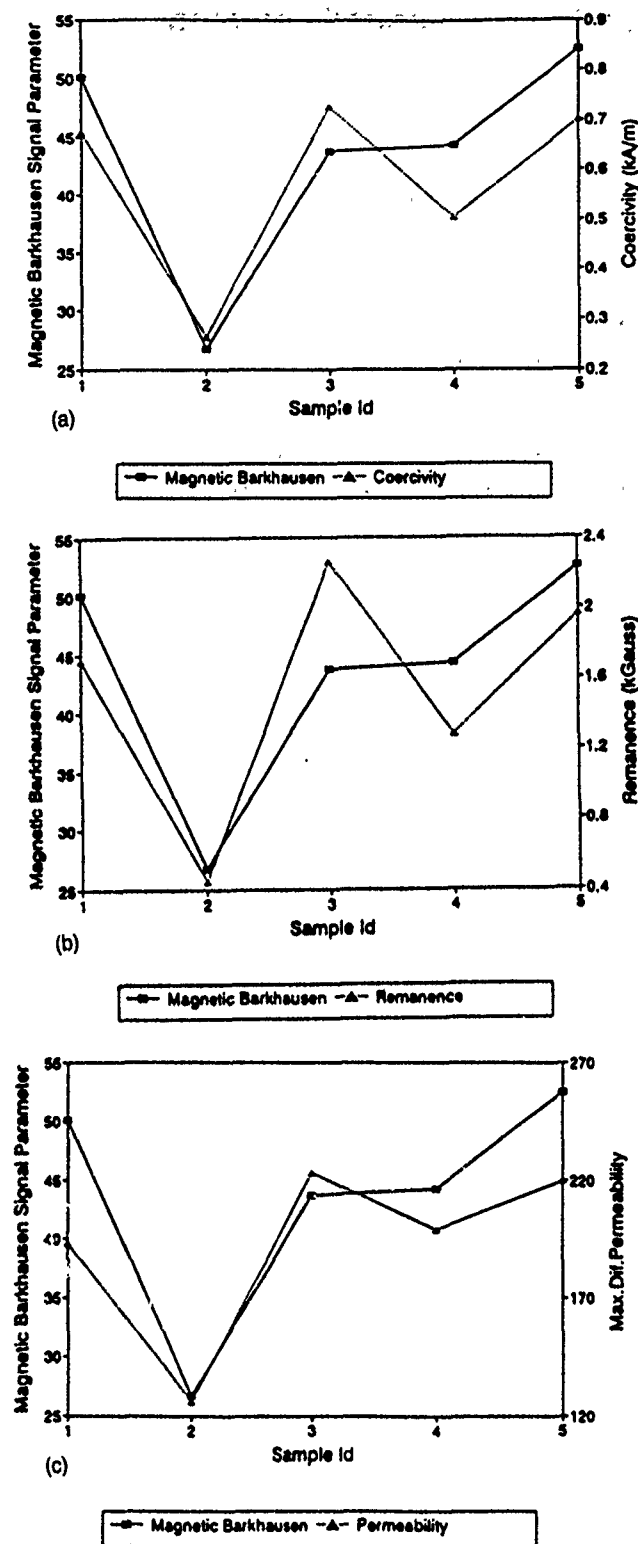


FIG. 3. Change in magnetic Barkhausen signal parameter: (a) coercivity, (b) remanence, and (c) maximum differential permeability with neutron irradiation. Identification of radiation and heat treatments on specimens as follows: spec. Id. 1: unirradiated; spec. Id. 2: 1st irradiation, 8.4×10^{18} n/cm²; spec. Id. 3: 1st irradiation and 1st annealing, 850 F/168 h.; spec. Id. 4: 2nd irradiation, 6.6×10^{18} n/cm²/spec. Id. 5: 2nd irradiation and 2nd annealing, same as the 1st annealing conditions.

case showed the same trend as the magnetic Barkhausen signal. The results of previous work⁸ on the same samples, which included magnetic hysteresis measurements are shown in Fig. 3 for comparison. The BH -loop parameters, coercivity, remanence, and differential permeability were plotted for each individual sample. As was indicated previously,¹⁰ the magnetic Barkhausen voltage maximum was proportional to the differential susceptibility. This is clearly seen in Fig. 3.

CONCLUSIONS

This investigation revealed the existence of a relationship between the extent of radiation damage by neutrons and the Barkhausen emission signals. There were significant correlations between mechanical properties of these materials and magnetic Barkhausen signals and these have been interpreted in terms of the effects of defects on both magnetic domain wall motion and dislocation movement. The results indicated that irradiation with neutrons caused damage throughout the volume of the material. It was anticipated that increased hardness would give rise to lower Barkhausen emissions due to increased pinning of domain walls. Successive neutron irradiation and annealing procedures also revealed a relationship between Rockwell hardness and the magnetic Barkhausen signal which resulted from neutron embrittlement.

ACKNOWLEDGMENTS

This work was supported by Science and Technology Center, Nuclear Advanced Technology Division at Westinghouse Electric Corporation, Pittsburgh, Pennsylvania. The authors wish to thank to P. K. Liaw of University of Tennessee, Knoxville and D. Drinon and R. Rishel of Westinghouse Electric Corporation, Pittsburgh, Pennsylvania.

¹ E. A. Little, D. J. Buttle, and C. B. Scruby, *Phys. Status Solidi A* **112**, 55 (1989).

² J. F. Stubbs, J. G. Williams, A. M. Ougou, J. U. Patel, and W. J. Shong, *Proceedings of the 5th International Symposium on Environmental Degradation of Materials in Nuclear Power Systems-Water Reactors*, edited by E. P. Simonen (American Nuclear Society, La Grange Park, IL, 1992).

³ M. J. Sablik, H. Kwun, G. L. Burkhardt, and D. G. Cadena, *Rev. Prog. Quantitative NDE* **12**, 1823 (1993).

⁴ C. W. Chen, *Magnetism and Metallurgy of Soft Magnetic Materials* (North-Holland, Amsterdam, 1977).

⁵ L. B. Sipahi and D. C. Jiles, *Nondestruct. Test. Eval.* **10**, 183 (1993).

⁶ L. B. Sipahi and D. C. Jiles, *J. Magn. Magn. Mater.* **104-107**, 385 (1992).

⁷ L. B. Sipahi, D. C. Jiles, and D. Chandler, *J. Appl. Phys.* **73**, 5623 (1993).

⁸ D. C. Jiles, Contract Report for Westinghouse Electric Corp. Pitt., 1992.

⁹ L. B. Sipahi, M. K. Devine, D. C. Jiles, and D. D. Palmer, *Rev. Prog. Quantitative NDE* **12B**, 1847 (1993).

¹⁰ D. C. Jiles, L. B. Sipahi, and G. Williams, *J. Appl. Phys.* **73**, 5830 (1993).

Experimental study on opening compensation for magnetic shields by current superposition

I. Sasada and Y. Oonaka

Department of Electronics, Kyushu University 36, Fukuoka 812, Japan

A new method is studied experimentally by which magnetic fields coming in through an opening of a magnetic shield can be compensated. The horizontal component of the earth's field is targeted as an external magnetic field to be compensated by the method, in which a single figure-eight coil is used. A cylindrical shielding case is developed for this study using a Permalloy cylindrical case (outer diameter=68 cm, length=180 cm) with an opening at an end and Metglas 2705M amorphous ribbons, which are wound helically on the outer surface of the Permalloy case by 16 layers. A magnetic shaking field of 200 Hz is applied to only the amorphous layers by a toroidal shaking coil of 36 turns. The size of the figure-eight coil used is 74 cm in diameter with 30 turns. Residual magnetic field measured by a flux gate magnetometer in the horizontal center plane of the shielding case shows that the area where the amplitude of the residual magnetic field is within ± 0.15 mG is extended by about 30 cm toward the opening.

I. INTRODUCTION

Magnetic shielding rooms of high performance are required for precise magnetic field measurements such as brain magnetic field measurements by superconducting quantum interference device magnetometers. Most of the magnetic shielding rooms presently used are built relying on the ferromagnetic enclosures to isolate the area to be shielded from the outside. As a result, they become heavy and expensive. If magnetic shielding rooms are allowed to have openings by incorporating a compensation technique, the above problems can be solved. In addition to that, we can get an easy access to the working space of the shielding room through the opening.

We have proposed a new method of compensating incoming magnetic field through an opening of magnetic shields by current superposition.¹ In this paper, we evaluate this method against the horizontal component of the earth's magnetic field (0.32 G in Fukuoka) using a cylindrical magnetic shielding case with an opening at an end and a single figure-eight coil. A large cylindrical shielding case (diameter=68 cm, length=180 cm) was developed for this study incorporating the magnetic shaking technique.^{2,3} The uniformly shielded area where the amplitude of the horizontal magnetic field was within ± 0.15 mG was extended by about 30 cm toward the opening by adjusting the compensation current.

The frequency characteristics of the shielding factor of the developed shielding case are also presented.

II. CYLINDRICAL SHIELDING CASE

A large cylindrical shielding case was developed using Metglas 2705M amorphous ribbons (width=5 cm, thickness ≈ 22 μ m) and a Permalloy cylindrical case (outer diameter=68 cm, length=180 cm, thickness=1.6 mm, weight ≈ 60 kg), incorporating the magnetic shaking technique.^{2,3}

Metglas 2705M amorphous ribbons were wound helically on the Permalloy case by 16 layers (total weight ≈ 12.1 kg) to cover the circumferential surface. A main reason we

used a Permalloy cylinder inside is to attenuate unwanted leakage of the magnetic shaking field into the area to be shielded. Two coils to give magnetic shaking field to the amorphous layers were installed. One is a toroidal coil of 36 turns surrounding only the amorphous layers and the other is a meander coil (line space=3 cm) consisting of a pair of meander coils connected in series, one of which is inserted between the fourth and the fifth layer and the other between the 12th and the 13th layer. One end of the Permalloy cylinder is left open and the other end is closed with the same Permalloy plate welded at all edges, on which there is a square hole of 6 cm \times 6 cm having been used during fabrication.

III. EXPERIMENT

The shielding case was laid on the floor perpendicularly to the direction of the earth's magnetic field as shown in Fig. 1. The coordinate system is defined with the origin at the center of the opening surface; z axis along the axis of the cylinder, x axis along the horizontal, and y axis along the vertical direction, respectively. We used the toroidal shaking coil rather than the meander one to obtain a large shaking effect. The amplitude of the shaking current was tuned to 110 mA (rms) at 200 Hz, because the shaking effect shows a peak for the shaking current.² The leakage flux density of the

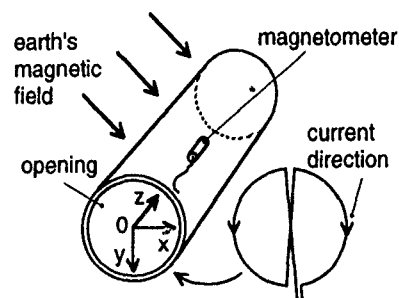


FIG. 1. Experimental setup. The opening is covered with the figure-eight coil.

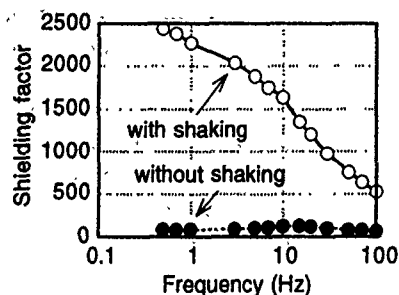


FIG. 2. Shielding factor of the developed cylindrical shielding case.

shaking field was less than $40 \mu\text{G}$ in most of the area inside the case. The shielding factor, as a basic characteristic of the developed shielding case, was measured as a function of frequency of the external magnetic field. In this case, the external magnetic field with an amplitude of 100 mG (rms) was applied transversely to the case by using a large Helmholtz coil of square shape ($4 \text{ m} \times 2 \text{ m} \times 1.5 \text{ m}$), and the magnetic field was measured at the center of the case. In the experiments of this paper, the magnetic field was measured by a triaxial flux gate magnetometer. The flux pattern appearing near the opening due to the horizontal component of the earth's magnetic field was also measured in the x - z plane.

To compensate the horizontal component of the earth's magnetic field (0.32 G in Fukuoka), a single figure-eight coil of 74 cm in diameter with 30 turns was set to cover the opening with the crossing part of the figure-eight coil being vertical as shown in Fig. 1. Horizontal components of residual earth's fields, B_x and B_z , inside the case were measured in the x - z plane.

Compensation current was adjusted by matching numerically the magnetic fields to be generated by the figure-eight coil with those measured inside the shielding case along the z axis, and we got 77 mA as the compensation current.

IV. RESULTS AND DISCUSSION

The shielding factor of the developed shielding case is shown in Fig. 2 for the frequency of the external magnetic field. The shielding factor (a ratio of external magnetic field versus residual magnetic field in the shield) with magnetic shaking on is 2400 at 0.5 Hz, which is enhanced 30 times as large as that with magnetic shaking off. This large enhancement cannot be explained by a single shell model of an infinite cylindrical shield. Spaces introduced to the magnetic shell for separating the Permalloy case and the amorphous ribbon layer and for inserting shaking coils bring about a multilayer structure. As the space between the Permalloy case and the innermost amorphous layer is largest (about 1 cm), using a double shell model,⁴ the Permalloy shell and the amorphous layer shell, the effective permeability of the amorphous layer is estimated as large as 6.3×10^5 at 10 Hz, and 9.3×10^5 at 0.5 Hz in relative permeability. The frequency characteristics of the enhanced incremental permeability at low frequency has already been reported.³

The flux pattern measured in the x - z plane near the opening is shown in Fig. 3. For the area $z \geq 40 \text{ cm}$, the vector

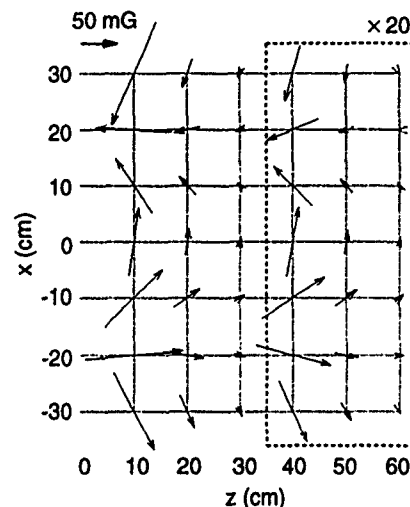


FIG. 3. Vector plot of the magnetic field measured near the opening of the cylindrical shielding case.

plot is magnified by 20 times. Although it is ideal to generate the magnetic field as close as possible to this but opposite in sign, it is also important to approach this by using as simple a coil as possible. Figure 4(a) shows the distributions of B_x along the z axis in the x - z plane with compensation off. Figure 4(b) shows those with compensation on. Similarly those for B_z are shown with compensation off in Fig. 5(a) and with compensation on in Fig. 5(b). From these results, we can see the uniformly shielded area is extended to about 30 cm toward the opening. It should be noted that the uniformly shielded area is extended toward the opening by

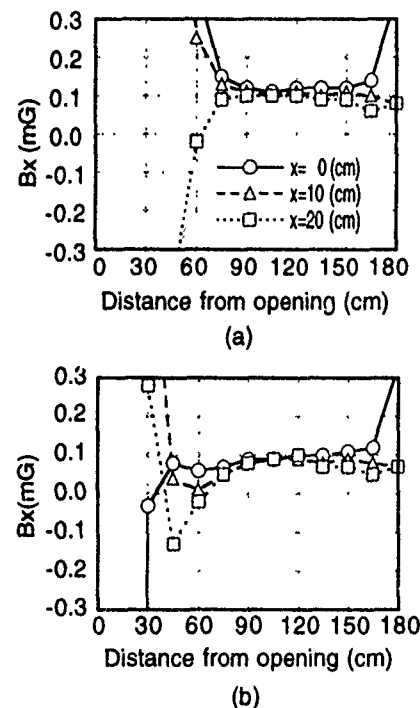


FIG. 4. Distributions of B_x , where the opening compensation is off in (a) and on in (b).

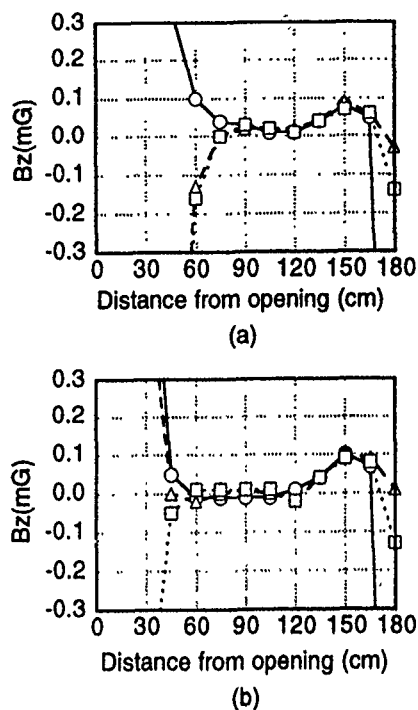


FIG. 5. Distributions of B_z , where the opening compensation is off in (a) and on in (b). Symbols are the same as in Fig. 4.

about half of the diameter of the case with a simple figure-eight coil. Disturbances found near distance=180 cm in all four figures are due to the square hole in the Permalloy plate

aforementioned. Due to the symmetry, these results also hold to vertical components. In this case, a figure-eight coil needs to be rotated by 90° .

Residual magnetic fields inside an infinite magnetic shield are theoretically uniform against uniform external fields. This is a very important nature of the cylindrical magnetic shield, because we can use gradiometer to measure very low magnetic field. The opening compensation discussed in this paper would be most suitable for cylindrical shields.

V. CONCLUSION

We demonstrated experimentally that the transverse magnetic field to the opening of cylindrical magnetic shields can be compensated by a figure-eight coil. The uniformly shielded area recovered by this method toward the opening is about half of the diameter in length.

ACKNOWLEDGMENTS

This work was supported by the Grant-in-Aid for Developmental Scientific Research from the Ministry of Education, Science and Culture of Japan.

¹I. Sasada and K. Harada, Proceedings of the 37th Conference on Magnetism and Magnetic Materials, Houston, TX 1992 (unpublished), Paper GQ-12.

²I. Sasada, S. Kubo, and K. Harada, J. Appl. Phys. **64**, 5696, (1988).

³I. Sasada, S. Kubo, R. C. O'Handley, and K. Harada, J. Appl. Phys. **67**, 5583 (1990).

⁴A. J. Mager, IEEE Trans. Magn. **MAG-6**, 67 (1970).

Effects of pole flux distribution in a homopolar linear synchronous machine

M. J. Balchin, J. F. Eastham, and P. C. Coles

School of Electronic & Electrical Engineering, University of Bath, Bath BA2 7AY, United Kingdom

Linear forms of synchronous electrical machine are at present being considered as the propulsion means in high-speed, magnetically levitated (Maglev) ground transportation systems. A homopolar form of machine is considered in which the primary member, which carries both ac and dc windings, is supported on the vehicle. Test results and theoretical predictions are presented for a design of machine intended for driving a 100 passenger vehicle at a top speed of 400 km/h. The layout of the dc magnetic circuit is examined to locate the best position for the dc winding from the point of view of minimum core weight. Measurements of flux build-up under the machine at different operating speeds are given for two types of secondary pole: solid and laminated. The solid pole results, which are confirmed theoretically, show that this form of construction is impractical for high-speed drives. Measured motoring characteristics are presented for a short length of machine which simulates conditions at the leading and trailing ends of the full-sized machine. Combination of the results with those from a cylindrical version of the machine make it possible to infer the performance of the full-sized traction machine. This gives 0.8 pf and 0.9 efficiency at 300 km/h, which is much better than the reported performance of a comparable linear induction motor (0.52 pf and 0.82 efficiency). It is therefore concluded that in any projected high-speed Maglev systems, a linear synchronous machine should be the first choice as the propulsion means.

INTRODUCTION

Linear induction motors (LIMs) have received much attention as the means of propulsion in many projected high-speed, ground transport systems. While this form of machine has many inherent advantages, it suffers from two major drawbacks. The first of these is due to the large mechanical clearances necessary in high-speed ground transport schemes. This demands a high reactive power component from the supply. An additional reactive power component is made necessary by the second disadvantage of LIMs, which is the longitudinal end effect. This effect is due to persistent induced transient current components in the induction motor secondary member. A convenient way of avoiding the problems associated with LIMs is to consider the advantages offered by synchronous machines. These machines are magnetized by direct current, and so large clearances (air gaps) will not demand ac reactive input. In addition it is not necessary to rely on induced secondary currents for torque (force) production in synchronous machines. This means that any practical method can be used to reduce or eliminate unwanted secondary currents. The choice of the form of a linear synchronous machine is important. In conventional synchronous machines the dc winding is normally on the rotating secondary member. This form of construction may be expensive to produce. An economical form of construction is offered by one of the "ac side excited" types of machine which are related to the inductor alternator. Two forms of this machine, known as the "heteropolar" and "homopolar" types have been developed and tested.¹⁻⁴ This paper concerns work performed on a homopolar type of machine, the details of which are shown in Fig. 1. The figure shows that the dc excitation winding is conveniently located on the primary member. This leaves the extended secondary as simple passive steel blocks which can be constructed in any convenient way to reduce induced currents.

On the basis of earlier work a design for a drive motor for a 100 passenger, 400 km/h vehicle has been produced. This machine has 40 poles and is approximately 12 m in length. Experimental work on such a large machine would clearly require an extensive and expensive test installation. It is, however, not necessary to test a complete machine. Because the persistence and magnitude of secondary induced currents can be made small, it is only necessary to perform measurements on short representative sections of the actual machine. In the apparatus constructed for this work a short 4-pole section of machine is used when the magnitude of end effects is of interest. When the part of the machine remote from the ends is of interest an 8-pole cylindrical form of machine is used. Measurements from the two forms of machine can be combined to give a very good indication of the performance of the actual 40-pole machine. In addition, the

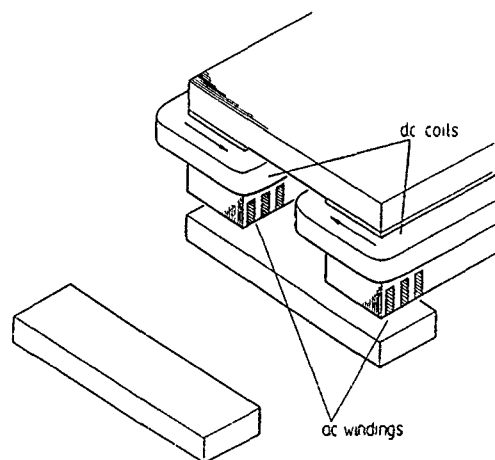


FIG. 1. Homopolar linear synchronous machine (LSM).

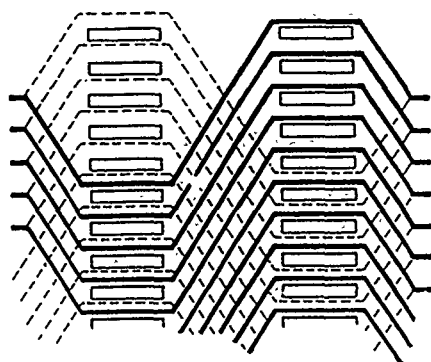


FIG. 2. LSM ac winding using figure-eight coils.

separate sets of results can be used in the verification of mathematical models. Figure 2 shows the novel "figure-eight"³ layout adopted for the ac armature winding, and Fig. 3 is a photograph of one of the complete 4-pole primary sections.

HIGH-SPEED HOMOPOLAR LSM TEST RIG

The testing of the two parts of the full-sized LSM is facilitated by using either one or two semicircular 4-pole primaries as shown in Fig. 4. The primaries have exactly the same transverse cross-section as the full-sized design of machine referred to in the Introduction. Electromagnetic forces produced by the machine are measured using piezoelectric transducers.

One of the more difficult parts of the design of this test apparatus has been that for the rotating secondary. It is necessary for this component (which has an o.d. of about 700 mm) to rotate at 3000 rev/min in order to achieve a linear speed of 400 km/h. It is also necessary to suspend the secondary steel pole pieces in magnetic isolation. Figure 5 shows the scheme adopted. The whole secondary assembly is supported on a mild steel shaft. Onto this shaft is shrunk a nonmagnetic stainless-steel boss. This part then supports the pole pieces (which are secured by radial bolts) which may be of either solid or laminated construction. The complete test stand of Fig. 4 is housed within a safety cell fabricated from

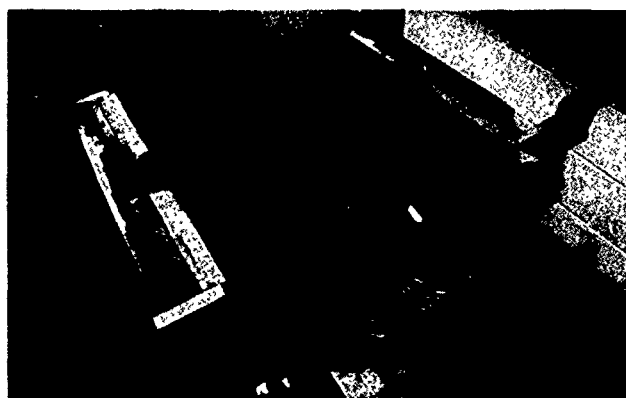


FIG. 3. Complete 4-pole LSM primary member.

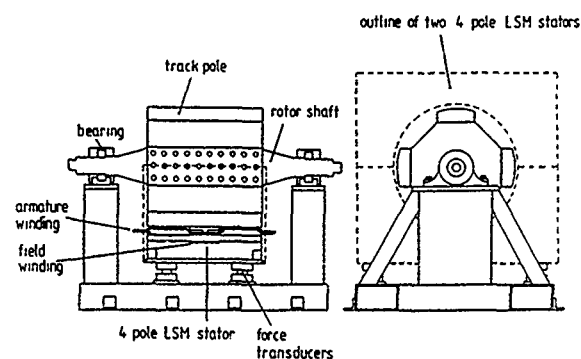


FIG. 4. Arrangement of LSM test rig.

approximately 300 Tonne of reinforced concrete. The cell is closed with doors manufactured from material designed to withstand ballistic impact.

A variable voltage and frequency electrical supply is necessary to power a LSM. One approach is to use a power electronic inverter, as has been demonstrated by the Toshiba Co. of Japan. In the LSM test apparatus being described, a corresponding form of supply is produced by an alternator which is coupled to the rotor shaft (Fig. 4). With this form of supply power can circulate between the machines in either electrical or mechanical form. By altering the angle between the LSM and alternator field poles the LSM torque (force) angle can be set up. Power to supply the ac and mechanical losses of the LSM and alternator system is provided by a dc drive on the same shaft. This is part of a Ward Leonard system with a speed control system to facilitate measurements at fixed frequency settings.

FIELD WINDING LEAKAGE

There are two possible positions for the dc excitation coils on the primary member, and they are shown in Fig. 6. The position shown at (A) is the more convenient from the point of view of mechanical construction, and it also has the benefit of slightly lower resistance. The position shown at (B) promises lower leakage. In order to explore this possibility both configurations were investigated practically using search coils and an integrating fluxmeter. The fluxes mea-

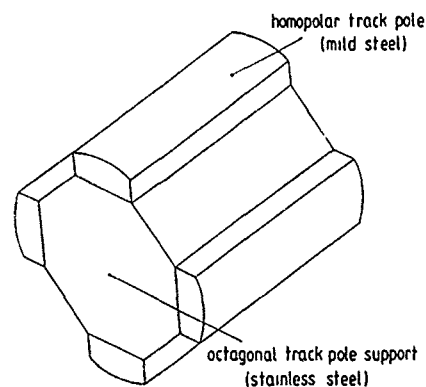


FIG. 5. Schematic of test LSM secondary member.

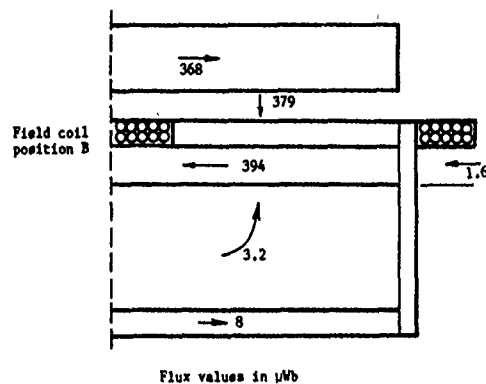
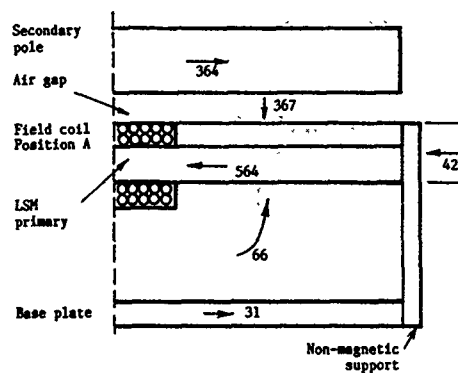


FIG. 6. Possible dc field coil positions for a homopolar LSM.

sured in the various parts of the machine are shown in Fig. 6. It will be observed that the amount of leakage is much smaller in position (B). This leads to the possibility of decreased primary iron core weight.

MEASUREMENT AND CALCULATION OF THE LONGITUDINAL END EFFECT

The excitation pole flux build up was measured using the short stator configuration provided by one primary member. The measurements were taken using a rectangular search coil

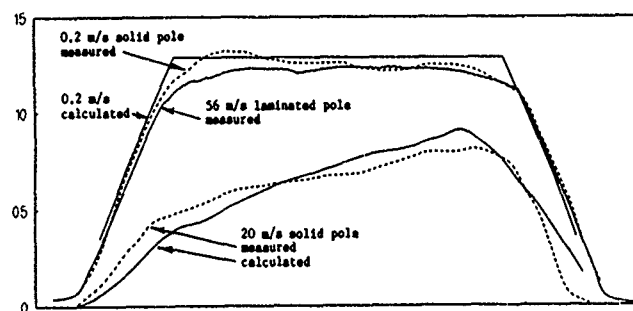


FIG. 7. Air gap longitudinal flux distribution at different speeds, with solid and laminated secondary poles.

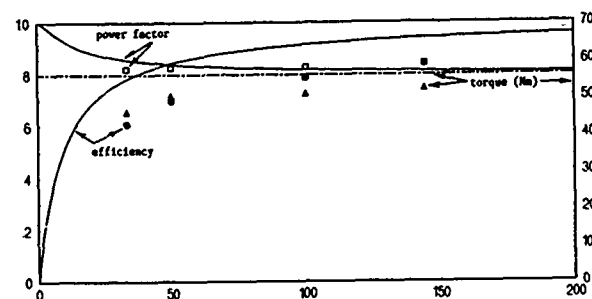


FIG. 8. LSM terminal characteristics at a 90° motoring torque (force) angle.

which spans one rotor pole. Figure 7 illustrates the test results. It is evident that the build up of flux using solid poles is considerably delayed even at 20 m/s (18% of the top speed). With laminated poles the flux builds up almost immediately. This behavior has been confirmed over the speed range of the tests. As an example, the results taken at 56 m/s are also shown on Fig. 7. The calculated results for the behavior of solid poles were obtained using a mesh calculation method which incorporates rotor movement.⁴

MOTRING CHARACTERISTICS

Variation of power factor, efficiency and torque with frequency is shown in Fig. 8. On this figure 200 Hz is equivalent to 112 m/s or 400 km/h. The results are given for a torque angle of 90°. It will be observed that the results are in broad agreement with the calculated values which are shown as continuous lines on Fig. 8. These calculated values were obtained using simple "round-rotor" synchronous machine theory neglecting pole face losses (due both to eddy currents induced by the entry and exit edges and the normal pole face loss which occurs in cylindrical machines).

In a previous paper⁴ results were given for a cylindrical machine. These showed closer agreement with the simple calculated lines. It can be inferred from this that the values which will be obtained from a 40-pole machine will lie in between the four pole short stator results shown on Fig. 8 and those taken earlier. This means that, for example, 300 km/h speeds will result in power factors and efficiencies in excess of 0.8 and 0.9, respectively. This is a much better performance than would be expected from a comparable linear induction motor, for which calculated results of 0.52 pf and 0.82 efficiency are given in Ref. 5.

¹J. F. Eastham, *Electron. Power*, IEE, London **23**, 239 (1977).

²M. J. Balchin and J. F. Eastham, *Proc. IEE (London)*, Part B **2**, 213 (1979).

³J. F. Eastham, M. J. Balchin, P. C. Coles, and D. Rodger, *IEEE Trans. Magn.* **MAG-23**, 2338 (1987).

⁴J. F. Eastham, M. J. Balchin, and P. C. Coles, *IEEE Trans. Magn.* **MAG-24**, 2892 (1988).

⁵J. F. Eastham, M. J. Balchin, and D. Rodger, *Proc. I Mech. E Conference on Maglev Transport Now and for the Future*, I Mech. E No. C406/84, October 1984, pp. 111-118.

Compensation of field distortion with ferromagnetic materials and permanent magnets

Manlio G. Abele, Henry Rusinek, Franco Bertora,^{a)} and Alessandro Trequattrini^{a)}
Department of Radiology, New York University School of Medicine, New York, New York 10016

This paper discusses a technique for improving the homogeneity of the magnetic field in structures of permanent magnets designed for magnetic resonance imaging, achieved by inserting layers of ferromagnetic plates and permanent magnets along the cavity of the structure. The analysis of the field in the magnet is performed using a boundary integral equation method. An example of optimization of the geometry and the amount of the magnetic material is presented.

I. INTRODUCTION

To design a permanent magnet for medical magnetic resonance imaging (MRI) applications one must determine the geometry and the distribution of magnetization that generate a nearly uniform field within a given region of interest. The exact solution of generating a perfectly uniform field is possible only if the magnetic structure totally encloses the volume of interest.¹

In a practical magnet used for imaging applications several factors contribute to the perturbation of the field inside the cavity. The most important cause of the field distortion is the opening of the magnet to access the cavity. For instance, ideal two-dimensional structures must be truncated at both ends. Since magnets used in MRI require high field uniformity within the region of interest, any field distortion must be compensated for.

There are several approaches to compensate for the effects of the magnet opening. In a traditional magnet the generation of the desired field characteristics, and in particular the achievement of the desired uniformity is accomplished by the design of the pole pieces, which are high magnetic permeability structures inserted within the cavity.

In the case of the magnetic structures introduced by the first author, the compensation of the effect of the magnet opening can be achieved by either the modification of the magnet geometry and the change in the distribution of magnetization or by addition of new components of high permeability materials.¹

This paper describes a technique based on the use of plates of high permeability materials which contain inserts of active components consisting of magnetized materials. Since the plates "sandwich" the active elements, these structures will be referred to as magnetic sandwiches. Magnetic sandwiches are inserted at the interface between the magnetic structure and the inner cavity and are arranged in layers perpendicular to the main field.

The mathematical procedure for determining geometry and composition of the layers is based on the elimination of increasing order of spatial harmonics in the potential expansion within the region of interest. The optimization of the magnetic structures will be illustrated below in the example of a prismatic hybrid magnet designed around a rectangular cavity.¹

II. MAGNETOSTATIC POTENTIAL GENERATED BY SANDWICH STRUCTURE

A basic schematic of the combination of plates and active material is presented in Fig. 1, which shows the two sandwich structures perpendicular to the direction of the field inside the cavity inserted within a rectangular cavity indicated by the dashed line in the figure. The plates are assumed to be built with an infinite magnetic permeability material and have zero thickness. As seen in the figure, the outer plate of each structure is continuous, and therefore maintained at a constant potentials Φ_1 and $-\Phi_1$. The inner layer is composed of several sections separated from each other. The figure also shows magnetic material polarized along the y axis and filling a portion of the peripheral section of the sandwiches. The magnetic material generates potential Φ_2 and $-\Phi_2$ on the peripheral section of the inner plates. It is assumed that the central portions of the inner plates are connected with the corresponding outer plates and therefore maintained at potential Φ_1 and $-\Phi_1$, as indicated in Fig. 1.

The potential difference $\Delta\Phi = \Phi_1 - \Phi_2$ depends on the geometry of the sandwich layers as well as the amount of the magnetic material inserted within the sandwich. The effect of the location of the active elements within the two plates is first investigated. The magnitude of the remanence J of the magnetic material and its orientation are kept fixed while the coordinates y_s, z_s shown in Fig. 2 are variable, simulating the amount of active material contained within the peripheral section of each plate.

The analysis is performed using a boundary integral equation method,² in which the surface charges σ on the

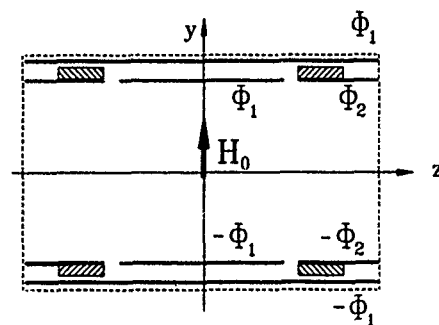


FIG. 1. A basic schematic of two sandwich structures containing active material in the peripheral section. The dashed line indicates the cavity of the magnet designed to generate a uniform field H_0 .

^{a)}At Esaote Biomedica, 16153 Genova, Italy.

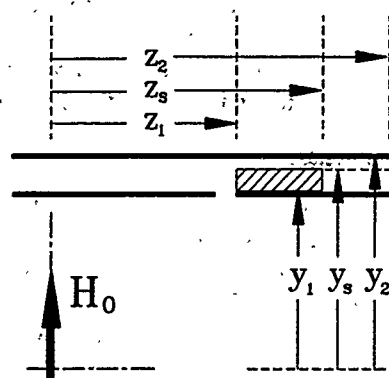


FIG. 2. Geometry of the active material in the peripheral section.

plates are first computed and then used to derive the scalar potential Φ as

$$\Phi = \frac{1}{4\pi\mu_0} \int \frac{\sigma}{\rho} dS. \quad (1)$$

Figure 3 illustrates the effect of filling the peripheral section with an increasing amount of the magnetized material. The plot corresponds to varying the z -axis filling, i.e.,

$$z_1 < z_s < z_2, \quad y_s = y_2. \quad (2)$$

The same plot is obtained by varying the y -axis filling of the peripheral plate

$$y_1 < y_s < y_2, \quad z_s = z_2. \quad (3)$$

The linearity of $\Delta\Phi$ versus the extent of the active material in both y and z directions implies that $\Delta\Phi$ is the function only of the amount of material, rather than of the location of the active material within the sandwich.

III. HYBRID MAGNET AND THE EFFECT OF OPENING

A methodology introduced by the first author led to the theoretical design of a novel permanent magnet device based on magnetic materials with linear demagnetization characteristics.¹ Structures designed using this methodology

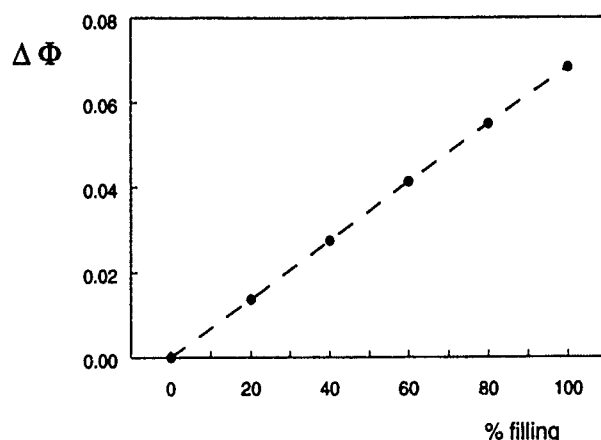


FIG. 3. The potential difference generated by increasing horizontal coverage of active material in the peripheral section on the sandwich structure.

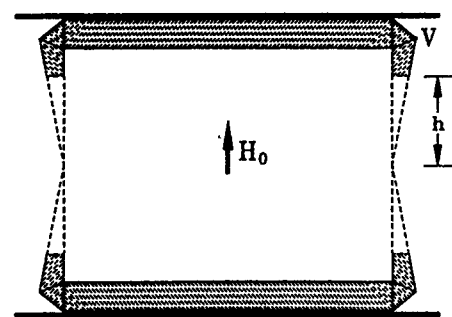


FIG. 4. Hybrid magnet with an opening. The heavy line represents the partial yoke.

generate uniform fields in arbitrary cavities completely enclosed by the magnetic material. Of practical interest is the category of hybrid magnets.³

In the particular case of a rectangular cavity of dimensions $z_0 = 1.5y_0$, the termination introduced by the hybrid magnet consists of two triangular prisms shown in Fig. 4. The coordinate of the vertex V of the magnet is given by

$$\begin{cases} y_V = \frac{y_0 \sqrt{1-K^2}}{K \sqrt{K(2-K)} + (1-K) \sqrt{1-K}} \\ z_V = z_0 + \frac{Ky_0}{K \sqrt{K(2-K)} + (1-K) \sqrt{1-K}} \end{cases}, \quad (4)$$

where K is a parameter of the design defined as

$$K = \frac{\mu H_0}{J}. \quad (5)$$

Assume that an increasingly large access to the magnet is created by removing a portion of the larger triangle of the height h as indicated in Fig. 4. The effect of the opening on the uniformity of magnetic field is analyzed by expanding the magnetostatic potential in a series of spherical harmonics within a region of cavity close to the origin. In the two-dimensional configuration the harmonic expansion of the potential in polar coordinates r, ψ reduces to

$$\Phi = \frac{1}{2\pi\mu_0} \sum_j q_j r^j \cos(j\psi). \quad (6)$$

The fundamental term q_1 provides the intensity of the field at the origin. The $j > 1$ terms, i.e., the distortion of the field, converge to 0 as $z_0 \rightarrow \infty$.

The values of coefficients q_j for the lowest order harmonics are listed in Table I for increasingly large value of the opening h . The results demonstrate a decrease in field homogeneity caused by the opening.

TABLE I. The effect of magnet opening on the lowest order harmonics.

h	q_1	q_3	q_5	q_7
0.2	0.1913	0.0004	0.000 24	-0.000 09
0.4	0.1871	0.0006	-0.000 15	-0.000 14
0.6	0.1848	0.0021	-0.000 84	-0.000 02
0.8	0.1834	0.0030	-0.001 40	0.000 19

TABLE II. The effect of increasing length of active element.

$z_2 - z_1$	q_1	q_3	q_5	q_7
1.0	-0.0055	-0.0099	0.0008	0.0013
0.8	-0.0061	-0.0065	0.0017	0.0010
0.6	-0.0057	-0.0037	0.0015	0.0003
0.4	-0.0043	-0.0018	0.0009	-0.0000

The values of the coefficient q_j of the harmonic expansion of Φ caused by the presence of a sandwich structure of different length $z_2 - z_1$ are listed in Table II. As seen by comparing Tables I and II, a significant improvement of the field uniformity, in particular a total elimination of the coefficient q_3 is possible. For example, in an open magnet characterized by $h = 0.8y_0$, elimination of coefficient q_3 is achievable either with a sandwich structure having length $z_2 - z_1 > 0.6$ and a partial filling of the peripheral compartment, or with a shorter length and active material of remanence larger than in the main magnetic structure. It should be noted that this compensation of the field distortion is achieved at the expense of a minor (approximately 3%) reduction of the field intensity at the center of the magnet.

A sandwich structure containing three compartments in each quadrant separated using two gaps has two degrees of freedom and can therefore be used to compensate the open magnet for the harmonics q_3 and q_5 simultaneously. Neglecting the cross coupling between the two sections, the field

generated by each section can be computed as the linear superposition of the individual fields, and the elimination of q_3 and q_5 in the open magnet can be achieved with practical values of the geometry and amount of active material.

IV. CONCLUSIONS

Active material placed between layers of ferromagnetic plates can be designed to eliminate the lowest order coefficients q_j of the open magnet. Because the active elements are shielded by layers of ferromagnetic material, a sandwich structure act as a spatial filter, eliminating lower order spatial harmonics without introducing high-order coefficients in the harmonic expansion.

Compared to the insertion of magnetic material alone, such sandwich structures offer the advantage that the precision of the fabrication procedure is confined to the shape of the ferromagnetic components. The final shimming of the magnet is achieved by changing the amount of magnetic material within the sandwich without concern about its location.

ACKNOWLEDGMENT

This work has been sponsored by Esaote Biomedica, Genova, Italy.

¹M. G. Abele, *Structures of Permanent Magnets* (Wiley, New York, 1993).

²M. G. Abele and H. Rusinek, Technical Report No. 24, Department of Radiology, New York University, 15 August 1991.

³M. G. Abele, Technical Report No. 21, Department of Radiology, New York University, 15 October 1989.

Equivalent structures of permanent magnets and electric currents designed to generate uniform fields

M. G. Abele

Department of Radiology, New York University School of Medicine, New York, New York 10016

Generation and confinement of a magnetic field by means of permanent magnets as well as time-independent electric currents are analyzed, and the conditions of existence of uniform field solutions are established in the general case of structures that enclose a region of arbitrary geometry. Basic properties of distributions of the electric currents are compared with the properties of yokeless structures of permanent magnets intended to generate the same uniform field within the same region.

I. INTRODUCTION

Both permanent magnets as well as electric currents can be designed to generate and confine the field without the need for shields of high magnetic permeability materials. In particular, a uniform field of intensity \mathbf{H}_0 can be generated in a volume V_0 of air, totally enclosed by a volume V_m which contains either a distribution of magnetized material or windings of electric currents designed to generate no field outside V_m . In the case of permanent magnets, if the magnetic material is assumed to have a linear demagnetization characteristic with zero magnetic susceptibility, the medium has the magnetic permeability of air everywhere.

II. STRUCTURES OF PERMANENT MAGNETS

Assume that \mathbf{H}_0 is uniform and V_m is composed of magnetized material where remanence \mathbf{J} , intensity \mathbf{H} , and induction \mathbf{B} satisfy the equation

$$\mathbf{B} = \mu_0 \mathbf{H} + \mathbf{J}, \quad (1)$$

where μ_0 is the magnetic permeability of a vacuum.

A uniform field \mathbf{H}_0 can be generated in a closed polyhedral region V_0 of arbitrary geometry.¹ In Fig. 1 s_h is a face of the polyhedron that interfaces with region V_m . In general V_m is a structure of polyhedrons V_{h1} that interfaces with V_0 and polyhedrons V_{h2} that interface with the surrounding medium. Vectors \mathbf{J}_{h1} and \mathbf{J}_{h2} are the remanences of regions V_{h1}, V_{h2} and the dotted line is the line of flux of \mathbf{B} . The computation of the remanences is provided by the vector diagram of Fig. 2, where μ_0 is assumed to be unity. One observes that \mathbf{B}_{h2} in region V_{h2} is parallel to interface u_h between V_{h2} and the surrounding medium.

On an interface between media of remanences $\mathbf{J}_{h-1}, \mathbf{J}_h$ the remanences induce a surface charge density σ_h

$$\sigma_h = \eta_h \cdot (\mathbf{J}_{h-1} - \mathbf{J}_h), \quad (2)$$

where η_h is a unit vector perpendicular to the interface and oriented from the medium of remanence \mathbf{J}_{h-1} to the medium of remanence \mathbf{J}_h . A uniform field is generated everywhere if the values of σ_h and the orientations of the interfaces satisfy the condition

$$\sum_{h=1}^n \sigma_h \tau_h = 0 \quad (3)$$

at a point common to n interfaces.¹ On each interface unit vector τ_h is parallel to the interface and is pointing away

from the interface. An example of a yokeless permanent magnet that satisfies Eq. (3) and encloses a rectangular prismatic cavity is shown in Fig. 3.

III. STRUCTURES OF ELECTRIC CURRENTS

Assume now that the same polyhedral region V_0 is enclosed by a distribution of electric currents and assume an ideal situation where the currents reduce to surface distributions over the plane interfaces. In Fig. 4 surface current densities ι_h, ι_{h+1} flow on interfaces s_h, s_{h+1} that are parts of the boundary of V_0 . Interfaces s_h, s_{h+1} intersect each other along a line that passes through point S_h and is perpendicular to the plane of Fig. 4. The normal components of the intensities are continuous across s_h and the tangential components suffer a discontinuity

$$\iota_h = \eta_h \times (\mathbf{H}_h - \mathbf{H}_0), \quad (4)$$

where η_h is the unit vector perpendicular to s_h and oriented from the region of intensity \mathbf{H}_0 to the region of intensity \mathbf{H}_h . The currents on all the interfaces are perpendicular, and the magnetic field is parallel to the plane of Fig. 4. A surface current density must be generated on an interface v_h in Fig. 4 in order to satisfy the boundary condition between the two regions of intensities $\mathbf{H}_h, \mathbf{H}_{h+1}$.

Assume that point S_h is common to n interfaces whose orientations are given by the unit vectors τ_h defined in Eq. (3). Assume that S_h coincides with the origin O of a polar coordinate system. The intensity \mathbf{H} of the magnetic field at a point P of coordinates (r, ψ) can be written in the form

$$\mathbf{H} = -\frac{1}{2\pi} \sum_{h=1}^n \iota_h \left[(\ln r) \eta_h + \left(\frac{\pi}{2} - \phi_h + \psi \right) \tau_h \right] + \mathbf{H}_e, \quad (5)$$

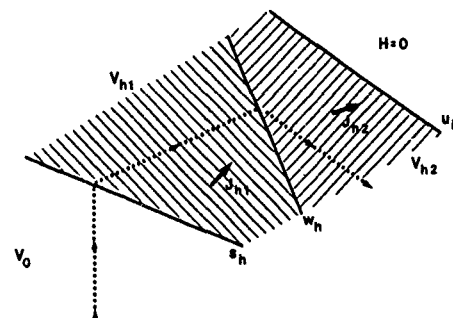


FIG. 1. Schematic of a yokeless structure of permanent magnets.

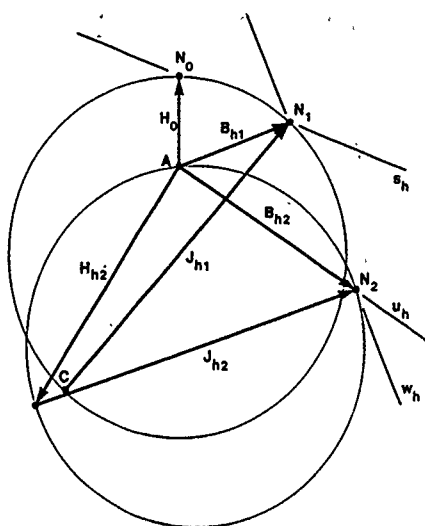


FIG. 2. Vector diagram of a yokeless magnetic structure.

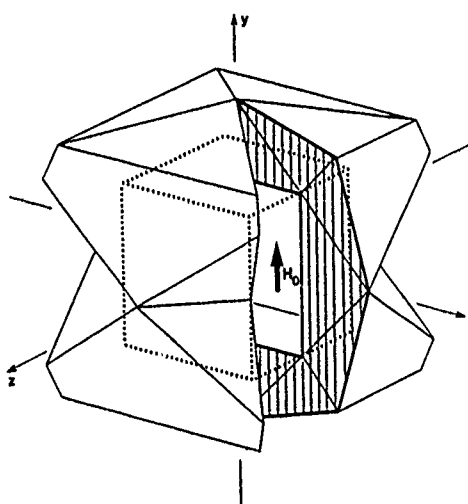


FIG. 3. Example of a permanent magnet. One octant is removed to show the details of the structure.

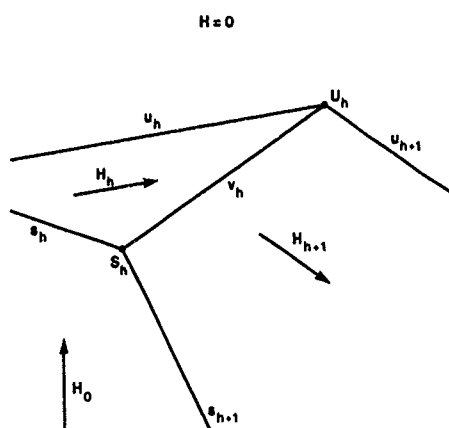


FIG. 4. Schematic of a yokeless structure of electric currents.

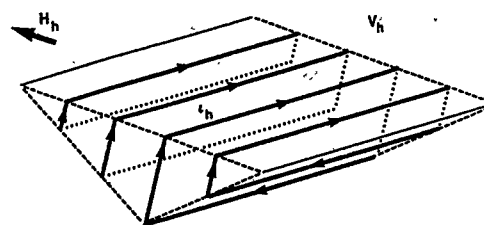


FIG. 5. Individual components of a structure of currents.

where ϕ_h is the orientation of the h th interface relative to $\psi=0$ and \mathbf{H}_e is the field intensity generated by the other edges of the n interfaces and all other sources.

In Eq. (5), the singularity of \mathbf{H} at $r=0$ cancels if the

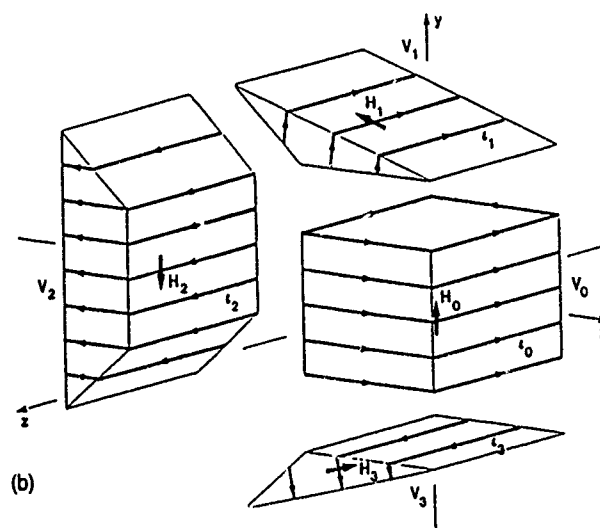
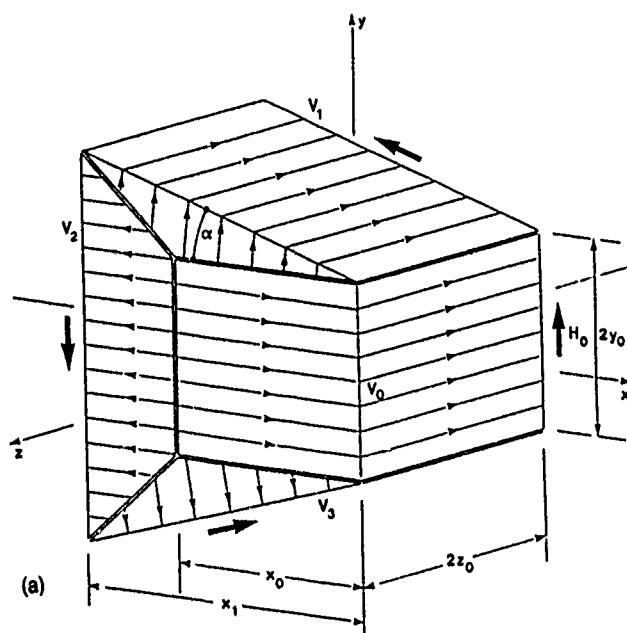


FIG. 6. Structure with rectangular prismatic cavity. Total structure (a). Exploded view (b).

current densities ι_h and the orientation of the interfaces satisfy the condition

$$\sum \iota_h \eta_h \times \sum \iota_h \tau_h = 0, \quad (6)$$

where ζ is the unit vector oriented along the line common to the n interfaces. If \mathbf{H}_e in Eq. (5) is uniform and Eq. (6) is satisfied at all points common to all the interfaces, a uniform field is generated in a region of arbitrary geometry enclosed by a structure of surface current densities, as in the case of a structure of magnetic materials described by Eq. (3).

The current distribution can be generated by a structure of independent windings around each region V_h where the field has the intensity \mathbf{H}_h (Fig. 5). The current density on the surface of V_h is perpendicular to \mathbf{H}_h and on each face of V_h it is equal to

$$\iota_{hk} = -\eta_{hk} \times \mathbf{H}_k, \quad (7)$$

where unit vector η_{hk} is perpendicular to the face and oriented outwards with respect to V_h . The superposition of the currents of the individual windings over the interfaces satisfies the boundary conditions between the regions of the structure. In particular, if interfaces u_h, u_{h+1} in Fig. 4 are parallel to $\mathbf{H}_h, \mathbf{H}_{h+1}$ and if current densities on u_h, u_{h+1} satisfy Eq. (6), then u_h, u_{h+1} can be the boundary of the structure of electric currents and the external medium where the field is zero.

Figure 6(a) shows a structure of four windings designed to generate a uniform intensity \mathbf{H}_0 within the rectangular prismatic cavity V_0 , and to confine the field within the structure. Intensity \mathbf{H}_0 is assumed to be perpendicular to a face of V_0 . Volume V_0 is enclosed by a winding with current density of magnitude $\iota_0 = H_0$ oriented perpendicular to \mathbf{H}_0 . The other three windings around regions V_1, V_2, V_3 channel and close the flux of \mathbf{B} . The exploded view of the structure is shown in Fig. 6(b), with heavy arrows indicating the field intensities in the four components of the structure. The current distribution on the faces of V_1, V_3 perpendicular to \mathbf{H}_0 , performs the function of deflecting the flux generated inside V_0 .

The quality of a magnet is measured by its figure of merit, M , defined as the ratio of the energy of the field inside

the region of interest V_0 , to the total energy stored in the structure.¹ In the case of a permanent magnet

$$M = \frac{W_0}{W_m}, \quad (8)$$

where W_0 is the energy inside V_0 and W_m is the energy stored within the magnetized material during the magnetization process. The absolute maximum of M is 0.25 for structures of permanent magnets.² In a three-dimensional structure M is usually of the order of 0.1 or smaller. In structures of electric currents

$$M = \left(1 + \frac{1}{H_0^2 V_0} \sum_h H_h^2 V_h \right)^{-1}, \quad (9)$$

where the sum is extended to all components V_h of the structure with the exception of V_0 . In the example of Fig. 6, Eq. (9) yields

$$M = \left[1 + \frac{x_1}{y_0} \frac{1}{\sin 2\alpha} + \frac{x_0}{x_1 - x_0} \left(1 + \frac{x_1}{2y_0} \tan \alpha \right) \right]^{-1}. \quad (10)$$

In the particular case of a cubic cavity V_0 with $x_0 = 2y_0 = 2z_0$, $x_1 = 2x_0$, and $\alpha = \pi/4$, Eq. (10) yields $M = 0.125$, which is significantly higher than what can be achieved in a three-dimensional permanent magnet.

IV. CONCLUDING REMARKS

A uniform field can be generated in a cavity enclosed by a structure of uniformly magnetized polyhedrons if the orientation of the interfaces between polyhedrons and the surface charge densities induced on the interfaces satisfy Eq. (3). The uniform field in the same cavity can be generated by a structure of electric currents uniformly distributed on plane surfaces if the orientation of these surfaces and the surface current densities satisfy the equivalent Eq. (6).

¹M. G. Abele, *Structures of Permanent Magnets* (Wiley, New York, 1993).

²M. G. Abele and H. Rusinek, *J. Appl. Phys.* **67**, 4644 (1990).

Thermal magnetic noise due to eddy currents in a strip wound ferromagnetic core at 4.2 K (abstract)

Yu. V. Maslennikov
Cryoton Co., Troitsk, Moscow

O. Snigirev
Department of Physics, Moscow University, Russia

M. Cerdonio, G. A. Prodi, and S. Vitale
Department of Physics, University of Trento, Italy

Many applications involving high impedance signal sources and use of the low input impedance SQUID magnetometer would take advantage of the use of low noise ferromagnetic cores in matching transformers. Noise in ferromagnetic cores at liquid helium temperatures has been shown to be limited by thermal fluctuation of the magnetization for the two following cases: for bulk cores,¹ where the skin effect sets a low frequency (<100 Hz) roll-off of the effective permeability, and the spectral density is white up to the roll-off, and for strip wound cores at frequencies lower than ≈ 100 Hz, where magnetic viscosity² gives origin to a frequency independent imaginary permeability and correspondingly to a $1/\omega$ shaped spectral density. Thanks to a high sensitivity dc SQUID magnetometer we have now been able to measure thermal noise due to the skin effect in a strip wound 15- μm -thick Ultraperm core where the roll-off frequency is ≈ 1 MHz. Data for the noise are in quite quantitative agreement with the prediction of the fluctuation dissipation formula and the measured values of $\mu(\omega)$. At frequencies lower than a corner ≈ 1 kHz the noise is again dominated by the $1/\omega$ tail due to magnetic viscosity. We discuss the relevance for applications.

¹S. Vitale *et al.*, J. Appl. Phys. **65**, 2130 (1989).

²G. A. Prodi *et al.*, J. Appl. Phys. **66**, 5984 (1989).

Design of fast acting actuators for cryogenic valve applications in the ARIANE5-program (abstract)

Peter Schiebener, Alfred Pfeiffer, and Karl Smirra
Deutsche Aerospace AG, Space Transportation Systems and Propulsion, 81663 Muenchen, Germany

Presently valve developments are being carried out for the new European space launcher ARIANE5. In the case of the tank pressurization and helium supply system valve actuation times in the order of 20–50 ms, liquid hydrogen and liquid helium temperatures, pressures of up to 210 bar, and the need of a very compact volume lead to a requirement profile of the valve actuation unit which is met by directly controlled solenoid actuators with an additional permanent magnet. The modeling of the magnetic circuit comprises the elements of permanent magnets, solenoids, ferromagnetic materials, and several airgaps. The solutions of the model are gained by means of FE program the SYSMAGNA (out of SYSTUS®) which is capable of taking into account not only the time transients of the developing current in the solenoid but also moving parts in the magnetic field, which themselves contribute to the magnetic flux change. The results of major interest being calculated are the force versus stroke curves and the current versus time curves. The mechanical and magnetic properties of the employed materials are taken either from available data sources or from critically reviewed measurement data. Additionally, subsequently needed material characterizations were performed at ambient down to $T=4$ K. The simulation results are compared to static and dynamic test results and show good agreement. Finally the simulation proves to be very helpful to predict and explain the behavior of the complete valve unit consisting of actuator and flow part. Even effects due to cryogenic operation, which occur in the integrated valve, may be analyzed.

Barkhausen transitions in single layer and bilayer thin permalloy films

G. P. Farrell and E. W. Hill

University of Manchester, Department of Electrical Engineering, Manchester M13 9PL, England

The low coercivity of uniaxial thin nickel-iron multilayer films, prepared according to E. W. Hill, J. P. Li, and J. K. Birtwistle [J. Appl. Phys. **69**, 4526 (1991)], makes them attractive for magnetic sensor applications. Barkhausen jumps, causing noise, limit the performance of such sensors. It has been reported [R. F. Soohoo, J. Appl. Phys. **69**, 5871 (1991)] that, for any given sample under identical initial conditions, these Barkhausen jumps are deterministic rather than noisy in nature. This is consistent with the fact that the defect structure of a given sample is deterministic. This study compares power spectra and coercivity distributions from Barkhausen pulses obtained by applying varying alternating fields to thin permalloy films. The effect of an orthogonal bias field is also examined. The samples under examination consist of both single layer and bilayer films, produced as continuous layers by vacuum evaporation and ion milled into 40 mm diameter discs. The permalloy is of 80/20 composition and has a total thickness of 100 nm. The bilayer films have a nonmagnetic tantalum interlayer of thickness 5 nm. The rate of change of the applied field was varied between 2918.4 and 11.4 Oe/s, at an initial amplitude of 90 Oe. The results show that the Barkhausen pulses have a strong deterministic trend, but also contain a smaller nondeterministic component. As the frequency and amplitude are decreased, this random effect becomes larger. As might be expected when an orthogonal bias field is applied to the samples, the amplitudes of the pulses are decreased. The films also exhibit a corresponding reduction in coercivity.

INTRODUCTION

Despite the lower coercivity offered by thin nickel-iron bilayer films as compared to single layer films of the same magnetic layer thickness, the noise performance of bilayer films may be a more important consideration in considering them as thin film flux-switching sensor cores. Examination of the switching properties of both single layer and bilayer films used as cores in fluxgate-type sensors shows that although there is a large deterministic effect, which provides an envelope for the shape of the overall transition, there is also a smaller random component which produces variations from cycle to cycle (Fig. 1). This random component remains even when identical initial conditions are ensured by completely sweeping all of the domains from the material, a

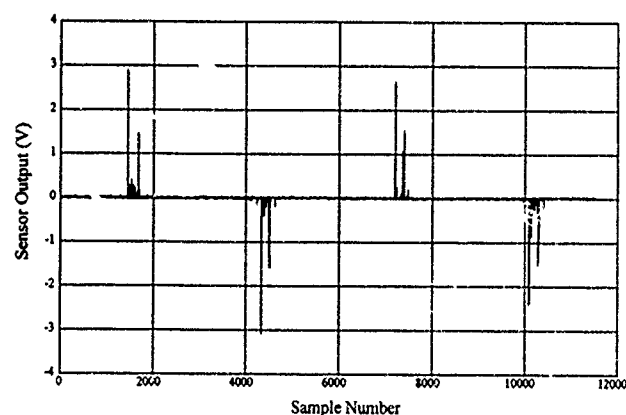


FIG. 1 Sensor output from consecutive cycles. Clear differences can be seen between the pulses, although the general shape remains similar.

process which may be verified by using the Bitter colloid method for domain observation. Such observation shows that a field of 30–40 Oe is required to sweep out all of the domains from a disc sample 100 nm thick and 40 mm in diameter. By treating the deterministic effect as the signal contribution and the random component as the noise contribution, an estimation of the Barkhausen noise in a sample may be made.

BACKGROUND

As the switching process is influenced by the microstructure of the magnetic layer, which is fixed and hence deter-

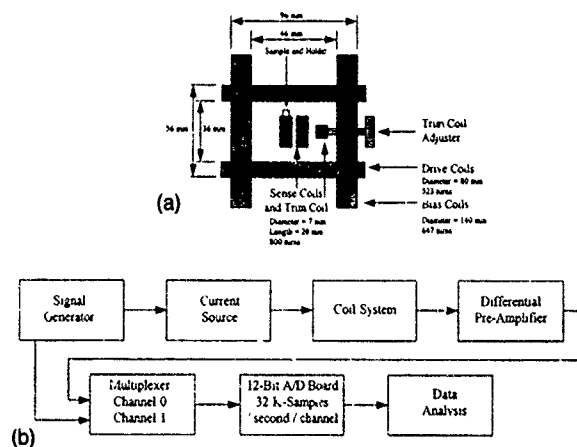


FIG. 2. (a) The coil measurement system. The sample was held in one of the sense coils and the trim coil used to balance offsets between the sense coils. The sample was swept around a hysteresis loop by the field generated by the drive coils, and an orthogonal field applied by the bias coils. (b) The data capture system. Data analysis was performed on a HP 700 workstation.

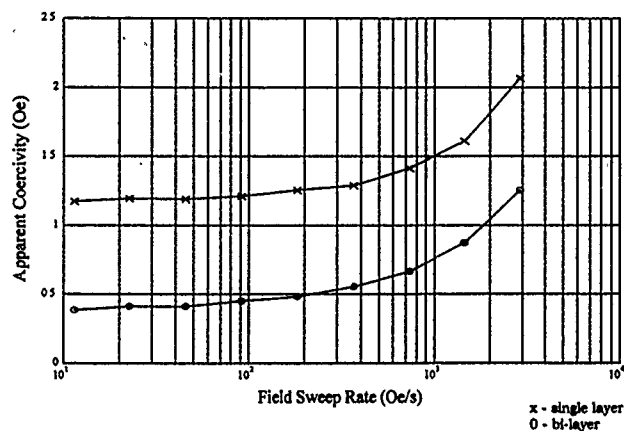


FIG. 3. The variation in coercivity with field sweep rate.

ministic for a given sample, it is reasonable to expect the Barkhausen transitions to also have a deterministic nature.¹ However, it is also important to consider the transitions as the movement of walls over energy barriers, which will be subject to the effect of random thermal perturbations. Thus, one measure of the noise in the material might be obtained by examining the variations in the coercivity from cycle to cycle. The distribution of such noise might be expected to be Gaussian, with the mean value equal to the true coercivity of the sample.

A second method of illustrating the random perturbations may be achieved by considering the integrated output of the sensor. In the absence of noise, this will have the form of a train of pulses at the same frequency as the sweep rate. If noise is present in the system, however, the pulses will exhibit small variations in frequency. Thus, a power spectrum should show an underlying trend giving the noise power, with spikes at the drive frequency and its harmonics. The ratio of the power at the fundamental frequency to the power at the same frequency, with the effect of the fundamental removed, might be used as a measure of the deterministic nature of the effect.

Assuming that one source of the noise might be a random variation in the direction of rotation of the magnetic moments during switching, it may be possible to reduce this noise by creating a preferred rotation direction. This is

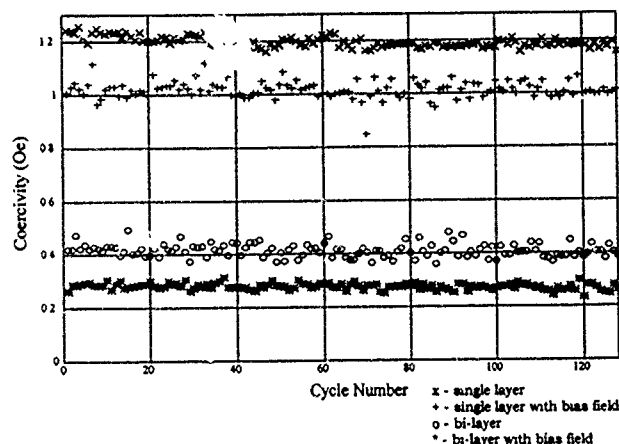


FIG. 4. (a)–(d) Variation in coercivity over 128 cycles. A reduction coercivity is observed when the bias field is applied.

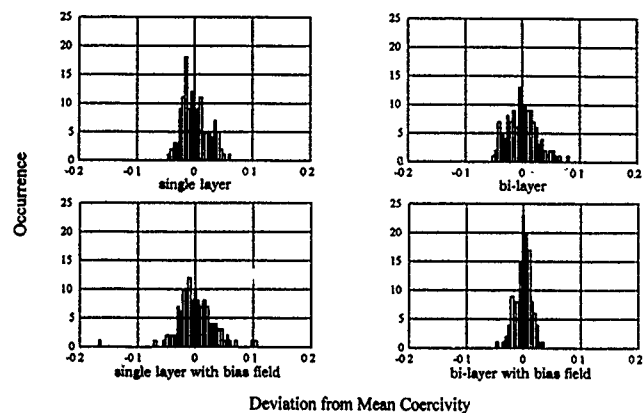


FIG. 5. (a)–(d) Distribution of coercivity from the mean value over 128 cycles. The application of a bias field causes the noise in the single layer film to increase and that in the bilayer film to decrease.

achieved by applying a small orthogonal hard axis bias field to the samples. One consequence of such a bias field will be a reduced output from the sensor as the dipoles will no longer be rotating through a full 180°. However, if the noise is reduced significantly, the signal to noise ratio (SNR) may be improved.

MEASUREMENT METHOD

The cores consist of 100 nm of magnetic material vacuum evaporated onto a 100 μm thick glass substrate, with a 5 nm tantalum spacer in the bilayer films.² Both types of film were produced on the same substrate as continuous layers, at a temperature of 300 °C and working pressure of 2×10^{-7} mbar. After the deposition, 40 nm diameter discs were masked off using a photolithographic technique and the films were ion milled to produce the disc shaped samples required. The discs were then mounted on thin plastic strips for ease of handling.

Measurements were performed by placing a sample in a coil system as shown in Fig. 2(a). The coil system was itself placed in a six layer mumetal enclosure. The field was swept linearly in time around the hysteresis loop in the direction of the easy axis of the sample, with at least 50 complete cycles

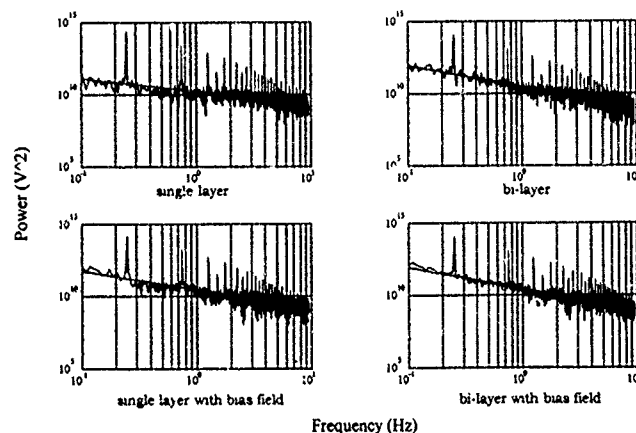


FIG. 6. (a)–(d) Power spectral densities. A linear trend to the Barkhausen noise is observed, with peaks at the effective drive frequency and its harmonics.

TABLE I. Power law dependence on frequency and signal to noise ratio results. The single layer film maintains a better SNR in the presence of a bias field, despite having an increased noise content. The bilayer film shows little change when the bias field is applied.

	Power law dependence on frequency (V^2/Hz)		Signal to noise ratio					
			0 Oe bias field			2 Oe bias field		
	0 Oe bias field	2 Oe bias field	Signal (V^2)	Noise (V^2)	SNR	Signal (V^2)	Noise (V^2)	SNR
Single layer	-0.88	-1.30	2.2×10^{14}	5.9×10^{10}	3729	1.5×10^{14}	1.7×10^{11}	882
Bilayer	-1.49	-1.47	1.1×10^{14}	2.3×10^{11}	478	1.1×10^{14}	2.2×10^{11}	500

being completed before any measurements were taken to provide a consistent starting point. The output of the sensor and the corresponding drive field were captured around each cycle via a 12-bit analog-to-digital (A/D) converter running at 32 K samples power second per channel. In all, 128 complete cycles were captured for each sample, at a range of field sweep rates varying between 2918.4 and 11.4 Oe/s with an amplitude of 90 Oe. Further measurements were then taken at a field sweep rate of 22.8 Oe/s and the same amplitude, with an orthogonal bias field of 2 Oe applied in the hard axis direction. The flow of data through the system is summarized in Fig. 2(b).

RESULTS

Figure 3 shows the apparent coercivity at each of the field sweep rates. A trend towards higher values appears at sweep rates greater than 100 Oe/s, possibly due to the inductance effects of the coil system, eddy currents in the sample, or the effect of sampling itself. Therefore, only results obtained at sweep rates lower than 100 Oe/s are considered here.

Figure 4 shows the variation in coercivity for each sample, with and without the bias field, at one sweep rate, namely, 22.8 Oe/s, over 128 cycles. The value for coercivity is obtained by integrating the pulses from each cycle, and taking the average of the field values at the median points. The mean coercivity for each sample in the absence of any bias field agrees well with the value measured by plotting the hysteresis loops on a magnetometer. Figure 5 shows the distributions of the coercivities, centered at zero for comparison purposes. With no bias field, the single layer film has a standard deviation of 0.0224 Oe, compared with 0.0260 Oe for the bilayer, suggesting that the noise in the two films is similar. The distributions are not truly normal, as expected, but instead exhibit some positive skew. This would suggest an asymmetrical hysteresis curve as the material is swept from one saturation state to the other, with more but smaller pulses as the film re-enters saturation due to the pinning of small domains at the edges of the material. When the film is subjected to an orthogonal hard axis bias field of 2 Oe, approximately one-half of the anisotropy field of the material, the standard deviations are 0.0324 Oe for the single layer and

0.0137 Oe for the bilayer. Thus, the noise in the single layer film has increased and that in the bilayer film has decreased. This is contrary to expectations, which suggested that the noise in both films should be decreased. The distributions appear to be more normally shaped, indicating more symmetry in the hysteresis loop around the switching point.

A comparison of the graphs in Fig. 4 shows that when the bias field is applied the coercivities of each film are reduced by around 0.2 Oe, probably due to an initial partial rotation of the magnetization.

Figure 6 shows power spectra for the samples, both with and without the bias field. The power law dependence on frequency is equal to the gradient of the line, and this value and the signal to noise ratio for each sample are given in Table I below.

These results show that for the single layer the bias field has a significant effect, increasing the power law dependence on frequency and dramatically reducing the SNR due to a reduced signal level and an increased noise level. For the bilayer film, the effect of the bias field is reversed; the power dependence on frequency is reduced and the SNR is increased, although this effect is small due to a similar reduction in both the signal and noise levels. Overall, however, the single layer film still has the better SNR.

CONCLUSIONS

Both the single layer and bilayer films show deterministic and nondeterministic components, with the nondeterministic components being similar in the absence of any bias field. A small hard axis bias field reduces the nondeterministic component in the bilayer film, but increases it in the single layer. Further work is required to relate this study to actual magnetization distributions in thin films.

ACKNOWLEDGMENTS

The authors would like to thank J. K. Birtwistle for his help in the preparation of the samples, and the Electrical Engineering workshop for the production of the coil system. Special thanks to Dowty Domain Magnetics and P. D. Austin for the financial support of this project.

¹R. F. Soohoo, J. Appl. Phys. 69, 5871 (1991).

²E. W. Hill, J. P. Li, and J. K. Birtwistle, J. Appl. Phys. 69, 4526 (1991).

Equation of motion of domain walls and equivalent circuits in soft ferromagnetic materials

G. Aguilar-Sahagun, P. Quintana,^{a)} E. Amano, J. T. S. Irvine,^{b)} and R. Valenzuela
Institute for Materials Research, National University of Mexico, Apartado Postal 70-360, Mexico D. F. 04510, Mexico

The equation of motion for ferromagnetic domain walls is compared with initial permeability measurements of Co-based soft ferromagnetic amorphous ribbons at frequencies in the range 100 Hz–13 MHz. The analysis of these results by complex permeability methods leads to an equivalent circuit formed by a parallel RL arrangement in series with a small resistance R_w due to resistance of the measurement coil. This equivalent circuit, however, cannot model the irreversible magnetization behavior for fields higher than the pinning (or propagation) field. It is shown that the equation of motion is also consistent only with the reversible magnetization mechanism, if the displacement term, x , represents instead the bulging of the pinned wall. The correlations between the terms in the equation of motion and the elements of the equivalent circuit are established.

I. INTRODUCTION

Domain wall dynamics in soft ferromagnetic materials are expected to be described by an equation of the form^{1,2}

$$m \frac{d^2x}{dt^2} + \beta \frac{dx}{dt} + \alpha x = 2M_s H(t), \quad (1)$$

where m is the effective wall mass, β is the viscous damping factor, α the restoring force, M_s the saturation magnetization, $H(t)$ the time-dependent field, x the wall displacement, and t the time. The domain structure is assumed to have a linear geometry with 180° walls with d spacing; magnetization variations are produced by displacements of flat walls. An interesting approximation, leading to the concept of propagation or pinning field, is the displacement of domain walls at a constant velocity, v , under the "pressure" of a constant field, H . Since the acceleration and restoring force terms disappear, Eq. (1) becomes

$$v = CH, \quad (2)$$

where $C = 2M_s/\beta$ is the mobility. Experimentally, these conditions clearly showed³ the existence of a "propagation" or "pinning" field, H_p , below which there is no wall displacement. Therefore, Eq. (2) should be written

$$v = C(H - H_p), \quad (\text{valid for } H \geq H_p). \quad (3)$$

Equation (1) can be solved⁴ for the stationary, forced oscillation condition of a driving field $H = H_0 \exp(-j\omega t)$, in terms of the real and imaginary parts of the susceptibility, χ . For high-permeability materials, $4\pi\chi \sim \mu$, the real and imaginary parts of the permeability can be written as

$$\mu' = \mu_0 \alpha / [\alpha^2 + (\beta\omega)^2], \quad (4)$$

$$\mu'' = \mu_0 \beta \omega / [\alpha^2 + (\beta\omega)^2], \quad (5)$$

where μ' and μ'' are the real and imaginary parts of the permeability, respectively, j is $(-1)^{1/2}$, μ_0 is the low-frequency limit of the permeability, ω is the angular frequency, and H_0 the amplitude of the applied field. Two

simple cases can be considered, depending on the relative values of the effective mass and the damping terms: if $m \ll \beta$, a relaxation occurs at a relaxation frequency

$$\omega_x = \alpha/\beta. \quad (6)$$

If $m \sim \beta$, the dispersion has a resonant character with a resonance frequency

$$\omega_s = (\alpha/m)^{1/2}. \quad (7)$$

To our knowledge, however, these equations have never been used to describe domain wall displacements ($H > H_p$) as a result of cyclic fields. Experimental spectra corresponding to the bulging mechanism (or initial permeability, $H < H_p$) are usually closer to the relaxation behavior, both in ceramic materials^{5,6} and in amorphous, metallic alloys;⁷ in a few cases, a resonant character has been observed,^{4,8} but this also for the initial permeability conditions.

In this article, we present measurements of complex permeability as a function of frequency in amorphous soft ferromagnetic ribbons for ($H < H_p$); these results are analyzed in terms of an equivalent circuit and compared with the equation of motion.

II. EXPERIMENT

The preparation of toroids by wound ribbons of Vitrovac[®] 6025 (nominal composition $\text{Co}_{66}\text{Fe}_4\text{Mo}_2\text{Si}_{16}\text{B}_{12}$, prepared by melt spinning by Vacuumschmelze), as well as the measurement techniques have been described elsewhere.⁷ Prior to magnetic measurements, ribbons were annealed at 300°C for 2 h in argon atmosphere to relieve stresses produced during the preparation process. Complex permeability, μ^* , is determined from impedance, Z^* , by

$$\mu^* = (-jK/\omega)Z^*, \quad (8)$$

where K is the geometrical factor.⁷

III. EXPERIMENTAL RESULTS

Real permeability spectra at low fields showed a constant behavior at low frequencies, followed by a dispersion with a relaxation character, Fig. 1. A small permeability value subsists for the high frequency range studied. All ex-

^{a)}Faculty of Chemistry.

^{b)}Department of Chemistry, University of Aberdeen, Meston Walk, Old Aberdeen, AB9 2UE, Scotland, U.K.

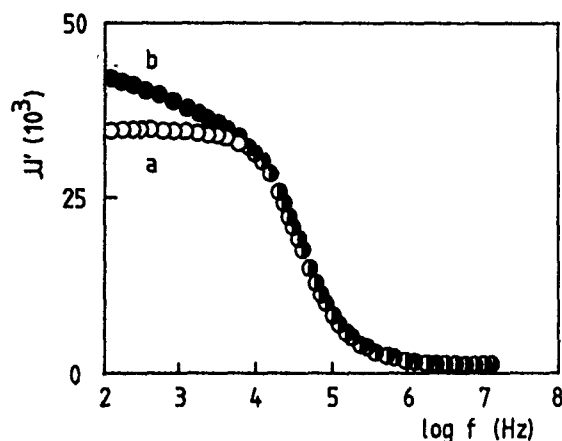


FIG. 1. Real permeability spectra (a) for field amplitude of $H=0.5$ A/m ($H_p \sim 0.6$ A/m), and (b) $H=0.8$ A/m.

periments performed at $H < 0.4$ A/m (5 mOe) resulted in the same curve. For higher fields, the permeability for low frequencies depended on the field value, but as frequency increased, all the curves merged into the low field plot, and therefore the relaxation behavior was the same for all of them, independently of the field, Fig. 1. A useful data representation is the complex permeability plot, μ' vs μ'' , Fig. 2. For $H < H_p$, a vertical spike is followed by a semicircle, as frequency increases, whereas for fields higher than H_p , the spike becomes inclined and deviates from the semicircle beginning. A third, complementary plot is the μ'' spectrum, Fig. 3, where the relaxation frequency appears as a maximum. In simple cases, it is possible to guess the equivalent circuit describing the experimental results from the geometry of this plot. In the present case, the obtained semicircle can be associated with a parallel, RL arrangement. The presence of a vertical "spike" in Fig. 2 and a (-1) slope for the low frequency range in Fig. 3 indicate an additional resistance term, R_w , in series with the parallel arrangement. It can be shown⁹ that this term is simply the coil resistance.

The permeability behavior at fields higher than the propagation field cannot be modeled by means of an equivalent circuit with ideal RL elements, since inclined spikes

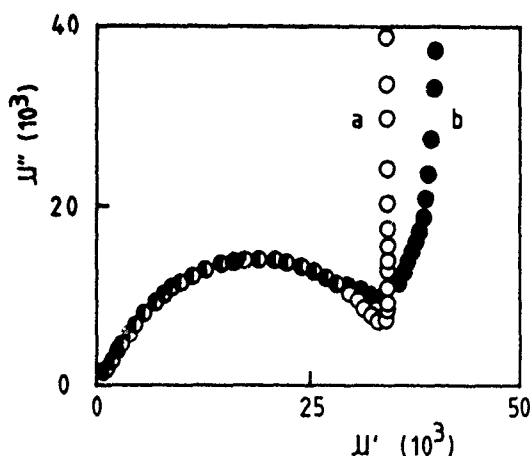


FIG. 2. Complex permeability plot for samples of Fig. 1.

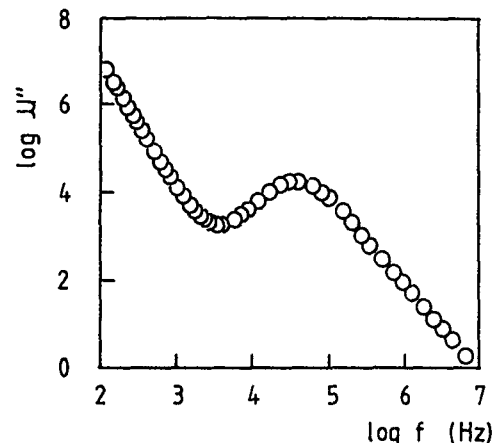


FIG. 3. Imaginary part of the permeability as a function of frequency for the low field experiment.

such as those in Fig. 2 involve impedances where the real part also depends on frequency. Warburg impedances of the form $Z_w = (1+j)\omega^\delta A$, where δ and A are constants, have been suggested¹⁰ to represent these results.

The relaxation frequency, ω_x , can be determined from the maximum in $\mu''(\omega)$ plots, Fig. 3; it corresponds to the condition $\mu' = \mu'' = \mu_0/2$ and is therefore related to the equivalent circuit elements given by the relationship

$$\omega_x = R/L. \quad (9)$$

Relaxation frequency ω_x has been verified⁹ to correspond to the intrinsic domain wall relaxation frequency and not to a parasitic, electrical relaxation.

IV. DISCUSSION

The complex permeability analysis allows the resolution of three magnetization mechanisms; at $H < H_p$, domain walls are pinned to defects and the field produces a reversible bulging, responsible for initial permeability. As frequency increases, a relaxation occurs resulting in a decrease of permeability; a small permeability value, presumably due to the spin rotation mechanism, which is expected to have the smallest time constant, persists at the highest measuring frequency in our system.

For high fields ($H > H_p$), domain walls are unpinned and displaced; however, this mechanism, possessing a large time constant, involves several steps (bulging, unpinning, displacement, repinning in a new position, debulging, etc.) in each cycle, and cannot be modeled by means of ideal elements in the equivalent circuit.

From this analysis, it appears that the mechanism responsible for the observed relaxation is wall bulging. If x is the bulging of the wall (and assuming a given geometry for the deformation), experimental results can be represented by Eq. (1), as well as by the parallel RL circuit. Since the use of the equivalent circuit approach has many advantages, it would be very useful to find some associations with the terms in the equation of motion approach.

The term of equivalent inductance L is clearly related to initial permeability by the geometrical factor ($\mu_0 = KL$). The

permeability value therefore depends on the extent of wall bulging, which in turn depends on the domain wall energy, γ . A domain wall pinned along two edges with a cylindrical bulging has a dc permeability¹

$$\mu_0 = (8\pi M_s^2 d)/(9\gamma), \quad (10)$$

where d is the distance between pinning edges and γ is the wall energy. The restoring force terms depends¹ on the wall energy as

$$\alpha = 18\gamma/d^2. \quad (11)$$

L is therefore related to α by the expression

$$L = [16\pi M_s^2/Kd](1/\alpha). \quad (12)$$

Due to its dissipative nature, the damping term, β , should be related to the equivalent resistance, R . From the expressions for the relaxation frequency, Eqs. (6) and (9), and taking into account Eqs. (10)–(12)

$$R = [16\pi M_s^2/Kd](1/\beta). \quad (13)$$

In order to obtain a resonance, a non-negligible effective mass and a capacitance are needed in the equation of motion and the equivalent circuit approaches, respectively. At this point, and taking into account the form of Eq. (7) and that of a resonant circuit, $\omega_s = (1/LC)^{1/2}$, it can be shown that

$$C = [Kd/16\pi M_s^2]m. \quad (14)$$

These correlations are extremely useful since some of the microscopic parameters such as wall energy, damping, and pinning can therefore be evaluated through the circuit elements from simple, macroscopic measurements as a function of frequency.

V. CONCLUSIONS

It has been shown that the equation of motion for domain walls, in its simple form, can describe the dynamics of pinned domain walls if the displacement term, x , represents instead the wall bulging. Domain wall displacements in real materials, involving a threshold field and bulging are too complex to be described by this equation. It has also been shown that the equivalent circuit approach is consistent with the equation of motion for the bulging mechanism. Finally, the correlations between the terms in both models, Eqs. (12), (13), and (14), have been established.

ACKNOWLEDGMENTS

Authors thank Dr. H. R. Hilzinger from Vacuum-schmelze GmbH, Germany, for providing the samples, and acknowledge partial funding from CONACyT-Mexico, DGAPA-UNAM (Mexico), the British Council, and the European Commission for this project.

¹E. M. Gyorgy, *In Treatise in Solid State Chemistry: Defects in Solids*, edited by N. B. Hannay (Plenum, New York, 1975), Vol. 2, p. 395.

²B. D. Cullity, *Introduction to Magnetic Materials* (Addison-Wesley, Reading, MA, 1972), p. 447.

³J. F. Dillon, Jr. and H. E. Earl, Jr., *J. Appl. Phys.* **30**, 202 (1959).

⁴G. P. Vella-Coleiro, D. H. Smith, and L. G. van Uitert, *J. Appl. Phys.* **43**, 2428 (1972).

⁵J. T. S. Irvine, A. R. West, E. Amano, A. Huanosta, and R. Valenzuela, *Sol. State Ionics* **40/41**, 220 (1990).

⁶M. Guyot, V. Cagan, and T. Merceron, *IEEE Trans. Magn.* **MAG-20**, 2157 (1984).

⁷R. Valenzuela and J. T. S. Irvine, *J. Appl. Phys.* **72**, 1486 (1992).

⁸A. Globus and M. Guyot, *IEEE Trans. Magn.* **MAG-6**, 614 (1970).

⁹G. Baca, E. Amano, and R. Valenzuela (to be published).

¹⁰J. T. S. Irvine, E. Amano, and R. Valenzuela, *J. Mater. Sci. Eng. A* **133**, 140 (1991).

Pinned domain-wall structure in magnetic field

Chai Tak Teh, Huei Li Huang, and Vladimir L. Sobolev^{a)}

Department of Physics, National Taiwan University, Taipei, Taiwan, Republic of China

The pinned domain-wall (DW) structure is investigated using a perturbational approach in terms of the inverse quality factor $1/Q$ and the ratio of H_{\parallel}/H_K (H_{\parallel} being the component magnetic field parallel to the anisotropy axis, H_K being the anisotropy field). The parallel component field gives rise to asymmetric boundary conditions which asymmetrize the DW structure. Dependence of the DW energy, static DW structure, and width on the orientation and the strength of the magnetic field has been evaluated and the corresponding Kondorsky function obtained.

I. INTRODUCTION

The structure of a resting domain wall (DW) under the action of an external magnetic field has already been treated in a number of articles (see Refs. 1 and 2 and the references therein). Nevertheless, the case of having the magnetic field arbitrarily oriented with respect to the wall normal and the anisotropy axis has not been sufficiently investigated to date. Such a problem may be considered as a reasonable one if the material has a high enough coercivity since otherwise, the presence of a component field along the anisotropy axis could lead to the DW movement.

Consider a uniaxial magnetic material with the material quality factor Q ($Q = K/2\pi M_s$, K being the anisotropy constant and M_s the saturation magnetization) larger than unity and a high enough coercivity field, but far less than the anisotropy field, $H_c < H_K$ ($H_K = 2K/M$). The DW is considered to be pinned and parallel to the x - z plane, and the z axis coincides with the anisotropy axis of the ferromagnet. The orientation of the external magnetic field is

$$\mathbf{H} = H(\sin \theta_H \cos \psi_H, \sin \theta_H \sin \psi_H, \cos \theta_H).$$

The polar axis is along the anisotropy axis. There is one restriction imposed on the external field. It requires the component field along the anisotropy axis, denoted as H_{\parallel} , to be less than the coercivity field of the material, $H_{\parallel} < H_c$.

In this article we present a detailed analysis of the effect of external field on the distribution of the magnetization inside domains and the DW. The variation of the DW energy, etc., are expounded. A new Kondorsky function⁴⁻⁶ based on the DW energy obtained herewith is also presented.

II. DOMAIN-WALL STRUCTURE

The energy density for a DW in a uniaxial ferromagnet may be written as follows:

$$W = K[\Delta_B^2(\vartheta'^2 + \sin^2 \vartheta \varphi'^2) + (\sin \vartheta \sin \varphi - \mu)^2 Q^{-1} - 2h_t \sin \vartheta \cos(\varphi - \psi_H) + \sin^2 \vartheta - 2h_{\parallel} \cos \vartheta], \quad (1)$$

where ϑ is the polar angle, φ the azimuthal angle of the magnetization vector, $\Delta_B^2 = A/K$ is the width of the Bloch wall; A is the exchange stiffness constant; $\vartheta' \equiv d\vartheta/dy$, $\varphi' \equiv d\varphi/dy$; $h_t = h \sin \theta_H$ is the transverse external field component; $h_{\parallel} = h \cos \theta_H$ is the longitudinal field compo-

nent; $h = H/H_K$; and μ is the limiting value of the magnetization component normal to the DW when it is at a distance from the DW inside domains. The term proportional to Q^{-1} describes the demagnetization field contribution to the energy. This term can be obtained naturally by means of solving the demagnetization integral³ subjected to continuity conditions normal to the DW plane.

The equilibrium orientations of the magnetization vectors inside domains are obtained by means of the variation of the energy density,

$$W_D = K[\sin^2 \vartheta - 2h_t \sin \vartheta \cos(\varphi - \psi_H) - 2h_{\parallel} \cos \vartheta], \quad (2)$$

from which it is easy to obtain

$$\sin \vartheta \cos \vartheta - h_t \cos \vartheta + h_{\parallel} \sin \vartheta = 0, \quad (3)$$

$$\varphi = \psi_H. \quad (4)$$

It is worthy of note that two solutions of the Eq. (3) have the form

$$\vartheta_1 = \vartheta_{10}, \quad \text{and} \quad \vartheta_2 = \pi - \vartheta_{20}, \quad (5)$$

which serve as the boundary conditions for the determination of the magnetization distribution inside DW. The angles ϑ_{10} and ϑ_{20} are the solutions of the equations⁵

$$\sin \vartheta_{j0} \cos \vartheta_{j0} - h_t \cos \vartheta_{j0} + (-1)^{j-1} h_{\parallel} \sin \vartheta_{j0} = 0, \quad j = 1, 2. \quad (6)$$

The equations describing the distribution of the magnetization inside the DW may be obtained by the variation of Eq. (1). As a result we obtain

$$\begin{aligned} \Delta_B^2 \vartheta'' - \sin \vartheta \cos \vartheta \varphi'^2 - \sin \vartheta \cos \vartheta \\ - Q^{-1}(\sin \vartheta \sin \varphi - \mu) \cos \vartheta \sin \varphi \\ + h_t \cos \vartheta \cos(\varphi - \psi_H) - h_{\parallel} \sin \vartheta = 0, \end{aligned} \quad (7)$$

$$\begin{aligned} (\sin^2 \vartheta \varphi')' - Q^{-1}(\sin \vartheta \sin \varphi - \mu) \sin \vartheta \cos \varphi \\ - h_t \sin \vartheta \sin(\varphi - \psi_H) = 0. \end{aligned} \quad (8)$$

To look for the solution of Eqs. (7) and (8) for materials with a large Q value we represent the magnetization angles in the following form:

$$\vartheta(y) = \vartheta^{(0)}(y) + Q^{-1} \vartheta^{(1)}(y), \quad \varphi = \varphi^{(0)}(y) + Q^{-1} \varphi^{(1)}(y), \quad (9)$$

where $\vartheta^{(0)}(y)$ and $\varphi^{(0)}(y)$ are the zeroth-order solution, respectively, of ϑ and φ . Upon substitution of Eq. (9) into Eqs.

^{a)}Permanent address: Institute for Single Crystal, Academy of Science of the Ukraine, Kharkov 310001, Ukraine.

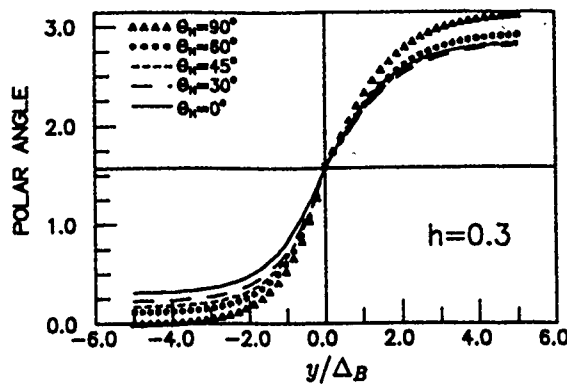


FIG. 1. Variation of the polar angle of the magnetization along the wall normal u ($=y/\Delta_B$) for several values of θ_H at $h=0.3$.

(7) and (8) we get a new system of equations in accordance with the order parameter Q^{-1} . In the zeroth order, we obtain

$$\Delta_B^2 \vartheta^{(0)''} - \sin \vartheta^{(0)} \cos \vartheta^{(0)} \varphi^{(0)'}{}^2 - \sin \vartheta^{(0)} \cos \vartheta^{(0)} = 0$$

$$-h_t \cos \vartheta^{(0)} \cos(\varphi^{(0)} - \psi_H) - h_{||} \sin \vartheta^{(0)} = 0, \quad (10)$$

$$(\sin^2 \vartheta^{(0)} \varphi^{(0)'})' - h_t \sin \vartheta^{(0)} \sin(\varphi^{(0)} - \psi_H) = 0. \quad (11)$$

Equation (11) has a solution $\varphi^{(0)} = \psi_H$ corresponding to a deviation of the azimuthal angle inside domain from its initial equilibrium value $\varphi=0$ due to the action of an external field. Substituting this into Eq. (10) we obtain

$$\Delta_B^2 \vartheta^{(0)''} - \sin \vartheta^{(0)} \cos \vartheta^{(0)} - h_t \cos \vartheta^{(0)} - h_{||} \sin \vartheta^{(0)} = 0, \quad (12)$$

This equation is exact. To solve this equation we need the boundary conditions set forth in Eq. (6) which describes the magnetization distributions inside domains. Note that $h_{||}$ is assumed to be small, satisfying the condition $H_{||} < H_c$, $H_{||} < H_K$, in keeping with the earlier assumption. From ϑ_{01} and ϑ_{02} given in Eqs. (5) and (6) one obtains

$$\begin{aligned} \sin \vartheta_{10} &= \sin \vartheta_0 - h_{||} \tan \vartheta_0 + h_{||}^2 \tan \vartheta_0 / \cos \vartheta_0, \\ \sin \vartheta_{20} &= \sin \vartheta_0 + h_{||} \tan \vartheta_0 + h_{||}^2 \tan \vartheta_0 / \cos \vartheta_0. \end{aligned} \quad (13)$$

These equations describe the boundary conditions for the magnetization distributions inside domains 1 and 2, in which

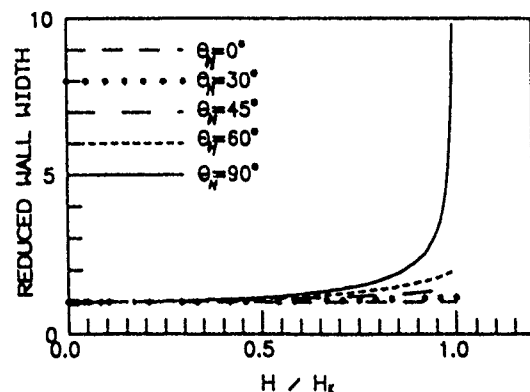


FIG. 2. Variation of the reduced DW width, Δ/Δ_B , vs the field strength for several field angle θ_H 's.

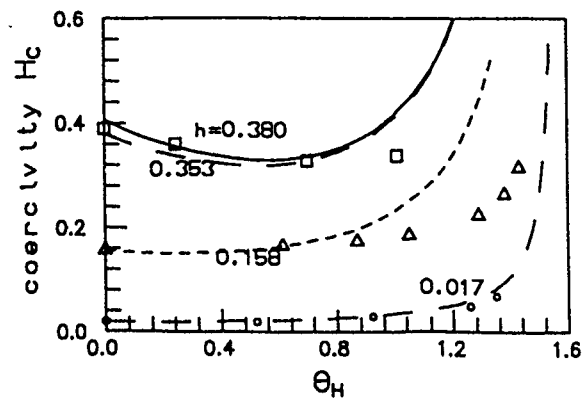


FIG. 3. Variation of the Kondorsky function vs the field angle θ_H for several h values. The data points were from Ref. 3 for barium ferrite.

$\sin \vartheta_0 = h_t$. Thus, the corresponding first integral in domains 1 and 2 is slightly different from each other. The first integral of Eq. (12) is expressed as

$$\left(\frac{d\vartheta}{du} \right)^2 = (\sin \vartheta - \sin \vartheta_0)^2 - 2h_{||} (\cos \vartheta \mp \cos \vartheta_0) + h_{||}^2 \tan \vartheta_0, \quad (14)$$

where $\vartheta(u) \equiv \vartheta^{(0)}(u)$ and $u = y/\Delta_B$ for brevity; the minus and plus sign refers to domains 1 and 2, respectively, separated by the DW.

The solutions describing the distribution of the magnetization inside domains 1 and 2, lying in the intervals $-\infty < u \leq 0$ and $0 \leq u \leq \infty$, are

$$\begin{aligned} \sin \vartheta_1 &= \sin \vartheta_0 + \frac{\cos^2 \vartheta_0}{\cosh w_1 + \sin \vartheta_0} \\ &+ \frac{h_{||}}{2} \frac{\sinh w_1}{\cosh w_1 + \sin \vartheta_0} \left(\tan \vartheta_0 + e^{w_1} \sec \vartheta_0 \right. \\ &\left. + \frac{3 \tan \vartheta_0 \sinh w_1}{\cosh w_1 + \sin \vartheta_0} \right), \end{aligned} \quad (15)$$

$$\begin{aligned} \sin \vartheta_2 &= \sin \vartheta_0 + \frac{\cos^2 \vartheta_0}{\cosh w_2 + \sin \vartheta_0} \\ &- \frac{h_{||}}{2} \frac{\sinh w_2}{\cosh w_2 + \sin \vartheta_0} \left(\tan \vartheta_0 + e^{-w_2} \sec \vartheta_0 \right. \\ &\left. - \frac{3 \tan \vartheta_0 \sinh w_2}{\cosh w_2 + \sin \vartheta_0} \right), \end{aligned} \quad (16)$$

up to the first order in $h_{||}$. In these formulae $w_{1,2} = u \cos \vartheta_0 / (1 \mp a h_{||})$, $a = 1 + 2 \sin^2 \vartheta_0 / 2 \cos^3 \vartheta_0$. For small $h_{||}$, the above results reduce exactly to the earlier one.⁷

III. DW ENERGY AND DW WIDTH

Equations (15) and (16) describe an asymmetric DW structure. Making use of these expressions the energy density of the DW is expressed as

$$\begin{aligned}\epsilon_{DW} &= \int dy (W_{DW} - W_D) \\ &= K \left(\frac{\Delta_B^2}{\Delta \cos \vartheta_0} f + \Delta g \cos \vartheta_0 \right) \quad (17)\end{aligned}$$

where Δ is a field-dependent DW width, and

$$f(\vartheta_0, h_{\parallel}) = 2 \left[\cos \vartheta_0 - \left(\frac{\pi}{2} - \vartheta_0 \right) \sin \vartheta_0 \right] + h_{\parallel}^2 F(\vartheta_0), \quad (18)$$

$$\begin{aligned}g(\vartheta_0, h_{\parallel}) &= 2 \frac{Q + \sin^2 \psi_H}{Q} \left[\cos \vartheta_0 - \left(\frac{\pi}{2} - \vartheta_0 \right) \sin \vartheta_0 \right] \\ &\quad + h_{\parallel}^2 G(\vartheta_0). \quad (19)\end{aligned}$$

In these expressions

$$\begin{aligned}F(\vartheta_0) &= -\sec^3 \vartheta_0 \left[1 - \sin^4 \vartheta_0 - \frac{1 + \sin^2 \vartheta_0}{2} \right. \\ &\quad \left. \times \left((\sqrt{2} - 1) \tan^2 \vartheta_0 + \ln \frac{1 - \sin \vartheta_0}{2 \cos^2 \vartheta_0} \right) \right], \quad (20)\end{aligned}$$

$$\begin{aligned}G(\vartheta_0) &\approx \sec^3 \vartheta_0 \left[\frac{2 \ln 2 \sin^2 \vartheta_0 + \ln 2 - 2}{4} \right. \\ &\quad \left. + \frac{1 + \sin^2 \vartheta_0}{4 \cos^3 \vartheta_0} \left[\cos \vartheta_0 - \left(\frac{\pi}{2} - \vartheta_0 \right) \sin \vartheta_0 \right] \right], \quad (22)\end{aligned}$$

in which the contributions on the order of Q^{-1} are omitted from the above expressions.

Upon minimization of Eq. (17) with respect to Δ the effective DW width can be expressed as

$$\Delta^2 = \frac{\Delta_B^2 f(\vartheta_0, h_{\parallel})}{\cos^2 \vartheta_0 g(\vartheta_0, h_{\parallel})}, \quad (23)$$

and the DW energy density is

$$\sigma = \frac{1}{2} \sigma_0 \sqrt{f(\vartheta_0, h_{\parallel}) g(\vartheta_0, h_{\parallel})}, \quad (24)$$

where $\sigma_0 = 4 \sqrt{AK}$ is the Bloch wall energy density in the absence of the external magnetic field.

The dependence of the DW energy on the external field orientation can be obtained easily by substitution of the expression $\sin \vartheta_0 = h \sin \theta_H$ into

$$\begin{aligned}\sigma &= \sigma_0 \left[\cos \vartheta_0 - \left(\frac{\pi}{2} - \vartheta_0 \right) \sin \vartheta_0 \right] + O(h_{\parallel}^2) \\ &= \sigma_0 \left[\sqrt{1 - h^2 \sin^2 \theta_H} - h \sin \theta_H \right. \\ &\quad \left. \times \left(\frac{\pi}{2} - \arcsin(h \sin \theta_H) \right) \right] + O(h_{\parallel}^2). \quad (25)\end{aligned}$$

Using Eq. (25) a new Kondorsky function can be expressed as

$$\begin{aligned}H_P(\vartheta) &= \frac{H_P(0)}{\cos \theta_H} \left[\sqrt{1 - h^2 \sin^2 \theta_H} - h \sin \theta_H \right. \\ &\quad \left. \times \left(\frac{\pi}{2} - \arcsin(h \sin \theta_H) \right) \right] + O(h_{\parallel}^2). \quad (26)\end{aligned}$$

IV. NUMERICAL RESULTS

The variation of the asymmetric DW structure versus polar angle across the DW at a constant h value based on Eqs. (15) and (16) is shown in Fig. 1. Due to the presence of h_{\parallel} , the terms in the large parentheses in Eq. (16) may change sign at some large field angle θ_H in domain 2 when the field strength h increases. This makes the curves for the variation of magnetization polar angles in domain 2 reverse its proper order for $\theta_H > \pi/2$. Note that there are three curves crowded together, almost falling onto a single one, with the $\theta_H = \pi/6$ curve coming down at the bottom, and that the two curves $\theta_H = \pi/4$ and $\pi/2$ cross at $u \sim 3$. Clearly, a symmetric wall will result provided only if $h_{\parallel} = 0$.

Figure 2 shows the variation of the reduced DW width Δ/Δ_B based on Eq. (23) versus the field strength for several θ_H 's. For small h values, the change in the wall width is seen to be relatively limited. At $\theta_H = 90^\circ$, we see that the wall width goes to ∞ as $h \rightarrow 1$, as expected.

The DW energy function along with the new Kondorsky function are shown to depend only on h_{\parallel} quadratically despite a linear dependence on h_{\parallel} in the boundary conditions, Eq. (13). Numerical evaluation of the new Kondorsky function shows an appreciable improvement over the previous results⁴⁻⁶ when the transverse field component gets more important, or as θ_H becomes larger than $\sim 75^\circ$. Figure 3 shows the variation of the Kondorsky function versus the field angle θ_H for several h values. The data points were taken from Ref. 4 for barium ferrite.

In summary, it is shown that the in-plane field parallel to the DW plane gives rise to asymmetric boundary conditions which asymmetrize the DW structure and modify the DW energy, and the corresponding Kondorsky function.

ACKNOWLEDGMENT

This research is supported by the National Science Council, ROC, through Contract No. NSC-82-0405-E02-124.

¹A. Molozemoff and J. Slonczewski, *Magnetic Domain Walls in Bubble Materials* (Academic, New York, 1979).

²G. A. Jones and B. K. Middleton, *Int. J. Magn.* **6**, 1 (1974).

³C. T. Teh, M.S. thesis, National Taiwan University, 1993.

⁴F. Schumacher, *J. Appl. Phys.* **70**, 3184 (1991).

⁵T. Y. Lee and H. L. Huang, *J. Appl. Phys.* **74**, 495 (1993).

⁶H. L. Huang and V. L. Sobolev, *IEEE Trans. Magn.* **29**, 2539 (1993).

⁷V. L. Sobolev, S. C. Chen, and H. L. Huang, *Chin. J. Phys. (Taipei)* **31**, 403 (1993).

Susceptibility of current-carrying iron whiskers

J. -G. Lee and A. S. Arrott

Simon Fraser University, Burnaby, British Columbia Canada V5A 1S6

The magnetization pattern of an iron whisker can be altered by passing a dc current along its axis. Changes in the resistance and the ac susceptibility are used to deduce the domain structures and how they change with dc currents and/or dc magnetic fields, applied along the axis. The magnetization curls around a central core that is magnetized along the whisker axis.

We attempt to deduce magnetization patterns in iron whiskers carrying current in magnetic fields from ac susceptibility and dc magnetoresistance measurements. When a sufficient current flows along the long [001] axis of an iron crystal with {100} surfaces, the magnetization pattern changes from a structure that is primarily magnetized in $\pm[001]$ to one where the magnetization circulates about that axis in the plane of the square cross section.¹ The observations of a decrease in the resistance and changes in the surface domain structures have provided strong evidence for these changes in iron whiskers.² Observations of flux changes also support this conclusion.³ Representations (not data) of the field dependence of the ac susceptibility at low frequency with and without a current along the axis of a typical whisker are shown in Fig. 1. The out-phase ac response χ'' is most sensitive to changes in magnetization patterns because the losses are dominated by the eddy currents produced by moving domain walls.

There are no noticeable effects on the ac susceptibility from currents below a critical value I_c . The susceptibility for zero current shows a characteristic response that is well documented in previous studies of domain configurations, Bloch walls and magnetization processes in iron whiskers from dc to 200 kHz.⁴⁻⁶ The magnetization pattern in zero field approximates, and sometimes is, the Landau structure of two long domains separated by a 180° domain wall with closure domains on each end.

If a small pickup coil is used to detect the changing flux Φ_B in the midplane of the whisker, the signal depends on the flux of magnetization Φ_M in the midplane, the applied field $H_0\hat{z}$, and the demagnetizing field $H_D(r)$. For the Landau structure, the contributions to Φ_B from $H_0\hat{z}$ and $H_D(r)$ cancel one another if the coil is tightly wound around the sample. Otherwise a correction is needed for the region between the coil and the sample. An effective susceptibility χ_{ext} is extracted from the ac voltage in the pickup coil and the ac current driving a solenoid. This is written in terms of a magnetic stiffness $\alpha(\omega)$ and a magnetic viscosity $\beta(\omega)$ as

$$\frac{1}{\chi_{\text{ext}}} = \alpha(\omega) + i\omega\beta(\omega). \quad (1)$$

In the current study, the frequency, 700 Hz, is sufficiently low that $\alpha(\omega) = \alpha(0)$ and $\beta(\omega) = \beta(0)$. The stiffness and viscosity can be calculated in the low-frequency limit for the whiskers without current. The stiffness $\alpha(0) \equiv 4\pi D \equiv AH_0/\Phi_M$, where A is the midplane area and is independent of magnetization until the flux of magnetization saturates in the midplane. This happens discontinuously

at the departure field H_d ; see Fig. 1. H_d is very close to $4\pi DM_s \equiv H_D$, where the magnetization in the central cross section is practically uniform and saturated. For the Landau structure, labeled as such in Fig. 1, the viscosity provides information on the position of the wall:

$$\beta(0) \equiv \beta_0 \{ \tanh[b(\pi/2)(1 - \Phi_M/\Phi_s)] + \tanh[b(\pi/2)(1 + \Phi_M/\Phi_s)] \},$$

where β_0 contains the conductivity and b is a numerical constant close to 1.05. The viscosity is greatest when the wall is centered in the midplane, decreasing to about one-half of the maximum just before saturation.

The various features of the ac response in the absence of current are a measure of the quality of the whisker. They are not observed if the whisker is subjected to strain. In experiments where wires are attached to measure resistance, it is necessary to be certain that the strains are less than those which would suppress the formation of the Landau structure. It was very difficult to insert a whisker, with current and potential leads attached, into the transformer, used to mea-

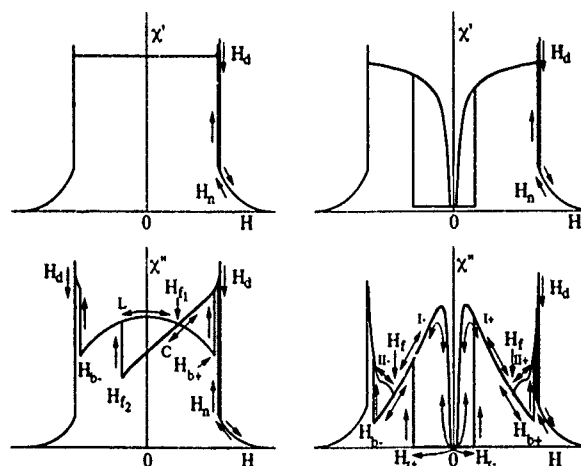


FIG. 1. Representations of the field dependence of components χ' and χ'' of the ac susceptibility for {100} iron whiskers. On the left-hand side: with no current along the axis, the responses corresponding to the Landau structure, labeled L, and to the Coleman structure labeled C, show the effects of magnetic viscosity in χ'' at low frequencies. On the right-hand side: with sufficient current to change the structure and to increase the departure field H_d by 50%, the responses corresponding to the structures of stages I and II are distinguished by differences in χ' . The magnetic viscosity increases with applied field in stage II. For stage I the magnetic response shows a low χ' for small fields. χ' increases sharply beyond an apparent threshold field for one field direction but not the other, depending on previous fields. The decrease in magnetic stiffness with field is accompanied by a decrease in magnetic viscosity.

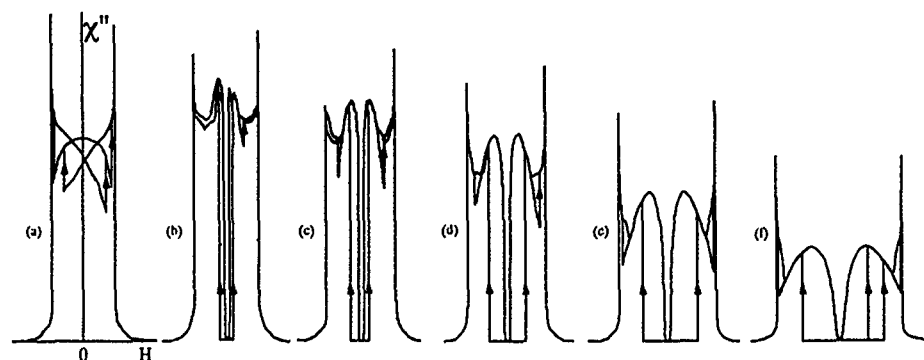


FIG. 2. Transcription of raw data for χ'' for a sequence of applied currents, $I=0.02, 0.075, 0.15, 0.2, 0.4$, and 0.6 A. These variations of χ'' with applied field at each current were recorded in a series of field cycles, showing the effects of hysteresis, which depend on previous maximum fields. The recorder traces have been scanned into bit maps from which this data is extracted. The response of this whisker is typical for many, but not all, of the various whiskers selected for their perfection with lengths between 2.0 and 2.5 cm and widths from 0.02 to 0.05 cm.

sure ac susceptibility, without creating such strains. It was more convenient to measure the ac susceptibility with only the current leads attached. Correspondences between the two sets of measurements provide evidence that the attachment of the potential leads did not change the dependence of magnetic structure on current and applied field.

When $I > I_c$, the field dependence of the ac susceptibility is quite different; see Fig. 1. The results are interpreted as arising from three different configurations. For $H > H_n \equiv H_d$ the midplane is saturated. As H is reduced below the nucleation field, the structure called stage II⁺ is nucleated. It is stable down to H_f where stage I⁺ forms. Stage I⁺ is stable for increasing as well as decreasing fields for all fields between H_{b+} and H_{r+} . Stage I⁺ reverts to stage II⁺ at H_{b+} . Stage I⁻ is nucleated at H_{r+} . Stage I⁻ and stage I⁺ apparently have some similarities and some differences in their structures. One may anticipate differences because the reversal of the applied field is not accompanied by a reversal in the constant applied current.

The most striking effects occur in low fields. If the field is decreased from H_{b+} to zero, the susceptibility becomes very small and remains small for negative fields until the negative field H_{r+} is reached. $|H_{r+}|$ is much larger than the fields for which the susceptibility decreases. If H_{r+} is not reached, the response is quite reversible all the way up to H_{b+} . Similar behavior is observed if the negative field H_{r+} is exceeded to produce stage I⁻ which is reversible between the negative field H_{b-} and the positive field H_{r-} .

Representative recorder traces of the ac response for a typical whisker are shown in Fig. 2. To explain these data we propose that the several stages resemble the patterns shown in Fig. 3. These structures require the presence of the field from the current. This field varies almost linearly with the distance from the center, except that it reaches a higher value at the centers of the edges than it does at the corners.⁷ This is the rationale for the stage-II configurations a and e. The direction of the magnetization (out of the paper for the + stages) is the same in the central region and the walls, except possibly for configuration d.

An estimation of the expected behavior of a model based on these configurations requires some approximations. It is

helpful to suggest that the response can be understood by considering what happens in the central cross section.⁸ One can approximate the power dissipation per unit length by considering from the motion of the walls as if the whisker were infinitely long. Perhaps the energy of the whisker scales with the energy per unit length E_L of the central cross section. E_L can be broken into terms reflecting the applied field, the demagnetizing field, the field from the current, and a contribution from the wall energy. To a fair approximation

$$E_L = -H_0\Phi_M + \frac{1}{2} \frac{4\pi D}{A} \Phi_M^2 + CIq^3 + Wq, \quad (2)$$

where q is the side of the inner square magnetized along the axis. The demagnetizing factor $4\pi D$ depends on the dimensions of the whisker. The coefficient C for the current term can be calculated from the geometry. The coefficient W for

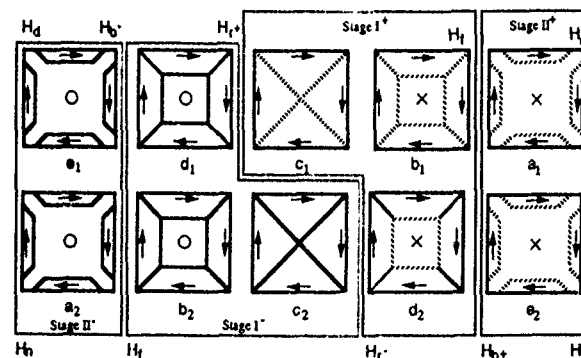


FIG. 3. Diagrams of the conjectured magnetic configurations in the midplane for stages I and II. The field is changing from H_n to H_d from right to left-hand side for a_1 to e_1 . From a_2 to e_2 , the field is changing in the opposite direction. In the transformation from a_1 to b_1 the domains coalesce. The magnetization in the center is + in stage I⁺ and stage II⁺ and - in stage I⁻ and stage II⁻. The transformation from c_1 to d_1 is nucleated away from the midplane. A Bloch line could cause a reversal of handedness somewhere along the diagonal wall in d_1 . On going from d_1 to b_2 to c_2 in stage I⁻, the handedness of that part of the diagonal wall closest to the origin is determined by the direction of the magnetization in the central core.

the wall term is calculable in the approximation that the wall energy densities σ_{110} and σ_{100} are those of walls of infinite extent:

$$W = -2\sqrt{2\sigma_{110}} + 4\sigma_{100} = -0.9\sigma_{100},$$

because $\sigma_{110} = \sqrt{3\sigma_{100}}$. This favors the expansion of the core from c_1 to b_1 in Fig. 3. It is a very small effect except at zero field.

To a first approximation $\Phi_M = q^2 M_s = q^2 \Phi_s / A$. The negative of the derivative of the energy with respect to Φ_M / A is the average internal field acting on the moving wall. This vanishes at equilibrium. When there are moving walls, it balances the field H_e from the eddy currents. To a first approximation H_e in stage I is given by

$$H_e = -4\pi \frac{\sigma \partial \Phi_M}{c^2 \partial t} \ln \left(\frac{A}{q^2} \right). \quad (3)$$

The response is found from the vanishing of the effective field

$$H_{eff} = -\frac{\partial E_L}{\partial \Phi_M} + H_e = H_0 - \frac{4\pi D}{A} \Phi_M - CI\Phi_M^{1/2} - \frac{W}{\Phi_M^{1/2}} - 4\pi \frac{\sigma}{c^2} \frac{\partial \Phi_M}{\partial t} \ln \left(\frac{\Phi_s}{\Phi_M} \right) = 0. \quad (4)$$

From this one obtains the dependence of H_0 , χ , $\alpha(0)$, and $\beta(0)$ on Φ_M :

$$\frac{H_0}{4\pi D M_s} = \frac{\Phi_M}{\Phi_s} + \frac{I}{I_1} \left(\frac{\Phi_M}{\Phi_s} \right)^{1/2} + W_1 \left(\frac{\Phi_s}{\Phi_M} \right)^{1/2}, \quad (5)$$

$$\frac{1}{\chi_{ext}} = \alpha(0) = 4\pi D \left[1 + \frac{I}{2I_1} \left(\frac{\Phi_s}{\Phi_M} \right)^{1/2} - \frac{W_1}{2} \left(\frac{\Phi_s}{\Phi_M} \right)^{3/2} \right], \quad (6)$$

and

$$\omega\beta(0) = 4\pi D \omega\beta_1 \ln \left(\frac{\Phi_s}{\Phi_M} \right). \quad (7)$$

For a 0.03-cm-thick 2.3-cm-long Fe whisker at 700 Hz, the quantity $\omega\beta_1 \approx 1/2$. The experiments have been performed with whiskers for which $I_{max}/I_1 \approx 1/2$. For all but the smallest fields, the terms in W_1 can be neglected. For parameters in this range, the model predicts the susceptibilities for stage I shown in Fig. 4. For stage II the model remains the same except the loss term is replaced by

$$\omega\beta(\omega) = 4\pi D \omega\beta_2 \ln [\Phi_s / (\Phi_s - \Phi_M)].$$

It would take a more detailed model for stage II than we possess to calculate β_2 . Experimentally it is observed that the loss in stage II matches the loss in stage I at the transition

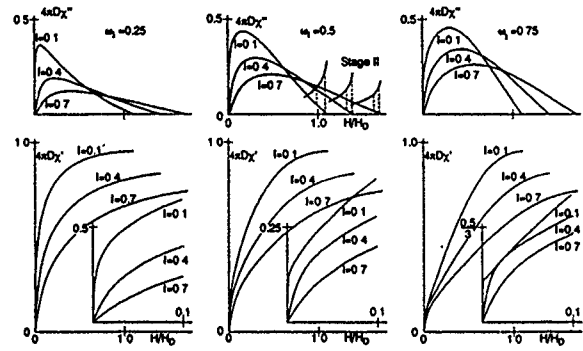


FIG. 4. Calculations of the field dependence of χ' and χ'' for three frequencies and three choices of current along the axis, including a blowup of the origin for χ' . The calculations are for the stage I. In addition, a simulation of stage II is presented in the panel for χ'' and $\omega_1 = 0.5$.

from stage II to stage I. This is used to pick a value for β_2 to calculate χ'' for stage II as shown for $\omega_1 = 0.5$ in Fig. 4.

This model accounts for much of the response in stage I⁺, for example, the linear increase in the departure field H_d with current, the low susceptibility at $H=0$, the maximum in χ'' , and the sharper rises in χ' and χ'' at lower currents for low fields. The model does not explain why the susceptibility stays low to a finite positive field. This effect is observed in the measurement of resistivity. The resistance remains constant for a small range of fields and then increases monotonically as Φ_M approaches Φ_s .

At present we do not know what accounts for the observations that the ac susceptibility and the resistivity remain constant for a small range of positive fields. That they remain constant for a range of negative fields is a direct consequence of the conjectured structure, whether W is positive or negative.

Except for low fields where the model appears incomplete, the behavior is well described by the first three terms in the model which come directly from Maxwell's equations and the assumption that the behavior of the whole system can be modeled by looking at the central cross section.

¹ E. Tatsumoto, Phys. Rev. **109**, 658 (1958).

² P. W. Shumate, Jr., R. V. Coleman, and R. C. Fivaz, Phys. Rev. B **1**, 394 (1970).

³ R. Berthe, A. Birkner, and U. Hartmann, Phys. Status Solidi A **103**, 557 (1987).

⁴ B. Heinrich and A. S. Arrott, Can. J. Phys. **50**, 710 (1972).

⁵ B. Heinrich, A. S. Arrott, and D. S. Bloomberg, in *Magnetism and Magnetic Materials 1972*, AIP Conf. Proc. 19, edited by C. D. Graham and J. J. Rhyne (AIP, New York, 1973), pp. 940-960.

⁶ D. S. Bloomberg and A. S. Arrott, Can. J. Phys. **53**, 1454 (1975).

⁷ K. Küpfmüller, *Einführung in die theoretische Elektrotechnik*, 8th ed. (Springer, Berlin, 1965), p. 242.

⁸ B. Heinrich and A. S. Arrott, *Magnetism and Magnetic Materials 1974*, AIP Conf. Proc. 24, edited by C. D. Graham and J. J. Rhyne (AIP, New York, 1975), pp. 702-720.

The effects of demagnetizing and stray fields on magnetoacoustic emission

D. H. L. Ng^{a)} and C. C. H. Lo

Department of Physics, The Chinese University of Hong Kong, Shatin, Hong Kong

J. P. Jakubovics

Department of Materials, University of Oxford, Parks Road, Oxford OX1 3PH, United Kingdom

Magnetoacoustic emission (MAE) has been measured from a Ni bar and a mild steel bar. The magnetizing field was produced by a c-core electromagnet, which was separated from the specimen surface by a nonmagnetic spacer layer (thickness l_a). In Ni, the MAE profile contains a single peak when l_a is small. As l_a increases, a second peak appears and then a third peak, indicating that MAE is not only caused by domain wall creation and annihilation, but also by domain wall motion. In the case of the mild steel bar, only two peaks are detected, which are increasingly separated as l_a increases. The different results between the two materials can be explained by the different mobility of non-180° domain walls. The present results also indicate that the MAE profile obtained from Ni is less sensitive to l_a than that obtained from mild steel. This difference can be explained by considering the reluctance of the magnetic circuit.

I. INTRODUCTION

Magnetoacoustic emission (MAE) is under development as a technique for the nondestructive evaluation of magnetic materials. The possibilities of measuring stress^{1,2} and detecting defects^{3,4} using MAE have already been demonstrated. One of the practical applications of MAE is to inspect surface smoothness in metallic assemblies and components. For such applications, the specimen is usually magnetized with a c-core electromagnet placed close to its surface. In the presence of defects such as buried voids and cracks, surface perturbations such as undercutting on flat surfaces, or when the surfaces are rough and curved, the coupling between the test piece and the magnet is poor. Demagnetizing fields and stray fields are therefore induced, resulting in the modification of the MAE profile. The purpose of this paper is to report the effects of these induced fields on the MAE signals obtained from Ni and mild steel by varying the thickness of an insulating spacer layer between the magnet and the specimen surface. This study will also provide information about the physical processes involved in the generation of MAE, and may help to settle some of the current disputes about these points.⁵

II. EXPERIMENT

MAE measurements were made on a Ni and a mild steel bar of dimensions 101.6 mm by 27.0 mm by 6.5 mm, and 190.0 mm by 20.1 mm by 5.8 mm, respectively. During the measurements, a 1 Hz magnetizing field of amplitude about 40 kA m⁻¹ was applied in the longitudinal direction by using a c-core electromagnet placed on the surface of the bar. The MAE signals (approximately in the range 35–200 kHz) were detected by a piezoelectric transducer, and were then amplified, rectified, and filtered. The mean signal amplitude was then plotted as a function of the applied field over half a hysteresis cycle. Ideally, the magnet and the bar should form a closed magnetic circuit with no demagnetizing field or

stray flux. A practical advantage of using a c-coil magnet over a conventional air-cored coil³ is that the magnet can be placed at any region of interest of the specimen. A similar arrangement was used in other MAE experiments.^{1,2} However, a nonmagnetic spacer must be used between the magnet and the test piece in order to minimize the everpresent electrical and acoustic noises. The spacer breaks the magnetic flux path in the circuit and introduces demagnetizing fields as well as stray fields. These effects alter the MAE signals detected by the piezoelectric transducer. The measurements were repeated at different spacer thicknesses l_a , ranging from 0.12 to 0.63 mm for mild steel, and from 0.05 to 1.55 mm for Ni. The MAE profiles obtained from both Ni and mild steel are shown in Fig. 1. Plots of peak amplitudes against spacer thickness for the two specimens are shown in Fig. 2.

III. MAE PROFILES

MAE profiles obtained from Ni usually contain a single peak. The profile obtained in our experiments with $l_a = 0.05$ mm is also of this form (Fig. 1, top left). With $l_a = 0.36$ mm, an additional peak appears to the left of the main peak, and with $l_a = 1$ mm, a third peak appears to the right. (The peaks are marked with arrows.) The peak heights generally decrease with increasing spacer thickness (Fig. 2). In the case of steel, the profiles always contain two peaks (Fig. 1, right). The peak heights in any particular profile become more nearly equal after the subtraction of noise (compare Figs. 1 and 2). It has been reported that MAE profiles obtained from a toroidal polycrystalline YIG sample change drastically as a result of demagnetizing effects, and also that the emission is related purely to domain wall creation and annihilation.⁵ As the results here show, if the above interpretation is correct, the peaks corresponding to the two processes would be increasingly separated as the effects of demagnetizing and field leakage increase, but there would not be a third peak in the low-field region. The existence of three peaks in the profile from Ni with larger l_a thus indi-

^{a)}Electronic mail: B108771@vax.csc.cuhk.hk.

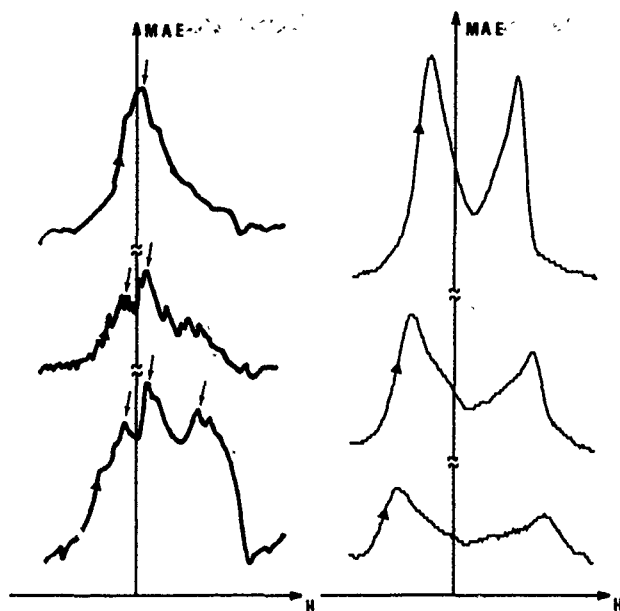


FIG. 1. MAE profiles (arbitrary units) as a function of applied field H obtained with various spacer thicknesses for Ni and mild steel. The three traces on the left were obtained from Ni with (from top to bottom) $l_a = 0.05, 0.95$, and 1.55 mm, respectively, and those on the right from mild steel with (from top to bottom) $l_a = 0.18, 0.31$, and 0.44 mm, respectively. Noise was not subtracted from these profiles. The three profiles from steel are to the same scale. The scales of the middle and bottom traces from Ni are enlarged by factors of 5 and 10, respectively, relative to the top trace.

cates that MAE is not only caused by domain wall creation and annihilation, but also by domain wall motion. The wall creation process involves the sudden release of trapped walls, the annihilation occurs when the walls abruptly collapse, and the wall motion involves the breaking away of walls from pinning centers. When the demagnetizing and flux leakage effects are small, the fields corresponding to domain wall creation and annihilation are close to the coer-

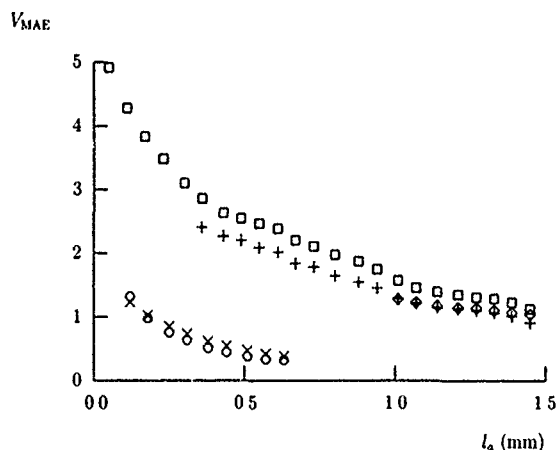


FIG. 2. Plots of peak amplitudes (V_{MAE} , arbitrary units) against l_a (mm) for Ni and mild steel. Crosses (+), squares, and diamonds correspond to the left, central, and right peaks from Ni respectively, and crosses (x) and circles correspond to the left and right peaks from steel respectively. The peak amplitudes shown were obtained after the subtraction of noise.

cive field. The MAE peaks due to all three processes therefore overlap, and the profile consists of a single peak.

The fact that a central peak does not appear in the MAE profiles from steel can be explained by the difference in the mobility of non-180° domain walls in steel and Ni. Gaunt⁶ has suggested that the pin restoring force f on a domain wall is given by

$$f = 2M_s A_p H_c, \quad (1)$$

where M_s is the saturation magnetization, A_p is the wall area associated with the pin, and H_c is the coercivity. Williams *et al.*⁷ also reported that the velocity of the domain walls is proportional to the resistivity and inversely proportional to M_s . Therefore a material with lower M_s , such as Ni tends to have a smaller f than one with a higher M_s , such as steel, and the domain walls would be more mobile in Ni than in steel. The existence of a strong central MAE peak in Ni resulting from wall motion suggests that the non-180° walls in Ni are more easily unpinned than in steel, giving rise to MAE in low fields. In mild steel, some 180° walls can move in small fields, but these walls do not give rise to MAE. Non-180° walls are less mobile and require a larger field to move them. The MAE activity contributed by the motion of the latter is so close to the annihilation process that the two processes are superimposed into one peak, and therefore only two peaks appear in the MAE profile from mild steel.

IV. THE MAGNETIC RELUCTANCE

The amplitude of the MAE peaks can be estimated by considering the magnetic circuit formed by the c-core magnet, the two spacers (one for each pole), and the specimen. A coil of N turns carrying a current I around a ferromagnetic core produces a magnetomotive force (mmf) given by NI . The magnetic flux Φ is related to the magnetic reluctance \mathcal{R} and the mmf NI by

$$\Phi = \frac{NI}{\mathcal{R}}, \quad (2)$$

where

$$\mathcal{R} = \sum_i \frac{l_i}{\mu_i A_i}, \quad (3)$$

and l_i , μ_i , and A_i are the length of the flux path, permeability, and cross-sectional area of the different sections of the circuit in series. In our magnetic circuit the magnetic flux is therefore given by

$$\Phi = NI \left(\frac{l_m}{\mu_m A_m} + \frac{2l_a}{\mu_a A_a} + \frac{l_s}{\mu_s A_s} \right)^{-1}, \quad (4)$$

where the subscripts m , a , and s refer to the magnet, the spacers, and the part of the specimen being magnetized, respectively. The magnetic flux in the circuit is reduced when the spacers are introduced, because it requires more energy to drive the same amount of flux across the spacers than through an equal volume of iron, since the permeability of the spacers is much lower. As l_a increases, the reluctance \mathcal{R} increases and Φ decreases. This effect is further enhanced by the existence of a demagnetizing field due to the free

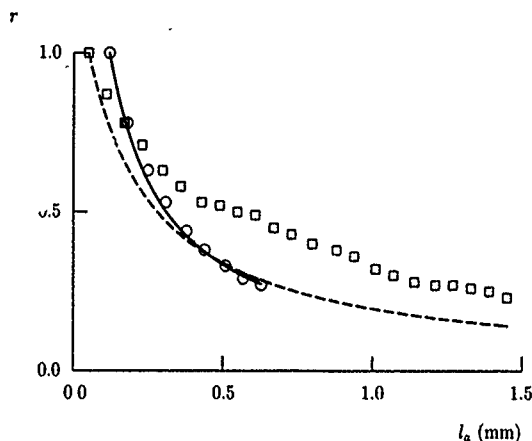


FIG. 3. Calculated R^{-1} (curves) and measured peak heights (points) plotted against l_a (mm). Squares and the dashed curve refer to Ni, circles and the full curve to steel. The values have been normalized as follows: for the dashed curve, $r = R^{-1}(l_a)/R^{-1}(0.05)$, for the full curve, $r = R^{-1}(l_a)/R^{-1}(0.12)$, for the squares, $r = V_{MAE}(l_a)/V_{MAE}(0.05)$, and for the circles, $r = V_{MAE}(l_a)/V_{MAE}(0.12)$.

poles at the two ends of the magnet. However, at a given mmf, Φ is still approximately inversely proportional to R . In the generation of MAE, the MAE activity is proportional to the rate of change of strain, and to the change of domain volume. The former is related to the amount of magnetic flux Φ inside the test piece, thus the MAE activity is also proportional to R^{-1} .

The permeability μ_s of the Ni bar was measured to be about 125. Assuming that μ_s of mild steel is 1000, and that $\mu_a = 1$ and $\mu_m = 1000$, the values of R for the magnetic circuits involving mild steel and Ni were calculated for different values of l_a . Figure 3 shows a comparison of MAE peak amplitudes with R^{-1} for both specimens, as a function of l_a . For steel, the agreement is very close, so that the magnitudes of the MAE signals can be predicted for different spacer thicknesses if an initial set of data (i.e., values of l_a and observed MAE) are given. For Ni, the agreement is less close, although a similar trend is followed. The results in

both Figs. 2 and 3 also show that l_a has a greater effect on the MAE in the mild steel bar. For example, in mild steel, a change of l_a from 0.12 to 0.63 mm decreases the normalized MAE signal from 1 to 0.27, while in Ni the change is from 0.87 to 0.49 when l_a changes from 0.11 to 0.61 mm. There are two reasons for this: (i) the large value of μ_s of mild steel leads to a smaller contribution of the specimen to the total reluctance R of the circuit, thus a small change of l_a will significantly alter R and also the observed MAE, and (ii) the value of spontaneous magnetization of mild steel is about 3.5 times of that of Ni, and the demagnetizing field created in the case of mild steel by the presence of the spacer would be 3.5 times larger than the field created in the case of Ni. Thus one would expect that the MAE signals decrease more rapidly with spacer thickness in mild steel than in Ni.

V. CONCLUSIONS

There is strong evidence that the generation of MAE is due to domain wall creation, motion, and annihilation during the process of magnetization. Movement of non-180° domain walls is involved in all three processes. The relative magnitude of the emission can be predicted by the magnetic circuit calculations.

ACKNOWLEDGMENTS

This work was funded by the Hong Kong UPGC Direct Grant-Mainline Research Scheme. The authors are also grateful to United College of the Chinese University of Hong Kong for financial support.

- ¹D. H. L. Ng, J. P. Jakubovics, C. B. Scruby, and G. A. D. Briggs, *J. Magn. Mater.* **104**, 355 (1992).
- ²D. H. L. Ng, J. P. Jakubovics, C. B. Scruby, and G. A. D. Briggs, *IEEE Trans. Magn.* **28**, 2214 (1992).
- ³D. J. Buttle, C. B. Scruby, G. A. D. Briggs, and J. P. Jakubovics, *Proc. R. Soc. London A* **414**, 469 (1987).
- ⁴D. H. L. Ng, J. P. Jakubovics, G. A. D. Briggs, and C. B. Scruby, *J. Appl. Phys.* **69**, 5868 (1991).
- ⁵M. Guyot and V. Cagan, *J. Appl. Phys.* **73**, 5348 (1993).
- ⁶P. Gaunt, *Can. J. Phys.* **65**, 1194 (1987).
- ⁷H. J. Williams, W. Shockley, and C. Kittel, *Phys. Rev.* **80**, 1090 (1950).

IR spectroscopy on FeNi and FePt Invar alloys

B. Buchholz, E. F. Wassermann, W. Pepperhoff, and M. Acet
Tiefemperaturphysik (SFB 166), Universität Duisburg, 47048 Duisburg, Germany

UHV IR emission spectroscopy has been carried out at energies 9–33 mRy (wavelength 2.8–9.8 μm) in the temperature range 430–800 K on single crystals of FeNi and FePt Invar, with Curie temperatures in the respective range. The results show a drastic (up to 30%) decrease of the IR absorptivity around T_c in the energy range 23–33 mRy (2.8–4 μm), while at small energies around 9 mRy (10 μm) the absorptivity is temperature independent, as expected for 3d metals, and found on pure Ni. The decrease in absorptivity on the Invar alloys cannot be understood by the common temperature dependence of interband transitions; rather, it calls for the existence of moment-volume instabilities, characterized by transitions between a high-spin ground state and a temperature-induced low-spin state. Qualitative agreement of the absorptivity with respective total density-of-states calculations on Fe₃Ni is demonstrated.

I. INTRODUCTION

In recent reviews^{1,2} we have shown that band calculations^{3,4} provide a new ansatz to understand the broad spectrum of Invar anomalies in 3d alloys. Particularly, the calculations reveal that the Fe moment in ordered Fe₃Ni and Fe₃Pt is unstable with respect to small changes in the atomic volume. The results call for the existence of moment-volume instabilities, characterized by a ferromagnetic high-spin-state (HS) with large atomic moment and volume (the ground state), and a low-spin-state (LS) with smaller magnetic moment and volume. Experimental evidence for the existence of these states has been given on ordered and disordered Fe₇₂Pt₂₈ as well as Fe_{68.5}Ni_{31.5} through low-temperature Mössbauer experiments under pressure,⁵ clearly revealing the HS-LS transition with increasing pressure, in quantitative agreement with the predictions from theory.

The situation at finite temperatures is less clear. Although the band calculations reveal that in the Invar concentration range the energy difference ΔE between the HS and LS states is of the order of 1–2 mRy (150–300 K), so that the LS state becomes thermally accessible, the physical nature of the excitations is still unknown. To shed more light on this situation, we carried out spin-polarized, angle-resolved photoemission on ordered Fe₇₂Pt₂₈.⁶ The observed difference in intensity below and above the Curie temperature T_c agreed well with the calculated density-of-states (DOS) difference for fcc Fe in the HS and LS state. Since, however, other interpretations of our data have been suggested,^{7,8} we think that new experiments are required to prove the correctness of our assumptions.

We have, therefore, for the first time, carried out IR emission spectroscopy in the range of wavelengths $\lambda=2.8$ –9.8 μm ($E=9$ –33 mRy) on FeNi and FePt Invar alloys in the temperature range 430–780 K, i.e., below and above the respective T_c 's of the alloys. Since the HS and LS states manifest themselves in sharp peaks in the DOS, lying ~ 20 mRy below and above the Fermi energy, respectively, IR spectroscopy

provides a suitable tool to investigate the changes in the DOS, when the sample temperature is raised through T_c . IR spectroscopy has an energy resolution of several tens of mRy, and in the range of wavelengths used the penetration depth of the radiation is some hundreds of angstroms. Both are advantageous in comparison to ultraviolet photoemission spectroscopy (UPS), where the energy resolution and the penetration depth are almost two orders of magnitude smaller.

In general, in 3d systems the temperature dependence of interband transitions and, therefore, the respective temperature dependence of the absorptivity is weak. It only depends on the smearing and the changes in bandwidth due to thermal agitation and expansion, respectively. Our results on FeNi and FePt Invar cannot be understood within these arguments; rather, it calls, as we will show, for an explanation within the HS-LS transition model as earlier claimed in our UPS measurements.⁶

II. EXPERIMENT

To determine the IR absorptivity via Kirchhoff law, we have set up an IR emission spectrometer with a grid monochromator and a thermocouple radiation detector. The light intensity is measured by a lock-in technique, chopping the beam with 11 cycles/s. To increase the sensitivity, we use a relative method, i.e., the emission of a sample is measured in comparison to a standard blackbody radiator, realized by a blackened hollow Cu block with a small hole. Sample and standard are placed in direct vicinity in the sample holder, so that they can be heated simultaneously and also kept at the same constant (± 30 mK) temperature. Focusing the emitted light of either sample or reference on the monochromator slit is achieved by a rotatable spherical mirror (glass, Al coated).

Although the penetration depth of the IR light in the spectral range used (2.8–9.8 μm) is roughly 200 Å, cleanliness and optical quality of the sample surface are of ample

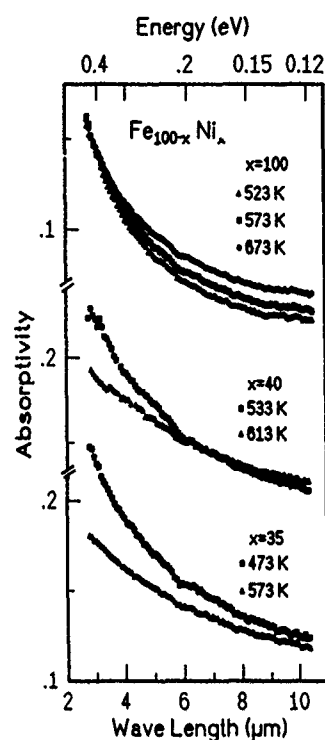


FIG. 1. Spectral absorptivity for Ni ($T_c = 624$ K), $\text{Fe}_{60}\text{Ni}_{40}$ ($T_c = 620$ K) and $\text{Fe}_{65}\text{Ni}_{35}$ ($T_c = 490$ K) at constant temperatures below and above the respective Curie temperatures.

importance. The samples are therefore placed in an UHV chamber (5×10^{-9} mbar). Surface preparation involves etching and polishing before mounting. They are annealed in vacuum at 900 K for 2 h to remove possible oxide layers.

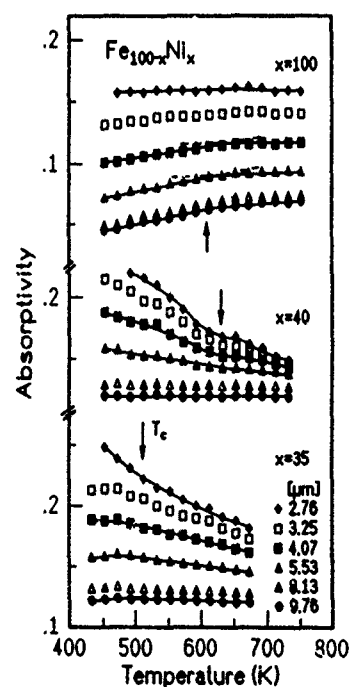


FIG. 2. Absorptivity vs temperature for Ni, $\text{Fe}_{60}\text{Ni}_{40}$, and $\text{Fe}_{65}\text{Ni}_{35}$ at constant wavelength. Note the 30% decrease in absorptivity, observed for the Invar alloys only at small wavelength. T_c 's are marked by arrows.

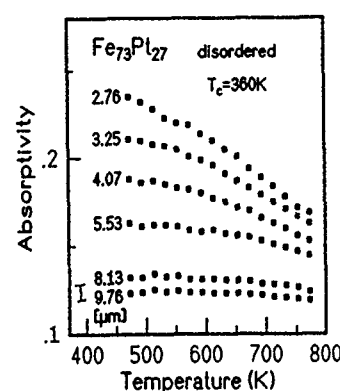


FIG. 3. Absorptivity vs temperature at constant wavelength for disordered $\text{Fe}_{73}\text{Pt}_{27}$ Invar.

III. RESULTS AND DISCUSSION

Figure 1 shows the spectral absorptivity for pure Ni and two FeNi Invar alloys at two temperatures, one above and one below the respective T_c 's. Note the difference in the absorption behavior between Ni and the FeNi alloys. While for Ni the absorptivity shows only a small increase with temperature at longer wavelength, a result in accordance with earlier findings,⁹ the Invar alloys exhibit opposite behavior. This is better revealed in Fig. 2, where the absorptivity is plotted as a function of temperature at constant wavelength. T_c 's are marked by arrows. In Ni there are small changes in slope of the absorptivity at T_c which increase with increasing wavelength. The effect is very likely due to the decrease of the band splitting, as shown in spin- and angle-resolved UPS investigation on Ni.¹⁰

The behavior of Ni is contrasted by the behavior of the Invar alloys, $\text{Fe}_{59.9}\text{Ni}_{40.1}$ and $\text{Fe}_{65}\text{Ni}_{35}$ (see Fig. 2), which at large wavelength, $\lambda = 8-10$ μm ($E \approx 10$ mRy), show hardly any change of the absorptivity with temperature. However, at small wavelength, $\lambda = 2-4$ μm ($E \approx 30-40$ mRy), a drastic (30%) decrease of the absorptivity is observed, when the temperature is raised through T_c . Equal results are shown in

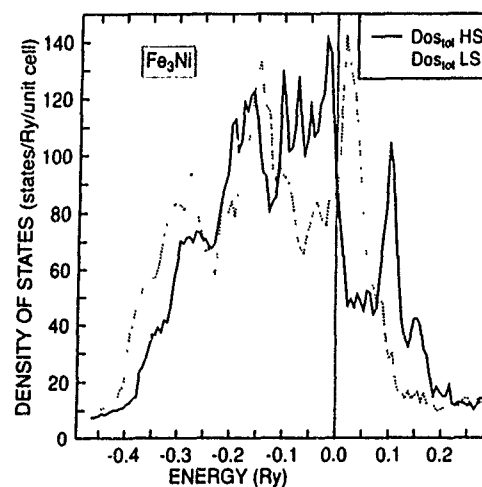


FIG. 4. Total density of states for Fe_3Ni in the HS state ($r_{ws} = 2.60$ a.u.; solid line) and LS state ($r_{ws} = 2.517$ a.u.; broken line).

Fig. 3, where the absorptivity versus temperature for disordered $\text{Fe}_{73}\text{Pt}_{27}$ Invar is given. They must consequently be caused by the Invar effect.

In contrast to the behavior at longer wavelength, the observed anomalies, maximum at short wavelength, call for a decrease in the combined DOS with increasing temperature. This can be made plausible within the band-structure calculations^{3,4} mentioned, i.e., within the HS-LS transition model. For this purpose we show in Fig. 4 the calculated¹¹ total DOS for Fe_3Ni in the HS (solid curve) and LS state (dashed curve). The HS state is characterized by the high peak in the DOS, lying about 20 mRy below E_F . For the LS state a similar feature is found. The observed reduction in the absorptivity can thus simply be understood by temperature-induced HS-LS transitions, which cause a drastic diminution of the HS DOS in the energy range in question.

Optical spectroscopy has the drawback that it averages over the total Brillouin zone, and the combined DOS is required to understand the microscopic processes in detail. Additionally, finite temperature effects result in some "rounding" of the DOS peaks, and indirect transitions might be of importance. Our present absorption experiment—as the UPS before—gives good experimental support for the correctness

of the HS-LS transition model, and the changes in electronic band structure accompanying it. Further support can result from absorption experiments at higher photon energies and lower temperature, where we expect the absorption anomaly in Invar to vanish. Experiments with a respective setup are presently under way.

ACKNOWLEDGMENT

This work was supported by DFG through SFB166.

- ¹E. F. Wassermann, in *Ferromagnetic Materials*, edited by K. H. Buschow and E. P. Wohlfahrt (North-Holland, Amsterdam, 1990), Vol. 5, p. 240.
- ²E. F. Wassermann, *J. Magn. Magn. Mater.* **100**, 346 (1991).
- ³M. Podgorny, *Phys. Rev. B* **43**, 11 300 (1991).
- ⁴P. Entel, E. Hoffmann, P. Mohn, K. Schwarz, and V. Moruzzi, *Phys. Rev. B* **47**, 8706 (1993).
- ⁵M. M. Abd-Elmeguid and H. Micklitz, *Phys. Rev. B* **40**, 7395 (1989).
- ⁶E. Kisker, E. F. Wassermann, and C. Carbone, *Phys. Rev. Lett.* **58**, 1784 (1987).
- ⁷Y. Kakehashi, *Phys. Rev. B* **38**, 12 051 (1988).
- ⁸H. Gollisch and R. Feder, *Solid State Commun.* **69**, 579 (1989).
- ⁹M. P. Stoll and C. Jung, *J. Appl. Phys.* **50**, 7477 (1979).
- ¹⁰H. Hepster, R. Raue, and G. Güntherodt, *Phys. Rev. Lett.* **51**, 829 (1983).
- ¹¹We are indebted to E. Hoffmann for calculation of the total DOS.

Anti-Invar in Fe-Ni

M. Acet, T. Schneider, H. Zähres, E. F. Wassermann, and W. Pepperhoff
Tiefemperaturphysik (SFB 166), Universität Duisburg, 47048 Duisburg, Germany

Anti-Invar behavior in a material can be characterized by an anomalously large and a weak temperature-dependent thermal-expansion coefficient, when compared to the respective Grüneisen lattice expansion. It is just the opposite of the Invar effect, which is characterized by an anomalously small thermal-expansion coefficient. Common to Invar and anti-Invar is the fact that both possess moment-volume instabilities. Anti-Invar is observed in the paramagnetic state. It occurs in γ -Fe and in a number of $3d$ fcc binary and ternary alloys. In $\text{Fe}_x\text{Ni}_{100-x}$ alloys it is observed in the concentration range $70 \leq x \leq 100$ at. % within the fcc stability range. The effect vanishes as the Invar concentration, $x=65$ at. %, is approached. To examine the valence electron concentration dependence of the anti-Invar effect the thermal expansion has been measured in the fcc state of $\text{Fe}_x\text{Ni}_{100-x}$ for $63 \leq x \leq 100$ at. %. Using a model based on moment-volume instabilities in conjunction with a thermal activation process the size of the anti-Invar effect in these alloys has been determined. The volume enhancement is found to decrease with increasing Ni concentration from 2.8% in γ -Fe to 0% at $x=65$ at. %.

I. INTRODUCTION

$3d$ Invar alloys are an important class of materials which owe their properties to moment-volume instabilities (MVI).^{1,2} Total energy calculations for Invar have shown the existence of a large-volume high-spin (HS) ground state and a small-volume low-spin (LS) state lying energetically a few mRy higher.³ The existence of these states have also been demonstrated in FeNi and FePt Invar alloys by Mössbauer experiments under pressure.⁴

Similar to Invar alloys γ -Fe is a material which also possesses a MVI. However, in contrast to Invar total energy calculations have shown that the ground state is an antiferromagnetic (AF) LS state and the higher-lying state is a ferromagnetic (FM) HS state.^{5,6} Mössbauer experiments at low temperatures on thin films of γ -Fe stabilized with different lattice constants have shown that below and above a critical lattice constant, $a_c=3.64$ Å (critical atomic volume, $V_c=12.05$ nm³), γ -Fe is AF and FM, respectively.⁷ These experiments confirmed the existence of these states in γ -Fe.

The signature of the Invar effect is a spontaneous volume magnetostriction starting near the magnetic ordering temperature and extending down to low temperatures. The anti-Invar effect, on the other hand, can be recognized by an anomalously large thermal-expansion coefficient, $\alpha(T)$, accompanied by an almost temperature-insensitive behavior at high temperatures in the PM state.^{8,9} $\alpha(T)$ of $\text{Fe}_{63}\text{Ni}_{37}$ Invar and γ -Fe anti-Invar are shown in Fig. 1. The shaded areas in this figure correspond to a spontaneous volume magnetostriction in the case of $\text{Fe}_{63}\text{Ni}_{37}$ and to a volume enhancement in the case of γ -Fe.⁹ An essential difference between Invar and anti-Invar is that in the former the volume effect occurs essentially in the magnetically ordered state, whereas in the latter it occurs in the magnetically disordered state.

In this work we initiate a systematic survey on the size of the anti-Invar effect as a function of valence electron concentration, e/a , in Fe-Ni alloys. With γ -Fe as a typical anti-Invar on one side and Ni a material with a "normal" thermal expansion on the other, one would expect the anti-Invar effect to disappear at some concentration of Ni when it is al-

loyed to Fe. At this concentration the AF-FM (LS-HS) MVI should no longer exist. For this purpose we have measured the thermal expansion of $\text{Fe}_x\text{Ni}_{100-x}$ alloys in their respective fcc stability ranges for $63 \leq x \leq 100$ at. % and examined the change in the size of the anti-Invar effect.

II. METHOD OF ANALYSIS OF $\alpha(T)$

Although the ground-state properties of the $3d$ metals and alloys can be adequately understood, a first-principles theory describing their thermal properties is not available. The problem becomes more complex in the event that a MVI exists as in the present case. In a previous study on $3d$ alloys we were able to discuss thermal properties using a two-level system based on the earlier hypothetical Weiss model.^{8,10} This had given a good description of the high-temperature anomalies in the specific heat and the thermal expansion. In a recent work⁹ we also used a similar model to understand the anti-Invar nature of γ -Fe, but this time with the support that a MVI in γ -Fe was a fact rather than a hypothesis. We use a similar approach here as well. The starting point is that the LS state and the HS state are separated by a small energy difference $\Delta\epsilon$, and thermal activation will lead to a mixture of these states. Although this method by no means describes the thermal evolution of the MVI, it provides a means for determining the size of the anti-Invar effect.

The observed thermal-expansion coefficient $\alpha(T)$ in anti-Invar is given by

$$\alpha(T) = \alpha_{\text{lat}}^{\text{LS}}(T) + \alpha_{\text{ex}}(T). \quad (1)$$

The first term, $\alpha_{\text{lat}}^{\text{LS}}(T)$, is approximately the lattice expansion of the pure LS state. It is determined from the Grüneisen relation,

$$\alpha_{\text{lat}}^{\text{LS}}(T) = \frac{c_V(T)}{3Q\{1 - K[E(T)/Q]^2\}^2}, \quad (2)$$

where c_V is the specific heat at constant volume, E is the internal energy, K is a constant associated with the indices of the Mie potential, and Q is a constant related to the Grün-

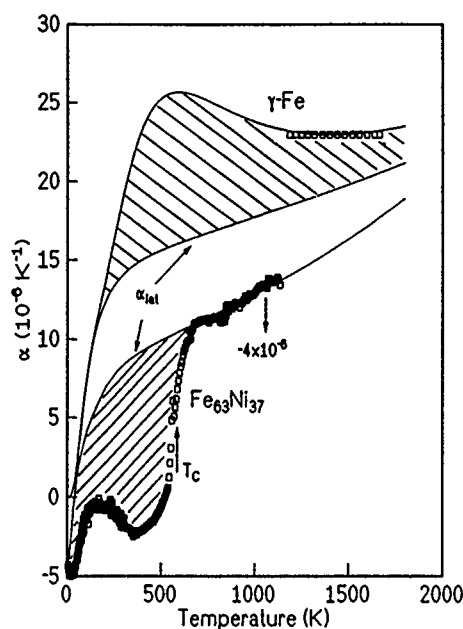


FIG. 1. The Invar in $\text{Fe}_{63}\text{Ni}_{37}$ and the anti-Invar effect in $\gamma\text{-Fe}$. Shaded areas show the associated volume magnetostriction. The ordinate for $\text{Fe}_{63}\text{Ni}_{37}$ is shifted by $-4 \times 10^{-6} \text{ 1/K}$. α_{lattice} denotes the lattice thermal expansion.

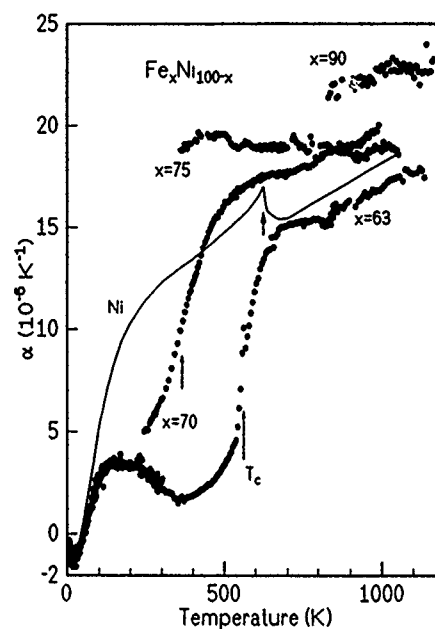


FIG. 2. $\alpha(T)$ of $\text{Fe}_x\text{Ni}_{100-x}$ for $x = 0, 63, 70, 75$, and 90 at. %. Arrows point to the Curie temperatures T_c of the samples which order ferromagnetically. The data for Ni have been shifted by $-1 \times 10^{-6} \text{ K}^{-1}$.

eisen constant γ . The second term in Eq. (1) is the excess thermal-expansion coefficient in a two-level system and is given by

$$\alpha_{\text{ex}}(T) = \frac{\Delta V}{3V_{\text{LS}}} \frac{\Delta \epsilon}{k^2 T^2} \frac{(g_{\text{LS}}/g_{\text{HS}}) \exp(\Delta \epsilon/kT)}{[1 + (g_{\text{LS}}/g_{\text{HS}}) \exp(\Delta \epsilon/kT)]^2}. \quad (3)$$

Here $\Delta V/V_{\text{LS}}$ is the relative volume difference between LS and HS states at 0 K. $\Delta \epsilon$ is the energy difference between the two states, $g_{\text{LS}}/g_{\text{HS}}$ is the degeneracy ratio, k is the Boltzmann constant, and T is the temperature.

III. EXPERIMENT

Samples of $\text{Fe}_x\text{Ni}_{100-x}$ with the concentrations $x = 63, 70, 75$, and 90 at. % were prepared by arc melting. They were then cut to 7-mm-long cylinders with a 6 mm diameter.

The thermal expansion of FeNi alloys was measured in their respective fcc stability ranges. Two capacitive dilatometers were used, operating in the temperature ranges $4.2 \leq T \leq 300 \text{ K}$ and $300 \leq T \leq 1000 \text{ K}$, respectively. The lower-temperature range measurements were made in a relative copper capacitance cell. The latter range was covered in a quartz push-rod-type cell. The coefficient of thermal expansion is calculated as the slope of consecutive data which were taken approximately 3 K apart in thermal equilibrium.

IV. RESULTS AND DISCUSSION

Figure 2 shows the results on $\alpha(T)$ in the fcc phases of $x = 0, 63, 70, 75$, and 90 at. %. The arrows mark the Curie temperatures T_c of the alloys which have FM order in the fcc state. $\alpha(T)$ of Ni was measured in order to demonstrate that the data for the alloys show no experimental artifact arising from experimental procedures. The data in the PM temperature range of the $x = 63$ at. % sample and Ni can be

described by Eq. (2). For $x \geq 70$ at. % $\alpha(T)$ in the PM range becomes more temperature insensitive with increasing Fe concentration, thus reflecting the anti-Invar effect. Therefore, one can conclude from this data that as the Invar concentration ($x = 65$ at. %) is approached from Fe-richer concentrations the anti-Invar effect disappears.

Attempting to analyze $\alpha(T)$ of alloys with $x \geq 70$ at. % only with Eq. (2) leads to unrealistic values of K and Q , hence to an unrealistic Grüneisen constant. Therefore, to ana-

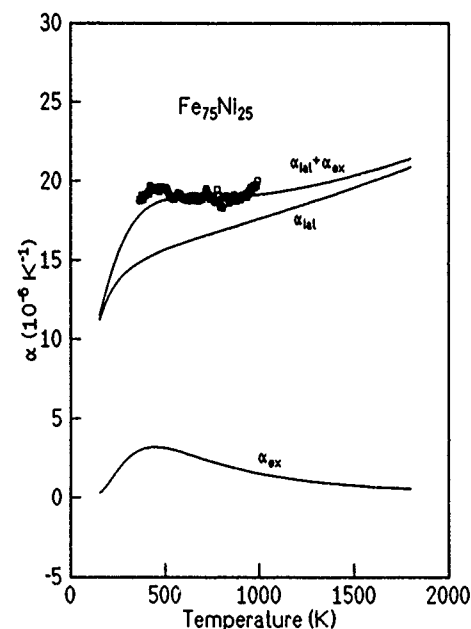


FIG. 3. The analysis of the excess and the lattice thermal expansions for the $x = 75$ at. % sample. The shaded area is the anti-Invar effect, which amounts to 0.77%. (Compare to $\gamma\text{-Fe}$ in Fig. 1.)

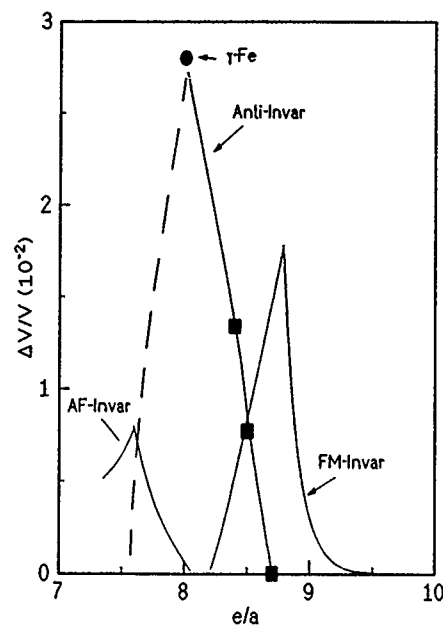


FIG. 4. Volume magnetostriction in AF Invar, FM Invar, and anti-Invar. The broken line is the anticipated behavior of anti-Invar on the AF side. The solid squares are the present data. The point for γ -Fe is from Ref. 9.

lyze the data for $x \geq 70$ at. % we first determine $\alpha_{\text{ex}}(T)$. This calculation is presented here for the $x = 75$ at. % sample. We estimate the values of $g_{\text{LS}}/g_{\text{HS}}$ and $\Delta\epsilon$, appearing in Eq. (3) from the e/a dependence of these quantities, determined from specific-heat measurements on fcc 3d alloys.^{8,9} $\Delta V/V_{\text{LS}}$ is estimated by interpolating between the value for γ -Fe, 0.7, and $x = 65$ at. %, where this quantity should vanish along with the disappearance of anti-Invar. There are therefore no adjustable parameters in Eq. (3). $\alpha_{\text{lat}}(T)$ is next determined to give the best fit to the data. Figure 3 shows the result of such an analysis. The curves in this figure are ex-

tended up to 1800 K which is near the melting point. The lack of data at these temperatures hinders a more accurate analysis, but nevertheless it allows for an estimation of the size of the anti-Invar effect. In this particular alloy the total volume enhancement amounts to 0.77%. A similar analysis for an alloy with $x = 80$ at. %, for which the data of an earlier measurement was used,⁸ yields 1.34 at. %. For $x = 65$ or 63 at. % there is no volume enhancement in the paramagnetic state.

The total volume enhancement in 3d systems as a function of e/a is plotted in Fig. 4. The curves for AF and FM Invar are adapted from Refs. 1 and 11. The broken line for $e/a < 8$ shows the anticipated behavior of anti-Invar on the AF side. The figure clearly demonstrates that the volume effects associated with anti-Invar can be larger than that in Invar.

ACKNOWLEDGMENTS

We are grateful to H. Bach for preparing the samples. Work was supported by Deutsche Forschungsgemeinschaft (SFB 166).

¹E. F. Wassermann, in *Ferromagnetic Materials V*, edited by K. H. J. Buschow and E. P. Wohlfarth (North-Holland, Amsterdam, 1990).

²E. F. Wassermann, *J. Magn. Magn. Mater.* **100**, 346 (1991).

³V. L. Moruzzi, *Phys. Rev. B* **41**, 6939 (1990).

⁴M. M. Abd-El Meguid and H. Micklitz, *Physica B* **161**, 17 (1989).

⁵V. L. Moruzzi, P. M. Marcus, and J. Kübler, *Phys. Rev. B* **39**, 6957 (1989).

⁶M. Uhl, L. M. Sandratskii, and J. Kübler, *J. Magn. Magn. Mater.* **103**, 314 (1992).

⁷W. Keune, T. Ezawa, W. A. A. Macedo, U. Glos, K. P. Schletz, and U. Kirschbaum, *Physica B* **161**, 269 (1989).

⁸W. Bendick, H. H. Ettwig, and W. Pepperhoff, *J. Phys. F* **8**, 2525 (1978).

⁹M. Acet, H. Zähres, E. F. Wassermann, and W. Pepperhoff, *Phys. Rev. B* (to be published).

¹⁰L. Kaufman, E. V. Clougherty, and R. J. Weiss, *Acta. Metall.* **11**, 323 (1963).

¹¹F. Richter and W. Pepperhoff, *Arch. Eisenhüttenwes* **47**, 45 (1976).

X-ray-absorption fine structure of selected R_2Fe_{17} nitrides

T. W. Capehart, R. K. Mishra, and F. E. Pinkerton

Physics Department, General Motors Research & Development Center, 30500 Mound Road, Warren, Michigan 48090-9055

X-ray-absorption fine structure from the rare-earth L_3 edges in $R_2Fe_{17}N_{3-x}$ ($R=Sm, Pr, \text{ or } Nd$), $x \sim 0.2$, establishes that these nitrides have 2.6 ± 0.6 nitrogen atoms bonded $2.54\text{--}2.57 \text{ \AA}$ from the rare-earth site. The observed enhancement of the nitrogen backscattering from magnetically oriented powders of $Sm_2Fe_{17}N_{3-x}$ establishes that between 80% and 100% of the nitrogen atoms occupy 9(e) sites of the $Sm_2Fe_{17}N_{3-x}$. No evidence is found for partial nitrogen occupancy of the 18(g) sites in $Sm_2Fe_{17}N_{3-x}$.

Compounds with the stoichiometry R_2Fe_{17} (R denotes rare earth) form for all the lanthanides, except lanthanum.¹ The structure of these compounds is a variant of the $CaCu_6$ structure with pairs of Fe atoms replacing one-third of the rare-earth atoms. Coey and Sun² discovered that interstitial nitrides can be prepared from the R_2Fe_{17} series, and that nitriding produces a remarkable increase in Curie temperatures.^{3,4} In general, the Curie temperatures for the resulting nitrides are approximately 700 K with only a weak dependence on the identity of the rare earth. The resulting nitrides have either the rhombohedral Th_2Zn_{17} or the hexagonal Th_2Ni_{17} structure depending on whether the rare earth is from the beginning or end of the lanthanide series. All the nitrides, except $Sm_2Fe_{17}N_{3-x}$, have basal-plane magnetocrystalline anisotropy.

X-ray-absorption fine structure (XAFS) investigations on randomly oriented powders of $Sm_2Fe_{17}N_{3-x}$ have been previously reported.^{5,6} While these studies concluded that N occupied the 9(e) sites in the Th_2Zn_{17} structure, they do not exclude the possibility of partial occupancy of other sites $2.54\text{--}2.56 \text{ \AA}$ from the rare-earth site. Neutron-diffraction studies on $Y_2Fe_{17}N_{3-x}$ and $Nd_2Fe_{17}N_{3-x}$ have also been reported.⁷ For Y nitride, neutron diffraction finds nitrogen occupies only the 9(e) sites. For $Nd_2Fe_{17}N_{3-x}$, however, the nitrogen is found to occupy both the 9(e) and 18(g) sites with maximal occupancies of 1.8 and 0.72 nitrogen atoms, respectively. Such a large dependence of the nitrogen site occupancy on the rare-earth site identity is unexpected; for example, the related $Nd_2Fe_{14}B$ structures are isomorphic, i.e., the structural parameters of these compounds are independent of the rare-earth species.

The existence of a second occupied nitrogen site in $Nd_2Fe_{17}N_{3-x}$ found by neutron diffraction prompted us to extend our previous EXAFS and x-ray appearance near-edge structure (XANES) studies on the technologically most interesting of the R_2Fe_{17} nitrides, $Sm_2Fe_{17}N_{3-x}$. In this work, we report measurements on magnetically oriented samples of $Sm_2Fe_{17}N_{3-x}$ to determine if there is significant partial occupancy of the 18(g) site in the Sm nitride. The EXAFS measurements on oriented samples provide a direct method to identify the plane(s) containing the N atoms, and a greater sensitivity to any partial N occupancy of the 18(g) sites in these systems. In addition, EXAFS and XANES measurements were made on unaligned samples of $Pr_2Fe_{17}N_{3-x}$ and $Nd_2Fe_{17}N_{3-x}$.

Polycrystalline powders of $R_2Fe_{17}N_{3-x}$ ($R=Pr, Nd, Sm$)

for this work were prepared following a procedure similar to that of Coey and Sun.² Details of our sample preparation of the Sm compounds have been given earlier.⁵ The ground powders had single-phase x-ray-diffraction patterns of the rhombohedral Th_2Zn_{17} structure (space group $R\bar{3}m$), with the lattice parameters given in Table I. Subsequently, a portion of each of the R_2Fe_{17} powders was heated in N_2 at 700–800 K for 16 h. The x-ray-diffraction peaks of these nitrated powders were shifted relative to those of the corresponding R_2Fe_{17} parent compound, consistent with the previous Th_2Zn_{17} structure, but with expanded lattice parameters. Also, a small amount of α -Fe was evident in the diffraction patterns. The parameters, given in Table I, are close to those previously reported by Buschow *et al.* for these nitrides.⁴ Samples for the measurements on aligned powders were made by suspending finely ground powders (~ 500 mesh) in paraffin. These samples were then placed in the field of an electromagnet to align the basal planes of these compounds in the same direction. Well-aligned samples were obtained by suspending these powders in melted paraffin and reversing the polarity of a ~ 15 kOe field several times.

X-ray-absorption spectra were measured initially on beamline A3 at the Cornell High Energy Synchrotron Source (CHESS), and repeated on beamline X11 at the National Synchrotron Light Source (NSLS) using Si(111) double-crystal monochromators. The L_3 -edge spectra from R_2Fe_{17} and $R_2Fe_{17}N_{3-x}$ are all dominated by a single peak near the absorption threshold similar to the spectra for the corresponding trivalent reference compounds. There were, however, small consistent differences in the L_3 -edge spectra between the parent R_2Fe_{17} compounds and their nitrides. First, the white line is higher and narrower in the nitrides. Second, the leading edge of the absorption spectrum for each nitride is shifted ~ 1 eV higher than its parent. The edge shifts produced by nitriding are analogous to the edge shifts caused by

TABLE I. Th_2Zn_{17} structure lattice parameters.

Compound	a (Å)	c (Å)
Pr_2Fe_{17}	8.5781	12.4509
$Pr_2Fe_{17}N_{3-x}$	8.7796	12.6237
Nd_2Fe_{17}	8.5638	12.4470
$Nd_2Fe_{17}N_{3-x}$	8.7635	12.6345
Sm_2Fe_{17}	8.5476	12.4354
$Sm_2Fe_{17}N_{3-x}$	8.7307	12.6300

oxidation, but are much smaller in magnitude.

The Fe *K*-edge XANES of these compounds also reflects an alteration of the Fe environment produced by nitriding. The near-edge threshold for R_2Fe_{17} is 0.4 ± 0.1 eV lower than the threshold for α -Fe. This suggests that, relative to α -Fe, there is a net electron transfer to the Fe. Assigning an approximate valence to Fe based on this shift is difficult. This is the result of the considerable variability in the rate with which 3*d* transition-metal edges shift with valence.⁸ Nominally, the threshold shifts for the 3*d* *K* edges are ~ 1 eV per unit valence,⁹ which suggests the average valence of the Fe sites in R_2Fe_{17} is anionically shifted by ~ 0.4 with respect to α -Fe. Indeed, this is qualitatively consistent with the valence of $-6/17$ that is anticipated from the formal rare-earth valence and the compound stoichiometry. The absorption thresholds of $R_2Fe_{17}N_{3-x}$ are shifted ~ 0.2 eV relative to their parents toward the α -Fe absorption thresholds. From this shift of the edge, it appears that Fe environment in the nitride is intermediate between its anionic state in R_2Fe_{17} and covalent state in α -Fe. We also note that the intensity of the pre-edge peak in α -Fe, $R_2Fe_{17}N_x$, and R_2Fe_{17} increases as the average volume of the Fe site decreases.

These XANES results imply a small negative charge transfer to the nitrogen for all three nitrides. These shifts imply that nitrogen is slightly anionic. While nitrogen cations are small, the covalent radius of nitrogen is 0.75 Å, and the anion is even larger. This steric consideration strongly suggests that for the R_2Fe_{17} lattice only the 9(*e*) and 18(*g*) sites are large enough to accommodate an interstitial nitrogen.

In the simplest approximation¹⁰ the EXAFS oscillations are given by

$$\chi = \sum_j \frac{N_j}{kr_j^2} F_j(k) \theta^{-\sigma^2 r_j^2 - 2r_j/\lambda} \sin(2kr_j + 2\theta_c + \theta_b), \quad (1)$$

where the summation extends over the coordination shells of the probed atom. For the *j*th component, N_j is the number of atoms in the shell, $F_j(k)$ the atomic backscattering amplitude, σ^2 the mean-square relative displacement¹¹ of the effective radius r_j , and $\theta_b(k)$ is the backscattering phase shift. The other factors determining $\chi(k)$ are the central atom phase shift $\theta_c(k)$ and the inelastic mean free path of the photoelectron λ . Due to the dependence of EXAFS on the chemical state of the atom, the most reliable determinations of bond distances and coordination numbers are made when the backscattering phase and amplitude functions are obtained from a chemically and structurally similar compound. In general, if the same atomic species occupies inequivalent lattice sites then the sum in Eq. (1) must be performed for each inequivalent site and averaged according to site multiplicity. In the Th_2Zn_{17} structure the rare earths occupy only one inequivalent lattice site [the 6(*c*)] while there are four inequivalent Fe sites. As a consequence, analysis of the rare-earth EXAFS is simpler and more direct than the Fe EXAFS.

Because of the close relationship between the parent compounds and these nitrides, the parent compounds are excellent models for the rare-earth backscattering shells in the nitrides. It is possible to isolate the R-N shell in $R_2Fe_{17}N_{3-x}$

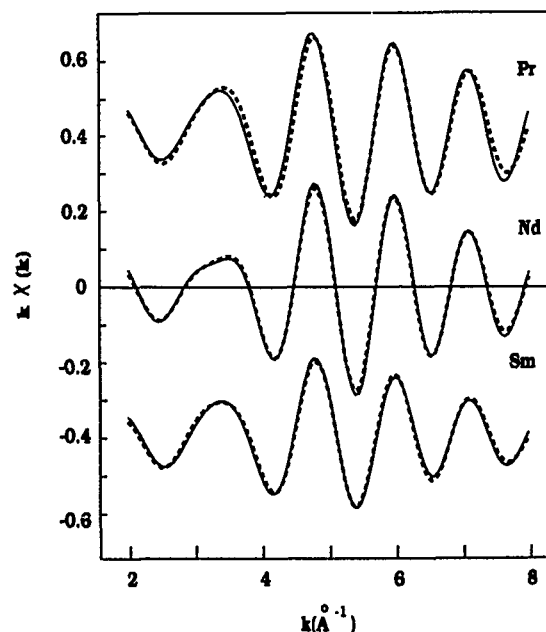


FIG. 1. Analysis of the filtered $\chi(k)$ EXAFS data from the first shell of randomly oriented powders of $R_2Fe_{17}N_{3-x}$ ($R=Pr, Nd, Sm$), using phase and backscattering amplitude functions from the parent compound for the R-Fe shell, and the rare-earth nitride for the R-N shell. The filtered data are given by the dotted lines, and the two shell fits are shown by the solid lines.

simply from the differences in the EXAFS oscillations in the following way: Since $f(k)$, $\theta_c(k)$, and $\theta_b(k)$ vary slowly with k , the phase difference in $\chi(k)$ due to a small (1%–2%) uniform lattice expansion, $r_j \rightarrow (1 + \epsilon)r_j$, can be accounted for by k rescaling $k \rightarrow k/(1 + \epsilon)$. By plotting $k^2\chi(k)$ for $k > 5$ Å⁻¹, which accentuates the Fe and rare-earth backscattering, and matching phases, an “average” expansion of the lattice can be readily determined. For the three sets of compounds we find that the lattice expansion determined by this procedure is very close to the average of the *c*- and *a*-axis expansions determined from x-ray diffraction.

We have analyzed the EXAFS data from the first shell of randomly oriented powders of $R_2Fe_{17}N_{3-x}$ using the phase and backscattering amplitude functions from the parent compound for the R-Fe shell, and the rare-earth nitride for the R-N shell. Since the central atom phase shifts of Pr and Nd are very similar, the Nd-N shell from NdN was used for analyzing the Pr compound. The R-N shell is not resolved from the first R-Fe shell in these nitrides, making it necessary to fit the Fourier-filtered data to a two-shell model. In general, both the parent compounds and the nitrides were Fourier filtered between 1.7 and 3.4 Å. Since the nitrogen backscattering contributes to the EXAFS only below 6 Å⁻¹, the uncertainties in this analysis are modestly large. We estimate the uncertainty in rare-earth–nitrogen shell radius and coordination number to be ± 0.02 Å and ± 1.0 , respectively. The fits to the filtered data are shown in Fig. 1, and the rare-earth–nitrogen shell radii and coordination numbers are reported in Table II.

A comparison of the Pr and Nd results to the earlier work on Sm shows only minor differences between the three systems: a small (0.03 Å) contraction of the rare-earth–

TABLE II. $R_2Fe_{17}N_x$ EXAFS results.

$R_2Fe_{17}N_{3-x}$	r_{R-N} (Å)	x
$Pr_2Fe_{17}N_{3-x}$	2.57 ± 0.02	0.5 ± 1.0
$Nd_2Fe_{17}N_{3-x}$	2.56 ± 0.02	0.5 ± 1.0
$Sm_2Fe_{17}N_{3-x}$	2.54 ± 0.02	0.2 ± 1.0

nitrogen shell between Pr and Sm, and a slight difference in the phase of the nitrogen backscattering (due to differences in the central atom phase shift).

Using oriented samples and utilizing the linear polarization of synchrotron radiation, we can further constrain the occupancy of the nitrogen site(s). To first order, the outgoing photoelectrons produced by the x ray follow a $\cos^2 \Theta$ distribution, where Θ is the angle between the polarization vector and the exit angle of the photoelectron. By using this cone as a "flashlight" to see an enhancement in backscattering from a particular species, it is possible to identify bond directions.

The (Fourier-filtered) difference in the EXAFS oscillations from magnetically aligned powders of the Sm_2Fe_{17} and $Sm_2Fe_{17}N_{3-x}$ oriented in the x-ray beam so the x-ray polarization was parallel to their basal planes is shown in Fig. 2. There is an enhancement of the intensity of the nitrogen backscattering, which is clearly evident in the difference $\chi(k)$ shown in Fig. 2. The backscattering for the oriented powder is enhanced by a factor of 1.6 ± 0.2 with respect to the randomly oriented powders. If all the nitrogen atoms are in the basal plane, i.e., in the 9(e) sites, the enhancement factor should be 1.5. For all nitrogen atoms in 18(g) sites the nitrogen backscattering should be diminished by a factor ~ 0.75 . Using the estimated uncertainty of the enhancement factor of ± 0.15 , the measured enhancement requires that $>80\%$ of the nitrogen atoms are in the basal planes containing the rare earth sites in these compounds, the 9(e) site. This is quite different from the neutron-diffraction results for the Nd compound where $\sim 40\%$ of the nitrogen was found in the 18(g) sites.

In summary, the small shifts observed in the rare-earth L_3 -edge and iron K -edge absorption thresholds between the parent R_2Fe_{17} compounds and their nitrides imply that nitrogen is nearly covalent in the nitrides. Based on the steric requirements of nearly covalent N, the only sites large enough to accommodate nitrogen are those of 9(e) and 18(g) symmetry. For $R_2Fe_{17}N_{3-x}$ the R-N shell radii range from 2.57 to 2.54 Å for $R=Pr, Nd$, or Sm. A composite estimate of the nitrogen occupancy from the three nitrides gives a R-N coordination of 2.6 ± 0.6 . The observed enhancement of the nitrogen backscattering from the oriented $Sm_2Fe_{17}N_{3-x}$ requires that $>80\%$ of the nitrogen occupies the 9(e) sites, though it is fully compatible with 100% occupancy of the 9(e) site. This is consistent with the structure

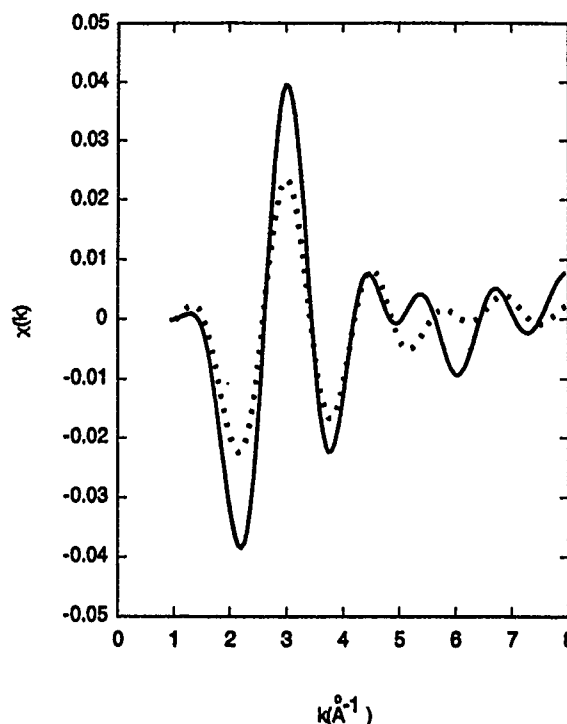


FIG. 2. A comparison of the Fourier-filtered difference between $Sm_2Fe_{17}N_{3-x}$ and the Sm_2Fe_{17} EXAFS oscillations $\chi(k)$ for magnetically aligned powders (solid line) and unaligned (dotted line).

found by neutron diffraction for the Y homologue of this series.

We thank CHESS and NSLS for the use of their facilities during these experiments. This research was carried out (in part) at the National Synchrotron Light Source, Brookhaven National Laboratory, which is supported by the U.S. Department of Energy, Division of Materials Science and Division of Chemical Sciences (D.O.E. Contract No. DE-AC02-76CH00016).

¹ K. H. J. Buschow, Rep. Prog. Phys. **40**, 1179 (1977).

² J. M. D. Coey and H. Sun, J. Magn. Magn. Mater. **87**, L251 (1990).

³ H. Sun, J. M. D. Coey, Y. Otani, and D. P. F. Hurley, J. Phys. Condensed Matter **2**, 6465 (1990).

⁴ K. H. J. Buschow, R. Coehoorn, D. B. de Mooij, K. de Waard, and T. H. Jacobs, J. Magn. Magn. Mater. **92**, 35 (1990).

⁵ T. W. Capehart, R. K. Mishra, and F. E. Pinkerton, Appl. Phys. Lett. **58**, 1395 (1991).

⁶ J. M. D. Coey, J. F. Lawler, H. Sun, and J. E. M. Allen, Appl. Phys. Lett. **xx**, xxx (1991).

⁷ S. S. Jaswal, W. B. Yelon, G. C. Hadjipanayis, Y. Z. Wang, and D. J. Sellmyer, Phys. Rev. Lett. **67**, 644 (1991).

⁸ F. W. Lytle and R. B. Gregor, Phys. Rev. B **37**, 1550 (1988).

⁹ J. Wong, F. W. Lytle, R. P. Messmer, and H. D. Maylotte, Phys. Rev. B **30**, 5596 (1984).

¹⁰ B. K. Teo, EXAFS: Basic Principles and Data Analysis, Inorganic Chemistry Concepts Vol. 9 (Springer, New York, 1986).

¹¹ G. Beni and P. Platzman, Phys. Rev. B **14**, 1514 (1976).

Exchange stiffness and magnetic anisotropies in bcc Fe_{1-x}Co_x alloys

X. Liu and R. Sooryakumar

Department of Physics, The Ohio State University, Columbus, Ohio 43210

C. J. Gutierrez and G. A. Prinz

Naval Research Laboratory, Washington, DC 20375

Brillouin scattering measurements from several bcc Fe_{1-x}Co_x epitaxial films are reported. The magnetic-field dependence of the spin-wave spectrum as well as the in-plane directional dependence of the surface magnon are determined. The saturation magnetization of the alloys was measured independently through superconducting quantum interference device magnetometry. Self-consistent fitting of the magnon dispersions determined from the separate Brillouin experiments provide values for the concentration dependence of the exchange stiffness D , the fourth-order crystalline cubic anisotropy K_1 , and surface anisotropies K_s and $K_{s,p}$. In agreement with ferromagnetic resonance data, K_1 is found to change sign for x beyond about 35 at. % while D steadily increases with cobalt concentration up to $x \sim 0.5$ and subsequently decreases in two Co-rich samples.

Despite tremendous recent progress, itinerant ferromagnets such as the 3d metals continue to provide challenges in understanding their electronic properties. The central problem remains that of electron correlations and their influence on various magnetic properties. On the one hand, magnetotransport¹ and existence of a Fermi surface² show that these electrons have a delocalized band-state character and display extended moment features. On the other, the Curie-type high-temperature magnetic susceptibility³ argues for localized atomlike behavior. It is important to recognize that these mutually opposite extremes are connected continuously by varying the relative strength of the electron-electron interaction U/W , where U and W are the intra-atomic Coulomb energy and bandwidth, respectively.

The recent successful growth of epitaxial bcc Fe_{1-x}Co_x films,⁴ that include elemental bcc Co (Ref. 5) and bcc Fe as end members, offers a unique opportunity to address some of the important issues relating to itinerant ferromagnets. The possibility to systematically vary a few critical parameters that influence the renormalization of bare interaction parameters and the occupation numbers in k space, allows for a study of their effects on the spin dynamics. Located toward the end of the 3d series, it is believed that the hcp phase of cobalt is more strongly correlated than bcc Fe.^{6,7} The bandwidth W of metastable bcc Co (Refs. 8 and 9) is approximately 1.5 eV smaller than that of hcp Co making this phase of Co one of the most strongly correlated 3d ferromagnets. Thus, in moving across the alloy series the strength of the correlation is directly varied from the strongly correlated bcc Co limit to the weak ferromagnet bcc Fe.

It is special that all Fe_{1-x}Co_x films ($0 \leq x \leq 1$) are grown in registry with the same substrate and stabilized in the bcc phase.⁴ Hence, the series is characterized by one crystal structure and essentially uniform lattice parameters. This feature thus allows for direct comparison of the magnetic properties of different alloys, without modeling the uncertain effects of lattice spacings and crystal structures.

A correct description of dynamical spin fluctuations in the intermediate regime between local and itinerant magne-

tism is essential to a unified theory, and thus the spin susceptibility $X(q, \omega)$ is a key parameter.¹⁰ The imaginary part of $X(q, \omega)$ is observed by light scattering from spin waves where the energy of long-wave magnons is given by $\hbar\omega = Dq^2$. For small q and ω , D can be calculated rigorously and its sign and magnitude are a direct measure of the stability of the ferromagnetic state.¹¹ D is also of interest, since the variation of the Curie temperature with composition seems to be largely controlled by the low-temperature value of D .¹² Magnetic anisotropies, both surface and volume contributions, also play a crucial role in the stabilization of long-range ferromagnetic order in laminar geometries.

In this article we report on Brillouin scattering measurements from thermal magnons in five Fe_{1-x}Co_x films (Table I). The magnetic-field dependence and anisotropies of the spin-wave characteristics relative to the crystalline axes are utilized to determine $D(x)$ and the anisotropy constants K_1 (volume magnetocrystalline), $K_{s,p}$ (surface in plane) and K_s (surface out of plane). With increasing Co concentration ($0.3 \leq x \leq 0.47$) D is found to increase from 470 to 800 meV Å² and then decrease in two samples for $x > 0.6$. We also determine that K_1 changes sign from being positive to negative at $x \sim 0.35$, a result consistent with ferromagnetic resonance measurements.⁴

The Fe_{1-x}Co_x (001) films several hundred angstroms thick were fabricated by molecular-beam epitaxy on ZnSe (001)-epilayered GaAs (001) substrates. The films were characterized by electron diffraction, Auger spectroscopy, and the final alloy composition measured by x-ray fluorescence.⁴ The average magnetic moments of the films were determined at room temperature with a superconducting quantum interference device (SQUID) magnetometer.

The Brillouin measurements were performed at room temperature utilizing up to 100 mW of p -polarized $\lambda = 514.5$ nm laser light.¹³ Two independent Brillouin experiments were carried out on each film. In one, the field dependence of the bulk ω_b and surface ω_s magnon frequencies was measured, since their response is particularly sensitive to D . In a second series of measurements, H was rotated in finite steps

TABLE I. Properties of bcc $\text{Fe}_{1-x}\text{Co}_x$ films deduced from Brillouin and magnetometry measurements. The alloy samples are (001) oriented and grown on ZnSe-epilayered GaAs. The pure bcc Co film was grown directly on GaAs and (110) oriented. The value for D for the latter film is that reported in Ref. 13, with the value of K_1 from Ref. 14.

	bcc Co	$\text{Fe}_{0.32}\text{Co}_{0.68}$	$\text{Fe}_{0.53}\text{Co}_{0.47}$	$\text{Fe}_{0.63}\text{Co}_{0.37}$	$\text{Fe}_{0.7}\text{Co}_{0.3}$
Thickness (\AA)	357	800	210	170	225
$4\pi M$ (kG)	15.5	18.1 ± 0.2	17.0 ± 0.3	20.1 ± 0.4	19.7 ± 0.2
$\gamma/2\pi$ (GHz/kG)	3.02 ± 0.03	3.03 ± 0.03	3.40 ± 0.05	3.20 ± 0.05	3.00 ± 0.03
K_1 (10^5 erg/cm ³)	-6.6	0.0 ± 0.1	-1.8 ± 0.3	-1.2 ± 0.2	2.0 ± 0.2
K_s (erg/cm ²)	-1.7	-1.5 ± 0.2	-0.21 ± 0.05	-0.54 ± 0.02	0.15 ± 0.02
$K_{s,p}$ (erg/cm ²)		0.00 ± 0.02	-0.06 ± 0.02	-0.04 ± 0.02	0.05 ± 0.01
D (meV \AA^2)	325 ± 40	476 ± 15	800 ± 50	530 ± 17	470 ± 14

away from the [100] axis by an angle ϕ_H and the magnon frequencies determined. These experiments provide for the magnetic anisotropies. Results for the spin-wave stiffness previously determined¹³ from pure bcc (110) Co films grown directly on to GaAs substrates are also included in the following section. Thus comparing its surface anisotropies with those of other samples should be done with caution.

Figure 1 shows a series of Brillouin spectra from $\text{Fe}_{0.53}\text{Co}_{0.47}$ in different applied magnetic fields. The strongest feature S in the spectra is the surface mode ω_s . With increasing H , ω_s increases steadily. The weaker peak at higher frequency shifts is the first bulk magnon ω_{B_1} . The corresponding spin-wave frequencies are plotted as a function of H in the inset to Fig. 1. The solid lines are a fit to the field dependence data based on the analysis discussed below. Figure 2 shows spectra of the surface mode from $\text{Fe}_{0.53}\text{Co}_{0.47}$ as a function of ϕ_H at $H=2$ kG. Reflecting magnetic anisotropies in the films, ω_s displays an oscillatory behavior with ϕ_H that is summarized in the inset to Fig. 2. The solid

curve is the result of calculations presented below. Similar Brillouin spectra with comparable quality of fits were obtained from the other samples. The results for M , the saturation magnetization, as determined from SQUID magnetometry, are summarized in Table I.

The Brillouin data for the H and ϕ_H dependence are utilized self-consistently to determine the important spin-wave parameters in $\text{Fe}_{1-x}\text{Co}_x$. The field-dependent data were analyzed as detailed in our previous studies.¹³ Briefly, we utilize Maxwell's equations and the equation of motion of M . Boundary conditions related to the continuity of the normal and in-plane magnetic fields at the film interfaces as well as the general exchange boundary conditions¹³ $\mathbf{M} \times (\nabla_{\text{M}} E_{\text{surf}} - D \partial \mathbf{M} / \partial \mathbf{n})$ where E_{surf} is the surface anisotropy energy density and \mathbf{n} the unit vector normal to the film are enforced. The resulting set of homogeneous equations yield nontrivial solutions only if the corresponding determinant is zero. The

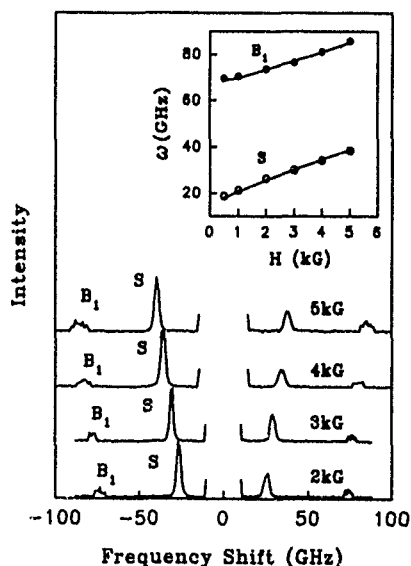


FIG. 1. Brillouin spectra of $\text{Fe}_{0.53}\text{Co}_{0.47}$. The magnetic field H was directed along [100]. The angle of incidence was 21° . The inset shows the surface ω_s and first bulk ω_{B_1} spin-wave frequencies as a function of H . The solid lines are a fit using our model.

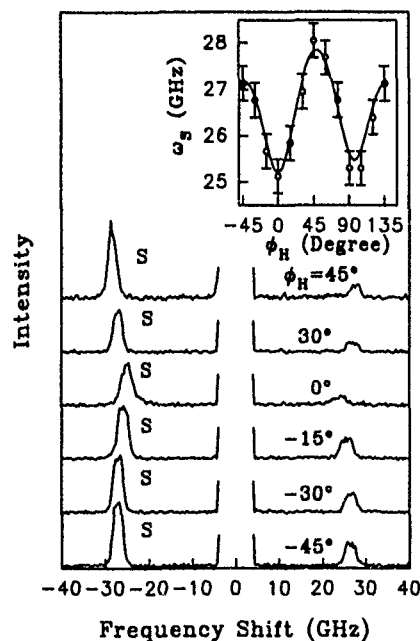


FIG. 2. Brillouin spectra of $\text{Fe}_{0.53}\text{Co}_{0.47}$ as a function of ϕ_H , the angle of the magnetization direction with respect to [100]. The measurement was done at $H=2$ kG and the angle of incidence was 21° . The inset summarizes the oscillatory behavior of $\omega_s(\phi_H)$. The solid line is a fit to the data.

determinant is employed in an iterative scheme where D , γ , K_1 , $K_{s,p}$, and K_s are varied to satisfy the condition of a vanishing determinant. The field dependence of ω_B and ω_s is most sensitive to D and γ .

The anisotropy constants have a strong influence on $\omega_s(\phi_H)$ and the ϕ_H dependence can be derived from the free-energy density to yield, for $qd \ll 1$, the expression¹⁵

$$\omega_s^2 = \frac{\gamma^2}{M^2} f_{\theta\theta} f_{\phi\phi} + 2\pi\gamma^2 \frac{f_{\theta\theta} + f_{\phi\phi}[1 + 2/(qd)] + 4\pi M^2}{1 + 1/(qd)}, \quad (1)$$

where, for (001) growth,

$$f_{\theta\theta} = MH \cos(\phi - \phi_H) + K_1(4 \sin^4 \phi - 4 \sin^2 \phi + 2)$$

$$+ \frac{4}{d} [K_s - K_{s,p} \cos^2(\phi - \phi_0)],$$

$$f_{\phi\phi} = MH \cos(\phi - \phi_H) + K_1(16 \sin^4 \phi - 16 \sin^2 \phi + 2)$$

$$+ \frac{4}{d} \{K_s - K_{s,p} \cos[2(\phi - \phi_0)]\}.$$

$f_{\theta\theta}$ and $f_{\phi\phi}$ are second derivatives of the free-energy density with respect to θ and ϕ , evaluated at the equilibrium angles. θ is the polar angle of M with respect to [001] and ϕ the azimuth angle with respect to [100]. ϕ_0 is the tilting angle of $K_{s,p}$ with respect to [100], q the in-plane magnon wave vector, and d the film thickness.

Dispersion of the $\omega(H)$ magnon branches is obtained from the numerical iteration scheme and provides excellent fit to the data. For example, calculations for $\text{Fe}_{0.53}\text{Co}_{0.47}$ are shown as solid lines in the inset to Fig. 1. Similarly data for $\omega_s(\phi_H)$ are fitted utilizing Eq. (1). The parameters K_1 , K_s , $K_{s,p}$, and ϕ_0 were used iteratively to provide the best fit to the $\omega_s(\phi_H)$ data. The anisotropy constants thus deduced agreed, within the error bars, with those values determined from the $\omega(H)$ behavior. A typical fit for $\omega_s(\phi_H)$ is shown in Fig. 2. The resulting parameters are listed in Table I.

Although elemental bcc Fe is ferromagnetic, fcc Fe is antiferromagnetic as is the neighboring element Mn. Thus, Fe is on the boundary between ferromagnetism and antiferromagnetism. The increasing values for D determined in the Fe-rich $\text{Fe}_{1-x}\text{Co}_x$ alloys indicate an intrinsic stability of ferromagnetism in these alloys. The variation of D with composition in bulk alloys of Fe with a limited Co concentration ($x \leq 0.50$) was measured by neutron scattering in 1965.¹⁶ While our values for D are generally consistent with these measurements for high Fe concentrations, D for the $x \sim 0.5$ sample deduced from the present study is about 60% larger. The reason for this deviation is unclear, and may be related to differences in sample quality; no details of structural or magnetic characteristics of the alloys utilized in Ref. 16 are available. The decrease in D we find for the $x = 0.68$ and $x = 1$ films suggest that, if the Curie temperature is largely determined by spin-wave excitations, T_c is decreasing in this Co concentration regime.

Model band calculations by Edwards and Muniz¹¹ yield an explicit formula for D for an alloy with varying electron concentrations. The theory has been applied¹⁷ to $\text{Fe}_{1-x}\text{Co}_x$ and predicts an increase in D of over 50% from the pure Fe value to that in $\text{Fe}_{0.5}\text{Co}_{0.5}$ and thus is qualitatively in agreement with our measurements. However, reasons for the decreasing trend in the measured magnitude of D for the two Co-rich films ($\text{Fe}_{0.32}\text{Co}_{0.68}$ and bcc Co), which is similar to reports on the dependence of D on x from bulk $\text{Fe}_{1-x}\text{Cr}_x$ alloys,¹⁶ are not readily apparent. Qualitative differences as $x \rightarrow 1$ in the local minority and majority density of states from which the local moments are derived are particularly relevant. Moreover, what effect do the strong electron correlations expected in bcc Co play in the spin-wave stiffness D ? Such questions have been addressed by Callaway and Wang,¹⁰ who considered the effect of electron correlations on D using spin-dependent local exchange plus correlation potential of a ferromagnetic electron gas. It is shown that in this simple, though unrealistic, model correlations do lead to a substantial reduction in D . In real correlated metals such as bcc cobalt, the reductions should continue to be present, but their magnitude is unknown.

In summary, Brillouin measurements on $\text{Fe}_{1-x}\text{Co}_x$ alloys have provided the composition dependence of the exchange stiffness, the cubic and surface anisotropy constants. $D(x)$ increases steadily until $x \sim 0.5$ beyond which it is found to decrease. The composition dependence of K_1 is strong and changes sign around $x \sim 0.35$. These measurements of $D(x)$ and $K_1(x)$ in well-characterized $\text{Fe}_{1-x}\text{Co}_x$ alloys should enable testing current first-principle calculations on spin fluctuations in the regime between local and itinerant magnetism and magnetic anisotropies without being burdened by extraneous issues such as structural and lattice constant modifications.

Work at OSU was supported by the NSF and that at NRL by the Office of Naval Research.

¹R. V. Coleman, W. H. Lowrey, and J. A. Polo, Phys. Rev. B **23**, 2491 (1981).

²A. Marshall, D. D. Pilgram, and G. G. Lonzarich, J. Phys. (Paris) **8**, 55 (1988).

³S. Arajs and R. V. Colin, J. Phys. Chem. Solids **24**, 1233 (1963).

⁴C. J. Gutierrez, J. J. Krebs, and G. A. Prinz, Appl. Phys. Lett. **61**, 2473 (1992).

⁵G. A. Prinz, Phys. Rev. Lett. **54**, 1051 (1985).

⁶W. Nolting, W. Borgiel, V. Dose, and Th. Fauster, Phys. Rev. B **40**, 5015 (1989).

⁷A. M. Oles and G. Stollhoff, Phys. Rev. B **29**, 314 (1984).

⁸Ph. Houdy et al., J. Appl. Phys. **69**, 5667 (1991).

⁹G. A. Prinz et al., J. Appl. Phys. **57**, 3024 (1985).

¹⁰J. Callaway and C. S. Wang, J. Phys. F **5**, 2119 (1975); D. M. Edwards and M. A. Rahman, J. Phys. F **8**, 1501 (1978).

¹¹D. M. Edwards and R. B. Muniz, J. Phys. F **15**, 2339 (1985).

¹²E. P. Wohlfarth, in *Quantum Theory of Atoms, Molecules and the Solid State*, edited by P. Lowdwin (Academic, New York, 1966), p. 485.

¹³J. Karanikas, R. Sooryakumar, B. Jonker, and G. Prinz, J. Appl. Phys. **69**, 6120 (1991).

¹⁴G. A. Prinz, C. V. Vittoria, J. J. Krebs, and K. B. Hathaway, J. Appl. Phys. **57**, 3672 (1985).

¹⁵B. Hillebrands, P. Baumgart, and G. Guntherodt, Phys. Rev. B **36**, 2450 (1987).

¹⁶R. D. Lowe et al., Phys. Rev. Lett. **14**, 698 (1965).

¹⁷R. B. Muniz, J. F. Cooke, and D. M. Edwards, J. Phys. F **15**, 2357 (1985).

Approach to the electronic structure of antiferromagnets

J. Callaway, D. G. Kanhere,^{a)} and A. Kolchin

Department of Physics and Astronomy, Louisiana State University, Baton Rouge, Louisiana 70803-4001

A study of a simple band model of a commensurate, two-dimensional antiferromagnet is briefly described. A self-consistent calculation shows a transition from a paramagnetic to a metallic antiferromagnetic state when an interaction is stronger than a critical value. The transition is accompanied by a change in size (large to small) of the Fermi surface. An insulating state may be obtained if there is exactly one electron per site.

I. INTRODUCTION

Although density functional theory is expected to give an exact description of the ground state of a system of electrons, calculations based on the local spin density approximation (LSDA) frequently give quite unsatisfactory results for antiferromagnetic insulating, transition-metal compounds.^{1,2} In some cases (CoO, La₂CuO₄, for example), the materials are predicted to be metallic, contrary to fact. In other cases (MnO, NiO) which are predicted to be insulating at $T=0$, the gap is too small, and the magnitude of the local moment is too small. Several different procedures have been advocated to avoid these difficulties: One can employ a model Hamiltonian approach which contains parameters representing LSD bands combined with other terms of the Hubbard type to represent short-range electron interactions. The methods of many-body theory can then be employed to obtain a more satisfactory description of the electronic structure.³ The self-consistent inclusion of a self-interaction correction has been proposed as a method for modifying the LSDA itself.⁴ However, the bands resulting from these calculations do not appear to agree well with results of photoemission measurements. Another approach modifies the LSDA energy functional by the addition of two Hubbard-like, orbital-dependent terms.⁵

Here we propose another procedure, similar to that of Anisimov and co-workers,⁵ but intended to retain what we consider to be an important feature of the LSDA, independence of an orbital basis. Specifically, we add to the exchange correlation potential of the standard LSDA, a "magnetic pseudopotential" which is determined from the spin density in the magnetic state. The pseudopotential contains an arbitrary constant which is intended to be adjusted so that some important calculated property, such as a spin moment, or an energy gap, agrees with experiment. Since the pseudopotential involves the spin density, a self-consistent calculation is required.

In this article we report the application of this procedure to a simple model, reserving the question of its utility in quantitative investigations of real materials to a subsequent publication.

II. MODEL

We discuss a simple two-dimensional (square) antiferromagnet in a two-sublattice approximation. Spiral, incommensurate, and disordered systems are not considered. We use for the ordinary potential of the chemical lattice

$$V(\cos 2\pi x/a + \cos 2\pi y/a), \quad (1)$$

where a is the chemical lattice constant. We investigate the possible establishment of an antiferromagnetic state by an interaction (the magnetic pseudopotential),

$$4U\rho_{-\sigma}(K_1)\cos \pi x/a \cos \pi y/a. \quad (2)$$

This term is added to the Schrödinger equation for electrons of spin σ ; a corresponding term which is, however, proportional to $\rho_{\sigma}(K_1)$ is added to the corresponding equation for spin $-\sigma$. The quantity K_1 is the magnitude of the smallest reciprocal lattice vector of the magnetic structure. A consequence of introducing the potential (2) is to add a term to the energy (i.e., to the exchange correlation functional),

$$N(K_1)U\rho_{\sigma}^2(K_1), \quad (3)$$

where $N(K_1)$ is the number of wave vectors in the star of K_1 (4 in the present example).

The calculation of the band structure with the use of Eq. (2) has to be made self-consistently, since it involves $\rho_{-\sigma}(K_1)$, which has to be obtained from the wave functions. Two features which result from the self-consistency requirement deserve comment as follows.

(i) The model obeys the theorem of Kohn and Nettel.⁶ In general, an antiferromagnetic solution can arise self-consistently in systems of two and three dimensions only for U greater than some minimum value. This does not apply in one dimension, and these are exceptions for band structures with special features, such as perfect nesting. In this respect, the present model differs significantly from the usual nearest-neighbor tight binding band often employed in the study of high- T_c superconductors, for which any repulsive Hubbard interaction, no matter how weak, leads to an antiferromagnetic state.

(ii) The model is not equivalent to the imposition of a staggered magnetic field, a device which has already been employed in some LSDA calculations⁷ and can also lead to antiferromagnetism. In the present case, the interaction involves a Fourier coefficient of the spin density. This Fourier coefficient depends on both the angular and the radial variation of the spin density. In contrast, a magnetic field couples only to the net spin excess on the site. We believe our approach is more flexible and capable of extension in that additional pseudopotential parameters may be introduced if desired. It is also more complicated because self-consistency is

^{a)}Permanent address: Department of Physics, University of Poona, Pune 411007, India.

required. Whether these differences in principle will lead to significantly different results remains to be determined by calculations for physical materials.

III. RESULTS

We summarize the essential results of our calculations on the two-dimensional model below. It is hoped to publish a more complete account elsewhere.⁸ First, we consider the half-filled band case, one electron per site.

In this case, as U is increased from zero, nothing happens until a critical value U_c is reached. At this point, antiferromagnetism develops but the system remains metallic. A gap develops around the point $(\pi/2, \pi/2)$ in the two-dimensional Brillouin zone which gradually diminishes along the diagonal line to $(\pi, 0)$. The lowest state at $(\pi, 0)$ is doubly degenerate. There is a pocket of holes around $(\pi, 0)$ and an electron pocket in the second band around $(\pi/2, \pi/2)$. As U is increased further, the system becomes insulating. The transition between antiferromagnetic metal and antiferromagnetic insulator occurs when a nondegenerate state in the third band falls below the doubly degenerate state. This causes a reconnection of the band structure. The lowest band is cut off from the others and is completely occupied. As U is further increased, the width of the occupied band decreases rapidly. Although the model is a band model, it is natural to describe the large U system as localized.

It is convenient, in presenting quantitative results, to remove the lattice constant from the problem by modifying the usual Rydberg atomic units so that the unit of energy is $(4\pi^2/a^2)Ry$, a being the lattice constant in Bohr units. One may observe that $2\pi/u$ is not very far from unity for many physical systems, so that for qualitative purposes, energies are roughly Rydbergs. The values we quote for U and V below are in these units.

Now we consider occupancies n_e per site different from 1. For small values of n_e the system is nonmagnetic. As n_e increases, there is a transition to an antiferromagnetic but still metallic state. In this state, the Fermi surface, which is shown in Fig. 1, comes into contact with the boundary of the Brillouin zone. The portion of the Fermi surface in contact with the zone boundary effectively disappears since there is an antiferromagnetic gap on the boundary. The Fermi surface consists of pockets of holes around the zone corners, which fill in as $n_e \rightarrow 1$. The value of the hole doping $\delta = 1 - n_e$ at which the transition between antiferromagnetic and paramagnetic states occurs depends on both U and V [the strength of the ordinary potential Eq. (1)]. In the case shown in Fig. 1, the transition occurs at about $n_e = 0.73$.

A diagram showing the critical value U_c as a function of n_e is presented in Fig. 2. This has been computed for a relatively small value of V (0.15). We see that U_c is rather flat as n_e decreases from 1. The curve turns up at about $n_e = 0.8$, which is close to the value $\pi/4$ at which a free-electron Fermi circle would come into contact with the (magnetic) zone boundary. For n_e smaller than this, U_c rises rapidly because large distortion of the free-electron Fermi circle is required to establish an antiferromagnetic state.

The value of the "hole" concentration required cause a transition to a nonmagnetic state in this example (≥ 0.2) is

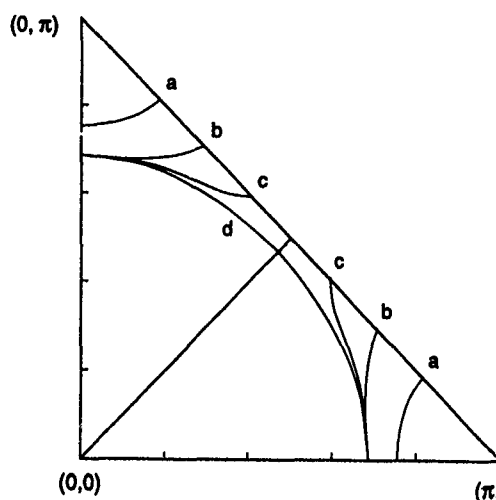


FIG. 1. Fermi "surfaces." Two irreducible wedges are combined to show symmetry. Curves: (a) $n_e = 0.90$; (b) $n_e = 0.80$; (c) $n_e = 0.75$; (d) $n_e = 0.72$. Parameters: $V = 0.15$, $U = 0.55$.

much larger than that for which it occurs in some cuprate superconductors; however, alternative parameters can readily be found for which the critical value of $\delta(\delta_c)$ is much smaller. As examples, we note that for $V = 0.5$ and $U = 1.6$, it occurs for $\delta_c \approx 0.07$, while for $V = 0.5$ and $U = 1.5$, $\delta_c = 0.01$. In general, when V increases, the curve of U_c vs n_e becomes steeper.

Luttinger's theorem⁹ asserts that the volume enclosed by the Fermi surface in an interacting system is the same as the volume enclosed by the Fermi surface in a noninteracting system of the same n_e . However, this theorem does not apply when there is a change in the spatial periodicity. This does change when antiferromagnetism disappears.

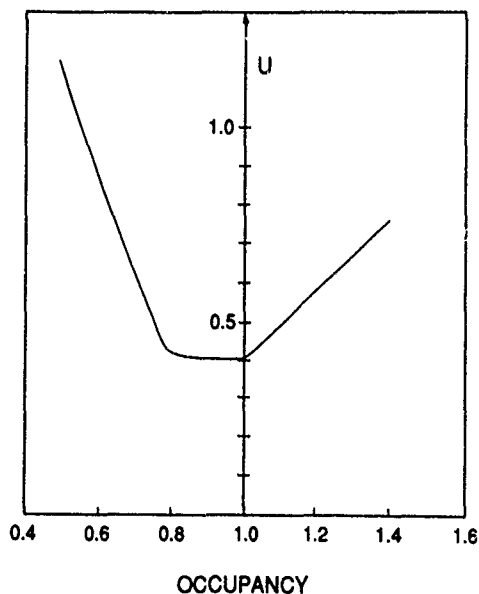


FIG. 2. The critical potential strength for a transition from a paramagnetic to a metallic antiferromagnetic state as a function of occupancy n_e . This diagram was calculated for $V = 0.15$. The antiferromagnetic insulating phase occurs only for $n_e = 1$ and $U > 0.46$.

An n_e increases beyond 1, qualitatively similar but quantitatively different behavior occurs. Elliptical electron pockets in the second band are formed around the point $(\pi/2, \pi/2)$. These expand toward X . Ultimately, the pockets reach X , antiferromagnetism disappears, and a large Fermi surface reappears. As n_e increases still further toward 2, the Fermi surface changes to holelike, corresponding to a nearly full band.

In summary, we have explored a simple, self-consistent band model which exhibits a transition between a paramagnetic and an antiferromagnetic state when an interaction is stronger than a critical value. The transition is accompanied by a change in size (large to small) of the Fermi surface. If there is exactly one electron per site, an insulating state may be formed. We believe this approach may be readily generalized to apply to realistic electronic structure calculations. Obviously, the utility of our approach in realistic calculations will depend on whether it is possible to obtain agreement with experiment with the use of a small number (one or two) magnetic pseudopotential parameters. This remains to be tested.

ACKNOWLEDGMENTS

This work was supported in part by the National Science Foundation under Grant No. DMR-91-20166. D.G.K. acknowledges the University of Poona for a grant of study leave.

- ¹T. Oguchi, K. Terakura, and A. R. Williams, Phys. Rev. B **28**, 6443 (1983); K. Terakura, T. Oguchi, A. R. Williams, and J. Kübler, *ibid.* **30**, 4734 (1984).
- ²L. F. Mattheiss, Phys. Rev. Lett. **58**, 1035 (1987); J. Yu, A. J. Freeman, and J. H. Xu, *ibid.* **58**, 1035 (1987).
- ³J. B. Grant and A. K. McMahon, Phys. Rev. B **46**, 8440 (1992).
- ⁴A. Svane and O. Gunnarson, Phys. Rev. Lett. **65**, 1148 (1990).
- ⁵V. Anisimov, J. Zaanen, and O. K. Andersen, Phys. Rev. B **44**, 943 (1991).
- ⁶W. Kohn and S. J. Nettel, Phys. Rev. Lett. **5**, 8 (1960).
- ⁷T. C. Leung, X. W. Wang, and B. N. Harmon, Phys. Rev. B **37**, 384 (1988).
- ⁸J. Callaway and D. G. Kanhere (to be published in Phys. Rev. B).
- ⁹J. M. Luttinger, Phys. Rev. **119**, 1153 (1960).

Magnetization density in URu₂Si₂ and URh₂Si₂

Alessandra Continenza and Patrizia Monachesi
Dipartimento di Fisica, Università dell'Aquila, I-67100 L'Aquila, Italy

The magnetic properties of the isostructural compounds URu₂Si₂ and URh₂Si₂ are compared in order to ascertain the different role played by Ru vs Rh. The total magnetic moment, obtained by spin-polarized electronic calculations with the full potential augmented plane-wave method within local spin-density approximation, agrees quite satisfactorily with the measured one in URh₂Si₂, whereas it is orders of magnitude too big in URu₂Si₂. However, important differences are found among the two compounds: These are the substantial contribution to the total magnetic moment of negative *d* spin polarization and the larger radial extension and asphericity of the magnetization density (in two crystal planes) in the Ru compound compared to the Rh compound. Also, the *f* positive spin-polarization density on U differs in the two compounds. This should result in different magnetic form factors in diffraction experiments.

URu₂Si₂ and URh₂Si₂ form in the tetragonal ThCr₂Si₂ structure whose atomic coordination is shown in Fig. 1. Both compounds order with a simple antiferromagnetic (AFM)¹⁻³ stacking along the *c* axis and their effective magnetic moment at high temperature is close to that of the U⁴⁺ ion. However, besides the structural similarities in the paramagnetic and ordered phases, the two compounds show dramatically different behavior below *T_N*.

The measured magnetic moment is $\approx 0.03\mu_B/\text{f.u.}$ and $1.96\mu_B/\text{f.u.}$ below *T_N*=17.3 and 138 K in URu₂Si₂ (Ref. 2) and URh₂Si₂,³ respectively. Moreover, URu₂Si₂ is a heavy-fermion antiferromagnet (specific-heat coefficient $\gamma=180$ mJ/mol K²), becomes a superconductor^{2,4} below *T_c* ≈ 1.2 K, and shows several other peculiarities in the specific heat, thermal expansion,⁵ magnetic excitations,¹ and susceptibility.⁶

Tentative explanations for the phenomenology of URu₂Si₂ have been given in terms of crystal field⁷ or quadrupolar order,^{6,8} but none is thoroughly consistent with all the experimental observations at the time. On the other hand, none of the anomalies found in URu₂Si₂ has been observed in URh₂Si₂, whose low-temperature behavior fits in the trend of other isostructural compounds.³

Presently, we undertake *ab initio* electronic structure calculations for the two compounds to investigate the different role played by Ru compared to Rh in the paramagnetic and ordered phases. Electronic effects due to the valence configuration of the metallic ion seem to be of extreme importance as suggested by magnetization measurements⁹ on polycrystals of URu_{1-x}Rh_xSi₂. In the ternary compound the behavior of *T_N* versus concentration changes drastically for values of *x* that do not affect the volume considerably. This behavior reminds us of the transition from a magnetic to a moment-reduced Kondo state [e.g., CeAg (Ref. 10)], due to the increase¹¹ of the Anderson hybridization.

The self-consistent calculations are made with a full potential augmented plane-wave (FLAPW) method¹² within the local spin-density approximation¹³ (LSDA). We use for both compounds the lattice constants² of URu₂Si₂, *a*=4.124 Å and *c*=9.582 Å, the actual volume difference among the two compounds amounting to $\approx 1\%$.

Numerical results in the paramagnetic state yield, at *E_F*,

a dominant density of states (DOS) *n_f* with *f* character on U and *d* character on the transition-metal ion, in both compounds (*n_f* is of the order of 4 states/eV U ce other *l* states as well as Si states contribute negligibly at *E_F* in both cases. The integrated density of occupied states amounts to about 2.8, 2.7 el/U for *f* states and 6.5 el/Ru, 7.5 el/Rh for *d* states in URu₂Si₂ and URh₂Si₂, respectively. The Stoner factor in the paramagnetic phase is found to be equal to 1.0 in URh₂Si₂ and to 0.88 in URu₂Si₂.

There are differences among the two compounds in the *f* and *d* density of states close to *E_F*. Worthy of notice in URu₂Si₂ is the occurrence of a partial splitting of the *f* DOS in a higher peak above and a lower peak below *E_F*. The latter has a ≈ 1 -eV-wide resonance below *E_F* with a high peak of *d* states from Ru.

The spin-polarized calculations are done in the ferromagnetic configuration for both compounds. Although not the ground state, the ferromagnetic phase is obtained in the presence of an external field.¹⁴ We focus on the ferromagnetic phase since we believe that the effects on the magnetic properties of the different valence configuration of Ru and Rh are qualitative the same as in the antiferromagnetic phase. Results of spin-polarized calculations are summarized in Table I.

In URh₂Si₂ the total moment agrees satisfactorily with

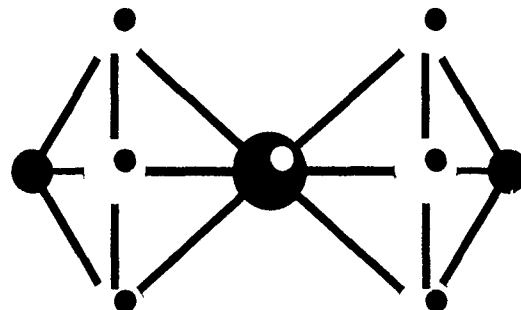


FIG. 1. Atomic coordination of the tetragonal structure of URu₂Si₂ and URh₂Si₂. The *c* axis passes through the U (black/white dot) atom and two Si (black) atoms. The plane (010) contains one U, four Ru/Rh, and two Si atoms. The basal plane (001) contains four Ru/Rh atoms (white/black dot).

TABLE I. Total magnetic moment and most relevant l partial components from different atoms (in parentheses) in UX_2Si_2 (where $X=Ru, Rh$) obtained from spin-polarized calculations in the ferromagnetic configuration.

Type	μ_T ($\mu_B/f.u.$)	μ_f (μ_B/U)	μ_d (μ_B/U)	μ_d (μ_B/X_2)
URu ₂ Si ₂	1.37	1.41	0.07	-0.22
URh ₂ Si ₂	1.83	1.75	0.07	-0.08

the experimental one: The f component contributes $\approx 96\%$ to the total magnetic moment. In URu₂Si₂ the LSDA total moment is lower due to a conspicuous antiparallel contribution from the d states on Ru (lacking on the Rh compound) and to a lower f polarization. μ_T is, however, in very bad agreement with the measured value in URu₂Si₂, as also found in previous¹⁵ electronic structure calculations for the antiferromagnetic phase. These results support *a posteriori* the idea that the type of magnetic order is not crucial to understand the different behavior of the two materials.

In Figs. 2 and 3 we report the most relevant partial DOS for the spin-polarized case in the two compounds. The splitting found in the paramagnetic f DOS of URu₂Si₂ is enhanced by the exchange field but only for the majority spin component. This fact, along with the different spin polarization of the d electrons in Ru and Rh, brings us to look at the spatial distribution of the magnetization density.

We plot in Figs. 4 and 5 the net spin polarization in two crystal planes parallel and perpendicular to the c axis (see Fig. 1). It can be seen that in the plane (010) the symmetry of

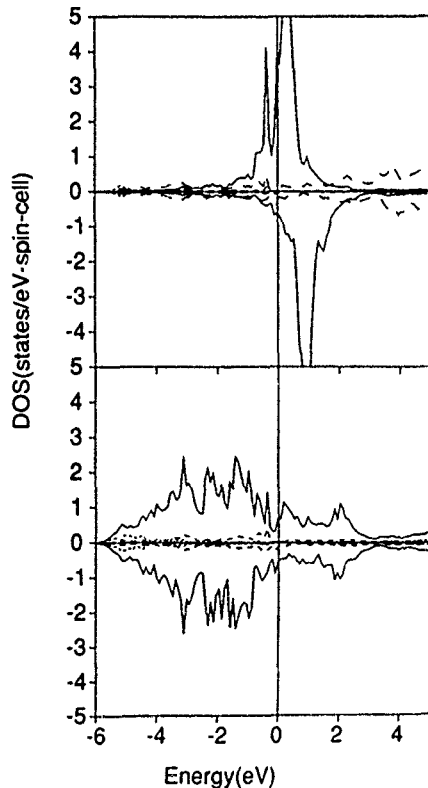


FIG. 2. Minority and majority spin DOS of URu₂Si₂ on U (top) and on Ru (bottom). The solid line refers to f states on U and d on Ru. Minor l components are also indicated by dotted lines.

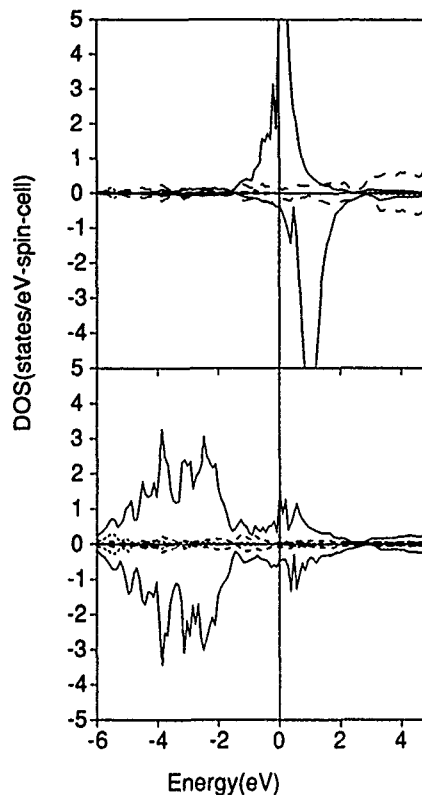


FIG. 3. Same as in Fig. 2, for URh₂Si₂.

the majority spin density on U, essentially f -like, as well as the minority spin density of essentially the d states on the metallic ion, is different in the two compounds. Also, in the basal plane (001), the negative spin density on Rh is quite

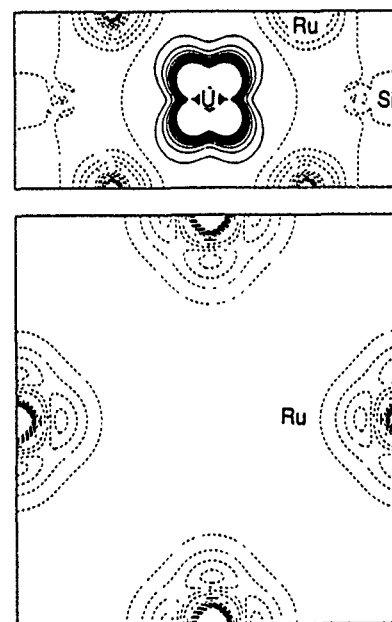


FIG. 4. Magnetization density in the crystal plane (010) (upper panel) and (001) (lower panel) of URu₂Si₂. Continuous and dotted lines indicate the contours of positive and negative spin density, respectively. Contours are equally spaced by 1.0 e/cell.

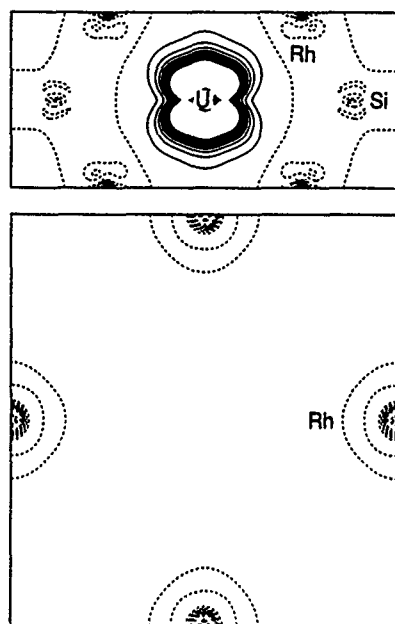


FIG. 5. Same as in Fig. 4, for URh_2Si_2 .

different from Ru, with a larger asphericity and inhomogeneity on the latter ion.

The results obtained so far suggest the following major conclusions.

There are two main differences found presently among URh_2Si_2 and URu_2Si_2 and must stem only from the outermost configuration of Ru compared to Rh and not from volume effects, as follows.

(i) The d minority spin polarization on Ru is about three times larger than on Rh. This substantial spin polarization has not been found in previous calculations¹⁵ in the AFM configuration nor pointed out explicitly in any experimental measurement. Worthy of notice is that the d spin polarization on Ru and Rh is not proportional to the Uf moment (see Table I).

(ii) The spatial distribution of the magnetization density calculated in the two planes (001), (010) has a different profile and magnitude in the two compounds. As a consequence, one would expect substantially different magnetic form factors in the two compounds, especially in the (001) plane since the contribution from the Ru minority spin density has a radial extension twice as large as Rh. The different magnetization density patterns, both on U and Ru/Rh atoms, suggest that the magnetic coupling in the two planes shown in Figs. 4 and 5 may differ considerably in the two compounds. From the analysis of the total valence-charge density in the same planes we find that in URu_2Si_2 the charge density on Ru near the nucleus is higher in the (001) than in the (010)

plane. In the latter case the interstitial charge density is substantially nonuniform. In URh_2Si_2 the role of the two planes is reversed and the interstitial charge density in the plane (010) is roughly half that of URu_2Si_2 . This raises the question of the validity of the point-charge model in the determination of the crystal-field parameters in URu_2Si_2 and the role of the crystal field in determining the superconducting pairing in heavy-fermion compounds.¹⁶

As found in several compounds of Ce with moderate or strong correlation, the strength of the hybridization, increased¹¹ by pressure or composition, may drive a transition from a (anti)ferromagnetic to a spin-compensated Kondo ground state. Since this behavior is actually shown by $\text{URu}_{1-x}\text{Rh}_x\text{Si}_2$ for $x > 0.3$, calculations of the hybridization in the two compounds is in progress. Worth noticing is that in URu_2Si_2 a strong hybridization is expected between the Uf , the Ru d states, and, possibly, Si p states. If this is the case, one would be in the presence of Anderson hybridization due to metallic superexchange. This might render the spin-spin coupling strongly dependent on the crystal-field state.

ACKNOWLEDGMENTS

We wish to thank P. Fazekas and P. Santini for helpful discussions. We acknowledge support by computing facilities in Lausanne (Switzerland) (through Grant No. 20.28846.90 of the Swiss National Science Foundation) and by CINECA (Italy) (through a grant of the Consiglio Nazionale delle Ricerche).

¹U. Walter, C. K. Loong, M. Loewenhaupt, and W. Schabitz, *Phys. Rev. B* **33**, 7875 (1986).

²C. Broholm, J. K. Kjems, W. J. L. Buyers, P. Matthews, T. T. M. Palstra, A. A. Menovsky, and J. A. Mydosh, *Phys. Rev. Lett.* **58**, 1467 (1987).

³H. Ptasiewicz, J. Leciejewicz, and A. Zygmunt, *J. Phys. F* **11**, 1225 (1981).

⁴T. T. M. Palstra *et al.*, *Phys. Rev. Lett.* **55**, 2727 (1985); M. B. Maple *et al.*, *ibid.* **56**, 185 (1986); W. S. Schabitz *et al.*, *Z. Phys. B* **62**, 171 (1986).

⁵A. de Visser, F. E. Kayzel, A. A. Menovsky, J. J. M. France, K. Hasielbach, A. Lacerda, L. Taillefer, J. Flouquet, and J. L. Smith, *Physica B* **165&166**, 375 (1990).

⁶A. P. Ramirez, P. Coleman, P. Chandra, E. Brueck, A. A. Menovsky, Z. Fisk, and E. Bucher, *Phys. Rev. Lett.* **68**, 2680 (1992).

⁷R. J. Radwanski, *J. Magn. Magn. Mater.* **103**, L1 (1992).

⁸P. Chandra and P. Coleman, *Phys. Rev. Lett.* **66**, 100 (1991); L. P. Gor'kov, *Europhys. Lett.* **16**, 301 (1991).

⁹H. Amitsuka, K. Tateyama, C. C. Paulsen, T. Sakakibara, Y. Miyako, *J. Magn. Magn. Mater.* **90&91**, 47 (1990).

¹⁰A. Eiling and J. S. Schilling, *Phys. Rev. Lett.* **46**, 364 (1981).

¹¹P. Monachesi and A. Continenza, *Phys. Rev. B* **47**, 14 622 (1993).

¹²H. F. Jansen and A. J. Freeman, *Phys. Rev. B* **30**, 561 (1984).

¹³U. von Barth and L. Hedin, *J. Phys.* **5**, 1629 (1972).

¹⁴K. Sugiyama and M. Date, *J. Magn. Magn. Mater.* **90&91**, 461 (1990).

¹⁵M. R. Norman, T. Oguchi, and A. J. Freeman, *Phys. Rev. B* **38**, 11 193 (1988).

¹⁶B. R. Trees and D. L. Cox (unpublished).

Spectroscopic studies of magnetic transitions in TbPO₄

G. K. Liu, C.-K. Loong, and F. Trouw

Chemistry and Intense Pulsed Neutron Source Division, Argonne National Laboratory, Argonne, Illinois 60439-4814

M. M. Abraham and L. A. Boatner

Solid State Division, Oak Ridge National Laboratory, Oak Ridge, Tennessee 37831-6056

In TbPO₄, an antiferromagnetic-phase transition is accompanied by a cooperative Jahn-Teller effect involving a Tb ion-lattice coupling that induces a tetragonal-to-monoclinic distortion of the crystal lattice and an associated readjustment of the Tb electronic states as required by the lowering of the rare-earth-site symmetry. The laser-excitation and emission spectra of TbPO₄ and 0.1% Tb-doped YPO₄ single crystals were studied at temperatures below and above the phase transitions. The line shapes of transitions in the stoichiometric compound are unusually broad and asymmetric while those observed for the dilute compound are relatively sharp. In addition, the TbPO₄ spectra show an anomalous temperature dependence near the phase transition, indicating strong interactions of the rare-earth ions with their local environments. In the present work, a comparison of the optical results with the results of new neutron-scattering measurements is made.

I. INTRODUCTION

Rare-earth orthophosphates, RPO₄ (R=Tb-Lu), crystallize in the tetragonal zircon structure (space group *I*4₁/*amd*) in which four equivalent rare-earth ions in a unit cell occupy sites of *D*_{2d} symmetry. The low-temperature magnetic properties of these compounds are strongly influenced by the symmetry of the rare-earth low-lying states that are split by crystal-field effects. The Tb, Dy, and Ho compounds have doublet ground states dominated by $|J \pm J_M\rangle$ components of large *J_M*, while the Er, Tm, and Yb compounds have ground states that are either energetically isolated singlets or Kramers doublets with a highly isotropic spin-magnetization density. Consequently, long-range antiferromagnetic ordering has been observed only in the former compounds with Néel temperatures *T_N*=2.28, 3.4, and 1.39 K for TbPO₄, DyPO₄, and HoPO₄, respectively.¹⁻³ The antiferromagnetic phase has a simple "two-sublattice" structure with the direction of the rare-earth magnetic moment lying parallel/antiparallel to the crystallographic *c* axis. Many magnetothermal properties, such as the magnetic susceptibility and heat capacity of these materials, can be adequately described by either a three-dimensional Ising model^{4,5} or by a molecular-field theory.⁶

TbPO₄ differs from the DyPO₄ and HoPO₄ antiferromagnets in the occurrence of an additional Jahn-Teller transition at 2.15 K where the Tb ion-lattice coupling induces a distortion of the tetragonal lattice to a monoclinic structure with a corresponding tilting of the Tb moments away from the tetragonal *c* axis in the (110) plane.⁷⁻⁹ A number of investigations, both experimental and theoretical, have previously been undertaken in attempts to understand the intriguing properties of TbPO₄. In particular, the interpretation of the optical-absorption and emission spectra (as well as electronic Raman-scattering data) of TbPO₄ are complicated by unusually broad transitions and asymmetric line shapes. Since the excited states of Tb³⁺ ions in a variety of materials are known to participate in various energy-transfer processes involving excitonic fluorescence, relaxation, and dispersion induced by magnetic-exchange interactions,¹⁰⁻¹³ we have performed optical-absorption and emission as well as neutron-

scattering experiments on both single-crystal and powder samples of Tb_xY_{1-x}PO₄ in an attempt to clarify the nature of the Tb-Tb interactions at low temperatures. This article presents results which provide new insight into the properties of the magnetic transitions within the Tb³⁺ ⁷F₆ ground multiplet and electronic transitions between the ⁷F₆ and ⁵D₄ multiplets in both the paramagnetic and antiferromagnetic phases of the Tb_xY_{1-x}PO₄ (*x*=0.01 and 1) compounds.

II. EXPERIMENTAL DETAILS

Single crystals of TbPO₄ and 0.1% Tb:YPO₄ were grown by dissolving and reacting the appropriate rare-earth oxides in molten lead pyrophosphate at high temperature¹⁴ followed by subsequent slow cooling. Polycrystalline powders of TbPO₄ were prepared by the technique of precipitation from molten urea.¹⁵ The resulting samples were examined by x-ray and neutron diffraction and were found to have the appropriate zircon structure. A tunable dye laser pumped by a pulsed Nd:YAG laser was used in the optical-absorption and fluorescence experiments. The laser linewidth was 0.4 cm⁻¹. Fluorescence emission from the lowest component of the ⁵D₄ multiplet was dispersed by a monochromator and detected by a cooled photomultiplier. Signals from the photomultiplier were averaged using a DEC minicomputer. The optogalvanic effect in a uranium-argon hollow-cathode lamp was used for wavelength calibration of the excitation spectra. The single-crystal samples were mounted in an optical cryostat with the *c* axis perpendicular to the incident laser beam. Low-temperature measurements (*T*≤4.2 K) were performed with the samples immersed in liquid helium, and the helium vapor was pumped in order to reduce the temperature to below the λ point.

Inelastic neutron-scattering measurements were performed using the QENS spectrometer at the Argonne spallation neutron source IPNS. The energy resolution of the QENS spectrometer varies smoothly from about 0.12 meV (0.96 cm⁻¹) at the elastic position to ≈0.45 meV (3.6 cm⁻¹) at an energy transfer of 10 meV. A sample consisting of

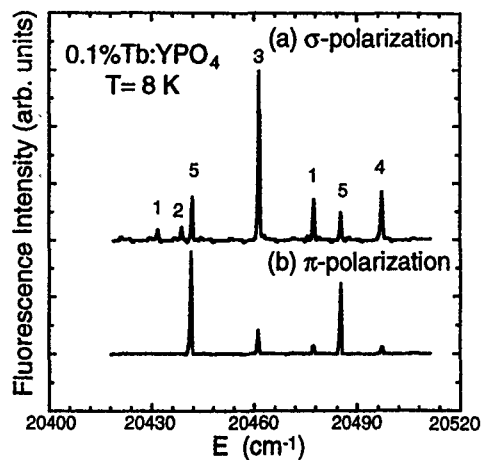


FIG. 1. Laser-excitation spectra of the ${}^7F_6 \rightarrow {}^5D_4$ transitions of Tb^{3+} (0.1%) in YPO_4 at 8 K: (a) σ polarization and (b) π polarization. The numbers label the symmetries of the excited states, e.g., 5 denotes a Γ_5 state.

approximately 30 g of polycrystalline TbPO_4 was cooled in a conventional helium cryostat and used in the neutron-scattering experiments.

III. RESULTS AND DISCUSSION

The ${}^7F_6 \rightarrow {}^5D_4$ excitation spectra of 0.1% $\text{Tb}^{3+}:\text{YPO}_4$ at 8 K obtained with both the σ (photon electric field $\mathbf{E} \perp$ the crystallographic c axis) and π ($\mathbf{E} \parallel c$ axis) polarization are shown in Fig. 1. Under the D_{2d} point-group symmetry, the $\text{Tb}^{3+} {}^7F_6$ ground multiplet is split by the crystal field into seven singlets, $2\Gamma_1 + \Gamma_2 + 2\Gamma_3 + 2\Gamma_4$, and three doublets, $3\Gamma_5$, and the excited 5D_4 multiplet is split into five singlets, $2\Gamma_1 + \Gamma_2 + \Gamma_3 + \Gamma_4$, and two doublets, $2\Gamma_5$. The Γ_5 doublet ground state has been previously identified by neutron and optical studies.¹⁶⁻¹⁸ The seven observed peaks shown in Fig. 1(a) can be interpreted as excitations from the Γ_5 ground state to the seven crystal-field-split states in 5D_4 . The selection rules for electric-dipole transitions allow only $\Gamma_5 \leftrightarrow \Gamma_5$ and $\Gamma_3 \leftrightarrow \Gamma_4$ transitions in the π -polarization and $\Gamma_5 \leftrightarrow \Gamma_{1,2,3,4}$ transitions in the σ -polarization configuration; however, some of the formally forbidden transitions were observed—probably due to imperfect polarization conditions. The energies and linewidths of the transitions, determined by nonlinear fits of the data to the reference uranium and argon lines, are listed in Table I. It can be seen that all of the optical transitions of the Tb^{3+} ions in the dilute sample are very sharp (Fig. 1) with measured linewidths between 0.4 and 0.5 cm^{-1} . Given that the laser-line resolution is 0.4 cm^{-1} , inhomogeneous line broadening in this sample cannot exceed 0.3 cm^{-1} . In addition, intrinsic broadening of the lines due to Tb-Tb interactions and zero-field hyperfine splitting are negligibly small.

In the case of the observed optical and neutron spectra of the stoichiometric compound TbPO_4 , the optical transitions in the 2.2–80 K temperature range are unusually broad and the lines are asymmetric. Figure 2(a) shows a typical excitation spectra of TbPO_4 observed at approximately 4.2 K in the π -polarization configuration. The transitions from the ground state to the two Γ_5 and the Γ_3 states of the 5D_4 multiplet are

TABLE I. The energies and linewidths (in cm^{-1}) of the ${}^7F_6 \rightarrow {}^5D_4$ transitions of Tb^{3+} in TbPO_4 and in YPO_4 .

States	TbPO ₄			0.1% Tb:YPO ₄ ^a energies 8 K
	Energies		Linewidths	
	1.5 K	4.2 K		
Γ ₁	20 443.2(1)	20 440	1.0	20 431.8(1)
Γ ₂	20 447.0(3)	20 438.6(1)
Γ ₃	20 456.0(5)	20 455	10.6	20 441.4(3)
Γ ₃	20 479.8(1)	20 478	1.8	20 461.3(1)
Γ ₁	...	20 492	...	20 473.4(1)
Γ ₃	20 502.5(5)	20 500	9.4	20 485.1(1)
Γ ₄	20 512.9(3)	20 509	3.4	20 496.9(1)

^aAll the linewidths are less than 0.3 cm^{-1} .

broadened into three bands with linewidths of more than 10 cm^{-1} . At the lower temperature of 1.5 K, we observed that these bands remained broad, and new weak narrow lines appeared [see Fig. 2(b)]. The assigned transition energies and the estimated linewidths for TbPO_4 are given in Table I. The small difference in the energies of the levels between the 0.1% $\text{Tb}:\text{YPO}_4$ and the stoichiometric TbPO_4 samples reflects the somewhat different crystal-field environments in these two materials.

The crystal-field excitations from the ground state to the next four higher states within the 7F_6 ground multiplet, as measured by neutron scattering at 1.5 and 4.2 K, are shown in Fig. 3. The observed transitions at both 4.2 and 1.5 K are significantly broader than the instrumental resolution. This indicates that the peaks are intrinsically broadened by interactions of the Tb magnetic moments with the environment. In fact, at 4.2 K the first three states at 0, 3.8, and 7.8 cm^{-1} , determined by a detailed inelastic neutron-scattering study,¹⁶ are merged into a band exhibiting an asymmetric profile. The strong peak evident at zero energy in the $T=4.2$ K spectrum originates from magnetic elastic scattering within the doubly degenerate Γ_5 ground state. At 1.5 K, the degeneracy is lifted by the reduction of site symmetry due to the tetragonal-to-monoclinic distortion of the lattice. As a result, the elastic

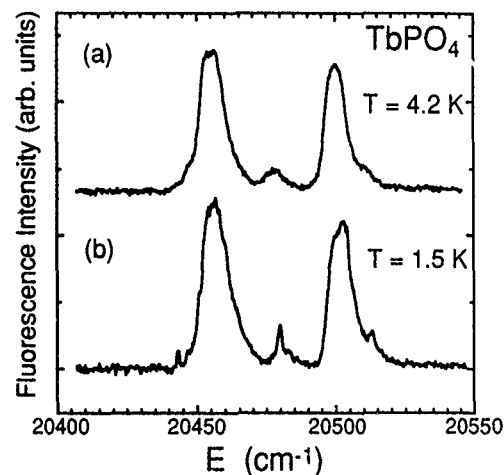


FIG. 2. Laser-excitation spectra of the ${}^7F_6 \rightarrow {}^5D_4$ transitions of Tb^{3+} in TbPO_4 in π polarization: (a) $T=4.2$ K and (b) $T=1.5$ K.

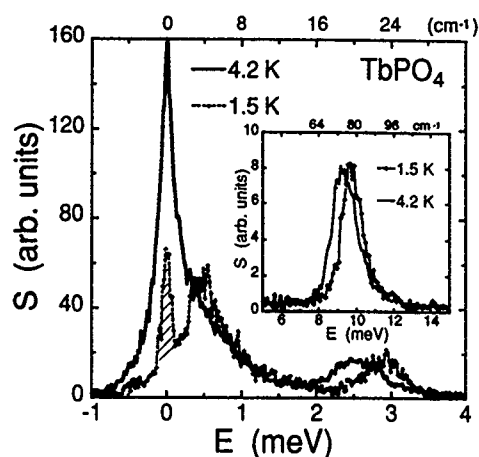


FIG. 3. The low-energy excitation spectra of TbPO_4 obtained by neutron scattering at 4.2 and 1.5 K. The energy resolution of the spectrometer varies smoothly from about 0.12 meV (0.96 cm^{-1}) at the elastic position to $\sim 0.45 \text{ meV}$ (3.6 cm^{-1}) at $E=10 \text{ meV}$. Both spectra contain a residual nuclear elastic-scattering component (shaded area) arising from the sample and container.

intensity diminishes and the spectrum shifts to higher energies by approximately 4 cm^{-1} . Long-range magnetic ordering has set in, and the neutron spectrum represents a measure of the magnon density of states. The energy-level scheme, as determined by neutron measurements, agrees well with that obtained from the optical emission spectra of the $^5D_4 \Gamma_1$ state to the 7F_6 ground multiplet.

The present optical and neutron-scattering measurements have provided new information regarding crystal-field effects and magnetic interactions in the $\text{Tb}_x\text{Y}_{1-x}\text{PO}_4$ system at low temperatures. In the dilute limit of 0.1% Tb in YPO_4 , the Tb-Tb interactions are determined to be negligible and single-ion crystal-field transitions give rise to sharp peaks which are observed in the optical spectra at all temperatures. The narrow linewidths of these excitations indicate that the effects of defect-induced inhomogeneous broadening, zero-field hyperfine splitting due to the nuclear spins, and the relaxations of the Tb^{3+} excited states are small. As the Tb concentration increases, the probability for interactions between a pair of Tb^{3+} excited states is enhanced under selective excitation by the laser field in an optical experiment. Such exciton-exciton interactions were, in fact, observed for $\text{Tb}_x\text{Y}_{1-x}\text{PO}_4$ through luminescence studies reported by Hirano and Shionoya¹⁰ and by Diggle and co-workers.¹¹

The present optical and neutron-scattering experiments on TbPO_4 have emphasized the study of superexchange interactions between the Tb^{3+} magnetic moments at low temperatures. Such interactions eventually lead to long-range antiferromagnetic ordering of the Tb^{3+} moments at 2.28 K and to a Tb ion-lattice coupling at 2.15 K. The exchange interaction, however, must intensify significantly at temperatures near the phase transitions, as manifested by the broadened transitions present in the optical and neutron spectra at 4.2 K. The effect of inhomogeneous broadening can be ruled out as

the cause of this effect due to the appearance of additional narrow peaks at 1.5 K, in the optical spectra. The significance of exchange interactions between the Tb ions at $T < 50 \text{ K}$ is also supported by the systematic deviation of the experimentally obtained values for the paramagnetic susceptibility χ_{\parallel} (i.e., with the applied field parallel to the crystallographic c axis), from the calculated values that are based solely on single-ion crystal-field effects.¹⁶ At 4.2 K, strong exchange interactions induce spin fluctuations that dynamically broaden the otherwise sharp crystal-field levels and reduce the lifetimes of the excitations. Consequently, the transition lines are broad and asymmetric. At 1.5 K, the Tb^{3+} wave functions are determined by the diagonalization of a Hamiltonian that includes the effects of crystal fields and long-range magnetic interactions. In general, the wave functions contain a number of components of $|JJ_M\rangle$ and they vary depending on the spin-wave propagation directions. The broad bands seen in the spectra at 1.5 K may be interpreted as magnon-to-optical exciton-band transitions. Such transitions have been found^{12,19} previously for the case of $\text{Tb}(\text{OH})_3$ and GdCl_3 and give rise to broad, asymmetric spectra. The magnon wave functions will also modify the selection rules for electric-dipole transitions. The additional narrow peaks in the 1.5 K spectra probably reflect such an enhancement of some transition intensities as favored by the selection rules.

ACKNOWLEDGMENTS

Work performed at Argonne National Laboratory and the Oak Ridge National Laboratory is supported by the U.S. Department of Energy, Office of Basic Energy Sciences, Chemical Sciences and Materials Sciences Divisions under Contracts No. W-31-109-ENG-38 (ANL) and No. DE-AC05-84OR21400 (ORNL), respectively.

- ¹J. N. Lee, H. W. Moos, and B. W. Mangum, *Solid State Commun.* **9**, 1139 (1971).
- ²J. C. Wright and H. W. Moos, *Phys. Lett. A* **29**, 495 (1969).
- ³A. H. Cooke, S. J. Swithenby, and M. R. Wells, *J. Phys. C* **6**, 2209 (1973).
- ⁴M. J. Metcalfe and H. M. Rosenberg, *J. Phys. C* **5**, 450 (1972).
- ⁵J. C. Wright, H. W. Moos, J. H. Colwell, B. H. Mangum, and D. D. Thornton, *Phys. Rev. B* **3**, 843 (1971).
- ⁶J. Sivardiere, *Phys. Rev. B* **8**, 2004 (1973).
- ⁷J. Coing-Bayat, F. Sayetat, and A. Apostolov, *J. Phys. (Paris)* **36**, 1165 (1975).
- ⁸W. Nägele, D. Hohlwein, and G. Domann, *Z. Phys. B* **39**, 305 (1980).
- ⁹S. Spooner, J. N. Lee, and H. W. Moos, *Solid State Commun.* **9**, 1143 (1971).
- ¹⁰M. Hirano and S. Shionoya, *J. Phys. Soc. Jpn.* **33**, 112 (1972).
- ¹¹P. C. Diggle, K. A. Gehring, and R. M. Macfarlane, *Solid State Commun.* **18**, 391 (1976).
- ¹²R. L. Cone and R. S. Meltzer, *J. Chem. Phys.* **62**, 3573 (1975).
- ¹³J. P. van der Ziel, L. Kopf, and L. G. Van Uitert, *Phys. Rev. B* **6**, 615 (1972).
- ¹⁴R. S. Feigelson, *J. Am. Ceram. Soc.* **47**, 257 (1964).
- ¹⁵M. M. Abraham, L. A. Boatner, T. C. Quinby, D. K. Thomas, and M. Rappaz, *Radioactive Waste Management* **1**, 181 (1980).
- ¹⁶C.-K. Loong, L. Soderholm, G. L. Goodman, M. M. Abraham, and L. A. Boatner, *Phys. Rev. B* **48**, 6124 (1993).
- ¹⁷W. Böhm, H. G. Kahle, and W. Wüchner, *Phys. Status Solidi B* **126**, 381 (1984).
- ¹⁸J. F. L. Lewis and G. A. Prinz, *Phys. Rev. B* **10**, 2892 (1974).
- ¹⁹R. S. Meltzer and H. W. Moos, *Phys. Rev. B* **6**, 264 (1972).

Magnetic structures of itinerant electron systems (abstract)

J. Kübler, L. Sandratskii, and M. Uhl

Institut für Festkörperphysik, Technische Hochschule Darmstadt, Germany

Under well-defined conditions itinerant electrons conspire to form magnetic moments that can show a variety of order phenomena in and near the ground state. We describe these quantitatively using energy-band theory which supplies a powerful conceptual and computational tool. Both the density functional and methodological bases are briefly reviewed and results are presented not only for noncollinear antiferromagnetic moment arrangements, but also for states having incommensurate helical order characterized by some wave vector q . In particular, we discuss the static nonuniform, exchange-enhanced magnetic susceptibility obtained for a selected set of transition metals.¹ The observed temperature variation of the electron density of states of bcc iron can be explained just as that of the $5d$ states of gadolinium. For fcc-iron precipitates we find an incommensurate antiferromagnet ground state² as observed by neutron-diffraction experiments. For other frustrated antiferromagnets, like the hexagonal Laves phase ThMn_2 , we obtain an incommensurate ground state, again in agreement with neutron diffraction experiments. Concerning the INVAR problem we add transverse magnetic fluctuations to the longitudinal fluctuations that recently have been quite successful in explaining magneto-volume anomalies of INVAR. Finally, we discuss the magnetization reversal in magnetic multilayers subject to an applied magnetic field.

¹L. Sandratskii and J. Kübler, *J. Phys. Condens. Matter* **4**, 6927 (1992).

²M. Uhl, L. Sandratskii, and J. Kübler, *J. Magn. Magn. Mater.* **103**, 314 (1992).

Electronic structure and spin-density distribution in Y_2Fe_{17} (abstract)

Ming-Zhu Huang and W. Y. Ching

Department of Physics, University of Missouri, Kansas City, Missouri 64110

We have calculated the spin-polarized band structure of the Y_2Fe_{17} compound in the rhombohedral structure using the first-principles self-consistent orthogonalized linear combination of atomic orbitals method in the local spin-density approximation. Using a real space integration scheme, we have obtained the site-decomposed magnetic moments as follows: $-0.28\mu_B$ on Y-6(c), $2.54\mu_B$ on Fe-6(c), $2.08\mu_B$ on Fe-9(d), $2.28\mu_B$ on Fe-18(f), and 2.10 on Fe-18(h). Similar values are obtained when the more traditional Mulliken scheme is used. The calculated spin magnetic moments are in good agreement with Mössbauer data but are somewhat larger than these obtained by Coehoorn using the linear muffin-tin orbitals (LMTO) method.¹ The calculated density of states are similar to that of Coehoorn's. In order to have a better insight on the magnetic structure of Y_2Fe_{17} , the real space spin density distributions are plotted and it is shown that the negative spin density on the Y site extends to a fairly large region. We will extend our calculation to $\text{Nd}_2\text{Fe}_{17}$ crystal and to cases in which the Fe atoms are selectively substituted by Al, Si, and Ga, as well as the effect of the N addition. Previous OLCAO calculations^{2,3} on $\text{Nd}_2\text{Fe}_{17}\text{N}$ systems were nonself-consistent and therefore less reliable.

Work supported by DOE Grant DE-FG02-84ER45170.

¹R. Coehoorn, Phys. Rev. B **39**, 13072 (1989).

²Z. Q. Gu and W. Lai, J. Appl. Phys. **71**, 3911 (1992).

³Z. Gu, W. Lai, X.-F. Zhong, and W. Y. Ching, Phys. Rev. B **46**, 13874 (1992).

Energetics of bcc-fcc lattice in Fe-Co-Ni compounds (abstract)

E. G. Moroni

Department of Theoretical Physics, Royal Institute of Technology, S-10044 Stockholm, Sweden

T. Jarlborg

Department of Condensed Matter Physics, University of Geneva, CH-1211 Geneva 4, Switzerland

The linear muffin tin orbital method is applied to compute the energy properties of several ordered binary Fe-Ni, Fe-Co, and ternary Fe-Ni-Co compounds near the bcc-fcc transition, from first principles. The calculations use the local spin density and the Perdew-Wang gradient corrected approximation to treat exchange and correlation. We address the importance of the gradient corrected approximation for the calculation of the fcc-bcc energetics for these 3D Fe-based systems near the Fe rich region. By adding Co to the Fe-Ni alloy it is possible to reduce the volume expansion accompanying the fcc to bcc transition. To study these effects we have considered the energetics in several ordered ternary systems with a fcc and bcc lattice. When increasing the e/a ratio from 8.5 (Fe_3Ni) to 8.75 (NiFe_2Co) and to 9 (Co or FeNi) one finds increased stability of the FM fcc phase compared to the bcc phase. We observe also that by increasing the e/a ratio the magnetic moment of the fcc lattice becomes more stable; this induces an augmentation of the spontaneous magnetostriction and a decrease of the volume change accompanying the fcc-bcc transition. A comparison of the different computed magnetic and ground-state properties with experimental data is provided.

Prediction of pressure-induced changes in magnetic ordering of correlated-electron uranium systems (invited)

Q. G. Sheng and Bernard R. Cooper

Department of Physics, West Virginia University, Morgantown, West Virginia 26506-6315

Experimentally, hydrostatic pressure experiments provide a very sensitive way to probe the development of magnetic ordering in correlated-electron systems. We have now developed and applied theory allowing us to understand and quantitatively predict the variation of ordering temperature with pressure in uranium-based correlated-electron materials on a wholly predictive calculated basis, i.e., without using any experimental data as input in the calculation. The theory physically captures the changes in the *f* spectral density distribution in space and time that are driven by pressure-induced increased band-*f* hybridization. As a test case, we have predicted behavior in good agreement with experiment for UTe where experimentally (Link *et al.*) T_c increases from 104 K to a maximum of 181 K at 7.5 GPa and then decreases to 156 K at 17.5 GPa. Our calculations: (1) using full-potential total-energy calculations match the experimental lattice parameter change with pressure within 2% and provide the decrease in average 5*f*-electron number; (2) extract information from the electronic structure calculation on the hybridization-induced changes and insert this into many-body theory to calculate the increase in two-ion coupling with pressure (from increased *f* spectral admixture into the bands) giving the initial increase in T_c ; (3) calculate the decrease in ordering temperature (in terms of coupling) with decreased 5*f* number (localized spectral density) which gives the ultimate decrease in T_c .

In correlated-electron uranium-based materials like UTe^{1,2} and UPt₃,³ the change in magnetic ordering in response to hydrostatic pressure has interesting characteristics: the ordering temperature rises with, or at least is insensitive to, pressure initially, while the low temperature ordered moment m_o decreases or indeed plunges dramatically. In the case of the weakly correlated ferromagnet UTe, in the measurements of Link *et al.*² T_c increases from 104 K at ambient pressure to a maximum of 181 K at 7.5 GPa and then decreases to 156 K at 17.5 GPa; while the decrease of m_o with the initial pressure in the measurements of Bartholin *et al.*,¹ while substantial, is not drastic in comparison to the results of Hayden *et al.*³ for the heavy-fermion antiferromagnet UPt₃.³ For UPt₃,³ the application of 2.05-kbar pressure causes no observable change in T_N ; while m_o is drastically reduced by 50%. If, as in the mean field theory, the ordering temperature T_{order} scales with the two-ion coupling J and the low temperature ordered moment m_o : $T_{order} \propto J m_o(m_o + 1)$, then, in both UTe and UPt₃, J increases and m_o decreases with pressure.

In order to understand this behavior, we consider the following effects: (i) the effect of pressure on the *f* spectral weight distribution in real space; (ii) the effect of this real space *f* spectral weight distribution on hybridization; (iii) the effect of hybridization on the *f* spectral weight distribution in energy space; and finally, the consequences of the effects in (i)–(iii) on magnetic ordering. These effects are described as follows.

(i) Localized 5*f* spectral loss in real space: When pressure increases, the system responds with the following reactions: the atomic distance decreases, \rightarrow the volume of the core region reduces, \rightarrow the core potential becomes less at-

tractive, \rightarrow the *f* states diffuse more of their waves outside the core region. This can be described by band structure calculations. In such calculations, the core regions are represented by muffin-tin spheres, supposing neighboring muffin-tin spheres touch, but do not overlap, with each other. The *f* waves (partial waves with orbital quantum number $l=3$ within a muffin-tin sphere) are singled out and filled up to the Fermi level, thus obtaining the real space localized *f*-electron number n_f . Table I shows the results of such calculations for UTe, from which one can see the decrease of n_f with pressure. As a result of crystalization, the *f* waves as a whole can no longer accommodate 14 electrons per atom, as a free atom can. The reason is that the parts of the *f* wave function at large radial distances (or, outside the muffin-tin spheres in band structure calculation) are distorted by the crystal field and lose the *f* characteristic, thus being excluded from the *f* waves. Such 5*f*-shell spectral loss in the real space is stronger when the atoms are closer to each other in a crystal. A consequence of this real space 5*f*-shell spectral loss is the reduction of the localized *f* moment. Notice that the n_f calculated from band structure theory is a time average.

(ii) Increase of hybridization: Hybridization V depends on the integral between the *f* state $\phi_f(r)$ and extended band state $\psi_{band}(r)$: $V = \langle \psi_{band}(r) | H | \phi_f(r) \rangle$, where $\phi_f(r)$ consists of both $l=3$ orbital wave function contained within the muffin-tin sphere and crystal-symmetry-dominated wave function diffusing outside the muffin-tin sphere. The more $\phi_f(r)$ is diffused in space, the more it overlaps with $\psi_{band}(r)$, thus the larger the V . As described in (i), pressure causes $\phi_f(r)$ to be more diffused, thus V grows with pressure. As a

TABLE I. Renormalized lattice volume V/V_0 , and $5f$ electron number n_f at different pressures P calculated for UTe from the LMTO band structure calculation.

P (GPa)	atmos	0.98	2.9	5.4	8.3	11.7	15.5	19.7
V/V_0	1.0	0.979	0.952	0.927	0.901	0.877	0.852	0.828
n_f	2.73	2.71	2.69	2.67	2.64	2.62	2.60	2.58

consequence, the hybridization-induced two-ion coupling also grows with pressure.

(iii) Localized $5f$ spectral loss in energy space: Without hybridization, the $5f$ states form a narrow f peak in energy space. When hybridization is turned on, parts of the f waves are stripped off from the narrow f peak and go to the extended regions in the energy space. This is schematically shown in Fig. 1. The parts of the f waves in the extended regions still keep the f characteristic; however, being extended states, they do not belong to a single atom, but to the whole crystal. In real space, electrons of these parts of the f waves hop around among neighboring atoms; and during their stay on a certain atom, they are contained within a muffin-tin sphere and are f -like in nature. The hopping is via non- f -extended bands, a result of hybridization. Thus, the f waves can be viewed as consisting of two parts: one in the narrow f peak, (these f waves are stable on a single atom, and therefore form the localized f waves); the other in the extended regions, (these f waves hop among neighboring atoms, and therefore form itinerant f waves). The division of these two parts is not clear cut. The addition of these two parts of the f waves on a certain atom, after time averaging, gives the f spectral weight in real space. The n_f calculated from the band structure calculation is such a time average: it is an accumulation of all the f waves, in the f peak as well as in the extended regions, up to the Fermi level. As a consequence, not all of n_f contributes to the stable local f moment; instead, parts of n_f , belonging to the extended states and being itinerant, do not always follow the magnetic polarization of the local moment. Since this effect is hybridization-induced, it also grows with the pressure.

We can see in the foregoing that as pressure increases, effects in (i) lead to effects in (ii), which further leads to effects in (iii). In other words, the f spectral loss in real space enhances hybridization; and hybridization enhances the f spectral loss in energy space. The f spectral loss in real space reduces the local moment by turning f waves into non- f waves [described in (i)]; the f spectral loss in energy space

reduces the local moment by turning localized f waves into itinerant f waves [described in (iii)]. Both effects in (i) and (iii) weaken the magnetic ordering. On the other hand, through increasing the two-ion coupling, hybridization strengthens the magnetic ordering [described in (ii)], thus competes with effects in (i) and (iii).

The varying magnetic ordering with pressure can be explained by the competing effects described above. The initial increase of T_c can be explained as the initial winning effect of the mechanism which strengthens magnetic ordering; the ultimate decrease of T_c can be explained as the eventual changeover of winning and losing effects. Whether it wins initially or not, ultimately the second, moment-reduction, mechanism discussed above wins.

In the following, we quantify this theory using techniques based on the theoretical framework we have developed.⁴ This involves the following procedures. (1) Using full-potential total-energy calculations, match the experimental lattice parameter change with pressure and provide the decrease in time averaged f -electron number in real space. This part of the calculation is of concern with regard to effects in (i) as mentioned above. (2) Extract information from the electronic structure calculation on the hybridization-induced changes and insert this into many-body model Hamiltonian to calculate the increase in two-ion coupling with pressure. This part of the calculation is of concern with regard to the effects in (ii). (3) Using Ising model to simulate the effect of the decrease in ordering temperature (in term of coupling) with decreased f spectral weight. This part of the calculation is of concern with regard to the effects in (iii). As a test case, this calculation is done for UTe.

(1) We perform a sequence of band structure calculations with a series of different lattice constants. We use a full-potential linearized muffin-tin orbital (LMTO) band structure (self-consistent relativistic LDA) calculation. The curve of the total energy versus unit cell volume is calculated. It has a minimum corresponding to the ambient pressure lattice constant, which is smaller than experiment by 3%. The result can be improved by including the orbital and spin polarization into the calculation (performed by S. P. Lim), and the error of lattice constant is reduced to less than 2%. The derivative of the total energy with regard to the unit cell volume is pressure. The lattice volume change with pressure and the f electron number (in the real space) n_f change with pressure are shown in Table I and Fig. 2. (The experimental results in Fig. 2 are from Gerward *et al.*, Ref. 5.) n_f changes from 2.73 at ambient pressure to 2.58 at 20 GPa, a loss of 0.15 electron per atom.

Figure 3 shows the results of the density of states (DOS) at three lattice constants. The DOS spectra have two peaks

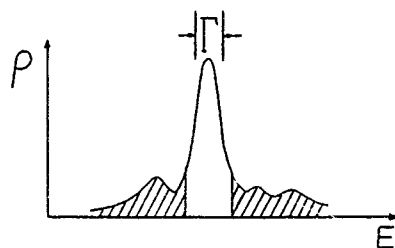


FIG. 1. f spectrum in energy space. The narrow peak, the localized f spectral weight, has a width Γ . The presence of f waves in the extended region is indicated by hatching.

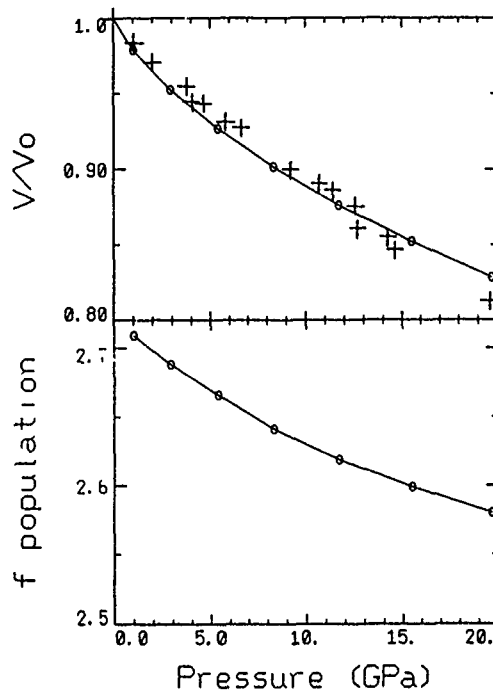


FIG. 2. Top: normalized lattice volume V/V_0 vs pressure. Bottom: $5f$ electron number n_f vs pressure. The open circles are points calculated from the LMTO band structure calculation. The crosses are experimental volume data from Gerward *et al.* (Ref. 5).

originating from the f states and split by spin-orbit coupling. The peak on the higher energy ($j=7/2$) side is empty. The other ($j=5/2$) peak contains electrons, and the physics of interest occurs there.

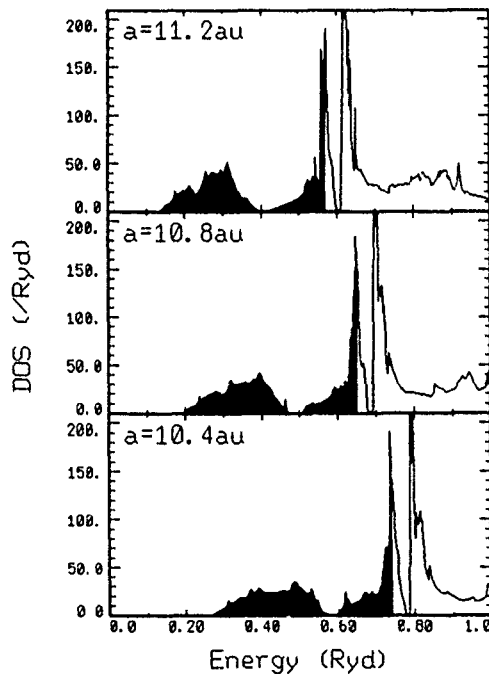


FIG. 3. Density of states of UTe, calculated with three lattice constants: $a=11.2$ a.u. (top); $a=10.8$ a.u. (middle); $a=10.4$ a.u. (bottom). The states below the Fermi level are indicated by shading.

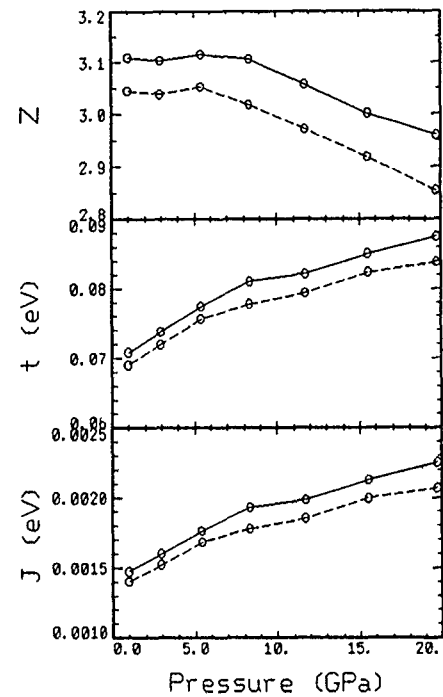


FIG. 4. Top: localized (corresponding to area of density of states peak) f spectral weight Z vs pressure. Middle: t vs pressure. Bottom: J vs pressure. The solid line is calculated for $\rho_{\text{cutoff}}=20\%\rho_{\text{max}}$; the dashed line for $\rho_{\text{cutoff}}=25\%\rho_{\text{max}}$.

(2) Comparing the three DOS spectra in Fig. 3, one can see that the ($j=5/2$) f peak becomes wider when the lattice constant is smaller. We define the width Γ for the f peak

$$\Gamma = \frac{[\int_{\rho > \rho_{\text{cutoff}}} (E - E_{\text{max}})^2 \rho(E) dE]^{1/2}}{\int_{\rho > \rho_{\text{cutoff}}} \rho(E) dE}, \quad (1)$$

where ρ is the density of states, E_{max} is the energy at the peak ρ_{max} . ρ_{cutoff} has to be chosen in the calculation, since, as mentioned above, the division of the localized f waves and itinerant f waves is not clear cut. In the following calculation, we choose ρ_{cutoff} to be 15%, 20%, 25%, and 28% of the peak value ρ_{max} , and results from different ρ_{cutoff} will be compared.

Since a bandwidth can be attributed to the interatomic interaction, Γ indicates the coupling of f states localized on neighboring atoms. Suppose such coupling only occurs for the first nearest neighbor; then Γ can be related to the two-ion coupling J in the following way. Consider the Hubbard model

$$H_H = \left(-t \sum_{i,n} c_{im}^+ c_{i+n,m'} + \text{h.c.} \right) + U \sum_{i,m \neq m'} n_{im} n_{im'}, \quad (2)$$

where t is the interatomic interaction, U the on-site Coulomb repulsion, m the magnetic quantum number, i an atomic site, $i+n$ the first neighbors of site i . A tight binding band results from using H_H

$$E_k = E_0 - t \sum_n \exp(-ikR_n). \quad (3)$$

For a fcc lattice, this band has a width $\Gamma = 1.04t$. This is obtained by projecting E_k onto the energy space using the tetrahedral technique.⁶ Thus, calculating Γ from the DOS spectra using Eq. (1) for a real system gives t . The middle panel of Fig. 4 shows the so calculated t vs pressure. t increases with pressure as expected.

If $U \gg t$, H_H can be converted into the following model:⁷

$$H = \left(-t \sum_{in} c_{im}^+ c_{i+n,m'} + \text{h.c.} \right) - J \sum_{in} \mathbf{S}_i \cdot \mathbf{S}_{i+n}, \quad (4)$$

where $J = t^2/U$. In going from Eq. (3) to Eq. (4), the approximation has been made that the quantum number of S_i^z can only be $m = \pm 1$. Clearly J is the two-ion coupling. U can be calculated from a supercell scheme.⁴ This gives $U = 3.4$ eV at ambient pressure, and U changes very little (less than 0.3 eV) with pressure up to 20 GPa. We take $U = 3.4$ eV for all the pressures. With t obtained as above, we can calculate $J = t^2/U$. J vs pressure is shown in the bottom panel of Fig. 4. J also increases with pressure as expected.

(3) The J interaction supposedly occurs between stable local moments. However, as mentioned above, in effect (iii), only the f waves in the narrow f peak in the energy space are localized. The rest of the f waves are itinerant and do not participate in the local magnetization. Define the localized f spectral weight Z :

$$Z = \int_{\rho > \rho_{\text{cutoff}}} \rho(E) dE, \quad (5)$$

where the choice of ρ_{cutoff} is taken according to that used in the definition of the width Γ of the f peak. From the DOS spectra, we calculate the Z change using Eq. (5). The results of Z vs pressure are shown in the top panel of Fig. 4.

U in UTe is close to an f^3 configuration. Suppose that the two-ion coupling occurs between the f^3 atoms. When an f^3 atom loses one unit of f spectral weight and reduces to an f^2 configuration, one unit of charge is moved into the extended band states located in a region surrounding this atom, and hence can screen this atom from magnetic interaction with its neighbors. Bearing in mind that the two-ion coupling in UTe is band mediated, such screening can be quite effective. Consequently, the magnetic coupling of an f^2 atom with its neighbors is much weaker, and f^2 atoms can be approximated as magnetically "empty" sites.

Define a baseline Z_0 as the localized f spectral weight corresponding to the situation that the system is in the f^2 configuration. Then $Z - Z_0$ gives the fraction of atoms which are in the f^3 configuration. Actually we do not know the local configuration for UTe at any pressure. However, since our purpose is to see the change with pressure, we artificially suppose that UTe is in the f^3 configuration at ambient pressure. This requires us to set the baseline Z_0 at the value so that $Z - Z_0 = 1$ at ambient pressure. With this setting of Z_0 , the fraction of f^3 atoms changes from 1 at ambient pressure to 0.8–0.85 at 20 GPa, depending on the choice of ρ_{cutoff} . We see that due to the localized f spectral loss, the fraction of magnetically empty sites increases with pressure.

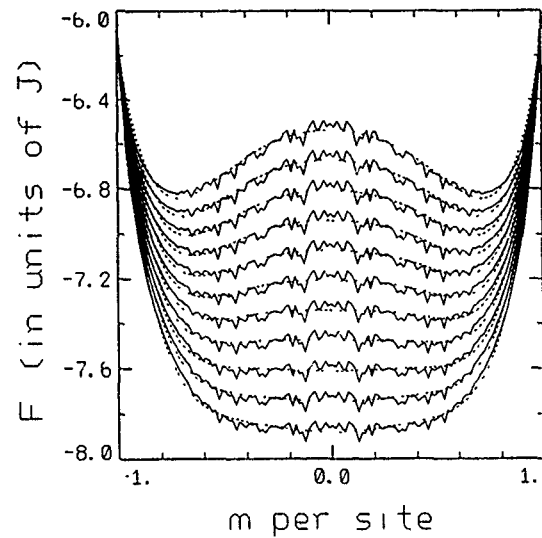


FIG. 5. Free energy F vs magnetization m at temperatures below and above T_c calculated from a computer simulation with an $8 \times 8 \times 8$ fcc Ising lattice for the case of no holes. The free energy (per site) is in units of coupling J . The solid lines are raw data from simulation; the dashed lines are results of the least square fitting to smooth out the noise. The curve on the top is for $T = 9.0J$, each of the curves below is for a temperature increment of $0.2J$ from the temperature corresponding to the curve above it. With increasing temperature, the double minimum disappears and m becomes zero at $T_c = 10.5J$.

The influence of localized f spectral loss on magnetic ordering can be simulated by an Ising model with holes. We use an Ising model in order to capture the very anisotropic nature of the two-ion hybridization-mediated interaction⁴ in a simple way; in future work we plan to treat this anisotropy more realistically as has already been done at ambient pressure.⁴ In this model, each lattice site fluctuates between being occupied by a moment or empty; the ratio of the average number of empty sites (holes) to the number of total sites is the fraction of magnetically empty sites in UTe as mentioned above; all the occupied sites are coupled to their nearest neighbors by an Ising interaction J , provided that neighbor is also occupied, while the holes do not couple to any sites.

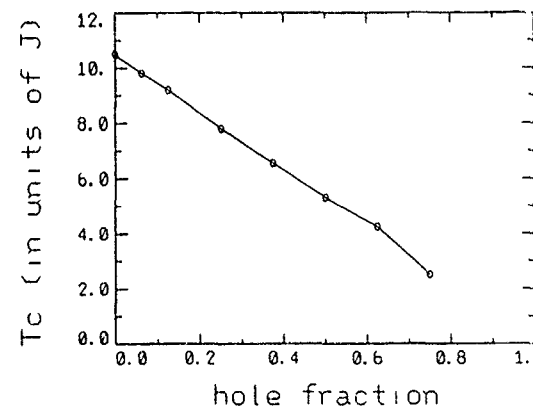


FIG. 6. T_c (in terms of two-ion coupling J) vs hole fraction. Calculated from a computer simulation with an $8 \times 8 \times 8$ fcc Ising lattice.

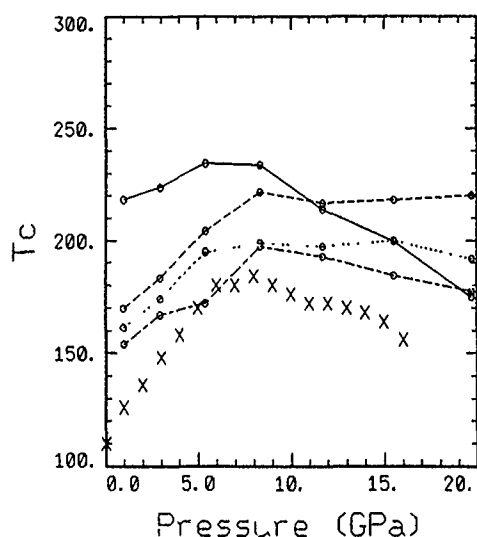


FIG. 7. T_c vs pressure for UTe. The solid line is calculated for $\rho_{\text{cutoff}} = 15\% \rho_{\text{max}}$; the long dashed line for $\rho_{\text{cutoff}} = 20\% \rho_{\text{max}}$; the short dashed line for $\rho_{\text{cutoff}} = 25\% \rho_{\text{max}}$; the long-short-dashed line for $\rho_{\text{cutoff}} = 28\% \rho_{\text{max}}$. The crosses are experimental data from Link *et al.* (Ref. 2).

Computer simulation calculates the curve of free energy versus total moment m of the Ising lattice at different temperatures. When the temperature is below T_c , the curves have double minima where $m \neq 0$; above T_c , the curves have a single minimum at $m = 0$. (see Fig. 5.) This provides the method of calculating T_c . By putting different numbers of holes in the Ising lattice, one can calculate the dependence of T_c on the hole fraction. In Fig. 6, we show the result for the dependence of T_c on the hole fraction calculated from a simulation using an $8 \times 8 \times 8$ fcc Ising lattice.

With the two-ion coupling J , the localized f spectral weight Z and their relation to the ordering temperature T_c obtained as discussed in the sequence numbered (1)–(3) above, we calculate T_c vs pressure. The results are shown in Fig. 7. Comparing with experiment, the initial increase of T_c is well predicted. Above 7.5 GPa, the calculated curves flatten, and do not go down as drastically as experiment. We believe that these results reflect the competing effects of hybridization as described at the beginning of this paper. But there are still some effects missing in the calculation: the transition from the increasing T_c to decreasing T_c region is more abrupt in experiment. We are in the process of looking for the reasons for this behavior.

In conclusion, we have performed 4 MTO band structure calculations for UTe at various pressures. The results match the lattice volume reduction with pressure. They also give the reduction of the real space $5f$ -electron number and the widening of the localized f spectral peak in energy space with pressure. We use a model Hamiltonian to relate to the localized f spectral peak in energy space, and then extract the effective two-ion interaction J from the width Γ of the localized f spectral peak. Bearing in mind that the $5f$ configuration fluctuates, we relate the area of this peak to the fraction of atoms which are in a configuration magnetically coupled to their neighbors. We use an Ising model with holes to simulate how the change of this fraction determines the change of

T_c . All the calculations are completely first principle based. A few artificial factors are involved, such as ρ_{cutoff} and Z_0 . This is legitimate since we are primarily interested in the change with pressure rather than the absolute scales of the calculated results.

The calculations capture the competing effects probed by pressure. These effects, namely the f spectral loss in real space and energy space and their interplay with hybridization, hold the key to understanding the correlated-electron systems. By probing these effects by pressure and calculating them from first principle, we are on the way to understanding these effects on a quantitative basis.

The behavior of UPt_3 ,³ a heavy-fermion antiferromagnet referred to in Sec. I, represents an especially interesting challenge for the theory discussed here. The scales of ordered moment and of pressures used are very different ($\sim 0.02 \mu_B/\text{U}$ atom and a few kbar) from those of UTe; and this is also true for the nature of the response, little change in T_N and a strong decrease in ordered moment. From the point of view of the theory described here, the behavior of UPt_3 would represent the extreme nonlinear limit of the magnetic ordering response under the combined effects of hybridization and band- f coulomb exchange prior to the “wash-out” of moment⁸ on entering the heavy-fermion regime. It would be interesting to see how the present theory fares once the anisotropy is treated more realistically under pressure as is already done at ambient pressure.⁴ Our educated guess is that in contrast to band theory⁹ which gives no magnetic ordering, our theory will give an overly large ordered moment. It would then be especially interesting to see the response to applied pressure. This would provide an important clue as to whether the non-Kondo on-site correlation effects included in our theory contain the essential ingredients for understanding heavy-fermion magnetic ordering or whether other omitted correlation effects are essential.

ACKNOWLEDGMENTS

This research was supported through the National Science Foundation under Grant No. DMR91-20333 and a grant from the European Institute for Transuranium Elements. Supercomputer time was provided by the San Diego Supercomputing Center. We have greatly benefited from discussions of the experimental situation with U. Benedict, P. Link, and G. H. Lander of the European Institute for Transuranium Elements. S. P. Lim performed the band theory total energy calculation which included polarization, as used in calculating the lattice constant.

¹H. R. Bartholin, J. Voiron, J. Schoenes, and O. Vogt, *J. Magn. Mater.* **63**, 175 (1987).

²P. Link, U. Benedict, J. Wittig, and H. Wühl, *J. Phys. Condens. Matter* **4**, 5585 (1992).

³S. M. Hayden, L. Taillefer, C. Vettier, and J. Flouquet, *Phys. Rev. B* **46**, 8675 (1992).

⁴B. R. Cooper, R. Siemann, D. Yang, P. Thayamballi, and A. Banerjee, in *Handbook on the Physics and Chemistry of the Actinides*, edited by A. J. Freeman and G. H. Lander (North-Holland, Amsterdam, 1985), Q. G. Sheng and B. R. Cooper, *J. Appl. Phys.* **69**, 5472 (1991); **70**, 6083 (1991); B. R. Cooper, Q. G. Sheng, and S. P. Lim, *J. Alloys Compounds* **192**, 223 (1993).

⁵L. Gerward, J. Staun Olsen, U. Benedict, S. Dabos, and O. Vogt, *High*

Pressure Research (Gordan and Breach, New York, 1989), pp. 235–251.

⁶G. Gilat and N. R. Bharatiya, *Phys. Rev. B* **6**, 1013 (1972).

⁷See, for instance, P. Fulde, *Electron Correlations in Molecules and Solids* (Springer, New York), p. 288.

⁸B. R. Cooper, Q. G. Sheng, S. P. Lim, C. Sanchez-Castro, N. Kioussis, and J. M. Wills, *J. Magn. Magn. Mater.* **108**, 10 (1992).

⁹M. B. Suvasini, G. Y. Guo, W. M. Temmerman, and G. A. Gehring, *Phys. Rev. Lett.* **71**, 2983 (1993).

Magnetic properties of the lattice Anderson model

H. Q. Lin

Department of Physics, University of Illinois at Urbana-Champaign, Urbana, Illinois 61801

H. Chen

Cray Research, Inc., Minneapolis, Minnesota 55121

J. Callaway

Department of Physics, Louisiana State University, Baton Rouge, Louisiana 70803-4001

We perform exact diagonalization studies of the one-dimensional lattice Anderson model for various clusters. The ground state energy and spin-spin correlation functions are calculated as functions of Hubbard U , hybridization V , and f level occupancies. For the symmetric case, we compare our results with weak and strong coupling perturbation theory.

We study the lattice Anderson model on finite, one-dimensional (1D), lattices in this paper. The model is defined by the Hamiltonian

$$H = -t \sum_{i\sigma} (c_{i\sigma}^\dagger c_{i+1\sigma} + hc) + E_f \sum_{i\sigma} n_{fi\sigma} + U \sum_i n_{fi\uparrow} n_{fi\downarrow} + V \sum_{i\sigma} (c_{i\sigma}^\dagger f_{i\sigma} + hc), \quad (1)$$

where $c_{i\sigma}^\dagger(c_{i\sigma})$ and $f_{i\sigma}^\dagger(f_{i\sigma})$ are creation (annihilation) operators for electrons in d and f orbitals on site i with spin σ , and $n_{fi\sigma} = f_{i\sigma}^\dagger f_{i\sigma}$. The d electrons hop with amplitude t , thus forming a conduction band e_k . The f electrons hybridize with d electrons with amplitude V , and have the usual Hubbard interaction U between spin up and down f electrons on the same site. The site energy E_f defines the relative position of f states with respect to the Fermi energy of the d electrons. An important special case is the so-called symmetric Anderson model in which $E_f = -U/2$.

When $U=0$, one can diagonalize Eq. (1) easily. Two bands are obtained with energies

$$E_k^\pm = \frac{1}{2} [e_k + E_f \pm \sqrt{(e_k - E_f)^2 + 4V^2}], \quad (2)$$

in which $e_k = -2t \cos(k)$ is the d electron band energy. A characteristic quantity in the Anderson lattice model is the gap Δ that separates the two bands. This is given for $U=0$ by $2\Delta = E_{k=0}^+ - E_{k=\pi}^- = \sqrt{4t^2 + 4V^2} - 2t$. The magnitude of the ratio U/Δ defines weak and strong coupling regions.

This model has been studied for many years in connection with valence fluctuation problems and an extensive literature exists.¹⁻³ Several approximation techniques have been applied to deal with many-body aspects of this model including renormalization group analysis,⁴ the Gutzwiller variational approach,⁵⁻⁷ the large-orbital-degeneracy $1/N$ expansion,^{8,9} and perturbation theory.^{10,11} Numerical calculations have also been carried out.¹¹⁻¹⁹

In this paper we use an exact diagonalization method to study the ground state properties of model of Eq. (1) for lattices with $N=2, 4, 6$, and 8 . We are restricted by computer memories so that we are unable to go beyond $N=8$. In order to obtain reliable answers in the thermodynamic limit, finite size extrapolation is needed and one may wonder if these

lattices are large enough. As we will show in the following, fortunately, we are able to achieve accurate extrapolation based on our finite lattice results.

One can show, without much difficulty, that, for a 1D tight binding band, the ground state energy per site on an N site lattice with total electron number $N_e = 4n$ is

$$\frac{E_{4n}}{N} = \frac{2}{N} \sum_k e(k) = -\frac{2t}{\pi} \sin\left(\frac{2n\pi}{N}\right) \frac{\pi/N}{\tan(\pi/N)}, \quad (3)$$

while for the infinite system with density N_e/N it is

$$\frac{E_\infty}{N} = -\frac{2t}{\pi} \sin k_f = -\frac{2t}{\pi} \sin\left(\frac{2n\pi}{N}\right), \quad (4)$$

where $k_f = (\pi/2)(N_e/N)$ is the Fermi wave number. Thus, finite lattice results for $N_e = 4n$ give an upper bound.

With total electron number $N_e = 4n + 2$, the ground state energy per site is

$$\begin{aligned} \frac{E_{4n+2}}{N} &= \frac{2}{N} \sum_k e(k) \\ &= -\frac{2t}{\pi} \sin\left(\frac{2n\pi}{N} + \frac{\pi}{N}\right) \frac{\pi/N}{\sin(\pi/N)}, \end{aligned} \quad (5)$$

while for the infinite system with density N_e/N it is

$$\frac{E_\infty}{N} = -\frac{2t}{\pi} \sin\left(\frac{2n\pi}{N} + \frac{\pi}{N}\right). \quad (6)$$

Thus finite lattice results for $N_e = 4n + 2$ give a lower bound.

For the symmetric Anderson lattice model, the oscillation between lattice size $N=4n$ and $N=4n+2$ is still present, as we found numerically. Therefore, we can use data obtained from $N=4n$ and $4n+2$ to set up upper and lower bounds for infinite system results. This approach can also be applied to other quantities to be discussed below. Hence we are able to obtain results for infinite systems with reasonable accuracy. We also tried other extrapolation schemes by assuming asymptotic forms of calculated quantities.

We have performed exact diagonalization calculations for the symmetric case with $t=1.0$, $V=0.5$ (hence $\Delta=0.12$), and U varying from 0 to 4, i.e., from weak coupling to strong coupling, in the $1/2$ -filled sector. Our results for the ground state energy per site are shown in Fig. 1. The estimated errors in extrapolations are within the size of the symbol.

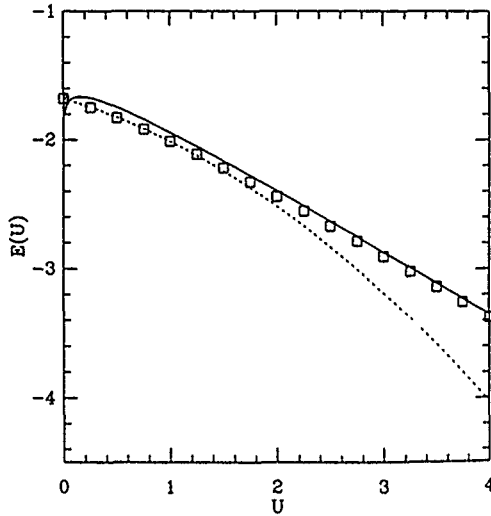


FIG. 1. The ground state energy per site as function of U for the symmetric Anderson lattice model with $t=1$, $V=0.5$. The dashed line is the weak coupling perturbation result from Eq. (7), and the solid line is the strong coupling perturbation result from Eq. (9). The squares are the exact diagonalization results and the uncertainties in the infinite system extrapolation are within the size of the symbol.

According to perturbation theory¹¹ for the symmetric case in the weak coupling limit where U/Δ is small, the ground state energy per site is

$$E(U) = \frac{2}{N} \sum_k E_k^- - \frac{U}{4} - \frac{U^2}{N^3} \sum_{pkq} \frac{v_p^2 u_{p+q}^2 v_{k+q}^2 u_k^2}{E_{k+q}^+ + E_p^+ - E_k^- - E_{p+q}^-} \quad (7)$$

with

$$u_p^2 = \frac{1}{2} [1 + e_p^2 / (e_p^2 + 4V^2)^{1/2}], \quad (8)$$

$$v_p^2 = \frac{1}{2} [1 - e_p^2 / (e_p^2 + 4V^2)^{1/2}]. \quad (9)$$

In the strong coupling limit where U/Δ is large, the ground state energy per site is

$$E(U) = -\frac{U}{2} + \frac{2}{N} \sum_k e_k f(e_k) - \frac{2V^2}{N} \sum_k \frac{1-f(e_k)}{U/2 + e_k}, \quad (10)$$

with $f(e_k)$ being the zero temperature Fermi factor.

We show weak coupling results as the dashed line and strong coupling results as the solid line in Fig. 1. Note that there is a singularity in strong coupling limit as $U \rightarrow 0$ [roughly $\ln(U)$] but it is hard to see from Fig. 1.

As U increases from 0 to ∞ , electrons tend to localize in the f orbitals and form local moments. We measure these moments by m_{fz}^2 , defined by

$$m_{fz}^2 = \langle (n_{f\uparrow} - n_{f\downarrow})^2 \rangle, \quad (11)$$

which varies from $\frac{1}{2}$ when $U=0$, to 1 when $U=\infty$. For weak coupling we have

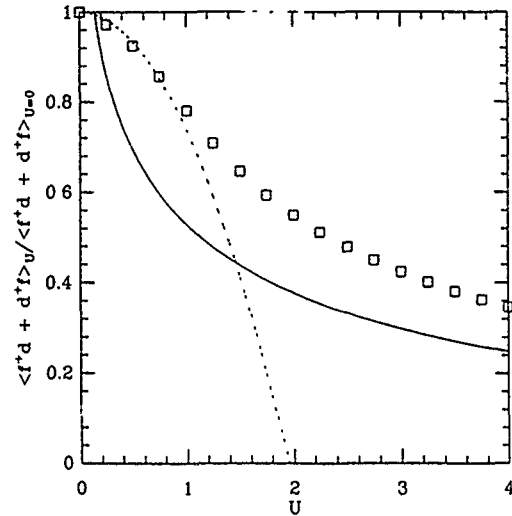


FIG. 2. Square of the f orbital local moment as function of U for the same case as in Fig. 1.

$$m_{fz}^2 = \frac{1}{2} + \frac{4U}{N^3} \sum_{pkq} \frac{v_p^2 u_{p+q}^2 v_{k+q}^2 u_k^2}{E_{k+q}^+ + E_p^+ - E_k^- - E_{p+q}^-}, \quad (12)$$

while for strong coupling we have

$$m_{fz}^2 = 1 - \frac{2V^2}{N} \sum_k \frac{1-f(e_k)}{(U/2 + e_k)^2}. \quad (13)$$

We show these results as the dashed line and solid line in Fig. 2, along with data points obtained from our exact diagonalization studies. Again, estimated errors in extrapolations are within the size of the symbol.

From Fig. 2, it is evident that weak coupling perturbation is invalid for $U/\Delta > 8$ and strong coupling perturbation gives bad answers for $U/\Delta < 20$. One may note that for energy calculations, both perturbation results are quite good over a much wider range of U/Δ . This behavior occurs in many highly correlated systems and our results show that a good ground state energy is not a sufficient criterion for the validity of an approximation scheme.

As U increases from zero, the effective hybridization is expected to be reduced due to correlations. To measure this reduction we calculate the matrix element $\langle c_{i\sigma}^\dagger f_{i\sigma} + hc \rangle$ and plot the ratio with respect to its $U=0$ value in Fig. 3. The weak and strong coupling results can be obtained from $\frac{1}{2} \partial E / \partial V$. We see that weak coupling perturbation is pretty good for $U/\Delta < 8$ again, but strong coupling perturbation is not good although qualitatively reasonable. This can be understood by observing that in weak coupling the perturbation was carried out to second order in U , while in strong coupling the perturbation was only carried out to first order in $1/U$.

Now we consider the nonsymmetric case in which $E_f \neq -U/2$. As E_f varies, one enters different physical regions. Basically, there are five regions.¹⁴ (1) Maximally occupied f states, where the f orbitals are doubly occupied ($n_f \sim 2$, $n_c \sim 0$). This region is characterized roughly by $E_f < -U - 2t$. (2) The first mixed valence region, $-U - 2t < E_f < -U - t$. The f occupation in this region

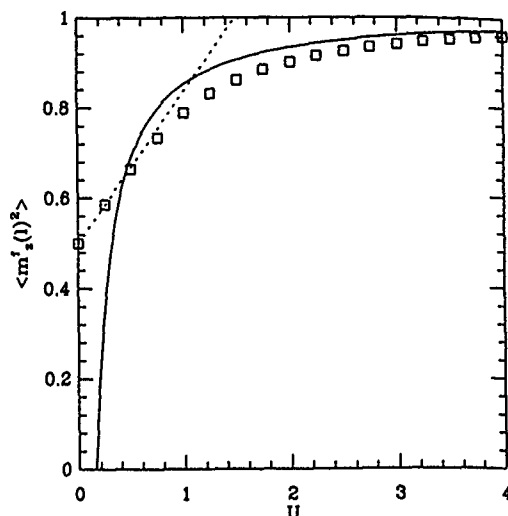


FIG. 3. The ratio of the hybridization matrix element $\langle c^\dagger_{f\sigma} + hc \rangle$ to its $U=0$ value as a function of U for the same case as in Fig. 1.

changes between 1 and 2. (3) The Kondo region, in which one has $n_f \sim 1$, $n_c \sim 1$. Its range is roughly $-U - t < E_f < t$. (4) The second mixed valence region, $t < E_f < 2t$. The f occupation in this region changes between 1 and 0. (5) The region of empty f levels ($n_f \sim 0$), $E_f > 2t$. Figure 4 shows f and c electron occupations and clearly demonstrates these five regions.

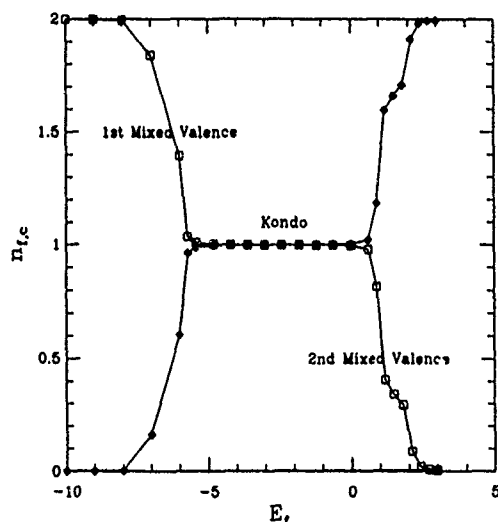


FIG. 4. The electron occupation of f orbitals (squares) and c orbitals (diamonds) as a function of E_f for $U=5.0$, $t=1.0$, and $V=0.1$.

In summary, we have studied some ground state properties of the one-dimensional Anderson lattice model by an exact diagonalization technique. We have performed finite size analysis and estimated results for infinite systems. Comparison with perturbation theory for the symmetric Anderson lattice model showed that weak coupling calculations are quite accurate for $U/\Delta < 8$ and strong coupling calculations are reasonably satisfactory for $U/\Delta > 20$. For the nonsymmetric case, we found that five distinct regions exist depending on the site energy E_f . The different types of physical behavior illustrated in Fig. 4 have been found in small system calculations for other geometries,¹⁴ and are presumably characteristic of the strong interaction-weak hybridization sector of the model generally, independent of the restriction of the present calculations to one dimension. Within the Kondo regime where n_c and n_f are close to 1, our finding that the energy and other physical quantities vary smoothly between weak and strong coupling limits is probably also independent of dimensionality.

Some of the computations were performed at the National Center for Supercomputing Applications, University of Illinois at Urbana-Champaign, and at National Energy Research Supercomputer Center, Lawrence Livermore National Laboratory. We are grateful for their support. The portion of the work performed at LSU was supported by the National Science Foundation under Grant No. DMR 91-20166.

¹P. Fulde, J. Keller, and G. Zwicknagel, in *Solid State Physics*, edited by H. Ehrenreich and D. Turnbull (Academic, New York, 1988), Vol. 41, p. 1, and references therein.

²D. M. Newns and N. Read, *Adv. Phys.* **36**, 799 (1987).

³N. E. Bickers, *Rev. Mod. Phys.* **59**, 845 (1987).

⁴H. R. Krishna-Murthy, J. W. Wilkins, and K. G. Wilson, *Phys. Rev. B* **21**, 1003 (1980).

⁵B. H. Brandow, *Phys. Rev. B* **33**, 215 (1986).

⁶T. M. Rice and K. Ueda, *Phys. Rev. Lett.* **55**, 995 (1985); **55**, 2093 (1985); *Phys. Rev. B* **34**, 6420 (1986).

⁷C. M. Varma, W. Weber, and L. J. Randall, *Phys. Rev. B* **33**, 1015 (1986).

⁸N. Read, D. M. Newns, and S. Doniach, *Phys. Rev. B* **30**, 3841 (1984).

⁹A. J. Millis and P. A. Lee, *Phys. Rev. B* **35**, 3394 (1987).

¹⁰K. Yamada and K. Yoshida, in *Proceedings of the Third Taniguchi Symposium*, Mount Fuji, Japan, 1980, edited by T. Moriya (Springer, Berlin, 1981), p. 210.

¹¹R. Blankenbecler, J. R. Fulco, W. Gill, and D. J. Scalapino, *Phys. Rev. Lett.* **58**, 411 (1987).

¹²J. E. Gubernatis, J. E. Hirsch, and D. J. Scalapino, *Phys. Rev. B* **35**, 8478 (1987); J. E. Gubernatis, *ibid.* **36**, 394 (1987).

¹³R. M. Fye, J. E. Hirsch, and D. J. Scalapino, *Phys. Rev. B* **35**, 4901 (1987); **44**, 7486 (1991).

¹⁴J. Callaway, D. P. Chen, D. G. Kanhere, and P. K. Misra, *Phys. Rev. B* **38**, 2583 (1988); Y. Ziang and J. Callaway, *ibid.* **38**, 641 (1988); J. Callaway, J. W. Kim, L. Tan, and H. Q. Lin, *Phys. Rev. B* **48**, 11 545 (1993).

¹⁵A. Reich and L. M. Falicov, *Phys. Rev. B* **34**, 6752 (1986).

¹⁶J. A. White, *Phys. Rev. B* **46**, 13905 (1992).

¹⁷P. Santini, L. Andreani, and H. Beck, *Phys. Rev. B* **47**, 1130 (1993).

¹⁸K. Ueda, *J. Phys. Soc. Jpn.* **58**, 3465 (1989); K. Yamamoto and K. Ueda, *ibid.* **59**, 3284 (1990).

¹⁹R. Jullien and R. M. Martin, *Phys. Rev. B* **26**, 6173 (1982).

Effects of doping in Kondo insulators (invited)

P. Schlottmann

Department of Physics, Florida State University, Tallahassee, Florida 32306

Kondo insulators like $\text{Ce}_3\text{Bi}_4\text{Pt}_3$ and CeNiSn are compounds with small-gap semiconductor properties. Nonmagnetic impurities, so-called Kondo holes, break the translational invariance and hence the coherence of the ground state. Impurity states can be introduced by (i) substituting the rare earth (actinide) ion or (ii) by replacing (or adding, removing) one of the ligand atoms. Isolated impurities usually give rise to bound states in the gap. Depending on the nature of the impurity (charge neutral or a dopand) the Fermi level is pinned by the impurity level or lies in the gap. In the former case the Kondo hole has magnetic properties (Curie susceptibility and Schottky anomaly in the specific heat), while in the latter situation the properties are nonmagnetic. For a finite concentration of Kondo holes the situations (i) and (ii) are qualitatively different. In (i) it gives rise to an impurity band inside the gap of the semiconductor. The height and width of the impurity band in the f -electron density of states are proportional to $c^{1/2}$ for small concentrations. If the impurities are charge neutral the Fermi level lies in the impurity band giving rise to a specific heat proportional to T and a Pauli-like susceptibility. If the impurities dope the bands the properties remain semiconducting with a strongly reduced gap. For ligand impurities [case (ii)] tails of impurity states develop close to the gap edges, suppressing in this way the gap. The system remains a semiconductor if the impurities are charge neutral, but $C \propto T$ and χ is finite if they are dopands.

I. INTRODUCTION

The effects of coherence in heavy-fermion systems are most pronounced in so-called Kondo insulators, which have small-gap semiconductor properties due to the hybridization gap at the Fermi level. The Kondo insulators SmS , SmB_6 , and TmSe were already an exciting topic more than ten years ago.¹ The more recent discovery of several Ce, Yb, and U based Kondo insulators (e.g., CeNiSn ,² $\text{Ce}_3\text{Bi}_4\text{Pt}_3$,³ YbB_{12} ,⁴ and UNiSn)⁵ has renewed the interest in this subject. All systems seem to be nonmagnetic at low T , except TmSe and UNiSn for which antiferromagnetic long-range order (for UNiSn accompanied by an insulator-metal transition) has been reported. In view of the small energy gaps involved the properties of these compounds strongly depend on strains in the crystal and impurities. Adding impurities, in particular small amounts of nonmagnetic impurities (Kondo holes), breaks the translational invariance of the lattice and gradually destroys the coherence of the heavy-fermion ground-state. Kondo holes are experimentally⁶ realized by substituting, e.g., Ce or U ions in a stoichiometric lattice by La or Th impurities, or by replacing, adding, or removing a ligand atom. Depending on the characteristics of the impurity (e.g., charge neutral or dopand) the properties of the Kondo hole can be magnetic or nonmagnetic. In this paper we discuss several possible situations that may arise, extending in this way our previous results.^{7,8}

In earlier publications^{9,10} we reported a microscopic theory of the Kondo hole, for both the metallic and insulating situations. The Kondo hole is a missing f electron at a given site, which is introduced by a very large local f level energy, preventing the occupation of the f level. Correlations within the f band are introduced via a self-energy, evaluated to second order in U . We studied the scattering off the Kondo hole in the local density of f states (DOS) in the neighborhood of the nonmagnetic impurity. The f DOS at the Kondo hole is zero. In a Kondo insulator a bound state develops in the

energy gap, whose spectral weight decreases rapidly with increasing distance from the impurity. These states only appear in the coherent phase. In this paper we generalize these results by including a potential scattering of the conduction electrons. If the Fermi level is pinned by the bound state the properties of the Kondo hole are magnetic; on the other hand, if the Fermi level lies in the gap (doping) the impurity is nonmagnetic. We furthermore consider here a defect causing a local change in the hybridization (e.g., missing or substituted ligand atom).

When the concentration of Kondo holes (locally missing f electrons) is increased an impurity band forms, gradually smearing the hybridization gap of the Kondo insulator. For a low density of impurities, c , the width and the height of this band depend nonanalytically on c .⁷ If the impurities are charge neutral (e.g., La replacing Ce) the Fermi level is pinned within this band and there is a small low T regime with the specific heat proportional to T with a strongly enhanced γ and a Curie-Weiss-like susceptibility. If the impurities dope the system with electrons or holes (e.g., Th replacing Ce) the Fermi level lies in the reduced gap and excitations have to overcome the gap (nonmagnetic semiconductor). Finally, if the impurity is a ligand defect (local perturbation of the hybridization) the band edges of the hybridization gap are strongly reduced. If the impurities are charge neutral the Fermi level lies in the gap, while doping converts it into a metal.

The remainder of this paper is organized as follows. In Sec. II we introduce the equations leading to the Kondo hole bound state and the impurity band in the case of a finite concentration. Properties of isolated Kondo holes are discussed in Sec. III, while in Sec. IV we present our results for finite c . Concluding remarks follow in Sec. V.

II. THE MODEL AND THE f DENSITY OF STATES

We consider the Anderson lattice without orbital degeneracy

$$H_0 = \sum_{\mathbf{k}\sigma} \epsilon_{\mathbf{k}} c_{\mathbf{k}\sigma}^\dagger c_{\mathbf{k}\sigma} + \epsilon_f \sum_{i\sigma} f_{i\sigma}^\dagger f_{i\sigma} + U \sum_i n_{i\uparrow} n_{i\downarrow} + V \sum_{\mathbf{k}\sigma} (c_{\mathbf{k}\sigma}^\dagger f_{\mathbf{k}\sigma} + f_{\mathbf{k}\sigma}^\dagger c_{\mathbf{k}\sigma}), \quad (2.1)$$

where V is the on-site hybridization, ϵ_f is the f level energy, U is the Coulomb repulsion in the f shell, $n_{i\sigma} = f_{i\sigma}^\dagger f_{i\sigma}$, $c_{\mathbf{k}\sigma}^\dagger$ ($f_{\mathbf{k}\sigma}^\dagger$) creates a conduction electron (f electron) with momentum \mathbf{k} and spin σ , and $f_{i\sigma}$ is the Wannier state at the site \mathbf{R}_i . An isolated Kondo hole at the site \mathbf{R} can be introduced by the following Hamiltonian:

$$H_1 = \frac{1}{N} \sum_{\mathbf{k}\mathbf{k}'\sigma} \exp[-i(\mathbf{k}-\mathbf{k}')\mathbf{R}] [\Delta \epsilon_f f_{\mathbf{k}\sigma}^\dagger f_{\mathbf{k}'\sigma} + W c_{\mathbf{k}\sigma}^\dagger c_{\mathbf{k}'\sigma} + \Delta V (f_{\mathbf{k}\sigma}^\dagger c_{\mathbf{k}'\sigma} + c_{\mathbf{k}\sigma}^\dagger f_{\mathbf{k}'\sigma})], \quad (2.2)$$

where N is the number of sites, and $\Delta \epsilon_f$, W , and ΔV are the scattering potentials experienced by the electrons. In earlier publications^{7,9} we only considered the scattering of the f electrons in the limit $\Delta \epsilon_f \rightarrow \infty$ and $W = \Delta V = 0$. $\Delta \epsilon_f \rightarrow \infty$ corresponds to a missing f electron at the site \mathbf{R} . In this paper we first solve the general scattering problem and discuss then special limits.

Since the impurity potential is factorizable, the $U=0$ scattering problem can be solved exactly.⁹ It is convenient to introduce the matrix Green's function

$$\hat{G}_{\mathbf{k},\mathbf{k}'}(z) = \begin{pmatrix} \langle\langle f_{\mathbf{k}}; f_{\mathbf{k}'}^\dagger \rangle\rangle_z & \langle\langle f_{\mathbf{k}}; c_{\mathbf{k}'}^\dagger \rangle\rangle_z \\ \langle\langle c_{\mathbf{k}}; f_{\mathbf{k}'}^\dagger \rangle\rangle_z & \langle\langle c_{\mathbf{k}}; c_{\mathbf{k}'}^\dagger \rangle\rangle_z \end{pmatrix}, \quad (2.3)$$

where we dropped the spin index, since for $U=0$ up and down spins decouple. Using the equation of motion for \hat{G} we obtain after some algebra

$$\hat{G}_{\mathbf{k},\mathbf{k}'}(z) = \hat{G}_{\mathbf{k},\mathbf{k}'}^0(z) \delta_{\mathbf{k},\mathbf{k}'} + \hat{G}_{\mathbf{k},\mathbf{k}'}^0(z) \hat{T}_{\mathbf{k},\mathbf{k}'}(z) \hat{G}_{\mathbf{k}',\mathbf{k}'}^0(z) \quad (2.4a)$$

with the t matrix given by

$$\hat{T}_{\mathbf{k},\mathbf{k}'}(z) = (1/N) e^{-i\mathbf{k}\mathbf{R}} \hat{M} \left(\hat{I} - (1/N) \sum_{\mathbf{k}''} \hat{G}_{\mathbf{k}'',\mathbf{k}''}^0(z) \hat{M} \right)^{-1} e^{i\mathbf{k}'\mathbf{R}}, \quad (2.4b)$$

where \hat{I} is the identity, and

$$\hat{M} = \begin{pmatrix} \Delta \epsilon_f & \Delta V \\ \Delta V & W \end{pmatrix}. \quad (2.4c)$$

Here $\hat{G}_{\mathbf{k}}^0(z)$ is the Green's function without impurity. The bound states in the gap of the Kondo insulator are given by the poles of the t matrix. The components of the quantity $\hat{G}^0(z) = (1/N) \sum_{\mathbf{k}} \hat{G}_{\mathbf{k}}^0(z)$ are related to the DOS of the conduction electrons. Assuming an elliptic DOS of half-width D [$g(z) = 1/(z - \epsilon_f)$],

$$F(z) = \frac{1}{N} \sum_{\mathbf{k}} \frac{1}{z - \epsilon_{\mathbf{k}}} = \frac{2}{D^2} (z - \sqrt{z^2 - D^2}), \quad (2.5)$$

$$\begin{aligned} G_{ff}^0(z) &= g(z) + V^2 g(z)^2 F[z - V^2 g(z)], \\ G_{cf}^0(z) &= G_{fc}^0(z) = V g(z) F[z - V^2 g(z)], \\ G_{cc}^0(z) &= F[z - V^2 g(z)]. \end{aligned} \quad (2.6)$$

The imaginary part of these quantities vanishes inside the gap, and depending on the scattering parameters the real part of the t matrix may diverge, giving rise to a bound state. Equations (2.4)–(2.6) then completely determine the f electron Green's function for one Kondo hole in the absence of Coulomb repulsion.

The main effect of the Coulomb repulsion is to introduce an f electron self-energy. For heavy electrons the momentum dependence of the self-energy is much less important than its energy dependence. We limit ourselves to a self-energy to second order in U about the Hartree–Fock solution.¹¹ Schweitzer and Czychoł¹² developed a systematic approach based on a $1/d$ expansion (d is the dimension)¹³ to overcome the tedious \mathbf{k} integrations for the periodic Anderson lattice. The calculation is greatly simplified in leading order ($d \rightarrow \infty$), which corresponds to the local approximation (momentum independent) and already contains the most relevant correlations. The \mathbf{k} dependence, introduced by the $1/d$ corrections,¹² is weak for $d=3$.

The self-energy to order U^2 and within the local approximation ($d \rightarrow \infty$) has the correct analytic properties and qualitatively the expected physical features. The correlations are momentum independent and incorporated into the $U=0$ solution for the Kondo hole by renormalizing the bare f level energy according to $\epsilon_f \rightarrow \epsilon_f + (1/2) U n_f + \Sigma_U(z)$, where n_f is the f level occupation. The self-energy is not calculated self-consistently¹⁴ with dressed Green's functions, i.e., propagators with a self-energy, since a renormalized vertex would also be needed to avoid violations of Ward identities. Similarly, we do not self-consistently incorporate the effects of the Kondo hole into $\Sigma_U(z)$. The impurity breaks the translational invariance; this affects the f electron propagator giving rise to an additional \mathbf{k} dependence in the self-energy, which is neglected here.

To second order in U and within the local approximation we have^{7,15}

$$\Sigma_U(z) = U^2 (-i) \int d\lambda e^{i\lambda z} [A(\lambda)^2 B(-\lambda) + B(\lambda)^2 A(-\lambda)], \quad (2.7a)$$

$$A(\lambda) = \int_{-\infty}^{\mu} d\omega e^{-i\lambda\omega} \rho(\omega), \quad B(\lambda) = \int_{\mu}^{\infty} d\omega e^{-i\lambda\omega} \rho(\omega), \quad (2.7b)$$

where μ is the chemical potential, and $\rho(\omega) = -(1/\pi) \text{Im } G_{ff}^0(z)$, with $z = \omega + i0$ and ϵ_f containing the Hartree–Fock shift due to the Coulomb interaction.

For the (electron-hole) symmetric case, i.e., $\epsilon_f = 0$ and exactly two electrons per site, the system is an insulator and the chemical potential lies in the gap, $\mu = 0$. The imaginary part of the self-energy has a gap of about three times the gap of the bare DOS (convolution of three propagators). The real and imaginary parts of $\Sigma_U(z)$ for this case as a function of ω are shown in Fig. (1). For the purpose of studying Kondo

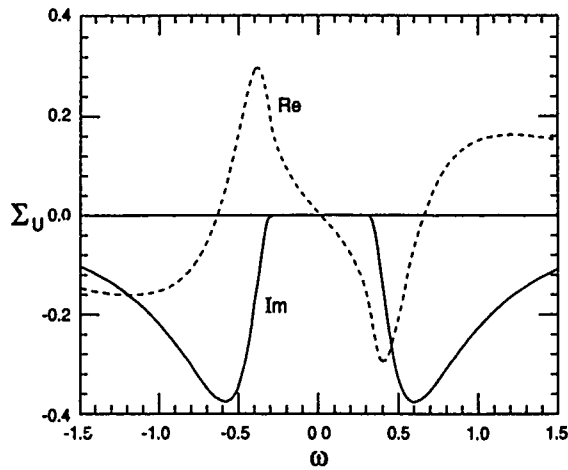


FIG. 1. Real (dotted) and imaginary (full line) parts of the Coulomb self-energy to second order in U as a function of ω for $V=1$, $D=10$, $\epsilon_f=0$ (Hartree-Fock shifted), $U=1$ and two electrons per site. As expected for an insulator the imaginary part vanishes in the interval $-3V^2/D < \omega < 3V^2/D$ and the slope of the real part is negative.

hole bound states in the gap of a Kondo *insulator*, the self-energy is then real over the range of interest of ω . Note that the real part of $\Sigma_U(z)$ has a negative slope, leading to the well-known Kondo mass enhancement also relevant for impurity bands (see below), and to a narrowing of the gap (reduction of the hybridization, Kondo temperature). A discussion of the insulating asymmetric and the metallic situations can be found in Refs. 8 and 9.

To generalize the above to a finite concentration of impurities, c , we rewrite the perturbed Green's function as a Dyson equation with an impurity self-energy $\hat{\Sigma}_{\text{imp}}(z, \epsilon_f, V) = cN\hat{T}_{\text{kk}}(z)$. This matrix self-energy renormalizes the frequency, the f level energy and the hybridization; a self-consistent treatment of this self-energy leads to

$$\tilde{z} = z - \Sigma_{cc}(\tilde{z}, \tilde{\epsilon}_f, \tilde{V}), \quad (2.8a)$$

$$\tilde{\epsilon}_f = \epsilon_f + \Sigma_{ff}(\tilde{z}, \tilde{\epsilon}_f, \tilde{V}) - \Sigma_{cc}(\tilde{z}, \tilde{\epsilon}_f, \tilde{V}) + \Sigma_U(z), \quad (2.8b)$$

$$\tilde{V} = |V + \Sigma_{fc}(\tilde{z}, \tilde{\epsilon}_f, \tilde{V})|, \quad (2.8c)$$

where the bare ϵ_f contains the Hartree-Fock shift $Un_f/2$, and we take the absolute value of the hybridization to keep it real (this corresponds to a gauge transformation, which has no effect on the f DOS). Equations (2.8) are equivalent to the sum of all diagrams with noncrossing impurity lines. They lead to a complex f level energy and finite imaginary part of \tilde{z} , which broaden the δ function of the Kondo hole bound state giving rise to an impurity band of finite width. Note that Σ_U is not renormalized; its effect on the Kondo hole band is more quantitative than qualitative.

III. RESULTS FOR ISOLATED KONDO HOLES

We have to distinguish the situations of a missing f electron (e.g., a La ion replacing a Ce atom) and a ligand defect. We first treat the missing f electron case, which corresponds to the limit $\Delta\epsilon_f \rightarrow \infty$. Carrying out the matrix products in Eq. (2.4) we obtain

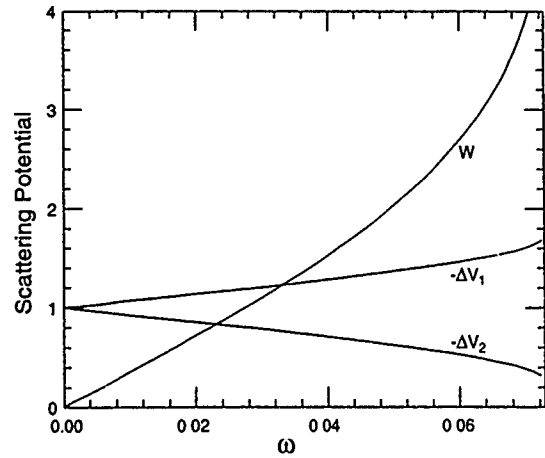


FIG. 2. Position of the bound state(s) in the hybridization gap for the symmetric Kondo insulator with $\epsilon_f=0$, $V=1$, $U=1$, $D=10$ and two electrons per site as a function of the scattering potential. The curve W refers to $\Delta\epsilon_f=\infty$, so that the only relevant scattering parameter is W . The energy of the boundstate is an odd function of W . The curves denoted with ΔV correspond to the ligand defect with $\Delta\epsilon_f=W=0$. There are two resonances for negative values of ΔV . $\Delta V(\omega)$ is an even function. Note that boundstates do not exist for all values scattering potentials.

$$\hat{\Sigma}_{\text{imp}}(z, \epsilon_f, V) = -c \{ G_{ff}^0(z) - W [G_{ff}^0(z) G_{cc}^0(z) - G_{cf}^0(z) G_{fc}^0(z)] \}^{-1} \times \begin{pmatrix} 1 - W G_{cc}^0(z) & W G_{fc}^0(z) \\ W G_{cf}^0(z) & -W G_{ff}^0(z) \end{pmatrix}. \quad (3.1)$$

This self-energy does not depend on ΔV , since the large $\Delta\epsilon_f$ potential inhibits the occupation of the f level. For $W=0$ we recover the results of Refs. 7 and 8. If W does not exceed a critical value, a δ -function-like bound state develops in the gap of the insulator. For the symmetric Kondo insulator ($\epsilon_f=0$ and two electrons per site) and $U=1$ Fig. 2 shows the position of the pole as a function of W , which moves from one band edge to the other. For larger values of W no bound state is formed. On a lattice the spectral weight of this bound state in the local f DOS falls off rapidly with the distance from the impurity,^{9,10} so that the bound state is almost completely localized on the nearest neighbor sites to the Kondo hole. Since there are no f electrons at the site of the Kondo hole, its local f DOS is zero. Both the size of the gap and the spectral weight of the bound state decrease with U via the self-energy as a consequence of the reduction of charge fluctuations. This bound state also appears in the d electron DOS.

The properties of the Kondo hole bound state depend on the nature of the impurity; for instance, if a trivalent Ce ion is replaced by La there is no change in valence and the Fermi level is pinned at the impurity boundstate. On the other hand, if Ce is substituted by Th, which is tetravalent, there is an additional conduction electron and the bound state will be filled. The Fermi level in this case lies in the gap between the bound state and the empty band edge and the properties remain those of a nonmagnetic insulator. In the former case, however, when the Fermi level is pinned by the impurity, the Kondo hole is magnetic: Despite the fact it originated from a

missing f electron its zero-field susceptibility follows a Curie law. A small magnetic field polarizes the localized state at $T=0$ and induces a Schottky anomaly in the specific heat in analogy to a spin 1/2. This effective spin could in principle be experimentally detected by electron paramagnetic resonance. In practice, however, the inhomogeneous broadening of this line will make its observation difficult. Due to slightly different surroundings the resonance energies of the defects have a distribution, whose width has to be of the order of 0.1 K or smaller to be observable. Kondo holes affect the low frequency infrared absorption in Kondo insulators. Large magnetic fields would still polarize Kondo holes with a distribution of bound state energies, but would also modify the bulk properties of the Kondo insulator, e.g., reduce its gap.¹⁶

In a metallic environment, on the other hand, low energy electron-hole excitations are allowed and the imaginary part of the self-energy $\Sigma_U(z)$ is nonzero everywhere except at the Fermi level. The hybridization gap is smeared to a pseudogap, i.e., the f DOS is nonzero everywhere over the entire range of interest. The Kondo hole now forms a pseudo-bound-state of finite width,¹⁰ which is small if we have very heavy fermions. The energy of the bound state lies in the pseudogap, i.e., not at the Fermi level, but its spectral weight is still located in the neighboring cells to the impurity. The magnetic and thermal properties of this pseudo-bound-state are those of a resonant level off-resonance with the Fermi level, i.e., a Curie-Weiss law and a Schottky-like specific heat with the Weiss temperature and the position of the maximum of C given by the energy of the resonance.

We now treat the ligand defect. In principle, all three scattering amplitudes in Eq. (2.2) could be nonzero, but the most relevant one now is ΔV . For simplicity we then consider $W=\Delta\epsilon_f=0$. Carrying out the matrix products in Eq. (2.4) we obtain

$$\begin{aligned} \hat{\Sigma}_{\text{imp}}(z, \epsilon_f, V) &= c \{ [1 - \Delta V G_{fc}^0(z)] [1 - \Delta V G_{cf}^0(z)] \\ &\quad - (\Delta V)^2 G_{ff}^0(z) G_{cc}^0(z) \}^{-1} \\ &\quad \times \begin{pmatrix} (\Delta V)^2 G_{cc}^0(z) & \Delta V - (\Delta V)^2 G_{fc}^0(z) \\ \Delta V - (\Delta V)^2 G_{cf}^0(z) & (\Delta V)^2 G_{ff}^0(z) \end{pmatrix}. \end{aligned} \quad (3.2)$$

The zeroes in the denominator of Eq. (3.2) determine the positions of the δ -function-like bound state. There are in principle two poles (quadratic equation in ΔV) both corresponding to negative values of ΔV . In general, it requires a threshold value of ΔV for a bound state to develop and ΔV should not exceed a critical value. The positions of the poles for the symmetric Kondo insulator ($\epsilon_f=0$ and two electrons per site) are displayed in Fig. 2.

The properties of the ligand defect again depend on the characteristics of the impurity. If the defect is a donor or acceptor the Fermi level will be pinned at one of the bound states and the impurity is magnetic as discussed above. If the defect is charge neutral, on the other hand, it does not pin the Fermi level and its properties are nonmagnetic.

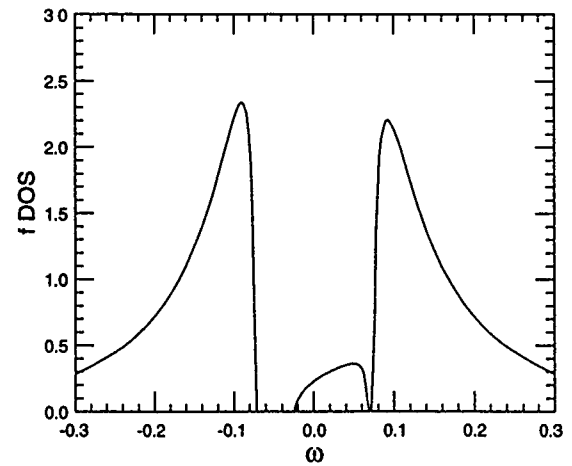


FIG. 3. f DOS for $V=1$, $U=1$, $D=10$, $\epsilon_f=0$ (Hartree-Fock corrected), $c=0.03$, $\Delta\epsilon_f=\infty$, $\Delta V=0$, and $W=1$. The structure inside the hybridization gap is the impurity band, which is separated by two gaps from the continuum of the Kondo insulator. The asymmetry arises from $W \neq 0$.

IV. IMPURITY BANDS

Finite concentrations of Kondo holes can give rise to impurity bands in the gap of the Kondo insulator. To gain insight we first analyze the symmetric situation ($\epsilon_f=\mu=0$) with $U=W=\Delta V=0$ in the limit $\Delta\epsilon_f \rightarrow \infty$. Since $W=0$ only ϵ_f is renormalized but not V and z when $\hat{\Sigma}_{\text{imp}}(z)$ is treated self-consistently. Due to the impurity self-energy the dressed f level energy acquires an imaginary part for small frequencies. In particular, for $\omega=0$ $\tilde{\epsilon}_f$ is purely imaginary and for small c we obtain $\tilde{\epsilon}_f = -2ic^{1/2}V^2/D$. Hence, the height of the band is not analytic in c . A similar analysis with $\omega \neq 0$ yields an impurity bandwidth of the order of $\tilde{\epsilon}_f$, so that the impurity band is approximately semielliptic with both height and width proportional to c for small c . Due to the nonanalytic dependence on $c^{1/2}$ the self-consistency condition Eq. (2.8b) and the limit $c \rightarrow 0$ cannot be interchanged. For $W \neq 0$ the impurity band becomes asymmetric, but the properties are otherwise similar.

To obtain more quantitative results we have to incorporate the Coulomb self-energy $\Sigma_U(z)$. As an example we show in Fig. 3 the f DOS for the symmetric host with $U=1$, $W=1$, $\Delta\epsilon_f=\infty$, and $c=0.03$. The asymmetry is due to the nonzero value of W . The f DOS does not show the van Hove saddle point singularities discussed in Refs. 9 and 10, since we consider a simple elliptic DOS for the conduction electrons. As discussed above the main effect of U is to narrow the gap of the Kondo insulator and to increase the height of (and to narrow) the peaks in the f DOS. The impurity band is separated from the continuum of the Kondo lattice by two gaps. The position of the band edges limiting the gap for $W=0$ (only one is shown, the other one is symmetric) and three values of U are displayed in Fig. 4(a). The gap is given by the region between the shown boundaries. The gap narrows with increasing U and increasing concentration of impurities, but within the range of validity of our approximations (noncrossing impurity lines in the self-energy) the gap never closes. For small c the $c^{1/2}$ dependence of the impurity

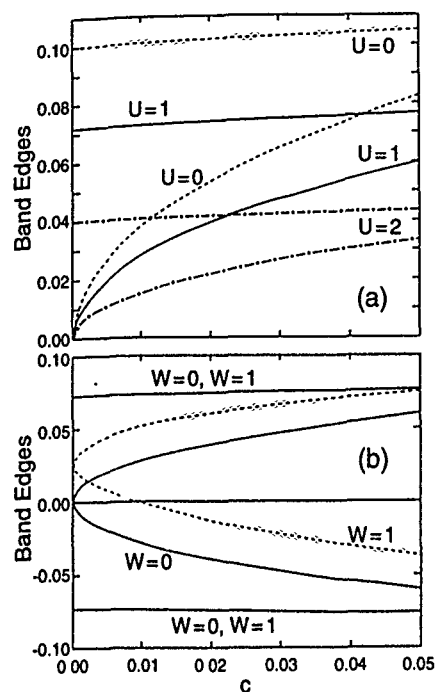


FIG. 4. Band edges of the hybridization gap and the impurity band for $V=1$, $D=10$, $\epsilon_f=0$ (Hartree-Fock corrected), and $\Delta\epsilon_f=\infty$ as a function of c . (a) $W=0$ and three values of U ; the dashed line refers to $U=0$, the solid curve to $U=1$ and the dash-dotted one to $U=2$. (b) $U=1$ and $W=0$ (solid curve) and $W=1$ (dashed line). Note that the gap narrows with U and the edges are symmetric only if $W=0$. The impurity band is always separated by a gap from the continuum of the insulator. Note the $c^{1/2}$ dependence for very low c .

band is observed. The band edge of the continuum of the Kondo insulator only increases slightly with c .

In Fig. 4(b) we show the four band edges for the symmetric Kondo insulator with $U=1$ for the cases $W=0$ and $W=1$. The $W=0$ case is the same as the solid curve in Fig. 4(a). The band edge of the Kondo lattice depends only very weakly on W . The impurity band for $W=1$ is strongly asymmetric and still has the $c^{1/2}$ dependence for small c . Consequently one gap is smaller than the other, but neither gap is closed within the range of validity of the theory.

The properties of the impure Kondo insulator once more depend on the characteristics of the impurities. We distinguish among dopands (e.g., Th replacing Ce) and charge neutral impurities (e.g., La substituting Ce). In the former case the Fermi level lies in one of the gaps discussed above and the system behaves like a nonmagnetic insulator. In the latter case the Fermi level lies in the impurity band. The chemical potential μ is determined self-consistently via $\mu = \text{Re}[\tilde{\epsilon}_f(\mu)]$ and is displayed in Fig. 5(a) as a function of ϵ_f for $W=0$ and $c=0.04$ ($\Delta\epsilon_f \rightarrow \infty$). Note that $\mu(\epsilon_f)$ is a linear function of ϵ_f with a slope that is only slightly smaller than one. The corresponding f electron DOS at the Fermi level is shown in Fig. 5(b). There is only a small increase of $\rho_f(\mu)$ with the asymmetry. On the other hand, $\rho_f(\mu)$ strongly depends on the concentration of Kondo holes; it grows monotonically with c , being proportional to $c^{1/2}$ for small c . The finite f DOS at the Fermi level gives rise to a specific heat contribution proportional to T . The range of this

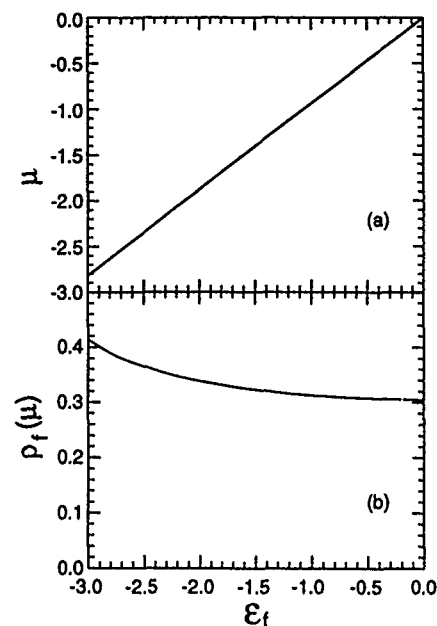


FIG. 5. (a) Chemical potential, μ , and (b) f DOS at the Fermi level, ρ_f , as a function of the (Hartree-Fock corrected) f level energy for $V=1$, $U=1$, $D=10$, $W=0$, $\Delta\epsilon_f=\infty$, and $c=0.04$ (see Ref. 7).

linear T dependence is of the order of the width of the impurity band. The γ coefficient^{7,8} is proportional to $\rho_f(\mu)$ and tracks the same weak ϵ_f dependence. The effective mass associated with γ for the parameters of Fig. 5 is about 15–20 times the mass of the conduction electrons. The susceptibility also follows the same trends.

For sufficiently small c all states in the impurity band are localized (charge neutral impurities), but an insulator-metal transition is expected as a function of c . When c is increased the bound states (located at the nearest neighbor sites to the impurity) start to overlap and electrons may percolate giving rise to conductivity and affecting the infrared optical properties. Magnetic order of the spin-glass-type is also possible.

Finally, we briefly address the situation $\Delta V \neq 0$ and $\Delta\epsilon_f = W=0$ by showing in Fig. 6 the f DOS for $\Delta V = -0.4$ and $c=0.05$ as compared to the pure symmetric Kondo insulator (dotted curve). The height of the main peaks decreases and impurity tails protrude into the gap. If the ligand defects are charge neutral the Fermi level remains within the gap and the system is a nonmagnetic insulator with a reduced gap. If the ligand impurity dopes the crystal the Fermi level lies in the continuum; hence $C \propto T$ at very low T and depending on the position of the mobility edge the system will be a metal or an insulator.

V. CONCLUDING REMARKS

We presented a summary of our results for various types of impurity states in a Kondo insulator. The formation of a Kondo insulator is perhaps the most dramatic implication of "coherent scattering." Kondo holes destroy the translational invariance and hence the coherence. We considered isolated Kondo holes, typically leading to a bound state in the hybridization gap, and finite concentrations of impurities, giving rise to impurity bands.

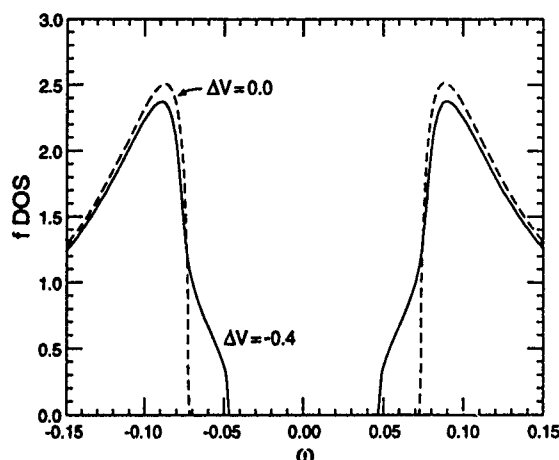


FIG. 6. f DOS for $V=1$, $U=1$, $D=10$, $\epsilon_f=0$ (Hartree-Fock corrected), $c=0.05$, and $\Delta\epsilon_f=W=0$. The solid curve corresponds to $\Delta V=-0.4$, while the dashed one is the pure Kondo insulator. Note that two tails appear at the band edges, but no impurity band develops in the gap.

So-called Kondo holes can be described by three scattering parameters, which correspond to a local change in the f level energy, a potential scattering of the conduction electrons and a local reduction of the hybridization matrix element. Depending on the characteristics of the impurity very different properties may arise. In most of the cases a bound state is formed in the hybridization gap of the Kondo insulator, but as shown in Sec. III not all scattering parameters will lead to a pole in the denominator of the t matrix, i.e., to a bound state. The two most important examples of impurities discussed are (i) the missing f electron (obtained in the limit $\Delta\epsilon_f \rightarrow \infty$), representing, e.g., the substitution of Ce by La or Th, and (ii) the ligand defect, characterized by $\Delta V \neq 0$ ($\Delta V \neq 0$ is typically negative). If the bound state pins the Fermi level (i.e., depending on the effective charge of the defect) the properties of the impurity are magnetic, i.e., it can be represented by an effective spin 1/2, although the origin of the defect is usually nonmagnetic. If the charge balance is such that there is no pinning of the Fermi level the bound state is nonmagnetic. The bound states are strongly localized, that is, they only extend over a few unit cells.

If the concentration of Kondo holes is finite the bound states acquire a finite lifetime and an impurity band (missing f electron) or impurity tails at the band edges (ligand defects) arise. Depending on the charge characteristics of the defects the Fermi level lies in the continuum or in the reduced gap. This determines the thermal properties of the impure Kondo insulator, i.e., either a specific heat proportional to T and a Curie-Weiss susceptibility or a thermally activated small effective gap semiconductor. The former case is unquestionably the more exciting one, which could lead to a spin-glass

phase or to an insulator-metal transition as a function of c . The impurity band is expected to affect the infrared optical properties.

There are several experimental studies on impure Kondo insulators. The predicted $c^{1/2}$ dependence of γ has been verified for La-substituted $\text{Ce}_3\text{Bi}_4\text{Pt}_3$.^{3,17} The valence instability and electrical properties of Yb and La-substituted SmB_6 have been studied long ago.¹⁸ The gap of CeNiSn was found to close with 15% La substitution¹⁹ and is also smeared with increasing x in $\text{CeNi}_{1-x}\text{Pt}_x\text{Sn}$.²⁰

The Coulomb interaction within the f shell is introduced perturbatively via a self-energy to second order in U . This approach is of course only valid for small U , but unless the Kondo insulator becomes antiferromagnetic we do not expect qualitative changes for larger U . For very large U in the asymmetric case the $1/N$ expansion (or mean field slave bosons) could be the more appropriate method to study the impurity bands.²¹

The support of the U. S. Department of Energy under Grant No. DE-FG05-91ER45443 is acknowledged.

- ¹See, e.g., *Valence Instabilities*, edited by P. Wachter and H. Boppert (North-Holland, Amsterdam, 1982).
- ²T. Takabatake, Y. Nakazawa, and M. Ishikawa, *Jpn. J. Appl. Phys. Suppl.* **26**, 547 (1987).
- ³M. F. Hundley, P. C. Canfield, J. D. Thompson, Z. Fisk, and J. M. Lawrence, *Physica B* **171**, 254 (1991).
- ⁴M. Kasaya, F. Iga, M. Takigawa, and T. Kasuya, *J. Magn. Magn. Mat.* **47** & **48**, 429 (1985).
- ⁵N. Bykovetz, W. H. Herman, T. Yuen, C. Jee, C. L. Lin, and J. E. Crow, *J. Appl. Phys.* **63**, 4127 (1988).
- ⁶N. B. Brandt and V. V. Moschalkov, *Adv. Phys.* **33**, 373 (1984).
- ⁷P. Schlottmann, *Phys. Rev. B* **46**, 998 (1992).
- ⁸P. Schlottmann, *Physica B* **186-188**, 375 (1993).
- ⁹R. Sollie and P. Schlottmann, *J. Appl. Phys.* **69**, 5478 (1991).
- ¹⁰R. Sollie and P. Schlottmann, *J. Appl. Phys.* **70**, 5803 (1991).
- ¹¹K. Yamada and K. Yosida, *Prog. Theor. Phys.* **76**, 621 (1986); V. Zlatic and B. Horvatic, *Phys. Rev. B* **28**, 6904 (1983); V. Zlatic, S. K. Ghatak, and K. H. Bennemann, *Phys. Rev. Lett.* **57**, 1263 (1986); H. Schweitzer and G. Czycholl, *Z. Phys. B* **74**, 303 (1989).
- ¹²H. Schweitzer and G. Czycholl, *Solid State Commun.* **74**, 735 (1990).
- ¹³W. Metzner and D. Vollhardt, *Phys. Rev. Lett.* **62**, 324 (1989); W. Metzner, *Z. Phys. B* **77**, 253 (1989); E. Muller-Hartmann, *ibid.* **76**, 211 (1989); H. Schweitzer and G. Czycholl, *Solid State Commun.* **69**, 171 (1989).
- ¹⁴H. Schweitzer and G. Czycholl, *Z. Phys. B* **79**, 377 (1990).
- ¹⁵Since we use an elliptic DOS for the conduction electrons, rather than a nearest neighbor tight binding band on a simple cubic lattice, our approach differs slightly from that of Ref. 12.
- ¹⁶A. Millis, in *Physical Phenomena at High Magnetic Fields*, edited by E. Manousakis, P. Schlottmann, P. Kumar, K. Bedell, and K. Mueller (Addison-Wesley, Reading, MA, 1991), p. 146.
- ¹⁷J. D. Thompson (private communication).
- ¹⁸M. Kasaya *et al.*, in *Valence Fluctuations in Solids*, edited by L. M. Falicov, W. Hanke, and M. B. Maple (North-Holland, Amsterdam, 1981), p. 251.
- ¹⁹F. G. Aliev *et al.*, *Physica B* **163**, 358 (1990).
- ²⁰S. Nishigori *et al.*, *Physica B* **186-188**, 406 (1993).
- ²¹R. Freytag and J. Keller, *Z. Phys. B* **80**, 241 (1990).

Structural and magnetic ordering in the cerium hydride (abstract)

R. R. Arons^{a)}

Institute für Festkörperforschung, KFA Jülich, D-52425 Jülich, Germany

J. K. Cockcroft

ILL, Grenoble, France

E. Ressouche

CENG/DRFMC/SPSMS/MDN, Grenoble, France

Depending on the H concentration at the octahedral (O) sites, $x(O)$, various tetragonal phases, due to H ordering, are observed in the Ce hydride at low temperatures. While our single crystal work showed that the tetragonal phase for $H/Ce \approx 2.7$, corresponding to $x(O) \approx 3/4$, is only stable in a region of $x(O) = \pm 0.05$, the other one was believed to be caused by a single H ordering process for $0.15 \leq x(O) \leq 0.5$ up to now. However, strong discrepancies in the structure were reported from different neutron diffraction studies.¹ We have studied both the structural H ordering and the magnetic ordering by neutron diffraction work for $0.2 \leq x(O) \leq 0.5$. It will be shown that the H ordering for $x(O) = 1/4$ and $1/2$ are completely different (Space groups: $I4/mmm$ and $I4_1/amd$, respectively). Accordingly, for $x(O) = 1/2$ the Ce atoms are crystallographically identical, while for $x(O) = 1/4$ two different Ce atoms are present in the lattice. Also the magnetic order is completely different for the two phases. For $x(O) = 0.5$, a commensurate magnetic phase appears below $T_N \approx 3.5$ K. The structure is described by a canted ferromagnet with $\mu_F = 1.3 \mu_B/\text{Ce atom}$ along the c axis and $\mu_{AF} = 1.1 \mu_B/\text{Ce atom}$ within the plane normal to c . On the other hand, for $0.2 \leq x(O) \leq 0.25$, an incommensurate AF phase with a long period, described by the wave vector $\tau = (0.12, 0.12, 0)$, is obtained at 1.4 K. Above 2.6 K, this phase is progressively replaced by the commensurate lines discussed before. For $x(O) = 0.265$, the two phases coexist at 1.4 K, while for $x(O) = 0.28$ only the commensurate phase is retained. Apparently, the long period phase is characteristic of the ideal H ordering around $x(O) = 1/4$, whereas it is strongly affected by the H occupation of the new positions for higher concentrations.

^{a)}Guest scientist at CEN-G/DRFMC/SPSMS/MDN, Grenoble, France.

¹R. R. Arons, in Landolt-Börnstein, *New Series*, Group III, Vol. 19d1, *Rare Earth Hydrides* (Springer, Berlin, 1991), pp. 280–393.

Recent developments in multi-channel Kondo physics (invited) (abstract)

Kevin Ingersent

Department of Physics, University of Florida, Gainesville, Florida 32611

Barbara A. Jones

IBM Research Division, Almaden Research Center, San Jose, California 95120

The two-channel Kondo model for a single spin-one-half magnetic impurity coupled to two degenerate bands of conduction electrons predicts the existence of a zero-temperature quantum critical point, leading to "marginal-Fermi-liquid" behavior at low temperatures. A two-channel Kondo description has been proposed¹ for several U and Ce-based heavy-fermion materials whose thermodynamic and transport properties exhibit anomalous temperature and magnetic field dependence.² This talk will review recent theoretical work on multi-channel Kondo behavior. Two factors may be particularly important in determining the relevance of the multi-channel Kondo effect for real systems: (1) Channel asymmetry: Any difference between the coupling of the two conduction bands to the impurities leads to the recovery of Fermi-liquid behavior at sufficiently low temperatures.³ (2) Inter-impurity interactions: Numerical renormalization-group calculations for a two-impurity model show that any nonzero Ruderman-Kittel-Kasuya-Yoshida (RKKY) coupling between the impurities destabilizes the single-impurity critical point.⁴ Depending on the strength and sign of the RKKY coupling, the system may be driven either to a Fermi-liquid or to a novel regime of non-Fermi-liquid behavior governed by nonuniversal critical exponents. The experimental implications of these findings will be discussed.

¹D. L. Cox, Phys. Rev. Lett. **59**, 1240 (1987).

²C. L. Seaman *et al.*, Phys. Rev. Lett. **67**, 2882 (1991); B. Andraka and A. M. Tsvelik, Phys. Rev. Lett. **67**, 2886 (1991).

³P. Nozières and A. Blandin, J. Physique **41**, 193 (1980).

⁴K. Ingersent, B. A. Jones, and J. W. Wilkins, Phys. Rev. Lett. **69**, 2594 (1992).

Giant magnetoresistance in $\text{Fe}_{0.95}\text{Cr}_{0.05}/\text{Cr}$ multilayer films

L. H. Chen, S. Jin, T. H. Tiefel, R. B. Van Dover, E. M. Gyorgy, and R. M. Fleming
AT&T Bell Laboratories, Murray Hill, New Jersey 07974

We have studied the effect of Cr alloying addition to the Fe layers on the magnetoresistance behavior of the Fe/Cr superlattice films $[\text{Fe}(15 \text{ \AA})/\text{Cr}(8\text{--}20 \text{ \AA})]_{30}$. The alloyed superlattice films $\text{Fe}_{0.95}\text{Cr}_{0.05}/\text{Cr}$ exhibited significantly improved giant magnetoresistance effect ($\Delta R/R \sim 12.2\%$ at 4.2 K), as compared to the unalloyed Fe/Cr multilayer films ($\Delta R/R \sim 6.9\%$). The M-H loops indicate that antiferromagnetic coupling exists in both films, which is believed to be responsible for the observed giant magnetoresistance. The improvement in $\Delta R/R$ in the Cr-alloyed superlattice films is attributed to the stronger spin-dependent scattering of conduction electrons caused by the introduction of Cr impurities in the ferromagnetic layers. The alloyed superlattice films also exhibit reduced coercivity and saturation magnetization.

I. INTRODUCTION

The giant magnetoresistance (GMR) phenomenon observed in the Fe/Cr type multilayer films¹⁻¹⁰ is attributed to the spin-dependent scattering at the interface of multilayer thin films, as well as the spin-dependent bulk scattering.³ In the applied field, the spins in ferromagnetic layers align in the field direction, and as a result, a reduced electrical resistance (ρ_F) is obtained in the film. However, if the field is removed, the ferromagnetic layers adjacent to the nonmagnetic spacer layer in between exhibit an antiferromagnetic coupling (antiparallel magnetization), and as a result a higher resistance (ρ_{AF}) is obtained (e.g., due to the spin-flip scattering when the conduction electrons cross the interfaces, and move into the neighboring ferromagnetic layers.) The change in magnetoresistance is defined as a resistivity ratio $\Delta\rho/\rho = (\rho_{AF} - \rho_F)/\rho_F$ or a resistance ratio $\Delta R/R$.

In the two current mode,¹¹ the current is carried by the spin \uparrow and spin \downarrow electrons. Here \uparrow and \downarrow indicate majority and minority spins. At high applied fields (ferromagnetic state), and low temperature, the total current of multilayer thin films is determined by the spin \uparrow and spin \downarrow current in parallel. The spin \uparrow and spin \downarrow currents could become significantly different if certain transition metal impurities are purposely introduced to a ferromagnetic material to disproportionately scatter the spin \uparrow and spin \downarrow electrons. In multilayer thin films, small-thickness nonmagnetic layers and the interface areas could be interpreted as the scattering impurities in ferromagnetic layers.^{2,3,5} However, a direct alloying of impurities into the ferromagnetic layer itself to modify the scattering behavior, and hence the GMR effect has not been attempted.

In this paper, we report a significant increase in GMR effect (almost twofold improvement) by intentional Cr alloying of the Fe layer in the Fe/Cr multilayer superlattice.

II. EXPERIMENT

Multilayer thin films of $(\text{Fe}_{0.95}\text{Cr}_{0.05})/\text{Cr}$ and Fe/Cr were prepared by DC magnetron triode sputtering system with

computer-controlled rotating shutter and substrate. These films, typically consisting of 30 double layers of Fe ($\sim 15 \text{ \AA}$ thick) and Cr ($\sim 11 \text{ \AA}$ thick), were deposited on the Si(100) substrate wafers, which were chemically cleaned (with a 10% HF solution) before deposition. As shown schematically in Fig. 1, a Cr overlayer of 50 \AA was added on top of the multilayer structure to protect the deposited films from oxidation. A Fe buffer layer of 40 \AA was used between the Si substrate and the multilayer to improve the quality of the superlattice interfaces. Because the magnetoresistance effect is very sensitive to the deposition parameters, such as applied accelerating voltage and distance between substrate and target, Ar atmosphere pressure, substrate temperature, and the nature of substrate materials, etc., the study of the Cr alloying effect was made on samples carefully prepared under the same sputtering conditions. Sputtering was carried out in a 3×10^{-3} Torr argon atmosphere; with a base pressure of 2×10^{-7} Torr before sputtering. A sputtering rate of $\sim 100 \text{ \AA/min}$ was used for all targets by adjusting the applied acceleration voltage between the substrate and target to be 90 V for the Cr target and 140 V for the Fe and $\text{Fe}_{0.95}\text{Cr}_{0.05}$ targets. The film thickness was determined by Rutherford Backscattering Spectrometry (RBS) using a calibration

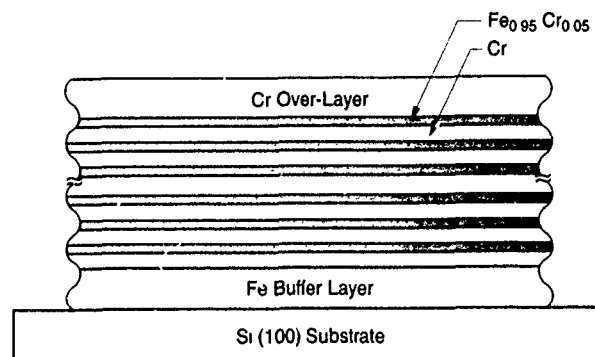


FIG. 1. Schematic illustration of the $\text{Fe}_{0.95}\text{Cr}_{0.05}/\text{Cr}$ superlattice film structure.

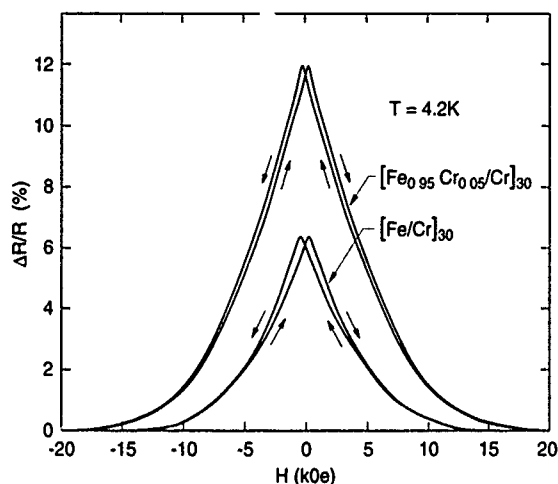


FIG. 2. $\Delta R/R$ vs H at 4.2 K.

sample of about 1000 Å thick single layer films of Fe, $\text{Fe}_{0.95}\text{Cr}_{0.05}$, and Cr, prepared under the same deposition conditions.

The crystal structure and texture of the deposited films were evaluated by x-ray diffraction (XRD) using $K_\alpha(\text{Cu})$ radiation. Small angle XRD was also carried out to characterize the interface roughness of the multilayer thin films. Conventional four probe method was used to measure the electrical resistance with a magnetic field applied in the film plane along the current flow direction. The measurements were carried out at various temperatures (4.2–295 K) and fields up to 30 K Oe. The in-plane magnetization loops were measured at room temperature and 4.2 K by using a vibrating sample magnetometer.

III. RESULTS AND DISCUSSION

The high-angle x-ray diffraction study indicates that the main diffraction peaks are Fe(110) and Cr(110). The low-angle diffraction measurements show a characteristic peak associated with the layer structure for both $\text{Fe}_{0.95}\text{Cr}_{0.05}/\text{Cr}$ and Fe/Cr superlattice films. The superlattice wavelength calculated from the peak position is within 10% of nominal thickness obtained from the calibration films. Comparison of the measured intensity versus 2θ curves suggests that the flatness of the interface in the Fe/Cr superlattice film is not drastically altered by Cr alloying to the Fe layers.

Shown in Fig. 2 are the magnetoresistance ratio [$\Delta R/R = (R - R_s)/R_s$, where R_s is the resistance at the saturation field] versus applied magnetic field curves (in-plane field parallel to the current flow direction) at 4.2 K for both $[\text{Fe}_{0.95}\text{Cr}_{0.05}(15 \text{ Å})/\text{Cr}(11 \text{ Å})]_{30}$ and $[\text{Fe}(15 \text{ Å})/\text{Cr}(11 \text{ Å})]_{30}$ films. As is evident from the figure, the magnetoresistance ratio of ~11.8% for the $\text{Fe}_{0.95}\text{Cr}_{0.05}/\text{Cr}$ superlattice is much larger, compared with ~6.4% for the Fe/Cr superlattice. (Slightly higher values of 12.2% and 6.9% are obtained if the Cr interlayer thickness is optimized to 10 and 9 Å, respectively, for the $\text{Fe}_{0.95}\text{Cr}_{0.05}/\text{Cr}$ and Fe/Cr superlattice films, as discussed later.) The $\Delta R/R$ vs H curves at 4.2 K for both superlattice films show the well-known hysteresis behavior because of the relatively large coercivity. Essentially similar

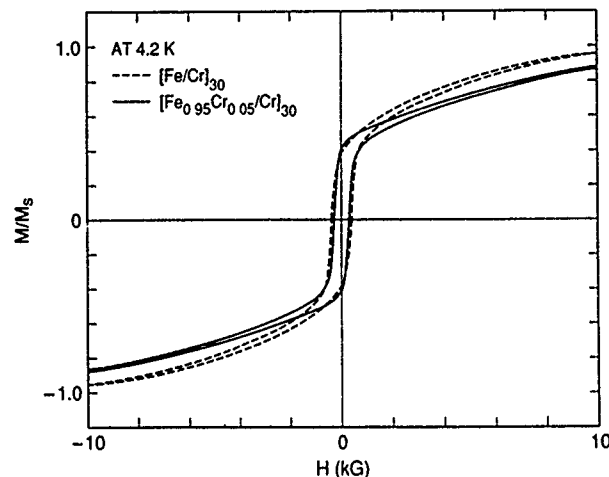


FIG. 3. M-H loops at 4.2 K.

$\Delta R/R$ behavior is observed at room temperature, except that the magnetoresistance ratios are somewhat lower than at 4.2 K, and the hysteresis is not as obvious due to the smaller coercivity at room temperature. A peak room temperature value of ~7% is obtained for the Cr-alloyed superlattice, and ~4% for the unalloyed superlattice film. The magnetoresistance ratios obtained in the present study are considerably smaller than the values previously reported by other researchers. The MR ratio in superlattice films is known to be very sensitive to various processing and materials parameters.^{10,12} The exact reason why the MR values in the present films are generally low is not clearly understood at the moment.

The M-H loops of the $[\text{Fe}_{0.95}\text{Cr}_{0.05}(15 \text{ Å})/\text{Cr}(11 \text{ Å})]$ and $[\text{Fe}(15 \text{ Å})/\text{Cr}(11 \text{ Å})]_{30}$ superlattice films are shown in Fig. 3 for 4.2 K. The Cr alloying reduces the coercivity, increases the remanence, and decreases the saturation moment. Essentially similar M-H characteristics are observed at room temperature, except that the coercivity values decrease from ~200 and ~150 Oe at 4.2 K to ~50 and ~35 Oe at room temperature for the Fe/Cr and $\text{Fe}_{0.95}\text{Cr}_{0.05}/\text{Cr}$ superlattice, respectively. All the M-H curves saturate at a relatively high field (above 12 KOe), and show the antiferromagnetic coupling effect between two neighboring ferromagnetic Fe layers separated by the nonmagnetic Cr layer. At a high saturation field, all the ferromagnetic Fe layers in the superlattice align the magnetic moment in the field direction. When the field is decreased to a certain low value, but still in the same direction, the magnetization direction of every other Fe layer is gradually reversed, due to the increasing antiferromagnetic coupling between two neighboring Fe layers. Thus, at low field, the magnetization of the superlattice is small and the magnetization direction of two neighboring Fe layers is antiparallel. When the field is raised to the saturation field in the opposite field direction, the previously antiparallel layers slowly reverse their magnetization over the range of ~0.5 to ~30 KOe until the superlattice is saturated.

The saturation moment (M_s) of the $[\text{Fe}_{0.95}\text{Cr}_{0.05}(15 \text{ Å})/\text{Cr}(11 \text{ Å})]_{30}$ film is estimated to be about 1190 emu/cm³ at 4.2 K which is slightly smaller, when compared with ~1300 emu/cm³ for the $[\text{Fe}(15 \text{ Å})/\text{Cr}(11 \text{ Å})]_{30}$ superlattice. The

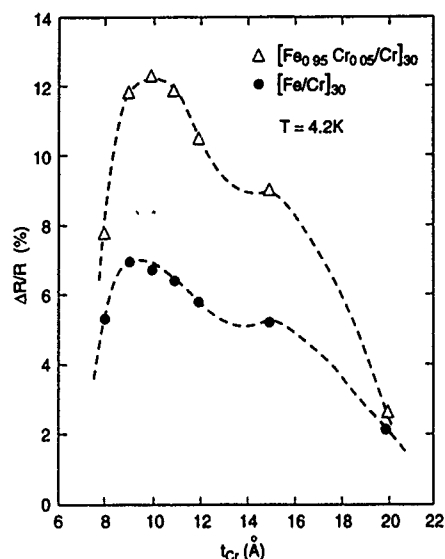


FIG. 4. $\Delta R/R$ vs Cr interlayer thickness at 4.2 K.

smaller saturation moment is believed to be caused by the Cr alloying of the Fe layers. As shown in Fig. 3, the remanent magnetization values of both superlattices are still substantial, around $0.35M_s$, which means the antiferromagnetic coupling between the Fe layers is not perfect.

Shown in Fig. 4 is the change in magnetoresistance at 4.2 K as a function of Cr interlayer thickness for both the $\text{Fe}_{0.95}\text{Cr}_{0.05}/\text{Cr}$ and Fe/Cr superlattices. As is evident from the figure, the maximum magnetoresistance ($\Delta R/R = 12.2\%$ and 6.9% , respectively for $\text{Fe}_{0.95}\text{Cr}_{0.05}/\text{Cr}$ and Fe/Cr superlattice) occurs at a Cr thickness of around 10 \AA , in agreement with a previous report,⁷ which showed an oscillatory change in magnetoresistance as a function of Cr thickness. It is seen that the magnetoresistance ratio for $\text{Fe}_{0.95}\text{Cr}_{0.05}/\text{Cr}$ is higher than that of Fe/Cr at all Cr thicknesses studied here. Such improved magnetoresistance ratio by adding Cr impurities directly to the Fe layer is attributed to stronger spin-dependent scattering of electrons in the $\text{Fe}_{0.95}\text{Cr}_{0.05}/\text{Cr}$ superlattice, and not to any significant difference in interface roughness, as discussed earlier. As mentioned previously, the Cr impurity (in the form of layers) in the Fe/Cr superlattice makes the spin \uparrow and spin \downarrow current very different.¹¹ When Cr impurities are mixed in Fe near the interface, the $\rho_{\uparrow}/\rho_{\downarrow}$ ratio is almost equal to 6 and very large compared with pure iron. Thus, it is believed that in the present $\text{Fe}_{0.95}\text{Cr}_{0.05}/\text{Cr}$ superlattices, the direct mixing of Cr impurities in the Fe layer should yield an additionally increased $\rho_{\uparrow}/\rho_{\downarrow}$ ratio and $\Delta R/R$, as compared to that in Fe/Cr , which is indeed observed in this work.

The temperature dependence of magnetoresistance and that of resistivity for the $[\text{Fe}_{0.95}\text{Cr}_{0.05}/\text{Cr}]_{30}$ and $[\text{Fe}/\text{Cr}]_{30}$ films are shown in Fig. 5. We find a general trend that the magnetoresistance ratio increases as the measurement temperature is decreased in both types of films. The increases in

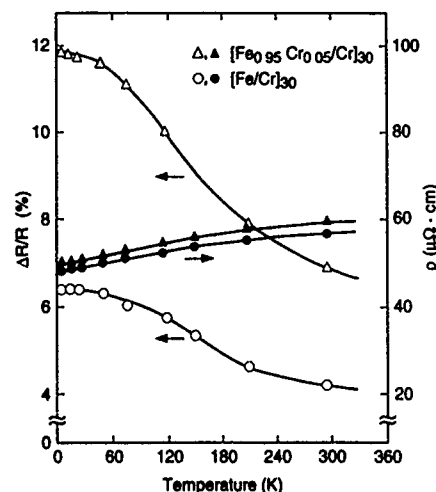


FIG. 5. $\Delta R/R$ and ρ vs temperature for the superlattice films.

magnetoresistance ratio for both films when temperature is lowered from room temperature to 4.2 K are caused mostly by the temperature-dependent increase in ΔR at low temperature as the resistivity (or resistance) of the films exhibit relatively small temperature dependence, as shown in the figure.

IV. SUMMARY

The giant magnetoresistance behavior and magnetization properties of the $[\text{Fe}_{0.95}\text{Cr}_{0.05}/\text{Cr}]_{30}$ superlattice films have been studied and compared with those of the $[\text{Fe}/\text{Cr}]_{30}$ films. Significantly improved magnetoresistance is obtained by direct alloying of Cr in the ferromagnetic Fe layers, which is attributed to the stronger spin-dependent scattering of electrons caused by the introduction of Cr impurities in the ferromagnetic layers.

- ¹P. Grunberg, R. Schreiber, Y. Pang, U. Walz, M. B. Brodsky, and H. Sowers, *J. Appl. Phys.* **61**, 3750 (1987).
- ²M. N. Baibich, J. M. Broto, A. Fert, F. Nguyen Van Dau, F. Petroff, P. Etienne, G. Greuzet, A. Friederich, and J. Chazelas, *Phys. Rev. Lett.* **61**, 2472 (1988).
- ³R. E. Camley and J. Barnas, *Phys. Rev. Lett.* **63**, 664 (1989).
- ⁴G. Binasch, P. Grunberg, F. Saurenbach, and W. Zinn, *Phys. Rev. B* **39**, 4828 (1989).
- ⁵A. Barthelemy, A. Fert, M. N. Baibich, S. Hachjoudi, F. Petroff, P. Etienne, R. Cabanel, S. Lequien, F. Nguyen Van Dau, and G. Greuzet, *J. Appl. Phys.* **67**, 5908 (1990).
- ⁶J. J. Kerbs, P. Lubitz, A. Chaiken, and G. A. Prinz, *Phys. Rev. Lett.* **63**, 1645 (1989).
- ⁷S. S. P. Parkin, N. More, and K. P. Roche, *Phys. Rev. Lett.* **64**, 2304 (1990).
- ⁸J. E. Mattson, M. E. Brubaker, C. H. Sower, M. Conover, Z. Qiu, and S. D. Bader, *Phys. Rev. B* **44**, 9378 (1991).
- ⁹B. A. Gurney, P. Baumgart, D. R. Wilhoit, B. Dieny, and V. S. Speriosu, *J. Appl. Phys.* **70**, 5867 (1991).
- ¹⁰E. E. Fullerton, D. M. Kelly, J. Guimpel, and I. K. Schuller, *Phys. Rev. Lett.* **68**, 859 (1992).
- ¹¹I. A. Campbell and A. Fert, in *Ferromagnetic Materials*, edited by E. P. Wohlfarth (North-Holland, New York, 1982), Vol. 3, p. 751.
- ¹²S. S. P. Parkin and B. R. York, *Appl. Phys. Lett.* **62**, 1842 (1993).

The effect of Au impurities at the interfaces on the magnetoresistance of MBE-grown Co/Cu multilayers

K. P. Wellock, B. J. Hickey, D. Greig, M. J. Walker, and J. Xu
Department of Physics, The University of Leeds, Leeds LS2 9JT, United Kingdom

N. Wiser
Department of Physics, Bar-Ilan University, Ramat-Gan, Israel

We have grown Co/Cu multilayers by MBE using a shuttering arrangement wherein half of the sample receives an amount of Au impurities at each interface. Under these controlled conditions, the differences in measurements between each half is attributed only to the effect of the impurities. The samples were characterized by x-ray diffraction and RHEED. We have found that small fractions of a monolayer of Au deposited at the Co/Cu interface significantly decreased the GMR. These results are discussed in the light of current theories on the role of bulk and interface scattering.

INTRODUCTION

The giant magnetoresistance (GMR) found in magnetic multilayers has recently been the subject of great interest, with Fe/Cr and Co/Cu being the most widely studied systems. It is interesting to note that there are important experimental differences regarding the GMR between Fe/Cr and Co/Cu. In Fe/Cr, for example, various methods of causing interdiffusion at the interface—annealing¹ or changing the growth conditions²—can lead to an increase in the magnitude of the GMR. On the other hand, Hall *et al.*³ found that for Cu/Co, the GMR decreased when interdiffusion was caused by annealing. Moreover, it was not until a growth technique of making the interfaces smoother was discovered,⁴ that a GMR was observed in MBE-grown (111)-oriented Co/Cu multilayers.

In the present investigation, we employ yet another experimental technique for changing the magnitude of the GMR. For Fe/Cr, it has been found¹ that the GMR is significantly increased if one deposits “extra” Cr impurities at the Fe/Cr interface. We have found that the opposite results apply to Co/Cu. That is, the deposition of Au impurities at the Co/Cu interface decrease the magnitude of the GMR. We note that various authors⁵ have deposited impurities at the interface of Fe/Cr, which resulted in a decrease in the GMR, however, in that work the thickness of the spacer layer (impurity+Cr) was not held constant, thus obscuring the effect of the impurity.

Before describing our data, it is useful to place these results in context. The theoretical model for the GMR suggested by Baibich *et al.*⁶ and developed by Camley and Barnas,⁷ which is based on separate currents flowing in parallel for different spin directions, explains rather well the general features of the GMR data. This model is based on spin-dependent electron scattering as the source of the GMR. Based on these ideas, we recently attributed³ the very different behavior between the Fe/Cr and the Co/Cu systems to the fact that whereas spin-dependent interface scattering is dominant in Fe/Cr, spin-dependent bulk scattering determines the GMR for Co/Cu, for the following reason. For the Fe/Cr system, the diffusion of Cr into Fe leads to a resonant virtual bound *d* state at the Fermi level,⁸ and hence to strong spin-dependent scattering at the Fe/Cr interfaces. However,

the scattering at the Co/Cu interface should be spin-independent because no such virtual bound state exists when Cu diffuses into Co. Recent results⁹ on the diffusion of Cu into NiFe by annealing lend credence to the idea that Cu as an impurity at the interface of magnetic and nonmagnetic layers causes only spin-independent scattering.

Further support for these ideas come from the measurements by Parkin *et al.*¹⁰ which have shown that for the Co/Cu system, the magnitude of the GMR as a function of the Cobalt thickness has a distinct maximum at about 10 Å. This result has been explained, both by Dieny *et al.*¹¹ and Mathon¹² on the basis on bulk spin-dependent scattering. Moreover, Dieny *et al.*¹¹ showed that the maximum in the GMR disappears if the interface spin-dependent scattering is also included in the calculation of the GMR.

These theoretical results are easy to understand. Increasing the Co thickness leads to an increase in the relative proportion of the bulk scattering to interface scattering, because a thicker Co layer leads to fewer interfaces per unit thickness of the multilayer. Therefore, if interface spin-dependent scattering were to be the most important for the GMR, then the GMR would always decrease with increasing Co thickness; this is not observed for Co/Cu multilayers. However, if bulk spin-dependent scattering is the most important for the GMR, then the GMR should initially increase with increasing Co thickness (which is in accordance with the Co/Cu data of Parkin *et al.*¹⁰) Finally, for sufficiently thick Co layers, the GMR must eventually decrease because the electron becomes “confined” to a single magnetic layer by its finite mean-free path. This explains the observed maximum in the GMR for Co/Cu multilayers as a function of the Co thickness.

Recent results¹³ on Co/Cu and Permalloy (Ni₈₁Fe₁₉)/Cu multilayers purport to show that in these systems the GMR is entirely determined by spin-dependent interface scattering. Interestingly, in these experiments where the GMR is measured as a function of the thickness of a Co layer inserted between permalloy and Cu, the GMR continues to increase until the Co is 8–10 Å thick (consistent with Ref. 10) and no observed decrease, surely if the GMR were determined by the interface alone, a decrease should be observed. It is also difficult to reconcile the interface-only argument in the light of thermopower measurements on Co/Cu,¹⁴ which show that the thermopower goes as the reciprocal of the magnetoresis-

tance. These authors point out the essential role of the *bulk* density of states in understanding these results. It also appears¹⁵ that the thermopower of permalloy Cu multilayers is very similar to that of Co/Cu, indicating that the *bulk* density of states of these systems is rather similar. We feel that aspects of both the interface and bulk scattering must be considered.

The purpose of the present investigation is to shed light on the question of the relative importance of interface versus bulk spin-dependent scattering for the Co/Cu system. In particular, we wish to elucidate the role played by impurities deliberately added at the Co/Cu interface. The results we present here are consistent with the conclusion that the dominant source of spin-dependent scattering in Co/Cu is located in the bulk. We have added small ($\ll 1$ monolayer) quantities of Au impurities at the interfaces, and have observed a decrease in the GMR that is related to the amount of Au deposited. For example, the GMR decreased from 22% to 6% when the Au shutter was opened for three seconds after each interface was formed. Thus, we have found yet another example of opposite behavior exhibited by the GMR for the Co/Cu system and for the Fe/Cr system. It should be pointed out that other explanations are also possible for the observed decrease in the GMR when Au impurities are added at the Co/Cu interface. Further experimental investigation of this point is in progress.

EXPERIMENTAL

The Co/Cu multilayers were grown in a VG80M MBE facility with a base pressure of 3×10^{-11} mbar. The substrate of GaAs(110) was heated to 600 °C to achieve the RHEED patterns characteristic of GaAs(110) surface reconstruction prior to growth. A 500 Å buffer layer of Ge was deposited at 500 °C at a rate of about 0.16 Å per second. During the evaporation of metallic layers the substrate temperature was held at 100 °C. The first metallic layer was 15 Å of Co deposited at a rate of about 0.2 Å/s, which grew as (100) BCC. A 10 Å layer of Au was then deposited on the Co, because it was found that such a layer is essential to produce a high-quality Co/Cu multilayer. The multilayers then consisted of 20 bilayers of Co(15 Å)Cu(9 Å) grown on the Au layer. To obtain the best samples the substrate is rotated at about 1 Hz. In order to minimize intersample differences, we prepared samples where the Au deposition at the interface affected half a large sample. At the point in the process where Au was to be introduced at an interface, a shutter was used to occlude half of the sample, thereby ensuring that the differences between the two halves were, as near as possible, due to just the Au. To obtain various amounts of Au, the evaporation source was exposed for different short periods of time. Resistivity measurements were performed using the standard four-probe DC method in fields up to 8 T and at temperatures between room temperature and 4 K. The magneto-optical Kerr effect was used to obtain magnetization curves at room temperature and in a maximum field of 0.5 T.

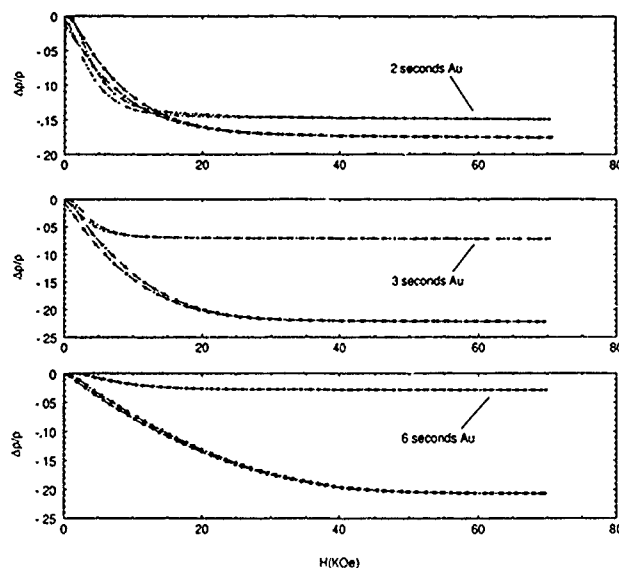


FIG. 1. The field dependence of the normalized resistivity at 4 K for (a) 2 s, (b) 3 s, and (c) 6 s exposure of the Au source.

RESULTS

Different samples were prepared with Au impurities by exposing the source for 1s, 2s, 3s, and 6s. We estimate that the Au deposition rate is about 0.05 Å s^{-1} . The samples were characterised *in situ* by RHEED and *ex situ* by low-angle x-ray diffractometry. The x-ray scans show that the first-order Bragg peak corresponding to the bilayer thickness for each sample agree within the experimental error. Qualitatively the data suggests that the Au has had only a small influence on the quality of the layers. Scans with and without Au are similar with many Kiessig fringes, which, if superimposed, are of similar intensity but slightly out of phase with each other. We will present more detailed results in a future publication. Figure 1 shows the magnetoresistance at 4 K for the 2s, 3s, and 6s samples. The 1s sample resulted in a less than 1% change in MR. It is evident that even small quantities of Au can result in large changes in MR, but importantly, in all cases the addition of Au at the Co/Cu interface resulted in a *decrease* in MR. It is interesting to note that in all samples, the addition of Au *did not* significantly increase the resistivity. For example, the largest change was in the 6s sample with only a $2 \mu\Omega \text{ cm}$ increase in resistivity with the addition of Au, yet the MR has decreased by 18%. By comparison, in our annealing work,³ such a large change in MR was accompanied by a fourfold increase in ρ . We have determined H_S as the saturation field of the MR, by fitting a straight line to the high field region and looking for the point of change in slope. In all cases the saturation field is substantially *less* when Au is deposited at the interfaces. The results for all samples are summarized in Table I.

Turning to the magnetization, Fig. 2 shows the room temperature results for the 3s sample. With the 5 KOe field available, it was impossible to saturate the magnetization of any of the samples. The data for the 3s sample was typical, in that at these fields and temperatures it was difficult to see a difference in $M(H)$ due to the Au. Figure 2 shows the low

TABLE I. Exposures of the Au source are in seconds and the resistivities are at 4 K. The percentage change in the magnetoresistance (MR%) is for measurements made at 4 K and H_S is the saturation field for the MR. The remanence and coercive field (H_C) are from measurements made at room temperature.

	1(a)	1(b)	2(a)	2(b)	3(a)	3(b)	4(a)	4(b)
Exposure/s	...	1	...	2	...	3	...	6
$\rho/\mu\Omega\text{ cm}$	16.7	18	13.5	14	17	18	12	14
MR%	19	18	18	15	22	7	21	3
H_S/kOe	31	35	40	25	34	16	47	22
Remanence%	52	55	60	45	59	44	64	...
H_C/Oe	36	42	34	41	39	32	41	...

field region of the same sample, 3s. From this data we have extracted the remanence and coercive field. For all the samples, the coercive field was about the same, 30–40 Oe, whereas the remanence for the samples with Au was less than their counterparts without Au (see Table I). It is not possible to connect the changes in MR with changes in the magnetic structure at this point. If one looks at the MR data at the same temperature and field range as the magnetization, there is little difference between samples. Further magnetization studies at low temperature are ongoing. We may qualitatively interpret these results in the same light as our anneal-

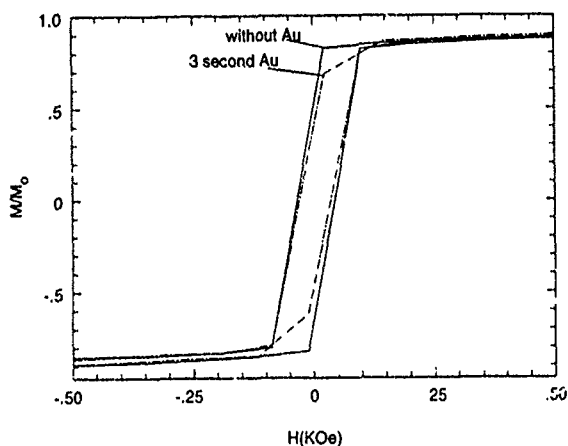


FIG. 2. Expanded field magnetization room temperature for no Au and 3 s exposure of the Au source at each Co/Cu interface.

ing work. The addition of Au at the Co/Cu interface has resulted in an increase in scattering that takes place at the interface. The bulk of the Co has been little affected by the Au, and thus scattering in the bulk is unchanged. Thus there is a net increase in scattering that takes place at the interface over that in the bulk. Since bulk scattering is the most important for the MR in Co/Cu, this has resulted in a decrease in the MR. This is another example of the difference between the Co/Cu system and the Fe/Cr system where in the latter, additional scattering at the interface resulted in an increase in the MR.

In conclusion we have found that depositing small amounts of Au at the Co/Cu interface has resulted in large decreases in MR in proportion to the amount of Au deposited, but without a significant increase in resistivity. The saturation field of the MR was found to fall by a factor of about 2 and the remanence by about 50%, for the samples with Au at the interface.

- ¹F. Petroff, A. Barthelemy, A. Harmzic, A. Fert, P. Etienne, S. Lequien, and G. Creuzet, *J. Magn. Magn. Mat.* **93**, 95 (1991).
- ²E. E. Fullerton, D. M. Kelly, J. Guimpel, I. K. Schuller, and Y. Bruynseraede, *Phys. Rev. Lett.* **68**, 859 (1992).
- ³M. J. Hall, B. J. Hickey, M. A. Howson, M. J. Walker, D. Greig, N. Wiser, *J. Phys. Condens. Matter* **4**, L495 (1992); M. J. Hall *et al.*, *Phys. Rev. B* **47**, 12 785 (1993); M. J. Hall *et al.*, *J. Magn. Magn. Mat.* **121**, 421 (1993).
- ⁴D. Greig, M. J. Hall, C. Hammond, B. J. Hickey, H. P. Ho, M. A. Howson, M. J. Walker, N. Wiser, and D. G. Wright, *J. Magn. Mat.* **110** L239 (1992).
- ⁵B. A. Gurney *et al.*, *IEEE Trans. Magn.* **26**, 2747 (1990); P. Baumgart *et al.*, *J. Appl. Phys.* **69**, 4774 (1991).
- ⁶M. N. Baibich, J. M. Broto, A. Fert, F. Nguyen Van Dau, F. Petroff, P. Etienne, G. Creuzet, A. Friederich, and J. Chazelas, *Phys. Rev. Lett.* **61**, 2472 (1988).
- ⁷R. E. Camley and J. Barnas *Phys. Rev. Lett.* **63**, 664 (1989).
- ⁸J. Friedel, in *Proceedings of the International School in Physics "Enrico Fermi," Course XXXVII, Theory of Magnetism in Transition Metals*, edited by W. Marshall (Academic, New York, 1967), pp. 283–318.
- ⁹J. P. Nozieres *et al.*, *J. Magn. Magn. Mat.* **121**, 386 (1993).
- ¹⁰S. S. P. Parkin, R. Bhadra, and K. P. Roche, *Phys. Rev. Lett.* **66**, 2152 (1991).
- ¹¹B. Dieny, V. S. Speriosu, J. P. Nozieres, B. A. Gurney, A. Vedyayev, and N. Ryzhanova, *Proceedings of the NATO ARW*, held in Cargese, June 1992, to be published as a NATO series.
- ¹²J. Mathon, *J. Magn. Magn. Mat.* **100**, 527 (1991).
- ¹³S. S. P. Parkin, *Appl. Phys. Lett.* **61**, 1358 (1992); S. S. P. Parkin, *Phys. Rev. Lett.* **71**, 1641 (1993).
- ¹⁴J. Shi, S. S. P. Parkin, L. Xing, and M. B. Salamon *J. Magn. Magn. Mat.* **125**, L251 (1993).
- ¹⁵M. B. Salamon (private communication).

Low field giant magnetoresistance in discontinuous magnetic multilayers

T. L. Hylton, K. R. Coffey, M. A. Parker, and J. K. Howard
IBM AdStar, San Jose, California 95193

Giant magnetoresistance of order 4%–6% has been observed in fields of 5–10 Oe at room temperature in annealed multilayers of $\text{Ni}_{80}\text{Fe}_{20}/\text{Ag}$ prepared by magnetron sputtering. For a wide range of NiFe and Ag thicknesses, no giant magnetoresistance was observed in the unannealed films. We attribute the appearance of giant magnetoresistance to a magnetostatic interlayer interaction that promotes antiparallel order of the moments in adjacent layers fostered by a breakup of the NiFe layers. We discuss the effects of variations in the underlayers, spacer thickness, and the sputtering process on the magnetoresistance. Our results suggest that maximizing magnetoresistance and minimizing hysteresis require samples with continuous Ag layers that prevent contact between the NiFe layers and NiFe layers that are discontinuous but not too severely disrupted.

Recently we reported¹ a giant magnetoresistance (GMR) effect of order 4%–6% with characteristic fields of 5–10 Oe in annealed multilayers of $\text{Ni}_{80}\text{Fe}_{20}/\text{Ag}$. Unannealed films are ferromagnetically coupled with negligible GMR. Upon annealing, GMR develops concurrently with a break-up of the magnetic layers. We have attributed the appearance of the GMR at low fields to magnetostatic interactions that favor antiparallel order of the moments in adjacent NiFe layers, which are prompted by the breakup of the magnetic layers. Devices based on these structures may be able to capitalize on the original promise of GMR, as observed in Fe/Cr multilayer systems^{2,3} by offering highly sensitive magnetic field sensors alternative to the “spin-value”⁴ and other low-field GMR structures^{5,6} for applications such as magnetoresistive heads used in magnetic recording systems. In this paper we concentrate on the role of process variations in the preparation of these structures, how they effect the GMR, and how they relate to our interpretation of the physics. Another paper at this conference will concentrate on the structure of these and related samples, as determined by transmission electron microscopy and x-ray diffraction.⁷

As we have previously discussed,^{1,8,9} greater low-field sensitivity in systems of magnetic particles embedded in a nonmagnetic matrix exhibiting GMR^{10–12} can be achieved if the particles can be given a flat, disk-like shape and oriented, such that all the particle surfaces are parallel to each other and to the applied field. The in-plane anisotropy induced by departures from a perfectly circular perimeter will be much smaller than in the case of similarly misshapen spherical particles. In an effort to achieve such a structure, we have prepared annealed multilayers of immiscible magnetic (NiFe) and nonmagnetic materials (Ag). Under appropriate annealing conditions, we expect penetration of the nonmagnetic material at the grain boundaries of the magnetic layer. While this may or may not result in a collection of flat, island-like magnetic particles, it will certainly promote a multidomain state within the magnetic layers. In addition, because the grains are columnar (with epitaxy between the NiFe and Ag layers) we expect that discontinuities at the grain boundaries in the magnetic layers will promote antiparallel alignment of the moments in adjacent layers.^{1,7}

The multilayers were prepared by S-gun magnetron sputtering in a mixture of 4% H_2 and 96% Ar at a pressure of

3 mTorr with substrates at ambient temperature. Substrates were 1 in. Si wafers with a 700 Å thermally grown oxide surface. A typical sample with n NiFe layers of thickness x and Ag layers of thickness y is given by $\text{Ta}(100 \text{ Å})/\text{Ag}(y/2)/[\text{NiFe}(x)/\text{Ag}(y)]_{n-1}/\text{NiFe}(x)/\text{Ag}(y/2)/\text{Ta}(40 \text{ Å})/\text{SiO}_2(700 \text{ Å})/\text{Si}$. A magnetic field of approximately 150 Oe applied during deposition resulted in a weak uniaxial anisotropy field of 2–3 Oe with significant dispersion. After deposition, the samples were broken into strips approximately 8 mm × 1.5 mm and annealed at atmospheric pressure in a mixture of 5% H_2 and 95% Ar in a rapid thermal processing oven at a variety of temperatures for 10 min. Magnetoresistance measurements were performed with a four-point, in-line geometry of the contacts, with the magnetic field applied parallel to the plane of the sample and either perpendicular or parallel to the current direction. In the figures that follow, all measurements were made at room temperature, with the applied field in the easy axis direction. Similar results have been obtained on samples with no significant uniaxial anisotropy deposited in the absence of an applied field.

As shown in Fig. 1, GMR develops after annealing to

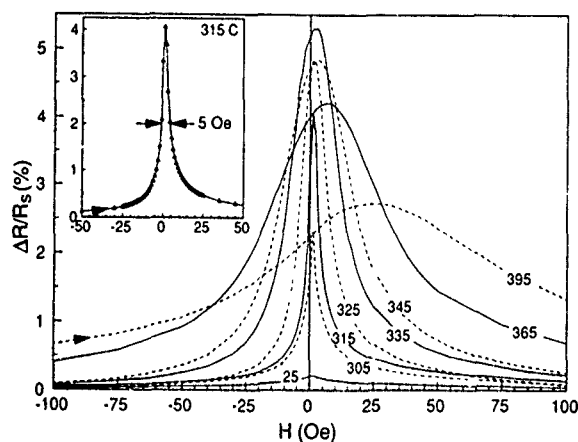


FIG. 1. $\Delta R/R_s$ vs H for a sample $\text{Ta}(100 \text{ Å})/\text{Ag}(20 \text{ Å})/[\text{NiFe}(20 \text{ Å})/\text{Ag}(40 \text{ Å})]_n/\text{NiFe}(20 \text{ Å})/\text{Ag}(20 \text{ Å})/\text{Ta}(40 \text{ Å})/\text{SiO}_2(700 \text{ Å})/\text{Si}$. The field is in the plane of the sample and perpendicular to the current. Arrows indicate the ramping direction of the field. Unannealed samples show only a small AMR effect, but for annealing temperatures above 300 °C, a large GMR effect is evident. Large sensitivities of order 0.8%/Oe are achieved in the sample annealed at 315 °C (inset).

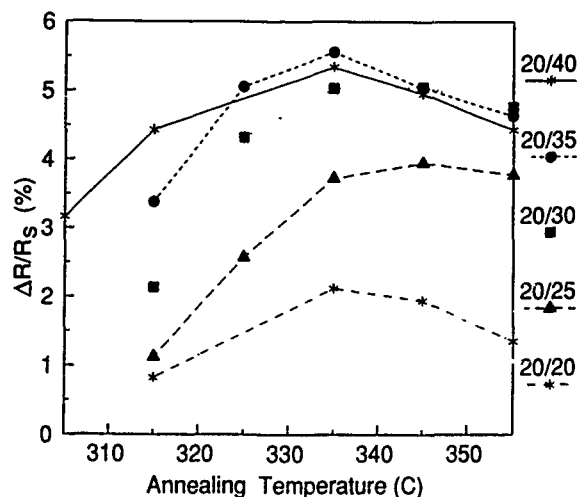


FIG. 2. The amplitude $\Delta R/R_s$ versus annealing temperature for samples Ta(100 Å)/Ag(x/2)/[NiFe(20 Å)/Ag(x)]₄/NiFe(20 Å)/Ag(x/2)/Ta(40 Å)/SiO₂(700 Å)/Si, where $x=20, 25, 30, 35$, and 40 Å. Unannealed samples (not shown) exhibit no GMR. Samples with thinner Ag spacers show systematically smaller $\Delta R/R_s$.

achieve magnitudes of typically $\Delta R/R_s=4\%-6\%$ for a sample with five NiFe layers, where $\Delta R=R-R_s$ and R_s are the change in resistance and the resistance at saturation, respectively. The resistance of the as-deposited sample drops about 15% after annealing at any temperature in the 300 °C–400 °C range. Thus, changes in ΔR dominate the variation in $\Delta R/R_s$ with annealing temperature. A difference in the magnitudes of the GMR for fields applied parallel and perpendicular to the current direction indicates a persistent anisotropic magnetoresistance effect (AMR) of magnitude 0.3%–0.5% in both the unannealed and annealed samples. As the anneal temperature increases, the width and hysteresis of $\Delta R/R_s$ versus the applied field H increase. We find a maximum $\Delta R/R_s=5.34\%$ after an anneal at 335 °C, with a full width at half-maximum (FWHM) of 22 Oe, but the sample annealed at 315 °C shows the largest change in resistance per unit field, $\Delta R/R_s/\text{FWHM}=4\%/5 \text{ Oe}=0.8\%/\text{Oe}$. As we have previously discussed,¹ the magnetoresistance becomes larger when the ratio of the magnetization remanence to that at saturation M_r/M_s becomes smaller, suggesting that ease of demagnetization plays an important role in determining $\Delta R/R_s$.

In Fig. 2, we show the dependence of the peak values of $\Delta R/R_s$ versus annealing temperature for a series of five-layer samples NiFe(20 Å)/Ag(y), where $y=20, 25, 30, 35$, and 40 Å. The dependence of the magnetoresistance on the applied magnetic field and its change with annealing temperature is qualitatively similar to that shown in Fig. 1 for all of these samples. In particular, none of the samples shows GMR prior to annealing, and all exhibit peaks in the magnitude of the GMR after annealing at temperatures in the range 335 °C–345 °C and peaks in sensitivity (i.e., the maximum change in $\Delta R/R_s$ per unit field) after annealing in the range 315 °C–325 °C. On the other hand, as the Ag spacer thickness decreases we see a gradual deterioration of GMR, such that $\Delta R/R_s$ and the sensitivity decrease while the hysteresis increases. At spacer thicknesses of 10 Å, we observe no GMR

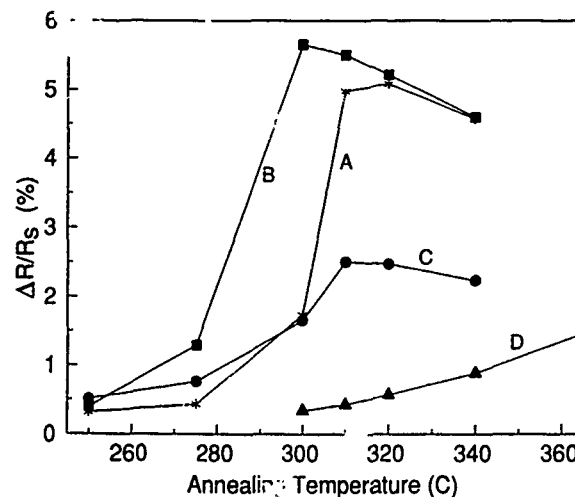


FIG. 3. The amplitude of $\Delta R/R_s$ versus annealing temperature for samples of the type Ta(100 Å)/Ag(20 Å)/[NiFe(20 Å)/Ag(40 Å)]_{n-1}/NiFe(20 Å)/Ag(20 Å)/Ta(40 Å)/SiO₂(700 Å)/Si prepared with different sputtering pressures and deposition temperatures: (a) 3 mTorr, 25 °C, (b) NiFe layers at 25 mTorr, Ag layers at 3 mTorr, 25 °C, (c) 25 mTorr, 25 °C, and (d) 3 mTorr, 100 °C.

before or after annealing. We point out that there is no evidence of oscillations in the magnitude of the magnetoresistance with changing Ag spacer thickness, contrary to what has been observed in many other transition metal multilayer systems.¹³

The changes that we observe in the GMR with change in Ag spacer thickness and annealing temperature may be the result of several competing interlayer interactions: (i) ferromagnetic exchange interaction mediated by the Ag spacer; (ii) ferromagnetic bridges or “pinholes” through the Ag spacer; and (iii) magnetostatic interactions caused by the breakup of the magnetic layers that promote an “artificial” antiferromagnetic state (i.e., antiparallel alignment of the moments in adjacent layers). Interactions (i) and (ii) inhibit GMR, while interaction (iii) promotes it. A breakup of the magnetic layers in a columnar microstructure serves to break the ferromagnetic order favored by (i) and (ii) in two ways: by providing an antiparallel interlayer coupling mechanism and by isolating regions dominated by pinholes. A possible explanation of the observed deterioration of the GMR with decreasing spacer thickness is that samples with thinner spacer layers have a greater density of ferromagnetic bridges, and that samples with spacers as thin as 10 Å are completely ferromagnetically coupled due to a very large density of pinholes. Others have made similar conclusions in NiFe/Ag multilayers with thin Ag spacers.^{14,15} As the annealing temperature increases, the pinhole density may increase and degrade the GMR, consistent with the results of Figs. 1 and 2. We also point out that magnetostatic interactions are very long range, and would not be expected to oscillate with layer thickness, consistent with our observations.

We now examine the effect of variations of the sputtering process parameters in an effort to influence the structure of the films and to determine its effect on the GMR. In Fig. 3, we show the change in amplitude of $\Delta R/R_s$ versus annealing temperature for several samples of [NiFe(20 Å)/Ag(40

Å)]₅ deposited at a variety of temperatures and pressures. Samples A and D, deposited at 3 mTorr and 25 °C and 100 °C, respectively, show a very different evolution of the magnetoresistance with annealing temperature. In particular, the sample deposited at low temperature shows a considerably larger $\Delta R/R_s$ appearing at much lower annealing temperature. A possible explanation for this observation is that the Ag layers in the sample deposited at 100 °C are more discontinuous due to increased Ag mobility on the sample surface during deposition. If so, then it is reasonable to expect a greater degree of NiFe bridging in the 100 °C sample, which would then require a greater degree of breakup of the NiFe (i.e., a higher annealing temperature) to effectively isolate the bridged regions and/or overcome the associated ferromagnetic interlayer coupling. A similar explanation can be offered to explain the difference between samples A and C, both sputtered at 25 °C, but at pressures of 3 and 25 mTorr, respectively. The sample sputtered at high pressure shows a uniformly smaller amplitude of $\Delta R/R_s$, again, suggesting a greater degree of interlayer ferromagnetic interaction. As high sputtering pressures are well known to produce more voided grain boundaries,¹⁶ greater bridging of the NiFe through the Ag might be expected. Sample B was prepared by alternately sputtering the NiFe layers at 25 mTorr and Ag layers at 3 mTorr. Interestingly, this sample shows a larger amplitude of $\Delta R/R_s$ at lower annealing temperatures than any of the other samples. The alternation of the sputtering pressure was an effort to create porous NiFe layers separated by continuous Ag layers, thereby enhancing the breakup of the NiFe layers while preventing bridging of the Ag layers. The data presented in Fig. 3 indeed suggest that it is exactly this structure that is desired to produce large $\Delta R/R_s$.

In Fig. 4 we show $\Delta R/R_s$ vs H at the annealing temperature yielding the largest amplitude of $\Delta R/R_s$ for each of the same samples in Fig. 3. Samples with smaller $\Delta R/R_s$ also show considerably greater hysteresis and characteristic fields. This trend is generally true in all the NiFe/Ag multilayer samples that we have examined, and is also evident in Fig. 1 for annealing temperatures higher than that which produces the peak amplitude of $\Delta R/R_s$. The hysteresis evident in these annealed multilayers may be the result of excessive breakup of the NiFe layers and bridging of the Ag spacer layers. We conclude that the ideal structure would have continuous Ag layers and NiFe layers that are not too severely disrupted. By carefully controlling the deposition and annealing parameters, structures such as these may not only yield very large $\Delta R/R_s$ at small fields, but also a nonhysteretic response.

Finally, we comment on the role of the Ta and Ag layers that sandwich the NiFe/Ag multilayer. The Ta underlayer was found to provide an enhanced (111) orientation of the multilayer and greatly improved the quality and reproducibility of the GMR effect. Ta underlayer thicknesses in the range 40–160 Å were found to have a roughly comparable effect. Samples with Cr, Y, or no underlayer showed a generally poorer quality GMR and reduced (111) orientation. For samples without Ta overlayers, Ag was seen to agglomerate on the sample surface after annealing, which we have also observed in annealed NiFeAg alloys exhibiting GMR.¹⁷ The

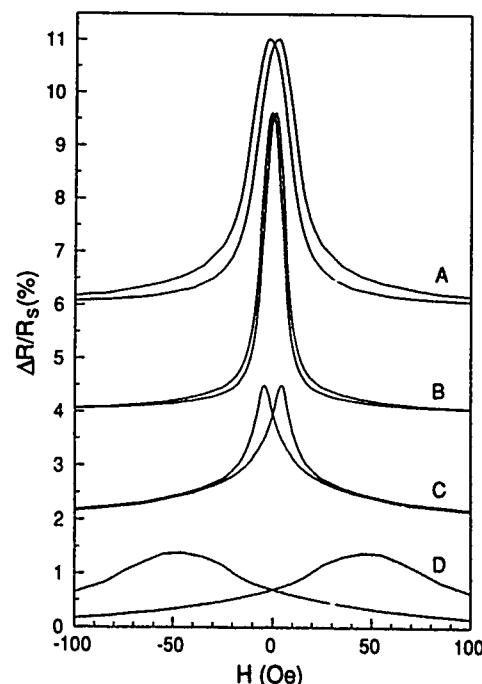


FIG. 4. $\Delta R/R_s$ vs H for the same samples shown in Fig. 3 at annealing temperatures of (a) 320 °C, (b) 300 °C, (c) 310 °C, and (d) 365 °C. Curves are offset along the vertical axis for clarity.

Ta overlayer prevents this agglomeration, as well as providing a thin passivating oxide on its surface. Better reproducibility and higher quality GMR is also obtained on samples that include Ag layers below the bottom NiFe layer and above the top NiFe layer. In these structures each NiFe layer is sandwiched between Ag layers, which may promote a more uniform breakup of the magnetic layers by annealing.

- ¹ T. L. Hylton, K. R. Coffey, M. A. Parker, and J. K. Howard, *Science* **261**, 1021 (1993).
- ² M. N. Baibich, J. M. Broto, A. Fer, F. Nguyen Van Dau, and F. Petroff, *Phys. Rev. Lett.* **61**, 2472 (1988).
- ³ G. Binasch, P. Grunberg, F. Saurenbach, and W. Zinn, *Phys. Rev. B* **39**, 4828 (1989).
- ⁴ B. Dieny, V. S. Speriosu, S. S. P. Parkin, B. A. Gurney, D. R. Wilhoit, and D. Mauri, *Phys. Rev. B* **43**, 1297 (1991).
- ⁵ C. Dupas, P. Beauvillain, C. Chappert, J. P. Renard, F. Trigu, P. Veillet, E. Vélú, and D. Renard, *J. Appl. Phys.* **67**, 5680 (1990).
- ⁶ T. Shinjo and H. Yamamoto, *J. Phys. Soc. Jpn.* **59**, 3061 (1990).
- ⁷ M. A. Parker, T. L. Hylton, K. R. Coffey, and J. K. Howard (these proceedings).
- ⁸ T. L. Hylton, *Appl. Phys. Lett.* **62**, 2431 (1993).
- ⁹ K. R. Coffey, T. L. Hylton, M. A. Parker, and J. K. Howard, *Appl. Phys. Lett.* **63**, 1579 (1993).
- ¹⁰ J. Q. Xiao, J. S. Jiang, and C. L. Chien, *Phys. Rev. Lett.* **68**, 3749 (1992).
- ¹¹ A. E. Berkowitz, J. R. Mitchell, M. J. Carey, A. P. Young, S. Zhang, F. E. Spada, F. T. Parker, A. Hutten, and G. Thomas, *Phys. Rev. Lett.* **68**, 3745 (1992).
- ¹² J. A. Barnard, A. Wakis, M. Tan, E. Haftek, M. R. Parker, and M. L. Watson, *J. Magn. Magn. Mat.* **114**, L230 (1992).
- ¹³ S. S. P. Parkin, *Phys. Rev. Lett.* **67**, 3598 (1991).
- ¹⁴ B. Dieny, V. S. Speriosu, S. Metin, S. S. P. Parkin, B. A. Gurney, P. Baumgart, and D. R. Wilhoit, *J. Appl. Phys.* **69**, 4774 (1991).
- ¹⁵ B. Rodmacq, G. Palumbo, and Ph. Gerard, *J. Magn. Magn. Mat.* **118**, L11 (1993).
- ¹⁶ J. A. Thornton, *J. Vac. Sci. Technol. A* **4**, 3059 (1986).
- ¹⁷ M. A. Parker, K. R. Coffey, T. L. Hylton, and J. K. Howard, *Proc. Mat. Res. Soc. Symp. Proc.* **313**, 85 (1993).

Epitaxial spin-valve structures for ultra-low-field detection

A. Schuhl and O. Durand

Laboratoire Central de Recherches, Thomson-CSF, 91404 Orsay, France

J. R. Childress, J.-M. George, and L. G. Pereira

Laboratoire de Physique des Solides, Université Paris-Sud, 91405 Orsay Cédex, France

A new epitaxial "spin-valve"-type system for low-field magnetoresistive detection is described. This system is based on Fe/Pd epitaxial multilayers grown on (100)MgO by MBE. These films show a very abrupt transition from positive to negative magnetization as the reverse field is applied during hysteresis measurements. We have used these sensitive magnetic properties to fabricate epitaxial spin-valve structures by epitaxial growth of Fe/Ag, Co/Ag, or Co/Cu bilayers on top of a Fe/Pd bilayer. Hysteresis loops and magnetoresistance curves clearly indicate a significant field range with antiparallel alignment of the two components. Magnetoresistive sensitivities of up to 0.3% per Oe at low temperatures have been observed in these structures. The efficiency of the spin-dependent scattering has subsequently been improved either through the addition of planar Co impurities, in both the soft and hard magnetic layer, or by increasing the number of active Fe/Pd interfaces. This approach leads to a drastic improvement of the sensitivity, up to 1.5% per Oersted at room temperature.

Sensitive magnetic field sensors, based on the magnetoresistive effect, require a large magnetoresistivity at low fields. The discovery of giant magnetoresistance (GMR) in antiferromagnetically exchange-coupled multilayers has opened new avenues for these applications.¹ The principal problem with coupled GMR systems is related to the magnetic field range of the effect, which is usually of 1 kOe or more. To decrease the field scale of GMR, the most promising approach is based on achieving antiparallel alignment *without* antiferromagnetic exchange coupling. This can be obtained by selective rotation of the magnetic layers, using various types of layers with different magnetic properties. For example, a magnetic multilayer can be grown using alternatively magnetically hard and magnetically soft layers.² Another method is to block one of the magnetic layers through an exchange coupling with an antiferromagnetic material.³ In practice, permalloy ($\text{Ni}_{79}\text{Fe}_{21}$) is often used as the soft material, and the growth of such materials is usually done by sputtering and leads to a polycrystalline structure. These systems, often referred to as a "spin-valve" structures, have led to sensitivities higher than 1% per Oersted⁴ at room temperature. Here we propose an alternative system, which makes use of the sensitive magnetic properties of epitaxial Fe/Pd bilayers grown by molecular beam epitaxy (MBE). In epitaxial Fe/Pd superlattices, complete rotation of the magnetization of Fe occurs on very small magnetic field scales (≈ 1 Oe). By combining a Fe/Pd bilayer with other epitaxial bilayers such as Fe/Ag or Co/Cu in a "spin-valve" structure, we have obtained highly field-sensitive epitaxial multilayers.

The present samples were grown in the same manner as the (100)Fe/Pd epitaxial multilayers studied previously.⁵⁻⁷ Briefly, we used 1 cm \times 1 cm (100)MgO substrates, annealed in UHV for 30 min at 450 °C immediately prior to deposition. Fe grows very well on (100)MgO, without any kind of buffer layer. A substrate temperature of $T_s \approx 80$ °C was chosen to yield the best structural properties, as determined by low- and high-angle x-ray diffraction and cross-sectional transmission electron microscopy.⁷ Measurements of the

magnetic properties of Fe/Pd superlattices show narrow hysteresis loops at all temperatures.^{5,6} Although the value of the coercive field H_c depends on the growth parameters such as temperature and deposition rate, and also on the thicknesses of the individual layers, it never exceeds 20 Oe at 15 K, and 5 Oe at 300 K. The Fe layers are ferromagnetically coupled to each other⁶ for Pd thicknesses as high as 40 Å. Most importantly, we observe a very abrupt transition from positive to negative magnetization as the reverse field is applied, with a transition width between 1 and 3 Oe. Measurements of the absolute magnetization using wedge-shaped Pd layers have provided evidence of a strong polarization of the Fe/Pd interface,⁷ and we have determined that the presence of this polarized interface is directly responsible for the low coercive fields.⁸

Following these results, we have used epitaxial Fe/Pd bilayers to develop new types of epitaxial "spin-valve" systems.⁸ For example, we have deposited by MBE an Ag/Fe/Ag trilayer ($H_c \approx 100$ Oe) on top of a Fe/Pd bilayer ($H_c \approx 20$ Oe), resulting in a compound structure of $\text{Fe}_{(20 \text{ Å})}/\text{Pd}_{(30 \text{ Å})}/\text{Ag}_{(30 \text{ Å})}/\text{Fe}_{(20 \text{ Å})}/\text{Ag}_{(30 \text{ Å})}$. RHEED patterns obtained during deposition indicate a fully epitaxial growth for the entire structure. The hysteresis loop of this structure [Fig. 1(b)] is essentially the sum of the two hysteresis loops obtained for separate $\text{Fe}_{(20 \text{ Å})}/\text{Pd}_{(30 \text{ Å})}$ and $\text{Fe}_{(20 \text{ Å})}/\text{Ag}_{(30 \text{ Å})}$ bilayers [Fig. 1(a)]. Thus, the two Fe layers in the structure are uncoupled, structurally as well as magnetically, by the $\text{Pd}_{(30 \text{ Å})}/\text{Ag}_{(30 \text{ Å})}$ interlayer. Antiparallel alignment of the two Fe layers is therefore achieved after reversal of the first Fe layer. Similar results are obtained as we replace Ag by Cu, and/or the second Fe layer by Co, which is a magnetically harder material. It is worth noting that although the growth proceeds epitaxially throughout the structure, RHEED patterns indicate a degradation of the layer flatness after the second bilayer system (i.e., Fe/Ag or Co/Cu) has been deposited. Therefore, it is not possible to repeat the layer sequence to form a thicker multilayer, since the subsequent

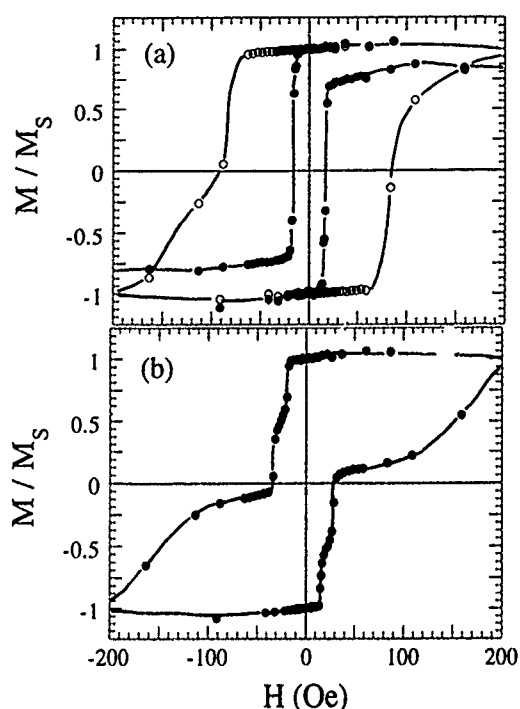


FIG. 1. Magnetic hysteresis loops at $T=15$ K of (a) a $\text{Fe}_{(20 \text{ Å})}/\text{Pd}_{(30 \text{ Å})}$ bilayer (filled circles) and a $\text{Fe}_{(20 \text{ Å})}/\text{Ag}_{(30 \text{ Å})}$ bilayer (open circles), and (b) a $\text{Fe}_{(20 \text{ Å})}/\text{Pd}_{(30 \text{ Å})}/\text{Ag}_{(30 \text{ Å})}/\text{Fe}_{(20 \text{ Å})}/\text{Ag}_{(30 \text{ Å})}$ structure.

Fe/Pd bilayers would not retain the required soft magnetic properties.

The magnetoresistive (MR) response is shown in Fig. 2 for the Fe/Pd/Ag/Fe/Ag structure. The rotation of the magnetization in the first Fe layer, at low fields, induces an abrupt increase of the resistivity when antiparallel alignment is achieved, as is seen in many other multilayer-based GMR systems. The maximum MR response at 4.2 K is 0.8% for Fe/Ag bilayers, 0.5% for Co/Ag bilayers, and 1.5% for Co/Cu bilayers (also shown in Fig. 2), each epitaxially grown on a Fe/Pd bilayer. The magnitude of the MR effect originates in the strength of the spin-dependent impurity scattering that occurs near the magnetic interfaces.¹ Although

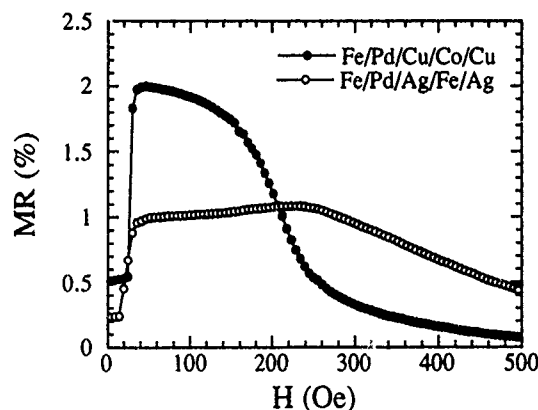


FIG. 2. Magnetoresistance as a function of applied magnetic field at $T=4.2$ K for $\text{Fe}_{(20 \text{ Å})}/\text{Pd}_{(30 \text{ Å})}/\text{Ag}_{(30 \text{ Å})}/\text{Fe}_{(20 \text{ Å})}/\text{Ag}_{(30 \text{ Å})}$ and $\text{Fe}_{(20 \text{ Å})}/\text{Pd}_{(30 \text{ Å})}/\text{Cu}_{(30 \text{ Å})}/\text{Cu}_{(30 \text{ Å})}/\text{Co}_{(20 \text{ Å})}/\text{Cu}_{(30 \text{ Å})}$ epitaxial structures.

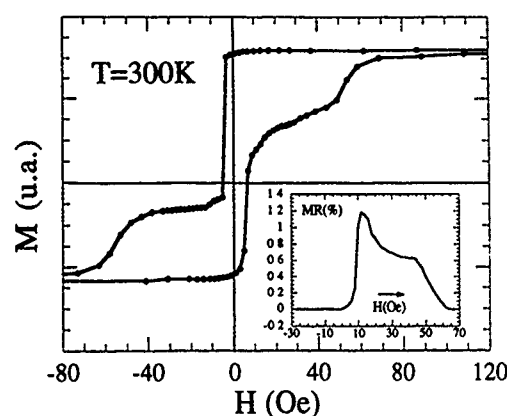


FIG. 3. Magnetic hysteresis loop at $T=300$ K of a $[\text{Fe}_{(20 \text{ Å})}/\text{Co}_{(4 \text{ Å})}/\text{Pd}_{(30 \text{ Å})}]/[\text{Cu}_{(30 \text{ Å})}/\text{Co}_{(20 \text{ Å})}/\text{Cu}_{(30 \text{ Å})}]$ structure. Inset: corresponding magnetoresistive response (shown for an increasing magnetic field).

small total magnetoresistance changes are observed, our interest lies in the small field scales (a few Oe) over which the MR increase is observed (up to 0.3% per Oe). At 300 K, the magnetoresistive effect is strongly decreased. For example, a value between 0.2% and 0.3% is observed for the Fe/Pd/Cu/Co/Cu structure above, depending on the precise value of individual layer thicknesses. Several factors contribute in limiting the maximum MR effect observed. First, the total thickness of the structure is on the order of the electronic mean-free path, therefore the efficiency of scattering within the structure is reduced. Second, unlike the case of exchange-coupled MMM's, "spin-valve" structures rely on spin-dependent scattering from different systems. Hence, in our multilayers, strong spin-dependent scattering must occur *both* within the Fe/Pd layers and within the other magnetic layers in order to achieve the maximum MR effect. Unlike the Co/Cu interface, which is well known to exhibit strongly spin-dependent electron scattering ($\alpha = \rho_{\uparrow}/\rho_{\downarrow} \ll 1$), the Fe/Pd interface is not expected to be particularly favorable. Nonetheless, because the field scales over which this MR is observed is actually smaller at room temperature than at 4.2 K, sensitivities close to 0.15% per Oe have still been observed at 300 K.

We have checked several ways to increase the magnetoresistive response of these structures. In particular, we have tried to increase the spin-dependent scattering within the Fe/Pd layers. In a first approach, we have introduced ultrathin layers of impurities (Cr, Cu, or Co) in the Fe layer. Whereas 3 Å of Cr in the Fe layer drastically increases the coercive field, no such adverse effect on the magnetic properties was observed with the use of Cu or Co impurity layers, while the magnetoresistive effect is significantly increased. For example, the introduction of a 4 Å-thick layer of Co in a $[\text{Fe}_{(20 \text{ Å})}/\text{Pd}_{(30 \text{ Å})}]/[\text{Cu}_{(30 \text{ Å})}/\text{Co}_{(20 \text{ Å})}/\text{Cu}_{(30 \text{ Å})}]$ structure leads to $\Delta R/R$ between 0.7% and 0.8% (a factor of 2 increase). Surprisingly, the effect does not depend on the precise position of the Co layer, i.e., whether it is placed at the Fe/Pd interface (shown in Fig. 3) or 5 Å below the interface. The addition of a second Co layer, resulting in a $[\text{Fe}_{(8 \text{ Å})}/\text{Co}_{(4 \text{ Å})}/\text{Fe}_{(8 \text{ Å})}/\text{Co}_{(4 \text{ Å})}/\text{Fe}_{(8 \text{ Å})}/\text{Pd}_{(30 \text{ Å})}]/$

Giant magnetoresistance with low saturation field in $(\text{Ni}_x\text{Co}_{100-x}/\text{Cu})$ multilayers

X. Bian, J. O. Ström-Olsen, and Z. Altounian

Centre for the Physics of Materials and Department of Physics, McGill University, 3600 University St., Montréal, Québec, H3A 2T8, Canada

Y. Huai

INRS-Energie et Matériaux, 1650 montée Ste-Julie, C. P. 1020, Varennes, Québec, J3X 1S2, Canada

R. W. Cochrane

Département de Physique et Groupe de recherche en physique et technologie des couches minces, Université de Montréal, C. P. 6182, Succ. A, Montréal, Québec, H3C 3J7, Canada

We have investigated giant magnetoresistance (GMR) in $\text{Ni}_x\text{Co}_{100-x}/\text{Cu}$ multilayers for x in the range 20–100. The GMR at room temperature is greater than 12% for magnetic alloys with x near 80, where the magnetocrystalline anisotropy is small. The smallest saturation fields are found near $x=60$ in the region where the magnetostriction vanishes. This combination of large GMR and small saturation field results in large MR field sensitivities up to 0.16%/Oe at room temperature. In order to maximize these parameters, we have also studied the dependence of the MR on the magnetic layer thickness and the number of bilayers.

I. INTRODUCTION

Giant magnetoresistance (GMR) in metallic multilayers composed of alternating magnetic and nonmagnetic layers has been extensively studied in a variety of layered magnetic transition metal and alloy systems. Among them, Cu-based multilayers such as Co/Cu ,¹ Fe/Cu ,² and $\text{Ni}(\text{Fe},\text{Co})/\text{Cu}$,^{3,4} which exhibit GMR at room temperature and an oscillatory exchange coupling, are important, both for a fundamental understanding of the effect as well as for its technological application. It is now generally agreed that GMR is associated with the reorientation of the magnetic moments in adjacent magnetic layers, and has been interpreted on the basis of spin-dependent electron scattering.⁵ A large number of studies have sought ways to increase the magnitude of the GMR. As a potential candidate for magnetic sensors however, a practical requirement along with large MR is high magnetic-field sensitivity, namely an appreciable resistance change upon the application of a small magnetic field.

$\text{Ni}_{80}\text{Co}_{20}/\text{Cu}$ multilayers have shown GMR and a well-defined oscillation in the MR as a function of the Cu spacer thickness at room temperature. Small saturation fields have also been observed for Cu thicknesses t_{Cu} near 20 Å, corresponding to the second peak of the oscillation in MR.⁶ In this paper, we report the composition dependence of MR and the magnetic properties of $\text{Ni}_x\text{Co}_{100-x}/\text{Cu}$ multilayers for x in the range 20–100 and for t_{Cu} around 20 Å. In addition, we have systematically varied the multilayer configuration, specifically the magnetic layer thickness and the number of bilayers, in order to maximize the magnetic field sensitivity. Throughout the paper, we emphasize the importance of the magnetocrystalline anisotropy and magnetostriction in this magnetically soft multilayer system.

II. EXPERIMENTAL DETAILS

Multilayers with structure $\text{NiCo}50 \text{ Å} / [\text{Ni}_x\text{Co}_{100-x} / \text{Cu}] \times 30$ with $t_{\text{Cu}}=20 \text{ Å}$ and a series of $\text{Ni}_{80}\text{Co}_{20}/\text{Cu}$ samples with the number of bilayers (from 8 up to 100) were pre-

pared by DC magnetron sputtering from separate targets of the appropriate $\text{Ni}_x\text{Co}_{100-x}$ alloy and Cu onto oxidized Si wafers at room temperature. 50 Å $\text{Ni}_{80}\text{Co}_{20}$ buffer layer was deposited between Si and multilayers for all the samples studied here. The base pressure in the deposition chamber before sputtering was less than 2×10^{-7} Torr. With a sputtering pressure of 8 mTorr of argon, the deposition rates (determined from the measured thicknesses of single films by low angle x-ray reflectivity measurements) were 1.5 Å/s for $\text{Ni}_x\text{Co}_{100-x}$ and 1.6 Å/s for Cu. The structural characterization of the samples was performed by low and high angle x-ray diffraction using $\text{Cu-K}\alpha$ radiation.⁷ The low angle x-ray reflectivity spectra reveal sharp superlattice peaks for all the samples studied here, indicating a well-defined compositional modulation along the growth direction. High angle x-ray diffraction data show that the films have coherent interfaces and textured polycrystalline structures with the FCC (111) direction normal to the film plane. The magnetoresistance measurements were carried out with four-terminal geometry and a high-resolution AC bridge at temperatures from 4.2 to 300 K and in magnetic fields of up to 1.0 T. Transverse MR is presented in this paper for which the magnetic field was either in the plane of the film or perpendicular to it.⁸ The room temperature magnetization of selected samples were also measured using a SQUID magnetometer.

III. RESULTS AND DISCUSSIONS

The saturation MR (measured at 77 and 300 K) of $\text{Ni}_{80}\text{Co}_{20}/\text{Cu}$ multilayers as a function of t_{Cu} for $t_{\text{NiCo}}=15 \text{ Å}$ is given in Fig. 1. Three well-defined peaks are found, with an oscillation period and phase quite similar to that found in other Cu-based multilayer systems. The fact that the period depends primarily on the Cu layer is consistent with an interpretation that the interlayer exchange coupling depends primarily on the electronic structure of the spacer material.⁹ Of particular interest for device applications is the broad second peak with a maximum MR comparable to that of the first

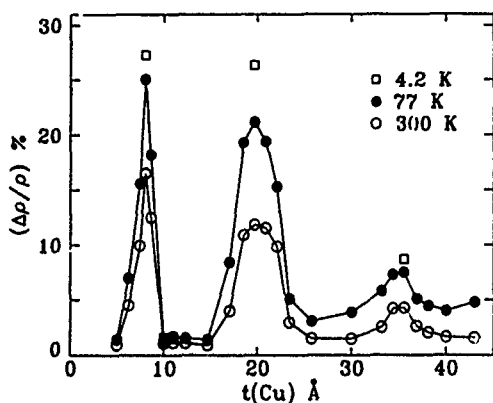


FIG. 1. Variation of the saturation MR with Cu spacer thickness t_{Cu} for a series of multilayer samples with structure $\text{Si}/\text{Ni}_{80}\text{Co}_{20}50 \text{ \AA} [\text{Cu } t_{\text{Cu}} \text{ \AA} / \text{Ni}_{80}\text{Co}_{20}15 \text{ \AA}] \times 30$

peak, and small saturation fields, which range between 100–150 Oe, depending on the degree of the antiferromagnetic coupling between the neighboring NiCo layers. As a consequence, large MR field sensitivities, up to 0.12%/Oe, at room temperature are obtained.

Figure 2 shows several room temperature MR curves of $\text{Ni}_x\text{Co}_{100-x}/\text{Cu}$ multilayers with $x=70$ and 80 obtained near $t_{\text{Cu}}=20 \text{ \AA}$. These data show a peak GMR between 8% and 12%, significantly larger than the anisotropy MR (AMR) at similar compositions. However, the saturation field H_S , determined from these curves as well as from magnetization versus field measurements varies considerably. For example, H_S is between 120 and 200 Oe for $x=80$, but is reduced to 60–110 Oe for $x=70$. Large H_S at $t_{\text{Cu}}=20 \text{ \AA}$ is the result of nearly ideal antiferromagnetic coupling, as can be inferred from magnetization curves and neutron scattering data.¹⁰

In the Ni–Co alloy system, the magnetocrystalline anisotropy K vanishes at 80% Ni, while the magnetostriction

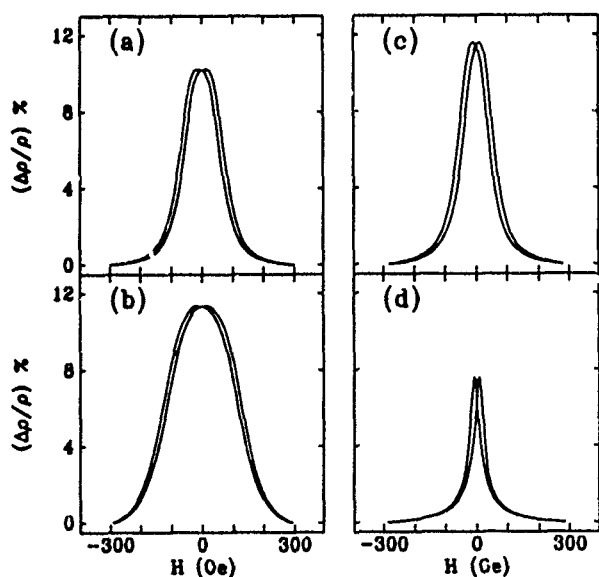


FIG. 2. Magnetoresistance $[\Delta\rho/\rho=(\rho_0-\rho_H)/\rho_H]$ vs the applied magnetic field at room temperature for (a) $\text{Ni}_{80}\text{Co}_{20}15 \text{ \AA}/\text{Cu}19 \text{ \AA}$, (b) $\text{Ni}_{80}\text{Co}_{20}15 \text{ \AA}/\text{Cu}20 \text{ \AA}$, (c) $\text{Ni}_{70}\text{Co}_{30}15 \text{ \AA}/\text{Cu}20 \text{ \AA}$, and (d) $\text{Ni}_{70}\text{Co}_{30}15 \text{ \AA}/\text{Cu}21 \text{ \AA}$.

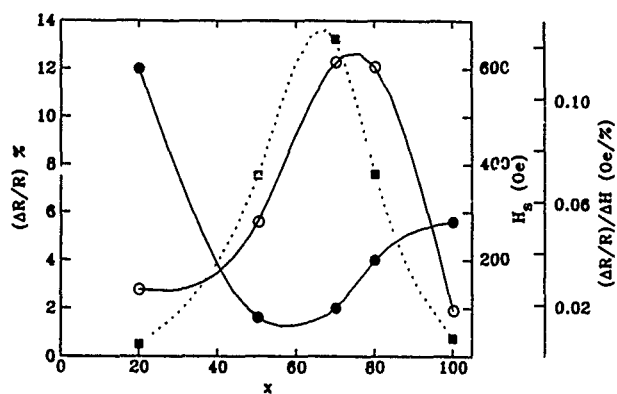


FIG. 3. Composition dependence of the MR (●), saturation field H_S (○), and MR field sensitivity (■) in $\text{Si}/\text{Ni}_{80}\text{Co}_{20}50 \text{ \AA} [\text{Cu}20 \text{ \AA}/\text{Ni}_x\text{Co}_{100-x}15 \text{ \AA}] \times 30$ multilayers for $20 \leq x \leq 100$.

coefficient λ_s vanishes at 60% Ni.¹¹ It is expected that the GMR and magnetostriction will depend, in part, on the competition between these two effects. The composition dependence of the MR, H_S , and the magnetic field sensitivity for $[\text{Ni}_x\text{Co}_{100-x}15 \text{ \AA}/\text{Cu}20 \text{ \AA}] \times 30$ multilayers with $20 \leq x \leq 100$ are shown in Fig. 3. A broad maximum MR of 12% is found in the range $x=70$ –80; a decrease of the Ni concentration leads to a decrease in the MR, which all but vanishes at $x=20$. In fact, the absence of GMR in $\text{Ni}_{20}\text{Co}_{80}/\text{Cu}$ multilayers over a wide range of Cu thickness (6–24 Å), together with magnetic measurements, suggests no antiferromagnetic coupling across the Cu spacer at this composition. The saturation field shows a broad minimum from $x=50$ –70, where the magnetostriction is also small. As clearly shown in Fig. 3, the maximum sensitivity appears at a composition between the maximum in the MR and the minimum in the saturation field. Therefore, selecting a magnetic component with intrinsically small magnetoelastic parameters at a weakly or partially coupled Cu thickness region will result in a substantial GMR with low H_S , and hence a large field sensitivity.

The distinctive features of these NiCo/Cu multilayers are the large amplitude and width of the second peak of the oscillation with Cu thickness, combined with the low value of saturation field, as illustrated in Figs. 1 and 3. To deter-

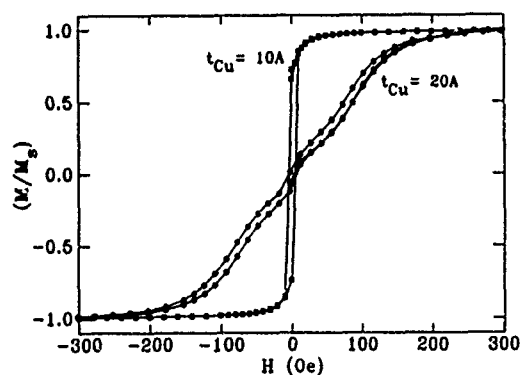


FIG. 4. Room temperature magnetization vs the applied magnetic field for (a) a FM sample $(\text{Ni}_{80}\text{Co}_{20}15 \text{ \AA}/\text{Cu}10 \text{ \AA}) \times 30$, and (b) an AF sample $(\text{Ni}_{80}\text{Co}_{20}15 \text{ \AA}/\text{Cu}20 \text{ \AA}) \times 30$.

TABLE I. Dependence of magnetoresistance parameters on t_{NiCo} and bilayer number n of (a) $(\text{Ni}_{80}\text{Co}_{20})_{t_{\text{NiCo}}}/\text{Cu}_{20} \text{ \AA} \times 30$ and (b) $(\text{Ni}_{80}\text{Co}_{20})_{15 \text{ \AA}}/\text{Cu}_{20} \text{ \AA} \times n$.

Sample (a)	R_0 (Ω)	ΔR_S (Ω)	$\Delta R/R_S$ (%)	H_S (Oe)	Sensitivity (%/Oe)
t_{NiCo}					
10 \AA	4.943	0.533	12.089	210	0.054
15 \AA	4.799	0.498	11.591	120	0.120
20 \AA	3.996	0.278	7.483	100	0.110
30 \AA	3.388	0.041	1.206	80.	0.016
(b) n					
8	21.205	1.146	5.658	90.	0.067
15	9.279	0.592	6.721	85.	0.094
30	4.769	0.443	10.843	100	0.112
45	3.077	0.245	11.509	105	0.107
60	2.339	0.236	12.401	115	0.110
100	1.538	0.153	11.061	120	0.089

mine the origin of the GMR in these soft multilayers, we have performed magnetization measurements and small angle neutron scattering on several samples. Figure 4 shows the magnetization versus field for a $\text{Ni}_{80}\text{Co}_{20}/\text{Cu}$ multilayer at $t_{\text{Cu}}=20 \text{ \AA}$; the contribution of the 50 \AA $\text{Ni}_{80}\text{Co}_{20}$ buffer layer was subtracted from the measured data. There is only small hysteresis and remanence associated with the magnetization curve, as also found in the MR curves. For comparison, we also show a typical magnetization curve for a ferromagnetically coupled sample ($t_{\text{Cu}}=10 \text{ \AA}$). Direct confirmation of the AF coupling for NiCo/Cu multilayers was obtained in neutron scattering experiments in an external magnetic field.¹⁰ GMR and small saturation fields measured in $\text{Ni}_x\text{Co}_{100-x}/\text{Cu}$ multilayers for $x=70-80$, particularly in the region near $t_{\text{Cu}}=20 \text{ \AA}$, is thus demonstrated in a sample, with weak AF coupling between magnetic layers. The estimated strength of AF coupling in this region is on the order of 0.003 erg/cm^2 . This value is much smaller than that found in other Cu-based multilayer systems, confirming that the interlayer coupling is indeed weak.

We have also studied the dependence of MR, H_S , and the MR field sensitivity on the multilayer structure, specifically the magnetic layer thickness and the number of bilayers, for a series of $\text{Ni}_{80}\text{Co}_{20}/\text{Cu}$ samples. As shown in Table I, both MR and H_S progressively decrease with increasing t_{NiCo} , while the field sensitivity shows a maximum at $t_{\text{NiCo}}=15 \text{ \AA}$. It is of interest to note that the magnetotransport properties are strongly correlated to the number of bilayers, n . The resistance change ΔR in a saturated magnetic field is maximum for n less than 10, and monotonically decreases with increasing n . The sheet resistance, however, decreases more rapidly as n increases and approaches a saturation value above $n=100$. The gradual increase of $\Delta R/R_S$ up to $n=60$ comes mainly from the rapid decrease of the sheet resistance. Structural studies by low and high angle x-ray diffraction have demonstrated that such behavior is strongly related to the multilayer structure. As the number of bilayers increases, the cumulative structural imperfections such as interface roughness and thickness fluctuations increase.¹² Strain built up at the interface become significant, and are reflected in the progressive increase of the saturation field as the bilayer number increases.

IV. CONCLUSIONS

$\text{Ni}_x\text{Co}_{100-x}/\text{Cu}$ multilayers offer a good combination of large GMR and low saturation field for a Cu thickness close to 20 \AA and x in the range 60–80. The maximum sensitivity occurs for $x=70$, roughly midway between the values for which the GMR is greatest ($x=80$) and H_S is least ($x=60$). It is shown that the GMR in multilayers with $t_{\text{Cu}} \sim 20 \text{ \AA}$ is related to the antiferromagnetic coupling, while the absence of GMR for alloys with $x < 50$ is most likely due to the effects of magnetocrystalline anisotropy. The magnetic and magnetotransport properties are strongly correlated with structural parameters, such as the thickness of the magnetic layer and the number of bilayer periods.

ACKNOWLEDGMENTS

We acknowledge the financial support from the Natural Sciences and Engineering Research Council of Canada, Fonds FCAR du Québec, and Martinex Science, Inc.

- ¹ S. S. Parkin, B. Bhadra, and K. P. Roche, Phys. Rev. Lett. **66**, 2152 (1991); D. H. Mosca, F. Petroff, A. Fert, P. A. Schroeder, W. P. Pratt, Jr., and R. Laloe, J. Magn. Magn. Mat. **94**, L1 (1991).
- ² W. R. Bennett, W. Schwarzacher, and W. F. Egelhoff, Jr., Phys. Rev. Lett. **65**, 3169 (1990).
- ³ S. S. P. Parkin, Appl. Phys. Lett. **60**, 512 (1992). M. Jimbo, T. Kanda, S. Goto, S. Tsunashima, and S. Uchiyama, Jpn. J. Appl. Phys. **31**, L1348 (1992).
- ⁴ B. Dieny, V. S. Speriosu, S. S. P. Parkin, B. A. Gurney, D. R. Wilhoit, and D. Mauri, Phys. Rev. B **43**, 1297 (1991).
- ⁵ R. E. Camley and J. Barnas, Phys. Rev. Lett. **63**, 664 (1989); P. M. Levy, S. Zhang, and A. Fert, Phys. Rev. Lett. **65**, 1643 (1990).
- ⁶ X. Bian, J. O. Ström-Olsen, Z. Altounian, Y. Huai, and R. W. Cochrane, Appl. Phys. Lett. **62**, 3525 (1993).
- ⁷ Y. Huai, R. W. Cochrane, Y. Shi, H. E. Fischer, and M. Sutton, Mat. Res. Soc. Symp. Proc. **238**, 671 (1992).
- ⁸ Y. Huai and R. W. Cochrane, J. Appl. Phys. **72**, 2523 (1992).
- ⁹ P. Bruno and C. Chappert, Phys. Rev. B **46**, 261 (1992).
- ¹⁰ X. Bian, J. O. Ström-Olsen, Z. Altounian, and B. D. Gaulin, unpublished.
- ¹¹ T. R. McGuire and R. L. Potter, IEEE Trans. Magn. **MAG-11**, 1018 (1975).
- ¹² Y. Huai, R. W. Cochrane, and M. Sutton, Phys. Rev. B **48**, 2568 (1993).

Hysteresis reduction in NiFeCo/Cu multilayers exhibiting large low-field giant magnetoresistance

S. Hossain,^{a)} D. Seale,^{a)} G. Qiu,^{b)} J. Jarratt,^{b)} J. A. Barnard,^{b)} H. Fujiwara,^{c)} and M. R. Parker^{a)}

The Center for Materials for Information Technology, The University of Alabama, Tuscaloosa, Alabama 35487-0209

Giant magnetoresistance (GMR) has been observed in $\text{Ni}_{66}\text{Fe}_{16}\text{Co}_{18}/\text{Cu}$ multilayered uniaxial magnetic thin films prepared by dc magnetron sputtering. Both easy and hard axis loops saturate at very low applied fields. The MR ratio reaches $\sim 80\%$ of its saturation value in less than 30 Oe. A maximum MR ratio of $\sim 10\%$ has been observed in the as-deposited state in a structure containing only ten bilayers. Typical hysteresis values for magnetoresistance loops are ~ 4 Oe in the as-deposited state. A gradual decrease of this hysteresis has been observed with annealing. An increase in the saturation field is also observed with annealing. Short-term annealing increases the magnitude of the magnetoresistance ratio; prolonged annealing causes a decrease. A field sensitivity of about 0.3% per Oe has been observed and dc magnetoresistance minor loops exhibit no measurable decrease in sensitivity.

I. INTRODUCTION

Many attempts have been made to produce multilayer structures with large magnetoresistance ratios, low magnetoresistance hysteresis, and low magnetostriction.¹ Recently, we have successfully produced NiFeCo/Cu multilayer GMR samples with low hysteresis and low saturation fields in a high rate dc magnetron sputtering deposition system. Interestingly, this system exhibits a nonhysteretic dc minor loop. We confirmed that the hysteresis in the MR loops can be substantially reduced by annealing. There are, however, some drawbacks to this post-deposition annealing process. The MR saturation field increases with annealing, and long-term annealing degrades the magnitude of the magnetoresistance. This effect has also been observed by another group.² The hysteretic behavior, saturation field, and magnetostriction in a ternary alloy system of Ni, Fe, and Co in multilayered structure with Cu interlayers largely depends on the ferromagnetic alloy composition. It also depends on the internal stress. Relieving internal stress by annealing may play a role in hysteresis reduction. Saturation magnetostriction numbers were measured for both single layer NiFeCo and NiFeCo, multilayered with Cu interlayers. A typical magnetostriction number is $\lambda_s = -1.8 \times 10^{-6}$. A gradual change in the MR magnitude and MR peak linewidth was observed with increasing Co in these multilayers.

II. SAMPLE PREPARATION AND EXPERIMENTAL TECHNIQUES

NiFeCo/Cu multilayered uniaxial magnetic thin films were prepared by dc magnetron sputtering (Vac-Tec Model 250 Sputtering System) at ambient temperature. Sputtering was done at 100 W power and at an argon pressure of 2

mTorr. A bias field was applied during deposition to induce uniaxial anisotropy by using a permanent magnet behind the substrate holder. The field strength of the magnet is ~ 80 Oe. Multilayered and reference films were grown on Corning 7059 glass and on SiO_2 coated [111] Si substrates. Samples grown on both glass and SiO_2 coated substrates exhibit similar properties. The composition of the films was determined by using a JEOL 8600 Electron Probe Microanalyser. Low and high angle XRD scans were performed on a Rigaku D/Max-2BX x-ray diffractometer with a thin film attachment. Magnetic annealing was carried out in flowing argon gas. An aligning field of ~ 100 Oe was applied in the easy direction during annealing. Magnetoresistance measurements were done on an IBM/Dascon 1 high resolution data acquisition system with a four-point linear probe. Magnetization measurements were performed on a Digital Measurement Systems VSM Model 880. All measurements were made at room temperature.

III. SINGLE COMPOSITION $\text{Ni}_{66}\text{Fe}_{16}\text{Co}_{18}/\text{Cu}$ MULTILAYER FILMS

Multilayers of $\text{Ni}_{66}\text{Fe}_{16}\text{Co}_{18}/\text{Cu}$ with ten repeats exhibit large low saturation GMR. The $\text{Ni}_{66}\text{Fe}_{16}\text{Co}_{18}$ layers were ~ 16 Å and Cu interlayers were ~ 22 Å thick. The magnetoresistance ratio measured at room temperature is customarily given by $d\rho/\rho = [\rho(H) - \rho(H_{\text{sat}})]/\rho(H_{\text{sat}})$. The saturation field resistance used for this calculation was measured at 1000 Oe applied field. Easy and hard axis magnetoresistance loops saturate at very low applied fields, as shown in Fig. 1(a). The MR ratio reaches $\sim 80\%$ of its saturation value in less than 30 Oe. A maximum MR ratio of $\sim 10\%$ was observed in the as-deposited state in a structure containing ten bilayers. We did not observe any significant increase in the MR magnitude with an increase in number of bilayers (from 8–14). Typical hysteresis values for these magnetoresistance loops are significantly lower than that reported earlier¹ (~ 4 Oe in the as-deposited state). A gradual decrease of the hysteresis of the magnetoresistance loops is observed with annealing (both at 200 °C and 250 °C) for the hard axis mea-

^{a)}The Department of Electrical Engineering, The University of Alabama, Tuscaloosa, Alabama 35487-0209.

^{b)}The Department of Metallurgical and Materials Engineering, The University of Alabama, Tuscaloosa, Alabama 35487-0209.

^{c)}The Department of Physics and Astronomy, The University of Alabama, Tuscaloosa, Alabama 35487-0209.

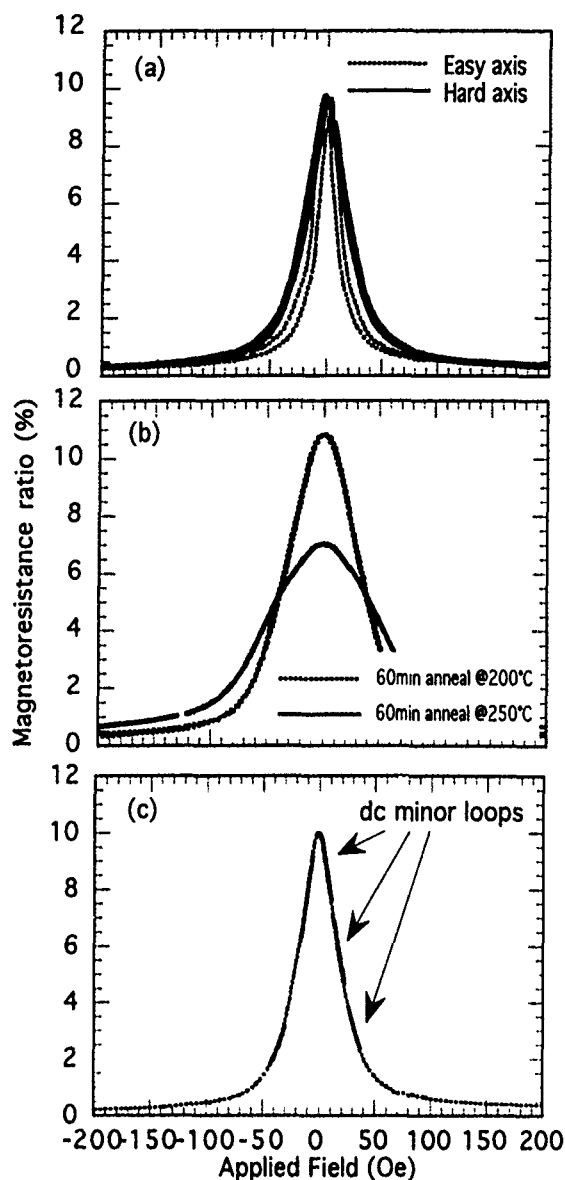


FIG. 1. Magnetoresistance loops in (a) as-deposited hard axis, and easy axis, (b) annealed, and (c) as-deposited with dc MR minor loops (plotted on 1/2 MR loop) for NiFeCo/Cu multilayers.

surement. This decrease may be due to the stress relief in the film caused by annealing. Figure 1(b) shows MR loops annealed for 1 h at 200 °C and 250 °C. Direct current magnetoresistance minor loops exhibit no measurable decrease in sensitivity, as shown in Fig. 1(c). MR and $M-H$ loops measured after annealing, however, indicate that there is an increase in the antiferromagnetic coupling strength. Interdiffusion of Cu and Ni with annealing can degrade the Cu interlayer, which results in a decrease in pure Cu interlayer thickness, but the aligning magnet helps preserve the uniaxial anisotropy. Figure 2 is a summary plot of MR%, $M-H$ loop coercivity, and MR hysteresis versus annealing time. The figure shows a decrease in H_c and MR hysteresis values with annealing for the hard axis magnetization loop. Short-term annealing produces a small increase in the magnitude of the magnetoresistance ratio; prolonged annealing causes a decrease. A field sensitivity of about 0.3% per Oe is

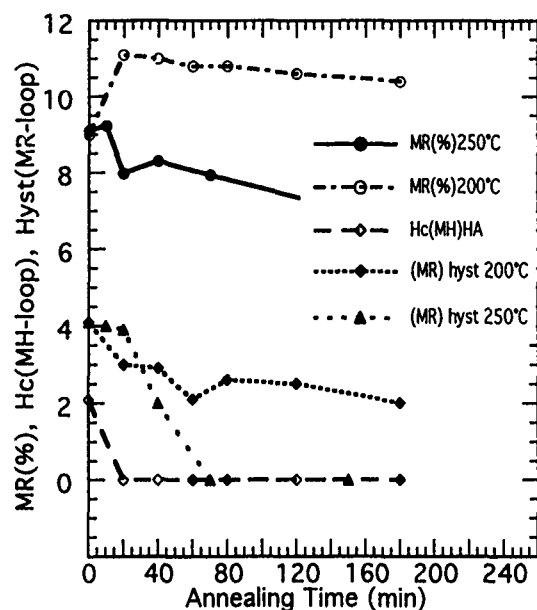


FIG. 2. Summary plot of MR%, $M-H$ loop coercivity, and MR hysteresis with annealing time in NiFeCo/Cu multilayers.

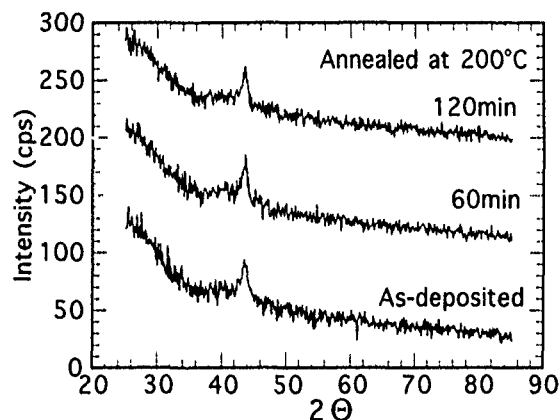


FIG. 3. High angle x-ray diffraction scans for as-deposited, and annealed NiFeCo/Cu multilayers.

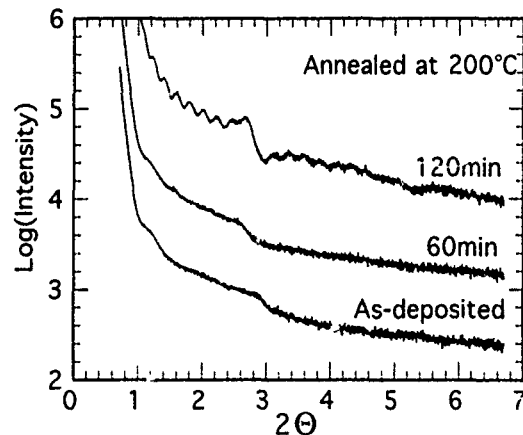


FIG. 4. Low angle x-ray diffraction scans for as-deposited, and annealed NiFeCo/Cu multilayers.

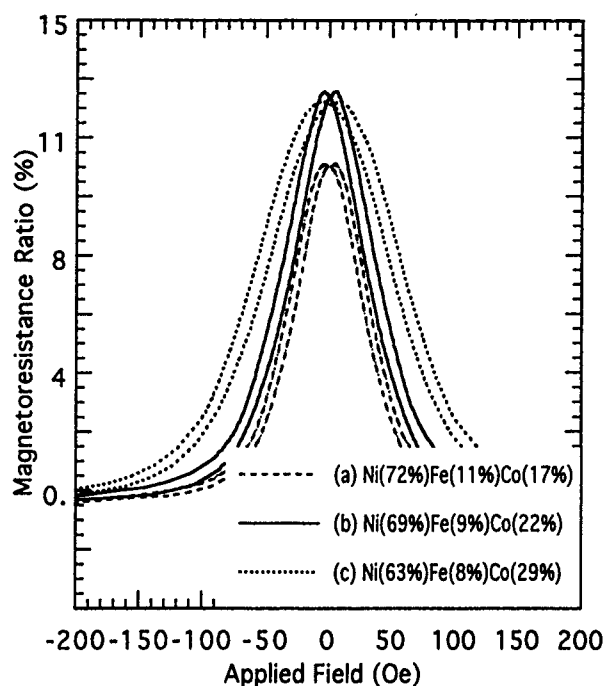


FIG. 5. As-deposited hard axis MR loops for (a) $\text{Ni}_{72}\text{Fe}_{11}\text{Co}_{17}/\text{Cu}$, (b) $\text{Ni}_{69}\text{Fe}_9\text{Co}_{22}/\text{Cu}$, and (c) $\text{Ni}_{63}\text{Fe}_8\text{Co}_{29}/\text{Cu}$ multilayered films.

observed. This is calculated by dividing the MR magnitude by the linewidth of the MR peak at the half-maximum. Figure 2 shows a gradual decrease in MR hysteresis with annealing. Figure 3 shows high angle diffraction patterns in as-deposited and in annealed states. The single weak peak suggests that the films are very fine grained. Low angle diffraction indicates that the layers as-deposited are very poorly formed, and may, in fact, be discontinuous (see Fig. 4). Sharpening of the first-order LXR peak with annealing is a qualitative indication of an improvement in the layered structure. NiFeCo films prepared by dc magnetron sputtering were found to be relatively more Ni-rich compared with the nominal target composition. This can be attributed to the differential sputtering yield of Ni, Fe, and Co. The small negative magnetostriction measured in these films is in agreement with the value of the measured film composition ($\text{Ni}_{76}\text{Fe}_{10}\text{Co}_{14}$).⁵

IV. NiFeCo/Cu MULTILAYER FILMS WITH DIFFERENT NiFeCo COMPOSITIONS

Very recently, we have made samples with several different Ni-Fe-Co alloy compositions layered with Cu spac-

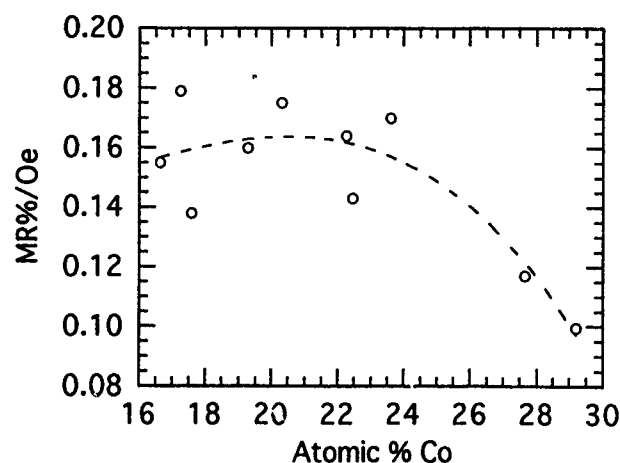


FIG. 6. Plot of MR sensitivity for changing Co concentration in NiFeCo/Cu multilayers.

ers. We observed a sizable (9%–14.5%) GMR effects from all of these samples. A set of representative MR loops are given in Fig. 5. MR loops (a), (b), and (c) correspond to the compositions $\text{Ni}_{72}\text{Fe}_{11}\text{Co}_{17}$, $\text{Ni}_{69}\text{Fe}_9\text{Co}_{22}$ and $\text{Ni}_{63}\text{Fe}_8\text{Co}_{29}$, respectively. These loops indicate a strong dependence of MR magnitude and sensitivity on ternary alloy composition. The compositional variation studied here essentially consists of partially replacing Ni with Co, while the Fe content remains nearly constant. Figure 6 displays the compositional dependence (in terms of Co content) of sensitivity.

V. SUMMARY

High field sensitivity GMR has been observed in NiFeCo alloy/Cu multilayers. The decrease in MR and $M-H$ loop hysteresis may be a result of increasing uniaxial anisotropy caused by magnetic annealing. Stress relief and reduction of imperfections by annealing may also help in reducing hysteresis.

ACKNOWLEDGMENTS

Acknowledgment is made to the NSIC-ATP funded by the Department of Commerce) and the Center for Materials for Information Technology at The University of Alabama for support of this work.

¹M. Jimbo, T. Kanda, S. Goto, S. Tsunashima, and S. Uchiyama, *Jpn. J. Appl. Phys.* **31**, L1348–L1350 (1992).

²S. Tsunashima, M. Jimbo, T. Kanda, S. Goto, and S. Uchiyama, *MRS Conference*, Spring 1993, San Francisco, CA, 1993.

Calculation of the temperature dependence of the giant MR and application to Co/Cu multilayers

J. L. Duvail, A. Fert, and L. G. Pereira

Laboratoire de Physique des Solides, Bât 510, Université Paris-Sud, 91405 Orsay, France

D. K. Lottis

School of Physics and Astronomy, University of Minnesota, Minneapolis, Minnesota 55455

Most theoretical models of the giant magnetoresistance (GMR) in metallic magnetic multilayers developed up to now are for the zero-temperature limit, thus neglecting the spin-flip scattering arising from spin fluctuations (magnons), as well as other scatterings from thermal excitations. To account for the temperature dependence of the GMR, we have introduced electron-magnon and electron-phonon scattering terms in a Camley-Barnas-like semi-classical model. We apply our calculation to the interpretation of the temperature dependence of the resistivity and GMR in Co/Cu.

I. INTRODUCTION

The giant magnetoresistance (GMR) of the magnetic multilayers, first discovered in Fe/Cr structures,¹ has now been observed in many systems. Its interpretation²⁻⁴ is generally based on the simplest version of the two current model for the conduction in ferromagnetic metals.⁵ One assumes that the electrical current is carried in *independent channels* by the spin \uparrow (majority spin direction) and spin \downarrow (minority) electrons, which is the *low temperature limit* of the two current model. However, at finite temperature, the *spin-mixing* by electron-magnon scattering, which is the transfer of momentum between the two channels, becomes an essential ingredient of the two current conduction in ferromagnets.⁵ In multilayers, the spin-mixing effect is expected to play an important role for the temperature dependence of the GMR and must be taken into account in the interpretation at finite temperature. In the paper, we present a model of the temperature dependence of the GMR, taking into account not only the contribution from thermally excited scatterings *within each channel* (that is the electron-phonon scattering and momentum nonconserving part of the electron-magnon scattering called "incoherent electron-magnon scattering" in the notation of Ref. 5), but also the (interchannel) *spin-mixing* contribution from *momentum conserving* (or *coherent* in the notation of Ref. 5) electron-magnon scattering. To our knowledge, the spin-mixing contribution (spin-flip scattering with momentum transfer) has never been taken into account in theoretical models, and only the intrachannel magnon scattering has been introduced in calculations.^{6,7}

II. MODEL

We consider an infinite multilayer composed of ferromagnetic metallic layers (Co, for example), separated by nonmagnetic metallic layers (Cu, for example). The current direction is in the plane of the layers.

Our starting point for the *low temperature* limit is the semi-classical model of Johnson and Camley,⁸ who take into account interfaces scattering by introducing interfacial layers in which the mean-free path (MFP) is shorter than inside the layers. The spin asymmetry of the MFP in the interfacial layer can also be different from that within the layers. The parameters of the model of Johnson and Camley include the resistivity of the nonmagnetic metal or what is equivalent,

the *MFP in the nonmagnetic layers* that we will call $\lambda_{\text{Cu}}(4.2 \text{ K})$, in the same way the *two MFP in the magnetic layers* that we call $\lambda_{\text{Co}}^{\uparrow}(4.2 \text{ K})$ and $\lambda_{\text{Co}}^{\downarrow}(4.2 \text{ K})$ for the spin \uparrow and spin \downarrow electrons respectively, the MFP $\lambda_{\text{I}}^{\uparrow}(4.2 \text{ K})$ and $\lambda_{\text{I}}^{\downarrow}(4.2 \text{ K})$ in the interfacial layers, the thickness of the interfacial layer t_{I} , and the thicknesses of the effective magnetic and nonmagnetic layers $(t_{\text{Co}}-t_{\text{I}})$ and $(t_{\text{Cu}}-t_{\text{I}})$, respectively. In Table I, we have listed the parameters of our fit expressed in terms of resistivity. We also introduce the cut-off in the angular integration suggested by Vedyayev *et al.*⁹

At *finite temperature*, we introduce the following temperature-dependent resistivity terms.

A. Within the layers

(i) A temperature-dependent contribution is added to the resistivity of each channel, i.e., we write

$$\rho_{\sigma}(T) = \rho_{\sigma}(4.2 \text{ K}) + \delta\rho_{\sigma}(T). \quad (1)$$

TABLE I. Resistivity terms used in our calculation $\rho_{\text{Cu}}^{(i)}$, $\rho_{\text{Co}}^{(i)}$, and $\rho_{\text{I}}^{(i)}$ are the intrachannel resistivities for the Cu, Co, and interfacial layers, respectively. Their temperature-dependent part $\delta\rho^{(i)}(T)$ are derived from experimental data on bulk materials for Cu and Co in Refs. 10 and 11 and is a free parameter for the interfacial layer. The spin-mixing resistivity $\rho_{\text{Co}}^{\text{I}}$ is derived from Ref. 11, while $\rho_{\text{I}}^{\text{I}}$ is a free parameter. (c) and (d) refer to two types of calculation, as explained in the text. The contribution of the resistivity term to the mean-free path inverse is $\rho_0\lambda_0 = (hk_F/ne^2) = 1940$ (Ref. 23). All the resistivities are given in $\mu\Omega \text{ cm}$.

T	4.2 K	100 K	200 K	300 K
$\rho_{\text{Cu}}^{\text{I}} = \rho_{\text{Cu}}^{\text{I}}$	8.1	8.8	10.2	11.5
$(\delta\rho_{\text{Cu}}^{\text{I}} = \delta\rho_{\text{Cu}}^{\text{I}})$	(0)	(0.70)	(2.12)	(3.40)
$\rho_{\text{Co}}^{\text{I}}$	24.9	25.6	27.3	29.3
$(\delta\rho_{\text{Co}}^{\text{I}})$	(0)	(0.73)	(2.47)	(4.42)
$\rho_{\text{Co}}^{\text{I}}$	176.4	183.0	198.0	210.9
$(\delta\rho_{\text{Co}}^{\text{I}})$	(0)	(7.3)	(22.2)	(35.3)
$\rho_{\text{I}}^{\text{I}}$	0	0.55	2.2	5.0
$\rho_{\text{I}}^{\text{I}}$ (c)	24.9	24.9	24.9	24.9
$(\delta\rho_{\text{I}}^{\text{I}})$	(0)	(0)	(0)	(0)
$\rho_{\text{I}}^{\text{I}}$ (d)	24.9	36.2	63.5	97.9
$(\delta\rho_{\text{I}}^{\text{I}})$	(0)	(11.3)	(38.6)	(73.0)
$\rho_{\text{I}}^{\text{I}}$ (c)	485	485	485	485
$(\delta\rho_{\text{I}}^{\text{I}})$	(0)	(0)	(0)	(0)
$\rho_{\text{I}}^{\text{I}}$ (d)	485	571	882	1212
$(\delta\rho_{\text{I}}^{\text{I}})$	(0)	(86)	(397)	(727)
$\rho_{\text{I}}^{\text{I}}$ (c)	0	4.73	12.5	25.9
$\rho_{\text{I}}^{\text{I}}$ (d)	0	0	0	0

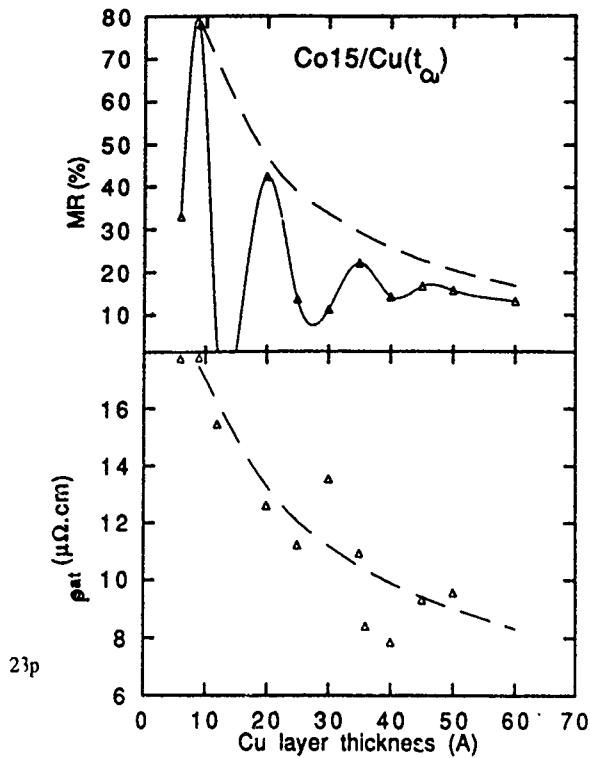


FIG. 1. Variation of the resistivity in the saturated state (bottom) and MR (top) as a function of the thickness of Cu for Co/Cu multilayers. Triangles: experimental data at 4.2 K for (Co 15 Å/Cu)×30 from Mosca *et al.* (Ref. 13). Dashed lines: calculation with the values of ρ_{Cu} , ρ_{Co}^I , ρ_{Co}^{II} , $\rho_{\uparrow\downarrow}^I$, and $\rho_{\uparrow\downarrow}^{II}$ indicated in the text and Table I.

The intrachannel term $\delta\rho_{\sigma}(T)$ includes contributions from electron-phonon scattering and also the incoherent part of the electron-magnon (e-m) scattering transferred to the lattice.⁵ For Cu, we will use the values of $\delta\rho_{\uparrow}(I) = \delta\rho_{\uparrow}(T)$ derived from the resistivity data of Ref. 10 for bulk Cu. For Co, we will use values of $\delta\rho_{Co}^I$ and $\delta\rho_{Co}^{II}$ derived from Ref. 10 and from resistivity measurements on Co-based dilute alloys.¹¹ All these resistivities are listed in Table I for several temperatures between 4.2 and 300 K.

(ii) A temperature-dependent spin-mixing term $\rho_{\uparrow\downarrow}^I(T)$ is introduced to couple the Boltzmann equations of the two channels [see Eq. (3) below]. It expresses the fact that the spin-flip scattering by magnons, a part of the electron momentum is coherently transferred to the channel with opposite spin and contributes to the interchannel term $\rho_{\uparrow\downarrow}^I$.⁵ Data for $\rho_{\uparrow\downarrow}^{Co}(T)$ are taken from Ref. 11 and extrapolated up to 300 K by assuming a variation as T^2 .

B. Inside the interfacial layers

We also introduce temperature-dependent resistivity terms, which, essentially, should express the scattering by enhanced spin fluctuations at the interfaces. We take into account either intrachannel resistivity terms $\delta\rho_{\uparrow}^I(T)$ and $\delta\rho_{\uparrow}^{II}(T)$, or, alternatively, an interchannel spin-mixing term $\rho_{\uparrow\downarrow}^I(T)$. The incoherent scattering should be predominant for a disordered interface. When the interchannel spin-mixing term is taken into account, the Boltzmann equation of the channel σ in a given layer is written as

$$\frac{m}{\hbar k_F} \frac{dg^{\sigma}(z, \mathbf{v})}{dz} + \frac{g^{\sigma}(z, \mathbf{v})}{\lambda^{\sigma} v_z} + \frac{g^{\sigma}(z, \mathbf{v}) - g^{-\sigma}(z, \mathbf{v})}{\lambda^{\uparrow\downarrow} v_z} = \frac{eE}{\hbar k_F v_z} \frac{\partial f_0(v)}{\partial v_x}, \quad (2)$$

where g^{σ} is the deviation of the electron distribution function from the Fermi-Dirac distribution $f_0(v)$ for the spin direction σ , z and x are the directions, respectively, perpendicular to the layers and parallel to the current, \mathbf{v} is the electron velocity, E is the electric field. The MFP inverses, $(\lambda^{\sigma})^{-1}$ and $(\lambda^{\uparrow\downarrow})^{-1}$, include the contributions from all the scattering mechanisms.

III. RESULT FOR THE Co/Cu SYSTEM

We have applied our calculation to the fit of experimental results by Mosca *et al.*¹³ NMR¹⁴ experiments on the same samples have established that the roughness of the interfaces can be modeled by a very dense distribution of monoatomic steps, so that we fix the thickness of the interfacial layer at 2 Å.

At low temperature, we begin by adjusting the MFP $\lambda_{Cu}^{\sigma}(4.2 \text{ K})$, $\lambda_{Co}^I(4.2 \text{ K})$, $\lambda_{Co}^{II}(4.2 \text{ K})$, $\lambda_{\uparrow}^I(4.2 \text{ K})$, $\lambda_{\uparrow}^{II}(4.2 \text{ K})$ to fit the absolute values of the resistivity and the MR ratio for several thicknesses. In Fig. 1 we show the fit of the variation of the resistivity and MR ratio with the thickness of Cu obtained for the values of $\rho_{Cu}^I(4.2 \text{ K})$, $\rho_{Co}^I(4.2 \text{ K})$, and $\rho_{\uparrow}^I(4.2 \text{ K})$ listed in Table I. We estimate the error bar on the MFP less than 15%.

To interpret the temperature dependence, we have focused on two samples with respectively thin (15 Å) and thick (60 Å) Co layers in order to determine the relative importance of the bulk and interface temperature-dependent scatterings. We have introduced the different temperature-dependent contributions successively.

The intra-channel terms $\delta\rho_{Cu}(T)$ (derived from Ref. 10), $\delta\rho_{Co}^I(T)$ and $\delta\rho_{Co}^{II}(T)$ (derived from Refs. 10 and 11) are introduced first. They are not free parameters. As shown by curves (a) in Fig. 2, the contribution from these terms accounts only for a small part of the variation of the resistivity and MR ratio with T .

Then, in addition, we introduce the spin-mixing term $\rho_{\uparrow\downarrow}^{Co}(T)$ derived from Ref. 11. As shown by the curves (b) in Fig. 2, this is still not sufficient to account for the variation with temperature, especially for the resistivity [we have tried fits with enhanced values of $\rho_{\uparrow\downarrow}^{Co}(T)$, without succeeding in accounting for the T dependence of the resistivity and MR ratio at the same time].

We are thus led to include T -dependent scattering by the interfaces, and we have begun by adding up a spin-mixed term $\rho_{\uparrow\downarrow}^I(T)$ (the values are listed in Table I). We obtain the curves (c) in Fig. 2, which mean that we can obtain a good fit of the variation with T for the resistivity, but not for the MR ratio (or vice versa).

We have then left out the term $\rho_{\uparrow\downarrow}^I(T)$ and introduced T -dependent intra-channel terms $\delta\rho_{\sigma}^I(T)$ in the interfacial layer (with the same values for the Co 15 Å/Cu 9 Å and Co 60 Å/Cu 9 Å samples). We could obtain a good agreement for the MR ratio of both samples and a good agreement for

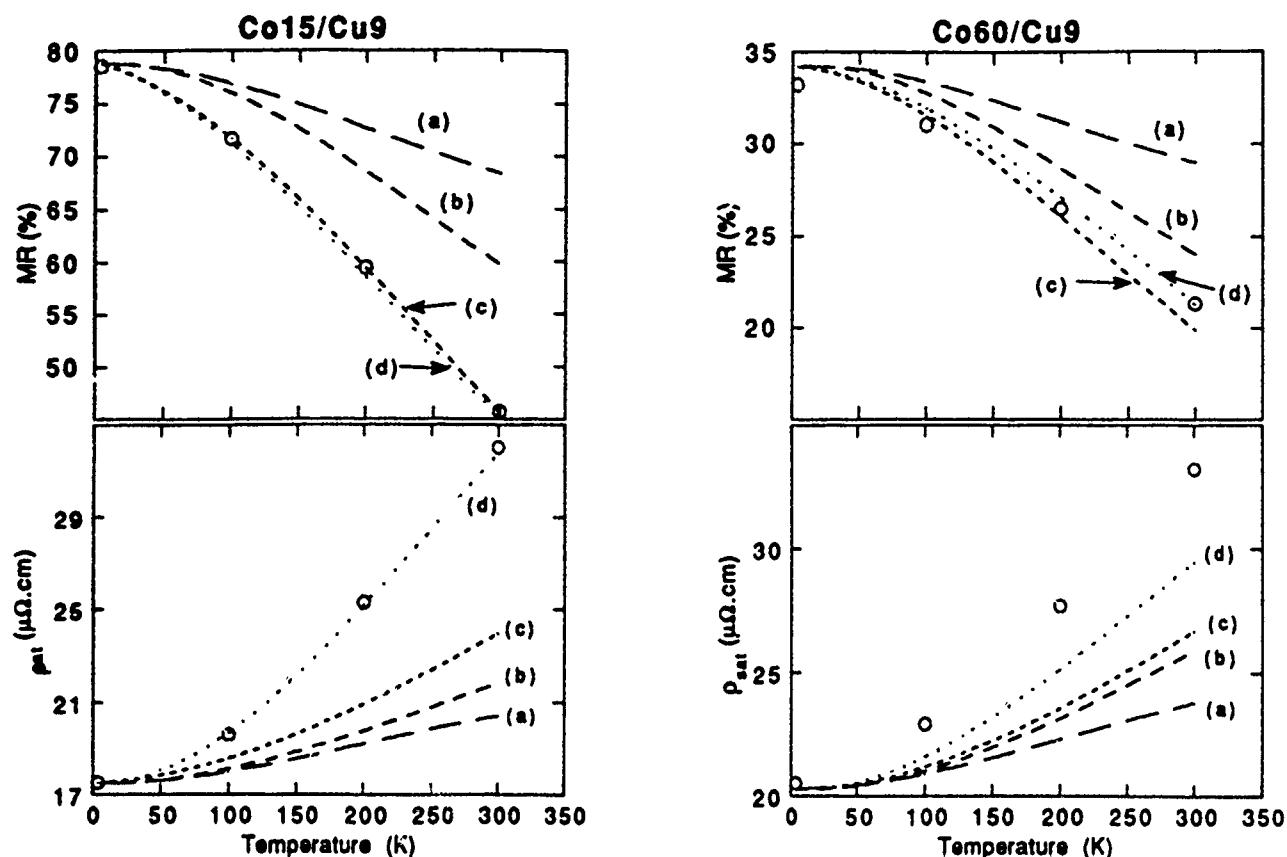


FIG. 2. Variation of the resistivity in the saturated state (bottom) and MR (top) as a function of temperature for (Co 15 Å/Cu 9 Å) (left) and (Co 60 Å/Cu 9 Å). Circles: experimental data from Mosca *et al.* (see Ref. 13). Curve (a): calculation taking into account the phonon and magnon intrachannel resistivities within Co and Cu layers. Curve (b): same calculation than (a) but also taking into account interchannel spin mixing terms within Co. Curves (c) and (d): calculation taking into account temperature-dependent scattering by the interfaces; (c) is calculated with an interchannel term, (d) is calculated with an intrachannel term.

the resistivity of Co 15 Å/Cu 9 Å; see curves (d) in Fig. 2. The variation with T we obtain for the resistivity of Co 60 Å/Cu 9 Å is slightly too small.

IV. DISCUSSION AND CONCLUSION

Our results can be summarized as follows. We have found that introducing within layers the temperature-dependent (intrachannel) resistivity and spin-mixing terms derived from data in bulk materials is not sufficient to account for the variation of the resistivity and MR ratio with T [the weak effectiveness of $\delta\rho_o(T)$ to reduce the MR is partly due to its pronounced spin dependence in Co].¹¹ The best fits have been obtained by also taking into account temperature-dependent interfacial scattering. It is interesting to notice that the best fit is obtained by introducing intrachannel resistivity terms, and no interchannel spin mixing term in the interfacial zone. This can be ascribed to incoherent scattering by the spin fluctuations at the interfaces. The incoherence is consistent with spin fluctuation within quite disordered interfaces.

The final conclusion is that the temperature dependence of the resistivity and MR of Co/Cu multilayers can be accounted for, at least approximately, by taking into account not only phonon and magnon resistivity terms determined in bulk materials, but also an additional contribution from interfaces.

ACKNOWLEDGMENTS

This work was supported in part by the European Economic Community [Esprit Project No. BRA6146] and by the CNRS Grant No. AI0693 (NSF-CNRS) collaboration].

- ¹M. N. Baibich, J. M. Broto, A. Fert, F. Nguyen Van Dau, F. Petroff, P. Etienne, G. Creuzet, A. Friederich, and J. Chazelas, *Phys. Rev. Lett.* **61**, 2472 (1988).
- ²R. E. Camley and J. Barnas, *Phys. Rev. Lett.* **63**, 664 (1989).
- ³J. Barnas, A. Fuss, R. E. Camley, P. Grünberg, and W. Zinn, *Phys. Rev. B* **42**, 8110 (1990).
- ⁴P. M. Levy, S. Zhang, and A. Fert, *Phys. Rev. Lett.* **65**, 1643 (1990); S. Zhang, P. M. Levy, and A. Fert, *Phys. Rev. B* **45**, 8689 (1992).
- ⁵A. Fert and I. A. Campbell, *J. Phys. F* **6**, 849 (1976); I. A. Campbell and A. Fert, *Ferromagnetic Materials*, edited by E. P. Wohlfarth (North-Holland, Amsterdam, 1982), p. 760.
- ⁶S. Zhang and P. M. Levy, *Phys. Rev. B* **43**, 11 048 (1991).
- ⁷M. Hasegawa, *Phys. Rev. B* **22**, 15 080 (1993).
- ⁸B. L. Johnson and R. E. Camley, *Phys. Rev. B* **44**, 9997 (1991).
- ⁹The angular integration is stopped at an angle corresponding to $\cos \Theta_c = 1/\sqrt{k_F^* \lambda}$ before the direction parallel to the layer plane, which can be justified by arguing that if the electron lifetime is finite, the uncertainty principle prevents its velocity from being exactly parallel to the layers. For details, see A. Vedyayev, B. Dieny, and N. Ryshanova, *Europhys. Lett.* **19**, 329 (1992).
- ¹⁰G. K. White and S. B. Woods, *Philos. Trans. Ser. A* **251**, 273 (1959).
- ¹¹B. Loegel and F. Gautier, *J. Phys. Chem. Sol.* **32**, 2723 (1971).
- ¹²B. Dieny, *Europhys. Lett.* **17**, 261 (1992).
- ¹³D. H. Mosca, F. Petroff, A. Fert, P. Schroeder, W. P. Pratt, Jr., R. Loloee, and S. Lequien, *J. Magn. Magn. Mat.* **94**, L1 (1991).
- ¹⁴C. Mesny, P. Panissod, and R. Loloee, *Phys. Rev. B* **45**, 12 269 (1992).

Magnetization reversal in CoFe/Ag/Fe/ZnSe thin layer sandwiches

D. Bilic and E. Dan Dahlberg

School of Physics and Astronomy, University of Minnesota, Minneapolis, Minnesota 55455

A. Chaiken, C. Gutierrez, P. Lubitz, J. J. Krebs, M. Z. Harford, and G. A. Prinz

Naval Research Laboratory, Washington, DC 20375-5320

In recent work [J. Appl. Phys. **70**, 10 (1991)] the spin valve effect (SVE) was measured in $\text{Co}_x\text{Fe}_{1-x}/\text{Ag}/\text{Fe}(x < 0.7)$ thin layer sandwiches grown by molecular beam epitaxy. The field dependence of the SVE was correlated with VSM magnetization data taken on the samples. It was found that only at low fields was there a correlation between the SVE resistance and the magnetization data. These results indicated a more complex reversal mechanism that included substantial magnetizations in directions not measured in traditional VSM measurements. In order to more accurately determine the field-dependent magnetization of the samples during reversal, the longitudinal and transverse Kerr effects were measured on the layers. The particular geometry used to measure the Kerr effects was for the light scattering plane to be perpendicular to the applied magnetic field. The transverse Kerr effect data, which in this geometry are sensitive to the magnetization parallel to the applied magnetic field, replicated the VSM data. The longitudinal Kerr effect, which is sensitive to the net magnetization perpendicular to the applied field (in the plane of the film), indicated a substantial perpendicular magnetization component. Based upon previous work on epitaxial iron films,²⁻⁴ it appears that the magnetization reversal process proceeds by transitions between easy axes. From these measurements, the anomalous resistances observed as a function of the applied magnetic field in J. Appl. Phys. **70**, 10 (1991), are explained by having one of the films soft, and two easy axes in the plane of the other film.

INTRODUCTION

Recently, considerable attention has been devoted to the study of multilayers and sandwiches composed of alternating magnetic and nonmagnetic layers. In part, this interest has been generated by the large magnetoresistance known as giant magnetoresistance or the spin valve effect (SVE) observed in a number of multilayers, such as Fe/Cr⁵ and sandwiches such as CoFe/Ag/Fe/ZnSe.¹ In the previous work¹ on CoFe/Ag/Fe/ZnSe sandwiches, both vibrating sample magnetometry (VSM) and SVE measurements were performed. It was found in that work that only the low field VSM data were correlated with the SVE data. This indicated that a more complex magnetic reversal process was occurring at higher magnetic fields, in at least one of the magnetic layers in the sandwich.

In the present work we describe a series of measurements of both the longitudinal (LKE) and transverse (TKE) magneto-optical Kerr effects on the same six samples used in the investigation detailed in Ref. 1. The six samples investigated varied in the alloy composition of the CoFe film and thickness of individual layers. Previous research²⁻⁴ has shown that measurements of the LKE and TKE provide information on the magnetization components, parallel and perpendicular to an applied magnetic field, of the magnetic material under investigation. Thus, measurements of the TKE, which is sensitive to the magnetization parallel to the applied magnetic field, should reproduce the VSM measurements and be well correlated with the SVE low field measurements. The LKE, being sensitive to the net magnetization perpendicular to the applied field, might be correlated with the high field SVE and/or provide extra magnetic information on the magnetization process.

EXPERIMENTAL DETAILS AND RESULTS

As stated in the Introduction, in the present work we focus on measurements of the Kerr effect, two of which are depicted in Fig. 1. The Kerr measurements are made with a fixed scattering plane, perpendicular to the applied magnetic field, and fixed polarizer angle. In these measurements, the analyzer is rotated to obtain the signals for longitudinal and transverse Kerr effects. The analyzer is held at an angle of $\Phi_a = 5^\circ - 15^\circ$ from the polarizer orientation to obtain the transverse magnetization (the LKE). The longitudinal magnetization component is obtained with the analyzer at an angle of $\Phi_a = 80 - 85^\circ$ from the polarizer orientation^{2,3} (the TKE).

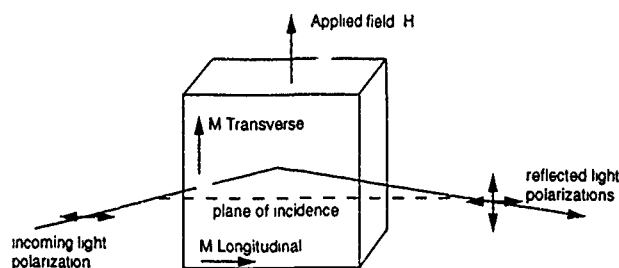


FIG. 1. Geometries of the transverse and longitudinal Kerr effects. The two Kerr effects measured are depicted. In the longitudinal Kerr effect, the magnetization measured is parallel to the plane of incidence, but perpendicular to the applied magnetic field. The longitudinal effect is characterized by a rotation of plane of polarization. The amount of rotation is proportional to the component of magnetization parallel to the plane of incidence. In the transverse Kerr effect, the magnetization is perpendicular to the plane of incidence, but parallel to the applied magnetic field. The transverse effect is depicted by a change in reflectivity of the light polarized parallel to the plane of incidence, not a rotation of polarization.⁶ The transverse Kerr effect thus measures the same magnetization variations as a VSM.

In the longitudinal Kerr effect, the detected magnetization is parallel to the plane of incidence. The longitudinal effect is characterized by a rotation of the plane of polarization between the incident and reflected light, where the amount of rotation is proportional to the component of magnetization parallel to the plane of incidence. In the transverse Kerr effect, the sensed magnetization is perpendicular to the plane of incidence. The transverse effect results in a change in the reflectivity of the light polarized parallel to the plane of incidence, not a rotation of polarization.^{2,3}

The six sandwiches used in this experiment were grown on gallium-arsenide (GaAs) substrates. The substrates were GaAs[001], which result in [001] Fe film grown on the ZnSe buffer layer. The zinc-selenide (ZnSe) epilayer was grown both to smooth or flatten the rough surface of the GaAs substrate and to inhibit the subsequently grown ferromagnetic film from chemically interacting with GaAs. The samples differed by the individual layer thicknesses and CoFe alloy composition. The sample structures were of the form $\text{Co}_x\text{Fe}_{1-x}/\text{Ag}/\text{Fe}/\text{ZnSe}/\text{GaAs}[001]$, where x is varied from 0 to 0.7. The alloy composition was varied to change the coercivity and other magnetic properties of one of the magnetic layers. The final Ag layer was a protective coating layer, while the buried Ag layer was a nonmagnetic, spacer layer. The thickness of the Ag spacer layer was large enough to decouple the CoFe and Fe layers.

The VSM measurements of the six $\text{Co}_x\text{Fe}_{1-x}/\text{Ag}/\text{Fe}/\text{ZnSe}$ samples were consistent with the film growth planes being (001) planes. This results in two magnetically intermediate (110) axes and two magnetically easy (100) axes of magnetization in the plane of the films. This is the same magnetic film configuration as was previously investigated in single layer epitaxial iron films.²

For brevity, only two of the samples from the series will be discussed. These samples both exhibited distinct SVE effects in applied fields, where there was no concomitant VSM signature. These are the $\text{Ag}(1.9)/\text{Fe}(8.1 \text{ nm})/\text{Ag}(3.9 \text{ nm})/\text{Co}_{30}\text{Fe}_{70}(8.4 \text{ nm})$ and $\text{Ag}(2.8 \text{ nm})/\text{Fe}(12.4 \text{ nm})/\text{Ag}(5.5 \text{ nm})/\text{Fe}(13.1 \text{ nm})$ sandwiches. The transport data from the previous study will be compared with the TKE and LKE data presented here.

Figure 2 shows both the VSM and SVE data for the sandwich containing the CoFe alloy film with the applied magnetic field close to a (110) axis (an intermediate axis). One should notice that the largest resistance signatures are well correlated with the VSM data. However, there is an extra SVE signature at fields on the order of 130 Oe, which does not have a VSM signature. The TKE data on this sample were consistent with the VSM data. The longitudinal Kerr effect measurement provided a signature that was correlated with the SVE at 130 Oe. These data are shown in Fig. 3.

Figure 4 again shows both the VSM and SVE data for the other sandwich, the one with only elemental Fe films. Again, the field is applied close to an intermediate (110) axis. Also, the VSM data and the SVE anomalies are well correlated at the lower magnetic fields, on the order of 75 Oe, but there is no VSM signal for the SVE peak at 250 Oe. Similar to the other film, Fig. 5 shows how the longitudinal Kerr

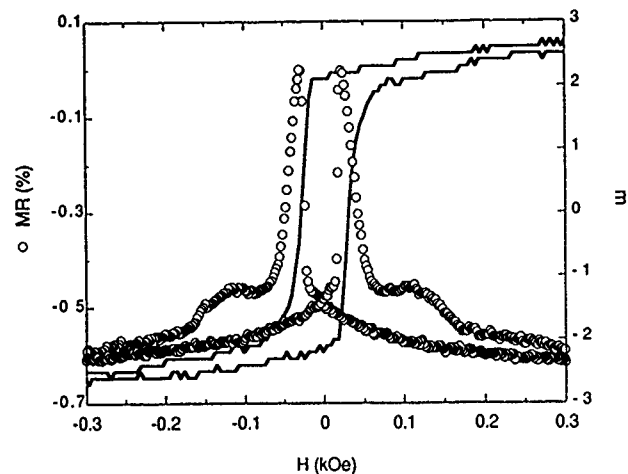


FIG. 2. Magnetization and magnetoresistance data for the $\text{Ag}(1.9)/\text{Fe}(8.1 \text{ nm})/\text{Ag}(3.9 \text{ nm})/\text{Co}_{30}\text{Fe}_{70}(8.4 \text{ nm})$ sample with the applied field along the (110) axis. The transport data were taken with the applied magnetic field parallel to the current direction. The main reversal of the magnetization occurs at the same field where the SVE has a maximum resistance. As the magnetization continues to rotate to the (110), parallel to the applied field, there is another SVE maximum. For this second maximum there is not a signature in the magnetization data.

effect data indicate the presence of a substantial magnetization component perpendicular to the applied field up to 250 Oe.

DISCUSSION AND CONCLUSIONS

The spin valve or magnetoresistance effect has been attributed to the antiparallel alignment of magnetic moments in thin film sandwiches. Three possible causes of the variation of SVE resistance with an applied field are exchange bias pinning of one of the ferromagnetic films, antiferromagnetic coupling between the layers, and different coercivities in sandwich layers. That in simple sandwiches like those investigated here, there are multiple resistance maxima, indicate a rather complex magnetization process in at least one of the

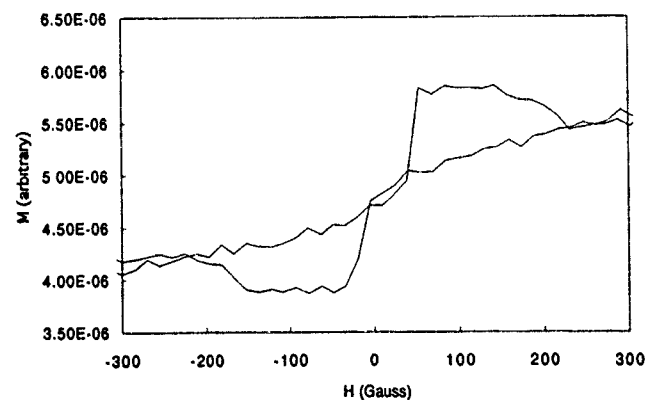


FIG. 3. Longitudinal Kerr effect data for the $\text{Ag}(1.9)/\text{Fe}(8.1 \text{ nm})/\text{Ag}(3.9 \text{ nm})/\text{Co}_{30}\text{Fe}_{70}(8.4 \text{ nm})$ sample, with the applied field along the (110) axis for the component of the magnetization. The more positive curve in positive applied magnetic fields was taken with increasing magnetic field. Notice that the maximum in the net perpendicular magnetization component from 50 to 200 Oe is correlated with the second SVE maximum shown in Fig. 2.

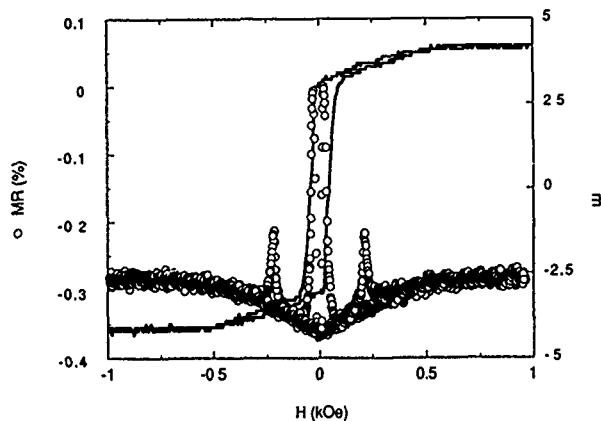


FIG. 4. Magnetization and magnetoresistance data for the Ag(2.8 nm)/Fe(12.4 nm)/Ag(5.5 nm)/Fe(13.1 nm) sample with the same field and current directions as in Fig. 1. As before, note the main reversal of the magnetization occurs at the same field where the SVE has a maximum resistance and that as the magnetization continues to rotate to the $\langle 110 \rangle$ direction there is another SVE maximum. For this second maximum there is not a signature in the magnetization data.

films. In order to understand this process, we will follow the magnetization of single layer Fe films as detailed in Ref. 2. The necessary information to be considered is that for these films and those in Ref. 2, there are two easy axes in the film planes, separated by intermediate axes.

With a saturating field close to, but not parallel to, an intermediate axis, the total magnetization is parallel to the applied field. As the field is reduced, the magnetization rotates toward an easy axis and a magnetization component perpendicular to the field develops. This is what occurs in both sandwiches, and can be seen in the magnetization data and the LKE data.⁷ When the major portion of the magnetization switches at the coercive field, the SVE signature is due to the slightly different coercivities or anisotropy energies of the films. In this process, the magnetization has flipped from one easy axis to another, but the net perpendicular magnetization has not changed. In other words, the magnetization has flipped or rotated from one easy axis to another, which is a 90° rotation.

The higher magnetic field transition occurs with the magnetization jumping to the other easy axis (the original one, but now with the magnetization in the opposite direction), resulting in the perpendicular magnetization changing sign. It is important to note that this process can, at most, only slightly alter the magnetization parallel to the applied field, and is thus undetected in the VSM data. It is during this later process that the extra SVE anomaly occurs. The remainder of the magnetization process is the rotation of the magnetization from the easy axis to parallel with the applied field (almost along the $\langle 110 \rangle$ direction). At the completion of the later process, the moments are again parallel, resulting in a low resistance state.

The above magnetization process is one scenario that would generate the data presented here. No quantitative cor-

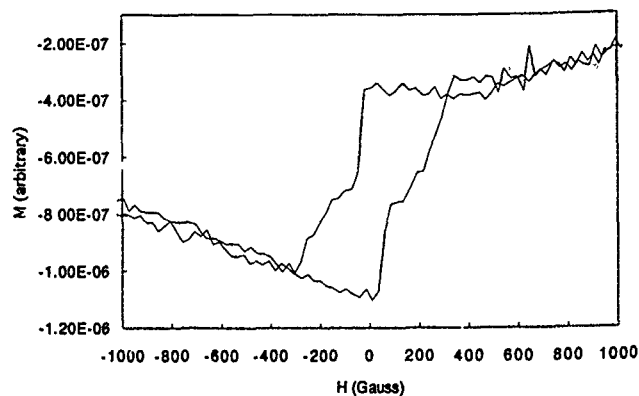


FIG. 5. Longitudinal Kerr effect data for the Ag(2.8 nm)/Fe(12.4 nm)/Ag(5.5 nm)/Fe(13.1 nm) sample, with the applied field along the $\langle 110 \rangle$ axis for the component of the magnetization. The more negative data at the zero applied field was taken with increasing magnetic fields. Notice that a transition in the perpendicular magnetization from 50 to 350 Oe includes the range where the second transition occurs in Fig. 4.

relation between the Kerr measurements and the SVE was attempted. In part, this is because the samples had deteriorated in the time between the SVE measurement and the Kerr studies. This study does point out that the two magnetic films in a single sandwich are not identical. This is true, even in the iron/silver/iron sandwich. One should note that this last statement does not require one of the iron films to be a polycrystal. It merely requires that the two iron films have different coercive fields for the magnetization processes described in the above.

In summary, the longitudinal Kerr effect has been shown to be correlated with SVE anomalies not understood by usual magnetization studies, i.e., VSM measurements. Although not accomplished in detail, it provides another tool to enable a detailed analysis of the reversal processes present in complex sandwiches possible.

ACKNOWLEDGMENTS

The work at the University of Minnesota was supported by a grant from the AFOSR (AF/FA9620-92-J-0185/P00001), and the work at the Naval Research Laboratory was supported by ONR.

¹A. Chaiken, C. J. Gutierrez, J. J. Krebs, and G. A. Prinz, *J. Magn. Mater.* **125**, 228 (1993).

²J. M. Florczak and E. D. Dahlberg, *Phys. Rev.* **44**, 9338 (1991).

³J. M. Florczak and E. D. Dahlberg, *J. Appl. Phys.* **67**, 7522 (1990).

⁴J. M. Florczak, E. D. Dahlberg, J. N. Kuznia, A. M. Wowchak, and P. I. Cohen, *J. Appl. Phys.* **69**, 4997 (1991).

⁵M. N. Baibich, J. M. Broto, A. Fert, F. Nguyen Van Dan, F. Petroff, P. Eitenne, G. Creuzet, A. Friederich, and J. Chazelas, *Phys. Rev. Lett.* **61**, 247 (1988).

⁶J. Zak, E. R. Moog, C. Liu, and S. D. Bader, "Universal approach to magneto-optics," *J. Magn. and Magn. Mat.* **89**, 107 (1990).

⁷It is interesting to note that it is also observed in the SVE data. This indicates that either the easy axes in the two films are not parallel or that the magnetizations break up into domains. It is not possible to distinguish between these two possibilities.

Effective internal fields and magnetization buildup for magnetotransport in magnetic multilayered structures

Peter M. Levy, Horacio E. Camblong,^{a)} and Shufeng Zhang
Department of Physics, New York University, New York, New York, 10003

Starting with the Kubo formula for electric conductivity we derive a set of equations that define the spin diffusion that is present when current is driven through inhomogeneous magnetic media. We show the spin accumulation, or nonequilibrium magnetization, attendant to charge transport through regions of inhomogeneous magnetization is governed by the same equations found in a thermodynamic approach to magnetoelectric transport.

There have been two approaches to understand the giant magnetoresistance (MR) of magnetic multilayered structures for currents perpendicular to the plane of the layers (CPP). The first has been a linear response theory based on either the Kubo formula^{1,2} or the Boltzmann equation,³ in which one calculates the current in response to an external electric field. The second is a thermodynamic approach,⁴ in which one introduces a magnetization potential H^* in addition to the electric potential V , to describe charge and nonequilibrium magnetization transport.^{5,6} For some systems both H^* and V are externally applied potentials, e.g., when one discusses the spin-polarized transport between the injector and detector in a spin-injection experiment,⁵ one introduces both electric and magnetization currents. However the CPP-MR, one applies *only* a voltage, and only an electric current flows into and out of the multilayered structure. While there may be a nominal magnetic field applied to the structure, it is largely irrelevant as a thermodynamic variable; the magnetization current and potential H^* are *internal* to the system. They represent the rearrangement of spin (magnetization) when an electric current is driven through the structure.

With this background in mind, there has been some questions⁷ as to whether the linear response approach,¹ which considers only the voltage V or electric field as the only variable in calculating the current neglects the effects of the nonequilibrium (current-driven) magnetization, or spin accumulation on the CPP-MR. Here we point out that the CPP-MR calculated by linear response theory *does* contain the effects of spin accumulation, even though one only considers the externally applied potential V . By using the Kubo formalism for charge transport in magnetic multilayered structures, we derive the equation that controls the spin accumulation. When one uses the approximation of a local self-energy, the spin-diffusion equation reduces to that assumed by the thermodynamic approach. We are able to clarify the conditions for the validity of the thermodynamic approach.

We begin with the linear response to an electric field, which for multilayered structures with *collinear* magnetization, i.e., ferro- and antiferromagnetically aligned layers, reduces to a one-dimensional problem²

$$j^s(z) = e \int \sigma^s(z, z') \frac{\partial}{\partial z'} V(z') dz', \quad (1)$$

where s is the spin index, and we have expressed the *external* electric field in terms of the classical potential, i.e., $E_{\text{ext}}(z) = e(\partial/\partial z')V(z')$. The conductivity is given in the Kubo formalism by the diagrams shown in Fig. 1. It includes the simple bubble diagram Fig. 1(a), the ladder diagrams due to non-spin-flip scattering Fig. 1(b) and the spin-flip diagrams represented by the wiggly lines [Fig. 1(c)]. Other diagrams, in which wiggled lines cross the shaded ladders have been neglected. Therefore, we only focus on spin-flip and non-spin-flip scattering processes, which are *local*. This type of scattering includes spin-orbit and paramagnetic impurity scattering, but excludes the magnon scattering, which is not local.

Rather than dealing with these diagrams explicitly in the conductivity $\sigma^s(z, z')$, we introduce an effective field $E^s(z')$,

$$j^s(z) = \int \sigma_b^s(z, z') E^s(z') dz', \quad (2)$$

where σ_b^s is the bubble diagram contribution to the conductivity, Fig. 1(a), and

$$E^s(z') = e \frac{\partial}{\partial z'} V(z') + e \int \Gamma^s(z', z'') \frac{\partial}{\partial z''} V(z'') dz'', \quad (3)$$

where Γ^s is the sum of the ladder diagrams, Figs. 1(b) and 1(c), without external legs. Γ^s is also called the diffusion propagator. The key difference between the diffusion propa-

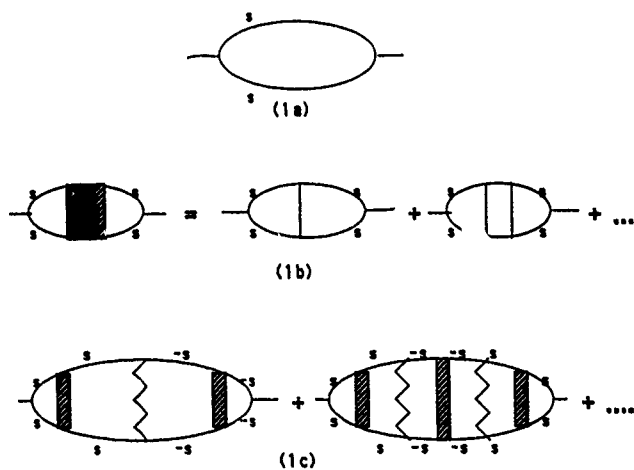


FIG. 1. Diagrams contributing to $\sigma^s(z, z')$. (a) is the bubble conductivity $\sigma_b^s(z, z')$ and (b) is the ladder contribution due to non-spin-flip processes and (c) is that due to spin-flip processes.

^{a)}Present address. Department of Physics, University of San Francisco, San Francisco, CA 94117.

gator and the bubble conductivity is that the former is long range while the latter has a length scale of the mean-free path. The asymptotic form of Γ in three dimensions is $1/|r'-r''|$.⁸ The main contribution of the diffusion propagator to the effective field, Eq. (3), is from the contribution for large separations of $z'-z''$, and one can assume that Γ^s in Eq. (3) only depends on the $z'-z''$. By integrating the second term in Eq. (3) by parts, and by using $(\partial/\partial z'')\Gamma^s(z', z'') = -(\partial/\partial z')\Gamma^s(z', z'')$, we find that Eq. (3) can be written as

$$E^s(z') = e \frac{\partial}{\partial z'} \left(V(z') + \int \Gamma^s(z', z'') V(z'') dz'' \right) \\ \equiv e \frac{\partial}{\partial z'} \mu^s(z'), \quad (4)$$

where the last identity defines the spin-dependent chemical potential μ^s .

In the following, we assume the spin-diffusion length is much larger than the mean-free paths, $\lambda_{sd} \gg \lambda_{mfp}$, i.e., that spin-flip processes are much rarer than non-spin-flip scattering. In this case $\sigma_b^s(z', z'')$ varies on the length λ_{mfp} (the Green's functions decay over distances given by the elastic mean-free paths), while the current $j^s(z)$ varies over distances λ_{sd} . We now invert Eq. (2) and treat the current density as a constant within the mean-free path. We can remove the current density from the integration, and arrive at

$$j^s(z) = \frac{e}{\rho^s(z)} \frac{\partial}{\partial z} \mu^s(z), \quad (5)$$

where

$$\rho^s(z) = \int \rho_b^s(z, z') dz', \quad (6)$$

and $\rho_b^s(z, z')$ is the inverse of the conductivity $\sigma_b^s(z, z')$. In the local relaxation time approximation, $1/\rho^s(z) = Cl^s(z)$, where $C = (e^2/h)(2k_F^2/3\pi)$ and $l^s(z)$ is a local mean-free path. This local relation between current density and the chemical potential is Ohm's law for each spin channel. It is valid as long as the current density for each spin channel does not change significantly within a mean-free path.

To obtain information about spin-diffusion, one has to calculate the ladder diagrams. From Figs. 1(b) and 1(c), the diffusion propagator satisfies the following integral equation:

$$\Gamma^s(z', z'') = d^s(z', z'') \\ + \int d^s(z', z_1) P_{sf}(z_1) \Gamma^{-s}(z_1, z'') dz_1, \quad (7)$$

where P_{sf} is the probability of spin-flip scattering and d^s is the diffusion propagator in the absence of the spin-flip scattering; see Fig. 1(b). In general, P_{sf} depends on energy. In our case we only consider nearly elastic spin-flip scattering, so that we set all the energy variables at the Fermi level. Equation (7) is the spin-diffusion equation in integral form. To write it in differential form, we use the fact that the diffusion propagator in the absence of spin-flip scattering satisfies^{8,9}

$$\frac{1}{3} \frac{\partial^2}{\partial z'^2} d^s(z', z'') = - \left\{ \frac{1}{l^s(z')} \right\}^2 \delta(z' - z''). \quad (8)$$

By taking the Laplacian of both sides of Eq. (7) and by using the above identity, we find

$$\frac{\partial^2}{\partial z'^2} \Gamma^s(z', z'') = -3 \left[\frac{1}{l^s(z')} \right]^2 \{ \delta(z' - z'') \\ + P_{sf}(z) \Gamma^{-s}(z', z'') \}. \quad (9)$$

Upon taking the derivative of the definition of the spin-dependent chemical potential Eq. (4) and by using Eq. (9), we arrive at

$$3 \{ l^s(z) \}^2 \frac{\partial^2}{\partial z^2} \mu^s(z) = - \frac{l^s(z) + l^{-s}(z)}{l_{sf}(z)} \{ \mu^{-s}(z) - V(z) \}, \quad (10)$$

where we have used $(\partial^2/\partial z^2)V(z) = 0$ for the classical potential, and we have defined the spin-flip mean-free path $l_{sf} \equiv (l^s + l^{-s})/P_{sf}$ to express the diffusion equation in terms of l_{sf} , as one usually does. Note that we have dropped the first term in Eq. (9) in calculating the chemical potential from the second term of Eq. (4) because it has already been included in the first term of Eq. (4).

Equation (10) is our main result; it controls the spin diffusion. To write it in a more familiar form for layered structures, we assume the local mean-free path is piecewise constant, i.e., $l^s(z)$ is a constant in a specific layer. In this case, Eq. (10), along with the equation given by interchanging s and $-s$ in Eq. (10), can be written as

$$\frac{\partial^2}{\partial z^2} [\mu^s(z) - \mu^{-s}(z)] = \frac{\mu^s(z) - \mu^{-s}(z)}{\lambda_{sd}^2(z)}, \quad (11)$$

where we have defined the spin-diffusion constant $\lambda_{sd}(z)$ as $1/\lambda_{sd}^2 \equiv [3l^s l_{sf}]^{-1} + [3l^{-s} l_{sf}]^{-1}$ and

$$\frac{\partial}{\partial z} \left\{ l^s(z) \frac{\partial}{\partial z} \mu^s(z) + l^{-s}(z) \frac{\partial}{\partial z} \mu^{-s}(z) \right\} = 0. \quad (12)$$

Equation (11) is exactly the one assumed by the thermodynamic approach,^{5,6} while Eq. (12) represents the conservation of charge, i.e., the total current is constant. These two equations determine the spin-dependent chemical potentials; then the electric current and the magnetization current are obtained from Eq. (5). We point out that one should use Eq. (10) rather than Eqs. (11) and (12) when the local mean-free paths and local spin-diffusion constant are not piecewise constants. For example, one could grow multilayers with continuously varying compositional differences.

We have reproduced and generalized the equations that define spin-diffusion in magnetic multilayered structures, when they are subject to an electric field. To understand the range of validity of these equations, we consider the different thicknesses of the layers d_{in} relative to the mean-free path and spin-diffusion length. The current derivation is in the limit $\lambda_{mfp} \ll \lambda_{sd}$, so that one can view it as a spin-diffusion process. The general solution of Eq. (11) contains an exponentially decaying part, with respect to the spin-diffusion length. For $d_{in} \ll \lambda_{sd}$, which includes the cases of $d_{in} \ll l^s$ (homogeneous limit) and $d_{in} \approx l^s$, the solution to Eq. (11) is simple; all the quantities, e.g., chemical potentials, are peri-

odic functions with a period of d_{in} , so that the exponential decay within the length of d_{in} is negligible and one can neglect the right side of Eq. (11).

We should point out that if one neglects spin-diffusion processes, this does not imply that one is omitting the spin accumulation or magnetization buildup. In fact, the magnetization buildup is largest when one neglects spin-flip processes. One can easily check this conclusion by calculating the chemical potential difference $\mu^s(z) - \mu^{-s}(z)$ from one layer to the next; the variation is largest when the spin-diffusion length is infinite. Most experiments are actually in this limit. Therefore, our original model¹ predicated on neglecting spin-flip processes can be used to analyze data on multilayered structures currently being studied. The diffusion equation begins to play a role when the layer thicknesses are comparable to the spin-diffusion length. In this case, one is in the local limit because the mean-free path is much smaller than the layer thicknesses. It is precisely in this limit that the diffusion equation, Eq. (10), has been derived. However, when λ_{mfp} is comparable with λ_{sdl} ,¹⁰ additional terms in Eqs. (5) and (10) will appear, and the derivation presented here fails. The derivation for the vertex corrections and effective fields where $\lambda_{mfp} \approx \lambda_{sdl}$ will be presented elsewhere.¹¹

In summary, we have shown that a linear response theory of transport for CPP is able to reproduce the spin-diffusion equations derived in the thermodynamic approach, provided one is in the limit where the concept of spin diffusion makes sense, i.e., far fewer spin-flip scattering processes than non-spin-flip ones, so that $\lambda_{mfp} \ll \lambda_{sdl}$.¹² When λ_{mfp} is comparable to λ_{sdl} , the concept of spin diffusion is not valid *nor are the spin-diffusion equations*. From this derivation, we can unequivocally respond in the affirmative as to whether linear response theory^{1,2} accounts for the spin accumulation, attendant to charge driven through regions of inhomogeneous magnetization, i.e., the case of CPP of magnetic multilayered structures. For currents in the plane of the layers (CIP) there is no spin accumulation, provided the size of the magnetic domains in the layers are larger than the spin-diffusion length. The reason is that, in the direction of magnetic inhomogeneities perpendicular to the layers, there is no net charge transport for CIP.

While not a difference in results, there is one in outlook between the linear response and thermodynamic approaches. In linear response theory single-site (local) spin-flip pro-

cesses contribute on an equal footing with nonlocal spin-flip processes due to magnons; although they produce quite different results, and we have not discussed magnons in this paper. In the thermodynamic approach the single-site spin-flip processes contribute to changing the magnetization potential and nonequilibrium magnetization, while the magnons contribute as momentum conserving spin-flip processes, and are accounted for by the potentials that fix the currents. This distinction that appears in the thermodynamic approach is a result of discriminating between spin accumulation and electric currents. This may be useful in spin injection experiments, where one applies spin-polarized (charge and magnetization) currents to a system. However, for CPP in magnetic multilayered structures, magnetization currents develop only *inside* the structures; these convert the external electric field into the internal fields seen by the electrons. When the medium is magnetized or when the scattering of the electrons is spin dependent, these effective internal fields are spin dependent. This accounts for both the electric and magnetization currents that develop in CPP in magnetic multilayered structures.

We would like to acknowledge useful discussions with Professor A. Fert and support from the Office of Naval Research Grant No. N00014-91-J-1695, NATO Grant No. 5-2-05/RG No. 890599, and the New York University Technology Transfer Fund.

¹ S. Zhang and P. M. Levy, J. Appl. Phys. **69**, 4786 (1991).

² H. E. Camblong, S. Zhang, and P. M. Levy, Phys. Rev. B **47**, 4735 (1993).

³ T. Valet and A. Fert, Phys. Rev. B **48**, 7099 (1993).

⁴ M. Johnson, Phys. Rev. Lett. **67**, 3594 (1991).

⁵ M. Johnson and R. H. Silsbee, Phys. Rev. B **35**, 4959 (1987); also, Phys. Rev. Lett. **60**, 377 (1988).

⁶ P. C. van Son, H. van Kempen, and P. Wyder, Phys. Rev. Lett. **58**, 2271 (1987).

⁷ G. E. W. Bauer, Phys. Rev. Lett. **69**, 1676 (1992); M. A. M. Gijs, Phys. Rev. Lett. **70**, 3343 (1993).

⁸ C. L. Kane, R. A. Serota, and P. A. Lee, Phys. Rev. B **37**, 6701 (1988); S. Zhang, to be published.

⁹ J. Rammer, Rev. Mod. Phys. **63**, 781 (1991).

¹⁰ By adding paramagnetic impurities to the nonmagnetic spacer layers one rapidly reaches the regime where $\lambda_{mfp} \approx \lambda_{sdl}$; J. Bass *et al.*, to be published in this proceeding.

¹¹ S. Zhang and P. M. Levy, to be published.

¹² By using the Boltzmann equation, T. Valet and A. Fert, see Ref. 3, also find the spin-diffusion equations found in the thermodynamic approach in the limit $\lambda_{mfp} \ll \lambda_{sdl}$.

Structure and giant magnetoresistance in sputtered and MBE grown Fe/Cr superlattices (invited) (abstract)

Ivan K. Schuller and David M. Kelly

Physics Department 0319, University of California, San Diego, La Jolla, California 92093-0319

R. Schad, M. Potter, and Y. Bruynseraede

Katholieke Universiteit Leuven, B-3001 Leuven, Belgium

We have performed a comparative study of Fe/Cr superlattices prepared by sputtering and molecular beam epitaxy. Detailed structural and magnetic measurements show that structural parameters are important in controlling the magnitude of the magnetoresistance. X-ray diffraction results show that films grown by molecular beam epitaxy (MBE) and sputtering are structurally different, and corresponding to these differences are large changes in the values of the magnetoresistance and its dependence on Cr thickness. The results indicate a strong dependence of the magnetoresistance on the structure of the superlattices.

Work supported by NSF-DMR 92-01698 at U.C.S.D. and Grant No. 88/93-130 of the G.O.A. and IUAP at KUL. International travel was provided by NATO

Direct measurement of spin dependent mean free paths in metals (abstract)

Bruce A. Gurney, Virgil S. Speriosu, Harry Lefakis, Dennis R. Wilhoit, and Omar U. Need

IBM Research Division, Almaden Research Center, 650 Harry Road, San Jose, California 95120-6099

We describe results obtained using a new spin valve structure that is specifically designed to measure the spin up and spin down mean free paths in ferromagnetic metals. We report how these mean free paths can be measured more directly and with greater accuracy than previous methods, which were based mostly on indirect evidence from magnetoresistance in ternary alloys. The technique is based on the "backed" spin valve layered structure: substrate/seed/80 Å FeMn/50 Å NiFe/23 Å Cu/20 Å NiFe/ t Å b /50 Å Ta where the back layer of material b with thickness t is probed by the rest of the structure, which forms a spin polarized conduction electron source. As t is varied the majority carrier mean free path λ_b^+ in the layer b is obtained directly from the form taken by the change in film conductance between parallel and antiparallel magnetization states, ΔG , whose solution of the Boltzmann transport equation shows is well approximated by the form $\Delta G = \Delta G_0 + \Delta G_b \{1 - \exp([t - t_x]/\beta \lambda_b^+)\}$, where ΔG_0 arises from the 20 Å NiFe layer, t_x is the high resistivity region of intermixing at the b layer interfaces, and $\beta \approx 1$ from observations with $b = \text{Cu}$. The minority carrier mean free path in a ferromagnetic layer b , λ_b^- , is obtained by comparing ΔG and λ_b^+ with $\Delta G'$, and $\lambda_{b'}^+$, of a nonmagnetic b' layer of similar resistivity to b ; it is a less direct measurement than that of λ^+ since it relies on the connection between conductivity and mean free path for the minority subband. We have obtained room temperature results for $\text{Ni}_{80}\text{Fe}_{20}$ ($\lambda^+ = 46 \pm 3$ Å, $0 < \lambda < 6$ Å), Fe ($\lambda^+ = 15 \pm 2$ Å, $\lambda = 21 \pm 5$ Å), and Co ($\lambda^+ = 55 \pm 4$ Å, $0 < \lambda < 8$ Å). The connection of spin dependent conductivity and mean free paths in ferromagnetic metals is crucial in exploring the mechanism of giant magnetoresistance and, more broadly, is central in all theories of transport in magnetic metals; this new technique should prove a powerful tool in measuring these fundamental quantities.

Giant magnetoresistance in epitaxial sputtered Fe/Cr(211) superlattices (abstract)

M. J. Conover, Eric E. Fullerton, J. E. Mattson, C. H. Sowers, and S. D. Bader
Materials Science Division, Argonne National Laboratory, Argonne, Illinois 60439

We report giant magnetoresistance (GMR) as high as 150% at 4.2 K in epitaxial Fe/Cr superlattices. Samples prepared by magnetron sputtering on MgO(100) produced the expected Fe/Cr(100) orientation; however, deposition on MgO(110) produced a novel (211) low-miller-index orientation. The crystallographic orientations and superlattice nature of the samples were confirmed by both low- and high-angle x-ray diffraction. The Fe/Cr(211) superlattices have an in-plane uniaxial anisotropy ($K_{||} = 9 \times 10^5$ ergs/cm³) along the Fe[011] which give the sample a rich magnetic behavior. The GMR with the current along the [011] is $\approx 20\%$ higher than that along the [111] direction of the (211) plane. The GMR for the (211) superlattices shows four oscillations with Cr thickness. Both orientations shows the expected long-period oscillation of 18 Å Cr and a GMR increase by a factor a 4 when cooled from room temperature to 4.2 K.

This work was supported by the U.S. Department of Energy, BES-Materials Sciences, under Contract W-31-109-ENG-38.

Compositional dependence of the structural and magnetic properties of PtMnSb films

R. Carey, H. Jenniches, D. M. Newman, and B. W. J. Thomas

Centre for Data Storage Materials, Coventry University, Coventry, CV1 5FB, United Kingdom

Nonstoichiometric, Pt deficient, PtMnSb films have been investigated for evidence of the increase in coercivity suggested by the work of Marinero [Appl. Surf. Sci. **43**, 117 (1989)]. Structural, magnetic, and magneto-optic properties of thin PtMnSb films of different compositions annealed in under 30 s using a rapid thermal processing (RTP) system [Carey *et al.*, IEEE Meeting on Current Topics in Applied Magnetism, Keele University, 4 November 1992 (unpublished), Paper 15; J. Magn. Soc. Jpn. **17**, 290 (1993)], have been determined. It is shown that the crystalline texture of the films can be controlled by adjustments in composition and RTP time and that Pt deficiency produces increases in coercivity. The production of coercivity does not correlate with the marked changes in texture but appears to be associated with the development of MnSb phases within the PtMnSb microstructure.

INTRODUCTION

The Heusler alloy PtMnSb is a half-metallic ferromagnet that, in its crystalline stoichiometric form, exhibits the largest polar Kerr rotation at room temperature of all known metallic systems. Following the first report of this large magneto-optic effect in the bulk material by van Engen *et al.* in 1983,¹ several authors have presented details of the preparation and properties of the alloy in thin film form.²⁻⁴ The large polar Kerr rotations of these films at wavelengths relevant to optical storage are clearly of interest for improved magneto-optic readout. Unfortunately, thin films of PtMnSb do not possess the magnetic properties, e.g., perpendicular anisotropy and high coercivity, required of magneto-optic data storage materials. A number of attempts have been made to develop significant perpendicular anisotropy.⁵⁻⁸ Limited success has been reported with the adoption of complex preparation techniques. Extensive post deposition annealing, necessary for the development of the crystalline structure for the material to exhibit spontaneous magnetization and a large polar Kerr effect, has been a common feature of the reports. Annealing usually occurs in a vacuum at temperatures $\approx 500^\circ\text{C}$ for at least one hour. Significant perpendicular magnetic anisotropy has only been achieved by annealing PtMnSb thin films in an Ar/O₂ atmosphere at 450°C for one hour.⁹

In this paper nonstoichiometric, Pt deficient, PtMnSb films have been investigated for evidence of the coercivity increase suggested by Marinero.¹

EXPERIMENT

The PtMnSb films used in this study were prepared by rf-sputtering from mosaic targets onto unheated glass substrates using a rf power of 30 W and an argon pressure of 10 mTorr. The films were all of similar thickness (≈ 200 nm) and the different compositions were produced by varying the number of Pt squares placed on top of a MnSb target. The range of compositions prepared in this way is shown in Table I.

All samples were subjected to between 15 and 30 s heat treatment in a rapid thermal processing (RTP) system.^{10,11} Film structure was determined using a Philips PW 1700

TABLE I. The compositions of the samples investigated.

Sample No.	Pt%	Mn%	Sb%
1	33.7	34.5	31.8
2	26.6	39.7	33.7
3	23.7	40.0	36.3
4	21.6	42.0	36.4
5	20.4	42.1	37.5

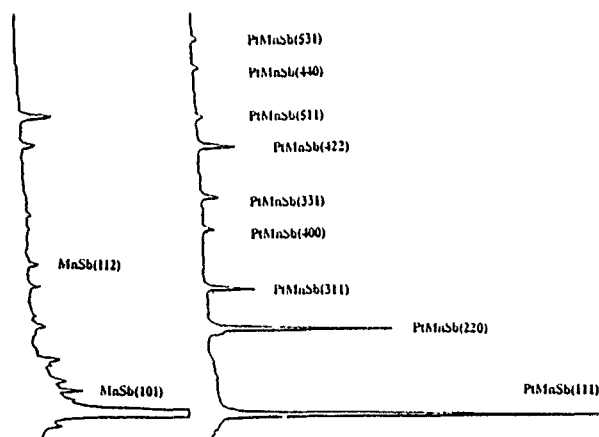


FIG. 1. X-ray diffraction structure of (a-top) near-stoichiometric film (sample 1) and (b-lower) Pt deficient (sample 5) film after identical RTP treatments.

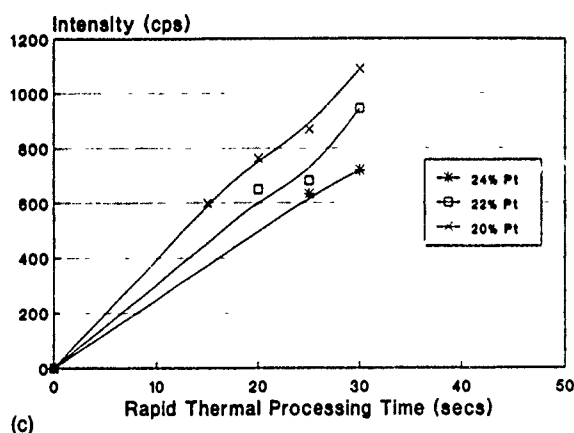
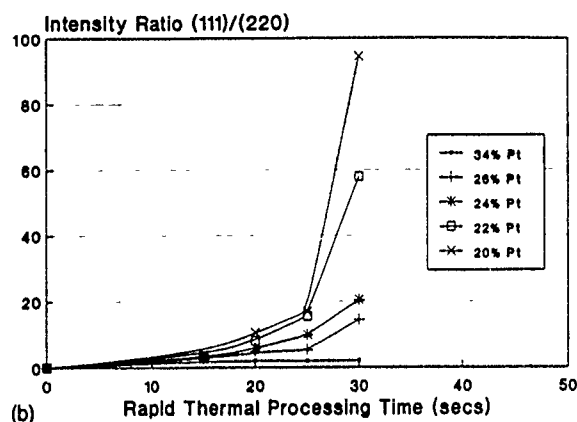
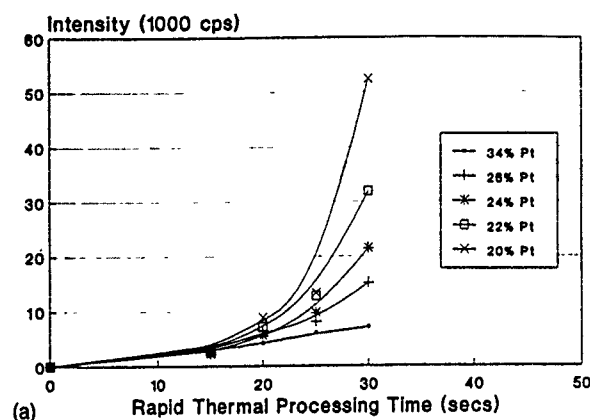


FIG. 2. (a) Development of PtMnSb (111) peak with RTP time. (b) Development of PtMnSb (111) texture with RTP time. (c) Formation of MnSb phases as measured by the development of MnSb (101) peak with RTP time.

x-ray diffraction system and their magnetic and magneto-optic properties investigated using a vibrating sample magnetometer (VSM) and polar Kerr hysteresis loop plotter operating at wavelengths of 670 and 825 nm.

RESULTS

All as deposited films evidenced no x-ray diffraction structure and no magnetic or magneto-optic activity. After RTP the near stoichiometric films (sample 1) developed the characteristic $C1_b$ structure, displaying the nine significant peaks shown in Figure 1(a). The dominant peak is the one representing the (111) plane with an intensity twice as large as the most significant of the other peaks, which is attributed

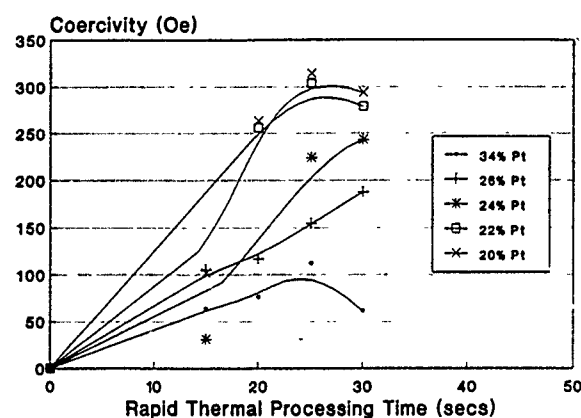


FIG. 3. Development of out of plane coercivity with RTP time.

to the (220) plane. The ratio of the two intensities for the (111) and the (220) planes is used as a measure of the (111) texture in the PtMnSb films. In contrast the Pt deficient samples, after the same RTP, exhibited marked changes in this (111) texture and evidence of growth of MnSb phases, as shown in Fig. 1(b) for sample 5.

The development of the (111) peak and its texture, as defined above, is displayed for all five compositions as a function of RTP time in Figs. 2(a) and 2(b). In Fig. 2(b) the texture is seen to increase rapidly with decreasing Pt content as the (111) peak height increases and the (220) peak height

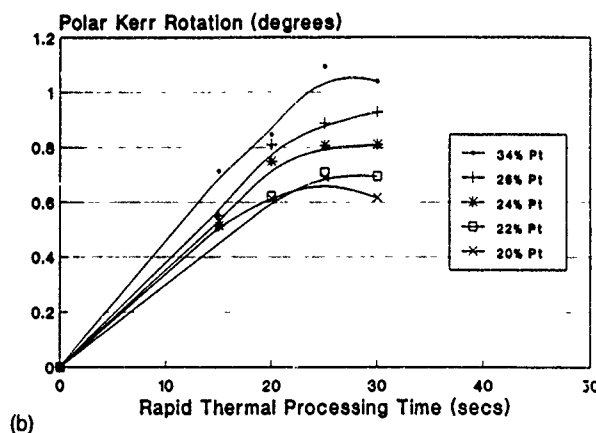
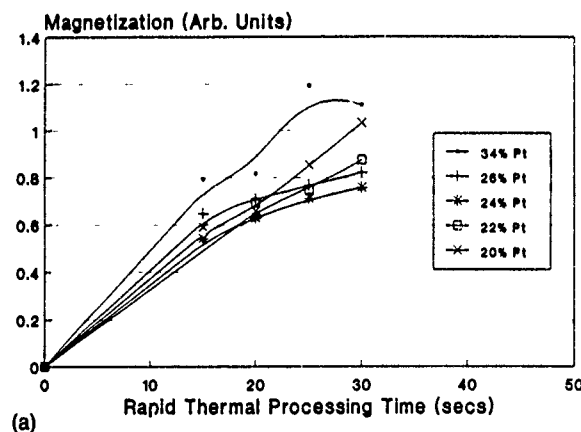


FIG. 4. (a) Development of magnetization with RTP time. (b) Development of polar Kerr rotation with RTP time.

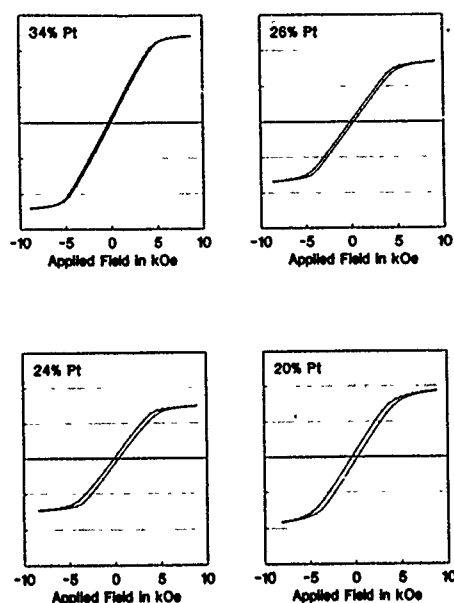


FIG. 5. VSM hysteresis loops (out-of-plane) for four different compositions after 30 s RTP.

decreases for processing times in excess of 20 s. Figure 2(c) demonstrates the development of MnSb phases in the most Pt deficient samples by plotting the growth of the identified MnSb (101) peak with processing time.

The corresponding variation of out of plane coercivity with RTP time is shown in Fig. 3 and the variations in magnetization and polar Kerr rotation in Figs. 4(a) and 4(b). Examples of the out of plane VSM hysteresis loops obtained for the various compositions after 30 s RTP are presented in Fig. 5.

DISCUSSION

The above results indicate very clearly that the texture of PtMnSb films can be effectively controlled by small adjust-

ments in composition and RTP time. It is also evident that the very marked changes in texture do not produce a significant change in coercivity although, in agreement with the suggestion made by Marinero,¹ an increase in coercivity is produced with Pt depletion. However, the clear correlation between the data presented in Figs. 2(c) and 3 suggests that, in line with the work of Kunimoto *et al.*,⁹ it is the increase in coercivity with the measured development of MnSb phases in the Pt deficient PtMnSb films that is of significance. Although the Pt deficient samples exhibit some reduction in polar Kerr rotation it still remains relatively large.

ACKNOWLEDGMENT

This work was supported by Johnson Matthey Technology Centre, Sonning Common, Reading, UK.

- ¹E. E. Marinero, Appl. Surf. Sci. **43**, 117 (1989).
- ²R. Ohya, J. Abe, and K. Matsubara, IEEE Transl. J. Magn. Jpn. **TJMJ-1**, 122f (1985).
- ³R. Ohya, T. Koyanagi, and K. Matsubara, J. Appl. Phys. **61**, 2347 (1987).
- ⁴S. Shiomi, A. Ito, and M. Masuda, J. Magn. Soc. Jpn. Suppl. No. S1 **11**, 221 (1987).
- ⁵S. Hatta, T. Shiono, and H. Adachi, IEEE Transl. J. Magn. Jpn. **3**, 445f (1988).
- ⁶K. Matsubara *et al.*, J. Magn. Soc. Jpn. Suppl. No. S1 **11**, 213 (1987).
- ⁷N. Sugimoto, T. Inukai, M. Matsuoka, and K. Ono, Jpn. J. Appl. Phys. **28**, 1139 (1989).
- ⁸K. Takanashi, K. Sato, J. Watanabe, Y. Sato, and H. Fujimori, Jpn. J. Appl. Phys. **30**, 52 (1991).
- ⁹A. Kunimoto *et al.*, IEEE Transl. J. Magn. Jpn. **TJMP-5**, 1016 (1990).
- ¹⁰R. Carey, H. Jenniches, D. M. Newman, P. A. Gago-Sandoval, and B. W. J. Thomas, IEEE Meeting on Current Topics in Applied Magnetism, Keele University, 4 November 1992 (unpublished), Paper 15.
- ¹¹R. Carey, H. Jenniches, D. M. Newman, and B. W. J. Thomas, J. Magn. Soc. Jpn. Suppl. No. S1 **17**, 290 (1993).
- ¹²P. G. van Engen, K. H. J. Buschow, R. Jongebreur, and M. Erman, Appl. Phys. Lett. **42**, 202 (1983).

Secondary ion bombardment effects on the magnetic properties and microstructures of ion-beam-deposited TbFe thin films

S. Yatsuya and M. B. Hintz

Information, Imaging and Electronics Sector Materials Application Laboratory, 3M Co.,
St. Paul, Minnesota 55144

TbFe films were produced by ion beam deposition both with and without 300 eV secondary ion bombardment (SIB). The magnetic properties and microstructures of the films were investigated. SIB was found to increase the perpendicular anisotropy coefficient, but decrease the magnetization-coercivity product (MH_c =energy product) of the films. The microstructure of the films changed dramatically; the film made in the absence of SIB is amorphous while the film made with SIB during deposition consists of nanocrystals in an amorphous matrix.

I. INTRODUCTION

It has been shown that secondary ion bombardment (SIB) during deposition, which is generally called ion assisted deposition, can alter the growth, density, and appearance of vapor-deposited films.¹

This paper compares the magnetic properties and microstructures of ion-beam-deposited (IBD) TbFe films made with and without 300 eV SIB.

II. EXPERIMENTAL

A dual ion beam system² was used to prepare specimens for this study. Base pressure prior to deposition was $\leq 5 \times 10^{-8}$ Torr. The Ar working gas pressure during deposition was 3×10^{-4} Torr. The Fe-Tb films were sandwiched between thin (15–20 nm) SiC films for environmental protection. The primary ion beam energy was 650 eV with a total beam current of 230 mA; this yields an ≈ 3 nm/min Fe-Tb deposition rate over the planetary swept area. The secondary ion source was operated at 300 eV energy and an average total current of 30 mA; it is estimated that this corresponds to an average current density of $\approx 10 \mu\text{A}/\text{cm}^2$ at the substrates. The secondary ion beam incidence angle is $\approx 45^\circ$ to the substrate surface normal. Fe-Tb film chemistry was determined by inductively coupled plasma analysis (ICP).

MH loops were measured using a vibrating sample magnetometer; torque measurements 45° to the film normal as a function of applied field³ were used to determine the uniaxial magnetic anisotropy constant, K_u .

Microstructural characterization of the films was carried out by transmission electron microscopy (TEM) using JEOL200CX and 2010 microscopes operated at 200 kV. Selected area diffraction and high resolution bright-field imaging were the primary modes of operation. Microbeam diffraction with a probe size of ≈ 2 nm was also employed. A film stack of SiC_x/TbFe/SiC_x was deposited on TEM grids with SiO support films, NaCl(100) single crystals, and Si(100) wafers. The first two substrates were used for plane view observation while the Si wafers were used for cross-sectional TEM specimen preparation and magnetic property measurements. The films grown on NaCl substrates were prepared for observation by floating off in water and transferring to TEM grids. Cross-section view samples were prepared by dimpling and ion beam milling.

Diffraction patterns and Kikuchi lines from the Si crystal substrate were used to align the specimens with the incident electron beam nearly parallel to the substrate surface.

III. RESULTS AND DISCUSSION

A. Specimen A: IBD TbFe film without SIB during growth

The ICP composition of the specimen A film is 74.1 at.% Fe and 25.9 at.% Tb. The film exhibits no magnetic compensation temperature from -160°C to the $\approx 145^\circ\text{C}$ Curie temperature, which is consistent with its Fe/Tb ratio. Saturation magnetization (M_s) and energy product (MH_c) at 20°C are $110 \text{ emu}/\text{cm}^3$ and $2.7 \times 10^5 \text{ ergs}/\text{cm}^3$, respectively. The squareness ratio of the loops is close to one. The uniaxial anisotropy constant, $K_u = 1.6 \times 10^6 \text{ ergs}/\text{cm}^3$.

An electron micrograph of the specimen A SiC_x/TbFe/SiC_x film stack on a SiO substrate is shown in Fig. 1 with the corresponding electron diffraction pattern. The TbFe film looks featureless and has one broad diffraction ring. The film is most likely amorphous.

Figure 2 shows a TEM cross-sectional view of the specimen A film stack. The individual layers of TbFe and SiC_x on the Si wafer can be seen. The region of the TbFe film close to the boundary with the SiC_x layer looks darker than the region away from the boundary because of the thickness. The Si single crystal film shows the structure image in the direc-

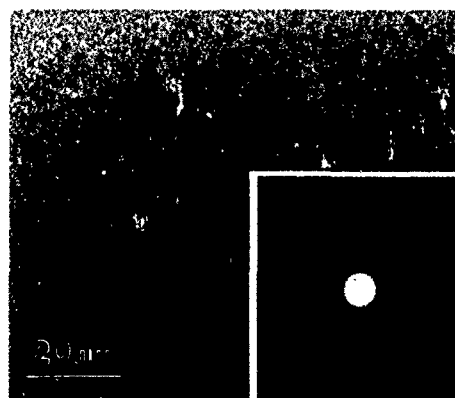


FIG. 1. Plane view of the specimen A SiC/TbFe/SiC film stack on SiO substrate and corresponding electron diffraction pattern.

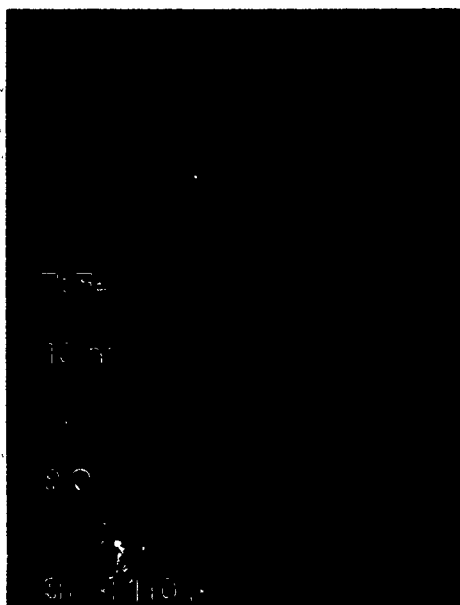


FIG. 2. Cross-sectional view of the specimen A SiC/TbFe/SiC film stack grown on a Si wafer (100)

tion of $\langle 110 \rangle$. It appears that the Si substrate surface is covered by an amorphous SiO_x layer around 2 nm thick. The interface between the SiC_x layer and the TbFe is quite sharp. The SiC_x layer grown on the Si substrate looks amorphous. The TbFe film grown on the SiC film does not have columnar structures and looks featureless. The film is most likely amorphous.

B. Specimen B: IBD TbFe film with SIB during growth

The ICP composition of the specimen B film is 79.8 at.% Fe and 20.2 at.% Tb. The reduced Tb concentration of this film relative to that of specimen A is probably due to preferential sputtering of the Tb by the secondary ion flux.⁴ The film exhibits a magnetic compensation temperature of -130°C . Saturation magnetization (M_s) and energy product (MH_c) at 20°C are 45 emu/cm^3 and $1.3 \times 10^5 \text{ ergs/cm}^3$, respectively. The squareness ratio of the loops is close to one. The uniaxial anisotropy constant, K_u , is $\approx 2.2 \times 10^6 \text{ ergs/cm}^3$. We have observed that SIB generally increases K_u in IBD TbFe films over a range of compositions.

The microstructure of the specimen A and B films is remarkably different. Figure 3 is a plane view of the specimen B $\text{SiC}_x/\text{TbFe}/\text{SiC}$ film stack on a SiO substrate, along with the corresponding diffraction pattern. The TbFe film contains dark particles or clusters of $\approx 2 \text{ nm}$ in size in an amorphous matrix. The diffraction pattern is composed of a strong broad ring which is broader than for the specimen A TbFe film, and exhibits a sharp intensity decline at the outer rim of the ring. The diffraction pattern shows that the film structure is significantly changed by SIB. The sharp intensity drop is considered to indicate the existence of small crystallites in the film.

Figure 4 shows the cross-sectional view of the specimen B film stack. The SiC films are most likely amorphous. The

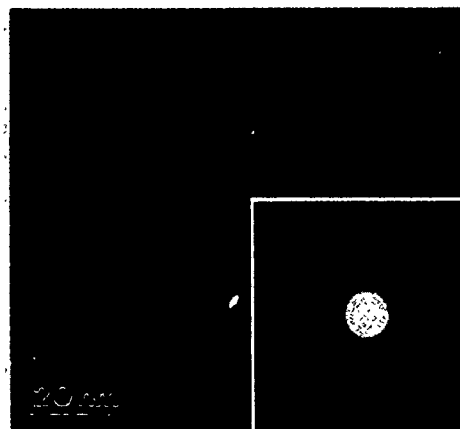


FIG. 3. The plane view of the specimen B SiC/TbFe/SiC film stack on SiO substrate and corresponding electron diffraction pattern.

cross-sectional view of the TbFe film also reveals $\approx 2 \text{ nm}$ clusters in the amorphous matrix, which is consistent with the data from the plane view. The fact that the clusters are seen both in the plane and cross-sectional views indicates that the clusters are not an artifact of TEM sample preparation or post-deposition oxidation. There is no evidence for columnar structure in the films.

Figure 5 shows a highly magnified micrograph of the TbFe film. The film contains 2–3 nm size nanocrystals with lattice fringes as shown by arrows. It is certain that the film contains nanocrystals. The microbeam diffraction pattern from the dark clusters in the specimen B TbFe film is shown in Fig. 6(a); the presence of diffracted spots indicates the dark regions are nanocrystals. On the other hand, microbeam diffraction from the light portions reveals diffuse rings characteristic of amorphous materials as shown in Fig. 6(b).

Inspection of the Figs. 1–6 micrographs clearly demonstrates that the SIB has resulted in a microstructural transformation from what appears to be an entirely amorphous structure (specimen A) to an amorphous matrix containing a nominally uniform distribution of nanocrystals (specimen B).

The presence of nanocrystals of $\alpha\text{-Fe}$ or Co in TbFeCo films made by sputtering has also been reported.⁵ Phase

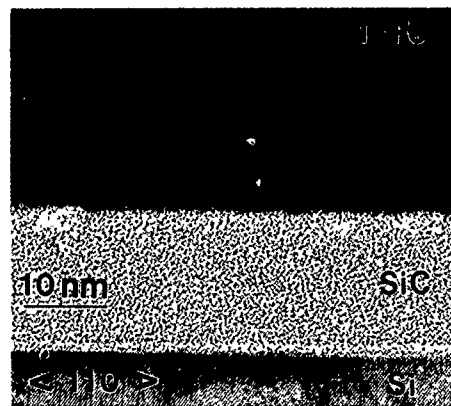


FIG. 4. The cross-sectional view of the specimen B SiC/TbFe/SiC film stack grown on a Si wafer (100).

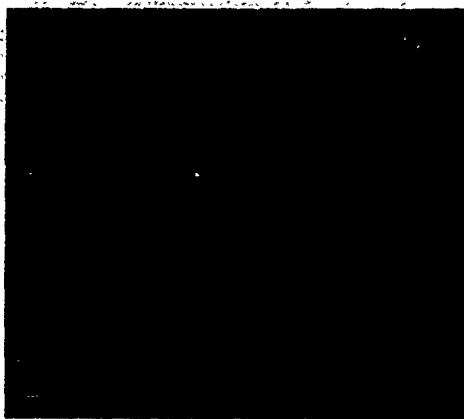


FIG. 5. High resolution electron micrograph of the specimen B TbFe. Arrows indicate nanocrystals with lattice fringes.

separation on a 2.5–3.5 nm scale as a function of the substrate bias voltage also have been observed in GdCoAu thin films.⁶ We are, however, unaware of any previous direct evidence that SIB can induce crystal formation in RE–TM alloys such as TbFe. SIB may be a useful tool for microstructure control in RE–TM films such as TbFe.

We speculate the reason why the ion assisted IBD film contains nanocrystals in the amorphous matrix as follows;



FIG. 6. Microbeam diffraction patterns from the dark portion (a) and from the light portion (b) of Fig 5.

ion bombardment played a role of making nucleation sites for the formation of the nanocrystals, because ion bombardment can create surface defects which act as nucleation sites for depositing film atoms.⁷ It is also known that ion bombardment of a growing film can influence crystalline orientation.^{8,9}

Several investigators have shown that ion bombardment during growth can influence the magnetic properties of rare earth-transition metal (RE–TM) alloys.^{10–14} For example the uniaxial magnetic anisotropy constant K_u was explained in terms of selective resputtering of atoms in different surface sites.^{12–14} However, none of the models considered a structure containing nanocrystals. We propose a possible model in which the presence of nanocrystals may affect K_u of the films made with SIB,⁵ and other magnetic properties.

ACKNOWLEDGMENT

We are very grateful to Masahiro Kawasaki of JEOL-US who took TEM pictures for us using the JEOL 2010.

- ¹J. M. E. Harper, J. J. Cuomo, R. J. Gambino, and H. R. Kaufman, *Modification of Thin Film Properties by Ion Bombardment During Deposition*, in *Ion Bombardment Modification of Surfaces: Fundamentals and Applications*, edited by O. Auciello and R. Kelly (Elsevier, Amsterdam, 1984).
- ²J. M. E. Harper, J. J. Cuomo, and H. T. G. Hentzell, *Appl. Phys. Lett.* **43**, 547 (1983).
- ³H. Miyajima, K. Sato, and T. Mizoguchi, *J. Appl. Phys.* **32**, 4669 (1976).
- ⁴J. M. E. Harper and R. J. Gambino, *J. Vac. Sci. Technol.* **16**, 1901 (1979).
- ⁵Z. G. Li, D. J. Smith, and K. Sickafus, *Appl. Phys. Lett.* **55**, 919 (1989).
- ⁶S. R. Herd, *J. Appl. Phys.* **50**, 1645 (1979).
- ⁷R. D. Bland, G. J. Kominiak, and D. M. Mattox, *J. Vac. Sci. Technol.* **11**, 671 (1974).
- ⁸R. M. Bradley, J. M. E. Harper, and D. A. Smith, *J. Appl. Phys.* **60**, 4160 (1986).
- ⁹Y. Nagai, A. Tago, and T. Toshima, *J. Vac. Sci. Technol. A* **5**, 61 (1987).
- ¹⁰T. Katayama, M. Miyazaki, Y. Nishihara, and T. Shibata, *J. Magn. Mater.* **35**, 235 (1983).
- ¹¹S. Yoshino, H. Takagi, S. Tsunashima, M. Masuda, and S. Uchiyama, *Jpn. J. Appl. Phys.* **23**, 188 (1984).
- ¹²R. J. Gambino and J. J. Cuomo, *J. Vac. Sci. Technol.* **14**, 152 (1977).
- ¹³H. R. Muller and R. Perthel, *Phys. Status Solidi B* **87**, 203 (1978).
- ¹⁴Y. Nishihara, T. Katayama, and Tsushima, *Jpn. J. Appl. Phys.* **17**, 1083 (1978).

Optical and magneto-optical constants of Pr substituted TbFeCo films

R. Carey, D. M. Newman, J. P. Snelling, and B. W. J. Thomas

Centre for Data Storage Materials, Coventry University, Coventry CV15FB, United Kingdom

Optimization of tri- or quadrilayer magneto-optic recording media requires knowledge of the optical and/or magneto-optical constants for all of the individual active or passive layers that together comprise the complete disk structure. The optical ($n+ik$) and first-order magneto-optical (Q_1+iQ_2) constants for two series (i) $(\text{Tb}_{23}\text{Fe}_{72.5}\text{Co}_{4.5})_{100-x}\text{Pr}_x$, (ii) $(\text{Tb}_{27}\text{Fe}_{65}\text{Co}_8)_{100-x}\text{Pr}_x$ of Pr substituted TbFeCo films, for which x varies between 0 and 30, have been determined by a combination of ellipsometry and Kerr polarimetry. Ellipsometry has also been used to determine independently the optical constants of the optimized SiN passivation layers developed to protect these samples. Using constants determined experimentally on thick samples, the variation of the polar Kerr rotation and ellipticity as a function of magnetic film thickness has been calculated for light incident from both the air and substrate side of a typical trilayer magneto-optic disk structure in which material from the above series, the magnetic and thermomagnetic properties of which have been previously reported [Carey *et al.*, J. Magn. Magn. Mater. (to be published)], forms the active storage layer. The agreement obtained with measurements demonstrates the self-consistency of the modeling process and the validity of the determined constants.

INTRODUCTION

Practical magneto-optic (MO) rare earth-transition metal (RE/TM) based recording media typically consist of tri- or quadrilayer structures in which a thin layer of active RE/TM material is sandwiched between dielectric protection/passivation layers and usually backed by a thin metallic reflector. Optimization of the readout properties of such structures requires the ability to model the magneto-optical behavior of the RE/TM material as a function of film thickness. This in turn requires knowledge of the optical and magneto-optical constants of the RE/TM material. Determination of these constants for such reactive material is not simple. Measurements must either be made *in situ* immediately following preparation or through the essential protection/passivation layers if the sample is to be removed from the preparation system.

In this paper we report the determination of the optical and magneto-optical constants for two series (i) $(\text{Tb}_{23}\text{Fe}_{72.5}\text{Co}_{4.5})_{100-x}\text{Pr}_x$, (ii) $(\text{Tb}_{27}\text{Fe}_{65}\text{Co}_8)_{100-x}\text{Pr}_x$ of Pr substituted TbFeCo films in which x varies between 0 and 30. All samples are identically protected between passivation layers of SiN prepared by rf magnetron sputtering from a Si_3N_4 target in a 9.5 mT Ar/ N_2 (10:1) atmosphere. The thickness and optical constants of the protection layers were independently determined.

A detailed description of the preparation and analysis of the samples, together with their magnetic and thermomagnetic properties, has already been reported.¹

EXPERIMENTAL TECHNIQUES

The samples used for the determination of the optical and magneto-optical constants were all 80 nm thick and protected above and below by SiN passivation layers 15 nm thick.

The ellipsometer used for the optical measurements is a semiautomated null instrument operating over the wavelength range 400–850 nm. Initially it was used to measure the optical constants of a single SiN layer, the thickness of

which had been previously determined by a multiple beam interferometric technique. Ellipsometric measurements on the SiN coated RE/TM films were then made through the SiN. Values for n and k were then evaluated over the above spectral range.

Further, a previous publication¹ has presented the measured normal incidence polar Kerr rotation θ_K and ellipticity ϵ_K for these samples at the diode laser wavelengths of 670 and 825 nm, and from these values (together with the optical constants of the SiN overlayer and the magnetic layer) the complex magneto-optical constants (Q) of the magnetic layers were calculated.²

RESULTS AND DISCUSSION

Table I shows the ellipsometric parameters and derived optical constants obtained from a 128-nm-thick silicon nitride layer deposited onto a glass substrate as a function of wavelength in the range 400–825 nm. For comparison it is noted that Serenyi *et al.*³ give $n=1.65$ and $k=0.12$ at 830 nm for equivalent sputtering conditions.

TABLE I. The measured ellipsometric parameters and optical constants for a reactively sputtered silicon nitride film (128 nm) deposited onto a glass substrate.

Wavelength (nm)	Principal angle (deg)	Principal azimuth (deg)	n	k
450	59.64	3.96	1.81	0.020
500	60.19	4.78	1.79	0.025
550	60.74	5.16	1.77	0.090
600	61.01	5.28	1.73	0.125
650	61.19	5.29	1.71	0.135
670	61.19	5.32	1.70	0.140
700	61.20	5.34	1.69	0.155
750	61.02	5.52	1.67	0.170
800	60.80	5.58	1.65	0.175
825	60.60	5.62	1.64	0.180

TABLE II. The optical constants (n, k) for the series $(\text{Tb}_{23}\text{Fe}_{72.5}\text{Co}_{4.5})_{100-x}\text{Pr}_x$.

Wave-length (nm)	TbFeCo 0% Pr		TbFeCoPr 6% Pr		TbFeCoPr 11% Pr		TbFeCoPr 16% Pr	
	n	k	n	k	n	k	n	k
450	2.05	2.10	2.05	2.45	2.25	2.85	2.10	2.30
500	2.40	2.65	2.10	3.00	2.40	3.00	2.15	2.35
550	2.50	3.00	1.95	3.25	2.45	3.25	2.00	2.80
600	2.65	3.65	2.00	3.30	2.50	3.30	2.25	2.85
650	2.50	3.55	2.25	3.05	2.55	3.45	2.15	2.85
670	2.55	3.60	2.45	3.55	2.60	3.60	2.15	3.00
700	2.55	3.65	2.60	4.05	2.65	3.65	2.10	3.35
750	2.10	3.60	2.30	4.05	2.40	4.00	2.15	3.75
800	2.15	3.85	2.15	4.05	2.45	4.30	2.20	4.30
825	2.20	3.95	2.25	4.15	2.50	4.35	2.25	4.35

Tables II and III similarly show the optical constants obtained for the Pr substituted TbFeCo samples that constitute series (i) and (ii), respectively. In comparison with some results⁴⁻⁶ reported in the literature the results for the real part of the refractive index (n) appear a little on the low side at the longer wavelengths (650–825 nm), although other results⁷ agree more closely to those presented here in this range. The radically different nature of the multitarget scanning preparation process¹ may be significant when comparing the present results with most in the literature.

Values evaluated for the first-order magneto-optic constants Q_1 and Q_2 are tabulated in Tables IV and V. At this time there are no Q values for Pr substituted TbFeCo available for direct comparison but values for the base TbFeCo alloys are in good agreement with those quoted elsewhere. Atkinson *et al.*,⁴ for example, have given values of $Q_1 \approx 0.016$ and $Q_2 \approx -0.005$ for $\text{Tb}_{27}\text{Fe}_{62}\text{Co}_{11}$ at 614 nm while McGahan *et al.*⁶ reporting on $\text{Tb}_{20.3}\text{Fe}_{71.7}\text{Co}_8$ at 670 nm cite $Q_1 \approx -0.024$ and $Q_2 \approx 0.004$. The sign reversal between these two measurements is due to the reversal in polar Kerr rotation between RE and TM dominant material.

Using the experimentally evaluated values of the optical and magneto-optical constants the thickness dependence of the polar Kerr rotation and ellipticity have been calculated for both series of Pr substituted TbFeCo compositions at the

TABLE III. The optical constants (n, k) for the series $(\text{Tb}_{27}\text{Fe}_{65}\text{Co}_8)_{100-x}\text{Pr}_x$.

Wave-length (nm)	TbFeCo 0% Pr		TbFeCoPr 8% Pr		TbFeCoPr 14% Pr		TbFeCoPr 30% Pr	
	n	k	n	k	n	k	n	k
450	2.25	2.55	2.20	3.65	2.15	3.00	2.30	3.10
500	2.45	2.70	2.10	3.70	2.25	3.30	2.50	3.30
550	2.50	3.00	2.15	4.30	2.25	3.80	2.60	3.65
600	2.55	2.85	2.25	4.00	2.30	4.00	2.55	4.10
650	2.55	3.05	2.40	4.10	2.35	4.30	2.70	4.25
670	2.60	3.15	2.50	4.15	2.35	4.40	2.70	4.35
700	2.65	3.25	2.55	4.15	2.40	4.45	2.70	4.50
750	2.50	3.70	2.50	4.80	2.25	4.65	2.50	4.95
800	2.35	3.80	2.45	4.55	2.20	5.05	2.40	5.45
825	2.40	3.80	2.40	4.60	2.20	5.10	2.45	5.50

TABLE IV. The magneto-optical constants (Q_1, Q_2) for the series $(\text{Tb}_{23}\text{Fe}_{72.5}\text{Co}_{4.5})_{100-x}\text{Pr}_x$.

Wavelength (nm)	TbFeCo 0% Pr		TbFeCoPr 6% Pr		TbFeCoPr 11% Pr		TbFeCoPr 16% Pr	
	Q_1	Q_2	Q_1	Q_2	Q_1	Q_2	Q_1	Q_2
670	12.2	-4.1	8.4	-5.1	6.5	-4.3	4.3	-2.4
825	15.1	-2.1	12.4	-0.8	11.1	-2.7	6.8	-1.0

two laser wavelengths of the Kerr polarimeter. Figure 1 compares the calculated thickness dependence of this magneto-optic behaviour for both the free surface (FS), and through the glass substrate (BS) side of the material, with experimental measurements made on films of varying thickness for the composition $\text{Tb}_{23}\text{Fe}_{72.5}\text{Co}_{4.5}$ at a wavelength of 825 nm. Figure 2 makes a similar comparison between calculated and experimental data for $(\text{Tb}_{23}\text{Fe}_{72.5}\text{Co}_{4.5})_{89}\text{Pr}_{11}$. The form of these results is typical of the samples in both series (i) and (ii). It can be seen that these plots establish that there is an acceptable correspondence between calculated and experimental data, thereby demonstrating the self-consistency of the evaluated material constants used in this modeling process.

Moreover, it is clear that the substitution of Pr into TbFeCo alloys degrades their magneto-optic behavior, at least for these compositions and wavelengths. An interesting feature though, to emerge from this investigation is the large increase in ellipticity with decreasing MO film thickness in these structures, being particularly large from the substrate side of the film. To a lesser extent there is a similar enhancement to the Kerr rotation from the substrate side of these films.

These through the substrate enhancements to θ_K and ϵ_K are simply explained by the limited coherence length of the diode laser radiation (≈ 1 mm) used in the Kerr polarimeter relative to the thickness of the glass substrate (1.2 mm). The resultant noncoherency of the light within the MO layer system for the substrate measurement can then be computed to be the cause of the improvement in MO signal. The free surface measurement does not similarly suffer as the film thickness is very much less than this coherence length.

CONCLUSION

The effective modeling of trilayer structures relevant to practical MO media has been demonstrated using experimen-

TABLE V. The magneto-optical constants (Q_1, Q_2) for the series $(\text{Tb}_{27}\text{Fe}_{65}\text{Co}_8)_{100-x}\text{Pr}_x$, for $x=30$ no polar Kerr signal could be obtained.

Wavelength (nm)	TbFeCo 0% Pr		TbFeCoPr 8% Pr		TbFeCoPr 14% Pr	
	Q_1	Q_2	Q_1	Q_2	Q_1	Q_2
670	11.7	-6.4	14.1	-5.3	11.2	-4.4
825	13.3	-4.6	17.7	-1.6	14.6	-1.9

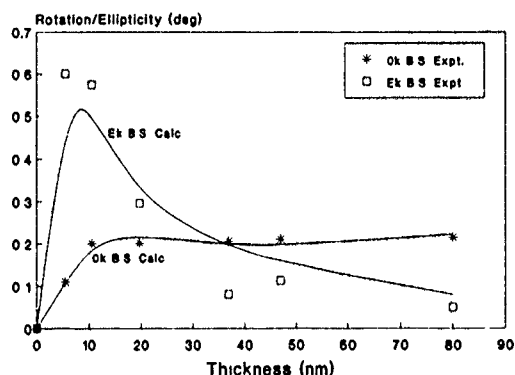
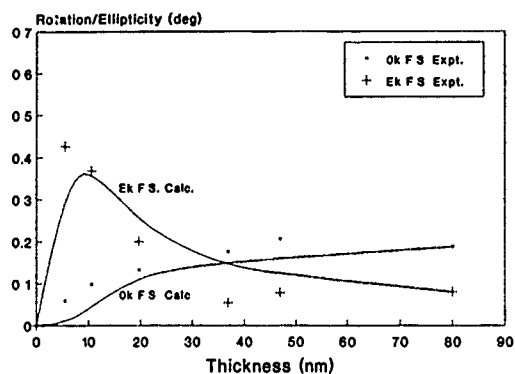


FIG. 1. The measured and calculated polar Kerr rotation and ellipticity from the free surface (top) and through the glass substrate (bottom) for $\text{Tb}_{23}\text{Fe}_{72.5}\text{Co}_{4.5}$ with film thickness at 825 nm.

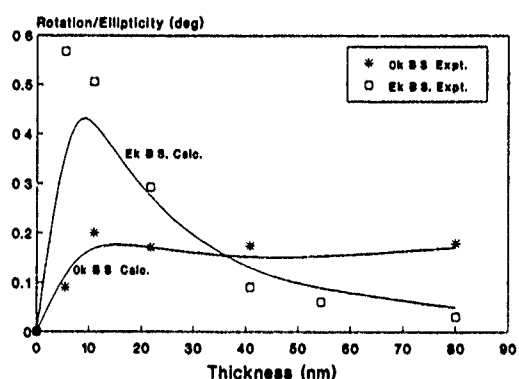
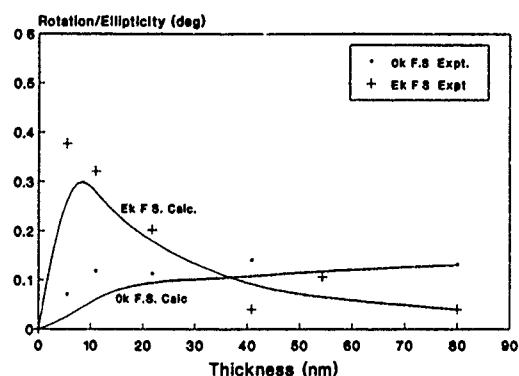


FIG. 2. The measured and calculated polar Kerr rotation and ellipticity from the free surface (top) and through the glass substrate (bottom) for $(\text{Tb}_{23}\text{Fe}_{72.5}\text{Co}_{4.5})_{89}\text{Pr}_{11}$ with film thickness at 825 nm.

tally evaluated optical and magneto-optical constants. The substitution of Pr into TbFeCo is shown not to enhance the magneto-optic behavior.

ACKNOWLEDGMENT

One of the authors (J.P.S.) was supported by the ESPRIT initiative.

- ¹R. C. Carey, D. M. Newman, J. P. Snelling, and B. W. J. Thomas, *J. Magn. Magn. Mater.* (to be published).
- ²J. P. Snelling, PhD thesis, Coventry University, 1993.
- ³M. Serenyi, W. Lauer, and H. U. Habermeier, *Nucl. Instrum. Methods Phys. Res. B* **18**, 659 (1987).
- ⁴R. Atkinson, I. W. Salter, and J. Xu, *J. Magn. Magn. Mater.* **95**, 35 (1991).
- ⁵W. A. Challener and S. L. Grove, *Appl. Opt.* **29**, 3040 (1990).
- ⁶W. A. McGahan, P. He, L.-Y. Chen, S. Bonafede, J. Woollam, F. Sequeda, T. McDaniel, and H. Do, *J. Appl. Phys.* **69**, 4568 (1991).
- ⁷G. A. N. Connell, *Appl. Opt.* **22**, 3155 (1983).

Thermal stability of NdGd/FeCo multilayers

X. Y. Yu, T. Suganuma, H. Watabe, S. Iwata, S. Tsunashima, and S. Uchiyama
Department of Electronics, Nagoya University, Nagoya 464-01, Japan

Thermal stability has been investigated for the structure and the perpendicular anisotropy K_u of $\text{Nd}_{44}\text{Gd}_{56}/\text{Fe}_{89}\text{Co}_{11}$ multilayer films with the bilayer period of 1 nm, where K_u becomes the maximum. From the results of isothermal annealing at temperature T_a , it has been found that the saturation magnetization M_s scarcely changes up to $T_a=400^\circ\text{C}$, while K_u is almost constant up to $T_a=200^\circ\text{C}$ but decreases rather quickly for T_a above 200°C . The decrease in K_u for $T_a>260^\circ\text{C}$ is accompanied by the decrease in the peak intensity of low angle x-ray diffraction, namely by the deterioration of the layered structure.

INTRODUCTION

Rare earth (RE)–transition metal (TM) amorphous films, especially Tb-FeCo films, are now commercially used as media for magneto-optic (MO) recording. In order to increase the recording density, shorter wavelength light such as 687 or 532 nm is going to be used in the next generation MO recording. As is well known, the Kerr rotation of Tb-FeCo, hence the figure of merit for readout, decreases with decreasing wavelength, and development of new media with a larger Kerr rotation at a shorter wavelength has been desired. In this connection, it was found that the MO effect of Nd-Co and Pr-Co amorphous films became larger than those of heavy RE-Co films at a shorter wavelength around 500 nm.^{1–3} However, since the magnetization of (Nd,Pr)-TM films is larger than that of heavy RE-TM, it is very difficult to prepare perpendicularly magnetized films.

Some efforts have been made on multilayer films with perpendicular magnetization by using interfacial anisotropy^{4,5} such as Nd/Fe⁵ and NdCo/Fe. We have prepared $\text{Nd}_{36}\text{Gd}_{64}/\text{Fe}_{89}\text{Co}_{11}$ and $\text{Pr}_{36}\text{Gd}_{64}/\text{Fe}_{89}\text{Co}_{11}$ multilayers with good Kerr hysteresis loop, which is expected as a candidate for the next MO media.^{6,7} However, like other MO media, we should be attentive to the thermal stability of the multilayers, especially interfacial structure. In this paper, thermal stability of the structure and the anisotropy is reported for NdGd/FeCo multilayers.

EXPERIMENTAL METHOD

All films under investigation were prepared on glass or fused quartz substrate by rf diode sputtering method as described in Ref. 6. A bilayer period of multilayer (ML) films was chosen as 10 Å, where the perpendicular anisotropy becomes the maximum as shown in Refs. 6 and 7. The thickness ratio of the RE layer to the TM one is 1:1. The ML films with total thickness of 1200 Å were covered by a SiAlON layer to prevent the films from oxidation. Compositionally modulated structure and crystal structure have been confirmed by low angle and high angle x-ray diffractometry, respectively. Magnetization and anisotropy were measured by a vibrating-sample magnetometer and a torque magnetometer. Annealing was done under a vacuum below 5×10^{-6} Torr.

RESULTS AND DISCUSSION

Figures 1 and 2 show the patterns of x-ray diffraction at low and high angle, respectively. It is seen that the peak intensity at low angle becomes smaller with increasing annealing temperature while the patterns of high angle have scarcely changed at the annealing temperatures below 370°C . The decrease of the low angle peak intensity means that interdiffusion occurs and compositionally modulated structure gradually changes into a uniform structure.

From the fact that some peaks appear at high angle after annealing, we can say that the amorphous film is crystallized above 450°C .

In Fig. 3, the change of the perpendicular magnetic anisotropy K_u with annealing time is shown. The values of K_u are almost constant by annealing at 100 and 185°C . By annealing at around 300°C , the anisotropy seemed to be decreased with annealing time, and at 400°C it was drastically reduced within half an hour.

The change of the saturation magnetization with the annealing time is shown in Fig. 4. In contrast to the change in

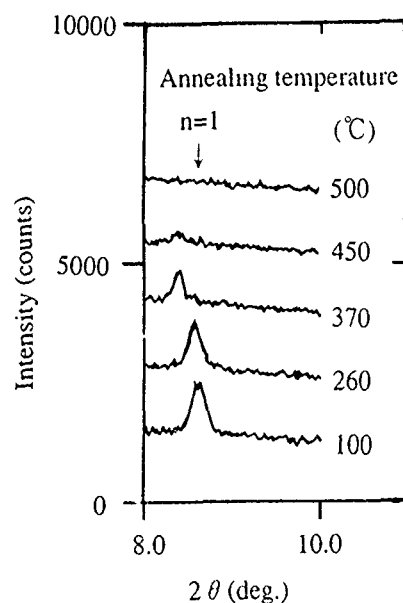


FIG. 1. X-ray diffraction patterns at low angle for $\text{Nd}_{44}\text{Gd}_{56}/\text{Fe}_{89}\text{Co}_{11}$ multilayers annealed at different temperatures for 1 h.

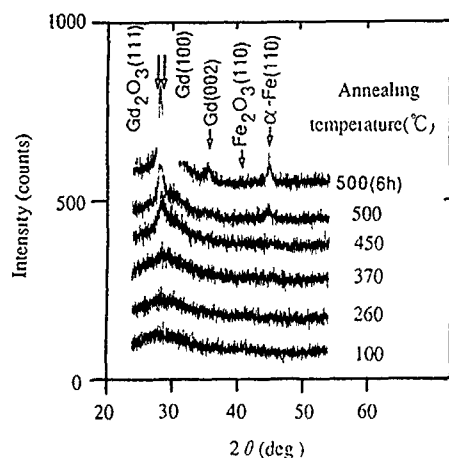


FIG. 2. X-ray diffraction patterns at high angle for $\text{Nd}_{44}\text{Gd}_{56}/\text{Fe}_{89}\text{Co}_{11}$ multilayers annealed at different temperatures for 1 h.

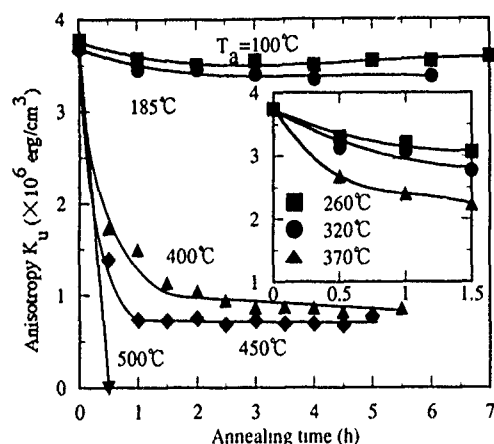


FIG. 3. Perpendicular magnetic anisotropy K_u as a function of annealing time for $\text{Nd}_{44}\text{Gd}_{56}/\text{Fe}_{89}\text{Co}_{11}$ multilayers.

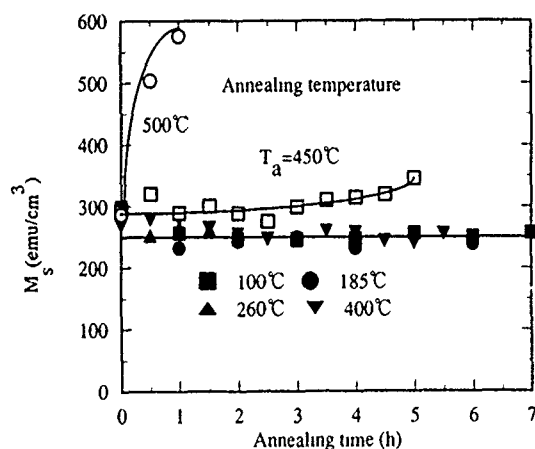


FIG. 4. Saturation magnetization M_s as a function of annealing time for $\text{Nd}_{44}\text{Gd}_{56}/\text{Fe}_{89}\text{Co}_{11}$ multilayers.

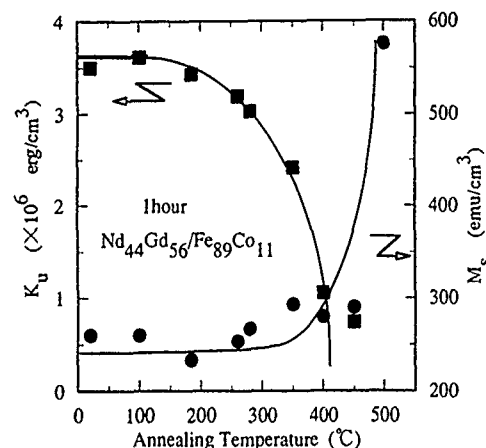


FIG. 5. Dependence of perpendicular magnetic anisotropy and saturation magnetization M_s on the annealing temperature

anisotropy, the saturation magnetization did not change with annealing time up to 400 °C. At 450 °C, however, it became slightly larger with annealing time and increased abruptly at 500 °C.

The dependence of the anisotropy and the saturation magnetization on the annealing temperature is shown in Fig. 5 for the annealing time of 1 h. The change starts around 200 and 400 °C for the anisotropy and the saturation magnetization, respectively. The difference between the change of the anisotropy and the magnetization may come from the difference in the mechanism. For example, anisotropic structures of atoms at the interface of multilayers are said to be of the origin of the perpendicular anisotropy while the effective composition of magnetic atoms is thought to decide the saturation magnetization.

The relationship between the anisotropy and the first peak intensity in low angle x-ray diffraction is shown in Fig. 6, where C/C_0 show the first peak intensity after annealing normalized with that before annealing. The samples plotted here are confined to the films annealed at temperatures below

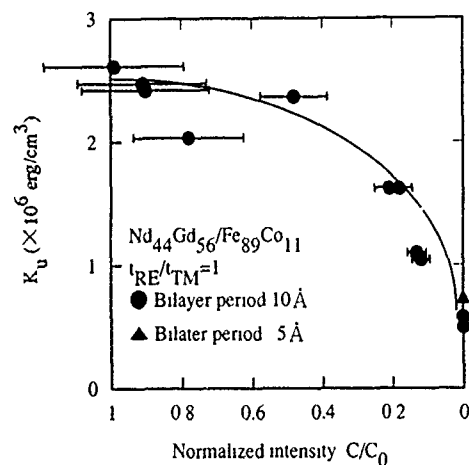


FIG. 6. The relationship between the perpendicular magnetic anisotropy K_u and the normalized intensity of the low angle first peak, C/C_0 for $\text{Nd}_{44}\text{Gd}_{56}/\text{Fe}_{89}\text{Co}_{11}$ multilayers.

400 °C, where the films keep the amorphous structure. Since the K_u decreases with decreasing C/C_0 , it is suggested that the K_u is closely related to and enhanced by the compositionally modulation structure.^{8,9}

CONCLUSION

Thermal stability of structure and magnetic properties has been investigated for GdNd/FeCo multilayers. The saturation magnetization M_s scarcely changes for annealing temperatures up to $T_a=400$ °C, while K_u decreases rather quickly for $T_a \geq 300$ °C. The decrease in K_u for $T_a > 300$ °C is accompanied by the decrease in the peak intensity of low

angle x-ray diffraction, namely by the deterioration of the layered structure, suggesting that K_u is closely related to modulation structure.

¹T. Suzuki and T. Katayama, IEEE Trans. Magn. **MAG-22**, 1230 (1980).

²Y. J. Choe, S. Tsunashima, T. Katayama, and S. Uchiyama, J. Magn. Soc. Jpn. **11**, Suppl. 273 (1987).

³Y. J. Choe, S. Tsunashima, and S. Uchiyama, J. Phys. **48(8C)**, 1953 (1988).

⁴N. Sato, J. Appl. Phys. **59**, 2514 (1986).

⁵D. J. Sellmyer, J. Appl. Phys. **61**, 4323 (1987); M. Nawate, T. Ohtani, S. Tsunashima, and S. Uchiyama, IEEE Trans. Magn. **MAG-26**, 1706 (1990).

⁶S. Tsunashima, T. Ohtani, X. Y. Yu, and S. Uchiyama, J. Magn. Magn. Mater. **104-107**, 1021 (1992).

⁷X. Y. Yu, S. Tsunashima, and S. Uchiyama, J. Magn. Soc. Jpn. **16**, 547 (1992) (in Japanese).

⁸Z. S. Shan, D. J. Sellmyer, S. S. Jaswal, Y. J. Wang, and J. X. Shen, Phys. Rev. Lett. **63**, 449 (1989).

⁹Z. S. Shan and D. J. Sellmyer, Phys. Rev. B **42**, 104 333 (1990).

Physical and magnetic microstructure of rapid thermally annealed thin film bismuth-doped garnets

W. R. Eppler, B. K. Cheong, D. E. Laughlin, and M. H. Kryder

Data Storage Systems Center, Carnegie Mellon University, Pittsburgh, Pennsylvania 15213

Bismuth-doped iron garnets are promising materials for blue light magneto-optic recording media. These materials have been deposited on glass substrates with bulk magnetic and magneto-optic properties suitable for magneto-optic recording. However, these films exhibit a very low carrier to noise ratio (CNR) when crystallized in conventional furnaces. The low CNR is due to the inability to write circular domains in these materials. Rapid thermal annealing (RTA) has been reported to produce films with a much finer grain size. We have confirmed by transmission electron microscopy that RTA does indeed reduce the grain size over an order of magnitude from films crystallized in a conventional furnace. Faraday microscopy has shown that films processed by RTA with smaller grain size (~ 30 nm) support circular magnetic domains of much greater regularity than films crystallized in conventional furnaces. The improved regularity of static thermomagnetically written domains, in films crystallized by RTA, lends promise that the noise in these materials can be reduced.

INTRODUCTION

Bismuth-substituted iron garnets are promising short wavelength magneto-optic recording materials since they have a strong magneto-optic effect at wavelengths less than 550 nm.¹ Shono *et al.*² demonstrated that bismuth-substituted garnet films grown on single crystal GGG substrates exhibit 54 dB of CNR (30 kHz bandwidth, 5 MHz writing frequency, 14 m/s linear velocity, 514 nm wavelength, and 1.4 μ m bit length). The single crystal GGG substrates are expensive and limited in size so a more practical substrate is needed. Garnet films deposited on glass disks, crystallized *in situ* by deposition at elevated temperatures, or by post-deposition annealing have exhibited low CNR's due to high media noise. The media noise is due in part to the inability to write regular circular domains when the grain size is comparable to the magnetic domain size.³ The magnetic domain walls follow the grain boundaries thus the irregularity in domain shape is a result of the average grain size being of the order of the written domain size.

Much effort has been made to control the grain size and film morphology through different dopants,^{4,5} underlayers,^{6,7} and annealing schedules^{8,9} with only limited success. Suzuki *et al.*¹⁰ reported that rapid thermal annealing (RTA), a process which employs arc lamps or flash lamps as the thermal source and can provide heating rates as high as 200 °C/s, was successful in reducing the grain size to about 30 nm. In a transmission electron microscope (TEM) study Bechevet *et al.*¹¹ observed an inhomogeneous microstructure of large crystallites (450 nm) embedded in a matrix of small crystallites (35 nm) in cerium-substituted iron garnets crystallized by RTA. The purpose of this work was to confirm Suzuki's results for bismuth-substituted garnets and to determine if the reduced grain size enables regularly shaped magnetic domains to be written in these materials.

EXPERIMENTAL DETAILS

Thin films were deposited by rf magnetron sputtering onto Corning No. 7059 glass substrates with the sputtering

conditions listed in Table I. The as-deposited films were amorphous and were crystallized by either conventional annealing at 670 °C for 3 h in an air atmosphere or by RTA in an AG Associates 610i heat pulse system with a heating rate of 100 °C/s and a dwell time of 2 min at 710 °C in a nitrogen atmosphere.

Microstructural investigations were conducted on planar ion-milled specimens in a Philips 420 T TEM. Micromagnetic investigations were conducted using Faraday microscopy (50 \times 0.5 or 125 \times 0.8 NA) with an argon ion laser (λ = 488 nm), modulated by an electro-optic modulator, as the writing source.

RESULTS AND DISCUSSION

A TEM image of a film annealed in a conventional furnace is shown in Fig. 1. This film has a polycrystalline microstructure with a grain size of the order of 1 μ m. A Faraday microscope image of thermomagnetically written domains in this film using a writing power of 20 mW, pulse width of 1 μ s, and a bias field of 70 Oe is shown in Fig. 2. The written domains are clearly irregularly shaped. In a previous paper³ it was shown that the domain walls are located along grain boundaries, thus the film microstructure plays a dominant role in determining the written domain shape. Further, it was shown that for films crystallized by post-deposition annealing the garnet phase nucleated at sites

TABLE I. rf magnetron sputtering conditions.

Target Composition:	Gd ₂ Bi ₁ Fe ₄ Al _{0.2} Ga _{0.2} O ₁₂
rf power	0.57 W/cm ²
Bleed gas	Argon
Bleed pressure	5 mTorr
Base pressure	5 \times 10 ⁻⁶ Torr
Deposition rate	150 nm/h
Deposition time	2 h



FIG. 1. Bright field TEM micrograph of garnet film annealed in a conventional furnace at 670 °C for 3 h in an air atmosphere.

spaced approximately 1 μm apart which grew rapidly until they impinged upon one another forming the grain boundaries. Therefore, the grain size is controlled by the density of garnet nuclei obtained before significant grain growth could occur.

A TEM image of an identical film crystallized by RTA is shown in Fig. 3. The average grain size is approximately 30 nm in agreement with Suzuki's results measured by scanning tunneling microscopy and x-ray diffraction. No evidence was found of the inhomogeneous microstructure, of large crystallites imbedded within a matrix of smaller crystallites, observed by Bechevet. A Faraday microscope image of domains written in this film using identical writing conditions as the conventionally annealed sample is shown in Fig. 4. These domains are much more circular than the domains written in the conventionally annealed sample, which lends promise that the noise in these materials can be reduced.

These results can be qualitatively understood in terms of the effects of different heat treatments on the nucleation and growth kinetics of the garnet phase. When the heating rate is

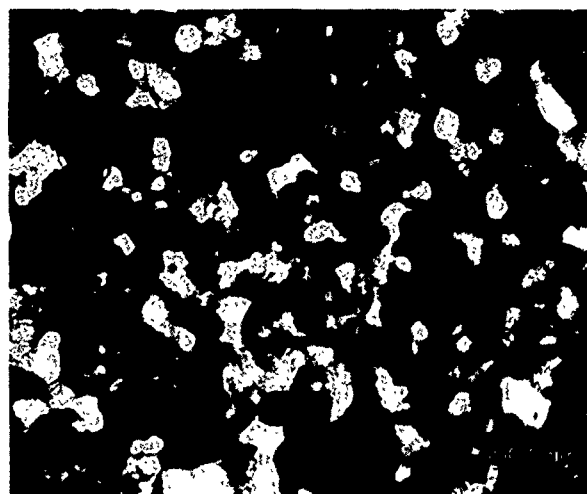


FIG. 3. Bright field TEM micrograph of a garnet film crystallized by RTA with a ramp rate of 100 °C/s and a dwell of 2 min at 710 °C in a nitrogen atmosphere.

slow (~ 0.1 °C/s) nucleation of the garnet phase will commence at a relatively low temperature. This means that the nucleation proceeds under a small driving force, thus leading to a low nucleation rate (number of garnet phase nuclei per unit volume of untransformed region per unit time). The small number of nuclei, which occur at the lowest temperatures, are given time to grow with the rising temperature and consume other possible nucleation sites. This produces a low effective nucleation density and therefore the large crystallite size observed of approximately 1 μm .

In the case of RTA, the rapid temperature rise will enable the nucleation to start at a relatively higher temperature (i.e., under a larger driving force). Further, the rapid temperature rise does not provide sufficient time for those nuclei which occur at the lowest temperatures to grow and consume the other possible nucleation sites. This creates a high effective nucleation density and the fine grained microstructure observed.



FIG. 2. Faraday micrograph of thermomagnetically written domains in post-deposition annealed garnet film (20 mW writing power, 1 μs pulse width, and 70 Oe bias field).

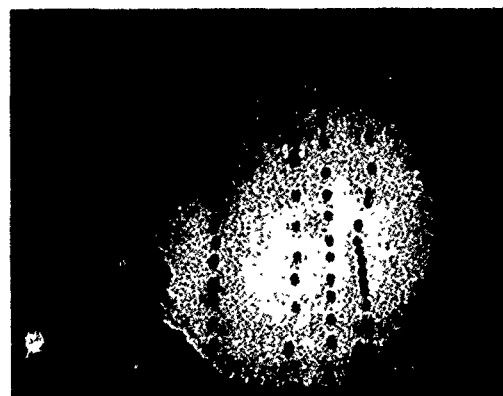


FIG. 4. Faraday micrograph of thermomagnetically written domains in RTA crystallized film (20 mW writing power, 1 μs pulse width, and 70 Oe bias field).

CONCLUSIONS

We have confirmed Suzuki's results that RTA significantly reduces the crystallite size of bismuth-doped iron garnet films on glass substrates. Further, we have shown that films crystallized by RTA with the smaller grain size support circular magnetic domains of much greater regularity than films crystallized in conventional furnaces. The improved regularity of static thermomagnetic written domains in these films lends promise that the media noise problems of these materials can be solved. We believe the reduced grain size in the RTA processed films is a result of improved nucleation of the garnet phase and suppression of grain growth from the rapid temperature rise. A quantitative understanding of the kinetics of the phase change in these materials would be helpful in determining the optimal heating rate and crystalli-

zation temperature and possibly point to better methods of controlling the crystallite size in these materials.

- ¹ P. Hansen and J. P. Krumme, *Thin Solid Films* **114**, 69 (1984).
- ² K. Shono, H. Kano, N. Koshino, and S. Ogawa, *J. Appl. Phys.* **63**, 3639 (1988).
- ³ D. J. Rogers, W. R. Eppler, D. E. Laughlin, and M. H. Kryder, *J. Appl. Phys.* **73**, 5788 (1993).
- ⁴ K. Nakagawa, K. Odagawa, and A. Itoh, *J. Magn. Magn. Mater.* **104-107**, 1007 (1992).
- ⁵ M. Gomi, K. Satoh, and M. Abe, *J. Appl. Phys.* **63**, 3642 (1987).
- ⁶ A. Itoh and K. Nakagawa, *Jpn. J. Appl. Phys.* **31**, L790 (1992).
- ⁷ J. Cho, M. Gomi, and M. Abe, *Jpn. J. Appl. Phys.* **27**, 2069 (1988).
- ⁸ A. Itoh and M. Kryder, *Appl. Phys. Lett.* **53**, 1125 (1988).
- ⁹ K. Shono, S. Kuroda, H. Kano, N. Koshino, and S. Ogawa, *Mater. Res. Soc. Symp. Proc.* **150**, 131 (1989).
- ¹⁰ T. Suzuki, *J. Appl. Phys.* **69**, 4756 (1991).
- ¹¹ B. Bechevet, D. Challeton, B. Rolland, M. F. Armand, B. Valon, and J. Mouchot, *J. Appl. Phys.* **60**, 4767 (1991).

Uniaxial anisotropy of double-layered garnet films and magneto-optical recording characteristics

Katsuji Nakagawa, Seiji Kurashina, and Akiyoshi Itoh

Department of Electronic Engineering, College of Science and Technology, Nihon University,
Funabashi, Chiba 274, Japan

For reducing the critical diameter of the written domain in magnetic garnet films for magneto-optical (MO) recording, double-layered garnet films were investigated. The coercivity of the double-layered garnet film was increased, when the upper layer was crystallized. This increase of the coercivity is caused by the increase of the uniaxial anisotropy energy. The increase of the uniaxial anisotropy energy also leads to a decrease in the noise level of the MO readout signal. As a consequence, the critical diameter of written domains was reduced to 0.2 μm . This critical diameter is smaller than the reading out beam spot for the case with a green laser and a high numerical aperture objective lens. The garnet films are sufficient for high density next generation MO recording.

INTRODUCTION

The fundamental characteristics required of magneto-optical (MO) recording media are high carrier to noise ratio (CNR) and high memory density. The high density is accomplished by small written domains and a small beam spot for reading out which is achieved by using short wavelengths. It is necessary for the candidates of the next generation of the MO media to have a large MO effect. Bi-substituted garnet films are excellent media for MO recording memory, because the figure of merit of the Bi-substituted garnet film is 3–6 times as large as those of the multilayered Co/Pt and the conventional TbFeCo media at a wavelength of 515 nm. The figure of merit is defined as the value of the Faraday or Kerr rotation angle multiplied by the reflection coefficient, and it is directly proportional to the MO readout signal strength. CNR of the garnet films was improved by reducing the grain size,¹ improving homogeneity of the film,² and using the double-layered structure.³ However, there are no reports of the critical diameter of written domains of garnet films for MO recording.

For the purpose of improving the memory density, the critical diameter of written domains was reduced by using the double-layered film. This decrease of the critical diameter is caused by the increase of the coercivity H_c . The mechanism of increasing the H_c was clarified by investigating the uniaxial anisotropy energy K_u .

EXPERIMENTAL

The under layer of the $\text{Bi}_{0.9}\text{Dy}_{2.1}\text{Fe}_{4.2}\text{Al}_{0.8}\text{O}_{12}$ garnet films doped with 1 at. % of Rb was prepared by pyrolysis on glass substrates. The films were post-annealed for crystallization, and the diameter of the grain of the Rb-doped garnet films was approximately 30 nm.¹ After the crystallization of the under layer, the upper layer of the garnet films was prepared by pyrolysis. The upper layer was also post-annealed for crystallization.

The critical diameter d_c is determined by the following:⁴

$$d_c = \sigma_w / (M_s \times H_c), \quad (1)$$

where σ_w is the wall energy density, M_s is the saturation magnetization, and H_c is the coercivity. σ_w is derived from the exchange stiffness constant and the uniaxial anisotropy energy K_u . The values of M_s , H_c , and K_u were measured by a vibrating sample magnetometer, a torque magnetometer,⁵ and a Faraday hysteresis loop tracer, respectively. The exchange stiffness constant at room temperature was approximated by using the Curie temperature T_c of the film.⁶ T_c was measured by the dependence of Faraday rotation coefficient on temperature.

The crystallization kinetics of the upper layer were evaluated by Johnson, Mehl, and Avrami as follows:

$$x = 1 - \exp[-(k \times t_a)^n], \quad (2)$$

where x is the transformation quantity, t_a is the annealing time, k is the rate constant, and n is the Avrami exponent. Since the models of the crystallization kinetics have been reported for the values of the Avrami exponent n ,^{7,8} the crystallization kinetics can be determined by the values of n . The transformation quantity x from the amorphous phase to the crystalline phase was determined by the change of the Faraday rotation coefficient of the films.

The MO recording and reading characteristics were measured by using 515 nm in wavelength of Ar ion laser. CNR was measured under the condition as follows. A frequency and a duty cycle for writing pulse were 500 kHz and 50%, respectively. Linear velocity of the films was 5.2 m/s. Bandwidth of a spectrum analyzer was 10 kHz.

RESULTS AND DISCUSSION

To know the crystallization kinetics of the upper layer, the Avrami exponent n for the upper layer was obtained from the Avrami plot as shown in Fig. 1. The value of n for the upper layer is approximately one. The model of the crystallization for $n=1$ is diffusion controlled growth of cylinders in an axial direction. This model of the upper layer is different from the model of the single layer, which is the disk-shaped diffusion controlled growth with a constant thickness.⁹ It was confirmed by using a transmission electron microscope that the grain shape of the cylinders was observed in a cross-sectional image.² The activation energy E_a

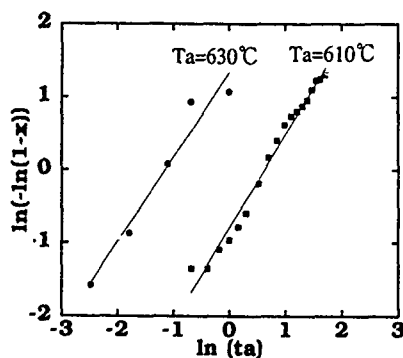


FIG. 1. The Avrami plot for the upper layer of $\text{Bi}_{0.9}\text{Dy}_{2.1}\text{Fe}_{4.2}\text{Al}_{0.8}\text{O}_{12}$ garnet on the under layer of 1 at. % of Rb-doped $\text{Bi}_{0.9}\text{Dy}_{2.1}\text{Fe}_{4.2}\text{Al}_{0.8}\text{O}_{12}$ garnet. Avrami exponent n is approximately one. The thickness of the upper and under layers are 100 nm, respectively.

of the upper layer for crystallization was derived from the Arrhenius plot as shown in Fig. 2. The value of E_a is due to both the processes of nucleation and growth of the nucleated crystallites. The value of E_a of the upper layer is 4.7 eV, while E_a of the under layer is 5.3 eV. This difference of E_a is probably caused by the difference of the nucleation mechanism between the upper and under layer. As a result, the model of the crystallization kinetics seems to be interpreted as follows. The crystallites of the upper layer are nucleated at the surface of the grain of the under layer, and the crystallites grow along the film normal with the shape of cylinders.

To increase the memory density of garnet films, it is important to increase M_s and H_c . We found the effect that H_c was increased without a change of M_s by using a double-layered film as shown in Fig. 3. H_c was increased to 3 kOe. H_c of the under layer before the deposition and crystallization of the upper layer was 1.8 kOe. After the coating of the upper layer without annealing, H_c of the double layer was not changed. However, H_c was increased to 3.0 kOe after the 10 min annealing for the double-layered film.

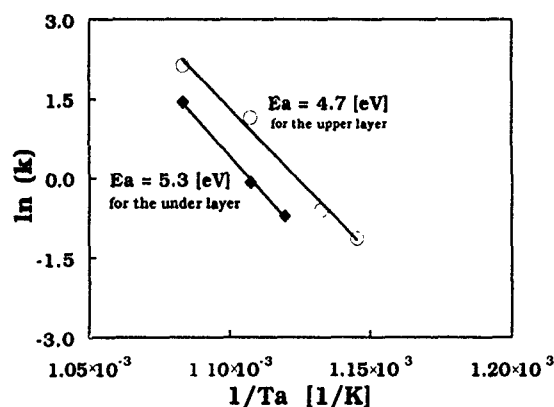


FIG. 2. The Arrhenius plots for the under layer of 1 at. % of Rb-doped $\text{Bi}_{0.9}\text{Dy}_{2.1}\text{Fe}_{4.2}\text{Al}_{0.8}\text{O}_{12}$ garnet and the upper layer of $\text{Bi}_{0.9}\text{Dy}_{2.1}\text{Fe}_{4.2}\text{Al}_{0.8}\text{O}_{12}$ garnet on the under layer. The activation energy E_a for the under and upper layer is 5.3 and 4.7 eV, respectively. The thicknesses of the upper and under layers are 100 nm, respectively.

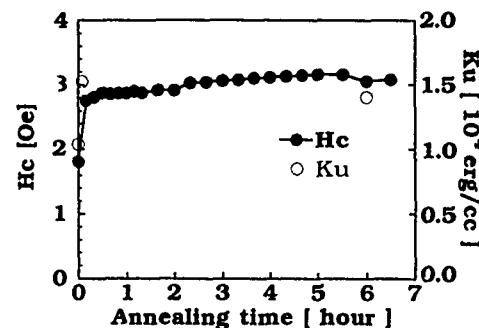


FIG. 3. The dependence of the coercivity H_c and the uniaxial anisotropy energy K_u of the double-layered garnet film on the annealing time for the crystallization of the upper layer. The composition of the under layer is 1 at. % of Rb-doped $\text{Bi}_{0.9}\text{Dy}_{2.1}\text{Fe}_{4.2}\text{Al}_{0.8}\text{O}_{12}$ garnet. The annealing temperature and time of the under layer are 630 °C and 3 h. The composition of the upper layer is $\text{Bi}_{0.9}\text{Dy}_{2.1}\text{Fe}_{4.2}\text{Al}_{0.8}\text{O}_{12}$ garnet. The annealing temperature of the upper layer is 610 °C. The thicknesses of the upper and under layers are 100 nm, respectively.

To know the reason why H_c was increased, the dependence of K_u on the annealing time was measured, as shown in Fig. 3. While K_u of the under layer was 1.0×10^4 ergs/cm³, K_u is increased to 1.4×10^4 ergs/cm³ after only a short annealing time. Since this dependence of K_u is very similar to the change of H_c , the increase of H_c may be caused by the increase of K_u .

This change of K_u can result from the shape anisotropy, the crystal growth anisotropy, or the stress-induced anisotropy. The shape anisotropy energy of the observed shape of cylinders is 0.07×10^4 ergs/cm³. This value of the shape anisotropy energy is lower than the change of K_u . After the short annealing time, the total volume of the crystallized grains of the upper layer is 3% of the coated upper-layer volume. This value was estimated from the transformation quantity x from the amorphous to the crystalline phase. Since the shape anisotropy is less than 0.07×10^4 ergs/cm³, the change of K_u is not caused by the shape anisotropy. For the single-layer film after the crystallization, H_c was not changed by the additional annealing. Therefore, the crystal growth anisotropy of the under layer does not seem to be increased by the annealing of the upper layer. If tensile stress is induced in the under layer, the stress-induced uniaxial anisotropy energy will be increased, because the magnetostriction constant of the under layer is negative. If the crystallites of the Bi-rich composition of the garnet are crystallized at the surface of the under layer, tensile stress can be induced in the under layer. Therefore, the increase of K_u of the under layer can be caused by the increase of the stress-induced anisotropy energy. However, it is necessary to measure the depth profile of the composition and the internal stress for the double-layered films.

The MO recording and reading characteristics were measured by using 515 nm in wavelength of Ar ion laser. The increase of K_u leads to the decrease in the noise level for reading out signal, because the fluctuation in the orientation of magnetic moments becomes lower by the increase of K_u .² By the effects of the increased H_c and K_u , CNR of 55 dB was achieved for the double-layered film by using 515 nm in

wavelength of Ar ion laser, while CNR was 52 dB for the single-layer garnet films. H_c and K_u of the double-layered film are 1.7 and 1.4 times as large as those of the single-layered film, respectively, and d_c is 0.7 times as small as the value of the single-layer film. As a result, the critical diameter d_c was reduced to 0.2 μm . This critical diameter is smaller than the reading out beam spot for the case with a green laser and a high numerical aperture objective lens. The garnet films are sufficient for high density next generation MO recording.

CONCLUSIONS

For the purpose of improving the memory density, the double-layered garnet films were investigated. The crystallization kinetics of the double-layered garnet films was investigated, and the model of the crystallization of the upper layer is the diffusion controlled growth of cylinders in the axial direction. The coercivity H_c of the garnet film was increased and the critical diameter d_c was decreased by using the double-layered film. This increasing of H_c is caused by the increasing the uniaxial anisotropy energy. By using this effect, the higher density MO recording memory can be achieved. The increase of the uniaxial anisotropy energy also leads to a decrease of the noise level for MO reading out

signal. In the future, it is necessary to measure the depth profile of the composition and the internal stress for the double-layered films.

ACKNOWLEDGMENTS

This work was partially supported by Grant-in-Aid for Encouragement of Young Scientists of the Ministry of Education, Science and Culture, and by CASIO Science Promotion Foundation.

- ¹K. Nakagawa, K. Odagawa, and A. Itoh, *J. Magn. Magn. Mater.* **104-107**, 1007 (1992).
- ²K. Nakagawa and A. Itoh, *Proceedings of the Magneto-Optical Recording International Conference '92*, Tucson, 1992 [*J. Magn. Soc. Jpn.* **17**, Suppl. No. S1, 278 (1993)].
- ³A. Itoh and K. Nakagawa, *Jpn. J. Appl. Phys.* **31**, L790 (1992).
- ⁴B. G. Huth, *IBM J. Res. Dev.* **18**, 100 (1974).
- ⁵H. Miyajima, K. Sato, and T. Mizoguchi, *J. Appl. Phys.* **47**, 4669 (1976).
- ⁶J. C. Slonczewski, A. P. Malozemoff, and E. A. Giess, *Appl. Phys. Lett.* **24**, 396 (1974).
- ⁷J. Burke, *Kinetics of Phase Transformations in Metals* (Pergamon, Oxford, 1965).
- ⁸J. W. Christian, *Transformation in Metal and Alloys*, 2nd ed. (Pergamon, Oxford, 1975).
- ⁹K. Nakagawa, K. Odagawa, and A. Itoh, *Proceedings of the Magneto-Optical Recording International Conference '91*, Tokyo, 1991 [*J. Magn. Soc. Jpn.* **15**, Suppl. No. S1, 231 (1991)].

Anisotropy and Faraday effect in Co spinel ferrite films

H. Y. Zhang, B. X. Gu,^{a)} H. R. Zhai, M. Lu, Y. Z. Miao, and S. Y. Zhang
Physics Department, Center of Materials Analysis, Nanjing University, Nanjing 210008, China

H. B. Huang
Analytical Center, Southeast University, Nanjing 210008, China

Crystalline Co spinel ferrite films were prepared by rf sputtering on glass substrates without buffer layer and annealed at temperatures from 400 to 600 °C for 2 h in air. (100) texture was obtained in these films. The anisotropy constant, magnetic hysteresis loops, and magneto-optical Faraday spectra of the films were measured. The texture became poor when the films were annealed below 500 °C, but the perpendicular anisotropy constant K_u , squareness ratio $R = (Mr/Ms)_\perp / (Mr/Ms)_\parallel$ increased and showed peak values of 2.2×10^5 ergs/cm³ and 0.94, respectively, at an annealing temperature $T_a = 500$ °C. For the film annealed at 600 °C (higher than the Curie temperature, 520 °C, of Co spinel ferrite), the texture recovered, but K_u and R dropped. The Faraday rotation spectra of Co spinel ferrite films showed a broad peak centered around 720 nm. The peak value increased monotonically with increasing annealing temperature. These results may be related to the Co ion-induced anisotropy and Co ion distribution in tetrahedral sites and octahedral sites.

I. INTRODUCTION

Thin ferrite films have attracted much attention in recent years as one of the candidates of magneto-optical (MO) recording media because of their large Faraday effect and good corrosion resistance.¹ An important problem people are concerned about is to make ferrite films which meet the requirements of MO recording such as perpendicular anisotropy by a technology that is as simple as possible. Co spinel ferrite films are promising candidates for having good MO properties and perpendicular anisotropy.¹⁻⁴ However the mechanism of perpendicular anisotropy and Faraday effect is not quite certain. In this paper the results of our study on the anisotropy and Faraday effect of Co ferrite films made by rf sputtering and annealed at different temperatures are reported.

II. EXPERIMENTS

CoFe₂O₄ films were prepared by rf sputtering with a sintered CoFe₂O₄ ceramic target. The base vacuum was 7.5×10^{-6} Torr. The pressure of sputtering gas, argon, was 20 mTorr without additional reactional oxygen gas. The films were deposited directly on glass substrates cooled by running water. The samples were annealed in temperatures ranging from 400 to 600 °C for 2 h in air and rapidly quenched to room temperature.

The atomic ratio between the content of Fe and Co in the as-sputtered samples determined by EDXA was found to be about 2:1. The structure and phase components of the sample were analyzed by x-ray diffraction with CuK α radiation. The thickness of the films measured by an optical interference technique was about 1 μ m. The room temperature hysteresis loops of the samples were measured by a vibrating-sample magnetometer with applied fields up to 20 kOe. Torque magnetometry was used to determine the effective perpendicular anisotropy constant of the films with a magnetic field of about 10 kOe. In our experiments, the angle of the torque

curve is that between the magnetic field and normal direction of the film. A setup was established using a polarization modulation technique to measure the Faraday rotation spectra of the films in the range 600–800 nm.

III. RESULTS AND DISCUSSION

The x-ray diffraction patterns of an as-prepared film and films annealed at different temperatures are shown in Fig. 1. The patterns of all the films show the diffraction lines corresponding to the spinel structure. The diffraction pattern of an as-prepared sample exhibits a strong (400) peak and a weak (311) peak compared with the diagram of isotropic Co ferrite powder, indicating a texture of [100] axis perpendicular to the film plane. The texture becomes poorer with increasing annealing temperature below 500 °C. It is noted that the (100) texture develops again when the annealing temperature reaches $T_a = 600$ °C. The same phenomena were also observed in annealed Co_{0.8}Fe_{2.2}O₄ with (111) texture and Co_{0.3}Fe_{2.7}O₄ with (110) texture under the same heat treatment conditions.

The anisotropy constants K_u and K_\perp shown in Fig. 2 were defined by $K_u = K_\perp + 2\pi Ms^2$, where K_\perp is the effective perpendicular anisotropy constant determined from the measured torque curves. The value of K_u increases with annealing temperature from negative to positive and reaches a maximum value of 2.2×10^5 ergs/cm³ at 500 °C. This trend of variation is in agreement with that of the squareness ratio $R = (Mr/Ms)_\perp / (Mr/Ms)_\parallel$. Figure 2 also displays the change of the squareness ratio $R = (Mr/Ms)_\perp / (Mr/Ms)_\parallel$ with annealing temperature. R is determined by measuring hysteresis loops in both directions perpendicular and parallel to the film plane. The change of R with annealing temperature is similar to that of K_u . The increase of R and positive K_u indicate that perpendicular anisotropy developed in the films after annealing.

The coercive forces ($H_{c\perp}$) were measured in a direction perpendicular to the film plane. With increasing annealing temperature, $H_{c\perp}$ increases below annealing temperature

^{a)}CCAST (World Laboratory), P.O. Box 8730, Beijing 100080, China.

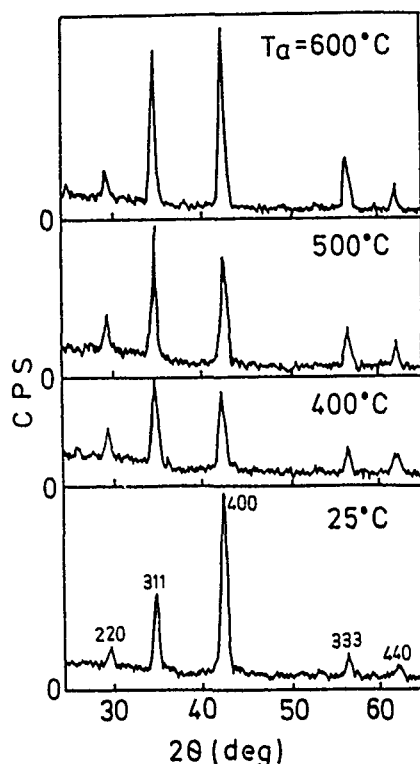


FIG. 1. X-ray diffraction patterns of CoFe_2O_4 films annealed at different temperatures (T_a), $T_a = 25$ (as prepared), 400, 500, and 600 °C.

$T_a = 500$ °C. The variation of coercive force $H_{c\perp}$ with annealing temperature goes parallel to the change of the perpendicular anisotropy constant K_u .

It is worthwhile noting that the pronounced (400) peak in as-sputtered film exhibits a preferential orientation of [100] axis normal to the film plane, which should lead to a positive perpendicular anisotropy constant in the films according to the literature.¹ But the values of K_u and R of as-sputtered films show in-plane anisotropy.

The possible origins of the anisotropy in Co spinel ferrite films were assumed as follows: (1) shape anisotropy of

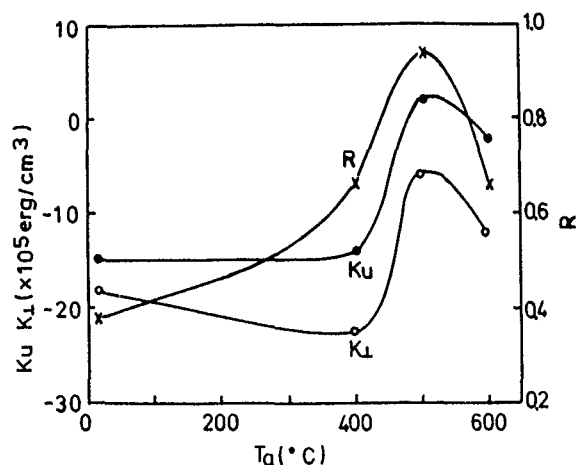


FIG. 2. The variation of anisotropy constants K_u , K_t and squareness ratio $R = (M_r/M_s)_\perp / (M_r/M_s)_\parallel$ with annealing temperature.

films, (2) thermal stress-induced anisotropy, (3) crystalline anisotropy, (4) Co^{2+} induced uniaxial anisotropy.

The shape anisotropy of films caused by the demagnetizing field of the film, expressed as $-2\pi Ms^2$, has been considered in calculating $K_u = K_t + 2\pi Ms^2$.

Thermal stress-induced anisotropy may exist in our films. There is tensile stress in our films prepared on glass substrates.¹ The effective anisotropy constant due to the thermal stress (K_σ) is $-3\lambda\sigma/2$. Here λ is the magnetostriction coefficient. For Co spinel ferrite: the (100) magnetostriction coefficient is $\lambda_{100} = -590 \times 10^{-6}$,⁴ the magnetostriction in isotropy polycrystalline samples is $\lambda_s = -110 \times 10^{-6}$. Thus thermal stress leads to a positive-induced perpendicular anisotropy which should be larger for the samples with (100) texture and smaller for isotropy samples. However the stress-induced anisotropy does not conform with the maximum perpendicular K_u , which appeared in the sample annealed at 500 °C, in which the (100) texture is poorer, thus the magnetostriction effect in the film plane is smaller. The variation of K_σ did not follow the experimentally observed variation of K_u . Thermal stress-induced anisotropy is therefore not the main origin of the presently observed K_u variation with annealing temperature.

Co spinel ferrite is of cubic symmetry and has a large positive anisotropy constant K_1 , 2.4×10^6 ergs/cm³. [100]-type axes are the easy magnetization axes. The magnetocrystalline anisotropy of the sample with (100) texture may give rise to a uniaxial anisotropy as measured by torque magnetometry. However the magnetocrystalline anisotropy cannot explain the large negative anisotropy constants of the films with (100) texture and there is an inconsistency between the variation of (100) texture and the measured perpendicular anisotropy. Therefore magnetocrystalline anisotropy is not the main origin of the anomalous variation of anisotropy in the films with T_a either.

Large uniaxial anisotropy induced by magnetic field annealing in Co spinel ferrite is well known. Penoyer and Bickford⁵ reported the mechanism of this induced anisotropy due to the migration of the cobalt ions. It has been reported that the distribution of divalent Co ions may change with thermal history of the sample.^{6,7} When our films were annealed without external magnetic field, the induced anisotropy also existed in the direction of the spontaneous magnetization. Thus Co^{2+} induced uniaxial anisotropy cannot be neglected in these films. The following is our tentative idea to explain our experimental results.

The magnetization is in the film plane during sputtering and annealing because of the demagnetizing field of the film, the induced anisotropy constant due to the anisotropic distribution of Co^{2+} should be negative, if present at all. During sputtering, the substrate temperature may be as high as about 300 °C and thus the as-sputtered film crystallizes. It is reasonable to assume that a negative-induced anisotropy K_t due to the anisotropic distribution of Co^{2+} ions develops during sputtering. Such induced anisotropy can also be assumed for the annealing and subsequent quenching process. Therefore the total anisotropy of the films is the sum of positive crystalline anisotropy K_a , positive stress anisotropy K_σ , and negative K_t , $K_u = K_a + K_\sigma + K_t$. For the as-sputtered film an

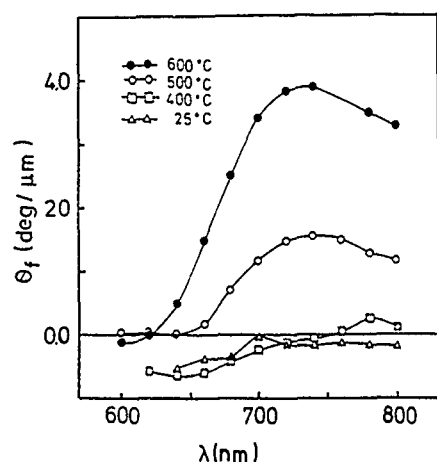


FIG. 3. The Faraday spectra of Co spinel ferrite films annealed at different temperatures.

absolute value of K_t is larger than $K_a + K_\sigma$ and may be the origin of negative K_u . For annealed films a positive K_a may decrease slightly due to a slight decrease of (100) texture and positive K_σ may increase due to higher annealing temperature, but the magnitude of negative K_t surely decreases for higher annealing temperature because $|K_t|$ is proportional to the square of magnetization at annealing temperature T_a which is lower for higher T_a and is inverse proportional to T_a . The increase of K_u from negative to positive, with annealing temperature for $T_a \leq 500^\circ\text{C}$, is mainly due to the decrease of $|K_t|$. But it remains a problem to explain the decrease of K_u at 600°C . It may be related to an increase of the number of divalent Co ions in tetrahedral sites, which we found from the Faraday spectra of films reported below. The single ion anisotropy of Co^{2+} in tetrahedral site is -79×10^{-17} ergs/ion which is $+850 \times 10^{-17}$ ergs/ion (at 0 K) in octahedral site.⁸

The Faraday spectra of prepared films shown in Fig. 3 were measured in the wavelength range from 600 to 800 nm. A peak centered near 720 nm in the spectra developed with increasing annealing temperature, reaching a maximum value of 3.8×10^4 deg/cm at wavelength 720 nm when $T_a = 600^\circ\text{C}$.

One origin of the increase of Faraday rotation angle with annealing temperature is the improvement of crystal structure including oxygen absorption of the film during annealing. The improvement of crystal structure can be reflected from the increase of magnetization with annealing temperature. The magnetization of as-sputtered film is 305 emu/cm^3 and increases to 384 emu/cm^3 at $T_a = 400^\circ\text{C}$, and 400 emu/cm^3 at $T_a = 600^\circ\text{C}$. The Faraday rotation peak increases

more rapidly than the magnetization for $T_a > 400^\circ\text{C}$. Mechanisms other than the improvement of the crystal structure may exist.

The mechanism of enhanced Faraday effect around 720 nm in Co spinel ferrites is associated with the crystal field transition of divalent cobalt ions in the tetrahedral sites.⁹ De Guire *et al.*¹⁰ reported the transformation of cobalt spinel ferrite from inverse to normal in a sample subjected to large cooling rates. An increase of the number of Co ions in tetrahedral sites was reported to enhance the Faraday effect at a wavelength of 720 nm.^{1,3,9} An increase of the number of divalent cobalt ions in tetrahedral sites may therefore be another reason for the observed increase of the Faraday rotation in our films annealed at higher temperature.

IV. CONCLUSION

(100) texture is necessary in Co spinel ferrite films to get perpendicular anisotropy according to the current literature.^{1,4} In contrast, our different experimental results indicate that the poorer (100) textured films exhibit a better perpendicular anisotropy. Thermal stress-induced anisotropy may be one origin of a positive perpendicular anisotropy in our films. The main reason of the variation of the perpendicular anisotropy in our films with annealing temperature, however, is thought to be annealing-induced anisotropy and Co ion distribution in tetrahedral sites and octahedral sites. The increase of Faraday rotation with annealing temperature seems to have two origins: (a) the improvement of crystal structure, (b) the increase of the number of divalent Co ions in the tetrahedral sites.

ACKNOWLEDGMENT

This work was supported by National Science Foundation of China and State Key Laboratory of Magnetism, Institute of Physics, Chinese Academy of Sciences.

¹M. Abe and M. Gomi, J. Magn. Soc. Jpn. **11**, 299 (1987).

²N. Hiratsuka and M. Sugimoto, IEEE Trans. Magn. **MAG-23**, 3326 (1987).

³N. N. Ectihiev, N. A. Economov, A. R. Krebs, and N. A. Zamjatina, IEEE Trans. Magn. **MAG-12**, 773 (1976).

⁴J. W. D. Martens and W. L. Peeters, J. Magn. Magn. Mater. **61**, 21 (1986).

⁵R. F. Penoyer and L. R. Bickford, Phys. Rev. **108**, 271 (1957).

⁶J. Ostorero, M. Guillot, M. Leblanc, and D. Rouet, J. Appl. Phys. **69**, 4571 (1991).

⁷G. A. Sawatzky, F. Vander Woude, and A. H. Morrish, J. Appl. Phys. **39**, 1204 (1968).

⁸H. R. Zhai, G. L. Yang, and Y. Xu, Progr. Phys. (in Chinese) **3**, 269 (1983).

⁹M. Abe and M. Gomi, J. Appl. Phys. **53**, 8172 (1982).

¹⁰M. R. De Guire, R. C. O'Handley, and G. Kalonji, J. Appl. Phys. **65**, 3167 (1989).

Magnetic and magneto-optical properties of (Tb,Dy)Nd/FeCo multilayers (abstract)

X. Y. Yu Y. Fujiwara, H. Watabe, S. Iwata, S. Tsunashima, and S. Uchiyama
Department of Electronics, Nagoya University, Nagoya 464-01, Japan

Nd-Co and Nd-FeCo amorphous films are known to have larger Kerr rotation θ_K at shorter wavelength and ultraviolet light compared with other RE-TM (rare earth-transition) amorphous films. This property is desirable for MO (magneto-optical) media for the next generation. In order to satisfy the perpendicular magnetization condition, we replaced a part of Nd by Gd to decrease the saturation magnetization M_s and applied the multilayer (ML) structure to enhance the perpendicular anisotropy K_u . Then we succeeded in getting a new ML medium of $\text{Nd}_{0.34}\text{Gd}_{0.66}/\text{Fe}_{0.9}\text{Co}_{0.1}$ with a bilayer period of 1 nm. However, the substitution of 66% Gd resulted in undesirable decreases of Kerr rotation and coercivity. In this experiment, a part of Nd is replaced by either Tb or Dy instead of Gd with an expectation that the amount of replacement to get the perpendicular magnetization configuration may be smaller since Tb and Dy have large one ion anisotropy compared with Gd. The magnetic and MO properties of Nd(Tb,Dy)/FeCo MLs will be reported. In the case of Tb, for example, a square Kerr hysteresis loop is obtained by the substitution of about 40%. However, θ_K at 400 nm is about 0.30° , which is larger than that of Tb-FeCo but smaller than NdGd/FeCo MLs.

Magnetization reversal dynamics in CoPt alloys and Co/Pt multilayers (abstract)

J. Valentin and Th. Kleinefeld
Universität Duisburg, FB10/Angewandte Physik, D-4100 Duisburg, Germany

D. Weller
IBM Almaden Research Center, 650 Harry Road, San Jose, California 95120

We have studied the dynamics of magnetization reversal processes in magneto-optic recording CoPt samples with perpendicular anisotropy. Thin films of subatomic layered $\text{Co}_{25}\text{Pt}_{75}$ alloys as well as Co/Pt multilayers with total thicknesses up to 300 Å were investigated. By means of polar Kerr microscopy we were able to obtain the magnetic domain pattern. High temporal resolution was achieved by using a rapid scanning CCD camera system. Depending on film parameters, we found wall motion dominated and nucleation dominated magnetic reversal processes. Detailed analysis of the domain topography shows evidence for a correlation of the fractal dimension of the domain shape to the macroscopic coercivity measured with a VSM and conventional Kerr hysteresis loops. In particular, we investigated the dynamics of magnetization reversal and observed magnetic aftereffect phenomenon. The time constant of the relaxation of the magnetization is strongly affected by the film structure and by the film thickness. We discuss our results in terms of the theoretical relaxation model of Fatuzzo and recent computer simulations.

This work was supported by Deutsche Forschungsgemeinschaft via Sonderforschungsbereich 166.

Amorphous to polycrystalline transformation of (BiDy)IG films (abstract)

H. Y. Zhang, B. X. Gu, H. R. Zhai, Y. Z. Miao, M. Lu, and T. Tang
Physics Department, Centre of Materials Analysis, Nanjing University, Nanjing, China

H. B. Huang
Analytical Centre, Southeast University, Nanjing, China

(BiDy)Fe₅O₁₂ films in the amorphous state were made by rf magnetron sputtering from a sintered Bi₂DyFe₅O₁₂ ceramic target onto quartz substrates and confirmed by x-ray diffraction. The films were annealed at different temperatures ranging from 500 to 800 °C for 1 h in air. The crystallization temperature was about 650 °C, as measured by DTA method. Magnetization M versus temperature relation of well crystallized films showed both a compensation temperature T_{comp} (80 K) and Curie temperature T_C (563 K). The M - T curve from 1.5 to 600 K of amorphous film showed no definite T_C or T_{comp} ; M measured in a field of 20 kOe decreased monotonously. The Faraday rotation (500–700 nm) of amorphous films was small. The M and Faraday rotation (633 nm) increased rapidly at the crystallization temperature. The Bi ion induced peak (550 nm) in the Faraday spectra got higher with the increasing annealing temperature and was up to 9.14 degree/ μm . The Faraday spectra of films annealed at 650 °C for different times showed that the films were well crystallized after annealing for 10 min. The optical absorption of the films in the visible region varied little during the transformation from amorphous to polycrystalline.

Epitaxial Bi-content ferrite-garnet film memory (abstract)

E. I. Il'yashenko

Applied Engineering Systems (A.E.S.), Moscow, Russia

V. P. Klin, A. D. Nickolsky, and A. G. Solovjov

Institute of Electronic Materials, Kaluga, Russia

Memory conception in epitaxial ferrite-garnet films on a compensation wall has been developed in recent work.¹ Further original solutions for memory element formation by heat treatment under Si layers have been found but this method has not been used in practice due to the difficulty of reproducing results. In this work the possibility of a memory matrix on the ferrite-garnet films by rf treatment has been investigated. In comparison with other work² this memory element formation method arrived at by an M_s decrease due to Ga redistribution from octahedral into tetrahedral positions provides the possibility to decrease significantly the device power intensity, to increase the speed of response, and to simplify the designing and technology. The work has been carried out with $(YBi)_3(FeGa)_5O_{12}$ films doped by Lu, Tm, Gd, Pr, and grown by the LPE method on GGG and GGG+CaMgZr substrates. The treatment mode and film composition influence upon the element switching stable threshold has been studied and read-only memory formation parameters have been found. Experimental results of rf-treatment influence upon epitaxial layer magnetic and magneto-optic features and main display parameters (optical transmission, contrast, speed of response) have been provided. The possibility of element formation from 1 up to 20 μm with a space of 12 μm and over has been shown. Figure 1 shows memory file elements with 60 and 20 μm space between them.

¹J. P. Krumme, P. Hansen; Appl. Phys. Lett. 22, 312 (1973).

²W. E. Ross, D. Psaltis, R. H. Anderson; Proc. SPIE 341, 191 (1982).

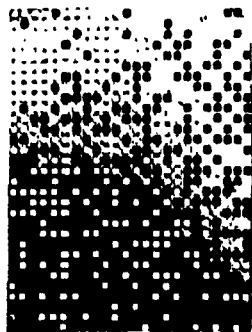


FIG. 1. Memory file elements with 60 and 20 μm space between them.

Ferromagnetism of YFe_2H_x

Kazuo Kanematsu

The Physical Science Laboratories, Nihon University at Narashino, Funabashi, Chibaken 274, Japan

Isothermal hydrogen absorption of YFe_2 at several temperatures forms four types of hydrides: δ , γ , β_1 , and β_2 . The δ hydrides with an orthorhombic MgCu_2 -type structure, $\text{YFe}_2\text{H}_{4.1}$, are ferromagnets of $3.8\mu_B/\text{f.u.}$ ($\text{YFe}_2\text{H}_{4.1}$) and $T_c=310$ K. The Mössbauer spectrum is analyzed with the direction of magnetization along [111]. The γ hydride $\text{YFe}_2\text{H}_{2.4}$ is a rhombohedral-type ferromagnet of $3.5\mu_B/\text{f.u.}$ and $T_c=500$ K. The spectrum is analyzed with the direction of magnetization along the c axis. Both β_1 hydride $\text{YFe}_2\text{H}_{1.9}$ and β_2 hydrides $\text{YFe}_2\text{H}_{1.3}$ are rhombohedral-type ferromagnets of $3.5\mu_B/\text{f.u.}$ and $T_c=570$ K. The β_1 hydride shows a smooth decrease of magnetization but the β_2 hydride shows a large decrease of magnetization between 200 and 400 K. The Mössbauer spectra of both hydrides are analyzed with the direction of magnetization in the c plane. The magnetization decrease in the β_2 hydride is discussed, assuming high- and low-magnetization phases.

I. INTRODUCTION

The cubic Laves phase compound YFe_2 forms a hydride, YFe_2H_4 , by hydrogenation at room temperature. The hydrogenation brings an increase in magnetization and a decrease of Curie temperature.¹⁻³ Recently, four kinds of YFe_2H_x hydrides were found in the isothermal hydrogen absorption at a temperature of $293\text{ K} \leq T \leq 573\text{ K}$.⁴ The hydrogenation at 293 K forms δ hydride with an orthorhombic $C15$ -type of structure. The hydrogenation in $323\text{ K} \leq T \leq 423\text{ K}$ forms γ hydrides with a hexagonal structure of $a=0.55\text{ nm}$ and $c=2.65\text{ nm}$. The hydrogenation in $473\text{ K} \leq T \leq 573\text{ K}$ forms β hydrides with a hexagonal structure of $a=0.515\text{ nm}$ and $c=2.46\text{ nm}$. The temperature dependence of magnetization shows that the β hydrides are classified in β_1 and β_2 hydrides formed at $473\text{ K} \leq T \leq 500\text{ K}$ and $523\text{ K} \leq T$, respectively. Mössbauer studies were performed for the representatives of δ , γ , β_1 , and β_2 hydrides and the spectra were analyzed. In the present article the details of experimental results and the analyzed results are reported and the ferromagnetism of each hydride is discussed.

II. EXPERIMENTAL PROCEDURE

The host compound YFe_2 was prepared by arc melting a mixture of Y (99.9% pure) and Fe (99.9% pure) with stoichiometric composition in argon atmosphere. Arc melting was repeated several times for homogeneity. Then the compound was sealed in an evacuated silica tube and annealed at 1100 K for 0.26 Ms (3 days). After the crystal structure was ascertained by x-ray diffraction, the powder with particles smaller than 0.3 mm was used for hydrogen absorption as the host compound. The isothermal hydrogen absorption was carried out in hydrogen pressure up to about 0.9 MPa after heating in vacuum at 670 K for about 4 ks (1 h). The γ and β hydrides used for magnetization and Mössbauer measurements were prepared with rapid cooling after eliminating the remaining hydrogen gas in the hydride capsule in order to avoid further hydrogenation at lower temperature. The num-

ber of absorbed hydrogen atoms was determined from gravimetric increase. The magnetization measurement was performed by a vibrating sample magnetometer in magnetic field of 0.84 MA/m (10.6 kOe). Mössbauer measurement was carried out for the samples used in magnetization measurements by a conventional constant acceleration-type spectrometer with ^{57}Co in Rh source.

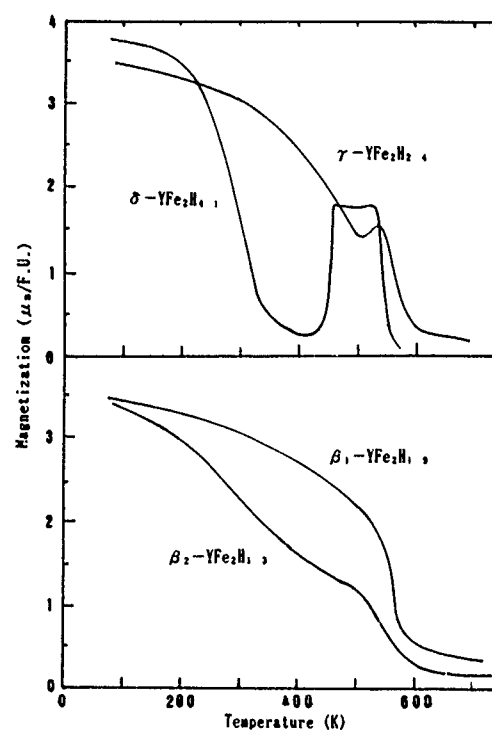


FIG. 1. Temperature dependencies of magnetization of δ hydride $\text{YFe}_2\text{H}_{4.1}$, γ hydride $\text{YFe}_2\text{H}_{2.4}$, β_1 hydride $\text{YFe}_2\text{H}_{1.9}$, and β_2 hydride $\text{YFe}_2\text{H}_{1.3}$ in $H=0.84\text{ MA/m}$ (10.6 kOe). Anomalies near 500 K in δ and γ hydrides come from β hydride formed by desorption of hydrogen.

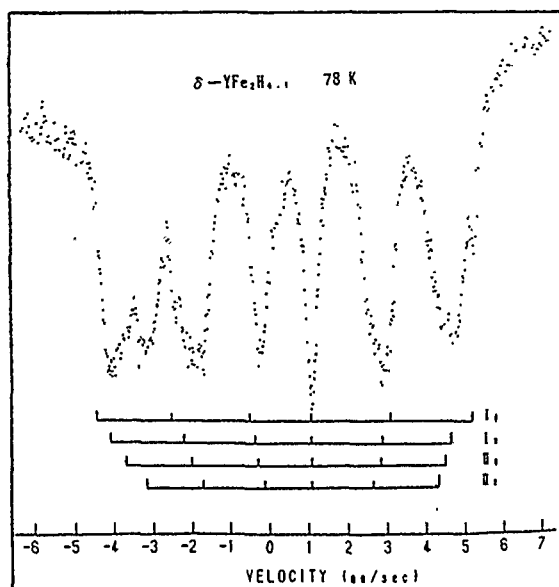


FIG. 2. Mössbauer spectrum of δ hydride $\text{YFe}_2\text{H}_{4.1}$ at 78 K, which is analyzed as the direction of magnetization is along [111].

III. RESULTS AND DISCUSSION

A. δ -hydride $\text{YFe}_2\text{H}_{4.1}$

The crystal structure of YFe_2 is C15 type with $a=0.737$ nm, and the magnetization and Curie temperature are $2.9\mu_B/\text{YFe}_2$ and $T_c=545$ K, respectively.

The δ hydride was prepared at 293 K. The crystal structure is an orthorhombic C15-type structure with $a=0.798$ nm, $b=0.783$ nm, and $c=0.807$ nm. The magnetization at 0 K estimated by extrapolation of the thermomagnetic curve is $3.8\mu_B/\text{f.u.}$ (formula unit, YFe_2H_x) and the Curie temperature is 310 K [Fig. 1(a)].

TABLE I. Hyperfine fields H_i , quadrupole splittings ΔE , and isomer shifts.

Hydride and temperature	Spectrum	Hyperfine field H_i (kOe)	Quadrupole splitting ΔE (mm/s)	Isomer shift (mm/s)
$\delta\text{-YFe}_2\text{H}_{4.1}$ 78 K	I ₁	307	0.09	0.39
	I ₂	288	-0.03	0.36
	II ₁	260	0.09	0.40
	II ₂	240	-0.03	0.45
$\gamma\text{-YFe}_2\text{H}_{2.4}$ 13 K	I ₁	275	-0.12	0.17
	I ₂	250	0.04	0.22
	II ₁	221	-0.15	0.39
	II ₂	195	0.05	0.14
$\beta_1\text{-YFe}_2\text{H}_{1.9}$ 290 K	I ₁	201	-0.30	-0.12
	I ₂	197	0.30	-0.05
	II	25		
$\beta_2\text{-YFe}_2\text{H}_{1.3}$ 290 K	I ₁	203	-0.30	-0.10
	I ₂	201	0.30	-0.09
	II	24		
13 K	I ₁	232	-0.30	-0.04
	I ₂	230	0.30	0.03
	II	42		

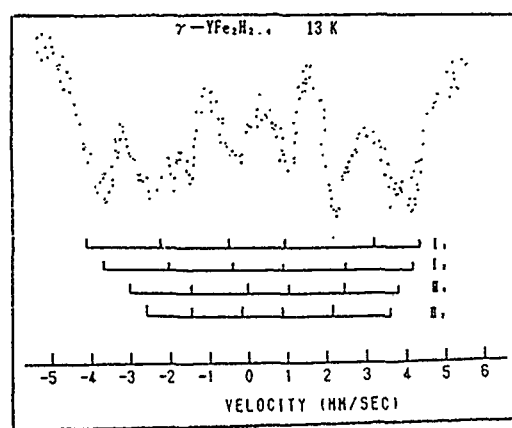


FIG. 3. Mössbauer spectrum of γ hydride $\text{YFe}_2\text{H}_{2.4}$ at 13 K, which is analyzed as the direction of magnetization is along the c axis.

The Mössbauer spectrum of C15-type compounds AFe_2 shows characteristic properties.^{5,6} If the direction is [111], the Mössbauer spectrum of AFe_2 compounds is a superposition of two subspectra with the intensity ratio of 1/3 and the

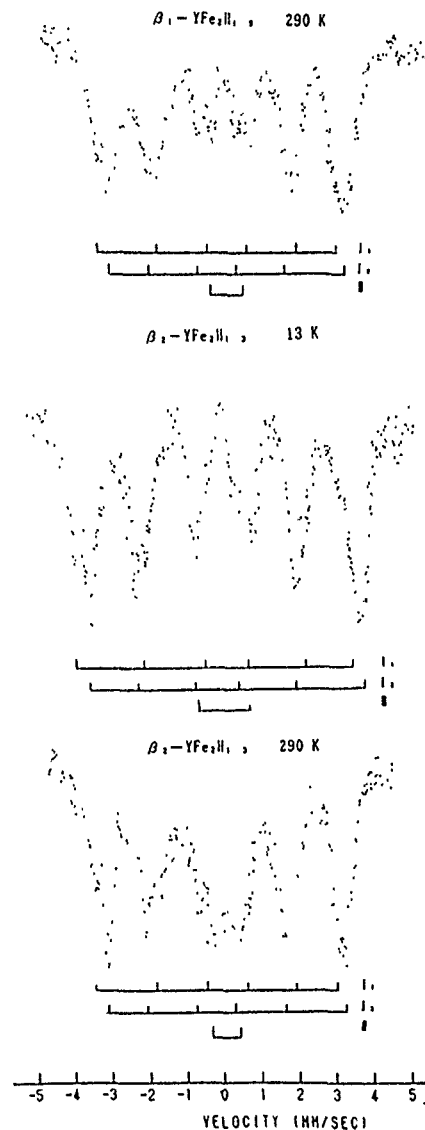


FIG. 4. Mössbauer spectra of β_1 hydride $\text{YFe}_2\text{H}_{1.9}$ at 290 K and β_2 hydride $\text{YFe}_2\text{H}_{1.3}$ at 290 and 13 K. The (I_1, I_2) are spectra when the direction of magnetization is in the c plane. The spectra (I_1, I_2) and II are interpreted to come from high- and low-magnetization phases.

ratio of quadrupole splitting of -3 . The $[110]$ direction of magnetization gives superposition of two subspectra with equal intensity and the ratio of quadrupole splitting of -1 . The $[100]$ direction gives a single spectrum.

The spectrum of δ -YFe₂H_{4.1} may be a superposition of many subspectra because of the orthorhombic distortion. The spectrum at 7 K (Fig. 2) is analyzed as a superposition of two pairs of subspectra (I_1, I_2) and (II_1, II_2), which are observed when the direction of magnetization is along $[111]$. The Mössbauer parameters are listed in Table I.

B. γ -hydride YFe₂H_{2.4}

The γ -hydride YFe₂H_{2.4} was prepared at 423 K. The x-ray-diffraction lines are indexed as a hexagonal structure of $a=0.566$ nm and $c=2.644$ nm. They are similar to, but not same as, those of rhombohedral ($R\bar{3}m$) PuNi₃-type YCo_{2.9} (Ref. 7) and YFe_{2.9}.⁸ The magnetization at 0 K estimated by extrapolation of the thermomagnetic curve is $3.5\mu_B/\text{YFe}_2\text{H}_{2.4}$ and the Curie temperature is about 500 K [Fig. 1(a)].

The iron atoms in rhombohedral YFe₃ form a tetrahedral network similar to those of YFe₂, and the c axis $[001]$ and the a axis in c -plane $[100]$ in hexagonal representation correspond to $[111]$ and $[110]$ directions in cubic structure, respectively. The spectrum at 13 K (Fig. 3) is analyzed as a superposition of two pairs of spectra, (I_1, I_2) and (II_1, II_2), which are observed when the direction of magnetization is along the c axis. The Mössbauer parameters are listed in Table I.

C. β_1 hydride YFe₂H_{1.9} and β_2 hydride YFe₂H_{1.3}

The β_1 hydride YFe₂H_{1.9} was formed at 500 K and the β_2 hydride YFe₂H_{1.3} was formed at 523 K. The x-ray-diffraction lines of both hydrides are nearly the same and are indexed as a hexagonal structure of $a=0.514$ nm and $c=2.467$ nm for YFe₂H_{1.9} and $a=0.514$ nm and $c=2.463$ nm for YFe₂H_{1.3}. They are similar to, but not same as, those

of γ -YFe₂H_{2.4}, YCo_{2.9}, and YFe_{2.9}. The extrapolated values of magnetization at 0 K are $3.5\mu_B/\text{YFe}_2\text{H}_x$. The Curie temperatures of both hydrides are about 570 K, but the magnetization decrease of β_2 hydride occurred reversibly with heating and cooling between 200 and 400 K. Although the decrease suggests another ferromagnetic phase of lower Curie temperature, the x-ray-diffraction pattern at room temperature shows no other phase. Therefore, it is assumed that the magnetization decrease results from a transition between two magnetic phases of high and low magnetization with same structure.

The spectra of β_1 hydride YFe₂H_{1.9} at 290 K and β_2 hydride YFe₂H_{1.3} at 13 and 290 K are analyzed as a superposition of subspectra (I_1, I_2), and II (Fig. 4). The pair (I_1, I_2) are the spectra when the direction of magnetization is along the a axis in the c plane. The parameters are listed in Table I. The pair of subspectra (I_1, I_2) come from the high-magnetization phase, and the subspectrum II comes from the low-magnetization phase. The increase of relative intensity of subspectrum II with increasing temperature supports the transition from the high-magnetization phase to the low-magnetization phase. At present, it is not clear whether the two magnetic phase exist separately or high and low spin states of iron atoms coexist in the rhombohedral lattice. This is a problem for future study.

¹K.-I. Kobayashi and K. Kanematsu, J. Phys. Soc. Jpn. **55**, 1336 (1986).

²K. H. J. Buschow, Solid State Commun. **19**, 421 (1976).

³K. H. J. Buschow and A. M. van Diepen, Solid State Commun. **19**, 79 (1976).

⁴K. Kanematsu, in *Proceedings of the 2nd International Conference on Rare Earth Development and Application*, edited by X. Guangxian et al. (International Academic, 1991), Vol. 1, p. 116.

⁵G. K. Wertheim, V. Jaccarino, and J. H. Wernick, Phys. Rev. **135**, 151 (1964).

⁶U. Atzmony, M. P. Dariel, E. P. Bauminger, D. Lebenbaum, I. Nowik, and S. Ofer, Phys. Rev. B **7**, 4220 (1973).

⁷K.-I. Kobayashi and K. Kanematsu, J. Phys. Soc. Jpn. **55**, 4434 (1986).

⁸K. Itoh, T. Okagaki, and K. Kanematsu, J. Phys. Soc. Jpn. **58**, 1787 (1989).

Longitudinal and transverse magnetoresistance and magnetoresistive anisotropy in ternary $(\text{Pd}_{1-x}\text{Fe}_x)_{95}\text{Mn}_5$ alloys

Z. Wang, H. P. Kunkel, and Gwyn Williams

Department of Physics, University of Manitoba, Winnipeg, Manitoba, Canada R3T 2N2

A summary of detailed measurements of the longitudinal and transverse magnetoresistance, and of the anisotropy in the magnetoresistance of ternary $(\text{Pd}_{1-x}\text{Fe}_x)_{95}\text{Mn}_5$ samples, is presented. While neither the longitudinal nor the transverse magnetoresistance saturate, these data suggest that the anisotropy (i.e., the difference) might become field independent in quite moderate fields. This feature enables a comparison to be made between this ternary system and binary PdFe, as a function of composition and temperature

I. INTRODUCTION

Unlike NiMn (Ref. 1) or PdMn,² ternary (PdFe)Mn remains as an example of a system in which initial indications of sequential paramagnetic to ferromagnetic to (transverse) spin-glass transitions have not been ruled out by subsequent detailed measurements. Early studies³ of the zero-field ac susceptibility χ_{ac} in (Pd+0.35 at. % Fe)+5 at. % Mn revealed the characteristic rapid increase in this response with decreasing temperature near 10 K as the ferromagnetic ordering temperature T_c was approached from the higher-temperature paramagnetic phase; this was followed by an essentially temperature-independent plateau region (in which χ_{ac} was not limited by demagnetization factor constraints) terminated by a sharp fall in χ_{ac} with decreasing temperature near 4 K, which was interpreted as evidence that the system had entered a phase with spin-glass-like ordering of the transverse spin components. A more quantitative set of criteria for establishing possible phase boundaries has recently been applied to this system⁴ which, in addition to providing estimates of the usual critical exponents near T_c , revealed the presence of an anomaly in the leading coefficient of the field-dependent response in the vicinity of the lower candidate transition. This latter anomaly, however, was weaker than predicted,⁵ so that the critical nature of this second transition remains in question.

Below we present a summary of detailed measurements of the longitudinal and transverse magnetoresistivities of $(\text{Pd}_{1-x}\text{Fe}_x)_{95}\text{Mn}_5$. These measurements not only supplement detailed field and temperature χ_{ac} studies, but also enable a comparison of the behavior of this ternary system to be made with the extensively investigated and well-understood binary system PdFe.

II. EXPERIMENTAL DETAILS

Samples with nominal composition $(\text{Pd}_{1-x}\text{Fe}_x)_{95}\text{Mn}_5$ ($x = 0.35, 1.6, 1.8, 2.0$, and 2.2 at. %) were prepared individually in an argon arc furnace from high-purity starting materials.⁶ A well-established sequence of inverting, remelting, cold rolling, and annealing procedures was implemented to ensure homogeneity of the final samples,⁷ which, for transport measurements, had typical dimensions $35 \times 2 \times 0.1$ mm.³ A low-frequency (37 Hz) ac method⁸ was used to measure the magnetoresistivities which were carried out in both the longitudinal and transverse configurations at 4.2 and 1.5

K in applied fields up to 1 T, and in the longitudinal configuration alone at the same two temperatures in fields up to 8.5 T.

III. RESULTS AND DISCUSSION

Figures 1 and 2 reproduce the longitudinal (\parallel) and transverse (\perp) magnetoresistivities in the liquid-helium range on (Pd+2.2 at. % Fe)+5 at. % Mn and on Pd+2.2 at. % Fe. These figures not only allow a direct comparison between the binary and ternary systems, but also demonstrate clearly the difficulties encountered in attempting to analyze the data on the ternary system quantitatively, as discussed below. As reported previously⁷ and confirmed in Fig. 2, although frequently referred to as a soft ferromagnet, applied fields ($\mu_0 H_a$) in excess of 1 T are necessary to produce full saturation in dilute PdFe, in agreement with magnetization measurements;⁹ in Fig. 2 $\rho_{\parallel}(H_a)$ at both 1.5 and 4.2 K can be seen to increase rapidly at low field (a result linked to domain effects) while above 0.1–0.2 T, ρ_{\parallel} decreases slightly with increasing field indicating incomplete saturation. The behavior of ρ_{\perp} is similar. In both orientations this higher-field slope increases with increasing temperature, as expected. Despite the presence of this weak noncollinear spin component the spontaneous resistive anisotropy (SRA), defined as

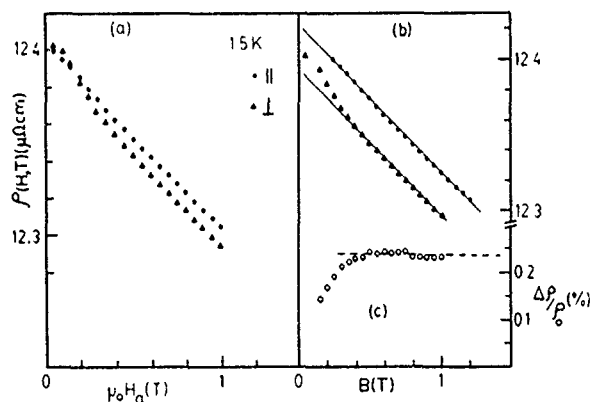


FIG. 1. (a) The longitudinal and transverse magnetoresistivities of the (Pd 2.2 at. % Fe) 5 at. % Mn sample plotted against the applied field $\mu_0 H_a$ at 1.5 K. (b) The data of part (a) plotted against the induction B . (c) The anisotropy ratio plotted against the induction B .

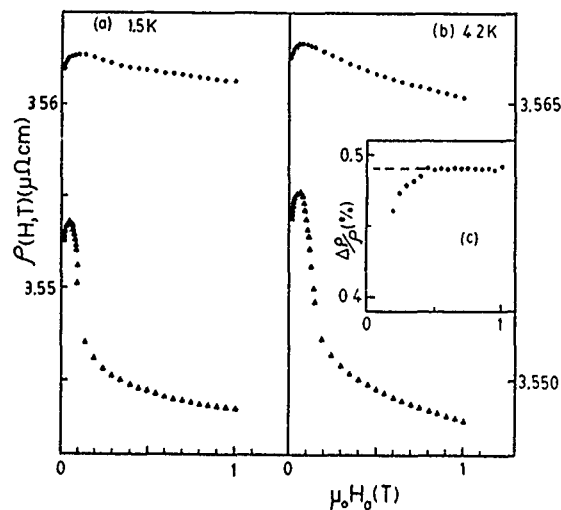


FIG. 2. (a) The longitudinal and transverse magnetoresistivities of the Pd 2.2 at. % Fe (designated as in Fig. 1) plotted against the applied field $\mu_0 H_a$ at 1.5 K. (b) Similar data acquired at 4.2 K on the same sample. (c) The anisotropy ratio from the data at 1.5 K plotted against the applied field.

$$\frac{\Delta\rho}{\rho_0} = \left(\frac{3(\rho_{\parallel} - \rho_{\perp})}{(\rho_{\parallel} + 2\rho_{\perp})} \right)_{B \rightarrow 0} \quad (1)$$

can be estimated with reasonable accuracy as $\Delta\rho(H_a) = \rho_{\parallel}(H_a) - \rho_{\perp}(H_a)$ appears to become field independent above $\mu_0 H_a \approx 0.5$ T [Fig. 2(c)], a field well below that necessary to achieve technical saturation. A similar result has been reported for amorphous FeZr .¹⁰ As discussed previously,^{7,10} valid arguments exist to base the extrapolations implicit in Eq. (1) on the induction¹¹ B [$B = \mu_0(H_a + M) - NM$, M being the magnetization and N the appropriate demagnetization factor] rather than H_a , but the use of the former rather than the latter proves unnecessary here because the magnetization is small at these compositions and the higher-field variation of the resistivity is weak⁷ (as confirmed in Fig. 2).

By contrast the behavior of the ternary sample at 1.5 K shown in Fig. 1 is dominated by a strong negative component in both orientations. This result is particularly striking since ac susceptibility measurements on Pd+2.2 at. % Fe yield⁷ $T_c \approx 81$ K whereas in ternary (Pd+2.2 at. % Fe)+5 at. % Mn T_c is similarly estimated at 48 K; thus, the 4.2 K data on the binary sample and the 1.5 K data on the ternary alloy were collected at essentially the same reduced temperature (T/T_c). These data on the ternary sample indicate unequivocally the presence of substantial spin noncollinearity (far in excess of that present in the corresponding binary alloy); nevertheless, the anisotropy in the magnetoresistance behaves in a similar manner to that in the binary system (apparently saturating in low field), and this forms the basis for subsequent analysis.

The extent of this noncollinearity is further demonstrated by the data reproduced in Fig. 3; in the longitudinal configuration the magnetoresistance continues to decrease in applied fields up to 8.5 T at 1.5 K, with little sign of saturation. Indeed, the fractional rate of change in resistivity ($1/\rho_0$)

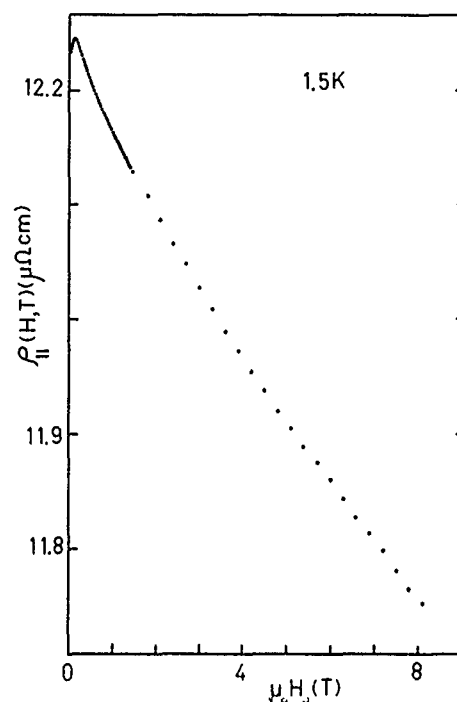


FIG. 3. The longitudinal magnetoresistance of the (Pd 2.2 at. % Fe) 5 at. % Mn sample vs applied field at 1.5 K, for an extended range of field.

($d\rho_{\parallel}/dH_a$) is nearly an order of magnitude larger at 8.5 T and 1.5 K in the ternary system than in the binary system at 1 T and 4.2 K.

The presence of such noncollinearity complicates estimates for the SRA through its influence on the field dependence of the resistivity. Figure 1(b) demonstrates the effects of replotting the data in Fig. 1(a) against the induction B , the latter being estimated with considerable care for the reasons outlined below. The induction was calculated by using directly, or scaling where necessary, previously published magnetization data (such as those of Sato *et al.*¹²) in conjunction with the corresponding demagnetizing factors, N_{\parallel} and N_{\perp} . The latter were found by evaluating the appropriate elliptic integrals using the carefully measured dimensions of each sample. These dimensions were specifically chosen so that $N_{\perp} \approx \mu_0$ [thus, there is essentially no difference between $\rho_{\perp}(H_a)$ and $\rho_{\perp}(B)$ in Fig. 1] while $N_{\parallel} \approx 5 \times 10^{-4} N_{\perp}$, so that $M(\mu_0 - N_{\parallel}) \approx \mu_0 M = 0.2$ T. This leads to a significant shift between $\rho_{\parallel}(H_a)$ and $\rho_{\parallel}(B)$, and while this shift plays an important role in estimates for the SRA, its reliability is determined by that of the available magnetization data (a property normally accurately measurable) not on estimates for the demagnetization factors (due to the sample geometry adopted). Figure 1(c) shows a plot of the ratio $\Delta\rho/\rho_0$ from Eq. (1) against the induction B ; this ratio increases rapidly as B increases, before appearing to saturate for $B \approx 0.4$ T despite the fact that neither $\rho_{\parallel}(B)$ or $\rho_{\perp}(B)$ show any indication of saturating; we suggest this approach to saturation in the ratio $\Delta\rho/\rho_0$ enables the SRA to be estimated in the manner shown, as indeed does the behavior of $\Delta\rho/\rho_0$ vs H_a in the binary sample [Fig. 2(c)]. In the binary system, of course, both $\rho_{\parallel}(H_a)$ and $\rho_{\perp}(H_a)$ show evidence of approach to saturation individually. It could certainly be argued that measurements

TABLE I. A summary of the transport properties of $(\text{PdFe})\text{Mn}$ and PdFe .

Fe conc. (at. %)	$(\text{Pd}_{1-x}\text{Fe}_x)_{95}\text{Mn}_5$						$\text{Pd}_{1-x}\text{Fe}_x$					
	1.5 K			4.2 K			1.5 K			4.2 K		
	ρ_0 ($\mu\Omega\text{ cm}$)	T_c (K)	$\Delta\rho$ ($\pi\Omega\text{ cm}$)	SRA (%)	$\Delta\rho$ ($\pi\Omega\text{ cm}$)	SRA (%)	ρ_0 ($\mu\Omega\text{ cm}$)	T_c (K)	$\Delta\rho$ ($\pi\Omega\text{ cm}$)	SRA (%)	$\Delta\rho$ ($\pi\Omega\text{ cm}$)	SRA (%)
2.2	12.40	48	30.5	0.25	29.9	0.24	3.55	81	17.7	0.50	17.2	0.49
2.0	11.89	45	27.8	0.23	27.9	0.23	3.37	75	15.8	0.47	15.7	0.47
1.8	11.49	42	23.5	0.20	24.0	0.20	2.99	69	12.1	0.41	11.5	0.38
1.6	11.12	38	19.0	0.17	17.5	0.16	2.70	62	10.6	0.39	10.4	0.38
0.35	8.33	9.3	3.8	0.04(5)	3.2	0.04	0.67	7.5	0.6	0.09	<0.1	...

at higher fields might reveal a change in the field derivative of the SRA in the ternary system; such an argument, however, could equally well be applied to binary PdFe and amorphous FeZr . Interestingly the anisotropy $[\rho_{\parallel}(B) - \rho_{\perp}(B)]_{B \rightarrow 0}$ so estimated is approximately twice as large in the ternary sample compared with the binary alloy, but due to a fourfold increase in the residual resistivity ρ_0 , the SRA is estimated to be twice as large in the binary system.

The results discussed above are typical for the composition range studied, viz., $(\text{Pd}_{1-x}\text{Fe}_x)_{95}\text{Mn}_5$ and $\text{Pd}_{1-x}\text{Fe}_x$ ($0.35 \leq x \leq 2.2$ at. % Fe), as summarized in Table I.

IV. CONCLUSIONS

Both the longitudinal and transverse magnetoresistivities of $(\text{Pd}_{1-x}\text{Fe}_x)_{95}\text{Mn}_5$ provide unequivocal evidence of noncollinearity in the impurity spins at temperatures as low as 3% of the ferromagnetic ordering temperature. Despite these complications, the SRA appears to saturate in low fields which, we suggest, enables estimates for the SRA to be made. Similar results have been reported in other systems,^{7,10} although the noncollinearity is admittedly weaker in them, the apparent saturation of the SRA being attributed to the fact that while the high-field slope of the magnetization curves reveals noncollinearity on a global scale, both the magnetoresistivity and SRA reflect changes on length scales on the order of the conduction-electron mean free path (a scale over which the noncollinearity may not be so marked). As demonstrated by Fig. 1, this is clearly not the case in $(\text{Pd}_{1-x}\text{Fe}_x)_{95}\text{Mn}_5$. Currently there is no theoretical guidance available for interpreting the SRA in noncollinear systems; we have recently¹³ applied an Ising model to successfully reproduce the characteristics of the SRA in the immediate vicinity of T_c in a number of ferromagnetic systems, however, the very nature of this model precludes its application to reentrant systems in which the noncollinearity arises from transverse spin-glass order combined with longitudinal ferromagnetic alignment. Furthermore, if indeed the spin configuration in $(\text{Pd}_{1-x}\text{Fe}_x)_{95}\text{Mn}_5$ is of this latter type then measurements in high fields (certainly those high enough to achieve technical saturation) should be avoided since they would disrupt the intrinsic spin polarization characteristic of the ground state. The situation is analogous to measuring the

nonlinear magnetization of spin glasses; the balance that needs to be achieved is one in which the applied field is not large enough to significantly alter the ground-state configuration yet does reveal any "incipient" anisotropy/nonlinearity. The results reported here represent an initial attempt to understand aspects of this complicated problem. Such difficulties notwithstanding, the concentration dependence of the SRA in binary PdFe and PdMn has been interpreted previously¹⁴ as indicating the absence of an orbital moment at the impurity sites in these systems, and the magnitude and composition dependence of the SRA in the ternary system (summarized in Table I) would, not surprisingly, lead to a similar conclusion for it.

ACKNOWLEDGMENTS

This work has been supported by grants from the Natural Sciences and Engineering Research Council (NSERC) of Canada, and the Research Board of the University of Manitoba.

- ¹H. P. Kunkel, R. M. Roshko, W. Ruan, and G. Williams, *Philos. Mag. B* **63**, 1213 (1991).
- ²G. Williams, in *Magnetic Susceptibility of Superconductors and Other Spin Systems*, edited by R. A. Hein, T. L. Francavilla, and D. H. Liebenberg (Plenum, New York, 1991), p. 475ff.
- ³B. H. Verbeek, G. J. Nieuwenhuys, H. Stocker, and J. A. Mydosh, *Phys. Rev. Lett.* **40**, 586 (1978).
- ⁴H. P. Kunkel and G. Williams, *J. Magn. Magn. Mater.* **75**, 98 (1988).
- ⁵K. Kornik, R. M. Roshko, and G. Williams, *J. Magn. Magn. Mater.* **81**, 323 (1989).
- ⁶Z. Wang, Ph.D. thesis, University of Manitoba, 1990.
- ⁷Z. Wang, H. P. Kunkel, and G. Williams, *J. Phys. Condensed Matter* **4**, 10 385 (1992); **4**, 10 399 (1992).
- ⁸W. B. Muir and J. O. Ström-Olsen, *J. Phys. E* **9**, 163 (1976).
- ⁹T. F. Smith, W. G. Gardner, and H. Montgomery, *J. Phys. C* **3**, S370 (1970).
- ¹⁰H. Ma, Z. Wang, H. P. Kunkel, and G. Williams, *J. Phys. Condensed Matter* **4**, 1993 (1992).
- ¹¹J. W. F. Dorleijn, *Philips Res. Rep.* **31**, 287 (1976).
- ¹²T. Sato, T. Nishioka, Y. Miyako, Y. Takeda, S. Morimoto, and A. Ito, *J. Phys. Soc. Jpn.* **54**, 1989 (1985).
- ¹³P. A. Stampe, H. P. Kunkel, and G. Williams, *J. Phys. Condensed Matter* **5**, L625 (1993).
- ¹⁴S. Senoussi, I. A. Campbell, and A. Fert, *Solid State Commun.* **2**, 269 (1977); A. Hamzić, Ph.D. thesis, Université de Paris-Sud, 1980; A. Hamzić, S. Senoussi, I. A. Campbell, and A. Fert, *Solid State Commun.* **26**, 617 (1978).

Formation and magnetic properties of $Y_2(Fe_{0.8}Ga_{0.2})_{17}C_x$ compounds

Fang-Wei Wang, Lin-Shu Kong, Lei Cao, Ming Hu, Bao-Gen Shen, and Jian-Gao Zhao
State Key Laboratory of Magnetism, Institute of Physics, Chinese Academy of Sciences, Beijing
100080, People's Republic of China

The alloys $Y_2(Fe_{0.8}Ga_{0.2})_{17}C_x$ ($x=0-2.5$) with the rhombohedral Th_2Zn_{17} phase were prepared by arc melting. The lattice parameters and the unit-cell volumes derived from x-ray-diffraction measurements increase linearly with the carbon content x . The Curie temperature T_c increases at first with increasing carbon concentration x , shows a maximum value of 558 K at about $x=1.0$, then decreases with x . The saturation magnetization at 1.5 K and the Fe magnetic moment have a slight change with the interstitial carbon content. The dilution of Fe by nonmagnetic Ga decreases the saturation magnetization and the Fe magnetic moment.

I. INTRODUCTION

Intermetallic compounds of the R_2Fe_{17} (R denotes rare earth) have attracted much attention recently because they can dissolve large amounts of interstitial nitrogen and carbon by the solid-gas reaction,^{1,2} which can enhance their magnetic properties considerably. The $Sm_2Fe_{17}N_x$ compound with excellent intrinsic magnetic properties¹⁻³ is a hopeful candidate for new permanent magnets. It is to be regretted that these nitrides and carbides are unstable at high temperatures. Early in 1988, de Mooij and Buschow⁴ reported on the ternary $R_2Fe_{17}C_x$ compounds by means of arc melting, but the interstitial carbon concentration is much lower and the intrinsic magnetic properties are unfit for permanent magnets. Last year, Shen *et al.*⁵⁻⁷ produced $R_2Fe_{17}C_x$ compounds with high carbon concentration which are stable at 1100 °C by melt spinning. However, it is difficult to gain a single 2:17-type phase carbide with high carbon if R is a light rare earth. Therefore, by substituting for Fe in $R_2Fe_{17}C_x$, we try to search for a path to gain high-carbon compounds with a single 2:17-type phase. We have reported some results of the $R_2(Fe,Ga)_{17}C_x$ compounds prepared by arc melting.^{8,9} In this article the structure and magnetic properties of $Y_2(Fe_{0.8}Ga_{0.2})_{17}C_x$ compounds are reported.

II. EXPERIMENT

The samples of compositions $Y_2(Fe_{0.8}Ga_{0.2})_{17}C_x$ ($x=0, 0.5, 1.0, 1.5, 2.0, 2.5$) were prepared by arc melting the appropriate amounts of Y, Fe, Ga, and Fe-C alloys in a high-purity argon atmosphere. The elements used were at least 99.9% pure. The ingots were melted several times to ensure homogeneity. Phase components and lattice parameters of the samples were determined by x-ray diffraction using $CoK\alpha$ radiation. Curie temperatures were derived from the temperature dependence of ac susceptibility in a field of less than 1 Oe. Saturation magnetizations were measured by an extracting sample magnetometer in a field of 70 kOe at 1.5 K.

III. RESULTS AND DISCUSSION

X-ray-diffraction measurements on $Y_2(Fe_{0.8}Ga_{0.2})_{17}C_x$ ($x=0-2.5$) ingots that were produced by arc melting show a single rhombohedral Th_2Zn_{17} phase (Fig. 1). We deduce from

the x-ray-diffraction patterns that there are not any amounts of α -Fe in any compounds. According to our previous work, alloys with compositions $Y_2Fe_{17}C_x$ ($x=0-2.5$) prepared by arc melting formed a single 2:17-type phase only for $x=0-1.0$. Some amounts of α -Fe exist as an impurity phase when

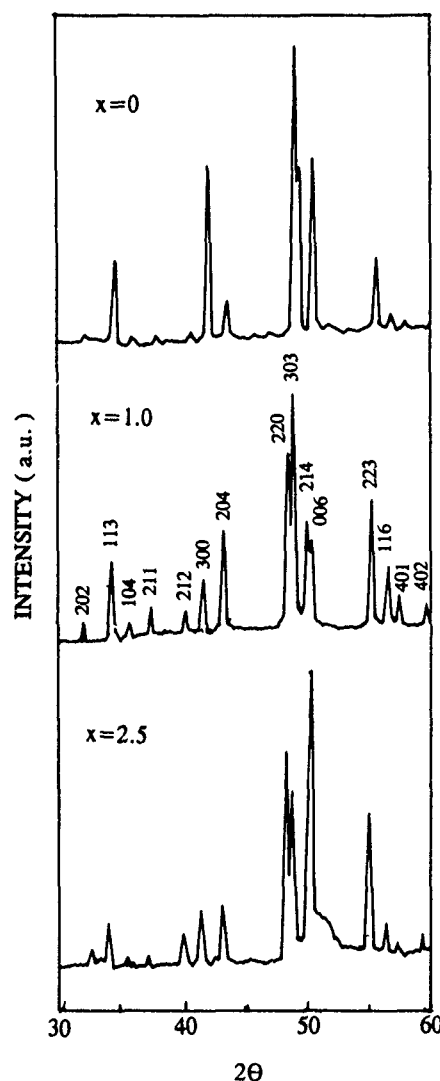


FIG. 1. The x-ray-diffraction patterns of $Y_2(Fe_{0.8}Ga_{0.2})_{17}C_x$ ($x=0, 1.0, 2.5$) with $CoK\alpha$ radiation.

TABLE I. The unit-cell parameters, the Curie temperatures, the saturation magnetizations, the saturation magnetizations at 1.5 K, and the Fe magnetic moments of the compounds $Y_2(Fe_{0.8}Ga_{0.2})_{17}C_x$.

x	a (Å)	c (Å)	v (Å ³)	T_c (K)	M_T (μ_B /f.u.)	μ_{Fe} (μ_B)
0.0	8.610	12.575	807.32	545	24.8	1.82
0.5	8.642	12.580	813.65	556	24.5	1.80
1.0	8.661	12.584	817.50	558	24.4	1.79
1.5	8.690	12.588	823.24	553	24.1	1.77
2.0	8.708	12.591	826.85	540	24.6	1.81
2.5	8.723	12.607	830.82	519	25.3	1.86

$x > 1.0$; the amount of α -Fe increases with the carbon content. If a single phase is wanted for the higher carbon concentrations, melt spinning must be adopted.⁶ Thus, it can be seen that Ga substituted for Fe makes it easy to construct a single 2:17 phase with high carbon concentration. The structure of compounds $Y_2(Fe_{0.8}Ga_{0.2})_{17}C_x$ ($x=0, 0.5$) turns to Th_2Zn_{17} type from hexagonal Th_2Ni_{17} type for Y_2Fe_{17} and $Y_2Fe_{17}C_{0.5}$. The lattice constants a, c and the unit-cell volumes v of $Y_2(Fe_{0.8}Ga_{0.2})_{17}C_x$ deduced from x-ray-diffraction measurements are listed in Table I. They increase linearly with the carbon content and the interstitial carbon extends the lattice constant a more obviously than the lattice constant c (Fig. 2). Comparing $Y_2(Fe_{0.8}Ga_{0.2})_{17}C_x$ with $Y_2Fe_{17}C_x$,⁶ it can be found that carbon has less effect on the lattice parameters of $Y_2(Fe_{0.8}Ga_{0.2})_{17}C_x$, and Ga substituted for Fe expands the unit-cell volume considerably so that there exists more space in the unit cell. It may be the reason why the high carbides of $Y_2(Fe_{0.8}Ga_{0.2})_{17}C_x$ can be obtained easily, and why the carbon has less effect on the lattice parameters of $Y_2(Fe_{0.8}Ga_{0.2})_{17}C_x$.

The concentration dependence of the Curie temperature T_c of the $Y_2(Fe_{0.8}Ga_{0.2})_{17}C_x$ compounds is shown in Fig. 3. T_c increases at first with carbon content x , and shows a maximum value of 558 K at about $x=1.0$, then decreases with increasing x . T_c does not increase monotonously with

increasing carbon concentration although the unit-cell volume is expanded linearly. In other words, the expansion of the unit-cell volume cannot cause continuous increase of T_c in the $Y_2(Fe_{0.8}Ga_{0.2})_{17}C_x$ series. T_c of $Y_2(Fe_{0.8}Ga_{0.2})_{17}$ is enhanced remarkably about 220 K over Y_2Fe_{17} . In the theory of the mean field, it is commonly accepted that the Curie temperature of rare-earth iron compounds is determined by the Fe-Fe, R-Fe, and R-R interactions. The Fe-Fe interaction is dominant, and the R-R interaction can be neglected relative to the R-Fe interaction and the Fe-Fe interaction. As result of this, the interstitial carbon in $Y_2Fe_{17}C_x$ improves the Fe-Fe interaction considerably; but, in $Y_2(Fe_{0.8}Ga_{0.2})_{17}C_x$ it only raises a little of the Fe-Fe interaction in a carbon content range x from 0 to 1.0, then reduces the Fe-Fe interaction at higher carbon concentrations.

The saturation magnetization M_s of $Y_2(Fe_{0.8}Ga_{0.2})_{17}C_x$ compounds is summarized in Table I. We find that the addition of interstitial carbon has a slight effect on M_s . Because yttrium, gallium, and carbon are nonmagnetic elements, the magnetic moment per Fe atom μ_{Fe} in $Y_2(Fe_{0.8}Ga_{0.2})_{17}C_x$ can be obtained according to $\mu_s = 0.8 \times 17 \mu_{Fe}$ (listed in Table I) and is constant about $1.81 \pm 0.03 \mu_B$. So, the Fe magnetic moment is approximately independent of the carbon concentration. These results have been obtained before for compounds $R_2Fe_{17}C_x$.^{5,6} The dilution of Fe by nonmagnetic Ga decreases the number of Fe atoms and varies the Fe atom environment. It probably causes the saturation magnetization and the Fe magnetic moment to decrease.

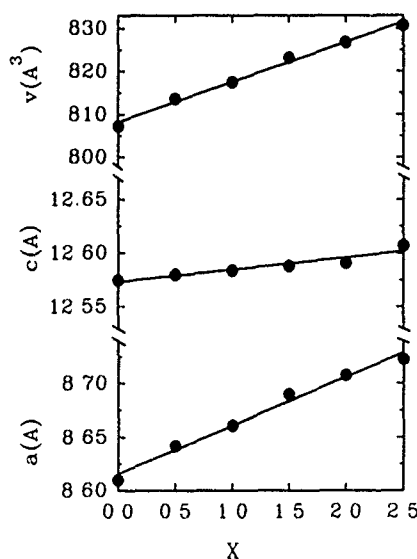


FIG. 2. The carbon content dependence of the lattice parameters a, c and the unit-cell volume v for compounds $Y_2(Fe_{0.8}Ga_{0.2})_{17}C_x$.

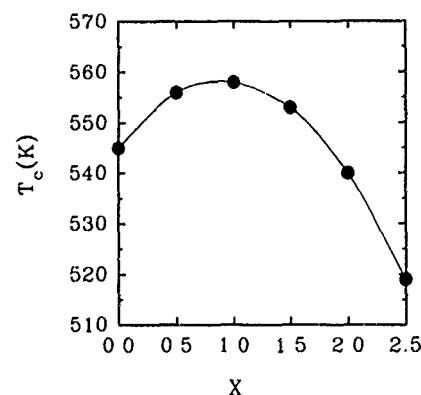


FIG. 3. The variation of the Curie temperature as a function of the carbon concentration for $Y_2(Fe_{0.8}Ga_{0.2})_{17}C_x$.

ACKNOWLEDGMENTS

This work was supported by the State's Sciences and Technology Commission and the National Nature Science Foundation of China.

¹J. M. D. Coey and H. Sun, *J. Magn. Magn. Mater.* **87**, L251 (1990).

²J. M. D. Coey, H. Sun, Y. Otani, and D. P. F. Hurley, *J. Magn. Magn. Mater.* **98**, 76 (1991).

³M. Katter, J. Wecker, L. Schultz, and R. Groosinger, *J. Magn. Magn. Mater.* **92**, L14 (1990).

⁴D. B. Mooij and K. H. J. Buschow, *J. Less-Common Met.* **142**, 349 (1988).

⁵B. G. Shen, L. S. Kong, and L. Cao, *Solid State Commun.* **83**, 753 (1992).

⁶L.-S. Kong, L. Cao, and B.-G. Shen, *Phys. Status Solidi A* **135**, K75 (1993).

⁷L.-S. Kong, L. Cao, and B.-G. Shen, *J. Magn. Magn. Mater.* **115**, L132 (1992).

⁸B. G. Shen, L. S. Kong, F. W. Wang, and L. Cao, *Appl. Phys. Lett.* **63**, 2288 (1993).

⁹B. G. Shen, F. W. Wang, L. S. Kong, L. Cao, and H. Q. Guo, *J. Magn. Magn. Mater.* **127**, L267 (1993).

Structural and magnetic properties of $\text{Nd}_2(\text{Fe,Ti})_{19}$

J. M. Cadogan and Hong-Shuo Li

School of Physics, University of New South Wales, Kensington, Australia, 2033

R. L. Davis

Australian Nuclear Science and Technology Organisation, Lucas Heights, Australia, 2234

A. Margarian

Department of Applied Physics, University of Technology, Sydney, Broadway, Australia, 2007

S. J. Collocott, J. B. Dunlop, and P. B. Gwan

CSIRO Division of Applied Physics, Lindfield, Australia, 2070

Alloys with the composition $\text{Nd}_2(\text{Fe,Ti})_{19}$ can exist in two crystal structures depending on the preparation technique. Melt-spun material has a hexagonal TbCu_7 -type structure ($a=4.902 \text{ \AA}$, $c=4.248 \text{ \AA}$) for a range of quenching speeds. Alloys prepared by arc melting, annealing at 1373 K and then water quenching have a complex monoclinic structure derived from a TbCu_7 superlattice ($a=10.644 \text{ \AA}$, $b=8.585 \text{ \AA}$, $c=9.755 \text{ \AA}$, $\beta=96.92^\circ$) and related to those of other intermetallics such as tetragonal $\text{Nd}(\text{Fe,Ti})_{12}$ and rhombohedral $\text{Nd}_2\text{Fe}_{17}$. Magnetic ordering temperatures for annealed (monoclinic) and melt-spun (hexagonal) $\text{Nd}_2(\text{Fe,Ti})_{19}$ are 411 and 454 K, respectively. ^{57}Fe Mössbauer spectroscopy at 295 K demonstrates that the local environments of the Fe atoms in the two structural modifications of $\text{Nd}_2(\text{Fe,Ti})_{19}$ are similar. The average ^{57}Fe magnetic hyperfine fields at 295 K for the monoclinic and hexagonal $\text{Nd}_2(\text{Fe,Ti})_{19}$ are 20.8 and 22.3 T, corresponding to average Fe magnetic moments of 1.33 and $1.43\mu_B$, respectively.

I. INTRODUCTION

Collocott *et al.*¹ recently identified a ternary phase, with a nominal composition $\text{Nd}_2(\text{Fe,Ti})_{19}$ (2:19) close to that of the well-established $\text{NdFe}_{11}\text{Ti}$ phase with the tetragonal ThMn_{12} -type structure. The crystal structure of this new phase is complex and x-ray diffraction patterns of arc-melted and annealed samples were tentatively indexed on a hexagonal TbCu_7 -type (1:7) superlattice structure with lattice parameters, $a_{2:19}=2a_{1:7}=9.88 \text{ \AA}$ and $c_{2:19}=4c_{1:7}=16.96 \text{ \AA}$.¹

There have been many reports on the presence of a phase with similar composition to that of $\text{Nd}_2(\text{Fe,Ti})_{19}$ in the Sm-Fe-Ti and Nd-Fe-Ti ternary alloy systems. Neiva *et al.*² reported the formation of $\text{Sm}(\text{Fe,Ti})_9$ with a hexagonal TbCu_7 structure at 1273 K, and also Hirose *et al.*³ observed the formation of a $\text{Nd}(\text{Fe,Ti})_9$ phase based on the same TbCu_7 structure. A Ti-stabilized NdFe_7 has been reported by Jang and Stadelmaier⁴ in as-cast alloys, and by Navarathna *et al.*⁵ in sputtered films. The formation of the TbCu_7 structure has also been reported in melt-spun samples, with Saito, Takahashi, and Wakiyama⁶ and Ohashi, Osugi, and Tawara⁷ observing a change from the ThMn_{12} structure to the TbCu_7 structure in $\text{SmFe}_{11}\text{Ti}$ with increasing quench rate. Similarly, Katter, Wecker, and Schultz⁸ observed a change from the rhombohedral $\text{Th}_2\text{Zn}_{17}$ structure to the hexagonal TbCu_7 structure in rapidly quenched binary Sm-Fe alloys.

This article presents magnetic and structural data on $\text{Nd}_2(\text{Fe,Ti})_{19}$ produced by high-temperature annealing and by rapid quenching.

II. EXPERIMENTAL PROCEDURE

Single-phase alloys of $\text{Nd}_2(\text{Fe,Ti})_{19}$ were prepared from Nd, Fe, and Ti of $\geq 99.9\%$ purity by argon arc melting followed by annealing at 1373 K for 72 h under an argon atmosphere in sealed quartz tubes, and then water quenching.

Melt-spun samples were prepared on a steel wheel in a helium atmosphere. Samples were characterized by x-ray diffraction using $\text{CuK}\alpha$ radiation, optical metallography, differential scanning calorimetry (DSC), and scanning electron microscopy using a JEOL 35CF equipped for backscattered electron imaging and energy-dispersive x-ray microanalysis. Magnetization measurements were carried out using a Quantum Design superconducting quantum interference device (SQUID) magnetometer. ^{57}Fe Mössbauer spectra were acquired at room temperature (295 K) using a constant acceleration, transmission spectrometer with a $^{57}\text{CoRh}$ source and calibrated with an α -Fe foil.

III. RESULTS AND DISCUSSION

Single-phase samples of $\text{Nd}_2(\text{Fe,Ti})_{19}$ can be prepared by arc melting and annealing for a range of Ti contents according to the formula $\text{Nd}_{9.4}\text{Fe}_{90.6-x}\text{Ti}_x$ with ($3.8 \leq x \leq 5.3$). No significant compositional range for Nd was detected. The samples reported here contain 4.1 at. % Ti.

Melt-spun samples of $\text{Nd}_2(\text{Fe,Ti})_{19}$ have the hexagonal TbCu_7 structure [Fig. 1(a)] with lattice parameters $a=4.902 \text{ \AA}$ and $c=4.248 \text{ \AA}$ over a range of wheel speeds from 5 to 30 m/s and contain less than 2% of α -Fe. Arc-melted samples also contain approximately 30% of the 1:7 phase prior to annealing.

Alloys prepared by arc melting and annealing at 1373 K exhibit a more complex structure. The x-ray diffraction data, shown in Fig. 1(b), which had originally been indexed¹ on a $2 \times a$ and $4 \times c$ superlattice of hexagonal TbCu_7 type has been reindexed using the Visser code⁹ on the basis of a monoclinic cell with lattice parameters $a=10.644 \text{ \AA}$, $b=8.585 \text{ \AA}$, $c=9.755 \text{ \AA}$, and $\beta=96.92^\circ$. Calculated and measured line positions and indices are shown in Table I for this structure. The relationship of the monoclinic $\text{Nd}_2(\text{Fe,Ti})_{19}$ structure to

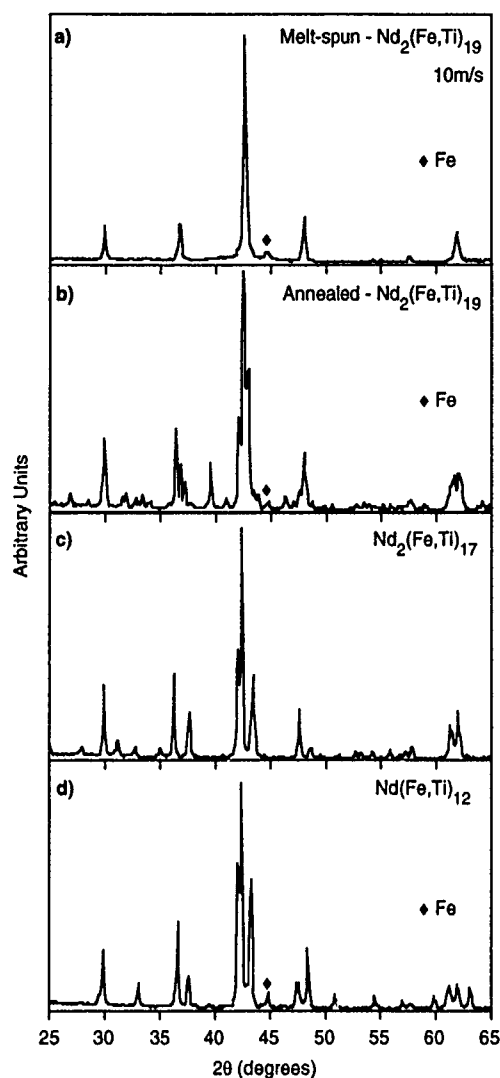


FIG. 1. X-ray-diffraction spectra for Fe-rich Nd-Fe-Ti phases: (a) melt-spun $\text{Nd}_2(\text{Fe,Ti})_{19}$; (b) annealed $\text{Nd}_2(\text{Fe,Ti})_{19}$; (c) $\text{Nd}_2(\text{Fe,Ti})_{17}$; and (d) $\text{Nd}(\text{Fe,Ti})_{12}$.

TbCu_7 is best illustrated by reference to Fig. 2, which shows the a - c plane of hexagonal TbCu_7 . The lattice parameters of the outlined cell are $a = 10.685 \text{ \AA}$ ($b_{2-19} \approx \sqrt{3}a_{1-7}$), $c = 9.809 \text{ \AA}$, and $\beta = 96.56^\circ$, all of which are very close to the measured values for monoclinic $\text{Nd}_2(\text{Fe,Ti})_{19}$. In the absence of single-crystal x-ray data or of a full profile refinement of the powder x-ray data, our identification of the annealed $\text{Nd}_2(\text{Fe,Ti})_{19}$ structure as monoclinic and based upon a superlattice of hexagonal TbCu_7 must remain provisional. A cell derived from an even larger TbCu_7 superlattice is possible. However, it is probable that the structure of annealed $\text{Nd}_2(\text{Fe,Ti})_{19}$ is related to that of melt-spun $\text{Nd}_2(\text{Fe,Ti})_{19}$ (i.e., TbCu_7) by an ordering of the atoms on the TbCu_7 sites, and a minor distortion of the hexagonal lattice. Therefore, it is also related to other rare-earth transition-metal structures such as $\text{Th}_2\text{Zn}_{17}$, $\text{Th}_2\text{Ni}_{17}$, and ThMn_{12} .

Figure 3 shows magnetization data for isotropic polycrystalline samples of annealed and melt-spun $\text{Nd}_2(\text{Fe,Ti})_{19}$ in applied fields of 0.1 and 5 T. Curie temperatures derived from low-field magnetization data are 411 K (annealed) and

TABLE I. X-ray-diffraction data for annealed $\text{Nd}_2(\text{Fe,Ti})_{19}$.

2θ observed	2θ calculated	$h k l$	Observed intensity (%)
13.80	13.77	0 1 1	<0.5
16.74	16.70	1 1 1	0.5
	16.77	2 0 0	
20.67	20.68	0 2 0	0.7
20.87	20.88	2 1 $\bar{1}$	1.7
21.07	21.05	0 1 2	0.7
	21.07	1 0 2	
22.33	22.34	1 2 0	0.6
23.36	23.36	2 0 $\bar{2}$	1.5
25.26	25.27	3 0 0	1.0
26.41	26.40	2 0 2	0.8
26.62*			1.7
26.76	26.74	2 2 0	3.7
27.80	27.75	0 2 2	0.8
28.45	28.41	2 1 2	45.1
29.66	29.69	1 2 2	16.2
29.86	29.87	3 1 1	26.6
30.76	30.64	2 0 $\bar{3}$	0.5
31.41	31.39	2 2 $\bar{2}$	4.0
31.70	31.68	1 1 3	5.8
32.59	32.60	0 3 1	3.3
32.87	32.87	3 2 0	3.0
33.21	33.18	3 0 2	4.3
33.77	33.77	2 2 2	2.3
33.97	34.00	1 3 1	2.1
35.76	35.83	2 1 3	2.1
36.32	36.29	3 2 $\bar{2}$	32.9
36.72	36.61	1 2 3	20.1
37.08	37.05	1 0 $\bar{4}$	12.3
	37.11	0 0 4	
37.82	37.98	1 3 2	1.9
39.02	38.98	2 0 $\bar{4}$	2.3
39.28	39.36	2 3 $\bar{2}$	4.4
39.45	39.42	3 2 2	18.4
40.83	40.96	3 3 $\bar{1}$	5.5
42.06	42.07	0 4 0	43.0
42.39	42.41	3 3 1	100.0
42.63	42.66	3 0 $\bar{4}$	64.7
42.89	42.89	2 0 4	72.1
43.76	43.77	1 3 3	6.9

*Unaccounted line.

454 K (melt spun), in agreement with the values measured by DSC.

Mössbauer spectra for the two structural modifications of $\text{Nd}_2(\text{Fe,Ti})_{19}$ are shown in Fig. 4. It is obvious from the data that the local environment of the Fe atoms in the two structures is similar. In the case of annealed $\text{Nd}_2(\text{Fe,Ti})_{19}$ a fit using five subspectra of sextets proved satisfactory,¹⁰ while for the melt-spun sample the data were fitted by a distribution of hyperfine fields using the program of LeCäer and Dubois.¹¹ The average hyperfine field at room temperature for the melt-spun material (22.3 T) is higher than for annealed samples (20.8 T), in line with the difference in their Curie temperatures.

IV. CONCLUSION

We have shown by x-ray diffraction that alloys of $\text{Nd}_2(\text{Fe,Ti})_{19}$ prepared by melt spinning, and by arc melting

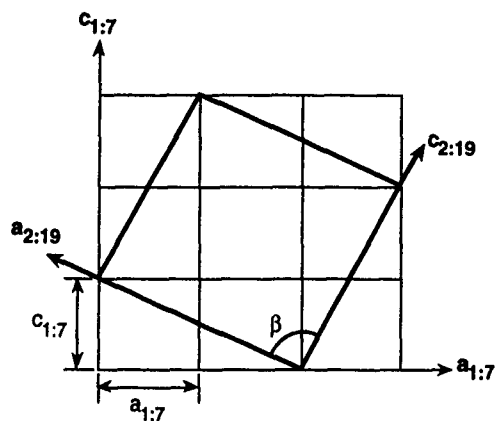


FIG. 2. Crystallographic relationship in the a - c plane between the unit cell of monoclinic $\text{Nd}_2(\text{Fe,Ti})_{19}$ and the hexagonal TbCu_7 superlattice.

and annealing crystallize in two distinct structures. Of the two structural modifications, the melt-spun material with the hexagonal TbCu_7 -type ($a=4.902 \text{ \AA}$, $c=4.248 \text{ \AA}$) structure is the simplest. The structure of arc-melted and annealed samples is more complex than the $2 \times a$ and $4 \times c$ superlattice of the TbCu_7 type proposed in our earlier report,¹ and even the monoclinic structure reported here ($a=10.644 \text{ \AA}$,

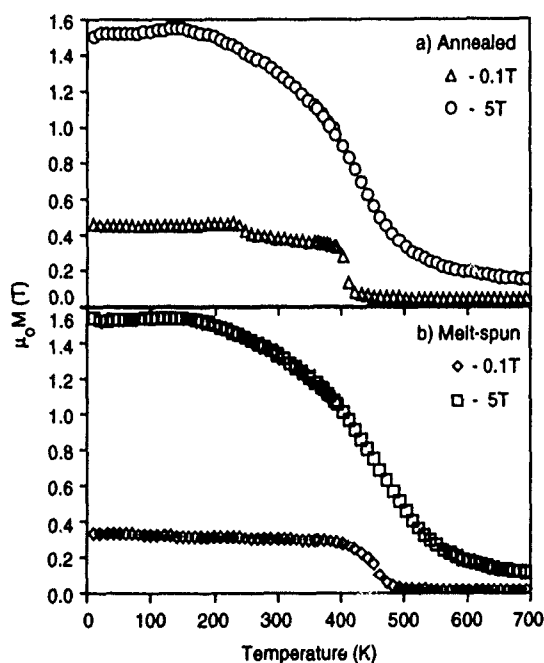


FIG. 3. Magnetization curves for (a) annealed and (b) melt-spun $\text{Nd}_2(\text{Fe,Ti})_{19}$ at 0.1 and 5 T.

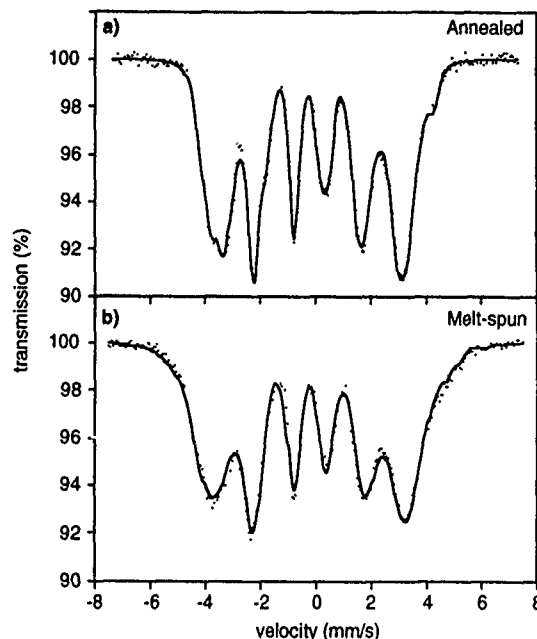


FIG. 4. Mössbauer spectra at 295 K for (a) annealed and (b) melt-spun $\text{Nd}_2(\text{Fe,Ti})_{19}$.

$b=8.585 \text{ \AA}$, $c=9.755 \text{ \AA}$, and $\beta=96.92^\circ$) must only be regarded as provisional until single-crystal x-ray data become available.

Mössbauer spectra of melt-spun, and arc-melted and annealed samples demonstrate that the local environments of the Fe atoms are similar. The average ^{57}Fe hyperfine field of 20.8 T for annealed and 22.3 T for melt-spun material corresponds to average Fe magnetic moments of 1.33 and $1.43 \mu_B$, respectively. The larger hyperfine field of the melt-spun material can be attributed to its higher Curie temperature.

- ¹ S. J. Collocott, R. K. Day, J. B. Dunlop, and R. L. Davis, in Proceedings of the Seventh International Symposium on Magnetic Anisotropy and Coercivity in Rare-Earth Transition Metal Alloys, Canberra, 1992, p. 437.
- ² A. C. Neiva, F. P. Missel, B. Grieb, E.-Th. Henig, and G. Petzow, *J. Less-Common Met.* **170**, 293 (1991).
- ³ S. Hirose, K. Makita, T. Ikegami, and M. Umemoto, in Proceedings of the Seventh International Symposium on Magnetic Anisotropy and Coercivity in Rare-Earth Transition Metal Alloys, Canberra, 1992, p. 389.
- ⁴ T. S. Jang and H. H. Stadelmaier, *J. Appl. Phys.* **67**, 4957 (1990).
- ⁵ A. Navarathna, H. Hegde, R. Rani, and F. J. Cadieu, *J. Appl. Phys.* **73**, 6242 (1993).
- ⁶ H. Saito, M. Takahashi, and T. Wakiyama, *J. Appl. Phys.* **64**, 5965 (1988).
- ⁷ K. Ohashi, R. Osugi, and Y. Tawara, in Proceedings of the Tenth International Workshop on RE Magnets and their Applications, Kyoto, 1989, p. 13.
- ⁸ M. Katter, J. Wecker, and L. Schultz, *J. Appl. Phys.* **70**, 3188 (1991).
- ⁹ J. W. Visser, *J. Appl. Crystallogr.* **2**, 89 (1969).
- ¹⁰ J. M. Cadogan, H.-S. Li, J. B. Dunlop, and A. Margarian, *J. Alloys Compounds* **201**, L1 (1993).
- ¹¹ G. LaCaer and J. M. Dubois, *J. Phys. E* **12**, 1083 (1979).

Possible ferrimagnetic coupling in light-rare-earth transition-metal intermetallic compounds

Z. G. Zhao, F. R. de Boer, and V. H. M. Duijn

Van der Waals-Zeeman Laboratory, University of Amsterdam, Valckenierstraat 65, 1018 XE, Amsterdam, The Netherlands

K. H. J. Buschow

Philips Research Laboratories, 5600 JA Eindhoven, The Netherlands

Y. C. Chuang

Institute of Metal Research, Academia Sinica, Wenhua Road, Shenyang, 110015, People's Republic of China

The possibility of ferrimagnetic coupling between the magnetic moments of the light-rare-earth (Nd, Pr) ions and of the transition-metal (Fe) ions in $\text{Nd}_6\text{Ga}_3\text{Fe}_{11}$ - and $\text{Pr}_6\text{Ga}_3\text{Fe}_{11}$ -based compounds is deduced from the high-field magnetization curves measured at 4.2 K on magnetically aligned and on free-powder samples and from the temperature dependence of the magnetization. The ferrimagnetic coupling is very weak: at 4.2 K, the rare-earth moments and the transition-metal moments can be forced to ferromagnetic alignment by application of an external magnetic field of about 4 T. Generally, in intermetallic compounds, the magnetic coupling is ferromagnetic between light-rare-earth and transition-metal ions and ferrimagnetic between heavy-rare-earth and transition-metal ions. The present results suggest that in some crystal structures ferrimagnetic coupling also may exist in the compounds formed by light-rare-earth and transition-metal elements.

I. INTRODUCTION

The compounds $\text{Nd}_6\text{Ga}_3\text{Fe}_{11}$ and $\text{Pr}_6\text{Ga}_3\text{Fe}_{11}$ crystallize in the $\text{La}_6\text{Ga}_3\text{Co}_{11}$ -type of structure with space group $I4/mcm$.¹ The crystal structure of $\text{La}_6\text{Ga}_3\text{Co}_{11}$ is shown in Fig. 1. The rare-earth atoms occupy two different crystallographic sites, La1 and La2. The Ga atoms occupy one site and share another site with Co. It can be seen from Fig. 1 that the crystal entails a stacking of layers of Co, rare-earth, and Ga atoms.

Magnetization transitions at low field strengths have been found at low temperatures in the $\text{R}_6\text{Ga}_3\text{Fe}_{11}$ compounds with $\text{R}=\text{Nd, Pr, Sm}$.² A previous investigation³ has shown that the transition fields in $\text{Nd}_6\text{Ga}_3\text{Fe}_{11}$ and $\text{Pr}_6\text{Ga}_3\text{Fe}_{11}$ almost do not change when B is substituted for Ga; however, the magnetic anisotropy of $\text{Nd}_6\text{Ga}_3\text{Fe}_{11}$ is influenced remarkably, leading to a spin-reorientation transition in $\text{Nd}_6\text{Ga}_{2.5}\text{B}_{0.5}\text{Fe}_{11}$ at about 130 K.³ These results suggest that the low-field transitions are not connected with the magnetic anisotropy. The aim of the present work is to obtain information about the origin of these transitions in $\text{Nd}_6\text{Ga}_3\text{Fe}_{11}$ and $\text{Pr}_6\text{Ga}_3\text{Fe}_{11}$.

II. EXPERIMENTAL PROCEDURE

The compounds $\text{Nd}_6\text{Ga}_{3-x}\text{B}_x\text{Fe}_{11}$ and $\text{Pr}_6\text{Ga}_{3-x}\text{B}_x\text{Fe}_{11}$ ($x=0, 0.5$) were prepared by melting together appropriate amounts of pure Nd, Pr, Ga, Fe, Fe-B alloy (20% B) in an arc furnace in a purified-argon atmosphere. To reach homogeneity, the ingots were inverted and melted twice. Wrapped in Mo foil, the as-cast ingots were annealed at 700 °C for 2 weeks in argon atmosphere. By x-ray diffraction, the annealed samples were found to possess the $\text{La}_6\text{Ga}_3\text{Co}_{11}$ -type structure and to contain small amounts of $\alpha\text{-Fe}$.

Magnetically aligned samples were prepared by mixing fine powder with a resin-doped epoxy solution at room temperature and by letting the mixture solidify in a mold with a

cylindrical hole in an external magnetic field of 0.8 T. High-field magnetization curves at 4.2 K were measured in the high-field installation at the University of Amsterdam with the field applied parallel and perpendicular to the alignment direction of the samples. The free-powder magnetization was measured on samples consisting of fine powder particles which could freely rotate in the sample holder under the influence of the applied external field. The temperature dependence of the magnetization was measured on free-powder samples between 4.2 and 260 K in a field of 3 T in an extracting-sample magnetometer.

III. RESULTS AND DISCUSSION

The magnetization curves of $\text{Nd}_6\text{Ga}_3\text{Fe}_{11}$ and $\text{Nd}_6\text{Ga}_{2.5}\text{B}_{0.5}\text{Fe}_{11}$, measured parallel and perpendicular to the alignment direction, are shown in Fig. 2. In the dotted magnetization curves recorded with increasing field, the transitions earlier reported³ to occur in low fields (below 5 T) are vaguely distinguishable, but they are very clearly visible in the dM/dB curves shown in Fig. 3. In the perpendicular

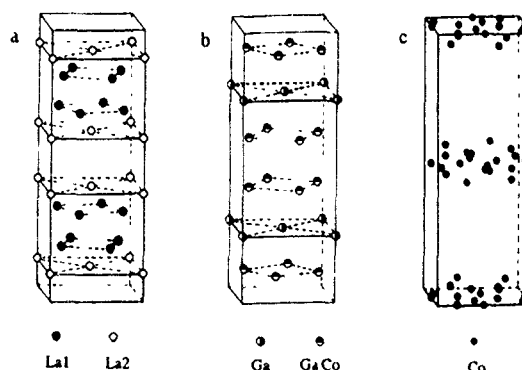


FIG. 1. Crystal structure of $\text{La}_6\text{Ga}_3\text{Co}_{11}$.

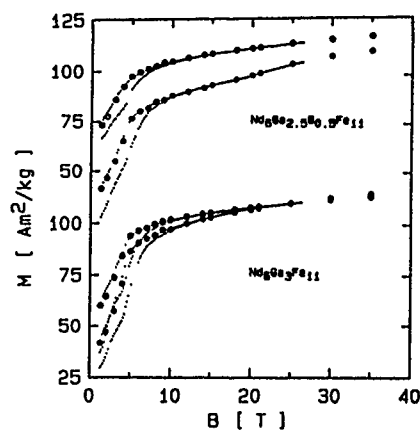


FIG. 2. Magnetization curves at 4.2 K of $\text{Nd}_6\text{Ga}_3\text{Fe}_{11}$ -based compounds for the field applied parallel (○) and perpendicular (●) to the alignment direction. The dotted lines correspond to data obtained by means of a triangular continuous-field pulse in which the field increases linearly with time up to 26 T and after that decreases linearly.

magnetization of $\text{Nd}_6\text{Ga}_{2.5}\text{B}_{0.5}\text{Fe}_{11}$ there is also a transition around 20 T. It is also seen in Fig. 3 that the critical fields of the low-field transitions hardly depend on the substitution of B for Ga. However, the magnetic anisotropy of $\text{Nd}_6\text{Ga}_3\text{Fe}_{11}$ is considerably enhanced upon substitution of B for Ga.

In $\text{Pr}_6\text{Ga}_3\text{Fe}_{11}$ (Fig. 4), the magnetic anisotropy is very small (<5 T), the parallel and perpendicular magnetization curves coinciding in relatively low fields. Similar to $\text{Nd}_6\text{Ga}_3\text{Fe}_{11}$, the substitution of B for Ga results in a higher magnetic anisotropy. Also in $\text{Pr}_6\text{Ga}_3\text{Fe}_{11}$ and $\text{Pr}_6\text{Ga}_{2.5}\text{B}_{0.5}\text{Fe}_{11}$, transitions are found at low fields in both the parallel and the perpendicular magnetization curves (Fig. 5). The critical fields of these transitions are again nearly independent of B substitution, as in the case of the $\text{Nd}_6\text{Ga}_3\text{Fe}_{11}$ -based compounds. For $\text{Pr}_6\text{Ga}_{2.5}\text{B}_{0.5}\text{Fe}_{11}$, additional transitions are found both in the parallel magnetization

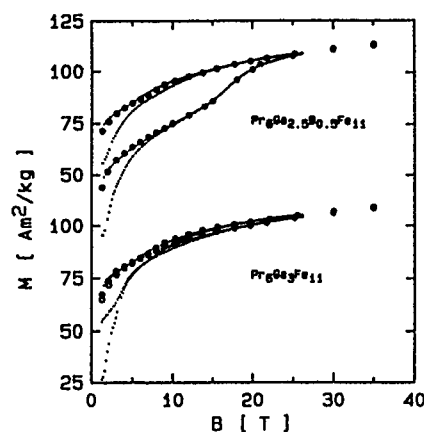


FIG. 4. Magnetization curves at 4.2 K of $\text{Pr}_6\text{Ga}_3\text{Fe}_{11}$ -based compounds for the field applied parallel (○) and perpendicular (●) to the alignment direction. The dotted lines correspond to data obtained by means of a triangular field pulse in which the field increases linearly with time up to 26 T and after that decreases linearly.

curve (at 9 T) and in the perpendicular magnetization curve (at 17 T). All magnetization curves of both the $\text{Nd}_6\text{Ga}_3\text{Fe}_{11}$ - and the $\text{Pr}_6\text{Ga}_3\text{Fe}_{11}$ -based compounds display a high differential susceptibility even in the highest applied fields indicating a noncollinear structure to be present. Assuming that the rare-earth moments and the Fe moments are nearly parallel at 35 T and that Nd and Pr have the free-ion moment values of $3.20\mu_B$ and $3.27\mu_B$, respectively, we can derive for both $\text{Nd}_6\text{Ga}_3\text{Fe}_{11}$ and $\text{Pr}_6\text{Ga}_3\text{Fe}_{11}$ an Fe moment of about $1.7\mu_B$ from the values of the parallel magnetization at 35 T. This value for the Fe moment is in good agreement with Mössbauer results.²

The experimental results presented above show that substitution of B for Ga in $\text{Nd}_6\text{Ga}_3\text{Fe}_{11}$ and $\text{Pr}_6\text{Ga}_3\text{Fe}_{11}$ hardly affects the low-field transitions in these compounds. In the Nd compounds, the transition fields are slightly higher than in the Pr compounds. Of substantial interest is the fact that

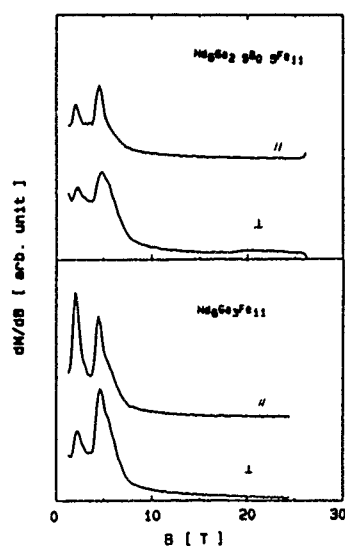


FIG. 3. Field dependence of dM/dB of $\text{Nd}_6\text{Ga}_3\text{Fe}_{11}$ -based compounds at 4.2 K for the increasing-field part of the continuous-field 26 T pulse.

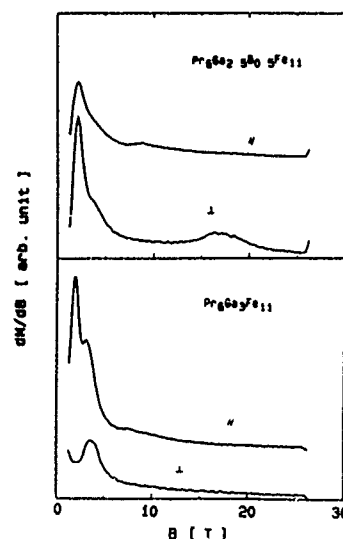


FIG. 5. Field dependence of dM/dB of $\text{Pr}_6\text{Ga}_3\text{Fe}_{11}$ -based compounds at 4.2 K for the increasing-field part of the continuous-field 26 T pulse.

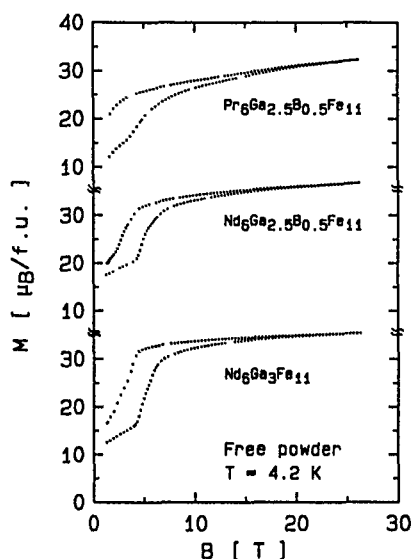


FIG. 6. Free-powder magnetization of $R_6Ga_{2.5}B_{0.5}Fe_{11}$ ($R=Nd, Pr$) compounds at 4.2 K.

the transitions are observed in both the parallel and perpendicular magnetization curves. Because there are at least two transitions in each magnetization curve, it is unlikely that all these transitions are first-order magnetization transitions (FOMP) as observed in $Nd_2Fe_{14}B$.⁴ Even more important in this respect is the fact that the transitions appear in both the parallel and the perpendicular magnetization curves. In the case of FOMP transitions one would also have the contradiction that the anisotropy fields of the compounds are strongly enhanced by substitution, whereas the critical fields of the low-field transitions do not change. These low-field transitions are therefore not to be associated with the overall anisotropy of the compounds.

To further investigate the nature of the observed transitions we performed free-powder magnetization measurements on $Nd_6Ga_3Fe_{11}$, $Nd_6Ga_{2.5}B_{0.5}Fe_{11}$, and $Pr_6Ga_{2.5}B_{0.5}Fe_{11}$ with the idea that transitions originating from discontinuous rotation of the total magnetization vector as occurs in a FOMP should not be observable in free-powder magnetization curves. Figure 6 shows that the magnetization jumps at about 20 and 17 T in $Nd_6Ga_{2.5}B_{0.5}Fe_{11}$ (Figs. 2 and 3) and $Pr_6Ga_{2.5}B_{0.5}Fe_{11}$ (Figs. 4 and 5), respectively, have completely disappeared in the free-powder magnetization proving these transitions to be of the FOMP type. Only at low fields are transitions observed in the free-powder data, which are of different origin and may be associated

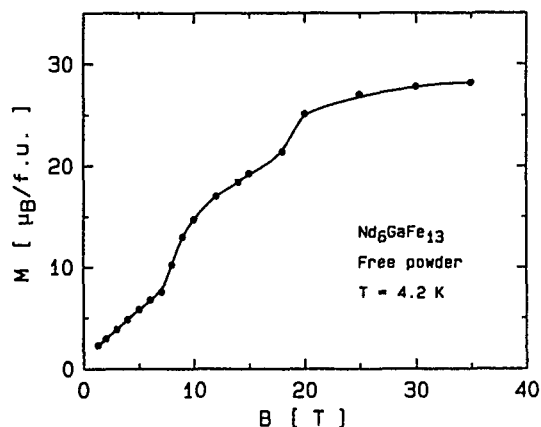


FIG. 7. Free-powder magnetization curve at 4.2 K of Nd_6GaFe_{13} . The line drawn is a guide to the eye.

with transitions from a ferrimagnetic spin structure to a ferromagnetic spin structure.

In order to obtain more information about the possible type of ferrimagnetic spin structure in these compounds, we measured the low-temperature magnetization of compounds of the type $Nd_6M_{3-x}Fe_{11+x}$ ($M=Al$ or Ga) and found⁵ that the transition fields strongly increase when Ga or Al are replaced by Fe . As an example, the result for $Nd_6Fe_{13}Ga$ is shown in Fig. 7. The substituted Fe atoms can be expected to occupy the Co positions in the $GaCo$ layers in Fig 1(b), which separate the R and the Co layers. In this case, the substituted Fe ions will very likely influence the strength of the interaction between the moments in the R and the Fe layers. The result in Fig. 7 shows that this interaction is negative, which makes it tempting to conclude that in these compounds the $Nd-Fe$ and the $Pr-Fe$ interaction may be of the ferrimagnetic type. This would be the first example of compounds in which the moment configuration deviates from the ferromagnetic alignment of light-rare-earth moments with respect to the transition-metal moments, which has been explained by Campbell.⁶

¹O. M. Sichevich, R. V. Lapunova, A. N. Sobolev, Yu. N. Grin, and Ya. P. Yarmolynk, *Sov. Phys. Crystallogr.* **30**, 627 (1985).

²H.-S. Li, B.-P. Hu, J. M. Gadoan, J. M. D. Coey, and J. P. Gavigan, *J. Appl. Phys.* **67**, 4841 (1990).

³Z. G. Zhao, X. K. Sun, Y. C. Chuang, and F. R. de Boer, *J. Alloys Comp.* **190**, 91 (1992).

⁴M. Sagawa, S. Fujimura, M. Togawa, H. Yamamoto, and Y. Matsuura, *J. Appl. Phys.* **55**, 2083 (1984).

⁵Z. G. Zhao, F. R. de Boer, and K. H. J. Buschow (unpublished).

⁶I. A. Campbell, *J. Phys. F* **2**, L47 (1972).

Magnetic properties of a novel Pr-Fe-Ti phase

Hong-Shuo Li, Suharyana, J. M. Cadogan, and G. J. Bowden
School of Physics, The University of New South Wales, Kensington, NSW 2033, Australia

Jian-Min Xu, S. X. Dou, and H. K. Liu
School of Materials Science and Engineering, The University of New South Wales, Kensington, NSW 2033, Australia

In a systematic study of the $(\text{Pr}_{1-x}\text{Ti}_x)\text{Fe}_5$ alloy series, the $(\text{Pr}_{0.65}\text{Ti}_{0.35})\text{Fe}_5$ alloy has been found to have a dominant phase with either the rhombohedral $\text{Th}_2\text{Zn}_{17}$ structure or the newly discovered $\text{Nd}_2(\text{Fe},\text{Ti})_{19}$ (S. J. Collocott, R. K. Day, J. B. Dunlop, and R. L. Davis, in *Proceedings of the Seventh International Symposium on Magnetic Anisotropy and Coercivity in R-T Alloys*, Canberra, July 1992, p. 437) structure, depending on the annealing procedure. Powder-x-ray-diffraction patterns and scanning electron microscopy show that the sample annealed at a temperature of 850 °C followed by 1000 °C has the 2:17 structure whereas annealing at 1000 °C directly leads to the new 2:19 structure. Energy-dispersive x-ray analysis yields Pr:Fe:Ti ratios of 10.7:86.2:3.1 for the $\text{Pr}_2(\text{Fe},\text{Ti})_{17}$ phase and 9.2:85.9:4.9 for the $\text{Pr}_2(\text{Fe},\text{Ti})_{19}$ phase. ^{57}Fe Mössbauer spectroscopy (at 295 K) gives values for the average ^{57}Fe hyperfine field of 15.7 T for the 2:17 phase and 17.5 T for the 2:19 phase, respectively.

I. INTRODUCTION

The discovery of the new $\text{Nd}_2(\text{Fe},\text{Ti})_{19}$ phase,¹ which is an intermediate phase between the well-known $\text{Nd}_2(\text{Fe},\text{Ti})_{17}$ and $\text{Nd}(\text{Fe},\text{Ti})_{12}$ phases, opens up an alternative choice for potential use as nitride permanent magnets similar to $\text{Sm}_2\text{Fe}_{17}\text{N}_x$.² Magnetic studies showed that both the magnetization and Curie temperature of the new 2:19 phase are very similar to those of the 2:17 phase.^{1,3} From a consideration of the dumb-bell replacement sequence, we have shown in a previous article⁴ that the 2:19 phase has a monoclinic structure³ derived from the orthorhombic ScFe_6Ga_6 structure.^{5,6} Both the $\text{Nd}_2(\text{Fe},\text{Ti})_{17}$ and $\text{Nd}(\text{Fe},\text{Ti})_{12}$ structures are formed by the replacement of a fraction of the Ca sites in the hexagonal CaCu_5 structure with transition-metal dumb-bells. This process may be illustrated by the formula

$$R_{1-x}(2T)_xT_5 \rightarrow RT_y,$$

with (i) the 2:17 structure corresponding to $x=1/3$ and (ii) the 1:12 structure corresponding to $x=1/2$. For the new 2:19 structure, we deduced a value of $x=2/5$, which is between 1/3 and 1/2. In this way, we revealed a possible structure chain for the CaCu_5 -related structures; namely 1:5, 1:7, 2:17, 2:19, ..., 1:12.⁴

In this article we report results from our systematic study of the Pr-Fe-Ti phase diagram. In particular, we report the formation of the new $\text{Pr}_2(\text{Fe},\text{Ti})_{19}$ phase and also preliminary results from a study of the magnetic properties of this new compound by ^{57}Fe Mössbauer spectroscopy.

II. EXPERIMENTAL METHODS

A series of $(\text{Pr}_{1-x}\text{Ti}_x)\text{Fe}_5$ samples with $x=0.1, 0.2, 0.25, 0.3, 0.35, 0.4$, and 0.5 were prepared by arc melting in an argon atmosphere. All samples were subsequently annealed at different temperatures in sealed quartz tubes under argon. The samples were wrapped in tantalum foil for the annealing process. They were characterized by (i) powder-x-ray diffraction (XRD) using $\text{CuK}\alpha$ radiation and (ii) scanning elec-

tron microscopy (SEM) with energy-dispersive x-ray analysis (EDAX). ^{57}Fe Mössbauer spectroscopy was carried out at 295 K in a standard transmission geometry using a $^{57}\text{CoRh}$ source. The spectrometer was calibrated with an α -Fe foil.

III. RESULTS

XRD, SEM, and Mössbauer analyses show that all the as-cast samples contain large amounts, ~30%, of α -Fe(Ti), which virtually disappear after annealing at 800 or 1000 °C for 3 days. Only the $(\text{Pr}_{0.65}\text{Ti}_{0.35})\text{Fe}_5$ samples show the existence of the new 2:19 phase, which we study in detail in the remainder of this article. Results for the remainder of the series will be presented elsewhere.

In Fig. 1 we show the SEM micrographs of the $(\text{Pr}_{0.65}\text{Ti}_{0.35})\text{Fe}_5$ samples: (a) annealed at 850 °C/3 days followed by 1000 °C/3 days and (b) at 1000 °C/3 days; we denote these two samples as samples A and B, respectively. For sample A, the dominant phase is 2:17 with a Pr:Fe:Ti ratio of 10.7:86.2:3.1 [Fig. 1(a)]. For sample B, the dominant phase is the new 2:19 structure with a Pr:Fe:Ti ratio of 9.2:85.9:4.9 [Fig. 1(b)]. Both samples contain small amounts of α -Fe(Ti) impurity.

These SEM/EDAX results were confirmed by the powder XRD data as shown in Fig. 2. The XRD pattern of sample A shows the typical reflections of the rhombohedral $\text{Th}_2\text{Zn}_{17}$ structure [Fig. 2(a)], while the XRD pattern of sample B gives a 2:19 structure, in which there is a characteristic peak located at $\sim 39.7^\circ$ [Fig. 2(b)] as observed in the XRD pattern of the $\text{Nd}_2(\text{Fe},\text{Ti})_{19}$ phase.^{1,3}

Figure 3 shows the ^{57}Fe Mössbauer spectra collected at 295 K for sample A [Fig. 3(a)] and sample B [Fig. 3(b)]. Our analysis of these two spectra employed three magnetically split sextets with variable linewidths. Inclusion of extra subspectra in the fitting procedure has little effect on the average hyperfine field value. It is reasonable to believe that the $\text{Pr}_2(\text{Fe},\text{Ti})_{19}$ phase should have multiple Fe sites since the x-ray-diffraction study indicates a quite complex crystal structure.^{1,3} As mentioned earlier, the 2-19 phase is an inter-

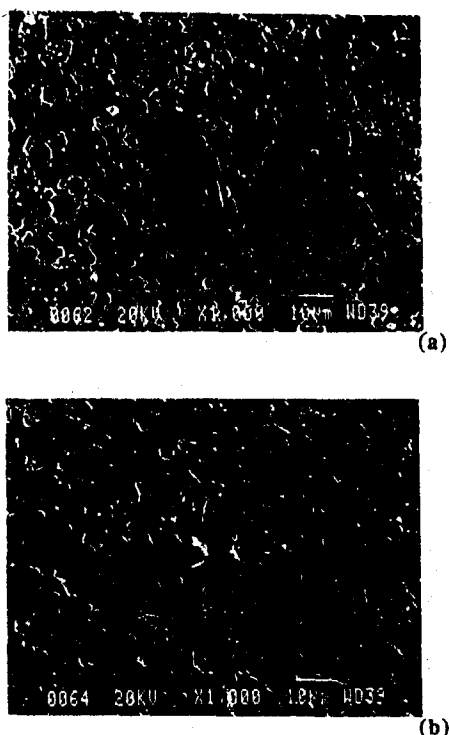


FIG. 1. SEM micrographs of $(\text{Pr}_{0.65}\text{Ti}_{0.35})\text{Fe}_5$: (a) sample A, annealed at 850 °C for 3 days followed by 1000 °C for 3 days; and (b) sample B, annealed at 1000 °C for 3 days.

mediate phase between well-known 2-17 and 1-12 phases; these two phases all have three or more Fe sites. The theoretical fits are represented by solid lines in Fig. 3; these fits yield an average ^{57}Fe hyperfine field of 15.7 T for the

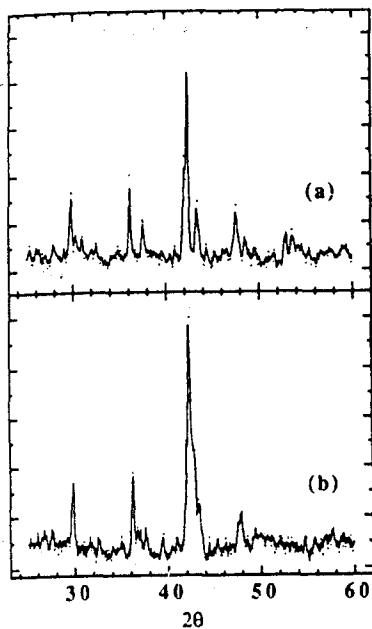


FIG. 2. Powder-x-ray-diffraction patterns ($\text{CuK}\alpha$) of $(\text{Pr}_{0.65}\text{Ti}_{0.35})\text{Fe}_5$: (a) sample A and (b) sample B (same as in Fig. 1).

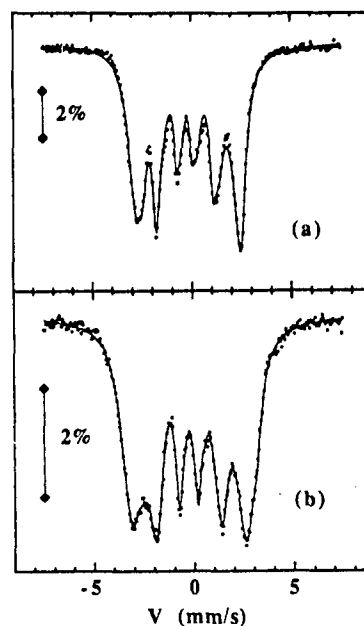


FIG. 3. ^{57}Fe Mössbauer spectra (at 295 K) of $(\text{Pr}_{0.65}\text{Ti}_{0.35})\text{Fe}_5$: (a) sample A and (b) sample B (same as in Fig. 1). Solid lines represent the theoretical fits.

$\text{Pr}_2(\text{Fe,Ti})_{17}$ phase and 17.5 T for the $\text{Pr}_2(\text{Fe,Ti})_{19}$ phase, respectively. The difference in the magnitude of the average hyperfine field between the 2:17 and 2:19 Pr-Fe-Ti phases is 1.8 T, compared to the corresponding value of 2.3 T in the Nd-Fe-Ti system (18.9 T for the 2:17 phase and 21.2 T for the 2:19 phase).⁴

IV. CONCLUSION

By using a combination of SEM/EDAX, powder-x-ray diffraction, and ^{57}Fe Mössbauer spectroscopy we have investigated the formation of a new ternary intermetallic phase in the Fe-rich corner of the Pr-Fe-Ti phase diagram, namely $\text{Pr}_2(\text{Fe,Ti})_{19}$, with a structure derived from the orthorhombic ScFe_6Ga_6 structure. Mössbauer data show a distinguishable difference in magnitude of the average ^{57}Fe hyperfine field (at 295 K) of the 2:17 (15.7 T) and 2:19 (17.5 T) phases.

ACKNOWLEDGMENTS

This work was supported by the award of a Research Fellowship to H.S.L. by the Australian Research Council (ARC). Research grants from the ARC and Post-Graduate Scholarships to Suharyana by the Indonesian Government and AIDAB are also gratefully acknowledged.

¹S. J. Collocott, R. K. Day, J. B. Dunlop, and R. L. Davis, in Proceedings of the Seventh International Symposium on Magnetic Anisotropy and Coercivity in R-T Alloys, Canberra, July 1992, p. 437.

²H.-S. Li and J. M. D. Coey, in *Handbook of Magnetic Materials*, edited by K. H. J. Buschow (Elsevier, Amsterdam, 1991), Vol. 6, Chap. 1, p. 1.

³J. M. Cadogan, H.-S. Li, R. L. Davis, J. B. Dunlop, A. Margarian, and P. B. Gwan, this Conference.

⁴H.-S. Li, J. M. Cadogan, J.-M. Xu, S. X. Dou, and H. K. Liu, ICAME '93, Aug. 8-13, 1993, Vancouver (to be published in *Hyperfine Interactions*).

⁵N. M. Belyavina and V. Ya. Markiv, *Dopov. Akad. Nauk. Ukr. RSR Ser. B* 12, 30 (1982).

⁶F. Weitzer, K. Hiebl, P. Rogl, and Yu. N. Grin, *J. Appl. Phys.* 68, 3512 (1990).

Magnetic properties of $\text{Gd}(\text{Fe}_{1-x}\text{Co}_x)_9\text{Ti}_2$ alloys

Suharyana, J. M. Cadogan, Hong-Shuo Li, and G. J. Bowden

School of Physics, The University of New South Wales, P.O. Box 1, Kensington, NSW 2033, Australia

Four samples of $\text{Gd}(\text{Fe}_{1-x}\text{Co}_x)_9\text{Ti}_2$ with $x=0.0, 0.1, 0.2$, and 0.3 were prepared by conventional arc melting followed by annealing at 1000°C for 3 days. Powder-x-ray-diffraction patterns of these samples show that all of the samples have a dominant phase with the tetragonal CeMn_6Ni_5 structure. Traces of TiFe_2 are also present. ^{57}Fe Mössbauer spectra have been collected at 80 and 295 K. X-ray-diffraction patterns and Mössbauer spectra on magnetically aligned samples indicate that the easy axis of magnetization is the crystallographic c axis. The Curie temperature increases monotonically with increasing cobalt concentration. The average hyperfine field at 80 K reaches a maximum of $26.8(5)$ T for $x\approx 0.2$.

I. INTRODUCTION

Rare-earth (R) transition-metal (T) intermetallic compounds, denoted as RT_{11} , with the tetragonal CeMn_6Ni_5 structure have been the subject of several investigations.¹⁻⁵ In particular, it has been shown¹ that the series of intermetallic compounds $\text{GdFe}_{9-x}\text{Co}_x\text{Ti}_2$ crystallize in the tetragonal CeMn_6Ni_5 structure with the space group $P4/mbm$.⁶ The Curie temperature T_c of the $\text{GdFe}_{9-x}\text{Co}_x\text{Ti}_2$ compounds for $x=0, 1$, and 3 has also been determined¹ and it was found that the T_c increased monotonically with Co concentration, from 280 to 450 K.

A special study has also been made of the tetragonal ThMn_{12} phase in $\text{GdFe}_{12-x}\text{Ti}_x$ compounds with $x=1$ and 1.5 ,² and Sm-Fe-Ti-Nb alloys in the atomic ratio of $14.5/75.0/9.5/1.0$.³ Even though the emphasis was on the 1-12 structure, the formation of a secondary 1-11 phase, with the CeMn_6Ni_5 structure, in annealed samples of both as-cast and melt-spun samples, was observed. A CeMn_6Ni_5 1-11 phase has also been reported in the Sm-Fe-Ti system near the tie line $\text{Sm}_2\text{Fe}_{17}\text{-TiFe}_2$.⁴ Finally, the CeMn_6Ni_5 structure has also been observed in $\text{YFe}_{11-x}\text{Ti}_x$ alloys,⁵ when $x=2$.

In this paper, we report ^{57}Fe Mössbauer experiments on both magnetically aligned and random powder samples of $\text{Gd}(\text{Fe}_{1-x}\text{Co}_x)_9\text{Ti}_2$. It is shown, both by Mössbauer spectroscopy and x-ray diffraction (XRD), that the direction of easy magnetization lies along the c axis, at least for $x>0$. It is also found that the average ^{57}Fe magnetic hyperfine field in $\text{Gd}(\text{Fe}_{1-x}\text{Co}_x)_9\text{Ti}_2$ reaches a maximum when $x=0.2$, in accord with expectations based on the Slater-Pauling curve for Fe/Co alloys.

II. EXPERIMENTAL DETAILS

The samples of $\text{Gd}(\text{Fe}_{1-x}\text{Co}_x)_9\text{Ti}_2$ with $x=0.0, 0.1, 0.2$, and 0.3 were prepared by arc melting, followed by annealing at 1000°C for 3 days. Powder XRD patterns were obtained using a Siemens diffractometer with $\text{CuK}\alpha$ radiation. The samples comprise a dominant phase with the tetragonal CeMn_6Ni_5 structure, but with traces of TiFe_2 . The ^{57}Fe Mössbauer spectra were collected at 80 and 295 K using a constant acceleration transmission spectrometer, with a $^{57}\text{CoRh}$ source. The low-temperature Mössbauer spectra were obtained using an Oxford Instruments CF506A continuous flow cryostat and an ITC-4 temperature controller (± 0.1 K). The spectrometer was calibrated using an $\alpha\text{-Fe}$ foil. The

magnetically aligned samples were prepared by mixing fine powder with epoxy resin and subsequently allowing the mixture to set in an applied magnetic field of 2.0 T at 295 K. For the Mössbauer experiments on aligned samples, the γ -ray direction was parallel to the direction of magnetic alignment. Curie temperatures were determined using ac susceptibility measurements with a frequency of 87 Hz. In addition, ac susceptibility measurements were also carried out in the temperature range 77–295 K, but no signs of magnetization reorientations were observed.

III. RESULTS

Typical XRD patterns on a random powder and a magnetically aligned samples of $\text{Gd}(\text{Fe}_{1-x}\text{Co}_x)_9\text{Ti}_2$ for $x=0.3$ can be seen in Figs. 1(a) and 1(b), respectively. Similar results were obtained for $x=0.1$ and 0.2 . For $x=0$ the Curie temperature T_c lies below room temperature, thereby precluding measurements on aligned samples. The main reflec-

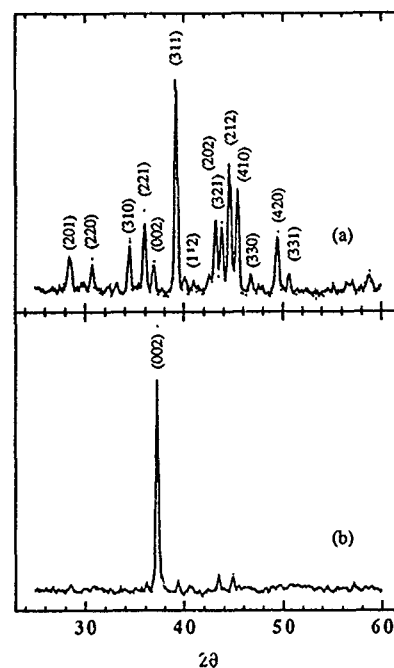


FIG. 1. X-ray-diffraction patterns for a (a) random powder and (b) magnetically aligned sample of $\text{Gd}(\text{Fe}_{0.7}\text{Co}_{0.3})_9\text{Ti}_2$.

TABLE I. Lattice parameters, Curie temperature, and average hyperfine field of $\text{Gd}(\text{Fe}_{1-x}\text{Co}_x)_2\text{Ti}_2$ compounds with $x=0.0, 0.1, 0.2$, and 0.3 .

x	a (Å)	c (Å)	T_c (K)	$\mu_0\langle H_{\text{hf}} \rangle$ (T)	
				295 K	80 K
0.0	8.247(7)	4.837(7)	285(5)	0.0	25.4(5)
0.1	8.244	4.830	314	14.3(5)	26.7
0.2	8.293	4.856	398	20.4	26.8
0.3	8.222	4.866	423	21.3	25.1

tion peaks were indexed according to the tetragonal CeMn_6Ni_5 structure, but with traces of the hexagonal Laves phase TiFe_2 . From a comparison of the random powder and aligned x-ray patterns, it is clear that the easy axis of magnetization is the crystallographic c axis of the tetragonal CeMn_6Ni_5 structure. Only the (002) reflection is important in the magnetically aligned sample. In Table I we give the lattice parameters as a function of the Co concentration. Also included in Table I are the Curie temperatures determined by ac susceptibility measurements, which rise monotonically with increasing Co concentration.

The ^{57}Fe Mössbauer spectra at 295 K obtained using polycrystalline powder samples can be seen in Fig. 2(a). The spectra were fitted with (i) four magnetically split sextets and (ii) a quadrupole doublet for the TiFe_2 contaminant. The TiFe_2 Laves phase appears in a rather wide compositional range, 26.9–35.4 at. % Ti.⁷ The measured quadrupole split-

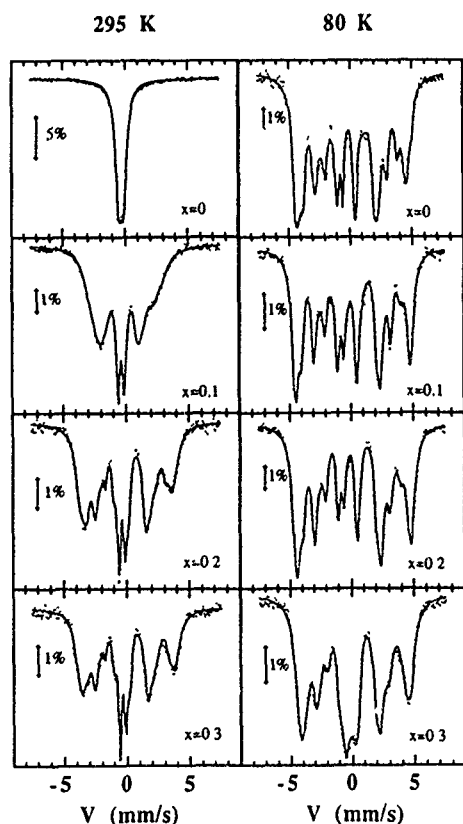


FIG. 2. ^{57}Fe Mössbauer spectra for random powder samples of $\text{Gd}(\text{Fe}_{1-x}\text{Co}_x)_2\text{Ti}_2$, where $x=0.0, 0.1, 0.2$, and 0.3 at (a) 80 K and (b) 295 K.

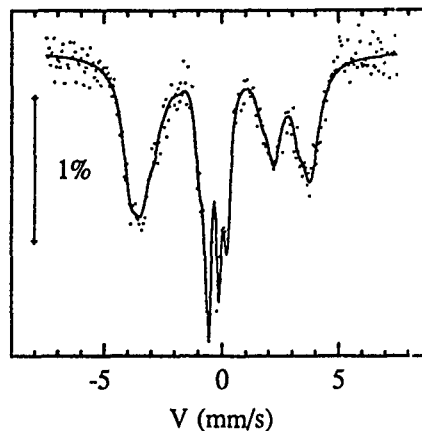


FIG. 3. ^{57}Fe Mössbauer spectra for a magnetically aligned sample of $\text{Gd}(\text{Fe}_{0.7}\text{Co}_{0.3})_2\text{Ti}_2$ at 295 K.

ting was found to be 0.35 mm/s, which is somewhat less than the value of 0.4 mm/s for pure crystalline TiFe_2 .⁸

Because of the considerable broadening of the hyperfine field distribution, caused by the Fe/Co occupations of the nearest-neighbor shells, the linewidths of the outer, middle, and inner lines of the magnetically split spectra were varied independently. In practice, the area of the Mössbauer spectrum associated with the contaminant TiFe_2 was found to be $\approx 15\%$. The ^{57}Fe Mössbauer spectra at 80 K can be seen in Fig. 2(b). The situation is now slightly more complicated because the TiFe_2 impurity phase is magnetically split below 280 K.⁷ At 80 K we find the magnetic hyperfine field of TiFe_2 in our compounds to be ≈ 7 T, which is in reasonable agreement with that determined by other workers.^{9,10}

The average ^{57}Fe magnetic hyperfine field as a function of the Co concentration can be seen in Table I. This reveals that at 80 K the magnetic hyperfine field reaches a maximum when $x \approx 0.2$. This is in reasonable agreement with expectations based on the Slater-Pauling curve for Fe-Co alloys.^{11,12} Similar behavior has been observed in the $\text{Y}(\text{Fe}_{1-x}\text{Co}_x)_2$,¹³ $\text{Y}(\text{Fe}_{1-x}\text{Co}_x)_3$, and $\text{Dy}(\text{Fe}_{1-x}\text{Co}_x)_3$ (Ref. 14) intermetallic compounds. This observation suggests that the magnitudes of both the Fe magnetic moments and hyperfine fields are determined, primarily, by the 3d bands associated with the Fe/Co sublattices.

In Fig. 3 the ^{57}Fe Mössbauer spectrum of a magnetically aligned $\text{Gd}(\text{Fe}_{0.7}\text{Co}_{0.3})_2\text{Ti}_2$ sample at 295 K can be seen. The solid line represents a theoretical fit, obtained using a variable angle θ , between the c axis and the direction of incident γ rays. The computed value of θ was found to be 21.0° , which strongly supports our conclusion based on the x-ray data, shown in Fig. 1(b). Thus, the easy direction of magnetization is the crystallographic c axis of the tetragonal CeMn_6Ni_5 structure. Since Gd^{3+} is in S state, the magneto-crystalline anisotropy of compounds under investigation must be determined by the properties of the Fe/Co sublattices.

IV. CONCLUSIONS

Both powder-x-ray diffraction and ^{57}Fe Mössbauer experiments on magnetically aligned samples show that the

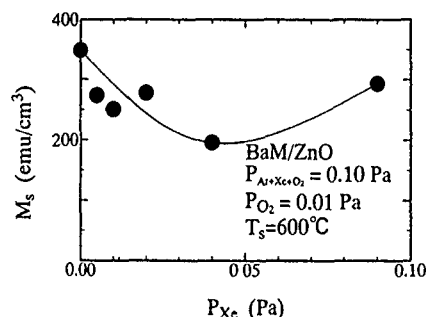


FIG. 5. Dependencies of saturation magnetization M_s on Xe pressure P_{Xe} .

arrive at the substrate after a few collisions with atoms of the working gas. The Fe, O, and even Ba atoms sputtered by Xe ions can arrive at the substrate with relatively high kinetic energy, enough to form BaM ferrite crystallites with good c -axis orientation. Therefore, the values of $\Delta\theta_{50}$ for both BaM layers deposited at P_{Ar+O_2} and P_{Xe+O_2} of 0.1 Pa were smaller and almost the same.

At P_{Xe} of 0.04 Pa, the sputtering phenomena and the collision of sputtered particles with the working gas seemed to be more complicated. There may be apparent differences in kinetic energies among deposited particles. Although the atoms sputtered by heavier Xe ions and collided with Ar or Xe atoms seem likely to possess relatively high energy and make a long walk on the substrate, the atoms sputtered by lighter Ar ions and collided with heavier Xe atoms seem likely to possess insufficient energy for a random walk on the substrate. Therefore, $\Delta\theta_{50}$ of the BaM layer deposited in mixed gases at P_{Xe} of 0.04 Pa might take a larger value than those at P_{Xe} of 0.00 and 0.09 Pa. It also seems that this nonuniformity of kinetic energy of deposited particles causes a very rough and nonuniform surface morphology for the films deposited in a mixture gases as seen in Figs. 3(c) and 3(d).

C. Magnetic characteristics

Figure 5 shows the P_{Xe} dependencies of the saturation magnetization M_s of the BaM layer. M_s of the BaM layer deposited at P_{Xe} of 0.00 Pa took the maximum value of 350 emu/cm³ and was not so different from the bulk M_s of 380 emu/cm³. M_s decreased with increase of P_{Xe} up to 0.04 Pa and took the minimum value of 196 emu/cm³ at P_{Xe} of 0.04 Pa, of which the value was as relatively large as 293 emu/cm³ at P_{Xe} of 0.09 Pa. These dependencies seemed to have a relationship distinctly close to the layer morphology and $\Delta\theta_{50}$ of films as seen in Figs. 3 and 4.

Figure 6 shows the P_{Xe} dependencies of the perpendicular and in-plane coercivities $H_{c\perp}$ and $H_{c\parallel}$, respectively. Al-

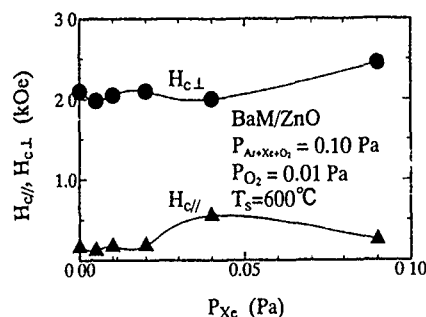


FIG. 6. Dependencies of perpendicular and in-plane coercivities $H_{c\perp}$ and $H_{c\parallel}$ on Xe gas pressure P_{Xe} .

though $H_{c\perp}$ was almost constant at about 2.0 kOe, $H_{c\parallel}$ took the maximum value of 0.6 kOe at P_{Xe} of 0.04 Pa. Since $H_{c\parallel}$ corresponds apparently to $\Delta\theta_{50}$, such a large $H_{c\parallel}$ at P_{Xe} of 0.04 Pa was attributed to the degradation of crystallinity implied by larger $\Delta\theta_{50}$ at P_{Xe} of 0.04 Pa as seen in Fig. 4.

IV. CONCLUSION

BaM ferrite layers were deposited on a ZnO underlayer at T_s of 600 °C at P_{Ar+Xe} of 0.09 Pa and O_2 at P_{O_2} of 0.01 Pa. The obtained results are as follows.

(i) BaM layers deposited at P_{Xe} of 0.09 Pa revealed a smooth surface appearance and excellent crystallinity with $\Delta\theta_{50}$ of 4°. In addition, they exhibited good magnetic characteristics such as M_s and $H_{c\perp}$ and $H_{c\parallel}$ of about 293 emu/cm³ and 2.0 and 0.3 kOe, respectively.

(ii) BaM layers deposited in the mixed gas at P_{Ar} , P_{Xe} , and P_{O_2} of 0.05, 0.04, and 0.01 Pa, respectively, had rough surface texture and worse crystallinity with $\Delta\theta_{50}$ of 8.7°. They exhibited smaller M_s and higher $H_{c\parallel}$ of 196 emu/cm³ and 0.6 kOe, respectively.

It seems to be possible to deposit the BaM layer with good crystallinity and magnetic characteristics on a ZnO underlayer using a mixture of O_2 and Xe instead of Ar as the sputtering gas.

¹ T. Fujiwara, IEEE Trans. Magn. **MAG-21**, 1480 (1985).

² E. Lacroix, P. Gerard, G. Marest, and M. Dupuy, J. Appl. Phys. **69**, 4770 (1991).

³ K. Yamamori, T. Tanaka, and T. Jitoshio, IEEE Trans. Magn. **MAG-27**, 4960 (1992).

⁴ M. Naoe, K. Noma, S. Nakagawa, and N. Matsushita, **73**, 6696 (1993).

⁵ M. Naoe, S. Hasunuma, Y. Hoshi, and S. Yamanaka, IEEE Trans. Magn. **MAG-17**, 3184 (1981).

⁶ I. Zaquine, H. Benazizi, and J. C. Mage, J. Appl. Phys. **64**, 5822 (1988).

⁷ M. Matsuoka and M. Naoe, J. Appl. Phys. **57**, 4040 (1985).

⁸ M. Naoe, S. Yamanaka, and Y. Hoshi, IEEE Trans. Magn. **MAG-16**, 646 (1980).

⁹ N. Matsushita, S. Nakagawa, and M. Naoe, IEEE Trans. Mag. **MAG-28**, 3108 (1992).

Magnetic resonance in PdFe alloys near T_c

A. N. Medina, V. S. Oliveira, and F. G. Gandra

Instituto de Física Gleb Wataghin, Universidade Estadual de Campinas, Campinas, SP, 13083-970, Brazil

A. A. Gomes

Centro Brasileiro de Pesquisas Físicas, R. Dr. Xavier Sigaud 150, Rio de Janeiro, RJ, 22290-180, Brazil

Magnetic resonance results in $\text{Pd}_{1-x}\text{Fe}_x$, with various Fe concentrations, are reported. The samples were prepared in the form of foils, 200 and 100 μm thick, and Fe concentrations of 0.2, 0.5, 1.0, and 1.5 at. %. The experiments were carried out at low temperature, close to the T_c of each alloy. For the more concentrated alloys and magnetic field perpendicular to the foil, more than one line is observed. The anomalies in the resonance spectrum are interpreted in terms of the existing giant moments in these alloys.

I. INTRODUCTION

$\text{Pd}_{1-x}\text{Fe}_x$ is ferromagnetic at low temperature, the Curie temperature $T_c(x)$, depending on Fe concentration. In an early magnetic resonance experiment,¹ made at temperatures between 1.5 and 25 K, a single line was observed for $x \leq 0.5$, and with the g value close to 2.18. No anomaly in the spectra was reported.

In our experiments, using samples of the same shape, we found extra resonance lines for Fe concentrations larger than 0.5%. It was also observed for low-concentration samples that the spectra are distorted. To investigate the origin of these lines, we observed the resonance as a function of sample thickness, Fe concentration, and for temperatures close to $T_c(x)$.

It is well known that Fe impurities dissolved in highly exchange-enhanced materials such as Pd induce giant moments due to the propagating polarization in the highly polarizable host.² Since the coupling of the Fe moment to this magnetic cloud is strong, one expects that the resonance spectrum may be different from that of isolated Fe atoms in, say, an insulating cubic material. Also, this complex metallic system requires a specific adaptation of the usual resonance theory. Although aware that Fe moments here are not localized in the same sense of a rare earth, we assume the resonance theory for local moments apply. The existence of polarized clusters, which follow the dynamics of the central Fe moment, will be included as an effective "anisotropy." Due to the shape of the samples, we derive parallel and perpendicular expressions for the field for resonance.

II. EXPERIMENTAL PROCEDURES

The samples were arc melted under argon atmosphere using 99.9% Fe and 99.99% Pd. The button was cold rolled to 200 μm and the thinner samples for the same concentration were obtained from this foil. All samples were annealed in argon at 810 °C for 3 days before the experiments.

The magnetic resonance experiments were carried out in a home-made homodine spectrometer with 3 mW microwave power in X band (9.34 GHz) and field modulation of 40 Oe peak to peak at 10 kHz. The samples were attached to the cold finger of the temperature variation system using thermal paste and Teflon tape. There was no contribution of the base

line to the spectra at low temperature because the signal of the sample is very intense.

III. EXPERIMENTAL DATA AND ANALYSIS

The magnetic resonance spectra of $\text{Pd}_{1-x}\text{Fe}_x$ foils of 200 μm thickness and several concentrations are shown in Fig. 1. Clearly the spectrum is composed of more than one line, in particular for concentrations above 0.5%. This observation induces a natural question about the existence of extra phases.

Since Fe is quite soluble in Pd, thermal annealing³ removes any existent sample inhomogeneity and other metallic phases such as Pd_3Fe . It remains to exclude other materials such as insulating oxides. To check this point the sample is reduced to powder, obtained from the same button. The result is a perfect Dysonian line, characteristic for metals, thus excluding the existence of oxides.

It is known that the lamination process can originate some degree of orientation of the foils. To find out the influence of the resulting (110) orientation of the foil on the resonance results, spectra were obtained for a 200 μm slab, cut

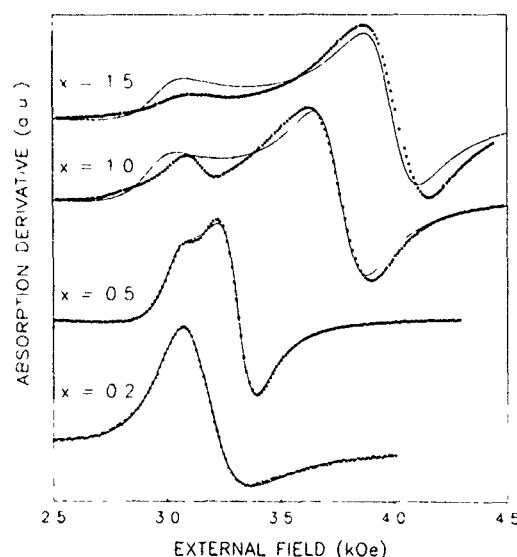


FIG. 1 $\text{Pd}_{1-x}\text{Fe}_x$, $x=0.2\%$, 0.5% , 1% , 1.5% resonance spectra at 7 K and 9.343 GHz of 200 μm foils with external field perpendicular to the surface. Dots indicate experiment and line indicates calculation.

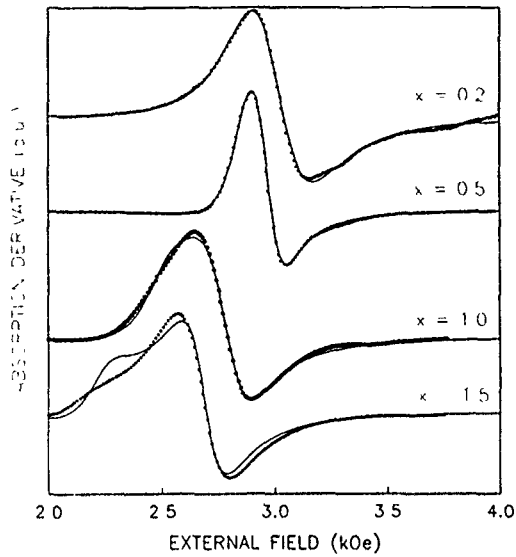


FIG. 2. Pd:Fe(x), $x=0.2\%$, 0.5% , 1% , 1.5% resonance spectra at 7 K and 9.343 GHz of 200 μm foils with external field parallel to the surface. Dots indicate experiment and line indicates calculation.

from the 1% button, using a 0.2-mm-thick diamond saw. The result as compared to Fig. 1 indicated the same spectrum, thus discarding the influence of orientation, since the button was completely nonoriented.

In Figs. 1 and 2 we show the spectra for 200 μm foils, for several concentrations, parallel and perpendicular external field orientation, at 7 K. The lower-field line shows less variation as compared to the high-field one when Fe concentration is changed.

A possible interpretation for this comes from the magnetization behavior. When Fe concentration is increased, $T_c(x)$ and M increase, the same occurring with the demagnetization field, thus shifting the position of the resonance line. Since the magnetization is not saturated, demagnetization is field dependent and consequently the two lines will not shift the same amount. For 0.2% and $T > T_c$ we observed one line with metallic shape but a field orientation dependence still persists.

The interpretation of our experimental spectra relies on two possibilities. The first one considers the existence of "good" moments, subjected to shape demagnetization and effective anisotropy field. The second contemplates long-range macroscopic ferromagnetic order. However, in usual ferromagnetic resonance one must fulfill special conditions⁴ to observe this two-line scenario.

We adopt then a modified version of the first possibility, taking into account the existence of the giant moments. Then one introduces effective spins submitted to anisotropy, the origin of the latter being associated with the existence of giant moments. These giant moments induced in Pd by the Fe impurity, confined in these foils, and strongly coupled to the Fe moments, will hinder the free rotation of the Fe moments. It is then reasonable to describe this effect through an effective anisotropy induced by these large magnetic clusters. This anisotropy acts on the effective local magnetic mo-

ments in such a way as to produce a spectrum with two possible g values.

From now on we assume the usual theory for resonance phenomena, taking into account, however, that Dysonian line shapes exist with two g values: g_{\perp} and g_{\parallel} . It is essential, however, to take into account that one has a polycrystalline sample, and thus a powder spectrum should be calculated. In principle, for temperatures larger than T_c we should get one distorted line, but corrections due to internal fields are necessary in both ordered and disordered magnetic phases.

The internal effective field for perpendicular [Eq. (1a)] and parallel [Eq. (1b)] orientations of the external field H to the foil are given by⁵

$$H_{\text{eff}} = (H - 4\pi M_s + H_a), \quad (1a)$$

$$H_{\text{eff}} = \sqrt{H(H + 4\pi M_s - H_a)}, \quad (1b)$$

where 4π is the demagnetization factor for the foil and H_a is the phenomenological effective anisotropy field attributed here to field inhomogeneities, surface effects, magnetocrystalline anisotropy, etc. M_s is the saturation magnetization, but since we are close to T_c , we use $M(H)$ instead. We assume that the alloy magnetization varies linearly with field, in the range from 0 to 4 kOe, such that $M = M_0 + H \, dM/dH$. Since we are close to T_c only terms proportional to H are retained. Here, $M_0 = 0$ and dM/dH is a fitting parameter.

The intensity of the first derivative of the powder spectrum is given by⁶

$$Y'(H) = C \int_{H_1}^{H_2} F'(H, H') \frac{[1 + (H_{\parallel}/H')^2]}{[1 - (H'/H_{\perp})^2]} dH', \quad (2)$$

where C is the amplitude, $H_{\parallel} = h\nu/\mu_b g_{\parallel}$, $H_{\perp} = h\nu/\mu_b g_{\perp}$ with ν the microwave frequency and μ_b the Bohr magneton. $F'(H, H')$ is the field derivative of the metallic line shape

$$F(H, H') \propto M \frac{1 + \alpha x}{(1 + x^2)}, \quad x = \frac{H_{\text{eff}} - H'}{\Delta H}. \quad (3)$$

In this expression, α is a dispersion parameter, ΔH is the linewidth, and the effective field H_{eff} is given by Eq. (1) using M in the limit of linear field dependence and neglecting H_a . The field derivative of the line is

$$F'(H, H') \propto \left[-\frac{B}{\Delta H} \frac{H^2}{H_{\text{eff}}} \left(1 - 2\pi \frac{dM}{dH} \right) + \left(A - \frac{2\pi B H^2}{\Delta H H_{\text{eff}}} \frac{dM}{dH} \right) \right], \quad (4a)$$

$$F'(H, H') \propto \left[A + \frac{B H}{\Delta H} \left(4\pi \frac{dM}{dH} - 1 \right) \right], \quad (4b)$$

respectively, for H parallel and perpendicular to the foil, where $A = (1 + \alpha x)/(1 + x^2)$, $B = -dA/dx$. Expressions (4a) and (4b) are substituted in expression (2) to fit the experimental data with an overall amplitude C , ΔH , H_{\parallel} , H_{\perp} , α , and dM/dH as fitting parameters.

The results are shown in Table I and Figs. 1 and 2 show the theoretical curves. Considering the degree of complexity presented by Eq. (2), the fitting to the experimental data is quite good. For $x=0.2$, there is no clear evidence for an extra

TABLE I. Fitting parameters of the powder spectra for $T=7$ K and $200\text{ }\mu\text{m}$. $g \pm 5\%$, $\Delta H \pm 10\%$. The symbols \perp and \parallel in the first column refer to the external field orientation to the sample surface.

Conc. at. %		g_{perp}	g_{\parallel}	ΔH (kOe)	dM/dH (10^{-4})
0.2	\perp	2.15	2.17	0.212	9
	\parallel	2.19	2.21	0.229	15
0.5	\perp	2.14	2.35	0.098	58
	\parallel	2.19	2.28	0.105	42
1.0	\perp	1.91	2.44	0.141	60
	\parallel	2.19	2.44	0.167	155
1.5	\perp	1.80	2.40	0.147	60
	\parallel	2.14	2.58	0.160	275

line and the g_{\perp} and g_{\parallel} values are very close to each other. We verify also that dM/dH is not large and with near values for both orientations. This fact seems reasonable since the working temperature is 7 K and T_c is about 4 K. For this sample, the linewidth as a function of temperature is linear, the g value close to 2.18. This behavior is appropriate for a paramagnet, but we should mention that the internal field is corrected by about 100 Oe due to the high susceptibility of the sample.

For higher concentrations, the difference between g_{\perp} and g_{\parallel} increases as concentration goes to 1.5%, showing that the anisotropy associated with the giant moment is also increasing. This is associated with the improvement of connectivity in the percolating and interacting magnetic clusters embedded in the foil-like sample.

The effective anisotropy field H_a is evaluated for $x \geq 0.5\%$ in the following way: Considering that $H_a/H \ll 1$ we note from Eqs. (1a) and (1b) that the correction to the internal field is very small for H parallel to the sample surface, so we assume that the correct g values are extracted from this configuration. H_a is then evaluated by the difference of the fields corresponding to g_{\perp} for both configurations of the external field (g_{\parallel} is not used here because it is more affected by error). The values for H_a are 70, 450, and 590 Oe, respectively, for 0.5%, 1%, and 1.5%. The obtained anisotropy fields are small as compared to the resonance field and increase with increasing Fe concentration. This results from the improved ferromagnetic properties of the samples.

In Fig. 3 we show the temperature dependence of the resonance spectra for $x=1\%$. When temperature increases g_{eff} decreases toward 2.1 and, for $T > T_c$ ($T_c \approx 38$ K), the spectrum shows a single line.

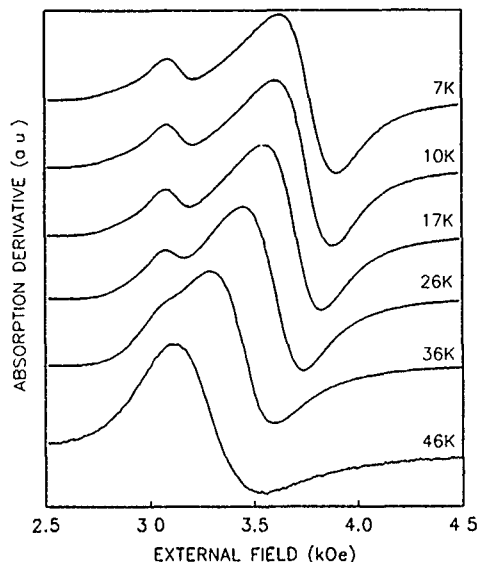


FIG. 3. Temperature dependence for Pd:Fe(1%), $200\text{ }\mu\text{m}$, and external field perpendicular to sample surface.

IV. CONCLUSIONS

We have presented a very simple model for the resonance in PdFe alloys, characterized by the existence of giant moments. We define effective localized moments to describe the resonance spectrum. Also, anisotropy associated with the giant moment is responsible for slightly different g values, originating the powder spectrum.

Using the g shift for the $x=0.2\%$ and 1.5% , the ρJ product ratio is estimated to be 1.4. This is consistent with a higher coupling of the interacting clusters, qualitatively understood in terms of an effective spin, via an increasing product ρJ .

ACKNOWLEDGMENTS

This work was partially supported by FAPESP, CNPq, and FAEP-Unicamp.

¹R. A. B. Devine, J. Phys. F 7, 461 (1977); Solid State Commun. 19, 351 (1976).

²T. Morya, in *Spin Fluctuations in Itinerant Electron Magnetism*, Springer Series in Solid State Sciences Vol. 56 (Springer, Berlin, 1985); Prog. Theor. Phys. 34, 329 (1965).

³J. Crangle and W. R. Scott, J. Appl. Phys. 36, 921 (1965); J. Crangle, Philos. Mag. 5, 335 (1960).

⁴C. Surig, K. A. Hempel, and F. Schumacher, J. Magn. Magn. Mater. 117, 441 (1992).

⁵Y. Li, M. Farle, and K. Baberschke, J. Magn. Magn. Mater. 93, 345 (1991).

⁶C. P. Poole, in *Electron Spin Resonance: A Comprehensive Treatise on Experimental Techniques*, 2nd ed. (Wiley, New York, 1983).

Effects of Co and Y substitution on magnetic properties of CeFe₂

Xianfeng Zhang and Naushad Ali

Department of Physics and Molecular Science Program, Southern Illinois University, Carbondale, Illinois 62901

CeFe₂ orders ferromagnetically (FM) below $T_C=227$ K; however, this FM state is inherently unstable and partial substitution of Fe by Co precipitates the instability of FM state and a ferromagnetic to antiferromagnetic (AFM) phase transition is observed at lower temperature. This second phase transition is a first-order phase transition. The dependence of T_C and T_N on the concentration of Co X for Ce(Fe_{1- X} Co _{X})₂ is presented. For Ce(Fe_{0.8}Co_{0.2})₂, the FM transition is at $T_C=160$ K, and the AFM transition is at $T_N=76$ K. The entropy change associated with the FM to AFM phase transition has been determined from magnetization measurements and found to be primarily associated with a change in the electronic density of states at E_F . If one starts with Ce(Fe_{0.8}Co_{0.2})₂ and partially substitutes Ce by Y, it is found that T_N gradually decreases with Y concentration; and for Y concentration greater than 10%, the AFM phase disappears and FM phase is fully restored. The dependence of T_C and T_N on the concentration of Y Z is presented for Ce_{1- Z} Y _{Z} (Fe_{0.8}Co_{0.2})₂. It is suggested that the second transition (FM to AFM) is a result of the competition between exchange energy and magnetic anisotropy energy. The measurements of magnetization, ac susceptibility, resistivity, and thermal expansivity are presented.

CeFe₂ is a ferromagnet that exhibits some anomalous magnetic properties such as a much lower Curie temperature ($T_C=227$ K) and a much lower magnetic moment per Fe atom ($1.15\mu_B$) than other compounds in the RFe₂ series (R denotes rare earth).¹ A number of investigations²⁻⁴ suggests that the anomalous magnetic properties of CeFe₂ may be due to some transfer of the Ce 4f electrons to the Fe 3d band. This suggestion is supported by experimental data of electronic specific heat coefficients, which are $53 \text{ mJ K}^{-2} \text{ mol}^{-1}$ for CeFe₂,⁵ and $21 \text{ mJ K}^{-2} \text{ mol}^{-1}$ for CeCo₂.⁶

The ferromagnetic state of CeFe₂ is inherently unstable. A small partial substitution of Fe by other elements such as Co, Al, and Ru precipitates the instability of ferromagnetic state and a ferromagnetic (FM) to antiferromagnetic (AFM) phase transition is observed at the temperature T_N , lower than T_C .⁷⁻⁹ This second phase transition is a first-order phase transition in case of Ce(Fe_{1- X} Co _{X})₂.⁷ The magnetic ordering of Ce(Fe_{1- X} Co _{X})₂ has been determined by Kennedy *et al.*¹⁰ using neutron diffraction. The ac susceptibility results by Roy and Coles¹¹ show that the T_C moves up but T_N is suppressed with the increase in Y concentration in Ce_{1- Z} Y _{Z} (Fe_{1- X} Al _{X})₂. They found that T_C increased to 235 K with $Z=0.1$ and went up further to 252 K for $Z=0.15$ in the case of $X=0.035$. The low-temperature transition is no longer present for X greater than 0.15.

According to the x-ray-diffraction studies by Nishihara, Tokumoto, and Yamaguchi,¹² there is a small volume change of 0.05% at T_N for the Ce(Fe_{1- X} Al _{X})₂ system. Kennedy *et al.*¹⁰ also reported a 0.05% cell volume change at T_N in the Ce(Fe_{1- X} Co _{X})₂ system. The 0.05% volume change is too small to apply an exchange-inversion model to explain the FM-AFM transition observed here.

In this article we present the effect of partial substitution of Fe by Co and Ce by Y on magnetic properties of the CeFe₂. Two magnetic phase diagrams are presented for the Ce(Fe_{1- X} Co _{X})₂ and for the Ce_{1- Z} Y _{Z} (Fe_{0.8}Co_{0.2})₂. The entropy change at the FM-AFM transition is determined for Ce(Fe_{0.8}Co_{0.2})₂ as a function of temperature. Some specific

measurements presented here include magnetization, ac susceptibility, resistivity, and thermal expansion for the Ce(Fe_{0.8}Co_{0.2})₂.

The sample preparation and experimental details are described in Refs. 7 and 13.

The magnetization M and ac susceptibility χ_{ac} as a function of temperature for Ce(Fe_{0.8}Co_{0.2})₂ are presented in Figs. 1(a) and 1(b), respectively. It is evident that partial substitution of Fe by Co causes a sharp transition from FM to AFM. The temperature dependence of the electrical resistivity [Fig. 1(c)] also clearly shows this magnetic transition. A significant slope change in the resistivity at 162 K is identified as being due to a paramagnetic (PM)-FM transition which occurs at 160 K in the magnetization measurement. The abrupt rise of the resistivity at 75 K corresponds to FM-AFM tran-

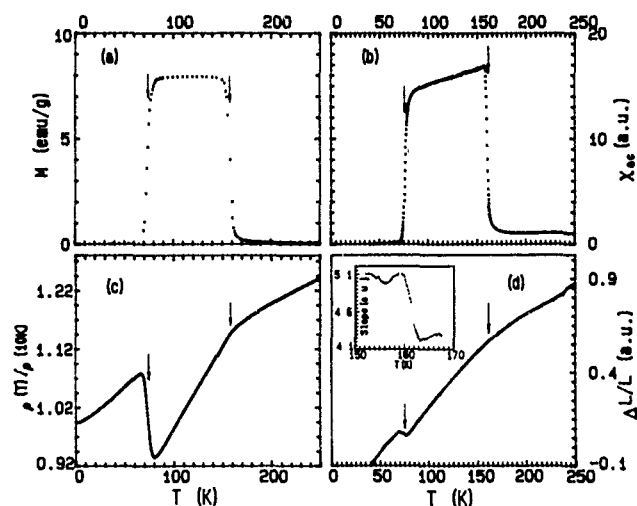


FIG. 1. (a) Magnetization M in an applied magnetic field of 100 G, (b) ac susceptibility χ_{ac} , (c) normalized electric resistivity, $\rho(T)/\rho(10 \text{ K})$, and (d) relative thermal expansivity $\Delta L/L$ as a function of temperature T for Ce(Fe_{0.8}Co_{0.2})₂. The insert of (d) shows the slope of $\Delta L/L$ around 160 K. The arrows indicate the T_C and T_N .

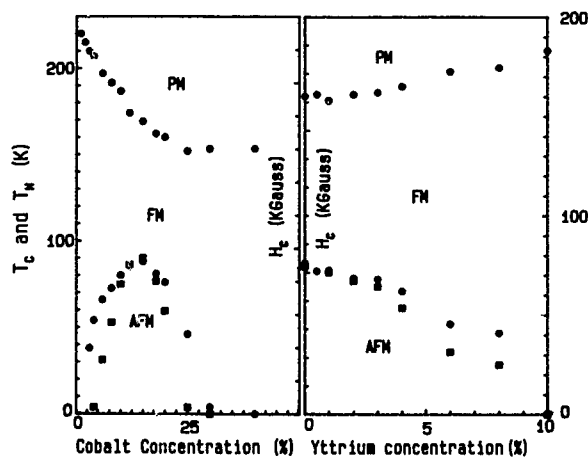


FIG. 2. (a) The T_N (●), T_C (○), and H_C (■) as a function of Co concentration X in $\text{Ce}(\text{Fe}_{1-x}\text{Co}_x)_2$ and (b) the T_N (●), T_C (○), and H_C (■) as a function of Y concentration Z in $\text{Ce}_{1-z}\text{Y}_z(\text{Fe}_{0.8}\text{Co}_{0.2})_2$.

sition. The result of thermal expansivity for $\text{Ce}(\text{Fe}_{0.8}\text{Co}_{0.2})_2$ is presented in Fig. 1(d). We observe a slope change in $(\Delta L/L)$ at $T \approx 162$ K as shown in the insert of the Fig. 1(d) and a step change in $\Delta L/L$ around $T = 75$ K. This result shows conclusively that the phase transition at 162 K is second order and the FM-AFM transition at 75 K is first order. Similar results are obtained for other samples.

Figure 2(a) shows the phase diagram for the system $\text{Ce}(\text{Fe}_{1-x}\text{Co}_x)_2$. The first transition temperature T_C decreases continuously as cobalt concentration increases for $X \leq 0.40$. Meanwhile, the second transition temperature T_N increases first with increasing X and then decreases after a maximum at 15% Co. For the Co concentration higher than 30%, no second transition has been observed down to the temperature of 4.2 K. Here the T_C and the T_N are defined as the temperatures at which the magnetization reaches the half-height of the on-set value.

Figure 3(a) shows magnetization versus temperature for $\text{Ce}_{1-z}\text{Y}_z(\text{Fe}_{0.8}\text{Co}_{0.2})_2$ with various Z values. The T_C increases while T_N decreases with the Z . For $Z = 0.1$, there is

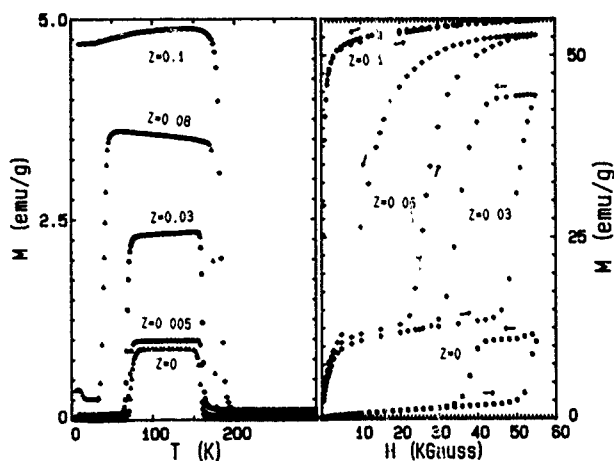


FIG. 3. (a) Magnetization M vs temperature T and (b) isothermal (at $T = 10$ K) magnetization M vs applied magnetic field H for $\text{Ce}_{1-z}\text{Y}_z(\text{Fe}_{0.8}\text{Co}_{0.2})_2$ with various Z values.

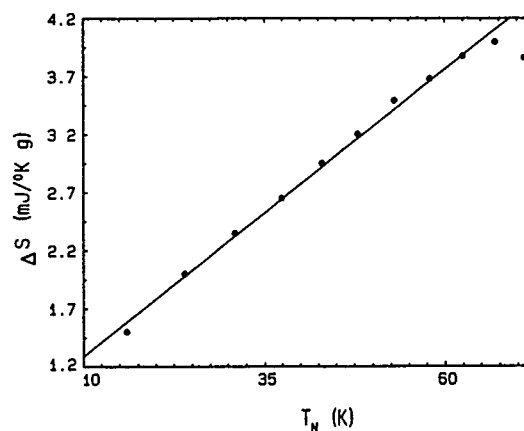


FIG. 4. Total entropy change ΔS as a function of temperature T for $\text{Ce}(\text{Fe}_{0.8}\text{Co}_{0.2})_2$ at the AFM-FM transition temperature.

no FM-AFM transition down to 5 K. A magnetic phase diagram for $\text{Ce}_{1-z}\text{Y}_z(\text{Fe}_{0.8}\text{Co}_{0.2})_2$ as a function of Y concentration is presented in Fig. 2(b). It is quite obvious that the partial substitution of Ce by Y in $\text{Ce}_{1-z}\text{Y}_z(\text{Fe}_{0.8}\text{Co}_{0.2})_2$ reduces the instability of the FM state; and for 10% Y substitution, a complete restoration of the FM state down to 5 K is achieved.

The results of isothermal (at $T = 10$ K) magnetization as a function of applied magnetic field for various Y concentrations is presented in Fig. 3(b). The magnetization increases very sharply at a critical field data H_C (for $Z = 0, 0.03$, and 0.06) with large field hysteresis. This sharp rise in magnetization at a critical field is associated with a field-induced AFM-FM first-order phase transition. We notice that the critical field decreases with increasing concentration of Y and it vanishes for 10% Y concentration.

The field-induced transition is also observed for all samples in the $\text{Ce}(\text{Fe}_{1-x}\text{Co}_x)_2$ system. The critical field H_C is plotted as a function of Co concentration X in Fig. 2(a) and as a function of Y concentration Z in Fig. 2(b). The H_C and T_N are closely associated with each other. In the system $\text{Ce}(\text{Fe}_{1-x}\text{Co}_x)_2$, the H_C and T_N show a maximum around the same X value of 0.15. In $\text{Ce}_{1-z}\text{Y}_z(\text{Fe}_{0.8}\text{Co}_{0.2})_2$, both H_C and T_N decrease monotonically with Y concentration. The field-induced transition and the magnetic hysteresis suggest the presence of magnetic anisotropy.¹⁴ Therefore, it is likely that magnetic anisotropy is a very important factor in the development of the AFM phase. Furthermore, we would like to propose that the competition between the exchange interaction energy and the temperature-dependent magnetic anisotropy energy is responsible for the FM-AFM transition in the itinerant system $\text{Ce}(\text{Fe}_{1-x}\text{Co}_x)_2$.

In an itinerant electron system the exchange interaction energy is directly related with the electronic density of states at the Fermi level.¹ We now present the result of entropy change across the FM-AFM transition, which we hope will provide us with some information on the electronic band structure in $\text{Ce}(\text{Fe}_{1-x}\text{Co}_x)_2$.

Figure 4 presents the change in entropy as a function of temperature for $\text{Ce}(\text{Fe}_{0.8}\text{Co}_{0.2})_2$ calculated using the thermodynamic relationship $\Delta S_T = -\Delta M(\partial H/\partial T)_{T_N}$. ΔS_T is total

entropy change which consists of the lattice entropy change and electronic entropy change across the transition; ΔM is the magnetization change between the AFM state and the FM state at T_N ; and $(\partial H/\partial T)_{T_N}$ is the derivative of the field dependence curve of the transition temperature T_N which can be calculated based on experimental data.¹³

The linearity of the entropy change with T_N suggests that it is the electronic entropy change that is primarily involved in the FM-AFM transition in our system because the electronic entropy can be written as $S_E = \int (C/T) dT = \gamma T$, where $C = \gamma T$ is used and γ is the electronic specific-heat coefficient. Since γ is proportional to the density of the electronic states at the Fermi surface, S_E is strongly influenced by the electronic band structure. At the FM-AFM transition, the electronic entropy change would be $\Delta S_E = (\gamma_{FM} - \gamma_{AFM})T_N$, where γ_{FM} and γ_{AFM} are the electronic specific-heat coefficients for FM and AFM states, respectively. The slope obtained from Fig. 4 is $10 \text{ mJ K}^{-2} \text{ mol}^{-1}$. The value of $\gamma_{FM} - \gamma_{AFM}$ by Wada, Nishigori, and Shiga¹⁵ is $13 \text{ mJ K}^{-2} \text{ mol}^{-1}$. The two values are in good agreement. The above results indicate that the main contribution to the total entropy change at the FM-AFM transition for this system is due to the electronic entropy change. The positive value of ΔS_E means that the electronic density of states at the Fermi level in the FM state is higher than that in the AFM state.

The FM state in CeFe_2 is inherently unstable. This has been recently suggested by the neutron-diffraction studies by Kennedy and Coles¹⁶ and Yang *et al.*¹⁷ They observed an antiferromagnetic component developing below $T \approx 80 \text{ K}$ in CeFe_2 . Wada and co-workers¹⁵ measured the Co concentration dependence of the electronic specific-heat coefficient γ for $\text{Ce}(\text{Fe}_{1-x}\text{Co}_x)_2$. They found that the γ value has a minimum around $x=0.16$. Thus, we may conclude that Co substitution for Fe in $\text{Ce}(\text{Fe}_{1-x}\text{Co}_x)_2$ has two effects: One is to modify the exchange interaction energy via altering the electronic density of states at the Fermi level; and the other is to modify the magnetic anisotropy energy. Generally from our data, the former is suppressed and the latter is enhanced by the Co substitution. Both effects enhance the instability of the FM state and, thus, the FM-AFM transition is likely to occur.

Up to now no experimental γ data for $\text{Ce}_{1-z}\text{Y}_z\text{Fe}_2$ have been reported. Khowash¹⁸ calculated the electronic band

structure for CeFe_2 . His results show that Y substitution for Ce in CeFe_2 may increase the electronic density of states at the Fermi level if we assume the rigid-band model is applicable to $\text{Ce}_{1-z}\text{Y}_z\text{Fe}_2$. On the other hand, our experimental results show that Y substitution for Ce suppresses the magnetic anisotropy. In contrast to the effects of the Co substitution for Fe, the Y substitution for Ce intensifies the stability of the FM state and, thus, prevents the FM-AFM transition.

In summary, the electronic band structure is modified at the FM-AFM transition in the $\text{Ce}(\text{Fe}_{1-x}\text{Co}_x)_2$ system. The FM phase has a higher electronic density of states at the Fermi level than the AFM phase. Co substitution for Fe in the $\text{Ce}(\text{Fe}_{1-x}\text{Co}_x)_2$ system intensifies the instability of FM phase. The Y substitution for Ce in the $\text{Ce}_{1-z}\text{Y}_z(\text{Fe}_{0.8}\text{Co}_{0.2})_2$ suppresses the magnetic anisotropy and gradually restores the stability of the FM phase. Finally, for 10% Y substitution for Ce, the stability of the FM phase is totally restored down to a temperature of 5 K. The competition between exchange interaction and the magnetic entropy is a possible mechanism for the FM-AFM transition observed in CeFe_2 and related pseudobinary compounds.

¹ K. H. J. Buschow, Rep. Prog. Phys. **40**, 1179 (1977).

² O. Eriksson, L. Nordstrom, M. S. S. Brooks, and B. Johansson, Phys. Rev. Lett. **60**, 2523 (1988).

³ P. K. Khowash, Phys. Rev. B **43**, 6170 (1991).

⁴ P. K. Khowash, Physica B **171**, 102 (1991).

⁵ A. K. Rastogi, G. Hilsher, E. Gratz, and N. Pillmayr, J. Phys. (Paris) Colloq. **49**, C8-277 (1988).

⁶ M. A. Sa, J. B. Oliveira, J. M. Machado da Silva, and I. R. Harris, J. Less-Common Met. **108**, 263 (1985).

⁷ N. Ali and X. Zhang, J. Phys. Condensed Matter **4**, L351 (1992).

⁸ A. K. Rastogi and A. P. Murani, in *Proceedings of the International Conference on Valence Fluctuations*, Banzalore, India (Plenum, New York, 1987), p. 437.

⁹ R. G. Pillay, A. K. Grover, V. Balasubramanian, A. K. Rastogi, and P. N. Tandon, J. Phys. F **18**, L63 (1988).

¹⁰ S. J. Kennedy, A. P. Murani, J. K. Cockcroft, S. B. Roy, and B. R. Coles, J. Phys. Condensed Matter **1**, 629 (1989).

¹¹ S. B. Roy and B. R. Coles, J. Phys. Condensed Matter **1**, 419 (1989).

¹² Y. Nishihara, M. Tokumoto, and Y. Yamaguchi, J. Magn. Mater. **70**, 173 (1987).

¹³ X. Zhang and N. Ali, J. Alloys Compounds (to be published).

¹⁴ E. Strykowski and N. Giordano, Adv. Phys. **26**, 487 (1977).

¹⁵ H. Wada, M. Nishigori, and M. Shiga, J. Phys. Condensed Matter **3**, 2083 (1991).

¹⁶ S. J. Kennedy and B. R. Coles, J. Phys. Condensed Matter **2**, 1213 (1990).

¹⁷ Y. S. Yang, B. D. Gaulin, J. A. Fernandez-Baca, N. Ali, and G. D. Wignall, J. Appl. Phys. **75**, 6066 (1993).

¹⁸ P. K. Khowash, Physica B **163**, 197 (1990).

Preparation and magnetic properties of BaM films with excellent crystallinity by Xe sputtering

N. Matsushita, K. Noma, S. Nakagawa, and M. Naoe

Department of Physical Electronics, Tokyo Institute of Technology, 2-12-1 O-okayama, Meguro-ku, Tokyo 152, Japan

M-type barium ferrite ($\text{BaFe}_{12}\text{O}_{19}$) films were deposited on a ZnO underlayer by sputtering with mixture of Ar, Xe, and O_2 gases. P_{O_2} and $P_{\text{Ar+Xe}}$ were set at 0.01 and 0.09 Pa, respectively, where P_{Xe} was changed from 0.00 to 0.09 Pa. The dependencies of surface morphology, $\langle D \rangle$, $\Delta\theta_{50}$, M_s , and $H_{c\perp}$ and $H_{c\parallel}$ on P_{Xe} were investigated. Both BaM layers deposited at P_{Xe} and P_{Ar} of 0.09 Pa possessed smooth surface and exhibited $\Delta\theta_{50}$, M_s , $H_{c\perp}$, and $H_{c\parallel}$ of about 4° , 300 emu/cm^3 , 2.0 and 0.3 kOe, respectively. The BaM layer deposited at P_{Xe} of 0.04 Pa possessed a rough surface and exhibited $\Delta\theta_{50}$ and $H_{c\parallel}$ as large as about 9° and 0.6 kOe, respectively, and M_s as small as about 200 emu/cm^3 .

I. INTRODUCTION

A magnetoplumbite type of Ba ferrite ($\text{BaM}:\text{BaFe}_{12}\text{O}_{19}$) has been intensively investigated due to its various attractive and useful properties for magnetic recording media and microwave filters, and so on.¹⁻⁷ In BaM ferrite, Ba ions occupy the same sites as oxygen ones in the *R* block where larger Ba^{2+} ions with a radius of 1.43 Å (see Fig. 2) should replace smaller O^{2-} ones with that of 1.32 Å. Therefore, it seems effective for the deposition of BaM ferrite films with good crystallinity that the Ba adatoms have a high kinetic energy for a sufficiently long walk on the substrate surface. However, since the atomic weight of Ba (137.3) is much heavier than that of Ar (40.0) as seen in Fig. 1, it is considered that Ba atoms ought to arrive at the substrate with a relatively low kinetic energy. Moreover, the Ar atoms recoiled by heavier Ba ions in targets might bombard the growing film with high kinetic energy during deposition and some of them not only may be incorporated into films as impurities, but also easily destroy the regularly packed lattice composed of lighter oxygen ions with a mass of 16.0. On the other hand, the atomic weight of Xe (131.3) is much heavier than that of O (16.0) and Fe (55.8), but is not so different from that of Ba. Therefore, Ba atoms as well as O and Fe ones seem to arrive at the substrate with relatively high kinetic energy for a sufficiently long walk and the number of the recoiled particles seems to decrease when Xe is used as the sputtering gas. It has also been found that ZnO underlayers are useful for the epitaxial growth of BaM layers as well as spinel ferrite layers.^{7,8} Therefore, BaM layers were deposited on the ZnO underlayer in mixture of Ar, Xe, and O_2 gases by using the facing target sputtering (FTS) apparatus; then, the crystallographic and magnetic characteristics of the specimen films on the partial Xe pressure P_{Xe} were investigated.

II. EXPERIMENTS

A. FTS apparatus

Figure 2 shows the schematic representation of the FTS apparatus for multilayers used in this study. The dc glow discharge is performed using the facing targets as cathodes and the grounded chamber wall and shield rings as anodes. The magnetic field for confining the plasma was about 140

Oe at the point of the center line between targets. Since the substrate is placed outside of the confined plasma, the deposited films can avoid the bombardment of high-energy particles such as γ electrons and negative ions.⁸ Moreover, since the highly ionized plasma is confined in a narrow space between targets, it can be maintained even at a very low working gas pressure below 0.1 Pa, the value of which is too low for a conventional sputtering system to generate the stable glow discharge.

B. Preparation of specimen films

Prior to the deposition of the BaM ferrite layer, the ZnO underlayer was deposited on a SiO_x/Si substrate. It is known that ZnO is composed of a densely packed structure of oxygen and since the distance between oxygen atoms in the densely packed plane of ZnO (3.24 Å) is not so different from that of CoFe_2O_4 with (111) orientation (2.96 Å) and BaM ferrite with *c*-axis orientation (2.95 Å), the ZnO underlayer is useful for the epitaxial growth of these ferrite layers.^{7,9} The preparation conditions are listed in the right-hand-side column of Table I. The thickness of the ZnO layer was about 4500 Å for the deposition of 1 h. The crystallite size $\langle D \rangle$ and the dispersion degree of *c*-axis orientation $\Delta\theta_{50}$ of the ZnO underlayer were about 500 Å and smaller than 4° , respectively.

The preparation conditions for BaM ferrite layers are listed in the left-hand-side column of Table I. The disk plates 85 mm in diameter used as targets were sintered from the

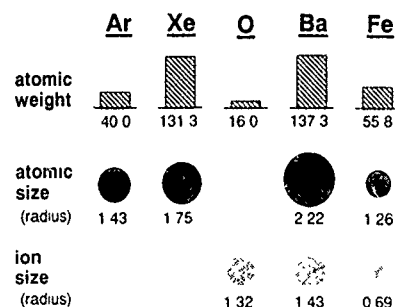


FIG. 1. Atomic weight and size of Ar, Xe, O, Ba, and Fe.

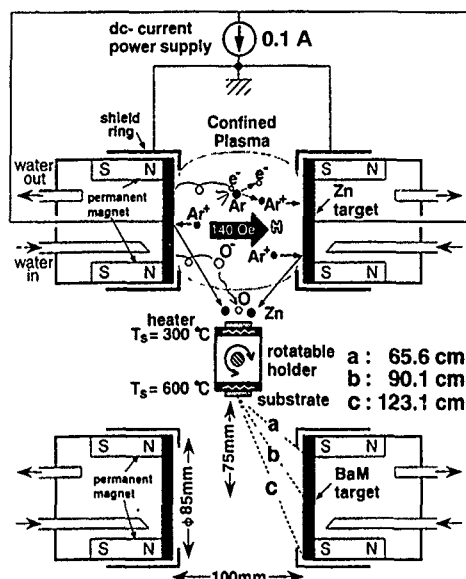


FIG. 2. Schematic representation of FTS apparatus for multilayers.

mixture of BaO and 5.5(Fe₂O₃) powders at 1350 °C in the air by a conventional dry method. The discharge current was set at 0.1 A and then the discharge voltage increased from 472 to 660 V with increase of P_{Xe} from 0.00 to 0.09 Pa.

III. RESULTS AND DISCUSSION

A. Composition and microstructure

The Ba and Fe content C_{Ba} and C_{Fe} was measured by using inductively coupled plasma spectrometry (ICPS). C_{Ba} normalized for C_{Fe} of 12 was about 0.9 at various P_{Xe} in the range between 0.00 and 0.09 Pa.

Figure 3 shows the scanning electron microscopy (SEM) photographs of the surface appearance of BaM layers deposited on a ZnO underlayer at P_{Xe} of (a) 0.00, (b) 0.01, (c) 0.04, and (d) 0.09 Pa. As seen in (a), the layer at P_{Xe} of 0.00 Pa revealed an almost smooth, dense, and uniform morphology, although very fine grains were slightly visible on the film surface; however, the surface smoothness was not ob-

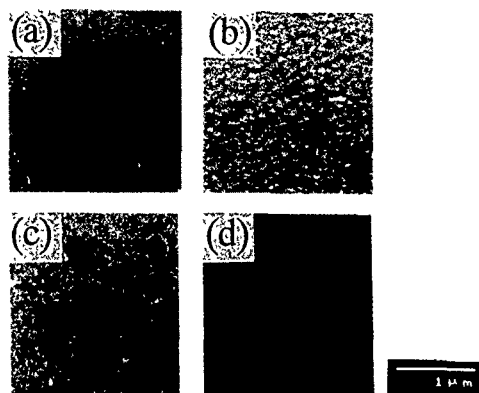


FIG. 3. SEM photographs for surfaces of BaM layers deposited at P_{Xe} of (a) 0.00, (b) 0.01, (c) 0.04, and (d) 0.09 Pa.

tained even when P_{Xe} was only 0.01 Pa as seen in (b). The layer deposited at P_{Xe} of 0.04 Pa revealed a very rough and nonuniform morphology as seen in (c). On the contrary, the layer at P_{Xe} of 0.09 Pa revealed a very smooth and flat morphology as seen in (d). These differences of surface morphologies between (a) and (c), or (d) and (c), seemed to have close relationships to the difference of the kinetic energy of deposited particles. These differences of energy of deposited particles cause the change of crystallographic and magnetic characteristics as seen in Secs. III B and III C.

B. Crystallinity

Figure 4 shows the P_{Xe} dependencies of $\langle D \rangle$ and $\Delta\theta_{50}$ of the BaM layer. $\langle D \rangle$ slightly decreased and $\Delta\theta_{50}$ was as small as 3.7° at P_{Xe} of 0.09 Pa and took a maximum value of 8.7° at P_{Xe} of 0.04 Pa.

The P_{Xe} dependencies of $\Delta\theta_{50}$ seemed to have a relationship remarkably close to the sputtering phenomena at the target and the collision times of sputtered particles to working gas atoms during the flight from target to substrate. The mean free path of sputtered particles in the working gas at the pressure of 0.1 Pa is about 50 and 100 mm for Ba and Fe atoms with radius of 2.22 and 1.26 Å, respectively, as shown in Fig. 1. The distances a , b , and c , which correspond to the shortest, mean, and the longest distance from target to substrate center, were 65.6, 90.1, and 123.1 mm, respectively, as seen in Fig. 2. Therefore, the sputtered particles seem to

TABLE I. Preparation conditions.

	BaM layer	ZnO underlayer
Target composition	Ba ₁₀ Fe ₁₁₀ O _{190-x}	Zn
Substrate	ZnO/SiO ₂ /Si	SiO ₂ /Si
Substrate temperature T_s	600 °C	300 °C
Residual pressure	8.0×10^{-5} Pa	
Total gas pressure $P_{Ar+Xe+O_2}$	0.10 Pa	0.26 Pa
Ar gas pressure P_{Ar}	0.09–0.00 Pa	0.13 Pa
Xe gas pressure P_{Xe}	0.00–0.09 Pa	...
O ₂ gas pressure P_{O_2}	0.01 Pa	0.13 Pa

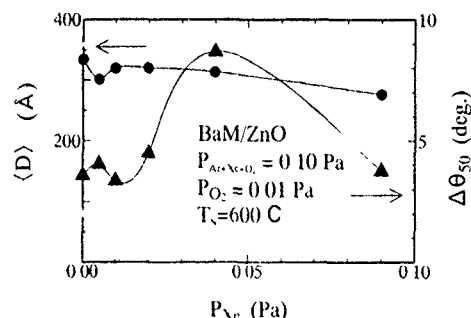


FIG. 4. Dependencies of crystallite size $\langle D \rangle$ and dispersion degree of c -axis orientation $\Delta\theta_{50}$ on Xe pressure P_{Xe} .

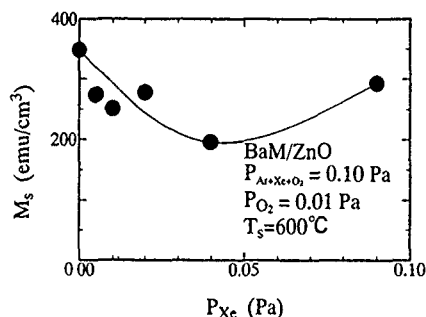


FIG. 5. Dependencies of saturation magnetization M_s on Xe pressure P_{Xe} .

arrive at the substrate after a few collisions with atoms of the working gas. The Fe, O, and even Ba atoms sputtered by Xe ions can arrive at the substrate with relatively high kinetic energy, enough to form BaM ferrite crystallites with good c -axis orientation. Therefore, the values of $\Delta\theta_{50}$ for both BaM layers deposited at P_{Ar+O_2} and P_{Xe+O_2} of 0.1 Pa were smaller and almost the same.

At P_{Xe} of 0.04 Pa, the sputtering phenomena and the collision of sputtered particles with the working gas seemed to be more complicated. There may be apparent differences in kinetic energies among deposited particles. Although the atoms sputtered by heavier Xe ions and collided with Ar or Xe atoms seem likely to possess relatively high energy and make a long walk on the substrate, the atoms sputtered by lighter Ar ions and collided with heavier Xe atoms seem likely to possess insufficient energy for a random walk on the substrate. Therefore, $\Delta\theta_{50}$ of the BaM layer deposited in mixed gases at P_{Xe} of 0.04 Pa might take a larger value than those at P_{Xe} of 0.00 and 0.09 Pa. It also seems that this nonuniformity of kinetic energy of deposited particles causes a very rough and nonuniform surface morphology for the films deposited in a mixture gases as seen in Figs. 3(c) and 3(d).

C. Magnetic characteristics

Figure 5 shows the P_{Xe} dependencies of the saturation magnetization M_s of the BaM layer. M_s of the BaM layer deposited at P_{Xe} of 0.00 Pa took the maximum value of 350 emu/cm³ and was not so different from the bulk M_s of 380 emu/cm³. M_s decreased with increase of P_{Xe} up to 0.04 Pa and took the minimum value of 196 emu/cm³ at P_{Xe} of 0.04 Pa, of which the value was as relatively large as 293 emu/cm³ at P_{Xe} of 0.09 Pa. These dependencies seemed to have a relationship distinctly close to the layer morphology and $\Delta\theta_{50}$ of films as seen in Figs. 3 and 4.

Figure 6 shows the P_{Xe} dependencies of the perpendicular and in-plane coercivities $H_{c\perp}$ and $H_{c\parallel}$, respectively. Al-

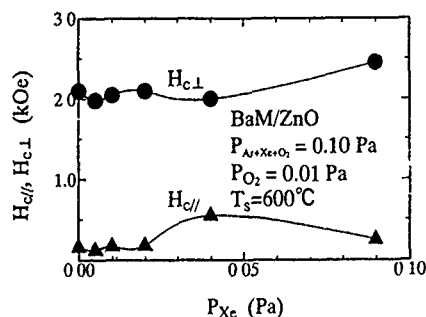


FIG. 6. Dependencies of perpendicular and in-plane coercivities $H_{c\perp}$ and $H_{c\parallel}$ on Xe gas pressure P_{Xe} .

though $H_{c\perp}$ was almost constant at about 2.0 kOe, $H_{c\parallel}$ took the maximum value of 0.6 kOe at P_{Xe} of 0.04 Pa. Since $H_{c\parallel}$ corresponds apparently to $\Delta\theta_{50}$, such a large $H_{c\parallel}$ at P_{Xe} of 0.04 Pa was attributed to the degradation of crystallinity implied by larger $\Delta\theta_{50}$ at P_{Xe} of 0.04 Pa as seen in Fig. 4.

IV. CONCLUSION

BaM ferrite layers were deposited on a ZnO underlayer at T_s of 600 °C at P_{Ar+Xe} of 0.09 Pa and O_2 at P_{O_2} of 0.01 Pa. The obtained results are as follows.

(i) BaM layers deposited at P_{Xe} of 0.09 Pa revealed a smooth surface appearance and excellent crystallinity with $\Delta\theta_{50}$ of 4°. In addition, they exhibited good magnetic characteristics such as M_s and $H_{c\perp}$ and $H_{c\parallel}$ of about 293 emu/cm³ and 2.0 and 0.3 kOe, respectively.

(ii) BaM layers deposited in the mixed gas at P_{Ar} , P_{Xe} , and P_{O_2} of 0.05, 0.04, and 0.01 Pa, respectively, had rough surface texture and worse crystallinity with $\Delta\theta_{50}$ of 8.7°. They exhibited smaller M_s and higher $H_{c\parallel}$ of 196 emu/cm³ and 0.6 kOe, respectively.

It seems to be possible to deposit the BaM layer with good crystallinity and magnetic characteristics on a ZnO underlayer using a mixture of O_2 and Xe instead of Ar as the sputtering gas.

¹T. Fujiwara, IEEE Trans. Magn. **MAG-21**, 1480 (1985).

²E. Lacroix, P. Gerard, G. Marest, and M. Dupuy, J. Appl. Phys. **69**, 4770 (1991).

³K. Yamamori, T. Tanaka, and T. Jitoshio, IEEE Trans. Magn. **MAG-27**, 4960 (1992).

⁴M. Naoe, K. Noma, S. Nakagawa, and N. Matsushita, **73**, 6696 (1993).

⁵M. Naoe, S. Hasunuma, Y. Hoshi, and S. Yamanaka, IEEE Trans. Magn. **MAG-17**, 3184 (1981).

⁶I. Zaquine, H. Benazizi, and J. C. Mage, J. Appl. Phys. **64**, 5822 (1988).

⁷M. Matsuoka and M. Naoe, J. Appl. Phys. **57**, 4040 (1985).

⁸M. Naoe, S. Yamanaka, and Y. Hoshi, IEEE Trans. Magn. **MAG-16**, 646 (1980).

⁹N. Matsushita, S. Nakagawa, and M. Naoe, IEEE Trans. Mag. **MAG-28**, 3108 (1992).

Magnetic ordering in UCoNiSi_2 and UCoCuSi_2 studied by ac-susceptibility and neutron-diffraction measurements

Moshe Kuznietz, Haim Pinto, and Mordechai Melamud
Nuclear Research Centre-Negev, P.O. Box 9001, 84190 Beer-Sheva, Israel

Polycrystalline samples of intermediate solid solutions of the UM_2Si_2 compounds ($\text{M}=\text{Co}, \text{Ni}, \text{Cu}$), namely UCoNiSi_2 and UCoCuSi_2 , were prepared and were found to have body-centered tetragonal ThCr_2Si_2 -type crystallographic structure. In UCoNiSi_2 ac susceptibility indicates a single antiferromagnetic (AF) transition at $T_N=115\pm 5$ K, confirmed by neutron-diffraction observation of the AF-I structure down to 10 K (with uranium moments of $1.6\pm 0.2\mu_B$, along the tetragonal c axis). In UCoCuSi_2 ac susceptibility indicates ferromagnetic transition at $T_C=107\pm 5$ K, and implies an AF transition at lower temperature, confirmed by the AF-I structure, observed in neutron diffraction below $T_0=95\pm 5$ K down to 10 K (with uranium moments of $1.6\pm 0.1\mu_B$, along the c axis). The magnetic properties are discussed in comparison with UM_2X_2 and $\text{U}(\text{M}, \text{M}')_2\text{X}_2$ materials ($\text{X}=\text{Si}, \text{Ge}$).

I. INTRODUCTION

The UM_2Si_2 compounds ($\text{M}=\text{Co}, \text{Ni}, \text{Cu}$) were studied previously^{1,2} and found to have ThCr_2Si_2 -type crystallographic structure. UCo_2Si_2 orders antiferromagnetically below 85 K into the AF-I structure (+ - + -) with a wave vector $\mathbf{k}=(0,0,1)$.¹ UNi_2Si_2 orders below 124 K into an incommensurate phase,² acquires AF-I structure below 103 K (Refs. 1 and 2) and ferrimagnetic (+ + -) structure with a wave vector $\mathbf{k}=(0,0,2/3)$ below 53 K.^{1,2} UCu_2Si_2 orders ferromagnetically below 103 K.¹ The ordered moments are along the tetragonal axis, and are found only on uranium.^{1,2}

Studying the $\text{U}(\text{M}, \text{M}')_2\text{Si}_2$ systems, we started with intermediate solid solutions $\text{UMM}'\text{Si}_2$. In UNiCuSi_2 ac susceptibility indicated³⁻⁵ antiferromagnetic (AF) transition at $T_N=150\pm 5$ and 155 ± 5 K, in two separately prepared samples, with four (or three) transitions below T_N with ferro/ferrimagnetic F character. Neutron diffraction on both materials showed^{4,5} that apart from the AF transitions at T_N (150 ± 1 and 152 ± 2 K, respectively) to the AF-I structure (+ - + -), in accordance with the ac susceptibility, none of the F transitions was observed. The AF-I structure persists down to 1.7(1.5) K. Short-range magnetic order involving several consecutive ferromagnetic planes in the AF-I phase detected by ac susceptibility, and not by neutron diffraction, is proposed to explain the differences between these measurements. Following our studies of UNiCuSi_2 , we have prepared polycrystalline samples of the other two intermediate solid solutions of the UM_2Si_2 compounds, namely UCoNiSi_2 and UCoCuSi_2 , and present here their magnetic properties, measured by ac susceptibility and neutron diffraction.

II. EXPERIMENTAL DETAILS

Polycrystalline samples of the solid solutions UCoNiSi_2 and UCoCuSi_2 were prepared by arc melting stoichiometric amounts of the constituents in an argon atmosphere. The obtained buttons were annealed at 750 °C in vacuum for 120 h, and were subsequently crushed into fine powders and examined by x-ray diffraction at room temperature ($\text{RT}=295$ K) to determine their quality, as well as their crystallographic properties.

ac-susceptibility measurements on polycrystalline samples were done on UCoNiSi_2 (456 mg) down to 80 K (Ref. 3) and later down to 20 K, and on UCoCuSi_2 (348 mg) down to 80 K. The ac magnetic field was rather weak (<10 Oe). Calibration of the ac-susceptibility values was done for UCoNiSi_2 with a polycrystalline sample of Gd_2O_3 (300 mg), for which the χ_M value at 293 K is 51×10^{-3} emu/mol (with $\theta=-15$ K and $\mu_{\text{eff}}=7.9\mu_B$), and for UCoCuSi_2 with a polycrystalline sample of Ho_2O_3 (20 mg), for which the χ_M value at 293 K is 89×10^{-3} emu/mol (with $\theta=-14$ K and $\mu_{\text{eff}}=10.5\mu_B$). These measurements determined the temperatures and types of magnetic transitions in near-zero magnetic fields, as well as the paramagnetic properties of these materials.

Neutron-diffraction measurements on 20 g polycrystalline samples (in cylindrical aluminium containers) were done in the IRR-2 reactor, with the diffractometers KANDI-II (at $\lambda=2.453$ Å) for UCoNiSi_2 and KANDI-III (at $\lambda=2.40$ Å) for UCoCuSi_2 . A DISPLEX (closed-cycle helium cooler made by Air Products, Inc.) was used for measurements at low temperatures (LT), down to 10 K, and the temperature was measured with Au(Fe)/Chromel thermocouple. These measurements determined the RT and LT crystallographic structure and LT magnetic structure of both materials.

III. RESULTS

At RT only $\{hkl\}$ reflections with $h+k+l=\text{even}$ are observed by x-ray and neutron diffraction from both UCoNiSi_2 and UCoCuSi_2 . These are consistent with the body-centered tetragonal ThCr_2Si_2 -type crystallographic structure (space group $I4/mmm$). The RT structure parameters are obtained from least-squares fits of the observed integrated and calculated neutron-diffraction intensities, assuming random occupation of the (M, M') site, yielding residuals $R=4.2\%$ and 3.7% , respectively. The RT lattice parameters (a, c) and derived tetragonal cell volume V , and the RT fitted position parameter (z) of the silicon atom, of UCoNiSi_2 and UCoCuSi_2 , are given in Table I. The parameters are compared in Table I with the averages of previously published values of the same parameters in the UM_2Si_2 compounds^{1,4} and in UNiCuSi_2 .³⁻⁵

TABLE I. RT lattice parameters and tetragonal cell volume in the UM_2Si_2 compounds (averages of reported values) and the $UMM'Si_2$ solid solutions (errors: in $a = \pm 0.010$ Å, in $c = \pm 0.02$ Å, in $z = \pm 0.002$).

Material	a (Å)	c (Å)	V (Å ³)	z (Si)	Ref.
UCo ₂ Si ₂	3.917	9.614	147.50	0.3715	1
UCoNiSi ₂	3.926	9.55	147.20	0.375	present ^a
UNi ₂ Si ₂	3.962	9.512	149.31	0.3715	1,4
UNiCuSi ₂	3.977	9.70	153.42	0.378	4
UCu ₂ Si ₂	3.984	9.946	157.87	0.3842	1,4
UCoCuSi ₂	3.967	9.755	153.51	0.382	present
UCo ₂ Si ₂	3.917	9.614	147.50	0.3715	1

The temperature dependence of the molar ac susceptibility of UCoNiSi₂, in the temperature range 20–295 K, is shown in Fig. 1. A single transition to an antiferromagnetic state is observed at $T_N = 115 \pm 5$ K, with a rather low $\chi_M = (6 \pm 1) \times 10^{-3}$ emu/mol at the transition. The temperature dependence of the molar ac susceptibility of UCoCuSi₂ in the temperature range 80–295 K, is shown in Fig. 2. A rather strong susceptibility peak, corresponding to a ferromagnetic ordering, is observed at $T_C = 107 \pm 5$ K, with a high $\chi_M = (165 \pm 5) \times 10^{-3}$ emu/mol at the transition. The sharp decrease of the ac-susceptibility curve at its low-temperature side, uncommon to a ferromagnetic phase, suggests a second transition, to an AF phase.

Inverse molar susceptibility curves of UCoNiSi₂ and UCoCuSi₂ in their paramagnetic states are deduced from Figs. 1 and 2, respectively. The paramagnetic Curie temperature θ is obtained from the intersection of the linear part of such a curve (above 200 K) with the temperature axis.

μ_{eff} (in μ_B) is obtained via the relation $(\chi_M)^{-1} = (2.83/\mu_{eff}^2)(1 - \theta/T)$, where χ_M is given in emu/mol and $(T - \theta)$ is given in K. The values for θ and μ_{eff} are listed in Table II, where they are compared with the respective values of UNiCuSi₂ (Refs. 3–5).

The LT neutron diffractograms of UCoNiSi₂ and UCoCuSi₂ (at 1 K) show additional reflections for which $h + k + l = \text{odd}$ (such as $\{010\}, \{012\}, \{111\}$), indicating AF ordering of at least the uranium sublattice, with a wave vector $\mathbf{k} = (0, 0, 1)$ and alternate stacking (+ -) of ferromagnetic layers along the tetragonal axis (AF-I). The absence of $\{00l\}$ reflections with odd l points out to ordered magnetic mo-

ments along the tetragonal axis. The LT diffractograms are similar to those shown for UCo₂Ge₂ (Ref. 6) and UNiCuSi₂.^{4,5}

The LT lattice parameters of UCoNiSi₂ and UCoCuSi₂ are obtained from least-squares fits of observed integrated and calculated intensities, with residuals $R = 4.9\%$ and 3.7% , respectively. The LT fitted parameters (a, c, z) fall within the experimental error range of the RT values. The integrated intensities of the reflections with $h + k + l = \text{odd}$ are in agreement with ordering of the uranium sublattice, with fitted (by the procedure of Ref. 6) ordered magnetic moments of $1.6 \pm 0.2 \mu_B$ (Table II).

Temperature variation of the integrated intensity of the magnetic $\{010\}$ reflection (Fig. 3) indicates that the AF-I structure exists in UCoNiSi₂ up to $T_N = 115 \pm 5$ K [Fig. 3(a)], in accordance with the transition observed in the ac susceptibility (Fig. 1). In UCoCuSi₂ the AF-I structure persists up to $T_0 = 95 \pm 5$ K [Fig. 3(b)], while the ac-susceptibility curve (Fig. 2) points out a ferromagnetic transition at $T_C = 107 \pm 5$ K. However, the poor statistical quality of the data in Fig. 3(b) does not allow us to confirm that T_C is indeed above T_0 , as expected. Moreover, due to the small ordered magnetic moment close to T_C , our neutron diffraction measurements in the T_0 to T_C temperature range are unable to detect the ferromagnetism.

IV. DISCUSSION

The measured lattice parameters in UCoNiSi₂ and UCoCuSi₂ fall between the respective parameters of the end

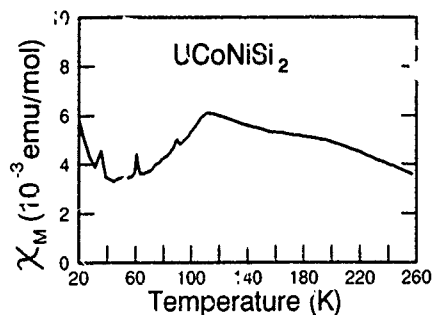


FIG. 1. Temperature dependence of the molar ac susceptibility in a polycrystalline sample of UCoNiSi₂ indicating antiferromagnetic ordering below $T_N = 115 \pm 5$ K. The inverse molar susceptibility above 200 K leads to $\theta = -175 \pm 50$ K and $\mu_{eff} = 3.5 \pm 0.3 \mu_B$.

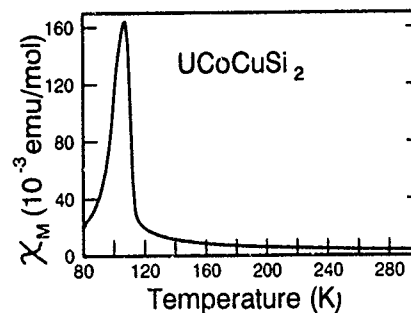


FIG. 2. Temperature dependence of the molar ac susceptibility in a polycrystalline sample of UCoCuSi₂ indicating initial ferromagnetic ordering below $T_C = 107 \pm 5$ K, followed by a transition to an antiferromagnetic phase. The inverse molar susceptibility above 200 K leads to $\theta = +40 \pm 10$ K and $\mu_{eff} = 2.8 \pm 0.2 \mu_B$.

TABLE II. Paramagnetic values (μ_{eff} and θ), ordering (T_N or T_C) and transition (T_0) temperatures, magnetic structures, and uranium ordered magnetic moments m in the UMM'Si₂ solid solutions.

Material	μ_{eff} (μ_B)	θ (K)	$T_N(T_C)$ (K)	Order below $T_N(T_C)$	T_0 (K)	Order below T_0	m (10 K) (μ_B)
UCoNiSi ₂	3.5 ± 0.3^a	-175 ± 50^a	115 ± 5^a	AF-I	1.6 ± 0.2
UNiCuSi ₂	2.4 ± 0.1^a	$+80 \pm 5^a$	$150 \pm 1^{a,b}$	AF-I ^b	2.2 ± 0.2^b
UCoCuSi ₂	2.8 ± 0.2	$+40 \pm 10$	107 ± 5	ferro	95 ± 5	AF-I	1.6 ± 0.1

^a) Reference 3.

^b) Reference 4.

compounds UM₂Si₂ (Table I), in agreement with the Vegard (Zen) law. In the case of UCoNiSi₂ a and c have different trends, while in the case of UCoCuSi₂ both a and c have similar trends, with respect to the end compounds.

The effective paramagnetic moments μ_{eff} in UCoNiSi₂ and UCoCuSi₂ are higher than the moment in UNiCuSi₂ (Table II), but all are still within a reasonable $5f$ configuration. This is the case also for UNi₂Si₂ and UCu₂Si₂.¹ The μ_{eff} values ($\leq 3.5\mu_B$) of all these materials seem to be correlated with the occurrence of localized magnetic moments on uranium atoms only. As an exception, a high effective paramagnetic moment, $4.85\mu_B$, is reported for UCo₂Si₂,¹ implying a certain paramagnetic moment on the cobalt.⁶

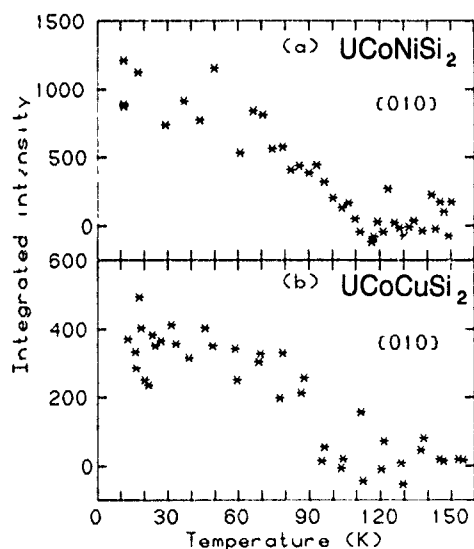


FIG. 3. Temperature dependence of the neutron-diffraction integrated intensity (above the background) of the magnetic {010} reflection: (a) in UCoNiSi₂, indicating $T_N=115 \pm 5$ K; (b) in UCoCuSi₂, indicating $T_0=95 \pm 5$ K. Each data point is an average of three consecutive scans of the {010} reflection, taken at increasing temperatures.

The additional small peaks on the ac-susceptibility curve of UCoNiSi₂ (see Fig. 1) are probably indicative of short-range-order transitions, but in a reduced extent when compared to the situation in UNiCuSi₂,³⁻⁵ outlined above. The reduced regions of irregular ferromagnetic (or ferrimagnetic) short-range order in UCoNiSi₂ indicate increased stabilization of the AF-I structure in this material compared with UNiCuSi₂.

The paramagnetic Curie temperature θ varies from negative in UCoNiSi₂ to positive and close to T_C in UCoCuSi₂ (Table II). Based on the trend of these θ values we expect an oscillatory variation of θ with x in the corresponding $U(M_{1-x}M'_x)_2Si_2$ systems, similar to that reported for $U(Ni_{1-x}Cu_x)_2Ge_2$.⁷

The occurrence of two magnetic phases in UCoCuSi₂, ferromagnetic below $T_C=107 \pm 5$ K and AF-I below $T_0=95 \pm 5$ K down to 10 K, is different from the magnetic behavior of the UCoNiSi₂ and UNiCuSi₂. The latter have single magnetic phases, both AF-I, below $T_N=115 \pm 5$ and 150 ± 1 K, respectively.

The oscillatory variations of θ with x in the $U(M_{1-x}M'_x)_2Si_2$ systems, and the magnetic phase diagrams of these systems are expected to be correlated with the change in the number of conduction electrons (RKKY-like behavior), as discussed for the $U(Ni_{1-x}Cu_x)_2Ge_2$ system.⁷

¹L. Chelomici, J. Leciejewicz, and A. Zygmunt J. Phys. Chem. Solids **46**, 529 (1985).

²H. Lin, L. Rebersky, M. F. Collins, J. D. Garrett, and W. J. L. Buyers, Phys. Rev. B **43**, 13 232 (1991).

³M. Kuznietz, H. Pinto, H. Ettegui, and M. Melamud, J. Magn. Mater. **104-107**, 13 (1992).

⁴M. Kuznietz, G. Andre, F. Bouree, H. Pinto, H. Ettegui, and M. Melamud, J. Appl. Phys. **73**, 6075 (1993).

⁵M. Kuznietz, G. Andre, F. Bouree, H. Pinto, H. Ettegui, and M. Melamud, Solid State Commun. **87**, 689 (1993).

⁶M. Kuznietz, H. Pinto, H. Ettegui, and M. Melamud, Phys. Rev. B **40**, 7328 (1989).

⁷M. Kuznietz, H. Pinto, H. Ettegui, and M. Melamud, Phys. Rev. B **48**, 3183 (1993).

Ferromagnetic ordering in dilute PdCo alloys

R. E. Parra and A. C. Gonzalez

Centro de Física, Instituto Venezolano de Investigaciones Científicas, Apartado 21827,
Caracas 1020A, Venezuela

The analysis of magnetization and neutron-scattering measurements shows that the ferromagnetic cloud in dilute PdCo alloys has a size of $7.92\mu_B$, with a Co moment of $2.02\mu_B$, for a range of concentrations of $0.3 \leq c \leq 2.0$ at. % Co. Using the values obtained by our analysis of the data, the neutron scattering and the critical temperatures of ferromagnetism are reproduced using a localized magnetic moment model with a Heisenberg type of interaction between clouds and Monte Carlo simulation methods. The calculated neutron scattering shows a strong component of critical scattering in the unpolarized neutron; this component is the cause of the larger value of the ferromagnetic cloud ($\sim 10\mu_B$) that can be inferred from the neutron scattering. Agreement is also found between calculated critical temperatures and experimental T_c 's at these values of concentrations.

I. INTRODUCTION

PdCo alloys have always been treated as one of the most typical giant moment systems, along with PdFe alloys. The size of the giant moment has been taken as $\sim 10\mu_B$, based on magnetization measurements made by Bozorth *et al.*¹ in 1961 and on unpolarized diffuse neutron-scattering measurements made by Low and Holden² in 1966. Although there has been subsequent analyses of the mentioned data, and also new experimental data, until now there has been no agreement on the size of the magnetization cloud and on several other magnetic characteristics of these alloys. It is the purpose of this work to present our results on these matters, using a new approach by analyzing the available experimental data with a local moment model in order to predict some of the magnetic properties of these alloys.

II. MAGNETIC MOMENTS

In 1961, Bozorth *et al.*¹ published their magnetization measurements on PdCo alloys. They found that ferromagnetism exists in compounds as dilute as 0.1 at. % Co. They also determined the average moment associated with each Co atom without making assumptions on whether the moment resides only on the Co atom, or partly on the Co with the rest of the moment scattered on the host atoms. The modern approach for this problem is to determine the individual average moment of the impurity and the magnetization cloud size $[M(0)]$ by neutron scattering and to verify the latter by magnetization measurements.³ $M(0)$ should be equal to $d\mu_{sat}/dc$, where μ_{sat} is the average magnetic moment of the alloy determined by magnetization measurements. Low and Holden² made unpolarized diffuse neutron-scattering measurements and determined the individual average moment of Co as $2.1 \pm 0.3\mu_B$. They also estimated that the giant moment size was about $10\mu_B$. Further analysis of the same data by Ododo⁴ in 1985 showed the same value for the impurity moment but a smaller value for the giant moment. There are only unpolarized neutron measurements on PdCo which, according to our analysis, have a nonelastic component in the scattering, therefore the $M(0)$ cannot be measured reliably at $K=0$, using this method. Moreover, there was no saturation in the available magnetization data.³

The best way to obtain $M(0)$ was to determine the average individual moments from the neutron scattering (critical scattering does not affect the neutron scattering at large K), and using the appropriate magnetic form factors, and then to calculate $d\mu_{sat}/dc$ using the fact that $\mu_{sat} = c\mu_i + (1-c)\mu_h$. With this method we find that $M(0)$ is equal to $7.92 \pm 0.29\mu_B$ and that $\mu_{Co} = 2.02 \pm 0.03$. These values are in agreement, within the errors, with the results obtained by Ododo.⁴

III. MODEL AND CRITICAL TEMPERATURES

We use a magnetic environment model that has been used for other giant moment systems. We only present here the necessary formulas; the complete model can be found in Ref. 5.

The giant moment is formed by the exchange enhancement of the Pd atoms. This enhancement is verifiable in the susceptibility of Pd which in this model can be written as

$$\chi = \frac{\chi_0}{1 - \Gamma}, \quad (1)$$

where Γ is an enhancement factor that has been determined as 0.947 ± 0.009 , and χ_0 is the nonenhanced susceptibility.

In this model we assumed no interaction between the magnetic impurities (we assume they are sufficiently isolated) and that the inducer of the ferromagnetism is the interaction between polarization clouds. This interaction is given by

$$H = -\frac{1}{2} \sum_{i,j} J_{ij} \mathbf{S}_i \cdot \mathbf{S}_j - \sum_i \mathbf{B} \cdot \mathbf{S}_i, \quad (2)$$

where \mathbf{S}_i are the spins of the system, \mathbf{B} is an external field, and J_{ij} are the exchange interactions between clouds. Using this interaction we determine, by Monte Carlo simulation, the critical temperatures of ferromagnetism from the maximum of $\tilde{\chi}$ which is given by

$$\tilde{\chi} = \frac{\langle (M - \langle M \rangle)^2 \rangle}{NkT}. \quad (3)$$

The quantity $\tilde{\chi}$ coincides with the susceptibility χ for infinite systems and is proportional to the fluctuation of the magni-

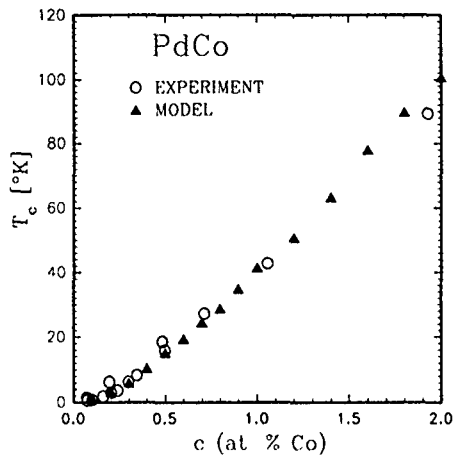


FIG. 1. Comparison of calculated critical temperatures of ferromagnetism with experimental values.

tude of the total moment. Critical temperatures were determined with 200 impurity spins in a fcc periodic lattice, with 2000 Monte Carlo steps per spin. The calculated temperatures are compared with experimental values in Fig. 1.

IV. NEUTRON SCATTERING

The diffuse unpolarized neutron scattering on *PdCo* alloys shows forward peaks which would give larger magnetization clouds than the values obtained by Ododo⁴ and by our analysis, for this concentration. This disagreement suggests the presence of a critical scattering contribution to the neutron measurements, which we decided to calculate. In order to do this, we used the following formula:⁶

$$T(\mathbf{K}) = \frac{1}{(0.27)^2 c(1-c)N} \frac{d\sigma}{d\Omega} \\ = |M(\mathbf{K})|^2 \left(\langle (\overline{S^\perp})^2 \rangle + \frac{1}{c(1-c)N} \right. \\ \left. \times \sum_{ij} e^{i\mathbf{K} \cdot (\mathbf{r}_i - \mathbf{r}_j)} [\langle \mathbf{S}_i^\perp \cdot \mathbf{S}_j^\perp \rangle - \langle (\overline{S^\perp})^2 \rangle] \right). \quad (4)$$

In this equation, S_i^\perp is the component of \mathbf{S}_i perpendicular to \mathbf{K} , $\langle \rangle$ indicate thermal averages, the overhead bar indicates spatial averages, and $M(\mathbf{K})$ is the form factor of the magnetization cloud.

The Monte Carlo calculations were made, using the Hamiltonian given in Eq. (2), the same way as before but with a field \mathbf{B} along the z axis assumed perpendicular to \mathbf{K} and obeying the condition

$$\frac{kT}{N} \ll B \ll kT_c. \quad (5)$$

This relation guarantees that the total magnetic moment keeps its orientation and that the local field of each spin is unaffected by the field B . Under the conditions expressed above, we calculated the quantities $\langle S_i^z \rangle$, $\langle \mathbf{S}_i \cdot \mathbf{S}_j \rangle$, and $\langle S_i^z S_j^z \rangle$ from which we obtained

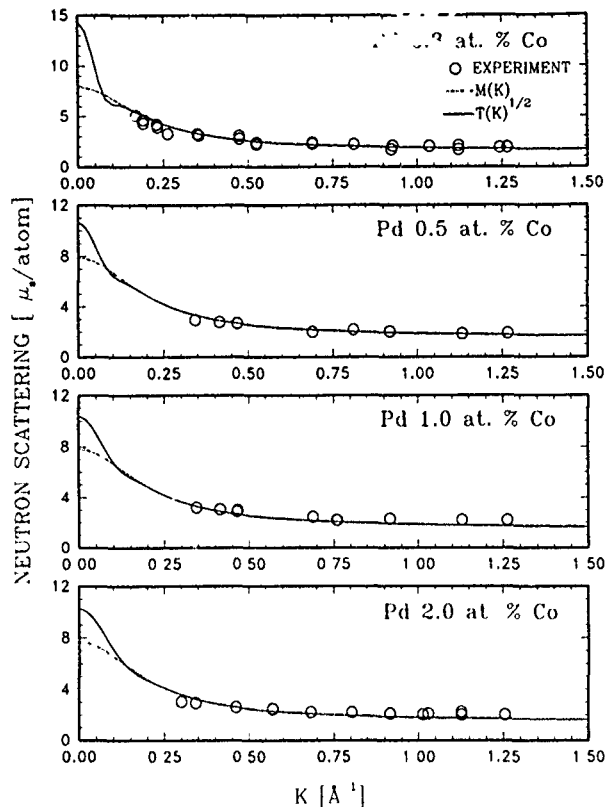


FIG. 2. Calculated neutron scattering compared with experimental values.

$$\langle \mathbf{S}_i^\perp \rangle = \langle S_i^z \rangle \hat{z}, \quad (6)$$

$$\langle \mathbf{S}_i^\perp \cdot \mathbf{S}_j^\perp \rangle = \frac{1}{2} (\langle S_i^z S_j^z \rangle + \langle \mathbf{S}_i \cdot \mathbf{S}_j \rangle). \quad (7)$$

Since the samples were polycrystalline, the spherically averaged diffuse scattering cross section was calculated as a function of wave vector \mathbf{K} . The calculation was performed at the temperature of the experiments. The results are shown in Fig. 2. $T(\mathbf{K})$ corresponds to a cross section normalized in order to be equal to $M(\mathbf{K})$ for large values of K ; the diffuse cross section without normalization is below the experimental data, since it was calculated for a nonsaturated system. The calculated neutron scattering shows that there is a strong component of critical scattering in the unpolarized neutron data of Low and Holden;² this component is the cause of the larger value of the ferromagnetic cloud that can be inferred from the neutron scattering.

V. CONCLUSIONS

Our results indicate that *PdCo* behaves as typical giant moment system, as expected. We find, however, that the magnetization cloud is not as large as has been reported earlier. This, we think, is reasonable because Co has a moment in a Pd host which is about one-third smaller than the moment of Fe in the same host. The cloud produced by Co must therefore be smaller and not of approximately the same value. The calculations of the critical temperatures and of the neutron scattering presented here and its verification against experimental values seem to confirm our conclusions.

¹R. M. Bozorth, P. A. Wolff, D. D. Davis, V. B. Compton, and J. H. Wernick, Phys. Rev. **122**, 1157 (1961).

²G. G. Low and T. M. Holden, Proc. Phys. Soc. London **89**, 119 (1966).

³R. Medina and J. W. Cable, Phys. Rev. B **15**, 1539 (1977).

⁴J. C. Ododo, J. Phys. F **15**, 941 (1985).

⁵R. Medina and R. E. Parra, Phys. Rev. B **26**, 5187 (1982).

⁶R. Medina, R. E. Parra, G. Mora, and A. C. González, Phys. Rev. B **32**, 1628 (1985).

Magnetic susceptibility of RCo_3B_2 ($\text{R}=\text{Y}, \text{Sm}, \text{Gd}, \text{and Dy}$)

H. Ido, M. Nanjo, and M. Yamada

Department of Applied Physics, Tohoku Gakuin University, Tagajo 985, Japan

The temperature dependence of magnetic susceptibility has been measured in a temperature region from about 100 to 500 K for the compounds RCo_3B_2 with $\text{R}=\text{Y}, \text{Sm}, \text{Gd}, \text{and Dy}$. Their magnetization curves at $T=5$ K have also been measured in a pulsed high field up to 170 kOe. YCo_3B_2 seems to have a Pauli paramagnetic nature down to $T=5$ K. In the paramagnetic temperature region, SmCo_3B_2 exhibits Van Vleck paramagnetism; however, GdCo_3B_2 and DyCo_3B_2 show Curie-Weiss character. The paramagnetic susceptibility for all compounds mentioned above is found to include a Pauli paramagnetic contribution from the Co sublattice. In the case of GdCo_3B_2 at $T=5$ K, the magnetic moment of $0.2\mu_B/\text{Co}$, which is antiparallel to the Gd moment, is considered to be induced by the exchange field from the Gd spin. A similar induced moment of $0.14\mu_B/\text{Co}$ is also estimated in DyCo_3B_2 . The Sm- and Dy-sublattice moments at $T=5$ K are smaller than the free-ion values, which can be explained by the crystal-field theory. A relatively large value of $B_2^0=7.0$ K for Dy^{3+} in DyCo_3B_2 can explain the experimental Dy^{3+} spontaneous moment and its increase by external field. The Sm moment in SmCo_3B_2 at $T=5$ K may be antiparallel to the induced Co-sublattice moment.

I. INTRODUCTION

The compounds RCo_3B_2 (R denotes rare earth) correspond to the case of $n=\infty$ of the compound systems expressed by the general formula $\text{R}_{n+1}\text{Co}_{3n+5}\text{B}_{2n}$ whose magnetic properties should reflect the systematic crystallographic change with n .¹⁻³ The above systems also include some possibility as a hard magnetic material.^{4,5} Therefore, magnetic study for the above systems seems very important from fundamental as well as applied view points. Ballou, Burzo, and Pop⁶ recently studied the magnetic properties of $(\text{Gd}_{1-x}\text{Y}_x)_2\text{Co}_7\text{B}_2$ compounds and pointed out that the Gd exchange field on the Co site significantly enhances the Co-sublattice moment. Similar suggestions have also presented by others.⁷⁻¹⁰ In order to clarify the induced moment on the Co site and also the magnetic state of the rare-earth sublattice, this work focuses on the compounds RCo_3B_2 with $\text{R}=\text{Y}, \text{Sm}, \text{Gd}, \text{and Dy}$. The magnetic susceptibility in the paramagnetic region in addition to the magnetic moment at $T=0$ K have been measured and are discussed for the above compounds.

II. SAMPLE PREPARATION AND X-RAY ANALYSIS

Samples examined in this work have been prepared by melting raw materials of 99.9% purity in an arc furnace. Generally the melting was repeated several times to homogenize the ingots which were then annealed at 800 °C for 1 day. The crystal structure of the samples thus prepared has been confirmed to be of the CeCo_3B_2 type which is constructed by replacing the $2c$ -site cobalts of the CaCu_5 -type structure by boron atoms.^{2,3} As seen in Table I, it is noted that the a axis of RCo_3B_2 remains almost unchanged; however, the c axis decreases significantly in comparison with those of the RCo_5 of the CaCu_5 -type structure.

III. MAGNETIC MEASUREMENTS

In order to determine the magnetic moment per formula unit ($\mu_B/\text{f.u.}$), magnetization curves of loose powder RCo_3B_2

with $\text{R}=\text{Y}, \text{Sm}, \text{Gd}, \text{and Dy}$ have been measured at $T=5$ K in a pulsed field up to 170 kOe. In the case of YCo_3B_2 , magnetization reached saturation at about 15 kOe, which gives a saturation moment of 0.6 emu/g or $0.032\mu_B/\text{f.u.}$ This small value must be attributed to ferromagnetic impurity which has been confirmed in the YCo_3B_2 sample.¹⁰ Therefore, the Co sublattice of YCo_3B_2 must be essentially in a nonmagnetic state at $T=5$ K.

Magnetization curves for RCo_3B_2 with $\text{R}=\text{Sm}, \text{Gd}, \text{and Dy}$ are illustrated in Figs. 1 and 2, respectively.

Spontaneous magnetization of SmCo_3B_2 is obtained to be 1.94 emu/g or $0.12\mu_B/\text{f.u.}$ by the linear extrapolation of the magnetization curve to zero field. The value of $0.12\mu_B/\text{f.u.}$ is much smaller than the Sm free-ion moment.

The linear part of the magnetization curve gives a high-field susceptibility $\chi_{\text{HF}}=6.9\times 10^{-6}$ emu/g, 4.5×10^{-4} μ_B/kOe . In the cases of GdCo_3B_2 and DyCo_3B_2 , the magnetizations do not reach the free-ion moments. Both magnetization curves with increasing field in Fig. 2 begin to have a linear part at around 60 kOe. The linear part for GdCo_3B_2 seems to be the saturation, which gives $6.4\mu_B/\text{f.u.}$, while the linear part for DyCo_3B_2 gives $8.2\mu_B/\text{f.u.}$ by extrapolation to zero field and $8.9\mu_B/\text{f.u.}$ at the maximum field

TABLE I Lattice constants (the values in parentheses are for RCo_5), Curie temperature, and magnetic moment per formula unit at $T=4.2$ or 5 K. Data from some references are also tabulated. The free ion moments μ_R^{3+} are also shown.

	a (Å)	c (Å)	T_c (K)	$\mu_B/\text{f.u.}$	μ_R^{3+}/μ_B
YCo_3B_2	5.051(4.914)		p.p.?	0.03, 0.09[10]	0
	3.035(3.982)				
SmCo_3B_2	5.110(4.982)		40[11]	0.12	0.71
	2.995(3.975)				
GdCo_3B_2	5.074(4.963)		58[9], 57[10]	6.4, 5.9[10]	7.0
	3.039(3.973)			6.4[9], 6.9[3]	
DyCo_3B_2	5.031(4.916)		27[3], 21[10]	8.2, 8.9($H=140$ kOe)	10.0
	3.018(3.990)			7.8[3], 7.6[9]	

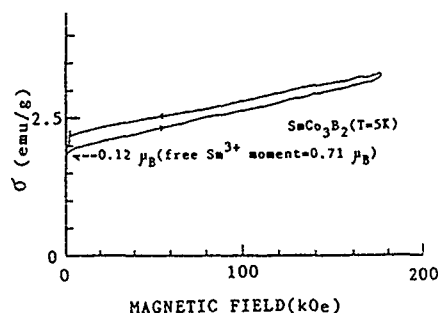


FIG. 1. Magnetization curve for loose powder of SmCo_3B_2 at $T=5$ K.

of 140 kOe. The specimens in this measurement are loose powder but may have some friction among powder particles; in addition, the pulsed field is used, so we regard only the linear part of the magnetization curve as an intrinsic magnetization process. The magnetic data are summarized in Table I.

Paramagnetic susceptibility has been measured for RCo_3B_2 in the temperature range from about 100 to 500 K. To remove the contribution from ferromagnetic impurities in the samples, we generally measured first a lot of thermomagnetic curves under various external magnetic fields up to 8 kOe, and then constructed magnetization curves from them at various temperatures above room temperature. In the temperature region below room temperature, magnetization curves have been measured in fields up to 12 kOe. The paramagnetic susceptibility has been determined from the linear part of each magnetization curve. Spontaneous moment contributed from the impurity in the case of DyCo_3B_2 has been determined to be 0.13 emu/g at room temperature.

In the case of YCo_3B_2 , the ferromagnetic impurity prevents us from determining the intrinsic magnetic susceptibility which is very small compared with those of GdCo_3B_2 and DyCo_3B_2 . The temperature dependence of magnetization mainly due to the temperature dependence of magnetization

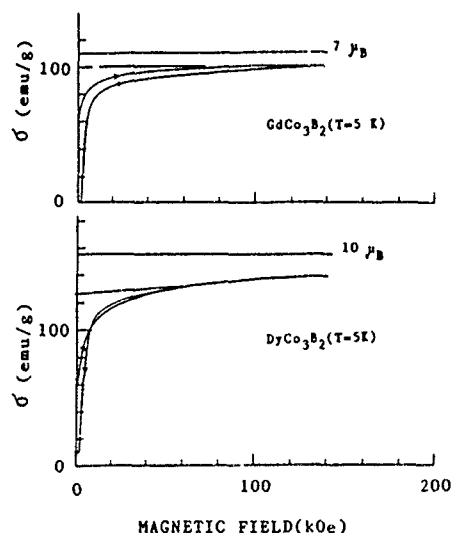


FIG. 2. Magnetization curves for loose powder of GdCo_3B_2 and DyCo_3B_2 .

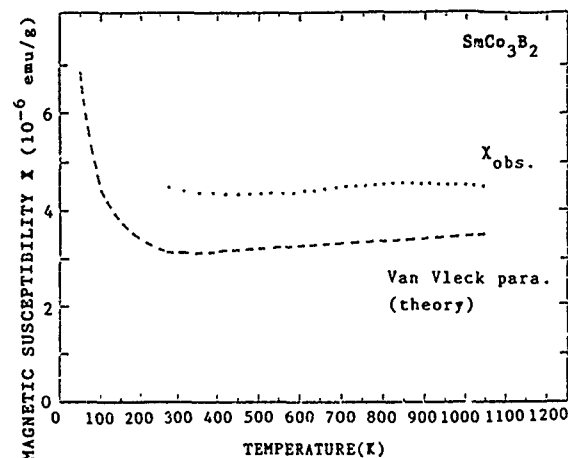


FIG. 3. Temperature dependence of magnetic susceptibility for SmCo_3B_2 powder.

of YCo_3B_2 in a constant magnetic field has been found to be almost independent of temperature in a wide range of temperatures, which also implies that YCo_3B_2 is essentially Pauli paramagnetic (see also Ref. 10).

The sample of SmCo_3B_2 is fortunately found not to contain ferromagnetic impurity with T_C higher than room temperature, so the temperature dependence of susceptibility has been easily determined as shown in Fig. 3. In the cases of GdCo_3B_2 and DyCo_3B_2 , their intrinsic magnetic susceptibilities have been determined by the method mentioned above. The data are shown in Fig. 4. These data deviate slightly from the Curie-Weiss law in the high-temperature region. The linear parts in the low-temperature region give 7.95 and $11.4\mu_B/\text{f.u.}$ for the effective moments of GdCo_3B_2 and DyCo_3B_2 , respectively. The former agrees well with the Gd^{3+} effective moment, however the latter is a little larger than the free Dy^{3+} value of $10.65\mu_B$. The paramagnetic Curie points agree fairly well with the ferromagnetic Curie temperatures listed in Table I

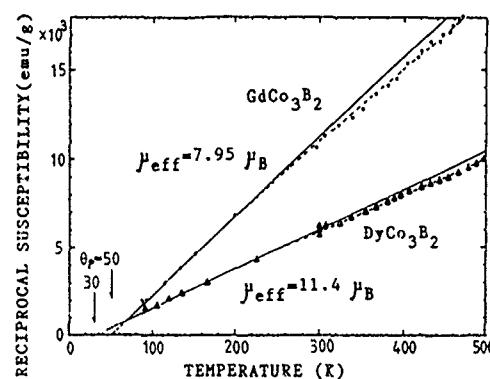


FIG. 4. Calculated magnetic moment m of Dy^{3+} at $T=0$ K as a function of $x = \mu_B(H_m + 2H)/D$. H_m : molecular field; H : external field; $D = 3B_2^0$.

IV. DISCUSSION OF THE RESULTS

As seen in Table I, the moment of the $0.01\mu_B/\text{Co}$ atom for YCo_3B_2 suggests nonmagnetic Co sublattice. As discussed in our previous article,³ the B atoms in the $\text{R}_{n+1}\text{Co}_{3n+5}\text{B}_{2n}$ systems have been considered to donate their valence electrons to the Co sublattice, which results in the nonmagnetic state of the Co sublattice. The moment of SmCo_3B_2 , $0.12\mu_B/\text{f.u.}$, at $T=5$ K suggests the influence of excited multiplets. The large high-field susceptibility of $6.9 \times 10^{-6} \text{ emu/g}$ in Fig. 1 must be explained mainly by the excited multiplets effect and partly by the Pauli paramagnetic Co sublattice. The saturation moment of $6.4\mu_B/\text{f.u.}$ for GdCo_3B_2 seems to be the most reliable value. The $-0.6\mu_B$ extra moment in comparison with $7.0\mu_B$ of a free Gd^{3+} moment must be attributed to the Co-sublattice negative polarization which is $0.2\mu_B/\text{Co atom}$.^{6,9} The large spin of the Gd atom ($S=7/2$) gives a strong exchange field to the Co $3d$ electrons. This result contrasts with the $0.6\mu_B$ extra moment parallel to the Gd moment in pure Gd metal at $T=0$ K.¹² The induced moment of the $0.2\mu_B/\text{Co}$ atom is smaller than $0.49\mu_B/\text{Co}$ estimated by Ballou and co-workers⁶ for $\text{Gd}_2\text{Co}_7\text{B}_3$ or $0.3\mu_B/\text{Co}$ estimated for GdCo_4B by Pedziwiatr *et al.*⁷ and Burzo *et al.*⁸ Since the B atoms in the $\text{R}_{n+1}\text{Co}_{3n+5}\text{B}_{2n}$ systems donate their valence electrons to the Co sublattice³ like $\text{RCo}_{5-x}\text{Al}_x$,¹³ the Co $3d$ band in RCo_3B_2 compounds must be nearly filled and distorted; therefore, the disagreement mentioned above is not surprising. Similar analysis is applied to the data for DyCo_3B_2 . The Dy atom has the same spin of $5/2$ as that of the Sm atom. If the exchange field on the Co site is proportional to the rare-earth spin, the Co polarization in DyCo_3B_2 as well as in SmCo_3B_2 is calculated on the basis of the data for GdCo_3B_2 to be $0.43\mu_B/\text{f.u.}$ or $0.14\mu_B/\text{Co atom}$.

Therefore, the $8.2\mu_B/\text{f.u.}$ of DyCo_3B_2 and $0.12\mu_B/\text{f.u.}$ of SmCo_3B_2 lead to $8.63\mu_B/\text{Dy}$ and $0.31\mu_B/\text{Sm}$ which are antiparallel to the induced Co moment. The latter case is especially noteworthy because the R moment is generally parallel to the moment of $3d$ metal atoms. The intrinsic Dy^{3+} spontaneous moment of $8.63\mu_B$ is now discussed by the crystal-field theory. We express the Hamiltonian for DyCo_3B_2 in a simple form by the following:

$$\mathcal{H} = DJ_z^2 + 2(g_J - 1)J_x\mu_B H_m, \quad (1)$$

where the first term in the right-hand side is the crystal field due to only A_2^0 , the second the exchange interaction between Dy ions with the molecular field H_m which is in the c plane, $D = 3B_2^0$, and the other notations are usual ones.

Solving the 16×16 determinant, we determined the ground-state wave function and then calculated the Dy^{3+} moment, $-g_J J_x \mu_B = m \mu_B$ at $T=0$ K as a function of $x = \mu_B H_m / D$.

The calculated result is shown in Fig. 5. When an external field H is applied, the H_m must be replaced by $(H_m + 2H)$. Point A in Fig. 4 gives a spontaneous Dy moment of $8.63\mu_B$, which results in $\mu_B H_m / D = 0.70$. The molecular field $\mu_B H_m / k$ is estimated to be 14.7 K or $H_m = 219$ kOe from $T_C = 27$ K, therefore $D = 3B_2^0$ is obtained to be 21.0 K or $B_2^0 = 7.0$ K, which is in good agreement with $B_2^0 = 6.37$ K

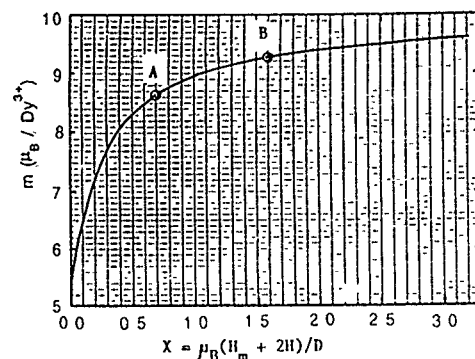


FIG. 5. Temperature dependence of reciprocal magnetic susceptibility for GdCo_3B_2 and DyCo_3B_2 .

estimated from the Mössbauer spectrum by Malik and co-workers.⁹ On the other hand, the maximum field in Fig. 3 is 140 kOe, which is comparable to the H_m . The summation of the two fields gives $\mu_B(H_m + 2H)/D = 1.60$, therefore $9.25\mu_B$ is expected for the Dy moment as seen from point B in Fig. 4. This expected value agrees very well with the experimental one, the intrinsic Dy moment of $9.33\mu_B$, which is the summation of $8.9\mu_B/\text{f.u.}$ at $H = 140$ kOe and the Co-induced moment of $0.43\mu_B$.

In the paramagnetic temperature region, SmCo_3B_2 behaves like the Van Vleck paramagnetism. The dashed line is calculated by taking the excited multiplets of $J=7/2$ and $9/2$ into account, and also by using $\lambda/k = 350$ K for the LS coupling constant. Therefore, the difference between the observed and calculated curves in Fig. 3 corresponds to the Pauli paramagnetic susceptibility contributed by the Co sublattice, $X_{\text{Co}} = 1.1 \times 10^{-6} \text{ emu/g}$. This Co contribution also appears in the magnetic susceptibilities of GdCo_3B_2 and DyCo_3B_2 . The deviations from the Curie-Weiss law are seen in Fig. 4. Rough estimation of X_{Co} from those deviations is about $2 \times 10^{-6} \text{ emu/g}$ for GdCo_3B_2 and about $4 \times 10^{-6} \text{ emu/g}$ for DyCo_3B_2 , which agree approximately with the X_{Co} for SmCo_3B_2 .

¹P. Rogl, in *Handbook on the Physics and Chemistry of Rare Earths*, edited by K. A. Gschneider and L. Eyring (North-Holland, Amsterdam, 1984), Vol. 6, p. 335.

²H. H. Smut, R. C. Thiel, and K. H. J. Buschow, *J. Phys. F* **18**, 295 (1988).

³H. Ogata, H. Ido, and H. Yamauchi, *J. Appl. Phys.* **73**, 5911 (1993).

⁴M. Q. Huang, B. M. Ma, S. F. Cheng, and W. E. Wallace, *J. Appl. Phys.* **69**, 5599 (1991).

⁵H. Ido, H. Ogata, and K. Maki, *J. Appl. Phys.* **73**, 6266 (1993).

⁶R. Ballou, E. Burzo, and V. Pop, *J. Appl. Phys.* **73**, 5695 (1993).

⁷A. T. Pedziwiatr, S. Y. Jiang, W. E. Wallace, E. Burzo, and V. Pop, *J. Magn. Magn. Mater.* **66**, 69 (1987).

⁸E. Burzo, N. Plugaru, I. Creanga, and M. Ursu, *J. Less-Common Met.* **155**, 281 (1989).

⁹S. K. Malik, A. M. Umarji, and G. K. Shenoy, *J. Appl. Phys.* **57**, 3252 (1985).

¹⁰H. Ido, H. Yamauchi, S. F. Cheng, S. G. Sankar, and W. E. Wallace, *J. Appl. Phys.* **70**, 6540 (1991).

¹¹H. Oesterreicher, F. T. Parker, and M. Misroch, *J. Appl. Phys.* **12**, 287 (1977).

¹²J. J. Rhyne, in *Magnetic Properties of Rare Earth Metals* edited by R. J. Elliot (Plenum, London, 1972), pp. 131 and 132.

¹³K. Konno, H. Ido, S. F. Cheng, S. G. Sankar, and W. E. Wallace, *J. Appl. Phys.* **73**, 5929 (1993).

¹³⁹La nuclear quadrupole resonance and relaxation in Zn-doped La₂CuO₄

M. Corti, A. Lasciari, A. Rigamonti, and F. Tabak^{a)}
Department of Physics "A. Volta," University of Pavia, 27100 Pavia, Italy

F. Licci and L. Raffo
Istituto MASPEC (CNR), 43100 Parma, Italy

¹³⁹La nuclear quadrupole resonance and relaxation measurements, aimed at the study of static magnetic properties and of the dynamical generalized susceptibility in La₂Cu_{1-x}Zn_xO₄, upon substitution of Zn²⁺ (*S*=0) for Cu²⁺ (*S*=1/2) inducing a spin vacancy in the antiferromagnetic matrix, are presented. From the doublet resulting from the mixed Zeeman-quadrupolar eigenstates, it is shown how the sublattice magnetization is only slightly *x* dependent, while its temperature dependence changes with respect to pure La₂CuO₄. The relaxation rates show moderate (compared to the case of itinerant spin vacancies, as in La_{2-x}Sr_xCuO₄) effects, which are related to the decrease of the correlation length and to the modifications induced in the spin-wave spectrum.

I. INTRODUCTION

The study of the effects of Zn for Cu substitution in La₂CuO₄ is motivated by the connections with the mechanism of superconductivity in cuprates, which is known to occur on the verge of antiferromagnetic (AF) order. The Zn doping of La₂CuO₄ decreases the Néel temperature, with the removal of a Cu²⁺ spin from the AF matrix, a situation somewhat equivalent to the spin vacancy induced by Sr doping, the relevant difference being that in this latter case the vacancy is itinerant. Zn doping has effects stronger than the conventional magnetic dilution. In fact, for two-dimensional (2D) Heisenberg AF on square lattice theoretical treatments,¹ and experimental findings,² indicate that the initial suppression rate

$$A = \frac{-1}{T_N(0)} \lim_{x \rightarrow 0} \frac{dT_N(x)}{dx} \quad (1)$$

should be π , while the AF order should persist up to the percolation threshold $x \approx 0.41$. In La₂Cu_{1-x}Zn_xO₄, *A* seems larger and for $x \approx 0.11$ *T_N* is already close to zero.³ The Cu magnetic moment and the magnetic exchange also stay practically constant for $x \leq 0.1$. Thus, one is led to the conclusion³ that novel microscopic features, such as effects on the electronic states, occur in La₂Cu_{1-x}Zn_xO₄.

A useful tool to study the microscopic magnetic properties in doped La₂CuO₄ is ¹³⁹La nuclear quadrupole resonance (NQR) and spin-lattice relaxation. A variety of experiments⁴ provided enlightening insights, particularly in La_{2-x}Sr_xCuO₄. In this article the results obtained in La₂Cu_{1-x}Zn_xO₄ are reported. The NQR spectra are used to derive the Cu sublattice magnetization $\langle \mu \rangle$ and its *x* and temperature dependence. The relaxation rates are interpreted in terms of magnetic excitations and of the modifications induced by the spin vacancy in the magnons spectrum.

II. EXPERIMENT

The Zn-doped La₂CuO₄ samples have been prepared by solid-state reactions in air, with annealing of the pellets for 24–48 h at 1050 °C. Particular attention has been devoted to

the problem of extra oxygen, which is known⁵ to cause a strong depression of *T_N*, particularly in Zn-doped YBCO.^{6,7} Measurements were first carried out in as-grown samples. Then a set of samples at various *x* was kept for 24 h at various temperatures from 600 to 900 °C in N₂ atmosphere. *T_N* was found to increase progressively, supporting the conclusion⁸ that the effect of interstitial oxygen simply adds on to one due to the magnetic vacancies. In the thermally treated samples, where for $x=0$ one has *T_N* = 315 K (close to the highest *T_N* achieved in La₂CuO₄), still some evidence of small amounts of extra oxygen, undetected by thermogravimetry measurements, was noticed from La NQR relaxation at $T \geq 300$ K.

The ¹³⁹La NQR spectra have been obtained with standard pulse techniques, from the echo envelope, by sweeping the frequency at moderate intensity of the radio-frequency field. The field at the La site was derived from the resonance lines originated from the mixed Zeeman-quadrupolar eigenstates of the $\pm 1/2 \leftrightarrow \pm 3/2$ NQR line.⁹ In particular, the shift δ of the doublet at higher frequency with respect to the quadrupole frequency ν_Q , obtained from the $(\pm 5/2 \leftrightarrow \pm 7/2)$ doublet, was measured. Since the asymmetry parameter of the electric-field gradient is small,⁹ δ is practically proportional to the effective field $|h|$ at the La site. Then, in the limit $T \rightarrow 0$, one has

$$\frac{\langle \mu_{Cu}(x,0) \rangle}{\langle \mu_{Cu}(0,0) \rangle} = \frac{|h(x,0)|}{|h(0,0)|} = \frac{\delta(x,0)}{\delta(0,0)} \quad (2)$$

The temperature dependence of $\langle \mu_{Cu}(x,T) \rangle$ was obtained from $|h(x,T)|$ in the assumption that the proportionality constant is temperature independent, which is the case when no modifications in the magnetic lattice occur. The field was derived from $\delta(x,T)$, through direct diagonalization of the matrix involving the Zeeman-perturbed quadrupole levels.

The ¹³⁹La NQR relaxation rate *W* has been obtained from the recovery, after saturation, of the echo signal of the $\pm 5/2 \leftrightarrow \pm 7/2$ line. One has⁴

$$2W = \frac{\gamma^2}{2} \int \langle h_+(0)h_-(t) \rangle e^{-i3\omega_Q t} dt \\ \approx \frac{\gamma^2}{2\pi^2} (h_{eff})^2 \frac{kT}{N} \sum_q \chi_q(0) J_q(3\omega_Q), \quad (3)$$

^{a)}On leave of absence from Hacettepe University, Ankara, Turkey

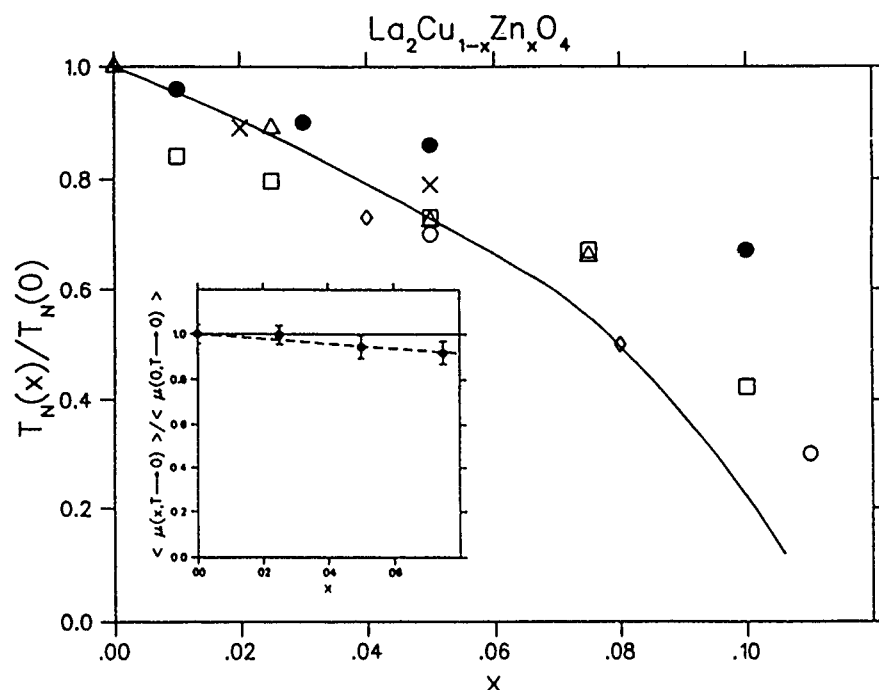


FIG. 1. x dependent of the Néel temperature and of the Cu sublattice magnetization $\langle \mu(x, T \rightarrow 0) \rangle$ (inset) in $\text{La}_2\text{Cu}_{1-x}\text{Zn}_x\text{O}_4$ after thermal treatment. [For the as-grown sample an analogous behavior is observed with $T_N(x=0)=225$ K, instead of $T_N(x=0)=315$ K of the thermally treated sample.] Representative data obtained by other authors with different techniques are also shown: (\diamond) susceptibility, Ref. 10; (\square) susceptibility and μ SR, Ref. 11; (\bullet) susceptibility, Ref. 5; (\times) neutron scattering, Ref. 8; (\circ) dc susceptibility, Ref. 12; (\triangle) present work. The solid and the dashed lines are the best-fit behaviors predicted by Acquarone and Pausco (Ref. 3) in correspondence to a model of metallic AF.

where h_{eff} is an effective field, mediated over the Brillouin zone and close to the value of the static field $|h| \approx 10^3$ G found in La_2CuO_4 at the lowest temperature.

III. RESULTS AND DISCUSSION

The Néel temperatures (obtained from the condition $\delta \rightarrow 0$ and from the concurrent peaks in the relaxation rate and/or in the dephasing time of the echo signals) and the x dependence of the sublattice magnetization are shown in Fig. 1. From our data the factor A [Eq. (1)] turns out close to 5.5. The x dependence of T_N appears well fitted by the theoretical behavior of a metallic AF.

In Fig. 2 the temperature dependence of the sublattice magnetization is shown. For $x=2.5\%$ the behavior of $\langle \mu_{\text{Cu}}(T) \rangle$ is close to the one for weakly itinerant AF (solid line), while at $x=7.5\%$ the data are better described by the behavior of the order parameter in 2D systems. For $(T/T_N) \ll 1$ one can try to analyze the decrease of $\langle \mu \rangle$ in terms of the law $1 - AT^\alpha$, expected to result from spin-wave excitations. One derives $\alpha \approx 1.95$ and $A = 1.4 \times 10^{-5} \text{ K}^{-1.95}$, a large value implying rapid decrease of the sublattice magnetization.

In Fig. 3 the ^{139}La NQR relaxation rates are reported and compared with the behavior in pure La_2CuO_4 . In the AF phases W decrease rapidly with decreasing temperature, as expected for the Raman two-magnon relaxation process.^{14,15} This can be interpreted in terms of an effective spectral density in the rf range which is negligible when the excitations are AF spin waves. Then, for 3D isotropic AF, one would have

$$J_{\text{eff}} = [4/(2\pi)^3 \omega_{\text{exch}}] (T/T_{\text{exch}})^3,$$

with ω_{exch} Heisenberg exchange frequency. However, estimates on the basis of this expression yield W considerably smaller than the experimental results. Even though a spin-

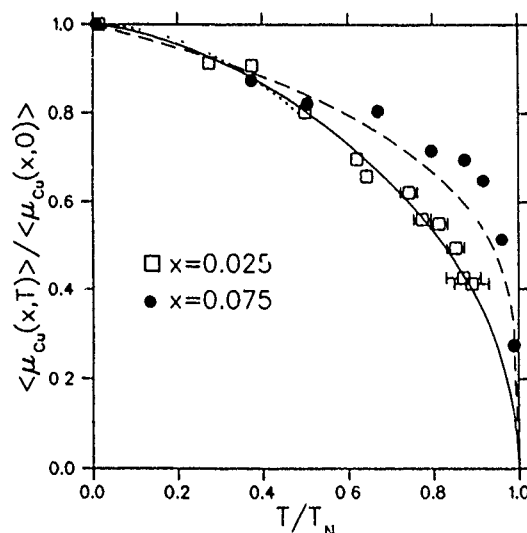


FIG. 2. Normalized temperature dependence of the Cu sublattice magnetization in $\text{La}_2\text{Cu}_{1-x}\text{Zn}_x\text{O}_4$. The solid line is the theoretical behavior predicted for a weakly itinerant AF (see Ref. 9) and fits rather well our data for $x=0$ (and those of Refs. 9 and 13 in pure La_2CuO_4 , practically coincident with ours). The dashed line is the function $\langle \mu_{\text{Cu}} \rangle \propto (T_N - T)^{1/4}$, of the form expected for the order parameter in low-dimensional systems. The dotted line corresponds to the function $(\langle \mu(0) \rangle - \langle \mu(T) \rangle) / \langle \mu(0) \rangle = AT^\alpha$ with $\alpha=1.95$ and $A = 1.4 \times 10^{-5} \text{ K}^{-1.95}$.

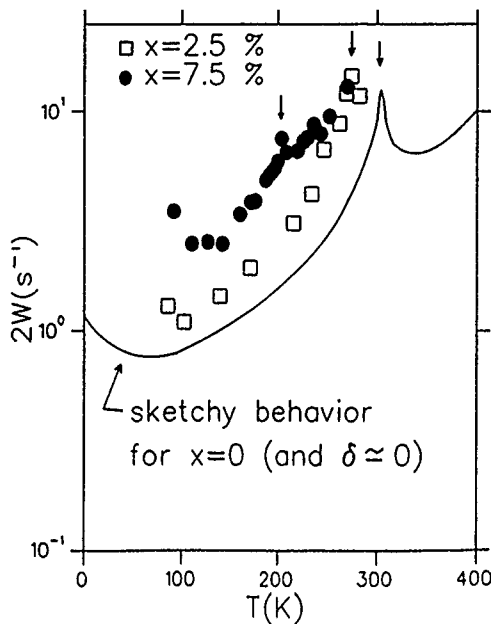


FIG. 3. ^{139}La NQR relaxation rates $2W$ in $\text{La}_2\text{Cu}_{1-x}\text{Zn}_x\text{O}_4$, for $x=0.025$ and $x=0.075$ as a function of temperature, and comparison with the sketched behavior (solid line) in $\text{La}_2\text{CuO}_{4+\delta}$ with $\delta \approx 0$. Some amount of extra stoichiometric oxygen δ , hardly detected in thermogravimetric measurements, is evidenced by the contribution to the relaxation occurring for $T \geq 250$ K and associated with quadrupolar mechanism, possibly through oxygen diffusion. The arrows mark the Néel temperatures indicated by the NQR spectra.

wave spectrum appropriate to 2D La_2CuO_4 is used,¹⁶ agreement is not found, as already observed for Cu relaxation.^{17,18}

In nominally pure La_2CuO_4 for T around T_N and particularly in the presence of AF disorder as in Zn-doped compounds, modifications in the conventional spin-wave spectrum can be expected.¹⁹ In particular, if $\xi \approx a/\sqrt{x}$ is the 2D magnetic correlation length, propagating spin waves can exist only for wave vector q larger than ξ^{-1} and one has regions of magnetization density short-range ordered in space which relax with a time scale related to ξ^{-1} . To discuss these effects we model the spectral density in Eq. (3) in the form

$$J_q(\omega) = \frac{1}{2\pi} \left(\frac{\Gamma_{\text{SF}}}{(\omega - \omega_q)^2 + \Gamma_{\text{SF}}} + \frac{\Gamma_{\text{SF}}}{(\omega + \omega_q)^2 + \Gamma_{\text{SF}}} \right), \quad (4)$$

suggested¹⁸ in the interpretation of neutron scattering in 2D AFs. Γ_{SF} heuristically describes the relaxational dynamics associated with the AF disorder or with finite size effects. By taking into account that in Eq. (3) $\chi(q,0) \propto |S_q|^2$ is only slightly q and x dependent^{3,8} and thus $kT\chi(q,0) \approx S(S+1)/3$, we can discuss the W 's in terms of the spectral density

$$J_{\text{eff}}(\omega \approx 0) = \frac{1}{N} \sum_q J_q(3\omega_Q \approx 0).$$

2D integration with $\omega_q = (c^2 q^2 + \Delta^2)^{1/2}$ yields

$$J_{\text{eff}} \approx \frac{1}{2\Gamma_{\text{SF}}} \left(\frac{\Gamma_{\text{SF}}}{\Gamma_{\text{SW}}} \right)^2 \ln \frac{\Gamma_{\text{SW}}^2 + \Delta^2 + \Gamma_{\text{SF}}^2}{\Gamma_{\text{SF}}^2 + \Delta^2}, \quad (5)$$

where $\Gamma_{\text{SW}} = cq_m(q_m \approx \pi/a$, maximum wave vector) is a typical spin-wave frequency that for order-of-magnitude estimates one can take as $\Gamma_{\text{SW}} \approx \omega_{\text{exch}} \sim 2 \times 10^{14}$ rad/s. In the light of Eq. (5), J_{eff} is expected to increase with x , in correspondence with the increased number of modes contributing to the central component. Furthermore, the decrease of the spin-wave velocity c with x^3 implies a decrease of Γ_{SW} and an increase in W , in agreement with the trend in Fig. 3.

Finally, we observe that in $\text{La}_2\text{Cu}_{1-x}\text{Zn}_x\text{O}_4$ the relaxation is affected by doping to a much smaller extent than the one due to itinerant spin vacancies, as in $\text{La}_{2-x}\text{Sr}_x\text{CuO}_4$,⁴ or $\text{Cu}_{1-x}\text{Li}_x\text{O}_4$,¹⁸ consistent with the predictions derived for the Zhang-Rice singlet in the framework of the t - J model.

ACKNOWLEDGMENTS

One of us (A.R.) gratefully acknowledges illuminating discussions with M. Acquarone. Thank are due to M. Bertassi for her help in the measurements. This work was supported by CNR of Italy in the framework of the "Progetto Finalizzato Tecnologie Superconduttive e Criogeniche" and by INFN (Istituto Nazionale di Fisica Nucleare).

¹A. R. McGurn, J. Phys. C **12**, 3523 (1979).

²D. J. Breed, K. Gilliamse, J. W. Sterkenburg, and A. R. Miedema, J. App. Phys. **41**, 1982 (1970); B. J. Dikken, A. F. M. Arts, H. W. De Wijn, W. A. H. M. Vlak, and E. Frikkee, Phys. Rev. B **32**, 1267 (1985).

³M. Acquarone and M. Piusco, Physica C **210**, 373 (1993).

⁴See, among others, F. Borsa, M. Corti, T. Rega, and A. Rigamonti, Nuovo Cimento D **11**, 1785 (1989); A. Rigamonti, F. Borsa, M. Corti, T. Rega, and F. Waldner, in *Earlier and Recent Aspects of Superconductivity*, edited by J. G. Bednordz and K. A. Muller (Springer, Berlin, 1990), p. 441; A. Rigamonti, M. Corti, T. Rega, J. Ziolo, and F. Borsa, Physica C **166**, 310 (1990); J. H. Cho, F. Borsa, D. C. Johnston, and D. R. Torgeson, Phys. Rev. B **46**, 3179 (1992).

⁵S. W. Cheong, A. S. Cooper, L. W. Rupp, B. Battlog, J. D. Thompson, and Z. Fisk, Phys. Rev. B **44**, 9739 (1991).

⁶H. Alloul, T. Ohno, H. Casalta, J. F. Marucco, P. Mendels, S. Arabsky, and G. Collins, Physica C **171**, 419 (1980).

⁷H. Alloul, P. Mendels, H. Casalta, J. F. Marucco, and J. Arabsky, Phys. Rev. Lett. **67**, 3140 (1991).

⁸B. Keimer, A. Aharony, A. Auerbach, R. J. Birgeneau, A. Cassanho, Y. Endoh, R. W. Frwin, M. A. Kastner, and G. Shirane, Phys. Rev. B **46**, 14 034 (1992).

⁹H. Nishihara, H. Yasuoka, T. Shimizu, T. Tsuda, T. Imai, S. Sasaki, S. Kanbe, K. Kishio, K. Kitazawa, and K. Fjzki, J. Phys. Soc. Jpn **56**, 4559 (1987).

¹⁰S. T. Ting, P. Pernambuco-Wise, J. E. Crow, E. Manusakis, and J. Weaver, Phys. Rev. B **46**, 11 772 (1993).

¹¹R. L. Lichti, C. Boekema, J. C. Lam, D. W. Cooke, S. F. J. Cox, S. T. Ting, and J. L. Crow, Physica C **180**, 358 (1991).

¹²D. Fiorani, F. Testa, and F. Licci (unpublished).

¹³I. Watanabe, K. Kumagai, Y. Nakamura, T. Kimura, Y. Nachamuchi, and H. Nakajima, J. Phys. Soc. Jpn **56**, 3028 (1987).

¹⁴T. Moriya, Prog. Theor. Phys. **16**, 641 (1956).

¹⁵D. Beeman and Pincus, Phys. Rev. **166**, 359 (1968).

¹⁶S. Chakravarty, M. P. Gelfand, P. Kopiez, R. Orbach, and M. Wollensak, Phys. Rev. B **43**, 2796 (1991).

¹⁷T. Tsuda, T. Ohno, and H. Yasuoka, J. Phys. Soc. Jpn **61**, 2109 (1992).

¹⁸See P. Carretta, M. Corti, and A. Rigamonti, Phys. Rev. B **48**, 3433 (1993).

¹⁹O. Scharpf and H. Capelmann, Z. Phys B **86**, 59 (1992).

³⁵Cl nuclear-magnetic-resonance study of magnetic ordering in Sr₂CuO₂Cl₂ single crystal

M. Corti and F. Borsa^{a)}

Dipartimento di Fisica "A. Volta," Università di Pavia, 27100 Pavia, Italy

L. L. Miller

Ames Laboratory and Department of Physics and Astronomy, Iowa State University, Ames, Iowa

A. Rigamonti

Dipartimento di Fisica "A. Volta," Università di Pavia, 27100 Pavia, Italy

³⁵Cl nuclear-magnetic-resonance (NMR) and relaxation measurements have been performed in a Sr₂CuO₂Cl₂ single crystal as a function of orientation between the external magnetic field H_0 and the tetragonal c axis. The onset is found of an anisotropic inhomogeneous broadening of the NMR line without paramagnetic shift starting below about 320 K. The broadening is strongly temperature dependent and it increases with increasing H_0 . The relaxation rate T_1^{-1} , on the other hand, diverges at $T_N \approx 260$ K in agreement with previous results in powder sample. It is suggested that the observed broadening is due to the onset at $T > T_N$ of a spontaneous nonzero thermal average of the Cu²⁺ moment lying in the a - b plane.

I. INTRODUCTION

Sr₂CuO₂Cl₂ is a layered perovskite with the body-centered-tetragonal K₂NiF₄ structure.¹ Neutron-diffraction,² magnetic susceptibility,² and μ SR (Ref. 3) studies have shown that Sr₂CuO₂Cl₂ orders magnetically with three-dimensional (3D) antiferromagnetic (AF) structure and an effective Cu²⁺ moment similar to the one in La₂CuO₄, well known as a parent compound of a series of high- T_c superconductors. The Cu²⁺ $S=1/2$ magnetic moments order in 3D, below $T_N \approx 260$ K, along the $[110]$ crystal direction, without the out-of-plane canting observed instead in La₂CuO₄ and related to the tetragonal to orthorhombic transition. Therefore, Sr₂CuO₂Cl₂ appears to be a good prototype of a 2D $S=1/2$ Heisenberg system.

A previous ³⁵Cl nuclear-magnetic-resonance (NMR) study in powder sample⁴ revealed a divergence of the nuclear spin-lattice relaxation rate (NSLR) with a sharp, magnetic-field-independent peak occurring at $T \approx T_N = 260 \pm 0.5$ K for $T \rightarrow T_N^+$. The critical behavior of the NSLR was interpreted in terms of strongly correlated 2D Cu²⁺ spin fluctuations. In the same study it was noted that the full width at half-intensity (FWHI) of the ³⁵Cl NMR line exhibited pretransitional broadening. The important message of the broadening is that it may indicate the occurrence of a nonzero thermal average of the Cu²⁺ moment even above T_N . In order to investigate this effect we present here the results of the ³⁵Cl NMR spectra as a function of the temperature in a single crystal.

II. EXPERIMENT

The single crystal consisted is a thin slab about 1 mm thick and 5×10 mm² wide with the c axis perpendicular to the plane of the slab. Some measurements were performed on a stack of about ten small slabs in order to increase the signal-to-noise ratio. At the temperatures where strong an-

isotropy of the line is present the measurements in the stack were found to be affected by misalignment effects.

The $I=3/2$, ³⁵Cl NMR measurements were carried out with a Fourier transform (FT) pulse spectrometer at two values of the external magnetic field: 5.9 and 2.3 T. The symmetry of the electric-field gradient tensor at the Cl site is axial with the principal axis in the c direction. In this case one expects a central line transition ($+1/2 \leftrightarrow -1/2$) and symmetric satellite transitions ($\pm 3/2 \leftrightarrow \pm 1/2$) displaced in frequency by an amount which depends upon the angle between H_0 and c .

Due to the small signal-to-noise ratio in the single crystal, the satellite lines could not be clearly detected. However, an estimate of $\nu_Q \leq 0.5$ MHz was inferred from the second-order shift of the central line. The measurements of the magnetic effects were performed on the central line transition only, for the two orientations $H_0 \parallel c$ and $H_0 \perp c$ for which the satellite lines are shifted by an amount greater than the line-width. The NMR spectra were obtained by FT of half of the echo signal following a two-pulse sequence (pulse width around 5–6 μ s). For the wider lines the spectrum was obtained by the frequency-swept echo intensity method. A few preliminary measurements of spin-lattice relaxation rate (NSLR) were performed by saturating the central line with a radio-frequency pulse sequence as described previously.⁴

III. RESULTS

The 3D Néel temperature was estimated from the peak in the ³⁵Cl NSLR shown in Fig. 1. Since the signal in the single crystal had an insufficient signal-to-noise ratio for reliable systematic relaxation measurements, particularly at low field H_0 , the measurements were carried out in the stack of single crystals. The NSLR is close to the values in the powder sample⁴ with a maximum at a slightly higher temperature ($T_N = 260 \pm 0.5$ K for the powder, $T_N = 265 \pm 3$ K for the stack of single crystals). No difference in the NSLR is detected within experimental error for the two magnetic-field orientations and for the two values of H_0 . A more precise

^{a)}Also at: Ames Laboratory and Department of Physics and Astronomy, Iowa State University, Ames, IA.

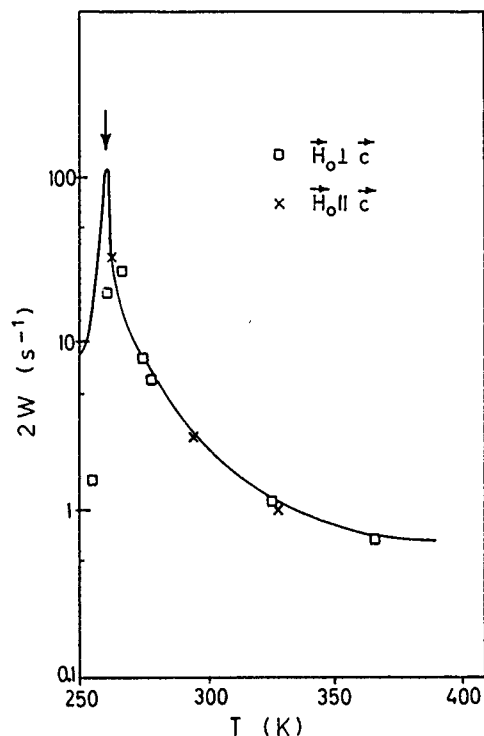


FIG. 1. ^{35}Cl nuclear spin lattice relaxation rate $2W$ as a function of temperature for a stack of single crystals, at $H_0=5.9$ T, for $H_0\parallel c$ and $H_0\perp c$. The solid line reports the behavior of $2W$ observed in the powder sample (Ref. 4), with T_N indicated by the arrow. An analogous behavior of the W vs T was observed at $H_0=2.3$ T (data not reported).

study of the critical spin dynamics through NSLR measurements has to wait for the availability of a larger single crystal.

The data for the linewidth as a function of temperature, magnetic-field intensity, and orientation of the crystalline c axis with respect to the external magnetic field are shown in Figs. 2 and 3. The remarkable result here is represented by the onset of a strongly anisotropic inhomogeneous broadening, for both field values, starting at $T\approx 320$ K. It is noted that for $H_0\parallel c$ there is only a small broadening while for $H_0\perp c$ the broadening below T_N exceeds 150 kHz. For $T<T_N$ the signal-to-noise ratio becomes too small to allow for reliable linewidth measurements. It should be stressed that for both orientations, no average shift of the center of the line with respect to the ^{35}Cl Larmor frequency could be evidenced.

IV. DISCUSSION

Let us first analyze the data in the 3D ordered phase below T_N . The lack of a detectable shift combined with the strongly anisotropic broadening is an unusual occurrence in a magnetically ordered single crystal. However, in the present case it is consistent with a dominant ^{35}Cl - Cu^{2+} nuclear-electron dipolar interaction and with the reported magnetic AF lattice structure with the Cu^{2+} magnetic moment along the equivalent $[110]$ directions.² The dipolar local field due to a moment μ at position r with respect to a nucleus at the origin is

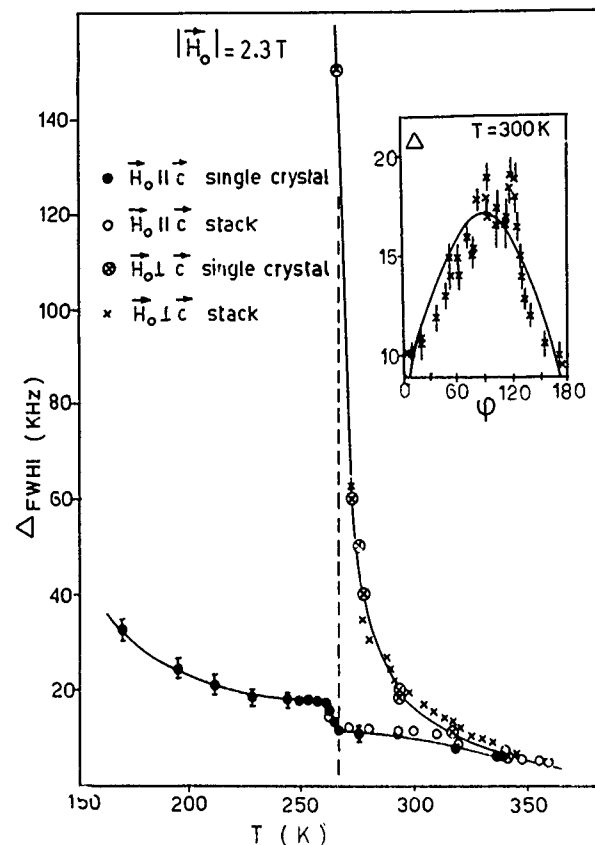


FIG. 2. ^{35}Cl NMR linewidth (full width at half-intensity) as a function of temperature for $H_0\parallel c$ and $H_0\perp c$ at $|H_0|=2.3$ T. (The solid lines are guides for the eye.) The dashed line indicates the Néel temperature as derived from the NSLR (Fig. 1). In the inset the angular dependence of Δ_{FWHI} at $T=300$ K is reported (the solid line is the function $\Delta=8+9\sin\phi$ kHz, ϕ being the angle between c and H_0).

$$h_d = \frac{\mu}{r^3} - \frac{3(\mu \cdot r) \cdot r}{r^5}. \quad (1)$$

Thus, for $H_0\parallel c$, the contribution of the Cu^{2+} nearest-neighbor magnetic moment at a given apical Cl site has a zero projection along the quantization axis H . On the contrary, for $H_0\perp c$, the projection of the dipolar field yields $h_d^z = (\mu/r^3)\cos\alpha$ where α is the angle between μ and H . For fixed a, b axis there are two possible magnetic domains and four possible angles α yielding four lines symmetrically shifted with respect to the Larmor frequency. Since our single slab might have more than one orientation with different (ab) directions the superposition of several four-line spectra are expected to give rise to an unresolved broadening without average shift. The dipolar field at the Cl site due to the dominant first Cu^{2+} neighbor contribution is 133 G for $\mu=0.34\mu_B$ and is directed perpendicular to the c axis. The complete dipolar sum evaluated for the AF arrangement described above yields a value of 115 G,⁴ with a direction still perpendicular to the c axis. Thus, in the presence of AF order and considering only dipolar local fields one expects a broadening which depends on the angle ϕ between H and c as

$$\Delta H(\phi) = \Delta H_{\parallel} + C|\sin\phi|, \quad (2)$$

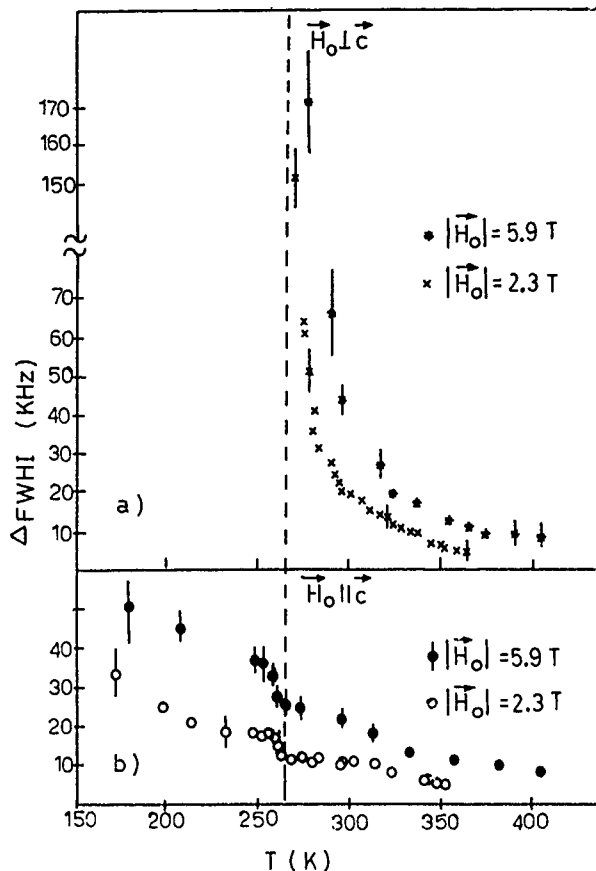


FIG. 3. ^{35}Cl NMR linewidth for (a) $\mathbf{H}_0 \perp \mathbf{c}$ and (b) $\mathbf{H}_0 \parallel \mathbf{c}$ as a function of temperature for two values of $|\mathbf{H}_0|$. The dashed line indicates the Néel temperature. Typical error bars are indicated.

where ΔH_{\parallel} is the NMR linewidth for $\mathbf{H}_0 \parallel \mathbf{c}$ and $C = \sqrt{\langle (h_z^2)^2 \rangle}$ is the rms value of the distribution of the dipolar field component along the quantization axis \mathbf{H}_0 due to the distribution of angles α .

The above considerations allow one to interpret the most striking result of the present study, i.e., the large anisotropic broadening of the NMR line above T_N . In fact, if the system were paramagnetic above T_N , one would expect a paramagnetic shift of the center of the NMR line of the order of magnitude of the broadening or more. Furthermore the dipolar shift due to the first Cu^{2+} neighbor should be larger for $\mathbf{H}_0 \parallel \mathbf{c}$ and of opposite sign than the one for $\mathbf{H}_0 \perp \mathbf{c}$ [see Eq. (1)]. Thus, the only plausible explanation for the broadening without shift occurring above T_N is the onset at $T \leq 320$ K of a static 2D order characterized by a local spontaneous moment $\langle \mu \rangle \neq 0$ lying in the a - b plane. In this case the local field at the ^{35}Cl site could be similar to the one predicted above for the AF 3D ordering since it is largely dominated by the first next-nearest-neighbor contribution. In fact, the rotation pattern for the linewidth at $T = 300 \text{ K} > T_N$ shown in the inset of Fig. 2 can be fitted with the behavior of Eq. (2).

For $T = 300 \text{ K}$ one finds $\Delta H_{\parallel} = 8 \text{ kHz}$ and $C = 9 \text{ kHz}$. The value of the intrinsic linewidth can be estimated from the linear extrapolation at $H_0 = 0$ of the linewidth at any temperature and for both orientations. The value so found is $\Delta H^0 = 4 \pm 1 \text{ kHz}$. The experimental value of ΔH_{\parallel} is temperature dependent and larger than the intrinsic width ΔH^0 for $T < 350 \text{ K}$ (see Fig. 2). The difference is too large to be due to misalignment effects. Thus, we conclude that the broadening for $\mathbf{H}_0 \parallel \mathbf{c}$ is due to the dipolar field of more distant Cu^{2+} moments not included in the simple model discussed above. The critical increase of the linewidth indicates that $\langle \mu \rangle$ increases rapidly as the 3D ordering temperature T_N is approached from above. While the anisotropy of the broadening can be explained in terms of the different effect of the dipolar fields for $\mathbf{H}_0 \parallel \mathbf{c}$ and $\mathbf{H}_0 \perp \mathbf{c}$ (as discussed above for $T < T_N$) the size of the constant C in Eq. (2) is too large to be explained only by the direct dipolar field at the Cl site and one should invoke a contribution due to nuclear-electron pseudodipolar interaction. Furthermore, the practically linear field dependence (see Figs. 2 and 3) of the broadening above T_N indicates that the static 2D effects are unconventional. It is noted that the field-dependent broadening cannot be due to the demagnetization effects which are negligible here, nor to random paramagnetic impurities which would not give rise to anisotropy. Also, the quadrupole broadening would have the opposite field dependence.

One is led to the tentative conclusion that there is a spontaneous average local moment $\langle \mu \rangle$ lying in the a - b plane, which arises above T_N and it is both temperature and field dependent. On the other hand, the fact that the NSLR still has a peak at T_N as in the powder sample indicates that the thermodynamic slowing down of the Cu^{2+} spin fluctuations is driven by the 3D transition. It should be pointed out that in the previous susceptibility measurements² a distinct slope discontinuity was seen in χ_{\parallel} at $T \approx 310 \text{ K}$ and it was ascribed to the onset of 3D order at T_N , arguing that the value higher than $T_N = 251 \text{ K}$ found by neutron scattering was due to the different sample employed. In the light of the present measurements it is conceivable that the effect observed at 310 K on the susceptibility is due to the onset of local 2D order as described here.

ACKNOWLEDGMENTS

This work was supported by CNR of Italy in the framework of the "Progetto Finalizzato Tecnologie Superconduttive e Criogeniche" and by INFN (Istituto Nazionale di Fisica Nucleare) under Project No. PV-MS-C.

¹ L. L. Miller, X. L. Wang, S. X. Wang, C. Stassis, D. C. Johnston, J. Faber, Jr., and C. K. Loong, Phys. Rev. B **41**, 1921 (1990).

² D. Vaknin, S. K. Sinha, C. Stassis, L. L. Miller, and D. C. Johnston, Phys. Rev. B **41**, 1926 (1990).

³ L. P. Le, G. M. Luke, B. J. Sternlieb, Y. J. Uemura, J. H. Brewer, T. M. Riseman, D. C. Johnston, and L. L. Miller, Phys. Rev. B **42**, 2182 (1990).

⁴ F. Borsa, M. Corti, T. Goto, A. Rigamonti, D. C. Johnston, and F. C. Chou, Phys. Rev. B **45**, 5756 (1992).

Effects of Co and Y substitution on magnetic properties of CeFe₂

Xianfeng Zhang and Naushad Ali

Department of Physics and Molecular Science Program, Southern Illinois University, Carbondale, Illinois 62901

CeFe₂ orders ferromagnetically (FM) below $T_C=227$ K; however, this FM state is inherently unstable and partial substitution of Fe by Co precipitates the instability of FM state and a ferromagnetic to antiferromagnetic (AFM) phase transition is observed at lower temperature. This second phase transition is a first-order phase transition. The dependence of T_C and T_N on the concentration of Co X for Ce(Fe_{1-x}Co_x)₂ is presented. For Ce(Fe_{0.8}Co_{0.2})₂, the FM transition is at $T_C=160$ K, and the AFM transition is at $T_N=76$ K. The entropy change associated with the FM to AFM phase transition has been determined from magnetization measurements and found to be primarily associated with a change in the electronic density of states at E_F . If one starts with Ce(Fe_{0.8}Co_{0.2})₂ and partially substitutes Ce by Y, it is found that T_N gradually decreases with Y concentration; and for Y concentration greater than 10%, the AFM phase disappears and FM phase is fully restored. The dependence of T_C and T_N on the concentration of Y Z is presented for Ce_{1-Z}Y_Z(Fe_{0.8}Co_{0.2})₂. It is suggested that the second transition (FM to AFM) is a result of the competition between exchange energy and magnetic anisotropy energy. The measurements of magnetization, ac susceptibility, resistivity, and thermal expansivity are presented.

CeFe₂ is a ferromagnet that exhibits some anomalous magnetic properties such as a much lower Curie temperature ($T_C=227$ K) and a much lower magnetic moment per Fe atom ($1.15\mu_B$) than other compounds in the RFe₂ series (R denotes rare earth).¹ A number of investigations²⁻⁴ suggests that the anomalous magnetic properties of CeFe₂ may be due to some transfer of the Ce 4f electrons to the Fe 3d band. This suggestion is supported by experimental data of electronic specific heat coefficients, which are $53 \text{ mJ K}^{-2} \text{ mol}^{-1}$ for CeFe₂,⁵ and $21 \text{ mJ K}^{-2} \text{ mol}^{-1}$ for CeCo₂.⁶

The ferromagnetic state of CeFe₂ is inherently unstable. A small partial substitution of Fe by other elements such as Co, Al, and Ru precipitates the instability of ferromagnetic state and a ferromagnetic (FM) to antiferromagnetic (AFM) phase transition is observed at the temperature T_N , lower than T_C .⁷⁻⁹ This second phase transition is a first-order phase transition in case of Ce(Fe_{1-x}Co_x)₂.⁷ The magnetic ordering of Ce(Fe_{1-x}Co_x)₂ has been determined by Kennedy *et al.*¹⁰ using neutron diffraction. The ac susceptibility results by Roy and Coles¹¹ show that the T_C moves up but T_N is suppressed with the increase in Y concentration in Ce_{1-Z}Y_Z(Fe_{1-x}Al_x)₂. They found that T_C increased to 235 K with $Z=0.1$ and went up further to 252 K for $Z=0.15$ in the case of $X=0.035$. The low-temperature transition is no longer present for X greater than 0.15.

According to the x-ray-diffraction studies by Nishihara, Tokumoto, and Yamaguchi,¹² there is a small volume change of 0.05% at T_N for the Ce(Fe_{1-x}Al_x)₂ system. Kennedy *et al.*¹⁰ also reported a 0.05% cell volume change at T_N in the Ce(Fe_{1-x}Co_x)₂ system. The 0.05% volume change is too small to apply an exchange-inversion model to explain the FM-AFM transition observed here.

In this article we present the effect of partial substitution of Fe by Co and Ce by Y on magnetic properties of the CeFe₂. Two magnetic phase diagrams are presented for the Ce(Fe_{1-x}Co_x)₂ and for the Ce_{1-Z}Y_Z(Fe_{0.8}Co_{0.2})₂. The entropy change at the FM-AFM transition is determined for Ce(Fe_{0.8}Co_{0.2})₂ as a function of temperature. Some specific

measurements presented here include magnetization, ac susceptibility, resistivity, and thermal expansion for the Ce(Fe_{0.8}Co_{0.2})₂.

The sample preparation and experimental details are described in Refs. 7 and 13.

The magnetization M and ac susceptibility χ_{ac} as a function of temperature for Ce(Fe_{0.8}Co_{0.2})₂ are presented in Figs. 1(a) and 1(b), respectively. It is evident that partial substitution of Fe by Co causes a sharp transition from FM to AFM. The temperature dependence of the electrical resistivity [Fig. 1(c)] also clearly shows this magnetic transition. A significant slope change in the resistivity at 162 K is identified as being due to a paramagnetic (PM)-FM transition which occurs at 160 K in the magnetization measurement. The abrupt rise of the resistivity at 75 K corresponds to FM-AFM tran-

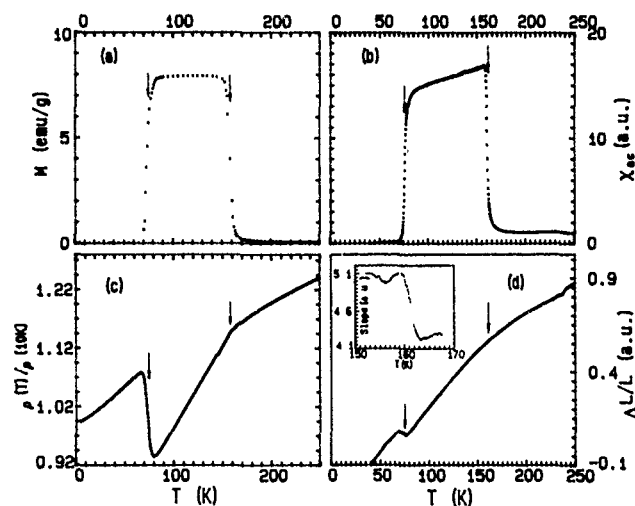


FIG. 1. (a) Magnetization M in an applied magnetic field of 100 G, (b) ac susceptibility χ_{ac} , (c) normalized electric resistivity, $\rho(T)/\rho(10 \text{ K})$, and (d) relative thermal expansivity $\Delta L/L$ as a function of temperature T for Ce(Fe_{0.8}Co_{0.2})₂. The insert of (d) shows the slope of $\Delta L/L$ around 160 K. The arrows indicate the T_C and T_N .

Magnetic effects in Cr-Mn alloy single crystals containing 0.05 and 0.1 at. % Mn

P. Smit and H. L. Alberts

Department of Physics, Rand Afrikaans University, P.O. Box 524, Auckland Park, Johannesburg 2006, South Africa

Measurements of the thermal expansion, ultrasonic wave velocity, and ultrasonic attenuation are reported for very dilute Cr-Mn alloy single crystals. The threshold Mn concentration needed to drive the first-order antiferromagnetic transition in Cr to second order is found to be smaller than 0.05 at. % Mn. This result is discussed in terms of recent theories. The critical behavior of the sound velocity and ultrasonic attenuation of Cr+0.1 at. % Mn is well described by a power law near T_N but not for the thermal expansion.

I. INTRODUCTION

Pure Cr condenses into an incommensurate I spin density wave (SDW) antiferromagnetic state below the Néel temperature T_N . The magnetic transition is weakly first order, showing a small discontinuity in the thermal expansivity¹ and neutron-diffraction intensity² at T_N . Both the magnetic structure and the first-order nature of the phase transition at T_N of pure Cr can be significantly altered through the addition of impurities (e.g., V or Mn), even for very small additions. Fishman and Liu³ recently addressed theoretically the problem of the effects of impurities on the order of the phase transition at T_N for pure Cr. The first-order nature of the transition is caused by a charge density wave (CDW) induced by the Coulomb interaction between two-hole Fermi surface sheets of pure Cr. Scattering by impurities suppresses the CDW and drives the transition to second order. As the first-order transition in pure Cr is weak, Fishman and Liu³ showed that only a very small impurity concentration is needed to accomplish this. They found that a threshold concentration c_t exists which separates the regions of first- and second-order phase transitions on the T - c magnetic phase diagram.

For Cr-V alloys, which remain in the ISDW phase up to about 4 at. % V where antiferromagnetism disappears,⁴ Fishman and Liu³ calculated a value $c_t=0.15$ at. % V, which corresponds well with experimental results. The addition of Mn to Cr drives the ISDW state of pure Cr to a commensurate C SDW state, and from theory³ a lower c_t value is expected for such a system than for Cr-V. An experimental study of c_t for Cr-Mn alloys has, however, not been done yet. In order to investigate this phenomenon in the Cr-Mn system, we conducted thermal-expansion ($\Delta L/L$) measurements on two Cr-Mn alloy single crystals containing 0.05 and 0.1 at. % Mn, respectively. This experimental parameter is a sensitive probe¹ in studying the order of the transition at T_N for Cr and its dilute alloys. We also report on an ultrasonic study of the Cr+0.1 at. % Mn crystal near T_N .

II. EXPERIMENT

Single crystals of pure Cr and Cr-Mn alloys containing nominal concentrations of 0.05 and 0.1 at. % Mn were grown by a floating-zone technique using rf heating in a pure Ar atmosphere. A bar of the alloy, roughly cylindrical in form,

about 10 cm in length and between 7 and 10 mm in diameter, was first prepared by rf melting in a horizontal cold crucible. To ensure homogeneity of the bar, it was prepared from seven separate smaller alloy ingots with a mass of about 8 g each and each prepared by arc melting in a purified Ar atmosphere. In the arc-melting process of the ingots, each was remelted five times, turning it upside down between melts, then taken out of the arc furnace and crushed to small pieces. It was then remelted five times, again turning it upside down between melts. The crushing and remelting procedures were repeated three times for each ingot in order to get the homogeneity as good as possible for the prepared alloy bar. The bar was then grown to a single crystal of length about 5 cm and diameter about 6 mm by the floating-zone technique with the bar in a vertical position. For the concentrations considered, Mn forms solid solutions in Cr. The starting materials were 99.996% pure Cr and 99.99% pure Mn. The homogeneity of the alloys was checked through electron microprobe analyses at different points on the samples (50 measurements done in total). Due to the very low impurity content the experimental error in obtaining absolute concentrations was relatively large, resulting in an error of observation of about 20% in the Mn concentration determined at each point. We were, nevertheless, able to verify that the alloys are homogeneous to within this error of observation, but could not tell whether the homogeneity was in fact even better than this. From previous experience on Cr-Si single⁵ crystals (containing up to 3 at. % Si) that we prepared in a similar manner as that above, we indeed expect the homogeneity of the two Cr-Mn crystals to be better than the above-quoted error of observation. The Si content in the Cr-Si crystals was large enough to allow for accurate concentration determination and they were found to be homogeneous to within 5%.

Thermal expansion ($\Delta L/L$) of the Cr-Mn crystals was measured relative to a Cr+5 at. % V sample using a strain gauge technique, while a standard pulse-overlap technique was used to obtain longitudinal ultrasonic wave velocities v_L and ultrasonic attenuation coefficients γ . The Cr+5 at. % V alloy remains paramagnetic at all temperatures and serves to simulate the nonmagnetic component of the thermal expansion of the Cr-Mn alloy single crystals, that is,

$$(\Delta L/L)_{\text{measured}} = (\Delta L/L)_{\text{Cr-V}} - (\Delta L/L)_{\text{sample}}$$

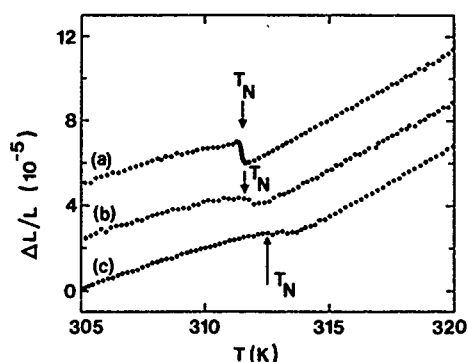


FIG. 1. The temperature dependence of the thermal expansion $(\Delta L/L)_{\text{sample}}$ near the Néel transition for (a) pure Cr, (b) Cr+0.05 at. % Mn, and (c) Cr+0.1 at. % Mn along [100]. The dots in curves (b) and (c) represent the measured points. In the case of pure Cr [curve (a)], measurements were recorded at 0.03 K temperature intervals near T_N . All the points are not plotted for the sake of clarity.

The $\Delta L/L$ measurements were conducted along [100] and v_L and γ were measured for 10 MHz ultrasonic waves propagating along [100]. The experimental error in the absolute $\Delta L/L$ values amounts to about 5% while changes in $\Delta L/L$ of 3×10^{-7} could be detected. Changes in v_L of 1 in 10^5 could be detected.

III. RESULTS AND DISCUSSION

Figure 1 shows the ISDW-P transition at T_N observed in the temperature dependence of $(\Delta L/L)_{\text{sample}}$ for the Cr, Cr+0.05 at. % Mn, and Cr+0.1 at. % Mn alloy single crystals. The T_N values, marked in Fig. 1, were taken at the minimum points in the $\alpha(T)$ curves, shown in Fig. 2. The ISDW-P transition shown in Fig. 1(a) for the pure Cr crystal occurs within a temperature range of approximately 0.3 K, which compares very favorably with that of 3 K observed by Fawcett *et al.*¹ in $\Delta L/L$ measurements. This indicates that our Cr crystal is of very good quality. The transition in pure Cr is furthermore characterized by an almost jumplike discontinuity, which is indicative of the transition's weak first-order nature. $\Delta L/L$ data around T_N were recorded for pure Cr at temperature intervals of approximately 0.03 K during both

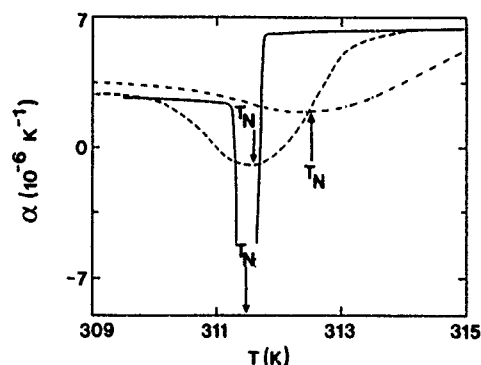


FIG. 2. Temperature dependence of the thermal-expansion coefficient α near the Néel transition for pure Cr (solid line), Cr+0.05 at. % Mn (dashed line), and Cr+0.1 at. % Mn (dashed-dotted line).

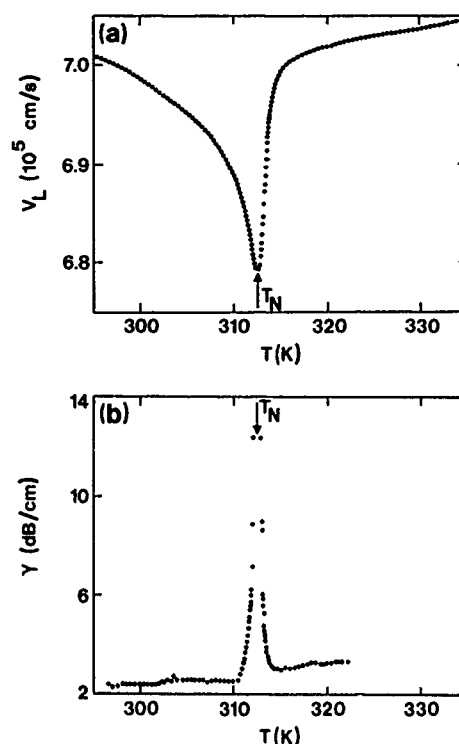


FIG. 3. Temperature dependence of (a) the longitudinal sound velocity v_L and (b) the ultrasonic attenuation coefficient γ near the Néel transition for Cr+0.1 at. % Mn. Wave propagation was along [100].

cooling and heating runs. Hysteresis effects of the order of 0.02 K in temperature, which is of the same order as the experimental error, were observed in the Néel transition for pure Cr. Curves (b) and (c) in Fig. 1 show that the transitions at T_N for the Cr+0.05 at. % Mn and Cr+0.1 at. % Mn crystals are continuous which is indicative of a second-order transition. One may reason that the continuous transitions in these crystals are the result of sample inhomogeneities. The observed width of the transitions, however, cannot be explained by sample inhomogeneities. As previously discussed, our crystals are expected to be homogeneous to better than 20%. The addition of 0.1 at. % Mn increases T_N of Cr by about 1 K (see the T_N values below). If the T_N transition in a perfectly homogeneous Cr+0.1 at. % Mn crystal was discontinuously first order, one therefore expects that variations as large as 20% in the Mn concentration throughout the volume of our Cr+0.1 at. % Mn crystal should result in broadening of the transition of about 0.2 K, which is smaller than the observed width of 2.3 K. The width of the transition was taken between the temperatures where the experimental $\Delta L/L - T$ points start to deviate from the roughly linear temperature behavior above and below the transition region. The width of 2.3 K on the $\Delta L/L - T$ curve of Fig. 1 for Cr+0.1 at. % Mn compares well with the width of about 3 K observed on the $\gamma - T$ curve of Fig. 3(b). For comparison the width of the transition for pure Cr in Fig. 1 is about 0.3 K. The effect of the addition of Mn on the first-order nature of the transition at T_N for pure Cr is clearly illustrated in the $\alpha(T)$ curves of Fig. 2 which display the Néel transitions for both Cr+0.05 at. % Mn and Cr+0.1 at. % Mn as shallow

and broad, compared to that of pure Cr. We obtain $T_N = (311.5 \pm 0.1)$ K for pure Cr, $T_N = (311.6 \pm 0.1)$ K for Cr + 0.05 at. % Mn, and $T_N = (312.5 \pm 0.2)$ K for Cr + 0.1 at. % Mn. The value $T_N = (312.5 \pm 0.2)$ K obtained from the $\Delta L/L$ measurements for Cr + 0.1 at. % Mn is confirmed by the $v_L(T)$ and $\chi(T)$ measurements shown in Fig. 3.

From the results in Figs. 1 and 2, we conclude that for an impurity concentration as small as 0.05 at. % Mn the first-order Néel transition at T_N for pure Cr is driven to a second-order one. The threshold impurity concentration c_t for Cr-Mn is therefore below 0.05 at. % Mn. The smaller c_t value for Mn impurities ($c_t < 0.05$ at. % Mn), compared to that for V ($c_t \approx 0.15$ at. % V), is expected from the theoretical analyses of Fishman and Liu³ and can be ascribed to two effects that influence the CDW. These effects are changes in commensurability of the SDW and impurity scattering as the solute concentration is varied. Doping Cr with Mn increases the commensurability (and decreases the energy mismatch z_0) of the SDW, while V doping decreases the commensurability. As $z_0 \rightarrow 0$, Fishman and Liu³ find that the CDW vanishes at T_N and the transition is always second order. With Mn doping, the CDW is suppressed both by decreasing z_0 and by impurity scattering. For V doping, the CDW is enhanced by increasing z_0 but suppressed by impurity scattering, with the last effect being dominant. Consequently, the threshold impurity concentration is smaller for Mn doping.

The observed second-order transition in the Cr + 0.1 at. % Mn crystal allows for an analysis of the critical behavior near T_N . Figure 3 shows the temperature dependence of v_L and χ for this crystal. The $v_L(T)$ curve [Fig. 3(a)] shows a minimum at $T_N = 312.5$ K, while a sharp attenuation peak is observed in the $\chi(T)$ curve at 312.4 K [Fig. 3(b)]. The criti-

cal behavior close to T_N for γ , $\Delta L/L$, and $\Delta v/v_0$, where Δv is the magnetic contribution and v_0 the nonmagnetic component of v , determined in the same manner as previously,⁵ was assessed for Cr + 0.1 at. % Mn in terms of a power law $A|1 - T/T_N|^{-\eta} + B$, where A and B are constants. Plots of $\ln(\Delta v/v_0 - B)$ and $\ln(\gamma - B)$ vs $\ln|1 - T/T_N|$ were found to be straight lines within temperature intervals, just below and just above T_N , of about 5 K in the case of $\Delta v/v_0$ and 1 K in the case of γ . The values of η , determined from the gradients of these straight lines, are $\eta_{T < T_N} = 0.13$ and $\eta_{T > T_N} = 1.00$ for $\Delta v/v_0$ and $\eta_{T < T_N} = 1.35$ and $\eta_{T > T_N} = 3.00$ for γ . Sato and Maki⁶ predicted $\eta_{T > T_N} = 0.5$ in the case of γ for ISDW antiferromagnets and no divergence at T_N for $\Delta v/v_0$. This does not compare well with the observed values for Cr + 0.1 at. % Mn. In the case of $\Delta L/L$, the data close to T_N could not be fitted to the power law.

In conclusion, the threshold Mn concentration that drives the antiferromagnetic transition in pure Cr to second order is found to be less than 0.05 at. % Mn. The critical behavior near T_N of $\Delta v/v_0$ and γ for Cr + 0.1 at. % Mn is successfully described in terms of a power law $A|1 - T/T_N|^{-\eta} + B$. This is, however, not the case for $\Delta L/L$.

¹E. Fawcett, R. B. Roberts, R. Day, and G. K. White, *Europhys. Lett.* **1**, 473 (1986).

²D. R. Noakes, T. M. Holden, and E. Fawcett, *J. Appl. Phys.* **67**, 5262 (1990).

³R. S. Fishman and S. H. Liu, *Phys. Rev. B* **45**, 12 306 (1992).

⁴R. B. Roberts, G. K. White, and E. Fawcett, *Physics B* **119**, 63 (1983).

⁵R. A. Anderson, H. L. Alberts, and P. Smit, *J. Phys. Condensed Matter* **5**, 1733 (1993).

⁶H. Sato and K. Maki, *Int. J. Magn.* **4**, 163 (1973).

Antiferromagnetism of metastable Cr-rich Cr-Gd alloys

Jen Hwa Hsu and Y. W. Fu

Department of Physics, National Taiwan University, Taipei, Taiwan, Republic of China

Cr is an antiferromagnet with a Néel temperature of 311 K. The addition of impurities will alter the antiferromagnetic properties of materials. Studies of the effect of magnetic Gd atoms on the Cr-rich $\text{Cr}_x\text{Gd}_{1-x}$ alloys are reported. The metastable $\text{Cr}_x\text{Gd}_{1-x}$ alloy films ($1.00 \geq x \geq 0.96$) have been prepared by the rapid-quenching method. It has been found from x-ray diffraction that the alloy films with $1.00 \geq x \geq 0.97$ have body-centered-cubic structure, the same as Cr. For higher Gd concentration, the alloy film contains both body-centered cubic and amorphous phases. The variation of the Néel temperature T_N as well as the spin-flip temperature T_F of metastable Cr-Gd alloys has been investigated by resistivity measurements between 10 and 300 K. It has been found that T_N decreases slowly from 311 K for pure Cr to about 290 K for $\text{Cr}_{0.97}\text{Gd}_{0.03}$. These results seem to indicate that magnetic Gd atoms show little effect on the antiferromagnetism of Cr. Furthermore, there is a broad resistivity minimum at low temperatures. This broad minimum occurs at higher temperature as Gd concentration is increasing. Thus, it suggests that a different mechanism accounts for this resistivity minimum. A detailed discussion is reported.

I. INTRODUCTION

Chromium is an itinerant antiferromagnet whose magnetism arises from some of the conduction electrons which condense through an exchange interaction to form a static spin-density wave (SDW) characterized by its wave vector \mathbf{Q} and its spin polarization \mathbf{S} . Its Néel temperature T_N is 312 K and its spin-flip temperature T_F has been determined to be 122 K. Between T_N and T_F , the SDW has transverse polarization ($\mathbf{S} \perp \mathbf{Q}$), and at T_F the spins rotate through 90° so that the SDW is longitudinally polarized.¹

In the past the antiferromagnetic properties of Cr alloys containing small amounts of the transition metals have been investigated extensively.² The results show that there is a strong and systematic dependence on the number of d elec-

trons of the impurity element. Elements with more d electrons than Cr raise T_N , while those with fewer d electrons depress T_N , the same conclusion as with Mn.³ It is also interesting to know whether the magnetism of Cr is altered by the introduction of magnetic Gd impurities; however, little work has been done related to it. This is because Gd and Cr are mutually immiscible. Previously, one of the authors has demonstrated that the rapid-quenching method is very useful to prepare metastable Gd-Cr alloys.⁴ In this matter, we are now able to investigate the effect of Gd atoms on the antiferromagnetism of Cr. Thus, we expect from this work to provide firmer experimental data in order to understand the theoretical aspect of antiferromagnetic coupling in the Cr system.

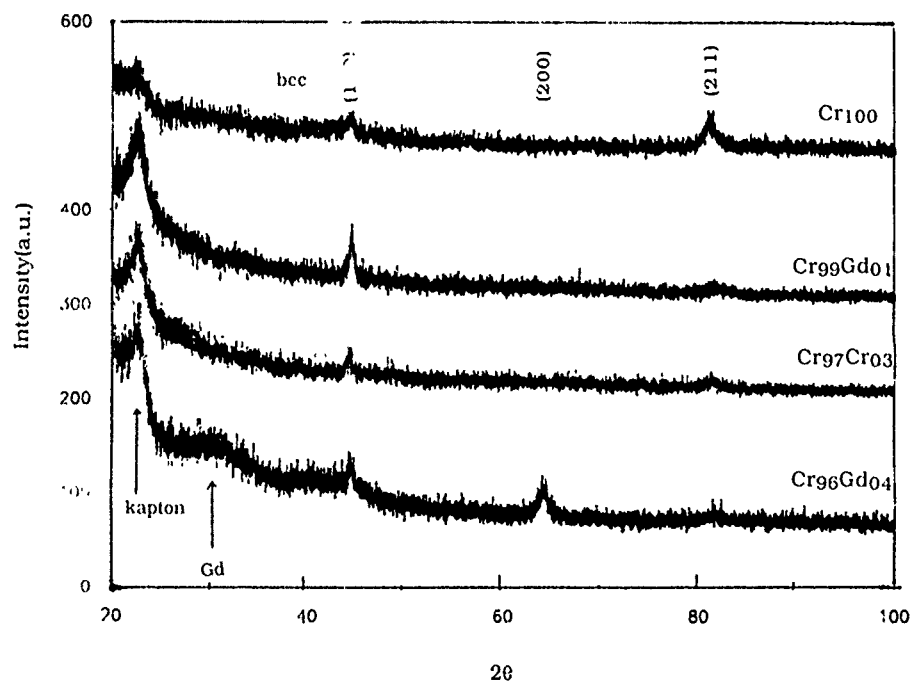


FIG. 1. Representative x-ray-diffraction patterns of metastable $\text{Cr}_x\text{Gd}_{1-x}$ alloys ($1 \geq x \geq 0.96$).

II. EXPERIMENT

The metastable $\text{Cr}_x\text{Gd}_{1-x}$ alloy films ($1 \geq x \geq 0.96$) were prepared by the dc magnetron sputtering method. Kaptons were used as the substrates which were cooled by liquid N_2 during sputtering. The thickness of films was estimated to be around $5 \mu\text{m}$. The film structures were determined from powder-x-ray diffraction in the θ - 2θ geometry.

The resistivity of alloy films has been determined from 10 to 320 K. The four-probe method was used. The Néel temperature T_N and spin-flip temperature T_F were determined from resistivity measurements. It has been shown that there are anomalies in the electrical resistivity of Cr around T_N and T_F .⁵⁻⁷ The selection of T_N and T_F are taken from either the points of minimum or the points of inflection.

III. RESULTS AND DISCUSSION

In Fig. 1 it is indicated that the the structure of the alloys with $1.00 \geq x \geq 0.97$ is a single body-centered phase, the same as with pure Cr. For the alloys with higher Gd concentration,

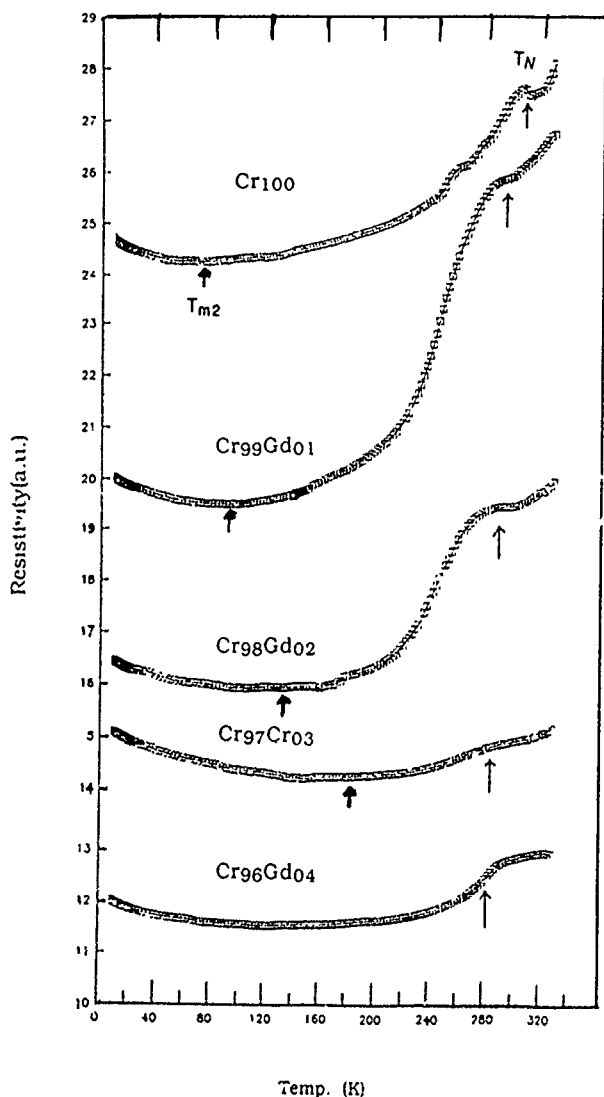


FIG. 2. Normalized resistivity of metastable $\text{Cr}_x\text{Gd}_{1-x}$ alloys ($1 \geq x \geq 0.96$) between 10 and 320 K.

an amorphous phase appears mixed with bcc phase. Thus, the concentration range chosen to investigate the effect on antiferromagnetism is between 1.00 and 0.96.

The normalized resistivity of metastable $\text{Cr}_x\text{Gd}_{1-x}$ is plotted in Fig. 2. It shows that the resistivity initially decreases as the temperature falls. At the temperature denoted as T_N , either a minimum or a drastic change of slope is found. With further decreasing temperature, a broad minimum denoted as T_{m2} is found. For pure Cr, the value of T_N from our experimental results is 311 K, which is identical to the Néel temperature of Cr. Therefore, T_N of all alloys in this work can be ascribed to the appearance of antiferromagnetism. As shown in Fig. 3, the Néel temperature of Cr alloys decreases slowly from 311 K for pure Cr to 286 K for 3 at. % Gd. This shift rate is much smaller than those of Cr alloys with other transition elements.² This suggests that the introduction of $4f$ electrons has little effect on the antiferromagnetism of Cr. This is consistent with the prediction of a two-band model.⁸

Regarding the occurrence of T_{m2} , the value of T_{m2} for pure Cr is around 78 K which is far below the spin-flip temperature of Cr. According to Meaden and Sze,⁵ a step-type change should be found around T_F . This is not true in our case. Therefore, the occurrence of T_{m2} is not related to the phenomenon of spin-flip transition. Again as shown in Fig. 3, T_{m2} rises rapidly from 78 K for pure Cr to 182 K for $\text{Cr}_{0.97}\text{Gd}_{0.03}$. Due to the small variation of resistivity in the low-temperature range, it is difficult to locate T_{m2} for $\text{Cr}_{0.96}\text{Gd}_{0.04}$, but a higher T_{m2} is still easily observed. We might first ascribe T_{m2} to the unexpected impurities in the sample; but, the systematic dependence of T_{m2} on Gd concentration excludes this possibility. It is evident that the existence of Gd is crucial to the occurrence of T_{m2} . As is known, the resistivity of Cr is very sensitive to the strain induced in the sample.⁹ Our samples were prepared using the quick-quenching method so that a large strain is expected to be induced during sample preparation. Furthermore, due to the larger size of the Gd atom, the substitution by the Gd atom will cause lattice mismatch; this will also create strain.

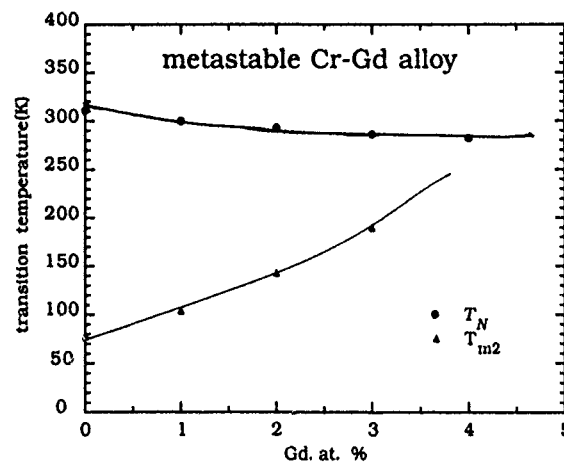


FIG. 3. The Néel temperature T_N and T_{m2} as a function of Gd concentration.

The process to clarify this possibility by using strain-free sample is underway.

¹W. B. Muir and J. O. Ström-Olsen, Phys. Rev. B **4**, 988 (1971).

²W. C. Kochler and R. M. Moon, Phys. Rev. **151**, 405 (1966); A. L. Trego and A. R. Mackintosh, *ibid.* **166**, 495 (1968).

³W. Williams Jr. and J. L. Stanford, J. Magn. Mater. **1**, 271 (1976).

⁴J. H. Hsu *et al.*, J. Appl. Phys. **70**, 6308 (1991).

⁵G. T. Meaden and N. H. Sze, Phys. Lett. A **30**, 294 (1969).

⁶S. Aarj, Phys. Lett. A **29**, 211 (1969).

⁷G. T. Meaden and N. H. Sze, Phys. Lett. A **29**, 162 (1969).

⁸W. M. Lomer, Proc. Phys. Soc. (London) **80**, 489 (1962).

⁹M. O. Steinitz, J. A. Marcus, E. Fawcett, and W. A. Reed, Phys. Rev. Lett. **23**, 979 (1969).

Magnetic properties of two new compounds: $\text{Gd}_2\text{Ni}_3\text{Si}_5$ and $\text{Sm}_2\text{Ni}_3\text{Si}_5$

Chandan Mazumdar

Indian Institute of Technology, Bombay, India 400 076

R. Nagarajan, L. C. Gupta, and R. Vijayaraghavan

Tata Institute of Fundamental Research, Bombay, India 400 005

C. Godart

UPR-209, C.N.R.S., 92195 Meudon Cedex, France

B. D. Padalia

Indian Institute of Technology, Bombay, India 400 076

The formation of two new materials, $\text{Sm}_2\text{Ni}_3\text{Si}_5$ and $\text{Gd}_2\text{Ni}_3\text{Si}_5$, of the rare-earth series $\text{R}_2\text{M}_3\text{Si}_5$ (R denotes rare earth and Y) and their magnetic and transport properties are reported here. These materials crystallize in the orthorhombic $\text{U}_2\text{Co}_3\text{Si}_5$ -type structure (space group Ibam). The magnetic susceptibility of $\text{Gd}_2\text{Ni}_3\text{Si}_5$ follows a Curie-Weiss behavior with an effective magnetic moment $8.1\mu_B/\text{Gd}$ ion. The material orders antiferromagnetically at ≈ 15 K. The magnetic susceptibility of $\text{Sm}_2\text{Ni}_3\text{Si}_5$ exhibits a deviation from the Curie-Weiss behavior which is attributed to the low-lying excited state of Sm^{3+} ions and also to crystal-field effects. This material also orders antiferromagnetically, but at ≈ 11 K. This value of the ordering temperature does not seem to follow the de Gennes scaling with respect to that of $\text{Gd}_2\text{Ni}_3\text{Si}_5$.

I. INTRODUCTION

Rare-earth (R) intermetallic materials have been of interest both in the area of fundamental physics and in application areas. Rare-earth-based materials have interested physicists because of the localized f -electron core and the related systematics emerging in the properties of the rare-earth series of a system. The well-known example is the lanthanide contraction often observed in the lattice parameters of isotypic compounds of a rare-earth series. However, the electronic properties of compounds within a series do get modified in the presence of other elements and deviations occur in the expected gradation of the properties with respect to the number of f electrons. These deviations provide us the means to study the physical mechanisms taking place in these materials and solids in general. For example, Ce compounds tend to exhibit anomalous phenomenon due to hybridization of the $4f$ electronic level with the $3d$ electronic level. This results in the phenomenon of heavy fermion behavior, valence fluctuation (VF), Kondo effect, etc. The effects of hybridization can also modify the magnetic interactions. In view of this, we are carrying out a program of synthesis and study of the physical properties of new rare-earth intermetallic compounds. We initiated the study of the series of compounds $\text{R}_2\text{Ni}_3\text{Si}_5$. In an earlier study, we showed the VF behavior of Ce and Eu in $\text{Ce}_2\text{Ni}_3\text{Si}_5$ (Ref. 1) and $\text{Eu}_2\text{Ni}_3\text{Si}_5$,² respectively. The formation of $\text{Ce}_2\text{Ni}_3\text{Si}_5$, $\text{Dy}_2\text{Ni}_3\text{Si}_5$, and $\text{Y}_2\text{Ni}_3\text{Si}_5$ has been reported in the literature.³ Here we report the synthesis of the two new compounds, $\text{Gd}_2\text{Ni}_3\text{Si}_5$ and $\text{Sm}_2\text{Ni}_3\text{Si}_5$, and the preliminary results of magnetic susceptibility and resistivity studies on them.

II. EXPERIMENT

The compounds $\text{Gd}_2\text{Ni}_3\text{Si}_5$ and $\text{Sm}_2\text{Ni}_3\text{Si}_5$ were prepared by the standard arc-melting technique using a water-cooled copper hearth in a flowing argon atmosphere. The purity of the starting materials was better than 99.9% for Sm, Gd, and

Ni and better than 99.999% for Si. Each of the arc-melted buttons was wrapped in tantalum foil, vacuum sealed in a quartz capsule, and annealed at 1100°C for 1 day and at 1000°C for 7 days. The materials were characterized at room temperature by powder-x-ray-diffraction using $\text{CuK}\alpha$ radiation in a commercial x-ray diffractometer (Jeol, Japan).

Magnetic susceptibility studies were carried out using a Faraday-type susceptometer (George Associates, U.S.A.). The measurements were performed over the temperature range from 4.2 to 300 K using a gas-flow-type helium cryostat. The temperature was measured by a gold-Chromel thermocouple.

Electrical resistivity studies over the temperature range 4.2–300 K were carried out using a home-built cryostat and employing the standard four-probe dc method. Thin silver wires were used as electrical leads and contacts to the samples were made using conducting silver paint. Commercial units were used in the electrical measurements (Keithley model 220 for current source and Keithley model 184 nanovoltmeter). In order to eliminate the effects of thermo emf, the resistance was first measured when the current was passing in one direction, then it was measured again with the current passing in the reverse direction, and then the average of these two readings was taken. The temperature was measured using a calibrated silicon diode.

III. RESULTS AND DISCUSSION

A. Structure

The room-temperature powder-x-ray-diffraction patterns (Fig. 1) confirmed the formation of single-phase materials of $\text{Gd}_2\text{Ni}_3\text{Si}_5$ and $\text{Sm}_2\text{Ni}_3\text{Si}_5$ in the orthorhombic $\text{U}_2\text{Co}_3\text{Si}_5$ -type crystal structure (space group Ibam) as is the case with other known materials of this series of Ni compounds.^{1–3} The unit-cell parameters of the materials were determined by a least-squares-fit procedure of the observed set of d spacing for each material. The resulting parameters were: $a = 9.616 \text{ \AA}$,

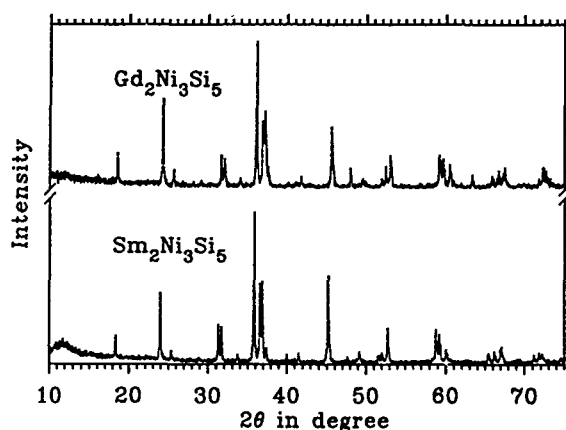


FIG. 1. Powder-x-ray-diffraction pattern for $\text{Gd}_2\text{Ni}_3\text{Si}_5$ and $\text{Sm}_2\text{Ni}_3\text{Si}_5$ at room temperature.

$b=11.292 \text{ \AA}$, $c=5.705 \text{ \AA}$ for $\text{Sm}_2\text{Ni}_3\text{Si}_5$; and $a=9.560 \text{ \AA}$, $b=11.197 \text{ \AA}$, $c=5.665 \text{ \AA}$ for $\text{Gd}_2\text{Ni}_3\text{Si}_5$. It is pointed out that the unit-cell parameters of $\text{Sm}_2\text{Ni}_3\text{Si}_5$ are smaller than those of $\text{Gd}_2\text{Ni}_3\text{Si}_5$ as it should be on the basis of "lanthanide contraction," in which one expects the unit cell to contract as the number of f electrons increase in a rare-earth series of compounds.

B. Magnetic and resistivity measurements

1. $\text{Gd}_2\text{Ni}_3\text{Si}_5$

The dc magnetic susceptibility result of $\text{Gd}_2\text{Ni}_3\text{Si}_5$ as a function of temperature is shown in Fig. 2. The material appears to order magnetically, $T_N \approx 15 \text{ K}$. From the cusplike behavior of the susceptibility peak we infer the nature of the ordering to be antiferromagnetic. The temperature dependence of the inverse susceptibility of $\text{Gd}_2\text{Ni}_3\text{Si}_5$ is linear above T_N (Fig. 2). A Curie-Weiss fit to this data yielded the magnetic moment per Gd ion to be $8.1\mu_B$. Generally, it is believed that in materials of this structure, the transition-metal ion does not carry the magnetic moment. In such a case, the entire observed moment would be attributed to the Gd ion. The moment per Gd ion in this case is slightly higher

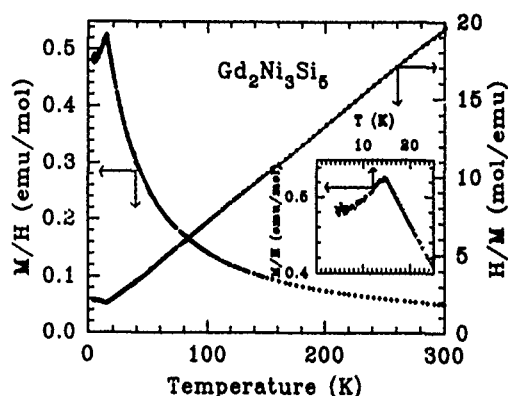


FIG. 2. dc magnetic susceptibility and its reciprocal for the compound $\text{Gd}_2\text{Ni}_3\text{Si}_5$. The solid line is a fit to the Curie-Weiss formula. The expanded region near T_N is shown in the inset.

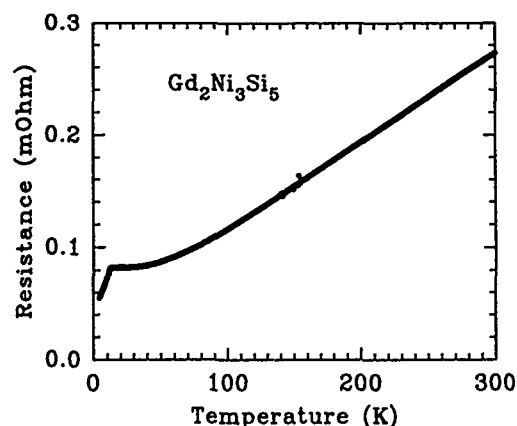


FIG. 3. The thermal variation of resistance (in $\text{m}\Omega$) for $\text{Gd}_2\text{Ni}_3\text{Si}_5$.

than the free-ion value of Gd^{3+} . At present we are not sure if this slightly higher value is due to any small impurity phase or due to intrinsic effects such as contribution from conduction electrons. We would like to point out that we synthesized and measured the magnetic susceptibility of $\text{Y}_2\text{Ni}_3\text{Si}_5$ also. It was found to behave in a Curie-Weiss manner with a magnetic moment of $0.27\mu_B/\text{formula unit}$.¹ Since the Y ion is not expected to carry any magnetic moment, if we assume that all the moment belongs to Ni and not to any impurity phase, then the observed moment indicates a value of $0.16\mu_B/\text{Ni ion}$ in $\text{Y}_2\text{Ni}_3\text{Si}_5$.

The temperature dependence of the electrical resistance of $\text{Gd}_2\text{Ni}_3\text{Si}_5$ is shown in Fig. 3. It shows a typical metallic behavior. The reduction in the magnetic scattering of electrons below the magnetically ordered state is clearly seen. The transition temperature seen here is consistent with that observed through magnetic susceptibility.

2. $\text{Sm}_2\text{Ni}_3\text{Si}_5$

The magnetic susceptibility of $\text{Sm}_2\text{Ni}_3\text{Si}_5$ is shown in Fig. 4 as a function of temperature. An antiferromagnetic transition is clearly seen at $\approx 11 \text{ K}$. It is interesting to note that the well-known de Gennes scaling seems to be breaking down here. The de Gennes factor for Sm with respect to Gd is 0.28. From this one would have expected an ordering tem-

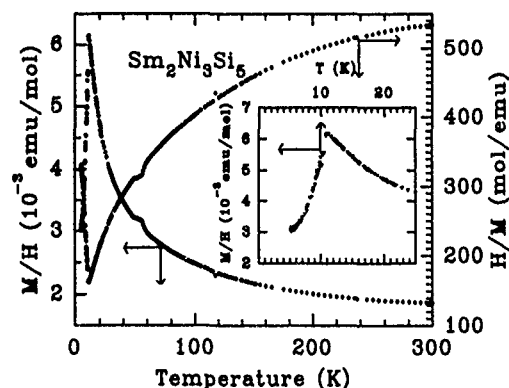


FIG. 4. dc magnetic susceptibility and its reciprocal for the compound $\text{Sm}_2\text{Ni}_3\text{Si}_5$. The expanded region near T_N is shown in the inset.

perature of ≈ 5 K. The observed value of T_N (≈ 11 K) is much higher than this. We believe that the small anomaly observed in the susceptibility near 55 K is due to a small impurity phase which is below the limit of detection in the x-ray-diffraction pattern. The temperature dependence of inverse susceptibility is not linear. This is not unexpected in a Sm-based material. This is primarily due to the fact that the ionic excited states are at a rather low level and, hence, they are also populated at moderate temperatures resulting in an effective value of magnetic moment which is different from that of the free Sm^{3+} ion in ground state. It is quite likely that at low temperatures, crystal-field effects also contribute to the deviation from the Curie-Weiss behavior.

IV. CONCLUSION

We have synthesized two new materials, $\text{Gd}_2\text{Ni}_3\text{Si}_5$ and $\text{Sm}_2\text{Ni}_3\text{Si}_5$, and shown that they form in orthorhombic

$\text{U}_2\text{Co}_3\text{Si}_5$ -type structure similar to other members of this rare-earth series. Both the materials seem to order antiferromagnetically ($T_N \approx 15$ and ≈ 11 K for $\text{Gd}_2\text{Ni}_3\text{Si}_5$ and $\text{Sm}_2\text{Ni}_3\text{Si}_5$, respectively). The ordering temperature of $\text{Sm}_2\text{Ni}_3\text{Si}_5$ does not follow the de Gennes scaling with respect to that of $\text{Gd}_2\text{Ni}_3\text{Si}_5$.

ACKNOWLEDGMENT

Part of this work was supported by Project No. 509-1 of Indo-French Centre for Promotion of Advanced Research, New Delhi, India.

¹C. Mazumdar, R. Nagarajan, S. K. Dhar, L. C. Gupta, R. Vijayaraghavan, and B. D. Padalia, Phys. Rev. B **46**, 9009 (1992).

²S. Patil, R. Nagarajan, L. C. Gupta, C. Godart, R. Vijayaraghavan, and B. D. Padalia, Phys. Rev. B **37**, 7708 (1988).

³B. Chabot and E. Parthe, J. Less-Common Met., **97**, 285 (1984).

Low-field ac magnetic susceptibility under pressure in GdMn_2 and TbMn_2 intermetallics

M. R. Ibarra,^{a)} Z. Arnold,^{b)} C. Marquina, L. García-Orza, and A. del Moral

Departamento de Física de la Materia Condensada e Instituto de Ciencia de Materiales de Aragón,
Universidad de Zaragoza-CSIC, 50009-Zaragoza, Spain

Low-field ac magnetic susceptibility experiments under pressure up to 10 kbar have been performed on the GdMn_2 and TbMn_2 compounds in the temperature range of 4–300 K. The results reveal the possible coexistence of two phases below T_N , one in which the magnetic moment of Mn is stable and other in which the Mn does not present any magnetic moment.

The RMn_2 compounds crystallize in the Laves phase structures. The hexagonal C14 phase is stabilized in the case of $\text{R}=\text{Pr}$, Nd , Sm , Ho , Er , Tm , or Lu and the cubic C15 for $\text{R}=\text{Y}$, Gd , Tb , Dy , and Ho . The magnetic properties of these compounds are strongly related to the intraatomic Mn-Mn distance.¹ The existence of a critical distance for these compounds is assumed (at room temperature $d_{\text{Mn-Mn}}=2.67$ Å). Below this value the magnetic moment on Mn (μ_{Mn}) is not stable. On the other hand, the appearance of a local magnetic moment takes place at a specific temperature through a first-order structural and antiferromagnetic transition, (T_N mostly around 100 K), when $d_{\text{Mn-Mn}}$ is greater than the critical value. At this transition very large spontaneous magnetovolume effects occur. The transition temperature is very sensitive to external parameters, such as the applied pressure² or the magnetic field.³ However, from nuclear magnetic resonance (NMR)⁴ on YMn_2 and neutron-diffraction experiments on YMn_2 and TbMn_2 ⁵ under pressure, a constant value for the μ_{Mn} was observed. Magnetostriction experiments using high pulsed magnetic fields up to 15 T demonstrated the stability of μ_{Mn} in YMn_2 , GdMn_2 , and NdMn_2 ,^{6,7} and the collapse of μ_{Mn} in the case of TbMn_2 .³

Up to now, pressure studies were related to the pressure sensitivity of the antiferromagnetic transition and little attention has been paid to the more tiny effects connected with the magnetic ordering observed at different temperatures on compounds with several rare earths. For our high-pressure studies of GdMn_2 and TbMn_2 compounds we used the low-field ac susceptibility $\chi(T)$ technique.

The polycrystalline RMn_2 compounds were prepared by arc melting the high-purity constituents. The sample annealing was carried out under a stabilized argon atmosphere at a pressure of 0.2 bar for 5 days at 800 °C. The nonexistence of secondary phases was checked by x-ray powder diffraction. Also, the low value of the $\chi(T)$ at room temperature was a more positive test of the absence of the ferromagnetic R_6Mn_{23} phase.

The $\chi(T)$ was measured using a low-frequency (15 Hz) mutual inductance bridge, with a peak value of the magnetic field of ≈ 30 mOe. The high-pressure measurements were done using a CuBe cell under fixed hydrostatic pressures up

to 10 kbar. The pressure was measured *in situ*, using a man-ganin pressure sensor.

GdMn₂:

In this compound $T_N=104$ K and below this temperature an antiferromagnetic behavior was observed. From magnetization measurements a magnetic ordering of the Gd sublattice below $T_c \approx 40$ K was observed,^{9–11} however from specific heat¹² and Mössbauer¹³ measurements, it was evident that the Gd sublattice is ordered up to T_N . There exists a large controversy about the magnetic structure due to the difficulty of performing neutron-diffraction experiments. Our recent results of magnetostriction⁷ clarified this magnetic behavior. We proposed a model¹⁴ considering a diffusionless (first-order) transformation at T_N with the existence of two phases below T_N ; one transformed phase (TP), which is the responsible for the huge thermal-expansion anomaly, and other nontransformed phase (NTP), in which $\mu_{\text{Mn}} \approx 0$ in the entire range of temperature. Evidence that the transition is not complete was found in $\text{Y}_{1-x}\text{Sc}_x\text{Mn}_2$ (Ref. 4) and TbMn_2 (Ref. 5) under pressure. The TP phase appears below T_N and both Gd and Mn magnetic sublattices become antiferromagnetically ordered. The Mn sublattice is ordered through the $3d$ - $3d$ exchange interaction and the Gd sublattice through the $3d$ - $4f$ exchange interaction. The NTP magnetically order at $T_c \approx 35$ K. This magnetic transition occurs because of the $4f$ - $4f$ exchange interaction between Gd ions (in this phase $\mu_{\text{Mn}} \approx 0$). The reliability of this model was tested by $\chi(T)$ under pressure and magnetostriction measurements performed on GdMn_2 .¹⁴ In the above-mentioned work an increase of T_c in the NTP and a decrease of T_N in the TP phase was observed for increasing pressures. The transition in both phases occurs simultaneously at $T_N=T_c=70$ K for a pressure of 6.9 kbar. At higher pressures it was observed that the first-order transition at T_N could take place in the ordered regime ($T_c > T_N$). Because the maximum pressure available in this range of temperature was 7.8 kbar, we performed $\chi(T)$ measurements in the series $\text{Gd}(\text{Mn}_{1-x}\text{Ni}_x)_2$ creating a chemical pressure¹¹ by substitution of smaller Ni atoms. We have selected Ni because the RNi_2 crystallizes in the same crystallographic structure and Ni does not carry a magnetic moment in this structure and, consequently, we cannot expect a perturbation of the $3d$ magnetism observed in pure GdMn_2 . In Fig. 1 we report the results obtained for selected concentrations. The $x=0$ compound shows a small anomaly at $T_c=35$ K which is associated with the establishment of magnetic order in the NTP phase and no anomaly is observed

^{a)} Author to whom correspondence should be addressed.

^{b)} Permanent address: Institute of Physics, Czech Academy of Sciences, Cukrovarnická 10, 162 00 Praha 6, Czech Republic.

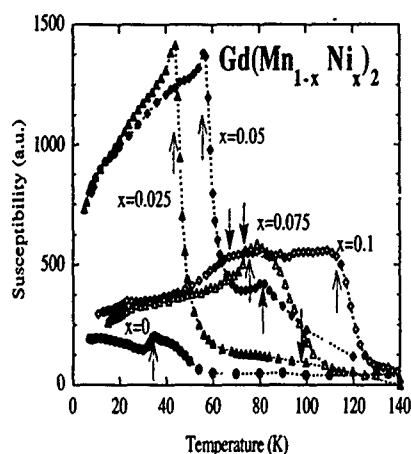


FIG. 1. $\chi(T)$ in $\text{Gd}(\text{Mn}_{1-x}\text{Ni}_x)_2$. The arrows indicate the values of the T_c (†) and T_N (‡).

at T_N . For $x=0.025$, a large anomaly in $\chi(T)$ is observed at 45 K which is associated with an increase of T_c and an anomaly in thermal-expansion measurements⁷ gave a value of $T_N=95$ K. For higher Ni concentrations, we start to observe an anomaly in $\chi(T)$ at T_N in good agreement with thermal-expansion results.⁷ The dependence of T_c and T_N on concentration can be clearly followed in Fig. 1 for the rest of the compounds. For $x=0.1$, we observe $T_c > T_N$, in close agreement with magnetization under pressure measurements in GdMn_2 .¹¹ These results constitute a good test of the model that we proposed¹⁴ and also clearly establish the stability of the TP, besides the existence of magnetic order in the R sublattice. Consequently, the appearance of local magnetic moment on Mn can take place below T_c . This conclusion is also in support of the stability of the μ_{Mn} and TP found in GdMn_2 up to applied magnetic field of 15 T.¹⁴

TbMn₂:

In RMn_2 compounds, TbMn_2 has the intraatomic Mn-Mn distance which is the closest to the critical distance below which $\mu_{\text{Mn}}=0$. It is assumed that this is one of the reasons why $T_N \approx 45$ K is significantly lower than in the rest of compounds (i.e., $\text{R}=\text{Sm}, \text{Pr}, \text{Nd}$, and Gd). Neutron-diffraction studies^{3,5} indicated the existence of two magnetic phases below T_N , which were called S_1 and S_2 . We can assume the S_1 phase is associated with the so-called TP. In this phase $\mu_{\text{Mn}} \neq 0$. Similarly the NTP presents a S_2 -type magnetic structure, reminiscent of that observed in DyMn_2 .¹⁵ Either under applied⁵ or chemical pressure a new ferrimagnetic phase appears as was observed in $\text{Tb}(\text{Mn}_{1-x}\text{Fe}_x)_2$ (Ref. 16) and $\text{Tb}_{1-x}\text{Sc}_x\text{Mn}_2$.^{17,18} In the present work we report $\chi(T)$ measurements under hydrostatic pressure. The thermal dependence of the $\chi(T)$ is presented in Fig. 2 for different applied pressures. In the range of pressure $p > 2$ kbar only one anomaly is observed, which is associated with T_c (para-ferrimagnetic transition) and increases with increasing pressures at the rate $dT_c/dp = 2$ K/kbar. The structural transformation is absent in this range of pressure and consequently a local magnetic moment on Mn atoms does not exist, in good agreement with neutron-diffraction and magnetization results.^{5,3} The low-pressure behavior is rather complex and

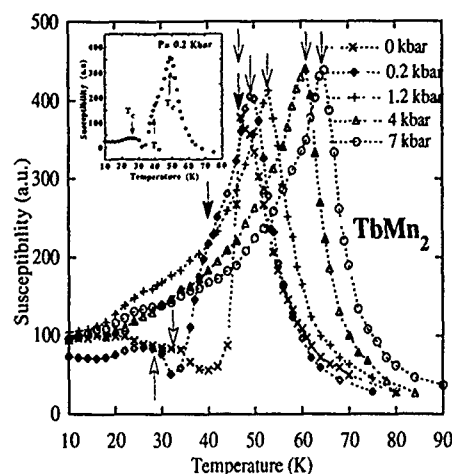


FIG. 2. $\chi(T)$ at different pressures in TbMn_2 . Inset $\chi(T)$ at $p=0.2$ kbar; T_c (†), T'_c (◊), T_N (‡).

can be understood from the results obtained at $p=0.2$ kbar. We analyze these results considering that both TP and NTP coexist. Three anomalies on the thermal dependence of susceptibility can be distinguished at 30, 40, and 50 K. We can assume $T_c=50$ K for the magnetic transitions in the NTP. The shoulder observed at $T'_c \approx 30$ K can be associated with the magnetic ordering temperature within the NTP, from the ferrimagnetic ordering at higher temperature toward the S_2 magnetic structure (DyMn_2 type). The other anomaly at $T_N \approx 40$ K—a sharp decrease of susceptibility—corresponds to the temperature at which the TP appears. The T_N is extremely pressure dependent ($dT_N/dp \approx -30$ K/kbar); in fact, TP disappears at a pressure above 2 kbar, in good agreement with former magnetization and neutron measurements.^{2,5} At normal pressure both T_c and T_N merge at $T_N \approx T_c \approx 45$ K, as can be observed in Fig. 2. At lower temperatures a shoulder appears at $T'_c = 35$ K, which can be associated with the transition to the S_2 magnetic structure within the NTP. Evidence of this NTP was found using neutron-diffraction experiments; at normal pressure this NTP only represents a few percent of the total sample volume.¹⁹ The volume of this phase rapidly increases with pressure. This result is in good agreement with the thermal-expansion results obtained on the same sample.⁸ Based on these arguments, we suggest the magnetic phase diagrams (T, p) of Figs. 3(a) and 3(b) for the TP and NTP, respectively. These results clarify some of the uncertainties implicit in the interpretation of the neutron-diffraction results in the region of temperature 35–50 K in $\text{Tb}(\text{Mn}_{1-x}\text{Fe}_x)_2$ (Refs. 3 and 16) and in $\text{Tb}_{1-x}\text{Sc}_x\text{Mn}_2$.¹⁸ The instability of the TP under pressure in this compound can be supported from other points of view. The existence of a ferrimagnetic phase at $T_c > T_N$ is not a stable situation for the existence of the TP in the case of TbMn_2 . Consequently, the increase of the molecular field induced by pressure in the NTP will have the same role as the increase of the applied magnetic field and will suppress the TP.

As a general conclusion from this systematic study of TbMn_2 and GdMn_2 compounds under pressure we propose an explanation for the complex magnetic behavior of these

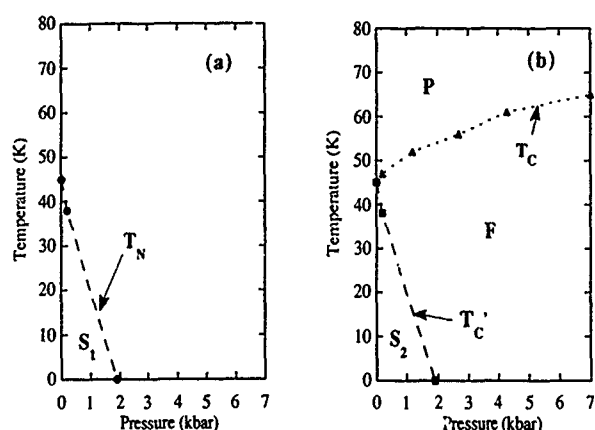


FIG. 3. Magnetic-phase diagram for the (a) TP and the (b) NTP in TbMn_2 .

compounds based on the coexistence of two phases TP and NTP originated by a diffusionless first-order phase transformation at T_N . The observed thermal dependence of the magnetic behavior under pressure is satisfactorily explained following the thermal pressure dependence of the different magnetic behaviors within each phase.

We acknowledge financial support from the CICYT under Grant No. MAT-1039 and PB90-1014 and from the European Commission under Project No. BRITE-EURAM BREU-C-68 and under Grant No. ERB-CIPA-CT-92-0137.

- ¹M. Shiga, *Physica B* **149**, 293 (1988).
- ²J. Voiron, R. Ballou, J. Deportes, R. M. Galera, and Lelievre, *J. Appl. Phys.* **69**, 5678 (1991).
- ³P. J. Brown, B. Ouladdiaf, R. Ballou, J. Deportes, and A. S. Markosyan, *J. Phys. Condensed Matter* **4**, 1103 (1992).
- ⁴H. Nakamura, H. Wada, K. Toshimura, M. Shiga, Y. Nakamura, J. Sakurai, and Y. Komura, *J. Phys. F* **18**, 981 (1988).
- ⁵S. Mondal, R. Ciwinsky, S. H. Kilcoyne, B. D. Rainford, and C. Ritter, *Physica B* **180-181**, 108 (1992).
- ⁶M. R. Ibarra, L. Garcia-Orza, and A. del Moral, *Solid State Commun.* **84**, 875 (1992).
- ⁷M. R. Ibarra, C. Marquina, L. Garcia-Orza, and A. del Moral, These proceedings.
- ⁸M. R. Ibarra, C. Marquina, L. Garcia-Orza and A. del Moral, *Solid State Commun.* **87**, 695 (1993).
- ⁹S. K. Malik and Wallace, *J. Magn. Magn. Mater.* **24**, 23 (1981).
- ¹⁰T. Okamoto, H. Fujii, Y. Makihara, T. Hihara, and Y. Hashimoto, *J. Magn. Magn. Mater.* **54-57**, 1087 (1986).
- ¹¹S. Endo, R. Tanaka, S. Nakamichi, F. Ono, H. Wada, and M. Shiga, *J. Magn. Magn. Mater.* **104-107**, 1441 (1992).
- ¹²T. Okamoto, H. Nagata, H. Fujii, and Y. Makihara, *J. Magn. Magn. Mater.* **70**, 139 (1987).
- ¹³J. Przewoznik, J. Zukrowski, and K. Krop, *J. Magn. Magn. Mater.* **119**, 150 (1993).
- ¹⁴M. R. Ibarra, Z. Arnold, C. Marquina, L. Garcia-Orza, and A. del Moral, in *Proceedings of the European Conference on Magnetic Materials, 1993 Kosice*.
- ¹⁵C. Ritter, S. H. Kilcoyne, and R. Ciwinski, *J. Phys. Condensed Matter* **3**, 727 (1991).
- ¹⁶S. Mondal, S. H. Kilcoyne, B. D. Rainford, and R. Ciwinsky, *Physica B* **180-181**, 111 (1992).
- ¹⁷R. Tanaka, S. Nakamichi, S. Endo, H. Wada, M. Shiga, and F. Ono, *Solid State Commun.* **78**, 489 (1991).
- ¹⁸E. Lelièvre-Berna, B. Ouladdiaf, R. M. Galera, J. Deportes, and R. Ballou, *J. Magn. Magn. Mater.* **123**, L249 (1993).
- ¹⁹R. Ballou (private communication).

Time evolution of magnetization in the FeRh system near antiferromagnetic-ferromagnetic transition temperature (abstract)

Shinji Yuasa, Yoshichika Oiani, and Hideki Miyajima

Department of Physics, Faculty of Science and Technology, Keio University, Hiyoshi 3-14-1, Kohoku, Yokohama 223, Japan

The body-centered cubic FeRh is known to exhibit a first-order phase transition from antiferromagnetic to ferromagnetic at about 400 K, accompanied by a volume expansion of about 1%. The time evolution of the magnetization M of ordered $\text{Fe}_{0.5}\text{Rh}_{0.5}$ and $\text{FeRh}_{0.958}\text{Pt}_{0.042}$ just below and above the transition temperature (T_0) was measured as functions of temperature and magnetic field. Around T_0 , the magnetization increased logarithmically with time up to M^* ($=41$ emu/g), the value of which indicates that the ferromagnetic grains occupy one third of the antiferromagnetic matrix. When $M=M^*$, there appeared a jump in M . After that, M varies as $M(t) = M_\infty[1 - \exp(-t/\tau)]$, where τ is a relaxation time. It should be noted that the value of M^* is independent of both temperatures and external magnetic fields. Microscopic observation and x-ray diffraction measurement showed that the ferromagnetic grains nucleated in the antiferromagnetic matrix began to grow with time just below T_0 . In this work, the time evolution of the phase transition was analyzed by considering the magnetic free energy, the elastic energy, and the strain energy at the surface of the grains. The above mentioned magnetic relaxation process is deeply related to the time evolution of the grain size.

Unusual magnetic properties and time dependent magnetization in ErCo_3Ga_2 (abstract)

Naushad Ali and Xianfeng Zhang

Department of Physics and Molecular Science Program, Southern Illinois University, Carbondale, Illinois 62901

In this abstract we will present the measurements of magnetization, ac susceptibility, and the time dependent effects on the magnetization of polycrystalline samples of ErCo_3Ga_2 and YCo_3Ga_2 . The field cooled (FC) and zero field cooled (ZFC) magnetization data suggest a spin glass transition in YCo_3Ga_2 below 160 K. The FC magnetization ErCo_3Ga_2 exhibits a negative minimum at 25 K and a compensation temperature at 150 K. It is suggested that ErCo_3Ga_2 has two magnetic phase transitions: one at 150 K (most likely a spin glass transition due to Co sublattice) and the other below 25 K (due to Er sublattice ordering). We have found an unusual time dependence of magnetization of ErCo_3Ga_2 at a constant temperature (below 150 K) and constant applied magnetic field. The magnetization M increases with time t and does not attain a constant value over a period of 64 h. The time dependence of magnetization follows the relation $M_{T,H}(t) = M_{T,H}(t_0) + a_{T,H} \ln t$. The slope $a_{T,H}$ is always positive and depends on temperature and the applied magnetic field. The field dependence of the slope shows a peak at a field H_a . The value of H_a decreases with increasing temperature. At a constant temperature the slope $a_{T,H}$ increases exponentially with the applied magnetic field and then decays towards zero values at high applied magnetic field. This suggests an activation energy process. Detailed experimental results on time effects will be presented.

Effects of magnetic fields on fibrinolysis

M. Iwasaka and S. Ueno

Biomagnetics and Biosystems Laboratory, Department of Computer Science and Communication Engineering, Faculty of Engineering, Kyushu University, Fukuoka 812, Japan

H. Tsuda

Clinical Laboratory, Kyushu University Hospital, Kyushu University, Fukuoka 812, Japan

In this study, we investigated the possible effects of magnetic fields on the fibrinolytic process. Fibrin dissolution was observed and the fibrinolytic activities were evaluated. First, fibrinolytic processes in magnetic fields were investigated by the fibrin plate method. We gathered solutions from the dissolved fibrin, and measured mean levels of fibrin degradation products (FDPs) in solutions. Mean levels of FDPs exposed to 8 T magnetic fields were higher than those not exposed to fields. Second, we carried out an experiment to understand how fibrin oriented in a magnetic field dissolves. FDPs in solutions of dissolved fibrins in fibrin plates were assayed. The result was that fibrin gels formed in a magnetic field at 8 T were more soluble than those not formed in a magnetic field. A model based on the diamagnetic properties of macromolecules was explained, and changes of protein concentrations in a solution in gradient magnetic fields were predicted.

I. INTRODUCTION

Fibrinogen, which is the prime factor in blood coagulation, changes to fibrin monomer by the action of protease thrombin, and fibrin monomers are polymerized. Fibrin polymers are diamagnetic materials that are oriented in a magnetic field. In the course of the polymerization process, when a magnetic field of intensity 10–20 T is applied, the fibrin fibers orient parallel to the magnetic fields.¹ When no magnetic field is applied, fibrin fibers become entangled in mesh, and no orientation is observed. This is an effect of strong static magnetic fields on the blood coagulation system.

On the other hand, the fibrinolytic process also occurs in vessels in a mutually compensating and balanced state with coagulation. Fibrin gels are dissolved when polymerized fibrins are degraded to fragments by plasmin. There have been some studies on the positive effect of weak magnetic fields (~ 0.3 T) on fibrinogen degradation products level in rabbits *in vivo*.² We have been studying the fibrinolysis in intense magnetic fields up to 8 T, to clarify the mechanism of enzyme reactions in magnetic fields, and reported about some *in vitro* studies of fibrinolysis.^{3,4} We have investigated how fibrin oriented in a magnetic field dissolves. Fibrin plates were prepared and the fibrinolytic process was observed. It was observed that the shapes of holes in dissolved fibrin changed to ellipsoidal patterns when fibrin plates were formed with a magnetic field at 8 T. The transversal axis of the ellipse was parallel to the magnetic fields.⁴

In the present study, we focus on the possibility that one of the enzyme reactions engaged in those coagulation and fibrinolysis cascades, could be influenced by magnetic fields. Fibrinolytic processes in magnetic fields are investigated by a fibrin plate method, and mean levels of fibrin degradation products (FDPs) in solutions are measured.

II. MATERIALS AND METHODS

A. Magnetic fields exposure system

We used a horizontal type of superconducting magnet with a bore 100 mm in diameter and 700 mm long. The magnet produced 8 T at its center, where the z axis was directed along the bore axis.

The distributions of magnetic fields at the center of a bore are shown in Fig. 1. In a sectional plane of a bore, the maximum field strength is in bore's wall, and the minimum field strength is in the center of the plane.

Figure 2 shows the distributions of magnetic fields on the z axis. This exposure system has a field distribution in which magnetic field strength changes from 7.84 to 4.30 T at $z=0\sim\pm 100$ mm in the center of a sectional plane of a bore. When the magnet produced 8 T at its center, the maximum product of the magnetic field and the gradient was $400\text{ T}^2/\text{m}$ at $z=\pm 75$ mm, where the z axis was along the bore axis.

B. Assay of FDPs released under magnetic fields

Fibrinolytic activity was evaluated by the fibrin plate method.⁵ Fibrin plates were prepared and the fibrinolytic process was observed. Thrombin ($80\text{ }\mu\text{l}$ 3.1 NIH units/ml) was

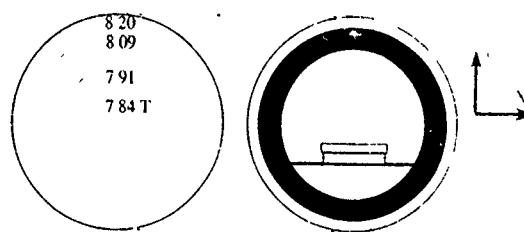


FIG. 1. Distribution of magnetic fields at the center of the bore.

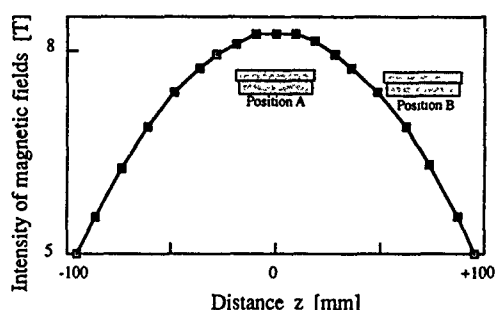


FIG. 2. Distribution of magnetic fields on the bore axis.

added to 3 ml of fibrinogen (4.8 mg/ml in 0.05 M Tris-HCl buffer, pH 7.4, containing 0.10 M NaCl). This solution was divided into two dishes and incubated at 25 °C for 60 min without magnetic fields. A hole was made in the centers of the fibrin plates by a gel puncher, and 20 μ l of plasmin (4 casein units/ml) was added to each hole.

Fibrin plates were incubated at 37 °C for 15 h, either with a magnetic field at 8 T or without magnetic fields, and dissolution of both types of fibrin was observed. The position of fibrin plates exposed to 8 T magnetic fields (position A) is shown in Fig. 2. We gathered solutions from the dissolved fibrin, and measured absorbencies at 280 nm with a spectrophotometer. Mean levels of FDPs in solutions were obtained using absorbance coefficients ($A_{1\% - 1 \text{ cm}}$ at 280 nm) of 1.51.⁶

The same experiment was carried out in gradient magnetic fields (position B: 350–400 T²/m).

C. Assay of fibrinolysis of fibrin colts formed in magnetic fields

We carried out an experiment to understand how the fibrin oriented in a magnetic field dissolves. Thrombin was added to a solution of fibrinogen. This solution was divided into two dishes; one was for magnetic field exposures and the other for the control. After incubation at 25 °C for 60 min, a hole was made in fibrin plates in which a protease plasmin was added. The dissolution of both fibrins was observed after incubation at 37 °C for 15 h. We gathered solutions from the dissolved fibrin, and measured mean levels of FDPs in solutions.

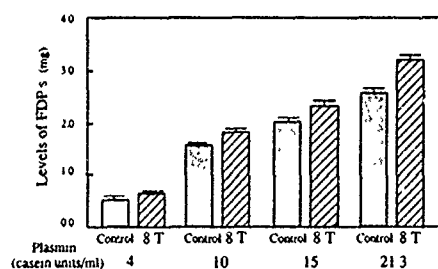


FIG. 3. Fibrinolytic processes in an 8 T magnetic field. Vertical axis shows the levels of FDPs. Various concentrations of plasmin (20 μ l) were added into a hole made in the center of fibrin plates. Data were expressed as means +SD for independent experiments.

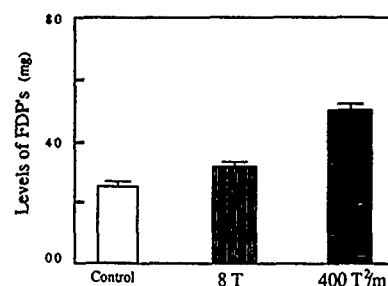


FIG. 4. Effects of gradient magnetic field on fibrinolytic process. Vertical axis shows the levels of FDPs. Plasmin (20 μ l, 21.3 casein units/ml) were added into the holes made in the center of fibrin plates. Data were expressed as means +SD for independent experiments.

III. RESULTS

A. Fibrinolysis under magnetic fields

Figure 3 shows the mean levels of FDPs in samples exposed to an 8 T magnetic field and in those not exposed. Fibrin plates exposed to fields were placed in the center of a magnet's bore axis, 20 mm below the center of the bore's sectional plane.

The maximum release of FDPs was observed when plasmin activity was 21.3 casein units/ml. Mean levels of FDPs in samples exposed to an 8 T magnetic field were higher than those not exposed by 18% on the average.

Figure 4 shows the effects of gradient magnetic fields on the fibrinolytic process. The mean level of FDPs released in a gradient magnetic field of 400 T²/m was more than 190% of the control samples, and 160% of the samples exposed to an 8 T magnetic field.

B. Fibrinolysis of fibrin colts formed in magnetic fields

FDPs in the dissolved holes in the fibrin prepared in either the presence or the absence of an 8 T magnetic field were assayed. The result is shown in Fig. 5. Plasmin concentrations were varied from 10 to 21.3 casein units/ml. Fibrin gels formed with a magnetic field were more soluble than those formed without a magnetic field.

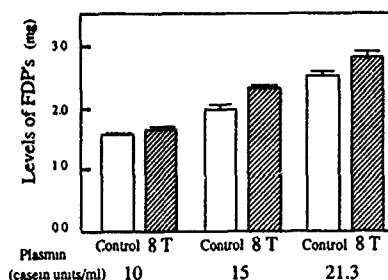


FIG. 5. Fibrinolysis in the fibrin that formed in a 8 T magnetic fields. Vertical axis shows the levels of FDPs. Various concentrations of plasmin (20 μ l) were added to the holes made in the center of fibrin plates. Data were expressed as means +SD for independent experiments.

IV. DISCUSSION

The results of the present study indicate that a reaction of the last cascade of fibrinolytic system, degradation of fibrin clots by protease plasmin, is influenced by magnetic fields up to 8 T.

In the first experiments, mean levels of FDPs in the center of a magnet's bore axis (position A; $z=0$ mm, $y=-19$ to -15 mm), were higher than those not exposed to magnetic fields by 18% on the average.

We have carried out the same experiment in the gradient magnetic fields area, where products of B and dB/dz are 350–400 T²/m at $z=\pm 60$ –95 mm (position B). Result shows that the effect of gradient magnetic fields is significant in this position.

We propose a model to explain these results. The model is the effect of magnetic fields on the kinetics of macromolecules, observed at macroscopic levels, that is caused by the diamagnetic properties.

Almost all materials in living systems are diamagnetic materials. Fibrin polymers have a distinguishable property, which is the large diamagnetic anisotropy resulting in magnetic torque energy $(1/2)\Delta\chi H^2$ which exceeds thermal energy kT . There is another kinetic property of diamagnetic materials. If there is a magnetic gradient, diamagnetic materials in this area can drift to less magnetic fields.

In the experiment of fibrinolysis under magnetic field, at position A, where the bottom of a fibrin plate is exposed to 7.90 T ($y=-19$ mm) and the top is exposed to 7.86 T ($y=-15$ mm), fibrin gel is in the gradient field of 7.5 T/m. Products of fields and gradient in this space are ~ 59 T²/m.

Let us introduce a situation in which there is a gradient magnetic field whose intensity decreases with the altitude increase. When there is a diamagnetic material, such as water, in gradient magnetic fields. A gravity force of $\rho_w g V_w$ acts downward on this material, where ρ_w is a mass of water per unit volume, g is the gravitational constant, and V_w is a volume of water cluster. On the other hand, a magnetic force $-\chi_w V_w \mu_0 \Delta(H^2)/2$ acts upward, where χ_w is a susceptibility of water.

Fibrin clots are gels that contain water clusters and ions, etc. When these clots are digested by the action of protease plasmin, many FDPs are released in the solution. If there are polymerized fibrins which have been isolated from clots, these fibrin polymers are adrift in the solution because of buoyancy. If we do not consider random movements caused by thermal energy, and viscosity is neglected, a force that acts on a diamagnetic material in the water is described as

$$F = \rho g V - \rho_w g V + (\chi_v - \chi_w) V \mu_0 \Delta(H^2)/2, \quad (1)$$

where ρ , χ_v , and V are constants of fibrin, FDPs, or plasmin.

If $(\rho - \rho_w)gV$ was small compared to $(\chi_v - \chi_w)V\mu_0 \times \Delta(H^2)/2$, and when magnetic energy $-(\chi_v - \chi_w)V\mu_0 H^2/2$ was larger than thermal energy kT , it is possible for the diamagnetic proteins in the solution to drift in a specific direction.

Drifting of fibrin polymers and FDPs in a specific direction results in the change of concentration of these proteins. When there is an increase of the concentrations of substrates and enzymes in a local space of a solution, an enzyme reaction such as fibrinolysis can be effected.

The effect of a gradient magnetic field of 400 T²/m was more distinguished as shown in Fig. 4. In this case, there are large gradients along the horizontal line. Solutions containing water, plasmin, and fibrin could diffuse to horizontal directions to promote the reactions of fibrinolysis.

An enhancement of fibrinolysis of clots formed with magnetic fields also seems to be due to magnetically induced changes in concentration of fibrins.

V. CONCLUSION

To investigate the effect of magnetic fields on the fibrinolytic process in thrombus, we carried out the above described experiments.

In the experimental results of the fibrin plate method, fibrinolysis under magnetic field gradient and fibrinolysis of clots formed with magnetic fields were enhanced.

ACKNOWLEDGMENTS

This work was supported in part by the Grants from the Ministry of Education, Science and Culture in Japan, and Nissan foundation.

¹J. Torbet, M. Freyssinet, and G. Hudry-Clergeon, *Nature* **289**, 91 (1981).

²E. Gorczynska, *J. of Hygiene, Epidemiology, Microbiol. and Immun.* **30**, 269 (1986).

³M. Iwasaka, S. Ueno, and H. Tsuda, in *Simulation and Design of Applied Electromagnetic Systems*, edited by T. Honma (Elsevier Science B.V., 1994), p. 435.

⁴S. Ueno, M. Iwasaka, and H. Tsuda, *IEEE Trans. Magn.* **29**, 6, 3352 (1993). (in press).

⁵C. Kluft, P. Brackman, and E. C. Veldhuyzen-Stolk, in *Progress in Chemical Fibrinolysis and Thrombolysis*, edited by J. F. Davidson, M. M. Samama, P. C. Desnoyers (Raven, New York, 1976), pp. 57–65.

⁶V. J. Marder, N. K. Shulman, and W. F. Carroll, *J. Biol. Chem.* **244**, 2111 (1969).

Early embryonic development of frogs under intense magnetic fields up to 8 T

S. Ueno and M. Iwasaka

Biomagnetics and Biosystems Laboratory, Department of Computer Science and Communication Engineering, Faculty of Engineering, Kyushu University, Fukuoka 812, Japan

K. Shiokawa

Zoological Institute, Faculty of Science, University of Tokyo, Tokyo 113, Japan

A possible influence of intense magnetic fields on the embryonic development of frogs was studied in reference to a potential hazard in magnetic resonance imaging technology. Some of the most serious hazardous effects that could be induced by intense magnetic fields are teratogenic effects on developing embryos. In the present experiment, the possible influence of intense magnetic fields up to 8 T on the early embryonic development of *Xenopus laevis* was studied. Embryos were exposed to magnetic fields up to 8 T for the period from the precleavage stage to neurula in a small glass vial. Embryos were then cultured in Brown-Caston's medium until the feeding-tadpole stage. No apparent teratogenic effects were observed when embryos were cultured for 20 h from the stage of uncleaved fertilized egg to the neurula stage under magnetic fields of 8 T. We conclude that static magnetic fields up to 8 T do not appreciably affect the rapid cleavage and the following cell multiplication and differentiation in *Xenopus laevis*. We have also studied the early embryonic development of *Xenopus laevis* in a 40 nT magnetic field, or 1/1000 of the earth's magnetic field, and obtained negative results. Thus, again under this very low magnetic field, fertilized eggs developed normally and formed tadpoles with no appreciable abnormality.

INTRODUCTION

The question of biological effects of magnetic fields has become serious recently in association with the appearance of superconducting magnets and magnetic resonance imaging (MRI) for medical applications.

One of the most serious hazardous effects that could be induced by intense magnetic fields is a teratogenic effect on developing embryos. Generally, fertilized eggs of animals divide quite actively. For example, a fertilized egg of the African clawed toad *Xenopus laevis* cleaves approximately every 25 min for the first 12 cycles of cell division,¹ and after such rapid and synchronous division, the embryo reaches the blastula and then gastrula stages to undergo formative movements to become a feeding tadpole, which is provided with all the necessary "organ anlage" to become a frog.

Thus embryos of *Xenopus laevis* provide a unique test system to examine both cytostatic and teratogenic effects of magnetic fields, because they first divide extremely rapidly during the cleavage stage, and then later differentiate various organs, the essential mechanisms of which are comparable to those of humans.

A preliminary study on embryogenesis in *Xenopus laevis* cultured in magnetic fields up to 1 T, 1000 T/m, and 6.34 T has been reported previously.^{2,3}

In these previous studies,^{2,3} embryos were exposed to the strong magnetic field after they reached 2–8 cell stages. In the initial phase of embryogenesis, *Xenopus* eggs undergo remarkable rearrangement of cytoplasmic substances and cortical rotation, which is induced by sperm entrance and determines the future dorsoventral polarity.⁴ Therefore, it is important to see if the developing embryos are affected by the strong magnetic field during such extensive cytoplasmic relocation.

To test the susceptibility of the egg rotation and accompanying changes to the strong magnetic field, it is necessary to expose the egg to the magnetic field shortly after insemination.

In the present experiment, the possible influence of intense magnetic fields up to 8 T on the early embryonic development of *Xenopus laevis* was studied by exposing eggs shortly after fertilization (before egg rotation).

MATERIALS AND METHOD

A female of *Xenopus laevis* which had not ovulated for at least six months was injected with 150 units of a gonadotropic hormone gonatropin,⁵ and unfertilized eggs squeezed out from the female were artificially inseminated following the methods of Wolf and Hedrick.⁶ About 20 min after fertilization, eggs were cultured at 21–22 °C in a Brown-Caston Ringer solution⁷ and eggs were exposed to magnetic fields up to 8 T in a small glass vial. Eggs that were arrested in development were counted as unfertilized and were eliminated from the culture within 2 h. Embryos were then cultured in Brown-Caston's medium until the feeding-tadpole stage, following the methods of Nieuwkoop and Faber.⁸ Tadpoles were fed a dried powder of alfalfa leaves.

We also studied embryonic development of *Xenopus laevis* in a magnetically shielded room where field strength is 40 nT.

The experimental design to expose eggs or embryos to magnetic fields is illustrated in Fig. 1. We used a horizontal type of superconducting magnet with a bore 100 mm in diameter and 700 mm long. The magnet produced 8 T at its center.

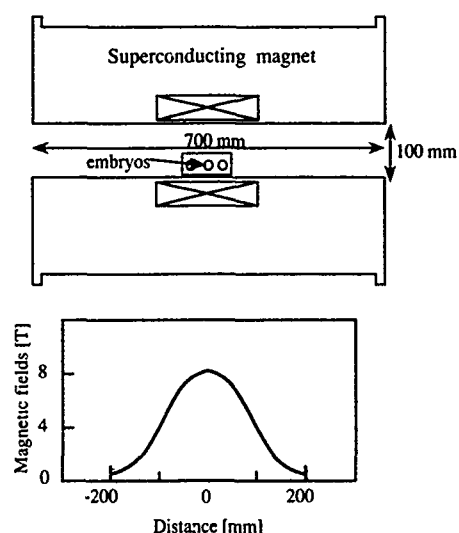


FIG. 1. Experimental setup to observe the embryonic development of frog embryos in a superconducting magnet.

RESULTS AND DISCUSSION

Figure 2 shows the outer appearance of exposed embryos at various stages. It is shown that embryos at the stages of blastula, neurula, and hatched tadpole treated with an 8 T or 40 nT magnetic field are quite similar in their outer appearance to the untreated control embryos.

The results are summarized in Fig. 3. The percentage of

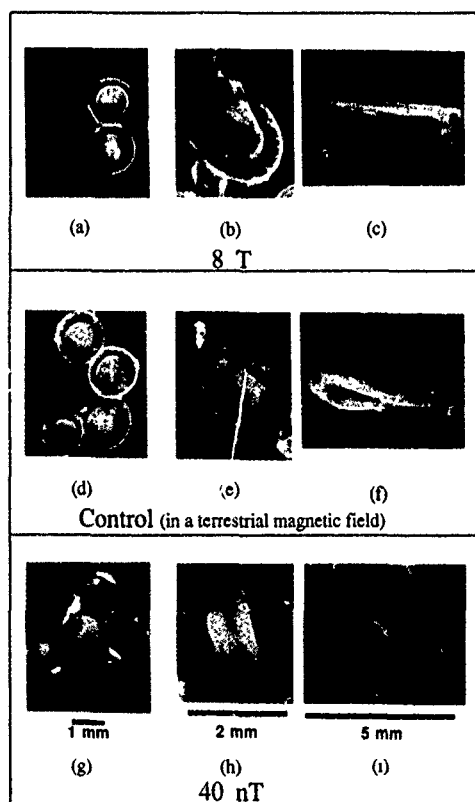


FIG. 2. Outer appearance of exposed embryos at various stages. (a),(d),(g) blastula stage; (b),(e),(h) tail bud-stage embryos; (c),(f),(i) tadpoles after hatching.

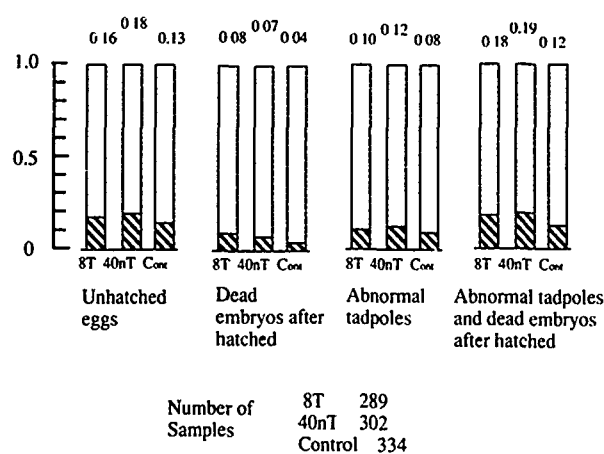


FIG. 3. The embryonic development under static magnetic fields. 8 T: embryos cultured in an 8 T magnetic field. 40 nT: embryos cultured in a 40 nT magnetic field. Cont: Control group. Samples 8 T 289, 40 nT 302, Cont 334.

embryos that reached late neurula stage was the same between the control and the embryos cultured in 8 T and 40 nT. The 14% of the embryos that died relatively early during the experiment is assumed to have been overripe eggs. Those designated as abnormal are tadpoles with faint coloring or albino formation, or axial bending including curled tail, edema formation, or a small head (microcephaly).

Neurath⁹ has done experiments on the embryonic development of frogs under gradient magnetic fields and obtained a significant difference in the hatching rate of the embryo. Neurath tried to explain the results through the movement of ferritin, a paramagnetic material in the cells.

Gradient magnetic fields will exert mechanical forces on heterogeneous materials of different magnetic susceptibility. Assuming that biomagnetic effects are due to forces between heterogeneous materials of different magnetic susceptibility in the body, the effect should be proportional to the product of the magnetic field and the gradient.

High gradient magnetic separation (HGMS) has made it possible to separate micron-sized paramagnetic particles from solution.¹⁰ Melville, Paul, and Roath¹¹ succeeded in separating red cells from whole blood by HGMS when the hemoglobin was in the completely deoxygenated state.

We have reported a study on the magnetic field effects on the embryonic development of *Xenopus laevis* by a similar technique used in HGMS.² Embryos were exposed to 1.0 T magnetic fields with different gradients of a range from 10 to 10^3 T/m during a period from cleavage to neurula stage. The results obtained suggested that strong magnetic fields with gradients higher than at least 10^4 T/m would be necessary to cause more clear teratogenic effects.

We have also reported results of a preliminary study on embryogenesis in *Xenopus laevis* cultured in static magnetic fields of 6.34 and 4.5 T.³ It is possible for diamagnetic materials in living systems to orient by static magnetic fields up to 10 T or more. The magnetic orientation of cellular constituents, especially of those in cytoplasmic membranes, could occur in the rapidly dividing cells of early embryos. It is also considered that magnetic fields could induce some effects on

the mitochondrial energy supplying system, which in turn induces some alteration in DNA and RNA metabolism. Results obtained showed that static magnetic fields up to 6.34 T did not appreciably affect the rapid cleavage and the following cell multiplication and differentiation in *Xenopus laevis*.

In the present study, the possible influence of intense magnetic fields up to 8 T on the early embryonic development of *Xenopus laevis* was studied by exposing eggs shortly after fertilization (before egg rotation). However, we observed no appreciable defect in the development of embryos. Also it was shown here that an almost zero or 1/1000 of the earth's magnetic field, has no teratogenic effect on *Xenopus* development.

Therefore, we concluded that as far as the rotation of cortical cytoplasm of fertilized eggs and subsequent cleavage and early development of *Xenopus laevis* are concerned, 8 T and 40 nT magnetic fields exert practically no appreciable effect.

ACKNOWLEDGMENT

This work was supported in part by the grants from the Ministry of Education, Science and Culture in Japan.

- ¹J. Newport and M. Kirschner, *Cell* **30**, 675 (1982).
- ²S. Ueno, K. Harada, and K. Shiokawa, *IEEE Trans. Magn.* **MAG-20**, 1663 (1984).
- ³S. Ueno, K. Shiokawa, and M. Iwamoto, *J. Appl. Phys.* **67**, 5841 (1990).
- ⁴J. Gerhart, G. Ubbels, S. Black, K. Hara, and M. Kirschner, *Nature* **292**, 511 (1981).
- ⁵K. Shiokawa and K. Yamana, *Dev. Biol.* **16**, 368 (1967).
- ⁶D. P. Wolf and J. L. Hedrick, *Dev. Biol.* **25**, 348 (1971).
- ⁷D. D. Brown and J. D. Caston, *Dev. Biol.* **5**, 412 (1962).
- ⁸P. D. Nieuwkoop and J. Faber, *Normal Table of Xenopus Laevis Daudin* (North-Holland, Amsterdam, 1956).
- ⁹P. W. Neurath, in *Biological Effects of Magnetic Fields*, edited by M. F. Barnothy (Plenum, New York, 1969), pp. 177-187.
- ¹⁰J. A. Oberteuffer, F. Paul, and S. Roath, *IEEE Trans. Magn.* **MAG-9**, 303 (1973).
- ¹¹D. Melville, F. Paul, and S. Roath, *IEEE Trans. Magn.* **MAG-11**, 1701 (1975).

Influence of spreading neuronal electric sources on spatio-temporal neuromagnetic fields

K. Iramina, K. Ueno, and S. Ueno

Biomagnetics and Biosystems Laboratory, Department of Computer Science and Communication Engineering, Kyushu University, Fukuoka 812, Japan

This study focuses on the influences of spreading multiple dipoles in the human head upon surface magnetic fields. A source model of the magnetoencephalogram (MEG) activity is proposed. This source model is expressed by spreading multiple dipoles which have time-varying dipole moments. Using this source model, spatio-temporal patterns of MEGs are simulated. Effects of spreading dipoles on spatio-temporal magnetic fields are investigated. The computer simulations show that the wave forms and amplitude of magnetic fields are affected significantly by the spread of the source and the conduction velocity of traveling dipoles. The latency of the peak magnetic field generated by spreading multiple dipoles varies with the measurements points on the surface of the head.

INTRODUCTION

It is difficult to solve the inverse problem in magnetoencephalography (MEG) and electroencephalography (EEG) because of the complexity of electrical sources and inhomogeneities of electrical conductivities in the human head. We have investigated the influence of inhomogeneous regions in the human head on surface magnetic fields.¹⁻⁵ We have also investigated spatial patterns of magnetic fields produced by multiple dipoles.^{6,7} MEG measurements have an advantage over EEG techniques in that the underlying neural source in the brain is localized. The conventional methods used to address the inverse problem have been concerned with estimation of positions and orientations of current sources which were modeled as a small number of dipoles. These inverse problems are solved using magnetic and electric signals at a fixed time. However, the neural sources in the brain are intricate in construction and electrical activities of neural sources change by the moment. There are many cases that cannot conform to the simple dipole model, such as single-current dipole or two-current dipoles.

Recently it became possible to measure magnetic fields at many points of the head simultaneously using the multichannel superconducting quantum interference device (SQUID) system. Multichannel SQUID measurements have revealed that sources of the N100 component of auditory evoked magnetic fields are represented by moving dipoles.^{8,9}

It is important to consider spatially distributed multiple dipoles as the sources of magnetic fields.

This study is focused on the influence of spreading dipoles upon spatio-temporal magnetic fields. Sources of electrical activity in the human brain are assumed as multiple traveling dipoles. Using this source model, spatio-temporal

patterns of magnetic fields are simulated. The computer simulation shows that the spread of the source and conduction velocity of traveling dipoles have significant effects upon the wave forms and amplitude of magnetic fields.

MODELS AND METHODS

The human head is assumed to be a homogeneous spherical volume conductor with 0.1 m radius. We assume that sources of MEG activity are diffused in the brain. The source area is represented by a square with 20 mm sides. This dipole layer exists under the vertex and orients perpendicular to the surface of the sphere. 10 000 current dipoles are arrayed in a lattice in the dipole layer. All dipoles orient perpendicular to the dipole layer. Each dipole has a time-dependent dipole moment. It is assumed that the dipole moment changes sinusoidally. The excitation of the adjacent cortical neuron propagates in the source area. The propagation of excitation is represented by the propagation of change of dipole moment. Magnetic fields are reflected by the spatio-temporal summation of these dipole activities. Figure 1 shows a schema of the propagation of the excitation of cortical neurons. The time-dependent dipole moment of the exciting dipole moves to the next dipole after a slight time lag. Figure 2 shows the head model and the dipole layer.



FIG. 1. Source model of spreading excitation of cortical neurons. The time-dependent dipole moment of the exciting dipole moves to the next dipole after a slight time lag.

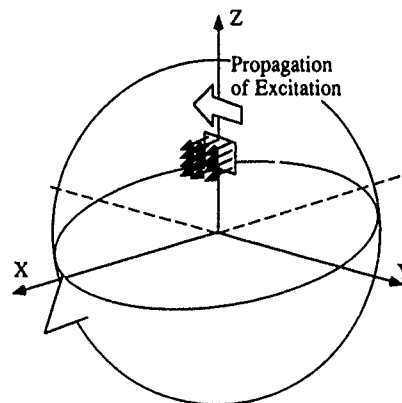


FIG. 2. Spherical head model and the locations of the dipole layer.

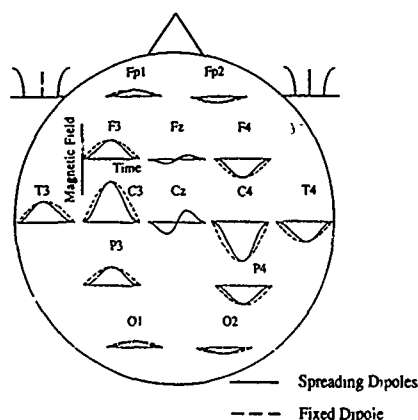


FIG. 3. The wave forms of magnetic fields generated by multiple dipoles that move in the source area (solid line), and the wave forms generated by a fixed single dipole that locates at the center of the source area (dashed line).

Magnetic field components perpendicular to the surface of the sphere are calculated by Biot-Savart law.

RESULTS AND DISCUSSION

Figure 3 shows the wave forms of magnetic fields generated by multiple dipoles that move in the dipole layer, and the wave forms generated by a fixed dipole that locates at the center of the dipole layer. The magnetic fields generated by a single dipole show the same pattern as the change of dipole moment, whereas the magnetic fields generated by multiple dipoles have various patterns which are different according to the measurement points. In particular, the peak latency varies with the measurement point. The delay of the latency is noticeable in the points away from the source area.

Figure 4 shows the distributions of the latency at the peak of the N pole of magnetic fields on the surface of the sphere. That is, the contour lines show the arrival time of the peak of magnetic fields. The depth of the dipole layer from the surface of the sphere is changed at 20, 50, and 70 mm. The contour of the latency is quantized by eight levels in the map. The patterns of distributions of peak latency vary in the positions of dipole layer. When the dipole layer is located deeper in the head, a widespread region is influenced in latency.

Figure 5 shows the change of wave forms of magnetic fields at the point C3 when the direction of traveling dipoles

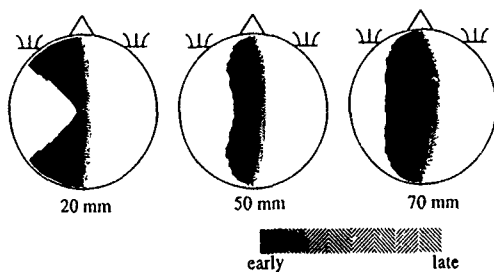


FIG. 4. Distributions of the latency of peak magnetic fields on the surface of the sphere. The depth of the dipole layer from the surface of the sphere is changed to 20, 50, and 70 mm.

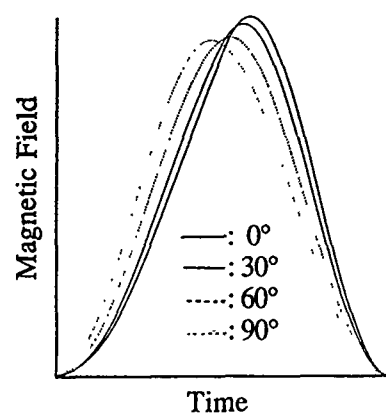


FIG. 5. Change of magnetic fields at C3 when the directions of propagation of multiple dipoles change from the horizontal direction to the vertical direction. 0° shows a direction from the left ear to the right ear and 90° shows the direction from the bottom to the vertex.

changes from the horizontal direction (along Y axis) to the vertical direction (along z axis). The peak of the wave forms occurs at an earlier time when the direction of traveling dipoles changes from horizontal to vertical.

Figure 6 shows the effects of conduction velocity of propagation of excitation in the source area. In this simulation, it is assumed that each dipole moment changes in 10 ms and the peak of the dipole moment is 3.0×10^{-13} A m. The length of the dipole layer is 10 mm. The dipole layer is located 50 mm under the vertex. Conduction velocity of traveling dipoles in dipole layer varies in six cases (1.25, 2.5, 5, 10, 20, and 40 mm/ms). These results show that wave forms and the amplitude of magnetic fields are remarkably different when the conduction velocity of traveling dipoles change. When the dipoles travel slowly, the amplitude of the magnetic field is small and the wave form shows a trapezoidal pattern. The amplitude of peak magnetic field is about 25 fT (2.5×10^{-14} T). The peak of wave forms becomes sharp as the conduction velocity increases. When the conduction velocity is 40 mm/ms, the amplitude of peak magnetic field is about 300 fT. These phenomena can be explained by the assumption that many dipoles in a wide area excite at the same time when the conduction velocity is fast. In contrast, when the conduction velocity is slow, the number of dipoles

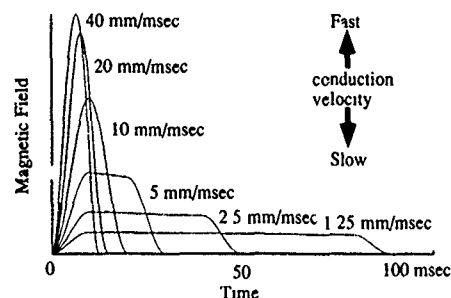


FIG. 6. The effects of conduction velocity of propagation of excitation. Conduction velocity of multiple dipoles in the source layer varies in six steps from 1.25 to 40 mm/ms.

excited at the same time is small and the excited region propagates slowly.

These simulated results suggest that it is possible to estimate the spreading area of the cortical excitation and conduction velocity of the propagation by using the spatio-temporal pattern of magnetic fields, in particular, peak latency, wave form, and amplitude. When both spatial and temporal distributions of the magnetic fields are considered in the inverse problem of MEG activities, the electrical activity in the brain can be estimated dynamically.

ACKNOWLEDGMENT

This work was supported in part by Grant No. 03505002 from the Ministry of Education Science and Culture, Japan.

- ¹S. Ueno, H. Wakisako, and S. Matsuoka, *IL Nuovo Cimento D* 2, 558 (1983).
- ²S. Ueno, H. Wakisako, and K. Harada, *Biomagnetism: Applications & Theory*, edited by H. Weinberg, G. Storoink, and T. Katila (Pergamon, New York, 1985), pp. 289-283.
- ³K. Iramina and S. Ueno, *Biomagnetism '87*, edited by K. Atsumi, M. Kotani, S. Ueno, T. Katila, and S. J. Williamson (Tokyo Denki University Press, Tokyo, 1988), pp. 106-109.
- ⁴K. Iramina and S. Ueno, *Advances in Bio:magnetism*, edited by S. J. Williamson, M. Hoke, G. Stroink, and M. Kotani (Plenum, New York, 1989), pp. 619-622.
- ⁵S. Ueno and K. Iramina, *Brain Topography* 3, 151 (1990).
- ⁶S. Ueno, K. Iramina, H. Ozaki, and K. Harada, *IEEE Trans. Magn. MAG-22*, 874 (1986).
- ⁷K. Iramina and S. Ueno, *J. Appl. Phys.* 67, 5835 (1990).
- ⁸B. Lütkenhöner and C. Pantev, *Biomagnetism: Clinical Aspects*, edited by M. Hoke, Y. Okada, and G. Romani (Elsevier, Amsterdam, 1992), pp. 143-152.
- ⁹R. L. Rogers, A. C. Papanicolaou, S. B. Baumann, C. Saydjari, and H. M. Eisenberg, *Electroenceph. Clin. Neurophysiol.* 77, 237 (1990).

Magnetite coating prepared by ferrite plating on expanded polytetrafluoroethylene membrane for medical use

Q. Zhang, T. Itoh, and M. Abe

Department of Physical Electronics, Tokyo Institute of Technology, Ookayama, Meguro-ku, Tokyo 152, Japan

As the first step to the study of increasing biocompatibility of expanded polytetrafluoroethylene (EPTFE) membranes, cardiovascular patches of EPTFE substrates were coated with Fe_3O_4 layer, which is expected to accelerate proliferation of endothelial cells. The ferrite layers were formed by the thin liquid film ferrite plating method at $T=75\text{--}90^\circ\text{C}$ and pH (in oxidizing solution) $=6.9\text{--}7.4$. At a fixed pH value, a single-phase Fe_3O_4 layer is obtained when T is higher than a threshold temperature, which increases with an increasing pH value; below the threshold temperature, the layer has an impurity phase of $\gamma\text{-FeOOH}$. The obtained Fe_3O_4 layers are polycrystalline with no preferred orientation, having magnetization and coercive force which agree with those reported for bulk samples.

I. INTRODUCTION

Ferrite plating facilitates the formation of crystalline films of spinel ferrites, $M_x\text{Fe}_{3-x}\text{O}_4$, containing various transition metals $M=\text{Ni}, \text{Co}, \text{Zn}, \text{Mn}, \text{Cr}$, etc.¹⁻³ Although prepared at low temperatures ($<100^\circ\text{C}$), the magnetic and electrical properties of ferrite-plated films are as good as those of the films prepared at high temperatures by conventional techniques (e.g., sputtering, pyrolysis). This opens the door to fabricating ferrite film devices using as substrates nonheat-resistant materials such as plastics and biomaterials. Furthermore, ferrite films prepared by ferrite plating from aqueous solution are strongly compatible with water and organic compounds.

Thus the ferrite-plated films have found novel applications to biomedical use. Fe_3O_4 films prepared by ferrite plating have been used as glucose (or urea) sensor electrodes, in which urease (or GOD), an enzyme decomposing glucose (or urea), is fixed on the film surface mediated by dextran (a saccharose).⁴ Polymer microspheres coated by ferrite plating have been used as carriers for a clinical enzyme immunoassay,^{5,6} in which antibodies are fixed on the ferrite layer. This novel type of enzyme immunoassay (CA19-9, CA125, etc., Fujirebio Inc.) is already on the market and is being used clinically as cancer markers.

It has been suggested that an artificial blood vessel improves in performance if its inner wall is coated with a ferromagnetic layer. This is because the leakage flux from the magnetic layer accelerates the proliferation of endothelial cells, which enhances the biocompatibility of the artificial vessel wall, preventing thrombi (blood clots) from sticking onto the wall.^{7,8} This idea was applied in an animal experiment in which magnetic flux was applied to the inner wall of an artificial blood vessel (embedded in the body of a living dog) by a ferromagnetic metal tape which surrounded the vessel. The results revealed that the endothelial reorganization on the surface of the vessel surrounded by the magnetic tape was enhanced significantly as compared to that obtained on a control (a vessel not surrounded by the magnetic tape). To realize this idea ultimately in a clinical environment, we must coat the inner wall of an artificial vessel with a ferrite layer (a metal layer is unsuitable because it is toxic to a

living body) at low temperatures, because artificial blood vessels are made of a polymer which lacks heat resistance. Conventional ferrite film preparation techniques (e.g., sputtering, pyrolysis, etc.) require heating of substrate at above several 100°C for crystallization of ferrite, and also they are inadequate to deposit ferrite film on inner wall of a tube, especially when it is long. Ferrite plating, on the other hand, can easily coat the inner wall of a long tube by flowing the aqueous solution inside the tube at low temperature.

Current artificial blood vessels are made of extended polytetrafluoroethylene (EPTFE). As the first step to the study of the ferrite-inner-wall-coated artificial vessel, a magnetite (Fe_3O_4) layer is deposited by the ferrite plating method on substrates of EPTFE patches.

In this paper we describe the conditions for which Fe_3O_4 layer is successfully deposited on the EPTFE patch, and report the structural and magnetic properties of the ferrite layer.

II. EXPERIMENT AND RESULTS

By the thin liquid film method⁹ Fe_3O_4 layers were deposited at $75\text{--}90^\circ\text{C}$ on substrates ($1.5\times1.0\times0.6\text{ mm}^3$) of an EPTFE patch [a cardiovascular patch (GORE-TEX, PC06)]. Prior to plating, the substrates were exposed to a rf-excited oxygen plasma (frequency: 13.56 MHz, power: 30 W, pres-

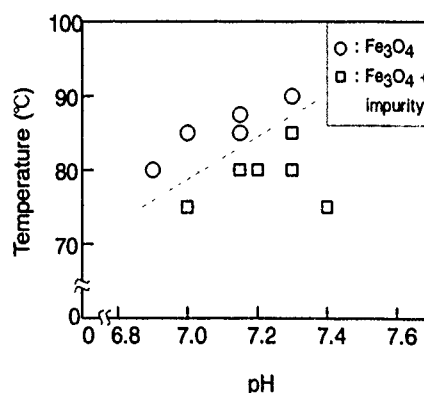


FIG. 1. Phase diagram of ferrite layers formed at various temperatures and pH values.

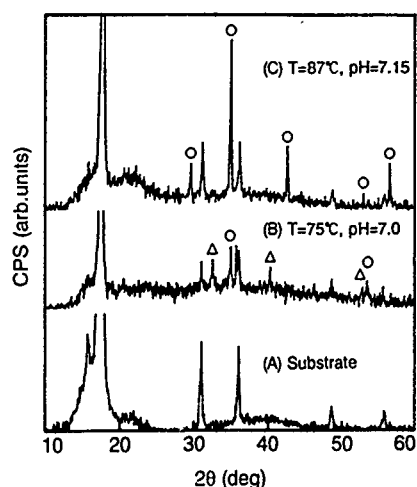


FIG. 2. X-ray diffraction diagrams of (A) EPTFE substrate and (B) and (C) ferrite layers formed under varying conditions. (O) scattering due to Fe_3O_4 , (∇) scattering due to $\gamma\text{-FeOOH}$.

sure: 0.2 Torr) for 1 min to increase the wettability of the surface.¹⁰ A reaction solution of FeCl_2 (3 g/l, $\text{pH}=6.8$) and an oxidizing solution were conducted for about 1 h through a gap (~ 1.0 mm) between substrate surface and glass cell wall.

The crystallographic phase, morphology, and magnetic properties of the plated layers were examined by a $\text{Cu K}\alpha$ x-ray diffractometer, a scanning electron microscope (SEM), and a vibrating sample magnetometer (VSM) at room temperature. The chemical composition of the ferrite layers was analyzed with an inductively coupled plasma (ICP) spectroscope, after dissolving the ferrite films in a 50% HCl solution. The thickness of the layer was calculated from the results of the chemical analysis assuming that the density of the layer is the same as that of a bulk sample.

Figure 1 shows a phase diagram of the layers deposited at various temperatures and pH values. Single-phase spinel (Fe_3O_4) type layers grow only when the temperature is higher than threshold temperature shown by a dashed line in

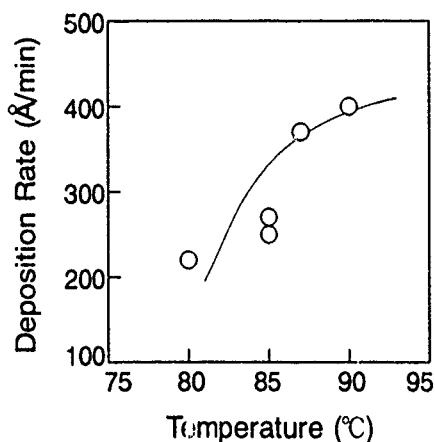


FIG. 3. Deposition rate of Fe_3O_4 layer plotted as a function of synthesizing temperature.

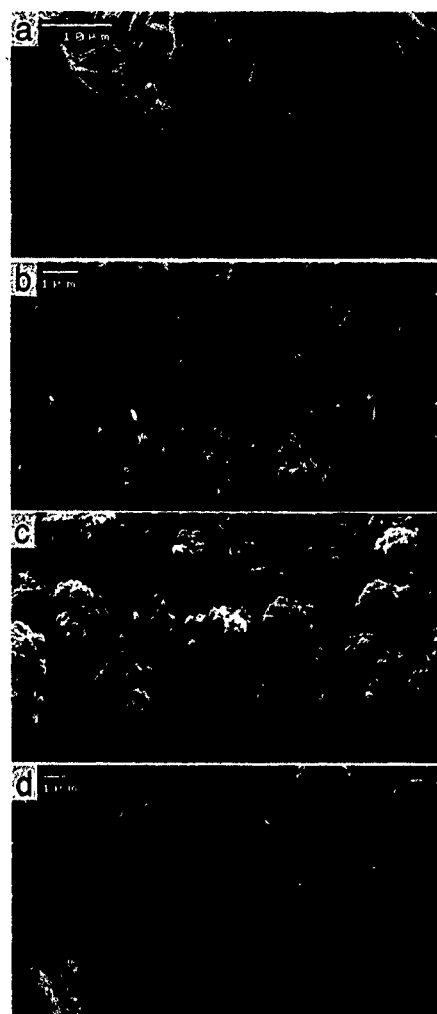


FIG. 4. SEM observations on (a) EPTFE patch substrate and ferrite layers formed on the EPTFE substrate at (b) $T=75^\circ\text{C}$, $\text{pH}=7.0$, (c) $T=80^\circ\text{C}$, $\text{pH}=7.2$, and (d) $T=87^\circ\text{C}$, $\text{pH}=7.15$.

the figure. The threshold temperature increases linearly with increasing pH value. Below the threshold temperature line, the impurity phase of $\gamma\text{-FeOOH}$ appears in x-ray diffraction diagram, as shown in Fig. 2. This is consistent with the known fact that, in ferrite plating of Fe_3O_4 , $\gamma\text{-FeOOH}$ is synthesized as a precursor from which Fe_3O_4 is produced.¹¹ The Fe_3O_4 layers are polycrystalline having no crystallographic orientation.

Figure 3 shows the deposition rate of the single-phase Fe_3O_4 layer plotted as a function of temperature. The rate increases with temperature, from ~ 200 Å/min at 80°C to ~ 400 Å/min at 90°C . These values agree with those obtained for Fe_3O_4 plating on substrates of continuous media [e.g., glass, polyethyleneterephthalate (PET), etc.].

Figure 4 shows SEM photographs for the EPTFE patch substrate and the layers deposited on it at various temperatures and pH values. The substrate [Fig. 4(a)] has a web structure of PTFE fibers with various thicknesses. The ferrite layer of single-phase Fe_3O_4 [Fig. 4(d)] forms a continuous layer on the porous substrate surface, while the layers with impurity phase [Figs. 4(b) and 4(c)] are discontinuous and porous with acicular or angular grains.

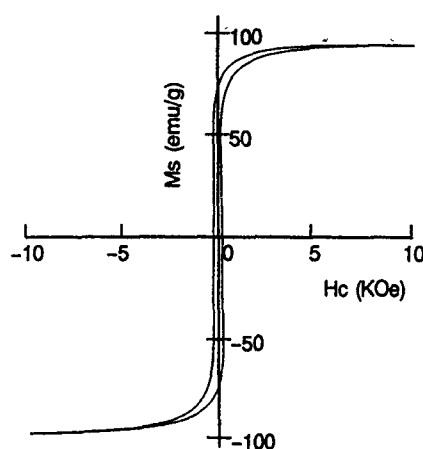


FIG. 5. Magnetization curve for a single-phase Fe_3O_4 layer (deposited at $T=87^\circ\text{C}$, $\text{pH}=7.15$), obtained applying external field parallel to layer plane.

A typical example of a magnetization curve for these specimens is shown in Fig. 5. Ferrite layers of single-phase Fe_3O_4 have magnetization of about 80–90 emu/g and coercive force of about 40–70 Oe, which agree with those reported for bulk samples of Fe_3O_4 .

III. CONCLUSIONS

By using the thin liquid film method, iron monooxide layers were successfully deposited on EPTFE patches at various temperatures and pH values of oxidizing solution. For a

fixed pH value, a threshold temperature exists, above which single-phase Fe_3O_4 layer is obtained. Below the threshold temperature, the layer has an impurity phase of $\gamma\text{-FeOOH}$, the precursor from which Fe_3O_4 is produced in ferrite plating. The Fe_3O_4 layers are polycrystalline with no crystallographic preferred orientation, and have magnetic properties which agree with those of bulk sample of Fe_3O_4 . Biocompatibility of the Fe_3O_4 layers will be examined in future investigations.

ACKNOWLEDGMENT

This study has been supported financially in part by a Grant-in-Aid for Developmental Scientific Research from The Ministry of Education, Science and Culture.

- ¹M. Abe and Y. Tamaura, *Jpn. J. Appl. Phys.* **22**, L511 (1983).
- ²M. Abe and Y. Tamaura, *J. Appl. Phys.* **55**, 2614 (1984).
- ³M. Abe, Y. Tanno, and Y. Tamaura, *J. Appl. Phys.* **57**, 3795 (1985).
- ⁴M. Abe, T. Itoh, Y. Tamaura, and K. Yoshimura, *Proceedings of the 5th International Conference on Ferrites*, Bombay, January, 1989, p. 1131.
- ⁵M. Abe, T. Itoh, and Y. Tamaura, *Mater. Res. Soc. Symp. Proc.* **332**, 107 (1991).
- ⁶M. Abe, T. Itoh, and Y. Tamaura, to be published in *Thin Solid Films*.
- ⁷M. Abe, *Proceedings of the 6th International Conference on Ferrites*, Tokyo and Kyoto, 1992, p. 472.
- ⁸F. Miyawaki, K. Suma, and H. Matumoto, "Jinkozoki" (*Artificial Organs*) **21**(5), 1377 (1992) [in Japanese].
- ⁹M. Abe, Y. Tamaura, Y. Goto, N. Kitamura, and M. Gomi, *J. Appl. Phys.* **61**, 3211 (1987).
- ¹⁰Q. Zhang, T. Itoh, M. Abe, and Y. Tamaura, *Proceedings of the 6th International Conference on Ferrites*, Tokyo and Kyoto, 1992, p. 478.
- ¹¹Y. Tamaura, K. Itoh, and T. Katsura, *Journal of Chemical Society Dalton Trans.*, 1983, p. 189.

Redistribution of dissolved oxygen concentration under magnetic fields up to 8 T

S. Ueno, M. Iwasaka, and T. Kitajima

Biomagnetics and Biosystems Laboratory, Department of Computer Science and Communication Engineering, Faculty of Engineering, Kyushu University, Fukuoka 812, Japan

The influence of static magnetic fields on the behavior of oxygen dissolved in an aqueous solution was studied in order to clarify the interaction mechanism of dynamic movements of dissolved oxygen with magnetic fields and to broaden the basic understanding of biological effects of magnetic fields. A horizontal type of superconducting magnet with a bore 100 mm in diameter was used. A cylindrical chamber filled with distilled water was exposed to magnetic fields up to 8 T and a gradient of 50 T/m. The spatial distribution of oxygen concentration dissolved in water was measured by a dissolved oxygen meter. A clear redistribution of oxygen concentration was observed, and the dissolved oxygen concentration increased more than 10% around the center of the magnet.

I. INTRODUCTION

It is an interesting problem for human beings whether or not magnetic fields have any influence on the life processes in living systems. Numerous investigations of magnetic field effects on biological systems have been reported.¹⁻⁴ However, the biological effects of static magnetic fields have not yet been clarified. Among several reviews and papers, the importance of the role of oxygen has been suggested by Aceto, Tobias, and Silver.³

Since oxygen is a paramagnetic molecule, recognition of a paramagnetic component has been emphasized in unraveling the underlying mechanisms in magnetic field effects on life processes. In spite of the importance of the topic, no experiment has been carried out to determine quantitative relationships between the intensity of dc magnetic fields and the behavior of oxygen gas dissolved in aqueous solution.

In our previously reported experiment using an electromagnet with 1.0 T and the gradient of 10 T/m, redistribution of dissolved oxygen was observed during oxygen desorption and absorption processes, but no redistribution of dissolved oxygen was observed in an equilibrium state of oxygen pressure.⁵

The effect of magnetic fields produced by a permanent magnet on oxygen dissolved in saline solution has also been studied by a Russian group.⁶

In relation to oxygen dynamics in water, we observed oxygen dynamics in air. We have observed the phenomenon that candle flames are pressed down by magnetic fields.⁷ We have also observed the phenomenon that flow patterns of gases are influenced by magnetic fields.⁸ A model called a magnetic curtain has been introduced to explain these phenomena.^{8,9} The magnetic curtain is an invisible barrier which is produced in air by the interaction between magnetic fields and paramagnetic oxygen molecules. We have demonstrated that candle flames are extinguished by the magnetic fields.¹⁰ The interception of oxygen by the magnetic curtain extinguishes flames. To explain the mechanism of magnetic curtain, a collision model has been simulated, introducing a technique of molecular dynamics.¹¹ We observed the oxygen concentration in air by a manometer, however, the oxygen concentration was not influenced.

The purpose of this paper is to investigate the influence of intense magnetic fields up to 8 T on oxygen gas dissolved in water. An experiment was carried out to determine the relationship between the applied magnetic field and spatial distributions of oxygen concentration in water. A definite redistribution of oxygen concentration was realized by magnetic fields with 8 T and the gradient of 50 T/m.

II. METHOD

The experimental setup is shown in Fig. 1. We used a horizontal type of superconducting magnet with a bore 100 mm in diameter and 700 mm long as shown in Fig. 2. It produces strong magnetic fields up to 8 T and the gradient of 50 T/m. When the magnet produces 8 T at its center, the maximum product of the magnetic field and the gradient is $400 \text{ T}^2/\text{m}$ at $z = \pm 75 \text{ mm}$, where the z axis is directed to the bore axis.

An acrylic cylindrical water chamber (30 mm in diameter, 620 mm long) was filled 100% with distilled water. The

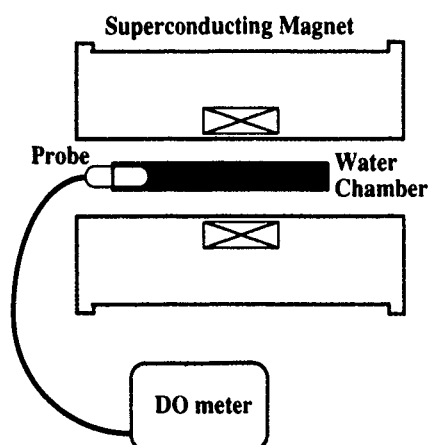


FIG. 1. Experimental setup. A horizontal type of superconducting magnet with a bore 100 mm in diameter produced magnetic fields up to 8 T. An acrylic chamber filled with distilled water was inserted into the bore of the magnet. The water chamber was exposed to magnetic fields, and the oxygen concentration was measured by a dissolved-oxygen (DO) meter.

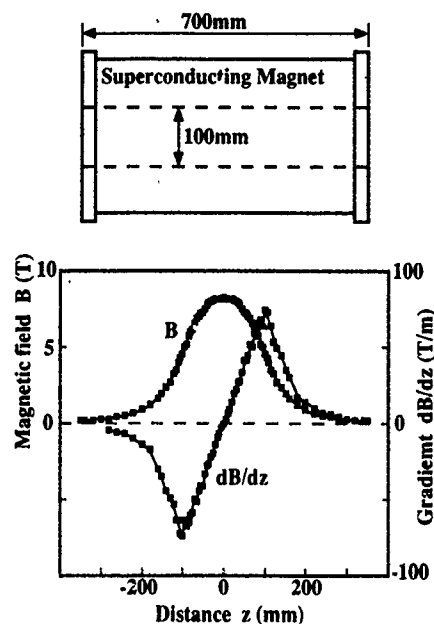


FIG. 2. The shape of the superconducting magnet and magnetic field B , and the gradient of magnetic field with respect to the bore axis, or z axis dB/dz .

dissolved oxygen concentration was controlled by introducing oxygen gases into the distilled water.

The cylindrical chamber was inserted into the bore, and the dissolved oxygen concentration was measured by a dissolved-oxygen meter (DO meter). The probe of the DO meter was fixed at the edge of the chamber. The chamber was moved together with the probe in the direction of bore of the magnet.

III. RESULTS AND DISCUSSION

The effect of an 8 T magnetic field on dissolved oxygen concentration is shown in Fig. 3. The probe fixed at the cylindrical chamber was inserted into the center of the magnet from the edge of the bore, the probe always looked toward the center of the magnet. Before the cylindrical chamber was inserted into the bore, the dissolved oxygen concentration in an equilibratory state was 7.8 mg/l at 25 °C. The chamber

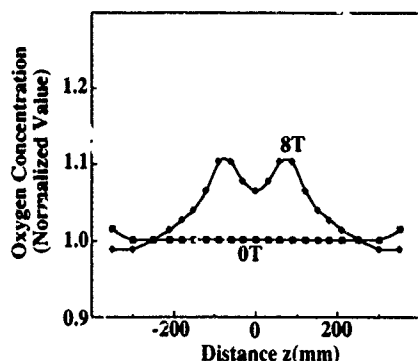


FIG. 3. Spatial distribution of oxygen concentration in water. The chamber was inserted into the center of the magnet from the edge. The probe of the DO meter always looked toward the center of the magnet.

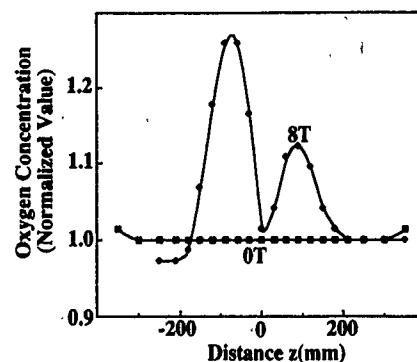


FIG. 4. Spatial distribution of oxygen concentration in water. The chamber was passed through the bore. The probe of the DO meter looked toward the edge of the bore after the probe passed through the magnet's center.

was exposed to 8 T magnetic fields. At the edge of the superconducting magnet, the dissolved oxygen concentration slightly decreased to 7.7 mg/l. The dissolved oxygen concentration gradually increased to 8.6 mg/l at $z = \pm 50$ mm, and 8.3 mg/l in the center of the magnet. The data in Fig. 3 were normalized by the value in an equilibratory state, i.e., 7.8 mg/l.

We also measured the oxygen concentration in a different procedure. The results are shown in Fig. 4. The probe was passed through the bore from one edge to the other. Before the probe passed through the center of the magnet, it detected increased oxygen concentration. When the probe passed through the center of the magnet, it detected an even higher oxygen concentration.

Because oxygen molecules were attracted toward the center of the magnet, the probe of the DO meter sensed more oxygen molecules when the head of the probe looked toward the edge of magnet's bore.

To observe more clearly the redistributions of oxygen concentration by gradient magnetic field, we introduced oxygen gases into the distilled water so that the oxygen concentration was saturated. The results are shown in Fig. 5. Compared to the distilled water, the oxygen concentration of the oxygen-bubbled water (oxygen introduced into the distilled water) in the center of the magnet increased about 20%. The

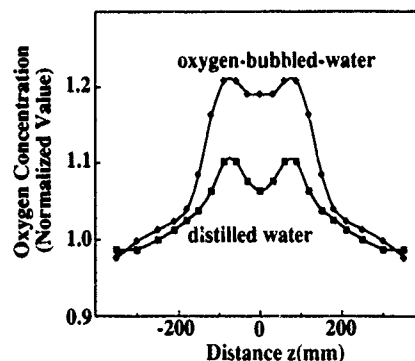


FIG. 5. Spatial distribution of oxygen concentration in water (comparing distilled water to oxygen-bubbled water).

results obtained show that the magnetic force affects dissolved oxygen in water.

In the present study we used a superconducting magnet which produced strong magnetic fields up to 8 T and a gradient of 50 T/m, and the magnetic force of 400 T²/m was strong enough to act on the movement of oxygen molecules dissolved in water.

ACKNOWLEDGMENTS

This work was supported in part by grants from the Ministry of Education, Science and Culture in Japan, and Nissan Foundation.

¹*Biological Effects of Magnetic Fields*, edited by M. F. Barnothy (Plenum, New York, 1964).

²*Biological Effects of Magnetic Fields*, edited by M. F. Barnothy (Plenum, New York, 1969), Vol. 2.

³H. Aceto, Jr., C. A. Tobias, and I. L. Silver, IEEE Trans. Magn. **MAG-6**, 386 (1970).

⁴E. H. Frei, IEEE Trans. Magn. **MAG-8**, 407 (1972).

⁵S. Ueno and K. Harada, IEEE Trans. Magn. **MAG-18**, 1704 (1982).

⁶B. E. Kraccen, *Magnetic Treatment of Water* (in Russian) (XHMNR, Moscow, 1982).

⁷S. Ueno and K. Harada, IEEE Trans. Magn. **MAG-22**, 868 (1986).

⁸S. Ueno and K. Harada, IEEE Trans. Magn. **MAG-23**, 2752 (1987).

⁹S. Ueno, J. Appl. Phys. **64**, 6030 (1988).

¹⁰S. Ueno, J. Appl. Phys. **65**, 1243 (1989).

¹¹S. Ueno and M. Iwasaka, J. Appl. Phys. **67**, 5901 (1990).

Properties of diamagnetic fluid in high gradient magnetic fields

S. Ueño and M. Iwasaka

Biomagnetics and Biosystems Laboratory, Department of Computer Science and Communication Engineering, Kyushu University, Fukuoka 812, Japan

This study focuses on the properties of diamagnetic fluid in static magnetic fields up to 8 T with the gradient of 50 T/m. We used a horizontal type of superconducting magnet with a bore 100 mm in diameter and 700 mm long. We observed the phenomenon that the surface of the water was pushed back by magnetic fields of higher gradients. Two "frozen" cascades were formed at $z = \pm 50-80$ mm; the surface of the water near the center of the magnet was parted, and the bottom of the water chamber appeared. The water level at both ends of the chamber was lifted up. In order to investigate the hydrodynamics of diamagnetic fluid in magnetic fields, we made a fluidic circuit with plastic tubing which passed through the superconducting magnet's bore. When magnetic fields in the center of the bore were changed from 0 to 8 T, the flow velocity of distilled water decreased, and the flow was stopped at 8 T. A stress analysis of diamagnetic fluid in magnetic fields was carried out to explain the mechanism of these phenomena. The hydrodynamics of diamagnetic fluid in $\sim 400 \text{ T}^2/\text{m}$ is able to compare with that of ferromagnetic fluid in weak magnetic fields. Studying the role of diamagnetic fluid in gradient magnetic fields is important in understanding the mechanism of biological effects of magnetic fields.

I. INTRODUCTION

Water, which is a diamagnetic material, is one of the most general and abundant diamagnetic fluids. It is an interesting problem for the human being whether or not magnetic fields have any influence on water. Diamagnetic water is often used for calibration and correction in determining magnetic susceptibilities of materials by the magnetic balance systems.

However, little has been observed about the hydrodynamic behavior of water, or diamagnetic fluid, in horizontal magnetic fields of 100–1000 T^2/m order.

In this paper, we investigate the dynamic behavior of water in high gradient magnetic fields, using a horizontal type of superconducting magnet, which produces magnetic fields up to 8 T. We carry out a stress analysis of a diamagnetic fluid in high gradient magnetic fields. Furthermore, we show a model experiment for effects of magnetic fields on water flow.

II. METHODS

A. Magnetic fields exposure system

We used a horizontal type of superconducting magnet with a bore 100 mm in diameter and 700 mm long. When the magnet produced 8 T at its center, the maximum product of the magnetic field and the gradient was 400 T^2/m at $z = \pm 75$ mm, where the z axis was directed to the bore axis. A distribution of magnetic fields is shown in Fig. 1.

B. Water chamber

A water chamber, 50 mm wide, 23 mm high, and 700 mm long was filled 50% with distilled water, which is a diamagnetic material. The water chamber was inserted into the bore of the magnet.

C. Hydrodynamic experiments

In order to investigate the hydrodynamics of diamagnetic fluid in magnetic fields, we formed a fluidic circuit with plastic tubing which passed through the superconducting magnet's bore as shown in Fig. 2. We used a plastic tubing made of vinyl chloride with 8 mm in inner diameter. Distilled water ran in the tube along the z axis of the magnet's bore. Changes of flow velocities were measured by a flow meter. The tubing was hard enough to eliminate contributions of any stress induced changes in the plastic tubing.

To investigate the effects of dissolved oxygen on the flow of diamagnetic fluid, oxygen gas was bubbled into distilled water, and the flow velocities were measured.

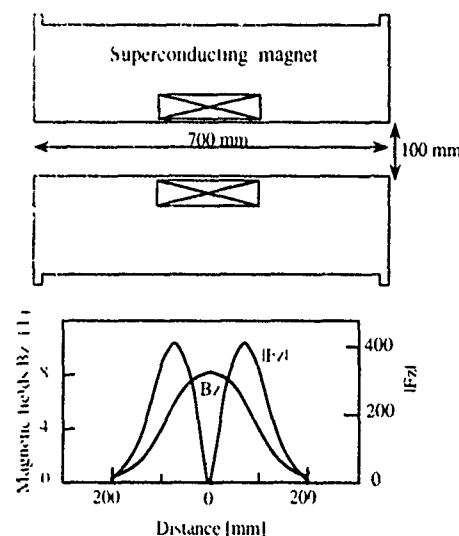


FIG. 1. Horizontal superconducting magnet and the distributions of magnetic fields. F_z is the product of magnetic fields and gradient.

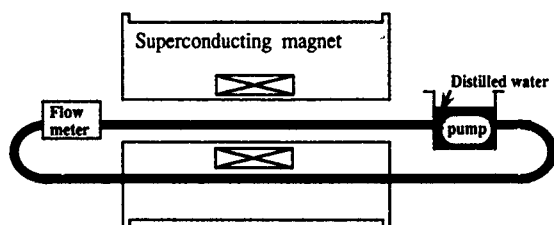


FIG. 2. Experimental setup for water flow experiment with a fluidic circuit with plastic tubing which is passed through the superconducting magnet's bore.

III. RESULTS AND DISCUSSION

A. Behavior of water in magnetic fields

When the water chamber was inserted into the bore of the magnet, we observed the phenomenon that the surface of the water was pushed back by magnetic fields of higher gradients. Two "frozen" cascades were formed at $z = \pm 50-80$ mm as shown in Fig. 3; the surface of the water near the center of the magnet was parted, and the bottom of the water chamber appeared. The water level at both ends of the chamber was lifted up.

We also realized the "frozen" cascades with agarose gel. The agarose solution was coagulated into a gel state in the superconducting magnet. Figure 4 shows that the surface of the agarose gel was formed in the same manner as in the water experiment.

A stress analysis was carried out to explain the mechanism of the formation of the "frozen" cascades.

The stress tensor of a diamagnetic fluid (in indicial notation) is given by

$$T_{ij}^m = (p^m + \mu_0 H^2/2 + \mu_0 M H/2) n_i, \quad (1)$$

$$p^m = -\mu_0 M H/2 + \mu_0 \int_0^H M dH - \rho g z + \text{const}, \quad (2)$$

where $\mathbf{n} = (n_i, n_j, n_k)$ is a unit vector that is perpendicular to the water surface, p^m is the static fluid pressure, μ_0 is the

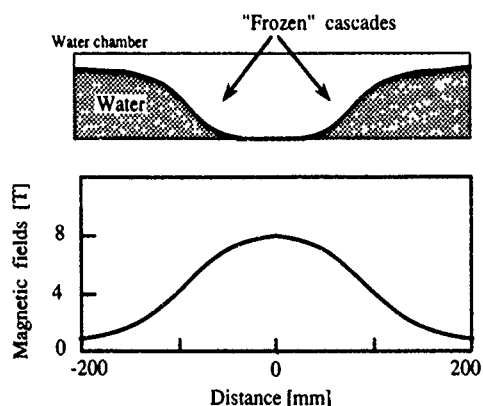


FIG. 3. An illustration of "frozen cascades" of water in gradient magnetic fields up to 8 T.

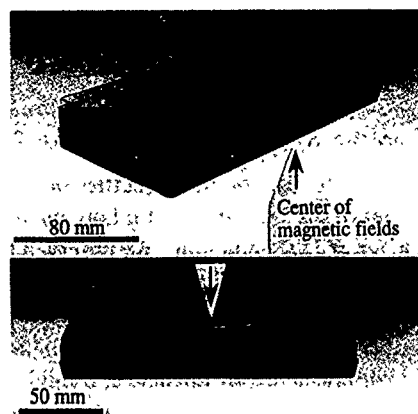


FIG. 4. A photograph of "frozen cascades" of agarose gel that formed in magnetic fields up to 8 T.

magnetic permeability, ρ is mass per unit volume, g is gravitational constant, M is the magnetization of diamagnetic fluid, and H is a magnetic field.¹

On the other hand, the stress tensor that is outside of the diamagnetic fluid is given by

$$T_{ij}^0 n_j = -(p^0 + \mu_0 H^2/2) n_i, \quad (3)$$

where p^0 is the environmental pressure.

On the surface of the "frozen" cascades, $T_{ij}^m n_j$ equal to $T_{ij}^0 n_j$.

Equations (1), (2), and (3) can be combined to give

$$z = h = (\mu_0/\rho g) \int_0^H M dH = \chi_m \mu_0 H^2/2 \rho g. \quad (4)$$

The distribution of h given by Eq. (4) is shown in Fig. 5. It seems that the curve in Fig. 5 corresponds to the surface lines of the "frozen" cascades. The behavior of water in

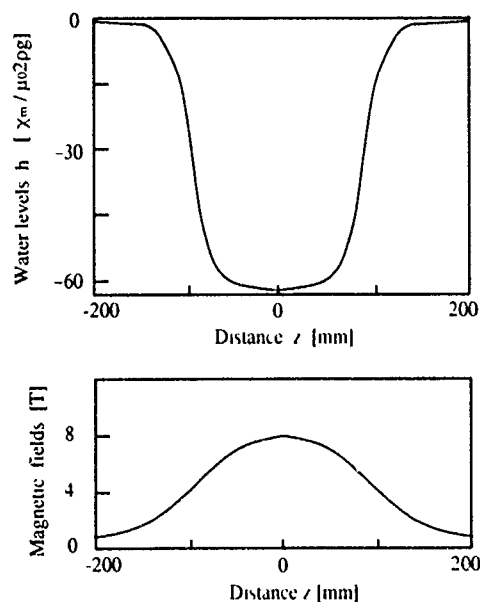


FIG. 5. Formation of "frozen cascades" of diamagnetic fluids. The curve is obtained by stress analysis.

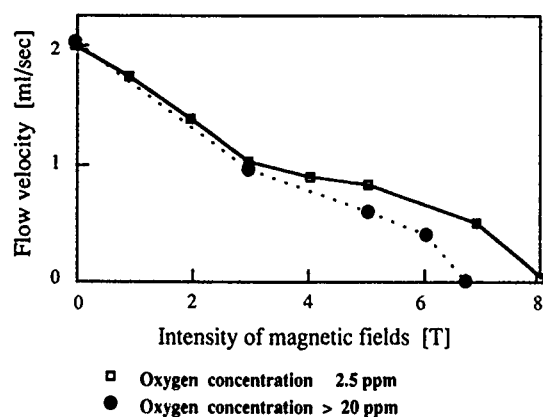


FIG. 6. Effects of magnetic fields up to 8 T on water flow.

horizontal high gradient magnetic fields and the formation of "frozen" cascades are understood by this stress analysis.

In reference to the properties of diamagnetic materials in vertical magnetic fields, there is a report about a numerical analysis of the necessary conditions for magnetic levitation of diamagnetic particles.²

B. Hydrodynamic experiments

Figure 6 shows the results of an experiment of water flow in magnetic fields. When magnetic fields in the center of the bore were changed from 0 to 8 T, the flow velocity of distilled water (2.0 ml/s, 18 mm/s) decreased and the flow was stopped at 8 T.

To investigate the effects of paramagnetic molecules, or dissolved oxygen, on the flow of diamagnetic fluid, oxygen gas was bubbled into distilled water. Changes of flow velocity resulting from the interaction of paramagnetic and diamagnetic materials with magnetic fields were observed. As shown in Fig. 6, the result was that flow velocity decreased compared to that of fluid without dissolved oxygen.

The flow of distilled water containing dissolved oxygen (2.0 ml/s, 18 mm/s) was stopped when the magnetic field in the center of the bore was 6 T. These results show that flow of diamagnetic fluid is controlled by 8 T magnetic fields.

IV. CONCLUSION

We have observed the phenomenon that diamagnetic fluid, such as water, behaves dynamically in high gradient magnetic fields of up to 8 T and 50 T/m. The hydrodynamics of diamagnetic fluid in $\sim 400 \text{ T}^2/\text{m}$ is able to compare with that of ferromagnetic fluid in weak magnetic fields.

Using a horizontal type of superconducting magnet with high gradient fields allowed us to observe a phenomenon; the surface of the water near the center of the magnet was parted, and the bottom of the water chamber appeared.

We also have shown experimental results that indicate a possibility in flow control of diamagnetic fluid by magnetic fields of up to 8 T and 50 T/m.

These results indicate that when a living body is exposed to magnetic fields of $100\text{--}500 \text{ T}^2/\text{m}$ order, diamagnetic liquids such as water in tissues are affected by magnetic forces. Remarkable effects of high gradient magnetic fields are expected in blood circulation, cerebral spinal fluid system, and other intracellular and extracellular solutions.

Studying the role of diamagnetic fluid in gradient magnetic fields is important in understanding the mechanism of biological effects of magnetic fields. The phenomena observed in the present experiments will provide a new aspect to applied physics and biomagnetics.

ACKNOWLEDGMENTS

This work was supported in part by grants from the Ministry of Education, Science and Culture in Japan, and Nissan foundation.

¹R. E. Rosensweig, *Ferrohydrodynamics* (Cambridge University, Cambridge, 1985).

²T. B. Jones, *J. Appl. Phys.* **50**, 5057 (1979).

Influence of ultraworking frequency alternating weak magnetic field on the microvasculature of mice (abstract)

Ningjiang Yang^{a)}

Department of Pathology, 465th Air Force Hospital, Jilin City 132011, China

Changmin Zhang^{b)}

Department of Physiotherapy, 465th Air Force Hospital, Jilin City 132011, China

The physical effect produced by the ultraworking frequency alternating weak magnetic field (UWFAWM) is demagnetization. We used two methods to study the influence of UWFAWM on the microvasculature of Kunmin mice. Method 1 (in vivo) included 21 mice (the experimental group 11 and the control group 10). Method 2 (in vitro) included 25 mice (the experimental group 13, the control group 12). Each group was put in the coil of the JDM-1 Type Demagnetometer which produced UWFAWM. The coil was electrified for the experimental groups, but not for the control groups, for 20 min, once a day. (1) Method 1. On the 10th day of demagnetization, the surface microvasculature diameters of liver and mesenterium were measured in two groups.¹ The results showed that those in the experimental group ($25.05 \pm 3.92 \mu\text{m}$ and $24.44 \pm 4.7 \mu\text{m}$, respectively) were markedly greater than those in the control group ($10.70 \pm 1.72 \mu\text{m}$ and $18.37 \pm 1.93 \mu\text{m}$, respectively). (2) Method 2. On the 40th day of demagnetizing, we killed all mice and immediately preserved the brain, heart, lung, liver, kidney, stomach, intestine, and submandibular gland in 10% formalin, then used continuous paraffin sections of $5 \mu\text{m}$ and HE stain, and measured the microvascular diameter of each group.² The results showed that mean diameters of the organs in the experimental group were also significantly greater than those in the control group ($p < 0.01$). This study confirms that UWFAWM can dilate the microvasculatures of various organs, resulting in local arterial hyperemia of the organ, advance local tissue metabolism, and an increase in organic function, thus providing a basis for treating some diseases and for health care.

^{a)}Member of Chinese Institute of Pathology.

^{b)}Member of Chinese Institute of Physiology.

¹C. Zhang *et al.*, Chin. J. Phys. Medicine 11, 117 (1989).

²N. Yang *et al.*, Chin. J. Biomagn. 5, 166 (1991).

Enzymatic oxidation-reduction processes under magnetic fields up to 8 T (abstract)

M. Iwasaka and S. Ueno

Department of Computer Science and Communication Engineering, Biomagnetics and Biosystems Laboratory, Faculty of Engineering, Kyushu University, Fukuoka 812, Japan

The question of whether magnetic fields affect enzymatic activities or not is of considerable interest in biochemistry and in biomagnetics. Xanthine oxidase, contained in liver, lungs, intestine, and other organs, catalyzes the degradation of hypoxanthine to xanthine, and xanthine to uric acid, which is the terminal waste of purine nucleotides in mammals. During the oxidation of xanthine, the enzyme releases superoxide anion radicals as intermediates which reduce ferricytochrome *c* (Fe^{3+}). Superoxide anion, as well as any type of free radical, is also paramagnetic. The study is focused on whether these magnetically related enzymatic activities can be affected by magnetic fields. There is a possibility that free radicals, as intermediates, can be modified by magnetic fields of specific intensities. In our previously reported study, we examined a possible effect of magnetic fields up to 1.0 T on biochemical reaction catalyzed by xanthine oxidase, and obtained negative results.¹ In the present abstract, we examine the effect of magnetic fields up to 8 T on this oxidation-reduction process. Reduced cytochrome *c* (Fe^{2+}) has an absorption maximum at 550 nm which can be detected by a spectrophotometer. Xanthine oxidase was assayed by superoxide dismutase—inhibitable reduction of cytochrome *c*. We measured optical absorbance of reduced cytochrome *c* by superoxide anion which was produced by the reaction catalyzed by xanthine oxidase. The absorbances of the mixture exposed to an 8 T magnetic field at 25 °C were higher than control samples in the re-oxidation process of cytochrome *c*. The results show that the 8 T magnetic fields altered the rate of reduction of cytochrome *c* by superoxide anion which was produced by the reaction catalyzed by xanthine oxidase. It may conclude that the electron transfer from xanthine to molecular oxygen or the transfer from superoxide anion to cytochrome *c*, can be affected by the magnetic fields up to 8 T.

¹ S. Ueno and K. Harada, IEEE Trans. Magn. MAG-22 (No. 5), 868 (1986).

Induction of mutations by magnetic field for the improvement of sunflower (abstract)

V. Kiranmai

Cytogenetics and Tissue Culture Lab., Dept. of Botany, Osmania University, Hyderabad 500 007, A.P., India

Mutagenic effect of magnetic field was studied in two varieties of *Helianthus annuus* L. var. S.S.56 and CO-2. Dry seeds of both the varieties were exposed to 1000, 2000, and 3000 G of magnetic field for over 90 min. The parameters screened were germination percentage, plant height, days to flowering, days to maturity, and yield of the plant. The mutants obtained were tall mutant, dwarf mutant, early flowering mutant, branched mutant, bold seeded mutant, and stripped seed mutant. The mutants were screened for biochemical analysis. Oil content and fatty acid analysis of the seeds were done by NMR and GLC techniques, respectively. Quantitative and qualitative analysis of the proteins in leaf and seeds were done for all the mutants obtained, along with the electrophoretic studies among the three doses studied, 2000 G was found to produce positive mutations in both varieties of sunflower.

The magnetic transformation of iron hydroxides under the action of micro-organism (*Azotobacter vinelandii*) (abstract)

Nadezda V. Verkhovtseva
State University, Yaroslavl, Russia

Irina V. Shpilkina
Polytechnical Institute, Yaroslavl, Russia

Vyacheslav F. Babanin
Polytechnical Institute, Yaroslavl, Russia

To analyze the action of *Azotobacter vinelandii* intact cells on synthetic high-dispersed iron hydroxides, Mössbauer spectroscopy and magnetic measurements were used for different conditions: for the nitrogen-free medium and for the NH-containing medium. The preparations of *Azotobacter vinelandii* obtained on the nitrogen-free medium with decreased acidity is characterized by relatively high contents of paramagnetic combinations ($\chi_{\text{par}} = (6.6 \dots 31.4) \times 10^{-6} \text{ sm}^3/\text{g}$, $I_{\text{sat}} = (0.12 \dots 0.73) \times 10^{-3}$ at 12 day cultivations, $\chi_{\text{par}} = (8.1 \dots 23.2) \times 10^{-6} \text{ sm}^3/\text{g}$, $I_{\text{sat}} = (0.07 \dots 0.93) \times 10^{-3}$ at 35 day cultivation). The quantity of magnetic ordered combinations in these samples is greater than 1.5–7 times that in bacteria at pH=7. The paramagnetic attributes of samples in the medium with NH is decreased more in 12 day culture (up to 50% compare to nitrogen-free variation) then in 35 day culture (up to 20%). The presence of doublets in Mössbauer spectra at different conditions (room temperature in damp, air-dry states, and frozen at the 100 K state) and strong differences in probability of sorption of Mössbauer radiation of damp preparations allow us to conclude that magnetic ordered combinations in the type of crystallines with particle size <10 nm are present in the composition of preparations. It is found from magnetic measurements that at pH<7 the paramagnetic component of susceptibility and magnetic saturation is high. At pH=7 the most intensive decrease of susceptibility and magnetic saturation is medium with nitrogen and at large aeration.

Magnetic properties of heterotrophic bacteria (abstract)

Nadezda V. Verkhovceva and Irina N. Glebova
University of Yaroslavl, Yaroslavl, Russia

Anatoly V. Romanuk
Polytechnical Institute of Yaroslavl, Yaroslavl, Russia

The magnetic properties (magnetic susceptibility and saturation magnetization) of six species of heterotrophic bacteria were studied: *alcaligenes faecalis* 81, *arthrobacter globiformis* BKM 685, *bacillus cereus* 8, *leptothrix pseudo-ochracea* D-405, *proteus vulgaris* 14, and *seliberia stellata*. It has been shown that the magnetic properties of bacteria depend on (1) the peculiarity of the micro-organism (species-specific and connected with cultivation conditions); (2) the source of the iron in the media. Most of the bacteria are diamagnetic in media with a minimum of iron ($\chi_{\infty} = -7.2 \dots -3 \times 10^{-6} \text{ sm}^3/\text{g}$). The spore forming species (*bacillus cereus*) has increased diamagnetism. Usually the bacteria are paramagnetic in iron-containing media because they concentrate into Fe compounds. The paramagnetism of the iron-concentrating species (*arthrobacter globiformis* — $\chi_{\text{par}} = 2.4 \times 10^{-6}$, *leptothrix pseudo-ochracea* $\chi_{\text{par}} = 11.0 \times 10^{-6}$ and *seliberia stellata* $\chi_{\text{par}} = 3.2 \times 10^{-6} \text{ sm}^3/\text{g}$) depends, in general, on magnetically ordered compounds. Iron compounds not accumulated by *proteus vulgaris* and these species are always diamagnetic.

Spin-glass structures in biological systems (abstract)

Alexandre I. Tsapin and L. A. Blumenfeld

Institute of Chemical Physics, Kosygina Strasse 4, 117977, Moscow, Russia

We have discovered spin-glass structures in different biological systems like animal and plant tissues, cells, chloroplasts, mitochondria, etc. These structures were detected by the ESR method. This work has been done using a synchronous culture of yeasts, *saccharomyces cer.* To detect spin-glass structures in a biological system, the sample must be cooled in the presence of a strong magnetic field, from 77 to 10 K. After such cooling, we recorded the ESR signal at g factor about 3.0 caused by spin-glass structures. The rotation of the sample at 10 K relative to the permanent magnetic field (always present in ESR experiments) leads to the significant change in the intensity of the ESR signal as well as in its shape. The curve of the dependence of the ESR signal intensity on the magnetic field in which the sample was cooled is S-shaped. The cooling of the same sample in zero magnetic field resulted in the absence of the ESR signal at $g=3.0$. It had been shown that the maximum ESR signal at g factor about 3.0 was reached 15 min before the beginning of mitosis. The study of the properties of the ESR signal at $g=3.0$ allowed us to make the conclusion that the paramagnetic centers responsible for this signal have been formed by Fe(II) ions localized at the chromosomes. Formed during mitosis, spin-glass structures which play a significant role in cell biology, can be detected only by the ESR method in field cooling experiments.

The testing of action of chemical extracts on soils by magnetic methods (abstract)

Vyacheslav F. Babanin, Irina V. Shpilkina, and Alexandr V. Ivanov

Yaroslavl Polytechnical Institute, Yaroslavl, Russia

The participation of soil iron in the formation of physics-chemical features in feed of plants and microorganisms is well known. Because of the active role of Fe in soil landscapes the Fe state is taken into account in investigations of the genesis of soils. In spite of a relatively high content of iron in soils up to 40%–45% (relative to Fe) its numerical forms are diagnosed in a complex way by Ronthgen diffractometry, differential thermal analysis, and microscopy. Thus, chemical extracts are widely used in soil science. Extracted Fe is considered to be of amorphous, strong or weak crystallized forms. These gradations are of wide use but they are not correct. This is established by some authors by means of magnetic measurements and Mössbauer spectroscopy [Jeanory *et al.*, *Sci. Solids* 135 (1986)] before and after magnetic separation and chemical extracts [Fine and Singer, *Soil Sci. Soc. Am. J.* 53, 191 (1989)]. We used the measurements of magnetic susceptibility and saturation and nuclear gamma resonance for the usual soils and electron paramagnetic resonance for weak magnetic Fe containing minerals (before the extract). Our results are comparable with the above research and lead to the next conclusions: (1) ordered alternations of magnetic parameters and results of action of extracts are absent; (2) the Mehra–Jackson extract (sometimes the Tamm's extract) often extracts the crystallized magneticordered and paramagnetic silicate and superparamagnetic forms of Fe; (3) magnetic susceptibility and magnetic saturation increase in some types of soils (brown earth, ferralsol, alluvial soil) at dissolution of the aluminosilicate part of soils because of enrichment by chemically strong particles of magnetite; (4) the conclusions on extracts (as far as crystallized silicate amorphous forms) do not have generalized characteristics.

The magnetic diagnostics of cosmic and industrial silt in humus horizons of soils (abstract)

Vyacheslav F. Babanin and Irina V. Shplkina
Polytechnical Institute, Yaroslavl, Russia

Sergei A. Shoba
Lomonosov University, Moscow

Alexander V. Ivanov
Polytechnical Institute, Yaroslavl, Russia

In the early 50s the increase of magnetic susceptibility in head horizons of soils has been observed. The reason was accepted to be forest and steppe fire. Later we discovered that the increasing of susceptibility and magnetic saturation was observed more clearly in the soils developed on weak magnetic native rock (loam, carbonate) and the magnetic fraction was separated from these soils in a more simple fashion. An abnormal increase in magnetic parameters is observed in primitive soils and the debris layer of dry forest (particularly of pine forest). The investigations have shown that magnetic particles (MP) are contained in ash of electrostations, in buried and modern soils, in humocoll and coal sheets, and in air of industrial cities and of the country. A high magnetic separated fraction (MV) contains particles (P) that differ by morphology and color. MF of soils is separated in a difficult manner from the rest mass (it also contains α -Fe, magnetite, hematite) and is contaminated by magnetic particles from native rock. We obtained that only spherical particles contribute to the soil magnetism from $(10...50) \times 10^{-6} \text{ sm}^3/\text{g}$ to $(100...150) \times 10^{-6} \text{ sm}^3/\text{g}$. MP come into modern soils from all sources. Magnetic particles are well conserved in automorphic and nonlogging buried soils, and in humocoll layers. Among humocoll layers investigated by us there were layers dating over 50 thousand years ago.

Dislocation etching of flux grown strontium hexaferrite single crystals (abstract)

Urvashi Raina, Sushma Bhat, and P. N. Kotru
Department of Physics, University of Jammu, India

F. Licci
Istituto MASPEC-ONR, via Chiavari, Param 18/A, Italy

Hexagonal hard ferrites like $\text{SrFe}_{12}\text{O}_{19}$ are technically interesting materials not only because they are the traditional permanent magnets but also as emerging magnetic recording media and as potential magneto-optic devices. For these reasons the study of dislocations in these samples is quite significant. Flux grown single crystals of $\text{SrFe}_{12}\text{O}_{19}$ are etched in 37% HNO_3 at 100 °C and 85% H_3P_4 at 120 °C. These two etchants produce hexagonal pits on (001) planes that are established as dislocation etchants by performing the following experiments: (1) successive etching for prolonged periods resulting in persistent point bottomed etch pits at all the stages; (2) etching of matched (0001) cleavages in similar, as well as dissimilar, etchants which produce 1:1 corresponding point bottomed etch pits on a pair of the matched cleavages; (3) etching of low angle grain boundaries which consist of a grid of equally spaced edge dislocations. An equally spaced row of etch pits is obtained along the grain boundaries. Hexagonal etch pits with smooth sloping planes are normally produced. Among such pits, unusual etch pattern features including pits with rhythmically and irhythmically spaced terracings, eccentric pits, small point bottomed pits within a large flat bottomed pit with differing geometrical centers, and flat bottomed pits with beaked centers, are obtained. Unusual deviations from the perfect match of etch patterns on certain matched (0001) cleavages are examined critically. It is thought that these unusual etch patterns are due to bending, branching, and stepping of dislocations. The terracing of pits is attributed to the segregation of impurities along dislocation lines.

Dipole-dipole interactions in $\text{KEr}(\text{MoO}_4)_2$ (abstract)

A. G. Anders, S. V. Volotskii, and O. E. Zubkov

B. I. Verkin Institute for Low Temperature Physics and Engineering, Ukrainian Academy of Science, Kharkov, Ukraine

The model of a dipole-dipole magnet previously developed^{1,2} has applied to a $\text{KEr}(\text{MoO}_4)_2$ crystal with two paramagnetic ions in an orthorhombic unit cell. The erbium ion in the compound has a large anisotropy of an effective g tensor which, in turn, leads to Ising-like behavior in the magnetic subsystem. As had been done earlier,² we had calculated the dipole configuration with the lowest energy, thus obtaining the ground-state structure that would appear at the magnetic phase transition. This dipole structure consists of ferromagnetic chains aligned along the c axis and antiferromagnetically coupled along a and b axes. The results were compared with recently done measurements of magnetic moment and low-temperature magnetic susceptibility.³ Calculated dipole ground energy $E_{\min} = -1.325$ K is in reasonable agreement with the experimental value of $T_n = 0.9$ K. The obtained easy-axis direction along the c axis also agreed with experiment. The phase transition observed in crystal at $H \parallel c$ in our model results in a transition to a ferromagnetic structure with $H_{cr} = 700$ Oe. The last agreed with measured $H_{cr} = 800$ Oe so one should conclude that a pure dipole model could well describe the main features of $\text{KEr}(\text{MoO}_4)_2$. At the same time our model could not explain the other phase transition that took place at $H = 1.5$ kOe ($H \parallel a$). To understand this transition one probably should also consider a small anisotropic exchange interaction.

¹J. M. Luttinger and L. Tisza, *Phys. Rev.* **70**, 954 (1946).

²T. Nimeyer, *Phys.* **57**, 281 (1972).

³E. N. Khatsko *et al.*, *Proceedings of the 18th Conference on Magnetism*, 1988, p. 714.

Database of magnetochemistry in solutions (abstract)

O. Ju. Tarasov and A. G. Vinogradov

Chemical Faculty, Kazan University, Kazan 420008, Russia

The database (DB) of magnetochemistry in solutions was created to systematize and to critically review data of the magnetic susceptibility of liquids, solutions, and substances in solutions. The database "MagChemSol 1.0" was made on a MFOXPLUS base and may be supported by DBASEIII PLUS or higher. Search fields include substances, solvent, condition and method of investigation, critical magnetochemistry characteristics, and references to literature. All material is printable and the database can change and expand itself. System requirements include IBM PC or compatible with 640 Kb of RAM, 5 in. and 3 in. diskette drive or hard-disk, and DOS 3.30 or higher; printers are Epson or compatible. The DB "MagChemSol 1.0" version includes about 1000 data entries according to the magnetochemical properties, the majority solvents in general use some diamagnetic and paramagnetic salts, and also the complex compounds of d and f elements in the solutions.

The Fund of Youth Grants of Kazan University is acknowledged for financial support of this work.

The magnetodynamic filters in monitoring the contaminants from polluted water systems (abstract)

R. Swarun and Bharat Singh^{a)}

Department of Physics, D. S. College, Aligarh 202001 U. P., India

The magnetic interaction seems to influence the "structural memory" of water systems which is quenched in ideally pure water. The sedentary lifetime of each water molecule is extremely short (10^{-10} s) and its molecular structures may be influenced by some physical effect like magnetic field treatment, its space time gradients, water velocity, pressure drop, etc. in the interpolar space, so as to yield a noticeable temporal magnetopotential development characterizing the properties of homogeneous and heterogeneous water systems. This principle is also extended to prevailing water systems which always contain various impurities, gas, molecules, ions, microscopic particles in random order. Still the existence of structural memory may be verified by reliable experimental data. The magnetopotential curves of different water systems depict the design and develop—software package for constructing the magnetodynamic-filters superior to the existing techniques on pollution studies like remote sensing, muon spin resonance, laser spectroscopy, nuclear techniques, the gamma ray peak efficiency method, trace elemental characterization due to NBS, neutron activation analysis, and graphite furnace atomic absorption spectrometer. The physiochemical characteristics of water calibrated in terms of magnetopotential curves change with the removal of dissolved gasses, impurities, thermal activation, etc. and the algae, bacteria, phosphates, etc. have been removed at a rapid rate. The magnetodynamic study of ganga water proves it to be an extremely pure and highly resourced fluid.

^{a)}Present address: Dept. of Electronic Science, Univ. of Delhi South Campus, New Delhi-110021, India.

AUTHOR INDEX

- aan de Stegge, J.-(10) 6424, 6440
aan de Stegge, J. B. F.-(10) 6709
Abad, H.-(10) 5725
Abd-Elmeguid, M. M.-(10) 6741
Abdul-Razzaq, W.-(10) 6567
Abe, M.-(10) 6094, 6804, 7171
Abele, M. G.-(10) 6993
Abele, Manlio G.-(10) 6990
Abell, J. S.-(10) 5850
Abraham, M. M.-(10) 7030
Acet, M.-(10) 6069, 7012, 7015
Adams, C. P.-(10) 6318
Adly, A. A.-(10) 5502
Aguilar-Sahagun, G.-(10) 7000
Aharoni, Amikam-(10) 5891
Ahmad, M.-(10) 6190
Ahmed, M. Ramadan-(10) 6030
Akioka, K.-(10) 6631
Aktas, B.-(10) 6819
Alba, M.-(10) 5826
Alberts, H. L.-(10) 5665, 7149
Albrecht, A. S.-(10) 5535
Alexander, Chester, Jr.-(10) 6754
Algarabel, P. A.-(10) 6223
Ali, K. F.-(10) 6030
Ali, Naushad-(10) 7128, 7161
Allen, Gary A.-(10) 6372
Allibert, C. H.-(10) 6277
Allibert, Colette H.-(10) 6658
Almeida, B.-(10) 6551
Alper, M.-(10) 6543
Al-Sharif, A. L.-(10) 6673
Altounian, Z.-(10) 5997, 6012, 6560, 7064
Amano, E.-(10) 6940, 7000
Amaral, V. S.-(10) 6513
Anders, A. G.-(10) 7186
Ankner, J. F.-(10) 6178, 6193, 6498, 6692
Antropov, V. P.-(10) 6366
Aoi, H.-(10) 6400, 6890
Araga, K.-(10) 6918
Aragoneses, P.-(10) 6315
Arai, A.-(10) 6631
Araki, S.-(10) 6379
Argyle, B. E.-(10) 6782
Arnold, Z.-(10) 5662, 7158
Arnoldussen, T. C.-(10) 6773
Arnoldussen, Thomas C.-(10) 5762
Arons, R. R.-(10) 6602, 7050
Arrott, A. S.-(10) 5695, 5713, 7006
Arroyo, J. Carlos-(10) 5568
Artigas, M.-(10) 6577
Artman, J. O.-(10) 5879, 5882
Asada, H.-(10) 6086, 6089
Asano, H.-(10) 6283
Atkinson, R.-(10) 6783, 6861
Atkinson, Ron-(10) 6786
Attenborough, K.-(10) 6543
Atwater, H. A.-(10) 6516
Auluck, S.-(10) 6298, 6301
Avgin, I.-(10) 5517
Awano, Hiroyuki-(10) 6852, 6893
Awschaloni, D. D.-(10) 6199
Ayers, J. D.-(10) 5801
Azevedo, A.-(10) 5613, 6763
Babanin, Vyacheslav F.-(10) 7182, 7183, 7184
Bach, H.-(10) 6069, 6072
Bacman, M.-(10) 6577
Bader, S. D.-(10) 6169, 6461, 7080
Baggio-Saitovitch, E.-(10) 6483, 6741, 6766
Bak, J.-(10) 5719
Balchin, M. J.-(10) 6987
Balentine, C. A.-(10) 6430
Ballantyne, Catherine C.-(10) 6959
Ballentine, C. A.-(10) 6427, 6429
Ballou, R.-(10) 6277
Banerjee, Subir K.-(10) 5925
Bao, Xiaohua-(10) 5870
Barandiarán, J. M.-(10) 6952
Barariu, Firuta-(10) 6949
Barbara, B.-(10) 5634, 6513
Barbara, Bernard-(10) 5642
Barlett, Darryl-(10) 6174
Barnard, J. A.-(10) 6930, 6934, 7067
Barnas, Jozef-(10) 6693
Barrom, Stacy-(10) 5578
Barrué, R.-(10) 6946
Barthélémy, A.-(10) 6412, 6623
Baryshev, V.-(10) 6543
Bass, J.-(10) 6699
Basso, V.-(10) 5677
Bauer, Gerrit E. W.-(10) 6704
Baumberg, J. J.-(10) 6199
Bayreuther, G.-(10) 6849
Beach, R. S.-(10) 6933
Beacom, T.-(10) 6723
Beauchamp, K. M.-(10) 6343
Bedrosian, G.-(10) 6027
Beers, K. L.-(10) 5940
Bellamy, B.-(10) 6623
Bellesis, George H.-(10) 6884
Bellouard, C.-(10) 5900
Belmans, Ronnie-(10) 6048, 6050
Belt, Roger F.-(10) 6363
Ben-Dor, L.-(10) 6720
Bennett, L. H.-(10) 5493
Bennett, W. R.-(10) 6144
Berger, A.-(10) 5598
Bergqvist, A.-(10) 5484, 5496
Berkowitz, A. E.-(10) 5562, 5639, 6097, 6613, 6622, 6912, 6933
Berry, S. D.-(10) 6124, 6688, 6691, 6692
Bertora, Franco-(10) 6990
Bertotti, G.-(10) 5490, 5677
Bertram, H. Neal-(10) 5765, 6385, 6779
Beyer, Adalbert-(10) 6049
Bhat, Sushma-(10) 7185
Bhushan, Bharat-(10) 5741, 5771, 6156
Bi, Y. J.-(10) 5850
Bian, X.-(10) 6534, 6554, 6560, 7064
Bie, Q. S.-(10) 6190
Bilic, D.-(10) 7073
Binek, C.-(10) 5856
Black, T. D.-(10) 6081
Blanco, J. M.-(10) 6315
Bland, J. A. C.-(10) 5586, 6458, 6501, 6508, 6528
Blevenec, Gilles Le-(10) 5647
Blumenfeld, L. A.-(10) 7183
Bluncson, Cherie R.-(10) 5538
Blythe, H. J.-(10) 6100
Boardman, A. D.-(10) 5630, 5631, 6804, 6804
Boatner, L. A.-(10) 7030
Bochi, G.-(10) 6430
Bödeker, P.-(10) 6492
Bødker, F.-(10) 6583
Boer, F. R. de-(10) 6522
Bogomolov, S. S.-(10) 6430
Bojarczuk, Nestor-(10) 6871
Booth, J. G.-(10) 5630
Booth, K. M.-(10) 5630
Borchers, J. A.-(10) 6477, 6498, 6592, 6691, 6692
Bornfreund, R. E.-(10) 5740
Borsa, F.-(10) 7146
Bortz, E.-(10) 5882
Bounds, C. O.-(10) 6628
Boursier, D.-(10) 6577, 6682
Bouterfas, N.-(10) 6476
Bowden, G. J.-(10) 7120, 7122
Bowen, Arlen-(10) 5750
Boyle, J.-(10) 5630
Braga, M. E.-(10) 6551
Bramwell, S. T.-(10) 5523, 5955
Brandisky, Kostadin-(10) 6050
Brard, Isabelle-(10) 5647
Brataas, Arne-(10) 6704
Bray, Ashley-(10) 5578
Breuer, M.-(10) 6741
Brewer, E. G.-(10) 6637
Brühl, K.-(10) 6184, 6492
Brooks, M. S.-(10) 6298, 6301
Broussard, P. R.-(10) 5595, 6679
Brown, L. M.-(10) 6501
Brown, P. J.-(10) 6816
Browning, V.-(10) 6610
Brubaker, W. W.-(10) 5529, 5940
Brück, E.-(10) 6522
Brunett, B.-(10) 5879
Brunsman, E. M.-(10) 5882
Bruynseraede, Y.-(10) 7079
Buan, J.-(10) 6344
Buchholz, B.-(10) 7012
Büchner, B.-(10) 6741
Buckley, M. E.-(10) 6508
Bue, M. Lo-(10) 5677
Burke, E. R.-(10) 5756, 5759, 5910, 6891
Burkhardt, G. L.-(10) 5673
Buschow, K. H. J.-(10) 5994, 6247, 7117
Cable, J. W.-(10) 6601
Cabral, Cyril, Jr.-(10) 6909
Cadieu, F. J.-(10) 6006, 6909, 6286, 6640
Cadogan, J. M.-(10) 7114, 7120, 7122
Callaby, D. Roy-(10) 6843
Callaway, J.-(10) 7024, 7041
Camblong, Horacio E.-(10) 6906, 7076
Cammarano, R.-(10) 5481
Cannell, P. Y.-(10) 5673
Cao, G.-(10) 6328, 6595
Cao, Lei-(10) 6250, 6253, 6256, 6259, 7111
Capehart, T. W.-(10) 7018
Carbucicchio, Massimo-(10) 5870
Cardoso, L. P.-(10) 6003
Carey, M. J.-(10) 6933
Carey, R.-(10) 6789, 7081, 7087
Cash, Andrew-(10) 6066
Castro, J.-(10) 6100
Cates, James C.-(10) 6754
Cava, R. J.-(10) 6603
Cavalleri, A.-(10) 5634
Cedell, T.-(10) 5656
Celinski, Z.-(10) 5583, 6187, 6473
Celotta, R. J.-(10) 6437, 6452
Cerdonio, M.-(10) 5634, 6996
Chaiken, A.-(10) 5808, 7073
Chandrapaty, S.-(10) 5940
Chang, C. R.-(10) 5794
Chang, Ching-Ray-(10) 5487, 5499, 5505, 5897
Chang, Chung-Hee-(10) 6864
Chang, J. W.-(10) 5923
Chang, Thomas-(10) 5553
Chang, W. C.-(10) 6244
Chantrell, R. W.-(10) 5574
Chao, B. L.-(10) 5667
Chappert, C.-(10) 5807
Charap, Stanley H.-(10) 5768
Chardarlapaty, S.-(10) 5529
Charles, S. W.-(10) 6583
Charrière, F.-(10) 6623
Châtel, P. F. de-(10) 6522
Chattopadhyay, T.-(10) 6072, 6816
Che, Xiaodong-(10) 6779
Checks, T. L.-(10) 5665
Chen, Baoxing-(10) 6174
Chen, C. J.-(10) 5897, 6112
Chen, C. T.-(10) 5808, 5810, 6378
Chen, Christina H.-(10) 6760
Chen, F. R.-(10) 5888
Chen, Guan-mian-(10) 6293
Chen, H.-(10) 7041
Chen, J.-(10) 6828
Chen, J. P.-(10) 5876
Chen, L. H.-(10) 6915, 7052
Chen, M.-(10) 5628, 5629
Chen, Ming-(10) 6084
Chen, S. C.-(10) 5577
Chen, Shaoan Chung-(10) 5797
Chen, X.-(10) 5997, 6012
Chen, Z. J.-(10) 5922, 6975
Cheney, S.-(10) 6828
Cheng, Song-(10) 5578
Cheng, Yuanda-(10) 6138, 6894
Cheong, B. K.-(10) 7093
Cheong, S. W.-(10) 6723
Cheong, S. W.-(10) 6819
Cherenkov, Valery A.-(10) 6746
Cherepanov, V. B.-(10) 5610
Chernakova, Ana K.-(10) 6066

- Chien, C. L.-(10) 5800
Chien, C.-L.-(10) 6489
Childress, J. R.-(10) 6412, 6623, 7061
Chin, Tsung-Shune-(10) 5888
Ching, W. Y.-(10) 6834, 7034
Chiriach, Horia-(10) 6949
Choi, Hyoung J.-(10) 5579
Choi, J. O.-(10) 5785
Choi, S. D.-(10) 6274, 6655
Choi, Y. S.-(10) 6937
Chou, T.-(10) 6379
Chow, Y. M.-(10) 5779
Chrissey, D. B.-(10) 5595, 6622
Chu, F.-(10) 6397
Chuang, D. S.-(10) 6427
Chuang, Y. C.-(10) 7117
Chubukov, Andrey V.-(10) 6345
Cinbis, C.-(10) 6763
Cingoski, Vlatko-(10) 6042
Cinquina, C. C.-(10) 5529
Cisneroz, P.-(10) 6397
Clark, A. E.-(10) 5656
Clarke, Roy-(10) 6174
Clemens, Bruce M.-(10) 5644
Cochran, J. F.-(10) 6181, 6187, 6473
Cochrane, R.-(10) 6546
Cochrane, R. W.-(10) 6534, 6554, 6560, 7064
Cockcroft, J. K.-(10) 7050
Coehoorn, R.-(10) 6659
Coe, J. M. D.-(10) 6235, 6921
Coffey, G. A.-(10) 5940
Coffey, K. R.-(10) 5960, 6382, 7058
Cohenca, C. H.-(10) 6720
Coles, P. C.-(10) 6987
Collocott, S. J.-(10) 7114
Colucci, C. C.-(10) 6303
Conover, M. J.-(10) 6461, 7080
Continentino, M. A.-(10) 6734
Continenza, Alessandra-(10) 7027
Cooper, Bernard R.-(10) 7035
Cordone, S. S.-(10) 5610
Correia, Vanessa M.-(10) 5838
Corti, M.-(10) 7143, 7146
Costa, U. M. S.-(10) 5811
Cottam, M. G.-(10) 5823, 6443
Coverdale, G. N.-(10) 5574
Cowen, J. A.-(10) 6489
Cox, T. J.-(10) 5562
Cressoni, J. C.-(10) 5820, 5841
Cresswell, A.-(10) 6619
Crook, Elizabeth M.-(10) 5565
Crooker, B. C.-(10) 5731
Cross, R. W.-(10) 6400
Crow, J. E.-(10) 6328, 6595, 6748, 6812
Cuccoli, Alessandro-(10) 5814
Cullen, James R.-(10) 6475
Cunha, S. F.-(10) 6766
- Drbo, C.-(10) 5586, 6458, 6459
Dagotto, Elbio-(10) 6340
Dahlberg, E. Dan-(10) 5475, 5776, 6567, 7073
Dahmen, Karin-(10) 5946
Daniel, D.-(10) 6921
Das, B. N.-(10) 6924
Das, Badri-(10) 6622
da Silva, B. L.-(10) 6563
da Silva, F. C. S.-(10) 5616
Dautain, M.-(10) 5707
Davies, K.-(10) 6583
Davis, R. L.-(10) 7114
Dawson, A. LeR.-(10) 6837
de Aguiar, F. M.-(10) 13, 5616
de Albuquerque, Douglas F.-(10) 5832
de Boe, F. R.-(10) 6247, 7117
DeFotis, G. C.-(10) 5529, 5940
- Defoug, S.-(10) 5707
De Graef, M.-(10) 5882
de Haan, S.-(10) 5508
de Jesus, J. C. O.-(10) 5520, 5862
de Jonge, W. J. M.-(10) 5728, 6440, 6709
Della Torre, E.-(10) 6106
Della Torre, Edward-(10) 5689, 5692, 5710, 6770
del Moral, A.-(10) 5662, 7158
del Moral, M. Ciria, A.-(10) 5850
den Broeder, F. J. A.-(10) 6424
Deng, Ming-Cheng-(10) 5888
de Oliveira, N. A.-(10) 6296
de Sousa, J. Ricardo-(10) 5835
De Ville, K.-(10) 6092
de Vries, J. J.-(10) 6440
Dewar, G.-(10) 5919
DeWeerd, Robrecht-(10) 6050
Deymier, P. A.-(10) 5571
DiBari, R. C.-(10) 6124
Dieter Storz, Hans-(10) 6049
Diggs, B.-(10) 5879
Ding, Juren-(10) 6150
Dingley, D.-(10) 6782
Dinia, A.-(10) 6548
Dionne, Gerald F.-(10) 6372
Di Pietro, C.-(10) 6039
Dissanayake, A.-(10) 5734
Djurberg, C.-(10) 5541
Dodge, J. S.-(10) 6872
Doi, T.-(10) 5907
Domański, Z.-(10) 5847
Dombrowski, R.-(10) 6054
Donner, W.-(10) 6421
Dormann, J. L.-(10) 5900
Dosanjh, P.-(10) 6334
dos Santos, R. J. V.-(10) 5820
dos Santos, Roberto J. V.-(10) 5838
Dou, S. X.-(10) 7120
Doyle, W. D.-(10) 5547, 5550, 5577, 6446
Driouch, L.-(10) 6309
Drucker, J. S.-(10) 5589, 5592
Drumheller, John E.-(10) 5952, 6081
Dube, D. C.-(10) 6744
Dufour, C.-(10) 6477
Duijn, V. H. M.-(10) 7117
Dumesnil, K.-(10) 6477
Dunham, D.-(10) 6890
Dunifer, G. L.-(10) 6190
Dunlop, J. B.-(10) 7114
Durand, O.-(10) 6412, 7061
Durrin, G.-(10) 5490
Duvail, J. L.-(10) 6412, 7070
- Eastham, J. F.-(10) 6987
Echer, C.-(10) 6900
Eckert, D.-(10) 6018
Edelstein, A. S.-(10) 6610
Edwards, G.-(10) 5873
Eggenkamp, P. J. T.-(10) 5728
Eibschutz, M.-(10) 6915
Elam, W. T.-(10) 5801, 6610
Eley, D. E.-(10) 5586
Elke, John-(10) 5578
Elkasaby, N. M.-(10) 6039
Ellison, A. J. G.-(10) 6825
Elstner, N.-(10) 5943
Emerson, K.-(10) 5952
Engdahl, G.-(10) 5484, 5496
Engel, B. N.-(10) 6498
Engel, Brad N.-(10) 6401
Eppler, W. R.-(10) 7093
Epstein, A. J.-(10) 5782
Erata, Tomoki-(10) 5903
Erdős, P.-(10) 5847
Eremenko, V.-(10) 6744, 6805
- Erickson, R. P.-(10) 6163
Ervin, A. M.-(10) 6610
Erwin, R. W.-(10) 6477, 6592, 6691, 6692
Escobar, M. A.-(10) 6946
Escorne, M.-(10) 6103
Evans, B. J.-(10) 5538, 6643
Everett, R. K.-(10) 6610
Everitt, B. A.-(10) 6592
- Fagan, A.-(10) 6921
Fahlander, M.-(10) 5656
Falco, C. M.-(10) 6498
Falco, Charles M.-(10) 6401
Fan, Hong-(10) 5578
Farle, M.-(10) 5601, 5604
Farle, Michael-(10) 5644
Farrell, G. P.-(10) 6997
Farrow, R. F. C.-(10) 6900
Fauth, F.-(10) 6334
Favorski, I. A.-(10) 5823
Fawcett, E.-(10) 6321
Fedoseev, B.-(10) 6743
Fejer, M. M.-(10) 6872
Felder, R. J.-(10) 6124, 6603
Fernandez-Baca, J. A.-(10) 6060, 6603
Fernando, A. S.-(10) 6303
Fert, A.-(10) 6412, 6623, 7070
Fert, Albert-(10) 6693
Feutrell, E. H.-(10) 5701
Filippi, J.-(10) 6513
Filoti, G.-(10) 6586, 6813
Fisch, Ronald-(10) 5544
Fischer, P.-(10) 6331, 6337, 6743
Fishman, R. S.-(10) 6290
Fisk, Z.-(10) 6723, 6819
Fittipaldi, I. P.-(10) 5829, 5832, 5835
Flanders, P. J.-(10) 5547
Flanders, Philip J.-(10) 5931
Fleming, R. M.-(10) 6124, 7052
Flynn, C. P.-(10) 6592
Folks, L.-(10) 6271, 6634
Fomin, V.-(10) 6744
Fondado, A.-(10) 6723, 6819
Foss, S.-(10) 6892
Foss, Sheryl-(10) 5776
Fraga, E.-(10) 6952
Frattini, Paul L.-(10) 5579
Fredkin, D. R.-(10) 6217
Freeland, J. W.-(10) 6464
Freeman, A. J.-(10) 5802, 6409
Freeman, M. R.-(10) 6194, 6205
Freitas, P. P.-(10) 6449, 6480, 6551
Friedberg, S. A.-(10) 5529
Friedman, G.-(10) 5683
From, M.-(10) 6181, 6187
Fruchart, D.-(10) 5988, 6577
Fruchart, R.-(10) 6577
Fu, L. P.-(10) 5714, 5725
Fu, Y. W.-(10) 7152
Fuerst, C. D.-(10) 6015, 6625, 6637
Fujii, H.-(10) 6522
Fujimoto, T.-(10) 6528
Fujiwara, H.-(10) 7067
Fujiwara, Hideo-(10) 6446
Fujiwara, Y.-(10) 6415, 7102
Fullerton, Eric E.-(10) 6169, 6461, 7080
Furrer, A.-(10) 6331, 6334, 6337, 6743
Furuya, T.-(10) 6658
Futamoto, M.-(10) 6126
- Gago-Sandoval, P. A.-(10) 6789
Galam, Serge-(10) 5526
Galtier, P.-(10) 6412
Gama, S.-(10) 6003
Gamachi, M.-(10) 6089
- Gambino, R. J.-(10) 6909
Gambino, Richard J.-(10) 6871
Gandra, F. G.-(10) 7125
Ganguly, B.-(10) 5873
Gao, Y. H.-(10) 6238
Garanin, D.-(10) 5958
García, N.-(10) 6580
García-Orza, L.-(10) 5662
García-Orza, L.-(10) 7158
Gardner, Richard A.-(10) 6138
Garifullin, I. A.-(10) 6492
Garshelis, I. J.-(10) 5670
Gautier, F.-(10) 6467
Gavrin, A.-(10) 6489
Gebel, B.-(10) 6018
Geerts, W.-(10) 6360
Gehring, P. M.-(10) 5959
Genon, A.-(10) 6036
Genova, D. J.-(10) 6858
George, J. M.-(10) 7061
Georges, Roland-(10) 5647
Gerasimchuk, V. S.-(10) 6092
Geri, A.-(10) 6024, 6033
Gester, M.-(10) 5586, 6458, 6501
Giesbers, J. B.-(10) 6709
Gijs, M. A. M.-(10) 6709
Gillespie, D. J.-(10) 6610
Gingras, M. J. P.-(10) 5523
Girt, Er.-(10) 5997
Givord, D.-(10) 6682
Glebova, Irina N.-(10) 7182
Glijer, Pawel-(10) 6141, 6150
Godart, C.-(10) 7155
Goldman, A. I.-(10) 6366
Goldman, A. M.-(10) 6343, 6344
Goltsev, A. V.-(10) 6742, 6747
Gomes, A. A.-(10) 6296, 7125
Gomez, R. D.-(10) 5756, 5759, 5910, 6891
Gómez Polo, C.-(10) 5791
Gomi, M.-(10) 6804
Gong, Wei-(10) 6649
Gonzalez, A. C.-(10) 7137
González, J.-(10) 6315
Gorlitz, D.-(10) 6054
Gorobets, Yu. I.-(10) 6092
Govindaraju, M. R.-(10) 6981
Granato, Enzo-(10) 6960
Grandjean, F.-(10) 5994
Gratz, E.-(10) 6602
Gray, S. J.-(10) 5586, 6458
Greaves, S. J.-(10) 6849
Green, M. A.-(10) 6811
Gregg, J. F.-(10) 6921
Greig, D.-(10) 7055
Grieves, S.-(10) 6921
Grigerit, T. E.-(10) 5952
Grimes, Craig A.-(10) 6959
Grimsditch, M.-(10) 6169
Gross, J.-(10) 6723
Grunberg, P.-(10) 6193
Grundy, P. J.-(10) 6361
Gu, B. X.-(10) 6955, 7099, 7103
Gu, E.-(10) 6501, 6528
Guillaume, M.-(10) 6331, 6334
Guillot, M.-(10) 5988, 6577, 6792
Gulyaev, Yu. V.-(10) 5619
Gunther, Leon-(10) 5642
Guo, Hui-qun-(10) 6250, 6312
Guo, Yimin-(10) 6388
Guo, Zhenzhou-(10) 5710, 6770
Gupta, B. K.-(10) 6156
Gupta, L. C.-(10) 7155
Gurney, Bruce A.-(10) 7079
Guruswamy, Sivaraman-(10) 6607
Guthmiller, G.-(10) 6397
Gutierrez, C.-(10) 7073
Gutierrez, C. J.-(10) 6286, 7021

- Gwan, P. B.-(10) 7114
 Gyorgy, E. M.-(10) 6124, 6603, 7052
- Ha, Min Yong-(10) 6078
 Haas, S.-(10) 6748
 Haas, Stephan-(10) 6340
 Hadjipanayis, G. C.-(10) 5876, 5885, 6000, 6507, 6623, 6624, 6646, 6649, 6676
 Hahr, C.-(10) 5782
 Hahn, Song-yop-(10) 6045
 Han, S. H.-(10) 5785
 Hanna, S. M.-(10) 5625
 Hanratty, C. M.-(10) 6861
 Harbison, J. P.-(10) 6665
 Hardner, H. T.-(10) 6531
 Harford, M. Z.-(10) 7073
 Harllee, Peter S., III-(10) 6884
 Harmon, B. N.-(10) 6366
 Harp, G.-(10) 6890
 Harper, J. M. E.-(10) 6909
 Harrell, J. W.-(10) 5550
 Harris, V. G.-(10) 5801, 6610, 6924
 Hart, A.-(10) 5574
 Hart, R.-(10) 6543
 Hartl, M.-(10) 5958
 Hasan, M. K.-(10) 6343
 Hashim, I.-(10) 6516
 Hastings, J. B.-(10) 5810
 Hathaway, Kristi B.-(10) 6475
 Hattori, K.-(10) 6415
 Hatwar, T. K.-(10) 6858
 Haushalter, Robert C.-(10) 5859
 Havela, L.-(10) 6522
 Hayano, S.-(10) 5904, 5907, 6887
 Hayashi, Hidetaka-(10) 6153
 Hayashi, K.-(10) 6540
 Hayashi, M.-(10) 6360
 He, Huahui-(10) 6795
 He, L.-(10) 5547, 5577
 He, P.-(10) 6495
 He, Y.-L.-(10) 5580
 Healy, S. D.-(10) 5589, 5592
 Hedge, H.-(10) 6286
 Hegde, H.-(10) 6006, 6009, 6640
 Heim, K. R.-(10) 5589, 5592
 Heinrich, B.-(10) 5583, 6181, 6167
 Heitbrink, Axel-(10) 6049
 Held, G.-(10) 5807
 Hellman, F.-(10) 6870
 Hembree, G. G.-(10) 5589, 5592
 Hempel, K. A.-(10) 5981
 Hendren, W. R.-(10) 6783
 Hendriksen, P. V.-(10) 6583
 Hennion, M.-(10) 5900
 Henry, Y.-(10) 5601
 Herbst, J. F.-(10) 6015, 6625
 Hermsmeider, B.-(10) 6890
 Hermsmeider, B. D.-(10) 5807
 Hernandez, A.-(10) 5791, 6952
 Herr, A.-(10) 6921
 Heuer, L. A.-(10) 5779
 Hicken, R. J.-(10) 5586, 6458
 Hickey, B. J.-(10) 6546, 7055
 Hikosaka, Takashi-(10) 5774
 Hill, E. W.-(10) 6997
 Hilton, D.-(10) 6124
 Hintz, M. B.-(10) 7084
 Hiram, Y.-(10) 5904
 Hirano, H.-(10) 5788
 Hirayama, Yukihiro-(10) 5903
 Hirota, K.-(10) 5959
 Hisatake, K.-(10) 6321
 Hisayama, Naoko-(10) 6162
 Ho, G.-(10) 5808, 6378
 Höchst, H.-(10) 6811
 Hoff, C. N.-(10) 6489
- Höier, R.-(10) 6268
 Holden, T. M.-(10) 6318
 Holdsworth, P. C. W.-(10) 5955
 Holody, P.-(10) 6699
 Honda, Naoki-(10) 5984
 Honda, Y.-(10) 6379
 Honda, Yukio-(10) 6893
 Horwitz, J.-(10) 6622
 Horwitz, J. S.-(10) 5595
 Hosaka, Sumio-(10) 6893
 Hosoe, Y.-(10) 5978
 Hossain, S.-(10) 7067
 Hota, R. L.-(10) 5737
 Howard, J. K.-(10) 5960, 6382, 7058
 Howson, M. A.-(10) 6546
 Hsieh, W. T.-(10) 6598
 Hsieh, C. S.-(10) 5577
 Hsu, J. H.-(10) 6616
 Hsu, Jen Hwa-(10) 7152
 Hsu, T. C.-(10) 6063
 Hu, B. P.-(10) 6226
 Hu, Bo-Ping-(10) 6235
 Hu, C.-(10) 6190
 Hu, Ming-(10) 6256, 7111
 Hu, Xiao-(10) 6486
 Hu, Z.-(10) 6000
 Huai, Y.-(10) 6534, 6554, 6560, 7064
 Huang, C. C.-(10) 6344
 Huang, D.-(10) 6351
 Huang, F.-(10) 6406
 Huang, H. B.-(10) 7099, 7103
 Huang, H. L.-(10) 5794
 Huang, Hui Li-(10) 5499, 5797, 7003
 Huang, M. Q.-(10) 6280, 6574
 Huang, Ming-Zhu-(10) 7034
 Huang, Y. H.-(10) 6616
 Huber, D. L.-(10) 5517
 Huber, W. H.-(10) 6343
 Huffman, G. P.-(10) 5873
 Humphrey, F. B.-(10) 6958
 Hurdequint, H.-(10) 6476
 Hwang, D. M.-(10) 6665
 Hylton, T. L.-(10) 5960, 6382, 7058
- Ibarra, M. R.-(10) 5662, 6223, 7158
 Ibrahim, M. M.-(10) 5873, 6822
 Ido, H.-(10) 6283, 7140
 Idzerda, Y. U.-(10) 5808, 5810, 6378, 6679
 Il'yashenko, E. I.-(10) 7104
 Imai, Yasuyuki-(10) 6162
 Imura, Ryo-(10) 6893
 Inaba, N.-(10) 6126
 Indeck, R. S.-(10) 5753
 Ingersent, Kevin-(10) 7051
 Inglefield, H. E.-(10) 6430
 Ings, John B.-(10) 6363
 Inoue, A.-(10) 6306
 Iramina, K.-(10) 7168
 Irurita, E.-(10) 6315
 Irvine, J. T. S.-(10) 6940, 7000
 Ishida, N.-(10) 5904, 5907
 Ishikawa, A.-(10) 5978, 6890
 Ishikawa, C.-(10) 6400
 Ishikawa, Tomohiro-(10) 6446
 Isnard, O.-(10) 5988
 Israeloff, N. E.-(10) 6344
 Itakura, A.-(10) 6769
 Ito, T.-(10) 6283
 Itoh, A.-(10) 6415
 Itoh, Akiyoshi-(10) 7096
 Itoh, Ikuro-(10) 6966
 Itoh, N.-(10) 6801
 Itoh, T.-(10) 6094, 7171
 Ivanov, Alexander V.-(10) 7184
 Ivanov, Alexandr V.-(10) 7183
 Ivanov, Valery A.-(10) 6729
 Ives, A. J. R.-(10) 5586, 6458
- Iwasaka, M.-(10) 7162, 7165, 7174, 7177, 7181
 Iwasaki, Shun-ichi-(10) 5984
 Iwata, S.-(10) 6769, 7090, 7102
- Jahnes, C. V.-(10) 5923
 Jahnes, Christopher V.-(10) 6159
 Jakubovics, J. P.-(10) 7009
 Jankowska, J.-(10) 6321
 Janssen, H. H. J. M.-(10) 6709
 Janstrom, Thomas J.-(10) 5747
 Japiassu, G. M.-(10) 6734
 Jardim, R. F.-(10) 6720
 Jarlborg, T.-(10) 6571, 7034
 Jarratt, J.-(10) 7067
 Jasmin, S.-(10) 6412
 Jaswal, D. Welipitiya, S. S.-(10) 6303
 Jaswal, S. S.-(10) 6346
 Jatau, J. A.-(10) 6106
 Jatau, James A.-(10) 6846
 Jen, S. U.-(10) 5667
 Jenniches, H.-(10) 7081
 Jhon, Myung S.-(10) 5579, 5747, 6867
 Jiang, H. X.-(10) 5734
 Jiles, D. C.-(10) 5511, 5676, 5922, 6975, 6981
 Jin, Q. Y.-(10) 6190
 Jin, S.-(10) 6915, 7052
 Jinfang, Liu-(10) 6289
 Johnson, E. D.-(10) 5810
 Johnson, M. T.-(10) 6424, 6440, 6659, 6709
 Johnson, Mark-(10) 6714
 Johnston, D. C.-(10) 6603
 Jones, Barbara A.-(10) 7051
 Jones, T. E.-(10) 6723, 6757
 Jonker, B. T.-(10) 5714, 5719, 5725
 Judy, Jack H.-(10) 5972, 6141, 6150
 Jung, C.-(10) 5571
 Jungblut, R.-(10) 6424, 6659
- Kaatz, F. H.-(10) 6610
 Kabos, P.-(10) 5632
 Kachur, I.-(10) 6744, 6805
 Kaczmarek, R.-(10) 5707
 Kagawa, K.-(10) 6540
 Kaiser, H.-(10) 6477
 Kamada, O.-(10) 6801
 Kameda, J.-(10) 6975
 Kamijima, A.-(10) 6379
 Kane, S. N.-(10) 6952
 Kanematsu, Kazuo-(10) 7105
 Kang, I. K.-(10) 5785, 6937, 6943
 Kang, T.-(10) 6943
 Kanhere, D. G.-(10) 7024
 Kano, H.-(10) 6540
 Kao, C. C.-(10) 5810
 Kapitulnik, A.-(10) 6872
 Karis, Thomas E.-(10) 6867
 Kartha, Sivan-(10) 5946
 Karube, Hiro-(10) 6855
 Kasai, Y.-(10) 6658
 Kashyap, A.-(10) 6298
 Kashyap, Arti-(10) 6301
 Kästner, J.-(10) 6072
 Katayama, T.-(10) 6360
 Kawano, S.-(10) 6060
 Kawazoe, Yoshiyuki-(10) 6486
 Keavney, D. J.-(10) 6464
 Kell, David M.-(10) 6178, 7079
 Kelly, Paul J.-(10) 6704
 Kemmler-Sack, S.-(10) 6813
 Kennedy, R. J.-(10) 6328
 Keramidias, V. G.-(10) 6665
 Kerch, H. M.-(10) 6840
 Kido, G.-(10) 6283
 Kikukawa, Atsushi-(10) 6893
- Kim, Chul Sung-(10) 6078
 Kim, H. J.-(10) 5785
 Kim, Jun-o-(10) 6045
 Kim, K. Y.-(10) 6943
 Kiranmai, V.-(10) 7181
 Kirby, R. D.-(10) 6346, 6348, 6418, 6495, 6670
 Kirby, Roger D.-(10) 6507
 Kirkpatrick, S.-(10) 5879, 5882
 Kishio, K.-(10) 6322
 Kita, E.-(10) 6455, 6531, 6918
 Kita, Eiji-(10) 5903
 Kitajima, T.-(10) 7174
 Klabunde, K. J.-(10) 5876, 5885
 Kleemann, W.-(10) 5856
 Klein, L.-(10) 6322
 Klein, V.-(10) 6813
 Kleinfeld, Th.-(10) 7102
 Klik, I.-(10) 5794, 5897
 Klik, Ivo-(10) 5487, 5499, 5505
 Klin, V. P.-(10) 7104
 Knappmann, S.-(10) 5598
 Ko, Heung Moon-(10) 6078
 Kobayashi, O.-(10) 6631
 Kodama, R. H.-(10) 5639
 Koetzier, J.-(10) 5958, 6566
 Koga, F.-(10) 5916
 Koh, Chang Seop-(10) 6045
 Koide, T.-(10) 5809
 Koike, K.-(10) 6890
 Koinkar, Vilas N.-(10) 5741
 Kojuharoff, Victor I.-(10) 6972
 Kolchin, A.-(10) 7024
 Komai, Tomoko-(10) 5774
 Kondoh, S.-(10) 6147
 Kong, Lin-Shu-(10) 6250, 7111
 Kong, Lin-shu-(10) 6253, 6256, 6259
 Kono, Raymond-Noel-(10) 6867
 Koon, N. C.-(10) 6622, 6924
 Kopeć, T. K.-(10) 5847
 Koranda, S.-(10) 6890
 Korman, Can E.-(10) 5478
 Kos, A. B.-(10) 6400
 Kotru, P. N.-(10) 7185
 Kotzler, J.-(10) 6054
 Kouvel, J. S.-(10) 5683, 6343
 Koyama, N.-(10) 6400
 Krajewski, J. E.-(10) 6603
 Kraus, L.-(10) 6952
 Krause, R. F.-(10) 6646, 6649
 Krebs, J. J.-(10) 6688, 7073
 Krishnan, Kannan M.-(10) 6900
 Krishnan, R.-(10) 6309, 6607
 Krumhansl, James A.-(10) 5946
 Kryder, M. H.-(10) 5966, 6391, 6394, 6763, 7093
 Kryder, Mark H.-(10) 6864
 Kutorov, Sergey A.-(10) 6745
 Kuanr, Bijoy Kumar-(10) 6115
 Kübler, J.-(10) 7033
 Kubrakov, Nikolai F.-(10) 6786
 Kuga, Kiyoshi-(10) 5987
 Kulakowski, K.-(10) 6315
 Kumar, Binod-(10) 6760
 Kumar, Sudha-(10) 6169
 Kunkel, H. P.-(10) 6510, 7108
 Kuo, P. C.-(10) 5577, 6244
 Kurashina, Seiji-(10) 7096
 Kushauer, J.-(10) 5856
 Kuwabara, Masago-(10) 6153
 Kuznietz, Moshe-(10) 7134
 Kwon, H. J.-(10) 6109
 Kwun, H.-(10) 5673
- Lacerda, F.-(10) 5829
 Lai, W. Y.-(10) 6226
 Lai, Wuyan-(10) 6504
 Lam, Irene-(10) 6138

- Lambeth, D. N.-(10) 6132
Lambeth, David N.-(10) 6884
Lambert, C. P.-(10) 5535
Lane, Alan M.-(10) 5578
Lane, L.-(10) 6397
Lang, J. C.-(10) 6366
Langman, R. A.-(10) 5673
Larica, C.-(10) 6766
Larionov, M.-(10) 6741
La Rosa, M.-(10) 6033
Lascialari, A.-(10) 7143
Lashmore, D. S.-(10) 6543
Lassri, H.-(10) 6309, 6607
Latha, K.-(10) 6118
Laughlin, D. E.-(10) 5966, 7093
Laulicht, I.-(10) 5607
Lawson, A. C.-(10) 6589
Leal, C. E.-(10) 6737
Leal, J. L.-(10) 6449, 6480
Lectard, E.-(10) 6277
Lectard, Eric-(10) 6658
Lederman, M.-(10) 6217
Lee, Heung Soo-(10) 6078
Lee, J.-(10) 5487, 5505
Lee, J. G.-(10) 7006
Lee, J. G.-(10) 5713
Lee, J. J.-(10) 5785
Lee, J. S.-(10) 6943
Lee, K. C.-(10) 6598
Lee, K. H.-(10) 5913
Lee, K. M.-(10) 5876
Lee, R. E.-(10) 6397
Lee, S. F.-(10) 6699
Lee, S. R.-(10) 6169
Lee, S. T.-(10) 5714
Lee, Sang Yout-(10) 6078
Lee, W. T.-(10) 6477
Lee, W. Y.-(10) 6274, 6655
Lee, Y. H.-(10) 5913
Lefakis, Harry-(10) 7079
Le Gall, H.-(10) 6103
Legros, W.-(10) 6036
Lenczowski, S. K. J.-(10) 6709
Leslie-Pelecky, D. L.-(10) 6489
Levy, M.-(10) 6286
Levy, Peter M.-(10) 6906, 7076
Lewis, V. G.-(10) 6927
Lewis, W. A.-(10) 5604
Lewis, William A.-(10) 5644
Li, D.-(10) 5844
Li, Hong-Shuo-(10) 7114, 7120, 7122
Li, L. X.-(10) 5734
Li, Shuxiang-(10) 6504
Li, W. Z.-(10) 6238
Li, W. H.-(10) 6598
Li, Yuet-(10) 6394
Li, Z. G.-(10) 6624
Lian, F. Z.-(10) 6289
Liang, Y. L.-(10) 6628
Liao, L. X.-(10) 6181, 6187
Liao, Simon H.-(10) 5800
Licci, F.-(10) 7143, 7185
Liew, Y. F.-(10) 5580
Lim, S. H.-(10) 6937
Lin, C. H.-(10) 5577
Lin, Gang Herbert-(10) 5765
Lin, H. J.-(10) 5808, 6378
Lin, H. Q.-(10) 7041
Lin, Jiang-Ching-(10) 5897
Lin, Ming-xi-(10) 6293
Lin, W. G.-(10) 6238, 6241
Lin, X.-(10) 6676
Lind, D. M.-(10) 6124, 6688, 6691, 6692
Linderth, S.-(10) 6583
Linderth, Søren-(10) 5867
Ling, Ji-wu-(10) 6293
Liu, C. J.-(10) 6244
Liu, C. S.-(10) 6112
Liu, F. H.-(10) 6391, 6394
Liu, G. C.-(10) 6226
Liu, G. K.-(10) 7030
Liu, H. K.-(10) 7120
Liu, J.-(10) 6624
Liu, J. P.-(10) 6247
Liu, J. Z.-(10) 6344
Liu, Jian-Min-(10) 6751
Liu, L.-(10) 5683
Liu, S. H.-(10) 6290
Liu, W. L.-(10) 6628
Liu, X.-(10) 7021
Lo, C. C. H.-(10) 7009
Lo, J.-(10) 6397
Lochner, E.-(10) 6124, 6688, 6691, 6692
Lodder, J. C.-(10) 5508
Loewenhaupt, M.-(10) 6602
Loloe, R.-(10) 6699
Long, Gary J.-(10) 5994
Loong, C. K.-(10) 6825, 7030
López-Quintela, M. A.-(10) 6757
Lorentz, Robert D.-(10) 6843
Lottis, D. K.-(10) 5475, 7070
Lu, Jing Ju-(10) 5499
Lu, M.-(10) 6190, 7099, 7103
Lu, Pu-Ling-(10) 5768
Lubitz, P.-(10) 5595, 7073
Lukin, J. A.-(10) 5529
Luo, C. P.-(10) 6351
Lussier, J. G.-(10) 6063
Lyberatos, A.-(10) 5704
Lynn, J. W.-(10) 6069, 6072, 6589, 6598, 6806
Ma, B. M.-(10) 6628
Ma, H.-(10) 6510
Macciò, M.-(10) 6431
Machado, F. L. A.-(10) 5862, 6563
MacLaren, J. M.-(10) 6428
Madabhushi, R.-(10) 5759
Maeda, K.-(10) 6321
Mackawa, M.-(10) 5559
Magni, A.-(10) 5490
Mahia, J.-(10) 6757
Majetich, S. A.-(10) 5879, 5882
Majkrzak, C. F.-(10) 6178
Majkrzak, C. F.-(10) 5959, 6193, 6498
Mak, Chee-leung-(10) 5719
Maley, C.-(10) 6723
Mangin, Ph.-(10) 6477
Mankey, G. J.-(10) 6406
Mao, Ming-(10) 6534
Maple, M. B.-(10) 5639, 6720
Marchal, G.-(10) 6477
Margarian, A.-(10) 7114
Margulies, D. T.-(10) 6097
Marinova, I.-(10) 5904, 5907, 6887
Marks, R. F.-(10) 6900
Marquina, C.-(10) 5662, 7158
Marshall, J. H.-(10) 6124
Martinez, D.-(10) 6100
Martins, C. S.-(10) 6563
Maruti, Sanchit-(10) 5949
Marx, Chr.-(10) 6054
Maslennikov, Yu. V.-(10) 6996
Masson, A.-(10) 6623
Mathur, S. C.-(10) 6744
Matson, M. E.-(10) 5475
Matsubara, I.-(10) 6321
Matsuda, Y.-(10) 6126
Matsumoto, Mitsunori-(10) 5969
Matsumura, Kunihiko-(10) 6855
Matsushita, N.-(10) 5975, 7131
Matsuyama, H.-(10) 6890
Matsuyama, K.-(10) 6086, 6089
Mattison, J. E.-(10) 6169, 6461, 7080
Mattsson, J.-(10) 5541
Mauger, Alain-(10) 5526
Maury, Claire-(10) 6658
Mayergoyz, I. D.-(10) 5686, 5756, 5910, 6027, 6891, 6963
Mayergoyz, Isaac D.-(10) 5478
Mazumdar, Chandan-(10) 7155
McCormick, P. G.-(10) 5481, 5701, 6634
McGuire, T. R.-(10) 6537, 6909
McHenry, M. E.-(10) 5879, 5882
McMichael, R. D.-(10) 5493, 5650, 5689, 5692
Meckenstock, R.-(10) 6492, 6508
Medina, A. N.-(10) 7125
Meigs, G.-(10) 5808, 6378
Melamud, Mordechai-(10) 7134
Melo, L. V.-(10) 6480, 6551
Merlin, Roberto-(10) 6340
Mesot, J.-(10) 6334
Messer, M. T.-(10) 6870
Metoki, N.-(10) 6421
Metzger, Robert M.-(10) 5870
Meys, B.-(10) 6036
Miao, Y. Z.-(10) 6190, 7099, 7103
Mibu, K.-(10) 6483
Micklitz, H.-(10) 6741
Mieski, Anders-(10) 6265
Midelfort, K.-(10) 5882
Migliori, A.-(10) 6625
Milham, Clive D.-(10) 5659
Miller, B. H.-(10) 6567
Miller, Joel S.-(10) 5782
Miller, L. L.-(10) 7146
Miller, M. S.-(10) 5779
Min, Tai-(10) 6129
Minemoto, H.-(10) 6801
Miotkowski, I.-(10) 5731
Mira, J.-(10) 6757
Miraglia, S.-(10) 5988
Mirebeau, I.-(10) 5900
Mirzamaani, Mohammad-(10) 6159
Mishra, R. K.-(10) 7018
Mishra, Raja K.-(10) 6652
Mishra, S.-(10) 5994
Misra, P. K.-(10) 5737
Mitchell, J. R.-(10) 6912
Miyajima, Hideki-(10) 5903, 7161
Miyamoto, Yasuyoshi-(10) 6525
Miyamura, M.-(10) 6147
Miyuchi, D.-(10) 6379
Moghadam, A.-(10) 5630
Mohammed, Osama A.-(10) 6045
Monachesi, Patrizia-(10) 7027
Montarroyos, E.-(10) 5862
Montenegro, F. C.-(10) 5520, 5862
Moorthy, V. N.-(10) 6740
Moreira, J. M.-(10) 6513
Morel, R.-(10) 6623
Moreland, John-(10) 6878
Mori, T.-(10) 6769
Morin, B. G.-(10) 5782
Morisako, Akimitsu-(10) 5969
Morisue, T.-(10) 6969
Morita, Osamu-(10) 6162
Moroni, E. G.-(10) 6571, 7034
Morrish, A. H.-(10) 5556
Mørup, S.-(10) 6583
Moskowitz, B.-(10) 6892
Moskowitz, Bruce-(10) 5894
Mostafa, Ibrahim-(10) 6030
Muir, W. B.-(10) 6534
Muller, Gerhard-(10) 5937, 6057, 6751
Müller, K. H.-(10) 6018
Muller, M. W.-(10) 5753
Muñoz, M. C.-(10) 6470
Murayama, A.-(10) 6147
Musa, S. O.-(10) 6546
Nagai, N.-(10) 5559
Nagamine, L. C. C. M.-(10) 6223
Nagarajan, R.-(10) 7155
Naik, R.-(10) 6190
Nakada, Masafumi-(10) 6855
Nakagawa, K.-(10) 6415
Nakagawa, Katsuji-(10) 7096
Nakagawa, S.-(10) 5975, 7131
Nakagawa, Shigeki-(10) 6525, 6568
Nakamura, A.-(10) 6126
Nakamura, Yoshihisa-(10) 6776
Nakanishi, Hiroaki-(10) 5969
Nakotte, H.-(10) 6522, 6589
Nanjo, M.-(10) 7140
Naoc, M.-(10) 5975, 7131
Naoc, Masahiko-(10) 5969, 5987, 6357, 6509, 6525, 6568
Narlikar, Anant V.-(10) 6740
Narumiya, Y.-(10) 6379
Nash, J. M.-(10) 5629
Nautiyal, T.-(10) 6298
Navarathna, A.-(10) 6006, 6009
Navas, C.-(10) 5535
Nedkov, I.-(10) 6726
Need, Omar U.-(10) 7079
Newman, D. M.-(10) 6789, 7081, 7087
Ng, D. H. L.-(10) 7009
Niarchos, D.-(10) 5853, 6232
Nichols, D. H.-(10) 6328
Nicklow, R. M.-(10) 6060
Nickolsky, A. D.-(10) 7104
Nicolaidis, G. K.-(10) 5853, 6306
Nicolet, A.-(10) 6036
Nikitov, S. A.-(10) 5630, 5631
Nikles, David E.-(10) 5565, 5578
Ning, Tai-shan-(10) 6250, 6256
Nishio, T.-(10) 6658
Noakes, D. R.-(10) 6321
Noguchi, K.-(10) 6379
Nogués, J.-(10) 5862
Nogues, M.-(10) 5826
Noh, T. H.-(10) 6937, 6943
Nolan, T.-(10) 6144
Noma, K.-(10) 5975, 7131
Nordblad, P.-(10) 5541
Nori, Franco-(10) 6340
Nuhfer, N. T.-(10) 5879
Numazawa, Junji-(10) 5987
Nunes, Jr., G.-(10) 6205
Nunzio, S. Di-(10) 6184
Nývlt, M.-(10) 6783
O'Barr, R.-(10) 6217
Ober, R.-(10) 5900
Obermyer, R. T.-(10) 6262, 6574
O'Brien, W.-(10) 6811
O'Bryan, H., Jr.-(10) 6124
O'Connor, Charles J.-(10) 5859
Oepen, H. P.-(10) 5598
O'Grady, K.-(10) 6921, 6927
O'Grady, K.-(10) 6849
Oh, J. H.-(10) 6109
Oh, Young Jei-(10) 6078
O'Handley, R. C.-(10) 6427, 6429, 6430
Ohnuki, Satoru-(10) 6852
Ohshima, N.-(10) 6160
Ohta, Norio-(10) 6852
Ohyama, T.-(10) 6086
Ojima, Masahiro-(10) 6852
Okabe, A.-(10) 6540
Okada, Osamu-(10) 6855
Oliveira, V. S.-(10) 7125
Oonaka, Y.-(10) 6984
O'Reilly, J. W.-(10) 6328, 6595
Orme, C.-(10) 6892
Oseroff, S.-(10) 6723, 6819

- Oseroff, S. B.-(10) 6757
 Osgood, R. M., Jr.-(10) 6286
 O'Shea, M. J.-(10) 5643, 6673
 Osipov, Sergey G.-(10) 6093
 Osofsky, M. S.-(10) 6679
 Ostorero, J.-(10) 6103, 6792
 Ostovic, Vlado-(10) 6048
 Ostrovskii, V. S.-(10) 5622
 O'Sullivan, J. A.-(10) 5753
 Otani, Yoshichika-(10) 5903, 7161
 Oti, John O.-(10) 6519, 6881
 Otsuka, Hiroaki-(10) 6966
 Ouchi, Kazuhiro-(10) 5984
 Ounadjela, K.-(10) 5601, 6434, 6467, 6548, 6921
 Ouyang, Jia-(10) 6795
 Ozaki, M.-(10) 6217
- Padalia, B. D.-(10) 6740, 7155
 Pahner, Uwe-(10) 6048, 6050
 Panagiotopoulos, I.-(10) 6232
 Panchanathan, V.-(10) 6652
 Papaethymiou, V.-(10) 6000
 Pardavi-Horvath, M.-(10) 6106
 Pardavi-Horvath, Martha-(10) 5864
 Parent, J. L.-(10) 5535
 Park, B. J.-(10) 6592
 Park, Jae Yun-(10) 6078
 Park, S. J.-(10) 6343
 Park, Yoon D.-(10) 5579
 Parker, D.-(10) 5574
 Parker, F. T.-(10) 5562, 6097, 6169, 6613, 6622, 6933
 Parker, M. A.-(10) 5960, 6382, 7058
 Parker, M. R.-(10) 6930, 7067
 Parker, Martin R.-(10) 5565
 Parkin, D. M.-(10) 6812
 Parkin, S. S. P.-(10) 6455, 6531, 6900
 Parra, R. E.-(10) 7137
 Pashkevich, Yu.-(10) 6741
 Passamani, E. C.-(10) 6483
 Patel, M.-(10) 6528
 Patterson, B. M.-(10) 6303
 Patton, C. E.-(10) 5628, 5629, 5632
 Patton, Carl E.-(10) 6084
 Patton, Steven T.-(10) 5771
 Paul, D. I.-(10) 6619
 Pázmándi, F.-(10) 5847
 Pechan, Michael J.-(10) 6178
 Pecheron-Guegan, A.-(10) 6103
 Peck, Paul R.-(10) 5747
 Peck, W. F., Jr.-(10) 6603
 Pedersen, Michael S.-(10) 5867
 Pedziwiatr, A. T.-(10) 6574
 Pelzl, J.-(10) 6492, 6508
 Pepperhoff, W.-(10) 7012, 7015
 Pereira, L. G.-(10) 7061, 7070
 Perera, P.-(10) 5643
 Pérez-Díaz, J. L.-(10) 6470
 Perlov, A. Ya.-(10) 5922
 Perron, J. C.-(10) 6946
 Peruyero, Jose-(10) 6066
 Petasis, D.-(10) 5879
 Petrakovskii, G.-(10) 6743
 Petrou, A.-(10) 5714, 5725
 Pettit, Kevin-(10) 6918
 Pfeiffer, Alfred-(10) 6996
 Phillips, J. M.-(10) 6124
 Pierce, D. T.-(10) 6437, 6452
 Pint, M. G.-(10) 6431, 6464
 Pinkerton, F. E.-(10) 6015, 7018
 Pinto, Haim-(10) 7134
 Pinto, R. P.-(10) 6551
 Piryatinskaya, V.-(10) 6744, 6805
 Pissas, M.-(10) 5853
 Planas, J.-(10) 5698
 Plaskett, T. S.-(10) 6480, 6537
 Podlesnyak, A.-(10) 6331
- Poinsot, R.-(10) 6921
 Politi, P.-(10) 6431, 6464
 Pollard, R. J.-(10) 6861
 Polstra, P. A.-(10) 5731
 Pomyalov, A. V.-(10) 5607
 Ponce, M.-(10) 6397
 Pop, Gheorghe-(10) 6949
 Popma, Th. J. A.-(10) 5508
 Porter, D. G.-(10) 5753
 Portwine, W.-(10) 6688
 Potter, M.-(10) 7079
 Pouget, S.-(10) 5826
 Pourarian, F.-(10) 6262, 6289
 Praino, A. P.-(10) 6782
 Prakash, Om-(10) 6740
 Pratt, W. P., Jr.-(10) 6699
 Préjean, J. J.-(10) 6682
 Price, Edward-(10) 6903
 Prikhod'ko, O.-(10) 6744
 Pringle, O. A.-(10) 5994
 Prinz, G. A.-(10) 5808, 6286, 7021, 7073
 Prinz, Gary-(10) 5776
 Prodi, G. A.-(10) 6996
 Prokeš, K.-(10) 6522
 Proksch, R.-(10) 6892
 Proksch, Roger-(10) 5776, 5894
 Prosser, V.-(10) 6783
- Qi, Qi-Nian-(10) 6235
 Qiu, G.-(10) 7067
 Qiu, Gan-(10) 6934
 Quandt, E.-(10) 5653
 Quintana, P.-(10) 6940, 7000
- Rabenberg, Lew.-(10) 6658
 Radhakrishna, P.-(10) 6601
 Raffo, L.-(10) 7143
 Raghavan, P. K. N.-(10) 6744
 Raghavan, S.-(10) 5571
 Raina, Urvashi-(10) 7185
 Ramesh, R.-(10) 6915
 Rani, R.-(10) 6006, 6009
 Ranjan, R.-(10) 6144
 Rao, D.-(10) 6622, 6933
 Rao, K. V.-(10) 5853, 5862, 6306
 Rao, X. L.-(10) 6226
 Rastelli, E.-(10) 5817, 6051
 Ratnam, A.-(10) 5634
 Ravinder, D.-(10) 6118, 6121
 Ravindran, K.-(10) 6081
 Re, M. E.-(10) 6782
 Rechenberg, H. R.-(10) 6223
 Reddy, M. Bhagavantha-(10) 6125
 Reddy, P. Venugopal-(10) 6125
 Reimers, J. N.-(10) 5523
 Reinders, A.-(10) 6424, 6440, 6659
 Reininger, R.-(10) 6811
 Remacle, J.-F.-(10) 6036
 Ressouche, E.-(10) 7050
 Restorff, J. B.-(10) 5656
 Rettori, A.-(10) 6431, 6464
 Rezende, S. M.-(10) 5613, 5616, 5862, 6563
 Rhee, J. R.-(10) 5913
 Rhyne, J. J.-(10) 6477
 Ribeiro, C. A.-(10) 6003
 Ricardo de Sousa, J.-(10) 5829
 Rice, Paul-(10) 6878, 6881
 Riera, Jose-(10) 6340
 Rigamonti, A.-(10) 7143, 7146
 Riley, L. A.-(10) 5673
 Ritter, J. J.-(10) 6840
 Rivas, J.-(10) 6100, 6757
 Rivero, G.-(10) 6952
 Roberts, Bruce W.-(10) 5946
 Robertson, N.-(10) 6397
- Robinson, R. A.-(10) 6589
 Robson, M. C.-(10) 6870
 Roessler, G. M., Jr.-(10) 6679
 Roessli, B.-(10) 6331, 6337, 6743, 6816
 Rojdestvenski, I. V.-(10) 5811, 5823, 6443
 Roky, K.-(10) 6831
 Romanuk, Anatoly V.-(10) 7182
 Rook, K.-(10) 5779
 Rosales-Rivera, A.-(10) 5862
 Rosales-Rivera, A.-(10) 5520
 Rosenberg, M.-(10) 6586, 6813
 Roshko, R. M.-(10) 5844
 Rosov, N.-(10) 6069, 6072
 Rubins, R. S.-(10) 6081
 Rubinstein, M.-(10) 5595, 6924
 Rubinstein, Mark-(10) 6557, 6622
 Ruf, Ralph R.-(10) 6871
 Rugar, D.-(10) 6211
 Runge, A. P.-(10) 6354
 Rusinek, Henry-(10) 6990
 Russak, M. A.-(10) 5923
 Russak, Michael A.-(10) 6159
 Russek, Stephen E.-(10) 6519, 6881
 Russell, P. E.-(10) 6132
 Ryan, D. H.-(10) 6837
- Sablik, M. J.-(10) 5673, 6769
 Sablina, K.-(10) 6743
 Sachdev, Subir-(10) 6345
 Sadamura, H.-(10) 5559
 Saenger, Dirk Uwe-(10) 6746
 Saffari, Haydee-(10) 6153
 Saffarian, Hassan M.-(10) 5568
 Safonov, Vladimir L.-(10) 6745
 Sahay, Satyam-(10) 6607
 Sahu, S.-(10) 6892
 Saito, Y.-(10) 5904, 5907, 6887
 Salamon, M. B.-(10) 6455, 6531, 6592, 6918
 Salter, I. W.-(10) 6783, 6861
 Salvini, A.-(10) 6024
 Samant, M.-(10) 6890
 Samant, M. G.-(10) 5807
 Samarasekara, P.-(10) 6640
 Samarth, N.-(10) 6199
 Sanders, Steven C.-(10) 6519
 Sandlund, L.-(10) 5656
 Sandratskii, L.-(10) 7033
 Sands, T.-(10) 6665
 Sankar, S. G.-(10) 6262, 6289, 6574
 Sano, Takanobu-(10) 6162
 Santini, H.-(10) 6397
 Sarkissian, B. V. B.-(10) 6766
 Sarmiento, E. F.-(10) 5820, 5841
 Sarrao, J. L.-(10) 6625
 Sasada, I.-(10) 5916, 6984
 Sato, Motoharu-(10) 6153
 Sato, T.-(10) 5788
 Saylor, C.-(10) 6723
 Scarmozzino, R.-(10) 6286
 Schad, R.-(10) 7079
 Schäfer, M.-(10) 6193
 Schäfer, R.-(10) 6782
 Schefer, J.-(10) 6331
 Scheinfein, M. R.-(10) 5589, 5592
 Scheinfein, Michael R.-(10) 6138
 Schep, Kees M.-(10) 6704
 Schiebener, Peter-(10) 6996
 Schlottmann, P.-(10) 5532, 6731, 7044
 Schneider, T.-(10) 7015
 Schneider-Muntau, H. J.-(10) 6812
 Schreiber, F.-(10) 6184, 6421, 6492, 6508
 Schrey, P.-(10) 6586
 Schreyer, A.-(10) 6193
 Schroeder, P. A.-(10) 6699
- Schuhl, A.-(10) 6412, 7061
 Schuller, Ivan K.-(10) 6178, 7079
 Schultz, S.-(10) 6217
 Schultz, T.-(10) 6723
 Schumann, F. O.-(10) 6508
 Schurer, P. J.-(10) 5583
 Schwarzacher, W.-(10) 6543
 Scorzelli, R. B.-(10) 6741
 Scott, D. W.-(10) 6628
 Seale, D.-(10) 7067
 Seaman, C. L.-(10) 5639
 Sechovsky, V.-(10) 6522
 Sedazzari, S.-(10) 5817
 Seddat, M.-(10) 6607
 Sedighi, Mojtaba-(10) 6138
 Seehra, M. S.-(10) 5873, 6822
 Self, Terry M.-(10) 5565
 Sellmyer, D. J.-(10) 6232, 6303, 6346, 6348, 6354, 6418, 6495, 6507, 6670
 Serena, P. A.-(10) 6580
 Sethna, James P.-(10) 5946
 Shah, S. I.-(10) 6676
 Shaheen, S. A.-(10) 6021, 6229
 Shalaev, Boris N.-(10) 6745
 Shan, Z. S.-(10) 6354, 6418
 Shand, P. M.-(10) 5731
 Shapiro, V.-(10) 6805
 Shaw, K. A.-(10) 6124, 6688, 6691, 6692
 Shelton, R. N.-(10) 6344
 Shen, B. G.-(10) 6955
 Shen, Bao-Gen-(10) 7111
 Shen, Bao-gen-(10) 6250, 6253, 6256, 6259, 6312
 Shen, J. X.-(10) 6346, 6348, 6418, 6495, 6507, 6670
 Sheng, Q. G.-(10) 7035
 Shi, Jing-(10) 6455
 Shi, X.-(10) 6394
 Shimazaki, Katsusuke-(10) 6852
 Shimoda, T.-(10) 6631
 Shin, J. Y.-(10) 6109
 Shin, Y. D.-(10) 5913
 Shinjo, T.-(10) 6483
 Shinoura, O.-(10) 6379
 Shiokawa, K.-(10) 7165
 Shirane, G.-(10) 5959, 6321
 Shiroishi, Y.-(10) 5978, 6890
 Shoba, Sergei A.-(10) 7184
 Shore, Joel D.-(10) 5946
 Shpilkina, Irina V.-(10) 7182, 7183
 Shpilkina, Irina V.-(10) 7184
 Shu, Xiao Zhou-(10) 6375
 Shull, R. D.-(10) 6840
 Shuming, Pan-(10) 6289
 Silva, C.-(10) 5879
 Simizu, S.-(10) 6289, 6574
 Simmons, Ralph-(10) 5765
 Simmons, Ralph F., Jr.-(10) 5747
 Sin, Kyusik-(10) 5972, 6150
 Sinclair, R.-(10) 6144
 Singh, Bharat-(10) 7187
 Singh, Okram G.-(10) 6740
 Singh, R. P.-(10) 5943
 Singleton, E. W.-(10) 6000
 Sinha, Urvija-(10) 6744
 Sipahi, L. B.-(10) 6978, 6981
 Sivertsen, John M.-(10) 5972, 6141, 6150
 Sivron, N.-(10) 5952
 Slade, S. B.-(10) 6613
 Slavina, A. N.-(10) 5610, 6443
 Slonczewski, J. C.-(10) 6474
 Smirra, Karl-(10) 6996
 Smit, P.-(10) 7149
 Smith, M.-(10) 5734
 Smith, N. V.-(10) 6378
 Smith, P.-(10) 5882

- Smith, R.-(10) 6723
Snelling, J. P.-(10) 7087
Snigirev, O.-(10) 6996
Soares, J. C.-(10) 6480
Sobolev, V. L.-(10) 5794
Sobolev, Vladimir L.-(10) 5797, 7003
Soderholm, L.-(10) 6740
Soghomonian, Victoria-(10) 5859
Sokoloff, J. B.-(10) 6075
Solanki, A. K.-(10) 6301
Soliman, A.-(10) 6492
Solovjov, A. G.-(10) 7104
Song, Kibong-(10) 6357
Song, L.-(10) 6226
Song, Oh Sung-(10) 6429
Song, Y. J.-(10) 5740
Sooryakumar, R.-(10) 5719, 7021
Sorensen, C. M.-(10) 5876, 5885
Soulette, J.-(10) 5512
Soulette, F.-(10) 6103
Sousa, J. B.-(10) 6513, 6551
Souza Azevedo, I.-(10) 6741
Sowers, C. H.-(10) 6169, 6461, 7080
Spada, E. J.-(10) 5923
Spada, F. E.-(10) 5562
Spalding, G. C.-(10) 6343
Speriosu, Virgil S.-(10) 7079
Sprague, J. A.-(10) 5801
Srinivasan, G.-(10) 5610, 6822, 6828
Srivastava, G. P.-(10) 6115
Srivastava, Niraj-(10) 6751
Staddon, C. R.-(10) 6921
Stageberg, F. E.-(10) 5779
Staley, S. W.-(10) 5879, 5882
Stampe, P. A.-(10) 6510
Stancil, Daniel D.-(10) 6066
Staub, U.-(10) 6334, 6337
Stearns, Mary Beth-(10) 6894
Stefanovskii, E. P.-(10) 6085
Stegge, J. aan de-(10) 6659
Steiner, M. M.-(10) 5719
Steinitz, M. O.-(10) 6318
Stelmazyk, P.-(10) 6813
Sternlieb, B. J.-(10) 6321
Stevens, R.-(10) 6546
Sticht, J.-(10) 6467
Stoeffler, D.-(10) 6467
Stohr, J.-(10) 5807, 6890
Stolze, Joachim-(10) 5937, 6057
Stom-Olsen, J. O.-(10) 6560
Storm, D. F.-(10) 6464
Story, T.-(10) 5728
Street, R.-(10) 5481, 5701, 6271, 6634
Ström-Olsen, J. O.-(10) 7064
Su, J. L.-(10) 6397
Suganuma, T.-(10) 7090
Sugita, N.-(10) 5559
Suharyana-(10) 7120
Suharyana, -(10) 7122
Sui, X.-(10) 5966
Suits, F.-(10) 5923
Sukstanskii, A. L.-(10) 5633, 6085
Sullivan, N.-(10) 6812
Sur, Jung Chul-(10) 6078
Suran, G.-(10) 6831
Surig, C.-(10) 5981
Sutton, M.-(10) 6554
Sutton, R.-(10) 5882
Suzuki, A.-(10) 6540
Suzuki, M.-(10) 6126
Suzuki, Y.-(10) 6360, 6400
Swagten, H. J. M.-(10) 5728
Swarup, R.-(10) 7187
Swüste, C. H. W.-(10) 5728

Tabak, F.-(10) 7143
Tagawa, Ikuya-(10) 6776
Takacs, Laszlo-(10) 5864

Takagi, F.-(10) 6631
Takahashi, H.-(10) 6769
Takahashi, Takakazu-(10) 6509
Takajo, M.-(10) 6958
Takayama, S.-(10) 6782
Takeo, Akihiko-(10) 6776
Takeshta, H.-(10) 6415
Takino, Hiroshi-(10) 6162
Tanahashi, K.-(10) 5978
Tanaka, M.-(10) 6665
Tanaka, N.-(10) 5788
Tanaka, Yoichiro-(10) 5774
Tang, D. D.-(10) 6397
Tang, H. C.-(10) 5493
Tang, N.-(10) 6238, 6241, 6247
Tang, T.-(10) 7103
Tanigawa, K.-(10) 5788
Taniguchi, K.-(10) 6086, 6089
Tarasenko, S. V.-(10) 5633
Tarasov, O. Ju.-(10) 7186
Tarnopolsky, G. J.-(10) 6144
Tasaki, A.-(10) 6918
Tasaki, Akira-(10) 5903
Tassi, A.-(10) 5817, 6051
Taylor, R. D.-(10) 5853
Teh, Chai Tak-(10) 7003
Tejada, J.-(10) 5637, 5642, 6557
Temiryazev, A. G.-(10) 5619
Templeton, T. L.-(10) 5695
ter Haar, Leonard W.-(10) 5949
Tessier, M.-(10) 6607
Testardi, L. R.-(10) 6595
Thangaraj, N.-(10) 6900
Thole, Bernard Theodoor-(10) 5807
Tholence, J. L.-(10) 6766
Thomas, B. W. J.-(10) 6789, 7081, 7087
Thompson, C. V.-(10) 6430
Thompson, G. K.-(10) 6643
Thompson, S. M.-(10) 6921
Thomson, T.-(10) 6849
Thornton, J. T.-(10) 6132
Thummes, G.-(10) 6566
Tiefel, T. H.-(10) 6915, 7052
Tikhomirova, M. P.-(10) 5619
Tindall, D. A.-(10) 6318
Ting, S. T.-(10) 6748
Tinklenberg, P.-(10) 6723
Tobin, J. G.-(10) 6369
Tognetti, Valerio-(10) 5814
Tomi-ita, K.-(10) 6769
Tomiyama, F.-(10) 6890
Tondra, Mark-(10) 6567
Tonner, B. P.-(10) 6890
Tonner, Brian-(10) 6811
Toporov, A. Yu.-(10) 6804, 6804
Torgn, Terry-(10) 5800
Torre, Edward Della-(10) 5775, 6846
Trequattrini, Alessandro-(10) 6990
Trindade, I. G.-(10) 6551
Tripathi, G. S.-(10) 5737
Troper, A.-(10) 6296, 6734, 6737
Trouilloud, P. L.-(10) 5923, 6782
Trouw, F.-(10) 7030
Tsameret, A.-(10) 6322
Tsankov, M. A.-(10) 5628, 5629
Tsapin, Alexandre I.-(10) 7183
Tsoukatos, A.-(10) 6507, 6623
Tsoukatos, T.-(10) 6624
Tsuda, H.-(10) 7162
Tsui, F.-(10) 6592
Tsui, Frank-(10) 6174
Tsunashima, S.-(10) 6769, 7090, 7102
Tucker, J. W.-(10) 5841
Tucker, Roy-(10) 6021, 6229
Tun, Z.-(10) 6063
Tung, M. J.-(10) 6112
Turnbull, M. M.-(10) 5535

Turpin, G. B.-(10) 5740

Uchiyama, S.-(10) 6769, 7090, 7102
Ueno, K.-(10) 7168
Ueno, S.-(10) 7162, 7165, 7168, 7174, 7177, 7181
Uher, Citrad-(10) 6174
Uhl, M.-(10) 7033
Uhrenius, Björn-(10) 6265
Ullah, M.-(10) 5960
Umphress, R.-(10) 5960
Ungurs, J.-(10) 6437, 6452
Utchkin, Sergey N.-(10) 6786

Vaia, Ruggero-(10) 5814
Vajda, Ferenc-(10) 5689, 5692, 5775
Vaknin, D.-(10) 6603
Valentin, J.-(10) 7102
Valenzuela, R.-(10) 6940, 7000
Valet, Thierry-(10) 6693
Val'kov, V.-(10) 6743
van de Veerdonk, R. J. M.-(10) 6709
Van Dover, R. B.-(10) 7052
van Dover, R. B.-(10) 6124, 6603
van Kooten, M.-(10) 5508
Van Leeuwen, R. A.-(10) 6498
VanWijland, F.-(10) 6489
Varga, L.-(10) 5547
Vasilyev, V. M.-(10) 5924
Vaurès, A.-(10) 6476
Vázquez, M.-(10) 5791, 6952
Vázquez, Manuel-(10) 6949
Vázquez-Vázquez, C.-(10) 6757
Veca, G. M.-(10) 6024, 6033
Vekhter, Benjamin G.-(10) 5863
Velázquez, J.-(10) 5791
Velicescu, M.-(10) 6586
Velu, E. M. T.-(10) 6132
Veneva, A.-(10) 6726
Vennegues, P.-(10) 5601
Vennix, C. W. H. M.-(10) 5728
Verkhovceva, Nadezda V.-(10) 7182
Verkhovtseva, Nadezda V.-(10) 7182
Verrucchi, Paola-(10) 5814
Vetoshko, P. M.-(10) 5922, 6804, 6804
Victoria, R. H.-(10) 6428, 6858
Vijayaraghavan, R.-(10) 7155
Vinogradov, A. G.-(10) 7186
Višňovský, S.-(10) 6783
Visokay, Mark R.-(10) 6153
Viswanath, V. S.-(10) 5937, 6057, 6751
Viswanathan, K. V.-(10) 6161
Vitale, S.-(10) 5634, 6996
Voiron, J.-(10) 6682
Volkovoy, V. B.-(10) 5922, 6804, 6804
Volotskii, S. V.-(10) 7186
von Geisau, O.-(10) 6508
Vorderwisch, P.-(10) 6334
Voronko, A. I.-(10) 5922, 6804, 6804
Vunni, G. B.-(10) 5535

Waby, N. A.-(10) 5631
Wadas, Andrzej-(10) 6878
Waddill, G. D.-(10) 6369
Wadewitz, Scott-(10) 5919
Wagner, J.-(10) 6825
Wakabayashi, N.-(10) 6601
Waknis, A.-(10) 6930
Waldfried, Carlo-(10) 5919
Walker, J. C.-(10) 6464
Walker, M. J.-(10) 6546, 6783, 7056
Wallace, W. E.-(10) 6280, 6574
Wallance, W. E.-(10) 6289
Wan, H.-(10) 6623, 6624
Wan, Hong-(10) 6507
Wang, D.-(10) 6232

Wang, Ding-sheng-(10) 6409
Wang, Dingsheng-(10) 5802
Wang, Fang-Wei-(10) 7111
Wang, Fang-wei-(10) 6250, 6253, 6259
Wang, G. C.-(10) 5580
Wang, Haiyun-(10) 5762
Wang, J. L.-(10) 6238, 6241
Wang, Jian-Qing-(10) 6604, 6903
Wang, Xindong-(10) 6366
Wang, Xun-Li-(10) 6603
Wang, Y. G.-(10) 6268
Wang, Y. J.-(10) 6351, 6418
Wang, Y. Z.-(10) 6226
Wang, Z.-(10) 7108
Wang, Z. R.-(10) 6603
Wang, Zhanwen-(10) 5859
Wanock, J.-(10) 5714, 5725
Warren, Garry W.-(10) 5568
Wassermann, E. F.-(10) 6072, 7012, 7015
Watabe, H.-(10) 7090, 7102
Watson, M. L.-(10) 6927
Watson, R. E.-(10) 5493
Watts, K. T.-(10) 5673
Weissman, M. B.-(10) 6531
Weller, D.-(10) 5807, 7102
Wellock, K. P.-(10) 7055
Wells, S.-(10) 6583
Wendhausen, P. A. P.-(10) 6018
Westphal, C. H.-(10) 6720
White, Robert L.-(10) 5644
Whitlock, Jonathan B.-(10) 6363
Wiedmann, M. H.-(10) 6498
Wiedmann, Michael H.-(10) 6401
Wierman, K. W.-(10) 6348, 6670
Wiese, G.-(10) 5632
Wigen, P. E.-(10) 5740, 6434
Wilhoit, Dennis R.-(10) 7079
Willett, R. D.-(10) 5952
Williams, C. W.-(10) 6740
Williams, G.-(10) 6510
Williams, Gwyn-(10) 7108
Williams, J.-(10) 5882
Willis, R. F.-(10) 6406
Winkelman, A. J. M.-(10) 6247
Wiser, N.-(10) 7055
Withanawasam, L.-(10) 6646
Wolf, J. A.-(10) 6193
Wolfe, R.-(10) 6286
Wong, B. Y.-(10) 5966
Woods, J. P.-(10) 6303
Woodward, R.-(10) 6271, 6634
Woollam, J. A.-(10) 6495, 6670
Wu, J. M.-(10) 6112
Wu, Rugian-(10) 5802, 6409
Wu, S. Y.-(10) 6598
Wu, Y.-(10) 5807, 6890
Wüchner, S.-(10) 6682
Wun-Fogle, M.-(10) 5656
Wynn, C. M.-(10) 5535

Xia, S. K.-(10) 6766
Xiao, Gang-(10) 6604, 6903
Xiao, John Q.-(10) 5800
Xu, J.-(10) 7055
Xu, Jian-Min-(10) 7120
Xu, Xie-(10) 6021, 6229
Xu, Y. B.-(10) 6190
Xu, You-(10) 6798
Xue, J. Simon-(10) 6740

Yacoby, E. R.-(10) 6322
Yagi, H.-(10) 6658
Yahisa, Y.-(10) 5978
Yajima, T.-(10) 6969
Yamada, M.-(10) 7140

Yamaguchi, Makoto-(10) 5903
 Yamamoto, M.-(10) 5904
 Yamasaki, J.-(10) 6958
 Yamashita, Hideo-(10) 6042
 Yamashita, T.-(10) 6144
 Yan, Mingliang-(10) 6504
 Yang, C. J.-(10) 6274, 6655
 Yang, F. M.-(10) 6238, 6241
 Yang, G.-(10) 5844
 Yang, H. D.-(10) 6598
 Yang, H. S.-(10) 6351
 Yang, Jie Hui-(10) 6798
 Yang, Lin-yuan-(10) 6312
 Yang, Ningjiang-(10) 7180
 Yang, Q.-(10) 6699
 Yang, Z. J.-(10) 5589, 5592
 Yang, Zheng-(10) 5556
 Yang, ZhiJun-(10) 6138
 Yao, Y. D.-(10) 6244
 Yatsuya, S.-(10) 7084
 Yatsuya, Shigeki-(10) 6843
 Yavari, A. R.-(10) 6946
 Ye, Xiao-Guang-(10) 6135
 Yelon, W. B.-(10) 6000
 Yeshurun, Y.-(10) 6322
 Yin, L.-(10) 6226

Yinfan, Xu-(10) 6289
 Yiping, L.-(10) 5885
 Yoneda, Yoshiro-(10) 5987
 Yoshida, K.-(10) 6400
 Yoshida, Y.-(10) 5695
 Yoshimoto, Hideaki-(10) 5987
 Yoshino, S.-(10) 6769
 Young, A. P.-(10) 5943
 Yu, Chengtao-(10) 6504
 Yu, W. Y.-(10) 5714, 5725
 Yu, X. Y.-(10) 7090, 7102
 Yu, Yongmin-(10) 5937
 Yu, Yuwu-(10) 5550
 Yuan, J.-(10) 6501
 Yuan, Samuel W.-(10) 6385
 Yuan, Sui hua-(10) 6375
 Yuasa, Shinji-(10) 7161
 Yumoto, S.-(10) 6160

Zabel, H.-(10) 6184, 6193, 6421
 Záhres, H.-(10) 7015
 Zaluska, A.-(10) 6560
 Zeidler, T.-(10) 6421
 Zeidler, Th.-(10) 6184
 Zeng, D. C.-(10) 6247

Zeng, Hua-Xian-(10) 5556
 Zhai, H. R.-(10) 6190, 6955, 7099, 7103
 Zhai, Y.-(10) 6190
 Zhan, Wen-shan-(10) 6253
 Zhang, Bo-(10) 6259
 Zhang, Changmin-(10) 7180
 Zhang, Guihua-(10) 6685
 Zhang, Guo Ying-(10) 6798
 Zhang, H.-(10) 6534
 Zhang, H. Y.-(10) 7099, 7103
 Zhang, M. J.-(10) 6094
 Zhang, Q.-(10) 6094, 7171
 Zhang, S. Y.-(10) 7099
 Zhang, Shu-(10) 5937
 Zhang, Shufeng-(10) 6685, 6906, 7076
 Zhang, W.-(10) 5535
 Zhang, X. W.-(10) 6351
 Zhang, X. X.-(10) 5637, 5642, 6557
 Zhang, Xianfeng-(10) 7128, 7161
 Zhang, Y.-(10) 6354
 Zhang, Y. B.-(10) 6495, 6670
 Zhang, Ying-(10) 6795
 Zhang, Z.-(10) 6434
 Zhao, Jian-Gao-(10) 7111
 Zhao, Jian-gao-(10) 6259, 6312

Zhao, R. W.-(10) 6241
 Zhao, Y. J.-(10) 5502
 Zhao, Z. G.-(10) 7117
 Zheng, Y.-(10) 6280
 Zhong, X. P.-(10) 6241
 Zhong, Xue-Fu-(10) 6834
 Zhou, A.-(10) 5879
 Zhou, H.-(10) 6334
 Zhou, L.-(10) 6434
 Zhou, R. J.-(10) 6586
 Zhou, S. X.-(10) 6268
 Zhou, X. Z.-(10) 5556
 Zhu, J. G.-(10) 6773
 Zhu, Jian Gang-(10) 5553
 Zhu, Jian-Gang-(10) 5762, 6129, 6135, 6150, 6388
 Zhuravlev, Michail Ye.-(10) 6729
 Zil'berman, P. E.-(10) 5619
 Zimmermann, G.-(10) 5981
 Zoll, S.-(10) 6548
 Zolliker, M.-(10) 6337
 Zubieta, Jon-(10) 5859
 Z'ubin, Pavel B.-(10) 6729
 Zubkov, O. E.-(10) 7186
 Züger, O.-(10) 6211
 Zvezdin, Anatoley K.-(10) 6786

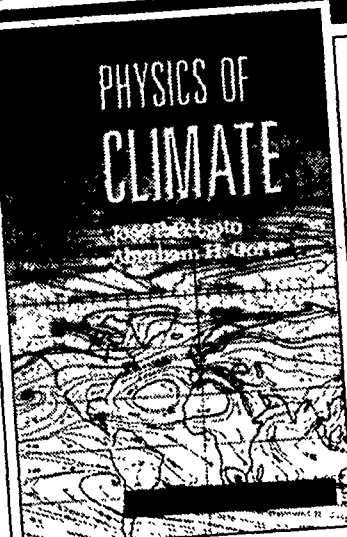
"Will become a classic text in climate research"

"A superb reference. . . . Belongs on the shelf of anyone seriously interested in meteorology and climatology."—Curt Covey and Karl Taylor, *Physics Today*

"This unique book offers a broad perspective on the Earth's climate system and will become a classic text in climate research."
—*Physics World*

"Informative and authoritative on a remarkably wide range of topics. . . . a unique and useful addition to the literature on climate dynamics."—*Nature*

"A modern treatment of the nature and theory of climate. . . . Having so many relevant statistical properties of the climate system under one cover is just one of the benefits that this volume bestows."
—Edward N. Lorenz, *Massachusetts Institute of Technology*



PHYSICS OF CLIMATE
José P. Peixoto, University of Lisbon
and Geophysical Institute de Luis
Abraham H. Oort, NOAA and
Princeton University
Foreword by Edward N. Lorenz

1992, 512 pages, 220 illustrations
0-88318-711-6, cloth
\$95.00 Your price \$76.00
0-88318-712-4, paper
\$45.00 Your price \$36.00

"Valuable to anyone who studies, models, or uses the climate of the earth."

—Walter Robinson, *Bulletin of the American Meteorological Society*

Using such contemporary tools as satellite data, acoustic tomography, infrared radiometers, and nonlinear mathematical models, *Physics of Climate* shows how environmental phenomena worldwide interact in a single, unified system. This integrated, global perspective unites all the key features of the climate system—oceans, atmosphere, and cryosphere—describing the structure and behavior of climate over time.

With more than 220 drawings, charts, and graphs, *Physics of Climate* is an absolutely indispensable text/reference for students and researchers in aeronomy, meteorology, oceanography, physics, and geophysics.

ALSO FROM THE AMERICAN INSTITUTE OF PHYSICS

CONTINENTS IN MOTION Second Edition

Walter Sullivan, former science editor
for *The New York Times*

"As entertaining as a good detective story—and considerably more informative."—*Time*

"*Continents in Motion* is a staggering assemblage of facts; it is also a history of discovery as revealing as . . . Watson's account of unraveling the genetic code."
—*The New York Times*

"Beautifully illustrated, superbly written, and thoroughly documented."
—*San Francisco Examiner & Chronicle*

Sullivan's absorbing history of the idea of continental drift includes findings by the Consortium for Continental Reflection Profiling; data from worldwide earthquake detectors analyzed by seismic tomography; analysis of ancient magnetism, fossils, and regional rock composition; and discoveries about the sea floor made by such unmanned devices as Alvin.

1991, 456 pages, illustrated
0-88318-703-5, cloth
\$50.00 Your price \$40.00

0-88318-704-3, paper
\$25.00 Your price \$20.00

CLIMATE CHANGE AND ENERGY POLICY

Edited by L. Rosen and R. Glasser,
Los Alamos National Laboratories

Integrating key voices in the climate change community and the energy policy-making and research communities, this book looks at climate change on many levels, including its economic impact on energy technologies.

1992, 564 pages
ISBN 1-56396-017-6, paper
\$55.00 Your price \$44.00

GLOBAL WARMING

Edited by D. Hafemeister, *California Polytechnic University*, B. Levi, *Physics Today*,
and R. Scribner, *Georgetown University*

"An excellent place to start for any physicist wishing to understand what global warming is all about."
—*Contemporary Physics*

AIP Conference Proceedings 247
1992, 350 pages
ISBN 0-88318-932-1, hardcover
\$95.00 Your price \$76.00

For faster service call toll free: 1-800-488-BOOK (In Vermont: 802-878-0315) Fax: 1-802-878-1102

ORDER FORM

- ☐ Check enclosed
(Payable in U.S. dollars to American Institute of Physics)
☐ MasterCard ☐ Visa ☐ AMEX

Exp. Date _____ Card No. _____
Signature (Required for all credit card orders) _____
Name _____
Institution _____
Street Address _____
City/State/Zip _____ 9364



MAIL TO:

American Institute of Physics c/o AIPC • 64 Depot Road • Colchester, VT 05446

Save 20%! Order today!			
Qty.	Title/Format	Save 20%	Total
	Physics of Climate, cloth	\$76.00	
	Physics of Climate, paper	\$36.00	
	Continents in Motion, cloth	\$40.00	
	Continents in Motion, paper	\$20.00	
	Climate Change and Energy Policy	\$44.00	
	Global Warming	\$76.00	

Subtotal _____

Shipping, Add \$2.75 for first book
(\$7.50 foreign), \$.75 for each additional book

Final Amount _____

PINET

THE PHYSICS INFORMATION NETWORK

The online information service serving your varied communication, research and information needs in physics with one affordable resource.

PINET is a full-service interactive network of searchable databases, communications services, news, announcements, and job listings. PINET is your network—created specifically for physicists and astronomers. It will plug you into the Internet, give you access to abstracts from over 70 AIP and AIP Member Society journals (including abstracts of articles not yet published), let you scan news releases and research results from national laboratories such as Brookhaven and Argonne, and much more.

You'll be able to research more effectively, get a jump on research before it's published, keep up to date with news and breakthroughs, and stay in touch with colleagues—all easily and inexpensively. With PINET and your PC, you'll be able to tap into:

SEARCHABLE DATABASES

- ☐ Advance Abstracts, with abstracts of papers up to three months prior to publication
- ☐ SPIN, containing nine years of abstracts from more than 70 journals and conference proceedings
- ☐ NASA, MIT, and dozens of other databases worldwide via the Internet—the world's largest network
- ☐ The Jobs Database, featuring nearly 200 job listings in academia, government, and industry

COMMUNICATIONS SERVICES

- ☐ Inexpensive international e-mail, online fax, and telex services
- ☐ Access to users of Internet, Bitnet, Compuserve, MCIMail, and other services

LATE-BREAKING NEWS/RESEARCH RESULTS

- ☐ AIP's *Physics News Update* and *FYI*
- ☐ The American Physical Society's *What's New*
- ☐ The American Geophysical Union's *KOSMOS*
- ☐ USENET bulletin boards, and more

PINET includes previews of articles to appear in *Physics Today*, *Computers in Physics*, and other publications; directories of physicists in the former Soviet Union and members of AIP and AIP Member Societies; a calendar of upcoming AIP Member Society meetings and conferences. PINET also gives you the ability to download research papers and software!

To order, or for more information, please contact:

AMERICAN INSTITUTE OF PHYSICS Electronic Products Division
Telephone: (516) 576-2262. Fax: (516) 349-9704
E-Mail: elecpub@aip.org

PLEASE REGISTER ME FOR:

☐ THE FLAT FEE PROGRAM—UNLIMITED USAGE

Access PINET via the Internet

- ☐ \$120 for a yearly subscription!
- ☐ \$32 for a 3-month subscription!

☐ THE HOURLY PROGRAM (RATES SHOWN BELOW)

Prime Time \$19/hr Weekdays 8am-5pm

Off-Peak \$14/hr Weekdays 5pm-11pm
Sundays 5pm-11pm

Night \$10/hr Every night 11pm-8am
Saturdays All Day
Sundays Until 5pm

- ☐ Enclosed is my check for \$_____ (Flat fee)
- ☐ Charge my subscription or monthly usage to my:
- ☐ VISA ☐ MasterCard ☐ American Express
- Card No. _____ Exp. Date _____

Signature _____

CREDIT CARD ORDERS MUST BE SIGNED

☐ Bill my organization: _____

Contact person: _____

Use the following for my User ID (8 alphanumeric characters or less):

1st choice _____ 2nd choice _____

☐ Send me more information about PINET service and payment options.

NAME _____

INSTITUTION _____

ADDRESS _____

CITY/STATE/ZIP _____

TELEPHONE _____ E-MAIL _____

Electronic Products Division, American Institute of Physics, 500 Sunnyside Boulevard, Woodbury, NY 11797-2999



AMERICAN INSTITUTE OF PHYSICS

500 Sunnyside Blvd., Woodbury, New York 11797-2999 · (516) 576-2262

Under U.S. copyright law, the transfer of copyright from the author(s) should be explicitly stated to enable the publisher to disseminate the work to the fullest extent. The following transfer must be signed and returned to the Editor's office before the manuscript can be accepted for publication. Please note that if the manuscript has been prepared as a Work Made For Hire, the transfer should be signed by both employer and employee. Address requests for further information or exceptions to the Office of Rights and Permissions, American Institute of Physics (AIP), 500 Sunnyside Blvd., Woodbury, New York 11797-2999 · (516) 576-2262.

TRANSFER OF COPYRIGHT AGREEMENT

Copyright to the unpublished and original article, including copyright to the abstract forming part thereof, entitled

submitted by the following author(s) (names of all authors) _____

is hereby transferred to American Institute of Physics (AIP) for the full term thereof throughout the world, BUT SUBJECT to the following rights reserved to the author(s) and to acceptance of the article for publication in

Name of Journal

AIP shall have the right to publish the article in any medium or form, or by any means, now known or later developed.

AIP shall have the right to register copyright in the article and the accompanying abstract in its name as claimant, whether separately or as part of the journal issue or other medium in which such work is included.

The author(s) reserve the following rights:

- (1) All proprietary rights other than copyright, such as patent rights.
- (2) The right, after publication by AIP, to grant or refuse permission to third parties to republish all or part of the article or translations thereof. In the case of whole articles, such third parties must obtain AIP's written permission as well. However, such permission will not be refused by AIP except at the direction of the author. AIP may grant rights with respect to journal issues as a whole.
- (3) The right, after publication by AIP, to use all or part of the article and abstract in compilations or other publications of the author's own works, and to make copies of all or part of such material for the author's use for lecture or classroom purposes.
- (4) If the article has been prepared by an employee within the scope of his or her employment, the employer reserves the right to make copies of the work for its own internal use. If the article was prepared under a U.S. Government contract, the government shall have the rights under the copyright to the extent required by the contract.

The author(s) agree that all copies of the article or abstract made under any of the above reserved rights shall include a copyright notice in the AIP's name. The author(s) represent and warrant that the article is original with them, that it does not infringe any copyright or other rights in any other work, or violate any other rights, and that the author(s) own the copyright in it or are authorized to transfer it. If each author's signature does not appear below, the signing author(s) represent that they sign this agreement as authorized agents for and on behalf of all the authors, and that this agreement and authorization is made on behalf of all the authors.

Signature

Date

Name (print)

If the manuscript has been prepared as a Work Made For Hire, the transfer should be signed by the employee (above) and by the employer (below):

Name of Employer (print)

Signature

Name (print)

Title

Date

A work prepared by a U.S. Government officer or employee as part of his or her official duties is not eligible for U.S. copyright; however, foreign copyright laws may differ. Thus, **this form should be signed even by U.S. Government officers or employees.** Signing of this form will not affect U.S. copyright law provisions in the case of works of the U.S. Government. If all the authors are in this category, check the box here and return the signed form. ☐

The American Institute of Physics is a not-for-profit membership corporation chartered in New York State in 1931 for the purpose of promoting the advancement and diffusion of the knowledge of physics and its application to human welfare. Leading societies in the fields of physics, astronomy, and related sciences are its members.

The Institute publishes its own scientific journals as well as those of its member societies; publishes both technical and general interest books; provides abstracting and indexing services; provides on-line database and e-mail services; disseminates reliable information on physics to the public; collects and analyzes statistics on the profession and on physics education; encourages and assists in the documentation and study of the history and philosophy of physics; cooperates with other organizations on educational projects at all levels; and collects and analyzes information on Federal programs and budgets.

Member Societies

The American Physical Society
Harry Lustig, Acting Executive Secretary
One Physics Ellipse
College Park, MD 20740-3844

Optical Society of America
David W. Hennage, Executive Director
2010 Massachusetts Avenue, N.W.
Washington, DC 20036

Acoustical Society of America
Charles Schmid, Executive Director
500 Sunnyside Blvd., Woodbury, NY 11797-2999

The Society of Rheology
Andrew M. Kraynik, Secretary
Department 1512
Sandia National Labs.
Albuquerque, NM 87185

American Association of Physics Teachers
Bernard V. Khoury, Executive Officer
One Physics Ellipse
College Park, MD 20740-3845

American Crystallographic Association
William L. Duax, Executive Officer
P.O. Box 96, Endicott Station
Buffalo, NY 14205-0096

American Astronomical Society
Peter B. Boyce, Executive Officer
1630 Connecticut Avenue, N.W.
Washington, DC 20009

American Association of Physicists in Medicine
Sal Trofi, Executive Director
One Physics Ellipse
College Park, MD 20740-3846

American Vacuum Society
William D. Westwood, Secretary
Bell-Northern Research, Ltd.
P.O. Box 3511, Station C
Ottawa, Ontario K1Y 4H7, Canada

American Geophysical Union
A. F. Spilhaus, Jr., Executive Director
1630 Connecticut Avenue, N.W.
Washington, DC 20009

Affiliated Societies

American Institute of Aeronautics and Astronautics, American Meteorological Society, American Nuclear Society, ASM International, Astronomical Society of the Pacific, Division of Physical Chemistry of ACS, Engineering Information, Inc., The Geological Society of America, Instrument Society of America, International Association of Mathematical Physicists, International Centre for Diffraction Data, Materials Research Society, Microscopy Society of America, Nuclear and Plasma Sciences Society of IEEE, Physics/Astronomy Section of the Council on Undergraduate Research, Physics Section of AAAS, Society for Applied Spectroscopy, SPIE—The International Society for Optical Engineering.

Corporate Associates: Approximately 175 leading corporations, by their membership, participate in and contribute to the support of AIP.

Publications

Physical Review A · Bernd Crasemann, *Editor*, Physics Dept., University of Oregon, Eugene, OR 97403
Physical Review B · P.D. Adams, *Editor*, The American Physical Society, 1 Research Rd., Box 1000, Ridge, NY 11961
Physical Review C · Sam Austin, *Editor*, Cyclotron Labs., Michigan State University, E. Lansing, MI 48824
Physical Review D · Lowell S. Brown and D.L. Nordstrom, *Editors*, APS, 1 Research Rd., Box 1000, Ridge, NY 11961
Physical Review E · Irwin Oppenheim, *Editor*, Dept. of Chemistry, Massachusetts Institute of Technology, Cambridge, MA 02139
Physical Review Abstracts · Reid Terwilliger, *Editor*, APS, One Physics Ellipse, College Park, MD 20740-3844
Physical Review Letters · J. Sandweiss, G. Basbas, S.G. Brown, and G.L. Wells, *Editors*, APS
APS News · Brian Schwartz, *Editor*, APS, One Physics Ellipse, College Park, MD 20740-3844
Bulletin of The American Physical Society · Brian Schwartz, *Editor*, APS, One Physics Ellipse, College Park, MD 20740-3844
Reviews of Modern Physics · David Pines, *Editor*, Loomis Lab. of Physics, 1110 W. Green St., Urbana, IL 61801
The Journal of the Acoustical Society of America · Daniel W. Martin, *Editor-in-Chief*, 7349 Clough Pike, Cincinnati, OH 45244
American Journal of Physics · Robert H. Romer, *Editor*, 222 Merrill Science Bldg., Box 2262, Amherst College, Amherst, MA 01002
The Astronomical Journal · Paul W. Hodge, *Editor*, Astronomy Dept FM-20, University of Washington, Seattle, WA 98195
Publications of the Astronomical Society of the Pacific · Howard E. Bond, *Editor*, Space Telescope Science Institute, Baltimore, MD 21218
Bulletin of the American Astronomical Society · Peter B. Boyce, *Editor*, AAS
The Astrophysical Journal · Helmut A. Abt, *Managing Editor*, Kitt Peak National Observatory, Box 26732, Tucson, AZ 85726
The Journal of Chemical Physics · J.C. Light, *Editor*, James Franck Institute, The University of Chicago, Chicago, IL 60637
Journal of Mathematical Physics · Roger G. Newton, *Editor*, Indiana Univ., The Poplars, Rm 324, Bloomington, IN 47405
Physics of Fluids · A. Activos, *Editor*, The Levich Institute, Steinman 202, CCNY, Convent Ave. at 140 St., New York, NY 10031
Physics of Plasmas · Ronald C. Davidson, *Editor*, Plasma Phys. Lab., Princeton Univ., P.O. Box 451, Princeton, NJ 08543
Journal of Applied Physics · Steven J. Rothman, *Editor*, Argonne Natl. Lab., Box 8296, Argonne, IL 60439-8296
Applied Physics Letters · Hartmut Wiedersich, *Editor*, Argonne Natl. Lab., Box 8296, Argonne, IL 60439-8296
Review of Scientific Instruments · Thomas H. Braid, *Editor*, Argonne Natl. Lab., Box 8293, Argonne, IL 60439-8293
Journal of Physical and Chemical Reference Data · Jean W. Gallagher, *Editor*, NIST, MS221/A3223, Gaithersburg, MD 20899
Physics Today · Gloria B. Lubkin, *Editor*, AIP, One Physics Ellipse, College Park, MD 20740-3843
Computers in Physics · Lewis Holmes, *Editor*, One Physics Ellipse, College Park, MD 20740-3843
Chaos · David K. Campbell, *Editor*, Dept. of Physics, University of Illinois—UC, Urbana, IL 61801
Journal of Vacuum Science and Technology A · Gerald Lucovsky, *Editor*, Dept. of Physics, N. Carolina State Univ., Raleigh, NC 27650
Journal of Vacuum Science and Technology B · Gary E. McGuire, *Editor*, MCNC, Research Triangle Park, NC 27709
Medical Physics · J.S. Laughlin, *Editor*, Memorial Sloan-Kettering Cancer Center, 1275 York Ave., New York, NY 10021
Noise Control Engineering Journal · Alan H. Marsh, *Editor-in-Chief*, DyTec Engineering, Inc., 5092 Tasman Dr., Huntington Beach, CA 92649
Powder Diffraction · Deane K. Smith, *Editor-in-Chief*, Dept. of Geosci. and Mineralogy, Penn State Univ., University Park, PA 16802
AAPT Announcer · Bernard V. Khoury, *Editor*, AAPT, One Physics Ellipse, College Park, MD 20740-3845
The Physics Teacher · Clifford E. Swartz, *Editor*, Phys. Dept., State University of New York, Stony Brook, NY 11794
Journal of Rheology · Arthur B. Metzner, *Editor*, Dept. of Chemical Engineering, University of Delaware, Newark, DE 19716
Journal of the Optical Society of America A · Bahaa E. A. Saleh, *Editor*, 2010 Massachusetts Ave., N.W., Washington, DC 20036
Journal of the Optical Society of America B · Paul F. Liao, *Editor*, 2010 Massachusetts Ave., N.W., Washington, DC 20036
Applied Optics · William T. Rhodes, *Editor-in-Chief*, Dept. of Electr. & Computer Eng., Univ. of Colorado, Boulder, CO 80309-0425
Optics Letters · Peter W. E. Smith, *Editor*, Bellcore, 331 Newman Springs Rd., Red Bank, NJ 07701
Optics and Photonics News · Andrea Pendleton, *Editor*, 2010 Massachusetts Ave., N.W., Washington, DC 20036
Journal of Lightwave Technology · Donald B. Keck, *Editor*, Corning Glass Works, Sullivan Park FR29, Corning, NY 14830
The Journal of Undergraduate Research in Physics · R.E. Adelberger, *Editor*, Physics Dept., Guilford College, Greensboro, NC 27410
AIP Conference Proceedings
Acoustical Physics
Astronomy Reports
Astronomy Letters
Crystallography Reports
JETP
JETP Letters
Low Temperature Physics
Optics and Spectroscopy
Physics-Doklady
Physics of Atomic Nuclei
Physics of the Solid State
Plasma Physics Reports
Physics of Particles and Nuclei
Semiconductors
Journal of Optical Technology
Technical Physics
Technical Physics Letters

Current Physics Index (CPI), quarterly and annual subject index with abstracts to all the above journals.
General Physics Advance Abstracts (GPAA), semimonthly advance abstracts of AIP-published physics literature.
Searchable Physics Information Notices (SPIN), monthly computer-readable tape of abstracts
Current Physics Microform (CPM), monthly microfilm edition of all the above journals
Current Physics Reprints (CPR), on-demand copies of any article in any of the above journals.
Physics Briefs (PB), semimonthly comprehensive index with abstracts to the world literature of physics
PINET, an online physics information network

Governing Board 1994–1995

Roland W. Schmitt, *Chair**
Reuben E. Alley
Benjamin Bederson
Roger A. Bell
Marc H. Brodsky (*ex officio*)*
Robert L. Byer*
Patricia E. Cladis
Charles Counselman, III
G. Brent Dalrymple*
Robert L. Dixon
William L. Duax
Judy R. Franz
Roderick M. Grant (*ex officio*)*
Joseph E. Greene
David Hennage
David W. Hoffman*
Karen L. Johnston
Frank J. Kerr
Bernard V. Khoury*
Carl Kisslinger
Patricia K. Kuhl
Donald N. Langenberg
Tingye Li
Harry Lustig*
Christopher H. Marshall
Gregory B. McKenna
Duncan T. Moore
Norman F. Ness
C. Robert O'Dell
C. Kumar N. Patel
Burton Richter
Barrett H. Ripin
J. William Rogers, Jr.
Charles E. Schmid*
Benjamin Snavely
A. F. Spilhaus, Jr.
Hugo Steinfink
Richard Stern
Howard G. Voss*
Martin Walt
* executive committee

AIP Officers

Marc H. Brodsky, *Executive Director and CEO*
Roderick M. Grant, *Secretary*
Arthur T. Bent, *Treasurer and CFO*
Theresa C. Braun, *Director of Human Resources*
Darlene Carlin, *Director of Publishing*
John S. Rigden, *Director of Physics Programs*

Publishing Services

James J. Donohue, *Director Publishing Services*
Edward P. Greeley, *Director Advertising and Exhibits*
Douglas LaFrenier, *Director of Marketing*
Peggy Judd, *Director of Information Technology*
Maria Taylor, *Publisher AIP Press*
Carol Fleming, *Manager Publishing II Branch*
Doreene A. Berger, *Manager Journal Production I Division*
Maya Flikop, *Manager Translation Program Division*
John T. Scott, *Manager Editorial Operations Division*
Cheryl Taub, *Manager Composition I Division*
Denise Weiss, *Manager Books/Special Projects*
Janice Wilmot, *Manager Production II Division*

APPLIED PHYSICS LETTERS: Current Table of Contents

Applied Physics Letters, a companion publication to the *Journal of Applied Physics*, is published weekly by the American Institute of Physics. Its letters are timely, short reports devoted to important new findings in applied physics. The contents list below is from a recent issue.

APPLIED PHYSICS LETTERS

Vol 64, No. 18, 2 May 1994
CODEN APPLAB ISSN 0003-6951

OPTICS

- 2329 Cr^{3+} : Ga_2Se_3 : Ga_2O_3 passive Q-switch for the Cr^{3+} : LiCaF_6 laser
Milton Barmham
- 2332 Noise suppression for photorefractive image amplification in the LiNbO_3 Fe crystal stack
Jingjun Xu, Guangqin Zhang, Shun Lu, Jiarun Lu, Lian Wen
- 2335 Polarization-independent wavelength filter using a grating-assisted vertical directional coupler in InP
F. Heismann, L. L. Buhl, B. I. Miller, M. J. R. Cantu, U. Koren, M. G. Young, R. C. Alenxas
- 2338 Optical near-field imaging with a semiconductor probe tip
J. Mertz, M. Hepp, J. Myrnek, O. Marti
- 2341 Phase configuration of BaTiO_3 by backward stimulated photorefractive scattering
Yong Zhu, Changqin Yang, Menglin Hu, Xiaojun Hu, Jiering Zhang, Tang Zhou, Xing Wu

CONDENSED MATTER: STRUCTURE, MECHANICAL AND THERMAL PROPERTIES

- 2344 Transmission electron microscopy characterization of $\text{In}_x\text{Ga}_{1-x}\text{As}$ substrates grown by heteroepitaxial lateral overgrowth
J. P. McCreary, B. Bykiewicz, T. Bykiewicz, E. Jan
- 2347 Anomalous laser-induced voltages in $\text{YBa}_2\text{Cu}_3\text{O}_7$ and "off-diagonal" thermoelectricity
Louis R. Testard
- 2350 Raman scattering and x-ray diffraction investigations of highly textured $(\text{Pb}_{1-x}\text{La}_x)_2\text{TiO}_5$ thin films
Z. C. Feng, B. S. Kwak, A. Erol, L. A. Bother
- 2353 Thermal expansion of polycrystalline diamond produced by chemical vapor deposition
D. J. Pickrell, K. A. Kline, R. E. Taylor
- 2356 Kinetic suppression of islanding in impurity-mediated heteroepitaxial growth of germanium on silicon
H. J. Oslan
- 2359 Absence of solute drag in solidification
J. A. Klotz, M. J. Aziz, D. P. Brunco, M. O. Thompson

SEMICONDUCTORS

- 2362 Threshold voltage shift of amorphous silicon thin film transistors with atmospheric pressure chemical vapor deposition silicon dioxide
Jeong Hyun Kim, Eun Yool Oh, Jung Kye Yoon, Yong Suk Park, Chan Hee Hong
- 2364 Blue electroluminescent devices with high quantum efficiency from alkyl-substituted poly(p-phenylene-vinylene)-oligomers in a polystyrene matrix
W. Tachibana, S. Jacobs, H. Nishiyama, H. J. Gase, Y. Gruber
- 2367 Optical properties of porous silicon superlattices
G. Vincent
- 2370 Long-wavelength excited SiGe/Si heterojunction internal photoemission infrared detectors using multiple SiGe/Si layers
J. S. Park, T. L. Lin, E. W. Jones, H. M. Del Castillo, S. D. Gunapala
- 2373 Photoluminescence of Si/SiGe/Si quantum wells on separation by oxygen implantation substrate
D. K. Nayak, N. Usami, S. Fukutani, Y. Shirai
- 2376 Photoluminescence of chemically vapor deposited Si on silica aerogels
Wenqiang Cao, Aron J. Hunt
- 2379 Single electron transport and current quantization in a novel quantum dot structure
Y. Nagamura, H. Sakai, L. P. Kouwenhoven, L. C. Mur, C. J. P. M. Hermans, J. Mochizuki, H. Noge
- 2382 Temperature dependence of cathodoluminescence from thin GaInAs/GaAs multiple quantum wells
U. John, J. Meninger, R. Hey, H. T. Grahn
- 2385 Unexcited carrier trapping and slow recombination in ion-bombarded silicon on sapphire measured via TLE at cryogenicity
Stuart D. Brown, Jucheng Zhang, Siem R. Kading
- 2388 Ultraviolet photoactivation of $\text{In}_x\text{Ga}_{1-x}$ compound semiconductors: A new approach to surface passivation
Carol I. H. Ashby, Kevin R. Zavadi, Arnold J. Howard, B. E. (Gene) Harmons

- 2391 Laser-induced epitaxial neutral mass spectrometry study of arsenic concentration profiles in a polycrystalline silicon/silicide-crystal silicon system
Yoshihiko Higashi, Tetsuya Maruo, Yoshitazu Homma, Junichi Kodate, Masayasu Miyake
- 2394 Electrofluorescence from porous silicon with conducting polymer film contacts
Kun-Hai U, Dennis C. Diaz, Yuesong He, Joe C. Campbell, Chaochen Tsai
- 2397 Low-temperature growth of high resistivity GaAs by photoassisted magnetron sputtering
J. C. Roberts, K. S. Boutsos, S. M. Bedair, D. C. Look
- 2400 Evidence for population inversion in excited electron states of a double barrier resonant tunneling structure
J. W. Coburn, M. S. Skolnick, D. M. Whitaker, P. D. Buckle, A. R. Wilcox, G. W. Smith
- 2403 Observation of resonant tunneling through localized continuum states in electron wave interference diodes
R. E. Camahan, M. A. Maldonado, K. P. Marth, R. J. Higgins, J. P. A. van der Walt, J. S. Harris, Jr
- 2406 Back side Raman measurements on GaP/In-GaAs ohmic contact structures
K. Worts, J. Wette, R. E. Silverman, M. Van Hove, G. Borgis, C. J. Palmstrom, L. T. Florez, H. Munder
- 2409 New interface structure for A-type $\text{CoSi}_2/\text{Si}(111)$
M. F. Chisholm, S. J. Pennycook, R. Jelsinski, S. Mani
- 2412 Threshold dose for ion-induced intermixing in InGaAs/GaAs quantum wells
L. B. Allard, G. C. Aers, P. G. Piva, P. J. Poole, M. Buchanan, I. M. Templeton, T. E. Jackman, S. Charbonneau, U. Alano, I. V. Mitchell
- 2415 High efficiency indium gallium arsenide photovoltaic devices for thermophotovoltaic power systems
David M. Wit, David S. Feleni, Richard W. Hoffman, Jr., Philip W. Jenkins, David J. Striker, David Scheiman, Roland Lowe, Maria Fauer, Raj K. Jain
- 2418 Dimerization induced incorporation nonlinearity in GaAsP
J. E. Cunningham, M. B. Santos, K. W. Goossen, M. D. Williams, W. Jan
- 2421 Full band structure calculation of the linear electro-optic susceptibility
Ed Gbureck, J. E. Sipe
- 2424 Observation of voids induced by mechanical stress and electroreorganization in passivated Al lines deposited at different purity levels
T. Marab, J. C. Brennan, P. Flinn, D. S. Gardner, M. Madden
- 2427 Dry etching and implantation characteristics of $\text{Al}_x\text{Ga}_{1-x}\text{P}$
S. J. Pearson, C. R. Abernathy, F. Ren
- 2430 Photoluminescence lifetime of GaP/AlP superlattices grown by gas-source molecular-beam epitaxy
Kumiko Asami, Hajime Asahi, Song Gang Kim, Joon Hong Kim, Atsuo Ishida, Setuo Takamuku, Shun-ichi Gonda
- 2433 Uncooled $\text{InSb/In}_{1-x}\text{Al}_x\text{Sb}$ mid-infrared emitter
T. Ashley, C. T. Elliott, N. T. Gordon, R. S. Hall, A. D. Johnson, G. J. Pryce
- 2436 Asymmetric dark current in quantum well infrared photodetectors
K. L. Tai, C. P. Lee, K. H. Chang, D. C. Liu, H. R. Chen, J. S. Tsang
- 2439 Extrinsic properties of ZnSe/ZnS superlattices
R. Cingolani, M. Lomascolo, N. Lovngaye, M. Dabbico, M. Ferrara, I. Summure

SUPERCONDUCTORS

- 2442 Superconducting readout of semiconductor memory at liquid nitrogen temperature
Claude Hilbert, Utam Ghoshal, Harry Kroger, Jon S. Matens, V. M. Hadda, T. A. Phil
- 2445 Influence of inductance induced noise in an $\text{YBa}_2\text{Cu}_3\text{O}_7$ dc-SQUID at high operation temperature
P. A. Nason, T. Ciesion, J. B. Hansen, A. Kühle

Subscription information may be obtained by writing Marketing Services at the American Institute of Physics.